ECCM

20

26-30 JUNE

2022

LAUSANNE

SWITZERLAND

Proceedings of the 20th European Conference on Composite Materials

COMPOSITES MEET SUSTAINABILITY

Vol 2 – Manufacturing

Editors : Anastasios P. Vassilopoulos, Véronique Michaud

Organized by :

EPFL

Under the patronage of :

CCLAB Composite Construction Laboratory

LPAC Laboratory for Processing of Advanced Composites

ESCM EUROPEAN SOCIETY FOR COMPOSITE MATERIALS

ECCM 20
26-30 JUNE 2022
LAUSANNE SWITZERLAND

EPFL CCLAB Composite Construction Laboratory LPAC Laboratory for Processing of Advanced Composites

Proceedings of the 20th European Conference on Composite Materials ECCM20 26-30 June 2022, EPFL Lausanne Switzerland

Edited By :

Prof. Anastasios P. Vassilopoulos, CCLab/EPFL
Prof. Véronique Michaud, LPAC/EPFL

Oragnized by:

Composite Construction Laboratory (CCLab)
Laboratory for Processing of Advanced Composites (LPAC)
Ecole Polytechnique Fédérale de Lausanne (EPFL)

ISBN: 978-2-9701614-0-0
DOI: http://dx.doi.org/10.5075/epfl-298799_978-2-9701614-0-0

Published by :

Composite Construction Laboratory (CCLab)
Ecole Polytechnique Fédérale de Lausanne (EPFL)
BP 2225 (Bâtiment BP), Station 16
1015, Lausanne, Switzerland

https://cclab.epfl.ch

Laboratory for Processing of Advanced Composites (LPAC)
Ecole Polytechnique Fédérale de Lausanne (EPFL)
MXG 139 (Bâtiment MXG), Station 12
1015, Lausanne, Switzerland

https://lpac.epfl.ch

Cover:

Swiss Tech Convention Center
© Edouard Venceslau - CompuWeb SA

Cover Design:

Composite Construction Laboratory (CCLab)
Ecole Polytechnique Fédérale de Lausanne (EPFL)
Lausanne, Switzerland

©2022 ECCM20/The publishers

Disclaimer:

The ECCM20 organizing committee and the Editors of these proceedings assume no responsibility or liability for the content, statements and opinions expressed by the authors in their corresponding publication.

Editorial

This collection gathers all the articles that were submitted and presented at the 20th European Conference on Composite Materials (ECCM20) which took place in Lausanne, Switzerland, June 26-30, 2022.

ECCM20 is the 20th edition of a conference series having its roots back in time, organized each two years by members of the European Society of Composite Materials (ESCM).

The ECCM20 event was organized by the Composite Construction laboratory (CCLab) and the Laboratory for Processing of Advanced Composites (LPAC) of the Ecole Polytechnique Fédérale de Lausanne (EPFL).

The Conference Theme this year was “Composites meet Sustainability”. As a result, even if all topics related to composite processing, properties and applications have been covered, sustainability aspects were highlighted with specific lectures, roundtables and sessions on a range of topics, from bio-based composites to energy efficiency in materials production and use phases, as well as end-of-life scenarios and recycling.

More than 1000 participants shared their recent research results and participated to fruitful discussions during the five conference days, while they contributed more than 850 papers which form the six volumes of the conference proceedings. Each volume gathers contributions on specific topics:

Vol 1 – Materials

Vol 2 – Manufacturing

Vol 3 – Characterization

Vol 4 – Modeling and Prediction

Vol 5 – Applications and Structures

Vol 6 – Life Cycle Assessment

We enjoyed the event; we had the chance to meet each other in person again, shake hands, hold friendly talks and maintain our long-lasting collaborations. We appreciated the high level of the research presented at the conference and the quality of the submissions that are now collected in these six volumes. We hope that everyone interested in the status of the European Composites’ research in 2022 will be fascinated by this publication.

The Conference Chairs

Anastasios P. Vassilopoulos, Véronique Michaud

ECCM 20
26-30 JUNE 2022
LAUSANNE SWITZERLAND

Hosting Organizations

Composite Construction Laboratory (CCLab)
Laboratory for Processing of Advanced Composites (LPAC)
Ecole Polytechnique Fédérale de Lausanne (EPFL)

Venue

Swiss Tech Convention Center (https://www.stcc.ch)

Conference Chairs

Chair : Prof. Anastasios P. Vassilopoulos, EPFL, Switzerland
Co-Chair: Prof Véronique Michaud, EPFL, Switzerland

International Scientific Committee

Prof. Malin Åkermo SE
Dr. Emmanuel Baranger FR
Prof. Christophe Binetruy FR
Prof. Pedro Camanho PT
Prof. Konstantinos Dassios GR
Prof. Brian Falzon UK
Prof. Kristofer Gamstedt SE
Prof. Sotiris Grammatikos NO
Prof. Christian Hochard FR
Prof. Marcin Kozlowski PL
Prof. Stepan Lomov BE
Dr. David May DE
Prof. Stephen Ogin UK
Prof. Gerald Pinter AT
Prof. Silvestre Pinho UK
Prof. Yentl Swolfs BE
Dr. Julie Teuwen NL
Dr. Panayota Tsotra CH
Prof. Wim van Paepegem BE
Prof. Dimitrios Zarouchas NL
Dr. Andrey Aniskevich LV
Prof. Christian Berggreen DK
Dr. Nicolas Boyard FR
Prof. Valter Carvelli IT
Prof. Klaus Drechsler DE
Prof. Bodo Fiedler DE
Dr. Nathalie Godin FR
Prof. Roland Hinterholzl AT
Prof. Ian Kinloch UK
Dr. Thomas Kruse DE
Prof. Theodoros Loutas GR
Prof. Veronique Michaud CH
Prof. Alessandro Pegoretti IT
Prof. Joao Ramoa Correia PT
Prof. Jose Sena-Cruz PT
Prof. Antonio T. Marques PT
Prof. Thanasis Triantafillou GR
Prof. Albert Turon ES
Prof. Anastasios P. Vassilopoulos CH
Prof. Martin Fagerström SE
Dr. Alexandros Antoniou DE
Prof. Lars Berglund SE
Prof. Michal Budzik DK
Prof. Lucas Da Silva PT
Dr. Andreas Endruweit UK
Prof. Mariaenrica Frigione IT
Dr. Larissa Gorbatikh BE
Dr. Martin Hirsekorn FR
Prof. Vassilis Kostopoulos GR
Prof. Jacques Lamon FR
Prof. Staffan Lundstrom SE
Prof. Peter Mitschang DE
Dr. Soraia Pimenta UK
Prof. Paul Robinson UK
Dr. Olesja Starkova LT
Prof. Sofia Teixeira de Freitas NL
Dr. Stavros Tsantzalis GR
Prof. Danny van Hemelrijck BE
Prof. Michele Zappalorto IT
Dr. Miroslav Cerny CZ

Local Organizing Committee

Prof. Anastasios P. Vassilopoulos, EPFL
Prof. Véronique Michaud, EPFL
Angélique Crettenand and Mirjam Kiener, Lausanne Tourisme
And all those who helped, colleagues who reviewed abstracts and chaired sessions, and CCLab and LPAC students and collaborators who worked hard to make this conference a success.

ECCM 20
26-30 JUNE 2022
LAUSANNE SWITZERLAND

Sponsors

SHIMADZU
Excellence in Science

Bristol Composites Institute

JEC GROUP

suprem

Surface Measurement Systems
World Leader in Sorption Science

INSTRON

9T LABS

Anton Paar

DIA-STRON
DELIVERING MEASUREMENT SOLUTIONS

AELER

HRC

ICCM 23
BELFAST 2023
30 JULY – 4 AUGUST

TEIJIN

Functional Composite Materials

materials
an Open Access Journal by MDPI

ELSEVIER

Supporting partners

JEC

CertBond
COST Action CA18120

EsSENce

Switzerland Tourism.

SWISS

SBB CFF FFS

sampe
Switzerland

COMPOSITES UNITED | SWITZERLAND

canton de vaud

Lausanne

Contents

NUMERICAL ANALYSIS OF THE THERMAL DECOMPOSITION IN THERMOPLASTIC BASED LAMINATES UNDER SEVERE TEMPERATURE CONDITIONS

David Philippe[a], Benoit Vieille[a], Fabrice Barbe[a], Yann Carpier[a]
a: INSA Rouen, Normandie Univ, CNRS, Groupe de Physique des Matériaux, 76800 Saint Etienne du Rouvray, (Rouen, FR) – david.philippe@insa-rouen.fr

Abstract: *This paper presents an experimental and numerical study over the behavior of thermoplastic matrix laminated composite materials reinforced with a carbon fiber fabric subjected to mechanical loading at temperatures leading to thermal decomposition of the matrix. During this process, the constitutive elements are progressively transformed into pyrolysis gases. As a result, the material properties and thermomechanical behavior greatly vary along temperature change and thermal decomposition. The proposed 3D Finite Element model is capable of capturing the porosity nucleation resulting from the thermal decomposition. Using an explicit representation of matrix and yarns, the progressive nucleation of elements based on the temperature distribution, time exposure and a probabilistic law is implemented according to experimental measurements. The proposed model predicts the evolution of the porosity volume ratio within the material as well as its influence on the mechanical response. Post-mortem microscopical observations allow a better understanding of porosity nucleation.*

Keywords: thermal decomposition; thermoplastic laminates; modelling

1. Introduction

Under critical service conditions, aeronautical structural parts consisting of polymer matrix composite materials may be subjected simultaneously to severe heat exposure (temperature up to 650°C) and mechanical loading. The analyses of the interactions between mechanics and thermal transfers taking place under such conditions rely on very specific experimental means. Indeed, it is necessary to reproduce these critical operating conditions (e.g. fire) of composite materials intended for applications in aircraft engine [1].

To this end, an approach based on both experimental and numerical analyses enables both a better understanding of the involved physics, and the development of a tool to predict the various phenomena. In the continuation of previous works [1,2], this study focuses on the thermomechanical behaviour of a carbon fiber / polyphenylene sulphide thermoplastic matrix laminates (C/PPS).

As exposed to the heat source, the temperature increases and the pyrolysis of the matrix progressively becomes a dominant mechanism. It takes place above the thermal decomposition temperature (450°C for PPS): the matrix undergoes a gradual transformation into pyrolysis gas and a carbon residue (named char, see [3]). As exposed to oxygen, oxidation of both char and fibers may occur [4]. During the process, porosities appear, which are cavities filled with pyrolysis gas. On a structural viewpoint, the nucleated porosities will induce the presence of high-pressure gas holes which, as they expand, will introduce an increase in the volume of the macro-structure through peeling. This behaviour is even more amplified by the fact that there is less matrix to insure the load transfer within the laminates. As a consequence on the

  doi:10.5075/epfl-298799_978-2-9701614-0-0

thermomechanical properties, the behaviour of the material is dramatically altered since solid matter is replaced by gas [5].

Porosities are classified in two categories: (i) open porosities which are connected to the external environment either directly or by a network of voids created during the progressive decomposition of the matrix within the laminate; the pyrolysis gases generated inside these porosities can then escape from the porosities (ii) closed porosities which remain trapped within the material and are still filled with pyrolysis gases. Their influence on the geometrical changes of the laminate also vary. Though closed porosities tend to induce a homogeneous swelling of the material (due to internal pressure), open ones disrupt this homogeneity especially on the borders of the sample. Indeed, the escape of the gases is an abrupt process making the edges of the composite spread far more than in the middle.

As porosities correspond to a third material phase nucleating in the composite during thermal decomposition, beside the matrix and the carbon fiber, and as this third phase has a prominent effect on both heat transfers and mechanical fields, to account for the kinetics of their formation within a numerical model is fundamental for comprehensively and accurately predicting the constitutive behavior of the composite under high thermal gradients. Following sections present (i) the experimental method to characterize this kinetics according to temperature and (ii) the way this kinetics is introduced into a meso-scale numerical model of the laminate.

2. Porosity volume fraction determination

2.1 Experimental methodology and technical means

Four different experimental techniques were considered: (i) mass loss (ii) volume density (iii) geometry (iv) microscopical observation. Their purpose is to determine the fraction of the porosity volume over the total volume. In that aim, they rely on the measurements of samples before and after they were subjected to homogeneous thermal conditions depending on both temperature and time. The volume chosen as the 'total volume' can be discussed as it could either be the initial volume or the final one. However, given the major swelling, the final volume was found to be more representative of the final state of the material. All four methods are briefly explained in Table 1 alongside their disadvantages.

After comparison of the different techniques, it was found that the most reliable methodology was to combine the mass and geometry ones. By naming the initial and final volume respectively V_i and V_f, and the volume lost due to mass loss V_l, the porosity volume ratio is given by:

$$\rho_p = \frac{V_f - V_i}{V_f} + \frac{V_l}{V_f} \quad (1)$$

It is worth reminding that the porosity volume ratio is the percentage of porosities within the matrix over the whole composite sample (whose initial matrix volume fraction is 50%).

  doi:10.5075/epfl-298799_978-2-9701614-0-0

Table 1: Experimental means for the measurement of the porosity volume ratio

	Technic description	Disadvantage(s)
Mass loss	Measurement of the mass before and after exposure and calculating the porosity volume as the volume related to the lost mass	Does not consider the swelling of the material
Density	Measurement of the density before and after exposure and calculating the porosity volume from the final mass and density	Very border-effects dependant (due to the measurement methodology)
Geometry	Measurement of the dimensions before and after exposure and calculating the porosity volume from the dimension change	Does not consider the mass loss
Microscopical observation	Cutting the samples and calculating the porosity surface at the center of the material (through microscopical imaging and a porosity detection script)	Loss of representativity (due to 2D + localised) / Subjectivity on the porosity detection

2.2 Experimental measures

Several tests were carried out on C/PPS woven laminates samples with quasi-isotropic (QI) and ±45° stacking sequences. The samples surface was of around 25x25 mm^2, with an average initial thickness around 2.20mm. They were placed in a furnace and subjected to isothermal temperature conditions in a range from 465°C (just above the beginning of the thermal decomposition [6]) up to 600°C with exposure times up to 15 minutes.

The evolution of ρ_p is represented in Fig. 1 for temperatures of 465°C, 530°C and 600°C. It appears that ρ_p changes qualitatively similarly for all considered temperature conditions: a rapid increase during the first ten minutes before a progressive saturation to an asymptotic value, depending on the temperature of treatment. A slight difference can be observed in the case of the 600°C scenario. The maximum value was reached very rapidly (5 min) and beyond that time the obtained value were not considered to be exploitable.

The decomposed samples were also used to analyse the porosity nucleation process at a microscopical level according to various configurations (temperature, exposition time, stacking sequence): Fig. 2 provides scans of samples (cross section at their center) at different states of the decomposition. It appears that increasing temperature and time result in increasing the surface occupied by porosities. The influence of temperature is mainly observed on the decomposition of the yarns, significantly debonding after a 600°C exposure, whereas time exposure mostly influences the overall decomposition state. Regarding the influence of the stacking sequence, porosity formation in ±45° laminates seems to more localized, and the yarns less degraded. It could be explained by the fact that matrix-rich are localized at the crimp (where weft fibers undulate over warp fibers bundles), which is less noticeable in QI laminates.

  doi:10.5075/epfl-298799_978-2-9701614-0-0

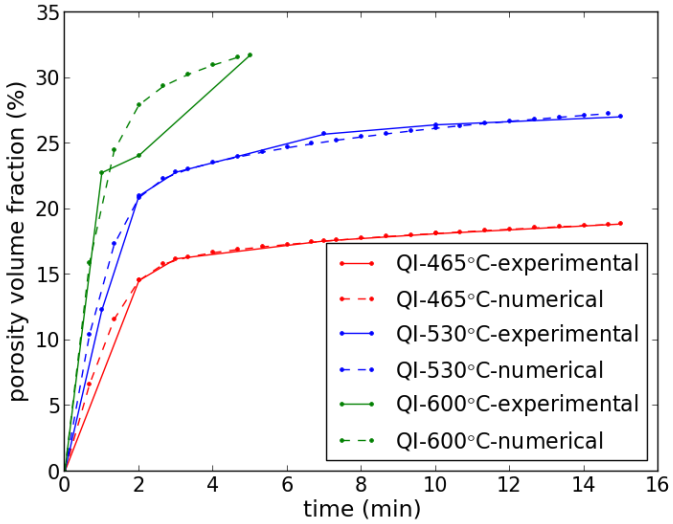

Figure 1. Evolution of porosity volume fraction according to time and temperature in QI stacking sequence (experimental and numerical)

(a) QI - Temperature: 465°C – Time: 7min – Porosity ratio: 28.6%

(b) QI - Temperature: 530°C – Time: 7min – Porosity ratio: 43.2%

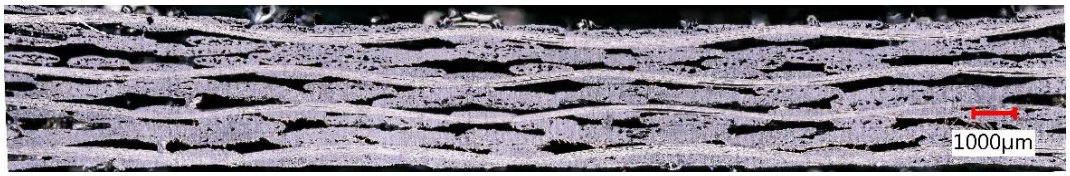

(c) QI - Temperature: 600°C – Time: 5min – Porosity ratio: 54.8%

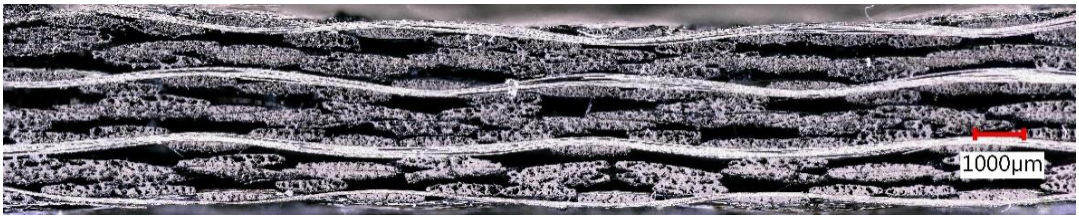

(d) ±45° - Temperature: 530°C – Time: 7min – Porosity ratio: 43.9%

(e) ±45° - Temperature: 530°C – Time: 10min – Porosity ratio: 53.8%

Figure 2. Post-mortem optical microscopy scans at the center of thermally decomposed samples. The overall length of the presented samples is 25mm

3. Application to numerical model

A three-dimensional numerical model of the composite was created representing explicitly matrix and yarns in 1/28th of a Representative Volume Element (RVE), i.e. a volume of 1.7x1.03x2.20mm^3 (Fig. 3(a)). The dimensions of study were chosen to get a fine enough discretization (5.15 million elements).

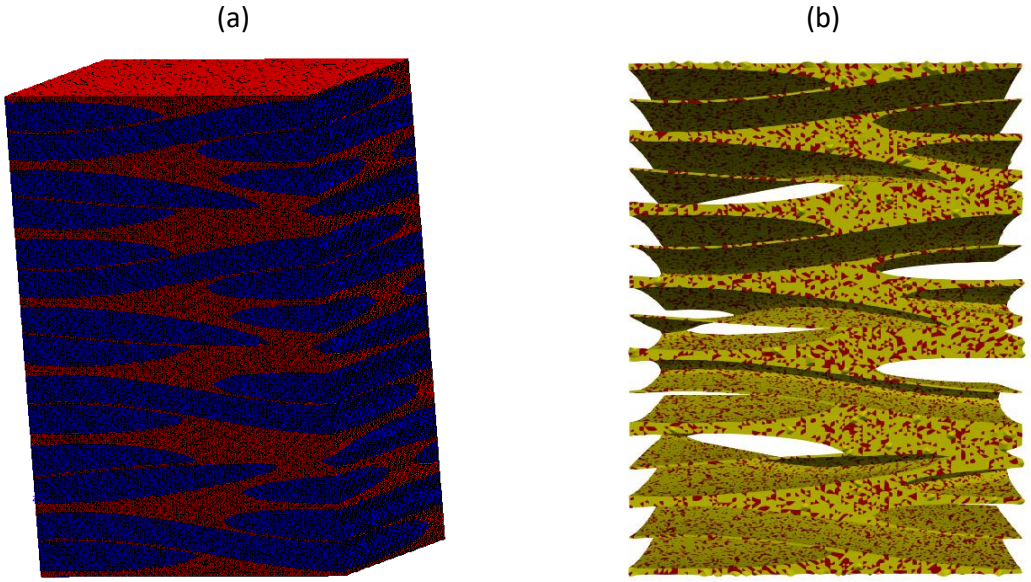

Figure 3. (a) Domain of study for the numerical modeling of thermal decomposition in a QI composites. Over 5x106 tetrahedral elements. (b) Front view of a 31.6% porosity material with only the matrix and porosities – matrix in red – porosities in yellow

3.1 Porosity creation

In order to reproduce the kinetics of porosity formation according to temperature, the previous experimental results were used as reference for temperatures up to 530°C. The nucleation was reproduced by meshing matrix elements progressively turning into gas, representing the process in the core of the samples. In that aim, a probabilistic law was introduced to account for the probability of matrix elements to turn into gas at each computation time. The retained probabilistic law (see Eq. 2) is derived from bimolecular autocatalytic reaction kinetics [7]. C(t), the probability of porosity nucleation at a time t, is expressed according to the three parameters A(T), A0, k(T) and B(t,T) which are described by time and temperature-dependent analytical laws.

$$[C](t) = \frac{A(T)}{A0 * exp(k(T) * t) + 1} + B(t,T) \quad (2)$$

This law is characterized by a high probability at the start of the heat treatment before rapidly dropping and reaching almost 0, as can be seen on Fig. 4 for three temperatures.

Using randomness through probability might appear not entirely representative, however it is consistent with experimental observations. Indeed, a significant disparity was observed in behavior for different samples in similar conditions (both in amplitude and distribution). Furthermore, the number of matrix elements is high enough so that the final porosity volume

  doi:10.5075/epfl-298799_978-2-9701614-0-0

ratio does not vary much between simulations with the same exposure conditions (scattering lower than 0.1%).

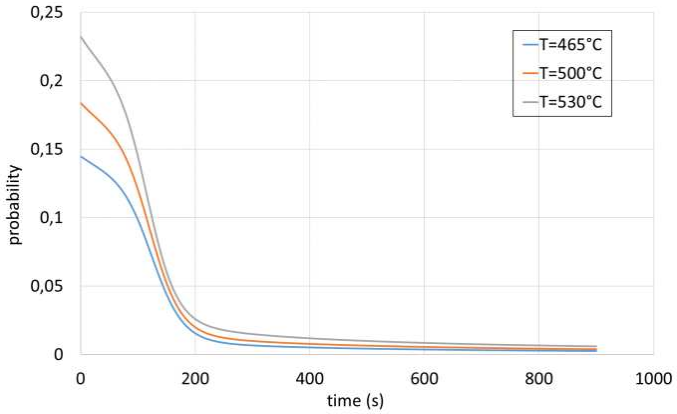

Figure 4. Evolution of the probability of porosity nucleation according to time for three temperatures.

This probabilistic law was used to numerically reproduce the material response to a thermal treatment. The comparison between experimental and numerical (through this probabilistic law) values of porosity volume fraction (Fig. 1) shows a good similarity between both. To a first approximation, the swelling of the material is not considered, which is a strong assumption. Fig. 3(b) shows the porosities in the numerical domain after 300s at 600°C. The total volume ration of porosities is then 31.6%. As previously stated, the large number of elements provides an almost regular distribution of the porosity elements.

It is worth recalling that given that the decomposition state of the composite is here only controlled via the porosity ratio. Indeed, the results would be similar for two couples (T1,t1) and (T2,t2) which, given the form of Eq. 2, might correspond to the same probability of nucleation.

3.2 Post-mortem mechanical analysis

This porosity-filled meshing was therefore used to conduct mechanical testing under compression in the in-plane and out-of-plane directions. The mechanical properties of the matrix and the fibers are well known (as long as the oxidization processes could be neglected), being considered as elastic isotropic for matrix and elastic orthotropic for yarns (using Chamis model [8]). However, it was not the case of the properties to assign to the porosities. Since porosities are filled with gas an accurate physics-based approach would be to consider a fluid exerting an internal pressure on the surrounding solid material. The implementation of such an approach is under progress. On the present state and as a first approximation, it was chosen to model the pyrolysis gas as an extremely soft elastic isotropic material.

This model was used to investigate the impact of porosity volume ratio on the overall stiffness of the simulated composite, see Fig. 5. It appears that the global stiffness decreases almost linearly as the porosity ratio increases: from 29.1GPa to 24GPa (18%) under axial (in-plane) compression and from 6.7GPa to 1.9GPa (72%) under out-of-plane compression. Therefore, the composite becomes softer and softer. Indeed, although the stiffness of the matrix is much lower than the one of the fibers, its effect is still not negligible, especially in preserving the cohesion of the reinforcement network. This is not the case of porosities whose presence will not only lower the stiffness of the global material but also disrupt the bonding between constitutive

  doi:10.5075/epfl-298799_978-2-9701614-0-0

elements as well. It is especially highlighted in the out-of-plane configuration for which the structural role of the matrix is stronger. It is confirmed by the stiffness drop which is much higher than in the axial configuration. It was also found that the Young Modulus applied to the porosities did not significantly influence the results, apart from a Young Modulus value much too high to be representative of a gas (around 100MPa).

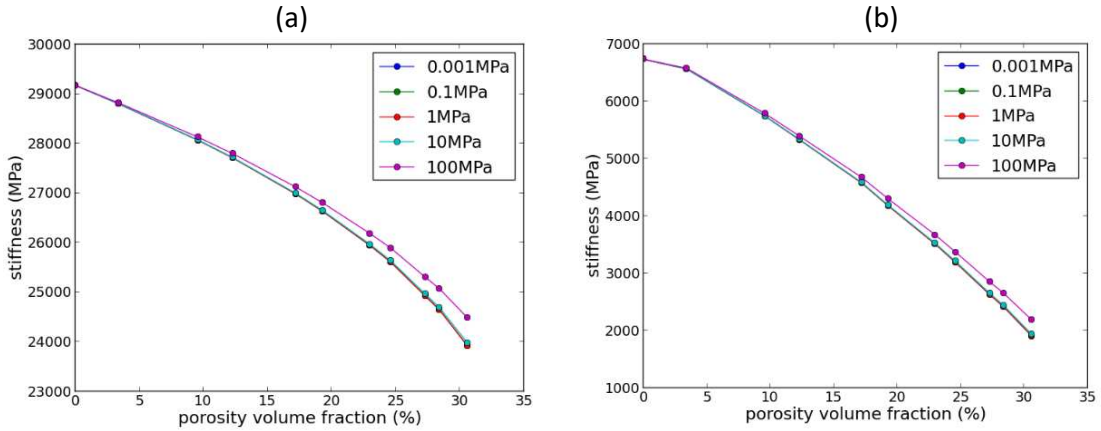

Figure 5. Evolution of the (a) axial (in-plane) and (b) out-of-plane Young Modulus of the numerical laminate according to the porosity volume ratio and for different set values of porosities Young Modulus

3.3 Swelling of the composite

It was observed experimentally that the thickness increase is a primary phenomenon of the thermal decomposition (referred to as swelling). Therefore, it was considered and an example is presented on Fig. 6, using the original mesh and another one less refined. A refined mesh is necessary because the pressure exerted by the porosities on the fiber bundles are more homogeneous and therefore do not completely change the structure of the fiber bundles.

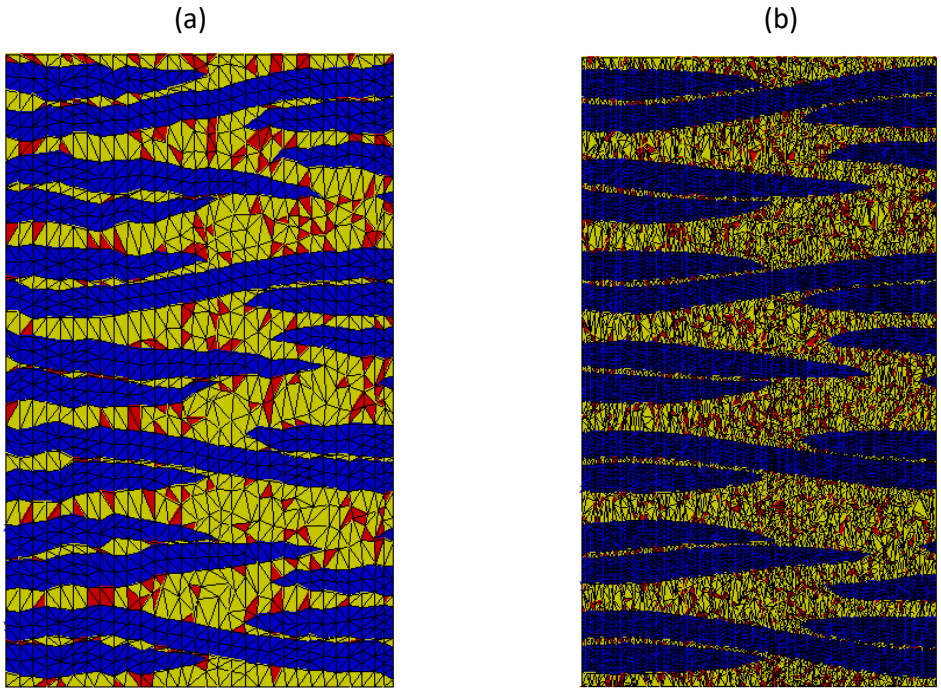

Figure 6. Swelling results on (a) a low refinement of mesh – (b) a high refinement of mesh - fibers in blue – matrix in red – porosities in yellow

  doi:10.5075/epfl-298799_978-2-9701614-0-0

4. Conclusion

This study first presents an experimental analysis on the kinetics of porosity formation in a thermoplastic matrix carbon-reinforced composite subjected to thermal treatments up to 600°C. On the basis of the evolution of the porosity volume fraction, a meso-scale numerical model of the composite has been developed. By means of a probabilistic law of porosity nucleation depending on time and temperature, it enables to explicitly represent the formation of porosities within the matrix and to well reproduce the overall kinetics of porosity formation. With such an approach, first analyses on the compressive behavior of the laminate have enabled to highlight the impact of the porosities, and thus of the matrix thermal decomposition on the elastic properties of the laminate.

5. References

[1] Carpier Y, Alia A, Vieille B, Barbe F. Experiments based analysis of thermal decomposition kinetics model. Case of carbon fibers PolyPhenylene Sulfide composites. Polymer Degradation and Stability 2021 ;186:109525.

[2] Carpier Y, Vieille B, Coppalle A, Barbe F. Study of thermomechanical coupling in carbon fibres woven-ply reinforced thermoplastic laminates: tensile behaviour under radiant heat flux. Polymer Composites, 2020.

[3] Duquesne S, Bourbigot S. Char Formation and Characterization, pp. 239– 259. 12 2009

[4] Vieille B, Coppalle A, Keller C, Garda MR, Viel Q, Dargent E. Correlation between post fire behavior and microstructure degradation of aeronautical polymer composites. Materials Design, 74:76–85, 2015

[5] Mouritz AP, Gibson AG. Fire Properties of Polymer Composite Materials. Solid Mechanics and Its Applications Vol. 143, Springer, 2006.

[6] Ma CCM, Hsia HC, Liu WL, Hu JT. Studies on Thermogravimetric Properties of Polyphenylene Sulfide and Polyetherether Ketone Resins and Composites. Journal of Thermoplastic Composite Materials 1988;1(1):39-49.

[7] Schuster P. What is special about autocatalysis? Monatshefte für Chemie - Chemical Monthly, 150. 05 2019

[8] Chamis CC. Mechanics of composite materials: past, present, and future. J. Compos. Technol. Res., 11. 1989

  doi:10.5075/epfl-298799_978-2-9701614-0-0

CLOSED-LOOP CONTROL OF LASER SURFACE TREATMENT VIA LASER INDUCED BREAKDOWN SPECTROSCOPY

Rodolfo Ledesma[a], Frank Palmieri[b], Elizabeth Barrios[a], John Hopkins[b], and John Connell[b]

a: National Institute of Aerospace, Hampton, VA 23666, USA – rodolfo.i.ledesma@nasa.gov
b: NASA Langley Research Center, Hampton, VA 23681, USA

Abstract: *Current composite manufacturing rates need to be improved to meet the projected demand of on-demand mobility (ODM) and commercial aircraft transports. Some processes in the composite manufacturing chain require touch labor such as manual sanding of surfaces prior to bonding and installing thousands of mechanical fasteners in bonded primary structures to achieve Federal Aviation Administration (FAA) certification. The consequences are insufficient repeatability in bond quality resulting in increased manufacturing time. The FAA has indicated that robust process control is one potential means of certifying bondlines in primary structure. This work describes an integrated closed-loop control system between a laser machining system and laser induced breakdown spectroscopy (LIBS) instrumentation as a means of assuring bond performance and achieving certified composite bondlines. Preliminary results from in-situ treatment and inspection are presented. Results indicate that LIBS inspection and laser treatment can be conducted simultaneously to achieve high quality, reliable adhesive bonds.*

Keywords: LIBS; laser ablation; automation; composite manufacturing; adhesive bonding

1. Introduction

Laser ablation is the removal of material by laser irradiation through photochemical, photothermal, or photophysical mechanisms, which is useful for preparation of an adherend surface for adhesive bonding. Laser surface treatment is a method that has been under research for the past decade at the NASA Langley Research Center (LaRC) to prepare aerospace materials [1-4] for adhesive joining. Laser ablation of composite materials removes the surface contaminants introduced during material handling and fabrication processes. The adjustment of laser parameters enables repeatable surface conditions, and superficial contaminants can be selectively and efficiently removed without damaging the underlying carbon fibers or the carbon fiber reinforced polymer (CFRP) structure [1-3].

At NASA LaRC, a single laser system has been used for both laser surface treatment and laser induced breakdown spectroscopy (LIBS), which enables in-situ monitoring of surface contaminants. The main contamination agent that has been investigated is silicone, which is ubiquitous in composites fabrication processes and, even at minute concentrations, can drastically decrease the performance of adhesive bonded structures. The complete removal and verification of removal of this contaminant is critical for the durability and performance of bonded parts. Silicones can be monitored using the silicon peak from the LIBS data. The silicon peak and carbon peak (mainly from the CFRP material) are used to determine the silicon to carbon ratio, Si/C, as an analytical parameter to quantify the silicone concentration.

This work describes the integration of a laser machining system and LIBS instrumentation to enable closed-loop control. The closed-loop control mechanism will ensure that treated surfaces

  doi:10.5075/epfl-298799_978-2-9701614-0-0

meet quality criteria prior to adhesive bonding. The main goal for this integrated system is assuring bond performance and achieving certified composite bondlines.

2. Laser induced breakdown spectroscopy

LIBS is a characterization technique that utilizes an intense laser source to excite a target material into a plasma state, and upon relaxation, the chemical species emit light, which provides information about the elemental composition. When LIBS uses short/ultrashort pulse widths (e.g., hundreds of ps to 10 fs), there is a short exposure of the material to the light irradiation and minimal heat transfer, thus, reducing the oxidation effects [5]. For polymers, when the laser intensity irradiated on the material is sufficient, mechanical stress is induced by multiphoton transition. If the mechanical stress is sufficient, it produces bond dissociation, and the material is removed from the target surface by fragmentation [6,7]. There is minimal energy transferred to the regions outside the irradiated material volume, thus, producing less thermal stress in the material [8].

A typical LIBS apparatus (Figure 1) is comprised of a laser source and a spectrometer, which includes a detector, e.g., charge-coupled device (CCD) array, and a spectrograph. The laser beam is usually focused to enhance spatial resolution and to deliver maximum laser intensity irradiation on the target surface.

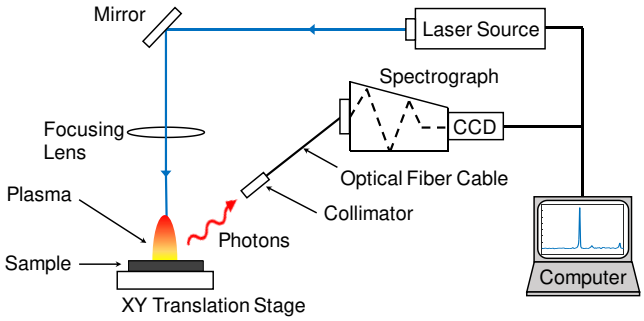

Figure 1. Typical LIBS apparatus comprised of a laser source, a spectrograph, a CCD-based detector, and a computer for data acquisition and laser control.

Significant advantages of LIBS measurements are that they can be conducted in open air and without sample preparation, and the results can be obtained near-instantaneously or in real-time. Advancement in the LIBS technique has shown that it can match or exceed the surface sensitivity of X-ray photoelectron spectroscopy (XPS) [9].

3. Laser ablation

At NASA LaRC, the laser ablative surface treatment is commonly conducted with a 355 nm wavelength, 10 ps pulse width, high repetition rates between 300 and 400 kHz, scan speeds in the order of 25.4 cm/s, and average laser powers of hundreds of mW. These conditions produce many overlapping low-energy (usually < 2 µJ) laser pulses [10,11]. The overlapping of the pulses increases the ablated material. However, the laser parameters used for surface treatment differ from the ones for LIBS [8,10,11]. Current LIBS inspections are conducted using a single laser pulse on a fresh (untested) surface and low energy pulses of at least 15 µJ to improve surface sensitivity and limit of detection [8], and to minimize the ablated material required to generate

a LIBS spectrum for analysis. The laser treatment parameters are being investigated to enable simultaneous in-situ LIBS inspections.

4. Closed loop control system

At NASA LaRC, efforts are being made to enable feedback control by integrating the laser system and the LIBS system [12]. By enabling synchronous control, the automation of the laser ablation and the spectral data collection will allow repeatable and instantaneous surface inspection while the surfaces are being laser treated for adhesive bonding. The automation of the processes will improve the surface inspection and bonded structure certification times. Figure 2 shows the main components and processes of the closed loop control system. The LIBS control system is used to set up the LIBS parameters for data collection such as the gate width, gate delay and number of pulses. After data collection, the LIBS control system calculates the Si/C ratio, which is used as a decision parameter. The communication and command exchange between the proprietary laser control system and the LIBS control system is through the transmission control protocol (TCP). The laser control system is used for the setup of the laser parameters and the XY stage movement. After the LIBS control system triggers the laser operation, the LIBS process begins. Each pulse generated by the laser system will trigger the spectrometer to record the plasma plume emission. Once the spectra collection is finished, the data processing and Si/C ratio determination are conducted automatically to assess the surface quality and determine whether the laser ablation process is complete or further treatment is needed.

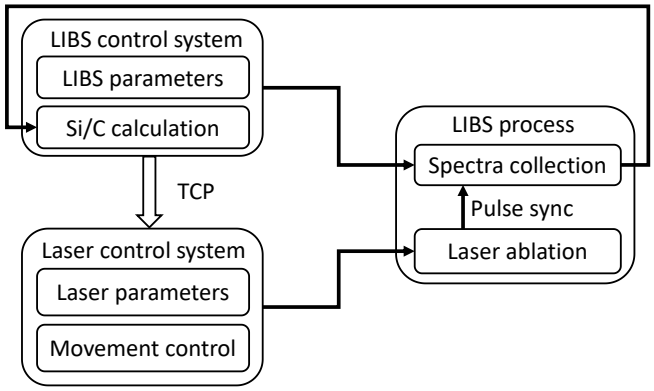

Figure 2. Diagram of the closed loop control system.

5. LIBS applications for CFRP

The applicability of LIBS has been documented [2,3,8,11]. The main focus of the research at NASA LaRC is on CFRP materials and the detection of minute amounts of silicone by monitoring the Si peak from the laser induced plasma. Relevant data are provided to support the feasibility of LIBS as a rapid means to enable quality control of CFRP surfaces prior to adhesive bonding. These results have established the fundamentals for the conception and current implementation of a closed loop control system based on laser technology [12].

Control (as fabricated) and purposely silicone contaminated surfaces were investigated to determine the effect of the residual contaminant on the bond performance [2]. A 355 nm, 10 ps laser system was used for LIBS and laser treatment (LT). Microjoule LIBS was used to detect silicone contamination before and after LT. Figure 3 shows the Si/C ratio as a function of the silicone areal density deposited on a surface prior to LT.

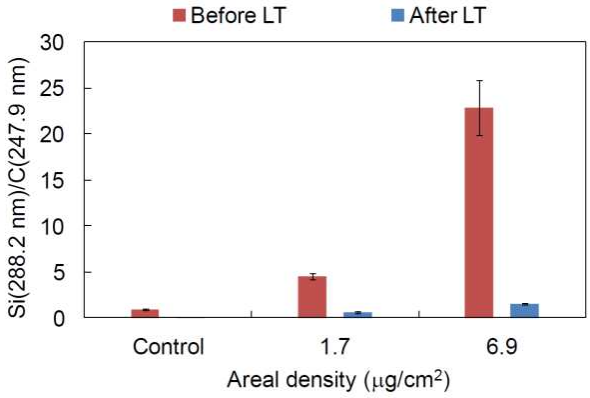

Figure 3. Si/C ratios from the LIBS measurements before and after laser surface treatment using picosecond pulses [2].

Surface characterization using LIBS (before and after laser treatment) with 355 nm, 10 ps pulses was performed on CFRP panels for detection of ultra-thin silicone contamination layers from 0.15 μg/cm^2 to 2 μg/cm^2 (thickness of 1.6 nm to 20 nm) [8]. LIBS was performed using 15 μJ pulses with a single shot on a fresh surface to maximize surface sensitivity. Optimization of laser parameters was studied to decrease the material ablation for LIBS inspection. Time-resolved analysis was conducted to determine optimal plasma conditions to detect Si. The LIBS instrument was sensitive enough to detect residual Si after laser surface treatment.

Surface sensitivity and the LIBS limit of detection (LOD) were investigated for the detection of silicone at various concentrations on CFRP surfaces [9]. XPS and LIBS analyses were performed on identical samples. XPS data were obtained from two different laboratories, BTG Labs (Cincinnati, OH) and NASA LaRC (Hampton, VA). For quantitative analysis, analytical calibration curves were constructed (Figure 4). From the calibration curves, it was possible to determine the detection limits of LIBS, which were below 0.6 at.%. These results demonstrated the advantages of LIBS over XPS for rapid detection of minute quantities of silicone contaminants, with high surface sensitivity and no special atmosphere or sample preparation.

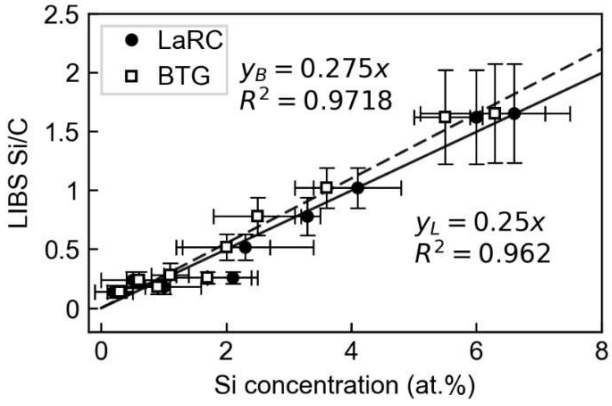

Figure 4. Analytical calibration curves with the Si/C ratio from LIBS and the Si concentration from XPS. The linear fits y_L (solid line) and y_B (dashed line) correspond to LaRC and BTG, respectively. (Reprinted from [9] with permission of SAGE Publishing).

5.1 Surface mapping

LIBS data can be collected at specific locations, and each location can provide a better understanding of the surface condition in that region. In Figure 5, the yellow dots represent the locations where LIBS was measured. The LIBS Si/C ratio from those locations can be correlated to the surface morphology or failure modes observed in failed bonded test specimens. The numbers in parentheses represent the Si/C ratios determined before (white) and after (orange) laser ablation at 200 mW, 355 nm, and a pulse width of 10 ps.

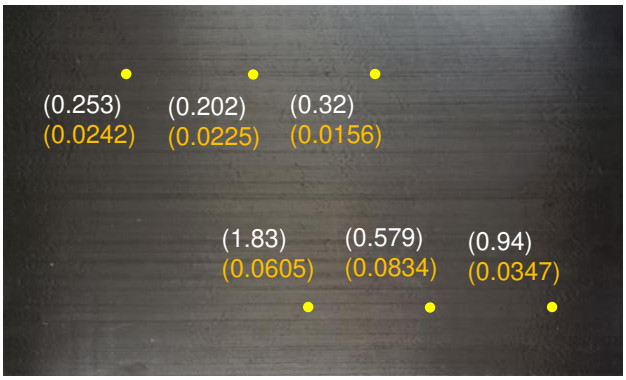

Figure 5. Surface mapping of a composite panel showing the LIBS Si/C ratios before (white) and after (orange) laser ablation.

Another example of surface mapping is when laser surface treatment and LIBS are conducted simultaneously to treat a specific area. In this case, four linearly arranged collimators continuously collected the plasma emissions as the laser was ablating the surface. Ten parallel lines (3.81 cm) were ablated at 200 kHz, 2 W average power (10 µJ pulse energy), and 254 cm/s scan speed, separated by 12.7 µm to produce a surface map using the Si/C ratios. Figure 6 shows the LIBS spectra for one line obtained from the first and second passes on the same location. After the first pass, there are strong Si peaks (between 250 nm and 255 nm, and at 288.2 nm). After the second pass, the Si peaks were not detected, indicating the removal of the silicone contaminant from the CFRP surface. The ablative overlap produced at 200 kHz pulse rate and 254 cm/s was enough for 10 µJ pulses to remove the silicone contaminant after two passes.

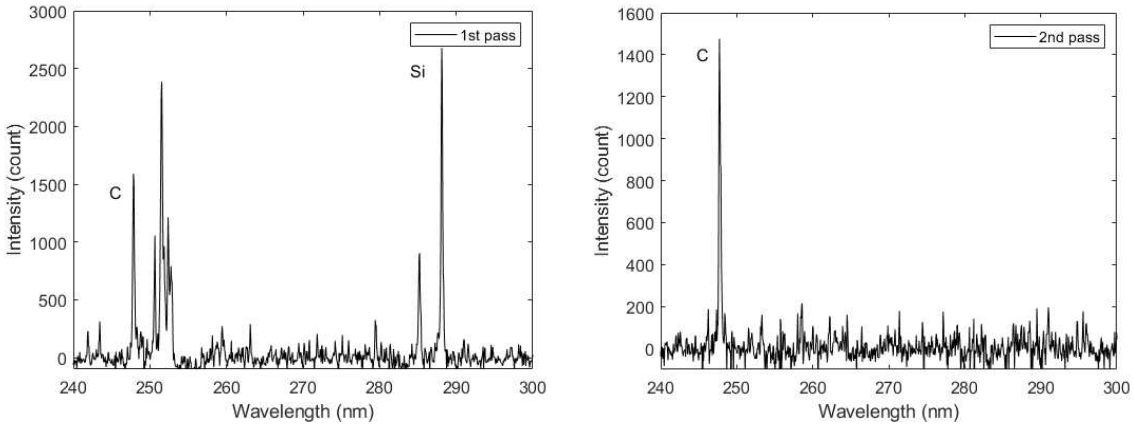

(a) (b)

Figure 6. LIBS spectra of one ablated line after (a) the first pass and (b) the second pass. After the second pass, the Si peaks were not present and only the C peak was detected.

Figure 7 shows the 2D surface maps using the calculated Si/C ratios from the LIBS measurements from the ten lines. Non-uniform distribution of silicone concentration was detected after the first ablation pass, as seen in Figure 7a. After the second pass on the same area, the silicone concentration was significantly reduced (Figure 7b).

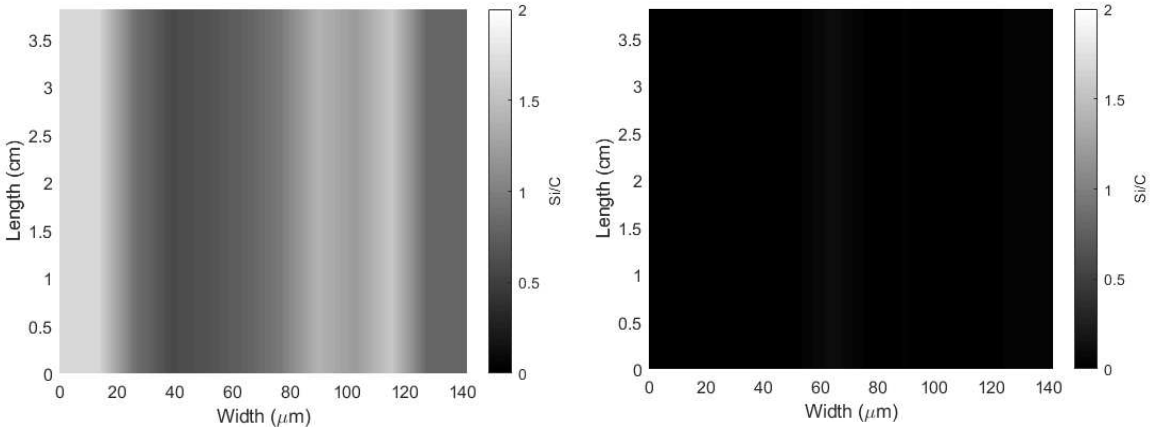

Figure 7. Surface mapping of an ablated region of 3.81 cm x 141.4 µm. Silicone contamination was observed for (a) the first ablation pass but was significantly reduced in (b) the second pass.

5.2 Mechanical testing

PEEK thermoplastic panels were laser treated and co-bonded with FM309-1 (Solvay) and AF-555 (3M Scotch-Weld) adhesives to IM7/8552 (Hexcel) thermoset prepreg to prepare double cantilever beam (DCB) samples (Figure 8). LIBS inspection was completed pre and post laser treatment and indicated that silicone contamination levels were reduced sufficiently to proceed with bonding. The specimens were configured by bonding one end of the panel with AF-555 and the opposite end with FM309-1. Precracks (fluorinated ethylene propylene (FEP) film, 12.7 µm thick) were inserted at both ends of the laminates so that each specimen could be tested from each end to double the number of tests conducted on each bonded panel. The laser treatment process was based on the legacy laser treatment parameters developed at NASA LaRC (Table 1). Figure 9 shows the fracture surfaces after DCB testing. The fracture surfaces show predominantly uniform cohesive failure mode, with some fiber tear on the AF-555 end. Cohesive failure in the adhesive indicates excellent bond performance of the surface treatment. At the time this report was written, no results were available to compare the LIBS-compatible laser surface treatment with the legacy process. Still, this result confirms that laser treatment and reduction of the Si/C ratio as measured by LIBS correlates with high performance bonding.

Figure 8. Sample configuration for DCB testing of laser treated IM7/PEEK. The orange line at the adhesive-IM7/PEEK interface shows the location of precrack (FEP film, 12.7 µm thick). Drawing not to scale.

Table 1. Laser treatment parameters based on legacy surface treatment process. Each laminate surface was treated with one laser pass. The laser wavelength was 355 nm and the pulse width was nominally 10 ps.

	Power (mW)	Frequency (kHz)	Scan speed (cm/s)	Line pitch (µm)
Panel 1	380	325	20	20.3
Panel 2	380	325	30	20.3

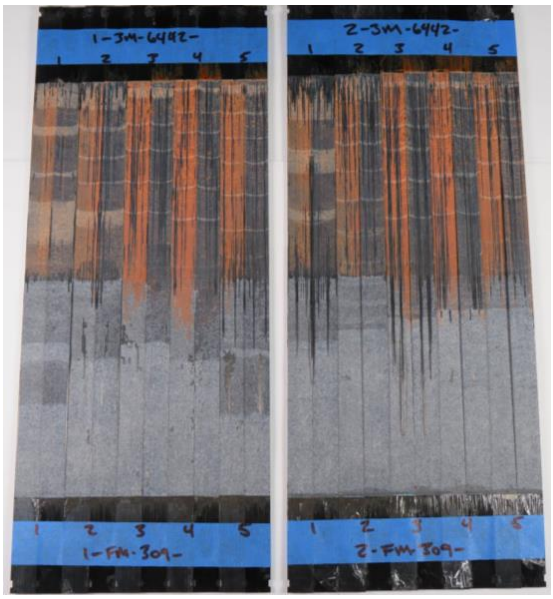

Figure 9. Fracture surfaces for two panels, previously laser treated, showing uniform cohesive failure mode. Panel 1 is left, Panel 2 is right (see Table 1 for details).

6. Summary

Laser surface treatment has been investigated at NASA LaRC to remove ultralow levels of surface contamination, chemically activate the surface, and increase surface area prior to adhesive bonding and coating processes. Silicones are ubiquitous in the fabrication process of CFRP substrates and, even at low concentrations, can significantly diminish adhesive bond performance. The LIBS system has been utilized and tuned as a surface quality control tool for the detection of silicone contaminants and was demonstrated to be an adequate and robust technique that can be integrated for in-line control of a bonding process.

The LIBS instrument developed at NASA LaRC was shown to be surface sensitive comparable to XPS. Extensive research has been conducted at NASA LaRC to prove the reliability of LIBS for the detection of ultralow levels of silicone species on CFRP surfaces prior to adhesive bonding.

The closed loop system described in this work is an advancement of the current apparatus to enhance the utility and speed of the LIBS and laser treatment processes. By integrating both systems, the LIBS and laser treatment can be automated to improve the repeatability and surface inspection times, and therefore, it can reduce the certification times of adhesive bonded structures. Preliminary results indicate that LIBS inspection and laser treatment can be conducted simultaneously to achieve high quality, reliable adhesive bonds.

  doi:10.5075/epfl-298799_978-2-9701614-0-0

Acknowledgements

This work was funded by the Advanced Composites Project (ACP) under the Advanced Air Vehicles Program (AAVP), the Internal Research and Development (IRAD) program, and the Transformational Tools and Technologies (TTT) program at the NASA Langley Research Center. The authors thank Tony Belcher (Boeing) for conducting the mechanical testing (under the Space Act Agreement SAA1-33748), John Hopkins (NASA LaRC) for conducting the laser ablation, and Hoa Luong and Sean Britton (NASA LaRC) for laminate fabrication.

7. References

1. Palmieri F, Belcher M, Wohl C, Blohowiak K, Connell J. Laser ablation surface preparation for adhesive bonding of carbon fiber reinforced epoxy composites. Int. J. Adhes. Adhes. 2016;68:95-101.
2. Palmieri F, Ledesma R, Fulton T, Arthur A, Eldridge K, Thibeault S, Lin Y, Wohl C, Connell J. Picosecond pulsed laser ablation for the surface preparation of epoxy composites. SAMPE Seattle; 2017 May 22-25.
3. Ledesma R, Palmieri F, Connell J. Laser induced breakdown spectroscopy of polymer matrix composites for real-time analysis of trace surface contaminants: A review. *Int. J. Adhes. Adhes.* 2020;98.
4. Palmieri F, Watson K, Morales G, Williams T, Hicks R, Wohl C, Hopkins J, Connell J. Laser ablative surface treatment for enhanced bonding of Ti-6Al-4V alloy. ACS Appl. Mater. Interfaces. 2013;5:1254-1261.
5. Pou-Alvarez P, Riveiro A, Novoa XR, Fernandez-Arias M, del Val J, Comesaña R, et al. Nanosecond, picosecond and femtosecond laser surface treatment of magnesium alloy: role of pulse length. Surf. Coat. Technol. 2021;427:127802.
6. Srinivasan R, Braren B. Ultraviolet laser ablation of organic polymers. Chem. Rev. 1989;89:1303-1316.
7. Gedvilas M, Raciukaitis G. Investigation of UV picosecond laser ablation of polymers. Proc. SPIE, Workshop on Laser Applications in Europe. 2005;6157:61570T.
8. Ledesma R, Palmieri F, Connell J, Yost W, Fitz-Gerald J. Surface characterization of carbon fiber reinforced polymers by picosecond laser induced breakdown spectroscopy. Spectrochim. Acta, Part B. 2018;140:5-12.
9. Ledesma R, Palmieri F, Campbell B, Yost W, Fitz-Gerald J, Dillingham G, Connell J. Correlation of trace silicone contamination analyses on epoxy composites using X-ray photoelectron spectroscopy (XPS) and laser-induced breakdown spectroscopy (LIBS). Appl. Spectrosc. 2019;73:229-235.
10. Palmieri F, Ledesma R, Cataldo D, Lin Y, Wohl C, Gupta M, Connell J. Controlled contamination of epoxy composites with PDMS and removal by laser ablation. SAMPE Long Beach; 2016 May 23-26.
11. Palmieri F, Ledesma R, Dennie J, Kramer T, Lin Y, Hopkins J, Wohl C, Connell J. Optimized surface treatment of aerospace composites using a picosecond laser. Composites, Part B. 2019;175.
12. Connell J, Palmieri F, Yost W, Hopkins J, Ledesma R. Laser surface treatment and spectroscopic analysis system. U.S. Patent Application Publication, US 2019/0033231; 2019 Jan. 31.

  doi:10.5075/epfl-298799_978-2-9701614-0-0

MANUFACTURE OF STEEL-CF/PA6 HYBRIDS IN A LASER TAPE PLACEMENT PROCESS: EFFECT OF SUBSTRATE SURFACE TEXTURE ON FIRST PLY PLACEMENT AND COMPRESSION SHEAR STRENGTH

Victoria Zinnecker[a,b,c], Chris Stokes-Griffin[a], Ludovic Rapp[b], Steve Madden[b], Andrei Rode[b], Paul Compston[a]*

a: ARC Training Centre for Automated Manufacture of Advanced Composites, Australian National University, Canberra, ACT 2600, Australia – Victoria.Zinnecker@anu.edu.au
b: Laser Physics Centre, Department of Quantum Science and Technology, Research School of Physics, Australian National University, Canberra, ACT 2600, Australia
c: Aerostructures Innovation Research Hub, Swinburne University of Technology, Hawthorn, Melbourne, VIC 3122, Australia – vzinnecker@swin.edu.au

Abstract: *This paper investigates the effect of steel substrate surface texture on the first ply placement and compression shear strength of metal-composite (carbon fibre/polyamide 6) hybrids manufactured in a laser-assisted automated tape placement (ATP) process. Texturing of the steel surface, using an ultrashort-pulsed laser, increased laser absorptance during ATP by 23%. Additionally, the scatter pattern changes from predominantly specular reflection for the pickled surface to a broad scatter for the grit blasted and the laser textured surface. The highest bond-line shear strength was obtained at a substrate temperature of 330°C for the grit blasted and laser textures surface due to a better flow of matrix in the surface asperities resulting in mechanical interlocking. High absorbing surface textures reduce the laser power required for the first ply placement by 25%.*

Keywords: automated tape placement; thermoplastic; metal-composite hybrid; laser texturing; mechanical testing

1. Introduction

Hybrid structures of metal and fibre-reinforced polymer composites provide great potential to manufacture lightweight automotive and aerospace components and combine the most desirable characteristics of each material. Composites with thermoplastic matrix exhibit high toughness, good crash performance, recyclability, and easy handling as material storage at ambient air temperature are possible. Furthermore, robot-guided laser-assisted tape placement (ATP) of carbon-fibre thermoplastics can be used to selectively reinforce metal parts along load bearing paths. However, manufacturing metal-composite hybrids is challenging due to the joining partners' mechanical, thermal, and chemical differences. In particular, placing the first ply of composite onto the steel substrate without an additional polymer coating will need special consideration due to differences in thermal behaviours of metals and composites, and the effects of the surface topography. The main challenge for manufacturing metal-composite hybrids is the order of magnitude difference in power needed to heat the steel substrate and the composite tape to the same temperature. With this difference in power required, it is crucial for a successful first ply placement to protect the feed tape from overheating and polymer degrading. It has been shown that roughening the metal substrates' surface improves processability through increased absorptance and broader scattering of the laser irradiation

  doi:10.5075/epfl-298799_978-2-9701614-0-0

during laser ATP compared to pickled steel [1]. However, no successful metal-composite bonding from direct placement of composite tape without a polymer interlayer has been reported.

In this study, the effects of the steel substrate's surface structure produced by grit blasting and femtosecond laser ablation on the automated laser-assisted tape placement process for the first ply placement and their bond-line shear strength are investigated. The metal surface is tailored to increase laser absorptance, diffuse reflected laser radiation, and increase mechanical interlocking. The substrate surfaces are optically analysed, and the angular dependent absorptance for the ATP laser is measured. A comparison of the qualitative scattering distribution for the different surface textures is presented, and their effect on the first ply placement ATP parameters is discussed. The compression shear strength for each specimen is also presented.

2. Materials, methods, and experimental set-up

2.1 Materials

Samples were manufactured with 2 mm thick low carbon, hot rolled, and pickled steel (*BRIGHTFORM®, BlueScope Limited, Australia*) and 15 plies of fully impregnated 0.13 mm x 12 mm 48% v/v CF/PA 6 unidirectional prepreg tape (*Celstran® CFR-TP PA 6 CF60-01, Celanese Corporation, Irving, Texas, USA*).

2.2 Surface pre-treatment

The surface area of the pickled steel substrate was increased by two different methods to increase mechanical interlocking, increase absorptance and reduce specular reflection. A subset of samples was uniformly abraded by grit blasting. A second subset was textured with an ultrashort pulsed (USP) Carbide CB3-40W laser *(Light Conversion, Lithuania*) at a wavelength of 1026 nm with a 2.75 mm output beam diameter ($1/e^2$). A quasi-telecentric f-Theta scanning lens with a 540 mm working distance *(S4LFT1420/449, Sill Optics GmbH, Germany)* produced a Gaussian focal spot of 87 µm FWHM diameter. A diffractive element *(ST-220-J-Y-A, Holo Or, Israel)* was placed in the laser beam path to redistribute the Gaussian beam intensity into a square top-hat profile with a rectangular focal spot size of 165 µm x 148 µm at FWHM. The scanning system consists of a 10-facet polygon scanner *(Precision Laser Scanning Inc., USA)* and a galvanometer scanner *(Cambridge Technology Inc., USA)* to create an X-Y raster scan of the laser beam across an area up to 280 mm × 280 mm. The material to be processed was fixed on a sample holder within an ablation chamber, filled with ambient air, and connected to an extraction system to exhaust ablated material. The laser settings for the surface texturing were: pulse width (t_p) 275 fs, single pulse energy on target (E_p) 245.8 µJ, laser pulse repetition rate (R_{rep}) 100 kHz, focal spot translation speed (v_{scan}) 86 m/s, and laser fluence (F) 1.1 J/cm^2 [2].

Figure 1 presents the white light interferometry images of the three distinct surface structures. Grit blasting results in a highly randomised roughened surface, whereas the square top-hat surface structure exhibits regular 70 µm deep grooves with a 300 µm spacing between each.

  doi:10.5075/epfl-298799_978-2-9701614-0-0

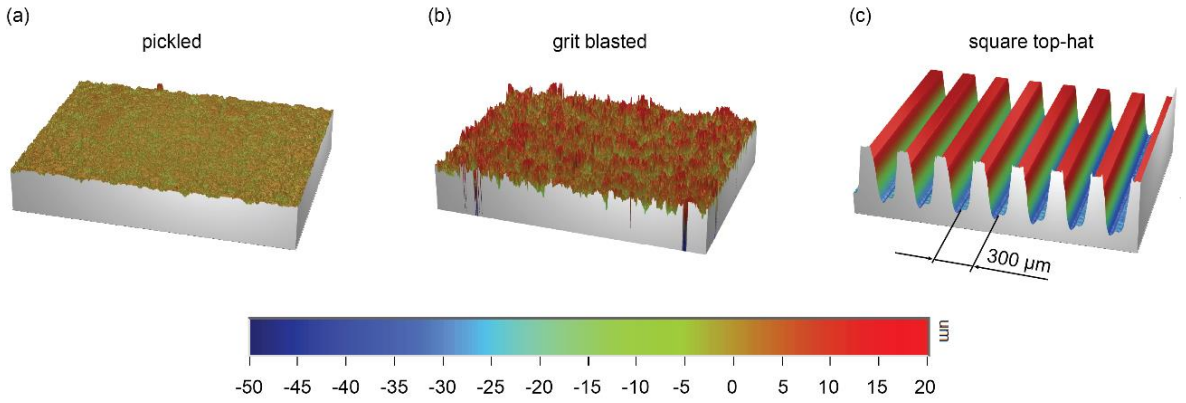

Figure 1. White Light Interferometry profiles for (a) pickled, (b) grit blasted and (c) square top-hat surfaces displayed with low frequency pass Fourier filter.

2.3 Optical analysis

Optical characterisations were performed on the substrates to analyse the influence of different surface pre-treatments on the laser absorptance (A), and the scattering distribution of the near-infrared (NIR) laser irradiation used during laser-assisted automated tape placement (ATP). Absorptance analysis was performed on a Lambda 1050 UV/Vis/NIR spectrophotometer *(Perkin Elmer Inc., USA)* equipped with a 150 mm integrating sphere. The integrating sphere is necessary to capture diffuse and specular reflectance, as the substrates show significant scattering behaviour. The 100% baseline was performed with a NIST (National Institute of Standards and Technology) traceable 99% reflectance standard mounted in the reflectance port. The angular dependent reflectance (in %) was measured for the 900 nm to 1060 nm wavelengths using the central sample holder for the integrating sphere. Measurements were performed at incident angles from 10° to 85°.

The transmittance (T) of the substrates was found to be zero at the wavelength of the laser (1060 nm). From the conservation of energy:

$$T + A + R = 1 \tag{1}$$

As the transmittance is zero, the absorptance is the complement of the reflectance:

$$A = 1 - R \tag{2}$$

Therefore, the absorptance can be determined indirectly from reflectance measurements.

For the qualitatively scattering distribution measurements, a low power HeNe laser (λ = 630 nm) was used to irradiate the specimen surfaces following the approach from other studies [1,3,4]. The laser spot was guided through a 2 mm wide iris and aimed at the textured samples at a fixed angle of θ = 60°. The scattering pattern was observed on a diffuse white target, assumed to be Lambertian, and placed at a distance of 100 mm behind the target. The orientation of the irradiated samples was in line with groove direction (ϕ = 0°), and the scattering pattern was recorded with a digital single-lens reflex (SLR) camera (Figure 2). The observed distributions should represent the relative irradiance as the radiance is proportional to the irradiance for a diffuse Lambertian target [5].

  doi:10.5075/epfl-298799_978-2-9701614-0-0

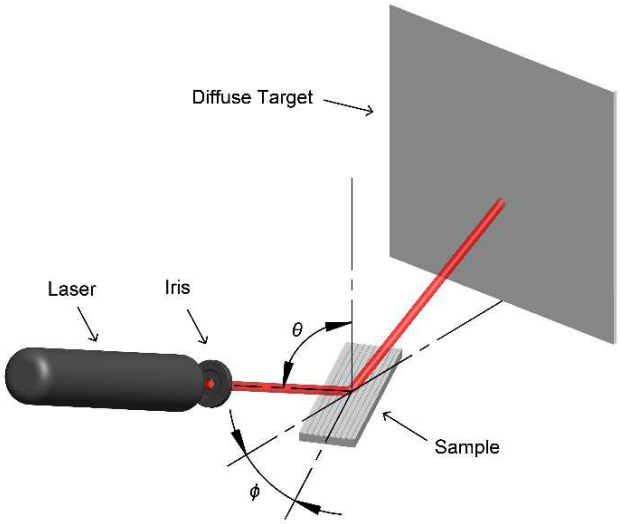

Figure 2. Experimental set-up for scattering observation. Adapted from [3].

2.4 Laser-assisted automated tape placement system

All specimens are manufactured using an automated tape placement system from AFPT GmbH (*AFPT GmbH, Germany*) equipped with two near-infrared diode lasers (*Laserline GmbH, Germany)* to heat the incoming tape and substrate independently (Figure 3 (a)). The tape and substrate were heated with 2 kW and 4 kW lasers, respectively. When using both laser sources, the positioning of the lasers result in equivalent heated lengths for normal placement as with single-laser systems. For first ply placement only the substrate laser was used (Figure 3 (b)).

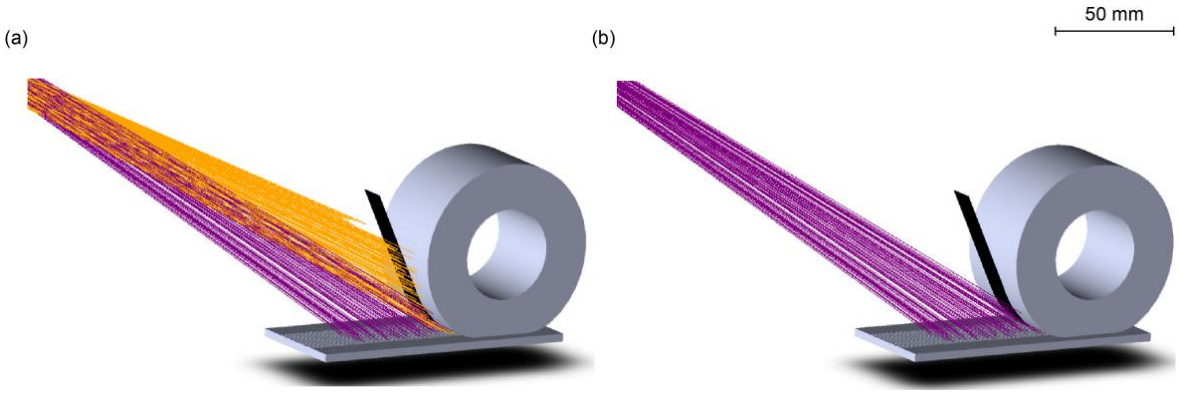

Figure 3. Schematic of dual-laser ATP system at ANU, (a) dual-laser nip-point heating with 2 kW tape laser (orange rays) and 4 kW substrate laser (purple rays), (b) substrate-only heating

2.5 Sample manufacturing

Fifteen (15) CF/PA6 plies were placed onto the prepared steel substrates. The placement parameters for the first ply, however, differ from the straightforward placement of the subsequent plies [6]. For the first ply placement, the biggest challenge is the order of magnitude difference in power required for the steel and composite to heat to the same processing temperature. To overcome this, an indirect heating strategy for the feed tape was used for the first ply placement: only the 4 kW substrate laser was used, while the feed tape was irradiated solely by the reflection of the substrate laser radiation off the substrate ((Figure 3 (b)). The feed tape temperature was monitored with a thermal camera and kept below the processing

  doi:10.5075/epfl-298799_978-2-9701614-0-0

temperature threshold of 450°C identified by [7]. The ratio of the heat flux on the tape and substrate depends on the specific substrate reflectance, making it difficult to achieve individual temperature targets on the tape and substrate. This was overcome by modulating the reflected radiation incident on the feed tape using a polished copper reflector. Two substrate temperatures of 200°C and 330°C were investigated and the substrate laser power adjusted accordingly. The substrate temperature was monitored with a thermocouple installed at the midpoint of the substrate's lower surface. A summary of the first ply placement settings is presented in Table 1. First ply placement was not successful for the pickled surface finish; hence no further investigations are included. For the placement of the subsequent plies, the dual-laser nip-point heating strategy was used with a placement rate of 400 mm/s, and consolidation force increased from 190 N to 370 N. Test specimens for mechanical characterisation were taken only from the locations where the ATP process had stabilised.

Table 1. First ply placement processing parameters

Surface texture	Substrate Temperature	Tape placement rate	Substrate laser power	Reflector
Grit blasted	200°C	100 mm/s	4000 W	no
	330°C	50 mm/s	4000 W	yes
Square top-hat	200°C	105 mm/s	4000 W	no
	330°C	50 mm/s	3000 W	no

2.6 Shear strength characterisation

The bond-line shear strength was characterised using a novel compression shear testing (CST) method [8] for tough thermoplastic composite laminates. Previous work with metal-composite hybrids demonstrated that the CST method yielded equivalent shear strengths with less scatter compared to single lap shear testing [9]. The metal-composite hybrid laminates were cut to 10 × 10 × 4.5 mm^3 (length × width × thickness). The gap between the loading noses, adjusted manually, was set to 0.5 mm. To ensure pure shear loading, the load points of the loading noses were aligned symmetrically with respect to the bond-line for the metal-composite hybrids.

Five specimens for every material configuration were tested at 1 mm/min under displacement control in a hydraulic testing machine *(model 8874, Instron, USA)* equipped with a 25 kN load cell. The shear strength was calculated according to Equation (3):

$$\sigma_S = \frac{F_{peak}}{l \times b} \tag{3}$$

Where σ_S is shear stress, F_{peak} peak load at failure, l length, and b width of the overlap area.

3. Results

3.1 Absorptance

The angular dependent absorptance *A* for a wavelength of 1060 nm of the different surface textures is plotted in Figure 4. The angle of incidence of the used laser source during ATP is

  doi:10.5075/epfl-298799_978-2-9701614-0-0

approximately 60° and highlighted in blue. For reference, the absorptance of UD-CF/PA 6 tape (*A* = 88%) is included in the graph. Grit blasting the steel substrate does not change the absorptance at 60° (*A* = 61%) compared to the pickled steel but provides a more constant absorptance for most angles of incidence. Laser texturing the pickled surface with the square top-hat beam profile (groove dimensions depth d = 70 µm and spacing s = 300 µm) increases the absorptance by 23%.

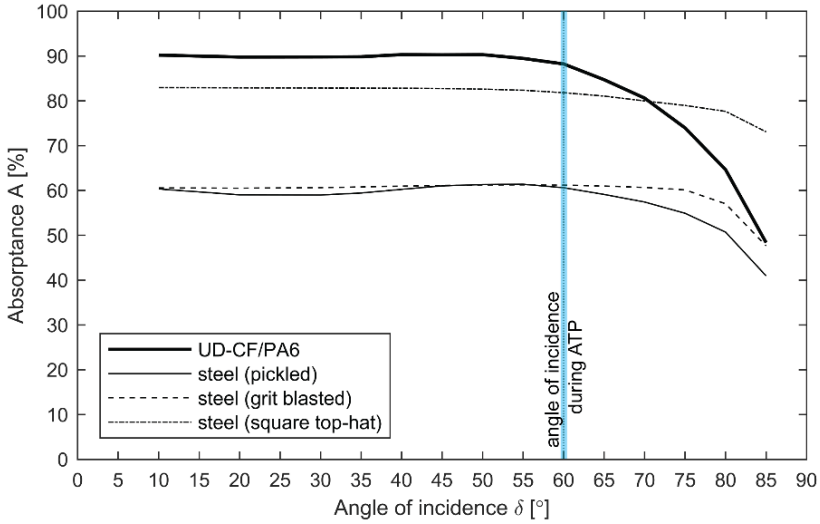

Figure 4. Angular dependent absorptance for distinct surface structures at 1060 nm. Measurements for UD- CF/PA 6 are included for reference.

3.2 Scatter distribution

The qualitative scattering distribution for different surface textures in $\phi = 0°$ direction (along the grooves) are presented in Figure 5. The darker the spot appears, the higher the laser power in this specific area. The pickled steel shows a dark spot in the centre of the recorded image, indicating specular reflection. Whereas the grit blasted surface scatters the light more broadly with the same symmetric shape. The square top-hat surface structure exhibits a wedged shaped scattering pattern induced by the two side walls of the groove with a small concentration spot in the centre, most likely induced by the pickled steel surface between the laser textured areas.

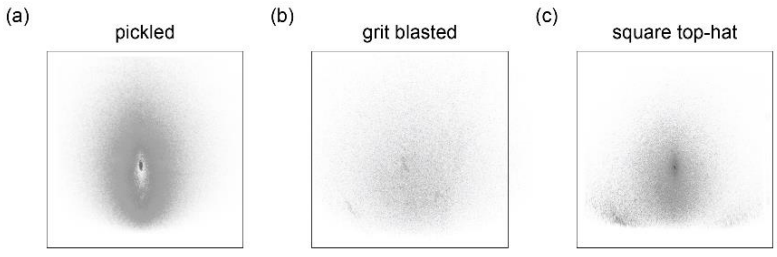

Figure 5. Scatter distribution for (a) pickled, (b) grit blasted, and (c) square top-hat surface structure.

3.3 Shear strength

The shear strengths for the steel-CF/PA 6 hybrids with different substrate surface pre-treatments are presented in Figure 6. No successful bonding was achieved for the pickled surface finish and therefore, the shear strength is zero. The grit blasted samples manufactured at a

substrate temperature of 200°C failed during cutting, hence the shear strength is also zero. The laser textured surface structure yields a shear strength of 4.8±0.4 MPa at low substrate temperature. Increasing the substrate temperature to 330°C doubles the shear strength of directly bonded steel-CF/PA 6 hybrids. A further increase of 50% in shear strength is achieved with the grit blasted surface structure at high substrate temperatures. This high shear strength is most likely caused by the undercuts introduced into the surface by grit blasting and therefore increasing the mechanical interlocking. The highest measured shear strength is 17.3 MPa for grit blasting and 14.7 MPa for the laser textured samples, respectively.

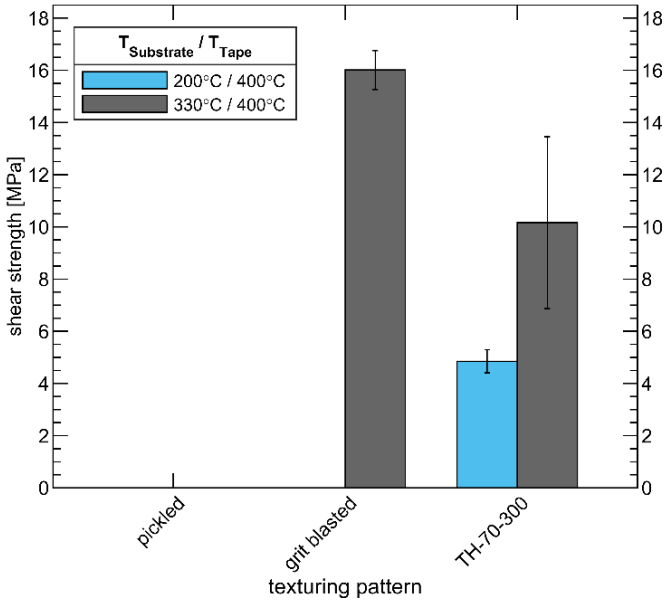

Figure 6. Shear strength for metal-composite hybrids without polymer interlayer for different metal surface structures

4. Discussion and Outlook

This study investigated the effect of different surface textures on the first ply placement of composite onto steel substrates without an additional polymer coating in a laser-assisted ATP manufacturing process and the shear strength of steel and CF/PA 6 hybrids. The main challenge for manufacturing metal-composite hybrids is the order of magnitude difference in power needed to heat the steel substrate and the composite tape to the same temperature. One approach is to increase the laser absorptance of the steel substrate such that the temperature profile of the substrate and the tape are more compatible. In this paper it was shown, that applying femtosecond laser ablation to a pickled steel surface increases the absorptance of the steel substrate by 23% compared to grit blasting. Additionally, the presented grit blasted, and laser textured surfaces scatter the laser light more broadly with less specular reflection than the pickled reference surface. The combination of increasing the surface area of the pickled steel, introducing undercuts, and broadening the scatter pattern resulted in successful metal-composite manufacture with high shear strengths without any additional coating. The shear strength test results suggest that high substrate temperature is necessary for successful metal-composite manufacturing with laser-assisted ATP. The high substrate temperature might be supporting the matrix flow into the asperities before re-solidification within the short time frame during thermoplastic ATP. Therefore, high absorbing substrates, manufactured in a clean,

  doi:10.5075/epfl-298799_978-2-9701614-0-0

precise, and repeatable way that decreases the required laser power for first ply placement are of interest. In this study, the laser power required was reduced by 25% and no additional reflector was required.

Future works could include development of tailored laser textured surfaces for a further increase in direct bond-line shear strength, such as inclined grooves to replicate the undercuts that are believed to be responsible for the high shear strength.

Acknowledgements

This research was supported by the ARC Training Centre for Automated Manufacture of Advanced Composites (IC160100040), supported by the Commonwealth of Australia under the Australian Research Council's Industrial Transformation Research Program and the Australian Government through the Australian Research Council's Linkage Project funding scheme (Project LP180100276), Transport for NSW, Australia.

References

1. Stokes-Griffin CM, Ehard S, Kollmannsberger A, Compston P, Drechsler K. A laser tape placement process for selective reinforcement of steel with CF/PA6 composites: Effects of surface preparation and laser angle. Materials & Design. 2017; 116:545–53.
2. Zinnecker V, Madden S, Stokes-Griffin C, Compston P, Rode AV, Rapp L. Ultrashort pulse laser ablation of steel in ambient air. Optics & Laser Technology. 2022; 148:107757.
3. Stokes-Griffin CM, Compston P. Optical characterisation and modelling for oblique near-infrared laser heating of carbon fibre reinforced thermoplastic composites. Optics and Lasers in Engineering. 2015; 72:1–11.
4. Kienle A, Forster FK, Diebolder R, Hibst R. Light propagation in dentin: influence of microstructure on anisotropy. Phys Med Biol. 2002; 48(2):N7–14.
5. Ramamoorthi R, Hanrahan P. On the relationship between radiance and irradiance: determining the illumination from images of a convex Lambertian object. J Opt Soc Am A, JOSAA. 2001 1; 18(10):2448–59.
6. Stokes-Griffin CM, Kollmannsberger A, Ehard S, Compston P, Drechsler K. Manufacture of steel–CF/PA6 hybrids in a laser tape placement process: Effect of first-ply placement rate on thermal history and lap shear strength. Composites Part A: Applied Science and Manufacturing. 2018; 111:42–53.
7. Stokes-Griffin CM, Kollmannsberger A, Compston P, Drechsler K. The effect of processing temperature on wedge peel strength of CF/PA 6 laminates manufactured in a laser tape placement process. Composites Part A: Applied Science and Manufacturing. 2019; 121:84–91.
8. Schneider K, Lauke B, Beckert W. Compression Shear Test (CST) – A Convenient Apparatus for the Estimation of Apparent Shear Strength of Composite Materials. Applied Composite Materials. 2001; 8(1):43–62.
9. Zinnecker V, Stokes-Griffin CM, Khudiakova A, Wolfahrt M, Compston P. A comparative study for shear testing of thermoplastic-based composites and metal-composite hybrids. Composites Part A: Applied Science and Manufacturing. 2020; 137:105953.

  doi:10.5075/epfl-298799_978-2-9701614-0-0

REAL-TIME MATERIAL MEASUREMENT FOR AUTOMATED FIBRE PLACEMENT

Iryna Tretiak[a], Jordan Jones, Duc Nguyen, Xiaochuan Sun, Mario Valverde, James Kratz

a: Bristol Composites Institute, University of Bristol, Bristol, UK

iryna.tretiak@bristol.ac.uk

Abstract: *Due to their mechanical characteristics, composite materials are commonly used in structural applications in industries such as aerospace and automotive. Among existing composites manufacturing methods, Automated Fibre Placement (AFP) is gaining interest thanks to its ability to provide higher production rates and tighter tolerances. However, variability in the incoming material, such as the thickness and width of the tape, can potentially affect the quality of the final AFP parts. Hence, there is a need for 'intelligent' AFP systems that can monitor the dimensions of the incoming material in real-time and adjust the process parameters accordingly, i.e., a closed-loop feedback system. The main purpose of this work is to investigate the possibility of laser sensor usage in real time AFP processing.*

Keywords: Composite manufacturing; Automated Fibre Placement; laser sensors.

1. Introduction

Composite materials are widely used in different industries due to their high specific stiffness and strength. Manufacturing of complex shapes requires new automated techniques that will reduce manufacturing waste, retain high quality and increase speed of production. Automated fibre placement (AFP) is one of the current manufacturing methods that involves robotic deposition of narrow strips of composite prepreg onto a mould to produce a desired lay-up. In doing so, AFP processes are able to provide high efficiency and repeatability (see Figure 1).

Process parameters, such as deposition speed, compaction pressure, temperature and tape tension need to be measured and controlled during the AFP process. These parameters are usually set prior to manufacturing and remain fixed during the entire process. However, variability in the incoming material [1], such as the thickness and width of the tape, can potentially affect the quality of the final part. Inspection of composite plies after deposition is currently made either by visual inspection, by dedicated personnel, or by using different inspection techniques, such as thermal imaging [2], eddy current inspection [2] or laser profiling [3]. In order to control the process, measurements need to be made before deposition at the roller. This can be done using sensors that can measure the chosen material property to a resolution smaller than the material variability. Furthermore, the chosen sensor will need to eventually operate in a factory, where variations in environmental conditions (e.g. lighting, temperature) and physical conditions (e.g. distance from the material, speed of material) might vary.

The aim of this paper is to investigate the effect of environmental and physical conditions on the measurements made by thickness and width sensors. A testbench was built to precisely monitor the environment conditions during an AFP process (e.g., temperature, compaction level) and identify their influence on the deposition quality. The results are used to select and

  doi:10.5075/epfl-298799_978-2-9701614-0-0

locate sensors in a research-based AFP deposition system to demonstrated closed loop control on composite manufacturing processes.

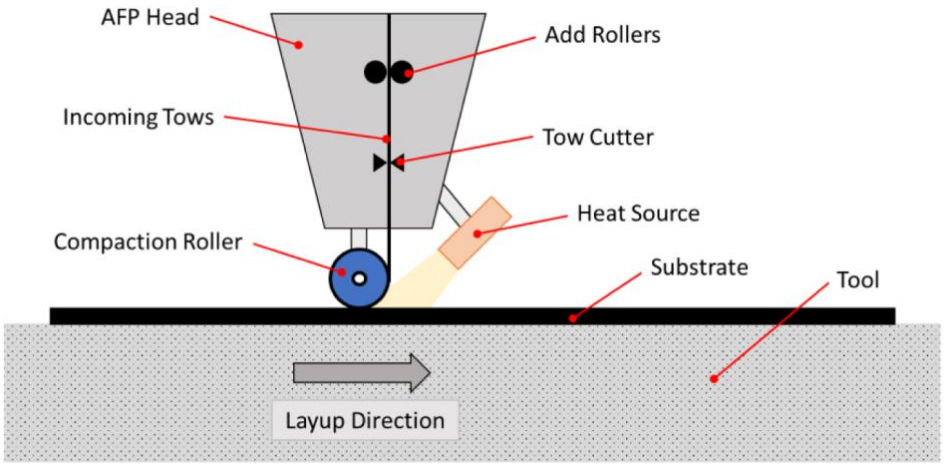

(a)

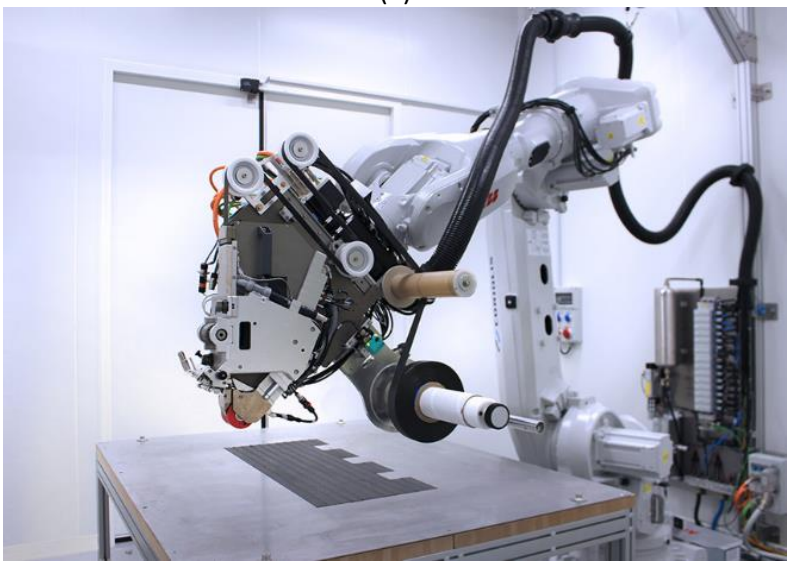

(b)

Figure 1. (a) Automated fibre process - schematic representation [4]*; (b) AFP machine (courtesy of Coriolis)*

2. Investigation of AFP machine features and parameters on laser sensors readings

2.1 Sensors selection

For this work, several sensors were selected that are able to measure the dimensions of the AFP tape before the deposition. At the pre-deposition stage, thickness measurement is done using two point -laser sensors placed opposite to each other. For this purpose, two *Micro-Epsilon OptoNCDT ILD2300-2* with the measuring range of 2 mm and the measurement resolution of 0.3 µm are placed opposite to each other to measure the thickness of the moving tape. There are several challenges involving this arrangement:

1. Sensor alignment: measured spots must coincide through the whole measuring range (no offset, tilt or inclination)
2. Mounting: Both sensors must be aligned
3. Synchronisation: movements during the AFP process can affect the reading of the sensors.
4. Field of measurement: the measured object should stay in the measuring field, so the tape needs to be in tension at all times.

All of these challenges have been addressed during the design and build of the experimental test frame that is discussed in the following section.

To measure the width of the tape (pre-deposition) *Micro-Epsilon ScanControl 2900-50* was selected, which provides 4 µm of line linearity and 1280 pixels per profile. This sensor needs to be positioned between 65 and 125 mm from the measuring object as the resolution is linked to this distance. For post-deposition measurements (thickness and width) *Micro-Epsilon ScanControl LLT30x0-25* was used, as this scanner provides good resolution in both thickness (1.5µm) and width direction (2048 points per profile).

2.2 Development of the test bench

To consider all the above limitations and challenges for usage of laser sensors, a new experimental test frame was designed and built (see Figure 2).

All the sensors are fixed on linear and rotational stages to ensure linearity of their positions. Moreover, this setup provides the opportunity to investigate the effect of the vertical and angular positions of the sensors on the readings. The composite tape was passed through the closed loop using a winder/unwinder unit, and the position of the additional rollers on the frame allowed the tension of the tape that it necessary for accurate thickness readings to be provided.

To read the data from all the sensors at the same time, a LabView programme was developed that collects width and thickness data in real time.

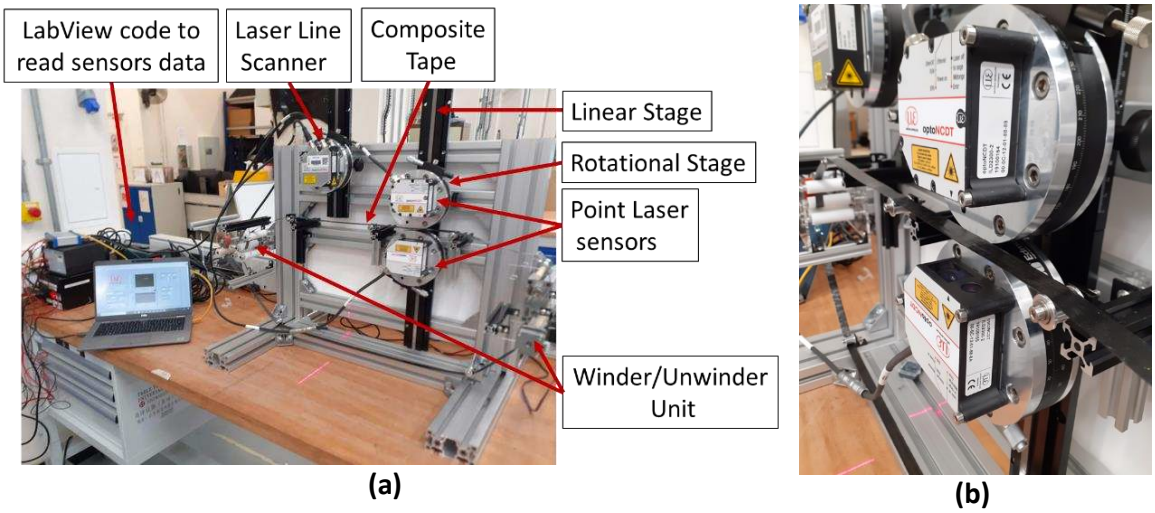

Figure 2. Experimental test frame: (a) general view of the set-up (b) close look of the tape passing through the sensors

2.2 Experimental testing and results

For this work, several machine and material features were selected to investigate their effect on the quality of sensors reading, such as:

- Light
- Vibration
- Position of the sensors
- Speed of material deposition
- Material topology

2.2.1 Effect of light intensity

To investigate the influence of light intensity, the tape stayed in a steady position, and the sensor positions were fixed in all tests to avoid the introduction of the other variabilities. Light intensity was controlled using UV lamps and measured using a lux meter. By changing the light intensity, dimensions of the tape were recorded. Results showed that the light doesn't have any effect on the sensors readings as shown in Table 1.

Table 1: Light intensity effect on thickness and width measurements

Light intensity, lux	Thickness, mm	Width, mm
445	0.31	6.4
1005	0.31	6.4
2700	0.31	6.4
6700	0.31	6.4

2.2.2 Position of the sensors

Having developed an experimental test frame with the sensors positioned on the linear and rotary stages, it is possible to investigate the position of the sensors on their readings (as the resolution might change with its position). This provides better guidelines for positioning the particular sensors on the AFP head.

Table 2: Measuring field for the laser line sensor ScanControl 2900-50

X axis, width, mm	Z axis, height, mm	Resolution, µm
42	70	32.8
50	95	39
58	120	45

As shown in Table 2, based on the vertical position of the line scanner, its resolution changes and the horizontal position (X-axis) needs to be adjusted in the LabView code (see Figure 3).

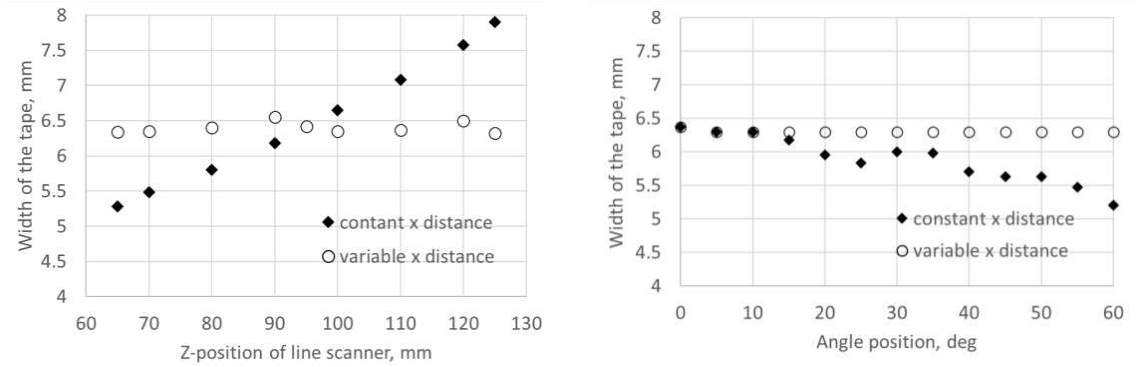

Figure 3. Effect of the laser line scanner position on the measuring values

2.2.3 Speed of material deposition and vibration

Deposition speed can potentially cause vibration of the machine, thus affecting the readings of laser sensors. To investigate this effect, a PCB Model 333M07 accelerometer was attached to the test frame. As the speed of the stepper motor varied from 20 to 150 revolutions per second, the vibration level was measured alongside the width and thickness of the tape. It was found that vibration level, thickness and width measurement were not affected by the deposition speed (see Figure 4)

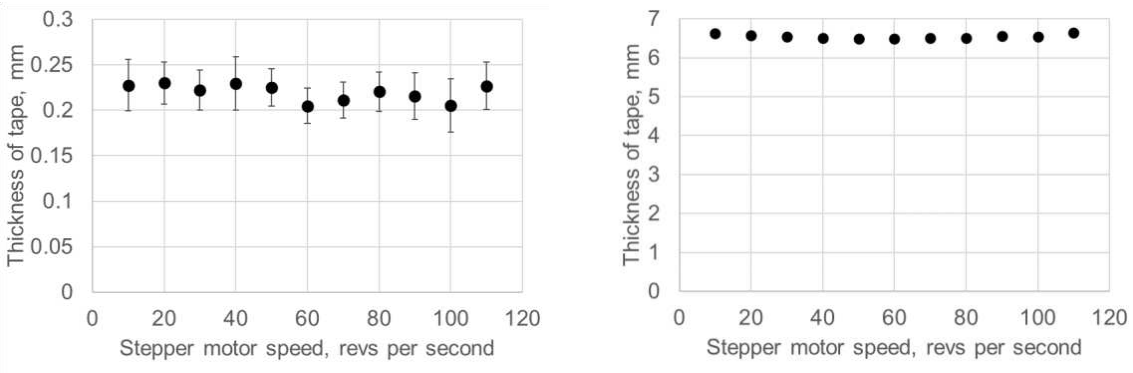

(a) (b)

Figure 4. The effect of the stepper motor speed on the thickness (a) and width (b) measurements

2.2.4 Material topology

Additional tests were done on the post deposition laser line scanner using different prepreg material types to identify their links to the quality of sensor readings (Figure 5). It was found that shiny and dark surfaces pose a significant challenge to the use of laser scanning techniques, as dark surfaces absorb the light and moreover shiny surfaces scatter light in uncontrollable directions. All of these issues could lead to measurement errors. Scattering behaviour of the composite material was investigated in the work of Meister et al [5]

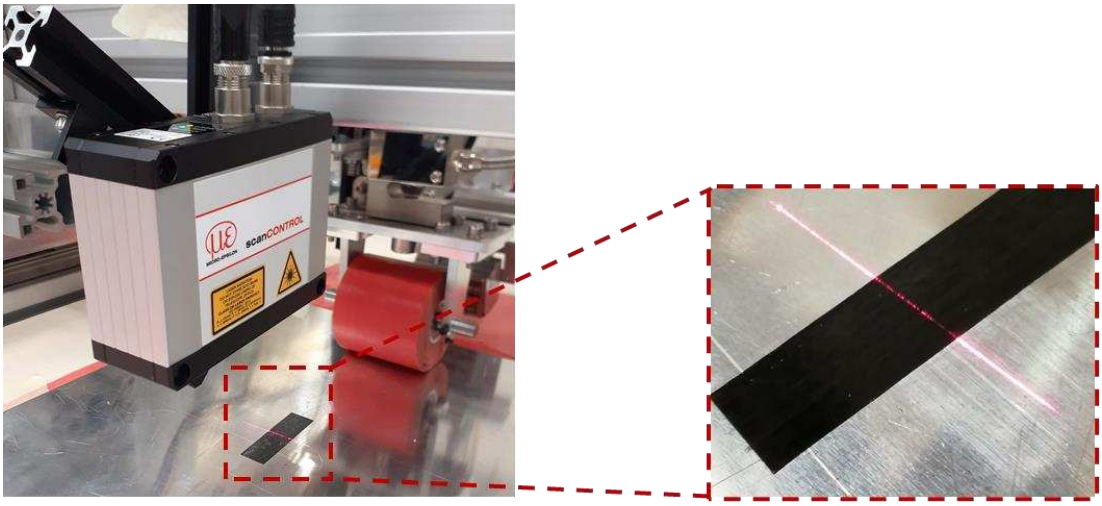

Figure 5. Experimental set-up for the post deposition line sensor quality measurements.

Three different types of composite prepregs with different surface roughness and different fibre areal weight were investigated. The results of these experiments are shown in Figure 6. Materials 1, 2, and 3 had different matrix systems. However, they all have a toughening phase within the matrix. Material 1 has the lowest number of points per profile, and this material has a shiny surface finish and the lowest fibre areal weight. With increasing fibre areal weight, the readings of the laser scanner improved. The results of this experiment provide guidelines on the suitable types of material for our project trials.

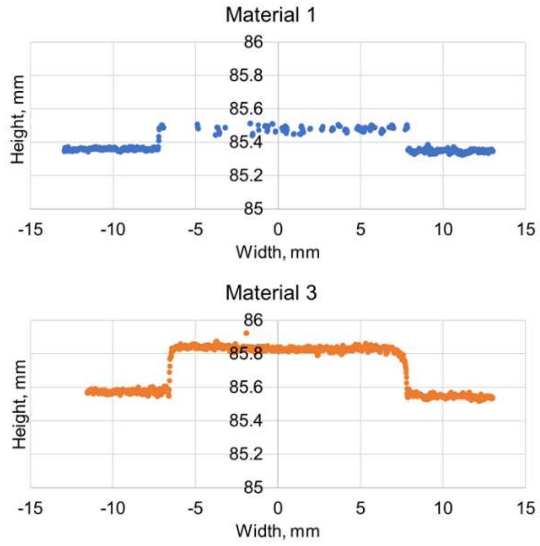

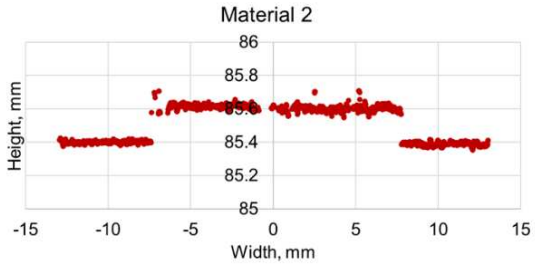

Material	Fibre areal weight, gsm	No of points in profile	Laser Scanner Resolution
Material 1	134	1067	2048
Material 2	194	1827	
Material 3	268	2033	

Figure 6. Composite tape profile using laser line scanner, showing different number of points based on different properties of the composite prepreg.

3. Conclusions

In this work, an experimental test set-up was designed and built, in order to evaluate the effect of environmental and physical conditions in an AFP process. Laser sensors were used to measure changes in the dimensions of a composite tape during AFP. It was shown that lighting, vibration, and deposition speed have little effect on the sensor's readings. However, the position of the line scanner affects its resolution, thus potentially influencing the accuracy of the readings. Moreover, the composite tape properties have been shown to have some effect on the number

of points per profile for the laser line scanner, as the experimental readings could be affected, with composite tape properties causing these effects potentially including fibre areal weight and reflectivity.

The results of this work are expected to be useful when selecting and locating sensors in a research-based AFP deposition system with fully-automatic feedback control.

Acknowledgements

This research was supported by the EPSRC grant Real-time *Material Measurements and Process Control in Automated Fibre Placement Composites Manufacture* (EP/S032533/1).

4. References

[1] D. H. J. A. Lukaszewicz and K. D. Potter, "The internal structure and conformation of prepreg with respect to reliable automated processing," *Compos. Part A Appl. Sci. Manuf.*, vol. 42, no. 3, pp. 283–292, 2011.

[2] E. D. Gregory and P. D. Juarez, "In-situ thermography of automated fiber placement parts," *AIP Conf. Proc.*, vol. 1949, no. April 2018, 2018.

[3] J. Cemenska, T. Rudberg, and M. Henscheid, "Automated In-Process Inspection System for AFP Machines," *SAE Int. J. Aerosp.*, vol. 8, no. 2, pp. 303–309, 2015.

[4] A. Brasington, C. Sacco, J. Halbritter, R. Wehbe, and R. Harik, "Automated fiber placement: A review of history, current technologies, and future paths forward," *Compos. Part C Open Access*, vol. 6, no. June, p. 100182, 2021.

[5] S. Meister, J. Stüve, and R. M. Groves, "Optical Material Characterisation of Prepreg CFRP for Improved Composite Inspection," *Appl. Compos. Mater.*, no. 123456789, 2021.

  doi:10.5075/epfl-298799_978-2-9701614-0-0

DESIGN OF AN OPTIMAL AUTOMATED TAPE LAYING PROCESS USING DIGITAL TWIN AND ARTIFICIAL BEE COLONY ALGORITHMS

Jhonny, de Sá Rodrigues[a], Paulo, Teixeira Gonçalves[a], Nuno, Correia[a], Luís Pina[b], Fernando, Gomes de Almeida[c]

a: INEGI - Institute of Science and Innovation in Mechanical and Industrial Engineering – jsrodrigues@inegi.up.pt
b: Strix Portugal
c: LAETA-INEGI, Faculty of Engineering, University of Porto

Abstract: *Automated systems are important to improve composite manufacturing processes for the aeronautics and automotive industry. Automated systems produce mechanically enhanced structures to meet a growing demand for efficient designs. Automated Tape Laying (ATL) is a process which has gained popularity in the last years. ATL objective is to raise a pre-impregnated composite temperature to weld material layers on top of a mould, applying pressure through a compaction roll, conforming the final structure. Process Digital Twin (DT) is a modelling strategy that which helps to improve the quality of the final product. DT allows to study ATL process parameters such as temperatures, electrical power, process velocity among others, and measure their effect upon the final product. Artificial Bee Colony (ABC) is a zero-order optimization technique selected as it does not require analytical derivatives and can take into account the process capabilities and constraints.*

Keywords: Artificial Bee Colony; Automated Tape Laying; Digital Twin; Process Design

1. Introduction

The Automated Tape Laying (ATL) process is a composite materials manufacturing technique which aims to produce mechanically enhanced structures out-of-autoclave by stacking thin composite material layers on top of a mould, minimizing scrap material, and reducing energy consumption. As this process is focused for thermoplastics, the process machine is mainly composed by a heater element to increase the material temperature, a compaction roll which presses the heated material against a mould which function is to lower the composite temperature while maintaining the mould shape to obtain the final structure.

As the main goal along the ATL process is focused on how to increase the composite material temperature at the process Nip Point located under the compaction roll to a defined value; a proper mathematical model is fundamental to understand the interaction between the composite material and the involved machine components, then obtain heat exchange relations. The first component to study is the heat source, some authors describe different types of heat sources such as gas torches, lasers, ultrasonic heating and infrared lamps [1,2] for this process. Another main component to study is the compaction roll, as it acts as a heat sink while compresses the composite material against the mould. Understanding the interactions allows to define a proper mathematical model for the temperature distribution along the composite material during the process, giving place to develop a Digital Twin (DT) [3].

  doi:10.5075/epfl-298799_978-2-9701614-0-0

The DT as a component of a Cyber-Physical System allows to understand the process response face any given inputs, from a design point of view [4,5] this means that it is possible to perform analysis for the ATL process related to the geometrical and spatial disposition of the machine components and process parameters such as temperatures, electrical power, and process velocity to study their effect upon the final product.

The analysis leads to a proper design of the ATL machine by systematically simulate the overall temperature distribution as a function of design parameters to obtain a suitable combination of them that meet defined requirements of temperature, time, or efficiency. The selection of the analysis technique depends on the degree of complexity of the DT, for processes defined using linear mathematical models, optimization techniques based on gradients are preferred, in case of mathematical models which derivative is not possible to obtain or to avoid linearization techniques which lead to information losses, a zero-order technique is preferred. Artificial Bee Colony (ABC) is a zero-order optimization algorithm that can deal with non-linear by exploring different proposed solutions and systematically converging to a minimization that could be defined inside a feasible region defined by constraints [6]. The use of non-linear DT implies high computational cost, which is not suitable for online implementation but when implemented using an offline approach, saves time and resources during the design stage

In this work it is presented a methodology to design an ATL process, which process unidirectional carbon fibres pre-impregnated with polyamide 6 composite, using a zero-order optimization technique in order to obtain a geometrical disposition of the machine components, minimizing the temperature error. The ATL mathematical model referenced as a 1.5-dimensional problem was developed in a previous research [3]. A numerical example is presented using one design parameter and one process parameter to demonstrate that the optimization algorithm is capable of handling multiple parameters simultaneously.

This methodology aims to be an offline manufacturing process design that can help to understand the capabilities of the equipment under development as well as to further design proper control systems which minimizes the control effort.

2. Automated Tape Laying Machine

The ATL machine presented in this work is mainly constituted by an infrared heater, a reflection plate, a compaction roll and a mould, which spatial disposition is presented in Figure 1. The compaction roll moves on top of the mould into the “x” direction as well as the rest of the assembly at the same process velocity. The goal with this design is to heat up the incoming composite material in order to reach a desirable temperature at the point of contact with the mould (Nip Point) located below the compaction roll.

The design parameters for this ATL machine can be numbered as follows: the moving speed, the compaction roll temperature which can be set at a constant value along the entire process, the mould temperature that can also be defined constant along the entire process, the compaction roll thermal conductivity constant, which is defined by its material, and the infrared heater power and position relative to the composite material.

2.2 Mathematical model

  doi:10.5075/epfl-298799_978-2-9701614-0-0

To mathematically describe the ATL machine, a 1.5-dimensional model is used. This model considers the Composite material as a straight line, see Figure 2.

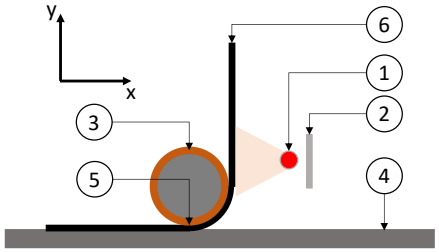

Figure 1. ATL machine components. (1) Infrared heating element. (2) Reflection plate. (3) Compaction roll. (4) Mould. (5) Nip point (6) Material feeding.

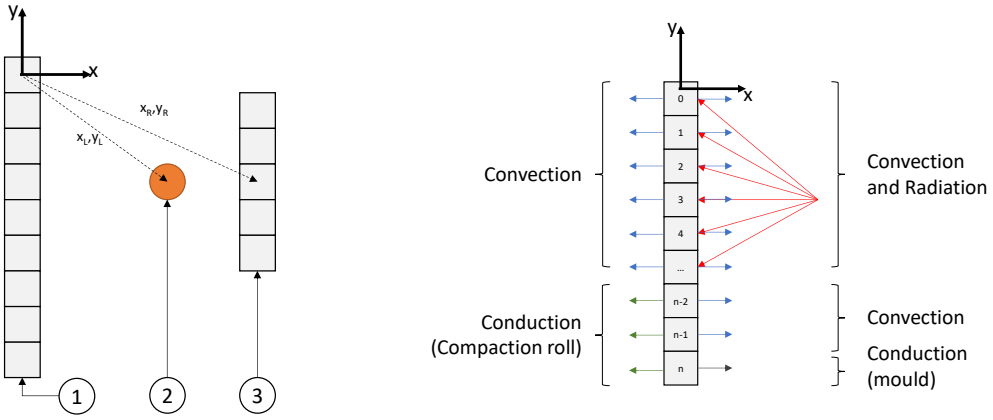

Figure 2. (a) General spatial distribution of the (1) composite material, (2) heat element and (3) reflection plate. (b) Heat exchange phenomena involved upon the composite material.

Figure 2(a) shows the reference from which the spatial disposition of the composite material, the heating element and the reflector plate are referenced to, and Figure 2(b) shows the heat exchange phenomena occurring on the composite material, were it is pointed the input heat coming from sum up the direct contribution of the heating element and the indirect contribution coming from the reflector plate (red lines), the convection with the ambient air (blue lines), the conduction along the contact between the material and the compaction roll (green lines) and the conduction along the contact between the material and the mould (grey line).

3. Optimization Algorithm

The Artificial Bee Colony was first proposed by [7] as an optimization algorithm, based on the behaviour of honey bees by performing a swarm exploration of the environment and communicate those findings to the rest of the hive.

3.2 Algorithm definition

The ABC algorithm consists of 3 types of bees namely *Employed bees, Onlooker bees and Scout bees.* The *Employed bees* are solutions generated using Eq. (1):

$$x_{i,j} = x_{min,j} + rand[0,1]\left(x_{max,j} - x_{min,j}\right) \quad (1)$$

where $x_{i,j}$ stands for a solution of the *Employed bee* i referenced to its parameter j, $x_{max,j}$ and $x_{min,j}$ stand for the maximum and minimum vales of said parameter respectively when constraints have to be applied, otherwise, for unbounded parameters, the choice is made randomly. After all the *Employed bees* are defined, those solutions are evaluated $f_j(x_j)$, and for each evaluation result it is calculated a fitness value using Eq. (2):

$$fit_i = \begin{cases} \dfrac{1}{1+f_j(x_j)} & (f_j(x_j) \geq 0) \\ 1+\left|f_j(x_j)\right| & (f_j(x_j) < 0) \end{cases} \quad (2)$$

After a fitness value is calculated for all the *Employed bees*, a probability function, Eq.(3), is used to determine solution x_j with the highest probability of being the optimal.

$$P_i = \frac{fit_i}{\sum_{n=1}^{SN} fit_n} \quad (3)$$

Once a solution has been selected by a process called *Greedy selection*, there are defined the *Onlooker bees*, which are based on the selected *Employed bee* using Eq. (4).

$$v_{i,j} = x_{i,j} + rand[-1,1](x_{i,j} - x_{k,j}) \quad (4)$$

Where $v_{i,j}$ are the *Onlooker bee* solutions for *Onlooker* j parameter i; with index $k \neq i$. The goal with this equation is to create new solutions by disturbing the selected *Employed bee*. Those new solutions are evaluated $f_j(v_j)$, and a *greedy selection* is performed after calculating the probability function (Eq. (3)). If the convergence condition is reached, the optimal solution is achieved, otherwise the selected *Onlooker bee* is defined as an *Employed bee* for the next iteration and *Scout bees* are generated using Eq. (1) to explore new solutions. The calculation process is repeated until the convergence condition is reached.

4. Numerical example

4.2 Materials and methods

The composite material used in this work is 0.14 mm thick Unidirectional carbon fibres pre-impregnated with Polyamide 6, which thermal properties are presented in Figure 3 from experimental data.

The material temperature distribution is described using a finite difference approach with one element in the thickness direction “x”, *Figure 2*. To solve the initial value problem for stiff systems of ordinary differential equations it is used the Implicit Runge-Kutta method of Radau of order 5.

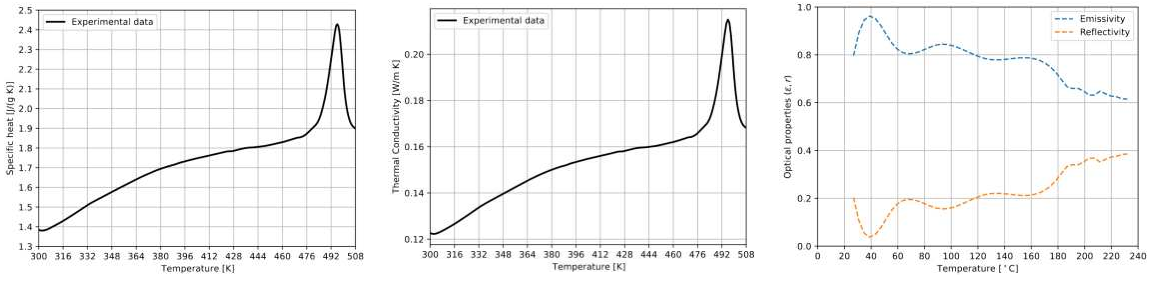

(a) (b) (c)

Figure 3. Thermal properties for the composite. (a) specific heat. (b) Thermal conductivity. (c) Thermal optical properties as function of temperature [3]

To demonstrate the design method proposed, two design variables are chosen, namely heater element position relative to the material along the "x" axis, Figure 2, and the voltage applied to the heating element. The values of the selected variables will be kept constant along a 30 seconds simulation, generating the data required to evaluate the objective function. Other design variables required for the mathematical model are presented in Table 1.

Table 1. Constant design parameters.

Parameter	Value	Parameter	Value
Heater element "y" position	0.058 m	Reflector plate "x" position	0.108 m
Material density	1342 kg/m^3	Reflector plate "y" position	0.02 m
Initial temperature	296.15 K	Process velocity	0.005 mm/s
Reflector plate length	0.05 m	Mould Temperature	296.15 K
Compaction roll diameter	0.055 m	Compaction roll temperature	343.15 K
Compaction roll thermal conductivity	0.25 W/m K	Mould thermal conductivity	12.1 W/m K

4.3 Objective function

The objective function to minimize is defined by a convex equation, Eq. (5).

$$f_j(x_j) = \sum_{k=0}^{K} \left(T_{k_{ref}} - T_{k_{calc}}\right)^2 + V^2 \tag{5}$$

Subjected to the following constraints Eq. (6) and Eq. (7).

$$0.01\ \text{m} < x_{heater} < 0.03\ \text{m} \tag{6}$$

$$50.0\ \text{V} < V_{heater} < 220.0\ \text{V} \tag{7}$$

Where $T_{k_{ref}}$ = 200 K, and $T_{k_{calc}}$ stands for the calculated temperature at the Nip Point at time k, and V stand for the voltage applied to the heating element; this last term refers to the actuation effort.

5. Results

The results of the optimization algorithm to design an optimal voltage applied to the heating element and its position relative to the composite material in the "x" direction, are presented in Figure 4(a) and Figure 4(b) respectively. The algorithm was capable to reach a minimization in four iterations handling two design parameters.

In Figure 5(a) and Figure 5(b), the results of the optimization algorithm are shown using a different seed for the random function, and while it took nine iterations to converge, the results

converged to the same values as in Figure 4, confirming that the algorithm is independent of the initial proposed solution.

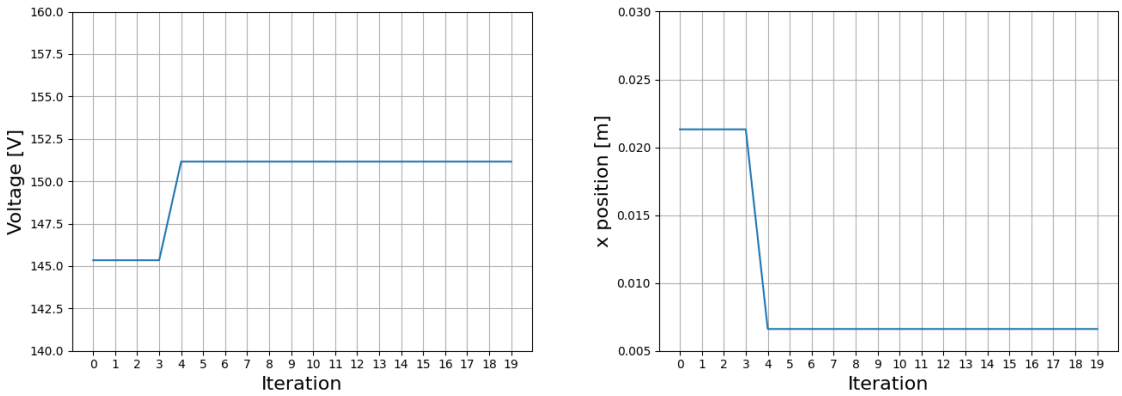

(a) (b)

Figure 4. Results of the optimization algorithm (seed 1). (a) Voltage applied to the heating element. (b) x position of the heating element

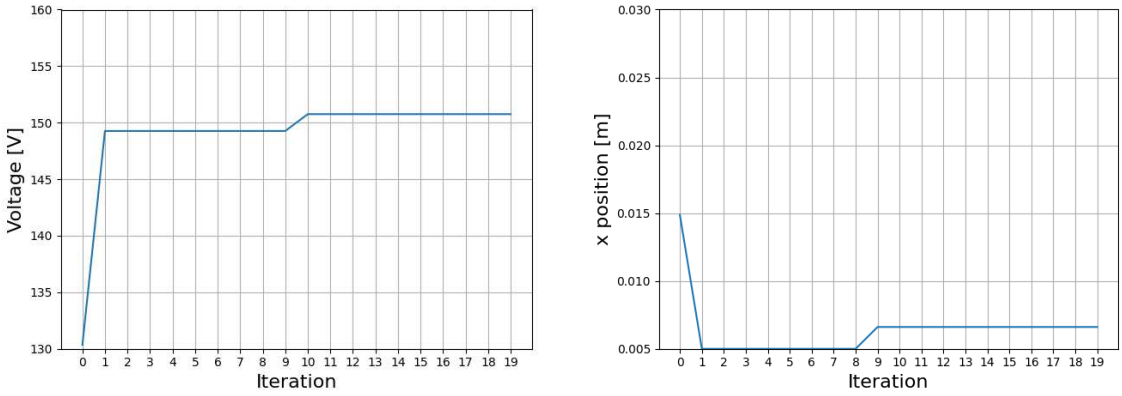

(a) (b)

Figure 5. Results of the optimization algorithm (seed 2). (a) Voltage applied to the heating element. (b) x position of the heating element

6. Conclusions

A relevant number of design and process variables adds a degree of difficulty when dealing with an optimal design for an Automated Tape Laying process, this difficulty can be minimized by using a suitable optimization technique that allows dealing with multiple variables.

The Artificial Bee Colony method proved to be suitable for designing an optimal ATL machine process by dealing with a mathematical problem in which derivatives are not possible to obtain excluding the use of classical derivative dependant algorithms, it is also capable to handle constraints and minimizing the risk to obtain a local minimum solution by using randomly generated solutions along the entire feasible domain.

It is worth to mention that even this is an offline procedure, multiprocessing or distributed computation can be used to design the ATL machine process to minimize the computational time required to converge to a solution. This is feasible due to every

  doi:10.5075/epfl-298799_978-2-9701614-0-0

employed and onlooker bee is independent from each other, this means that each bee is treated as a separate problem.

Acknowledgements

This research has received funding from the European Union's Horizon 2020 research and innovation programme under grant agreement No 768710.

7. References

1. de Sá Rodrigues J, Teixeira P. Model for an Automated Tape Laying Process: Heat source Identification. In: Oliveira A, Areias B, Amorim J, Ribeiro P, editors. DCE21: Symposium on Mechanical Engineering: Book of Abstracts and Invited Lectures. Porto: FEUP Edições; 2021. p. 29–31.

2. Yassin K, Hojjati M. Processing of thermoplastic matrix composites through automated fiber placement and tape laying methods. J Thermoplast Compos Mater [Internet]. 2018 Dec 26;31(12):1676–725. Available from: http://journals.sagepub.com/doi/10.1177/0021998397031003O2

3. de Sá Rodrigues J, Gonçalves PT, Pina L, Gomes de Almeida F. Modelling the Heating Process in the Transient and Steady State of an In Situ Tape-Laying Machine Head. J Manuf Mater Process [Internet]. 2022 Jan 11;6(1):8. Available from: https://www.mdpi.com/2504-4494/6/1/8

4. Lu Y, Liu C, Wang KIK, Huang H, Xu X. Digital Twin-driven smart manufacturing: Connotation, reference model, applications and research issues. Robot Comput Integr Manuf [Internet]. 2020;61(April 2019):101837. Available from: https://doi.org/10.1016/j.rcim.2019.101837

5. Tao F, Qi Q, Wang L, Nee AYCC. Digital Twins and Cyber–Physical Systems toward Smart Manufacturing and Industry 4.0: Correlation and Comparison. Engineering [Internet]. 2019 Aug 1 [cited 2019 Oct 24];5(4):653–61. Available from: https://linkinghub.elsevier.com/retrieve/pii/S209580991830612X

6. Karaboga D, Akay B. A comparative study of Artificial Bee Colony algorithm. Appl Math Comput [Internet]. 2009 Aug 1 [cited 2022 Apr 18];214(1):108–32. Available from: https://linkinghub.elsevier.com/retrieve/pii/S0096300309002860

7. Karaboga D. An idea based on honey bee swarm for numerical optimization [Internet]. Kayseri; 2005. Available from: https://abc.erciyes.edu.tr/pub/tr06_2005.pdf

INVESTIGATION OF THE INFLUENCES OF AFP PROCESS PARAMETERS ON THE CRYSTALLINITY AND MECHANICAL PROPERTIES OF LM-PAEK COMPOSITES

Francisco Ansedes, Ivette Coto, Noelia Gonzalez, Ricardo Losada, Adrian Rodriguez, Elena Rodriguez

AIMEN Technological Centre – francisco.ansedes@aimen.es

Abstract: *AFP (Automated Fiber Placement) is a composite material manufacturing process that allows parts to be manufactured in an automated way. It consists of depositing tows or tapes of composite material with an AFP head (mounted on a robotic arm or on a gantry or column type structure) that applies pressure and temperature, and that moves at a specific speed. Until now, AFP technology has been widely used in the aeronautical industry to manufacture large parts, such as wings or fuselages, mainly using thermosetting matrix composite materials. In recent years, the aeronautical industry has begun to investigate the use of thermoplastic matrix composite materials, since their properties allow for shorter manufacturing processes, taking advantage of their reprocessing properties. Currently, one of the main research goals on the processing of thermoplastic materials with AFP is the In-Situ Consolidation (ISC), which allows to manufacture the piece and consolidate the material at the same moment of its deposition, resulting in the part being finalized at the end of its lay-up, avoiding the need to perform an autoclave cycle.*

In this work, ISC manufacturing with AFP of LM-PAEK tapes is studied, trying to optimize the quality of the composite specimens by understanding the relationship between the manufacturing parameters, crystallinity, and the obtained mechanical properties.

Keywords: Automated Fiber Placement (AFP); In-Situ Consolidation (ISC); Thermoplastic composites; Low melting Poly aryl ether ketone (LM-PAEK); Mechanical properties; Crystallinity

1. Introduction

The use of composites in the aeronautical industry has been present for decades. Automated manufacturing technologies, such as AFP (Automated Fibre Placement) have allowed the manufacturing of large structures, such as wings or fuselages, reducing production times, and increasing the repeatability and final quality of the parts. Thermoset based materials represent most composites used in aerospace, but in recent years, thermoplastic based composites are gaining relevance. The main advantage of thermoplastics over thermosets is that prior to curing, they have an unlimited shelf life at room temperature and do not require refrigeration. Also, recycling is possible, they can be remelted and reformed post cured, offering flexibility and sustainability advantages [1].

The processing of thermoplastics in AFP is one of the main technologies on which the development of thermoplastic materials is based. In this technology, the material is deposited automatically, heating it with a laser system and applying pressure, to achieve consolidation

  doi:10.5075/epfl-298799_978-2-9701614-0-0

between the material that is applied and the one that is already part of the substrate deposited in previous layers.

Several works [2],[3], indicate that the processing temperature of the Nip Point (point of contact between the incoming tape and the substrate) should be high enough to decrease the matrix viscosity and allow an intimate contact between the tapes when the pressure is applied. This contact is essential for allowing the polymeric chain reptation and diffusion between the tapes, and thus, for a good bonding. Also, other publications[4],[5], make reference to the importance of crystallinity in the bonding of thermoplastic tapes, characterizing interlaminar fracture toughness as a combined effect of matrix ductility (inversely proportional to crystallinity) and fibre-matrix interface bond (proportional to crystallinity).

In the present work, the structural performance of the union between AFP deposited tapes isbe studied and correlated with the processing temperature and the crystallinity in the union area. The processing temperature in the nip point and the crystallinity is studied also in relation to the layup tool temperature (and thus, the cooling rates in the processed tape).

2. Materials and Methods

2.1 Materials

The material studied in this work is a unidirectionally reinforced composite tape, composed by a semi-crystalline low melt PAEK thermoplastic matrix (LM-PAEK TC1225) and a T800G carbon fibre reinforcement. The material was supplied by TORAY and is commercially identified as Cetex® TC1225 LMPAEK / T800G UD tape.

The material properties of the neat resin used as matrix is listed in *Table 1*, and the format of the composite tape is specified in *Table 2*.

Table 1: Material properties of matrix.

Material	Tm (°C)	Tg (°C)	Recommended processing temperature by supplier (°C)
LM-PAEK TC1225	305	147	340-385

Table 2: Composite tape format.

Material designation	Fiber Areal Weight, FAW (g/m²)	Resin content (%)	Ply Thickness (mm)	Width (mm)
TC1225 LMPAEK / T800G UD	145	36	0.145	25.4

2.2 AFP manufacturing

The equipment used in this work is an AFP (Automated Fibre Placement) head system, a PrePro3D model from Conbility manufacturer. The AFP system is mounted in a FANUC R-2000iC/165F Robotic Arm. The AFP system controls (among other parameters not listed for clarity) the placement speed, the applied compaction force (that defines the applied pressure, together with the application area resulting from elastomeric roller deformation), and the applied laser power, that sets the processing temperature in a closed control loop, receiving temperature feedback from two pyrometers pointing at the Nip point (one focused on the incoming tape and the other focused on the substrate). Temperature measurements at the nip point are taken from both pyrometers, and in this work are presented as an average of both of them for determining the nip point temperature. Also, measures from all the coupons of every case of study are averaged. The temperatures are selected from the third ply of each coupon, since this is the ply where the interlaminar properties are studied in the mechanical experiments, as described in 2.4.

The main parameters used in this work are listed in *Table **3***.

The laser used for heating up the nip point (incoming tape and substrate) is a Laserline diode laser source, model LDF6000-40, of 6300W and operating wavelengths ranging from 940 to 1060 nm.

The material is deposited on a heated layup tool that consists of an aluminum plate heated with resistances.

Table 3: AFP parameters used in this work.

AFP Parameter	Value
Layup speed [m/s]	0.25
Pressure [bar]	5.5

2.3 Annealing

Heat treatments of the samples were carried out in a furnace at equal annealing cycles for all the coupons subjected to annealing. The temperature was increased at the rate of 10°C/min until 220°C, and this temperature was maintained for 90 min. After this, the samples were cooled at 5°C/min until they reach ambient temperature.

2.4 Mechanical testing

Single Lap Shear Strength properties were evaluated according to the experimental procedure and specimen preparation proposed in [6]: four tapes where laid-up with the AFP process, on top of each other and in the same direction. In the middle of the stacking, two Kapton film strips of 20 mm width were placed with a separation of 5 mm, so that the top two plies and the bottom two plies are overlapped 5 mm. The separation in the bottom and top plies was made cutting the tapes on top of the Kapton film strips.

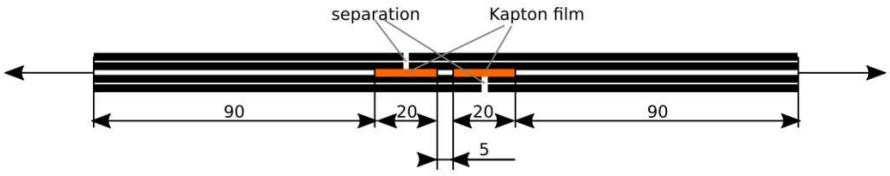

Figure 1. Simplified Single Lap Shear test specimen proposed in [6].

Single Lap Shear Strength tests were performed to characterize the samples using a 250 kN capacity standard tensile/compression machine (MTS®). Shear strength was measured at a constant speed of 1 mm min^{-1}. At least five repeated specimens were tested, and the data was averaged.

2.5 Differential Scanning Calorimetry (DSC)

The thermal properties of the materials were analyzed by Differential Scanning Spectroscopy (DSC). The experiments were carried out in a DSC Q2000 (TA Instruments). The DSC tests were performed with N_2 as the purge gas. The samples were sections cut from the fabricated specimens, in the area of study of the mechanical tests. Samples with a mass of 20-30 mg (7-10 mg of neat resin) were put on an alumina crucible and subjected to a heating cycle from r.t to 360 °C at a rate of 10 °C/min. After the first heating cycle, the temperature is held at 360 °C for 15 min, that is about 50 °C above the melting temperature to erase the thermal history, then cooling to r.t at 10 °C/min, and finally, a second heating from r.t to 360 °C at 10 °C/min. Crystallinity was determined by the equation 1.

$$\chi = \frac{\Delta H_m}{130} \times 100\% \qquad 1$$

Where ΔH_{endo}, ΔH_{exo} are the integral area of the endothermic peak and exothermic peak, respectively, and 130 J/g is the melting enthalpy of a 100% crystalline LMPAEK sample.

3. Results and Discussion

3.1 Thermal analysis

In this work, several coupons were manufactured with different layup tool temperature conditions, to have different scenarios regarding cool down rates. The heated layup tool, that acts as a substrate to the material, was heated up to 3 different temperatures: 25, 160 and 220°C. For each layup tool temperature, two groups of 5 coupons were manufactured. One of this groups was submitted to the annealing cycle described in Section 2.3, and then tested following the mechanical test procedure described in Section 2.4. The other group was mechanically tested (as described in Section 2.4) without a prior annealing cycle.

Crystallinity of the samples was measured using DSC technique (as described in section 2.5), resulting in the values listed in *Table **4***. Our results show that, the coupons manufactured with low layup tool temperatures (25°C) have crystallinity levels around 5%. The layup tool temperature of 160°C, despite being higher than the Tg of the material (147°C), renders also crystallinity values similar to the previous. However, the coupons manufactured at the highest layup tool temperatures (220°C) give markedly higher crystallinity levels (around 25%), similar to the post-processed samples.

Table 4: Average transitions temperatures, enthalpies, and estimated crystallinities correspondent to the first heating cycle.

Layup tool temperature [°C]	T_g (°C)	T_{cc}(°C)	ΔH_{cc} (J/g)	T_m(°C)	ΔH_m (J/g)	X (%)
25	149.36	192.20	9.37	305.58	12.08	5.8
160	149.89	191.33	9.53	307.4	12.79	7.0
220	152.28	235.00	-0.81	304.43	10.15	26.5
Annealed coupons*	159.74	206.60	-1.06	307.12	11.24	26.3

*(independently of layup tool temperature)

3.2 Mechanical properties

In a first round of experiments, coupons were manufactured to study the influence of the tool temperature on the processing nip point temperature, and in the interlaminar shear strength properties. The layup tool temperature was increased from 25°C to 220°C in five steps, and five coupons were manufactured in each step. The laser power and incidence angle on the nip point was maintained, and consequently the temperature in the substrate material was different in all the iterations. The nip point temperature at the substrate and shear strength values are listed in *Table 5* and represented in *Figure **2***.

Table 5: Nip point temperatures and Shear Strength values (variable nip point temperature).

Layup tool temperature [°C]	Nip point temperature (substrate)*[1] [°C]	Shear Strength [MPa]
		Without Annealing
25	265	26.70±5.09
160	335	36.00±5.10
220	385	42.58±5.45

*[1] Temperature measured at the substrate in the nip point area. The incoming tape was kept at a stable temperature of 350±15°C.

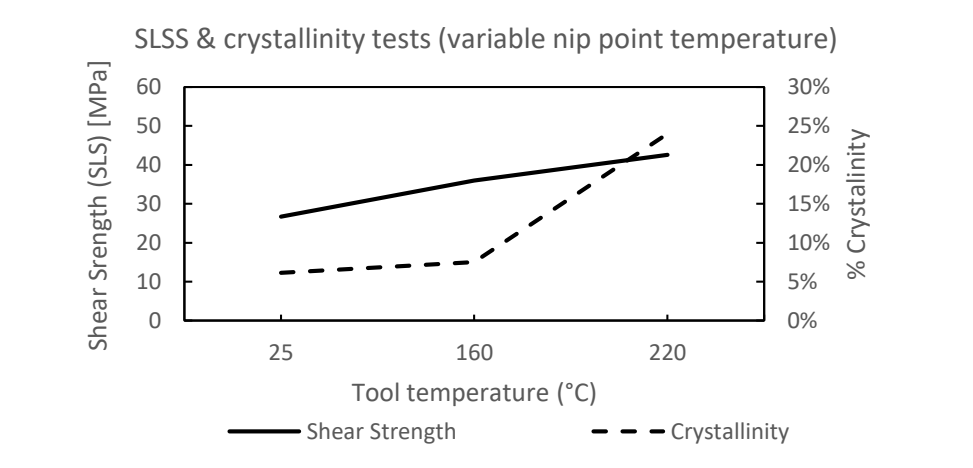

Figure 2. Interlaminar Shear Strength values with variable nip point temperature.

As it can be appreciated, lower tool and nip point temperatures result in lower SLSS values.

The increment of the nip point temperature decreases the polymer matrix viscosity, allowing a better flow and contact between the tapes, and enhancing the interdiffusion of the polymeric chains between tapes [2]. A higher processing temperature benefits the interlaminar union, as showed in the data from this first round of experiments, where the nip point temperature ranges from 265°C to 385°C, causing a variation on the SLSS values, that range from 27 MPa to 43 Mpa.

A second round of coupons was manufactured to study the influence of the tool temperature and the crystallinity in the SLSS values, without the influence of the nip point temperature. The laser power and orientation parameters were modified to obtain a uniform temperature distribution between the incoming tape and the substrate tape. The influence of the layup tool temperature in the processing temperature at the nip point was considerably reduced (but not eliminated) as it can be appreciated in the results listed in *Table 6*.

For each layup tool temperature two sets of 5 coupons were manufactured. Out of these 2 sets, one was subjected to an annealing cycle before the mechanical testing, and the other one was mechanically tested directly.

The mechanical results are listed on *Table 6*. In *Figure 3* are represented the mechanical test values of the samples manufactured, comparing the samples that were subjected to an annealing cycle and those that were directly tested after manufacturing. In *Figure **4*** are graphically represented the mechanical test results and crystallinity values of the coupons, without and with an annealing cycle, respectively. As it can be appreciated, the mechanical values of the SLSS tests of not annealed coupons are slightly higher than that of the annealed coupons. Accumulated tensions resulting from the annealing cycle, or the fragilization of the interlayer union caused by the higher crystallinity could be responsible of the slightly lower SLSS values in the annealed coupons, but further study should be do confirm this. Also, there is no significant difference on the SLSS values between the coupons manufactured with different tool temperatures, since there are no great differences on the nip point temperature.

Table 6 : Nip point temperatures and Shear Strength values (fixed nip point temperature).

Layup tool temperature [°C]	Nip point temperature*[2] [°C]	Shear Strength [MPa]	
		Without Annealing	With Annealing
25	330	31.11±4.85	23.82±2.69
160	350	30.00±3.37	28.16±3.71
220	360	28.67±1.77	26.37±2.78

*[2] Temperature averaged from the substrate and the incoming tape in the nip point area.

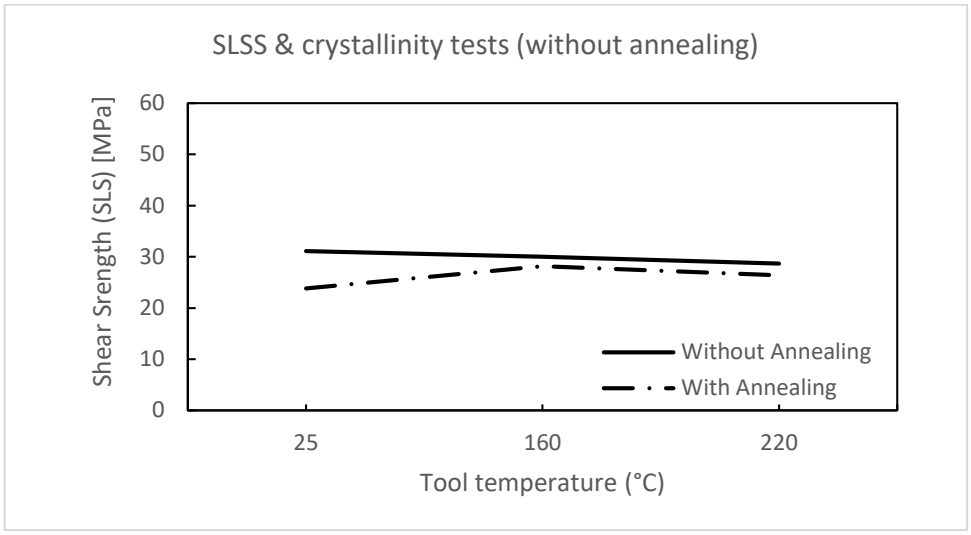

Figure 3. Interlaminar shear strength values comparison between annealed and not annealed coupons.

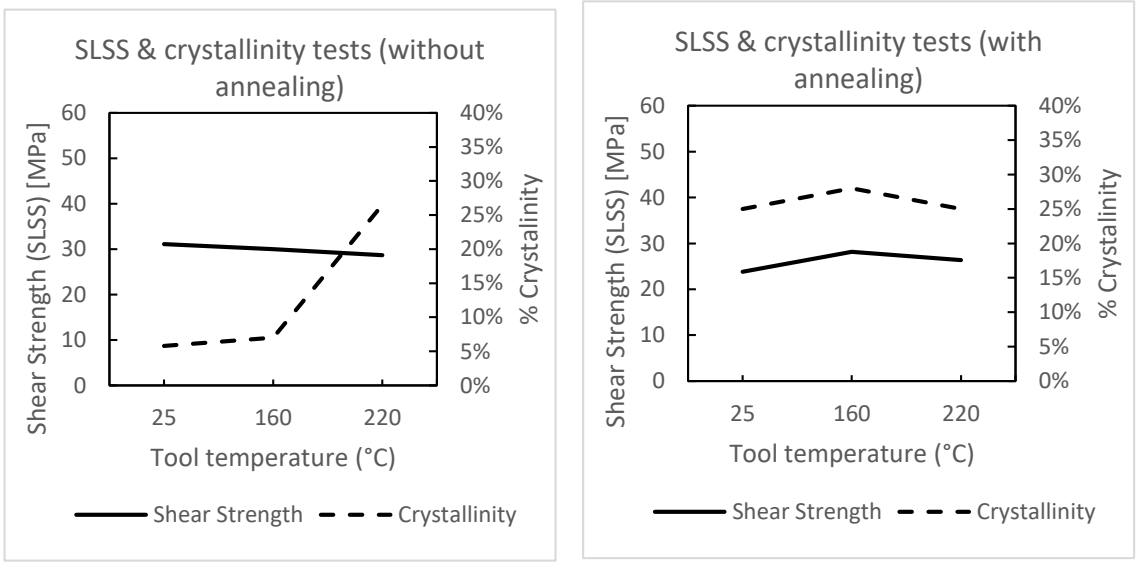

Figure 4. Graphical representation of crystallinity and SLSS load values of coupons tested without a previous annealing cycle (left) and with a previous annealing cycle (right).

4. Conclusions

This work has studied the thermoplastic AFP process, focusing on the influence of the layup tool temperature on the crystallinity and on the interlaminar mechanical properties (studied by SLSS method) and the influence of the crystallinity obtained with an annealing cycle in the mechanical properties.

The experiments performed show that achieving a sufficient nip point temperature has a great influence on the interlaminar shear strength values, showing a clear correspondence between the increment on the nip point temperature and obtained SLSS values.

Also, the results show that higher crystallinities do not improve the interlaminar shear strength properties of the coupons, when tested on a SLSS test. Low crystallinity specimens were compared with high crystallinity specimens obtained both by subjecting the specimen to an annealing cycle or by decreasing the cool down rates with the layup tool temperature, and the higher crystallinity specimens did not achieve higher shear strength values.

5. Acknowledgments

This work is developed in DOMMINIO project, which has received funding from the European Union's Horizon 2020 research and innovation programme under grant agreement No 101007022."

References

1. Veldman, S. L., Kortbeek, P., Wölcken, P. C., Herrmann, R., Kos, J., & Villegas, I. F. (2020, February). Development of a multifunctional fuselage demonstrator. In Aerospace Europe Conference 2020 (pp. 25-28).

2. Khan, M.A.; Mitschang, P.; Schledjewski, R. Identification of some optimal parameters to achieve higher laminate quality through tape placement process. Adv. Polym. Technol. 2010, 29, 98–111.

3. Levy A, Heider D, Tierney J, et al., Inter-layer thermal contact resistance evolution with the degree of intimate contact in the processing of TP composite laminates. J Compos Mater., 2014 48: 491–503.

4. Gao, Shang-Lin, and Jang-Kyo Kim. "Cooling rate influences in carbon fibre/PEEK composites. Part 1. Crystallinity and interface adhesion." Composites Part A: Applied science and manufacturing 31.6 (2000): 517-530.

5. Gao, Shang-Lin, and Jang-Kyo Kim. "Cooling rate influences in carbon fibre/PEEK composites. Part II: interlaminar fracture toughness." Composites Part A: Applied science and manufacturing 32.6 (2001): 763-774.

6. Dreher P, Chadwick AR, Nowotny S. Optimization of in-situ thermoplastic automated fiber placement process parameters through DoE. In: Proceedings of the 40th SAMPE Europe conference; 2019, p. 1–13.

THE EFFECT OF SEMI-CURING ON INFUSED LAMINATE INTERFACIAL PROPERTIES

Michael, O'Leary[a], Robin, Hartley[a], Turlough, McMahon[b], James, Kratz[a]

a: Bristol Composites Institute, University of Bristol, Bristol UK – Michael.oleary@bristol.ac.uk
b: Airbus, Pegasus House, Filton UK

Abstract: *Post cure joining operations and complex preform integration prior to resin infusion processes are two issues facing advanced composite manufacturing. A multistage cure process known as "Semi-curing" has the potential to remove post cure joining operations, inspect for quality as value is added to composite parts, and reduce the complexity of integrated structures. Semi-curing is a process whereby elements of an integrated structure are infused and semi/partially cured prior to integration into preforms comprising the remainder of the structure. Semi-cured laminates with elements initially cured to varying initial degrees of cure were manufactured and tested in mode I and mode II. Mode I testing showed interfacial properties to be broadly unaffected by the degree of cure of the semi cured element up to the gel point, only deteriorating thereafter, whereas in mode II, interfacial properties were retained at all degrees of cure. These results demonstrate the usefulness of the Semi-curing approach up until gelation.*

Keywords: Liquid composite moulding; Fracture; Joining; Co-curing; Staged Curing

1. Introduction

Aerospace manufacturers have been relying more and more on composite structures as has been seen through the Boeing 787, Airbus A350 and A220 programs. These sort of programs have historically relied heavily on prepreg and autoclave curing to manufacture separate composite components, which are the trimmed/drilled and mechanically joined together. However recently there has been a noticeable shift towards more highly integrated structures, out of autoclave (OOA) processes, and resin infusion processes [1–3]. Creating a more integrated structure and using resin infusion in conjunction with OOA processes can reduce the cost of manufacturing parts while also lowering manufacturing time [4,5]. However, there are also key risks associated with these manufacturing methods, namely the potential need for time consuming post cure joining operations to join sections of the structure. This is coupled with the risks associated with preform misalignment and complex infusions.

Semi-curing may help overcome the challenge of post cure joining operations while also de-risking large-scale infusions. The key steps in the semi-curing process are highlighted in Figure 1., showing how elements of the integrated structure are taken and initially semi-cured, after which they can be inspected for quality. This creates a simplified and modular set of semi-cured preforms which can be combined with dry preforms to manufacture the integrated part in a final infusion/cure step requiring few or no additional post cure joining operations.

The origins of semi-curing date back to ideas around staged curing of prepreg to reduce thermal spiking and non-uniform consolidation in thick composite parts [6]. This has progressed to exploring how prepreg structures can be "melded" together through selective curing of sections while leaving areas uncured so that there are still chemically active surfaces

  doi:10.5075/epfl-298799_978-2-9701614-0-0

available for reacting and forming new bonds, thus avoiding the need for adhesives [7]. Infusion technology were laminates were initially semi cured before being integrated with another preform prior to final infusion and curing step have also been proposed [8–10]. Studies investigating surface preparation indicate that there is interdependence between the interfacial properties and the degree of cure of the semi-cured element [8].

The current work builds on the state-of-the-art in semi-curing by exploring the interlaminar resistance of fully-cured laminated that had initially semi-cured elements. The Mode I and Mode II interfacial properties are experimentally determined. Mode II allows for a greater understanding of the interfacial properties under shear. This is critically important should a semi-cured interface ever be present in a structure expected to fail under shear loading and this failure has yet to be characterised where semi-curing has been employed. Additionally, any form of surface treatment, contamination or preparation has been avoided in the manufacture of the semi-cured elements. The aim is to investigate how the residual chemical activity alone in the semi-cured elements preforms when compared to a baseline laminate produced through a single infusion and cure.

This paper will first give the materials used before the manufacturing methods and specimen preparation are outlined. From this the test procedure is explained and the results given. Following this the results are discussed and conclusions as to the feasibility of semi-curing given for the used materials systems.

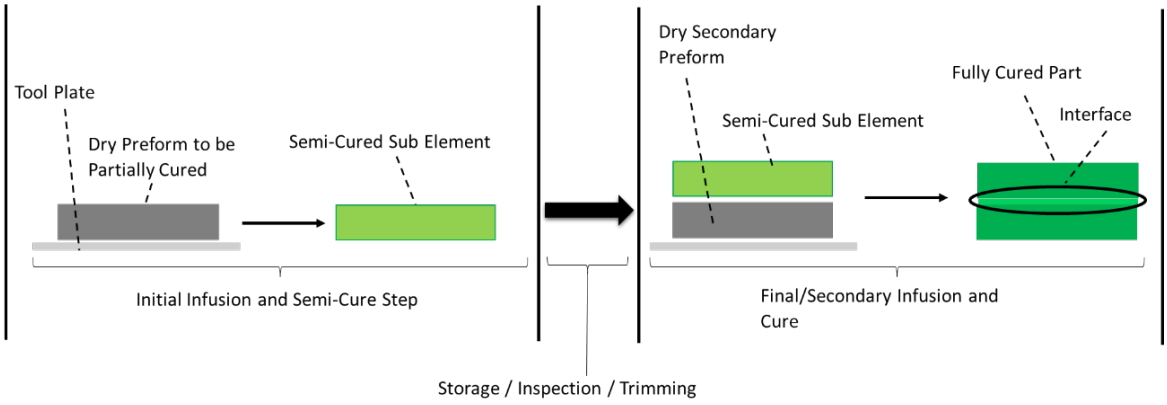

Figure 1. Schematic outlining the steps in the semi-curing process

2. Materials

A commercially available, single part epoxy resin infusion system was used to produce all laminates manufactured and tested in this work. This epoxy material is representative of the class of infusion epoxies used by the aerospace industry. The fibre reinforcement was a carbon fibre biaxial non-crimp fabric (NCF) with a 3,1mm tricot stitch in a 0°/90° orientation, with an areal weight of 480g/m^2 and had powder binder applied.

  doi:10.5075/epfl-298799_978-2-9701614-0-0

3. Methods

3.1 Specimen Manufacture

Flat panels consisting of two sub elements stacked on top each other with a horizontal interface between them were manufactured in two stages as illustrated in Figure 1. In the first stage, the upper semi cured sub element was made by infusing and partially curing a preform. This was then placed on top of the lower element (a dry secondary preform) and in the second stage the interface between the two was formed by a final infusion and cure process.

Six of these panels were made to investigate the effect the degree of cure reached by the upper sub element in stage one on the properties of the interface in the final fully cured part. The degrees of cure investigated are shown in Table 1, along with a baseline panel for comparison made through a traditional single stage infusion and curing process. All laminates had a final layup of $[(90/0)_4,(+95/+5),(-5/-95),(0/90)_4]$. The mid plane contained fibres in a +5/-5 orientation to avoid the fibres nesting, which could cause bridging during Mode I testing, leading to artificially high interlaminar fracture toughness values being reported. The manufactured dimensions of each panel was 350mm × 350mm and 4.7mm thick. PTFE film (12µm thick) inserts were included at the midplane to act as crack initiators for testing.

Two types of test specimen were machined from the panels using a CNC diamond saw:

i)148 mm × 20 mm Mode I double cantilever beam (DCB) specimens with a 75 mm PTFE insert.

ii) 170 mm × 20 mm Mode II end notch flexure (ENF) specimens with a 50 mm PTFE insert.

Table 1. outlines the laminate names, manufacturing process, partial degree of cure of the initially semi cured sub element, and reasons for choosing said degree of cure.

Table 1: Laminate Manufacturing Details

Laminate I.D	Manufacturing Process	Initial DoC	Reason for choosing DoC listed
BL0	Baseline	N/A	Comparison with traditional bulk curing.
SC0.2	Semi-cure	0.2	DoC below gel and Tg below room temperature
SC0.3	Semi-cure	0.3	DoC below gel and Tg around room temperature
SC0.5	Semi-cure	0.5	DoC below gel and Tg above room temperature
SC0.7	Semi-cure	0.7	DoC at gel
SC0.9	Semi-cure	0.9	Comparable to adhesive bonding

3.3 Testing Methodology

3.3.1 Mode I Testing

Double Cantilever Beam (DCB) testing was carried out to assess the Mode I performance of the interfaces in the manufactured laminates according to ASTM D5528-13 [11]. Steel strap hinges were bonded to the top and bottom surfaces with Araldite paste adhesive to apply an opening load to the specimen arms. The sides of the specimens were spray painted with a fine layer of white paint to follow the progress of the crack as it grew.

  doi:10.5075/epfl-298799_978-2-9701614-0-0

A Shimadzu AGS-X Series universal tester fitted with a 500N load cell was used for Mode I testing. It was used in conjunction with an iMetrum Video Gauge to record the tests so that the crack length could be measured. The test was performed under displacement control at a rate of 2mm/min up until crack extension exceeded 50mm. While loading the specimen, the crosshead displacement, applied load, and crack growth were recorded.

To calculate the Mode I interlaminar fracture toughness from the specimens (G_{Ic}) Eq. (1) was used:

$$G_{Ic} = \frac{3P\delta}{2b(a+|\Delta|)} \quad (1)$$

where P is the applied load, δ is the load point displacement, b is the specimen width, and a is the delamination length. The $|\Delta|$ term is a correction factor which is determined by generating a least squares plot of the cubed root of the compliance (were the compliance is defined as δ/P) versus delamination length and finding the distance on the x axis which is intercepted by the plotted line.

3.3.2 Mode II Testing

The Mode II performance of the laminates was assessed using End-Notched Flexure (ENF) tests in a three-point-bend test setup. ENF testing was carried out as per ASTM D7905, with the testing comprising of an initial non-pre-crack test (NPC) and a second pre-cracked test (PC) [12].

Mode II testing was conducted using a Shimadzu AGS-X Series universal tester fitted with a 10kN load cell. Tests used 0.5mm/min constant displacement. A video gauge was used to record the crack growth so that an updated crack length could be used in the NPC tests. Cross head displacement, load, and time were all recorded.

Eq. 2 was used to determine the Mode II interlaminar fracture toughness (G_{IIc}).

$$G_{IIc} = \frac{3mP_{max}^2 a_0^2}{2b} \quad (2)$$

where m is a calibration coefficient found through compliance testing before the fracture NPC and PC tests, P_{max} is the maximum force from the fracture test, a_0 is the crack length used in the fracture and B is specimen width.

4. Results and Discussion

4.1 Manufacturing Observations

Having manufactured half laminates to varying initial degrees of cure prior to their integration in the second step of the semi-curing process (Figure 1), it was possible to make observations regarding the usability and ease of working with the semi-cured materials. At low degrees of cure (0.2-0.3) the material displayed similar levels of tack to an aerospace grade prepreg material. However, as the degree of cure advanced towards 0.5 the material was stiff and boardy and began to handle like a cured part at degree of cure around the gel point at 0.7.

  doi:10.5075/epfl-298799_978-2-9701614-0-0

4.2 Mode I Performance

The values of G_{Ic} from the DCB testing of the six laminates are shown in Figure 2. The trend in the plot indicates that the interfacial properties are largely retained in a fully-cured laminate with an initial degree of semi-cure up to 0.7, when compared to the baseline values (DoC 0). The laminate at 0.7 represents a DoC at roughly the gel point for the resin. Past this value results can be seen to fall off. Similar trends are observed in the literature where semi-curing was not wholly detrimental to Mode I performance [13]. However, some work where peel ply was used in the initial semi-curing stage as surface treatment prior to secondary integration found better interfacial performance at higher degrees of cure/past gelation and this may be due to the use of the peel ply alone [8].

4.3 Mode II Performance

Figure 3 shows the results of both the NPC and PC ENF tests. The results showed good agreement between the NPC and PC tests. Results would appear to indicate that the semi-curing process has no detrimental effect on the Mode II performance of the composite laminates produced. This result is very encouraging since load transfer between composite plies happens in shear between layers.

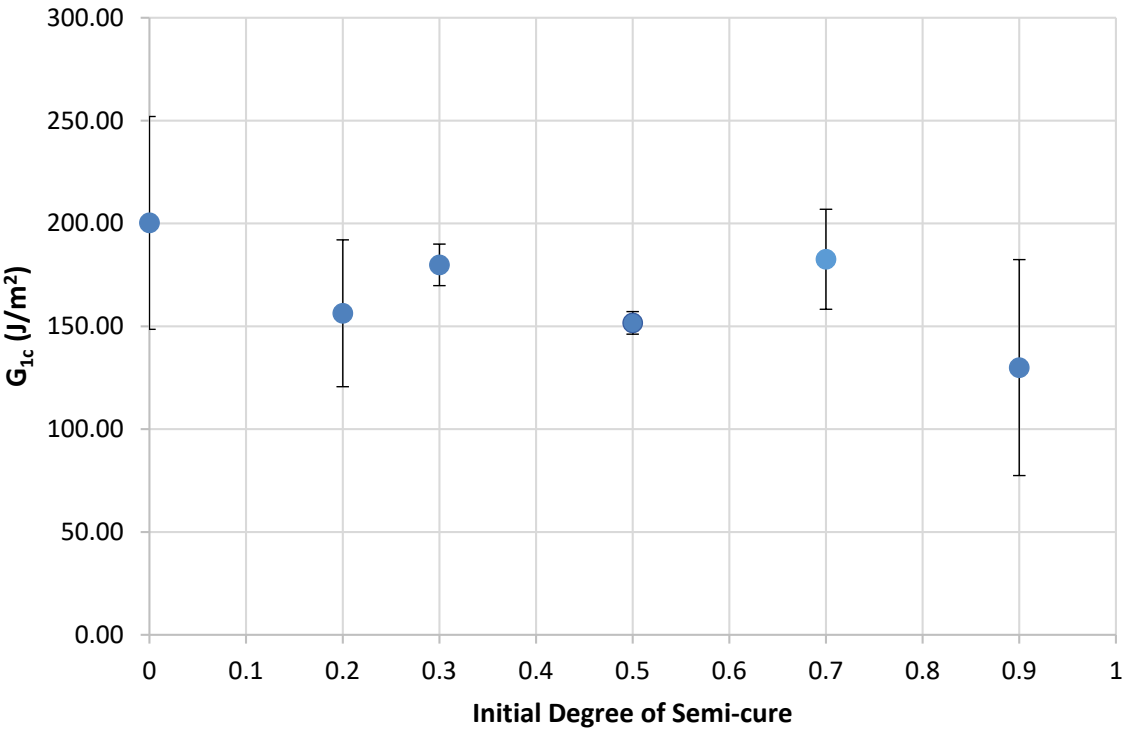

Figure 2. Mode I Test Results

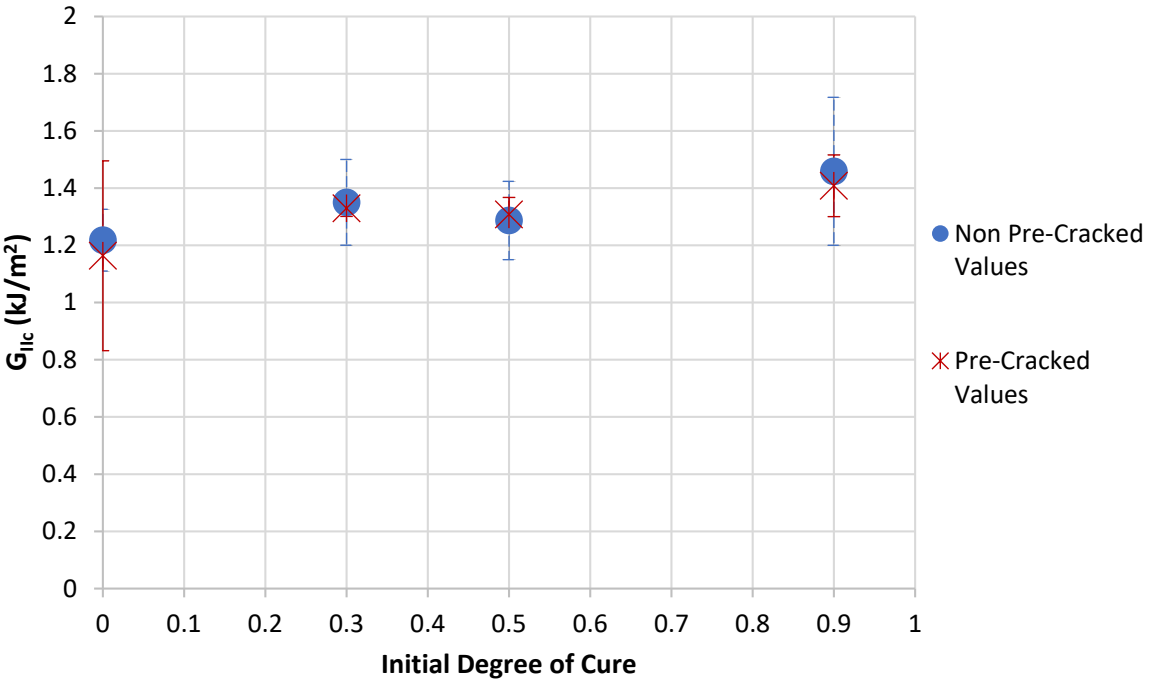

Figure 3. Mode II Test results with Circles representing the NPC test results and the crosses representing the PC tests

5. Conclusions

The effect of introducing a semi-cured interface in the mid-plane of an epoxy resin infused carbon fibre laminate was studied in this paper. Once the laminate was fully cured, semi-curing was seen to have little effect on interfacial properties when the initial degree of semi-cure is kept below gelation. In Mode I there was approximately a 30% reduction in interfacial properties if the initial degree of cure was above gelation, while in Mode II there was no such effect. It is also clear that Mode I testing is a far more sensitive test for quantifying the effect of semi-curing on interfacial properties.

Overall, semi-curing seems to be a promising technique to de-risk preform integration before infusion of complex composite structures. Further work will assess how the interfacial properties change around gelation (i.e. finer granularity in degrees of cure from 0.6–0.8) and it is hoped that the results may be available in the near future.

Acknowledgments

This work was funded by Airbus and the EPSRC through the Centre for Doctoral Training in Advanced Composites for Innovation and Science (EP/L016028/1) and the Future Composites Manufacturing Hub (EP/P006701/1) Layer by Layer Curing project.

References

1. Diaz S, Torres M. IIAMS- Innovative Infusion Airframe Manufacturing System. 2020;
2. Gardiner G. Advancing the OOA infused wing box [Internet]. Composites World. [cited 2022 Mar 11]. Available from: https://www.compositesworld.com/articles/advancing-the-ooa-infused-wing-box
3. Chamorro FJ, Domínguez F. Highly integrated composite structures: Process and tooling challenges. 16th Eur Conf Compos Mater ECCM 2014. 2014;(June):22–6.

  doi:10.5075/epfl-298799_978-2-9701614-0-0

4. Giacchetta R, Bueno G, Moreno JM, Cruza JF. Nuthic: Non-contact ultrasound inspection machine of highly integrated composite parts. In: 7 th International Symposium on NDT in Aerospace. 2015.
5. Herbeck L, Wilmes H, Kleineberg M. Materials and processing technology for a CFRP Fuselage. In 2004.
6. White SR, Kim YK. Staged curing of composite materials. Compos Part A Appl Sci Manuf. 1996 Jan;27(3):219–27.
7. Corbett T, Forrest M, Gac P Le, Fox BL. Characterization of melded carbon fibre/epoxy laminates. Compos Part A Appl Sci Manuf. 2007 Aug;38(8):1860–71.
8. Moosburger-Will J, Sause MGR, Horny R, Horn S, Scholler J, Llopard Prieto L. Joining of carbon fiber reinforced polymer laminates by a novel partial cross-linking process. J Appl Polym Sci. 2015 Jul 15;132(27).
9. Motsch N, Rieger F, Rief T, Hausmann J. Investiagtion of pre-cured carbon fiber/epoxy laminates for modified co-curing process. In: SAMPE Europe Conference. Nantes; 2019.
10. Motsch-Eichmann N, Rieger F, Rief T, Hausmann J. Experimental investigation of modified co-curing process for carbon fiber/epoxy-laminates. J Micromechanics Mol Phys. 2021 Sep 8;06(03):1–12.
11. ASTM D5528-01. Standard test method for mode I interlaminar fracture toughness of unidirectional fiber-reinforced polymer matrix composites. ASTM. 2013;
12. ASTM D7905. Standard test method for determination of the mode II interlaminar fracture toughness of unidirectional fiber-reinforced polymer matrix composites. ASTM. 2019;
13. Rieger F, Rief T, Motsch N, Hausmann JM. Manufacturing CFRP-Parts Using a Modified Co-Curing Method – Fundamental Experimental Analysis. Key Eng Mater. 2019 Jun;809:372–7.

  doi:10.5075/epfl-298799_978-2-9701614-0-0

CONTINUOUS RESISTANCE HEATING TECHNOLOGY – RISKS AND OPPORTUNITIES OF A NOVEL HEATING METHOD

Yannis Grohmann[a]

a: Deutsches Zentrum für Luft- und Raumfahrt e.V., Institute of Composite Structures and Adaptive Systems, Lilienthalplatz 7, 38108 Braunschweig, Germany – yannis.grohmann@dlr.de

Abstract: *CoRe HeaT, the Continuous Resistance Heating Technology, is a novel heating method that can be used for carbon fibre placement processes such as the Automated Fibre Placement method, tape winding or alike. The paper gives a short overview of the technology and its main properties. The main disadvantage and risk of the technology is that it is not compatible with all common production materials. Only suitable carbon fibre materials can be heated using CoRe HeaT. While dry fibre tape material seems to be unproblematic, some prepreg tapes were found to be critical. Microscopic analysis and electrical resistance measurements seem to be an easy and fast method to determine whether a tape is suitable for continuous resistance heating or not. Aside from this risk, the technology offers the opportunity to increase productivity while reducing costs through high-speed heating and superior energy efficiency.*

Keywords: Automated Fibre Placement (AFP); Joule/ohmic/resistive/intrinsic heating; Carbon fibre reinforced plastic (cfrp); Manufacturing process

1. Introduction

Automated Fibre Placement (AFP) is one of the most common manufacturing processes for series production of carbon fibre reinforced plastic parts (cfrp) [1]. An important aspect for those processes is the heating technology. The increasing interest for thermoplastic part production and dry fibre process routes has pushed the development of new and improved heating technologies. The VCSEL laser [2], the Xenon Flashlamp [3] or use of ultrasonic heating [4] for example, have all been developed and tested for the AFP process within the last 5-10 years. Furthermore, the laser, as state of the art technology, has made a lot of progress [5].

An alternative to these AFP heating methods that has been in development for the past years, is direct electrical resistance heating, based on heating the electrically conductive carbon fibres using the Joule effect [6-9]. While static Joule heating of carbon fibres is known and has already been used for different purposes over the years [10], the focus of the Continuous Resistance Heating Technology (CoRe HeaT) is the AFP process and therefore heating unidirectional (UD) tapes or tows that are in movement. The electrical current is induced into the fibres via direct surface contact. Figure 1 shows how an AFP end effector heating zone configuration could be set up. In this example, the first electrical contact is in front of the consolidation roller. The second contact is the tooling. However, different electrode setups are possible with their own specific pros and cons. Within one of the electrical contacts, a current is induced. While flowing through the carbon tapes to the next electrical contact, the current produces heat within the fibres via the Joule effect.

  doi:10.5075/epfl-298799_978-2-9701614-0-0

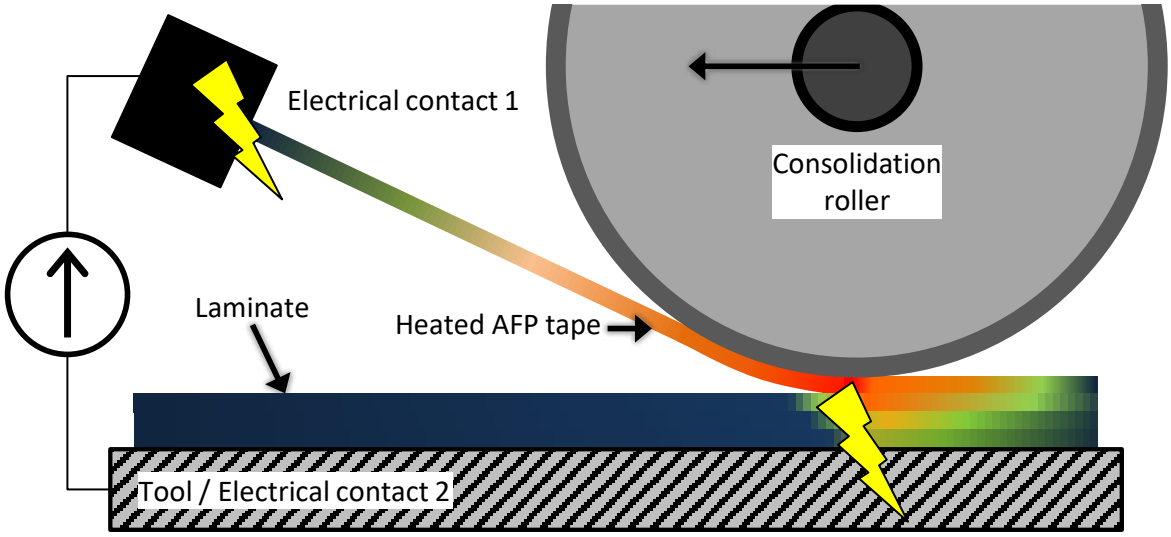

Figure 1. Basic principle of a possible CoRe HeaT setup for the AFP process

The resistive properties of carbon fibres are well suited for intrinsic ohmic heating. Theoretically heating rates much higher than other state of the art technologies are possible, even when limiting the applied electric voltages to the extra low voltage level (ELV), to prevent the dangers of an electric shock for humans [11]. ELV allows working directly next to the layup process without any special safety measures like laser proof housing or alike. Furthermore, in comparison to other high-speed heating technologies, the technology is cheaper, very compact and potentially easy to be integrated into an AFP end effector. In addition, directly heating the material with the Joule effect is highly energy efficient. Biggest drawback however is the limited compatibility of the technology to tape materials with suitable electrical properties.

2. Analysis of the pros and cons of CoRe HeaT

Focus of the current research is using the CoRe technology within the AFP process. It is one of the most common automated manufacturing processes and allows an automated test sample production. Furthermore, there is a wide variety of available research and literature focused on AFP [1]. Nevertheless, the findings and knowledge gained can also be used for all other manufacturing methods and technologies were carbon fibre materials need to be heated during dynamic transport. However, due to the need for direct electrical contact to the carbon fibres, not all materials that are common, are suitable for using CoRe HeaT. Next to the requirement of mainly being composed out of electrically conductive carbon fibres, the fibre distribution and especially the surface texture and composition play a major role. As long as raw and untreated carbon fibres are used, a general compatibility should be given. However, often the carbon fibres have been processed or modified, so that they are suitable for a chosen manufacturing method. With a focus on the AFP process, appropriate tape types were investigated.

2.1 Investigating material compatibility

Three main material types are common for the AFP process. The most common type is still the thermoset prepreg, available as tape or tow. However, this type of material needs only low process temperatures, typically below 70°C [1], reducing the need for high-intensity heating technologies. Also, the sticky thermoset matrix system covering the fibres is a potential problem for direct electrical surface contacts due to contamination. Furthermore, alternate process

  doi:10.5075/epfl-298799_978-2-9701614-0-0

routes that use dry fibre tape material with a separate matrix infusion or injection offer a lot of advantages. First aircraft wings are already being manufactured in this way [12] and several research projects have focused on dry fiber placement [13].

Dry fibre tapes are fundamentally different to pepreg tapes. They are usually composed out of spread raw carbon fibre rovings that are stabilized with the help of auxiliary materials like non-woven veils, hotmelt powder binders or a combination of those or similar products. Their process temperatures go up to 200°C and above, making faster heating technologies beneficial. The auxiliary veils and binders are normally electrically isolating. However, their weight-based percentage is normally below 10 %. Figure 2 shows microscopic images of the surfaces of different dry fibre materials. The two pictures on the left show the bindered surfaces of different AFP tape materials where large areas of raw carbon fibres are still clearly visible. These tapes were well suited for the CoRe heating technology due to good contact properties. The surface in the right picture is covered with an electrically isolating veil. Even though the carbon fibres are also still visible in the background, the veil surface of this tape was not well suited for the process, since the three-dimensional structure of the veil in combination with its stiffness, made it nearly impossible to get a good contact to the fibres. However, the other side of the tape did not have a veil, had good contact properties and therefore could still be used. For dry fibre tapes, without an isolating matrix within, it is sufficient if at least one side of the tape has good electrical contact properties. So far, all tested dry fibre tapes and tows composed of high strength (HS), high tenacity (HT) or intermediate modulus (IM) carbon fibres in combination with epoxy or thermoplastic based veil or powder binders of several different suppliers were well suited for using CoRe HeaT.

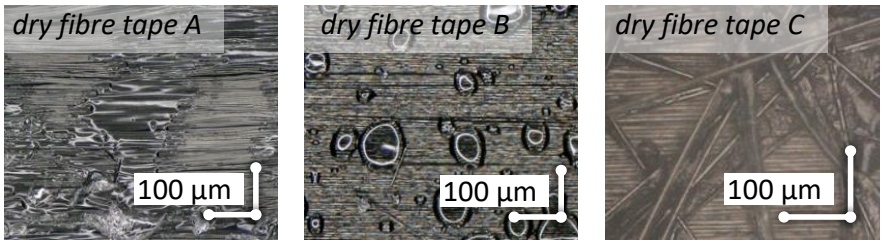

Figure 2. Microscopic look at the surface of different dry fibre tows and their composition

Thermoplastic prepreg tapes are the third type of tapes that are in focus. They have received increasing attention in recent years, due to their advantages in regard to increased toughness, better recyclability and especially faster manufacturing and assembling because of their welding capabilities [14]. With process temperatures of up to 400°C and above, they are the most demanding material type. An important aspect of these tapes in regard to CoRe HeaT is that the fibres are already pre-impregnated with the matrix system. The electrically isolating properties of the matrix can be a problem. For a good compatibility to direct electrical heating, the tapes need a high fibre volume content, a homogeneous fibre distribution within the tape and enough uninsulated fibres on the surface of the material. Figure 3 shows the micrographs of two different tapes, with the left one having much better properties in regard to Joule heating than the right one. Since the electrical current always seeks the path of least resistance, a fiber distribution that is as uneven as in the picture on the right, can lead to an equally uneven temperature distribution.

  doi:10.5075/epfl-298799_978-2-9701614-0-0

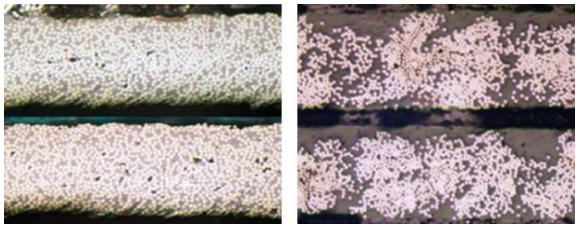

Figure 3. Two different thermoplastic prepreg tapes and their fibre distribution [15]

The requirement of a good electrical contact resistance of the surface of the tape is even more important for an even temperature distribution without hotspots. Available thermoplastic prepreg tapes differ a lot in this regard. A first visual inspection can help to determine whether the tape is potentially compatible or not. Smooth flat shiny tapes indicate a resin-rich surface with a high electrical resistance and only a few contact zones, leading to severe hotspots. A matt looking surface where the fibres can be seen, could indicate a potential compatibility. However, a closer look is needed to understand why some prepreg tapes can be used for continuous high speed direct electrical resistance heating and others are not. Figure 4 shows a microscopic image of the surface of different prepreg tapes. The investigated tapes belong to the group of polyaryletherketones (PAEK), except for tape D, which is a polyamide 6 (PA6) prepreg. The right picture shows the PA6 tape, with a smooth and shiny surface that is nearly completely covered by resin and is therefore unsuitable. The left picture shows the matt surface of a PAEK tape, where the fibre structure can be seen. Nevertheless, a very close look with a magnification of 2000x shows that there is a thin shiny thermoplastic film covering most of the fibres completely. Layup trials using this tape revealed the problematic consequences of such a surface condition, which were uneven temperature distributions during layup. Especially at higher layup speeds from 0.5 m/s and above, severe hot spots with clearly visible damage to the material surface occurred. The second picture on the right shows a microscopic look on the surface of another PAEK prepreg tape, that seemed well suited for the process. In contrast to *prepreg tape A* on the left, it can be seen that the fibers on the surface are not completely covered by resin. The rough structured look of the raw carbon fibers can be clearly distinguished from areas where they are covered with resin. This tape was tested with a layup speed of up to 1 m/s with seemingly good results.

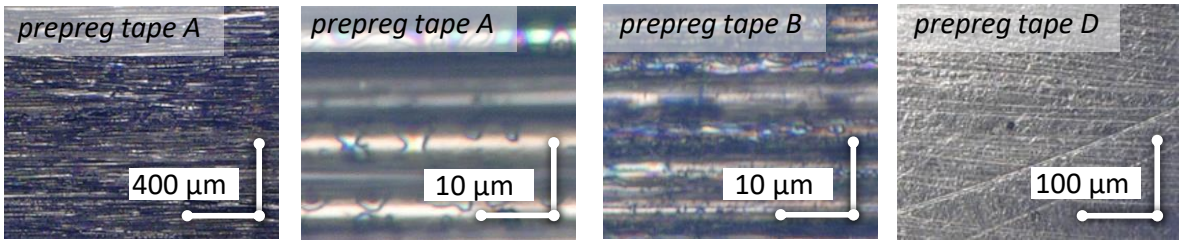

Figure 4. Different thermoplastic prepregs and their surfaces in detail

The optical inspection however is just a way to further understand why certain tapes are more suitable than others. A practical attempt to determine the compatibility is by testing the materials electrical properties in detail. An important factor that is expected to correlate with the compatibility to continuous resistance heating, is the surface contact resistance. Therefore, the electrical properties of different tape materials were tested, to get an indicator on how well they are suited for CoRe HeaT.

  doi:10.5075/epfl-298799_978-2-9701614-0-0

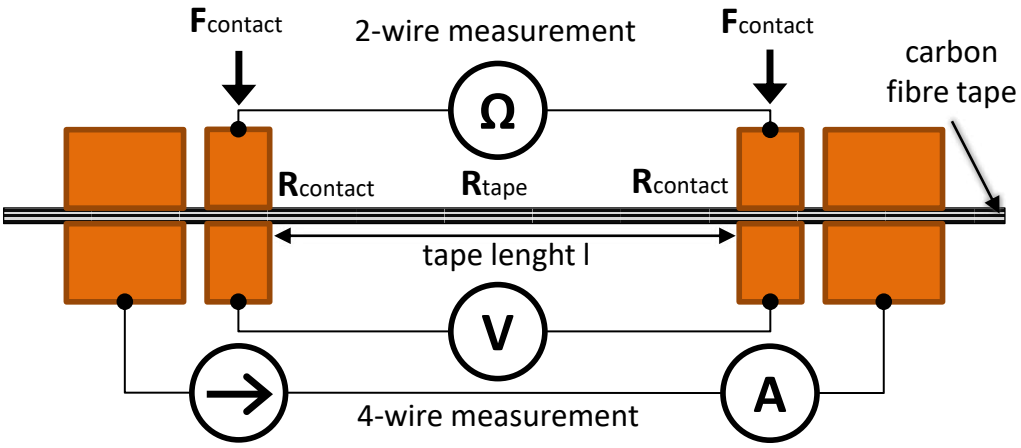

Figure 5. Sketch of the resistance test setup

The test setup used to determine the contact resistance can be seen in figure 5. It is a 4-wire resistance measurement setup with pneumatically actuated contacts, so that the contact forces can be varied, in combination with a standard 2-wire test circuit.

The 4-wire measurement gives an exact reading of the tape's resistance (R_{tape}) without the contact resistances ($R_{contact}$). The 2-wire setup measures the total resistance (R_{total}), including these. Therefore, the contact resistance can be determined by subtracting the value of the 4-wire resistance measurement (R_{4w}) of the 2-wire resistance value (R_{2w}).

$$R_{contact} = R_{total} - R_{tape} = R_{2w} - R_{4w} \quad (1)$$

Table 1 shows the average contact resistances with a low contact force (R_{c-lcF}), a high contact force (R_{c-hcF}) and the maximum difference between the lowest and the highest measured contact resistances (Δmax) in a series of 5 measurements. The investigated tapes *A*, *B* and *D*, are the same that have been discussed in the microscopic analysis above. *Prepreg tape C* is another newly introduced PAEK tape, which is a thin-ply prepreg with an aerial weight of only 40 g/m². The *bindered dry fibre tape A*, from figure 2, is listed as a reference. It has already been thoroughly tested and seems to be very well suited for the CoRe heating technology. Layup speeds with up to 2 m/s were unproblematic and an inter laminar shear strength (ILSS) test series showed no negative influences of high intensity resistance heating on the specimen [7]. The *thermoplastic prepreg tape A* has been tested with layup speeds of up to 0.25 m/s with an acceptable result in regard to temperature homogeneity and optical inspection of the layup quality. At higher speeds however, hot spot severity increased to a point that was unacceptable. P*repreg tape B* is the tape that has been tested with a layup speed of 1 m/s without any problems. The thin-ply *prepreg tape C* was already successfully tested with a maximum layup speed of 2 m/s, also without any noticeable problems. *Thermoplastic prepreg tape D* has not yet been tested with the AFP prototype. Even though the average contact resistance is lower than *prepreg tape A*, it is expected that *prepreg tape D* will perform worse, due to a much higher scattering of the contact resistances (Δmax). The experience made so far, supports the theory that high contact resistance with high scatter corresponds to poor compatibility with the CoRe heating technology.

  doi:10.5075/epfl-298799_978-2-9701614-0-0

Table 1: Different tape materials and their electric properties

Material type	R_{c-lcF} [Ω]	R_{c-hcF} [Ω]	Δmax [Ω]
Bindered dry fibre tow A	2,6	0,6	3,6
Thermoplastic prepreg tape A	43,1	13,3	60,3
Thermoplastic prepreg tape B	3,7	2,0	5,7
Thermoplastic prepreg tape C	4,0	0,3	5,0
Thermoplastic prepreg tape D	31,5	7,4	115,0

2.2 Highly dynamic heating

One of the reasons why CoRe HeaT could be interesting to use in a process, is the highly dynamic heating capability. Extreme process acceleration and process speeds faster than current state of the art technologies, allow an increase in productivity. The maximum estimated speed for different types of materials, that are listed in table 2, are mainly limited by the extra low voltage limitations [11]. In theory, specialized machines were human interaction during processing is not needed, raising the electric process voltage would allow even higher process speeds. Another technology related aspect that has an influence on the maximum process speed when a voltage limit is given, is the heating zone length and design details regarding the heating unit [16]. Besides technical related influences, the tape material properties are an important factor. As described before, critical temperature distribution due to bad compatibility might limit the maximum layup speed. Furthermore, the required process temperature, the tapes specific weight, its specific heat capacity and the electrical properties all have an influence on the maximum process speed. Table 2 is therefore only intended to give an idea of the potential maximum layup speeds, with this estimation being constrained by a maximum process voltage that remains within the ELV limit.

Table 2: Maximum estimated layup speeds in regard to materials contact resistances, the area specific weight, the layup temperature and tested layup speeds

Material type	Materials R_{c-hcF} [Ω]	Materials weight [g/m²]	Layup temperature [°C]	Max speed tested [m/s]	Max speed estimated [m/s]
Dry fibre tow A	0,6	210	160	2,0	> 32
Prepreg tape A	13,3	145	> 380*²	1,0	< 0,5*
Prepreg tape B	2,0	194	> 340*²	1,0	2,7
Prepreg tape C	0,3	40	> 340*²	2,0	>7,0

* Higher layup speeds led to severe hot spots and heat damages to the tape material.

*² Estimated layup temperatures based on materials melting point or measured temperatures ahead of nip point (maximum) temperature.

  doi:10.5075/epfl-298799_978-2-9701614-0-0

2.3 Green low-cost technology

Since the technology is not yet commercially available, it is not possible to compare exact prices. However, based on hardware costs of the prototype and known costs for comparable laser or flashlamp systems, it is expected that the price for a CoRe heating unit will be significantly lower, by at least 30 %. In comparison to laser systems, another big cost reduction factor is that no laser proof housing is needed. Especially for larger production facilities, laser proof housing could easily cost 100.000 € or even much more, depending on the machines size. Another aspect making CoRe HeaT a green low-cost technology is the superior energy efficiency. Using the Joule effect, the electrical energy flowing through the fibres is directly transformed into heat without energy losses [17]. As with the maximum process speed, the material properties, the design of the heating unit and the selected process parameters have an influence on the final energy efficiency. Table 3 is listing the used power for different layup trials using CoRe HeaT and data found in publications regarding the use of a laser or a flashlamp heating system, to get a rough comparison of energy usage. Since the materials weight, the layup speed and especially the process temperature generally have a significant impact on the energy efficiency, the final results listed for power consumption in watts per tape and process speed should only be understood as a very rough estimate. Furthermore, the information found in publications are often not detailed enough or instead of the electrical power usage of a laser, the optical power is given.

Table 3: Energy consumption for different materials and process parameters in comparison to different heating technologies

Material type	Materials weight [g/m²]	Layup speed [m/s]	Layup temperature [°C]	Heating technology	Power usage [W/tape]	Power usage [W/tape·m/s]
Bindered dry fibre tape A	210	0,75	160	CoRe HeaT	150	200
Thermoplastic prepreg tape B	194	1,0	> 340*	CoRe HeaT	1500	1500
Thermoplastic prepreg tape A	145	0,15	> 380*	CoRe HeaT	320	2133
Thermoplastic prepreg tape A	194	0,11	365	Flashlamp	975*²	8864
Cytec APC-2 C/PEEK	<200*³	0,2	450	Laser	1000	5000

* Estimated values based on materials melting point or measured temperatures ahead of nip point (maximum) temperature.
*² Multitow Layup unit, therefore total power divided by tows that were processed [18]
*³ No information on aerial weight, but with a mentioned thickness of 0.135 mm per ply, the estimated aerial weight is lower than 200 g/m² [19]

  doi:10.5075/epfl-298799_978-2-9701614-0-0

3. Summary and conclusion

A critical aspect of the CoRe Heating technology is that it only works with carbon fibre materials, that have a surface where the fibres themselves are easily contactable. Therefore, the main question whether this novel heating method could be usable with a certain process in mind, must be answered by looking at the desired process materials first. The main requirement of being mainly composed out of carbon fibres is just the start. With a focus on AFP carbon fibre tapes, two different ways how to analyze the materials and estimate their compatibility are presented. A close up look with a microscope and a 2000x magnification allows to see whether individual fibres are lying open or if they are covered by an electrical isolator. However, other aspects of the materials properties might hinder direct electrical contact. For example, the stiffness of surface covering electrically isolating veils, which could not directly be determined via a microscope. Another method that seems to give good values for compatibility evaluation is resistance measurement. The results of a test setup were the resistance between contact electrodes and the carbon fibre material could be determined, seems to have a good correlation to practical process experiences in regard to material compatibility.

Nevertheless, further research is needed to determine whether a material is fully compatible and therefore without any risks regarding part manufacturing, since high process speeds might become a problem for some materials.

The low costs of the technology and the extremely high potential process speeds however, make this an interesting new alternative for future carbon fibre processing machines.

Acknowledgements

The Author would like to thank the German Federal Ministry of Education and Research (BMBF) for supporting the research by funding the project ThermoPros (03INT713BG).

4. References

1. Brasington A, Sacco C, Halbritter J, Wehbe R, Harik R. Automated fiber placement: A review of history, current technologies, and future paths forward. Composites Part C: Open Access. 2021
2. Weiler T, Striet P, Janssen H, Emonts M. Optical Modelling of VCSEL-Assisted Thermoplastic Tape Placement. Proceedings of the 17th European Conference on Composite Materials. 2016
3. Williams D, Brown M. Xenon Flashlamp Heating for Automated Fibre Placement. Third Symposium on Automated Composites Manufacturing (ACM 3). 2017
4. Rizzolo RH, Walczyk DF. Ultrasonic consolidation of thermoplastic composite prepreg for automated fiber placement. Journal of Thermoplastic Composite Materials. 2016
5. Assadi MD. High Speed AFP Processing of Thermoplastics. SAMPE nexus. 2021
6. Grohmann Y, Stüve J. Continuous Resistance Heating Technology for fast and efficient high-volume production processes. 28th SICOMP. 2017
7. Grohmann Y. A new heating method for faster fibre placement. 11th International Conference on Manufacturing of Advanced Composites. 2018
8. Evans AD, Turner TA, Endruweit A. Development of Automated Dry Fibre Placement for High Rate Deposition. ICCM22. 2019

  doi:10.5075/epfl-298799_978-2-9701614-0-0

9. Grohmann Y. Continuous Resistance Heating Technology for High-Speed Carbon Fibre Placement Processes. SAMPE Europe. 2020
10. Forintos N, Czigany T. Multifunctional application of carbon fiber reinforced polymer composites: Electrical properties of the reinforcing carbon fibers - A short review. Composites Part B: Engineering. 2019
11. DIN EN 61140 - VDE 0140-1:2016-11. Protection against electric shock – common aspects for installation and equipment - (IEC 61140:2016)
12. Sloan J. Infused wing sheds light on aerocomposites future [Internet]; 2018 [cited 2022 April 20]. Available from: https://www.compositesworld.com/articles/infused-wing-sheds-light-on-aerocomposites-future
13. Gardiner G. Dry fiber placement: Surpassing limits [Internet]; 2016 [cited 2022 April 20]. Available from: https://www.compositesworld.com/articles/dry-fiber-placement-surpassing-limits
14. Nishida H, Carvelli V, Fujii T, Okubo K. Thermoplastic vs. thermoset epoxy carbon textile composites. Conference Series: Materials Science and Engineering. 2018
15. Risteska S. Unidirectional Carbon Fiber Reinforced Thermoplastic Tape in Automated Tape Placement Process [Internet]; 2021 [cited 2022 April 20]. Available from: https://www.intechopen.com/chapters/79552
16. Grohmann Y, Stüve J. High speed tape placement with CoRe HeaT. ITHEC 2020 – International Conference and Exhibition on Thermoplastic Composites. 2020
17. Zeller W, Franke A. Das physikalische Rüstzeug des Ingenieurs. Technik-Tabellen-Verlag Fikentscher & Co. 1977
18. Stefaniak D, Haschenburger A, Kolbe A, Menke N, Ucan H. Alternativen in der automatisierten thermoplastischen Bauteilfertigung [Internet]; 2022 [cited 2022 April 20]. Available from: https://www.youtube.com/watch?v=bZxBK5Bv4bY
19. Slange TK, Buser YM, Wijskamp S, Warnet L, Grouve WJB, Akkerman R. Rapid Manufacturing of a Tailored Spar by AFP and Stamp Forming. 4th International Conference and Exhibition on Thermoplastic Composites. 2018

  doi:10.5075/epfl-298799_978-2-9701614-0-0

A STEPWISE METHOD FOR THE CHARACTERIZATION OF NON-ISOTHERMAL CRYSTALLIZATION KINETICS OF POLY(ETHER ETHER KETONE) AT PROCESSING-RELEVANT COOLING RATES

Théo Baumard[a], Elissa El Rassy[a], Nicolas Boyard[a], Steven Le Corre[a], Jean-Luc Bailleul[a], Jérôme Bikard[b], Lise Trouillet-Fonti[b]*

a: Nantes Université, CNRS, Laboratoire de thermique et énergie de Nantes, LTeN, UMR 6607, F-44000 Nantes, France
b: Solvay, Rue Prosper Monnet, 69190 Saint Fons, France
*: Corresponding author : theo.baumard@univ-nantes.fr

Abstract: *Isothermal and non-isothermal crystallization kinetics of PEEK are investigated experimentally using fast scanning calorimetry. A stepwise method to derive the kinetics from interrupted crystallization tests is introduced. The evolution of crystallinity as a function of time is evaluated from the variation of specific heat capacity to avoid taking into account melt-recrystallization phenomena when integrating the melting enthalpy. This experimental work allows the construction of a continuous cooling transformation diagram, at cooling rates close to those of industrial processes.*

Keywords: Crystallization kinetics ; Fast scanning calorimetry ; PEEK

1. Introduction

The use of thermoplastic composites is expanding in the transportation industry, particularly in response to stricter emission regulations that make it necessary to lighten structures. To achieve the production rates required by this high-volume market, forming and assembly processes that allow short cycle times (injection, thermoforming, thermoplastic welding) are used. These processes, which are generally non-isothermal, are based on processing above the melting temperature of the thermoplastic matrix. The microstructure of the final part depends on the cooling conditions from the molten state. The characterization of the crystallization of these semi-crystalline polymers is necessary to understand the relationship between process parameters and final part properties. In thermoplastic welding processes for example, the interaction between chain diffusion at the interface and crystallization can lead to significant variations in the quality of adhesion as a function of the imposed temperature cycle.

Poly(ether ether ketone) (PEEK) is a high performance semi-crystalline thermoplastic polymer with excellent mechanical properties and good thermal stability, used in particular for structural applications in the aerospace and automotive industries. Crystallization of PEEK under isothermal and non-isothermal conditions at rates up to 90K/min has been the subject of numerous differential scanning calorimetry (DSC) studies [2,3,4]. However, no study presents results under non-isothermal conditions for cooling rates close to those of industrial processes (10-100K/s).

  doi:10.5075/epfl-298799_978-2-9701614-0-0

2. Experimental protocol

2.1 Fast scanning calorimetry (FSC)

Fast differential scanning calorimetry (FSC) is a recent extension of standard differential calorimetry, allowing to reach heating and cooling rates up to 10^6 K/s [5]. This technique allows the investigation of very fast phase change phenomena, which are often inaccessible for conventional devices. The tests were carried out using a power-compensated Mettler Toledo Flash DSC1 instrument, equipped with UFS1 chip sensors allowing a heating rate up to 10000K/s and cooling up to 5000K/s.

The study material is a low viscosity PEEK grade developed by Solvay and supplied in pellet form. After drying, a small sample of the material is cut from the pellet with a scalpel, positioned in the center of the sensor measurement area and melted at a rate of 10K/s to allow good thermal contact with the chip prior to further analysis (Figure 1). A relatively high sample mass compared to other literature studies (about 500ng) is used to ensure that the crystallization phenomena are representative of those of the bulk material.

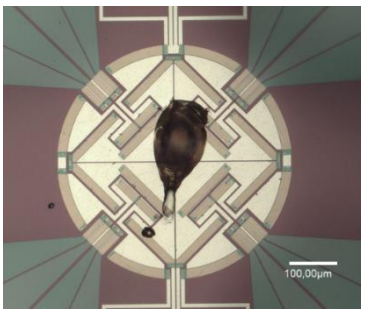

Figure 1 – PEEK sample on a UFS1 chip

2.2 Stepwise method for the characterization of crystallization kinetics

2.2.1 Isothermal crystallization

Preliminary tests have shown that the characterization of crystallization kinetics directly from the integration of the crystallization peak during cooling is not possible due to a low signal to noise ratio, i.e. the crystallization heat flow is too low to be directly measured. A discrete method based on a sequential approach is therefore applied to characterize the crystallization. The isothermal protocol, developed in a previous study [6] and described in Figure 2a., consists in (1) erasing the thermal history of the material by heating above the melting temperature, (2) cooling at high rate (2000K/s, which is shown to be sufficient to ensure that no crystallization takes place during cooling) to the isothermal crystallization temperature, (3) performing an isothermal step of a defined duration, (4) cooling at 2000K/s to room temperature and (5) heating at 2000K/s to 380°C. This protocol is repeated by varying the time and temperature of the isothermal step. Isothermal crystallization is studied here between 160°C and 320°C (i.e. a temperature range between Tg+10°C and Tm-20°C approximately), and for step times varying between 0.01s and 3600s.

  doi:10.5075/epfl-298799_978-2-9701614-0-0

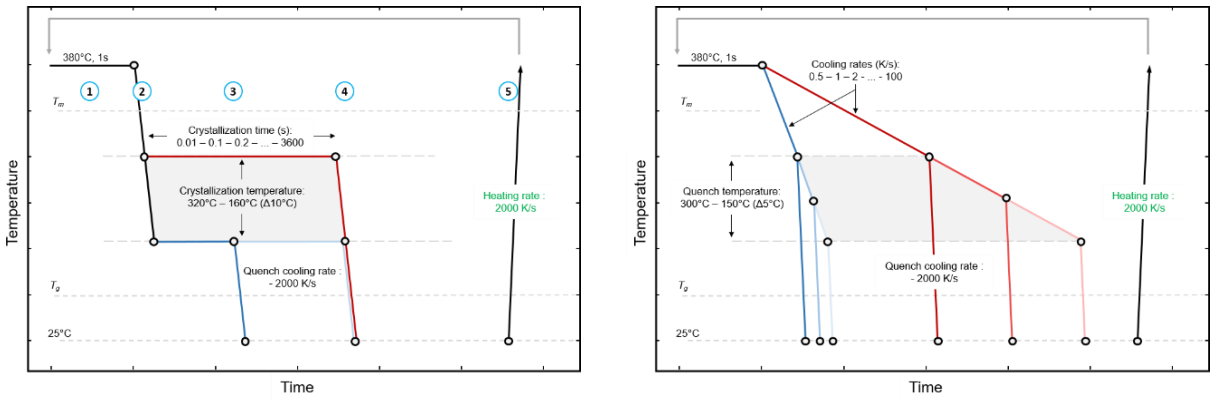

a. Isothermal crystallization *b. Non isothermal crystallization*

Figure 2 – FSC temperature cycle

2.2.2 Non-isothermal crystallization

The discrete method presented above is extended to study non-isothermal crystallization (Figure 2b.). After the thermal history erasure step, the sample is cooled at the rate of interest to a fixed temperature T_{quench} before quenching the resulting microstructure at 2000K/s. The sample is then heated at 2000K/s to melt the crystals formed during cooling. The test is repeated for several values of T_{quench} (between 150°C and 300°C) and several values of cooling rate (from 0.5 to 100K/s) to discretely reconstruct the crystallization kinetics.

3. Experimental results

3.1 Isothermal crystallization

An example of curves corresponding to the raw heat flux measured during the heating step following isothermal crystallization, obtained by varying the dwell time for a temperature of 220°C, is shown in Figure 3.

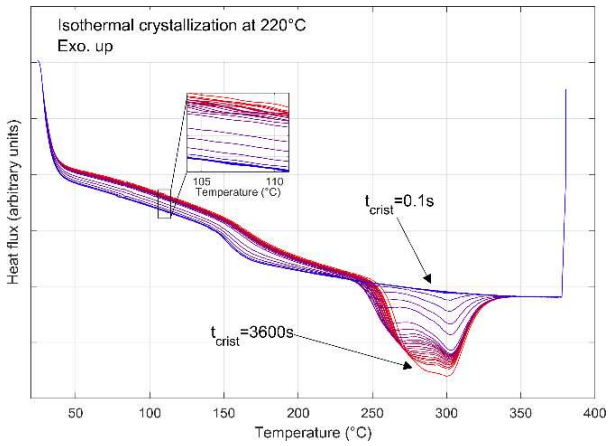

Figure 3 – Heat flux during heating following isothermal crystallization at 220°C varying dwell times

The curves show a marked transition near 160°C, corresponding to the glass transition of the amorphous phase, followed by a melting peak of variable amplitude depending on the duration of the isothermal crystallization stage. Two distinct melting peaks are apparent; this double melting phenomenon, classical for PEEK, corresponds to the melting of two crystal populations.

However, it has been shown in the literature that the peak corresponding to the higher melting temperature is due to a melt-recrystallization phenomenon during heating [5,6]: as soon as the crystalline phase starts to melt, the oriented chains can recrystallize into more stable lamellae. This phenomenon occurs continuously until recrystallization is no longer possible. Therefore, the method consisting in measuring the crystallization generated during the isothermal stage from the direct integration of the global melting peak is not directly applicable: this peak being the sum of the melting enthalpy associated to the crystals generated during the isotherm, and the melting/recrystallization enthalpy. Moreover, the phenomenon being continuous, the deconvolution of the melting peaks which would allow to consider only the enthalpy associated to the first peak is also not adapted.

To avoid the error associated with taking into account the melt-recrystallization, the direct measurement of the variation of the specific heat capacity of the sample is proposed. The heat capacity depends linearly on the crystallinity ratio α by equation (1), and the heat flux measured by calorimetry is proportional to the specific heat capacity (equation 2).

$$C_p^{tot}(\alpha, T) = (1-\alpha)C_p^{am.}(T) + \alpha C_p^{cr.}(T) \quad (1)$$

$$\phi = \frac{dH}{dt} = mC_p^{tot}\frac{dT}{dt} \quad (2)$$

The new approach is therefore to observe the variation of the heat flow φ measured by FSC during heating after isothermal crystallization as a function of the step time, and for a temperature below the glass transition temperature so as to prevent any modification of the crystalline structure. In practice the observed variation is averaged over the range 105°C - 110°C (see inset in Figure 3). Figure 4 shows the evolution of the relative crystallinity of the sample as a function of time, calculated with the two methods presented (integration of the global melting peak and variation of the specific heat capacity) and for plateau temperatures between 230°C and 290°C.

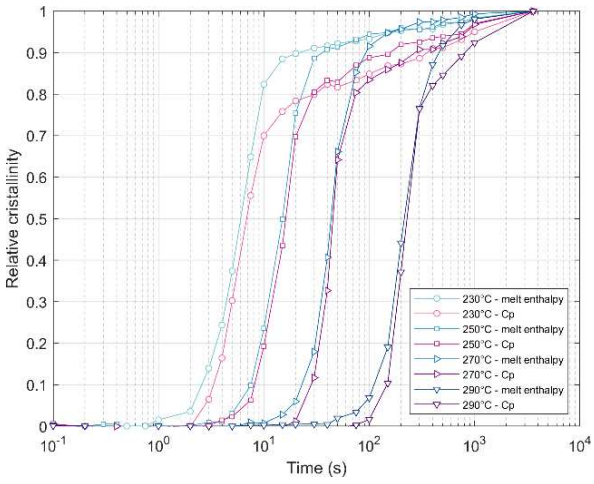

Figure 4 – Relative cristallinity evolution measured from the total melting enthalpy and specific heat capacity

The curves obtained (independently of the method) show at first a sigmoidal evolution of the crystallinity attributed to the primary crystallization, then a linear evolution with the logarithm of time attributed to the thickening of the crystalline lamellae (secondary crystallization). Both

  doi:10.5075/epfl-298799_978-2-9701614-0-0

approaches lead to equivalent half-crystallization times. The approach based on the direct integration of the melting peak leads to an overestimation of the crystallinity, associated with the enthalpy of fusion/recrystallization.

3.2 Non-isothermal crystallization

An example of curves corresponding to the raw heat flux measured during the heating step following non-isothermal crystallization, obtained by varying the temperature before quenching, is shown in Figure 5 for a cooling rate of 5K/s. We can observe in the same way as for the isothermal crystallization a double melting peak whose enthalpy increases with the decrease of the temperature before quenching.

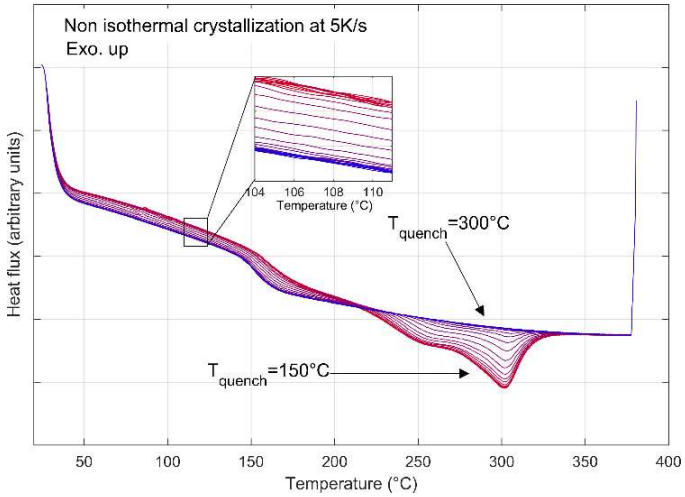

Figure 5 – Heat flux measured during heating after non-isothermal crystallisation at 5K/s interrupted at different temperatures

The double melting peak is also due to a melting/recrystallization phenomenon during heating. Therefore, the analysis of the crystallization kinetics is performed from the observation of the evolution of the specific heat as presented previously. The evolution of the maximum relative crystallinity under non-isothermal conditions is presented in Figure 7 as a function of the cooling rate. A marked decrease in crystallinity is observed for cooling rates above 10K/s with complete amorphization above 100K/s. This validates the choice of a cooling rate of 2000K/s in the protocol employed as adequate to quench the crystalline microstructure.

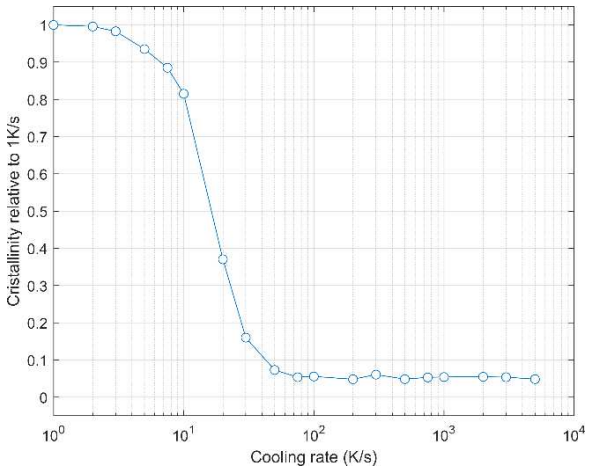

Figure 6 – Relative cristallinity as a function of cooling rate

The evolution of the specific heat capacity as a function of temperature for the different cooling rates evaluated shows a classical sigmoidal pattern of non-isothermal crystallization. The derivation of the curves allows to reconstruct the evolution of the endothermic heat flux related to the crystallization (Figure 7). The proposed experimental protocol thus allows to obtain the shape of the crystallization peak, which is not accessible in FSC by direct method, and this for cooling rates up to 5000 times higher than in DSC. We observe a decrease in the amplitude of the crystallization peak with the increase of the cooling rate, as well as a shift of the extremum towards lower temperatures: from 270°C at 0.5K/s to 220°C at 15K/s.

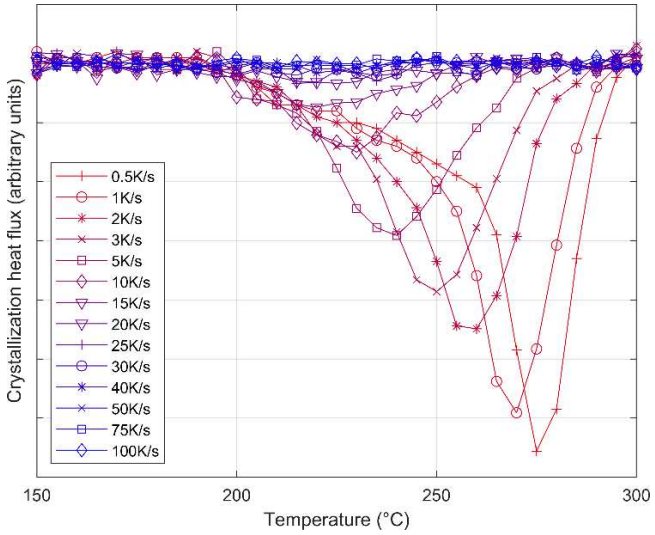

Figure 7 –Crystallization heat flux obtained from the stepwise method

This experimental campaign also allows to edit a CCT process diagram (continuous cooling transformation diagram, Figure 8) of PEEK, in a range of cooling rates corresponding to the industrial forming processes. This diagram makes it possible to determine the relative crystallinity of the material under non-isothermal conditions, and thus to define the adequate cooling rates according to the desired crystal structure. This graph shows that the crystallization phenomenon takes place mainly between 270°C and 200°C, temperature below which the molecular mobility is too limited. An analytical model to describe the non-isothermal crystallization kinetics of PEEK from the experimental results obtained remains to be developed.

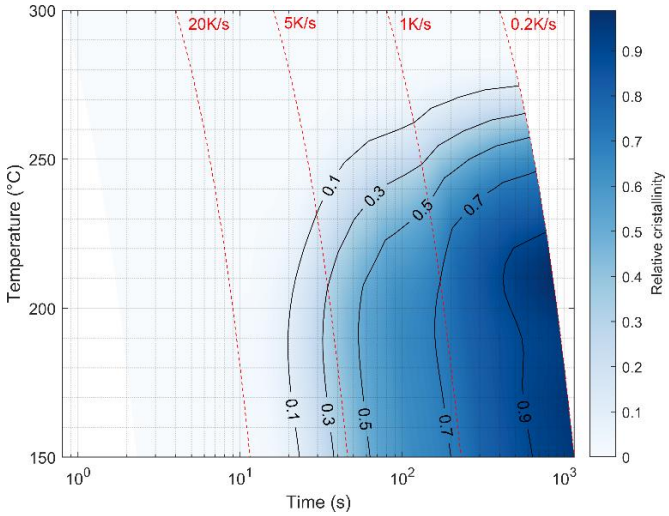

Figure 8 – CCT diagram of PEEK

4. Conclusion

This experimental work has allowed the characterization of isothermal and non-isothermal crystallization kinetics of PEEK by rapid differential scanning calorimetry. The protocol based on the analysis of interrupted crystallization tests allows to override the relatively slow crystallization mechanisms of the studied material. The use of the specific heat capacity as a measure of crystallinity also allows to avoid the error induced by taking into account melt-recrystallization phenomena when integrating the melt enthalpy.

Results obtained for isothermal crystallization show a secondary crystallization mechanism with a logarithmic evolution in time, attributed to lamellae thickening. Interrupted non-isothermal crystallization tests provide for the first time a description of the crystallization kinetics of PEEK in a range of cooling rates comparable to industrial processes. A model to describe the non-isothermal kinetics is under development. Moreover, the proposed experimental methodology is currently used to extend the study to the degradation of the material, in order to characterize the impact of thermo-oxidation phenomena on the ability of PEEK to crystallize.

5. References

1. J. Avenet, T. Cenders, S. Le Corre, J-L. Bailleul, A. Levy, Experimental correlation of rheological relaxation and interface healing times in welding thermoplastic PEKK composites, *Composites: Part A*., 149 (2021), 1064-1089.
2. C. Bas, P. Battesti, N. Albérola, Crystallization and melting behaviors of poly(aryletheretherketone) (PEEK) on origin of double melting peaks, Journal of Applied Polymer Science, 53-13(1994), 1745-1757.
3. P. Cebe, Non-isothermal crystallization of poly(etheretherketone) aromatic polymer composite, Polymer Composites, 9-4 (1988), 271-279
4. E. Bessard, O. De Almeida, G. Bernhart, Unified isothermal and non-isothermal modelling of neat PEEK crystallization, *Journal of Thermal Analysis and Calorimetry,* 115 (2014), 1669-1678
5. A. Toda, R. Androsch, C. Schick, Insights into polymer crystallization and melting from fast scanning chip calorimetry, *Polymer,* 91 (2016), 239-263
6. X. Tardif, B. Pignon, N. Boyard, J. Schmelzer, V. Sobotka, D. Delaunay, C. Schick, Experimental study of crystallization of PolyEtherEtherKetone (PEEK) over a large temperature range using a nano-calorimeter, *Polymer Testing*, 36 (2014), 10-19.
7. H. Marand, Z. Huang, Isothermal lamellar thickening in linear polyethylene: correlation between the evolution of the degree of crystallinity and the melting temperature, *Macromolecules*, 37 (2004), 6492-6497
8. J. Weeks, Melting temperature and change of lamellar thickness with time for bulk polyethylene, *Journal of Research of the National Bureau of Standards*, 67-5 (1963), 441-451.

Composites Meet Sustainability – Proceedings of the 20th European Conference on Composite Materials,
ECCM20. 26-30 June, 2022, Lausanne, Switzerland

Effect of dwell stage in the cure cycle on toughening of epoxy using thermoplastic multilayers

Ujala Farooq [*a], *Julie Teuwen* [a], *Clemens Dransfeld*[a]

[a] Faculty of Aerospace Engineering, Aerospace Manufacturing Technologies, Delft University of Technology, Kluyverweg 1, 2629 HS Delft, the Netherlands

[*]Corresponding author: U.Farooq @tudelft.nl

Abstract:

A second micro-phase (i.e. thermoplastic) can be added to epoxies to overcome their intrinsic brittleness. This addition of thermoplastics to epoxy resin results in reaction-induced phase separating morphologies in the micrometer range. In this paper, the influence of a two-dwell cure cycle on interphase formation, by hot stage microscopy experiments and final morphology, by scanning electron microscopy, of a poly(ether imide) (PEI) and high Tg epoxy system was investigated. The parameters changed in the cure cycle were the first dwell temperatures and first dwell times (up to the onset of phase separation (OPS) or up to the 80% degree of cure (80% DOC)). Especially at lower first dwell temperatures, the diffusion distance was higher in the OPS case compared to the 80% DOC case. This behavior was ascribed to the fact that, in the case of OPS, the epoxy polymer oligomers were still mobile and could diffuse further during the second dwell, while at 80% DOC, the epoxy cross-linked network was already bound but could still diffuse due to non-stoichiometric curing. The restricted mobility of the polymer chains for the 80% DOC case resulted in a larger part of a finer phase separated morphology, compared to the OPS case.

Keywords: Epoxy; Poly(ether imide) (PEI); Interphase formation; Curing cycle; Reaction induced phase separation

1. Introduction

Epoxies (EP) with high cross-linking densities are brittle and hence have a low fracture toughness. However, different methods are known to increase fracture toughness. Several approaches incorporate a second phase into the epoxy matrix, such as rubber, inorganic nanoparticles or thermoplastics [1]. In the case of thermoplastic (TP) tougheners, the second phase is created by diffusion and dissolution, followed by reaction induced phase separation, leading to a morphology in the micrometer range [2]. During the curing process, the liquid epoxy monomers diffuse into the glassy TP and partially swell or dissolve it, resulting in the diffusion of TP polymer chains into the epoxy resin. This inter-diffusion process tends to slow down and eventually stops after reaching the gel point due to the constrained mobility of the epoxy [3]. The inter-diffusion diffusion of the TS and TP components creates a concentration gradient in the interfacial region. The interfacial region, surrounded by the pure phases (epoxy and PEI), can be divided into three distinct regions, (1) infiltration layer, (2) gel layer, and (3) liquid layer. The liquid layer contains a diluted polymer solution with relatively free motions of entire polymer chains. The gel layer is a swollen polymer in a rubber-like state. In the infiltration layer, Fickian diffusion of the solvent molecules is observed. The epoxy penetration front between the gel and infiltration layer advances at a constant rate and this is usually referred to as case II diffusion

  doi:10.5075/epfl-298799_978-2-9701614-0-0

[4]. The proceeding reaction between the epoxy co-monomers eventually results in a reaction-induced phase separation leading to a gradient morphology [4], where epoxy rich droplets can be observed, reducing in size towards the pure TP.

Curing of epoxy-based composites is typically done by performing two dwell cure cycles. In literature, the effect of cure cycle parameters such as cure temperature and time on the interphase formation, final morphology of EP and TP systems for single dwell cure cycles has been researched. Harismendy et al. [5] reported an increase in droplet size with the increasing cure temperature (140, 160, 180°C) for an epoxy/PEI system. Bian et al. [6] showed that both cure temperature and cure conversion of epoxy resin influences the morphology spectrum of a epoxy/PEI system. Previously, it was assumed that the diffusion process stops at the onset of phase separation for a single dwell cure cycle [4]. Recently, Voleppe et al. [7] reported that the penetration front of thermoset seemed to continue beyond phase separation for an epoxy and polyethersulfone (PES) system using a single dwell cure cycle.

The influence of the cure cycle with varying dwell time/degree of cure at the first dwell, on the interphase dimension and final morphology for Poly(ether imide) (PEI)/EP systems, is not well understood. PEI could be a potential modifier for epoxy resins for aerospace applications due to its high glass transition temperature (217°C), good miscibility due to its amorphous state and compatibility with epoxy systems, enhanced rigidity, and strength at higher temperatures [8]. The research presented in this work aims to understand the interphase formation and morphology, to attain the desired droplet size and interphase morphology for improved material toughness. This aim is achieved by analyzing the influence of dwell time by considering two main cases for each selected first dwell temperature (120-180˚C): (i) wait until the onset of phase separation (OPS) before increasing the temperature to 200°C (second dwell), (ii) wait until 80% degree of cure (80% DOC) before the second dwell.

2. Methodology

2.1 Materials

A blend of TGMAP (Araldite MY 0610 CH), and bisphenol-F epoxy resin monomer (DGEBF, Araldite PY 306 CH) was used as the epoxy resin, while DDS (Aradur 9719-1) was used as a hardener, all supplied by Huntsman, Switzerland. The epoxy system is characteristic for aerospace composites prepregs with a cure temperature of 180°C. 60 µm thermoplastic PEI films (Ultem 1000) were provided by SABIC, Saudi Arabia.

2.2 Cure Cycle

To study the effect of first dwell time and temperature of two-dwell cure cycles, the first dwell times and temperatures (t_{dwell} and T_{dwell} resp.) were varied while the second dwell was kept constant during the experiments: 200°C for 20 min to reach full cure (Figure 1). The selection of the dwell temperatures and times was based on the cure kinetics model of the epoxy system

[2]. Two different first dwell times (t_{dwell}) corresponding to (1) onset of phase separation (OPS) and (2) 80% degree of cure (80%DOC), were selected for each investigated first dwell temperature: 120°C, 140°C, 160°C, or 180°C.

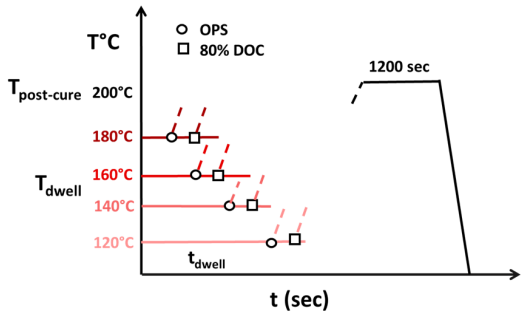

Figure 1. Representative two-dwell cure cycle used for experiments with variable first dwell time and temperature [9].

2.3 Hot stage experiments

Hot stage microscopic analysis was performed to observe the epoxy/PEI interphase formation during the cure cycle. The experimental setup used for hot stage analysis was described by [2]. A PEI film having 2-3 mm wide central slit was sandwiched between two cover glasses and was placed on a temperature-controlled microscope stage THMS600 (Linkam Scientific, UK). The reactive liquid epoxy was then injected into the slit region, where the resin drop immediately reached the specimen temperature by having contact with the hot stage and filled the slit by capillary forces. Upon resin contact with the hot stage, the selected cure cycle was started. An optical microscope (Keyence VHX-2000) was used to attain 30-second interval time-lapse allowing to observe the region of the epoxy/PEI interface.

2.4 Optical interphase analysis

To study the interphase and the morphology of the cured samples, scanning electron microscopy (SEM) (JEOL JSM-7500F, Germany), see Fig. 2a, and confocal laser scanning microscopy (CLSM) (Keyence 3D, VK-X1000) were used. Samples were first embedded in a fast-cure epoxy resin, then grinded and polished after which they were etched with N-Methyl-2-pyrrolidone for qualitative observation of the interphase morphologies.

2.5 Image Analysis

The micrographs obtained with SEM were further used to quantify the droplet sizes and their distribution. To obtain the droplet sizes from the images, the multi-stage thresholding and marker-based watershed image segmentation procedure was used using Weka - a machine learning segmentation tool in ImageJ. The Python packages (Scikit-Image, SciPy, Numpy, and matplotlib) and blob detection within OpenCV were used to calculate the droplet size across the interphase region (Fig. 2c).

  doi:10.5075/epfl-298799_978-2-9701614-0-0

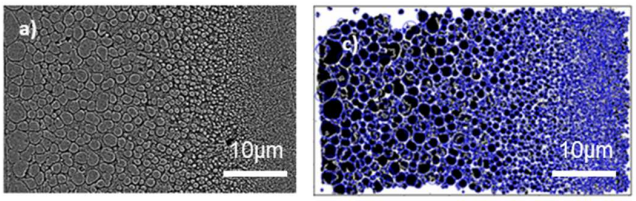

Figure 2. a) SEM image of sample at 180°C, c) blob detection from segmented image [9]

3. Results

3.1 Interphase formation

In Figure 3, the micrographs of a sample with a first dwell at 180°C for two different first dwell times are shown, at different stages during the cure cycle. Fig. 3a shows the presence of (1) a penetration front of epoxy in the PEI film, (2) a darker region close to the penetration front, consisting of swollen thermoplastic resulting from the dissolution of the epoxy monomers (i.e. gel layer) and (3) a clear interface between the gel layer and epoxy (PEI front), indicating the onset of phase separation [2]. Fig. 3a-c presents the evolution of the interphase region when the second dwell is started at the time of onset of phase separation (OPS case). It can be seen that both the epoxy and PEI front progress significantly over time during the second dwell, even beyond the onset of phase separation. Fig. 3d-f shows the evolution of the interphase region when the second dwell started after achieving 80% degree of cure (80% DOC case): in Figure 3d, the onset of phase separation is shown and in 3e-f the progression of the diffusion front, which is small compared to Figure 3b-c.

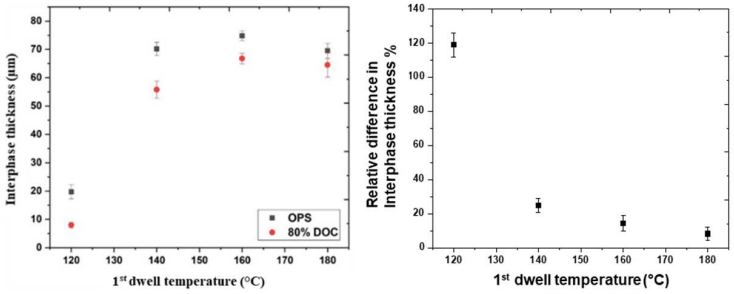

Figure 4. (left) final interphase thickness against first dwell cure temperature at different first dwell times. (right) Relative difference in final interphase thickness between OPS and 80% DOC first dwell times as a function of first dwell temperature [9].

In Figure 4 (left), the interphase thickness as a function of first dwell temperature is shown for both the OPS and 80% DOC case. The interphase thickness increases with first dwell temperature until 160°C for both cases, after which it slightly decreases for a first dwell temperature of 180°C. To evaluate the effect of both first dwell cure temperature and time on the interphase formation, the relative difference in interphase thickness between the two cases (OPS and 80% DOC) is plotted as a function of first dwell temperature, see Figure 4

(right), with 80% DOC as a reference. The results show that the relative difference in interphase thickness is higher at lower first dwell cure temperatures, that is ≤ 140°C.

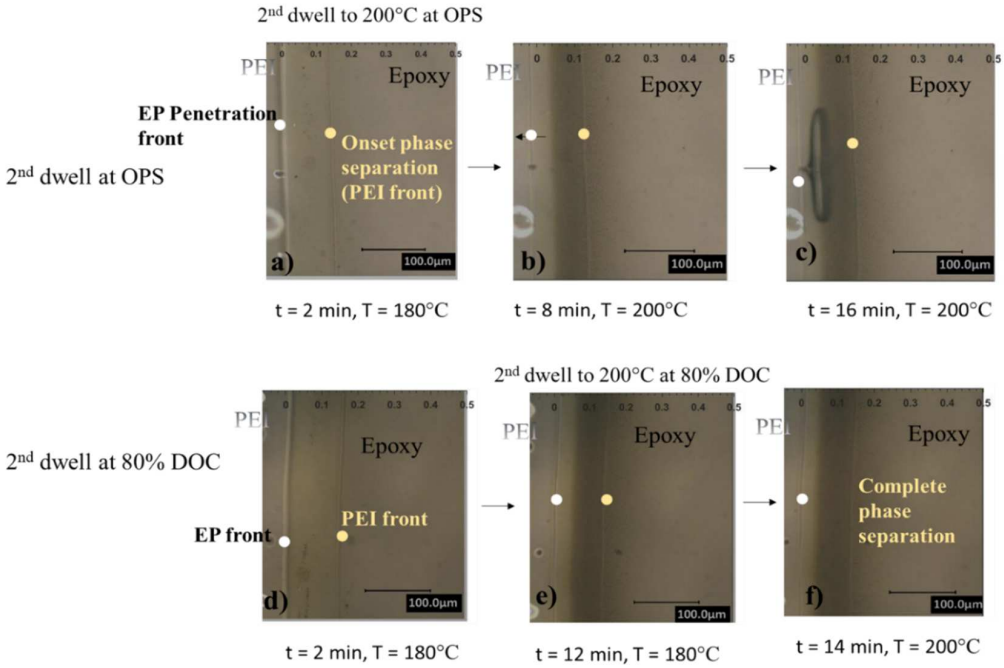

Figure 3. Optical micrographs for 180°C first dwell temperature; a) second dwell started just after OPS b, c) showing change in position of EP and PEI front through pointer. d,f) second dwell started after 80 % DOC (d) OPS, (e,f). showing change in position of EP and PEI front through pointer (the 0 mark is the initial interface between PEI and EP, the scale is in mm) [9].

3.2 Morphological analysis

For most cases studied, an epoxy/PEI biphasic region separated by a distinct interface of pure epoxy (left) and pure PEI (right) was observed, see Figure 5a and 5c-f. Close to the pure epoxy interface, the epoxy/PEI biphasic morphology was described by epoxy-rich droplets dispersed in a PEI matrix, i.e. phase-inverted morphology [2]. The phase inversion occurs due to a viscoelastic phase separation phenomenon, also observed for other epoxy/thermoplastic blends [10]. The epoxy droplet size and frequency is shown as a function of the position along the interphase in Fig. 5 for the different cure cycles. The size of these epoxy droplets was observed to decrease gradually towards the pure PEI region, due to the increase in PEI content. The droplet size close to the epoxy interface increased as a function of first dwell cure temperature until 160°C. Additionally, the frequency of smaller droplets was higher in the case of 80% DOC as compared to the OPS (see for instance Fig. 5e and 5f).At a first dwell temperature of 120°C, with 80% DOC, (Fig. 5b), no gradient morphology was observed but rather a narrow droplet size distribution.

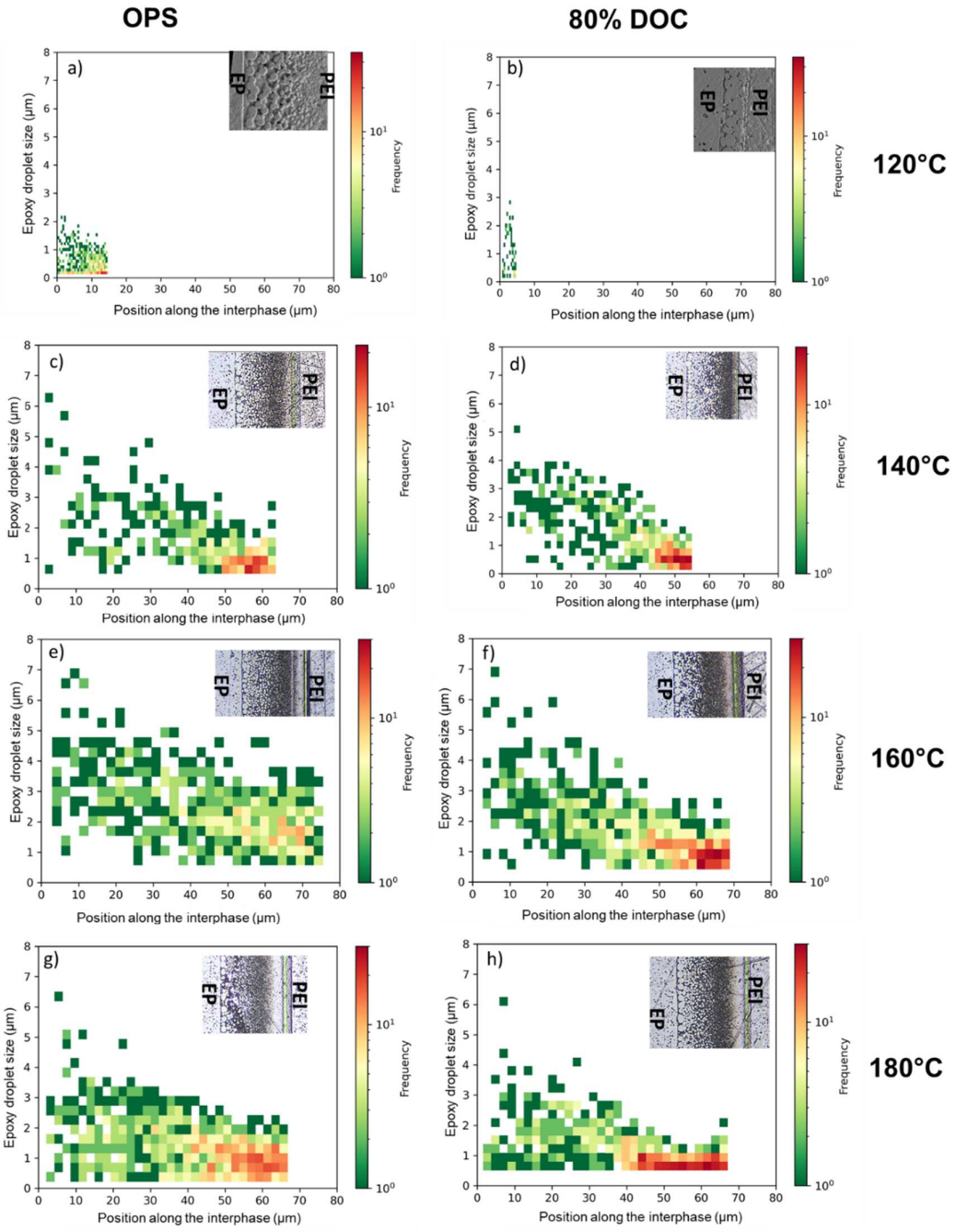

Figure 5. The epoxy droplet size histograms plotted as a function of position along the interphase (0 = pure EP) for samples cured until OPS or 80% DOC at different first T_{dwell} [9].

4. Discussion

Figure 3 showed higher diffusion distances in the OPS case which may be attributed to the fact that the gel point was not attained in the OPS case resulting in a higher diffusivity. The degree of cure ranged from 0.15 to 0.36 for the OPS cases while the gelation point was estimated to

be at a degree of cure of 0.43 (based on Flory–Stockmayer). Therefore the epoxy polymer chains are still in a mobile state and can diffuse further during the second dwell phase [6]. At 80% DOC however, the degree of cure was beyond gelation, and therefore the epoxy network should be completely bound due to infinite molecular weight. Nonetheless a considerable diffusion distance was still observed for the 80% DOC case. Due to the different diffusion speeds of three constituents of the epoxy system, demixing and/or non-stoichiometric curing may take place, which was more prominent at higher first dwell temperatures. This could imply that at the diffusion front, the reaction rates predicted from the reaction kinetic model are inaccurate: a slower reaction between epoxy monomers seems to take place, resulting in a longer mobility and diffusion time, even after achieving the nominal gel point.

An increase in interphase thickness with increasing first dwell temperature (Fig. 4 left) can be explained by the competition between the rate of phase separation and curing rate. When the phase separation rate is higher than the curing rate, the interphase thickness is primarily controlled by the rate of phase separation (i.e. first dwell temperatures ≤ 160°C) and vice versa for first dwell temperature greater than 160°C [2]. A similar trend of increase and then decrease in interphase thickness as a function of increasing first dwell temperature was observed for DGEBA epoxy toughened with polysiloxanes [11]. The authors attributed this behavior to the chemical reaction, coalescence, and inter-diffusion of DGEBA and polysiloxanes. The high relative difference in interphase thickness between OPS and 80% DOC (Fig. 4 right) at lower first dwell temperature shows the higher diffusion/dissolution of polymeric chains by starting second dwell at OPS for lower first dwell temperatures. These results indicate that, both first dwell temperature and time (i.e. OPS and 80% DOC) influence the interphase thickness, especially at lower first dwell temperatures.

When looking at the morphology, influence of both first dwell temperature and time was seen. The absence of gradient morphology at 120°C (Fig. 5b) suggests that there is no concentration gradient, indicating the occurrence of case II diffusion for shorter diffusion lengths. At higher first dwell temperatures, a clear concentration gradient was seen (Fig. 5c-f), indicating a mixed-mode between case I and case II diffusion. The droplet size in the vicinity of pure epoxy increased for increasing first dwell temperatures until 160°C (Fig. 5), possibly caused by higher mobility of polymeric chains at the start of the second dwell, favoring a longer growth phase after nucleation. The frequency of smaller droplets increased in the case of 80% DOC (compared to OPS), which may be linked to the restricted mobility of the polymer chains after gelation, eventually preventing growth of particles and resulting in smaller droplets [9]. This hypothesis was further verified by the absence of smaller droplets at 120°C for 80% DOC case.

5. Conclusions

The main objective of this work was to study the effect of dwell time and temperature in the first dwell on the droplet size formation and interphase morphology. Hot stage microscopy experiments showed that the epoxy and PEI diffusion fronts continued to progress, even after the onset of phase separation. The diffusion distance was higher in the case of OPS, compared to the 80% DOC case, especially at lower first dwell temperatures, resulting in a larger interphase region. The interphase thickness increased with first dwell temperature until 160˚C for both cases, after which it slightly decreased for a first dwell temperature of 180˚C. Furthermore, the size of bigger droplets near the pure epoxy region was mainly controlled by dwell temperature, while the frequency of smaller droplets was controlled by dwell time. A higher interphase thickness was obtained for the OPS case while a larger number of smaller particles were observed for 80% DOC. Therefore, the influence of both interphase thickness and droplet size on fracture toughness will be investigated in the future. This work highlights the importance of the curing process beyond phase separation to control interphase dimension and morphology.

6. References

1. Deng, S et al. Thermoplastic–epoxy interactions and their potential applications in joining composite structures–A review. Composites Part A: Applied Science and Manufacturing (2015), 68, 121-132
2. Teuwen J. et al., Gradient interphases between high-Tg epoxy and polyetherimide for advanced joining processes, in: 18th European Conference on Composite Materials (2018)
3. Vandi, L et al. Interface diffusion and morphology of aerospace grade epoxy co-cured with thermoplastic polymers. In Proceedings of 28th Intl Congress of the Aeronautical Sciences (2012)
4. Lestriez, B et al. Gradient interphase between reactive epoxy and glassy thermoplastic from dissolution process, reaction kinetics, and phase separation thermodynamics. Macromolecules (2001), 34
5. Harismendy, I et al. Dicyanate ester–polyetherimide semi-interpenetrating polymer networks. II. Effects of morphology on the fracture toughness and mechanical properties. Journal of Applied polymer science (2001), 80, 2759-2767
6. Bian, D et al. Interlaminar toughening of GFRP—part i: Bonding improvement through diffusion and precipitation. Journal of Manufacturing Science and Engineering (2017), 139
7. Voleppe, Q et al. Interdiffusion and phase separation upon curing in thermoset-thermoplastic interphases unravelled by the characterization of partially cured systems. Polymer (2016), 106, 120-127
8. Farooq, U; Teuwen, J.; Dransfeld, C. Toughening of Epoxy Systems with Interpenetrating Polymer Network (IPN): A Review. Polymers (2020), 12, 1908
9. Farooq, U. et al. Effect of a Dwell Stage in the Cure Cycle on the Interphase Formation in a PEI/High Tg Epoxy System, ACS Applied Polymer Materials (2022) 3 (12), 6111-6119
10. Surendran, A. et al. An overview of viscoelastic phase separation in epoxy based blends. Soft matter (2020), 16, 3363-3377
11. Cabanelas, J.et al. Confocal microscopy study of phase morphology evolution in epoxy/polysiloxane thermosets. Polymer (2005), 46, 6633-6639

UPSCALING OF IN-SITU AUTOMATED FIBER PLACEMENT WITH LM-PAEK – FROM PANEL TO FUSELAGE

Dominik Deden[a], Lars Brandt[a], Olivia Hellbach[a] & Frederic Fischer[a]

a: German Aerospace Center (DLR) Augsburg – Center for Production Technology (ZLP)
dominik.deden@dlr.de web Page: www.DLR.de/zlp

Abstract: *The application of thermoplastic CFRPs in large aerospace components enables a modern and differential approach to Aircraft manufacturing. Most importantly the opportunity of dust-free joining of components by means of thermoplastic welding technologies allow subassemblies to be pre-equipped with system and cabin elements that are then subsequently joined. The Institute for Structures and Design of the German Aerospace Center (DLR) has been working on in-situ Automated Fiber Placement (AFP) with different thermoplastic matrix materials with the goal to develop a suitable single stage manufacturing process for thermoplastic CFRPs. Different aspects of the scale-up were investigated including the overall ply design, manufacturability of complex areas of a fuselage, first ply adhesion, and the overall laminate quality with regard to weldability. The manufacturing of a test shell with 4 m diameter is presented in this work. It identified key areas of the process that require further refinement in order to assure manufacturability and weldability of AFP-produced parts. Using the results, a holistic approach to the manufacturing process is proposed for the direct manufacturing of large-scale components made with the in-situ AFP Process.*

Keywords: In-Situ AFP, Thermoplastic AFP, Full-Scale Demonstrator, Lightning Strike Protection, Aircraft Fuselage

1. Introduction

In recent years the development of thermoplastic in-situ AFP (T-AFP) process as a slim single stage production method for carbon fiber reinforced plastics (CFRPs) has been a focus of the Center for Lightweight Production Technology (ZLP) in Augsburg. Such a process is seen as an enabler towards the utilization of thermoplastic CFRPs in Aeronautics. Especially the omission of size limitations caused by ovens or autoclaves as well as the possibility of pre-equipping and dust-free joining of the differential designs make in-situ AFP a very promising process if mechanical performance and the scaling of the process can be demonstrated. The mechanical performance has been shown in the past on coupon level [1,2].

Upscaling of the process to manufacture a full-scale fuselage skin results in specific challenges: the composite design for TAFP has to be established, first ply adhesion and lightning strike protection integration has to be managed and a suitable machine layup for large component production has to be established. This paper provides a comprehensive overview on how these problems can be solved, shows specific experiments and results that have been conducted to solve these issues and indicates areas where additional work has to be investigated to upscale T-AFP.

  doi:10.5075/epfl-298799_978-2-9701614-0-0

2. Demonstrator Design

The design of AFP components is largely influenced by the existing and applied principles from the production of thermoset prepreg AFP components. Parts are designed to the nominal width and height of the prepreg tapes. Overlapping material and resin pockets that form in areas of wide gaps or missing tows are considered defects that weaken the AFP laminate [3]. One tool used to meet geometric requirements are defined gaps that are tolerated within certain limits dependent on the given component and material. Due to the downstream autoclave process necessary when using thermoset prepregs small gaps are filled with resin, resulting in a smooth laminate. Since this is not viable for an in-situ AFP process due to its transience, process specific design principles need to be defined. Viable design strategies must manage the gaps. On a process side this can only be achieved if either the process or the material is adjusted to a predetermined width. From a design perspective the two most effective measures are the inclusion of planned gaps or the adjustment of the ply geometry.

2.1 Design to Manufacture for in-situ T-AFP

The most important difference between the thermoset prepreg AFP and the thermoplastic in-situ AFP with regards to the design is the width of a single placed tape. With the in-situ process it is not feasible to calculate laminates based on the nominal width of the prepreg material. The material will be flattened due to resin flow and fiber movement and thus widened by the process itself. This behavior is highly dependent on the process parameters as well as the quality of the prepreg material. Apart from the material and process, the specific hardware and its attributes can limit the freedom of design. The design principles for in-situ AFP are as follows:

A consolidated tow width must be determined for a given set of process parameters and materials. The strategy for the lay-up is a zero gap/overlap strategy. Any deviation from a gap- and overlap-free lay-up will cause a noticeably grooved laminate as depicted in Figure 1. The grooves are visible through multiple layers and are not smoothed by consecutive layers.

Figure 1 : Grooved laminate due to insufficient gap sizes placed with in-situ T-AFP

The design is constrained in size to multiples of the consolidated tape width (CTW) perpendicular to the lay-up direction. Conclusively, it is not possible to design the transition between patches in ramps with consistent step sizes. This is not a problem for the performance of the laminate but is a significant difference to traditional AFP design. In order to maximize the design freedom despite this constraint it is desirable to have a standard CTW which is as small as possible. Consequently, the capability to drop tows and place single tapes is beneficial in order to realize intricate laminate designs for T-AFP. The design and the hardware are therefore codependent. This is also the case for the minimum length of track that can be placed. The minimum cut length

(MCL) determines the minimal size of single plies and the amount of excess material in the corners. It is therefore a crucial measurement for the design. Both CTW and MCL need to be defined for a certain set of process parameters, materials and the given hardware before the design can be tailored to the process.

2.2 Definition of Process limits for the Design

The MCL is machine specific. There will always be a free length between the nip-point and the point where the tape is cut. For the MTLH this length is approximately 125 mm. The MCL that can be placed with the MTLH at acceptable quality is 150 mm.
The CTW was experimentally determined for the TC1225 LM-PAEK at 125 mm/s lay-up speed and 500 °C control temperature. Three tapes in parallel were placed in two layers. The width was measured at 41.2 mm. Then multiple tracks with distances of 41.1 mmm, 41.2 mm, 41.3 mm and 41.4 mm were placed alongside each other and gaps and overlaps were measured. The results showed that 41.3 mm is the ideal CTW for the given operating point resulting in a smooth butt joint between tracks. The CTW was confirmed by the placement of full laminates with high lay-up quality.

2.3 Final Design

The final design of the test shell is shown in Figure 2. The overall height is 2270 mm, the width measures 3950 mm and the radius of the half shell is 1930 mm. The layer structure consists of 98 plies in total with fiber direction angles auf 0°, 45°, 90° and 135°. Besides the full-covering and partly covering layers covering the manufacturing edge of part (MEOP) there are three distinct reinforcement features: On the left side there is the octagonal antenna patch consisting of eight individual layers of all fiber angles, which will be placed with a gap/overlap strategy of dispersed gaps. On the right side there is a rectangular reinforcement consisting only of 0° and 90° layers. Finally, there is the octagonal center reinforcement with 34 individual layers which resembles the reinforcement of a door corner.

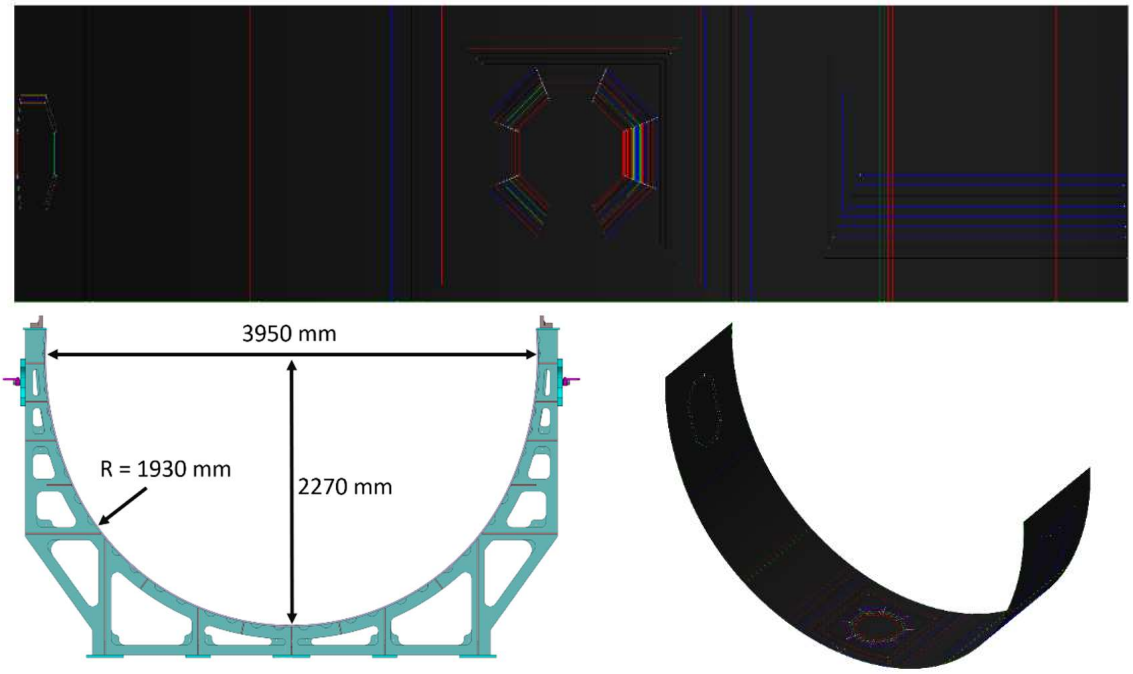

Figure 2 : Final design of the test shell – Measurements (bottom left) and two CAD views

  doi:10.5075/epfl-298799_978-2-9701614-0-0

Both octagonal reinforcements are designed with a 1:20 ramp angle. The rectangular reinforcement on the right is designed with a shallow ramp of 1:200 inclination. All features are designed like a real aircraft fuselage with the goal of a subsequent welding of support structures like stringers and frames. Except for the antenna patch all plies are done in an interleaved design, which is in accordance with typical CFRP fuselage designs. The antenna patch is placed on top of the last fully covering layer. This has been done to investigate a potential differential approach in which the reinforcement patches can be placed after the much larger covering layers – which are also more time consuming in production – are placed. The design consists of 9986.2 m of tape placed in 98 individual plies. The estimated weight is 38 kg.

3. First Ply Adhesion

A first ply adhesion is necessary for the process since there is no direct adhesion between a metal mold and the thermoplastic tapes. Therefore, an additional layer is necessary that is temporarily fixed to the mold and that allows a bonding of the placed tapes in order to transmit forces between the mold and the laminate. The bind between the adhesion layer and the tape can be a temporary or permanent.

3.1 Materials

A typical material used as a first layer between the mold and thermoplastic lay-up is polyimide. On the one hand polyimide has a sufficient temperature range of up to 400°C. On the other hand, polyimide forms a temporary bond with the LM-PAEK material which can be separated by mechanical force. Scaling has also been demonstrated before [4]. The polyimide film used in this study is 200HN Kapton from Dupont with a thickness of 50 µm. Another material used by the ZLP in the past is a pristine resin layer for first layer adhesion. The concept was proven for male tooling geometries such as pressure vessels. The pristine resin foil should be the same material as the placed tape. In this case VICTREX 150 LM-PAEK with a thickness of 60 µm. A major drawback however is the additional weight of the added layer, since it does not contribute significantly to the overall mechanical performance [5].
Thus, an adhesion layer that is also functional is desirable. In CFRP fuselages such as the Airbus A350 a lightning strike protection (LSP) layer is vital and is currently placed manually by trained workers [6]. An LSP layer consists of a copper mesh embedded in a matrix foil. Therefore, using LSP as a first adhesion layer dismisses the need for an additional process step altogether. Two different LSP versions were available to the DLR – a version with pristine resin and a blackened version.

3.2 Fixation Methods

The fixation of the laminate needs to transmit forces to the mold, thus ensuring the accurate position of the laminate throughout the entire manufacturing process. Easy demolding of the finished part is also a requirement for the fixation method that needs to be addressed. A vacuum strategy is generally suited for this purpose, but considering the size of the mold and the scale up the application is work intensive and prone to leakage. Thus, an alternative method of fixation using double sided adhesive tape certified for CFRP production is considered. This method has shown decent results on male tooling geometries in the past [5].

3.3 Experiments and Results

A first ply adhesion layer was set up on a planar lay-up surface with different combinations of material and fixation methods. Afterwards at least five tracks of 800 mm length were placed next to each other for four layers – totaling to at least 20 tracks per lay-up. The results were compared after the first and the last layer. Double-sided adhesive tape works well for male tooling geometries but proofed unsuitable for planar or female molds. Wrinkles occurred at the end of the track or at splices of the adhesion layer. This was observed for all materials and can be seen in Figure 3. The wrinkles show that material has been displaced by the process forces and the first layer needs to be fixed over its entire surface.

Figure 3: Wrinkles at the end of tracks caused by displacement of material

A vacuum setup is the most feasible approach and was tested for all materials. A breather layer that distributes the vacuum evenly is necessary for all investigated materials. This will cause the laminate to have a textured surface on the outside.

Table 1 : Performance of different adhesion layer materials

Material	Pro	Contra
Dupont 200HN Kapton	▪ Good lay-up quality ▪ Temporary bond	▪ No temperature control in first ply
VICTREX 150 LM-PAEK	▪ Good lay-up quality ▪ Comparably cheap	▪ No temperature control in first ply ▪ Prone to rupture at edged during process ▪ Additional weight without further advantage
LM-PAEK/LSP	▪ Good lay-up quality ▪ Additional functional layer enhances overall process ▪ Temperature control of first ply if blackened	▪ No temperature control in first ply ▪ Stiff and hard to handle for vacuum setup ▪ Limited size impedes scale up ▪ Material still in development

The trials showed that all materials are suited for the process. An overview of pros and contras for each material is given in *Table 1*. Due to the most logical benefits for the overall production of large fuselage panels the blackened LSP was chosen for the demonstrator.

  doi:10.5075/epfl-298799_978-2-9701614-0-0

3.4 Scaled LSP First Ply

The first step of production is the application of the adhesive layer. One major difference is the necessity for splicing two sheets of the LSP foil in order to cover the entire part with one vacuum system. The splice is done with Kapton adhesive tape which faces the mold. The vacuum connectors towards the pump are located on both sides of the mold at the top edges of the MEOP as well as at the bottom of the mold. In order to secure leakage from the vacuum the LSP was double sealed towards the mold – one seal with double sided adhesive encircling the MEOP and in addition a Kapton adhesive band on all edges. The stacking of the entire vacuum setup is displayed in Figure 4. Using this setup, the vacuum was successfully kept under 50 mBar over the entire production time. However, an optimized distribution of connectors for the vacuum pump is necessary for larger parts.

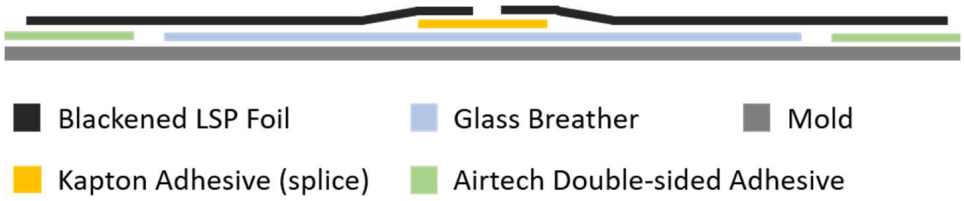

Figure 4 : Stacking of the vacuum fixed adhesive layer

4. Full Scale T-AFP Manufacturing

The design presented in 2.3 was placed on the LSP adhesive layers with the T-AFP process. Used machinery and the results of the manufacturing process are discussed in the following.

4.1 Machine Setup

The manufacturing of the test shell was done with a Multi Tow Lay-up Head (MTLH) by AFPT mounted on a KUKA Quantec KR120 R2700 extra HA industrial articulated robot. The robot is mounted on an additional linear drive. The MTLH places three ½" tapes in parallel. Its heat source is a 6.6 kW pulsed diode IR laser emitting a wavelength of 1090 nm. The lay-up speed of the process is 125 mm/s. The Tooling used for the layup is made from invar steel. The MTLH and the entire setup is depicted in Figure 5.

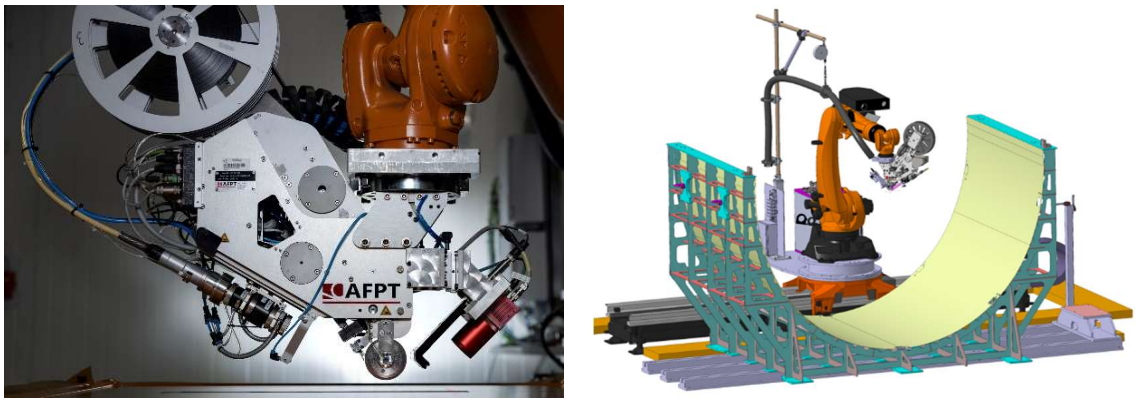

Figure 5 : Machine setup - MTLH AFP endeffector (left) & CAD layout of the robotic cell (right)

The offline Programming of the robot is done using the software 'Vericut Composite Programming' (VCP) from CGTech.

  doi:10.5075/epfl-298799_978-2-9701614-0-0 published under CC BY-NC 4.0 license

4.2 Machine Lay-up

The lay-up worked well at a process speed of 125 mm/s. The maximum deployment rate at this speed is 5 kg/h and is therefore relatively low especially compared to industry standard thermoset AFP where process speeds reach over 1500 mm/s. The transfer of the zero gap/overlap strategy worked well from panel to the large mold. The result of the first ply is shown in *Figure 6* (top left). The result was a smooth surface without noticeable wrinkles.

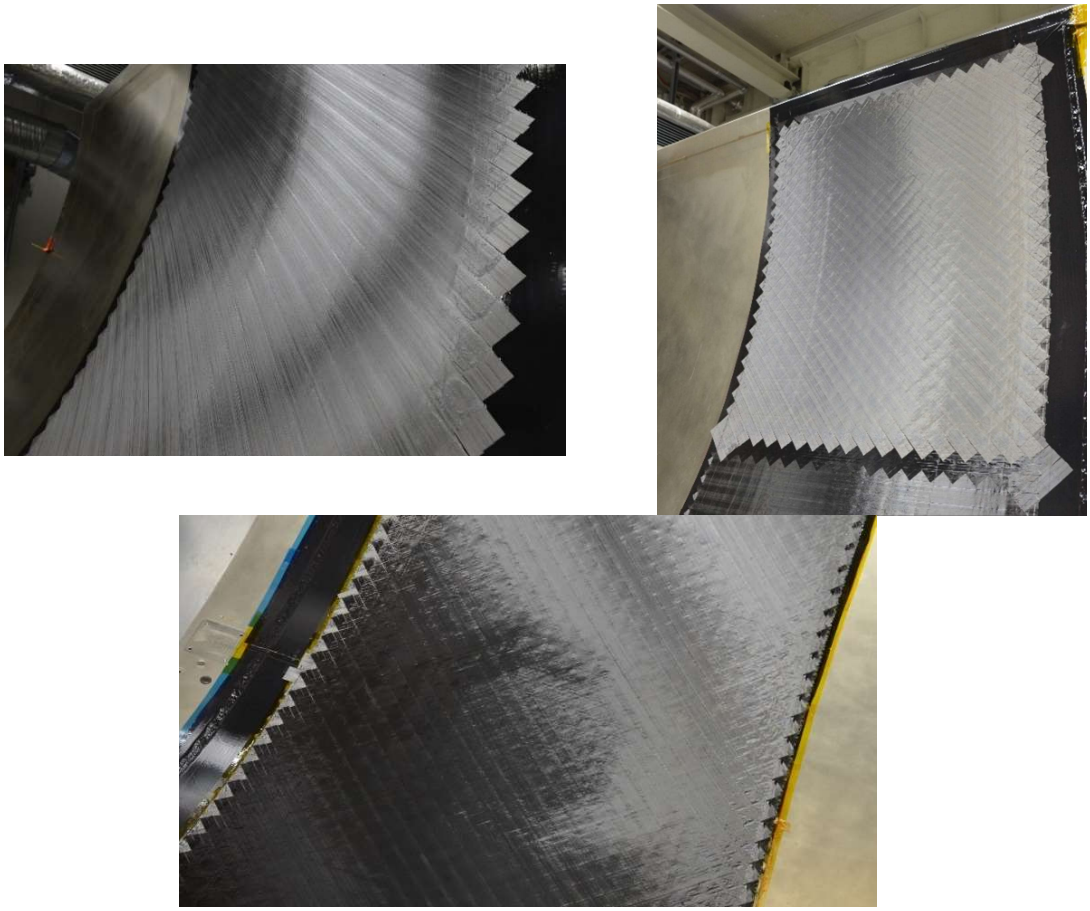

Figure 6 : Examples of laminate quality after plies 1 (top left), 22 (top right) and 98 (bottom)

The quality of the lay-up and the surface quality was found to be good for the first layer as well as consecutive layers. This was observed for the entire part. Even at the thickest area of the test shell – the octagonal door corner support with 70 layers – the lay-up quality was good on visible inspection Figure 6 (bottom). Thus, the proposed design principle for zero gaps and overlaps is successful for the in-situ T-AFP process. The second design strategy of dispersed gaps was applied to the final reinforcement layer. The resulting surface quality after eight placed layers is rough. Since staying within the designed boundaries of a ply is the main focus of this placement strategy, additional staggering cannot be implemented. The combination of defined gaps and no staggering results in a laminate which is holey for several layers down. Figure 7 shows the final result of the antenna patch. The difference in layup quality is apparent compared to the first lay-up strategy. The rough laminate quality is also impacting the overall process due to overheating in the trenches resulting in an inhomogeneous temperature measurement via thermal imaging. This is not acceptable for the internal power control loop which relies on the observed temperature to adjust the laser power.

  doi:10.5075/epfl-298799_978-2-9701614-0-0

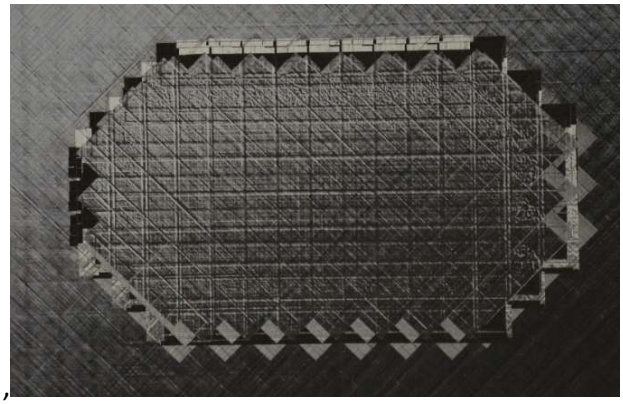

Figure 7 : Antenna patch placed on top of the laminate with dispersed gaps

There were two major problems regarding the scale up. Firstly, the staggering of plies caused issues with the lay-up. Secondly, the durability of the compaction rollers made from silicone is problematic for a smooth flow in production.

The staggering was done in steps of ⅕ of the tape width. Thus, after five consecutive staggering steps placement started from the initial position relative to the edges. This however led to issues with tape placed on a slant with at least one of the tapes not in contact with the laminate. The main defect caused by this was bridging of the tapes in 90° tracks. This can be easily avoided if staggering is done in only one direction over the entire laminate.

Two different silicones have been used in the past as compaction rollers for the T-AFP process. Both silicones were recommended by the machine manufacturer for use with the MTLH. Sylgard 184 from DOW with a shore hardness of 43 A and SF45 a casting silicone with a shore hardness of 45 A. The MTLH has a cooled compaction roller with a silicone cover. Since the silicone is a thermal isolator it heats up from the process significantly and despite the active cooling from its inside. The accumulated heat and the resulting residual temperature are therefore directly linked to the length of placed tracks and the duration respectively. The temperature of the silicone was not constantly monitored, however the thermal camera measured temperatures of up to 230 °C during the production. The longest tracks had a length of 6500 mm. The two silicones started to disintegrate after approximately 180 m (Sylgard 184) and 350 - 450 m (SF45) respectively. After this operating length the silicone covers became increasingly brittle and showed visible cracks. The Sylgard 184 silicone lost material debris if used further, which contaminated the laminate. Further, once the silicone becomes dull and brittle the process leaves a mark on the placed material and the placed surface is noticeably dull. Therefore, a regular change of silicone roller is essential.

Figure 8: Degraded silicone covers: Sylgard 184 after 170 m (left) & SF45 after 450 m (right)

  doi:10.5075/epfl-298799_978-2-9701614-0-0

4.3 Lessons Learned

The successful placement of the entire test shell helped to understand the dynamic of the scale-up of a part manufactured with T-AFP. Specific actions for the overall process can be derived from the result.

First Ply Adhesive Layer
Beginning with the build-up of the adhesive layer there are three major points of improvement. The quality of the LSP foil needs to be increased. Splicing of the foils needs to be refined with a focus on vacuum tightness. Lastly, more vacuum connection points are needed for an even distribution of the vacuum and thus a secure fixation of the laminate within the mold.

Silicone Compaction Roller
The durability of current rollers is not acceptable for a large-scale production. High temperatures caused by long tracks accelerate the decay of the silicone. There are several actions that can mitigate the problem. Another silicone which is more durable and heat resistant can be used for the compaction unit. In addition, the geometry of the silicon can be adapted for a better heat transfer (e.g. thinner silicone layer). Last, the heat flux of the cooling system can be significantly increased to further cool and thus preserve the silicon layer.

Design
A design with dispersed gaps planned over a fixed geometry of a ply is not feasible for in-situ T-AFP. Further, the stacking needs to be planned in a way, that the direction of the staggering is always the same in order to prohibit edges on which the endeffector cannot deploy material without noticeable defects.

5. Conclusion & Outlook

A total of 9986.2 m of LM-PAEK tape in 98 plies were placed to build the half shell demonstrator with in-situ T-AFP. The lay-up was done on a functional LSP layer. The scaling of the LSP adhesive layer for larger parts will require an improved slicing of the individual sheets. The deployment of tape with zero gap and overlap strategy resulted in a smooth surface and laminate of high quality. The design of the laminate needs to be suited to the specific consolidated tape width of the used material. This may limit certain designs in the future. The biggest issues of the process with regards to scale-up are frequent material changes and a high degradation rate of the compaction rollers made from silicone. This will cause down times and ultimately limit productivity. Increased cooling of the compaction roller as well as alternative silicones with better heat resistance will be investigated for improvement. In general, the T-AFP process has proofed to be scalable to large components. With a maximum deployment rate of 5 kg/h at current process speeds the productivity is relatively low. However, due to the slim single stage process, manufacturing times can be viable – especially if additional measures such as deployment of more tape in parallel are taken. Investigation of laminate quality at higher speeds are ongoing. The next step for the test shell is the integration of stiffeners by means of ultrasonic and resistance welding. A larger demonstrator with 8 m length is planned to be built in summer 2022 which will demonstrate the improved process on an even larger fuselage with more complex features such as a fully reinforced door surround and stepped longitudinal edges for the joining of two shells.

  doi:10.5075/epfl-298799_978-2-9701614-0-0

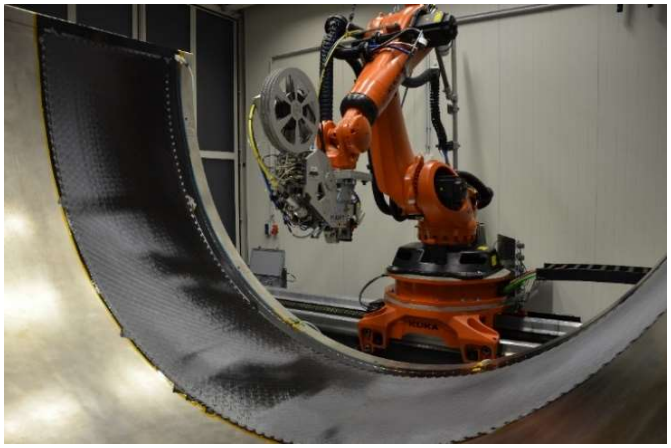

Figure 9 : In-situ AFP-manufactured half-shell in the DLR facility in Augsburg

Acknowledgements

This project has received funding from the Clean Sky 2 Joint Undertaking (JU) under grant agreement No 945583. The JU receives support from the European Union's Horizon 2020 research and innovation program and the Clean Sky 2 JU members other than the Union.

Disclaimer

References

[1] I. Schiel, L. Raps, A.R. Chadwick, I. Schmidt, M. Simone, and S. Nowotny, "An investigation of in-situ AFP process parameters using CF/LM-PAEK," *Advanced Manufacturing: Polymer & Composites Science*, Oct. 2020, pp. 1–7.

[2] L. Raps, A.R. Chadwick, I. Schiel, and I. Schmidt, "CF/LM-PAEK: Characterisation and sensitivity to critical process parameters for automated fibre placement," *Composite Structures*, vol. 284, Mar. 2022, p. 115087.

[3] A. Brasington, C. Sacco, J. Halbritter, R. Wehbe, and R. Harik, "Automated fiber placement: A review of history, current technologies, and future paths forward," *Composites Part C: Open Access*, vol. 6, Oct. 2021, p. 100182.

[4] Netherlands Aerospace Centre Press Release, "NLRs stunning project departs for next generation composite planes," Jun. 2021.

[5] L. Brandt, D. Deden, F. Bruckner, M. Engelschall, M. Mayer, A. Schuster, D. Nieberl, C. Frommel, F. Krebs, S. Jarka, F. Fischer, and L. Larsen, "Development of a Lean Production Process for a Thermoplastic Composite Upper Stage Propellant Tank," *SAMPE Europe 2020 Conference Proceedings*, 2020.

[6] C. Nguyen, A. Kolbe, and C. Bäns, "Application of Lightning Strike Protection on Thermoplastic Structures by Automated Fiber Placement," *ITHC 2020 Conference Proceedings*, 2020.

COMPARING MEASUREMENT TECHNIQUES FOR THE CHARACTERISTICS OF LAY-UP DEFECTS IN THE AFP PROCESS USING 3D LASER SENSOR DATA

Fabian Diemar[a], Marc Klingenberg Campoy[a], Benno Böckl[a], Klaus Drechsler[a]
a: Chair of Carbon Composites, Department of Aerospace and Geodesy, TUM School of Engineering and Design, Technical University of Munich, Boltzmannstraße 15, 85748 Garching, Germany
Email: fabian.diemar@tum.de

Abstract: *Automated Fiber Placement is a fully established process that is widely used for the serial production of aerospace parts. However, the process still offers high potentials in terms of automation and digitization. This is especially the case for the automated quality inspection. This paper presents an approach for a precise measurement of the size and the position of lay-up defects such as gaps and overlaps. In order to acquire the necessary data of the surface, thermoset prepreg layers are placed on a planar tool where they are scanned inline with an optical inspection system. The output is a grayscale image based on laser profile height data and a 3D point cloud, which stores point coordinates in a world coordinate system. Based on both data types different approaches for the automated defect detection and measurement are developed. Both approaches showed satisfactory results in terms of detection and measurement accuracy.*

Keywords: AFP; Defect Detection; Point Cloud Analysis; Quality Inspection

1 Introduction

Automated Fiber Placement (AFP) is an established technology used to automate the layup of prepreg. During the production, a robot guided laying head automatically places multiple prepreg tapes in parallel on a mold. Depending on different process parameters, the quality of the lay-up can deviate. The so-called lay-up defects can have a severe impact on the final part stability and production tolerances [1]. Visual inspections in current production lines after each ply aim at finding and removing lay-up defects before the final consolidation of the material. These actions can cover up to 32 % of the overall production time and are prone to human error [2]. Therefore, investigations towards an automated quality inspection can help to improve the reliability of the process and to reduce material waste.

A robust data acquisition and analysis of the lay-up is crucial in order to ensure a reliable defect detection. Several measurement techniques exist where surface data is acquired during the material lay-up. The data acquisition can be performed either by laser profilometry or by thermography. The measurement device can be integrated in the AFP laying head or it can be part of a stand-alone solution [3,4].

In the field of data processing and defect detection, a strong focus in literature is on grayscale based image processing for the segmentation of defects. The work of Schulz et al. [5] introduced a digital image processing pipeline for the segmentation for gaps and overlaps. The authors Tao et al. [6] presented an online detection method for the tow width measurement via an histogram analysis. Meister et al. [7] compared multiple segmentation techniques for AFP lay-up defects. Schuster et al. [8] developed a generic inline measurement system with a 2D profile evaluation to detect defects via curve fitting.

  doi:10.5075/epfl-298799_978-2-9701614-0-0

The disadvantage of the pixel-based representation of the surface is that geometrical information is not easily accessible. This is especially relevant if 3D position information of the defect is required. To overcome this problem, point cloud analysis is used, which deals with 3D point coordinates in a specified coordinate system. In this context, Tang et al. [9] developed a first approach for the classification of lay-up defects by analyzing each laser profile separately. The authors Jovančević et al. [10] implemented a pipeline for the point-cloud based analysis of defects on an airplane exterior surface.
This paper investigates techniques to deal with 3D point cloud data and compares the results with an image processing pipeline. The focus is thereby on the measurement accuracy of different techniques, which are compared to a manual measurement of the defect characteristics. The paper concludes with further improvements of the current solutions and defines possible applications.

2 Methodology

2.1 Data Acquisition

Material lay-up is performed using a *Coriolis Composites* AFP machine. Eight UD prepreg tapes of 1/8'' (3,175 mm) width are placed in parallel on an aluminum mold with each track. Defects like gaps and overlaps are introduced manually in an adjacent step.
The data acquisition of the digital surface representation of the lay-up is realized using a customized CNC controlled 3-axis system provided by *Walter Seikowsky GmbH*. This setup allows linear movements of a laser line profile scanner over a planar surface. Depending on the maximal measurement width of the laser sensor, the trajectory of the robot system is programed by moving the sensor forward and backward allowing the coverage of the whole surface. An image of the setup and an exemplary trajectory is depicted in Figure 1. The laser sensor used is a *Micro Epsilon* scanCONTROL 2660. The following process parameters were set: scanner frequency 166,66 Hz (6 ms), Lay-Up Speed 1000 mm/min, resulting in a pixel resolution in *x* and *y* direction of 0,1 mm/px.

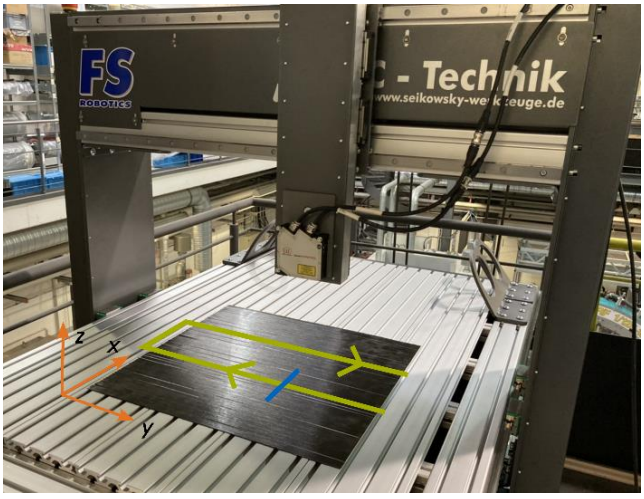

Figure 1 - Data Acquisition Setup: the laser line in blue, the trajectory (2 tracks) in green

2.2 Data Formats

The system outputs three matrices *X, Y, Z* containing the corresponding *x*, *y*, *z* coordinates for each linear track of the trajectory. The *z*-value represents the height data whereas the position

is set by *x* and *y*. The matrix data is acquired by synchronizing laser profiles of the sensor and the position coordinates of the robot system. In this case real position information of each laser profile is stored. This data format allows an easy conversion of the surface information into a PNG file or a point cloud data (PCD) file. The grayscale image for each track is generated by normalizing the *z*-values and assigning them a value between 0 and 255. This results in an 8-bit PNG file. For the point cloud, every single point P_i (x_i, y_i, z_i) is added to a binary encoded point cloud object in PCD-format.

3 Implementation

For both data types, this paper presents different approaches for the automated defect detection. The first approach is based on digital image processing using Computer Vision functions to process the surface data. The second solution focuses on point cloud analysis. The algorithms are implemented in C++ using the open source libraries *OpenCV* for image processing and *Point Cloud Library (PCL)* for the point cloud analysis. Both solutions aim for the defect classification and measurement of gaps and overlaps in planar lay-ups.

3.1 Digital Image Processing

Figure 2 gives an overview of the different steps of the developed image processing pipeline for defect detection and measurement.

Figure 2 - Pipeline for digital image processing

In a first preprocessing step, the raw image data is smoothened with a median filter with a kernel size of 10x10 pixels. To avoid effects of inclination in the image due to uneven molds or substrates a customized function rotates the image around the *x*-axis in order to get a homogeneous distribution of grayscale values. A closing operation serves as an additional filtering operation and eliminates small gaps and spots in the image. Figure 3 depicts the resulting images for each operation. The segmentation of the defects is performed by binarizing the image with different thresholds. A histogram analysis distinguishes between the different height levels in the image and outputs zero to two threshold values depending on the distribution of the grayscales. In the example of Figure 3, three grayscale levels are determined (orange peaks) resulting in two threshold values (in green). Afterwards two binarization steps result in two separated binary images where gaps and overlaps are segmented individually. The classification into gaps and overlaps depends on the position of the threshold in relation to the highest value in the histogram. A simple bounding box is set around the segments to highlight them in the resulting image. In the following, gaps are framed in orange and overlaps are visualized in blue.

The bounding box outputs relevant information about the defect size, like centroid position, length and width. The transformation of the pixel-based data via the pixel resolutions and positions stored in the matrix data *X, Y, Z* containing the *x, y, z*-coordinates leads to a representation of the defect characteristics in absolute coordinates.

  doi:10.5075/epfl-298799_978-2-9701614-0-0

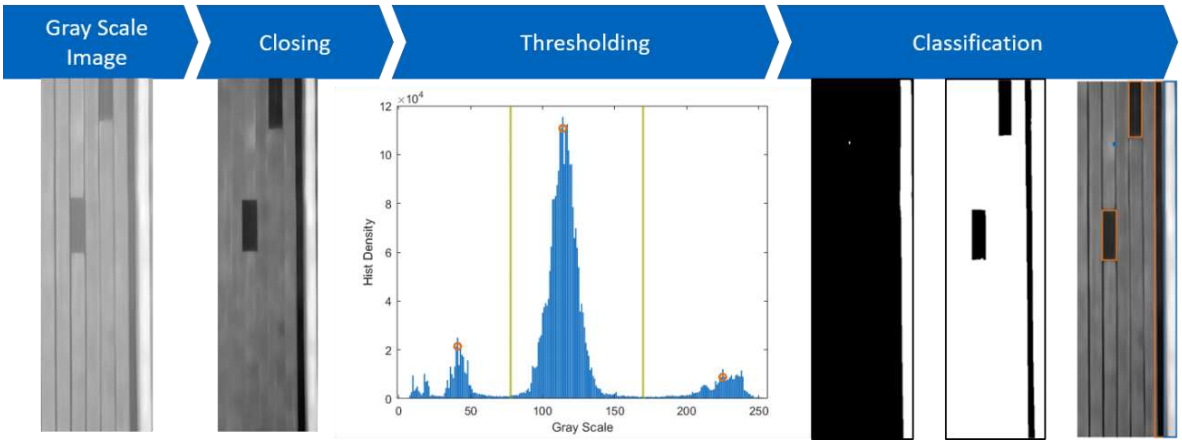

Figure 3 - Approach for defect segmentation and classification based on digital image processing

In addition, a line-fitting algorithm tries to improve the segmentation of the contours of a detected defect. Figure 4 shows the different steps. Each extracted bounding box is used to cut out the defective areas of the original image. In each cut out, the Sobel Algorithm outputs in a next step a binary image for the detection of vertical edges. An additional closing operation connects single pixels to a closed area. Afterwards the algorithm fits a line by linear regression using those pixels that belong to one edge. This allows a subpixel precise measurement of the defect width.

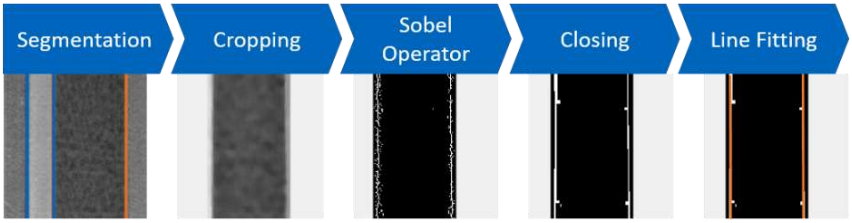

Figure 4 – Pipeline for edge extraction and line fitting

3.2 Point Cloud Analysis

The second approach focuses on the implementation of a point cloud based analysis of the surface data. The advantage is the treatment of real position data that makes it easier for defect measurement and positioning. Figure 5 shows the different steps executed by the algorithm.

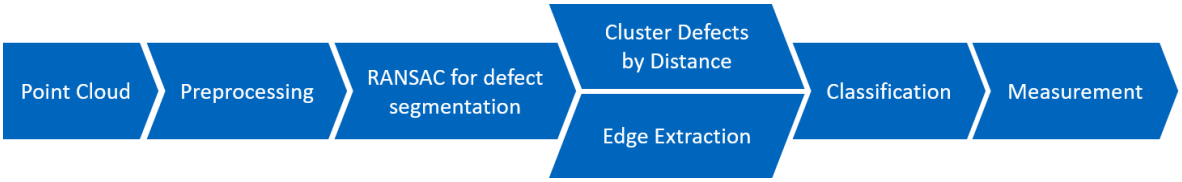

Figure 5 - Pipeline for Point Cloud Analysis

The preprocessing of the raw point cloud covers a filtering and an optional downsampling operation. Therefore, a Voxel Grid filter with a defined leaf size can be applied. This reduces measurement noise and decreases the amount of points stored in the point cloud. The mean point distance is equal to the previously defined pixel resolution of 0,1 mm. The RANSAC algorithm aims to detect outliers in the point cloud outside a reference surface fitted in all points [11]. RANSAC is useful for anomaly detection and defect segmentation and stores in this case all

  doi:10.5075/epfl-298799_978-2-9701614-0-0

points corresponding to a defect in an outlier point cloud. Figure 6 shows an exemplary cut view of a cloud with gaps (orange) and overlaps (blue). It illustrates the RANSAC method where the inlier points are marked in black and the outliers in blue and orange.

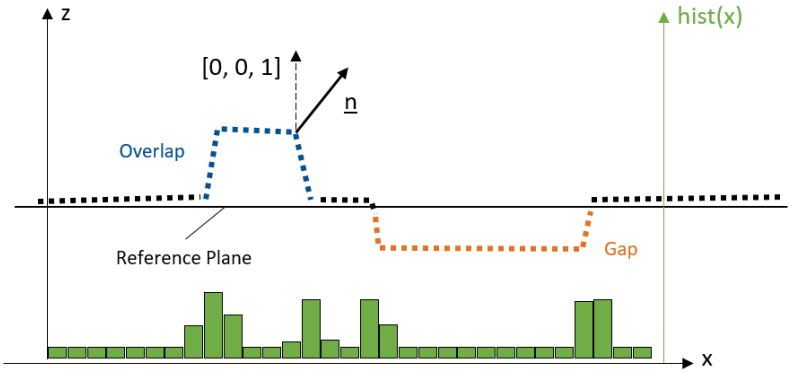

Figure 6 - Defect Segmentation and Classification

The position of any outlier point in relation to the reference plane leads to the classification of gaps and overlaps in a subsequent step.

In order to segment multiple defects in the outlier point cloud, a clustering algorithm groups points by evaluating their Euclidian distance to each other. It is possible to extract all defects separately with a cluster tolerance of 0,2 mm.

An additional segmentation technique based on point normals estimation already successfully implemented by Jovančević et al. [10] distinguishes between the orientation of the normal. The approach is also visualized in Figure 6. The normal corresponds to the normal vector of a plane fitted through six neighboring points. In this case, edge extraction is performed by computing the point cloud normals and afterwards thresholding the angle between the normal vector and the *z*-axis [1 0 0]. An absolute value inside the range of 45° ± 30° refers to a detected edge in the surface data. The corresponding point is therefore stored in a separate point cloud. In order to cluster the points into separated edges a histogram evaluation of the *x*-coordinate helps to identify points belonging to the same edge. The histogram in Figure 6 depicted in green shows peaks in the intervals of the edges. The algorithm automatically identifies the corresponding *x*-limits and splits the outlier point cloud into separated point clouds for each detected edge.

For the classification, the algorithm extracts the area between two edges in the outlier point cloud and checks if the point density exceeds a defined threshold. With the analysis of the position in relation to the reference plane it is possible to separate gaps and overlaps.

Figure 7 depicts the results for each step from the original to the output.

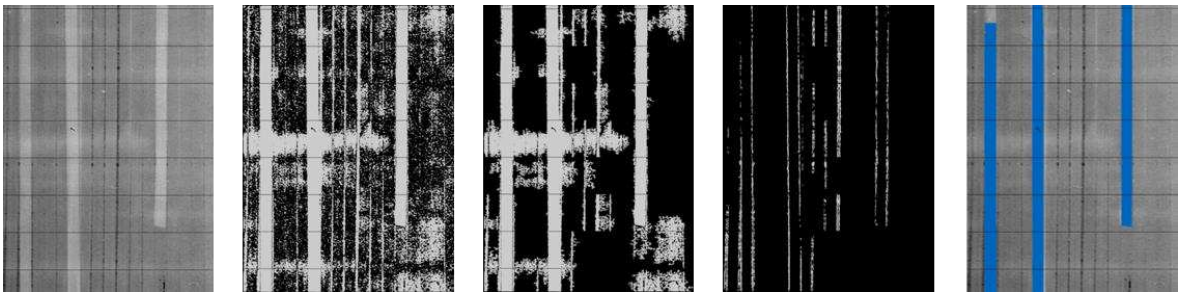

a) Original | b) RANSAC outliers | c) Euclidian distance clustering | d) Edge extraction | e) Segmented and classified defect

Figure 7 – Point cloud processing with different pipeline steps

  doi:10.5075/epfl-298799_978-2-9701614-0-0

The last step covers the output of the geometrical information of each defect. The mean value of all *z*-coordinates in the point cloud of each defect is set as the height of the defect. This refers to the distance to the RANSAC fitted planed. A prerequisite is that only few defects occur in the lay-up in order to guarantee a good fitting of the plane in the reference surface without defects. Similar to the image based approach, a linear function is fitted into all points in the edge point clouds. With the mathematical description of the edges, it is possible to determine the length in *y*-direction and the distance between two adjacent lines referring to the width of the defect in *x*-direction.

4 Results & Validation

Figure 8 and Figure 9 give an overview of the output for two different lay-ups. The defects are numbered from 1 to 5. The left image shows the original PNG for the lay-up. In both cases, the image size is 638 x 892 pixels. The second image depicts the bounding boxes for each detected defect. A gap is framed with an orange box and the overlaps are shown in blue. In the third image, the fitted lines in the corresponding color represent the extracted edges. The fourth output indicates the result from the point cloud analysis. This approach clusters all points corresponding to one defect in a separate cloud and visualizes the cluster in the right color.

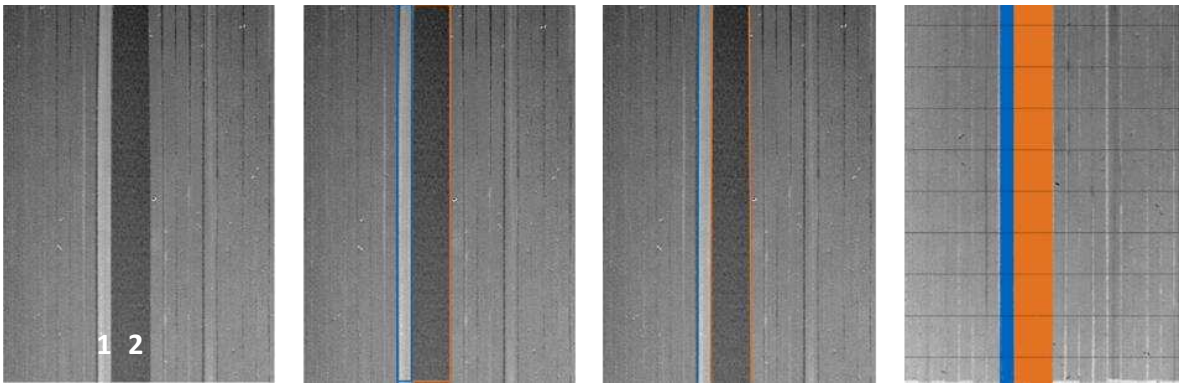

a) Original grayscale image | b) segmentation with bounding box | c) segmentation with extracted edges | d) point cloud based approach

Figure 8 - Results of gap (orange) and overlap (blue) detection

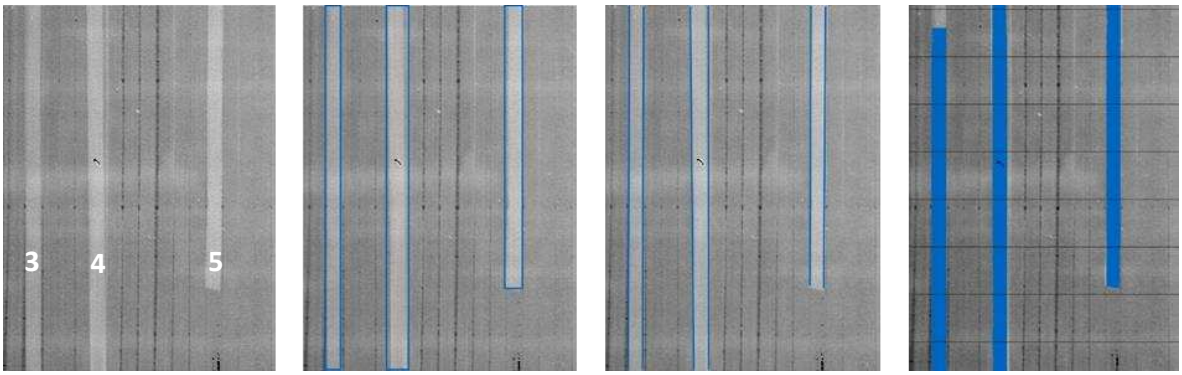

a) Original grayscale image | b) segmentation with bounding box | c) segmentation with extracted edges | d) point cloud based approach

Figure 9 - Results of overlap detection in blue

A total number of eight samples with 21 defects were tested and correctly classified by the algorithms. All solutions clearly distinguish between gaps and overlaps and visualize the defected area in a PNG image or the original point cloud. The point cloud analysis fails in some cases to segment the whole defect correctly as seen in Figure 9 on the right. Here the left overlap is not classified completely.

Table 1 shows the results for the measurement of the width of the defects in the depicted images in Figure 8 and Figure 9. For the reference, the distance is determined manually by measuring the width of each defect in a 2D-plot of the surface scan at three different values of *y* according the approach of Schmitt et al. [12]. The sign indicates whether the value is smaller (< 0) or greater (> 0) than the reference value.

It can be seen that the bounding box approach, which is the simplest solution, can measure accurately if the defect is well aligned with the scanning direction. For overlap (4) and overlap (5) major deviations to the reference value can be observed. This is due to the fact, that the bounding box always frames the defect area with a rectangle. In this case, the line fitting approach or the point cloud analysis get results that are more precise.

Table 1 - Results of the measurement approaches in relation to reference value in %

Example	Defect type	Measurement Approach		
		Bounding Box	Line Fitting	Point Cloud Analysis
Figure 8	Overlap (1)	0,86 %	0,28 %	-2,4 %
	Gap (2)	3,25 %	-3,91 %	0,66 %
Figure 9	Overlap (3)	0,36 %	6,7 %	- 3,1 %
	Overlap (4)	38,55 %	2,32 %	-1,5 %
	Overlap (5)	14,74%	8,7 %	-7,47 %

5 Conclusion & Outlook

This paper presents two different solutions for the automated defect detection of lay-up defects in the AFP process. Both approaches can reliably detect overlaps and gaps and output their characteristics in terms of width, height, length and position. They are limited to planar lay-ups where the fiber direction is equal to the scanning direction during the data acquisition. The results show that a performant image-processing pipeline delivers as good results as the point cloud analysis. The advantage of the point cloud analysis is the fact, that it can be transferred to 3D analysis and that it is applicable to unorganized point clouds. A prerequisite for both approaches is the fact that the amount of defective areas in one image or point cloud does not exceed the amount of areas with no defects. This scenario would lead to wrong results in the histogram approach and the RANSAC method.

In a future step, the algorithms will be extended to a broader range of defect types like ply boundary deviations or twists. In addition, the data acquisition will focus on the scanning of 3D surfaces. For the detection and measuring of defects on 3D surfaces the use of point cloud analysis will be essential.

Acknowledgements

The authors would like to thank the German Federal Ministry for Economy Affairs and Climate Action for funding the work in the context of the research project “ECHTZEIT” (funding code: ZF4004323FH9).

6 References

[1] Lukaszewicz DH-J, Ward C, Potter KD. The engineering aspects of automated prepreg layup: History, present and future. Composites Part B: Engineering 2012;43(3):997–1009.

[2] Rudberg T, Nielson J, Henscheid M, Cemenska J. Improving AFP Cell Performance. SAE Int. J. Aerosp. 2014;7(2):317–21.

[3] Denkena B, Schmidt C, Völtzer K, Hocke T. Thermographic online monitoring system for Automated Fiber Placement processes. Composites Part B: Engineering 2016;97:239–43.

[4] Schmitt R, Mersmann C, Damm B. In-process 3D laser measurement to control the fiber tape-laying for composite production. In: Schelkens P, Ebrahimi T, Cristóbal G, Truchetet F, Saarikko P, editors. SPIE Photonics Europe: SPIE; 2010, 77230R.

[5] Schulz M, Janssen H, Brecher C, Evertz A. Online Analysis of Geometrical Inaccuracies During the In-situ Automated Fiber Placement of Tailored Composite Blanks out of Thermoplastic Tape. In: 5th International Conference & Exhibition on Thermoplastic Composites, Bremen, 13.-15.10.2020.

[6] Tao Y, Jia S, Duan Y, Zhang X. An online detection method for composite fibre tow placement accuracy. Proceedings of the Institution of Mechanical Engineers, Part B: Journal of Engineering Manufacture 2016;230(9):1614–21.

[7] Meister S, Wermes MAM, Stueve J, Groves RM. Algorithm assessment for layup defect segmentation from laser line scan sensor based image data. In: Zonta D, Huang H, editors. Sensors and Smart Structures Technologies for Civil, Mechanical, and Aerospace Systems 2020: SPIE; 2020, p. 45.

[8] Schuster A, Mayer M, Willmeroth M, Brandt L, Kupke M. Inline Quality Control for Thermoplastic Automated Fibre Placement. Procedia Manufacturing 2020;51:505–11.

[9] Tang Y, Wang Q, Wang H, Li J, Ke Y. A novel 3D laser scanning defects detection and measurement approach for automated fibre placement (AFP) in-process inspection. Meas. Sci. Technol. 2021.

[10] Jovančević I, Pham H-H, Orteu J-J, Gilblas R, Harvent J, Maurice X et al. 3D Point Cloud Analysis for Detection and Characterization of Defects on Airplane Exterior Surface. J Nondestruct Eval 2017;36(4).

[11] Fischler MA, Bolles RC. Random sample consensus: a paradigm for model fitting with applications to image analysis and automated cartography. Commun. ACM 1981;24(6):381–95.

[12] Schmitt R, Orth A, Niggemann C. A method for edge detection of textile preforms using a light-section sensor for the automated manufacturing of fibre-reinforced plastics. In: Osten W, Gorecki C, Novak EL, editors. Optical Measurement Systems for Industrial Inspection V: SPIE; 2007, p. 661609.

  doi:10.5075/epfl-298799_978-2-9701614-0-0

CONTACTLESS DIELECTRIC PROCESS MONITORING (CDPM) OF POLYMER COMPOSITES MANUFACTURING

Tasnuva Khaleque[a], Ioannis Vagias[b], Alex Skordos[b], Hamed Yazdani Nezhad[c]

a: Tun Abdur Razak Research Centre, email: t.khaleque13@alumni.imperial.ac.uk
b: Cranfield University
c: City University of London

Abstract: *A feasibility study has been performed systematically to develop a real-time contactless measurement of the dielectric properties (DP) of composite surface by means of a high-frequency, free-space vector network analyser (VNA) associated with one steel conical horn antenna (mono- static method). Examinations of the dielectric spectra of thermoset epoxy systems over a frequency range of 1kHz to 10GHz have shown α and γ relaxations across a range of cure temperatures [1]. The γ relaxation occurring at relatively high frequencies is related to the motion of the molecules while the α relaxation is attributable to epoxide groups in the reacting systems . A thermoset epoxy resin was selected for this feasibility study to assess its relaxation characteristics (sensitive to the degree of cure) in real-time using a remote VNA. The assessments were carried out at 60 °C and 80 °C curing temperatures.*

Keywords: polymer composites ; real-time cure monitoring; dielectric properties ; vector network analyser (VNA).

1. Introduction

Carbon fibre-reinforced polymer (CFRP) composites are widely used for high performance, light weight structures in various industrial sectors and applications due to their superior mechanical properties (e.g. high stiffness and low weight), thermal and chemical resistance and low shrinkage properties [2]. Therefore, different manufacturing techniques for CFRP composites have been developed. However, Conventional CFRP composites manufacturing techniques (autoclaved or out-of-autoclave) can be expensive at large scales, and are time consuming (mainly due to allow thermal energy conducting through the polymer medium and the composite), and are associated with effects from uncertainties associated with the manufacturing process parameters control (e.g. temperature, pressure and resin flow) which may have a significant effect on the quality of the composite structure and thus the structure's mechanical performance.

In recent years various real-time manufacturing process monitoring technologies (e.g. embedded dielectric sensors, pressure sensors, fibre optic sensors etc.) have been developed to track the critical process parameter variations during the composite manufacturing, and to associate reliable closed-loop feedback systems with the manufacturing. However, all the techniques mentioned above are point contact type and suffer from several limitations such as possible interference with the in-process composite, not fully scalable to relatively large scale, non-flat, curved structures, and may require severe considerations in terms of practical implementations (e.g. increasing number of sensors for large scales hence, increasing the overall cost and associated electronics). Such challenges must be overcome for real-time measurement

  doi:10.5075/epfl-298799_978-2-9701614-0-0

of a composite process before it can be applicable to large structures and/or for mass manufacturing.

The present study focuses on the development of a real-time contactless dielectric process (cure) monitoring (CDPM) technique for polymer composite manufacturing. The main objective of the present study is real-time measurement of the dielectric properties (DP) of composite surface, remotely, by means of a high-frequency, free-space vector network analyser (VNA) associated with two steel conical horn antenna.

Thermal imaging of the composite surface, which produces a real-time heat pattern (HP) is the sole existing measurement relying upon remote sensing with no interference with the composite structure. Developing a HP of the surface is necessary for a closed-loop process, however, a temperature increase at a specific point occurring for a relatively short period of time may not mean a high degree of cure at that location, and indeed may result from a contribution from uncertainties about the material such as an area enriched by carbon fibres. On the other hand, non-uniform heating (and cure) can be caused by the combination of material uncertainties (e.g. fibre volume fraction). Hence, process control relying solely on the HP measurement over the composite surface may not be reliable. Moreover, it has been shown that there is a strong correlation between dielectric data and the cure state (e.g. degree of cure) at a specific location in the material, as it interprets the polymerisation state in real-time [3]. Therefore, using dielectric sensing technique to identify the dielectric pattern (DP) across the surface of the composite is advantageous as it correlates with the material's characteristics under cure.

Since the change in the dielectric properties of composites during the curing is mainly contributed by the matrix material, current work focuses on the study of a pure epoxy resin, as a first step to fibre reinforced composite. Therefore, a thermoset epoxy resin was selected for this feasibility study to assess its relaxation characteristics (sensitive to the degree of cure) in real-time using a remote VNA. The assessments were carried out at 60 °C and 80 °C temperatures.

2. Experimental Methods

2.1 Materials and Manufacturing

A low viscosity thermoset epoxy resin, 'Araldite LY 5052' (Huntsman, UK), was used. The epoxy was crosslinked using 'Aradur HY 5052' (Huntsman, UK), a mixture of polyamines curing agent. The epoxy and the hardener were liquid at room temperature. Araldite LY 5052 and the hardener Aradur HY 5052 were mixed using a mixed ratio of 100:38 by weight. The epoxy-hardener system was cured at two different temperatures (60 °C and 80 °C) using a hot plate 'Stuart SD500' from Cole-Palmer, UK (Figure 1). Firstly, the hot plate was cleaned using acetone and a layer of vacuum bagging film of 50 µm thickness, 'VB200' (supplied by Easycomposites, UK), was attached to the hot plate, using flash tape, 'Flash/release tape' (supplied by Easycomposites, UK), to protect the surface of the hotplate. An 8 mm thick sealed wall was built around the edge of the hotplate using layers of 'Tacky tape' ('Vacuum Bagging Gum Sealant Tape' supplied by Easycomposites, UK) in order to make a mould for curing the epoxy system, as seen in Figure 1.

  doi:10.5075/epfl-298799_978-2-9701614-0-0

Figure 1. Hot-plate mould for curing epoxy-hardener system

The dielectric properties of approximately 718 ml (6 mm thickness layer) of epoxy-hardener system was monitored during the curing cycle using a (VNA) equipped with a steel conical antenna. The temperature variation of the epoxy during the curing cycle was observed using a FLIR T420 thermal imaging camera at every 5 min. The Schematic of the experimental set-up is illustrated in Figure 2.

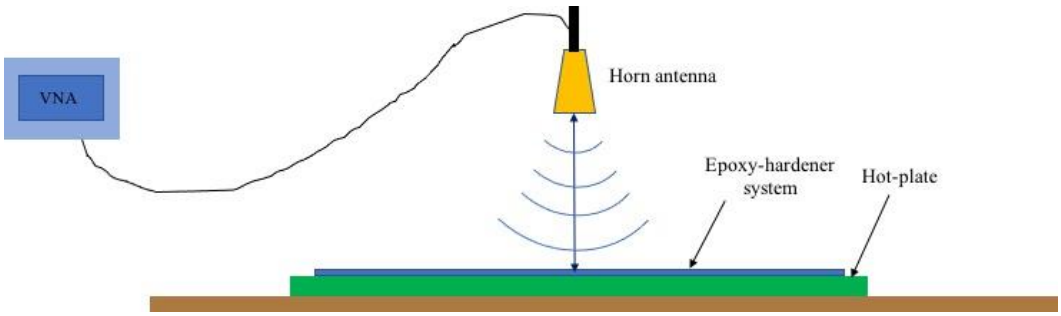

Figure 2. Schematic of the experimental set-up equipped with remote dielectric measurement

The equipment used for the dielectric measurement are VNA 37937c, Anritsu; phase stable cables, K-connector; GPIB-to-USB cable, National Instruments; Horn Antennae, Narda 640, Standard Gain; coaxial cables, SMA-to-SMA; photographic tripod; Laser rangefinder; Digital inclinometer, DXL360, 2-axis; Plexiglas flat plate of 30cm × 30cm × 6mm; Four (4) RF foam absorbers and tyrofoam block of 30cm × 30cm× 15cm .The experimental setup is show in Figure 3. Four RAM panels were positioned around the hot plate where the resin was later poured for curing. Above the hot plate, the horn antenna, mounted on a metal base and fixed onto the tripod, which regulated in pitch and roll. The hot plate was aligned with the antenna through the use of a 2-axis digital inclinometer (pitch and roll) and a laser rangefinder for the antenna to point towards the centre of the hot plate (see Figure 4). The width and height of the horn lips were 8 cm, thus producing, at 8.2 GHz (f_{min}, λ_{max}), a maximum beam width of 26.18 degree The far field at the aforementioned frequency was 0.35 m and at this downrange the beam footprint was 0.16m in both directions (azimuth and elevation). The Plexiglass block was placed at 1.176895 m downrange (1.176895, 1.188895) m, thickness 6 mm, while the resin was placed at (1.18007, 1.18607) m, thickness 6 mm. At these distances, the footprint of the beam was no greater than 54.3 cm × 54.3 cm. The size of the usable surface of the hot plate was 50 cm × 30 cm. Of this surface, an area of 46 cm × 26 cm was utilised to cure the resin. A 2 cm margin in width and length was reserved for the restraining wall (see Figure 5) as mentioned above.

  doi:10.5075/epfl-298799_978-2-9701614-0-0

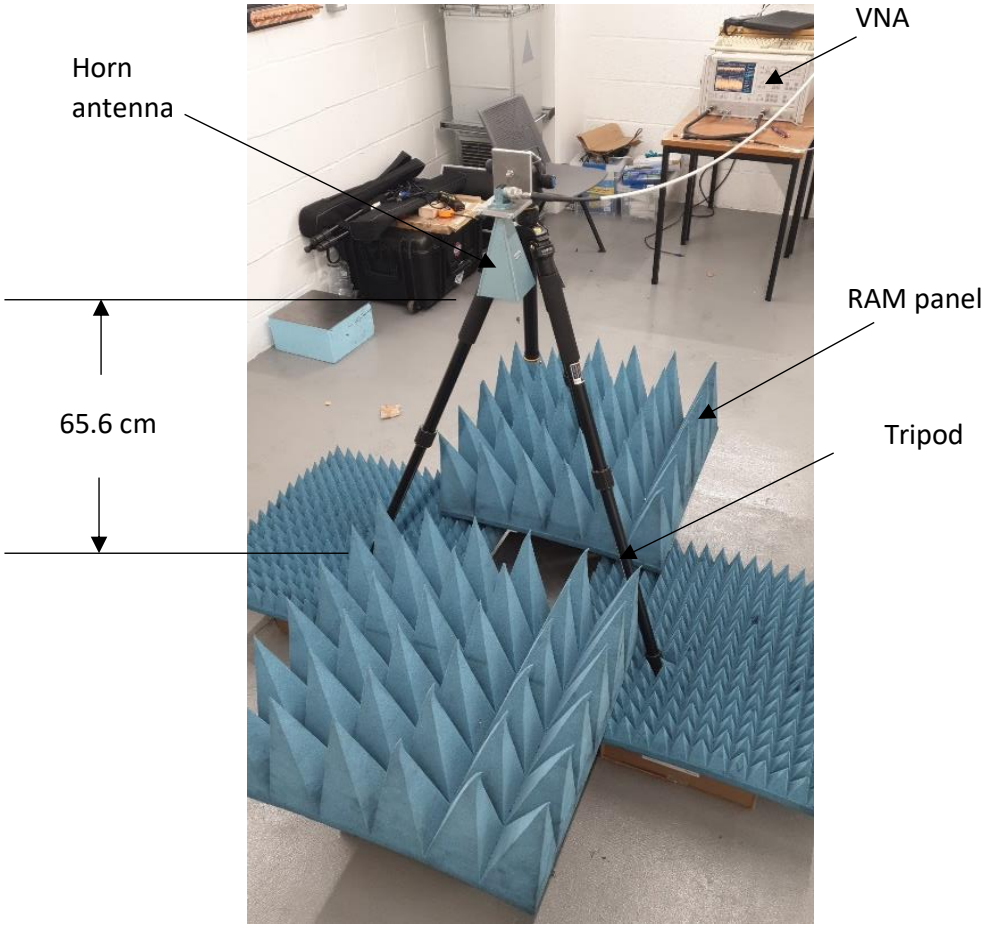

Figure 3. Dielectric Measurement set-up

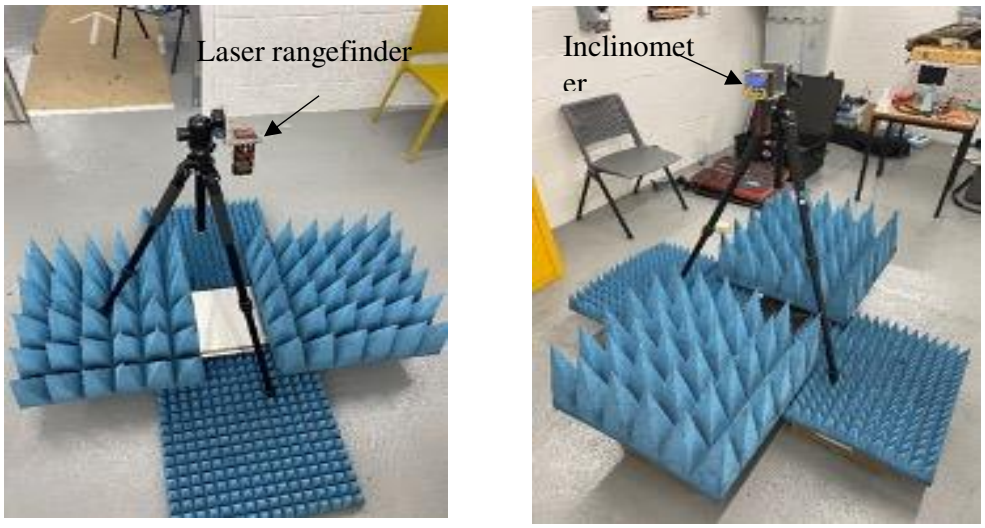

Figure 4. Hot-plate and antenna mount alignment

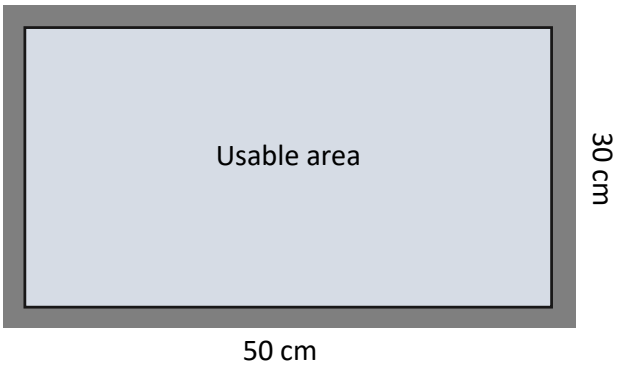

Figure 5. Experimentation area for resin curing and dielectric measurement

2.2 Data Acquisition and Processing

Two measurements were made; one on a Plexiglas 50 cm ×30 cm × 6 mm plate which was mounted on a 50 cm × 30 cm × 30 cm styrofoam block on top of the hot plate, and a second measurement of the resin over two hours in five minute intervals. Two separate backgrounds were captured for coherent background subtraction. The S_{11} channel of the VNA was captured using the GBIP cable and a laptop. The captured data were magnitude (dB) and phase (deg) and enabled the recreation of the complex signal.

3. Results

3.1 Curing of Epoxy Resin

The surface temperature of the epoxy during the curing process was observed using a thermal imaging camera. Figure 6 shows the temperature variation of the resin during the epoxy curing at 60 °C. The plot clearly shows that the temperature of the resin overshoot the mould temperature (60 °C) confirming the cure progression of the resin as the cure reaction of epoxy is exothermic.

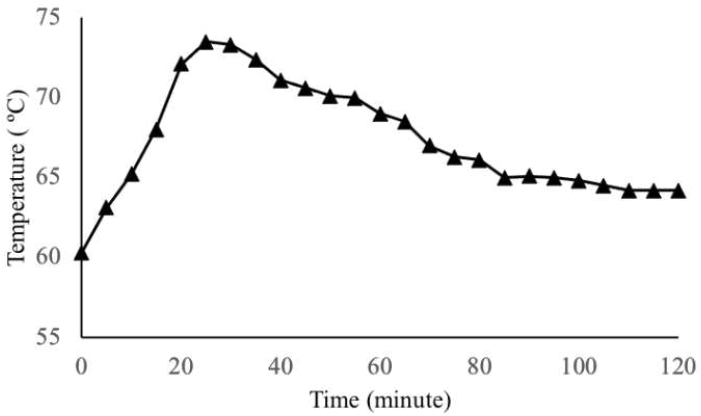

Figure 6. Temperature variation during cure of the Araldite LY 5052/Aradur HY 5052 epoxy resin

The decrease in temperature at 35 min indicates the slowdown of the exothermic reaction. The foam RAM panels used in the experiment were not heat resistant, and therefore a slight burning

  doi:10.5075/epfl-298799_978-2-9701614-0-0

and melting of one of the panels were observed at the end of the epoxy curing cycle. The burnt portion of the foam absorber stuck to the tacky tap boundary on the hot plate. The epoxy was set to cure at 80 °C, however within 7 min the epoxy temperature increased dramatically to 150 °C due to exothermic reaction and smoke was also detected. Therefore, further heating of the epoxy was stopped to avoid the hazardous situation. Extreme caution must be taken as such extreme state as in the previous case.

3.2 Post Processing of Dielectric Data

A measurement was performed to check that the plexiglass background was free of unintentional interference. The signal in the frequency domain should be Gaussian white noise. In particular, when subtracting two background signal captures, only the hot plate surface and the minimum signal duration should be visible, and one or two multipath features of the room. It was found that the presence of the floor, the signal duration, the frequency dependence of clutter and not perfect subtraction cause phase linearity from 8.2 GHz to approximately 9 GHz. This was corrected by range gating.

The epoxy resin was cured for 1 hour at 60 °C and the S_{11} VNA channel was captured every 5 minutes (Figure 7, Figure 8 and Figure 9). The permittivity was calculated for every time slot.

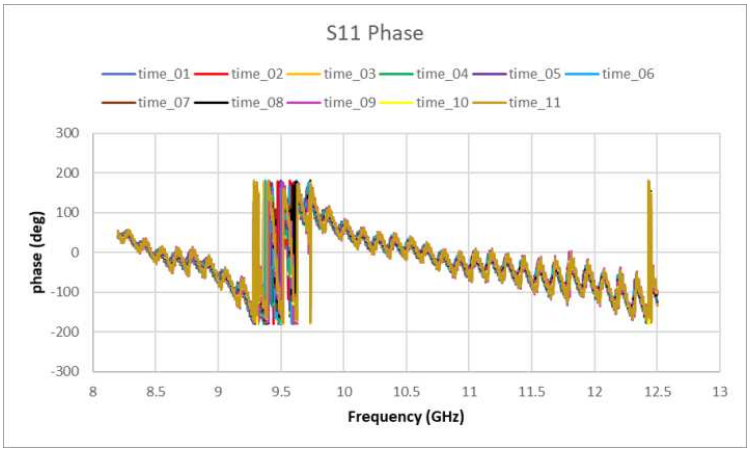

Figure 7. Resin S11 phase (background subtracted and range gated)

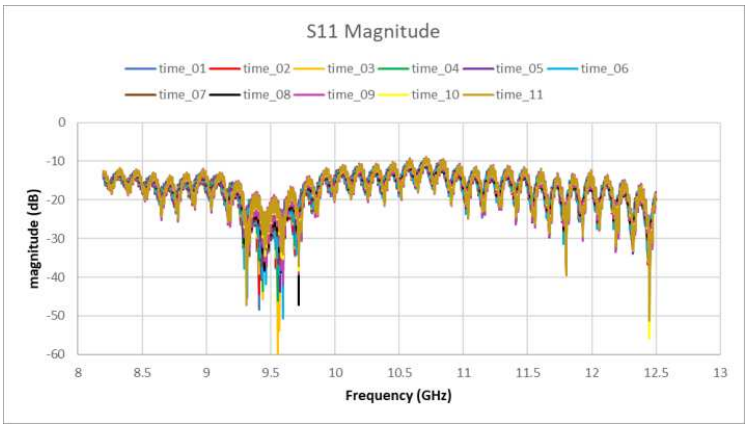

Figure 7. Resin S11 magnitude (background subtracted and range gated)

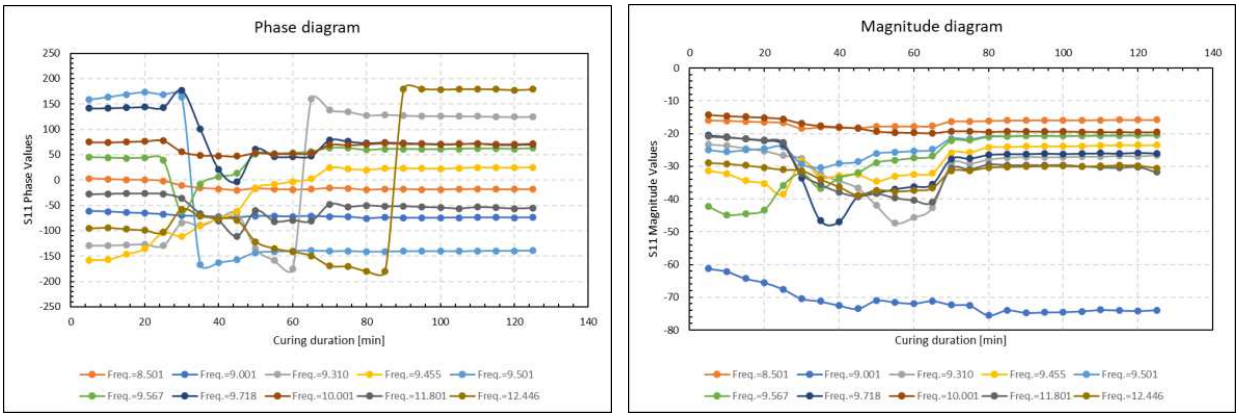

Figure 9. Resin S11 phase and magnitude vs curing time (background subtracted and range gated)

Three main regimes in the evolution of S11 phase data with time are identified (Figure 9). Regime 1: constant phase with increasing time for all frequencies for time < 25 min ; regime 2: varied phase with increasing time for all frequency for 25 min <time < 70 min; regime 3: constant phase with increasing time for all freq. for time > 70min at frequency 8.5 zero phase occurs with varied (increasing) frequency, swapping signs in the non-zero phase data, all phase values drop after time = 25 min at all frequencies except for frequency = 9.310 and 9.455. Frequency 9.310 exhibits an abrupt increase in the phase values between 25 min and 45 min, and an abrupt decrease between 45 min and 60 min. Frequency 9.455 exhibits a gradually increasing trend with time, indicates an abrupt change (drop) at time 25min (starting of regime 2), continue to rise within regime 2, and change to constant trend at time 70 min. Frequency 12.446 constant regime 3 starts later than the others' regime 3 point, post 85 min. All frequencies exhibit a short term sudden increase at the end of regime 2 at 65min, before reaching regime 3's constant values.

Three main regimes in the evolution of S11 magnitude data with time are identified (Figure 9). Regime 1: constant magnitude with increasing time for all freq. for time <25 min; regime 2: varied magnitude with increasing time for all freq. for 25 min < time < 70 min; regime 3: constant magnitude with increasing time for all frequencies for time > 70 min; all S11 magnitude data are negative across all curing time; with varied (increasing) frequency, fluctuations (rise and drop) in the magnitude data, across all times; magnitude values drop after time = 25 min at all frequencies except for frequency 9.455 and 9.567; frequency 9.455 exhibits an abrupt increase in the magnitude values between 25min and 30min, and a slight decrease between 30 min and 60 min. Frequency 9.567 exhibits a gradually increasing trend with time, indicates an abrupt change (drop) at time 30 min (approximately at the starting of regime 2), continue to rise within regime 2, and change to constant trend at time 70 min. All frequencies exhibit a short term sudden increase at the end of regime 2 at 65 min, before reaching regime 3's constant values. Frequency 9.001 is an anomaly in the magnitude trend with no indicative representation of regimes 1 and 2, however clearly shows a constant trend within regime 3 which consistent with the data from the other frequencies.

4. Conclusions

The focus of this feasibility study was to develop a real-time contactless measurement of the dielectric properties (DP) of composite surface by means of a high-frequency, free-space vector network analyser (VNA) associated with one steel conical horn antenna (monostatic method), therefore making it portable and scalable with no structural interference with the composite. A thermoset epoxy resin (Aradur HY 5052/Araldite LY 5052) was selected for this feasibility study to assess its relaxation characteristics (sensitive to the degree of cure) in real-time using a remote VNA. The assessments were carried out at 60 °C and 80 °C curing temperatures.

The methods used in the feasibility study proved to be reliable to measure the variation of electrical permittivity of thin layer of epoxy or composites over a wide bandwidth. However, further research should be performed to understand the interference of the hot plate surface with the material under test.

The feasibility study has been performed systematically to develop a real-time contactless measurement of the dielectric properties (DP) of composite surface by means of a high-frequency, free-space vector network analyser (VNA) associated with one steel conical horn antenna (mono- static method). However, through the course of this study some potential areas of further research have emerged and are addressed.

Acknowledgements

The research has been funded by the UK Engineering & Physical Sciences Research Council (EPSRC) Hubs of Future Metrology and Future Composites Manufacturing (CIMCOMP), Ref. EP/P006930/1.

5. References

1. Zong L, Zhou S, Sgriccia N, Hawley MC, Sun R, and Kempel LC. Dielectric properties of an epoxy-amine system at a high microwave frequency. Polym Eng Sci, 45: 1576-1580, 2005
2. Sims FA. Applications of resins in bridge and structural engineering. International Journal of Cement Composites and Lightweight Concrete 1985; 7:225-32.
3. Michels J, Sena-Cruz J, Czaderski C, Motavalli M. Structural strengthening with prestressed CFRP strips with gradient anchorage. Journal of Composites for Construction 2013; 17:651-661.

  doi:10.5075/epfl-298799_978-2-9701614-0-0

INVESTIGATION OF VARIOTHERMAL MOULD HEATING SYSTEMS FOR PROCESSING OF HIGH TEMPERATURE THERMOPLASTIC COMPOSITES IN SHORT CYCLES

Veit Würfel[a], Jan Condé-Wolter[a], André-Luca Pietsch[a], Stefan Scheitz[b], Davide Schultz[b], *Patrick Först[c], Christian Garthaus[d], Johannes Lindenau[d], Tobias Weber[e] and Maik Gude[a]*

a: Technische Universität Dresden, Institute of Lightweight Design and Polymer Technology, Holbeinstraße 3, 01307 Dresden, Germany, veit.wuerfel@tu-dresden.de
b: Fraunhofer Institute for Material and Beam Technology IWS, Winterbergstraße 28, 01277 Dresden, Germany
c: Siegfried Hofmann GmbH, Siegfried-Hofmann-Straße 1+3, 96215 Lichtenfels, Germany
d: herone GmbH, Meschwitzstraße 21, 01099 Dresden, Germany
e: Boeing Deutschland GmbH, Brabanterstr.4,80805, München, Germany

Abstract: *Due to their good mechanical and physical properties as well as the potential for short cycle manufacturing, high performance thermoplastic composites offer a promising alternative to thermoset composites, especially in the aerospace industry. In this study, a new out-of-autoclave tooling concept is presented to manufacture tape-braided CF/PEKK composites in a bladder assisted moulding process. In order to reduce cycle times to less than 20 minutes, four different heating systems are investigated, including infrared heaters and three different resistive heating systems. The heating rates, the temperature distribution and the efficiency of the systems are examined in a technical benchmark to evaluate production at an early stage.*

Keywords: Thermoplastics; Heating system; PEKK; Mould; Tooling

1. Introduction

Fibre reinforced thermoplastic (FRTP) composites prove to be a valuable material for the design and manufacture of high performance lightweight structures with high production rates. By using pre-impregnated unidirectional thermoplastic tape material combined with the tape-braiding process with its high grade of automation, high performance composite hollow structures can be manufactured efficiently in a bladder assisted moulding (BAM) process [1]. Without the need of impregnation of the fibres, parts can be formed by heating the fibre-polymer tape over its melting temperature with the subsequent consolidation and cooling under pressure. Thereby, variothermally heated moulds lead the processing temperature. In this work, various variothermal heating systems for thin walled moulds are benchmarked regarding heating rates, homogenity of temperature distribution and overall energy efficiency. For large structures autoclaves or out-of-autoclave processing in convection ovens are being used for the manufacture of aerospace parts in which cycle times can take up to multiple hours. For technical thermoplastic polymers and thermosets, moulds are commonly heated with fluids in fluid channels close to the part surface, as demonstrated in [2]. Heating rates of 95 K/min are reached, but due to the large oil tempering unit and large steel mould a high amount of energy is required with high environmental impact. For the processing temperatures of high performance thermoplastics in the range of 380 °C, tempering media like water and oil are only applicable if the system is pressurized to maintain the liquid aggregate state of the heating fluid, which increases system complexity. Inductive heating with smart susceptors and air cooling is

  doi:10.5075/epfl-298799_978-2-9701614-0-0

used in [3]. Very high heating rates can be reached with the use of ferromagnetic alloys and complex thin walled mould systems. Inductive heating is used in [4] to pre-heat a metallic insert for an injection moulding process in less than ten seconds. In [5] the light induction tooling technology enables the manufacture of aerospace shell parts with heating rates of up to 150 K/min by thin shell tooling with a supporting structure. The production to functional specification (PtFS) technology by Surface Generation Ltd is studied in a rapid isothermal stamp forming process [6] and in a BAM process [7]. Thin steel shell moulds are heated and cooled with compressed air and cartridge heaters to achieve heating rates up to 90 K/min. In [8] an one-piece thin aluminium tubular mould was heated with an induction coil in a BAM process in which a cycle time of 10 min was reached for FRTP tapes. Various heating systems are developed in order to realize out-of-autoclave processes. Yet, complex shaped hollow profiles made out of high temperature thermoplastic composites are still often times manufactured in oven or autoclave processes and tooling and heating systems are not available or very capital intensive. Therefore, a comparative study of different mould heating systems for complex thermoplastic hollow profiles is performed to demonstrate the possibilities for efficient high rate manufacture.

2. Test equipment and methods

2.1 Mould specimen geometry and material

A thin walled multi-part mould design is chosen for the investigation and the manufacture of hollow-shaped FRTP-structures (Figure 1). The necessary internal pressure in the BAM process is below 10 bar. Combined with the high stiffness and strength of hollow shapes in resistance to internal pressure, this enables a thin walled mould design.

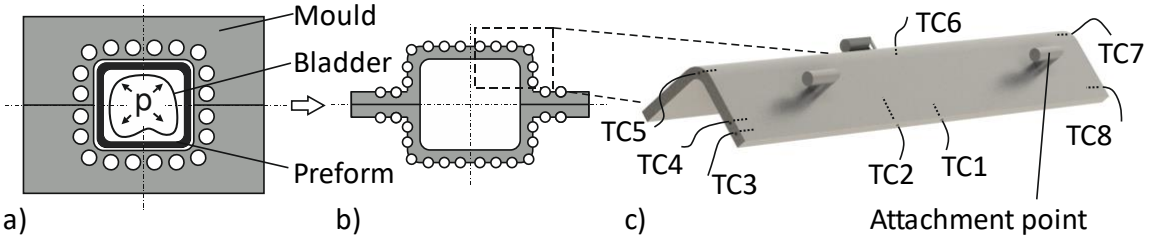

Figure 1. a) Classical two-part mould design with fluid heating channels for the BAM process, b) novel thin-walled mould design with heating elements on the outside of the tool, c) mould specimen used and positions of temperature measurement by thermocouples (TC)

The low mass drastically reduces the heat capacity of the tool. For this study, a representative geometry is chosen. The specimen is an L-shaped sheet of 1.4301 stainless steel, which has two flat areas and a tight corner radius. The sheet is 256 mm long and 75 mm wide when unfolded. The area of the outside of the specimen body is 19 200 mm². There are three attachment points on the specimen. A minimum sheet thickness of 5 mm is chosen to limit complications in machining of the final mould design. Several thermocouples (TC) are attached inside of the specimen in machined holes. In Figure 1 the position and in Table 1 the depth of the TC inside of the specimen are given.

Table 1: Depth of the thermocouples

Thermocouple	TC1	TC2	TC3	TC4	TC5	TC6	TC7	TC8
Depth of hole [mm]	5	17	5	17	5	2.5	5	5

  doi:10.5075/epfl-298799_978-2-9701614-0-0

2.2 Variothermal mould heating systems

Following a market screening, four different heating systems are chosen for the investigation: mineral-insulated conductors **(MIC)**, **thick-film** technology, thermally sprayed **thin-film** and infrared **(IR) heaters** (Figure 2). These systems are either integrated in or on the thin-walled mould or used to heat the mould externally.

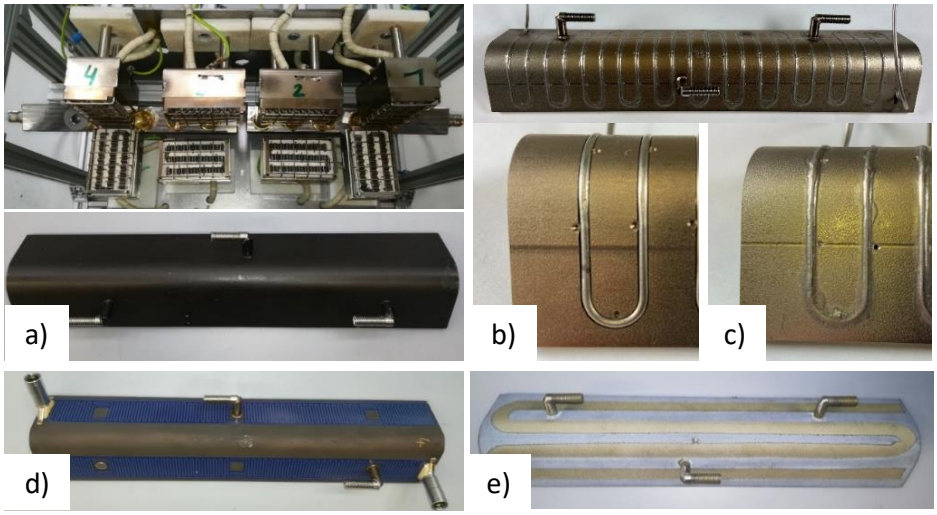

Figure 2. Mould heating systems investigated: a) Infrared heaters and coated specimen, b) MIC form closure, c) MIC brazed, d) Thick-film technology and d) Thermal sprayed thin-film

Eight **IR heaters** of the Micro-G3-6 series from Krelus AG are used the experimental investigation, see Figure 2 a). Each emitter has an operating voltage of 10.5 V and a current consumption of 12.5 A. The specimen for the IR heating is coated black with a high temperature resistant coating 'SUPERTHERM black 800°C' to increase the absorption of the infrared light. There are gaps of 10 mm to 30 mm between the radiators and 8 mm between the radiators and the specimen. A 5-stage manual control unit VLC 20 BK FI/80V from Krelus AG is used. Secondly, **MIC** (Figure 2 b) and c)) from ThermoExpert Deutschland GmbH are tested. These are mineral-insulated heating cables with seamless cold ends of the type SMH-I20/1500. They consist of a Ni20Cr wire conductor and an Inconel 600 isolation jacket. The length of the heating cable is 1500 mm, the length of the cold lead is 250 mm. The minimum bending radius of 5 mm is used for the heating track. Two variants of integration are investigated. The first variant is inserted into machined grooves on the outside of the specimen and fixed in a form closure by a punching operation. The second variant was additionally connected by means of vacuum brazing. The variants will be referred to as **MIC form closure** and **MIC brazed** respectively. A hot runner controller Thermonom 12 from Intronik is used for the heating wires together with a variable transformer 2422-529-07411 by Filec. The **thick-film** technology 'BlueFlow', visible in Figure 2 d), is also investigated in this study. Thick-film heating elements are multilayer systems. A dielectric layer is applied to the specimen. This is followed by the actual heating conductor track. Both layers are applied by screen-printing and later burnt in. The total thickness of the thick-films 120 µm. A thick-film layer is applied to each of the straight outer surfaces of the test specimen. Thus, there are two independent heating layers. They are 254 mm long and 22 mm wide. Each layer has an electrical round plug-in connection for power supply. With the empty spaces for attachment points considered, there is a heated area of 5300 mm² per layer. The power output is 525 W for each layer. Based on this, the power per area equals 99 kW/m².

  doi:10.5075/epfl-298799_978-2-9701614-0-0

Considering the specimen surface area, the power per area is reduced to 54.7 kW/m². A DPT6 multi-channel control unit from Günther Heisskanaltechnik is used for controlling the temperature. The last studied heating concept in this study are **thin-film** resistance heating layers which are applied by atmospheric plasma spraying (APS) [9], see Figure 2 e). First, a 50 µm thick Ni20Cr bond coat is applied which improves the adhesive bond between substrate and spray additives. Additionally, an aluminium titanium oxide (Al_2O_3-$3TiO_2$) insulating base layer is applied. In this work, a thickness of 200 µm is used. Afterwards, the standard alloy Ni20Cr is also used as a heating layer. A conductor width of 9 mm, thickness of 120 µm and an operating voltage of 85 V is chosen. 47 % of the specimen surface is covered by the heating track geometry, which is adapted to the specimen geometry as well as the attachment points. In this study an insulating cover layer is not used. A 3000 W DC power supply unit HEAPS 8360-30 2U from Heiden Power GmbH is used. Two high-temperature resistant cables of the series ÖLFLEX HEAT 350 SC are used per supply line. Mechanical clamps are used for the electrical contact due to difficulties with brazed contacts in preliminary investigations. The characteristic electrical data of the heating systems investigated is listed in Table 2. The power per area is calculated considering the outside area of the mould of 19 200 mm² on which the heating systems are applied on. The **IR heater** system is limited by the power of the available heaters and the gaps between the emitters. The achievable length of the **MIC** variants is restricted by the minimum bending radius of the heating cable. Their fixation method of either form closure or vacuum brazing limits the applicable power. The **MIC brazed** have a better thermal contact to the tool than **MIC form closure**, allowing them to be operated at a higher voltage without damaging the inner heating core due to overheating. The **thick-film** can only be applied on the flat surface areas due to manufacturing reasons. The **thin-film** has the highest power per area and in this study it is limited by the available power supply unit.

Table 2. Technical data of the investigated mould heating systems

	IR heater	**MIC form closure**	**MIC brazed**	**Thick-film**	**Thin-film**
Current [A]	11.9	10.6	13.0	2.3	29.6
Voltage [V]	80	55	65	230	85
Total power [W]	952	585	845	1050	2516
Power/area [kW/m²]	49.6	30.5	44.0	54.7	131.0

2.3. Test setup and evaluation method

The testing rig is shown in Figure 3. The frame of the testing oven is made of aluminium profiles and is completely enclosed with steel sheets to minimise convective effects. The specimen is positioned in the middle of testing oven by three attachment rods. Cooling nozzles are integrated in the testing oven and are fed by an external compressed air supply. The power supply and the thermocouples are passed through holes into the oven. Type K thermocouples (nickel/chrome-nickel/aluminium) with a diameter of 0.75 mm and a length of 500 mm with an insulating Inconel 600 jacket are used. The temperature is measured with a custom temperature logger at a frequency of 10 Hz and analysed in Labview. Additionally, an infrared-camera 'VarioCam hr' from Infratec GmbH is positioned in front of the oven to measure the temperature distribution on the inner surface of the specimen in separate heating trails with the front cover removed. The frame rate is one frame per second and the emission coefficient is set to 0.93.

  doi:10.5075/epfl-298799_978-2-9701614-0-0

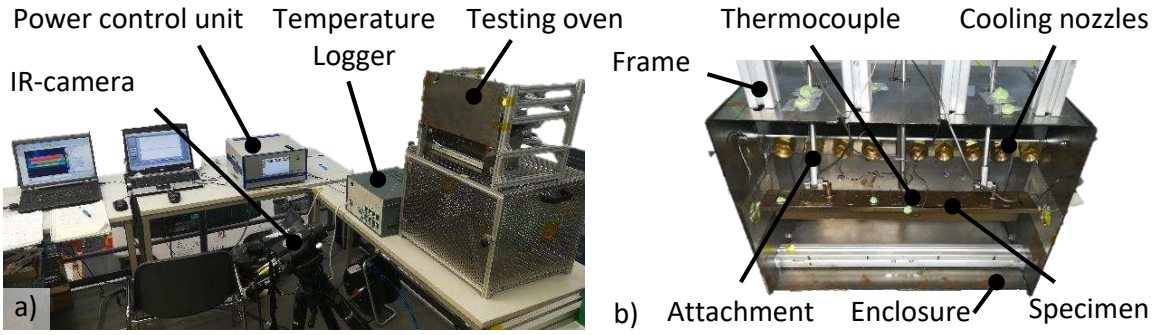

Figure 3. a) Testing rig consisting of b) testing oven, temperature logger, IR-camera, different power control units and measuring equipment

2.4. Temperature cycle

The targeted application of the investigated mould heating systems is the consolidation of high-temperature thermoplastic composites. Thus, a processing temperature of 376 °C is chosen for the consolidation of CF-PEKK. The consolidation cycle consists out of a heat-up phase, a consolidation dwell phase of 330 s and a cool-down phase. The maximum possible heating rates are to be experimentally investigated. The presented heating rate is measured by the thermocouples which determine the control loop and the fastest thermocouple during the IR heater experiments as the **IR heaters** needed manually control.

2.5 Energy consumption

The energy consumption along the whole process chain of a composite is of high relevance to evaluate the environmental impact in a life cycle analysis as well as the operational costs during manufacturing. In the heating interval t_{Heat} from 30 °C to 350 °C, in which the different control units heat with the full power available, the required electrical energy of the heating methods is determined. Due to the different control units and controls, the electrical operating variables are measured individually for each heating method. Once the current I and voltage U have been determined, the required electrical work W_{el} can be calculated with with Eq.1:

$$W_{el} = U * I * t_{Heat} \quad . \tag{1}$$

The DC power supply unit of the **thin-film** supplies the heating layer with a constant 85 V. The current measured by the power supply unit during this process is recorded every 10 s. The voltage supply to the **MIC** is constant and is set at the transformer at the beginning of the experiments and checked with a multimeter. The changing current over time is measured with a power meter PCE-830 of PCE Deutschland GmbH at 0.5 Hz. The **IR heaters** each have a resistance of 0.84 Ω. The eight radiators are connected in series. The control unit supplies the radiators with a constant 80 V during the heating interval. This results in an electric current of 11.9 A. The electrical current cannot be measured over time due to the experimental setup. For the calculation of the required electrical energy, the current must therefore be considered constant. The DPT6 controller of the **thick-film** automatically records the output power at 1 Hz.

3. Results

A representative heating cycle for each heating system investigated is shown in Figure 4. All heating systems reached the targeted processing temperature of 376 °C at the controlled TC.

  doi:10.5075/epfl-298799_978-2-9701614-0-0

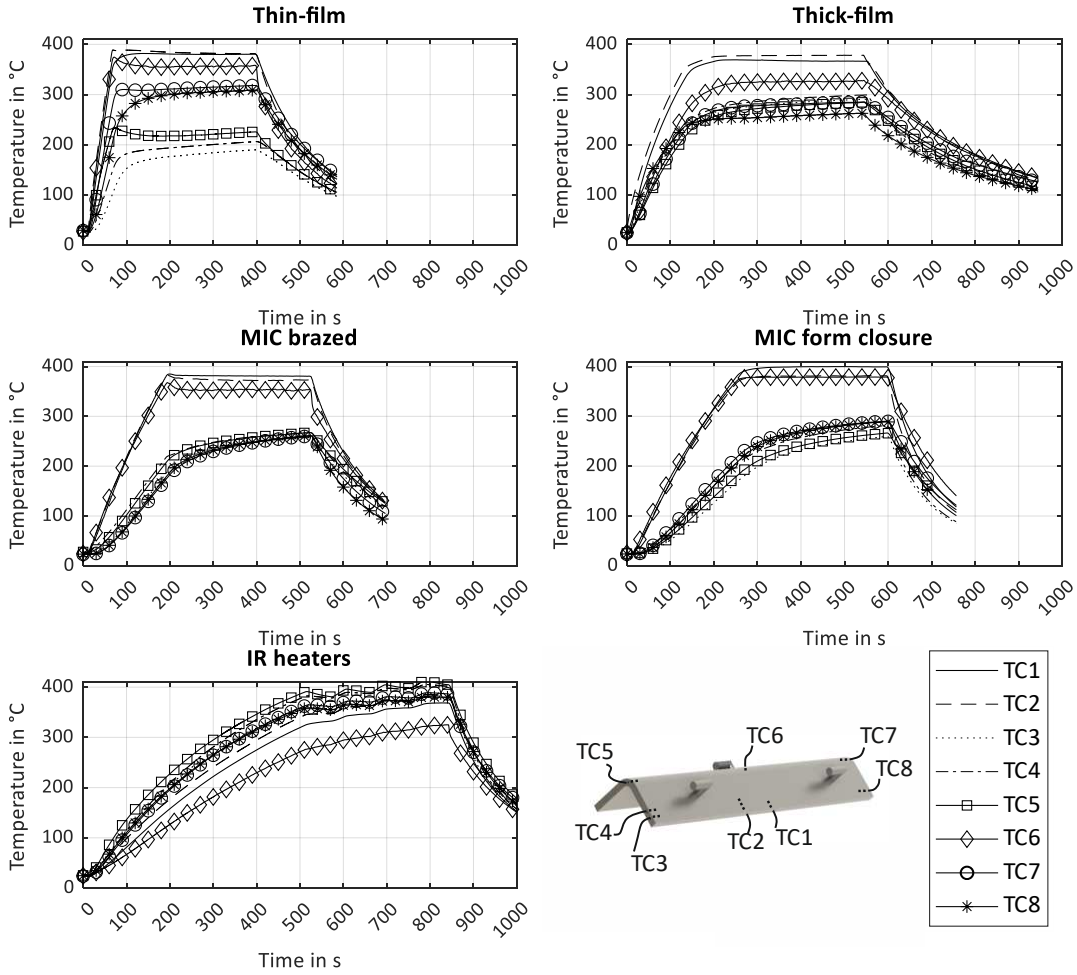

Figure 4. Measured temperature cycles of the different variothermal heating systems

All resistive heating variants show a similar temperature distribution and heating cycle. In the center of the resistive heating specimen, the targeted temperature is reached quickly and is controlled by the power control units accurately. The temperature on the outer edges of the specimen lags with a high amount of deviation to the center. The temperature evolution in the **IR heater** specimen is slower and less linear than for the resistive heating variants. The total temperature deviation is smaller compared to the resistive heating specimen. In Figure 5 the temperature distribution is shown in thermal images for the **MIC form closure** specimen and the **IR heater** specimen during the heating phase.

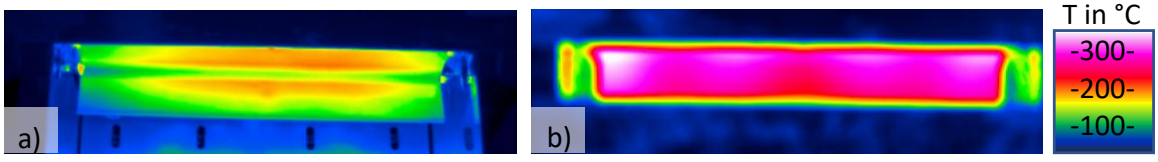

Figure 5. Thermal image showing the temperature distribution in the heating phase on the specimen surface for a) MIC form closure specimen and b) IR heater specimen

The temperature gradient from the edges to the center for the resistive heating variants is mostly attributed towards the electrical contacts for the **thick-** and **thin-film** specimen and cold

ends of the **MIC** specimen. Additionally, higher convective losses are expected at the outer edges. The temperature distribution on the **IR heater** specimen is caused by the gaps between the emitters. The heating rates and temperature deviations are listed in Table . The temperature deviation is measured at the end of the consolidation dwell time before cooling down. The **thin-film** is the fastest heating system investigated. The **IR heaters** achieved the lowest overall temperature deviation, although the deviation in the center of the specimen is the highest. It is caused by the radius section not being directly radiated from the heaters. The higher possible voltage enabled the **MIC brazed** to achieve higher heating rates. The radius section not being covered by the heating system causes a high temperature deviation in the center of the specimen of the **thick-film** specimen. The **thick-film** control unit already regulated before reaching the target temperature of 376 °C, which is why the heating rate is lower at the end of the heating phase.

Table 3. Comparison of the measured heating rates and temperature deviations

	IR heaters	**MIC form closure**	**MIC brazed**	**Thick-film**	**Thin-film**
Power/area [kW/m²]	49.6	30.5	44.0	54.7	131.0
Heating time 30 °C – 376 °C [s]	449.4	244.5	174.7	206.0	53.3
Heating rate 30 °C – 350 °C [K/min]	49.8	89.5	121.0	146.6	395.1
Heating rate 30 °C – 376 °C [K/min]	46.2	84.9	118.8	100.8	389.5
Max. temperature deviation [K]	80.1	140.2	120.5	115.6	191.8
Max. temperature deviation in specimen center (TC1, TC2, TC6) [K]	75.9	20.5	27.2	50.9	22.3
Electrical work W_{el} 30 °C – 350 °C [kWs]	367.5	130.0	122.1	136.6	120.1

The **thin-film** specimen is the most efficient system with the least amount of electrical work required for the heating operation. This is due to the high contact area of the heating conductor track with the specimen as well as the conductive heat transfer. Vacuum brazing enabled the **MIC brazed** to require less electrical work than **MIC form closure**. The **IR heaters** required the highest amount of electrical work to heat the specimen, roughly about a multiple of three compared to the resistive heating systems.

4. Discussion

The design of the heating systems affects the effectivity and efficiency to a large degree. The electrical contact of the resistive heating systems as well as the cold ends of the **MIC** have to be compensated in the mould design to avoid large temperature deviations. The power per area of the **thick-film** is reduced by 45 % because the radius section cannot be covered due to manufacturing reasons. A flat face mould design would improve the effectivity and efficiency of the **thick-film** system. The **IR heater** system achieved the lowest heating rates and lowest efficiency due to the energy dissipation during the process. Gaps between the emitters introduce high temperature deviation. The layout of the **IR heaters** needs to be improved to minimize gaps and the associated negative results. The effects of deviations in the coefficients of thermal expansion of the mould and the heating systems attached need to be investigated especially for large aerospace tooling. Stainless steel was used as a mould material in the experiments, even though it has a low thermoconductivity of 15 W/mK compared to other steel

  doi:10.5075/epfl-298799_978-2-9701614-0-0

alloys. To improve temperature distribution in the mould, other alloys can be more favourable. The heating rates are only measured for the mould. With composite material in the mould during the manufacturing process, the heating rates will be reduced. A higher efficiency and lower cycle time can be achieved when the manufactured cycle starts and ends at temperatures like the glass transition temperature of the composite material.

5. Conclusion

Tooling technology plays an important role in the industrialisation of high temperature thermoplastic composites in aerospace in order to exploit the potential of short cycle times of the materials and to reduce manufacturing efforts in out-of-autoclave processes. In this study, a thin-walled mould design and four different variothermal heating systems have been introduced and experimentally tested. Short cycle times of less than 20 minutes are achieved for all systems. Future work has to be done to optimize the design of the heating systems in order to improve the temperature distribution in the mould. Even though the **IR heater** system reached the lowest heating rates and comparably low efficiency, its contactless heating capability enables the heating system to be adjusted to different moulds. This reduces capital investment and increases the modularity of the system significantly, especially for similar but different parts in the aerospace industry. The implementation of the heating systems to manufacture complex composite structures is subject of future research.

Acknowledgements

The authors gratefully acknowledge the funding of this work by the Federal Ministry for Economic Affairs and Climate Action, BMWK, within the Federal Aviation Research Programme LuFo V-3 and GÜNTHER Heisskanaltechnik GmbH for the support and the supply of specimen.

6. References

1. Garthaus C, Barfuss D, Witschel B, Gude M. Tape braiding: high-performance fibrereinforced thermoplastic profile structures. 2015 Apr;JEC Composites Magazine(Issue #96):62–4.
2. Liebsch A, Müller-Pabel M, Kupfer R, Gude M. LIFE CYCLE ASSESSMENT OF THERMOPLASTIC HYBRID STRUC- TURES WITH HOLLOW PROFILES. 2020;11.
3. Matsen MR. Induction Consolidation/Molding of Thermoplastic Composites Using Smart Susceptors [Internet]. United States; 2012 Jun p. 81. Available from: doi:10.2172/1043163
4. Koshukow MW. Entwicklung und Aufbau einer automatisierten Prozesskette für die Herstellung komplexer Kunststoff-Metall-Hybridstrukturen. :13.
5. Schaal L. Roctool LIT: A high performance and cost-effective solution for automotive and aeronautical applications. Reinforced Plastics. 2018 Dec;62(6):307–13.
6. Reynolds N, Awang-Ngah S, Williams G, Hughes DJ. Direct Processing of Structural Thermoplastic Composites Using Rapid Isothermal Stamp Forming. Appl Compos Mater. 2020 Apr;27(1–2):107–15.
7. Singh A, Reynolds N, Carnegie CR, Micallef C, Keating EM, Winnett J, et al. A novel route for volume manufacturing of hollow braided composite beam structures. Advanced Manufacturing: Polymer & Composites Science. 2019 Oct 2;5(4):224–9.
8. Barfuss D, Würfel V, Grützner R, Gude M, Müller R. Integral blow moulding for cycle time reduction of CFR-TP aluminium contour joint processing. In Palermo, Italy; 2018 [cited 2021 Oct 29]. p. 050003. Available from: http://aip.scitation.org/doi/abs/10.1063/1.5034876
9. Scheitz S, Toma F-L, Berger L-M, Puschmann R, Sauchuk V, Kusnezoff M. Thermally sprayed multilayer ceramic heating elements. Thermal spray bulletin 4. 2011;(Nr. 2):88–92.

A COMPARISON OF INFRARED AND XENON FLASHLAMP HEATING FOR THERMOSET AUTOMATED FIBRE PLACEMENT

Dr David Williams

Consultant, Heraeus Noblelight Ltd., Unit 163, Cambridge Science Park, Milton Road, Cambridge, CB4 0GQ, UK – david.williams@heraeus.com

Abstract: *Xenon flashlamp heating has shown significant promise as an alternative to laser and infrared heating in Automated Fibre Placement (AFP). Although research has primarily been focused on high-power heating of thermoplastic composites, there is still a pressing need to improve automated processing of thermoset composites for current aerospace applications. This paper focusses on a comparison of infrared heating (the state-of-the-art on many AFP systems) and flashlamp heating applied to AFP of thermoset materials.*

Three aspects of the AFP process are investigated: the maximum achievable lay-up speed; the homogeneity and extent of the heating across the material width (perpendicular to the lay-up direction); and the ability of the heating systems to achieve fast heat-up and cool-down rates.

Keywords: Flashlamp; Infrared; Automated Fibre Placement; Thermoset

1. Introduction

As the automated processing of composite materials using AFP has developed over the last decade, there has been a significant body of research focused on new materials such as bindered dry fibre and thermoplastics. These materials typically require higher processing temperatures and more sophisticated heating technologies in order to manufacture high quality components. The Xenon flashlamp heating technology was developed with these materials in mind, to offer an alternative to lasers and hot gas guns ([1], [2], [3], [4]).

At the same time, industries such as aerospace have continued to manufacture using lower-temperature thermoset materials, and there is now a growing need to increase manufacturing rates and part quality due to the high demand for new aircraft. It is perhaps surprising then that the heating technologies typically used for thermoset AFP have remained relatively unchanged, with the standard infrared (IR) lamp being the state-of-the-art on the majority of thermoset AFP systems. While IR lamps are simple and can achieve the 30-60°C temperature required for AFP lay-up, they are known to have several deficiencies. Lichtinger et.al. ([5]) showed that IR lamps are prone to heating outside the lay-up zone and risk advancing the cure of thermoset materials in these areas, whilst Hormann et.al. ([6]) identified the importance of controlling the heat source in variable speed lay-up to achieve a defined surface temperature. Calawa & Nancarrow ([7]) also recognized the need for a high-power and fast-acting heat source that could maintain the required temperature through the variable-speed AFP processing typical of complex geometries.

This paper investigates the application of the Xenon flashlamp heating technology to thermoset AFP, comparing it to the standard IR lamp in its ability to reach high processing speeds, minimize heating outside the lay-up zone and give fast heat-up and cool-down rates.

  doi:10.5075/epfl-298799_978-2-9701614-0-0

2. Experimental Configuration

Experimental trials were conducted in partnership with Compositadour, Bayonne, France. A Coriolis "C-Solo" AFP system, laying up a single ¼" epoxy prepreg tape of Hexcel 8552/AS4/135gsm material, was used for all trials. Lay-up was performed onto an Aluminium tool with a glass fibre surface layer vacuumed to the table under a thin thermoplastic film. An elastomeric compaction roller of Shore Hardness 40 was used with a compaction force of 300N in all cases. In order to limit the effects of heat conduction into the tool, two substrate plies were placed in advance, each of 8 ¼" tapes (a total of 2" width), to create a base substrate onto which a single ¼" tape could be applied for each of the subsequent trials.

An Optris thermal imaging video camera was installed onto the robot head to follow the lay-up and focus on the "nip point" (the point where the incoming tape adheres to the substrate). The material emissivity was set at 0.85 to match previous studies at this viewing angle. Figure 1 shows a typical image from a thermal video during lay-up.

IR Trials

For the IR trials, two 600W lamps were used in the positions shown in figure 2. These lamps are supplied in this configuration as the default heating system for the C-Solo AFP machine and are twin-tubed (figure of 8 cross-section) with their output energy concentrated in the 1 – 1.4µm wavelength band. As the figure suggests, the majority of the lamp energy is directed towards the substrate some distance from the nip point. The closest lamp is approximately 81mm from the nip point and 16mm above the substrate.

The lamps heat in a continuous manner, and the heating power can be modulated by varying the current flowing through the lamp filaments. This is typically achieved by setting a percentage power value on the AFP machine interface and can be set to vary with robot speed.

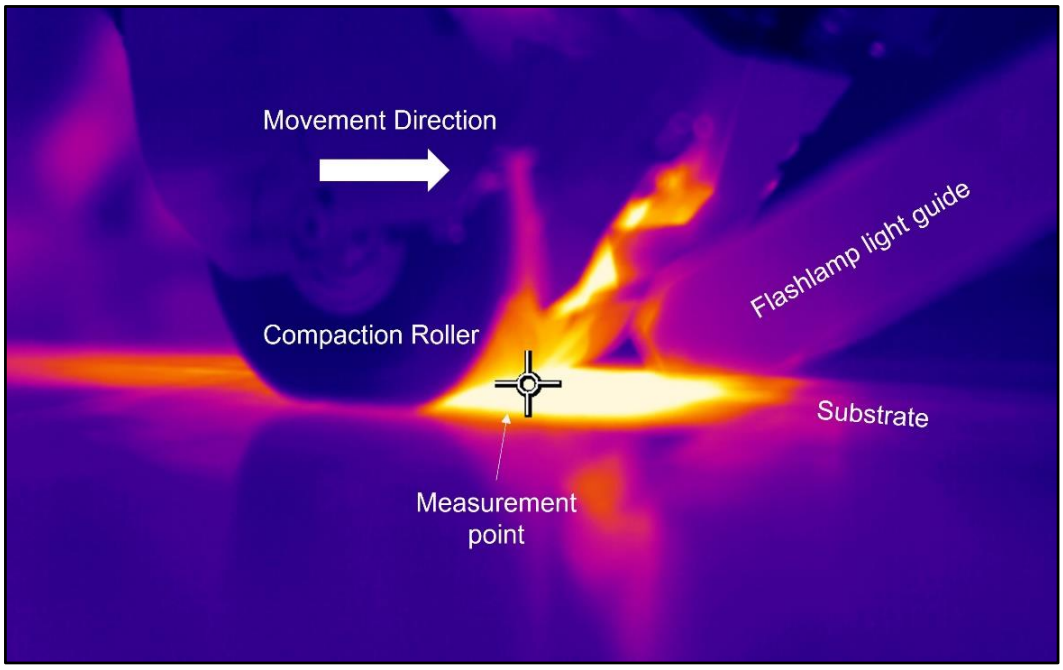

Figure 1: Typical thermal image showing the geometry around the nip point during lay-up and the temperature measurement position used in all trials.

  doi:10.5075/epfl-298799_978-2-9701614-0-0

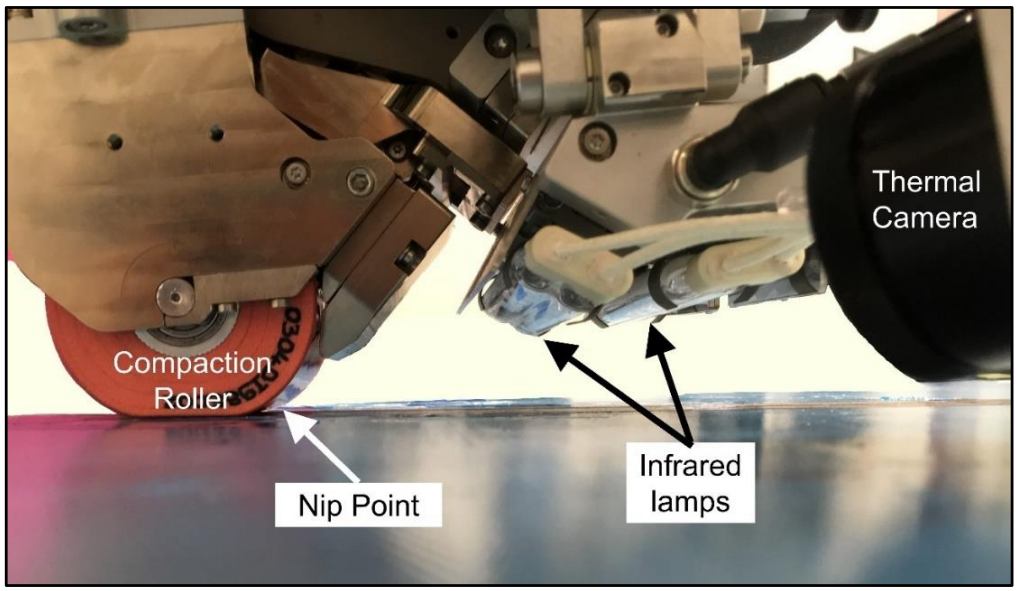

Figure 2: Side view of lay-up showing position of IR lamps. (Note that the image has been edited to remove background details for clarity).

Flashlamp Trials

The Xenon flashlamp system used in the trials provides heat in the form of high-energy pulses with a very broad spectral output, with energy in the UV, visible and infrared spectral regions. Three pulse parameters: pulse voltage (typically 150-250V); pulse frequency (number of pulses per second – typically 60-100 Hz); and pulse duration (typically 2-5ms) are varied to modulate the average output power of the system. The pulses superimpose as the flashlamp passes across a moving target, resulting in a constant nip point temperature. The flashlamp system used in this work was limited to 6kW electrical input power, which equates to approximately 3kW optical output power.

The flashlamp is contained in a head with a shaped reflector behind and an aperture in front, to guide the energy into a solid quartz light guide, as shown in figure 3. The light guide acts to guide the flashlamp energy to the target surfaces by means of total internal reflection. The end of the light guide is shaped into three output surfaces, to give control over the thermal profile on the incoming tow, the substrate, and the nip point. The flashlamp and the head materials are cooled by a flow of deionized water in an annular jacket that surrounds the lamp, meaning very little latent heat builds up in the system. The output from the light guide is diffuse and broadband, giving some safety benefits over laser heat sources. Further background information on the flashlamp system can be found in [1] and [2].

For the trials in question, the flashlamp light guide was positioned approximately 45mm from the nip point at an angle of 25 degrees and 5mm offset from the substrate, as shown in figure 3. This angle allows the lower output surface of the light guide to lie parallel to the substrate. Previous work has shown that the nip point temperature is weakly dependent on the offset and angle of the light guide.

  doi:10.5075/epfl-298799_978-2-9701614-0-0

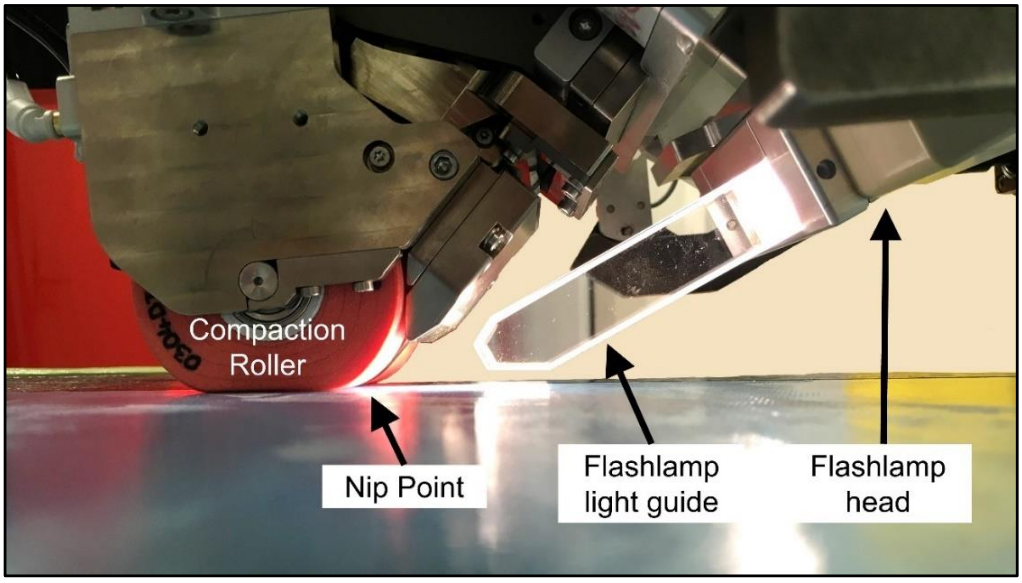

Figure 3: Side view of lay-up showing position of flashlamp head and light guide. Note that the image has been edited to remove background details for clarity.

3. Maximum Lay-Up Speed

A series of trials was conducted with both heating systems at lay-up speeds of 0.2, 0.4, 0.6, 0.8 and 1m/s. For each speed, a total of 5 power levels were used for each heater – 20%, 40%, 60%, 80% and 100% heating for the IR lamps (set on the Coriolis AFP system), and 1, 1.5, 2, 2.5 and 3.5kW electrical input power for the flashlamp system (set on the flashlamp control software). It was not possible in the short duration of the testing to measure the absolute power levels for the IR lamps. Note that the maximum output power of the flashlamp system is 6kW, but lower power values were employed to avoid heat degradation of the material.

Thermal videos were captured for each trial and a nip point temperature was extracted in each case by monitoring the measurement area at the nip point (figure 1) and taking an average temperature over the full lay-up run.

In the case of the IR trials, it was observed that the nip point temperature for 100% power decreased for each increase in speed, as expected. At 0.2m/s, the maximum nip point temperature achieved was 75°C and this reduced to 60°C at 0.4m/s. Therefore, if the target surface temperature is set at 60°C in this study, the maximum lay-up speed to reach this target for the IR heating system is 0.4m/s.

For the flashlamp system, at 0.2m/s the maximum temperature observed was 95°C at the 3.5kW power level, at 0.4m/s the maximum was 70°C and at 0.6m/s it was 53°C. As the full power capabilities of the flashlamp system were not deployed in the trials, it was desirable to extrapolate the results to the higher power values available (up to 6kW for this system). The power law technique employed by Di Francesco et.al. [8] and Monnot et.al. [9] was used to estimate the results at higher speeds from the trial results at lower speeds and powers. This empirical procedure, described in [9], makes some assumptions on the shape of the speed vs. power graph and enables the graph to be drawn for any chosen nip point temperature. Figure 4 shows the estimated power vs. speed graph for a chosen 60°C nip point temperature. Several data points from the trials are added for reference.

  doi:10.5075/epfl-298799_978-2-9701614-0-0

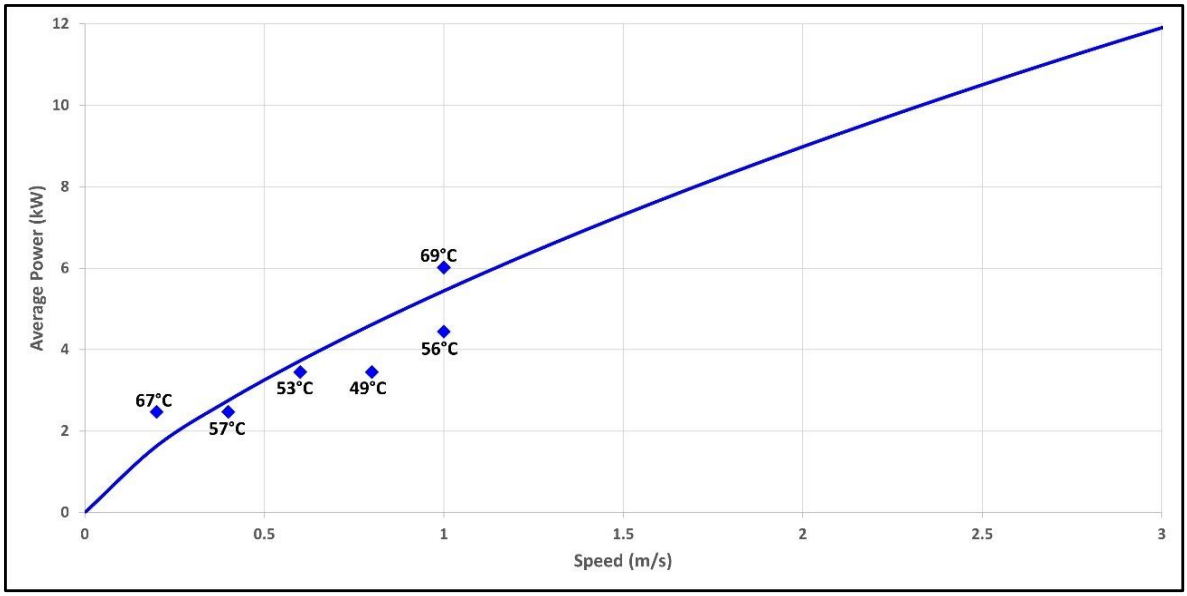

Figure 4: Estimated power law for flashlamp system obtained using empirical method of [9]. The blue line estimates the speed vs. Power relation for a nip point temperature of 60°C.

The graph in figure 4 estimates that, had the flashlamp been deployed at its maximum power of 6kW, the maximum lay-up speed for a 60°C nip point temperature would have been approximately 1.2m/s. For alternative flashlamp systems at higher powers, the graph indicates that higher lay-up speeds are achievable.

4. Homogeneity Across Lay-Up Width

In order to investigate the homogeneity of each heating system across the width of the lay-up, a total of 13 parallel tapes was laid as a substrate, giving a total width of 3¼" on which trials could be performed. The compaction roller was removed (as it was found to have a cooling effect on the substrate) and the temperature generated on the substrate was measured perpendicular to the lay-up direction, with the camera positioned behind the robot head, as shown in figure 5. Note that a heated zone width of 2" is typical for AFP lay-up, where 8 parallel tows are placed in one robot pass.

A representative result is shown in figure 6, where the blue line shows the flashlamp heating concentrated on the central 2" zone and the red line shows the IR lamp heating more outside this central zone. Both lines are normalized to allow comparison of the profiles.

The flashlamp heated zone is relatively homogeneous in the central 2" zone as the flashlamp light guide has a width of just over 2". The thermal profile rolls off quickly at the edges and minimizes the heating of already-laid material outside the central zone. The light guide can be designed for different heating widths, and additional work has shown that a wider light guide (60mm) can move the roll-off zones to beyond the central 2".

The red line in figure 6 shows that the IR heating is less homogeneous in the central zone and significant heating occurs outside the 2" target width. As observed by Lichtinger et.al. [5], this heating of the already-laid material is undesirable and may cause unwanted advancement of the material cure in these areas.

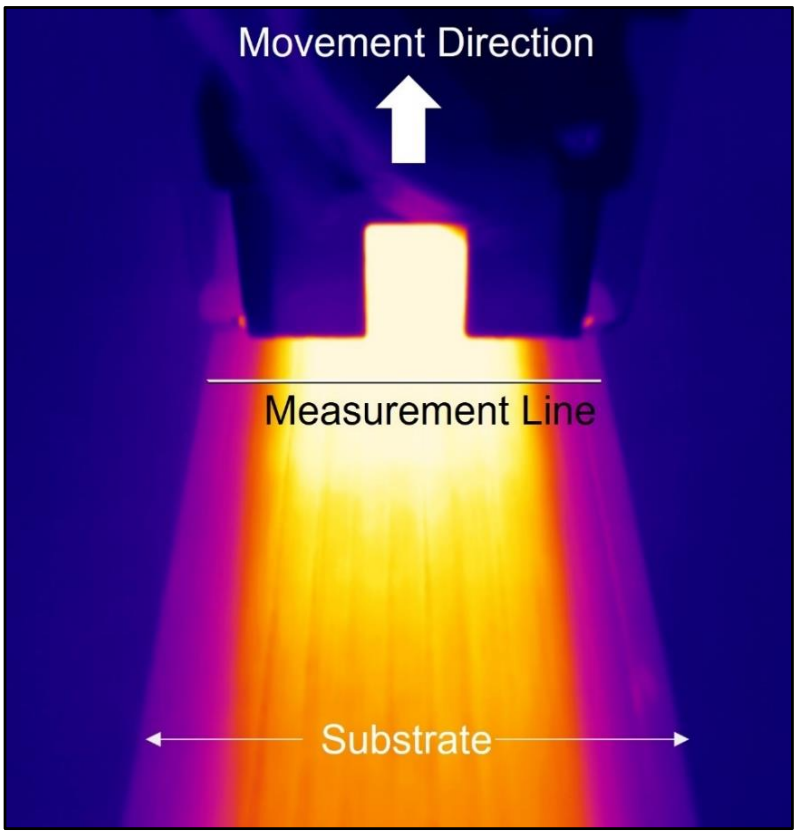

Figure 5: Thermal image showing the thermal profile across the substrate from behind the robot head. This example shows a result for the flashlamp system.

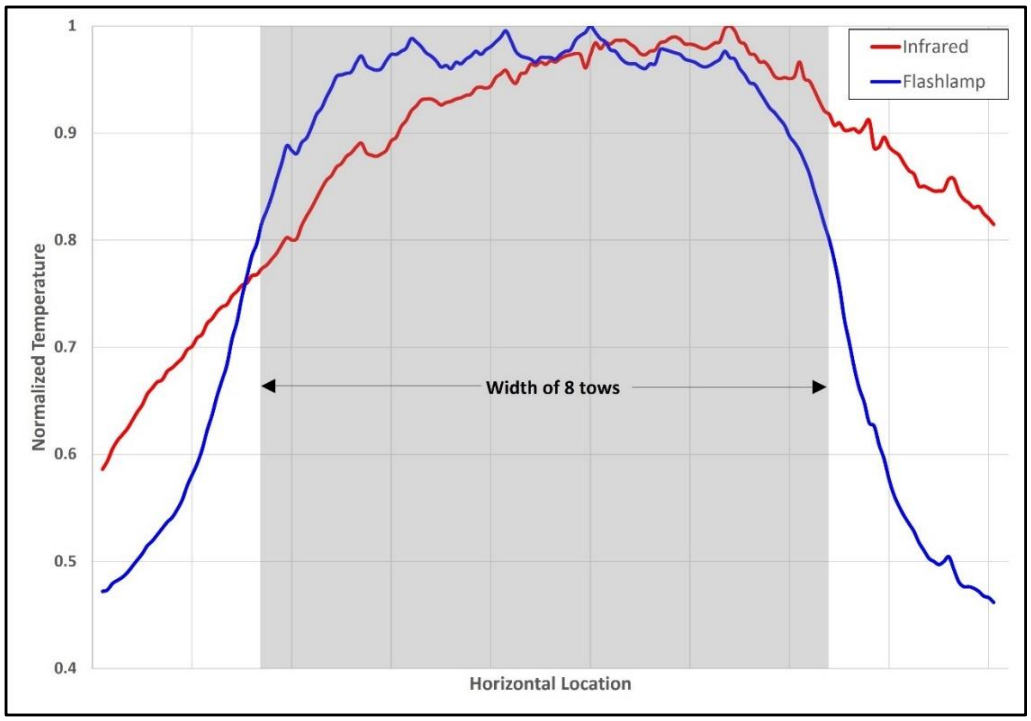

Figure 6: Graph of thermal profiles across the substrate. The blue line shows the flashlamp result and the red line shows the IR result. The grey area shows the position of a typical 8 tows. Results have been normalized to facilitate the comparison between heating systems.

  doi:10.5075/epfl-298799_978-2-9701614-0-0

5. Heat-Up and Cool-Down Rate

Further trials were conducted to assess the heat-up and cool-down rates of the two heating systems. Figures 7 and 8 show representative results where heating was switched on 1.5 seconds into the lay-up run, then switched off at 8.5 seconds.

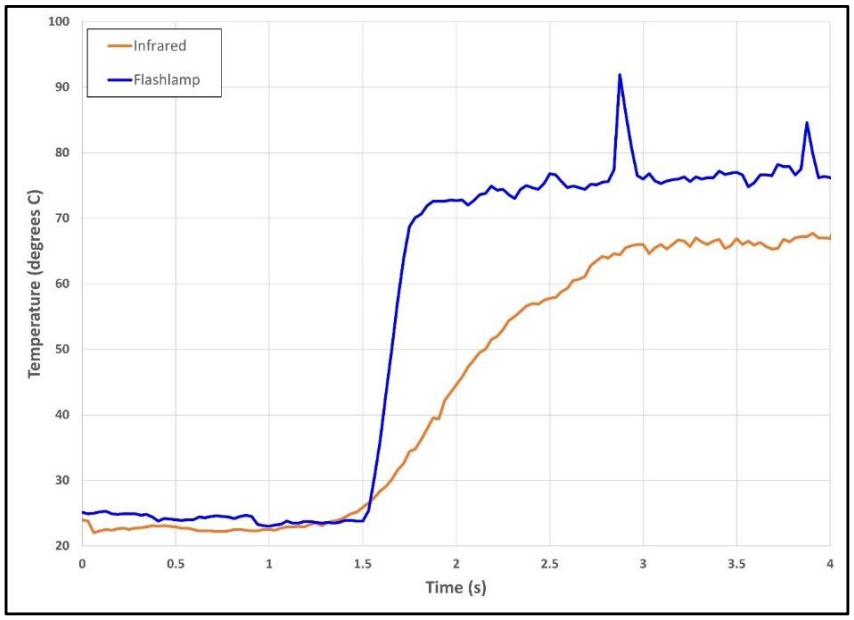

Figure 7: Graph of nip point temperature for heater switch on at 1.5s

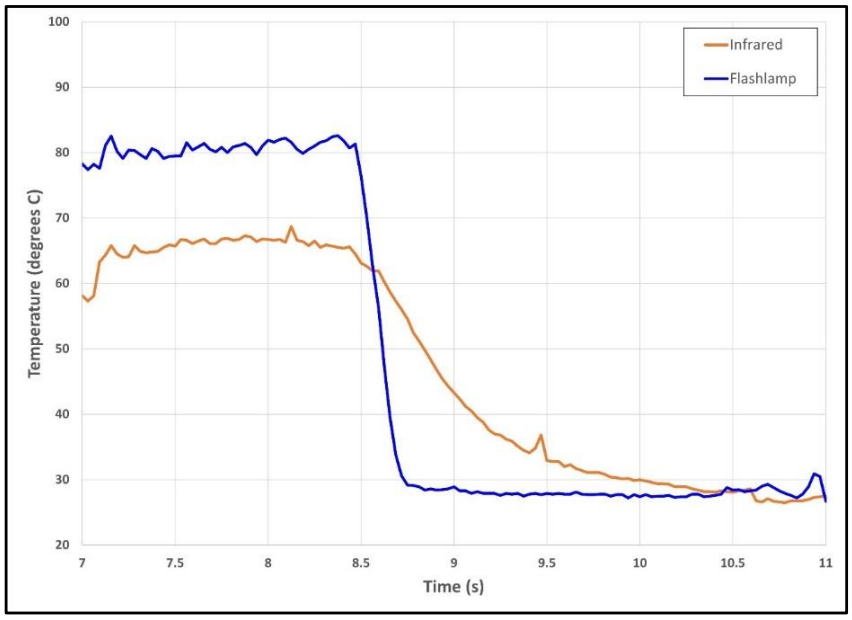

Figure 8: Graph of nip point temperature for heater switch off at 8.5s

The graphs in figures 7 and 8 show that the reaction time of the flashlamp system is approximately 0.1s for both heat-up and cool-down in this case, whereas the equivalent reaction time for the IR system is approximately 1.5s. This reaction time has important consequences for the lay-up of a complex component, where lay-up speed may vary quickly, and the heater must be able to modulate its power to maintain the target surface temperature.

  doi:10.5075/epfl-298799_978-2-9701614-0-0

6. Conclusions and Further Work

The experimental results described here facilitate a comparison between IR and flashlamp heating in a representative thermoset AFP application. The flashlamp system has been shown to offer higher achievable lay-up speeds, due to the greater power available and its ability to focus that power via its light guide. There is also a marked difference in the thermal profiles across the heated zone. The flashlamp concentrates the majority of its energy onto the central 2” zone, whereas the IR lamp spreads its energy outside this zone. The relative reaction times of the two heat sources are also significantly different, with the flashlamp system reacting at switch-on and switch-off in approx. 0.1s and the IR system reacting in approx. 1.5s.

The results described here, highlighting three important aspects of AFP lay-up, suggest that the flashlamp system is worthy of further investigation. Further work will include investigation of higher power flashlamp systems and the effects of flashlamp position on lay-up performance.

Acknowledgements

This work was performed at Compositadour, Bayonne, France. The assistance of engineers at Compositadour is gratefully acknowledged.

References

1. Williams, D. and Brown, M. “Developments in Xenon Flashlamp Heating for Thermoplastic Automated Fibre Placement”, Proceedings of the Fourth International Symposium on Automated Composites Manufacturing, Montreal, Canada, April 2019.
2. Williams, D., “A New Light on Composites Heating”, JEC Composites Magazine 111, Special JEC Issue, March 2017
3. Brandt, L., Deden, D., Fischer, F., Dreher, P. N., Williams, D., Engelschall, M., Nieberl, D., and Nowotny, S. “Xenon flashlamp based in-situ automated fiber placement of thermoplastic composites”. In: Twenty-Second International Conference on Composite Materials (ICCM22), Melbourne, Australia, August 2019.
4. Deden, D., Bruckner, F., Brandt, L. and Fischer, F. J. C. “Comparison of Heat Sources for Automated Dry Fibre Placement: Xenon Flashlamp vs. Infrared Heating”, In: Twenty-Second International Conference on Composite Materials (ICCM22), Melbourne, Australia, Aug 2019.
5. Lichtinger, R., Hörmann, P., Stelzl, D. and Hinterhölzl, R., “The effects of heat input on adjacent paths during automated fibre placement”, Composites: Part A (2014), Volume 68, January 2015, Pages 387-397.
6. Hörmann, P., Stelzl, D., Lichtinger, R., Van Nieuwenhove, S., Mazón Carro, G., Drechsler, K. ”On the numerical prediction of radiative heat transfer for thermoset automated fiber placement”, Composites Part A: Applied Science and Manufacturing 67, 282–288, 2014.
7. Calawa, R. and Nancarrow, J., "Medium Wave Infrared Heater for High-Speed Fiber Placement," SAE Technical Paper 2007-01-3842, 2007.
8. Di Francesco, M., Veldenz, L., Dell'Anno, G. and Potter, K. “Heater power control for multi-material, variable speed Automated Fibre Placement.” Composites Part A: Applied Science and Manufacturing, 101:408–421, 2017.
9. Monnot, P., Williams, D. and Di Francesco, M., "Power control of a flashlamp-based heating solution for Automated Dry Fibre Placement," In: 18th European Conference on Composite Materials (ECCM 18), Athens, Greece, June 2018.

  doi:10.5075/epfl-298799_978-2-9701614-0-0

MONITORING PROCESS PARAMETERS ON LIQUID RESIN INFUSION FOR SHAPE DISTORTION ANALYSIS

Andrea Torre-Poza[a], Ana M. R. Pinto[b], Tania Grandal[b], Raquel Travieso-Puente[a], Elena Rodríguez-Senín[a]

a: Advanced Materials, AIMEN Technology Centre, O Porriño, Spain
b: Smart Systems and Smart Manufacturing, AIMEN Technology Centre, O Porriño, Spain
Email: andrea.torre@aimen.es

Abstract: *This paper presents a real-time monitoring experimental approach for investigation of key manufacturing parameters for shape distortions prediction starting with early manufacturing stages until the post-curing phase. Fiber Bragg Grating (FBG) sensors and Direct Current (DC) dielectric sensors were used to monitor temperature, strain and resin curing evolution during the infusion of small coupons. The combination of both sensors allowed detection of resin arrival, the point of minimum viscosity, the gel point, the temperature gradients, and the strain distribution across the coupon. At the end of the manufacturing cycle, the geometry of the coupons was evaluated by means of 3D coordinate measuring over the course of several days after tool extraction. The experimental data was used as input for the calibration of a numerical FEM-based tool for shape distortions prediction of complex structures.*

Keywords: Liquid resin infusion; process monitoring; FBG sensors; dielectric analysis; shape distortions

1. Introduction

The use of carbon fiber reinforced polymers in the manufacturing of structural parts in the aerospace sector has increased significantly in the last decades. Nowadays up to 50% of an aircraft can be made from these materials [1]. In this context, autoclave curing pre-impregnated fibres (pre-preg) has been the predominant manufacturing technique. However, the high operational cost and limitations regarding its storage and expiration dates has increased the interest in other technologies [2]. Out-of-Autoclave (OoA) Liquid Resin Infusion (LRI) processes are gaining interest in the sector as they benefit from lower operational costs, lower material waste and it is possible to reach up to 56% fiber volume fraction with them [3,4].

Shape distortions are a common problem in liquid composite moulding. The geometrical deviations from the tool (namely warpage on flat parts and spring-in/spring-back on curved parts) are undesired defects that eventually can result in discarding those parts that do not meet the tolerances during assembly operations. Several studies [5,6,7] have attributed the main cause of these defects to the residual stresses generated during the manufacturing phase. The main mechanisms responsible for these stresses are [7]: thermal anisotropy, polymerization shrinkage, tool-part interaction, temperature gradients, resin flow and compaction.

Process monitoring is a powerful tool for understanding process induced defects as it gives an insight into the process parameters affecting these mechanisms. Especially during the design phase, in which this information can help identifying causes of distortions, predict them, and

  doi:10.5075/epfl-298799_978-2-9701614-0-0

optimize the manufacturing process. Thermocouples and pressure transducers are commonly used in liquid composite moulding processes for temperature and pressure monitoring, respectively [8]. Although these sensors are simple to use, they are not very accurate for measuring resin arrival or curing evolution, which are key parameters in the manufacturing of thermoset composites [8]. Other monitoring techniques such as dielectric analysis [9] and fiber optic sensors [10] offer a better understanding of the resin curing process.

In this context, the project ELADINE (Evaluation of LAminate composite Distortion by an Integrated Numerical Experimental approach) proposes a solution based on process monitoring for the calibration of a FEM-based numerical simulation tool able to predict shape distortions on complex aircraft structural components, such a wing box. A methodology for monitoring parameters during the manufacturing of small-scale coupons by liquid resin infusion is presented in this article. A sensor network of Fiber Bragg Gratings (FBG) was used for strain and temperature monitoring in combination with dielectric Direct Current (DC) sensors for resin cure monitoring.

2. Materials and methods

2.1 Sensors for process monitoring

For the process monitoring, FBG and DC sensors were selected. FBG sensors are a minimally invasive, robust, a mature technology and a cost-effective option for strain and temperature monitoring [11]. FBG is an optical fiber with a morphological change in a small portion of its core that reflects the light at a particular wavelength (namely the Bragg's wavelength) letting the rest of wavelengths pass through. When the FBG portion of the optical fiber is expose to any external variation, there is a shift in the wavelength reflected [12]. This wavelength shift is due to strain and temperature variations, and so both signals need to be decoupled.

Dielectric sensor's working principle is based on the existence of dipoles on the resin monomers, which are oriented to conduct electricity in the presence of an electric field. As the resin curing proceeds, the monomers are combined into polymeric chains which form a complex cross-linked network hindering ion mobility and increasing electrical resistance [13]. DC sensors (provided by Synthesites) were used, since no additional insulation is needed to directly measure onto carbon fiber parts. These sensors are capable of indirectly measure the resin degree of cure in real time which later was quantified by Differential Scanning Calorimetry (DSC).

2.2 Manufacturing of composite coupons

Small scale C-shape coupons (Figure 1) resembling a spar section of the wing box of an aircraft were manufactured for understanding of the main variables affecting the spring-in on its curved parts. For these coupons, 3 mm thick HiTape dry carbon fiber (HEXCEL) flat preforms manufactured by automated fiber placement (AFP) were used as reinforcement material and RTM6 (HEXCEL) was used as resin matrix. The consolidated flat preforms were shaped into the C form by applying heat and vacuum. A composite tool was used to reduce part-tool interaction since both have similar thermal expansion coefficient.

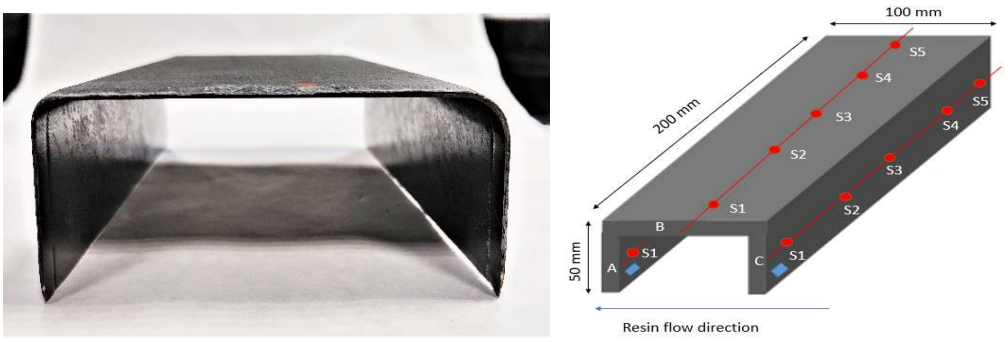

Figure 1. Photograph of a C-spar coupon manufactured by LRI (left) and sensor's schematic distribution on a C-spar coupon (right).

Before infusion, the sensors were placed between tool and dry fiber and between dry fiber and vacuum bag, following the scheme presented in Figure 1. The temperature FBG sensors were encapsulated in a 1,2 mm external diameter stainless steel tube to ensure isolation from strain induced variations. Next, the infusion consumables were placed, and the vacuum bag was closed protecting the optical fiber's exit, so that its integrity was preserved during the whole manufacturing process and without compromising the vacuum level inside the bag. After that, the tool was set in the oven, the sensors were connected, and the infusion process was carried out, for which the tool had been previously heated at 120°C and the resin at 80°C (these conditions were used during the infusion process). Once the whole laminate was saturated with resin the inlet was closed and the curing cycle begun; starting with a heating ramp from 120°C to 185°C, followed by a 2h dwell at 185°C. Finally, the coupon was cooled down by natural convection and demoulded after the temperature was below 50°C. Pictures of the manufacturing process are presented in Figure 2.

Figure 2. C-spar coupon experimental process: A) shaping of flat preforms into C-shape; B) sensors positioning and bagging configuration; C) monitoring of infusion and oven cure; D) post-manufacturing monitoring with 3DCMM and strain sensors.

2.3 Shape distortion analysis

The demoulding operation was performed very carefully to prevent the optical fibers from breaking since extra force was applied to extract the coupon from the tool. Then, the coupon geometry was assessed by means of a 3D Coordinate Measuring Machine (3DCMM). Up to 80 measuring points were controlled during two weeks after demoulding, as well as the angle formed between the spar caps and the web of the coupon. Moreover, strain variations were

also monitored during that time. The sensors were disconnected during the demoulding phase but reconnected right after for measuring the strain changes in the coupon during the days after demoulding. In this way, the same sensors used during the infusion phase also monitored the post-manufacturing phase since they were properly embedded. The resulting geometry was compared with that of the tool.

3. Results

3.1 Monitoring the LRI manufacturing process

After manufacturing, the response of each sensor embedded in the coupon was analysed. In *Figure 3* the results of one DC sensor, one strain FBG sensor and one temperature FBG sensor positioned close to each other are presented. Resin arrival was detected by the DC sensor and was identified as an abrupt decreased in the values of resistivity, since in the liquid resin the ion mobility is as its maximum, thus, conducting electricity. At the same time (1h), the FBG temperature sensor detected the same event by the decreased in the value of temperature registered, as the resin was injected at lower temperature than that of the tool. Once the whole coupon was infused, the heating ramp started and so did the curing reaction of the resin, and the polymeric chains started to form which increased rapidly the resistivity. The gel point (at 2,56h) was identified as a tendency shift in the part with upward slope of the resistivity graph. At such point, the strain sensor registered a shift in the strain signal towards negative values, which was attributed to resin cure shrinkage. From that point almost until the end of the temperature dwell, both sensors' signal stabilized marking the end of the cure because, at that moment, the resin had formed a complex network and the polymeric chains' movement was limited, thus, hindering electrical conductivity or strain evolution. When the cooling phase started, there was an abrupt decrease in the strain signal due to thermal contraction.

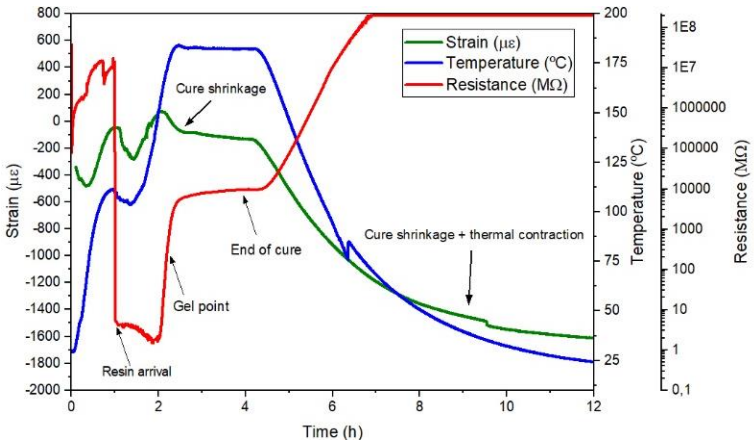

Figure 3. Results from DC sensor (red), FBG for temperature monitoring (blue) and FBG sensor for strain monitoring (green) during the manufacturing cycle of a C-spar coupon.

These results prove that the sensors offer useful information about the manufacturing procedure, even though they are from a single sensor of each type. It follows that by using a multi-sensor distribution scheme, more information can be extracted from different zones within the coupon in order to obtain a complete overview of the process in the entire geometry. With that purpose, 30 FBG sensors and 2 DC sensors were used. The arrival of the resin was detected in several points of the coupon showing a faster flow front in the surface in contact with the infusion consumables, whereas the flow front in the tool side was slightly slower and

less homogeneous, which is due to the absence of flow media on this side of the coupon. Another interesting result observed was the existence of temperature gradients during the dwell phase at 185°C (see left graph of *Figure 4*). Regarding the strain results, as explained before, the strain related to the resin curing reaction was calculated after the gel point. This point was considered as the starting point for the evaluation of strain development, for comparison purposes between sensors located at different parts of the coupon. It was observed that sensors positioned between the tool and the coupon exhibited a lower strain variation than those placed between the coupon and the infusion consumables. This effect might be attributed to the higher resin content accumulated in that area, since the infusion bagging can act as a resin reservoir causing a higher contraction of the sensors. Moreover, the tool/part interaction might influence the strain felt by the sensors since a composite tool was used for the manufacturing and it may have a similar behaviour to the manufactured coupon. An example of these results is presented in the right graph of *Figure 4*, where to ease the analysis of this effect only the results from a few sensors are presented. Moreover, it is worth noticing that at the end of the curing cycle just before demoulding, all the sensors were registering negative strain values, which means they were being contracted.

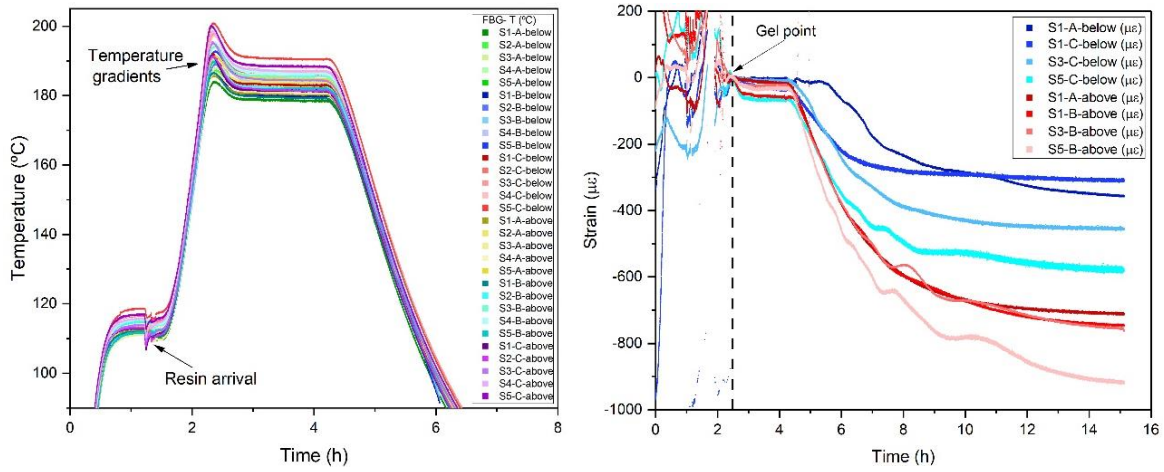

Figure 4. Temperature (left) and strain (right) results from several FBG sensors monitoring the manufacturing cycle of a C-spar coupon.

3.2 Analysis after manufacturing: shape distortion analysis

3DCMM measurements performed on the coupon right after demoulding revealed mismatches with respect to the tool geometry. An average decreased of 1,2 ± 0,4° in the angles formed by the web and the spar caps of the coupon was already observed on the first day of measurement. Moreover, a reduction in the distance between the tips of the two spar caps was detected which confirmed the spring-in effect. Daily measurements were performed for the following 20 days; however, the coupon did not experiment further distortion as shown on the left side of *Figure 5*.

On the other hand, the strain variations obtained after demoulding present lower values with opposite sign when compared with those obtained during the manufacturing, indicating de-compression of the coupon. After the first 6 days, the strain variation's magnitude was significantly lower, but did not completely stabilize. An explanation for this may be extracted by relating this data with the strain results observed during the manufacturing phase. At the end

of the curing cycle (before demoulding), the coupon had internal stresses accumulated due to resin cure shrinkage and the coupon is pressing against the tool. When the coupon was released from the mould (demoulded), those internal stresses were released in the form of macro-distortions right after demoulding (spring-in caused by bending deformation) and micro-distortions during several days after manufacturing (but not significant to cause shape distortions). Moreover, an uneven distribution of strain values within the coupon was obtained at the end of the manufacturing cycle, which can explain the shape distortions observed in the geometrical assessment.

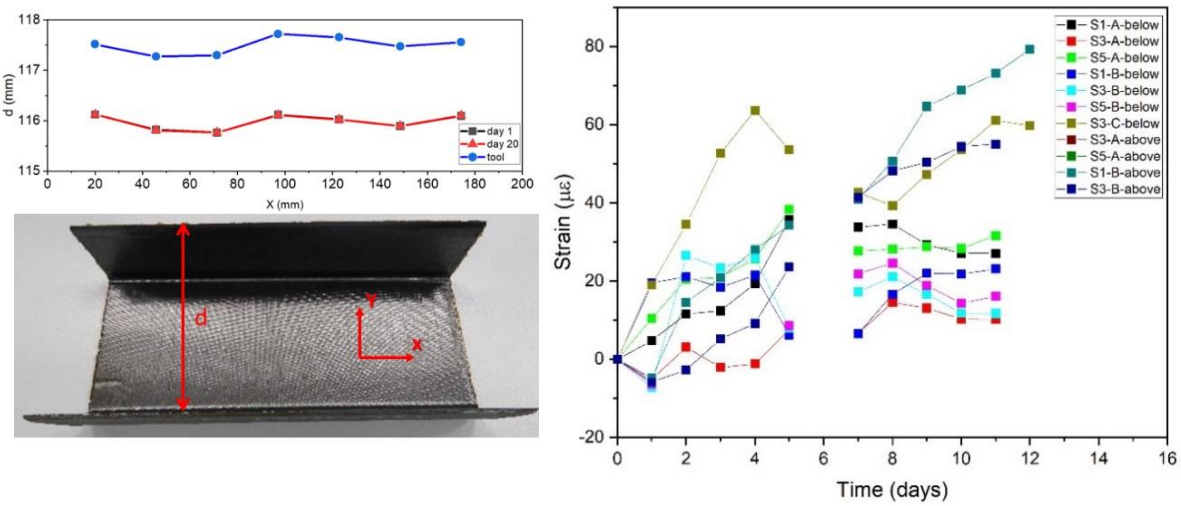

Figure 5. Evolution of the distance between spar caps obtained by 3DCMM (left) and strain results (right) after demoulding of a C-spar coupon.

Within the framework of the ELADINE project, the presented process monitoring methodology was tested and validated in coupons with other geometries, such as slightly curved coupons simulating the covering skin of an airplane wing box. The data generated during the monitoring phases was used to calibrate a FEM-based model for shape distortion prediction in complex structural components [14]. In addition, the same procedure was successfully implemented in oven cured prepreg coupons extending the applicability of this methodology to other composite manufacturing techniques.

4. Conclusions

This study presents a method for the monitoring of the manufacturing process of thermoset composites by oven cured LRI and its post-manufacturing phases. A combination of two sensing technologies, namely DC and FBG sensors, were implemented to effectively identify key parameters affecting the main phases of a resin curing process: resin arrival, minimum viscosity, gel point, end of cure, temperature gradients, cure shrinkage and thermal contraction. A strategic sensor distribution was used to gather this information in different zones of C-shaped coupons to relate them to the shape distortions occurring after manufacturing. Spring-in phenomena was observed after the manufacturing process and attributed to the residual strain accumulated at the end of the manufacturing phase. The results obtained can be used for developing predictive simulation models.

  doi:10.5075/epfl-298799_978-2-9701614-0-0

Acknowledgement

This project has received funding from the Clean Sky 2 Joint Undertaking (JU) under grant agreement No 865431. The JU receives support from the European Union's Horizon 2020 research and innovation programme and the Clean Sky 2 JU members other than the Union

5. References

1. Bachmann J, Hidalgo C, Bricout S. Environmental analysis of innovative sustainable composites with potential use in aviation sector—A life cycle assessment review. Science China Technological Sciences. 2017;60(9):1301-1317.
2. Witik R, Gaille F, Teuscher R, Ringwald H, Michaud V, Månson J. Economic and environmental assessment of alternative production methods for composite aircraft components. Journal of Cleaner Production. 2012;29-30:91-102.
3. Hindersmann A. Confusion about infusion: An overview of infusion processes. Composites Part A: Applied Science and Manufacturing. 2019;126:105583.
4. Liu Y, Yuan C, Liu C, Pan J, Dong Q. Study on the resin infusion process based on automated fiber placement fabricated dry fiber preform. Scientific Reports. 2019;9(1).
5. Baran I, Cinar K, Ersoy N, Akkerman R, Hattel J. A Review on the Mechanical Modeling of Composite Manufacturing Processes. Archives of Computational Methods in Engineering. 2016;24(2):365-395.
6. Takagaki K, Minakuchi S, Takeda N. Process-induced strain and distortion in curved composites. Part I: Development of fiber-optic strain monitoring technique and analytical methods. Composites Part A: Applied Science and Manufacturing. 2017;103:236-251.
7. Wisnom M, Gigliotti M, Ersoy N, Campbell M, Potter K. Mechanisms generating residual stresses and distortion during manufacture of polymer–matrix composite structures. Composites Part A: Applied Science and Manufacturing. 2006;37(4):522-529.
8. Torres M. Parameters' monitoring and in-situ instrumentation for resin transfer moulding: A review. Composites Part A: Applied Science and Manufacturing. 2019;124:105500.
9. Amirova L, Brauner C, Grob M, Gort N, Schadt F, Pantelelis N et al. Online Cure Monitoring and Modelling of Cyanate Ester-Based Composites for High Temperature Applications. Polymers. 2021;13(18):3021.
10. Aktas A, Boyd S, Shenoi R. Cure and strain monitoring of novel unsaturated polyester/phenolic resin blends in the vacuum infusion process using fibre Bragg gratings. Journal of Composite Materials. 2015;49(29):3599-3608.
11. Zhang G, Zhou Z, Ding G, Xu S, Xie C, Zhang J. Cure monitoring and mechanical properties measurement of carbon fibre-reinforced plastics laminate using embedded fibre Bragg grating sensors. Materials Research Innovations. 2015;19(sup5):S5-718-S5-725.

12. Luyckx G, De Waele W, Degrieck J, Paepegem W, Vlekken J, Vandamme S et al. Three-dimensional strain and temperature monitoring of composite laminates. Insight - Non-Destructive Testing and Condition Monitoring. 2007;49(1):10-16.
13. Lee H. The Handbook of Dielectric Analysis and Cure Monitoring. Cambridge: Lambient Technologies LLC; 2017.
14. Torre-Poza A, Pinto A, Grandal T, González-Castro N, Carral L, Travieso-Puente R et al. ELADINE: sensor monitoring and numerical model approach for composite material wing box shape distortions prediction. IOP Conference Series: Materials Science and Engineering. 2022;1226(1):012001.

  doi:10.5075/epfl-298799_978-2-9701614-0-0

CO-CONSOLIDATION AND STAMP-FORMING AS AN ONE-SHOT PROCESS TO MANUFACTURE COMPLEX CF/PEEK PARTS

Julian Weber[a], Jens Schlimbach[b]

a: Processing Technology, Institut für Verbundwerkstoffe GmbH, Kaiserslautern, Germany - Julian.weber@ivw.uni-kl.de
b: Processing Technology, Institut für Verbundwerkstoffe GmbH, Kaiserslautern, Germany

Abstract: *Stamp-forming of thermoplastic 2D-Tape-Preforms is a time-efficient process to manufacture structural parts for aircraft industry. In the scope of an aviation research project, the novel process route stamp-forming with simultaneous co-consolidation as an one-shot process is being developed. In this study, the feasibility to manufacture CF/PEEK C-frames with fusion bonded local stiffeners is investigated. Thereto, a special tool design was initiated to place 3D-stiffener parts in the cavity while being heated above melting temperature at the joining surface. Partially consolidated 2D-Tape-Preforms are heated in the attached IR-panel and transferred to the mold when process temperature of both joining partners is reached. Cycle time, comprising heating, molding and joining to manufacture C-frames of an arc length of 1600 mm and 8 local stiffeners, is less than 10 minutes. Validation comprises thickness measurement, angular measurement as well as microsection analysis.*

Keywords: Co-consolidation; carbon fiber/polyether ether ketone; automated-tape-laying; stamp-forming; fusion bonding; direct bonding

1. Introduction

The extension of out-of-Autoclave (OOA) processes as well as the use of thermoplastics instead of thermosets to manufacture carbon fiber reinforced plastic (CFRP) parts is one method to increase efficiency in order to compete with conventional metal design. It is key to decrease cycle time and application of non-reusable process materials during manufacturing. Laborious assembly can be improved by increasing integral one-shot designs instead of differential assembly designs. Thereto, thermoplastics offer great opportunities concerning direct bonding, since their molecular structure allows fusion bonding processes in order to reshape structures and to join contact surfaces during manufacturing, service-life and end-of-service time [1–5].

To understand thermoplastic fusion-bonding, a so-called polymer-polymer healing process is reflected [6]. Wool and O'Connor [7, 8] subdivided this procedure, which is required for (co-)consolidation, in five sequential stages: 1. surface rearrangement, 2. surface approach, 3. wetting, 4. diffusion and 5. randomization. Until molecule diffusion sets in, intimate contact development emerges, which was originally developed by Dara and Loos [9]. Resin flow causes squeezing of air and resin out of the interface, network deformation takes place and potential barriers associated with inhomogeneities at the interface disappear [10]. The time until full intimate contact is achieved can be considered as a function of polymer viscosity [11, 12], depending on the polymer temperature, initial surface roughness and the applied pressure. With intimate contact being fully developed, molecules begin to migrate through the interface and entangle with the ones of the counterparty. The strength of the bond increases until full

  doi:10.5075/epfl-298799_978-2-9701614-0-0

bonding is achieved – that is when the interface cannot be distinguished from the bulk material [13]. To complete the bonding process, cooling under pressure is required. Thereby the rate of cooling is of great importance to set morphological and mechanical polymer properties [6, 13–15]. Process hybridization of stamp-forming and co-consolidation is characterized by short time intimate contact development and high cooling rates, which is challenging to create polymer healing and thus, needs thorough investigations.

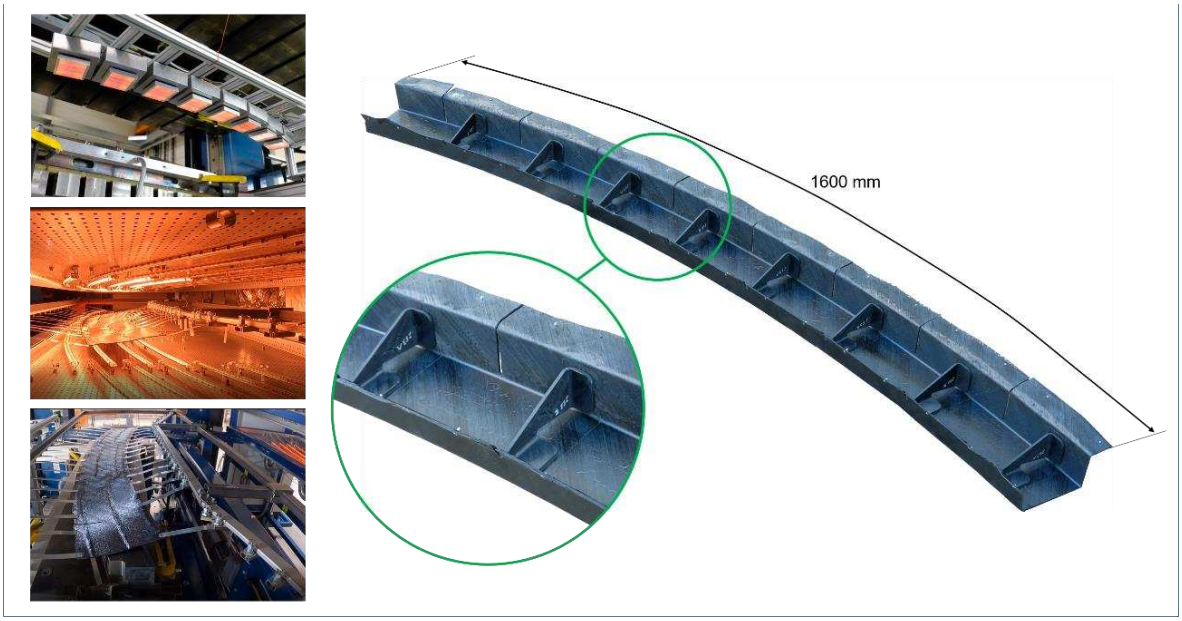

Figure 1: Hybrid processing to manufacture integral C-frames with local reinforcements

In this study, local reinforced C-frames for aircraft fuselages are manufactured by means of stamp-forming and co-consolidation. In preliminary processes, 2D-Tape-Preforms are manufactured in Automated-Tape-Laying and 3D-reinforcements are processed in stamp-forming process. The aim of the hybrid-process stamp-forming and co-consolidation is to fully consolidate the - initially partially-consolidated - Tape-Preforms and fusion bond reinforcements. General process feasibility is validated by manufacturing demonstrator parts of an arc length of 1600 mm and a radius of 3000 mm. Eight reinforcements are fusion bonded while molding the Tape-Preform to its C-shape.

2. Materials and experimental

The material used in this investigation is Solvay's CF/PEEK Tape (APC-2 Polyether-Ether-Ketone, AS4 carbon fiber) with a fiber volume content of 0.58 and a cured ply thickness of 0.14 mm according to data sheet. Both laminates, partially consolidated Tape-Preforms as well as stamp-formed reinforcements, are manufactured in preliminary processes.

2.1 Tape-Preform manufacturing

C-frame Tape-Preforms are manufactured in Automated Fiber Placement at Fraunhofer IGCV in Augsburg by using a Coriolis C1 robot based Fiber Placement machine. To process 8 ¼ " adjacent tapes at a speed of 0.2 m/s, the laser is set to a power of 2300 W; detecting temperature at the nip point through infrared measurement is 400 °C.

  doi:10.5075/epfl-298799_978-2-9701614-0-0

2.2 Co-consolidation tool design

The tooling to mold the 2D-Tape-Preforms to a C-shape comprises an upper and a lower part, whereas the lower part features eight cut-outs to insert carriers for reinforcements (see *Figure 2*). The carriers consist of several components in order to demold undercut geometry of the joint between Tape-Preform and reinforcement. The surface that is surrounding the joining area is to achieve Tape-Preform equivalent cavity height in order to fully consolidate the thermoplastic material. Since spring-in between web and flanges of the C-frame due to residual stresses during cooling is evident, the angular between nominal geometry of the final part and tooling differ. Fusion bonding reinforcements between web and flange would prevent spring-in and cause additional residual stresses, which is why bond between C-frame and reinforcement is only realized at the web and not at the flanges. Consequently, angular of reinforcements exhibit C-frame angular instead of tool geometry. The wedge-shaped void resulting in the angular difference between tooling and reinforcement is filled with carrier components to match nominal cavity height to consolidate Tape-Preform.

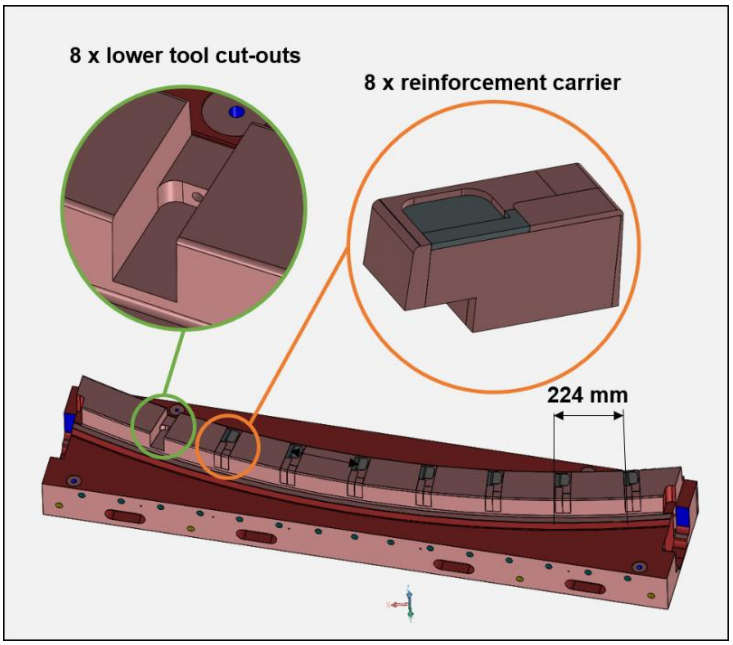

Figure 2: Co-consolidation tool design to carry reinforcements

The positioning of the cut-outs to place the reinforcement carriers respects thermal expansion of the tooling due to temperature increase from room temperature to process temperature (ΔT = 180 K).

2.3 Stamp-forming and co-consolidation setup

Setup to manufacture C-frames with reinforcements comprises the tooling including eight carriers to insert the reinforcements, an IR-panel that is attached to the press to heat the Tape-Preforms and an IR-panel that is attached on a sledge to be transferred and are placed above the lower tool to heat the reinforcements, which are placed in the lower part of the tool and placed in the reinforcement carriers respectively. Preliminary heating trials were carried out to synchronize the heating of the Tape-Preforms and the reinforcements placed in the carriers.

  doi:10.5075/epfl-298799_978-2-9701614-0-0

To start the process, the Tape-Preform is attached in a transfer frame, which is moving between the tool and the IR-panel. Eight reinforcements are placed in the cavity of the lower part of the tool. Tape-Preform and joining surfaces of the reinforcements are heated well above melting temperature until set temperature is reached. The Tape-Preform is transferred to the tool and the IR-panel sledge is removed from its heating position to place the Tape-Preform above the tool and the reinforcements. The press moves to close the tool in order to mold the Tape-Preform and fusion bond the reinforcements at the joining surfaces by means of co-consolidation.

C-frames are manufactured at four different pressure settings, whereas values are given in percentage in relation to maximum pressure setting.

3. Characterization

Manufactured C-frames are examined for the extent of spring-in or deviation from nominal geometry by measuring the angle between web and outer flange on the outside of the C-frame at each reinforcement position . Part thickness is determined at web, outer and inner flange. Thickness measurements identify unequal pressure distributions. Microsection evaluation provides information on consolidation quality of the Tape-Preform at the outer flange, the web, and the position of the reinforcement joint. Images are analyzed by using greyscale analysis.

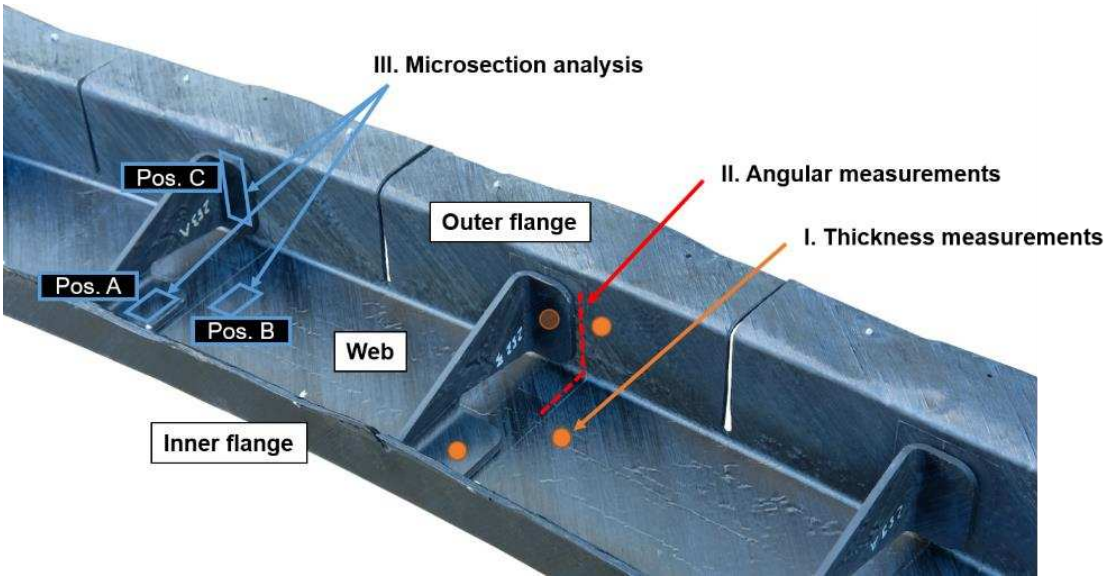

Figure 3. Overview of characterization methods of manufactured C-frames

4. Results and discussion

4.1 Thickness measurement

Figure 4 shows the results of thickness measurements at web, inner and outer flange in relation to different molding pressures. Applicable to all C-frames, inner flange thickness and outer flange thickness are lower than web thickness. Average web thickness is greater than nominal laminate thickness of 2.66 mm and average flange (outer and inner flange) thickness is lower than nominal thickness. It is assumed, that the lower thickness at the flanges occurs due to

interlaminar tape-shearing, when the Tape-Preform surface contacts upper and lower mold in combination of elevated holding forces during molding at the attachment points of the Tape-Preform to prevent fiber undulations. Dependencies between pressure and thickness cannot be assigned with this data.

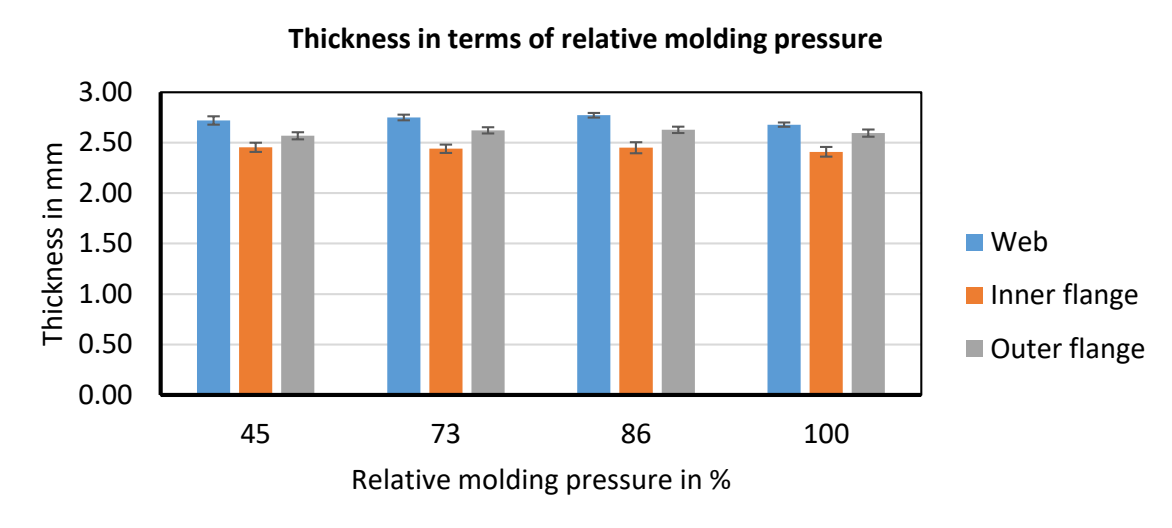

Figure 4: C-frame thickness at different measurement positions and different molding pressure

4.2 Angular measurement

Angular at outer flanges are measured from left hand side to right hand side and named 1 to 8. Results are given as deviation from tooling geometry in percentage (compare Figure 5), revealing the change of geometry after demolding due to residual stresses. Angle deviation of outer flanges to tooling range between 0.15 % and 1.63 %. Results reveal disparity between left hand side and right hand side of the parts, which is interpreted as inhomogeneous tooling temperature. There is no dependency between pressure and angular measurement according to this data.

  doi:10.5075/epfl-298799_978-2-9701614-0-0

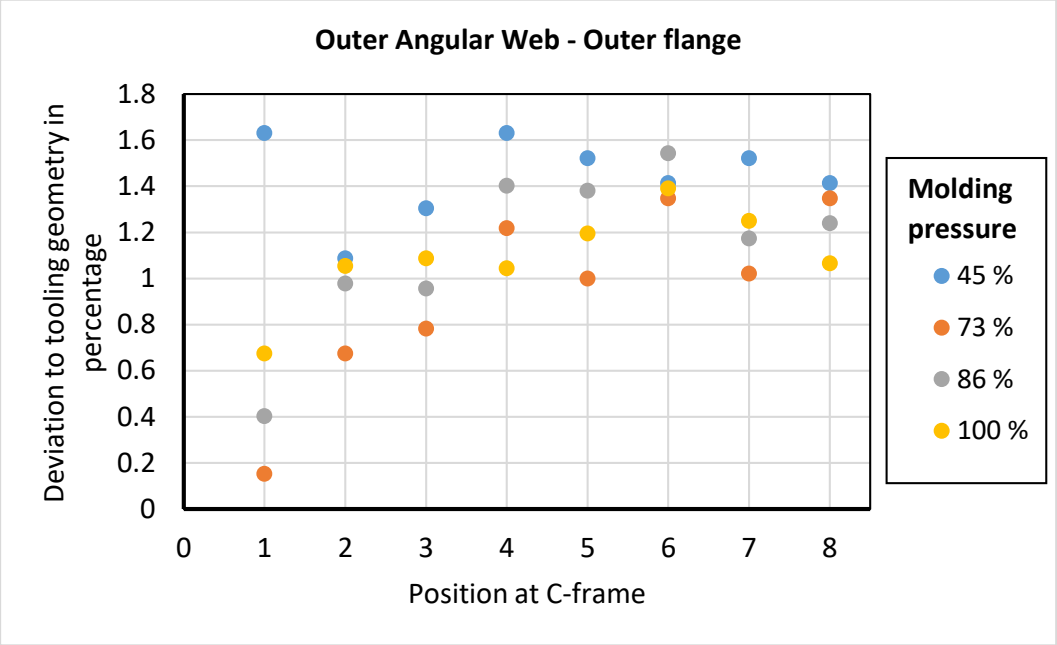

Figure 5: Angular measurement expressed as deviation from tooling geometry in percentage

4.3 Microsection analysis

Figure 6 shows typical microsections of the reinforced C-frame specimen at different positions . According to the analyzed images, the joining zone is consolidated to the same extent as the Tape-Preform and the reinforcement. In the considered microsections, no voids in-between contacting layers of reinforcement and Tape-Preform can be located. Voids are entrapped rather intralaminar than interlaminar, homogenously distributed throughout the entire laminate thickness. It is assumed to be a phenomena of poor tape impregnation and not related to process of stamp-forming, co-consolidation respectively. Figure 7 shows the results of porosity determination by means of grey scale analysis, presenting least porosity, advanced consolidation respectively, at the joint position between Tape-Preform and reinforcement (Pos. A). Maximum average porosity is detected at Pos. B representing the consolidated Tape-Preform after stamp-forming at the web with no reinforcement. The strong dependency between cavity height, laminate thickness and consolidation leads to the assumption of too great thickness of laminates (Tape-Preform plus reinforcement) in comparison to cavity height resulting in pressure peaks.

  doi:10.5075/epfl-298799_978-2-9701614-0-0

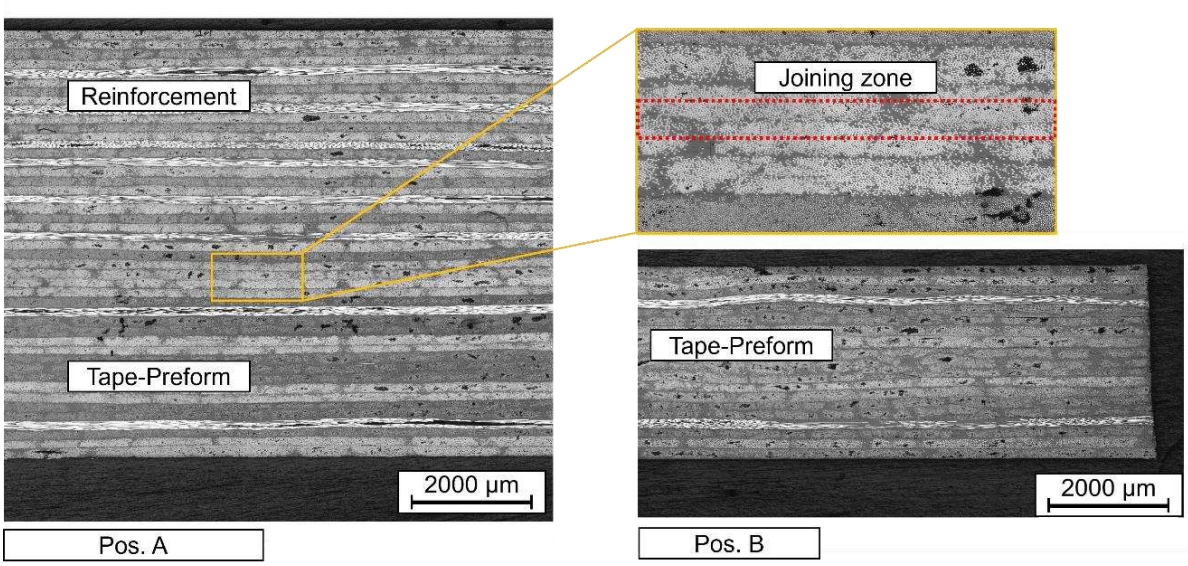

Figure 6: Microsection of reinforced C-frames at different positions

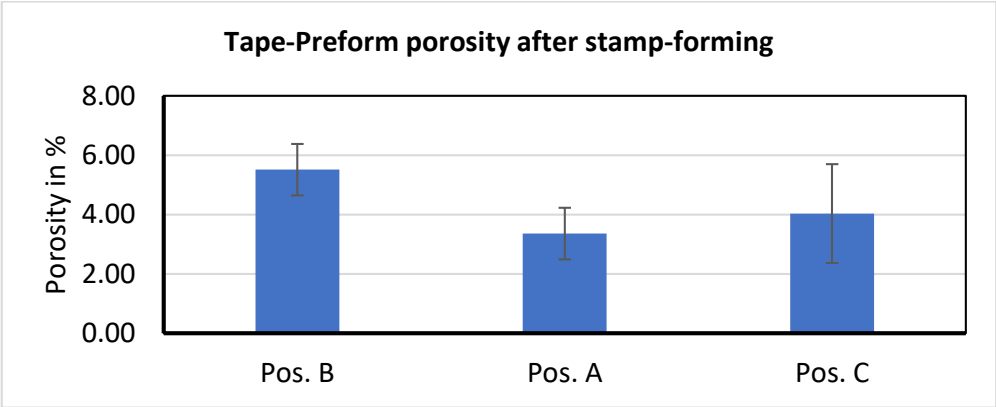

Figure 7: Tape-preform porosity after stamp-forming at different positions

5. Conclusion and Outlook

In this study, the general feasibility of a hybrid process comprising stamp-forming and co-consolidation to manufacture local reinforced structures in a novel one-shot process is demonstrated. A special tool design was initiated to carry 3D-reinforcements in order to exclusively melt the reinforcement's joining surface and prevent the remaining laminate from deconsolidating due to heat transfer. Thickness measurements reveal inhomogeneous pressure distribution resulting in locally different consolidation. Angular measurement indicates spring-in being evident as well as imparity between left hand side and right hand side of the C-frames, which is assumed to be an effect of inhomogeneous cooling during the molding process. Microsection analysis shows no peculiarity in the joining zone in the matters of interlaminar void entrapment compared to other existing layers. Interaction between laminate thickness and cavity height requires revision in order to achieve homogeneous pressure distribution.

The next step is to optimize the molding process parameters for consistent Tape-Preform consolidation. By deploying hydraulic slides at the joint-position between reinforcement and Tape-Preform, fusion bonding pressure can be controlled and further knowledge of bond-strength influencing parameters can be generated. Furthermore, the choice of cavity height for

  doi:10.5075/epfl-298799_978-2-9701614-0-0

reinforcements to set consolidation pressure becomes obsolete. Poor Tape-Preform consolidation after stamp-forming is either to be enhanced by different stamp-forming parameter settings or by the choice of tape material with better impregnation. Overall process robustness can be improved by monitoring and adjusting temperatures of both, laminates and tooling.

Acknowledgements

The project “OSFIT-Frame - One-Shot Fully Integrated Thermoplastic-Frame" is funded by the Federal Ministry for Economic Affairs and Climate Action (BMWK) on the basis of a decision by the German Bundestag (funding reference 20W1706C).

6. References

[1] A. R. Offringa, “Thermoplastic composites—rapid processing applications,” *Composites Part A: Applied Science and Manufacturing*, vol. 27, no. 4, pp. 329–336, 1996, doi: 10.1016/1359-835X(95)00048-7.

[2] J. Sloan, *TAPAS 2: Next steps in thermoplastic aerostructures.* [Online]. Available: https://www.compositesworld.com/articles/tapas-2-next-steps-in-thermoplastic-aerostructures (accessed: Nov. 23 2019).

[3] J. W. van Ingen, “Thermoplastic Orthogrid Fuselage Shell,” *Sampe Journal*, pp. 7–15.

[4] J. Weber, “Mit thermoplastischen Faserverbundkunststoffen zur Großserienreife: Methodik Integralbauweise,” *Technikforum VDE Kurpfalz e.V. und VDI Nordbadisch-Pfälzischer Bezirksverein e.V.*, pp. 14–15.

[5] J. Weber and J. Schlimbach, “Co-consolidation of CF/PEEK tape-preforms and CF/PEEK organo sheets to manufacture reinforcements in stamp-forming process,” *Advanced Manufacturing: Polymer & Composites Science*, vol. 5, no. 4, pp. 172–183, 2019, doi: 10.1080/20550340.2019.1673961.

[6] C. Ageorges and L. Ye, *Fusion Bonding of Polymer Composites*. London: Springer, 2002.

[7] R. P. Wool and K. M. O’Connor, “A theory crack healing in polymers,” *Journal of Applied Physics*, vol. 52, no. 10, pp. 5953–5963, 1981, doi: 10.1063/1.328526.

[8] R. P. Wool and K. M. O'Connor, “Time dependence of crack healing,” *J. Polym. Sci. B Polym. Lett. Ed.*, vol. 20, no. 1, pp. 7–16, 1982, doi: 10.1002/pol.1982.130200102.

[9] A. C. Loos and P. H. Dara, “Processing of Thermoplastic Matrix Composites,” in *Review of Progress in Quantitative Nondestructive Evaluation*, D. O. Thompson and D. E. Chimenti, Eds., Boston, MA: Springer US, 1987, pp. 1257–1265.

[10] F. Yang and R. Pitchumani, “Fractal Description of Interlaminar Contact Development during Thermoplastic Composites Processing,” *Journal of Reinforced Plastics and Composites*, vol. 20, no. 7, pp. 536–546, 2001, doi: 10.1177/073168401772678580.

[11] F. Yang and R. Pitchumani, “Healing of Thermoplastic Polymers at an Interface under Nonisothermal Conditions,” *Macromolecules*, vol. 35, no. 8, pp. 3213–3224, 2002, doi: 10.1021/ma010858o.

[12] F. Yang and R. Pitchumani, “Interlaminar contact development during thermoplastic fusion bonding,” *Polym. Eng. Sci.*, vol. 42, no. 2, pp. 424–438, 2002, doi: 10.1002/pen.10960.

[13] Y. H. Kim and R. P. Wool, “A theory of healing at a polymer-polymer interface,” *Macromolecules*, vol. 16, no. 7, pp. 1115–1120, 1983, doi: 10.1021/ma00241a013.

[14] S. C. Mantell and G. S. Springer, “Manufacturing Process Models for Thermoplastic Composites,” *Journal of Composite Materials*, vol. 26, no. 16, pp. 2348–2377, 1992, doi: 10.1177/002199839202601602.

[15] L. Moser, *Experimental analysis and modeling of susceptorless induction welding of high performance thermoplastic polymer composites*. Zugl.: Kaiserslautern, Techn. Univ., Diss., 2012. Kaiserslautern: Inst. für Verbundwerkstoffe, 2012.

AUTOMATED DETECTION OF YARN GAPS DURING RADIAL BRAIDING OF CARBON FIBER BY MEANS OF LIGHT BARRIERS

Stephan Maidl[a], Leoni Putze[a], Kalle Kind[a], Klaus Drechsler[a]

a: Chair of Carbon Composites, Department of Aerospace and Geodesy, TUM School of Engineering and Design, Technical University of Munich, Boltzmannstr. 15, 85748 Garching, Germany – stephan.maidl@tum.de

Abstract: *Braiding of carbon fiber is a highly automated process for manufacturing preforms directly from carbon fiber yarns. The quality of braided textiles from reinforcement yarns and the stability of the process can however be negatively affected by irregularities that occur during braiding. In order to detect such process defects as early as possible during their formation and in an effort to limit the effects of defects, the development of online monitoring systems for the braiding process is desirable. Currently available sensor modules involve problems of either insufficient data acquisition, process impairments or high costs and complexity. The paper at hand outlines a newly developed form of a sensor module that only requires one stationary sensor (thereby being cost-efficient) and that is able to gather process data without causing any additional yarn damage (no process impairments) by means of an optical inspection of the braid formation zone.*

Keywords: Braiding; Braiding defects; Online process monitoring; Quality control

1. Introduction

Braiding of reinforcement yarns is an advantageous process when low scrap material and high production rates of predominantly tubular preforms are required. However, irregularities and defects which occur during the process can significantly reduce the mechanical performance of the braided part, negatively affect the output rate of a braiding machine and can moreover cause additional costs for error cause analysis and error correction time. In their work (1), Mierzwa et. al. set out that the so-called fibrous ring was one of the most common irregularities during braiding of carbon fiber. The fibrous ring is understood as a circular accumulation of broken carbon filaments at the braiding spool (bobbin) which impedes the yarn from unwinding properly from the bobbin. The subsequent anomalous increase in yarn tension causes yarn gaps in the braided preform and can eventually induce a breakage of the yarn. Mierzwa et. al. (2) delineated on the effect of local yarn gaps on the mechanical performance of braided coupons. In their experiments with preforms that were infiltrated by means of the Vacuum Assisted Process, they discovered a deterioration of 36 % in tensile and a deterioration of 33 % in compressive strength when the yarn gap was oriented perpendicularly to the loading direction. In (3), Mierzwa purposefully introduced local yarn gaps in braided torsional shafts and found similar effects on their torsional strength. Ebel et al. (4, 5) mention yarn loops in braided preforms and a generally “fuzzy” braid due to frictional filament abrasion as further typical process defects. Nevertheless, they state that the fibrous ring had the most significant effect on machine productivity. In their endurance braiding tests, they found that typical braiding defects can lead to a machine downtime of up to 26 % of the total production time. This was due to the time it took to locate a defect in the braiding machine as well as due to the manual work it

  doi:10.5075/epfl-298799_978-2-9701614-0-0

required to repair or rethread yarns that had broken due to yarn tension increases that could be traced back to fibrous rings.

2. State of the Art

In order to avoid the effects of braiding defects described above, some sensor systems for monitoring the braiding process are already available. Based on the mounting of the sensors, these monitoring systems can be subdivided into bobbin carrier independent and bobbin carrier dependent approaches. Generally speaking, bobbin carrier independent approaches offer the possibility to monitor all braiding yarns with a limited number of stationary sensors. Thereby, installation effort and costs are minimized. By contrast, bobbin carrier dependent approaches require the use of as many sensors as there are braiding yarns in the machine because the sensing elements are directly mounted onto the carriers. The operator is provided with data at a high level of detail on each braiding yarn at any time during the process. However, this usually comes with comparatively high installation effort and costs. Since such high costs can often not be justified in a production scenario, the emphasis shall be on bobbin carrier independent approaches within the scope of this paper.

An important representative of bobbin carrier independent systems are circuit breakers which jut into the tracks of the bobbin carriers. At each bobbin carrier, there is a yarn tensioning unit in place which brakes the bobbin. The yarn tensioning unit features a lever or a slider that is deflected upwards by the acting yarn tension against a spring force. Upon breakage of a yarn, the lever or slider of the yarn tensioning unit is pushed down by the spring force. When the respective bobbin carrier reaches the said circuit breaker, the lever or slider, which is now in its lowest position, pushes the switch. Consequently, a signal is generated that stops the braiding machine. Systems of this kind are currently the only standard sensor modules that are commercially available for braiding of reinforcement yarns. Another approach of carrier independent monitoring systems was invented by Lenkeit (6). His concept comprises a skid with a force sensor attached to it. The skid is placed into the braid formation zone in a way that every time a yarn passes by, it slides along and touches the skid. By measuring the normal force that acts onto the skid, yarn tension irregularities can be discovered. The major advantage of this approach over to the commercially available switches is that it enables the detection of an anomalously tensed yarn before the yarn actually breaks. A drawback is however that it requires additional yarn contact by the skid, which may damage brittle reinforcement yarns. The sensor module proposed by Maidl et. al. (7, 8) also makes use of the yarn tensioning units of the bobbin carriers. They attached magnets to the levers of the yarn tensioning units and arranged hall sensors around the circumference of the braiding machine in a way that the position of the lever of the yarn tensioning unit could be measured each time a bobbin carrier passed by a sensor. This way, they were able to estimate the acting yarn tension without any additional yarn contact and detect yarn tension irregularities before they had led to a yarn breakage. However, as with the previous two concepts, the discrete nature of the monitoring system remained. A yarn always needed to pass by the sensing element in order to be able to state whether it is correctly tensed or not (dead time between measurements). Therefore, Maidl et al. (9) developed sensor integrated braiding rings for the measurement of reaction forces that the braiding yarns induce when they are deflected at the braiding ring before they are deposited onto the mandrel. Since all braiding yarns are in contact with the braiding ring at any time during the process, the yarns can continuously be monitored without any significant dead time. From

  doi:10.5075/epfl-298799_978-2-9701614-0-0

the occurrence of uneven distributions in reaction forces, the sensor integrated braiding rings are however only able to localize a defective yarn within a group of numerous yarns. They cannot narrow down the defect localization to a single yarn, which the commercially available switches, the invention by Lenkeit (6) or the approach by magnets and stationary hall sensors (7, 8) are able to. Branscomb and Beale (10) pursued an approach that is particularly suitable for braiding of cords or ropes. They observed movement of the point at which the individual braiding yarns form the cord or the rope (braiding point) by means of a camera. A computer vision algorithm was able to distinguish between regular and defective braiding by tracking the position of the braiding point. The concept is however not applicable to braiding of composite parts. This is because reinforcement yarns are usually braided onto rigidly guided mandrels. This way, the braiding point cannot move as it is the case during braiding of cords or ropes.

The idea of optically inspecting the braid formation zone is yet still worthwhile to be further enhanced and adapted to composite application scenarios. This is because it conceptually opens the possibility to both continuously monitor all braiding yarns without significant dead time and at the same time allow a precise identification of a defective yarn. Brockmanns et al. mention a possible detection concept tailored to braiding of reinforcement fibers in their patent application (11) by means of a stationary optical sensor in the braid formation zone. However, they do not provide any data on the sensitivity or stability of their approach. In the paper at hand, their detection concept is tested in braiding experiments on a radial braiding machine RF 1/128-100 from Herzog GmbH as an initial verification of the idea of an optical inspection of the braid formation zone for defect detection purposes. It is demonstrated that an implementation of the detection concept by a stationary light barrier can detect defect-related anomalies. However, for a reliable defect detection, it is shown that the discrete measurement approach by light barrier needs to be extended to a continuous camera-based inspection of the braid formation zone in order to even out naturally occurring process deviations.

3. Detection Concept

During braiding of reinforcement fibers, the yarns do not follow a straight path from the bobbin carriers to the braid formation point. Instead, due to frictional interaction between the braiding yarns themselves as well as between the braiding yarns and the braiding ring, they show curved, evolvent-like shapes (cf. white-dotted straight line in Figure 1 for reference). During regular braiding, all yarns are similarly tensed. This results in similar curvatures of the braiding yarns. When a braiding defect such as a fibrous ring is present, then the elevated yarn tension causes the defective yarn to show less curvature since the frictional forces remain essentially unchanged. This results in deviating distances of the defective yarn to its neighboring yarns. The distance between the defective yarn and its preceding yarn is reduced (cf. orange color in Figure 1). In turn, the distance between the defective yarn and its succeeding yarn is increased (cf. blue color in Figure 1). When a yarn with an anomalously reduced yarn tension is present, then its curvature in the braid formation zone would be increased compared to the other braiding yarns. Hence, its distance to the preceding yarn would be increased and its distance to the succeeding yarn would be reduced. Figure 1 shows the curved yarns in the braid formation zone of a radial braiding machine. In the paper by van Ravenhorst et al. (12), it can be seen that this effect also occurs in axial braiding machines. For a detailed derivation of a model to quantify the frictional yarn interaction during braiding, the reader is referred to the said paper (12).

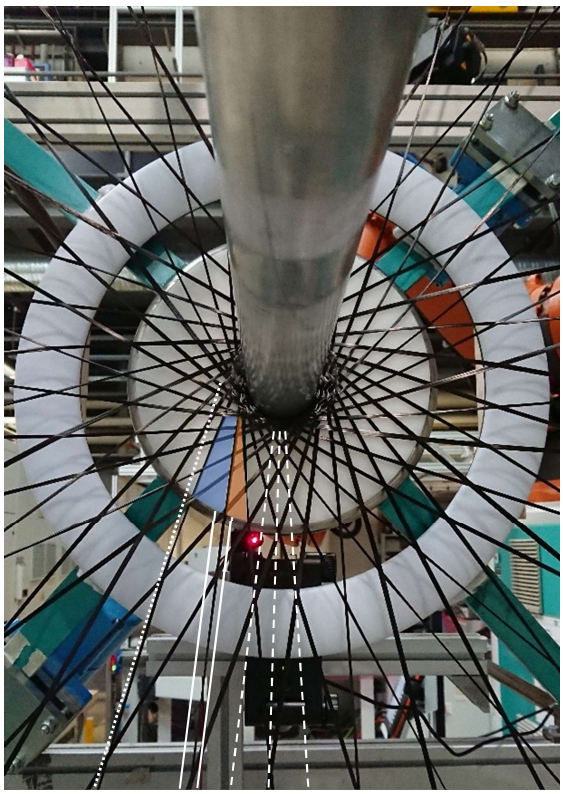

Figure 1. Braid formation zone of n_{yarns}=64 Tenax®-E HTS40 F13 24k carbon fiber yarns during overbraiding of a cylindrical mandrel with a diameter of d=65 mm in an RF 1/128-100 braiding machine from Herzog GmbH; tangential white-dotted line to a carbon yarn indicates its curvature; two solid white lines mark the yarn with elevated yarn tension; the reduced distance to the preceding yarn is marked with orange color; the increased distance to the succeeding yarn is indicated with blue color; exemplary centric white-dashed lines mark positions of yarn intersections

In Figure 1, a laser behind the plane of braiding yarns is also visible. This laser is part of the light barrier for the initial verification of the defect detection concept by yarn curvatures. The light barrier is completed by a photodiode which is located at the other side of the plane of braiding yarns. The defect detection described in the following sections 4 and 5 relies on measuring the different time intervals between the transits of the moving yarns through the light barrier due to their deviating distances as explained above.

4. Experimental Setup

The light barrier was made up of a DG650-1-5(12x34) laser from Picotronic GmbH and a BPW46 photodiode from Vishay Intertechnology, Inc. The photodiode was operated in the mode of a photovoltaic cell. Its output voltage was measured by a USB-6210 data acquisition device from National Instruments, Inc. at a rate of 1000 scans per second. To enable an automated peak detection as shown in Figure 2, left, the raw data from the photodiode was processed by a moving average filter over ten data points. Since yarns moving in clockwise direction intersect with yarns moving in counterclockwise direction at certain positions (cf. white-dashed lines in Figure 1) it was necessary to position the light barrier in the middle of two adjacent lines of yarn intersection in order to reliably detect the transit of each individual yarn. The data shown in the subsequent section 5 was acquired with the photodiode placed directly behind the braid

  doi:10.5075/epfl-298799_978-2-9701614-0-0

formation plane and the laser positioned at a distance of about 1.5 meters to the braid formation plane. This way, the laser could be focused to a spot diameter of about 0.5 mm in the braid formation plane by means of its internal focusing lens. Thereby, the yarn transits through the light barrier could precisely be detected. Note that the opposite arrangement as shown in Figure 1 with the laser directly behind the braid formation plane is meant for illustration purposes and a proper visibility of the laser light only.

For the experimental verification of the detection principle, a cylindrical mandrel with a diameter of $d = 65\,mm$ and a length of $l = 1.5\,m$ was overbraided with $n_{yarn} = 64$ carbon fiber yarns of the type Tenax®-E HTS40 F13 12k. The braiding angle φ, which describes the angle of fiber orientation with respect to the longitudinal axis of the mandrel, was varied between $\varphi = \{30°; 45°; 60°\}$. The speed of horn gear rotation of the braiding machine was set to $r = 65\,rpm$. For each configuration, a flawless reference measurement and measurements with elevated yarn tensions of a single braiding yarn in counterclockwise direction of ~20 N, ~35 N and >45 N were conducted in order to simulate a braiding defect. The elevated yarn tension was created by a yarn brake that was attached to a single bobbin carrier (cf. Maidl et al. (9) for an illustration of the yarn brake). In order to be able to explain anomalous signals from the light barrier, the movement of the yarns in the braid formation plane was additionally recorded by an SLR camera.

5. Results and Discussion

Figure 2, left shows exemplary measurement data from the photodiode acquired during a flawless reference experiment under a braiding angle of $\varphi = 45°$. It is observable that the photodiode saturates at approximately 0.48 V upon full exposure to the laser light. When a braiding yarn transits through the light barrier and shades the laser, the photovoltage drops significantly. These drops in photovoltage were marked with red circles by means of the "findpeaks" function in MATLAB R2021a. Since the light barrier is positioned in a way that the laser beam intersects the braid formation plane between the lines of yarn intersection (cf. white-dashed lines in Figure 1) the drops in photovoltage alternatingly correspond to a yarn circulating in clockwise and to a yarn circulating in counterclockwise direction through the braiding machine. This is why for an analysis of the yarn distances and an inference on yarn curvatures, the time intervals between every second drop in photovoltage need to be calculated. The annotations I_C and I_{CC} in Figure 2, left indicate time intervals between the transits of two successive yarns going in clockwise (C) direction and counterclockwise (CC) direction (view as in Figure 1), respectively. The assignment of the direction of circulation of the yarns was done by consulting the video recordings which yarn of which direction first passed through the light barrier. The clockwise intervals are drawn into the diagram in Figure 2, right with respect to the left y-axis (blue) and the counterclockwise intervals are drawn into the diagram with respect to the right y-axis (orange). The diagram starts at a braiding distance of 30 cm in order to cut off any settling effects at the beginning of the process. From this starting point on, the diagram shows five full revolutions of the yarns through the braiding machine. It can be seen that the yarn transit intervals through the light barrier show a significant scatter for both directions of circulation. The mean value of the scattered interval lengths can be read to about $0.46\,s$. This can be explained by the relation of the number of horn gears in the machine $n_{horn\ gears} = 32$ and the set rotational speed of the horn gears $r = 65\,rpm$. From these values, the time for a bobbin carrier to complete a full 360°-revolution through the machine calculates to

  doi:10.5075/epfl-298799_978-2-9701614-0-0

$$t_{360°} = \frac{n_{horn\ gears}}{2 \cdot \frac{r}{60\ \frac{s}{min}}} = \frac{32}{2 \cdot \frac{65\ rpm}{60\ \frac{s}{min}}} \approx 14.77\ s \quad (1).$$

The theoretical interval length between the transits of yarns of the same direction of circulation can be determined by

$$length_{transit\ interval} = \frac{t_{360°}}{\frac{n_{yarn}}{2}} \approx \frac{14.77\ s}{\frac{64}{2}} \approx 0.4615\ s \quad (2).$$

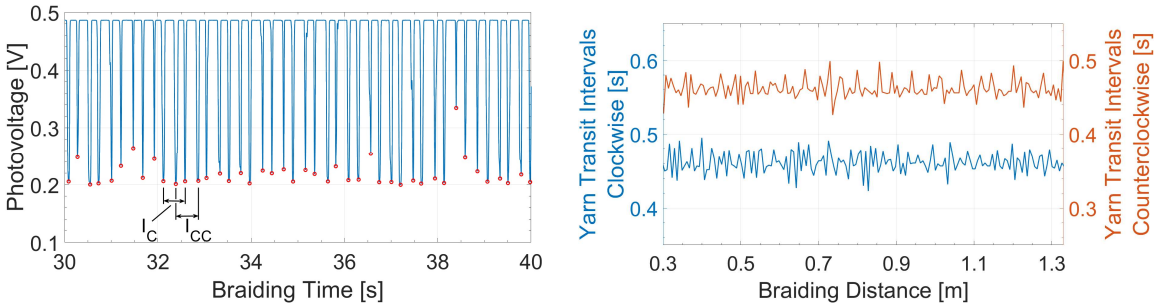

Figure 2: Exemplary measurement data from the photodiode (left); transit intervals by direction of yarn circulation (right); both diagrams obtained from flawless braiding at a braiding angle of 45°

Figure 3, left illustrates the yarn transit intervals for the case of a single yarn in counterclockwise direction that shows an elevated yarn tension of approximately 20 N. The intervals in relation to the defective yarn are marked with red circles. It can be observed that when the defective yarn travels through the light barrier, a shorter interval is directly followed by a longer interval. However, the intervals corresponding to the defective yarn cannot clearly be distinguished from the natural scatter of the process. The picture is different when the defective yarn showed a yarn tension of approximately 35 N (cf. Figure 3, right). As can be seen from the defect-related intervals marked by the red circles, they stand out more prominently compared to the natural fluctuations of the braiding process. Furthermore, a regular disruption of the sequence of the intervals in clockwise direction is observable. In contrast to the anomaly in the signal analysis for the counterclockwise yarns (which contain the yarn with deliberately elevated tension), a longer transit interval is directly followed by a shorter interval in case of the clockwise yarns. An isolated occurrence of such an anomaly would hint at the presence of a yarn with too low tension and hence higher curvature.

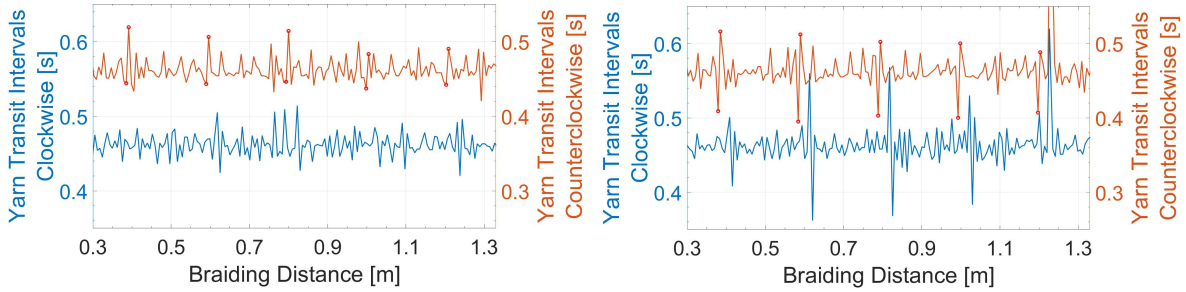

Figure 3: Transit intervals by direction of yarn circulation during defective braiding at a braiding angle of 45°; elevated tension of a single yarn of ~20 N (left) and ~35 N (right)

Consulting the video recording from the braid formation zone however reveals that this is due to the yarn with the elevated tension interfering and holding back a yarn of the opposite

direction of circulation. At a braiding distance of approximately 1.25 m, this effect is so strong that two yarns of opposite direction of circulation do not intersect on the usual lines of yarn intersection any more (cf. dashed lines in Figure 1) but exactly where the laser beam intersects the braid formation plane (cf. Figure 4, left). This even swaps and therefore falsifies the assignment of clockwise and counterclockwise yarns in Figure 3, right from approximately 1.25 m braiding distance on.

Figure 4, right shows the yarn transit intervals per direction of circulation for the case of an elevated yarn tension of >45 N. In principle, the same defect characteristic anomalies in both directions of circulation as with the elevated tension of 35 N are observable. However, the transit intervals at about 1.2 m marked with red circles show that it is, even with this high tension, not always guaranteed that an anomaly is clearly visible in the data. This is due to the fact that the braiding yarns naturally vibrate during the process which may coincidentally even out defect-characteristic data patterns. Further data from the experiments with braiding angles of $\varphi = 30°$ and $\varphi = 60°$ are not further discussed within the scope of this paper because they showed the same features as the presented data on a braiding angle of $\varphi = 45°$.

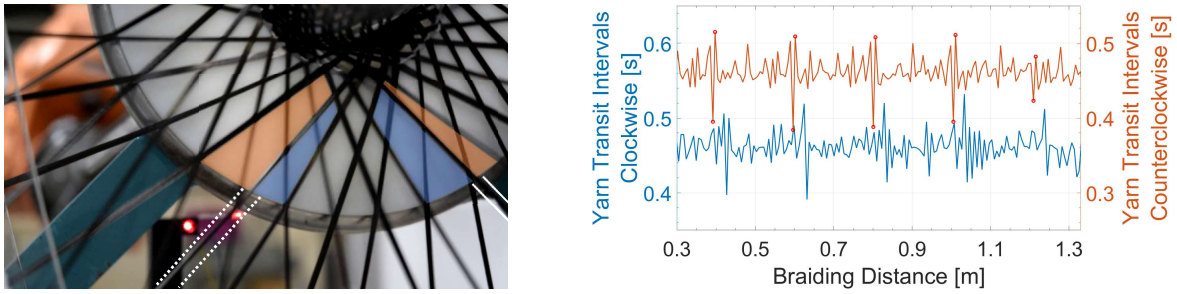

Figure 4: Still image of the disruption in assignment of direction of yarn circulation from Figure 3, right at 1.25 m braiding distance (left); yarn with elevated tension marked with two solid lines, held-back yarn of opposite direction marked with two dotted lines; distance to the respective preceding yarn marked with orange and distance to the respective succeeding yarn marked with blue color; transit intervals by direction of yarn circulation during defective braiding at a braiding angle of 45° and elevated tension of a single yarn of >45 N (right)

6. Conclusion and Outlook

The authors conclude that the method of measuring deviating yarn distances due to different yarn curvatures in the braid formation is in principle a suitable method for the detection of yarn tension anomalies during braiding of reinforcement fibers. The implementation of the detection method by a stationary light barrier showed that especially at higher levels of elevated yarn tension of 35 N and beyond, a defect characteristic succession of a short yarn transit interval through the light barrier directly followed by a longer transit interval hints at the presence of a defective yarn. However, due to the discrete nature of the detection method in combination with the natural scatter of the process (e.g. vibration of the yarns) a clear defect detection is not always guaranteed. Furthermore, the discrete detection by light barrier does not offer an unequivocal assignment of the yarn transits to the respective direction of yarn circulation.

The authors therefore propose the implementation of a camera-based inspection method for the whole braid formation zone. This way, all yarns could continuously be monitored. By tracking each individual yarn through the acquired frames, an averaging of the yarn distances to the

  doi:10.5075/epfl-298799_978-2-9701614-0-0

neighboring yarns could be carried out. Natural process fluctuations could be evened out by means of an averaging of the yarn distances over a certain time period and process anomalies could be more distinct in the acquired data. This would particularly be beneficial for an automated data analysis algorithm. Additionally, the direction of circulation of each yarn could clearly be identified by a camera-based approach, thereby enhancing the reliability of the detection concept.

Acknowledgements

The authors thankfully acknowledge the funding provided by the German Federal Ministry of Education and Research under the scheme “KMU-innovativ” for the project “InSensoFlecht” (funding code: 02P16K553) and the funding provided by the German Federal Ministry for Economic Affairs and Climate Action under the scheme “Zentrales Innovationsprogramm Mittelstand (ZIM)” for the project “IMoFlecht” (funding code: ZF4004324HB9).

7. References

1. Mierzwa A, Ebel C, Harbers T, Drechsler K. Investigation on Creation of Fibrous Rings and Their Influence on the Braided Preform Quality; ECCM17 - 17th European Conference on Composite Materials. Munich, Germany; 2016 Jun 26.
2. Mierzwa A, Ebel C, Drechsler K. Influence of yarn gaps on the mechanical performance of braided carbon fiber reinforced plastics. Zeitschrift Kunststofftechnik / Journal of Plastics Technology 2018; 14(2):146–73.
3. Mierzwa A. Zur Entstehung und Auswirkung von Garnlücken in Carbonbiaxialgeflechten [Dissertation]. Garching, Germany: Technische Universität München; 2019.
4. Ebel C, Brand M, Drechsler K. Effect of Fiber Damage on the Efficiency of the Braiding Process; 11th Composites Week @ Leuven and TexComp-11 Conference. Leuven, Belgium; 2013 Sep 16.
5. Ebel C, Mierzwa A, Kind K. Yarn damage during braiding of reinforcement fibers for composites. In: Advances in Braiding Technology. Elsevier; 2016. p. 319–54.
6. Lenkeit J, inventor; Tensometric-Meßtechnik Ströhmann & Co GmbH. Verfahren zur Zugkraftmessung an laufenden Fäden einer Fadengruppe sowie Vorrichtung zur Ausübung des Verfahrens. German Patent DE19730965C1. 1999 Jun 10.
7. Maidl S, Sabieraj M, Mierzwa A, Ebel C, Drechsler K. Investigating the unwinding behavior of technical yarns and development of a new sensor system for the braiding process. IOP Conf. Ser.: Mater. Sci. Eng. 2018; 406:12065.
8. Maidl S, Mierzwa A, Matschinski A, inventors. Thread Tension Anomalies Detection: European Patent Specification. EP3784826B1. 2021 Mar 3.
9. Maidl S, Fernández Villalba Á, Kind K, Drechsler K. Development of sensor integrated braiding rings for the automated detection of braiding defects. Materials Today: Proceedings 2020.
10. Branscomb DJ, Beale DG. Fault detection in braiding utilizing low-cost USB machine vision. The Journal of The Textile Institute 2011; 102(7):568–81.
11. Brockmanns K-J, Kümpers F-J, Baumgart G, Leifeld M, inventors. Radialflechtmaschine. German Patent Application DE102012223127A1.
12. van Ravenhorst JH, Akkerman R. A yarn interaction model for circular braiding. Composites Part A: Applied Science and Manufacturing 2016; 81:254–63.

  doi:10.5075/epfl-298799_978-2-9701614-0-0

INFLUENCE OF AUTOMATED FIBRE PLACEMENT PROCESSING PARAMETERS ON THE CONSOLIDATION OF OUT-OF-AUTOCLAVE PREPREGS

Axel Wowogno [1], Iryna Tretiak [1], Stephen R. Hallett [1], James Kratz [1]

[1] Bristol Composites Institute, University of Bristol, Queen's Building, University Walk, Bristol BS8 1TR, United Kingdom – Corresponding author: A. Wowogno (axel.wowogno@bristol.ac.uk)

Abstract: Composite materials are widely used in the aerospace industry due to high performance needs. This study investigates the thickness change of cross-ply samples (2mm thickness and 30x30mm^2 compaction area), using a representative out-of-autoclave (OOA) carbon fibre reinforced epoxy prepreg system. Two experimental programs were used to examine the consolidation behaviour of the material by varying Automated Fibre Placement (AFP) process parameters, such as pressure magnitude (from 0.05MPa to 0.25MPa), pressure application time (from 1s to 20 min) and temperature (from 30°C to 210°C). Upon analysis of the thinning and widening of the samples, a minimum pressure value of 0.1 MPa was defined to reach compaction and optimal parameters for dimension stability were proposed (150°C for 2.5s). Voids were analysed and showed that higher temperature and longer time exposure led to smaller and fewer voids, with 0.45% porosity being achieved at 210°C for 10s. This shows that hot debulking is a promising route for thickness control during prepreg deposition, but that further analysis is needed to properly replicate specific processing conditions such as fast deposition speeds.

Keywords: Advanced Manufacturing; Carbon Fibre / Epoxy Prepreg; Compaction; Thickness control.

1. Introduction

Thickness control is an important part of the manufacturing of composite components with prepregs. It guarantees the quality of preforms for the steps before the cure and then ensures the production of reliable parts. Several technologies can potentially be used to properly control the consolidation and the dimensions of the preforms. One approach is the deposition of plies during the Automated Fibre Placement (AFP) process (Figures 1a and 1b). This method would be suitable for both thermosets and thermoplastic composites [1][2].

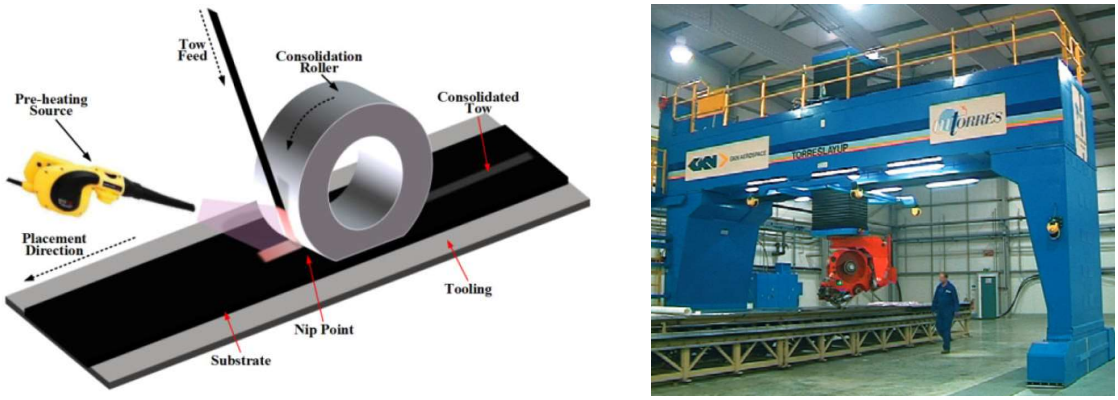

Figure 1 : AFP process - (a) Schematic representation [3] and (b) Full scale Gantry style AFP [4]

  doi:10.5075/epfl-298799_978-2-9701614-0-0

Recent reviews of the possibilities offered by the AFP are proposed through both models and experiments [5][6]. Upon further investigation, it emerged that an analysis combining a commercially available Out-of-Autoclave (OOA) prepreg [7], such as the IM7/M56 supplied by Hexcel [8][9] and a consolidation program focused on thickness control is yet to be proposed. Indeed, no literature also considering specially designed OOA thermoset prepreg could be found, although the influence of consolidation force on the performance of AFP manufactured laminates has been studied [10]. Dong et al. [11] have proposed a rapid cure procedure, but with independently developed OOA resin and prepregs. Lee et al. [12] have used the material considered here, but their focus was on the process and not on the material behaviour.

There are nonetheless studies that focus on material properties and dimensional tolerances in automated processes [13][14]. The authors have investigated the resin content and the voidage of uncured prepregs and have shown that high temperatures reduced the amount of low fibre density areas as well as the size of the voids. This shows how increasing temperature increases consolidation where OOA processing becomes possible.

The new concept presented in this paper is the monitoring of the thickness of laminates over a range of high temperatures and short contact times that are found in AFP processing. Increasing the temperature allows the resin to flow more easily, which might offset the pressure application times needed to achieve the required thickness control during deposition. This will permit to estimate the effects of phenomenons observed in prepregs handled at elevated temperature (such as bleeding and squeezing [14]) and later on, to control the width and thickness of preforms. Finally, the void level of the samples was analysed.

2. Materials and Methods

2.1. Materials

The material selected for this study is the M56/35%/UD268/IM7-12K [8], a high-performance Epoxy / Carbon Fibre prepreg developed for OOA curing of composite aircraft structures and suitable for automated processing. The cross-ply configuration was chosen to create the samples (see Figure 2a). Using 8 unidirectional (UD) 30x50mm plies, of a thickness of 0.25 mm (hence a thickness of 2mm), the prepared samples offer a compaction area of 30x30 mm2 (see Figure 2b). The lay-up was performed using a specially designed tool, permitting to properly align the plies in the 0° and 90° directions. Each sample was debulked for 10 min at room temperature to ensure the removal of the air trapped between the hand laid-up plies.

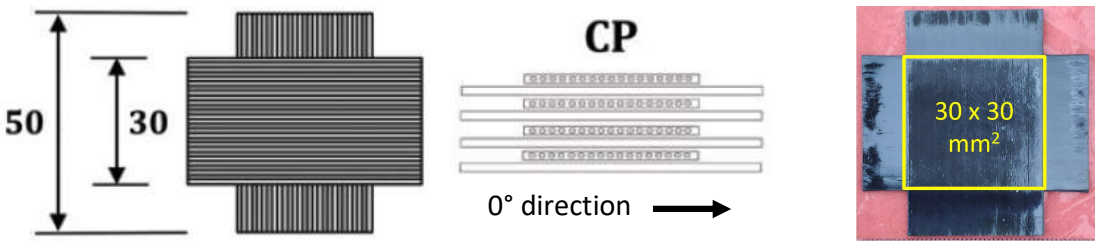

Figure 2 : (a) 8-plies cross-ply sample configuration and (b) compaction area

  doi:10.5075/epfl-298799_978-2-9701614-0-0

2.2. Materials

Before and after the tests (Figure 3a), sample dimensions were taken with a micrometre for the thickness and a calliper for the width and the length. The zones of interest are indicated in Figures 3b and 3c. To evaluate thickness evolution in time, the final thickness after test was measured and thickness values were calculated by subtracting the displacement values given by the Instron from the measured final thickness.

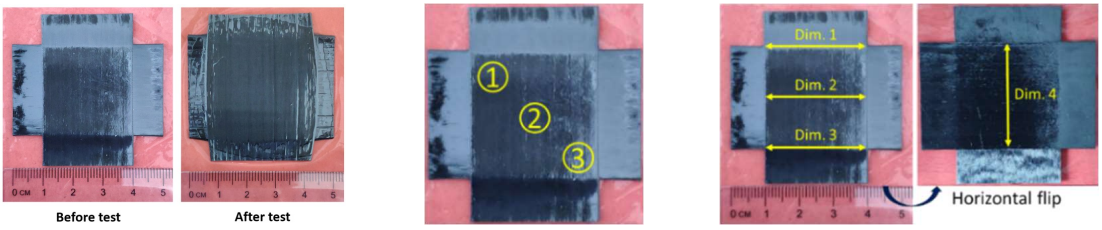

(a) (b) (c)

Figure 3 : Measurement zones of (a) thickness and (b) compaction area.

The compaction tests were performed using custom made heater plates, that were installed on an INSTRON™ 5969 machine, equipped with a 50 kN load cell (Figure 4a). The temperature of the plates was controlled using a Watlow controller connected to thermocouples. This set-up allowed to precisely control force and temperature during experiments. The software Bluehill Universal was used to monitor force and displacement simultaneously and extract this information. Figure 4b shows the positioning of samples in the test set-up (unrestrained and centred). The samples were placed on a release film to prevent the flowing resin from sticking to the heated plates.

Once the machine compliance test was performed, the specimen was placed on the bottom plate and a 1 minute timer was started, as this has been judged useful to have a homogenized temperature throughout the sample, even at its core. During this time, the force and displacement balances were completed. The test was then launched, after which the top plate was lifted and the sample was retrieved. Before taking measurements, the hot samples were given time to cool down (5 min) while the data was being saved.

After each sample was tested, the compaction area was cut off with an ultrasonic knife and was scanned using a Nikon™ XTH320 CT-scanner. A source voltage of 140 kV and a source current of 140 µA were applied using four images per projection. A scan resolution (voxel size) of 32 µm was achieved. The void analysis was done with VG Studio™ MAX 3.5.1 and a threshold of 50% was used for image processing.

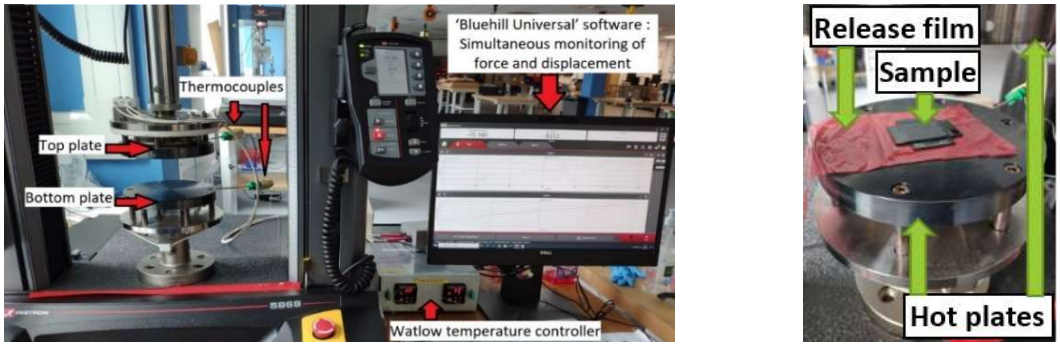

(a) (b)

Figure 4 : (a) Test set-up and (b) Sample positioning

2.3. Test Programs

Nixon-Pearson et al. [14] presented experimental procedures that will be followed for this research project. As depicted in Figure 5a, the first adapted test method uses a regime where the fast application of load is followed by long creep intervals. Called "Ramp & Dwell (RD) program", it was made to incrementally cover a range of pressures commonly seen in the AFP conditions. This is to assess the effect of temperature and identify the compaction limit after which pressure has less impact. The second method (shown in Figure 5b), the "Hold program" is performed with a fixed pressure (selected from the Ramp & Dwell program), at higher temperatures, with varying time and temperature, which will offer information about the influence of both processing parameters. 28 samples were tested for the RD program and 24 were tested for the Hold program.

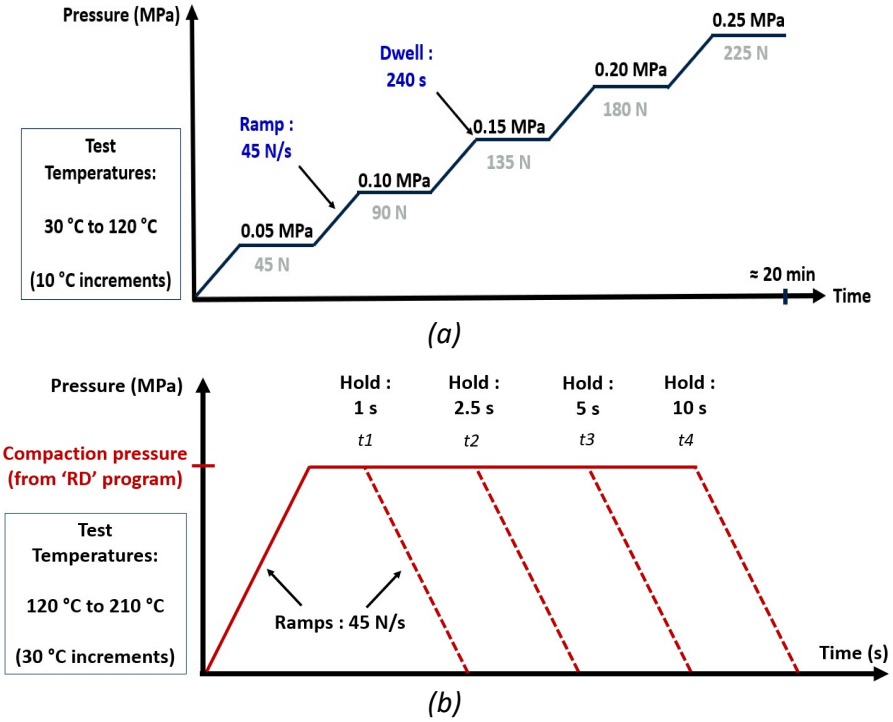

Figure 5 : Investigation process – (a) "Ramp & Dwell" program and (b) "Hold" program

3. Results and Discussion

3.1. Test Programs

For each temperature in the Ramp-Dwell program, analysis of the thickness change after each load increment showed that the thickness reductions after the 0.1 MPa, 0.15 MPa and 0.20 MPa steps are similar, but that all three are far lower than the thickness change after the 0.05 MPa section. This could be due to the squeezing effect (resin pushing the fibres transversely, making the system deform as an incompressible fluid), being predominant at first and the bleeding effect (resin flowing out the ply following the direction of the fibres, without shifting them) being predominant afterwards.

These observations allowed us to select a pressure level of 0.1 MPa to reach acceptable levels of consolidation for this material. From this, 0.1 MPa was selected as the compaction pressure for the subsequent "Hold program". The measured thickness and visual observations of width for this program are shown in Figure 6.

  doi:10.5075/epfl-298799_978-2-9701614-0-0 published under CC BY-NC 4.0 license

In Figure 6a, the '1s' curves show that the pressure application time should be longer. Indeed, for these curves, even after the load has been removed, there is a delay in the displacement response. This is certainly due to the fact that the machine could not properly apply and remove the requested load for such a short time. In Figure 6b, it can also be noted that with the increase of temperature, the gap between the final thicknesses for each temperature reduces (i.e., 0.17 mm reduction between 120°C and 150°C, then 0.08 mm reduction between 150°C and 180°C). This may be linked to the change in viscosity, allowing the resin to flow more efficiently along the fibres as the temperature increases. No machine response delay was observed for pressure application times of 2.5s and longer.

As anticipated, it was also observed that increasing the test temperatures led to lower thicknesses and wider compaction areas. Figures 7a and 7b respectively show the progress of the final thicknesses and widths. Knowing at which rate the thickness evolves at high temperature will then allow to control it more efficiently.

In Figure 8, it is shown that the compaction areas get gradually bigger with the increase of temperature. It is also the case with the increase of pressure application time, but to a smaller extent. Moreover, it can be seen that some compaction areas have curved edges. This starts with the sample tested at 180°C for 5s and appears for higher times and temperatures. The cause for this could be that the squeezing flow still being in effect even after the compaction limit has been reached. It would then be recommended to perform at lower temperatures and times (hence 150°C and 2.5s), to enable the control of the dimensional stability.

In Figure 8, it is shown that the compaction areas get gradually bigger with the increase of temperature. It is also the case with the increase of pressure application time, but to a smaller extent.

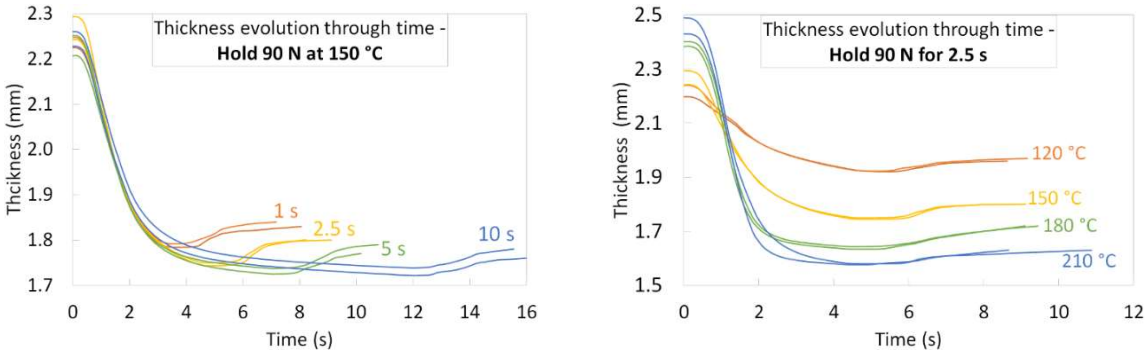

(a) (b)

Figure 6 : Hold program – Thickness change – (a) "Hold 150°C" and (b) "Hold 2.5 s"

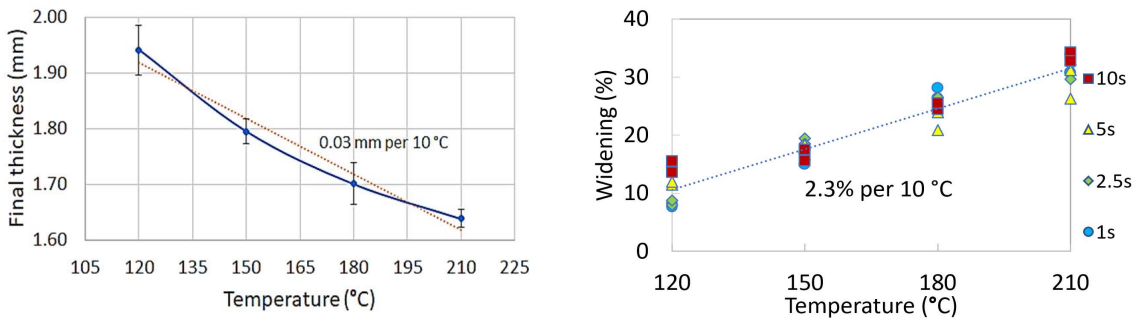

(a) (b)

Figure 7 : Hold Program – Evolution of (a) final thicknesses and (b) final widths

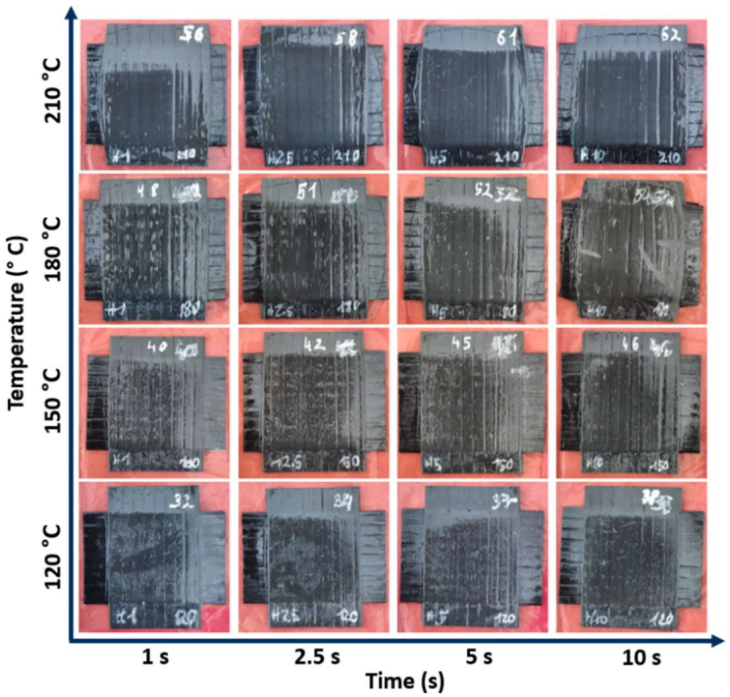

Figure 8 : Hold program samples – Evolution of the compaction area in terms of time and temperature

3.2. Void analysis

The VG Studio software was used to analyse the size of the voids and their distribution within the compacted samples.

Table 1 : Void network (3D view)

Parameters	Uncured	120 °C – 1 s	210 °C – 10 s
Voids (%)	7.39	1.91	0.45
Voids distribution (3D)	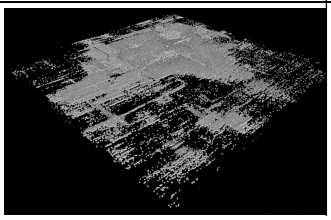	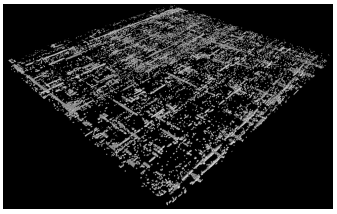	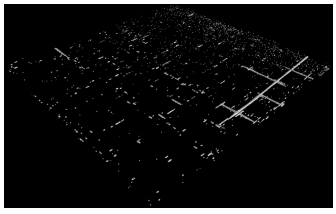

Table 2 : Effect of time and temperature on voids (Side sample view)

Parameters	**Void size and distribution**
Uncured *(7.39 % voids)*	
120 °C – 1 s *(2.63 % voids)*	
120 °C – 10 s *(1.91 % voids)*	
210 °C – 1 s *(0.88 % voids)*	
210 °C – 10 s *(0.45 % voids)*	

As might be expected, a decreasing void level was observed as compaction temperature and time were increased. This is shown in Table 1, where the uncured sample has the highest void volume. This table also shows the extreme parameters of the Hold program (lowest temperature with shortest time vs. highest temperature with longest time) and their respective average void contents Table 2 shows the void features of selected samples. The results indicate that longer pressure application time and higher compaction temperature lead to smaller and fewer voids. The same scale was used to show the decrease of thickness with the increase of temperature.

4. Results and Discussion

The aim of this study was to investigate the compaction behaviour of the Out-Of-Autoclave Carbon/Epoxy prepreg IM7/M56 and to verify the possibility to control the dimensions of samples with a set of parameters. Experimental results showed that a pressure level of 0.1 MPa generated enough consolidation. With this pressure applied, the thickness and width change rates were 0.03mm/10°C and 2.3%/10°C. Furthermore, 2.5s and 150°C were selected as the best parameters for dimension stability control during lay-up. Shorter times are too susceptible to lead to a significant machine implication in the results. Longer times and higher temperatures lead to uncontrolled compaction area shape. Porosity was also analysed, as the presence of voids has an influence on final part thickness and integrity. Defect analysis was performed by investigating the average void content and voids sizes in the compacted samples and showed that higher temperature and longer pressure application time led to smaller and fewer voids, going from an average void content of 7.39% in an uncured sample, down to 0.45% in a sample compacted at 210°C for 10s. Predicting and controlling material behaviour will permit to better analyse and understand the influence of process conditions and hence enhance final part quality. This is only achievable by guaranteeing enough consolidation and thickness control. Having explored extreme parameters has helped to define which limits of deposition time, temperature and force should be used with the chosen material. Future experiments will explore if these parameters can produce desirable laminate quality without the need for autoclave pressure.

5. Acknowledgements

The authors would like to acknowledge the support of Rolls-Royce plc through the Composites University Technology Centre (UTC) at the University of Bristol and the EPSRC through the CoSEM Centre for Doctoral Training (EP/S021728/1) and the Future Composites Manufacturing Hub (EP/P006701/1).

6. References

[1] M. Di Francesco and L. Veldenz, “On the development of multi-material automated fibre placement technology National Composites Centre – Bristol , UK,” *Int. Conf. Manuf. Adv. Compos. (Icmac 2015)*, no. June, 2015.

[2] V. Dhinakaran, K. V. Surendar, M. S. H. Riyaz, and M. Ravichandran, “Review on study of thermosetting and thermoplastic materials in the automated fiber placement process,” *Mater. Today Proc.*, vol. 27, pp. 812–815, 2020.

[3] Z. Han, S. Sun, H. Fu, and Y. Fu, “Multi-Scale Low-Entropy Method for Optimizing the Processing Parameters during Automated Fibre Placement,” pp. 1–18, 2017, doi: 10.3390/ma10091024.

[4] G. Marsh, “Automating aerospace composites production with fibre placement,” *Reinf.*

  doi:10.5075/epfl-298799_978-2-9701614-0-0

Plast., vol. 55, no. 3, pp. 32–37, 2011.

[5] L. Zhang, X. Wang, J. Pei, and Y. Zhou, "Review of automated fibre placement and its prospects for advanced composites," *J. Mater. Sci.*, vol. 55, no. 17, pp. 7121–7155, 2020, doi: 10.1007/s10853-019-04090-7.

[6] J. Frketic et al. "Automated manufacturing and processing of fiber-reinforced polymer (FRP) composites: An additive review of contemporary and modern techniques for advanced materials manufacturing," *Addit. Manuf.*, vol. 14, pp. 69–86, 2017.

[7] T. Centea, L. K. Grunenfelder, and S. R. Nutt, "A review of out-of-autoclave prepregs - Material properties, process phenomena, and manufacturing considerations," *Compos. Part A Appl. Sci. Manuf.*, vol. 70, pp. 132–154, 2015.

[8] Hexcel, "HexPly M56 - 180°C Out-Of-Autoclave curing matrix - Material Datasheet," 2020.

[9] S. Mortimer, M. J. Smith, and E. Olk, "Product development for out-of-autoclave (O.O.A.) manufacture of aerospace structures," *Int. SAMPE Symp. Exhib.*, 2010.

[10] E. Oromiehie, B. G. Prusty, P. Compston, and G. Rajan, "The influence of consolidation force on the performance of AFP manufactured laminates," *ICCM Int. Conf. Compos. Mater.*, vol. 2017-Augus, no. August, pp. 20–25, 2017.

[11] A. Dong, Y. Zhao, X. Zhao, and Q. Yu, "Cure cycle optimization of rapidly cured out-of-autoclave composites," *Materials (Basel).*, vol. 11, no. 3, 2018, doi: 10.3390/ma11030421.

[12] J. Lee *et al.*, "Advanced carbon fiber composite out-of-autoclave laminate manufacture via nanostructured out-of-oven conductive curing," *Compos. Sci. Technol.*, vol. 166, pp. 150–159, 2018, doi: 10.1016/j.compscitech.2018.02.031.

[13] D. H. J. A. Lukaszewicz and K. D. Potter, "The internal structure and conformation of prepreg with respect to reliable automated processing," *Compos. Part A Appl. Sci. Manuf.*, vol. 42, no. 3, pp. 283–292, 2011.

[14] O. J. Nixon-Pearson et al. "An experimental investigation of the consolidation behaviour of uncured prepregs under processing conditions," *J. Compos. Mater.*, vol. 51, no. 13, pp. 1911–1924, 2017.

DEVELOPMENT OF A DIRECT INJECTION MOLDING PROCESS FOR THE PRODUCTION OF LONG GLASS FIBER-REINFORCED PHENOLIC RESINS COMPONENTS

Robert Maertens[a,b]
Wilfried V. Liebig[a]
Kay A. Weidenmann[c]
Peter Elsner[b]
a: Karlsruhe Institute of Technology (KIT), Institute for Applied Materials – Material Science and Engineering (IAM-WK), Engelbert-Arnold-Straße 4, 76131 Karlsruhe, Germany
robert.maertens@kit.edu
b: Fraunhofer Institute for Chemical Technology ICT, Joseph-von-Fraunhofer-Straße 7, 76327 Pfinztal, Germany
c: Augsburg University, Institute of Materials Resource Management (MRM), Am Technologiezentrum 8, 86159 Augsburg, Germany

Abstract: *Parts made from phenolic molding compounds reinforced with glass fibers have a good heat resistance, a high dimensional accuracy, and an excellent chemical resistance. However, these parts typically have a low tensile strength. Conventional glass fiber-reinforced phenolic molding compounds have an average fiber length which is below the critical fiber length for this material combination. To increase the fiber length and to mitigate this disadvantage, a new injection molding process variant was developed, which allows the direct addition of long glass fibers. For opening and dispersing long fiber bundles, a thermoset-specific screw mixing element was developed and compared to the conventional conveying screw geometry. Despite the increased fiber shortening when using the mixing element, the mechanical properties were improved compared to the standard conveying screw geometry, which is attributed to the better fiber-matrix homogenization.*

Keywords: thermoset molding compound, long fiber injection molding, screw mixing element, fiber length measurement, phenolic resin

1 Introduction

1.1 Fiber-reinforced phenolic molding compounds

Since their invention by Baekeland in 1909 [1], phenolic resins have been used in a wide variety of applications and serve as important constituents in wood composite adhesives, foams and insulation material, refractories as well as in fiber-reinforced molding compounds [2]. These composite parts have a high maximum operating temperature, an excellent chemical resistance, and a very good dimensional accuracy, which is why they are often used in the direct vicinity of the internal combustion engine [3] or electric motors [4]. One of the biggest challenges for the wider use of phenolic molding compounds is their brittle deformation behavior [5, 6]. To increase the mechanical strength, reinforcement fibers are compounded into the resin. In general high average fiber lengths are desirable [7–9]. However, in the state-of-the-art thermoset injection molding process of phenolic molding compounds, small weighted average fiber length val-

  doi:10.5075/epfl-298799_978-2-9701614-0-0

ues of L_p = 0.3 mm … 0.35 mm are typical [10]. To quantify the required fiber length for a significant improvement of the mechanical properties, the critical fiber length L_c, which is the minimum fiber length that is required for fully utilizing the reinforcement potential of the fibers [11], is used. A fiber length $L < L_c$ still leads to a reinforcing effect, but does not fully utilize the available potential. Even though the literature values for the critical fiber length L_c in glass fiber-reinforced phenolic resins vary between L_c = 2 mm [12] and L_c = 8 mm [13], it can be assumed that the fiber length in typical, commercially available materials is significantly below L_c.

1.2 Long fiber injection molding processes

A logical first step for increasing the fiber length in the molded component is to increase the fiber length in the base material. For thermoplastic polymers, long fiber granulates are available in a variety of different lengths and matrix materials. For thermoset matrix systems, no long fiber granulate for injection molding is available, but there are long fiber phenolic molding compounds for compression processing. They have a plate-like shape and are available in length classes of 5 mm, 12 mm and 24 mm. For compression molding applications, impact strength values that are 10 … 20 times superior to conventional short fiber molding compounds are claimed [5]. However, according to studies by Saalbach et al. [14] and Raschke [15], this material causes significant processing problems during injection molding, such as sticking to the screw and the barrel, without offering any beneficial mechanical properties of the molded parts.

Several injection molding process variants with a direct long fiber feeding have been developed for thermoplastic materials. In the injection molding compounder (IMC), a co-rotating twin-screw extruder is combined with an injection unit [16]. Direct rovings are pulled into the extruder and are wetted by the thermoplastic polymer. The continuous compounding process is coupled to the discontinuous injection process with a melt buffer. Another inline compounding process has been developed by Composite Products, Inc. (CPI). This process combines a continuous single-screw compounding process with the injection process using a melt buffer [17]. To make the direct compounding feasible for lower volume applications, several processes with the common aspect that the melting and compounding is carried out discontinuously have been developed. This removes the need for a melt buffer and therefore reduces capital investment costs. The direct compounding injection molding (DCIM) process couples a single screw compounding extruder with a traditional injection molding machine [18]. In the DIF process (direct incorporation of continuous fibers), continuous fibers are directly pulled into the screw of the injection molding machine [19]. Mixing elements on the injection molding screw are required for obtaining a good fiber dispersion. The fiber direct compounding process (FDC) works by pulling the unreinforced thermoplastic granulate passively into the screw and melting it like in a conventional injection molding machine [20]. In contrast the DIF process, the continuous fibers are cut to a length of L = 2 mm … 100 mm using a fiber chopper and are fed to the injection molding machine via a twin-screw sidefeed. At the position of the fiber feed, the screw diameter is reduced to facilitate the incorporation of the fibers.

Within this work, the effect of a newly developed long fiber thermoset molding process on the fiber length in the molded component and on the tensile strength of the glass fiber-reinforced phenolic resins is evaluated. It enables the manufacturing of parts with a flexible composition of long and short glass fibers.

  doi:10.5075/epfl-298799_978-2-9701614-0-0

2 Materials and methods

2.1 Materials and manufacturing processes

The phenolic molding compound used within this work is based on the Vyncolit® X6952 short glass fiber-reinforced compound by Sumitomo Bakelite (Gent, Belgium). Short glass fibers (SGF) were sourced from 3B fibreglass (Hoeilaart, Belgium) in the form of their DS5163-13P D = 13 µm chopped strands. The SGF content in the molding compound was adjusted from fractions of ϕ = 0 wt.-% up to ϕ = 30 wt.-% by twin-screw extruder compounding on a lab scale extruder with a screw diameter of d = 27 mm (Leistritz Extrusionstechnik GmbH, Nürnberg, Germany) [21]. For the long glass fibers (LGF), the Tt = 2400 tex direct roving 111AX11 with a filament diameter of D = 17 µm by 3B fibreglass was used. The nomenclature of the material formulations follows the scheme PF-SGF*x*-LGF*x*. The variable x stands for the fiber content ϕ of the short or long glass fibers. The long fiber thermoset injection molding process enables a flexible combination of SGF and LGF by separating the two mass flows, see Figure 1

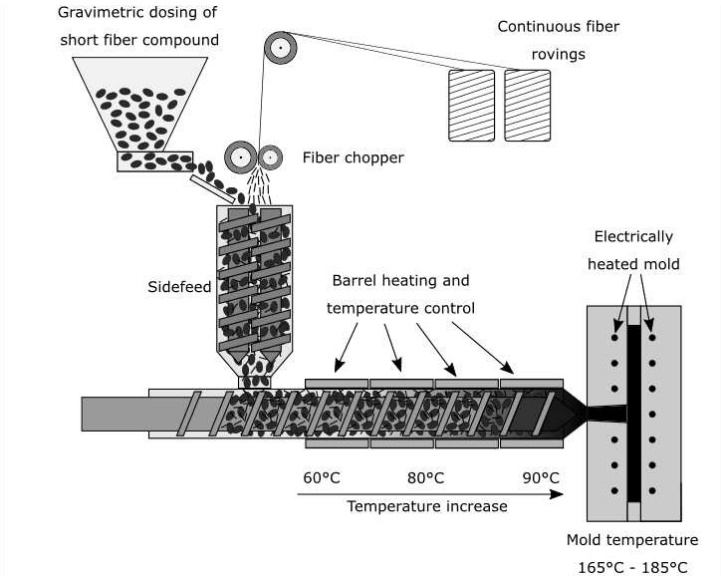

Figure 1. Process scheme long fiber thermoset injection molding process

The SGF are gravimetrically fed as a part of the phenolic molding compound, whereas the LGF are chopped from the continuous rovings. Both are fed into the plasticizing unit with a twin-screw sidefeed. The injection molding screw is a conveying screw with an interchangeable screw tip, which allows the adaption of either a conventional conveying geometry or a newly designed, thermoset specific Maddock mixing element, which is shown in Figure 2 a).

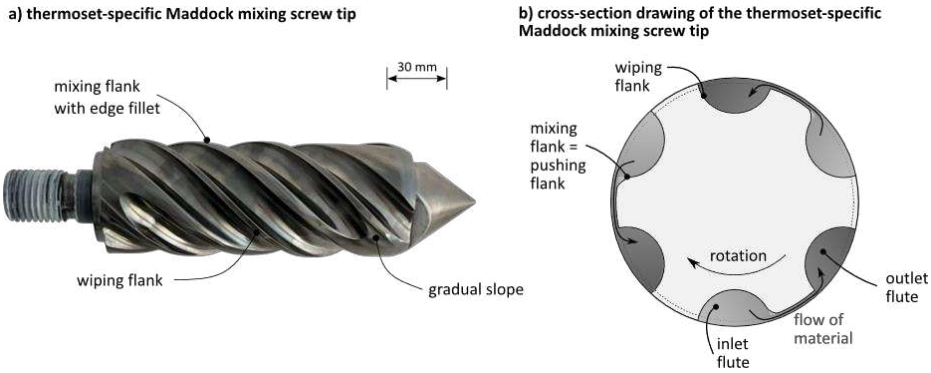

Figure 2. Thermoset-specific Maddock mixing element image (a) and cross-section drawing (b)

  doi:10.5075/epfl-298799_978-2-9701614-0-0

The mixing element features three distinct differences to a conventional Maddock mixing element. First, the inlet channels feature a gradual slope at their ends to facilitate the flow of material and to avoid material accumulations, which additionally narrows down the residence time distribution. The second feature difference to the traditional Maddock mixing element is the edge fillet on the mixing flight. Due to the radius on this edge, the material must undergo additional elongational stresses when passing through the shear gap. The third main feature is that the positions of the mixing flight and wiping flight are reversed compared to the state-of-the-art, which is visible from Figure 2b). Traditionally, the pushing flank is also the wiping flank of the mixing element. This makes sense for thermoplastic materials which enter the mixing element in a completely molten state. However, due to the low shear conveying screw design, the thermoset molding compounds only start to melt in the foremost screw flights under the influence of the pressure from the flanks of the conveying screw. This means that the material close to the pushing screw flanks is molten, whereas the material distant from the screw flanks might still be granular [22]. If the molding compound entered a traditional mixing element in such a state, the granular fraction would be pushed through the shear gap, possibly blocking it. The thermoset-specific design ensures that only molten material is pushed through the shear gap.

2.2 Material characterization techniques

In the injection molding trials, rectangular plates with a size of 190 mm × 480 mm and a thickness of h =4 mm were molded. The plates were filled via a central sprue with a diameter of d = 15 mm and post-cured up to T = 180 °C The test specimens were cut out of the plates by waterjet-cutting both in parallel (0°) and perpendicular (90°) orientation to the flow of material. The tensile testing was carried out according to the standard DIN EN ISO 527-2 [23].

For the fiber length measurement, a sample cut from the molded part with a diameter of d = 25 mm and a typical weight of m = 3 g was used. The matrix was removed pyrolytically at T = 650 °C for t = 36 h under air atmosphere by using a LECO TGA 701 (St. Joseph, USA). The ash residue was transferred into distilled water and a small amount of acetic acid was added. The suspension was subjected to t = 2 min in an ultrasonic bath to open the fiber bundles. Further dilution steps were done by using a beaker with an outlet tap and a propeller stirrer. The measurement samples were taken through the outlet tap and transferred to a petri-dish, which was then analyzed by using the FASEP device by IDM systems (Darmstadt, Germany). Per petri-dish, approximately n = 3000 … 6000 fibers were measured. The process was repeated at least four times per specimen [10]. The weighted average fiber length L_p can be calculated according to Equation (1) using the length L_i of each individual fiber i.

$$L_\mathrm{p} = \frac{\sum_{i=1}^{n} n_i L_i^2}{\sum_{i=1}^{n} n_i} \tag{1}$$

3 Results

Figure 3 shows the tensile strength parallel and perpendicular to the flow of material for samples with an overall total fiber content of ϕ = 30 wt.-%.

  doi:10.5075/epfl-298799_978-2-9701614-0-0

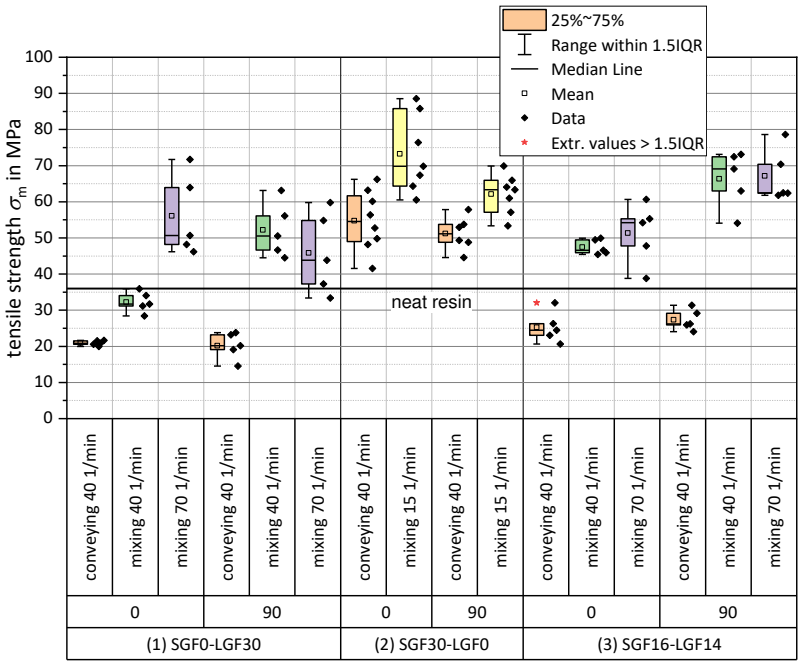

Figure 3. Tensile strength of test specimens with 30 wt.-% glass fiber content

Switching from the conveying screw geometry to the Maddock mixing screw element increases the tensile strength for all formulations and for both specimen orientations. Increasing the plasticizing screw speed when using the mixing element leads to a further significant increase in tensile strength for the PF-SGF0-LGF30 formulation in 0° orientation. For the other formulations and orientations, the tensile strength mostly increases but within the standard deviation of the measurement. The scattering of the measurement results also increases when using the mixing element. While the positive effect of the mixing element on the tensile strength of the LGF materials is clearly visible from the measurement results, it must be noted that the overall highest absolute strength value is reached by the SGF compound. The fiber length measurement results for PF-SGF0-LGF30 are shown in Figure 4.

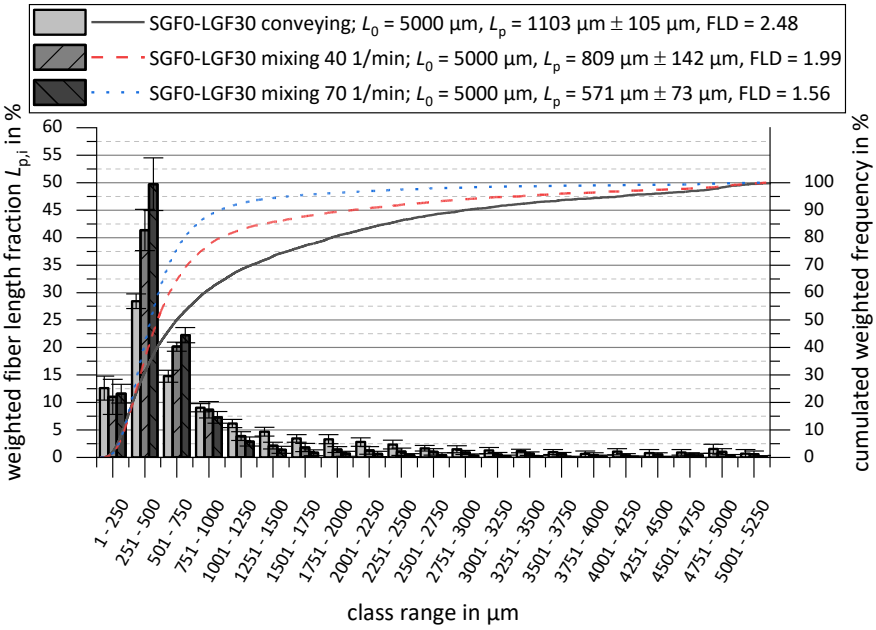

Figure 4. Weighted average fiber length for PF SGF0 LGF30 using mixing element

  doi:10.5075/epfl-298799_978-2-9701614-0-0

A stronger fiber shortening is visible with increasing mixing energy input, this means when using the mixing element and when increasing the screw speed. The weighted average fiber length in the molded part is reduced from L_p = 1103 µm for the conveying screw tip to $L_{p,\ 40\ 1/min}$ = 809 µm and to $L_{p,\ 70\ 1/min}$ = 571 µm for the Maddock mixing element. The ratio of the weighted average fiber length and the numerical average fiber length, FLD=L_p/L_n, which is an indirect measure for the fiber dispersion quality [24], is also improved when using the mixing element. At the highest screw speed setting that was investigated, $FLD_{mix,70\ 1/min}$=1.56 indicates a good fiber dispersion.

4 Discussion

Switching from the conveying screw to the mixing element leads to a stronger shortening of the fibers, which is further increased by using a higher plasticizing screw speed. In this regard no difference to thermoplastics was found. Most studies for thermoplastics state that the fiber length in the molded part decreases with increasing screw speed. Moritzer and Bürenhaus [25] confirmed this for glass fiber-reinforced polypropylene (PP-GF), Lafranche et al. have drawn the same conclusions for glass fiber-reinforced polyamide 6.6 (PA66-GF) [26]. As an exception to the general consensus, Rohde et al. [27] only found a slight, but not statistically significant shortening effect of the screw speed for PP-GF.

The mechanical characterization results have shown that using the mixing element leads to an increased strength, despite the accompanying fiber shortening. This means that the advantages of additional mixing outweigh the disadvantages of shorter glass fibers. This stands in contrast to most studies for fiber-reinforced thermoplastics. The findings of Thomason et al. [7] confirm the Kelly-Tyson model of the critical fiber length. They found an increase in tensile strength up to a fiber length of L = 3 mm … 6 mm for PP-GF. Similar results are reported by Fu and Lauke [8], who observed a rapid increase in tensile strength with increasing fiber length. However, the fiber length is only one factor that determines the strength of the composite material. According to Šahinović and Mušič [28], a homogeneous distribution of the fibers in the polymer matrix is equally important. Especially in the case of bundle-shaped material constituents such as long fiber granulate pellets or chopped long fibers, opening the bundles is important for achieving good mechanical properties. Stress concentrations under mechanical load occur at imperfections in the material [29], for example at fiber bundles. The magnitude of these stress concentrations generally increases with the size of the defect [29, 30]. Especially for composites with a brittle matrix material such as thermosets, the stress concentrations cannot be relieved by plastic deformation of the matrix. As shown in [31], using the mixing element in the long fiber thermoset injection molding process significantly improves the homogeneity of the molded parts by reducing the number of fiber bundles. This increased homogeneity leads to less stress concentrations and consequently to the improvement in tensile strength, despite the fiber shortening.

5 Summary and Conclusions

A newly developed injection molding process variant enabled the manufacturing of parts with varying compositions of short and long glass fibers. With a purpose-designed, thermoset-specific injection molding screw mixing element, varying degrees of dispersive mixing were introduced. The molded parts were characterized regarding their tensile strength and the residual fiber length. The long fiber thermoset injection molding process enabled an up to fourfold increase of the fiber length in the parts compared to conventional phenolic molding compounds when using the standard conveying screw geometry and an approximately two times increase when

  doi:10.5075/epfl-298799_978-2-9701614-0-0

using the mixing element screw. The tensile properties of the parts increased with increased mixing energy input and thus with decreasing fiber length. It is concluded that for achieving a high tensile strength, the fiber homogenization is more important than the fiber length.

Acknowledgements

This work is funded by the Deutsche Forschungsgemeinschaft (DFG, German Research Foundation) projects EL 473/9-1 and WE 4273/18-1.

6 References

1. Baekeland LH, inventor. US942700A Condensation product of phenol and formaldehyde and method of making the same.
2. Pilato L. Phenolic resins: 100 Years and still going strong. React. Funct. Polym. 2013; 73(2):270–7.
3. Beran T, Hübel J, Maertens R, Reuter S, Gärtner J, Köhler J et al. Study of a polymer ejector design and manufacturing approach for a mobile air conditioning. Int. J. Refrig. 2021; 126:35–44.
4. Langheck A, Reuter S, Saburow O, Maertens R, Wittemann F, Berg LF et al. Evaluation of an integral injection molded housing for high power density synchronous machines with concentrated single-tooth winding. 2018 8th International Electric Drives Production Conference (EDPC) 2018:187–92.
5. Koizumi K, Charles T, Keyser HD. Phenolic Molding Compounds. In: Pilato LA, editor. Phenolic Resins: A Century of Progress. Berlin, Heidelberg: Springer; 2010. p. 383–437.
6. Paulke B-R, Börner F, Hahn M, Jobmann M, Englich S, Gehde M et al. Thermosets Impact Modification by Means of Phase-Compatilizing, Amino Resin-Coated Latex Particles. CIT 2015; 87(10):1342–7.
7. Thomason JL, Vlug MA, Schipper G, Krikor H. Influence of fibre length and concentration on the properties of glass fibre-reinforced polypropylene: Part 3. Strength and strain at failure. Compos. Part A Appl. Sci. Manuf. 1996; 27(11):1075–84.
8. Fu S-Y, Lauke B. Effects of fiber length and fiber orientation distributions on the tensile strength of short-fiber-reinforced polymers. Compos. Sci. Technol. 1996; 56(10):1179–90.
9. Asoodeh F, Aghvami-Panah M, Salimian S, Naeimirad M, khoshnevis H, Zadhoush A. The Effect of Fibers' Length Distribution and Concentration on Rheological and Mechanical Properties of Glass Fiber–Reinforced Polypropylene Composite. J. Ind. Text. 2021:152808372110432.
10. Maertens R, Hees A, Schöttl L, Liebig WV, Elsner P, Weidenmann KA. Fiber shortening during injection molding of glass fiber-reinforced phenolic molding compounds: Fiber length measurement method development and validation. Polym.-Plast. Tech. Mat. 2021; 60(8):872–85.
11. Kelly A, Tyson WR. Tensile Properties of Fibre-Reinforced Metals: Copper/Tungsten and Copper/Molybdenum. J. Mech. Phys. Solids 1965; 13(6):329–50.
12. Chen F, Tripathi D, Jones FR. Determination of the Interfacial Shear Strength of Glass-Fibre-Reinforced Phenolic Composites by a Bimatrix Fragmentation Technique. Compos. Sci. Technol. 1996; 56(6):609–22.

  doi:10.5075/epfl-298799_978-2-9701614-0-0

13. Gore CR, Cuff G. Long-Short Fiber Reinforced Thermoplastics. In: ANTEC 1986. Boston. p. 47–50.
14. Saalbach H, Maenz T, Englich S, Raschke K, Scheffler T, Wolf S et al. Faserverstärkte Duroplaste für die Großserienfertigung im Spritzgießen: Ergebnisbericht des BMBF-Verbundprojektes FiberSet. Munich; 2015.
15. Raschke K. Grundlagenuntersuchungen zur Prozess- und Struktursimulation von Phenolharzformmassen mit Kurz- und Langglasfaserverstärkung. Chemnitz: Technische Universität Chemnitz; 2017.
16. Putsch P, inventor. Compunding-Injection Moulding Process and Device. WO 92/00838.
17. Weber C, Ledebuhr S, Enochs R, Busch J. A Novel, New Direct Injection Technology for In-Line Compounding and Molding of LFT Automotive Structures. In: SAE Technical Paper Series; 2002.
18. Hirsch P, Menzel M, Klehm J, Putsch P. Direct Compounding Injection Molding and Resulting Properties of Ternary Blends of Polylactide, Polybutylene Succinate and Hydrogenated Styrene Farnesene Block Copolymers. Macromol. Symp. 2019; 384(1):1800167.
19. Truckenmüller F. Direct Processing of Continuous Fibers onto Injection Molding Machines. J. Reinf. Plast. Comp. 1993; 12(6):624–32.
20. Holmes M. Expanding the market for long fiber technology. Reinf. Plast. 2018; 62(3):154–8.
21. Maertens R, Liebig WV, Elsner P, Weidenmann KA. Compounding of Short Fiber Reinforced Phenolic Resin by Using Specific Mechanical Energy Input as a Process Control Parameter. J. Compos. Sci. 2021; 5(5).
22. Singh R, Chen F, Jones FR. Injection molding of glass fiber reinforced phenolic composites. 2: Study of the injection molding process. Polym. Compos. 1998; 19(1):37–47.
23. DIN EN ISO. 527 Plastics – Determination of tensile properties.
24. Franzén B, Klason C, Kubát T, Kitano T. Fibre Degradation During Processing of Short Fibre Reinforced Thermoplastics. Compos. 1989; 20(1):65–76.
25. Moritzer E, Bürenhaus F. Influence of processing parameters on fiber length degradation during injection molding. In: ANTEC 2021. Online. p. 219–23.
26. Lafranche E, Krawczak P, Ciolczyk J-P, Maugey J. Injection moulding of long glass fiber reinforced polyamide 66: Processing conditions/microstructure/flexural properties relationship. Adv. Polym. Tech. 2005; 24(2):114–31.
27. Rohde M, Ebel A, Wolff-Fabris F, Altstädt V. Influence of Processing Parameters on the Fiber Length and Impact Properties of Injection Molded Long Glass Fiber Reinforced Polypropylene. IPP 2011; 26(3):292–303.
28. Šahinović A, Mušič B. Improvement of the mechanical properties of thermosetting-binding-system-based composites by means of kneading procedure modification and composite formulation. Processes 2020; 8(5):625.
29. Joffre T, Miettinen A, Wernersson EL, Isaksson P, Gamstedt EK. Effects of defects on the tensile strength of short-fibre composite materials. Mechanics of Materials 2014; 75:125–34.
30. Faudree MC, Nishi Y. Tensile Strength Enhancement by Shortening Glass Fibers with Sub-Millimeter Length in Bulk Molding Polymer Compound. Mater. Trans. 2010; 51(12):2304–10.
31. Maertens R, Schöttl L, Liebig WV, Elsner P, Weidenmann KA. Study of material homogeneity in the long fiber thermoset injection molding process by image texture analysis. Adv. Manuf.: Polym. Compos. 2022:1–11.

  doi:10.5075/epfl-298799_978-2-9701614-0-0

MODULAR INFUSIONL: NOVEL APPROACHES TO SEGREGATION AND CONTROL OF FLOW FRONTS WITHIN LIQUID RESIN MOULDING

Joseph, Soltan[a], Janice, Dulieu-Barton[b], James, Kratz[c], Jamie, Hartley[d]

a: National Composites Centre and University of Bristol –joe.soltan@nccuk.com

Abstract: Modular Infusion is a novel liquid resin moulding method which aims to decrease variance across components, reduce frequency and magnitude of flow-based defects and enable fibre or matrix design optimisation. The term 'modular' refers to creating independent zones during a single liquid resin moulding process, which will be achieved by segregating regions, so that a favourable flow front progression is developed. Application of integral barrier film and compaction barrier methods resulted in successful segregation of out-of-plane and in-plane flow fronts, respectively. Complex multiarchitecture parts fabricated through modular infusion methods exhibited a significant improvement in void frequency and the elimination of dry spots.

Keywords: Liquid composite molding; scrap reduction; flow front control and segregation; component optimisation; complex preform infusion

1. Introduction

Liquid resin molding of composites is a widely adopted group of manufacturing processes based on variations of vacuum assisted resin transfer molding (VARTM) and resin transfer molding (RTM). Such processes often require costly development cycles to reach an industrially acceptable standard [1]. The component architecture and final net shape that can be achieved with liquid resin molding is limited by variations in the material permeability and consequent increasing risk of resin flow-based defects [2]-[3]. As components become larger and more complex, the risk of flow-based defects increases resulting in increased scrappage [4]-[5]. Traditional liquid resin molding processes are also limited to using a single matrix material as they typically do not allow for flow front segregation. Therefore, there is a need for a right first time, low variance liquid resin molding process that allows for local design tailoring within complex parts.

Studies showed control of resin flow involves tailoring free volume (FV), i.e., the volume of free space within a dry fibre preform [6]-[9]. Decreasing free volume arrests flow front progression whereas increasing free volume promotes it. Manipulating free volume enables the segregation and control of flow fronts within a single liquid resin molding process. Such segregation could directly prevent many common LCM defects while also enabling fibre and matrix material optimisation. Such control could be employed in-plane or out-of-plane as illustrated in Figure 1.

  doi:10.5075/epfl-298799_978-2-9701614-0-0

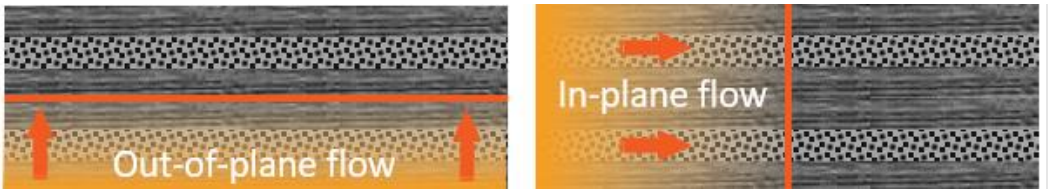

Figure 1. Out-of-plane and in-plane barrier schematics

External vacuum has been applied to increase FV of the fibre bed, therefore, reducing wet out times [10]. A similar method could be employed to reduce crimp imparted by FV reducing methods. In the work presented, identification, development, and appraisal of suitable flow front segregation and control methodologies has been completed to determine whether modular methods can be utilised, within an industrial context, to de-risk processing and optimise performance of typical liquid resin moulded components.

2. Materials

A range of reinforcement materials were down selected for barrier method development to determine the impact of varying material architectures on the barrier methods. These materials are shown below in Table 1.

Table 1: Reinforcements used in modular infusion development

Architecture	Supplier	Known constituents	Rule of mixtures density
2x2 Twill	Sigmatex	245 gsm FT300B Carbon	1.78 g/cm^3
Biax Non-crimp Fabric (NCF) (0/90 and 45/135)	Toray	~536 gsm T800G carbon ~12 gsm powder binder ~8 gsm veil ~3gsm stitch yarn	~1.76 g/cm^3
TX1100 Automated Fibre Placement (AFP) dry tape	Solvay	~194 gsm IM7 Carbon ~4 gsm Veil ~10 gsm Binder	~1.75 g/cm^3
Angle Interlock 3D woven fabric	Axis Composites	3020 gsm 24K/12K/6K T700	1.78 g/cm^3

For early barrier method development, a two-part room temperature curing infusion epoxy system, RIMR 135 and RIMH 137 supplied by PRF, was utilised as a process efficient option. Once barrier methods had been matured, a low viscosity, single component epoxy RTM system from Toray was used in industrial demonstrator manufacture. For out-of-plane barrier trials and subsequent industrial demonstrator manufacture Toray TC310 adhesive film (137 gsm) with glass scrim was employed.

3. Methods

To split a component into independent zones, each with normalised flow front behaviour, a resin film barrier applied during layup as well as mechanical compaction coupled with vacuum relaxation were applied as respective out-of-plane and in-plane barriers illustrated in Figure 2.

  doi:10.5075/epfl-298799_978-2-9701614-0-0

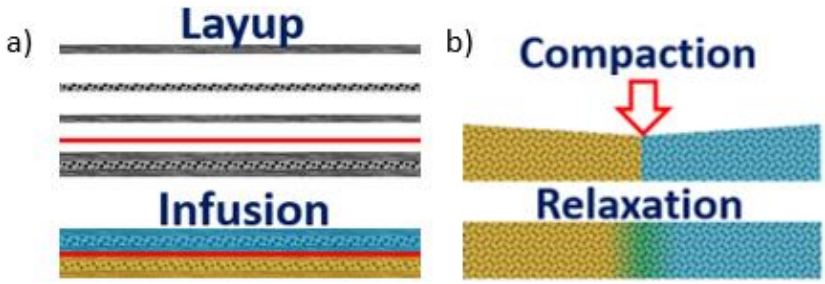

Figure 2. Barrier methods a) Resin barrier film segregation, b) Compaction barrier segregation

3.1 Compaction barrier development

Initial compaction barrier methods were developed through iterative trials on tooling pictured in Figure 3. This consisted of aluminium extrusions with sliding fittings, where frame elements were oriented to resist bending. Threaded inserts and M8 bolts housed within the compaction frame allowed compaction application into the preform below. Index pins ensured repeated alignment while allowing for rapid assembly and disassembly. A machined intensifier was used to transmit compaction force from the bolts. To maintain consistency between material architectures, a nominal preform thickness of 1.8mm was selected. This resulted in 9 plies of twill fabric, 4 plies of NCF, and 9 layers of AFP tape. A quasi-isotropic layup was selected in each case. A vacuum dead zone was included in the region directly under the intensifier by replacing breather with Mosites 1453D elastomer as highlighted in Figure 3**Error! Reference source not found.**b. Vacuum was drawn and monitored in each zone independently. TC310 resin film was added to tool surfaces in some trials to reduce fibre bridging against rigid boundaries. RIMR 135/RIMH 137 resin mixture was introduced through a lower central port as shown in Figure 3c.

  doi:10.5075/epfl-298799_978-2-9701614-0-0

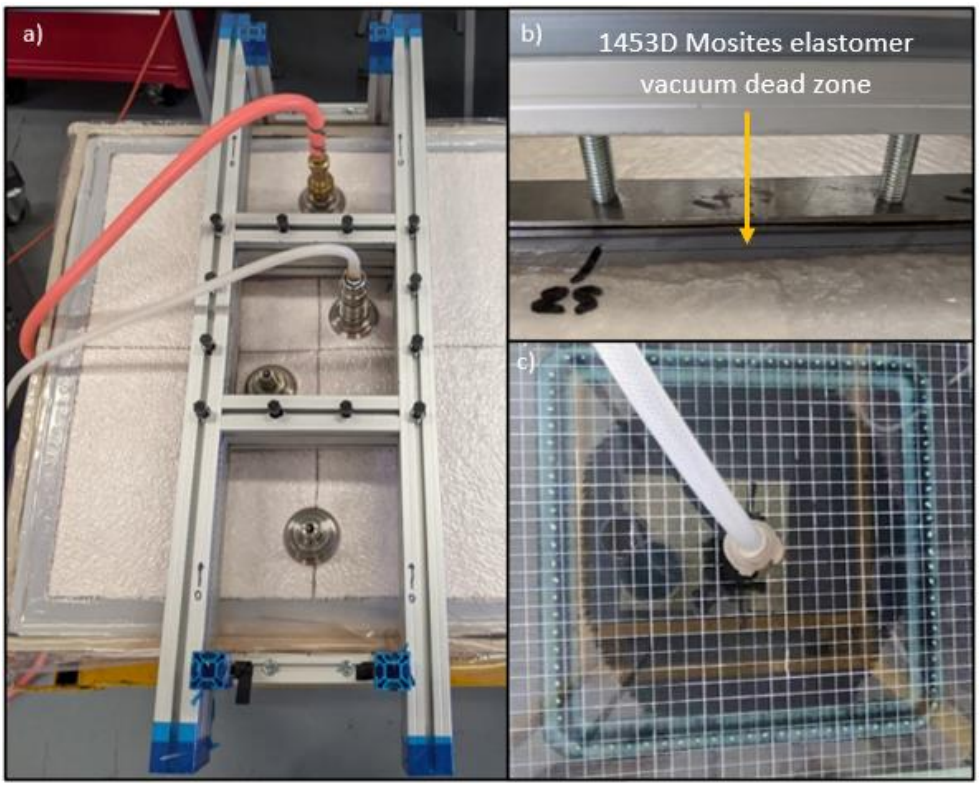

Figure 3. Compaction barrier development tooling a) Compaction frame b) Compaction transmission from bolts to intensifier c) Dark compaction witness mark against light TC310 film

3.2 Resin barrier film development

Figure 4 shows the bagging method used in resin film barrier trials. A flow media dead zone was incorporated to give the infused resin additional time to flow out of plane instead of "race tracking" through the vent. A VAP layer encapsulated the preforms to allow vacuum driving force through the laminate. Tacky tape was butted against test samples to dam resin flow along the periphery of the preform. Three tests were run using unsupported TC310 material with one sample consisting of a single layer and the other samples consisting of a double layer.

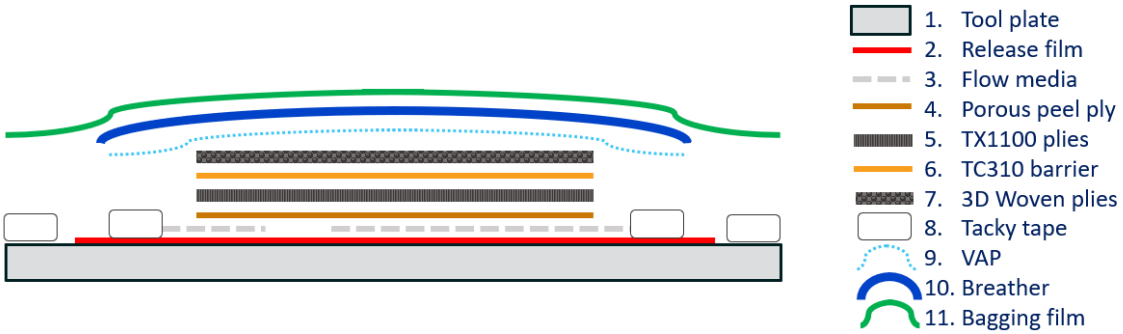

Figure 4. Out-of-plane barrier trial bagging method

3.3 Demonstrator manufacture

Following barrier method development a representative industrial demonstrator component, depicted in Figure 5, was fabricated to demonstrate how modular infusion methods could be applied to complex preforms as well as confirm part quality improvements against a VARTM

  doi:10.5075/epfl-298799_978-2-9701614-0-0

baseline. The component consisted of three zones: an NCF skin, AFP T-stiffener and 3D woven rib cleat. The VARTM approach infused the component as one through zone 1 and 2 inlets. The modular infusion approach fed each zone with resin independently where, a compaction barrier was utilised at the skin stiffener interface and resin film barrier between stiffener and rib cleat. Once the target resin weight had been infused the compaction barrier was removed and external vacuum bag was placed on top of the barrier region to encourage fibre bed relaxation as per [8].

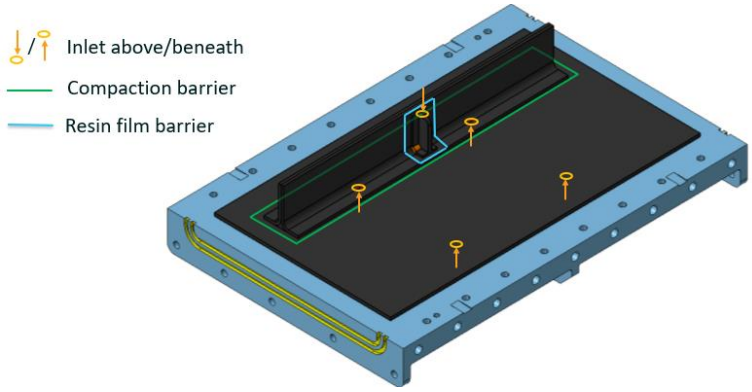

Figure 5. Demonstrator infusion strategy

4. Results

Initial compaction barrier trials found that an independent vacuum source for each zone was required to form the desired preferential flow. TC310 film used against rigid tool surfaces exhibited improvements in barrier integrity due in part to better control of vacuum differential between zones, but largely because of the filling of fibre architecture driven bridging. TC310 in Figure 6 exhibits clear repeat banding which suggests regular regions of low pressure caused by bundling of 90° plies referred to as ‘beach matting’. Such areas of low pressure indicate preferential flow paths for resin to breach the compaction barrier.

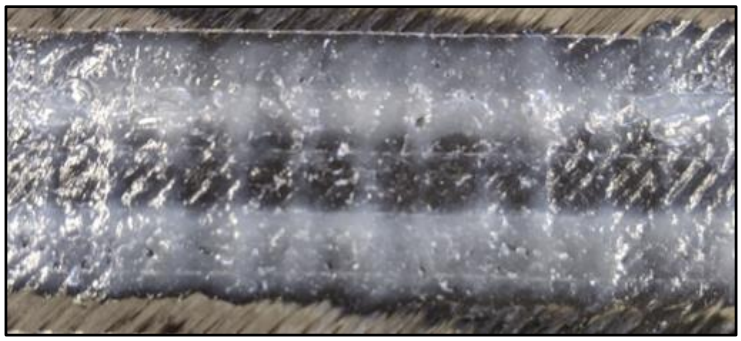

Figure 6. Banding on tool surface TC310

As shown in Figure 7a, NCF exhibits the highest degree of flow front conformity to barrier geometry. Leaks can be observed at flash tape windows where a thickness change resulted in low pressure areas. In Figure 7b, barrier boundaries are visible yet ATL material architecture exhibits the furthest flow front migration away from the barrier bounds. A clear 45° orientation can be seen which corresponds to channels between tapes on the upper 45° oriented plies. Sub-surface channelling is also evident as patches of wet-out material are observed on the surface which are not directly linked to the central zone. In Figure 7c the flow

  doi:10.5075/epfl-298799_978-2-9701614-0-0

front within the twill weave material architecture has conformed well to the barrier bounds, where all visible leaks present in this case developed after the inlet had been clamped. A probable cause of flow front migration in this case is the woven architectures inherent bridging for tow crossing which results in small areas of FV which resin can be driven through.

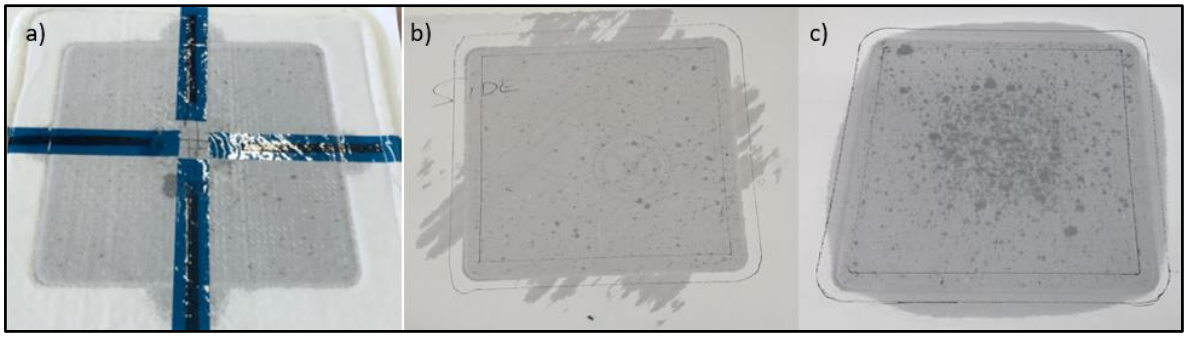

Figure 7. Compaction barrier performance on different material forms a) NCF b) AFP c) Twill

An out-of-plane barrier film trial coupon is pictured in Figure 8**Error! Reference source not found.** where a lower permeability AFP preform was fully wet out while a much more permeable 3D woven preform remained dry. A subsequent demonstrator trail demonstrated the effectiveness of both barrier methods on a single component whereby a stiffener was infused while skin and rib cleat elements were left dry as pictured in Figure 9.

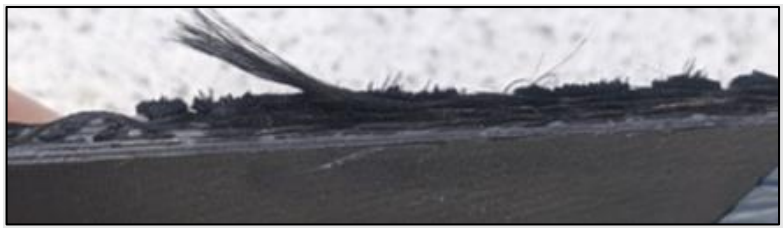

Figure 8. Cross section of a test coupon exhibiting clear interlaminar zone boundary

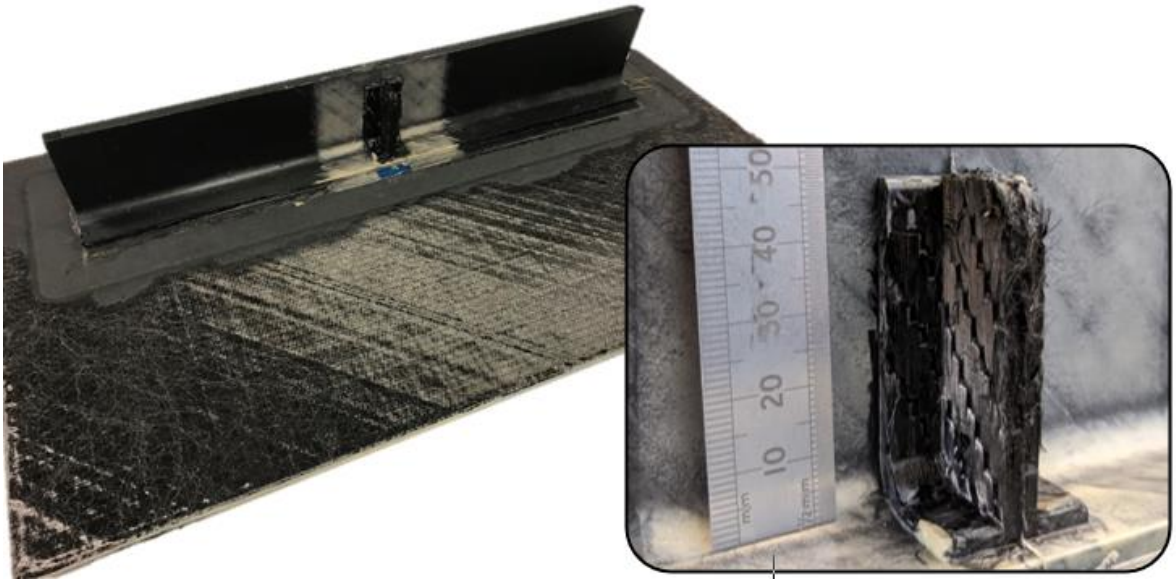

Figure 9. Stiffener only infusion trial Left) Complete assembly showing flow front bounds on skin Right) Closeup of dry rib cleat

Crimp imparted by compaction barriers was minimised with the application of external vacuum. Figure 10 demonstrates that when no relaxation cycle is applied a significant divot remains as witness to applied compaction. Here maximum crimp was measured to be ~20%. Upon application of a five-minute vacuum induced preform relaxation cycle a much smoother transition is observed with a maximum measured crimp of ~13%. It's noted that compaction regions are particularly void free. This is likely due to changes in pressure driving resin in as flushing voids as compaction is released.

Figure 10. Microsections of compaction barrier region. Top) No relaxation Bottom) 5-minute relaxation cycle

During industrial demonstrator manufacture the VARTM baseline component exhibited a much lower flow rate than its modular infusion counterpart. Initial x-ray, microsection and acid digestion analysis revealed modular infusion components are of superior quality to those created through traditional liquid resin moulding processes. These indicative findings are to be corroborated by further manufacturing trials. Figure 11 exhibits component quality enhancements made possible through application of modular infusion methods. Early stalling of resin flow in VARTM component manufacture is a likely cause of the dry spots observed in the stiffener region. Modular methods avoided such stalling by splitting a large flow problem into smaller discrete zones, therefore, reducing the maximum distance from inlets which in turn increased average flow front velocity.

  doi:10.5075/epfl-298799_978-2-9701614-0-0

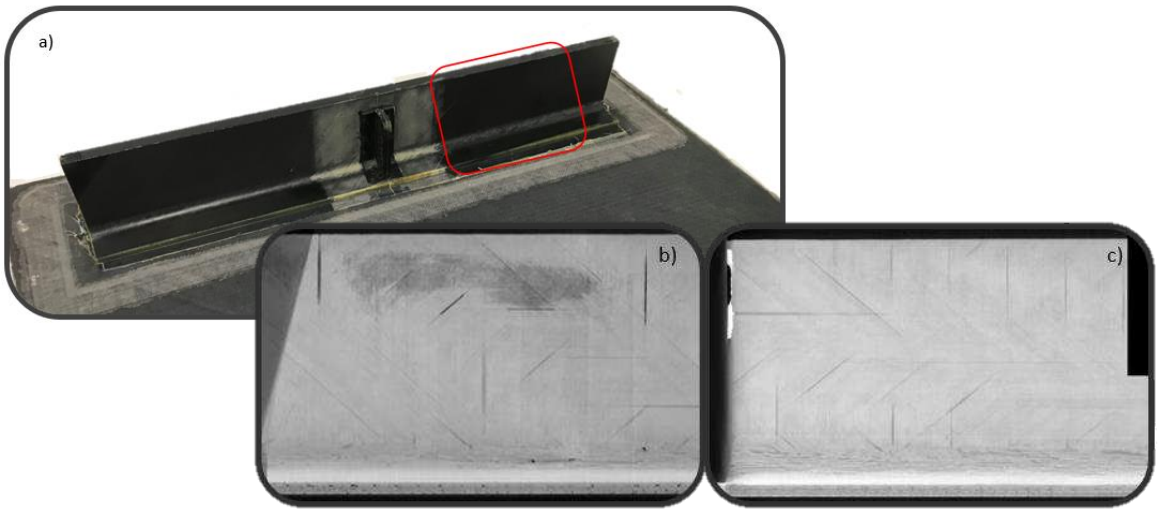

Figure 11. X-ray CT image a) X-Ray region b) Benchmark VARTM component C) Modular infusion component

5. Conclusion

This work has outlined the development of in-plane and out-of-plane barrier methods for the control of resin flow within liquid composite molding processes. Initially proven in small scale trials before being scaled to demonstrator components, both methods resulted in the successful segregation and control of flow fronts within a single infusion.

In-plane barrier methods demonstrated that preform compaction is effective in stemming resin flow. Additionally, the use of torqued bolts to apply compaction force presents an interesting alternative to pneumatic or press based systems. An observed risk to compaction barrier adoption is permanent out of plane deformation of the laminate imparted by the high forces inherent within the process. Suitable methods to reduce this, such as the use of an additional vacuum source to relax the preform should be explored further.

For out-of-plane segregation, it was found that off the shelf TC310 resin performed well with no need for thermal staging to increase viscosity. A significant risk to resin film barriers lies in their conformability to part geometries. Bridging or wrinkling over features can result in channels between zone boundaries leading to resin leak paths. Downstream processing of preform elements leading to high bulk, spring back or other geometric deviation makes application of resin film barriers during layup more challenging.

Further developments are planned to optimise modular infusion methods and related tooling, scale modular methods to larger demonstrator components, develop understanding of modular processing through sensor application and develop further understanding on the mechanical impact of modular methods through element and component testing.

Acknowledgements

I would like to acknowledge the University of Bristol, Bristol Composite Institute and National Composite Centre for allowing access to equipment and software which made this research possible. I would also like to acknowledge the Engineering and Physical Sciences Research Council for the financial backing of the project.

  doi:10.5075/epfl-298799_978-2-9701614-0-0

6. References

1. Advani SG. Role of process models in composites manufacturing [Internet]. Vol. 2, Comprehensive Composite Materials II. Elsevier Ltd.; 2017. 24–41 p. Available from: http://dx.doi.org/10.1016/B978-0-12-803581-8.09898-2

2. Luo J, Liang Z, Zhang C, Wang B. Optimum tooling design for resin transfer molding with virtual manufacturing and artificial intelligence. Compos - Part A Appl Sci Manuf. 2001;32(6):877–88.

3. Pearce NRL, Summerscales J, Guild FJ. Improving the resin transfer moulding process for fabric-reinforced composites by modification of the fabric architecture. Compos Part A Appl Sci Manuf. 2000;31(12):1433–41.

4. González C, Vilatela JJ, Molina-Aldareguía JM, Lopes CS, LLorca J. Structural composites for multifunctional applications: Current challenges and future trends. Prog Mater Sci. 2017;89:194–251.

5. Verma KK, Dinesh BL, Singh K, Gaddikeri KM, Sundaram R. Challenges in Processing of a Cocured Wing Test Box Using Vacuum Enhanced Resin Infusion Technology (VERITy). Procedia Mater Sci [Internet]. 2014;6(Icmpc):331–40. Available from: http://dx.doi.org/10.1016/j.mspro.2014.07.042

6. Gillio EF, Mcknight GP, Gillespie JW, Advani SG, Bernetich KR, Fink BK. Processing and properties of Co-Injected Resin Transfer Molded vinyl ester and phenolic composites. Polym Compos. 1999;20(6):780–8.

7. Krollmann J, Snajdr R, Paz M, Zaremba S, Drechser K. Hybrid-matrix approach: How to overcome the conflict of matrix selection? AIP Conf Proc. 2016;1779.

8. Alms JB, Advani SG, Glancey JL. Liquid Composite Molding control methodologies using Vacuum Induced Preform Relaxation. Compos Part A Appl Sci Manuf [Internet]. 2011;42(1):57–65. Available from: http://dx.doi.org/10.1016/j.compositesa.2010.10.002

Composites Meet Sustainability – Proceedings of the 20th European Conference on Composite Materials,
ECCM20. 26-30 June, 2022, Lausanne, Switzerland

Manufacturing Advances for Pultruded Rod Based Structural Members and Thick Ply Systems

Laura Rhian Pickard[a], Giuliano Allegri[a], Michael R. Wisnom[a]

a: Bristol Composites Institute, Faculty of Engineering, University of Bristol BS8 1TL, UK
laura.pickard@bristol.ac.uk

Abstract: *Fibre-reinforced composite components based around pultruded rods are under investigation with the intention to deliver structural members with improved compressive performance compared to standard fibre-reinforced composites, through a novel hierarchical approach inspired by natural composites. These components present new challenges in manufacturing, as the cured rods become constituents in the larger composite parts. This work highlights advances in manufacturing two representative components, cylindrical struts and flat thick plies, each built around the rods. Key considerations are optimising rod alignment, manufacturing of suitably sized components for representative mechanical testing and minimising defects. Manufacturing methods for both of these components are presented and discussed.*

Keywords: Fibre-reinforced composites; pultruded rods; compression; infusion; prepreg

1. Introduction

Natural composites such as bamboo (Figure 1) or bone (Figure 2) are lightweight structures which perform well under compression. They have hierarchical structures, with features at multiple length scales. NextCOMP seeks to improve the performance of fibre-reinforced composites under compression by creation of similar hierarchical structures.

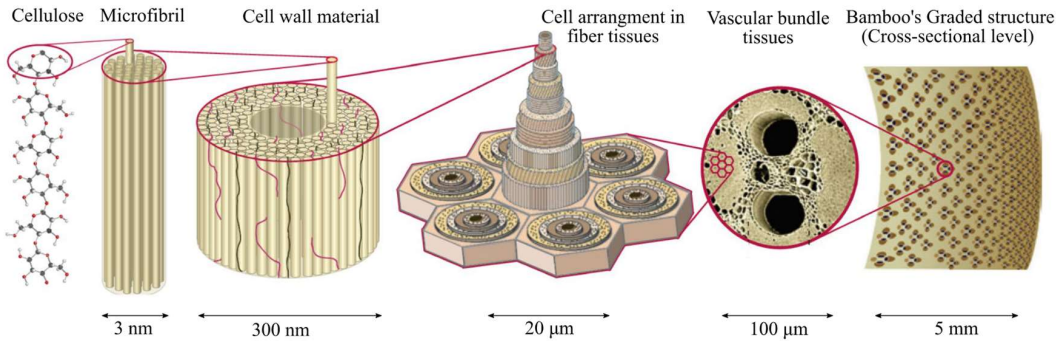

Figure 1. Illustration of hierarchical structure of bamboo. Reproduced from [1]

This work focuses on hierarchical composites based around pultruded carbon fibre-epoxy rods.

For a planar structure, rods must be organised into a flat thick ply. When infused in a channel and constrained at either end, rods are seen to flex between the ends, leading to misalignment. Therefore an adaptation of the 'prepreg sandwich' structure proposed by Clarke [2] is employed to keep the rods in place.

The sandwich structure is suitable for trialling rods of various diameters and cross sections. Using a resin film compatible with the prepreg, the structure may be cured in an autoclave. Use of thin-ply prepreg minimises the additional material.

  doi:10.5075/epfl-298799_978-2-9701614-0-0

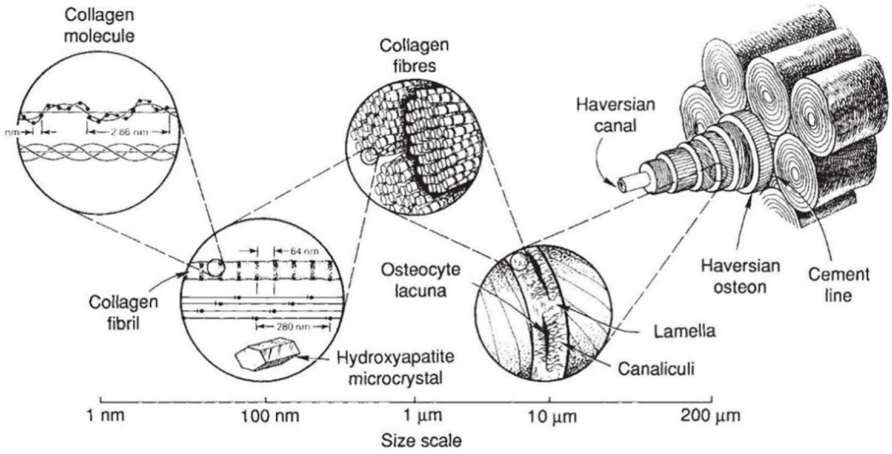

Figure 2. Illustration of hierarchical structure of bone. Reproduced from[3]

Wisnom [4] described use of an overwind on a solid carbon fibre-epoxy rod such as these to radially compress the rod in order to suppress splitting. Cylindrical struts, consisting of carbon-fibre epoxy pultruded rods of circular cross section plus an infused resin, were manufactured by Potter et al [5] for compression after impact testing. This work demonstrated that a Kevlar overwind around the strut could deliver improvement in compressive performance (Figure 3).

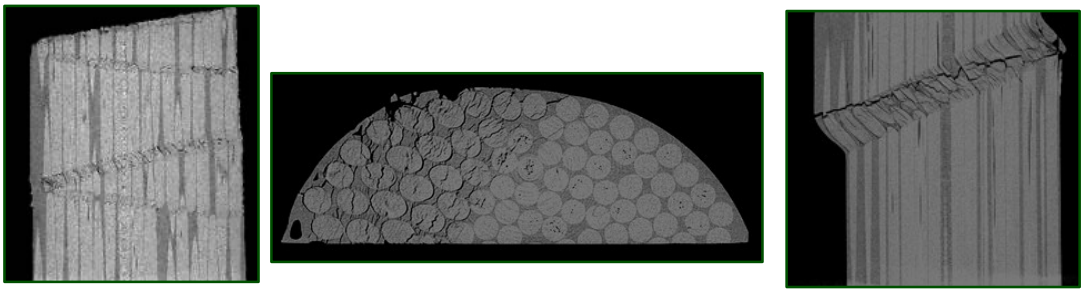

Figure 3. Samples from [5]*, CT scans L R Pickard. Following compression after impact tests. Overwound strut (left, showing zig-zag kink band propagation) exhibited greater compressive strength than without overwind (centre and right, showing single kink band)*

Similar cylindrical struts are discussed here, manufactured using different materials.

As we intend to construct a hierarchical composite, with layers of structure at different length scales designed to constrain compressive failure, individual pultruded rods may be overbraided, with the intention of ultimately using overbraided rods within structures such as cylindrical struts or thick plies.

2. Materials and manufacturing methods

While NextCOMP ultimately aims to incorporate novel fibres and resins; each with micro- or nano- structures designed to control compressive failure; into the hierarchical composites with ply and/or rod based higher level structures, for the initial development stage we use commercially available rods, resins and prepregs so that these can proceed in parallel.

  doi:10.5075/epfl-298799_978-2-9701614-0-0

2.1 Flat Thick Ply

Preliminary trials of infusion of loose, stitched and end-taped 'plies' of rods resulted in poor alignment and rolling of stitched groups of rods at the edge of infusion channels. Rods are sufficiently flexible to move during infusion despite constraint at the ends.

The 'prepreg sandwich' approach pioneered by Clarke [2], shown in Figure 4, requires rods to be precisely aligned between two layers of prepreg, with the addition of resin film between the rods to ensure wet-out.

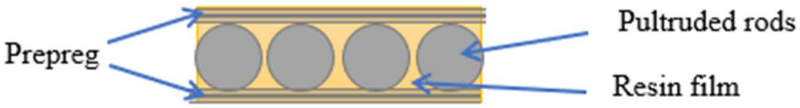

Figure 4. Diagram of 'prepreg sandwich' construction for thick ply containing pultruded rods

Manual lay-up of prepreg sandwich samples ~10cm in length each containing 15-20 rods was carried out using Hyperflight 0.7mm diameter carbon fibre-epoxy rods [6] and Skyflex K51 resin [7], with both Skyflex K51 unidirectional thin ply carbon fibre [7] and Hexcel 913 unidirectional E-glass [8] prepreg outer layers. The samples were cured in an autoclave for 90 minutes at 125°C, 7 bar pressure. The stated rod T_g is 170°C.

2.2 Cylindrical strut.

Cylindrical struts were manufactured using Easy Composites 0.8mm diameter carbon fibre-epoxy rods [9] and Prime 27 resin. Initial trials used a hollow glass tube of internal diameter 12.5mm, coated with release agent, as a tool. Rods were trimmed and fitted into the tool.

The glass tool was held vertically during infusion and cure, with the resin inlet at the base of the tool, to facilitate air bubbles rising to the outlet at the top. Infusion speed was manually controlled using clamps. Each strut was cured at 80°C for 4 hours in an oven.

Struts manufactured using flexible tubing followed the same method, with the addition of a vacuum bag surrounding the flexible tube to provide external radial compression.

2.3 Overbraiding

A Herzog 16 carrier microbraider, used at half capacity with 8 tows, was employed for overbraiding of 0.8mm diameter pultruded rods. A horngear rotary speed of 120±5 rpm was used and a variety of lay lengths tested. Lay length describes the length of braid constructed while a single tow travels a full 360° around the rod during the braiding process, so as lay length decreases braid angle is expected to increase. Overbraiding was carried out with Teijin Twaron 2200 aramid [10], Toyobo high modulus Zylon [11] and Toray T300 carbon fibre [12].

3 Results

3.1 Flat Thick Ply

Cured 'prepreg sandwich' thick plies retained rod alignment as shown in Figure 5. Microscopy (Figure 6) shows the Hyperflight rods contain voids and have an uneven fibre distribution. The rods have become ovalized during the cure, despite the temperature being lower than the stated rod T_g, and there are some gaps in rod spacing.

Figure 5. A cured thick ply prepreg sandwich: Skyflex K51 thin ply unidirectional carbon fibre, Skyflex K51 resin and Hyperflight 0.7mm diameter carbon fibre-epoxy pultruded rods

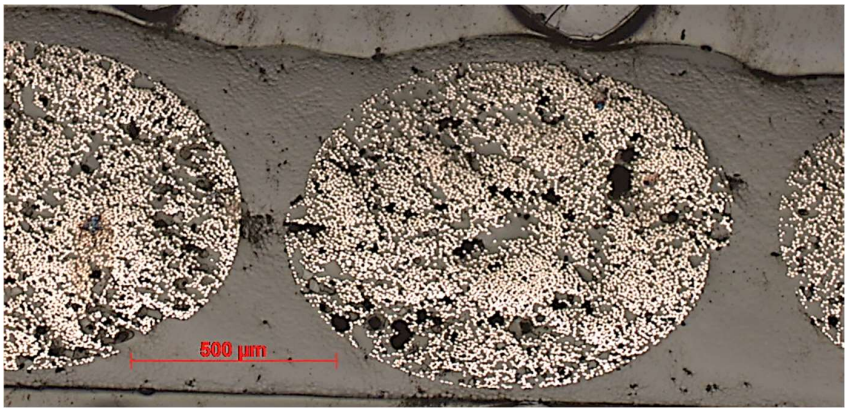

Figure 6. Microscope image showing rods between layers of 913 E-glass prepreg. Skyflex K51 resin film used between rods.

3.2 Cylindrical strut

Struts manufactured using a solid glass tube retain a circular cross section, however quality was variable (Figure 7). While the rods were packed tightly during setup, movement during infusion and cure was sufficient to result in non-uniform rod density. Voids were present throughout and racetracking between the rods and inner surface of the tube was seen, in one instance resulting in a large central void.

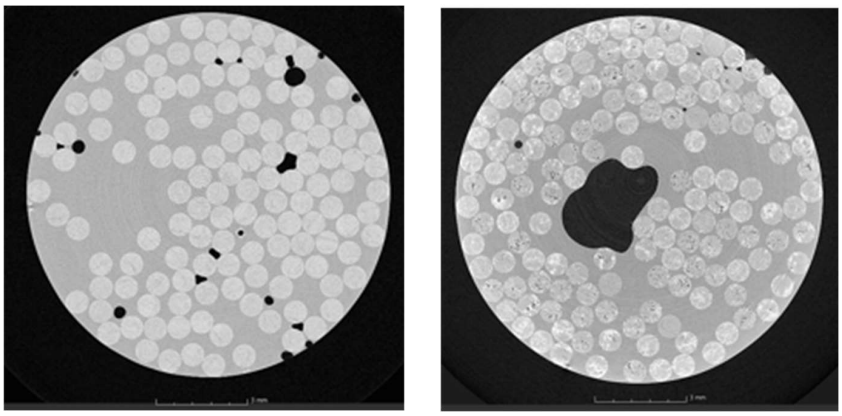

Figure 7. CT scan slices of struts manufactured using glass tools, 0.8mm diameter rods.

  doi:10.5075/epfl-298799_978-2-9701614-0-0

Struts manufactured using flexible tooling (Figure 8) showed much improved rod distribution and very little porosity. However the strut cross section was not circular.

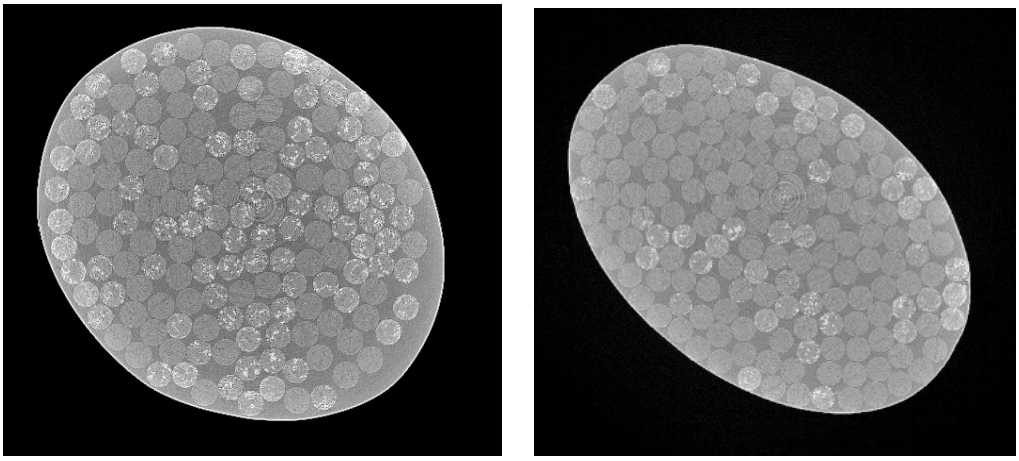

Figure 8. CT scan slices of struts manufactured using flexible tools, 0.8mm diameter rods.

3.3 Overbraiding

Overbraiding (Figure 9) of a relatively small diameter pultruded rod core requires small tows in order to achieve conformation to the rod at larger braid angles (shorter lay lengths). The aramid supplied, of 1610dtex, was too large to conform to a 0.8mm diameter rod at a lay length of 2mm causing bunching. However the braiding at this angle showed little fibre breakage, indicating this may be a suitable material in a smaller tow size.

For all materials, the input lay length was not always achieved in practice, with variation in braid angle and movement of the braid point seen.

273dtex Zylon showed relatively good conformation down to 1mm lay length, though braid angle was not consistent and some bunching was seen. No breakage was observed. A

1k T300 carbon fibre showed significant breakage, resulting in a 'fuzzy' overbraid with a minimum achievable lay length of 2mm, with only a small amount braided before tows snapped.

  doi:10.5075/epfl-298799_978-2-9701614-0-0

Figure 9. Overbraids of 0.8mm rod using 1K T300 carbon fibre at 2mm lay length (left), 273dtex high modulus Zylon at 1mm lay length (centre) and 1610dtex Twaron at 2mm lay length (right).

4. Discussion and next steps

Finite element modelling suggests that increased shear support in the matrix region between the rods may deliver improved compressive performance. The 'fuzzy' carbon overbraids may therefore be beneficial, as the broken fibres increase the effective interphase region and bridge the gaps between rods. A multi-material braid, combining zylon and carbon, may therefore be useful. Smaller tow sizes are to be trialled in overbraiding, and both single overbraided rods and the larger structures manufactured from them to be tested in compression. Reliable compression testing is also a challenge, with new methods under development by NextCOMP colleagues.

Thick plies can be made by hand in small sizes, using the prepreg sandwich model, however achieving precise rod alignment and sufficient resin content in larger samples becomes more difficult. We therefore propose to trial a human-robot collaborative approach, following the work of Elkington et al [13]. A robot can precisely place and hold components of the rod based composite while a human operator applies pressure to consolidate the part.

The work presented here is an initial step towards achieving manufacture of hierarchical, pultruded rod based composites. Future challenges will include integration of novel fibres and resins, which may have non-standard manufacturing requirements, into rod-based systems and integration of the struts and thick plies shown here into larger structures.

As a new way of thinking about composites, the hierarchical approach has the potential to change our approach to the design and manufacture of composite parts. This brings opportunities to develop novel architectures and the manufacturing techniques required to create them.

Improved performance under compression may expand the potential markets for composite products, and could deliver advantages in lightweighting and efficiency through redesign of existing systems. Future composites may not be restricted to the ply model, with rod-based structures among many options for the next generation of fibre-reinforced composites.

5. Conclusions

The two pultruded rod based systems discussed here, cylindrical struts and thick plies, are under development as demonstrators for the hierarchical approach.

Use of a flexible tool with vacuum bag when manufacturing cylindrical struts has been shown to deliver fewer voids and better rod density than a solid glass tool, where voids and racetracking between rods and the tool sides appear evident. Changes in tool fixings and/or post manufacture machining may be used to decrease the eccentricity of the resulting strut to achieve a circular cross section.

Simple infusion of a thick ply, with rods constrained outside the gauge section by stitching, results in poor alignment as the rods flex during infusion, and the stitched thick ply can roll at the edges of the infusion channel. A 'prepreg sandwich' approach, with rods between two layers of prepreg and the regions between rods packed with resin film has delivered better

alignment at the proof of principle stage. The next stage of this work will involve trialling a human-robot collaborative approach to manufacture, intended to enable the repeatable manufacture of larger thick plies with precision.

Acknowledgements

The authors kindly acknowledge the funding for this research provided by UK Engineering and Physical Sciences Research Council (EPSRC) programme Grant EP/T011653/1, Next Generation Fibre-Reinforced Composites: a Full Scale Redesign for Compression in collaboration with Imperial College London.

Supporting data can be requested from the corresponding author but may be subject to confidentiality obligations.

References

[1] T. Gangwar, D. J. Heuschele, G. Annor, A. Fok, K. P. Smith, and D. Schillinger, "Multiscale characterization and micromechanical modeling of crop stem materials," *Biomechanics and Modeling in Mechanobiology*, vol. 20, no. 1, pp. 69–91, Feb. 2021, doi: 10.1007/S10237-020-01369-6/TABLES/5.

[2] A. Clarke, "Mechanical properties and process conversion of a novel form of unidirectional carbon fibre/epoxy rod.," University of Bristol, 1998.

[3] R. Lakes, "Materials with structural hierarchy," *Nature*, vol. 361, no. 6412, pp. 511–515, Feb. 1993, doi: 10.1038/361511a0.

[4] M. R. Wisnom, "Suppression of splitting and impact sensitivity of unidirectional carbon-fibre composite rods using tensioned overwind," *Composites Part A: Applied Science and Manufacturing*, vol. 30, no. 5, pp. 661–665, May 1999, doi: 10.1016/S1359-835X(98)00174-2.

[5] K. D. Potter, F. Schweickhardt, and M. R. Wisnom, "Impact Response of Unidirectional Carbon Fibre Rod Elements with and without an Impact Protection Layer," *Journal of Composite Materials*, vol. 34, no. 17, pp. 1437–1455, Sep. 2000, doi: 10.1106/3QGB-7PJ0-P129-4XRR.

[6] "0.8mm Carbon Rod - Materials." https://www.hyperflight.co.uk/products.asp?code=CARBON-ROD-08MM&name=0-8mm-carbon-rod (accessed Apr. 12, 2022).

[7] "Green Chemicals Biz. SKYFLEX Team Materials Selection Guide SKYFLEX Prepreg," 2014.

[8] "HexPly ® 913 125°C curing epoxy matrix Rheology Gel Time," 2020, Accessed: Apr. 12, 2022. [Online]. Available: https://www.hexcel.com/contact

[9] "0.8mm Carbon Fibre Rod; 1m, 2m - Easy Composites." https://www.easycomposites.co.uk/0-8mm-carbon-fibre-rod (accessed Apr. 12, 2022).

  doi:10.5075/epfl-298799_978-2-9701614-0-0

[10] "Twaron® Filament Yarn - Teijin Aramid." https://www.teijinaramid.com/en/product-details/twaron-filament-yarn/ (accessed Apr. 12, 2022).

[11] "ZYLON ® (PBO fiber) Technical Information (2005)."

[12] "T300-Technical-Data-Sheet-1.pdf".

[13] M. Elkington, C. Ward, A. Kirby, M. Libby, and N. Gandhi, "Collaborative Human-Robotic layup." Dec. 14, 2017. Accessed: Dec. 07, 2021. [Online]. Available: https://research-information.bris.ac.uk/en/publications/collaborative-human-robotic-layup

  doi:10.5075/epfl-298799_978-2-9701614-0-0

ZONALLY HEATED TOOLING FOR MOUDLING COMPLEX AND HIGHLY TAPERED COMPOSITES PARTS

Vincent K. Maes[a], Arjun Radhakrishnan[a], James Kratz[a]

a: Bristol Composites Institute, University of Bristol, Queens Building, University Walk, BS8 1TR, Bristol, United Kingdom – vincent.maes@bristol.ac.uk

Abstract: *Moulding composite materials is an energy-intensive activity and to meet quality requirements, slower heat rates and longer dwells are often used. This is especially true for larger, thicker and/or geometrically complex parts, due to the unevenness of convection heating in ovens and autoclaves. An alternative technology for moulding is using heated tooling, which improves the energy efficiency of the process but can also significantly increase the tooling costs. However, the true power of heated tooling is in the ability to tailor the temperature profile in different regions. By introducing zonal heating, significantly faster process cycles can be achieved, hence improving production rates. Using cure simulation, two identical components are analysed, one part using convection heating (i.e. oven) and the second using direct heating (i.e. heated tooling). The zonal approach was tuned based on numerical models and show a reduction 17.5% time.*

Keywords: moulding; zonally heated tooling; tapered composites

1. Introduction

Moulding composite materials is an energy-intensive activity required to produce the final shape and achieve the desired material properties. To meet quality requirements, slower heat rates and longer dwells are often used, especially for larger, thicker and/or geometrically complex parts. This is because ovens and autoclaves, which transfer heat through convection, can leave such parts with significant thermal gradients leading to residual stresses and potential damage in the final cured part if not mitigated. Even with slower heating rates and intermediate dwells introduced to cure cycles, thick and complex parts can often experience huge variations in the rate of cure resulting in some regions transitioning from liquid to glassy before other regions, further increasing risk of part warpage and microcracking. To this end, studies have looked into using optimization to manage the exotherm and cure time for thick large parts with success [1].

Alternatively, rather than attempting to make the most of the oven/autoclave as heat sources, heated tooling can be used instead. With heated tooling heat is introduced directly to the tool surfaces or volume through heated fluid circulation [2] or heating elements [3]. While this improves the energy efficiency of the process, it also significantly increases the tooling costs and is hence generally not adopted in the industry for large parts. However, the true power of heated tooling is not in reducing the energy consumed for a standard cure cycle (i.e. as a direct replacement to an oven or autoclave process), but rather in the ability to tailor the temperature profile applied to different regions [4]. By introducing zonal heating, significantly faster process cycles can be achieved while reliably meeting the optimal part quality by reaching moulding temperatures quicker and more uniformly [5] even for complex parts with thick tooling. A faster cure cycle using heated tooling then brings savings both in reducing the energy bill as well as in

  doi:10.5075/epfl-298799_978-2-9701614-0-0

allowing greater throughput, hence allowing more parts to be produced using a smaller factory footprint.

This work seeks to demonstrate the ability of zonal heated tooling to produce large thickness variation parts to the same quality standards with faster cure cycles. Assisted by cure simulation, two identical components were simulated. One part relied on the oven for heat with a traditional convection heating cycle and the second used the electric cartridges with different temperature profiles in an accelerated and zonally defined heating cycle. Future work will focus on validating these simulations with experimental trials.

2. Specimen Design and Numerical Model

2.1 Part and Tooling Material and Geometry

The part design was chosen to contain both thick and thin regions, as well some overall geometric complexity that would influence the heat flow around it when heated using an oven. The cross-section of the design is shown in Figure 1 with some key dimensions given in millimetres. The physical part is then intended to be a 150 mm deep extrusion of this shape. The tooling shown is made from 3 parts of 8 mm thick stainless steel which are brought together to form a two sided tool. Cork is used as shown in to fill intentional gaps introduced in order to allow a nearly closed mould at the start of cure while also accommodating compaction during cure.

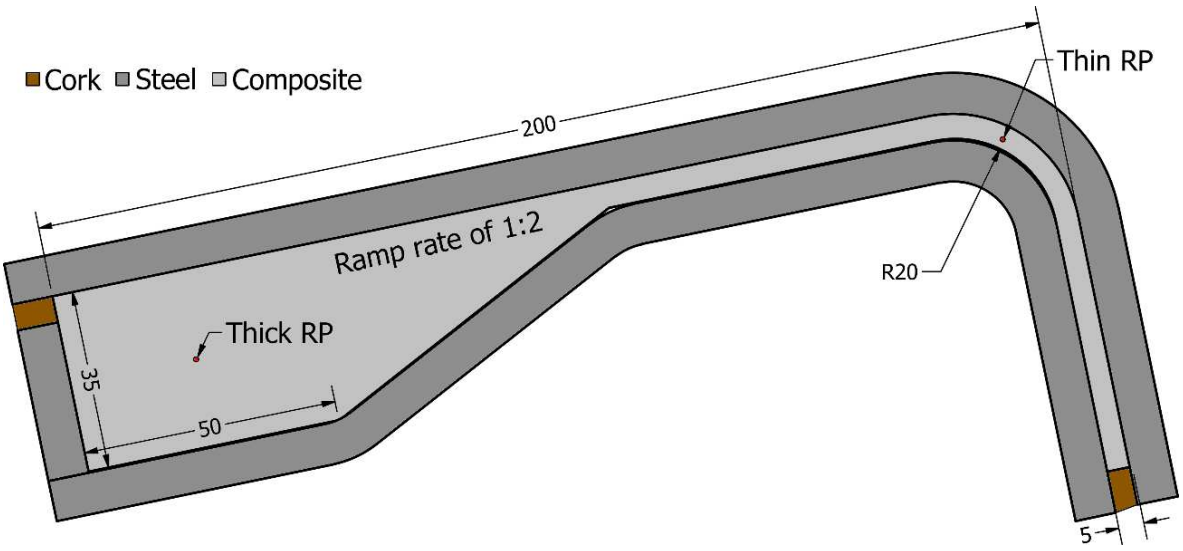

Figure 1. 2D cross-sectional view of design, incl. tooling, with key dimensions in millimetres.

The composite material chosen in this work is SHD MTC400 which is reinforced with a twill fabric made of T700 carbon fibre. This material was chosen in part due to its reactivity which makes it challenging to cure thicker parts without incurring significant exotherms. For the analysis and prediction of this thermal behaviour, the key material parameters are the density, ρ, specific heat capacity, c_p, and the conductivity, κ. These are provided in Table 1, for both the composite and tooling material, as well as the cork. For the composite material the specific heat capacity and conductivity in-plane and through-thickness are given as functions of temperature, T, and Degree of Cure (DoC), α, as given in Eq. (1), and Eq. (2) and Eq. (3), respectively.

Table 1: Thermal properties of composites material, steel, and cork.

Property	Unit	Composite Material	Steel	Cork
ρ	[kg/m^3]	1586.0	7850.0	240.0
c_p	[J/(kg·K)]	Eq. (1)	500.0	1900.0
κ	[W/(m·K)]	Eq. (2) and Eq. (3)	45.0	0.04

$$c_p(T) = 2.411 \cdot T + 1168.0 \tag{1}$$

$$\kappa_{11}(T,\alpha) = \kappa_{22}(T,\alpha) = 4.2207 + 0.0085818 \cdot T + 0.027922 \cdot \alpha \tag{2}$$

$$\kappa_{33}(T,\alpha) = 0.7344 - 0.001 \cdot T + 0.3924 \cdot \alpha - 0.0015 \cdot T \cdot \alpha \tag{3}$$

The final component required to define the material system is the cure kinetics, defined by the DoC rate function, see Eq. (4), and the total heat of reaction, H, which is taken as 543 J/g. The coefficients of the cure kinetics [6] are given in Table 2.

$$\frac{d\alpha}{dt}(T,\alpha) = \frac{\left(A_1 \cdot \exp\left(-\frac{E_1}{R \cdot T}\right) + A_2 \cdot \exp\left(-\frac{E_2}{R \cdot T}\right) \cdot \alpha^m\right) \cdot (1-\alpha)^n}{1 + \exp\left(D \cdot (\alpha + \alpha_{c0} - \alpha_{cT} \cdot T)\right)} \tag{4}$$

Table 2: Cure kinetic parameters for MTC 400 resin system [6].

Parameter	Units	Value
A_1	[1/s]	2.97e6
E_1	[J/mol]	1.36e5
A_2	[1/s]	1.28e11
E_2	[J/mol]	9.82e4
m	[-]	0.8473
n	[-]	2.4065
D	[-]	28.504
α_{c0}	[-]	1.326
α_{cT}	[1/K]	5.73E-3
R	[J/(mol·K)]	8.314

2.2 Numerical Model and Cure Cycle Selection

The numerical model used to run the cure simulations was set up using the heat transfer analysis in ABAQUS. For speed, a 2D cross-sectional mesh was chosen to simulate the mid-plane of the part geometry shown in Figure 1. Meshing was done using a target element edge length of 1 mm, to ensure sufficient elements in the thinner region to capture any through thickness gradients. The analysis was transient with an initial time stepping of 30 seconds and a constraint on the maximum change in temperature in any material point of 2°C for any single time step. This was needed to ensure any exotherms were sufficiently time resolved.

For the oven cure simulation the entire outer edge of the tooling and cork was simulated as having convection heating with a heat transfer coefficient of 25 W/(m^2·K). The sink temperature profile was then set to be the air temperature profile. For the heated tooling the boundary edge was divided into two regions to allow separate temperature profiles to be applied. The first region contained the boundaries of the thick and ramped regions and the second region contained the boundaries of the thin and corner regions.

For each of these set-ups, a two stage cure cycle was manually tuned to limit the exotherm to be around the target final cure temperature of 120°C. For the heated tooling model the zonal heating was further used to target a more even heat up rate and DoC development throughout the composite material volume. To check these metrics, two reference points (RP) were used to extract the local temperature and DoC throughout the cycle in the centre of the thick region, Thick RP, and in the centre of the corner, Thin RP, as indicated in Figure 1.

3. Numerical Results

3.1 Cure Cycles

The baseline cure cycle for this material for standard thickness laminates is a single hold cure at a temperature anywhere between 80°C and 135°C, with a hold time of 16 hours for the low temperature cure and only an hour at the higher temperature. Due to the reactivity of the material and the thickness of the chosen part, however, the higher hold temperature is not viable due to the exothermic peak of up to 235°C that would generate, according to the model. For this reason, an intermediate dwell at 90°C was introduced. At this temperature the material begins to react and the thick region experiences a mild exotherm up to around 120°C. The second rise up to the final cure temperature of 120°C then brings the whole part to this temperature for the final hold.

The final cure cycles are given in Figure 2, where it can be seen that the initial ramp rate and hold temperature are identical for both the single zone and the dual zone cure cycles. However, while for the single zone the second ramp is delayed to allow thick region exotherm to pass, for the dual zone it is possible to initiate the second ramp earlier in the thin region only. This separation of the regions also allows the overall cure cycle to be reduced by 10% while still achieving the same final DoC throughout the whole part. In the single zone cure, due to the delay in ramping up to the final temperature, the thin region lags behind in cure development requiring the overall cure cycle to be extended in order to allow it to catch up and achieve a part with roughly even cure throughout.

  doi:10.5075/epfl-298799_978-2-9701614-0-0

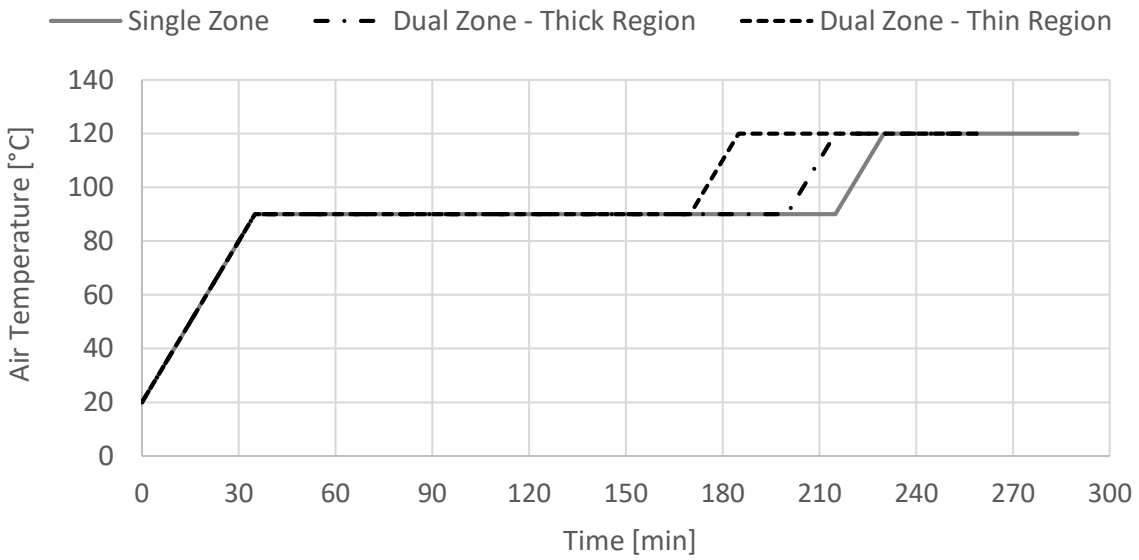

Figure 2. Air temperature profiles for single and dual zones.

3.2 Exotherm and Degree of Cure progression

As can be seen more clearly in Figure 3, the single zone oven curing results both in a significant thermal gradient during the exotherm of the part as well as a significant variation in DoC development between the thick and thin regions of the part. The maximum difference in temperature, at the peak of the exotherm, is around 20°C and the maximum difference in DoC, occurring just after the exothermic peak, is around 0.3, with the thick region surpassing a DoC of 0.9 while the thin region is still below 0.6. Such a large DoC variation implies that the polymer in the thick region will begin to gel and carry load while the thin region is still in liquid form. Combined with the thermal gradient this will result in thermal stresses and potential micro-cracking at the interface of these two regions.

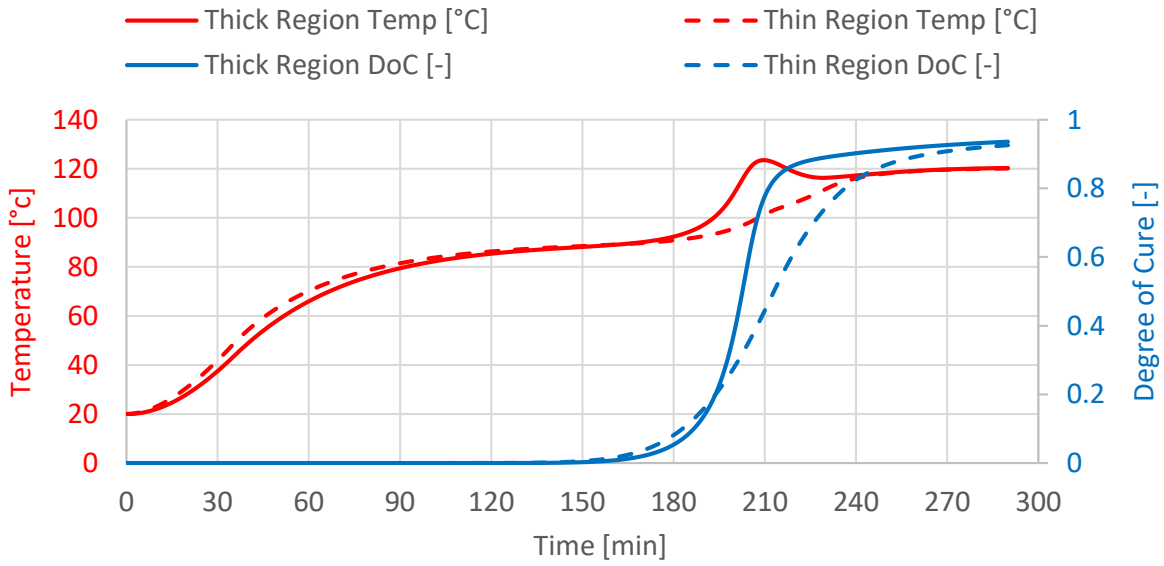

Figure 3. Temperature and Degree of Cure simulated at mid-thickness in thick and thin region for single zone cure.

The dual zone approach, as shown in Figure 4, avoids these complications as it is able to create a closer match both in the thermal history and DoC development in both regions. In the dual zone approach the maximum temperature difference is roughly halved down to around 10°C and the maximum difference in DoC is also halved to around 0.15. Overall it can be observed that the dual zone heating approach allows very close match in thermal history and DoC development even though the thickness ratio is 1:7 and the thick region exotherms while the thin region does not.

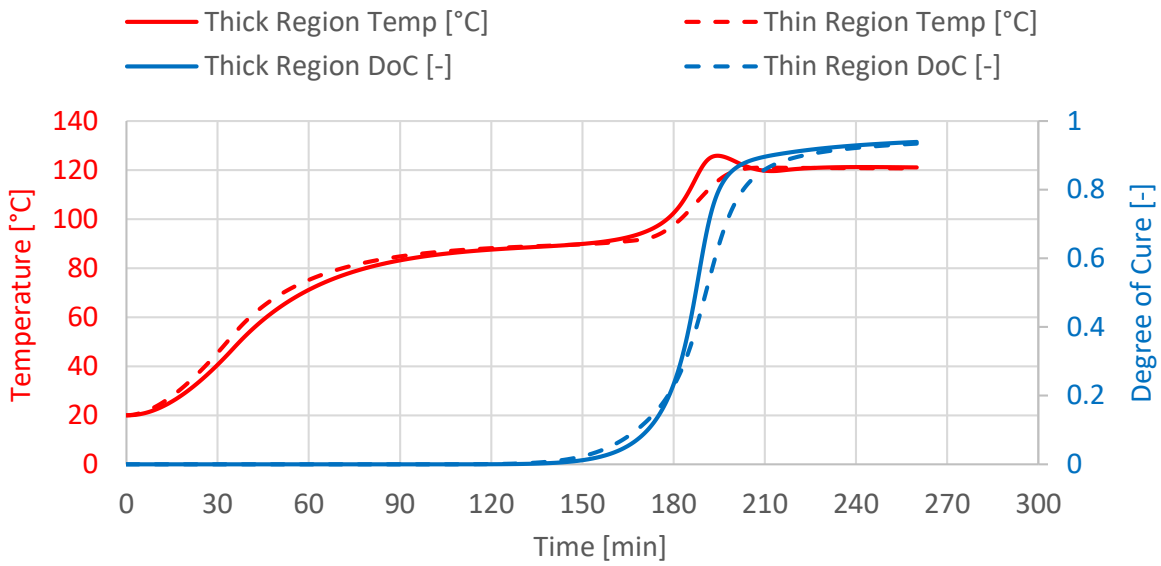

Figure 4. Temperature and Degree of Cure simulated at mid-thickness in thick and thin region for dual zone cure.

4. Conclusions

In this study a thick and complex part was simulated using a reactive system to evaluate the ability of zonally controlled heated tooling to better manage the exotherm and allow for a more even thermal and cure development profile. Using manual tuning of the air temperature profiles for both a single zone and dual zone approach to heating a complex part with a large thickness variation, this was shown to be successful.

The dual zone approach allowed both the temperature and DoC differences between the thick and thin region to be halved, while also allowing a reduction in total cure cycle time of 10%. This improvement can be attributed to the ability to separately heat up the thin region before the thick region exotherm has completed, allowing both regions to experience a more similar thermal history and DoC development.

In future work, these numerical simulations will be experimentally validated using trial parts with embedded thermocouples. The use of both heating, active cooling, and reheating [7] will also be explored to further improve the management of the exotherm and reduce the cure cycle time and thermal history and DoC development mismatch even further.

Acknowledgements

This work was supported through the Bristol Impact Acceleration Account under the EPSRC grant EP/R511663/1. The support is gratefully acknowledged.

5. References

1. Struzziero G, Skordos AA. Multi-objective optimisation of the cure of thick components. Compos Part A Appl Sci Manuf. 2017 Feb 1;93:126–36.
2. Abdalrahman R, Grove S, Kyte A, Rizvi MJ. Numerical simulation and experimental verification of heating performance of an integrally water-heated tool. J Reinf Plast Compos. 2016;35(8):655–71.
3. Athanasopoulos N, Koutsoukis G, Vlachos D, Kostopoulos V. Temperature uniformity analysis and development of open lightweight composite molds using carbon fibers as heating elements. Compos Part B Eng. 2013;50:279–89.
4. Weiland JS, Hubert P, Hinterhölzl RM. Thermal dimensioning of manufacturing moulds with multiple resistively heated zones for composite processing. J Compos Mater. 2017;51(28):3969–86.
5. Smith AW, Goyette K, Kazanas C, Hubert P. Development of a heated tooling solution to improve process flexibility for out-of-autoclave prepregs. Int SAMPE Tech Conf. 2013;
6. Gaska K. SHD MTC400 Cure Kinetics and Rheology. 2021.
7. Kim JS, Lee DG. Development of an Autoclave Cure Cycle with Cooling and Reheating Steps for Thick Thermoset Composite Laminates. J Compos Mater. 1997;31(22):2264–82.

  doi:10.5075/epfl-298799_978-2-9701614-0-0

ADDITIVELY MANUFACTURED METAL TOOLING FOR CURE OPTIMISATION IN COMPOSITE MANUFACTURING

Arjun Radhakrishan [a], Max Valentine [b], Vincent Maes [a], Maria Valero[a], Elise Pegg[b], Vimal Dhokia[b], James Kratz[a]

a: Bristol Composite Institute, Department of Aerospace Engineering, University of Bristol, U.K.

b: Department of Mechanical Engineering, University of Bath, U.K.

Abstract: *The selection of tooling for composite manufacturing is a critical step in ensuring the quality of the resultant composite parts. The energy consumed during part manufacturing is used to evolve the composite properties but a substantial proportion of it is used to heat the tooling. Additive manufacturing (AM) offers a viable solution to reducing the tooling mass by generating complex tool architectures that can withstand the manufacturing process reduce mass and provide additional functionalities. A series of 16 lattice steel tools were additively manufactured and used to cure flat composite specimens. The thermal profile of the composite curing was monitored to characterise the thermal responsiveness of the tools. The curing of composites on equivalent solid monolithic tools of constant thickness was numerically simulated using a cure-coupled heat transfer model. The results indicate that AM tools with lattice architectures can achieve heating rates higher than 83% of the set rate while keeping the exothermic overshoot temperature below 30% of the setpoint, which its monolithic counterparts couldn't achieve. Hence lattice structures enabled by AM can push the design space into regions previously unavailable to tooling design.*

Keywords: AM tooling; Lattice structures; Thermal light weighting; Heat Transfer

1. Introduction

The composites landscape faces significant challenges presented by increasingly compressed design timescales, growing demand in productivity and the soaring complexity of products. Additionally, sustainability is a priority for the UK to achieve its pledge to reduce greenhouse gas emissions by at least 68% before 2030 and achieve net-zero by 2050 [1]. While lightweight composite structures are expected to help reduce emissions during operation, energy is the single biggest factor in the life-cycle analysis of the manufacturing process. However, how composite curing equipment and tooling are designed and manufactured has not changed since high-performance composites were first used in aerospace applications in the 1970s.

A significant step towards reducing cure cycle times is through reducing the tooling mass and improving tool architecture to enhance heat transfer. A simple estimation indicates that the tooling for composites parts is typically 10-40 times heavier than the finished part itself. Furthermore, current curing methods involve heating large volumes of air either using autoclaves or ovens. As a result of these, energy is wasted heating the environment as well as the tool during the curing cycle. Therefore, an immediate increase in thermal efficiency can be achieved via the improvement of the tool design which currently focuses on monolithic designs where there is a single block of material through-thickness of the tool. AM can be a useful route in designing complex lightweight architectures unachievable through subtractive processes such as machining. This opens up the possibility to tailor the tool design to manage the heat transfer

  doi:10.5075/epfl-298799_978-2-9701614-0-0 published under CC BY-NC 4.0 license

and optimise the cure cycle while maintaining key tool characteristics such as shape accuracy and specific stiffness.

AM tooling has been trialled using various polymers, composites and metal as feedstock [2]. Among these, metal tooling would be more attractive for its durability leading to a higher number of moulding cycles, hence lower running costs. Metal Big Area Additive Manufacturing (MBAAM) system has been trialled by Oak Ridge National Laboratory using low-cost steel wire [3]. The study showcased the feasibility of producing large AM tools however the process has lower print resolution leading to considerable post-processing to improve the surface finish. On the other hand, laser powder bed fusion (L-PBF) processes, or more specifically selective laser melting (SLM), has higher resolution and opens the possibility of creating durable, bespoke, and complex designs to lightweight tools not only to withstand the manufacturing cycles but also to provide additional functionalities such as finer cooling channels and integrated sensors.

This study aims to assess the feasibility of using metal AM tools to improve composite curing in conventional ovens. This is evaluated by monitoring the temperature during experimental curing trials on AM tools and comparing it to their simulated mass-equivalent monolithic tools. This work develops a platform for characterising the thermal responsiveness of various lattice geometries and volume densities. Furthermore, this study highlights the expanded design space available for tooling designs for composite curing.

2. Materials and methods

2.1 Tool design, manufacturing, and quality characterisation

The key requirements for the tools were to be as thermally light as possible while maintaining the stiffness required for composite manufacturing. The tools were made thermally light through the choice of different lattice architectures with faceplates. Such a design helps to reduce the mass of the tool while providing sufficient stiffness for countering the stresses observed during the composite manufacturing process. Hence, a series of tools, enclosing a volume of 100 mm × 100 mm × 10 mm, were manufactured using the SLM process at the University of Bath to manufacture flat composite laminates of 45 mm × 45 mm. Lattices were designed using Gen3D Sulis Lattice software (Sulis V1.9.10, Gen3D, Bath, UK) [4]. The lattice geometries selected to test were planar diamond, a diamond with cut-outs, gyroid and graded gyroid. The tools were built using a RenishawAM250 SLM machine using 316L Stainless Steel (SS316L) powder in an inert argon atmosphere. A total of 16 tools were manufactured on a single build plate as shown in Figure 1. As this study is focused on the preliminary evaluation of the as-built metal tools, no post-build treatments of the tools were done to either improve the surface finish or strength properties.

A planar diamond lattice was the simplest geometry that was selected that provides strength, however, it may not allow for the same airflow through the lattice volume as the gyroid lattices. The diamond geometry was selected as a honeycomb-style geometry whose 45° angle ensures it can be manufactured by SLM without any need for support structures and no constraints in terms of the cell size. On the other hand, a diamond with cut-outs was used to improve the convective flow through architecture which, in a simple planar diamond lattice would be restricted due to the partially enclosed unit cells.

  doi:10.5075/epfl-298799_978-2-9701614-0-0

A gyroid is a specific type of triply periodic minimal surface (TPMS) as it contains no joints or discontinuities throughout its volume. TPMS lattices are advantageous in maximising surface area for a given volume, a key characteristic required for heat exchangers [5]. Such lattices are manufacturable due to the availability of additive processes and challenging via subtractive processes. Another architecture selected was a variation of the gyroid architecture where the volume density progressively increases closer to the faceplate. This design would promote conductive heat transfer closer to the part surface which is crucial for control of exothermic reactions in the composite part while optimising the tool mass.

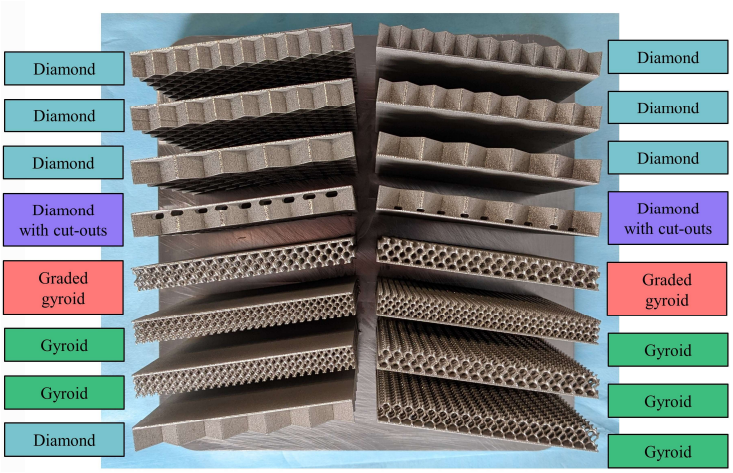

Figure 1 AM tools of varying configurations on the build plate

2.2 Composite materials and manufacturing

The composite was prepared using 14 plies of 40 mm x 40 mm prepreg (SHD) comprised of MTC400 Epoxy resin as the matrix and 415 gsm twill weave fabric made of T700 carbon fibre as the reinforcement. The as-built faceplate surface was used to manufacture the composite sample and the bagging scheme is illustrated in Figure 2 (a). A thermocouple was placed in the centre of the prepreg stack to capture the thermal history through the cure cycle. The first series of 8 tools were connected using Teflon tubes to reduce the number of oven cycles required to experiment, as shown in Figure 2 (b).

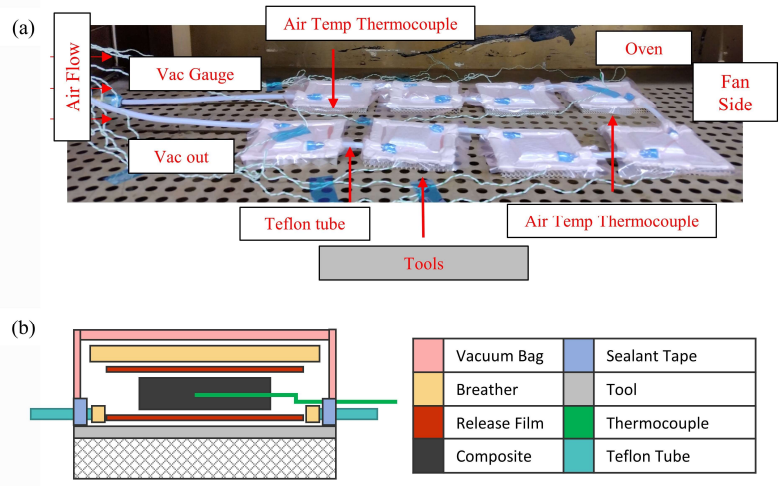

Figure 2 Bagging and curing scheme for the AM tools.

  doi:10.5075/epfl-298799_978-2-9701614-0-0

To understand any effect arising from the location of the tool in the oven, two additional thermocouples were placed at the extreme ends of the series of tools to capture the air temperature. The vacuum in this series was ensured to be 29 inHg in both of the runs. The prepared tools were then placed in a conventional oven (Carbolite) for curing. The thermocouples were connected to a datalogger (Pico Logger), and temperature data were collected at a sampling rate of 1 Hz. The cure schedule was, to ramp up from room temperature at a heating rate of 3°C/min to reach 135°C, dwell for 1 hour, and followed by a cool down at 2°C /min to reach 30°C.

2.3 Numerical model and cure simulation

The numerical model used to run the cure simulations for monolithic tools was set up using a cure-kinetics coupled transient heat transfer analysis in ABAQUS. The composite thickness was 6.2 mm based on the average thickness measured from the experimental trial and was modelled with homogenised properties. A monolithic tool of 100 mm in width was used with four different thicknesses: 1 mm, 2 mm, 5 mm, and 10 mm. The key parameters for the composite material are the specific heat capacity, and thermal conductivities (in-plane and through-thickness) which are expressed as functions of temperature, T, and Degree of Cure (DoC), α, as given in Eq. (1), and Eq. (2) and Eq. (3), respectively. The physical and thermal properties of the composite and tool are summarised in Table 1.

$$c_p(T) = 2.411 \cdot T + 1168.0 \tag{1}$$

$$\kappa_{11}(T,\alpha) = \kappa_{22}(T,\alpha) = 4.2207 + 0.0085818 \cdot T + 0.027922 \cdot \alpha \tag{2}$$

$$\kappa_{33}(T,\alpha) = 0.7344 - 0.001 \cdot T + 0.3924 \cdot \alpha - 0.0015 \cdot T \cdot \alpha \tag{3}$$

The previously developed cure-kinetic model and parameters shown in Eq (4) for the resin system were used in this work [6]. The coefficients of the cure kinetics are given in Table 2.

$$\frac{d\alpha}{dt}(T,\alpha) = \frac{\left(A_1 \cdot \exp\left(-\frac{E_1}{R \cdot T}\right) + A_2 \cdot \exp\left(-\frac{E_2}{R \cdot T}\right) \cdot \alpha^m\right) \cdot (1-\alpha)^n}{1 + \exp\left(D \cdot (\alpha + \alpha_{c0} - \alpha_{cT} \cdot T)\right)} \tag{4}$$

A target element size of 1 mm for meshing was used on the tools and the composite meshed with 6 elements through thickness. The initial time-stepping for the transient analysis was 20 s and the constraint on the maximum change in temperature at any material point of 10°C for any single time step. These parameters were chosen to sufficiently resolve the curing process time to capture the exothermic behaviour of the resin system which typically results in a rapid increase in temperature in a short time.

The outer surfaces in contact with the environment were simulated as having a convection heat transfer with a 20 W/(m2.K) heat transfer coefficient. The sink temperature profile was then set to be the air temperature profile. The cure cycle was the same as that was applied for the experimental work on lattice structures detailed in Section 2.2.

  doi:10.5075/epfl-298799_978-2-9701614-0-0

Table 1 Thermal properties of composite material and steel

Property	Unit	Composite Material	Steel
ρ	[kg/m^3]	1586.0	7850.0
c_p	[J/(kg·K)]	Eq. (1)	500.0
κ	[W/(m·K)]	Eq. (2) and Eq. (3)	45.0

Table 2 Cure kinetic parameters for MTC 400 resin system [6].

Parameter	Units	Value
A_1	[1/s]	2.97×10^{-6}
E_1	[J/mol]	1.36×10^{-5}
A_2	[1/s]	1.28×10^{-11}
E_2	[J/mol]	9.82×10^{-4}
m	[-]	0.8473
n	[-]	2.4065
D	[-]	28.504
α_{c0}	[-]	1.326
α_{cT}	[1/K]	5.73×10^{-3}
R	[J/(mol·K)]	8.314
H	J/g	543

3. Results and discussion

All the samples, both the simulation and experimental, exhibit varying extents of exothermic reaction as observed from the overshoot in temperature above the setpoint as shown in Figure 3. There was a negligible difference in the temperature profile of 0.5°C at the two extreme ends of the series of tools, indicating the location in the oven was not a factor. Since there was a negligible difference arising from the location and the thickness of the part, the thermal response observed for various samples could be attributed to the tool itself.

These thermal profiles were used to calculate the initial heating rate, overshoot temperature and the final cooling rate observed by these samples. Both the heating and cooling rates were calculated from the linear region of the thermal profile to capture only the effects the of tool and not that of the exothermic reaction. The overshoot temperature was calculated as the increase in temperature above the oven setpoint of 135°C. The heat transfer in these cases occurs through convection at the tool surfaces followed by conductive heat transfer through the tool. The surface area exposed to the airflow is a dominant factor in the convective heat transfer

  doi:10.5075/epfl-298799_978-2-9701614-0-0

while the tool mass is the primary driver in conductive heat transfer. To understand these effects, the heating rate, cooling rate and overshoot temperature are plotted against the tool mass and surface area as shown in Figure 4.

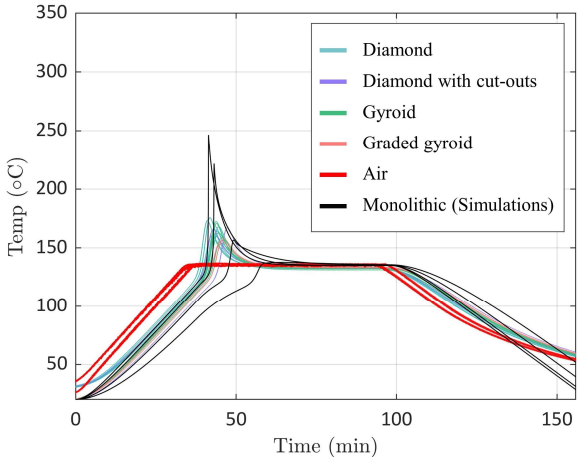

Figure 3 Thermal profile of different AM tools monitored during the experiments along with the simulated profiles for monolithic tools.

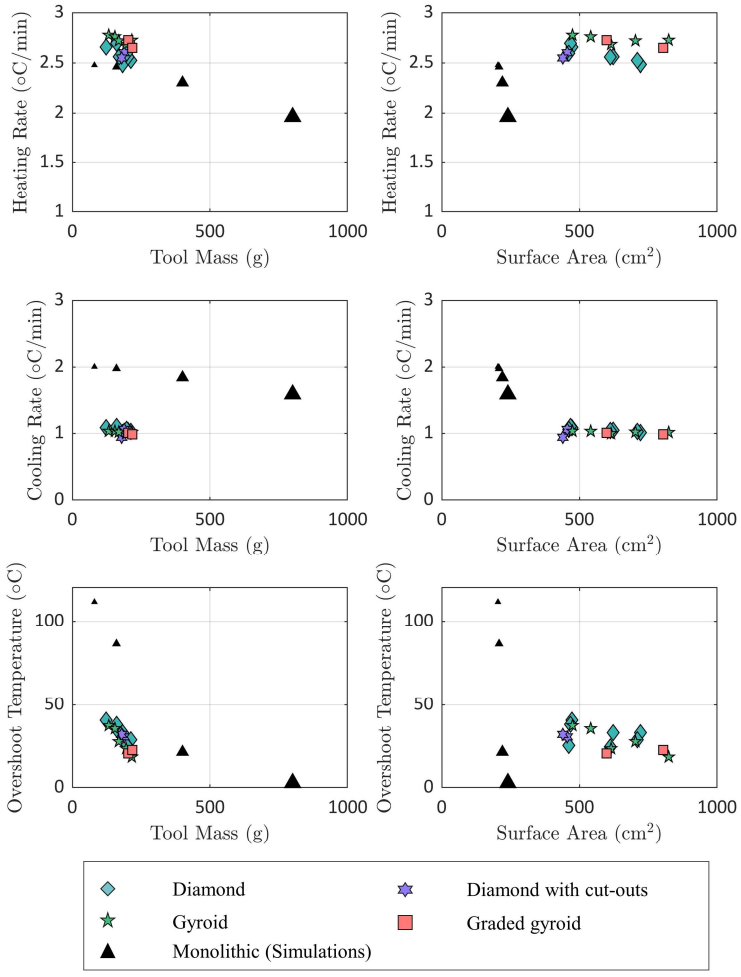

Figure 4 Heating rate, cooling rate and overshoot temperature vs. tool mass and surface area for various AM tools and the simulated monolithic tools.

  doi:10.5075/epfl-298799_978-2-9701614-0-0

All the AM tools performed better than monolithic tools with higher heating rates and above 2.5°C/min. The heating rates observed by the samples on monolithic tools almost linearly increase with reduced tooling mass, but no such relation could be made for AM tools given the tools had similar masses. Increasing the surface area of the tools has improved the heating indicating increased contribution from the convective heat transfer. However, the performances had minimal difference between varying AM tool configurations. On the other hand, the cooling rates were lower for the AM tools than for their monolithic counterparts with average at 1°C/min. The conductive heat transfer from the cured part to the tool could potentially dominate the cooling rates. Hence, tools with a larger mass concentrated towards the faceplate would be beneficial. Hence the monolithic tool performing better could be attributed to this effect. However, further investigation is required to explore this hypothesis. The overshoot temperature is expected to increase with reduced tool mass as tools act as heat sinks in composite curing. Both, monolithic and AM tools exhibit this trend independently, however, AM tools can perform better at controlling the overshoot compared to their monolithic counterparts.

To assess the performance in cure optimisation, the tools have to be able to achieve high heating rates while controlling the exothermic temperature by conducting heat away from the part. Hence, the performance plot using these two parameters was prepared as shown in Figure 5 for the various configurations. The reduction of tool mass in monolithic mass results in high heating rates, however, results in overshoot temperatures passing well over the degradation temperature of the epoxies. But, through the use of lattice architectures an innovative design space opens up where thermal lightweight does not lead to runaway exothermic reaction. These lattice designs were able to withstand the manufacturing procedure from layup to curing.

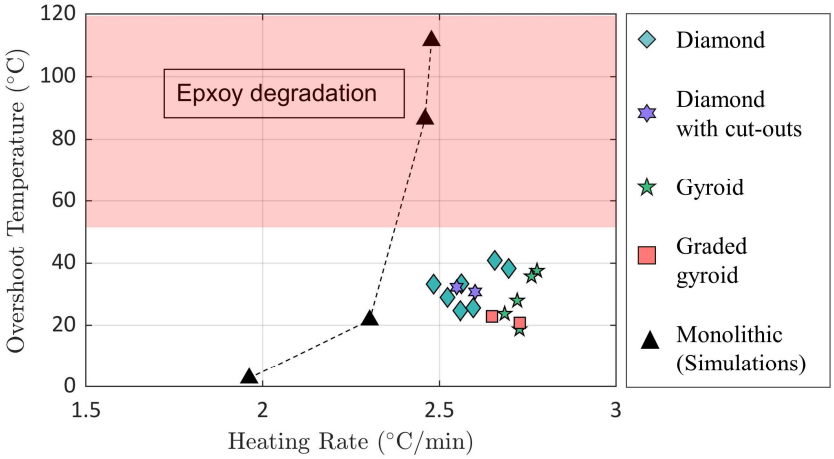

Figure 5 Design space comparison between monolithic and AM lattice tools to achieve low overshoot temperature and high heating rate.

4. Conclusion and future work

In this study, AM tools with different lattice architectures were used to cure composites and the thermal response within the composites was compared to their simulated monolithic counterparts. The key factors such as heating rate, overshoot temperature and cooling rate were used to assess the tools.

  doi:10.5075/epfl-298799_978-2-9701614-0-0

The lattice architectures enabled by AM were shown to achieve higher heating rates than their monolithic counterparts while controlling the exotherm. This was achieved by reducing the tool mass while exposing a larger surface area to convective heat transfer, thus improving the overall heat transfer. Such geometries expand the available design space for tooling leading to reduced cycle times and optimised curing. This study shows various tool designs that could be beneficial in convective curing methods. Such lattice tools can also be designed to account for other curing methods such as heated tooling to form a cyclic design methodology considering composite chemistry, curing method and tool architecture.

However, challenges remain when using AM tools, particularly in achieving surface finish without the use of additional machining as well as manufacturing larger tools using SLM. Future work would look into curing complex geometries where temperature gradients are sharper. Such a study will also have to look into including additional tooling requirements such as the surface finish, design for a layup and grading of the tooling architectures.

Acknowledgements

The work was supported by the EPSRC Future Composites Manufacturing Hub (EP/P006701/1) project titled Additively Manufactured Cure Tooling.

5. References

1. Sharma, Alok Johnson B. “UK sets ambitious new climate target ahead of UN Summit.” Technical report no. 2020. 2020. https://www.gov.uk/government/news/ Uk-sets-ambitious-new-climate-target-ahead-of-un-summit.
2. Li Y, Xiao Y, Yu L, Ji K, Li D. A review on the tooling technologies for composites manufacturing of aerospace structures: materials, structures and processes. Compos Part A Appl Sci Manuf 2022;154:106762.
3. Hassen AA, Noakes M, Nandwana P, Kim S, Kunc V, Vaidya U, et al. Scaling Up metal additive manufacturing process to fabricate molds for composite manufacturing. Addit Manuf 2020;32:101093.
4. Gen3D. “Sulis Lattice.” (2018) 2018. https://gen3d.com/ sulis-lattice/.
5. Catchpole-Smith S, Sélo RRJ, Davis AW, Ashcroft IA, Tuck CJ, Clare A. Thermal conductivity of TPMS lattice structures manufactured via laser powder bed fusion. Addit Manuf 2019;30:100846.
6. Gaska K. SHD MTC400 Cure Kinetics and Rheology. 2021.

  doi:10.5075/epfl-298799_978-2-9701614-0-0

2D FIBER PLACEMENT OF INTEGRAL THERMOPLASTIC FRAME STRUCTURES

Kilian, Seefried[a], Kevin, Scheiterlein[a]

a: Fraunhofer Research Institute for Casting, Composite and Processing Technology IGCV, Am Technologiezentrum 2, 86159 Augsburg, Germany
E-mail: kilian.seefried@igcv.fraunhofer.de, web page: https://www.igcv.fraunhofer.de/en.html

Abstract: *State-of-the-art aircraft frames are built with thermoset resin systems necessitating time and cost-consuming autoclave curing cycles. The substitution of these materials by unidirectional tapes with thermoplastic matrices offers potential to use out-of-autoclave, highly automated and therefore cost-efficient manufacturing technology. Within a collaborative research, the manufacturing of highly integrated frame structures using laser-assisted automated fiber placement combined with stamp forming and co-consolidation to develop a cost- and time-efficient process chain has been investigated. This study mainly presents the investigation results of the laser-assisted fiber placement process including manufacturing engineering investigations regarding guide curve design as well as the effect of variable angle guide curves on the mechanical properties. Therefore, various guide curve geometries have been investigated and resulting fiber angle deviations as well as cover ratios analyzed. In addition, coupon laminates with straight and curved fiber paths have been manufactured and tensile testing done.*

Keywords: Aerospace applications; Automated Fiber Placement; guide curve design; thermoplastic composites; tensile testing

1. Introduction

The automated cost-efficient manufacturing of composite parts becomes more and more important for the aerospace industry due to the need to reduce costs and environmental impact. Currently, main of the composite parts for aircrafts are made by thermoset composites. Thermoplastic matrices but offer several advantages compared to thermoset composites such as the possibility for highly productive manufacturing processes or the weldability for functional integration [1]. One of these manufacturing processes is the Automated Fiber Placement (AFP). With the thermoplastic AFP pre- or fully consolidated preforms can be manufactured rapidly to realize high layup rates. In addition, by the robot-based layup complex geometries can be realized and fiber angles adjusted precisely [2]. Especially for primary aircraft structures, there are several research projects on the manufacturing by thermoplastic composites [3]. One of the most complex primary aircraft structure is the frame. Currently, aircraft frames are mainly manufactured by thermoset composites in automated processes. Due to high curing cycles within autoclaves, the productivity of the processes is limited. Following, thermoplastic composites offer a potential to optimize the productivity for frame structures [4]. Additionally, thermoplastic structures allow functional integration enabling an optimization of assembly processes. For these reasons, the manufacturing of integral frame structures by means of thermoplastic AFP was investigated. The pre-consolidated 2D-preforms are then stamp formed into the final shape. Hereby, one-shot processes were developed by investigating the stamp-

  doi:10.5075/epfl-298799_978-2-9701614-0-0

forming plus co-consolidation and stamp-forming plus overmoulding [5]. For the assembly of the integral frame structures and the associated tolerance management additive manufacturing technologies have been included. For the thermoplastic AFP process the available concepts regarding path planning and avoiding defects for thermoset AFP had to be adopted and optimized. Various layup and coverage strategies as well as guide curve (GC) design concepts, like geodesic guide curves or variable angle guide curves, are available nowadays [6]. In this study the optimized guide curve design for frame structures is investigated in terms of reaching low fiber angle deviations and parallel high cover ratios under taking into account the available know-how for the thermoplastic AFP process. In addition, the influence of steered guide curves on the mechanical properties is researched by tensile testing.

2. Experimental work

2.1 Part geometry and process route

The target part is a generic frame structure as can be seen in Figure 1. The frame structures are laid in laser-assisted 2D fiber placement process and afterwards stamp formed without any further consolidation step into the final 3D shape.

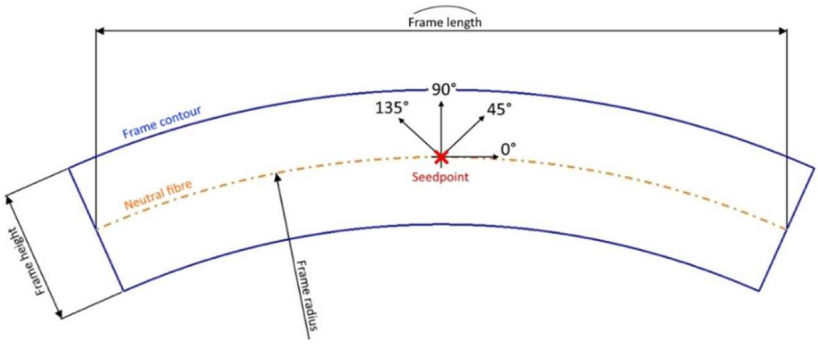

Figure 1: Geometry and fiber angle orientations for a generic frame structure

2.2 Fiber Placement system

The used Fiber placement system is a Coriolis C1 from Coriolis Composites, France. For the processing of thermoplastic material the end effector is additionally equipped by a diode laser system from the company Laserline GmbH, Germany. The laser type is the LDF 6000-100 VGP with a wavelength range of 900 to 1,070nm and a maximal power of 6kW. The focal distance is 240mm and the rectangular laser field has dimensions of about 58x8mm. By default, for all tests a deformable compaction roller was used.

2.3 Material

The material used is C/PEEK APC-2/AS4 supplied by Solvay S.A., Belgium with an aerial weight of 145gsm and a resin content of 34%.

2.4 Process monitoring

For the monitoring of the process and the measuring of the derived Nip-point temperature a FLIR A325sc with 60Hz and a 320x240 pixel resolution is used. The emissivity of the used material was determined to 0.96 by a static test set-up within a high-temperature oven.

  doi:10.5075/epfl-298799_978-2-9701614-0-0

2.5 Guide curve design

One of the key challenges for the guide curve design is the part geometry. Due to the radius of curvature of the preforms a novel guide curve design is required to ensure a high cover ratio and low fiber angle deviation at the same time. Furthermore, the steering radius of these novel guide curves must be regarded to ensure a high layup quality. With the CATFiber© software of Coriolis Composites, France the mentioned characteristics were analyzed and evaluated for the defined design methods. The cover ratio was determined by the ratio between total surface of the Manufacturing Edge of Part (MEOP) and the simulated covered surface by the tapes given by CATFiber© software. The tolerances to be observed are 5° for fiber angle deviation and greater than or equal to 97% for the cover ratio. At the same time any resulting gaps and overlaps must not exceed 2.5mm.

As methods, mainly the sectorization as well as variable angle guide curves were analyzed. The sectorization method describes the procedure of dividing the part geometry into a defined number of sectors. In these sectors, defined guide curves are used which are constant within the sectors and changing between the sectors. In addition, the sector boundary can be designed by adjusting the sector overlap between 0% and 100% as can be seen in Figure 2.

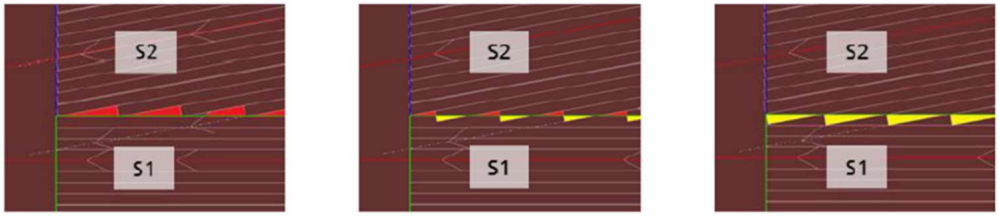

Figure 2: Illustration of sectorization concept with design of boundary with 0% sector overlap (left), 50% sector overlap (middle) and 100% sector overlap (right) [7]

The variable angle method describes the creation of guide curves based on geometric curve types. Following curve types were investigated: Circle, Ellipse, Involute and logarithmic spiral.

The focus of the GC investigations was on 45/135deg and 90deg orientation. Finally, the steering of the individual orientations were analyzed. The non-geodesic layup of the material can have several effects on the quality of the layup such as fiber waviness or tow buckling [2]. Therefore, an analysis of the steering radius is required to check for limiting radii of curvature. For steering radii below 1000mm there can be seen significant deviations in regards to Nip-Point temperature as well as tow buckling [2].

2.6 Tensile testing of straight and variable angle guide curve concept

In addition to the guide curve design and the engineering characteristics, the effect of curved tow paths on the mechanical properties was investigated. Therefore, tensile specimens with straight guide curves and fiber angle deviations of 2.5° and 5° as well as specimens with curved guide curves and comparable fiber angle deviations were manufactured. The specimens were compared to a reference specimen with no fiber angle deviation as well as to each other in terms of the maximal stress and E-modulus. Five specimens with 350x350mm and $[0]_8$ stacking were laid. Subsequently, the coupons were consolidated in an autoclave to avoid influences on the results by the degree of consolidation. The used autoclave cycle was based on the material specifications given in the datasheet of the supplier. Finally, the specimens were trimmed

  doi:10.5075/epfl-298799_978-2-9701614-0-0

according to DIN EN ISO 527-5. In addition, an Aramis system of the company GOM, Germany was used to monitor the failure behavior of the specimens. Therefore, the tensile specimens were painted white and a stochastic pattern of black dots was applied with an airbrush system. Figure 3 shows the specimens after layup as well as a schematic illustration of the tensile specimens. A layup speed of 200 mm/s, a compaction force of 500N, a Nip-Point temperature of about 400°C and a tooling temperature of 150°C were defined as process parameters.

The curved GC coupons were designed to have the defined maximal angular deviation at 75mm from the line of symmetry and following at the edge of the specimen. It must be regarded that the angular deviation for the curved GCs changes along the specimen and is even nearly to 0° in the line of symmetry. The straight GC coupons, on the other hand, have a constant fiber angle deviation along the specimen. However, it must be taken into account that only a certain proportion of the fibers are continuous along the specimens due to the angular deviation. The proportion of non-through fibers has a significant influence on tensile properties and especially on tensile strength [8].

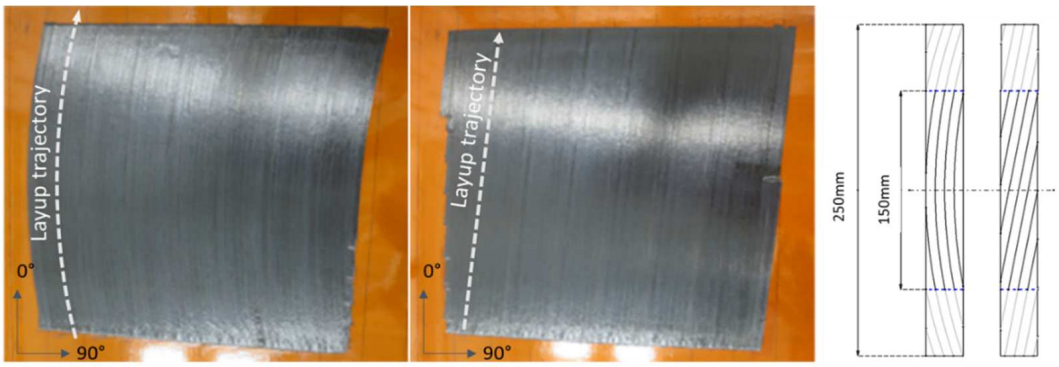

Figure 3: Manufactured specimens for the determination of the effect of curved guide curves on the mechanical properties. Left: Curved guide curve design with defined fiber angle deviation. Middle: Straight guide curve design with defined fiber angle deviation. Right: Schematic illustration of the tensile specimens

3. Results and discussion

3.1 Maximal fiber angle deviation and cover ratio

45deg/135deg-orientation

Sectorization concept and variable angle method were investigated for 45 and 135deg oriented layers. For the sectorization straight guide curves were used within the sectors for tape generation. With this method the maximal fiber angular deviation is reduced to 6° by dividing the part into 25 sectors. The maximal fiber angle deviations of 6° are laying at the inner and outer contour of the frame and a cover ratio of 92.9% is reached.

For the variable angle method ellipsis, involutes, circles and spirals were investigated. All these geometries lead to comparable results regarding fiber angle deviation and cover ratio. However, the elliptical guide curves ensure the best results in terms of gaps and overlaps across the preform as these guide curves lead to longitudinal gaps instead of commonly known triangular gaps. With this concept a maximal fiber angle deviation at the inner and outer contour of 4.9° and a cover ratio of 99.4% is realized.

Figure 4 shows the simulated fiber angle deviation for the sectorization concept with 25 defined sectors as well as for the elliptical guide curves.

  doi:10.5075/epfl-298799_978-2-9701614-0-0

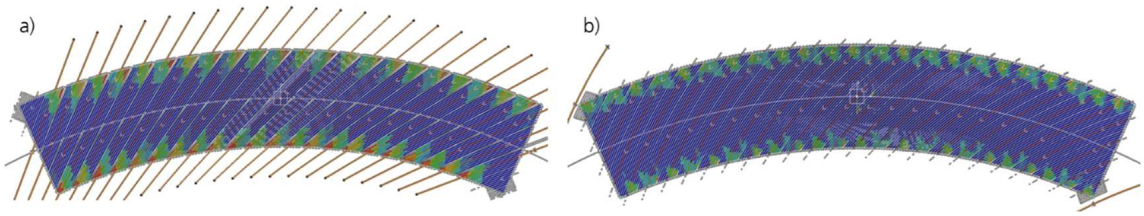

Figure 4: Illustration of fiber angle deviation for a) sectorization concept with 25 defined sectors and b) elliptical guide curves. Red areas are illustrating angular deviation above 5° whereas blue areas mean angular deviations below 1°. The green to orange areas are angular deviations between 1° and 5°.

For designing the guide curves linear dependencies between the part geometry and the length of the primary and secondary axes of the ellipse were found in order to enable an automatic design of optimized guide curves by a VBA-macro. These linear dependencies are seen in Equation (1) and (2). Figure 5 illustrates the designing of the elliptical guide curves.

$$A=0.4005*Rn+96.541mm \quad (1)$$

$$B=0.2327*Rn+54.748mm \quad (2)$$

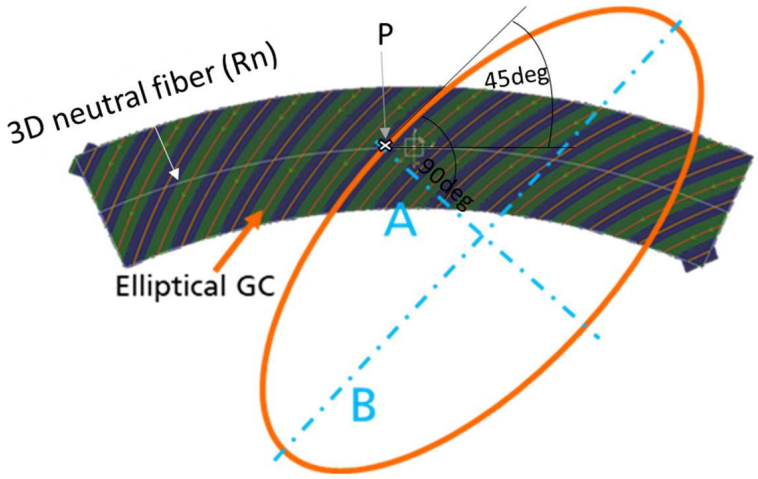

Figure 5: Design of elliptical guide curves for 45deg-oriented layers. A und B are the two axes defining the ellipsis. P is the intersection Point of the ellipsis with the 3D neutral fiber and lies additionally on a 45°-tangent to the ellipsis as well as a tangent to the neutral fiber.

The positioning of the ellipsis in the geometry is done by the intersection point P that lies on the neutral fiber and additionally on a 45°-tangent to the ellipsis as well as a tangent to the neutral fiber. For the replication of the ellipsis across the whole geometry the distance between the points P is set to 72.35mm.

90deg-orientation

For the 90deg oriented layers the sectorization concept as well as circular guide curves were investigated. For the sectorization the geometry was divided into 7 sectors with 5 tapes per sector. With this concept a maximal fiber angle deviation of 4.3° and a cover ratio of 98% is derived. The cover ratio is hereby derived by setting the overlap between the sectors in CATFiber© to 0%. By setting the overlap between the sectors to 50% or even 100% the cover ratio can be increased under the condition that the implemented overlaps also increase. At the sector boundaries a high number of triangular gaps are resulting as well as high fiber angle deviations are concentrated.

  doi:10.5075/epfl-298799_978-2-9701614-0-0

For the circular guide curves various diameters were investigated. Circular guide curves with a diameter of 3000mm showed the best results regarding fiber angle deviation. With this concept the fiber angle deviation can be decreased to maximal values of about 3.5° at the outer contour. On the other hand the gaps and overlaps between the single tapes increased to about 2.2mm gap and 1.25mm overlap. Figure 6 shows the simulated fiber angle deviation for the sectorization concept with seven defined sectors as well as for the circular guide curves.

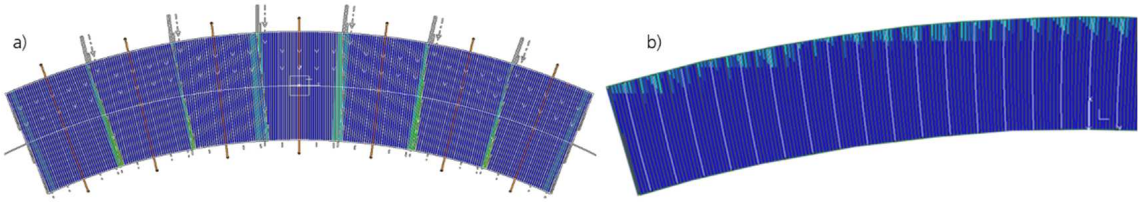

Figure 6: Illustration of fiber angle deviation for a) sectorization concept with seven defined sectors and b) circular guide curves with diameters of 3000mm. The color scale is identical to Figure 5.

Summary

Figure 7 shows an overview of the obtained results for the 90deg and 45deg sectorization as well as for the 45deg variable angle concepts regarding fiber angle deviation and cover ratio. The permitted tolerance range for the fiber angle deviation and the cover ratio is highlighted in green. It can be seen that for 90deg orientation the sectorization concept is well suited to observe low fiber angle deviations and high cover ratios. The circular guide curves reduces the fiber angle deviation but on the other hand the cover ratio decreases and further defects in form of overlaps are brought into the layup. For 45 and 135deg orientation the design of variable angle guide curves is necessary to get into the permitted tolerance range. Ellipsis showed the best possible compromise of fiber angle deviation, cover ratio as well as gap and overlap management.

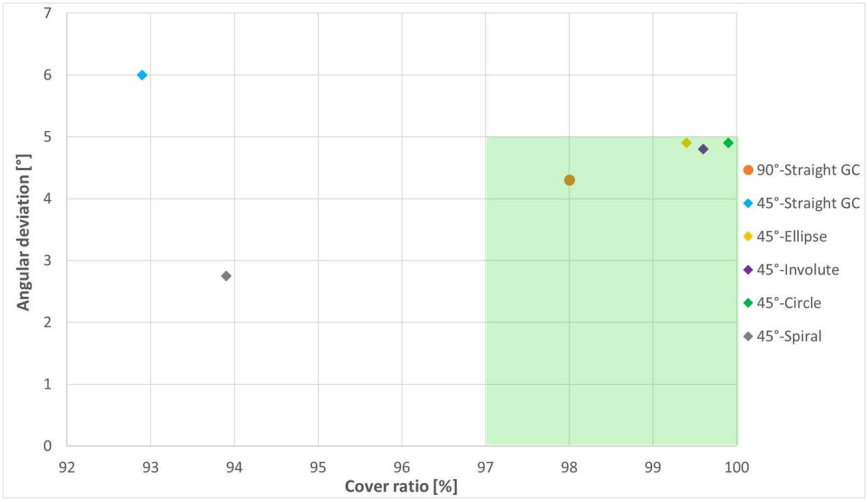

Figure 7: Overview of maximal fiber angle deviation and reachable cover ratio for the observed guide curve concepts.

3.2 Steering analysis

Figure 8 shows the steering analysis for the 45deg oriented layer. The limits were set to 3000mm and 1500mm radius. This means that the blue areas visualize a steering radius larger or equal to 3000mm. In the red areas the radius is even or below 1500mm. The green to yellow areas have

  doi:10.5075/epfl-298799_978-2-9701614-0-0 published under CC BY-NC 4.0 license

a radius between 3000 and 1500mm. According to Zenker et. al. [2] a steering radius below 1000mm is critical in terms of temperature distribution and undulations. Since the steering radius for the defined guide curve concept is about 1500mm in the edge-near areas and is above 1500mm in the inner areas, it is assumed that no significant defects are introduced by the steering.

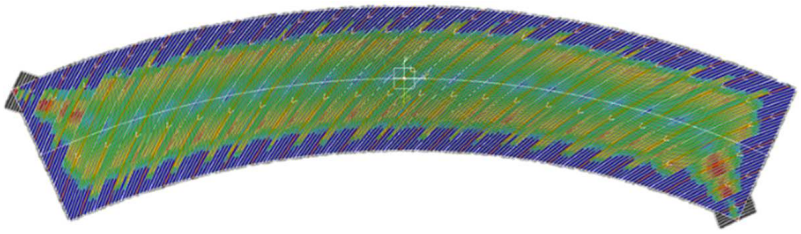

Figure 8: Analysis of steering radius for 45deg-oriented layer.

3.3 Effect of fiber angle deviation of straight and variable angle guide curves on tensile properties

As mentioned in chapter 2.6 only a proportion of the fibers for the tensile specimens are through-fibers. Consequently, these proportions must be taken into account for calculation of the stress since the loads are mainly taken by the trough-fibers. As the effect of non-trough fibers on E-modulus is less than on the strength, only the results of maximal stress were modified by the effective width [8]. Figure 9 shows the measured results of tensile testing as well as the modified results by taking into account the effective width. For the consideration of the effective width, the theoretical maximal values were used.

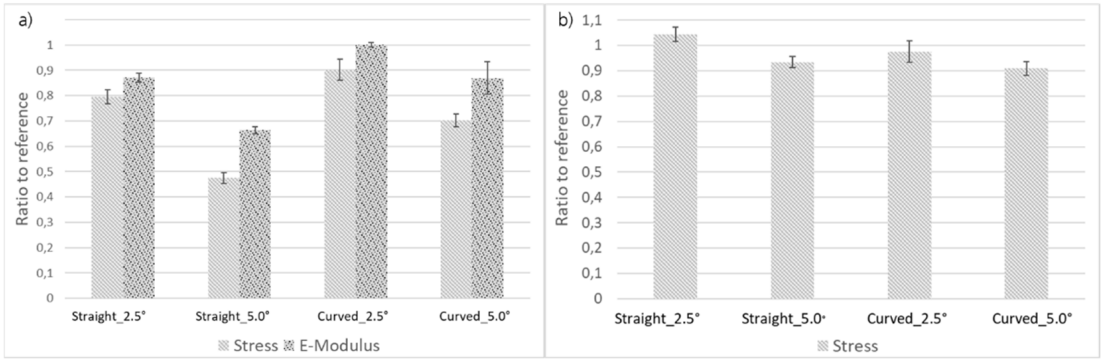

Figure 9: a) Measured results of tensile testing, b)Modified tensile stress by effective width. Results are given as ratio to tested reference with no fiber angle deviation

For the straight guide curve specimen with a fiber angle deviation of 2.5° it is seen that the average maximal stress of the specimens is about 4% higher than for the reference with a standard deviation of 2.9%. Taking into account the standard deviation of 2.4% for the reference there is no significant deviation of the results. It is assumed that the small angular deviation in combination with the subsequent consideration of the effective width using the theoretical value results in no decrease in maximum stress being seen.

The situation is similar for the results of the curved specimens with an angular deviation of 2.5°. Taking into account the standard deviations of the reference as well as these specimens no significant deviation of the maximum stress is seen. In terms of failure behavior, the straight specimen fails due to shear stresses and matrix failure. The curved specimens, on the other

  doi:10.5075/epfl-298799_978-2-9701614-0-0

hand, also shows first matrix failure due to shear stresses resulting in a stress drop. However, the stress increases again until fiber breakage finally occurs. Figure 10 shows the results of failure behavior of the curved specimen for angular deviation of 2.5°.

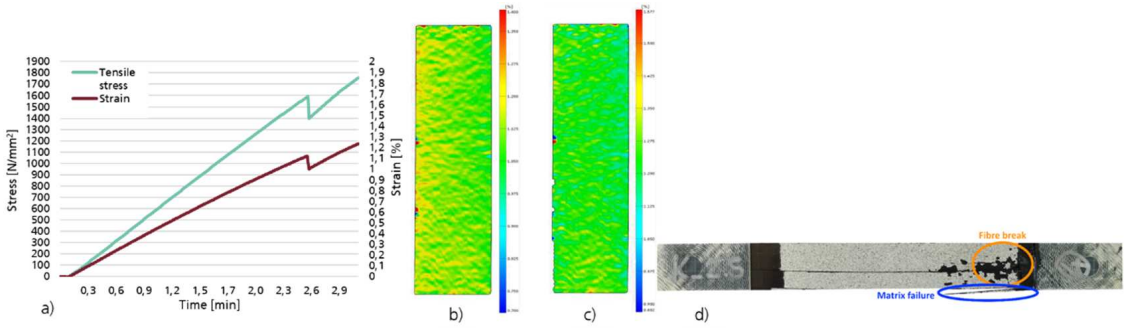

Figure 10: a) Measured stress and strain during tensile testing, b) Strain distribution during tensile testing before matrix failure and c) after matrix failure, d) Failed curved tensile specimen with 2.5° fiber angle deviation

For the specimens with an angular deviation of 5° a significant decrease of the maximum stress is seen. For the straight specimens the maximum stress decreases by 6.6% with a 2.1% standard deviation. For the curved specimens the maximum stress decreases by 9.1% with a 2.6% standard deviation. This result is fundamentally to be expected due to the anisotropy of the fibers. In the direct comparison of the results between straight and curved specimens, there is no significant difference taking into account the standard deviations. In terms of failure behavior, both specimens failed due to shear stresses and matrix failure. It can be concluded that curved tow trajectories does not involve a significant decrease of tensile properties.

4. Conclusion and outlook

Based on the results of guide curve design investigations ellipses are well suited to define the guide curves for 45deg and 135deg layers in regards to fiber angle deviations, cover ratio and gap and overlap management. In addition, longitudinal instead of commonly known triangular gaps are created with this method. These gaps can often partially or completely be closed for thermoplastic tapes by squeeze flow mechanism. For 90deg layers the sectorization concept is well suited to design the robot trajectories while maintaining the defined tolerances. With the investigation of the tensile strength of curved and straight specimens with defined fiber angle deviations it is shown at a basic level that curved guide curves have no significant disadvantageous effect on the tensile properties. In order to be able to make more comprehensive statement and to define safety factors for the design of the frame structures, further investigations are still required here.

Acknowledgements

The researches performed in the described studies were funded by the Federal Ministry for Economic Affairs and Energy (BMWi LuFo V-3 OSFIT, 20W1706C). The authors acknowledge all project partners of BMWi LuFo V-3 OSFIT for the fruitful cooperation. In addition, the authors acknowledge the assistance of Ms. Katharina Backes for the investigation and automatization of guide curve design for frame structures as well as Mr. Christoph Wieland for the optimization and investigation of variable angle guide curves on the mechanical properties.

5. References

[1] Slange TK. Rapid Manufacturing of Tailored Thermoplastic Composites by Automated Lay-up and Stamp Forming: A Study on the Consolidation Mechanisms. Enschede, the Netherlands: University of Twente; 2019.

[2] Zenker T, Schwab M. Analysis of fiber steering effects in thermoplastic automated fiber placement. In: ECCM18 - 18th European Conference on Composite Materials. Athens, Greece; 2018.

[3] Comer AJ, Ray D, Obande WO, Jones D, Lyons J, Rosca I et al. Mechanical characterisation of carbon fibre-PEEK manufactured by laser-assisted automated-tape-placement and autoclave. Composites Part A: Applied Science and Manufacturing 2015.

[4] Heß C. Beitrag zur Qualitätssicherung für die serientaugliche Herstellung von textilen Preformen [Dissertation]. München: Technische Universität München; 2015.

[5] Weber J, Schlimbach J. Co-consolidation of CF/PEEK tape-preforms and CF/PEEK organo sheets to manufacture reinforcements in stamp-forming process. Advanced Manufacturing: Polymer & Composites Science 2019; 5(4):172–83.

[6] Rousseau G, Wehbe R, Halbritter J, Harik R. Automated Fiber Placement Path Planning: A state-of-the-art review. CAD&A 2018; 16(2):172–203.

[7] Zenker T, Schuerger C, Drechsler K. Experimental analysis of gaps and overlaps caused by intra-ply sectorization in the thermoplastic automated fiber placement process. In: ECCM17 - 17th European Conference on Composite Materials. Munich, Germany, 2016

[8] Yang X, Nanni A, Haug S, Sun CL, Rolla R. Strength and Modulus Degradation of CFRP Laminates from Fiber Misalignment. In: Journal of Materials in Civil Engineering, ASCE, 2002.

  doi:10.5075/epfl-298799_978-2-9701614-0-0

QUALIFICATION METHOD FOR AUTOMATED FIBRE PLACEMENT TO OPTIMIZE PROCESS PARAMETERS REGARDING LAYUP QUALITY

Kevin, Scheiterlein[a], Oussama, Etlijani[a], Sebastian, Müller[a] and Klaus, Drechsler[b]

a: Fraunhofer IGCV - Institute for Casting, Composite and Processing Technology, Am Technologiezentrum 2, 86159 Augsburg, Germany – email: kevin.scheiterlein@igcv.fraunhofer.de
b: Chair of Carbon Composites, TUM School of Engineering and Design, Technical University of Munich, Boltzmannstr. 15, 85748 Garching, Germany

Abstract: *Automated Fibre Placement (AFP) is an advanced process for the manufacturing of high-performance composite structures and is established in the aerospace industry. The main challenge is the optimization of the process parameters, such as layup speed, compaction force and heating temperature, to minimize the common AFP layup defects. The evaluation of these defects is an important topic during the development of new components. Defect detection is usually done by visual inspection of the layup and manual recording of the occurred defects. This paper developed a methodology to determine the defect characteristics, focused on out-of-plane wrinkles, which are typical during a curved layup of thermoset tape material in respect to process parameters, geometry and material width. This methodology offers the possibility to compare different materials and process parameters on a basic level to get a detailed understanding of the influence on layup quality within the AFP process.*

Keywords: Automated Fibre Placement; fibre steering; optical measurement; quality analysis; machine learning

1. Introduction

Due to their density-related and mechanical properties, composites are potential lightweight construction materials today and will continue to be so in future [1, 2]. However, their use in series applications poses enormous challenges for manufacturing technologies and can only be realised economically through a high degree of automation. The goal here is to substitute manual work steps with automated processes. Theoretically, this can be implemented for the entire process chain ranging from engineering and manufacturing to recycling. Automated fibre placement (AFP) is already being used and is part of this process chain. AFP is a highly automated process and therefore entails a high degree of complexity [3, 4]. For efficient use, this technology requires a comprehensive understanding of the process. This applies to engineering, manufacturing engineering and the production itself. There are a multitude of influencing factors (plant technology, materials, environmental conditions, etc.) that affect the manufacturing process and the perfect interaction of these factors results in the process window [5–7]. The determination of this process window is currently a time-consuming and manual process, which must be validated and adapted for new materials or new component geometries. The digitalisation of process variables and their further processing is one way of reducing complexity for the user, increasing process understanding and thereby establishing a robust process chain [8–10].

  doi:10.5075/epfl-298799_978-2-9701614-0-0

To get an objective standard for the determination of the influences of different material, machine or environmental parameters a method was developed to qualify a standard layup for parameter evaluation using the AFP machine Csolo from the manufacturer Coriolis Composites. The outcoming qualification method consist of the AFP layup, its digitalisation and the algorithmic evaluation with the machine-learning algorithms and delivers as result the number of defects, the defect area and a self-defined quality parameter.

2. Methods

2.1 AFP experiments & material

The single-fibre AFP machine Csolo (Figure 1 left) from the manufacturer Coriolis Composites available at Fraunhofer IGCV was used for the lay-up trials. The machine can process thermoplastic, dry and thermoset tape materials in widths from ¼" (6.35 mm) to 1.5" (38.1 mm) [11]. To validate the qualification method, a serie of trials were carried out with the variation of different process parameters shown in Table 1. For each parameter configuration five individual tapes were laid-up inside of the scanning area of the optical measurement system (two sets per scan). As reference one single tow was laid up with no curvature, to get the nominal thickness of the processed material without any defects. In contrast to serial applications, no infrared lamp was used to heat the material. Instead, a heating plate was used to constantly preheat the lay-up surface to the desired temperature. The reason for this is the long heating rate of the infrared lamp and the resulting differences in the heating rate of the individual tows. The tooling was prepared with the lay-up foil Securelon® L-2000 from Airtech.

As material a typical aerospace thermoset carbon fibre prepreg in ¼" width, 0.2 mm thickness and an epoxy resin matrix was used. The material was manufactured within the tack life and stored in ambient conditions during the trials, regarding the AFP machine configuration.

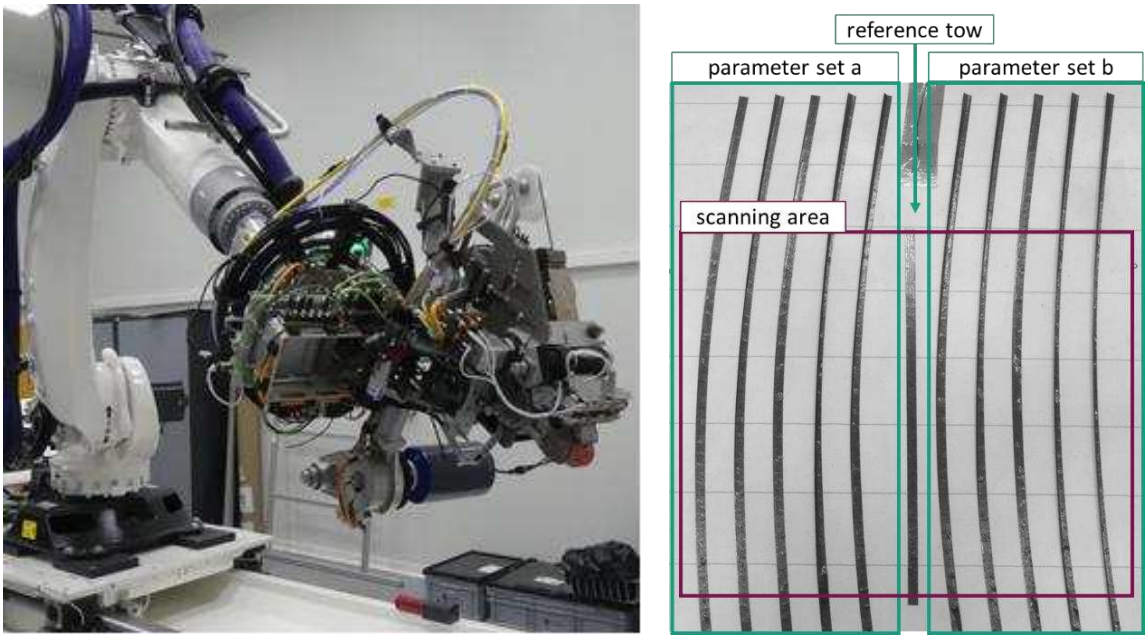

Figure 1. Csolo (Coriolis Composites) AFP machine (left), lay-up configuration of the experimental study used for two parameter sets, including the reference tow and the scanning area for the optical measurement system (right)

  doi:10.5075/epfl-298799_978-2-9701614-0-0

Table 1 : AFP process parameters and their variation step during the layup trials

Process parameter	Value	Step
Layup velocity [m/s]	0.04 – 0.2	0.04
Compaction force [N]	500	-
Tooling temperature [°C]	21.5 – 60	10
Layup radius [mm]	300 – 1500	300

2.2 optical measurement system

To generate the digital twin of the AFP layup for further processing and analysis of the quality, an optical 3D scanner is used. Herby different light patterns are used to generate a three dimensional shape of the surface. The 3D scanning sensor is the GOM ATOS Core 300 which combined two stereo cameras and a light source. The sensor operates with narrow-band blue light so that the distributing ambient light can be filtered by polarization. The measuring surface covers 300×230 mm and reaches a maximum resolution of 0.12 mm [12]. For geometrically complex or large-scale components, multiple scans must be performed and later superimposed using reference points. In order to avoid the effects of material reflections regarding the tape-surface on the scans, the surfaces is sprayed with an industrial matting developer.

2.3 point cloud processing

Since point clouds are usually noisy, sparse and unorganized, extracting features and information from them can be a very challenging task. A Python based approach was established using the point cloud library Open3D. Moreover the most relevant algorithms which were applied for this paper are the random sample consensus RANSAC (supervised) for the segmentation. RANSAC was developed for robust regression in data with noise. It is an iterative method for estimating a mathematical model from a data set that contains outliers. The RANSAC algorithm works by identifying the outliers in a data set and estimating the desired model using data that does not contain outliers [13]. In this paper the algorithm is used to segment the point cloud vertically. For this the point cloud containing n points is needed, then the algorithm picks at least 3 points to estimate a plane model. In the next step the distance between this plane and every other points is calculated. With the selected tolerance the classification of the points into inliers (inside the tolerance) and outliers (outside the tolerance) is performed. This routine is repeated until the set value of maximum iterations is reached. The chosen plane is the one with the highest value of inliers.

The second algorithm is the density-based spatial clustering of applications with noise DBSCAN (unsupervised) for the clustering of the generated point clouds. It relies on a density-based notion of clusters which is designed to discover clusters of arbitrary shape. It requires two parameters, the radius (Ɛ) of the sphere around the point and the minimum number of points (minPts) which has to be inside of this sphere. The algorithm creates a sphere with the specified radius around every point and classifies the points in three categories Core Point (number of points is bigger or identical as minPts), Border Point (number of points is lower than minPts) or Noise (no surrounding points). Afterwards the cluster is expanding, by randomly selecting a Core

  doi:10.5075/epfl-298799_978-2-9701614-0-0

point and adding all Core points close to it (inside Ɛ), repeating this routine with all the added Core points as the next starting point. Border points are also added, but not used as starting points. [14]

3. Results

3.1 Layup quality qualification method

The outcome is a standardized routine, which starts from the layup and reaches till the algorithmic evaluation of the recorded point cloud to get the number of defects, the defect area and a self-defined quality parameter. The method considers all out-of-plane effects, like wrinkles, twists or tow pull off as defects. The routine is divided in the following steps:

- Apply the AFP Layup as shown in Figure 1
- Preparing the scanning area with matting developer to reduce the reflections on the tape surface
- scan the AFP layup with the ATOS Core 300 using the GOM Inspection software (Figure 2 left), the scan area of the layup was defined to the size of the one image in the ideal distance of the sensor ~300x230 mm and is shown in Figure 1 right
- Polygonise and export of the point cloud as ASCII using the GOM Inspection software to get a raw point cloud out of the scanned layup (Figure 2 right). The point cloud has its main coordinate system in respect to the sensor position.

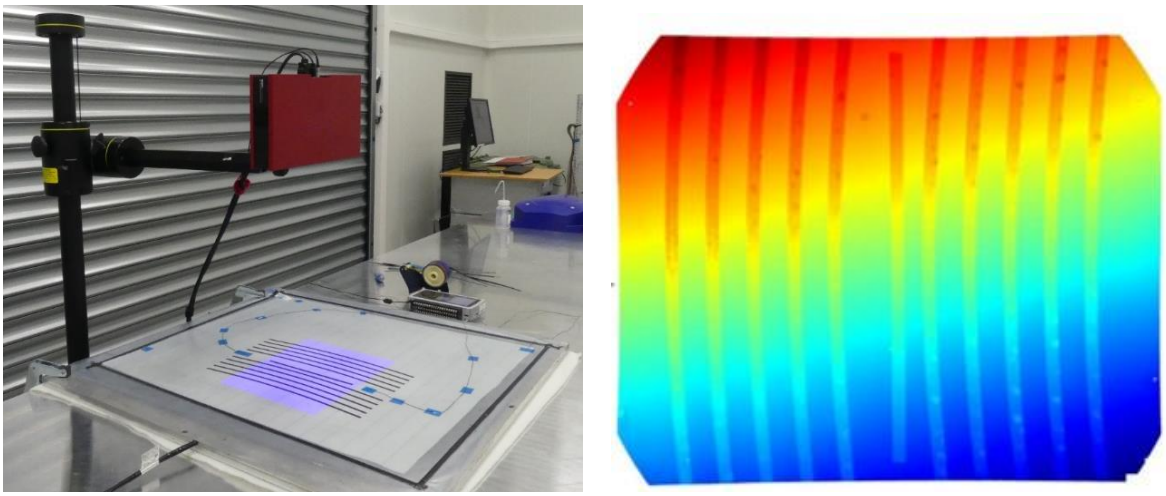

Figure 2. Setup of the scanning process using the GOM ATOS Core 300 (left) to generate a point cloud (right) for the algorithmic evaluation routine.

- Coordinate transformation using a fitted plane of the tooling surface to get a coordinate system in respect to the layup, z-direction will be layup direction (Figure 3 left).
- Segmentation of the steering ply from the tooling surface using the RANSAC algorithm with a tolerance considering the tape thickness (Figure 3 centre). The result is the tooling surface as inliers (Figure 3 centre, red area) and the tape surface and their defects as inliers (Figure 3 centre, green area).
- Clustering and labelling of the individual tapes with the DBSCAN (1) algorithm to separate them combined with their defects. To get rid of the noise clusters a minimum number of points was defined. (Figure 3 right)

  doi:10.5075/epfl-298799_978-2-9701614-0-0

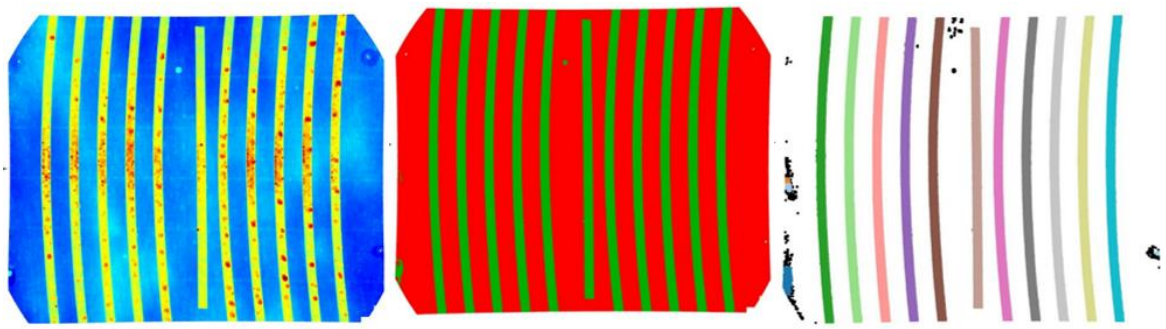

Figure 3. Individual steps of the algorithmic evaluation routine, coordinate transformation using a fitted plane (left), segmentation of the tapes and the tooling surface using RANSAC (centre), clustering of the individual tapes with DBSCAN

- Segmentation of the defect areas inside of the individual Tapes using the RANSAC algorithm to get defect area inside of the individual tapes
- Clustering of the individual defect areas with the DBSCAN (2) algorithm to separate the defects inside of one tape to get the number of defects
- Calculation of the defect size using a mesh generated with a ball pivoting algorithm

The parameters used for the algorithms are shown in Table 1 and are manually adjusted regarding the density of the point cloud and the thickness of the tape material.

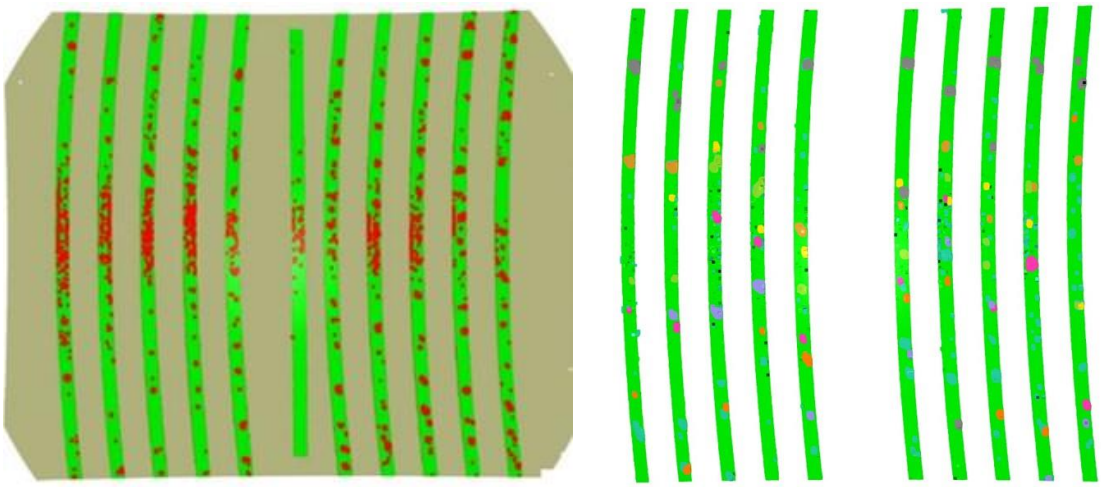

Figure 4. Using RANSAC to separate the defects from the tape area within the tolerance (left), clustering of the individual defects using DBSCAN (right)

Finally all calculations come together in the evaluation of the number of defects, the relative size of defects and the self-defined quality parameter. The quality parameter combines the defect area and the defect size relative to the mean value as shown in Eq.(1). This parameter considers a poor tape quality either with few huge defects or a large number of small defects and is a first approach to define such parameter.

$$Q = X * R \; ; \; with \; X = \frac{z_{max}}{z_{mean}} \; and \; R = \frac{A_{defect}}{A_{tape}} \tag{1}$$

  doi:10.5075/epfl-298799_978-2-9701614-0-0

Table 2 : Parameters of the used algorithms

Algorithm	Parameter	Value
RANSAC	Distance tolerance	0.12
	$RANSAC_n$	3
	$max_{iterations}$	1000
DBSCAN (1)/(2)	Radius Ɛ	2.5 (1)/(2)
	minPts	100 (1); 20 (2)
Estimate normal KDTree	Radius	1.6
	$N_{neigbours}$	16
Ball pivoting	Radii	[0.7, 0.8, 0.9, 1]

3.2 Validation of the qualification method

To validate the qualification model a process parameter variation was performed and the routine was used for the evaluation. Figure 5 shows the evaluation of one experiment presenting two parameter sets and heat maps of all performed experiments on the tooling surface heated to 40 °C with the number of defects, the relative size of defects and the resulting quality parameter. If there is no value in the heat map it wasn't possible to perform a representing experiment due to no tack of the material within this process window.

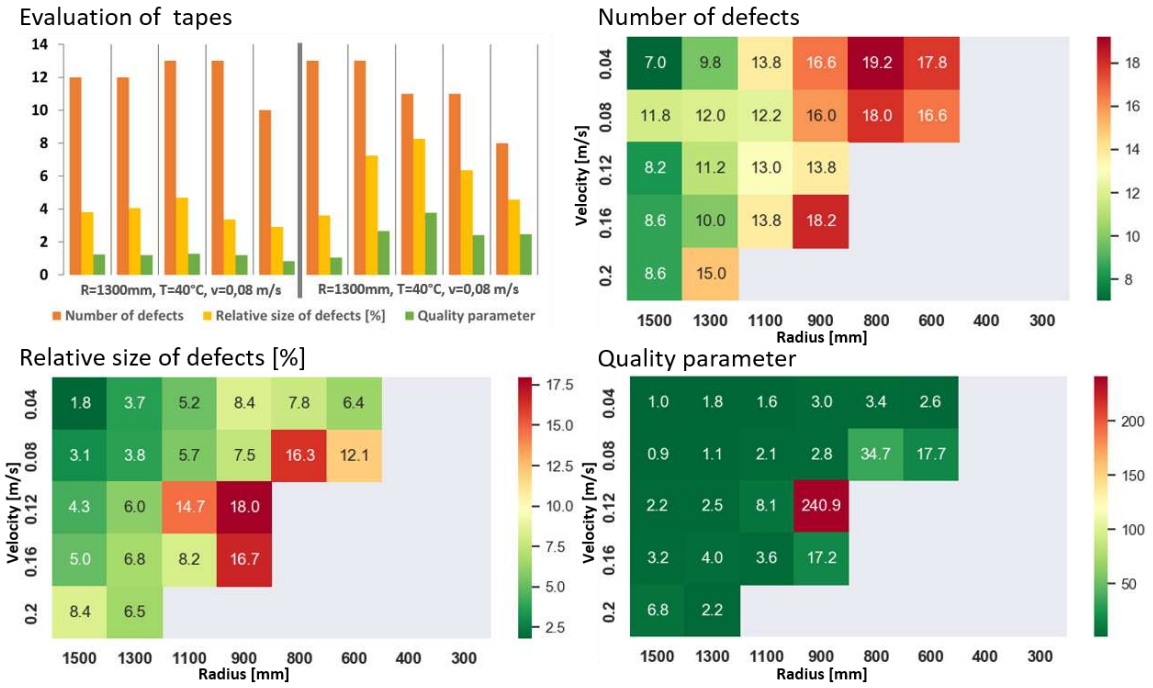

Figure 5. Evaluation of two parameter sets for every individual tape (upper left) and of all experiments performed on the 40 °C heated tooling summarized over 5 tapes regarding number of defects, relative size of defects and quality parameter (bottom left and right side)

4. Discussion

Regarding to the qualification method, the main factors for the quality and accuracy of the method are the repeatability of the robotic system and the resolution and quality of the point cloud captured with the optical sensor. The robot repeatability and accuracy is the same as in the later manufacturing process so it is valid to use it within this method. In this paper the quality of the point cloud is next to the optical sensor also influenced by the needed industrial matting developer, which is applied manually. This human factor should be eliminated for further optimisation of the method. To reach this goal a laser scanning system described in [15–17] could be used. On the other hand the developed algorithmic evaluation routine is robust and could be used for similar point clouds of AFP layups of various machinery and sensor systems for point cloud generation with a sufficient resolution for AFP tape materials. Moreover it is applicable for out-of-plane defects, other AFP defects like in-plane waviness, tow drop or drift are not considered in the current status of the qualification method.

The results of the validation shown on every tooling temperature, that the relative size of the defects and the number of defects increase for higher velocities and smaller radii, like it is shown for example in [17, 18]. Another point is the investigation on different tooling temperatures, it shows first, that the number of possible process parameters increases with the temperature and second the number of defects decrease within the same parameter sets if the temperature is increased. From 50 °C to 60 °C there is a higher reduction of the defect number, in this case the point clouds show in-plane waviness occurred more than on any other tooling temperature and these defects couldn't be detected with the developed method. For the used material it means, that the viscosity changes significant over 50 °C and the steering leads to in-plane waviness instead of out-of-plane defects.

5. Conclusions

A qualification method for standardized AFP layups to detect out-of-plane effects and qualify them regarding their size and number including a self-defined quality parameter was developed. The method is based on the algorithmic evaluation of point clouds, captured with an optical measurement system, using different machine learning algorithms like RANSAC and DBSCAN. The validation showed that the method is applicable for the investigation of different process parameters like steering radii, velocity and tooling temperature and could be used for any other AFP process parameter or material variation. Regarding the Python and Open3D approach it offers the possibilities to integrate other analysis to implement the detection of further defects occurring during fibre steering. For research aspects it gives the opportunity to get a better understanding of fibre steering in an experimental manner and a possibility to compare it with simulation. Regarding digitalisation and automation of AFP production there is the opportunity to implement the method the AFP machine interface and define routines to check the status of the manufactured material or generate an ideal process window for various materials and conditions.

  doi:10.5075/epfl-298799_978-2-9701614-0-0

6. References

1. U.S. Government Accountability Office, http://www.gao.gov. GAO-11-849 Aviation Safety: Status of FAA's Actions to Oversee the Safety of Composite Airplanes.
2. Nelson ES, Reddy DR. Green Aviation: Reduction of Environmental Impact through Aircraft Technology and Alternative Fuels: CRC Press; 2018.
3. Lukaszewicz DH-JA, Ward C, Potter KD. The engineering aspects of automated prepreg layup: History, present and future. Composites Part B: Engineering. 2012:997–1009.
4. Grimshaw MN, Grant CG, Diaz JML. Advanced Technology Tape Laying For Affordable Manufacturing Of Large Composite Structures.
5. Heller K, Böckl B, Ebel C, Drechsler K. Influence of Prepreg Aging and Tack on Lay-up Effects/Defects in Thermoset Automated Fiber Placement. In: 18th European Conference on Composite Materials ECCM18.
6. Hörmann P. Thermoset automated fibre placement - on steering effects and their prediction [PhD Thesis].
7. Kim BC, Hazra K, Potter K. Limitations of fibre placement techniques for variable angle tow composites and their process induced defects. In: 18th International Conference on Composite ICCM.
8. Maass D. Progress in automated ply inspection of AFP layups. Reinforced Plastics. 2015:242–5.
9. Rudberg T, Nielson J, Henscheid M, Cemenska. Improving AFP Cell Performance. SAE Int. J. Aerosp. 2014:317–21.
10. Halbritter A, Harper R. Big parts demand big changes to the fiber placement status quo. SME Composites Manufacturing. 2012.
11. Coriolis. Csolo - Automated Fibre Placement machine. https://www.coriolis-composites.com/fiber-placement-machines/coriolis-csolo/. Accessed 20 Apr 2022.
12. ZEISS - GOM. ATOS Compact Scan. https://www.gom.com/de-de/produkte/3d-scanning/atos-compact-scan. Accessed 20 Apr 2022.
13. Fischler MA, Bolles RC. Random sample consensus: A Paradigm for Model Fitting with Applications to Image Analysis and Automated Cartography. Commun. ACM. 1981:381–95.
14. Ester M, Kriegel H-P, Sander J, Xu X. A Density-Based Algorithm for Discovering Clusters in Large Spatial Databases with Noise.
15. Gardiner G. InFactory Solutions with Airbus. 23.3.2017. https://www.compositesworld.com/articles/infactory-solutions-qualifies-afp-sensor-on-mtorres-equipment. Accessed 16 Aug 2021.
16. Gardiner G. Coriolis Composites and Edixia develop inline inspection for AFP. https://www.compositesworld.com/articles/coriolis-composites-and-edixia-develop-inline-inspection-for-afp. Accessed 16 Aug 2021.
17. Veldenz L, DiFrancesco M, Astwood S, Giddings P, Kim BC, Potter K. Assessment of Steering Capability of Automated Dry Fibre Placement Through a Quantitative Methodology. Automated Composites Manufacturing - Third International Symposium. 2017.
18. Matveev MY, Schubel PJ, Long AC, Jones IA. Understanding the buckling behaviour of steered tows in Automated Dry Fibre Placement (ADFP). Composites Part A: Applied Science and Manufacturing. 2016:451–6.

  doi:10.5075/epfl-298799_978-2-9701614-0-0

INVESTIGATING THE EFFECT OF PLY ORIENTATION ON THE SURFACE THERMAL HISTORY OF NEWLY PLACED TAPE DURING THERMOPLASTIC COMPOSITE MANUFACTURING WITH LAFP PROCESS

Ali Barzegar [a, b, c], Sasan Karimi [a, b, c], Hatice S. Sas [a, b, c], Mehmet Yildiz [a, b, c]

a: Integrated Manufacturing Technologies Research and Application Center, Sabanci University, Tuzla, Istanbul, 34956, Turkey
b: Composite Technologies Center of Excellence, Sabanci University-Kordsa, Istanbul Technology Development Zone, Pendik, Istanbul 34906, Turkey
c: Faculty of Engineering and Natural Sciences, Department of Manufacturing Engineering, Sabanci University, Tuzla, Istanbul, 34956, Turkey
Email: abarzegar@sabanciuniv.edu

Abstract: *One of the effective factors on the temperature distribution during the automated fiber placement is the thermal contact resistance. The analysis of microscopy images indicated that by changing the fiber orientation from unidirectional to cross-ply stacking sequences, the degree of intimate contact decreases. This phenomenon raises the issue of thermal contact resistance, threreby leading to the poor heat flux through the interface of the tape-substrate and the heat tends to flow to the top surface of the tape. Accordingly, in the next lay-up on the top of the previous laminate, the inlet temperature of the substrate surface for cross-ply configuration will be higher and by increasing the number of layers, more heat can accumulate on the top of the laminate. This issue highlights the importance of cooling time in cross-ply laminates, especially when the length of the domain is short or the lay-up is performed with a higher placement rate.*

Keywords: Automated fiber placement; fiber orientation; heat transfer

1. Introduction

Automated fiber placement (AFP) has opened up new possibilities for manufacturing composite materials efficiently. Recent research on laser-assisted automated tape placement (LATP) has attempted to develop online consolidation procedures that would allow composite components to be manufactured without a post-consolidation step, such as autoclave or hot press [1].

In the AFP process, the thermal history of consolidation has a considerable impact on the quality of a manufactured part. One of factors that affects thermal history is fiber orientation difference between subsequent layers from an intimate contact perspective. In laminates produced by the AFP process, the amount of heat transfer between layers is directly related to the degree of intimate contact (D_{ic}). In the case of poor intimate contact, the presence of air gaps leads to the exertion of thermal contact resistance (TCR) between layers. This phenomenon causes the temperature of the upper surface of the newly placed tape to be different for different fiber orientations. In cases in which time is insufficient for cooling and the next lay-up on previous laminate must be done immediately, the inlet temperature of the upper surface of the substrate is not the same for different ply orientations. This temperature difference gradually accumulates at each lay-up and can affect the quality of the in-situ consolidated part. The objective of this work is to investigate this phenomenon experimentally and numerically for two different ply

  doi:10.5075/epfl-298799_978-2-9701614-0-0

orientations: unidirectional and cross-ply. First, to obtain the degree of intimate contact and calculate the thermal contact resistance for $[0°/0°]$ and $[0°/90°]$ interfaces, specimens with $[0°/0°/0°]$ and $[0°/90°/0°]$ stacking sequences were manufactured with a 400 mm/s deposition rate. Then, cross-sectional microscopy images were taken for the top interface and analyzed with ImageJ software to obtain D_{ic} and subsequently calculate TCR. Furthermore, a 2D steady-state thermal model was constructed and coupled with TCR to predict the temperature of the upper surface of the newly placed tape. It should be noted that the existence of TCR was only considered for the interface between new incoming tape and substrate (top interface), and for the remaining interfaces inside the substrate, the full degree of intimate contact was assumed.

2. Material and Methods

2.1 Specimen manufacturing

To manufacture composite laminates, a robotic-based automated fiber placement (AFP) approach was used, as shown schematically in Figure 1.

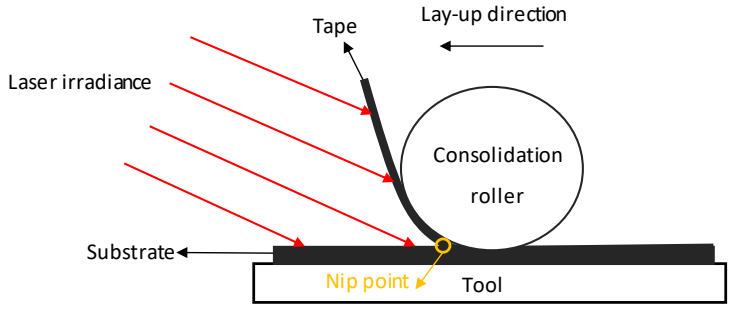

Figure 1. Schematic diagram of the LAFP process

This machine has the capability to simultaneously lay up to eight 6.35 mm wide slit continuous tapes at a nominal maximum speed of 800 mm/s. The heat source was a 6 kW Laserline LDF series diode laser system, and the optic lens created a rectangular laser spot with an 8 mm × 56 mm illuminated area of 250 mm focal distance. A conformable consolidation roller with a 70 mm diameter and 60 shore hardness was used for compaction. During consolidation, the tool temperature was calibrated to 155°C. A thermal camera was mounted on the placement head, next to the laser heat source, to measure the temperature of the heated surface.

The prepreg material used in this study was TC1320 CF/PEKK tapes provided by Toray Cetex with a fiber volume fraction of 66%, a nominal thickness of 0.15 mm and 6.35 mm width. The AFP manufactured thermoplastic laminates have a length and width of 1100 mm and 50.8 mm, respectively, and consist of three layers with $[0°/0°/0°]$ and $[0°/90°/0°]$ stacking sequences. The specimens were produced with the following process conditions: 400 mm/s deposition speed, 500 N roller consolidation pressure and 3427 W laser power. The manufactured parts were then used to measure the average degree of intimate contact for the $[0°/0°]$ and $[0°/90°]$ interfaces experimentally.

2.2 Temperature measurement

During the lay-up process, the material surface temperature in the heated region (with laser heat source) up to the nip point was measured using a long-wave infrared (LWIR) camera (the

Optris PI 400i). The thermal camera has an 80 frame per second recording capability and an IR detector with a resolution of 382 × 288 pixels; the camera was calibrated in the temperature range of -20 °C and 900 °C with an accuracy of ± 2 °C or ± 2 %. The collected data were used to validate the accuracy of the developed thermal model.

2.3 Thermal contact resistance

When an inter-laminar void between the two layers is present, due to the low thermal conductivity of the air, the heat flux through the interface is poor. Because of this phenomenon, the heat flux (q) from the bottom surface of newly placed tape to the top surface of the substrate is affected by thermal contact resistance, which can be expressed as:

$$q = (T_t - T_s)/R_c \tag{1}$$

where T_t and T_s are the bottom and top surface temperature of the tape and substrate, respectively. R_c is the thermal contact resistance, which can be computed as follows [2]:

$$R_c = D_{ic,t_0} a_0 \left(\frac{1}{k_y D_{ic}^2} + \frac{1-D_{ic}}{k_{air} D_{ic}} + \frac{1}{k_y} \right) \tag{2}$$

where D_{ic,t_0} is the initial degree of intimate contact, a_0 is depth of the asperities for the unprocessed tape, and D_{ic} is after lay-up interface degree of intimate contact. k_y and k_a are the thermal conductivities of the CF/PEKK composite in the through-thickness direction and air, which are 0.73 W/mK and 0.0043 W/mK, respectively [3,4].

2.4 Intimate contact measurement

In order to obtain D_{ic,t_0} and a_0, the real surface profile measurement of the raw tape is needed. For this aim, µsurf laser profilometer from nanofocus® was used to extract the surface topology. The a_0 is equivalent to twice the standard deviation of the surface profile and D_{ic,t_0} was calculated based on the Lee and Springer model [5] which represents the initial tape surface irregularities as a series of identical rectangles. Through this approach, the degree of intimate contact for unprocessed tape can be calculated as follow:

$$D_{ic,t_0} = b_0/(b_0 + w_0) \tag{3}$$

where, b_0 is the width of the rectangular element and w_0 is the gap between two adjacent rectangular elements for unprocessed tape. These geometrical parameters were calculated by using a similar procedure proposed by Schaefer et al. [6]. Finally, the numerical values of D_{ic,t_0} and a_0 were obtained as 0.392 and 4.02, respectively.

Another important parameter that is required to calculate the thermal contact resistance is the final degree of intimate contact (D_{ic}). For measurement of D_{ic}, the specimens were taken from the mid-section of the manufactured components (Figure 2), where the robot head experiences approximately constant placement speed. The samples were then embedded in epoxy for handling purposes and polished to attain high quality cross-sectional microscopy images. A Nikon ECLIPSE LV100ND microscope with a 50x-magnification lens was used for this aim. For each specimen, several photos were taken along the width of the interface of the two plies; these photos were then stitched together with ImageJ image processing software.. After the image was binarized, thresholding was used to specify the percentage of inter-laminar voids that

existed at the interface, from which consequently we were able to calculate D_{ic}. The obtained D_{ic} for the $[0°/0°]$ and $[0°/90°]$ interfaces were only used to find TCR for the topmost interface; for the other interfaces inside the substrate, the full degree of intimate contact was assumed.

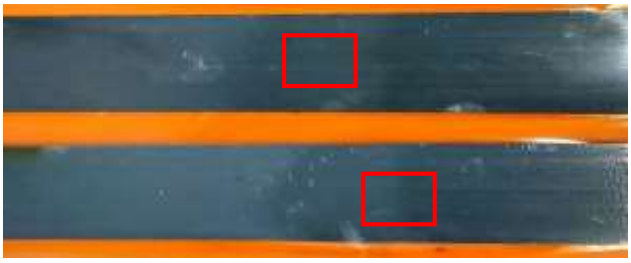

Figure 2. The positions of g the samples taken from the manufactured parts for microscopy images

3. Thermal model

The purpose of developing a thermal model was to predict the temperature distribution on the top surface of the laminate during the fiber placement process. As it was assumed that there is uniform heat across the width of the plies, a two-dimensional Finite Difference Model was implemented in MATLAB® software by using an Eulerian framework attached to the moving head. In this approach, the roller and heat source were considered fixed, but the material moved in the opposite direction with velocity (v), which was equal to the placement speed. In this case, advection occurring through a fixed frame and velocity term was added to the energy equation, as follows:

$$\rho c_p \left(v \frac{\partial T}{\partial x}\right) = \ddot{q} + k_x \left(\frac{\partial^2 T}{\partial x^2}\right) + k_y \left(\frac{\partial^2 T}{\partial y^2}\right) \quad (4)$$

In this equation, ρ is the density; c_p is the heat capacity; v is mass velocity in the lay-up direction; T is temperature; $\ddot{q}$ is heat generation per unit area; k_x and k_y are the conductivity of the material in the direction of the lay-up and in the thickness direction, respectively. It should be noted that the heat generation term was ignored in this study since laser heat flux was assumed to be the dominant heat input [7]. The presence of a velocity term in Eq. (4) imposes a limitation on element size in the lay-up direction. Hence, to ensure that the solution is convergent, the dimensionless Peclet number should be less than unity . The thermal properties of the CF/PEKK tape were selected from the reference [3] as $c_p = 1675\ J/kg.℃$, $\rho = 1506\ kg/m^3$, $k_x = 6\ W/m.K$, and $k_y = 0.73\ W/m.K$ at 200 °C .

3.1 Laser heat flux calculation

For calculation of laser heat flux, the proposed correlation in [8] was used. In this approach, it is assumed that the heated surfaces receive homogeneous radiation from a laser heat source and that heat flux is dependent on laser power and setup geometry. The correlations are as follow:

$$q_s = \left(P \frac{h_s}{h}\right) \frac{1}{h'_s w_s} a,\ q_{t=} \left(P \frac{h_t}{h}\right) \frac{1}{h'_t w_t} a \quad (5)$$

where q_s and q_t are the heat fluxes; h_s/h and h_t/h are the fractions of laser irradiances; h'_s and h'_t are the illuminated lengths; w_s and w_t are the are illuminated widths on the surfaces of the substrate and tape, respectively; and a is the absorptance, which was obtained based on the laser incident angle [9]. The geometrical parameters h'_s, h'_t, w_s, w_t and laser incident angle, θ

were obtained by on-site measurements, and related parameters, h_s, h_t and h were calculated using simple geometrical relations. The parameters are shown in given *Figure 3* and the value of them are provided in *Table 1*.

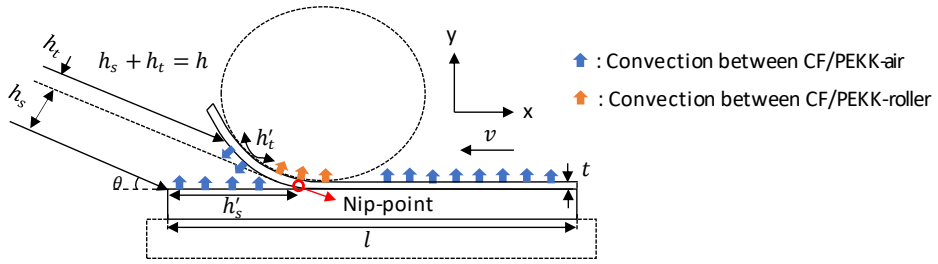

Figure 3. A schematic geometry of the thermal model along with boundary conditions

3.2 Boundary conditions

The implemented boundary conditions in the thermal model are shown in *Figure 3*. To simplify the problem, the physical body of the tool and roller were not considered, and only their boundary conditions were taken into account. The temperature of ambient, roller and tool were considered to be constant as $25℃$, $25℃$ and $155℃$, respectively. The convection coefficient between the tape-ambient was assumed as $20\ W.\frac{K}{m^2}$, and for the tape-roller was considered as $200\ W.K/m^2$. The substrate and tape inlet temperatures were assumed as $155℃$ and $25℃$, respectively, for both $[0°/0°/0°]$ and $[0°/90°/0°]$ laminates, but for the next lay-ups, the substrate inlet temperature was updated based on the simulation results of the previous step. As stated before, thermal contact resistance exiting at the top interface of the laminate (Eq. (1)) was implemented in the thermal model.

Table 1: Overview of the required input parameters for the heat transfer model.

Parameter	Value	Parameter	Value
Domain length, l	300 [mm]	Substrate illuminated width, w_s	56 [mm]
Tape thickness, t	0.15 [mm]	Fraction of the laser incident on the substrate, h_s/h	0.64
Tape illuminated width, w_t	50.8 [mm]	Length of the illuminated substrate, h'_s	20.3 [mm]
Fraction of the laser incident on the tape, h_t/h	0.36	Absorptance	0.6 [9]
Length of the illuminated tape, h'_t	10.5 [mm]	Laser angle, θ	15°

4. Results and discussion

4.1 Thermal model validation

The thermal camera recording data during the laying-up of the third layer for the $[0°/0°/0°]$ and $[0°/90°/0°]$ configurations were used to verify the developed thermal model. It should be noted that these data were related to the temperature distribution of the substrate and tape surface in the heating zone, as a function of distance from the nip point. As can be seen in Figure 4, the simulation results and experiments for both the tape and substrate were very similar, with

maximum differences of 3.75% and 3.21%, respectively. Based on these accurate predictions of temperature distribution, we relied on this thermal model in predicting the surface temperature of new incoming tape.

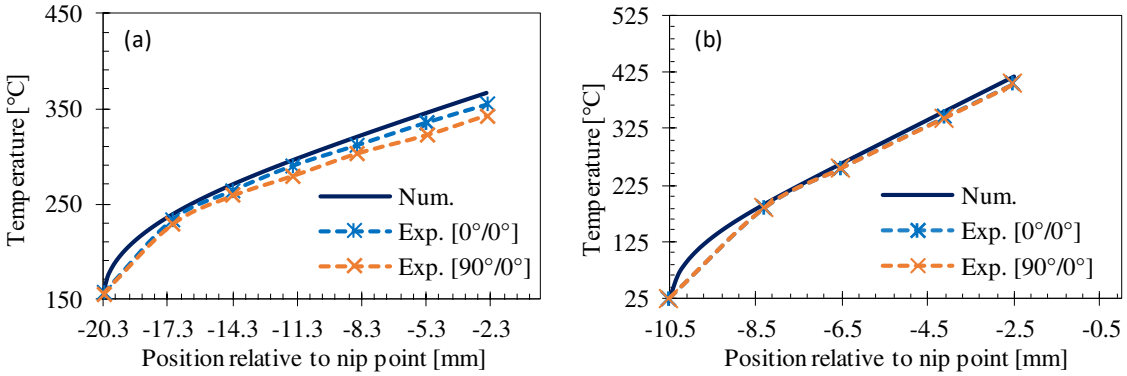

Figure 4. Validation of thermal model with experiments for (a) substrate and (b) tape

4.2 The effect of fiber orientation on the degree of intimate contact

After analyzing the microscopic images using ImageJ software, the degree of intimate contact for $[0°/0°]$ and $[0°/90°]$ interfaces were obtained as 0.917 and 0.761, respectively. This means that as the ply orientation difference increases, the degree of intimate contact decreases. As mentioned earlier, these values were used to calculate the thermal contact resistance (Eq. (2)) at the topmost interface, but for other interfaces inside the substrate, the full degree of intimate contact was assumed. The TCR for $[0°/0°]$ and $[0°/90°]$ interfaces were obtained as 3.789e-5 and 1.209e-4, respectively.

4.3 The effect of fiber orientation on the upper surface temperature of laminate

In Figure 5(a), the upper surface temperatures of the newly placed tape for $[0°/0°/0°]$ and $[0°/90°/0°]$ stacking sequences are shown. One can see that the top surface temperature for $[0°/90°/0°]$ laminate was higher than that of $[0°/0°/0°]$ so that the temperature difference between the peaks was equal to 45℃. This phenomenon can be explained by our observation that by increasing the fiber orientation difference between subsequent layers, the degree of intimate contact at the interface decreased, and consequently the thermal contact resistance increased. Hence, in our model less heat flux transferred from the bottom surface of the newly placed tape to the upper surface of the substrate and the remaining heat flows to the top surface of the tape. This surface temperature difference between the two configurations continued during the cooling zone. Based on this, we can understand that for the next lay-up on the previous laminate, if insufficient time exists for the domain temperature to reach the tool temperature, the substrate inlet temperature will not be the same for the two laminates.

Figure 5(b), (c), and (d), shows the temperature profile for the upper surface of the newly placed tape for the fourth, fifth, and sixth lay-ups, respectively, on both unidirectional and cross-ply laminates. To simplify the simulation, the time gap for the robot head to return to the initial point for the next lay-up was ignored, and it was assumed that the inlet temperature of the substrate was equal to the most recent temperature of the laminate in the cooling zone of the previous step. As expected, the upper surface temperature difference of the unidirectional and cross-ply laminates increased with the number of layers, so that the temperature difference between the peaks for fourth, fifth, and sixth lay-ups was equal to 60℃, 72℃, and 83℃,

respectively. This phenomenon can be explained as follows: As the lay-ups continued, in the cross -ply laminate, due to the higher thermal contact resistance at the top interface on the one hand and the lower temperature gradient between the top and bottom surfaces of the substrate and new incoming tape, respectively, on the other hand, less heat was transferred from the tape to the substrate. This phenomenon was repeated in each lay-up, and as a result, the surface temperature difference between the unidirectional and cross-ply laminates increased. These results indicate that for laminates with a fiber orientation difference between the plies, more time for cooling is needed at each step to prevent the laminate from overheating, especially when the substrate with high top surface inlet temperature is exposed to laser irradiance. Otherwise, heat may accumulate gradually and cause degradation of components. This understanding may prove highly important in applications in which tape placement is performed at a higher placement rate or the laminate has a short lay-up length (for example in a tape winding process) and the the robot head quickly returns to the starting point.

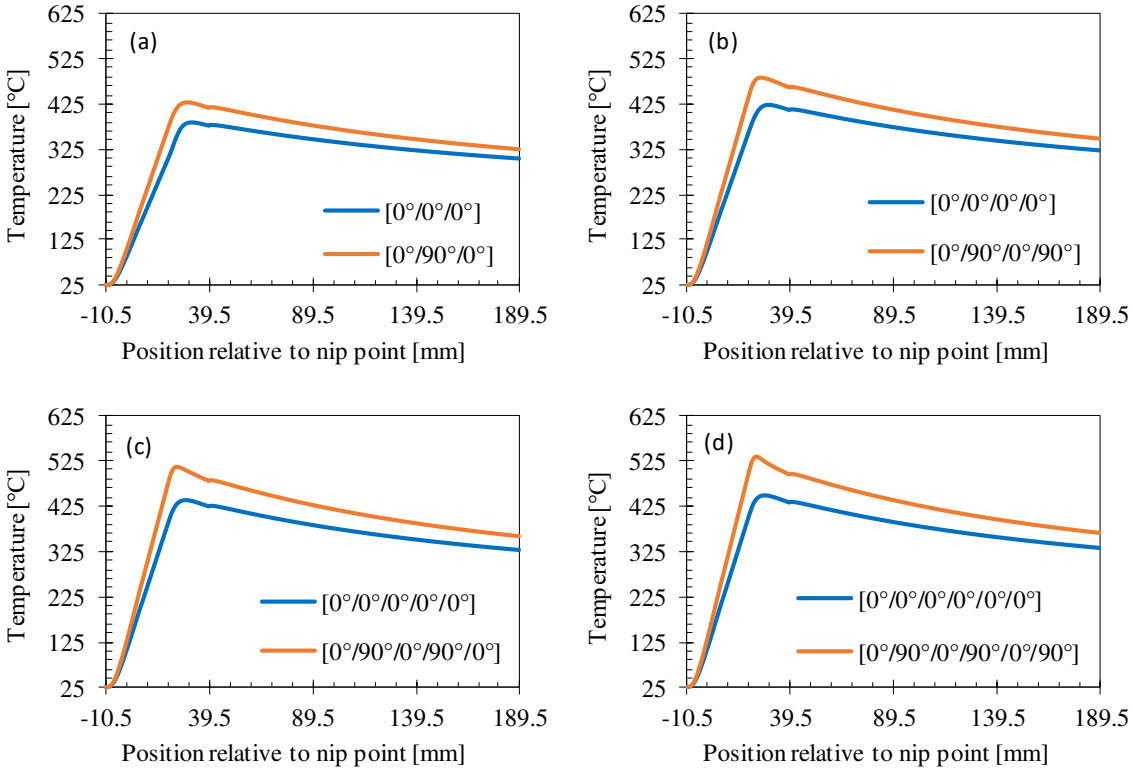

Figure 5. Temperature profile for top surface of newly placed tape for unidirectional and cross-ply stacking sequnces with increasing the number of layers

5. Conclusion

In this work, during the LAFP process, the effects of fiber orientation difference on the top surface temperature of a laminate when the number of layers increases was investigated. The results showed that by increasing the fiber orientation difference between two subsequent plies, the degree of intimate contact is reduced, highlighting the issue of thermal contact resistance (TCR). The existence of higher TCR at the [0°/90°] interface led to lower heat transfer in the thickness direction of the laminate than that of the [0°/0°] interface, and as a result, the top surface temperature of newly placed tape in the cross-ply laminate was higher. Moreover, with continuous lay-up on top of previous layers, when cooling time was insufficient, more heat

gradually accumulated on the top surface of the cross-ply laminate at each step, leading the temperature difference on the top surface of the laminate between unidirectional and cross-ply to increase. This phenomenon highlights the importance of cooling time for cross-ply configurations, especially when the laminate length is short or lay-up is accomplished with a higher placement rate.

6. References

1. Yassin K, Hojjati M. Processing of thermoplastic matrix composites through automated fiber placement and tape laying methods: A review. Journal of Thermoplastic Composite Materials. 2018;31(12):1676–725.

2. Levy A, Heider D, Tierney J, Gillespie JW. Inter-layer thermal contact resistance evolution with the degree of intimate contact in the processing of thermoplastic composite laminates.

3. Çelik O, Peeters D, Dransfeld C, Teuwen J. Intimate contact development during laser assisted fiber placement: Microstructure and effect of process parameters. Composites Part A: Applied Science and Manufacturing. 2020 Jul 1;134:105888.

4. Ageorges C, Ye L, Mai YW, Hou M. Characteristics of resistance welding of lap shear coupons. Part I: Heat transfer. Composites Part A: Applied Science and Manufacturing. 1998 Aug 1;29(8):899–909.

5. Lee W il, Springer GS. A Model of the Manufacturing Process of Thermoplastic Matrix Composites: http://dx.doi.org/101177/002199838702101103 [Internet]. 2016 Jul 27 [cited 2022 Apr 2];21(11):1017–55. Available from: https://journals.sagepub.com/doi/abs/10.1177/002199838702101103

6. Schaefer PM, Guglhoer T, Sause MGR, Drechsler K. Development of intimate contact during processing of carbon fiber reinforced Polyamide-6 tapes: http://dx.doi.org/101177/0731684416687041 [Internet]. 2017 Jan 9 [cited 2022 Apr 2];36(8):593–607. Available from: https://journals.sagepub.com/doi/full/10.1177/0731684416687041?casa_token=lrHQAH_071oAAAAA%3Asf-sk81oWkbOP0P08iyd8iC-7LeYJAi9N29idbKHRK3nCT2Ih87p82XVcdp1gU_OmyBPcAVZSsdCEA

7. Kok T. On the consolidation quality in laser assisted fiber placement: The role of the heating phase. 2018 Sep 6 [cited 2022 Apr 2]; Available from: https://research.utwente.nl/en/publications/on-the-consolidation-quality-in-laser-assisted-fiber-placement-th

8. di Francesco M, Veldenz L, Dell'Anno G, Potter K. Heater power control for multi-material, variable speed Automated Fibre Placement. Composites Part A: Applied Science and Manufacturing. 2017 Oct 1;101:408–21.

9. Stokes-Griffin CM, Compston P. Optical characterisation and modelling for oblique near-infrared laser heating of carbon fibre reinforced thermoplastic composites. Optics and Lasers in Engineering. 2015 Sep 1;72:1–11.

EFFICIENT AND COMPONENT-SPECIFIC FIBRE LAYUP PROCESSES

Dominik, Delisle[a], Christian Ueckert[b], Christian Krombholz[a]

a: German Aerospace Center, Institute of Composite Structures and Adaptive Systems, Department of Composite Process Technologies, Stade – dominik.delisle@dlr.de
b: German Aerospace Center, Institute of Composite Structures and Adaptive Systems, Department of Composite Design, Brunswick

Abstract: *Against the background of sustainability, efficient and resource-saving manufacturing processes must not be disregarded, especially when using carbon fibre-reinforced plastics. This also means that part design and manufacturing process must be highly harmonised. Focused on automated fibre-layup processes, the Institute of Composite Structures and Adaptive Systems at the German Aerospace Center (DLR) is therefore currently developing a closed-loop approach to part and process design. A simulation-based, process-analytical approach is used for a comparative evaluation of different machine and process configurations as well as a subsequent optimisation of the design based on the selected configuration. Complex process configurations such as the simultaneous use of several layup units can be considered. The procedure as well as the potential of the approach is demonstrated by considering a generic wing shell.*

Keywords: Automated fibre placement; Process assessment; Process design; Analytical process model

1. Introduction

When considering the production of large fibre composite components, such as wing shells, processes such as Automated Fibre Placement (AFP) or Automated Tape Laying (ATL) are primarily used to increase process efficiency. In these processes, unidirectional semi-finished fibre products are automatically placed on a shaping tool with a high degree of repeatability [1]. As shown in Table 1, there are a number of different machine configurations for implementing the AFP process, which differ not only in the machine kinematics but also primarily in the width of the semi-finished fibre product used and the number of material tracks.

Table 1: Extract of existing machine configurations

Config. #	Material width [mm]	Rows	Laying width [mm]	Representatives
1	6.35	16	101.6	Coriolis C1; Brötje Staxx Flex
2	6.35	24	152.4	Coriolis C2
3	12.7	16	203.2	Coriolis C3; Fives Viper
4	38.1	6	228.6	Coriolis C5 (robotic)
5	38.1	20	762	Coriolis C5 (gantry)

Given the challenge of achieving a certain production rate, the question of a system's productivity is central to process design. The productivity of a system is defined here as the achievable number of components per unit of time. This is influenced, among other things, by the maximum feedrate and the overall laying width, i.e. the achievable material throughput of the machine. A common method of increasing productivity is therefore to use the widest possible semi-finished product.

  doi:10.5075/epfl-298799_978-2-9701614-0-0

With regard to sustainable production, but also to the component costs incurred, the consideration of the productivity of a machine is not sufficient. Rather, the entire process must be considered and the process efficiency evaluated. In addition to the process time, a multitude of other boundary conditions and influencing factors must be considered. One example is the resulting material expenditure. Due to the lower contour accuracy, the use of a wider material to increase the material throughput often means a higher material input and possibly a higher mass of the final component. This is in contrast to the advantages of saving time. This also illustrates that the alignment of component design and machine configuration from Table 1 also has a considerable influence on process efficiency. Thus, there is no uniform solution for the most suitable machine and plant design for all components. The methodology presented here therefore pursues the approach of replacing the mostly linear process of component development, as shown in Figure 1, with a closed loop of component and process design.

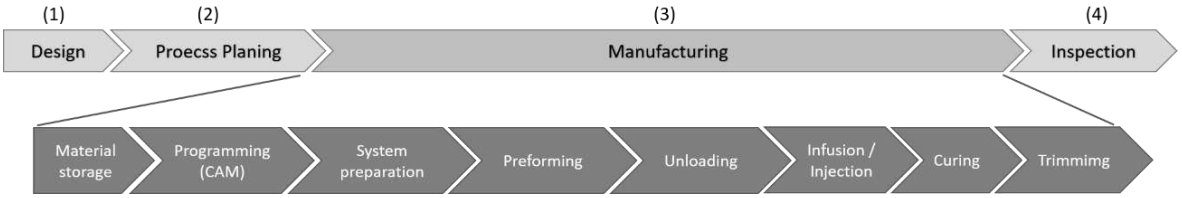

Figure 1. Linear steps of the entire manufacturing process

2. Methods and approach

Two fundamental requirements result from the objective of closed component and process design. On the one hand, a high level of detail must be ensured. This is necessary in order to be able to consider even small changes in the design or machine configuration in the analysis and evaluation. Secondly, in addition to the variation of machine configurations, it should also be possible to consider innovative plant concepts such as the approach of coordinated layup units of the GroFi® research platform of the DLR in Stade [2].

Due to the requirements, empirically based top-down approaches can be excluded. This is due to the low level of detail and the necessary empirical values, which are not available for the evaluation of innovative concepts. The methods of component-specific process design presented here are therefore based on a process-analytical bottom-up approach. Since these methods strongly depend on the quality and the level of detail of the input data [3], the process models presented here are based on the results of a reference simulation. The basic approach is shown in Figure 2.

Based on a structure-optimised design, a reference process is first analysed. In the first step, a single-head process is simulated using a reference configuration of the machine. In a second step, the entire process is considered. Considering a specified process scenario, the resource expenses of the material deposit process step determined via the simulation are supplemented by further expenses of the overall process. For the comparative evaluation of different process scenarios and system configurations, the necessary data for further machine configurations can be derived from the reference simulation. The comparative evaluation forms a solid basis for the decision-making process of the machine and plant configuration. Finally, an optimisation of the structure-optimised design takes place, considering the boundary conditions of the selected machine configuration.

  doi:10.5075/epfl-298799_978-2-9701614-0-0

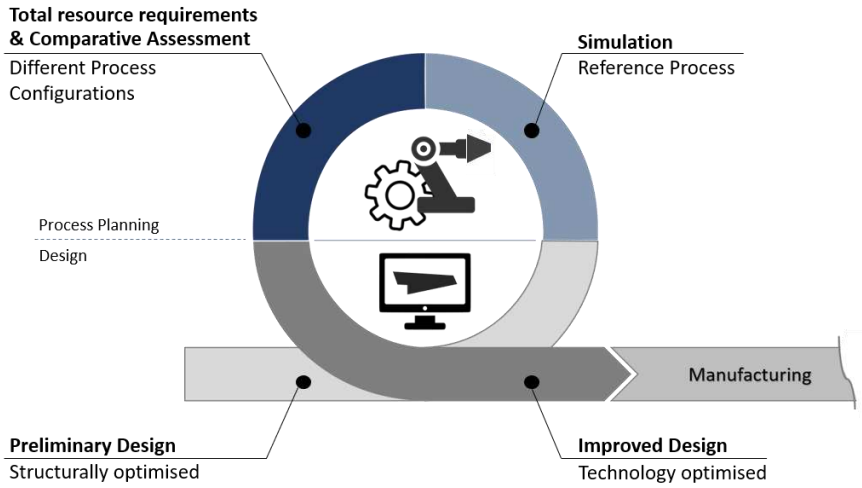

Figure 2. "Closed loop" approach of component and process design

Hereafter, the elaborated methods of component-specific process design are discussed in more detail. The focus is on the methods and procedures of process analysis and process evaluation. With regard to the methods of technology-specific design optimisation, only the basic approach is presented. For more detailed information, please refer to [4].

2.1 Process analysis and process evaluation

In the following, the part of the process planning shown in Figure 2 will be dealt with in more detail. By means of the elaborated methods, a solid basis for the decision-making process of the plant and machine design is to be created already in the early stage of the component design. The essential components of the input generation, the methodology of the process evaluation and the output are shown in Figure 3.

Input

The input is basically made up of two blocks of information. On the one hand, there is information describing the process scenarios to be considered. In addition to the specification of the industrial boundary conditions, the machine configurations to be used are also determined for the individual scenarios. Furthermore, it is defined how many machines are in operation at the same time during production or are available as redundancy. In addition, it is possible to define further data of plant and machine components, such as monetary expenses, energy consumption or necessary maintenance effort.

Since the underlying component design and thus the stacking is not changed, different material types are not considered. Only the width of the semi-finished product and the available amount of material per spool varies analogously to the defined machine configurations (Table 1). This has an influence on the time of material deposition as well as on the mass of the component and the number of necessary maintenance operations during the production process.

The second information block of the input contains component-specific information and comes from the data of an offline programming and simulation environment (OLP). Depending on a defined reference configuration of the machine, the time and material expenditures for the process step of the material deposit are determined here for a single-head process. The data has a high granularity, which enables the evaluation of individual courses and thus also the evaluation of different design features.

  doi:10.5075/epfl-298799_978-2-9701614-0-0

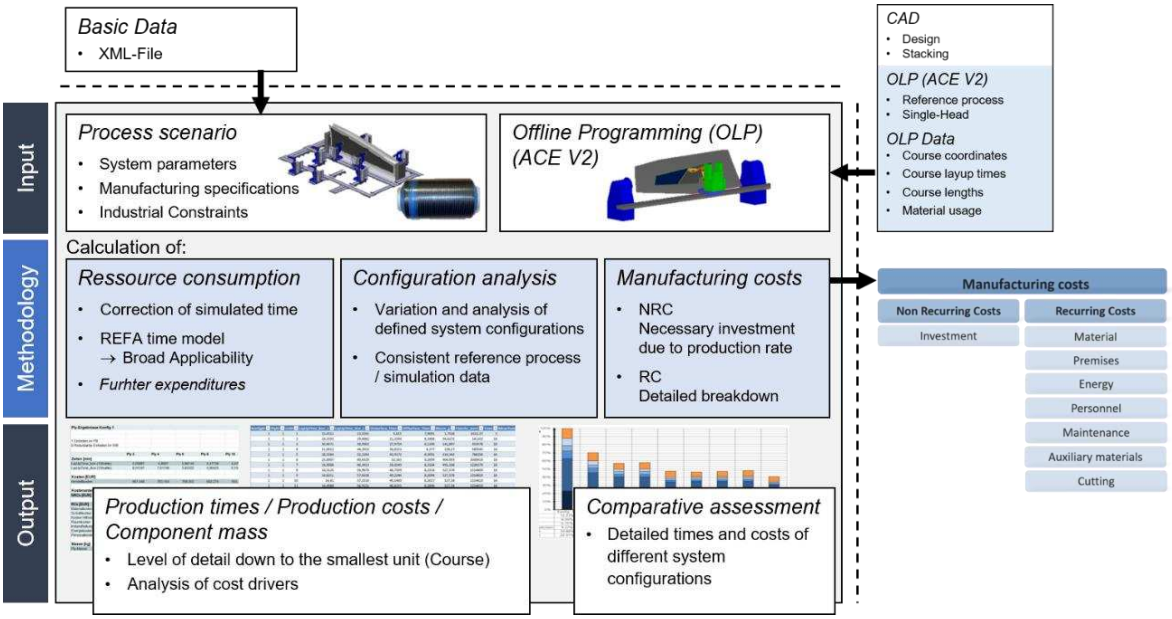

Figure 3. Basic approach of process analysis and process evaluation

By using the data of an OLP, a high quality of information is achieved which is necessary for the subsequent process analytical methods to determine the resource requirements of the overall process. However, a disadvantage resulting from this procedure is the limitation to kinematic systems that are mapped by the OLP. In the present case, an extended version of the ACES V2.0 software from the company Fives Cincinnati is used, which restricts the consideration to 6-axis kinematics with linear rails [5].

Methodology

For a given input, the central step is the analysis and evaluation of the entire process. Here, the resource expenses of the reference process determined with the OLP are corrected considering the boundary conditions defined in the input. In addition, the resource calculation is supplemented by further expenses, such as the expenses for any loading of the layup units during the layup process.

To define the system boundaries of the process evaluation, the sub-process steps of the manufacturing process, according to Figure 1, were further analysed. Hereby, the process evaluation was limited to the process steps which are influenced by a variation of the variables defined in the input. The result is shown in Figure 4.

Process steps that depend on the specifications of the process configurations were analysed in terms of their workflows and transferred to corresponding process models. The individual process models are linked in such a way that the full complexity of an AFP process with several layup units is represented. Depending on the available machines and personnel resources, it can thus be considered, for example, whether sub-processes can be parallelized or whether they run in a linear fashion and may require a temporary standstill of production.

Through the possibility of considering the effects of different process and machine configurations in the time calculation, the respective rate capability can also be considered in the comparative evaluation. By specifying a target rate, the necessary number of production plants and thus the necessary investment costs can be determined.

  doi:10.5075/epfl-298799_978-2-9701614-0-0 published under CC BY-NC 4.0 license

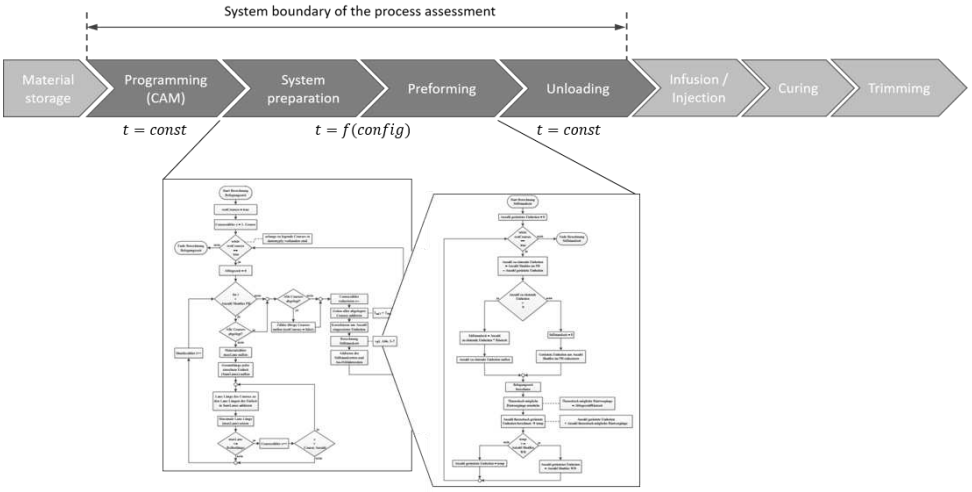

Figure 4. System boundaries and schematic representation of time determination (adapted from Figure 1)

The analysis of the overall process is carried out for all process scenarios and configurations specified in the input. For machine configurations that deviate from the reference, the resource expenses of the material placement sub-step are derived from the results of the simulation. Hereby it is assumed that the kinematic behaviour of the machine is not significantly influenced by a change in the geometry of the machine's end effector. The effects on the production time when using several layup units are currently considered by knock-down factors, which were determined in previous studies [6, 7]. In order to ensure a broad applicability of the elaborated methods, the time models according to the Association for Work Design, Business Organization and Business Development (REFA) are used to determine the process times [8].

Output

In the current status, the determined resource expenses of the specified process scenarios and configurations are converted into production costs per component according to Figure 3 and compared with the corresponding component masses. The output is provided in two granularities. On the one hand, an overview is given at the level of the process scenarios. On the other hand, there is a detailed output in which the proportional resource expenses of the individual courses are shown. This enables the determination of cost drivers depending on the design and the selected machine configuration.

2.2 Design optimisation

After selecting a machine configuration on the basis of the comparative evaluation, the initial design is optimised for the respective configuration. The aim is to achieve a further increase in the efficiency of the process without negatively affecting the structural performance of the component. The approach to design optimisation is to utilise the maximum laying width of the machine configuration as much as possible. This leads to an adaptation of the ply contours and ramp architecture in such a way that the extension of a ply is a multiple of the machine's laying width and, in addition, the ply edges are aligned parallel to the fibre orientation, as shown in Figure 5. On the one hand, this reduces the total number of courses. On the other hand, deceleration and acceleration processes within a course caused by necessary cutting processes are avoided.

For further information on technology-specific design optimisation, please refer to [4].

  doi:10.5075/epfl-298799_978-2-9701614-0-0

3. Case study

To illustrate the potential, the described methodology is applied to a generic wing shell model, which is shown in Figure 5. The wing shell model was developed as part of the "Efficient Wing Cover Manufacturing" (EWiMa) project [7]. The results of the design optimisation listed below were also generated within the framework of this project [4]. The key data of the wing shell can be found in Figure 5.

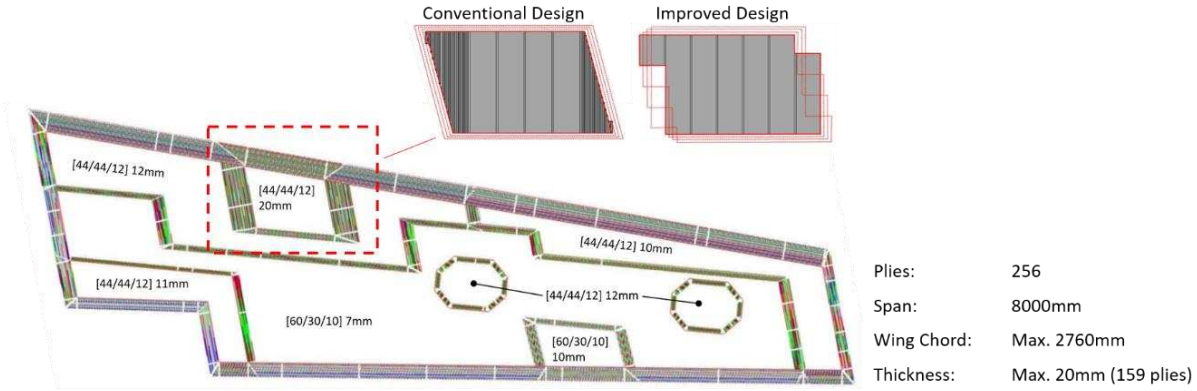

Figure 5. Generic wing cover design

In the following process analysis, the first step is limited to a comparison of different machine configurations. A uniform process scenario is taken as a basis for all configurations. It is also assumed that the rate capability of all configurations is sufficiently high, which means that differences in production time do not affect the investment costs. The comparative evaluation of the different configurations is therefore limited to the resource costs per component that arise directly in the process, which are subsequently represented by recurring costs (RCs) and the component mass.

The comparative evaluation of the different machine configurations is shown in Figure 6. The configuration designations refer to the information in Table 1. It can be seen directly that in the present design the mass of the component correlates with the width of the material used. Regarding the recurring costs the correlation is less straightforward. Although the material costs constitute an important share of the manufacturing costs, which means that a lower mass of the component initially also has a positive effect on the costs. However, this is countered by the higher time required for a smaller laying width of the machine configuration.

As can be seen in the left part of Figure 6, machine configuration 4 was chosen as the reference from Table 1. This has both the highest material width (38.1mm) and the highest laying width (228.6mm), excluding gantry systems. In accordance with the OLP, the consideration is limited to robotic machines. It can be seen that using only 6.35mm wide material in the present case, 5% of the material expenditure can be saved. When using machine configuration 2, the cost saving caused by the mass saving also outweighs the higher time expenditure, so that an additional 2% of the recurring costs can be saved compared to the reference. The further considerations are therefore made with machine configuration 2.

For the sake of completeness, configuration 2 is compared with a gantry system. Configuration 5 from Table 1 is used here, as this also has the highest material width (38.1mm) but also the highest laying width (762mm) and thus the highest material throughput. This comparison is not

  doi:10.5075/epfl-298799_978-2-9701614-0-0

permissible without further assumptions, as the speeds from the OLP are still used. Therefore, as mentioned before, the additional assumption must be made that the maximum layup speed is limited by the process and not by the kinematics.

A look at the right part of Figure 6 shows that in this case the cost of configuration 2 compared to configuration 5 is 6% higher. Compared to gantry systems, however, robotic systems offer the advantage of dynamic workspace distribution among several units. If one therefore considers the use of 2 simultaneously acting units, the additional cost is reduced to only 2%.

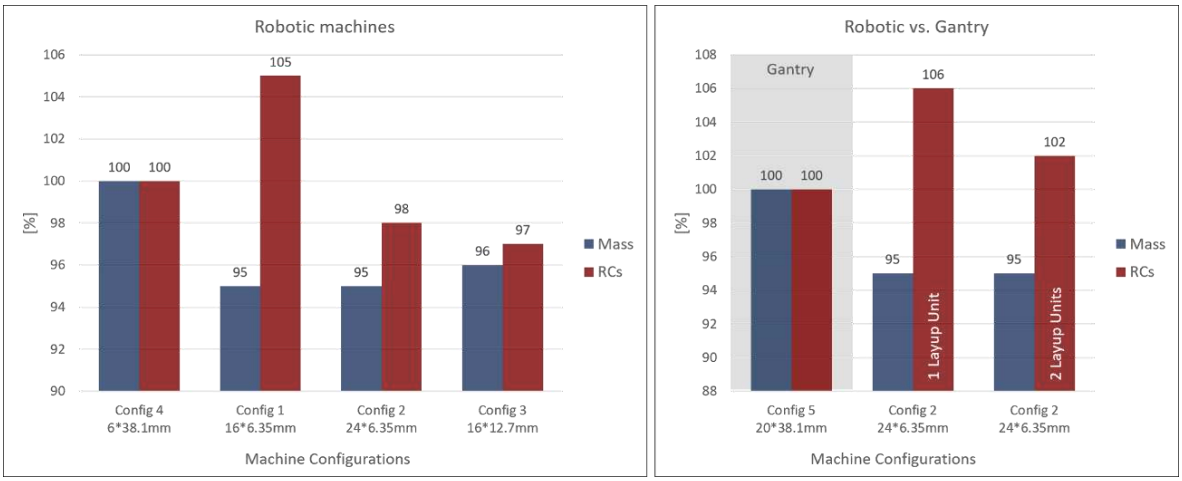

Figure 6. Comparative assessment of different machine configurations

There is further potential for increasing process efficiency in the final step of closed component and process design (Figure 2). Here, the initial design is optimised for the selected machine configuration. Using the patch area shown in Figure 5, a reduction in lay-up time of 3.4% was achieved when using 6.35mm wide material [4]. The extent to which the advantages of the design optimisation achieved in the patch area can be transferred to the complete wing shell must be shown in further investigations. Nevertheless, an increase in efficiency can also be expected for the entire wing shell.

Considering the left side of Figure 6, it can be seen that the use of the widest possible material for the present design does not result in any advantages with regard to the resulting component mass and the recurring manufacturing costs. If the multi-head potential of robotic systems is utilised, a mass saving of 5% can even be achieved in comparison to gantry systems at comparable manufacturing costs.

The rate capability of the different configurations was disregarded in the consideration carried out here. Thus, it must be mentioned in addition that the time saving of the gantry system compared to the robotic system with 2 production units is approx. 40% in the present case.

4. Conclusion and outlook

For the decision-making process of technology and process design in the early stage of component design, a method was presented which represents a closed loop between component and process design. The potential of this approach was demonstrated by considering a generic wing shell. It became apparent that the sole consideration of the productivity of a machine configuration is not sufficient in the decision-making process. Rather, the question

  doi:10.5075/epfl-298799_978-2-9701614-0-0

always arises of optimisation under consideration of several target parameters, in which a suitable solution can be found under definition of a concrete limit ratio of the selected target variables. The determination of the target parameters as well as the limit ratio must be made individually from design case to design case. The detailed knowledge of the resource requirements necessary for this can be ensured by means of the methods presented here.

Material-side influences are not yet considered in the process analysis. For example, the selection of a material width can have an effect on the maximum possible layup speed and thus on the process efficiency. Appropriate approaches are currently being considered and will be linked to the analysis tool in the future [9]. In addition, the consideration of several simultaneously acting robots is still carried out via non-part-specific factors. For component-specific statements, a coupling of the analysis with corresponding optimisation algorithms is conceivable. The technology-specific design optimisation is currently the final step of the closed design cycle. Since it is to be expected that the component-specific optimisation potential also depends on the material width, an integration into the comparative assessment is conceivable when the automation of the methods is advanced.

Acknowledgements

This research is part of the project DHiiP-AIR and was financially supported by the Federal Ministry for Economic Affairs and Energy, Germany. This project has received funding from the Federal Ministry for Economic Affairs and Energy, Germany under the funding code No. 20W1911F.

5. References

[1] Brasington A, Sacco C, Halbritter J, Wehbe R, Harik R. Automated fiber placement: A review of history, current technologies, and future paths forward. Composites Part C: Open Access. 2021 Oct;6(100182).

[2] Krombholz C, Delisle D, Perner M. Advanced Automated Fibre Placement. In: 11th International Conference on Manufacturing Research (ICMR2013). Cranfield University Press; 2013. p. 411-6.

[3] Schlimbach J. Oekonomische Prozessanalyse und Modellintegration zur Kostenberechnung von Faser-Kunststoff-Verbunden [phdthesis]. Institut fuer Verbundwerkstoffe GmbH - Kaiserslautern; 2006.

[4] Ueckert C, Delisle D, Bach T, Huehne C, Stueve J. Design Optimization of a CFRP Wing Cover for the AFP Process. In: 6th Aircraft Structural Design Conference; 2018. Efficient Wingcover Manufacturing (EWiMa), LuFo V-1, Förderkennzeichen 20W1309B.

[5] Krombholz C, Boelke J, Kruse F, Beykirch B, Bock M, Delisle D, et al. Abschlussbericht: Faserverbundgerechte Großbauteile und Online-Qualitätssicherung im Autoklaven (GRONQA). Institut für Faserverbundleichtbau und Adaptronik; 2014.

[6] Krombholz C, Delisle D. Zeiteffiziente und koordinierte Faserablage. Institut für Faserverbundleichtbau und Adaptronik; 2013. Available from: https://www.dlr.de/fa/-Portaldata/17/Resources/dokumente/publikationen/Innovationsbericht_2013.pdf.

[7] Huehne C, Ueckert C, Bach T, Nickel J, Delisle D, Ucan H. EWiMa - Efficient wingcover manufacturing. Institut für Faserverbundleichtbau und Adaptronik; 2018.

[8] Schlick C, Bruder R, Luczak H. Arbeitswissenschaft. Berlin, Heidelberg: Springer; 2010.

[9] Saar D. Entwicklung eines Modellansatzes zur Beschreibung des Tack-Verhaltens im Dry Fiber Placement [mathesis]. Technische Universitaet Kaiserslautern; 2021.

  doi:10.5075/epfl-298799_978-2-9701614-0-0

THE EFFECT OF PICK-UP POINT LOCATION ON FIBRE ANGLE DEVIATIONS IN NON-CRIMP FABRICS

Chantal, de Zeeuw [a,c], Daniël, Peeters[b,c], Otto, Bergsma[a], Rinze, Benedictus[a,c]

a: Structural Integrity and Composites Group, Faculty of Aerospace Engineering, Delft University of Technology, Delft, Netherlands – Email address corresponding author: C.M.deZeeuw@tudelft.nl
b: Aerospace Structures and Computational Mechanics, Faculty of Aerospace Engineering, Delft University of Technology, Delft, Netherlands
c: SAM|XL, Delft University of Technology Campus, Delft, Netherlands

Abstract: *The automated handling of non-crimp fabrics using pick-and-place processes will subject the fabrics to forces due to e.g. gravity and movement. These forces can result in undesired fiber angle deviations. The current work looks at predicting and preventing in-plane shear induced fiber angle deviations by studying the positioning of pick-up points. Experimental work shows that the layers of non-crimp fabrics should be expected to deform as individual layers unless they are fixed using an external mechanism. This is to be taken into account when choosing the gripping mechanism for the pick-up points to avoid unexpected behavior. The experimental work is also used for the preliminary validation of a numerical model based on deflections. Results from the current work are a basis for further research on the influence of pick-up point location on the fibre angle deviations in non-crimp fabrics.*

Keywords: Pick-and-place; automation; fabrics/textiles; non-crimp fabrics

1. Introduction

For pick-and-place processes to become widely implemented in industry a consistent product quality needs to be achieved. One important quality criterion is the fiber angle deviations in the reinforcement. Handling a reinforcement will subject it to forces due to e.g. gravity and movement. These forces can result in in-plane shear and subsequently in fiber angle deviations.

In the state of the art the positioning of individual pick-up points is typically either not discussed or is based on the mold where the fabric is to be draped on – not on the effect of the handling on the fabric. In the work where the positioning of pick-up points is studied the positioning is based on the deflection of the fabric or the minimization of strain energy, e.g. [1-4]. These parameters do however not give a clear indication of the influence of pick-up point location on the quality of the reinforcement.

This work is a step towards predicting and preventing in-plane shear induced fiber angle deviations by studying the positioning of pick-up points. Finite Element Simulations validated through experimental work will be used to study the influence of pick-up point location on the in-plane shear strain for a bi-axial Non Crimp Fabric [NCF]. In de Zeeuw et al. [5] tolerances have been set for the fiber angle deviations, additionally the relationship between in-plane shear strain and fiber angle deviations has been demonstrated for the NCF used in the current and

  doi:10.5075/epfl-298799_978-2-9701614-0-0

future work. The results from the current work will be used in future work to validate the results from the simulations.

In de Zeeuw et al. [6] pick-up point strategies for the handling of single and multiple layers of reinforcement are discussed. The current work studies whether an NCF can be considered as a single layer or should be treated as multiple layers when it comes to the selection of gripping mechanisms for pick-up points.

This paper presents the initial steps taken to study the effect of pick-up point location on plane shear induced fiber angle deviations in non-crimp fabrics. First, Section 2 presents the materials that are used. This is followed by the experimental and numerical methods in Section 3. The results are presented in Section 4 and discussed in Section 5. Finally, the conclusions are presented in Section 6.

2. Materials

The current work uses an E-glass based Biaxial $\pm 45^o$ NCF with a chain stitch pattern produced by R&G Faserverbundwerkstoffe GmbH. The choice for a chain-stitch type NCF is based on a chain stitch giving a high form stability, making the fabric appropriate for automated handling [3]. The NCF has stabilizing tows in the 0 and 90 direction. Table 1 presents the details for the NCF selected for the present work.

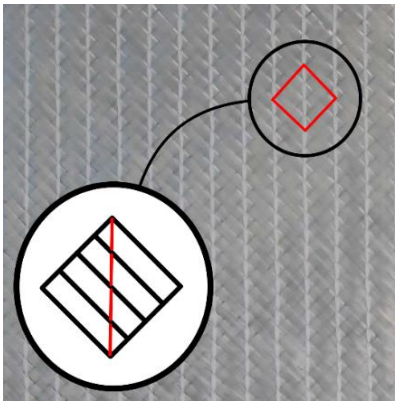

Figure 1. Stitch pattern of NCF

Table 1: Specifications of selected fabric as provided by manufacturer

Fabric type:	Biaxial $\pm 45^o$ NCF
Weight:	430 g/m^2
Fibres:	100% E-glass (300 tex)
Stitch:	Chain stitch
Finishing:	Silane treated

Table 2 presents the homogenized elastic properties that have been determined in de Zeeuw et al. [5] for the bi-axial NCF used in this work.

  doi:10.5075/epfl-298799_978-2-9701614-0-0

Table 2: Homogenized elastic properties as determined in de Zeeuw et al. [5]

E_{11} [MPa]	E_{22} [MPa]	E_{33} [MPa]	μ_{12} [-]	μ_{13} [-]	μ_{23} [-]	G_{12} [MPa]	G_{13} [MPa]	G_{23} [MPa]
196	196	0.16	0.5	0.5	0.5	2.39	0.24	0.24

3. Methods

During the experiments $\pm 45^o$ specimens of 300 x 300 mm and 550 x 550 mm are subjected to gravity while being suspended from a fixed pick-up point in each corner that's attached to a frame. Figure 2 shows one of these tests.

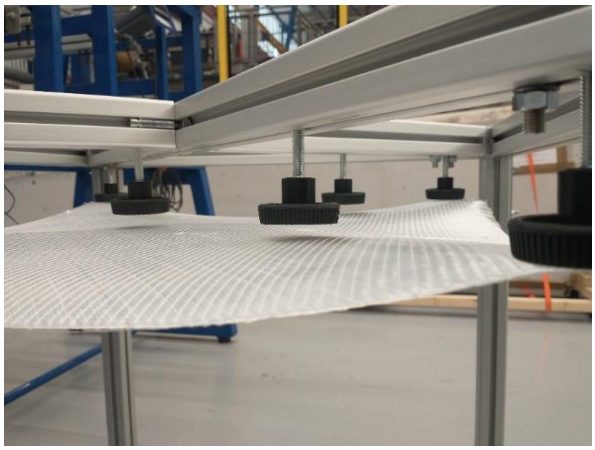

Figure 2. Frame with a 550 x 550 mm reinforcement suspended from the pick-up points

The in-plane positioning of the pick-up points is accurate op to 0.5 mm. The pick-up points with a diameter of 46 mm are attached to the reinforcements using double sided tape. From the moment the NCF is delivered on a roll to when the reinforcements are attached to the frame care is taken that they are always fully supported to avoid any preliminary in-plane shear or other deformations. Once the specimens are suspended from the frame the deflection is obtained through 3D scanning using a FARO 3D scanner.

Two different configurations are used for the specimens. This is done to determine whether an NCF can be treated as a single layer reinforcement or should be treated as multiple layers when selecting gripping strategies. In the first series the specimens are tested as is. For the second series a round piece of foil is adhered to the bottom side of the specimens at the location of the pick-up points using an silane modified polymer based adhesive. Care is taken that the adhesive fully penetrates the fabric to ensure the two layers of the NCF are fixed together.

Specimen dimensions are chosen with a pick-up point diameter of 50 mm in mind. For the 300 x 300 mm specimens this would result in a distance between the centers of two pick-up points of 250 mm. For the 550 x 550 mm specimens this distance would be twice as large, 500 mm. The 50 mm knobs that were ordered for the current work did however turn out to be 46 mm.

The numerical models are created using Abaqus/CAE 2021. The reinforcement is modeled as a shell using S4R elements with the material properties as defined in Table 2. A gravity load of 9.81 m/s^2 is applied. Figure 3 shows the partitions used for the current work. The lines across the diagonal are used to obtain the simulated deflection. This is later compared to the experimental

  doi:10.5075/epfl-298799_978-2-9701614-0-0

work for an initial validation step based on deformation. The partitions for the pick-up points are used to apply the translational and rotational displacement boundary conditions observed for the pick-up points during the experiments. To facilitate modeling of the rotation of the pick-up point the material for these areas is modeled as a very rigid material instead of the properties presented in Table 2.

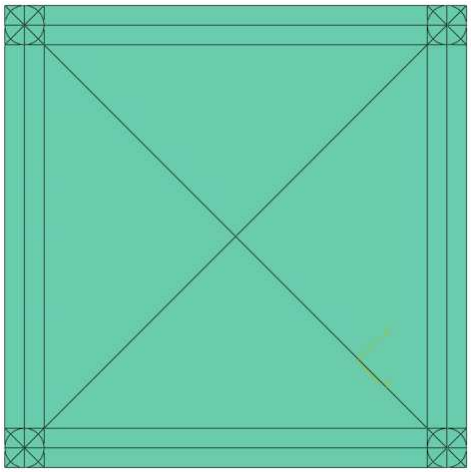

Figure 3. Partitions for the 550 x 550 mm numerical model

4. Results

Figure 4 shows a color map of the obtained point cloud for one of the 550 x 550 mm specimens from the first series. This first series did not include the adhesive gluing the layers together at the corners. The deflection pattern is not the one typically observed for $\pm 45^o$. In this figure the tows of the top layer lay in the direction indicated with a solid line. The tows of the bottom layer lay in the direction indicated with a dashed line.

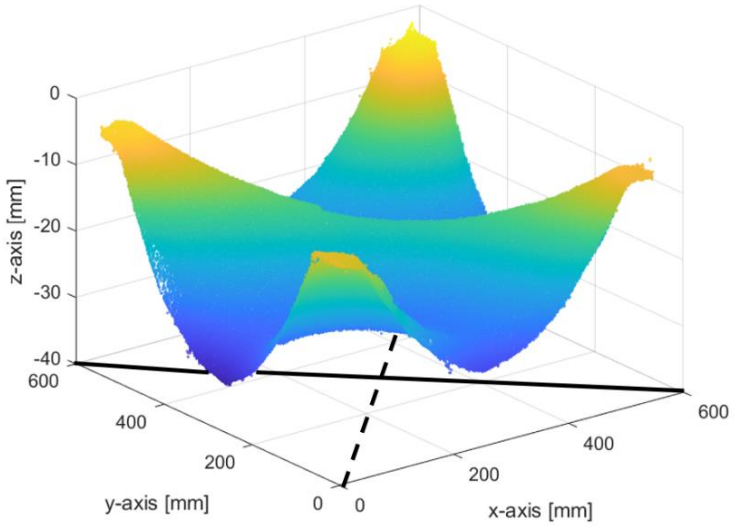

Figure 4. Point cloud with color map for one of the specimens from series 1.

Figure 5 shows the deformation result for one of the 550 x 550 mm specimens from the second series. The second series did include the adhesive gluing the layers together at the corners. For these specimens the deflection pattern is as expected for a $\pm 45^o$ fabric. These specimens show a smaller deflection than the specimens without adhesive applied at the corners.

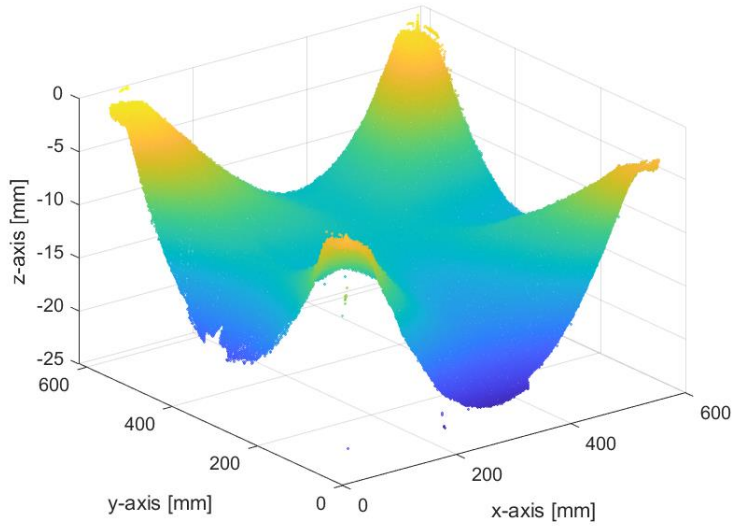

Figure 5. Point cloud with color map for one of the specimens for series 2.

The results show that the method chosen to grip the reinforcement is important for the behavior during handling. For the first series as shown in Figure 4 the double sided tape results in a firm connection between the pick-up point and the upper layer of the reinforcement. Within the NCF the two layers are held together by the stitches. The bottom layer is free to slide, the stitches do not prevent movement along the tows. With the tows of the bottom layer not being fixed they are unable to resist the gravity load and slide, resulting in the pattern as seen in Figure 4.

An initial validation step is done using the deformation results from the series 2 experiments. This is done by comparing the deflections along the diagonal of the numerical and experimental results. Figure 6 and 7 show this comparison for respectively the 300 x 300 mm specimens and the 550 x 500 mm specimens. The experimental results showed that there were small off-sets in the y-direction for the different pick-up points. These off-sets have been included in the numerical models.

  doi:10.5075/epfl-298799_978-2-9701614-0-0

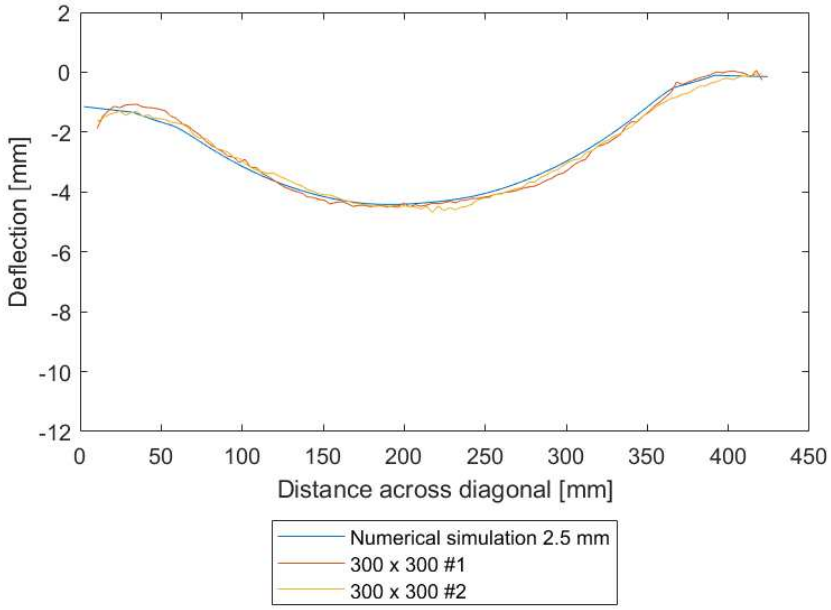

Figure 6. Comparison between numerical and experimental results for dimensions of 300x300

The results show that the numerical model is better able to predict the behavior of the 300 x 300 mm specimens than for the 550 x 550 mm specimens. For the 300 x 300 mm specimens the numerical results lay within 8% from the mean experimental results. For the 550 x 550 mm specimens this is 18.5%. The numerical model is shown to overestimate the deflection.

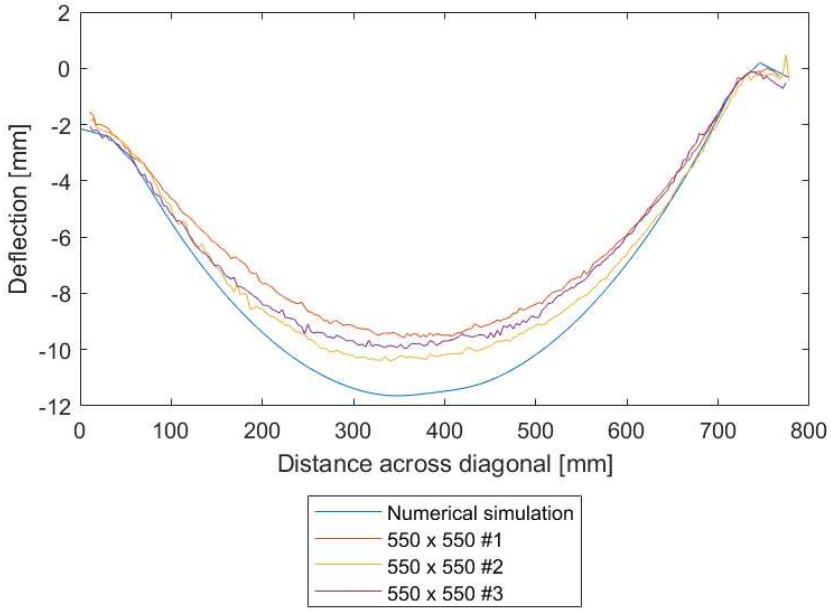

Figure 7. Comparison between numerical and experimental results for dimensions of 550x550

The actual values of interest for the current work are not the displacements but the in-plane shear strains. These in-plane shear strains are directly related to the fiber angle deviations.

Figure 8 shows the simulated in-plane shear strains for a 550 x 550 mm specimen. For the in-plane shear strains the regions closer to the pick-up points are of interest while for deflections the maximum values will be roughly in the center of the reinforcement.

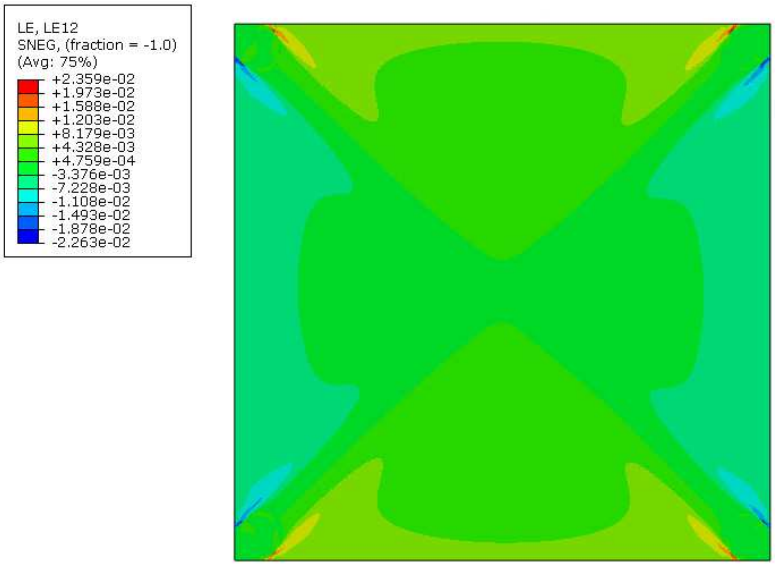

Figure 8. Simulated in-plane shear strains for 550 x 550 mm non-crimp fabric reinforcement

5. Discussion

The current work shows that when handling a dry non-crimp fabric it is important that both layers are supported and that the stitches should not solely be relied on to ensure the bottom layer stays in place. When handling multiple layers of reinforcement needle grippers are the only gripping technology discussed in Zeeuw et al. [6] that can reliably pick up all layers. The bi-axial NCF of the current work consists of only two layers, still gripping technologies will need to be evaluated before they are implemented to ensure all layers are gripped.

The FEM model assumes that the two layers of the NCF cannot act independently. It can therefore not predict the behavior observed for the first series of experiments. An initial validation based on the displacement measured has been performed. The results show that the model is able to give a reasonable prediction for the deflections along the diagonal. The simulated result is more accurate for the 300 x 300 mm specimens than for the 550 x 550 mm specimens. For practical reasons it is more desirable for the simulations to overestimate the deflections than to underestimate them. When designing the pick-and-place process an overestimate in the deflections will ensure there is always enough clearance between reinforcements and other surfaces.

It is suggested that the differences between experimental and numerical results are a side effect of the way the material is modeled. The numerical model does not consider the individual tows and stitches but uses homogenized elastic properties. A biaxial NCF has a variety of mesoscopic fabric deformation mechanisms [8]. A representative volume element [RVE] is used to obtain homogenized elastic properties based on displacements in the 1, 2 and 3 directions. The deformation mechanisms that occur when a reinforcement is picked up at four corners will however be more complex than those that occur in the RVE.

  doi:10.5075/epfl-298799_978-2-9701614-0-0

The area of interest of the work is not the deflection of the reinforcements during handling but the in-plane shear strains and the fiber angle deviations. The deflections give an indication of the ability of the model to predict the behavior of the reinforcement. However, the deflections are not necessarily directly linked to the in-plane shear strains. A small difference in the in-plane shear strains near the pick-up points could for example result in a significantly larger deflection in the middle of the fabric. The model will need to be validated based on in-plane shear strains in future.

6. Conclusions

The current work presents the initial steps taken to study the influence of pick-up point positioning on in-plane shear induced fiber angle deviations. The experimental work found that for dry NCFs it cannot be assumed that the whole NCF will behave as a homogeneous material during handling. The results show that if a gripping technology is used that just grips the top layer, the bottom layer will be free to slide. To ensure predictable handling, gripping technologies will need to be chosen such that all layers are fixed.

The experimental results are used to take a preliminary look at the ability of the numerical model to simulate the behavior of bi-axial NCFs under gravity loading. The simulation is shown to give reasonable predictions for the deflections along the diagonal. The validation strategy used in the current work is however not the most appropriate one for validating the model. Further validation will be carried out based on in-plane shear strains.

7. References

1. Lankalapalli S, Eischen JW. Optimal pick-up locations for transport and handling of limp materials: Part I: One-dimensional strips. Textile Research Journal 2003; 787-796
2. Ragunathan S, Karunamoorthy L. Genetic algorithm-based optimal locations for handling fabric materials in garment automation. International Journal of Robotics and Automation 2006; 288:294
3. Lankalapalli S, Eischen JW. Optimal pick-up locations for transport and handling of limp materials: Part II: Two-dimensional parts. Textile Research Journal 2003; 867-874
4. Ballier FJ. Systematic gripper arrangement for a handling device in lightweight production processes. PhD Thesis 2019;
5. de Zeeuw CM, Peeters DMJ, Bergsma OK, Benedictus R. Setting bounds for in-plane shear induced fiber angle deviations in bi-axial non-crimp fabrics. Under review/Unpublished 2022; -:-
6. de Zeeuw CM, Peeters DMJ, Bergsma OK, Benedictus R. Strategies for swift automated pick-and-place operations of multiple large-sized layers of reinforcement-a critical review. Advanced Manufacturing: Polymer & Composites Science 2020; 57:71
7. Krieger H, Gries T, Stapleton SE. Design of tailored non-crimp fabrics based on stitching geometry. Applied Composite Materials 2018; 113:127
8. Creech G, Pickett AK. Meso-modeling of non-crimp fabric composites for coupled drape and failure analysis. Journal of material science 2006; 6725:2736

  doi:10.5075/epfl-298799_978-2-9701614-0-0

INFLUENCE OF TEXTILE DESIGN PLAN ON THE PERFORMANCE OF 3D WOVEN CARBON/EPOXY COMPOSITES

Monali Dahale[a], Anto Antony Samy[a], Calvin Ralph[a], Edward Archer[a], Roy Brelsford[a], Glenda Stewart[a], Simon Hodge[a], and Alistair McIlhagger[a]

a: Engineering Research Institute, Ulster University, Shore Road, Newtownabbey, Co. Antrim, BT37 0QB, United Kingdom

Email: m.dahale@ulster.ac.uk

Abstract: *3D fibre reinforced composites have the potential to reduce delamination, improve through-thickness strength and damage tolerance, the full potential of these materials in the aerospace and automotive industry is yet to be explored. This can be partly attributed to the fact that the manufacturing process of 3D woven composites can be challenging due to the requirement of unfamiliar processes and a limited understanding of the influence of textile weaving parameters on the performance of final 3D woven composites. The structure of the 3D woven composites is predominantly controlled by the textile design plan during the 3D weaving process. A lack of in-depth understanding between the textile design plan and the physical/mechanical performance of 3D woven composites has inspired this investigation. This paper presents a detailed investigation of the influence of two textile design plans for the same architecture on the physical and mechanical properties such as tension, compression, and flexure in 3D layer-to-layer carbon/epoxy woven composites. The two textile design plans (design 1 and design 2) for 3D layer-to-layer architectures were achieved by changing the grouping of warp and binder yarns without modifying the loom set-up, which significantly reduced the manufacturing time and cost. The two designs in 3D woven layer-to-layer architecture were woven with a constant warp density of 12 warps/cm using T700-50C-12k carbon fibres. On the transition from design 1 to design 2 of 3D woven composite, the resin rich areas, tow misalignment and yarn crimp were significantly reduced. The tensile properties were improved by 55% and 37% along warp and weft directions, respectively. The compression properties were improved in the longitudinal direction with a slight deterioration in the transverse direction. This work has helped prove how slight fundamental changes in textile preforms can significantly change the performance of 3D woven composites without increasing the manufacturing cost and time.*

Keywords: 3D woven composite; textile design plan; mechanical properties; microstructural properties

1. Introduction

Traditionally metals have been used for wide applications in automotive and aerospace industries due to their superior toughness, ductility and uniform weight distribution properties (1). However, due to the design flexibility, high strength, reduced weight, low density and optimised levels of stiffness/strength as per the loading conditions (2), metals have been increasingly replaced by laminated composites. The problem with the UD or 2D laminated composites is their propensity to delaminate under the influence of out-of-plane loading. With the addition of through-thickness binders in 3D woven composites, delamination failure is initiated, allowing the composite to carry increasing loads well beyond first crack initiation (3). Moreover, 3D weaving is gaining popularity in the industry over 2D weaving due to its capability

  doi:10.5075/epfl-298799_978-2-9701614-0-0

to manufacture near-net-shape preforms reducing the manufacturing/machining cost (4). However, the ability to produce complex integrated structures and excellent through-thickness strength and toughness of 3D woven composites is tempered by lower in-plane performance compared to 2D woven or unidirectional composites (5). This may be further exacerbated by process induced defects or variability. In order to obtain optimum high-performance composite structures, it is essential to have a comprehensive knowledge of the effect of 3D fibre content, architecture and manufacturing defects on the properties of composites. Although 3D woven composites show promising potential for various applications, their practical utilisation in structural components on a mass scale is limited by high initial equipment cost and the lack of a thorough understanding of the effect of weaving parameters in the textiles on the mechanical and impact performance.

A substantial amount of work has been performed to characterise three fundamentally different architectures of 3D woven composites (layer-to-layer, angle interlock, and orthogonal) for their failure mechanisms and mechanical performance (6)(7)(4). In addition, there are limited studies on geometrical flaws like misalignment, voids, resin rich areas, and some topological features caused by changing the weave architecture and its influence on the mechanical properties and their subsequent failure mechanism (8)(9). However, the effect of weaving parameters in one constant architecture on the mechanical and impact performance along with their failure mechanisms has not yet been explored substantially in the literature.

This paper investigates the influence of textile design, an easily adjustable weave parameter, on the physical and mechanical performance of 3D woven layer-to-layer composites. In this study, the architecture was kept constant, and only the textile design was changed, which dictated the arrangement of warp and binder yarns in the unit cell. The textile design changes in 3D woven preforms can be achieved by a slight change in the manufacturing process (by changing the lift plan) instead of rethreading the entire loom, which takes up to over 100 hours. Also, rethreading the entire loom can cause severe damage to the warp yarns which knockdowns the mechanical properties of the subsequent composite materials (10). Textile design controls the grouping of warp/binder yarns in a unit cell, which dictates the spacing between yarns, indirectly influencing the composite material's tow misalignment, resin-rich areas and void content. Hence in this study, keeping the warp density constant of 12 warps/cm, two textile designs with two grouping plans were developed and compared against each other for their mechanical and physical properties. In-depth failure mechanism analysis in both the designs of layer-to-layer 3D woven composites under different loading was carried out using optical microscopy.

2. Material

2.1 Manufacturing of 3D woven preforms

Two different textile designs (design 1 and design 2) with a constant warp density of 12 ends/cm in a layer-to-layer architecture were designed using ScotWeave software (Figure 1). Design 1 and design 2 textile design plans were created by splitting the unit cell structure (12 warps/cm) into two and four groups respectively. In design 1, binder and stuffer/warp yarns were placed alternatively, whereas, in design 2, three binders were followed by three stuffer/warp yarns. To manufacture these two designs on the DATAWEAVE controlled jacquard loom, the creel was set up for 600 bobbins to weave 12 ends/cm for a 50 cm wide textile preform. The architecture consisted of three warp layers, four weft layers and three warp binder layers which connect weft layers immediately above and below each binder. In Figure 1, binder

  doi:10.5075/epfl-298799_978-2-9701614-0-0

yarns are shown in red, stuffer/warp yarns in blue and weft yarns are light green. T700S-50C-12k (800 Tex) (11) carbon fibre was used to manufacture all specimens in all three directions.

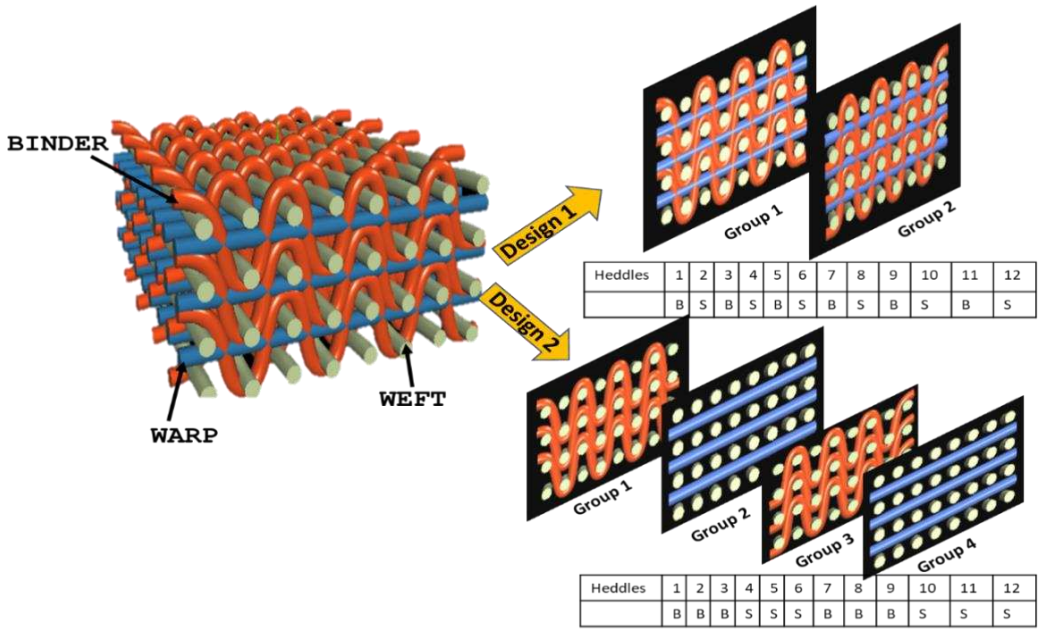

Figure 1: Grouping of two textile designs of layer-to-layer 3D woven preforms

According to the grouping of a unit cell, two textile design plans for design 1 and design 2 were developed on the ScotWeave CAD software to operate the Jacquard loom (1152 hooks) at Ulster University (Figure 2). Both the textile design plans were divided into 12 warp yarns (X-axis) and 8 weft yarns (Y-axis). By manipulating the lift of the heddles in a jacquard loom, grouping determined the placements of these yarns in the architecture. It can be understood from the textile design plan for design 1 (Figure 2a) that for the first weft insertion, heddle one was lifted, for the second weft insertion, the first, second, third and seventh heddles were lifted. This was continued until the 8th weft insertion, which completed a one-unit cell.

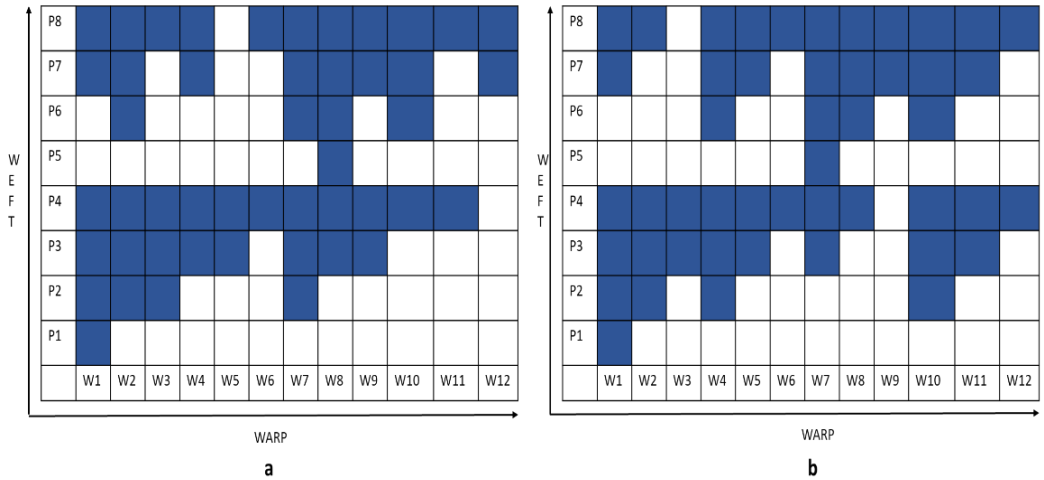

Figure 2: Textile lift plan (a) design 1 (b) design 2 of 3D woven layer-to-layer architectures

2.2 Manufacturing of 3D woven composites

The textile preforms woven in two textile designs (design 1 and design 2) were consolidated via Resin Transfer Moulding (RTM) using a Gurit Prime 37 epoxy resin system (12). Resin and hardener were mixed in 100:29 by weight ratio and stirred for two minutes in order to ensure uniform mixing. Before infusion, the mixture was degassed in a homogeniser for 30 minutes and then injected into a room temperature RTM tool designed to consolidate 400x400 mm preforms. The injection pressure was maintained at 1.5 bar throughout the infusion. After injection, the part was cured at 50℃ for 16 hours.

3. Experimental

The physical properties of the textile preforms, such as the weft density (number of transverse yarns per cm of the fabric), warp density (number of longitudinal yarns per cm of the fabric) and thickness were measured according to ASTM standards, respectively. In addition, crimp measurements were made in accordance with BS 2863:1984. Percentage crimp is the ratio of the difference between the yarn length and fabric length over fabric length. It is calculated using the following equation:

$$\% \text{ Crimp} = \frac{L_{yarn} - L_{fabric}}{L_{fabric}} \quad (1)$$

Five specimens each in warp and weft directions were tested under tension in accordance with ASTM 3039 using a Zwick Universal Testing System (UTS) with a 100kN load cell. A crosshead displacement of 2mm/min was used to perform these tests. An extensometer was used to record strains up to 0.6%, after which it was detached to prevent it from damaging due to shock waves. Five specimens in each direction (warp and weft) were tested for compression in accordance with a Boeing modified ASTM D695 using an electromechanical Instron 5500R UTS machine with a 100kN load cell and anti-buckling fixture. The original test was modified by changing the specimen shape and reducing the gauge length to 4.8mm in order to avoid buckling of the test specimens. Three-point bending tests were performed on five specimens in each direction in order to obtain the flexural strength and the modulus. This test was performed in accordance with ASTM D7264 standard on an electromechanical Instron 5500R UTS machine with a 100kN load cell. Five specimens with a span to thickness ratio of 32 were tested oriented in both the warp and weft directions at a crosshead displacement of 1mm/min. An Olympus sZ3 stereo microscope was used to study the surface of the area of interest of fracture specimens, which were polished using a Struers TegraPol-31 machine.

4. Results and Discussion

4.1 Physical properties

Physical properties of 3D woven preforms and composites for design 1 and design 2 iterations are listed in Table 1. On the transition from design 1 to design 2, the structure becomes more compact with small inter yarn spacing. As shown in Table 1, the crimp is reduced by 33% and 28% in the warp and weft yarns, respectively, on the transition from design 1 to design 2. Due to the less compact structure in design 1, the yarns are not stacked uniformly compared to design 2 (Figure 3). This resulted in a smaller unit cell size and fewer resin rich areas in design 2 compared to design 1. Although the warp density was maintained constant at 12 warps/cm due to the arrangement of yarns, there is significant yarn distortion evident in design 1 compared to design 2 (Figure 3). Yarn distortion or misalignment quantified in terms of peak crimp angle decreases by 61% in design 2 compared to design 1 (Table 1).

  doi:10.5075/epfl-298799_978-2-9701614-0-0

Table 1: Preform and composite properties of Design 1 and Design 2 3D woven composite

Fabric	Weft /cm	Warp/cm	t* (mm)	Yarn content (%)			% Tow crimp in uncompressed preform		Peak crimp angle (°)	$V_{f\,(\%)}$
				Warp	Weft	Binder	Warp	Weft		
Design 1	8	12	2.6	30	40	30	5.5	1.8	27.9	36.7
Design 2	10	12	3	27.2	45.5	27.2	3.7	1.3	10.8	42.8

t: thickness of uncompressed 3D woven preforms*

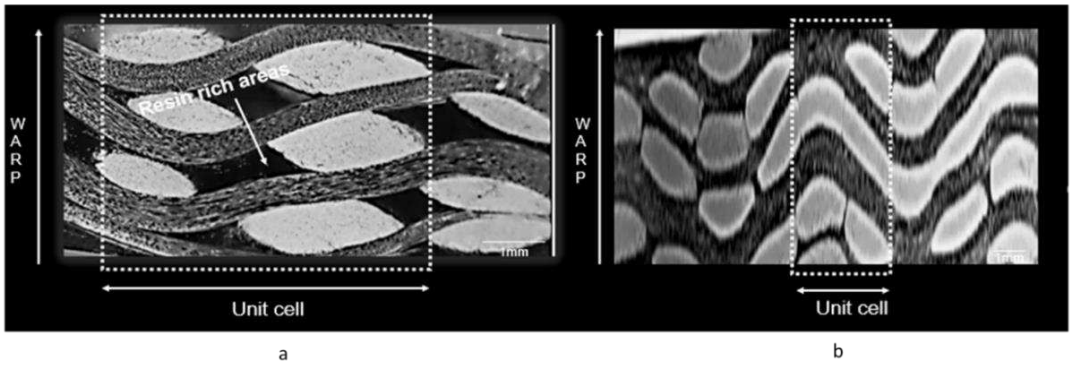

Figure 3: Micrographs (a) Design 1 (b) Design 2 3D woven layer-to-layer composite

4.1 Tensile properties

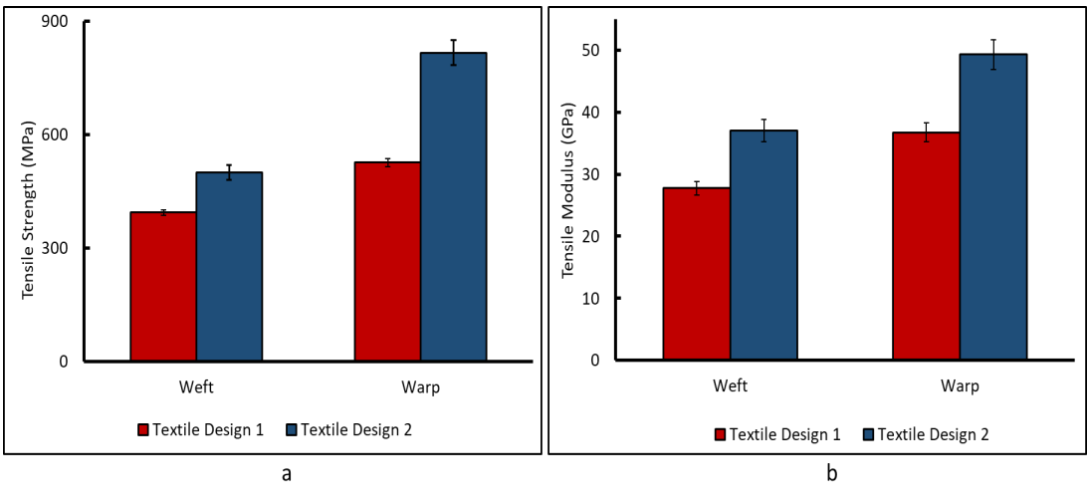

Figure 4: (a)Tensile Strength (b) Tensile Modulus of two designs of 3D woven layer-to-layer composites

Figure 4 represents the comparative bar graphs of tensile strength and modulus of design 1 and design 2 3D woven composites specimens in both warp and weft directions. In the warp direction, there is a 55% increase in the tensile strength and a 36% increase in the tensile modulus, which can be partially attributed to a decrease in crimp of 33% (Table 1) from design 1 to design 2 specimens. Binder tow straightening and matrix cracking around the binding

positions were observed visually on the surface of all the specimens. In design 2 specimens, 54% more transverse surface cracks along the entire specimen were observed than in design 1 specimens. This is thought to result from a greater number of stress concentration bands which corresponds to more frequent binding points at the specimen surface. These stress concentrations result from resin rich regions, which are associated with binding points as well as the tendency of the binders to straighten out during loading. This is accompanied by fibre-matrix debonding, which is likely to initiate at those points. Warp direction failure transitions from being predominantly fibre-matrix debonding dominated in design 1 compared to being dominated by fibre pull out and fibre fracture in design 2 specimens. Also, design 1 specimens have significantly more resin rich regions (Figure 3), whereas negligible resin rich areas are observed in design 2 specimens due to their more compact structure. The presence of numerous resin rich areas in design 1 specimens promotes clean fracture rather than fibre pull-out or fibre fracture.

In weft direction specimens, there is a 27% and 37% increase in the tensile strength and modulus, respectively. This is to be expected as the fibre content of the load carrying yarns was increased to maintain the dimensional stability, leading to a more compact architecture in the design 2 specimens, which results in less crimped weft tows (28% less) and a higher fibre volume fraction (17% more) (Table 1). Design 1 specimens displayed more numerous and larger resin rich regions, larger than in design 2 specimens. These fibre devoid areas promoted clean matrix fracture in the design 1 specimens with only little resistance from weft yarns and no visible interlaminar cracking.

4.3 Compression properties

On the transition from design 1 to design 2, the compressive strength increased by 20% and 9% in warp and weft directions, respectively (Figure 5). Due to the grouping pattern which dictated the arrangement of yarns, the unit cell size in design 2 decreased significantly compared to design 1 (Figure 3). This implies that it takes more than double the length of textile architecture to repeat itself in design 1 compared to design 2. This further implies that the binder interlacement points in design 1 specimens are spread apart in a longer unit cell with a higher yarn spacing. Whereas the binder interlacement points are more concentrated in design 2 specimens, which results in a higher energy failure mechanism under compression loading like through-thickness shear compared to delamination matrix cracks in design 1 specimens in the warp direction. Although the fibre content in the warp direction for design 1 and design 2 specimens remains constant at 12 warps/cm, there is still a significant increase in the compressive properties. The role of fibre strength is insignificant in deciding the compressive properties where the tow misalignment in the yarns is significant (13). Instead, under compression loading, the failure of composite is dictated by the tow misalignment angle and matrix shear strength (14). Peak crimp angles (Table 1), a quantifier for the tow misalignment, decrease from 27.9° to 10.8° on the transition from design 1 to design 2 specimens. The increased tow misalignment is an outcome of the fact that in design 1 architecture due to, improper yarn stacking resulted in increased tow misalignment in the in-plane and out-of-plane yarns. The improvements in the compressive properties in the warp direction on the transition from design 1 to design 2 are an outcome of several properties: 1. increase in the binder interlacement points, 2. decrease in unit cell size results in more resistance for crack arrest mechanism and 3. decrease in the geometrical flaws or irregularities.

  doi:10.5075/epfl-298799_978-2-9701614-0-0

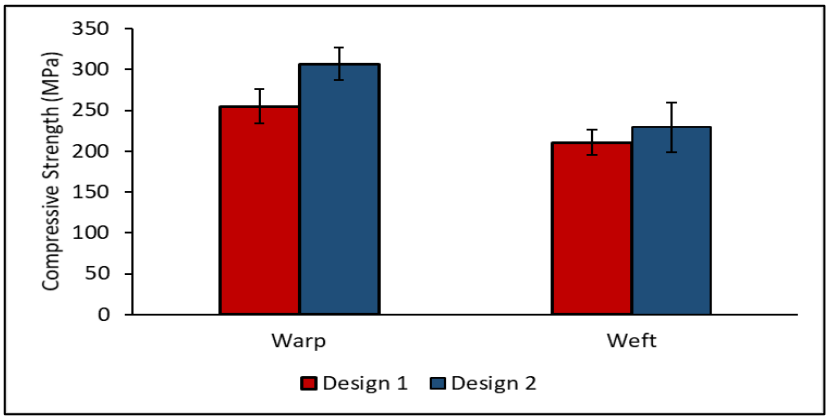

Figure 5: Compressive Strength of two designs of 3D woven layer-to-layer composites

4.4 Flexure properties

Table 2: Flexural properties of two designs of 3D woven layer-to-layer composites

			Warp		Weft	
			Value	% COV	Value	%COV
Flexure	Design 1	Strength (MPa)	310.7	6.4	360.5	2.4
		Modulus (GPa)	12.7	1.8	14.6	0.8
	Design 2	Strength (MPa)	434.4	4.6	470.8	3.1
		Modulus (GPa)	20.9	2.3	26.7	5.1

Table 2 lists the flexural properties of two designs of 3D woven composites in both warp and weft directions. Although the warp density remained constant at 12 warps/cm in design 1 and design 2 specimens, the flexural strength and modulus in the warp direction increased by 40% and 64% in design 2 specimens. This is an outcome of higher interlacement points per unit cell in design 2 specimens compared to design 1 specimen, which has a more spread out unit cell due to non uniform stacking of yarns. The increased binder interlacement points in design 2 tend to resist the cracks compared to design 1 specimens. This is supported by the micrographs of the failed flexure specimens of design 1 and design 2 specimens (Figure 6). It is evident from Figure 6 the cracks are not very well resisted (due to more resin rich areas), and extensive through-thickness cracks are evident in design 1 specimens. Cracks initiate at the resin rich areas at the surface and propagate through the thickness with matrix cracking, debonding, and fibre breakage observed. In design 1 specimens, significant through-thickness cracks were evident, indicating lower flexural properties than in design 1 specimens. Also, tow misalignment (Table 1), quantified in terms of peak crimp angle, is known to have a detrimental effect on the flexural properties (15) in design 1 compared to design 2.

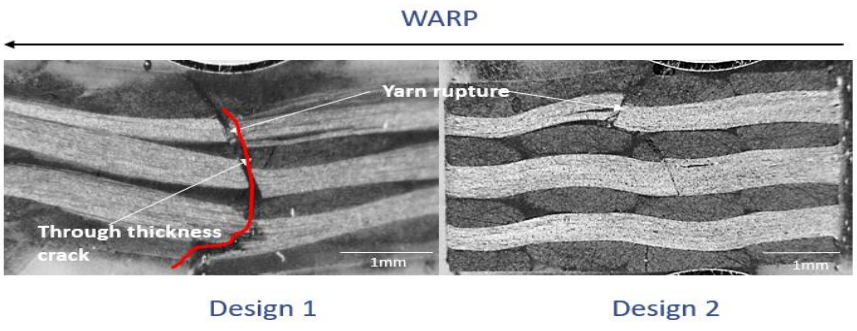

Figure 6: Micrographs of failed flexure specimens of design 1 and design 2 3D woven composite

5. Conclusion

The main objective of this paper was to study the influence of easily adjustable textile design plan on the physical and mechanical properties (tension, compression and flexure) of 3D woven warp interlock layer-to-layer carbon/epoxy composites. The mechanical properties were improved in both the warp and weft directions with a increase in number of groups in the textile design plan. The tensile strength was improved by 27% in the weft and 55% in the warp direction, compressive strength by 9% in the weft and 20% in the warp direction and flexural strength by 30% in the weft and 40% in the warp direction. It was found that althought the fibre content was kept constant along the longitudinal direction, by changing the textile design plan, increases its mechanical properties in both warp and weft directions. This is thought to be result of a combination of several factors- V_f, tow misalignment, interyarn spacing, tow arrangement, crimp, binding points/ unit cell and size/distribution of resin rich areas. The improvements in mechanical performance from design 1 to design 2 were achieved with a relatively small change in manufacturing parameter (lift plan change) rather than a rethreading the entire loom, which is an expensive and time cosuming process.

6. Acknowledgements

This work is supported by UKRI Strength in Places Fund (SIPF) Artemis Project. The authors acknowledge the support from Artemis Technologies Ltd and The Engineering Research Centre (ECRE) of Ulster University.

7. References

1. Sierakowski RL. Strain rate behavior of metals and composites. Convegno IGF XIII Cassino 1997 [Internet]. 1997;1–28. Available from: http://www.gruppofrattura.it/ocs/index.php/cigf/igf13/paper/view/206
2. Huang T, Wang Y, Wang G. Review of the Mechanical Properties of a 3D Woven Composite and Its Applications. Polym Plast Technol Eng [Internet]. 2017;2559(July):1–17. Available from: https://www.tandfonline.com/doi/full/10.1080/03602559.2017.1344857
3. Chen F, Hodgkinson JM. Impact behaviour of composites with different fibre architecture. Proc Inst Mech Eng Part G J Aerosp Eng. 2009;223(7):1009–17.
4. Saleh MN, Soutis C. Recent advancements in mechanical characterisation of 3D woven composites. Mech Adv Mater Mod Process [Internet]. 2017;3. Available from: http://mammp-journal.springeropen.com/articles/10.1186/s40759-017-0027-z
5. Ansar M, Xinwei W, Chouwei Z. Modeling strategies of 3D woven composites: A review. Compos Struct [Internet]. 2011;93(8):1947–63. Available from: http://dx.doi.org/10.1016/j.compstruct.2011.03.010
6. Umer R, Alhussein H, Zhou J, Cantwell W. The mechanical properties of 3D woven composites [Internet]. Journal of Composite Materials. 2016. 1–36 p. Available from: http://journals.sagepub.com/doi/pdf/10.1177/0021998316681187%5Cnhttp://jcm.sagepub.com/cgi/doi/10.1177/0021998316681187
7. Potluri P, Hogg P, Arshad M, Jetavat D, Jamshidi P. Influence of Fibre Architecture on Impact Damage Tolerance in 3D Woven Composites. 2012;799–812.
8. Cox BN, Dadkhah MS, Morris WL, Flintoff JG. Failure mechanisms of 3D woven composites in tension, compression, and bending. Acta Metall Mater. 1994;42(12):3967–84.
9. Dahale M, Neale G, Lupicini R, Cascone L, McGarrigle C, Kelly J, et al. Effect of weave parameters on the mechanical properties of 3D woven glass composites. Compos Struct. 2019;223.
10. Archer E, Buchanan S, McIlhagger A, Quinn J. The effect of 3D weaving and consolidation on carbon fiber tows, fabrics, and composites. J Reinf Plast Compos. 2010;29(20):3162–70.
11. TORAYCA. T700S TECHNICAL DATA SHEET CARBON. :6–7.
12. Adesah RS, Zakaria R, Ghazali AF, Ismail AF, Daud A. Literature review of tufted reinforcement for composite structures Literature review of tufted reinforcement for composite structures. 2017;
13. Stig F, Hallström S. Influence of crimp on 3D-woven fibre reinforced composites. Compos Struct. 2013 Jan;95:114–22.
14. Mahadik Y, Hallett SR. Effect of fabric compaction and yarn waviness on 3D woven composite compressive properties. Compos Part A Appl Sci Manuf. 2011 Nov;42(11):1592–600.
15. Dai S, Cunningham PR, Marshall S, Silva C. Influence of fibre architecture on the tensile, compressive and flexural behaviour of 3D woven composites. Compos Part A Appl Sci Manuf [Internet]. 2015;69:195–207. Available from: http://dx.doi.org/10.1016/j.compositesa.2014.11.012

  doi:10.5075/epfl-298799_978-2-9701614-0-0

THE ROLE OF MELTING ON INTIMATE CONTACT DEVELOPMENT IN LASER-ASSISTED TAPE PLACEMENT OF CARBON FIBRE REINFORCED THERMOPLASTIC COMPOSITES

Alejandro Jiménez del Toro[a,b,], Julie Teuwen[b], Tomas Flanagan[a], William Finnegan[c,d]*
a: ÉireComposites – a.jimenezdeltoro@eirecomposites.com
b: Delft University of Technology – a.jimenezdeltoro@tudelft.nl
c: National University of Ireland Galway
d: SFI MaREI Centre for Energy, Climate and Marine

Abstract: *Laser-assisted tape placement (LATP) and thermoplastic composites (TPCs) pre-impregnated (prepreg) tapes are a promising combination of technologies, combining in-situ consolidation of the TPCs and the high degree of automation achievable with LATP. Laminate quality tends to decrease when increasing placement speed due to the shortening of heating and consolidation window. Such heating windows require high laser power to achieve the desired nip point temperature, which can hinder through-thickness temperature distribution within the incoming tape during the heating stage. The effect of placement speed, laser power and thermal conductivity model on the temperature and melt profile of tapes prior the compaction phase will be investigated through simulations for carbon fibre reinforced polyphenylene sulphide unidirectional tapes. Results show that significant through-thickness thermal gradients occur within a tape at high laser power; and the obtained gradients differ for each thermal conductivity model used.*

Keywords: laser-assisted tape placement; melting, heat transfer model; thermal conductivity; heating stage

1. Introduction

Laser-assisted automated tape placement (LATP) of carbon fibre (CF) reinforced thermoplastic composites (TCs) is a versatile technology with the potential to utilise the in-situ consolidation capabilities of TCs to bring one-step manufacturing of composite parts. The in-situ consolidation of the part is achieved by continuous bonding of the incoming tape to the substrate, in which the interface between the two heals and restores bulk-like properties[1]. Such properties are developed when a high degree of bonding is achieved; which results from the contribution of the degree of autohesion and intimate contact, D_{ic}. However, current in-situ consolidation in LATP is not a robust process.

Prior to autohesion, it is crucial to achieve a high degree of intimate contact. Current intimate contact development models[2,3] rely on resin squeeze flow to describe the flattening of the surface's asperities upon compaction, and are unable to successfully predict experimental D_{ic} measurements[4]. Recent work has revealed that tape's surfaces are heterogeneous and can have resin poor areas. Kok[5] found a logarithmic relationship between D_{ic} and the resin poor surface depth, achieving D_{ic} approximately to 1 when that depth was close to zero, meaning the surface was resin rich. This shows that contrary to what current D_{ic} models, due to resin poor surface areas, both squeeze and through-thickness percolation flow are relevant in D_{ic} development. Hence, since through-thickness resin flow is required, not only surface

  doi:10.5075/epfl-298799_978-2-9701614-0-0

temperature but also its distribution within the tape become relevant parameters to analyse in LATP.

To improve deposition rates, both placement speed and/or tape's fibre areal weight can be increased. Elevated placement speeds can lead to significantly reduced processing times and impose very elevated heating rates regardless of the tape's thickness. Time scales in the order of tens of milliseconds and heating rates well above 5 000 °C/s can be expected. Polymers are thermal insulators and composites' through-thickness thermal conductivity, k_z, is highly influenced by this fact[6], which could compromise the temperature distribution within a tape upon heating in such short processing times. Thermal conductivity, k, is a function of thermal diffusivity, α, density, ρ, and specific heat capacity, c_p, as per Eq.(1).

$$k = \alpha \rho c_p \ [\mathrm{W/m \cdot K}] \tag{1}$$

It is worth noticing that all these properties depend on temperature and porosity, among others[7]. For several neat polymers[8], including polyphenylene sulphide (PPS)[9], α decreases with temperature. Also, k_z for CF/PPS composite has been reported to decrease with temperature[10], whereas an increase with temperature has been identified for CF reinforced polyether-ether-ketone (CF/PEEK)[7]. Several models have been developed to predict k_z values in composites and some of them will be used in this work. Examples of LATP modelling of heat transfer in composites with constant[11] and temperature-dependent[12] values of k_z can be found.

Given the low k_z of composites and the rapid surface heating due to elevated placement speeds, thermal gradients within the tape might occur and hinder percolation flow and intimate contact development. The presence and influence on intimate contact development of these thermal gradients has not been studied yet. The aim of this work is to evaluate the presence of through-thickness thermal gradients within a tape during the heating phase, prior to consolidation, using different placement speeds, laser powers and k_z models, by means of a finite element model (FEM). The steps followed in the study are: (1) a laser source and CF/PPS unidirectional composite are modelled based on previously reported studies; (2) the thermal history and through-thickness temperature profile of a CF/PPS unidirectional tape heated up by a laser source at different placement speeds, laser powers and thermal conductivities is simulated by finite element method; (3) the influence of k_z on the simulation results is evaluated.

2. Numerical modelling methodology

The finite element model was performed in COMSOL Multiphysics® 5.6, using the Backward Differentiation Formula solver for a transient heat transfer problem in which a moving laser heat source passes over a static rectangle of CF/PPS unidirectional composite. The geometry used was a 150 mm length and 0.15 mm thick rectangle. A triangular mesh with a maximum element size of 7 µm was sufficiently refined to observe no significant difference in the simulation results. The laser source have been modelled following the irradiance distribution described by Grouve [11], which has been simplified to an skewed top hat distribution to mimic the effect of the laser losing sight of the tape as it rolls under the roller. The reflection from the substrate are not accounted for in this model, and the roller is considered transparent to the laser and at constant temperature. The initial tape, ambient and roller

  doi:10.5075/epfl-298799_978-2-9701614-0-0

temperatures are 293.15 K. The upper surface of the geometry receives the radiation from the laser, and loses energy by means of convection with the environment and radiation. The lateral surfaces lose energy by the same means as the upper one but do not receive heat input. The bottom surface is always in perfect contact with the roller and loses energy by conduction. All parameters regarding geometry, placement and laser are listed in Table 1. The matrix-reinforcement distribution is considered homogeneous throughout the composite and its properties are listed in Table 2.

Table 1. Placement and laser simulation parameters.

Property	Symbol	Units	Value
Sample length	s_l	cm	1.5
Sample thickness	s_t	mm	0.15
Laser power	L_p	kW	1, 3, 6
Laser length	L_l	mm	45
Laser width	L_w	mm	28
Laser shadow length	L_{shadow}	mm	3
Placement speed	S	mm/s	100, 400, 800
Time step	t_{step}	s	0.001

Table 2. Composite, PPS and CF material properties.

Property	Symbol	Units	Value
Composite surface emissivity[10]	ϵ	$-$	0.9
Composite absorptivity[11]	A	$-$	0.9
PPS molecular weight	M_w	kg/mol	1
PPS melting temperature	T_m	°C	298
PPS density[13]	ρ_m	kg/m^3	1300
CF density[14]	ρ_f	kg/m^3	1790
Specific heat capacity of PPS[13]	$c_{p,m}^{solid}(298\ \mathrm{K})$	J/g·K	1100
Heat capacity change of PPS at T_g[15]	$\Delta c_{p,m,a}(T_g)$	J/g·K	0.27
CF specific heat capacity[14]	$c_{p,f}$	J/kg·K	$750 + 2.05 \cdot T[K]$
Fibre volume fraction	χ_f	$-$	0.55
CF/PPS-air heat transfer coeff.[10]	h_{air}	W/m^{2}K	2.5
CF/PPS-roller heat transfer coeff.[11]	h_{roller}	W/m^{2}K	100

The heat capacity of CF/PPS, c_p, as a function of temperature was calculated from the individual heat capacities of each component applying the rule of mixtures. The specific heat of PPS, $c_{p,m}$, results from the heat capacity of solid, $c_{p,\mathrm{m}}^{\mathrm{solid}}(T)$, and molten, $c_{p,\mathrm{m}}^{\mathrm{melt}}(T)$, PPS which were estimated as described elsewhere[16]. $c_{p,m}^{\mathrm{melt}}(298\ \mathrm{K})$ was estimated as $c_{p,m}^{\mathrm{melt}}(298\ \mathrm{K}) = c_{p,m}^{\mathrm{solid}}(298\ \mathrm{K}) + \Delta c_{p,m,a}(T_g)$. It is assumed that the heat capacity of the molten polymer is achieved above T_g. Both, CF, ρ_f, and PPS, ρ_m, densities are assumed constant and the composite density, ρ, results from applying the rule of mixtures. Values for thermal diffusivity of PPS, $\alpha_m(T)$, are based on Chukov's[13] experimental work. In the presented thermal model,

  doi:10.5075/epfl-298799_978-2-9701614-0-0

they are calculated by means of cubic spline interpolation from 25 to 250 °C, and considered constant outside that interval. Thermal conductivity of PPS, k_m, has been estimated by Eq. (1) , using $\alpha_m(T)$, ρ_m and $c_{p,m}$ previously described. The thermal conductivity of carbon fibre in the longitudinal, $k_{x,f}$, and transverse, $k_{y,f}$ and $k_{z,f}$, direction have been estimated as described elsewhere[14].

2.2 Composite thermal conductivity

In this work, the influence on the temperature distribution of a tape has been studied for four different k_z models for the CF/PPS composite. These models are listed in Table 3.

Table 3. Composite through-thickness thermal conductivity, k_z, model equations used in the present study.

Model	k_z [W/m·K]
Rule of mixtures[17]	$\frac{k_{z,f}k_m}{k_{z,f}\chi_m + k_m\chi_f}$
Halpin-Tsai[18]	$k_m\left(\frac{1+\zeta\eta\chi_f}{1-\eta\chi_f}\right), \eta = \frac{(k_{z,f}/k_m)-1}{(k_{z,f}/k_m)+\zeta}, \zeta = 1$
Linear[10]	$0.5 - 3.5 \cdot 10^{-4}T$
Constant[7]	0.72

3. Results

The presented simulation results have been obtained at the vertical middle section of the geometry, 0.75 cm, at the end of heating stage for each placement speed, including the laser shadow. The simulation times are therefore a function of the placement speed as: 555 ms ($S = 100$ mm/s), 138 ms ($S = 400$ mm/s) and 69 ms ($S = 80$ mm/s). The laser shadow length is kept constant at 3 mm, as defined in Table 1. To assess the validity of results of this study, they have been compared to those experimentally produced by Grouve[11] for CF/PPS composites. The order of magnitude of the simulations results seem to agree with the experimental observations.

3.2. Laser power and placement speed effect on thermal history

As previously discussed, higher laser power is required for shorter heating times in order to achieve the desired temperatures, which leads to higher heating rates. The effect of the heating rates in the through-thickness temperature distribution, using Halpin-Tsai model for k_z calculation, can be observed in the solutions obtained for the configurations in Table 4 , shown in Figure 1. The temperature at the top surface (T_{ts}), which is heated by the laser, and the bottom surface (T_{bs}), which is on the opposite side of the tape, are evaluated at each time step during the heating phase for the middle section of the tape. An initial temperature plateau is seen before the laser reaches the middle section of the geometry, since $T_t = T_{ts} = T_{bs}$. Once the laser heats up the middle section, T_{ts} and T_{bs} increase differently as a function of L_P and k_z, generating a through-thickness temperature difference, $\Delta T_t = T_{ts} - T_{bs}$. As the tape enters the laser shadow region, a sudden temperature drop is experienced. Two ΔT_t are

  doi:10.5075/epfl-298799_978-2-9701614-0-0

of interest: $\Delta T_t^{end} = T_{ts}^{end} - T_{bs}^{end}$, which defines the through-thickness temperature difference at the end of the heating phase; and that between the maximum and final T_{ts}, $\Delta T_t^{drop} = T_{ts}^{max} - T_{ts}^{end}$, which represent the required tape superheating to achieve T_{ts}^{end}.

Table 4. Temperature evolution through the heating stage of the upper, T_{ts}, and bottom, T_{bs}, faces for two distinct LATP configurations: (1A) $L_P = 1.0$ kW and $S = 100$ mm/s; and (1B) $L_P = 6.0$ kW and $S = 800$ mm/s.

Configuration	L_P [kW]	S [mm/s]	$Time$ [ms]	T_{ts}^{max} [°C]	ΔT_{ts}^{drop} [°C]	T_{ts}^{end} [°C]	T_{bs}^{end} [°C]	ΔT_t^{end} [°C]
1A	1.0	100	555	427	15	412	409	4
1B	6.0	800	69	471	66	405	296	109

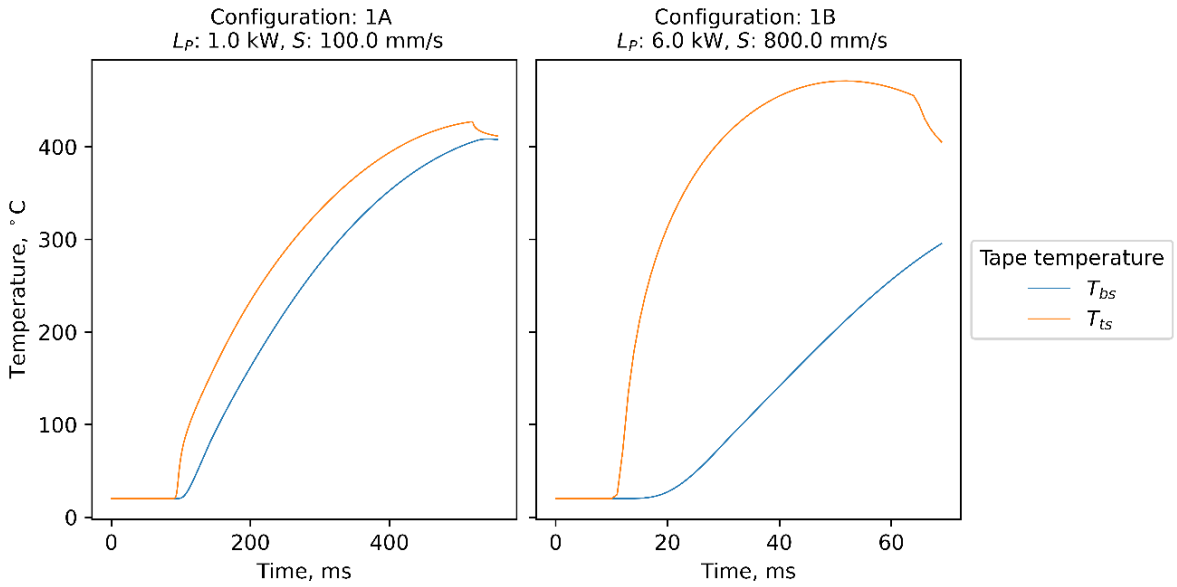

Figure 1. Upper, T_{ts}, and bottom, T_{bs}, surface temperatures of a tape heated by (1A) a 1.0 kW laser at 100 mm/s; and (1B) a 6.0 kW laser at 800 mm/s.

Similar T_{ts}^{end} are estimated for these two laser power and placement speed configurations, 405 and 412 °C for configurations 1A and 1B, respectively. As expected, to reach similar temperatures higher heating rates are seen in configuration 1B, since the heating window is approximately 10 times shorter. ΔT_t^{end} changes significantly with the power of the heat source, from 4 to 109 °C for configurations 1A and 1B, respectively. In addition, T_{bs} is below 298 °C, the melting point of PPS, for configuration 1B. The superheating required to achieve similar final temperatures is greater for configuration 1B than 1A, 471 and 427 °C, respectively; which results in smaller ΔT_{ts}^{drop} for configuration 1A than 1B, 15 and 66 °C, respectively. The temperature drop for configuration 1A occurs right at the start of the laser shadow, whereas the drop for configuration 1B starts, with a lower slope, several milliseconds earlier.

3.2. Effect of k_z model on thermal history

The role of k_z on ΔT_t^{end}, being 0 µm the bottom surface and 150 µm the top surface heated by the laser, is shown in Figure 2. The melting line for PPS is plotted as temperature references.

  doi:10.5075/epfl-298799_978-2-9701614-0-0

All four k_z models used show different behavior as a function of the laser power. For configuration 2A, all models show similar ΔT_t^{end} except for the linear model, which predicts a higher value. In configuration 2B, all predictions show larger ΔT_t^{end} than in configuration 2A, being Halpin-Tsai and constant models the most moderate and closer to each other in their predictions; whereas the rule of mixtures and linear models show significantly wider temperature ranges. It is worth noticing that the linear model already predicts T_{bs}^{end} does not reach the melting temperature at the end of the laser shadow. For configuration 2C, the predicted ΔT_t^{end} has broaden up for all models and values considered. The linear model produces results with a T_{bs}^{end} below the melting line, respectively. The rule of mixture and Halpin-Tsai models show $T_{bs}^{end} < T_m$ too. The constant model is the only one predicting a full melt of the tape in configuration 2C. As the laser power increases from configuration 2A to 2C, the relative difference of T_{bs}^{end} and T_{ts}^{end} between the different models became larger as well.

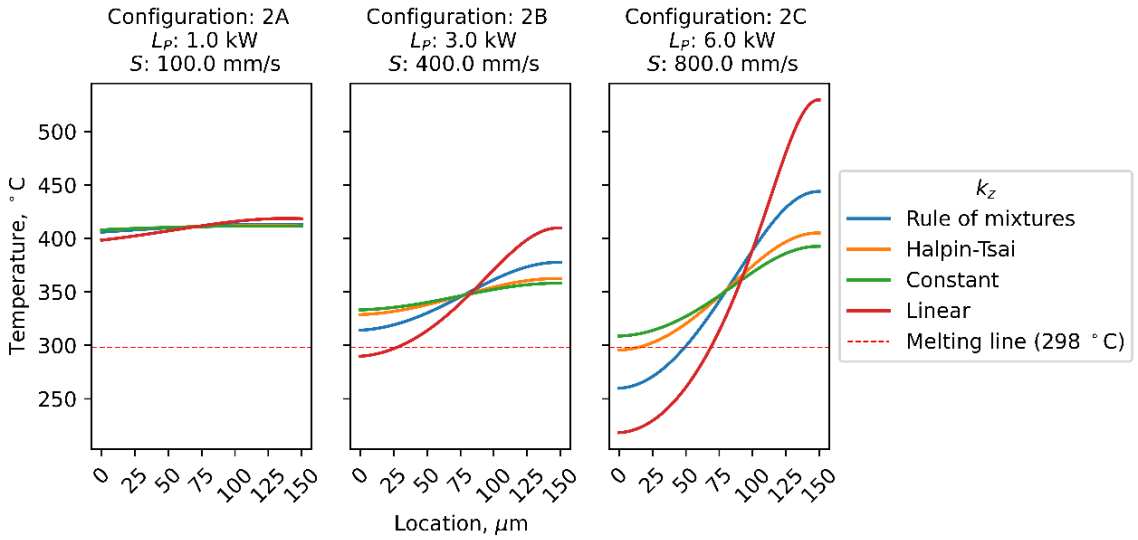

Figure 2. Estimated through-thickness temperature distribution (from the bottom surface, 0 µm, to the upper surface, 150 µm) at the end of the heating stage as a function of different k_z models for tapes heated up by (2A) a 1.0 kW laser at 100 mm/s, (2B) a 3.0 kW laser at 400 mm/s; and (2C) 6.0 kW laser at 800 mm/s.

4. Discussion

The simulated through-thickness thermal histories of a laser heated tape show results which depend on LATP configurations and k_z. Using Halpin-Tsai k_z model, as seen Figure 1, higher heating rates are produced to achieve similar T_{ts}^{end} as the placement speed and laser power increase; as a results, larger ΔT_t^{end}, ΔT_{ts}^{drop} and T_{ts}^{max} are experienced in the tape. Hence, choosing elevated nip point temperatures with high laser powers may produce polymer degradation upon heating. According to the simulations, this effect is not likely to occur at lower laser powers, since the tape superheating is not significant.

The effect of the LATP configuration and k_Z model used on ΔT_t^{end} is shown in Figure 2. As laser power and heating rate increase, the larger ΔT_t^{end} becomes, which results in measurements of the tape's surface temperature not being representative of the actual tape through-thickness temperature. In fact, the rule of mixtures, Halpin-Tsai and the linear models

  doi:10.5075/epfl-298799_978-2-9701614-0-0

predict T_{bs}^{end} below T_m. This is not the case for low placement speeds, in which temperature homogenisation occurs prior compaction, as seen in Figure 2 (configuration 2A).

As the heating rates increase, the through-thickness temperature distributions obtained with the different k_z models also diverge from each other, as seen for the different configurations in Figure 2. Hence, the significant differences found between the k_z models as a function of the laser power make it necessary to experimentally determine the thermal conductivity to reach a higher confidence on the simulation results.

The existence of large through-thickness temperature distributions would also generate gradients in temperature dependent properties, such as viscosity and thermal expansion, among others. According to Darcy's law on percolation, it would hinder percolation towards the surface as the viscosity would increase from the heated surface into the tape. To the best of our knowledge, the effect of thermal gradients in the tape on the development of intimate contact has not yet been explored in literature

5. Conclusions

This work studied the development of through-thickness temperature gradients within a CF/PPS tape upon heating in LATP, as a function of different placement speeds and laser powers, by means of FEM analysis; as well as the influence of different k_z models on the obtained solutions. For all k_z models used, temperature gradients appear, and increase their value, as the laser power, and therefore heating rate, increase; some of them predict $T_{bs}^{end} < T_m$ for 6 kW laser power. For those configurations where through-thickness thermal gradients are present, readings of T_{ts} by means of a thermal camera would not represent the actual temperature of the tape. Different k_z models predict significantly different through-thickness temperature distributions for laser powers 3 and 6 kW; hence generating experimental data on this magnitude as a function of temperature seems necessary to improve the accuracy of the simulations. Resin flow may be hindered by the existence of thermal gradients within the tape thickness, which could be a negatively contributing factor to the development of intimate contact at high placement speeds.

Future work includes (1) the study of thermal history within a tape by experimental means, especially for elevated placement speeds; (2) the adequate characterisation of the composite properties as a function of temperature; (3) improvement and validation of the presented thermal model; (4) the possible role that the existence of thermal gradients might have on intimate contact development in LATP of CF/PPS composites.

Acknowledgements

This work is supported by the European Union's Horizon 2020 research and innovation programme (project STEP4WIND, grant agreement no. 860737).

6. References

1. Yassin K, Hojjati M. Processing of thermoplastic matrix composites through automated fiber placement and tape laying methods: A review. Journal of Thermoplastic Composite Materials. 2018 Dec;31(12):1676-725.
2. Lee WI, Springer GS. A model of the manufacturing process of thermoplastic matrix composites. Journal of composite materials. 1987 Nov;21(11):1017-55.

  doi:10.5075/epfl-298799_978-2-9701614-0-0

3. Yang F, Pitchumani R. A fractal Cantor set based description of interlaminar contact evolution during thermoplastic composites processing. Journal of materials science. 2001 Oct;36(19):4661-71.
4. Çelik O, Peeters D, Dransfeld C, Teuwen J. Intimate contact development during laser assisted fiber placement: Microstructure and effect of process parameters. Composites Part A: Applied Science and Manufacturing. 2020 Jul 1;134:105888.
5. Kok T. On the consolidation quality in laser assisted fiber placement: the role of the heating phase (Doctoral dissertation, University of Twente).
6. Tavman IH, Akinci H. Transverse thermal conductivity of fiber reinforced polymer composites. International Communications in Heat and Mass Transfer. 2000 Feb 1;27(2):253-61.
7. Cogswell FN. Thermoplastic aromatic polymer composites: a study of the structure, processing and properties of carbon fibre reinforced polyetheretherketone and related materials. Elsevier; 2013 Oct 22.
8. dos Santos WN, De Sousa JA, Gregorio Jr R. Thermal conductivity behaviour of polymers around glass transition and crystalline melting temperatures. Polymer Testing. 2013 Aug 1;32(5):987-94.
9. Dydek K, Latko-Durałek P, Sulowska A, Kubiś M, Demski S, Kozera P, Sztorch B, Boczkowska A. Effect of Processing Temperature and the Content of Carbon Nanotubes on the Properties of Nanocomposites Based on Polyphenylene Sulfide. Polymers. 2021 Jan;13(21):3816.
10. Y Carpier, Barbe F, B Vieille, A Coppalle. Identification of thermal properties and decomposition modelling of carbon fibers-PPS composites exposed to fire. In Proceeding of the 18th European Conference on Composite Materials (ECCM-18). ECCM, Athens, Greece. 2018. p. 24–8.
11. Grouve W. Weld strength of laser-assisted tape-placed thermoplastic composites (Doctoral dissertation, University of Twente).
12. Stokes-Griffin CM, Compston P, Matuszyk TI, Cardew-Hall MJ. Thermal modelling of the laser-assisted thermoplastic tape placement process. Journal of Thermoplastic Composite Materials. 2015 Oct;28(10):1445-62.
13. Chukov DI, Stepashkin AA, Tcherdyntsev VV, Olifirov LK, Kaloshkin SD. Structure and properties of composites based on polyphenylene sulfide reinforced with Al-Cu-Fe quasicrystalline particles. Journal of Thermoplastic Composite Materials. 2018 Jul;31(7):882-95.
14. Johnston AA. An integrated model of the development of process-induced deformation in autoclave processing of composite structures (Doctoral dissertation, University of British Columbia).
15. Wunderlich B. Thermal analysis of polymeric materials. Springer Science & Business Media; 2005 Apr 4.
16. Feldman D. Properties of polymers, by DW van Krevelen, Elsevier Science Publishers, Amsterdam, Oxford, New York, 1990, 875 pages, US $337.25. Journal of Polymer Science B Polymer Physics. 1991 Dec;29(13):1654-.
17. McCullough RL. Generalized combining rules for predicting transport properties of composite materials. Composites Science and Technology. 1985 Jan 1;22(1):3-21.
18. Affdl JH, Kardos JL. The Halpin-Tsai equations: a review. Polymer Engineering & Science. 1976 May;16(5):344-52.

  doi:10.5075/epfl-298799_978-2-9701614-0-0

3D FLOW AND FIBRE ORIENTATION MODELLING OF COMPRESSION MOULDING OF A-SMC: SIMULATION AND VALIDATION IN SQUEEZE FLOW

Gustaf Alnersson[a], Yvonne Aitomäki[b], Anna-Lena Ljung[c], T. Staffan Lundström[c]

a: Gestamp Hardtech/Luleå University of Technology – gustaf.alnersson@associated.ltu.se
b: RISE AB
c: Luleå University of Technology

Abstract:

Keywords: Sheet Moulding Compound; Numerical Simulation, Fibre Orientation Modelling

1. Introduction

Sheet Moulding Compound (SMC) is a class of composite materials that have the possibility to be useful in automotive industrial applications, due to the possibility of obtaining comparatively short cycle times. More recently, Advanced SMC (A-SMC) has also been introduced, the main difference compared to earlier materials being that the fibres are now carbon and the volume fraction of fibres is higher (35% and higher compared to earlier 20-25%). Another important advancement is the rapid development cycles in the automotive industry means that it is necessary to be able to reliably numerically predict both the manufacturability and the mechanical properties of parts.

For the moulding process, fitted pieces of sheets consisting of fibres and resin are placed inside a heated mould; when the mould closes the SMC stack melts, flows out and fills the mould.

Process modelling of SMC is however rather complicated for a number of reasons, chief among these the complex material properties of SMCs and the presence of high volume fractions of fibres. These fibres and in particular their orientations will also greatly affect the mechanical properties of the parts. The focus of this work will thusly be on fibre orientation prediction.

The squeeze test rig that is studied in the work presented here is used for determining the viscous properties of materials. This initial study uses the geometry to compare the results of different simulation techniques.

Two different approaches are discussed here. In one a general fluid mechanics code, Ansys CFX, is used for modelling the movement of the SMC during the compression process, the results of which are then used as input for a Python script that calculates the evolution of the fibre placement and fibre orientation distribution. In the other approach, the more specialized composite software 3DTimon is used for determining both charge deformation and fibre evolution.

2. Methods

2.1 General code

  doi:10.5075/epfl-298799_978-2-9701614-0-0

The movement of the charge during the compression of the mould is modelled using fluid mechanics by numerically solving the Navier-Stokes equations (see for instance Cengel and Cimbala [1]). Here the viscosity is modelled using the semi-empirical model suggested by Kluge [2],

$$\eta = 3\eta_0\left(1 + 100f_f + 1000f_f^2\right)e^{-B\left({}^1/_{T_0} - {}^1/_{T}\right)}\left(\frac{\dot{\varepsilon}}{\dot{\varepsilon}_0}\right)^{n-1}\left(1+\dot{\gamma}^2\right)^{{}^{(n-1)}/_2} \quad (1)$$

in which η is the viscosity, T is temperature, B is a temperature constant, $\dot{\varepsilon}$ is a factor connected to how compressed the material is compared to its initial state, $\dot{\gamma}$ is the shear rate, n is a power law constant, and the subscript 0 indicates initial conditions.

The fibre orientation evolution is modelled using the model suggested by Folgar and Tucker [3] and Advani and Tucker [4], in which the fibres are assumed to be rigid ellipsoidal particles with a large aspect ratio, and that they are sufficiently large that Brownian motion can be neglected. There are a number of issues with this approach [5], but it is the approach taken in most commercial codes specializing in composites. Orientation tensors are used to describe the alignment with the principal axes. The time evolution of the orientation tensors can be described as

$$\frac{Da_{ij}}{Dt} = -\frac{1}{2}\left(\omega_{ik}a_{kj} - a_{ik}\omega_{kj}\right) + \frac{1}{2}\lambda\left(\dot{\gamma}_{ik}a_{kj} + a_{ik}\dot{\gamma}_{kj} - 2\dot{\gamma}_{kl}a_{ijkl}\right) + 2D_r(\delta_{ij} - \alpha a_{ij}) \quad (2)$$

where a_{ij} is the orientation tensor, ω is the vorticity tensor, $\dot{\gamma}$ is the shear rate tensor, α relates to how many spatial dimensions are considered and D_r is the rotary diffusivity. The fourth-rank tensor a_{ijkl} is approximated with the hybrid approach suggested by Advani and Tucker [6]

$$a_{ijkl} \equiv (1-f)\hat{a}_{ijkl} + f\tilde{a}_{ijkl} \quad (3)$$

in which $\hat{a}$ is a linear approximation, $\tilde{a}$ is a quadratic approximation and f is a scalar measure of the orientation. This approach has been implemented in a Python code, which uses the time evolution of the flow field predicted by CFX as input.

2.2 3D Timon

For the second approach, the software 3D TIMON is used, which is a software for modelling of composites manufacturing developed by Toray Engineering. The viscosity model used in these calculations is described as

$$\eta = \frac{\eta_0}{1+\left(\frac{\eta_0\dot{\gamma}}{\tau^*}\right)^{1-n}},\ \eta_0 = De^{-\frac{A_1(T-T^*)}{A_2+(T-T^*)}}, \quad (4)$$

where η is the viscosity, T is temperature, $\dot{\gamma}$ is the shear rate, n is a power law constant, D and A_1 are temperature constants and T^* and A_2 are factors connected to the flow pressure.

For fibre orientation modelling an approach referred to as Direct Fibre Simulation is used (see for instance [7]) in which the fibres are modelled as sequences of rigid rods.

2.3 Comparison

  doi:10.5075/epfl-298799_978-2-9701614-0-0

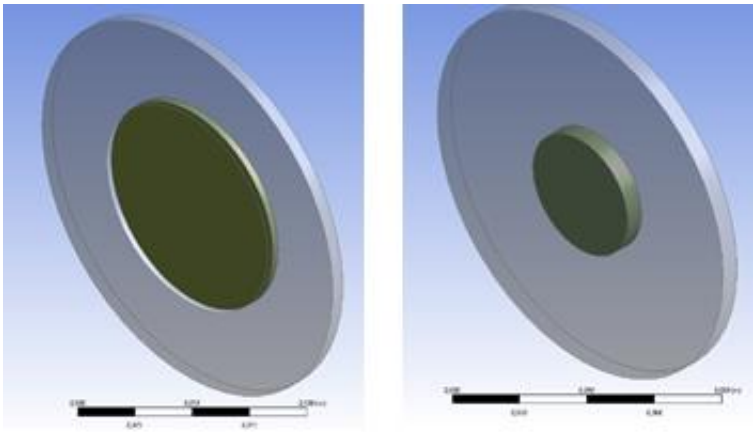

Figure 1: An isometric view of the geometry used in the first case (left) and the second case (right). The highlighted area indicates the initial position of the charge.

The geometries that are studied can be seen in Figure 1. It is a press tool used for rheological tests. Two different cases are set up, one in which the material initially covers the entire area under the press tool providing a constant area of applied pressure. In the simulation the tool is slightly larger so that there exists a cavity for the material to flow into. The second case has a higher stack with a smaller initial area of contact.

For comparison between the two approaches only the particles that remain below the press itself are studied. Using a Python script, several equidistant lines are drawn from the midpoint along the principal axes to the edge of the press, which are then further subdivided into segments. The orientation tensors obtained from both approaches can then be compared in the different subsegments.

3. Results and Discussion

3.1 Results for Case 1

The fibre orientation results for the two different approaches for the first case can be seen in Figures 2 and 3. In both these figures, the different zones indicate the distance to the midpoint, i.e., zone 1 is right at the centre and zone 4 is at the edge of the press and the values presented are based on averaging the component aligned with that axis. It can be seen in Figure 2 that the results are mostly in agreement in the inner zones and are in relatively good agreement in the out zones as well, even if the spread of results for the Python code is far greater. In Figure 3 it can be seen that the Python code predicts a significantly greater out-of-plane component than 3D Timon does.

  doi:10.5075/epfl-298799_978-2-9701614-0-0

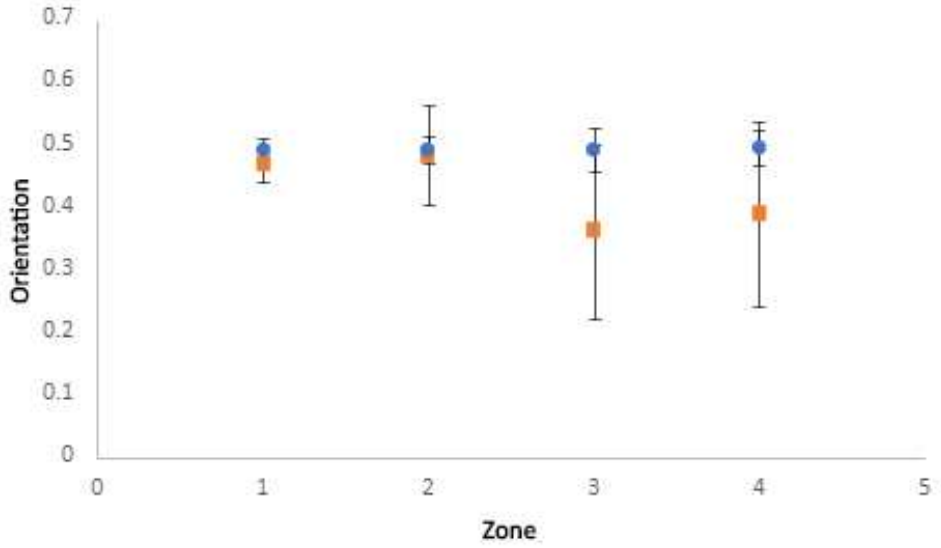

Figure 2: Average values with error bars of the components aligned with the principal flow direction, i.e. a_{11} in the lines along the x axis and a_{22} in the lines along the y axis. Blue circles are taken from 3DTimon, and orange squares are taken from Python.

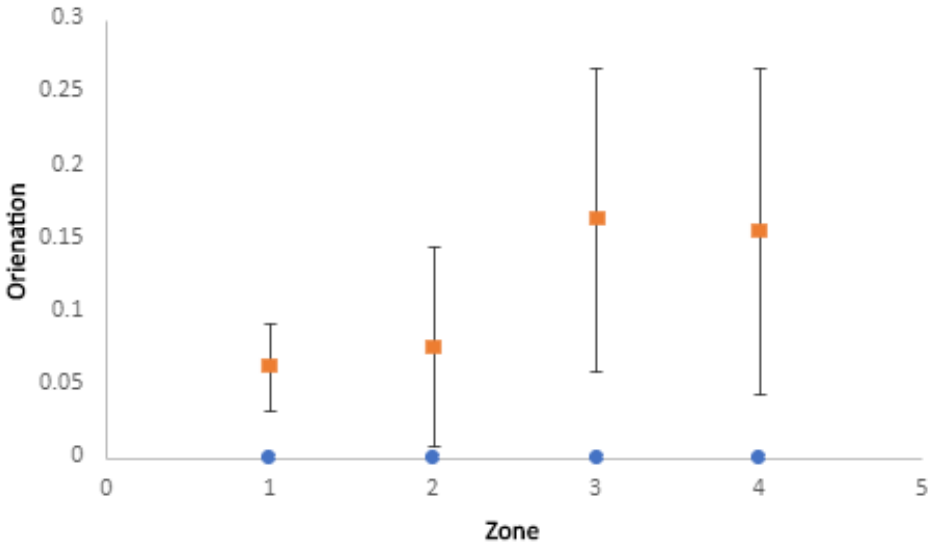

Figure 3: Average values with error bars of the out-of-plane components. Blue circles are taken from 3D Timon, and orange squares are taken from Python

3.2 Results for Case 2

The fibre orientation results for the two different approaches can be seen in Figures 4 and 5 It can be seen in Figure 4 that the results align very well in the centre of the press, but that they diverge significantly as the distance from the midpoint increases. A trend for greater flow direction alignment can be seen for the 3DT Timon results; no such trend can be seen for the Python implementation. It can also be seen in Figure 5 that 3D Timon here as well predicts almost no out-of-plane orientation, while the Python implementation once again predicts far more significant out-of-plane components, especially in the zones farther from the midpoint.

  doi:10.5075/epfl-298799_978-2-9701614-0-0

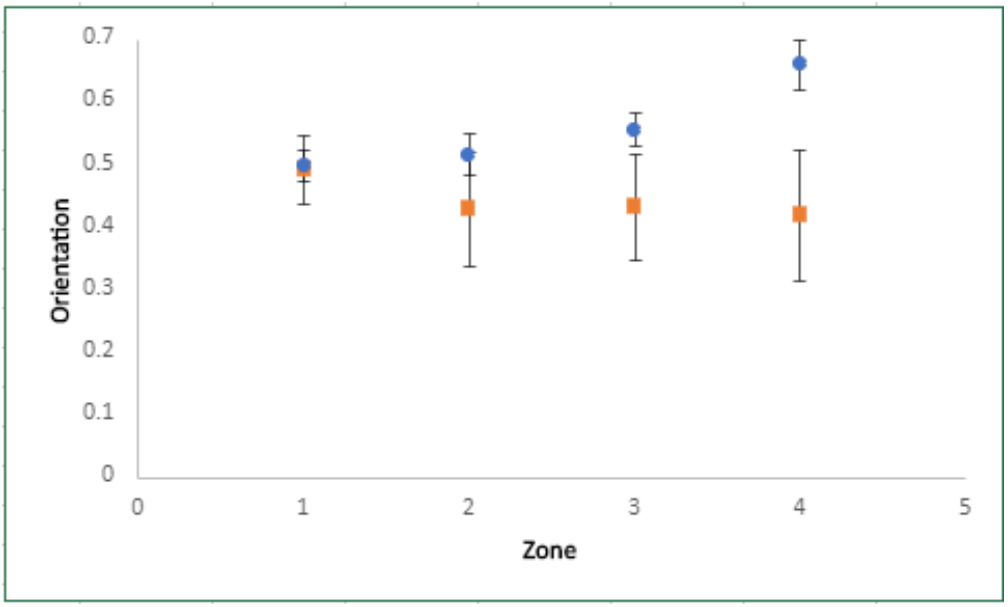

Figure 4: Average values with error bars of the components aligned with the principal flow direction, i.e. a_{11} in the lines along the x axis and a_{22} in the lines along the y axis. Blue circles are taken from 3DTimon, and orange squares are taken from Python.

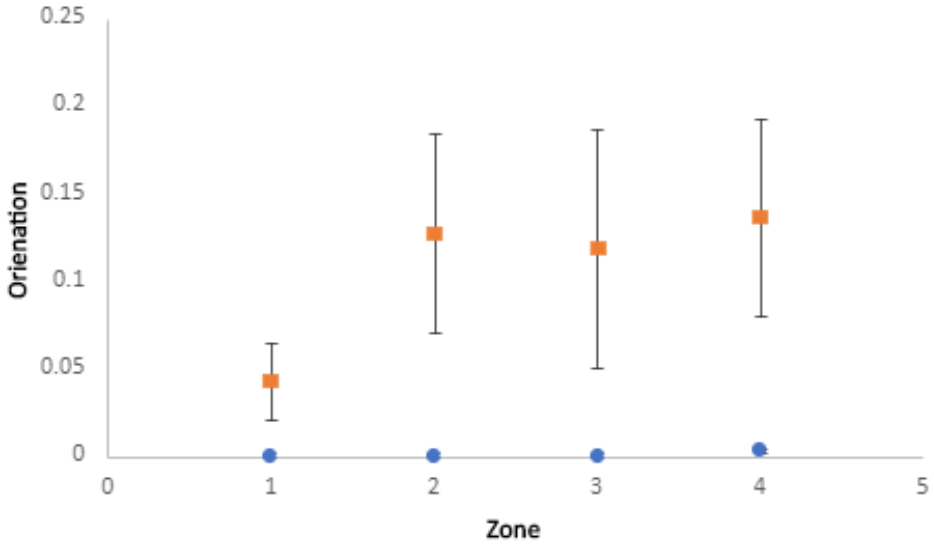

Figure 5: Average values with error bars of the out-of-plane components. Blue circles are taken from 3D Timon, and orange squares are taken from Python.

3.3 Discussion

A general trend that can be observed from these results is that the Python implementation has a far greater variation in results overall than 3D Timon. It can also be observed that the Python implementation predicts far more motion in the out-of-plane direction than the 3D Timon model does. In both Figure 2 and 4 the trends are different between the two methods with the greater out-of-plane alignment being a likely explanation for these results. While the reason for this discrepancy is not entirely clear, the greater focus on three-dimensional modelling in the general software is one possible cause.

  doi:10.5075/epfl-298799_978-2-9701614-0-0

4. Conclusions

Comparisons between two fibre orientation approaches for two different cases have been presented. One approach is based on a general fluid mechanics code, the results of which are then used as input for a Python code based on [4] for modelling fibre orientation, while the other uses a specialized composite code where fibre orientation is calculated in accordance with [7]. The trends in the two different codes are slightly different with a main factor being greater out-of-plane components predicted by the general approach. The results from the Python code also have a greater spread. Continued refinement of the Python code, as well as comparisons to experiments will be the subject of future work.

5. Acknowledgements

This work is a part of the PROSICOMP II project funded by the Swedish Research Innovation Agency (VINNOVA), through Lighter – a strategic innovation program funded by Vinnova, Swedish Energy Agency and Formas and FFI, Vehicle Strategic research and Innovation supported by Vinnova, the Swedish Transport Administration and the Swedish Energy Agency) and the automotive industry.

6. References

[1] Cengel, Y. A., & Cimbala, J. M. (2014). Fluid Mechanics: Fundamentals and Applications (3rd ed.). McGraw-Hill.

[2] Kluge, N. J., Lundström, T. S., Westerberg, L. g., & Olofsson, K. (2015). Compression moulding of sheet moulding compound: Modelling with computational fluid dynamics and validation. Journal of Reinforced Plastics and Composites, 34(6), 479–492.

[3] Folgar, F., & Tucker, C. L. (1984). Orientation Behavior of Fibers in Concentrated Suspensions. Journal of Reinforced Plastics and Composites, 3(2), 98–119.

[4] Advani, S. G., & Tucker, C. L. (1987). The Use of Tensors to Describe and Predict Fiber Orientation in Short Fiber Composites. Journal of Rheology, 31(8), 751–784.

[5] Sepehr, M., Carreau, P. J., Moan, M., & Ausias, G. (2004). Rheological properties of short fiber model suspensions. Journal of Rheology, 48(5), 1023–1048.

[6] Advani, S. G., & Tucker, C. L. (1990). Closure approximations for three-dimensional structure tensors. Journal of Rheology, 34(3), 367–386.

[7] Kobayashi, M., Dan, K., Baba, T., & Urakami, D. (2015). Compression Molding 3D-Cae of Discontinuous Long Fiber Reinforced Polyamide 6 : Influence on Cavity Filling and Direct Fiber Simulations of Viscosity Fitting Methods. 20th International Conference on Composites Materials, July, 1–12.

  doi:10.5075/epfl-298799_978-2-9701614-0-0

SQUEEZE FLOW OF CARBON FIBRE SHEET MOULDING COMPOUND IN COMPRESSION MOULDING

Connie Qian, Hao Yuan, Mona Jesri, Muhammad Khan, Kenneth Kendall*

Automotive Composites Research Centre, WMG, University of Warwick, Coventry, United Kingdom, CV4
*Corresponding author: connie.qian@warwick.ac.uk

Abstract: *A novel material model specifically developed for SMC flow simulation has been proposed in this paper, where the experimental material characterisation is performed using the squeeze flow testing method. The model has been validated through simulation of the squeeze flow testing and the accuracy of the model is assessed by comparing the predicted compression forces against experimental data collected from the squeeze flow testing. The new material model has also been adopted to perform a full-component simulation using a flat plaque geometry. The proposed new model has demonstrated significant improvement in comparison to existing commercial models in both compression force and filling pattern predictions.*

Keywords: SMC; compression moulding; squeeze flow; process simulation.

1. Introduction

Compression moulding of long discontinuous carbon fibre based Sheet Moulding Compound (SMC) has attracted growing interests in the automotive industry for manufacturing high-volume vehicle structures due to a number of advantages such as lower material wastage compared to continuous fibre prepregs and relatively fast processing speed compared to many other composites manufacturing processes.

Several commercial process simulation packages have been developed for compression moulding of SMC, such as Moldflow by Autodesk, Moldex3D by CoreTech and 3D TIMON by Toray. The constitutive models employed in these packages are commonly adapted from models originally developed for injection moulding of short fibre composites. The co-authors recently conducted a full assessment of the predictive accuracy for all three commercial packages mentioned above [1]. This study found that all these simulation packages failed to correctly predict the compression forces as well as the filling patterns. Therefore, it was suggested that a dedicated material model will need to be developed for compression moulding of SMC.

The key barrier in reliable SMC compression moulding simulation is the lack of understanding in the flow behaviour and suitable material characterisation techniques. The deformation mechanism of long discontinuous fibre composites (such as SMC) during compression moulding processes is very different from that of short fibre composites during injection moulding processes. Firstly, the physical behaviours of the two types of material are different due to differences in the organisation of the fibres. Short fibre composites, especially those with low fibre content typically experiences suspension flow behaviour, where the resin carries the fibres as a suspension and material deformation is dominated by the resin. Long fibre composites (e.g. SMC) on the other hand, contains a network of entangled fibre bundles, and the material deformation is dominated by the interactions between fibre bundles [2]. From a continuum

  doi:10.5075/epfl-298799_978-2-9701614-0-0

mechanics point of view, the former only requires analysis of viscous stresses, while the later might also require analysis of elastic stresses. Secondly, the loading conditions in compression moulding processes and injection moulding processes are also different. In compression moulding processes, the material flows under large compaction force applied over a large surface area, which means the deformation is dominated by compressive stresses. In injection moulding processes, the material flows under high injection pressure applied at one or a few discrete points known as gate, which means the deformation is dominated by shear stresses.

This study aims to develop a new modelling approach to enable accurate process simulation for SMC compression moulding. The squeeze flow testing setup is adopted for investigating the flow behaviour of SMC under the typical compression moulding conditions. The force-displacement history for different compressing speeds is recorded and used for derivation of the correct compressive stress-strain relationship. A new constitutive model is developed based on these data and implemented in ABAQUS/Explicit using in-built plasticity model. The accuracy of the model is assessed in terms of predicted compression forces and pressures.

2. Experimental Material Characterisation

The material used in this study was a vinylester based carbon fibre SMC with 12.5mm fibre length, and 47% fibre weight fraction. The material is specifically designed for high volume automotive applications. Experimental material characterisation was conducted using a squeeze flow rig attached to a Zwick 250kN servo-hydraulic testing machine. The squeeze flow rig features a pair of heated steel platens coated with silicon release agent resembling the surfaces of typical compression moulding tools (see *Figure 1*). During the squeeze flow test, a circular SMC sample was positioned in the centre of the bottom platen using a removable sample locator, and the top platen moves down at a constant speed until the sample was compressed to a target thickness. No preheating was performed in this study, which means the initial sample temperature equalled the room temperature. All samples presented in this paper had initial diameter of 50mm and were compressed to a final thickness of 0.2mm (see Figure 2). The initial sample thickness was found to range between 1.4mm to 1.8mm for the material studied. It should be noted that due to the nature of the compounding process, raw SMC samples typically have highly irregular thickness, creating extra challenges in material characterisations. In this study it was assumed that the raw SMC use had a thickness variation of ±20%, therefore the actual force-displacement data were taken after the sample had been compacted by 20% of its original thickness. Squeeze flow tests were performed at three compression speeds (2 mm/s, 5 mm/s and 10 mm/s) and two platen surface temperatures (80°C and 120°C) to understand the rate dependency and temperature dependency of the material.

  doi:10.5075/epfl-298799_978-2-9701614-0-0

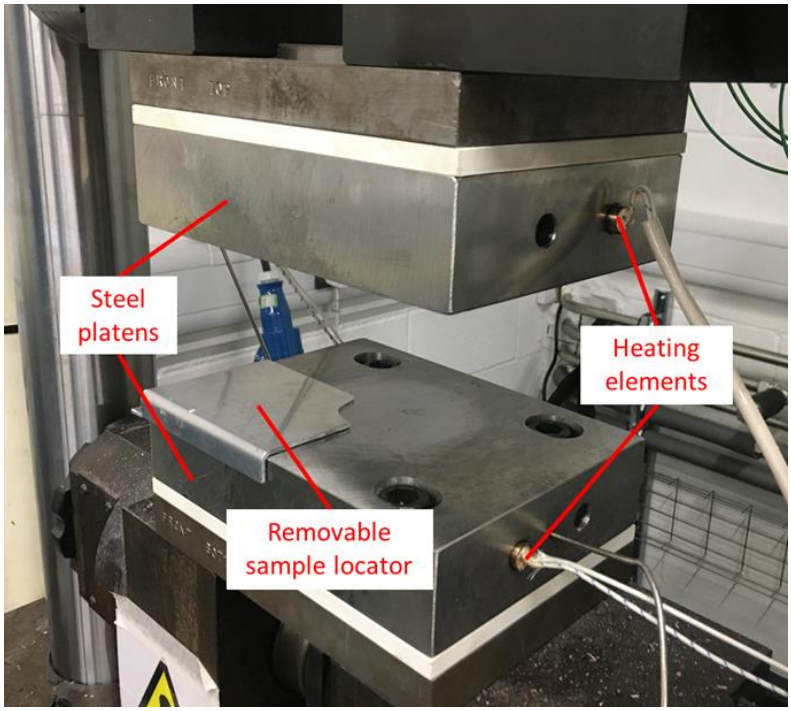

Figure 1: The squeeze flow testing rig

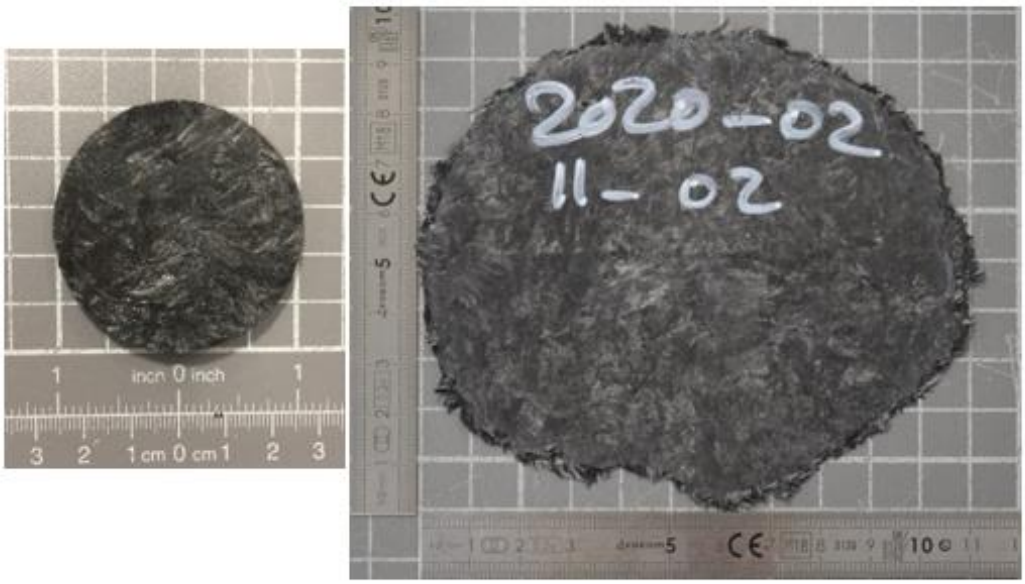

Figure 2: An example squeeze flow testing sample tested at 80°C and 2mm/s closing speed. Left: before compression. Right: after compression.

Figure 3 presents the compressive stress-strain curves from the squeeze flow tests performed at different speeds and temperatures. It should be noted that data recording terminated at lower strain values as the testing speed increased, which was due to a fault with the current data acquisition system rather than the testing machine itself and expected to be fixed in the future. Nevertheless, existing data suggest that all curves seem to experience very similar characteristic shapes. Comparison between the curves also suggests that the material

  doi:10.5075/epfl-298799_978-2-9701614-0-0

experiences both temperature dependency and rate dependency, such that the compression forces increase with increased speed and decreased temperature.

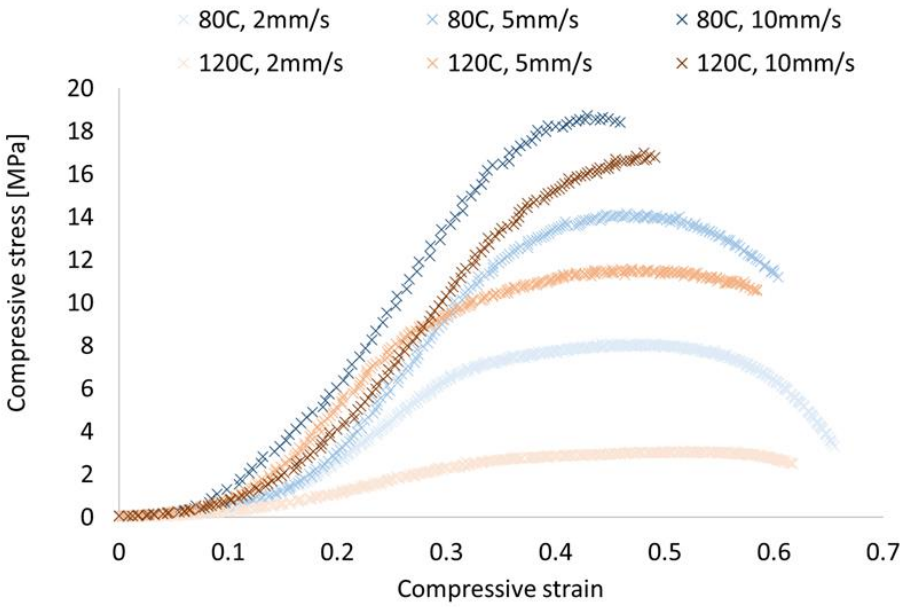

Figure 3: Compressive stress-strain curves from the SMC squeeze flow tests at various platen temperatures and closing speed

3. Numerical Simulation Methodology

3.1 Constitutive material modelling

The stress-strain relationship in (Figure 3) was implemented in ABAQUS using the in-built plasticity model with isotropic hardening. ABAQUS offers the option of defining plasticity behaviour using discrete (tabulated) yield stress vs. plastic strain data. Rate dependency and temperature dependency can also be incorporated using this method. Other material parameters defined in the material model included density of 1500 kg/m^2, elastic modulus of 30GPa and Poisson's ratio of 0.49. Note that it was not possible to physically determine the elastic modulus and Poisson's ratio of the material using the current squeeze flow testing setup, therefore these values were arbitrarily determined by assuming the material is virtually homogeneous, isotropic, and incompressible.

3.3 Validation of the constitutive material model

The proposed material model was validated by simulating the squeeze flow test and comparing the predicted force-displacement curve against the experimental curve. Due to the large deformation in SMC flow, adaptive meshing was required to prevent excessive element distortion. Therefore, the analysis was performed in ABAQUS/explicit utilising the Arbitrary-Lagrangian-Eulerian (ALE) remeshing function.

The SMC sample was modelled as a 3D deformable body and meshed using 8-node linear brick elements with reduced integration (C3D8R). The testing surfaces on the top and bottom platens were modelled as discrete rigid shells and meshed using 4-node rigid elements R3D4. The kinematic contact was applied at the sample-platen interfaces and the contact properties were

  doi:10.5075/epfl-298799_978-2-9701614-0-0

frictionless in the tangential direction, and "hard contact" in the normal direction. Encastre boundary conditions were applied to the bottom platen and velocity boundary conditions were applied to the top platen. The velocity was increased from 0 to the full magnitude within the first 0.05s using a smooth step profile to minimise the fluctuation in forces caused by the explicit solver. The test was modelled isothermally meaning that temperature dependency was currently not captured in the analysis. The force-displacement curve for the top platen was extracted from the simulation results and compared with the experimental force-displacement curve.

3.4 Compression moulding process simulation

Compression moulding process simulation was performed using a flat plaque geometry of 550mm x 550mm x 3mm. The initial charge measured 426mm x 426mm (approximately 60% coverage) and consisted of 3 plies of SMC. The initial charge was modelled using two different approaches (Figure 4): the regular thickness approach, where each ply of SMC was modelled with uniform thickness, such that the plies were in perfect contact with each other at the beginning; the irregular thickness approach, where each ply of SMC was modelled with randomly varied thickness (±20%), creating loft between plies. The model setup was similar to the squeeze flow simulation, but charge was modelled using 6-node linear wedge element (C3D6R), as the irregular thickness would introduce warped surfaces on brick elements, cause errors in job execution in ABAQUS.

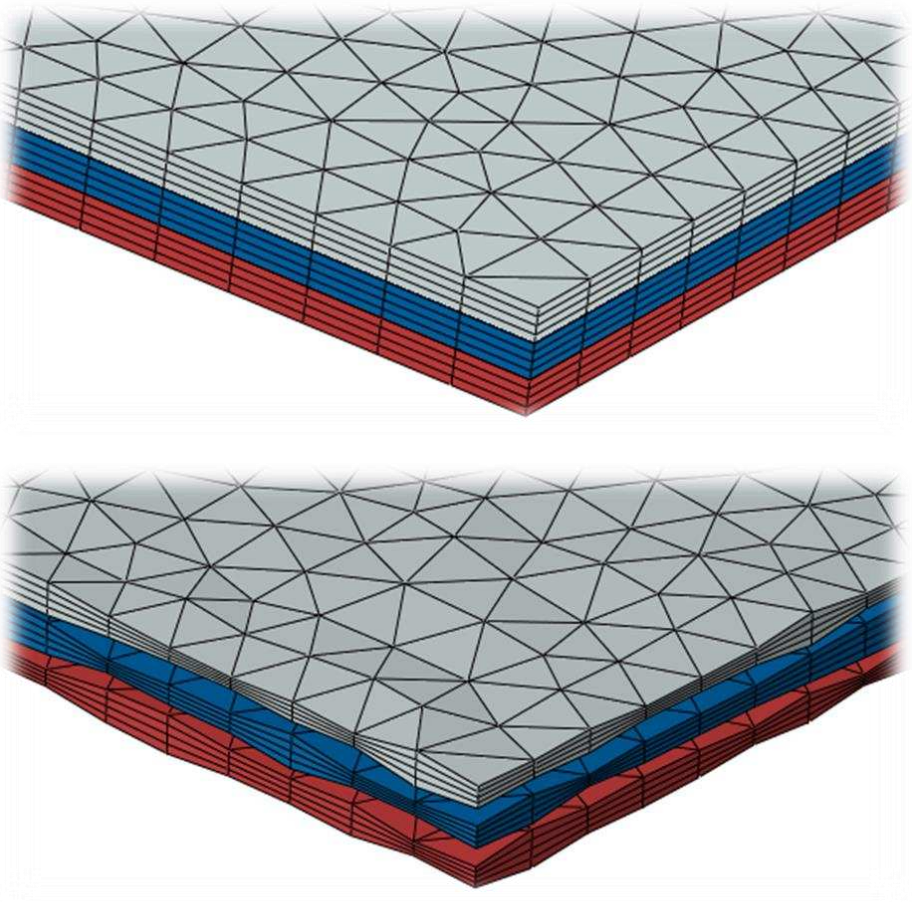

Figure 4: Initial charge modelled using regular thickness approach (top) vs irregular thickness approach (bottom).

  doi:10.5075/epfl-298799_978-2-9701614-0-0

4. Results and Discussions

4.1 Validation of the constitutive material model

Figure 5 compares the compression force-displacement curve predicted using the newly proposed model against the experimental data and the curves predicted using commercial process simulation packages 3D TIMON and Moldex3D. Overall speaking, the predictions from the proposed model show very good agreement with the experimental results until the displacement reaches ~0.8mm The discrepancy beyond this point is because the final softening in the stress-strain curve in Figure 3 cannot be modelled using ABAQUS's in-built plasticity model, instead, the stress will continue to plateau, cause the predicted force to be greater than reality. The commercial models on the other hand, show poor agreement with the experimental results in terms of both the magnitude of the compression forces and the characteristic shape of the curve. It is also interesting to notice that both commercial models have predicted non-zero compression force at zero displacement, which has also been observed in [1].

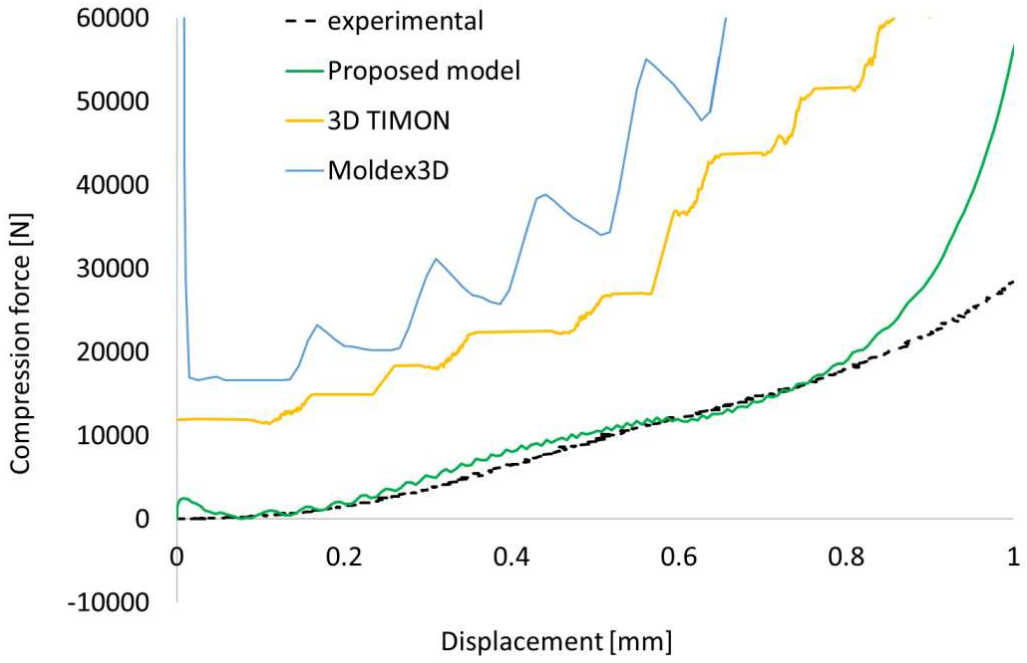

Figure 5: Comparison of compression force-displacement curves predicted by different models against the experimental curve.

4.2 Compression moulding process simulation

Figure 6 compares the filling patterns predicted using different process simulation models against the filling pattern taken from the experimental partial closure. It can be observed from Figure 6a that the SMC experienced solid-like deformation, such that the corners on the original charge still presented. However, the filling pattern predicted by Moldex3D showed a more rounded shape, similar to that's commonly seen in liquid moulding process such as RTM. The filling patterns predicted using the proposed new model on the other hand, showed much better agreement with the experimental filling pattern. The filling pattern predicted using the irregular thickness approach was more realistic compared to that predicted using the regular thickness approach, as it ccould capture the irregular flow front seen in the experimental filling pattern.

  doi:10.5075/epfl-298799_978-2-9701614-0-0

It should be noted that the compression force and pressures predicted using the proposed new model have not been benchmarked against experimental data in this paper. This is because in an actual compression moulding process, the closure speed is usually non-constant, especially during the force switch-over. As the rate dependency has not been incorporated into the current constitutive material model, the compression force and pressured predicted by the process simulation will not be accurate. A more sophisticated material model including rate dependency and temperature dependency will be developed as a part of the future work.

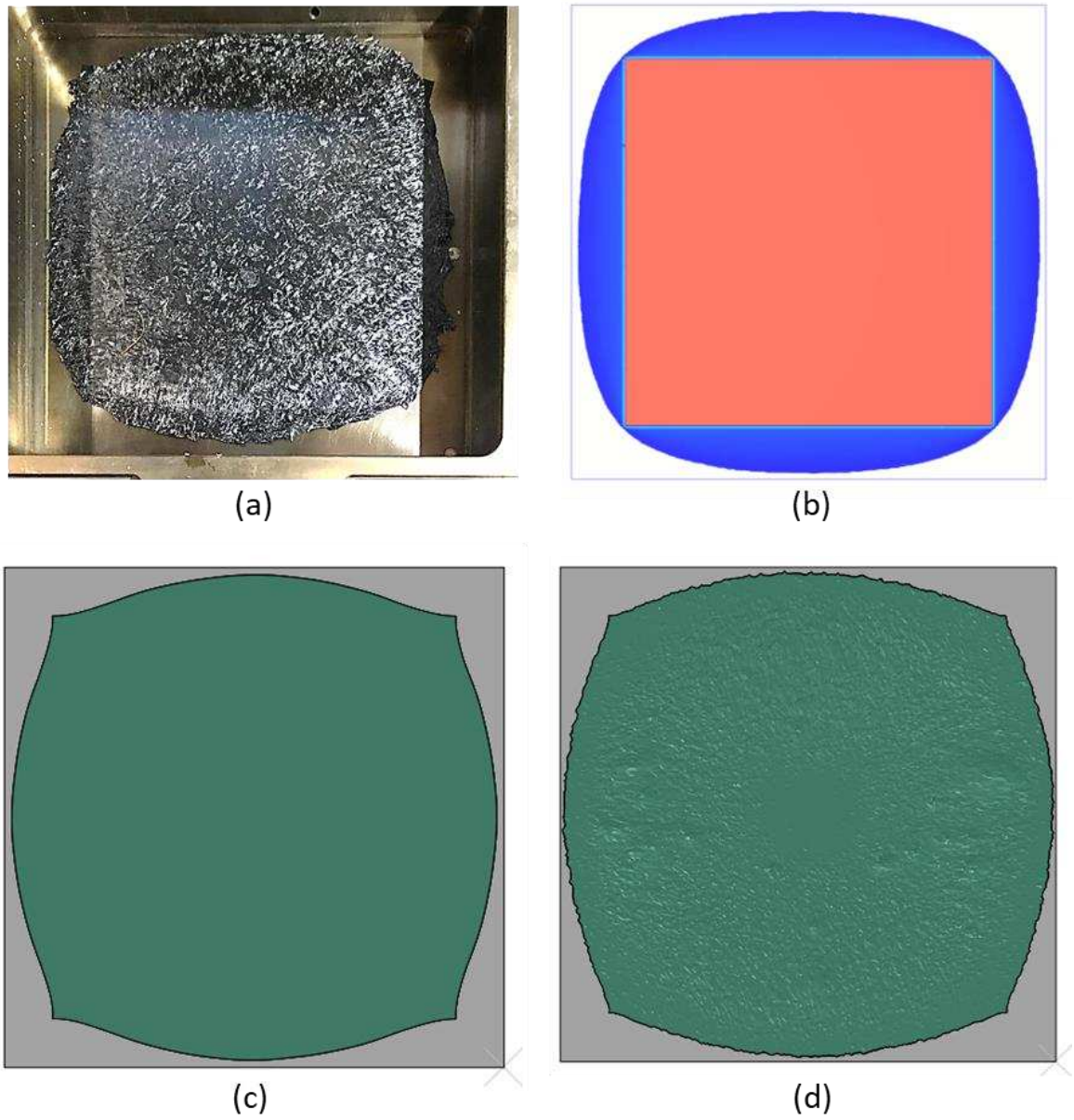

Figure 6: Filling pattern comparison for the flat plaque geometry. (a) Experimental. (b) Moldex3D. (c) Proposed new model with regular charge thickness. (d) proposed new model with irregular charge thickness.

  doi:10.5075/epfl-298799_978-2-9701614-0-0

5. Conclusions

A dedicated material model has been developed for flow simulation of SMC compression moulding. The model describes the flow behaviour of SMC using a compressive stress-strain relationship and the squeeze flow test has been employed to determine the material input data. The squeeze flow testing results have suggested that the material behaviour is both rate dependent and temperature dependent. The new material model has been implemented in ABAQUS using an in-built plasticity model and validated through simulation of the squeeze flow test. The proposed model has demonstrated significant improvement compared to commercial packages. A compression moulding process simulation has also been performed using a flat plaque geometry, where the proposed new model has achieved much better filling pattern prediction compared to commercial package Moldex3D. It has been demonstrated the most realistic filling pattern prediction has been achieved by modelling the initial charge using an irregular thickness approach.

The proposed new modelling technique is simple and accurate and can be implemented in most generic FEA packages. Potential future work will include future material model development to incorporate the rate dependency and temperature dependency.

Acknowledgements

The authors would like to acknowledge the financial support from the EPSRC Future Composites Manufacturing Hub (grant number EP/P006701/1) and the China Scholarship Council.

References

1. Qian C, Deshpande, A., Jesri, M., Groves, R., Reynolds, N., & Kendall, K. A Comprehensive Assessment of Commercial Process Simulation Software for Compression Moulding of Sheet Moulding Compound. 24th International Conference on Material Forming; Liège, Belgique2021.

2. Toll S. Packing mechanics of fiber reinforcements. Polymer Engineering & Science. 1998;38(8):1337-50.

  doi:10.5075/epfl-298799_978-2-9701614-0-0

A MULTI-SCALE MECHANICAL MODEL FOR HIGH FIBER CONTENT SMC IN COMPRESSION MOLDING

François Mahé[a], Christophe Binetruy[a,b], Suresh Advani[b,a], Julien Férec[c], Benedikt Eck[d]

a: Nantes Université, Ecole Centrale Nantes, CNRS, GeM, UMR 6183, 44000 Nantes, France – francois.mahe@ec-nantes.fr
b: Mechanical Engineering, University of Delaware, DE, USA
c: Univ. Bretagne Sud, UMR CNRS 6027, IRDL, F-56100 Lorient, France
d: Faurecia, 14 Rue des Petits Bois, 35400 Saint-Malo, France

Abstract: *High-Performance SMC (HP-SMC) materials have been recently developed with higher fiber volume fraction and long fiber length, where collimated filaments are assembled in the form of bundles. These denser SMC materials exhibit complex behaviors which are not predicted by the suspension theory, especially concerning bundle orientations. They also induces difficulties in compression molding, hence the need for the development of more advanced models to anticipate issues. A generalized deformation measurement is proposed to separate macroscopic deformations from internal rearrangements based on a statistical description of mesostructures. On this basis, a multi-scale formulation is obtained to relate the rheological behavior of HP-SMCs to the material design parameters, with a mixed viscous/friction approach. A comparison with experimental compression molding results confirms the significance of this mixed approach. The proposed model allows to predict the molding force and internal solid stress as a function of the material design parameters.*

Keywords: SMC; process; multi-scale modeling; statistical description

1. Introduction

Sheet Molding Compounds (SMC) are chopped fiber bundle thermoset composite materials used in compression molding processes to manufacture composite structures [1]. Recently, High-Performance SMC (HP-SMC) materials have been developed. They have higher fiber volume fractions and even longer fiber lengths, where collimated filaments are assembled in the form of fiber bundles (Fig. 1). The rheological behavior of these High-Performance SMC (HP-SMC) materials is known to be complex and introduces practical difficulties in compression molding [2-4]. This work focuses on the description of these highly concentrated fiber suspensions used in compression molding, and proposes more advanced models to improve the material design and process parameters.

2. Multi-scale mechanical model

It is assumed that the contact and the friction forces play a major role in the evolution of the high fiber content SMC materials. Indeed, the fiber bundle volume fraction in HP-SMC is in the range of 25%-40%, which is much higher than the dilute suspension limit defined as the inverse of the fiber bundle aspect ratio $1/r \simeq 4\%$ (for a usual aspect ratio of 25). Then, the number of contacts between the fiber bundles is large. The SMC mesostructure is a dense fibrous network subjected to compressive mechanical loadings. These contact forces induced friction stress opposed to the displacements and rotations of the fiber bundles.

  doi:10.5075/epfl-298799_978-2-9701614-0-0

3.1 Friction model

A simple model is proposed to capture friction forces and their consequences on the mesostructure evolution. It is assumed that the frictional stress can be expressed by a Coulomb-type friction law:

$$\tau \leq \eta\sigma \tag{1}$$

where τ is the in-plane tangential contact stress, σ is the average normal contact stress between the bundles and η is a friction coefficient defined by the material of the roving. It is noted positive for a compression. Then, the SMC material can deform and the fiber bundles can move only if the viscous stress applied on the fiber bundles is greater than the frictional stress.

3.2 Fibrous network constitutive law

The normal stress σ is a function of the fibrous mesostructure characteristics. The simplest model is to consider a linear elastic relationship between σ and a deformation metrics of the mesostructure ε:

$$\sigma \sim k\varepsilon \tag{2}$$

where k is a material parameter of the fiber bundle related to its shear modulus.

To express k and ε, let us consider a contact point within the fibrous network. The SMC material is considered to be layers of thin and slender fiber bundles oriented mainly in the plane, immerged in a viscous matrix. The fibrous mesostructure is viewed as a random stack of horizontal fiber bundles [5] placed between two parallel planes separated by a distance h. The fiber bundles have length l, width w, thickness e and an elliptical cross-sectional area $\frac{\pi we}{4}$. As the orientations are mostly in-plane and the fiber bundles are thin slender bodies, the contact areas are all vertically oriented. An increment of the contact force df is proportional to the increment of the vertical relative displacement between the planes du with the proportional coefficient K:

$$2df = Kdu \tag{3}$$

In a displacement-based mechanical problem, the deformation of the fibrous mesostructure is the same across the thickness. The displacement increment can be expressed in terms of vertical stretch $\lambda = h/h^*$ where h^* is the bulky thickness for which there is no contact loading [5]. It leads to:

$$du = e\frac{d\lambda}{\lambda} \tag{4}$$

In a linear approach, the stress inside the bundle is related to its shear. The proportional coefficient is related to the shear modulus of the fiber bundle G, its cross-sectional area and the average distance between the contact points l_c by:

$$k = \frac{G}{l_c}\frac{\pi we}{4} \tag{5}$$

Assuming that the average number of contacts along a fiber bundle is proportional to λ^{-1}, it comes:

$$l_c \simeq \frac{l\lambda}{2} \tag{6}$$

The contact force df is related to the local contact normal stress $d\sigma'$ by the contact area which is for slender fiber bundles $s_c = w^2$. Combining Eq. (3) to (6), we obtained the expression of an increment of the average contact stress:

$$d\sigma' = \frac{df}{w^2} = G\frac{\pi}{4}\left(\frac{e}{w}\right)^2 \frac{1}{r}\frac{d\lambda}{\lambda^2} \tag{7}$$

where $r = \frac{l}{w}$ is the fiber bundle aspect ratio. Integrating Eq. (7) leads to:

$$\sigma' = \frac{G}{r}\frac{\pi}{4}\left(\frac{e}{w}\right)^2 (\lambda^{-1} - 1) \tag{8}$$

This stress is redistributed over the surface of the bundle, which defines the effective contact stress:

$$\sigma = \sigma' \times \frac{lw}{w^2} = \sigma' \times r = G\frac{\pi}{4}\left(\frac{e}{w}\right)^2 (\lambda^{-1} - 1) \tag{9}$$

A comparison with Eq. (2) allow us to define the deformation metrics for a random stack of fiber bundles with a linear shear behavior by $\varepsilon = \lambda^{-1} - 1$. Then, the mechanical modulus is defined from the shear modulus of the fiber bundle and its geometrical dimensions with $k = G\frac{\pi}{4}\left(\frac{e}{w}\right)^2$. In HP-SMC materials, the fiber bundles are made of parallel thin fibers coated with a sizing. As the glass or carbon fiber shear modulus is very large compared with the shear modulus of the sizing, it comes that G is of the same order of magnitude as the shear modulus of the sizing. Eq. (8) relates the mesoscale and microscale.

Eq. (8) involves the stretch of the mesostructure defined from the bulky thickness of the unloaded fibrous mesostructure. The particularity of Eq. (8) compared to the classical continuum mechanics is that the fibrous network is a discontinuous random media. The fiber bundles can be rearranged to increase the fiber content (and decrease the thickness h) without compressive loadings ,for example by aligning the fiber bundles in a shear flow. The thickness of the unloaded configuration h^* can evolve during the transformation, in contrast to the classical continuum mechanics. In [5], we demonstrated from a statistical geometry point of view that $\lambda = \frac{h}{h^*} = \frac{1}{\phi\alpha r}$ where ϕ is the fiber bundle volume fraction, r is the aspect ratio of the bundles and α is a measure of the isotropy of the mesostructure. It is equal to 1 for a 2D isotropic mesostructure, and it tends to zero for aligned fiber bundles. It is a measure of the mesostructure shear considering the average over the fiber bundle population of their relative contact angles θ:

$$\alpha = \frac{\pi}{2}\langle|\sin\theta|\rangle \tag{10}$$

Combining Eqs. (8) and (10) and the expression of λ, we obtain the constitutive law of a concentrated SMC fibrous mesostructure which relates the microscale mechanical properties and the mesoscale random description:

$$\sigma = G\frac{\pi}{4}\left(\frac{e}{w}\right)^2 (\phi\alpha r - 1) = k(\phi\alpha r - 1) \tag{11}$$

Eq. (11) defines the friction stress for a dense fibrous network with a fiber bundle volume fraction in the range $\phi \in \left[\frac{1}{\alpha r}, 1\right]$.

3.3 Homogenized SMC multi-scale constitutive equations

The SMC material is composed of two phase that contribute to the mechanical response of the material. We assume that the matrix phase is modeled as a simple incompressible fluid characterized by its shear viscosity μ_{fluid} and represented by its velocity field $\vec{v}_f$. For a quasi-static transformation, inertia forces are negligible. The conservation equations for the fluid phase are:

$$-\nabla p + \mu_{fluid}\nabla^2\vec{v}_f = 0 \quad ; \quad \nabla \cdot \vec{v}_f = 0 \tag{12}$$

The intrinsic phase averages of the velocity fields of the solid and fluid phases are related to the average phase velocity by the fiber bundle volume fraction:

$$\langle\vec{v}_s\rangle^s = \phi\langle\vec{v}_s\rangle \quad ; \quad \langle\vec{v}_f\rangle^f = (1-\phi)\langle\vec{v}_f\rangle \tag{13}$$

In SMC materials, we assume there is no segregation, i.e., the average velocities of both phases are equal. This assumption is valid as long as there is no interfacial rupture between the two phases, but it may be invalid in some extreme cases encountered in industrial processes.

Taking the spatial average of Eq. (12), we obtain the homogenized conservation equations for the SMC material:

$$-(1-\phi)\nabla\langle p\rangle^f + (1-\phi)\mu_{fluid}\nabla^2\langle\vec{v}_f\rangle^f + \phi\mu_{solid}\nabla^2\langle\vec{v}_s\rangle^s = 0 \quad ; \quad \nabla\cdot\langle\vec{v}_s\rangle = \nabla\cdot\langle\vec{v}_f\rangle \tag{14}$$

The solid viscosity comes from Eq. (1) and is defined as the ratio between the friction threshold stress and the shear rate in the case where the criterion is equality.

Using Eq. (13), Eq. (14) can be reformulated into the more compact form:

$$-(1-\phi)\nabla\langle p\rangle^f + \mu_{fluid}[1+M]\nabla^2\langle\vec{v}\rangle = 0 \quad \text{with } \langle\vec{v}_s\rangle = \langle\vec{v}_f\rangle = \langle\vec{v}\rangle \tag{15}$$

where the adimensional number M is the ratio between the friction stress and the fluid stress:

$$M = \frac{\eta\sigma}{\mu_{fluid}\dot{\gamma}} = \frac{\eta k}{\mu_{fluid}\dot{\gamma}}(\phi\alpha r - 1) \tag{16}$$

This number characterizes the type of flow. For $M = 0$, the flow is suspension-like and is governed by the usual equations of suspension theory. For $0 < M$, the mesostructure is compacted in a fibrous network. The contacts govern the mechanical response of the fibrous mesostructure and the effective viscosity of the media increases compared to the fluid viscosity by the factor $1 + M$.

Based on the friction approach, it is proposed to extend the usual description of the evolution of the orientation tensor field through a new model respecting the Folgar-Tucker equation [7]:

$$\dot{\boldsymbol{A}}_{\boldsymbol{2}} = 2(\boldsymbol{L}\cdot\boldsymbol{A}_{\boldsymbol{2}})^{sym} - 2\boldsymbol{A}_{\boldsymbol{4}}\boldsymbol{:}\boldsymbol{D} \tag{17}$$

where $\boldsymbol{L}$ is the velocity gradient applied on the fibrous mesostructure. In this approach, this velocity gradient is no longer equal to the fluid phase velocity gradient as in suspension theory, but from the ratio between the local friction stress obtained from Eq. (8) and the shear stress. It

is naturally defined by $\boldsymbol{L} = (1 - M)\nabla\langle\vec{v}\rangle$ for $0 \leq M < 1$ and $\boldsymbol{L} = 0$ for $M > 1$. This new model expresses the local slipping between the fiber bundles and the fluid phase in the case of important friction for high-fiber content materials.

3. Compression experiments on custom-designed SMC materials

To characterize the macroscopic mechanical response of SMC materials, lab-scale compression tests are carried out to measure the compression force of different custom-designed SMC materials with different fiber bundle volume fractions and fiber lengths. The same roving and resin are used for all the SMC materials. Design parameters are given in Table 1.

The mold is made of two parallel circular plates of radius 50 mm, heated to a temperature of 140°C. Circular SMC samples of initial radius 50 mm, consisting of three plies of thickness 2 mm, are compressed at a constant velocity. Two compression velocities of 1 mm/s and 5 mm/s as used for each material. Three samples are realized for each configuration.

Table 1: Design parameters of the different SMC materials tested in the compression experiment.

	Fiber bundle Mass fraction	Fiber bundle volume fraction	Fiber bundle length
SMC 1	25 %	18 %	25 mm
SMC 2	32 %	24 %	25 mm
SMC 3	47 %	37 %	25 mm
SMC 4	25 %	18 %	50 mm

To confirm the friction-based model, we propose to compare the dependencies of the SMC effective viscosity with the different design parameters and the compression rate. In the experiment, the compression velocity $\dot{h}$ is constant. For a gap h between the mold plates of radius R, the compression pressure imposed by the mold is [6]:

$$P = 3\left(\frac{R}{h}\right)^2 \mu_{eff}\dot{\varepsilon} \quad \text{with } \dot{\varepsilon} = \frac{\dot{h}}{h} \quad \text{and} \quad \mu_{eff} = \mu_{fluid}[1 + M] \tag{18}$$

The measured compression pressure corresponds to the average of the pressure field. Using definitions of phase average operators Eq. (13):

$$P = (1 - \phi)\langle p\rangle^f \tag{19}$$

With Eq. (18) and (19), we define the reduced viscosity:

$$\mu_{red}^{(\text{exp})} = \frac{\mu_{eff}}{1-\phi} = \frac{\langle p\rangle^f}{3(R/h)^2\dot{\varepsilon}} \tag{20}$$

According to the proposed friction-based model Eq. (15), the averaged pressure $\langle p\rangle^f$ is proportional to the reduced pressure which is obtained by:

$$\mu_{red}^{(\text{theory})} = \mu_{fluid}\frac{(1+M)}{1-\phi} \sim \frac{\phi\alpha r - 1}{1-\phi} \tag{21}$$

  doi:10.5075/epfl-298799_978-2-9701614-0-0

This reduced viscosity depends on the material parameters through the term $\frac{\phi\alpha r-1}{1-\phi}$, which is different for each SMC materials in Table 1. The reduced viscosity is supposed to evolve linearly in this term, which will be verified experimentally. Due to the stochastic variability of such random materials, the determination of the effective viscosity is difficult and can evolve in a compression test with long flow length and material evolutions. In our case, the flow length is small enough to neglect the mesostructure evolutions as reorientations of the fiber bundles. To apply Eq. (18), we have to characterize the effective viscosity at the initial time when the SMC material begins to flow so as not to depend on the evolution of viscosity due to resin curing.

4. Comparison of experimental and theoretical results

From the compression tests on the different SMC materials, the reduced viscosity is calculated from Eq. (20) and compared to the factor $\frac{\phi\alpha r-1}{1-\phi}$ which is contained in the definition of M in Eq. (21). The results are plotted in Fig. 1.

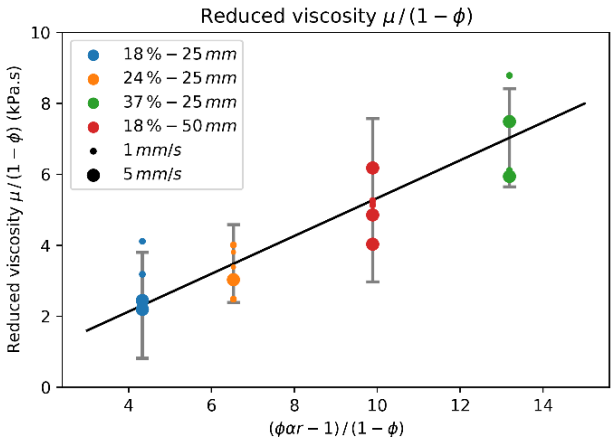

Figure 1. Evolution of the experimental reduced viscosity for various fiber bundle volume fractions, fiber bundle length and compression velocities. The error bars represent the interval $[-2\sigma, +2\sigma]$ *where σ is the standard deviation of the experimental values.*

It is shown that the reduced density varies linearly with respect to $\frac{\phi\alpha r-1}{1-\phi}$ where this dimensionless number involves the different mesostructure descriptors. It comes that the effective viscosity of the SMC material is governed by friction forces according to Eqs. (15) and (16). This model gives a non-trivial relationship between the effective viscosity of a SMC material and its mesostructural descriptors.

5. Conclusion

Based on the assumption that the large number of contacts between fiber bundles in SMC materials induces compressive loading in the fiber network, we proposed a friction-based model to predict the internal solid stress. This frictional stress modifies the effective viscosity of the SMC material according to the mesostructure parameters. Model predictions are compared with compression tests involving different custom-designed SMC materials. This model shows that the macroscopic behavior of SMC materials can be related to internal mesostructural properties. A dimensionless number is defined to characterize the regime of flow of high-fiber content SMC materials and the kinematics of the evolving mesostructure.

  doi:10.5075/epfl-298799_978-2-9701614-0-0

Acknowledgements

We thank Faurecia for their technical and financial supports and Owens Corning for providing the custom SMC materials.

6. References

1. Orgéas L, Dumont P. Sheet molding compounds. Wiley encyclopedia of composites 2011; 1-36.
2. Dumont P, Vassal J, Orgéas L, Michaud V, Favier D, Månson J. Processing, characterisation and rheology of transparent concentrated fibre-bundle suspensions. Rheologica acta 2007; 46(5):639-651.
3. Schommer D, Duhovic M, Hausmann J. Development of a Solid Mechanics Based Material Model Describing the Behavior of SMC Materials. Proceedings of the 14th International Conference on Flow Processes in Composite Materials; 2018; Lulea, Sweden.
4. Meyer N, Schöttl L, Bretz L, Hrymak A, Kärger L. Direct Bundle Simulation approach for the compression molding process of Sheet Molding Compound. Composites Part A: Applied Science and Manufacturing 2020; 132:105809.
5. Mahé F, Binetruy C, Advani S, Férec J, Eck B. A multi-scale statistical description of stacks of non-cohesive thin particles. Powder Technology 2022; 399:116988.
6. Béreaux Y. Écoulement dans la mise en oeuvre des polymères. 2014.
7. Advani S, Tucker C. The use of tensors to describe and predict fiber orientation in short fiber composites. Journal of rheology 1987; 31(8):751-784.

  doi:10.5075/epfl-298799_978-2-9701614-0-0

FFF MANUFACTURING OF HIGH PERFORMANCE THERMOPLASTICS. CRYSTALLINITY AND MECHANICAL PROPERTIES LINKED TO THE PROCESSING PARAMETERS

Ricardo Losada, Francisco Ansedes, Celia Martin, Xabier Pérez, Alberto Pedreira, Elena Rodriguez, Adrian Rodriguez

AIMEN Technological Centre – ricardo.losada@aimen.es

Abstract: *Fused filament fabrication (FFF) technology has been mostly restricted to polymers with relatively low melting temperatures, and this has limited the use of FFF in very demanding sectors such as aerospace. The development in the last years of highly stable thermoplastics such as the PAEK's (polyaryletherketones) open the way to widespread the use of FFF in aerospace. One of the goals of the H2020 RETPAIR project is to gain knowledge in the 3D printing of PAEK´s, by understanding the link between the polymer characteristics, the printing parameters, annealing treatment, and the resulting mechanical properties. It was compared the 3D printing of two different PAEK´s, the pseudo-amorphous PEKK 60:40 and the slow crystallizing LM-PAEK. Results showed a significant variation of crystallinity and mechanical properties with the annealing treatments. The overall mechanical performance of PEKK is superior to LM-PAEK. Surprisingly, a stronger orientation dependency for PEKK 60:40 is also reported.*

Keywords: Poly aryl ether ketones (PAEK´s); Fused filament fabrication (FFF); 3D printing; Annealing; Crystallinity

Introduction

Poly aryl ether ketone polymers (PAEK´s) are widely used as high-performance thermoplastics due to its excellent thermal and mechanical properties. They also offer excellent chemical resistance and good chemical and physical properties at high temperatures. During the last years, different additive manufacturing (AM) technologies have been developed for thermoplastic materials. Fused filament fabrication (FFF) systems typically require smaller set up and running costs than other systems and FFF has become a fast-growing polymer AM technology. By extruding solid filament through a computer-controlled hot nozzle onto a building plate, the system creates parts layer by layer. FFF printed parts are generally less mechanically capable than their conventionally manufactured, polymer-processed counterparts, such as via injection molding (IM) [1]. These deficiencies are primarily a result of the nature of the FFF mechanism. Important drawbacks of FFF are porosity and interlayer adhesion, that are mostly due to a limited coalescence between filaments. Coalescence occurs above the melting temperature of the polymer when the crystalline phases have turned into amorphous phases. The coalescence in semi-crystalline polymers is strongly affected by the kinetics of crystallization and the thermal gradient during the processing. If the crystallization process is very fast, the filaments solidify rapidly and there is no time for the macromolecular interdiffusion between adjacent layers. Further, imbalanced crystallization at the interface, in the bulk, and in previously deposited layer leads to warpage, residual stress accumulation and interlayer delamination [2]. Therefore, it is essential to ensure appropriate control of the temperature during processing, especially for fast crystallizing PAEK´s such as PEEK, which is

  doi:10.5075/epfl-298799_978-2-9701614-0-0

probably the most widely known material within this family and is commonly used in industry as a suitable metal alloy replacement in numerous structural applications. However, such thermal control is very difficult in FFF. These limitations have restricted the use of PEEK and its composites in FFF. Alternatively, other slow crystallizing PAEK matrices such as LM-PAEK and PEKK 60:40 are interesting alternatives. These slow crystallizing polymers can be initially printed in amorphous phase followed by an annealing treatment to increase the crystallinity, which in turn can increase some mechanical properties of semi-crystalline polymers [3].

The aim of this work is to investigate the FFF processing of two different PAEK polymers, the PEKK 60:40 and LM-PAEK. The mechanical properties of printed PEKK 60:40 and LM-PAEK samples in horizontal (X) and vertical (Z) build directions were evaluated, and the impact of annealing on crystallinity and on the mechanical properties is also reported. The present work is limited to filaments from two different manufacturers. The printing settings and annealing conditions for each material were set based upon manufacturer recommendations and prior experience.

1. Materials and Methods

2.1 Materials

Two different PAEK filaments were studied. These were a PEKK 60:40 filament acquired from 3DXTECH, commercial name PEKK-A, and a LM-PAEK filament supplied by VICTREX and commercially identify as AM200. The material properties of both filaments are presented in *Table 1*.

Table 1: Material properties of filaments.

Material	Tg (°C)	Tm (°C)	Filament diameter (mm)
PEKK-A	162	305	1.75
AM200	151	303	1.75

2.2 FFF printing

The filaments were used to manufacture samples for tensile and flexural tests according to standards ISO 527-2 and ISO 178 and using a commercially available printer (3NTR A2V4). A scheme of the manufactured specimens are shown in Figure 1. The samples were printed using a 0.5 mm nozzle with a layer height of 0.25 mm using a perimeter printing speed of 25 mm min^{-1}, and an infill printing speed of 30 mm min^{-1}. The printing temperatures were adjusted for both materials. A comprehensive collection of the printing settings is summarized in *Table **2***. Two different printing directions have been tested; X specimens (horizontal build) were fabricated laying on the print bed in the XY plane as shown in *Figure 1*, while Z specimens (vertical build) were fabricated standing vertically on the print bed as individual samples unsupported in the XY plane.

  doi:10.5075/epfl-298799_978-2-9701614-0-0

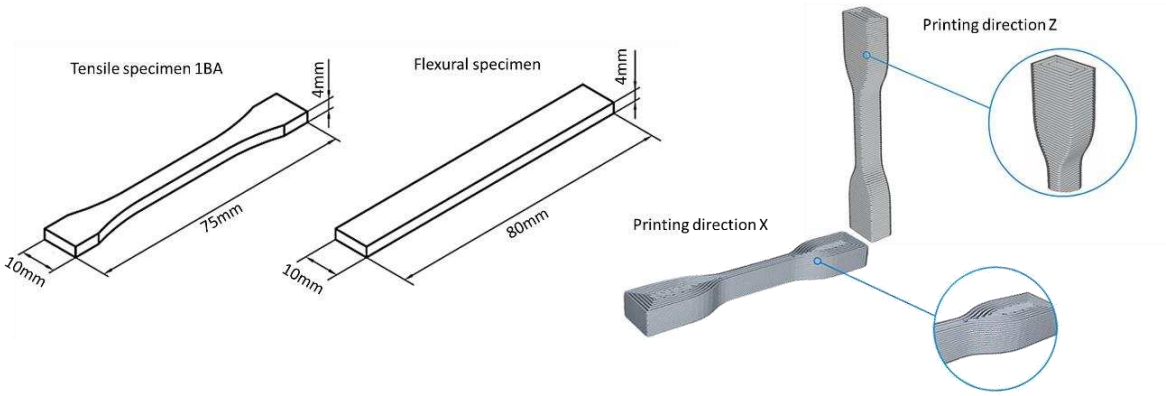

Figure 1: 3D printed tensile and flexural test specimens according to ISO527-2 and ISO 178, respectively(left), and printing direction scheme (right).

Table 2: Printer settings used in this work.

Printing parameter	PEKK-A Y	PEKK-A Z	AM200 Y	AM200 Z
Slicer	KISSLICER			
Nozzle temperature (°C)	370		385	
Build chamber temperature (°C)	90	80	75	75
Bed temperature (°C)	140		135	
Nozzle diameter (mm)	0.5			
Layer height (mm)	0.25			
Perimeter width (mm)	0.6			
Infill width (mm)	0.6	0.5	0.5	0.5
Flow	1	0.97	0.96	0.95
Perimeter infill overlap	1	0.75	1	0.75
Cooling fan (%)	0	100	50	100
Retraction	0			
Perimeter printing speed (mm s^{-1})	25			
Infill printing speed (mm s^{-1})	30			
Filament diameter (mm)	1.75			
Build plate material	Glass			
Adhesive	Nano polymer			

2.3 Annealing

Heat treatments of the samples were carried out in a furnace. The thermal cycle was the same for both materials. The temperature was increased from r.t to 160 °C at 10 °C/min, and held at 160 °C for 30 min, and the raised at 10 °C/min to 200 °C and maintained there for 90 min. Finally, the samples were cooled down at 1 °C/min until they reach ambient conditions.

2.4 Mechanical testing

Tensile and flexural tests were performed to characterize the samples using a 5 kN capacity standard tensile/compression machine (Shimazdu®). Tensile properties were evaluated according to ISO 527-2, moduli were measured at a constant speed of 1 mm min^{-1} whilst tensile strengths and elongation at break were measured at 5 mm min^{-1}. Flexural tests (under three

  doi:10.5075/epfl-298799_978-2-9701614-0-0

points bending configuration) were carried out according to ISO 178 with a span length of 64 mm, the radius of two supports and central loading edge were 5 mm, and the test speed was 2 mm/min. At least five repeated specimens were tested, and the data was averaged.

2.5 Differential Scanning Calorimetry (DSC)

The thermal properties of the materials were analyzed by Differential Scanning Spectroscopy (DSC). The experiments were carried out in a DSC Q2000 (TA Instruments). The DSC tests were performed with N_2 as the purge gas. The samples were filaments and cuts from the fabricated specimens. Samples with a mass of 5-7 mg were put on an alumina crucible and subjected to a heating cycle from r.t to 360 °C at a rate of 10 °C/min. After the first heating cycle, the temperature is held at 360 °C for 15 min, that is about 50 °C above the melting temperature to erase the thermal history, then cooling to r.t at 10 °C/min, and finally, a second heating from r.t to 360 °C at 10 °C/min. Crystallinity was determined by the equation 1.

$$\chi = \frac{\Delta H_m}{130} \times 100\% \qquad 1$$

Where ΔH_{endo}, ΔH_{exo} are the integral area of the endothermic peak and exothermic peak, respectively, and 130 J/g is the melting enthalpy of a 100% crystalline PEEK sample [4].

2. Results and Discussion

3.1 Thermal analysis

The DSC thermograms show that, for both materials, at low build temperature samples are printed mostly amorphous. In the first heating cycle, PEKK-A and AM 200 present a cold crystallization transition prior to melting, see Figure 2. Interestingly, the melting signal for the PEKK-A sample has a shoulder that probably results from the presence of a different crystalline structure. To determine the melting enthalpy, the total area under the melting peak is used for calculations. The resulting crystallinity degree of “as printed parts” is, as expected, slightly higher for AM 200 7.5% than for PEKK-A 2.4%. The much slower crystallization rate of PEKK-A is evidenced in the second heating cycle, after erasing the thermal history, where the PEKK-A sample still shows a cold crystallization process proving that this material hardly crystallizes at a cooling rate of 10 °C/min from the melt.

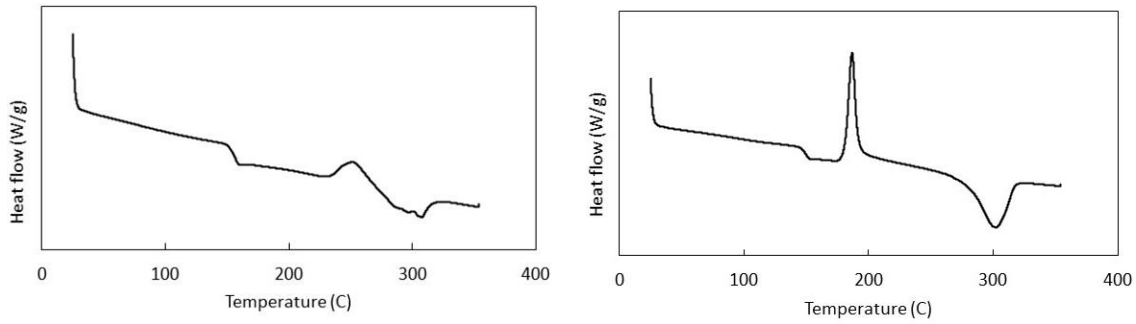

Figure 2: DSC, first heating cycle for “as printed” samples, left PEKK-A, right AM 200. Exo up

After annealing, the first heating cycle shows significant differences respect to the “as printed” samples, see Figure 3. Both materials exhibit a secondary melting peak, at 20-30 °C above the annealing temperature that has already been reported in previous studies with PAEK´s [5]. This

secondary peak is attributed to a population of small crystals formed during the annealing. The calculated total crystallinity is similar for both materials 24% for PEKK and 27% for AM 200. Table 3 displays the measured and calculated parameters for the first heating cycle for as printed and annealed samples.

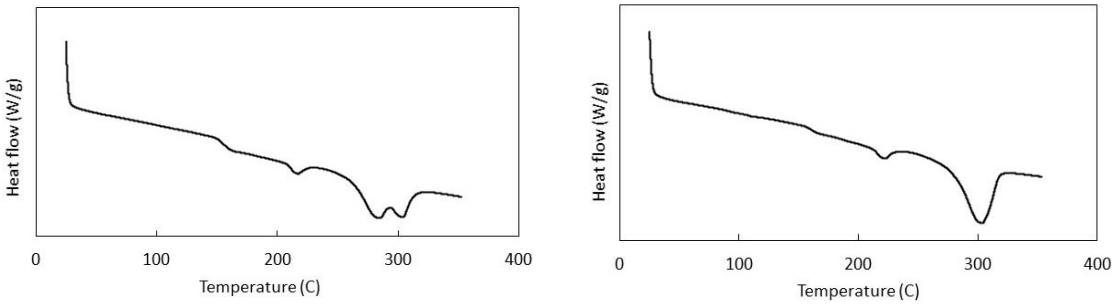

Figure 3: DSC, first heating cycle for "annealed" samples, left PEKK-A, right AM 200. Exo up

Table 3: Transitions temperatures, enthalpies, and estimated crystallinities correspondent to the first heating cycle.

	Material	T_g (°C)	T_{cc}(°C)	ΔH_{cc} (J/g)	T_m(°C)	ΔH_m (J/g)	X (%)
As printed	PEKK-A	156.9	252.7	8.1	307.3	11.2	2.4
	AM 200	150.0	186.7	24.1	301.1	33.8	7.5
Annealed	PEKK-A	155.8	-	-	216.7/303.8	29.9	24.7
	AM 200	159.6	-	-	222.0/302.9	35.6	27.4

3.2 Mechanical properties

Tensile and flexural properties were tested to evaluate the mechanical performance of both materials "as printed" and after annealing. Experimental results of tensile and flexural performances in terms of average strength, stiffness, and elongation at break are displayed in Table 4 and Table 5.

Table 4 : Tensile and flexural properties of PEKK-A.

Material	Printing direction	Tensile			Flexural	
		Strength / MPa	Modulus /GPa	Elongation at break %	Strength / MPa	Modulus / GPa
As printed	X	83.9±3.0	3.2±0.3	160.2	136.0±4.0	3.1±0.1
	Z	69.2±2.3	2.5±0.2	4.9±0.6	60.0±7.0	2.1±0.1
Annealed	X	96.4±9.8	3.6±0.1	5.0±3.3	161.0±5.0	3.4±0.1
	Z	64.3±5.0	2.9±0.2	2.4±0.3	91.0±12.0	2.6±0.2

  doi:10.5075/epfl-298799_978-2-9701614-0-0

Table 5:Tensile and flexural properties of AM 200.

Material	Printing direction	Tensile			Flexural	
		Strength / MPa	Modulus /GPa	Elongation at break %	Strength / MPa	Modulus / GPa
As printed	X	60.7±0.8	2.5±0.7	123.0	96.8±2.1	2.4±0.9
	Z	46.9±5.0	2.2±0.2	11.3±4.8	70.4±1.1	1.9±0.1
Annealed	X	71.2±8.3	2.8±0.6	11.8±7.7	134.0±7.0	2.8±0.2
	Z	49.3±10.6	2.4±0.6	2.8±1.3	102.0±9.0	2.4±0.1

According to theory [6], the mechanical properties of polymers are closely related to crystallinity, the chains in crystalline state are better ordered and present stronger intermolecular forces causing greater strength and rigidity. Contrary, the macromolecular chains in amorphous state are looser, showing good extensibility (plastic behavior). Further, the strong orientational arrangement of the macromolecular chains deposited by FFF has a big impact on the mechanical properties of the part depending on the testing direction. The advantage of using slow crystallizing polymers in FFF is proved by the analysis of the mechanical properties in the Z samples. For those samples, the loading direction is perpendicular to the fabrication direction and mechanical parameters such as tensile strength are related to the interlayer bonding. For the as printed samples, tensile strength for Z samples have values of 59 MPa for PEKK-A and 47 MPa for AM 200, which are markedly higher than the previously published for other PAEK, such as PEEK [7], that are in the range of 10 to 25 MPa. In fast crystallizing polymers like PEEK, the quick formation of crystals on the surface limits the chain interdiffusion, leading to weak interlayer bonding and reduced Z properties.

The comparison between the as printed PEKK-A and AM 200 shows the following: for X samples, PEKK-A exhibits tensile and flexural strength values, which are around 40% higher than for AM 200. For the Z samples, the same trend is observed for the tensile strength but for the flexural strength the values are slightly lower for PEKK-A. As well, when analyzing the anisotropy, regarding the tensile properties there are not big differences for both materials. However, for the flexural properties the quasi amorphous PEKK-A results far more anisotropic than AM 200, Table 6.

Table 6: Anisotropic character (as printed specimens)

Material	Ratio properties Z build direction respect to X build direction	
	Tensile strength	Flexural strength
PEKK-A	82%	44%
AM 200	78%	72%

Upon annealing, regardless the material, for the X samples the increase in crystallinity has a strengthening effect. Accordingly, an increase of 15-20% is observed in the tensile and flexural properties. However, for the Z samples the situation is different, the annealing increases notably the flexural strength, but there was practically no effect on the tensile strength. We speculate that such differences between the flexural and tensile properties for Z samples are related to the fabrication process. Though the processing conditions are the same for both type of samples, the different cross section may lead to local environmental variations that affect the

  doi:10.5075/epfl-298799_978-2-9701614-0-0

performance of the samples. During the fabrication of flexural and tensile samples, the cooling fan is set at 100%, but the cross section of the flexural samples is twice larger than that of the tensile samples. The molecular interdiffusion is strongly affected by the temperature at the interlayer surface, and we believe that the small cross-section of the tensile samples allows its faster cooling leading to a more restricted molecular interdiffusion between adjacent layers compared to the flexural samples. As consequence, transcrystallization after annealing is very limited for the tensile samples, and thus the tensile strength remains practically unaffected.

3. Conclusions

This work analyzes the effect of polymer characteristics, build orientation, and annealing on the mechanical performance of 3D printed parts produced from commercially available filaments of "quasi amorphous" PEKK 60:40 and slow crystallizing LM-PAEK by fused filament fabrication (FFF). Flexural and tensile strength and stiffness analysis demonstrated a higher overall higher mechanical performance of PEKK 60:40 under ambient conditions. As well, differences in the mechanical properties in the horizontal (X) and vertical (Z) build directions indicate more anisotropy in the printed samples of PEKK 60:40.

Upon annealing, the mechanical properties showed some variations. Regardless the build direction, the increase in crystallinity has a strengthening effect on the flexural strength and stiffness of both polymers. However, while for the tensile properties the strengthening is clear in the horizontal build direction, in the vertical direction the effect is almost negligible for both materials. Variations of temperature near the interface due to the different geometries of flexural and tensile Z samples may justify those results. However, further research is needed to put more light on it.

Acknowledgments

This work was developed in the frame of the RETPAIR project, which has received funding from the Clean Sky joint Undertaking (JU) under grant agreement No 101008183.

4. References

1. Fico D, Rizzo D, Casciaro R, Esposito Corcione C. A review of polymer-based materials for Fused Filament Fabrication (FFF): Focus on sustainability and recycled materials. Polymers. 2022; 14:465.
2. Basgul C, Yu T, MacDonald DW, Siskey R, Marcolongo M, Kurtz SM. Does annealing improve the interlayer adhesion and structural integrity of FFF 3D printed PEEK lumbar spinal cages?. Journal of the Mechanical Behavior of Biomedical Materials. 2020; 102:103455.
3. Regis M, Bellare A, Pascolini T, Bracco P. Characterization of thermally annealed PEEK and CFR-PEEK composites: Structure-properties relationships. Polymer Degradation and Stability. 2017; 136:121-130.
4. Blundell DJ, Osborn BN. The morphology of poly(aryl-ether-ether-ketone). Polymer. 1983;414 24(8):953-958.
5. Gardner KCH, Hsiao BS, Matheson Jr RR, Wood BA. Structure, crystallization and morphology of poly(aryl ether ketone ketone). Polymer. 1992;33 12:2483-2495.

  doi:10.5075/epfl-298799_978-2-9701614-0-0

6. Yang C, Tian X, Li D, Cao Y, Zhao F, Changquan S. Influence of thermal processing conditions in 3D printing on the crystallinity and mechanical properties of PEEK material. Journal of Materials Processing Technology. 2017;248:1-7.
7. Rinaldi M, Ghidini T, Cecchini F, Brandao A, Nanni F. Additive layer manufacturing of poly (ether ether ketone) via FDM. Composites Part B Engineering. 2018;145:162-172

  doi:10.5075/epfl-298799_978-2-9701614-0-0

DIGITIZING THE PRODUCTION OF CARBON FIBER SHEET MOLDING COMPOUNDS

Miro Duhovic[a], Thomas Hoffmann[a], Dominic Schommer[a], Jürgen Ernst[b], Katja Schladitz[c], Ali Moghiseh[c], Florian Gortner[a], Joachim Hausmann[a], Peter Mitschang[a], Konrad Steiner[c]

a: Leibniz-Institut für Verbundwerkstoffe GmbH, 67663 Kaiserslautern, Germany – miro.duhovic@ivw.uni-kl.de
b: Fraunhofer IIS, Am Wolfsmantel 33, 91058 Erlangen, Germany
c: Fraunhofer ITWM, Fraunhofer-Platz 1, 67663 Kaiserslautern, Germany

Abstract: *Recently, it has been discovered that carbon fibers polarize light, providing an opportunity to detect the fiber orientation on the surface of carbon fiber-reinforced polymer parts using polarization imaging. In this work, the orientation of the fibers on the surface of a carbon fiber-reinforced Sheet Molding Compound (C-SMC) semi-finished product is measured during continuous production, enabling real-time quality control and complete digitization of the material's fiber orientation information. The polarization camera captures images of the material at defined time intervals, creating an image stack. These images are then stitched to create a continuous image of the entire semi-finished material product roll. Fiber orientation information at any location can then be digitally extracted to create virtual-cutting and stacking plans for optimal usage of material from the roll for compression molding parts. Moreover, the images provide the initial fiber orientation information, essential for accurate numerical simulation of the C-SMC compression molding process.*

Keywords: Sheet Molding Compound; Polarization imaging; Fiber orientation

1. Introduction

Fiber orientation strongly influences the stiffness and strength of composite components. Ideally, it is an attribute of the material, which should be digitally documented throughout the entire processing chain for numerical simulation and quality control. There are several methods for measuring fiber orientation in composite parts. The most common are; image analysis via optical microscopy [1], [2], the Eddy current measurement technique for carbon fiber reinforced plastics (CFRPs) [3-5] and X-ray computed tomography (CT) [1], [6-9]. All three methods require expensive equipment or elaborate specimen preparation. In this paper, another method for fiber orientation measurement is demonstrated using the so-called polarization imaging technique [10-13]. This method takes advantage of the fact that carbon fibers reflect polarized light when illuminated with non-polarized light [11]. The angle of polarization (AOP) can then be correlated to the in-plane fiber orientation angle [12], [13]. The method provides a cost effective way of directly photographing or filming the surface of a material/component and obtaining complex fiber orientation information in real–time without special preparation and with no restriction on the specimen size. The technology is seen as one of the key elements for the digitization of carbon fiber based polymer composites in the material processing chain. Potential applications for polarization imaging of CFRP surfaces include quality assurance of CFRP semi-finished products and components as well as the automation, control, and optimization of the many different manufacturing routes for CFRP components.

  doi:10.5075/epfl-298799_978-2-9701614-0-0

2. Polarization Camera – Principle of Operation

Figure 1 (a) illustrates the basic working principle of the polarization effect by reflection. Light is termed non-polarized if the light wave has no defined angle of oscillation about its axis of propagation. Almost all natural and artificial light sources emit non-polarized light. If these light waves hit a polarizing object, the reflected or transmitted light waves will all be oriented at the same angle, as shown in the figure by the single reflected wave. If unpolarized light strikes the surface of a CFRP, linearly polarized light is reflected. The angle of the reflected wave about its axis of propagation corresponds to the fiber orientation at the point of reflection. The resin system does not affect the measurement, as many polymer resins in their natural (uncoloured) state are amorphous and therefore relatively transparent. The exact working principle of the polarization on CFRP surfaces has not yet been researched in detail. However, an effect similar to that of the wire-grid polarizer is suspected [11]. Furthermore, wire-grid polarizers are an important element of the polarization camera itself.

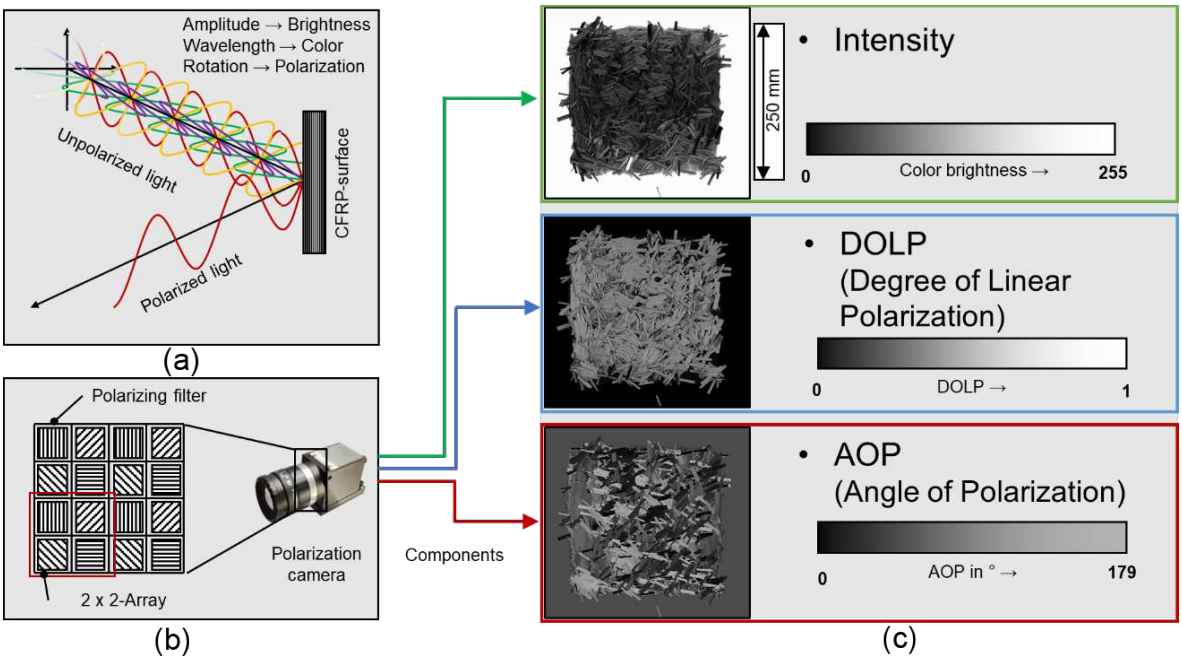

Figure 1. a) Basic working principle of light polarization by reflection, b) wire-grid based pixel filter used in the polarization camera to detect the angle of polarization and c) the three simultaneously captured images (Intensity, DOLP and AOP) demonstrated on a specimen containing randomly dispersed carbon fiber rovings

2.1 Wire-grid polarizers

Wire-grid polarizers are small structures consisting of a transparent substrate on which thin, parallel conductive metal wires are deposited. When the polarizer is exposed to incoming (unpolarized) light, the wires transmit the component of the electric field perpendicular to the wires, and reflect the component parallel to the wires. For a wire-grid polarizer to work, the distance between the wires must not be greater than the wavelength of the light used [14]. The conventional approach to measure the polarization direction of light is to use a rotating polarizer placed directly in front of the camera. By changing the amplitude of the transmitted light waves measured behind the polarizer as a function of the rotational orientation of the polarizer, it is possible to analytically determine the polarization angle of the incident light. [11] Direct

  doi:10.5075/epfl-298799_978-2-9701614-0-0

integration of differently oriented wire-grid based polarizing filters on the pixel sensors of a camera eliminates the need for an upstream polarizing filter. The filters on the pixel sensors are arranged in a 2 x 2 array (Figure 1 (b)) with differently oriented polarizers (0°, 45°, 90°, 135°) which attenuate the amplitude of the incident light depending on its polarization direction. Using the four intensities measured at the pixel sensors, the angle of polarization (AOP) can then be calculated and displayed in real-time. [11, 13]

In a recent paper by Ruan et al. [15], it was shown that the surface of carbon fibers contains grooves of varying shape, most of which have a width in the range of 400 – 700 nm (which is exactly the wavelength range of visible light). This geometric characteristic, in addition to the fact that carbon fibers are electrically conductive, seem to be the two prerequisites enabling this measurement technique for carbon fibers.

2.2 Image components

The polarization camera used in this work (type: VCXU-50MP, manufacturer: Baumer GmbH) supports 8-bit (256 grayscale), 10-bit (1024 grayscale), and 12-bit (4096 grayscale) pixel formats. It is able to process (practically instantaneously) the light measured at the individual pixel sensors into three image components, capturing complementary information about the reflected light (see Figure 1 (c)):

Intensity: This display mode corresponds to that of a conventional grayscale image and represents the color brightness of the imaged object.

DOLP: Degree of Linear Polarization (DOLP), represents the ratio of polarized to unpolarized light. The higher (brighter) the grayscale value, the higher the degree of polarization. In this work, surfaces without polarizing properties are therefore depicted in black, while surfaces with ideal polarizing properties appear in white.

AOP: The Angle of Polarization (AOP), represents the polarization direction of the incident light as a grayscale value. The spectrum of unprocessed AOP images ranges from black (polarization angle = 0°) to white (polarization angle = 180°). In the cases presented in this paper, this means that the orientation of the unprocessed AOP component represents the fiber orientation as a grayscale value between 0 (polarization angle = 0°) and 255 (polarization angle = 180°).

ADOLP: The Angle & Degree of Linear Polarization (ADOLP) combines the two display modes DOLP and AOP into a color image. The DOLP is represented as color brightness and the AOP as color value. This display mode is mainly used for visualization as shown later in Figure 2.

3. Polarization imaging during C-SMC material production

Using the principles described in the previous section, the fiber orientation of a carbon fiber-reinforced Sheet Molding Compound (C-SMC) semi-finished product is measured during continuous production, enabling real-time quality control and complete digitization of the material's fiber orientation information. A polarization imaging system is used to analyze the fiber orientation distribution for a complete roll of manufactured C-SMC semi-finished material. Figure 2 shows the set-up of a standard SMC production line schematically, including the position of an integrated polarization imaging system. Initially, a resin system is applied to a carrier film (1) before passing through a cutting unit, which distributes chopped carbon fibers with a length of 25.4 mm onto the resin and carrier film (2). The polarization camera is positioned

directly behind the cutting unit, providing a clear planar field of view of the chopped carbon fiber rovings passing beneath (3). Positioning the camera at about a 1 meter height makes good use of the camera's 5MP image sensor (2448 x 2048 pixels) capturing images at sufficiently high resolution at the complete width of the material roll. The camera captures images of the material at defined time intervals and is capable of capture speeds of up to 73fps, creating an image stack. In the present work, the semi-finished material was processed on the SMC production line at system belt speeds of up to 2 m/min with similar areal weights (1000-1250g/m^2) to commercially available materials at image capture rates of <10fps. Using more powerful computer hardware and more sophisticated image processing algorithms would allow the capture of material information through the entire thickness, even at higher areal weights. These images are then stitched to create a continuous image of the entire semi-finished material product roll (4). In addition to real-time material quality control, the fiber orientation information at any location of the roll can be extracted to create virtual-cutting and stacking plans for optimal usage of material from the roll for compression molding parts. Moreover, the images provide the initial fiber orientation information, essential for accurately simulating the C-SMC compression molding process [16, 17].

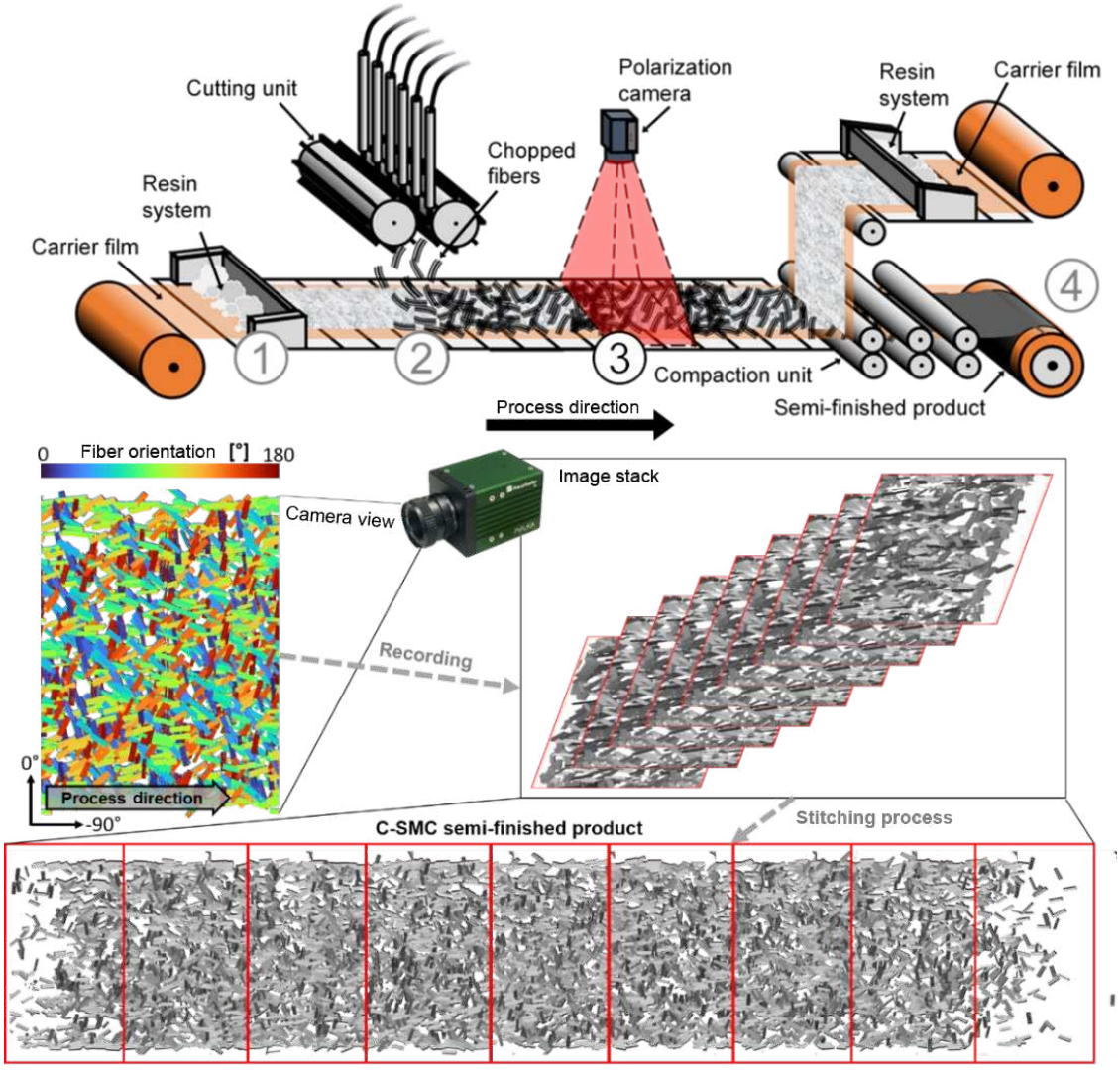

Figure 2. Schematic showing the production stages of a C-SMC semi-finished product and measurement of fiber orientation during material production using polarization imaging

  doi:10.5075/epfl-298799_978-2-9701614-0-0

4. Digitization and image processing

The digitization process consists of several steps, from the acquisition of raw data by means of polarization imaging, to the processing of this raw data and the calculation and visualization of the material's in-plane fiber orientation tensors (FOTs). The FOTs are used to define the initial state fiber orientation in the C-SMC material charge, which is important for accurate compression molding simulations. C++ is used throughout as the programming language and Microsoft Visual Studio 2019 is used as the development environment. The following section summarizes the main hardware and software components used for digitization, also shown schematically in Figure 3:

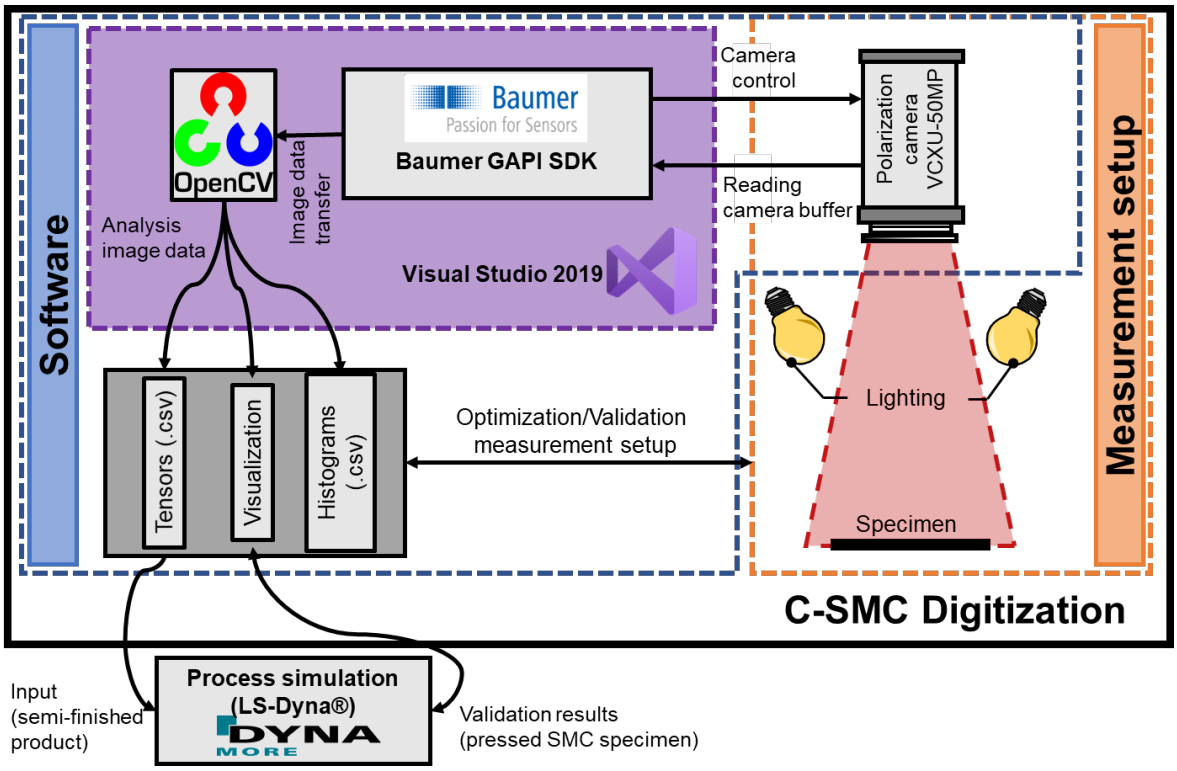

Figure 3. Schematic of the developed individual software and hardware components for digitizing C-SMC semi-finished products

Polarization Camera (hardware + internal software): The polarization camera software captures raw images and derives intensity, DOLP, and AOP images from the data. These three data components remain in the camera's memory buffer until retrieved.

Baumer GAPI SDK (programming library): The "Baumer Generic Application Programming Interface" (Baumer GAPI) serves as an interface between the PC and the camera for reading the data from the camera's buffer memory and communicating with the camera. Furthermore, Baumer GAPI passes the captured image data on to OpenCV for storage and further processing (version 2.11 for C++ was used in this work). Baumer also provides the free software "Baumer Camera Explorer" (current version at the time of this work: 3.1.0) for more simple polarization image acquisition and equipment calibration.

OpenCV (programming library): OpenCV (Open Computer Vision) is an open source-programming library used for image processing and computer vision. OpenCV version 4.5.2 is

used for the image processing steps, creating the data for analysis, visualization, and simulation input.

Parallel to the development of the software environment, the measurement setup, consisting of camera, illumination and specimen configuration, including the application of a measurement scale on the SMC carrier foil, was continuously optimized and validated. The measurement scale is a requirement for the creation of the digital cutting plan, which is discussed in the following section.

5. Digital cutting plan and OpenCV outputs

Before the AOP images of the semi-finished product can be used to create the input for compression molding simulations, a digital cutting plan needs to be created. This is applied to the stitched panoramic image of the complete C-SMC semi-finished product roll. The digital cutting plan also serves as a cutting template for real material cut-outs taken from the prepreg roll, which are then stacked to form the SMC charge. Here, an additional program was written to automate the creation of the digital charge layers, documenting the position, size and shape of each cut-out. Initially, a zero point must be chosen at any location along the measuring tape (see Figure 4), providing the x and y reference point for the cut-out. After defining the origin, the shape (square or circular) and the in-plane coordinate positions of the cut-outs are determined. The cut-outs can be freely defined anywhere within the panoramic image of the digital semi-finished product. They are numbered and documented along with their coordinates (in mm) on the panoramic image of the semi-finished product. A copy of the panoramic image is then saved as a cutting plan. In addition, each cut-out is saved as a separate image. These digital cut-outs can then be visualized or analyzed in the form of colored FO images, FO distribution histograms, and tensor data (see Figure 4). Depending on the desired complexity of the compression molding simulation model, the individual layer information can be used discretely or averaged over the SMC charge thickness. A more detailed description of the three main forms of data output is given below:

Colored FO images: For better visualization, a cleaned AOP grayscale image can be colored. Each gray value is assigned a color value from the RGB color space using a similar color pallet to that used when visualizing the FO in flow simulations.

Histograms: The AOP images' gray level histograms, restricted to the angle range [0,179] yields the respective experimental fiber orientation distributions, see Figure 4. The normalized histogram of the fiber orientation distribution of a cut-out stored as .csv data can later be used to evaluate the global degree of isotropy or to plan or influence the isotropy/anisotropy of C-SMC charges assembled from the roll.

Orientation tensors: 2nd order fiber orientation tensors calculated from the AOP images serve as the interface between polarization camera measurements of fiber orientations and C-SMC compression molding simulations, see Figure 4. For the direct derivation of the input parameters required for the simulations, the latter are virtually coarsened to a grid adapted to the mesh size used in the FE simulations. The image is divided into square regions of interest (ROI) representing the element size. For each ROI, the orientation tensor is calculated and visualized by an ellipse whose axes correspond to the eigenvectors and whose color represents the main orientation direction, see Figure 4.

  doi:10.5075/epfl-298799_978-2-9701614-0-0

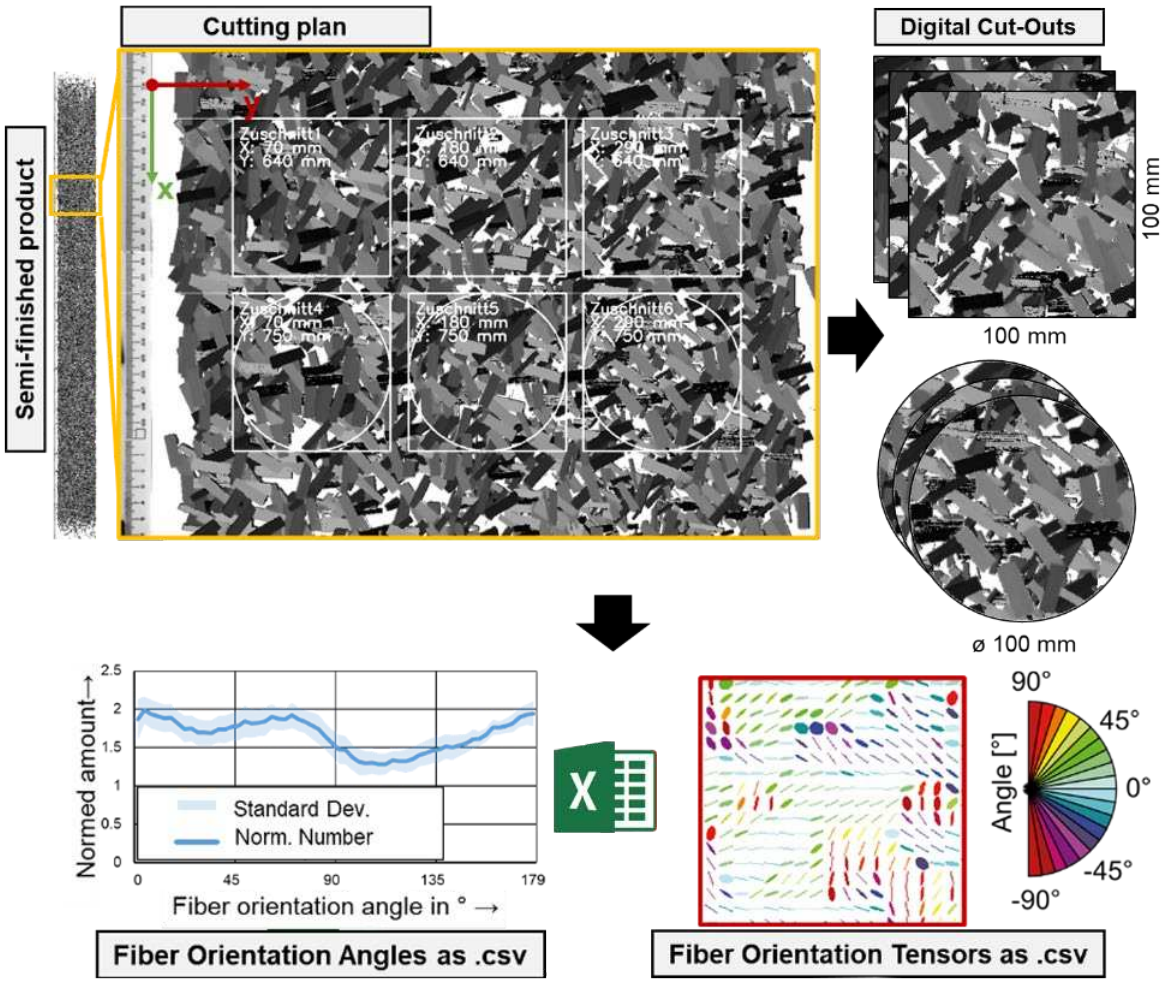

Figure 4. Example of a generated digital cutting plan with cut-outs of varying shape and their resulting fiber orientation distributions visualized as a histogram and FO tensor plot

6. Conclusions

This paper describes a comprehensive digitization pathway for C-SMC materials using polarization imaging. The principle of the polarization effect is explained. Hardware and software components for a polarization imaging system for monitoring continuous C-SMC material production have been developed. The system has proven applicable in an actual SMC production line. It captures and processes image data, which is used for online process monitoring and for extracting fiber orientation input for simulation of the C-SMC compression molding process.

Acknowledgements

This project was funded by the Fraunhofer Institute for Industrial Mathematics (ITWM) within the framework of the High Performance Center Simulation and Software Based Innovation.

7. References

1. Desplentere F, Lomov SV, Woerdeman DL, Verpoest I, Wevers M, Bogdanovich A. Micro-CT characterization of variability in 3D textile architecture. Composites Science and Technology, 2005. Vol. 65: pp. 1920–1930. https://doi.org/10.1016/j.compscitech.2005.04.008

2. Hayes BS, Gammon LM. Optical Microscopy of Fiber-Reinforced Composites. ASM International, Ohio, 2010.
3. Lange R, Mook G. Structural analysis of CFRP using eddy current methods. NDT&E International, 1994, Vol. 27, Nr. 5: pp. 241-248.
4. Romanenko V. Materialcharakterisierung und durchgängige 3D-Prozesssimulation für kohlenstofffaserverstärktes Sheet Molding Compound. Dissertation, TU Kaiserslautern, 2020. https://doi.org/10.26204/KLUEDO/6302
5. Bardl G, Nocke A, Cherif C, Pooch M, Schulze M, Heuer H, Schiller M, Kupke R, Klein M. Automated detection of yarn orientation in 3D-draped carbon fiber fabrics and preforms from eddy current data. Composites Part B, Vol. 96, 2016: pp. 312-324.
6. Vogtmann J, Klingler A, Rief T, Gurka M. 3D X-ray Microscopy as a Tool for in Depth Analysis of the Interfacial Interaction between a Single Carbon Fiber and an Epoxy Matrix after Mechanical Loading. Journal of Composites Science, 2021, 5, 21.
7. Garcea S, Wang Y, Withers P. X-ray computed tomography of polymer composites. Composites Science and Technology, 2018. Vol. 156: pp. 305-319.
8. Wirjadi O, Godehardt M, Schladitz K, Wagner B, Rack A, Gurka M, Nissle S, Noll A. Characterization of multilayer structures in fiber reinforced polymer employing synchrotron and laboratory X-ray CT. International Journal of Materials Research, 2014, Vol. 105: pp. 645-654. https://doi.org/10.3139/146.111082
9. Baranowski T, Dobrovolskij D, Dremel K, Hölzing A, Lohfink G, Schladitz K, Zabler S. Local fiber orientation from X-ray region-of-interest computed tomography of large fiber reinforced composite components. Composites Science and Technology, 2019. Vol. 183, https://doi.org/10.1016/j.compscitech.2019.107786.
10. Schreiber J, Gudelev V, Smirnov A. New polarization interferometry Approaches for In-situ Process Control and Product Quality Assessment. 18th World Conference on Nondestructive Testing, 16.-20. April 2021, Durban, South Africa.
11. Schöberl M, Kasnakli K, Nowak A. Measuring Strand Orientation in Carbon Fiber Reinforced Plastics (CFRP) with Polarization. 19th World Conference on Non-Destructive Testing, 2016.
12. Ernst J, Junger S, Tschekalinskij W. Messung einer Faserrichtung eines Kohlefaserwerkstoffes und Herstellung eines Objekts in Kohlefaserverbundbauweise. DE Patent, 10 2012 220 923.9, 15.05.2014.
13. Ernst J, Junger S, Tschekalinskij W. Measurement of a fiber direction of carbon fiber material and fabrication of an object in carbon fiber composite technique. US Patent, US 9,234,836 B2, 12.01.2016.
14. Peterson, EW. Wire Grid Infrared Polarizer. Applied Optics, vol. 4, no. 8, pp. 6–9, 1965.
15. Ruan R, Cao W, Xu L. Quantitative characterization of physical structure on carbon fiber surface based on image technique. Mater Des 2020;185:108225. https://doi.org/10.1016/j.matdes.2019.108225.
16. Schommer D, Duhovic M, Romanenko V, Andrae H, Steiner K, Schneider M, Hausmann J. Material Characterization and Compression Molding Simulation of CF-SMC Materials in a Press Rheometry Test. Key Engineering Materials, 2019, Vol. 809: pp. 467-472. https://doi.org/10.4028/www.scientific.net/KEM.809.467
17. Romanenko V, Duhovic M, Schommer D, Hausmann J, Eschl J. Advanced process simulation of compression molded carbon fiber sheet molding compound (C-SMC) parts in automotive series applications. Compos Part A Appl Sci Manuf 2022;157:106924. https://doi.org/10.1016/j.compositesa.2022.106924.

ADDITIVE MANUFACTURING OF COMPOSITE STRUCTURES WITH INTEGRATED INTERNAL HEATING AND DAMAGE SENSING

Bartosz Gackowski[a, b], Mohit Sharma[b], Sridhar Idapalapati[a]

a: School of Mechanical & Aerospace Engineering, Nanyang Technological University, 50 Nanyang Avenue, Singapore 639798, Singapore – gack0001@e.ntu.edu.sg; msridhar@ntu.edu.sg
b: Institute of Materials Research and Engineering (IMRE), Agency for Science, Technology and Research (A*STAR), Institute of Materials Research and Engineering, 2 Fusionopolis Way, Singapore 138634, Singapore – stubartoszm@imre.a-star.edu.sg

Abstract: *In this study, conductive paths made of carbon nanotubes, short carbon fibres, and epoxy resin were incorporated into the composite structure using a hybrid additive manufacturing method. The films were made on-site from a suspension and deposited on demand, allowing the number and location of the films to be controlled. Because the electrical and thermal conductivities of nanotubes were preserved, the films were connected to a power supply and used to generate heat via Joule heating. The maximum generated temperature was determined by the thickness of the conductive film. The paths were also strain-sensitive due to the piezoresistivity and were used to detect damage by measuring changes in resistivity. This work focuses on the method's underlying concepts, problems, and potential solutions.*

Keywords: additive manufacturing; multifunctional composites; carbon nanotubes; short carbon fibres

1. Introduction

Additive manufacturing (AM) offers a considerable enhancement in design freedom and shorter supply chains through the possibility of at-point-of-demand manufacturing, while the scrap production, energy consumption, weight, and cost of the produced components can be reduced (1). One of the most popular AM methods is Fused Filament Fabrication (FFF) due to its low cost, scalability, and compatibility with many thermoplastics (2, 3). Thus, the global market value of extrusion-based additive manufacturing (AM) is expected to increase almost four times between 2020 and 2026 (4). However, structures obtained with this method suffer from porosity and interlaminar bonding issues, which reduce mechanical properties (5). Traditional methods for solving these problems include applying temperature and pressure, e.g., during post-processing with an autoclave or a hot press. However, these methods require a high capital investment and are energy-intensive, which increases the manufacturing costs (6).

An alternative approach has been proposed in recent years where a resistive heater made of a carbon nanotube film was used to generate heat under a vacuum bag, which reduced energy consumption by two orders of magnitude in comparison to autoclave curing (7). The CNT films have also been proposed for other applications, including de-icing (8), lightning strike protection (9), and energy storage (10). The films have also been used for structural health monitoring of composites due to the piezoresistive effect of carbon nanotubes (11). However, none of the

  doi:10.5075/epfl-298799_978-2-9701614-0-0

widely available AM methods, like FFF, SLS, or SLA, can embed a sufficient quantity of CNT films into the composite structure to make these applications possible.

Recently, a new hybrid AM method has been proposed that creates a continuous film with CNTs and short carbon fibres (SCFs) from a suspension. The film (so-called hybrid buckypaper) can be covered with a layer of a thermoplastic, making a laminate (12). This work aims to explore the possibility of using this AM method for the manufacturing of composite structures with integrated self-heating and damage sensing.

2. Materials and methods

2.1 Materials

The acrylonitrile butadiene styrene (ABS) filament (with a diameter of 1.75 mm) was purchased from Element14, Singapore. Carbon fibre powder had a diameter of 7.5 µm, a length of 100 µm and a density of 1800 kg/m3, and was supplied by Easy-Composites, UK. Multiwalled carbon nanotubes had an outer diameter of between 30-50 nm, a length in the range of 10-20 µm and a purity of above 95 wt.% with an ash content below 1.5 wt.% and were obtained from Cheap Tubes (Grafton, VT, USA). The surfactant, Triton X-100, in laboratory grade, was procured from Sigma-Aldrich, Singapore. A room-temperature curing epoxy resin (Epicote 2009) was purchased from Polymertec, Singapore.

2.2 Additive manufacturing

All samples were 3D-printed using a custom-built prototype, which uses one nozzle to extrude the ABS filament and the second one to discharge a suspension of CNTs and SCFs, forming the hybrid buckypaper (HBP). The suspension was prepared by mixing 2 wt.% of CNTs, 4 wt.% of SCFs, 1 wt.% of the surfactant, and 10 wt.% of epoxy resin in a solvent. The mixture was subsequently homogenised for 30 min using a probe sonicator (Q500, Qsonica, USA).

The models of specimens were prepared in 3D software (Autodesk Inventor, USA) and sliced using Simplify3D software (version 4.1.2). The printing speed was set to 30 mm/s and was the same for ABS and the 3D-printing ink. The ABS nozzle was maintained at 240°C, while the manufacturing bed was set at 90°C to speed up evaporation of the carrying solvent and formation of the HBPs. More details about the method are available elsewhere (12).

2.3 Self-heating and post-processing

One HBP with a thickness of 0.1 mm, 0.2 mm, or 0.3 mm was embedded in a 2 x 15 x 150 mm ABS sample with 0.1 mm layers. Two access points (150 mm^2 each) were designed on the top of the sample, which allowed to connect wires directly to the HBP using silver paint. The wires were connected to a power supply that was set to 60V. The temperature generated by Joule heating was measured using a multimeter with a probe located in the middle of the top surface of the sample, 0.3 mm above the HBP layer. To determine the impact of the heat-treatment on the mechanical properties and microstructure of the samples, each series of samples was post-processed under vacuum bagging (1 bar) for 30 min. The tensile tests were conducted in accordance with ASTM D3039/D3039M-14 using a universal testing machine (Shimadzu Co., Japan) with a 10 kN load cell under displacement control at a crosshead speed of 1 mm/min. The grip areas (45 mm on each side) were covered with an emery cloth in order to prevent any slippage or failure at the access points to the HBP. The strain was measured with a video

extensometer. Scanning Electron Microscope (SEM, JEOL JSM6700F, Japan) was used to examine the microstructure of the fracture surfaces.

2.4 Damage sensing during three-point bending

The samples for three-point bending had a size of 100 x 12.7 x 3 mm and had one embedded HBP with a 0.1 mm thickness under the top layer of ABS. Similarly to tensile samples, two access points with an area of 127 mm^2 were located on the top surface, which gave direct access to the HBP. The flexural properties were measured according to D7264/D7264M–15. The support span was 51 mm, and was loaded under displacement control at a rate of 1 mm/min. The resistivity of the HBP was recorded in real-time using a multimeter.

3. Results and discussion

3.1 Joule heating

The temperatures recorded at the top surface of the 3D-printed laminates are shown in Fig. 1A. The maximum generated temperatures directly corresponded with the increased thickness (0.1 mm, 0.2 mm, and 0.3 mm) of the embedded HBPs and increased to 30°C, 45°C and 60°C, respectively. The temperatures reached their peaks within the first few minutes. After turning off the power supply, the temperatures started to drop rapidly and decreased to room temperatures within 1-2 minutes.

The thermal images (see Fig. 1B) indicate non-uniformity in the thermal conductivity of HBPs with 0.1 mm and 0.2 mm thickness. This could be caused by a partial removal of the HBP by the nozzle during covering it with the top ABS layer. Using HBPs with a 0.3 mm thickness increased the probability of preserving the electrical continuity within the HBP, which also allowed to generate higher temperatures. The approx. 60°C generated using this method is in good agreement with the other reported 3D-printed CNT films (13), but remains lower than the 150-180°C obtained by Joule heating of commercial CNT films (7), or those made by Chemical Vapor Deposition (14) or mask-assisted blade-coating printing (15).

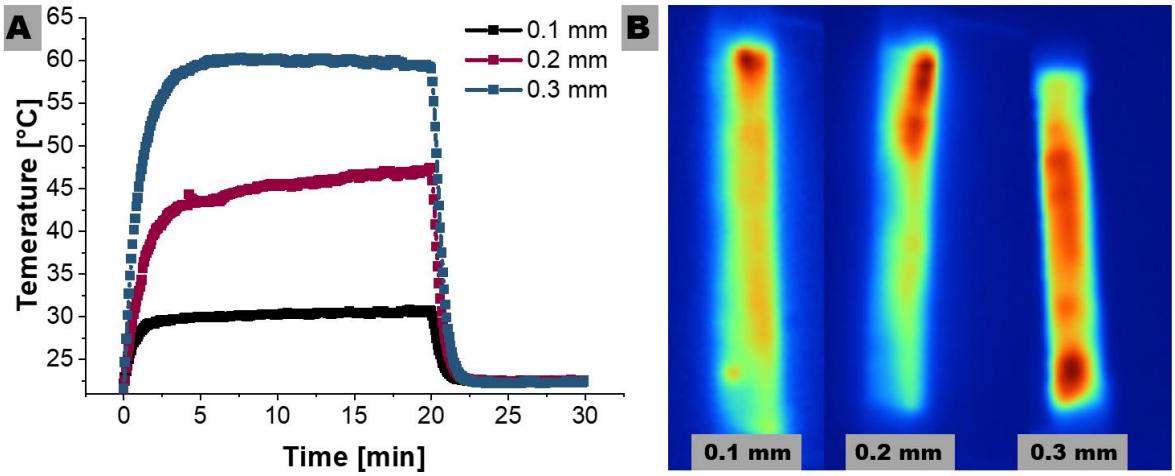

Figure 1. Temperature recorded at the top surface during Joule heating (A) and thermal images (B) after 5 mins of Joule heating (the size of the conductive path is 110 mm).

3.2 Tensile testing

As shown in Fig. 2, the tensile strength and elastic modulus of as-printed ABS equaled 33 MPa and 1.8 GPa, respectively. The Joule heating treatment under vacuum-bagging did not have any noticeable impact on tensile properties. It indicates that the HBPs did not impair the integrity of the laminates, but the relatively low weight percentage of HBPs and their non-symmetrical location prohibited the composites from reaching higher properties, which is generally observed for nanocomposites. The generated temperature (30–60°C) is still lower than the glass transition temperature of ABS (approximately 100°C), so heat-related changes in the morphology of these samples are unlikely to happen.

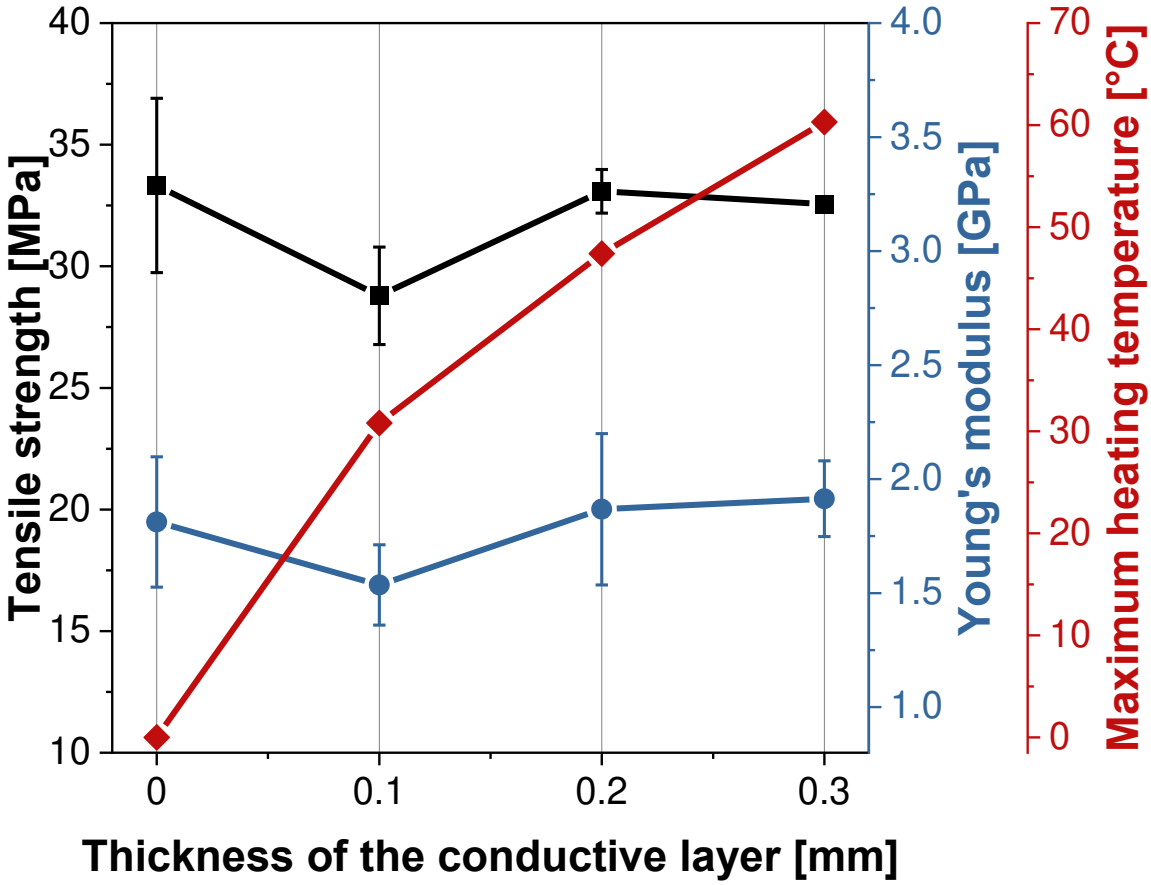

Figure 2. Tensile properties of as-printed ABS and post-processed composites by Joule heating under vacuum-bagging.

The fracture surface of the as-printed ABS sample (see Fig. 3A) shows a stack of voids with lengths between 10-100 µm. These voids are typical for 3D-printed polymers and can be useful in some applications, but they can also reduce the strength and interlayer bonding (16). After vacuum bagging post-processing, there was no discernible difference in porosity between the composites with 0. 1 mm and 0.2 mm HBPs. On the other hand, a small reduction in the number and size of voids can be noticed on the fracture surface of the composite with 0.3 mm HBP, which also generated the highest temperature during Joule heating. Nevertheless, the porosity is still present, and as the tensile properties indicated, the impact on mechanical properties is negligible. The low heating temperature could be caused by a relatively high weight percent of

epoxy in the HBP (62 wt.%), which is detrimental to electrical conductivity. Thus, a potential solution to this problem is to find another, less obstructing polymer binder for the HBP. However, this range of temperatures is still sufficient for electrothermal de-icing (17).

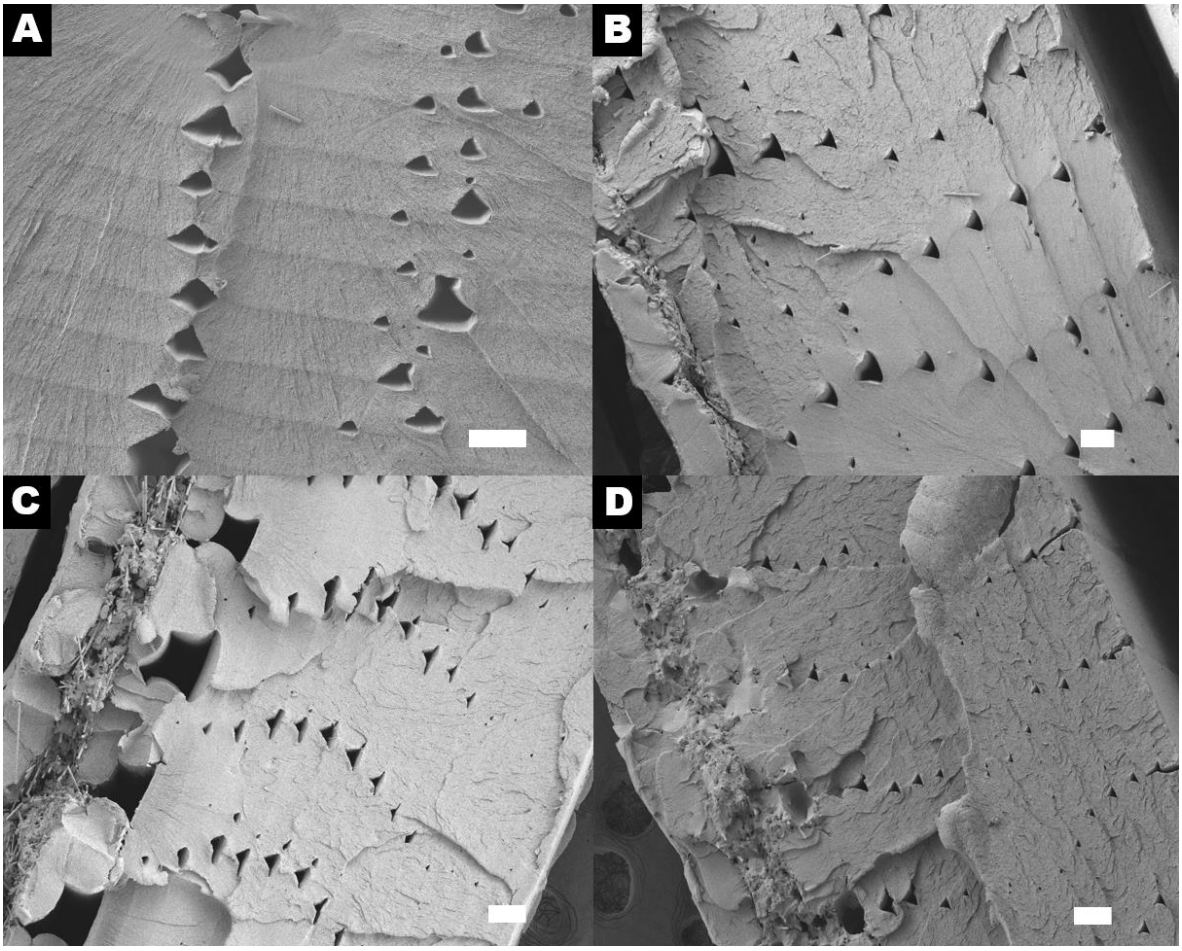

Figure 3. Fracture surfaces of as-printed ABS (A) and post-processed composites with 0.1 mm (B), 0.2 mm (C) and 0.3 mm (D) HBPs. The size of the scalebar is 100 µm.

3.3 Damage sensing

The possibility of using HBP as strain and damage sensors in real-time was investigated during three-point bending. The curves showing strength vs strain and change in resistivity vs strain were plotted together in Fig. 4, revealing three distinct regions. The initial region took place until 3% of strain and indicated a linear behaviour of both flexural strength and the change in resistivity of the embedded HBP. The linearity of the piezoelectric response is crucial for using it as a strain sensor (13). In the second region, the strength and HBP response reached an intermittent plateau, which ended with crazing at the bottom layer of the ABS sample. Subsequently, the strength started to sharply drop in the third region and led to the failure of the sample. However, the HBP did not break and continued to experience an increase in resistivity with a sharp spike that correlated with the breakage of the sample. It indicates that the HBP can be used as a strain sensor and for structural health monitoring.

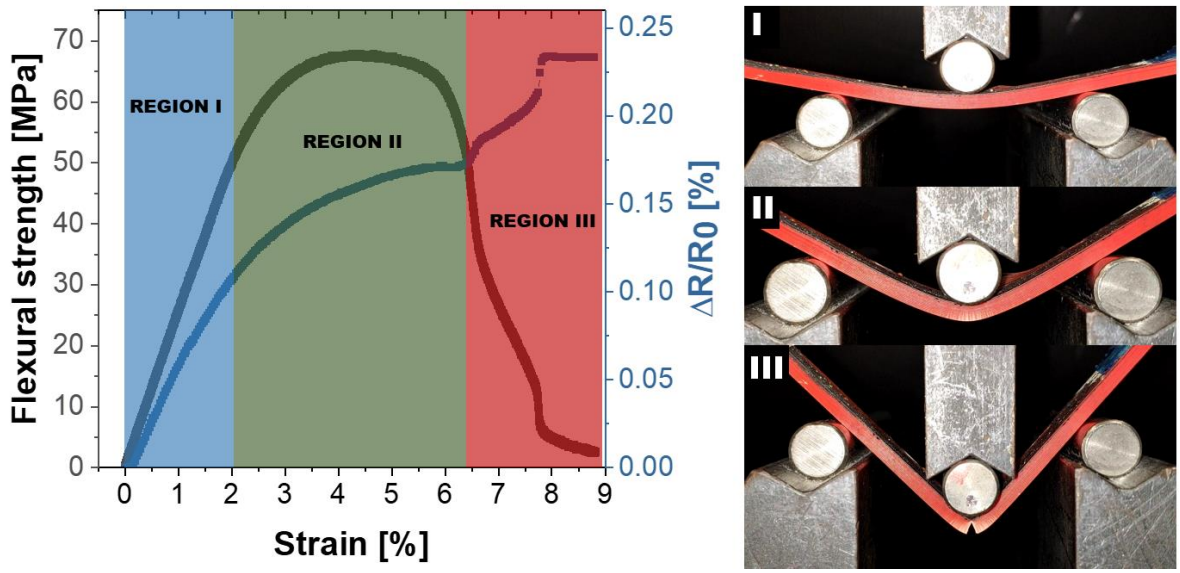

Figure 4. Flexural and piezoelectric response of the HBP composite during three-point bending.

4. Conclusions

This work investigated a new approach towards additive manufacturing of multifunctional composite structures. Hybrid buckypapers containing carbon nanotubes, short carbon fibres, and epoxy resin were embedded into the ABS matrix using a suspension-based precursor. This method preserved the design freedom of AM and allowed to build a conductive path inside the composite structure. Depending on the thickness of the embedded film (0.1-0.3 mm), the maximum generated temperature ranged between 30-60°C. The samples were post-processed by vacuum-bagging for 30 min with heat generated by Joule heating. Tensile properties did not significantly change with respect to as-printed ABS samples, which indicated a good cohesion of HBPs with the matrix, but the impact on porosity was negligible. The resistivity of the HBP was recorded in real-time during three-point bending and showed a linear initial response and a spike in resistivity during fracture. Therefore, the 3D-printed composites with HBPs can be used for de-icing, strain sensors, and structural health-monitoring.

Acknowledgements

B.G. wishes to acknowledge the support from the Agency for Science, Technology and Research (A*STAR) through the Singapore International Graduate Award (SINGA).

References

1. Seppala JE, Kotula AP, Snyder CR. Polymer-based additive manufacturing: recent developments: ACS Publications; 2019.

2. Ngo TD, Kashani A, Imbalzano G, Nguyen KTQ, Hui D. Additive manufacturing (3D printing): A review of materials, methods, applications and challenges. Composites Part B: Engineering. 2018;143:172-96.
3. Penumakala PK, Santo J, Thomas A. A critical review on the fused deposition modeling of thermoplastic polymer composites. Composites Part B: Engineering. 2020;201:108336.
4. McWilliams A. Global Markets for 3D Printing. Wellesley: BCC Publishing; 2021.
5. Caminero MA, Chacón JM, García-Moreno I, Reverte JM. Interlaminar bonding performance of 3D printed continuous fibre reinforced thermoplastic composites using fused deposition modelling. Polymer Testing. 2018;68:415-23.
6. Shaik F, Ramakrishna M, Varma PD. A Review on fabrication of thermoset orepreg composites using out-of-autoclave technology. INCAS Bulletin. 2021;13(2):133-49.
7. Lee J, Ni X, Daso F, Xiao X, King D, Gómez JS, et al. Advanced carbon fiber composite out-of-autoclave laminate manufacture via nanostructured out-of-oven conductive curing. Composites Science and Technology. 2018;166:150-9.
8. Yao X, Hawkins SC, Falzon BG. An advanced anti-icing/de-icing system utilizing highly aligned carbon nanotube webs. Carbon. 2018;136:130-8.
9. Zhang X, Zhang J, Cheng X, Huang W. Carbon nanotube protected composite laminate subjected to lightning strike: Interlaminar film distribution investigation. Chinese Journal of Aeronautics. 2021;34(2):620-8.
10. Ito H, Murata T, Fujisaki M, Tsuji R, Morita Y. High capacity and energy density organic lithium-ion battery based on buckypaper with stable π-radical. ChemSusChem. 2021;14(5):1377-87.
11. Wang X, Li B, Zhang D, Lu J, Lin L, Lu S, et al. Strain monitoring using carbon nanotube Buckypaper sensor on composite repaired structure. Applied Physics A. 2021;127(12):1-14.
12. Gackowski BM, Phua H, Sharma M, Idapalapati S. Hybrid additive manufacturing of polymer composites reinforced with buckypapers and short carbon fibres. Composites Part A: Applied Science and Manufacturing. 2022;154:106794.
13. Wang X, Gou J. 3D Printing of functional composites with strain sensing and self-heating capabilities. 3D Printing for Energy Applications. 2021. p. 69-89.
14. Lee J, Stein IY, Kessler SS, Wardle BL. Aligned carbon nanotube film enables thermally induced state transformations in layered polymeric materials. ACS applied materials & interfaces. 2015;7(16):8900-5.
15. Karalis G, Tzounis L, Dimos E, Mytafides CK, Liebscher M, Karydis-Messinis A, et al. Printed single-wall carbon nanotube-based joule heating devices integrated as functional laminae in advanced composites. ACS Applied Materials & Interfaces. 2021;13(33):39880-93.
16. Tao Y, Kong F, Li Z, Zhang J, Zhao X, Yin Q, et al. A review on voids of 3D printed parts by fused filament fabrication. Journal of Materials Research and Technology. 2021.
17. Abdulkareem Muhsan A, Lafdi K. Fabrication and characterization of graphene-based de-icing heater. Materials Today: Proceedings. 2021.

ICE HAIL STONE IMPACT TESTING OF TAILORED FIBRE PLACED COMPOSITE STRUCTURAL GUIDE VANES FOR NOVEL CFRP-TI INTERMEDIATE CASES OF FUTURE JET ENGINES

Richard König[a], Sebastian Spitzer[a], Holger Böhm[a], Tim Bätzel[a], Reyya Nitin Rao[b], Maik Gude[a]

a: Institute of Lightweight Engineering and Polymer Technology, Technische Universität Dresden, 01307 Dresden, Germany – richard.koenig@tu-dresden.de
b: Rolls-Royce Deutschland Ltd & Co KG, 15827 Blankenfelde-Mahlow, Germany – Reyya-Nitin.Rao@Rolls-Royce.com

Abstract: *Variable-axial carbon fibre reinforced polymers (CFRP) can be used to substitute titanium in structural-mechanical engine components. Such structures can be impacted by hailstones during operation. A validation strategy for a composite outlet guide vane of a hybrid titanium-CFRP-intermediate case is presented based on physical ice impact experiments starting at coupon level up to component level. For this, high velocity impact tests with spherical ice impactors were performed on the leading edge of plate specimens. An evaluation of the impact related amount of mechanical damage can be considered for the further design process and for the validation of analysis models in the virtual testing procedure. The work focuses on spherical ice impactors and the acceleration with a gas gun impact rig in regard to a reliable and reproducible testing procedure.*

Keywords: hail stone; impact testing; validation strategy; composite structural vanes

1. Impact loaded Composite Structures in Aircraft Engines

The utilization of lightweight materials in the aviation industry contributes to reach the ambitious goal of CO2 reduction by 75 % until 2050 announced by the European Green Deal [5]. One of the most weight bearing components in the engine (cf. Figure 1, left) is the intermediate case (IMC, centre). Here, the application of novel fibre-reinforced composite materials and their application in a structural design adapted to the stress path, realized by tailored fibre placement (TFP), shows high potential for weight reduction, which is a key factor in reducing specific fuel consumption. A key element for the implementation of new fibre composite designs are aerodynamically and structurally stress able guide vanes (cf. Figure 1, right) [3, 6].

However, the design of composite structures is complex and the assessment of its load-bearing capacity is challenging due to a strong relationship and interaction between structural and material design as well as the applied manufacturing process. The design process of jet engine structures becomes more difficult under complex high-dynamic impact loading conditions, which may cause local mechanical damage leading to loss of function. To enable a robust design of composite guide vanes, a consistent validation strategy is required for the assessment and evaluation of the impact related damage. For this purpose, a virtual-physical combined validation process is performed [7].

  doi:10.5075/epfl-298799_978-2-9701614-0-0

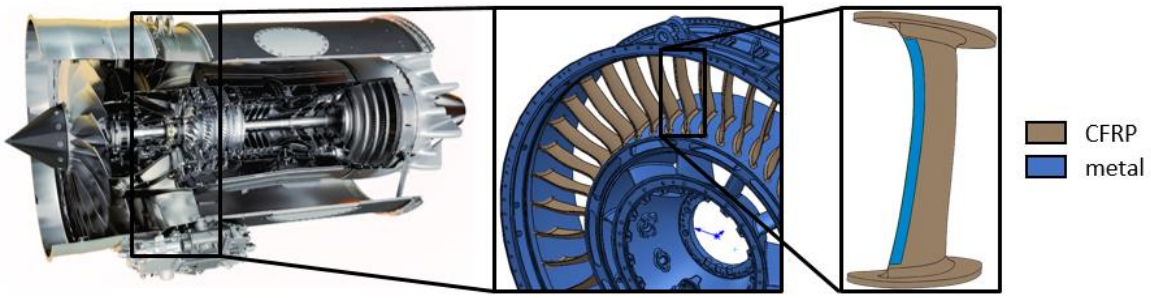

Figure 1. Rolls-Royce Pearl 700 (left), section of a hybrid intermediate case (centre) and composite structural vanes (right)

During operation, the guide vanes of the intermediate case are exposed to certain ice impact loads due to hailstones or ice shreds from icing phenomena on the fan blades or the inside of the fan casing. In this context, the impact energy of hailstones is considered more critical due to their volume and density. Hailstones are formed in thunderclouds where a 0 °C boundary exists. In the lower area are the strong warm upwinds that cause water droplets to rise above the boundary into the colder area of the cloud. There, the droplets begin to freeze, creating the hail embryo. By alternately ascending and descending the embryo, more and more water droplets accumulate in the lower and freeze in the upper part of the cloud (cf. Figure 2, left). This creates the typical layered structure of the hailstone (cf. Figure 2, right).

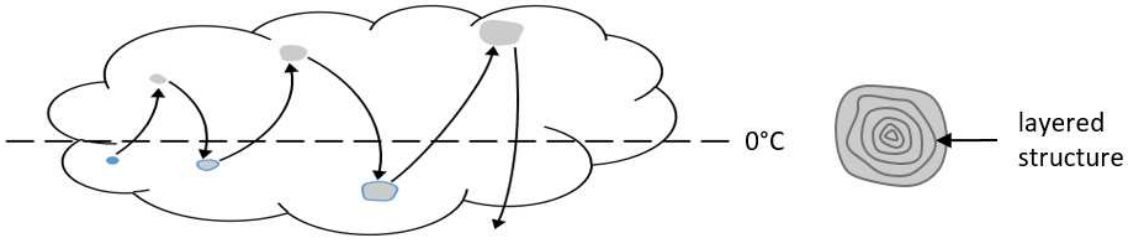

Figure 2. Formation of hailstones (left) and layered structure (right)

The impact of a hailstone on composite structures can cause significant damages. Due to the high velocity, combined with a localised impact load, the composite material behaves brittle, as the elastic deformation limit is usually exceeded in such scenarios. The consequences of such an impact are often delamination or fibre fractures, which reduce the residual strength of the structure [8]. It is therefore important that safety-relevant components are validated for hail impact before they are used. Complex virtual models enable the behaviour of the structure under impact of hailstones to be estimated using e.g. finite element analyses [2]. To create realistic models, experimentally determined data are required, which can be acquired using test rigs such as the impact and crash test rig at TU Dresden (cf. Figure 3).

  doi:10.5075/epfl-298799_978-2-9701614-0-0

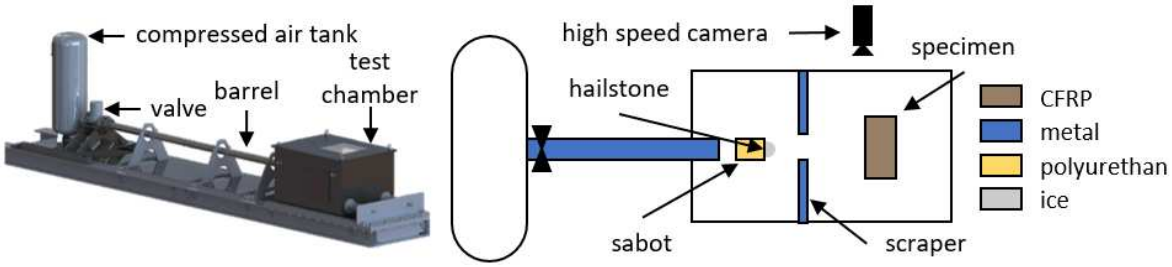

Figure 3. Impact and crash test rig at TU Dresden as a CAD-model (left) and the schematic structure and mode of operation (right)

2. Validation Strategy for a Composite Vane with regard to Hail Impact

EASA CS-E 790 specifies the requirements for hail impact tests [4]. The hailstones should have diameters of 25 mm and 50 mm and need to be accelerated to a velocity of 177 m/s during testing. Before the tests are carried out, it must be ensured that a reliable test performance in terms of reaching the target speed and preventing damage of the impactors during acceleration is given. The artificial hailstones must be manufactured in such a way that they do not contain any air pockets, as these cause residual stresses in the impactor, which would lead to less energy being transferred to the test specimen during the impact. Furthermore, the test rig must be designed variably so that the testing of different specimen geometries can be implemented in a straightforward manner.

To implement a resource-efficient hailstorm validation strategy, a building block was elaborated (cf. Figure 4). Following the VDI 2221: Break down the complex problem into sub-problems [9], the overall topic of hail impact on the intermediate case of the engine is divided into sub-areas, which are first examined individually. Various impact tests are carried out on simplified test specimens before the vane is tested. The simplified plate test specimens can be used to obtain information regarding the behaviour of composite materials in the impact case and to identify damage critical areas of the vane.

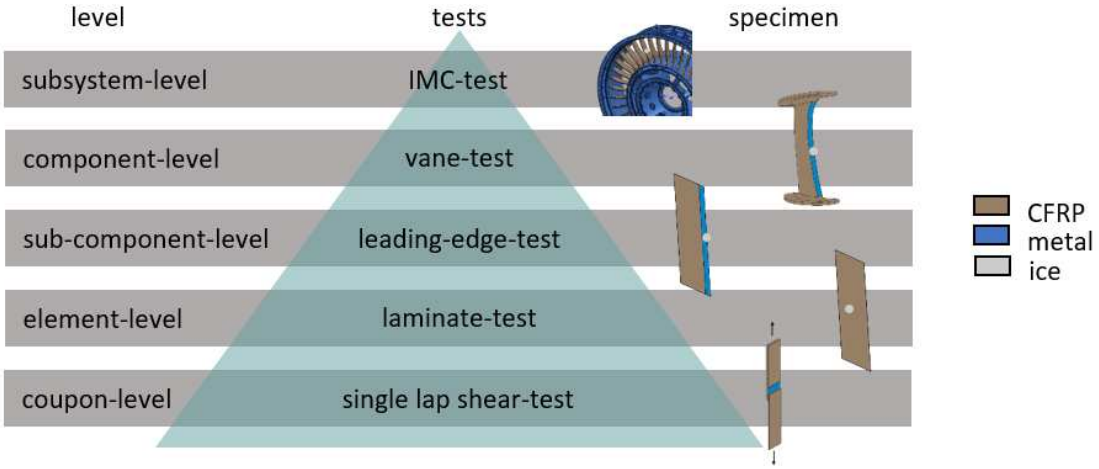

Figure 4. Validation pyramid using the building block approach for hail impact testing

When carrying out the impact tests, a sabot is used to store and fix the artificial hailstone in the barrel of the test rig. The sabot is made of polyurethane and has a cavity corresponding into which the hailstones are pressed. It must be ensured that the impactor does not fall out of the sabot due to the acceleration impulse in the barrel. After the sabot with the artificial hailstone

  doi:10.5075/epfl-298799_978-2-9701614-0-0

has left the barrel, there is a short free flight phase before the sabot hits a sabot stripper and thus-releases the hailstone. The hailstone maintains its trajectory and finally hits the target (cf. Figure 5).

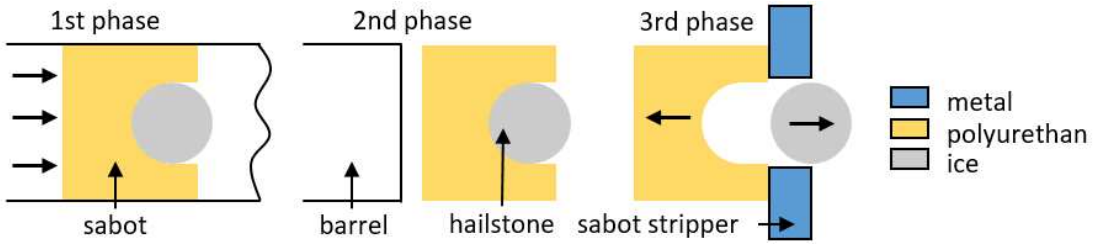

Figure 5. System of sabot and hailstone during the phases of the shooting procedure

3. Development of a reproducible Test Procedure for Hail Impact Tests

Two different moulds are used to produce the artificial hailstones. The 50 mm hailstones are made in a silicone mould, while a 3D-printed three-part mould made of polylactide acid (PLA) is used for the 25 mm hailstones. The principle for producing the artificial hailstones without air pockets is identical for both moulds. A directional freezing process is used to freeze the moulds from top to bottom. The moulds are placed in an insulated cup and filled with water. The water covers the upper part of the cup. Due to the insulation, the water in the upper area of the mould starts to freeze first. The frozen front spreads downwards into the cup and pushes trapped air in front of it. This pushes the air into the lower area of the cup so that the hailstone, which is placed in the upper part, has no air pockets. In total, the 25 mm diameter hailstones were placed at -18 °C for 8 hours and the 50 mm diameter hailstones for 24 hours before they were demoulded (cf. Figure 6). For storing, the artificial hailstones were placed back in the fridge at -18 °C in sealable plastic bags.

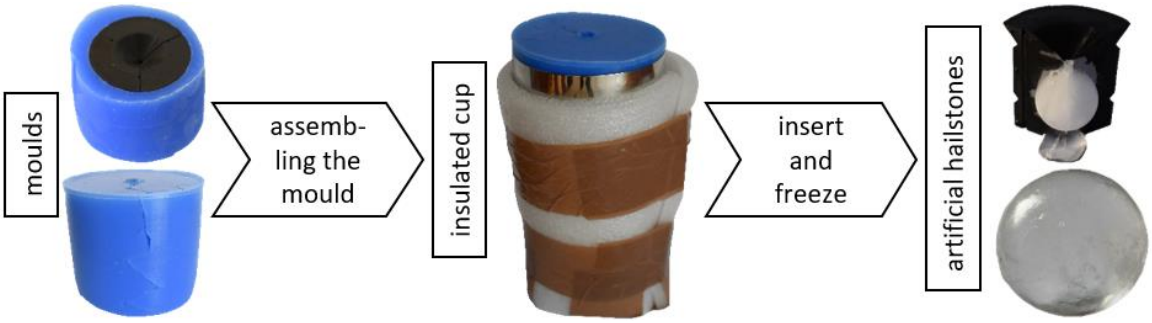

Figure 6. Manufacturing methodology for air free hailstones

First, clear artificial hailstones were manufactured to check that they did not contain any air pockets. Then, impactors were also made with a cotton filling. The cotton is intended to stop the crack growth in the artificial hailstone that occurs during the impact and thus simulate the less brittle behaviour of real hailstones. Less energy is used for crack expansion in the artificial hailstone, which means that more energy can be transferred to the test specimen [1].

For the clamping of the test specimens, a test set-up was designed to enable various test setups according specimen geometry and impact position (cf. Figure 7). For this purpose, a cost-effective structure made of aluminium profiles was designed, in which the clamping for the test

specimen can be fixed and the angle of the plates as well as the horizontal and vertical alignment can be variably adjusted.

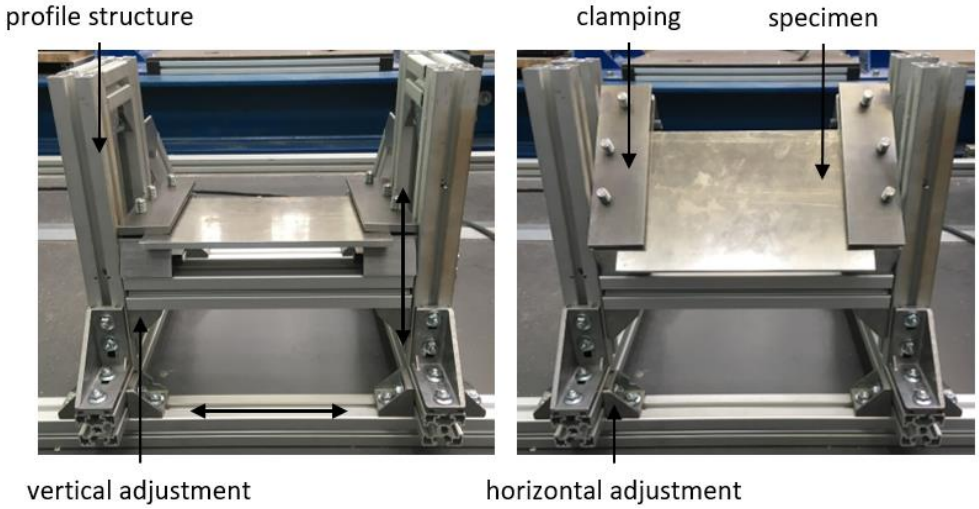

Figure 7. Test set-up with clamping for the test plates

Two high-speed cameras recording 40,000 fps were used to capture the impact tests. This allows for the velocity to be determined optically with a scale located in the test stand as well as the integrity and impact behaviour of the impactors to be checked during the test. The master camera on top records the free-flight phase of the hailstone, while the side camera records the impact location on the specimen via a mirror installed in the test chamber (cf. *Figure 8*).

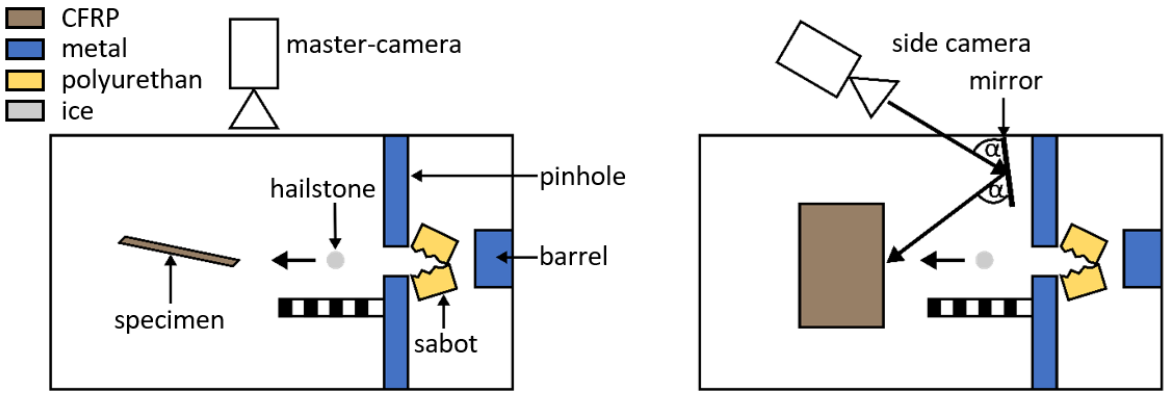

Figure 8. Experimental setup in the test chamber side view (left) top view (right)

4. Hail Stone Impact testing

To prove the integrity of the artificial hailstones before they hit the test specimen and to be able to localise the point of impact, the first tests were carried out with unfilled hailstones. The illumination of the test chamber allows to detect cracks or damage in the projectiles on the high-speed images and to determine the impact area.

It was evident from the first tests that the undamaged release of the hailstone from the sabot did not work properly right from the start. Various parameters were determined, evaluated and adjusted with different efforts. For example, the inner contour of the sabots was first manually modified so that the hailstones were fixed in the sabot in the best possible way during the acceleration process. In addition, an external fixation of the hailstones in the sabot was tested

using Tacky Tape. After the fixation of the artificial hailstone was in the sabot was verified with the help of the high-speed cameras, the pinhole could be identified as an additional source of faults (cf. Figure 9). An expansion of 2 mm meant that the hailstones no longer touched the edge of the aperture and could therefore pass it without being damaged.

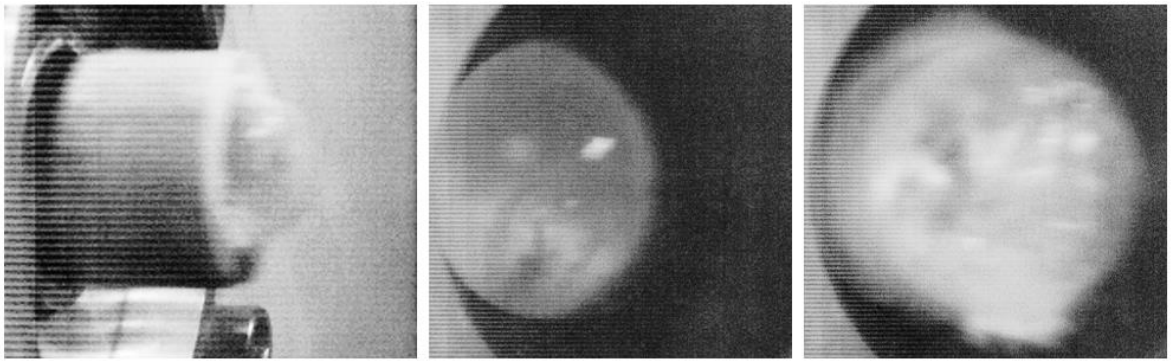

Figure 9. Undamaged artificial hailstone leaving the barrel (left), undamaged hailstone before contact with scraper (centre), damaged hailstone after stripping process (right)

Due to the environmental temperatures in the test hall, it was not possible to fix the 25 mm hailstones in the sabot by press fitting. Loading the test rig with closing the test chamber and connecting the high-speed cameras took about 15 min prior each test. During this time, the small artificial hailstones begin to melt and lose some of their volume, which is enough to cause them to lose their adhesion in the sabot and fall out of it. Therefore, before the experiments, the sabot was filled with 1 ml of water and stored together with the impactor for at least 12 hours at -18 °C. The frozen water reinforces the fixation of the hailstone in the lower part of the sabot (cf. Figure 10). In addition, the barrel of the test stand was cooled down from the outside with the help of cooling pads during the subsequent tests.

Figure 10. Freezing of sabot hailstone system before tests with 25mm artificial hailstones

The parameter with which the velocity of the hailstones is adjusted is the applied pressure from the gas reservoir. From the preliminary tests, a ratio *x* is determined between the kinetic energy of the hailstone sabot system to be achieved and the acceleration work required for this (cf. Eq. (1)):

$$x = \frac{E_{kin}}{W_{acc}} = \frac{mv^2}{2p\left(\frac{\pi}{4}d^2 - A_2\right)s}. \quad (1)$$

The determined ratios *x* are plotted over the measured velocities of the hailstones (cf. Figure 11). The ratio *x*, which must be set to reach the target velocity, can be estimated by means of the comparison tests.

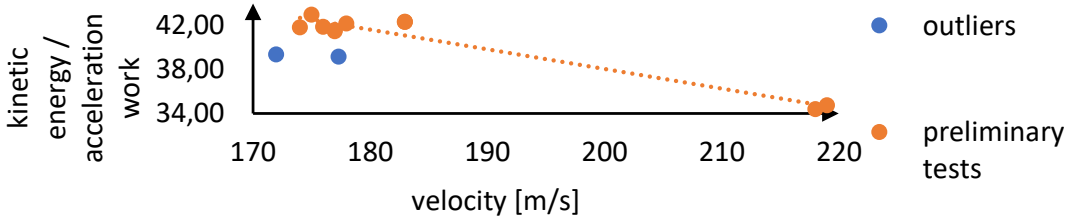

Figure 11. Ratio of x and the velocity of the artificial hailstones

As soon as sufficient values have been determined for an estimation of the curve, equation (1) can be converted according to the pressure and the required pressure can be determined as a function of the mass of the sabot hailstone system, since the other parameters remain constant (cf. Eq. (2)):

$$p = \frac{mv^2}{2x\left(\frac{\pi}{4}d^2 - A_2\right)s}. \tag{2}$$

After the velocity of the impactors could be set with an accuracy of ± 5 m/s, the different behaviours of unfilled and cotton-filled hailstones were examined. From high-speed recordings it could be seen that the unfilled hailstones developed cracks in the entire body of the impactor at the moment of impact on an aluminium test plate (cf. Figure 12, top). As a result, the force transmission to the plate was low and caused only elastic deformation of the test specimen. In contrast, the cotton filling interrupted the crack propagation in the hailstone, which meant that significantly more energy could be transferred into the test body (cf. Figure 12, bottom).

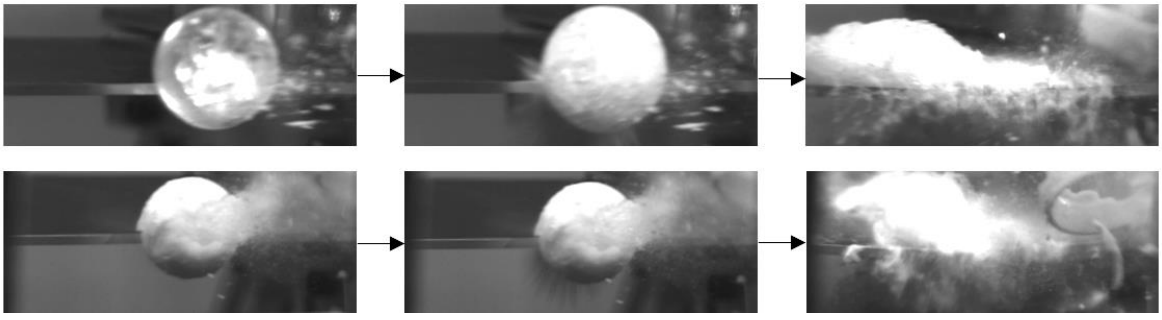

Figure 12. Behaviour of unfilled (top) and cotton-filled (down) hailstones at impact

For the subsequent tests, it was therefore decided to carry out the impact tests with the filled hailstones. The impact of the hailstone caused an elastic deformation of the composite plates in the impact area, which spread out in waves throughout the test specimens (cf. Figure 13).

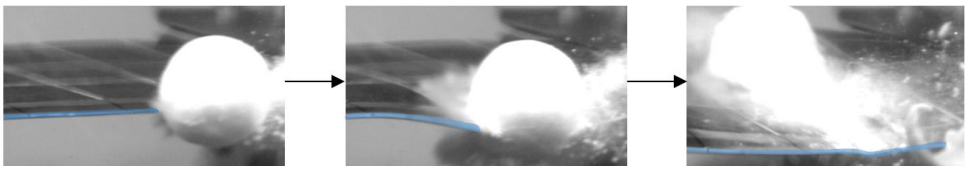

Figure 13. Impact of cotton-filled hailstone on composite specimen plate with metallic leading edge

5. Conclusions

For the validation of new composite outlet guide vanes, the resistance against high dynamic loads, as they occur in the case of a hail impact, has to be verified. For this purpose, a suitable validation strategy has been developed in this paper, which enables the effects of hailstones on the structure to be reproduced as realistically as possible. A method for the production of artificial hailstone was described, reliable impact tests on a variable test fixture were carried out and the behaviour of unfilled and cotton-filled hailstones was investigated. The knowledge obtained can be used to advance the physical validation of composite components for hailstorm. The results from high dynamic out-of-plane impact tests on composite specimen can be used to improve virtual validation and to calibrate the virtual twin model of the component.

Acknowledgements

The work took place as part of the project "Development of a highly efficient linked product engineering process (PEP) for hybrid lightweight structures in the context of Industry 4.0" (PEP4.0, funding code 20X1717B). The project is funded as part of the fifth Luftfahrforschungsprogramm of the Bundesministerium für Wirtschaft und Klimaschutz BMWK.

References

[1] A. International. 2010. Test Method for Hail Impact Resistance of Aerospace Transparent Enclosures. ASTM International, West Conshohocken, PA.

[2] Böhm, H., Hornig, A., Gude, M., Högner, L., and Meyer, M. 2022. A method for a coupled structural - CFD analysis of compressor rotor blades subjected to ice impact with uncertain impactor parameters. ASME Turbo Expo 2022: Turbomachinery Technical Conference & Exposition 2022.

[3] Dargel, A., Kluger, J., Klaus, C., Spickenheuer, A., Bittrich, L., Spitzer, S., Schubert, K., Feltin, D., and Gude, M. Design, modelling and manufacturing of a variable-axial composite structural guide vane for a jet engine intermediate case in the context of industry 4.0. SAMPE Europe Conference 2021 Baden/Zürich - Switzerland 2021.

[4] EASA. 2018. Certification Specifications and Acceptable Means of Compliance for Engines CS-E.

[5] Europäische Kommission. 2011. Flightpath 2050. Europe's vision for aviation; maintaining global leadership and serving society's needs; report of the High-Level Group on Aviation Research. Policy / European Commission. Publ. Off. of the Europ. Union, Luxembourg.

[6] Kluger, J., Spitzer, S., Spickenheuer, A., Bittrich, L., Klaus, C., and Gude, M. 2022. Design and dimensioning of aerodynamic and structural vanes for jet engines made of multi-axial and variable-axial CFRP and comparison of these approches with titanium vanes. ECCM20 2022.

[7] Spitzer, S., Folprecht, F., Dargel, A., Klaus, C., Langkamp, A., and Gude, M. 2021. Effiziente und Robuste Entwicklung Komplexer Faserverbund-Triebwerkstrukturen. Entwerfen Entwickeln Erleben in Produktentwicklung und Design 2021.

[8] Verein Deutscher Ingenieure. 1989. VDI 2014 - Entwicklung von Bauteilen aus Faser-Kunststoff-Verbund.

[9] Verein Deutscher Ingenieure. 2019. VDI 2221 - Methodik zum Entwickeln und Konstruieren technischer Systeme und Produkte.

  doi:10.5075/epfl-298799_978-2-9701614-0-0

PHYSICAL AND CHEMICAL FOAM INJECTION MOULDING OF NATURAL FIBRE REINFORCED PP COMPOUNDS WITH CONTROLLED MOULD OPENING

Matthias Mihalic[a], Claudia Pretschuh[a], Thomas Lummerstorfer[b], Wolfgang Kienzl[c]

a: Kompetenzzentrum Holz - Wood K plus, Altenberger Strasse 69, 4040 Linz, Austria;
m.mihalic@wood-kplus.at
b: Borealis Polyolefine GmbH; St. Peter Strasse 25, 4021 Linz, Austria
c: ENGEL Austria GmbH, Ludwig-Engel-Strasse 1, 4311 Schwertberg, Austria

Abstract: *In this study, physical (MuCell technology) and chemical foam injection moulding was used to produce plates made from wood fibre and cellulose fibre reinforced polypropylene, respectively. For both technologies, the used core-back method enabled precise mould opening during injection and thus allowed for a variation of plate thickness and density. The simpler short-shot technology, used only for the chemical foaming trials with differing shot volume, provided plates with constant thickness.*

The foam structure and finally the mechanical properties of the plates depend on the filler type, the foaming method and the density. The latter is directly linked to the plate thickness or the shot volume. Overall, the results demonstrate the considerable weight saving potential of foam- compared to conventional injection moulding.

Keywords: Foam injection moulding; natural fibre composite; weight reduction; polypropylene;

1. Introduction

Lightweight design is a key focus in the automotive industry to lower vehicle fuel consumption, thereby reducing CO_2 emissions and contributing to a more sustainable mobility. Among other possibilities, foam injection moulding is an effective method to produce lightweight structural parts. Further part weight reduction is achieved by substituting conventional mineral fillers like talc for natural fibres due to the lower density of the latter. The mechanical properties of natural fibre reinforced composites (NFCs) are comparable to their mineral filled counterparts [1] and they bear the potential for a reduction of greenhouse gas emissions [2,3].

Foam injection moulding can in general be divided into two main categories – physical and chemical foaming. Physical foaming, also known as microcellular injection moulding [4] is achieved by dissolving a supercritical gas (like N_2 or CO_2) in the polymer melt, followed first by cell nucleation and then cell expansion when the melt reaches the mould cavity, where a rapid pressure drop occurs. In contrast, in chemical foaming, gas formation occurs by decomposition of a chemical blowing agent [5] when the melt reaches a certain temperature. While chemical foaming has the advantage that it can be performed basically with conventional injection moulding equipment (only a shut-off nozzle is required), its main drawbacks are typically a less homogeneous bubble formation and potential problems caused by the chemical by-products of the blowing agent [6].

  doi:10.5075/epfl-298799_978-2-9701614-0-0

Besides the obvious benefit of a reduced part weight, further advantages of foam injection moulding compared to compact injection moulding are a reduced melt viscosity, which leads to reduced injection pressures, the possibility of using lower processing temperatures, and a reduction of cycle times [7,8].

The aim of the present study was to assess the weight reduction potential of both physical and chemical foaming for two NFCs and to evaluate the influence of the different foaming processes on their mechanical performance.

2. Materials and methods

2.1 Materials

The materials used for this study were a commercial wood reinforced PP composite ("PPWood") and a self-made cellulose reinforced PP composite ("PPCell"). The fibre content was 20 w% in both cases. The PPCell compound was prepared at Wood K plus using a Brabender DSE20/40D twin screw extruder with a 20 mm screw diameter. A throughput of 10 kg/h and a screw speed of 375 rpm were chosen; a decreasing temperature profile ranging from 210 °C in the melting zone to 180 °C at the die was used in order to keep thermal degradation of the fibres to a minimum. All materials were dried overnight at 80 °C prior to injection moulding.

2.3 Injection Moulding

2.3.1. Physical foaming

Physical foaming was achieved by nitrogen injection according to the MuCell® process. The trials were carried out at ENGEL Austria GmbH using a hydraulic/hybrid ENGEL Duo 12060/1700 injection moulding machine with 120 mm screw diameter. The temperature profile increased from 180 °C in the melting zone to 200 °C at the nozzle. Tool temperatures of 60 °C ("T60") and 40 °C ("T40") were used. After the initial gas loading of 0.3 w% N_2 in the melt ("N03") resulted in insufficient cavity filling at larger mould opening gaps, the loading was increased to 0.6 w% ("N06") for all remaining trials.

A plate tool of 800x400 mm with three gates distributed along the central "axis" of the plates was used. The nominal thickness of the plate tool was 2.5 mm; for the core-back trials opening gaps of 0 / 0.1 / 0.2 / 0.3 / 0.4 / 0.5 / 0.75 / 1 mm were used, resulting in nominal plate thicknesses ranging from 2.5 mm to 3.5 mm. The specimens for the mechanical and microscopic characterisation were milled out of the plates using a CNC machine.

2.3.2. Chemical foaming

The chemical foaming trials were performed at Wood K plus using a Wittmann Battenfeld SmartPower 120 servo-hydraulic injection moulding machine with 35 mm screw diameter and 120 kN clamping force. The temperature profile increased from 145 °C near the hopper to 190 °C at the nozzle. Foaming was achieved by adding 3 m% of a chemical blowing agent (Hydrocerol® ITP845 by Clariant Masterbatches GmbH, Germany) via an automatic dosing unit. Besides the core-back ("CB") foaming trials with mould opening gaps of 0 / 0.2 / 0.4 / 0.8 / 1 mm (resulting

  doi:10.5075/epfl-298799_978-2-9701614-0-0

in plate thicknesses ranging from 3 mm to 4 mm), additional trials in short-shot mode ("SSh"), with the dosage volume of 100% / 95% / 90% of the switchover volume, were carried out.

The majority of the chemical foaming trials were performed using a 200x150x3 mm plate tool with a wedge-shaped film gate. In order to investigate the influence of the gate geometry, additional core-back trials were performed using a 180x180x3 mm plate tool with a central gate.

2.4. Characterisation of the injection moulded samples

Density measurements were performed according to the Archimedes principle following EN ISO 1183-1, using a Sartorius YDK01 density kit and analytical balance. The flexural properties were determined via a 3-point bending test according to EN ISO 178 using a Messphysik Beta 50 universal testing machine, with a preload of 5 N and a test speed of 2 mm/min. The notched and unnotched Charpy impact strength according to EN ISO 179 were characterised using a CEAST 9050 pendulum impact tester, with a 0.5 J pendulum hammer for the notched samples and a 2 J or 7.5 J hammer, depending on the impact strength, for the unnotched samples.

Tensile tests according to EN ISO 527 were performed on the physically foamed samples, using a Messphysik Beta 20-10 universal testing machine, with a preload of 3 N and a test speed ranging from 1 mm/min (for the determination of the E-modulus) to 50 mm/min. No such test was performed on the chemically foamed samples, as the plates produced at Wood K plus were not large enough to produce standardised shoulder bars.

In addition to the mechanical characterisation, the foam structure was analysed via optical microscopy of embedded and polished samples using an Olympus BX-RLA2 reflected light microscope.

3. Results and discussion

3.1 Mechanical properties

3.1.1. Physical foaming trials

3.1.1.1. Density versus plate thickness

Figure 1 shows a correlation of the densities of the foamed samples with the nominal plate thickness. Both materials show roughly the same trend of the density-versus-thickness curves. There is a drop in the density of approx. 10% from the compact samples to the foamed samples at equal thickness. The density of the foamed samples at maximum thickness (3.5 mm) is approx. 30% lower (ranging from 28.6% to 30.8%) than at minimum thickness (2.5 mm) in all cases, which is similar to the relative difference in thickness (28.6%). Assuming a constant part weight for all samples, a reciprocal correlation between the density and the part thickness can be expected; this is roughly the case for all the foamed specimens. In addition, the following observations were made:

- In the compact specimens and at low foaming degrees (small mould opening gaps) the absolute density of PPWood is slightly lower than the density of PPCell. At higher foaming degrees (large mould opening gaps) this difference becomes negligible.

  doi:10.5075/epfl-298799_978-2-9701614-0-0

- A lower gas loading results in a higher density, indicating a lower foaming degree (see the curve of PPCell_N03_T60 in Figure 1).
- The influence of the tool temperature on the density-versus-thickness curve is negligible for PPCell, whereas for PPWood slightly lower densities were achieved at 40 °C tool temperature than at 60 °C (except for an outlier at a thickness of 2.6 mm).

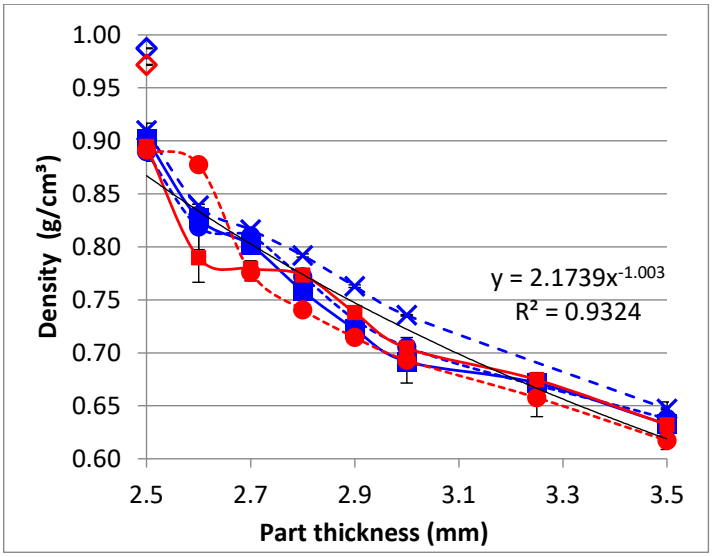

Figure 1: Dependence of the part density on the nominal part thickness (left); correlation of the density with the inverse part thickness, foamed samples only (right).
*Legend: **PPCell**, **PPWood**. Compact samples – ◇◇; Samples N03_T60 – ✕, dashed line; Samples N06_T60 –■■, solid lines; Samples N06_T40 – ●●, dotted lines.*

3.1.1.2. Tensile and flexural properties

Both materials show a linear dependency of the tensile modulus and strength on the density; this trend also extends to the compact samples. There is no noticeable influence of the gas loading and tool temperature on the tensile modulus and strength. While both materials show very similar values for the tensile modulus in relation to the density, the PPCell compound is clearly superior to the PPWood in terms of the tensile strength (cf. Figure 2, left). This indicates the effect of the larger aspect ratio of the cellulose fibres in PPCell compared to the roughly cubic wood particles in PPWood. The flexural modulus and strength follow the same trends as the respective tensile properties; this is the case for all samples. However, the flexural data show a significant amount of scattering which makes it difficult to assess any possible influence of the processing conditions or even the filler type.

3.1.1.3. Impact properties

While the discrepancy between the two materials is almost negligible for the tensile and flexural modulus and in the range of +25-30% in favour of PPCell in the tensile and flexural strength, the differences in the impact properties are much more significant – roughly +250-300% in the unnotched impact strength and around +100% in the notched impact strength, both in favour of PPCell. There is again a roughly linear correlation between the notched impact strength and

the density, albeit with some scattering, which also extends to the compact samples (cf. Figure 2, right). In contrast, the dependency of the unnotched impact strength on the density is not quite linear but appears to become steeper with higher density resp. lower degree of foaming. In particular there is a significant drop in the unnotched impact strength of both materials going from the compact samples to the respective foamed samples at equal thickness, i.e. without mould opening (approx. -45 % for PPCell and approx. -30 % for PPWood).

Similar to the tensile and flexural properties, no clear statement can be made regarding the influence of the gas loading and tool temperature on the impact properties in relation to the density, as the observed differences are in the same range as the standard deviations of the measured values.

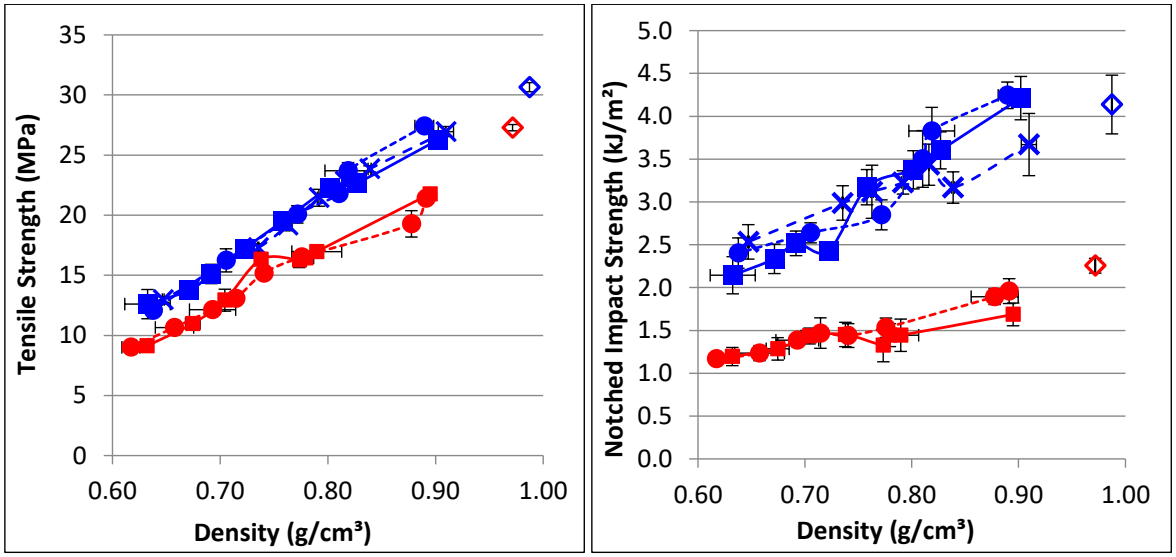

Figure 2 Dependence of the tensile strength (left) and Charpy notched impact strength (right) on the density of the foamed parts.
*Legend: **PPCell**, **PPWood**. Compact samples – ◇◇; Samples N03_T60 – ×, dashed line; Samples N06_T60 –■■, solid lines; Samples N06_T40 – ●●, dotted lines.*

3.1.2. Comparison with chemical foaming trials

Similar to the results from the physical foaming trials, a roughly linear relation between the density and the flexural modulus and strength was observed for the chemical foaming trials. This was the case for both materials, PPCell and PPWood, as well as for the different methods – core-back foaming with the film-gate plate tool ("CB_film") or with the central-gate plate tool ("CB_cent"), and short-shot foaming with the film-gate tool ("SSh_film"). The flexural properties of the chemically foamed samples in relation to the density are clearly superior to those of the physically foamed samples (see the left-hand graph in Figure 3 for the flexural modulus of PPCell). A very similar observation is made for the Charpy notched impact strength (cf. Figure 3, right, for PPCell), although here the differences between the results from the physical and chemical foaming appear slightly less prominent.

Besides the different foaming techniques, one should bear in mind the different injection moulding machines that were used for the physical and chemical foaming trials, respectively,

and also the use of a hot-runner system (physical trials) vs. a cold-runner system (chemical trials). In any case, the fact that all the results from the chemical trials fall approximately onto the same line shows that the plate geometry – film gate or central gate – does not appear to be a major factor.

The flexural and impact properties of the samples prepared by short-shot foaming are comparable to those prepared by core-back foaming. However, for the short-shot samples an interpretation of the relation between the density and the mechanical properties is less reliable because of a notable density gradient in flow direction, which results in significant scattering of the data.

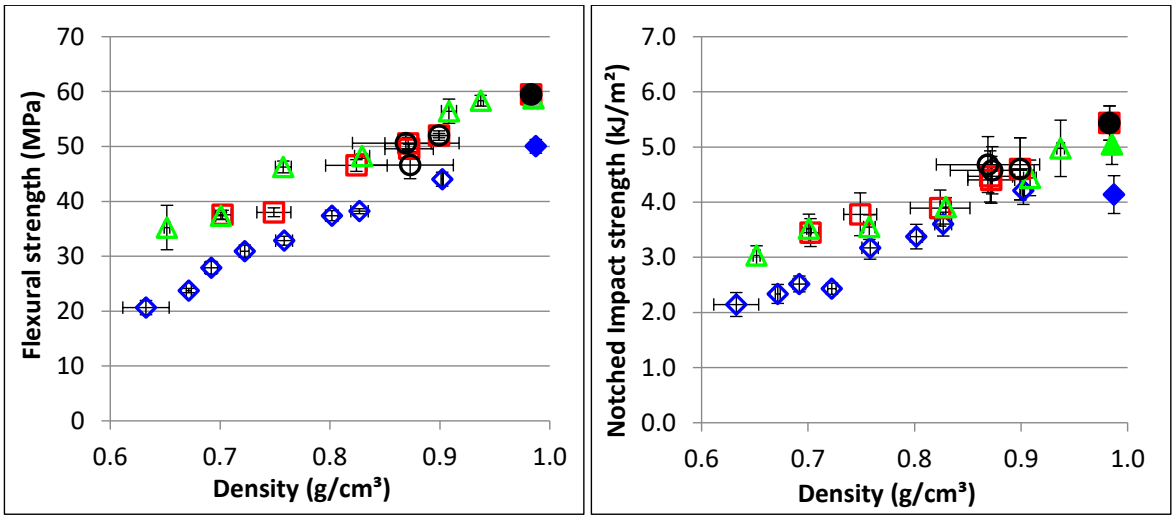

Figure 3 Flexural strength (left) and Charpy notched impact strength (right) of PPCell, foamed with different methods.
Legend: Core-back physical (N06_T60) – ◇; CB_film – □; CB_cent – △; SSh_film – ○.

3.2. Optical microscopy

In order to relate the mechanical properties to the foam structure, optical microscopic images of the cross-sections of the foamed plates were taken. The foam structures of samples from the physical (series N06_T60) and chemical (series CB_film) foaming trials at selected mould opening gaps are shown in Figure 4 (PPWood) and Figure 5 (PPCell).

While there are clear differences in the foam structure not only between the two materials but also between the chemically and physically foamed samples, the evolution of the foam structure with increasing plate thickness is quite similar in all cases. Without mould opening, the foam structure seems to consist mainly of a relatively small number of relatively large pores. With increasing mould opening gap, a layered structure develops where a core layer of large pores is surrounded on both sides by an intermediate layer containing a large number of small pores, and a compact outer layer. With increasing mould opening gap, the pore size increases as well, until in the case of PPWood even large voids of several hundred microns are formed.

A comparison of the two materials shows that the foam structure of PPCell is in general much finer than that of PPWood. This observation suggests a smaller particle size and, given equal mass percentages of the fillers in the two compounds, a larger number of the cellulose fibres

compared to the wood particles, which directly results in a larger number of nucleating sites for the pore formation.

For both materials the foam structure of the chemically foamed samples is more homogeneous than that of the physically foamed samples. In addition, the thickness of the compact outer layer is visibly larger for the chemically foamed samples (approx. 400-800 µm) than for the physically foamed samples (approx. 200-350 µm). Both observations are in accordance with the superior mechanical properties of the chemically foamed samples that have been discussed above.

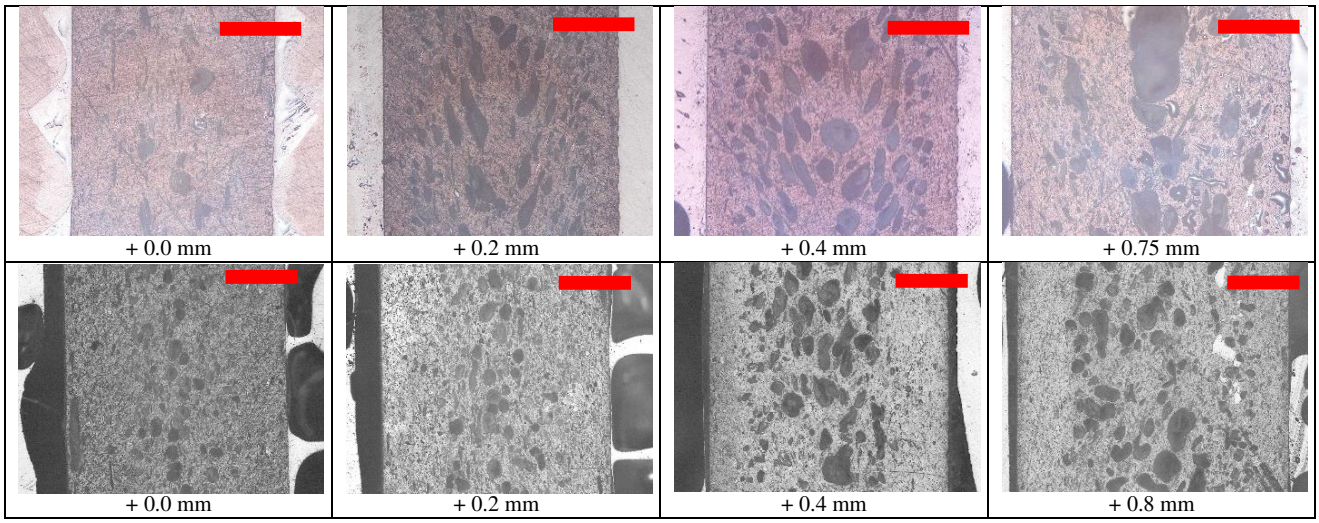

Figure 4 Foam structure of physically (top row; N06_T60) and chemically (bottom row; CB_film) foamed specimens of PPWood at different mould opening gaps. Dark spots in the samples represent pores respectively voids. Bright spots represent pores filled with resin from the sample preparation. The red bars represent 1 mm.

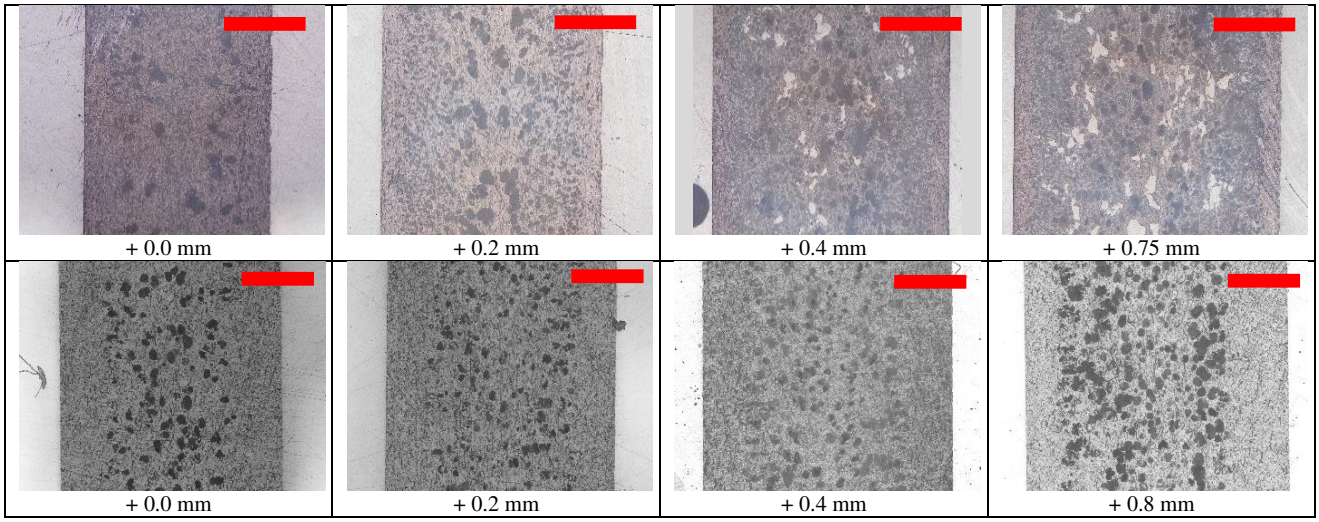

Figure 5 Foam structure of physically (top row; N06_T60) and chemically (bottom row; CB_film) foamed specimens of PPCell at different mould opening gaps. Dark spots in the samples represent pores respectively voids. Bright spots represent pores filled with resin from the sample preparation. The red bars represent 1 mm.

  doi:10.5075/epfl-298799_978-2-9701614-0-0

4. Conclusions

It could be demonstrated that the core-back method allows for precise control of the part thickness in both physical and chemical foam injection moulding. The roughly reciprocal correlation between the density and the part thickness, and the roughly linear correlation between the tensile and flexural properties and the density show that a constant and reproducible foaming process was achieved in all core-back trials. The simpler short-shot method led to comparable mechanical properties in relation to the density, but the results were less reproducible, most likely due to an inhomogeneous density distribution along the flow path.

While physical foaming appeared to be slightly more effective regarding the achievable density reduction, the physically foamed parts had worse mechanical properties at equal density than their chemically foamed counterparts. This can be related to the foam structure and the thicker compact outer layer that was formed in the chemically foamed samples.

The overall mechanical properties of the cellulose reinforced compound PPCell were clearly superior to the wood reinforced compound PPWood, particularly in terms of the impact performance, which can be related to the larger aspect ratio of the cellulose fibres, and also to the more homogeneous foam structure.

Finally, the results show that foam injection moulding of NFCs offers considerable weight-saving potential compared to conventional injection moulding.

5. References

1. Sobczak, L., Lang, R.W., Haider, A. Polypropylene Composites with Natural Fibers and Wood - General Mechanical Property Profiles. Compos.Sci.Technol. 2012, 72(5), 550-557
2. D. Civancik-Uslu, L. Ferrer, R. Puig, P. Fullana-i-Palmer. Are functional fillers improving environmental behavior of plastics? A review on LCA studies. Science of the Total Environment 626 (2018) 927–940.
3. Hesser F. Environmental advantage by choice: Ex-ante LCA for a new Kraft pulp fibre reinforced polypropylene composite in comparison to reference materials. Composites Part B 2015; 79:197-203.
4. Ding, Y.; Hassan, M.H.; Bakker, O.; Hinduja, S.; Bártolo, P. A Review on Microcellular Injection Moulding. Materials 2021, 14, 4209. https://doi.org/10.3390/ma14154209.
5. Štěpek, J.; Daoust, H. Chemical and physical blowing agents. In Additives for Plastics; Springer: New York, NY, USA, 1983; Volume 5, pp. 112–123.
6. Kutz, M. Applied Plastics Engineering Handbook: Processing and Materials; Elsevier Science: Amsterdam, The Netherlands, 2011, pp. 1–574.
7. Chong, T.-H., Ha, Y.-W., Jeong, D.-J. Effect of Dissolved Gas on the Viscosity of HIPS in the Manufacture of Microcellular Plastics. Polym. Eng. Sci. 2003, 43(6), 1337-1344
8. Mallick, P.K. Thermoplastics and thermoplastic-matrix composites for lightweight automotive structures. In: Mallick, P.K. (Ed.) Materials, Design and Manufacturing for Lightweight Vehicles, Woodhead Publishing, 2010, pp. 174-207.

  doi:10.5075/epfl-298799_978-2-9701614-0-0

FOAM INJECTION MOULDING OF CELLULOSE FIBRE REINFORCED PP - INFLUENCE OF PROCESSING PARAMETERS

Claudia Pretschuh[a], Romana Welser[a], Matthias Mihalic[a], Thomas Lummerstorfer[b], Christian Sponner[c], Andreas Steurer[c]

a: Kompetenzzentrum Holz - Wood K plus, Altenberger Strasse 69, 4040 Linz, Austria, c.pretschuh@wood-kplus.at
b: Borealis Polyolefine GmbH, St. Peter Strasse 25, 4021 Linz, Austria
c: ENGEL Austria GmbH, Ludwig-Engel-Strasse 1, 4311 Schwertberg, Austria

Abstract: *Cellulose fibre reinforced polypropylene (PP) composites are known to support lightweight design of injection moulded (IM) parts. For an additional weight reduction, foam injection moulding can be used. The presentation provides an overview of achievements for physical (MuCell®) foam injection moulding of PP-cellulose fibre compounds with CO_2 or N_2 and a comparison to chemical foaming. The trials used the same experimental setup (machine and screw) to ensure comparable residence times. The studied variables include gas type and concentration, injection moulding parameters like injection volume and velocity, and the additional use of mould opening (core-back process). The impacts of the different processing parameters on the local foam structure, the achievable density reduction, the overall weight reductions and the mechanical properties of foam IM plates are discussed.*

Keywords: Foaming; injection moulding; cellulose fibre; polypropylene; weight reduction

1. Introduction

Natural and cellulose fibres as filler in PP composites are well-known for their potential reduction of primary energy use and GHG emissions [1-4]. Additionally, they support lightweight design by a reduced composite density compared to glass fibre or talcum filled PP composites. The selection of different available lightweight and natural filler types – fibrous cellulose powder, fine wood powder, larger wood particles and other natural fibres - helps to adjust and optimize the composite properties, and further combinations of different fillers can be used [5].

By the production of injection moulded parts, foam injection moulding (FIM) can be applied for an additional reduction of weight and the development of ultra-light-weight thermoplastic parts. It was shown [6] that fibrous cellulose powder (Tencel® FCP) improves the foamability of a polyolefin in the foam injection moulding process. Two methods can be used to produce such ultra-lightweight plastics: direct gas injection (MuCell® technology; “physical FIM”) or the application of a chemical foaming agent (e.g. sodium hydrogencarbonate; “chemical FIM”).

In previous own trials the chemical FIM process often resulted in improved mechanical properties. In the present study, a comparison between physical FIM and chemical FIM was carried out, focusing on CO_2 as used gas type. By using the same machinery, screw and mould type, influences on the residence and cooling time could be prevented. Injection moulding parameters were varied to study their impact on the density and weight reduction potential of PP-cellulose compounds.

  doi:10.5075/epfl-298799_978-2-9701614-0-0

2. Materials and methods

2.1 PP-cellulose compound

Fibrous cellulose powder TENCEL® FCP 10/300/M (FCP) was used as lightweight and reinforcing filler for PP. Tencel® is a registered trade mark of Lenzing AG and commercially produced from sustainably grown wood by using the Lyocell process. These cellulose fibres are homogenous and highly available. The FCP type used in this study possesses a comparably high aspect ratio with a particle length of 300 µm and a filament diameter of 10 µm. Such fine fillers can help to improve foamability by introducing interfaces. FCP was used in an amount of 20 weight%.

PP is a light plastic material with good mechanical performance and a suitable processing temperature range in combination with natural fibers. PP BJ400HP from Borealis, a special low viscosity type, with density of 908 kg/m³ and a melt flow rate (230 °C/2.16 kg) of 100 g/10min, was used for the compounding. As coupling agent, 2 wt% of a maleic anhydride grafted PP with 1.4% grafting level, Scona TPPP 8112 FA from Byk Altana were added.

A parallel, co-rotating twin screw extruder Brabender DSE20 comprising a screw diameter (d) of 20 mm, and a length of 40 d was used for compounding. A twin screw sidefeeder was employed for feeding FCP. All components were fed via Motan-Colortronic gravimetric dosing scales. 2 vertical ports were used for venting. The maximum melt temperature, measured at the screw tip, was 180°C. For granulation, an ECON EUP50 under-water pelletizer was used. The granules were dried at 80°C before injection moulding, until moisture content was 0.08%.

2.2 Foam injection molding

Injection moulding was performed on an ENGEL e-victory 220. Plates were produced via a 200 x 150 x 3 mm plate tool equipped with one film gate. The used temperature profile started at 180°C for the heating zones and ended with 200°C at the nozzle; tool temperature was set to 40°C, if not otherwise mentioned. The used processing parameters are summarized in Table 1.

Table 1: Processing parameters used for PP-cellulose prepared by compact IM, MuCell® FIM and chemical FIM (chem).

	Shot volume [cm³]	*Gas/FA content [%]*	*Mold opening [mm]*	*Injection speed [cm³/s]*	*Screw rotational speed [m/s]*	*Back or process pressure [bar]*	*Cooling time [s]*	*Cycle time [s]*
Comp	*114*	*0*	*0*	*114*	*0.3*	*70*	*25*	*42*
CO_2	*95-108*	*1.0-1.6*	*0-0.6*	*110-250*	*0.3-0.5*	*150-175*	*22-30*	*37-45.5*
N_2	*95*	*0.6*	*0.3-0.6*	*200*	*0.5*	*160*	*22*	*45.5*
Chem	*96.5*	*3-4*	*0.3-0.5*	*193*	*0.3-0.5*	*83-160*	*22*	*31-45.5*

For compact reference plates, packing pressure was 505 bar for 10s. For the MuCell® FIM, packing pressure was reduced to 0.2s, by employing similar cooling and cycle time.

  doi:10.5075/epfl-298799_978-2-9701614-0-0

For the MuCell® process CO_2 and N_2 were used. Gas content (weight percent) of CO_2 dosing was varied, gas content of N_2 was 0.6 %. Shot volume was varied and reduced to 108 cm³, 100 cm³ and 95 cm³. Injection speed was varied and core back process with mold opening was additionally applied. For core-back process, the cooling time was reduced to 22s. Total cycle time was 37 s, for core-back process at 45.5 s, if not otherwise mentioned.

For chemical foam injection moulding, the foaming agent (FA) Hydrocerol ITP 845 from Clariant was used. It is an endothermic foaming and nucleating agent masterbatch with 40% effective components, their decomposition starts at 150°C. Back pressure was set to 155 - 160 bar, one trial was performed with 83 bar. 0.3mm to 0.5 mm mould openings were applied. Two temperature profiles were used, one from 180°C to 200°C; the other from 150°C to 185°C at the nozzle.

Weight reduction was determined from the rectangular plates by weighing up; density values were determined at the middle of the plates by a buoyancy method, employing a Sartorius analytical balance, according to ISO 1183-1. Flexural properties were determined according to EN ISO 187; Charpy impact strength, notched (1eA) and unnotched (1eU), were tested according to ISO 179. For the preparation of microscopy images, cross sections were cut from the middle part of the plates, embedded and polished. Pictures were taken by an Olympus BX-RLA2 reflected light microscope in bright field mode.

3. Results and discussion

MuCell® foam injection moulding of PP-cellulose with CO_2 injection resulted in high weight and density reductions, see Figure 1. The extent of reduction could be adjusted among others by the reduction of the shot volume. The weight reduction reached values of up to 16% in relation to the compact plates.

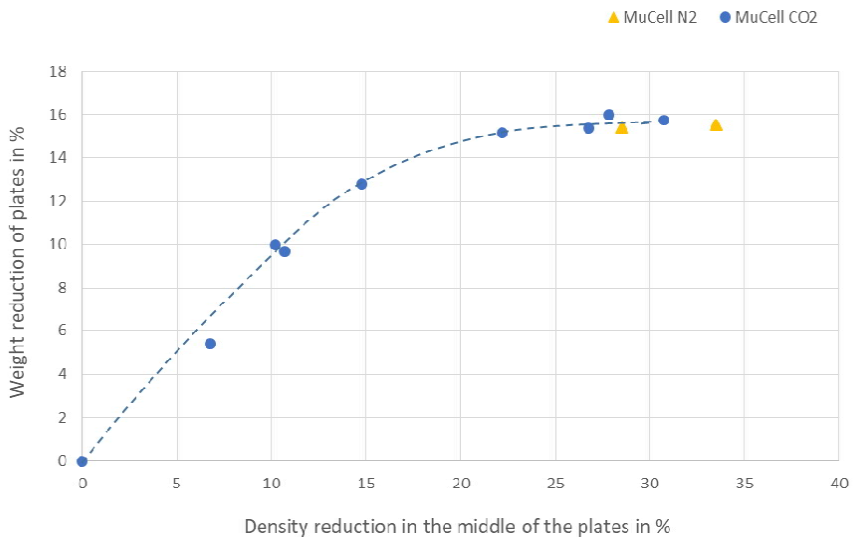

Figure 1. Relation of weight reductions and density reductions for several PP-cellulose plates prepared by MuCell® foam injection moulding.

Density reductions measured from the middle part of the plates reached values of over 30%. Up to around 15% density reduction, the relation between overall weight reduction and the density

  doi:10.5075/epfl-298799_978-2-9701614-0-0

reduction in the middle seems to be quite linear; however, higher density reductions from the middle part did not result in higher overall weight reductions. Probably, the higher foaming effect from the middle part, is compensated by a lower foaming effect in the other parts of the panel. Interestingly, the use of CO_2 or N_2 resulted in identical weight reduction.

Results from flexural testing were related to the density measured at the middle part, see Figure 2, as the specimens for testing had been prepared from spots close to the middle of the plates. The flexural modulus decreased, as soon as a density reduction of 15% was attained. Flexural strength follows a similar trend. At density reductions below 20%, it is therefore possible, by using MuCell® process with CO_2 injection, to obtain PP-cellulose composite plates with low density and only slightly reduced flexural properties.

At low density values, the two gas types used in the MuCell® process, resulted in quite similar flexural properties for the PP-cellulose plates, and the FIM process with chemical foaming agent gave as well similar results. However, for chemical FIM, the achievable density reduction range was much narrower.

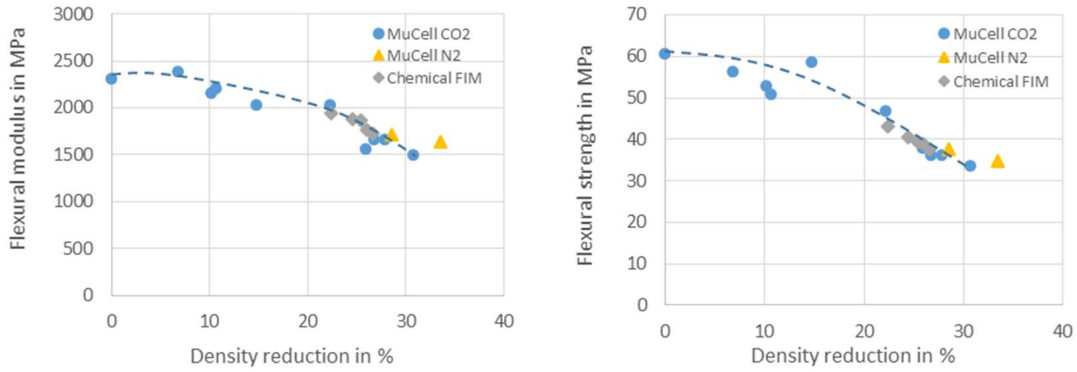

Figure 2. Flexural modulus (left) and flexural strength (right) of PP-cellulose related to the density reduction of the plates prepared by MuCell® or by chemical FIM.

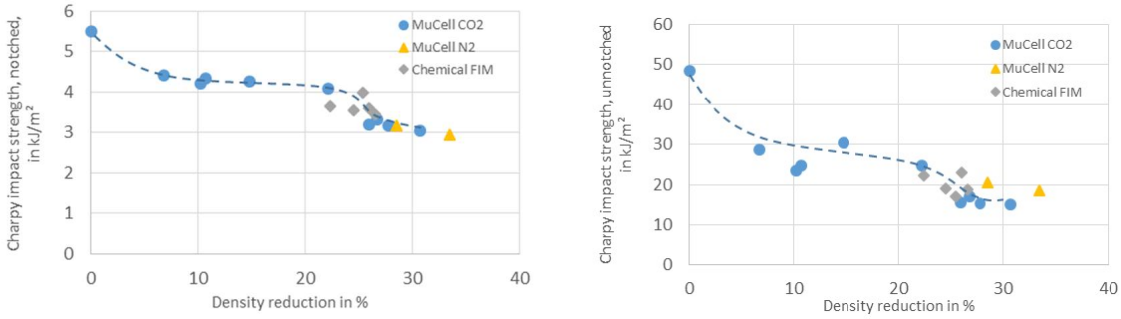

Figure 3. Charpy impact strength, notched (left) and unnotched (right), of PP-cellulose related to the density reduction of the plates prepared by MuCell® or by chemical FIM.

Charpy impact strength decreases by using foam injection moulding, see Figure 3; notched specimens lost 20% of their value, the unnotched ones lost even more than 40%. The introduction of several gas cavities probably prevents the energy absorption due to crack propagations. In addition, the cells act as crack initiation sites, which also explains the drop of the unnotched impact strength for FIM specimens. If the density reduction is above 20%, the

  doi:10.5075/epfl-298799_978-2-9701614-0-0 published under CC BY-NC 4.0 license

impact strength reductions are even higher. In these cases, more or bigger foam cells were visible.

Table 2 shows the density and weight reductions related to the studied processing parameters for the MuCell® FIM process. In general, with decreasing shot volume, density and weight reductions increased. No significant differences in density or weight reductions were observed by variation of the CO_2 gas content, which is an indication, that the gas was sufficiently solved in the polymer matrix. By applying mould opening, an additional reduction of the density in the middle part of the plates could be clearly achieved; however, the weight of the total plate was only slightly changed, probably due to the fact that the edges of the plates contain less foam cells. Higher injection speed resulted generally in lower density reductions. This can be explained by the reduced time, which is available for the expanding of the foam in the mould, and as well by the higher pressure which exists in the mould. Reduction of the mould temperature and, the variation of the screw speed gave no significant influence on the weight reductions; therefore, they are not presented in Table 2.

*Table 2: Density and weight reductions for PP-cellulose prepared by MuCell® FIM; related to the studied processing parameters. (*Sample 9: processed at mould temperature of 30°C).*

Sample		*Shot volume [cm³]*	*Gas content [%]*	*Mould opening [mm]*	*Injection speed [cm³/s]*	*Density reduction middle [%]*	*Weight reduction plate [%]*
0	*compact*	*114*	*0*	*0*	*110*	*0*	*0*
1	*MuCell CO_2*	*108*	*1.2*	*0*	*110*	*6.8*	*5.4*
2	*MuCell CO_2*	*100*	*1.0*	*0*	*200*	*10.2*	*10.0*
3	*MuCell CO_2*	*100*	*1.6*	*0*	*170*	*10.7*	*9.7*
4	*MuCell CO_2*	*100*	*1.2*	*0.6*	*200*	*25.9*	*10.8*
5	*MuCell CO_2*	*95*	*1.6*	*0*	*250*	*14.8*	*12.8*
6	*MuCell CO_2*	*95*	*1.2*	*0*	*200*	*22.2*	*15.2*
7	*MuCell CO_2*	*95*	*1.2*	*0.3*	*200*	*27.8*	*16.0*
8	*MuCell CO_2*	*95*	*1.2*	*0.5*	*200*	*30.7*	*15.7*
*9**	*MuCell CO_2*	*95*	*1.2*	*0.3*	*240*	*26.8*	*15.4*
10	*MuCell N_2*	*95*	*0.6*	*0.3*	*200*	*28.6*	*15.4*
11	*MuCell N_2*	*95*	*0.6*	*0.6*	*200*	*33.5*	*15.5*

When the flexural moduli of the MuCell® specimens are related to density or weight (specific modulus), best results were achieved by sample 1 and sample 6; either by applying a lower weight reduction of 5% or by using a low shot volume and optimum injection speed of 200 cm³/s;

  doi:10.5075/epfl-298799_978-2-9701614-0-0

the core-back process was not necessary. Highest flexural strength related to density was achieved by applying the highest injection speed of 250 cm^3/s (sample 5). Unfortunately, impact strength was generally reduced through the foaming process; highest impact strength values related to weight were also obtained for sample 5. As explained by microscope images, see Figure 4, the higher injection speed during production of sample 5 resulted in a finer cell morphology compared to sample 6, as there was less time for expanding.

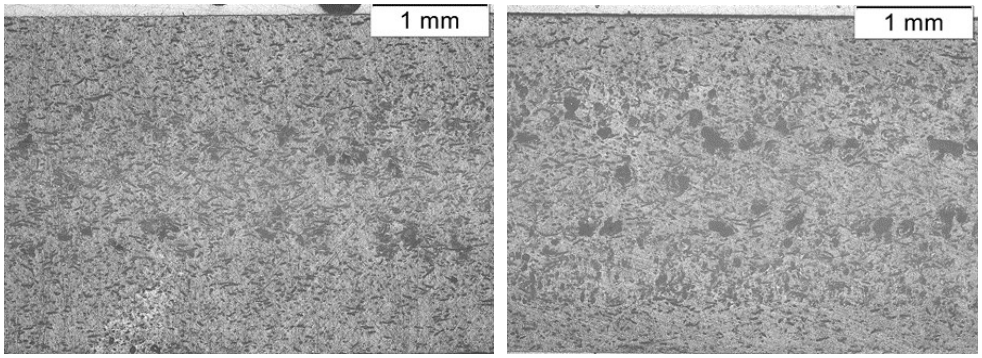

Figure 4a. Microscopy images of foamed PP-cellulose, sample 1 (left) and sample 5 (right).

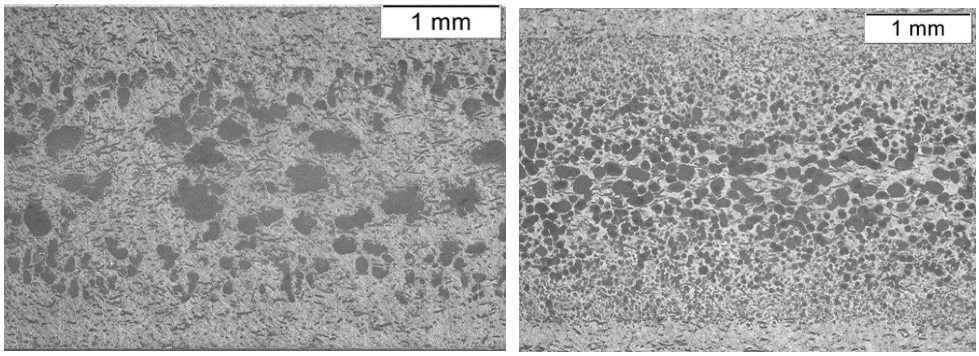

Figure 4b. Microscopy images of foamed PP-cellulose, sample 6 (left) and sample 10 (right).

Microscope images of PP-cellulose, see Figure 4, present on the one hand the foam cells as circular dark phases, and on the other hand the dispersion of the cellulose fibres, as well as a dark phase. Differences in the foam structures are clearly visible in the presented samples. Sample 1 shows less foam cells. In sample 5, several more foam cells are observable. Sample 6 presents very big foam cells in the middle layer. Sample 10, prepared by N_2 injection, resulted in a lot of foam cells, arranged in different layers. Sample numbers are explained in Table 2.

Table 3 presents density and weight reductions related to the studied processing parameters for the chemical FIM of PP-cellulose. Increasing the mould opening showed only a minor influence on density reduction. The raise of the foaming agent content to 4% could not increase the weight reduction. Lowering of the screw speed rather decreased the weight reduction of the plate, probably caused by an insufficient dispersion of the foaming agent in the melt. Weight reduction could be slightly increased again by decreasing the melt temperature; thereby, the chemical decomposing reaction of the foaming agent can be decelerated and this can result in a more homogenous foaming. The weight reduction could be further increased by softening the shear process through reduction of the back pressure and by lowering dwell time during the plasticization.

  doi:10.5075/epfl-298799_978-2-9701614-0-0

Table 3: Density and weight reductions for PP-cellulose prepared by chemical FIM; related to the studied processing parameters.

Sample	*Foaming agent content [%]*	*Mould opening [mm]*	*Temp. nozzle [°C]*	*Screw speed [m/s]*	*Density reduction middle [%]*	*Weight reduction plate [%]*	*Note*
12	*3*	*0.3*	*200*	*0.5*	*24.5*	*14.7*	
13	*3*	*0.5*	*200*	*0.5*	*26.6*	*14.6*	
14	*4*	*0.5*	*200*	*0.3*	*26.0*	*11.2*	
15	*4*	*0.5*	*185*	*0.3*	*22.4*	*11.8*	
16	*4*	*0.5*	*185*	*0.3*	*25.4*	*13.3*	*Reduced back pressure and cycle time (30s)*

Highest specific stiffness and specific flexural strength values, for chemical FIM samples, were received by sample 15, which was produced at lower melt temperature. Highest specific notched impact strength was attained by sample 16, and the highest specific unnotched impact strength by sample 14; both samples were prepared at a foaming agent content of 4 weight percent.

4. Conclusions

The results of this study confirm the foamability of PP-cellulose compounds by MuCell® FIM with CO_2 and N_2 injection, and by chemical FIM. Resulting weight reductions, homogeneity of the foam structure, size of the foam cells and mechanical properties depend highly on the adjusted processing parameters, which have to be optimized for each foaming process. If a foaming degree below 15% is applied, it is possible to simultaneously decrease weight while sustaining flexural modulus and strength. However, impact strength was reduced in all cases by foaming.

Acknowledgements

This study was supported by the Austrian Research Promotion Agency FFG (COMET program).

5. References

1. Civancik-Uslu D, Ferrer L, Puig R, Fullana-i-Palmer P. Are functional fillers improving environmental behavior of plastics? A review on LCA studies. Science of the Total Environment 2018; 626: 927–940.
2. Hesser F. Environmental advantage by choice: Ex-ante LCA for a new Kraft pulp fibre reinforced polypropylene composite in comparison to reference materials. Composites Part B 2015; 79:197-203.
3. Shen L, Patel MK. Life cycle assessment of man-made cellulose fibres. Lenzinger Berichte 2010; 88:1-59.

  doi:10.5075/epfl-298799_978-2-9701614-0-0

4. Broeren MLM, Dellaert SNC, Cok B, Patel MK, Worrell E, Shen L. Life cycle assessment of sisal fibre e Exploring how local practices can influence environmental performance. Journal of Cleaner Production 2017, 149:818-827.
5. Vardai R, Lummerstorfer T, Pretschuh C, Jerabek M, Gahleitner M, Bartos A, Moczo J, Anggono J, Pukanszky B. Improvement of the impact resistance of natural fiber–reinforced polypropylene composites through hybridization. Polymers for Advanced Technologies 2021; 1-9.
6. Pretschuh C, Steidl E, Lehner P, Müller N, Marsche M, Steinbichler G, Haider A. Regenerated cellulose fibers Tencel® FCP as filler in PP for improved foam injection molding. Biocomposites Conference Cologne, Köln, 2017.

  doi:10.5075/epfl-298799_978-2-9701614-0-0

IN-LINE QUALITY ASSURANCE AND PROCESS CONTROL IN FULLY AUTOMATED WELDING PROCESSES

Stefan, Weidmann[a], Peter, Mitschang[a]

a: Leibniz-Institut für Verbundwerkstoffe GmbH – stefan.weidmann@ivw.uni-kl.de

Abstract: *Induction welding of hybrid metal-composite structures offers a number of advantages, but at the same time possesses major challenges with implementing in-line quality assurance (QA) and process control. Process control by contactless measurement of the surface temperature is - usually - not possible, because the conditions on the surface do not accurately reflect all the effects in the joining zone. A new approach for in-line QA is based on the thickness change (TC) of the hybrid structure before and after welding. The results show, that an increasing TC reduces the number of voids in the joining zone and can be correlated with tensile-shear strength. It was also found, that a correlation between the progress of the TC and the temperature of the steel specimen is present. This approach is implemented in the fully automated FlexHyJoin production cell (www.flexhyjoin.eu) for hybrid welding.*

Keywords: quality assurance; induction welding; hybrid joining; thickness change

1. Introduction

The increasing use of composite structures made of thermoplastic fiber reinforced polymer composites (TP-FRPC) requires the development of suitable joining processes [1]. Induction welding is particularly suitable as a thermal joining process due to the efficient and contact-free energy input. Especially for hybrid metal-composite structures, the metallic joining partner can be efficiently heated by induction. When the metal is heated above the melting temperature of the TP-FRPC, the matrix polymer melts to the interface of the metal. Due to a simultaneously applied consolidation force, the metallic joining partner is pressed into the molten TP-FRPC to establish an intimate contact. When using physical surface pretreatments - such as laser structuring of the metal part - the matrix polymer flows into the cavities of the structuring and solidifies after cooling, resulting in a hybrid bond. Using chemical surface pretreatments, e. g. by bonding agents, bonding mechanisms act on a molecular level.

Other hybrid joining processes such as vibration welding or ultrasonic welding mostly use energy-time controlled approaches. Resistance welding also usually uses a predefined energy-time profiles, since direct temperature measurement is difficult or less accurate due to the hidden joining zone. Non-contact thermal joining processes - such as laser welding - can use an infrared camera or pyrometer for temperature monitoring in addition to a predefined power input, but often the joining zone is hidden by components or it is difficult to measure on a reflective metal surface, for example. Similar challenges are present in induction welding, where the joining zone area with the highest temperature is also covered by, for example, a consolidation stamp. [2, 3, 4, 5]

An alternative QA approach is to monitor the thickness change (TC) during thermal joining instead of temperatures. The major advantage is the monitoring TC to be very simple. In addition TC can easily be incorporated as a process parameter into existing plant technology and can be

  doi:10.5075/epfl-298799_978-2-9701614-0-0

used as QA parameter for many thermal joining processes, even beyond metal-FRPC hybrid joining. The state of the art on this approach is fairly limited and only a few authors investigated the approach of using the TC as process control parameter or its progress during joining [6, 7, 8, 9]. Due to the simplicity of the QA approach and its broad use in other thermal joining processes it is being further researched, especially to prepare the QA approach for industry.

1.1 Preliminary work

In [10], the influence of TC on joint strength and void content has already been investigated in detail, when joining laser-structured steel (deep-drawing steel, thickness 1 mm, laser structure spacing 0.3 or 0.6 mm) with continuous glass-fiber-reinforced polyamide 6 (Tepex dynalite 102-RG600, thickness 1.5 mm). The definition of TC is shown in Figure 1.

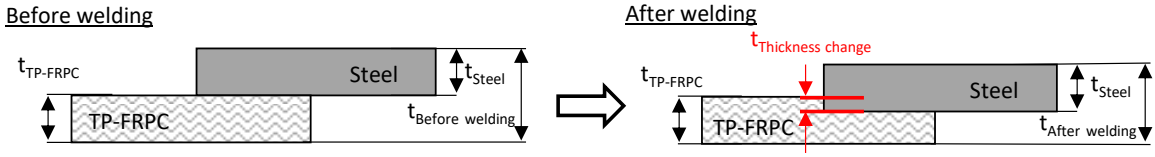

Figure 1: Definition of TC [10]

The result shows, that higher TC lead to higher lap shear strengths and the void content decreases. Furthermore, it was found that from a certain TC onwards, the lap shear strength does not increase further and almost all pores are squeezed out from the joining zone. Reaching this TC can thus be defined as a QA criterion for a laser-structured steel surface, which must be exceeded in order to consider that a defect-free joint has been achieved. It was also found, that the TC for maximum lap-shear strengths varies depending on the structuring distance. Shorter structuring distances require less TC for maximum lap-shear strength than larger structuring distances. This is due to the smaller total volume of cavities that must be filled with molten polymer.

Aim of this study is to investigate, if QA by TC monitoring is also suitable for other surface pre-treatments without laser-structuring. For this investigation deep drawing steel sheets pretreated with bonding agent were used. In addition, the influence of the joining temperature and the surface pretreatment on the TC progress is examined.

2. Methology and experimental

Lap shear specimens were manufactured according to DIN 1465 by using the induction welding test rig shown in Figure 2. In order to be able to set the TC precisely, spacers were placed next to the specimens on the aluminum positioning tool and varied according to the targeted TC. Furthermore, the thickness of each steel test specimen and each TP-FRPC test specimen was measured with a micrometer at the joining zone before welding. Thus, by subtracting the sum of the specimen thicknesses before welding by the final thickness of the joint, it can be verified that the target TC was achieved. For each target TC five specimens were joined and tested according to DIN 1465 (Zwick 1474; hydraulic clamping, test speed 1 mm/min, free test length 112.5 mm). One further specimen was used to prepare a micrograph of the joining zone. The specimens were all joined with a consolidation force of 300 N, a generator power of 10 A and a holding time of 10 s. Figure 2 shows the specimen geometry, the weld test rig and an exemplary process diagram.

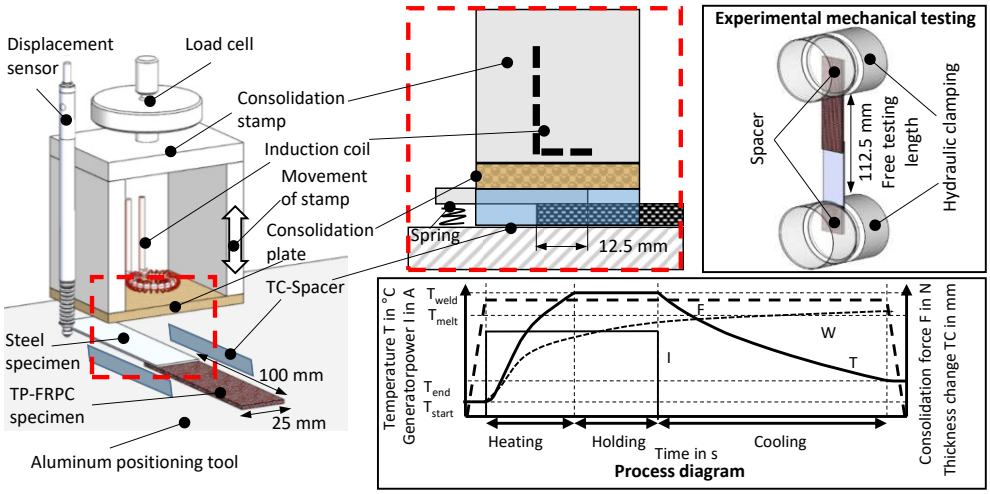

Figure 2: Experimental specimen manufacturing, mechnaical testing and process diagram

3. Materials

Two different bonding agents were used as coating for the steel sheets. In combination with GF-PA6 or GF-PP specimen, in total 7 different material combinations, were investigated. The material combinations are defined in Table 1. The results for pretreatments by laser structuring were taken from [10].

Table 1: Investigated material combinations (results transferred from* [10]*)*

		Acronym	Surface pretreatment of mild steel	TP-FRPC	Welding temperature T
Related to chapter	4.1	GF-PA6/HL400	Bonding agent Köratac HL 400	BondLaminates Tepex dynalite 102-RG600, thickness 1.5 mm	280 °C
	4.1	GF-PA6/HL403	Bonding agent Köratac HL 403	BondLaminates Tepex dynalite 102-RG600, thickness 1.5 mm	280 °C
	4.1	GF-PP/HL400	Bonding agent Köratac HL 400	BondLaminates Tepex dynalite 104-RG600, thickness 2 mm	240 °C
	4.2				180, 210, 240 °C
	4.1	GF-PP/HL403	Bonding agent Köratac HL 403	BondLaminates Tepex dynalite 104-RG600, thickness 2 mm	240 °C
	4.2				180, 210, 240 °C
	4.1*	LS0.6/GF-PA6	Laser structuring in line pattern	BondLaminates Tepex dynalite 102-RG600, thickness 1.5 mm	290 °C
	4.1*	LS0.3/GF-PA6	Laser structuring in line pattern	BondLaminates Tepex dynalite 102-RG600, thickness 1.5 mm	290 °C
	4.2	LS0.3/GF-PP	Laser structuring in line pattern	BondLaminates Tepex dynalite 104-RG600, thickness 2 mm	180, 210, 240 °C

Köratac HL400 [11] and Köratac HL403 [12] bonding agents are epoxy-based coating materials and are applied to the metals before welding, cured and can then be further processed without any special storage or transport conditions. They have been especially optimized for joining metal to polypropylene. The special feature of Köratac HL403 is, that it is also conditionally suitable for joining with polyamide 6.

4. Results

4.1 Influence of TC on bond strength

Figure 3 summarizes the lap-shear results of the hybrid joints manufactured with different material combinations for different target TCs and the results with laser structuring from [10].

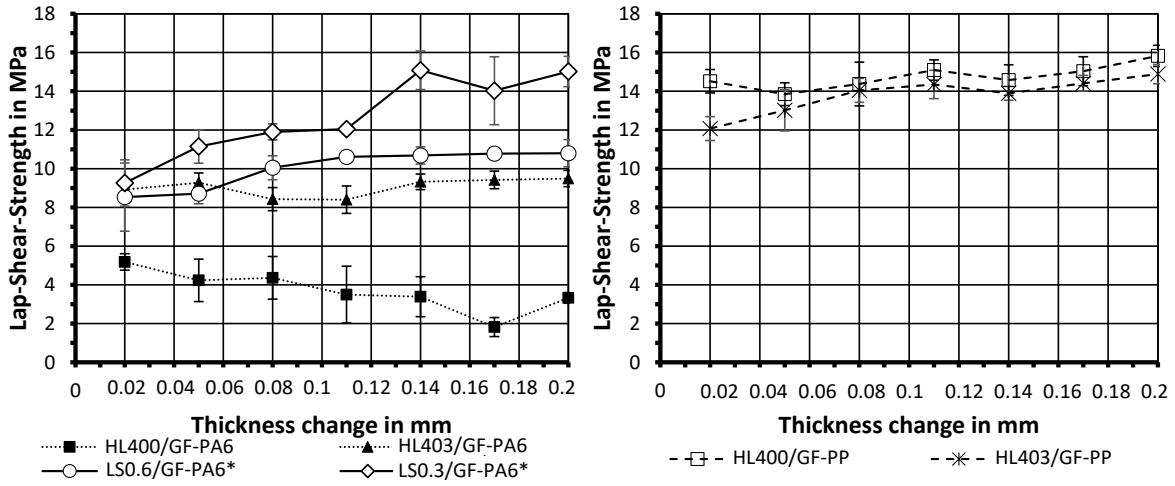

HL400/GF-PA6	HL403/GF-PA6	LS0.6/GF-PA6	LS0.3/GF-PA6	HL400/GF-PP	HL403/GF-PP
-35.71%	6.39%	26.49%	62.20%	9.02%	23.36%
Influence of thickness change from 0.02 to 0.2 mm					

Figure 3: Influence of TC on bond strength. Left: Steel joined to GF-PA6, Right: Steel joined to GF-PP. (* results transferred from *[10]*)

Overall, for the material combination steel with GF-PA6, it can be stated that higher bond strengths are achieved with laser structuring than with the Köratac bonding agents, described in [11] and [12]. Furthermore, it is evident that in contrast to the hybrid specimens with a laser-structured surface, the hybrid joints with a bonding agent coating tend to show a lower increase in strength at higher TC. In the case of HL400/GF-PA6, the strength decreases when the TC increases. It is obvious, that in the case of the bonding agents, no cavities have to be filled with molten polymer and therefore a faster wetting of the entire surface takes place. Thus, the bonding mechanisms are fully established - even at small TC. In the case of HL400/GF-PP and HL403/GF-PP, lap shear strengths are close together at all TC, except 0.02 mm. The deviation at 0.02 mm may be caused as a result of the small TC, as some areas of the joining zone were not wetted with molten polymer, resulting in lower lap shear strength. Considering TC ≥ 0.05 mm, it was found that higher TC affect the lap shear strength much less than compared to laser-structured metal specimen. Therefore with bonding agents, no further increase in joint strength is to be expected once the complete wetting of the joining zone is achieved. In order to check, at which TC full wetting of the steel surface was achieved, micrographs were prepared of each TC, which are shown in Figure 4. In addition, the fracture surfaces of HL403/GF-PA6 and HL403/GF-PP are also shown at the lowest and highest TC. Since the micrographs of both bonding agents are similar, only HL403 is shown in detail.

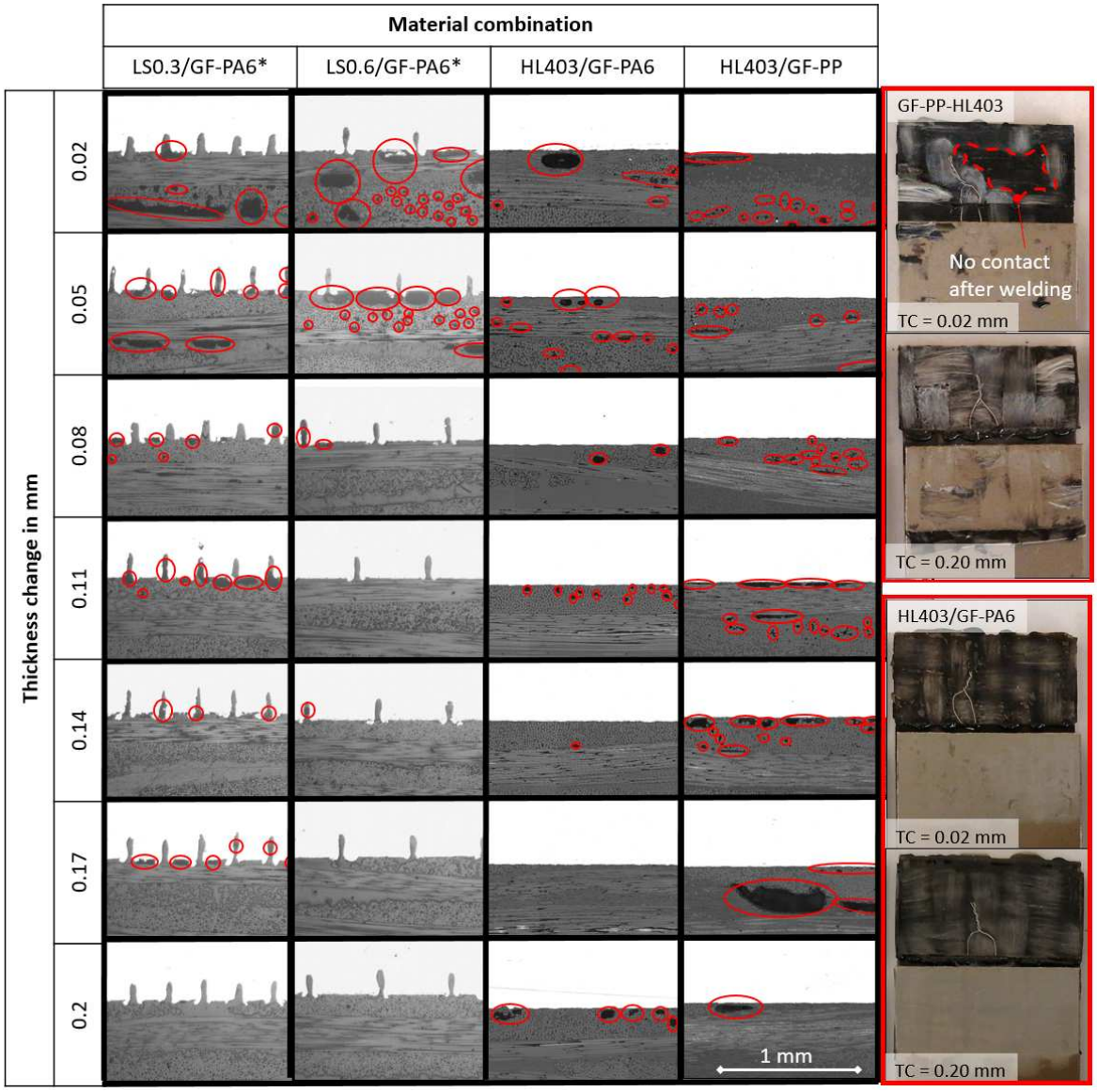

Figure 4: Micrographs of welded specimen at different TC and fractured surfaces after testing

The micrographs show, that wetting of the joining zone took place at TC of 0.02 mm. However, a closer look at the fracture surfaces reveals, that some areas in the joining zone of HL403/GF-PP at a TC of 0.02 mm show no contact between the joining partners. In contrast, the HL403/GF-PP specimens with a TC of 0.2 mm show full contact. Depending on the material combination and the TC, the number and size of voids in the hybrid joints using bonding agents varies. In contrast to the void content in the hybrid specimens with the laser-structured steel surface, no clear correlation can be seen between the decrease in void size and number with increasing TC. One reason is, that the laser structuring can better evacuate the air through the cavities when the TC increases. In the case of bonding agents, the air can only be evacuated in in-plane direction together with molten matrix. This is associated with long flow paths and the fiber reinforcement also hinders the squeezing out of the air, resulting in more air inclusions after cooling.

In addition, it can be noticed that the voids are significantly larger with HL400/GF-PP or HL403/GF-PP compared to HL400/GF-PA6 or HL403/GF-PA6. Polypropylene shrinks more during

solidification than polyamide 6. The greater shrinkage increases the tendency for voids formation during cooling in the isochoric process, in which spacers are used to adjust the TC, and thus a lack of compression may favor the formation of voids during cooling.

In order to determine the extent of the influence of the voids on the lap shear strength, the next step is to compare test specimens with isobaric process control, i.e. process control without spacers, with test specimens produced by isochoric process control (TC = 0.2 mm). Since this effect occurred in particular in material combinations using GF-PP, only these will be examined in more detail. The results of the mechanical testing are shown in Figure 5. In order to show that less voids are present using isobaric processing, the micrographs are also shown in Figure 5.

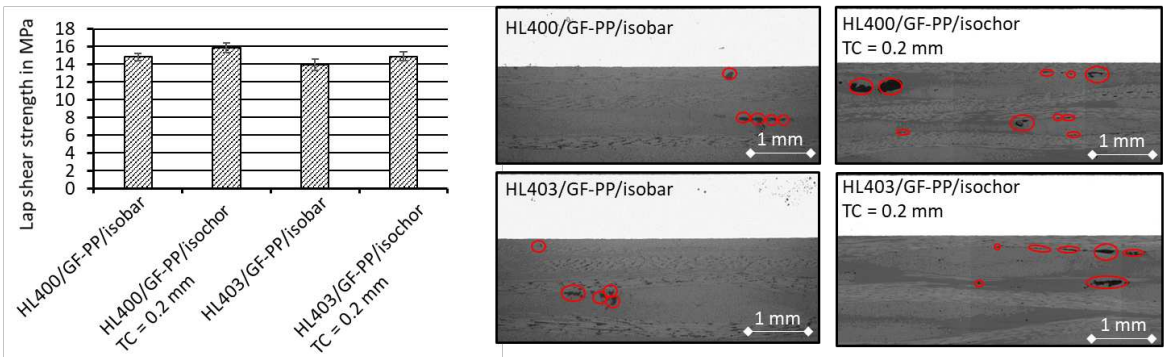

Figure 5: Influence of isobar and isochor consolidation on lap shear strength

Although there are more voids in specimen with isochoric process control, no significant difference can be found in the strengths of the hybrid specimens of an isobaric or isochoric process control.

4.2 Influence of welding temperature and surface pretreatment on TC progress

In this chapter, the influence of the welding temperature and the surface pretreatment on the TC progress is examined, the results are shown in Figure 6. The process control investigated here is isobaric, i. e. no spacers were used and the consolidation pressure was thus applied to the joining zone during the entire process time. The material combinations being used are listed in Table 1. The welding temperatures and the surface pretreatments were varied according to the information given in Table 1.

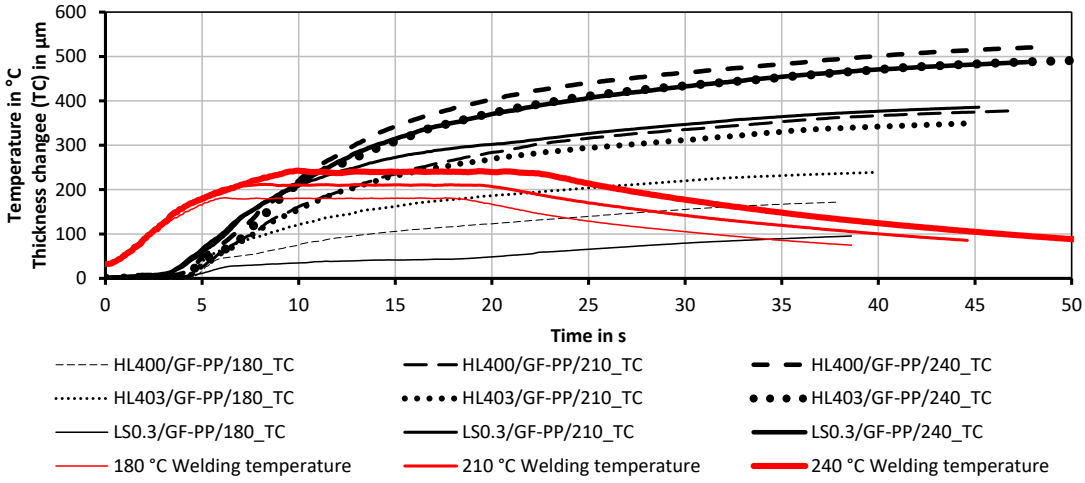

Figure 6: Influence of welding temperature and surface pretreatment on TC progress

It was found, that higher welding temperatures lead to higher TC for all surface pretreatments. This is due to the decreasing matrix viscosity at higher temperature as well as to the longer welding time at higher welding temperatures, since more time is needed to reach the higher welding temperature and also more time is needed to cool down the specimens. No significant influence of the surface pretreatment on the TC can be detected. At a welding temperature of 180 °C, larger deviations in TC can be identified. The TC also increases when the specimens are cooled, because the specimens and the test rig also cool down and a TC can thus be measured as a result of thermal expansion. As a consequence, the final measured TC in the test rig does not correspond to the real TC at the specimen, because other influences (also deflection of the consolidation plate, consolidation of the specimens, settlement effects, etc.) are also measured.

5. Implementing as in-line quality assurance (QA) in industrial scale

It was shown on a laboratory scale that in-line QA can be implemented and provides meaningful results with regard to the quality of the hybrid joint. In order to demonstrate, that in-line QA is also suitable for an industrial scale, this in-line QA approach was implemented in a fully automated production cell for hybrid joining as part of the FlexHyJoin project. The constructive implementation is shown in Figure 7.

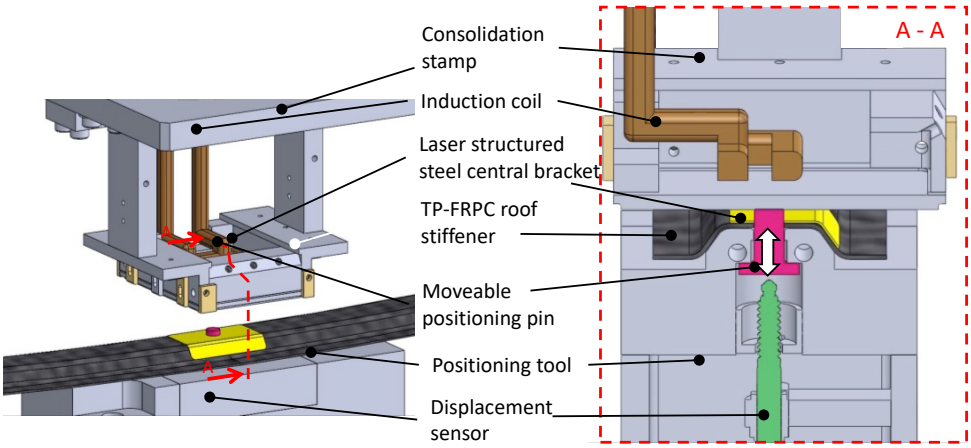

Figure 7: Implementation of TC in-line-QA in industrial production process

The TP-FRPC roof stiffener and the laser-structured steel central bracket are positioned to each other by a linearly movable positioning pin. When the consolidation stamp moves onto the joining partners at the beginning of the process, the positioning pin is pushed into the mold. This displacement is recorded by the displacement sensor. During heating and cooling, the displacement, i.e. the TC, is recorded and can be used as a QA criterion in the same manner as in the laboratory scale.

6. Summary

The investigations prove, that the thickness change (TC) during welding can be used as in-line quality control parameter for both laser structured and coated metal-FRPC hybrid joints. With regard to a void-free joint, laser structuring in line pattern seem to be well suited to support evacuation of the air out of the joining zone. For surface pretreatments, here in particular coated steel sheets with Köratac bonding agents, the TC can also be used as an in-line quality assurance feature, since it has been shown, that a small TC (0.05 mm) leads to high joint strengths. But if void-free joints have to be produced, high attention must be paid to the shrinkage of the

  doi:10.5075/epfl-298799_978-2-9701614-0-0

polymer in an isochoric process when using high crystalline polymers like PP. It was found, that there is no influence of isochoric and isobaric process control on the lap-shear strength for hybrid joints made of bonding agents and GF-PP. In order to avoid voids in the joining zone, isobaric process control is recommended. A process control, which targets a certain TC in the process and remains at this position seems to be promising and must be further investigated.

Acknowledgements

This study has been conducted in the frame of the research project "Automated hybrid welding of metallic fasteners to fiber-reinforced polymer components (HyBe)", funded by the Central Innovation Program for SMEs (ZIM) of the German Federal Ministry of Economic Affairs and Climate Action (BMWK), funding code: KK5003706FF1

7. References

1. A. Yousefpour, M. Hojjati und J.-P. Immarigeon, „Fusion Bonding/Welding of Thermoplastic Composites," Journal of Thermoplastic Composite Materials. , pp. 303-341, 2004.
2. B. Harras, K. Cole und T. Vu-Khanh, „Opimisation of the ultrasonic welding of PEEK-carbon composites," Journal of Reinforced Plastics and Composites, pp. 174-182, 1996.
3. C. Ageorges, L. Ye und M. Hou, „Experimental investigation of the resistance welding of thermoplastic- matrix composites," Composites Science and Technology, pp. 1027-1039, Mai 2000.
4. S. Katayama und Y. Kawahito, „Laser joining carbon fiber-reinforced plastic to stainless steel," Industrial Laser Solutions, pp. 22-30, 15 Juli 2014.
5. D. Maurer und P. Mitschang, „Quality controlled induction welding by adapted process parameters," SAMPE Journal, Vol. 53, No. 1, pp. 42-50, 2017.
6. I. F. Villegas, „Strength development versus process data in ultrasonic welding of thermoplastic composites with flat energy directors and its application to the definition of optimum processing parameters," Composites Part A: Applied Science and Manufacturing, Nr. Volume 65, pp. 27-37, Oktober 2014.
7. R. C. Don, J. W. Gillespie Jr. und C. L. T. Lambing, „Experimental characterization of processing-performance relationships of resistance welded graphite/polyetheretherketone composite joints," Polymer Engineering and Science, Bd. Volume 32, Nr. Issue 9, pp. 620-631, Mai 1992.
8. H. Shi, I. F. Villegas und H. Bersee, „A displacement-detection based approach for process monitoring and processing window definition of resistance welding of thermoplastic composites," Composites Part A: Applied Science and Manufacturing, Bd. Volume 74, pp. 1-9, Juli 2015.
9. T. Zhao, C. Broek, G. Palardy, I. F. Villegas und R. Benedictus, „Towards robust sequential ultrasonic spot welding of thermoplastic composites: Welding process control strategy for consistent weld quality," Composites Part A: Applied Science and Manufacturing, pp. 355-367, June 2018.
10. S. Weidmann, M. Hümbert und P. Mitschang, „Suitability of thickness change as process control parameter for induction welding of steel/TP-FRPC joints," Advanced Manufacturing: Polymer & Composites Science, pp. 55-68, 2 April 2019.
11. Kömmerling Chemische Fabrik GmbH Data sheet Köratac HL 400, 2017.
12. Kömmerling Chemische Fabrik GmbH Data sheet Köratac HL 403, 2013.

  doi:10.5075/epfl-298799_978-2-9701614-0-0

DETERMINING THE INFLUENCE OF THE LEVEL OF DETAIL IN FEA MODELING ON THE WARPAGE PREDICTION OF PCBS

Peter Filipp Fuchs[a], Philipp Michael Novak[a], Margit Lang[a], Tao Qi[b], Julia Zündel[b], Mario Gschwandl[a], Thomas Antretter[c]

a: Polymer Competence Center Leoben GmbH, 8700 Leoben, Austria, peter.fuchs@pccl.at
b: AT & S Austria Technologie & Systemtechnik Aktiengesellschaft, 8700 Leoben, Austria
c: Institute of Mechanics, Montanuniversität Leoben, 8700 Leoben, Austria

Abstract: *Due to ongoing miniaturization and feature integration efforts, the complexity of new PCBs increases significantly. Hence, the size of all structures such as copper vias, connection areas or plated through-holes decreases. Consequently, the application of numerical methods such as finite element analysis (FEA) requires either highly simplified models or enormous computing power to enable virtual evaluation. An in-house developed Virtual PCB builder allows the automatic FE-model generation for any given PCB design. Thereby, the complexity of the investigated design can be reduced by means of material homogenization approaches to a desired level of detail; thus, controlling the computational effort for planned calculations. In order to validate the influence of the chosen level of detail on the prediction quality, a specific test coupon was created and warpage tests were conducted using a Dantec Q400 TCT digital image correlation (DIC) system. During testing, the coupon is heated from room temperature to 180°C and the resulting displacement respectively warpage is measured. Nine FE-models with different levels of detail are generated using the established tool. Thereby, the model resolution is increased step by step. Finally, each modeling approach is evaluated in terms of computational efficiency and accuracy. Based on the results a best practice procedure for warpage analysis is defined for local or global effects of the investigated PCB. Thus, future product developments as well as product designs can be facilitated and improved.*

Keywords: warpage; finite element analysis; discretization; advanced modeling; PCB

Introduction

Printed Circuit Boards (PCBs) and IC substrates are the backbone of high-performance microelectronic products and ensure the electrical interconnection of all components. However, trends as miniaturization and heterogeneous integration pose a challenge to their reliability. This is driving the demand for fast reliability assessment tools as a basis for intelligent design solutions. Current approaches are based on a combination of both, virtual analyses and experiments [1]. However, the requirement of experimental tests and prototype iterations is a significant cost and time factor [2]. Trends towards a virtual product release are yet restricted by the complexity of microelectronics and the thus insufficient prediction quality [3]. The quality of simulations of microelectronic products is dominated by two main sub criteria: the accurate description of the behavior of the different individual materials featured in the system [4,5] and the discretization of the very fine and complex structures [6,7]. This work focuses on the assessment of the influence of the chosen discretization approach. The analyzed effect of an increased level of detail is indicated schematically in Figure 1.

  doi:10.5075/epfl-298799_978-2-9701614-0-0

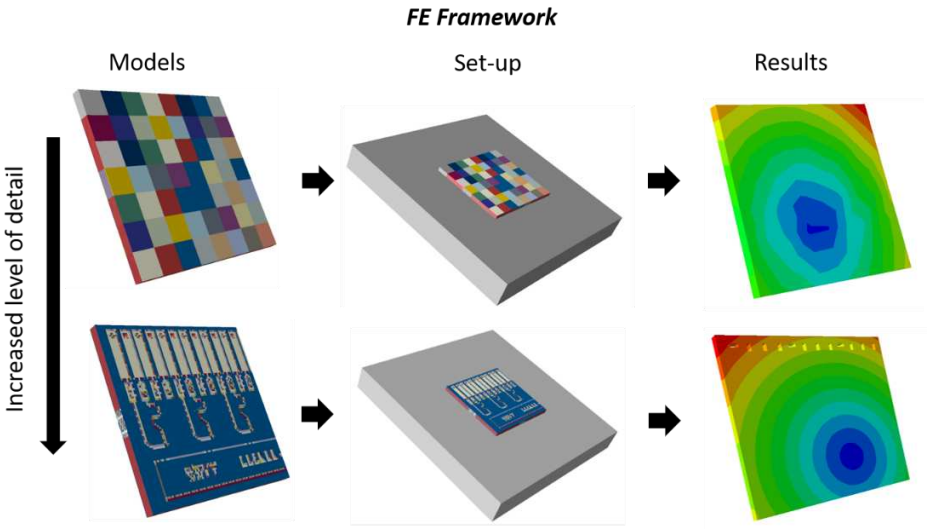

Figure 1. Schematic representation of the influence of the level of discretization on the FE model results in a thermo-mechanical simulation

1. Materials and Design

The study is carried out on an exemplary multilayer PCB design built of insulating (glass-fibre reinforced epoxy prepregs) and conducting layers (inhomogeneous copper structures) connected with each other by vias. Eight samples are prepared and measured. Due to its size the PCB is cut in half with a size of 31x31mm to fit the experimental boundary conditions (compare Figure 2). The thickness of the PCB is 1.6mm.

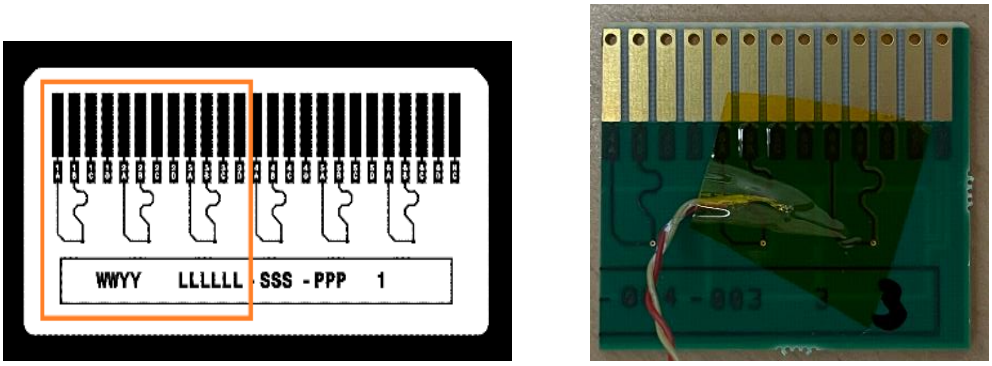

Figure 2. Multilayer PCB design (left) and a specimen (right).

2. Experimental

For the experimental analysis a Dantec Q400 system (Dantec Dynamics, Ulm, Germany) is used [8]. The device consists of two cameras, a heating stage as well as a cooling system based on liquified nitrogen as shown in Figure 3. During the test a time series of pictures of the measured sample is recorded, which is then compared to the initial picture. Once the images are matched, using the software Istra 4D (Dantec Dynamics, Ulm, Germany) the relative displacement between the reference and deformed pictures is evaluated.

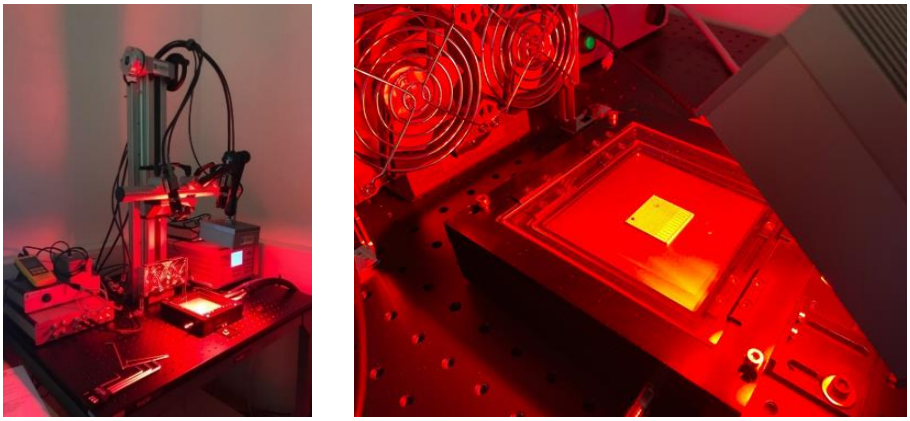

Figure 3. Experimental test set up with the Dantec Q400 system (Dantec Dynamics, Ulm, Germany)

The DIC measurement requires a speckle pattern on the layer facing the two cameras, in order to match the distortion of the reference (virgin material) and deformed images. For this measurement the speckle pattern employs a white base coating with black speckles. The base coating is applied by using a NORD-TEST Developer U89 and the pattern is created by using the graphite spray “Kontakt Chemie GRAPHIT 33”.

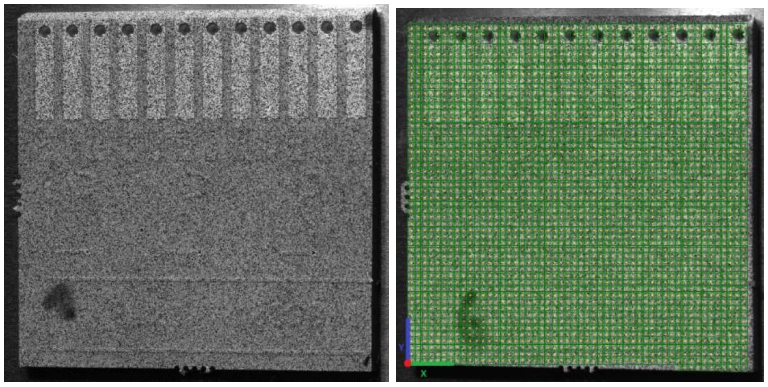

Figure 4. Specimen with applied speckle pattern (left) and a representation of the facets defined for the strain evaluation(right)

The prepared specimens are placed in the temperature chamber. A heating rate of 1K/min is applied starting from room temperature to 180°C. The temperature is held constant for 5 minutes every 10K to ensure a homogenous temperature whenever a picture is recorded. For the strain evaluation the facet size it is set to 31px (0.02mm/px) and the grid spacing distance is set to 25px. The coordinate system point of origin is defined to be at the lower left corner of the sample.

3. Simulation

In order to allow a fast and efficient virtual assessment of new PCB designs a dedicated in-house tool for FE-modeling, the “Virtual PCB Builder (VPB)” [6], was applied. This tool allows the fully automated generation of FE-models based on design data and material data. The VPB allows to decrease the complexity of a given PCB design by means of clustering, segmentation and material homogenization. Thereby, the design data is transferred to the necessary input data format, already allowing for simplifications. To investigate the influence of the design input quality on the global prediction quality three levels were introduced: 96 dpi, 150 dpi and 300

  doi:10.5075/epfl-298799_978-2-9701614-0-0

dpi. With decreasing quality, the precision of small features in the design data is reduced. Further, the VPB allows to choose between different cluster sizes for the segmentation procedure described in Gschwandl et al. [6]. Three different cluster sizes: 4x4, 8x8 and 16x16 are investigated (compare Figure 5).

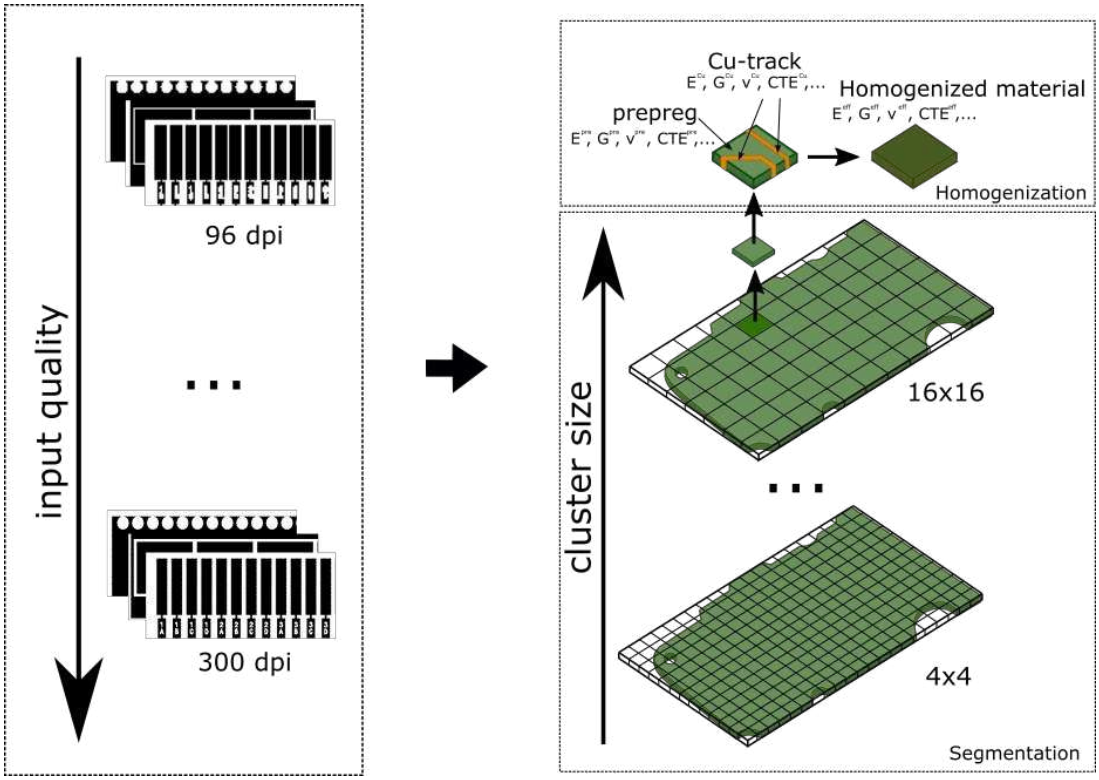

Figure 5. Schematic representation of the discretization approach via input quality, clustering and homogenization

The combination between input quality and cluster size finally defines the cluster size dimension in mm as illustrated in Table 1.

Table 1: Analyzed discretization

discretization	input quality [dpi]	cluster size	cluster size [mm]
1	96	4x4	1.06 x 1.06
2	96	8x8	2.13 x 2.13
3	96	16x16	4.40 x 4.40
4	150	4x4	0.67 x 0.67
5	150	8x8	1.35 x 1.35
6	150	16x16	2.70 x 2.70
7	300	4x4	0.34 x 0.34
8	300	8x8	0.67 x 0.67
9	300	16x16	1.35 x 1.35

  doi:10.5075/epfl-298799_978-2-9701614-0-0

A total of nine different discretizations were analyzed using the commercial FE-software Abaqus (R2020, Dassault Systèmes, France). Each model was generated by the VPB tool. Within the FE-software the model boundary conditions (BC) are applied as follows:

- BC1 is fixing one node at the lower left side for all translational degrees of freedom (DOF) (U1=U2=U3=0). Thus, all obtained displacements are referenced to this point; identically to the experimental evaluation of the DIC measurements.
- BC2 fixes the translational degrees of freedom of the upper-left node in x and z-direction (U1=U3=0). Thus, the model is prevented from rotating around the x and z-axis.
- BC3 fixes translational degrees of freedom of the lower-right corner node in y- -direction (U3=0), preventing any rotation around the y-axis.
- Finally, a temperature profile is applied in two steps to the entire model via a predefined field. The heat distribution is assumed constant to be constant troughout the entire model, due to the slow heating in the experiments. Initially the temperature is set to 23°C. In the consecutive step the temperature is linearly increased to 180°C.

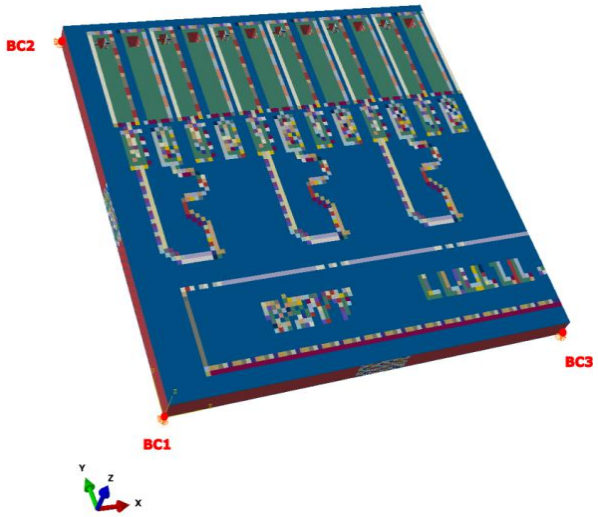

Figure 6. Simulation model with indicated boundary conditions

4. Results

To compare the simulation results with the experimental results, the deformation of the total expansion of the PCB is evaluated based on the DIC measurements at the maximum temperature reached (180°C). The full field displacement is given exemplary in Figure 6 for direction x (see coordinate system indicated in Figure 5 as a reference). As a scalar comparison value the maximum displacement in x any y direction was averaged over the specimen width and length respectively and all eight measured samples. The measured out of plane values (z displacement) were below $5e^{-3}$ mm and are therefore not considered within further evaluations.

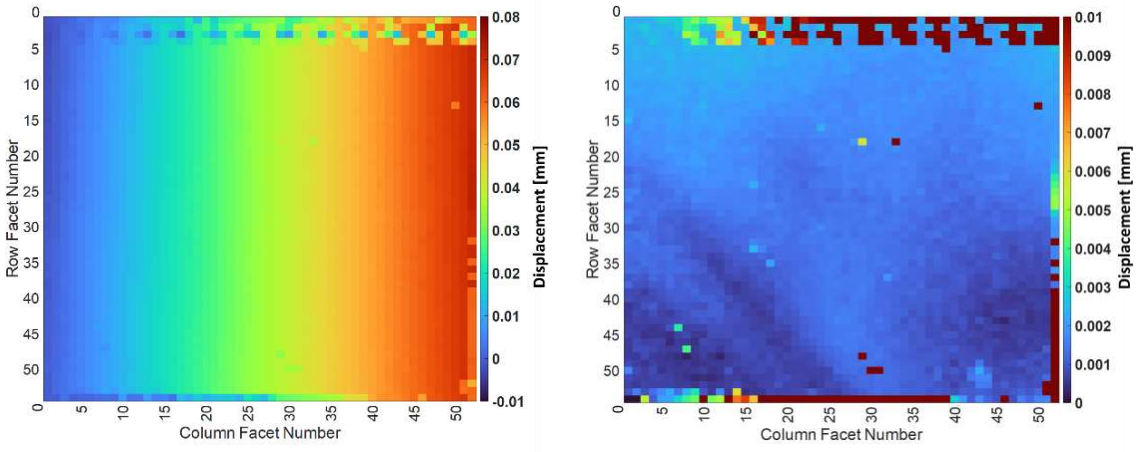

Figure 7. Experimental results for the full field displacement distribution for the x-direction (left) and the associated measurement standard deviation (right)

The simulation data was evaluated the same way as the experimental data. The averaged maximum x and y displacement were evaluated for all different discretizations. An example for the simulated full field displacement field is given for input quality 96 dpi and 300 dpi and the different cluster sizes in Figure 7.

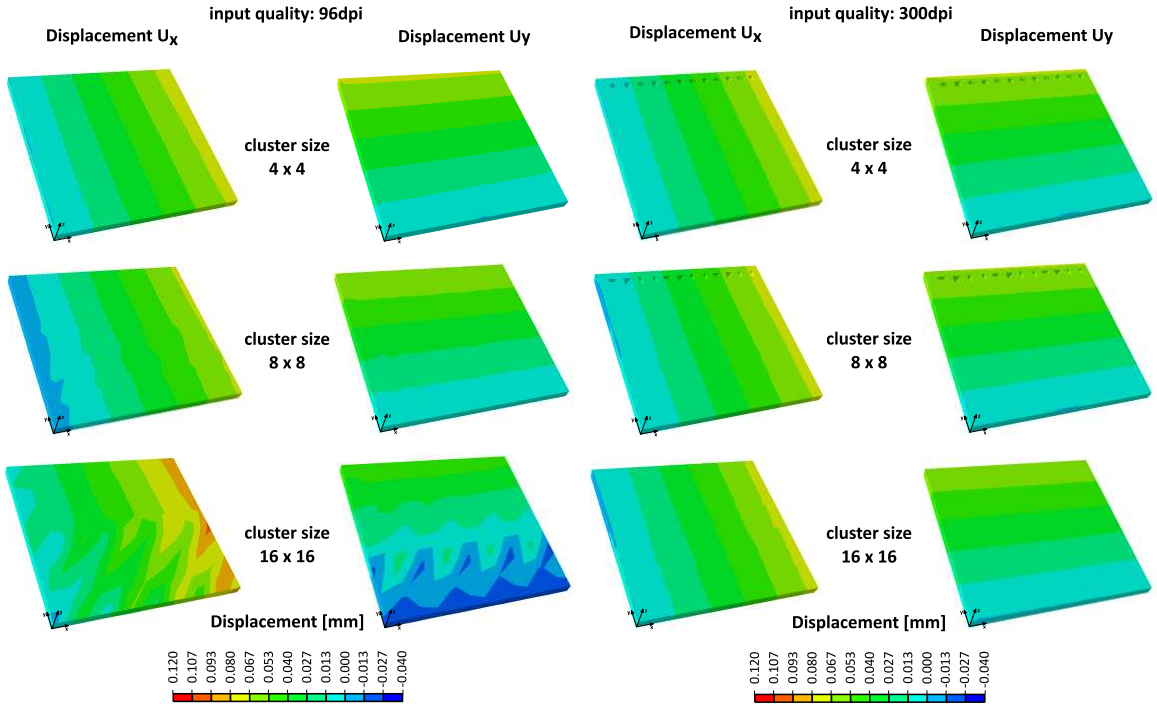

Figure 8. Simulation results for full field displacement x and y for the different discretizations for input quality 96 dpi and 300 dpi

The results of the experimental analysis are compared against the simulation results of all discretizations as shown for the x-direction in Figure 8. As expected, simulation models based on higher input qualities and smaller cluster sizes lead to results with a better agreement with the experimental data.

  doi:10.5075/epfl-298799_978-2-9701614-0-0

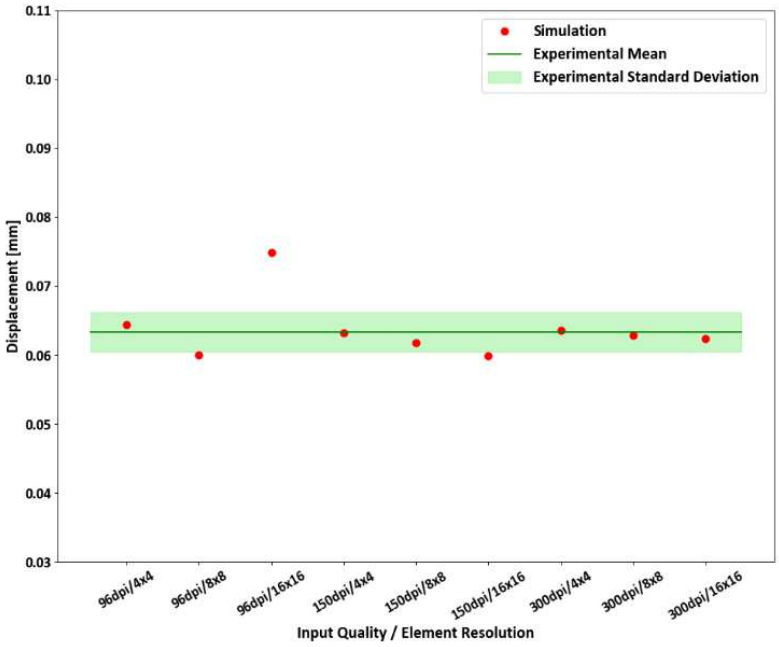

Figure 9. Comparison simulation results against experimental results (x-direction)

All simulation results based on the 300 dpi input quality or 4x4 cluster size show deviations below 2%. However, a combination between 96 dpi input quality and a large cluster size leads to deviations of more than 18%. The results also show that an over- or underestimation of the measurement results cannot be predicted, as both is observed for the different discretizations. The total CPU time for all models, run on the same system (Intel Xeon Silver 4216, 256 GB RAM, 64 logical cores), is given in Figure 9. The results of Figure 8 and Figure 9 can be used to identify the optimum trade-off between computation time and accuracy. The best combination with respect to efficiency and accuracy is a 300 dpi input quality with a large cluster size. Using this discretization, the calculation time is reduced by a factor of 5 when compared to the best performing 300 dpi input quality with a small cluster size, while the deviation to the experimental result is at acceptable 1.5 %.

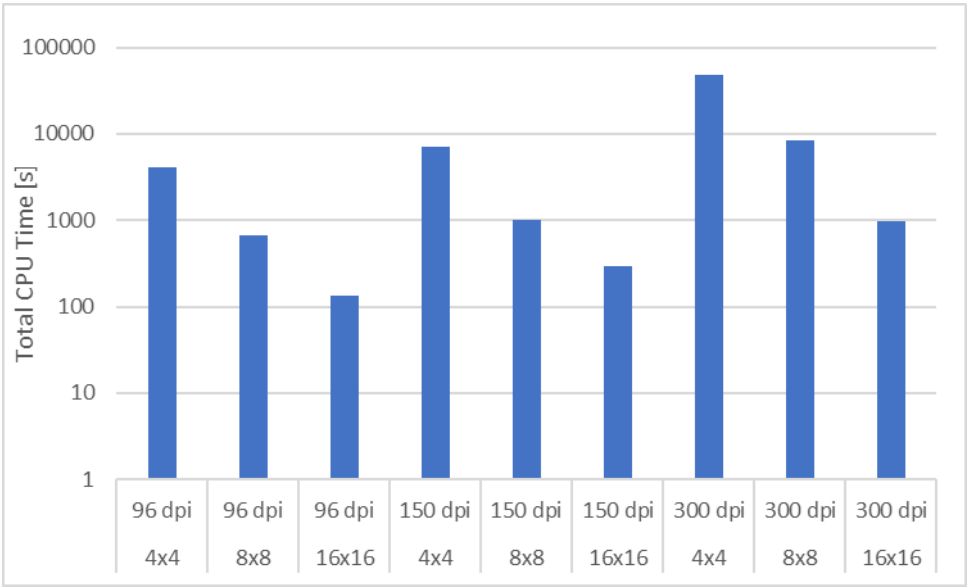

Figure 10. Total CPU time for all different discretizations analyzed

5. Conclusions

Different FE discretization strategies of a PCB build up have been evaluated against experimental thermal expansion results. The results show that either a high design input quality or a low cluster size is import for reliable results. The best trade-off between accuracy and total CPU time is a 300 dpi input quality and a 16x16 cluster. Due to the physics-based clustering approach the accuracy loss is acceptable while the computation time can be significantly reduced.

Acknowledgements

The research work was performed within the COMET-project „ ENSURING SYSTEM RELIABILITY VIA HYBRID POLYMER–METAL COMPOSITE SIMULATION “ (project-no.: VII-3.04) at the Polymer Competence Center Leoben GmbH (PCCL, Austria) within the framework of the COMET-program of the Federal Ministry for Climate Action, Environment, Energy, Mobility, Innovation and Technology and the Federal Ministry for Digital and Economic Affairs with contributions by Montanuniversitaet Leoben (Chair of Materials Science and Testing of Polymers and Chair of Mechanics) and AT&S Austria Technologie & Systemtechnik AG. The PCCL is funded by the Austrian Government and the State Governments of Styria, Lower Austria and Upper Austria.

References

[1] Fuchs PF, Pinter G, Krivec T. Design independent lifetime assessment method for PCBs under low cycle fatigue loading conditions. EuroSimE;2014. https://doi.org/10.1109/EuroSimE.2014.6813787.

[2] Gschwandl M, Pfost M, Antretter T, Fuchs PF, Mitev I, Tao Q et al. Electro-Thermo-Mechanical Reliability Assessment of Arbitrary Power Electronics. In: 2021 22nd International Conference on Thermal, Mechanical and Multi-Physics Simulation and Experiments in Microelectronics and Microsystems (EuroSimE). Piscataway, NJ: IEEE; 2021, p. 1–8.

[3] Prisacaru A, Guerrero EO, Chimmineni B, Gromala PJ, Yang Y-H, Han B et al. Towards virtual twin for electronic packages in automotive applications. Microelectronics Reliability 2021;122:114134. https://doi.org/10.1016/j.microrel.2021.114134.

[4] Fuchs PF, Pinter G, Tonjec M. Determination of the orthotropic material properties of individual layers of printed circuit boards. Microelectronics Reliability 2012;52(11):2723–30. https://doi.org/10.1016/j.microrel.2012.04.019.

[5] Fellner K. Method development for the cyclic characterization of thin copper layers for PCB applications.

[6] Gschwandl M, Fuchs P, Fellner K, Antretter T, Krivec T, Qi T. Finite Element Analysis of Arbitrarily Complex Electronic Devices. IEEE 18th Electronics Packaging Technology Conference (EPTC) :497–500.

[7] Frewein M, Krivec T, Tao Q, Zuendel J, Rosc J, Gschwandl M et al. Package level warpage simulation of a fan out system in board module. 2019 20th International Conference on Thermal, Mechanical and Multi-Physics Simulation and Experiments in Microelectronics and Microsystems, EuroSimE 2019 2019. https://doi.org/10.1109/EuroSimE.2019.8724518.

[8] Gschwandl M, Frewein M, Fuchs PF, Antretter T, Pinter G, Novak P. Evaluation of Digital Image Correlation Techniques for the Determination of Coefficients of Thermal Expansion for Thin Reinforced Polymers. EMAP 2018 - 2018 20th International Conference on Electronic Materials and Packaging 2019. https://doi.org/10.1109/EMAP.2018.8660763.

BUILD QUALITY ANALYSIS OF ADDITIVELY MANUFACTURED LOCALLY ENDLESS FIBER REINFORCED POLYAMIDE

Manuel Frank[a], David Mrozek[a], Jonathan Glinz[a], Sascha Senck[a], Roland Hinterhoelzl[a]

a: Research Group of Lightweight Design and Composite Materials, University of Applied Sciences Upper Austria, Stelzhamerstraße 23, 4600 Wels, Austria, manuel.frank@fh-wels.at

Abstract: *Within this study, additively manufactured (AM) polyamide samples were locally reinforced with 1,5K endless carbon fiber to modify the achievable bending stress and the load bearing capability under temperature. Using non- destructive testing methods, it was shown that a void gradient exists within the manufactured samples not only within the build-plate plane, but also in build height direction. This gradient was detected using automated grey-scale analysis of section cuts generated using three-dimensional computational tomography. The interaction analysis of the performed coupon tests showed dependencies between the relative fiber content and the extrusion direction of the supporting thermoplastic polyamide matrix material.*

Keywords: additive manufacturing; carbon fiber; material characterization

1. Introduction

Additive manufacturing methods like fused deposition modelling have become increasingly popular due to their inherent possibility to reduce material usage and energy consumption as well as the possibility to fabricate components without the need for expensive production equipment. In past years additional functionalization in terms of integration of endless fibers were developed and studied e.g. by Zhuo et al. [1] and allow for tailored structures with minimal fiber usage. Nevertheless, it seems unclear to a certain point, how combinations of different build parameters like matrix extrusion direction and amount of integrated reinforcement fibers affect the overall performance of such structures since the internal geometry is strongly influenced by printing parameters. For instance, Pyl et al. investigated fiber placement and extrusion strategies on their effect on open-hole tensile strength [2]. Within the presented work, bi-matrix CFC (composite fiber co-extrusion) was chosen to manufacture samples to be evaluated in terms of their bending as well as their heat deflection temperature behavior. Furthermore, samples were produced to be analyzed in terms of their porosity. A polyamide 6/6.6 copolymer (polymaker PolyMide CoPA) was used as main matrix material, while local fiber reinforcement was integrated consisting of a pre-impregnated endless fiber consisting of a 1,5K carbon fiber tow (Anisoprint CCF 1.5K). Selected pre - investigations were additionally done using transparent PET-G as matrix material to increase the visibility of the fiber tows.

1.1 Additive manufacturing with local endless fiber reinforcement

Since mechanical, but also thermophysical properties of composite materials strongly depend not only on the fibre direction but also on the build strategy and therefore porosity and the achievable fibre volume fraction, it is important to investigate influencing factors during processing as was done by Kabir et al., who set up a list of preparatory, machine, process and environmental factors affecting quality of 3D printed composites [3] but also investigated by Brenken et al. [4]. For fused filament fabrication, next to the flow rate, it was shown by Patil et

  doi:10.5075/epfl-298799_978-2-9701614-0-0

al. that for instance surface roughness, print speed and filament length had a significant effect on the thermoplastic filling density of the desired geometry but also on the quality of the filling pattern [5], whereas Zhang et al. showed that also too high print speeds resulted in lower filling density due to higher porosities resulting from the narrowing extruded melt [6]. Regarding resulting effects, it was shown by Van de Werken et al. that regions with low filling density were prone to crack initiation and -propagation [7]. Within this work, those aspects should be further investigated when applying those findings to locally endless fibre reinforced structures and to develop an understanding of the filling density and possible porosity gradients. Especially the factor combination of extrusion direction and fiber coverage should be investigated in terms of dependencies and interactions since this – as to the best knowledge of the authors - has not been covered until now.

1.2 Methodology

Selected coupon samples were produced using an Anisoprint composer A3 desktop printer. CAD design was done using Dassault systems CATIA V5 to prepare sample geometries and then submitted to Anisoprint Aura 2 for slicing operations. The created NC code files were then transferred to the printer. Samples were assessed according to HDT - 75 -3 and DIN EN ISO 14125 standards in terms of their bending and heat deflection behavior, but also additional tensile tests similar to AITM 1 0007 standards were additionally carried out to investigate filament adhesion on a microscopic level. Micrographs as well as EDX and XCT scans were created to investigate the micro and macrostructure of the samples. All fabrication processes were planned using a statistical test plan (two stage 2^x) to investigate effects and interactions of parameter variations during manufacturing. Manufacturing was performed while monitoring extruder hot-end and build plate temperatures using thermocouples to assess process stability.

2. EXPERIMENTAL

2.1 NC code generation

NC code creation was done using the AURA 2 slicer software from Anisoprint followed by manual code modifications, namely adaption of build plate temperatures, fan speeds and first layer heights to improve adhesion to the build platform. Furthermore, local fiber trajectories were defined to integrate additional build volumes inside the sample geometry as explained in chapter 3.

2.2 Sample production

Manufacturing was performed while monitoring extruder hot-end and build plate temperatures, where a decreased warpage of the specimen by minimizing of the temperature gap between hot end and build plate could be observed and can be explained by residual stresses occurring in extrusion processes as was shown by Zhang et al. [8]. Next to the z Offset gap between extruder hot end and the substrate (be it the build plate or previously manufactured layers), pre-trials with a 1,75mm PET-G thermoplastic filament were done investigating the fiber federate (with respect to the velocity of the printhead) to supply stable fiber placement. It also must be stated that the offset between the fiber nozzle and the build plate additionally influences spreading of the fiber tows and therefore the width of the fiber reinforcement and has a direct influence on fiber coverage.

  doi:10.5075/epfl-298799_978-2-9701614-0-0

3. ANALYSIS AND TESTING

3.1 Filling density and porosity

Next to the relative amount of reinforcement fibers inside the desired fiber trajectory, the thermoplastic material extrusion direction was defined as factor for the design of experiments. As an example, for the effect of filling density (which directly depends on the extrusion direction) Figure 1 depicts a section cut of a polyamide 6/6.6 specimen, which was investigated perpendicular to the extrusion direction using SEM. It can be seen, that using optimized settings for filling density and flow rate of the printhead, voids within the thermoplastic structure can be minimized, whilst single filament contours still can be distinguished in single areas. Those areas show filaments, which did not fully develop a diffusion of entangled polymer chains between each other due to locally higher cooling rates and therefore solidification.

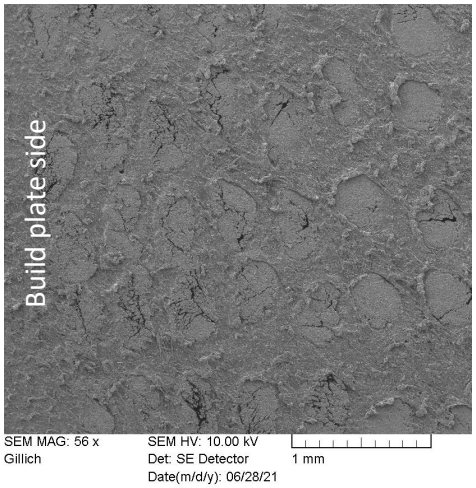

Figure 1. Section cut perpendicular to material extrusion direction

To investigate those inter-bead voids and the quality of the local reinforcement fiber placement on a macroscopic level, a generic test specimen geometry (60x30x30mm) with a combination of unidirectional reinforcement fibers and unidirectional extrusion direction was developed to be analyzed using a Dual source XCT Rayscan 250E computer tomograph. Within this specimen, multiple parallel square fiber trajectories (0.65 x 0.65mm) were defined, in which carbon fiber tows were placed. For the investigation, virtual section cuts in the XY-, YZ- and ZX plane (Figure 2) were created using myVGL.

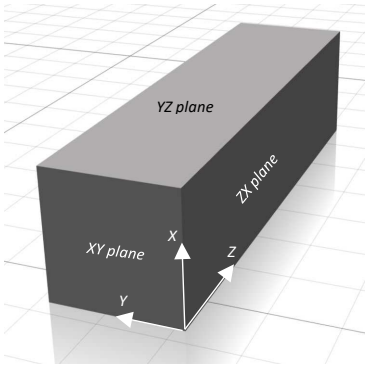

Figure 2. Main axis system and -planes of the specimen (x-axis facing the build plate side)

After that, resulting greyscale pictures were converted into black and white images by applying two different threshold levels to separate thermoplastic and fibre areas from voids using a MATLAB script to identify black and white areas with a pixel counting algorithm. Figure 3 shows an example of such a greyscale section cut parallel to the build plate.

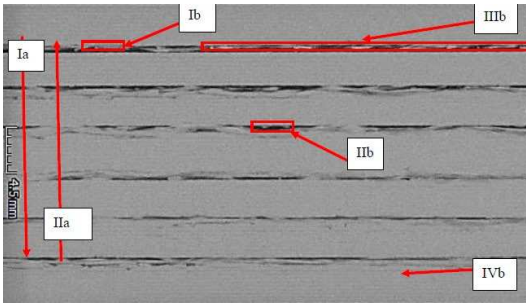

Figure 3. Section cut parallel to the build plate plane

The as – designed fibre trajectories are still visible in some areas (IIIb), which – even in this unidirectional scenario - show not-fully fibre – filled areas leaving voids as can also be seen in (IIb). In contrast, an area with largest fill density (comparable to Figure 1) is highlighted in (IVb) in a non-fibre – reinforced segment of the specimen. Further investigations showed that in certain regions fibre paths as-built deviate from the trajectories as planned in the slicer software (Ib). Figure 3 already indicates a gradient of the void content perpendicular to the fibre direction (Ia and IIa) and can also be seen when investigating the specimen perpendicular to the build-plate plane (Figure 4). Furthermore, alongside the fiber direction (Z) a void gradient (porosity function) can be detected.

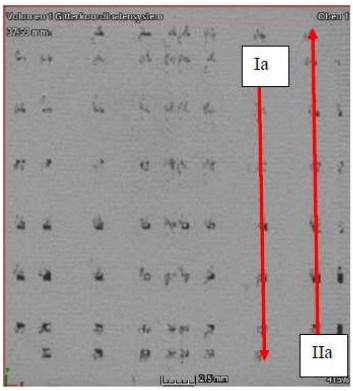

Figure 4. Section cut perpendicular to the fiber direction

  doi:10.5075/epfl-298799_978-2-9701614-0-0

For quantification alongside the X-, Y- and Z – direction (main axis), the void area per section cut area, the matrix area per section cut area but also the ratio between those two (void gradient function Δ_{Ext}) was derived using a pixel counting algorithm in MATLAB. The results are shown in Figure 5.

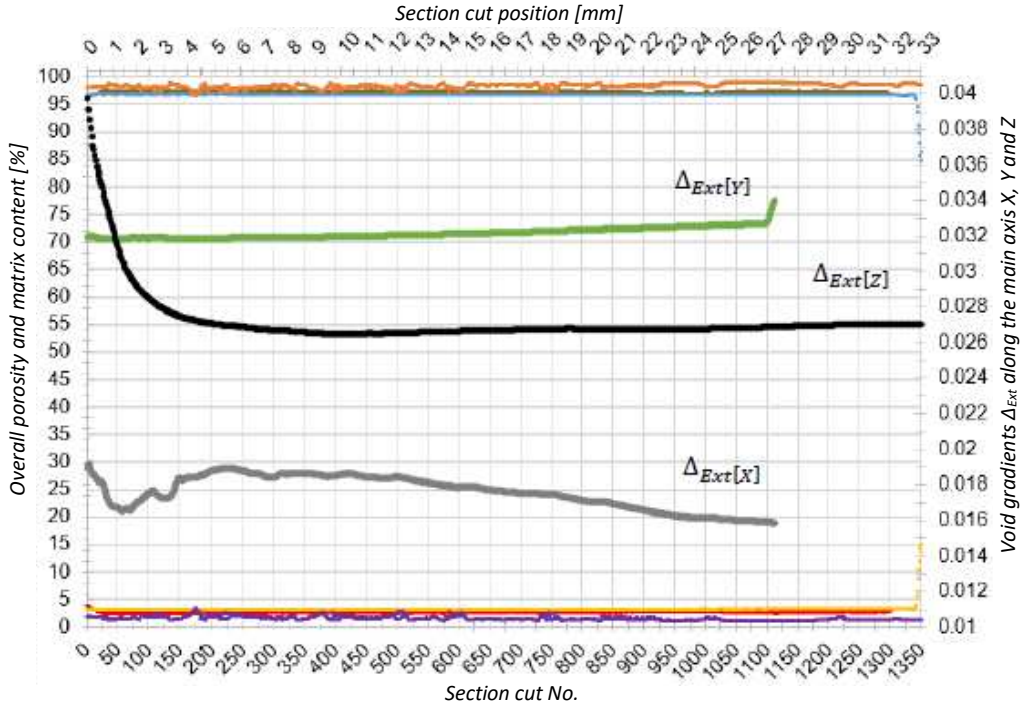

Figure 5. Void gradients Δ_{Ext} alongside the main axis directions, porosity content [%] within the XY, YZ and ZX planes and matrix content [%] within the XY, YZ and ZX planes

For $\Delta_{Ext\,(Z)}$, the void gradient - starting from 0,040 - drops to a stable ratio of 0,027 alongside the longitudinal print direction Z. This corresponds with the observation of air entrapment within the extruder nozzle at the beginning of the print paths which is being released after the extrusion pressure within the nozzle reaches a certain level at around 15% of the extrusion path length. For $\Delta_{Ext\,(Y)}$, the void gradient also shows a decrease at the beginning followed by a more constant behaviour on a higher absolute ratio of around 0.033 although a rapid incline is visible towards the end of the specimen at around 25mm which correspond with reduced material flow of the last extrusion paths alongside the specimen. For $\Delta_{Ext\,(X)}$, the void gradient perpendicular to the print bed shows a decrease of the void gradient up to 4% of the specimen height, followed by an increase up to 0,019 at 17% which is then followed by a nearly linear decrease to 0,016 at the end (top side) of the specimen. Table 1 shows mean values of the porosity but also the matrix and fiber content of the analysed section cuts alongside the main directions of the specimen.

Table 1: Porosity of the specimen's section cuts alongside the main directions (mean values).

		Area share [%]	
Direction	Section cut plane	Void	Matrix, fiber
X	YZ	1,564	98,436
Y	XZ	3,303	96,697
Z	XY	2,681	97,319

To validate XCT results, section cuts were investigated concerning the void share but also used to inspect the accuracy of the placed carbon fiber reinforcement within the designated fiber trajectory like it is shown in Figure 6.

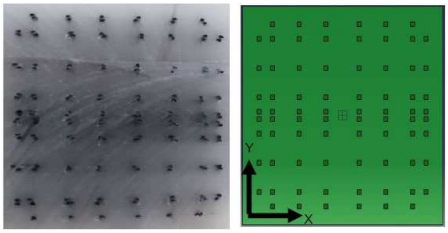

Figure 6. Section cut of a printed specimen (l.) and as-designed fiber trajectory positions

3.2 Bending behavior

To reduce parameter combination settings and therefore manufacturing trials, the extrusion direction with respect to the specimen geometry but also the degree of fiber coverage within a defined volume element were chosen as primary and secondary factor during design of experiments. To investigate the effects of the selected parameters, rectangular test coupons for bending tests were fabricated whilst taking the primary and secondary factor settings into account. The first factor (A) was defined as the thermoplastic matrix extrusion direction in 0° (A-) and 90° (A+) with respect to the longitudinal direction of specimen as is shown in Figure 7 as this was one of the significant influencing factors identified by Dickson et al. [9].

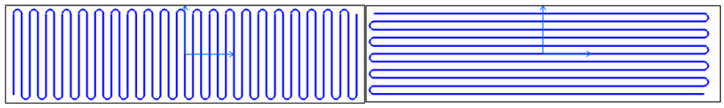

Figure 7. Thermoplastic matrix extrusion direction transversal (l.) and longitudinal (r.) to the specimen direction

Since factor A depicts a matrix build geometry parameter, relative fiber coverage within a specified volume element was defined as fiber – relevant build parameter (factor B). This *fiber coverage FC* – as can be seen in Eq. (1) – can be described as the desired amount of fiber tows per volume element $FC_{def.}$ divided by the maximum amount of fiber tows which can be placed inside this area within the technical limits $FC_{max.}$.

$$FC = \frac{FC_{def.}}{FC_{max.}} \tag{1}$$

Following the method of a variation of n_f variables, factor B was set using n_l values for $FC = 1$ (B+) as well as $FC = 0.5$ (B-), followed by the design of experiments using factor combination with resulting n_r experiments:

$$n_r = {n_l}^{n_f} \tag{2}$$

For better understanding, Figure 8 shows two different settings for *FC* for an open-hole test specimen with circumferential fiber reinforcement using a PET-G matrix for visibility reasons:

Figure 8. Test specimen using maximum (l.) and halved (FC=0.5, r.) fiber coverage

4. RESULTS AND DISCUSSION

Tests were conducted following DIN EN 14125 (3 point bending test) using a Zwick/Roell ZMART.PRO and 75-3 (heat deflection temperature) using a Coesfeld VIC/HDT tester. For testing of the bending stress σ_f as can be seen in Eq. (3), it must be said that the cross-member travel had to be limited at 20mm since the maximum bending stress at break could not be reached.

$$\sigma_f = \frac{3FL}{2bh^2}\left\{1 + 6\left(\frac{s}{L}\right)^2 - 3\left(\frac{sh}{L^2}\right)\right\} \tag{3}$$

Figure 9 shows that - as assumed previously – the bending stress increases with a higher fiber coverage. However, due to a higher main effect of factor A, this can be significantly weakened by the extrusion direction of the surrounding thermoplastic matrix and even can lead to lower absolute achievable bending stresses in the case of a perpendicular extrusion direction using a higher share of fiber coverage. Also, the non – parallel effects show an interaction between extrusion direction and fiber coverage.

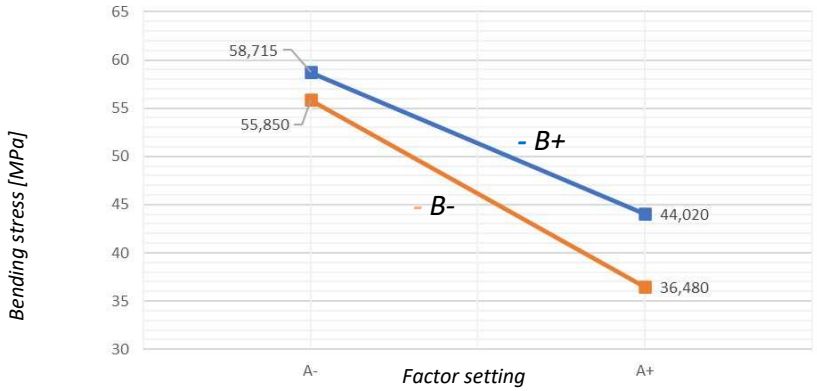

Figure 9. Interaction chart of the bending stress at 20mm cross member travel

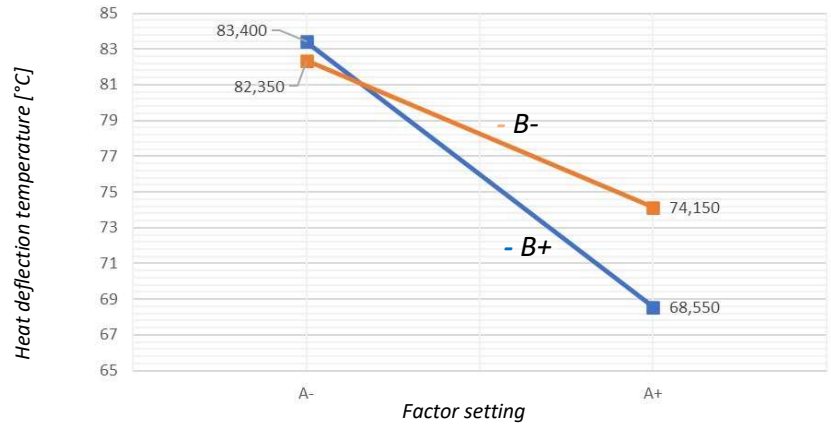

Figure 10. Interaction chart of the heat deflection temperature

Figure 10 shows, that - due to the parallel orientation of the extruded material to the principal stress direction – the properties under temperature load increase and result in a higher heat deflection temperature. A main effect of factor A of $\hat{\alpha} = -7{,}683$ in comparison to the main effect of factor B of $\hat{\beta} = 1{,}517$ shows that the extrusion direction has a more significant influence on this property than the total amount of fibers, which can be explained by interfilament adhesion phenomena caused by the extrusion direction dependent void areas within the structure as shown in chapter 3.

  doi:10.5075/epfl-298799_978-2-9701614-0-0

5. CONCLUSION

Within this work, it was shown that – starting from analysis of manufactured specimen and identifying relevant process parameters like extrusion direction and fiber coverage- significant dependencies exist between those parameters and build quality. If parameter interactions are considered during the design of an endless fiber reinforced AM structure like a geometry under bending and thermal loads, it is possible to tailor its characteristics and therefore decrease the needed amount of reinforcement fibers to fulfill its target properties. 3D CT scans showed a dependency of void formation and porosity not only with respect to the build-plate plane but also a gradient in the other two main directions. The presented investigation does not only show a dependency of process parameters and material combination on the build quality but also the existence of a geometrical influence. Combining this knowledge with future process parameter studies allows not only the optimization of AM structures but should also lead to design guidelines for such processes.

Acknowledgements

The authors are grateful to the State Government of Upper Austria for providing financial support for the project: “Selective use of carbon composites in efficient structures”.

6. References

1. Zhuo P et al. Material extrusion additive manufacturing of continuous fibre reinforced polymer matrix composites: A review and outlook. Composites Part B: Engineering 2021; Volume 224: 109143
2. Pyl Let al. Exploration of the design freedom of 3D printed continuous fibre-reinforced polymers in open-hole tensile strength tests. Composites Science and Technology 2019; Volume 171: 135-151
3. Kabir S et al. A critical review on 3D printed continuous fiber-reinforced composites: History, mechanism, materials and properties. Composite Structures 2020; Volume 232: 111476
4. Brenken B et al. Fused filament fabrication of fiber-reinforced polymers: A review. Additive Manufacturing 2018; Volume 21: 1-16
5. Patil P et al. Multi-objective optimization of process parameters of Fused Deposition Modeling (FDM) for printing Polylactic Acid (PLA) polymer components. Materials Today: Proceedings 2021; Volume 45 , Part 6: 4880-4885
6. Zhang W et al. Characterization of residual stress and deformation in additively manufactured ABS polymer and composite specimens. Composites Science and Technology 2017 ; Volume 150: 102-110
7. Van de Werken N. et al. Design considerations and modeling of fiber reinforced 3D printed parts. Composites Part B 2019 ; Volume 160: 684-692
8. Zhang Y et al. A parametric study of part distortions in fused deposition modelling using three-dimensional finite element analysis. Proceedings of the Institution of Mechanical Engineers, Part B: Journal of Engineering Manufacture. 2008; Volume 222, issue 8: 959-968
9. Dickson A et al. Fabrication of continuous carbon, glass and Kevlar fibre reinforced polymer composites using additive manufacturing. Additive Manufacturing 2017; Volume 16: 146-152

  doi:10.5075/epfl-298799_978-2-9701614-0-0

ADDITIVE MANUFACTURING AND COMPRESSION MOLDING: TWO CONCEPTS INTEGRATED IN A SINGLE MANUFACTURING PROCESS FOR FIBER-REINFORCED THERMOPLASTIC COMPOSITES

Giovangiuseppe Giusto[a, b], Giorgio Fusco[c], Claudio Campagnoli[c], Giovanni Barletta[d], Nicola Gallo[b, d] and Felice De Nicola[a]

a: CIRA - Italian Aerospace Research Centre, Via Maiorise, 81043 Capua (CE); Italy – g.giusto@cira.it
b: IMAST S.c.ar.l. - Technological District on Engineering of polymeric and composite Materials and Structures, Vico II San Nicola alla dogana, n. 9, 80133 Napoli; Italy
c: Aerosoft SpA - Via Maiorise, 81043 Capua (CE); Italy
d: Leonardo S.p.A. – Aerostructure Division – Via per Monteiasi sp.83, 74023 Grottaglie (TA); Italy

Abstract: *This work presents a new process for Continuous Fiber Reinforced Thermoplastic Composites integrating an additive manufacturing approach in a current industrial automated production line. This technology combines additive manufacturing concept with continuous carbon fiber reinforcement and compression molding to create strong and light components.*

The starting material is not a filament or a continuous reinforced thermoplastic tow/tape, as FDM or fiber placement processes, but a prepreg fabric containing gaps with the necessary shapes to obtain the final 3D component once stacked and processed by compression molding. So, the 3D component is obtained from addition of 2D fiber reinforced thermoplastic prepregs (layers) with appropriate geometries.

This process can be completely automatic and integrates several steps, such as the cutting of the fabric with the appropriate geometries, pick and place, the filling of the gaps with appropriate materials and the compression molding.

Each step of the whole process was validated on lab scale. The scale-up on industrial production line is in progress.

Keywords: 3D printing; Additive manufacturing; Carbon fiber; Thermoplastic composites.

1. Introduction

The interest for Continuous Fiber Reinforced Thermoplastic Composites (CFRTPCs) is increasing significantly in recent years. The CFRTPCs are becoming an interesting alternative to the conventional thermosetting polymers and metals due to excellent mechanical performance, chemical resistance, recycling and potential used in lightweight structures [1].

Although the Compression Molding (CM) represents the most used technology at the moment to process this family of materials, the additive technics are invading the manufacturing processes, thanks to the advantages they bring in terms of getting complex geometries, reducing expensive metal molds, product near to final shape and waste reduction.

  doi:10.5075/epfl-298799_978-2-9701614-0-0

To date, the dominant part of the 3D printing industry has immensely relied on single material printing, but the need to increase the mechanical properties and get materials with specific functionalities is leading on the one hand to the development of innovative materials (multi material printings, charged polymers and fiber reinforced composites), on the other hand to the integration of the additive approach into current processes, developing new Additive Manufacturing (AM) methods [2].

The process here proposed follows the second way, traying to integrate additive concepts with CM processes, in order to transfer the advantages of AM in the current thermoplastic production lines.

A thermoplastic bushing for aeronautical application is proposed in this paper to show the progress of the technology. It is actually done using CNC machining of a Polyetheretherketone (PEEK) bar and is used to hold and connect hydraulic hoses through a composite structure.

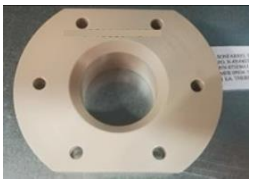

Figure 1. Thermoplastic bushing in PEEK for aeronautical application

2. Manufacturing approach: integrating compression molding and additive concepts

2.1 Step definition

The developed process, named TERM-AM, was meant to exploit the advantages of additive technologies trying to integrate them on the current thermoplastic production lines and mitigating the technological impact, as much as possible. TERM-AM can be completely automatic. It opportunely combines several consolidated and widely used processes in the composite field, such as the cutting of the plies, pick and place, the extrusion and the compression molding.

TERM-AM realizes the final 3D component from addition of 2D fiber reinforced thermoplastic prepregs (layers) with appropriate geometries. The basic scheme is represented in the following figure.

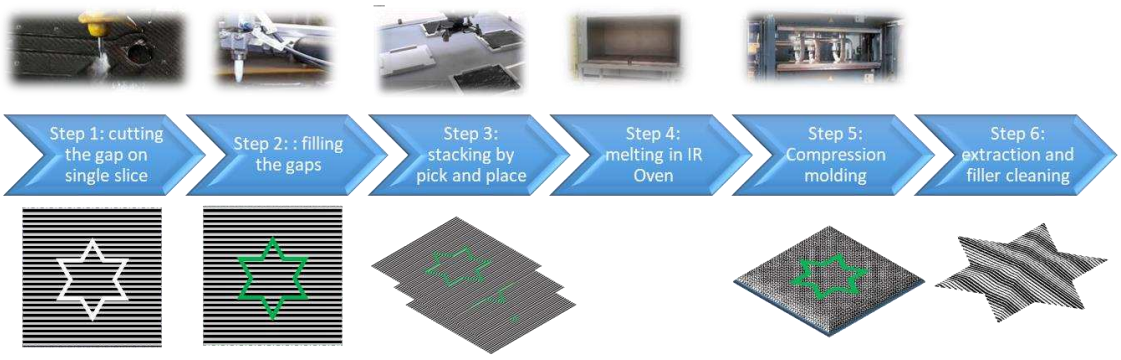

Figure 2. Flow chart TERM-AM process

  doi:10.5075/epfl-298799_978-2-9701614-0-0

The starting material for TERM-AM is not a filament or a continuous thermoplastic carbon/glass tape, as Fused Deposition Modeling (FDM) or fiber placement processes, but a prepreg fabric.

On each prepreg, the gaps necessary to obtain the final 3D shape at the end of the process once stacked are cut in step1. Then, they are filled with suitable materials (step 2) able to resist to the melting temperature of the matrix (step 4), to contain its flow during the compression (step 5) and which are easily cleaned at the end of the process (step 6).

After the filling of the gaps, the TERM-AM follows the classical approach of an automated thermoplastic industrial line, that is the IR Oven for the melting, compression molding and final refinement of the parts.

Obviously, the base scheme TERM-AM can be customized according to the specific requirements of the component to be realized. For example, in order to reduce the process time, as starting material a consolidated carbon reinforced panel can be preferred with respect to the single layer, if a high resolution in "*z*" direction is not required or the gaps on several layers have the same shape or very similar. Otherwise, in some cases, the gap can be filled after the stacking, if the final shape permits it.

In the next figure an alternative scheme for TERM-AM process is shown. The starting materials are pre-consolidated reinforced thermoplastic composite panels

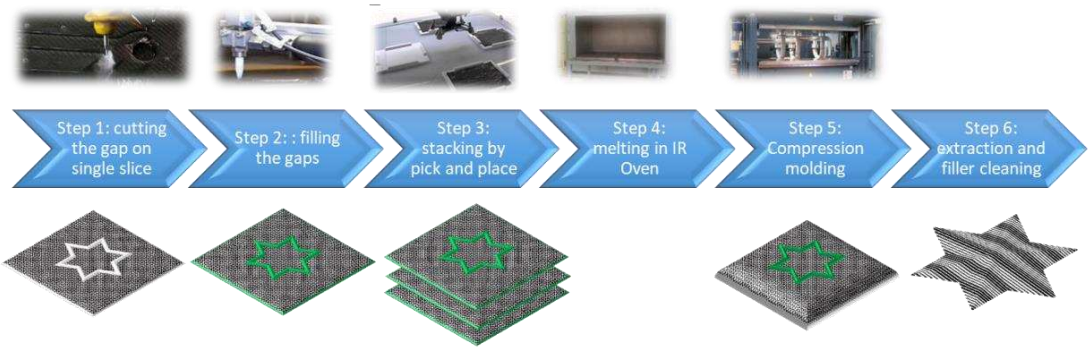

Figure 3. TERM-AM process starting from pre- consolidated reinforced panel

2.2 Materials selection

The choice of the thermoplastic matrix is selected on the base of the component requirements to be realized (mechanical and thermal properties, as well as specific functionalities). In the specific case-study here presented, the selected matrix for the aeronautical bushing is Polyetherketoneketone (PEKK).

The development of TERM-AM process implied, above all, the selection of the consumables, including the filler. Their selection is mainly driven by process parameters, that for high perform thermoplastic materials, such as PEKK, PEEK, Poly Phenylene Sulfide (PPS) and so on, are very strict.

Regarding the materials to be used to fill the gaps (fillers), their selection is a key aspect for the success of the TERM-AM approach. It must:

- confine the matrix during CM and avoid that it flows from the dummy area to the useful one and vice versa;

  doi:10.5075/epfl-298799_978-2-9701614-0-0

- resist to the thermal condition of the process (T>380°C for PEKK matrix);
- have an adequately high viscosity to be laid down in the gap by extrusion and remain in position during the pick and place phases and general handling;
- be soluble in some solvent or brittle post process to be easily removed;

Several materials were characterized in order to verify all aspects impacting on the process. Thermal and viscosity analysis, as well as dedicated tests to evaluate several technological aspects to be integrated, were performed on a large number of commercial materials. Several kinds of materials were considered, from polymeric to silicon one, including refractory materials. In the following figure some representative thermal analysis is reported.

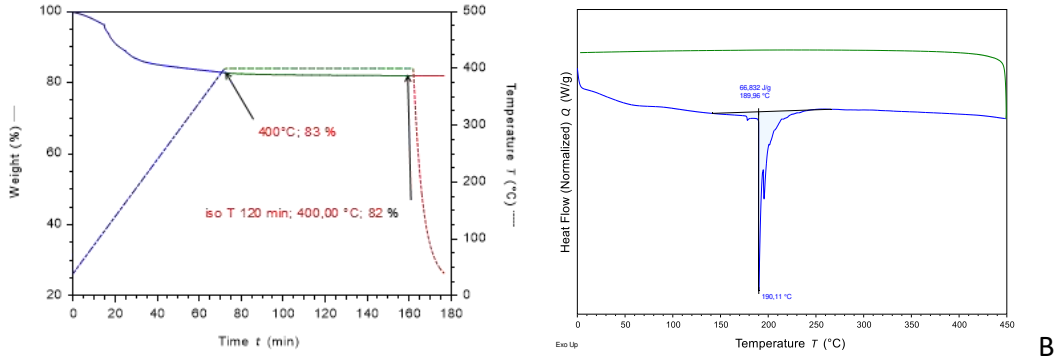

A B

Figure 4. Thermo Gravimetric Analysis (A) and Differential Scanning Calorimetry Analysis (B) of a one-component refractory paste

The trade-off activity selected as filler three commercial products, which resist to the temperature and pressure process, can be applied by extrusion and can be removed easily at the end of the process. They are:

- commercial FDM Support Removal to be applied by extrusion or technics similar to FDM;
- one-component silicone rubber (acetic cross-linking) to be applied by applicator gun (manual or pneumatic)
- one-component refractory paste glass-based filler to be applied by applicator gun (manual or pneumatic)

Their application, as well as each step of the TRM-AM, was validated on Lab-scale realizing the bushing demonstrator in carbon reinforced PEKK (CF/PEKK) and carbon reinforced Polyaryletherketone (CF/PAEK).

2.3 Lab-Scale validation

All identified steps for TERM-AM were studied on lab scale in order to verify the applicability, optimize the key parameters and resolve the technological aspects. Although the experiments aimed at studying the single steps, the whole process was designed to be fully automated. So, the single steps were investigated on lab scale, but always keeping in mind the solution to automate and integrate them in the whole process.

Three steps in particular were analyzed in depth: the realization of the gap (step 1), the deposition of the filler (step 2) and the compression molding of the stacking, including the filled gaps (step 5).

  doi:10.5075/epfl-298799_978-2-9701614-0-0

These three steps, although consequential, are strictly connected to each other, especially the shape of the gap, in terms of the width, and the deposition of the filler.

The shape of the gap on each layer defines the “useful area” (green line in Figure 2) which, once stacked, processed and cleaned form the waste area, will return the 3D volume of the component to be realized (step 6 in Figure 2 and Figure 3). In other words, the “useful area” of a layer is the basic 2D element which, added to the other layers, forms the final 3D component.

On the other hand, a good and uniform filler deposition in the gap (green line in Figure 2) guarantees a clear separation between the useful area and the waste one, avoiding the migration of the matrix between from one side to the other and facilitating the extraction of the 3D final component at the end of the process.

For this reason, these aspects were studied at the same time, customizing appropriate tests. Starting from simple geometries, more and more complex shapes have been investigated. In the next picture the adopted flow is shown.

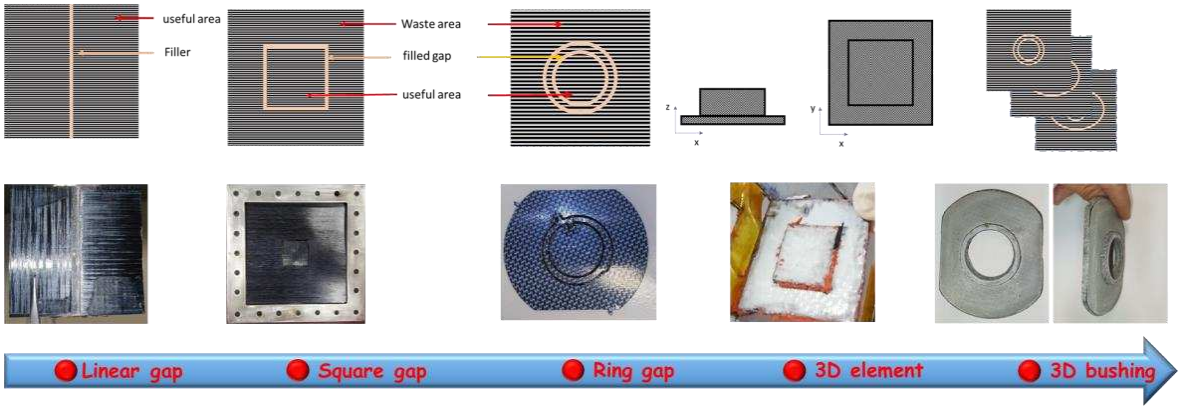

Figure 5. Adopted logical flow with increasingly complex geometries.

The development of the process has allowed to investigate and optimize several technological aspects related to the cutting and the deposition of the filler, manly, identifying and overcoming the various met criticalities.

An important aspect, for example, is homogeneity of the filler in gap during the deposition. The presence of the defects or voids (figure 6 B) during the deposition of the filler causes important problems essentially due to the migration of the matrix in that area (figure 6 C), such as the adhesion between the useful area and the waste area.

A B C

Figure 6. Stacking of 10 plies with square gaps (A), where the filler in the gap is not homogeneous (B); Microscopic analysis after the CM step (C)

In order to improve the homogeneity of the filler in the gap and evaluate the possible automation of this step a 3Dpen was tested for the deposition. This tool allowed to optimize the

  doi:10.5075/epfl-298799_978-2-9701614-0-0

process and define a theoretical aspect ratio of the gap, i.e. the ratio of width to depth. This aspect ratio proved to be fundamental for a good quality of the deposition.

Figure 7. Deposition of the filler in the gaps by 3DPen and microscopic analysis before the CM

Regarding the cutting of the gaps, automatic processes were considered. In particular for single layer prepreg an US cutter was used, while for pre-consolidated thermoplastic reinforced panel the Water Jet technic.

The final validation on lab scale of the whole TER-AM was performed step by step by manufacturing of representative elements of the thermoplastic bushing identified as aeronautical demonstrator. The most representative bushing elements were manufactured starting from pre-consolidated carbon reinforced thermoplastic panels based on the PAEK e PEKK matrix. The main phases of the TERM-AM are shown below.

The gaps with the appropriate geometries were made by WJ, while the filler deposition was performed by pneumatic applicator gun. In the shown sample below the refractory paste was used. In order to guarantee the adhesion only where it is necessary, a release film for high temperature (Kapton) was applied in the waste area or where the adhesion is not required.

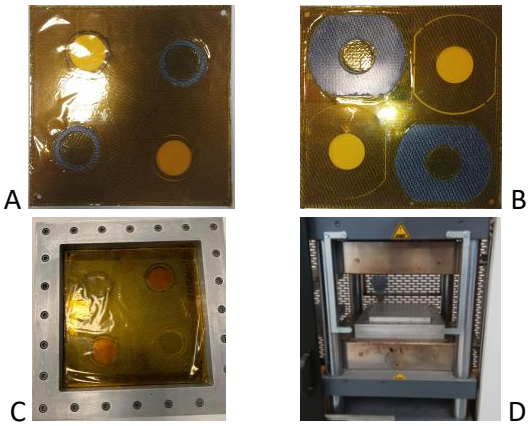

Figure 8. Carbon fiber reinforced PEKK panels with filled gaps ready to be stacked (A and B); stacking in the mold (C) and ready to press (D)

At the end of the process the final 3D component was extracted applying a low pressure on the area to be removed (Figure 9). A light cleaning completes the process.

Figure 9. Extraction step of the 3D final component (bushing) after the CM

  doi:10.5075/epfl-298799_978-2-9701614-0-0

A bushing component made of carbon reinforced PAEK with external glass skins (CF/GF/PAEK) was manufactured to improve the thermal insulation. In the next picture the main steps are reported.

Figure 10. Main steps of the TERM-AM process to realize the bushing made with (CF/GF/PAEK)

3. Scale-up process

The scale-up of the TERM-AM is currently in progress and is taking place on the fully robotized manufacturing process line of Aerosoft Company. This plant is able to realize CFRTPCs using a fast thermoforming CM (Out of Autoclave technology).

Starting from development on the Lab scale, a massive test campaign was carried out, in order to understand the key parameters. These experimental activities were implemented changing the process parameters and verifying by Non-destructive Inspection (NDI) technics (thermography and US, manly) the quality of samples.

The main key process variables and the necessary manufacturing line upgrade were identified studying different recipes. The final set-up tuning is still in progress. The thermoplastic composites used are CF/PPS and CF/PEKK. Some pictures of molds and tools realized to test the scale-up of the process are presented.

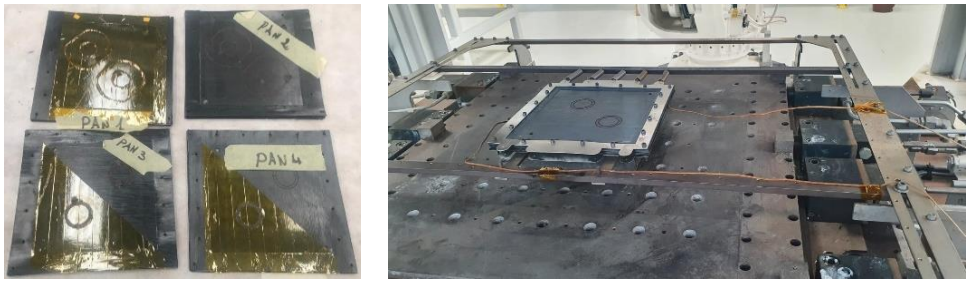

Figure 10. Slices preparation including filler and kapton insertion and its positioning in the robotized handling tool frame of thermoforming line

Figure 11. Frame with slices positioned in Aerosoft thermoforming line: IR Oven (A) and temperature controlled (B).

Figure 12. TERM-AM extraction steps and bushing sub-component in C/PEKK

4. Conclusions

The presented work shows a new process for CFRTPCs integrating an additive manufacturing approach in a current industrial automated production line. This technology combines Additive manufacturing concept with continuous carbon fiber reinforcement and compression molding to create strong and light components. The feasibility has been confirmed even though the studies are currently in progress.

The original component is manufactured in PEEK using the CNC machining technology.

A preliminary cost analysis performed taking into account only the Recurrent Costs (RC) of the prototype manufacturing phase, provides a value of the cost ratio (TERM-AM prototype/Original Component) comparable considering the realization of a couple of prototypes for each manufacturing cycle.

By the way, a scale-up of the manufacturing line in terms of more components realized in each compression moulding cycle could, of course, drastically reduce the cost of the TERM-AM component. Other cost saving could be obtained buying big quantities of the raw material.

Another important consideration is the possibility to use continuous fibers with different orientation improving mechanical properties.

Further investigations are still in progress. The process could be competitive in different contest:

- using recycled composite materials
- needing some particular low or high thermal conductivity
- needing big series of simple vertical extractable components
- having a geometry that is difficult to be manufactured by CNC machining
- needing a robust and reliable automated process

Acknowledgements

This work has been supported by the Research Project AMICO (code ARS01_00758) co-funded by the Italian Ministry of Education, University and Research.

5. References

1. Chacóna et al. Additive manufacturing of continuous fibre reinforced thermoplastic composites using fused deposition modelling: Effect of process parameters on mechanical properties. Composites Science and Technology 2019; 18: 107688.
2. Parandoush P., Lin D. A review on additive manufacturing of polymer-fiber composites. Composite Structures 2017; 182: 36–53

  doi:10.5075/epfl-298799_978-2-9701614-0-0

MECHANICAL CHARACTERISATION OF IN-SITU BONDING BETWEEN PEEK FILAMENTS AND LAMINATES IN THE FFF PROCESS

Simon Hümbert[a], Isabell Schmidt[a], Fynn Atzler[a], Michael Lengowski[b]

a: Institute for Structures and Design (BT), German Aerospace Center (DLR), Stuttgart Germany
simon.huembert@dlr.de
b: Institute of Space Systems, University of Stuttgart, Stuttgart, Germany

Abstract: *Fused filament fabrication (FFF) of high-temperature, aerospace-grade thermoplastics like PEEK has made significant progress in recent years and has become an established process for 3D-printing of complex parts. However, possibilities of adding long or continuous fibres are still limited and the introduced thermal stresses limit the maximum part dimensions. To overcome these limitations, this work investigates the potential of bonding FFF printed parts in-situ onto continuous fibre reinforced laminates. This process allows the combination of the complexity of 3D-printing with large scale manufacturing processes for high-performance structures. The investigation is divided in two steps. Firstly, the effect of process temperatures on the inter-layer bonding of printed PEEK is investigated. On this basis, the optimal process parameters for the bonding of printed PEEK onto PEEK laminates are analysed. The results show a strong correlation between the process temperatures and the inter-layer bonding as well as the bonding between filament and laminates. The process influences shown form the basis for future hybrid component and process designs.*

Keywords: Fused Filament Fabrication; thermoplastic composites; in-situ bonding; PEEK; 3D-printing

1. Introduction

Fused filament fabrication (FFF) of high-temperature thermoplastics like PEEK (Polyether ether ketone) or PEI (Polyethylenimine) has made significant progress in recent years and has become an established process for 3D-printing complex parts. Several studies have shown that high process temperatures are required to provide sufficient interlayer bonding and thus sufficient mechanical properties of printed high temperature parts [1], [2]. Theoretical and mechanical investigations of the bond formation in FFF have shown, that bonding only accrues above the glass transition temperature Tg and that most of the bond forms close to the melting temperature [3], [4]. The latest generations of commercial FFF machines allow the additive manufacturing of high temperature, aerospace grade materials like PEEK or PEI by providing heated print beds and chambers up to 300 °C.

However, the mechanical properties of 3D-printed, thermoplastics high-temperature parts are still below the properties of injections moulded parts [5]. Furthermore, possibilities of adding long or even continuous fibres are still very limited and the high introduced thermal stresses can cause warpage and fractures within the part, limiting the parts maximal dimensions [6], [7].

One approach to overcome these limitations is the combination of thermoplastic 3D-printing with large scale manufacturing processes for high-performance structures like automated tape placement or compression moulding. This combination is intended to unite the complexity of

  doi:10.5075/epfl-298799_978-2-9701614-0-0

3D printing with the excellent material properties of continuous fibre-reinforced thermoplastics and their high production rate. There are several approaches to achieve this goal. [8] investigated sandwich structures with different 3D-printed core geometries which are joined with continuous fibre reinforced laminates by adhesive bonding. Similar tailored composite designs have been proposed by [9], where the consolidation between is achieved during a thermoforming process. Another approach has been proposed by [10]. In this case the 3D-printing is not used for structural components, but for moulds or substrates for automated fibre placement.

All these approaches have in common that the continuous fibre-reinforced laminates and the 3D-printed components are manufactured independently of each other and are then joined downstream. Other investigations focus on direct bonding of 3D-printed structures onto laminates, comparable to overmoulding. [11] demonstrates the process development of "Over 3D-prining" using PA 6 (Polyamide 6) organo-sheets. A more detailed analysis of the bond strength and the influence of process parameters for PA 6 has been shown in [12] and [13]. A comparable study, including the direct comparison with injection moulding, using PLA (Polylactic acid) has been conducted by [14]. In all of these studies, the process temperatures as well as the surface condition play major roles for the bonding quality

The Institute for Structures and Design (BT) at the German Aerospace Center (DLR) develops multifunctional 3D printed sandwich structures as described in [15] and [16], in which the in-situ bonding between core and laminate plays a decisive role. The hybrid process not only ensures that the mechanical requirements are met, but also enables completely new design methods, such as those described in [17] and [18].

In order to be able to use the hybrid manufacturing process for such high-performance applications as in aerospace, it is imperative to characterise the process precisely and to determine stable process windows for the high-performance materials used. For this purpose, the influence of the process parameters in 3D printing on the joining quality between printed PEEK and PEEK laminates is characterised in this work. To this end, the limits of the process window for the printing of PEEK itself are first determined by mechanical tests. On the basis of this process window, a parameter study is carried out to determine the most important influences on the joining quality. The results of this investigation will form the basis for future process development of additive manufacturing of hybrid structures as well as the upscaling for automated, large-scale production processes.

2. Material and Methods

The 3D-printing process is performed using a GEWO HTP-260 [19] high temperature FFF printer. The printer provides a heated bed up to 270 °C and a heated chamber up to 260 °C. The nozzle can be heated up to 450 °C. Tensile test specimens for the PEEK printing characterisation are printed from 1.75 mm Fil-A-Gehr PEEK [20] filament. All specimens for the bonding characterisation are printed from Ensinger TECAPEEK CF30 [21], a PEEK filament filled with 30 % carbon fibres. The laminate used for the shear specimens is a Toray Cetex 1200 UD laminate. Material properties are summarized in Table 1.

Table 1: Material Properties of pure PEEK and carbon fibre reinforced PEEK filament [20], [21]

Property	PEEK	PEEK-CF
Density	1.29 [g/cm^3]	1.38 [g/cm^3]
Young's modulus	3500 [MPa]	17500 [MPa]
Ultimate strength	94.5 [MPa]	190 [MPa]
Nozzle temperature	380-410 [°C]	400-440 [°C]
Bed temperature	N/A	130-160 [°C]
Chamber temperature	180 [°C]	230-250 [°C]

The in-situ bonding of FFF parts onto thermoplastic laminates includes two different bond formations, the inter-layer bonding of the part itself and the bonding between the part and the laminate. Therefore, the investigation is divided in two parts.

2.1 Characterisation of PEEK Printing

Mechanical properties of 3D-printed structures and the relation between such properties and the process parameters have been studied intensively. A wide range of experimental characterisations have been summarized by [5] and [7]. Both reviews state the process temperatures as well as print speeds and raster angles as most important factors for static mechanical properties. However, most research has been done on ABS (Acrylnitril-Butadien-Styrol) and PLA [7]. Regarding the high-temperature thermoplastic PEEK, the review of [22] gives a good overview on the state of research. Overall, process temperatures as well as print speed and raster angle show significant impact on the material properties.

In this study the focus is on the processing temperatures. Tensile specimens have been printed with different nozzle temperatures as well as bed and chamber temperatures. Setting large differences between bed and chamber temperature is only possible in a limited range with the used printer. Moreover, temperature gradients within the chamber are not desired for this investigation. Therefore, bed and chamber temperature are summarized in a low, intermediate and high ambient temperature. The most important print settings are shown in Table 2. Using these settings, tensile specimens according to ISO 527-2 type BA [23] are printed and tested. Additionally, crystallinity of the specimens is measured. The microstructure of the inter-layer bonding is analysis using microsections.

Table 2: Process parameters of the PEEK printing characterization

Process Parameter	Range		
Nozzle Temperature [°C]	426; 434; 442; 450		
	Low	**Intermediate**	**High**
Bed Temperature [°C]	160	215	270
Chamber Temperature [°C]	150	205	260
Speed [mm/s]	15		
Layer Height [mm]	0.2		
Nozzle Diameter [mm]	0.4		
Infill Raster [°]	+- 45		

2.2 Characterisation in-situ Bonding

Based on the process window for printing PEEK, a range of process parameters for the in-situ bonding of printed PEEK onto laminates is defined. Additionally to the process temperatures, also print speed, extrusion factor and the height of the first printing layer are investigated. The parameter variation is shown in Table 3.

Table 3: Process parameters of the joining characterization

Process Parameter	Range
Nozzle Temperature [°C]	430-450
Substrate Temperature [°C]	200-270
Chamber Temperature [°C]	200-260
Speed [mm/s]	5-20
First Layer Height [mm]	0.1-0.3
Extrusion Factor [%]	100-200
Nozzle Diameter [mm]	0.4
Layer Height other layers [mm]	0.2
Infill Raster [°]	+-45

Using these parameters, single lap shear specimens based on ASTM D3846-08 [24] are printed and tested. Therefore, six specimens are printed onto one laminate, from which one is used for temperature measurement and the remaining five are used for testing. The specimens are then separated and notched with a disk saw. The printing and test setup are shown in Figure 1.

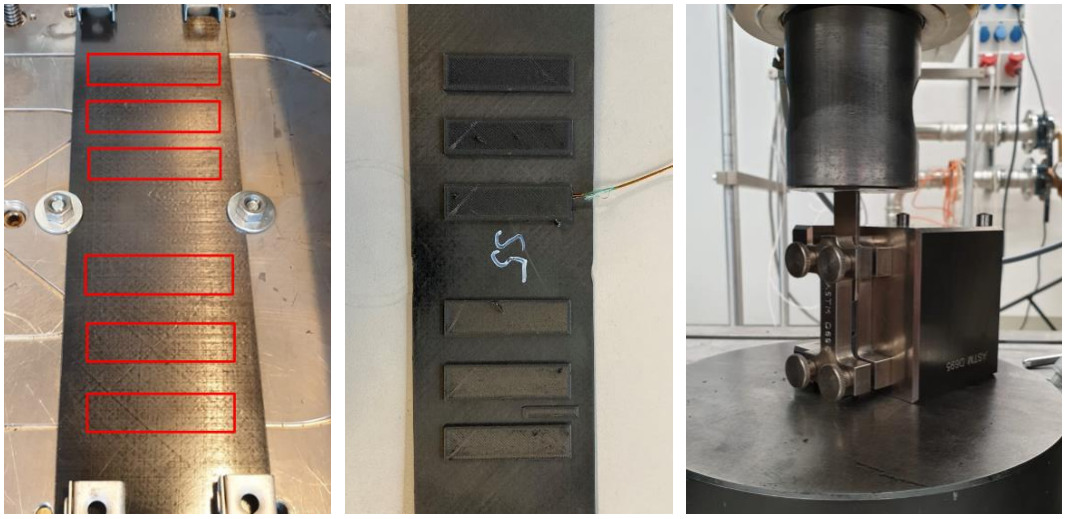

Figure 1: Printing and specimen preparation of shear specimens. Left: laminate before printing; Middle: printed specimens on laminate; Right: shear specimen in compression test

3. Results

3.1 Characterisation of PEEK Printing

The analysis of the inter-layer bonding showed a strong correlation between the processing temperatures and the mechanical properties of the printed part. The results of Young's Modulus and ultimate strength are shown in Figure 2. Especially a high ambient temperature (bed and chamber temperature) is required to optimize mechanical properties.

  doi:10.5075/epfl-298799_978-2-9701614-0-0

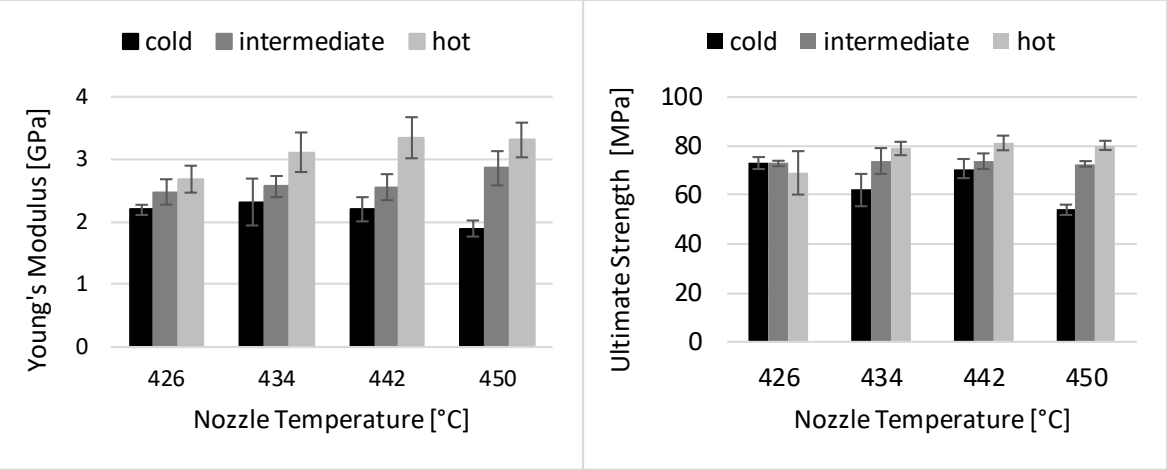

Figure 2: Results of Youngs' Modulus (left) and ultimate strength (right)

Microsections of the printed specimens show that high ambient temperatures improve the layer adhesion significantly. Additional, residual stresses due to high thermal gradients during the printing process increase at lower ambient temperatures. The effects of poor layer adhesion and high thermal gradients is illustrated in Figure 3. While there is no distinct layer interface visible at high ambient temperatures, clear interfaces are identifiable at low temperatures leading to cracking and layer separation.

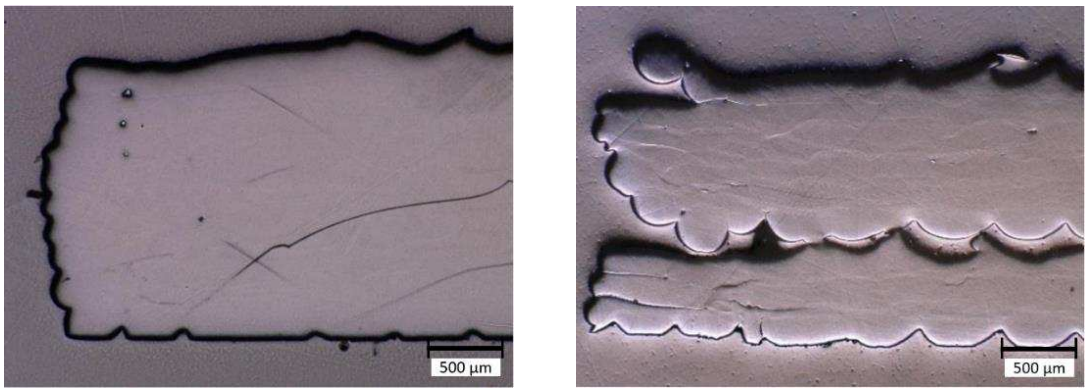

Figure 3: Cross-section of printed PEEK at high 260 °C chamber temperature (left) and at 150 °C chamber temperature (right)

3.2 Characterisation in-situ binding

Similar to the bond formation in the printed part itself, the bonding between printed PEEK and PEEK laminates highly depends on the process temperatures. In this case, the critical factor is the temperature in the interface between both boding partners. The parameters that influence this temperature directly are the nozzle temperature and the temperature of the substrate, which is regulated by the bed temperature. The effect of both parameters is shown in Figure 4.

Beside the process temperatures, also other factors effectively influence the temperature in the interface and thereby the bond formation. Two important examples are shown in Figure 4. Lower printing speed improves the bonding. Furthermore, the layer thickness of the first layer, and thereby the distance between the hot nozzle and the bonding zone, has a major impact on the bonding strength.

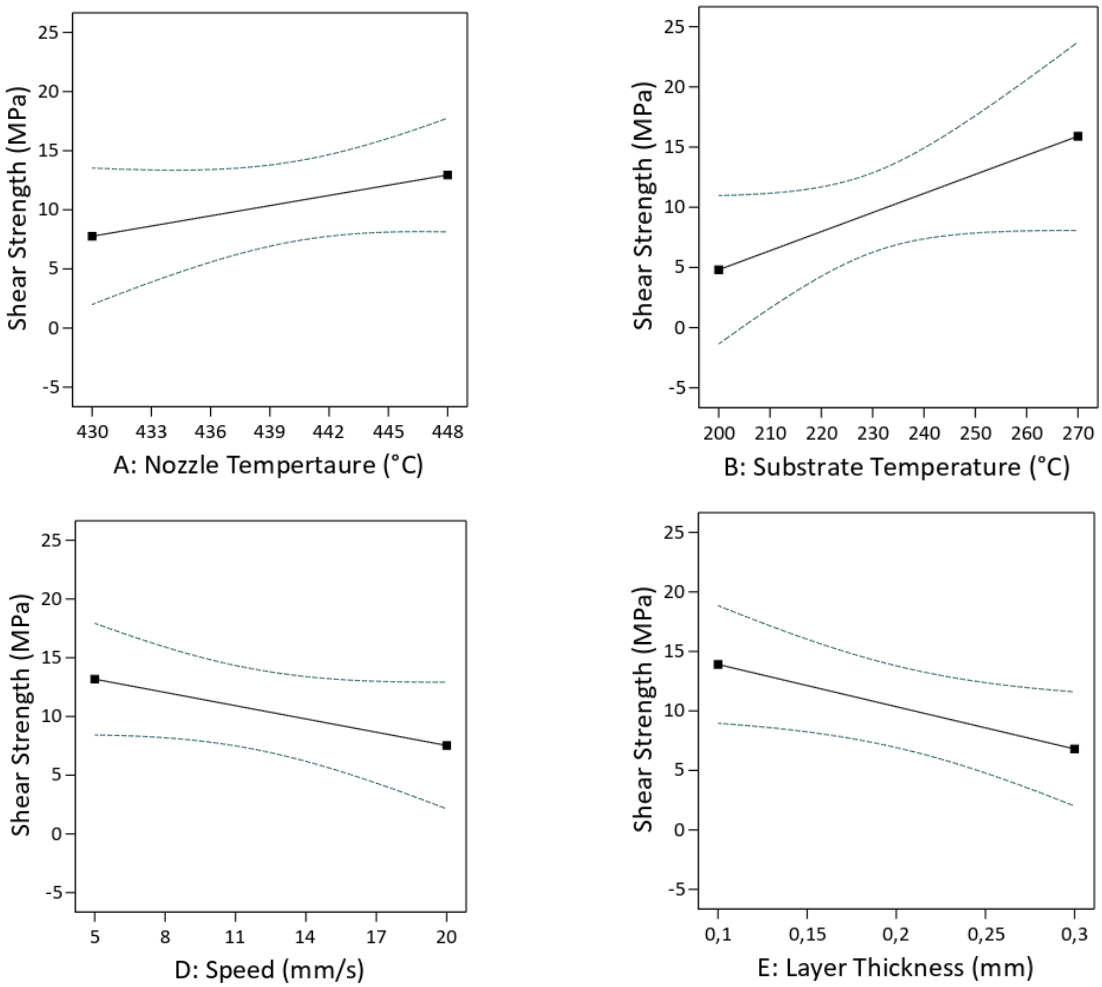

Figure 4: Influence of nozzle temperature, substrate temperature, print speed and layer thickness on the bonding between printed PEEK and PEEK laminates

4. Conclusion

This work shows the first results of in-situ bonding of 3D-printed PEEK onto PEEK laminates during the printing process. In order to determine a reasonable process window for the print process, the impact of process temperatures on the interlayer bonding of printed PEEK itself is analysed first. Results show that high process temperatures, especial ambient temperatures resulting from bed and chamber temperatures a crucial for sufficient interlayer bonding during the printing process. Low temperatures result in cracking and layer separation, limiting the mechanical properties of printed parts. These results are in line with correlated research activities on 3D-printing of PEEK and give a guideline for the required temperatures for a successful in-situ bonding onto continuous carbon fibre reinforced laminates.

In order to characterise the strength of the in-situ bonding, shear tests with different process parameters have been conducted. The results show that the shown correlations of PEEK 3D-printing also apply to the bonding strength. High temperatures in the interface between printed PEEK and the laminate enable a successful bonding. Beside the process temperatures, also parameters like speeds and layer thickness influence the strength. With bonding strengths of up to 15 MPa, the bonding process provides reasonable potential to compete with other bonding processes and paves the way for new design and process developments.

  doi:10.5075/epfl-298799_978-2-9701614-0-0

Acknowledgements

This work is financed by the Ministry of Economic Affairs, Labour and Tourism Baden-Württemberg reference numbers 3-4332.62-DLR/49 (IRAS), 3-4332.62-DLR/56 (IRAS II) and 3-4332.62-DLR/59 (IRAS III)

5. References

[1] C. Yang, X. Tian, D. Li, Y. Cao, F. Zhao, and S. Changquan, 'Influence of thermal processing conditions in 3D printing on the crystallinity and mechanical properties of PEEK material', *J. Mater. Process. Technol.*, vol. 248, May 2017, doi: 10.1016/j.jmatprotec.2017.04.027.

[2] S. Xiaoyong, C. Liangcheng, M. Honglin, G. Peng, B. Zhanwei, and L. Cheng, 'Experimental Analysis of High Temperature PEEK Materials on 3D Printing Test', in *2017 9th International Conference on Measuring Technology and Mechatronics Automation (ICMTMA)*, Jan. 2017, pp. 13–16. doi: 10.1109/ICMTMA.2017.0012.

[3] T. J. Coogan and D. O. Kazmer, 'Healing simulation for bond strength prediction of FDM', *Rapid Prototyp. J.*, Apr. 2017, doi: 10.1108/RPJ-03-2016-0051.

[4] U. Yilmazer and M. Cansever, 'Effects of processing conditions on the fiber length distribution and mechanical properties of glass fiber reinforced nylon-6', *Polym. Compos.*, vol. 23, no. 1, Art. no. 1, Feb. 2002, doi: 10.1002/pc.10412.

[5] E. Cuan-Urquizo, E. Barocio, V. Tejada-Ortigoza, R. B. Pipes, C. A. Rodriguez, and A. Roman-Flores, 'Characterization of the Mechanical Properties of FFF Structures and Materials: A Review on the Experimental, Computational and Theoretical Approaches', *Materials*, vol. 12, no. 6, Art. no. 6, Jan. 2019, doi: 10.3390/ma12060895.

[6] M. F. Arif, S. Kumar, K. M. Varadarajan, and W. J. Cantwell, 'Performance of biocompatible PEEK processed by fused deposition additive manufacturing', *Mater. Des.*, p. 11, 2018.

[7] S. Vyavahare, S. Teraiya, D. Panghal, and S. Kumar, 'Fused deposition modelling: a review', *Rapid Prototyp. J.*, vol. 26, no. 1, pp. 176–201, Jan. 2020, doi: 10.1108/RPJ-04-2019-0106.

[8] T. Li and L. Wang, 'Bending behavior of sandwich composite structures with tunable 3D-printed core materials', *Compos. Struct.*, vol. 175, no. Supplement C, Art. no. Supplement C, Sep. 2017, doi: 10.1016/j.compstruct.2017.05.001.

[9] H. Janssen, T. Peters, and C. Brecher, 'Efficient Production of Tailored Structural Thermoplastic Composite Parts by Combining Tape Placement and 3d Printing', *Procedia CIRP*, vol. 66, pp. 91–95, Jan. 2017, doi: 10.1016/j.procir.2017.02.022.

[10] F. Raspall, R. Velu, and N. M. Vaheed, 'Fabrication of complex 3D composites by fusing automated fiber placement (AFP) and additive manufacturing (AM) technologies', *Adv. Manuf. Polym. Compos. Sci.*, vol. 5, no. 1, pp. 6–16, Jan. 2019, doi: 10.1080/20550340.2018.1557397.

[11] U. Morales, A. Esnaola, M. Iragi, L. Aretxabaleta, and J. Aurrekoetxea, 'Over-3D printing of continuous carbon fibre composites on organo-sheet substrates', *AIP Conf. Proc.*, vol. 2113, no. 1, p. 020015, Jul. 2019, doi: 10.1063/1.5112520.

[12] L. Penter, J. Maier, B. Kauschinger, T. Lebelt, N. Modler, and S. Ihlenfeldt, '3D printing technology for low cost manufacturing of hybrid prototypes from multi material composites', in *Production at the leading edge of technology*, Berlin, Heidelberg, 2021, pp. 396–405.

[13] J. Maier *et al.*, 'Adhesion Studies during Generative Hybridization of Textile-Reinforced Thermoplastic Composites via Additive Manufacturing', *Materials*, vol. 14, p. 3888, Jul. 2021, doi: 10.3390/ma14143888.

[14] R. Boros, P. Kannan Rajamani, and J. G. Kovacs, 'Combination of 3D printing and injection molding: Overmolding and overprinting', *Express Polym. Lett.*, vol. 13, no. 10, pp. 889–897, 2019, doi: 10.3144/expresspolymlett.2019.77.

[15] S. Hümbert, L. Gleixner, E. Arce, P. Springer, M. Lengowski, and I. Sakraker, 'MATERIAL CHARACTERIZATION OF ADDITIVELY MANUFACTURED PA12 AND DESIGN OF MULTIFUNCTIONAL SATELLITE STRUCTURES', presented at the ECSSMET 2018, Noordwijk, Netherlands, May 2018.

[16] T. Stäbler *et al.*, 'Integrated Research Platform for Affordable Satellites', presented at the 70th International Astronautical Congress, Washington D.C., 2019.

[17] M. Echsel, P. Springer, and S. Hümbert, 'Production and planned in-orbit qualification of a function-integrated, additive manufactured satellite sandwich structure with embedded automotive electronics', *CEAS Space J.*, vol. 13, Jul. 2020, doi: 10.1007/s12567-020-00328-2.

[18] S. Hümbert, J. Meth, M. Echsel, M. Lengowski, and T. Stäbler, 'Additive manufacturing of radiation shielding for small satellites', presented at the IAC 2021, Dubai, 2021.

[19] 'Überblick', *GEWO3D*. https://gewo3d.com/de/htp-260/ueberblick.html (accessed Sep. 26, 2021).

[20] 'FIL-A-GEHR PEEK', *FIL-A-GEHR SHOP*. https://shop.filagehr.com/filament/3/fil-a-gehr-peek (accessed Jan. 09, 2022).

[21] 'Datasheets plastics | Ensinger'. https://www.ensingerplastics.com/en-us/datasheets (accessed Jan. 09, 2022).

[22] A. R. Zanjanijam, I. Major, J. G. Lyons, U. Lafont, and D. M. Devine, 'Fused Filament Fabrication of PEEK: A Review of Process-Structure-Property Relationships', *Polymers*, vol. 12, no. 8, Art. no. 8, Aug. 2020, doi: 10.3390/polym12081665.

[23] Deutsches Institut für Normung (DIN) and Deutsches Institut für Normung (DIN), Eds., *[DIN EN ISO 527-2] Kunststoffe: Bestimmung der Zugeigenschaften. Teil 2: Prüfbedingungen für Form- und Extrusionsmassen (ISO 527-2:2012); Deutsche Fassung EN ISO 527-2:2012*. Berlin (de): Beuth, 20120600.

[24] ASTM International, 'ASTM D3846-08(2015), Standard Test Method for In-Plane Shear Strength of Reinforced Plastics', West Conshohocken, PA, 2015. [Online]. Available: www.astm.org

ADDITIVE MANUFACTURING OF DYNAMIC THERMOSET COMPOSITES WITH SELF-HEALING AND SHAPE MEMORY CAPABILITIES

Yinglun, Hong[a], Itxaso, Azcune[b], Alaitz, Rekondo[b] and Eduardo, Saiz[a]

a: Centre for Advanced Structural Ceramics, Department of Materials, Imperial College London, London SW72AZ, UK – Email: yinglun.hong15@imperial.ac.uk
b: CIDETEC, Basque Research and Technology Alliance (BRTA), Paseo Miramón, 196, 20014 Donostia-San Sebastián, Spain

Abstract: *The development of polymer composites combining self-healing and shape memory responses with the mechanical properties required for structural applications, could benefit a wide range of fields, from transportation to construction. In this work, we investigate the shaping of epoxy vitrimer composites using direct ink writing, an additive manufacturing technology that enables the fabrication of parts with complex shapes. The composition of these epoxies can be designed to achieve self-healing and shape memory capabilities. Direct ink writing is based on the continuous extrusion of a filament. Reduced graphene oxide is used as an additive to prepare vitrimer-based pastes able to flow through a narrow printing nozzle (510 μm in diameter) and hold the weight of the printed part. The composites contain BN platelets to enhance thermal conductivity. The thermal and mechanical properties of the printed composites have been assessed. We show that the alignment of the BN platelets during extrusion can result in thermal conductivities above 2 Wm/K in the direction of platelet alignment.*

Keywords: shape memory; vitrimer composites; additive manufacturing.

1. Introduction

The development of self-healing (SH) and shape memory (SM) materials attracts much interest. Vitrimers are a new class of thermosetting polymers.[1] Unlike conventional thermosets, vitrimers can be reprocessed and repaired through the rearrangement of chemical bonds upon heating. They could be used to create structures able to self-repair and change shape in response to external stimuli for applications such as self-deployable assemblies, actuators, airfoils. The challenges are to combine these properties with the mechanical performance required for structural applications and integrate the materials into the shaping technologies capable of producing the complex parts required for these applications.

Additive manufacturing technologies such as direct ink writing can create new opportunities in the fabrication of bespoke components using thermoset composites. These composites are very attractive due to their chemical resistance, stiffness, and strength. Direct ink writing uses the continuous extrusion of a paste at room temperature to build parts layer by layer. This paste should exhibit the viscoelastic response required to combine continuous extrusion (through nozzles ~0.1-1 millimeters in diameter) and shape retention after deposition and during thermal curing. This is usually done by incorporating additives to manipulate rheology, for example, nanoclays [2], fumed silica [3] and carbon nanofibers [4]. However, these additives may have a detrimental effect on the performance of the composites.

  doi:10.5075/epfl-298799_978-2-9701614-0-0

In this work, we develop a printable epoxy vitrimer-based feedstock for direct ink writing using relatively low contents (< 6wt.%) of reduced graphene oxide (rGO) flakes to manipulate the viscoelastic response. The vitrimers are re-processable and exhibit SM properties derived from aromatic disulfide exchange reactions [1]. We studied the thermal and mechanical response of the materials (including their SM capabilities) and quantified the effect of the introduction of anisotropic reinforcements, boron nitride platelets, on their thermal and mechanical properties.

2. Experimental

2.1 Materials

The vitrimer epoxy was prepared using bisphenol A diglycidyl ether (DGEBA)-based epoxy resin (ARALDITE LY1564) with an epoxide equivalent weight 161-173 g eq^{-1}, Poly(propylene glycol) diglycidic ether (DGEPPG, Mn=380; epoxy equivalent weight of 190 g eq^{-1}), and 4-Aminophenyldisulfide (4-AFD). Graphene oxide (GO) was prepared using graphite flakes (SKU332461, 150-500 µm sieved, Sigma Aldrich) whereas the composites incorporated H-BN (AB134567, abcr) platelets (d(0.5) = 4-6 µm).

2.2 rGO synthesis

GO water suspensions were synthesized through the chemical exfoliation of graphite following a Modified Hummers Method in a 5L reactor [5]. The as-prepared suspensions were washed with deionized water to remove unreacted reagents in a centrifuge (Thermo Scientific Sorvall LYNX 6000 Superspeed Centrifuge) at 8000 rpm for 30 min. After more than 15 centrifugation cycles, GO suspensions with pH ~ 6 were achieved.

The GO water suspension was dried in a convection oven at 37 ℃ for 48 hours. The oven-dried GO film was then placed in a glass petri dish with a lid and reduced through microwave irradiation in air in a microwave oven (Daewoo electronics, 1000 W) for 2 min to produce reduced graphene oxide (rGO).[6]

2.3 Epoxy resin preparation

DGEBA was mixed with DGEPPG in a weight ratio of 23:77 using centrifugal mixing (Thinky Mixer AR-100) at 2000 rpm. After complete mixing, the hardener 4-AFD was added to the mixture and dissolved at 80 ℃. The weight ratio between the mixture and hardener was 100:37. The homogenous mixture was defoamed in the Thinky Mixer at 2200 rpm for 10 min followed by further degassing in a vacuum desiccator until no visible air bubbles were left. Pristine epoxy parts were prepared by casting in silicone moulds and then cured at 120 ℃ in an oven for 2.5 hours, followed by a post-curing at 150 ℃ for 2 hours.

2.4 Paste preparation

rGO/epoxy pastes were prepared by dispersing the rGO flakes (5 wt.%) in the pre-mixed epoxy resin through a series of 2-minute mixing cycles using the Thinky Mixer at 2000 rpm until the flakes were completely incorporated. Degassing was done at 2200 rpm for 20 min. The same preparation procedure was applied to prepare the BN/rGO/epoxy pastes.

  doi:10.5075/epfl-298799_978-2-9701614-0-0

2.5 Direct Ink writing of composites

The as-prepared slurry was loaded in a 3 ml syringe barrel with 510 µm diameter printing nozzle. The direct ink writing process was carried out in a robocaster system (3dInks, USA) at room temperature. The ink was continuously extruded from the nozzle at a speed of 6 mm/s and deposited onto a PTFE substrate layer by layer. The printed parts were cured at 120 ℃ for 2.5 hours followed by a post-curing at 150 ℃ for 2 hours.

2.6 Assessments of thermal properties

Thermogravimetric analysis (TGA) was done to cured neat epoxy vitrimer fabricated by mold-casting, rGO/epoxy and BN/rGO/epoxy composites fabricated by direct ink writing under 20 ml/min air flow at temperatures ranging from 20 to 800 °C. Differential scanning calorimetry (DSC) was done between 20 and 100 °C to measure the glass transition temperatures. The heating rate for both TGA and DSC was 10 °C/min. Laser flash analysis has been used to compare the room temperature thermal conductivity of each material, using 10 × 10 × 5 mm^3 cuboids. The BN composite has been tested in two different directions: in-plane (along the extrusion direction) and out-of-plane (perpendicular to the extrusion direction).

2.7 Dynamic mechanical analysis (DMA)

The shape memory properties of printed 5wt% rGO/epoxy composites were tested using a TA Instruments DMA Q800 system under controlled force mode. The specimens were printed into 12 × 1.5 × 17.5 mm^3 plates. The samples were heated from room temperature to 80 °C at 10 °C/min, then uniaxial tensile loading was applied at 1.5 N/min until reaching 1.5 N. The force was held for 10 min. After that, the sample was released at a rate of 1.5 N/min until it was stress free. This process was repeated 3 times and the strain rate was recorded.

2.8 Mechanical testing

The tensile strength of the materials has been tested using dog-bone shaped specimens in a Deben 300 N tensile test stage at a displacement rate of 0.1 mm/min. The fracture toughness (K_{IC}) has been measured in 3-point bending using the method described in ASTM E1820 − 20b. The specimens were fabricated into single edge-notched beams and tested in a Deben 300 N tensile test stage. The notches were sharpened manually with a razor blade. The corresponding fracture surfaces have been observed in the scanning electron microscope (SEM).

3. Results

3.1 Printability

The epoxy mixture exhibits a Newtonian behaviour with a viscosity of 0.3 Pa.s. After adding rGO all the pastes are shear thinning with a yield stress (Bingham pseudoplastic) and there is a clear hysteresis when performing shear cycles of increasing and decreasing shear rates. The static yield stresses (σ_y^{st}) needed to start flow are always higher than the dynamic ones, σ_y^{dy}, reached after one cycle (Figure 1). These yield stresses increase with increasing rGO content in the ink and also with the addition of BN platelets. The dynamic yield stress varies between 17 MPa and 3640 MPa for pastes containing 2 wt% and 5 wt% rGO respectively. Only pastes with a dynamic yield stress above 1000 MPa exhibited good shape retention after printing.

  doi:10.5075/epfl-298799_978-2-9701614-0-0

The maximum shear rate that the ink experiences during extrusion through a 510 µm diameter nozzle at a rate of 6 mm/s can be estimated using Eq. (1).

$$\dot{\gamma}_{max} = \frac{4\dot{Q}}{\pi r^3} \quad (1)$$

Where $\dot{Q}$ is the volumetric flow calculated through $\dot{Q} = Sr^2$, S represents the printing rate and r represents the radius of the nozzle [7]. This shear rate is around 30 s^{-1}.

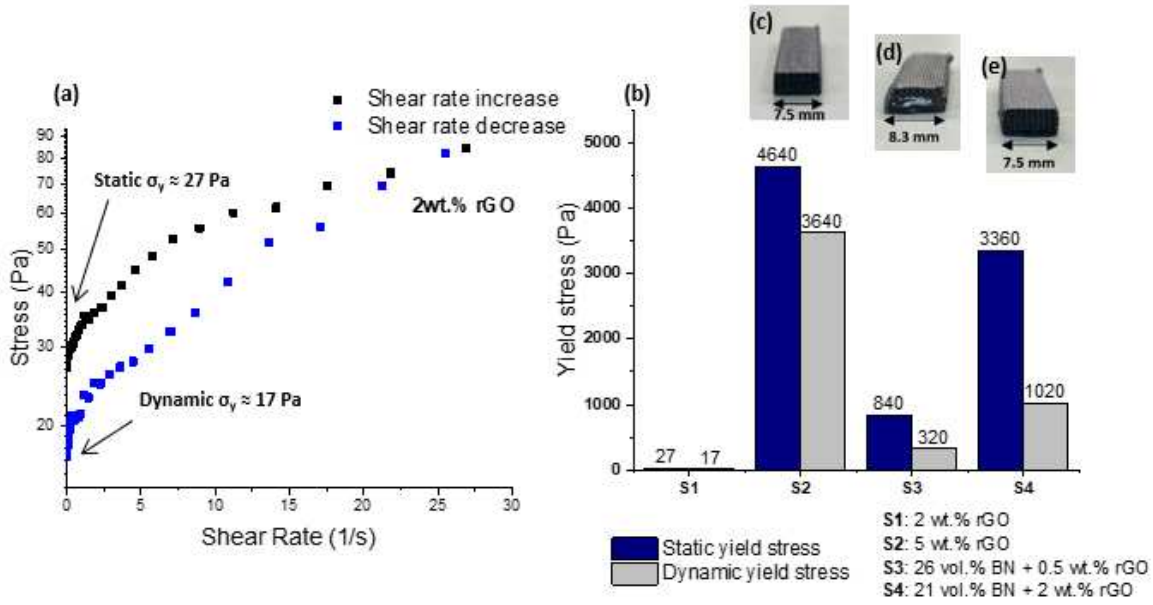

Figure 1. (a) Stress vs. shear rate cycles for epoxy vitrimer based slurries containing 2 wt.% rGO flakes. (b) Comparison between static and dynamic yield stress of pastes containing different amounts of additives. (c) (d) (e) Pictures of printed and cured epoxy-based composites with corresponding ink formulations: S2, S3 and S4.

3.2 Thermal properties

TGA has been used to measure the thermal stability of the materials (Figure 2(a)). The fully cured epoxy resin, rGO/epoxy and BN/rGO/epoxy printed composites start losing mass at a similar temperature of around 250 °C. The glass transition temperatures (T_g) of each composition have been measured using DSC differential scanning calorimetry (Figure 2(b)). The cured neat epoxy vitrimer and rGO/epoxy composite have the same T_g at ~ 50 °C while the addition of BN reduces slightly the T_g (~ 42 °C).

The results from laser flash analysis (Figure 3) showed that the introduction of 5 wt.% rGO into the epoxy matrix led to a small increment in the thermal conductivity from ~0.2 W/m.K to 0.6 W/m.K, while the inclusion of 21 vol. % BN and 2 wt.% rGO resulted in a significant increase in the in-plane direction up to 2.2 W/m.K.

  doi:10.5075/epfl-298799_978-2-9701614-0-0

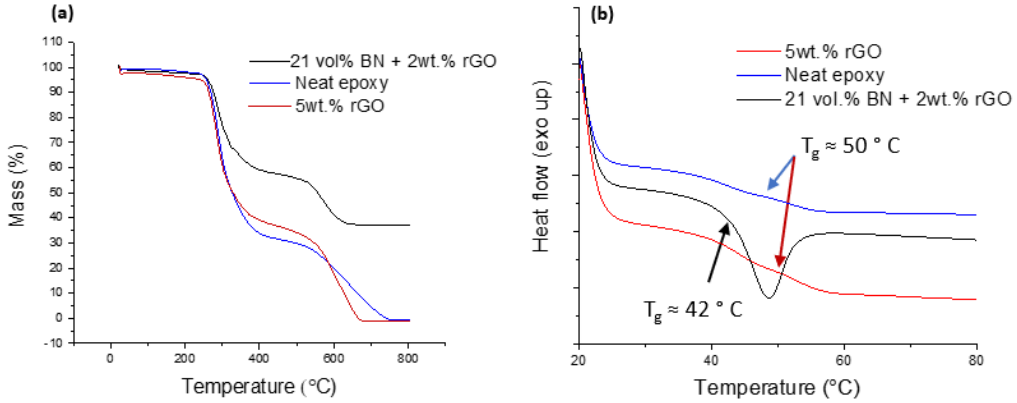

Figure 2. Thermal analysis: (a) TGA and (b) DSC of cured pristine epoxy resin and cured epoxy-based composites fabricated by direct ink writing.

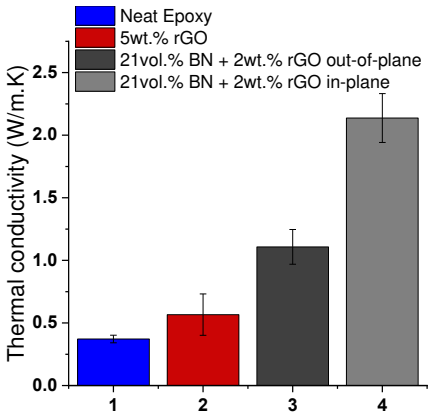

Figure 3. Room temperature thermal conductivities of cured epoxy resins and cured epoxy-based composites fabricated by direct ink writing at room temperature.

3.3 Shape memory performance

The shape memory behaviour of the rGO/epoxy composites fabricated by direct ink writing has been quantified using DMA. The rate of strain fixity (R_f) and recovery (R_r) in each cycle were calculated using Eqs. 2 and 3 and shown in Table 1.

Table 1: Strain fixity rate and strain recovery rate calculated for each thermomechanical cycle.

Cycle	Fixity	Recovery
1	65 %	72 %
2	61 %	95 %
3	61 %	98 %

$$R_f = \frac{\varepsilon_u(n)}{\varepsilon_m} \times 100\ \% \quad (2)$$

$$R_r = \frac{\varepsilon_m - \varepsilon_p(n)}{\varepsilon_m - \varepsilon_p(n-1)} \times 100\ \% \quad (3)$$

Where n indicates the cycle number, ε_u indicates the strain when the stress is removed after the deformation step, ε_m is the maximum strain in this cycle and ε_p is the strain in the stress-free state before the deformation step.

3.4 Mechanical properties

The average Young's modulus, tensile strength, and maximum elongation before failure for each material are summarized in Table 2. The force-displacement curves from the 3-point flexural tests on notched samples are plotted in Figure 6 (a). While the neat epoxy breaks in a brittle manner, the addition of rGO and BN induces a more gradual failure. The corresponding fracture surfaces (Figure 6c-e) exhibit the characteristic morphology of a brittle fracture for pure epoxy, but they become microscopically rougher with rGO and BN additions. These additions also introduce some porosity that is larger in samples containing 5wt% rGO.

Table 2: Young's modulus, tensile strength and maximum elongation of dog-bone samples.

Specimen	Young's modulus	Tensile strength	Max Elongation
Neat Epoxy	2.8 ± 0.3 GPa	52 ± 1 MPa	16 ± 4 %
5 wt.% rGO/epoxy	2.1 ± 0.1 GPa	22 ± 1 MPa	1.7 ± 0.2 %
21 vol.% BN/2wt.% rGO/epoxy	3.4 ± 0.1 GPa	41 ± 4 MPa	1.4 ± 0.4 %

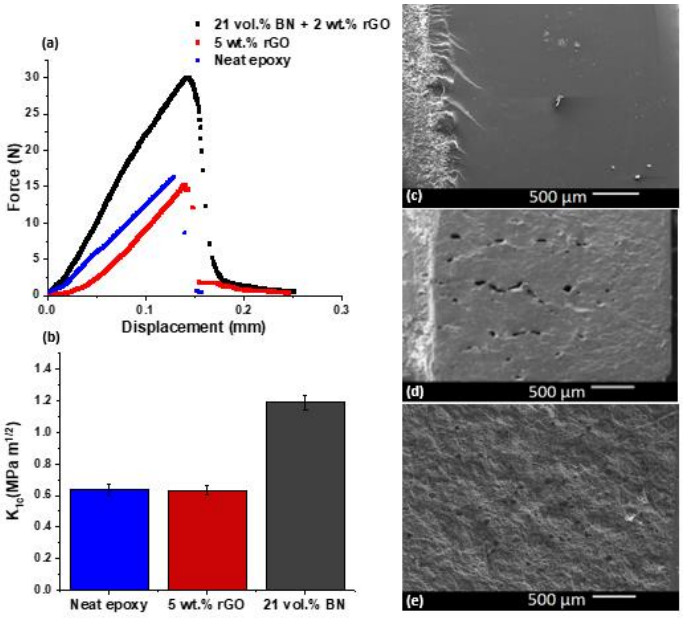

Figure 4. (a) Force vs. displacement curves measured using 3-point flexural tests; (b) K_{IC} calculated for casted neat epoxy vitrimer, printed 5wt.% rGO/epoxy and printed 21 vol.% BN/2wt.% rGO/epoxy composites. SEM images of fracture surfaces on (c) neat epoxy, (b) 5wt.% rGO/epoxy composite, and (c) 21 vol.% BN/2wt.% rGO/epoxy composite.

4. Discussion

One of the key properties of a printable paste is its yield stress. It has to be high enough to maintain the printed shape but low enough to enable smooth extrusion. The epoxy resin is a

  doi:10.5075/epfl-298799_978-2-9701614-0-0

Newtonian liquid before curing and does not exhibit any yield stress. After adding a small amount of rGO (2 wt.%), the epoxy-based slurry started to exhibit a low σ_y^{st} of around 27 Pa. When the rGO content in the slurry reached 5 wt.%, the flakes started to get physically entangled and resulted in an increase of σ_y^{st} to around 4640 Pa. The hysteresis observed after the shear rate cycle is probably due to the breakup of this entanglement during the increase in shear rate, the entanglement is not fully recovered, and some large flakes might have been broken into smaller ones. Although the σ_y^{dy} of the slurry is ~1-2 kPa lower than the static one, it is still high enough for shape retention after printing, as shown by the photograph of the printed 5wt.% rGO/epoxy bar with well-defined shape in Figure 1 (c). This formulation was used to fabricate rGO/epoxy composites in this project. The goal in the development of the BN-composites was to incorporate as much boron nitride as possible in order to increase the thermal conductivity. To achieve this goal with a printable ink, it is necessary to decrease the rGO content as otherwise the static yield stress becomes too high for extrusion. Parts printed with a paste containing 26 vol.% BN and 0.5 wt.% rGO slumped after depositing a few layers (Figure 1 (d)). The poor shape retention was due to the low dynamic yield stress. To prevent the printed part from slumping, a new formulation with lower amount of BN (21 vol. %) and higher amount of rGO (2 wt.%) was developed. It was found to possess very good shape retention (Figure 1(e)) consistent with its dynamic yield stress that is more than 2 times greater than that of the previous formulation. Therefore, in this work the paste containing 21 vol.% BN and 2 wt.% rGO has been chosen for the direct ink writing fabrication of composites.

The addition of BN and rGO did not have a large effect in the thermal stability that is mainly determined by the properties of the epoxy (Figure 2 (a)). The effect on the T_g was also small, the neat epoxy resin and the rGO composite have the same glass transition temperature of ~ 50 °C. The T_g of BN composite was found to be slightly lower (~ 42 °C). This could be caused by the enhanced thermal conductivity due to the addition of BN platelets (Figure 3). The printed BN composites exhibit a thermal conductivity much higher than that of the epoxy resin and a directional thermal transport that depends on the printing direction. This is due to alignment of the BN platelets in the direction of extrusion when the filament was squeezed out through the narrow nozzle. This BN composite has an in-plane thermal conductivity of ~ 2.2 W/m·K which is comparable to that of the hot-pressed BN/epoxy materials reported in the literature [8].

In the first thermomechanical cycle, the rate of strain recovery was 72 %. There was a large change in strain that has not recovered which could be caused by plastic deformation. In the next 2 cycles the recovery was higher than 95 %. In all the three cycles the rate of strain fixity is almost constant in between 60 and 65 %. All these SM properties are similar to the pristine epoxy [9].

The mechanical performance of the material was found to be affected by the additives (Figures 5 and 6). After introducing the rGO flakes in the polymer matrix, the Young's modulus, tensile strength, and maximum elongation were reduced due to the increase in porosity and the weak rGO-epoxy interface in the printed structure. The rGO flakes seem to stabilize bubbles in the paste. The BN composites are denser, probably due to their lower rGO content that facilitates removal of gas bubbles. As a result, the strength of the BN composites is similar to the one of the epoxy (albeit a bit lower). Its maximum elongation is also lower. However, their fracture toughness and Young's modulus were found to be higher due to the high stiffness of the BN platelets.

  doi:10.5075/epfl-298799_978-2-9701614-0-0

5. Conclusions

We have developed pastes for the direct ink writing of epoxy vitrimer composites based on the addition of rGO. These composites can contain up to 26 vol% of microscopic BN platelets. The hysteresis in the yield stress of the pastes and their corresponding printing performance indicated the importance of dynamic yield stress on the shape retention capability. The thermal properties of the printed composites were found to be comparable to the matrix material, whereas for the thermal conductivity, there was a significant enhancement from 0.3 W/m.K to 2.2 W/m·K due to the introduction of BN platelets. With regards to the SM response, the rGO/epoxy composite possesses a strain fixity and recovery that is consistent with the neat epoxy resin. However, this rGO composite was found to be mechanically weaker than the epoxy resin in terms of Young's modulus and tensile strength, because of the internal porosity and the weak rGO-epoxy interface. These properties were substantially recovered with the reduction in rGO content and the addition of BN.

Acknowledgements

This work has been financially supported by the Office of Naval Research (ONR) under award number N62909-18-1-2056.

6. References

1. Azcune I, Odriozola I. Aromatic disulfide crosslinks in polymer systems: Self-healing, reprocessability, recyclability and more. European Polymer Journal. 2016;84:147-60.
2. Hmeidat NS, Kemp JW, Compton BG. High-strength epoxy nanocomposites for 3D printing. Composites Science and Technology. 2018;160:9-20.
3. Chandrasekaran S, Duoss EB, Worsley MA, Lewicki JP. 3D printing of high performance cyanate ester thermoset polymers. Journal of Materials Chemistry A. 2018;6(3):853-8.
4. Lewicki JP, Rodriguez JN, Zhu C, Worsley MA, Wu AS, Kanarska Y, et al. 3D-printing of meso-structurally ordered carbon fiber/polymer composites with unprecedented orthotropic physical properties. Scientific reports. 2017;7(1):1-14.
5. Picot OT, Rocha VG, Ferraro C, Ni N, D'elia E, Meille S, et al. Using graphene networks to build bioinspired self-monitoring ceramics. Nature communications. 2017;8(1):1-11.
6. Voiry D, Yang J, Kupferberg J, Fullon R, Lee C, Jeong HY, et al. High-quality graphene via microwave reduction of solution-exfoliated graphene oxide. Science. 2016;353(6306):1413-6.
7. M'barki A, Bocquet L, Stevenson A. Linking rheology and printability for dense and strong ceramics by direct ink writing. Scientific reports. 2017;7(1):1-10.
8. Zhang T, Sun J, Ren L, Yao Y, Wang M, Zeng X, et al. Nacre-inspired polymer composites with high thermal conductivity and enhanced mechanical strength. Composites Part A: Applied Science and Manufacturing. 2019;121:92-9.
9. Azcune I, Huegun A, de Luzuriaga AR, Saiz E, Rekondo A. The effect of matrix on shape properties of aromatic disulfide based epoxy vitrimers. European Polymer Journal. 2021;148:110362.

  doi:10.5075/epfl-298799_978-2-9701614-0-0

New 3D-Printing Platform Produces Structural CFRTP Parts with OPTION FOR Unique Aesthetic Surfaces

Yannick Willemin[a], Dr. Martin Eichenhofer[b]

a: 9T Labs AG – yannick@9tlabs.com
b: 9T Labs AG

Abstract: *The comparatively high cost of producing structural parts in carbon fiber-reinforced composite versus metallic counterparts of comparable performance remains a constraining factor in many industries. Higher freedom to optimize part geometry and better control of fiber layout to optimize performance, cost, and mass, coupled with increased automation during production would help reduce current constraints. As such, composite 3D printing, an additive manufacturing technology, is starting to deliver on those needs. For example, additive fusion technology (AFT)—a hybrid manufacturing process combining 3D printing of thermoplastic composite tapes and neat monofilaments plus consolidation/forming of the printed preform in a compact compression press using matched metal dies—offers excellent surfaces, high dimensional control, very-low voids and material waste, 100% traceability, and high levels of repeatability and reproducibility in a scalable system that makes high-performance carbon composites competitive in more markets.*

Keywords: 3D printing; structural composites, serial/series production, carbon composites; aesthetics

1. A Need Previously Unfulfilled

When producing structural parts in the small-to-medium size, low-to-moderate production volumes (<10,000 units/year), industry has long had needs that until recently went unfulfilled. The University of Delaware reported [1] that 80% of small or thick-section structural parts are specified in metals due to high fabrication costs associated with structural composite materials, which can be 3x higher than comparably performing and easier to process metals. The same report noted that only when the size of carbon fiber-reinforced plastic (CFRP) structures exceeded 9.1 kg was investments in automation cost justified. Unfortunately, CFRP manufacturing processes producing the highest-performing parts have tended to be the slowest and least automated, which has effectively locked this valuable class of materials out of consideration for small and thick structural parts in many industries—especially when production volumes fall below 10,000 units annually.

This unfulfilled need for a fast, accurate, scalable, and cost-effective method of producing small and/or thick-section structural CFRP parts in low-to-moderate volumes is changing thanks to two converging trends. The first is expansion of unidirectional (UD) carbon fiber-reinforced tape-based intermediates into a broader range of thermoplastic matrices and the second is new developments in 3D printing that permit fiber-reinforced thermoplastic parts to be printed. This paper will report on one technology that combines two types of materials—UD carbon fiber-reinforced thermoplastic (CFRTP) tapes plus unreinforced or chopped fiber reinforced filaments of the same matrices—and offers very-accurate control of filament orientation, the ability to print fine geometric detail, with design flexibility rarely attainable in composites manufacturing. In this technology platform, 3D printing is combined with a compact compression press that both preheats/consolidates the printed preform, then finish

  doi:10.5075/epfl-298799_978-2-9701614-0-0

forms it into a (near-)net-shape part with very little waste and very-low voids quickly, repeatedly, and at lower costs than metals.

2. Additive Fusion Technology

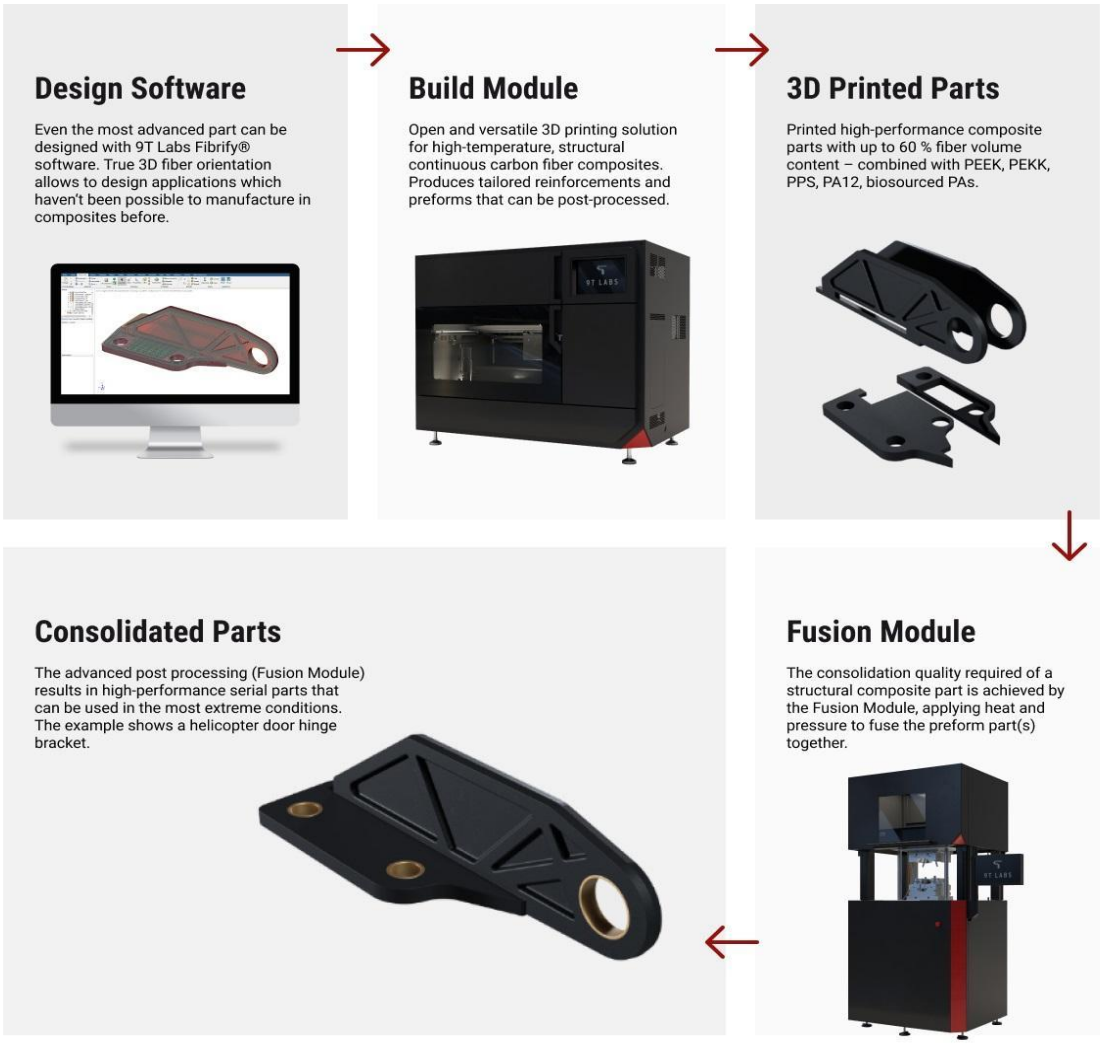

Figure 1. Additive fusion technology consists of advanced design software, a 3D printer that produces (near-)net-shape preforms, and a compact compression press equipped with matched metal dies in which preforms are heated, shaped, and consolidated.

The patented technology referenced above was developed by Zürich-based 9T Labs AG, a 2018 spinoff from ETH Zürich (Swiss Federal Institute of Technology) with the goal of leveraging automation, software, and materials to make high-performance structural composites parts more affordable to industry. This hybrid manufacturing process—called additive fusion technology (AFT)—combines the best of polymer additive manufacturing (e.g., freedom to achieve high design complexity, unmatched fiber layout control, 100% traceability, and low energy usage and waste) with conventional manufacturing via compression molding in matched metal dies (e.g., rapid cycle times, tight tolerance control, high repeatability and reproducibility (R&R), low material waste, very-low voids, and excellent surface finish) and it does so at consistently lower piece costs than metallic alternatives. Advanced design tools help a variety of design and filament layout options to be considered rapidly and efficiently while

  doi:10.5075/epfl-298799_978-2-9701614-0-0

interfacing with standard CAE design tools. The process also uses established thermoplastic materials broadly available from global supply chains. Parts produced via AFT are being used or evaluated in the aerospace/aviation, automotive/motorsports, medical device, industrial/machinery, robotics/automation, sporting goods, and consumer luxury goods segments.

2.1 Design

The process begins by accessing the cloud-based Fibrify software suite, which interfaces with common structural analysis packages via plugins and is used to quickly evaluate multiple filament-layup options to optimize parts in terms of performance, cost, and mass. The package has been designed to simplify and speed design work for novice users but also to offer high levels of flexibility for more experienced users. Designs can be built from scratch or CAD files can be imported and solid models can be filled with straight and curved lines (UD fibers), neat resin, and even holes, which in turn can be reinforced by laying out reinforcing fiber bands. More complex designs can incorporate both 2D fiber patterns in a 3D solid with additional vertically distributed fibers (in the Z axis) to speed up the design optimization process. Rules can be applied to parameterize vertical fiber distribution, and layouts can be modified layer by layer. Layup options can then be checked in structural packages to verify performance. Cost to produce the preferred layout can also be calculated in Fibrify after selecting the final design, the materials to be used, and setting production targets. Once the entire design is validated, the software's manufacturing execution system (MES) generates G-Code, which is sent to the printer, instructing it how to produce the part. The MES also manages production flow by acting as an ERP (enterprise-resource planning) package to manage part build and molding.

2.2 Preform Printing/Layup with Material Options

3D printing is done in the Red Series Build Module, which produces a near-net- or net-shape preform with very little waste. The printer permits filament positioning at nearly any angle in X, Y, and Z axes to produce preforms with fiber-volume fractions (FVF) up to 60%; neat filaments (1.75 mm diameter) of the same matrix can be used in part areas with lower structural requirements to reduce both mass and cost. Since matrix resins are matched between tapes and monofilaments, excellent bonding between reinforced and unreinforced material is achieved.

High-quality carbon fiber-reinforced UD tapes with excellent impregnation and very-low voids are used for fiber layup. These tapes are supplied pre-slit to the equivalent of 1-2K tows and wound onto spools, which are loaded into the printer. As tape is pulled into the unit, it is roll-formed into tiny tubular filaments, permitting fine detail to be printed (minimum section thickness=1.5 mm; minimum section height=0.6 mm; minimum fiber radius=1.5 mm). Currently, PEKK, PEEK, PPS, PA12, and bio-based PA materials are available, although nearly any high-quality commercial thermoplastic tapes and filaments may be used.

2.3 Preform Consolidation and Shaping

Once the preform has been printed, it is moved to the forming step (Red Series Fusion Module) where it is heated, shaped, consolidated, then chilled/solidified. Consolidation is necessary since the printing process produces a bumpy surface. This step also helps ensure excellent bonding between layers, elimination of void, and release of residual stresses. Heating/consolidation and forming/chilling take place in matched metal dies mounted inside

  doi:10.5075/epfl-298799_978-2-9701614-0-0

the unit's compact compression press, which assure short molding cycle times, high R&R, and a high-quality surface on both A and B sides of the part. Just like conventional compression molding, the process permits insertion of metallic hardware into the preform before consolidation/forming for added functionality.

2.4 Structure, Function and Unique Surface Aesthetics

Neat polymer can be used to print the final layers of a part, which increases printing speed and lowers total part cost and mass, while also ensuring that, after consolidation/forming, the part offers a resin-rich, homogeneous surface.

Another option exists to create unique surface aesthetics—even biomimetic effects—by applying specific types of commercial tapes or monofilaments in transparent, translucent, or opaque colors for decorative rather than mechanical purposes during printing of those final layers. For example, a material like gold leaf filament has been selectively incorporated over the 3D-printed composite before printing of clear resin and subsequent consolidation, creating a rich and interesting surface. Or the carbon fiber itself can be laid down in unique patterns that suggest burled wood or flowing waves found in long hair or Japanese wood prints or even to create 3D patterns with depth of image (DOI) currently unattainable from woven fabrics. Still another option is to apply various black or "colored" carbon fiber fabrics, non-crimp fabrics, or even decorative films to part surfaces after printing and before consolidation.

These options extend aesthetic possibilities and enable CFRTP to move beyond solely structural and functional capabilities and into luxury and consumer goods ranging from motorsports to watch bezels, to cases, and even decorative wall panels for homes and businesses.

Figure 2. AFT offers options to create unique surface finishes by way of surface fiber layups that can even produce biomimetic looks. This feature is currently being used to produce structural, functional parts with unique surfaces in the motorsports and luxury consumer goods markets.

2.5 Manufacturing Benefits

Depending on dimensions, a single Build Module can produce up to 5,000 preforms/year and a single Fusion Module can mold up to 10,000 parts/year. As manufacturing volumes increase, more units can be added, making the system easily scalable. The current build envelope for

  doi:10.5075/epfl-298799_978-2-9701614-0-0

both Build and Fusion Modules is 350 x 270 x 250 mm, although larger structures can be produced by printing subcomponents and welding them together—either during the consolidation step or after demolding (another benefit of thermoplastic matrices). Or adhesive bonding and/or mechanical fasteners may also be used to join smaller components into larger assemblies.

By building the AFT platform around thermoplastic instead of thermoset matrices, printers and printing are greatly simplified and molding cycles are reduced significantly since thermoplastics are already prepolymerized and do not need additional time to polymerize and crosslink as thermosets do. Additionally, scrap can be repurposed elsewhere and end-of-life parts can be melt reprocessed (recycled).

Combining preform production and consolidation/forming with a robust design tool integrated with common structural FEA packages eliminates traditional, costly, and time-consuming "make & break" cycles where parts are designed, produced, tested, then prototype designs are further modified to more closely meet performance and cost targets. In turn, this helps manufacturers bring parts to market faster. As such, the AFT process enables companies large and small to produce high-performance composite parts that are significantly stiffer, stronger, lighter, and less costly than metals and plastics while addressing challenging serial part application needs in industries whose needs were previously unmet or poorly met.

3. Feasibility Studies

To date, 9T Labs has performed more than 100 feasibility studies for customers in industries as diverse as aerospace/aviation, sporting goods, medical device, motorsports, and leisure/luxury goods. Many companies have gone on to purchase systems. What follows are examples of studies that were conducted, incumbent materials that were benchmarked, and results that were achieved after fully designed parts were printed, formed, and tested.

3.1 Helicopter Hinge

9T Labs and the University of Applied Sciences Northwestern Switzerland (FHNW) collaborated on a research project to determine if the AFT process could be used to produce a structural CFRTP hinge, one of a pair that articulates each of two doors on a composite-bodied helicopter. The benchmark material was a 1-piece machined stainless steel hinge fastened to a rigid plate with 4 M8 bolts. The part was designed to withstand maximum static loads of 2.172 kN of force perpendicular to the bearing force when the door was open. Production quantity is 1,000 pieces/year. A team in France had earlier benchmarked the same part using hand laminated and compression molded chopped CFRTP tapes in a PEEK matrix. Both the French and 9T Labs teams maintained the external geometry and attachment locations but changed internal hinge geometry to optimize composite properties and enhance moldability/printability. Goal of the 9T Labs team was to improve performance vs. benchmark and French design. As such, 3 different designs were developed and printed using tapes and monofilaments with a PEKK matrix (the closest high-temperature offset to PEEK 9T Labs had at the time). Design 1 used the same internal and external geometry as the benchmark part and no attempt was made to optimize it to take advantage of composite properties. Dimensions on Designs 2 and 3 were both modified slightly to enhance printability and take full advantage of composite properties. Both designs were topology optimized using different fiber layups. Results are shown below.

  doi:10.5075/epfl-298799_978-2-9701614-0-0

Figure 3: Benchmark steel hinge with key properties

Table 1: Comparison of 5 Helicopter Hinge Designs

Property / Design	Mass (g)	Dimensions (mm)	Max. Static Load (kN)	Relative Cost (1,000 parts/year)
Machined Steel *Benchmark*	135	112 x 42 x 22.5	3.0 (Yield point)	€70
Laminated Chopped CF/PEEK Tapes *French Team*	21*	112 x 42 x 22.5	4.2	––
Design 1: 3DP CF/PEKK (non-optimized) *9T Labs*	20*	112 x 42 x 22.5	1.6	––
Design 2: 3DP CF/PEKK (Topology Optimized) *9T Labs*	25*	112 x 44 x 30	4.8	€35
Design 3: 3DP CF/PEKK (Topology Optimized) *9T Labs*	27.5*	112 x 44 x 30	6.9	€35

**Weight without metal insert, which adds 4.2 g*

All four CFRTP designs were significantly lighter than the benchmark steel hinge. The topology-optimized 9T Labs designs were 80% lighter but demonstrated 160% and 230% improvements in maximum static load. Additionally, both designs could be produced at roughly half the cost of the benchmark in quantities of 1,000 parts/year.

3.2 Surgical Aiming Arm

Another feasibility study conducted in a very different industry was a surgical aiming arm allowing orthopedic surgeons to align pins, bolts, holes, and other instruments with the bone plate during operations to repair shattered bones. While such parts see relatively low loads during use, they must maintain very tight dimensions throughout their use life, which consists of repeated cycles of autoclave sterilization. They also must be radiolucent to permit in situ position verification of the bone fixation system by X-ray during surgery.

Commercial aiming arms tend either to be machined from aluminum or from blocks of composite. 9T Labs' goal was to determine if a 3D printed CFRTP aiming arm could meet the

  doi:10.5075/epfl-298799_978-2-9701614-0-0

performance requirements of the application while also reducing cost. Owing to the heat and humidity of autoclave sterilization, the team chose PEKK as the matrix for both CFRTP tapes and monofilaments. Numerous layup options were considered. Owing to the criticality of maintaining dimensional stability and absolute position of the aiming arm holes, researchers locally reinforced holes with aligned fibers to prevent holes from shifting due to linear displacement or in-plane shear loads. To prevent in-plane flexure, fiber bands were also applied along the load path. Additionally, bands were added along the external perimeter to reinforce against out-of-plane flexure through the thickness of the part. Finally, designs incorporated stiff face skins that could stand up to post-print deburring, polishing, and engraving, creating a sandwich of composite skins enclosing the part's bulk volume filled with neat resin.

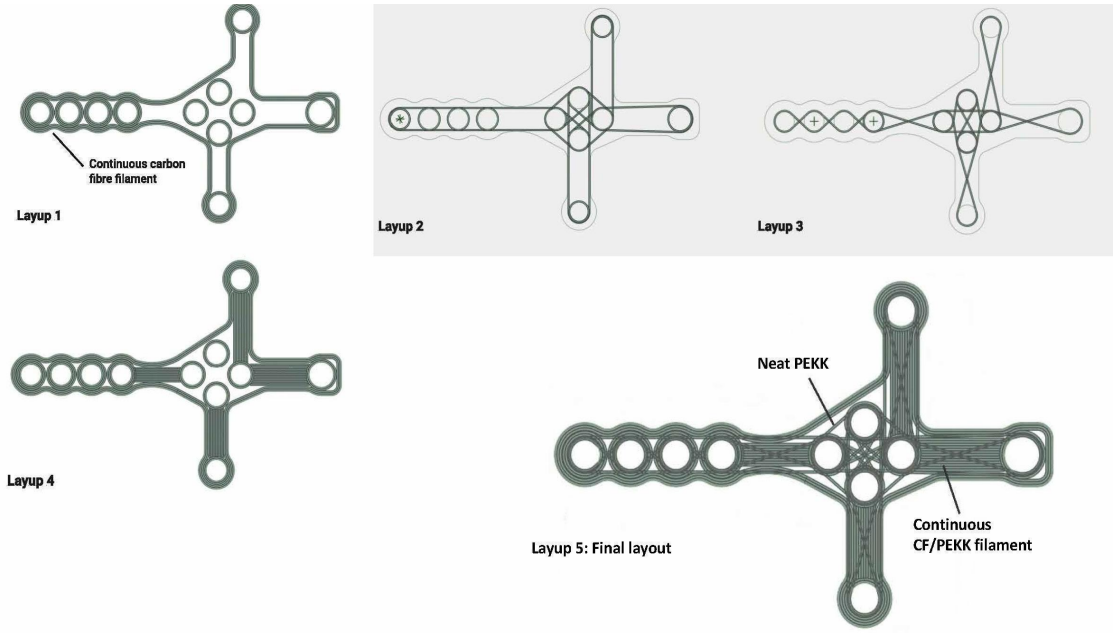

Figure 4: Fiber layout options with different methods of reinforcing critical hole dimensions

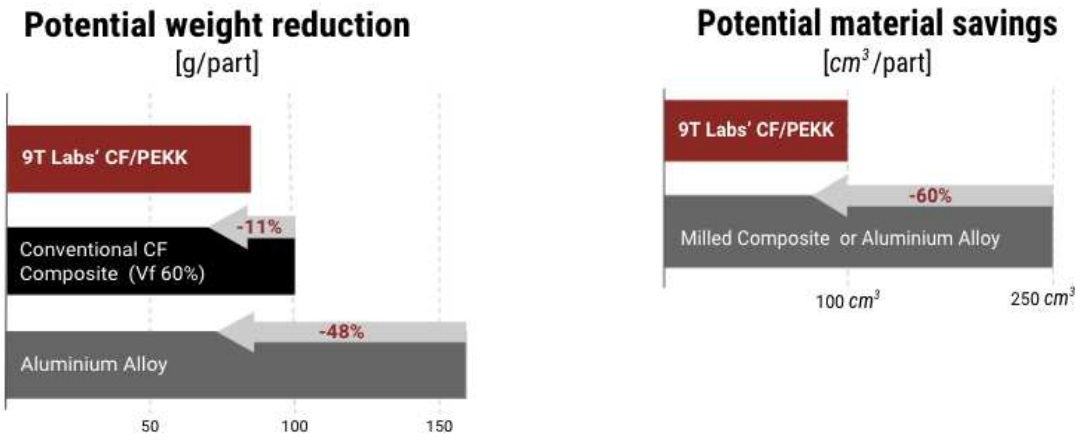

Figure 5: Potential weight and material (waste) savings for machined aluminum (grey), CF/PEEK composite block (black), and 3D printed CF/PEKK (red).

  doi:10.5075/epfl-298799_978-2-9701614-0-0

The design that best met the multiple loading conditions while minimizing weight and cost featured 90 printed layers and produced a part that was 174 x 107 x 15 mm and weighed 88 g. Its performance was compared against two incumbent materials: machined blocks of aluminum and carbon fiber-reinforced PEEK. Both the machined CF/PEEK composite block and the 3D printed CF/PEKK were, respectively, 37% and 48% lighter than the aluminum part. Since milling metal or composite produces significant waste, the 3D printed part was estimated to reduce material loss by 60%, helping lower part costs. At production volumes of 3,000 aiming arms/year, piece costs for the 3D printed parts would be ≈€90, and at 6,000 units/year, costs would drop to ≈€78. Included in the AFT cost estimates are 5% labor, 35% material, and 60% equipment usage, including the cost of producing a metal mold.

3.3 Exoskeleton Winglet

Still another interesting feasibility study was conducted by 9T Labs, Centre de développement des composites du Québec (CDCQ), MAWASHI Science & Technology, Développement économique Canada pour les régions de Québec, the Province of Québec, and Cégep de Saint-Jérôme. This study involved a 3D printed exoskeleton element called a winglet, which helps support heavy backpacks to reduce back strain. Goals were to reduce mass and cost without increasing deflection under load vs. the titanium benchmark.

Figure 6: Benchmark exoskeleton winglet element produced in machined titanium.

This time, a PA 12 matrix was selected for the component, which featured a very challenging double curvature surface that had never been 3D printed by 9T Labs before. The compound surface also proved challenging to mold, since printed preforms needed to be somewhat flexible to fit into the metal mold for consolidation and forming. The part was produced in 9 layers with different fiber patterns and sizes to fit the mold cavity. Researchers also considered compaction and material flow in their designs.

As before, the AFT process enabled parts with high mechanical performance to be produced owing to the ability to place continuous fiber bands along load paths, align fibers in multiple axes to maximize performance, and subsequently to consolidate the material to yield parts with very-low porosity/voids. The final part weighed 60% less and cost 50% less than the machined titanium benchmark. Deflection under load values were nearly identical.

  doi:10.5075/epfl-298799_978-2-9701614-0-0

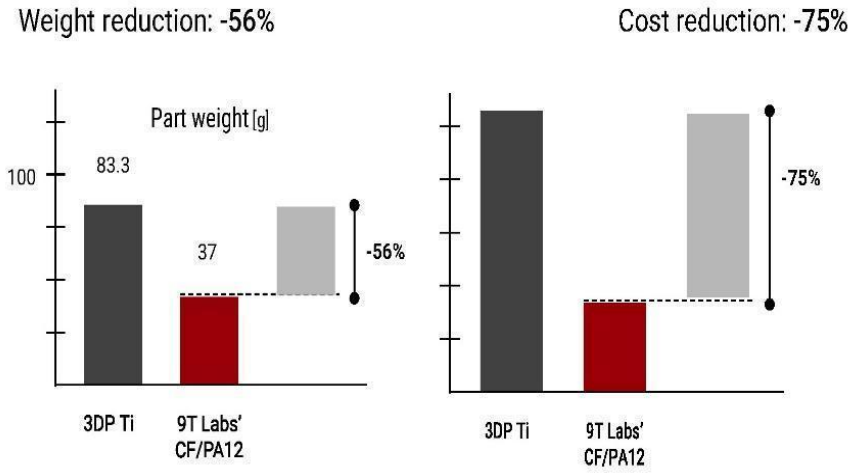

Figure 7: Weight and cost savings for printed CFRTP winglet vs. machined titanium.

These examples have demonstrated how the hybrid AFT process offers industry new options for producing structural CFRTP parts in smaller and/or thicker sizes and modest production volumes while lowering mass and cost and achieving comparable or better performance. The ability to optimize geometry and fiber layup, produce net-shaped parts, and the automation AFT offers help reduce cost, increase production speeds, and enable more markets to take advantage of the many performance, functional, and aesthetic benefits that CFRTP brings.

4. References

1. Yarlagadda S, Deitzel J, Heider D, Tierney J, Gillespie Jr. J. Tailorable Universal Feedstock for Forming (TUFF): Overview and Performance. SAMPE 2019; 10.33599/nasampe/s.19.1605.
2. Willemin, Y. New 3D-Manufacturing Platform, Composites United/CU reports #02, 2021, pp. 58-59.
3. Willemin, Y. Development of CFRTP Structural Hinge for Helicopter Door through additive fusion technology (AFT). Compositi magazine, March 2022, pp. 32-35.
4. Willemin, Y. Addressing key challenges in composite AM for maritime parts. Compositi magazine, Feb. 2022, 44-46.
5. Willemin, Y. New Hybrid Process for Converting Small Structural Parts from Metal to CFRP. Reinforced Plastics, December 2021, pp. 56-58.

  doi:10.5075/epfl-298799_978-2-9701614-0-0

3D PRINTING UNDER HIGH AMBIENT PRESSURE

Jens, Schuster[ab], Yousuf Pasha Shaik[a]

a: Institute for Polymer Technology West-Palatinate - Institut für Kunststofftechnik Westpfalz (IKW), Department for Applied Logistics and Polymer Sciences, University of Applied Sciences Kaiserslautern
b: Corresponding author – jens.schuster@hs-kl.de

Abstract: *Contrary to other polymer processing methods additively manufacturing processes do not use any pressure during the consolidation of layers. This study investigates the effect of high ambient pressure and temperature on the mechanical consolidation properties of filaments during the FDM process. To achieve high strength properties as of injection-moulded specimens, a setup has been made which consists of a 3D printer integrated into a customized autoclave. The autoclave can maintain 135 bar of pressure and a maximum temperature of 185°C. Autoclave preheating before and autoclave pressure effect while printing improves the consolidation of filaments immensely and nullifies voids. The pressure inside the autoclave provokes a more intimate contact between the contacting surfaces and results in higher mechanical properties such as yield strength and Young´s modulus. Additionally, 3D-printing was performed under a nitrogen atmosphere of 5 bar additional pressure resulting in a further increase in mechanical properties. Currently, short fiber reinforced polyamide 6 is printed using the previously mentioned process.*

Keywords: Mechanical properties; 3D printing; Additive manufacturing; Layer consolidations; Preheating; Nitrogen Atmosphere.

1. Introduction

Additive Manufacturing (AM) is the most emerging plastic process that promises a single processing step to fabricate complex and multifunctional parts/products using the CAD model [1]. It is defined as a "Process of joining of material such as polymer, metal, concrete, ceramics, or rubber in the form of successive layers on top of each other" [2]. Additive manufacturing, also known as 3D printing or rapid prototyping, has existed for many years. In 1984, the very first 3D printing technology was developed by Charles W. Hull of 3D Systems Corporation and named Stereo Lithography (SL), which was very expensive [3]. Initially, designers and architects because of their potential to make functional prototypes mainly used rapid prototyping. Later, extensive research was done, and tremendous advancements were created. This led to the development of many other AM methods like fused deposition modelling (FDM), materials jetting, inkjet printing, powder bed fusion, etc. These advancements in AM have reduced its costs, productivity, and wastage and have increased printing quality, accessibility, sustainability, and user-friendliness. These improvements have amplified their usage in automotive, aviation, medical, construction, and other applications [4].

Among all AM techniques, FDM plays a dominant role in all kinds of industries from small-scale to large-scale due to its low cost and feasibility and can be operated by individuals.

  doi:10.5075/epfl-298799_978-2-9701614-0-0

FDM is a process, in which a circular cross-sectional filament of predefined diameter made to push into the hot-end through a feeder with a defined speed, and melted material exiting from the nozzle attached to the hot-end follows a defined path to construct a specimen layer-by-layer. It is a cost-effective way to quickly produce prototypes and functional parts, aside from cheap machines and simple technological processes. By contrast, FDM parts have drawbacks in their mechanical properties. These parts possess the least dimensional accuracy and resolution among all other 3D printing technologies [5]. Moreover, FDM model's parts have visible layer lines that require post-processing to achieve a smooth, flat surface and less consistent behavior. Even though FDM rapid prototyping has a wide range of applications, it is not helpful to produce structural parts due to the anisotropic mechanical properties [6]. This drawback restricts their usage in many applications.

Research reveals that a typical FDM printer inserted into a nitrogen atmosphere to print parts shows a 30% increment in the tensile strength of its printed parts [7]. Another research investigation specifies heat treatment of 3D-printed parts enhances adhesion between the interlayers and reduces internal stresses [8]. However, an annealing process has constraints, as some polymers are temperature-sensitive and leading to thermal shrinkage or warping.

The effect of pressure and temperature on 3D-printed samples were analyzed. In previous studies, the post-processing treatment of 3D-printed and injection-molded specimens with autoclaving pressure and temperature treatment increased properties in all areas, including modulus and strength. This is because the samples' residual stresses are released during the post-treatment process. In the autoclave, samples absorb moisture from hot compressed air, causing internal crystalline growth, resulting in a larger grain structure. This increased the modulus and the yield strength. The combined effects of pressure and temperature, the reduced residual stresses, increased crystallinity, enhanced the mechanical properties by approximately 20 % [9, 10].

The objective of this research is to 3D print specimens in a customized autoclave under the ambient pressure and elevated temperature conditions and to measure the improvement of mechanical properties such as yield strength, yield strain, Young's modulus, flexural and impact strength. The samples were printed with the same infill density and same process parameters at 0 bar, 5 bar and 10 bar in the transverse and longitudinal directions to the hot-end nozzle. Every mechanical test is carried out with a sample batch. The results were averaged, analyzed and conclusions drawn. First tests, were 3D-printing was performed under a nitrogen atmosphere of 5 bar additional pressure were carried out.

1.1 Material

In this work, pure PLA (Polylactic Acid) filament (red) of high quality from Real Filament Company, Netherlands, was used. PLA filaments usage in FDM is common because of its low melting point (180°C-220°C), and it supports quality surface prints, is non-toxic, has high UV resistance, and low moisture adsorption allows easy handling.

1.2 FDM 3D-Printer

In this research, an Ender-3, V2 model FDM 3D-Printer from Creality-2020 was used. The maximum possible dimensions are 250×220×220 mm (H×B×L) [11]. General specifications like

  doi:10.5075/epfl-298799_978-2-9701614-0-0

Maximum bed temperature, maximum extruder temperature, and maximum printing speed are 100°C, 250°C, and 180 mm/sec, respectively.

1.3 Autoclave

A customized autoclave chamber from Haage Anagram GmbH, Germany, which had been specially designed to support polymer-processing methods, was used in this research. This autoclave maintains a maximum pressure of 135 bar and a maximum internal temperature of 185°C.

1.4 Fabrication of Specimens

The testing specimens were printed at 0 bar, 5 bar, and 10 bar of additional pressure in the autoclave. Since the material was PLA, the printing process was done with 205°C nozzle temperature and 60°C at the bedplate and the temperature was kept at 50°C inside the autoclave while printing. In addition, samples were printed in a nitrogen atmosphere inside the autoclave. For each test eight samples were tested which were printed in two different printing patterns (longitudinal and transverse to the printing direction) in three different pressure conditions (0 bar, 5 bar and 10 bar) in an autoclave. The test parameters include nozzle diameter, layer thickness, voltage capacities of printer and samples printing environment conditions are shown in Table 1.

1.5 Experimental setup

The 3D printing was carried out in the autoclave described previously (Fig. 1). The pressure was buildup inside the autoclave by sending compressed air into it using a compressor. In this research work, different mechanical tests like tensile, flexural, and Charpy impact were conducted on the printed samples.

1.6 Tests on samples

- The tensile strength, stiffness, and elongation properties were measured according to DIN ISO 527, using a tensile testing machine from Zwick (Proline-Z005) along with Zwick´s Test Expert software. The strain measurement was done optically with the Video extensions system also from Zwick.
- Flexural properties of materials are examined through the 3-point bending test according to DIN ISO 178 using the Zwick -UTM mentioned previously.
- Charpy impact test DIN ISO 179 was carried out with a pendulum from the company Ray-Ran with an impact energy of 4 joules and an impact velocity of 2.9 m/sec.
- The density of the samples was measured by applying the Archimedes principle.

1.7 Test results

- The Young´s modulus depicted in Fig. 2 improved by 39.3% if printed in the 10-bar pressure condition, which indicates a better improvement in the consolidation of layers and strength in a longitudinal direction. In the transverse direction, an improvement by 147.8 % can be noticed. The yield strength is a criterion that indicates the maximum load a part can withstand elastically. In the vertical direction, an increase of 40.3 % and, as expected, in the transverse direction and of 96% is achieved. The yield strain was also raised by 50 % in both directions, represented on the secondary scale in Fig. 3. The

  doi:10.5075/epfl-298799_978-2-9701614-0-0

samples printed in nitrogen atmosphere derived even better results in terms of the Young's modulus and yield strength in both the directions. The properties are far higher than those of the samples printed compressed air.

- The flexural test results shown in Fig. 4, indicate an improvement of 11 %, and 54 % in longitudinal and transverse direction printed samples flexural modulus respectively. The Flexural strength comparison indicates in Fig.5, an increment of 113 %, and 153 % in the longitudinal and the transverse direction of printed samples respectively, which is a significant improvement in the bending strength.
- An improvement of 75.4 % and 37.7 % in the impact strengths of samples is achieved in longitudinal and transverse direction printed samples in 0 bar to 10 bar ambient pressure conditions in autoclave respectively (Fig. 6).
- The density test results in Table 2, indicate the increase in density of samples printed in longitudinal and transverse direction. The internal structures of specimens are more firmly packed and produced a dense grain structure and resistance to porosity. All together helps to increase strength and utmost void-free samples

1.8 Conclusions

Fig. 7 illustrates a pictorial view of the effect of autoclave pressure while printing on the consolidation of printing layers. The pressure gradient positively affects the layer consolidation and facilitates the better compaction of polymeric material.

The analysis of the results of the mechanical tests shows, that the pressure environment during 3D printing significantly improves the mechanical properties of the samples. The flexural strength increased almost 150 % in both transverse and longitudinal directions. In the longitudinal direction, improvement in flexural modulus is low in vertical but high in the transverse direction. In the impact test, the impact strength increased up to 80%. There is notable growth in tensile properties because of pressure conditions.

Fig. 7 explains the effect of autoclave pressure while printing on the consolidation of the layer printed. Three effects that individually be identified in future work are made responsible for this enormous increase in mechanical properties.

- Increase of shear strength between layers due to better consolidation.
- Shear strength between layers increases due to reduced distances between layers and hence increased secondary bonding.
- Drastic reduction in voids.

Some results have been published under "3D Printing Composites", a special issue of the Journal of Composites Science (ISSN 2504-477X) [12].

1.9 Perspectives

Currently, short fiber reinforced polyamide 6 is printed using the same experimental setup and the test results are yet to get. Furthermore, the 3D-printing process should be improved by using a miniature extruder for providing the molten thermoplastic material and a hot air gun to preheat the already printed material for better adhesion to the next filament. However, both devices have to be qualified for use under high ambient pressure.

  doi:10.5075/epfl-298799_978-2-9701614-0-0

2. Figures, Tables, and citations

Table 1. 3D Printer parameters while printing in an autoclave

	3D-printing at 0 bar	3D-printing at 5 bar	3D-printing at 10 bar
Nozzle Diameter	0.5mm	0.5mm	0.5mm
Printing Speed	150%	150%	150%
Layer Thickness	0.12mm	0.12mm	0.12mm
Hot end and Bed temperature	200°C and 50°C	205°C and 60°C	205°C and 60°C
Voltage Capacity of Printer	24V	25.7V	25.9V

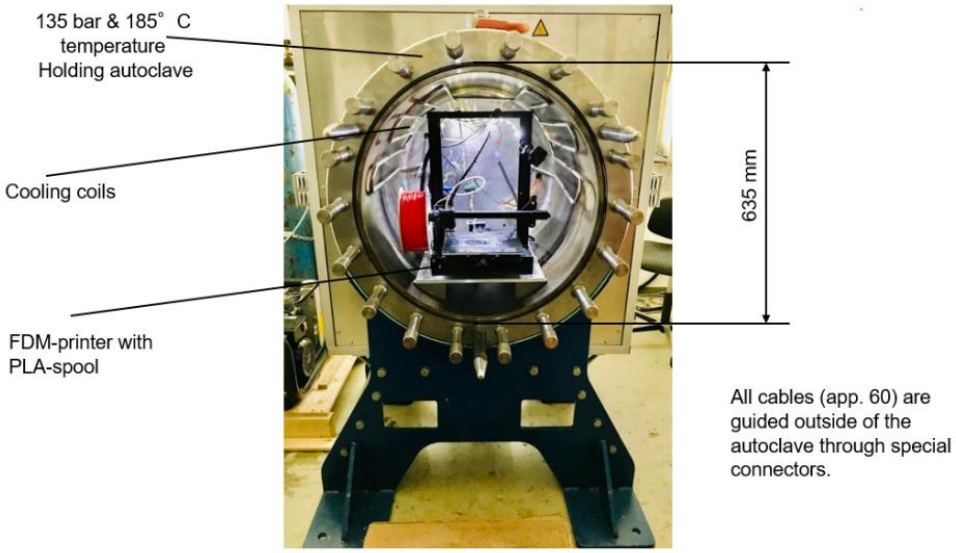

Figure 1. 3D-Printer setup in autoclave

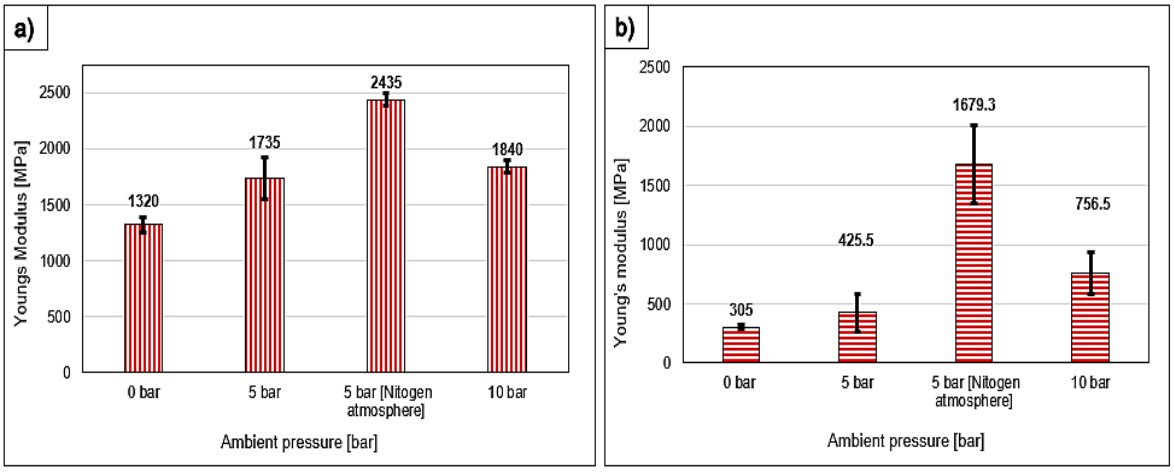

Fig. 2. Young´s modulus comparison of samples printed in different pressure conditions longitudinal (a) and transverse (b) to the printing direction

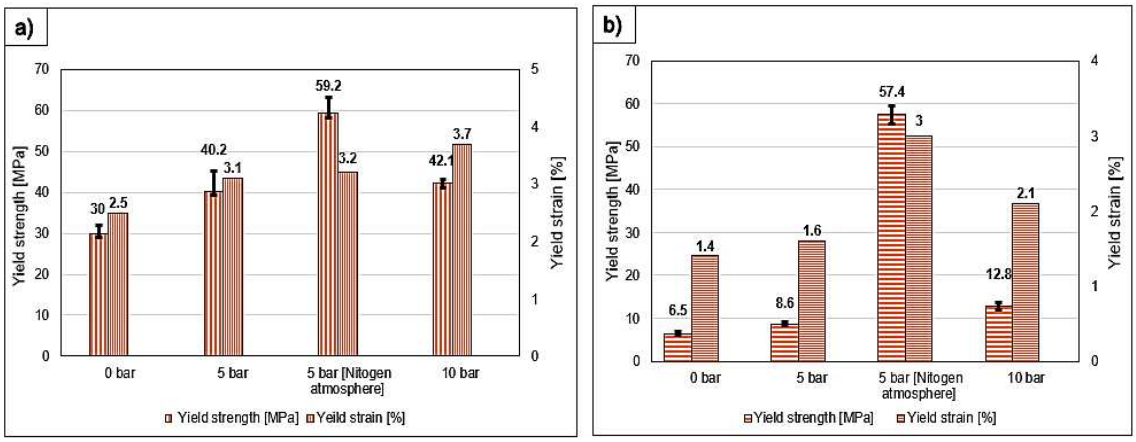

Fig. 3. Yield strength and Yield strain comparison of samples printed in different pressure conditions longitudinal (a) and (b) transverse to the printing direction

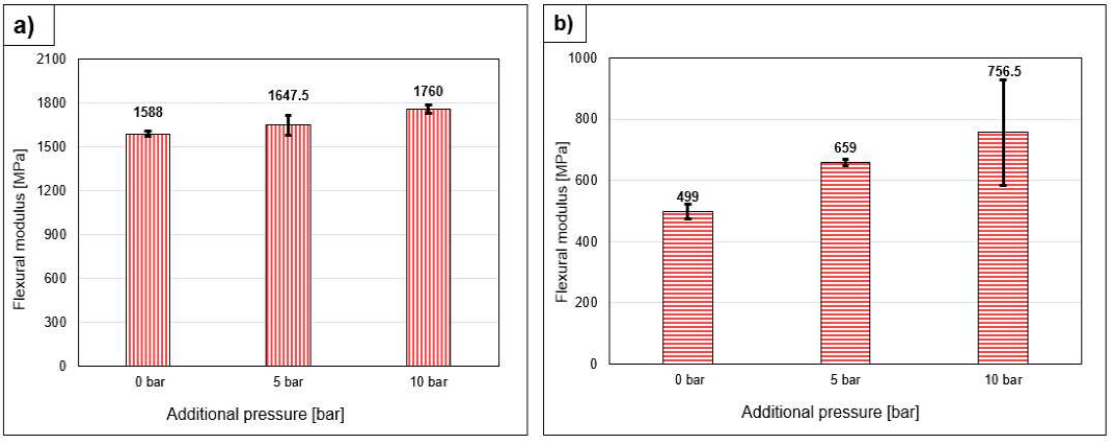

Fig. 4. Flexural modulus comparison of samples printed in different pressure conditions longitudinal (a) and (b) transverse to the printing

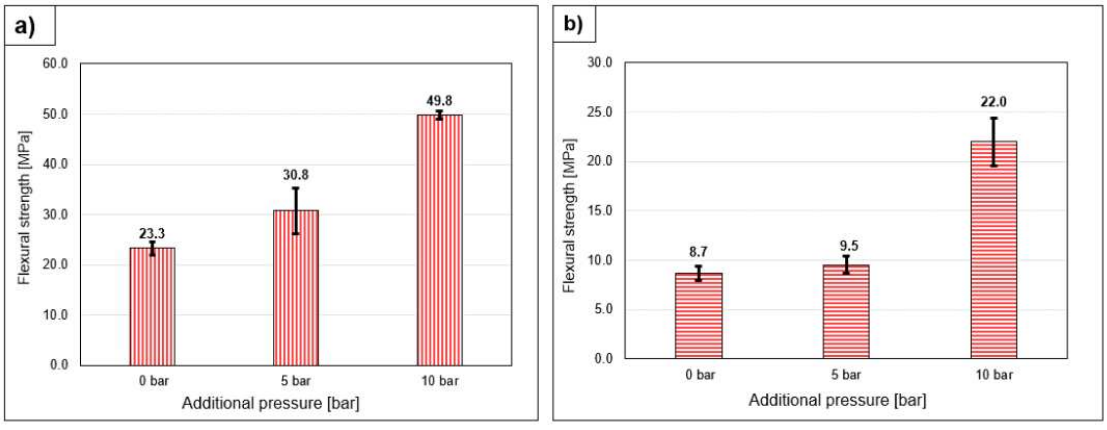

Fig. 5. Flexural strength comparison of samples printed in different pressure conditions longitudinal (a) and (b) transverse to the printing

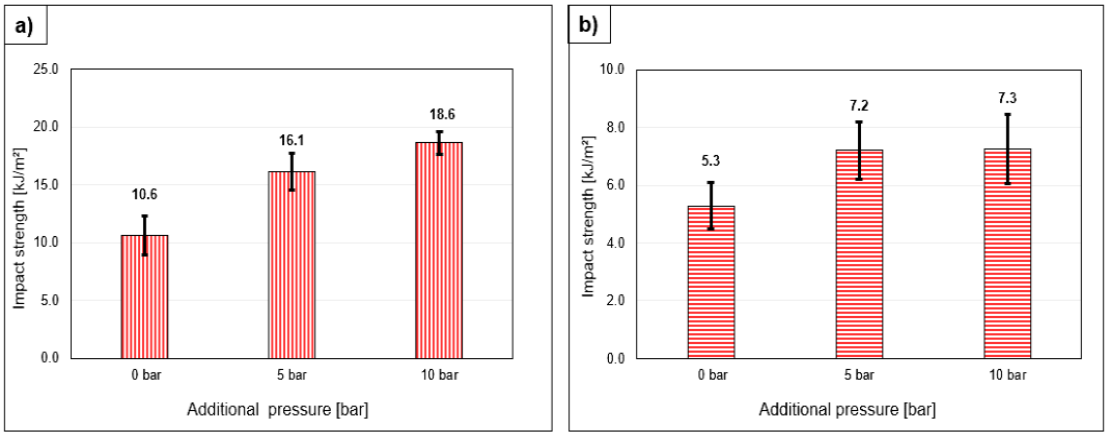

Fig. 6. Impact strength comparison of samples printed in different pressure conditions longitudinal (a) and (b) transverse to the printing

Table 1. 3D Printer parameters while printing in the autoclave

	3D-printing at 0 bar	**3D-printing at 5 bar**	**3D-printing at 10 bar**
Longitudinal printed samples (Average Density)	1.0765 gm/cm^3	1.1340 gm/cm^3	1.1439 gm/cm^3
Transverse printed sample's (Average Density)	1.0288 gm/cm^3	1.0735 gm/cm^3	1.0943 gm/cm^3

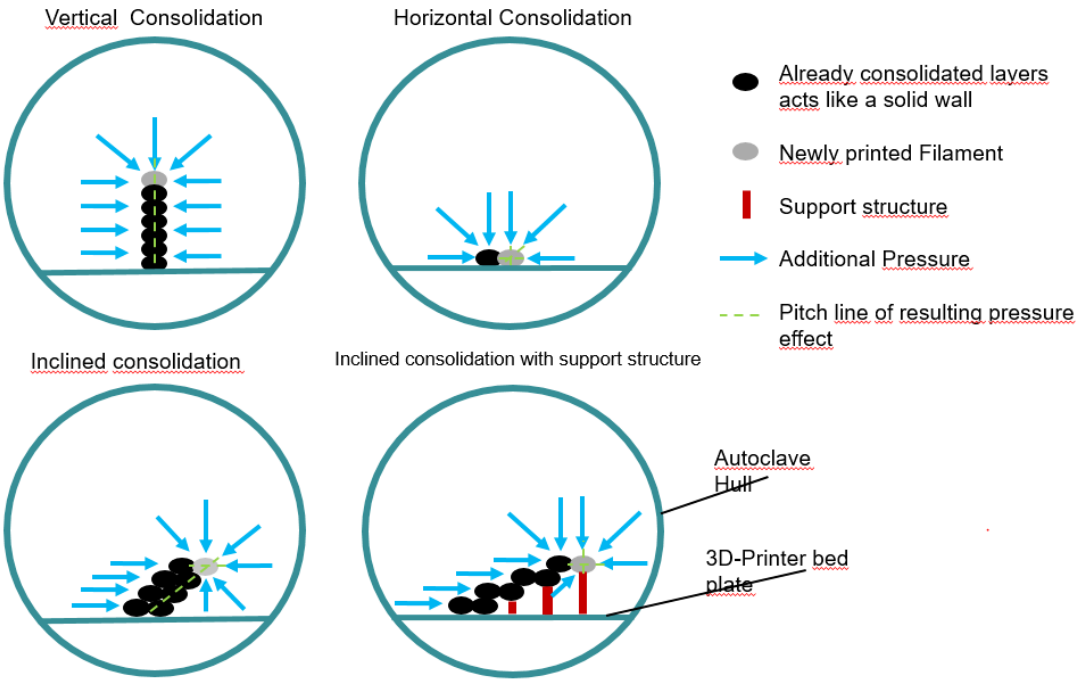

Fig. 7. Pressure gradient during FDM 3D-printing under ambient pressure 'p'

Acknowledgements

The authors would like to thank Hochschule Kaiserslautern for funding the project and providing laboratory equipment and its facilities at University of Applied Sciences Kaiserslautern, Germany & IKW.

3. References

1. Schirmeister CG, Hees T, Licht EH, Mülhaupt R. 3D printing of high-density polyethylene by fused filament fabrication. Addit. Manuf. 2019, 29, 152–159.
2. Zhao. Y, Chen Y, Zhou Y. Novel mechanical models of tensile strength and elastic property of FDM AM PLA materials: Experimental and theoretical analyses. Mater. Des. 2019, 181, 3–7.
3. Ngoa TD, Kashania A, Imbalzanoakate G, Nguyena T, Huib D. Additive manufacturing (3D printing): A review of materials, methods, applications and challenges. Compos. Part B 2018, 2, 56–67.
4. Ning F, Cong W, Qiu J, Wei J, Wang S. Additive manufacturing of carbon fiber reinforced thermoplastic composites using fused deposition modelling. Compos. Part B 2015, 80, 369–378.
5. Behalek L, Safka J, Seidl M, Habr J, Bobek J. Fused Deposition Modelling vs. Injection Molding: Influence of Fiber. MM Sci. J. 2018, 1, 1–5.
6. Zou R, Xia Y, Liu S, Hu P, Hou W, Hu Q, Shan C. Isotropic and anisotropic elasticity and yielding of 3D printed material. Compos. Part-B Eng. 2016, 99, 506–513.
7. Lederle F, Meyer F, Brunotte GP, Kaldun C, Hübner EG. Improved mechanical properties of 3D-printed parts by fused deposition modelling processed under the exclusion of oxygen. Progress. Addit. Manuf. 2016, 1, 3–7.
8. Butt J, Bhaskar R. Investigating the Effects of Annealing on the Mechanical Properties of FFF-Printed Thermoplastics. J. Manuf. Mater. Process. 2020, 4, 38.
9. Shaik YP, Schuster J, Chowdary R. Impact of 3D printing patterns and post-consolidation pressure on mechanical properties of FDM printed samples. Am. Res. J. Mater. Sci. 2020, 1, 1–10.
10. Shaik YP, Schuster J, Shaik A, Mohammed M, Katherapalli HR, Effect of Autoclave Pressure and Temperature on Consolidation of Layers and Mechanical Properties of Additively Manufactured (FDM) Products with PLA. J. Manuf. Mater. Process. 2021, 5, 114.
11. N.N. Creality Ender 3 V2. Creality, January 2020. Available online: https://www.creality.com/goods-detail/ender-3-v2-3d-printer
12. Shaik YP, Schuster J, Katherapalli HR, Shaik A. 3D Printing under High Ambient Pressures and Improvement of Mechanical Properties of Printed Parts. J. Compos. Sci. 2022, 6, 16.

  doi:10.5075/epfl-298799_978-2-9701614-0-0

ESTABLISHING SYNERGISTIC EFFECTS OF BN AND CNT ON THE THERMAL CONDUCTIVITY OF PEEK FILAMENTS FOR 3D PRINTING

Yunus Emre, Bozkurt[a,c], Alptekin, Yildiz[a,c], Ugur, Emanetoglu[c], Hulya, Cebeci[b,c],

a: Aviation Institute, Istanbul Technical University, Istanbul, 34469, Turkey
b: Department of Aeronautical Engineering, Istanbul Technical University, 34469, Istanbul, Turkey
c: Aerospace Research Center, Istanbul Technical University, Istanbul, 34469, Turkey
bozkurtyu@itu.edu.tr

Abstract: *Additive manufacturing (AM) is a novel technology for fabrication of the objects that may come in complex shapes. Fused filament fabrication (FFF) is one of the most widely used techniques to fabricate polymer composites with advantages such as cost efficiency, high speed, and simplicity. FFF technique suffers from mainly limited polymeric feedstock materials requiring suitable viscosity with limited functionality. Adding nanofillers to polymeric matrices to gain such multifunctional properties are alternative route for advanced applications. In here, polymer composites with thermally conductive fillers of BN and CNTs were explored in a semi-crystalline engineering thermoplastic polyether ether ketone (PEEK) matrix. The results presented that the thermal conductivity of neat PEEK composites increased from 0.32 W/mK to 1.56 W/mK with 40 wt.% BN fillers. Besides, the hybridization through 1 wt.% CNTs/30 wt.% BN filler addition enhanced thermal conductivity to 1.62 W/mK. Also, the composite filaments were successfully fabricated and 3D printed.*

Keywords: Fused Filament Fabrication; Thermal conductivity; Polyether ether ketone;

1. Introduction

The main aim of thermal management applications is to cool off electronic devices by dissipating the heat. One of the main components of the thermal management systems is heat exchangers which enable transferring of heat (1,2). The conventional heat exchangers have been fabricated using metals such as copper and aluminum. To meet the high demands of the electronic industry, the challenges that were arisen by conventional materials such as corrosion, heaviness should be overcome. Polymers are ideal candidates to defeat these challenges with their lightweight, corrosion resistance, and cost-efficiency, (3–5). However, polymers suffer from low thermal conductivity properties. Incorporating nano- or micro-fillers into polymers and dispersing them uniformly may help to overcome challenges arising from the low thermal conductivity of thermoplastics with a minimal weight penalty (6–8). To achieve high thermal conductivity in polymeric structures, various types of fillers such as metals (copper, silver, aluminum, gold, *etc*.) ceramics (aluminum nitride, boron nitride, silicon carbide), and carbon-based materials (carbon nanomaterials, graphene nanoplatelets) are used (9–11).

Additive manufacturing (AM) which is also known as three-dimensional (3D) printing or rapid prototyping (RP), is a novel technology for the fabrication of objects that may come in complex shapes. This method enables the fabrication of complex objects from the 3D model guided by computer-aided design (CAD) by usually adding materials layer by layer (12). Fused filament fabrication (FFF) is one of the most widely used techniques to fabricate polymer composites thanks to advantages such as cost efficiency, high speed, and simplicity. Thermoplastic polymers

  doi:10.5075/epfl-298799_978-2-9701614-0-0

such as polylactic acid (PLA), acrylonitrile butadiene styrene (ABS), polycarbonate (PC), polyetherimide (PEI), polyether ether ketone (PEEK), and polyphenylene sulfide (PPS) are commonly used as feedstock materials in the FFF technique (13–16). The production of 3D parts is completed by melting the polymers in the nozzle and depositing their layers on each other (16). The quality of the final product mainly depends on the processing parameters such as layer thickness, raster width, raster angle, and air gap (17). FFF technique suffers from mainly limited feedstock materials requiring suitable viscosity and limited functionality if fillers were not employed (16). Therefore, novel materials such as reinforced with fillers can be considered as a potential solution to these problems. The fabrication of thermally conductive filaments for the FFF has been studied by various researchers. Hwang et al. fabricated thermally conductive Cu/ABS filaments and investigated the effect of Cu content on different parameters. They achieved a 41% increase in thermal conductivity of ABS with the addition of 50 wt.% copper and reached 0.912 W/m K (18). In another study, Liu et al. investigated the behavior of thermal conductivity and coefficient of thermal expansion (CTE) of BN/TPU polymer composites in two directions as printing direction (PD) and thickness direction (TD) (19). The BN/TPU polymer composites were fabricated with various BN fractions by an internal mixer and twin-screw extruder processes, respectively. The CTE values in the PD decrease with the increasing BN loading with a negative CTE value of BN fillers along the in-lane direction. However, CTE values in the TD increased with the increasing BN concentration because of the high CTE value of BN filler along the out-line direction. The thermal conductivity behavior of BN/TPU composites differs based on whether printing or thickness directions are considered. Even though the thermal conductivity of the composites increased with the addition of BN in the TPU matrix, the increase in thermal conductivity in the PD was higher than that of in the TD. To assess the hybridization effect on the thermal conductivity, Lebedev et al. fabricated PLA matrix composite filaments reinforced with carbon nanotubes (CNTs) and graphite (G) for the FFF by the melt-compounding method. Thermal conductivity of PLA improved by more than 14 times and reached 2.73 W/mK from 0.193 W/mK with the incorporation of 30 wt.% G. Through these promising results, hybrid CNTs/G/PLA composites were fabricated. Thermal conductivity of the 1 wt.% CNTs/30 wt.% G/PLA composite was improved by approximately 40% and reached 3.8 W/mK (20).

In this study, PEEK was selected as the polymer material with its high mechanical properties, high service temperature, and corrosion resistance. Multiwalled carbon nanotubes (MWCNTs) and hexagonal boron nitride in micron sizes (h-BN) were selected as fillers having high thermal conductivities. Hence, BN/PEEK polymer composites and MWCNTs/BN/PEEK hybrid polymer nanocomposite filaments were fabricated. The morphology and thermal conductivity results of polymer composites were investigated using field emission scanning electron microscopy (FE-SEM) and laser flash method, respectively. The results showed that incorporation of 30 wt.% BN fillers into the PEEK matrix improved the thermal conductivity from 0.32 W/mK to 1 W/mK. When the hybridization process was carried out with CNTs and BN addition, the thermal conductivity of composites was increased to 1.62 W/mK for 1 wt.% CNTs/30 wt.% BN/PEEK. Also, 3D printing of these composites can be achieved at relatively high filler loadings compared to literature.

2. Experimental Approach

2.1 Materials

PEEK granules were obtained from Victrex (PEEK151G) as a matrix material with a density of 1.3 g/cm3, glass transition temperature (T_g) of 143 ℃, and melting temperature (T_m) 343 ℃. PEEK is a semi-crystalline thermoplastic polymer and is compatible with melt-processing and FFF. BN supplied from Civelek Porselen, exhibits a particle size between 4 and 10 µm, and a purity of 99.5%. CNTs were purchased from Nanokomp (industrial-scale multi-walled CNTs with carbon purity: min. 90 %, diameter: 5–15 nm, length: 1.5–2 µm).

2.2 Fabrication of BN/PEEK and CNTs/BN/PEEK Composite Filaments

BN/PEEK filaments with 30 wt.% and 40 wt.% BN fractions and CNTs/BN/PEEK filaments with 1 wt.% CNTs/30 wt.% BN and 1 wt.% CNTs/40 wt.% BN fractions were fabricated by melt compounding without using any solvents or additives. The melt compounding process was carried out by a twin-screw extruder. PEEK granules were dried before the extrusion process in an oven at 150 ℃ for overnight to remove moisture from granules. Then the granules and the fillers were fed through the main and side feeders, respectively as illustrated in Fig. 1. The resulting granules obtained from the twin-screw extruder process were fed to the single screw extruder through the main feeder to fabricate BN/PEI and hybrid CNT/BN/PEI composite filaments with a standard diameter of 1.75 mm.

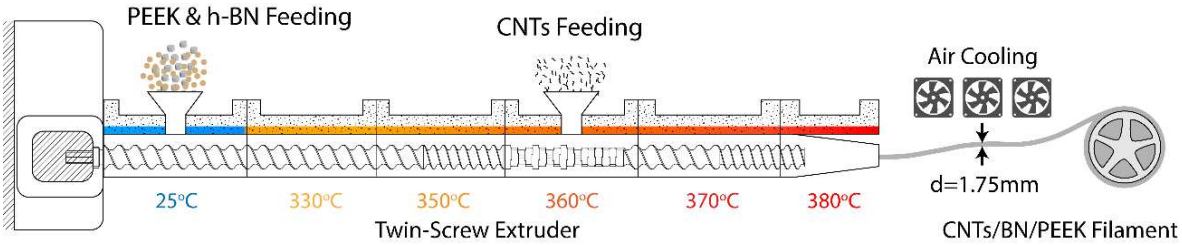

Figure 1. The fabrication process for PEEK matrix polymer composites by melt-processing.

2.3 Characterization

2.3.1 Thermogravimetric analysis

The thermal decomposition behaviors of neat PEEK and BN/PEEK and CNTs/BN/PEEK composites were investigated using a TA Instrument-TGA55 thermogravimetric analyzer at a heating rate of 10 ℃/min under the N_2 flow of 2 mL/min within a temperature range of 30–850 ℃. The measurements were conducted using samples with varying weights between 5 and 10 mg.

2.3.2 Morphological investigations

The surface morphologies of neat PEEK, BN/PEEK, and CNTs/BN/PEEK composites were observed using a field emission scanning electron microscope (FEG-SEM). SEM analysis was performed by using SEM, Quanta FEG 450 operating at 15 keV. Before SEM measurements, specimens were fractured in cryogenic liquid and coated with a thin layer of gold-platinum alloy. Thereafter, samples were placed in a vacuum chamber to focalize the electron beam on the fractured edge.

  doi:10.5075/epfl-298799_978-2-9701614-0-0

2.3.3 Thermal conductivity measurements

The through-plane thermal conductivity measurements were carried out by laser flash method (Netzch LFA 457 Microflash). The thermal conductivity (k) was calculated using the Eq. (1),

$$k = \alpha \times \rho \times C_p \quad (1)$$

where k, α, ρ, and C_p, are the thermal conductivity (W/mK), thermal diffusivity (mm^2/s), density (kg/m^3), and specific heat capacity (J/kg) of the composite, respectively. The hot-pressed composites were cut into samples of 12.5 mm in diameter, 2 mm in thickness and placed onto a metal holder to measure the thermal conductivity. All measurements were carried out for five times of each sample.

3. Results and Discussion

3.1 Thermal Analysis

Thermogravimetric analysis was performed to investigate the effect of BN and CNTs fillers in the PEEK matrix. Figure 2 presents the TGA curves of the neat PEEK, BN/PEEK, and CNTs/BN/PEEK composites. The onset degradation temperatures were detected at ca. 570 °C for neat PEEK and PEEK matrix composites. The incorporation of BN and CNTs fillers did not affect significantly onset temperatures. Besides, CNTs and BN addition did not exhibit a significant change in T_5 and T_{15} as shown in Table 1.

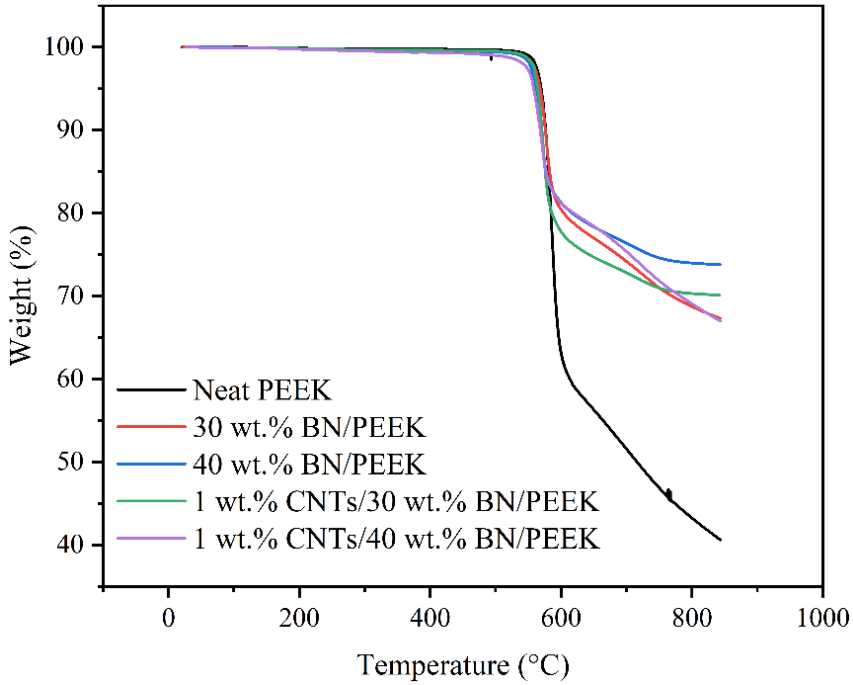

Figure 2. Thermogravimetric analysis of neat PEEK and PEEK composites.

Table 1: TGA results of neat PEEK and PEEK composites.

Sample	Weight loss temperature (°C)	
	T_5	T_{15}
Neat PEEK	560.9	572.3
30 wt.% BN/PEEK	568.2	582.5
40 wt.% BN/PEEK	561.3	577.4
1 wt.% CNTs/30 wt.% BN/PEEK	564.3	575.8
1 wt.% CNTs/40 wt.% BN/PEEK	558.2	576.7

3.2 Morphological Investigations

The SEM images of neat PEEK, BN/PEEK composites with 30 and 40 wt.% fractions and CNTs/BN/PEEK hybrid nanocomposites with 1 wt. CNTs/30wt.% and 1 wt.%/40 wt.% BN fractions were shown in Fig. 3. At loadings higher than 30 wt.% fillers, BN/PEEK and CNTs/BN/PEEK polymer composites demonstrated that with the increasing concentration, BN and CNTs particles were packed densely such as decreasing the particle-particle distance which leads to the formation of thermally conductive pathways for effective phonon transport (Fig. 3). Hence, the increased thermal conductivity can be attributed to decreasing distance between filler and matrix in polymer composites.

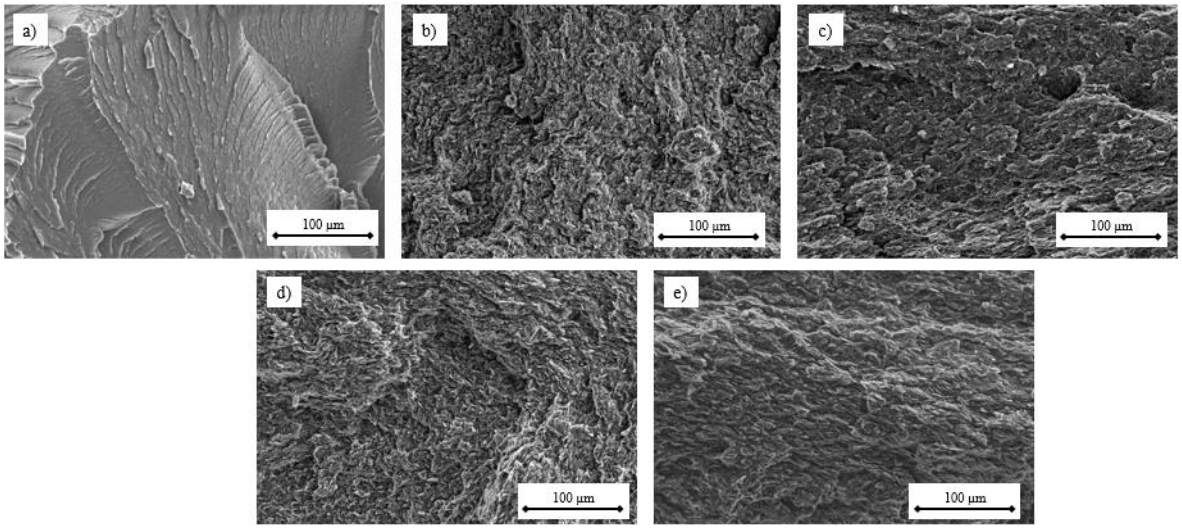

Figure 3. SEM images of a) 30 wt.% BN/PEEK, b) 40 wt.% BN/PEEK, c) 1 wt.% CNTs/30 wt.% BN/PEEK and d) 1 wt.% CNTs/40 wt.% BN/PEEK composites.

3.3 Thermal Conductivity

As already presented in earlier studies (21–24) the thermal conductivity of BN was much higher than PEEK; therefore, the addition of BN fillers into the PEEK matrix increased the thermal conductivity of BN/PEEK composites. Table 2 shows the thermal conductivities of BN/PEEK

composites. The thermal conductivity of the neat PEEK was obtained as 0.32 W/mK, which is similar to given in the product technical datasheet. When the BN concentration reached 30 and 40 wt.%, the thermal conductivities of the composites were increased to 1.56 W/mK, respectively. The increase in thermal conductivity can be associated with the formation of an effective thermal conductivity network through establishing BN-BN interaction. The 1 wt.% CNTs addition to 30 wt.% BN/PEEK composite showed a clear hybridization effect and increased the thermal conductivity up to 1.62 W/mK. However, 1 wt.% CNTs addition to 40 wt.% BN/PEEK composite did not lead to an increase in thermal conductivity. The results can be related to the high viscosity resulting with BN concentration when 40 wt.% was added. Thus, wettability and dispersion of CNTs into the matrix became more difficult and the expected increase in thermal conductivity could not be achieved for 1 wt.% CNTs/40 wt.% BN/PEEK composite.

Table 2: Thermal conductivity results of neat PEEK and PEEK composites.

Sample	Thermal Conductivity (W/mK)
Neat PEEK	0.32 ±0.01
30 wt.% BN/PEEK	1±0.06
40 wt.% BN/PEEK	1.56±0.03
1 wt.% CNTs/30 wt.% BN/PEEK	1.62±0.05
1 wt.% CNTs/40 wt.% BN/PEEK	1.56±0.01

4. Conclusion

In conclusion, BN/PEEK composites were produced using 30 percent and 40 percent BN additives. In addition, CNTs/BN fillers were incorporated into the Peek matrix at a rate of 1%/30% and 1%/40%, respectively, using the hybridization technique. All of the composites were fabricated with a twin-screw extruder with a screw diameter of 12 mm and a L/D ratio of 22. The thermal conductivity of neat PEEK composites increased from 0.32 W/mK to 1.56 W/mK with 40 wt.% BN fillers. Besides, the hybridization through 1 wt.% CNTs/30 wt.% BN filler addition enhanced thermal conductivity up to 1.62 W/mK. Also, the incorporation of BN and CNTs into the PEEK matrix did not lead to a serious change in thermal decomposition temperatures. These polymer composites are suitable candidates for 3D printing and injection molding processes.

Acknowledgments

The authors are grateful to the Boeing Company, United States for financial support and technical discussions with the project of 2019000191. Yunus Emre Bozkurt is also thankful to TUBITAK 2224-A Grant Program for Participation in Scientific Meetings Abroad for covering the ECCM 20 travel, participation, and accommodation expenses.

  doi:10.5075/epfl-298799_978-2-9701614-0-0

References

1. Hussain ARJ, Alahyari AA, Eastman SA, Thibaud-Erkey C, Johnston S, Sobkowicz MJ. Review of polymers for heat exchanger applications: Factors concerning thermal conductivity. Appl Therm Eng [Internet]. 2017;113:1118–27. Available from: http://dx.doi.org/10.1016/j.applthermaleng.2016.11.041

2. Lu MC. A synergistic model for thermal conductivity with hybrid fillers in polymeric matrix composites. Annu IEEE Semicond Therm Meas Manag Symp. 2016;Part F1214:151–6.

3. Qin Y, Li B, Wang S. Experimental investigation of a novel polymeric heat exchanger using modified polypropylene hollow fibers. In: Industrial and Engineering Chemistry Research. American Chemical Society; 2012. p. 882–90.

4. T'Joen C, Park Y, Wang Q, Sommers A, Han X, Jacobi A. A review on polymer heat exchangers for HVAC&R applications. Int J Refrig [Internet]. 2009;32(5):763–79. Available from: http://dx.doi.org/10.1016/j.ijrefrig.2008.11.008

5. Leung SN. Thermally conductive polymer composites and nanocomposites: Processing-structure-property relationships. Vol. 150, Composites Part B: Engineering. Elsevier Ltd; 2018. p. 78–92.

6. Hussain ARJ, Alahyari AA, Eastman SA, Thibaud-Erkey C, Johnston S, Sobkowicz MJ. Review of polymers for heat exchanger applications: Factors concerning thermal conductivity. Vol. 113, Applied Thermal Engineering. Elsevier Ltd; 2017. p. 1118–27.

7. Mehra N, Mu L, Ji T, Yang X, Kong J, Gu J, et al. Thermal transport in polymeric materials and across composite interfaces. Vol. 12, Applied Materials Today. 2018. p. 92–130.

8. Chen H, Ginzburg V V., Yang J, Yang Y, Liu W, Huang Y, et al. Thermal conductivity of polymer-based composites: Fundamentals and applications. Progress in Polymer Science. 2016.

9. Lee GW, Park M, Kim J, Lee JI, Yoon HG. Enhanced thermal conductivity of polymer composites filled with hybrid filler. Compos Part A Appl Sci Manuf. 2006 May;37(5):727–34.

10. Ngo IL, Jeon S, Byon C. Thermal conductivity of transparent and flexible polymers containing fillers: A literature review. Int J Heat Mass Transf [Internet]. 2016;98:219–26. Available from: http://dx.doi.org/10.1016/j.ijheatmasstransfer.2016.02.082

11. Burger N, Laachachi A, Ferriol M, Lutz M, Toniazzo V, Ruch D. Review of thermal conductivity in composites: Mechanisms, parameters and theory. Prog Polym Sci [Internet]. 2016;61:1–28. Available from: http://dx.doi.org/10.1016/j.progpolymsci.2016.05.001

12. Rengier F, Mehndiratta A, Von Tengg-Kobligk H, Zechmann CM, Unterhinninghofen R, Kauczor HU, et al. 3D printing based on imaging data: Review of medical applications. Vol. 5, International Journal of Computer Assisted Radiology and Surgery. Springer Verlag; 2010. p. 335–41.

13. Valino AD, Dizon JRC, Espera AH, Chen Q, Messman J, Advincula RC. Advances in 3D printing of thermoplastic polymer composites and nanocomposites. Vol. 98, Progress in Polymer Science. Elsevier Ltd; 2019.

14. De Leon AC, Chen Q, Palaganas NB, Palaganas JO, Manapat J, Advincula RC. High performance polymer nanocomposites for additive manufacturing applications. Vol. 103, Reactive and Functional Polymers. 2016. p. 141–55.

15. Mulholland T, Falke A, Rudolph N. Filled Thermoconductive Plastics for Fused Filament Fabrication [Internet]. [cited 2020 Mar 22]. Available from: www.functionalize.com

16. Wang X, Jiang M, Zhou Z, Gou J, Hui D. 3D printing of polymer matrix composites: A review and prospective. Compos Part B Eng [Internet]. 2017;110:442–58. Available from: http://dx.doi.org/10.1016/j.compositesb.2016.11.034

17. Sood AK, Ohdar RK, Mahapatra SS. Parametric appraisal of mechanical property of fused deposition modelling processed parts. Mater Des. 2010 Jan;31(1):287–95.

18. Hwang S, Reyes EI, Moon K sik, Rumpf RC, Kim NS. Thermo-mechanical Characterization of Metal/Polymer Composite Filaments and Printing Parameter Study for Fused Deposition Modeling in the 3D Printing Process. J Electron Mater [Internet]. 2015 Mar 29 [cited 2020 Mar 22];44(3):771–7. Available from: http://link.springer.com/10.1007/s11664-014-3425-6

19. Liu J, Li W, Guo Y, Zhang H, Zhang Z. Improved thermal conductivity of thermoplastic polyurethane via aligned boron nitride platelets assisted by 3D printing. Compos Part A Appl Sci Manuf [Internet]. 2019;120(October 2018):140–6. Available from: https://doi.org/10.1016/j.compositesa.2019.02.026

20. Lebedev SM, Gefle OS, Amitov ET, Berchuk DY, Zhuravlev D V. Poly(lactic acid)-based polymer composites with high electric and thermal conductivity and their characterization. Polym Test. 2017 Apr 1;58:241–8.

21. Zhou W, Qi S, Li H, Shao S. Study on insulating thermal conductive BN/HDPE composites. Thermochim Acta. 2007;452(1):36–42.

22. Che J, Jing M, Liu D, Wang K, Fu Q. Largely enhanced thermal conductivity of HDPE/boron nitride/carbon nanotubes ternary composites via filler network-network synergy and orientation. Compos Part A Appl Sci Manuf [Internet]. 2018;112(May):32–9. Available from: https://doi.org/10.1016/j.compositesa.2018.05.016

23. Zhang X, Shen L, Wu H, Guo S. Enhanced thermally conductivity and mechanical properties of polyethylene (PE)/boron nitride (BN) composites through multistage stretching extrusion. Compos Sci Technol [Internet]. 2013;89:24–8. Available from: http://dx.doi.org/10.1016/j.compscitech.2013.09.017

24. Gu J, Guo Y, Yang X, Liang C, Geng W, Tang L, et al. Synergistic improvement of thermal conductivities of polyphenylene sulfide composites filled with boron nitride hybrid fillers. Compos Part A Appl Sci Manuf. 2017;95:267–73.

INFLUENCE OF PRE-CURING STAGE IN ADDITIVE MANUFACTURING OF ADVANCED THERMOSETTING COMPOSITES

Francesco, Taddei[a], Michel, Barbezat[a], Enrico, Troiani[b], Giacomo, Struzziero[a]

a: Laboratory for Mechanical Systems Engineering, Swiss Federal Laboratories for Materials Science and Technology (Empa), Überlandstrasse 129, 8600 Dübendorf, Switzerland (first author's email: francesco.taddei@empa.ch)
b: Department of Industrial Engineering DIN, University of Bologna, Via Fontanelle 40, 47121 Forlì, Italy

Abstract: *The arising of cure-related defects during manufacturing of thermosetting composites and their hardly predictable effect on mechanical-performance is often cause for part rejection, which is detrimental for both cost and sustainability. Additive Manufacturing (AM) of continuous fibre-reinforced thermosets is envisaged to bring significant benefits in terms of reducing temperature overshoot, and consequently residual stresses. The work investigates the influence of the introduction of a pre-curing phase upon the exothermic overshoot and the defects induced during deposition of pre-cured tows (i.e. microbuckling). A Finite Element Analysis (FEA) addressing the cure simulation has been developed, and pre-cured specimens have been tested. The findings point out that a pre-cure level between 20% and 30% reduces the temperature overshoot within the laminate by 90%, generating in-plane waviness with a severity that should not compromise its performance.*

Keywords: Additive Manufacturing; residual stresses; exothermic overshoot; pre-curing; in-plane waviness

1. Introduction

Composite materials have considerably expanded their applications due to their excellent mechanical performance together with lightweight. Nevertheless, the high non-linearity of the cure stage often introduces unexpected defects (i.e. thermal gradients, residual stresses, matrix cracking) which undermine part quality and lead to part rejection. Due to the low thermal conductivity through-thickness, the scenario worsens for thicker parts [1-4].

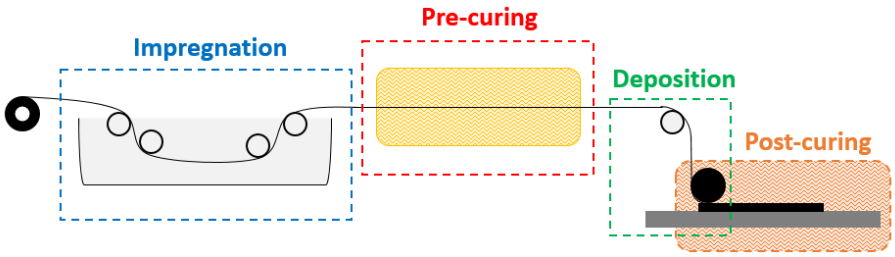

Figure 1. AM process scheme

Additive curing of Carbon/Epoxy composites can strongly reduce the exothermic overshoot during cure and the related residual stresses [5,6]. The addition of a pre-curing stage between the impregnation and deposition units (Fig. 1) shows the potential to further exploit these benefits, allowing for the manufacturing of high-quality thick components and for the design of

  doi:10.5075/epfl-298799_978-2-9701614-0-0

more aggressive cure cycles with the consequent reduction in process time. However, the deposition of pre-cured tows might induce other stresses inside the material that could result in phenomena like microbuckling [7,8]. This work investigates the twofold influence of pre-curing upon exothermic overshoot and deposition induced defects.

2. Materials and methodology

2.1 Resin system characterization

The resin under characterisation is a system composed of hot-melt epoxy resin XB3515, hardener paste Aradur® 1571 and Accelerator 1573 [9]. Characterization of the cure kinetics and resin specific heat was performed via Differential Scanning Calorimetry (DSC) in isothermal (*90°C*, *100°C*, *110°C*, *120°C*, *140°C*), dynamic (*1°C/min*, *2°C/min*, *10°C/min*, *50°C/min*) and temperature-modulated scans (*3°C/min* with a modulation amplitude of *1°C* every *60 s*) [10,11]. The gel point was estimated using oscillatory mode in a rheometer during isothermal tests with frequencies of *0.5 Hz* and *1 Hz* and temperatures of *100°C*, *110°C*, *120°C* [11]. An autocatalytic model with a diffusion term in Eq. (1) was used to fit experimental data. The glass transition was modelled using the DiBenedetto curve of Eq. (2). Finally, Eq. (3) expresses the specific heat capacity as a function of temperature and degree of cure.

$$\frac{d\alpha}{dt} = \frac{A\cdot\exp(-\frac{E}{R\cdot T})}{1+\exp[C(\alpha-(\alpha_C+\alpha_T\cdot T))]}\alpha^m(1-\alpha)^n \tag{1}$$

$$T_g = T_{g_0} + \frac{(Tg_\infty - Tg_0)\cdot\lambda\cdot\alpha}{1-(1-\lambda)\cdot\alpha} \tag{2}$$

$$C_p = C_r + C_{r_T}\cdot T + \frac{Cg-Cr-Cr_T\cdot T}{1+\exp(C(T-Tg-\sigma-\sigma_T\cdot T))} \tag{3}$$

Where $d\alpha/dt$ is the reaction rate, α the degree of cure, T the temperature, n the 1st reaction order, m the 2nd reaction order, A the pre-exponential Arrhenius factor, E the activation energy, C the coefficient controlling the breadth of the transition, α_C the coefficient governing the chemical-controlled part of the reaction, α_T the coefficient governing the diffusion-controlled part of the reaction, Tg is the glass transition temperature, Tg_0 the glass transition temperature for the uncured resin, Tg_∞ the glass transition temperature for the fully cured material, λ a fitting parameter controlling the convexity of the non-linear regression, C_p is the specific heat, C_r and C_g are respectively the intercepts in the rubbery and glassy state, Cr_T controls the dependence on temperature in the rubbery state, σ, C and σ_T are the parameters governing respectively the position, breadth and temperature dependence of the specific heat transition from rubbery to glassy state.

2.2 Cure simulation

A 1D Heat Transfer (HT) model is built in *Abaqus/CAE* with user-subroutines [1,3,12], governed by the energy balance in Eq. (4).

$$\rho_c C_p \frac{\partial T}{\partial t} = \left(1-v_f\right)\rho_r H_{tot}\frac{d\alpha}{dt} + \nabla\cdot(\overline{K}\,\nabla T) \tag{4}$$

Where H_{tot} is the total heat of reaction and K is the thermal conductivity matrix. The thermal conductivity and thermal properties of the composite have been computed using the laws and the rule of mixtures reported in [3]. The geometry is modelled as a squared-base solid with

  doi:10.5075/epfl-298799_978-2-9701614-0-0

dimensions *10x10x14.5 mm*, representing the central region of the laminate, and partitioned along the vertical direction in *80* eight-node linear brick elements. For the validation of the model, the temperature profiles recorded on top and at the bottom of the laminate (see Section 2.3) are used as boundary conditions, while the subroutines FILM and DISP are used in all the other simulations. The initial conditions, in particular degree of cure and temperature, are defined using SDVINI. The convection coefficient for the air in the oven is estimated as $h_{conv} = 43$ by tuning it so that the model matches as best as possible the measurement on the top of the laminate. On the sides, insulation is set as a boundary condition (Fig. 2). Sub-material thermal properties and their evolution are implemented in the subroutine UMATHT.

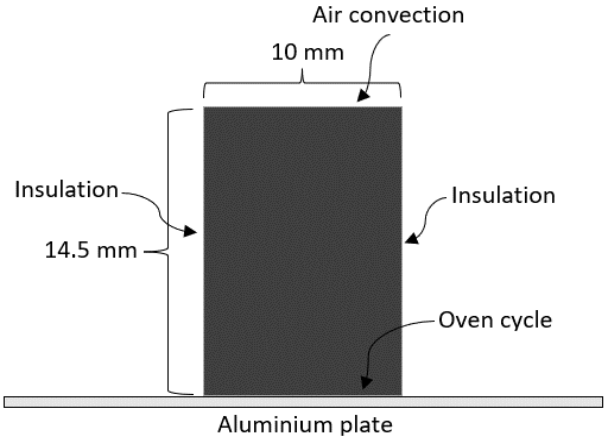

Figure 2. Schematic of geometry and boundary conditions

Once the cure model is built and validated, it can be used to simulate the thermal behaviour of an additively manufactured thermosetting laminate for a certain length (*100 mm*), number of layers (*80* layers of *0.181 mm* each), level of pre-cure (*0-50%*) and printing speed (*600 mm/min*). The model assumes that the HT analysis starts when all the layers have been deposited. However, the initial degree of cure of each layer is estimated through the cure kinetics with a temperature of *120°C,* for duration according to the printing speed selected and thickness position, and fed to the solver as initial condition. Then, the cure is completed by implementing the Manufacturer Recommended Cure Cycle (MRCC).

2.3 Laminates manufacturing

Two UD laminates were manufactured from *80* layers of prepreg strips (*50x100 mm*) for validation of the HT model. The temperature was recorded during every process phase by inserting thermocouples at the bottom, in the middle and on top. One laminate was subjected to the MRCC and its final thickness was *14.5 mm* in the central region where thermocouples were placed. The second laminate was cured with a two-stage procedure: it consisted of pre-curing two sub-laminates made of *40* layers without vacuum bagging up to *26%* and *42%* degree of cure; afterwards, the less cured part was put on top of the other one, and their cure was progressed under vacuum conditions using the MRCC.

2.4 Deposition analysis

Metallic fixtures for a bending test were designed as shown in Fig. 3 to mimic the deposition process. Their geometry mimics a deposition from the vertical direction onto a horizontal flat mould, namely a deflection of *90°*, for four different punch diameters (*20*, *30*, *40*, *50 mm*). Single

  doi:10.5075/epfl-298799_978-2-9701614-0-0

strips of prepreg were used as specimens for the test (thickness about *0.195 mm*, length *50-70 mm*, width *5-8 mm*). They were pre-cured in the oven without vacuum to achieve the four different levels of conversion *22*, *31*, *41* and *52%*. The bending test was run at a temperature *20°C* higher than the glass transition temperature. After reaching thermal stability and homogeneity, the unclamped specimen was bent at a down speed of *2 mm/min*. Afterwards, the chamber was cooled below the glass transition temperature, the punch head was raised, and the specimen removed. Because of the slowness of the reaction at the testing temperatures, the degree of cure was reasonably assumed constant throughout the experiment. Four specimens were obtained for each of the *16* cases.

Figure 3. Bending setup

The surface of the specimens was inspected using optical microscopes and pictures were taken. The analysis revealed the presence of in-plane waviness, which was geometrically characterised via the three parameters depicted in Fig. 4. Measured parameters are representative of a set of waves with similar geometry, meaning that each value catches the shape of a group of adjacent waves. Since edges are more subjected to defects related to cutting and handling of the material, any defect close to them was ignored.

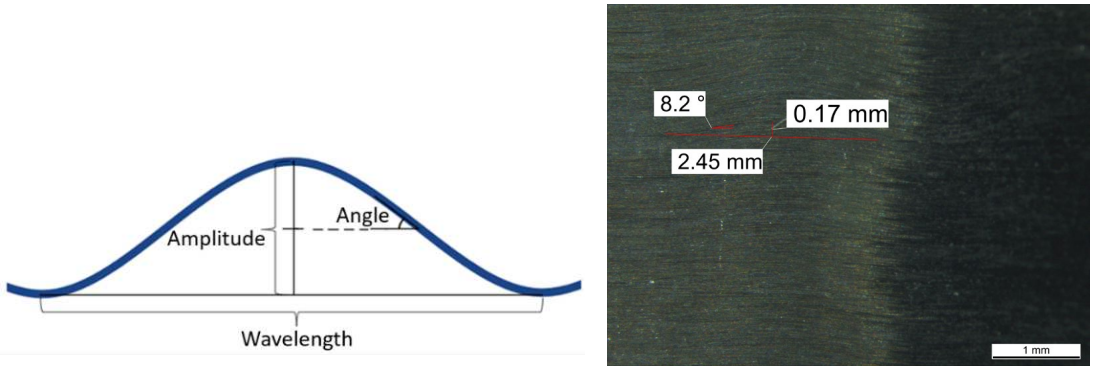

Figure 4. Geometrical parameters of waves

3. Results and discussion

3.1 Resin characterisation

The parameters of the materials models to fit the experimental data for cure kinetics, DiBenedetto and specific heat are reported in Tab. 1. Two practical rules are commonly used to define gelation: the point where dynamic viscosity reaches *10 kPa·s* or where storage and loss moduli cross over [11]. In this study, both methods show similar results and gelation occurs at an averaged degree of cure of *48% ± 7%*.

  doi:10.5075/epfl-298799_978-2-9701614-0-0

Table 1: Parameters of the models used for resin characterisation

Parameter	Value	Unit	Parameter	Value	Unit
n	*0.915*	/	C_r	*1.588*	J g^{-1} K^{-1}
m	*0.564*	/	Cr_T	*0.002575*	J g^{-1} K^{-2}
A	*2.1E+10*	s^{-1}	C_g	*1.485*	J g^{-1} K^{-1}
E	*96874*	J mol^{-1}	C	*0.171*	K^{-1}
C	*33.54*	/	σ	*71.82*	K
α_C	*-2.613*	/	σ_T	*-0.7458*	/
α_T	*0.00913*	K^{-1}			
Tg_0	*2*	°C			
Tg_∞	*141*	°C			
λ	*0.48*	/			

3.2 Exothermic overshoot and Finite Element Analysis

The exothermic overshoot was computed from temperature measurements during the cure of the two laminates manufactured in this project. Its maximum was recorded between the middle and the bottom and was equal to *10.0°C* for the standard cure case, while it was equal to *6.4°C* for the multistage cure (reduction of *36%*). These measurements were compared to simulated values in order to validate the HT analysis (in Fig. 5 the comparison in the standard cure case at the centre location of the laminate). The results of the simulations are reported in Fig. 6. The reduction in percentage is quantified using as reference the simulated temperature difference between the middle and the bottom of a standard manufactured laminate without pre-curing at the occurrence of the maximum overshoot, which is represented by the contour maps in Fig. 7. The use of fixed temperature boundary conditions for the nodes in touch with the tool explains why the overshoot in Fig. 7 differs from measured values.

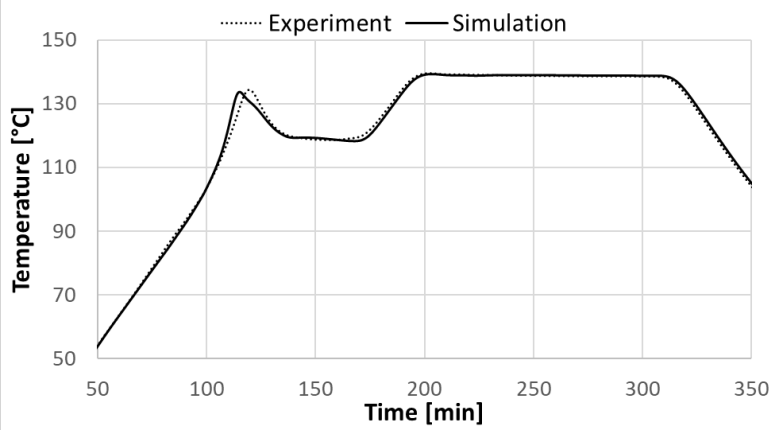

Figure 5. Temperature evolution comparison at the centre of the laminate between measurements and FE prediction

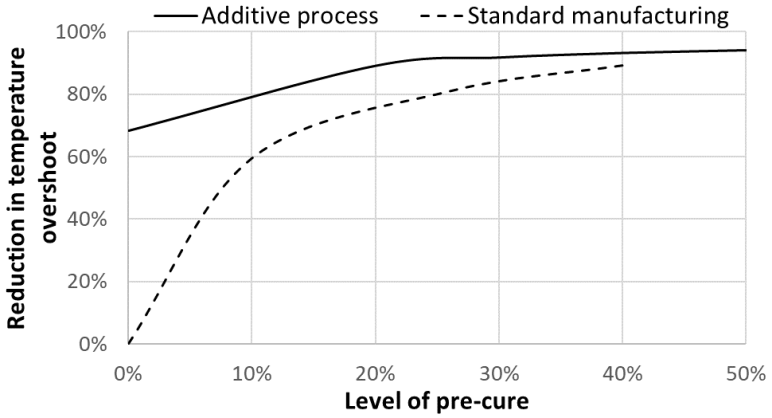

Figure 6. Reduction in temperature overshoot due to pre-cure in AM

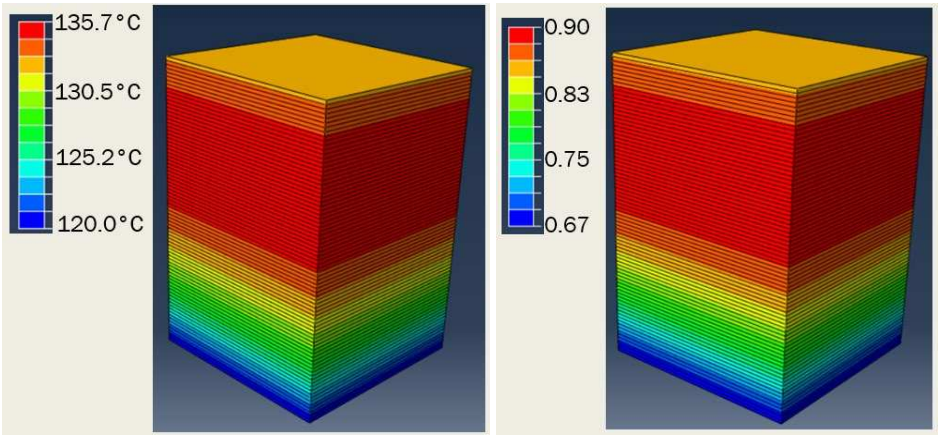

Figure 7. Through thickness results when MRCC is applied: Temperature (left); Degree of cure (right).

From Fig. 6 it can be inferred that the temperature overshoot is strongly reduced by using an additive process. Since the material is being deposited while curing, the process effectively deals with a fraction of the entire thickness resulting in lower temperature overshoot. Moreover, an increasing level of pre-cure translates into a weaker exothermic phenomenon for both processes since chemical potential has been partially exhausted in the pre-cure phase. Finally, beyond *25%* pre-cure level benefits in temperature overshoot reduction become less significant. At the same time, a higher pre-cure level is anticipated to introduce more defects upon deposition, therefore a trade-off is necessary.

3.3 Defects from deposition – in-plane waviness

Optical microscopy revealed the presence of in-plane waviness on the surface of the specimens, the source of which is to be found in the compressive stresses generated during curing and bending that exceed the critical microbuckling stress [7,8]. This analysis assumes the waviness as fully developed along the surface, which makes the approach strongly conservative. The outcomes of the geometrical characterization are plotted against the degree of cure in Fig. 8 using the average value of the four specimens available for each condition. The plot shows no trend between the severity of the waves and the dimension of the punch; this means that there is a margin of freedom to vary that parameter since a smaller compaction roller is more suitable during the printing of concave and complex shapes. On the other side, there is a relationship

  doi:10.5075/epfl-298799_978-2-9701614-0-0

between the degree of cure and the severity of the waviness. Waves become shorter and wider if the degree of cure increases, or equivalently if the level of pre-cure is higher. Below gelation (*48%* for the system under study) stresses are able to relax. The increasing severity of the waviness shown in Fig. 8 reflects the increasing difficulty of the resin to relieve stresses as gelation is approaching. Another phenomenon leading to this trend is that curing in its first phase is chemical-dominated, therefore compressive stresses induced by resin shrinkage are more pronounced if the cure has lasted longer. Finally, the mismatch in coefficient of thermal expansion (CTE) between fibres and resin during heating and cooling phases generates stresses while testing the specimens. In UD laminates, waviness is expected to have the strongest effect on compressive strength because the component might end up into buckling mode of failure [7,8,13]. It is also proved that the number of wavy plies plays a crucial role and this would occur in every layer since it is generated during the additive deposition of tows. Being aware of the differences between this work and the cited papers [13], it is still possible to state that a waviness with the geometrical characteristics measured for pre-cured specimens up to *30%* should lead to a compressive strength reduction between *2%* and *10%* of the nominal value. Instead, more severe waves like the ones detected for cure levels of *40%* and *50%* might reduce the resistance to compression of a value between *9%* and *24%*.

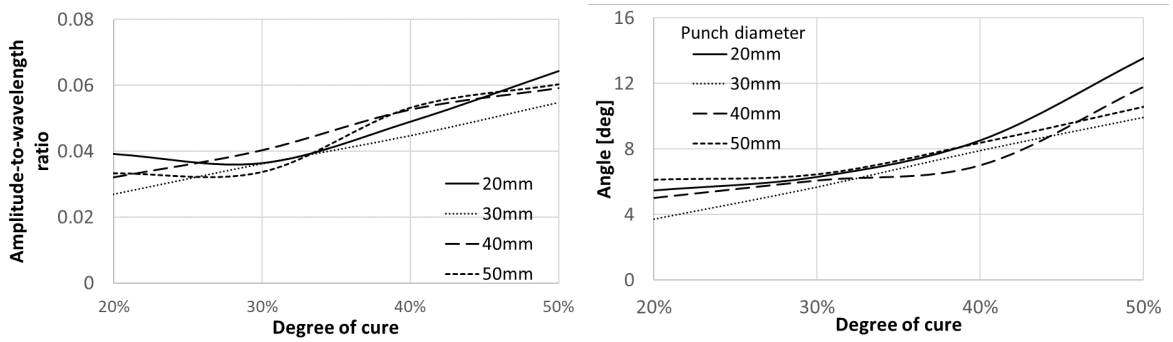

Figure 8. Influence of pre-cure level on in-plane waviness

4. Conclusion and future works

This project reveals that the splitting of the cure in a pre-curing and a post-curing stage in AM has the potential to reduce temperature overshoot generated inside thick CFRP thermosetting composites during their cure. Two competing phenomena are observed. On one hand, pre-curing reduces the temperature overshoot; on the other hand, a higher level of pre-cure induces more severe defects during deposition (i.e. microbuckling). The optimal level of pre-cure is the one that reduces the exothermic overshoot without creating relevant defects during the deposition stage. A level of pre-cure between *20%* and *30%*, for the resin system under investigation, reduces temperature differences inside the material by more than *90%,* generating in-plane waves with a severity that should not compromise the mechanical performances of the component. In order to further progress the understanding of the process under investigation, future research should delve into the characterisation of in-plane waviness generation during the deposition stage and into other types of defects related to this manufacturing technique.

  doi:10.5075/epfl-298799_978-2-9701614-0-0

Acknowledgements

This work was supported by the Laboratory for Mechanical Systems Engineering, Swiss Federal Laboratories for Materials Science and Technology (Empa) through the Empa board of directors (project code AP304-2124).

5. References

1. Struzziero G, Nardi D, Sinke J, Teuwen JJ. Cure-induced residual stresses for warpage reduction in thermoset laminates. Journal of Composite Materials 2020; 54(22):3055-3065.
2. Kravchenko OG, Kravchenko SG, Pipes RB. Cure history dependence of residual deformation in a thermosetting laminate. Composites Part A: Applied Science and Manufacturing 2017; 99:186-197.
3. Struzziero G, Teuwen JJ. A fully coupled thermo-mechanical analysis for the minimisation of spring-in and process time in ultra-thick components for wind turbine blades. Composites Part A: Applied Science and Manufacturing 2020; 139:106105.
4. Bogetti TA, Gillespie JW. Process-induced stress and deformation in thick-section thermoset composite laminates. Journal of Composite Materials 1992; 26(5):626-660.
5. Skordos AA, Kratz J. Layer by layer curing (LbL) - Feasibility study. 2018.
6. Struzziero G, Barbezat M, Skordos AA. Assessment of the benefits of 3D printing of advanced thermosetting composites using process simulation and numerical optimisation. Additive Manufacturing 2022; 54:102719.
7. Slaughter WS, Flecks NA. Microbuckling of fiber composites with random initial fiber waviness. Journal of the Mechanics and Physics of Solids 1994; 42(11):1743-1766.
8. Liu D, Fleck NA, Sutcliffe MPF. Compressive strength of fibre composites with random fibre waviness. Journal of the Mechanics and Physics of Solids 2004; 52(7):1481-1505.
9. Datasheet Huntsman - Resin XB 3515 / Aradur® 1571 / Accelerator 1573. 2009.
10. Karkanas PI, Partridge IK. Cure modeling and monitoring of epoxy/amine resin systems. i. cure kinetics modelling. Journal of applied polymer science 2000; 77(7):1419-1431.
11. Zarrelli M, Skordos AA, Partridge IK. Investigation of cure induced shrinkage in unreinforced epoxy resin. Plastics, Rubber and Composites: Macromolecular Engineering 2002; 31(9):377-384.
12. Yan X. Finite element modeling of curing of epoxy matrix composites. Journal of applied polymer science 2007; 103(4):2310-2319.
13. Mandell J, Samborsky D, Wang L. Effects of fiber waviness on composites for wind turbine blades. International SAMPE symposium and exhibition 2003; 2653-2666.

  doi:10.5075/epfl-298799_978-2-9701614-0-0

CRYSTALLINITY PREDICTION OF SHORT CARBON FIBRE REINFORCED POLYAMIDE 6 COMPOSITES MANUFACTURED BY FUSED FILAMENT FABRICATION

Yifan, Zhu[a,b], Lenny, Van Daele[c], Sandra, Van Vlierberghe[c], Lincy, Pyl[a]
a: Department of Mechanics of Materials and Constructions (MeMC), Vrije Universiteit Brussel (VUB), Pleinlaan 2, B-1050
Brussels, Belgium – yifan.zhu@vub.be
b: SIM vzw, Technologiepark 48, B-9052 Zwijnaarde, Belgium
c: Polymer Chemistry and Biomaterials Group (PBM), Centre of Macromolecular Chemistry (CMaC), Department of Organic and Macromolecular Chemistry, Ghent University, Krijgslaan 281 S4-bis, B-9000 Ghent, Belgium

Abstract: *Polymer additive manufacturing has transformed itself from a technology that is mainly focused on rapid prototyping to a widely received manufacturing technique for highly customised products. In fused filament fabrication (FFF), due to the fast heating and cooling of the polymer, the printed part's crystallinity and mechanical properties are inevitably affected. This research proposes a numerical approach to predict the final crystallinity for FFF printed polyamide 6/short carbon fibre composite. To do so, samples were built with the FFF technique with their temperature history recorded by infrared camera measurements. Differential scanning calorimetry (DSC) was conducted on the FFF filament to calibrate the numerical model. Temperature history was used as input for the model and the printed part's final crystallinity is predicted. Tensile tests were carried out to examine the influence of crystallinity on the printed part's mechanical performance.*

Keywords: Fused filament fabrication; Short fibre reinforced thermoplastic; Crystallinity

1. Introduction

The availability and accessibility of fused filament fabrication (FFF) have made it a popular choice among the public and some industries. Despite the ease of having access to such technology, the intrinsic complexity of this manufacturing process remains an obstacle to fully unleash its potential. A direct correlation between the inputs and the performance of the final product is still not fully understood. It is known that higher crystallinity leads to an increased modulus of the material [1]. Being able to predict the level of crystallinity in the printed part is an interesting development, as it economises the cost of testing and gives a non-destructive way of estimating the level of crystallinity.

In literature, several approaches were proposed to predict the crystallinity evolution of FFF printed semi-crystalline polymers. Pu et al. [2] considered the crystallisation process to be quiescent and used the Schneider rate equations. The predicted level of crystallinity was correlated to the mechanical performance of the printed part. Samy et al. [3] utilised the Nakamura crystallisation kinetics model to investigate the evolution of crystallinity. The printed part's distortion and residual stress were deduced from the calculated crystallinity.

In this study, the crystallinity development of short carbon fibre reinforced polyamide 6 processed by FFF is examined. The prediction is done by employing Velisaris' crystallisation model [4]. The predicted level is compared against the experimental one and similar values

  doi:10.5075/epfl-298799_978-2-9701614-0-0

were found. The influence of different levels of crystallinity on mechanical performance was examined by tensile tests.

2. Experimental

2.1 Material and manufacturing

The material used for this study was Onyx from Markforged, a type of filament made of polyamide 6 with short carbon fibre reinforcement. The diameter of the filament is 1.75mm and it is constantly stored in a desiccator or dry box to prevent moisture absorption. The detailed info like molecular weight or chemical composition of Onyx is not disclosed by Markforged.

Markforged Mark Two printer was used for the manufacturing of the samples. The sample dimension is 70 x 10 x 0.7 mm^3 (L x H x T) and the printing path for each layer could be seen in figure 1a, the sample is made to have two parallel tracks per layer. The layer thickness for the printing was set to be 200 µm and in total each sample has 50 layers. Other key process parameters like printing speed, nozzle temperature or extrusion speed are not adjustable by users and Markforged's default slicer software Eiger sets them automatically.

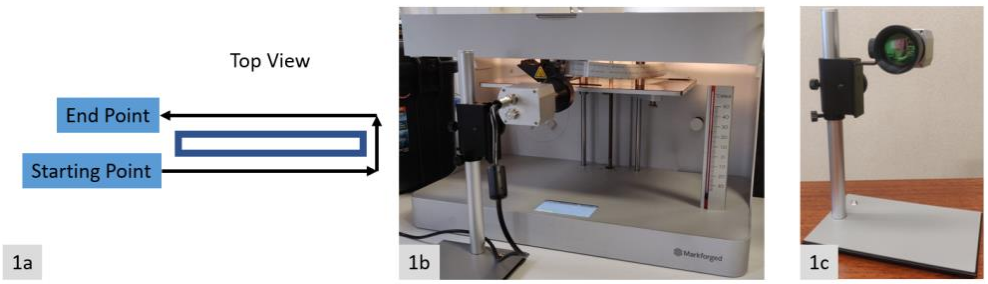

Figure 1a. Layer printing path of the sample, 1b. The setup used during printing, 1c. Infrared camera.

3D printing of samples was performed under two environmental conditions. The first one is printing without the cover which exposes the entire build chamber to the ambient air. In the second condition, the build chamber is covered with a plastic envelope that traps the extruder's heated air. A thermometer is placed near the build plate to measure the chamber temperature. In the first and second condition, the chamber temperature was 25°C and 35°C, respectively.

2.2 Process temperature monitoring

The temperature measuring during the printing process was performed with an Optris PI640i infrared camera equipped with microscope optics. The camera detects infrared signals at a spectral range of 8 – 14 µm and records at a resolution of 640 x 480 pixels, the maximum framerate at this resolution is 32 Hz. At a working distance of 100 mm, it has a field of view (FOV) of 25.4 x 17.5 mm^2 which provides a spatial resolution of 25.2 µm per pixel. Given the layer thickness is 200 µm, 7 measurements could be made per height of a layer. The camera was set up to point at the front face of the sample. Figure 1b shows the setup during printing while figure 1c is the infrared camera used. The lengthwise middle section of the sample was inside the FOV and it corresponds to the gauge section for tensile testing. An emissivity value of 0.95 is adopted in this study [5]. Temperature measurements in the concave regions in

between layers give underestimated values as the view angle between the normal surface and the camera gets close to 90°. To circumvent this, measurement of layer temperature was done at the mid-height pixel of the layer. The recorded temperature data was used as input for the crystallinity calculation.

2.3 Differential scanning calorimetry

To obtain the coefficients for calibrating the numerical model and predict the final crystallinity, isothermal and non-isothermal crystallisation experiments are conducted with standard differential scanning calorimetry (DSC) on the Onyx filament. For the isothermal tests, crystallisation temperatures of 165°C, 170°C, 175°C and 180°C were chosen. The samples quickly cool from 275°C to the desired isothermal temperature at a rate of 50°C/min. It then holds at the isothermal temperature for an extra 60 minutes. The non-isothermal tests were carried out at cooling rates of 5°C, 10°C, 20°C, 30°C, 40°C, and 50°C per minute. All samples cool from 275°C at the specific cooling rate to 40°C and the experiment is concluded.

To find the final crystallinity of the printed samples and compare the experimental results with the prediction, modulated differential scanning calorimetry (mDSC) analyses were used. Tests were made up of a single heating run at a heating rate of 2°C/min to 275°C with modulation of ±0.32°C every 60 seconds. The level of absolute crystallinity (X_{abs}) of the printed samples was then calculated from equation 1.

$$X_{abs} = \frac{\Delta H_f - \Delta H_{cc}}{\Delta H_f^{\infty}} \quad (1)$$

Where ΔH_f represents the enthalpy of fusion, ΔH_{cc} is the cold crystallisation enthalpy and ΔH_f^{∞} is the enthalpy of fusion for fully crystalline polyamide 6. Due to the material being a blend of around 90% by weight polyamide 6 and 10% short carbon fibre [6], the mixture rule was used and obtained a value of 169.2 J/g.

The equipment selected to conduct both the mDSC and DSC experiments was Q2000 from TA instruments installed with refrigerated cooling systems. All experiments were performed under a nitrogen environment. To process the experimental data, Universal Analysis from TA Instruments was used.

2.4 Tensile test setup

Tensile tests were performed on printed samples to examine the influence of the level of crystallinity on mechanical properties. An Instron 5885 testing system equipped with mechanical grips and a 10 kN load cell was used for the tensile tests. All tests were performed under displacement control at a crosshead displacement rate of 1 mm/min to avoid any dynamical effect. A 2620-601 dynamic extensometer from Instron was utilized for the strain measurement. For each environmental condition (build chamber without cover and with cover), 4 tensile samples were tested.

3. Modelling

Velisaris' phenomenological model captures both the primary and secondary stages of polymers crystallisation [7]. For the detailed derivation of the model, readers are referred to the original paper. The applicability of this model to additively manufactured composites was

demonstrated by Brenken et al. [8] on 50% by weight carbon fibre reinforced polyphenylene sulphide. Tierney et al. [9] validated the appropriateness of this model by predicting the final crystallinity of polyether ether ketone (PEEK)/carbon fibre composite.

The model is shown from equation 2 till 4:

$$w_1 + w_2 = 1 \tag{2}$$

$$X_{vc} = X_{vc\infty}(w_1 F_{vc1} + w_2 F_{vc2}) \tag{3}$$

$$F_{vci} = 1 - exp\left\{-C_{1i}\int_0^t T * exp\left[\frac{-C_{2i}}{T - T_g + T_{ci}} - \frac{C_{3i}}{(T(T_{mi} - T)^2)}\right] n_i \tau^{n_i - 1} d\tau\right\} \tag{4}$$

$$i = 1{,}2$$

Where $X_{vc\infty}$ is the maximum level of crystallinity achievable by the material and X_{vc} represents the actual level of crystallinity. The primary and secondary crystallisation mechanisms are described by function $F_{vc1}$and F_{vc2}, and the extent of each mechanism relative to the other is given by the weight factor w_1 and w_2. Inside functions $F_{vci,}$ parameter C_{1i} describes the crystallisation rate's temperature dependence, C_{2i} is associated with the temperature dependence of the growth mechanism and C_{3i} is related to the enthalpy of nucleation. n_i is the Avrami exponent for each mechanism and is extracted from the isothermal crystallisation experiments. T, T_g are used to represent the temperature of the process and glass transition temperature of the material, respectively. T_{mi}, T_{ci} are the melting temperature and empirical fitting temperature for primary or secondary crystallisation, respectively. From the mDSC heating run, the glass transition temperature of the material was identified at 44°C.

4. Results and discussion

4.1 Infrared thermal imaging

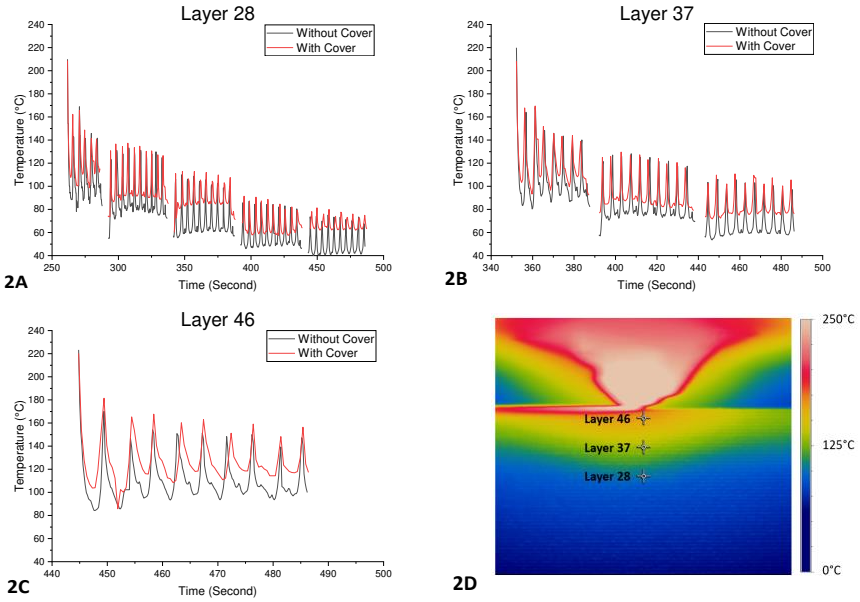

Figure 2. 2a – 2c, Temperature profile of the points from just extruded till the end of printing. 2d, Locations of the measuring points.

  doi:10.5075/epfl-298799_978-2-9701614-0-0

Three measuring points, situated at the midpoint in terms of both length and height of each layer, were chosen on layer 28, 37 and 46, as shown in figure 2D. The temperature history of these three points could be observed in figure 2A to 2C respectively.

The fresh extrudate has a temperature above 200°C and it drops to around 100°C within one second. As the nozzle travels to print the backside of the layer, the next peak appears when the new extrudate is in contact with the front track at the measuring point. Thus, every two consecutive peaks represent a layer that is finished. Due to the mechanism of the Markforged printer, the machine lowers the build plate by 4 mm for around 5 seconds when every 5 layers are printed. This causes a portion of the sample to disappear from the FOV of the infrared camera and creates discontinuities in the measured temperature profile as can be seen in figure 2a and 2b. After the 5 seconds of disappearance, the build plate returns to the previous height. It is observed that the layer temperature decreases as it is away from the nozzle. As more layers are deposited, the measured points get further away from the top layer and hence an overall cooling trend is observed. By comparing the temperature profile of printing with or without cover, it could be seen that both conditions have similar peak temperatures. However, printing with cover has a slower cooling rate as demonstrated in the higher valley temperatures in between successive peaks, this is due to the higher build chamber temperature which creates a lower temperature gradient.

4.2 Crystallisation analysis

The absolute and relative crystallisation evolution for filaments that underwent non-isothermal crystallisation at different cooling rates is shown in figure 3. All plots have a typical sigmoidal shape and with a higher cooling rate, the plot translates towards the left which means that the onset and end of crystallisation are at lower temperatures. The maximum crystallinity achieved is 23.57% for filaments cooled at 5°C/min and this value is used in the model's calibration.

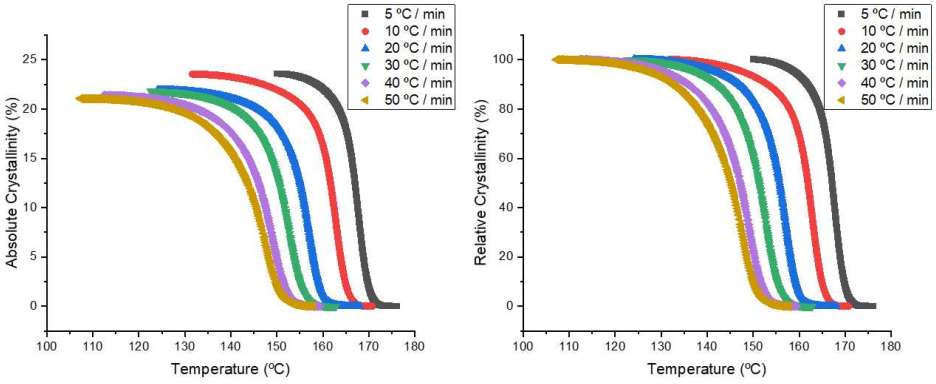

Figure 3. Absolute and relative crystallinity evolution for Onyx filament at various cooling rates.

Equations 5 and 6 are used to compute the absolute crystallinity and relative crystallinity, respectively.

$$X_{abs} = \frac{\Delta H_C}{\Delta H_f^{\infty}} \tag{5}$$

$$X_{rel}(t) = \frac{\int_{t_o}^{t} (\frac{dH}{dt})\, dt}{\int_{t_e}^{t} (\frac{dH}{dt})\, dt} \quad (6)$$

Where ΔH_C represents the enthalpy of crystallisation and ΔH_f^{∞} is the enthalpy of fusion for fully crystalline polyamide 6/short carbon fibre composite. Concerning equation 6, t_o and t_e are the onset crystallisation and end crystallisation time, *H* is the heat flow, and *t* represents the time during crystallisation. DSC results from the isothermal crystallisation experiments are processed and used to create Avrami plots [10] as shown in figure 4. The Avrami exponents are derived from the slope of the plots.

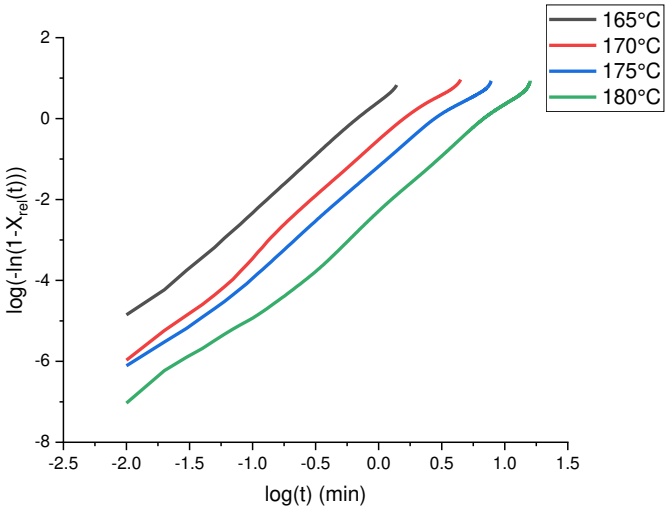

Figure 4. Avrami plot for isothermal crystallisation at various temperatures.

4.3 Modelling result

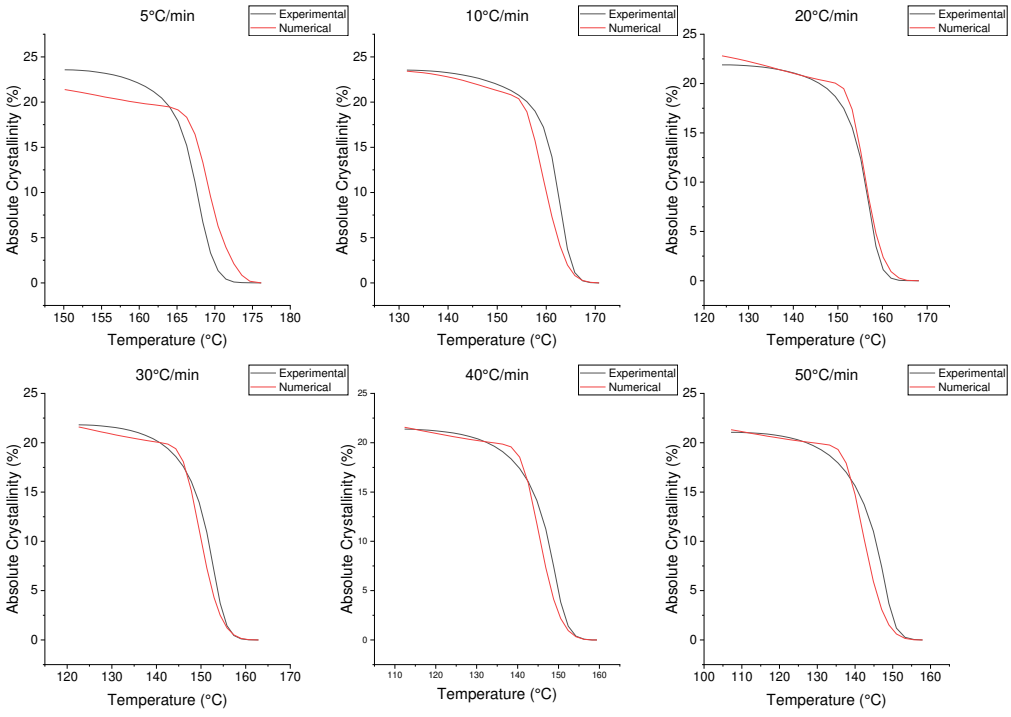

Figure 5. The numerical model fitted to non-isothermal crystallisation data.

Data obtained from both the isothermal and non-isothermal crystallisation experiments are used to characterize all the parameters for the numerical model. From the isothermal result, the calculated Avrami exponents for each mechanism are adopted. The model was then fitted to the non-isothermal experimental result at all cooling rates by using Matlab. Figure 5 shows the experimental and fitted curve of the absolute crystallinity as a function of temperature. From the curve fitting, all the parameters in equation 4 to 6 are found. The time-temperature data from the infrared recording are then used as input for the crystallinity prediction of the printed samples. Table 2 shows the results of the prediction compared to the experimental results.

Table 2: Prediction of absolute crystallinity of printed samples.

Condition	$X_{experiment,abs}$ [%]	$X_{prediction,abs}$ [%]	Deviation [%]
Printed With Cover	19.44	21.99	+ 13.12
Printed Without Cover	18.64	19.39	+ 4.02

The predicted values have deviation up to 13.12% from the experimental result which demonstrated the approach's feasibility in estimating crystallinity. For both conditions, the prediction of absolute crystallinity of printed samples is higher than the experimentally determined crystallinity. This could be due to the model being fitted to filament data at cooling rates up to 50°C/min. The temperature gradient during fused filament fabrication is more than 10^2 higher (> 5000°C/min). Such difference may cause the model to overestimate the level of crystallinity. According to Winkelmann et al. [11], further improvement to the model can be done by fitting to experimental data at the anticipated cooling rate by using flash DSC.

4.4 Mechanical properties

Table 3 summarizes the tensile properties of the printed samples. Samples printed in a build chamber with cover condition have marginally higher values in all tensile properties. This is attributed to the slightly higher level of crystallinity which gives it more mechanical strength. However, lower ultimate strain is observed on samples with lower crystallinity which is not coherent with the literature finding [1]. This peculiarity is hypothesised to be due to the surface effect as samples printed without cover tend to have a rougher surface.

Table 3: Tensile strength of printed samples.

Condition	Young's modulus [GPa]	Ultimate stress [MPa]	Ultimate strain [%]
Printed With Cover	1.45 ± 0.12	48.04 ± 0.17	24.03 ± 1.13
Printed Without Cover	1.39 ± 0.19	46.40 ± 0.13	22.48 ± 1.97

5. Conclusion

This study presented a methodology for estimating the level of crystallinity of polyamide 6/short carbon fibre composite made by FFF. The infrared thermal data show that printing with a cover creates a relatively slower cooling rate as compared to printing without. Also, a feasible way of estimating the final crystallinity of the printed part by using thermal history along with the calibrated numerical model is demonstrated. Fitting non-isothermal crystallisation data at a much higher cooling rate could further enhance such a model and improve its accuracy.

  doi:10.5075/epfl-298799_978-2-9701614-0-0

Acknowledgements

The authors acknowledge the support of the Agency for Innovation and Entrepreneurship Flanders via the Strategic Initiative Materials in Flanders in the framework of the SIM-SBO PET2VALUE project, running in the NANOFORCE program.

6. Reference

1. Babs V, Amalia K, Lincy P, Sandra V.(2022). Effect of extrusion and fused filament fabrication processing parameters of recycled poly(ethylene terephthalate) on the crystallinity and mechanical properties. Additive Manufacturing 2022; 50: 102518

2. Pu, J, McIlroy C, Jones A, Ashcroft I. Understanding mechanical properties in fused filament fabrication of polyether ether ketone. Additive Manufacturing 2021; 37:101673.

3. Samy A, Golbang A, Harkin E, Archer E, McIlhagger A. Prediction of part distortion in Fused Deposition Modelling (FDM) of semi-crystalline polymers via COMSOL: Effect of printing conditions. CIRP Journal Of Manufacturing Science And Technology 2021; 33: 443-453.

4. Velisaris N, Seferis C. Crystallization kinetics of polyetheretherketone (peek) matrices. Polym Eng Sci 1986; 26: 1574-1581

5. Faust L, Kelly G, Jones D, Roy D. Effects of Coefficient of Thermal Expansion and Moisture Absorption on the Dimensional Accuracy of Carbon-Reinforced 3D Printed Parts. Polymers 2021; 13: 3637.

6. Pascual C, Iragi M. An approach to analyse the factors behind the micromechanical response of 3D-printed composites. Composites Part B: Engineering 2020; 186: 107820.

7. Kelly C, Jenkins M. Modeling the crystallization kinetics of polymers displaying high levels of secondary crystallization. Polymer Journal 2021; 54(3): 249-257.

8. Brenken B, Barocio E, Favaloro A, Kunc V, Pipes R. Development and validation of extrusion deposition additive manufacturing process simulations. Additive Manufacturing 2018; 25: 218-226.

9. Tierney J, Gillespie Jr J. Crystallization kinetics behavior of PEEK based composites exposed to high heating and cooling rates. Composites Part A: Applied Science And Manufacturing 2003; 35(5): 547-558.

10. Lorenzo A, Arnal M, Albuerne J, Müller A. DSC isothermal polymer crystallization kinetics measurements and the use of the Avrami equation to fit the data: Guidelines to avoid common problems. Polymer Testing 2007; 26(2): 222-231.

11. Winkelmann F, Hein R. Further development of a simulation model for the description of the crystallization kinetics of semi-crystalline thermoplastics. NAFEM World Congress. 2021.

12. Brenken B. Extrusion Deposition Additive Manufacturing of Fiber Reinforced Semi-Crystalline Polymers. Purdue University ProQuest Dissertations Publishing. 2017.

  doi:10.5075/epfl-298799_978-2-9701614-0-0

DEVELOPMENT OF A NOVEL 3D PRINTING PROCESS: CHARACTERISATION OF MATERIAL AND PROCESS PARAMETERS

Joshua Hares, Piaras Kelly, Mark Battley, Simon Bickerton

Centre for Advanced Composite Materials, University of Auckland –
josh.hares@aucklanduni.ac.nz

Abstract: *A novel continuous carbon fibre reinforced 3D printing process is being developed. By applying a process-science based understanding to each stage of the printing process, higher fibre volume fractions and improved mechanical properties can be achieved in the printed material. In this paper, a selection of material and process characterisation experiments which are used to develop the process-science based understanding are presented. First, solid epoxy resins are characterised using DSC to define a practical processing temperature window between the glass transition temperature and the cure onset temperature. Secondly, an experiment to test in-line fibre infiltration unit geometries is developed. Finally, a novel experimental facility is used to characterise radial tow compaction behaviour.*

Keywords: Composite 3D printing; Fibre compaction; Fibre friction; Resin characterisation; Process characterisation

1. Introduction

High-performance fibre reinforced plastics see widespread use across industries such as marine, automotive, and aerospace for lightweight, high strength and stiffness components. However, current polymer composite manufacturing technology require the formation of a part in a mould, incurring significant tooling costs, then skilled and costly manual labour is required to laminate the part onto the mould. Automated Tape Layup and Automated Fibre Placement are recent technologies that are applied to automate composite manufacture. However, these processes are limited in the geometry of parts that can be created and require application of high local consolidation pressure, and therefore do not negate the need for a mould.

3D printing of continuous fibre reinforced plastics is an emerging technology with the potential to both fully automate composite manufacture and remove the requirement for a mould. The technology has the potential to offer additional benefits such as fibre steering for highly optimised lightweight structures [1]. While there are examples of continuous fibre printing processes commercially available today, applications are limited as the resulting mechanical properties are lower than those achieved by traditionally manufactured composite materials [2].

Within the literature, a range of fibre reinforced 3D printing processes are being developed including short [2] and long [3] fibre reinforced thermoplastics, and short [4] and long [5] fibre reinforced thermosets. Of these, 3D printed long fibre reinforced thermoset polymers have been shown to exhibit the highest mechanical properties. Ming et al. [5] achieved mechanical properties comparable to traditionally manufactured composites by attaining a high fibre volume fraction ($V_f > 0.6$). In the presented process, a pre-impregnated carbon fibre reinforced epoxy feedstock was supplied to a printing head. No processes could be identified within the literature by the authors, in which a continuous fibre reinforced thermoset could be 3D printed, without using a pre-impregnated feedstock.

  doi:10.5075/epfl-298799_978-2-9701614-0-0

A novel composite 3D printing process is being developed with the aim to print continuous carbon fibre thermoset polymers at a high fibre volume fraction (V_f > 0.5), with mechanical properties comparable to composite materials manufactured using traditional methods. In-situ mixing of resin and fibre will be incorporated into the process (Figure 1), so a pre-impregnated feedstock is not required, thus reducing material costs. Taking the constituent materials as inputs to the process removes the need for a separate pre-impregnation processing stage, which simplifies the process and reduces the time and cost of processing and handling. It also has the potential to improve the versatility of the final printing process, where the fibre reinforcement type could be changed throughout the printing process for multi-material printing.

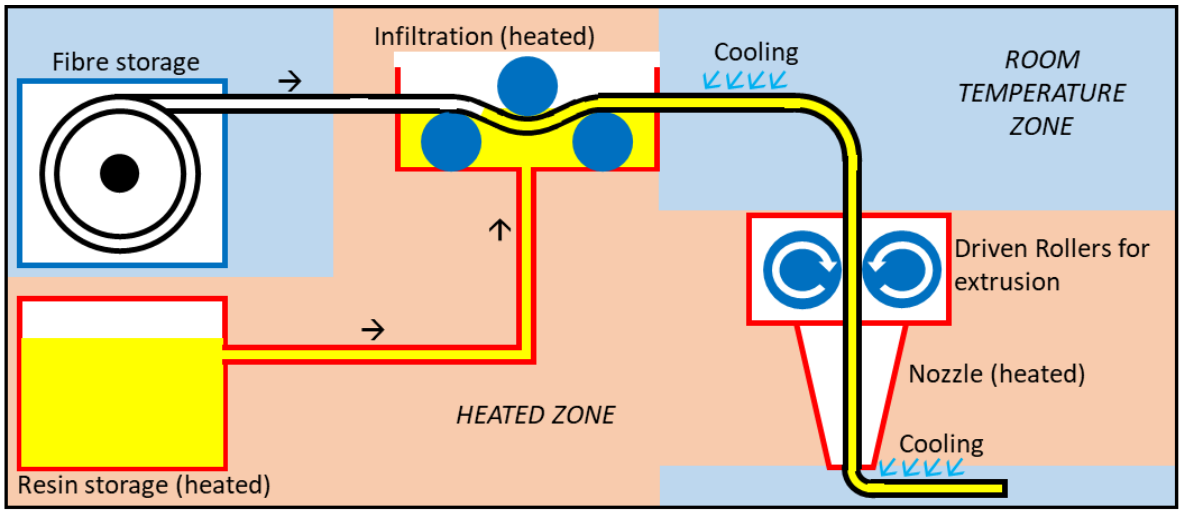

Figure 1. Schematic of proposed continuous fibre reinforced thermoset 3D printing process, showing in-situ infiltration and heated and cooled zones.

A process-science based approach has been followed for the development of the proposed process. In the wider research project, several materials and processes have been characterised to inform a basic process model, which will be used to enable better process design. In this paper, a selection of the material and process characterisation experiments carried out as a part of the research project will be presented, including 'solid' epoxy resin characterisation, in-line resin infiltration, and a novel experiment characterising radial fibre tow compaction behaviour.

2. Resin Characterisation

To provide greater compatibility with the 3D printing process, a 'solid' epoxy was selected, which is solid at room temperature (initially in powder form), with a cure onset temperature significantly higher than its glass transition temperature. This allows for a processing temperature window within which the resin is liquid, but can be cooled down and solidified without initiating crosslinking. This behaviour is suited to the proposed 3D printing process, as the fibre bundle can be impregnated with resin in a liquid form before being cooled down and transported as a solid to the print head using driven rollers. The material system can then be heated by a small amount to a temperature that allows processing through the printing nozzle, and finally cooled to solidify the printed filament after nozzle exit (Figure 1). Curing of the printed composite part will occur in a separate processing step, once the entire part has been printed.

  doi:10.5075/epfl-298799_978-2-9701614-0-0

Differential Scanning Calorimetry (DSC) was carried out on two single-component solid epoxy resin products (E2020 and E2040) supplied by Swiss CMT AG to determine their glass transition temperature and cure onset temperature. Using a temperature ramp rate of 10°C/min, the temperature of each sample was raised from 0°C to 100°C, and then returned to 0°C three times, before being raised continuously until cure had completed. A TA Instruments Q1000 was used for the experiments. Two 10mg samples of each resin type were tested in this way, and the averaged results are shown in Table 1.

Table 1: Measured glass transition and cure onset temperatures for solid epoxy resins.

Resin	T_G first cycle [°C]	T_G second cycle [°C]	T_G third cycle [°C]	Cure onset temperature [°C]
E2020	42.93	43.28	43.65	158.83
E2040	39.16	39.42	39.32	170.52

From Table 1, E2020 and E2040 solid epoxy resins show a potential processing temperature range of over 100°C. The consistency of the glass transition temperature through repeated melting and solidification cycles demonstrates the suitability of these resins for the multiple heat cycles involved in the proposed 3D printing process.

To fully characterise the behaviour of these resins for use in the proposed continuous fibre printing process, two additional tests are required (and are not completed at the time of writing). Rheometric tests will be carried out to determine target temperatures for resin infiltration, and Dynamic Mechanic Analysis (DMA) tests will be undertaken to measure stiffness of the uncured solid resin varies with temperature, which will be used to determine post-nozzle cooling rates and target temperatures in the 3D printing process.

3. Development of In-Line Fibre and Resin Infiltration Unit

A key part of the proposed 3D printing process is the in-situ combination of fibre and resin, which will be achieved within an in-line infiltration module. In collaboration with the Leibniz-Institut für Verbundwerkstoffe (IVW), a solid-state unit is being developed to ensure complete infiltration of resin and fibre can be achieved in-line (Figure 2). Advantages of an infiltration module of this design include lower maintenance due to less moving parts, less resin wastage, and a more compact unit than traditional resin bath or high-pressure resin injection systems [6]. The curvature of the channel in which the fibre tow and resin pass through applies transverse pressure, forcing resin to impregnate the tow.

Although initially developed as a technology for high-speed filament winding applications up to 30m/min [6], the concept is being adapted here for slower speed 3D printing at 50-500mm/min. The main parameters that affect infiltration are tow tension and channel curvature [6]. Testing is required to determine the ideal channel parameters for application to the proposed 3D printing process. At the time of writing, preliminary testing is underway to measure how resin infiltration is affected by tow tension and channel curvature. Figure 2 presents the experimental setup. Low, medium, and high curvature channel geometries, as well as a uncurved control channel, are being tested utilising multiple tow tensions. The fibre is pulled from an adjustable

braked creel through the infiltration module and on to a winding mandrel. The mandrel is comprised of eight evenly spaced bars so that infiltrated and cured specimens, untouched by the mandrel, can be analysed. TS2B-10K in-line tension sensors are placed on either side of the infiltration module to measure the fibre tension, and the force required to pull the tow through the module. Cured specimens cut from the mandrel will be examined using microscopy to determine the percentage of the tow infiltrated by resin.

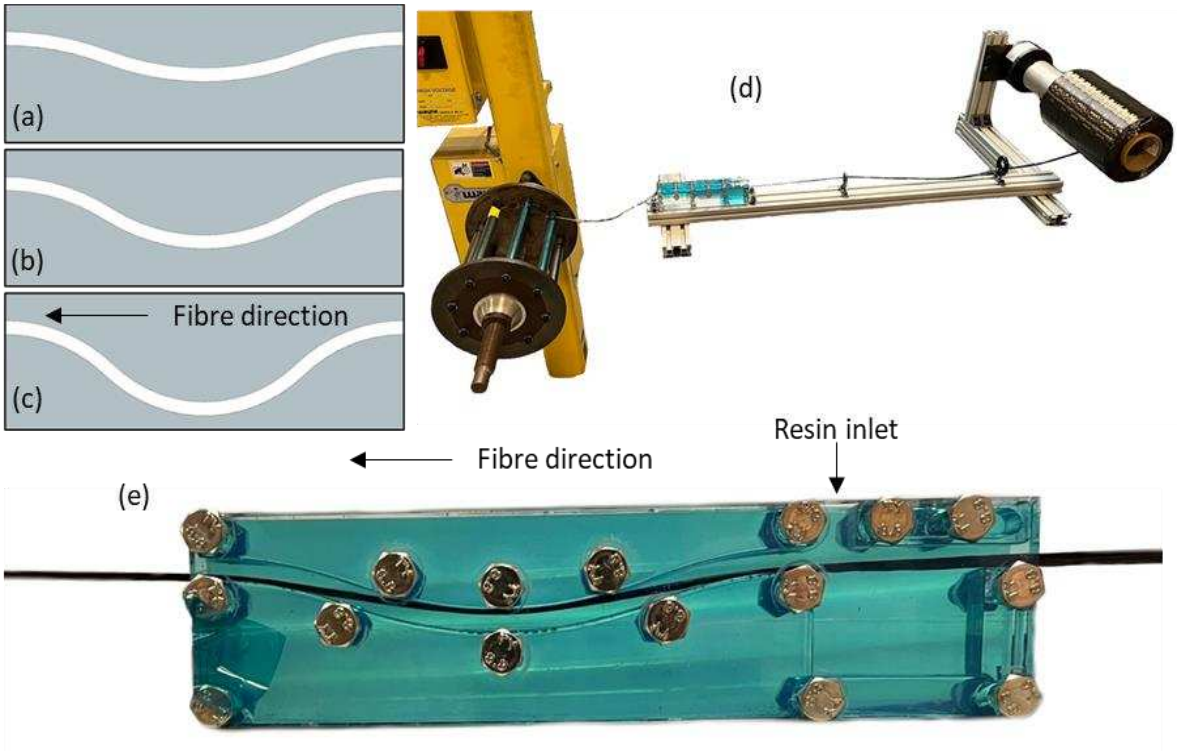

Figure 2. (a-c) Low, medium and high curvature infiltration geometries. (d) Experimental setup for testing in-line tow infiltration. (e) Fibre passing through the low curvature geometry.

4. Radial Tow Compaction

As a part of the proposed printing process, a saturated continuous fibre tow will pass through the nozzle of the printing head to be extruded. Within the nozzle, some compaction of the saturated fibre tow is necessary so that an appropriate fibre volume fraction is achieved at the nozzle exit, where the fibre and resin can then be deposited and solidified. Within the nozzle, the mode of tow deformation is radial compaction, rather than transverse compaction of 2D textiles, which occurs within most traditional composite manufacturing methods. While previous studies have extensively characterised the transverse compaction response of fibre reinforcements [7], the authors could find only one publication addressing radial compaction response [8]. Batch et al. [8] have demonstrated that fibre tows under radial compaction display a sharper exponential increase in compaction pressure with increasing fibre volume fraction compared to transverse compaction, although only for bundles of multiple tows and not single tows. To address this literature gap, a novel experiment has been established to characterise the radial compaction response of single fibre tows, as well as groups of tows, contributing to required material processing understanding for the proposed continuous fibre 3D printing process.

  doi:10.5075/epfl-298799_978-2-9701614-0-0

The presented experimental facility is based on measuring the force required to pull a fibre bundle through an opening with a known area. By measuring the friction coefficient between the material of the opening walls and the fibre bundle along with the pulling force, the compaction force, and thus, the required radial compaction pressure can be calculated. By carefully measuring the cross-sectional area of the opening, the fibre volume fraction can be calculated. In order to collect data at a range of fibre volume fractions for a single fibre tow, an iris mechanism has been developed which has a controllable, variable diameter opening (Figure 3).

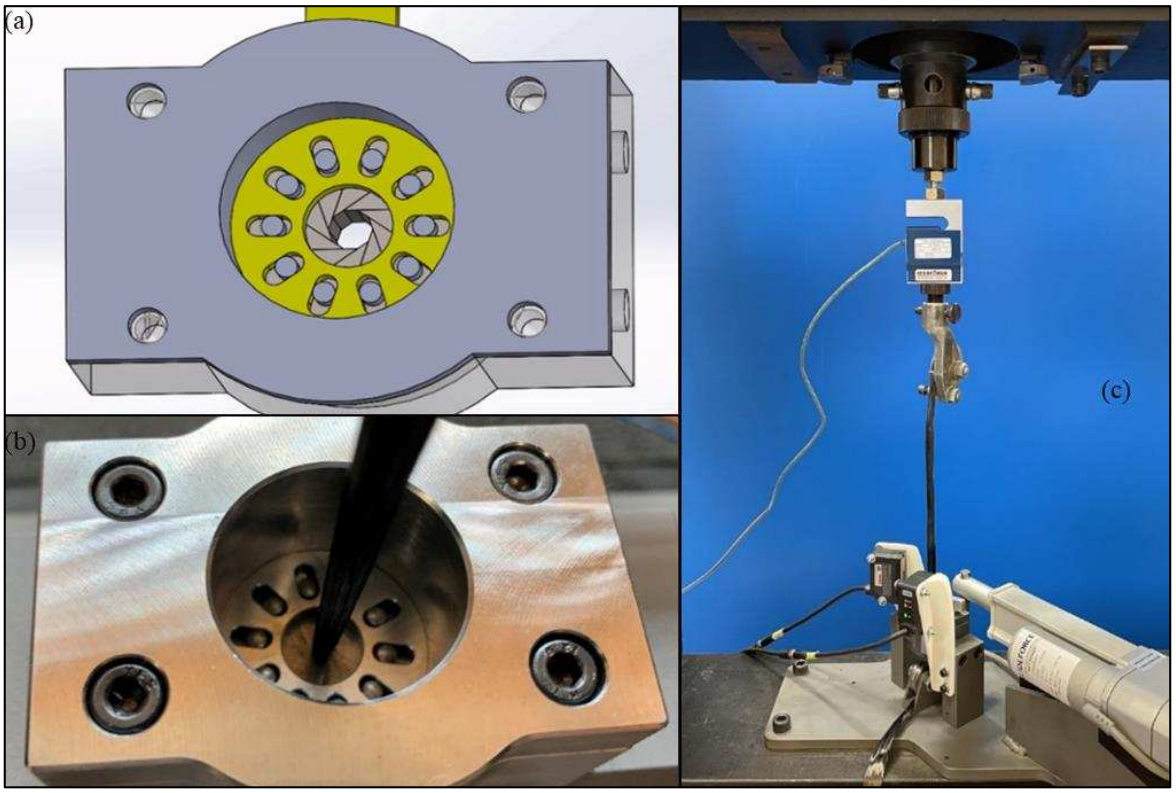

Figure 3. (a) CAD model of iris mechanism. (b) Image of carbon fibre tow being radially compacted by iris mechanism. (c) Experimental setup of radial compaction facility set up on universal testing machine including iris mechanism, fibre clamps, load cell, and linear actuator.

4.1 Friction Measurements

To measure the friction coefficient between the walls of the iris opening and the fibre bundle, a separate experiment was developed. Here, a tensioned fibre tow is pulled over a drum with an equivalent material and surface finish to the walls of the iris opening. The iris opening walls are made from 4340 steel and were manufactured by wire cutting, resulting in an estimated isotropic surface roughness of 2-4Ra. To match this, the friction drum was made from 4340 steel and bead-blasted to give an equivalent surface finish. The force required to pull the fibre bundle over the friction drum is measured, and a friction coefficient is calculated using Eq. (1), the Capstan Equation.

$$\mu = \ln\left(\frac{T_1}{T_2}\right)\frac{1}{\theta} \tag{1}$$

  doi:10.5075/epfl-298799_978-2-9701614-0-0

Where μ is the friction coefficient, T_1 and T_2 are the fibre tensions on each side of the drum, and θ is the wrap angle around the drum.

Average pulling forces over a pulling distance of 240mm can be seen for pulling speeds of 50mm/min, 150mm/min, and 450mm/min in Table 2, along with the friction coefficients calculated. The results indicate a positive relationship between pulling speed and friction coefficient, and the measured values for friction coefficients are consistent with similar measurements presented in the literature [9].

Table 2: Average pulling force and friction coefficient measurements for each pulling speed.

Pulling speed [mm/min]	Average pulling force [N]	Force coefficient of variation	Friction coefficient
50	2.30	0.089	0.044
150	2.43	0.071	0.077
450	2.63	0.041	0.089

4.2 Compaction Response Measurements

The force required to draw the fibre bundle through the iris opening is measured directly, using an Interface SM-2000N load cell mounted to the moving crosshead on the Instron 4465-5900R universal testing machine used for the experiment (Figure 3). To measure the diameter of the opening, a spatially calibrated IDS UI-1490SE camera was used to measure the position of wedges forming the iris mechanism. A Pololu Glideforce MD122004-P linear actuator is used to control the opening area of the iris mechanism, with an Interface SM-1000N in-line load cell utilised to ensure consistency between closing force and pulling force measurements. To calculate the compaction pressure, Eq. (2) is used.

$$\sigma_C = \frac{F_P/\mu}{\pi d t} \tag{2}$$

Where σ_C is the compaction pressure, F_P is the pulling force, d is the diameter of the iris opening, and t is the depth of the iris opening.

The radial compaction behaviour of a single 50K carbon fibre tow was measured using the experimental facility described above at three pulling speeds: 50mm/min, 150mm/min, and 450mm/min. Figure 4 shows a plot of fibre volume fraction and compaction pressure, as calculated from the radial compaction measurements, across the three pulling speeds. Five tow samples were measured at each pulling speed. Each datapoint represents an average from data collected through 240mm of fibre tow displacement through the iris.

The measured radial compaction response is as expected, with an exponential increase observed for compaction pressure with increasing fibre volume fraction, in agreement with the literature [8]. Based on the work by Batch et al. [8], it is expected that the radial compaction response shows exponential behaviour with a more sharply increasing gradient compared to transverse compaction. There appears to be no significant relationship between pulling speed and compaction response.

  doi:10.5075/epfl-298799_978-2-9701614-0-0

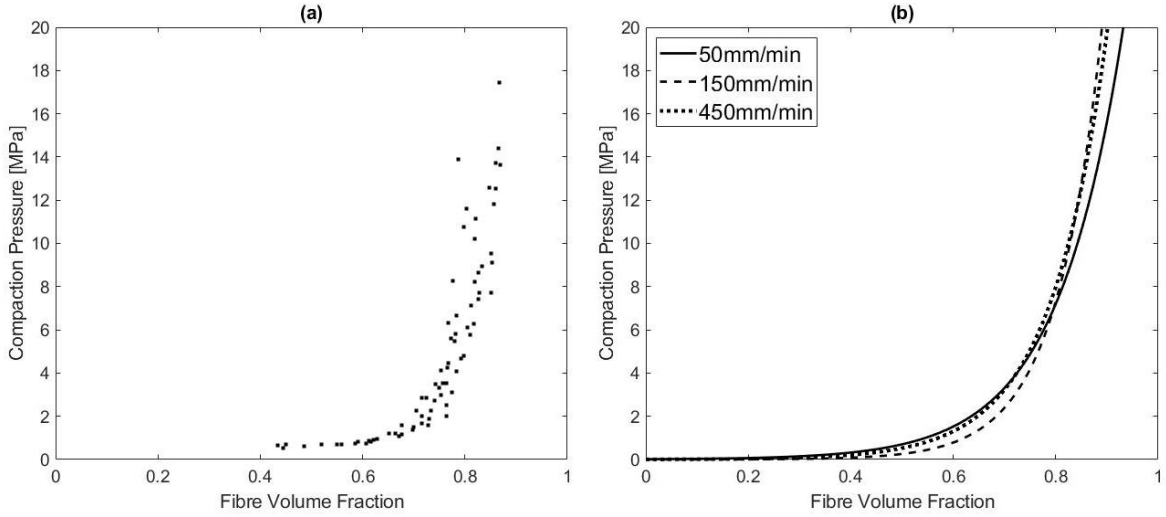

Figure 4. (a) Measured compaction response of 50K carbon fibre tow at 150mm/min pulling speed. (b) Exponential fit of compaction responses of 50K carbon fibre tows at all pulling speeds.

5. Conclusion

As part of the development of a novel continuous fibre reinforced thermoset 3D printing process, several material and process characterisation experiments have been carried out:

DSC measurements of 'solid' type epoxy resins confirmed the temperature window between glass transition and onset of cure is wide enough to be suitable as a temperature processing window for the proposed printing process. The resins displayed stability of glass transition temperatures across several melting and solidification cycles, indicating no crosslinking had occurred. This behaviour shows their suitability to the multiple melting and solidification cycles of the printing process. Additional experiments including rheometry and DMA are required to fully characterise the resin for its role in the printing process.

An experiment to test in-line resin infiltration units was developed, but at the time of writing no testing had been completed. This facility will be used to measure the influence of processing parameters including infiltration unit geometry and fibre tension on fibre infiltration.

A novel experiment to characterise the radial compaction behaviour of a fibre tow was developed. The facility measured an expected exponential relationship between fibre volume fraction and compaction pressure, and a positive relationship was found between fibre pulling speed and fibre-steel friction coefficient. No relationship was found between fibre pulling speed and fibre tow radial compaction response.

The results of these experiments will be used within the wider research project to develop models of the proposed printing process, which will in turn inform the design of the physical process to achieved higher fibre volume fractions and improved mechanical properties of the printed material.

  doi:10.5075/epfl-298799_978-2-9701614-0-0

Acknowledgements

The authors would like to thank Swiss CMT AG for the supply of the solid epoxy resins used, and the Leibniz-Institut für Verbundwerkstoffe (IVW) for collaboration on impregnation unit design. The first author also thanks the University of Auckland for providing funding to this project in the form of the University of Auckland Doctoral Scholarship.

6. References

1. Zhang H, Li A, Wu J, Sun B, Wang C, Yang D. Effectiveness of fibre placement in 3D printed open-hole composites under uniaxial tension. Compos Sci Technol. 2022 Mar;220(June 2021):109269.
2. Blok LG, Longana ML, Yu H, Woods BKS. An investigation into 3D printing of fibre reinforced thermoplastic composites. Addit Manuf. 2018 Aug 1;22:176–86.
3. Dickson AN, Barry JN, McDonnell KA, Dowling DP. Fabrication of continuous carbon, glass and Kevlar fibre reinforced polymer composites using additive manufacturing. Addit Manuf. 2017 Aug 1 [cited 2019 Mar 5];16:146–52.
4. Compton BG, Lewis JA. 3D-printing of lightweight cellular composites. Adv Mater. 2014;26(34):5930–5.
5. Ming Y, Duan Y, Wang B, Xiao H, Zhang X. A Novel Route to Fabricate High-Performance 3D Printed Continuous Fiber-Reinforced Thermosetting Polymer Composites. Materials (Basel). 2019 Apr 26;12(9):1369.
6. Miaris A, Paessler M, Schledjewski R, Mitschang P. Modeling the Impregnation Process of a Siphon Impregnation System During Filament Winding. In: Volume 6: Materials and Fabrication, Parts A and B. ASMEDC; 2011. p. 79–87.
7. Gutowski TG, Morigaki T, Cai Z. The Consolidation of Laminate Composites. J Compos Mater. 1987;21(2):172–88.
8. Batch GL, Cumiskey S, Macosko CW. Compaction of fiber reinforcements. Polym Compos. 2002;23(3):307–18.
9. Mulvihill DM, Smerdova O, Sutcliffe MPF. Friction of carbon fibre tows. Compos Part A Appl Sci Manuf. 2017 Feb;93:185–98.

  doi:10.5075/epfl-298799_978-2-9701614-0-0

NANO-HYDROXYAPATITE REINFORCED, 3D PRINTED PHOTOPOLYMER-BASED COMPOSITES FOR BIOMEDICAL APPLICATIONS

Kolos Molnár[a,b], Haijun He[a], Bálint Budavári[c], Krisztina S. Nagy[c], Angéla Jedlovszky-Hajdú[c], Yahya Kara[a]*

a: Budapest University of Technology and Economics, Faculty of Mechanical Engineering, Department of Polymer Engineering, Műegyetem rkp. 3., H-1111 Budapest, Hungary – molnar@pt.bme.hu
b: MTA–BME Research Group for Composite Science and Technology, Műegyetem rkp. 3., H-1111 Budapest, Hungary
c: Semmelweis University, Department of Biophysics and Radiation Biology, Laboratory of Nanochemistry, Nagyvárad tér 4, H-1089 Budapest, Hungary

Abstract: In this study, we added hydroxyapatite (HAP) nanoparticles into an acrylic-based photopolymeric 3D printing resin. The original formula is recommended for stereolithographic 3D printing of dental surgical guides. We wanted to improve the material's toughness and other mechanical properties without compromising the biocompatibility. For that aim, we applied a two-step mixing process and a co-monomer as carrier to properly disperse the nanoparticles. We found that both the HAP nanoparticles and the co-monomer greatly influenced the mechanical properties. With 30% MMA and 1 phr HAP nanoparticle loading the flexural and the tensile strength improved by 76% and 115%, respectively. Besides, the strain at break became three-fold higher than that of the reference resin. The cytotoxicity test results were also promising, since the morphology and adherence of the cells did not change.

Keywords: 3D printing; Hydroxyapatite; Nanocomposites; Surgical guide; Stereolithography

1. Introduction

The flexibility of 3D printing systems (to use variety of materials and create any object) makes them an attractive technology. There are several 3D printing approaches based on mechanical, electrical, or photochemical principles (*e.g*. fused deposition modelling, direct metal laser sintering, selective laser sintering, two-photon polymerization, and stereolithography) [1, 2]. The liquid-based 3D printing technologies, such as stereolithography (SLA) and digital light processing (DLP) offer a dimensional precision much better than that of the fused filament fabrication methods [3]. During the processing, a photopolymeric liquid resin is cured by UV light according to the desired layer geometry. Because photopolymerization can cure a resin rapidly, it is one of the most widely used methods in 3D printing. This is evidenced by the fact that photopolymers are the most consumed 3D printing materials, claiming almost half of 3D printed materials market [4,5].

In dental applications, the primary usage of polymers has been in prosthetics such as denture bases, their application has expanded to include artificial teeth, direct tooth restorations, crown and bridge facings, implants, impressions, and temporary crowns [6]. The current applications of medical-related 3D printing include surgical guides, dental splints, *etc.,* in which the 3D printed part is put into the oral cavity for shorter or longer times. Certain resins, such as the Dental SG by Fromlabs are compatible for this purpose, but these systems provide moderate

mechanical properties. Reinforcing these photopolymers can be a feasible, but challenging approach, because the reinforcement decreases the UV transmittance of the resin and hinders the polymerization.

Surgical guides in the field of dentistry were already established for oral surgery applications. By transferring radiographic digital information of computed tomography (CT) or cone beam CT to surgical templates, dental implants can be positioned more precisely. It plays a major role in difficult anatomical situations allowing a better prosthetic to fit consequently. These guides have been restricted to implant dentistry. Recent case reports have shown that modern 3D-printed templates can also be successfully used in auto-transplantation of teeth and guided osteotomy and root resection [7]. The production of surgical guides requires biocompatible biomaterials which do not induce adverse effects when they are in contact with the tissue. Biocompatibility and the response of the oral soft tissue to materials used in conventional, as well as in subtractive processed dental materials are well documented, whereas the impact of resins used in desktop SLA 3D printers is currently not entirely clear [8]. For most resins used in SLA printers additional post curing is required.

In this study, we tried to improve certain mechanical properties of a commercial photopolymer resin without worsening its biocompatibility. Using solid phase additives is challenging in liquid-based 3D printing, because the additive worsens the transmittance of the resin for UV light. For this reason, we chose hydroxyapatite nanoparticles as reinforcement and we also tried to compensate the changes in viscosity with a co-monomer, namely methyl-methacrylate.

2. Materials and Methods

2.1. Materials used

The photopolymeric resin used in this study was FormLabs Dental SG type photopolymeric resin (SG). The Dental SG resin is principally a mixture of methacrylic ester olygomers (>90 m%) and phosphine oxide as photoinitiator (<3%). According to the description of the manufacturer, the resin is autoclavable, biocompatible and designed for Class 1 dental surgical guides to help dentists guarantee accurate implant placement. The polymerized resin can be used for 24 h in the oral cavity without issues [9].

Synthetic hydroxyapatite (HAP) powder of spherical nanograins was purchased from Sigma-Aldrich. The purity was higher than 97% and the average particle size is smaller than 200 nm (BET) according to the producer. The specific surface are of the powder was greater than 9.4 m^2/g. Methyl-methacrylate monomer (MMA), also obtained from Sigma-Aldrich, was applied as a reactive solvent. The solvent was used without further purification.

2.2. Dispersion of the nanoparticles

To achieve a dispersive mixing of the nanoparticle agglomerates, we needed to empoly a high specific energy mixing technique. We chose ultrasonic mixing that is widely used for such purposes at mixing CNTs, graphene, *etc*. [10].

We found that the dispersion of the HAP nanoparticles was challenging. The ultrasonic mixing leads to a sudden and significant temperature increase of the mixture in the vicinity of the sonotrode due to the high energy density. At that high temperature, the decomposition of the photoinitiator takes place leading to the non-desired polymerization and crosslinking of the

photopolymeric resin during mixing. That leaves no chance to print the resulted gel-like resin. We had to overcome this issue, and for the dispersion of the HAP nanoparticles, we decided to use a two-step mixing process and used a co-monomer (MMA). The co-monomer had a double-role: 1. to be a carrier medium for nanoparticles during mixing, 2. The HAP nanoparticles increased the viscosity of the resin, so to compensate it by dilution.

In the first step, we mixed the MMA monomer with the desired amount of HAP by an ultrasonic homogenizer (*i.e.* no initiator included in the batch). We used a Bandelin (Germany) Sonopuls 4200 HD type mixer with a standard geometry cylindrical sonotrode at 20 kHz frequency, and the power set at 50 W. The ultrasonic mixing was carried out in a thin-wall plastic container. To avoid the warmup of the mixture, we put the box in a water bath to promote heat release. The temperature was monitored throughout the mixing, and we never let it go above 40 °C. The mixing was going on for 15 minutes. With this, we not only avoided the problems of unintentional curing during the mixing, but we found that the low viscosity of the solvent can enhance the dispersion of the nanoparticles.

In the second step, we admixed the HAP/MMA mixture to the SG resin, by mechanical mixing. It took place in a non-transparent container to avoid the decomposition of the photo-initiator. The mechanical mixing was done for 5 minutes at low rotation speed by an IKA-made (Germany) RW 16 basic type laboratory mixer with a propeller agitator.

Specimens of various HAP and MMA concentrations (Table 1.) were 3D printed by a FormLabs (USA) Form2 type stereolithographic 3D printer. We printed dogbone specimens (75 mm long x 7.5 mm wide x 2 mm thick) for the tensile tests and 80x10x4 mm oblong specimens for 3D printing and Charpy-impact tests, 5 pieces from each group.

Table 1: The material compositions used for 3D printing.

Specimen	SG resin content [%]	MMA content [%]	HAP content [phr]
SG (reference)	100	-	0
0 HAP	70	30	0
1 HAP	70	30	1
2 HAP	70	30	2
3 HAP	70	30	3

The specimens were washed by general-purpose isopropyl alcohol, deburred and then post-cured for 30 minutes at 60 °C in a FormLabs UV chamber.

2.3. Material testing

The material characterization included mechanical tests (tensile and 3-point bending), and we tested the morphology of the materials by scanning electron microscopy (SEM). As the materials may be used as surgical guides in the future, therefore we also tested the cytotoxicity of the SG, 0 HAP and 3 HAP samples.

Fracture surfaces of the tensile specimens were investigated by a JEOM (Japan) 6380LA type scanning electron microscope (SEM), coupled with an energy dispersive X-ray detector (EDS). The specimens were gold-sputtered by a Jeol (Japan) JFC-1200 type sputter coater before the tests.

The specimens were tested by a Zwick Z005 (Germany) type tensile testing machine with a load cell of 5kN. For the tensile tests, the gripping distance was 40 mm and the test speed was set at 2 mm/min. For the 3-point bending tests the support distance was 64 mm and the test speed was 5 mm/min.

The geometry of all the specimens was measured respectively by a digital caliper, with a precision of 0.01 mm, prior to the execution of the tests. In case of both type of tests, 5 specimens were tested from each material composition.

We also assessed the biocompatibility of three of the SG resin based polymer samples (SG, 0 HAP and 3 HAP) by indirect cytotoxicity tests according to the ISO-10993-5 standard. For this purpose, we used the MG-63 human osteosarcoma cell line (Sigma-Aldrich) and discs with a diameter of 12 mm. The mass of these discs varied between 45-125 mg. The culture medium of the MG-63 cells was composed of Minimal Essential Medium (MEM, 87%), Fetal Bovine Serum (FBS, 10%), non-essential amino-acids (NEAA, 1%), L-Glutamine (1%, final concentration: 2 mM), as well as 100 units/ml penicillin and 100 mg/ml streptomycin. The cells were maintained under standard conditions (37°C, 5% CO_2 and 100% humidity).

On the first day of the experiment, 10 000 cells in 200 µl of cell culture medium per well were seeded in a 96-well tissue culture plate. The selected polymer discs were sterilised in chlorine dioxide solution (diluted to 1% in phosphate buffered saline, PBS) for 30 min in 24 well plates and then soaked in cell culture medium for 24 hours. The amount of the medium for each polymer disc was determined by the following ratio: 100 mg polymer in 1.5 ml medium. After 24 h incubation of the cells, their old medium was replaced by the supernatants of the polymer discs (namely with the extracts of the polymer samples). In case of the untreated control group, the old cell culture medium was also changed by fresh medium. After 24 h, morphological investigations and cell viability tests were performed.

The morphology of the cells was monitored by a phase-contrast microscope (Nikon Eclipse TS100) with a 10x objective lens. Images were taken with a high-performance CCD camera (COHU) applying the Scion image software. For colorimetric evaluation of cell viability, firstly the WST-1 cell proliferation reagent (Roche) was diluted (1:20) with MEM without Phenol Red. The wells were washed with 200 µl of PBS and afterwards 200 µl of the diluted WST-1 reagent was added to the cells. After 3h incubation at 37°C, the absorbance was measured by a microplate reader (Bio-Rad Model 3550) at 450 nm with 650 nm reference wavelength. Wells containing only the reagent but no cells were used as blank while untreated cells were used as control.

3. Results and discussion

We were able to 3D print all the tensile and bending specimens with the desired dimensional precision. Beides that, the appearance of the specimens was also fine. The samples were not tacky, indicating a high conversion rate of the olygomers. The MMA addition well-balanced the viscosity increase originating from the HAP additive. The initially transparent resin turned white

as a result of the HAP addition. But neither the MMA co-monomer nor the HAP loading affected the quality of printing significantly.

The SEM images of the fracture surfaces can be seen in Figure 1. The samples showed a rather rigid fracture at 1000 x maginfication, especially the reference sample. The HAP loading affected the fracture surface considerably. The fractured surface became larger that indicates some improvement in the fracture energy. At the HAP-containing samples tiny white dots appeared that can be identified as the spherical HAP nanoparticles and their agglomerates. The dispersion and distribution of the HAP nanoparticles can be considered fair.

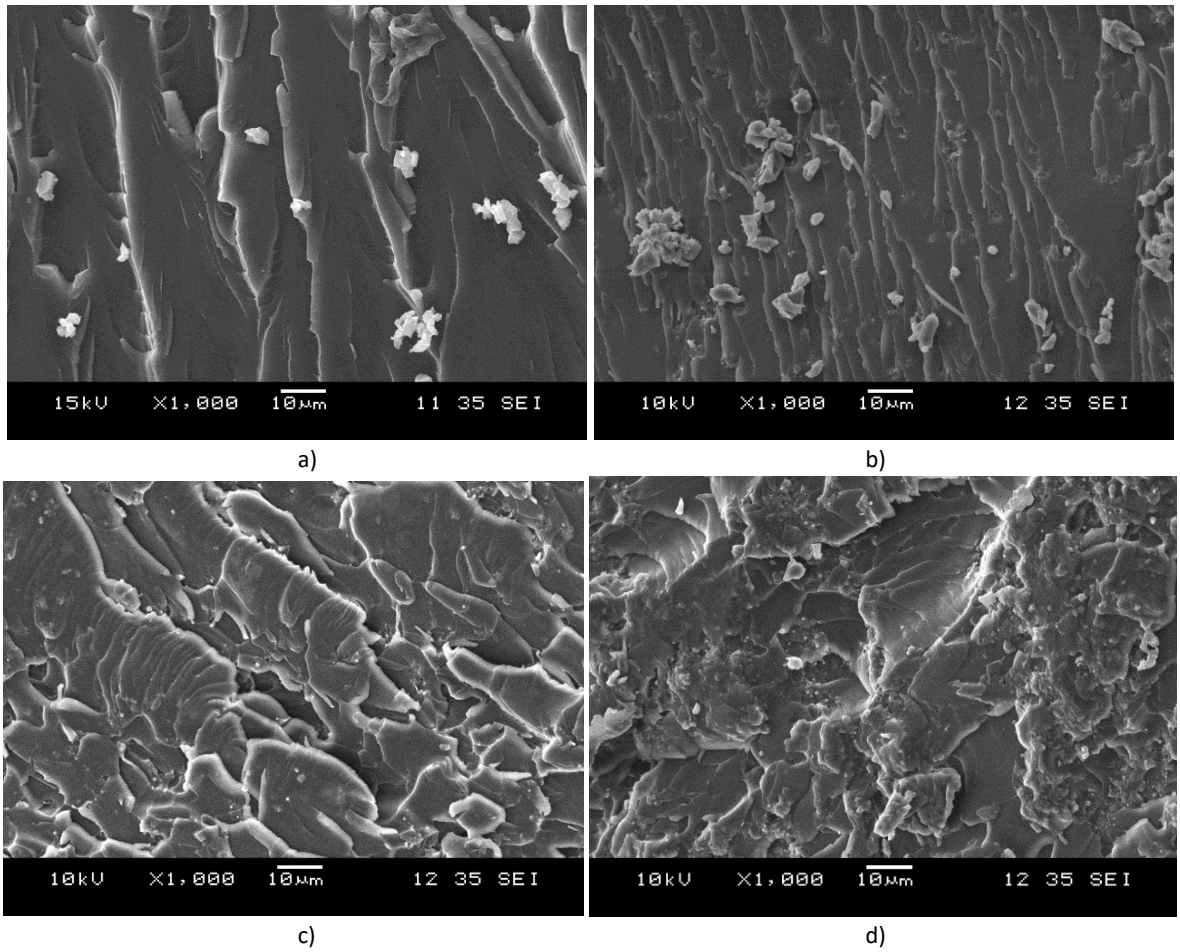

Figure 1. SEM images of the fracture surfaces of the 3D printed samples. a) 0 HAP, b) 1 HAP, c) 2 HAP, d) 3 HAP

In order to see if it is really HAP that can be observed at the fracture surfaces, we used the EDS detector of the SEM and created maps of the elements (see Figure 2.). Since the chemical formula of HAP is $Ca_{10}(PO_4)_6(OH)_2$ therefore we tried to detect the *Ca* and *P* atoms. In Figure 2. the *Ca* is indicated in green, while the *P* is indicated in blue color. At the higher concentration, minor aggregation of HAP can be observed (see the small green islands in the figure). At low HAP contents the particles seemed to be well-dispersed.

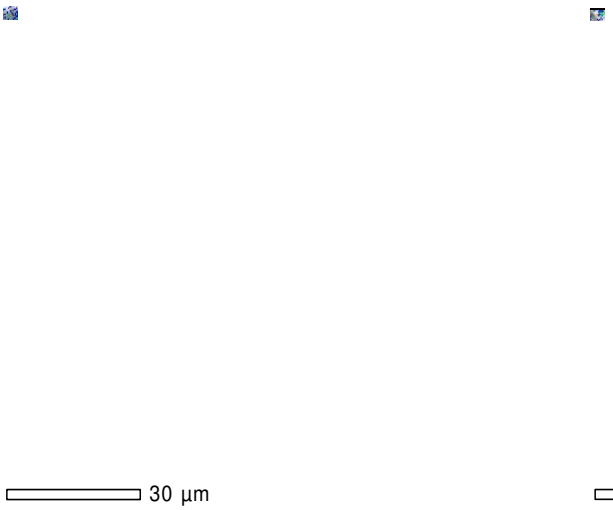

a) b)

Figure 2. EDS map of the HAP loaded samples (green: Ca, blue: P) a) 1 phr HAP, b) 3 phr HAP.

The results of the 3-point bending test are presented in Figure 3. The HAP content improved the flexural strength greatly. In the case of the SG resin reference the average flexural strength was 62.8 MPa. The MMA co-monomer together with 1 phr HAP loading improved that to 110.7 MPa. Considering the deviations (15.6 MPa *vs.* 3.4 MPa), this is a significant change. In the case of the 1 HAP and 2 HAP samples the flexural strength improved by 76% and 66%, respectively. Unfortunately, the flexural modulus decreased. On the other hand, the strain at break was 2.2% for the neat SG resin, while for the SG+MMA sample it was 9.1% and for the HAP loaded samples it was in the range of 6.4-12.8%. That implies that the MMA made the samples significantly tougher. One of the biggest issues with the SLA printing resins is their rigidity [11] that is clearly a disadvantage at surgical guides. It is easy to break them by accident during application. The co-monomer improved the strain at break greatly and made the material tougher.

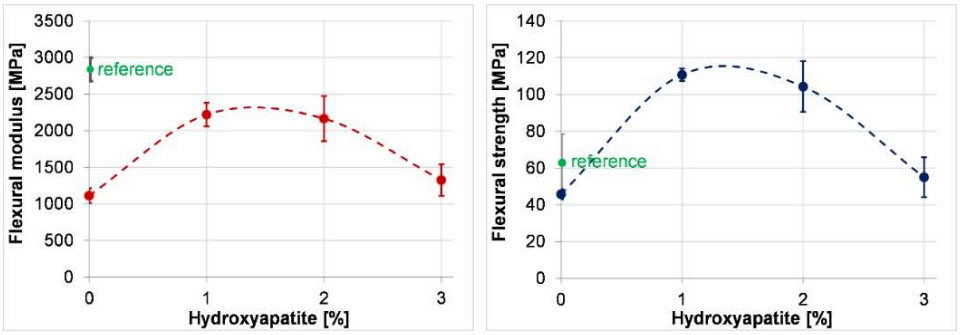

a) b)

Figure 3. The main results of the 3-point bending tests. Flexural modulus (a) and flexural strength (b) of the composites with various HAP contents

The main results of the tensile tests can be seen in Figure 4. Interestingly, the tensile modulus of the specimens did not change considerably. However, high HAP content decreased it slightly. The tensile strength of the material increased due to both the MMA co-monomer and the HAP additive. In the case of the reference sample, it was 25.43 MPa, while in the case of 1 phr HAP loading it was 54.75 MPa that is a 115% improvement.

The strain at break again improved greatly. The SG reference material had a strain at break of 1.06%, while the MMA co-monomer (without HAP) had 2.44%. The HAP further improved this, up to 3% (strain). Again, the MMA and the HAP helped to make the resin much tougher.

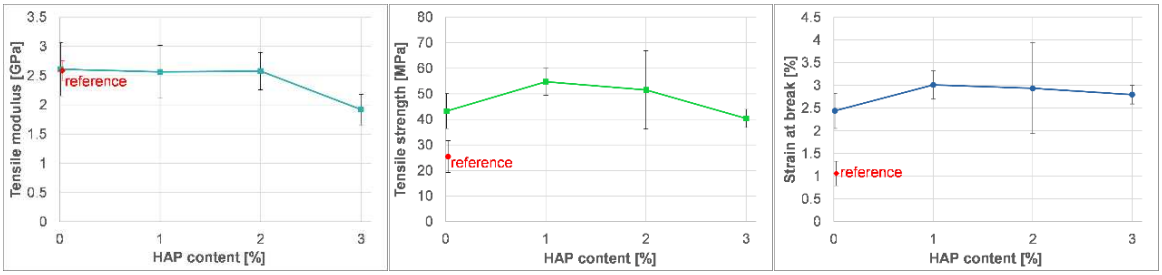

a) b) c)

Figure 4. The main results of the tensile tests. Tensile modulus (a) tensile strength (b), and strain at break (c) of the composites with various HAP contents

The microscopic images of the growing MG-63 human osteosarcoma cells on the samples together with the control sample can be seen in Figure 5. All the samples show a similar morphology of the cells, neither the MMA nor the MMA+HAP changed this. Besides that, the cells adequately adhered to the samples in all the cases that shows the material promotes cell growth and they are not cytotoxic.

The relative cell viability is presented in Figure 6. All the samples showed smaller values than the control sample. The neat SG resin produced a value lower than the mixture of SG/MMA. Concerning the deviations, it seems that the MMA co-monomer improved the cell viability significantly. Regarding the 3 HAP sample, the results a but contradictory. The cell viability tests shows that the material is slightly cytotoxic at 24 h. On one hand, the surgical guide is usually used only for shorter time. On the other hand, the cell morphology and adhesion did not show a significant cytotoxicity of the materials. Therefore, further investigations are needed to better understand this phenomenon.

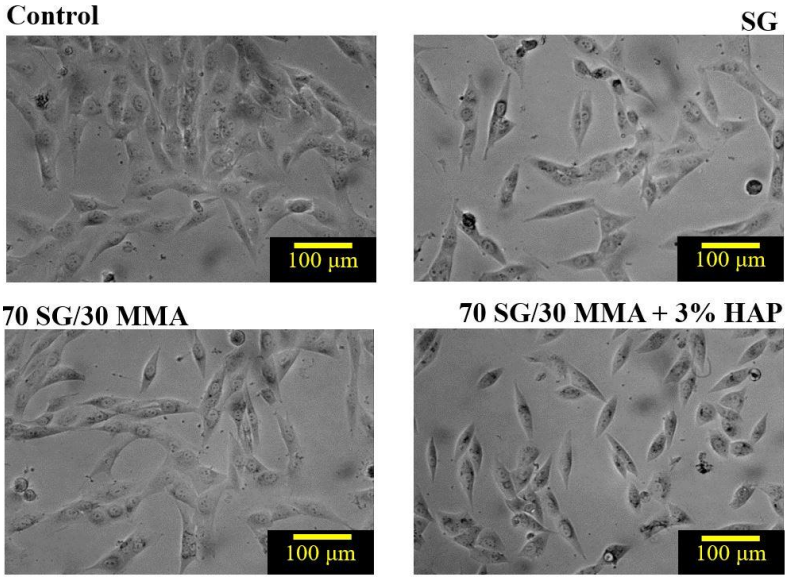

Figure 5. Phase-contrast microscopic images of MG-63 human osteosarcoma cells growing in the absence or the presence of the extracts of the different polymer sample types for 24 h.

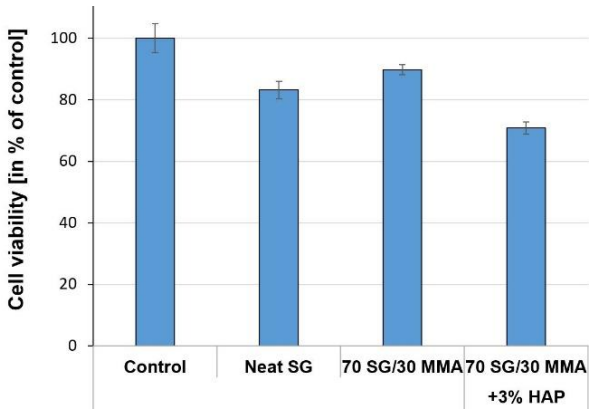

Figure 6. Relative cell viability of MG-63 cells treated with the extracts of the different polymer samples for 24 h. The viability was normalized to untreated control cells.

4. Conclusions

In this study, we tried to improve the mechanical performance of an SLA 3D printing resin, which is recommended to be used as dental surgical guides. We added HAP nanoparticles to the resin and used MMA as a co-monomer. For this purpose, we developed and applied a special, two-tier mixing process. The MMA co-monomer not only helped to compensate for the viscosity increase caused by the HAP nanoparticles, but it was a carrier for them during the mixing. We were able to 3D print the nanoparticle loaded resins and obtained the specimens with suitable geometry.

The SEM/EDS investigations confirmed that the mixing method applied resulted in a good quality distribution and dispersion of the HAP nanoparticles. At higher HAP contents, small agglomeration of HAP was observed.

The mechanical tests showed that the MMA helped to make the material tougher. The strain at break considerably improved in the case of both the tensile and the 3-point bending tests. The HAP loading further improved the toughening effect. We obtained the best results (tensile strength, flexural strength) at the 1 phr HAP-loaded samples. The cytotoxicity test results were also promising, since the morphology and adherence of the cells did not change, but further studies are required to confirm these results.

Acknowledgments

The research reported in this paper was supported by the National Research, Development and Innovation Office (NKFIH FK 138501) and by the NVKP_16-1-2016-022 project entitled: Developing a new generation of manufacturing process of tailor-made medical implants and tailor-made medical aids for additive technologies. Kolos Molnár is thankful for the János Bolyai Research Scholarship of the Hungarian Academy of Sciences, and for the ÚNKP-21-5 New National Excellence Program of the Ministry for Innovation and Technology. The research was further financed by the Higher Education Institutional Excellence Programme of the Ministry for Innovation and Technology in Hungary, within the framework of the Therapeutic Development thematic program of the Semmelweis University.

  doi:10.5075/epfl-298799_978-2-9701614-0-0

5. References

1. Li X, Zou Q, Wei J, Li W. The degradation regulation of 3D printed scaffolds for promotion of osteogenesis and in vivo tracking. Composites Part B: Engineering 2021; 222:109084.
2. Manapat J, Qiyi C, Piaoran Y, Advincula R. 3D printing of polymer nanocomposites via stereolithography. Macromolecular Materials Engineering 2017 ; 302 :1600553.
3. Naeem OA, Bencharit S, Yang I-H, Stilianoudakis SC, Carrico C, Tüfekçi E. Comparison of 3-dimensional printing technologies on the precision, trueness, and accuracy of printed retainers. American Journal of Orthodontics and Dentofacial Orthopedics 2022; 161 :582-91.
4. Horne R, Hausman K. 3D printing for dummies, Wiley. 2017.
5. Gibson L, Rosen D. Additive manufacturing technologies. Springer. 2010.
6. Gladwin M, Bagby M. Clinical aspects of dental materials: theory, practice, and cases. Lippincott Williams & Wilkins. 2004.
7. Strbac GD, Schnappauf A, Giannis K., Bertl MH, Moritz A, Ulm C. Guided autotransplantation of teeth: a novel method using virtually planned 3-dimensional templates. Journal of Endodontics 2016, 42 :1844-50.
8. Öztürk F, Malkoc S, Ersöz M, Hakki SS, Bozkurt BS. Real-time cell analysis of the cytotoxicity of the components of orthodontic acrylic materials on gingival fibroblasts. American Journal of Orthodontics and Dentofacial Orthopedics 2011; 140:243-9.
9. FormLabs. Material data sheet. 2016. https://formlabs-media.formlabs.com/datasheets/DentalSG-DataSheet.pdf
10. Tyurnina AV, Morton JA, Subroto T, Khavari M, Maciejewska B, Mi J, Grobert N, Porfyrakis K, Tzanakis I, Eskin DG. Environment friendly dual-frequency ultrasonic exfoliation of few-layer graphene. Carbon 2021; 185: 536-45.
11. Kurzmann C, Janjić K, Shokoohi-Tabrizi H, Edelmayer M, Pensch M, Moritz A, Agis H. Evaluation of resins for stereolithographic 3D-printed surgical guides: the response of L929 cells and human gingival fibroblasts. BioMed Research International. 2017; 4057612.

HIGHLY ALIGNED DISCONTINUOUS FIBRE COMPOSITE FILAMENTS FOR FUSED DEPOSITION MODELLING: OPEN-HOLE CASE STUDY

Narongkorn, Krajangsawasdi [a], Benjamin K.S., Woods [a], Ian, Hamerton [a], Dmitry S., Ivanov [a], Marco L., Longana [a]

[a] Bristol Composites Institute, Department of Aerospace Engineering, School of Civil, Aerospace, and Mechanical Engineering, University of Bristol, Queen's Building, University Walk, Bristol, BS8 1TR, UK

Abstract: *Fused filament forming (FFF), a thermoplastic layer-by-layer additive manufacturing technique, can build complex geometries, reducing manufacturing defects created with conventional methods, e.g. the interruption of fibre continuity by machining through-holes, by defining an alternative printing path. Aligned discontinuous fibre composites (ADFRC) preforms, produced with a novel fibre alignment technology, High Performance Discontinuous Fibre (HiPerDiF), were used as a reinforcement for poly(L-lactic acid) (PLA) and then reshaped to a circular-shaped filament for FFF using a specially designed rolling machine. The physical and mechanical properties of the produced HiPerDiF-PLA filament was investigated. After that, the filament was printed by a general 3D printer to fabricate an open-hole sample with a curvilinear printing path around the hole. The printed open-hole specimen strength was compared to a hand lay-up of the HiPerDiF-thin tape with a same-size cut hole to examine the difference between the printed and the conventionally manufactured structures.*

Keywords: Aligned discontinuous fibre composites; fused filament forming; thermoplastic composite; additive manufacturing

1. Introduction

A novel fibre alignment technology, called High Performance Discontinuous Fibre (HiPerDiF), invented and patented at the University of Bristol, allows the production of aligned discontinuous fibre preforms as reinforcement for various types of polymeric matrices. The short fibres are dispersed in water, then the fibre-water suspension is sprayed between a series of parallel plates, the sudden momentum change upon impact aligns the fibres. After that, the fibres fall onto a conveyor mesh belt where the water is extracted, and the aligned dry fibre pre-form is obtained [1]. The produced preform is finally impregnated with a matrix, either thermosetting or thermoplastic, to obtain a thin prepreg tape. The overall process is illustrated in Figure 1 [2].

Fused filament forming (FFF), a thermoplastic layer-by-layer additive manufacturing technique, can build complex geometries, reducing the manufacturing defects generated by conventional methods, while also reducing stress concentrations through customized printing paths [3-5]. However, general materials for FFF, *e.g.* poly(acrylonitrile-butadiene-styrene) (ABS) or poly(L-lactic acid) (PLA), have low mechanical performance [6]. To expand the application of FFF from prototypes or secondary structures to more structural parts, the thermoplastics used in the process needs to be reinforced and the HiPerDiF fibre is one of the suitable reinforcements. This is because of the high formability of the discontinuous fibre that would favour the complex shape forming of the FFF [7].

  doi:10.5075/epfl-298799_978-2-9701614-0-0

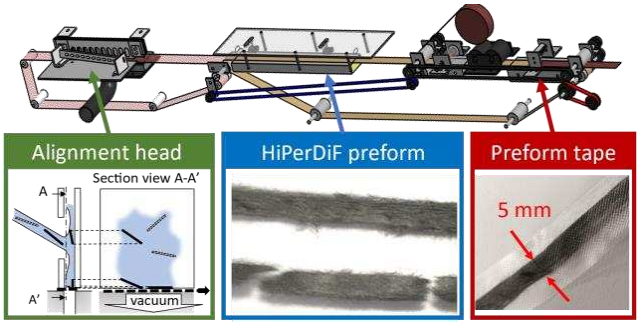

Figure 1. Schematic describing HiPerDiF process starting from spraying fibre to a plate obtaining an aligned fibre preform about 5 mm in width and ending with impregnated preform tape [2].

In a previous study [8], the HiPerDiF thin preform was used to reinforce PLA: this thin HiPerDiF-PLA tape was re-shaped manually by compression in a metal mould under high temperature and finally pultruded to a circular cross section. The manual method is time and labour consuming. A new industrially scalable filament forming method has been implemented to continuously produce filament automatically with minimum human interaction. This paper is investigating the advantages of using the HiPerDiF reinforcement as a 3D printing filament format rather than the original thin tape by fabricating an open-hole sample with the fine diameter filament printing with an predetermined printing path that can avoid fibre cutting by machining or drilling, then compared the open-hole strength with the ones of a conventional hand laid-up 5-mm wide HiPerDiF thin tape with an open hole obtained by punching.

2. Filament preparation and properties

2.1 Filament preparation

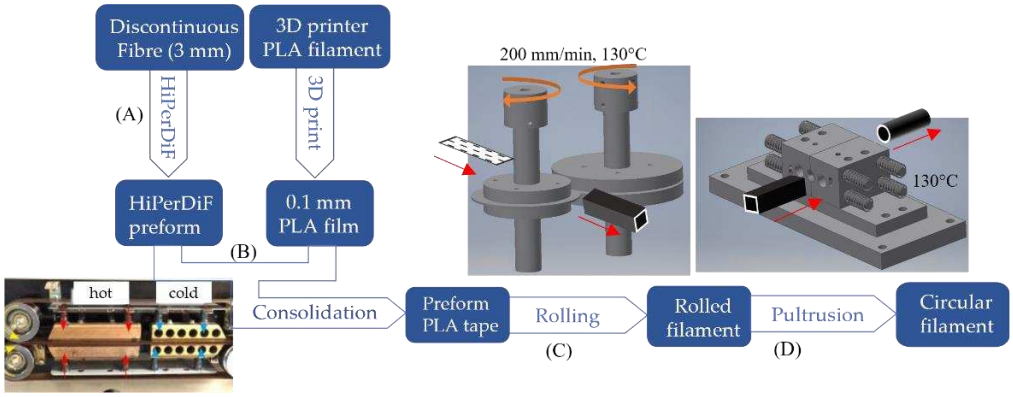

Figure 2. Overall filament forming process starting from (A) HiPerDiF preform fibre and thin PLA matrix preparation, (B) consolidation of HiPerDiF preform and PLA tape, (C) bulking tape by designed rolling technique and (D) pultrusion through a series of nozzles.

The filament was made by two constituents: commercial 3 mm chopped C124 carbon fibre with a fibre diameter of 7 µm, supplied by Toho Tenax GmbH and PLA for 3D printing supplied by 3D4Makers B.V. The PLA was prepared as a thin film, with 0.1 mm thickness, using a 3D printer to obtain a 200 x 13 mm^2 rectangular sheet. After passing the fibre through the HiPerDiF process mentioned in the introduction, the HiPerDiF preform was impregnated with the PLA film using heat and compression force followed by cooling in a dedicated consolidation machine to produce the HiPerDiF-PLA impregnated tape. The tape with a nominal cross section of 0.2 x 5 mm^2 is the starting point of the re-shaping to a circular filament. Figure 2 shows the overall

filament forming process starting from the preparing constitutive materials and ending with a pultrusion of a circular 3D printing filament.

The tape was re-shaped in a designed heated roller with a tuned gap (approximately 1 x 1 mm^2). The roller is heated up to 130°C to allow the thermoplastic to soften and fuse with itself, but not to melt. The roller moves with a linear speed of 200 mm/min to drive the material to the gap and another stepper motor with a synchronized speed is used to pull the bulked filament from the rollers. The rollers fold and compress the thin tape. As the pressure applied is not entirely uniform, the process produces a square-like filament with the variable cross-section characteristics, *e.g.* containing microvoids (Figure 3 (a)) and material overflow into the gap between two rollers (Figure 3 (b)).

To refine the filament cross section of the square to a circular that is ready to be fed to a 3D printer, the square filament (with the imperfections) was finally pultruded through a convergent nozzle from 1.4 mm to 1 mm (stage D in Figure 2) at a temperature of 120°C. Then, the filament was finally pultruded through a straight drilled polymer nozzle with a diameter of 1 mm under the same temperature as the previous pultrusion to improve the shape and surface finishing. The perfect circular shape cross section that is ready to feed to a 3D printer is shown in Figure 3(c).

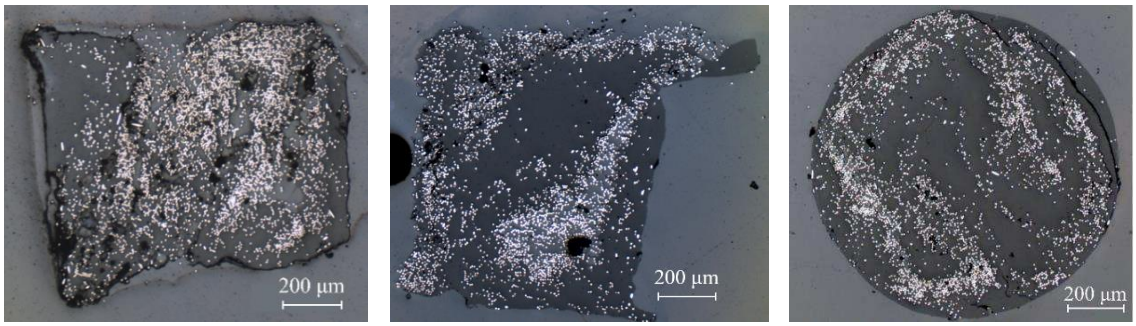

(a) (b) (c)

Figure 3. (a) Square filament present as microvoids in the filament due to not enough compression; (b) square filament present as material overflow at the corners due to the excess compression and too small gap; (c) the final perfect circular cross section filament.

2.2 Tensile specimen preparation

The printing path of a 100 mm x 100 mm spiral square was designed as shown in Figure 4(a) to produce a single layer specimen for tensile properties investigation. The printed part with this path was cut into four 100 mm x 10 mm tensile testing samples. The sample was fabricated with a commercial 3D printer, Ender3, with the nozzle replaced with a modified 1.4-mm diameter flat-end brass nozzle. The printing set-up was: nozzle temperature 210°C, bed temperature 80°C, speed 300 mm/min, set nozzle height 0.4 mm, and raster gap 1.6 mm. The printed large square, Figure 4(b), shows a well-laid raster along the defined linear path. At the corners, there are some deviations from the sharp 90° turning path, as seen in Figure 4(b), this is caused by the poor adhesion of the filament to the printing bed which is more severe at the sudden direction changes. All the corners were discarded in this study by cutting them following the cutting line shown in Figure 4(b), with a hack saw for metals to make four straight 10 x 100 mm single layer tensile specimens. The dimensions, width and thickness, of the sample were measured. Then,

  doi:10.5075/epfl-298799_978-2-9701614-0-0

the 20 mm fibreglass end-tabs were attached at both ends of the specimens leaving a 60 mm gauge length.

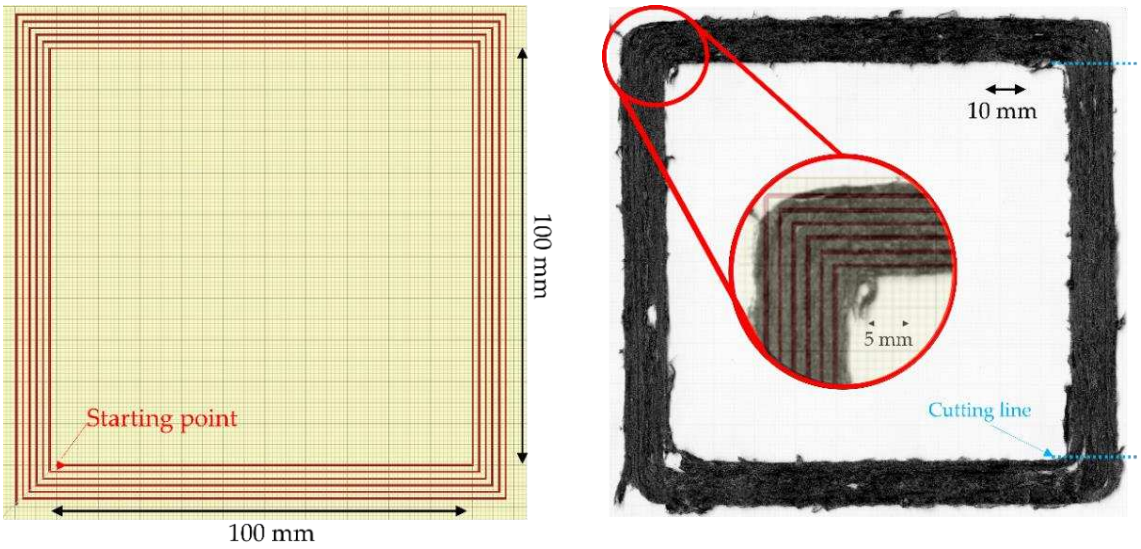

(a) (b)

Figure 4. (a) Printing path of large square shape with 90° sharp turning corners to produce four tensile samples starting from inside; (b) top surface of the sharp corner printed part with a zoom-in of a corner.

2.3 Tensile testing and result

A servo-electric tensile testing machine (Shimadzu AGS-X, Japan) with a 1 kN load cell operated at a cross-head displacement speed of 1 mm/min was used. The strain was measured using a video extensometer (Imetrum, UK). The tensile properties of the tested samples are shown in Table 1. The stiffness is similar to the HiPerDiF-PLA tape investigated earlier [2]. However, the strength is slightly lower. This may be caused by the poor raster bonding that shows as the breakage along with the inter-raster bonding rather than perpendicular to the raster.

Table 1: Tensile properties of the single-layer 3D printed part.

Tensile stiffness (GPa)	Tensile strength (MPa)	Breaking strain (με)
19 ± 3	122 ± 26	7004 ± 1000

3. Open-hole testing

3.1 Open-hole specimen fabrication

To illustrate the benefit of using the HiPerDiF as a 3D printing material, open hole samples were fabricated with two different methods: 3D printing with a curvilinear predetermined path and thermally annealed hand layup with a punched hole.

3.1.1 Open-hole printing

The printing path, shown in Figure 5(a), was designed to steer around a hole in the middle of the sample in the shape of a half-circle. The steering can avoid the cutting of material to make a hole that may result in the discontinuity of the structure and a weak point. The path was inspired by curvilinear 3D printing path to fabricate an open hole specimen from literature [3, 5]. The G-code was generated to print the specimen as five upwards and downwards half circles with a

  doi:10.5075/epfl-298799_978-2-9701614-0-0

straight line before and after reaching the curvature. This will leave one straight-continuous line and four short linear lines just attached to the outer curvature on each side to fill the rectangle specimen. The printing was performed with the same setting as the tensile sample. The curvilinear printed sample is shown in Figure 5(b). The achieved hole dimension measured in the direction perpendicular to the load is 5-6 mm. This dimension is smaller than the designed path, *i.e.* 10 mm diameter. The smaller hole results from the poor adhesion between the printing bed and the heated filament. The material cannot make enough adhesion to the bed during sudden direction changes. This drags the deposited material leaving an eye-shaped hole.

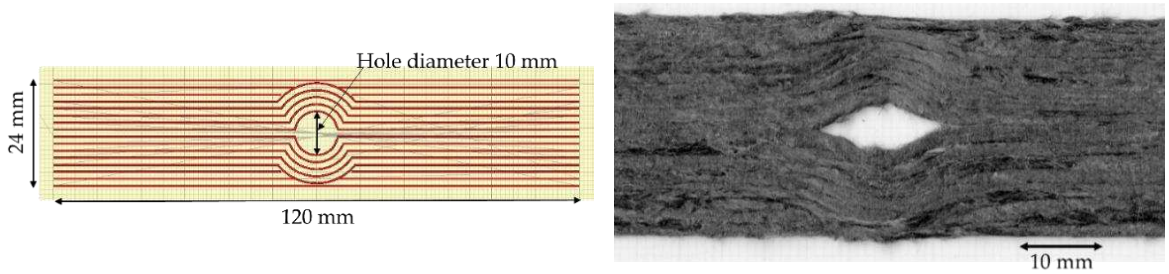

(a) (b)

Figure 5. (a) Designed curvilinear 3D printing path for 10 curvilinear rasters sample; (b) high magnification at the curvature hole of 10 curvilinear rasters sample on the bottom side (sticking to the printing bed).

3.1.2 Open-hole layup

The benchmark specimens were made using a conventional tape layup process, using 5-mm wide HiPerDiF-PLA pre-impregnated tapes. On the odd layer, six tapes were placed side by side to make a 30-mm wide layer, then the even layer was stacked with a half-width overlap to close the butt joint of the tapes on the previous layer. There are four stacking of the overlap layers as the cross section schematic shown in Figure 6(a) to obtain a total thickness of ~0.6 mm. The layup was compressed in a vacuum bag (-1 bar) and heated at a temperature of 190°C for 1 hour to achieve a consolidated panel. Then, the protruded edges of around 2.5-mm on each edge were trimmed with a knife, to achieve a 25-mm-wide sample. Finally, the middle circular 6-mm hole was punched with a hollow punching tool with a hammer. The layup specimens with a punched hole are shown in Figure 6(b).

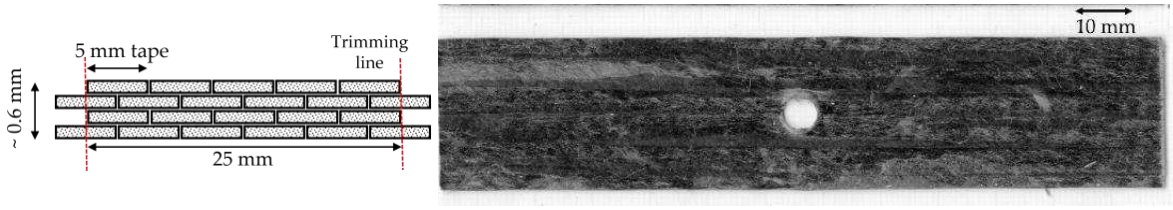

(a) (b)

Figure 6. (a) Stacking sequence of the layup sample showing four overlap layers with the final cutting line; (b) an example of a layup part with a 6-mm punched hole.

3.2 Open-hole testing result

The hole size was measured from the scanned image of the sample at the widest position of the hole. The cross-section area used to calculate the strength is the specimen width minus the hole diameter multiplied by the thickness measured at the position around the hole. The samples were tested using the same testing machine and procedure as the tensile tests described above.

  doi:10.5075/epfl-298799_978-2-9701614-0-0

The maximum load was recorded for the calculation of open-hole ultimate strength using the cross section area of the sample disregarding the hole. The ultimate strength of both specimen types is shown in Figure 7(a). It can be seen that the printing part has lower ultimate strength than the lay-up. This is because of (i) the presence of fibres misaligned from the load direction due to the rasters printing pattern; (ii) the inconsistency of the printing and imperfect welding of rasters during printing; (iii) the higher compaction of the lay-up and the removal of voids through the thermally annealing and vacuum. The stress-strain curve of a sample from each tested group are shown in Figure 7(b). This also shows the different mechanical behaviour between the two groups: a highly non-linear behaviour in the curvilinear 3D printing and a linear behaviour with a sudden failure in the layup with a cut hole.

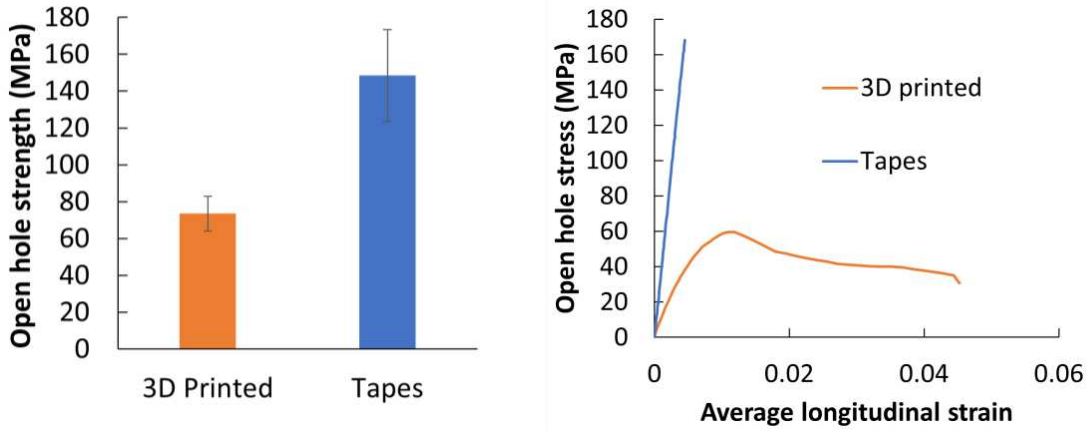

(a) (b)

Figure 7. (a) Open-hole strength of different sample types; (b) open-hole stress versus average longitudinal strain curves of each sample type showing different failure behaviours.

Despite the lower strength of the printed part, the curvilinear raster changes the load direction and stress concentration around the hole. The initial failure of the printed samples was the breaking of the inter-raster around the hole, then the curve rasters moved and the hole closed before the breakage perpendicular to the load direction. The final breakage of the sample occurred to some of the rasters so the overall sample was not completely separated. The failure of the open-hole printed part shows in Figure 8(a). By contrast, the lay-up fails suddenly in one rupture which breaks perpendicular to the load at the position of the hole, as seen in Figure 8(b). It can be implied that the printing part has higher non-linearity and shows less brittle behaviour compared to the lay-up sample.

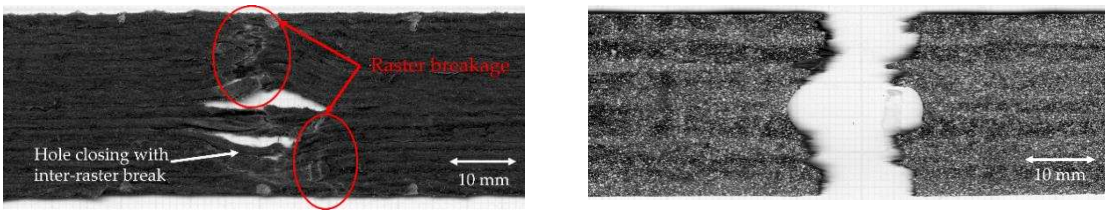

(a) (b)

Figure 8. Breakage of the open-hole samples: (a) 3D printed curvilinear part showing hole closing by the inter-raster separation following raster breakage; (b) tape lay-up showing breakage perpendicular to the fibre/load direction at the middle of the hole.

4. Conclusions

  doi:10.5075/epfl-298799_978-2-9701614-0-0

In this study, the ADFRC tapes, produced with the HiPerDiF technology, and a PLA matrix, have been transformed, with an specially industrially scalable designed method, into circular cross-section filaments suitable for 3D printing. The tensile performance of the part 3D printed with the filament was evaluated by printing the produced filament into a single layer specimen. The stiffness and strength are approximately 19 GPa and 122 MPa, respectively. The benefits of fabricating the HiPerDiF tape into circular cross section 3D printing filament were emphasized by making an open-hole specimen for the tensile testing. 3D printing can fabricate the open hole sample by steering around the hole without cutting the rasters or the fibres. This results in a change of failure mechanism from brittle breakage that occurred in the layup with oven-cured to the more progressive failure mode by breaking at the inter-raster bonding around the curvature. Although the open hole sample fabricated with 3D printing to the curvilinear printing path shows lower strength than the layup, the 3D printed curvilinear may benefit some applications that require a non-linear behaviour rather than a high strength with a catastrophic failure. Future work will investigate modifications to the printing process to increase further the strength and dimensional accuracy of the open hole specimens.

Acknowledgements

This work was supported by the Engineering and Physical Sciences Research Council (EPSRC) through the ACCIS Doctoral Training Centre [EP/L016028/1] and the EPSRC “High Performance Discontinuous Fibre Composites a sustainable route to the next generation of composites” [EP/P027393/1] grant.

5. References

1. Yu H, Potter KD, Wisnom MR. A novel manufacturing method for aligned discontinuous fibre composites (High Performance-Discontinuous Fibre method). Composites Part A: Applied Science and Manufacturing. 2014;65:175-85.
2. Blok LG, Longana ML, Woods BKS. Fabrication and characterisation of aligned discontinuous carbon fibre reinforced thermoplastics for automated manufacture. Materials. 2020;13(20):4671.
3. Zhang H, Li A, Wu J, Sun B, Wang C, Yang D. Effectiveness of fibre placement in 3D printed open-hole composites under uniaxial tension. Composites Science and Technology. 2022:109269.
4. Sanei SH, Arndt A, Doles R. Open hole tensile testing of 3D printed continuous carbon fiber reinforced composites. Journal of Composite Materials. 2020;54(20):2687-95.
5. Khan S, Fayazbakhsh K, Fawaz Z, Nik MA. Curvilinear variable stiffness 3D printing technology for improved open-hole tensile strength. Additive Manufacturing. 2018;24:378-85.
6. Krajangsawasdi N, Blok LG, Hamerton I, Longana ML, Woods BKS, Ivanov DS. Fused Deposition Modelling of Fibre Reinforced Polymer Composites: A Parametric Review. Journal of Composites Science. 2021;5(1):29.
7. Such M, Ward C, Potter K. Aligned discontinuous fibre composites: a short history. Journal of Multifunctional Composites. 2014;2(3):155-68.
8. Krajangsawasdi N, Longana ML, Hamerton I, Woods BK, Ivanov DS. Batch production and fused filament fabrication of highly aligned discontinuous fibre thermoplastic filaments. Additive Manufacturing. 2021;48:102359.

  doi:10.5075/epfl-298799_978-2-9701614-0-0

ANALYSIS OF THE REMOTE LASER CUTTING PROCESS OF CARBON FIBRE REINFORCED POLYMERS AND ITS INFLUENCE ON MECHANICAL PROPERTIES

Benjamin Schmidt[a], Markus Husert[a], Martina Zimmermann[b], Markus Kästner[a,c]

a: Institute of Solid Mechanics, TU Dresden, Germany – Benjamin.Schmidt@tu-dresden.de
b: Institute of Materials Science, TU Dresden, Germany
c: Dresden Center for Computational Materials Science (DCMS), TU Dresden, Germany

Abstract: In machining technologies for fibre reinforced polymers, remote laser cutting plays a special role as it can minimize the drawbacks of other laser cutting methods. In remote laser cutting, the laser spot is moved with tilt-able mirrors, instead of a translational movement of the optics. This means smaller masses need to be moved, which enables higher accelerations and thus it allows for precise cutting results even at high spot velocities and sharp edges. This results in a reduction of the heat input and thus thermal damage, like charred edges and matrix evaporation. For a reliable structural analysis, it is necessary to quantify these damages and to create a linkage to the mechanical properties of the machined structures.

In the first part of this contribution the remote laser cutting process is analysed. Cyclic holes, that are cut with three different cutting parameter configurations are analysed. A two-dimensional heat conduction simulation is used to determine the time dependent temperature field during cutting and cooling phase. Based on the maximum local temperature reached during this process, two characteristic zones can be identified: the heat affected zone, where starting with glass transition temperature thermally induced changes in the chemical and mechanical properties occur, and the matrix evaporation zone, where matrix evaporation temperature is exceeded. Here only the fibres are still present. The latter is also visible in micro-sections, which are used for validation.

In a second part, a linkage to the mechanical properties of the machined structures is created. Therefore, tensile tests of open hole specimens are simulated with consideration of the thermally induced damage. In the heat affected zone material is modelled with temperature dependent reduction parameters for the mechanical parameters. Additionally, during the tensile test mechanically induced damage is described by a macroscopic, orthotropic damage model. Three remote laser cutting parameter configurations and milled specimens as a thermally undamaged reference are compared.

Finally, an extension of the thermal cutting simulation from 2D to 3D is presented is presented. The effective thermal material parameters are calculated with a rule of mixture from the microscopic parameters for the fibre, the matrix and the process gas. The evaporation of matrix and fibre material is modelled with phase transitions. The laser spot is modelled with a Gaussian distribution as a heat input on the upper side. The emerging process gas is assumed to absorb a part of the laser power according to the Beer-Lambert law.

Keywords: Process-Structure-Property-Linkage, Laser Cutting, Thermal Degradation, Carbon Fibre Reinforced Polymers, Process Simulation, Mechanical Properties

1 Introduction

Laser beam cutting, as a non-contact and wear-free cutting technology with consistent quality, is one approach to minimise mechanical damage during the production of carbon fibre reinforced polymers (CFRP). Remote laser cutting has advantages over gas-assisted laser cutting for processing CFRP: the shorter interaction times between the material and the laser beam are made possible by the higher spot speeds. This decreases the amount of heat that is absorbed by the surrounding material. However, this cutting process has downsides as well: porosity and matrix deterioration occur near the cutting gap as a result of the heat input.

Herzog et al. [1] provide a comprehensive analysis of the Heat Affected Zone (HAZ) and the damage it causes. They examined CFRP plates that had been cut using three different laser sources. Matrix damage occurred in the HAZ area in micro-sections. The strength of laser cut, water jet cut and milled specimens was evaluated in tensile tests. The tensile strength was lowered as the HAZ width increased. The use of notched specimens might be beneficial for a more complete comparison of the technologies. Different methodologies for the investigation of process-generated damage and the cutting process optimisation were also provided.

Frayssinous et al. [2] researched laser cutting of polymers using a fibre laser with a diameter of 3.44 µm. The results were compared to a CO_2 laser and revealed that the fibre laser had a better cutting quality due to the wavelength being resonant with the polymer's carbon-hydrogen bond.

Canisius [3] created a numerical laser cutting process model for CFRP structures that allows for gap and HAZ predictions for arbitrary cutting settings.

The majority of these studies place a considerable emphasis on the process itself and the quantification of the resulting thermal damage. However, because CFRP are mostly utilised for structural parts, it is worth to investigate the impact of process-induced damage on the mechanical material properties and the failure behaviour of the processed structures. In two publications this challenge is addressed in different ways by Young [4] and Stock and Kerschreiter [5]. In [4] the mechanical damage to CFRP caused by micro hole laser drilling (d = 120 µm) is analysed. In static and cyclic tensile tests, drilled specimens are compared to intact specimens. During the static tests, a 10% stiffness loss and a 29% strength reduction were measured as a result. It is not suggested to use these values in material modelling since the influence of the HAZ is difficult to distinguish from the increased stress concentration at the holes. In [5] stress concentrations in laser cut woven CFRP specimens are examined with open hole tensile testing. The stress concentrations surrounding the hole are computed analytically. When comparing laser cut and water jet cut specimens, a reduction in stiffness was observed in the HAZ, resulting in lower stress peaks at the holes and hence greater allowable maximum forces for laser cut specimens.

In this paper, the influence of thermal damage on the mechanical properties of CFRP structures is analysed systematically with a comparative experimental and numerical study of the milled and laser cut processes, as well as a structural characterisation of the treated specimens. A model for the thermally damaged material based on the investigation of process-induced damage utilizing 2D thermal analysis and micro sections is presented. Tensile tests of specimens created with different processing parameters are then used to quantify the impact on the

mechanical properties of the CFRP. A finite element analysis of specimens prepared with the different process configurations was used to validate the material model for the HAZ.

As presented in [6], the 2D thermal approach has some drawbacks, as it is less accurate for large gaps and micro sections are needed in order to identify the input parameters. For this reason, as an outlook, a proof of concept for a 3D thermal simulation which regards the laser as a heat source, and matrix- and fibre sublimation as phase transitions is presented.

2 Material and process description

In this contribution, CFRP plates were remote laser cut with three different parameter configurations, as described in Table 1. The resulting cutting gap was analysed by means of micro sections. Additionally, open hole tensile tests with holes prepared with the different laser cutting parameter configurations were examined. A detailed description of the experimental and numerical setup can be found in [6].

Table 1 Process parameters for three different laser cutting process configurations L12, L25 and CO_2.

Parameter	Unit	L12	L25	CO_2
Beam source	-	Fibre laser	Fibre laser	CO_2laser
Wavelength	µm	1.07	1.07	10.6
Laser power	W	1860	4650	2870
Focal spot diameter (86 %)	µm	36	36	482
Spot velocity	m s^{-1}	5	1	0.5
Cool down time	s	1	1	2
Cutting cycles	-	40	4	7
Gap width	µm	66.5	166.6	482

The laminates of the composite material were pressed from Sigrapreg C U150-0/NF-E340/38 % prepregs consisting of Torayca T700 carbon fibres and an E340 epoxy matrix. In this analysis plates with a $[0/90]_{6s}$ stacking sequence and a thickness of 1.9 mm are used. A fibre volume content of V_f = 0.54 was measured.

In remote laser cutting, the laser spot is deflected by two tilt-able mirrors. This allows for a high spot velocity, which minimises the interaction time with the laser and thus reduces the HAZ. The laser source is a 5 kW fibre laser with a wavelength of 1070 nm and a focal diameter (86 %) d_f = 36 µm. Additional process parameters can be found in Table 1.

In order to analyse the influence of the cutting process on the mechanical properties, open hole tensile test specimens are utilised, as illustrated in Figure 1. The specimens have a length of 240 mm and a width of 28.8 mm. In grey, the clamping area with a length of 50 mm is highlighted. The hole diameter is 4.8 mm.

3 Cutting process simulation

For the structural analysis of remote laser cut CFRP structures, it is necessary to identify the HAZ. Since large portions of the HAZ are invisible in micro sections, a numerical identification allows for a higher accuracy. The laser has a high spot velocity, so the interaction time is very short, and what is more important for the formation of the HAZ is the heat transport inside the material, which is on a much larger time scale. The layer thickness is large compared to the gap width, so only a negligible small heat transport occurs out of plane and therefore a layer-wise 2D approach is a good approximation.

The cutting process is modelled thermally with the two-dimensional heat equation

$$\rho c \dot{T} = \lambda \nabla^2 T \tag{1}$$

with the mass density ρ, the heat capacity c, the temperature T, and the homogenised thermal conductivity λ of a single layer. For the initial state of the simulation, it is assumed that in the gap area the fibre evaporation temperature T_{fib} is reached, while the remaining area is still at reference (room) temperature T_0, as illustrated in Figure 1 (right). Out of plane heat conduction is neglected, which is a reasonable approximation because the heat conductivity in fibre direction is much higher than perpendicular to them. Due to symmetry, only a quarter specimen is simulated. There are 90 elements over the quarter circumference.

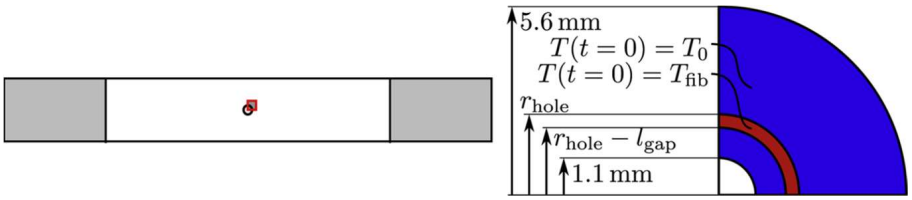

Figure 1. Open hole tensile test specimen (left) and simulation area for heat simulation with initial temperatures T_{fib} in the area of the cutting gap and T_0 in the remaining area (right).

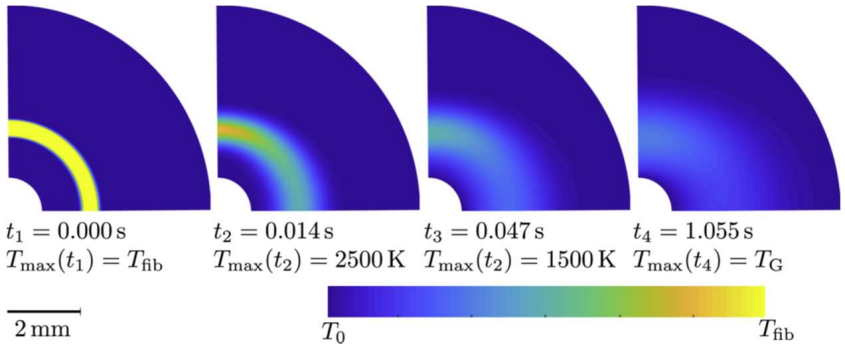

Figure 2. Temperature field in the simulation area at various times.

Figure 2 shows the temperature fields at different times for the CO_2 laser cutting configuration. The heat spreads into the gap environment, whereby the maximum temperature in the field decreases. When the maximum temperature falls below the glass transition temperature T_G after about one second ($t = t_4$), the simulation terminates. Since the fibre direction is from left to right, the temperature decreases faster in the lower part of the quarter circle and stays for a longer time in the upper part.

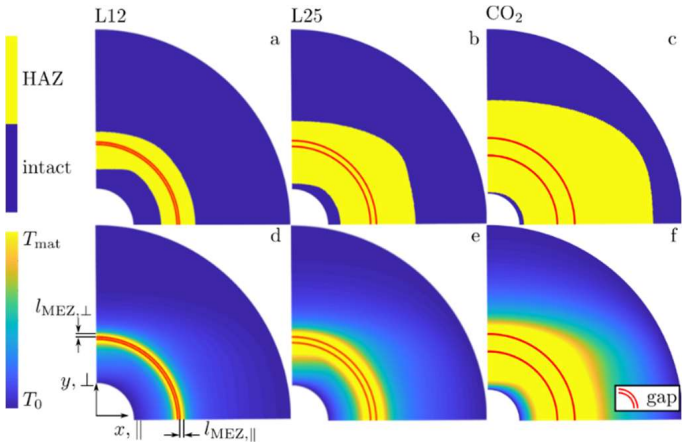

Figure 3. Heat affected zone (top) and maximum temperature (bottom) reached in the cutting process as well as the resulting gap for three cutting parameter configurations L12 (a) and (d), L25 (b) and (e), and CO_2 (c) and (f).

In Figure 3 the cutting process simulation results for the three process configurations introduced in Table 1 are presented. Figure 1 (a) to (c) show the HAZ, which is the area where the glass transition temperature was reached. At this temperature, chemical reactions start, which can lead to irreversible changes in the mechanical properties of the material. Figure 1 (d) to (f) show the distribution of the maximum temperature reached during the simulation. The yellow area, which is the area where the matrix evaporation temperature was exceeded, can be used for validation, as the matrix evaporation zone (MEZ) is visible in the micro sections and was also measured.

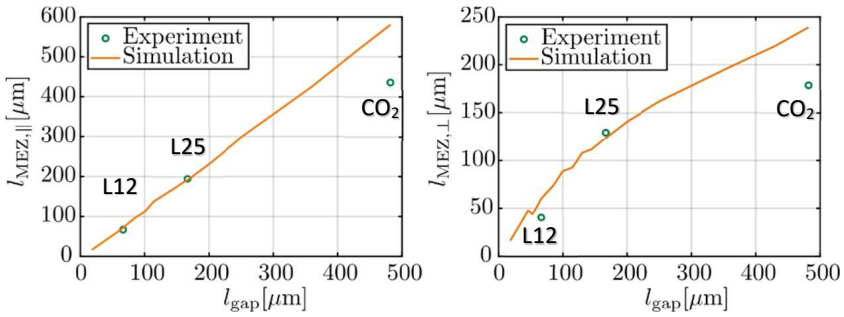

Figure 4. Matrix evaporation zone length parallel (left) and perpendicular (right) to fibre direction for varying gap width in simulation and experiment.

In Figure 4 the comparison of numerically and experimentally obtained MEZ in fibre parallel and fibre perpendicular directions is presented. For the two fibre laser cut configurations, there is a good agreement. The simulation of the CO_2 laser cut specimen overestimates the MEZ area (Figure 4). The reason can be found in the broad gap, which allows for a relatively free gas flow, so hot process gas can leave out of plain, which is not yet taken into account in this simulation. Therefore, the heat energy in the simulated gap is overestimated, and thus the MEZ.

4 Mechanical simulation

In order to analyse the influence of the cutting process on the mechanical properties and the failure behaviour of the material, tensile tests were performed experimentally and numerically. In the simulation, the open hole tensile test specimen introduced in Figure 1 (left) is discretised

three dimensionally layer-wise with fully integrated solid elements. The area around the hole is discretised with 100 elements over the circumference. The $[0/90]_{6s}$ CFRP is modelled on a macroscopic level by a stack of twelve orthotropic material layers. For every single layer failure initiation and propagation is considered with the model introduced by Pinho et al. [7]. The model uses damage variables for the fibre tensile, fibre compression and the matrix mode with linear degradation.

In order to model the thermally damaged material in the HAZ, the initial model parameters are reduced with reduction factors, so instead of the values for intact material, lower values are used for stiffnesses, strengths and fracture toughnesses. Stock and Kerschreiter [5] performed tensile tests on thermally damaged specimens and identified a strength reduction of $f_{strength}$ = 68 % and f_{Young} = 22 % at the cutting gap. These values are used as maximum reduction values in this simulation as well, since both composites are made of carbon reinforced epoxy. In this model, the parameters are degraded linearly over the length of the HAZ.

In Figure 5, the results of the tensile tests are presented. The reference is the milled specimen without thermal damage. For each cutting configuration five specimens were tested, and the maximum strength reached during the tensile test is plotted with black dots. For the two fibre laser cut specimens, an increase in the HAZ length leads to increased strengths. At first glance, this seems unintuitive, since the material strength is decreased in the HAZ. However, in addition to the strength, the material stiffness is also reduced and this has a contrary effect: due to the smaller stiffness, the notch effect of the hole is mitigated and the stress peak at the hole is smaller. This leads to a more homogeneous stress field and thus a higher effective stress. For the CO_2 laser cut specimen, again a different trend can be observed: for a large HAZ the maximum effective strength is decreased. The reason for this can be found in the reduction of the load bearing area due to the large HAZ. The simulation can reproduce this general trend but overestimates the effective strength of the CO_2 laser cut specimens, since the simulation result is not in the scatter range of the experimental results. There are two main reasons for the discrepancy. First, the process model already showed a deviation in the results for this configuration, so the error in the mechanical simulation might be caused by the wrong input parameters. A second reason can be found in the slow spot velocity leading to a large interaction time of the CO_2 configuration, see Table 1. Additionally, to the matrix evaporation, there is also a time-dependent decomposition, which has a stronger influence at longer interaction times. This effect is not regarded in the simulation, as the overall modelling approach only depends on the maximum temperatures.

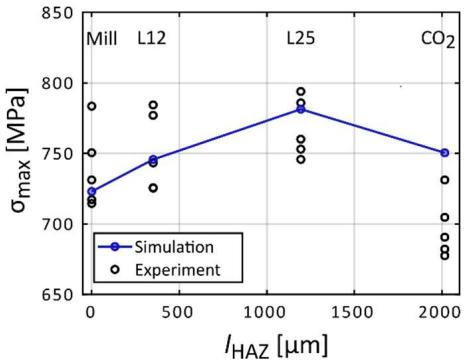

Figure 5. Simulation and experimental results for the open hole tensile tests for different processing configurations.

5 Conclusions

Investigations into the effect of the remote laser cutting process on CFRP failure were presented in this article. An experimental and numerical examination of open hole specimens produced with various cutting procedures was carried out for this objective. A process modelling approach was developed to estimate the width of the HAZ, which was further incorporated into a parametrised damage model to study the resulting structure properties of open hole specimens.

It is possible to replicate the complicated interactions between different process configurations and the resulting mechanical behaviour. Fibre laser cut specimens had a greater tensile strength than thermally intact milled specimens. The highest tensile strength was observed with a medium HAZ size, demonstrating that the goal of a cutting process optimisation does not have to be a minimal HAZ. A contrary trend occurred for CO_2 laser cut specimens with a greater HAZ, where the tensile strength was reduced. The simulation correctly predicts that the tensile strength will grow initially for greater HAZ and decrease thereafter.

6 Outlook

Despite the generally good accordance of experimental and numerical results, the presented process model has one major drawback: The gap width of a cutting configuration is used as an input parameter. This means, that no true prediction of the cutting process is possible, as for each new process parameter configuration a specimen has to be cut and measured.

An alternative approach that solves this problem is the full 3D process model as recently presented in [8], based on a similar approach introduced by Canisius [3]. The simulation area is a hollow cylinder as presented in Figure 6 a). Here the laser is modelled with a Gaussian distribution. The interaction between laser and material is modelled with a Lambert-Beer approach as a heat source. Matrix and fibre evaporation are modelled as phase transitions (see Figure 6 b). After reaching the evaporation temperature in an element, the temperature cannot rise, but energy is absorbed until the evaporation enthalpy is reached and the phase variable *p* rises. Depending on the phase variables, the constituents of the rule of mixture which are used to calculate the homogenised thermal properties are changed. Epoxy resin and carbon fibre are used for intact material. After matrix evaporation, CO_2 as process gas, and carbon fibre are applied. After fibre evaporation only hot process gas is left, so it is used for both constituents.

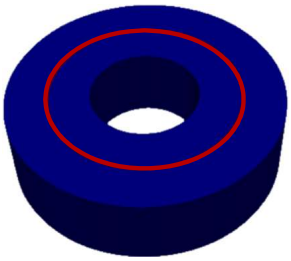

(a) Simulation domain of the laser cutting process simulation with the cutting contour (red).

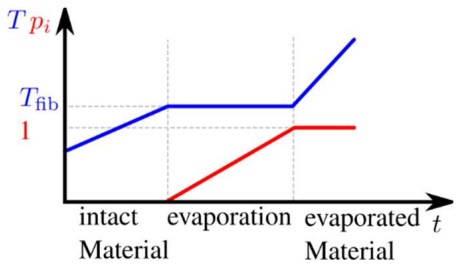

(b) Temperature and phase variable for a constant energy input during the fibre sublimation.

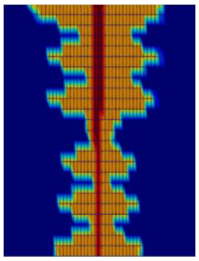

(c) Cross section after the cutting process, with intact material ■, complete matrix evaporation ■ and complete fibre and matrix evaporation ■.

Figure 6. Visualisations of the simulation domain, fibre evaporation and the cutting gap.

Acknowledgements

This work was supported by the Deutsche Forschungsgemeinschaft (DFG, KA 3309/6-3 and ZI 1006/12-3). The authors gratefully acknowledge the support.

7 References

1. Herzog D, Jaeschke P, Meier O, Haferkamp H. Investigations on the thermal effect caused by laser cutting with respect to static strength of CFRP. International Journal of Machine Tools and Manufacture. 2008;48:1464–73. doi:10.1016/j.ijmachtools.2008.04.007.
2. Frayssinous C, Fortin V, Bérubé J-P, Fraser A, Vallée R. Resonant polymer ablation using a compact 3.44 µm fiber laser. Journal of Materials Processing Technology. 2018;252:813–20. doi:10.1016/j.jmatprotec.2017.10.051.
3. Canisius M. Prozessgüte für das Laserstrahltrennen kohlenstofffaserverstärkter Kunststoffe. Berlin, Heidelberg: Springer Berlin Heidelberg; 2018.
4. Young TM. Impact of Nd-YAG Laser Drilling on the Fatigue Characteristics of APC-2A/AS4 Thermoplastic Composite Material. Journal of Thermoplastic Composite Materials. 2008;21:543–55. doi:10.1177/0892705708091283.
5. Stock JW, Kerschreiter J. Modelling the Stress Concentration in CFRP at Notches with a Thermally Influenced Cut Edge. AMR. 2016;1140:288–95. doi:10.4028/www.scientific.net/AMR.1140.288.
6. Schmidt B, Rose M, Zimmermann M, Kästner M. Analysis of process-induced damage in remote laser cut carbon fibre reinforced polymers. Journal of Materials Processing Technology. 2021;295:117162. doi:10.1016/j.jmatprotec.2021.117162.
7. Pinho ST, Iannucci L, Robinson P. Physically based failure models and criteria for laminated fibre-reinforced composites with emphasis on fibre kinking. Part II: FE implementation. Composites Part A: Applied Science and Manufacturing. 2006;37:766–77. doi:10.1016/j.compositesa.2005.06.008.
8. Schmidt B, Husert M, Rose M, Zimmermann M, Kästner M. Analysis of the remote laser cutting process induced damage in carbon fibre reinforced polymers. Proc. Appl. Math. Mech. 2021. doi:10.1002/pamm.202100099.

THE INFLUENCE OF REPAIR GEOMETRY ON THE STRENGTH OF REPAIRED COMPOSITE STRUCTURES

Spyridon Psarras[a], George Sotiriadis[a], Theodoros Loutas[a], Vassilis Kostopoulos[a]

a: University of Patras, Department of Mechanical Engineering & Aeronautics, 26500, GR – spsarras@upatras.gr

Abstract: *In the scenario deployed in this study, tests were carried out on repaired 300x250mm composite stiffened panels. The initial damage was assumed to be extended in a depth of the first six plies and a repair with scarf ratio of 1:50 was employed. A circular repair took place, utilizing laser-assisted ablation and the wet patches approach. The panels were tested in Detailed Finite Elements (FE) models were validated against the test findings and their performance as a prediction tool for the performance of repairs on composite aeronautical structures was assessed.*

Keywords: Repairs; Composites; Stepped Scarf; Finite Elements

1. Introduction

Low velocity impacts in CFRP's structures cause a variation of size, type and area of damages thus different types of repair methods have to take place [1]. For an ensured and controlled repair selection, numerical models have to be developed and verified against the acquired experimental results.

According to [2] the adhesive's mechanical behavior and more specifically the ultimate strain at failure is a primary factor regarding the strength of a bonded joint if the peel stresses can be neglected. Ductile adhesives have a higher strain to failure and as a result they can provide higher durability in a well-designed joint. Epoxy adhesives such as FM-300 have been widely used in previous research [3, 4]. The bondline thickness influence on the efficiency of the joint has been investigated in [4, 5]. It was determined that an adhesive to ply thickness ratio of 2/3 reduces stress concentration on the joint. In [6], it was observed that a 1% increase in void content in the adhesive film can reduce the recovered strength by 5%.

Despite the fact that adhesive bonding offers great advantages, it is only permitted in secondary structures of an airplane. The inability to completely detect flaws such as kissing bonds in the adhesive bondline with non-destructive testing is a major issue that hinders the utilization of adhesive bonding in primary structures. This type of flaw occurs when the two joined parts are in perfect contact but there is no mechanical connection between them. Researchers have tried to address the problem by proposing various configurations such as the impedance method or non-linear ultrasonics [7, 8].

Many studies have been carried out to optimize the scarf repair technique. In [9], the effect of repair geometry, patch type and surface treatment is studied for 8 plies repair. Yoo et al. [10] conducted a parametric study on the effect of different scarf ratios. They observed that for scarf ratios of 1:5-1:10, the recovered properties are low (below 20%) and by increasing the ratio (1:30) the recover percentage increased. However, in their research they used overplies at the

  doi:10.5075/epfl-298799_978-2-9701614-0-0

repair. In [11], they studied the effect of fiber oriented repairs, both experimentally and numerically. Despite the reduction in repair length, no significant improvement on the recovered strength was observed, compared to stepped scarf repair. Whittingham et al. [3] conducted an extensive study on the effects of the type of repair patch used on the bondline's quality.

In this study, we climb the test hierarchy from [12] and go to generic aircraft structures elements testing i.e. Repaired composite stiffened panels were manufactured and tested. The findings of the test campaign were used in order to validate the performance of FE models as a predictive tool for the performance of repaired structures.

2. Experimental campaign

2.1 Manufacturing and repairing the single stiffener panels

For this set of experiments, it was decided to add a stiffener to repaired plates. A common omega-shaped stiffener common in fuselage subcomponents was used. It consists of 7 layers of CFRP material, same as the plate. The layup is 45/-45/0/90/0/-45/45. . The material removal was done by using laser, the frequency was 600 kHz and the speed was 3600 mm/min. These parameters were the result of a statistical investigation about the laser parameters. A wet repair method was employed. The prepreg layers for the repair, were cut in a turning machine, to the desired diameters. Instead of the exact diameters originating from the scarf ratio, which were around 18mm, a more standard value was chosen, 20mm. This was decided as it was easier to find the required equipment to cut the pre-preg sheets circularly. The adhesive film was laid in the cavity and the prepreg plies were put one by one. Ultrasound (C-scan) was used to evaluate the uniformity of the repair. The quality after the treatment is visible in the figure bellow, *Figure 1*.

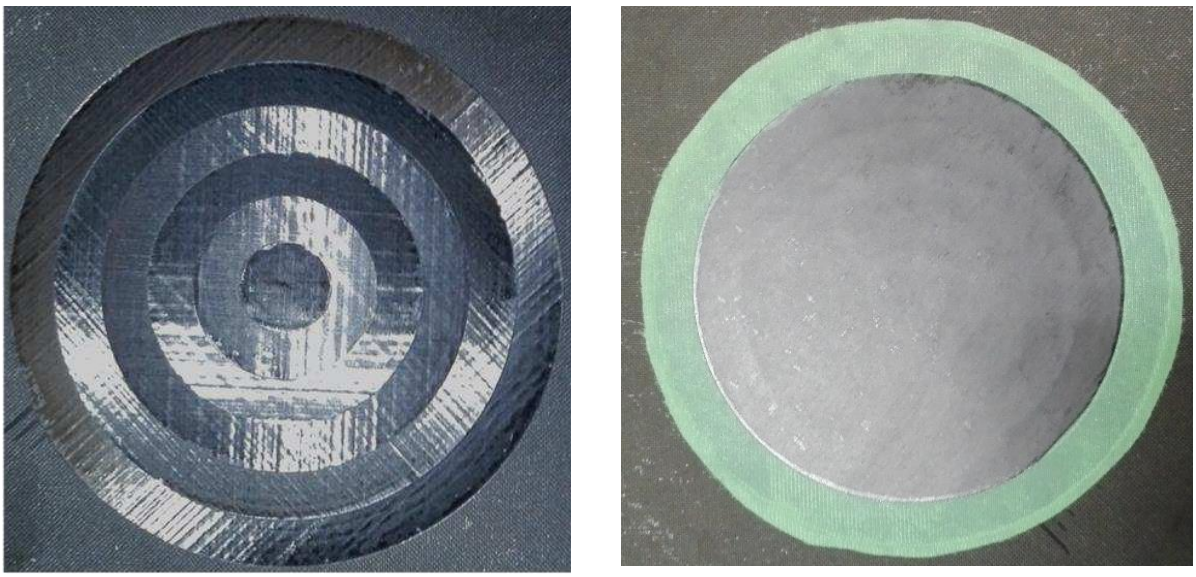

Figure 1: Plate after laser treatment (left) and wet patch application (right).

2.2 Testing in compression the repaired panels

The compression tests took place in an INSTRON hydraulic universal testing machine. The panels' loading edges were potted in resin, in order to achieve uniform loading conditions. The monitoring equipment is illustrated in *Figure 2*.

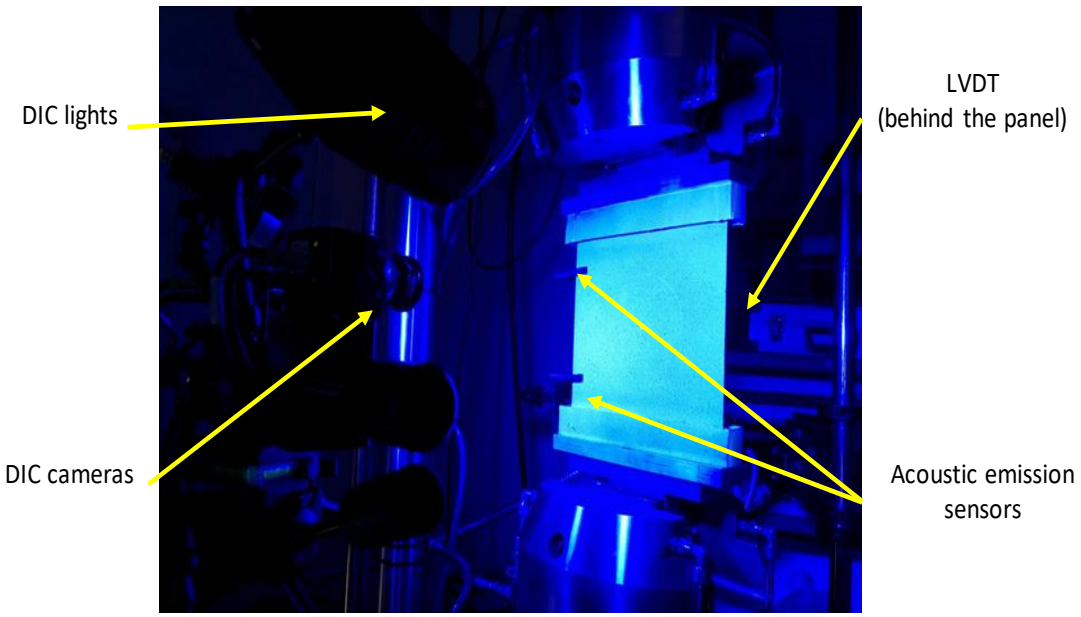

Figure 2: test setup

The first buckling was observed at around 35 kN. A cracking sound was recorded at 76 kN, and a second one at 96 kN, however no visible damage was seen, on either side of the panel. No adhesive debonding was observed at the patch, or the visible sides of the stiffeners. The experiment was cut short at around 100 kN, and the collapse load was not reached, however significant post-buckling was observed. The maximum displacement recorded by the machine was approximately 2.0 mm.

3. FE models of single stiffened panels with repair

The Finite Element (FE) models of the CFRP composite panels with stiffener and repair patch were develope. Lay-ups of the composite parts, as mentioned before, were continuum shell elements and were used to mesh the skin, the stiffener and patch. Within each element, one through-thickness integration point was defined to represent each ply. Layers of cohesive elements were inserted between sublaminates and skin/stiffener and patch/skin in order to model delamination and debonding initiation and growth. The materials properties that were used are listed in *Table 1* and *Table 2* and have previously validated [12, 13]. All the parts of the tested panels were designed in detail in order to increase the accuracy of the FE model. *Figure 3* presents an overview of the panel with its parts.

  doi:10.5075/epfl-298799_978-2-9701614-0-0

Table 1: Material properties (MPa)

Graphite/Epoxy UD IMS 24K 977-2	
Young's modulus in fibre direction	125000
Young's modulus in matrix direction	8680
Shear modulus	4700
Fibre tension strength	3325
Matrix tension strength	66
In-plane shear strength	90
Fibre compression strength	911
Matrix compression strength	170

Table 2: Parameters used to define mechanical behaviour of cohesive elements.

Material		FM300	IMS/9772
ρ (kg/m^3)		1300	1530
Penalty stiffness (kN/mm^3)	K_n	100	143
	K_s	35	73
	K_t	35	73
Interfacial strength (MPa)	t_n	14	66
	t_s	40	99
	t_t	40	99
Fracture toughness (J/m^2)	G_{Ic}	400	370
	G_{IIc}	600	590
Mixed mode coefficient (Benzeggagh-Kenane critetion)		2	2

  doi:10.5075/epfl-298799_978-2-9701614-0-0

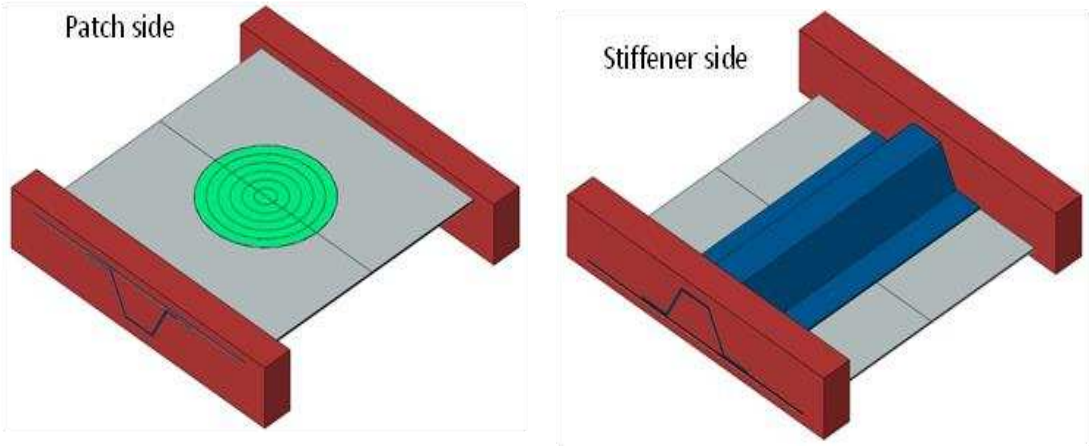

Figure 3: The two sides of the stiffened panel FE model. Different parts are illustrated with different colours.

Surfaces of stiffener and patch were tied to the surface of the skin. The end regions of the panel, which were inserted in the resin, were tied to the skin and stiffener. Contact was defined between all surfaces. For the compression tests, the ends of the panel were potted in resin and the channel encasing the resin loaded by the platens of the test machine. All degrees of freedom of the ends were therefore consisted to the constraints of the panel except displacement in longitudinal direction. To replicate this boundary condition, rigid plates were tied to the potting and their reference points (RPs) were constrained so that they can only move in longitudinal direction. The panel was loaded by defining a ramp displacement in longitudinal direction.

The numerical problem was solved using explicit solver, available in ABAQUS, as nonlinear geometric effects were considered. The explicit solver takes into account these terms, however the structure should be loaded very slowly so that the influence of these terms becomes negligible before buckling (the explicit solver is also suitable when initiation and growth of interlaminar and translaminar damages need to be modelled). The first predictions of the failure load were made and were compared with the test results as can be seen in Figure 4. From the FE curve the buckling starts at the load level of 50kN and the waviness of the curve is the result of the change in buckling shapes. It seems that the FE models is slightly stiffer than the tested panels but this has to do with the actual thicknesses of the tested panels against the perfection of the FE models.

An indication of the debond grade of the patch before failure was seen in Figure 4. These results of the tested panel can be compared with the results of the FE analysis. The model predicts that the debond of the patch will start from the outer step and as the panel is compressed is moving to the inner section. But this is not happening step by step as the second step seems to be bonded while in the actual test the third step remains bonded. The trend seems to be the same and if considering the possible manufacturing imperfections and the overall complexity and random nature of damage accumulation then the predictions of the FE model are in a very good level.

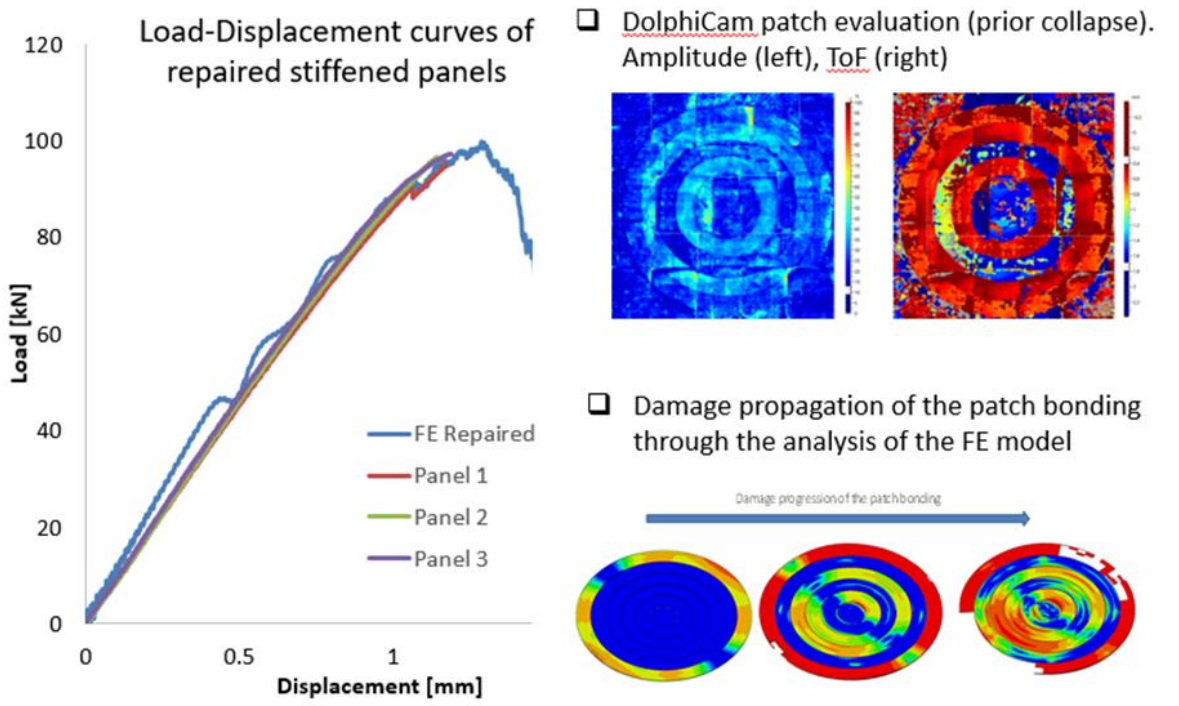

Figure 4 Left: Comparison of the load displacement curves between the experimental data and the FE prediction. Right: On the top the patch failure during testing is illustrated and on the bottom the FE prediction for the patch failure

4. Conclusions

In this work the effectiveness of stepped repair to damaged fibre reinforced composite materials was investigated by using extensive testing accompanied by validated FE numerical modelling. These tests were the benchmarks for the FE models and the capabilities of the FE models were evaluated. Attention was given at the actual failure modes of composites including delamination. The FE models were capable to predict the failure load of the panel in compression as well as the way it failed. Also, the comparison of the PA images with the FE models gave a clear insight of the loads and the way the patch debonds during compression

The outcome was that the optimized stepped scarf repair increases the strength of the damaged panel with main advantage the decreased material removal during the repair process, which relates to saving time, material and cost in comparison with the conventional repair shapes. Clearly these models can be used for further repair studies.

Acknowledgements

The research leading to the results has received funding from European Union's H2020 Programme under Grant Agreement N° [814581] - OASIS.

  doi:10.5075/epfl-298799_978-2-9701614-0-0

5. References

1. Katnam, K.B., L.F.M. Da Silva, and T.M. Young, *Bonded repair of composite aircraft structures: A review of scientific challenges and opportunities.* Progress in Aerospace Sciences, 2013. **61**: p. 26-42.
2. L., H.-S., *Adhesive-bonded scarf and stepped-lap joints.* Tech. Rep. NASA CR 112237, Langley Research Center, Hampton: VA, 1973.
3. Whittingham, B., et al., *Micrographic studies on adhesively bonded scarf repairs to thick composite aircraft structure.* Composites Part A: Applied Science and Manufacturing, 2009. **40**(9): p. 1419-1432.
4. Bendemra, H., P. Compston, and P.J. Crothers, *Optimisation study of tapered scarf and stepped-lap joints in composite repair patches.* Composite Structures, 2015. **130**: p. 1-8.
5. Gunnion, A.J. and I. Herszberg, *Parametric study of scarf joints in composite structures.* Composite Structures, 2006. **75**(1): p. 364-376.
6. Préau, M. and P. Hubert, *Effects of processing conditions on bondline void formation in vacuum bag only adhesive bonding: Modelling, validation and guidelines.* International Journal of Adhesion and Adhesives, 2018. **80**: p. 43-51.
7. Kim, C.-H., J.-H. Choi, and J.-H. Kweon, *Defect detection in adhesive joints using the impedance method.* Composite Structures, 2015. **120**: p. 183-188.
8. Najib, M.F. and A.S. Nobari, *Kissing bond detection in structural adhesive joints using nonlinear dynamic characteristics.* International Journal of Adhesion and Adhesives, 2015. **63**: p. 46-56.
9. Ellert, F., I. Bradshaw, and R. Steinhilper, *Major Factors Influencing Tensile Strength of Repaired CFRP-samples.* Procedia CIRP, 2015. **33**: p. 275-280.
10. Yoo, J.-S., et al., *Parametric study on static and fatigue strength recovery of scarf-patch-repaired composite laminates.* Composite Structures, 2016. **140**: p. 417-432.
11. Niedernhuber, M., J. Holtmannspötter, and I. Ehrlich, *Fiber-oriented repair geometries for composite materials.* Composites Part B: Engineering, 2016. **94**: p. 327-337.
12. Psarras, S., et al., *Evaluating experimentally and numerically different scarf-repair methodologies of composite structures.* International Journal of Adhesion and Adhesives, 2019: p. 102495.
13. Loutas, T.H., et al., *Investigation of a pulsed laser ablation process for bonded repair purposes of CFRP composites via peel testing and a design-of-experiments approach.* International Journal of Adhesion and Adhesives, 2019: p. 102407.

FORMING OF HYBRID (UD-ASMC) COMPOSITES

Abhik, Dutta[a], Mathilda, Karlsson Hagnell[b], Yvonne, Aitomäki[b], Malin, Åkermo[a]

a: Department of Engineering Mechanics, KTH Royal Institute of Technology, Sweden – abhikd@kth.se

b: Department of Polymers, Fiber and Composites, Division of Material and Production, RISE Research, Sweden.

Abstract: *Combining short and long fibre reinforcement in the same component, enables establishing an optimum combination between cost and production efficiency while still maintaining good structural characteristics of the produced component. This can be done in a single compression molding step. However, producing defect free hybrid components require a good understanding of the deformation mechanisms during manufacturing. Traditionally, unidirectional (UD)-prepreg forming models involve the study of mechanisms such as shear and ply bending. On the other hand, manufacturing of advanced SMC (ASMC) relies on enabling a significant amount of squeeze flow. However, little is known about the interaction of these mechanism. This study aims to look at the interaction between long, aligned fibres and short fibre composite material during the first phase, forming, of a compression molding process. A two-stage modelling approach consisting of draping and squeeze flow respectively, is suggested and material properties for the first stage of modelling the UD-ASMC hybrid stack is presented. The material system studied consists of a combination of UD "snap-cure" prepreg and ASMC, both having fibre volume fraction greater than 50% and are suitable for use in serial production.*

Keywords: UD-ASMC; Hybrid Composite; Forming; Compression Molding.

1. Introduction

Reducing the time and costs associated with manufacturing composite components is key to large scale adoption of composites in the automotive industry. This requires finding a balance between the stiffness/strength properties and manufacturing methods. One way to achieve this, is combining short and long fibre reinforcements in the same part. With long fibres providing high strength/stiffness along with the low cost and production efficiencies associated with short randomized fibres. In addition, the short randomized fibres can be made from recycled fibres thereby helping improve sustainability of the final product.

Traditionally, hybrid components are manufactured by using the over-molding process, where a backing structure, such as ribs, is injected onto a thin composite shell. However, this method requires several distinct manufacturing steps. To increase its feasibility, a hybrid combination out of unidirectional (UD) prepreg and advanced sheet molding compound (ASMC) is studied in this work. Prior studies [1] have found a sizeable increase in the flexural modulus and stiffness of a component made by combining SMC and UD as compared to one made by SMC alone. Moreover, this UD-ASMC hybrid component can be manufactured with traditional SMC manufacturing processes, such as "Compression Molding". This can be done simultaneously, by forming the ASMC and UD material together making the process more efficient and cost-effective as compared to over-molding . Figure 1 illustrates the compression molding process for a hybrid component where the SMC material is placed between the UD. Similarly, other layups and orientations can also be accommodated in this process.

  doi:10.5075/epfl-298799_978-2-9701614-0-0

However, producing defect free hybrid components will require a good understanding of the deformation mechanisms that the prepreg and ASMC material undergo during manufacturing.

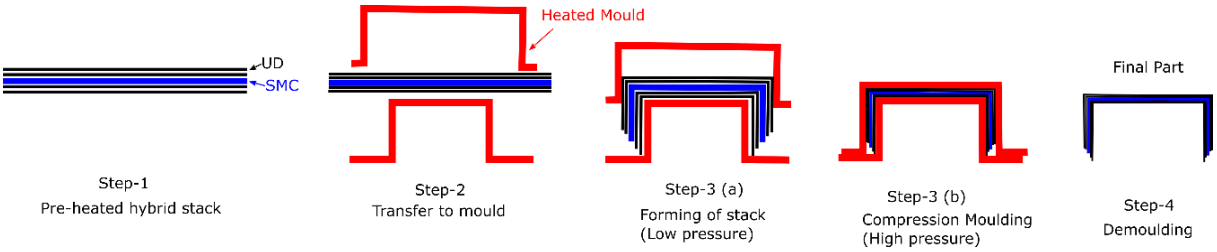

Figure 1: Compression moulding process for hybrid composite components

Three major mechanisms determine the deformation of the prepreg material from a flat stack to complex geometry, they are inter-ply shear, intra-ply shear and ply bending. Inter-ply shear is the relative motion between adjacent layers of prepregs. As the flat stack takes the shape of a complex geometry, the individual layers of prepreg must slide on top of each other. On the other hand, intra-ply shear describes in-plane shear of individual layers of prepregs. The last major deformation mechanism is the out of plane bending of the prepreg material. Generally, the out-of-plane bending stiffness of the prepreg is uncoupled from the in-plane properties of the prepreg and is much lower.

As opposed to the deformation mechanisms that the prepreg undergoes, manufacturing of SMC component relies on enabling a significant amount of squeeze flow. This is influenced by several factors such as; the rheological properties of the charge, 3D effects of flow front, temperature gradients and re-orientation of fibres as the charge flows [9] and can result in defects such as uneven skin thickness.

Extensive work has been performed in the past to study these deformation mechanisms for UD-Prepreg and SMC in isolation. However, little is known about the interaction of these mechanisms, during both forming and curing. A better understanding of these interactions can allow activating these mechanisms in a tailored order, ensuring the best part quality possible.

One way to model the interaction of these mechanism is by simplifying the compression molding process into two stages that occur successively. The first stage includes the forming of the hybrid stack into the required shape (Figure 1, Step 3 (a)). This takes place at a relatively low pressures as the mold starts to close. In this stage the relevant deformation mechanisms are inter and intra-ply shear and ply bending. Note that there is no flow of ASMC in this stage and the ASMC act almost as a deformable solid with in-plane properties such as a Youngs modulus and a yield stress, out-of-plane bending stiffness and undergoes inter-ply shear with the adjacent prepreg material. The second stage begins as the mold is closed and pressure starts building up between the molds. This results in the squeeze flow of the ASMC (Figure 1, Step 3 (b)). This is a fair simplification for two reasons. Firstly, it has been noted that forming of a prepreg stack usually occurs at low normal pressures [2] and even before the tool is completely closed. Secondly, squeeze flow of the ASMC requires high pressure, this is generally achieved after the tool closes. High pressure is also important to reduce voids formed during compression molding of SMC [3].

This proposed two step modelling approach can provide a good first approximation about the quality of final part manufactured. However, this requires extensive material characterization of both the UD prepreg and the ASMC. This study focusses on the first step of the approach.

  doi:10.5075/epfl-298799_978-2-9701614-0-0

Modelling this first stage requires several material parameters for both the UD and ASMC material. The required parameters include intra-ply shear, inter-ply shear and ply bending for the UD prepreg material, these are presented in this study. Further, material parameters for the ASMC, such as bending stiffness, in-plane properties and intra-ply shear against the UD prepreg is also presented.

Finally, this study aims to build knowledge on the interaction of the different deformation mechanisms from a forming perspective, thus enabling optimized compression molded hybrid components. The material system studied consists of a combination of UD "snap-cure" prepreg and advanced SMC (ASMC), both having fibre volume fraction greater than 50%. A two-stage modelling approach consisting of draping and squeeze flow is suggested and material properties for the first stage of modelling the UD-ASMC hybrid stack is presented.

2. Test Method

2.2 Materials

The prepreg material used for this study consisted of a unidirectional carbon fiber reinforced epoxy prepreg with T700S fibres and "snap-cure" resin system. The resin system has a cure time of 120 seconds at 130° C. The prepreg had a fiber volume fraction of 58%. The ASMC material used in this study was carbon fibre reinforced with a vinylester based resin system with a volume fraction similar to that of the prepreg. The resin system the ASMC material was also a "snap-cure" type resin system with a slightly higher cure time than the prepreg at 130° C. The ASMC material was received as plies consolidated to a thickness of 1.88 mm. Both material systems were supplied by Toray.

2.3 Test Setup

Four types of tests were performed in this study. Firstly, bias-extension tests were performed to measure the intra-ply shear characteristics of the prepreg. Second, inter-ply friction tests were performed to measure the shear properties for the UD-UD and UD-ASMC interface. Third, bending tests were performed on both the UD and the ASMC material to measure the out of ply bending characteristics. Finally, tensile tests were performed on uncured ASMC to measure its in-plane stiffness and yield characteristics. All tests were performed at isothermal conditions at a temperature of 60° C. This was achieved by placing the test apparatus in a temperature chamber designed to fit in an Instron testing machine. This temperature was selected due to a combination of factors such as; recommended charge temperature from material supplier, previous experience with forming the UD material at this temperature and practical limitations of the test setup.

The intra-ply shear properties for prepreg material was measured with a test method commonly known as bias-extension test. This can be described as a tensile test performed on a stack of UD prepregs, generally consisting of fibres in the +-45 orientation. This method has been well described in [4] and [5]. The exact test setup used in this study is described in [6]. The test specimens had a layup of [+45/-45]s. The loading speed was kept relatively fast, 50 mm/min, to emulate the fast-forming conditions that may be experienced by the stack in the compression molding process.

Interply shear/friction tests were performed on a custom-made test rig. An older version of the test apparatus has been described in [2]. Modifications were made to this test setup, to

decrease the heat up time by heating the sliding interface by in-situ heater, rather than placing the test rig in a temperature chamber. This resulted in a heat-up time of 10 minutes to reach a stabilized condition. The interply shear characteristics of the UD-ASMC interface was measured by attaching UD plies on the side plates and ASMC on the center plates. Previous works have shown that interply shear is highly dependent on the processing conditions under which the sliding takes place [7]. These conditions may be dynamic and change as the mold closes. This study focused on performing tests over a wide range of sliding speed with a low normal pressure (Table 1). The normal pressure was selected because it was the lowest repeatable pressure that could be obtained in the test setup. Further, as stated before, it has been shown that forming occurs at low normal pressure. A large range of sliding speeds were chosen to obtain an overview of the effect of sliding speed on the interply shear for the UD-ASMC interface. This was done, because, to the best of our knowledge, there are no previous works that have characterized interply shear for UD-ASMC interface.

Interface	Normal Pressure (bar)	Sliding Speed (mm/min)	No. of Tests
UD-UD	0.1	50/5/0.1	3
UD-ASMC	0.1	50/30/10/5/0.5	3

Table 1: Test Matrix for interply shear/ friction tests.

Out of plane bending was measured as per the ASTM D1388 standard [8]. The UD prepreg was tested in the 0 direction. The ASMC samples were cut from different regions of the prefabricated roll received from the material supplier. Three tests were performed for each configuration.

Lastly, tensile tests were performed on the ASMC material to characterize the in-plane properties of the ASMC. The test procedure was as follows. First, test specimens were cut from the consolidated ASMC plies. The specimen had overall dimensions of, 246*29 mm, with the narrow region having a width of 19 mm, as specified in ASTM D638 (Type III) [8]. Next, the specimens were consolidated under vacuum pressure at room temperature. Thereafter, the specimens were heated to test temperature, 60°C, for 10 minutes before being clamped in the grips. Tensile tests were performed in a temperature chamber installed inside an Instron machine to maintain isothermal conditions. These tests were performed at two loading speeds, 50 mm/min and 5 mm/min. Five tests were performed for each configuration. The load was measured by a 500 N loadcell, and the strain was measured by the crosshead movement.

3. Test results and suggested modelling approach

This section presents the test results along with suggestions for modelling the observed material characteristics in process simulations.

3.1 Bias- Extension Tests

Figure 2 presents the results of the bias extension test performed on the UD material. The specimen tested had a layup of [+45/-45]s and was tested at 60 ° C. The results are presented first as the load measured by the loadcell as a function of the displacement. The observed response is similar to that recorded by previous works characterizing intra-ply shear for UD material [6]. No undesirable effects like ply buckling or splitting was observed during the tests.

The recorded load-displacement response was then normalized to a shear angle (γ)- shear stress (σ) curve using Pin Joint Net assumption [10] (Figure 2 (Right)).

Since the in-plane shear behavior of UD prepreg material has been a topic of intense study in the past, most modelling solutions used for forming are able to capture this behavior. For instance, AniForm [11] offers a reinforced Kelvin-Voigt model that can capture this shear behavior. Some other general purpose finite element software also include material models that can capture this behavior. For instance, LS-DYNA, where *MAT_249 can capture the shear behavior based on an input curve of the in-plane shear test data [12].

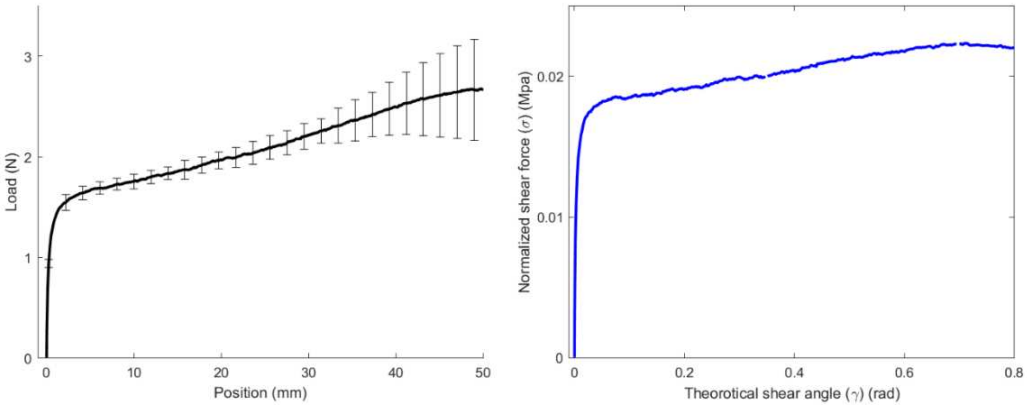

Figure 2: Bias-extension test results for UD specimen.(Left) Recorded load-position response. Plot represents a mean of 3 tests with error bars indicating standard deviation. (Right) Normalized shear force-shear angle response extracted from bias-extension test with pin joint net assumption.

3.2 Interply Shear

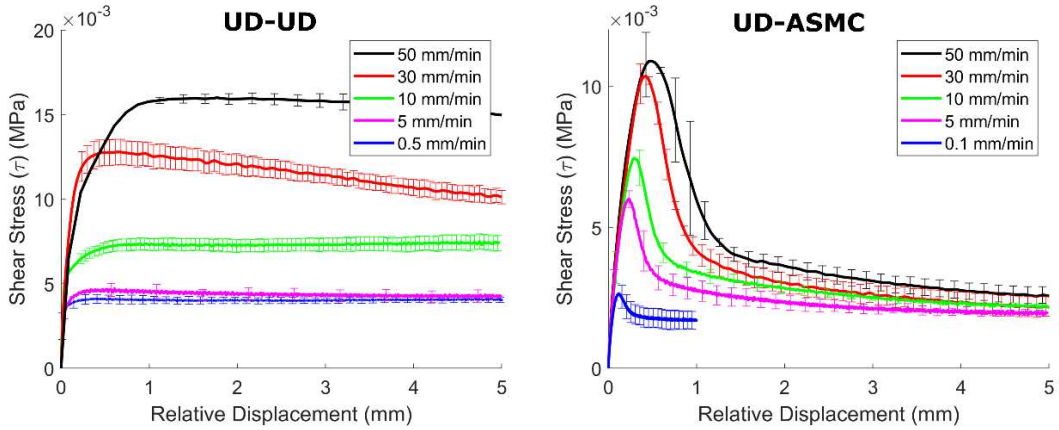

Figure 3: Interply shear response for (Left)UD-UD interface and (Right) UD-ASMC interface at 0.1 bar normal pressure. Note that the Y-scale for the graphs differ by a factor of two.

As shown in Figure 3 the interply shear behavior of both interfaces varied greatly both in the nature of the curve and the shear stress levels. Note that the Y-scale in Figure 3 differs by a factor of two. The UD-UD interface exhibited a bi-linear shear stress response with an initially stiff interface followed by gradual yield and a stable shear stress level. On the other hand, the UD-ASMC exhibited a very high initial peak which decomposed to a low stable level. In fact, this initial peak was almost as high as that of the UD-UD interface. In addition, the stable shear

stress level for all sliding speeds tested tended to converge to the same value. This value is approximately half of the UD-UD interface at the lowest sliding speed.

If the forming speed of the process is known, a simple contact model with static and dynamic coefficient of friction can be used to replicate this behaviour. However, it is possible that the sliding speed may change as the forming occurs. Further, different regions may experience different sliding speeds. This will require a more complex model dependent on among other parameters, sliding speed and normal pressure.

3.3 Out of plane Bending

Due to the anisotropic nature of the material, the out of plane bending stiffness for the uncured UD prepreg and ASMC prepreg are much lower than their in-plane stiffness. In this study the out-of-plane bending stiffness was measured by a cantilever bending test as per ASTM D1388 standard. The results are presented in Table 3.

Material	Overhang Length (mm)	Deviation (mm)	Bending Length (mm)
UD (0°)	191.6	2.8	54.2
ASMC	227.3	22	36.5

Table 2: Bending and overhang length measured by the cantilever test.

The bending behaviour can be modelled by several different approaches. A common method is to use a model where the in-plane behaviour is captured by a membrane element and the out of plane bending behaviour is modelled by shell elements. These two elements are then coupled to deform together [13], providing a bending response that is independent of the in-plane properties of the material. Another method that is more suitable in a general finite element solution is to vary the location and weight factors of the through thickness integration point, this results in the material bending with a much lower bending stiffness than it's in-plane modulus. This requires reverse calibrating the material model with several parameters, for instance one shell element may use 3 through thickness integration points and a weight factor for each point resulting in 6 variables to be optimized, to replicate the bending stiffness of the material. Further, this requires caution from the user since the bending stiffness would then be isotropic.

3.4 Tensile tests

The in-plane properties of the ASMC were strongly dependent on the loading rate (Figure 4). In general, the initial shear stress response was linear. In addition, a higher loading rate resulted in a higher modulus. However, note that the tests at the higher loading rate exhibited a large spread between tests. The initial response was followed by yielding at around 1% strain. All specimens tested, failed in the narrowest region of the specimen as intended (Figure 5). The region between yielding and complete separation (strain ~1- 2.5%) was marked by a decrease in the shear stress as the randomly oriented fibers and resin were pulled away from each other.

Based on these findings, the following can be said about modelling this behavior. First, the initial part of the curve can be modelled as linear elastic. Secondly, the linear elastic region is followed by a yield point. Thirdly, the failure is gradual as the fibres and matrix are pulled away

from each other. This gradual failure behavior can be tricky to model. As a first approximation, a brittle type failure criteria based on the shear stress can be used to indicate tearing. Finally, both the elastic modulus and the yield point are dependent on the loading rate, this would have to be accounted for in the model.

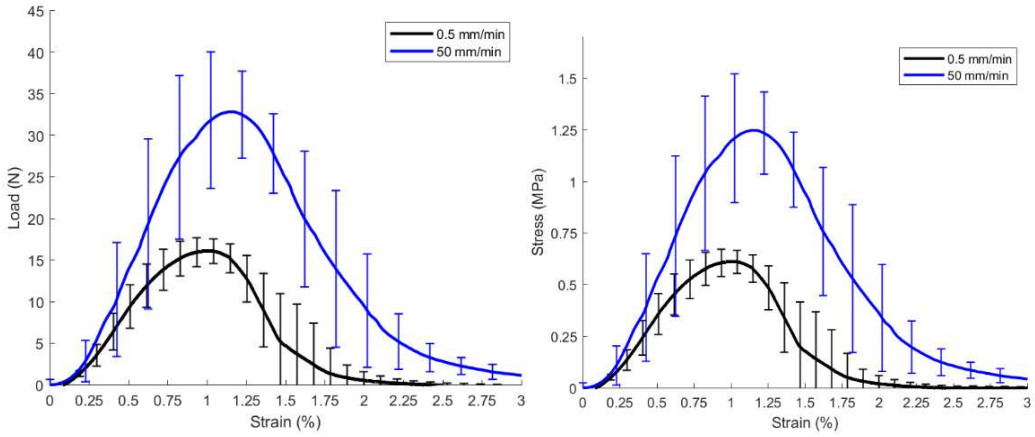

Figure 4: In-plane tensile response of ASMC Material at varying loading rates. (Left) Load-Strain. (Right) Stress-Strain.

Figure 5: A sample Tensile test specimen after test

4 Conclusion

One way to model the compression molding process for a UD-ASMC hybrid stack is by dividing it into two stages, forming and squeeze flow, that occur sequentially. Modelling the first stage by this method requires both a qualitative and quantitative understanding of the deformation mechanisms that the hybrid stack will undergo during forming. This study investigates these deformation mechanisms along with their interaction with each other. This was done by characterizing the material in intra-ply shear, interply friction and bending for the UD material and in-plane tension and bending for the ASMC material. In addition, interply friction tests for the combination of UD-ASMC material was also performed. The results show a large difference in friction between UD-UD and UD-ASMC interface. These large variations observed in the friction behavior of the interfaces provides opportunities to tailor the forming behavior where needed.

Due to the large number of tests involved, this study was limited to isothermal conditions and was aimed towards exploring the interaction of different deformation mechanisms. Despite its explorative nature, the results presented here along with the modelling approach are a crucial foundation to model the first stage, forming, of the compression molding process. This work is currently ongoing and will be presented in future studies.

Accurately capturing the material behaviour across different interfaces would be crucial to predict the boundary conditions for the second stage of the simulation. For instance, a stack

  doi:10.5075/epfl-298799_978-2-9701614-0-0

having a layup [+45/-45/ASMC]s being formed such that the +45/-45 on either side of the ASMC are being sheared in-plane. Three deformation mechanisms are competing against each other here. First, the UD layers will tend to undergo intra-ply shear. Second, the interply friction between the UD-ASMC will oppose the UD layer from shearing. Finally, the ASMC itself will be pulled in tension and tend to fracture. The interaction of these mechanism will determine the final size and position of the ASMC and therefore the starting condition of flow during the second stage of modelling. A better understanding of these deformation mechanisms also allows coupling and tailoring these mechanisms as needed. This results in several parameters that can be optimized that will finally result in better part quality and reduce overall time and cost.

Acknowledgements

The authors acknowledge funding by Centre for Excellence in Production Research (XPRES) and the Swedish Innovation Agency, VINNOVA, via LIGHTer Academy and PROSICOMP II.

5 References

[1] Wulfsberg J, Herrmann A, Ziegmann G, Lonsdorfer G, Stöß N, Fette M. Combination of carbon fibre sheet moulding compound and prepreg compression moulding in aerospace industry. Procedia Engineering, vol. 81, Elsevier Ltd; 2014.

[2] Larberg YR, Åkermo M. On the interply friction of different generations of carbon/epoxy prepreg systems. Composites Part A: Applied Science and Manufacturing 2011.

[3] Odenberger PT, Andersson HM, Lundström TS. Experimental flow-front visualisation in compression moulding of SMC. Composites Part A: Applied Science and Manufacturing 2004.

[4] Wang J, Page JR, Paton R. Experimental investigation of the draping properties of reinforcement fabrics. Composites Science and Technology 1998.

[5] Potter K. Bias extension measurements on cross-plied unidirectional thermoset prepreg. ICCM International Conferences on Composite Materials 2017.

[6] Larberg YR, Åkermo M, Norrby M. On the in-plane deformability of cross-plied unidirectional prepreg. Journal of Composite Materials 2012.

[7] Sjölander J. Improving Forming of Aerospace Composite Components through Process Modelling. Stockholm: 2018.

[8] Standard Test Method for Stiffness of Fabrics. ASTM D1388-18.

[9] Alnersson, Gustaf, Lundström, T Staffan and Ljung, Anna-Lena. Twenty-second international conference on composite materials (ICCM22) . Numerical study of the 3d-flow characteristics during compression moulding of

[10] Lebrun G, Bureau MN, Denault J. Evaluation of bias-extension and picture-frame test methods for the measurement of intraply shear properties of PP/glass commingled fabrics. Composite Structures 2003.

[11] ANIFORM VIRTUAL FORMING. www.aniform.com (accessed April 12, 2022).

[12] LS-DYNA User Manual. https://www.dynasupport.com/manuals.

[13] ten Thije RHW, Akkerman R. A multi-layer triangular membrane finite element for the forming simulation of laminated composites. Composites Part A: Applied Science and Manufacturing 2009.

  doi:10.5075/epfl-298799_978-2-9701614-0-0

NUMERICAL MODELLING OF A DEMONSTRATOR TO INVESTIGATE GEOMETRIC PARAMETER INFLUENCES ON THE THERMOFORMING OF FIBER-REINFORCED THERMOPLASTICS

Jan Middelhoff[a], André Hürkamp, Klaus Dröder

a: Technische Universität Braunschweig, Institute of Machine Tools and Production Technology, Langer Kamp 19b, 38106 Braunschweig, j.middelhoff@tu-braunschweig.de

Abstract*: In conventional thermoforming processes of fiber-reinforced thermoplastics (FRTPs), material damage or material failure quickly occurs due to complex cavities, especially with large cavity depths and sharp geometric transitions and three-dimensional corners. To overcome these challenges the use of segmented punches in the thermoforming process is considered. This leads to an extended process parameter spectrum with the number of segments, which is numerically investigated in this paper. For this purpose, a material characterisation of the used* glass fiber-reinforced organic sheet with polyamide 6 matrix (Tepex dynalite 102RG600(4)/47%) *as well as a calibration of the material card is carried out. After validation of the material card, a numerical model of a demonstrator geometry with a fix segmentation was build up to investigate different sequencing strategies. A suitable segmentation strategy including a sequencing strategy was shown to contribute to a more material-sensitive process control.*

Keywords: Segmented Thermoforming; FRTP; Numerical Process-Modelling

1. Introduction

With regard to the manufacturing of FRTPs, production technologies similar to sheet metal processing are increasingly establishing themselves in series applications. Therefore, continuously fiber reinforced thermoplastic sheets (organo sheets) are heated above melting temperature, formed and consolidated. Process cycle times for the manufacturing of FRTP are rapidly approaching those of sheet metal forming processes. The thermoforming of organo sheets is therefore one of the most promising processes [1]. However, the field of application for this process is very limited in terms of component complexity, due to the material properties of the organo sheet.

The essential drawback is insufficient formability depending on the fiber orientation in the plastified state due to the poor elongation at break of the fibers [2]. In consequence, this process reaches its limits by forming complex components like battery housings, which consists of large cavity depths and sharp geometric transitions and three-dimensional space corners [3, 4]. Additional forming steps or sequential manufacturing can overcome these challenges. However, it decreases the economic efficiency due to an increasing number of process steps. Since an economical process is imperative for the large-scale production in automotive applications using thermoplastic fiber-reinforced plastic components, new innovative tooling concepts suitable for the material have to be developed. A promising solution for a process that reduces material damage while also being economical is the use of segmented stamping tools in the thermoforming process. However, segmentation expands the parameter spectrum in the thermoforming process by the required number of segments, the segmentation strategy as well

  doi:10.5075/epfl-298799_978-2-9701614-0-0

as the possibility of different control and thus sequencing of the segments. The optimal configuration of these additional process parameters therefore entails a series of cost- and time-intensive experiments. Thus, the complex development process of the segmentation and sequencing strategy requires numerical models.

2. Strategies for segmented tools in composite manufacturing

In conventional thermoforming processes of thermoplastic FRP, material damage or material failure quickly occurs due to complex cavities. Typical critical areas are especially corners, which occur in many manufactured parts [5]. Main cause for such damages is shear and bending deformation mechanisms. Shearing of the fibers in the region of the case corners causes wrinkles to form, which are due to an increased shear angle above the shear-locking angle [6]. The formation of wrinkles can be counteracted by introducing in-plane tensile stresses, which are realised in the process by blank holders or a clamping systems [7]. However, even when using such systems, high shear angles are induced, so that material failure also occurs in complex geometric cavity areas [5]. For this reason, segmented punches are studied in order to exert a positive effect on the material to be formed and to realise a material-specific step-by-step forming as schematically illustrated in Figure 1.

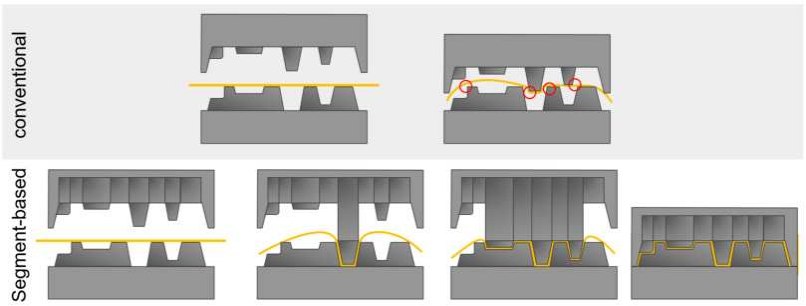

Figure 1. Schematic of the comparison of conventional and segment-based thermoforming

So-called multi-point forming tools are already used and investigated in the forming of metallic materials and plastics in the deep-drawing process [8, 9]. The adaption of such processes would result in using too small punch segments for the thermoforming of plastic components, which leads to deviations in the shape accuracy of the component. Accordingly, the surface quality is reduced by too small punch segments due to the induction of pressure points in the moulded part [10]. Therefore, a compromise between multi-point application and a geometry-mapping punch system has to be chosen for thermoforming FRTP. The use of individual segments close to the geometry can reduce the disadvantages of both approaches and avoid defects and material damage with targeted process control [11].

3. Numerical Model and Material Characterization

3.1 Geometry

A determining factor for process control is the implementation of a suitable segmentation strategy. For testing such strategies for geometrically critical cavities, a numerical model can reduce material costs and experimental effort. In addition to segmentation, sequencing, i.e. the controlled deflection of the individual segments in relation to each other, is decisive for the quality of the formed component. This results in an ever-increasing number of possible sequencing options as the number of segments increases. The segmentation is feasible with

  doi:10.5075/epfl-298799_978-2-9701614-0-0

regard to the identification of critical curvature regions [12]. In this paper, the approach of segmentation according to different partial geometries as well as according to the design of the individual segments suitable for production is pursued. For this purpose, a geometry of the cavity is selected that combines typical forming part geometries (shell, hemisphere, bridge) shown in Figure 2. These also occur in a similar form in the example of the battery housing and were combined into a demonstrator geometry that has a lower geometric complexity. This also reduces the numerical effort. In addition to simple parabolic surfaces (radius area), the demonstrator geometry contains both planar and elliptical surface components (area of the case corner) and thus represents a large proportion of the types of curvature that occur.

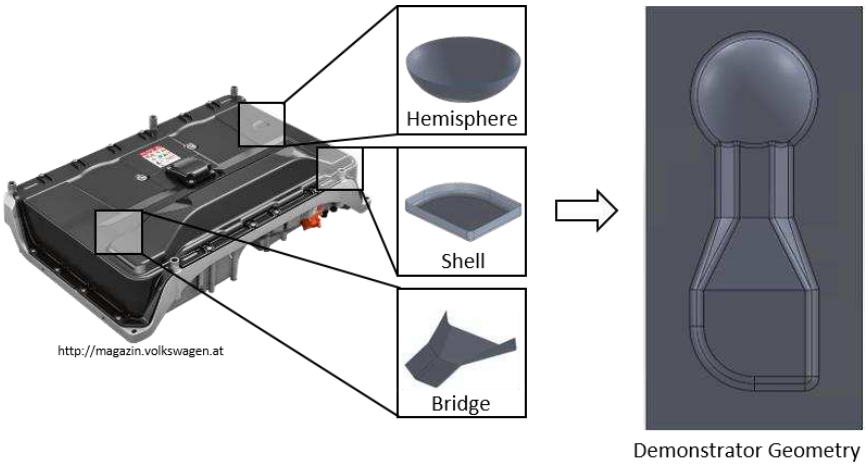

Figure 2. Developed demonstrator geometry derived from the example of the battery housing

3.2 Material Characterization and Calibration

The observed material is a glass fiber reinforced organic sheet with polyamide 6 matrix (Tepex dynalite 102RG600(4)/47%). The fabric is an E-Glass roved in twill 2/2 style with 47% fiber content. The total thickness of the organo sheets is 2 mm, with one layer having a thickness of 0.5 mm. For characterisation, quasi-static (test speed 2 mm/min) tensile and bias extension tests were carried out according to the standards DIN EN ISO 527 and DIN EN ISO 14129 on a tensile testing machine Z050 TH with temperature chamber [13, 14]. The tests were carried out on speciments with 0°-, 90°- and 45°-orientation of the specimen fiber direction to the centre axis of the tensile testing machine at 24°C, 140°C, 200°C and 230°C ambient temperature in the test chamber. The choice of temperature levels related to the glass transition temperature and melting temperature of the polyamide 6 matrix, so that testing was carried out below and above these temperatures. The samples were prepared with a stochastic pattern before the test in order to record the transverse and longitudinal strains of the samples with the help of digital image correlation (DIC). For this purpose, a point cloud was created over the entire measurement range of the specimen geometry. The strains measured at the individual points were averaged in a subsequent step. In addition, the force-time histories were used as output from the tensile testing machine to obtain stress-strain or shear-strain-shear angle curves for the individual temperature levels. The results of the stress-strain curves for 0° are shown in Figure 3a. Due to the symmetrical ply structure, the results90° orientation of the load directionare similar. In Figure 3b, the shear stress over the shear angle for the specimens in 45° fiber orientation Are displayed.

  doi:10.5075/epfl-298799_978-2-9701614-0-0

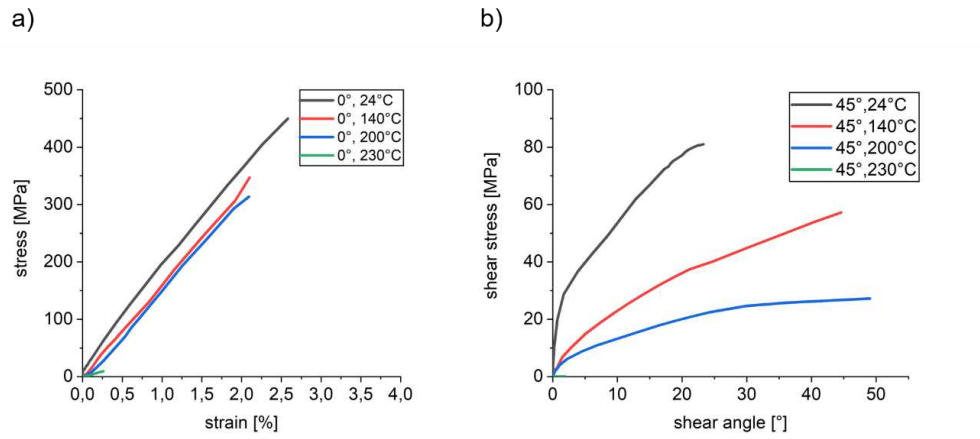

Figure 3. Results of the tensile test in a) 0° fiber orientation and b) 45° fiber orientation

With increasing temperature, the strength of the 0° samples of FRTP decreases slightly. With regard to the 45° specimens, the maximum shear stress decreases with increasing temperature while the maximum shear angle increases. The data obtained were integrated into the MAT_249_reinforced thermoplastics material model in the multipurpose FEM software LS-Dyna, which is suitable to simulate the forming behaviour of thermoplastic composites [15]. The material model consists of an anisotropic hyper-elastic material behaviour for the fiber reinforcement, and a temperature dependet elasto-plastic material formulation for the matrix material. The results of the simulations of the bias-extension tests and the numerical model are shown in Figure 4.

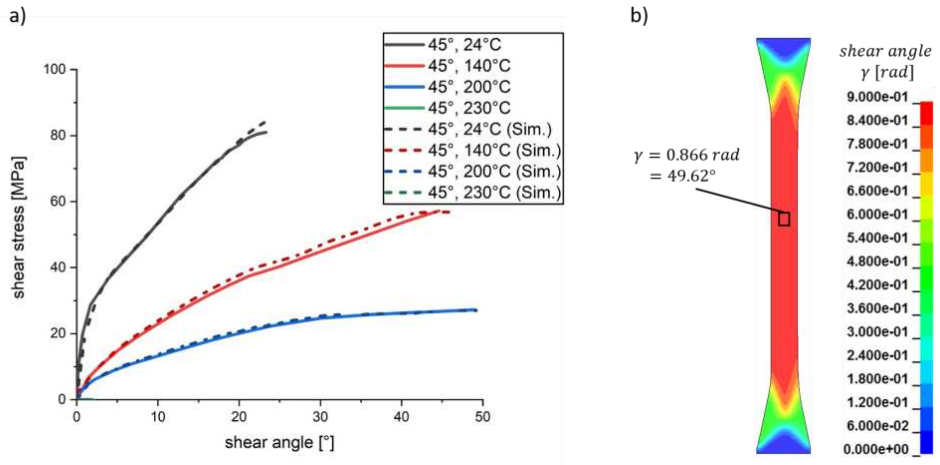

Figure 4. a) Comparison of simulative and experimental results of the bias-extension test in 45° fiber orientation; b) numerical Model of the bias-extension test for 200°C

The material parameters used are validated by comparing the results obtained experimentally with those provided by the numerical model. As can be seen qualitatively in Figure 4 a) on the bias-extension test, the curves of the experiments are reproduced accurately. The deviation between the numerical model and the experimental results is below 5%. The same applies in the comparison of experiments and simulations of the tensile tests on 0° specimens.

In addition to the mechanical properties, the thermal behaviour is also represented in the numerical model. For this purpose, reference values for the required characteristic values

thermal conductivity and specific heat capacity of comparable materials were considered. For comparison, the specific heat capacity was determined using a DSC analysis and compared with the reference values. Due to the good agreement of the values, the measured values were used in the numerical model. Therefore, the thermal conductivity was set at 0.28 W/K m and the specific heat capacity at 1.30 J/gK. [16]

3.3 Finite Element Model for segmented forming

The validated material model was used to develop a numerical model of a demonstrator geometry consisting of typical forming sub-geometries. Figure 4 shows the numerical model of the demonstrator geometry including segmentation.

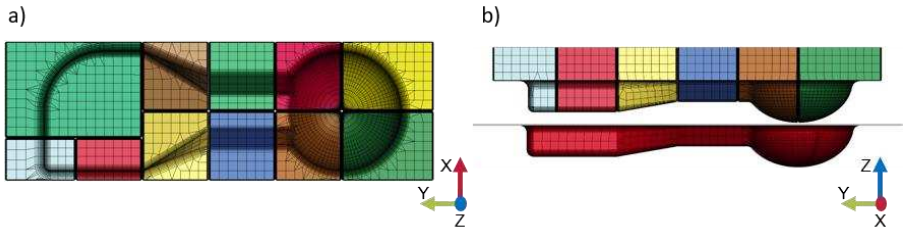

Figure 4. a) Top view and b) side view of the developed demonstrator geometry

To avoid non-physical zero-energy modes of deformation leading to zero stress and strain, fully integrated shell elements (ELFORM 16) are used. The Bathe-Dvorkin transverse shear treatment eliminates w-mode hour-glassing. In addition to the tensile and shear behaviour, the numerical model must also contain the bending behaviour and other parameter settings for a realistic representation of the thermoforming process. The MAT_249 does not allow the definition of temperature-dependent bending stiffness at material level. However, to achieve bending stiffness, the bending properties are provided by increasing the number of integration points through the thickness of the blank. Varying the number of integration points and their distances to the neutral axis of the component influences the bending behaviour of the blank. [17]

The segmentation was initially chosen for manufacturing reasons and is symmetrical. The asymmetrical design of the partial geometry of the shell is based on preliminary investigations, shown in Figure 5.

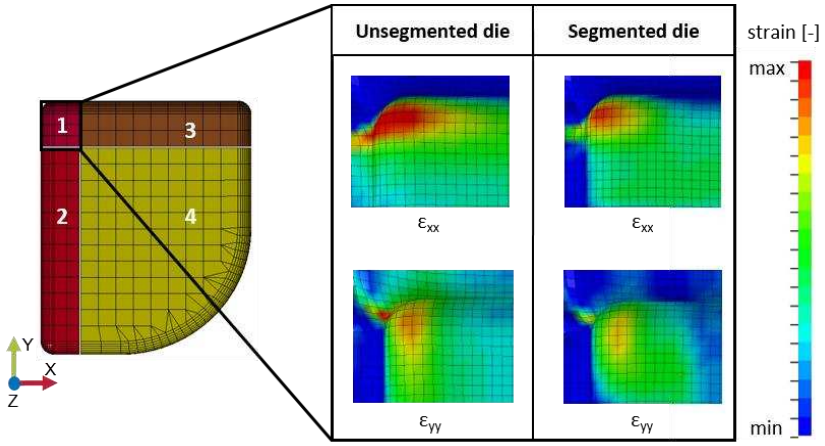

Figure 5. Reduction of the occurring strains through segmentation of the shell geometry

In the preliminary tests, it was shown that the sequence Segment 1 - Segment 2 - Segments 3 & 4 lead to reduced strains in the area of the corner in the formed component. With smaller segments in the case corner area, lower strains are achieved in the component after forming compared to forming without segmentation. In contrast, the organo sheets experiences higher loads in the process, which leads to higher strain peaks in the numerical model. Therefore, a compromise between slightly higher strain peaks during the forming process combined with lower strains in the formed component compared to the process without segmentation was chosen in the demonstrator geometry.

With regard to reducing computing time, the simulation was accelerated by a factor of 100. This is accompanied by considerably higher kinetic energies in the system, which may lead to convergence problems [18]. Global damping and 20 % of critical viscous damping (VDG) are recommended by the literature to counteract these convergence problems [18]. At the same time, the global damping factor cannot be chosen too high, as it reduces the wrinkle heights in out-of-plane direction.

4. Numerical Results

The developed numerical model of the demonstrator geometry was used to test different sequencing strategies. The simulation results of the forming with, unsegmented moulds serve as a reference.

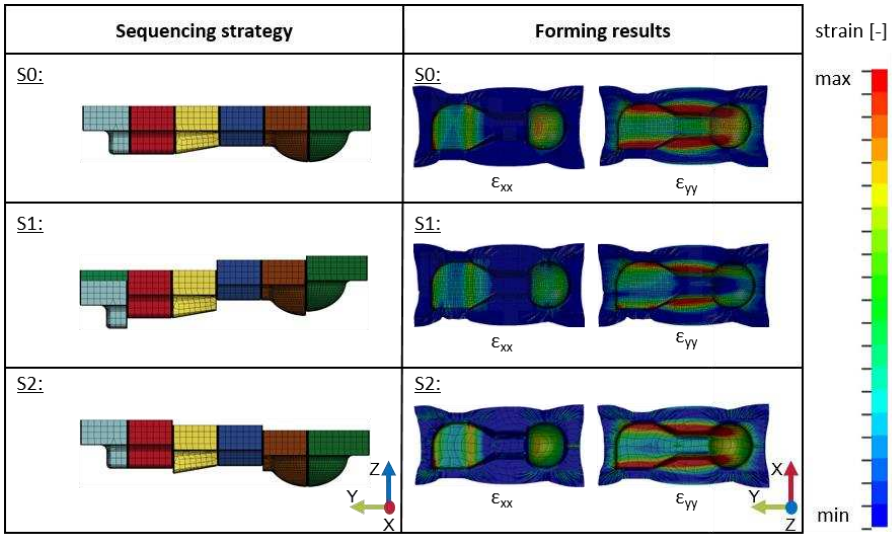

Figure 6. Examples of selected sequencing strategies and representation of the occurring strains ε_{xx} and ε_{yy} in the formed component

Figure 6 shows two sequences next to the reference configuration (S0). Sequence 1 (S1) starts in the area of the case corner of the shell geometry and ends with the forming in the area of the partial geometry "hemisphere". Sequence 2 (S2) starts in the hemisphere area and ends with the shell segments. By displaying the strains ε_{xx} and ε_{yy}, a more material-sensitive forming in the real process is assumed in the case of a globally considered strain reduction in the component. Comparing the strains occurring in the reference configuration with those of sequence S2, no improvement can be shown with regard to a more material-sensitive forming process. Sequence S1, on the other hand, shows a reduction with regard to the strain distributions in the component. Strain reduction is also achieved in the shell area by S1 when considering ε_{xx}.

  doi:10.5075/epfl-298799_978-2-9701614-0-0

Furthermore, a reduction in the simulation results can be observed in the hemisphere area in the transition area from hemisphere to bridge. A clearer strain reduction is visible in the comparison of ε_{yy}. Especially in the edge area of the shell geometry, but also in the transition from hemisphere to bar.

The results lead to the assumption that starting the forming process in critical areas such as a corner of a cavity (cf. Figure 6 S1) leads to a more material-sensitive forming process than starting in the area of a hemisphere geometry (cf. Figure 6 S2). This is mainly due to the temperature control in the process. In sequence 2, the corner area is formed last, so that the organic sheet cools down and thus the organo sheet loses its draping ability. As a result, the matrix solidification increases in the temperature range around the matrix melting temperature of 220°C [16]. In consequence, higher strains occur in the corner of the partial geometry of the shell compared to the result of S1.

5. Conclusion and Future Work

The use of segmented punches for thermoforming FRTPs has a decisive influence on the material-sensitive forming of such parts. In this paper, a suitable segmentation and sequencing strategy was shown leading to reduced strain characteristics in the component and thus to a more material-sensitive forming process. In a next step, automated parameter studies in combination with Machine Learning are carried out to analyse and optimised the material-sensitive forming with respect to different geometric characteristics. Furthermore, the numerical model itself can be optimised with regard to the contact conditions and validated by experimental tests.

Acknowledgements

The IGF-Project “Material-specific thermoforming through controlled mould elements” of the European Research Association for Sheet Metal Working (EFB e.V.) was funded by the Federal Ministry of Economics and Energy (BMWi) under the funding number 20677BG of the German Federation of Industrial Research Associations (AiF) on the basis of a decision by the German Bundestag. The authors are thankful for this financial support.

6. References

1. Hopmann C, Michaeli W (2017) Einführung in die Kunststoffverarbeitung, 8., aktualisierte Auflage. Hanser eLibrary. Hanser, München
2. Neitzel M, Mitschang P, Breuer U (eds) (2014) Handbuch Verbundwerkstoffe: Werkstoffe, Verarbeitung, Anwendung, 2., aktualisierte und erw. Aufl. Hanser, München
3. Schwarzmann P (ed) (2016) Thermoformen in der Praxis, 3., neu bearbeitete und erweiterte Auflage. Hanser eLibrary. Hanser, München
4. Dröder K, Vietor T (eds) (2019) Technologies for economical and functional lightweight design. Zukunftstechnologien für den multifunktionalen Leichtbau. Springer Berlin Heidelberg, Berlin, Heidelberg
5. Allaoui S, Hivet G, Soulat D et al. (2014) Experimental preforming of highly double curved shapes with a case corner using an interlock reinforcement. Int J Mater Form 7:155–165. https://doi.org/10.1007/s12289-012-1116-5

6. Behrens B-A, Chugreev A, Wester H (2019) Experimental and numerical characterization method for forming behavior of thermoplastics reinforced with woven fabrics. Procedia Manufacturing 29:443–449. https://doi.org/10.1016/j.promfg.2019.02.160
7. Breuer U, Neitzel M, Ketzer V et al. (1996) Deep drawing of fabric-reinforced thermoplastics: Wrinkle formation and their reduction. Polym Compos 17:643–647. https://doi.org/10.1002/pc.10655
8. Cao JH, Fu WZ, Li MZ (2013) Research on the Dimpling in Multi-Point Thermoforming of Polycarbonate Sheet. AMR 738:34–37. https://doi.org/10.4028/www.scientific.net/AMR.738.34
9. Li M-Z, Cai Z-Y, Liu C-G (2007) Flexible manufacturing of sheet metal parts based on digitized-die. Robotics and Computer-Integrated Manufacturing 23:107–115. https://doi.org/10.1016/j.rcim.2005.09.005
10. Zitzlsberger SG (2015) Flexibles Werkzeug zur Umformung von Polycarbonatplatten unter besonderer Beachtung der optischen Qualität. Dissertation, Herbert Utz Verlag
11. Abosaf M, Essa K, Alghawail A et al. (2017) Optimisation of multi-point forming process parameters. Int J Adv Manuf Technol 92:1849–1859. https://doi.org/10.1007/s00170-017-0155-y
12. Coutandin S (2020) Prozessstrategien für das automatisierte Preforming von bebinderten textilen Halbzeugen mit einem segmentierten Werkzeugsystem. Dissertation, Shaker Verlag
13. DIN EN ISO 527-4:2022-03, Kunststoffe_- Bestimmung der Zugeigenschaften_- Teil_4: Prüfbedingungen für isotrop und anisotrop faserverstärkte Kunststoffverbundwerkstoffe (ISO_527-4:2021); Deutsche Fassung EN_ISO_527-4:2021
14. DIN EN ISO 14129:1998-02, Faserverstärkte Kunststoffe_- Zugversuch an 45°-Laminaten zur Bestimmung der Schubspannungs/Schubverformungs-Kurve des Schubmoduls in der Lagenebene (ISO_14129:1997); Deutsche Fassung EN_ISO_14129:1997
15. Hürkamp A, Lorenz R, Ossowski T et al. (2021) Simulation-based digital twin for the manufacturing of thermoplastic composites. Procedia CIRP 100:1–6. https://doi.org/10.1016/j.procir.2021.05.001
16. Kern Polyamid 6 mit 50 % Glasfaser 8PA 6 GF50). https://www.kern.de/de/technisches-datenblatt/polyamid-pa-6-gf50?n=1115_1
17. Grubenmann M, Heingärtner J, Hora P et al. (2018) Influence of temperature on in-plane and out-of-plane mechanical behaviour of GFRP composite. J Phys.: Conf Ser 1063:12146. https://doi.org/10.1088/1742-6596/1063/1/012146
18. Morris CD, Dangora LM, Sherwood JA (2014) Using LS-DYNA to Simulate the Thermoforming of Woven-Fabric Reinforced Composites

ONLINE CHARACTERIZATION OF FIBER-REINFORCED THERMOPLASTIC COMPOSITE DECONSOLIDATION

Luc, Amedewovo[a,b], Steven, Le Corre[a], Basile, de Parscau du Plessix[b], Laurent, Orgéas[c], Arthur, Lévy[a]

a: Université de Nantes, CNRS, Laboratoire de Thermique et Energie de Nantes, LTeN, UMR6607, 44000 Nantes, France – steven.lecorre@univ-nantes.fr
b: IRT Jules Verne, Chemin du Chaffault, 44340 Bouguenais, France
c: CNRS, Université Grenoble Alpes, Laboratoire 3SR, 38000 Grenoble, France

Abstract: *Deconsolidation occurs in a fiber-reinforced thermoplastic composite when it is heated above a certain temperature. During heating in manufacturing processes (for example in welding, AFP, thermostamping, …), when low pressure is applied, porosities can appear in different forms (bubbles, delaminations, etc.). Various works have been carried out in the literature to understand this phenomenon. In most of these works, deconsolidation is characterized by post-mortem analyzes or thermomechanical analyzes (TMA). However, these methods do not highlight deconsolidation mechanisms. In order to overcome these limitations, a new device for deconsolidation characterization is developed. It makes it possible to characterize online and continuously the deconsolidation of fiber-reinforced thermoplastic composite laminates. First results on moisture and residual stress effect on deconsolidation, were obtained on aerospace grade composite material (Carbon fiber/PEKK laminates).*

Keywords: Fiber-reinforced Thermoplastic composite; Deconsolidation; Porosity; Real time Characterization; Thickness Variation

1. Introduction

In recent years, the demand for fiber-reinforced composite materials has continued to grow in the aeronautical sector. The interest of composite materials lies in their specific mechanical properties (mechanical property/density ratio) which are better, compared to metals or other families of materials. This property of composite materials gives the possibility of considerably reducing the weight of structures in order to reduce gas emissions. In aeronautics, fiber-reinforced thermosetting matrix composites are the most widely used today. Fiber-reinforced thermoplastic composites are a better alternative to address assembly-related issues encountered with thermosetting composites, e.g., with the possibility of being welded [1][2].

However, during thermoplastic prepregs manufacturing processes involving fusion (continuous welding, thermostamping, AFP, …), when a low pressure is applied, the deconsolidation of the composites occurs during heating leading to detrimental porosities [3][4]. Given the negative effect of porosities on the mechanical performance of parts [5][6], a better control is necessary to prevent or minimize deconsolidation. The conditions for the porosities appearance and the mechanisms that govern their growth is to be investigated.

Two major hypotheses exist in the literature to explain deconsolidation mechanisms. On the one hand, some authors suggest that the deconsolidation is due to a relaxation of the residual stresses initially present in the composite plates after their consolidation [4] [7] [8]. On the other

  doi:10.5075/epfl-298799_978-2-9701614-0-0

hand, other authors explain the deconsolidation by the diffusion, under the effect of temperature and pressure, of volatiles (including water) dissolved in the laminates during their storage or during the prepregs manufacture [3][9][10].

In most of these works, deconsolidation is characterized by *post-mortem* analyzes (thickness measurements before and after deconsolidation, micrographs, …). However, they do not informe on the *in-situ* mechanisms involved during heating. Another method used to characterize deconsolidation is thermomechanical analysis (TMA) [10][11], allowing *in-situ* (continuous) characterization of deconsolidation during the heating phase. However, standard TMAs requires samples of small dimensions (few mm only) which are not representative of the size of the composite structures.

In this work, a novel TMA device has been developed (section 2) and validated (section 3) for the continuous and online characterization of the deconsolidation of large high-performance fiber-reinforced thermoplastic matrix composite laminates carbon/PEKK (section 4).

2. Experimental setup

The developed device, called CODEC bench (COmposite DEconsolidation Characterization), allows continuous and online monitoring of the deconsolidation of a composite plate subjected to a temperature variation, representative of a manufacturing process. The characterization is done by continuous measurement of the composite thickness which is related to structural change in the composite such as porosities. The CODEC setup is shown in Figure 1.

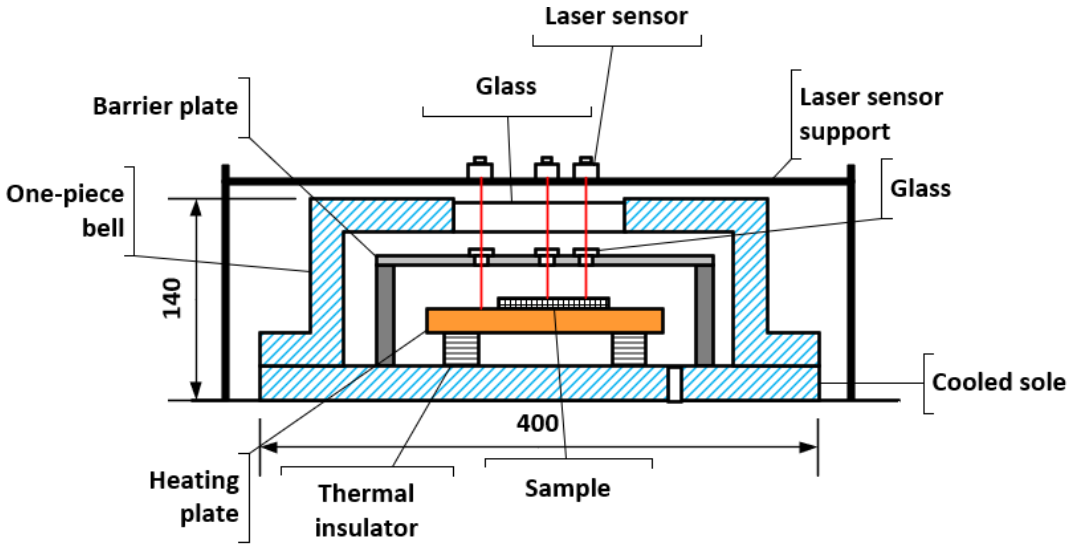

Figure 1. Scheme of the CODEC device designed for online characterization of deconsolidation of large fiber-reinforced thermoplastic composite plates, using laser sensors for thickness measurement, during its processing on a hot plate. This gives insight on the deconsolidation

The device is composed of a copper heating plate, which is placed in a closed thermal chamber (in aluminium) with a 25 mm thick borosilicate glass window. Water circulation channels are machined in the sole to cool the chamber walls. Two blocks of Pamitherm thermal insulators are placed between the sole and the heating plate, to reduce heat transfer by conduction. In order to vent the chamber during heating, a hole is machined in the sole to maintain atmospheric pressure inside.

  doi:10.5075/epfl-298799_978-2-9701614-0-0

The hot plate temperature is measured by a K-type monitoring thermocouple located in the middle of the hot plate, 1 mm underneath its surface. The thickness variation of the samples is measured using 3 Keyence IL-S065 laser sensors through the borosilicate window. The three distance measurement sensors have a measurement range of 55 to 75 mm and a linearity of ±0.075% of the full scale. The laser emitted by the sensors has a wavelength of 655 nm (visible light), to which the borosilicate is transparent. The maximum environmental temperature that the sensors can withstand is 50°C. For this reason, the sensors are positioned in a box located on a structure outside the chamber.

Thermocouples, laser sensors, and power controller are connected by means of modules to a single NI CompactDAQ acquisition system. The heating power is generated by cartridge heaters and regulated according to the temperature measured by the control thermocouple. The control is performed automatically using a single software developed on labVIEW. Thus, the temperature, thickness data acquisition and temperature control are synchronized.

3. Thickness variation measurement validation

In order to validate the CODEC Bench, the Coefficient of Thermal Expansion (CTE) obtained on a homogeneous material, *i.e.*, 6061 Aluminum, using a standard dilatometer (Linseis L75HS500LT), was compared with the CTE obtained with the same material on the CODEC setup.

For standard dilatometry, the test was performed on a 10 mm × 10 mm × 2.98 mm sample of 6061 aluminum which was heated at 2°C/min from 20°C to 300°C. Aluminum does not experience phase change or deconsolidation during heating. Strain as a function of temperature is ploted in Figure 2. From this curve, the linear CTE was determined along the thickness direction (Table 1).

Another test was thereafter carried out with the CODEC device, with a bigger plate of the same alloy (125 mm × 25 mm × 2.98 mm. The sample placed in the device was heated at the same heating rate as on the dilatometer up to 250°C.

Two laser sensors were used to measure the thickness variation of the sample. One sensor aims the center of the sample (sensor 2) and another 40 mm from the center (sensor 3). The last sensor (sensor 1) aims the heating plate (Figure 2.c). During the heating, the distances between the sensors and the targets (sample and heating plate) were recorded. The sample elongation was obtained by the difference between the actual distance and the initial ones. The heating plate elongation (baseline, sensor 1) was subtracted from the total elongation calculated on the sample. This operation allowed us the intrinsic sample elongation to be estimated. From these data, the linear CTE of the sample was determined along the thickness direction (Figure 2.b).

The curve obtained with the CODEC device is non-linear. This non-linearity is due to the macroscopic movements of the heating plate and air convection which disturbed the laser measurement. However, the comparison of the CTEs obtained by standard dilatometry and with the CODEC device, at the measurement points (Table 1) shows that the CODEC device is able to characterize small strains with a measurement resolution of ± 36 µm.

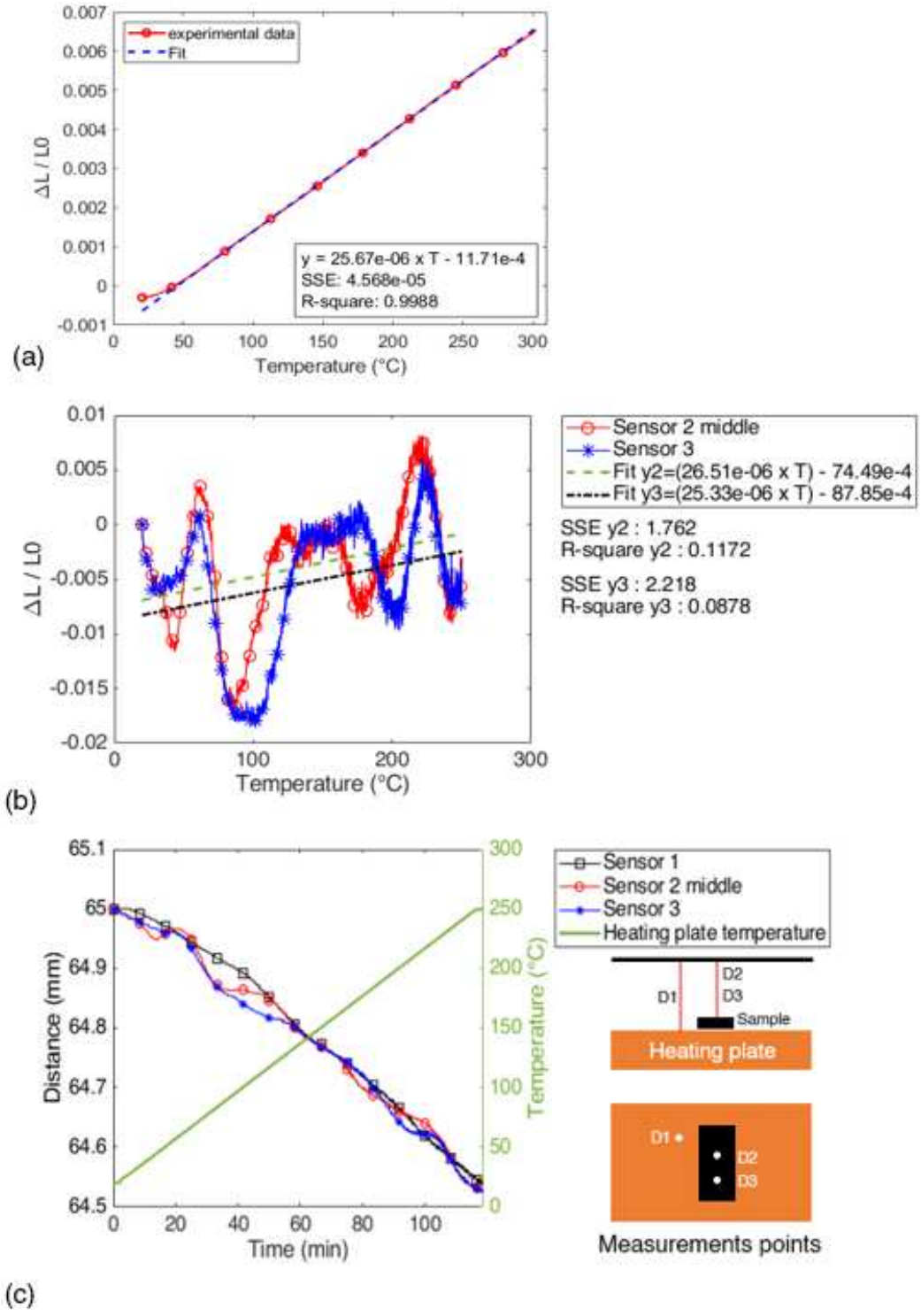

Figure 2. computed strain of a 6061 Aluminum reference material during (a) standard dilatometry (b) on CODEC device at two measurement points (c) Raw distances measured over time during ramp up on the reference material

  doi:10.5075/epfl-298799_978-2-9701614-0-0

Table 1: Comparison of CTEs obtained by standard dilatometry and on the CODEC bench.

Dilatometry ($°C^{-1}$)		25.68e-06	
	Sensor 2	Sensor 3	Mean
Codec setup ($°C^{-1}$)	26.51e-06	25.33e-06	25.92e-06
Absolute error ($°C^{-1}$)	0.84e-06	0.34e-06	0.25e-06
Relative error (%)	3.27	1.32	0.97

4. Composite deconsolidation characterization

In this section, the moisture and residual stress effect on the deconsolidation of a high-performance thermoplastic composite is investigated. Using the CODEC setup, deconsolidation tests were carried out on unidirectional (UD) laminates composed of carbon fibers (CF) and PEKK 7002 resin.

4.1 Materials

Prepregs CF/PEKK plies are supplied by Toray Advanced Composite. The plies have a fiber areal weight (FAW) of 194g/m² and a theorical thickness of 0.185 mm. The resin mass content is 34%. The glass transition temperature (Tg) and melting temperature (Tm) of PEKK 7002 are 160°C and 337°C, respectively (according to the manufacturer).

First, the plies were stacked in a mold following the same orientation $[0]_{16}$. Consolidation was then carried out on a PEI 50t press according to the following cycle: heating at 10°C/min up to 380°C under a pressure of 0.1 MPa; holding of the temperature for 20 min under a pressure of 4 MPa; cooling at 10° C./min at the same pressure, then demolding. 16 UD plies of 350 mm × 350 mm × 2.90 mm were manufactured accordingly. Optical micrographs on the consolidated plates validate the absence of porosities (Figure 4).

4.2 Pretreatments and testing procedure

In order to investigate the moisture and residual stress effect, the deconsolidation tests were carried out on two groups of samples: Ambient storage (AS) samples and dried samples (DS). The AS samples were cut by water jet from the consolidated plates stored in the workshop for 5 months in ambient conditions. A weight measurement after a drying test at 180°C on an 80 mm × 80 mm sample, cut from the stored plates, showed that the water content of the plates is 0.013% at the end of the storage.

The dried samples were also cut from the stored pates and then dry at 180°C for 72 hours. This drying condition was defined by continuous weight measurement during drying tests at different temperatures (140°C, 180°C, 250°C). Drying at 180°C for 72 hours fully eliminated the effect of humidity without any thermal degradation of the material.

The samples dimensions for the deconsolidation tests were 125 mm × 25 mm × 2.90 mm. Within the codec setup, the samples were heated at 60°C/min up to 380°C and then maintained at this temperature for 5 min, follow by a cooling (natural convection between the sample and the air). This cycle is representative of typical temperature for CF/PEKK during its processing (resistance welding, thermostamping, …). Each testing condition was repeated three times. At the end of

each test, the thickness variation was also measured by *post mortem* analysis, using a 0.01 mm precision micrometer. *Post mortem* optical micrographs were also performed on the samples.

4.3 Results and Analysis

Figure 3.a shows the evolution of deconsolidation strain $\varepsilon_d = ln(e/e_0)$ (e_0 and e being the initial and actual sample thicknesses, respectively) vs time, during deconsolidation of the DS and AS sample. The sample strain brutal increase during the ramp up, is a signature of deconsolidation. In the absence of humidity, the maximum deconsolidation strain reaches 0.17, which is mainly ascribed to the residual stress relaxation. Indeed, when the material temperature reaches the melting temperature range, the sample begins to melt and behaves like a viscoelastic liquid. The phase change from a viscoelastic solid to a viscoelastic liquid favors the residual stress relaxation.

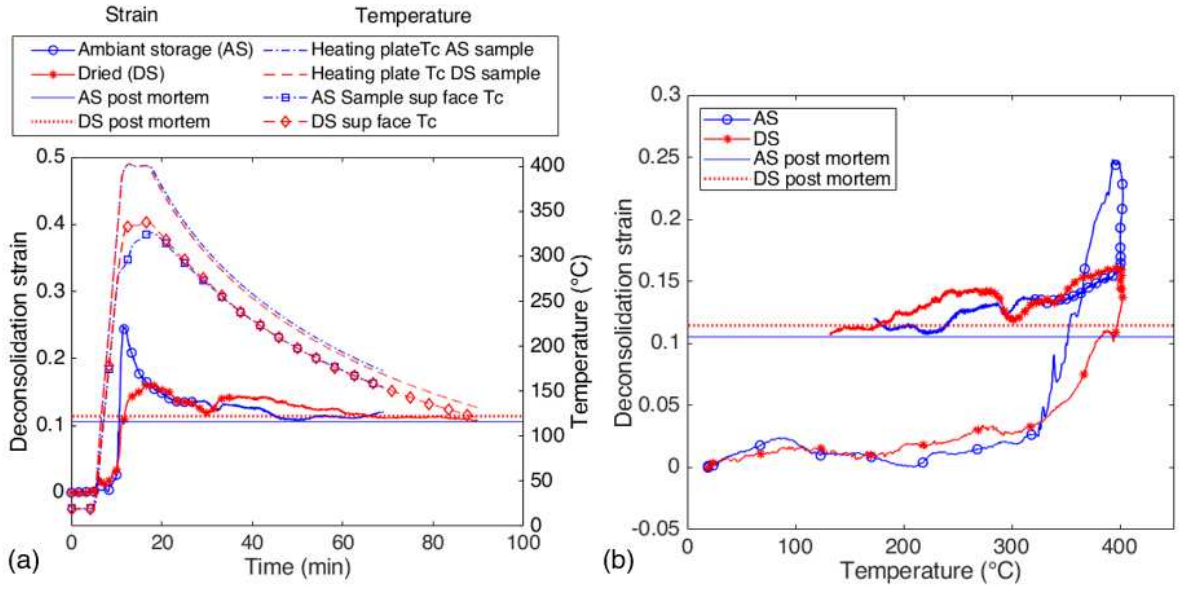

Figure 3. deconsolidation strain (a) vs time (b) vs temperature measured at the center of the AS and DS sample

Figure 3.b shows the deconsolidation strain *versus* the heating plate temperature. The sample strain behavior can be divided into 3 phases. During the first phase, the sample experiment thermal expansion. In the second phase, when the temperature reaches the melting temperature range, the deconsolidation begins and lead to an important strain increase followed by a slight strain decrease. This decrease, mostly visible in the AS samples, is probably linked to the collapse of the large porosities under gravity effect. In the third phase, the sample strain decreases due to the sample shrinkage during the cooling.

In the case of AS samples, the maximum strain observed is 0.09 higher than the DS samples maximum strain. This difference is related to the combination of the moisture effect with the residual stress relaxation. The moisture effect is linked to the water molecules diffusion in the porosities (due to the temperature increase) leading to the porosities internal pressure increase. The porosities start to grow when their internal pressure is greater than the external pressure applied by the composite. According to the small difference between the maximum strain, it can be noted that, on the material studied and under the defined test conditions, the effect of humidity is small but not negligible compared to the effect of residual stresses. The diffusion

phenomenon strongly depends on the heating rate. To be able to draw a conclusion on the predominant phenomenon, it will be necessary to carry out tests at other heating rates.

The *post mortem* optical micrographs also highlight the moisture effect. In the AS samples, micrographs show larger porosities, mainly located at the subsurface (Figure 4.b). In the DS samples, the porosities have small sizes and are homogeneously located in the middle of the sample (Figure 4.c). However, the measured *post mortem* thickness indicates a small difference between the AS sample and dried sample strains ($\Delta\varepsilon_d = 0.01$, see Figure 3.b). The *post mortem* thickness measurement solely cannot therefore explain the microstructure differences.

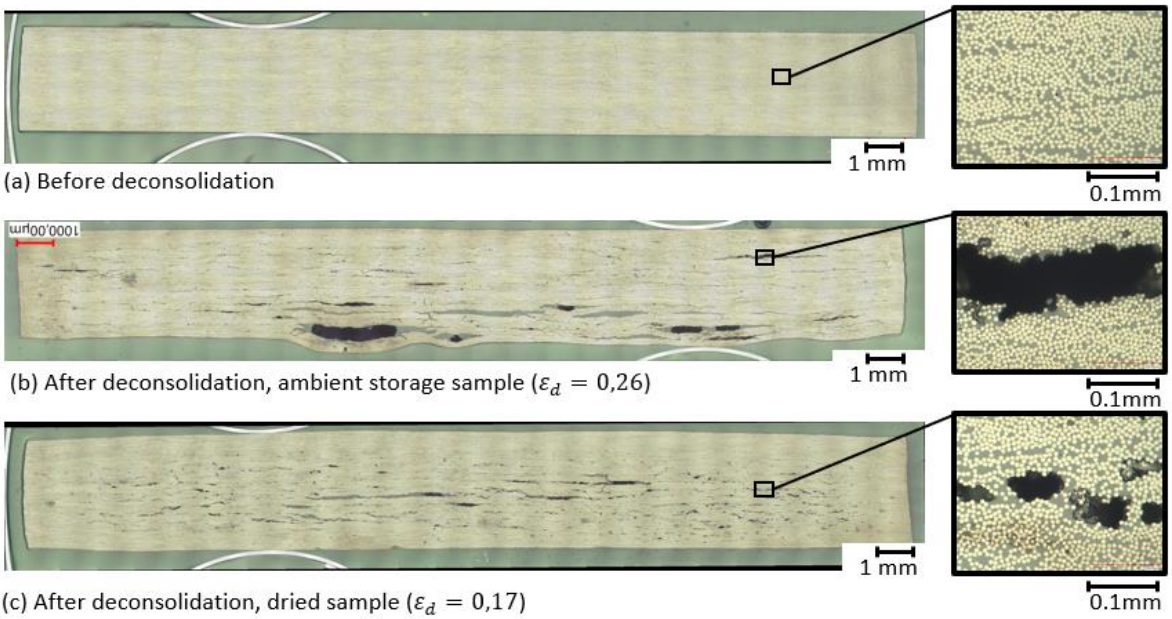

Figure 4. cross-sections micrograph of a 25mm wide sample after (a) press consolidation, material is fully consolidated (b) after ambient storage for 5 months (c) after drying at 180°C for 72 hours

Unlike the *post mortem* thickness measurement, the online deconsolidation strain characterization shows that the porosities final morphology and distribution is highly affect by the *in-situ* mechanisms during heating. The difference between the final content, distribution and morphology of the porosities can now be explained and highlighted by the deconsolidation strain history. The large porosities observed in the AS sample are due to the fast and high increase of the porosities size visible the deconsolidation strain evolution. The low porosities content observed in the DS samples is related to the slow growth of the porosities size during the heating also visible in the deconsolidation strain evolution. Thanks to the online characterization on the CODEC setup, these two observations allowed a better understanding of the moisture diffusion effect and residual stress relaxation effect on deconsolidation.

5. Conclusion

In order to better understand the mechanisms involved during deconsolidation, the CODEC device has been developed in this study. The device allows continuous and online characterization of composite laminates deconsolidation, under industrial conditions, using thickness measurement with a resolution of ±36 µm.

  doi:10.5075/epfl-298799_978-2-9701614-0-0

Using the CODEC setup, deconsolidation tests were carried out on a CF/PEKK composite sample dried at 180°C for 72h and sample stored in ambient conditions for 5 months. The tests results show a small (but not negligible) effect of moisture on deconsolidation, compared to residual stress effect. The deconsolidation kinetics measured correlates well with the final porosities content and morphologies observed on post mortem micrographs. This provide a better understanding of the mechanisms involved during the deconsolidation of a press consolidated thermoplastic composite laminate. In the future the codec will be updated and used to investigate the effect of heating rate and pressure on deconsolidation, in order to have a deep comprehension of deconsolidation, under different industrial conditions.

Acknowledgements

The authors would like to thank Julien Aubril and Arnaud Arrive for the help on the design and machining of the CODEC bench. The authors would like to acknowledge the funding of PERFORM project led by IRT Jules Verne (France Institute for Advanced Research and Technology Manufacturing technologies for composites, metals and Hybrid Structures) who made this work possible. Authors wish to associate the industrial partners of PERFORM project: Airbus, Daher, Safran, Latecoere, Stelia Aerospace, Clayens NP, Naval Group and Faurecia.

6. References

1. Mays GC, Hutchinson AR. Adhesives in civil engineering. Cambridge University Press. 1992.
2. Crane RL, Dillingham G. Composite bond inspection. J Mater Sci. oct 2008;43(20):6682-94.
3. Banea MD, da Silva LFM. Adhesively bonded joints in composite materials: An overview. Proc Inst Mech Eng Part J Mater Des Appl. 1 janv 2009;223(1):1-18.
4. Donadei V, Lionetto F, Wielandt M, Offringa A, Maffezzoli A. Effects of Blank Quality on Press-Formed PEKK/Carbon Composite Parts. Materials. 23 juin 2018;11(7):1063.
5. Saenz-Castillo D, Martín MI, Calvo S, Rodriguez-Lence F, Güemes A. Effect of processing parameters and void content on mechanical properties and NDI of thermoplastic composites. Compos Part Appl Sci Manuf. juin 2019; 121:308-20.
6. Liu X, Chen F. A Review of Void Formation and its Effects on the Mechanical Performance of Carbon Fiber Reinforced Plastic. :19.
7. Wan Y, Takahashi J. Deconsolidation behavior of carbon fiber reinforced thermoplastics. J Reinf Plast Compos. sept 2014;33(17):1613-24.
8. Brzeski M, Mitschang P. Deconsolidation and Its Interdependent Mechanisms of Fibre Reinforced Polypropylene. Polym Polym Compos. oct 2015;23(8):515-24.
9. Simacek P, Advani SG, Gruber M, Jensen B. A non-local void filling model to describe its dynamics during processing thermoplastic composites. Compos Part Appl Sci Manuf. mars 2013;46:154-65.
10. Slange TK, Warnet LL, Grouve WJB, Akkerman R. Deconsolidation of C/PEEK blanks: on the role of prepreg, blank manufacturing method and conditioning. Compos Part Appl Sci Manuf. oct 2018;113:189-99.
11. Shi H, Villegas IF, Bersee HEN. A study of process induced voids in resistance welding of thermoplastic composites. 2015;13.

  doi:10.5075/epfl-298799_978-2-9701614-0-0

EFFECT OF RELEASE AGENT ON PROCESS-INDUCED DEFORMATION IN AUTOCLAVE CURING OF LAMINATE COMPOSITES

Arnon LERDWONGPAISAN[a,b], Bruno CASTANIE[a], Philippe OLIVIER [a]

a: Institut Clément Ader, Université de Toulouse, 3 rue Caroline Aigle, Toulouse 31400, France
b: Burapha University, 169 Long Had Bangsaen Rd, Saensuk, Muang, Chon Buri 20131, Thailand
Email: lerdwong@insa-toulouse.fr

Abstract: *During manufacturing, composite laminated parts undergo process-induced stresses and frequently exhibit some deformations at the end of cure. Among the different sources inducing these stresses and deformations, our work focusses upon tool/part interaction and more especially on the effects of bagging products. A series of cross-ply and angle-ply laminates were autoclave-cured on aluminium flat mould. Liquid release agent, ETFE release film and peel-ply were placed between the laminates bottom face and the mould. The deflection of all laminates was measured at the end of cure and numerical simulations were performed by FEM (Abaqus) for comparison. These numerical simulations propose an original modelling enabling the behaviour of releasing film and peel-ply to be taken into consideration. It reveals that cross-ply laminates* are sensitive to presence of peel-ply layer while angle-ply laminates are less. In this case, the thermal behaviour of releasing film and peel-ply need to be investigated by thermomechanical analysis.

Keywords: Out-of-Plane deflection; Autoclave process; Laminate composite; tool/part interaction

1. Introduction

During autoclave curing, composite parts are subjected to the pressure and variation of temperature, residual stress can be generated and the geometric distortion may result due to various parameters [1]. This is a problem in tolerances control especially when the part need to be assembled with other parts, it might have to be forced to fit in and internal stress is built up. Worst-case scenario, those parts can be scrapped.

Several parameters can be considered to be the source of part distortion. These parameters are classically separated into two groups between intrinsic and extrinsic sources. The intrinsic one are related to the characteristic of the part including the original properties of prepreg material, part shape and layup orientation. The extrinsic parameter mainly refers to the manufacturing process including the characteristic of tool/mould and autoclave condition.

The sources of distortion were greatly studied in various literatures and tool/part interaction is the one that is remarkable. Different part geometry and layup directly affect to part deformation. Thicker parts are supposed to have lower distortion compared to thinner part while bigger part is considered to provide larger distortion compared to smaller part. Metallic mould with high coefficient of thermal expansion (CTE) is assumed to induce larger part warpage. The characteristic of mould surface and releasing agent may or may not have an

  doi:10.5075/epfl-298799_978-2-9701614-0-0

importance on geometrical distortion. However, the comparison in the midst of research work might be difficult due to various unknown conditions.

Therefore, this work aims to investigate the influence of tool/part interaction to the part deflection. We decided to start from the symmetrical flat laminate with thin layer. The effects of the interface between part and mould surfaces is considered. This work relies on the basis of our previous research [2-5].

2. Experimental method

2.1 Material and manufacturing

The raw material is a unidirectional prepreg M21EV/IMA provided by Hexcel Composites. 250 x 250 mm cross-ply [0°$_1$/90°$_1$]s and angle-ply [+45°$_1$/-45°$_1$]s laminates were autoclave-cured using a 2024 aluminium mould. Choosing a 2024 mould with its high CTE enables process-induced deformations to be exacerbated (when compared to the ones that could be obtained with steel or INVAR moulds).

Liquid release agent (Freekote C-600®), ETFE releasing film, and peel-ply were placed between the laminates bottom face and the mould. Freekote was applied on the mould surface as a liquid release agent prior placing releasing film and peel-ply. Four different tool/part interfaces were used: 1) Freekote and one layer releasing film, 2) Freekote and one layer peel ply, 3) Freekote and two layers releasing film, 4) Freekote and three layers releasing film. The bagging arrangement is presented in Figure 1. Four samples were provided for each interface configuration, 32 laminate plates were manufactured in total.

The cure cycle consisted in a first isothermal dwell at 150 °C for 1h30 followed by a second isothermal dwell of 1h30 at 180 °C. Heating and cooling rates were set at 1 °C/min. Autoclave pressure was set up to 7 bar (0.7 Mpa).

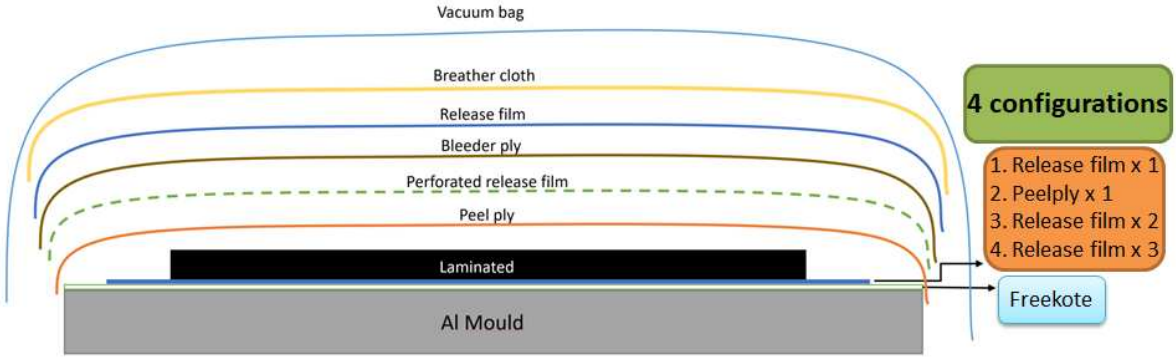

Figure 1. Bagging arrangement for experiment.

2.2 Measurement methods

Bagging products were unpacked and all laminates were removed from the mould. There was no difficulty during demoulding due to the existing releasing agent and interfaces. Physical distortion of all specimens was initially observed. The warpage of cross-ply laminate is quite

  doi:10.5075/epfl-298799_978-2-9701614-0-0

small and prevalent at the center of the plate while the warpage of angle-ply laminate is large over the whole specimen (see Figure 2).

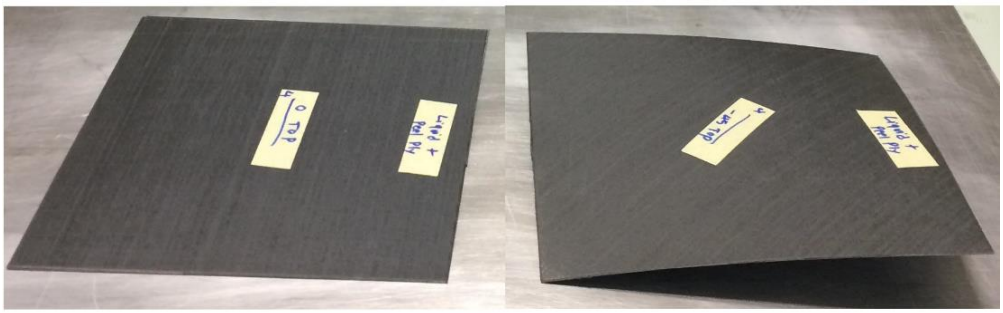

a) Cross-ply b) Angle-ply

Figure 2. Specimens distortion pattern.

Two measurement methods, Digital Image Correlation (DIC) and Laser Displacement Sensor (LDS) were employed to determine the magnitude of deformation of all laminates. Technically, the DIC can provide both shape and magnitude of deformation but the LDS was used to ensure the result by measuring the position of maximum distortion size. All laminate plates were spray painted by white and filled with random circular speckle dots on the top surface for DIC image processing. After the DIC measurement was done, the positions of coordinate were provided for 17 measurement points by LDS (see Figure 3). These points are assumed to be able to provide the actual shape of the specimens.

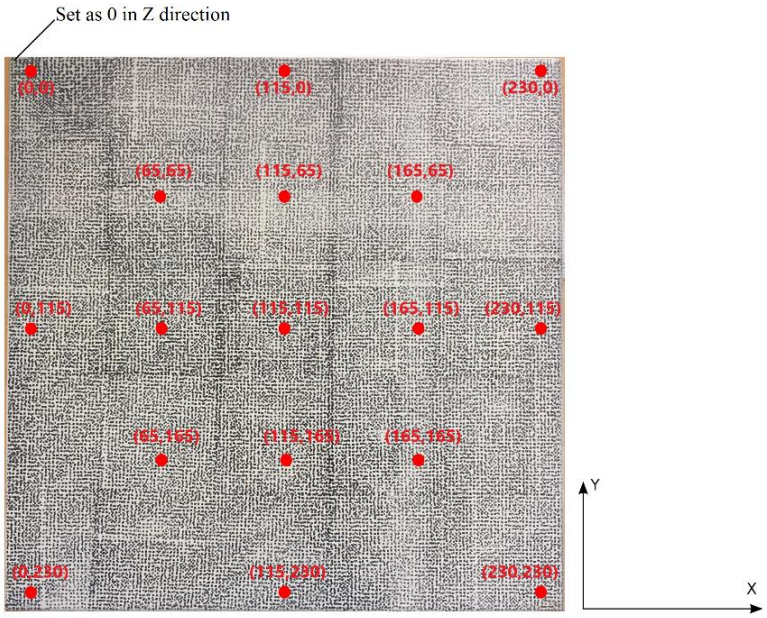

Figure 3. Specimen preparation before measurement and location of the 17 LDS points.

The DIC was operated by two cameras and sufficient light sources installed on the top of laminate in order to capture the specimen's images. Afterward, the magnitude and shape of deformation can be computed by VIC 3D software. For LDS, a semi-automated milling machine was utilised to install the laser head and the use of machine table to change the measuring

  doi:10.5075/epfl-298799_978-2-9701614-0-0

positions. Finally, the results from both measurement were compared to ensure the accuracy. The measurement set up for DIC and LDS are showed in Figure 4 a) and b) respectively.

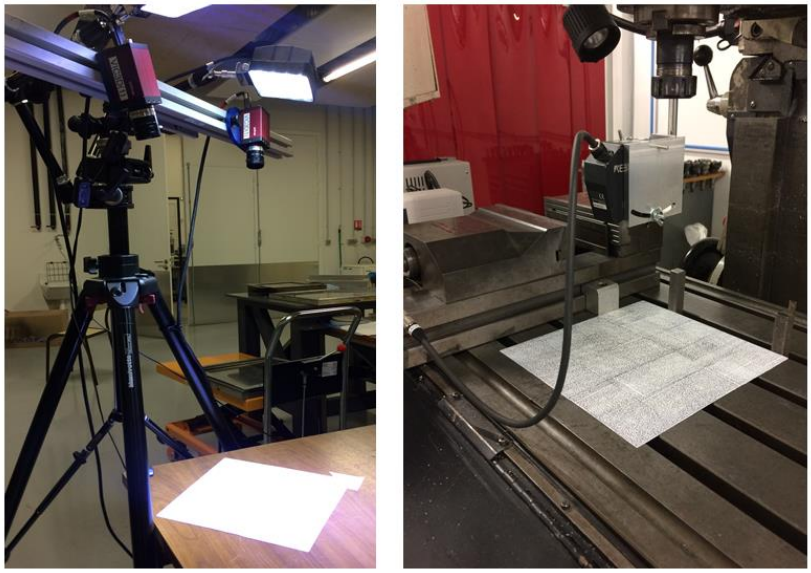

a) Digital Image Correlation (DIC) b) Laser Displacement Sensor (LDS)

Figure 4. Measurement set up

3. Experimental results

DIC provided distortion shape with magnitude in positive and negative values respected to the mid-plane, these two values are summed to gain the total deformation size.

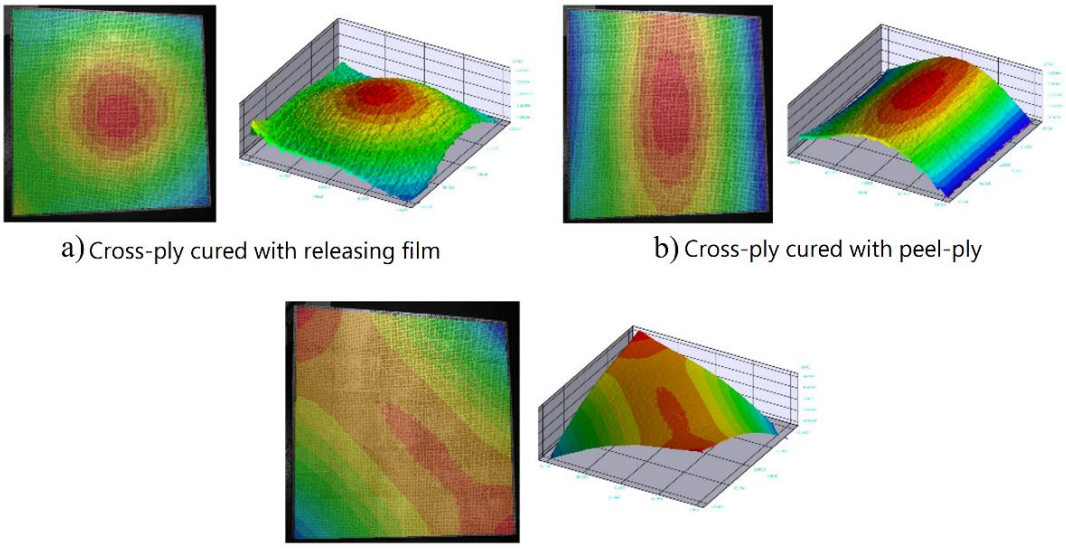

a) Cross-ply cured with releasing film b) Cross-ply cured with peel-ply

c) Angle-ply cured with releasing film and peel ply

Figure 5. Distortion shape from DIC

This communication only presents the example of distortion pattern for cross-ply and angle-ply laminates cured with releasing film and peel-ply. The different number of releasing film layers has no impact on cross-ply laminate, the distortion pattern is illustrated in Figure 5 a). Out-of-

  doi:10.5075/epfl-298799_978-2-9701614-0-0

plane deflections in Figure 5 b) shows that cross-ply laminate is sensitive to presence of peel-ply layer while the deflection of angle-ply laminate does not exhibit any sensitivity to any interfaces presence (see Figure 5 c)). Moreover, The presence of peel-ply increases the magnitude of deformation compared to the use of one, two and three layers of releasing film while no significant difference is observed for angle-ply with various interfaces, these results are indicated in Figure 6. In addition, the maximum distortion valued measured by LDS are consistent with the results from DIC.

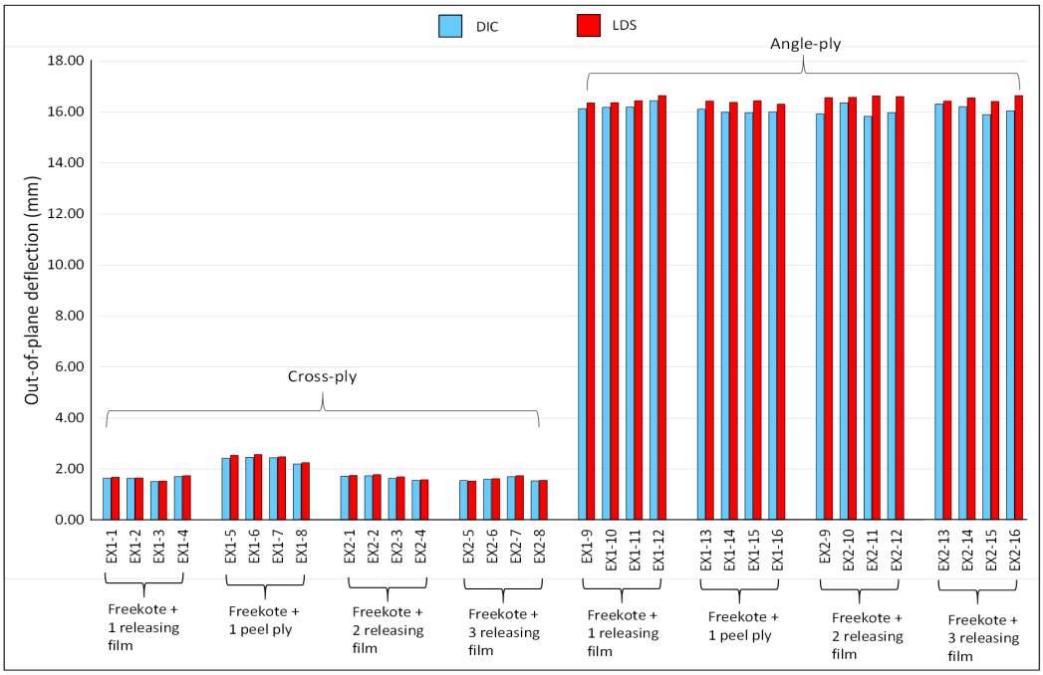

Figure 6. Magnitude of deformation measure from DIC and LDS

4. Numerical Simulation

In order to ensures the accuracy of experimental data, the numerical simulations were performed by FEM (ABAQUS). These numerical simulations propose an original modelling enabling the presence and the behaviour of releasing film and peel-plies to be taken into consideration. Effectively our aim was to improve the multiphysics numerical solution developed previously by the authors [4, 5] to provide a better understanding and modelling of the real influence of releasing agents during curing.

Abaqus 2016 was used to create 3D numerical simulation. The model contains full size of three main 3D solid deformable parts including laminate plate, interface and mould plate (see Figure 7), their properties were collected from many sources [6-12] as presented in Table 1. The thermomechanical model of M21EV/IMA was developed by Moretti et al. and is integrated with this simulation under the form of FORTRAN subroutines, thermo-kinetic, thermo-chemical, chemical shrinkage and thermo-mechanical behaviour were provided please refer to the reference [4, 5].

The simulation consists of three main step including initial, curing and de-moulding steps. Initial temperature of 20 °C was assigned in initial step while the amplitude of pressure and curing

  doi:10.5075/epfl-298799_978-2-9701614-0-0

profile are implemented in curing step, interface and mould is deactivated at de-moulding step to let the laminate to deform at the end of simulation. The model is connected by contact modelling with mesh element type C3D20T standard quadratic with Coupled Temperature-Displacement family.

Table 1 : The properties of aluminum mould and release materials used for simulation

	Density (t/ mm^3)	Thermal conductivity (T.mm/s^3 ° C)	Young modulus(E) (Mpa)	Poisson ratio	CTE (1/° C)	Specific heat (C_p) (mm^2/ s^{2}° C)
Aluminium	$2.7x10^{-9}$	237	69000	0.346	$2.31x10^{-5}$	$910x10^{6}$
ETFE releasing film	$1.7x10^{-9}$	0.238	800	0.45	$9x10^{-5}$	$1900x10^{6}$
Peel-ply	$64x10^{-15}$	0.28	3550	0.402	$9.5x10^{-5}$	$1670x10^{6}$

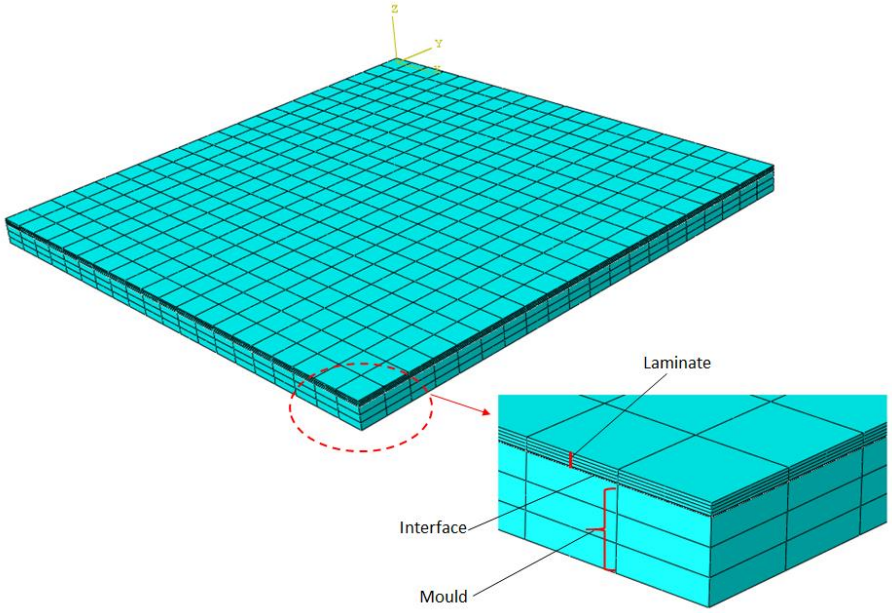

Figure 7. Abaqus model construction

The simulation results are presented in Figure 8. Compare to Figure 5, the agreement between experiment and simulation results is satisfying for both cross-ply and angle-ply laminates, this ensure the efficiency of thermomechanical modelling and curing environment assigned to the model. Simulation results from Figure 8 c) and d) support the experiment in Figure 5 c), it can be concluded that the variation of tool/part interface has no influence on angle-ply laminate. However, the discrepancy between experimental and simulation results is observed for the presence of peel-ply (see Figure 5 b) and Figure 8 b)), further investigation might be required for thermos-mechanical characterisation of textile sheet.

  doi:10.5075/epfl-298799_978-2-9701614-0-0

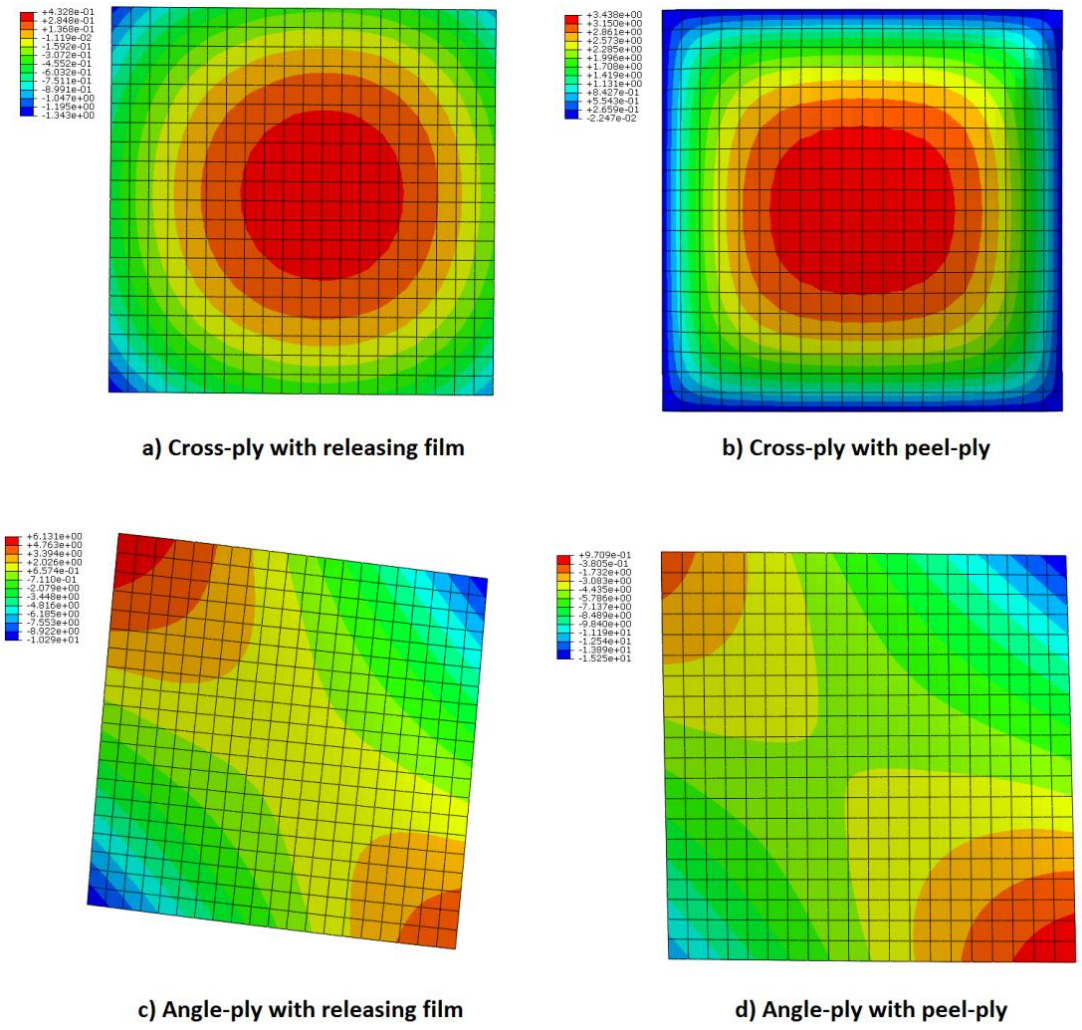

Figure 8. Simulation results

5. Conclusion

This study aims to investigate the effect of tool/part interaction to the geometrical distortion of symmetrical flat laminate at the end of cure. The variation of tool/part interface does not play significant role on the distortion of angle-ply laminate while cross-ply laminate is sensitive to the presence of peel-ply and the number of releasing film has no any effect on their distortion so only one layer of releasing film is suitable.

The numerical simulation that employed thermomechanical modelling integrated with tool/part interaction assigned to the model is consistent with the experimental result. However, further studies are required for the modelling of interface materials in order to improve the numerical result.

  doi:10.5075/epfl-298799_978-2-9701614-0-0

6. References

1. Patricia P, Harald EN, Beukers A. Residual stresses in thermoplastic composites—A study of the literature—Part I: Formation of residual stresses. Composites: Part A 2006; 37(11): 1847–1857.

2. Mezeix L, Seman A, Nasir M, Aminanda Y, Rivai A, Castanié B, Olivier P, Ali KM. Spring-back simulation of unidirectional carbon/epoxy flat laminate composite manufactured through autoclave process. Composite Structures 2015; 124: 196-205.

3. Fiorina M, Seman A, Castanié B, Ali KM, Schwob C, Mezeix L. Spring-in prediction for carbon/epoxy aerospace composite structure. Composite Structures 2017; 168: 739-745.

4. Moretti L, Castanié B, Bernhart G, Olivier P. Characterization and modelling of cure-dependent properties and strain during composite manufacturing. Journal of composite materials 2020; 54(22): 3109-3124.

5. Moretti L, Castanié B, Bernhart G, Olivier P. Experimental study and in-situ FBG monitoring of process-induced strains during autoclave co-curing, co-bonding and secondary bonding of composite laminates. Composites Part A: Applied Science and Manufacturing 2021; 142: 106224.

6. FLUOROTHERM™. Materials Overview: ETFE Properties. [Online].; 2021 [cited 2021 January 15. Available from: https://www.fluorotherm.com/technical-information/materials-overview/etfe-properties/.

7. fabrix360. What is ETFE? [Online]. [cited 2021 January 15. Available from: https://www.fabrix360.com/what-is-etfe.

8. Faserverbundwerkstoffe. Peel ply. [Online]. [cited 15 January 2021. Available from: https://shop1.r-g.de/en/art/190181.

9. Ertalon. Technical Data Sheet for Nylon 66 Rod, Sheet & Tube. [Online]. [cited 2021 January 15. Available from: https://www.theplasticshop.co.uk/plastic_technical_data_sheets/nylon_66_technical_data_sheet.pdf.

10. Plastics P. Thermal Properties of Plastic Materials. [Online]. [cited 2021 January 15. Available from: https://www.professionalplastics.com/professionalplastics/ThermalPropertiesofPlasticMaterials.pdf.

11. MatWeb. Overview of materials for Nylon 66, Unreinforced. [Online]. [cited 2021 January 15. Available from: http://www.matweb.com/search/datasheettext.aspx?matguid=a2e79a3451984d58a8a442c37a226107.

12. MatWeb. Aluminum, Al. [Online]. [cited 2021 January 15. Available from: http://www.matweb.com/search/datasheet.aspx?bassnum=AMEAL00&ckck=1.

  doi:10.5075/epfl-298799_978-2-9701614-0-0

COMPARATIVE STUDY ON THE HEATING METHODS IN THE POST-FORMING OF CARBON REINFORCED THERMOPLASTIC TUBULAR STRUCTURES

Mengyuan, Li[1,a], Chris, Stokes-Griffin[1], Paul, Compston[1]

1: ARC Training Centre for Automated Manufacture of Advanced Composites, Australian National University, Canberra, ACT 2600
a: mengyuan.li@anu.edu.au

Abstract: *This paper presents a localised heating technique for the post-forming of polyamide 6 carbon (CF/PA6) thermoplastic tube. Straight CF/PA6 tubes can be post-formed into desired curvatures via rotary draw bending at elevated temperatures. Localised heating restrains fibre movements during forming to be within the forming zone only, while forming under isothermal conditions allows for fibre movement throughout the heated tube. The localised heating technique utilises an induction heating set-up, where a mild steel mandrel is first heated to 340 °C and radiates heat to the CF/PA6 tube until it reaches its formable temperature. The tube is then moved by a linear actuator to simulate feeding during post-forming. Heating experiments revealed that tube heating times increase with fibre angles. The feeding rate is 2.42 mm·s^{-1} for all fibre angles. Localised induction heating is shown to be significantly faster than oven heating, enabling the post-forming operation to be performed within 180 s.*

Keywords: thermoplastic composite tube; CF/PA6; induction heating; post-forming; rotary draw bending

1. Introduction

The combination of high stiffness-to-weight ratios of composites and high design versatility of tubular structures makes carbon fibre reinforced thermoplastic tubes highly desirable for an extended range of lightweight and high strength applications [1,2]. Currently, straight thermoplastic tubes can be rapidly produced from pre-impregnated carbon reinforced thermoplastic tapes by laser assisted thermoplastic automated tape placement (TP-ATP) [3]. The use of thermoplastic matrix system allows for fibre relocation and re-orientation upon re-heating of the matrix into its soft and formable state [4]. This, therefore, enables customisation of more complexed geometries and curvatures like coil springs and handlebars from straight thermoplastic tubes via post-forming operations such as rotary draw bending (RDB) akin to metallic tubing [5].

RDB at elevated temperature is a relatively simple post-forming technique with high design freedom, reduced instrument cost, and the possibility of automation [6]. In this process, a straight thermoplastic tube (section) is first heated to its matrix softening temperature, then formed to the desired curvature through fibre relocation and re-orientation resulted from bending. RDB of a tube can be performed either under isothermal conditions or with localised heating of tube bending zone only.

  doi:10.5075/epfl-298799_978-2-9701614-0-0

In previous studies, tubes formed under isothermal conditions were observed to show slight geometrical distortions including reduction in tube diameters and extension of tube extrados (outer arc) beyond their designed bending zones [7]. This was due to fibre movement throughout the whole tube under isothermal conditions instead of within its designated forming zone. The oven heating process for forming under isothermal conditions took approximately 5 hours per tube [7], which was inefficient especially considering its industrial application. Localised heating allows for the partial melting of tube matrix system at designated heating zone only, while the rest of the tube stays relatively cool. This restrains fibre movements during forming to be within the heated section only, preventing geometrical distortions caused by fibre movements beyond the forming zone. Engel and Böcking has presented a localised heating technique to pre-heat the entire tube bending zone using four infrared (IR) heaters placed at every 90° around the tube [8]. The tube was then formed after its bending zone was heated to its formable temperature. This method took about 200 s to heat up the tube surfaces facing the IR heaters while the rest of the bending zone showed a maximum temperature gradient of 50 °C, which created uneven tube temperature profiles [8]. In this study, a localised heating technique utilising an induction heating set-up is presented. Heating experiments will be conducted using $[\pm30°]_4$, $[\pm45°]_4$, and $[\pm60°]_4$ polyamide 6 carbon (CF/PA6) thermoplastic tubes to determine feasible parameters including tube heating time and tube feeding rate, which will be compared with those of oven heating used in post-forming under isothermal conditions.

2. Heating experiments

The heating experiments aim to simulate the heating process prior to RDB in the post-forming of CF/PA6 tubes. In this process, a metal mandrel was first heated by induction heating; the tubes were heated by radiative heat transfer from the mandrel before being fed to the bending die to be post-formed.

The matrix of the tubes starts to soften at 220 °C as defined by [7]. In the heating experiments, heating parameters were determined for tubes to reach 250 °C, where the heated zone is fully formable, while being moved. Using an output current, I_{out} = 105 A, the mandrel was heated to and maintained at temperatures from 220 °C to 340 °C in 20 °C intervals for 7 sets of experiments corresponding to each temperature. In each experiment, the tubes were heated while stationary and measured for their heating times, t_{tube} to 250 °C and equilibrium temperature, $T_{tube,e}$ if they could not reach 250 °C. Once a tube section was heated to 250 °C, the tube was moved at different rates to measure the change in tube temperature profile. From this, the moving rate that maintains a constant maximum tube temperature of 250 °C could be determined, corresponding with the conditions required for continuous forming. This rate determines the forming rate of the bending process.

2.1 Experimental set-up

The experimental set-up consists of three main apparatus, namely an induction heater (Across International IH8A), a mild steel mandrel, and a linear actuator to simulate the feeding of tube during rotary draw bending as shown in Fig. 1.

The induction heater has a maximum output power of 8 kW. The output current can be adjusted between 105 A and 605 A, and its output frequency is between 30 and 80 kHz. A three-turn copper induction coil with an internal diameter of 55 mm, an external diameter of

  doi:10.5075/epfl-298799_978-2-9701614-0-0

67 mm, and a total length span of 25 mm was connected to the heating unit and used to perform heating.

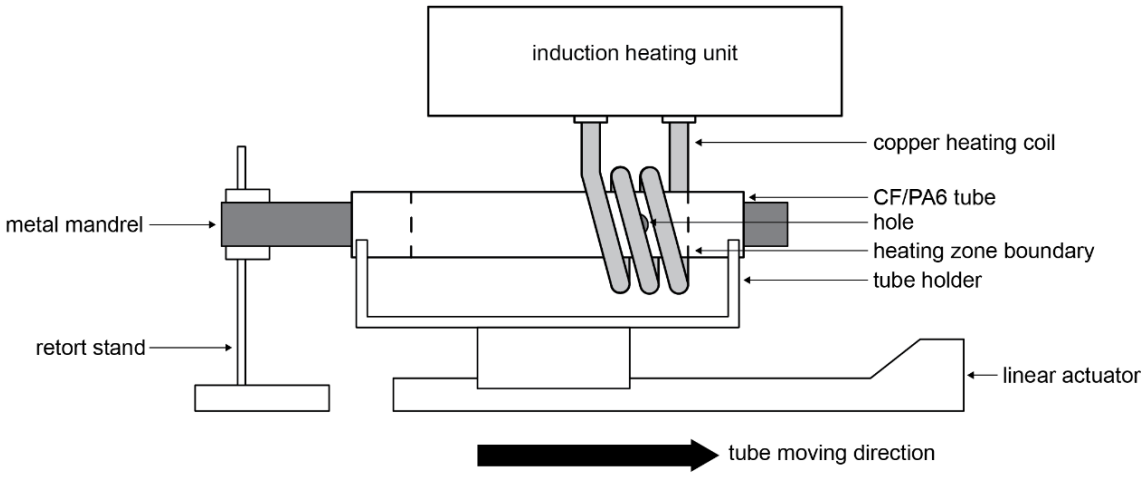

Figure 1. Induction heating set-up

A mild steel mandrel was used in this study as it is ferromagnetic, making it highly responsive to induction heating, thus ensuring quicker induction heating time with lower power output as compared to non-magnetic materials such as stainless steel and aluminium [9]. The mandrel is 225 mm in length, sufficient for the movement of tube to simulate feeding. The mandrel diameter is 16 mm, allowing for a 2 mm clearance between the mandrel and the tube inner wall to avoid direct contact which could damage the latter at high temperature. The mandrel was coated with thermal resistant, matte black paint to maximise black-body radiatiative heat transfer. The coating additionally has a high emissivity (0.97) which aids long-wave infrared (LWIR) temperature measurements.

The tube and the metal mandrel were held concentric to the induction coil by a tube holder attached to the linear actuator and a retort stand respectively to ensure uniform heating. The tube can be moved at rates from zero to 8.33 $mm \cdot s^{-1}$ along the axis in both directions, adjusted by the control unit of the stepper motor.

2.2 Experimental materials

The heating experiments used straight CF/PA6 tubes manufactured by AFPT GmbH via TP-ATP of Celstran® CFR-TP PA6 CF60-01 tapes. Each tape has a thickness of 0.13 mm and a width of 12 mm, with a fibre volume content of 48%. The tapes were placed at a rate of 12 $m \cdot min^{-1}$. The consolidation force and the process temperature were 200 N and 280 °C respectively. Following a conventional helical filament winding pattern, the tapes were wound around a 20 mm diameter chrome steel bar with a shift parameter of one (N_s = 1) as defined by [10] and 5, 4, and 3 circuits (P) per ±30°, ±45°, and ±60° layer pair respectively. The tube fibre orientations are defined from its axial direction to its transverse direction, where a fibre at 0° is parallel to the longitudinal direction, and a fibre at 90° is perpendicular to the longitudinal axis or parallel to the hoop axis. The manufactured tubes were measured to have on average a ±2° variation from their designed fibre angles. All tubes have an average emissivity of 0.87, determined by K-type thermocouple, for the LWIR temperature measurements.

  doi:10.5075/epfl-298799_978-2-9701614-0-0

The manufactured CF/PA6 tubes have 8 plies and were measured with an average tape width of 12.5 mm, inner diameter (d_i) of 20 mm, and outer diameter (d_0) of 22.6 mm, which resulted in the average wall thickness of 1.3 mm. The lengths of the tubes are 120 mm, and a heating zone of 72.5 mm was marked on each tube to simulate the bending zone of a tube post-formed to the bending angle of 90° with a bending radius of 46 mm (bending ratio = 2). A 4 mm diameter hole was drilled at 12.5 mm from one side of the heating zone boundaries, corresponding to the centre of the induction coil span, to enable temperature measurement of the metal mandrel during heating. Three tubes of each fibre orientation, namely $[\pm30°]_4$, $[\pm45°]_4$, and $[\pm60°]_4$ were used in the heating experiments.

2.3 Tube characterisation

Temperatures of the tubes and the mandrel were recorded by a Xenics Gobi-640-GigE long-wave infrared (LWIR) camera placed at 400 mm away from the heating zone (Fig. 2). The average tube temperature was measured at region A (excluding the hole), and the mandrel temperature, $T_{mandrel}$, was measured at point B in the hole. Tube heating times, t_{tube}, were recorded by the timer on the induction heating unit as the tubes were heated from ambient to 250 °C. If a tube was unable to reach 250 °C at a given $T_{mandrel}$, the temperature at which it reached equilibrium for 10 seconds was taken as its $T_{tube,e}$.

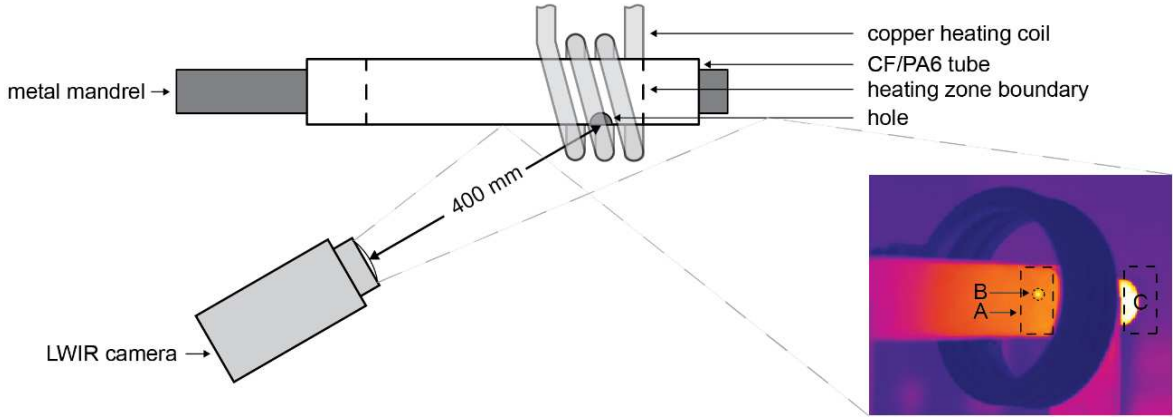

Figure 2. LWIR camera measurement set-up

After determining t_{tube}, a feasible tube feeding rate was determined based on the temperatures measured at region C while the tube was moving. The average temperature of region C was taken as the tube moved through the coil and covered the region. A feasible moving rate was determined to be when the temperature drop is no greater than 5°.

3. Results and discussion

3.1 Stationary tube heating time

From the heating experiments, the $[\pm30°]_4$, $[\pm45°]_4$, and $[\pm60°]_4$ tubes reached equilibrium at temperatures below 250 °C with $T_{mandrel}$ maintained at or below 320 °C, 300 °C, and 280 °C respectively as shown in Fig. 3 (a). The $[\pm60°]_4$ tubes had the highest equilibrium temperature, $T_{tube,e}$ at any given $T_{mandrel}$, which are on average 10% higher than those of the $[\pm45°]_4$ tubes, while the $[\pm30°]_4$ tubes had the lowest $T_{tube,e}$ which are on average 9% lower than those of the $[\pm45°]_4$ tubes. The tubes were then measured for their heating time, t_{tube} to 250 °C with $T_{mandrel}$ set to 340 °C. From Fig. 3 (b), the $[\pm60°]_4$ tubes had the shortest average t_{tube} of 46 s while the

$[\pm30°]_4$ tubes had the longest average $t_{tube,e}$ of 77 s, which are 31% shorter and 28% longer than that of the$[\pm45°]_4$ tubes (87 s) respectively.

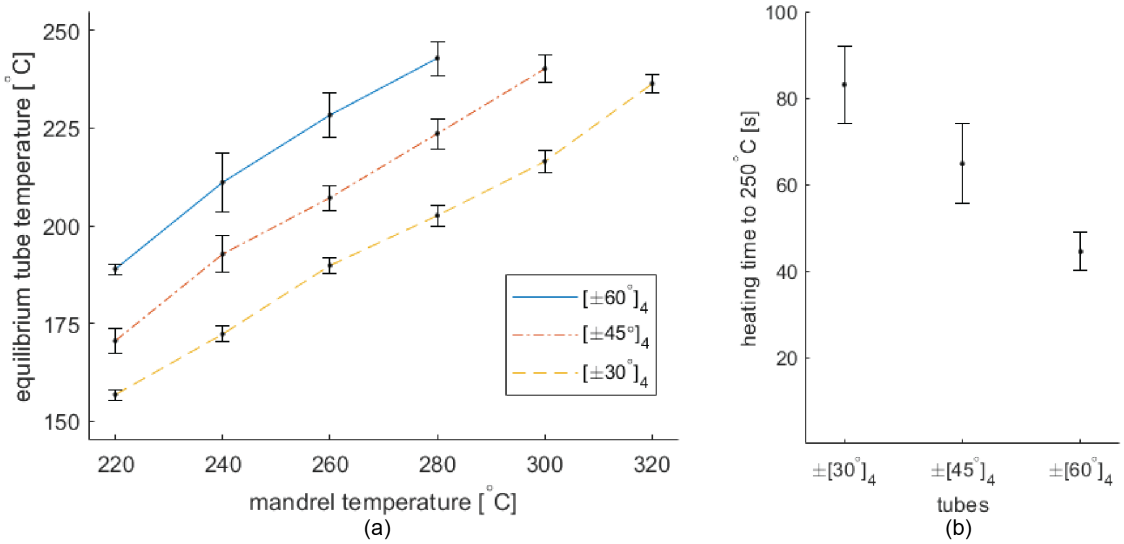

Figure 3. (a) Changes in $T_{tube,e}$ for different fibre angles, (b) t_{tube} at $T_{mandrel}$ = 340 °C

In this case where all parameters except for fibre orientation were kept constant, an approximately linear increase in t_{tube} and $T_{tube,e}$ take place as fibre angle increases. Tubes with larger fibre angles have their fibres more transversely aligned. During induction heating, these fibres are also more aligned to the current direction, allowing for a higher efficiency in heating in addition to the radiation from the heated mandrel. As the heating rate is influenced by fibre angle, induction heating of the tube itself also affects the heating parameters despite the main thermal body being the mandrel. With the minimum I_{out} = 105 A, uncertainties in heating parameters caused by slight fibre angle variations were minimised for the set-up.

3.2 Tube feeding rate

The feasible feeding rate is found to be 2.42 mm·s^{-1} for the heating parameters found in Section 3.1. This feeding rate corresponds to a bending rate of 3 °·s^{-1} for the bending parameters defined in [7], taking a total of 30 s to bend a tube to 90° for example. At this feeding rate, the temperature profiles of tubes of the three fibre angles measured at their region Cs are similar while more noise is observed as fibre angles decrease. For which, the mean temperatures of the $[\pm30°]_4$, $[\pm45°]_4$, and $[\pm60°]_4$ tubes in motion are 250.8 °C, 252.5 °C, and 252.8 °C respectively with standard deviations of 2.6, 2.2, and 1.8 as shown in Fig. 4.

Considering a total of 60 s for tube loading and unloading, a 90° bend can be rapidly post-formed in 173 s, 154 s, and 135 s for the $[\pm30°]_4$, $[\pm45°]_4$, and $[\pm60°]_4$ tubes respectively using the induction heating set-up.

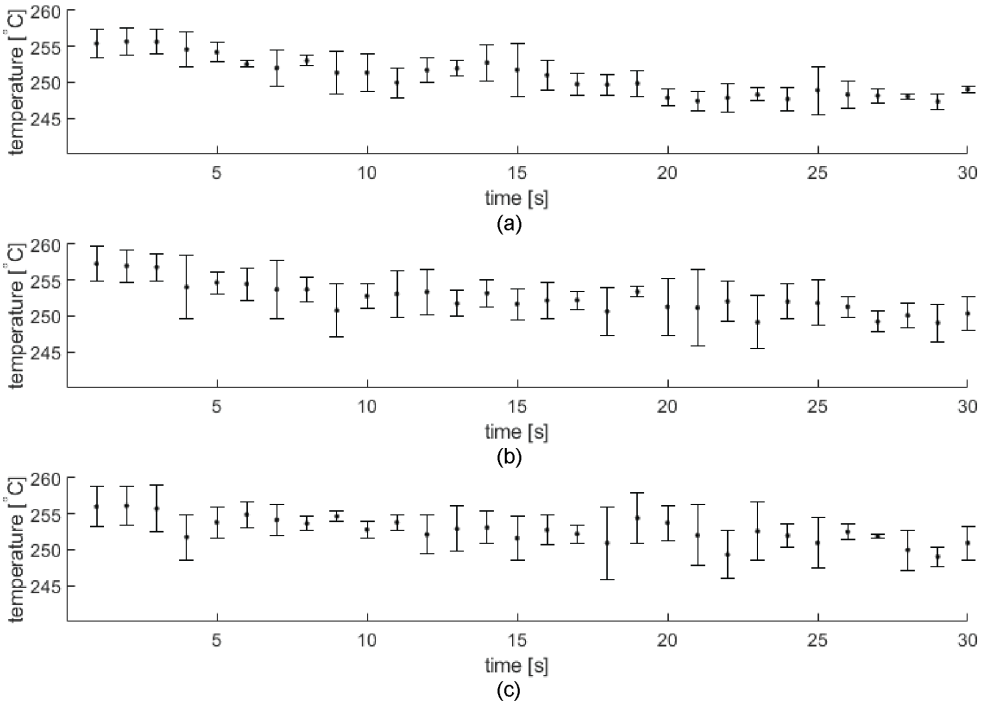

Figure 4. Region C tube temperature profiles for (a) [±30°]$_4$, (b) [±45°]$_4$, and (c) [±60°]$_4$ tubes

3.4 Comparison with forming under isothermal conditions

The presented localised heating technique is significantly more efficient than the oven heating method for forming under isothermal conditions. In terms of the heating time, heating of [±30°]$_4$, [±45°]$_4$, and [±60°]$_4$ tubes using the induction heating set-up took 0.45%, 0.36%, and 0.25% of the time taken by the oven, which took an average of 5 hours to heat a tube of any fibre angle [7]. Similarly, localised induction heating of [±30°]$_4$, [±45°]$_4$, and [±60°]$_4$ tubes is quicker than localised heating using IR heaters by taking 40.5%, 32.4%, and 22.5% of the time taken the latter, which took an average of 200 s [8]. On the other hand, the localised induction heating technique is more sensitive to tube fibre angles, hence an additional step of determining tube heating time for each fibre angle is needed, whereas for oven heating, the heating time is independent of fibre angle.

The forming rate for localised induction heating is limited by the heating rate of the tube at 3 °·s^{-1}, which is significantly slower than the forming rate of 45 °·s^{-1} used in the previous studies using isothermal heating [7]. The effect of the forming rate therefore warrants investigation.

4. Conclusion

In this study, the localised heating technique for CF/PA6 tubes utilising an induction heating set-up and its corresponding heating parameters and tube feeding rate for post-forming are presented. The identified parameters allow for the efficient heating of the tube forming zone, allowing for localised fibre relocation and re-orientation during post-forming to better maintain tube geometrical integrity during forming. For this purpose, heating experiments of [±30°]$_4$, [±45°]$_4$, and [±60°]$_4$ tubes were performed.

The set-up utilises heating of a mild steel mandrel with a 2 mm clearance to the tube inner wall, which radiates heat to the tube in an efficient and controllable manner without direct

  doi:10.5075/epfl-298799_978-2-9701614-0-0

contact which may damage tube surface at high temperature. A linear actuator was used to move the tube to simulate feeding of tube to be post-formed. Heating was performed with mandrel temperatures from 220 °C to 340 °C and output current of 105 A. The tubes were first heated stationary, then moved when they reach 250 °C. Stationary heating results revealed that:

- The $[\pm 30°]_4$, $[\pm 45°]_4$, and $[\pm 60°]_4$ tubes reached equilibrium at temperatures below the formable temperature of 250 °C when mandrel temperatures were 320 °C, 300 °C, and 280 °C respectively;
- equilibrium temperature increases linearly as tube fibre angle increases; and
- Tubes of all three fibre angles can be heated to 250 °C by a 340 °C mandrel, for which their heating times followed a linear trend as the fibre angles change.

Based on the temperature measurements of tube sections moving through the coil, the corresponding feeding rate was found to be 2.42 $mm \cdot s^{-1}$ to maintain the tube at a constant forming temperature. In this case, all tube had similar temperature profiles despite of their different fibre angles.

Overall, localised heating is a more efficient heating technique as compared to oven heating and heating using IR heaters despite additional estimation of heating parameters required for varying fibre angles.

Future work will include integration of the induction heating set-up into the RDB set-up for the complete CF/PA6 tube post-forming operation. Effects of aluminium RDB dies placed next to the heater and tube bending mandrel on tube heating parameters upon integration will also need to be investigated to warrant consistent and effective heating.

Acknowledgements

This project was conducted within the ARC Training Centre for Automated Manufacture of Advanced Composites (IC160100040), supported by the Commonwealth of Australia under the Australian Research Council's Industrial Transformation Research Program.

5. References

1. Osborne J. Automotive Composites – in Touch with Lighter and More Flexible Solutions. Metal Finishing. 2013 Mar 1;111(2):26–30.

2. Tornero RG. Composite materials are more present today than ever before in cars. Reinforced Plastics. 2015 May 1;59(3):131.

3. Schäkel M, Hosseini SMA, Janssen H, Baran I, Brecher C. Temperature analysis for the laser-assisted tape winding process of multi-layered composite pipes. Procedia CIRP. 2019 Jan 1;85:171–6.

4. Asim M, Jawaid M, Saba N, Ramengmawii, Nasir M, Sultan MTH. 1 - Processing of hybrid polymer composites—a review. In: Thakur VK, Thakur MK, Gupta RK, editors. Hybrid Polymer Composite Materials [Internet]. Woodhead Publishing; 2017 [cited 2021 May 5]. p. 1–22. Available from: https://www.sciencedirect.com/science/article/pii/B9780081007891000010

  doi:10.5075/epfl-298799_978-2-9701614-0-0

5. Eckardt S, Barfuß D, Condé-Wolter J, Gude M, Würfel V, Böcking J. Study on Bend-Forming Behaviour of Thermoplastic Tape-Braided CFRTP Profiles. In: SAMPE Europe Conference 2020. 2020. p. 9.

6. Banno T, Rashidi A, Crawford B, Milani AS, Nakai A. DEVELOPMENT OF BEND-FORMING TECHNOLOGIES ON CFRTP TUBE. In: TWENTY-SECOND INTERNATIONAL CONFERENCE ON COMPOSITE MATERIALS. 2019. p. 6.

7. Li M, Stokes-Griffin C, Sommacal S, Compston P. Fibre Angle Prediction for Post-Forming of Carbon Fibre Reinforced Composite Tubular Structures. Composites Part A: Applied Science and Manufacturing. 2022 Apr 1;106948.

8. Engel B, Böcking J. BENDING OF FIBRE-REINFORCED THERMOPLASTIC TUBES. In: 20th International Conference on Composite Materials. 2015. p. 9.

9. Moosbrugger C. ASM Ready Reference: Electrical and Magnetic Properties of Metals. ASM International; 2000. 298 p.

10. Rousseau J, Perreux D, Verdière N. The influence of winding patterns on the damage behaviour of filament-wound pipes. Composites Science and Technology. 1999 Jul 1;59(9):1439–49.

  doi:10.5075/epfl-298799_978-2-9701614-0-0

Tailoring mechanical properties of randomly oriented tape composites: An experimental study

Huub H. Urselmann[a], Deniz E. Gülmez[a], Clemens A. Dransfeld[a]
a: Technische Universiteit Delft – Aerospace Manufacturing Technology – H.H.Urselmann@tudelft.nl

Abstract: Discontinuous tape composites (DTC) have properties such as notch insensitivity, short processing times, and large shaping freedom. However, the mechanical behaviour of randomly oriented tape (ROT) composites is less predictable compared to continuous fibre composites due to the mesoscopic heterogeneity of the material. Controlling the tape alignment is a compelling approach for tailoring the mechanical properties of ROT composites, enabling better control and prediction of the material properties such as tensile strength and stiffness. However, for a successful implementation of the alignment method in industry, a fast tape alignment method is needed. A quantitative assessment has been made between different alignment methods. The presented alignment method has been used to manufacture aligned DTC samples for the characterisation of the material. This study showed an average tensile stiffness of randomly orientated, 0˚ centred, and ±45˚ centred tapes of 32.5, 79.5, and 25.3 GPa respectively.

Keywords: Randomly Orientated Tapes; Discontinuous Fibre Composites; Tow alignment; Computer vision; Mechanical Properties

1. Introduction

Discontinuous tape thermoplastic composites can contribute to waste reduction, low-cost production in the aerospace and automotive industries, and allow for large shaping freedom. However, mechanical performance of DTC show high variability due to their discontinuous structures [1]. To apply this material group with higher confidence into structures, more knowledge has to be gained on how to predict and improve their material properties. By aligning the properties of the tapes with the direction of loading, the mechanical response can be influenced [2]. This can be done by orienting the fibres inside the material in the loading direction to make the material stronger and stiffer.

This study focuses on the alignment and the effect of alignment of DTC. Tapes have been aligned by means of a mechanical alignment method as suggested by Gan et al [3]. The selected tape alignment method makes use of vertical slits to align and deposit tapes into a mould. This method is a fast and dry method which is suitable for large-scale manufacturing processes. For this study, tapes with dimensions 22.5 x 7.5 x 0.2 mm made out of carbon fibre with a thermoplastic matrix and a fibre volume fraction of 55% have been used. In this paper, a tape alignment technique is described and characterized by means of measuring the orientation distribution of tapes on a surface. These measurements have been obtained using the OpenCV library in Python [4].

For the determination of the effect of alignment on the mechanical response, three type of samples have been manufactured with a random, 0° centred, and ±45° centred tape orientation distribution. For the latter two, the alignment technique has been applied to create a single

  doi:10.5075/epfl-298799_978-2-9701614-0-0

aligned layer and a $[+45°,-45°]_s$ quasi-layup. The test samples have been tested in tensile loading for the determination of the tensile and shear response of the material.

The recorded tensile stiffness where found to be 32.5, 79.7, and 25.3 GPa respectively for the randomly orientated, 0˚ centred and ±45˚ centred tape distributions respectively. The obtained results give insight in the effect of tape alignment in discontinuous fibre composites on the tensile modulus. The effect of manufacturing on the overall tape orientation distribution has become more quantifiable than research has shown until now.

2. Experimental Procedure

Discontinuous tapes were obtained by cutting unidirectional continuous tape composites with a fibre volume ratio of 55%. The dimensions of tapes are 22.5 x 7.5 x 0.2 mm.

2.1. Tape Alignment Method

The used alignment method has been proposed by Gan et al. [3]. Although this method was used for thermoplastic composite tapes, the design has been altered to be suitable for thermoplastic tapes with the described dimensions. This alignment method has been selected from a group of potentially successful concepts which have been graded based on their process time, development time and level of alignment that each of them reached. With OpenCV as image recognition software, a large number of measurements have been executed for the determination of the tape orientation distribution.

The final method has been selected due to its fast and dry deposition of tapes which makes it suitable for large scale manufacturing. The method uses an alignment tool which exist out of multiple parallel walls. These walls have varying height and chamfers at the edges to ensure that the tapes do not clog the tool and are evenly spread out into the mould. This resulted into the alignment tools as shown in Figure 1a. This design has been used for the development of alignment tools for the +45˚ and -45˚ direction which can be seen in Figure 1b/c. All three different tools have been designed for manufacturing with FDM.

(a) (b) (c)

Figure 1, Alignment tools for manufacturing, a) 0° orientation, b) +45° orientation, c) -45° orientation.

For the manufacturing of aligned DTC plates, an alignment tool is placed in a mould cavity after which tapes are deposited. By shaking the tool, the tapes align between the walls of the tool and are left inside the mould when the tool is removed (as can be seen in Figure 2). The spacing between the walls has been set at 1 mm more than the width of the tapes. This allows for good alignment of tapes in combination with easy deposition and avoids clogging of the tool.

  doi:10.5075/epfl-298799_978-2-9701614-0-0

(a) (b) (c)

Figure 2, Deposited tapes inside mould, a) Random tape distribution, b) 0° centred tape distribution, c) ±45° centred tape distribution.

2.2. Alignment Characterisation Using Digital Image Recognition

The selection and characterization of the alignment method has partially been executed by means of position (1,1) of the orientation tensor [5-6]. For this, aligned tapes have been deposited onto a moving surface. Of these tapes, images have been captured which allows for the determination of their orientation by means of the OpenCV library in Python. During this characterization, multiple test runs have been executed with the alignment tool which resulted in the tape orientation distribution as shown in Figure 3 and an in-plane orientation tensor as shown in equation 1 [5-6].

$$a_{ij} = \frac{1}{N_t}\sum_{k=1}^{N_t} p_i^k p_j^k \quad [1]$$

Hereby N_t is the number of measured tapes and p is the component of the unitvector of the measured tape projected onto one of the principle axis. This study used the first position of the orientation tensor, a_{11} which is zero when all tapes are perpendicular to the loading direction and one when they are all aligned in the loading direction. With a random orientation, this value is assumed to be 0.5. The orientation vector below shows the values of the selected alignment method. In here it can clearly be seen that the use of the alignment tool resulted in an overall alignment of the deposited tapes into the 0˚ direction.

$$a_{in-plane} = \begin{bmatrix} 0.87 & 0.00 \\ 0.00 & 0.13 \end{bmatrix}$$

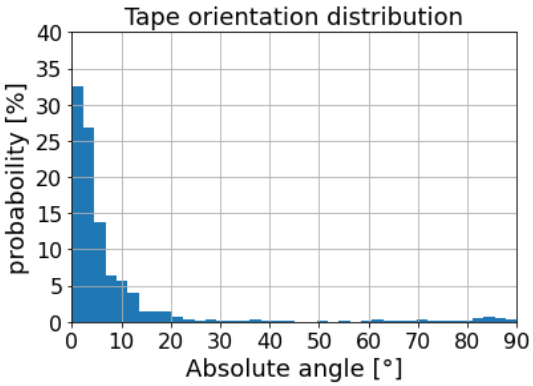

Figure 3,Measurements orientation distribution of alignment tool

2.3. Sample Manufacturing

Three different types of DTC samples have been manufactured; six with a random layup, six with 0° centred alignment, and four with ±45° centred alignment. For each sample type, the corresponding alignment tool has been used as described in section 2.1. The mould has been heated up to 385°C at 45 bar followed by a 20 minute dwell and cool-down to room temperature. The manufactured plates are cut with a Proth diamond blade cutting machine according to Figure 4. These dimensions are based on previous studies [4,7,8], and the available mould size. Tabs have been glued onto the 30 mm of each end for better load transfer resulting in a gauge length of 80 mm.

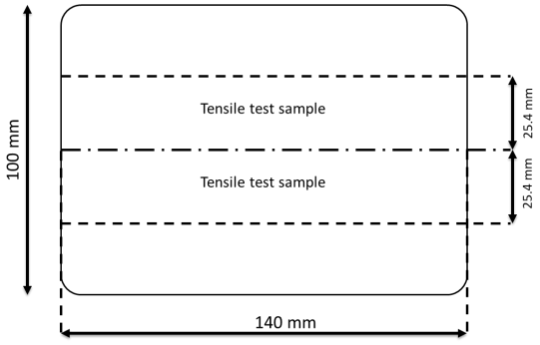

Figure 4, Cutting pattern for sample manufacturing.

3. Test Methodology and Results

3.1. Tensile response

The tensile test setup has been shown in Figure 5. The test samples have been hydraulically clamped in a *250KN Zwick tensile test machine* and elongated with displacement control with a displacement rate of 1 $mm\ s^{-1}$. Two 5 MP cameras have been used with the ViC3D DIC system of Correlated Solutions Inc. With this, the force readings of the load cell are linked to the measurements of the DIC system for the determination of the average tensile modulus in the range between 1000 micro-strain [9] to half the failure load [10].

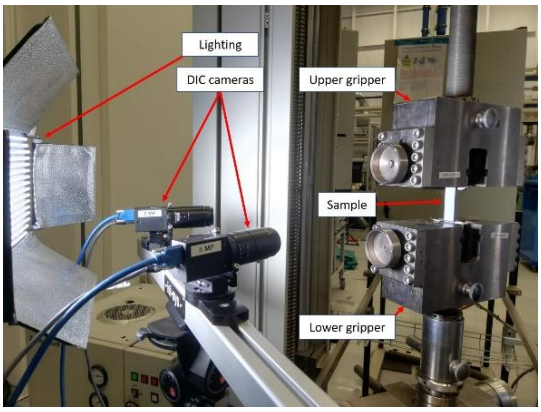

Figure 5, Tensile test setup.

During the study, the effect of tape orientation on strain distribution was investigated. For this, only tensile tests have been performed, and thus, only the strains in loading direction is presented. In Figure 6 and 7, the strain characteristics are shown which shows similar variety in

the strain field found in literature [11]. Based on the strain patterns in Figure 6, significant varieties in distributions could not be identified. When comparing the strains of the three types of samples in Figure 7, it is found that the randomly orientated tapes have the highest spread in strains. This stochastic distribution is most likely caused by the large variety in local stiffness due to the deposition process. The samples with tapes aligned in the loading direction show the smallest spread.

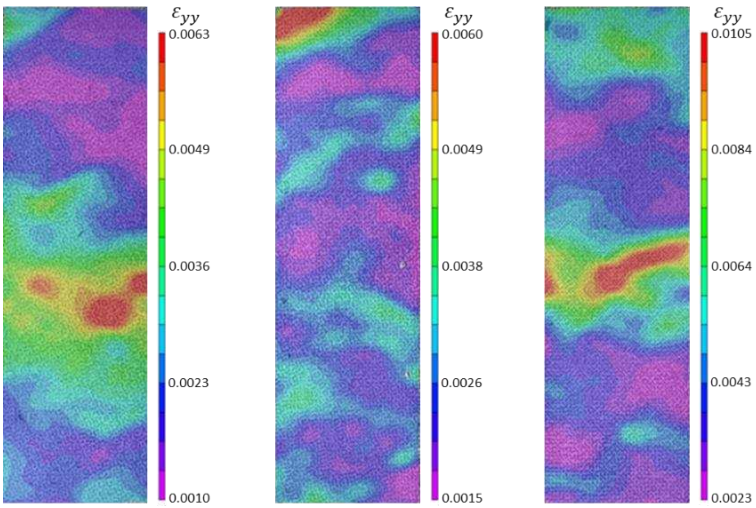

Figure 6, Examples of strain distributions, a) Random tape distribution, b) 0° centred tape distribution, c) ±45° centred tape distribution.

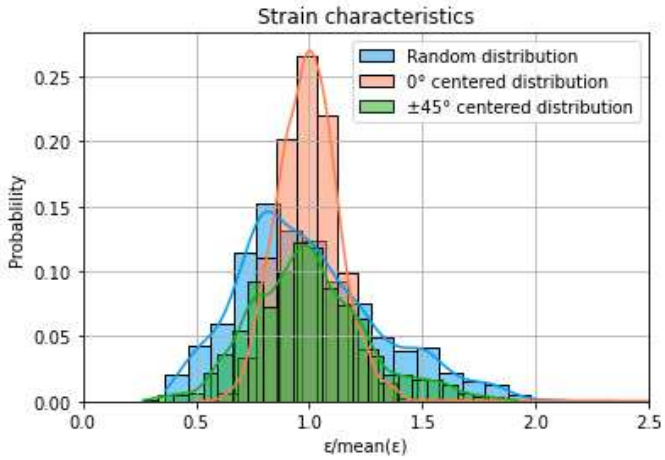

Figure 7, Longitudinal Lagrange strain characteristics of tape orientation distributions at half the failure load. Strains are normalized to the mean value of each sample

By combining the DIC strain data and the tensile force measurements, the stress strain curves of the samples have been obtained as shown in Figure 8. Within the different tape orientation distributions, differences are observed with regards to the stiffness, ultimate tensile stress, and strain at failure. These can be caused by the stochastic nature of the material but is most likely also caused by the manufacturing process. This is assumed because the tensile response of samples from the same plates are relatively similar.

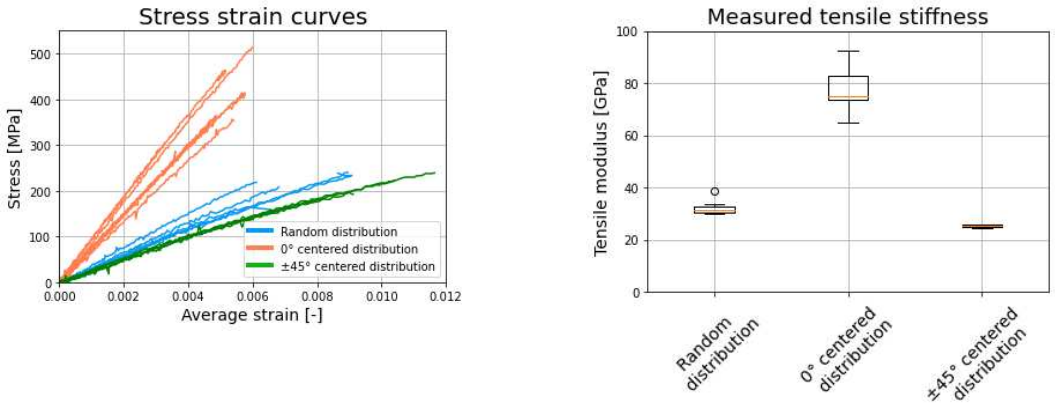

Figure 8. Tensile response of mechanical test, a) stress strain curves b) statistical results of tensile modulus.

As mentioned, the tensile modulus is taken as the average slope of the curves between 1000 micro-strain and half the failure stress. On average, it was found that the samples with randomly orientated tapes and 0° centred tapes have a tensile modulus of 32.5 GPa and 79.7 GPa respectively. The ±45˚ orientation centred samples showed an average tensile stiffness of 25.3 GPa. What should be noted is that the ±45˚ samples showed the lowest spread in stiffness. This is expected to be because tape misalignment in both directions compensate each other, while the alignment tool limits the possible variations in tape orientations as well.

Based on the measurements, the minimal average UTS of 0° centred tapes is 396 MPa compared to 202 MPa for the random tape orientation. Due to failure at the tabs of the samples, the UTS of 0° centred tapes is expected to be higher. The ±45˚ centred samples show a tensile strength comparable to the randomly orientated samples of 210 MPa. This tape orientation showed the highest strains at failure. Because the main failure modes of this type was matrix failure, it is assumed the failure was in shear. This results in a shear strength of the material of 105 MPa.

3.2. Failure analysis

The failure surfaces of the tested samples have been inspected using optical microscopy to see the differences in failure modes that are present in each of the samples. Three of the observations are shown in Figure 9. It was found that the samples with randomly orientated tapes show a large variety of failure modes that are (A) tape splitting, (B) fibre failure , and (C) matrix failure. The samples with a 0˚ centred tape orientation showed a more fibre related failure and less matrix failure which is linked to the tensile stresses in the fibre direction. Opposite to this was ±45˚ centred samples which showed mainly matrix failure whereby the different orientation layers have been separated from each other.

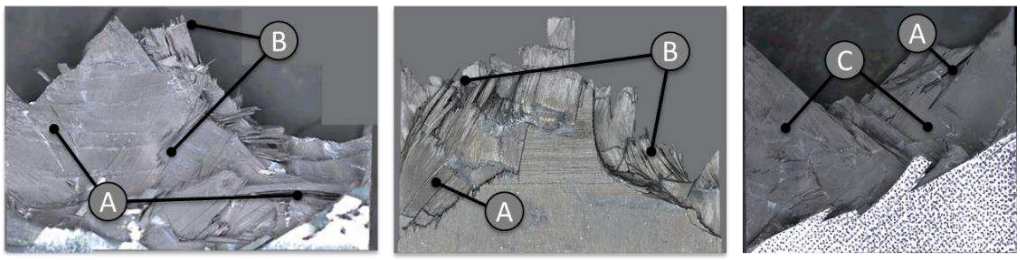

(a) (b) (c)

Figure 9, Fracture surfaces, a) Random tape distribution, b) 0° centred tape distribution, c) ±45° centred tape distribution. (A) tape splitting, (B) fibre failure , and (C) matrix failure.

4. Conclusions & Recommendations

Recent research into DTC has resulted in many insights into the mechanical behaviour and design parameters. This study has documented the tools and manufacturing needed for a fast dry alignment of DTC (in 0˚, +45˚, and -45˚ direction) and quantified the tensile modulus of the material with random, 0° centred, and ±45˚ centred DTC.

First an alignment method has been presented which is quantified using the tape orientation distribution using OpenCV. With the described method, test samples have been manufactured and tested in tension. By means of the obtained DIC data, it was found that the differences in tape orientation caused differences in strain characteristics. Hereby the randomly orientated tapes showed the largest spread and the 0˚ centred tape distributions showed the lowest.

By combining the tensile force readings and DIC strain measurements, stress strain curves have been obtained for all the samples. It was found that due to the alignment in loading direction, the average tensile modulus in loading direction was increased by 145% compared to randomly orientated tapes, from 32.5 to 79.7 GPa. The samples with the ±45˚ centred tapes showed a tensile stiffness and strength of 210 MPa and 25.3 GPa respectively.

The described alignment method and its characteristics can be used for the development and testing of more complicated tape alignment (such as steering). The results of the material characterization can be used for large scale alignment, reference values for design, or for validation of future research in numerical and experimental material characterisation.

3. Acknowledgements (For Clemens)

The authors of this paper would like to thank Prof. Dr. Christian Brauner from the FHNW University of Applied Sciences for supplying the material that has been used during this study.

4. References

[1] Pimenta, S., & Robinson, P.. An analytical shear-lag model for composites with ‘brick-and-mortar’architecture considering non-linear matrix response and failure. Comp. Science and Technology, 104, 111-124, 2014.

[2] Martulli, L. M., Muyshondt, L., Kerschbaum, M., Pimenta, S., Lomov, S. V., & Swolfs, Y. Carbon fibre sheet moulding compounds with high in-mould flow: Linking morphology to tensile and compressive properties. Comp. Part A: Applied Science and Manufacturing, 126, 105600, 2019.

  doi:10.5075/epfl-298799_978-2-9701614-0-0

[3] Gan, K. W., Ho, Y. W., Ow, Z. Y., Israr, H. A., & Wong, K. J. Aligned discontinuous carbon fibre tows in hybrid composites and their tensile behaviour: An experimental study. Journal of Comp. Materials, 53(26-27), 3893-3907, 2019.

[4] Bradski, G., & Kaehler, A. Learning OpenCV: Computer vision with the OpenCV library. " O'Reilly Media, Inc.", 2008.

[5] Advani, S. G., & Tucker III, C. L. The use of tensors to describe and predict fiber orientation in short fiber composites. Journal of rheology, 31(8), 751-784, 1987.

[6] Ranganathan, S., & Advani, S. G. (1990). Characterization of orientation clustering in short-fiber composites. Journal of Polymer Science Part B: Polymer Physics, 28(13), 2651-2672.

[7] Yamashita, S., Hashimoto, K., Suganuma, H., & Takahashi, J. Experimental characterization of the tensile failure mode of ultra-thin chopped carbon fiber tape-reinforced thermoplastics. Journal of Reinforced Plastics and Comp., 35(18), 1342-1352, 2016.

[8] Feraboli, P., Peitso, E., Deleo, F., Cleveland, T., & Stickler, P. B. Characterization of prepreg-based discontinuous carbon fiber/epoxy systems. Journal of reinforced plastics and comp., 28(10), 1191-1214, 2009.

[9] Siddiqui, M. Z., Tariq, F., Naz, N., & Ahmed, M. F. Determination of Young's modulus of metallic and composite materials by digital image correlation. Journal of Space Technology, 1(1), 32-37, 2012.

[10] Cuartas, VM, Perrin, M., Pastor, ML, Welemane, H., Cantarel, A., & Karama, M. Identification of the elastic properties in CFRP composites. In International Symposium on Aircraft Materials ACMA 2014 (pp. pp-61), 2014, April.

[11] Feraboli, P., Cleveland, T., Stickler, P., & Halpin, J. Stochastic laminate analogy for simulating the variability in modulus of discontinuous composite materials. Comp. Part A: Applied Science and Manufacturing, 41(4), 557-570, 2010.

STRAIGHTENING OUT THE ADOPTION OF VARIABLE STIFFNESS COMPOSITE LAMINATES IN THE AEROSPACE INDUSTRY

Thore, Roepman[a], Mohamed, Gomaa[a], Julien, van Campen[b]
a: Laminance Technologies B.V. – t.roepman@laminance.com
b: Aerospace Structures and Computational Mechanics, Technische Universiteit Delft –
j.m.j.f.vancampen@tudelft.nl

Abstract: *In the late 1960s fibre reinforced composites were first applied in civil aviation. Since their introduction they have made commercial aircraft significantly lighter, and thereby more fuel efficient and cheaper to operate. It is not uncommon that the structure of a modern aircraft consists for more than 50% of composite materials. The concept of variable stiffness (VS) composite structures was first introduced in the 1990s. The performance improvements associated with VS laminates are comparable to the improvements of conventional composite structures over metallic structures. Despite their potential, VS laminates have not been adopted in commercial aviation yet. In this paper we investigate what requirements need to be fulfilled to adopt VS laminates in civil aviation. As a specific example we look at straight-fibre variable stiffness laminates (SFVS), which have been developed at TU Delft to be a low-cost alternative to VS laminates that rely on automated fibre placement.*

Keywords: Variable Stiffness; Performance Improvement; Structural Optimization; Adoption of Technology; Aerospace Industry

1. Introduction

The use of composite materials in civil aviation has steadily gained terrain since their introduction in the late 1960s [1,2]. In 1982 the first primary structure made of carbon fibre-epoxy was certified for the Boeing 737 [1]. The Boeing 787 in terms of structural weight consist for more than 50% of composite materials [2]. The adoption of composite materials in civil aviation can safely be called successful. Composite materials have delivered on the expected improvements: 10-20% weight reduction compared to metallic structures, integrated manufacturing instead of manufacturing and assembling a large number of parts, better fatigue performance, and structural efficiency. Of course, composite materials have also introduced new challenges, but these are outweighed by the benefits.

The transition from metallic structures to composite structures has been very successful. Similar significant improvements in the mechanical performance of a laminated composite structure can be achieved by spatial variation of the stiffness properties within the laminate. Such a variable stiffness (VS) laminate, typically is created by steering the fibres within the laminae, result in in an in-plane variation of stacking sequence and thus an in-plane variation of mechanical properties of the laminate and subsequent load-redistribution within the laminate.

Since the early work on VS laminates [3–5] more than 30 years have passed. In these years, significant improvements in the design, analysis and manufacturing of VS composite laminates have been made. Buckling load improvements more than 100% (compared to the best constant stiffness design) are reported for VS laminates [5], and there are numerous examples of case studies on (aerospace) structures [6]. Nevertheless, to the knowledge of the authors, there is

  doi:10.5075/epfl-298799_978-2-9701614-0-0

still no widespread adoption of VS laminates in the aerospace engineering industry. This raises the question, why VS laminates are not being adopted, and what can be done to change this.

Recent work done at the TU Delft has demonstrated that it is possible to achieve variable stiffness laminate designs by means of laminate blending and patching operations, instead of fiber steering. The result is a straight-fiber variable stiffness (SFVS) laminate. These laminates stay very close to conventional laminates in terms of required manufacturing infrastructure but offer performance improvements similar to those of VS laminates.
In this paper we investigate which boundary conditions in terms of structural performance, certification and cost need to be met to introduce a new type of composite material to civil aviation, and we will try to answer the question whether it is likely for variable stiffness laminates to find their way into civil aviation in the coming two decades. First, an overview of the potential performance improvements associated with variable stiffness laminates is given. Second, we will look at the drivers for the adoption of a new technology in civil aviation and the obstacles that need to be overcome. Then, the class of straight-fibre variable stiffness (SFVS) laminates is considered as a case study. This is followed by a discussion and outlook for the coming two decades.

2. The Potential of Variable Stiffness Laminates

Hyer and Lee [3] were the first to spatially optimize the fibre orientation to increase the strength of a rectangular plate containing a circular cut-out at its center. Iteratively the fibre orientation was matched to the “principal stress direction” in 120 unique elements and a curvilinear design was generated that fails at a 60% higher tensile load. An adoption to their model and optimization procedure resulted in a design optimized for buckling in uni-axial compression of the same model. Load alleviation to simple supported sides away from the central cut-out results in a load carrying capability increase of more than 100%.

The concept of variable stiffness laminates was formulated by Gürdal and Olmedo [5]. In the following decades many sophisticated design frameworks addressing stiffness, strength and manufacturing constraints have been developed for a range of applications as can be found in a comprehensive review paper by Sabido et al [6]. Design methods for plates, shells, cylinders, and beams have been developed, optimizing, strength, stiffness or thermal response. There seems to be the capability to design VS composite structures, and the performance improvements reported are in the double digits. The manufacture of VS composite structures at an industrial scale seems to be slightly more challenging, but manageable. The biggest hurdle for adoption in aerospace seems to be lacking certifiability criteria for VS laminates [6].

3. Adoption of a new Technology in Aerospace Industry

In the previous section it has been established that variable stiffness (VS) laminates offer a significant improvement in mechanical performance over conventional laminates. In this section the question will be addressed what boundary conditions need to be met before we will see adoption of VS laminates in civil aviation. Above all else, civil aviation has a high price elasticity and is therefore very sensitive to cost. The hypothesis underpinning this work, is therefore, that VS laminates will only be adopted, if the benefits outweigh the cost incurred when introducing the new technology. Below, we will focus on the expected benefits when VS laminates are adopted. Furthermore, we look at the expected cost of certification and manufacturing. Here we point out, that this analysis is by no means complete.

  doi:10.5075/epfl-298799_978-2-9701614-0-0

3.1 Benefits of implementation

The main benefit of adopting VS laminates in civil aviation will be weight reduction of the aircraft structure, which in turn will lead to a reduced fuel consumption. Our preliminary analysis showed that application of VS laminates to an A320-type aircraft would result in a 7% reduction in fuel consumption.

Apart from weight reduction, VS laminates do not offer any apparent benefits compared to conventional laminates. Therefore, it can be concluded that the adoption of VS laminates in civil aviation will be strongly dependent on fuel cost. It will only be attractive to develop VS laminate technology for civil aviation if fuel cost stays at its current elevated level or increases even further, e.g. by increasing the taxation of fuel.

From a financial standpoint the authors do not expect it to be likely that the weight benefit offered by VS laminates would be used to offset the increased weight of alternative powertrains in civil aviation. This is because, the development budget is more likely to be used for the development of the alternative powertrain itself, than to optimize the structure of the aircraft.

3.2 Manufacturing

Adopting VS laminates in aviation would likely require an investment in manufacturing capability. Automated fibre placement and continuous tow shearing using multiple tows [8] seem to be likely candidates. Next to the investment in new manufacturing equipment, manufacturing time may also be expected to increase. The combination of investment in new manufacturing tools and the increased production time and therefore production cost per part, make the adoption of VS laminates in civil aviation less attractive.

3.3 Certification

The adoption of VS laminates in civil aviation would require a departure from the so-called building block approach, in which first coupons, then elements, sub-components and then components are tested. For a structure with a continuous variation of stacking sequences, such an approach would no longer be tractable. Instead, new analysis techniques and virtual testing may replace the more conventional certification procedure. Making this transition may make for cheaper certification in the longer term, but in the short term it will mean increased certification cost, which may be prohibitive for the introduction of a new technology.

4. Straight-Fibre Variable Stiffness Laminates

In recent work we have demonstrated that it is possible to achieve variable stiffness laminate designs by means of laminate blending and patching operations, instead of fibre steering (Fig. 1). This results in a straight-fibre variable stiffness (SFVS) laminate. Stacking sequence continuity is assured by enforcing relaxed generalized blending guideline [7]. The developed method is computationally efficient. Preliminary results show similar improvements in buckling load improvement as have been reported in literature for fibre-steered variable stiffness laminates. The advantage of the proposed design method is that variable stiffness laminates can be achieved by a wide range of manufacturing techniques.

  doi:10.5075/epfl-298799_978-2-9701614-0-0

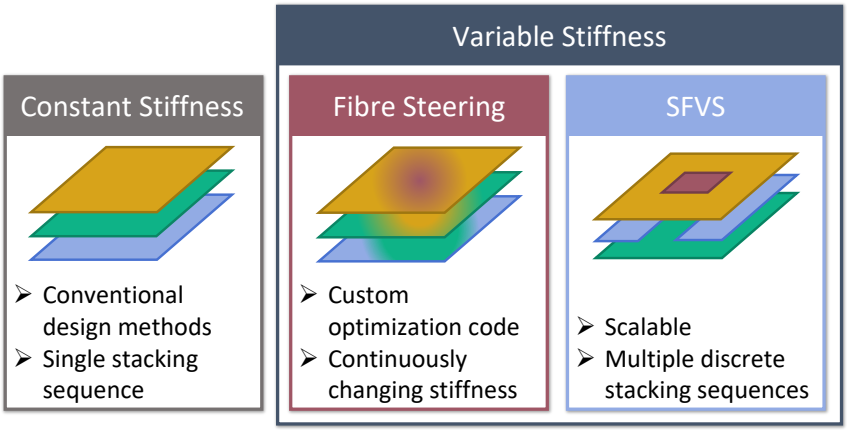

Figure 1: Straight-fibre variable stiffness laminates

A preliminary analysis showed that application of SFVS laminates to an A320-type aircraft would result in a 6% reduction in fuel consumption. SVFS laminates can be manufactured using existing manufacturing techniques, meaning no extra cost will be incurred when manufacturing. Because the manufacturing process remains unchanged, it is expected that the extra effort to certify the new structure will also be minimal. Additionally, there is reason to believe that the architecture of SFVS laminates will be beneficial to its damage tolerance [9], thereby reducing cost that would be incurred by inspection and potential repair.

5. Discussion and Outlook

Variable stiffness (VS) laminates have a lot of potential when it comes to the improvement of structural performance and can therefore are a prime candidate to reduce structural weight in civil aviation. The performance improvement compared to conventional composite structures is similar to the performance improvement that composite structures seemed to provide over metallic structures when they were introduced in the late 1960s. Nevertheless, VS laminates have not been adopted by civil aviation yet.

The analysis presented in the paper is purely qualitative in nature. It indicates that the adoption of VS laminates in aviation would only be likely if there is a prolonged increase in fuel cost, which would make the expected weight savings, and therefore cost savings, outweigh the expected increased cost in terms of manufacturing and certification.

Straight fibre variable stiffness (SFVS) laminates, developed by the authors of this paper, offer performance improvements which are comparable to those of VS laminates, with the added benefit that they can be manufactured and certified within the existing infrastructure for composite structures in civil aviation. This means, that SFVS laminates will be economically viable at lower fuel cost than VS laminates would. Therefore, SFVS laminates could be used to introduce the concept of variable stiffness within civil aviation.
The experience that would be gathered using SFVS laminates could used to develop a certification strategy for more complex VS laminates, such that the certification process for VS laminates is ready, as soon as the technology for mass production of VS laminates becomes available.

The authors are convinced that it will only be a matter of time before VS laminates are adopted by civil aviation. SFVS laminates can play an important role in expediting the process.

  doi:10.5075/epfl-298799_978-2-9701614-0-0

6. References

1. Mouritz, A.P. (2012), '15 - Fibre-polymer composites for aerospace structures and engines', Introduction to Aerospace Materials, Woodhead Publishing, Pages 338-393, ISBN 9781855739468, https://doi.org/10.1533/9780857095152.338.
2. Giurgiutiu, V. (2016), 'Structural Health Monitoring of Aerospace Composites', Introduction, Academic Press, ISBN 9780124096059.
3. Hyer, M.W. and Charette, R.F. (1991), 'The use of curvilinear fiber format in composite structure design', AIAA Journal 29(6), 1011 – 1015.
4. Hyer, M.W. and Lee, H.H. (1991), 'The Use of Curvilinear Fiber Format to Improve Buckling Resistance of Compsoite Plates with Central Circular Holes', Composite Structures 18, 239 – 261.
5. Gürdal, Z. and Olmedo, R. (1993), 'In-plane response of laminates with spatially varying fiber orientations: Variable stiffness concept', AIAA Journal 31(4), 751 -758.
6. Sabido, A., Bahamonde, L., Harik, R. and Van Tooren, M.J.L. (2017), 'Maturity assessment of laminate variable stiffness design process', Composite Structures 160, 804–812.
7. van Campen, J.M.J.F., Seresta, O., Abdalla, M.M., and Gürdal, Z, (2008), 'General Blending Definitions for Stacking Sequence Design of Composite Laminate Structures'. In 49th AIAA/ASME/ASCE/AHS/ASC Structures, Structural Dynamics, and Materials Conference 16th AIAA/ASME/AHS Adaptive Structures Conference; 10t, Schaumburg, IL, April 2008. American Institute of Aeronautics and Astronautics. ISBN 978-1-60086-993-8. (doi: 10.2514/6.2008-1798).
8. Zympleoudis, E. Potter, K., Weaver, P.M, and Kim, B.C., (2015) 'Automated high volume production of complex composites parts: CMTS (continuous multi-tow shearing)', 20TH INTERNATIONAL CONFERENCE ON COMPOSITE MATERIALS
9. Nagelsmit, M.H., Kassapoglou, C. & Gürdal, Z. (2010). 'A new fibre placement archi- tecture for improved damage tolerance'. Pitea, Sweden, 21st SICOMP Conference.

RCF-TAPES FOR SUSTAINABLE HIGH PERFORMANCE LIGHTWEIGHT CONSTRUCTION

Julian Theiss[a], Violetta Schumm[b], Michael Sauer, Dr.-Ing. Frank Manis

a: Fraunhofer IGCV (s) – Julian.theiss@igcv.fraunhofer.de
b: Fraunhofer IGCV (s) – violetta.schumm@igcv.fraunhofer.de

Abstract*: This study addresses the production and the processing of highly aligned tapes from recycled carbon fibers (rCF). Starting from a modified carding process, the rCF are stretched and fixed into semi-finished tape products along subsequent processing steps. The characterization methods used in this study to test the composite include tensile and bending tests, the determination of fiber volume content, and eddy current technology to measure fiber orientation. Composites build on basis of these rCF-tapes reaches a bending strength of approx. 800 MPa in fiber direction and stiffness about 70 GPa at a fiber volume content of around 36 %. Such properties are approximately double those of nonwovens made by comparable state of the art technology routes. By using various fiber placement technologies, those high properties can be used in a load-path-compliant manner.*

Keywords: Recycling; Carbon fibers; rCF-tapes; Automated fiber placement; Composites

1. Introduction

The use of carbon fiber reinforced plastics and the associated material efficiency compared to metallic materials plays an essential role in lightweight constructions [1]. However, the production of carbon fibers is based on fossil raw materials and is very energy intensive [2]. Therefore, it makes sense to use carbon fibers in more than one lifecycle. By recycling carbon fibers, a sustainable material closed loop is possible [3], but currently two major limitations of this approach still exist. State of the art materials made from recycled carbon fibers are most often processed into nonwoven mats that have a very limited fiber alignment and therefore just a moderate fiber volume content (FVC) [4]. Due to the isotropically orientated and tangled arrangement of the fibers in the semi-finished product, it is difficult to achieve a FVC above 35 % without risking significant fiber shortage by single-fiber breaking [4]. However, with increasing fiber orientation, higher fiber packing densities are made possible. These two characteristics are particularly important when processing rCF, as fiber orientation and high FVC are directly correlating with enhanced properties of the subsequent composite. One way to increase the fiber orientation is the production of so called tapes, which includes an additional stretching process after the nonwoven formation [5]. The aim of this study is the development of a manufacturing chain that makes it possible to increase the properties of rCF-composites and therefore use them in applications as substitutes for other classes of materials or even virgin fibers.

2. Materials and methods

2.1 Materials

The tapes used in this study are produced with a combination of carbon fibers (CF) and thermoplastic fibers. A comparison is made between cut off waste and pyrolyzed carbon fibers.

  doi:10.5075/epfl-298799_978-2-9701614-0-0

In order to simplify the naming the term rCF is used in the following. The exact fiber type descriptions are summarized in Table 1.

Table 1 : Fiber material overview

Fiber	Manufacturer	Type	Linear density [dtex]	Fiber length [mm]	Density [g/cm3]	Tape material
rCF1	SGL Carbon	C T50-4.4/255 T140	0,69	≈ 80	1,78	1/2/3
rCF2	ELG Carbon Fibre	Carbiso C SM 45R	0,69	30-60	1,80	4
PA6	EMS-Chemie	Grilon P300	6,7	60	1,14	1/2/3/4

The polyamide 6 (PA6) fibers act directly as matrix material in the subsequent consolidation. Due to the textile processes, the matrix fibers are already very evenly distributed in the material, which finally benefits the impregnation. In addition, the processing in the carding line can be facilitated by adding more ductile polymer fibers.

2.2 Tape making process

At the beginning, carbon and matrix fibers are weighed according to desired FVC. Then the rCF are manually pre-opened to obtain a better homogeneity of the fiber pile. Next, the fiber mixture is spread evenly on the feed table and opened again by hand. The first mechanical fiber opening is now started and the fibers are separated, aligned and mixed by the interaction of the so-called tambour and several pairs of worker-turner-rolls according to the carding principle [6]. A chopper removes the fibers from the tambour and deposits them on a wooden roller.. As soon as sufficient pile is available, it is fed through a belt hopper and taken off by a subsequent pair of rolls. The funnel bundles the fiber pile and a sliver is produced which is suitable for further processing. The schematic structure of such a system is shown in Figure 1 on the left. In technical language, the direction of production is called machine direction (MD) and the direction across it is called cross direction (CD).

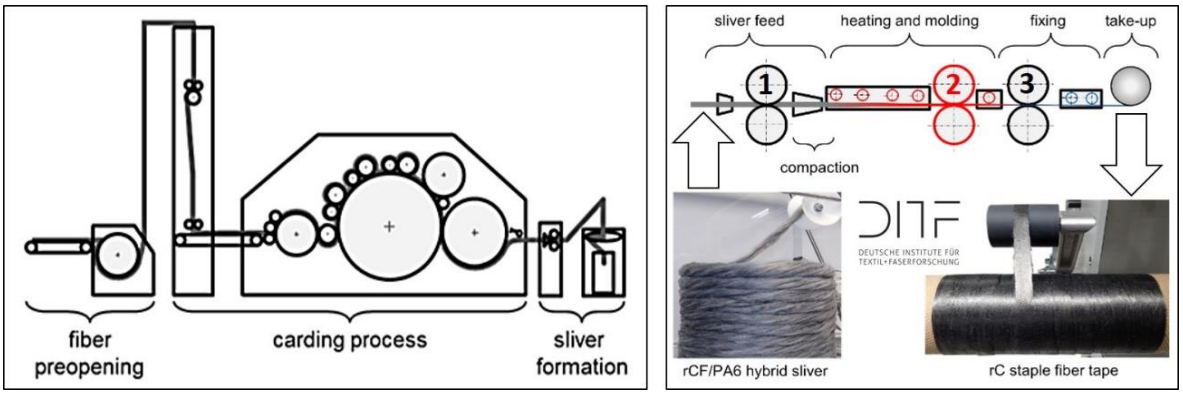

Figure 1: Schematic structure of the tape production with fiber opening, carding unit [7], sliver formation and the drafting system with 3 roller pairs and heating station, compacting and cooling unit (in cooperation with DITF Denkendorf).

The next step is the stretching and consolidation of the fiber sliver. For this purpose, the sliver is fed to the drafting system via a guide unit and a compactor. The drafting system is made up

  doi:10.5075/epfl-298799_978-2-9701614-0-0

of three pairs of rollers, each consisting of a drive roller and a free-turning pressure roller (see Figure 1 right). Due to the different size of the gears, drive roll 2 rotates at a higher speed than drive roll 1. This speed difference leads to the desired drafting of the sliver and thus to fiber parallelization. The width of the sliver can be influenced by adjusting the compactor. This regulation has a significant influence on the degree of consolidation and shape of the final tape. A hot air blower is then used to melt the thermoplastic part of the fiber sliver, which allows roller pair 3 to perform the consolidation. Between roller pair 2 and 3, the main draft acts. The rCF tape produced is then wound onto a spool.

2.3 Fiber placement and testing panel production

The production of carbon fiber-reinforced plastics consists of several steps: the production of semi-finished products (in this case the tape production), the fiber placement and the consolidation. In the following part of the study, the manual fiber placement, the automated fiber placement (AFP) and the final consolidation of test panels will be explained.

The tool required for pressing the test panels has dimensions of 350 x 350 mm. In order to compensate for any inaccuracies in the manual layup, the width and length of the so-called layup is set to 360 x 360 mm in order to cut it exactly to the tool dimension afterwards. As a first step, 360 mm long pieces of tape are cut to size and fastened next to each other with adhesive tape on a metallic base. Starting with the second layer, the tapes are placed on top of the first layer, offset by half the tape width. The fixation between the layers is done by means of an ultrasonic hand welder from the company EUROSONIC Neumann GmbH (Typ HS 800/35). Heat is generated by mechanical vibration, causing the thermoplastic part of the tape to melt. By pressing the sonotrode onto the layup, welding points are created which fix the tape. This process is repeated layer by layer.

In Automated Fiber Placement, a narrow tape is placed on a delivery table by means of a robot. For this purpose, the tape is fed by the material transport unit to the consolidation unit. As soon as the desired tape length is reached, it is shortened by the cutting device. At the nip point, an infrared (IR) laser melts the thermoplastic matrix. The compaction roller uses the laser to fix the tape in place and to increase the degree of compaction of the layer structure. By simultaneously depositing several tows next to each other, AFP technology can be used to realize complex three-dimensional geometries with a high degree of coverage. In addition, it is possible to create curved webs due to the narrow width of the tape. Then the stacks are cut to the mold dimension.

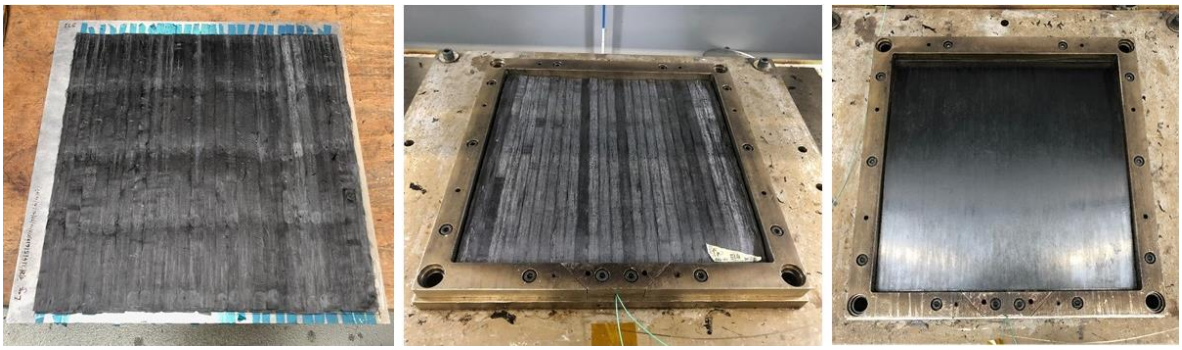

Figure 2: Manual tape laying process from left to right side: 360 x 360 mm layup, cut and inserted layup before and after consolidation of the rCF-tapes.

  doi:10.5075/epfl-298799_978-2-9701614-0-0

Before the material can be placed in the heating press, it must also be dried in a convection oven at 80 °C for approx. 4 hours. This is necessary because the PA6 used absorbs moisture from the ambient air, which can influence the consolidation characteristic. Then the stacks are processed into test panels in the heating press of Fraunhofer IGCV using a variothermal heating cycle in a dipping edge tool. A release agent is applied to the surface of the tool to prevent the test panel from sticking. After drying, the stack can be inserted into the mold and the process starts with heating up to 245 °C with a force of 50 kN. The temperature is controlled with the help of thermocouples in the edges of the material. Once this temperature is reached, the force applied by the heating press increases to 245 kN (equivalent to approx. 20 bar pressure) and the cooling process to 80 °C begins. These values are adapted to the melting temperature of the polymer, which is about 220 °C. The cycle time for the above parameters is approx. 80 min. After cooling, the consolidated test panel can then be removed. The entire process from layup preparation to placing the stack into the mold and the consolidated test panel can be seen in Figure 2.

2.4 Characterization methods

The characterization methods used include eddy current measurement, fiber volume content determination, and tensile and bending testing. Eddy current measurement is a non-destructive test performed by using the EddyCus CF lab 4040 measuring system from Suragus. The method uses local conductivity differences of the carbon fibers and thus enables characterization of fiber orientation and material homogeneity. The fiber volume content measurements are carried out on three specimens of the consolidated test panels and performed according to DIN EN 2564 using sulfuric acid and hydrogen peroxide. Tensile testing is carried out to DIN EN 527-4 with a load cell of 50 kN, clamping length of 50 mm, test speed of 2 mm/min and specimen of type 1B in 0° on the Z050 universal testing machine from Zwick & Roell. The 4-point-bending test is performed to DIN EN 14125 with a load cell of 10 kN, test speed of 1 mm/min and specimens of material class 2, also on the Z050 universal testing machine. The bending properties are determined in 0°, 90° +45° and -45°. Based on the mechanical tests, stress-strain curves of the materials can be evaluated. In addition, a single fiber length measurement is carried out according to DIN 53808-1. For this purpose, 150 fibers each are taken and measured before and after the fiber sliver production.

3. Results

3.1 Tape manufacturing process

The tape production starts with an evaluation of suitable carding parameters. A comparison of three different settings can be found in Figure 3. The most optimal compromise between the mechanical stress on the fibers and the mixing effect of both fiber components is provided by setting 2, which is why this setting serves as the basis for the upcoming tape production.

During nonwoven production, approx. 34 % of the weighed-in fiber quantity is deposited within the carding line. Due to the mechanical stress within the carding process, the carbon fibers are also shortened. Therefore a fiber length measurement is carried out before and after the carding process. The fiber length of the rCF1 shortens on average from an input of 65.3 mm in the sliver to 35.9 mm. The short fiber content (≤ 12 mm fiber length) increases on average from 2.7 % to 12 %. The fiber length of the rCF2 shortens on average from an input of 19.4 mm in the fiber sliver to 14.1 mm. The short fiber content increases for this fiber type on average from 9.3 % to 36.7 %.

  doi:10.5075/epfl-298799_978-2-9701614-0-0

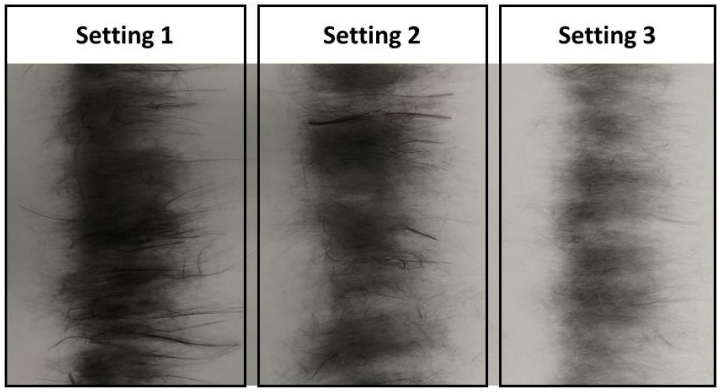

Figure 3: Comparison of three different carding settings: Fiber blending, but also fiber shortening still increases from left to right.

Based on this, four different tape variants with 0.5 inch widths are produced in this study. For the production of the 1st tape material (named as material 1), one fiber sliver out of rCF1 is stretched to a tape areal weight of 75 gsm. For the production of the 2nd tape (named as material 2), two fiber slivers made out of rCF1 are stretched to a tape areal weight of 155 gsm. The initial and main draft can therefore be the same for the tape production of material 1 and 2. When producing material 3, the draft is increased in comparison to material 1 and 2 in order to maximize the fiber orientation. For this, three fiber slivers are stretched to a tape areal weight of 155 gsm. The tape made from the pyrolyzed rCF2 (named as material 4) is processed in the same way as material 2 and weighs approx. 155 gsm.

3.2 Fiber placement of rCF-tapes

First, the tapes are deposited manually as described in chapter 2.3. Depending on the tape areal weight and homogeneity, different numbers of layers are required for a test panel thickness of approx. 2 mm. The test panel made of material 1 is produced of 35 layers, those made of material 2 and 4 of 19 layers each and those made of material 3 of 21 layers. After consolidation, test panels 1-3 have a weight between 360 g and 365 g and a thickness between 2.13 mm and 2.17 mm. Test panel 4 weights about 336 g with a thickness of 2.03 mm.

Figure 4: Picture of the AFP system used (left) and the processing of rCF-tapes with their challenges as homogeneity (middle) and wrinkling (right).

The suitable parameters for the automated fiber placement of the rCF-tapes are determined iteratively. The used system is shown in Figure 4 left. The starting point is the experience gained in processing vCF tapes (virgin carbon fiber tapes) with a similar fiber-matrix combination in pre-trials. Finally, the tests are carried out with the following parameters: A target temperature of 260 °C, applied force of 500 N, laying speed of 0.4 m/s and laser power ply 1 of 540 W and ply 2

  doi:10.5075/epfl-298799_978-2-9701614-0-0

about 410 W. Although the parameters are based on the before mentioned pre-trials, the temperature profile of the laydown test with the rCF-tapes shows significant fluctuations. These temperature fluctuations are related to the inhomogeneous structure of the tape. Compared to vCF tapes, the rCF-tapes also show variations in terms of the geometric dimensions and the stiffness. Therefore, small adjustments have to be made to the laying system of the machine. Especially by changing the fiber guide plate (see Figure 4 middle) and the resulting widening of the guide from ½" to 1", the continuity of the tape laydown is greatly improved. Mainly as a result of the thickness variations, wrinkling of the tape occurs, as shown in Figure 4 on the right. This leads to clogging of the system and to an interruption of the laying process. Due to the comparatively low stiffness of the rCF tape, caused by the discontinuous fiber structure, it can slip during the transitions in the laying head and interruption occurs again.

3.3 Characterization

The characterization of the composites is based on the test methods described in chapter 2.4. Since the mechanical properties are strongly dependent on the fiber volume content, this value is the basis for assessing the properties of this material and is measured with the method described above. The fiber volume content is 34.6 % by volume for material 1 and 35.0 % by volume for material 2 and 36.15 % for material 3 and 32.0 % by volume for material 4. These values are very high compared to the fiber volume contents of other rCF products with an isotropic fiber structure. Due to the high degree of orientation, the rCF tapes can be processed much more easily and higher packing densities can be achieved. Figure 5 also shows that the impregnation quality of the CFRP is very good despite the high fiber volume content.

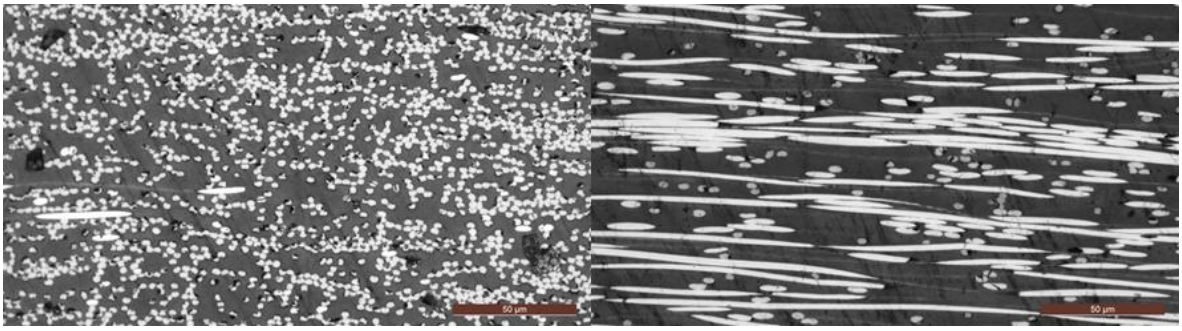

Figure 5: Micrographs in 0° (fiber direction – left) and 90° (across fiber direction - right) of material 3.

The fiber orientation measurement is based on the determination of the MD/CD ratio (0°/90°). With the help of the test methods carried out, the results of the eddy current measurement and bending test can be compared with each other. The determined MD/CD ratios based on the transmission value of the eddy current measurement, bending strength and bending modulus are summarized in Figure 6. The highest MD/CD ratio is achieved with material 3, as a ratio of 2.6/1 is reached based on eddy current measurement, a ratio of 7.3/1 based on bending strength and a ratio of 11.7/1 based on bending stiffness. The higher degree of stretching therefore has a positive effect on the fiber orientation. The calculated MD/CD ratios of material 1 and 2 are between 15 % and 20 % below the level of material 3. Accordingly the different basis weights of the tapes show no significant influence on their fiber orientation. Material 4 shows a lower fiber orientations, which is probably a result of the use of the pyrolyzed CF. Due to the shortened fibers, the stretching of the sliver within the drafting system is probably not as efficient as with longer fibers, but this level with a ratio of 8.2/1 based on bending stiffness is still very high.

  doi:10.5075/epfl-298799_978-2-9701614-0-0

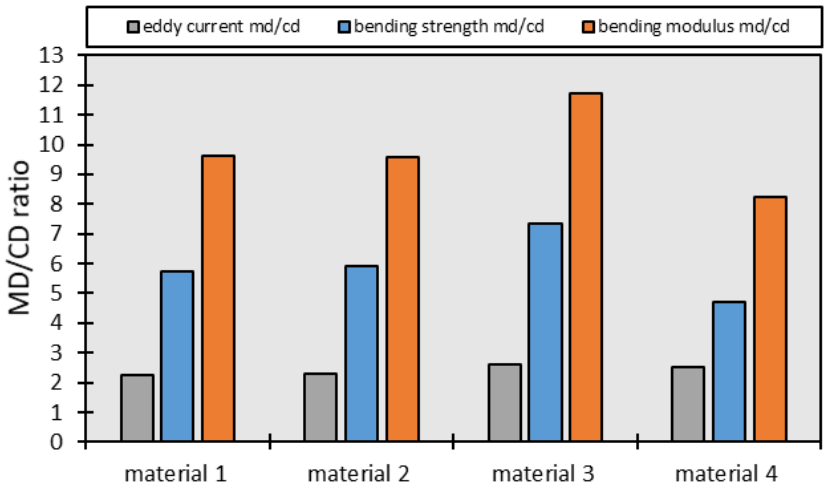

Figure 6: MD/CD ratio of the materials on the basis of eddy current measuring, bending strength and bending modulus.

The mechanical properties of the tensile and bending test of the materials are shown in Figure 7. As in the tensile tests, the values of the bending tests are very high compared to semi-finished products consisting of less oriented short fibers. The bending results in this figure are limited to 0°, as the material has the lowest properties at 90° and the values at +45° and -45° are located between the characteristics at 0° and 90°. The increased values of material 3 are, as already mentioned, due to an increased fiber orientation in 0°. There is no significant difference in the bending properties achieved between material 1 and 2. When comparing the tensile strength and stiffness of these two materials, material 2 achieves slightly higher properties. These higher values are probably due to the increase in the areal weight of the tape or local inconsistencies. The lower properties of material 4 in the tensile and bending test are probably due to the lower degree of orientation and the slightly lower FVC.

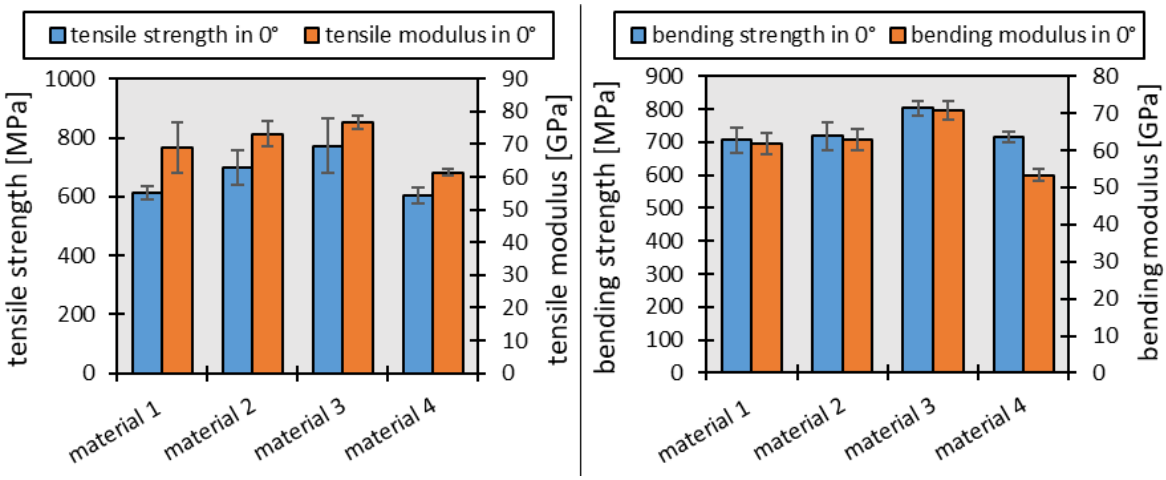

Figure 7: Tensile and bending properties of different materials in 0° (fiber alignment in this direction).

4. Conclusion

The above-mentioned tests have shown that rCF-tapes with high fiber alignment have a very high potential with regard to various areas. Indeed, the described manufacturing process makes it possible to exploit the specific properties of recycled carbon fibers already quite promising. With a maximum tensile force of 773 MPa achieved in the tests described, the properties of this

  doi:10.5075/epfl-298799_978-2-9701614-0-0

material are about three times higher than those of comparable semi-finished rCF-products such as nonwovens. This is mainly due to the very high degree of orientation of the tapes. Thus, this technology plays a key role in the processing of rCF semifinished products. Nevertheless, there is still room for improvement. Among other things, work still needs to be done on the dimensional accuracy of the tapes in terms of thickness and width. In addition, the tapes still have potential in terms of homogeneity (thick and thin spots) and, in order to be able to compete with vCF products, the fiber volume content must be further increased. In addition, the drafting systems can still be adapted to the fiber length of recycled carbon fibers in order to achieve even higher orientation. In the course of the currently ongoing research project “Infinity” it can be assumed that wider tapes will be produced, which can be precisely cut to the desired width. This goes hand in hand with significantly improved processability. In addition, the quality in relation to the above-mentioned variations can be strongly increased and thus a general improvement in the processability of the rCF tape can be assumed. The processing of rCF-tapes in the AFP process represents a milestone in research on recycled fiber. However, there is still further potential here as well. Following the production of larger quantities of tape material, further deposition trials will be carried out. An additional attempt will aim at the development of wider tapes and either process them directly or slit them in an additional step. Furthermore, the finite fiber length in the tape has a positive effect on the steering behavior and, in the subsequent forming process, on the drapeability of the organic sheet. This potential will also be evaluated as part of the publicly funded project “Infinity”.

Acknowledgements

The results were obtained from the project "Infinity - High-performance tapes made from recycled carbon fibers for lightweight construction - CO2 reduction through high-quality recycling processes and materials" (funding code 03LB3006F), which is funded by the BMWK. We would like to thank Olaf Reichert from DITF for his development work in rCF-tape production and Thomas Zettel for carrying out numerous tests as part of his thesis.

References

1. M. Neitzel, P. Mitschang, U. Breuer, Handbuch Verbundwerkstoffe – Werkstoffe, Verarbeitung, Anwendung. Kaiserslautern: Hanser-Verlag, 2014.
2. Y. S. Song, J. R. Youn, T. G. Gutowski, Life cycle energy analysis of fiber-reinforced composites. Composites Part A, 2009, 40, 1257-1265.
3. G. Oliveux, L. O. Dandy, G. A. Leeke, Current status of recycling of fibre reinforced polymers: Review of technologies, reuse and resulting properties. Progress in Materials Science, 2015, Bd. 72, pp. 61-99.
4. F. Manis, G. Stegschuster, H. Osburg, H. Paulus, S. Keller, P. Seiwald, MAI CC4 CaRinA - Carbonfaser Recyclingwerkstoffe für industrielle Anwendungen. Abschlussbericht, 2021.
5. O. Rimmel, D. May, C. Georgen, A. Poeppel, P. Mitschang, Development and validation of recycled carbon fiber-based binder tapes for automated tape laying processes. Journal of Composite Materials, 2018, 53, 3257-3268.
6. C. Cherif, Textile Werkstoffe für den Leichtbau. Dresden: Springer Verlag, 2011.
7. C. Goergen, S. Baz, P. Mitschang und G. T. Gresser, „Highly drapable organic sheets made of recycled carbon staple fiber yarns“ at 21. International Conference on Composite Materials. Xi, August 20-25, 2017.

  doi:10.5075/epfl-298799_978-2-9701614-0-0

BOND STRENGTH ANALYSIS IN CONTINUOUS FIBER REINFORCED THERMOPLASTICS

Jiakuan, Zhou[a], Frederik, Desplentere[b], Jan, Ivens[a]

a: KU Leuven, Department of Materials Engineering, Campus De Nayer, Sint-Katelijne-Waver, Belgium – jiakuan.zhou@kuleuven.be
b: KU Leuven, Department of Materials Engineering, Campus Brugge, Brugge, Belgium

Abstract: *Bond strength development is essential in the continuous processing of fiber reinforced thermoplastic laminates. A wedge peel test is an easy to perform test to assess the bond strength development as a function of processing parameters. In this research, compression molded glass fiber reinforce polypropylene (GF/PP) and glass fiber reinforced styrene-acrylonitrile (GF/SAN) unidirectional laminates exemplified the relationship between processing parameters and bond strength by wedge peel tests. Results showed that bond strength was dominated by cooling rate with around 20% (amorphous SAN) to 100% (semicrystalline PP) increase under higher cooling rate, together with the effect of fiber interpenetration and interlaminar resin pockets. This was illustrated by failure mode analysis through fracture surface morphology under light microscope and SEM, fiber interpenetration analysis by μCT measurements, and crystallization analysis by XRD. In conclusion, high cooling rate and relaxation time enhance bond strength of continuous fiber reinforced thermoplastics in present research.*

Keywords: Bond strength; Continuous fiber reinforced thermoplastics; Wedge peel test; Fiber interpenetration; Crystallization

1. Introduction

Processing and manufacturing of thermoplastics plus their composites rely on fusion bonding, and the final product quality is significantly affected by the bond strength development. The promising automated tape placement (ATP) of continuous fiber reinforced thermoplastics (CFRT) enables digital, efficient, environmentally friendly manufacturing of lightweight and high-performance structures in aeronautics, automotive and wind power industry etc.. However, for such a fast in-situ non-isothermal consolidation process, achieving a high-quality bonding is challenging due to that intimate contact may not completely finish prior to healing, overheating induced thermoplastics degradation etc.[1]. This puts forward demands of an easy and efficient method of bond strength characterization.

The characterization of bond strength is to quantify the interlaminar shear strength of fusion bonded laminates. This is probably the most complicated property to determine as the difficulty of obtaining a uniform and stable stress state. Some standard test methods are widely used, like double cantilever beam (DCB) test[2] (e.g. ASTM D5528), lap shear test[3] (e.g. ASTM D5868), or short beam strength (SBS) test[4] (e.g. ASTM D2344). However, these tests normally require a thick bulk laminate, which means relatively long sample preparation time. Moreover, Schäfer[5] reported that undesired failure mode happened when performing SBS tests on carbon fiber reinforced polyamide 6, and bond strength by lap shear test can also be strongly affected by

  doi:10.5075/epfl-298799_978-2-9701614-0-0

moisture. Instead, some peel tests can be used, like T-peel test[6] (e.g. ASTM D1876), mandrel peel test[7] (e.g. DIN EN 2243) and wedge peel test. For the T-peel test and mandrel peel test, at least one flexural peel leg is prerequisite, and large fluctuation of peel force might occur[8]. The wedge peel test has not been standardized yet, but it's proved that bond strength by wedge peel test is significantly correlated with that by DCB test[9,10], and it's easy to prepare specimens and perform tests in the meanwhile. This makes it suitable for tests on thin laminates like those made by ATP, and a reliable alternative to widely used standard tests.

The present research focuses on the exploration of bond strength development as a function of processing parameters that are decisive for high laminates quality through wedge peel tests. Glass fiber reinforce polypropylene (GF/PP) and glass fiber reinforced styrene-acrylonitrile (GF/SAN) unidirectional (UD) tapes were compression molded into 4-ply laminates under different processing temperatures and cooling rates. Then their bond strength was quantified by wedge peel tests, and further analyzed. The difference in bond strength level between GF/PP and GF/SAN was demonstrated by fracture surface morphology under light microscope and SEM. The bond strength comes from fiber interpenetration and waviness between plies was emphasized and quantified by µCT measurements, as this differentiate the bond strength in CFRT from pure polymers. Moreover, the significant bond strength increase in GF/PP under high cooling rate was illustrated by crystallization analysis with X-ray diffraction (XRD).

2. Materials and Experiments

2.1 Materials and sample preparation

Commercial GF/PP UD tapes (UDMAX^{TM} GPP 45-70 TAPE, sourced by FRT Tapes) and GF/SAN UD tapes produced by authors' project partners were selected for the present research. Both of them are 0.25 mm thick. Besides, the melting point (T_m) of semi-crystalline PP is around 166 ^oC, and the glass transition temperature (T_g) of amorphous SAN is around 102 ^oC.

Samples for wedge peel tests were manufactured by compression molding, since the processing parameters can be accurately controlled in such a bulk-consolidation process as compared to ATP. Two hot press machines were used for different cooling rate, namely Fontijne press TP 400 and Pinette press zenith 2. First the UD tapes were cut into 24 cm long ones, and then 4 plies of tapes were stacked together. A small piece of Teflon film as crack starter, was placed between the second and third ply on one end of the stack, this way a non-bonded area can be obtained for crack initiation. Finally some $[0]_4$ laminates were made with Fontijne press and Pinette press separately for each processing parameters. Each plate was trimmed and cut along fiber direction, resulting in six wedge peel test specimens that are around 15 mm wide, with two non-bonded free legs. Besides, samples for µCT and XRD were cut from the center of the bonded areas.

2.2 Processing parameters

At first the hot press was pre-heated to the designated isothermal temperature, which is from 190 ^oC, 200 ^oC to 240 ^oC for GF/PP, according to the recommended range on the data sheet, and 220 ^oC, 230 ^oC as well as 240 ^oC for GF/SAN. The pressure for all experiments was set to 7 bar for both holding and cooling process. After stabilizing at the isothermal temperature, the stacked tapes were put in the hot press for 10 min holding, at the set temperature and pressure. For the cooling process, samples were forced cooled until the temperature below 30 ^oC, and then demolded. There are some differences in the cooling between Fontijne press and Pinette press.

  doi:10.5075/epfl-298799_978-2-9701614-0-0

For the Fontijne press, samples are kept between 2 plate molds with set pressure for both holding and cooling process, and the forced cooling is achieved with flow water in plate molds. For the Pinette press, there are separate hot stage and cold stage, and the forced cooling is achieved by transferring samples from hot stage to cold stage that stays at room temperature all the time. As a result, the cooling rate of Pinette is much higher than that of Fontijne press. Besides, it's worth mentioning that the transfer manipulation results in around 20 s pressureless relaxation time for Pinette samples. The temperature profile of whole process was measured by thermocouples inside the stacked tapes, and the approximate cooling rate for Fontijne press and Pinette press is given in Table 1.

Table 1: Approximate cooling rate at specific temperature in the cooling process

	Cooling rate at 200 °C	Cooling rate at 166 °C	Cooling rate at 102 °C
Fontijne samples	51 K/min	42 K/min	23 K/min
Pinette samples	604 K/min	484 K/min	206 K/min

2.3 Wedge peel tests

The present research used the wedge peel test setup mentioned by ref.[5], see Figure 1. An aluminum frame is vertically mounted onto the bottom of a static universal testing machine Instron 4467, with a wedge fixed on its top. A 3.2 mm thick wedge was rounded, with an angle of 20° and a radius of 0.5 mm, for a valid failure mode. Two free legs of the tested specimen were put on either side of the wedge, wrapped by a sand paper to prevent slippage, and then clamped by pneumatic grips above the wedge. A 1 kN load cell was used to record the wedge peel force, and 10 data points were sampled per second.

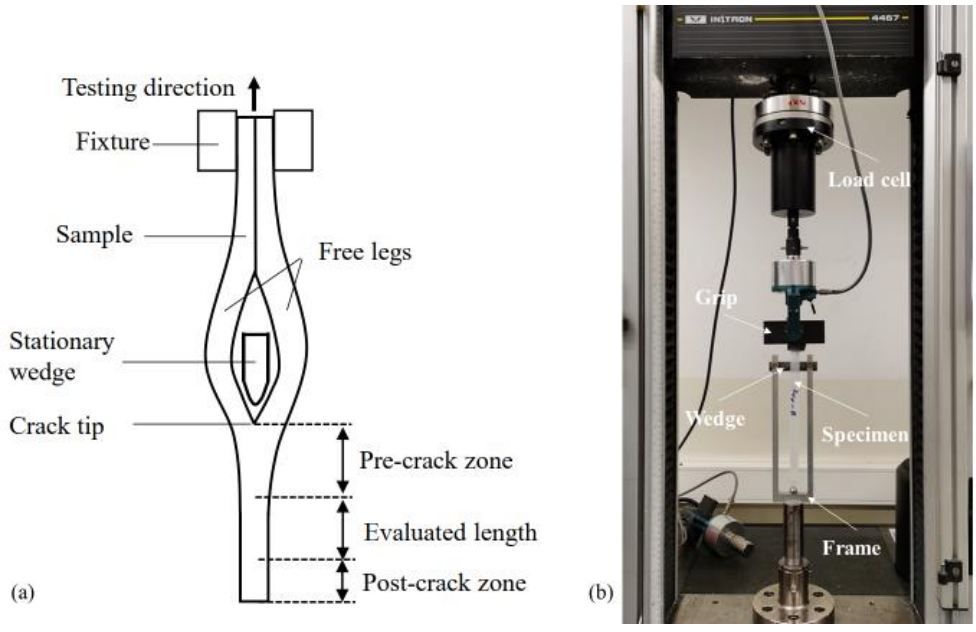

Figure 1. Schematic setup (a) and practical setup (b) of wedge peel tests

Before starting tests, the specimen width was measured at 3 different locations of the bonded area, and the average value was used as the nominal width. When performing tests, the upper cross-head rose vertically at the speed of 60 mm/min, pulling the specimens upward. Naturally, the wedge cut through the interface and peeled the second and third ply.

  doi:10.5075/epfl-298799_978-2-9701614-0-0

3. Results and discussion

3.1 Wedge peel strength

An example of typical wedge peel force – displacement curves is gives in Figure 2. The "F" in legend means Fontijne samples and the "P" means Pinette samples. Due to the running-in effect at the beginning of peeling, the data points before 60 mm were discarded. For each specimen, the selected data points for statistical evaluation ranged from 60 mm to 140 mm, as they were relatively stable. The wedge peel force in this region was averaged, and then normalized by the nominal width of the corresponding specimen, yielding the wedge peel strength.

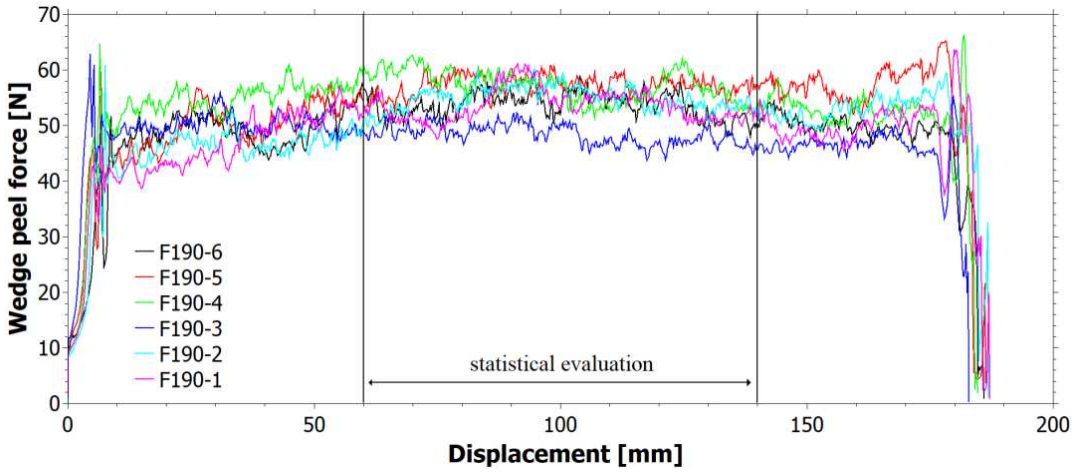

Figure 2. An example of typical wedge peel force – displacement curves for GF/PP Fontijne samples made at 190 °C

The results of the wedge peel strength is presented in Figure 3. All GF/PP samples show a higher level of wedge peel strength than GF/SAN samples, no matter they were made by Fontijne press or Pinette press. Moreover, there is a significant difference in the increase of wedge peel strength from low cooling rate to high cooling rate. Specifically, wedge peel strength of Pinette samples is 100% and 20% higher than Fontijne samples for GF/PP and GF/SAN respectively. However, wedge peel strength for both GF/PP and GF/SAN is not sensitive towards the set temperatures, keeping at a close level for the same material and the same hot press machine.

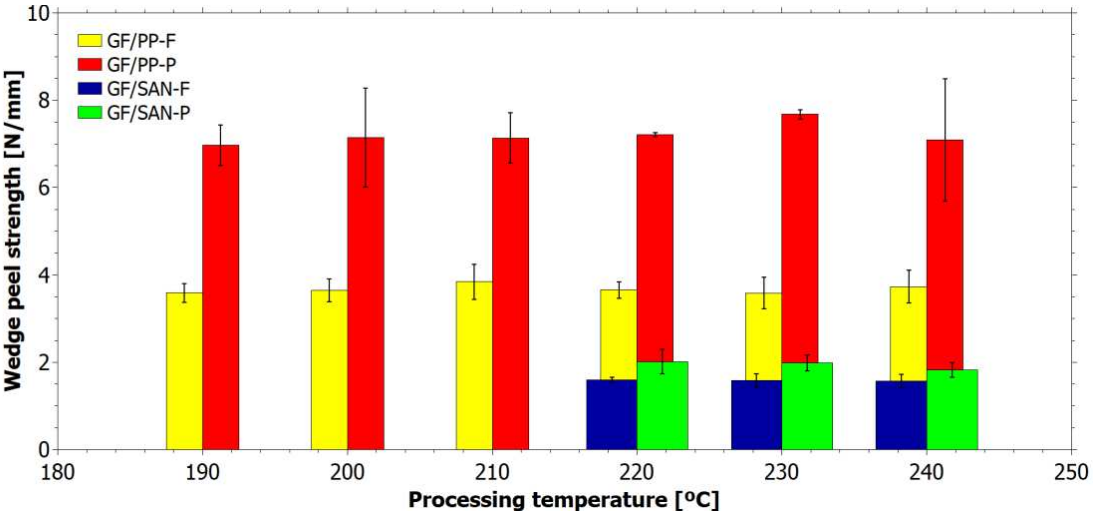

Figure 3. Wedge peel strength of both GF/PP and GF/SAN samples

3.2 Light microscopy and scanning electron microscopy

The delaminated surfaces were observed. Light microscopy showed fibers were pulled out for both GF/PP and GF/SAN, which indicated that there were fibers of one ply interpenetrated into the adjacent plies. Besides, stress whitening phenomenon was also found on PP matrix. The interpenetrated fibers worked like entangled polymer chains while even stiffer, diverting some strain energy from the crack tip and increasing the interlaminar toughness. A further observation on pulled-out fibers was done under SEM, see Figure 4. It shows that resin was still tightly adhered and wrapped on pulled-out fibers for GF/PP but not for GF/SAN. All these morphologies illustrate different failure modes (plastic yielding with stress whitening, cohesive failure for GF/PP, while brittle damage and fiber-matrix interfacial failure for GF/SAN), and explain the much higher bond strength of GF/PP as compared to GF/SAN.

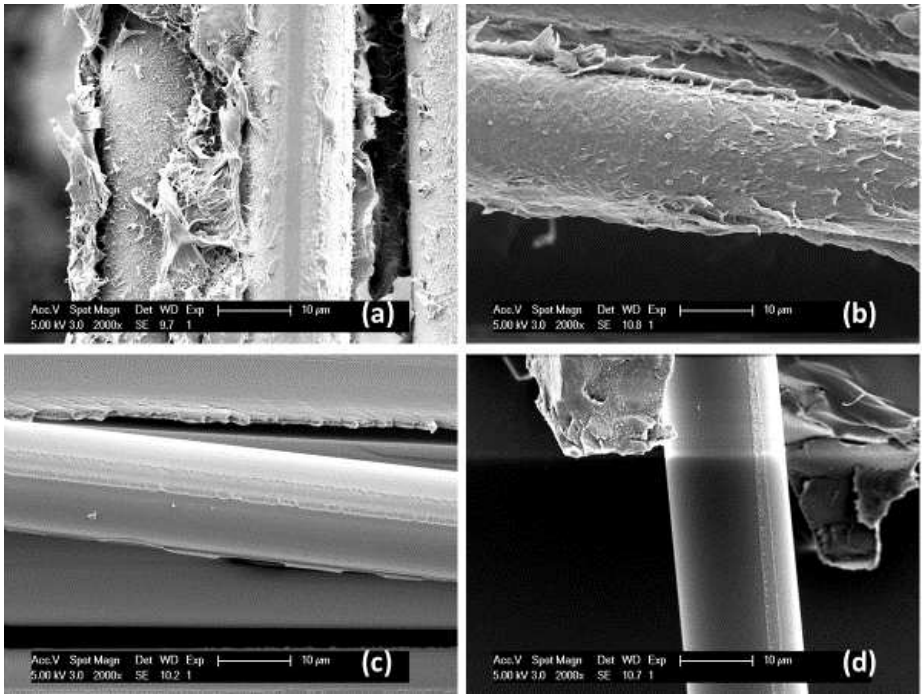

Figure 4. Pulled-out fibers of (a) GF/PP-F, (b) GF/PP-P, (c) GF/SAN-F and (d) GF/SAN-P under SEM

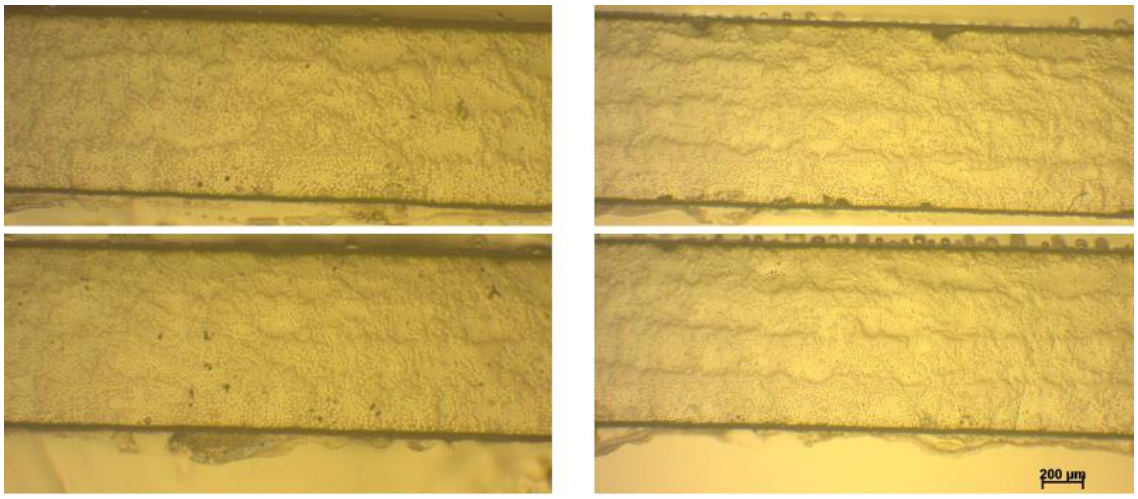

Figure 5. Cross-sections of GF/PP-F240 on the left and GF/PP-P240 on the right as examples

  doi:10.5075/epfl-298799_978-2-9701614-0-0

The cross-sections of compression molded laminates were also observed with light microscope as presented in Figure 5. It's obvious that Pinette samples have more inhomogeneous fiber distribution and more resin pockets at the interfaces, possibly due to capillary percolation during pressureless relaxation time. This contributes to the higher bond strength of Pinette samples as the bond strength is polymer matrix dominating.

3.3 µCT measurement

The classical bond strength development theory by Yang and Pitchumani[11] considered fusion bonding between 2 pure polymer substrates. However, the materials in present research are thermoplastics reinforced by fibers. Although the bond strength between 2 CFRT tapes is still dominated by polymer matrix, fiber interpenetration as mentioned above, should also be considered. The interpenetrated fibers differ from their counterparts on the orientation, which will be reflected by the deviation of fiber's orientation angles. This was analyzed on VoxTex software developed by the authors' group[12], with corresponding µCT data.

Multi-scan (5 scans with 10 mm intervals) was performed on each sample with same X-ray parameters and voxel size. The µCT images showed similar cross-section morphology with micrographs presented in Figure 5. Then the orientation analysis were performed on VoxTex with the YZ plane (parallel to the laminate surface) as the projection plane, yielding the orientation distribution functions of in-plane angle φ and the out-of-plane angle θ. The root mean square (RMS) value of φ and θ was chosen as an indicator for the comparison of fiber interpenetration and waviness, and RMSs of 5 scans were averaged as the RMS of that sample, as presented in Table 2. It's clear that both RMS of φ and θ of Pinette samples are higher than those of Fontijne samples, which reflects the higher degree of interpenetration and (in-plane) waviness for Pinette samples. This is also attributed to the pressureless relaxation time.

Table 2: RMS values of fiber orientation angles for all GF/PP and GF/SAN samples

Sample	RMS of φ	RMS of θ	Sample	RMS of φ	RMS of θ
GF/PP-F200	0,8282	0,4120	GF/PP-P200	1,3202	0,4592
GF/PP-F210	0,8771	0,4342	GF/PP-P210	1,0619	0,4616
GF/PP-F220	0,9297	0,4187	GF/PP-P220	1,6568	0,5756
GF/PP-F230	1,3678	0,4622	GF/PP-P230	1,4708	0,5348
GF/PP-F240	1,0495	0,4263	GF/PP-P240	1,3086	0,4998
GF/SAN-F220	0,9885	0,4322	GF/SAN-P220	1,6860	0,8468
GF/SAN-F230	1,1750	0,5420	GF/SAN-P230	1,4230	0,6816
GF/SAN-F240	1,2434	0,4972	GF/SAN-P240	1,3772	0,6804

3.4 X-ray diffraction

However, fiber interpenetration and interlaminar resin pockets cannot totally explain the giant differences in strength increase between GF/PP (~100%) and GF/SAN (~20%) by Pinette press compared with that by Fontijne press. As bond strength is highly dominated by matrix, a critical difference, that PP is semi-crystalline while SAN is amorphous, should be considered. As the crystallization of PP may play a significant role, the XRD measurements were performed with 2θ range from 5° to 60° and a step length of 0.02°. The measured XRD patterns are showed in Figure 6. The strongest crystal peaks located at 2θ of around 14.1°, 16.9°, 18.6°, 21.1° and 21.9°, as well

  doi:10.5075/epfl-298799_978-2-9701614-0-0

as some small peaks afterwards, represent the α – PP which exists in both Fontijne samples and Pinette samples. However, another small peak marked by black arrow at 2θ of around 16.2° demonstrates the existence of β – PP in Pinette samples. Differential scanning calorimetry (DSC) results also support the this, but wouldn't be discussed here due to paper length limitation.

Next, further crystallization analysis was done through profile fitting on Jade. The crystallinity X_c and the crystallite size X_s can be seen from Table 3 and 4 respectively. It's clear that for Pinette samples, high cooling rate induced lower crystallinity, smaller crystallite size and β-crystals. The fine α – PP and β – PP exhibit higher ductility, significantly enhancing the bond strength of GF/PP.

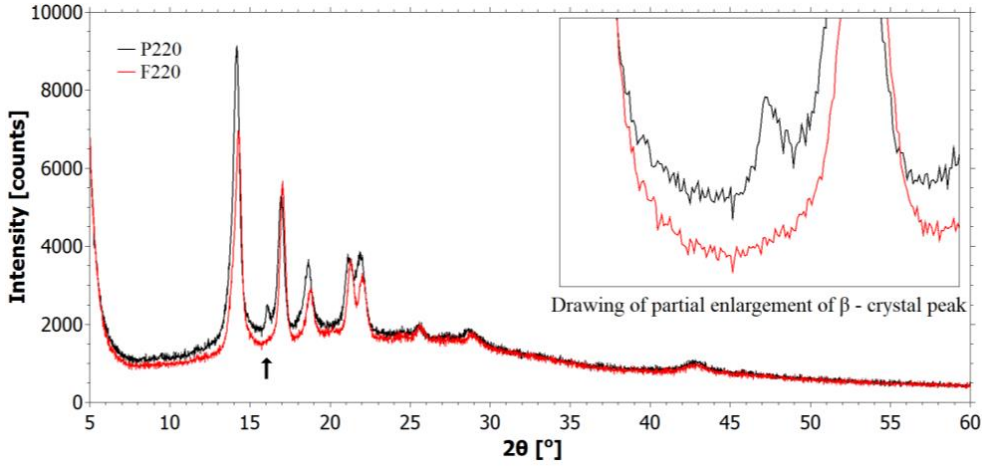

Figure 6. Typical XRD patterns of GF/PP, with F220 and P220 as examples

Table 3: Crystallinity X_c of GF/PP samples made at set temperatures

	Crystallinity X_c of GF/PP made at set temperatures					
	190 °C	210 °C	220 °C	230 °C	240 °C	250 °C
Fontijne samples	49,79%	48,21%	47,07%	50,20%	49,45%	49,98%
Pinette samples	40,93%	42,21%	41,07%	42,21%	40,89%	41,29%

Table 4: Average crystallite size X_s of GF/PP samples made by Fontijne and Pinette press

	Average X_s [Å] of α – PP crystals at different 2θ				
	14,14°	16,87°	18,58°	21,11°	21,86°
Fontijne samples	165,17	221,83	195	185,83	168,33
Pinette samples	167,67	207,17	162,17	144,17	145,33

4. Conclusion

In this paper, wedge peel tests were performed on GF/PP and GF/SAN laminates to characterize their bond strength. Results showed that bond strength was dominated by cooling rate with around 20% (amorphous SAN) to 100% (semicrystalline PP) increase under higher cooling rate. Different failure modes explain the higher bond strength of GF/PP in general. The pressureless transfer of laminates from the hot stage to the cold stage induced interlaminar resin pockets and fiber interpenetration between plies, which contributes the minor part (20%) of bond strength increase for both materials. The major part (80%) of the increase for semicrystalline

  doi:10.5075/epfl-298799_978-2-9701614-0-0

GF/PP relies on crystallization effects, as the lower crystallinity, smaller crystallite size and existence of β-PP under higher cooling rate resulted in more ductile PP matrix. In conclusion, high cooling rate and relaxation time enhance bond strength of CFRT in present research.
In the future, some more works on the quantitative relation between degree of fiber interpenetration and bond strength is promising. Regarding the wedge peel test, the compression molded laminates can be used as reference materials that already reach 100% degree of bond, and then the degree of bonding for the same materials by the same or other processing techniques as well as processing parameters can be estimated on this basis. Besides, the effects of friction force, wedge geometry, and test parameters like cross-head speed etc. on wedge peel tests deserve further investigation.

Acknowledgements

The present research was supported by SIM ICON ProUD project (HBC.2020.2457).

5. References

1. Tierney J, Gillespie Jr JW. Modeling of in situ strength development for the thermoplastic composite tow placement process. J Compos Mater. 2006;40(16):1487–506.
2. Ray D, Comer AJ, Lyons J, Obande W, Jones D, Higgins RMO, et al. Fracture toughness of carbon fiber/polyether ether ketone composites manufactured by autoclave and laser-assisted automated tape placement. J Appl Polym Sci. 2015;132(11).
3. Qureshi Z, Swait T, Scaife R, El-Dessouky HM. In situ consolidation of thermoplastic prepreg tape using automated tape placement technology: Potential and possibilities. Compos Part B Eng. 2014;66:255–67.
4. Carlsson LA, Adams DF, Pipes RB. Basic experimental characterization of polymer matrix composite materials. Polym Rev. 2013;53(2):277–302.
5. Schäfer PM. Consolidation of carbon fiber reinforced polyamide 6 tapes using laser-assisted tape placement. Technische Universität München; 2017.
6. Awaja F. Autohesion of polymers. Polymer (Guildf). 2016;97:387–407.
7. Marinosci VM, Grouve WJB, de Rooij MB, Wijskamp S, Akkerman R. Effect of grit-blasting on the fracture toughness of hybrid titanium-thermoplastic composite joints. Int J Adhes Adhes. 2021;109:102893.
8. Boiko YM, Lyngaae-Jørgensen J. Fracture energy–fracture stress relationship for weak polymer–polymer interfaces. Polymer (Guildf) [Internet]. 2005;46(16):6016–24.
9. Hulcher B, Marchello JM, Hinkley JA. Correlation between double cantilever beam and wedge peel tests for automated tow placement. Mater Process affordability- Keys to Futur. 1998;1955–65.
10. Hulcher AB, Marchello JM, Hinkley JA. Wedge peel testing for automated fiber placement. J Adv Mater. 1999;31(3):37–43.
11. Yang F, Pitchumani R. Nonisothermal healing and interlaminar bond strength evolution during thermoplastic matrix composites processing. Polym Compos. 2003;24(2):263–78.
12. Straumit I, Lomov S V, Wevers M. Quantification of the internal structure and automatic generation of voxel models of textile composites from X-ray computed tomography data. Compos Part A Appl Sci Manuf. 2015;69:150–8.

  doi:10.5075/epfl-298799_978-2-9701614-0-0

FIBRE STEERING EFFECT ON BEND-TWIST RESPONSE OF A FLEXIBLE COMPOSITE PROPELLER

Phyo Thu Maung [a], Phil Filippou, Md Shamsuddoha [a], Gangadhara Prusty [a]*

a: ARC Training Centre for Automated Manufacture of Advanced Composites, (AMAC), School of Mechanical & Manufacturing Engineering, UNSW Sydney, Australia(s) – P.maung@unsw.edu.au*

Abstract:

Traditional rigid marine propellers operate efficiently for a specific speed but perform suboptimal at off-design conditions. Flexible composite propellers overcome such efficiency losses through passive shape-adaptivity but are limited by its deflection and strength allowance. Advances in automated composite manufacturing provide fibre steering at a ply level, allowing for more design freedom to improve the efficiency. A realistic marine propeller blade with 36° skew and 25° pitch angle was thus studied for the fibre steering effect on the structural responses of the blade such as deflection, twist and stress. The responses were analysed using response surface method with design of experiments formulated by Central Composite Design. Second-order regression was fitted to obtain response equations, and multi-objective genetic algorithm was then used to achieve optimal steered fibre angles within a set of objectives and manufacturing constraints.

Keywords: Propeller; automated fibre placement; optimization; tow steering; design of experiment

1. Introduction

The use of fibre-reinforced composite materials in marine propellers have many advantages including light-weight, corrosion resistance, delayed cavitation and improved hydrodynamic performance. The ability to tailor fibre orientations in laminate layup provides a key advantage in developing shape adaptive flexible composite propellers. By taking advantage of inherent bend-twist coupling, flexible propeller blades under hydrodynamic loads can utilise the resulting twist to adapt their pitch angle for superior efficiency at off-design conditions. A number of studies [1-3] have been carried out to understand the bend-twist flexibility of propeller blades and their optimization through advantage in performance. These conventional optimisations usually tailor laminate layup design using straight fibre orientations. However, recent advances in automated manufacturing technology allows for fibre steering and curvilinear fibre path optimisation, increasing design freedom for further shape-adaptive enhancement. In curvilinear fibre orientation, local fibre angles vary spatially producing variable stiffness across the laminate, which is commonly referred to as a variable stiffness laminate (VSL) [4]. Tailoring fibre paths within the variable stiffness laminate provides designers with the ability to direct stress away from less well-supported areas, change the buckling modes, and adjust the natural frequency of a panel [4-6].

While the curvilinear fibre paths greatly open the available design space, it also increases the complexity of both the structural analysis and layup selection due the variability of fibre angles across the laminate. Defining a reference path and repeating this reference across the laminate

  doi:10.5075/epfl-298799_978-2-9701614-0-0

provides a practical simplification to lower the number of variables to represent the curvilinear layup. The reference path can be defined as an equation in terms of two fibre angles [4]or polynomial coefficients [7]. The use of mathematical expression for curvilinear reference path helps to ensure fibre continuity and the manufacturability of the layup (Sobhani Aragh et al., 2021). There are several reference path formulations such as non-linear variations using Bezier curves [6, 8], geodesic curves [9] and constant in-plane curvature [10]. In optimisation of steered fibre paths for propeller blade, previous studies have shown to improve the bend-twist response [11] and lower overall fuel cost [12]. However, these studies used genetic algorithm and other types of optimisations, which requires several iteration and simulation runs which is not suitable for high fidelity model.

The focus of this study aims to further investigate the suitability and benefits of fibre steering when applied to a true marine propeller geometry. This study has used curvilinear paths with three control points for varying fibre angles across the blade surface. Besides, this work ventures into extending the current body of knowledge towards the use of curved fibre orientations and response surface optimisation, which will enrich knowledge within the field and allow for more efficient optimisation framework and more effective controllable shape adaptive designs.

2. Numerical modelling

In order to investigate the impact of various layups on the composite propeller, a finite element model (FEM) was established for a single blade structural response study. The blade geometry was created in SolidWorks before importing into the commercial software ANSYS 2020 R2, where the ACP and static structural modules were used for structural analysis.

2.1 Blade geometry

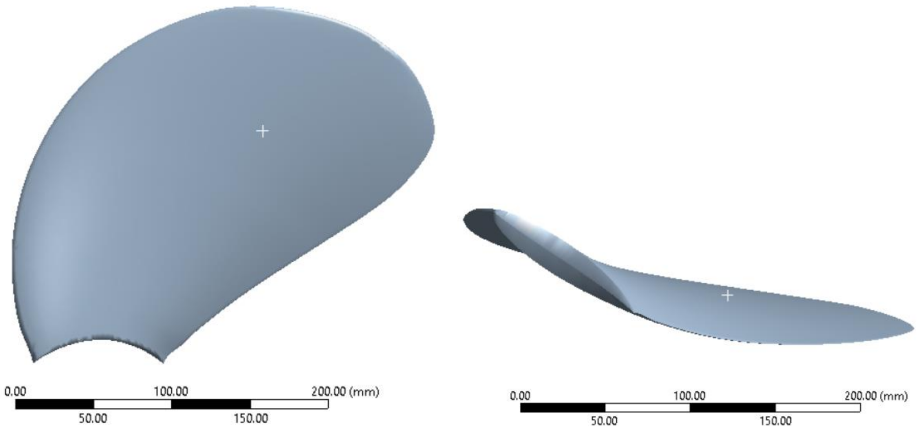

Figure 1. Marine propeller blade with 36° skew and 25° pitch angle used in the current study

The DSTN 4382 marine propeller blade with the propeller diameter of 0.65 m has been selected as an initial reference geometry as its geometry has both high levels of pitch changes and skew [13]. This blade provided a good basis for the features typical of a practical shape adaptive propeller where it has been shown higher pitch and skews generally promote superior shape adaptive properties [1, 2]. In addition, the introduction of pitch and skew provides a significant departure from simple hydrofoils studied previously in that they lacked any pitch or skew characteristics. The geometry of the blade was ultimately iterated upon to ensure practicality for future automated fibre placement (AFP) manufacturing and experimental testing. These

  doi:10.5075/epfl-298799_978-2-9701614-0-0

changes included reducing the thickness of the blade along its radius and reducing the pitch of the undeformed blade. The blade is based on a NACA α =0.5 mean line, with a modified NACA 66 profile. The blade model was illustrated in Figure 1.

2.2 Layup definition

The layup was defined within the ACP Pre Module. HTS45E23/E752-LT unidirectional carbon prepreg material from Park Aerospace was used for the current study. The cured ply thickness of the material was assumed to be 0.14 mm. Therefore, a total of 144 layers would be required at the maximum thickness point. The following layup $[[\theta]_{32}/[0/90/45/(-45)]_{10}]_S$ was used; the inner 40 plies are grouped into a quasi-isometric scheme providing general stability and stiffness to the laminate, these may be substituted for a core material in the future experimental study. The remaining 32 ply angles denoted by θ may be freely defined as a single fibre angle in straight fibre layup or as $<T_0|T_1|T_2>$ in curvilinear layup.

2.3 Loading and boundary conditions

The loading on a propeller blade is usually produced by hydrodynamic forces acting on the two propeller faces as the blade rotates. The high-pressure side is typical on the lower half of the blade, and the low-pressure side on the top half of the blade. The exact pressure distribution is highly dependent on the vessel hull shape, and operating velocity with the local pressure field varying in time due to wake field interaction effects. As this study only investigates the structural impacts of the fibre orientation paths, the loading on the blade has been simplified to a uniform pressure distribution applied to the high-pressure side of the blade. A 22.4 kPa nodal pressure, the equivalent to a 1 kN load was applied to the pressure face nodes. The root of the blade was given a fixed condition to mimic the connection to a blade hub or in the case of the experimental blade the clamping region.

2.4 Mesh configuration

Mesh configuration was completed within the ANSYS Composite PrepPost module (ACP). A solid 3D blade model was created using ANSYS Composite PrepPost module, with SOLID185 hexahedral elements and eight through-thickness elements. A mesh sensitivity study for stress convergence was completed to understand the minimal level of mesh refinement required to ensure mesh independence within the structural results while maintaining computational efficiency. The stress value was found to differ by less than 0.02% between the final two refinements – element sizes of 2.0 mm and 1.5 mm. Given the small improvement for a relatively large increase in solving time, the mesh was considered to achieve convergence at 2.0 mm sizing, which produced a total of 66,914 elements and 75684 nodes.

3. Optimisation Strategy

3.1 Formulation of piecewise curvilinear paths

Curved fibre path methods allow for spatial variation in the local material properties. Generally, a reference path is defined by a set of variables, where the variables considered differ based on the type of reference path being considered. Subsequently, the reference path could be replicated over the laminate either using a shifting or parallel method. The shifting path is simpler, however often results in deviations in replicated paths including gaps and overlaps, particularly when surfaces with large curvatures such as exhibited by propeller blade considered

  doi:10.5075/epfl-298799_978-2-9701614-0-0

in this study [14]. The parallel method has thus instead been chosen as it better accounts for curvature along the surface. In order to effectively study the effect of curvilinear fibre path on the shape-adaptive response of the propeller blade, fibre angle variations at three locations (root, middle and tip of the blade) was incorporated in the current curvilinear fibre definition, forming a piecewise variation function.

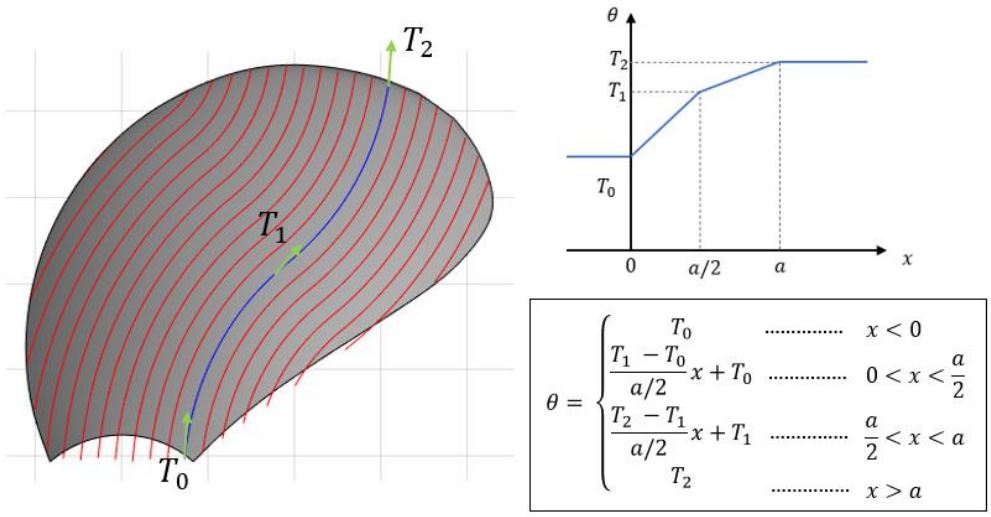

Figure 2. Illustration of curvilinear fibre paths on the blade model

The mathematical implementation of the curvilinear fibre angle was thus represented by a piecewise function as shown in Figure 2. T_0, T_1 and T_2 are the fibre angles at the start, the middle and the end of the curvilinear fibre path, respectively. The reference path orgin starts at the root of the blade and ends at the tip, with the x-axis (0-deg reference direction) pointing from the centre of the effective propeller disk to the blade tip. Positive fibre orientations are defined towards the leading edge, while negative fibre orientations rotate towards the trailing edge. This definition also allowed for easy comparison to previous straight fibre studies [15], where it has been proposed fibre angles facing towards the leading edge to maximise twist, while those away minimize twist.

3.2 Response surface optimisation

A response surface methodology (RSM) correlates the relation between two or more independent variables known as factors and a given dependant variable known as the response using polynomial regression fit equations. These polynomial equations can be used to predict the responses based on the factors and form the response surface to understand the correlation. In the case of a larger set of factors, however, the number of experiments or simulations required to properly understand the desired response increases. The consideration for a proper Design of Experiments (DOE) is important to reduce the required number of simulation samples to a feasible amount. Central composite design (CCD) is one such experimental technique that allows the investigation of the influence of several factors on different responses. The CCD provides the minimal set of DOE required to perform surface fitting using quadratic equations. While it is possible to use designs for higher-order polynomials, these are often discouraged as they require a significantly greater quantity of sample points. Additionally, cubic and higher fits

  doi:10.5075/epfl-298799_978-2-9701614-0-0

introduce a higher likelihood of further complications relating to statistical issues and model construction. The general form of the full quadratic multivariate least square's regression considered is shown in Eq. (1). This full form regression was applied to each response and refined as required based on the quality of the initial fits and suitability of coefficients. A detailed discussion on the terminology and concepts used in RSM can be found in [16].

$$y_{response} = b_0 + \sum_{i=1}^{3} b_i x_i + \sum_{i=1}^{3} b_{ii} x_i^2 + \sum_{i=1}^{2} \sum_{j=2, j>i}^{3} b_{ij} x_i x_j \quad (1)$$

Where, $y_{response}$ is the response variable. b_0, b_i are the constant and the coefficient, whereas x_i refers to the factor value.

Circumscribed enhanced rotatable CCD was used for the approximation of the quadratic polynomial model in this study. A Central Composite Design (CCD) contains an embedded factorial or fractional factorial design with centre points associated with a set of high and low boundary points, which are usually coded as +1, 0, -1 and additional factorial of $\alpha > 1$. A 3-factor central composite design (CCD) with $\alpha = 1.682$ was chosen in this case, resulting in *29* simulations with various combinations of three factors. The three factors are the curvilinear fibre angles (T_0, T_1 ,T_2), and their boundary values (+1 and -1) were determined by performing structural analysis on the blade with the straight fibre layup. The responses in interest are twist, tip deflection and stresses obtained from the simulation. The RSM modelling andanalysis have been carried out by using Minitab 19 software.

The quadratic equations obtained from RSM were then used in multi-objective genetic algorithm (MOGA) to determine the optimal combination of curvilinear parameters. Genetic algorithms are proven to be exceptionally well empirical techniques, which have been effectively in machine learning based optimization. Genetic algorithm (GA) was used to find a set of the combination of twist angles to obtain a set of twist and deflection as optimum outputs. The aim was to maximize the twist angle ($\phi_{0.75R}$) and minimize the tip deflection (δ_{tip}). However, for practical considerations, a set of constraints was also imposed during the execution of the GA, which are shown in Table 1. Transverse stress-to-strength ratio (σ_{22}/S_{22}) was constrained to be less than 0.25 to allow for a higher load, while the difference between curvilinear fibre angles were also constrained to produce a manufacturable layup.

Table 1: Objectives and constraints used for curvilinear fibre angle optimisation in GA

Performance	**Objectives**	**Constraint**
Twist at 0.75 R ($\phi_{0.75R}$)	Maximise $\phi_{0.75R}$	$\phi_{0.75R}$ >1°
Tip deflection (δ_{tip})	Minimise δ_{tip}	-
Transverse stress (σ_{22})	-	σ_{22}/S_{22}< 0.25
Fibre angles (T_0, T_1 ,T_2)	-	$\lvert T_1 - T_0 \rvert$, $\lvert T_2 - T_1 \rvert$ < 15°

4. Results and discussion

4.1 Straight fibre angle results

In order to determine the high and low boundary values for curvilinear fibre angles, the propeller blade model with various straight fibre layups were first studied for their structural responses. Various layups were considered from -90° to +90° with an increment of 15°. Tip deflection as

well as edge deflections at 0.75R and corresponding twist angle were plotted against the layup angles in Figure 3 (left). It can be seen that the lowest deflection with minimal twist was obtained with -15° orientation, whereas the highest twist was achieved using +30° fibre angle. Beyond +30°, (from +45° to +90°) twist angle decreases while tip deflection increases. As low deflection with high twist is desired to maximise bend-twist coupling in a composite blade, the suitable range for curvilinear fibre angles in RSM would be from -15° to +30°.

In-plane stresses ($\sigma_{11}, \sigma_{22}, \sigma_{12}$) and corresponding failure indexes from stress-based quadratic failure criteria (Maximum stress and Tsai-Wu) were also plotted in Figure 3 (right). It can be seen that the trend of failure indexes against the layup angle is very similar to that of transverse stress, indicating that transverse stresses is the most critical parameter in determining the failure index values. This is in line with what was observed in the previous study [11]. Reducing transverse stress would improve the failure index and thus, transverse stress was studied as one of the three responses in RSM.

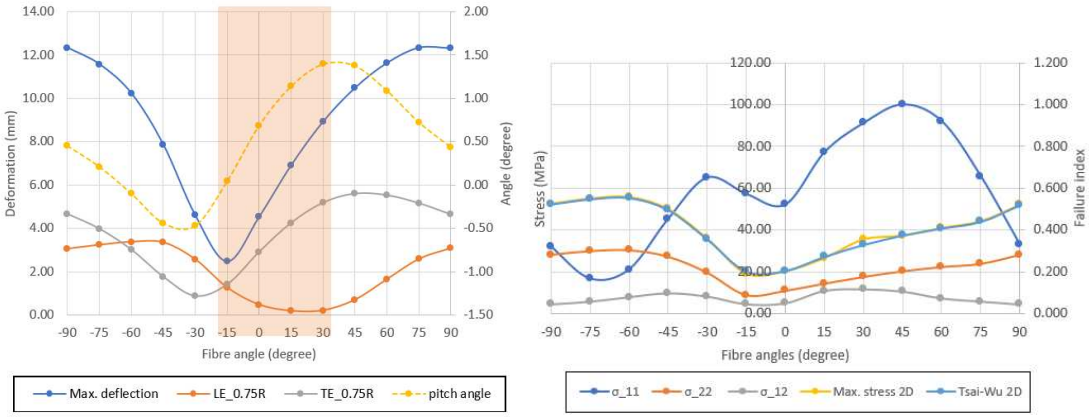

Figure 3. (Left) Tip deflection and twist against fibre angles; (right) In-plane estresses and failure indexes against fibre angles

4.2 Curvilinear fibre angle results for response prediction

The blade model with different combinations of curvilinear fibre angles set out by CCD was simulated in ANSYS using static structural analysis system. The responses (tip deflection, twist and maximum transverse stress) were obtained for each set of curvilinear fibre angles. The twenty-nine sets of responses were imported into Minitab 19 tool for regression fit, and the coefficients (b_i) for quadratic model as shown in Eq. (1) were determined. Stepwise selection of terms was used for model reduction with the application of a 0.15 significance level. In other words, if the p-value of the coefficient term was less than or equal to 0.15, the term is statistically significant to be included in the regression equation. Otherwise, the term is determined as statistically insignificant and the coefficient for the term equals to zero.

While the deflection and twist responses (δ_{tip} and $\phi_{0.75R}$) were readily fit into the second-order polynomials, logarithmic transformation was required for transverse stress prior to the regression to achieve R-square of above 0.9. The regression equations for each response are presented in Eq. (2)-(4). The R-square for each response was presented in Table 2. It can be seen from the equations that the second-order term of T_2 and the interaction term of T_0T_2 were not statistically significant in both δ_{tip} and $\phi_{0.75R}$ responses. In the case of logarithmic transverse stress, all the second-order terms were excluded in correlation, making it as the linear

  doi:10.5075/epfl-298799_978-2-9701614-0-0

polynomial fit. Moreover, T_0 terms were not critical in predicting transverse stress, which means that only the fibre angles between the middle and tip of the blade were essential for failure stress reduction. This could be explained by the observation found in the reference [11], where the transves stress were maximum in the region between the middle and tip of the blade and steering fibre angles in that critical region would largely impact the trasverse stress.

$$\delta_{tip} = 4.5461 + 0.03458\,T_0 + 0.08940\,T_1 + 0.01250\,T_2 + 0.000363\,T_0^2 - 0.000234\,T_1^2 + 0.000226\,T_0T_1 - 0.000153\,T_1T_2 \quad (2)$$

$$\phi_{0.75R} = 0.66497 + 0.016281\,T_0 + 0.017683\,T_1 + 0.000668\,T_2 - 0.000096\,T_0^2 - 0.000155\,T_1^2 - 0.000106\,T_0T_1 - 0.000016\,T_1T_2 \quad (3)$$

$$Ln(\sigma_{22}) = 2.3961 + 0.015249\,T_1 + 0.003328\,T_2 - 0.000090\,T_1T_2 \quad (4)$$

Table 2: Adjusted R-square from the response fit of deflection, twist and logarithmic stress

	$\boldsymbol{\delta_{tip}}$	$\boldsymbol{\phi_{0.75R}}$	$\boldsymbol{Ln(\sigma_{22})}$
Adjusted R-square	0.9973	0.9982	0.9272

The reliability of regression equations were also verified by comparing the finite element result of three verification points, which were not included in the DOE, against that obtained from the RSM predictions. The comparison results are shown in Table 3. It can be ssen that the maximum difference in variation was less than 3% between the computed and the predicted results.

Table 3: Verification of the response prediction using verification points

Verifcation points			***FE results***			***RSM prediction***			***% difference***		
T_0 [°]	T_1 [°]	T_2 [°]	δ_{tip} [mm]	$\phi_{0.75R}$ [°]	σ_{22} [MPa]	δ_{tip} [mm]	$\phi_{0.75R}$ [°]	σ_{22} [MPa]	δ_{tip} [mm]	$\phi_{0.75R}$ [°]	σ_{22} [MPa]
23.44	9.77	-2.09	6.49	1.12	12.86	6.44	1.13	12.68	*-0.9%*	*0.6%*	*-1.4%*
5.29	-10.63	15.12	3.93	0.57	10.10	3.96	0.56	9.96	*0.9%*	*-0.8%*	*-1.4%*
-14.81	-3.41	21.22	3.99	0.34	11.31	4.09	0.35	11.26	*2.5%*	*2.9%*	*-0.5%*

4.3 Optimisation results

By using the regression equations in multi-objective genetic algorithm (MOGA) , the curvilinear fibre angles were optimised for a given set of objectives and constraints, as provided in Table 1. As a multi-objective optimisation problem, the optimal solution would not converge to a single solution. Rather, a number of pareto optimal solutions were produced. In this case, three different candidates (the largest twist candidate, the lowest deflection candidate and medium twist and deflection candidate) were presented as C1, C2 and C3 respectively,as shown in Table 4. In addition to optimisation using 15° curvilinear angle variation constraint for the manufacturable layup, optimisations with a larger angle variation allowance (20° and 25°) were also performed. These larger angle variation are impractical in the current propeller size as they would produce narrow fibre curvature and would create undesirable tow defects. But, in the case of a larger propeller size, tows would become effectively smaller and such large angle

  doi:10.5075/epfl-298799_978-2-9701614-0-0

variation could be achieved easily. The results show that greater twist (11.6% increase) albeit with higher deflection could be achieved when the curvature constraint was allowed to 20° difference between T0 and T1 or T1 and T2. The increment in twist was not pronounced when it further relaxed the curvature constraint to 25°angle variation allowance.

Table 4: Optimal curvilinear fibre angles for different fibre angle variation constraint

Fibre angle variation	Candidates	T_0 [°]	T_1 [°]	T_2 [°]	δ_{tip} [mm]	$\phi_{0.75R}$ [°]	σ_{22}/S_{22}
15°	C1-D15	23.44	9.77	-2.09	6.46	1.12	0.229
	C2-D15	16.60	7.01	-2.98	5.84	1.00	0.219
	C3-D15	19.12	8.51	-5.08	6.08	1.05	0.222
20°	C1-D20	30.46	14.29	-0.88	7.26	1.25	0.250
	C2-D20	29.00	9.70	-5.17	6.71	1.18	0.248
	C3-D20	26.76	12.31	11.63	6.99	1.20	0.249
25°	C1-D25	34.60	12.50	8.25	7.44	1.27	0.248
	C2-D25	28.81	11.50	-10.95	6.80	1.20	0.234
	C3-D25	33.05	12.06	4.04	7.26	1.25	0.244

5. Conclusion

A numerical framework was developed for characterizing and optimising the effect of fibre steering angles on the mechanical performance in the form of twist and deflection for a scaled composite propeller. The analysis was carried out using Ansys Composite PrepPost (ACP) module, while the responses in the properties were idealized using response surfaces arising from central composite design (CCD) based design of experiments and regression analysis. The numerical framework for optimising fibre steered angles using response surface methodology (RSM) aligns well with the predicted verification points indicating veracity of using such methodology. Followed by this was an efficient multi-objective genetic algorithm (MOGA) optimisation due to the usage of the the mathematical response equations obtained from the RSM. The optimistion efficiently provides the optimal steered fibre angles for a given pair of objectives and manufacturing constraints. Further optimisation with narrower fibre curvature constraint was performed, which showed upto about 12% increase in twist leading to a potential of more efficient propeller. This exercise indicated a potential of optimizing the steered fibre paths especially crucial during automated manufacturing, which is the planned pathway for the advancement of this work.

Acknowledgements

This project also received the support through the following funding schemes of the Australian Government: (a) ARC LIEF: An Australasian facility for the automated fabrication of high-performance bespoke components (LE140100082). (b) ARC ITTC: ARC Training Centre for Automated Manufacture of Advanced Composites (IC160100040).

6. References

1. Khan MM, Daniel OA, Vinay D, M. J, A. V. Effects of bend-twist coupling on composite propeller performance. Mechanics of Composite Materials and Structures. 2000;7(4):383-401.

  doi:10.5075/epfl-298799_978-2-9701614-0-0

2. Chen B, Neely S, Michael T, Gowing S, Szwerc R, Buchler D, et al., editors. Design, fabrication and testing of pitch-adapting (flexible) composite propellers. SNAME Propellers/Shafting Symposium '06; 2006: SNAME.
3. Herath MT, Natarajan S, Prusty BG, St John N. Isogeometric analysis and genetic algorithm for shape-adaptive composite marine propellers. Comput Methods Appl Mech Eng. 2015;284:835-60.
4. Gürdal Z, Olmedo R. In-plane response of laminates with spatially varying fiber orientations - Variable stiffness concept. AIAA J. 1993;31(4):751-8.
5. Marouene A, Boukhili R, Chen J, Yousefpour A. Buckling behavior of variable-stiffness composite laminates manufactured by the tow-drop method. Compos Struct. 2016;139:243-53.
6. Thomas MA, Hallett SR, Weaver PM. Design considerations for variable stiffness, doubly curved composite plates. Compos Struct. 2020;244:112170.
7. Parnas L, Oral S, Ceyhan Ü. Optimum design of composite structures with curved fiber courses. Compos Sci Technol. 2003;63(7):1071-82.
8. Kim BC, Potter K, Weaver PM. Continuous tow shearing for manufacturing variable angle tow composites. Compos Part A: Appl Sci Manuf. 2012;43(8):1347-56.
9. Zhao C, Xiao J, Huang W, Huang X, Gu S. Layup quality evaluation of fiber trajectory based on prepreg tow deformability for automated fiber placement. J Reinf Plast Compos. 2016;35(21):1576-85.
10. Sobhani Aragh B, Borzabadi Farahani E, Xu BX, Ghasemnejad H, Mansur WJ. Manufacturable insight into modelling and design considerations in fibre-steered composite laminates: State of the art and perspective. Comput Methods Appl Mech Eng. 2021;379:113752.
11. Maung PT, Prusty BG, Phillips AW, St John NA. Curved fibre path optimisation for improved shape adaptive composite propeller blade design. Compos Struct. 2021;255:112961.
12. Blasques JP, Berggreen C, Andersen P. Hydro-elastic analysis and optimization of a composite marine propeller. Mar Struct. 2010;23(1):22-38.
13. Carlton J. Marine Propellers and Propulsion. Saint Louis, UNITED KINGDOM: Elsevier Science & Technology; 2018.
14. Oromiehie E, Prusty BG, Compston P, Rajan G. Automated fibre placement based composite structures: Review on the defects, impacts and inspections techniques. Compos Struct. 2019;224:110987.
15. Phillips AW, Nanayakkara A, Cairns R, St John N, Herath MT, Zarruk GA, et al., editors. Effect of material anisotropy on the structural response of flexible composite hydrofoils. SAMPE Baltimore 2015; 2015.
16. Anderson MJ. RSM simplified : optimizing processes using response surface methods for design of experiments. Second edition. ed. Whitcomb PJ, editor. Boca Raton: Boca Raton Taylor & Francis; 2017. 304 p.

  doi:10.5075/epfl-298799_978-2-9701614-0-0

EFFECTS OF DIFFERENTIAL TAPE AND SUBSTRATE TEMPERATURES ON CF/PEEK LAMINATES MANUFACTURED IN AN INDEPENDENTLY CONTROLLED DUAL-LASER TAPE PLACEMENT PROCESS

Christopher Stokes-Griffin[a], Silvano Sommacal[a], Paul Compston[a]

a: ARC Training Centre for Automated Manufacture of Advanced Composites, Australian National University, Canberra, ACT 2600, Australia – chris.stokes-griffin@anu.edu.au

Abstract: *This study investigates the effects of using independently controlled tape and substrate processing temperatures with a novel dual-laser tape placement head for manufacturing thermoplastic composite laminates. Unidirectional $[0]_{32}$ CF/PEEK laminates were manufactured at 400 mm/s. The effect of differential heating was investigated for tape and substrate setpoint temperatures between 400-600 °C. The interlaminar bond quality was assessed by compression shear tests. Laminate quality in terms of void content and distribution were analysed by micro-CT. High compression shear strengths were observed for lower substrate temperatures of 400 °C and 500 °C, in combination with higher tape temperatures of 500 °C and 600 °C. The void content was relatively high at both extremes of low and high temperature combinations, suggestive of limited void compression for low temperatures and void re-expansion at high temperatures due to the polymer remaining molten after consolidation.*

Keywords: automated tape placement; thermoplastic composites; laser heating; mechanical testing; micro-CT

1. Introduction

The advantages of thermoplastic composites are being realised by industry and are already beginning to displace traditional thermoset components [1–4]. Laser-assisted automated tape placement (ATP) is one of the key manufacturing technologies for the next generation of composite structures. It is an automated manufacturing approach for high performance thermoplastic composite laminates. A laser ATP head uses a high-power laser(s) to simultaneously melt the surfaces of the thermoplastic prepreg feed tape and the substrate, which are immediately consolidated by pressure applied by a conformable roller (Figure 1). Typical modern laser tape placement heads have used single near-infrared source producing a rectangular spot aimed at the nip point, with heating bias controlled by closed-loop electromechanical adjustment of the laser angle. Downsides of this approach include inconsistent heated lengths on the tape and substrate, and heating bias control that is slow to react, creating challenges for placement around rapid changes in geometry. A dual-laser head with independent lasers for the tape and substrate respectively (Figure 1) overcomes these limitations as the laser spots remain fixed, and the tape and substrate temperatures are independently controlled solely by digital modulation of the respective laser powers in real-time. It also makes it possible to study the effects of differential processing temperatures while maintaining constant heated lengths.

  doi:10.5075/epfl-298799_978-2-9701614-0-0

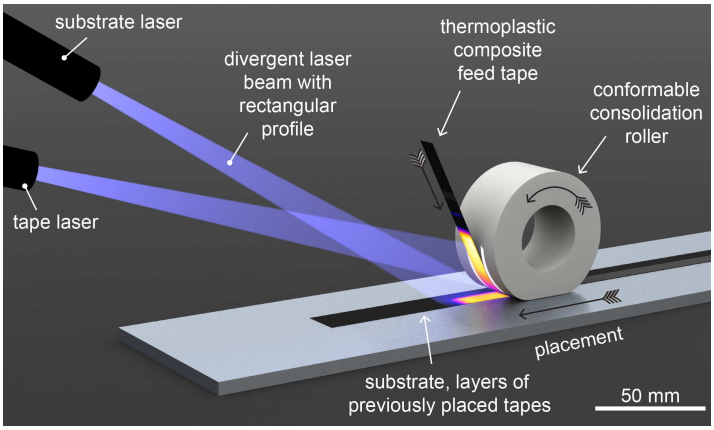

Figure 1. A diagram of the dual laser ATP process. The tape and substrate are heated before the nip-point by independently controlled lasers.

Studies have shown the thin feed tape is relatively heat-soaked [5,6], while a large temperature gradient exists in the substrate due to conductive heat loss. High process temperatures have been shown to maximise the bond development [7], but can also result in degradation of the polymer matrix, cause matrix squeeze-out [8] and greater residual stress. Knowledge of the effect of differential process temperatures can be used to enhance process efficiency and laminate quality.

This paper investigates the effects of using independently controlled tape and substrate processing temperatures with a novel dual-laser tape placement head for manufacturing thermoplastic composite laminates. Unidirectional $[0]_{32}$ CF/PEEK laminates will be manufactured with a placement rate of 400 mm/s. The effect of differential heating will be investigated for tape and substrate setpoint temperatures between 400-600 °C. The interlaminar bond quality will be assessed by compression shear tests. Laminate quality in terms of void content and distribution will be analysed by micro-CT.

2. Experimental

2.1 Laser ATP system

Placement trials were performed using a bespoke dual-laser automated tape placement system from AFPT GmbH. Independent closed-loop control systems control the power of each laser to maintain independent setpoint temperatures on the surfaces of the tape and substrate respectively prior to the nip point. The apparent surface temperatures are monitored using a non-contact long wave infra-red (LWIR) sensor array. The process control temperatures are calibrated to a black-body source and the emissivity during placement is assumed to be unity ($\varepsilon = 1.0$). The configuration of the placement head for the experimental trials, including laser beam geometry is summarised in Table 1.

2.2 Placement trials

The purpose of this study is to investigate the effect of differential tape and substrate process temperatures on the laminate quality for a laser ATP process. Process setpoint temperatures of 400 °C, 500 °C and 600 °C, corresponding with the temperatures reported in literature for laser ATP of CF/PEEK, will be applied for the tape and substrate surfaces, resulting in a total of nine permutations for sample manufacture. A relatively high placement rate of 400 mm/s was

  doi:10.5075/epfl-298799_978-2-9701614-0-0

Table 1: Placement head configuration

Parameter	Value	Unit
Substrate laser:		
Spot dimension, focus	24 × 17, 300	mm
Heated length, approx.	55	mm
Tape laser:		
Spot dimension, focus	24 × 17, 300	mm
Heated length, approx.	50	mm
Consolidation roller:		
Diameter	80	mm
Material	Silicone, water cooled.	

selected as high laminate quality is typically more difficult to achieve at this speed, and therefore expected to reveal larger differences in laminate interlaminar strength and void content. *Suprem*^{TM} *T* 55% v/v AS4/PEEK tape with a nominal cross-section of 0.15 × 12 mm was used to manufacture $[0]_{32}$ single-tape-width samples 500 mm in length. To minimise the heat-sink effect of the tooling and provide similar through-thickness thermal properties to a full laminate, the samples were placed onto a *Porcher Pipreg®* CF/PEEK 4-ply plain woven consolidated sheet (Figure 2). The samples were manufactured simultaneously in parallel to ensure the consolidation roller overhang was supported on either side by the neighbouring sample of the same thickness. This ensures consistent pressure throughout manufacture for all samples and simulates the state of the roller when manufacturing full laminates. Additional redundant samples were placed either side of the first and last test sample to ensure consistent conditions for the characterised laminates. The placement parameters are summarised in Table 2.

Figure 2. Nine test samples manufactured by laser tape placement with different permutations of tape and substrate temperature. The plain-woven CF/PEEK substrate and redundant samples at each end are also visible.

  doi:10.5075/epfl-298799_978-2-9701614-0-0

Table 2: Placement trial parameters.

Parameter	Value	Unit
Placement rate	400	mm/s
Control setpoint temperature:		
Substrate (T_{subst})	[400, 500, 600]	°C
Tape (T_{tape})	[400, 500, 600]	°C
Consolidation cylinder pressure	3.0	bar

2.3 MicroCT analysis

X-ray micro-computed tomography (µCT) was utilised to investigate the microstructure and characterise void content and distribution of the samples. Specimens were scanned at the ANU CT laboratory (CTlab) using an HeliScan™ micro-CT instrument equipped with a flat panel detector with 3040 x 3040 pixels and a micro-focus X-ray source of 60 kV. Total number of 2D projections acquired per sample and utilised to reconstruct 3D composite volumes varied between ~4500 and ~4800, image acquisition time varied between ~5.5 and ~6 hours, while the scanning resolution (i.e. voxel size) is 4.2 µm for all. From each image, a subset of ~1.5 x ~5 (cross section) ~10 (length) mm was then digitally extracted from the region inside the samples where the compression shear strength was measured. Voids were then segmented and the void content measured for all nine subsets.

2.4 Interlaminar strength characterisation

The interlaminar shear strength was characterised with the compression shear test (CST) method [9,10] which is suitable for measuring the interlaminar strength of tough thermoplastic composites. Specimens were extracted from halfway along the length of the 500 mm long samples, where the placement head speed and process temperatures are at steady state. Five 10 mm × 10 mm samples were precisely milled to size with tungsten carbide tooling, ensuring the loading surfaces were both parallel and square. Testing was performed with a bespoke CST fixture mounted in an *Instron* universal testing machine equipped with a 25 kN load cell. The mid-planes of the laminates were tested to failure at a rate of 1 mm/min, with a gap of 0.5 mm between the loading noses. The compression shear strength was calculated as the peak load divided by the nominal shear area (10 mm × 10 mm).

3. Results and Discussion

3.1 Compression shear strength

The compression shear tests for all samples resulted in sudden catastrophic failure parallel with the plane of shear. No plastic deformation was observed at the loading nose contact points. The results of the tests are presented in Figure 3. The scatter in the results was very low except for samples processed with a substrate temperature of T_{subst} = 600 °C. For T_{subst} = 400 °C, there is no statistically significant difference in strength for 500 °C and 600 °C tape temperatures, indicating that high levels of bonding have been achieved for both.

  doi:10.5075/epfl-298799_978-2-9701614-0-0

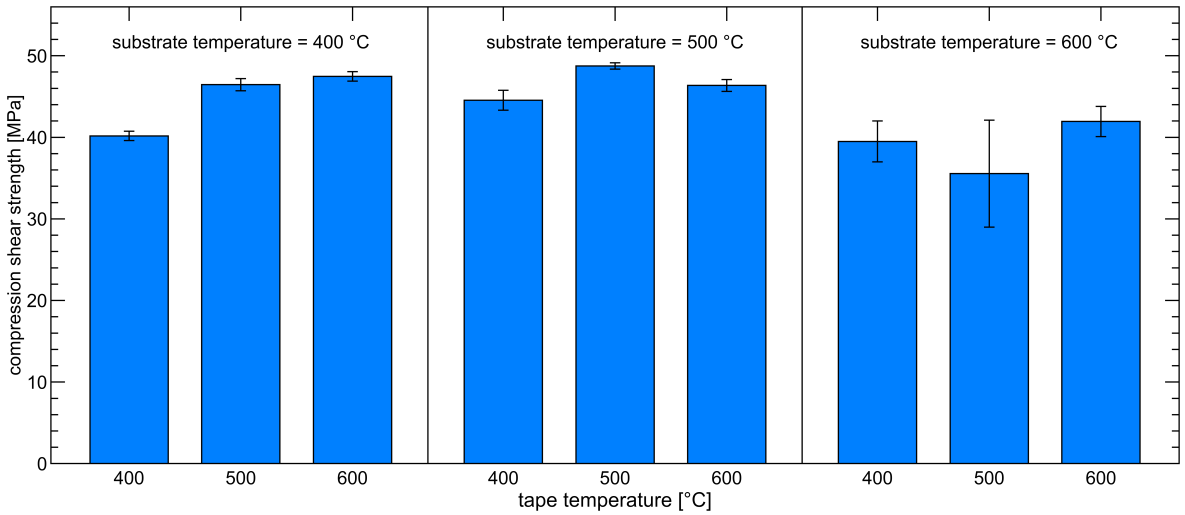

Figure 3. Compression shear strength vs. tape and substrate setpoint temperature. Error bars represent ±σ.

However, with T_{tape} = 400 °C, the lower strength suggests incomplete bonding. When increasing the substrate temperature to 500 °C, the strength also increases for T_{tape} = 400 °C and 500 °C, indicating increased laminate quality; however, for T_{tape} = 600 °C there was no statistically significant difference in strength. At the highest substrate temperature of 600 °C, all compression shear strengths decreased by more than 10% and had significantly greater scatter. This is indicative of decreased laminate quality, with contributing factors including polymer degradation, void content, and greater residual stress due to the deeper melt zone that would occur with high process temperature. Polymer degradation would appear to be unlikely, as at other substrate temperatures, T_{tape} = 600 °C resulted in high strengths. In summary, the highest compression shear strengths are observed for low and moderate substrate temperatures of 400 °C and 500 °C, in combination with moderate and high tape temperatures of 500 °C and 600 °C.

3.2 Void content analysis

The void content of each sample determined analytically from the micro-CT scans is presented in Figure 4. When the substrate temperature setpoint is 400 °C, there is an inverse correlation between the compression shear strength and void content which decreases significantly from 3.0% to 1.7%. This implies that at low tape temperature the melt viscosity of the polymer is too low (specifically during consolidation under the roller) for rapid compression of the voids. Increasing the substrate temperature to 500 °C further decreases the melt viscosity and void content for T_{tape} = 400 °C (1.8%) and T_{tape} = 500 °C (1.5%). However, a significant increase to 2.6% is seen when a tape temperature of 600 °C is used. This is likely attributed to void re-expansion due to the polymer remaining molten after the consolidation roller has passed. This effect is more pronounced at the highest substrate temperature of 600 °C, where the void content increases from 2.2% to 3.2% as the tape temperature is increased from 400 °C to 600 °C. The lowest void contents are observed for either a combination of T_{tape} = 600 °C and T_{subst} = 400 °C or T_{tape} = 500 °C and T_{subst} = 500 °C. An interesting observation is the fact that at T_{subst} = 500 °C, when increasing the tape temperature from 500 °C to 600 °C, a dramatic ~73% rise in void content (from 1.5% to 2.6%) is observed, while the compression shear strength only diminishes by 5%, suggesting that tough thermoplastic composites such as CF/PEEK are less sensitive to

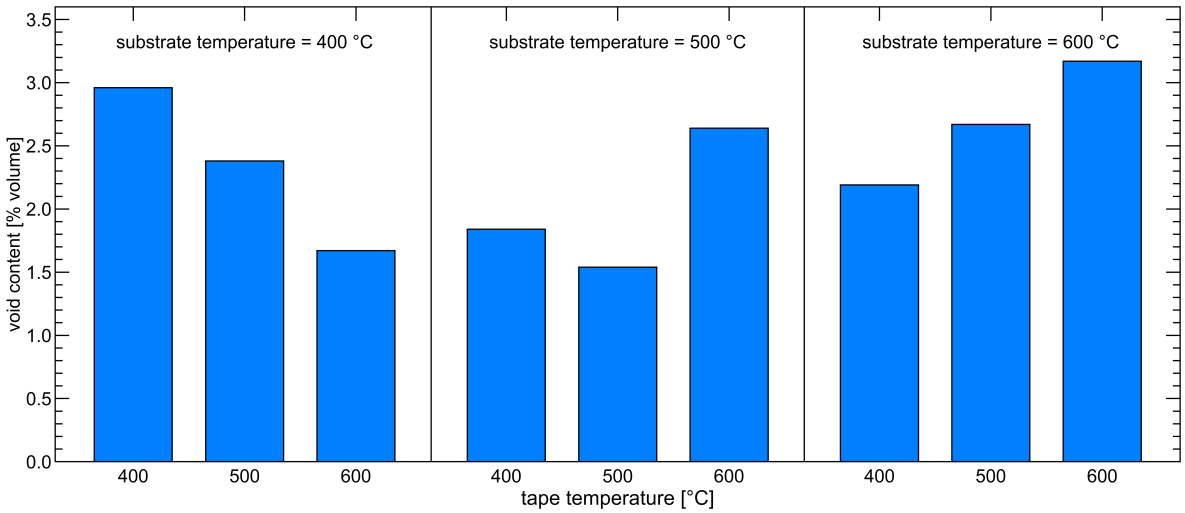

Figure 4. Void content vs. tape and substrate setpoint temperature.

void content. Figure 5 shows 3D visualisations of the subset digitally extracted from the micro-CT image of the sample processed with T_{tape} = 500 °C and T_{subst} = 500 °C, which corresponded with the highest compression shear strength of 48.7 MPa and lowest void content of 1.5%. The fibres (orange colour) are evenly distributed within the matrix (grey), and a small interlaminar resin-rich region is present. The voids (black or blue) are generally distributed in the intra-ply regions, with a combination of small round voids and elongated voids adjacent to fibres.

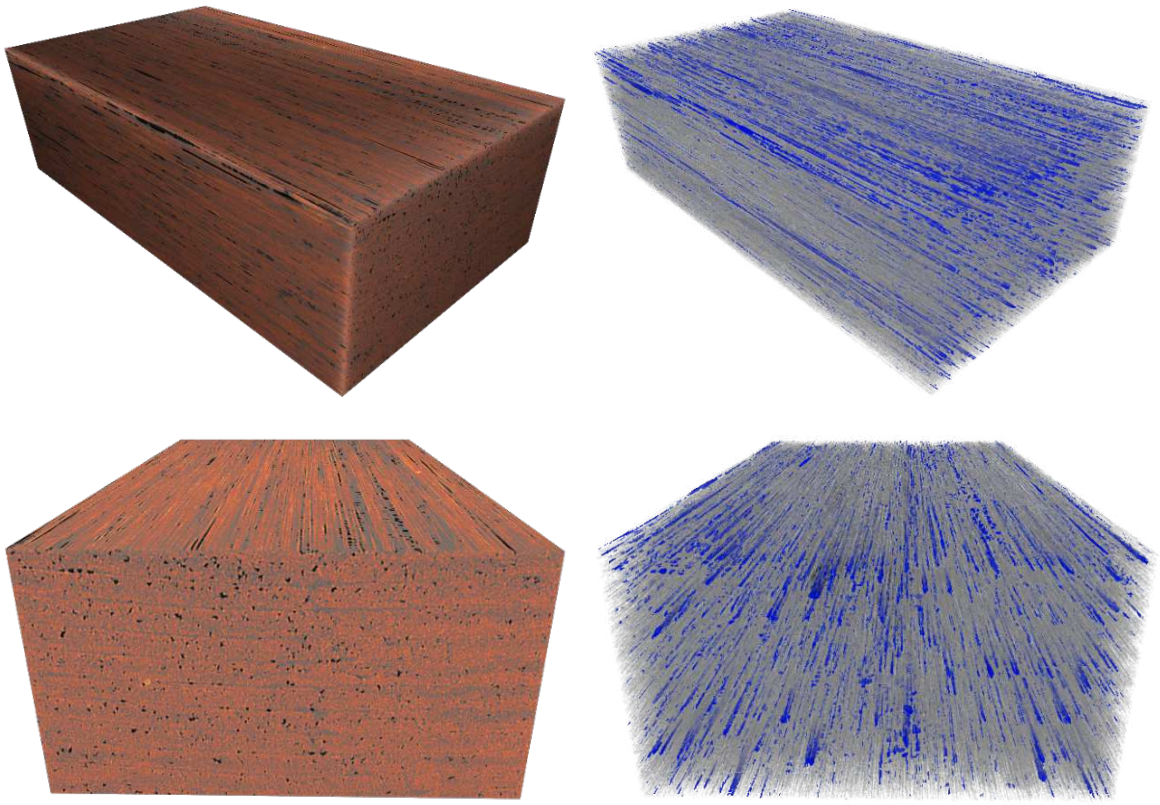

Figure 5. Micro-CT images showing the distribution of fibres and matrix (left) and internal voids (right) within the composite processed at 400 mm/s with T_{tape} = 500 °C and T_{subst} = 500 °C.

  doi:10.5075/epfl-298799_978-2-9701614-0-0

4. Conclusion

This study investigated the effects of using independently controlled tape and substrate processing temperatures with a novel dual-laser tape placement head for manufacturing thermoplastic composite laminates. Unidirectional $[0]_{32}$ CF/PEEK laminates were manufactured at 400 mm/s. Processing temperature setpoints of 400 °C, 500 °C and 600 °C were applied to the tape and substrate surfaces resulting in 9 permutations for sample manufacture. The interlaminar bonding was assessed by compression shear tests. Laminate quality in terms of void content, fibre and void distribution were analysed by micro-CT scans. The key findings are as summarised below:

- The consistently high compression shear strengths are observed for lower substrate temperatures of 400 °C and 500 °C, in combination with higher tape temperatures of 500 °C and 600 °C.
- The void content was found to be high for both low and high temperature combinations, suggestive of limited void compression for low temperatures and void re-expansion at high temperatures due to the polymer remaining molten post-consolidation.
- The lowest void contents of 1.6% and 1.5% were observed for either a combination of T_{tape} = 600 °C, T_{subst} = 400 °C and T_{tape} = 500 °C, T_{subst} = 500 °C respectively.
- For T_{subst} = 500 °C, when increasing the tape temperature from 500 °C to 600 °C, a dramatic rise from 1.5% to 2.6% void content is observed, however the compression shear strength only diminishes by 5%, suggesting that tough thermoplastic composites such as CF/PEEK are less sensitive to void content.
- The best properties were observed for T_{tape} = 500 °C and T_{subst} = 500 °C, which corresponded with the highest compression shear strength of 48.7 MPa and lowest void content of 1.5%.

Future directions include a more detailed study of the void dynamics including model implementation. Processing with differential temperatures will also influence the residual stress state within the laminates, therefore this would also be of interest to study.

Acknowledgements

This research was supported by the ARC Training Centre for Automated Manufacture of Advanced Composites (IC160100040), supported by the Commonwealth of Australia under the Australian Research Council's Industrial Transformation Research Program.

5. References

1. Thermoplastic composites: Poised to step forward [Internet]. [cited 2022 Jan 17]. Available from: https://www.compositesworld.com/articles/thermoplastic-composites-poised-to-step-forward.
2. Airbus and Clean Sky 2 support environmental protection | Airbus [Internet]. [cited 2022 Jan 17]. Available from: https://www.airbus.com/en/newsroom/news/2021-04-airbus-and-clean-sky-2-support-environmental-protection.
3. Chadwick AR, Kotzur K, Nowotny S. Moderation of thermoplastic composite crystallinity and mechanical properties through in situ manufacturing and post-manufacturing

  doi:10.5075/epfl-298799_978-2-9701614-0-0

tempering: Part 1 – Mechanical characterisation. Composites Part A: Applied Science and Manufacturing. 2021;143:106286.
4. Valverde MA, Belnoue JP-H, Kupfer R, Kawashita LF, Gude M, Hallett SR. Compaction behaviour of continuous fibre-reinforced thermoplastic composites under rapid processing conditions. Composites Part A: Applied Science and Manufacturing. 2021;149:106549.
5. Weiler T, Emonts M, Wollenburg L, Janssen H. Transient thermal analysis of laser-assisted thermoplastic tape placement at high process speeds by use of analytical solutions. Journal of Thermoplastic Composite Materials. 2018;31:311–38.
6. Stokes-Griffin CM, Compston P. An inverse model for optimisation of laser heat flux distributions in an automated laser tape placement process for carbon-fibre/PEEK. Composites Part A: Applied Science and Manufacturing. 2016;88:190–7.
7. Stokes-Griffin CM, Compston P. The effect of processing temperature and placement rate on the short beam strength of carbon fibre–PEEK manufactured using a laser tape placement process. Composites Part A: Applied Science and Manufacturing. 2015;78:274–83.
8. Stokes-Griffin CM, Kollmannsberger A, Compston P, Drechsler K. The effect of processing temperature on wedge peel strength of CF/PA6 laminates manufactured in a laser tape placement process. Composites Part A: Applied Science and Manufacturing. 2019;121:84–91.
9. Schneider K, Lauke B, Beckert W. Compression Shear Test (CST) – A Convenient Apparatus for the Estimation of Apparent Shear Strength of Composite Materials. Applied Composite Materials. 2001;8:43–62.
10. Zinnecker V, Stokes-Griffin CM, A. Khudiakova, Wolfahrt M, Compston P. A comparative study for shear testing of thermoplastic-based composites and metal-composite hybrids. Composites Part A: Applied Science and Manufacturing. 2020;137:105953.

  doi:10.5075/epfl-298799_978-2-9701614-0-0

AN EXTENDED ANISOTROPIC APPROACH FOR TAILORED FIBER PLACEMENT STRUCTURES COMBINING TOPOLOGY AND BASE MATERIAL OPTIMIZATION

Johannes Schwingel[a], Stefan Carosella[a], Peter Middendorf[a]

a: Institute of Aircraft Design, University of Stuttgart, D-70569 Stuttgart, Germany
Email: schwingel@ifb.uni-stuttgart.de, web page: http://www.ifb.uni-stuttgart.de

Abstract: *Several approaches have been developed to introduce anisotropic materials into the topology design process where most researches focus only on single-ply laminates without considering complex load states in intersections. Fiber placement technologies especially Tailored Fiber Placement are suitable to fabricate the complex shapes regarding material sustainability. This technology introduces an additional base material component which may have an influence on the structural behavior but is currently not considered for a combined optimization. A homogenization is used in this work to combine the topology optimization approach with its extended material design space and the base material optimization. To compare the results parametric studies have been conducted. Both, the new mixed cross-ply design space and the combination with the base material show significant improvements regarding structural stiffness and their interaction.*

Keywords: Anisotropic Topology Optimization; Tailored Fiber Placement; Optimized Base Material

1. Introduction

The role of resource efficiency is becoming increasingly important for all industrial sectors. Especially the mobility sector benefits from smart solutions for materials and processes. For ECCM20 theme of "Composites meet sustainability," automated fiber placement techniques such as Tailored Fiber Placement (TFP) hold great potential for maximizing lightweight design.

Therefore, suitable design methods are required to maintain or even increase structural stiffness by simultaneously reducing mass. TFP is selected whenever near-net-shape designs are desired for smaller components or local reinforcements on existing preforms are necessary. This preforming technology is a stitching process that allows fiber tows to be placed on a base material according to the actual stresses occurring in the component. Thus, regarding sustainability, less material can be used, preform waste is reduced to a minimum and the specific stiffness increases. To achieve these aims, complex design methods and suitable optimization algorithms for anisotropic materials have to be developed. TFP structures can be divided into two use cases, stand-alone components and local reinforcements with(out) base material and an already existing base laminate, respectively. In order to achieve a maximum performance both interdepending components, TFP reinforcement and base material and their effects have to be considered for design optimization.

The most effective method and the first step in a design process is a topology optimization. First introduced only for isotropic materials [1] various publications concentrated on a further development for anisotropic unidirectional materials [2–4]. These methods are sufficient for the

  doi:10.5075/epfl-298799_978-2-9701614-0-0

truss members in a topological design but in the overlap regions the approach has its limitations since more than one fiber orientation is necessary to capture the stress state. For fiber placement technologies smoother fiber distributions in those areas are beneficial to simplify the subsequent machine path generation. In literature most approaches for anisotropic topology focus on the actual optimization of fiber orientations but not on the effects of the surrounding material. In summary, a lot of potential for fiber placement approaches exists when those two problems, design space and additional affecting components, can be solved.

Therefore, this paper presents an extended optimization approach that attempts to address these topics. The algorithm is based on an objective function approximation which has first been introduced by Ijsselmuiden [5] and was further developed by Peeters [6] for Automated Tape Laying to apply a topology optimization using lamination parameters. Although these parameters return a global optimized laminate, only specific types of laminates are required for a topological design. Hence, a design space is introduced in this work to extend the often-used unidirectional laminates to a "mixed cross-ply" design space that includes UD, cross-ply and a transition zone between both laminate types to avoid ambiguous solutions. Often only local TFP reinforcements are required for an existing composite preform. Therefore, the laminate stiffness matrix is considered separately from the local element-wise material optimizations and subsequently homogenized for the finite element analysis (FEA).

The results are generated for benchmark models, e.g. a classic symmetric cantilever beam and the MBB beam ("Messerschmidt-Bölkow-Blohm"). Several parameter studies are conducted and compared to quasi isotropic solutions as well as the general lamination parameter results. Furthermore, all values are normalized to the quasi isotropic case and mass to provide relative improvements regarding lightweight design.

The contribution of this paper can be summarized as follows. The original approach using lamination parameters as design variables is replaced by a simpler composite material design space that is sufficient for topology optimization. Furthermore, the base material for TFP applications is additionally considered and simultaneously optimized.

To describe the approach section 2 provides basic information of the optimization procedure for the local topology reinforcement component using the extended design space. In the third section "base material extension" the objective function is reformulated to include base material and the individual components are explained. The results section shows validated parameter studies and comparisons to existing approaches for selected benchmark models. Finally, concluding remarks and an outlook for future investigations are given.

2. Basic method

2.1 Optimization formulation

The presented approach focuses on the minimization of the inner structural energy (maximum stiffness) for a constrained volume fraction which is typical for a topology optimization step. For the latter part the SIMP method (Solid isotropic material penalization) is chosen which creates virtual densities scaling the elements initial material modulus or laminate stiffness matrices. For anisotropic considerations it is important to mention that material orientations and densities have to be optimized simultaneously as follows:

  doi:10.5075/epfl-298799_978-2-9701614-0-0

$$\min_{\boldsymbol{x},\rho} U_\Omega \;\rightarrow\; \min_{\rho}\left(\min_{\boldsymbol{x}} U_\Omega\right) \tag{1}$$

where *U* is the inner structural energy for a region *Ω*, the vector ***x*** defines the selected design space of material orientations and ρ is the virtual density. Simultaneous optimization means that for each iteration of the iterative loop a finite element analysis is performed. The subsequent local optimizations are conducted based on this fixed strain field until the next FEA. This process continues until convergence is achieved.

The overall objective function is used as

$$U_\Omega = \boldsymbol{\Phi}_\Omega : \boldsymbol{A}_\Omega^{-1} \quad \text{with} \quad \boldsymbol{\Phi}_\Omega = \frac{\partial U_\Omega}{\partial \boldsymbol{A}_\Omega^{-1}} \tag{2}$$

where the region *Ω* can describe local elements or the part level, e.g. for the optimization of the base material. The sensitivity matrix ***Φ*** describes the derivation of the system stiffness matrix according to the inverse membrane stiffness matrix $\boldsymbol{A}^{-1}$. For further details the reader is referred to IJsselmuiden [5].

2.2 Anisotropic topology optimization

For a topologically optimized design the intersection points need more than one unidirectional orientation to catch the shear loads. Hence, cross-ply laminates are required in addition to a unidirectional layup for the truss members [7]. In order to describe the material design space with a minimum of design variables lamination parameters are used as an intermediate step. A full laminate stiffness matrix requires a set of four laminate parameters $V_{1\text{-}4}$. Since only balanced and symmetric are assumed the set can be reduced to V_1 and V_3. Figure 1 shows the *"mixed cross-ply"* design space on the left.

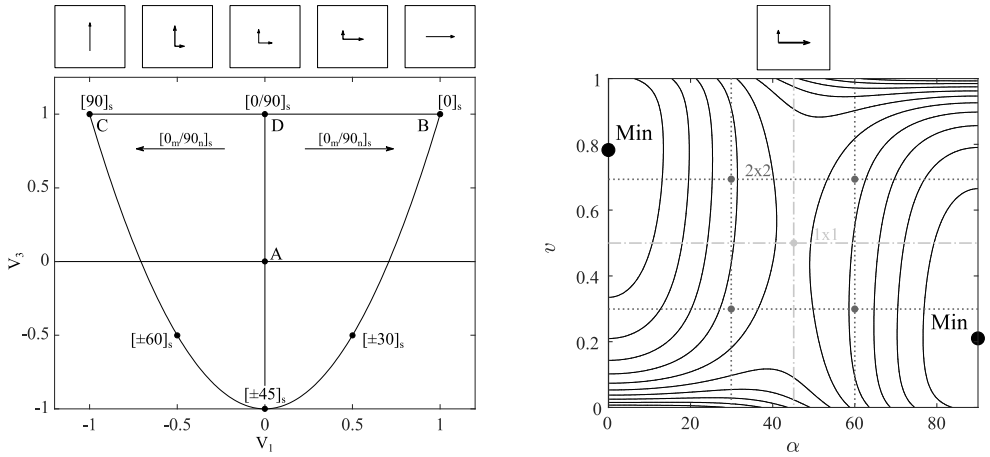

Figure 1. Mixed cross-ply definition: General balanced design space using lamination parameters (l.), exemplary inner structural energy for two material parameters (r.)

The two-parameter optimization is driven by the layer fraction *v* (Eq. (3)) and the layer orientation *α* where the second layer has a general angle difference of 90°.

$$\begin{aligned} V_1 &= v \cdot \cos 2\alpha + (1-v)\cos 2(\alpha - 90°) \\ V_3 &= v \cdot \cos 4\alpha + (1-v)\cos 4(\alpha - 90°) \end{aligned} \tag{3}$$

Based on these parameters the laminate stiffness matrix can be built using the laminate thickness *h* and the constant material matrices ***Γ*** as follows:

$$\boldsymbol{A} = \rho \cdot h(\boldsymbol{\Gamma}_0 + V_1 \cdot \boldsymbol{\Gamma}_1 + V_3 \cdot \boldsymbol{\Gamma}_3) = \rho \cdot \widetilde{\boldsymbol{A}} \tag{4}$$

  doi:10.5075/epfl-298799_978-2-9701614-0-0 published under CC BY-NC 4.0 license

To find the minimum of the two-dimensional space a gradient-based algorithm is used starting from multiple start points (see Figure 1 r.) to avoid local minima or saddle points [7]. Once the local material optimization is done for all elements, the topology optimization step is conducted in the specific iteration. The topology algorithm follows the classic SIMP method (Solid Isotropic Material with Penalization, see [1]).

Once the optimum density and material distribution is found, an FE-analysis is conducted to update the structural behavior and the objective value is monitored to previous steps to check the convergence behavior.

3. Base material extension

The extended anisotropic topology optimization approach shown in the previous section is used for the local reinforcement component in a TFP structure. The other part is the base material which is mainly investigated in this work. The structural behavior for the optimization of the base material can be described by changing Eq. (2) to

$$U_B = \boldsymbol{\Phi}_B : \boldsymbol{A}_B^{-1} \quad \text{s.th.} \quad U_{total} = \boldsymbol{\Phi}_B : \boldsymbol{A}_B^{-1} + \sum_e \boldsymbol{\Phi}_e : \boldsymbol{A}_e^{-1} \tag{5}$$

Both sensitivity matrices $\boldsymbol{\Phi}_B$ and $\boldsymbol{\Phi}_e$ are calculated separately based on the individual membrane stiffnesses. The base material (index "*B*") has a constant stiffness and thickness over the whole structural region (see Figure 2) so that only one sensitivity matrix has to be determined. According to the formulation from [5] the matrix is calculated as follows:

$$\boldsymbol{\Phi}_{\alpha\beta,B} = \sum_{\gamma,\delta} A_{\beta\gamma,B} \cdot A_{\delta\alpha,B} \left(\boldsymbol{u}_{sys}^T \cdot \frac{\partial \boldsymbol{K_{sys}}}{\partial A_{\delta\gamma,B}} \cdot \boldsymbol{u}_{sys} \right) \quad \text{with} \quad \alpha, \beta, \gamma, \delta \in \{1,2,3\} \tag{5}$$

The gradient of the system stiffness matrix is determined using classic FE stiffness matrix assembly methods. The membrane stiffness matrix ***A*** is based on the previous step. To simplify the FE-model, both, the base material and the TFP reinforcement part are combined into the same element using a superposition of the laminate stiffness matrices.

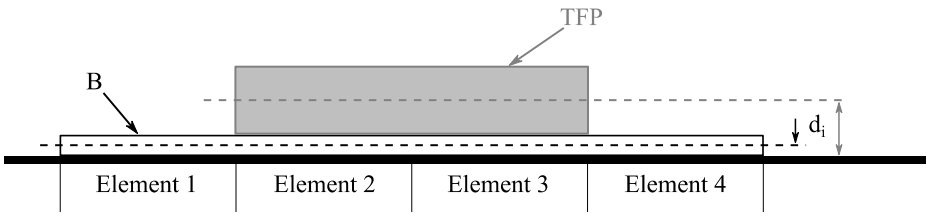

Figure 2. Principle of combining base material and TFP reinforcement

Since the sensitivities of both components are separately calculated and common nodes are used, the system displacement vector $\boldsymbol{u}_{sys}$ is treated as the relationship inside the same iteration. This ensures the consideration of all stiffness effects on the global structural behavior and the response is determined based on all optimum parameters from the previous optimization step.

The topology optimization step is conducted according to the formulation in the previous section. Since the base material does not depend on any virtual density of the TFP reinforcement, the gradient is zero for this part. The shape of the topology is only influenced by the base material stiffness considered in the system displacement vector.

  doi:10.5075/epfl-298799_978-2-9701614-0-0

4. Results

The results for the anisotropic topology optimization and the considered base material are based on a classic benchmark model. In Figure 3 a cantilever beam is shown with an applied symmetric load on the right and an aspect ratio of 3.

E_1	E_2	ν_{12}	G_{12}
1	1/14	1/4	1/24

Figure 3. Benchmark model for the optimization: symmetric load on the right and fixed boundary condition on the left (aspect ratio 3:1)

For all results an initial isotropic material distribution is used. For the topology optimization the volume is uniformly constrained to 50 %. ABAQUS/Standard is considered as the FE solver with a general shell section combined with a material distribution to implement the optimum membrane stiffness matrices directly instead of individual laminates.

4.1 Topology optimization results for TFP reinforcement

In *Figure 4*a the new mixed cross-ply laminate type is opposed to four other design spaces. The normalized stiffness of the mixed cross-ply shows a significant improvement compared to simple ±α-balanced laminates and a quasi-isotropic material. The main advantage is shown in *Figure 4*a and 4b in the highlighted intersection area. In this region shear loads are dominant which cannot be captured by a single laminate orientation as demonstrated with the UD design space.

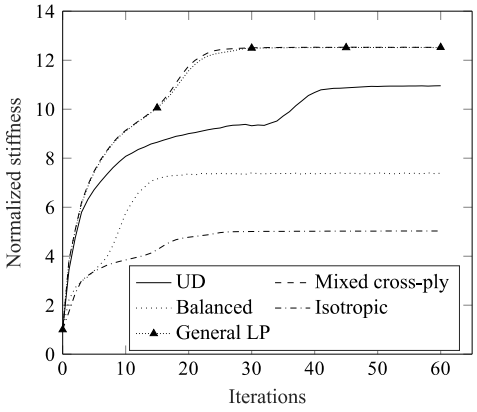

Design space	Normalized stiffness
UD	11.0
Mixed cross-ply	12.5
Balanced	7.4
Isotropic	5.0
General LP	12.5

a) Stiffness behavior of different design spaces compared and normalized to the initial isotropic material design

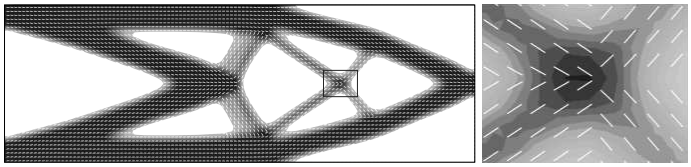

b) Anisotropic topology design for UD design space

  doi:10.5075/epfl-298799_978-2-9701614-0-0 published under CC BY-NC 4.0 license

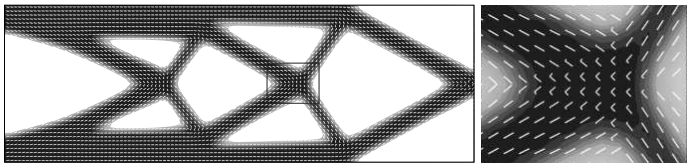

c) Anisotropic topology design for mixed cross-ply design space

Figure 4. Results of the anisotropic topology optimization

Furthermore, a solution is likely to be ambiguous in the center. In contrast, mixed cross-ply laminates are aligned to those shear loads and provide a smooth transition towards the individual truss members. Furthermore, it is obvious that the general approach with a full set of optimized lamination parameters gives the same results as the mixed cross-ply laminate type. This indicates that for a topology optimization it is not necessary to consider all possible stacking sequences which reduces the number of design parameters as well as the computation effort.

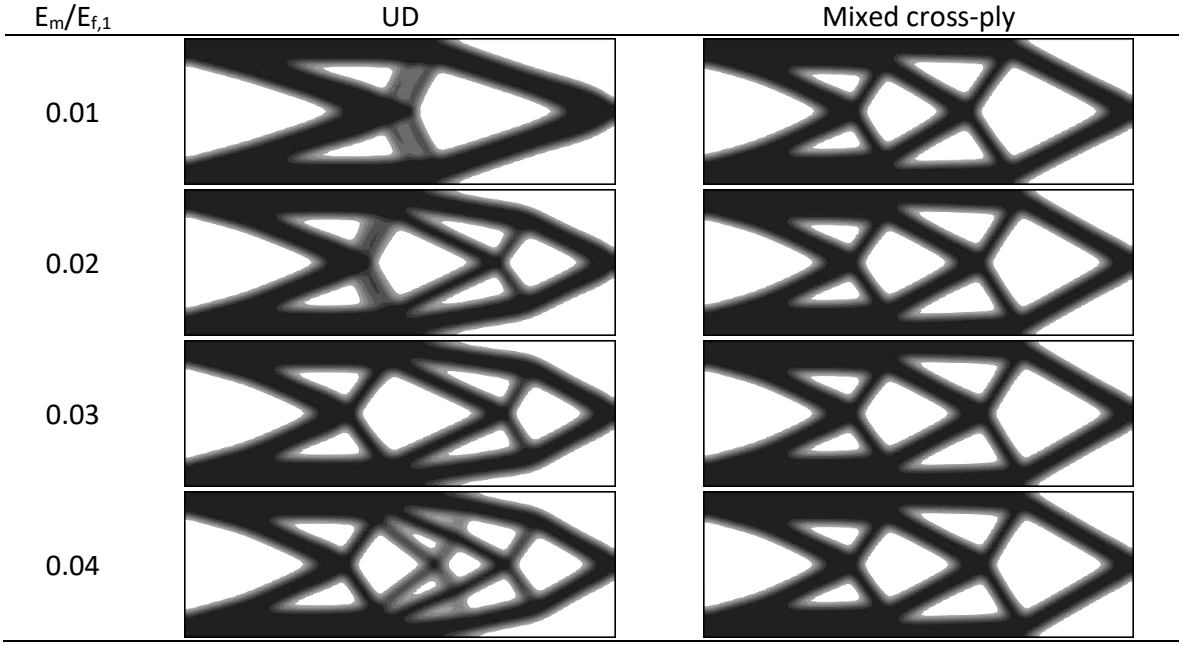

Figure 5. Design comparison for different material property variations

A further advantage is shown in Figure 5 where topology designs for UD and mixed cross-ply are compared with a varying resin modulus E_m. It is obvious that the UD designs depend significantly on the varying properties whereas the mixed cross-ply designs are stable for all changes. This indicates a better adaptability for the mixed cross-ply design space.

4.2 Combined base material and topology investigation

In a first step to combine the base material optimization with anisotropic topology optimization approach the individual effects are separated using a constant base material orientation. In Figure 6 the normalized specific stiffness is compared for different constant base material orientations. The corresponding resulting topological designs are presented in Figure 8. The used thickness ratio $R = t_{TFP}/t_B$ is chosen as eight for this investigation. It can be seen that the optimizer for the anisotropic topology is influenced by the additional stiffness component. For

  doi:10.5075/epfl-298799_978-2-9701614-0-0

example, the ±45°-configuration shows a reduced number of truss members placed in shear direction since the base material carries a high fraction of the shear loads in the center.

Furthermore, the constant stiffness designs are compared to the topology design without base material and the combined optimization of base material stiffness and reinforcement topology. The first indicates the best solution of all considered configurations in terms of mass normalization. In cases where a base material is necessary, e.g. for local reinforcements of a closed-walled skin the combined optimization is most suitable. In this work the base material design space is chosen to be simple balanced laminates but other design spaces are also applicable. From a manufacturing perspective the base material can be fabricated using the Dry Fiber Placement technology [8].

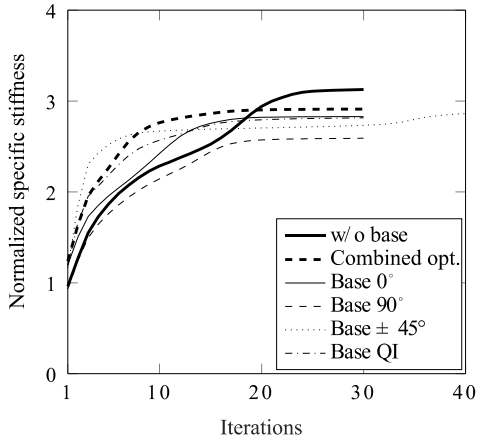

Figure 6. Normalized specific stiffness for different base material configurations

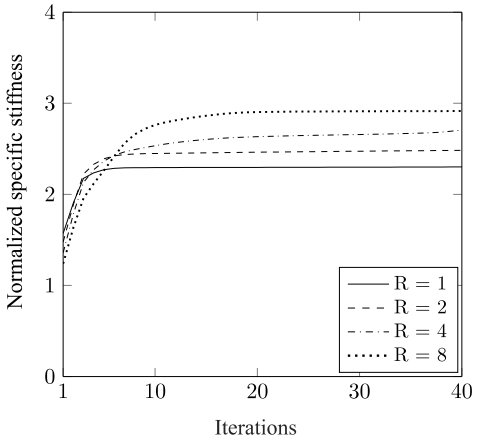

Figure 7. Normalized specific stiffness for various thickness ratios R

The final study is presented in Figure 7 andFigure *9* where different thickness ratios between TFP reinforcement component and base material have been investigated. In this context both components are optimized simultaneously. It is obvious that the thickness ratio has a major impact on the topological design. For the first two ratios the base material is still dominant resulting in two unconnected regions of the reinforcement. In general, the best designs result from a connection between support areas and load introduction which is the major advantage of TFP structural designs. For the given benchmark example, a continuous material distribution has formed for a thickness ratio of at least four which indicates an efficient application of local TFP reinforcements.

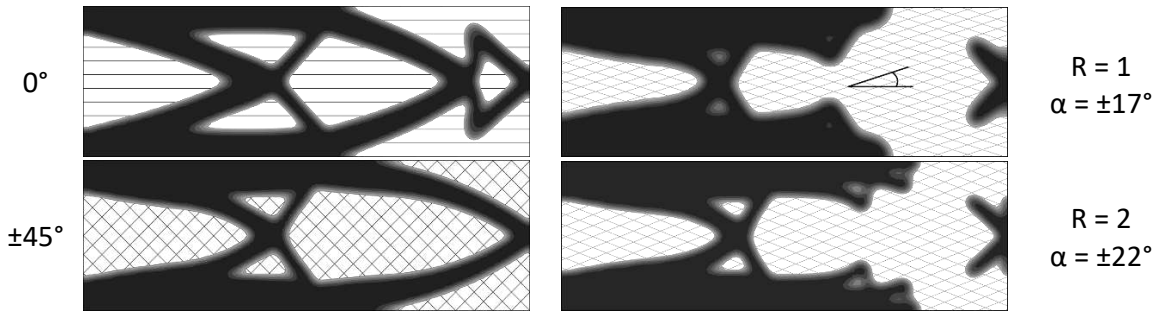

  doi:10.5075/epfl-298799_978-2-9701614-0-0

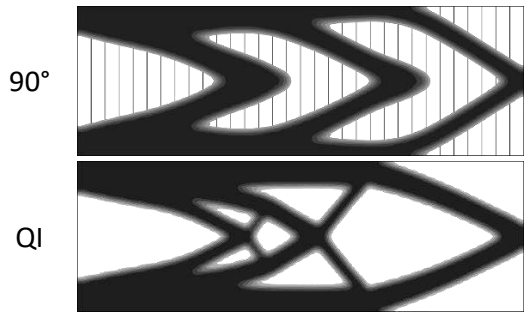

Figure 8. Topology design for constant base material orientations

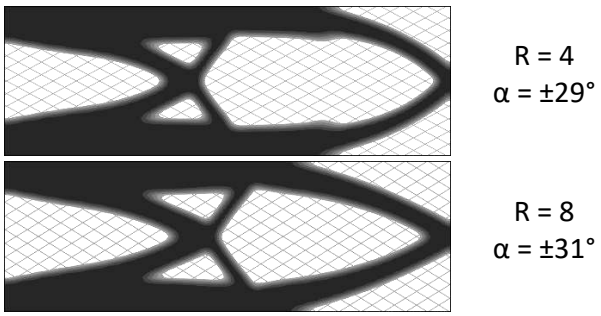

Figure 9. Combined optimization for different thickness ratios $R = t_{TFP}/t_B$

5. Conclusion

A combined optimization approach is presented in this work for the Tailored Fiber Placement technology. The proposed method considers the interaction of the local reinforcement component and the base material. For the first part an extended design space has been introduced for the anisotropic topology optimization step while the material orientations of the base material have been optimized simultaneously. Different parameters were investigated to show the efficiency of the approach. The mixed cross-ply design space has demonstrated significant stiffness improvements compared to other laminate types such as single-ply materials. The next step, the combination of base material and topology optimization demonstrated the additional interaction and design changes to enable the future application of this approach for the design of larger assemblies with local TFP reinforcements.

6. References

1. Bendsoe MP, Kikuchi N. Generating Optimal Topologies in Structural Design using a Homogenization Method. Computer Methods In Applied Mechanics And Engineering 71. 1988:197–224.
2. Nomura T, Kawamoto A, Kondoh T, Dede EM, Lee J, Song Y, Kikuchi N. Inverse design of structure and fiber orientation by means of topology optimization with tensor field variables. Composites Part B: Engineering. 2019;176:107187. doi:10.1016/j.compositesb.2019.107187.
3. Jantos DR, Hackl K, Junker P. Topology optimization with anisotropic materials, including a filter to smooth fiber pathways. Struct Multidisc Optim. 2020;61:2135–54. doi:10.1007/s00158-019-02461-x.
4. Li D, Kim IY. Modified element stacking method for multi-material topology optimization with anisotropic materials. Struct Multidisc Optim. 2020;61:525–41. doi:10.1007/s00158-019-02372-x.
5. IJsselmuiden ST. Optimal Design of Variable Stiffness Composite Structures Using Lamination Parameters: Wohrmann Print Service; 2011.
6. Peeters, D. Design Optimisation of Practical Variable Stiffness and Thickness Laminates. 2017.
7. Schwingel J, Middendorf P. Topological design using multivariate laminate stackings for tailored fiber placement. Journal of Composite Materials. 2022. doi:10.1177/00219983221085721.
8. Grisin B, Carosella S, Middendorf P. Dry Fibre Placement: The Influence of Process Parameters on Mechanical Laminate Properties and Infusion Behaviour. Polymers (Basel) 2021. doi:10.3390/polym13213853.

  doi:10.5075/epfl-298799_978-2-9701614-0-0

MANUFACTURING AND EXPERIMENTAL TESTING OF COMPOSITE/METAL JOINTS WITH TEXTILE MESOSTRUCTURE

Andrejs, Pupurs[a], Inita, Bramane[a], Inga, Ļašenko[a], Māris, Maniņš [a], Mārtiņš, Irbe[a], Alens, Šņepsts[a]

a: Riga Technical university – andrejs.pupurs@rtu.lv

Abstract: *The present paper investigates novel composite/metal joint designs based on gradual interweaving of carbon fiber yarns with metallic fiber yarns obtaining a textile meso-structure. Various configurations of knitted and woven hybrid fabrics were produced from carbon and steel fibers and composite plates were manufactured using vacuum infusion of epoxy resin. Mechanical properties such as elastic modulus, ultimate tensile strength and strain at failure were experimentally determined. Results show rather similar values of strength for steel fiber knitted and woven composites, while for carbon fiber notably higher properties were obtained for woven composites. For different hybrid carbon/steel fiber composites a rather wide variety in properties was obtained depending on the actual meso-structure. The paper summarizes initial test results of a large-scale parametric analysis from which composites with highest strength and strain to failure will be selected for analysys of micro-damage evolution moving toward development of joints with enhanced mechanical properties.*

Keywords: composite/metal joints; knitted fabrics; woven fabrics; mechanical properties

1. Introduction

In many engineering applications, the improvement of structural performance and reduction of weight is achieved by replacing the metallic parts with polymeric composites. However, an immediate shift to fully composite structures is often not possible due to technology limitations. In result, research work on composite/metal joints has significantly increased in the last decades. A comprehensive summary of state-of-the-art composite/metal joint types, manufacturing technologies and their properties are summarized in [1, 2]. The most common composite/metal joint types include bolted, self-piercing rivet (SPR), adhesive, hybrid penetrative reinforced (HYPER) joints. Alternatively, hybrid joints in form of combination of SPR, bolted joints and adhesive joints are presently investigated in the literature to create a joint with higher strength than those gained from each individual technique [3]. Study in [4] stated that, although the limitations of bolted and adhesively bonded joints are addressed by combining the two processes, this often defeats the original objective of size, weight and cost savings.

Unlike the previously described bolted, riveted and adhesive composite/metal joints, HYPER joints use integrated joint elements. Such joints usually contain small pins, raising from the surface of the metallic component, which are integrated in the uncured composite substrate. This provides a mechanical interlocking and additional epoxy adhesion around the pins [5]. The HYPER technology is time and cost-intensive, due to the requirement of special tools and know-how. In literature different concepts of pin building are described, which includes additive and subtractive manufacturing processes. Main advantage of HYPER technology is the positive

  doi:10.5075/epfl-298799_978-2-9701614-0-0

mechanical failure behavior comparing to other joining methods [6]. Detriments are the elaborated manufacturing process and the difficult separating and recycling of the components.

Several techniques have been developed that involve creating features on the metallic part to reinforce the joint [4]. This includes the Comeld process which uses an electron beam to create features on the metal surface that improve strength. Comeld joint is based on form locking load transmission, so the stress is introduced over the entire composite thickness. However, the manufacturing of joint requires high accuracy and is time-consuming. Furthermore, an abrupt transition from composite to metal properties associated with stress concentrations is present in such joints.

In [7] a new type of joint was investigated with an interleaved stack of metal and dry carbon fibers, across which a welding joint was made at the first stage. The second stage involved epoxy resin infusion into the carbon fibre fabric [7]. More favorable characteristics of mechanical behaviour of joint were observed in [7] compared to typical adhesive or bolted joints, however, the manufacturing process is resource and time consuming.

To overcome these disadvantages, a novel type composite/metal joints will be developed and experimentally tested within the present study. The composite/metal joint is based on gradual interweaving of carbon fiber yarns with metallic wire yarns into a single textile, achieving significant advantages in mechanical properties. Textile based composites compared to laminated pre-preg composites exhibit more resistance to delamination and splitting and they have much higher notched strength [8,9]. The main hypothesis of the study is that, due to gradual interweaving of carbon and metallic yarns, a smooth transition of thermo-mechanical properties from purely composite to purely metallic part will be achieved thus significantly improving the stress-state in the joint region that will allow for full utilization of the strength of carbon fibers and metallic material. In such way, a significant increase in mechanical strength of the joint is expected, compared to the currently existing composite/metal joint types both in static and cyclic mechanical loading. In addition, such composite/metal joints have a potential for other significant advantages such as reduction of residual manufacturing-induced stresses, elimination of stress concentrations, ductility of the joint failure, and manufacturing cost reduction due to pre-fabricated textiles.

The present paper describes manufacturing of fabrics and composite plates with knitted and woven textile meso-structure with different combinations of carbon and steel fibers. The paper also summarizes experimental test results showing the basic mechanical properties of manufactured hybrid composites such as the elastic modulus, ultimate tensile strength and the maximum tensile strain at failure.

2. Materials and Manufacturing

2.1 Fiber yarns

Three types of carbon fiber filaments and one type of stainless steel fibers (in continuous yarns) were selected and purchased from the commercially available assortment to perform manufacturing of fabrics. Following types of carbon fibers were selected: Toray T300-1K 50A (Japan), Toray T700SC-12K50C (Japan) and Toray FT300B-3K-50B (France) fibers.

  doi:10.5075/epfl-298799_978-2-9701614-0-0

Regarding metallic fibers, stainless steel yarn SY 11/1 (91 tex) filaments manufactured by Bekintex (Belgium) from short steel fibers by Fujibo (Japan) were used. The SY 11/1 fibers were specifically selected based on their suitability for weaving applications, according to the manufacturer's information.

2.2 Manufacturing of knitted fabrics

Knitting of fabrics was performed on a manual knitting machine Brother (Japan). Manual knitting machines are typically designed for knitting commercial fabrics for clothing and household applications using cotton, wool, synthetic and other types of yarns. However, provided that the filament size and the needle grades are compatible, the manual knitting machines can also be successfully adapted for manufacturing of textiles from commercial carbon fiber and other types of high performance fibers, such as steel fibers.

The first challenge for knitting carbon fiber fabrics is to select the compatible size (grade) of the needles of the knitting machine. For larger filaments, such as T700SC-12K50C fibers, lower grade needles were used than for T300-1K 50A fibers. Compared to cotton and wool yarn filaments typically used on the knitting machines, carbon fibers are more brittle and may break when subjected to extreme bending and twisting during the knitting process. Furthermore, when subjected to friction (filament against another filament) the carbon fibers tend to form fluff, which can stop the filament from passing through the needles and channels of the knitting machine and can lead to defects and imperfections in the textile fabric. For metallic fibers such as yarns of SY 11/1 stainless steel fibers, while bending and passing through the needles is not an issue, the friction between the filaments is distinctly higher than for most of the commercial cotton, wool and synthetic yarns. The above mentioned challenges must be addressed in order to manufacture textiles with dense filament packing and repeatable properties. Teflon, paraffin and silicon lubricants were used for reducing the friction between the filaments, when necessary, however, it was followed that not an excessive amount of lubricants were applied to the fabrics to prevent potential reduction of bonding between the filaments and the epoxy resin in the composite manufacturing stage. List of manufactured knitted fabrics is presented in Table 1.

Table 1: List of manufactured knitted fabrics.

Nr.	Fabric notation	Type	Yarn materials
1	SY 11/1, 1 filament	Single jersey	SY 11/1 , 91 tex, FUJIBO/Bekintex, steel
2	T300-1K 50A, 1 filament	Single jersey	Toray T300, 1K 50A, carbon
3	SY 11/1, 3 filaments	Single jersey	SY 11/1 , 91 tex, FUJIBO/Bekintex, steel
4	SY 11/1, 1 filament + T300-1K 50A, 1 filament	Single jersey	Filament hybrid of SY/1 and T300

  doi:10.5075/epfl-298799_978-2-9701614-0-0

2.3 Manufacturing of woven fabrics

Weaving of carbon and stainless steel fiber fabrics was performed using a manual weaving loom. To develop a robust and efficient method for weaving of carbon and steel fiber fabrics, a custom-made weaving loom was elaborated which minimizes friction between the warp filaments. The used set-up requires manual and labour intensive winding of the weft yarns in the full length of the fabric, however, it was verified that such approach gives a very good and repeatable quality of the fabric and eliminates the friction. The list of manufactured woven fabrics is summarized in Table 2.

Table 2: List of manufactured woven fabrics.

Nr.	Fabric notation	Type	Yarn materials
1	T300 1x	Plain weave	T300-1K 50A
2	SY 11/1 2x	Plain weave	SY 11/1
3	SY 11/1 2x warp, T300FR 1x weft	Plain weave	SY 11/1, FT300B-3K-50B
4	T300 FR 1x warp, SY 11/1 2x weft	Plain weave	FT300B-3K-50B, SY 11/1

Examples of manufactured knitted fabrics (reference and hybrid) are shown in Fig.1a. Fig.1b shows the process of weaving of steel fiber fabric.

a) b)

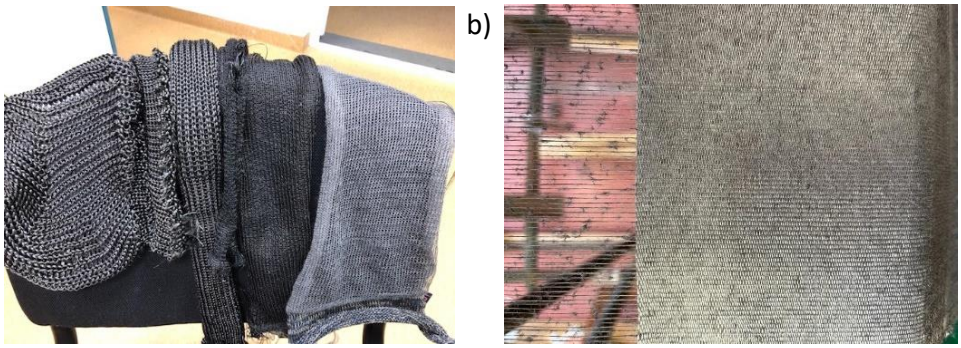

Figure 1. a) samples of manufactured knitted fabrics; b) manufacturing of woven fabrics

2.4 Manufacturing of composites

Previously produced dry knitted and woven fabrics (see Table 1 and 2) were stacked in various layups to manufacture composite plates representing various concepts of mechanical joints with textile meso-structure according to the objective of the work. After stacking in desired lay-ups, the fabrics were infused with epoxy resin by the vacuum infusion process. The epoxy resin used for manufacturing of composites was Epoxy LY1564 with XB 3404-1 hardener from Huntsman (USA). Curing of the plates was performed at +80°C temperature for 8 hours. List of

  doi:10.5075/epfl-298799_978-2-9701614-0-0

manufactured composite plates (lay-ups) and the notation used is summarized in Table 3 for knitted composites and in Table 4 for woven composites.

Table 3: List of manufactured knitted composites.

Nr.	Lay-up	Type	Notation
1	$[(T300)_8]$	Knitted	C1
2	$[(SY\ 11/1)_8]$	Knitted	M1
3	$[(SY\ 11/1\ 3filaments)_8]$	Knitted	M2
4	$[(Hybrid\ SY11/1+T300)_8]$	Knitted	H1
5	$[(T300/SY11/1)]_{2s}$	Knitted	H2
6	$[(T300)_2/(SY11/1)_2]_s$	Knitted	H3
7	$[T300/(\ SY\ 11/1\ 3filaments)]_{2s}$	Knitted	H4

Table 4: List of manufactured woven composites.

Nr.	Lay-up	Type	Notation
1	$[T300\ 1x]_4$	Woven	C3
2	$[SY\ 11/1\ 2x]_4$	Woven	M3
3	$[T300\ FR\ 1x + SY\ 11/1\ 2x]_4$	Woven	H5
4	$[SY\ 11/1\ 2x + T300\ FR\ 1x]_4$	Woven	H6

3. Mechanical testing

Standard size rectangular shape test specimens (according to ASTM D3039) were cut from the composite plates, specimen ends were reinforced with glass fiber composite tabs to prevent failure within grips of the testing machine during loading. Mechanical testing was performed on Zwick/Roell Z150 universal testing machine equipped with 1 kN and 150 kN capacity load cells. Tensile strain was measured using non-contact video-extensometer from Messphysik. Tests were performed at a rate of tensile strain equal to 1% per minute consisting of initial loading-unloading step up to 0.30% of tensile strain for measurement of elastic tensile modulus followed by loading step until the ultimate failure. 3 test specimens from each laminate lay-up were tested from which the average results were calculated

  doi:10.5075/epfl-298799_978-2-9701614-0-0

4. Results and discussion

Results of mechanical tests are summarized in Table 5 for knitted composites and in Table 6 for woven composites. Regarding the properties of knitted composites, it is notable that elastic modulus for different studied composites is rather low due to high waviness of the reinforcement yarns and due to relatively low fiber volume fraction. On the other hand, the maximum tensile strain for knitted composites is well above 1% for all studied configurations. Results for different hybrid carbon/steel knitted composites indicate a rather wide range in mechanical properties due to rather large differences in their meso-structure and reinforcement volume fraction.

Table 5: Summary of tensile test results for knitted composites.

Notation	E [GPa]	σ^{max} [MPa]	ε^{max} [%]
C1	12.18	138.61	1.30
M1	6.43	66.42	1.26
M2	8.01	70.62	1.04
H1	12.03	110.94	1.18
H2	8.62	88.30	1.12
H3	10.00	95.60	1.36
H4	6.78	74.39	1.24

Regarding mechanical test results for woven composites it is notable that for carbon fiber/epoxy composites notably higher properties are obtained, as expected, due to reduced waviness and increased fiber volume fraction compared with knitted composites (e.g., C1 in Table 5). As for steel fiber/epoxy composites (M3 in Table 6) only a slight increase in elastic modulus was noted. A slight reduction in strength was also noted compared to knitted composites (M1 and M2 in Table 5), however, the reasons for this are due to be investigated in more detail. The two woven hybrid composites (H5 and H6) demonstrate significantly different results since for H5 the warp yarns are carbon while for H6 the warp yarns are SY 11/1 steel fibers.

Table 6: Summary of tensile test results for woven composites.

Notation	E [GPa]	σ^{max} [MPa]	ε^{max} [%]
C3	37.36	326.14	1.15
M3	9.46	57.62	0.61
H5	35.83	428.78	1.01
H6	9.87	63.04	0.63

  doi:10.5075/epfl-298799_978-2-9701614-0-0

5. Conclusions

Prototypes of composite/metal mechanical joints with textile mesostructure were manufactured and experimentally tested in the present study. Manufacturing of reference and hybrid carbon/steel fabrics were produced using knitting and weaving. Reference and hybrid composite plates were manufactured with vacuum infusion technique. Basic mechanical properties of the hybrid composites such as elastic modulus, tensile strength and strain at failure were determined from uniaxial tensile tests. Results show rather similar values of strength for steel fiber knitted and woven composites, while for carbon fiber notably higher properties were obtained for woven composites. For different hybrid carbon/steel fiber composites a rather wide variety in properties was obtained depending on the actual meso-structure.

Acknowledgements

This work was supported by Latvian Council of Science, project LZP-2019/1-0357 “Development and behavior analysis of novel textile composite/metal joints with enhanced mechanical properties”

6. References

1. Jahn J, Weber M, Boehner J, Steinhilper R. Assessment Strategies for Composite-metal Joining Technologies-A Review. Procedia CIRP 2016; 50:689-694.
2. Pramanik A, Basak AK, Dong Y, Sarker PK, Uddin MS, Littlefair G, Dixit AR, Chattopadhyaya S. Joining of carbon fibre reinforced polymer (CFRP) composites and aluminium alloys – A review. Composites Part A: Applied Science and Manufacturing 2017; 101:1-29.
3. El Zaroug M, Kadioglu F, Demiral M, Saad D. Experimental and numerical investigation into strength of bolted, bonded and hybrid single lap joints: Effects of adherend material type and thickness. International Journal of Adhesion and Adhesives 2018; 87:130-141.
4. Zhang H, Wen W, Cui H. Study on the strength prediction model of Comeld composites joints. Composites Part B: Engineering 2012; 43(8):3310-3317.
5. Parkes PN, Butler R, Meyer J, de Oliveira A. Static strength of metal-composite joints with penetrative reinforcement. Composite Structures 2014;118(1):250-256.
6. Ucsnik S, Scheerer M, Zaremba S, Pahr DH. Experimental investigation of a novel hybrid metal-composite joining technology. Composites Part A: Applied Science and Manufacturing 2010; 41(3):369-374.
7. Joesbury AM, Colegrove PA, Van Rymenant P, Ayre DS, Ganguly S, Williams S. Weld-bonded stainless steel to carbon fibre-reinforced plastic joints. Journal of Materials Processing Technology 2018; 251:241-250.
8. Yudhanto A, Watanabe N, Iwahori Y, Hoshi H. The effects of stitch orientation on the tensile and open hole tension properties of carbon/epoxy plain weave laminates. Materials and Design 2012; 35:563-571.
9. Yudhanto A, Iwahori Y, Watanabe N, Hoshi H. Open hole fatigue characteristics and damage growth of stitched plain weave carbon/epoxy laminates. International Journal of Fatigue 2012; 43:12-22.

  doi:10.5075/epfl-298799_978-2-9701614-0-0

CHARACTERIZATION OF STATIC FAILURE IN LAMINATES CONTAINING TRANSVERSE PREFORM TRANSITIONS BY IMAGE PROCESSING

Asbjørn Malte Olesen[a], Brian Lau Verndal Bak[a], Jens Jakob Bender[a], Esben Lindgaard[a]*

a: CraCS research group (cracs.aau.dk), Department of Materials and Production, Aalborg University, Fibigerstræde 16, Aalborg, Denmark,

* asbjoernmo@mp.aau.dk

Abstract: *Preform laminates are introduced to reduce costs when manufacturing large composite structures such as wind turbine blades. A preform is defined as a stack of unidirectional and biaxial dry non-crimp fabric glass fibre plies weakly bonded using a polymeric binder material. In using preforms, potentially weak interfaces are created between preforms in the cured laminate, called preform transitions. The failure of transverse preform transitions subject to static tension is characterized in terms of crack density by a novel automated image processing method for crack quantification. It is found that for static tension, the transverse preform transition geometry has equal or lower crack density compared to the equivalent continuous laminate.*

Keywords: glass fibre reinforced polymers; discontinuous plies; transverse matrix cracking; digital image processing

1. Introduction

As the demand increases for more and larger wind turbines, demand for automated manufacturing of fibre composite structures also increases [1,2]. One approach is using bindered preforms to replace some or all of the manual process of placing fibre material into the casting mould. A bindered preform is defined as a stack of dry unidirectional (UD) and biaxial (BX) non-crimp fabric (NCF) glass fibre mats assembled separately from the casting mould and made into a coherent unit using a polymeric binder material to bond the individual fibre mats. Multiple preforms are typically needed to create a structure such as a wind turbine blade (WTB). The interface between preforms is potentially weak – this region is termed the preform transition. Due to manufacturing constraints, this region consists of many ply terminations in close proximity and arranged in the manner of a staircase, see Figure 1. The staircase occurs because a preform is moved as a single piece, making interleaving of the individual mats impossible in the preform transition. In current designs of WTBs, only transverse preform transitions (as shown in Figure 1) are relevant, as the transition from root laminate to the rest of the blade is made by manual layup.

Before the preform transition can be used in structural models, the failure mechanisms and design loads of the transition must be determined. It is well known that discontinuities in laminates typically lead to a knockdown of structural strength compared to laminates with exclusively continuous fibre plies. Investigations into the failure of laminates made from bindered preforms find that failure is highly dependent on the material system used, as both stiffness and strength may be negatively affected or unaffected by the presence of binder materials [3]. The preform transition is a combination of bindered preforms and discontinuous

  doi:10.5075/epfl-298799_978-2-9701614-0-0

laminates, and the failure of this combination is not addressed in the literature. The effects of binder material are particularly pronounced in the case of loads applied transverse to the fibre direction, where more matrix cracks are formed in specimens made with binder material compared to a reference laminate without binder material [3]. While matrix cracks typically do not immediately lead to failure of the WTB, matrix crack evolution must be understood as the cracks can act as initiators of delaminations [4]. Matrix cracks are initiated and grow in response to both static and fatigue loads; however, only the static case of hoop stresses is considered for certification of WTBs [5].

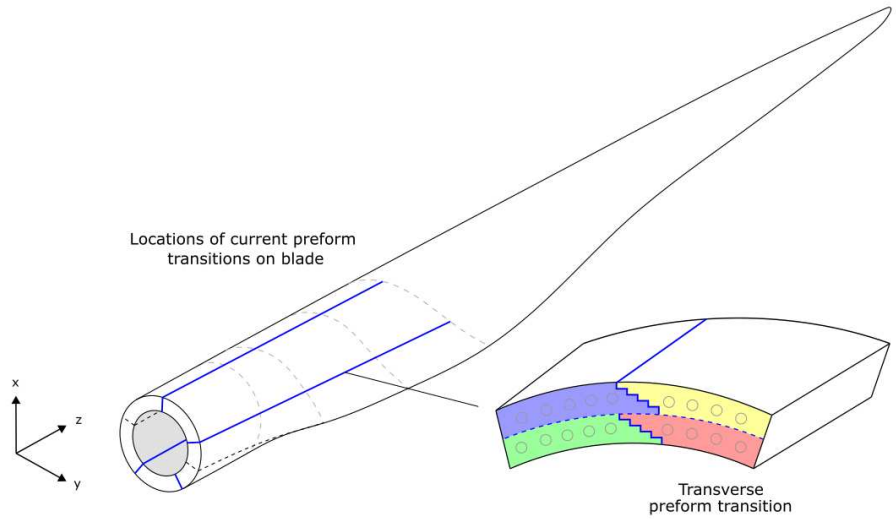

Figure 1. The root section of a wind turbine blade is sectioned into multiple preforms, creating interfaces between preforms, marked by the blue lines. The interface created along the UD fibre direction is described as the transverse preform transition and consists of four individual preforms.

Matrix crack density as a function of applied stress or strain is often used for characterization, as it gives a scalar value for the damage state of the laminate. A wide range of methods for observing full-field intralaminar and interlaminar cracks in glass fibre reinforced polymer (GFRP) laminates exist [6,7]; transilluminated white light imaging (TWLI) is especially suited for the transverse preform transition. TWLI exploits that GFRPs are translucent to some extent, and by shining a light through the laminate, internal damage appears as shadows or darker regions, where internal surfaces caused by fractures transmit less light. The developing crack state is captured by taking multiple images during a test [8]. The difference between a reference image of the undamaged laminate and an image of the damaged laminate corresponds to damage in the form of cracks. High dynamic range imaging may be used to improve the image quality (and thus accuracy of finding cracks), where multiple images of a single crack state are captured at different exposure levels [9]. TWLI has been successfully used to characterize matrix cracks caused by fatigue loads [8-10], but no examples of static loading are found in the literature. In fatigue loading scenarios, it is exploited that the applied load/displacement is cyclical, such that a specimen will always return to a predictable position and same strain. For quasi-static loading, the test cannot return to a reference position for each image, as the loading rate must be constant and high enough to avoid potential viscoelastic effects in the matrix and crack formation. The high loading rate severely limits the possible timeframe for capturing a crack state, as cracks will be continuously developing. The postprocessing of image data (i.e.,

  doi:10.5075/epfl-298799_978-2-9701614-0-0

quantifying the crack density) is preferred to be automated [11], as manually counting cracks: (1) can be a labour-intensive process even for small data sets, (2) introduces test-extrinsic measurement variation dependent on human error, and (3) makes it difficult to ensure/prove that cracks are counted exactly the same across data sets.

This paper aims to determine whether the transverse preform transition is prone to accelerated failure and to develop an automated method for quantifying matrix cracks in GFRP laminates subject to static loads.

2. Method

2.1 Test specimens

Specimens are made to mimic transverse preform transitions from a WTB. Three sets of specimens are made (see Figure 2): (1) containing a nominal preform transition geometry, with a total transition length of 210 mm, (2) containing an aggressive preform transition geometry with halved ply termination distances and a total transition length of 105 mm, and (3) control specimens containing no ply discontinuities. All specimens are made from the same material system with 45% UD and 55% BX with polymeric binder coating and polyester matrix. All the layups are made with backing material facing down. All preforms are consolidated by activating the binder material before the laminate is infused with polyester. Cured specimens are cut by a diamond blade saw, and the cut edges are sanded to remove all surface cracks and then polished to 500 ANSI grit size, such that specimens are 400±3.0 mm long and 50±0.2 mm wide. Width and thickness are then measured at 10 equally spaced positions along the length of the laminate. 3 specimens are tested for types (1) and (2), and 10 specimens are tested for type (3).

2.2 Experimental setup and procedure

A hydraulic 100 kN load frame with hydraulic grips is used to apply static load to the laminate specimens. The test is performed at a constant load rate of 1 kN/s up to 23 kN, whereafter the specimen is unloaded – delaminations start to occur at higher loads, which is out of scope for this study. Cameras are placed facing the smooth side of the specimen (i.e., the side of the laminate facing the mould surface during infusion) at a distance of 3 meters. Camera settings are given in Table 1. Two cameras are used to capture as much of the specimen as possible. Images are acquired such that the first image from both cameras is of the unloaded specimen, and the last image is at the max load. Two constant light sources are placed behind the specimen such that only the light that passes through the specimen reaches the camera sensor.

Table 1: Camera settings. Settings are identical for both cameras.

Camera	Flir Blackfly 2/3" CCD (BFLY-PGE-50H5M-C)
Resolution	2448 x 2048
Image scale	0.087 mm/pixel
Exposure time	17 ms
Frame rate	5 Hz
Lens	Edmund Optics 75mm DG Series Lens

  doi:10.5075/epfl-298799_978-2-9701614-0-0

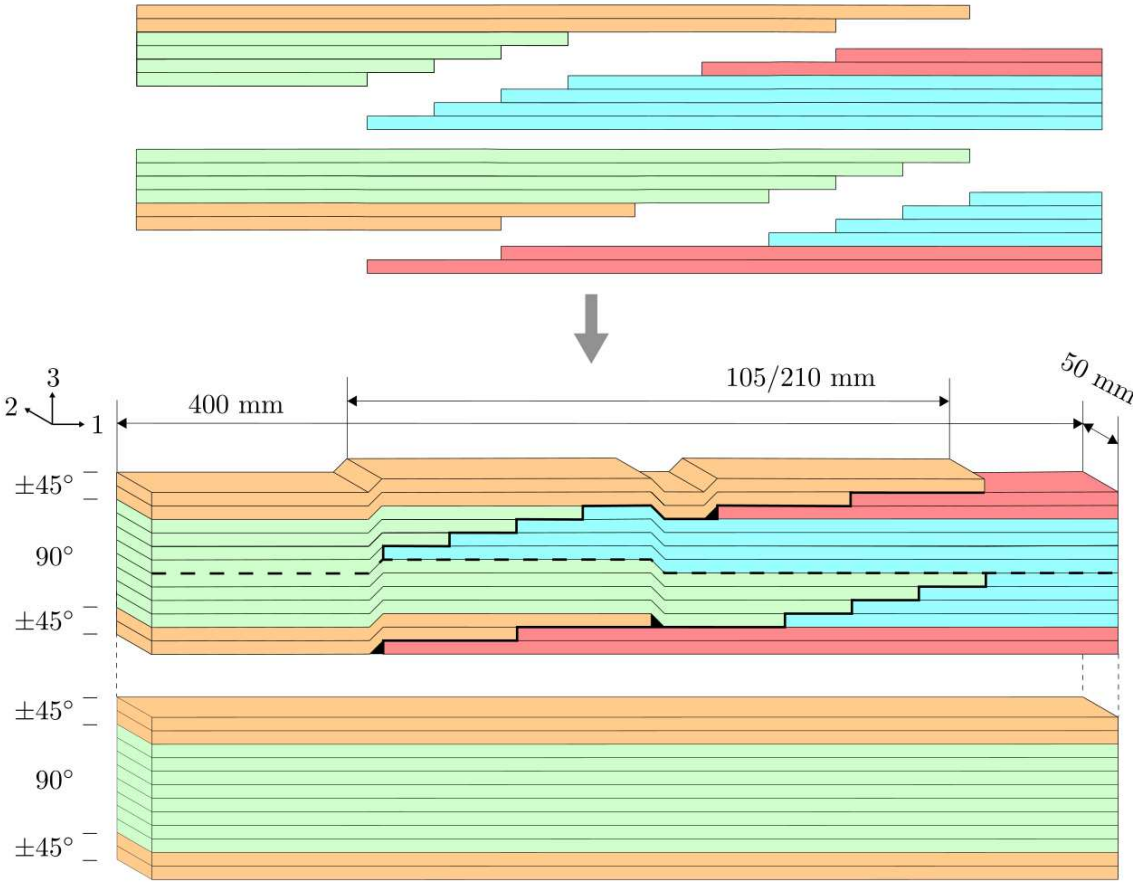

Figure 2. Top: four individual preforms are made stacked in the order shown. Middle: the transverse preform transition. The bold black line indicates the transverse transition between preforms, and the dashed line is the midline between preforms. Bottom: a control specimen consists of a single preform.

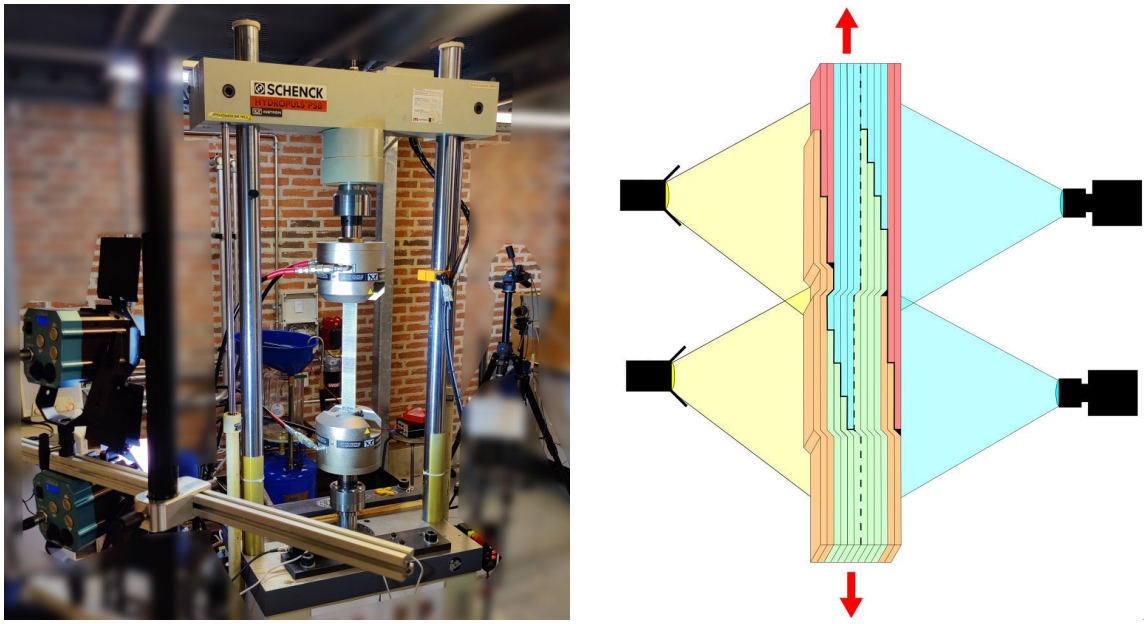

Figure 3. Left: real test setup. Right: schematic representation of test setup.

2.3 Automated image processing

A MATLAB program is developed to compute the crack density automatically. The program execution is split into four main functions: (1) compensation for specimen movement and strain, (2) image difference, (3) crack detection, and (4) crack density calculation.

Images are first rotated such that the expected orientation of cracks is horizontal. A region of interest (ROI) R_{ref} is then selected on reference image I_{ref}. The image data inside R_{ref} is used to perform histogram matching on the target image I_n, such that I_{ref} and I_n have equal brightness histograms. This is necessary to compensate for an observed darkening effect (or reduced transillumination) of the laminate that increases with strain. To compensate for displacement and strain in I_n, the function `estimateGeometricTransform2D` [12] is used to detect features in R_{ref} and match them to features on I_n, illustrated in Figure 4. By enforcing an affine transformation mapping of I_n onto R_{ref}, the transformation applies only constant strain and displacement compensation everywhere on I_n. This operation rescales all images to have no strain or displacement relative to I_{ref} and crops images to be consistent with R_{ref}.

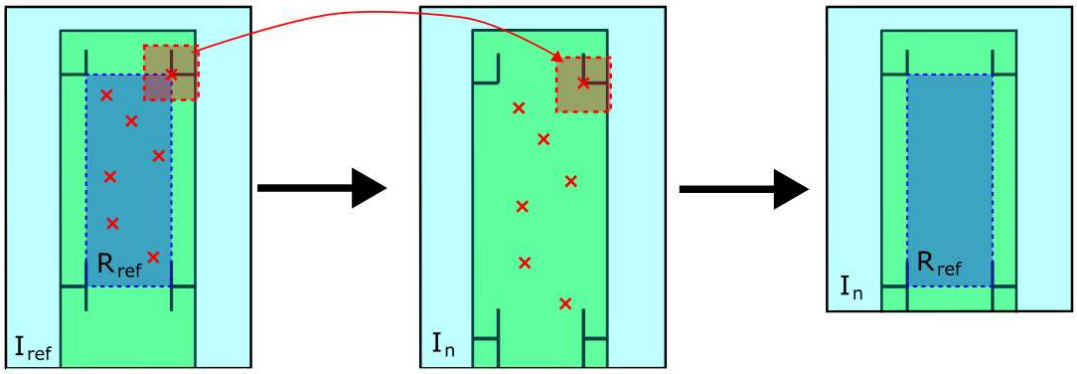

Figure 4. The affine transformation of I_n onto I_{ref}, used to compensate for strain and displacement. The red crosses represent locations that are matched between the reference and target image.

The image pixel difference $\Delta I_n = I_{n-1} - I_n$ is computed to find changes between sequential images and morphological "open" and "close" filters are applied to ΔI_n to remove noise. A rectangular filter kernel is used, with height and width corresponding to the expected width of a crack shadow and minimum crack extension, respectively. As the filter settings are related to physical dimensions, the settings can be determined a priori, meaning heuristic tuning of the filter is avoided. The morphological filter operations will remove features smaller than either dimension of the filter kernel, such that the filtered difference image ΔI_n^* only contains new crack growth and no noise (assuming that noise does not generate features of similar to or greater than the size of a crack). An example is shown in Figure 5.

Using the sequential image difference deviates from what has been done for fatigue tests, where all images are compared to a single reference [7,9]. The reason for introducing the sequential difference is to counteract noise caused by stitching threads in the laminate. The stitching threads are opaque and thus create shadows that appear as lines parallel with actual matrix cracks. If strain is constant everywhere in the laminate, the position of the stitching will be proportional to the normal strain. However, due to the locally varying strain caused by laminate

  doi:10.5075/epfl-298799_978-2-9701614-0-0

variations and cracks, the position is not predictable and cannot be compensated for. Comparing the I_{ref} to an image with new cracks (where the strain is significantly larger) means that the stitching thread will move and thus appear in ΔI_n as a line indistinguishable from a crack, and is thus not removed from ΔI_n^* either. This noise is avoided by only making comparisons between images with smaller differences in strain and crack development. A consequence of this approach is that only crack increments can be observed directly and the absolute damage state must be calculated instead.

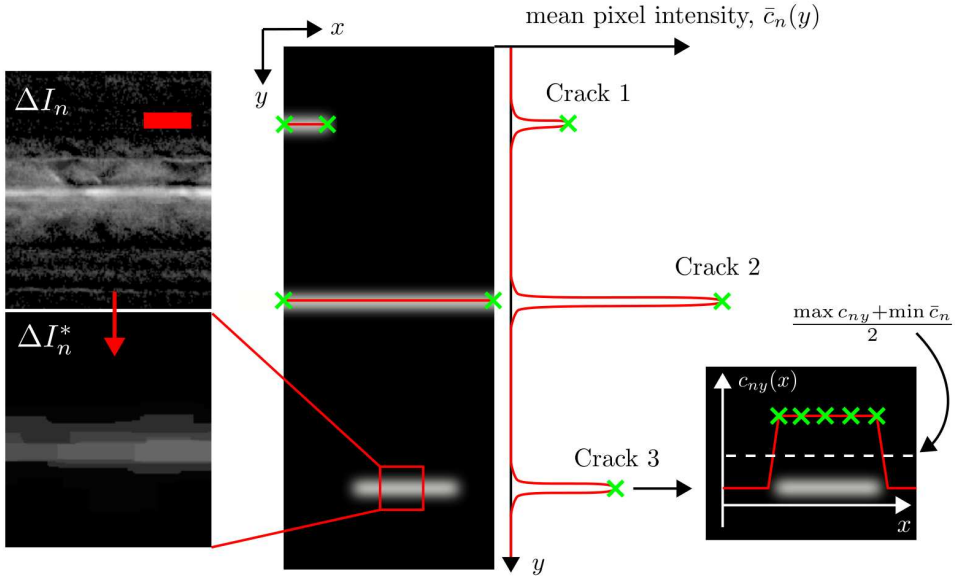

Figure 5. Using a rectangular filter kernel (shown as the red rectangle), noise is removed from difference image ΔI_n (shown as a zoomed view). Cracks are detected by evaluation of the pixel intensity value $c_n(x, y)$.

Detection of cracks is done in two steps (illustrated on Figure 5), working first along the vertical axis to detect cracks and next along the horizontal axis to determine position of crack tips. First the mean pixel intensity is found along the vertical axis, as a signal $\bar{c}_n(y)$:

$$\bar{c}_n(y) = \frac{1}{N_x} \sum_{x=1}^{N_x} c_n(x, y) \tag{1}$$

Where $c_n(x, y)$ is the pixel brightness values of ΔI_n at coordinate (x, y) on and N_x is the width of R_{ref} in pixels. $\bar{c}_n(y)$ is smoothed by a moving average half as wide as the filter kernel height and the signal peaks are found. The corresponding y-coordinates are saved. Using the y-coordinates, the signal $c_{ny}(x)$ is extracted, and every x that satisfies

$$c_{ny}(x) \geq \frac{\max c_{ny}+\min \bar{c}_n}{2} \tag{2}$$

is saved. These are the x-coordinates of the new crack growth, along with y calculated from Eq. (1). With the (x,y) pixel positions of crack growth, the absolute damage state at a given point in time is calculated by populating a blank image with all computed crack growth up to that point and discarding all pixels that occur more than once. This is then used to calculate the crack density ρ_n on I_n as the sum of crack lengths over the area of the ROI:

$$\rho_n = \frac{\Sigma L_n}{A} = \frac{P_n}{N_x N_y} \frac{1}{p} \tag{3}$$

Where ΣL_n is the sum of crack lengths, A is the area of R_{ref}, P_n is the number of pixels with a crack detected in Eq. (2), N_y is the height of R_{ref} of pixels, and p is the image scale as given in Table 1.

3. Results

Computed crack densities are shown in Figure 6. In experiments, the only fracture/failure observed was matrix cracks in the UD plies. Two observations are made on the local crack density: (O1) the control specimens have an evenly distributed crack density, showing no particular concentration of crack density (as would be expected from a continuous laminate), and (O2) the specimens with preform transitions have a lower crack density in the preform transition zone in the specimen. Another three observations are made on crack density development as stress is increased: (O3) there is little difference in crack density between preform specimens, (O4) the control specimens have a higher crack density for a given stress, and (O5) the first failure stress is equal or lower for control specimens, where cracks start developing at ~45 MPa compared to ~50 MPa for preform specimens.

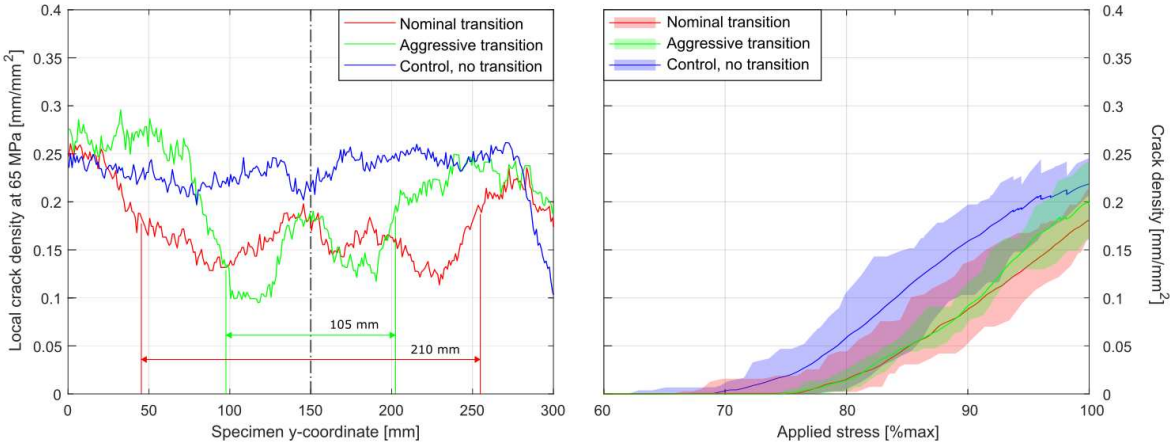

Figure 6. Left: local crack density at 65 MPa applied load, calculated as the crack density in an 50 mm x 50 mm area and averaged across specimens. The lengths shown correspond to the preform transitions sizes. Right: full specimen crack density. The solid line indicates mean values for the series, and the coloured area represents the range (min and max) of crack densities observed.

From the observations it is concluded that preform transitions do not cause a premature failure, as the crack density of the control specimens is higher both locally on the specimen and in an average sense. Given that the specimens (as presented in Figure 2) effectively have an additional BX in the preform transition itself, and cracks are only observed in UD plies, it is concluded that this difference in layup is more important than the internal ply discontinuities. Additionally, the aggressive preform transition does not seem to perform worse than the nominal preform transition, which suggests that the preform geometry has some robustness toward inaccurate placement. Along with the conclusion that the BX plies are governing the level of crack density, it is concluded that the current designs of preform transitions are safe to use, provided the transverse preform transition includes BX overlaps.

  doi:10.5075/epfl-298799_978-2-9701614-0-0

4. Conclusion

It is found that the transverse preform transition is not prone to accelerated failure under static tension, as only transverse matrix cracks are observed in experiment and the crack density is lower in specimens containing preform transitions as compared to a control laminate with no transitions. These findings are made possible by a novel automated method for quantifying matrix cracks in GFRP laminates, also presented in this paper. The novel developments concern compensating for large displacements and strains, noise caused by internal stitching threads, and images taken at a single exposure level. The method can accurately track in situ development of transverse matrix cracks, even when large amounts of noise are present.

5. Acknowledgements

The project is supported by EUDP (grant 64019-0514). The support is gratefully acknowledged.

6. References

1. Ohlendorf JH, Richrath M, Franke J, Brink M, Thoben KD. Towards automation of wind energy rotor blade production: a review of challenges and application examples. Advanced Manufacturing: Polymer & Composites Science 2020; 6(4):173-190
2. Zangenberg J, Brøndsted P, Koefoed M. Design of a fibrous composite preform for wind turbine rotor blades. Materials and Design 2014; 56:635-641
3. Schmidt S, Mahrholz T, Kühn A, Wierach P. Powder binders used for the manufacturing of wind turbine rotor blades. Part 2. Investigation of binder effects on the mechanical performance of glass fiber reinforced polymers. Journal of Composite Materials 2019; 53(16):2261-2270
4. Suiker ASJ, Fleck NA. Modelling of fatigue crack tunneling and delamination in layered composites. Composites Part A 2006; 37:1722-1733
5. DNVGL-ST-0376 Standard. Rotor blades for wind turbines. DNV GL AS 2015
6. Battams G. The use of optical techniques to assess the damage tolerance of composite materials. University of Southampton 2014; PhD Thesis
7. Glud JA, Dulieu-Barton JM, Thomsen OT, Overgaard LCT. Automated counting of off-axis tunnelling cracks using digital image processing. Composites Science and Technology 2016; 125:80-89
8. Bak BLV; Lindgaard E. A method for automated digital image-based tracking of delamination fronts in translucent glass fibre-laminated composite materials. Strain, 2020, 56.4: e12345
9. Bender JJ, Glud JA, Lindgaard E. Optical high dynamic range acquisition of crack density evolution in cyclic loaded GFRP cross-ply laminates affected by stitching. Composites Part A 2018; 112:207-215
10. Bender JJ, Bak BLV, Jensen SM, Lindgaard E. Effect of variable amplitude block loading on intralaminar crack initiation and propagation in multidirectional GFRP laminate. Composites Part B: Engineering, 2021, 217: 108905.
11. Brunner AJ. Fracture mechanics testing of fiber-reinforced polymer composites: The effects of the “human factor” on repeatability and reproducibility of test data. Engineering Fracture Mechanics 2022; 264:108340
12. MATLAB - Image Processing Toolbox user guide, MathWorks, 2022

  doi:10.5075/epfl-298799_978-2-9701614-0-0

OPEN HOLE TENSION AND DOUBLE LAP JOINT TESTS FOR INLAY KNIT NATURAL FIBER COMPOSITES

Ryuya Furukawa[a],Satoshi Bando[a], Satoshi Tamaki[b], Junji Noda[a]

a: Kindai University-2233730013j@waka.kindai.ac.jp
b: Shima Seiki MFG.,LTD.

Abstract: *Natural fiber reinforced composites with excellent environmental friendliness are significant expectations. General structure consists of multi-materials were assembled by mechanically fastener with circular holes. However when a mechanical fastener was applied in the composite material, it was reported that the strength will be significantly reduced due to stress concentration and fiber discontinuity. Therefore, an inlay-type flax knit base material was used by inserting inlay into a knit with excellent shape followability using buttonhole knitting technology. In addition, open hole specimens with discontinuous fiber and continuous fiber using this knitted fabric were molded by VaRTM and evaluated for OHT and bearing pressure strength.*

Keywords: knit fablic ; Natural fiber composite ; bearing ;

1. Introduction

Joint technology is very important from the viewpoint of multi-material products using fiber reinforced composites. Mechanical joints using bolts and rivets have the advantage of high joint strength and ease of disassembly and inspection. It was well-known that the mechanical properties such as tensile strength of open-holed composite considerably decrease due to the occurrence of stress concentration near hole. The discontinuous fibers near hole also cause a decrease in mechanical property. In recent years, the natural fiber composites made from natural resources have been expected due to their environmental friendliness and specific stiffness and strength. Since the natural fiber has a high failure strain, the woven and knit structure using natural fibers have been used in the clothing industry from a long time ago. Inlay knit is one of knit structures, that is weft yarns are inserted into the knit to reduce knit elasticity. Therefore, we focused on the drape capability of inlay knit structure to use as reinforcements of composites. Using this knit structure, the fibers detoured the open hole are retained as a continuous fiber alike a button hole with clothes. Then the Discontinuous fiber open Hole specimen(DH) and the Continuous fiber open Hole specimen(CH) as shown in Fig. 1. A compressive force is generated at the joint in the load direction and a tensile force is generated in the opposite direction. Therefore, it is necessary to evaluate not only the bearing strength by the bearing test but also the tensile strength by the open hole tensile (OHT) test. The purpose of this study is to evaluate the OHT strength and the bearing strength of the mechanical joint of natural fiber composite based on inlay knit.

  doi:10.5075/epfl-298799_978-2-9701614-0-0

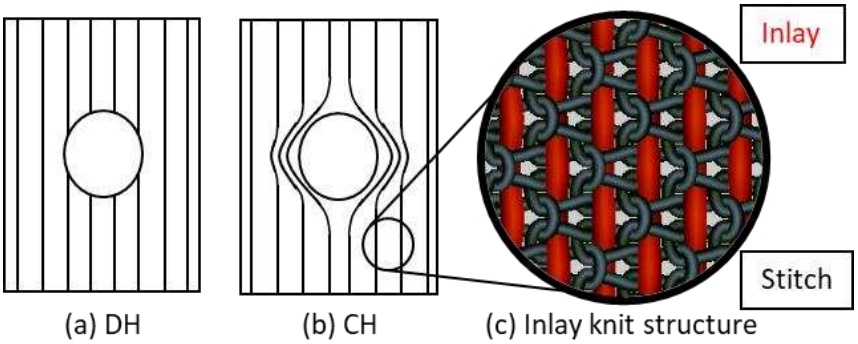

Figure 1. Schematics of circular hole specimens

2. Materials and experimental methods

In this study, a unidirectional flax inlay yarns of 2.6 knitted by flax knit yarn of 7.2 was used. These number were the number of yarns. Loop length was 10.53mm. A two-layered laminate was formed by Vacuum assisted resin transfer molding (VaRTM). Epoxy resin (EPOLAM5015 Resin and Hardener, AXSON) was used as the matrix. The mixing ratio of resin and hardener is 10:3. After curing at room temperature for 48 hours or more, the specimen was cut out with a length of 100 mm, a width of 24 mm (W), and a thickness of 2 mm. At this time, the inlay was placed in the load direction. After that, in order to prevent stress concentration at the grip of the specimen, a tab with a length of 15 mm, a width of 24 mm, and a thickness of 1 mm was created and pasted on an aluminum plate. A circular hole was made using a drill after molding for the DH specimen, and a brass rod was inserted to make a circular hole before molding for the CH test piece. Fig. 2 shows the circular holes in CH and DH of the knit used before and after molding. Since natural fibers have a large fiber shape change, the circular holes are continuously present in a single knit in order to bring the conditions of the CH and DH specimens closer together. After forming, the inlay in CH was curved along the circular hole, and DH was cut at the circular hole. Circular hole diameters of DH and CH specimen were 4, 6, 8 mm, and the number of test was 3. For the OHT test, a circular hole was provided at the edge distance of 50 mm. The bearing test was performed with a ratio E/D of 5 in which edge distance E and pin diameter D with reference to the JIS K7080 B method. The bearing jig shown in Fig. 3 was used for the joint, and stainless steel rods were attached with bearing jig to perform a bearing test. The testing machine used was a precision universal testing machine (Autograph AG-X SHIMADZU CORPORATION).

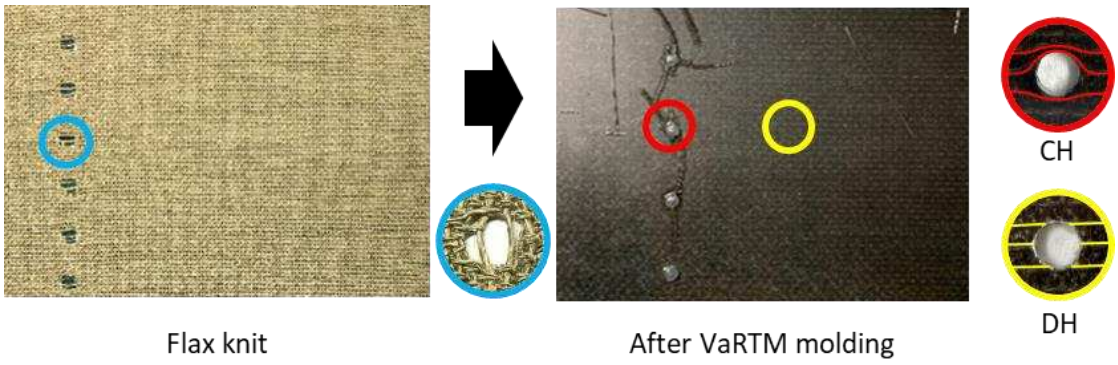

Figure 2. State of the circular hole

  doi:10.5075/epfl-298799_978-2-9701614-0-0

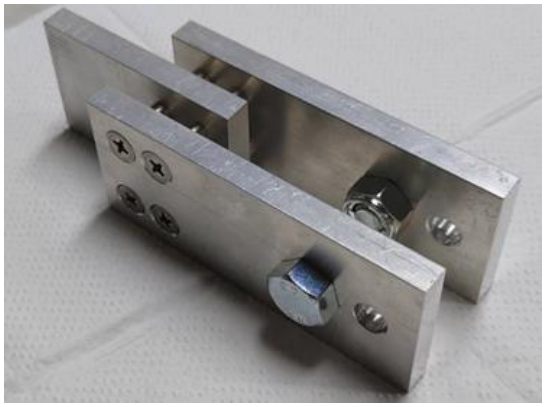

Figure 3. Bearing jig

3. Experimental results and discussion

3.1 OHT strength

The relationship between OHT strength and circular hole diameter ratio was shown in Fig. 4. As a conventional method, both Russo [1] and Pipes [2] conducted open hole tensile tests on CFRP laminates made of discontinuous fibers. Additionally, the results of OHT tests for CFRP laminates from previous studies by us were also shown in this figure. The normalized strength was defined by divided from that strength of non-hole composite, was approximately the same in all cases. Compared to conventional methods, the normalized strength of current knit laminates was significantly increased for continuous fibers compared to discontinuous fibers. The normalized strength of CH was approximately 1.0, which was comparable to that of the no-hole natural fiber composite. Therefore, in the case of 4 mm circular holes, the effect of strength reduction due to stress concentration is considered to be almost negligible.

  doi:10.5075/epfl-298799_978-2-9701614-0-0

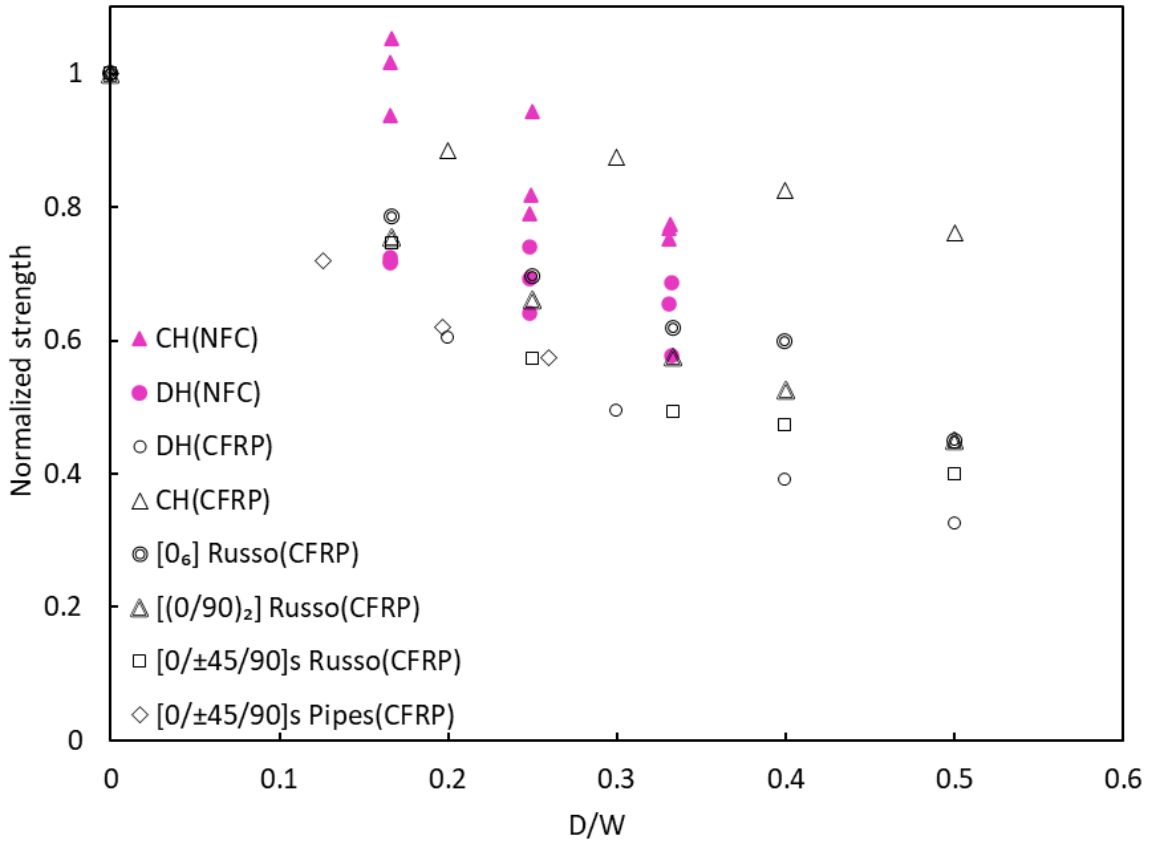

Figure 4. Relation between OHT strength and circular hole diameter ratio

3.2 Bearing strength

The relationship between bearing strength and the circular hole diameter ratio was shown in Fig. 5. The bearing strength σ_b was calculated using Eq. (1). Where *P* is the maximum load, *d* is the diameter of the circular hole, and *t* is the lamination thickness.

$$\sigma_b = \frac{P}{dt} \tag{1}$$

No difference in bearing strength was observed between DH and CH. When the diameter of the circular hole was 6 mm(D/W=0.25), the bearing strength of DH and CH was reversed, but no significant difference was observed between DH and CH for each diameter of the circular hole. There was a decrease in strength in proportion to the diameter of the circular hole. Therefore, the bearing test by inserting the pin depends on the strength of the knit around the circle, not the strength of the inlay, so the effect of the hole is considered to be small.

  doi:10.5075/epfl-298799_978-2-9701614-0-0

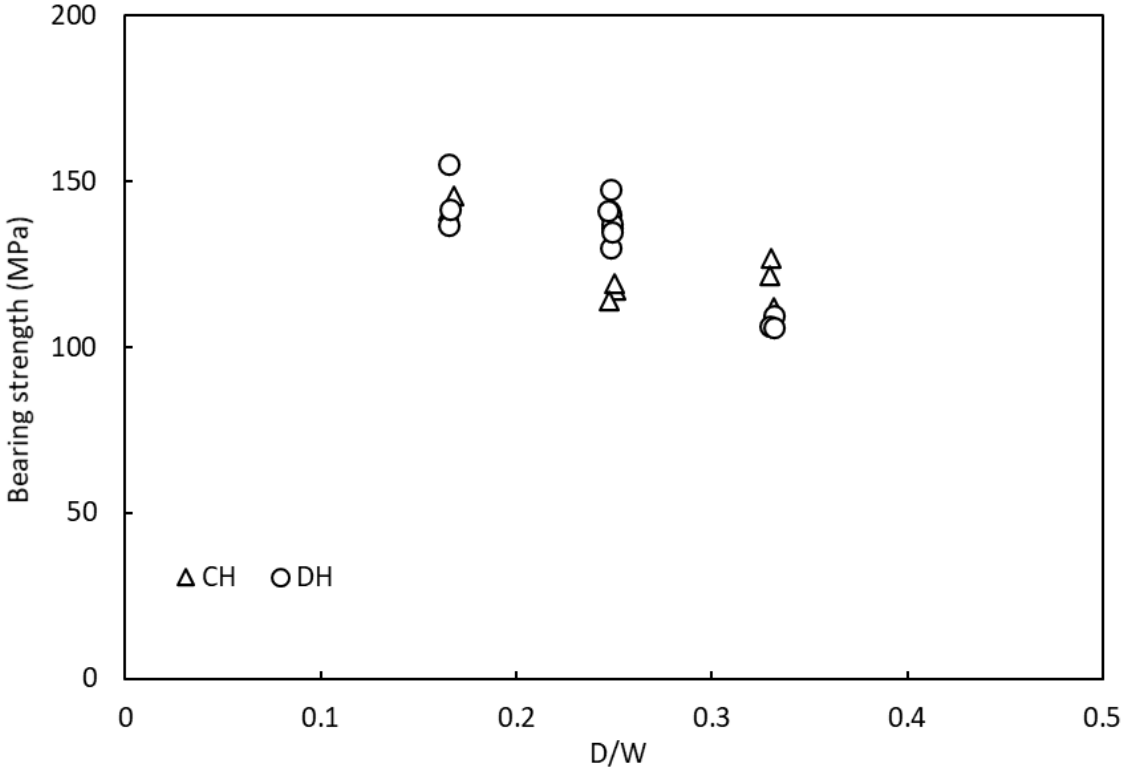

Figure 5. Relation between Bearing strength and circular hole diameter ratio

The results of the bearing test showed that under the condition of E/D=5, the bearing stress decreases as the circular hole diameter increases. However, the use of inlay knit as a reinforcement material exhibits different behavior from that of Unidirectional (UD) material due to the restraint of the inlay by the knit. Therefore, we created a NFC UD material with the same thickness as the knit NFC material and conducted a bearing test. Results were shown in Fig. 6.

  doi:10.5075/epfl-298799_978-2-9701614-0-0

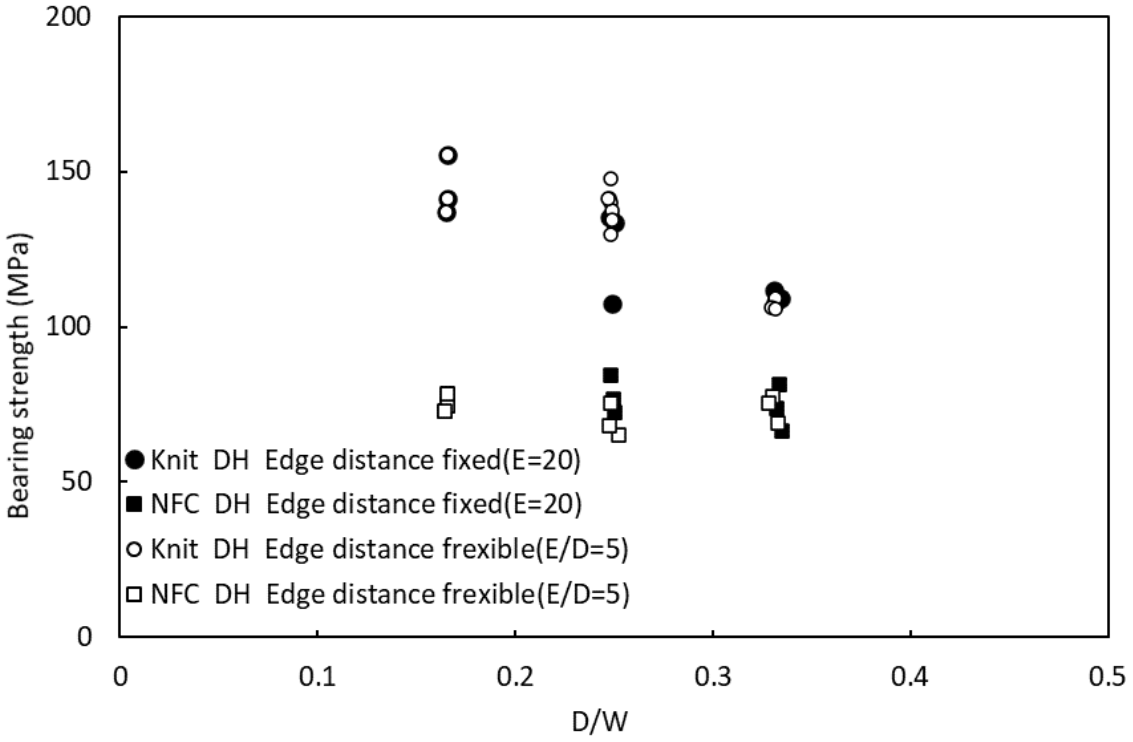

Figure 6. Relation between Bearing strength and circular hole diameter ratio (UD)

As a result, the bearing strength of the knit NFC was higher than that of the NFC UD even when the diameter of the circular hole was increased. This is because only the matrix is responsible for the load transfer between the fibers in the NFC UD. On the other hand, in the knit NFC, it was considered that not only the matrix but also the knit was responsible for the load transfer. In addition, a comparison was made between E/D=5 and the case in which the edge distance was fixed at 20mm. However, the results did not differ. This is because stress is concentrated in near the circular hole in the bearing test.

3.3 Fracture behavior in OHT and bearing test

Fig. 7 shows the fracture of the specimen during the OHT test. In the DH specimen, the fracture was observed from the edge of the hole to the width of the specimen for all hole diameters due to the stress concentration caused by the hole and the cut fiber. In the case of CH, the fracture was observed at a distance from the circular hole at a diameter of 4 mm. Fig. 8 shows the fracture of the specimen during the bearing test. For diameters of 4 and 6 mm, bearing failure occurred in the direction load. For diameters of 8 mm, the force was transmitted vertically to the direction of load, resulting in tensile failure. As shown in Fig. 9 when a bearing load is applied to the circular hole, three types of failure occur: bearing failure, tensile failure, shear failure[4]. The bearing fracture shown in Fig. 9(a) is a form in which a constant load increase occurs, and the tensile fracture shown in Fig. 9(b) is a form in which a rapid load decrease occurs, and the shear fracture shown in Fig. 9(c) is a form in which fracture progresses while repeatedly increasing and decreasing the load. At this time, from the viewpoint of structural design, it is desirable that the bearing progressive failure to stable fracture with a gradual decrease in strength.

  doi:10.5075/epfl-298799_978-2-9701614-0-0

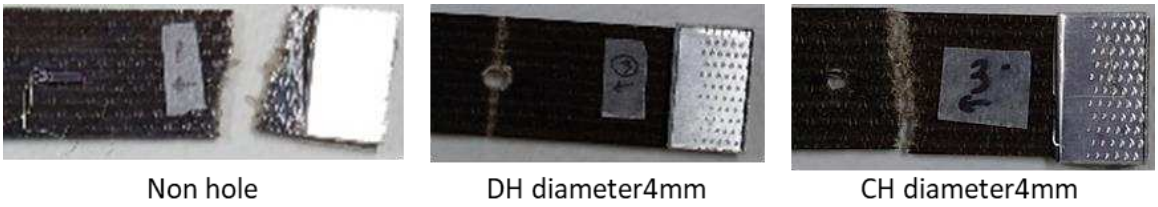

Figure 7. Fracture modes in OHT tests

Figure 8. Fracture modes in bearing tests

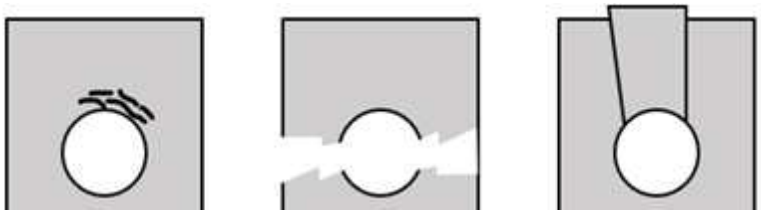

Figure 9. Types of failure modes

  doi:10.5075/epfl-298799_978-2-9701614-0-0

4. Conclusions

In the OHT test, CH showed higher strength due to fiber continuity than DH. On the other hand, in the bearing test, the knit bore the strength because the inlay was placed in the loading direction of the pin that penetrated the specimen, and the strength was not different between DH and CH. In the bearing test, stress concentration occurs around the pin, so it can be said that changing the edge distance does not affect the bearing strength. In addition, compared with NFC flax UD material, knit NFC material showed an improvement in bearing strength because knit also plays a role in load transfer. From these results, a perforated plate made of inlay type knit base material with continuous fibers. Can be said to be suitable as a mechanical joint member.

5. References

1. Russo A, etal., Mechanics of Comp. Materials. 2007; 43:359-376.
2. Pipes R B, etal., Tecnomic publishing company. 1997.
3. Koya Motoyama, Daisuke Hirakawa, Junji Noda, Koichi Goda. OHT strength of plain weave CFRP with uncut circular holes. The 4th Japan Composite Materials Joint Conference. 2013
4. Hiroshi Tsuda, Atsushi Takahashi, Jun Watanabe, Kiyoshi Kumochi. Bearing strength characteristics of plain weave C / C composite material. Proceedings of the Japan Society of Mechanical Engineers 1998;4 Vol. A, 64. No. 620.

  doi:10.5075/epfl-298799_978-2-9701614-0-0

DELAMINATION BEHAVIOR OF WELDING JOINT FOR CRUCIFORM NATURAL FIBER COMPOSITES

Junji Noda[a] and Taisei Yamanaka[a]

a: Kindai University – nodaj@waka.kindai.ac.jp

Abstract: *For the development of tsunami shelter consisted of natural fiber composite tapes, a novel dome structure was proposed and the compressive behavior was investigated experimentally and numerically. Then, it was found that delamination at the crossbeam intersection caused structural failure. Therefore, a cruciform coupon was prepared by crossing unidirectional tapes, then out-plane mode I delamination test and in-plane shear delamination test were newly proposed and performed using cruciform specimens. For out-plane mode I delamination test, the arm length was adjusted to contribute the mode I delamination propagation. For in-plane shear delamination test, the restraint plates near cruciform specimen were attached to apply a pure shear state along mode II and III directions. Additionally, delamination analysis using cohesive element was conducted to evaluate the delamination behavior of the joint at the crossbeam intersection.*

Keywords: Natural fiber composite; joint; delamination; cohesive element; dome

1. Introduction

In the event of a tsunami caused by an earthquake, it is effective to evacuate to the nearest high ground, but if there is no high ground, temporary evacuation facilities such as tsunami shelters are effective. The tsunami shelters are required to be unsinkable, high specific modulus, strength and impact resistant, and some of them are made of short fiber FRP. Then, it is often composed of curved surfaces such as spheres and ellipses to allow them to float in the turbulent waters where collapsed houses and cars are swept away. It is well known that FRP have the high relative modulus and strength, however FRP have trouble in molding a corner-less shape using long fibers. In order to form a three-dimensional spherical structure such as a tsunami shelter using a long fiber-reinforced composite material with high specific strength, it is necessary to development a crossbeam structure. On the other hand, although a lot of research has been done on the recycling of FRP in various fields [1,2], the separation of fiber and resin is still costly, and most of the waste is disposed of in landfills. Therefore, the practical application of natural fiber composite (NFCs) is attracting attention for sustainable societies. NFCs have some merits for the development of tsunami shelter. Firstly, the composites achieve a carbon neutral and low cost in resources for mass production. Secondly, the composites have a high crash-proof due to the high failure strain of natural fibers. However, due to the fact that NFCs is derived from biomass, its long-term durability has been an issue, and the general application of NFCs has not grown as much as expected. Since the tsunami shelters are to be used only in emergencies, the durability of the NFCs is not a problem if it can be used for a week or so. This is a practical example where the advantages of mass production and mass installation of shelters at low cost can be utilized. We proposed a hemispherical crossbeam structure using unidirectional NFC tape in order to develop a low-cost and high-strength tsunami shelter [3]. Proposed tsunami shelter concept was shown in Fig. 1.

  doi:10.5075/epfl-298799_978-2-9701614-0-0

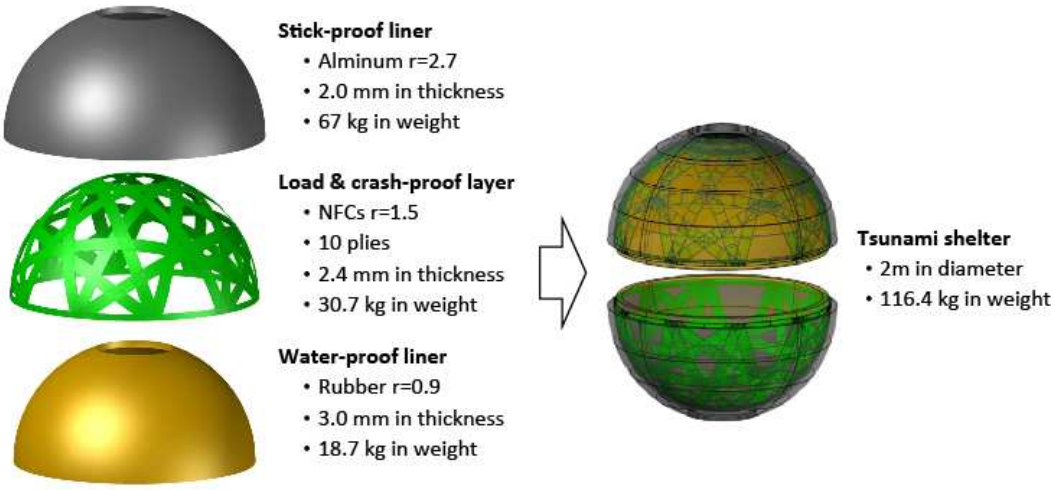

Figure 1. Proposed tsunami shelter concept

Off-axis compressive analysis and progressive compression tests were conducted on the hemispherical crossbeam structure. Representative off-axis compressive analysis results and laboratory-scale compression tests are shown in Fig. 2. It was found that the occurrence of delamination between crossbeams leads to the failure of the whole structure. C. Blondeau et al. [4] performed the DCB test, a Mode I interlaminar fracture toughness test method, on the interface of three different types of inversely symmetrical CFRP laminates to investigate the effect of orientation angle on resistance to crack growth. Although the fracture resistance of angle-ply interfaces is much stronger than that of unidirectional laminates, unstable crack growth was found to occur, as observed in their study. These findings could be applied to the phenomenon of delamination at crossbeam joints because the direction of loading and the direction of crack propagation are different.

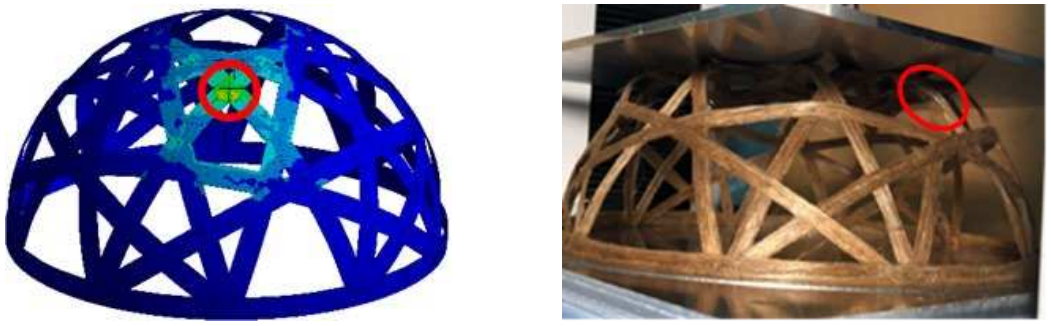

(a) Equivalent stress distribution (b) Progressive compressive test

Figure 2. FEM analysis and compression test

In this study, out-of-plane delamination tests and in-plane shear delamination tests were proposed and conducted using cruciform specimens formed by thermally bonding unidirectional NFC tapes, focusing on the intersection of the crossbeam structure. In addition, delamination analysis was performed using the cohesive zone model (CZM) at the bonded interface of the cross-shaped specimens. The validity of the proposed test methods were confirmed by comparing the analysis results. Finally, the interface characteristics were evaluated and the CZM parameters were identified to obtain data for the design criteria of the crossbeam joint, which is important for the structural reliability of the NFC dome for tsunami shelter development.

  doi:10.5075/epfl-298799_978-2-9701614-0-0

2. Out-of –plane delamination

2.1 Cruciform specimen and jig

From the off-axis compression analysis of the hemispherical crossbeam structure, it was considered that the occurrence of delamination between crossbeam affects the failure of the entire structure, and the joint strength at the intersection of crossbeam was focused on. In this section, the out-of-plane delamination test with Mode I (out-of-plane direction) crack propagation was conducted using a cruciform specimen as the basic shape and failure mode.

Firstly, cruciform specimens were prepared by crossing the unidirectional tapes. The cruciform specimens were preformed by cutting FLAXPREG T-UD PP tape (CAP SEINE FLAX UNIT, France), crossing it in a cross shape, covering it with a backing film, and heating it in an oven at 200°C for 20 minutes under vacuum as shown in Fig. 3. The size of the crossbeam was 200 mm in length and 10 mm in width. When forming the crossbeams, the bending modulus of the crossbeam was too low to be tested with a single layer, so three layers were formed by crossing each other. As a result, the thickness was 1.05 mm. Next, a novel out-of-plane delamination test jig was designed and fabricated from steel. The cruciform specimen and the jig were mounted on a small tabletop testing machine as shown in Fig. 4.

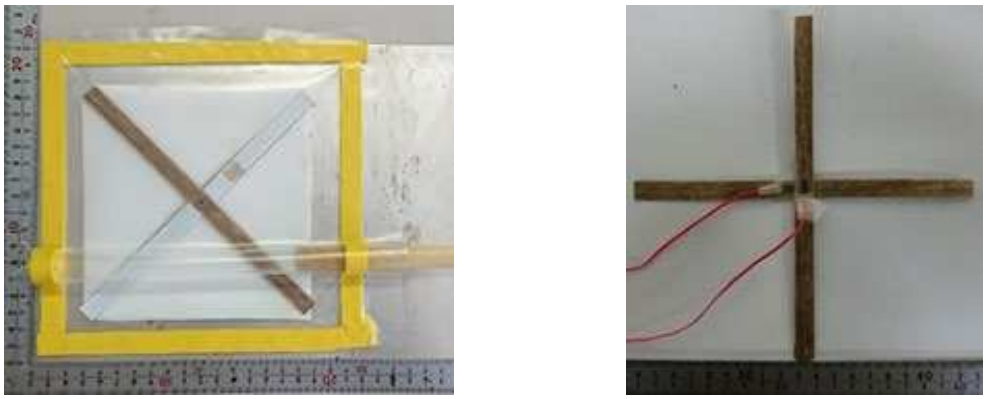

(a) Vacuumed preform state (b) Cruciform specimen

Figure 3. Cruciform specimen preparation

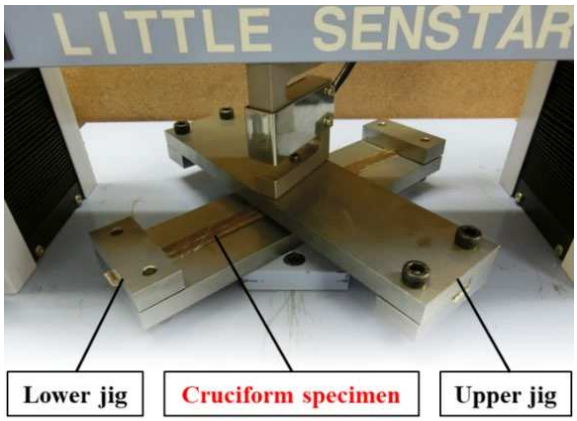

Figure 4. Out-of-plane delamination test setup

2.2 Out-of –plane delamination test results

As a result of out-of-plane delamination tests, delamination was observed at the intersection of the crossbeams. Fiber bridging was observed on the delaminated surface, and the cruciform specimens, which were welded together at a pressure of about vacuum pressure assistance, were bonded quite tightly. The relationship between the load and stroke of the out-of-plane delamination test is shown in Fig.5. Figure 5 also shows the deformation of the cruciform specimen observed from a 45-degree angle in the plane. From this figure, it was clear that the specimen exhibits the following three deformation and fracture phases. First, (a) the load increased in the bending mode in which the upper and lower pairs of three-point bending deformations were dominant. Next, (b) the load shifted to the four-crossbeam tensile mode after the stroke exceeded 8 mm. Finally, (c) delamination started and the final separation occurred. In this test, it was considered that the dominant fracture mode changed depending on the relationship between the crossbeam length of the cruciform specimen and the size of the thermally bonded interface.

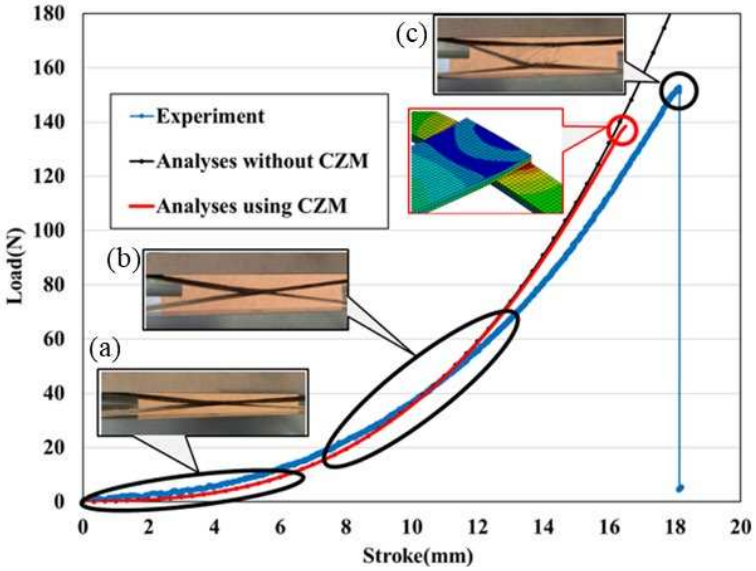

Figure 5. Load-stroke diagrams of Mode I delamination tests using cruciform specimens

2.3 Finite element analyses for out-of-plane delamination

A finite element model for out-of-plane delamination using CZM was conducted to investigate the interface delamination conditions at the joint of cruciform specimens. The finite element model was shown in Fig. 6. Workbench of ANSYS version 19.1 was used as the solver. An auto-mesh was performed using hexahedral 20-node solid elements, and the aspect ratio of the elements ranged from 1.04 to 1.07, with an average of 1.05. The boundary conditions were as follows. The symmetry of the shape of the cruciform specimen was used to fabricate a half model. The thickness was set to 1.05 mm assuming a three-ply laminate, and orthotropic anisotropy was introduced into the crossbeam. The material properties of the assumed flax fiber/PP composite tape are shown in Table 1. Based on the test results, the CZM parameters fitted in the analysis were Mode I traction force TI of 20 MPa and Mode I cohesive energy dissipation GIC of 1000 J/m^2. The number of nodes in the model was 20,736 and the number of elements was 12,800. In order to confirm the validity of CZM, the analysis was also conducted

  doi:10.5075/epfl-298799_978-2-9701614-0-0

with the same boundary conditions by constructing shared nodes without using the cohesive elements.

The load-stroke relationships for the analysis results with CZM and without CZM were appended in Fig. 5. By fitting the experimental results with CZM parameters, the delamination phenomenon could be simulated in the analysis. However, not only Mode I but also Mode II (in-plane shear direction) delamination occurred due to the long crossbeam arms and the dominance of the four crossbeam tensile modes. It was found that this phenomenon could be eliminated by shortening the length of the specimen arms between the restraints, however this was omitted here.

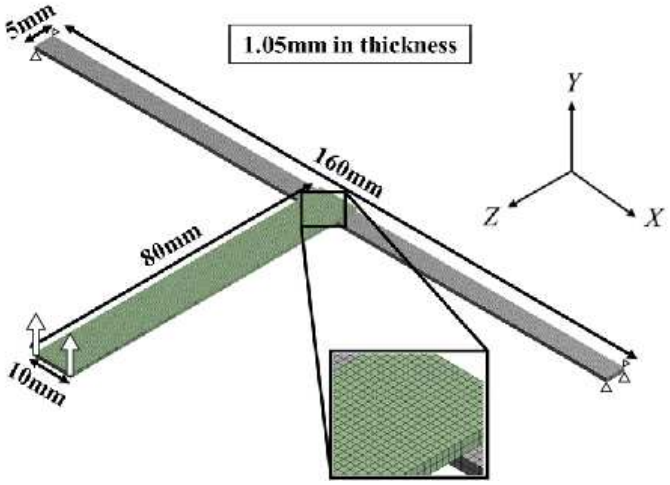

Figure 6. FE model and boundary conditions for out-of- plane delamination model

Table 1 Material properties of flax/PP for FEM analysis

Longitudinal elastic modulus E_{L} [GPa]	Transverse elastic modulus E_{T} [GPa]	Poison's ratio ν_{LT} [-]	Poison's ratio ν_{TT} [-]	Shear modulus G_{LT} [GPa]	Shear modulus G_{TT} [GPa]
20.0	1.79	0.0261	0.442	1.432	1.074

3. In-plane shear delamination

3.1 Cruciform specimen and jig for in-plane delamination test

Since not only Mode I but also Mode II delamination has a significant influence on the failure of crossbeam joints in GC domes, CZM parameters (tractions and cohesive energy dissipations) for Mode II delamination propagation must also be identified. To simulate Mode II crack-dominated delamination, a novel test jig was fabricated to prevent out-of-plane bending and torsion of the cruciform specimens. Fig. 7 shows the in-plane shear type delamination test jig with a restrained cruciform specimen mounted on a small table-top testing machine. The cruciform specimen has a crossbeam length of 200 mm, a width of 20 mm, and a thickness of 2.1 mm. Thin aluminum foil with a thickness of 11 μm was formed between the corners of the joint interface to introduce a pre-crack and stabilize crack propagation. In addition, a cruciform specimen with a circular hole of 10 mm in diameter was also introduced to examine the effect of friction at the center of the bonding interface, and delamination tests were conducted.

  doi:10.5075/epfl-298799_978-2-9701614-0-0

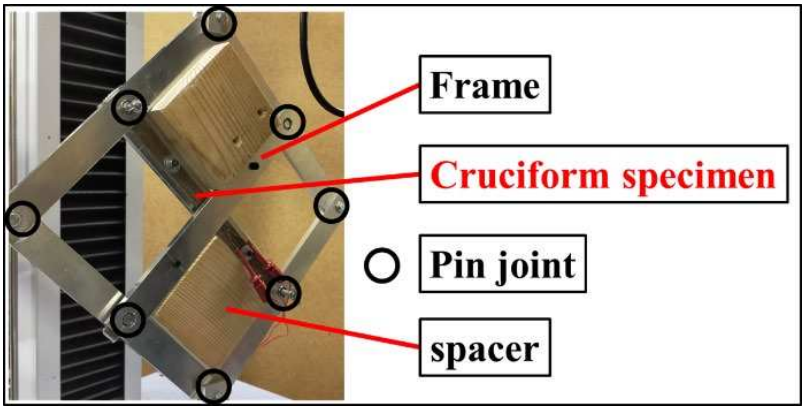

Figure 7. In-plane shear delamination test setup

3.2 Finite element analyses for in-plane delamination

A finite element model for in-plane delamination using CZM was conducted to investigate the interface delamination conditions at the joint of cruciform specimens. The finite element model was shown in Fig.8. These analyses were performed to validate the proposed test method and identify CZM parameters. Auto-mesh was performed using rigid and shell elements, and the aspect ratio of the elements ranged from 1.0~4.5, with an average of 1.1. The model had 4,441 nodes and 4,007 elements. The boundary conditions were set so that the pin joints were free to rotate, and the out-of-plane deformation was suppressed by constraining the out-of-plane direction of the cruciform specimen section. The CZM parameters fitted in the analysis were a Mode II traction force TII of 2 MPa and a Mode II cohesive energy dissipation GIIC of 200 J/m^2. The in-plane delamination analyses and experimental results with and without a 10 mm diameter circular hole were shown in Fig. 9, respectively. Comparison of the in-plane shear delamination test and the analysis showed good agreement in the initial deformation due to the in-plane shear delamination test being performed with reduced out-of-plane deformation. However, fiber bridging and friction at the delaminated interface caused the load gradient to increase even after delamination. It was found that the load increase due to interfacial friction after delamination was suppressed by opening a 10 mm-diameter circular hole in the center of the bonded interface.

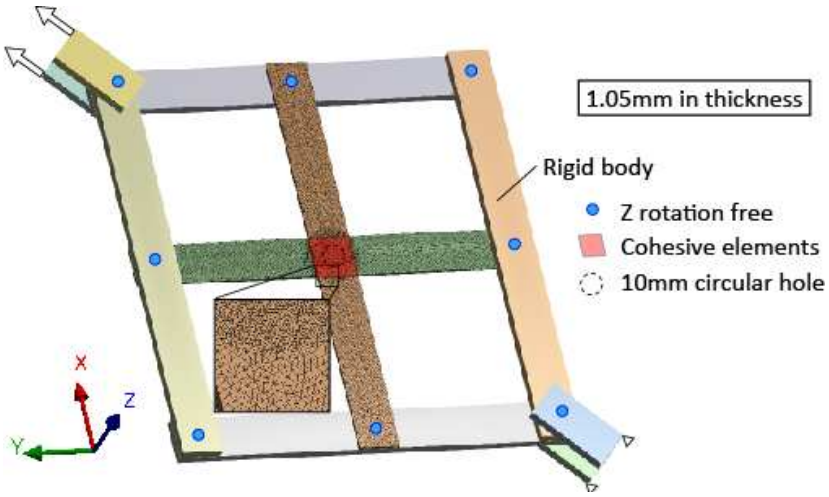

Figure 8. FE model and boundary conditions for in-plane delamination model

  doi:10.5075/epfl-298799_978-2-9701614-0-0

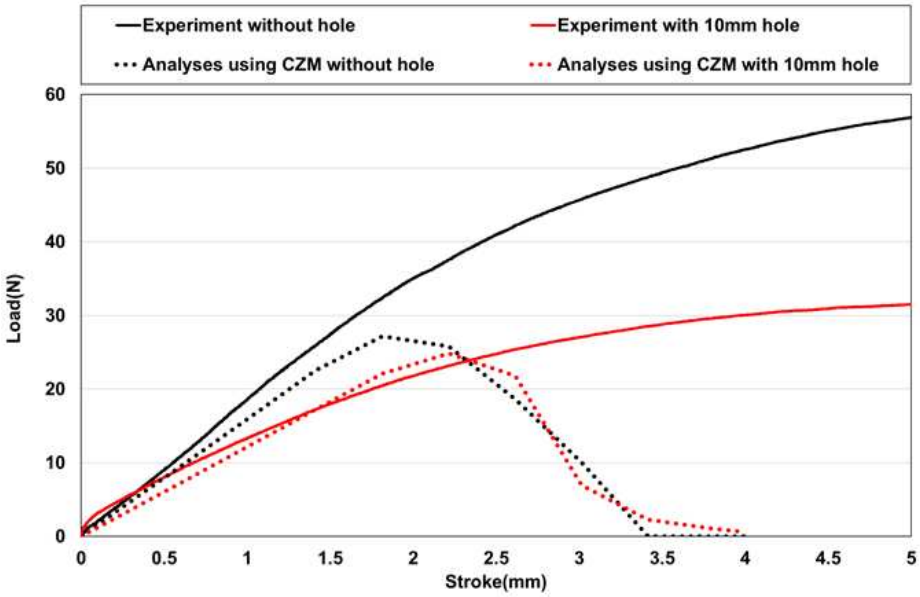

Figure 9. Load-stroke diagrams of in-plane delamination tests using cruciform specimens

4. Conclusions

In this study, out-of-plane delamination tests and in-plane shear delamination tests using cruciform specimens were conducted to experimentally verify the fracture behavior. The validity of the proposed delamination test method and analysis was examined by performing a delamination analysis using CZM and comparing it with the test results. As a result, the following were found.

1. Shortening the crossbeam length suppresses the Mode II crack stress ratio at the CZM interface edge and increases the Mode I crack stress ratio, making it possible to conduct Mode I crack-dominated out-of-plane delamination tests.

2. By comparing the out-of-plane delamination test results with the CZM analysis, the out-of-plane delamination behavior could be simulated by fitting the traction force and cohesive energy dissipation for Mode I.

3. In in-plane shear delamination tests, the introduction of a pre-crack at the edge of the welded-joint interface of a cruciform specimen was effective because it stabilizes crack propagation and reduces the initial slope variation.

4. Fiber bridging and friction continue to occur at the delaminated interface, causing the load gradient to increase even after delamination. This increase in load due to interfacial friction after delamination could be suppressed by opening a circular hole in the center of the bonding interface.

5. By constraining the out-of-plane deformation and simulating Mode II crack-dominated delamination in the initial loading phase, the CZM parameters, i.e., Mode II traction force and cohesive energy dissipation, could be identified.

Acknowledgements

This work was supported by JSPS KAKENHI Grant Number JP21K03760.

5. References

1. Hanaoka H, Ikematsu H, Takahashi S, Ito N, Ijuin N, Kawada H, Arao Y, Kubouchi M, Recovery of carbon fiber from prepreg using nitric acid and evaluation of recycled CFRP. Composites Part B 2022; 231:109560.
2. Rosa ADL, Greco S, Tosto C, Cicala G, LCA and LCC of a chemical recycling process of waste CF-thermoset composites for the production of novel CF-thermoplastic composites. Open loop and closed loop scenarios. Journal of Cleaner Production 2021; 304:127158.
3. Noda j, Yamanaka T, Miyamoto T, Development of tsunami shelter structure using green composites. 1st Russia-Japan Joint workshop on composite materials 2019; IS12
4. Blondeau C, Pappas G, Botsis J, Influence of ply-angle on fracture in antisymmetric interfaces of CFRP laminates. Composite Structures 2019; 216, 15:464-476.

  doi:10.5075/epfl-298799_978-2-9701614-0-0

INFLUENCE OF HIGH-RATE TESTING ON THE INTERLAMINAR FRACTURE BEHAVIOR OF METAL-COMPOSITE JOINTS

Georgios Kotsinis[a], George Sotiriadis[a], Theodoros Loutas[a]*

a*: Laboratory of Applied Mechanics and Vibrations, Department of Mechanical Engineering and Aeronautics, University of Patras, Patras University Campus, GR-26504, Rio-Patras, Greece – kotsinisgeorgios@gmail.com

a: Laboratory of Applied Mechanics and Vibrations, Department of Mechanical Engineering and Aeronautics, University of Patras, Patras University Campus, GR-26504, Rio-Patras, Greece

Abstract: *In this work the Mode I and Mode II fracture behavior of an asymmetric metal-composite joint under high opening displacement rate is studied. The testing on Mode I and Mode II loading was achieved via a Split Hopkinson Pressure Bar (SHPB) apparatus. For the mode I test the Wedge Insert Fracture method (WIF) was used on Double Cantilever Beam (DCB) specimens. Mode II tests on End Notched Flexure (ENF) specimens was carried out with the use of a cylindrical impactor on the edge of the incident bar. A novel hybrid analytical-experimental method based on digital image correlation (DIC) measurements as well as on the dynamic J-integral is proposed for the calculation of the fracture toughness. To validate the hybrid method, static experimental results are used, applied on a metal to composite joint while, finite element analysis (FEA) is used for verification.*

Keywords: Split Hopkinson Pressure Bar; Interlaminar Fracture; Strain Energy Release Rate; High-Rate Testing; Dissimilar Adhesive Joint

1. Introduction

The increasing use of metal-composite adhesive joints in engineering structures makes it necessary to have a good understanding of their damage tolerant behavior under different ranges of loading speeds. The fracture toughness of a joint is a usual metric used to evaluate that. Under static loads there are standardized procedures for the calculation of fracture toughness, but when high load rates are considered additional effects such as the propagation of stress waves, the specimen's vibration, and the increase of the kinetic energy are presented. Analytical models which consider the vibration of DCB [1] and ENF [2] specimens for similar and symmetric joints are proposed in the literature. For the case of more complex adhesive joints like metal-composite joints which contain additional effects such as the dissimilarity of the materials, the asymmetric geometry of the joint, and the thermal effects, the creation of a time dependent analytical model which considers all these effects is analytically rigorous. The digital image correlation (DIC) method is used in the literature to investigate the behavior of adhesive joints. In [3] DIC is used for the investigation of the kinematics of a single leg bending specimens, in [4] the DIC is used for the calculation of traction separation laws. Several works like [5], [6] use DIC for the calculation of fracture toughness based on the virtual crack closure technique (VCCT) and the J-integral respectively. In this work the interlaminar toughness of the adhesive joint, at the initiation of a crack, will be calculated based on the strain energy release rate (SERR) using the DIC combined with the analytical formulation. The calculation of the total SERR is based on the dynamic J-integral and the partitioning method applied to the VCCT.

  doi:10.5075/epfl-298799_978-2-9701614-0-0

2. Materials - Test Configuration

2.1 The metal-composite adhesive joint

In this study the adhesive joint consists of two adherents: one titanium sheet and a woven composite. During the characterization of the interfacial toughness of the joint under static loading, plastic deformation on the titanium is presented [7]. Thus, two aluminum backing beams are added. The final joint is presented in Figure 1(a) and the properties of each layer are given on Table 1. It must be mentioned that during the curing of the titanium and the composite, thermal stresses arise on the joint due to the high temperatures. More details about the manufacturing and the static tests of the joint can be found on [7].

Table 1: Material properties of the joint

Material	E_1, E_2 **(GPa)**	G_{12} **(GPa)**	ν_{12} **(-)**	σ_{yield} **(MPa)**	**CTE** α_i **(·10^{-6}/°C)**	**Thickness (mm)**	ΔT **(°C)**
Composite	66	4.5	0.035	-	3.0	1.4	-155
Titanium	105	45	0.34	368	9.0	0.8	-155
Aluminum	73	28	0.33	345	-	5.0	-

2.2 Quasi-static and dynamic fracture tests

For the fracture testing, DCB and ENF specimens are selected. Static fracture tests are performed on a 25 kN Instron 8872 universal testing machine at room temperature conditions (25°C, 50–60% RH). The displacement rates for the Mode I and II experiments are 1mm/s. High-rate tests on mode I and Mode II loading are performed on a Split Hopkinson Pressure Bar (SHPB) apparatus Figure 2(a). The SHPB consists of an incident and a transmitted bar with 2 m length each and a diameter of 25 mm. The transmitted bar is clamped with the use of steel clamps, so no axial movement of the transmitted bar is allowed. A gas gun is employed to accelerate the striker bar. For the Mode I testing the Wedge Insert Method (WIM) is used (Figure 2(b)). The specimen was clamped on the non-cracked side using a metal block. The wedge is placed on the incident bar and is made from stainless steel. During the tests no natural pre-crack was created. For the Mode II tests, the ENF specimen was placed perpendicular to the slender bars on a metal base (Figure 2(c)). On the edge of the incident bar a small cylinder was placed to act as the loading nose and transfer the excitation to the specimen. Due to the presence of the aluminum and titanium beams the energy used for the test must be carefully selected through trial and error to avoid plastic deformations. So, a specific range of energies were used to achieve crack propagation. Due to the very high speed of the crack propagation, strain gages are placed in front of the crack tip to capture the crack initiation through the change of the compressive strain on the top of the adherent. The length of the specimens and the crack tip are presented in Figure 1(b). Because the region of interest is close to the crack tip, the high-speed camera is focused on a region 20 mm close to the crack. Thus, to measure the input velocity of the wedge a CFRP component is bolted on the wedge to access wedges movement on the camera window.

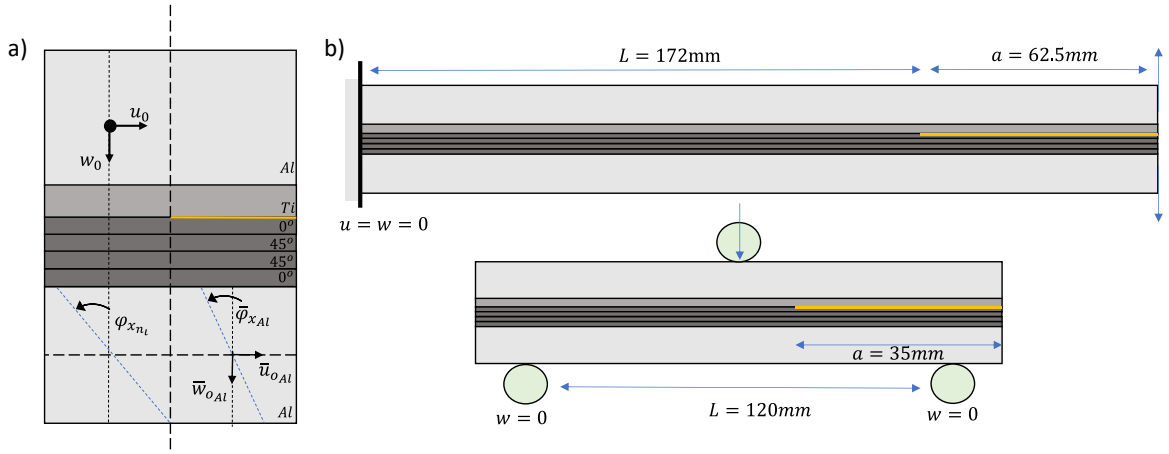

Figure 1: (a) The final adhesive joint with the kinematic assumptions of the analytical model (presenting fully only in the bottom aluminium part for brief), (b) The geometry and the boundary conditions of the DCB and ENF specimens

An optical method is utilized for the monitoring of the crack initiation using a high-speed camera. A Photron® Fastcam SA4 camera recording from 60.000 and 100.000 frames per second with 320x160 and 128x96 pixels resolution is used with two incandescent lamps. To measure the desirable displacements of the joint a DIC software (GOM Correlate©) is used based on a stochastic pattern (Figure 2(d)). The pattern is created using an airbrush to achieve the desirable average size of 3–7 pixels in the acquired image [8]. The frame rate of the camera is selected to capture the first three eigenfrequencies of the adhesive joint.

3. Analytical background

As mentioned previously, the extraction of an analytical data reduction scheme for such a complex joint considering vibrational effects is very complex. In this work the theoretical formulation from [9] will be used, adding though the vibration effects, based on the Lagrange multipliers method for the modelling of the interface bonding. The adhesive joint is considered as an elastic beam containing a through the width crack. Its adherent consists of several layers with arbitrary material properties and thicknesses. The Timoshenko beam theory [10] is used to describe the beam kinematics as:

$$u_i(x,z,t) = u_{o_i}(x,t) + z\varphi_{x_i}(x,t),\ w_i(x,z,t) = w_{o_i}(x,t) \tag{1}$$

where: $u_{o_i}, \varphi_{x_i}, w_{o_i}$, are the mid-plane displacements and rotations, respectively. More information about the analytical model is presented in [1] and [9]. The fracture toughness can be expressed as the energy flow around a contour Γ divided by the crack speed [11], referred also as generalized J-integral.

$$J = \frac{F(\Gamma)}{c} = \frac{\lim_{\Gamma\to 0}\int_{\Gamma}\left(\sigma_{kl}\hat{n}_l\frac{\partial u_k}{\partial t} + (U^d + T^d)c\hat{n}_1\right)ds}{c} \tag{2}$$

where: σ_{kl}, u_k, are the stress and displacement tensors, $\hat{n}$, is the normal unit vector and c, is the velocity of the crack. U^d, T^d are the strain and kinetic energy densities respectively.

  doi:10.5075/epfl-298799_978-2-9701614-0-0

The contour integral is path independent only in a vicinity close to crack tip. By considering a rectangular path around the crack tip the total fracture energy can be presented as a function of the beam's kinematics and their derivatives as:

$$J = \frac{1}{2}\sum_{i=1}^{n_l}\left(C_i\left\|\left(\frac{\partial w_i}{\partial x}\right)^2\right\| + A_i\left\|\left(\frac{\partial u_i}{\partial x}\right)^2\right\| + D_i\left\|\left(\frac{\partial \varphi_i}{\partial x}\right)^2\right\| + 2B_i\left\|\left(\frac{\partial u_i}{\partial x}\right)\left(\frac{\partial \varphi_i}{\partial x}\right)\right\| - N_{xi}^T\left\|\frac{\partial u_i}{\partial x}\right\| - M_{xi}^T\left\|\frac{\partial \varphi_i}{\partial x}\right\|\right) \quad (3)$$

where: A_i, B_i, C_i, D_i, are the extensional stiffness, bending-extension coupling stiffness, shear stiffness and bending stiffness of sub-laminate i, respectively. N_{xi}^T and M_{xi}^T are the thermal components of the axial force and bending moments resultants. The symbol $\|.\| = (.)^+ - (.)^-$ stands for the difference of a quantity before (-) and after (+) the crack tip. To find the individual components of the SERR a VCCT based method is used [9]. VCCT states that the energy required for the opening of the crack is the same as the energy required for closure. The SERR components can be expressed using the interfacial forces and relative displacement in front of the crack tip as [11]:

$$J_I = \frac{1}{2\delta\alpha}\lambda_y \Delta w,\ J_{II} = \frac{1}{2\delta\alpha}\lambda_x \Delta u \quad (4)$$

where: λ_y, λ_x are the Lagrange multipliers model the interracial stresses at the crack tip, $\Delta w, \Delta u$ are the relative displacements in front of the crack tip and $\delta\alpha$ is the crack extension. Thus, the individual components of the fracture toughness are expressed as:

$$J_I = \frac{1}{2}\sum_{i=1}^{n} C_i\left\|\left(\frac{\partial w_i}{\partial x}\right)^2\right\| \quad (5a)$$

$$J_{II} = \frac{1}{2}\sum_{i=1}^{n}\left(A_i\left\|\left(\frac{\partial u_i}{\partial x}\right)^2\right\| + D_i\left\|\left(\frac{\partial \varphi_i}{\partial x}\right)^2\right\| + 2B_i\left\|\left(\frac{\partial u_i}{\partial x}\right)\left(\frac{\partial \varphi_i}{\partial x}\right)\right\| - N_{xi}^T\left\|\frac{\partial u_i}{\partial x}\right\| - M_{xi}^T\left\|\frac{\partial \varphi_i}{\partial x}\right\|\right) \quad (5b)$$

Eq. (5) have the hypothesis of linear elastic fracture mechanics (LEFM). To make the use of Eq. (3), (5) applicable, the kinematics measured by the DIC must fulfil the assumptions of the Timoshenko beam theory and the continuity of the displacements and rotations at the crack tip. Timoshenko's beam theory assumes that the axial and transverse displacements are linear and constant through the beams section respectively. But a DIC analysis represents a 2D problem. Works in literature [3], [4] used the averaged value of the displacements through joint thickness. The problem is that as the measurement gets closer to the crack tip the transverse displacement field is starting to deviate importantly from a constant value. To investigate this, a case study for a simple joint under static loading is used (details from the adhesive joint under investigation can be found on [1] for a geometric ratio, initial crack/ bonded part length equals to 20) by using as the DIC results a 2D plane stress model (this selection is used to have a comparison using the numerical VCCT). The SERR was calculated based on Eq. (5a) thus, the derivative $\partial w_i/\partial x$ in front of the crack tip must be calculated (behind the crack tip it equals to zero due to the symmetry of the joint). To be in tune with the analytical model the derivative must be calculated at the node of the midplane of the adherent at $x = L$. But in 2D model due to the elastic deformation of the section the value at this node is not equal to zero as the analytical model describes. Thus, there is a mismatch in the assumptions made. To include all the assumptions of the beam theory, the analytical solution for the transverse displacement from [1] is used as a fitting equation of the mid-plane displacements of a path through the length of the cracked region in the model.

Then the term $\partial w_i/\partial x$ can be calculated from the derivative of the fitted equation at the crack tip. The analytical and the fitted equation respectively are:

$$w_{analytical} = 21.52 - 485.088\,x + 3483\,x^2 - 7740\,x^3 \quad (6a)$$

$$\mathrm{w_{fit}} = 19.74 - 447.772x + 3228.341\,x^2 - 7174.092\,x^3 \quad (6b)$$

It is noted that the total deflection is described very well by the Timoshenko theory but close to the crack tip the difference is non negligible with a deviation of 67% from the VCCT solution.

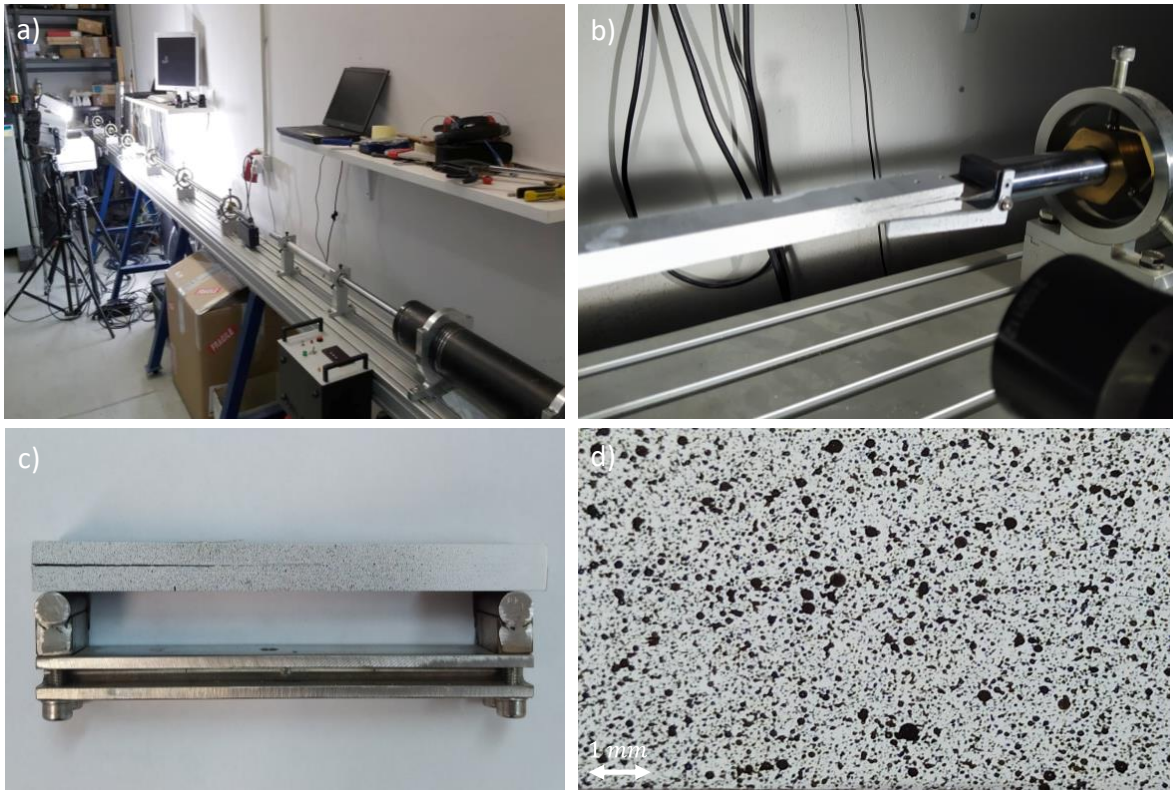

Figure 2: (a) The SHPB apparatus, (b), (c) the configuration of the dynamic DCB and ENF experiments respectivelly (d) The stochastic pattern used for the DIC analysis

Timoshenko beam theory cannot describe the kinematic field of transverse displacements precisely close to the crack tip but very well for the axial displacements. This occurs since the Timoshenko theory presents a linear distribution of the axial displacements through thickness. To use Eq. (5a) in the field of Timoshenko theory and considering that the shear stresses are minimum near the crack tip, the following assumption is made $\partial w_i^+/\partial x \cong \varphi^+$ at the crack tip. The use of the rotation $\varphi_{x_i}(x,t)$ also provides the advantage that is different for each layered material so the proposed method can be applied to a different number of layers with result better description of the axial displacements through the thickness. A similar assumption was also made in [5]. It must be mentioned that the averaged value of the displacements in the bonded part gives good results, so the assumption is only for the calculation at $x = L^+$

The rotation by the y-axis is calculated as [3]:

$$\varphi_{x_i}(x,t) = \frac{\left(\vec{u}_{o_i}\left(x,\frac{h_i}{2}\right)\vec{x} - \vec{u}_{o_i}\left(x,\frac{-h_i}{2}\right)\vec{x}\right)}{h_i} \quad (7)$$

The kinematics derivates will be calculated using finite differences. The distance Δx between the points is investigated in Section 4.1.

For a variable f the forward and backward derivatives are given as:

$$\frac{\partial f}{\partial x} = \frac{f_{j+1} - f_j}{\Delta x}, \quad \frac{\partial f}{\partial x} = \frac{f_{j-1} - f_{j-2}}{\Delta x} \tag{8}$$

4. Validation and numerical modelling

The proposed methodology is validated numerically and experimentally using the VCCT and static experiments. The results only for the DCB specimen will presented for brief.

4.1 Validation with 2D plane stress FEA

The 2D model consists of two solid parts bonded together in the interface. Each layer is modelled separately taking the geometry and the material properties from Table 1. The applied velocity is 1 m/s, and the boundary conditions match that from the SHPB apparatus. An explicit solver is used in the commercial finite elements software Abaqus©. The thermal stresses were added as initial stresses at increment 0 of the analysis. 0.125 mm elements are used for the convergence of the kinematic field in a 3 mm region close to crack tip. The distance Δx for the convergence of the finite difference is calculated to be 0.125 mm. By using the hybrid model with the assumptions of Section 3 the SERR for the proposed method and the VCCT are presented in Figure 3.

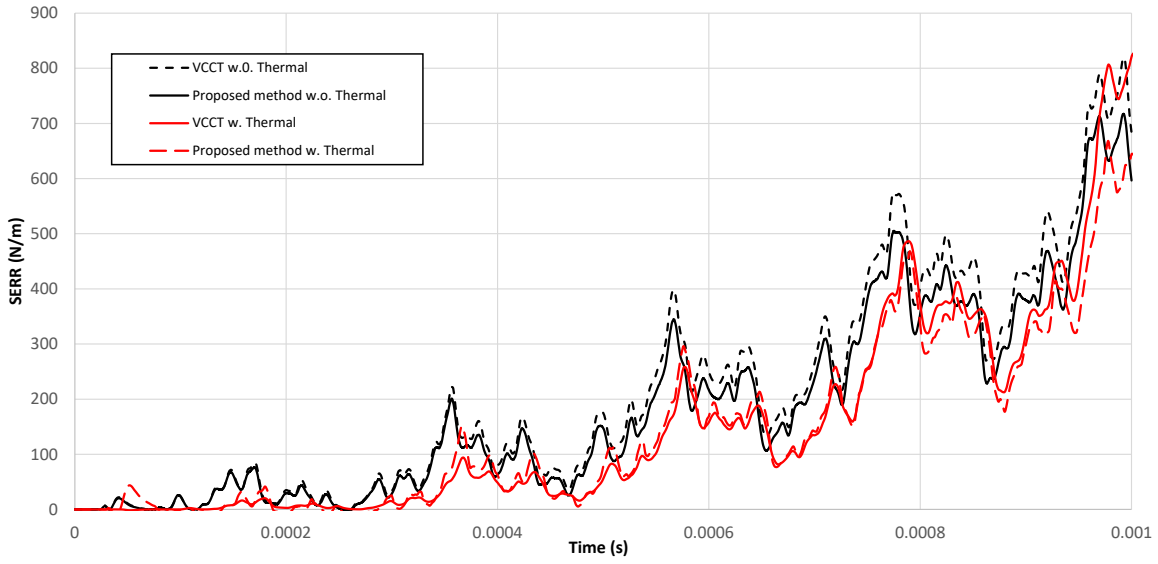

Figure 3: Comparison of the predictions of the proposed model and the VCCT for the calculation of the fracture toughness with and without the effect of thermal stresses

The results are in good agreement either with or without the presence of thermal stresses, making Eq. (3) applicable under the assumption $\partial w_i^+ / \partial x \cong \varphi^+$.

4.2 Validation with experimental results

To investigate if the method is applicable using the kinematic field obtained from DIC as an input, the following procedure is followed. First, 3D FEA models are calibrated using the force-

  doi:10.5075/epfl-298799_978-2-9701614-0-0

displacement curve from static experiments. Only the linear elastic part is considered in this work since Eq. (3), (5) are used only for the initiation of a crack. Then the SERR is calculated using the VCCT and Eq. (5) using the kinematics from the DIC. The 3D model has the same model assumptions as the plane stress one. The results are presented in Figure 4**.**

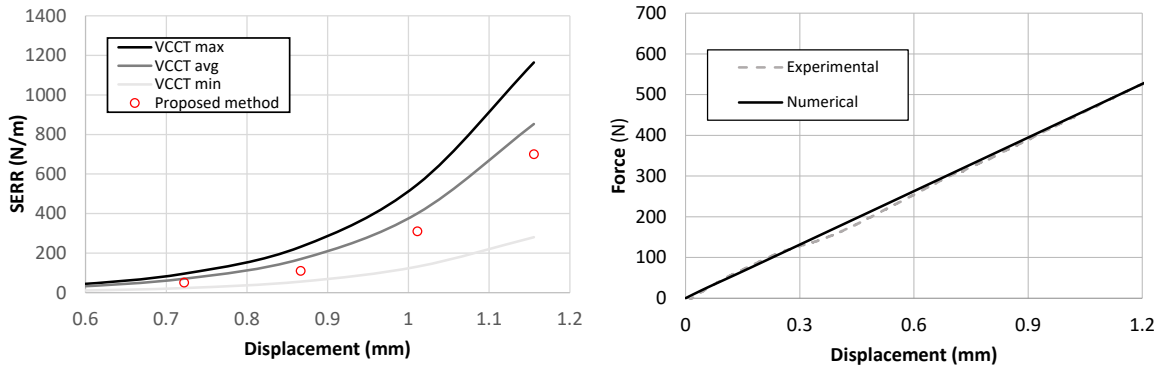

Figure 4: Comparison of the results of the proposed model and the VCCT ones based on the DIC input for the kinematics

The results from the proposed method seem to be close to the averaged value of the SERR. The deviation of the SERR through the width are large so the averaged value is taken as reference.

5. Results from the high-rate experiments

The results from the Mode I experiment are presented on Figure 5. The applied velocity is constant and equal to 0.97 m/s. Based on the camera frame rate the first three eigenfrequencies are captured by the DIC analysis. The imported noise due to camera or rigid body motions are removed using the DIC software.

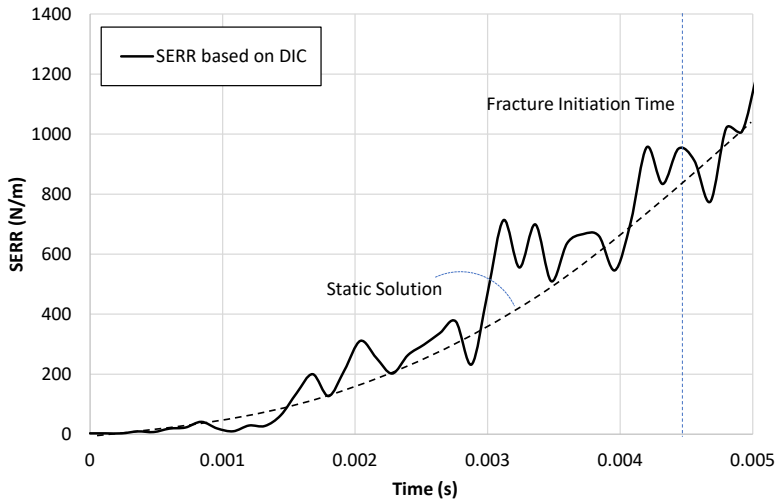

Figure 5: Stain energy release rate versus time calculated with the proposed methodology

For the ENF specimens the crack propagation time for the specific adhesive joint was smaller than the time for the creation of the standing waves. Thus, no vibration data was collected by

the high-speed camera. Also due to the elastic deformation of the metal base, the kinematics measured from the DIC was not reliable. Thus, the results for the ENF are not presented in this work and will be investigated by the authors in the future.

6. Conclusions

- A novel hybrid analytical-experimental method for the calculation of the dynamic SERR based on the Timoshenko beam theory is proposed.
- The proposed methodology is validated with numerical modelling via FEA.
- Vibrational effects due to the propagation of elastic waves affect the value of the fracture toughness at the initiation of the crack propagation.

Acknowledgment

The research work was supported by the Hellenic Foundation for Research and Innovation (H.F.R.I.) under the "First Call for H.F.R.I. Research Projects to support Faculty members and Researchers and the procurement of high-cost research equipment grant" (Project Number: 2573).

7. References

1. Kotsinis G, Loutas T. Strain energy release rate under dynamic loading considering shear and crack tip root rotation effects. European Journal of Mechanics, A/Solids. 2022 Mar 1;92.
2. Chen T, Harvey CM, Wang S, Silberschmidt V. Theory of dynamic mode-II delamination in end-notched flexure tests. Composite Structures. 2021 Oct 15;274.
3. ben Salem N, Jumel J, Budzik MK, Shanahan MER, Lavelle F. Analytical and experimental investigations of crack propagation in adhesively bonded joints with the Mixed Mode Bending (MMB) test Part I: Macroscopic analysis & Digital Image Correlation measurements. Theoretical and Applied Fracture Mechanics. 2014;74(1):209–21.
4. Gorman JM, Thouless MD. The use of digital-image correlation to investigate the cohesive zone in a double-cantilever beam, with comparisons to numerical and analytical models. Journal of the Mechanics and Physics of Solids. 2019 Feb 1;123:315–31.
5. Huo X, Luo Q, Li Q, Sun G. Measurement of fracture parameters based upon digital image correlation and virtual crack closure techniques. Composites Part B: Engineering. 2021 Nov 1;224.
6. Leitão N, Gilabert FA. A unified J-Integral-based procedure to investigate at different loading regimes the fracture by FEM simulations and image analysis. Journal of the Mechanics and Physics of Solids. 2021 Apr 1;149.
7. Tsokanas P, Loutas T, Kotsinis G, Kostopoulos V, van den Brink WM, Martin de la Escalera F. On the fracture toughness of metal-composite adhesive joints with bending-extension coupling and residual thermal stresses effect. Composites Part B: Engineering. 2020;185.
8. Quino G, Chen Y, Ramakrishnan KR, Martínez-Hergueta F, Zumpano G, Pellegrino A, et al. Speckle patterns for DIC in challenging scenarios: Rapid application and impact endurance. Measurement Science and Technology. 2021 Jan 1;32(1).
9. Greco F, Lonetti P. Mixed mode dynamic delamination in fiber reinforced composites. Composites Part B: Engineering. 2009 Jul;40(5):379–92.
10. Timoshenko S. Theory of Elasticity. 1951
11. Anderson T. Fracture Mechanics Fundamentals and Applications. 2005

  doi:10.5075/epfl-298799_978-2-9701614-0-0

FRONTAL POLYMERIZATION IN NON-ADIABATIC SYSTEMS: THE INFLUENCE OF NATURAL CONVECTION

Laurence, Rongy[a], John A., Pojman[b], Reda, Tiani[a]

a: Nonlinear Physical Chemistry Unit, Université libre de Bruxelles (ULB), Faculté des Sciences, CP231, 1050 Brussels, Belgium – laurence.rongy@ulb.be
b: Department of Chemistry, Louisiana State University, Baton Rouge, Louisiana 70803, United States

Abstract:

Thermal frontal polymerization (FP) converts a monomer-initiator mixture into polymer through the propagation of a front resulting from the coupling between an exothermic polymerization reaction and the diffusion of heat. Such fronts are usually described with one-dimensional (1D) reaction-diffusion (RD) theories modeling the spatio-temporal evolution of the monomer and/or the initiator concentrations and of the temperature. We have recently shown that those 1D models cannot fully describe FP in the presence of heat losses (non-adiabatic conditions). Here, we show, with a 2D model, that the layer thickness and the reactants' viscosity, two parameters that cannot be accounted for in 1D models, are crucial parameters controlling not only the dynamics of the front but also determining its very existence. Natural convection arising from density gradients of thermal origin across the front is incorporated in our 2D model. Such results supplement recent coatings experiments by FP on wood substrates.

Keywords: Frontal polymerization; heat losses; 2D modeling; buoyancy-driven convection

1. Introduction

Thermal polymerization fronts (hereafter named simply polymerization fronts) are initiated by the local application of a heat source at the boundary of a system that contains initially a monomer-initiator mixture (see Figure 1) [1]. In Figure 1, the monomer is trimethylolpropane triacrylate (TMPTA) and the initator is Luperox 231 (1,1-bis(tert-butylperoxy)-3,3,5-trimethylcyclohexane) chosen due to its stability at room temperature and compatibility with TMPTA [2]. The heat locally triggers the activation of the initiator for the free-radical polymerization of the monomer that produces heat, which by diffusion further drives the reaction. A polymerization front is then formed that converts the initiator-reactants mixture into the polymer. Hence, such as for wildfires, (thermal) polymerization fronts are sustained by reaction and heat diffusion.

Thermal frontal polymerization (FP) has been known for long but has regained interest lately due to promising applications [3,4]. Since the reaction is localized, and no input of energy is required except for the initiation of the front, FP allows the fast and controlled formation of polymers that is expected to allow low energy cost as compared to bulk polymerizations. Recently, the ring-opening metathesis polymerization of dicyclopentadiene using a ruthenium catalyst and an alkyl phosphite inhibitor (that increases the stability of the monomer) has been shown to lead to the fast energy-efficient synthesis of high-performance thermosets and fibre-reinforced polymer composites similar to those used, in particular, on airplanes [5]. We could therefore expect FP to open the way to new faster, energy efficient, and greener routes for the

  doi:10.5075/epfl-298799_978-2-9701614-0-0

synthesis of high-performance polymers in manufacturing industries (namely chemical, aerospace and wind turbines industries) [5].

Recent applications in coatings industry have also been highlighted [2]. More specifically, FP has recently been tested for on-demand curing of resins on solid substrates. However, experimental difficulties were observed that strongly restrict applications in this direction. In particular, a workable coating requires a minimum value for the layer thickness and for the viscosity of the initiator-monomer mixture. Such results highlight the limits of the widely used 1D non-adiabatic reaction-diffusion models to describe the dynamics of polymerization fronts [6,7].

In this context, we have analyzed the dynamics of a polymerization front numerically and analytically in a rectangular two-dimensional (2D) layer. The article is organized as follows. In section 2, we present our model obtained by coupling reaction-diffusion-convection equations, to describe the space and time evolution of the monomer and initiator concentrations as well as of the medium temperature, to the Navier-Stokes equations. Indeed, buoyancy-driven convection arising from thermal gradients across the front is likely to play a role in the system dynamics. In section 3, we present and discuss the results. We first analyze the front dynamics in the high-viscosity limit to prevent any convection so as to focus on the effects of the layer thickness on the system dynamics. We find that, for a fixed surface cooling coefficient controlling the rate of heat losses, a minimum value of the layer thickness is required for front propagation [8]. For large-enough layer thicknesses, the front propagates whatever the rate of heat losses [8]. Next, we extend the analysis so as to include convection with a focus on the effects of the reactants' viscosity on the front propagation. We predict that front extinction occurs below a critical value of the reactants' viscosity at any fixed value of the layer thickness.

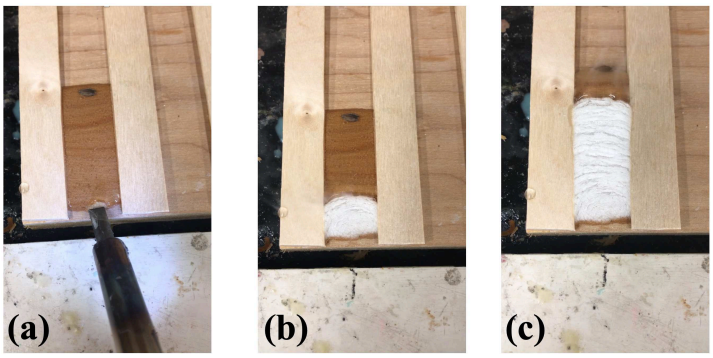

Figure 1. (Top view) (a) Initiation of a thermal polymerization front by a heat gun. The liquid is the monomer-initiator mixture. (b) Front propagation shown after 10 s and (c) 20 s. The system size is of the order of the centimeter. The product (white) invades the reactants mixture in time.

2. Model system

We consider a 2D system of length L_x and thickness L_z, which initially contains a liquid monomer-initiator mixture. Due to the local application of heat source, a spatially localized reaction zone (a polymerization front) travels in the system with a direction perpendicular to the gravity field. Due to changes in temperature and composition, the solution density changes across the front driving buoyancy-driven flows. We shall assume the solution density $\rho(T)$ to depend only on temperature, while we neglect its dependence on composition. We assume the polymer to be in the liquid phase whose viscosity is either constant or increasing with the degree of conversion quantified by $(M(x,z,t) - M_0)/M_0$, where M is the monomer concentration and M_0 its initial

  doi:10.5075/epfl-298799_978-2-9701614-0-0

concentration. The model is obtained by coupling the spatio-temporal evolution equations for the monomer $M(x,z,t)$ and the initiator $I(x,z,t)$ concentrations and for the medium temperature $T(x,z,t)$ to the Navier-Stokes equations describing the velocity field $\underline{v} = (u,w)$ evolution. The model system then reads,

$$\frac{\partial M}{\partial t} + \underline{v}.\underline{\nabla}M = D_M \nabla^2 M - k_{\mathrm{eff}}(T) M\sqrt{I}, \quad (1)$$

$$\frac{\partial I}{\partial t} + \underline{v}.\underline{\nabla}I = D_{\mathrm{I}} \nabla^2 I - k_{\mathrm{d}}(T) I, \quad (2)$$

$$\rho_0 c_p \left(\frac{\partial T}{\partial t} + \underline{v}.\underline{\nabla}T\right) = \lambda \nabla^2 T - \Delta H\, k_{\mathrm{eff}}(T) M\sqrt{I}, \quad (3)$$

$$\rho_0 \left(\frac{\partial \underline{v}}{\partial t} + (\underline{v}.\underline{\nabla})\underline{v}\right) = -\underline{\nabla}p + \underline{\nabla}.\underline{\underline{\tau}} + \rho(T)\underline{g}, \quad (4)$$

$$\underline{\nabla}.\underline{v} = 0, \quad (5)$$

where p is the pressure, $\underline{g} = (0,-g)$ is the acceleration due to gravity, $\rho_0 = \rho(T = T_0)$ is the density of reactants (monomer-initiator) mixture at temperature T_0 (ambient temperature). The effective rate constant $k_{\mathrm{eff}}(T)$ and $k_{\mathrm{d}}(T)$, respectively associated to the monomer consumption and initiator decomposition, follow the Arrhenius laws, $k_j(T) = {k^0}_j exp\left(-E_j/RT\right)$, with $j =$ eff or d, and ${k^0}_j$ the pre-exponential factor. The last terms (reaction terms) in Eq. (1) and (2) are well-known to accurately describe the kinetics of free-radical polymerizations with a thermal initiator [9]. The Laplacian operator is defined as $\nabla^2 = \frac{\partial^2}{\partial x^2} + \frac{\partial^2}{\partial z^2}$, and the viscous stress tensor $\underline{\underline{\tau}} = 2\mu\,\underline{\underline{S}}$ where $\underline{\underline{S}} = \frac{1}{2}\left(\underline{\nabla}\otimes\underline{v} + \left(\underline{\nabla}\otimes\underline{v}\right)^T\right)$ is the strain-rate tensor, and μ the dynamic viscosity which may generally depend on composition and temperature (see section 3.2). The model parameters in Eqs. (1)-(5), i.e., the specific heat capacity c_p, the thermal conductivity λ, the molecular diffusion coefficients D_M and D_I, and the reaction enthalpy per mole of monomer ΔH (here negative since the polymerization reaction is exothermic) are all assumed constant. The Navier-Stokes equations (4)-(5) are written in the Boussinesq approximation, which assumes that the density variation is only important in the buoyancy term. This approximation also implies that the density of the solution does not depend on pressure, which should be valid in the context of FP when there are no bubbles in the experiments. In Eq. (4), the solution density is assumed to depend linearly on temperature, $\rho(T) = \rho_0 + \frac{\partial \rho}{\partial T}(T - T_0)$, with $\frac{\partial \rho}{\partial T}$ constant and negative meaning that the density decreases with increasing temperature.

The initial conditions are no flow and $I\,(x,z,t=0) = I_0, M(x,z,t=0) = M_0$ and $T\,(x,z,t=0) = T_0$.

To specify the boundary conditions (BCs), we take a rectangular domain with 2 rigid side walls (at $x = 0$ and $x = L_x$), a rigid bottom (at $z = 0$) and a rigid top boundary (at $z = L_z$). At each boundary, we require zero-flux BCs for the monomer and initiator concentrations. For the temperature, we apply a constant heat source T_s at the left system boundary ($x = 0$) to initiate FP and we assume heat losses to occur at the top ($z = L_z$) system boundary (non-adiabatic conditions). The two other boundaries are assumed insulated. The BCs for the fluid velocity field at the four rigid boundaries are no-slip conditions, $u = 0 = w$. The BCs then read,

  doi:10.5075/epfl-298799_978-2-9701614-0-0

$$T = T_s\,, \frac{\partial M}{\partial x} = 0 = \frac{\partial I}{\partial x} \quad \text{at } x = 0, \tag{6}$$

$$\frac{\partial M}{\partial x} = 0 = \frac{\partial I}{\partial x}\,, \quad \frac{\partial T}{\partial x} = 0 \quad \text{at } x = L_x, \tag{7}$$

$$\frac{\partial M}{\partial z} = 0 = \frac{\partial I}{\partial z}\,, \quad \frac{\partial T}{\partial z} = 0 \quad \text{at } z = 0, \tag{8}$$

$$\frac{\partial M}{\partial z} = 0 = \frac{\partial I}{\partial z}\,, \quad \lambda \frac{\partial T}{\partial z} = -h\,(T - T_0) \quad \text{at } z = L_z, \tag{9}$$

where h is the convective heat transfer coefficient that quantifies the rate of heat losses from the top boundary to the surrounding. The length L_x is taken large enough so as not to affect the system dynamics on the time of interest. In Eq. (6), the fixed BC could be replaced by a non-flux BC after a minimum heating time. However, this does not affect the long-time front dynamics that we are typically interested in analyzing. Thus, we have kept this fixed BC for the temperature for simplicity. Note that the absence of a free surface prevents the formation of Marangoni-driven flows induced by surface tension gradients across the front.

In the absence of convection, Eqs. (1)-(3) with appropriate BCs Eqs. (6)-(9) and the above mentioned initial conditions are solved using finite-difference and the fourth-order Runge-Kutta methods for discretization of space and time, respectively. The temporal and spatial step sizes are dt = 5 × 10^{-5} and dx = 0.05, dz = 0.1, respectively. In the presence of convection, the highly non-linear set of equations, Eqs. (1)-(9), are numerically solved with the finite-element based COMSOL Multiphysics software by using a custom free triangular mesh with a Jacobian matrix updated on every iteration as the program computes the solutions at each time step with the Newton's method (see [10] for technical details). The accuracy (within few % of relative errors) is achieved by varying the finite element parameters and mesh size.

Below, we focus on the effects of the heat transfer coefficient, the layer thickness and the reactants' viscosity on the system dynamics. Those parameters are therefore varied while we keep fixed all the other parameters in the range of typical experimental values [2,6,9,11,12].

3. Results and discussion

3.1 In the absence of convection

In the high-viscosity limit, we can neglect the effects of convection, and Eqs. (1)-(5) reduce to the reaction-diffusion equations Eqs. (1)-(3) with $\underline{v} = \underline{0}$.

Here, our goals are to evaluate the effects of heat losses and of the layer thickness quantified by h and L_z, respectively, on the front propagation with no influence of convection.

To do so, we can define the Biot number, which quantifies the rate of heat losses (in the same way as h) to the surrounding as, $Bi = hL_c/\lambda$, where L_c is the characteristic length scale of the problem [8]. This number is obtained by making Eq. (9) dimensionless with the dimensionless procedure introduced by Heifetz et al. [6].

A typical numerical solution for the front visualized with the polymerization reaction rate is shown in the absence ($Bi = 0$) and presence of heat losses ($Bi \neq 0$) (see Figure 2). The translational symmetry of Eqs. (1)-(3) with no flow and insulated top and bottom BCs impose a planar geometry of the front as it propagates in the system (see Figure 2 (a)). In the presence of heat losses, this symmetry is broken as the reaction zone is colder near the top boundary where

  doi:10.5075/epfl-298799_978-2-9701614-0-0

heat losses occur than at the bottom of the system. Hence, the front propagates in the form of a plume (see Figure 2 (b)).

The long-time dynamics of the non-adiabatic front depend on both the values of the Biot number and of the layer thickness [8]. In the small layer thickness limit, Eqs. (1)-(3) with BCs (6)-(9) are equivalent to 1D models with heat losses encoded in an effective cooling coefficient inside the heat equation [6]. Such models always predict the possibility to quench the front when the cooling coefficient, or equivalently the Biot number, exceeds a critical value. When increasing the layer thickness, however, the effects of the second dimension (z) becomes important and predictions based on 1D models break down. In particular, as a signature of 2D modeling, we find that beyond a critical value of the layer thickness (of a few centimeters), the front cannot be stopped, whatever the intensity of the heat losses [8].

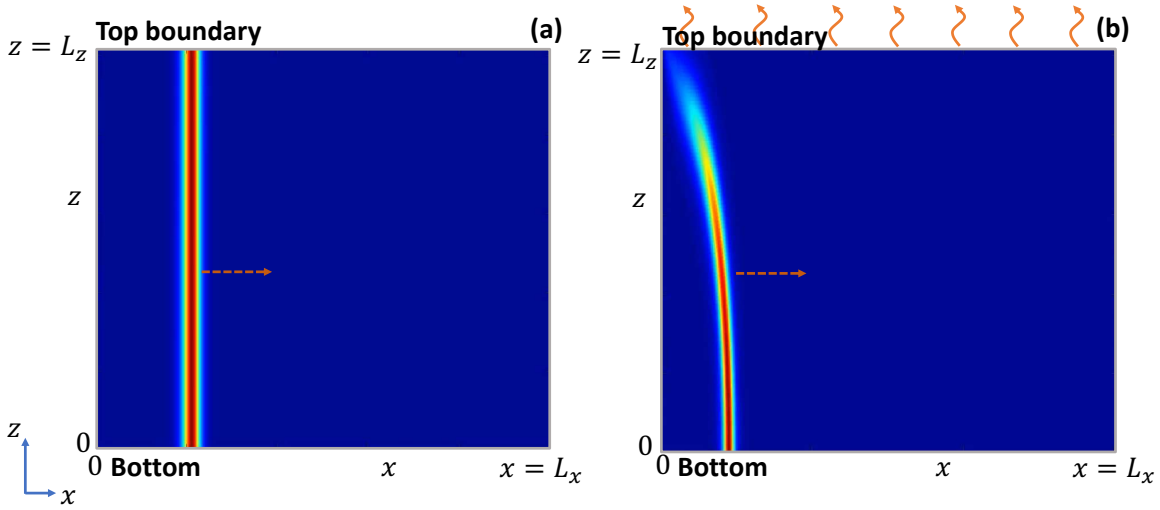

Figure 2. Front propagation as quantified by the polymerization reaction rate (last term of Eq. (1)) in the absence of convection and in (a) adiabatic (Bi = 0), and (b) non-adiabatic (Bi = 0.60) conditions. Heat losses are shown schematically with arrows. The red and blue colors represent the maximum and minimum of the reaction rate, respectively. The front travels in a 2D rectangular domain of thickness L_z and length L_x of order of mm sizes after the initiation of the front at the left system boundary (the horizontal dashed arrow indicates its direction).

3.2. In the presence of buoyancy-driven flows

When the medium viscosity decreases, convective effects become important and the complete set of equations, Eqs. (1)-(9), needs to be considered. The goal of this section is to highlight the effects of convection and in particular, of reactants' viscosity, on the front properties in the absence and presence of heat losses. To do so, we first assume the viscosity of the medium as independent of any variable of the system. In this case, the viscosity is constant in space and time.

Additionally, it is common to assume in the context of FP that an appreciable amount of the initiator is consumed in the wake of the moving front and thus, we can neglect the effects of variation of the initiator concentration on the front dynamics [7]. The latter assumption does not affect the system dynamics qualitatively [7,12].

  doi:10.5075/epfl-298799_978-2-9701614-0-0

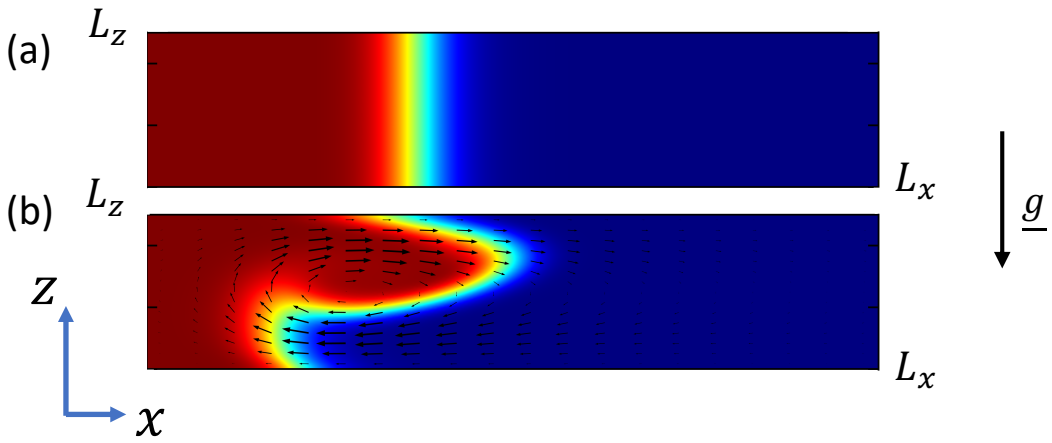

Figure 3. Front propagation visualized with the degree of conversion, $(M(x,z,t) - M_0)/M_0$, with M_0 the initial monomer concentration, in the (a) absence and (b) presence of buoyancy-driven convection and zoomed around the transition zone between the polymer region (red, degree of conversion equals 1) and the reactants mixture (blue, degree of conversion is zero). The thickness $L_z = 1\ mm$ and length $L_x = 10\ mm$. The constant dynamic viscosity is 1.5 mPa.s.

In Figure 3, we show the typical adiabatic propagation of the front perpendicular to the gravity field visualized here with the degree of conversion in the presence of convection. For the sake of comparison, we have also drawn the RD solution (no flow). Since it is assumed that density decreases with increasing temperature, the hot polymer (in red) rises while the cold reactants mixture (in blue) sinks in the gravity field (see Figure 3 (b)). If we compare with Figure 3 (a), this leads to a clockwise convective roll that deforms the planar RD interface.

The self-sustained character of FP drives the system into asymptotic dynamics where the front travels at constant speed and width with a stationary vortex surrounding it. This result is similar to what was observed when buoyancy-driven flows travel with autocatalytic fronts (fronts driven by an autocatalytic instead of a polymerization reaction) [13].

In non-adiabatic conditions, however, this asymptotic regime can be disrupted due to heat losses that quench the front. In that case, front extinction occurs when the reactants' viscosity is below a critical value. A hypothesis is that buoyancy-driven flows bring cold fluid to the reaction zone, quenching propagation except for very viscous monomer solutions.

Those results can be extended if we consider the medium viscosity as variable. In particular, the polymer is typically more viscous than the reactants mixture. In this case, one needs an equation of state for the viscosity. One particular choice could be to assume that the viscosity is an exponential function of the degree of conversion to model the rapid increase of viscosity from the reactants mixture to the polymer side as the front travels in the system.

Preliminary results show that one of the important effects of the product viscosity on the system dynamics is to quantitatively affect the value of the critical reactants' viscosity. Indeed, we note that the higher the polymer viscosity, the less intense the flows, and the smaller the critical reactants' viscosity. This is work in progress.

  doi:10.5075/epfl-298799_978-2-9701614-0-0

Acknowledgements

The authors thank the F.R.S.-FNRS for their financial support. This work was partially supported by the NSF EPSCoR-Louisiana Materials Design Alliance (LAMDA) program (Grant No. OIA-1946231).

4. References

1. Pojman JA. Frontal Polymerization. In: Polymer Science: A Comprehensive Reference. Elsevier. 2012. p. 957-80.
2. Bansal K, Pojman JA, Webster D, Quadir M. Frontal polymerization of a thin film on a wood substrate. ACS Macro Letters 2020; 9(2):169–73.
3. Pojman JA. Cure-on-Demand Composites by Frontal Polymerization. In: Reference Module in Materials Science and Materials Engineering. Elsevier. 2022. p. 1-17.
4. Li Q, Shen H-X, Liu C, Wang C-F, Zhu L, Chen S. Advances in Frontal Polymerization Strategy: From Fundamentals to Applications. Progress in Polymer Science 2022; 127: 101514.
5. Robertson ID, Yourdkhani M, Centellas PJ, Aw JE, Ivanoff DG, Goli E, et al. Rapid energy-efficient manufacturing of polymers and composites via frontal polymerization. Nature 2018; 557(7704):223–7.
6. Heifetz A, Ritter LR, Olmstead WE, Volpert VA. A numerical analysis of initiation of polymerization waves. Mathematical and Computer Modelling 2005; 41(2–3):271–85.
7. Volpert VA. Dynamics of thermal polymerization waves. In: Proceedings of NATO ASI. Springer. 2006.
8. Tiani R, Pojman JA, Rongy L. Critical role of the layer thickness in frontal polymerization. Journal of Physical Chemistry B 2022; under minor revision.
9. Goldfeder PM, Volpert VA, Ilyashenko VM, Khan AM, Pojman JA, Solovyov SE. Mathematical modeling of free-radical polymerization fronts. Journal of Physical Chemistry B 1997; 101(18):3474.
10. Multiphysics C. COMSOL Multiphysics Reference Manual v. 5.5. COMSOL AB. Stockholm, Sweden. 2019.
11. Goldfeder PM, Volpert VA. Nonadiabatic frontal polymerization. Journal of Engineering Mathematics 1998; 34(3):301-18.
12. Spade CA, Volpert VA. Linear stability analysis of non-adiabatic free-radical polymerization waves. Combustion Theory and Modelling 2001; 5(1):21–39.
13. Rongy L, Goyal N, Meiburg E, De Wit A. Buoyancy-driven convection around chemical fronts traveling in covered horizontal solution layers. Journal of Chemical Physics 2007; 127(11):114710.

  doi:10.5075/epfl-298799_978-2-9701614-0-0

RAPID-CURE OF FIBER-REINFORCED COMPOSITES BY FRONTAL POLYMERIZATION

Nil Parikh[a,b], Sagar Vyas[a,b], Douglas Ivanoff [a,c], Philippe Geubelle[a,b], Nancy Sottos [a,c]

a: Beckman Institute for Advanced Science and Technology, University of Illinois at Urbana-Champaign – (nilp2@illinois.edu)
b: Department of Aerospace Engineering, University of Illinois at Urbana-Champaign
c: Department of Materials Science and Engineering, University of Illinois at Urbana-Champaign

Abstract: *Frontal polymerization (FP) is a rapid energy-efficient curing technique that substantially reduces the manufacturing burdens for thermoset polymers and composites by leveraging the monomer's enthalpy of polymerization to provide the energy necessary for conversion rather than relying on an external source. Our current research focuses on frontal ring-opening metathesis polymerization (FROMP) of dicyclopentadiene and integration within carbon fiber-reinforced polymer composites (FRPCs). We manufacture carbon FRPCs utilizing a combination of iso-static pressing, vacuum-assisted resin transfer molding (VARTM), and FP to rapidly manufacture composites with fiber volume fractions up to 65%. Properties of the FRPC are improved with the incorporation of a norbornene-based short-chain ester cross-linker.*

Keywords: Frontal polymerization; Fiber-reinforced polymer composites (FRPC); out-of-autoclave; dicyclopentadiene

1. Introduction

Frontal polymerization (FP) is a self-sustaining reaction driven by the exothermic heat of polymerization from the resin system [1-4]. Heat produced from a local reaction zone acts to polymerize the adjacent monomer, forming a self-propagating polymerization wave or front. FP presents the advantages of fast and energy-efficient curing in a growing library of monomers [1-4]. Recently the frontal ring-opening metathesis polymerization (FROMP) of dicyclopentadiene (DCPD) has been demonstrated as a viable means to cure high-performance fiber-reinforced polymer composites (FRPC) with fiber volume fraction, V_f, ca. 51% with similar performance to conventionally cured counterparts [1].

In prior work, FP for high-performance applications was limited by relatively low values of fiber volume fraction. Successful curing by FP relies on the chemical energy stored in the resin and increased V_f leads to the front stalling and lower degree of cure [2]. The present study focuses on alleviating this bottleneck by through-the-thickness cure of the FRPC and the incorporation of co-monomers for increased thermomechanical performance.

2. Materials and Methodology

2.1 Resin Materials

The base resin constituents for the fabrication of carbon fiber-reinforced polymer composites using FP include dicyclopentadiene (DCPD), 5-ethylidene-2-norbornene (ENB), second-generation Grubbs' catalyst (GC2), and tributyl phosphite (TBP), which were purchased from

  doi:10.5075/epfl-298799_978-2-9701614-0-0

Millipore-Sigma and used as received without further purification. To depress the melting point of DCPD, 5 wt% ENB was blended with DCPD at 50°C. The liquid mixture was then degassed overnight at room temperature and under vacuum (100kPa) with stirring. All references to DCPD refer to the 95:5 DCPD:ENB mixture. GC2 (36 mg, 1 equivalence) was carefully weighed out in a 100 mL glass media bottle. In a separate polyethylene container, TBP (11.4 µL, 1 equivalence) was added to DCPD (56.05 g, 6.67 x 10^3 equivalence). The monomer/inhibitor solution was transferred to the bottle containing GC2 and the mixture was sonicated for 10 minutes to ensure complete dissolution of the catalyst (Figure 1a). The resin was then filtered with a 0.22 µm filter to remove any remaining debris.

Dinorbornenyl short chain ester: The short chain ester was synthesized according to previous work [5]. Comonomer resins were prepared analogously, and the total monomer concentration was maintained.

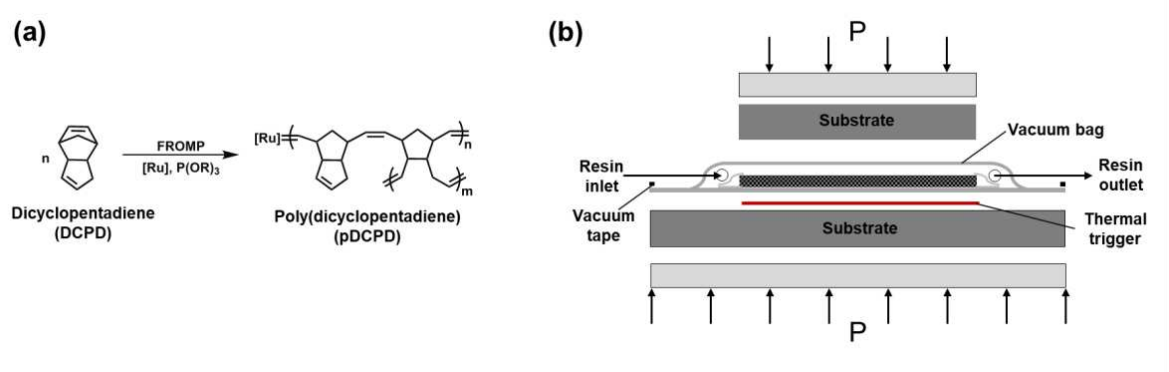

Figure 1. Overview of frontal polymerization of carbon fiber-reinforced composites. (a) Base chemical scheme for frontal polymerization. (b) Side view of VARTM composite layup for the FP-based fabrication of composite in hot press using through-thickness curing.

2.2 Vacuum-Assisted Resin Transfer Molding (VARTM)

Carbon fiber-reinforced composites were fabricated using a single-bag vacuum assisted resin transfer molding (VARTM) technique coupled with isostatic pressing. The VARTM layup was prepared on a rigid thermally nonconductive substrate under which a resistive heating mat was placed to initiate the reaction. The reinforcement phase of the carbon FRPC consists of 12 plies of 10 cm x 12 cm Toray T300 carbon fabric (2 × 2 twill weave, tow size 3,000, areal density 204 g m^{-2}) oriented in the 0 direction (Figure 1b). A vacuum of 40 kPa is applied to the fabric preform to infuse the desired resin system. An additional thermally nonconductive substrate is placed on top of the laminate with spacers. The entire laminate is placed within an isostatic press while retaining vacuum. The layup is then pressed at room temperature (22°C) and 308 kPa with FP initiated using the resistive heating mat set to a specific target temperature, T_{target}, to produce composites with ca. V_f = 65%.

2.3 Composite Material Characterization

In-situ temperature measurements were conducted during FP using T-type thermocouples embedded at the bottom, mid-ply, and top of the fabric preform. The peak temperature recorded by each thermocouple was defined as the maximum temperature experienced by the laminate at that position. The rate of cure or the velocity of front propagation was determined by measurement between successive peaks monitored by the thermocouples. The cure time for

each carbon FRPCs was determined by time required to initiate the reaction – the onset of the reaction, and the end of prescribed heating (start of the cooling step). The void content of the cured carbon FRPC was determined by casting, polishing, and imaging of the composite cross section. ImageJ software was used to calculate the total void content relative to the area of composite cross section.

Degree of cure, α, was measured using a combination of differential scanning calorimetry (DSC) and thermogravimetric analysis (TGA). Flat 8 mg samples were cut and sealed at the bottom of an aluminum pan with hermetic lids. The residual exotherm was determined by heating samples from -50°C to 250°C at 10 °C/min. After DSC, the matrix to fiber mass is determined using TGA. α was determined using

$$\alpha = 1 - \frac{H}{H_R}, \quad (1)$$

where H is the residual exotherm (corrected for matrix mass) and H_R is the enthalpy of reaction of the liquid resin system.

Dynamic mechanical analysis (DMA) was used to determine the glass transition temperature (T_g) and thermomechanical response of the carbon FRPCs. Rectangular specimens were cut from the composite panel and polished to final dimensions of 44 mm x 5 mm x 2.2 mm. Samples were loaded on a three-point bend fixture with a span of 40 mm. A fixed force (2 N) with strain of 0.01% and frequency of 1 Hz at 2°C min^{-1} from 0°C to 250°C is used for all samples. T_g is taken from the peak of tanδ (ratio of loss and storage modulus) is reported using the TRIOS software analysis from TA Instruments.

3. Results and Discussion

3.1 Effect of Energy Input on Composite Fabrication

The properties exhibited by composites are directly correlated to the degree of cure governed by the temperature reached during the curing process [6]. We hypothesize the properties of the carbon FRPCs prepared using FP are also governed by the degree of cure and temperature attained during cure. We impose a target temperature (T_{target}) ranging from the onset of the reaction (70°C) to temperatures observed during cure of the polymer system (200°C), corresponding to an energy input of 9 kJ and 48 kJ. A representative heating profile obtained from thermocouples located at the bottom, mid-ply, and top of the composite laminate is shown in Figure 2. As the temperature increases beyond the onset temperature, the FP curing reaction dominates the temperature signal after which the sample heats to the desired temperature. From these temperature curves, we extract the front temperature and front velocity for each target temperature.

We observe that the energy input has limited impact on the front characteristics as it propagates through the composite, indicating that these characteristics are driven by the chemical energy stored within the resin. Optical micrographs of the samples were comparable as the sample preparation and fabrication mitigated the formation of voids, with values summarized in Table 1. The degree of cure, α, of the composite showed the largest change because of the increased energy input resulting from the higher temperature. As the energy input increases, the degree of cure of the composite also increased reaching α=0.89. The thermomechanical response of the composite sample illustrates the impact of the energy input (Figure 3a). At T_{target} =70°C, multiple

  doi:10.5075/epfl-298799_978-2-9701614-0-0

onsets are present in the storage modulus indicating the possibility of beta-transitions resulting from the lower degree of cure of the composite. As T_{target} increases to 200°C, the presence of these transitions are minimized. The glass transition temperature, T_g, of each sample increased with T_{target} maximizing at T_{target} =200°C (Figure 3b). The rubbery plateau shifts up with increasing energy input indicating an increase in the crosslinking density of the composite matrix material.

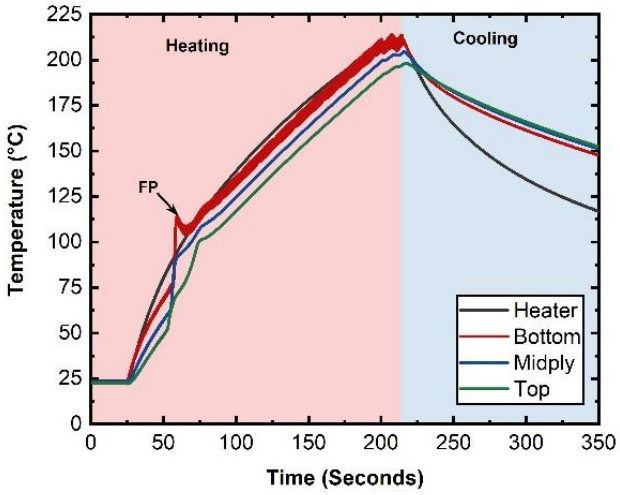

Figure 2. Representative thermocouple profile for the composite using a through-thickness curing scheme. A target temperature of 200°C was applied to the bottom surface of the composite laminate. Frontal polymerization initiates at ca. 55 sec, as evidenced by the peak in the heating curve.

Table 1: Carbon FRPC Properties for Varying Energy Input.

Sample	Target Temperature T_{target} (°C)	Max Front Temperature (°C)	Front Velocity, v_f (cm/min)	Fiber Volume Fraction, V_F (%)	Void Volume Fraction, V_v (%)	Energy Input (kJ)	Degree of Cure, α
1	70	115 ± 2.5	1.24 ± 0.09	64.8 ± 1.2	0.05 ± 0	9	0.80 ± 0.03
2	200	125 ± 3.3	1.20 ± 0.11	64.3 ± 1.1	0.04 ± 0	48	0.89 ± 0.03

  doi:10.5075/epfl-298799_978-2-9701614-0-0

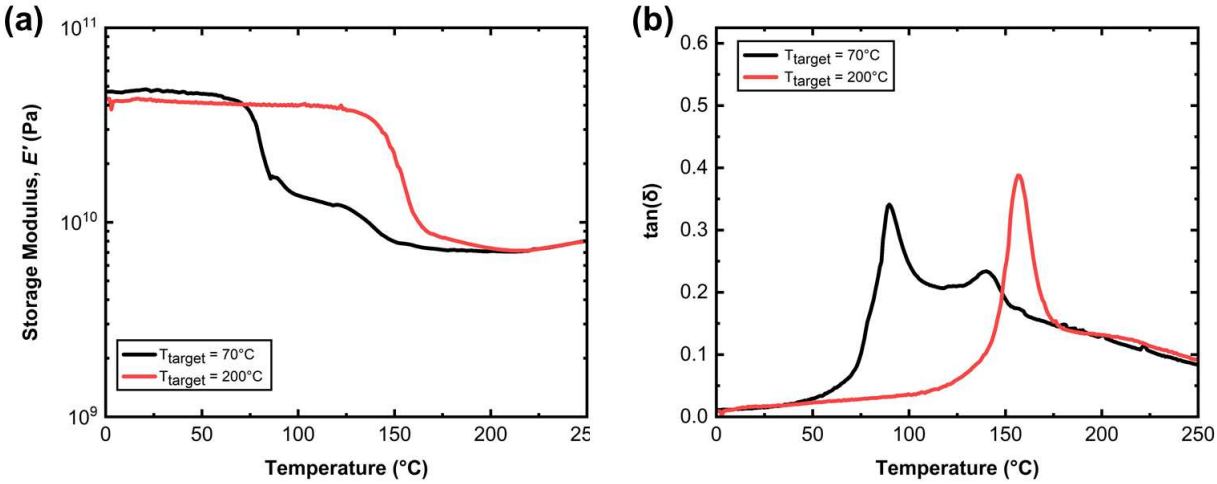

Figure 3. Representative DMA curves for target maximum surface temperatures of 70°C and 200°C. (a) Evolution of the storage modulus demonstrating the increase in target temperature's effect on the thermomechanical response of the composite. (b) Ratio of the storage and loss modulus from DMA used for determination of the glass transition temperature.

3.2 Effect of Co-monomers on thermomechanical properties

With the increase in the energy input to the carbon FRPCs, we have demonstrated that maximum properties are achieved at temperatures around 200°C, indicating that the increase in energy input to the system alleviates the need to rely exclusively on the chemical energy stored within the resin system. Increasing the energy input permits the inclusion of monomers with lower enthalpy that functionally participate in the frontal ring-opening metathesis polymerization to imbue a property increase or functionality. Examples of such co-monomer systems include those explored by Ivanoff et al. using norbornene-based cross-linkers that enable tuning of the cross-link density leading to increased thermomechanical properties [5]. We included a norbornene-based short chain ester (SCE) co-monomer into the resin system and characterized the resulting carbon FRPC. At 30 *wt%* of SCE we observe a 10% increase in T_g of the composite with a noticeable shift in the rubbery plateau (Figure 4a, b) because of the increased crosslinking.

  doi:10.5075/epfl-298799_978-2-9701614-0-0

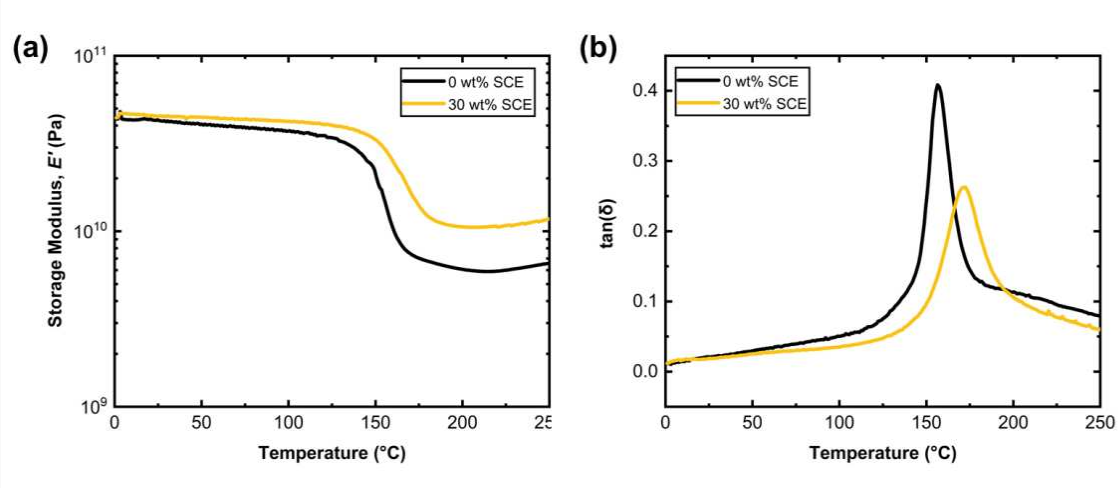

Figure 4. Representative DMA curves for increase in co-monomer concentration. (a) Evolution of the storage modulus demonstrates an increase in the rubbery modulus; (b) Ratio of the storage and loss modulus from DMA with increase in the glass transition temperature with incorporation of co-monomer.

4. Conclusion

In this work, we manufactured carbon FRPCs using a rapid through-thickness FP curing scheme to investigate the effect on the composite quality and properties of the energy input achieved by varying the target temperature, T_{target}, of the resistive heating mat. The processing window permitted the inclusion of co-monomers that increased properties and added functionality. Panels manufactured with higher T_{target} achieved a higher degree of cure and an improved thermomechanical response compared to those with lower T_{target}. The inclusion of the norbornene-based short chain ester crosslinker resulted in a 10% increase in the glass transition temperature and a shift in the rubbery plateau compared to the base resin. These results suggest a promising future for the implementation of frontal polymerization as a strategy of fabricating high-performance carbon FRPCs.

Acknowledgements

This work was supported by the National Science Foundation (NSF Grant No. 1830635) through the LEAP-HI: Manufacturing USA program. We thank Dev Patel and Thien Le for assistance with layup materials preparation and thermal characterization. N.A.P acknowledges the support of a graduate followship from the Beckman Institute at the University of Illinois at Urbana–Champaign. The authors extend gratitude to the late Prof. Scott White for his guidance and inspiring outlook on materials.

5. References

1. Robertson, I. D., Yourdkhani, M., Centellas, P. J., Aw, J. E., Ivanoff, D. G., Goli, E., Lloyd, E. M., Dean, L. M., Sottos, N. R., Geubelle, P. H., Moore, J. S., and White, S. R. (2018) “Rapid energy-efficient manufacturing of polymers and composites via frontal polymerization.” Nature, 557, 223-227.

  doi:10.5075/epfl-298799_978-2-9701614-0-0 published under CC BY-NC 4.0 license

2. Goli, E., Parikh, N. A., Yourdkhani, M., Hibbard, N. G., Moore, J. S., Sottos, N. R., and Geubelle, P. H. (2020) “Frontal polymerization of unidirectional carbon-fiber-reinforced composites.” Composites Part A, 130, 105689.
3. Sangermano, M., D’Anna, A., Marro,C., Klikovits, N., and Liska, R. (2018) “UV-activated frontal polymerization of glass fibre reinforced epoxy composite.” Composites Part B, 143, 168-171.
4. Tran, A. D., Koch, T., Knaack, P., and Liska, R. (2020) “Radical induced cationic frontal polymerization for preparation of epoxy composites.” Composites Part A, 132, 105855.
5. Ivanoff, D. G., Sung, J., Butikofer, S. M., Moore, J. S., and Sottos, N. R., (2020) " Cross-linking agents for enhanced performance of thermosets prepared via frontal ring-opening metathesis polymerization.” Macromolecules, 53, 8360-8366.
6. Gutowski, TG, Advanced Composites Manufacturing. New York: Wiley. 1997.

  doi:10.5075/epfl-298799_978-2-9701614-0-0

ADDRESSING THE CHALLENGES IN FRONTAL CURING OF HIGH-PERFORMANCE CARBON FIBER REINFORCED COMPOSITES

Muhammad Salman Malik[a], Valerie Grasser[a], Markus Wolfahrt[a], Sandra Schlögl[a], Gerald Pinter[b]

a: Polymer Competence Center Leoben GmbH, Rossegerstraße 12, 8700, Leoben, Austria
muhammad.malik@pccl.at
b: Chair of Materials Science and Testing of Polymers, Department Polymer Engineering and Science, Montanuniversität Leoben, 8700, Otto Glöckel-Straße 2, Leoben, Austria

Abstract: *Curing epoxy-based carbon fiber composites via the thermal frontal polymerization technique is a potential alternative to conventional thermal curing that offers short cycle time and reduced energy consumption costs. This technique, which is based on a cationic curing mechanism, utilizes the heat of polymerization in an autocatalytic traveling front that cures the composite with an induction time of few seconds. In recent years, frontal polymerization has been used to cure composites with very low fiber volume content (<40 %) so that the curing front can be activated with UV light. However, the thermo-mechanical properties of these composites do not meet the requirements for high performance aerospace and automobile applications since most of those composites have a very high fiber content (>50 %). Along with the thermal conductivity, the high fiber content compromises on the optical transparency of the composites. Herein, we address this issue by reporting thermo-mechanical properties of heat activated frontally cured composites and compared them with conventionally thermally cured ones.*

Keywords: Frontal polymerization; unidirectional; carbon fiber, composite

1. Introduction

The potential of carbon fiber reinforced epoxy composites (CF-epoxy) as high-performance and lightweight construction materials is being exploited in a broad range of industries, especially in the transport sector. The amount of CF-epoxy used in industry is increasing steadily as are the variety of application fields (1). However, the most common curing type-thermal curing, restricts the application fields due to some inherent drawbacks. Firstly, the prolonged time of curing in an oven or an autoclave consumes a lot of energy. Secondly, due to the low heat conductivity of epoxy in comparison to reinforcement and the need for uniform curing, the thickness of the part is restricted. Thirdly, the manufacturing process is often limited by the resin's pot life. Consequently, further research is being conducted in the field of rapid curing methodologies that could cut down cycle time of composite manufacturing and at the same time, allow a uniform and high degree of cure (2–4). One promising curing technology is frontal polymerization.

Frontal polymerization was first investigated back in the 1970s on methyl methacrylate monomers, where a thermal initiator was used for generating a self-sustaining heat curing front (5). As the cationic ring-opening polymerization of epoxide monomer is a highly exothermic reaction, it can also be exploited to dissociate a radical thermal initiator. Carbon-centered

  doi:10.5075/epfl-298799_978-2-9701614-0-0

radicals are formed, which are oxidized to carbocations in the presence of a iodonium salt, and a self-sustaining polymerization front is formed by following a reaction mechanism known today as radical induced cationic frontal polymerization (RICFP) (6). Curing of epoxy monomers via RICFP is a fast and self-sustaining technique to achieve a high degree of crosslinking, whilst requiring only a localized stimulus either through UV or thermal initiation (7). Moreover, the manufacturing process via frontal polymerization provides longer pot life, typically several months. Furthermore, energy and time can be saved by the rapid autocatalytic curing process. Additionally, FP provides more freedom in product design, such as the aforementioned possible higher wall thickness and bigger part size. The costs for long heating cycles and expensive equipment, such as autoclaves can be prevented by frontal polymerization (4). Currently, there is no reported industrial-scale set-up for curing via frontal polymerization while on the contrary, conventional curing is already well studied and resins and hardeners, optimized for a wide variety of applications, are commercially available (8–10).

Several authors reported promising results with frontal polymerization of various fiber or filler reinforced composites (3, 11–13). These composites were confined to a low fiber or filler content due to limited penetration of UV light making it difficult for the polymerization to initiate deep within the composite layers. Endless carbon fiber-based epoxy composites are characterized by a high fiber volume fraction (>50 %) that qualifies them for several engineering applications such as aerospace, transportation and construction. Therefore, the target of the current study was to compare the properties of composites with unidirectional (UD) fiber orientation and a fibre volume content greater than 50 %. In this work, we compared thermo-mechanical properties of different CF-epoxies cured via two methods- conventional anhydride cured and via thermo-activated radical induced cationic frontal polymerization (RICFP). The latter method has not yet been used for manufacturing carbon fiber reinforced composites on a large scale. Consequently, the results from the performed thermo-mechanical characterization mark the first step towards applying frontal polymerization as a rapid and efficient curing alternative to conventionally cured composites employed in industry.

2. Materials and test methods

Materials and test specimen manufacturing

A commercially available bisphenol A-based epoxy resin was used as matrix material. Unidirectional 50k (UD-50) 200 gsm carbon fiber fabric was used as a reinforcement to manufacture composite test specimens. All composites were manufactured with the help of vacuum assisted resin infusion method (VARI) as depicted in figure 1. After the impregnation of the dry fibers with the resin, the curing time and temperature was set as follows. For conventional curing, the composites were cured for 5 h at 120 °C in an oven. On the contrary, composites cured via frontal polymerization were subjected to the heating plate for 30 min at 150 °C. The minimum onset temperature of curing for frontal polymerization was determined with a rheometer (MCR501 Anton Paar, Austria) in temperature time sweep mode. Since frontal polymerization requires only a localized initiation to sustain the front, we deliberately provided a heating time of 30 min so that there is no premature quenching of the front at such low epoxy volume content in the composite (<40 %). The fiber volume fraction was experimentally determined from thermo-gravimetric analysis (Mettler Toledo, Schwerzenbach, CH) to ensure a fiber content >50%, whereas, the test results of composite specimens were averaged from a

  doi:10.5075/epfl-298799_978-2-9701614-0-0

minimum of 5 specimens. On average, a fiber volume fraction of 55 ± 3% was achieved for both thermo-activated and conventional thermal cured composite test specimens.

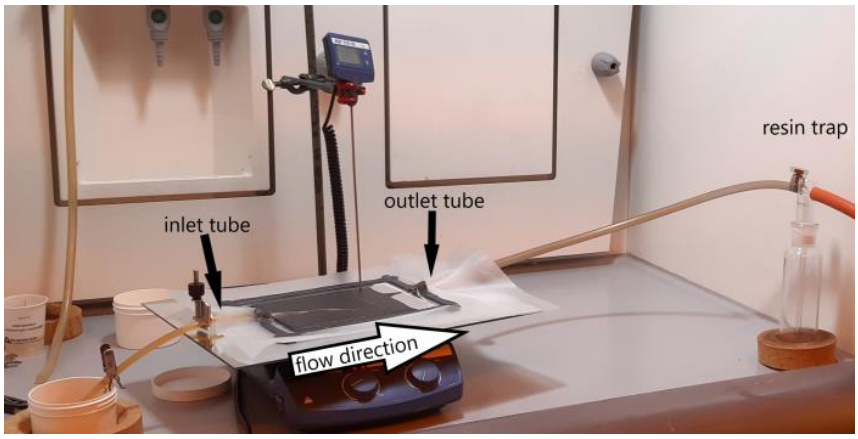

Figure 1 Setup of a vacuum assisted resin infusion process at the laboratory.

For the optical investigations via light microscope (MAT7, Carl Zeiss AG, Germany), samples were embedded in an epoxy matrix, grinded and polished. Optical micrographs of specimens manufactured with these two curing methods showed basically no voids. Two examples are depicted in figure 2.

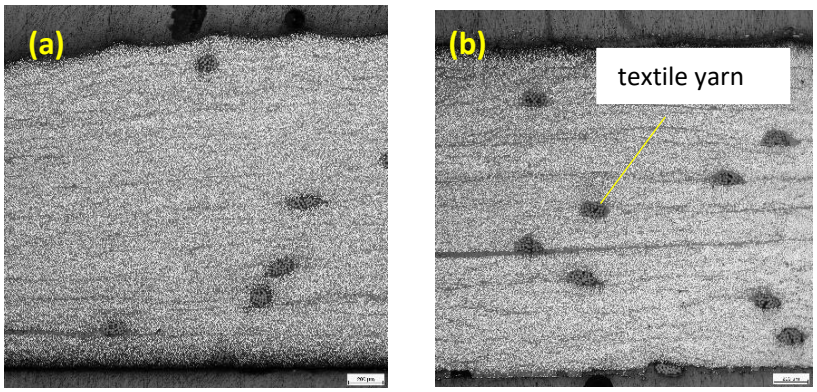

Figure 2. Examples of polished micrographs of 2mm UD composite plates used for compression, DMA, ILSS tests cured via (a) conventional thermal cured and (b) thermo-activated frontal curing.

Specimens for tensile and compression tests were manufactured according to DIN EN ISO 527-4 (14) (specimen type 1B) and DIN ISO EN 14126 (15), respectively. For interlaminar short beam shear tests, rectangular test specimens were prepared in accordance to DIN ISO EN 14130 (16).

Test methods

Dynamic mechanical measurements (DMA) were done on a Mettler-Toledo DMA861e (Mettler Toledo, Schwerzenbach, CH) under three-point bending mode in accordance to DIN ISO EN 6721-5 (17) and specimens manufactured accordingly. All measurements were performed in a temperature range from 25 to 225 °C at a heating rate of 2K/min and a frequency of 1 Hz. In order to ensure material deformation within the linear viscoelastic region, the auto offset force was set to 400% and an amplitude of 10 µm was chosen. The tensile properties were determined

in accordance with DIN EN ISO 527-4 (14). A 250kN universal tensile/compression testing machine (Z010, Zwick/Roell, Ulm, D) was used with a displacement rate of 2 mm/min and the strain was measured with a mechanical extensometer. The compression properties were determined according to DIN ISO EN 14126 (15). The cross-head speed applied was 1 mm/min. Each specimen was loaded parallel to the fiber direction on a universal tensile/compression testing machine (Z250, Zwick/Roell, Ulm, D). To measure the local strain distribution of the test specimens, optical full-field strain measurements were performed using a 3D image correlation photogrammetry system. Short beam shear testing was carried out according to DIN ISO EN 14130 (16) using Z10 machine from Zwick/ Roell (Ulm, D).

3. Results and discussions

Figure 3 shows typical results from DMA measurements for specimens cured via thermo-activated frontal polymerization in comparison to the conventional thermal curing technique. From the storage modulus curves, the glass transition temperature T_g (onset value) for the frontally cured composite is higher (134 °C) than the $T_{g,onset}$ (121 °C) for conventionally cured composite. The tan delta peak for frontally cured composite is broader than the one of conventionally cured composites indicating a different type of network structure. Moreover, a slight increase in storage modulus after the Tg is observed for the conventional cured composite that indicates a slight post-curing effect. The results confirm that frontal polymerization rapidly cures the composite to a high degree, resulting in high Tg values and negligible post-curing effects. In addition, frontal polymerization is characterized by very high temperatures (typically >200 °C), which is way above the glass transition temperature of the cured network. As a result, a homopolymerized and tight cross-linked network is formed rapidly , trapping any unreacted initiating radicals and preventing post curing (7).

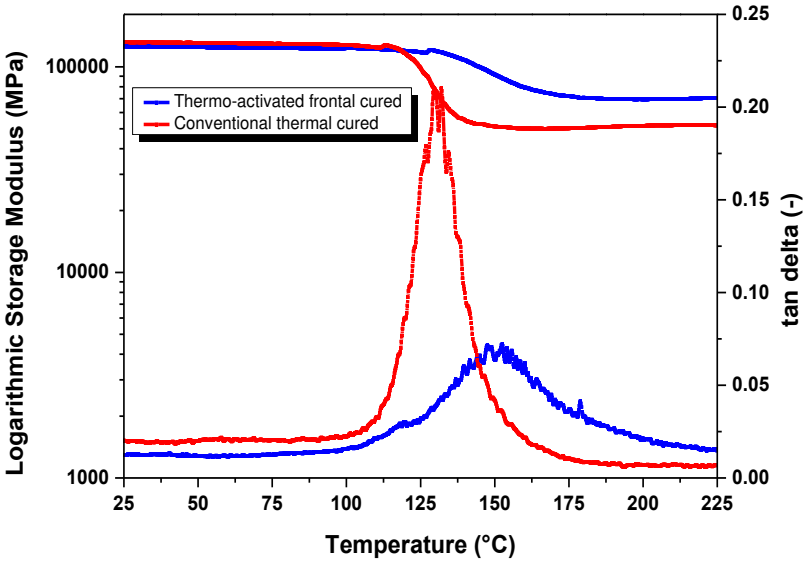

Figure 3. Comparison of storage modulus and tan delta as a function of temperature between thermo-activated frontally and conventional thermal cured UD-50 reinforced composite.

The results of mechanical tests for the composite specimens are summarized in table 1. This table shows the comparison between frontally and conventionally cured composites subjected to tensile, compression and inter-laminar shear loading.

Table 1: Results from mechanical testing conducted on UD-50 reinforced composite specimens cured via thermo-activated frontal and conventional thermal curing techniques.

Property	Conventional thermal curing	Thermo-activated frontal curing
Tensile Modulus, GPa	131 ± 6	135 ± 6
Tensile strength, MPa	1816 ± 61	1196 ± 219
Strain at break, %	1.38 ± 0.08	0.85 ± 0.18
Compression Modulus, GPa	117 ± 13	125 ± 7
Compression strength, MPa	912 ± 83	1107 ± 88
Inter-laminar shear strength, MPa	88 ± 8	93 ± 8

The tensile test results for frontal cured specimens show a lower tensile strength and a slightly higher modulus in comparison to conventional cured specimens. These frontally cured specimens had a strain of 0.85%, i.e. nearly 2 times lower than the fiber, exhibiting a matrix dominated failure. This behavior can be explained by the high degree of cross-linking formed during frontal polymerization promoting the fiber-matrix adhesion and resulting in overall reduced ductility of the composite. In addition, the higher value of compressive strength and modulus for frontally cured composite is also in good agreement to the fact that frontal polymerization results in more matrix dominated behavior.

The inter-laminar shear strength for the two types of composites was evaluated via the classical short beam shear test valid for unidirectional reinforced composites. The frontal cured composite exhibited a slightly higher shear strength (93 MPa) than conventional thermal cured composite (88 MPa). The frontally cured composites showed single shear deformation but not prominent multiple shear deformations. These results were almost similar to the findings by Tran et al. (3) who showed multiple shear deformation for frontally cured composites and single shear for conventionally cured composites. Since ILSS is a matrix dominated failure, we presume that this might be due to a more heterogenous cross-linking network formed during frontal polymerization in comparison to conventional thermal curing (refer to figure 3).

4. Summary and outlook

In this work, we have demonstrated the possibility to frontally cure fiber-reinforced composites upon brief heating that possess more than 50% of fiber content and could not be cured via UV induction. The rapid curing front can be initiated with a short contact of medium temperature heat (150°C) for 30 min in an oven. The thermo-mechanical test results from these high fiber-content reinforced composites are promising as they either surpass or are equal to the thermo-mechanical properties of composites cured conventionally by a hardener. These results showed slightly higher glass transition temperatures (onset values), compression strength and inter-

  doi:10.5075/epfl-298799_978-2-9701614-0-0

laminar strength than conventionally cured composites. A low elongation to failure from tensile test and high compression strength further revealed that frontally cured composites exhibit a brittle behavior. This is due to rapid formation of a high cross-linked network thanks to high temperature curing front (>200 °C) that exceeds the glass transition temperature of the cured network. Hence, it is assumed that a stronger fiber-matrix adhesion is achieved with frontal cured composites.

These composites are under full scale development in order to demonstrate their feasibility in high-fiber content composites sector such as aerospace and automobile industries. With these studies we have demonstrated that it is still possible to rapidly cure composites by frontal polymerization when UV light becomes a major drawback for in-depth composite curing.

Acknowledgements

This research was funded by the Austrian Research Promotion Agency (FFG), grant number 854178. The work was performed within the COMET-project ‘‘Development of new curing technologies for the rapid and efficient production of epoxy based composites title’’ (project-no.: VII.1.02) at the Polymer Competence Center Leoben GmbH (PCCL, Austria) within the framework of the COMET-program of the Federal Ministry for Climate Action, Environment, Energy, Mobility, Innovation and Technology and the Federal Ministry for Digital and Economic Affairs with contribution by Montanuniversität Leoben (Chair of Chemistry of Polymeric Materials and Chair of Materials Science and Testing of Polymers). The PCCL is funded by the Austrian Government and the State Governments of Styria, Lower Austria and Upper Austria.

Literature Cited

1. Klein B, Gänsicke T. Leichtbau-Konstruktion: Dimensionierung, Strukturen, Werkstoffe und Gestaltung / Bernd Klein, Thomas Gänsicke. Eleventh edition. Wiesbaden: Springer Vieweg; 2019.

2. Mgbemena CO, Li D, Lin M-F, Liddel PD, Katnam KB, Thakur VK et al. Accelerated microwave curing of fibre-reinforced thermoset polymer composites for structural applications: A review of scientific challenges. Composites Part A: Applied Science and Manufacturing 2018; 115:88–103.

3. Tran AD, Koch T, Knaack P, Liska R. Radical induced cationic frontal polymerization for preparation of epoxy composites. Composites Part A: Applied Science and Manufacturing 2020; 132:105855.

4. Robertson ID, Yourdkhani M, Centellas PJ, Aw JE, Ivanoff DG, Goli E et al. Rapid energy-efficient manufacturing of polymers and composites via frontal polymerization. Nature 2018; 557(7704):223–7.

5. Chechilo NM, Khvilivitskii RJ, Enikolopyan NS. On the Phenomenon of Polymerization Reaction Spreading. Dokl. Akad. Nauk SSSR 1972; 204:1180–1.

6. Malik MS, Schlögl S, Wolfahrt M, Sangermano M. Review on UV-Induced Cationic Frontal Polymerization of Epoxy Monomers. Polymers (Basel) 2020; 12(9).

  doi:10.5075/epfl-298799_978-2-9701614-0-0

7. Malik MS, Wolfahrt M, Sangermano M, Schlögl S. Effect of a Dicycloaliphatic Epoxide on the Thermo-Mechanical Properties of Alkyl, Aryl Epoxide Monomers Cured via UV-Induced Cationic Frontal Polymerization. Macro Materials & Eng 2022:2100976.

8. Guadagno L, Raimondo M, Vittoria V, Vertuccio L, Naddeo C, Russo S et al. Development of epoxy mixtures for application in aeronautics and aerospace. RSC Advances 2014; 4(30):15474–88.

9. Sukanto H, Raharjo WW, Ariawan D, Triyono J, Kaavesina M. Epoxy resins thermosetting for mechanical engineering. Open Engineering 2021; 11(1):797–814.

10. Rafique I, Kausar A, Anwar Z, Muhammad B. Exploration of Epoxy Resins, Hardening Systems, and Epoxy/Carbon Nanotube Composite Designed for High Performance Materials: A Review. Polymer-Plastics Technology and Engineering 2016; 55(3):312–33.

11. Sangermano M, Antonazzo I, Sisca L, Carello M. Photoinduced cationic frontal polymerization of epoxy–carbon fibre composites. Polym. Int. 2019; 68(10):1662–5.

12. Sangermano M, D'Anna A, Marro C, Klikovits N, Liska R. UV-activated frontal polymerization of glass fibre reinforced epoxy composites. Composites Part B: Engineering 2018; 143:168–71.

13. Tran AD, Koch T, Liska R, Knaack P. Radical-induced cationic frontal polymerisation for prepreg technology. Monatsh Chem 2021; 152(1):151–65.

14. ISO 527-4. Plastics — Determination of tensile properties — Part 4: Test conditions for isotropic and orthotropic fibre-reinforced plastic composites. Available from: URL: https://www.iso.org/standard/80369.html [cited 2022 Apr 20].

15. ISO 14126:1999. Fibre-reinforced plastic composites — Determination of compressive properties in the in-plane direction. Available from: URL: https://www.iso.org/standard/23638.html [cited 2022 Apr 20].

16. ISO 14130:1997. Fibre-reinforced plastic composites — Determination of apparent interlaminar shear strength by short-beam method. Available from: URL: https://www.iso.org/standard/23642.html [cited 2022 Apr 20].

17. ISO 6721-5. Plastics - Determination of dynamic mechanical properties: Part 5: Flexural vibration - Non-resonance method. Available from: URL: https://www.iso.org/standard/73145.html [cited 2022 Apr 20].

PROCESSING OF FIBRE REINFORCED POLYMERS BY CONTROLLED RADICAL INDUCED CATIONIC FRONTAL POLYMERISATION

Jeroen Staal[a], Edgar Smit[a], Baris Caglar[b], Véronique Michaud[a]

a: Laboratory for Processing of Advanced Composites (LPAC), Institute of Materials, Ecole Polytechnique Fédérale de Lausanne, Station 12, Lausanne CH-1015, Switzerland
b: Aerospace Manufacturing Technologies, Faculty of Aerospace Engineering, Delft University of Technology, Kluyverweg 1, Delft 2629HS, the Netherlands
Email correspondence: jacobus.staal@epfl.ch

Abstract: *Radical Induced Cationic Frontal Polymerisation (RICFP) has recently been proposed as a promising strategy for processing of epoxide carbon fibre reinforced polymers. Control of the local heat balance is crucial towards the production of industrial-quality composites, which is typically achieved via controlling the heat generation. In this work we present a comprehensive overview of RICFP processing of cycloaliphatic epoxide composites with enhance heat insulation. The thermal initiating compound was identified as the main component to control heat generation, which correlated well with the front velocity. A processing window was defined as function of the fibre and initiator contents and composites with to 45.8% V_f were successfully produced. Optimisation of resulting mechanical properties was made possible by optimisation of the heat balance, with matrix glass transition temperatures of up to 187°C achieved for the used cycloaliphatic system. Post-curing was found beneficial to overcome suggested inhomogeneous curing due to the dual-scale nature of fabrics.*

Keywords: Frontal polymerization, Fiber reinforced polymer, Composite processing

1. Introduction

Frontal polymerisation has emerged as a promising technique for out-of-autoclave processing of fibre reinforced polymers (FRPs), offering significant potential enhancements in processing time, cost and environmental impact[1]. Thermal frontal polymerisation is driven by thermal gradients formed by the distinct separation, i.e. a front, between the hot polymer and cold monomer resin. After an initial, e.g. thermal or UV-irradiation, trigger, an autocatalytic reaction mechanism allows the front to progress through the resin solution as long as a threshold temperature is exceeded. The approached steady-state temperature, assuming an FRP with constant thickness and fibre volume fraction (V_f), is a direct result of the local heat balance. As schematically illustrated in Figure 1, the local heat balance for a polymerisation front progressing through a fibrous preform is between the enthalpy of polymerisation, counterbalanced by thermal diffusion to the neighbouring resin layer, heat losses to the mould and heat uptake by the fibrous reinforcement.

  doi:10.5075/epfl-298799_978-2-9701614-0-0

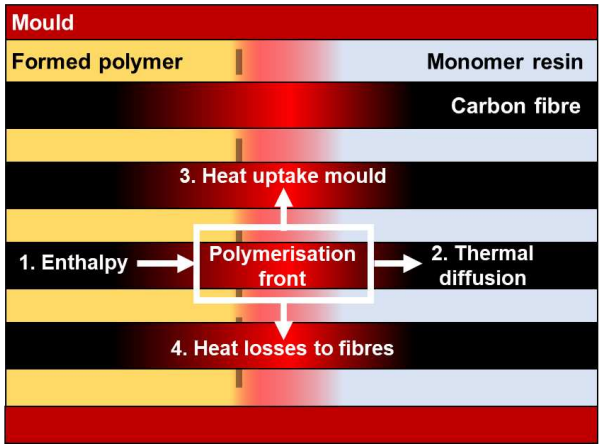

Figure 1 Schematic representation of local heat balance in frontal polymerisation. 1. Generated enthalpy of polymerisation, 2. Thermal diffusion to boundary layer, 3. Heat uptake by the mould material and 4. carbon fibres

First discovered by Chechilo and Enikolopyan[2,3] in the early 1970s, systems undergoing free-radical polymerisation are traditionally used for frontal polymerisation due to their beneficial high reactivities in combination with limited exothermicities. Promising systems based on dicyclopentadiene, following a frontal ring opening metathesis polymerisation (FROMP) mechanism, have recently been proposed. Robertson et al.[1] were able to produce carbon FRP panels with fibre V_fs of up to 51% and resulting properties comparable to oven-cured FRPs. While strong advances have subsequently been recorded e.g. further functionalisation[4,5], additive manufacturing[6,7] and simulation[8,9] of FROMP systems, their potential for use in industrial FRP processing is currently limited by the pot life of several hours in the presence of alkyl phosphite inhibitors[10].

Mariani et al.[11] were the first to propose so-called radical induced cationic frontal polymerisation (RICFP) to induce frontal polymerisation in epoxide systems. Based on radical induced cationic polymerisation proposed by Crivello[12], the autocatalytic mechanism in RICFP comprises the thermal initiation by the elevated front temperature of a free-radical thermal initiator, followed by an excitation of a cationic photoinitiator that creates new active polymer chains. This dual-initiator configuration allows RICFP systems to be uniquely stable, e.g. resins remained stable for over a month while being kept in a dark environment at 50°C[13], while fronts can be initiated both thermally and by UV-irradiation.

A number of studies have been dedicated to FRP processing by means of RICFP. While first articles mainly assessed the compatibility of RICFP systems with different fibre types[14–16], recent advances have paved a way for RICFP as a technique to produce industrial-quality FRPs. Using a system consisting of bisphenol A diglycidyl ether (BADGE), the highly reactive diaryliodonium (perfluoro-tert-butoxy) antimonate[17] and benzopinacol as monomer, photoinitiator and thermal initiator, respectively, Dung Tran et al.[18] were able to produce woven carbon FRPs with V_fs of around 35%. The resulting mechanical properties were comparable to those of anhydride-cured FRPs while glass transition temperatures exceeded 160°C. Gachet et al.[19] synthesised novel sulfonium-based initiators and were able to successfully cure carbon FRPs with 50 w% (40% V_f) carbon content with high front velocities of over 13 cm/min.

  doi:10.5075/epfl-298799_978-2-9701614-0-0

The influence of filler materials on the front characteristics was observed experimentally by Dung Tran et al.[18], who quantified the maximum volume fraction of different filler types that allowed for the formation of a front. The insulating nature of glass microspheres resulted in a nearly double allowed maximum filler content compared to the more conductive short carbon fibres and aluminium particles. This was explained by the increased spreading of the reaction zone, as also observed in numerical studies [9,20,21], which can significantly enhance front velocities at the cost of front temperature. Moreover, the dispersion of fillers was found of large influence on the reported slope of the front velocity as a function of the filler content[18]. The role of external heat losses on the other hand has merely been investigated. Knaack et al.[22] found a minimum thickness required to overcome external heat losses and hence the threshold temperature for successful front progression. Goli et al.[23] demonstrated that these heat losses acted as boundary effects, lowering the front temperature and potentially the degree of cure in the thin layers adjacent to the mould of which the thickness increases with the heat flow rate.

The control of the local heat balance is therefore crucial towards the production of high-performance composites. While significant effort is paid to the development of novel RICFP systems with increased reactivities[17,24,25] and thereby heating rates, the heat loss terms are generally left out of consideration. In this work we demonstrate the potential of reducing heat losses by the design of well-insulated system for RICFP processing. Minimising heat losses can increase the maximum possible fibre volume fractions that exceed those previously achieved using RICFP systems. Tailoring the local heat balance via the heat generation term is moreover demonstrated via adjustment of initiator concentrations. This can be used to optimise the mechanical performance of resulting FRPs, while the inhomogeneous curing due to the fabrics' dual-scale pore distribution can be overcome by post-curing.

2. Experimental

2.1 Materials

Omnilane OC1005 (IGM Resins, the Netherlands) resin, consisting of 3,4-epoxycyclohexyl-3',4'-epoxycyclohexane carboxylate (ECC) monomer was used in combination with photoinitiator p-(octyloxyphenyl)phenyl iodonium hexafluoro antimonate (IOC-8, ABCR, Germany) and benzopinacol (Acros Organics, Belgium) as thermal initiating compound. Isopropyl thioxanthone (Genomer ITX, Rahn, Switzerland) was used as photosensitiser to shift the initiation wavelength spectrum. 2x2 twill weave carbon textiles were acquired from Swiss Composites (Switzerland) and had an areal weight of 285 g/m^2, an ends/picks count of 3.5/3.5 cm^{-1} and 6K fibres per yarn. Moulds were produced from a PVC foam, glass fabric and breather fabric (Swiss Composites, Switzerland). High-temperature Diatex Polyimide HM 25 µm were obtained from Global Tools (Switzerland). An EXFO Omnicure S2000 Standard UV-light source was used for front initiation.

2.2 Methods

Resins were purified under vacuum after which the thermal initiator, photosensitiser and photoinitiator were dissolved by mixing at high shear rate. Degassing under vacuum was done at room temperature for about 30 minutes.

  doi:10.5075/epfl-298799_978-2-9701614-0-0

Polymerisation enthalpy of resins was characterised by Differential Scanning Calorimetry (DSC) using a TA Instruments DSC Q100. Resin samples of 2-3 mg were weighed in closed aluminium hermetic pans and measured at a heating rate of 5 °C/min over a range of -20 - 105°C, followed by an isothermal procedure of 30 minutes. The procedure was subsequently repeated as baseline. Maximum heat outputs corresponded to peak maxima after baseline correction.

Front velocities were characterised for systems with varying compositions containing about 12% V_f carbon fibres. For this scan, only compositions capable of forming a front in a neat resin system were selected while low carbon fibre V_fs were chosen to ensure frontal polymerisation to occur for all selected compositions. Carbon fibre tows were weighed and placed in an in-house made silicon mould with cavity dimensions of 45x12x7 mm that was subsequently filled with resin. A silicon mould half with an opening at one extreme of the cavity was placed on top. A schematic representation of the experimental setup is shown in Figure 2. Temperatures were recorded at an acquisition rate of 100 Hz via three thermocouples integrated in the top mould half, placed 15, 25 and 35 mm from the opening. Front velocities were determined by linear regression of the peak temperature times.

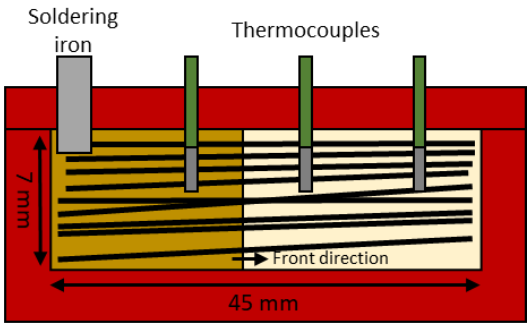

Figure 2 Schematic representation of the experimental setup (longitudinal cut) for front velocity characterisation.

Composites were produced by a hand layup method with fabrics and resin being alternately placed in a 5 mm mould cavity. A well-insulated system was designed to minimise heat losses to the ambient environment, which consisted of a Teflon-coated foam core that was subsequently enclosed by an envelope vacuum bag. The vacuum level was regulated to 0.5 bar and maintained for about 30 minutes to allow for further compaction of the impregnated fabric stack. Initiation was done by irradiation at an intensity of at least 500 mW/cm^2 from one of the resin-rich corners until the formation of a front was observed. The sample was kept under vacuum until cooled down to room temperature.

Dynamic Mechanical Analysis (DMA, TA Instruments DMA Q800) was carried out in three-point bending mode to characterize moduli and glass transition temperatures (T_gs) of composite samples. Samples were cut in strips of 55x10x5 mm and measured at 3°C/min over 2 heating cycles; a first cycles ranging from 15-250°C followed by a cycle of 15-300°C. Set amplitudes and frequencies were 10 µm and 1 Hz, respectively.

3. Results & Discussion

The heat generation term of a passing polymerisation front is defined by heat release of growing active cationic chains. Variation of the initiator concentrations has been reported[11,26] to

  doi:10.5075/epfl-298799_978-2-9701614-0-0

allow for control of heat generation and thereby RICFP front characteristics. Nevertheless, no clear consensus on the role of individual initiating components has been reached and relations are generally established based on indirect observations, i.e. via front velocities or temperatures, while the resin enthalpy is generally overlooked. Figure 3a shows a comparative overview of the maximum heat output recorded by DSC and front velocities in 12% V_f composites as function of the photoinitiator, photosensitiser and thermal initiator concentrations. Both the photo- and thermal initiators showed increased resin heat outputs with increasing concentration, which is supported by their Spearman correlation coefficients listed in Table 1. The recorded front velocities, shown in Figure 3b, moreover followed similar trends as observed in Figure 3a, which is in line with the observations made by Refs. [13,26], suggesting that the recorded heat output in DSC measurements is a good indicator to assess the behaviour of RICFP resins.

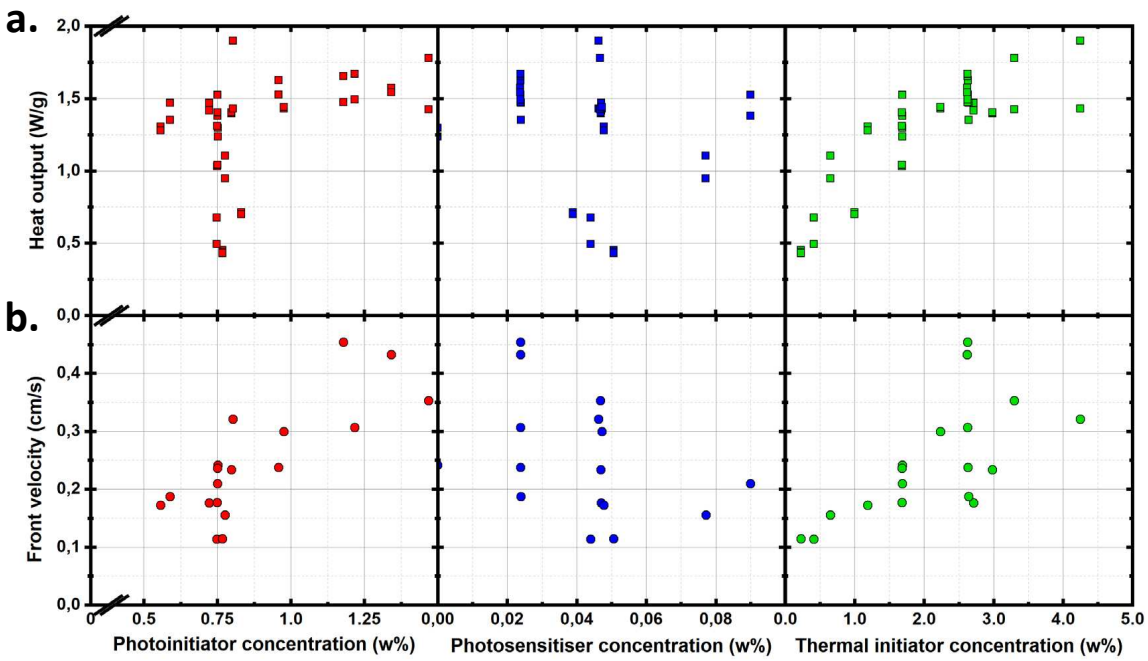

Figure 3 Composition dependence of: a) Heat output recorded in DSC measurements and b) front velocities recorded by integrated thermocouples.

The apparent slopes and larger Spearman coefficients moreover give rise to the hypothesis that, within the considered range of concentrations, the thermal initiator is of larger influence on both the heat output and front velocity. This would be in agreement with observations of Mariani et al.[11] who reported, despite the use of different initiator types in an ECC resin, a continuous increase of front velocity as a function of thermal initiator concentration while the photoinitiator concentrations resulted in a plateau of front velocity after a steep increase at low photoinitiator concentration. Hence, the significance of the photoinitiator concentration would be largely dependent on the chosen range of concentrations, while this would not be the case for the thermal initiator concentrations.

Table 1 also shows that the Spearman correlation coefficient for the photosensitiser concentration is slightly negative and significant, suggesting the increasing presence of a

  doi:10.5075/epfl-298799_978-2-9701614-0-0

photosensitiser negatively impacts the enthalpy generated by the resin, while a significant correlation was absent for the front velocities. Although these observations gives rise to a hypothesis that a photosensitising compound slightly reduces heat output that does not affect the front propagation, which is in line with the work of Bomze et al.[13], further investigation is needed to elucidate the role of photosensitisers in RICFP and confirm this hypothesis.

Table 1 Spearman correlation parameters of the composition dependence of heat outputs and front velocities

Resin component	Heat output [W/g]		Front velocity [cm/s]	
	Coeff.	p < 0.05	Coeff.	p < 0.05
Photoinitiator	0.529	$4.6 \cdot 10^{-4}$	0.643	0.018
Photosensitiser	-0.418	$7.3 \cdot 10^{-3}$	-0.258	0.394
Thermal initiator	0.759	$1.4 \cdot 10^{-8}$	0.846	$2.7 \cdot 10^{-4}$

Carbon FRPs were subsequently produced with a varying initiator concentration, while the molar ratio between photo- and thermal initiating compounds was fixed at 1:2.3. Three different scenarios could take place upon initiation in the resin-rich zone: a self-sustaining front forms that polymerises the complete fabric stack, the formation of a front that can only propagate through the fabric stack when followed by the light source and the inability to form a front. As shown in Figure 4, it was possible to induce self-sustaining fronts in fabric stacks with V_fs up to 45.8% with a thermal initiator concentration of 1 w%, which exceeds the previously published maxima reported for RICFP systems[18,19]. While partially a result from the use of the highly exothermic ECC monomer, e.g. compared to BADGE resin of Dung Tran et al.[18], this improvement is mainly attributed to the mould design, which aimed to minimise heat uptake and heat transfer to approach a quasi-adiabatic system.

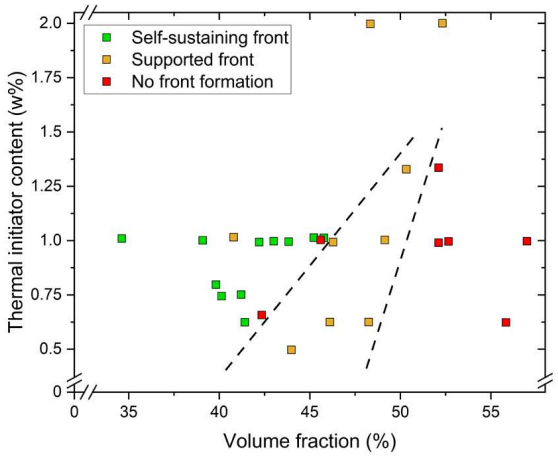

Figure 4 Ability of front formation in an carbon FRP system with varying V_f and thermal initiator concentrations

Figure 4 shows a clear cut-off between the different scenarios, i.e. for systems containing 1 w% of thermal initiator, samples with V_fs above 46% required additional heat input by UV-irradiation

  doi:10.5075/epfl-298799_978-2-9701614-0-0

to re-initiate the front while this also did not suffice for V_fs above ±50%. These cut-offs can be directly related to the local heat balance since the increasing fibre content results in increased heat losses up to the point that the front temperature drops below the threshold temperature for the autocatalytic mechanism. Figure 4 moreover shows that the cut-off V_f increases with increasing thermal initiator concentration since it enhances the heat generation term in the local heat balance. Large initiator concentrations were found unable to induce a front despite the V_f being lower than the observed cut-off. This could hypothetically be attributed to a rapid conversion as a result of these high concentrations, polymerising and heating the resin before heat transfer to the fibres could take place. This subsequently introduces a strong gradient between polymer and fibres, cooling down and potentially quenching the propagating front.

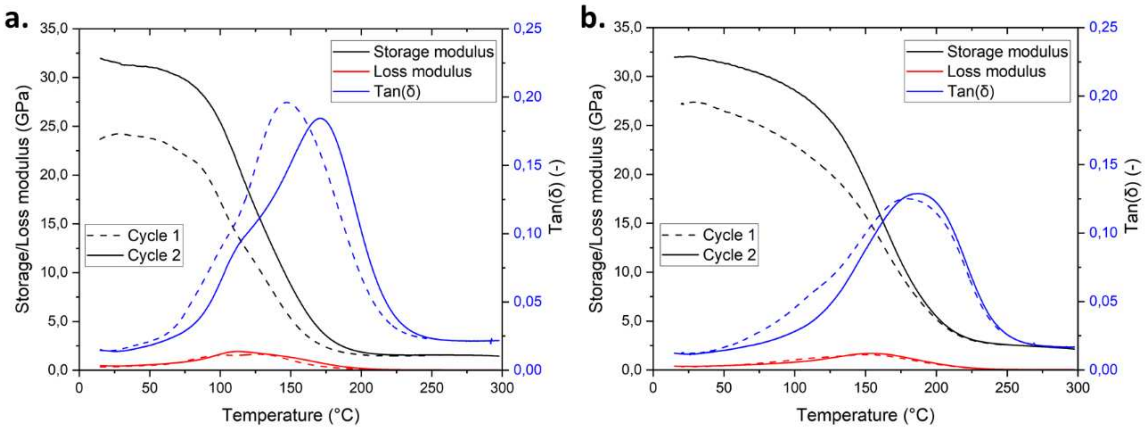

Figure 5 Typical DMA curves of samples with 40% Vf and a) 0.624 and b) 1.001 w% thermal initiator

Thermal management moreover impacts the mechanical behaviour of RICFP-produced FRPs. Assessment of the flexural modulus and the T_g by DMA showed a shift of both parameters after one completed measurement cycle. This is attributed to post curing effects most likely taking place within yarns, where carbon fibres are closely packed and hence heat losses are more severe. Figure 5 shows two typical DMA curves of FRPs with V_fs around 40% and two different initiator concentrations. Counterintuitively, the moduli recorded in the first measurement cycle were higher at lower initiator concentration, which recovered to the roughly equal moduli after post curing. The T_g was moreover 30°C higher than that when a higher concentration was used, reaching a T_g of 187.4°C after the second measurement cycle. An explanation for this behaviour follows the hypothesis that a slower heat release, and thereby gradual heating of the resin-fibre region near the front, reduces local cooling or quenching of the front and hence improves the resulting FRP properties.

4. Conclusion

The current work aimed for the production of high-volume fraction carbon FRPs in a well-insulated system by RICFP induced in a cycloaliphatic epoxide resin system. While previous investigations mainly focussed on the maximisation of system reactivities, front temperatures and velocities, control of the local heat balance was found crucial towards the optimisation of the resulting FRP properties. A correlation between heat outputs recorded in DSC measurements and front velocities was observed. The concentrations of both the photo- and

  doi:10.5075/epfl-298799_978-2-9701614-0-0

thermal initiating compounds were found of significant influence on both the heat generation and front propagation of the system. A processing window was identified that relates the formation of a self-sustaining or supported front to a required range of fibre V_fs and the initiator concentrations. This window was moreover related to the mechanical properties. Lower initiator concentrations, hence slower heat generation, was suggested beneficial for the resulting properties while a rapid post-treatment was found necessary to maximise the mechanical behaviour of FRPs. Confirmation of this suggestion is the subject of future work in combination with an extension of the processing window to gain a better insight in the role of the mould types and filler materials on the RICFP processing of FRPs.

Acknowledgements

The authors acknowledge the support from the Swiss National Science Foundation (SNF n° 200021_182669).

5. References

[1] I. D. Robertson *et al.*, *Nature*. **557**, 223–234 (2018).
[2] N. M. Chechilo, N. S. Enikolopyan, *Dokl. Phys. Chem.* **221**, 391–394 (1975).
[3] N. M. Chechilo, E. I. Khvilivitskii, N. S. Enikolopyan, *Dokl. Akad. Nauk SSSR*. **204**, 1180–1181 (1972).
[4] M. Garg *et al.*, *Nat. Commun.* **12**, 1–9 (2021).
[5] Y. Gao *et al.*, *Small*. **17**, 1–9 (2021).
[6] Y. An, J. H. Jang, J. H. Youk, W. R. Yu, *Smart Mater. Struct.* **31** (2022), doi:10.1088/1361-665X/ac41ea.
[7] Z. Zhang *et al.*, *J. Manuf. Process.* **71**, 753–762 (2021).
[8] E. Goli, I. D. Robertson, P. H. Geubelle, J. S. Moore, *J. Phys. Chem. B*. **122**, 4583–4591 (2018).
[9] E. Goli *et al.*, *Compos. Part A Appl. Sci. Manuf.* **130**, 105689 (2020).
[10] I. D. Robertson *et al.*, *ACS Macro Lett.*, 609–612 (2017).
[11] A. Mariani *et al.*, *J. Polym. Sci. Part A Polym. Chem.* **42**, 2066–2072 (2004).
[12] J. V. Crivello, S. Liu, *Chem. Mater.* **10**, 3724–3731 (1998).
[13] D. Bomze, P. Knaack, T. Koch, H. Jin, R. Liska, *J. Polym. Sci. Part A Polym. Chem.* **54**, 3751–3759 (2016).
[14] M. Sangermano, I. Antonazzo, L. Sisca, M. Carello, *Polym. Int.* **68**, 1662–1665 (2019).
[15] M. Sangermano, A. D'Anna, C. Marro, N. Klikovits, R. Liska, *Compos. Part B*. **143**, 168–171 (2018).
[16] C. Noè *et al.*, *Macromol. Mater. Eng.* **2100864**, 1–11 (2022).
[17] N. Klikovits, P. Knaack, D. Bomze, I. Krossing, R. Liska, *Polym. Chem.* **8**, 4414–4421 (2017).
[18] A. Dung Tran, T. Koch, P. Knaack, R. Liska, *Compos. Part A Appl. Sci. Manuf.* **132**, 105855 (2020).
[19] B. Gachet *et al.*, *RSC Adv.* **10**, 41915–41920 (2020).
[20] E. Goli *et al.*, *J. Appl. Polym. Sci.* **47418**, 1–9 (2018).
[21] Y. Gao *et al.*, *Chaos*. **31** (2021), doi:10.1063/5.0052821.
[22] P. Knaack *et al.*, *J. Polym. Sci. Part A Polym. Chem.* **57**, 1155–1159 (2019).
[23] E. Goli, T. Gai, P. H. Geubelle, *J. Phys. Chem. B*. **124**, 6404–6411 (2020).
[24] R. Taschner, P. Knaack, R. Liska, *J. Polym. Sci.*, 1–14 (2021).
[25] D. Bomze, P. Knaack, R. Liska, *Polym. Chem.* **6**, 8161–8167 (2015).
[26] B. R. Groce, D. P. Gary, J. K. Cantrell, J. A. Pojman, *J. Polym. Sci.*, 1–8 (2021).

  doi:10.5075/epfl-298799_978-2-9701614-0-0

MODELING AND OPTIMIZATION OF FRONTAL-POLYMERIZATION-BASED MANUFACTURING OF FIBER-REINFORCED COMPOSITES

Philippe Geubelle[ac], Sagar Vyas[ac], Aditya Kumar[ac], Yuan Gao[ac], Nil Parikh[ac], Nancy Sottos[bc]

a: Department of Aerospace Engineering, University of Illinois (geubelle@illinois.edu)
b: Department of Materials Science and Engineering, University of Illinois
c: Beckman Institute for Advanced Science and Technology, University of Illinois

Abstract: *Frontal polymerization (FP) has recently been proposed as a faster, energy efficient, out-of-autoclave manufacturing method for thermosetting polymer matrix composites. In this paper, we first derive a closed-form approximation of the front speed based on an asymptotic analysis of the thermal and degree-of-cure solutions in the vicinity of the propagating front. Theoretical results are compared with numerical predictions and experimental measurements for the case of carbon and glass fibers embedded in a dicyclopentadiene (DCPD) resin, showing very good agreement. We then combine a reaction-diffusion finite element solver and an adjoint-based sensitivity analysis to perform a gradient-based optimization of a through-thickness FP-based manufacturing of thick carbon-DCPD composite panels with high fiber volume fractions.*

Keywords: Frontal polymerization; Reaction-diffusion model; Process optimization; Thermoset composites.

1. Introduction

Current manufacturing techniques of thermoset-matrix fiber-reinforced composites rely primarily on the bulk polymerization of the resin. In addition to the substantial capital investments associated with the need for autoclaves, ovens, or heated molds, the long and complex heat and pressure cycles involved in the thermal curing process result in a time-consuming and energy-intensive manufacturing process. Frontal Polymerization (FP), which involves a polymerization wave that propagates through a monomer or a gel to convert it to polymer, has been recently demonstrated by the Autonomous Materials Systems research group at the University of Illinois in [1] as an alternative approach to eliminate the need for autoclaves and make the process substantially (by orders of magnitude) faster and more energy efficient.

The key parameters describing the propagation of a polymerization front in a fiber-reinforced composite, i.e., the front speed and temperature, depend on a large number of parameters, including those that define the cure kinetics of the resin (heat of reaction, activation energy, time constant, etc.), the process conditions (initial temperature and degree of cure of the resin, and heat losses to the surrounding), the volume fraction and orientation of the fibers, and the thermal properties of resin and fibers.

To capture the impact of most of these parameters, a reaction-diffusion model expressed in terms of the transient temperature field of the composite and the degree of cure of the resin and based on the homogenized thermal properties of the composite has been developed, implemented, validated, and applied to the FP-based manufacturing of carbon/DCPD and glass/DCPD composites [2-4].

  doi:10.5075/epfl-298799_978-2-9701614-0-0

The first part of this paper summarizes some recent advances made in the theoretical and numerical analysis of FP in unidirectional composites, with emphasis on the prediction of the impact of the fiber content, cure kinetics, and thermal properties on the steady-state propagation speed of the front.

In the second part of this paper, we combine a reaction-diffusion finite element solver and an adjoint-based sensitivity analysis to perform a gradient-based optimization of the through-thickness FP-based manufacturing of thick carbon-DCPD composite panels with high fiber volume fractions. The reaction-diffusion solver is validated through comparison between numerical predictions and experimental measurements of the thermal histories at various locations across the thickness of the manufactured part. The process optimization aims at reducing the energy input and process duration while achieving high values of the degree of cure throughout the manufactured panel. The optimized manufacturing processes are compared with experimental observations.

2. Polymerization front propagation in DCPD-based composites

2.1 1D reaction-diffusion model

As described in [2], frontal polymerization (FP) in unidirectional composites with a fiber volume fraction ϕ can be modeled by the following reaction-diffusion partial differential equations involving homogenized properties:

$$\begin{cases} \overline{\rho C_p}\dfrac{\partial T}{\partial t} = \bar{\kappa}\dfrac{\partial^2 T}{\partial x^2} + (1-\phi)\rho_{\mathrm{m}} H_{\mathrm{r}}\dfrac{\partial \alpha}{\partial t}, \\ \dfrac{\partial \alpha}{\partial t} = A\exp\left(-\dfrac{E}{RT}\right) f(\alpha). \end{cases} \tag{1}$$

In the first relationship of Eq. (1), the temperature T (in K) and degree of cure α (dimensionless) are the two dependent variables, x (in m) is the spatial coordinate in the direction that aligns with the fiber orientation, t (s) denotes time, and ρ_{m} (in kg/m^3) and H_{r} (in J/kg) represent the density and heat of reaction of the resin, respectively. The homogenized thermal properties $\bar{\kappa}$ and $\overline{\rho C_p}$ can be captured by the rule of mixture as

$$\begin{cases} \bar{\kappa} = \kappa_{\mathrm{m}}(1-\phi) + \kappa_{\mathrm{f}}\phi, \\ \overline{\rho C_p} = \rho_{\mathrm{m}} C_{p,\mathrm{m}}(1-\phi) + \rho_{\mathrm{f}} C_{p,\mathrm{f}}\phi, \end{cases} \tag{2}$$

where the subscripts 'm' and 'f' respectively denote the matrix and the fibers, while κ (in W/m·K), ρ (in kg/m^3), and C_p (in J/kg·K) represent the thermal conductivity, density, and heat capacity, respectively.

The second relationship of Eq. (1) describes the polymerization kinetics in terms of the Arrhenius equation, where A (in 1/s), E (in J/mol) and R (= 8.314 J/mol·K) stand for the pre-exponential factor, activation energy, and the ideal gas constant. A generalized Prout-Tompkins model with a molecular diffusion term $f(\alpha) = (1-\alpha)^n \alpha^m \left[\frac{1}{1+e^{c_d(\alpha-\alpha_d)}}\right]$ was adopted to describe the cure kinetics, where n and m (both dimensionless) denote the reaction order, while c_d and α_d (both dimensionless) incorporate the molecular diffusion effect. The material properties and cure kinetics parameters in the model are given in Tables 1 and 2, respectively.

Table 1: Thermal properties of the DCPD resin and the carbon and glass fibers

Materials	κ (W/m·K)	ρ (kg/m^3)	C_p (J/kg·K)
DCPD (m)	0.15	980	1,600
Carbon fibers (f)	9.38	1,800	753.6
Glass fibers (f)	1.28	2,575	802.5

Table 2: Cure kinetic parameters for DCPD

A (1/s)	E (J/mol)	H_r (J/kg)	n	m	c_d	α_d
8.55×10^{15}	110,750	350,000	1.72	0.77	14.48	0.41

As described in [3], the governing PDEs (1) can be converted into a system of steady-state ordinary differential equations by defining a moving coordinate system attached to the steadily propagating front, $X = x - v_{\mathrm{f},\parallel}\, t$, where $v_{\mathrm{f},\parallel}$ is the speed of the polymerization front in the fiber direction. Then, using the idea that the value of front velocity is closely related to the amount of energy *instantaneously* released at the reaction front [4], we can derive the following asymptotic estimates for the front velocity for FP in a unidirectional composite with arbitrary fiber volume fraction:

$$v_{\mathrm{f},\parallel} = \max_{\varepsilon} \sqrt{\frac{A\,\overline{\kappa}}{(1-\phi)\rho_\mathrm{m} H_\mathrm{r}} \frac{R\tilde{T}(\varepsilon)^2}{E}\, exp\left(\frac{-E}{R\tilde{T}(\varepsilon)}\right)\frac{1}{\sigma}}, \tag{3}$$

where

$$\begin{cases} \tilde{T}(\varepsilon) = T_0 + \dfrac{(1-\phi)\,(1-\alpha_0-\varepsilon)\;\rho_\mathrm{m} H_\mathrm{r}}{\overline{\rho C_p}}, \\ \sigma = \displaystyle\int_0^{1-\alpha_0-\varepsilon} \frac{y}{(y+\varepsilon)^n (1-\varepsilon-y)^m} \left(1+\exp(c_\mathrm{d}\,(1-\varepsilon-\alpha_d-y))\right) dy. \end{cases} \tag{4}$$

In Eq. (3) and (4), T_0 and α_0 respectively denote the initial values of the temperature and degree of cure. The theoretical formula (3) is used to study the dependence of front speed on the fiber volume fraction ϕ for two composites: carbon/DCPD and glass/DCPD. As observed in Figure 1, the front velocity for carbon/DCPD composite has a non-monotonic dependence on ϕ as the velocity first increases upon addition of a small amount of carbon fibers, reaches a maximum at $\phi\sim0.1$ before progressively decreasing as the amount of heat of reaction associated with the exothermic frontal polymerization is reduced with increasing fiber volume fraction. For the glass/DCPD composite, however, Figure 1 shows that the front velocity monotonically decreases with increasing fiber volume fraction. This contrasting behavior is due to the higher thermal diffusivity ($\delta = \kappa/\rho C_p$) of carbon fibers compared to glass fibers. The higher thermal diffusivity of carbon fibers allows for the carbon/DCPD composite to overcome the effect of lower effective heat of reaction ($(1-\phi)H_\mathrm{r}$ term in Eq. (1)) for low values of ϕ resulting in a higher front velocity. Such behavior is also confirmed numerically and experimentally as shown in Figure 1. Analytically, we can carry out a Taylor series expansion of (3) around $\phi = 0$, and obtain that non-monotonic dependence of front velocity on ϕ is observed when

$$\frac{\delta_{\mathrm{f}}}{\delta_{\mathrm{m}}} - \left(\frac{1}{1 + T_0\, C_{p,\mathrm{m}}/H_{\mathrm{r}}} + \frac{E}{2\,R}\, \frac{C_{p,\mathrm{m}}}{H_{\mathrm{r}}}\, \frac{1}{(1 + T_0\, C_{p,\mathrm{m}}/H_{\mathrm{r}})^2} \right) > 0, \tag{5}$$

which demonstrates the key role played by the thermal diffusivity of the fibers.

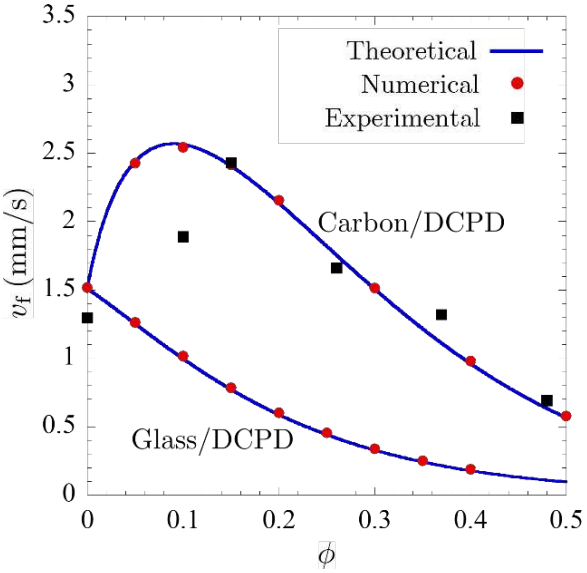

Figure 1. Effect of the fiber volume fraction ϕ on the steady-state propagation speed v_f of a polymerization front in carbon/DCPD and glass/DCPD composites: theoretical (solid curves) and numerical (red symbols) predictions. The analytical predictions for the carbon/DCPD composite are compared with experimental measurements (black symbols) taken from [2].

2.2 Reaction-diffusion modeling of anisotropic FP

To investigate the direction-dependent propagation of the polymerization front in unidirectional composites, the model in Eq. (1) can be extended to 2D as follows:

$$\begin{cases} \overline{\rho C_p}\, \dfrac{\partial T}{\partial t} = \overline{\kappa_{ij}}\, \dfrac{\partial^2 T}{\partial x_i \partial x_j} + (1-\phi)\rho_{\mathrm{m}} H_{\mathrm{r}}\, \dfrac{\partial \alpha}{\partial t}, \\ \dfrac{\partial \alpha}{\partial t} = A \exp\left(-\dfrac{E}{RT}\right) f(\alpha), \end{cases} \tag{6}$$

where the dimension x_i and x_j represent the x (parallel to fibers) and y (perpendicular to fibers) in the schematic presented in Figure 2a, and $\overline{\kappa_{ij}}$ is the homogenized thermal conductivity matrix given by

$$\overline{\kappa_{ij}} = \begin{bmatrix} \overline{\kappa_{\parallel}} & 0 \\ 0 & \overline{\kappa_{\perp}} \end{bmatrix}. \tag{7}$$

In this work, the homogenized thermal conductivities in the directions parallel ($\overline{\kappa_{\parallel}}$) and perpendicular ($\overline{\kappa_{\perp}}$) to the fiber orientation were determined by the rule of mixture and the extended Rayleigh model [5]:

$$\begin{cases} \overline{\kappa_{\parallel}} = \kappa_{\mathrm{m}}(1-\phi) + \kappa_{\mathrm{f}}\phi, \\ \overline{\kappa_{\perp}} = \kappa_{\mathrm{m}} + \dfrac{2\phi\kappa_{\mathrm{m}}}{\dfrac{\kappa_{\mathrm{m}} + \kappa_{\mathrm{f}}}{\kappa_{\mathrm{f}} - \kappa_{\mathrm{m}}}\phi + \dfrac{\kappa_{\mathrm{f}} - \kappa_{\mathrm{m}}}{\kappa_{\mathrm{f}} + \kappa_{\mathrm{m}}}(0.30584\phi^4 + 0.01336\phi^8 + \cdots)}. \end{cases} \tag{8}$$

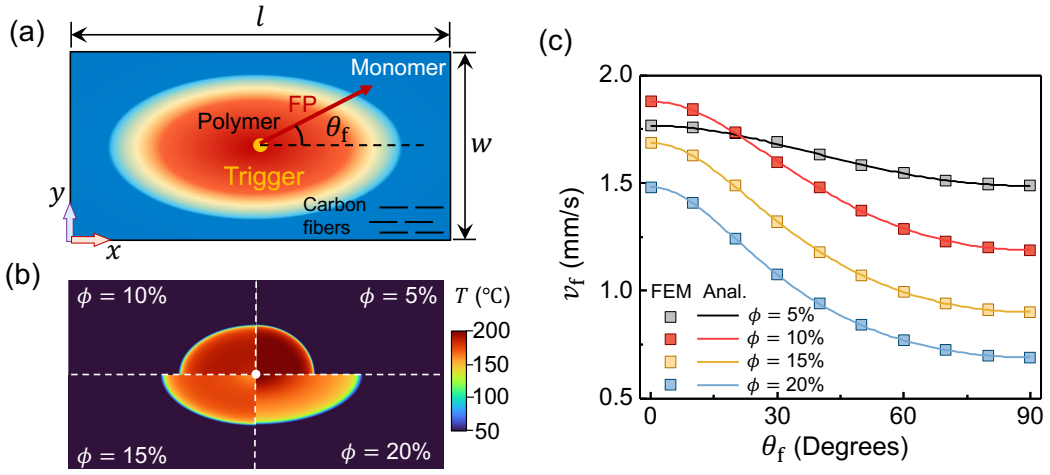

Figure 2 Anisotropic FP in unidirectional carbon/DCPD composite. (a) Problem description. The 2D numerical domain has a length $l = 40$ mm and a width $w = 20$ mm. (b) Effect of fiber volume fraction ϕ on the extent of the front at a time when the front has propagated by 10 mm in y-direction. (c) Comparison between analytical (solid curves) and numerical (symbols) results for the angular dependence of the front speed v_f for four values of ϕ.

Typical results obtained for an initial temperature $T_0 = 20$ °C and an initial degree of cure $\alpha_0 = 0.05$ are presented in Figure 2b. As the volume fraction ϕ increases from 5% to 20%, the thermal properties of the composites are increasingly anisotropic, and the front adopts an elliptical shape with an increasing aspect ratio. The numerical snapshots of the temperature field correspond to the moment at which the front has propagated by 10 mm in the y-direction. Figure 2c demonstrates the angular dependence of the front velocity v_f (with the $0 \leq \theta_f \leq 90°$ defined in Figure 2a) for different values of the fiber volume fraction. In Figure 2c, the numerical results (symbols) are compared with the following analytical expressions (curves):

$$v_f(\theta_f) = \sqrt{\frac{\left(v_{f,\parallel} v_{f,\perp}\right)^2 (1 + \tan^2 \theta_f)}{v_{f,\parallel}^2 \tan^2 \theta_f + v_{f,\perp}^2}}, \tag{9}$$

where $v_{f,\parallel}$ and $v_{f,\perp}$ denote the front velocities in directions parallel ($\theta_f = 0°$) and perpendicular ($\theta_f = 90°$) to the fiber orientation.

3. Through-thickness FP-based manufacturing of thick composites

As indicated in the previous section, the polymerization front speed in high fiber-volume fraction composite decreases with ϕ as the exothermic heat of reaction available to sustain the front is reduced as quantified by the $(1-\phi)$ term in the thermal diffusion Eq. (1). To address this issue, a through-thickness FP-based process has been adopted for the manufacturing of thick high-volume-fraction composites, with the thermal trigger generated through a heat source located at the bottom of the composite part. In this last section, we simulate and optimize a through-thickness FP-based manufacturing process for a 2.2 mm thick carbon/DCPD woven composite with $\phi = 0.65$.

3.1 Process modeling and validation

For this through-thickness FP process, the computational domain consists of a 2.2 mm long 1-D model of the composite and of a 25.4 mm thick PTFE insulation. FP in the composite (0 mm $\leq x \leq$ 2.2 mm) is modeled using Eq. (1) with the expression of the homogenized through-thickness thermal conductivity of the woven composite $\bar{\kappa}$ taken from [6]. The transient thermal solution in the insulation layer (2.2mm $\leq x \leq$ 27.6 mm) is modeled as

$$\rho_{\mathrm{i}} C_{p,\mathrm{i}} \frac{\partial T}{\partial t} = \kappa_{\mathrm{i}} \frac{\partial^2 T}{\partial x^2}, \tag{10}$$

where ρ_{i}, $C_{p,\mathrm{i}}$, κ_{i} are the density, specific heat capacity, and thermal conductivity of the insulation, respectively. Equations (1) and (10) are solved with the following boundary conditions along the bottom side of the composite:

$$\begin{aligned} -\bar{\kappa}\frac{\partial T}{\partial x}(0,t) &= Q^*(t), \qquad \text{for } t \leq t_{\mathrm{trig}} \\ -\bar{\kappa}\frac{\partial T}{\partial x}(0,t) &= 0, \qquad \text{for } t > t_{\mathrm{trig}} \end{aligned} \tag{11}$$

where $Q^*(t)$ is the time-dependent heat flux applied by the heating unit to trigger the FP and t_{trig} is the duration of the trigger. The initial temperature in the entire domain, T_0, is set to 20^0C while the initial degree of cure of the composite, α_0, is set to 0.01. The top end of the domain ($x = 27.6$ mm) is insulated throughout the simulation. The model is discretized spatially using 1D linear finite elements and temporally using the Crank-Nicolson method, and the resulting nonlinear algebraic equations are solved at each time step using the Newton-Raphson method. A very fine uniform grid (200 elements) and a small time step (set at 0.01 s) are adopted to capture accurately the transient evolution of the temperature and degree of cure throughout the composite layer.

Figure 3 presents the result of a validation study of the 1-D thermo-chemical solver by comparing the thermocouple measurement (solid red curve) and the finite element simulation (dashed red curve) of the evolution of the temperature at the top of the composite layer. The solid black curve denotes the temperature of the heater.

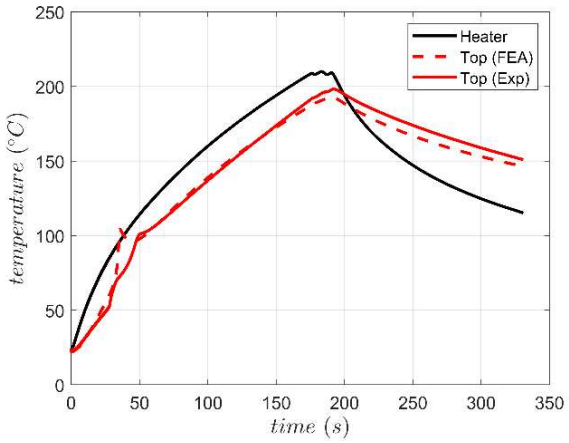

Figure 3. Comparison between numerical (dashed red curve) and experimental (solid red curve) results obtained by applying the heater profile shown by the black curve. The numerical and

experimental results show good agreement for the heating ($t \leq 190\ s$) and cooling ($t > 190\ s$) phases of the trigger thereby validating the numerical model.

As apparent in Figure 3, the model and experimental results are in good agreement, thereby validating the model. The energy cost associated with the trigger is computed by converting the temperature-time trigger to a flux-time trigger, calculating the energy density (in J/m^2) by computing the area under the flux-time curve, and then multiplying the energy density by the area of the panel (0.013 m^2) resulting in an energy cost of 14,381 J.

3.2 Process optimization

The second component of this numerical analysis of the through-thickness FP-based manufacturing process consists in minimizing the energy input to the composite while achieving a high-quality part characterized by a minimum degree of cure of 0.95 throughout the thickness of the composite at the time the trigger is turned off. The optimization problem is formulated by expressing the flux-time trigger profile as a piecewise linear curve consisting of ten flux design variables equally spaced in time. Hence, the objective of the process optimization consists of reducing the area under the applied-flux-time curve. In this gradient-based optimization scheme, the sensitivities for the objective function are computed analytically whereas those associated with the constraint function are obtained using the adjoint method.

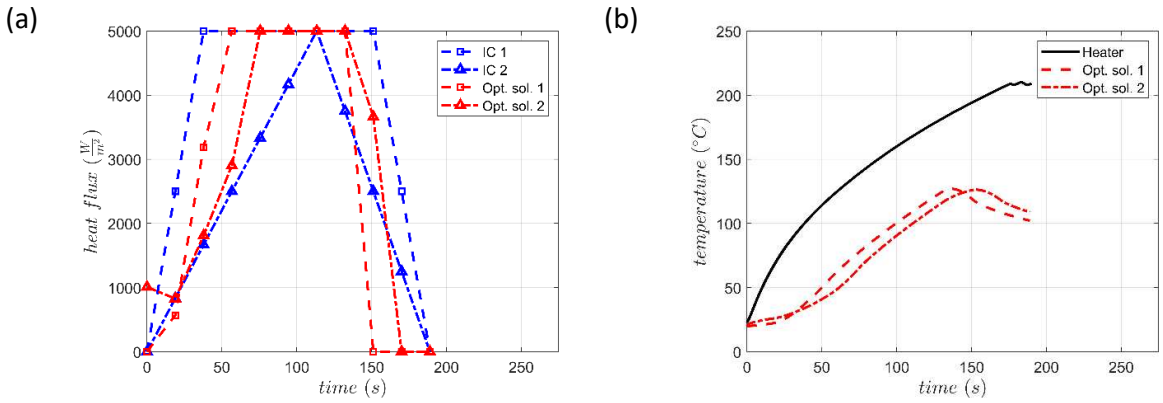

Figure 4. (a) Two different initial trigger profiles (blue curves) with a trigger duration of 190 s and their corresponding optimal results (red curves). The difference between the optimal trigger profiles indicates the existence of local optima, although the predicted optimal profiles are relatively similar. (b) Optimal flux-time triggers converted to temperature-time triggers for the two optimal solutions shown in (a) compared to the reference trigger (black solid curve).

We constrain the flux design variables (square and triangular symbols in Figure 4a) to lie between 0 and 5000 W/m^2 and set the trigger duration to 190 s to facilitate a direct comparison with the experimental results. Additionally, we adopt multiple different initial guesses for the trigger profile as local minima are expected in this optimization problem. Two of these initial guesses denoted by IC 1 and IC 2 are shown as blue curves in Figure 4a. The corresponding optimized trigger profiles are shown as red curves in Figure 4a for the applied heat flux versus time and in Figure 4b for the trigger temperature-time profile. When compared with the reference experimental curve (solid black curve in Fig. 4b), the optimization results indicate energy savings of approximately 50%.

4. Conclusions

  doi:10.5075/epfl-298799_978-2-9701614-0-0

Frontal polymerization (FP) is a promising approach for the out-of-autoclave, rapid, and energy-efficient manufacturing of thermoset composite materials. Through the numerical and analytical solutions of a reaction-diffusion model expressed in terms of the homogenized thermal properties of the composite, this study has quantified the impact of the thermal diffusivity of the reinforcing phase on the amplitude and directionality of the polymerization front velocity. In the second part of this manuscript, we have summarized the results of finite-element-based simulations of the FP-based through-thickness 'flash curing' of a composite laminate. The associated gradient-based optimization results indicate the potential for further reduction of the energy input for the FP-based manufacturing process.

Acknowledgements

This work was supported by the National Science Foundation for Grant No. 1933932 through the GOALI: Manufacturing USA: Energy Efficient Processing of Thermosetting Polymers and Composites. The authors also acknowledge the support from the U. S. Air Force Office of Scientific Research through Award FA9550-20-1-0194 as part of the Center of Excellence in Self-healing and Morphogenic Manufacturing.

5. References

1. Robertson, I. D., Yourdkhani, M., Centellas, P. J., Aw, J. E., Ivanoff, D. G., Goli, E., Lloyd, E. M., Dean, L. M., Sottos, N. R., Geubelle, P. H., Moore, J. S., and White, S. R. (2018) "Rapid energy-efficient manufacturing of polymers and composites via frontal polymerization." Nature, 557, 223-227.
2. Goli, E., Parikh, N. A., Yourdkhani, M., Hibbard, N. G., Moore, J. S., Sottos, N. R., and Geubelle, P. H. (2020) "Frontal polymerization of unidirectional carbon-fiber-reinforced composites." Composites Part A, 130, 105689.
3. Vyas, S., Goli, E., Zhang, X., and Geubelle, P. H. (2019) "Manufacturing of unidirectional glass-fiber-reinforced composites via frontal polymerization: a numerical study". Composites Science and Technology, 184, 107832, 1-6.
4. Kumar, A., Gao, Y., and Geubelle, P. H. (2021) "Analytical estimates of front velocity in the frontal polymerization of thermoset polymers and composites." Journal of Polymer Science, 59,1109–1118.
5. Pietrak, K., and Wisniewski, T. S. (2014). "Methods for experimental determination of solid-solid interfacial thermal resistance with application to composite materials." Journal of Power Technologies, 94, 270.
6. Ning, Q., and Chou, T. (1995). "A closed-form solution of the transverse effective thermal conductivity of woven fabric composites." Journal of Composite Materials, 29, 2280–2294.

  doi:10.5075/epfl-298799_978-2-9701614-0-0

IN-SITU MONITORING OF WELD LINE THICKNESS IN CONTINUOUS ULTRASONIC WELDING OF THERMOPLASTIC COMPOSITES

Erdem Akay[a], Filipp Köhler[a,b], Irene Fernandez Villegas[a]

a: Aerospace Structures and Materials Department, Faculty of Aerospace Engineering, Delft University of Technology, Kluyverweg 1, 2629 HS Delft, The Netherlands – e.akay@tudelft.nl
b: CTC GmbH, Airbusstraße 1, 21684 Stade, Germany

Abstract: *Continuous ultrasonic welding is a very fast and efficient composite joining technique that has been developed in recent years and especially aimed for aerospace applications. Researchers have put a significant amount of effort into revealing the capabilities of continuous ultrasonic welding and the current study was aimed to complement prior work by suggesting a potential in-situ monitoring methodology for the process. Within the scope of this study, a correlation between the weld line thickness and weld quality was experimentally shown by using a robotic continuous ultrasonic welding system located at* CTC GmbH in Stade. *The aforementioned correlation then used to demonstrate a possible laser sensor based monitoring methodology for continuous ultrasonic welding process by utilizing the frame based continuous ultrasonic welding system located in the Faculty of Aerospace Engineering at Delft University of Technology.*

Keywords: Thermoplastic Composites; In-situ Monitoring; Continuous Ultrasonic Welding; Thickness Measurement; Laser Sensors

1. Introduction

Continuous ultrasonic welding (i.e. “CUW” in an abbreviated form) is one of the most efficient integration methods of thermoplastic composites. Researchers from our group have already utilized CUW method by using both frame based and robotic welding platforms to achieve sufficient amount of joint strength for aerospace applications and they have also improved CUW process in many aspects [1-6]. On the other hand, the implementation of this method into an industrial manufacturing process still requires the ability of consistent and high-quality welding in a controlled manner. It is obvious that a sophisticated monitoring system, which is developed for ensuring the highest-level of weld quality in each practice will play a key role to transform CUW process into a commonly relied on industrial tool.

Typically, experimental techniques like micrography, mechanical testing and fracture surface examinations are used to determine the quality of a welded composite joint. Information gathered from these evaluation techniques are always convenient to correlate the process parameters and other process data with the welded joint performance. On the other hand, aforementioned examinations can only be a part of the baseline research, if the ultimate goal is performing in-situ quality evaluations in an industrialized manufacturing process. To achieve this goal, several studies were conducted within the past decade. Villegas showed that monitoring welding process can be an efficient way to define a desired parameter envelope for high strength

  doi:10.5075/epfl-298799_978-2-9701614-0-0

welds and also power and displacement data obtained from the microprocessor-controlled ultrasonic welding machine can be effectively used for in situ monitoring of the static ultrasonic welding process [7 - 9]. Previous research indicates that, a specialized monitoring technique for continuous ultrasonic welding process can be beneficial to take a step forward for industrialization of this joining method for thermoplastic composite structures. Therefore, within the context of this study, a possible way for in-situ monitoring of the CUW process was investigated by performing weld line thickness measurements.

2. Weld-line thickness investigation for robotic ultrasonic welding process

2.1 Experimental setup and specimen preparations

Within this part of the study, the correlation between the weld line thickness and the quality of the welds was assessed. The quality of the welds was determined by the lap shear strength of welded adherends. The study was performed on a robotic ultrasonic welding cell at the CTC GmbH in Stade as seen in Figure 1. A Kuka KR125 using a KR C2 controller is used to move the welding head along a predefined and programmed weld path. The welding head itself consists of the welding train which is supplied by Herrmann Ultraschalltechnik. The welding head is complemented by a pre-clamping and a consolidation unit to allow for sufficient consolidation. This setup was already used by our research group in a previous study [6].

Figure 1. Robotic ultrasonic welding cell at CTC GmbH in Stade

Welding was performed on coupons in a single lap configuration. The total weld length was 250 mm. The adherends were made out of high performance unidirectional material from the PAEK family. A multiaxial layup was used which resulted in a adherend thickness of 2.2 mm. After welding the adherends were cut into single lap shear specimen and were tested according to ASTM D1002 with a crosshead speed of 1.3 mm/min. In total 8 samples were extracted while areas at the beginning and at the end of the weld line were discarded. The sample dimensions and the cutting plan are shown in Figure 2. A discontinuous energy director with an areal weight of 160 g/m² made out of the same polymer material as the adherends' matrix was used throughout the study.

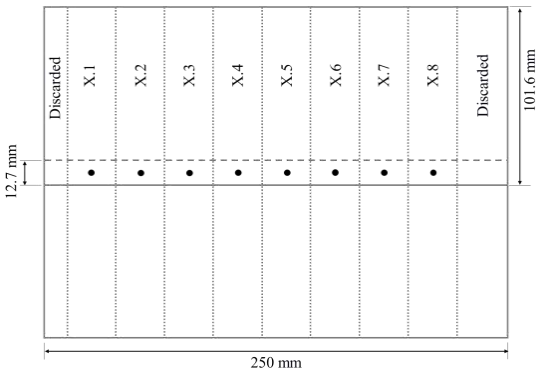

Figure 2. Sample dimension and cutting plan of the coupons used for welding. The black dots mark the point of measurement for the weld line thickness

2.1 Measurements and results

To determine the weld line thickness (i.e. t_{weld_line}), the thickness of the coupons (i.e. $t_{upper\_adherend}$ and $t_{lower\_adherend}$) in the intended weld area was measured before welding. After welding the total thickness of the welded area was measured. To obtain the resulting weld line thickness the thicknesses of the upper and lower adherends are subtracted from the thickness in the weld area according to the equation below:

$$t_{weld\_line} = t_{welded\_area} - (t_{upper\_adherend} + t_{lower\_adherend}) \quad (1)$$

All measurements were done using a caliper. To correlate the weld line thickness to the achieved lap shear strength, measurements were taken in the center of each specimen prior to welding and prior to final testing. The locations of the measurement points are shown in Figure 2. Within the study, a constant vibration amplitude and only one type of energy director was used while the welding speed was varied between 18-32 mm/s.

Figure 3 shows the lap shear strength as a function of the calculated weld line thickness. The lap shear strength is given as percentage of the highest lap shear strength achieved within this study. The weld line thickness is given in relation to the energy director thickness before welding, while 100% (vertical line) marks the original energy director thickness. Each color represents a coupon welded with a specific welding speed. The graph indicates a correlation between the weld line thickness and the lap shear strength which can be achieved. Weld line thicknesses which are higher than the original energy director thickness tend to result in lower final lap shear strength. Those samples also showed porosity within the weld line which is a sign of poor welding quality and, in those cases, insufficient consolidation. In contrast, specimens with a weld line thickness of 10-30 % of the original energy director thickness show lap shear strength values around 80% or higher compared to the maximum achieved value. Those specimens also show no signs of porosity or un-welded areas. For those specimens showing a negative weld line thickness it has to be noted that the chosen method of determining the weld line thickness cannot distinguish between thickness decrease happening in the weld line and a decrease in thickness of the adherends itself. Negative thickness therefore can be caused by significant through-the-thickness heating and fiber squeeze out. Although the resulting lap shear strength values are not affected by this, through-the-thickness heating and fiber squeeze out should be prevented as much as possible as it can lead to porosity within the weld line especially at the edges of the weld area. It is assumed that even lower weld line thicknesses would also have an effect on the lap shear strength as the integrity of the adherends is reduced.

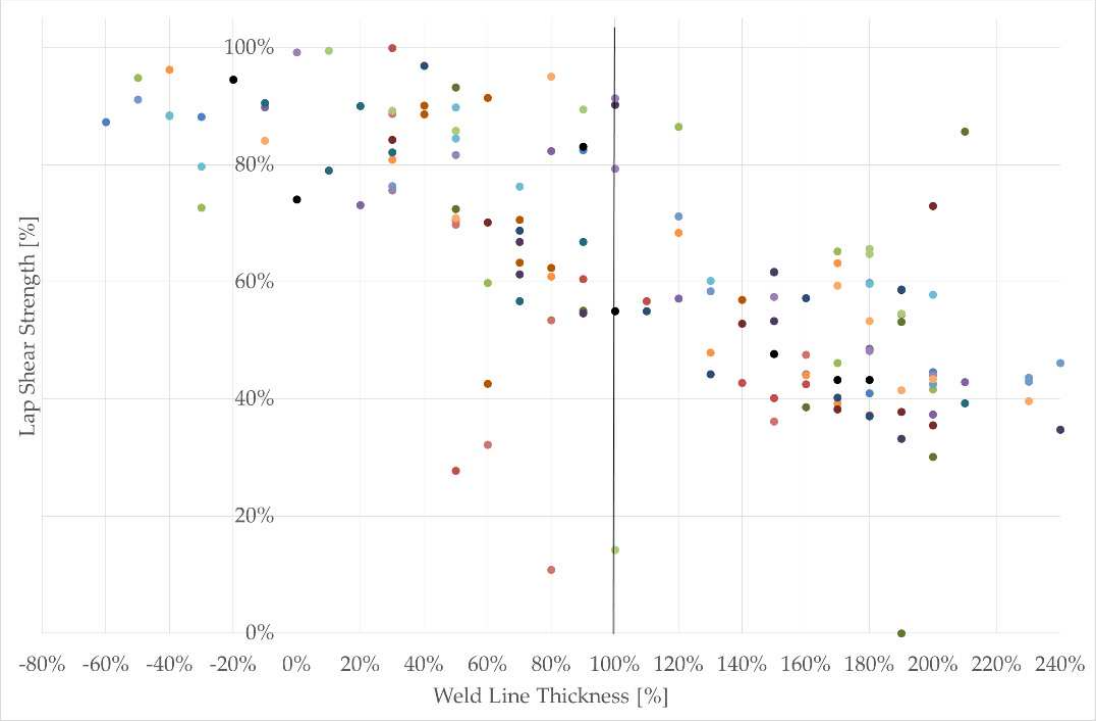

Figure 3. Graph shows the lap shear strength in relation to the weld line thickness. Lap shear strength is given as percentage to highest achieved lap shear strength. Weld line thickness is given in relation to energy director thickness prior to welding (marked as vertical line). Each color stands for one specific welding speed.

3. Monitoring system development for weld-line thickness measurements

3.1 Continuous ultrasonic welding machine and welding experiment details

The correlation between weld-line thickness and weld quality observed from the experiments performed with the robotic continuous ultrasonic welding system indicated the possible benefits of a well established in-situ monitoring methodology for continuous ultrasonic welding process based on thickness measurements. Consequently, it was decided to develop a weld-line thickness monitoring system for performing in-situ measurements and quality evaluations with dedicated sensors. For this purpose, the continuous ultrasonic welding frame-based machine located in the Faculty of Aerospace Engineering at Delft University of Technology was chosen. This particular CUW machine utilizes a very stiff frame structure and consists of four main subsystems, namely ultrasonic welding machine, consolidation system, movable X-Y table and the welding fixture, as seen in Figure 4a. The sketch in Figure 4b shows the lay-out of the adherends and energy director within the welding clamping fixture for welding process.

Composite adherends for the welding experiments were manufactured out of 5 harness-satin CF/PPS thermoplastic powder-impregnated material . The dimensions of the adherends cut from the manufactured laminate were 220 mm x 101.6 mm. The nominal thickness for each adherend was measured as 1.8mm and the overlap length was 12.7mm. A 0.2mm-thick discontinuous PPS energy director (i.e. the woven mesh introduced in [2]) was used for the experiments. A specific set of welding parameters (i.e., welding force, amplitude, consolidation force and distance between consolidator and sonotrode) were applied along the entire study. During the welding experiments, only the welding speed was changed between 7mm/s to 30mm/s, to differentiate the weld line properties in a controlled manner.

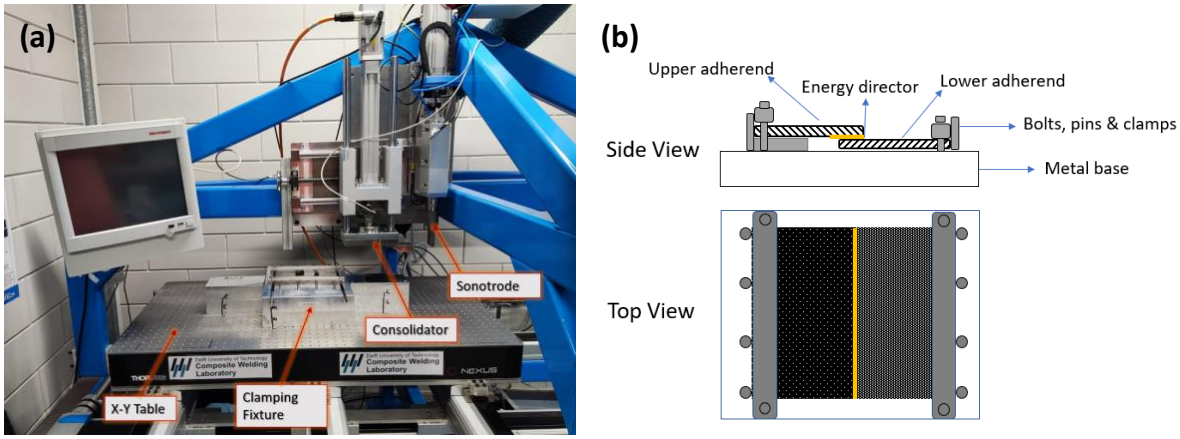

Figure 4. (a) Continuous ultrasonic welding system, (b) the welding clamping fixture that is used for adherend and ED placement for CUW experiments

3.2 Monitoring setup and measurement methodology

The stiff structural frame of CUW machine was able to accommodate any size of sensors while keeping them attached rigidly in place, which was important for creating a system without any complexities or calibration problems. Initially, two different types of laser sensors (i.e. spot laser sensor and 2D line laser sensor) for weld-line thickness measurement and a thermal camera for temperature measurement were utilized along with the designed sensor frame. All of these components were integrated into the CUW system for performing in-situ monitoring experiments as seen in Figure 5. After conducting some preliminary experiments with this initial design of the in-situ monitoring system, it was soon understood that subsequent sensor frame iterations had to be performed to achieve an optimal measurement experience, which resulted five different iterations of monitoring setups in total. In each setup, different equipment configurations and consequently different variations of the data processing and analysis algorithm were generated due to the modifications on the sensor locations and measurement methodologies.

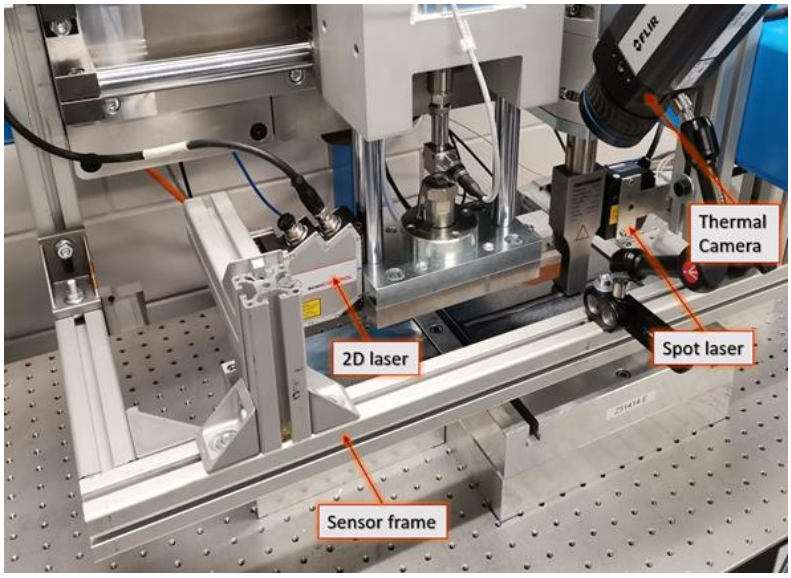

Figure 5. The initial design of in-situ monitoring setup for CUW process

Using the least possible number of sensors is desirable for achieving an efficient and easy to apply in-situ monitoring system for CUW process, since there is a direct proportion between the

number of sensors, data size, computation time and system complexity. Therefore, the configuration that utilizes a single 2D laser sensor was chosen for the demonstration purposes in this study. For this purpose, a single 2D laser sensor (i.e. Micro-Epsilon scanCONTROL 2950-25) was used to scan the upper and lower adherends before the weld process, and it is used to scan the welded area after the weld process as seen in Figure 6. By performing these 2D scans, three set of data files were obtained. Following that, recorded data files were processed within the Python algorithm to calculate the thickness of the upper adherend, lower adherend and welded area at thousands of equally spaced stations along the weld direction, respectively. Finally, the thickness information obtained from each scan were used to calculate the actual weld-line thickness values at the same stations along the weld direction by utilizing Equation 1.

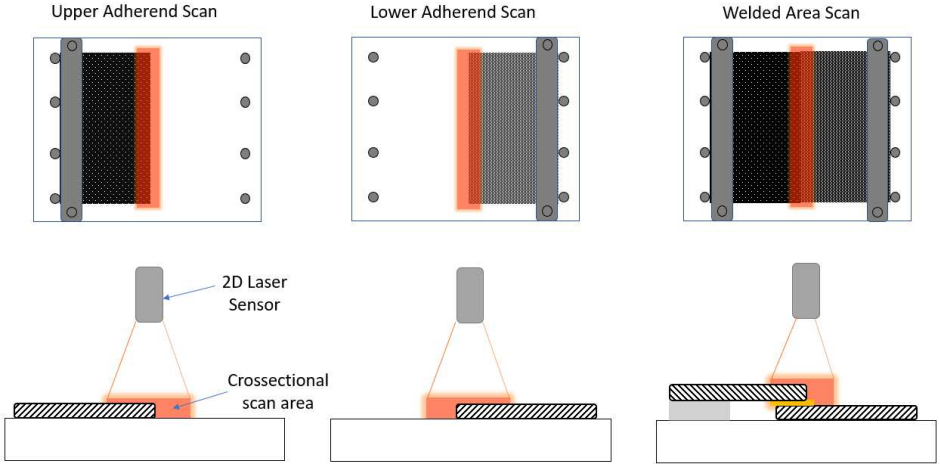

Figure 6. Adherend and welded stack thickness measurement

3.3 Weld-line thickness monitoring

The output of a weld-line thickness measurement analysis for the experiment performed at 15mm/s weld speed is provided in Figure 7 as an example. For this experiment, the welding process was started at approximately 15mm away from the starting edge of the adherends and continued up to the point of 205mm from the same edge resulting with a 190mm long weld. Y axis of the given curve in this plot indicates the weld line thickness of the welded stack calculated by moving-average of the data and x-axis shows the weld direction starting from the edge. It can be seen that a significant weld line thickness decrease occurs in the first 15mm, then a relatively flat weld line thickness behavior is visible and lastly the calculated weld line thickness increases significantly after around 205mm. From the experiment, it is known that the initial and final areas with steep thickness variation in this plot falls out the actual welded area, therefore it can be stated that the gap between the unwelded adherends is misleading the thickness measurement in these locations and the actual weld line thickness (i.e. the flat area in the plot) of this welding experiment deviates around approximately 60µm. Within the monitoring algorithm, the first derivative of the moving-average data was analyzed to designate these unwelded areas. By using the result of this analysis, the start and end locations of the actual welded area were calculated, and initial & final unwelded areas were automatically indicated as seen in Figure 7.

The variations in weld line thickness were also used for identifying local quality issues. In Figure 8a, the blue plot indicates the weld-line thickness measurement output of the monitoring system for the experiment that previously discussed (i.e. performed at 15mm/s weld speed).

  doi:10.5075/epfl-298799_978-2-9701614-0-0

Here, the single lap shear strength percentage values (i.e. with respect to the maximum achieved strength value) of individual specimens cut from the same welded plate are also shown as green bars. Additionally, in Figure 8b, actual fracture surface images of each specimen are shown in the picture. From the figure, it can be observed that the general correlation of the calculated thickness variation with the lap shear strength values seems promising. Especially the reflection of one of the larger unwelded areas (i.e. area indicated with the red rectangle) onto the thickness measurement output and lap shear strength values indicates the potential advantage of the developed system for precise quality monitoring along the weld line.

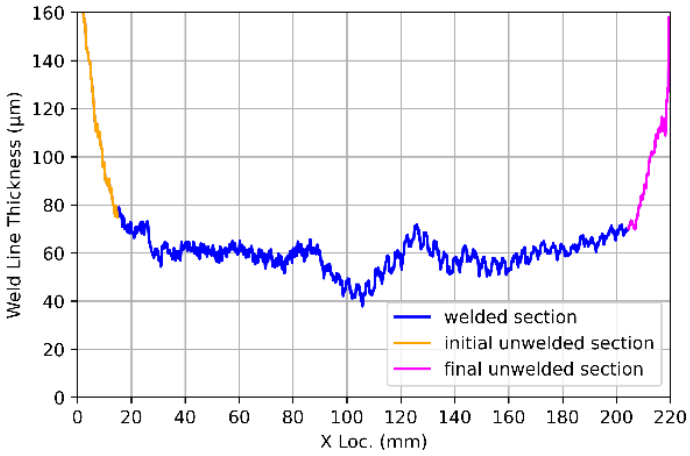

Figure 7. Weld line thickness measurement and unwelded area detection

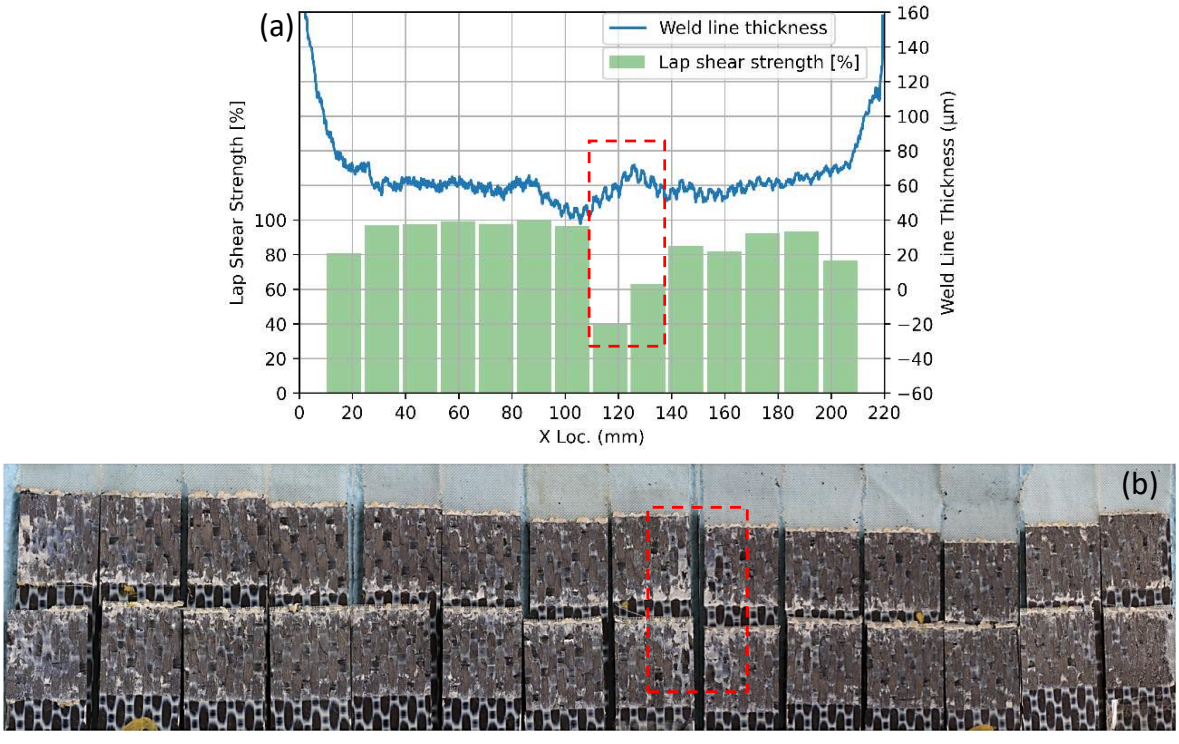

Figure 8. (a) Weld-line thickness (in blue) and SLS strengths (in green) comparison, (b) fracture surface image of single lap shear test specimens

4. Conclusion

Even though continuous ultrasonic welding promises a very fast and efficient joining capabilities for aerospace grade thermoplastic composites, the requirement of consistency in high quality

  doi:10.5075/epfl-298799_978-2-9701614-0-0

results is one of the main challenges for industrialization of this technology. Investigations performed within the first part of this study (i.e. with the robotic CUW system) revealed that there is a significant correlation between the weld line thickness and lap shear strength values. Since lap shear strength is one of the most reliable indicators of the weld quality, it is obvious that the correlation between these parameters can play a key role as a monitoring tool to maintain high quality welds during each CUW process. The conducted experimental work during the second part of this study (i.e. with the CUW frame based system) indicated that a 2D laser sensor monitoring system can be potentially utilized to track this correlation, which is believed to be an important step forward to industrialize continuous ultrasonic welding technology for aerospace applications. The tested monitoring configuration that consists of a single 2D laser sensor provides the opportunity to analyze the weld-line thickness in a relatively fast and efficient way. On the other hand, the analysis methodology is heavily dependent on the data of the utilized single laser sensor. Consequently, different sensor configurations should be tested to develop the most sensitive and accurate measurement methodology and to acquire reliable results. Moreover, the demonstrated monitoring setup can only be used as an off-line system (i.e. after the actual welding process) in its current state. Therefore, the proposed laser sensor setup should be integrated in the CUW machine to perform its tasks simultaneously with the continuous welding process as an effective in-situ monitoring system.

5. References

1. Köhler F, Jongbloed B, Filipe T, Hermann A, Fernandez Villegas I, Benedictus R. A Roadmap for developing an industrial continuous ultrasonic welding process for thermoplastic composites. 4th International Conference and Exhibition on Thermoplastic Composites. 2018 October 30-31.
2. Jongbloed B, Teuwen J, Palardy G, Fernandez Villegas I, Benedictus R. Continuous ultrasonic welding of thermoplastic composites: Enhancing the weld uniformity by changing the energy director. Journal of Composite Materials. 2020; 54(15):2023-2035.
3. Jongbloed B, Teuwen J, Benedictus R, Fernandez Villegas I. On differences and similarities between static and continuous ultrasonic welding of thermoplastic composites. Composites Part B: Engineering. 2020; 203:108466.
4. Jongbloed B, Teuwen J, Benedictus R, Villegas IF. A study on through-the-thickness heating in continuous ultrasonic welding of thermoplastic composites. Materials. 2021; 14:6620.
5. Jongbloed B, Vinod R, Teuwen J, Benedictus R, Villegas IF. Improving the quality of continuous ultrasonically welded thermoplastic composite joints by adding a consolidator to the welding setup. Composites Part A. 2022; 155:106808.
6. Köhler F, Villegas IF, Dransfeld C, Herrmann A. Industrialization aspects for ultrasonic welding of large thermoplastic aerospace structures. ITHEC 2020. 2020 October 12-13.
7. Villegas IF. Strength development versus process data in ultrasonic welding of thermoplastic composites and its application to the definition of optimum process parameters. Composites Part A. 2014; 27-37:65.
8. Villegas IF. In situ monitoring of ultrasonic welding of thermoplastic composites through power and displacement data. Journal of Thermoplastic Composites. 2015; 28:1.
9. Villegas IF. Ultrasonic welding of thermoplastic composites. Frontiers in Materials. 2019; 6:291.

MONITORING THE PROPERTIES OF CEMENT-BASED COMPOSITE MATERIALS WITH IMPEDANCE SPECTROSCOPY

Aikaterini Gkaravela[a], Ioanna Vareli[a], Nektaria-Marianthi Barkoula[a] and Alkiviadis S. Paipetis[a]
a: Department of Materials Science & Engineering, University of Ioannina, Ioannina, Greece – a.gkaravela@uoi.gr

Abstract: *In the current study the properties of cement-based composites reinforced with single-, multi-walled carbon nanotube (SWCNTs and MWCNTs, respectively) and carbon fibers (CF) were studied using Electrochemical Impedance Spectroscopy (EIS). EIS was applied for the online monitoring of the dispersion process of the CNTs in aqueous solutions and subsequently for the monitoring of the hydration process of cement-based composites. Depending on the CNT content and type, the values of the complex resistance, i.e., Impedance |Z| showed a dramatic change during sonication which indicates the formation of a conductive network. The existence of a percolated network in aqueous dispersions was illustrated by approximately seven orders of magnitude drop of |Z|. The changes of |Z|, as a function of the frequency, during hydration reveal changes in the microstructure and the formation of a conductive network. As the hydration process progresses, the cement-based composites reinforced with SWCNTs have better electrical properties than the respective ones with MWCNTs or CFs. The lowest values of |Z| are presented by the 0.5 wt.% SWCNTs nanocomposite.*

Keywords: cement-based composites; carbon nanotubes; impedance spectroscopy

1. Introduction

Cement-based materials are the most widely used structural materials in a wide range of applications due to their easily accessible raw materials, simplicity in the preparation process, low cost, etc. However, the goal in the construction industry is to develop new materials with ''smart'' abilities that will meet the high expectations of modern buildings. Part of this research is focused on the use of materials with high conductivity such as carbon nanotubes (CNTs) or carbon fibers (CFs) as additives in cementitious composite matrices, towards nano or/and micro cement-based composite materials for multifunctional purposes [1][2][3]. Adding CNTs or/and CFs into a cement matrix could not only enhance the mechanical properties [4], but also impart new functionalities, such as damage sensing capabilities through monitoring of the electrical conductivity [5][6]. Over the years there is an increasing understanding of the electrical properties of cement-based composites [7][8]. Typical cementitious materials display high electrical resistivity [9]. In wet condition they can act as semiconductors with resistivity values in the range of 10^5 Ω/mm but in dry condition they are consider as insulators as the resistivity increases in the range of 10^{12} Ω/mm. The difference in the resistivity of wet and dry condition of typical cementitious materials can be attributed to the presence of the free water [10]. The dispersion of conductive fillers into a cementitious matrix could result in the creation of conductive paths. However, due to their structure and hydrophobic behavior, CNTs have the tendency to form agglomerates so their dispersion is a major challenge [11]. The combination of a surfactant, which lowers the Van der Waals attraction forces, with a dispersion technique, such as ultrasonication, could further reduce the self-attraction of CNTs and result in their adequate dispersion in aqueous solutions [12][13] before their addition in the cementitious

  doi:10.5075/epfl-298799_978-2-9701614-0-0

matrix. The performance of cement-based composite materials depends on a variety of factors such as the water-to-cement ratio, the amount of the filler, the admixture procedure etc. The use of nano-fillers along with surfactants could greatly affect the evolution of the hydration process, which determines the physical and mechanical properties of the nanomodified materials. Therefore, the monitoring of the hardening process is of paramount importance for the evaluation of the proposed materials. Electrochemical Impedance Spectroscopy (EIS) is a non-destructive technique, which can be used for monitoring the hydration and structural evolution of cement-based composite materials [14][15][16]. EIS is also a promising tool for on-line monitoring of the dispersion of the CNTs in aqueous solution [17]. EIS is based on the application of a sinusoidal voltage which in turns create an electric field in a range of frequencies and the material under test is subjected to this electric field. When the material does not interact with the electric field, dipoles and ions of the material have a random orientation. When the sinusoidal voltage is applied dipoles begin to orient, and ions begin to conduct an electrical current. The dielectric response of the material is quantified in terms of a complex Resistance, the Impedance |Z|. From an electrical standpoint, the Impedance, |Z|(ω), of a material at any angular frequency, ω, follows equation 1 where the resistive impedance Z'(ω) is the real part, and the reactive impedance Z''(ω) is the imaginary part of the impedance, in Ohm [18].

$$|Z|(\omega) = \sqrt{Z'(\omega)^2 + Z''(\omega)^2} \quad (1)$$

In this study, EIS was used to monitor the dispersion of CNTs in aqueous solutions as well as the hydration process of cement-based composites. The results of |Z| as a function of frequency showed a dramatical change since a drop by many orders appeared in |Z| values which is regarded as an indication of the formation of a conductive path. EIS was also used for monitoring the hydration process. It is particularly interesting that the values of |Z| are lower in relation to the cement reference as the concentration of the CNTs and the CFs in the composite increases. Additionally, a difference in |Z| magnitude regarding the type of the filler was observed. The changes of the magnitude of |Z| as the hydration process progresses demonstrate the existence of a conductive network which is formed by the addition of the CNTs and the CFs.

2. Experimental

2.1 Materials

In this study two different types of CNTs were used. MWCNTs in powder form under the brand name of Nanocyl were provided by Nanocyl. The CNTs had average diameter of $9.5*10^{-9}$ m, average length of 1.5 μm, carbon purity of 90% and a transition Metal oxide < 1%. SWCNTs also in powder form were provided by OCSiAl. The product name was TUBALL, with the specific characteristics of, average diameter 1.8±0.4 nm, length> 5 μm, carbon content: >85 wt.%, and metal impurities <15 wt.%. Sodium dodecylbenzene sulfonate (SDBS) purchased from Sigma Aldrich was used as surfactant. Carbon Fibers T700 were provided by Torray Industries, INC. For the integration of the CFs into the cement matrix a carbon fiber cutting machine was used to chop the fibers in a specific size (5mm). Ordinary Portland cement (OPC) CEM I 42.5 R was provided from TITAN S.A. GREECE. All the samples were prepared with deionized water. The dispersions contained predetermined amount of CNTs and CFs of 0.1 wt.% and 0.5 wt.% by cement weight, while the ratio of CNTs/SDBS was kept constant at 1:1.

  doi:10.5075/epfl-298799_978-2-9701614-0-0

2.2 Experimental Procedure

The dispersion of the CNTs in the deionized water was performed for 60 min using a tip-ultrasonic probe processor (UP400S, Hielscher Ultrasonics) with an amplitude of 25%, which resulted in a total sonication energy of 18.6W. To keep the temperature of the aqueous dispersion constant, the sonication process was performed in a water bath. For the dispersion monitoring an interdigital ceramic sensor was immersed into the solution medium. The sonication process was stopped every 30 min and an EIS measurement was obtained. using an Advanced Dielectric Thermal Analysis System (DETA-SCOPE) supplied by ADVISE, Greece in a frequency range of 10^{-2} Hz – 10^{5} Hz.

The cement composites were prepared using the CNT-based dispersions, the chopped CFs, and Portland cement at a water-to-cement ratio (w/c) of 0.5 by weight. The mixtures were stirred for 10 min using a mechanical stirrer (IKA® EUROSTAR control 200P4) equipped with an R1381 propeller stirrer and casted into a polymer-based mold. EIS measurements were conducted using a digital Impedance Analyzer in a frequency range from 10^{-1} Hz to $5*10^{6}$ Hz provided by Zurich Instruments, Switzerland. Two titanium mesh electrodes were directly inserted into the fresh mixture to monitor the changes of |Z| from the beginning of the hydration procedure until the age of 28 days.

3. Results and Discussion

3.1 Dispersion monitoring

Table 1 presents the values of the impedance |Z| (complex resistance) at the frequency of 0.05Hz after 30 and 60 min of dispersion. This frequency was selected as in low frequencies the impedance |Z| is within the region that follows the Ohm's law. In this region, there is no contribution of the imaginary resistance of the impedance |Z|, only the real resistance is contributing, proportional to DC resistance of the sample. For the first 30min of the dispersion process, the |Z| values for all the samples were very high and were considered unreal as they are within the set-up measurement limits. After a total time of 60min of sonication, at 0.1 wt.% of MWCNTs, no changes were observed in the Impedance |Z|, indicating that a conductive network was not formed. On the other hand, for the same SWCNTs content (i.e., 0.1 wt.%) after 60min of sonication, a drop of |Z| by seven orders of magnitude was observed, a fact which demonstrates the formation of a conductive CNTs network. The difference in the |Z| values between MWCNTs- and SWCTNs-based dispersions at 0.1 wt.% loadings could be related with the inherent conductivities of MWCNTs and SWCNTs, as well as their ability to be dispersed. SWCNTs have higher aspect ratio (up to 10000) than MWCNTs (50–4000), they also present stronger Van der Waals forces [19] making their dispersion more difficult in comparison to MWCNTs. Moreover, the electrical conductivity of SWCNTs has been reported to be on the order of 10^{2} to 10^{6} S/cm while the MWCNTs are 10^{3} to 10^{5} S/cm[20].

Dispersions with 0.5 wt.% MWCNTs and SWCNTs presented a drop of impedance |Z| by eight orders of magnitude after 60min of sonication. In both cases a conductive network was achieved. The dispersion of 0.5wt.% SWCNTs illustrates the lowest values of |Z| of all the samples.

  doi:10.5075/epfl-298799_978-2-9701614-0-0

Table 1. Values of |Z|(Ohm) after 30min and 60min of sonication time for the dispersions of the CNTs in the frequency of 0.05Hz.

Sample	$\|Z\|(Ohm)_{30min}$	$\|Z\|(Ohm)_{60min}$
0.1 wt. %MWCNTs	$1.54*10^{12}$	$1.54*10^{12}$
0.1 wt. % SWCNTs	$2.94*10^{12}$	$1.41*10^{5}$
0.5 wt.% MWCNTs	$2.46*10^{12}$	$9.64*10^{4}$
0.5 wt. % SWCNTs	$1.63*10^{12}$	$5.95*10^{4}$

3.2 Hydration monitoring

The results of the magnitude of |Z| as a function of frequency and hydration duration are presented in Figure 1.

As observed in Fig. 1a right after mixing the impedance |Z| presented low values since the presence of the water was dominant in the cement paste composites. The highest values appeared for the reference cement paste followed by the composites with low concentration of conductive additives. The type of the additive plays an important role in the electrical properties of the composite since the admixture with 0.1 wt.% SWCNTs presented the lowest values in comparison to the pastes with 0.1 wt.% MWCNTs and CFs. Additionally, for the cement composites with 0.5 wt.% the lowest values of |Z| corresponded to 0.5 wt.% SWCNTs content. Based on the above, it can be deduced that the presence of the SWCNTs had a positive effect on the formation of a conductive network from the beginning of the hydration process.

Generally, during the first 24 hours of the hydration process (wet condition) of cementitious materials the concentration of the ions is quite high leading to ionic association. This association causes the formation of C-S-H gel and the phase of ettringite which in turn lead to a decrease in ions mobility, therefore an increase in the complex resistance (impedance |Z|). This increase was obvious in all the specimens except of the specimen enhanced with 0.5wt.% SWCNTs (Fig.1b). In this case the conductive path dominated therefore the |Z| values were not affected from the decrease of ions mobility. This is further supported by the fact that at low frequencies the addition of SWCNTs resulted in even lower values of |Z| within the first 24h of the hydration process.

  doi:10.5075/epfl-298799_978-2-9701614-0-0

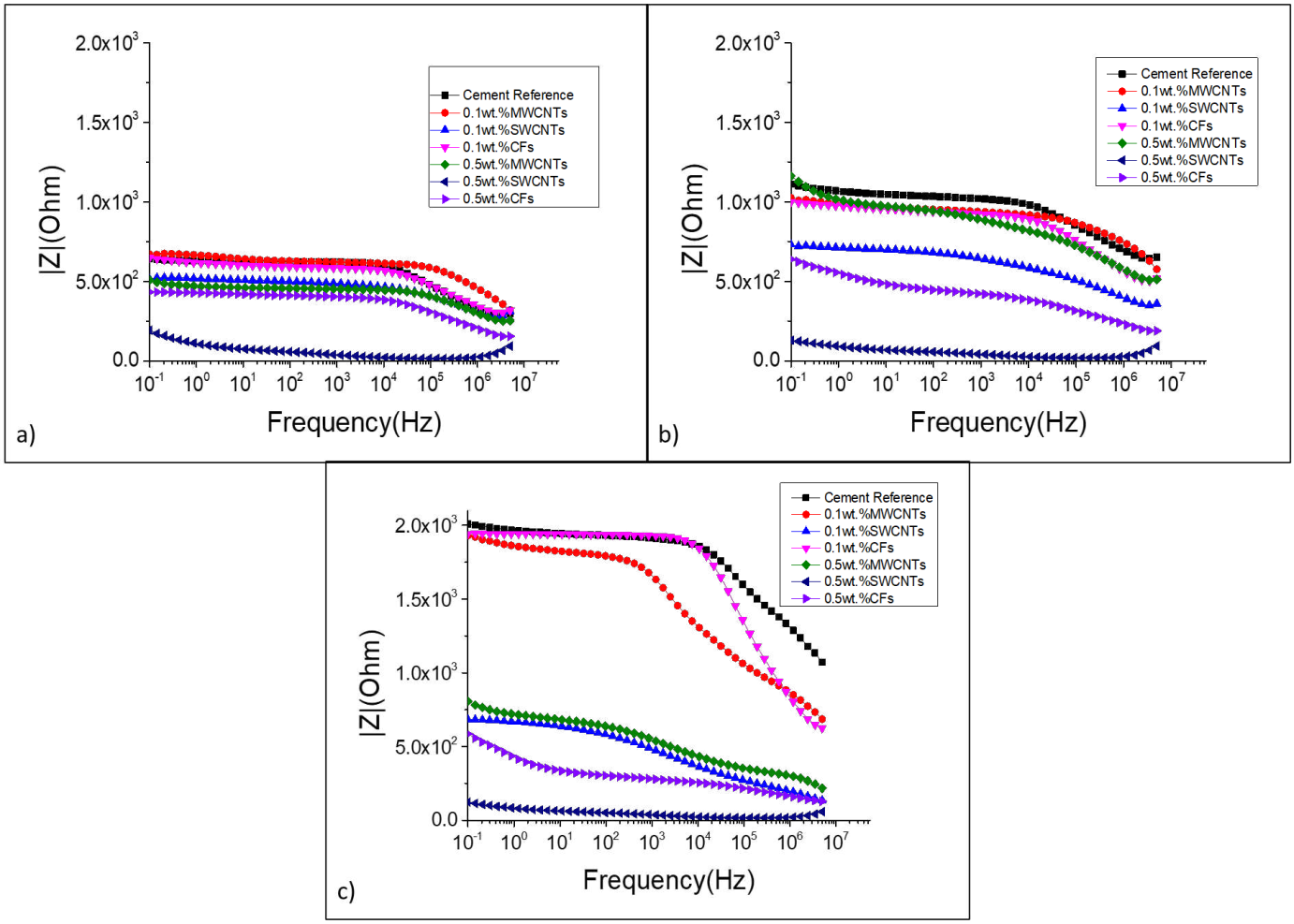

Figure 1. Bode plots of the hydration process monitoring: a) After Mixing, b) 1 day of Hydration and c) 28 days of Hydration.

At the end of the hydration process (Fig.1c), for the composites with low concentration of MWCNTs and CFs the values of |Z| are approximately the same in relation to the cement reference. The amount of the additives is below the percolation threshold therefore it was not feasible the formation of a conductive network. On the other hand, the composite with 0.1wt.% SWCNTs presented lower values in the impedance |Z| as the addition of this amount of SWCNTs is above the percolation threshold and the conductive network has been achieved.

As the concentration of the CNTs or the CFs in the composites increased, the values of |Z| were lower in relation to the cement reference. The type of the reinforcement affects the electrical properties of the composites since the lowest values in the impedance |Z| are presented by the composite with 0.5wt.% SWCNTs followed by the composite with 0.5wt.% CFs and the composite with 0.5wt.%MWCNTs.

4. Conclusions

In this research EIS was proposed as a method to evaluate the dispersion of CNTs in aqueous solution. The accuracy and the sensitivity of EIS make it a technique which can characterize the dispersion of the CNTs as it was able to detect changes linked with state of the solutions. The

  doi:10.5075/epfl-298799_978-2-9701614-0-0

drop of the |Z| values by many orders of magnitude, for the dispersions above the percolation threshold, after 1 hour of the sonication process indicated the formation of a conductive CNTs network. Furthermore, EIS was used for monitoring the hydration process of cementitious composites though the changes of the impedance Z. The composites in which the reinforcement was below the percolation threshold presented similar behaviour with the reference cement. Above that, lower values of the impedance Z were obtained as the hydration process progressed. Not only the amount but also the type of the reinforcement affected the electrical properties of the cement composites since the composite reinforced with 0.5wt.% SWCNTs presented the lowest values of |Z|.

Acknowledgements

This research has been co-financed by the European Union and Greek national funds through the Operational Program Competitiveness, Entrepreneurship, and Innovation, under the call RESEARCH – CREATE – INNOVATE (project code: HICOTEG-T1EDK-03482).

5. References

1. Lee SJ, You I, Zi G, Yoo DY. Experimental investigation of the piezoresistive properties of cement composites with hybrid carbon fibers and nanotubes. Sensors (Switzerland). 2017;17(11).

2. Shi T, Li Z, Guo J, Gong H, Gu C. Research progress on CNTs/CNFs-modified cement-based composites – A review. Constr Build Mater [Internet]. 2019;202:290–307. Available from: https://doi.org/10.1016/j.conbuildmat.2019.01.024

3. Vareli I, Tzounis L, Tsirka K, Kavvadias IE, Tsongas K, Liebscher M, et al. High-performance cement/SWCNT thermoelectric nanocomposites and a structural thermoelectric generator device towards large-scale thermal energy harvesting. J Mater Chem C. 2021;9(40):14421–38.

4. Kang J, Al-Sabah S, Théo R. Effect of single-walled carbon nanotubes on strength properties of cement composites. Materials (Basel). 2020;13(6):1–12.

5. Cerro-Prada E, Pacheco-Torres R, Varela F. Effect of multi-walled carbon nanotubes on strength and electrical properties of cement mortar. Materials (Basel). 2021;14(1):1–13.

6. Konsta-Gdoutos MS, Aza CA. Self sensing carbon nanotube (CNT) and nanofiber (CNF) cementitious composites for real time damage assessment in smart structures. Cem Concr Compos [Internet]. 2014;53:162–9. Available from: http://dx.doi.org/10.1016/j.cemconcomp.2014.07.003

7. Cosoli G, Mobili A, Tittarelli F, Revel GM, Chiariotti P. Electrical resistivity and electrical impedance measurement in mortar and concrete elements: A systematic review. Appl Sci. 2020 Dec 2;10(24):1–43.

8. Berrocal CG, Hornbostel K, Geiker MR, Löfgren I, Lundgren K, Bekas DG. Electrical resistivity measurements in steel fibre reinforced cementitious materials. Cem Concr Compos. 2018;89:216–29.

9. Yousuf F, Wei X, Zhou J. Monitoring the setting and hardening behaviour of cement paste by electrical resistivity measurement. Constr Build Mater [Internet].

  doi:10.5075/epfl-298799_978-2-9701614-0-0

2020;252:118941. Available from: https://doi.org/10.1016/j.conbuildmat.2020.118941

10. Lamastra FR, Chougan M, Marotta E, Ciattini S, Ghaffar SH, Caporali S, et al. Toward a better understanding of multifunctional cement-based materials: The impact of graphite nanoplatelets (GNPs). Ceram Int [Internet]. 2021;47(14):20019–31. Available from: https://doi.org/10.1016/j.ceramint.2021.04.012

11. Kim GM, Park SM, Ryu GU, Lee HK. Electrical characteristics of hierarchical conductive pathways in cementitious composites incorporating CNT and carbon fiber. Cem Concr Compos [Internet]. 2017;82:165–75. Available from: http://dx.doi.org/10.1016/j.cemconcomp.2017.06.004

12. Jiang L, Gao L, Sun J. Production of aqueous colloidal dispersions of carbon nanotubes. J Colloid Interface Sci. 2003;260(1):89–94.

13. Kharissova O V., Kharisov BI, De Casas Ortiz EG. Dispersion of carbon nanotubes in water and non-aqueous solvents. RSC Adv. 2013;3(47):24812–52.

14. Hu X, Shi C, Liu X, Zhang J, de Schutter G. A review on microstructural characterization of cement-based materials by AC impedance spectroscopy. Cem Concr Compos [Internet]. 2019;100(March):1–14. Available from: https://doi.org/10.1016/j.cemconcomp.2019.03.018

15. Wansom S, Kidner NJ, Woo LY, Mason TO. AC-impedance response of multi-walled carbon nanotube/cement composites. Cem Concr Compos. 2006;28(6):509–19.

16. Suryanto B, Kim J, McCarter WJ, Starrs G, Aitken MW. Assessing the performance and transport properties of concrete using electrical property Measurements. J Adv Concr Technol. 2020;18(7):437–55.

17. Tsirka K, Foteinidis G, Dimos K, Tzounis L, Gournis D, Paipetis AS. Production of hierarchical all graphitic structures: A systematic study. J Colloid Interface Sci [Internet]. 2017;487:444–57. Available from: http://dx.doi.org/10.1016/j.jcis.2016.10.075

18. Martinsen G. Impedance Basics. 2013;(1):1–55.

19. Saifuddin N, Raziah AZ, Junizah AR. Carbon nanotubes: A review on structure and their interaction with proteins. J Chem. 2013;2013.

20. Earp B, Dunn D, Phillips J, Agrawal R, Ansell T, Aceves P, et al. Enhancement of electrical conductivity of carbon nanotube sheets through copper addition using reduction expansion synthesis. Mater Res Bull [Internet]. 2020;131(April):110969.

ACCELERATE GROWTH OF THE COMPOSITE INDUSTRY BY STANDARDIZED QUALITY MANAGEMENT BASED ON THE SUCCESSFUL MODEL OF WELDING AND ADHESIVE BONDING TECHNOLOGY – DIN SPEC COMPOSITES

Milan Kelch[a], Stefan Simon[a], Andreas Groß[a]

a: Fraunhofer Institute for Manufacturing Technology and Advanced Materials IFAM – milan.kelch@ifam.fraunhofer.de

Abstract: *What can the composite industry learn from welding and adhesive bonding technology? When these joining technologies emerged, they were first mistrusted, since the load bearing capacity cannot at 100 % be tested in a non-destructive way after the joining process. However, both technologies are today accepted as trustworthy technologies. One of the crucial points that led to the success of these technologies was the implementation of a standardized technology-specific quality management system from an early stage. There are a lot of similarities between the mentioned processes and the manufacturing and repair of composite materials. However for composite materials there is a big gap between universal standards such as ISO 9001 and very specific standards e.g. for individual test methods. Against this background a cross-industry standard for the quality assurance during manufacturing and repair of composite materials is proposed to increase acceptance of composite materials in more application areas.*

Keywords: standardization; quality assurance; safety requirements, professional training, verification management

1. Introduction

Fiber composite materials have gained more importance during the last decades in numerous sectors of industry due to their high potential to design complex and lightweight components with a high resistance towards corrosion, high specific energy absorption, good damping properties and numerous other advantages. Market surveys from different sectors report a continuous growth of composite industry only interrupted by the global economic crisis and corona pandemic situation [1],[2],[3]. However there are still untapped markets and even in sectors that already apply composite technology the potential of these materials and especially the lightweight design potential is often not fully exploited.

A major challenge for companies implementing composites in their production is that the material and thus also the material properties are only defined during the manufacturing process. Even small deviations during production (e.g. incorrect mixing ratio of the matrix, incorrect fiber orientation, contaminations etc.) can lead to large variations in the material properties, and the manufacturer thus bears a large part of the responsibility for the material properties. As a result, many companies are still suspicious of the material or components are oversized to account for unmanageable variations in material properties. In this way, potential for saving resources and avoiding emissions through lightweight construction, which is actually already available according to the current state of the art, remains unused.

  doi:10.5075/epfl-298799_978-2-9701614-0-0

A frequently made mistake in the introduction of composite materials is the unreflected transfer of design and handling principles of conventional materials like metals to composite materials due to insufficient knowledge of the material, as a result of which the material cannot meet the requirements of the component. The negative experiences made in the process are then attributed to the material "composites".

Another challenge often perceived as an obstacle in the manufacture and repair of composite components is that neither the individual manufacturing steps nor the finished composite product can be verified one hundred percent non-destructively. Accordingly, the manufacturing and repair processes fall under the definition of so-called "special processes" according to EN ISO 9001 [4].

2. Quality assurance through standardization

In order to transfer “special processes” in the direction of "controllable processes" and to ensure consistent product quality, the core idea, largely already established in industry according to EN ISO 9001, is to avoid errors from the outset by means of a quality management system in the respective company through organizational measures. In order to counter the obstacles in the manufacture and repair of composite components, this basic idea can be applied, but it must be specified in a technology-specific, cross-industry and standardized manner.

EN ISO 9001 thus lays down the (process) organizational foundations for a functioning quality management system, but does not specify it in technological terms. Although a large number of standards and guidelines already exist for the manufacture and repair of composites (an overview of these standards can be found in DIN's Composites standardization portal[1]), these relate to technical imponderables such as the standardization of certain test methods or processes. With regard to the consideration of organizational imponderables, no cross-industry and product-independent standardization document exists worldwide.

The technological standards are undoubtedly necessary and provide orientation for detailed technological issues, but are only relevant in individual industries and applications. Standards which attempt to close the gap between EN ISO 9001 and the specific technology-related standards relate only to individual industries and processes [5], [6], [7], [8], [9] and do not include a holistic, organizational view of all the necessary aspects of quality assurance across all the disciplines involved. They do not represent a generally valid guide in the quality assurance of FRPs for the development of new industries and applications.

3. Welding and adhesive bonding technology as a role model

Two joining technologies that are also closely associated with lightweight construction, welding technology and adhesive bonding technology, have faced a similar challenge in the past. As with the manufacture and repair of composite components, these joining methods are "special processes", which means that neither the individual manufacturing steps nor the finished product can be fully inspected in a non-destructive manner. Here too, therefore, a great deal of responsibility lies with the user. Accordingly both technologies were initially met with great mistrust, which stood in the way of cross-industry application.

[1] https://www.din.de/en/services/standards-portals/composites (accessed 22.03.2022)

  doi:10.5075/epfl-298799_978-2-9701614-0-0

In the meantime, however, it is impossible to imagine industrial production without both technologies. In addition to R&D activities, the essential confidence-building element in the successful establishment of welding and bonding technology was and is provided by cross-industry, product-independent quality assurance standards for the technology-specific organization of the respective processes in the form of national and international standards[10], [11], [12), [13], [14], [15], [16], [17], [18], [19], [20], [21], [22].

These quality standards - all of which are purely user standards - are compatible with each other and, in relation to the respective technology, specify the ingenious core idea of EN ISO 9001, namely to avoid possible errors in a "special process" according to the state of the art by supplementing it in the quality management system (QMS) of the respective company through organizational measures from the outset (figure 1).

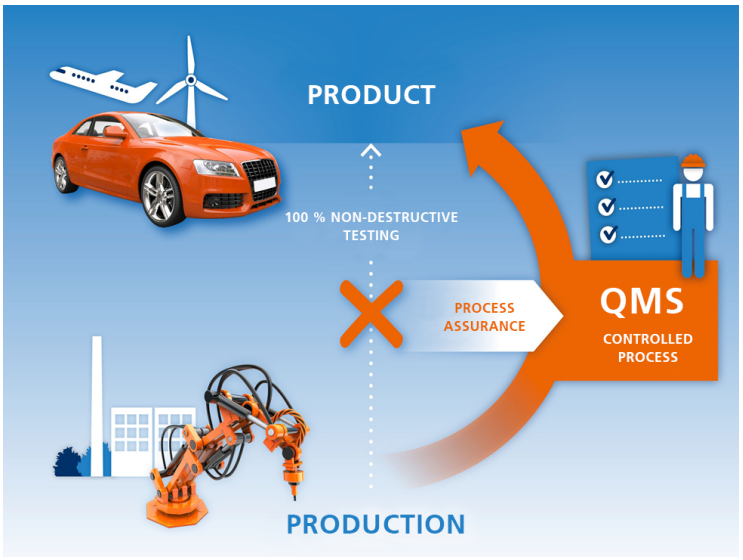

Figure 1. For processes like adhesive bonding or composite manufacturing, the quality of the product can't be tested at 100 % after the process. Therefore the process needs to be controlled by a defined quality management system (QMS).

These standards, with a corresponding certification system, have now become established worldwide across all industries. These, for example, explicitly simplify the approval of suppliers significantly and replace their time-consuming individual audits. And, as both have shown, the improvement in image, the increase in acceptance and the gain in confidence in both technologies are also the result. All factors that have a positive economic impact.

In the joining technologies of relevance to lightweight construction, welding technology and adhesive bonding technology, it has thus been possible to successfully bridge the gap between EN ISO 9001 and process- or industry-related standards with national and now also international quality assurance standards.

The success of these standards in effectively assuring the quality of special processes such as welding or bonding lies in the three core elements contained in each of these standards.

Core element 1: Classification of components according to safety requirements

The effort of quality management is based on the safety requirements or the effect of the potential failure of a component ("high safety requirements": direct or indirect danger to life

  doi:10.5075/epfl-298799_978-2-9701614-0-0

and limb in case of failure up to "no safety requirements": no damage to persons or the environment in case of failure of the component).

Core element 2: Appointment of supervisory and execution personnel with objectively verifiable competences.

This core element substantiates the EN ISO 9001 requirement for technologically adequate and demonstrably qualified personnel for operational supervisory and execution personnel for "special processes". This requirement is implemented through the cross-hierarchical and certifying qualification of operational supervisory and execution personnel. In both welding technology and adhesive bonding technology, three-level personnel qualification systems have been established for the technical decision-making personnel, supervisory personnel and executive personnel.

Core element 3: Verification/conformity assessment of the design and layout:

It must be ensured by the user, with the assistance of supervisory personnel qualified in accordance with core element two, that the real load on the component in operation is always less than the maximum load capacity. This must be demonstrated by calculation, experiment or a combination of calculation and experiment.

The purpose of these three core elements is to take a holistic view of a technology by combining the competencies from design/construction, production execution and planning, purchasing, occupational health and safety, environmental protection, maintenance and quality management with the specific competencies of the respective technology.

Experience with the aforementioned methods shows that the process-related concretization of QM principles through product-independent and cross-industry standards noticeably simplifies business processes, significantly reduces development risk and greatly increases product reliability [24], [25], [26], [27], [28]. Figure 2 demonstrates these effects using the example of rail vehicle manufacturing. Ten years after the introduction of corresponding standards for bonding, the number of bonds has roughly tripled, while the number of defects noticed has been significantly reduced.

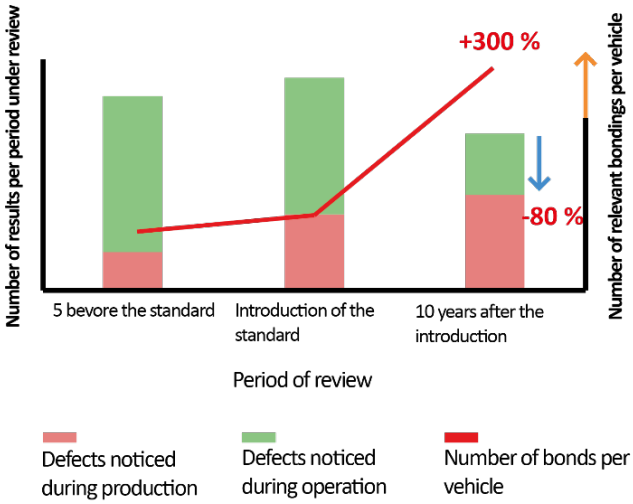

Figure 2. Results of a long-term study on the effectiveness of the adhesive bonding QM standards in rail vehicle construction [adapted and translated from 23]

4. DIN SPEC Composites

In order to build a bridge between ISO 9001 and the application and process-specific standards in the field of composites, a committee has been working together since 2019 to develop a cross-industry quality assurance standard in the form of a DIN SPEC based on the model of welding and bonding technology. Representatives from various industries as well as participants from research institutes and certification bodies are contributing their experience in order to develop a standard that will make it easier for companies already using composite technology to guarantee high and reproducible quality in the manufacture and repair of composite components in their own operations or those of their suppliers, and will provide companies wishing to integrate composite technology into their products with guidance on the quality-assured introduction of this technology.

In terms of content, the three core elements, which are also successful in adhesive bonding and welding technology, provide the structure of the standard.

The first core element is the classification of composite components according to safety requirements. The consequences in the event of component failure are assessed by evaluating the probability of occurrence and the expected effects on people, the environment and the serviceability of the overall system. If the failure of a component is expected to result in an unavoidable danger to life and limb or to have serious ecological consequences, correspondingly high requirements must be met in the quality assurance measures. If the failure only leads to a loss of comfort or functionality, the requirements for quality assurance measures requested by the standard are low. By grading into a total of four safety classes along the lines of welding and bonding technology, the quality management requirements for a specific component can be precisely defined.

Depending on the safety classification of the component, the function, tasks and competences for the executing personnel, supervisory personnel and testing personnel are defined within the DIN SPEC. The supervisory personnel play an important role. They are the central point of contact for all factors influencing quality and check all relevant processes such as contract coordination, design, verification, storage and transport of components, production planning and the qualification of subcontractors. The supervisory personnel must regularly demonstrate that their competencies have been maintained or expanded. Depending on the safety requirements of the component, three levels of competence are defined that personnel must demonstrate when performing certain processes. The competence levels are based on the structure used in many companies, consisting of technical decision-making personnel, supervisory personnel and executive personnel.

As an important criterion for the proof of corresponding competences, it is defined that, in accordance with DIN EN ISO/IEC 17024 [29]:

- the acquisition of knowledge or training and further training,
- the examination of this competence, knowledge and experience, and
- the recognition of this competence, this knowledge and this experience

are to be strictly separated from each other and that there are no economic or legal relations between the involved actors.

  doi:10.5075/epfl-298799_978-2-9701614-0-0

By executing and monitoring the manufacturing and repair processes by personnel with defined and verifiable competencies, errors can be avoided or detected already in the process. Furthermore, a uniform further training system promotes cross-hierarchical communication.

In addition to the involvement of appropriately qualified personnel, the requirements for verification also depend on the respective safety class of the component. In the case of components with high safety requirements, the user, with the assistance of supervisory personnel, must ensure that the stress on the component in use is less than the stressability at all times. On this basis, more detailed specifications for verification are currently being worked out by the working group.

5. Conclusions

The implementation of the three core elements should enable companies to apply the composite technology with a holistic view from the idea to the product in a quality-assured way. As welding and bonding technology have shown, the life of a comparable standard can prevent a reduction in the number of errors identified during operation, thus boosting confidence in the technology of composites, expanding fields of application and unlocking the potential for lightweight construction with an impact on the ecological balance sheet.

A prerequisite for this, however, is broad acceptance of the standard in the industry. Once the standard has been completed, it will initially be implemented on a pilot basis at the companies in the working group by setting up a corresponding quality management system and also transferring it to suppliers. The expected success should convince more and more companies of the usefulness of such a standard. It helps that the adhesive bonding QM standards have long been accepted in many composite processing companiesmany FRP companies, since adhesive bonding technology supports the use of lightweight FRP components on account of its technological potential, or even makes it possible in the first place.

Acknowledgements

Our acknowledgements go to all the members of the DIN SPEC COMPOSITES work group for their engagement, input and supporting for this project by name: BÜFA Composite Systems GmbH & Co. KG, DB Fahrzeuginstandhaltung GmbH, DLR German Aerospace Center Institute of Composite Structures and Adaptive Systems, FR Fassmer GmbH &Co. HKG, F & E Technologiebroker Bremen GmbH - Zertifizierungsstelle TBBCert, TechnologieCentrum Kleben GmbH, thyssenkrupp Marine Systems GmbH, Voith Group.

6. References

1. Witten E, Mathes V. (2020). The Market for Glass Fibre Reinforced Plastics (GRP) in 2020. Market Developments, Trends, Outlooks and Challenges. Federation of Reinforced Plastics 2020 Frankfurt, Germany.
2. Composites Germany. Composites Germany – results of the 18th Composites Market Survey [press release 2022]. https://composites-germany.org/index.php/en/news-en/market-information

  doi:10.5075/epfl-298799_978-2-9701614-0-0

3. Sauer M. Composites Market Report 2020 – The global CF-Market 2020 – Market Development, Trends, Outlook and Challanges. Composites United e.V. 2020, Berlin, Germany.
4. EN ISO 9001:2015-11: Quality management systems – Requirements
5. CSN EN 16245-1:2013 - Fibre-reinforced plastic composites - Declaration of raw material characteristics - Part 1: General requirements, Beuth Verlag, Berlin, 2013.
6. DIN SPEC 2305-2 Klebtechnik - Qualitätsanforderungen an Klebprozesse - Teil 2: Kleben von Faserverbundkunststoffen
7. VDI 2014 Blatt 1: Entwicklung von Bauteilen aus Faser-Kunststoff-Verbund; Grundlagen
8. Germanischer Lloyd WindEnergie GmbH 'Richtlinie für die Zertifizierung von Windenergieanlagen
9. Germanischer Lloyd: Klassifikation- und Bauvorschriften II – Werkstoffe und Schweißtechnik Teil 2 – Nichtmetallische Werkstoffe Kapitel 1 – Faserverbundwerkstoffe und Kleben
10. ISO 21368:2022, Adhesives — Guidelines for the fabrication of adhesively bonded structures and reportingprocedures suitable for the risk evaluation of such structures, ISO copyright office, CP 401, Ch. de Blandonnet 8, CH-1214 Vernier, Geneva, 2022
11. Normenreihe DIN EN ISO 3834, Quality requirements for fusion welding of metallic materials, Beuth-Verlag: Berlin, 2006
12. DIN EN 1090:2012-02, Execution of steel structures and aluminium structures, Beuth-Verlag: Berlin, 2012
13. DIN EN 13455:2012-07, Unfired pressure vessels, Beuth-Verlag: Berlin, 2012
14. Normenreihe DIN EN 15085, Railway applications - Welding of railway vehicles and components, Beuth-Verlag: Berlin, 2008
15. Normenreihe DIN EN ISO 15607, Specification and qualification of welding procedures for metallic materials, Beuth-Verlag: Berlin, 2004 - 2018
16. Standards series DIN 6701, Adhesive bonding of railway vehicles and parts, Beuth-Verlag: Berlin, 2006 - 2015, Beuth-Verlag: Berlin, 2006 - 2015
17. DIN 2304:2020-04, Adhesive bonding technology - Quality requirements for adhesive bonding processes, Beuth-Verlag: Berlin, 2008
18. DIN SPEC 2305-1:2018-05, Adhesive bonding technology - Process chain adhesive bonding - Part 1: Advice for manufacturing, Beuth-Verlag: Berlin, 2018
19. DIN SPEC 2305-2:2018-10, Adhesive bonding technology - Quality requirements for adhesive bonding processes - Part 2: Adhesive bonding of fibre composite materials, Beuth-Verlag: Berlin, 2018
20. DIN SPEC 2305-3:2019-02, Adhesive bonding technology - Quality requirements for adhesive bonding processes - Part 3: Requirements for the adhesive bonding personnel, Beuth-Verlag: Berlin, 2019
21. Technische Lieferbedingungen TL A0023, Kleben und verwandte Prozesse – Qualitätsanforderungen an Herstell- und Instandsetzungsbetriebe für militärische Produkte, Urheber: Bund 2017, zu beziehen beim: BAAINBw, Koblenz, www.baainbw.de/TL
22. EN 17460, Railway applications - Adhesive bonding of rail vehicles and parts, CEN-CENELEC Management Centre: Rue de la Science 23, B-1040 Brussels, 2019
23. Hellwig, P. Siemens Transportation, Workshop „Umsetzung der DIN 2304 in die Praxis", Fraunhofer IFAM, 27.10.2015

  doi:10.5075/epfl-298799_978-2-9701614-0-0

24. Mayer B, Groß A. In Kreislaufwirtschaft und Klebtechnik; Fraunhofer-Verlag: Stuttgart, 2020; S.61, Kapitel: Kleben- aber sicher: die Entwicklung von Qualitätsnormen zur Gewährleistung sicheren Klebens.
25. Behnisch H, Aichele G. In Die Schweißtechnik im Wandel der Zeiten; DVS-Verlag GmbH: Düsseldorf, 2006; S.219 - 228, Kapitel: Von der genieteten zur geschweißten Stahlkonstruktion.
26. Behnisch H, Aichele G. In Die Schweißtechnik im Wandel der Zeiten; DVS-Verlag GmbH: Düsseldorf, 2006; S. 251 – 252, Kapitel: Regelwerke wurden angepasst.
27. Groß A, Meiß E. In Dichtungstechnik Jahrbuch 2019; K-F. Berger, S. Kiefer (Hrsg.); ISGATEC GmbH: Mannheim / Silber Druck oHG: Niestetal, 2018; S. 367 – 374, Wissen und verstehen, was man tut – Das Potenzial der Klebtechnik und die Notwendigkeit der Qualitätssicherung.
28. Gross A., Lohse H. adhesion ADHESIVES & SEALANTS 2015, 4, 12 – 17, Topic of the month: New DIN 2304 standard and its use in practice.
29. DIN EN ISO/IEC 17024:2012-11 - Conformity assessment - General requirements for bodies operating certification of persons, Beuth Verlag, Berlin 2012

  doi:10.5075/epfl-298799_978-2-9701614-0-0

Experimental investigations on accelerated curing of adhesively bonded G-FRP tube connections

Morten Voß[a], Marvin Kaufmann[a], Till Vallée[a]

a: Fraunhofer Institute for Manufacturing Technology and Advanced Materials IFAM, Bremen

Abstract: *For the joining of FRP components, adhesive bonding is increasingly preferred to mechanical fasteners as poorer transfer of loads resulting from interrupted fibres represents problematic. However, polymerisation remains a comparatively slow process that is usually bound to limited manufacturing temperatures. This article shows, that curing by inductive heating can compensate for both disadvantages. For that, Curie particles (CP) susceptible to electromagnetic fields (EMF) were added to two adhesives (epoxy and polyurethane), and the effect thereof on the adhesive was assessed. The particles relieved all requirements regarding temperature control during the induction process. Subsequently, different series of G-FRP single lap tubular joints (SLTJ) were assembled, cured following different protocols, and subjected to tensile tests. Mechanical testing showed that inductively cured SLTJ achieved equal or higher shear strengths, if compared to reference sets, which was accompanied by a reduction in curing time by the factor of 100 for the epoxy and 1400 for the polyurethane.*

Keywords: Accelerated curing, inductive heating, Curie particles, electromagnetic induction, G-FRP tube

1. Induction curing with particles

By reviewing the existing literature, it quickly becomes clear that the field of particle-induced curing by induction is yet quite open, and very young—with most of the available literature originating from the current decade. Many of the available studies ignore the fact that used particles can be heated significantly above acceptable curing temperatures of polymers (80–120 °C, for 2K adhesives, 150–200 °C, for 1K adhesives) if tight control of induction power is disregarded. These include e.g. magnetite (Fe_3O_4, T_c = 576 °C (1, 2)), iron (Fe, T_c = 770 °C (3)), nickel (Ni, T_c = 358 °C[125,135] (4, 5)) or ferrites of different types (T_c = 60-460 °C, depending on composition (6)).

Ambitious efforts to control adhesive temperatures via embedded particles are often missing. To prevent overheating, some researchers tried to control bond temperatures by using external monitoring techniques and adjustment of induction power(7, 8). However, this involves additional experimental effort and does not prevent local adhesive damages, as measured temperatures always represent temperatures of the adhesive-particle mix and not the susceptors temperature. Moreover, the approach represents no satisfactory solution for practical application, as it entails additional technical as well as human resources. The outlined circumstances reveal the strong need for an in-depth analysation with particles that circumvent the problem of temperature monitoring.

  doi:10.5075/epfl-298799_978-2-9701614-0-0

2. Objectives

The aim of the paper was to investigate the use of Curie particles (CP) for controlled accelerated curing of structural composite tubes. The roadmap of the publication has been illustrated in Figure 1. The following scientific objectives were defined:

- Device an experimental setup to accelerate the cure of two exemplary structural 2K adhesives used to bond several series of G-FRP single lap tubular joints (SLTJ).
- Application of suitable temperature monitoring techniques to validate homogeneity of developing curing temperatures during the process.
- Assessment of effects resulting from the addition of CP as well as the inductive heating on mechanical joint performances.

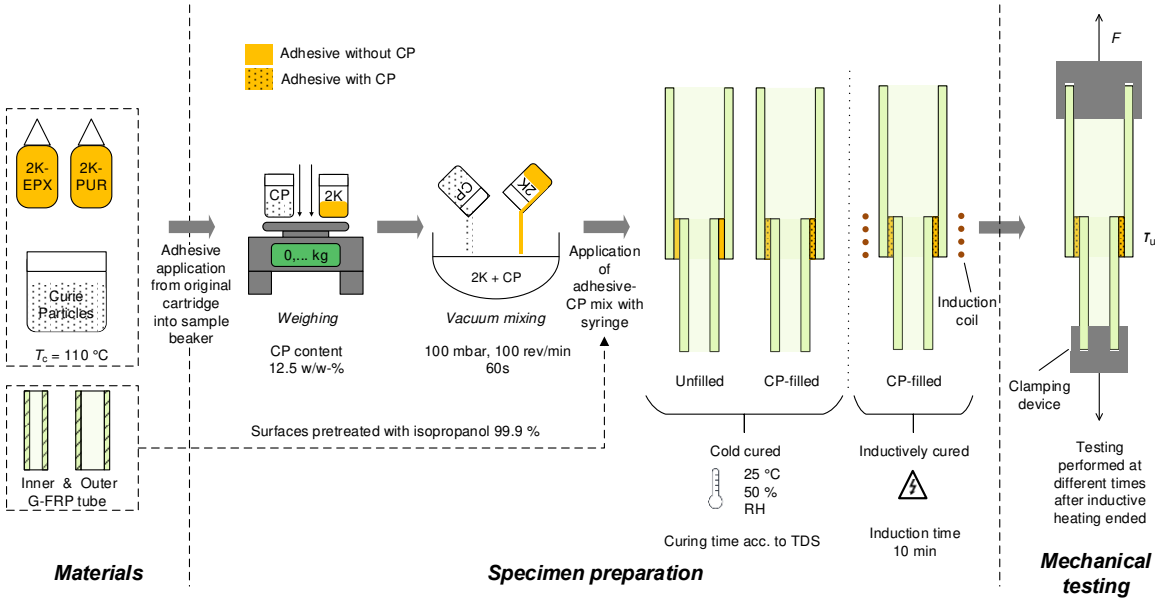

Figure 1: Roadmap of the paper

3. Materials & methods

3.1 Adhesives

Two commercially available two-component (2K) structural adhesives were selected for the accelerated curing experiments. For the adhesive class of 2K epoxy (2K-EPX), Fischer EM390S (abbreviated from here on as Fi390, Fischerwerke GmbH & Co. KG, Germany) was chosen. In contrast, Loctite Purbond CR821 (LP821, Henkel AG & Co. KGaA, Germany), a 2K polyurethane (2K-PUR), was selected to extend the findings towards a second class of polymers. Essential adhesive properties have been listed in Table 1.

Table 1: Materials properties of the adhesives taken from manufacturer's technical data sheet (TDS)

Adhesive	Class	Density [g/cm^3]	Pot life at RT [min]	Curing time at RT [h]	E / σ_u [MPa]
Fi390	2K-EPX	1.50	15-30	18	5230 / 40
LP821	2K-PUR	1.32	30	240	1000 / 45

3.2 Curie particles

Soft magnetic Manganese-Zinc-Ferrite (Mn-Zn-Fe) particles (Hengdian Group Magnetics Co. Ltd., China), hereinafter referred to as Curie particles (CP), served as susceptors. The CP had the shape of small flakes with sizes thereof ranging from 0.5–25.0 µm ($\overline{\emptyset}$ = 11.8 µm) and 90 % of all CP being smaller than 21.3 µm. The CP were selected because their Curie temperature, T_c, of 110 °C was closest to the range of temperatures relevant for the accelerated curing of the selected 2K adhesives (80–120 °C).

3.3 Single lap tubular joints

The structural joint configuration investigated consisted in G-FRP single lap shear tubular joints (SLTJ). These consisted of inner tubes with an external diameter of Ø40 mm, and outer tubes with an internal diameter of Ø42 mm; both exhibited a thickness of 3 mm. Discarding imperfections and tolerances, the combination of inner and outer tube leaves a gap of 1 mm to be filled by the adhesive.

Table 2: Material properties of the G-FRP SLTJ taken from manufacturer's TDS

Property	Glass weight [% by mass]	Tensile strength [MPa]		Tensile stiffness [GPa]		Poisson's ratio [-]		Thermal conductivity [W/m·K]	
		0°	90°	0°	90°	v_{13}	v_{23}	0°	90°
Value	60 ± 5	>250	>65	>22	>8	0.29	0.11	0.36	0.3

3.4 Experimental program

The experimental program has been summarised in Table 3. In the following, the label 'Cc' stands for RT-cured joints, while 'Ic' labels inductively cured series. Mechanical testing was performed 1 h, 24 h as well as 240 h after inductive heating. All RT-cured series have been manufactured under laboratory conditions (23 ± 2 °C, 50 ± 10 % RH).

Table 3: Experimental program of produced SLTJ series

Series	Short name	Adhesive type	CP content	Curing method	Curing conditions [h / min*]	Tested after	Joints
1	Fi_Cc_24 h	2K-EPX	0	RT	24	24	3
2	Fi_Cc_24 h_CP	2K-EPX	12.5	RT	24	24	3
3	Fi_Ic_1 h	2K-EPX	12.5	Inductively	10*	1	3
4	Fi_Ic_24 h	2K-EPX	12.5	Inductively	10*	24	3
5	Fi_Ic_240h	2K-EPX	12.5	Inductively	10*	240	3
6	LP_Cc_240h	2K-PUR	0	RT	240	240	3
7	LP_Cc_240h_CP	2K-PUR	12.5	RT	240	240	3
8	LP_Ic_1 h	2K-PUR	12.5	Inductively	10*	1	3
9	LP_Ic_24 h	2K-PUR	12.5	Inductively	10*	24	3
10	LP_Ic_240h	2K-PUR	12.5	Inductively	10*	240	3

3.5 Induction curing of SLTJ

The manufacturing approach of the SLTJ has been visualised in Figure 2. In order to inject the adhesive-CP mixes, a feedhole with a diameter of 4 mm was drilled into the tubes of the larger diameter at the height of the overlap length (see Figure 2-a). During inductive heating, temperatures at different points in the adhesive-CP mixture were monitored with thermocouples fixed to the outer surface of the inner tube, as illustrated in Figure 2-b or d. Three thermocouples were placed in the middle of the overlap, at equal angles of 120°.

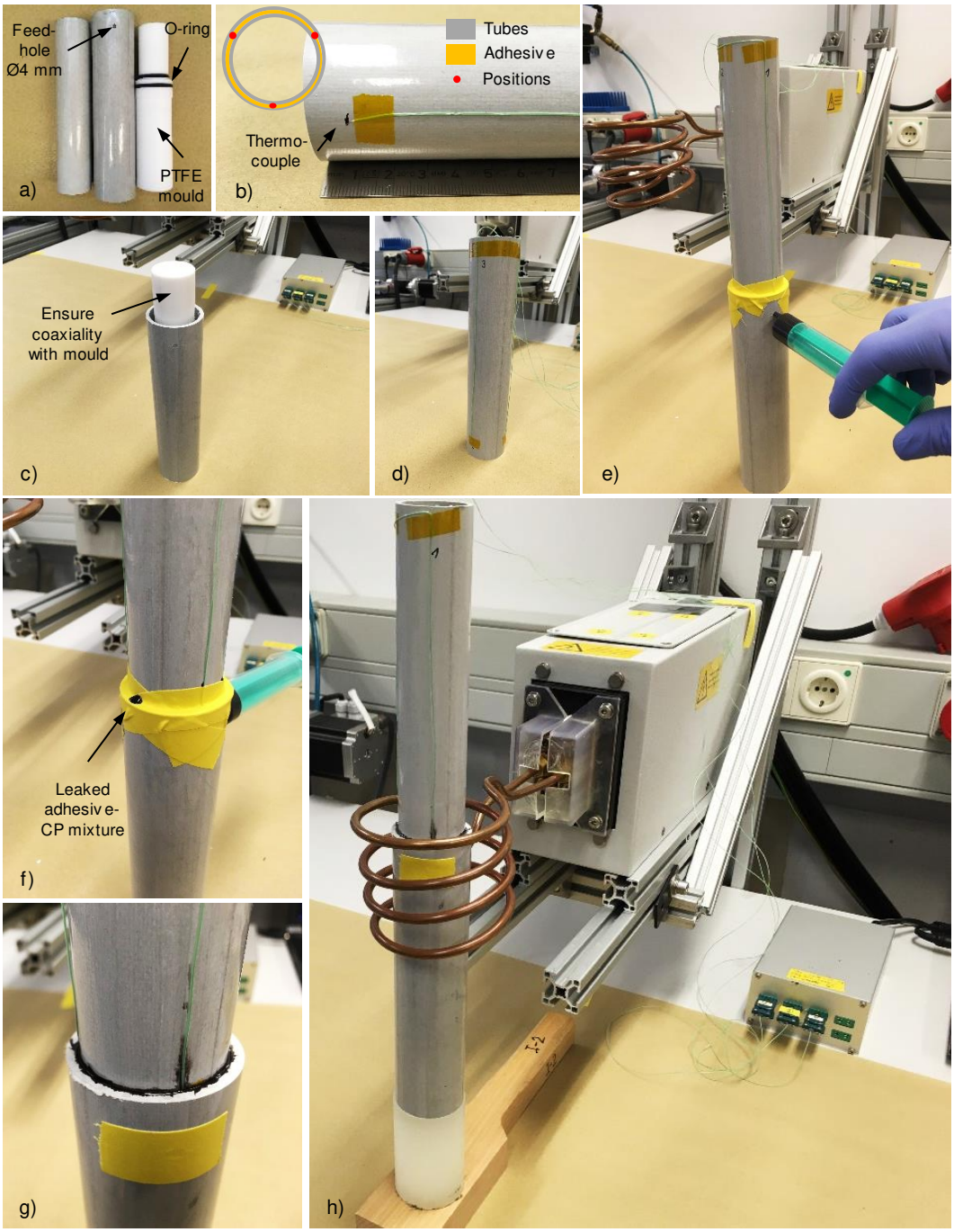

Figure 2: *Manufacturing process of SLTJ with a) inner tube, outer tube and PTFE mould, b) thermocouple fixed with temperature resistant polyamide adhesive tape on outer surface of inner tube, c) outer tube cast placed in PTFE mould, d) inner tube with attached thermocouples, e) application of adhesive-CP mixture (herein Fi390) over feedhole, f) leaked adhesive from slit in the tape, g) completely filled joint after removing of adhesive tape and h) positioning of bonded SLTJ specimen during inductive heating with thermocouples attached to the temperature control unit*

A PTFE mould was used to assemble the two G-FRP tubes, ensure coaxiality and maintain a constant adhesive layer thickness of 1 mm. The manufacturing process is amply described by Figure 2. Mechanical testing was performed using a specifically designed fixture.

4. Results and discussion

3.1 Temperature development

The temperature recordings for Fi390 and LP821 have been illustrated in Figure 3. In general, all temperature curves appear as arc-shaped. Temperatures – regardless of the considered adhesive – begin to flatten after about 4–6 min of inductive heating. After 5 min, inductive heating of the two adhesives filled with 12.5 w/w-% (~4 vol-%) resulted in satisfactory heating rates of 12 K/min (Fi390), and 11.8 K/min (LP821), respectively.

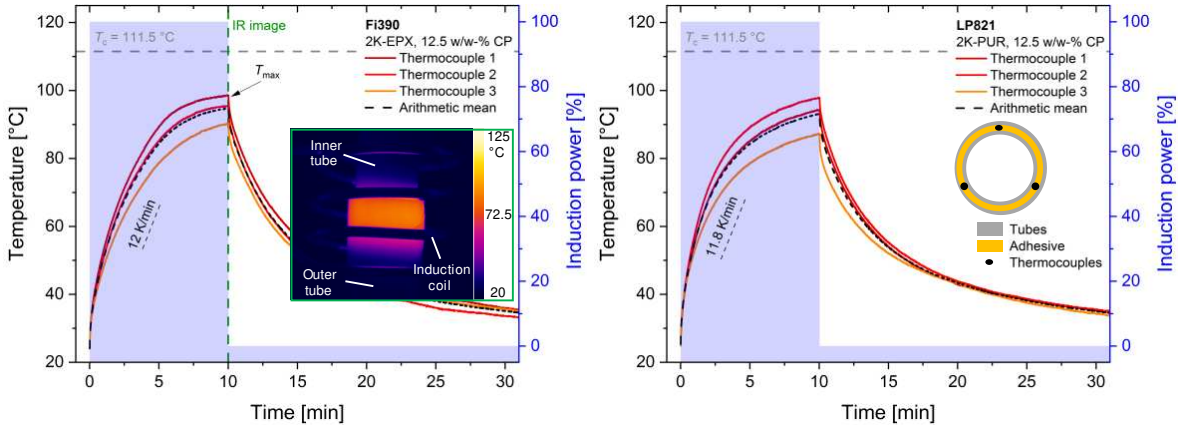

Figure 3: Temperature profiles recorded with thermocouples inside adhesive-CP mixtures during inductive heating of SLTJ for a) Fi390 and b) LP821; Exemplary IR image for Fi390 at t = 10 min (a, green frame)

At the end of the inductive heating phase, maximum end temperatures of 94.7 °C, for Fi390, and 93.2 °C for LP821, respectively, were recorded. Maximum deviations from the arithmetic mean over the period of heating amounted to 6.1 °C (Fi390) and 7 °C (LP821); heating of the two adhesives was very similar, with the comparatively small differences being attributable to differing enthalpy release.

3.2 Mechanical results

During data evaluation, shear strength was defined as the joint strength divided by the overlap surface, with the outer surface of the inner tube considered for the calculations. Shear strengths of all series were calculated, and opposed to each other, in Figure 4 in form of a bar chart, sorted by adhesive. The average shear strength for Fi390 increases from 9.2 MPa to 10.4 MPa after RT-curing with added CP. The same is, save for the figures, true for LP821. Longer conditioning times after induction lead to an increase of shear strength for Fi390; the opposite is true for LP821. From aforementioned observations, it can be concluded that a differing build-up of stiffness and strength throughout the SLTJ results, which turns out to be different depending on the considered adhesive. Thus, it may be that full cure – and consequently strength – has already been achieved 1 h after the EMF became inactive, but stiffness has not yet fully developed. As a result, a changing state of stress with conditioning time occurs, which is either in favour (Fi390) or to the disadvantage (LP821) of strength.

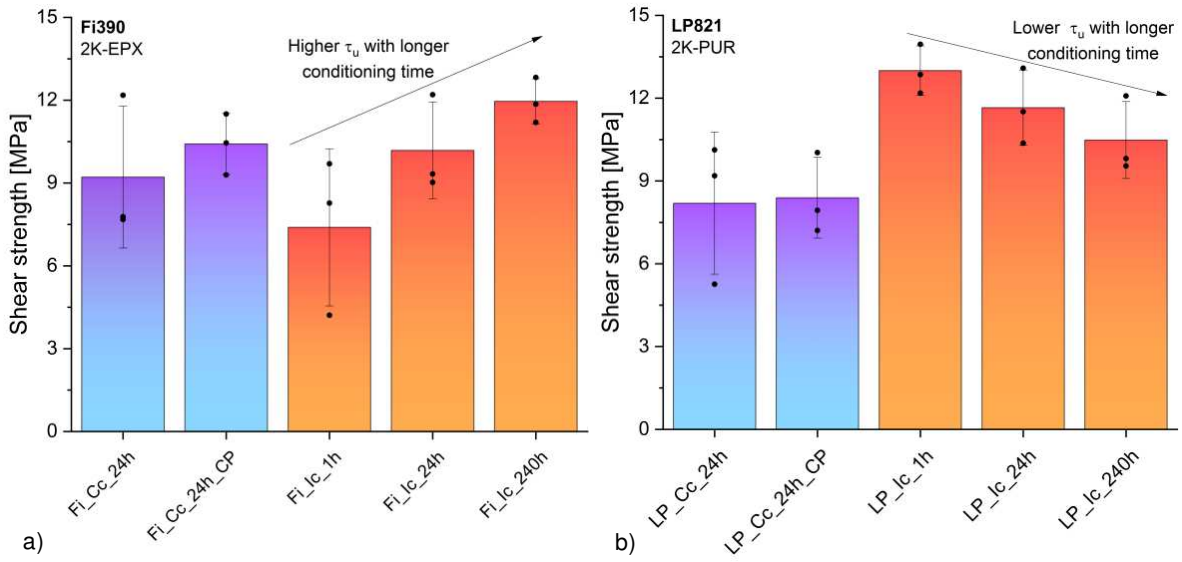

Figure 4: Comparison of achieved shear strength of SLTJ bonded with a) Fi390 and b) LP821; Zwick|Roell UTM (100 kN), v = 2 mm/min, all tests performed at RT

5. Conclusion

In this paper, induction curing with Curie particles (CP) was used to cure different series of G-FRP single lap shear joints (SLTJ) bonded with two commercially available adhesives (epoxy and polyurethane) For that, a manufacturing and accelerated curing procedure was devised and the process conditions and associated effects were analysed by means of thermal and mechanical metrics. After evaluation of all data, the following important conclusions were drawn:

- Temperature development during induction depended on the adhesive type. These differences are linked to differences in the release of enthalpy, both in terms of magnitude and timing.
- Failure occurred by tearing-off the G-FRP. The adhesives did thus not limit joint strength, but rather the substrate. Accordingly, joint capacity proved almost independent on the adhesive type, and the condition under which curing occurred.
- The experimental results presented show that thanks to induction heating, significant reductions in curing times of SLTJ are possible.

Acknowledgements

Acknowledgements can be added at the end of the paper, before the references if applicable.

Literature Cited

1. Bae D, Shon M, Oh S, Kim GN. Study on the Heating Behavior of Fe3O4-Embedded Thermoplastic Polyurethane Adhesive Film via Induction heating. Bulletin of the Korean Chemical Society 2016; 37(8):1211–8.

2. Vattathurvalappil SH, Haq M. Thermomechanical characterization of Nano-Fe3O4 reinforced thermoplastic adhesives and single lap-joints. Composites Part B: Engineering 2019; 175:107162.

3. Bae D, Shin P, Kwak S, Moon M, Shon M, Oh S et al. Heating behavior of ferromagnetic Fe particle-embedded thermoplastic polyurethane adhesive film by induction heating. Journal of Industrial and Engineering Chemistry 2015; 30:92–7.

4. Taegyu L, Yongsung K, Seungyong C, Minyoung S, Hokyoon J, Sangtaek O et al. Heating behavior and adhesion performance of induction-heated multilayered thermoplastic polyurethane adhesive film. The Journal of Adhesion 2019.

5. Suwanwatana W, Yarlagadda S, Gillespie Jr. JW. Influence of particle size on hysteresis heating behavior of nickel particulate polymer films. Composites Science and Technology 2006; 66(15):2825–36.

6. Cebrián AS, Moser P, Zogg M, Ermanni P. Paste adhesive modification for induction curing. In: Available from: URL: https://www.research-collection.ethz.ch/handle/20.500.11850/48700.

7. Hubbard JW, Orange F, Guinel MJ-F, Guenthner AJ, Mabry JM, Sahagun CM et al. Curing of a bisphenol E based cyanate ester using magnetic nanoparticles as an internal heat source through induction heating. ACS applied materials & interfaces 2013; 5(21):11329–35.

8. Vallée T, Adam M. Inductively cured glued-in rods in timber using Curie particles. International Journal of Adhesion and Adhesives 2016; 70:37–45.

MODELLING OF ACCELERATED CURING OF ADHESIVELY BONDED G-FRP TUBE CONNECTIONS

Till, Vallée[a], Morten, Voß[a], Marvin Kaufmann[a]

a: Fraunhofer IFAM, Bremen/Germany – till.vallee@ifam.fraunhofer.de

Abstract: *This paper presents the analysis of a series of adhesively bonded tube-in-tube (TiT) joints composed of glass-fibre reinforced polymers (G-FRP) for which induction heating with Curie-particles (CP) was used to accelerate curing. It focuses on the prediction of their load capacity using a probabilistic method (PM). First, the G-FRP material was characterised with regard to transverse (tensile) and shear stresses, which allowed to determine a valid failure criterion, including the related statistical description subsequently required for the PM. Then, finite element analysis (FEA) was used to determine the stresses within the TiTs, for not only a perfect geometry, but also considering a series of possible geometrical imperfections (offset and misalignment of the centrelines, and ovalisation) with three degrees of severity. The influence of aforesaid imperfections on stresses was determined, and discussed. Based thereupon, load capacity was numerically determined, compared to the experimental values, and the influence of imperfections highlighted. Predicted joint capacities agreed well with the experimental ones. The influence of centreline offset and ovalisation was found to be of minor importance, if compared to that of the misalignment. By an extension of the procedure, scattering of the experimental data was also predicted in form of upper and lower quantiles, which also agreed well.*

Keywords: adhesive; bonding; strength; prediction; probabilistic

1. Introduction

In the first part of this series, inductive heating of adhesively bonded composite tubular joints, whose curing was accelerated through adjunction of Curie-particles (CP) subjected to an oscillating electromagnetic field (EMF), was investigated in depth in [1]. The experimental investigations resulted in tubular joints in essence exhibiting the same quasi-static strength after accelerated curing within minutes, if compared to cold-cured reference sets. Two major questions requiring modelling arose.

Firstly, a better understanding of the curing kinetics, i.e. the relationship between the intrinsic curing-related properties of the adhesive, their interaction with the added particles, and the EMF. Modelling this aspect allows practitioners to estimate curing times based upon fundamental material, and system, parameters, and, *in extenso*, the optimisation in curing duration, and resources, for their practical issues. Secondly, the mechanical performance of the resulting joints, in particular their load capacity. Prediction thereof is arguably one of the most important task engineers have to accomplish. Due to the multi-physical nature of the problem, its appropriate treatment depends on several disciplines—these will be briefly addressed below.

1.1 Curing kinetics

For epoxies [2], the curing process is an important factor affecting the performance of the hardened adhesive, which in the uttermost cases undergoes a transition from the liquid to the

  doi:10.5075/epfl-298799_978-2-9701614-0-0

solid state, transitioning through a state called gelation (or vitrification). Initially, the epoxy curing reactions are kinetically controlled; however, with reduced mobility of the monomers, the reaction is more and more diffusion controlled, and corresponding reaction rate drops by orders of magnitude below that in the liquid region until it is eventually satiated. For polyurethanes [3], similar concepts apply, although made slightly more complicated owing to the fact that moisture is frequently an important ingredient for the reaction, making its diffusion an additional aspect to consider. As almost all chemical reactions, the rate of adhesive's polymerisation strongly depends on temperature. In its original formulation, Arrhenius' equation [4] deals with the term reaction rate, e.g. the rate at which two reactants A and B form the compound C, all expressed in terms of quantities. Usually, proxies other than quantities rate are considered, e.g. through monitoring of viscosity [5], dielectric cure monitoring [6], Fourier transform infrared spectroscopy (FTIR) [7], and most notably enthalpy via Differential Scanning Calorimetry (DSC) [8]. The relationship between adhesive formulation, temperature, and curing kinetics has been discussed on several occasions, including by Yousefi et al. in [9], or more recently by Ratsch et al. in [8]. It will suffice at this point to remind that curing of almost all adhesives is accelerated by supplying thermal energy or temperature, a fact that is adequately rendered by a large variety of kinetic models, as for example that of Kamal-Sourour [10, 11].

From a formal point of view, induction heating involves three main different physical phenomena, electromagnetism, heat transfer, and mechanics. A complete mathematical model for induction heating processes therefore needs to consider and tightly couple the equations modelling these phenomena. Such coupling, although not trivial, has been repeatedly reported [12–14]. They mostly rely on temperature independent electromagnetic properties. When Curie-temperature (T_C) is taken into account, modelling is made significantly more complicated, as resistances and inductance meaningfully drop, and relative permeability decreases to 1, in essence resulting in a nonmagnetic material [15]; different strategies have been developed to circumvent associated numerical problems [16].

1.2 Strength prediction

Decades of research have confirmed that joint strength cannot be determined by means of a stress-based approach [17–19].The singularity at the end of the adhesive layer and the significant mismatch in stiffness between the adherends and the adhesive require either adapting such approaches with methods such as stress-at-a-distance [20, 21], model refinement [22, 23], stress-intensity factors [17, 18], and stress-over a zone [24, 25], or higher-order mechanical concepts, most notably fracture mechanics (FM) [26–28], and probabilistic methods (PM) [19, 29, 30] to tackle the question of joint strength prediction.

2. Materials and methods

2.1 Induction heating and adhesive curing

Curing kinetics of the two adhesives, and adhesive-CP mixes, as characterised by dynamic DSC measurements [31] in a Discovery DSC (TA Instruments, Inc., USA). In these tests, constant heating rates (2, 5, 10, 15, and 20 K/s) were considered in a temperature range of 0 °C to 250 °C and a rate of 2K/s. Based upon the experimental data gathered by dynamic DSC, the software Netzsch Kinetics Neo® determined appropriate kinetic parameters considering the Kamal-Sourour model [10, 11]. Modelling the heating behaviour of the bonded joint was carried out using the finite element analysis (FEA) package Ansys® v19. The sample geometry amply

  doi:10.5075/epfl-298799_978-2-9701614-0-0

described in [1] and represented in Figure 1, inner tubes with an external diameter of ø40 mm, and outer tubes with an internal diameter of ø42 mm, both exhibiting a thickness of 3 mm, overlapping by 20 mm, were bonded via an adhesive layer of 1 mm. Besides modelling a perfectly coaxial joint, three different geometrical imperfections were also considered: an offset of the tube's centrelines, a misalignment thereof, and their ovalisation.

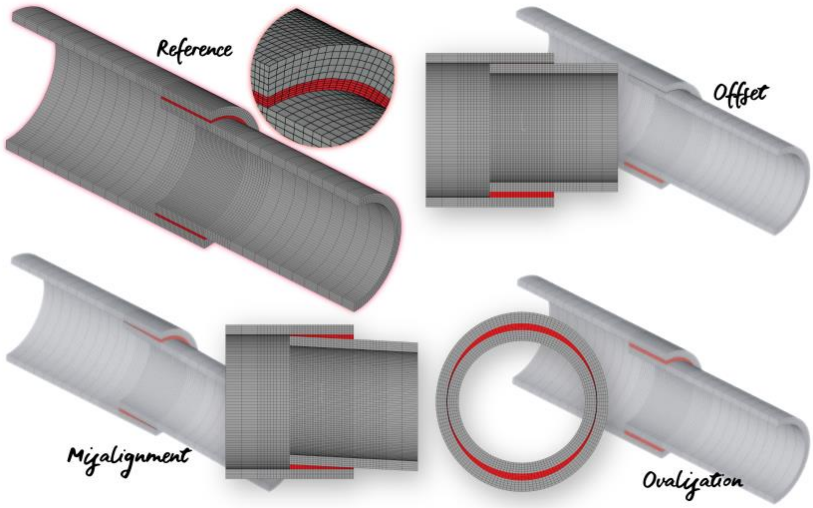

Figure 1 : The meshed FE model, top-left: the reference joint, top-right: the offset series, bottom-left: the misalignment series, and bottom-right: the (tube) ovalisation series; in all case, simple symmetry was considered.

The thermal modelling required two distinct aspects: firstly, modelling the thermal load resulting from the heat released by the exposure of the embedded CP to the inductively generated electro-magnetic field (EMP). For the modelling, it was assumed that temperatures generated within the adhesive layer are attributable to two distinct heat sources: heat originating from CP exposed to the EMF, H_{cp}, and heat released by the exothermic polymerisation, H_{cure}. In addition to exothermy, heat originating from the CP exposed to the EMF over time, $H_{cp}(t)$, and the Curie effect (switch-off at T_c) had to be integrated into the numerical model. Secondly, modelling the transient heat flux within the joint and its surroundings, in particular determining the time-dependent temperature development in the various locations of the adhesive mass.

2.2 Mechanical modelling

Joint capacity was modelled using a probabilistic approach, which has been used on various occasion in recent years, as discussed in the introduction. In essence, joint capacity prediction is substituted by the prediction of its probability of survival (P_S) or failure (P_F) under a given load, and not by comparing strength to resistance. A suitable proxy for the deterministic term strength is then the load for which $P_S = 0.5$, as then sample size would be equally divided into joints failing, and not. The probability of survival of the joint is tracked down to the "sum" of that of its contituents. As the bonded joint was modelled numerically, it appeared convenient to consider each finite element ϵ_i as such a contituent, to determine its probability of failure $P_{S,i}$, and to consider that the total probability of failure equals the product of that of its constituents, or $P_{S,Total} = \Pi\ P_{S,i}$, see Eq. (2) below. Because of the significant difference in size of the individual finite elements (V_i), and that of the samples based upon which strength has been determined (V_0), it is paramount to readjust strength according to Weibull's statistical size effects: $\sigma_i/\sigma_0 =$

$(V_i/V_0)^{1/m}$, with *m* the Weibull modulus. It is posited for the following that two stress components dominate the failure behaviour of the G-FRP within the bonded joints: through-thickness stresses σ_Z, and shear stresses τ_{XZ}. The simultaneous action thereof being described by a failure criteria $\Phi(\sigma_Z,\tau_{XZ})$, to be derived from the mechanical testing. Values of the failure criterion, $\phi_i = \Phi(\sigma_{Z,i},\tau_{XZ,i})$, were then computed for each element of the considered domain, and attributed a Weibull-probability of failure, P_s. Following the weakest-link assumption, the probability of survival of the complete domain corresponds to the product of the probabilities of survival of the individual links thereof. With aforesaid in mind, Equation (2) below, already derived 1968 by Freudenthal [32], results.

$$P_{s,\text{total}} = \prod_{i=1}^{n} P_{s,i} = \prod_{i=1}^{n} \exp\left[-\frac{V_i}{V_0}\left(\frac{\phi_i - \gamma}{\beta}\right)^{\alpha}\right] = \exp\sum_{i=1}^{n}\left[-\frac{V_i}{V_0}\left(\frac{\phi_i - \gamma}{\beta}\right)^{\alpha}\right] \quad (2)$$

It is known from previous investigations on that specific joint typology [29], and on that material [33], both transverse tensile and shear stresses act conjunctly to trigger failure. Accordingly, material strength was characterised with regard to both stress components acting conjunctly. For that, a specific device shear-tensile device (STD) [17] has been devised, which allows for the simultaneous application of the eponymous stresses on small samples of dimensions 40 x 40 mm². Pairs of corresponding τ-σ-points were then reported in a Cartesian grid, and an appropriate failure criterion $\Phi(\tau,\sigma)$ determined using the software OriginPro®. The data was then characterised statistically through modelling into a 3P-Weibull distribution using the statistical package EasyFit®.

Stresses were determined using the commercial FEA package Ansys. Material properties, all considered linear elastic, were determined from technical datasheets; the adhesive was considered isotropic, the G-FRP transverse isotropic. The element type SOLID226 was used, and the mesh refined at the level of the adhesive layer (with 5 layers of elements) and the G-FRP in the overlap zone (with 4 layers of elements), as illustrated in Figure 1, so to correctly render any stress peaks.

3. Results and discussion

3.1 Modelling temperatures and curing progress

The temperatures generated by the induction heating process were generally well rendered by the numerical model, as show a comparison between experimental and numerical data at different time steps, cf. Figure 2. The model validation was successfully carried out using thermocouple data recorded during CP heating at various locations of the GiR, which showed very good qualitative – and mostly quantitative – agreement with the numerical predictions. Based thereupon, predictions of the curing progress, i.e. the evolution of the curing degree with time, were also made. These simulations show that the adhesive reached a high level of curing (> 95%) at the end of the induction heating process, with further curing occurring during the cooling phase. Additional parametric studies have also revealed that the polymerisation enthalpy proved to be very important. Its significance increases with the thickness of the adhesive layer, duration of the induction time and magnitude of the curing temperature of the GiR. This indicates upper limits of the sheer adhesive mass so to avoid runaway curing reactions.

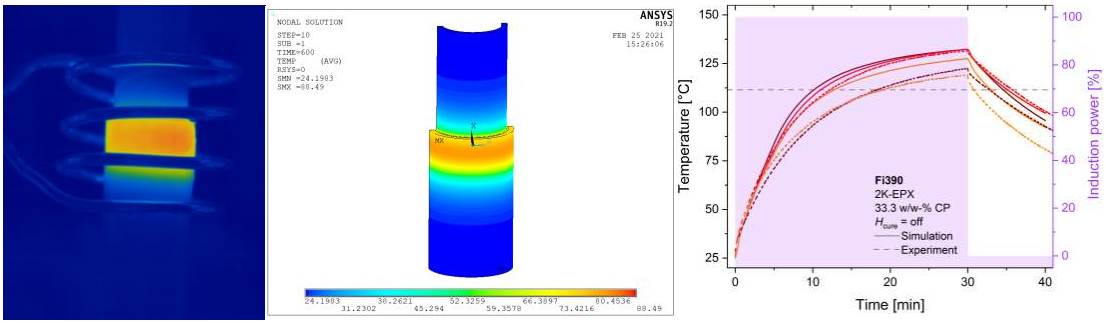

Figure 2 : Experimental and numerically determined temperatures around the overlap region

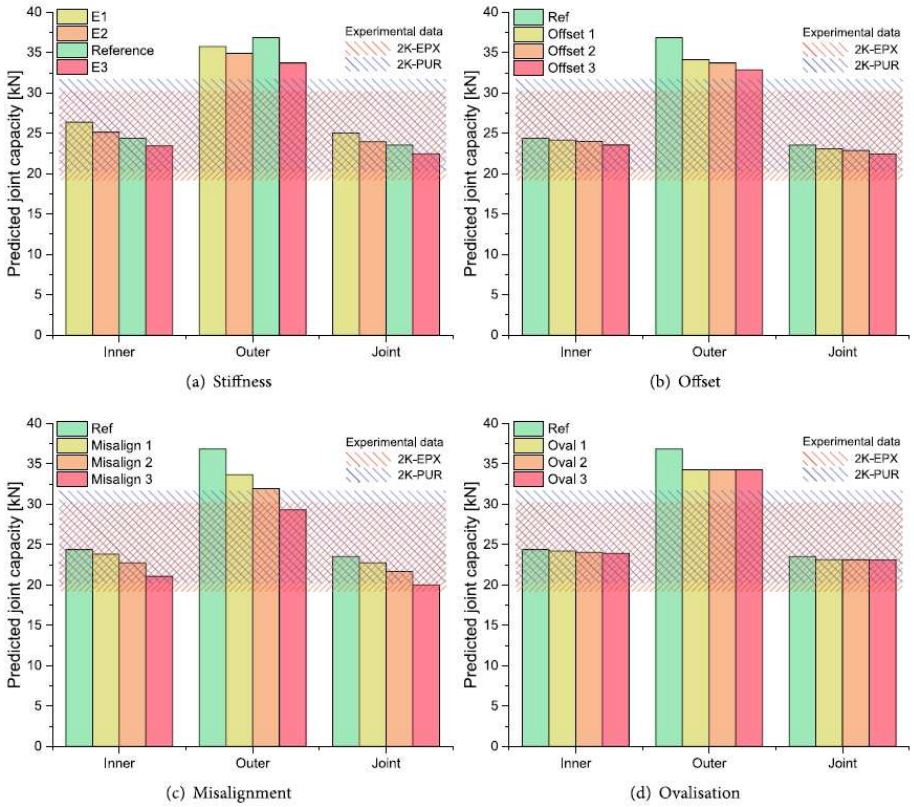

Figure 3 : Predicted joint capacities for different imperfections, and compared to the experimental data

3.2 Modelling strength

All predicted joint strengths, or load capacities, are summarised in Figure 3. Offsetting the centrelines of the tubes had relative little effect on predicted joint capacities, in particular for that of the inner tube alone, and of the joint (inner and outer tubes), respectively. Differences remained below 4%, if comparing the perfectly aligned tubular joints with those featuring the maximum possible deviation. This result has to be seen in combination with the influence of stresses, not detailed in this conference paper [34], where it was shown that offsetting almost doubled the magnitude of stresses at the beginning of the overlap. The influence of tilting the tube's centrelines resulted in a more significant differentiation of predicted capacities, which dropped by around 20% (comparing the joint with the highest misalignment to the reference). The FEA, also not detailed in this conference paper, highlighted that misalignment significantly influenced stress magnitudes, which were increased by as much as 25% in magnitude. However,

  doi:10.5075/epfl-298799_978-2-9701614-0-0

unlike offsetting, which ultimately proved to result in very localised increased, FEA revealed that misalignment altered the stress field all over the overlap length, thus significant for the probabilistic approach. Ovalisation of the tube proved to have an almost negligible effect on predicted joint capacity, with differences barely noticeable. Already FEA showed that ovalisation resulted in localised changes in the stress pattern, both in terms of axial and radial distributions. Accordingly, as the change affected only a relatively limited number of elements, little reduction of the probability of survival, and thus load capacity, resulted.

4. Conclusions

In a first step, the temperature development resulting from the inductive heating process was numerically modelled, including the expected curing degrees of the adhesives in function of time. In a second step, the G-FRP was characterised with regard to the stresses acting in the TiT, namely transverse and shear stresses. The G-FRP was shown to exhibit a quadratic failure criterion, for which adequate fitting parameters were derived, and statistically described. In the next step, stresses acting in the TiT were numerically computed, and the influence of a series of geometrical imperfections thereon determined, and discussed. Lastly, combining the information gathered during the characterisation of the G-FRP with the FEA performed on the TiTs, the probabilistic strength prediction was rolled out, and load capacities were predicted. Predicted joint capacities of the reference cases compared well with the previously determined experimental values. The influence of offsetting the centreline of the tubes, and their ovalisation, on strength was found to be negligible. Only tube's misalignment proved to have a noticeable influence on strength.

5. References

1. Morten Voß, Marvin Kaufmann, Till Vallée. Experimental investigations on accelerated curing of adhesively bonded G-FRP tube connections. 20th European Conference on Composite Materials (ECCM20). 2022.
2. Ellis B, editor. Chemistry and Technology of Epoxy Resins. London, New York: Blackie Academic & Professional; 1993.
3. Malucelli G, Priola A, Ferrero F, Quaglia A, Frigione M, Carfagna C. Polyurethane resin-based adhesives: curing reaction and properties of cured systems. International Journal of Adhesion and Adhesives. 2005;25:87–91. doi:10.1016/j.ijadhadh.2004.04.003.
4. Arrhenius S. Über die Dissociationswärme und den Einfluss der Temperatur auf den Dissociationsgrad der Elektrolyte. Zeitschrift für Physikalische Chemie 1889. doi:10.1515/zpch-1889-0408.
5. Hesekamp D, Pahl MH. Curing effects on viscosity of reactive epoxy resin adhesives. Rheola Acta. 1996;35:321–8. doi:10.1007/BF00403532.
6. Hussain F, Chen J, Hojjati M. Epoxy-silicate nanocomposites: Cure monitoring and characterization. Materials Science and Engineering: A. 2007;445-446:467–76. doi:10.1016/j.msea.2006.09.071.
7. SANCHEZSOTO M, PAGES P, LACORTE T, BRICENO K, CARRASCO F. Curing FTIR study and mechanical characterization of glass bead filled trifunctional epoxy composites.

Composites Science and Technology. 2007;67:1974–85. doi:10.1016/j.compscitech.2006.10.006.
8. Ratsch N, Böhm S, Voß M, Adam M, Wirries J, Vallée T. Accelerated curing of glued-in threaded rods by means of inductive heating – part II: modelling. The Journal of Adhesion. 2019:1–31. doi:10.1080/00218464.2019.1654865.
9. Yousefi A, Lafleur PG, Gauvin R. Kinetic studies of thermoset cure reactions: A review. Polym. Compos. 1997;18:157–68. doi:10.1002/pc.10270.
10. Kamal MR, Sourour S. Kinetics and thermal characterization of thermoset cure. Polym. Eng. Sci. 1973;13:59–64. doi:10.1002/pen.760130110.
11. Sourour S, Kamal MR. Differential scanning calorimetry of epoxy cure: isothermal cure kinetics. Thermochimica Acta. 1976;14:41–59. doi:10.1016/0040-6031(76)80056-1.
12. Chaboudez C, Clain S, Glardon R, Mari D, Rappaz J, Swierkosz M. Numerical modeling in induction heating for axisymmetric geometries. IEEE Trans. Magn. 1997;33:739–45. doi:10.1109/20.560107.
13. Dreyfuss P, Rappaz J. Numerical Modelling of Induction Heating for Two Dimensional Geometries; 2001.
14. Bay F, Labbe V, Favennec Y, Chenot JL. A numerical model for induction heating processes coupling electromagnetism and thermomechanics. Int. J. Numer. Meth. Engng. 2003;58:839–67. doi:10.1002/nme.796.
15. Martín-Segura Guillermo, Ferrater-Simón Coia, López-Mestre Joaquim, Montesinos-Miracle Daniel, Bergas-Jané Joan, Eng. Ahmed Masmoudi. Simulation of an induction hardening system during Curie temperature transition considering converter's performance. COMPEL - The international journal for computation and mathematics in electrical and electronic engineering. 2013;32:396–411. doi:10.1108/03321641311293957.
16. Paya B, Fireteanu V, Spahiu A, Guérin C. 3D magneto-thermal computations of electromagnetic induction phenomena. COMPEL - The international journal for computation and mathematics in electrical and electronic engineering. 2003;22:744–55. doi:10.1108/03321640310475164.
17. Keller T, Vallée T. Adhesively bonded lap joints from pultruded GFRP profiles. Part II: Joint strength prediction. Composites Part B: Engineering. 2005;36:341–50. doi:10.1016/j.compositesb.2004.11.002.
18. Vallée T, Keller T. Adhesively bonded lap joints from pultruded GFRP profiles. Part III: Effects of chamfers. Composites Part B: Engineering. 2006;37:328–36. doi:10.1016/j.compositesb.2005.11.002.
19. Vallée T, Correia JR, Keller T. Probabilistic strength prediction for double lap joints composed of pultruded GFRP profiles – Part II: Strength prediction. Composites Science and Technology. 2006;66:1915–30. doi:10.1016/j.compscitech.2006.04.001.
20. Khoramishad H, Akhavan-Safar A, Ayatollahi, da Silva LF. Predicting static strength in adhesively bonded single lap joints using a critical distance based method: Substrate thickness and overlap length effects. Proceedings of the IMechE. 2017;231:237–46. doi:10.1177/1464420716666427.
21. Martiny P, Lani F, Kinloch AJ, Pardoen T. A maximum stress at a distance criterion for the prediction of crack propagation in adhesively-bonded joints. Engineering Fracture Mechanics. 2013;97:105–35. doi:10.1016/j.engfracmech.2012.10.025.

22. Zhao X, Adams RD, Silva LFMd. Single Lap Joints with Rounded Adherend Corners: Experimental Results and Strength Prediction. Journal of Adhesion Science and Technology. 2011;25:837–56. doi:10.1163/016942410X520880.
23. Vallée T, Tannert T, Murcia-Delso J, Quinn DJ. Influence of stress-reduction methods on the strength of adhesively bonded joints composed of orthotropic brittle adherends. International Journal of Adhesion and Adhesives. 2010;30:583–94. doi:10.1016/j.ijadhadh.2010.05.007.
24. Clark JD, McGregor IJ. Ultimate Tensile Stress over a Zone: A New Failure Criterion for Adhesive Joints. The Journal of Adhesion. 1993;42:227–45. doi:10.1080/00218469308026578.
25. Towse A, Potter KD, Wisnom MR, Adams RD. The sensitivity of a Weibull failure criterion to singularity strength and local geometry variations. International Journal of Adhesion and Adhesives. 1999;19:71–82. doi:10.1016/S0143-7496(98)00058-X.
26. Chaves FJP, da Silva LFM, Moura MFSF de, Dillard DA, Esteves VHC. Fracture Mechanics Tests in Adhesively Bonded Joints: A Literature Review. The Journal of Adhesion. 2014;90:955–92. doi:10.1080/00218464.2013.859075.
27. Li S, Thouless MD, Waas AM, Schroeder JA, Zavattieri PD. Mixed-mode cohesive-zone models for fracture of an adhesively bonded polymer–matrix composite. Engineering Fracture Mechanics. 2006:64–78.
28. Ripling EJ, Mostovoy S, Patrick RL. Application of Fracture Mechanics to Adhesive Joints. In: Adhesion. 100 Barr Harbor Drive, PO Box C700, West Conshohocken, PA 19428-2959: ASTM International; 1964. 5-5-15. doi:10.1520/STP44560S.
29. Albiez M, Vallée T, Ummenhofer T. Adhesively bonded steel tubes – Part II: Numerical modelling and strength prediction. International Journal of Adhesion and Adhesives 2018. doi:10.1016/j.ijadhadh.2018.02.004.
30. Vallée T, Fricke H, Myslicki S, Kaufmann M, Voß M, Denkert C, et al. Modelling and strength prediction of pre-tensioned hybrid bonded joints for structural steel applications. The Journal of Adhesion. 2021:1–41. doi:10.1080/00218464.2021.1928498.
31. Roşu D, Caşcaval C, Mustată F, Ciobanu C. Cure kinetics of epoxy resins studied by non-isothermal DSC data. Thermochimica Acta. 2002;383:119–27. doi:10.1016/s0040-6031(01)00672-4.
32. Freudenthal AM. Statistical approach to brittle fracture. Fracture, An Advanced Treatise, II. 1968:591–619.
33. Vallée T, Tannert T, Meena R, Hehl S. Dimensioning method for bolted, adhesively bonded, and hybrid joints involving Fibre-Reinforced-Polymers. Composites Part B: Engineering. 2013;46:179–87. doi:10.1016/j.compositesb.2012.09.074.
34. Voß M, Vallée T, Kaufmann M. Accelerated curing of adhesively bonded G-FRP tube connections — Part III Strength prediction. Composite Structures 2021. doi:10.1016/j.compstruct.2021.113900.

MANUFACTURING, MECHANICAL AND DEGRADATION BEHAVIOR OF MG/PLA BIORESORBABLE COMPOSITE LAMINATES FOR ORTHOPEDIC APPLICATIONS

Wahaaj Ali[a,b,c], Leon Tillmann[c], Alexander Kopp[c], Carlos González[a,d] and Javier LLorca [a,d]

a: IMDEA Materials Institute, Madrid 28906, Spain (E-mail: syed.rizvi@imdea.org)
b: Department of Material Science and Engineering, Universidad Carlos III de Madrid, Leganés, Madrid 28911, Spain
c: Meotec GmbH, Aachen 52068, Germany
d: Department of Materials Science, Polytechnic University of Madrid, 28040 Madrid, Spain

Abstract: *A strong and tunable bioresorbable composite material offers the potential to replace conventional non-degradable metals and render defects of bioresorbable metallic and polymeric implants for orthopedic applications. In this investigation, magnesium fibers (WE43 alloy) of 300 microns in diameter were used to reinforce medical-grade PLA to manufacture a bioresorbable composite material for orthopedic applications. Afterward, unidirectional and multidirectional laminates of Mg fiber (WE43)/PLA (medical grade) composites with 15% Mg volume, are fabricated by hot compression process. The mechanical behavior of composite is studied in longitudinal and transverse directions utilizing tensile tests, while the ±45 coupon tensile test studies in-plane shear response. Lastly, we discuss insights into the degradation mechanism of composite by in vitro degradation tests.*

Keywords: PLA; magnesium; bioresorbable; composite; characterization

1. Introduction

Biodegradable polymers entered long ago in the commercial markets for orthopedic applications. But their low mechanical properties, slow degradation rate, and adverse effects motivated researchers to find new biomaterials (1). As an alternate, last decade, magnesium and its alloys got generous attention from the scientific community. It offers mechanical properties comparable to bone and high osteointegration. There are numerous *in vivo*, pre-clinical, and clinical studies on magnesium for bone fixation applications with positive outcomes. However, magnesium corrosion control is still a challenge because it is highly corrosive in the physiological environment causing unpredictable mechanical failures. Another main concern is hydrogen gas, a by-product of magnesium corrosion that traps in tissues around the implant causing inflammation (2)(3)(4). Considering the drawbacks of both potential biodegradable materials, using them as a composite is appealing because magnesium can reinforce polymer matrix increasing their mechanical properties. In contrast, polymer slows down magnesium corrosion. Furthermore, the composite's resultant mechanical properties and degradation rate are tailorable by shape, volume fraction, and nature of magnesium reinforcement, which is the requirement for an ideal bioresorbable implant. The available literature on Mg/PLA composite reported properties on unidirectional (longitudinal) laminates such as, tensile, flexural and impact, overall mass loss of composite, molecular weight on PLA matrix, effect of coatings and processing methods, etc. (5) (6) (7). But ply behavior in 3 major directions i.e., longitudinal, transverse, and shear has not been reported yet, which is critical to designing an optimized

  doi:10.5075/epfl-298799_978-2-9701614-0-0

multidirectional laminate of this material. In this study, we present the mechanical behavior of composite is studied in longitudinal and transverse directions utilizing tensile tests while the ±45 coupon tensile test studies in-plane shear response.

2. Experimental

2.1 Materials

Billets of WE43 MEO Mg alloy were produced by casting, machining, and heat-treatment processes and then converted into 6 mm diameter rods by indirect extrusion (Meotec GmbH, Germany). Rods were cold drawn to fibers of 0.3 mm diameter (Meotec GmbH, Aachen and Fort Wayne Metals Research Products Corp., Indiana, USA) which were used as reinforcement. Pellets of Medical grade PLA (PURASORB PLDL 7038) were hot-pressed into films to make up the matrix phase of the composite.

2.2 Composite manufacturing

The laminas of Mg fiber reinforcement and PLA matrix were separately prepared and then hot pressed at 180°C with pressure to prepare a void-free composite. Three types of laminates were manufactured: Unidirectional longitudinal (UL - $[0]_4$), Unidirectional transversal (UT - $[90]_4$), and multidirectional cross ply laminate (US - $[\pm 45]_s$) with 15% volume fraction of magnesium fibers as shown in Figure 1. The manufacturing strategy has been described in detailed in references (8)(9).

Figure 1. Bioresorbable composite of Mg (WE43) fiber/Medical grade PLA. Unidirectional laminate

2.3 Mechanical tests on Mg/PLA composite

Mechanical tests were performed on a Universal Testing Machine (Instron) with a 10 KN load cell while displacement rate was 3 mm/min, 1 mm/min, and 1 mm/min for UL, UT, and US laminates. Tabs of glass fiber composite were bonded to Mg/PLA composites for gripping. Strains were computed using the Digital Image Correlation technique (VIC, Correlated Solutions Inc.). Shear modulus and strength were calculated as per the guidelines in Standard ASTM D 3518/D 3518M – 94 (10).

3. Results and discussion

3.1 Tensile behavior in the longitudinal direction

  doi:10.5075/epfl-298799_978-2-9701614-0-0

Longitudinal Tensile (UT) response of the Mg/PLA composite is shown in Figure 2. The initial response is linear with Elastic modulus of 9.1 ± 0.4 GPa. The elastic zone ends with a non-linear response which is attributed to the plastic deformation of annealed Mg fibers. Finally, a catastrophic failure is produced. This catastrophic failure corresponds to two possibilities i.e., either PLA matrix strain reaches its tensile strain, or one Mg fiber fails, which propagates the cracks in the matrix.

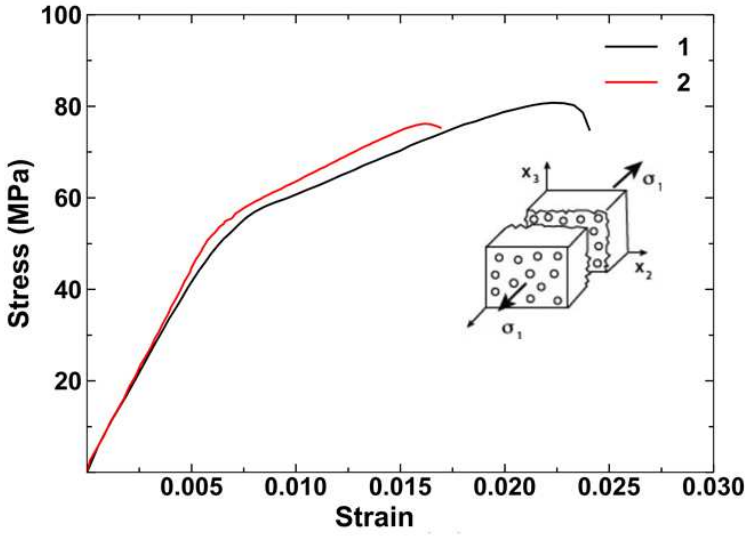

Figure 2. Stress-Strain plot of tensile behavior of composite in longitudinal direction

3.2 Tensile behavior in the transverse direction

In the Transverse Tensile (UT) direction, the initial linear elastic response gives an elastic modulus of 4.1 ± 0.2 GPa. It is well known that the matrix and interfacial properties affect the failure mode in the transverse direction. Figure 3 infers that the failure of Mg/PLA composite is accompanied by PLA matrix cracking and matrix/fiber debonding (11). The tensile strength in this direction is 27.3 ± 1 MPa. The low scatter stress-strain curves show the homogeneous distribution of fibers.

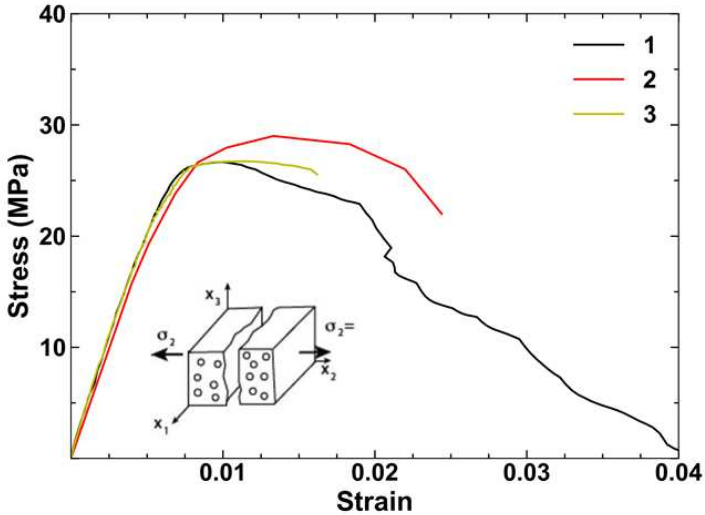

Figure 3. Stress-Strain plot of tensile behavior of composite in transverse direction

3.4 Degradation mechanism of composite

The degradation mechanism of Mg/PLA composite during *in vitro* conditions has been explained in our previous publication (8), where we used 0.1 mm diameter fiber (smaller than current 0.3 mm) and non-medical grade PLA matrix, but the degradation principles should be similar. First, water present in the simulated solution diffuses through the PLA matrix and reaches the Mg fiber surface reacting with magnesium and forming the layer of Mg $(OH)_2$. This layer becomes weak in the presence of Chlorine ions present in the simulated solution, and corrosion of magnesium continues in the following manner: formation and dissolution of Mg $(OH)_2$. The corrosion by-products occupy more volume and increase the pressure on the surrounding PLA matrix, which ultimately cracks. The crack facilitates the supply of fresh body fluids and migration of degradation species and thus, increases the pit size at the crack nucleation point. On the other hand, PLA degradation is prolonged as compared to Mg and is accompanied by hydrolytic degradation, which has been explained in detail in references (9) (12).

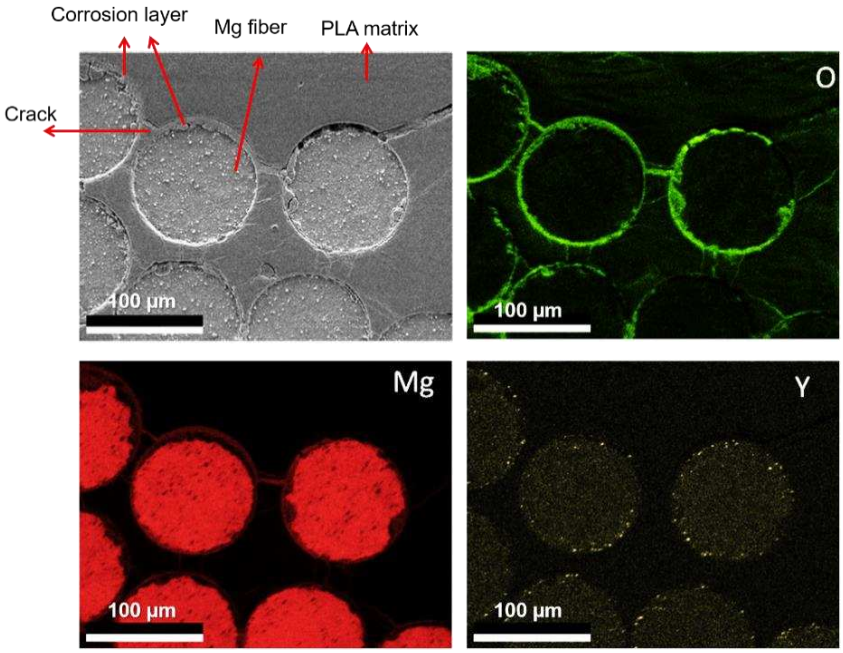

Figure. 5. (a) Secondary electron micrograph showing the details of corrosion at the fiber/matrix interface after 148 h in PBS at 37 ◦C with element map of O, Mg and Y obtained by energy-dispersive X-ray spectroscopy (8)

4. Conclusion

The experimental study presents the mechanical behavior of Mg/PLA composite ply in three major directions. The properties have been summarized below:

Table 1: Ply properties of Mg/PLA composite with 15% Mg volume

Test type	Laminate configuration	Modulus (GPa)	Strength (MPa)
Unidirectional longitudinal tensile (UL)	$[0^o]_4$	9.1 ± 0.4	77.8 ± 3.3

  doi:10.5075/epfl-298799_978-2-9701614-0-0

Unidirectional transversal tensile (UT)	$[90^o]_4$	4.1 ± 0.2	27.3 ± 1.0
In-Plane shear cross ply laminate (US)	$[\pm 45^o]_s$	-	24.6 ± 1.6

The study revealed that Mg/PLA composite follows the rule of mixture (ROM) for composites. The slight deviation from ideal ROM value has attributed to minor fiber misorientations that originated during fabrication process. Mg fiber properties dominantly control the mechanical behavior in the UL direction, while for UL and US directions, it is controlled by PLA matrix and fiber/matrix interfacial properties. These ply properties can be further used to design a bioresorbable Mg/PLA composite implant with optimal mechanical behavior. However, more insights are needed about the mechanical behavior in compression and shear mode when composite starts to degrade.

5. Acknowledgments

This investigation was supported by the European Union's Horizon 2020 research and innovation programme under the Marie Skłodowska-Curie grant agreement No 813869.

6. References

1. Ambrose CG, Clanton TO. Bioabsorbable implants: review of clinical experience in orthopedic surgery. Ann Biomed Eng. 2004;32(1):171–7.

2. Biber R, Pauser J, Brem M, Bail HJ. Bioabsorbable metal screws in traumatology: A promising innovation. Trauma Case Reports. 2017 Apr 1;8:11–5.

3. Zhao D, Witte F, Lu F, Wang J, Li J, Qin L. Current status on clinical applications of magnesium-based orthopaedic implants: A review from clinical translational perspective. Biomaterials [Internet]. 2017;112:287–302.

4. Meischel M, Hörmann D, Draxler J, Tschegg EK, Eichler J, Prohaska T, et al. Bone-implant degradation and mechanical response of bone surrounding Mg-alloy implants. J Mech Behav Biomed Mater [Internet]. 2017;71(February):307–13.

5. Guo C, Liu X, Liu L, Bai J, Xue F, Lin P, et al. Impact behaviors of poly-lactic acid based biocomposite reinforced with unidirectional high-strength magnesium alloy wires. Prog Nat Sci Mater Int [Internet]. 2014;24(5):472–8.

6. Ali W, Mehboob A, Han M-G, Chang S-H. Experimental study on degradation of mechanical properties of biodegradable magnesium alloy (AZ31) wires/poly(lactic acid) composite for bone fracture healing applications. Compos Struct [Internet]. 2019;210(December 2018):914–21.

7. Li X, Chu C, Wei Y, Qi C, Bai J, Guo C, et al. In vitro degradation kinetics of pure PLA and Mg/PLA composite: Effects of immersion temperature and compression stress. Acta Biomater [Internet]. 2017;48:468–78.

8. Ali W, Echeverry-Rendón M, Kopp A, González C, LLorca J. Strength, corrosion resistance and cellular response of interfaces in bioresorbable poly-lactic acid/Mg fiber

  doi:10.5075/epfl-298799_978-2-9701614-0-0

composites for orthopedic applications. J Mech Behav Biomed Mater. 2021;123(June):104781.

9. Ali W, Mehboob A, Han MG, Chang SH. Effect of fluoride coating on degradation behaviour of unidirectional Mg/PLA biodegradable composite for load-bearing bone implant application. Compos Part A Appl Sci Manuf [Internet]. 2019;124(March):105464.

10. Standard Test Method for In-Plane Shear Response of Polymer Matrix Composite Materials by Tensile Test of a 45° Laminate. ASTM Int. 2001;

11. Tang Z, Wang C, Yu Y. Failure response of fiber-epoxy unidirectional laminate under transverse tensile/compressive loading using finite-volume micromechanics. Compos Part B Eng [Internet]. 2015;79:331–41.

12. Buchanan F. Degradation rate of bioresorbable materials, prediction and evaluation. Woodhead Publishing Limited; 2008. 634 p.

  doi:10.5075/epfl-298799_978-2-9701614-0-0

Cyclic behavior and crack propagation in adhesively-bonded assemblies under mixed mode and negative load ratios

C. Bernolin[a], G. Stamoulis[b], P. Bidaud[a], W. Albouy[c], N. Dagorn[c], D. Thévenet[a]

a: ENSTA Bretagne, UMR CNRS 6027, IRDL, F-29200 Brest, France
b: Univ. Bretagne Occidentale, UMR CNRS 6027, IRDL, F-29200 Brest, France
c: Safran Composites, A Technology platform of Safran Tech, 33 Avenue de la Gare, 91760 Itteville

Keywords: crack propagation; adhesive, fatigue

The use of adhesives to bond different structures is more and more investigated in domains such as aeronautics, automobile or marine systems. In many industrial cases, adhesively-bonded joints are submitted to complex fatigue loadings. In previous studies, fatigue tests based on Scarf samples [1] were performed in order to assess the crack initiation and define a criterion for fatigue crack initiation. Nevertheless, the strength of adhesively-bonded structures can also be predicted under the scope of the fracture mechanics theory. In order to study different loadings cases (mode I, mode II, mode I+II), the crack propagation was investigated with a modified Arcan device [2]. The identification of the Strain Energy Release Rate (SERR) was based on a Benzeggagh-Kenane criterion in the plane I+II. An inverse identification method built on the use of a linear finite element model was used to define the critical value of the strain energy release rate. Monotonic and fatigue tests were performed under different fatigue load ratios: a specific experimental fixture was developed in order to generate positive and negative load ratios and characterize the effects of compression on the crack propagation. In this presentation, experimental results are presented plotting the crack propagation rate vs. the SERR range and the influence of the different fatigue load ratios is investigated. Experiments were performed using hydraulic tensile-compression machine. The Arcan specimens were loaded under displacement control. Three different angles γ were tested (Figure 1): 0° (tensile), 45° (tensile-shear) and 90° (shear).

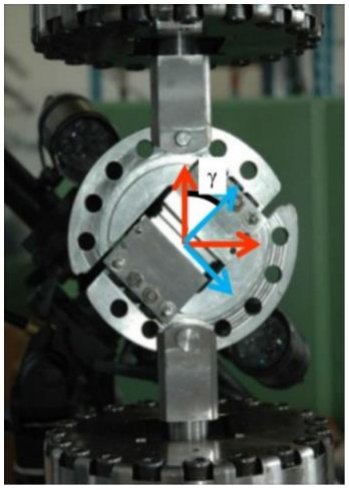

Figure 1: Arcan fixture

  doi:10.5075/epfl-298799_978-2-9701614-0-0

The profile displacements along the adhesive joint are extracted and measured using a 3D Digital Image Correlation (DIC - GOM Aramis 5M). A CCD camera (Qimaging Retiga 1300 B) was placed behind the specimens in order to monitor, if possible, the crack propagation during loading. The global experimental set-up is shown in Figure 2. A trigger is set to get images at the maximum and minimum value of the displacement actuator. All the cameras were synchronized in order to get the experimental loading force for each recorded image. Tests were performed at a fixed loading frequency f = 1Hz and a positive displacement ratio $R_u = \frac{u_{min}}{u_{max}}$ = 0.2.

Figure 2: Arcan experimental set-up for fatigue tests

Different fracture surfaces were observed on the fatigue specimens, and are illustrated in Figure 3, where cohesive and adhesive failures are observed, depending on the loading angle.

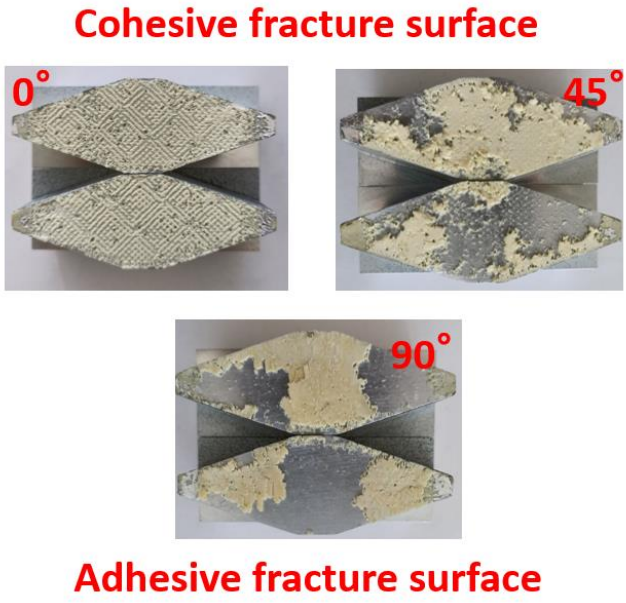

Figure 3: Different fracture surfaces

[1] N. Carrere, C. Badulescu, J-Y. Cognard, D. Leguillon, Int. J. Adhes. Adhes., 62, 154 (2015).

[2] G. Stamoulis, N. Carrere, J.-Y Cognard, P. Davies, C. Badulescu, Int. J. Adhes. Adhes., 66, 147 (2016).

  doi:10.5075/epfl-298799_978-2-9701614-0-0

A FOUR-POINT BENDING TEST TO STUDY BOTH FAILURE INITIATION AND CRACK PROPAGATION AT THE INTERFACE OF AN ADHESIVE JOINT

Pierre Bidaud[a], Nicolas Carrère[a], Thomas Bonnemains[b], Eric Lolive[b]

a: IRDL, UMR CNRS 6027, Ensta Bretagne, F-29200 Brest, France;
b: IRDL, UMR CNRS 6027, UBO, F-29200 Brest, France;

Abstract: *In this study the authors propose a test specimen developed to study both failure initiation and crack propagation at the interface with the aim to determine its strength and toughness. The two-substrate specimen used were bonded with a thin joint of structural adhesive, to conform to most of the industrial applications. Then, geometry of the specimen and parameters of the four-point bending were designed to localize failure initiation at one interface and in order to have a stable evolution of the crack propagation at this interface. This optimization work was performed using 3D Finite Element Model for an interface of metallic substrates and an industrial epoxy based adhesive. An experimental campaign was carried out on the optimized configuration of the specimen and the four-point bending flexural loading. The failure properties identified at the interface for a specific surface preparation are compared to the one characterized for "cohesive" failures on the structural adhesive.*

Keywords: Adhesive; Interface; Fracture mechanics; Failure initiation; Crack Propagation.

1. Introduction

Failure occurring at an interface in an adhesively bonded joint is considered as non-conform. This is the reason why most of the results in the literature concerns failure occurring within the adhesive. Thus, tests designed to characterize "adhesive" failure properties at the interfaces, remains a few. Based on the work of Roche et al. [1], which lead to the development of a standard for the characterization of interfaces [2], three point bending was carried to assess failure initiation at epoxide-aluminum interfaces [3-4]. Concerning fracture mechanics, using a four-point bending test, Zebar et al. developed a notched specimen in order to determine interfacial fracture toughness of different metal-polymer samples [5].

2. Experimental configuration

2.1 Bonded samples

Unlike the sample proposed by the standards, the tested configuration has a second substrate and a thin adhesive joint. The aim was to reproduce the industrial bonding processes. All the specimens were assembled using a dedicated bonding device in order to have the required precision on the dimensions. The interface studied in this paper was constituted with an epoxy based adhesive and aluminum substrates. Specific surface preparations were performed on the two interfaces. The main dimensions of the configuration are presented on Figure 1.

  doi:10.5075/epfl-298799_978-2-9701614-0-0

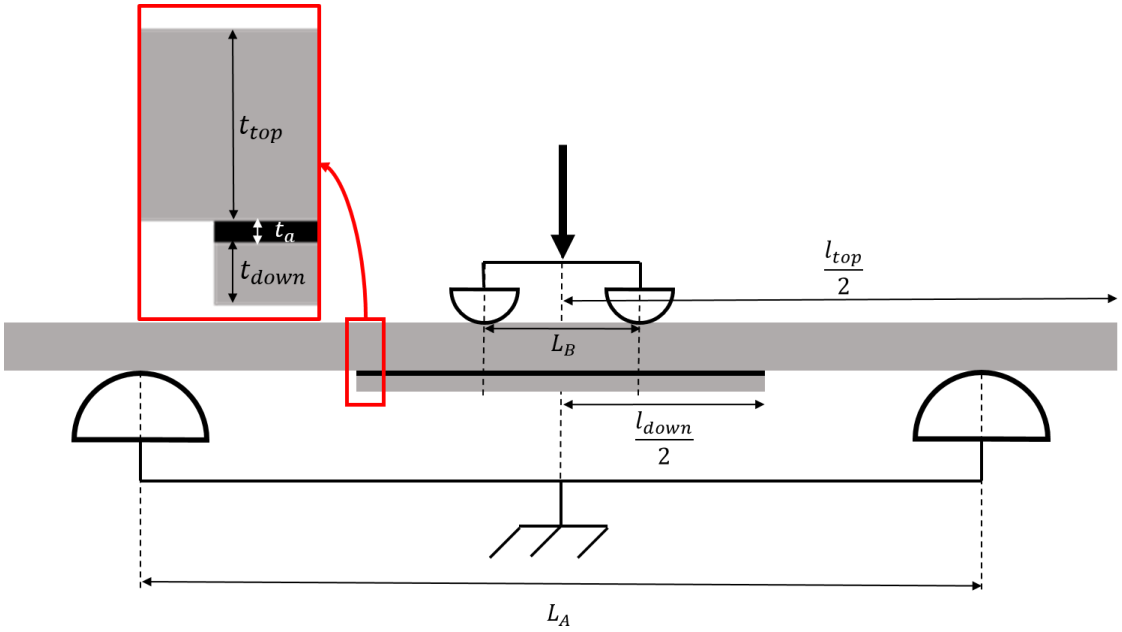

Figure 1. Configuration of the four-point bending test.

2.2 Testing procedure

A bending using four-point was preferred for the flexibility of its configuration introducing a second span on the upper rolls L_B. All the tests were performed driven in displacement using an electrical testing machine. The experimental results are not presented in this paper.

3. Numerical simulation

3.1 Parameters for an optimized geometry

Due to its novelty, geometry of the specimen and spans between rolls for the bending were not fixed by any standard. In order to achieve an interfacial failure they constitute parameters we can change. Changes in these dimensions involve modifications in the stress states in the adhesive joint. A parametric study on three dimensions were so modified in the numerical simulations in order achieve failures at the upper interface: length and thickness of the lower substrate respectively l_{down} and t_{down}, and the span between the upper rolls L_B.

3.2 Cohesive Zone Models

Simulations were performed with Abaqus® Finite Element Models (FEM) introducing Cohesive Zone Models (CZM) at the interface or in the middle of the adhesive joint. The material behavior was considered as linear elastic and all the material parameters were taken from the state of the art. Similar parameters were implemented for the failure criteria in the cohesive and interfacial CZMs. Loading, symmetries, boundary conditions and parameters taken for the simulations are summarized on the Figure 2. Changing the set (l_{down} ,t_{down} , L_B) of parameters an optimized configuration was found maximizing the following ratio :

$$R = {}^{F_{Coh}}/_{F_{int}}$$

where F_{Coh} is the load for a cohesive failure and F_{int} for an interfacial failure. These loads were considered as the maximum value obtained in the numerical simulations for CZM in the middle

  doi:10.5075/epfl-298799_978-2-9701614-0-0

of the adhesive joint (mid. Join CZM) or at the upper interface (interface CZM). Simulation results are presented in terms of load-displacement curves in figure 3 with a first optimized set of parameters showing a significant in the numerical load to failure.

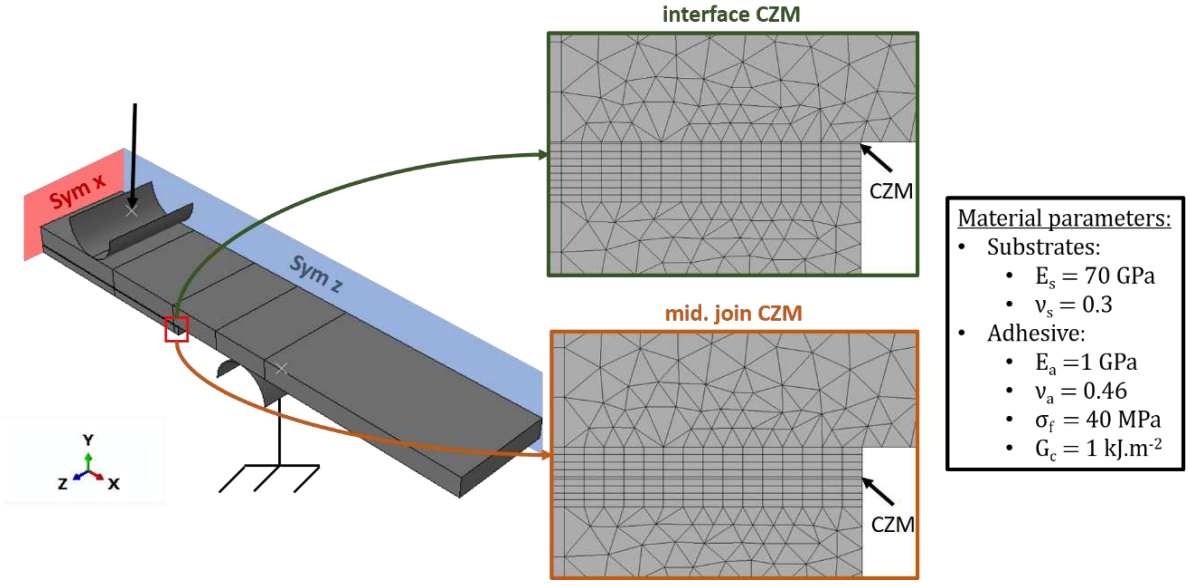

Figure 2. Finite Element Models and material parameters.

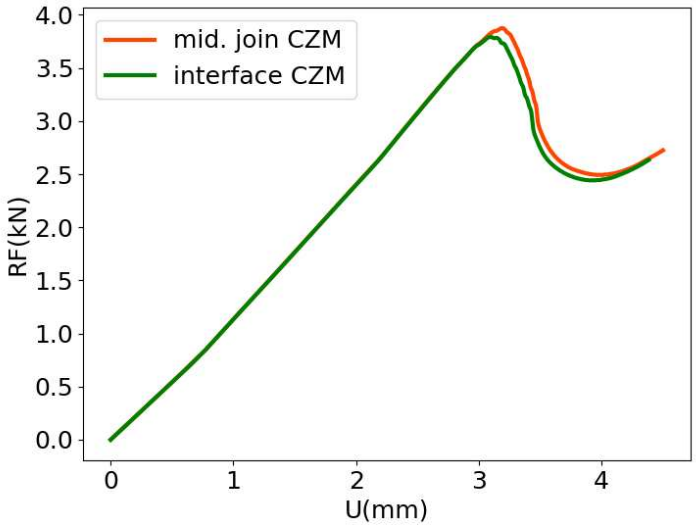

Figure 3. FEM load displacement results for the two CZM configurations.

4. Prospects

More numerical and experimental results are coming and will be publicized in future volumes of scientific journals.

5. References

1. Roche A, Behme A, Solomon J, A three-point flexure test configuration for improved sensitivity to metal/adhesive interfacial phenomena, IJAA 1982.

  doi:10.5075/epfl-298799_978-2-9701614-0-0

2. ISO 14679, Adhesives – measurement of adhesion characteristics by a three-point bending method, 1997.

3. Sauvage JB, Aufray M, Jeandrau JP, Chalandon P, Poquillon D, Nardin M, Using the 3-point bending method to study failure initiation in epoxide-aluminium joints, IJAA 2017.

4. Birro TV, Aufray M, Paroissien E., Lachaud F., Assessment of the interface failure behaviour for brittle adhesive using the three point bending test, IJAA 2021.

5. Zebar MEM, Hattali ML, Mesrati N, Interfacial fracture toughness measurement in both steady state and transient regimes using four-point bending test, IJF 2020.

  doi:10.5075/epfl-298799_978-2-9701614-0-0

BEARING STRENGTH PREDICTION BY CFRP AND FFRP DAMAGE ONSET CRITERIA FOR RIVETED JOINTS

Jarno Jokinen[a], Oscar Rodera Garcia[a], Pauli Hakala[a], Farzin Javanshour[a], Mikko Kanerva[a]*

a: Faculty of Engineering and Natural Sciences, Tampere University, Finland
* Corresponding author: jarno.jokinen@tuni.fi

Abstract: *Fasteners are a typical method for providing load transfer between different parts. The current interest by the industry is to use natural fibres, such as flax, in composite laminates. The failure modes in flax fibre reinforced plastic (FRP) composite joints are clearly less known. This work studies the damage onset of a fastener joint using three-dimensional finite element models. The damage onset is analysed using the Hashin 3D and Puck's failure criterion. In the analysis, carbon and flax FRP joints are simulated. The analyses remark that the Puck criterion's parameters have an influence on the damage onset and specific parameters are needed for the flax FRP in joints.*

Keywords: bearing; joint; Hashin; Puck; flax

1. Introduction

Mechanical joints are a critical part in lightweight composite structures. Mechanical joints have several advantages, which include applicability to inspections and disassembly. The challenge is the stress peaks caused by fasteners. For studying the load-carrying capability of these mechanical joints, both analytical and numerical methods are used. These are mainly based on stress-based methodologies. The stress field around the fastener in orthotropic composite plies is complex and requires a fitting failure criterion for taking into account different stress components. Several different stress and strain-based criteria have been developed [1].

In addition to strength values, certain criterion includes parameters dependent on the laminate. This is a challenge when new material combinations are taken into use. The current trend of many industrial fields is sustainability, which evokes further interest in natural engineering materials, such as flax fibres. Currently, there is no long-term experience about the using of flax laminates in the structural applications, including mechanical joints [2,3].

The target of this work is to study the damage onset in carbon fibre reinforced plastic (CFRP) and flax fibre reinforced plastic (FFRP) laminate joints with fasteners. The study is performed using finite element (FE) analyses where Hashin 3D and Puck criteria are implemented. The work compares the damage onset and studies the influence of Puck criterion's parameters. In addition, the location of the damage and the influence of friction are covered.

2. Methods

2.1 Finite element model

The three-dimensional FE model presenting a riveted joint was created using Abaqus/Standard 2021 (Fig. 1). The model consisted of three laminates and one rivet. All three laminates had the same geometry (length 48 mm and width 24 mm). The rivet diameter was 4 mm. The simplicity

  doi:10.5075/epfl-298799_978-2-9701614-0-0

of the fastener was considered, e.g. countersinks were not modelled. The circular fastener ends (heads) had 8 mm outside the hole region (1 mm in thickness). The 'rivet edge' distance was 12 mm in the longitudinal direction and 12 mm in the width direction. Eight ply laminates' stacking sequence was $[0/45/-45/90]_{SE}$. The thicknesses of CFRP and FFRP laminates were respectively 1.12 mm and 2.96 mm. The 0-direction was parallel to the loading direction. The ply properties for CFRP and FFRP are presented in Table 1.

Table 1: Material properties used in this study. [4–6]

	CFRP	FFRP
Ply thickness [mm]	0.14	0.37
E_1 [GPa]	140	24.98
E_2, E_3 [GPa]	10	4.51
ν_{12}, ν_{13}, ν_{23}	0.3	0.3
G_{12}, G_{13}, G_{23} [GPa]	5.17	5.21
X_T [MPa]	2080	260
X_C [MPa]	1560	260
Y_T, Z_T [MPa]	59	18.58
Y_C, Z_C [MPa]	203	18.58
S (S_{12},S_{13},S_{23}) [MPa]	93	33.51
E_f [GPa]	230	58.9
E_m [GPa]	3	2.9

The laminates were connected using a titanium fastener. The fastener's Young's modulus was 110 GPa, and Poisson's ratio was 0.3. The contacts between fastener and laminates and laminate and laminate were modelled. These contacts were modelled as frictionless and frictional. The effects of fastener tightening were also covered in the numerical analyses. The tightening effect was modelled by pressure loading at the fastener socket region.

The FE models were loaded by tensile loading simulating the mechanical load. The loading was performed using the enforced displacement at the left side edge of the middle laminate. The (same) edge width and vertical displacements were restricted. The value of enforced displacement was 0.1 mm in the CFRP joint and 0.05 mm in the FFRP joint. The outside laminates were restricted in all the three directions at the laminate end edge, as shown in Figure 1. The FE model laminates were modelled using fully integrated solid elements (C3D8) and the rivet using reduced integrated solid elements (C3D8R). The typical element dimension was 1 mm, which provided approximately 28,000 elements for the CFRP and FFRP models.

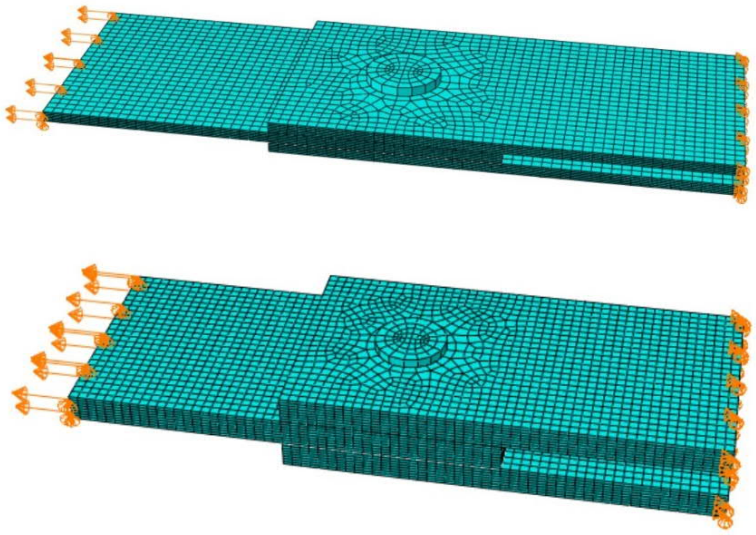

Figure 1. The finite element models of the CFRP (top) and the FFRP (bottom) joints.

2.2 Damage onset criterion

The damage onset for the joint laminates was studied using the Hashin 3D and Puck stress criteria [7,8]. Both criteria were implemented to the analysis using the user-defined material subroutine (UMAT) in Abaqus [9]. The Hashin 3D and Puck criteria can be extracted in the following form:

Hashin 3D Fibre failure

$$f_{FF} = \left(\frac{\sigma_{11}}{X_T}\right)^2 + \left(\frac{\sigma_{12}}{S}\right)^2 + \left(\frac{\sigma_{13}}{S}\right)^2, \text{when } \sigma_{11} > 0 \quad (1)$$

$$f_{FF} = \left(\frac{\sigma_{11}}{X_C}\right)^2, \text{when } \sigma_{11} < 0 \quad (2)$$

Hashin 3D Matrix Failure

$$f_{IFF} = \left(\frac{\sigma_{22}+\sigma_{33}}{Y_T}\right)^2 + \frac{\sigma_{23}^2-\sigma_{22}\cdot\sigma_{33}}{S^2} + \frac{\sigma_{12}^2+\sigma_{13}^2}{S^2}, \text{when } \sigma_{22} + \sigma_{33} > 0 \quad (3)$$

$$f_{IFF} = \frac{1}{Y_C}\left[\left(\frac{Y_C}{2S}\right)^2 - 1\right](\sigma_{22} + \sigma_{33}) + \frac{(\sigma_{22}+\sigma_{33})^2}{4S^2} + \frac{(\sigma_{23}^2-\sigma_{22}\sigma_{33})}{S^2} + \frac{(\sigma_{12}^2+\sigma_{13}^2)}{S^2}, \text{ when } (\sigma_{22} + \sigma_{33} < 0) \quad (4)$$

Puck Fibre failure

$$f_{EFF} = \frac{1}{R_{\parallel}^{t,c}}\left[\sigma_{11} - \left(\nu_{\perp\parallel} - \nu_{\perp\parallel f} m_{\sigma_1}\frac{E_{\parallel}}{E_{\parallel f}}\right)(\sigma_{22} + \sigma_{33})\right] = 1, \text{when } \sigma_{11} > 0 \quad (5)$$

$$f_{EFF} = \frac{1}{-R_{\parallel}^{t,c}}\left[\sigma_{11} - \left(\nu_{\perp\parallel} - \nu_{\perp\parallel f} m_{\sigma_1}\frac{E_{\parallel}}{E_{\parallel f}}\right)(\sigma_{22} + \sigma_{33})\right] = 1, \text{when } \sigma_{11} < 0 \quad (6)$$

Puck Matrix failure

$$f_{EIFF} = \sqrt{\left(\left(\frac{1}{R_{\perp}^{At}} - \frac{p_{\perp\psi}^t}{R_{\perp\psi}^A}\right)\sigma_n(\theta)\right)^2 + \left(\frac{\tau_{nt}(\theta)}{R_{\perp\perp}^A}\right)^2 + \left(\frac{\tau_{n1}(\theta)}{R_{\perp\parallel}^A}\right)^2} + \frac{p_{\perp\psi}^t}{R_{\perp\psi}^A}\sigma_n(\theta), \text{when } \sigma_n(\theta) > 0 \quad (7)$$

$$f_{EIFF} = \sqrt{\left(\left(\frac{1}{R_{\perp}^{At}} - \frac{p_{\perp\psi}^{t}}{R_{\perp\psi}^{A}}\right)\sigma_n(\theta)\right)^2 + \left(\frac{\tau_{nt}(\theta)}{R_{\perp\perp}^{A}}\right)^2 + \left(\frac{\tau_{n1}(\theta)}{R_{\perp\parallel}^{A}}\right)^2} + \frac{p_{\perp\psi}^{t}}{R_{\perp\psi}^{A}}\sigma_n(\theta), \text{when } \sigma_n(\theta) > 0 \quad (8)$$

$$\text{with } \frac{p_{\perp\psi}^{t,c}}{R_{\perp\psi}^{A}} = \frac{p_{\perp\perp}^{t,c}}{R_{\perp\perp}^{A}}\cos^2\psi + \frac{p_{\perp\parallel}^{t,c}}{R_{\perp\parallel}^{A}}\sin^2\psi. \quad (9)$$

Puck criterion's $p_{\perp\parallel}^{t}$, $p_{\perp\parallel}^{c}$, $p_{\perp\parallel}^{t}$ and $p_{\perp\parallel}^{c}$ were modified during the analyses. For the detailed description of the Puck and Hashin parameters, the work by Rodera Garcia [9] is referred.

3. Results

3.1 Stress distributions

The analyses were performed using the enforced displacement, and the corresponding reaction forces were calculated at laminate ends (Table 2). The bearing and by-pass stresses were evaluated in the middle laminate, which had a higher loading than the outside (strap) laminates. The bearing stress can be estimated based on the simplified analytical equation

$$\sigma_{BR} = P/dt \quad (10)$$

where P is the force, d is the fastener diameter, and t is the adherend thickness. The by-pass stresses were estimated using the area based on the laminate width excluding rivet hole and multiplied by laminate thickness.

Table 2: Joint reaction forces, average bearing, and by-pass stress in this study.

	CFRP	FFRP
Reaction force [N]	1124	400
Bearing stress [MPa]	251	34
By-pass stress [MPa]	50	7

3.2 Hashin failure criterion

Firstly, the damage onset was studied using the Hashin failure criterion. The values were evaluated in three nodal lines (A, B and C) in the middle laminate, as shown in Figure 2. The nodal (lines) locations had an angle (of 0, 54 and 90) over the loading direction. The failure criterion's values were studied in these locations for different ply orientations.

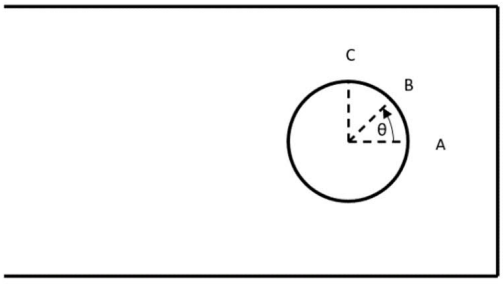

Figure 2. Nodal lines in the middle laminate.

The margin of safety (MoS) per ply provided by the Hashin's criterion are shown in Figures 3 and 4 for CFRP and FFRP laminates, respectively. In both laminates, the nodal line A and the ply angle 0° are shown to be the most critical. The minimum values in the CFRP and FFRP laminates are -16 % and -51 %. This indicates that the applied loading provides the damage onset for both laminates based on the Hashin criterion. However, the loading is more critical to the FFRP laminate.

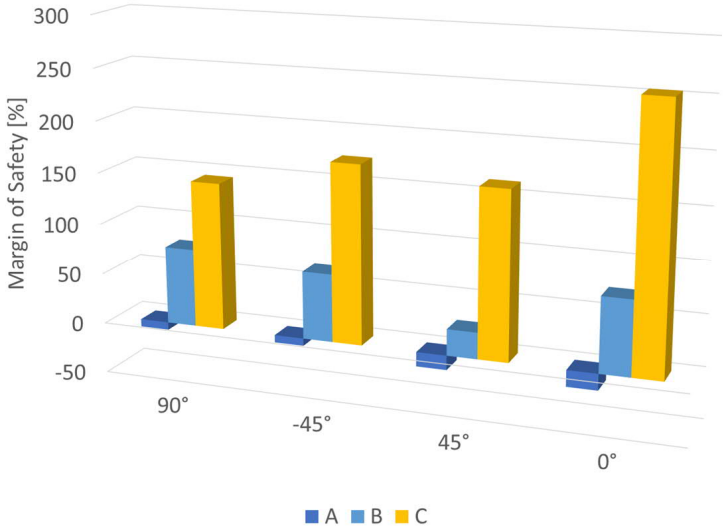

Figure 3. The margin of safety provided by the Hashin criterion's maximum value for the four-ply angles and three nodal lines in the CFRP laminate.

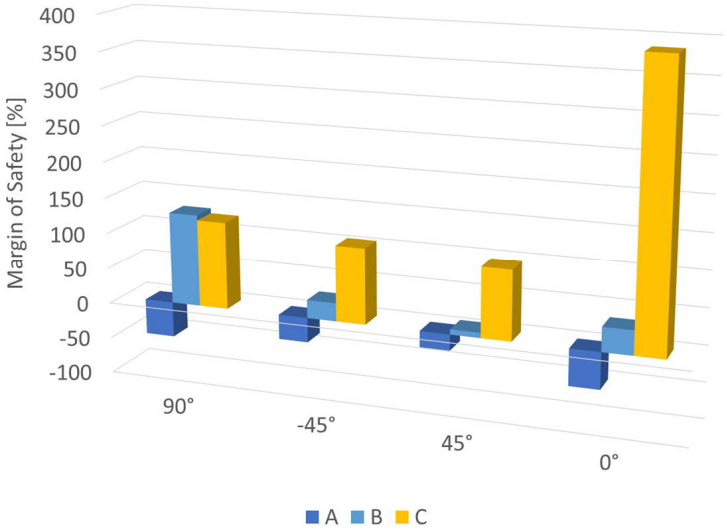

Figure 4. The margin of safety provided by the Hashin criterion's maximum value for the four-ply angles and three nodal lines in the FFRP laminate.

3.3 Puck criterion

Secondly, the Puck stress criterion was used in the analysis. The Puck criterion-related analyses for the CFRP and FFRP laminates are shown in Figures 5 and 6. The Puck criterion has parameters in it, which were modified during the analyses. In the CFRP laminate (Figure 5), the parameters

influence was around 5 % among the results gained. The comparison to the Hashin criterion remarked a difference of 10 % when compared to the highest value (of criterion) provided by the Puck criterion.

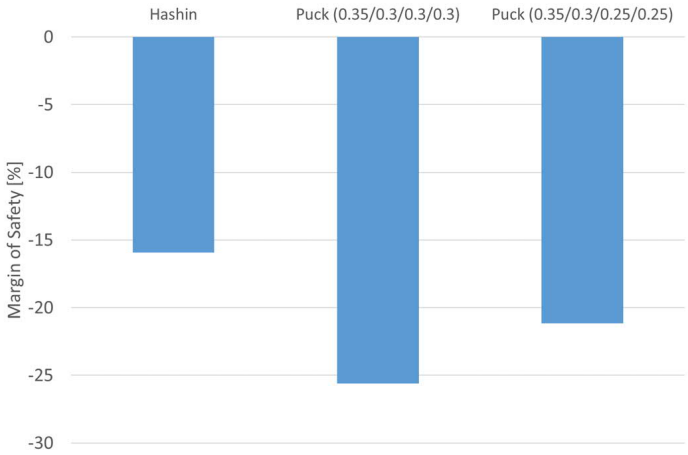

Figure 5. The influence of the Puck criterion's parameters on the MoS and its comparison to the MoS by the Hashin criterion for the CFRP laminate.

The Puck parameters are typically provided for CFRP and glass FRP (i.e., GFRP) laminates. In the FFRP laminate case of this study, both GFRP and CFRP parameters were used. The CFRP parameter values (0.35/0.3/0.3/0.3) provided the values close to the Hashin's criterion. The GFRP parameter values (0.3/0.25/0.2/0.2) provided almost a 10 % difference (at a maximum). The GFRP values lead to more conservative prediction of failure.

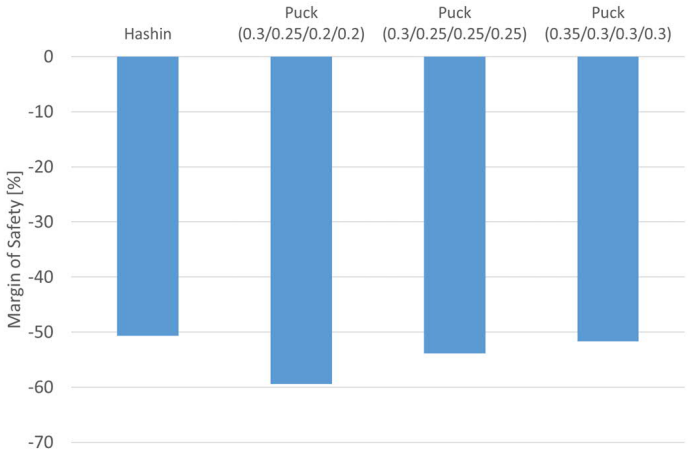

Figure 6. The influence of the Puck criterion's parameters on the MoS and its comparison to the MoS by the Hashin criterion for the FFRP laminate.

3.4 Friction and pressure

Finally, friction and rivet pressure were analysed. These analyses were performed using the Hashin criterion. The results for the CFRP and FFRP joints are shown in Figures 7 and 8. According to the results, friction has an influence on the MoS of the laminate. The pure (emulated tightening) pressure did not provide significant change for the MoS of the laminate. For that reason, only the combination of friction and pressure is provided in the results in Figures 7 and

Error! Reference source not found.. This combination improves the MoS value. Results clearly indicate that the friction distributes the loading over a large area, and the rivet is less loaded.

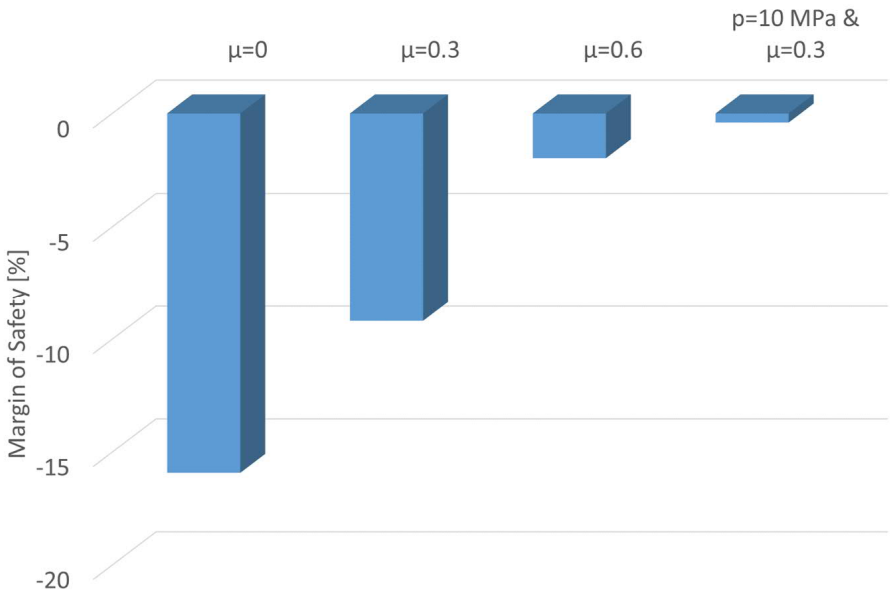

Figure 7. The effect of joint friction and rivet pressure on the MoS of CFRP laminate.

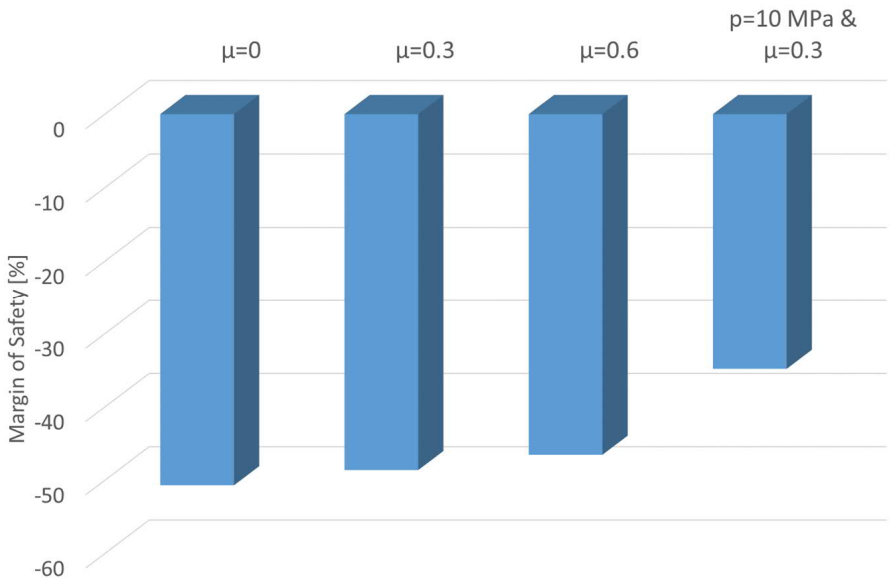

Figure 8. The effect of joint friction and rivet pressure on the MoS of FFRP laminate.

4. Conclusion and discussion

In this work, the damage onset in mechanical joints with composite laminates and fasteners was studied. The damage onset was based on two stress-based criteria, Hashin 3D and Puck. The criterion is using stress components provided by the finite element used. The stress distribution at the edge of the fastener hole is highly concentrated. Based on the preliminary analyses, the damage onset prediction is highly dependent on the applied finite element mesh. The joint modelling requires modelling the fastener-to-laminate and laminate-to-laminate contacts correctly.

The Hashin 3D criterion in the analysis showed that the loading direction in the fastener hole was the most critical parameter. This states that the bearing stress state would predict the damage onset. The most critical ply angle was 0° in both laminates studied. The damage onset was expected in all the plies. The FFRP laminate's 0° and 90° angles were exceeding the damage onset (prediction) of that made for plies 45° and -45°. The damage onset was more even in the CFRP plies compared to FFRP. The analysis using the Puck criterion resulted in higher values and indicated the likeliness of the damage onset. The parameters (constants) in the Puck criterion were studied in the FFRP plies where established values do not exist and should be covered in future studies. The friction facilitates a uniform stress distribution around the fastener and delays the damage initiation (onset) in the composites. This is a useful result for a practical analysis in that the ignorance of the bearing friction would yield more conservative designs of joints.

Acknowledgements

This research is partly based on the funding related to the ecosystem project SmartTram2 (5136/31/2019) for Tampere University funded by Business Finland.

5. References

[1] Orifici AC, Herszberg I, Thomson RS. Review of methodologies for composite material modelling incorporating failure, Compos Struct 2008;86:194-210.

[2] Fiore V, Calabrese L, Scalici T, Valenza A. Evolution of the bearing failure map of pinned flax composite laminates aged in marine environment. Compos Part B Eng 2020;187:107864.

[3] Estrada RG, Santiuste C, Barbero E. Failure maps of biocomposites mechanical joints reinforced with natural fibres. Compos Part C Open Access 2021;5:100159.

[4] Skytta V, Saarela O, Wallin M. Progressive Failure of Composite Laminates; Analysis vs Experiments. Fract Nano Eng Mater Struct - Proc 16th Eur Conf Fract 2006:341–2.

[5] Javanshour F, Prapavesis A, Pärnänen T, Orell O, Lessa Belone MC, Layek RK, et al. Modulating impact resistance of flax epoxy composites with thermoplastic interfacial toughening. Compos Part A Appl Sci Manuf 2021;150:106628.

[6] Prapavesis A, Tojaga V, Östlund S, Willem van Vuure A. Back calculated compressive properties of flax fibers utilizing the Impregnated Fiber Bundle Test (IFBT). Compos Part A Appl Sci Manuf 2020;135:105930.

[7] Hashin Z. Failure criteria for unidirectional fiber-reinforced materials, J Compos Mater, 1980;7:48-464.

[8] Puck A, Schürmann H. Failure analysis if FRP laminates by mans of physically based phenomenological models, Compos Sci Technol, 1998;58:1045-1067.

[9] Rodera Garcia O. Damage onset modelling of curved composite laminates. Master of Science thesis, Tampere University of Technology, 2018.

  doi:10.5075/epfl-298799_978-2-9701614-0-0

INVESTIGATION ON FASTENING BEHAVIOUR AND JOINING STRENGTH OF UD-CF/PEEK RIVET TO MULTIMATERIALS

Takeshi Eguchi[a,b], Mikitaka Ito[a], Kazuaki Nishiyabu[a]

a: Kindai University – nishiyabu@mech.kindai.ac.jp
b: Dai-chi Dentsu Ltd. – eguchi@daiichi-dentsu.co.jp

Abstract: *This study aims to develop the high reliable and efficient fastening process for a joining of multimaterials using carbon fibre reinforced thermoplastic rivet. The simple thermoplastic tape pultrusion machine with unique tape feeding system and compressive moulds was developed in laboratory, and the round-rod was fabricated using unidirectional carbon fibre reinforced poly-ether-ether-ketone (UD-CF/PEEK) prepreg tape. From the round-rod, the head forming and fastening of rivet were performed with compact servo-press unit. The effects of type of round-rods, heating and fastening conditions on the fastener and its joining strengths were investigated by cross-sectional observation, tensile shear strength test and pull through strength test. The tensile shear strength and the pull through strength of UD-CF/PEEK rivet showed sufficient high compared to Aluminium rivet, because the structure where the rivet head and body are united with continuous fibres. These experimental results prove that the rivet fastening process using UD-CF/PEEK rods developed was a highly availabe for multimaterials joining.*

Keywords: CFRTP, CF/PEEK, Rivet fastening, Joining strength, Multimaterials

1. Introduction

Multimaterials are composed of metals and polymer composites and recently are focusing as one of candidate materials with a high cost-performance for light-weighting. To manufacture the large structures with complex shape, it must be assembled by any joining methods with these materials, but such dissimilar materials have much lower joining strength than polymer composites themselves. Thus, they are often joined by any mechanical fastenings in addition to adhesive bonding by thermosetting resin. However, the metallic rivets or bolts have a significant problematic such as weight increase and galvanic corrosion in addition to the increased fastening work costs. On the other hand, advanced thermoplastic composites are focusing from several properties better than thermosetting ones. Especially, it has an advantage of enabling secondary process by re-heating like plastic working of metals. However, the thermoplastics are not suitable for adhesive bonding, because the adhesion has no chemical reaction to thermoplastics. Therefore, several fusion joining methods such as electric-resist welding, induction welding and ultrasonic welding have been proposed recently for advanced thermoplastic composites. However, in either matrix-based composite, the joining strengths are not sufficient, and the reliability and durability are reduced due to the delamination occurred under cyclic and impact loadings. Whereas the mechanical fastenings such as bolts and rivets are traditional joining methods, they are superior for high reliability and durability in addition to easy dis-assembly in changing the components. However, when using bolts or rivets, it is necessary to cut the continuous fibres of the laminates and open many holes. This has the serious drawbacks of the damage caused by stress concentration around the holes, in addition to increasing the weight of the fasteners and the operation costs. These problems remain in

  doi:10.5075/epfl-298799_978-2-9701614-0-0

practice, but in addition to these adhesive and welded joints, it is believed that any mechanical fastenings are compensatory or guaranteed joining method required for a higher reliability in strength and a longer durability. In particular, the rivets made of thermoplastic CFRP [1] will be desirable for joining of multimaterials that combine high-performance composites with metals, which is difficult for adhesive and fusion bonding.

In this study, the laboratory-scale prepreg tape pultrusion machine was developed, and the round-rod was fabricated using unidirectional carbon fibre reinforced poly-ether-ether-ketone (UD-CF/PEEK) prepreg tape. The head forming and fastening of the rivet for joining of multimaterials was performed precise-controllably with compact servo-press with near-infrared heater. The effects of type of round-rod, heating and fastening conditions on the strength of rivet head and its joining strengths were investigated by cross-sectional observation and tensile test of rivet head, single lap tensile test and pull through test of fastened multimaterials.

2. Experimental materials and apparatus

2.1 Manufacturign of round rod by prepreg tape pultrusion process

Manufactruing process of round rod by laboratory-scale prepreg tape pultrusion machine developed is shown in Fig. 1. It is configured by slitter, heating die, pressing die, holding die, cooling die and drawing device, and a compact and high-quality manufacturing can be realized by two main features; one is a unique tape feeding system realizing in-situ slitting to reduce the size of the equipment, another is using continuous compressive die for high consolidation of pultruded parts. A commercial product of unidirectional carbon fibre reinforced poly-ether-ether-ketone (UD-CF/PEEK) prepreg sheet (Toray Advanced Composites, Cetex®, TC1200) was used to manufacture the round rod with outer diameter of 6.5mm. This sheet has already been consolidated completely, then it does not have to struggle to impregnate the high viscous polymer into the fibre bundle. The slitter cuts a prepreg sheet to any width and the tapes are supplied directly to the pultrusion dies which are composed of cavity insert with taper and compressive die insert. The compressive die insert improves the density by pressurizing from square-shaped cavity to the round one. It is cooled down near the glass transition temperature of matrix polymer in the cavity of straight. Finally, after cooling below the glass transition temperature, it is continuously pulled out with a drawing device.

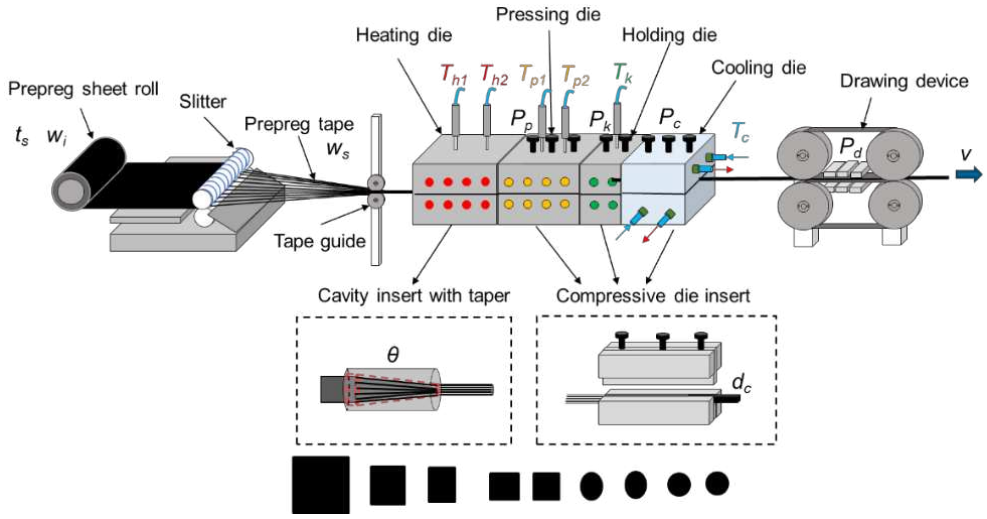

Figure 1. Manufactruing of round rod by laboratory-scale prepreg tape pultrusion machine

  doi:10.5075/epfl-298799_978-2-9701614-0-0

2.2 Thermoforming and fastening process of CFRTP rivet

The thermoforming and fastening processes of CFRTP rivet are shown in Fig. 2. In the thermoforming process of rivet head (Fig. 2(a)), a CFRTP round rod is inserted into the hole of lower die. And the upper end-part of the rod is rapidly heated by ring-heater above the melting temperature. The rivet head is formed by the upper die attached to the servo-press unit. At that time, the pressing load and moving distance of the upper mould are controlled appropriately. The rivet head formed is cooled down while maintaining the load, and then it is de-moulded from the upper mould. Next, in the fastening process by CFRTP rivet (Fig. 2(b)), the CFRTP rivet is inserted into the hole opened in the plates to be joined, and the only upper end of the rivet is rapidly heated up with ring-heater. The rivet is fastened by the upper mould attached to the servo-press unit. The pressing load and travel distance of the upper mould are controlled appropriately. The rivet is released from the upper mould after cooling down below the glass transition temperature while maintaining the compressive load. Then, the rivet fastening process is completed.

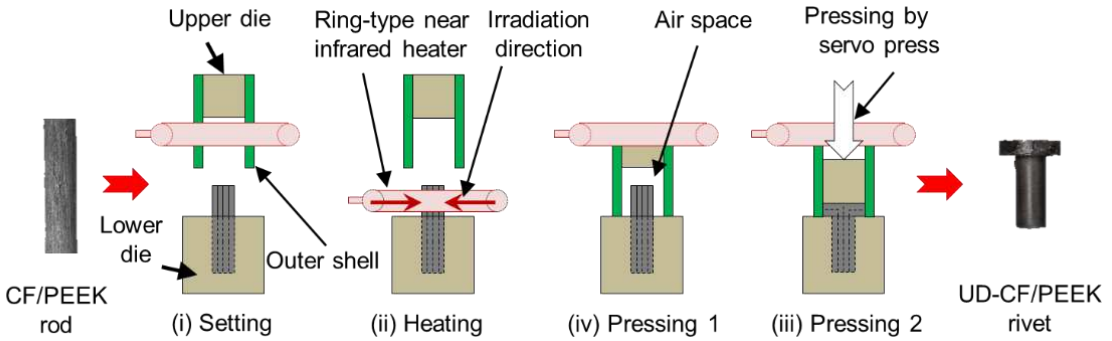

(a) Thermoforming process of CFRTP rivet head

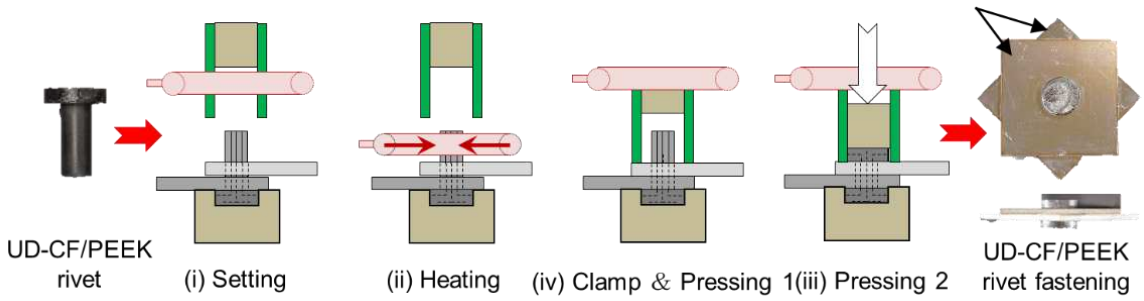

(b) Fastening process of CFRTP rivet

Figure 2. Thermoforming and fastening process of CFRTP rivet

2.3 Evaluation of CFRTP rivets by mechanical tests

The mechanical property of CFRTP rivets were evaluated by several strength tests as shown in Fig. 3. It was also tested for comparison with UD-CF/PEEK rivet prepared using CFRTP rod (Suprem™ supplied from Suprem SA, Switzerland). In single lap tensile test shown in Fig. 3(a), the stainless-steel plate was fastened by CFRTP and Aluminum alloy rivets. Also, in the pull-through strength test (NASM 1312-8) shown in Fig. 3(b), 38mm square stainless-steel plates fastened by CFRTP and Aluminum alloy rivets was used. The head tensile test of CFRTP and Aluminum alloy rivets were also performed using the special device as shown in Fig. 3(c).

  doi:10.5075/epfl-298799_978-2-9701614-0-0

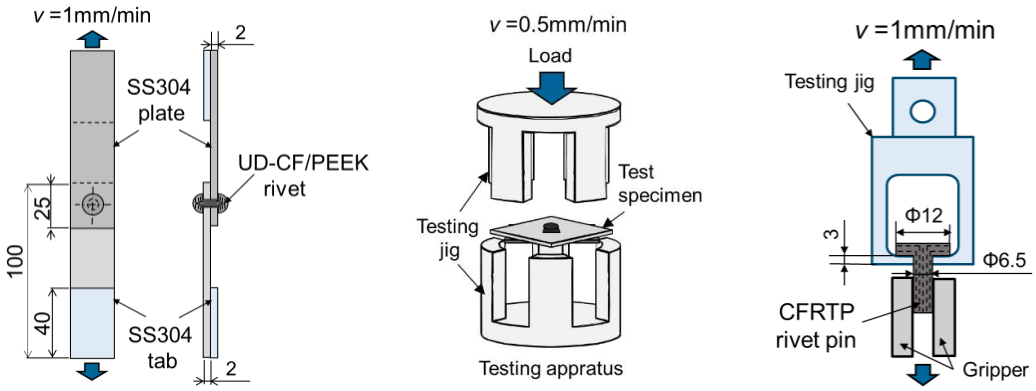

(a) Single-lap tensile test *(b) Pull-through test* *(c) Head tensile test*

Figure 3. Testing methods for evauationg of rivet head

3. Experimental results and discussions

3.1 Quality of CFRTP round rod

Fig. 4 shows the outer diameters of UD-CF/PEEK rod in the horizontal and vertical directions, and weight of small samples, plotted by position from die gate. In heating die, the outer diameter in the vertical direction are larger than that in the horizontal ones. But, in pressing and holding die, it is closing to the same outer diameter. In the meantime, the weight of the rod increases largely. The outer diameter and weight of rod are almost at constant from in holding die to after drawing. As shown in Fig. 5, as the results, the density is increasing, and the porosity is conversely decreasing in heating and pressing dies. As the pultrusion process progresses, the density is almost at constant, and the porosity is closing to almost zero.

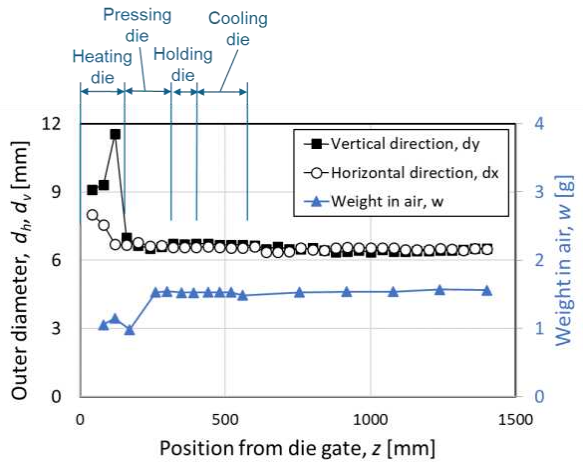

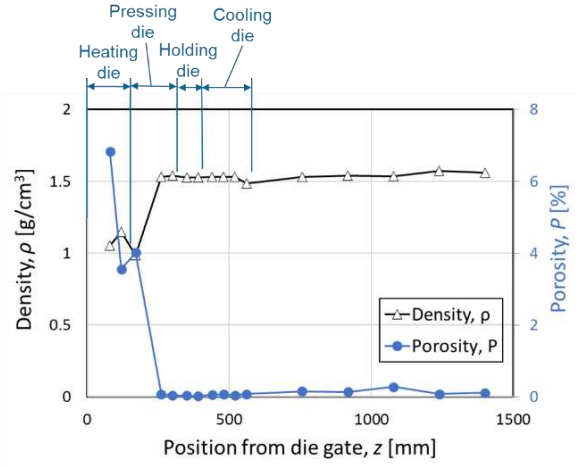

Figure 4. Change in diameter and weight *Figure 5. Change in apparent density and porosity*

Fig. 6 shows the cross-sectional images in pultrusion of UD-CF/PEEK rod. In prepreg sheet, there are no visible voids, because the consolidation has been completed. However, after these slitted tapes are inserted into heating die, the tapes were melted and softened at suitable location by heating. There are many air-gaps between prepreg tapes, and the tapes are expanded in the thickness direction, some voids are visible into these laminas as shown in Fig. 6(i). In pressing die, the shape is not circular, but is vertical ellipse, and some linear voids remain between those

  doi:10.5075/epfl-298799_978-2-9701614-0-0

tapes as shown in Fig. 6(ii) and (iii). And they were applied the compressive load gradually in pultrusion for high-densification. In holding and cooling die, the shape becomes circle, and small burrs occurred at the both sides, where is a partition line of matched die as shown in Fig. 6(iv) and (v). After going out the die, the shape is circular and there are no visible voids as shown in Fig. 6(vi). Also, it is seen from the longitudinal-sectional image of the rod shown in Fig. 6(vii) that a striate grooves are caused on the rod surface along the longitudinal direction of carbon fibre. Also, it was confirmed from the cross-sectional images of the rod shown in Fig. 6(viii) that the uniformly and highly-dispersed carbon fibres and polymer are observed inside the rod.

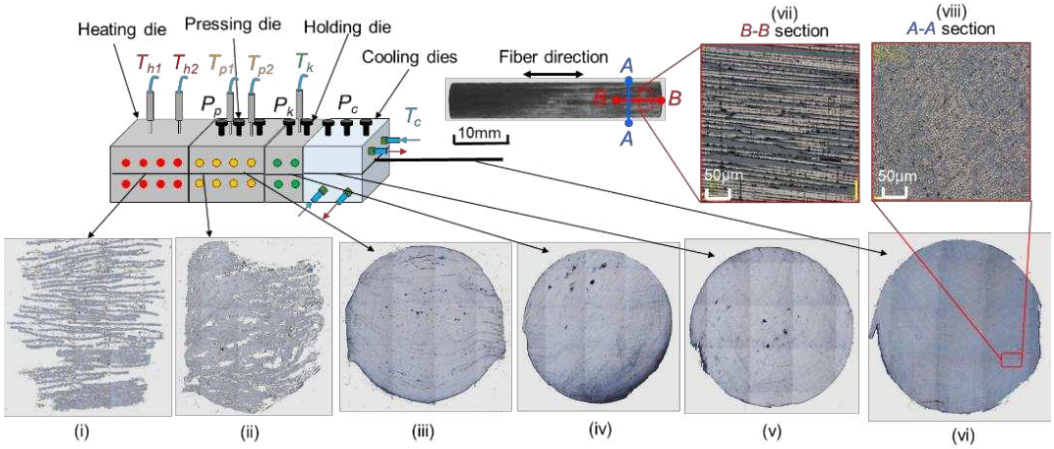

Figure 6. Cross-sectional images in prepreg tape pultrusion processing of UD-CF/PEEK rod

3.2 Heating behaviour of CFRTP round rod

A ring-type of near-infrared heater which is a high thermal transmittance, compact and low cost was used. Fig. 7 shows the result of surface temperature distribution observed by infrared-camera on the rod surface, heated by radiating the light from horizontal direction to surrounding outer of round rod. From the thermal images shown in Fig. 7(a), it is seen clearly that the temperature of rod surface is increased quickly to the bottom direction of rod with increasing of the heating time. However, the bottom of the rod is lower temperature than the tip of the rod. In this case, from Fig. 7(b), it can be seen that most part of rod was heated higher than the melting temperature of PEEK polymer, when the heating time is 30s.

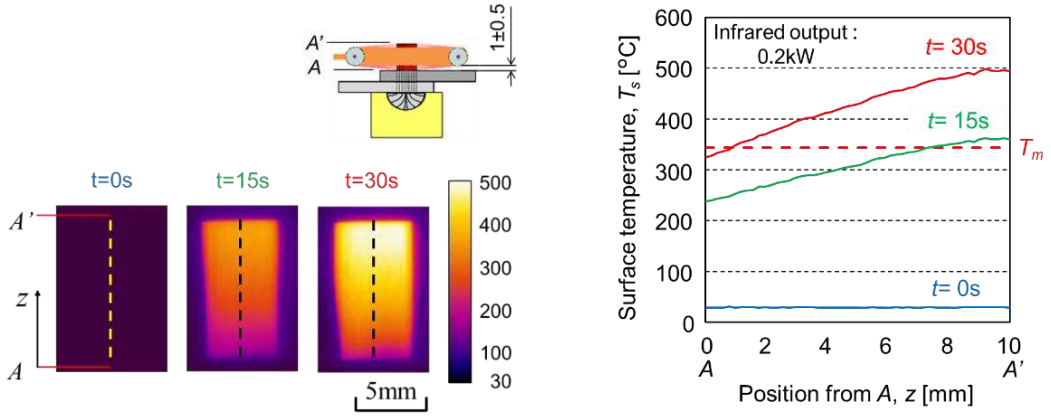

(a) Thermal images *(b)* Surface temperature at tip of rod

Figure 7. Change of surface temperature distribution in heating of UD-CF/PEEK *rivet pin*

3.3 Load and displacement control

The fastening of CFRTP rivet was performed under the below condition: heating time, 30s, surface heating temperature, 400-420 °C, max press load, 5kN and press speed, 100mm/s. The change of load, folding force and displacement of upper mould measured or controlled by compact servo-press unit are shown in Fig. 8(a). In this graph, at position (i), the folder and punch are located at the upper portion away from the round rod when it is heated. Immediately after heating for the specified time, at position (ii), the folder moves downward in 0.4s and comes into contact with the plate surface, and the load begines to increase by reaction force with the coil spring. At position (iii), the punch moves further downwards and contacts on the tip end of the rod. At position (iv), in 0.6s, the control method is switched from the displacement control to the constant load control. At position (v), as the upper mould moves down slowly, the load increases remarkably. At position (vi), in 0.8s, the constant load control starts to work, and the load is keeping at constant of 5kN. In this way, the fastening of CFRTP rivet can be performed by controlling the load and displacement precisely with servo-press unit.

Fig.8 (b) shows the cross-sectional and appearance images of CFRTP rivet-head at each position marked in Fig. 8 (a). From these images, at position (iii), the buckling of fibres are seen in the portion away from the tip of the rod, and there are many gaps between tapes. At position (iv) and (v), the disc-shaped head is forming unstably, and large gaps are generated around the disk. This seems because the re-heating increased the distance between the tapes. At position (vi), there are no cracks and no voids in the head with smooth surface, and the height of this head is considerably larger than the other ones. This is because the only head part is highly pressed with appropriated load control. From the cross-sectional images (vi), it is seen that the rivet head formed in disk-shape with high-density. In the rivet-head part, the carbon fibres spreads laterally, and the whole of carbon fibre is re-oriented. The surrounding parts are pressed high-densely, and the obvious voids are not visible inside the head part. And it can be seen the un-melted original area on the bottom of the rod.

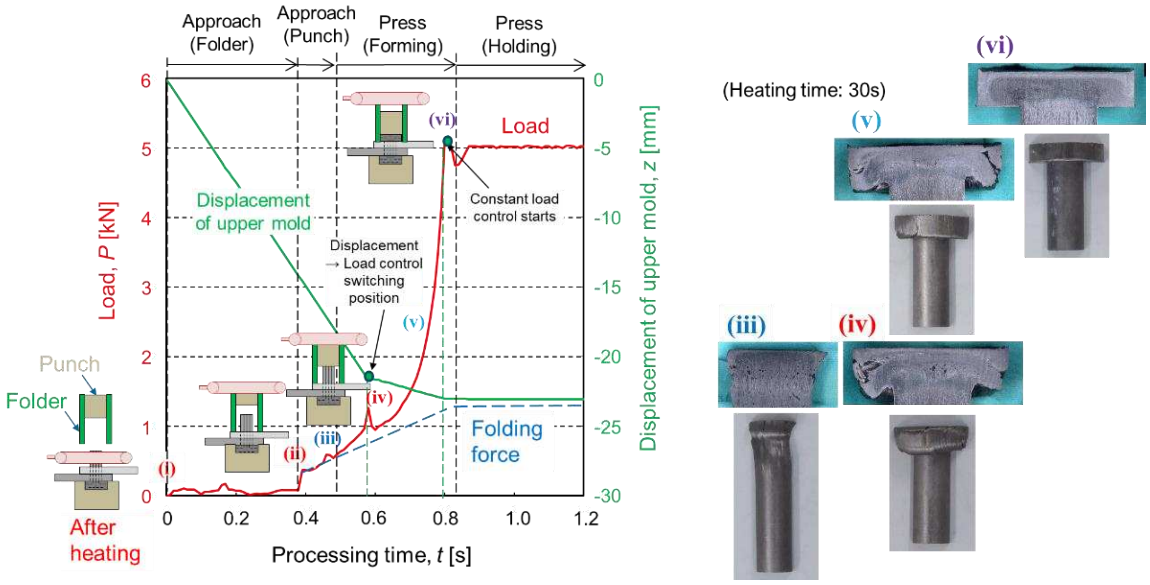

(a) Change of load and displacement *(b) Sectional and appearance images*

Figure 8. Change of load and displacement and images in thermo-forming of rivet head

  doi:10.5075/epfl-298799_978-2-9701614-0-0

3.4 Single lap shear strength

Fig. 9 (a) shows the appearance of single lap shear strength test specimen which is stainless-steel plates fastened by UD-CF/PEEK rivet. The rsults of single lap shear strength test are shown in Fig. 9 (b). Aluminum alloy rivet was also tested for comparison with UD-CF/PEEK ones prepared using CFRTP rods supplied from Suprem, Switzerland and our CFRTP rod. It can be seen from this bar graph, the both CFRTP rivet specimens showed the same or slightly higher tensile shear strength than Aluminum alloy one. This is because the unidirectional carbon fibres are positioned vertically between the two plates, and the rigid carbon fibres have greatly resisted the shear deformation of the two plates.

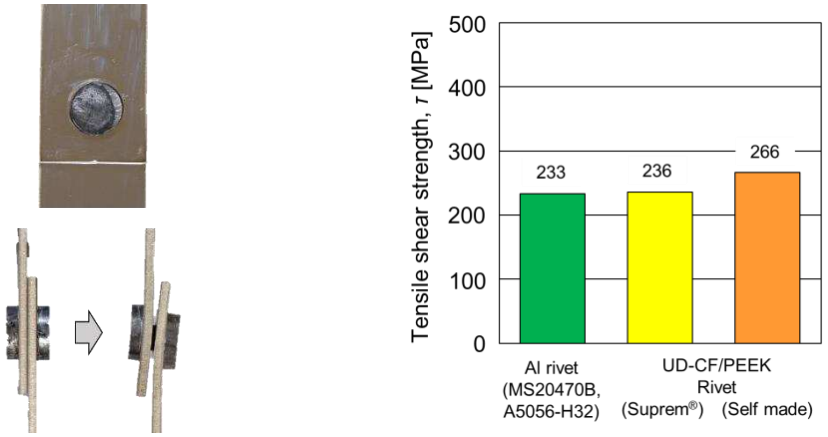

(a) Appearance of single lap test specimen *(b) Tensile shear strength*

Figure 9. Results of single lap shear strength test

3.5 Pull-through strength

Fig. 10 shows the pull-through strength test used a NASM tool and a 38mm square test specimen. It is confirmed from the photograph after testing shown in Fig. 10(a) that the stainless-steel plates bent largely, but did not break at the head part of any CFRTP rivets. It is shown from this bar graph shown in Fig. 10(b) that the both UD-CF/PEEK rivets had the almost same or slightly lower maximum pull-through force than Aluminum alloy one.

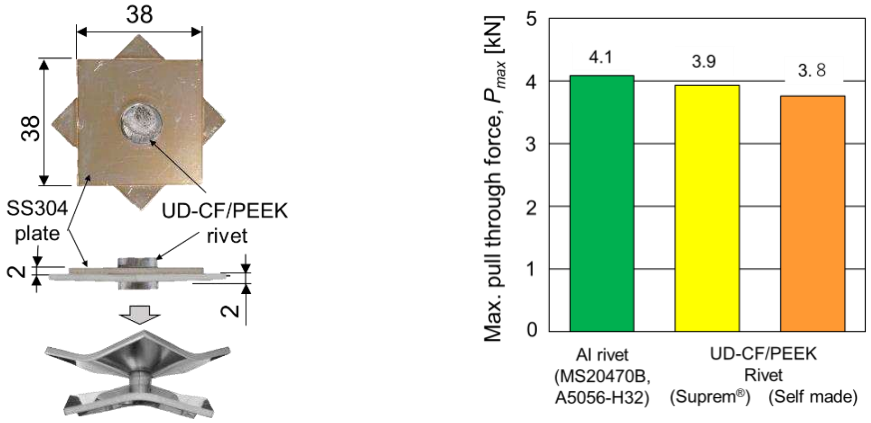

(a) Appearance of *pull-through test* specimen *(b) Maximum pull-through force*

Figure 10. Results of pull-through strength test

  doi:10.5075/epfl-298799_978-2-9701614-0-0

3.6 Tensile stregth of rivet head

The head tensile test of CFRTP and Aluminum alloy rivets was carried out. From the tensile load-displacement curves shown in Fig. 11(a), Aluminum alloy rivet shown a very high tensile load and elongation, because it was large-deformed locally in the gripping part. However, it is obvious from the bar graph shown in Fig. 11(b) that the maximum tensile loads are relatively low in any CFRTP rivet-heads comapared with Aluminum alloy one. This is because the significant cracks occurred between the tapes in the head part as shown in the photographs after head tensile test (Fig. 12). In case of this head tensile test, it is considered that the load acts transversely to the fibre into the head part, therefore, significant cracks occurred at a low tensile load.

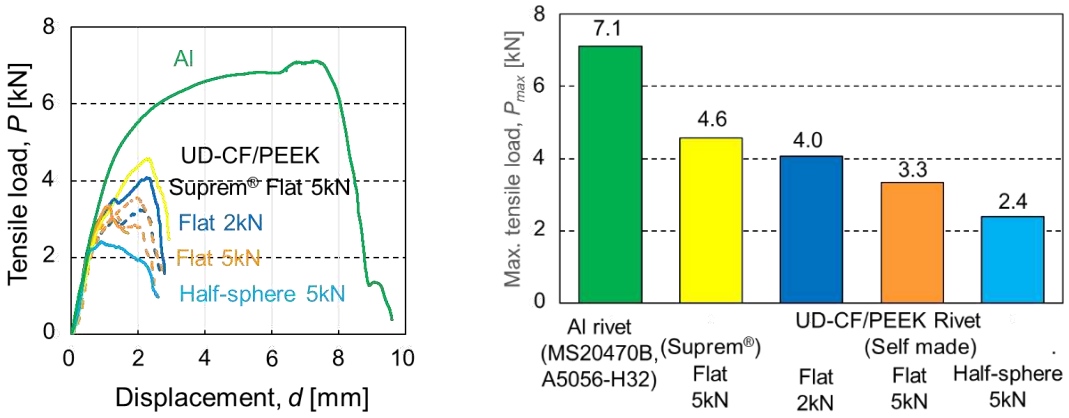

(a) Tensile load-displacement curves *(b) Maximum tensile loads*

Figure 11. Results of tensile test of rivet head

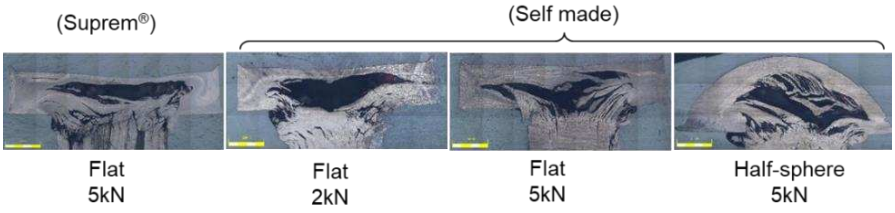

Figure 12. Cross-sectional images of rivet head after tensile test

4. Conclusion

In this study, the laboratory-scale thermoplastic tape pultrusion machine was developed, and the fabrication of round-rod with high properties was realized using UD-CF/PEEK prepreg sheet. Also, severla head types of CFRTP rivets were moulded from the pultruded rod and fastened with precisely control by compact servo-pressing with near-infrared heater. The high-dense structure where rivet head and body are integrated by continuous carbon fibres, consequently, the CFRTP rivet joint has the same high tensile shear strength and pull-through strength as the Al alloy. From the experimental results, it was proven that the thermoplastic CFRP rivet fastening process developed had a high availability to the practical joining of multimaterials.

5. References

1. Christophe Absi, Nawaf Alsinani, Louis Laberge Lebel, Carbon fiber reinforced poly(ether ether ketone) rivets for fastening composite structures, Compos Struct, 280 (2022) 114877.

  doi:10.5075/epfl-298799_978-2-9701614-0-0

NUMERICAL MODELLING OF WELDED THERMOPLASTIC COMPOSITES INTERFACES BEHAVIOUR UNDER QUASI-STATIC AND DYNAMIC LOADING

Pauline Bourda[a,b], Patrick Rozycki[a], Mamadou Abdoul Mbacké[b]

a: Nantes Université, Ecole Centrale de Nantes, CNRS, GeM, UMR 6183, F-44000 Nantes, France, pauline.bourda@ec-nantes.fr
b: Nantes Université, IRT Jules Verne, F-44000 Nantes, France

Abstract: *In the transport industry, the study of structures' crashworthiness is essential to ensure the safety of passengers. The increasing use of thermoplastic composites in this area induces design difficulties because of the materials' anisotropy, their strain rate dependency or novel joining methods such as welding. Joints need proper modelling as they constitute a structure's weakness. Despite many studies on composites welding processes and dynamic behaviour of bonded joints or delamination, no study focuses on the evolution of welded composites joints behaviour with the increase of loading speed. This study investigates the numerical modelling of welded thermoplastic composites from quasi-static loading up to 7 m/s. An experimental campaign served to identify the behaviour of the laminate and its welded joints using single lap joint specimens. The numerical part aims to determine the interface behaviour by an inverse method.*

Keywords: Thermoplastic composites; Ultrasonic welding; Strain rate; Cohesive elements

1. Introduction

Thermoplastic composite welding is a joining method competing with usual mechanical fastening or bonded interfaces [1]. The speed of the process and the quality of welded interfaces have led many authors to investigate the process experimentally and numerically to improve the weld strength. Most of the studies focus on the influence of the process settings to achieve the highest interface strength, for low-speed loadings, with a suitable reproducibility [2]. Recently, authors such as Murray and al. [3], Koutras and al. [4] and Rohart and al. [5] studied the influence of the loading and environmental parameters on the welded interface behaviour. These investigations are essential as the structures deal with such environmental parameters during service. Murray and al. have shown that welded joints are more performant than bonded joints under fatigue loadings for wind turbines [3]. Concerning the influence of temperature and relative humidity (RH) on the joints, the interface strength reduces with increasing temperature and RH, with an evolution of the fracture mechanism in the case of PPS/glass fibre joints [4,5]. The influence of such parameters on the joint behaviour results from a significant sensitivity of thermoplastic resin to environmental conditions. In addition to temperature and RH, strain rate also affects the behaviour of resins and their composites. For example, polyamide 6-6/glass fibre composite shear behaviour and PA66 resin stiffen with strain rate for various conditions of RH [6]. Therefore, the influence of strain rate on the interface may be significant as it constitutes a resin-rich zone between substrates. Despite the strain rate dependence of thermoplastic composites and their potential applications in the transport industry, no authors studied the evolution of welded interface behaviour with the loading speed, as far as the authors know.

  doi:10.5075/epfl-298799_978-2-9701614-0-0

Data from several studies suggest that interfaces, such as bonded ones or inter-ply zones, can be sensitive to loading speeds [8-13]. Most investigations in the literature studied composites or metallic joined specimens using Double Cantilever Beam, End Notched Flexure, and lap shear joints. Previous research has established that fracture toughness of carbon/epoxy decreases when strain-rate increases, whether in mode I or II [7,8]. In the case of bonded interface, the results are more dependent on the adhesive and substrate type. However, a decreasing trend is observed for fracture toughness while fracture strength increases for higher loading speeds [9,10]. In addition to the experimental study on delamination and bonded interface behaviour under several loading conditions, many authors investigated the modelling of such evolution on the interface behaviour using cohesive elements. Some authors defined an extended cohesive law using viscous functions to change the law parameters according to strain rate or loading speed [11,12]. For these applications on delamination and bonded interface, viscous laws have enabled the modelling of jointed structures from quasi-static to large strain rates. Moreover, as May [13] identified, the consideration of the strain rate influence on delamination strongly affects the extent of the damaged area.

This study provides new insight into the behaviour of welded thermoplastic composite interface with the influence of loading speed. An experimental campaign was conducted on the laminate and welded specimens (single lap joint). These tensile tests were performed for several loading speeds, and they furnished data for two purposes. Firstly, they permit the set-up of the behaviour law developed previously for the laminate by Mbacké and Rozycki [14]. Secondly, data obtained on welded samples help to model the interface behaviour using the global response of the specimen and the exhaustive model for laminate in-plane behaviour. The evaluation of the interface law parameters is conducted for several loading rates. These results will show whether it is necessary to include an influence of the loading speed in the interface law.

2. Methods and material

This study conducted tensile tests on the laminate to confirm the in-plane shear, longitudinal and transverse behaviour. In addition, tensile tests on welded specimens allow the study of the welded joint behaviour at various loading rates.

2.1 Laminate and welding process

The studied material is a polyamide 6-6 reinforced by glass fibres twill woven 2x2. The reinforcement is equilibrated with a fibre volume content of 50%. The laminate was produced as four ply plates of 2 mm total thickness. Specimens were water-jet cut. The laminate behaviour was investigated with tensile tests on $[0]_4$ and $[45]_4$ specimens to define in-plane properties. Welded specimens were joined by ultrasonic welding using a static method and specific equipment to limit substrate movements and ensure planarity. A 20 mm wide ultrasonic horn was used, vibrating at 20 kHz and 60 µm. The welding process was energy controlled. Linear energy directors, made of neat PA6 resin, were placed at the interface to improve the weld quality. Single lap joint (SLJ) configuration is considered in this study with various substrate assemblies: $[0/45]_S/[0/45]_S$, $[45]_4/[45]_4$ and $[0/45]_S/[45]_4$. The same settings were used for the several configurations: welding energy, welding force, holding force and holding time. All specimens were dried before the experimental campaign to ensure a homogeneous relative humidity among samples as PA66 resin behaviour is highly sensitive to

humidity. The desorption process was performed at 90°C in a desiccator, and a regular weighing of the reference samples allowed to monitor the moisture loss over time until stabilisation. Specimens were stored in sealed bags of 4 layers (PET Alu OPA PE (+/-10%)) until the testing to avoid the regrowth of humidity.

2.2 Tensile tests

Dumbbell shaped specimens are used in this study to concentrate the stress in the effective zone and at the interface. A width of 20 mm is considered to ensure at least one and a half RVE size in the zone of interest. An overlap of 20 mm x 20 mm is set for the welded. Tensile tests were performed in quasi-static using an Instron 5584 machine (1.2 mm/min), and in dynamic thanks to a MTS 819 dynamic tensile test machine (2 mm/s, 0.2 m/s, 2 m/s and 7 m/s). A camera registered the tests to explore the displacement/strain field. Ufreckles was used to post-process data by Digital Image Correlation [15]. Three tensile tests were performed for each condition. Specimen bending leads to a mode I loading on the free edges of the overlap besides the mode II loading. Modes I and II were determined from SLJ tensile behaviour.

2.3 Numerical modelling

A complete description of the material in-plane behaviour is used in this study based on the previous work of Mbacké and Rozycki [14]. The model describes the behaviour of one layer at a mesoscale. A damageable elastoplastic behaviour defines the ply in shear with the evolution of elastic, plastic and damage properties according to the strain rate. The influence of strain rate is negligible for longitudinal and transverse orientations compared to shear. Hence, longitudinal and transverse directions are defined by an elastic-damageable behaviour non influenced by strain rate. The law was implemented in Abaqus through a VUMAT user subroutine. Parameters were identified from the results of the tensile test campaign carried out on the in-plane shear behaviour of PA66/GF.

The welded interface is described by cohesive elements, as the fracture path is known to be along the weld. The interface is considered homogeneous despite the variation in the local aspect of the interface. The interface thickness was evaluated from measurements at the microscale (for a few samples) and mesoscale (for all specimens tested). A value of $2.39\ 10^{-2}$ mm is used, which is in the same order of magnitude as the resin-rich layer between plies. The displacement boundary conditions applied were extracted from the experimental campaign near the load application zone. The cohesive law used is the build-in law from ABAQUS. The bi-linear law is described in Figure 1.

The stiffness of elements in modes I and II are assumed to be identical to the resin's Young's modulus and shear modulus, respectively (E = 3.9 GPa and ν = 0.4 [16], thus G = 1 GPa). A quadratic criterion is considered for damage initiation [17]. A mode mix is considered for the damage evolution using a fixed value of 2.284 for the B-K criterion power parameter identified by Camanho and al [18] on the delamination of AS4/PEEK. Both bold parameters in Figure 1 were determined for each mode by an inverse method: σ^0, the damage initiation stress and G_c, the fracture toughness. Mode II and mode III parameters are supposed to be equal. A first study of the influence of traction-separation law modulus has shown the limited influence of these parameters on the specimen's behaviour.

  doi:10.5075/epfl-298799_978-2-9701614-0-0

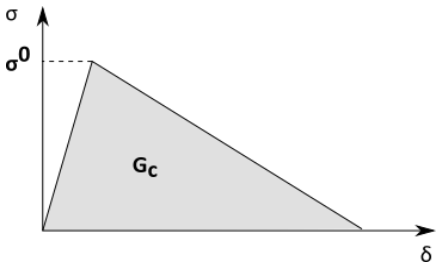

Figure 1: Cohesive element bilinear traction separation law

3. Results and discussion

3.1 Experimental results

The shear behaviour of the PA66/GF laminate is strongly sensitive to strain rate in the environmental state considered (room temperature and dry state). Stiffening is observed with an increase of shear modulus as well as yield stress with increasing strain rate up to 250 s^{-1}, as shown in Figure 2. Longitudinal and transverse behaviours are supposed to be equal (equilibrated woven). Elastic, plastic and damage properties are identified from tensile tests performed at 1.2 mm/min.

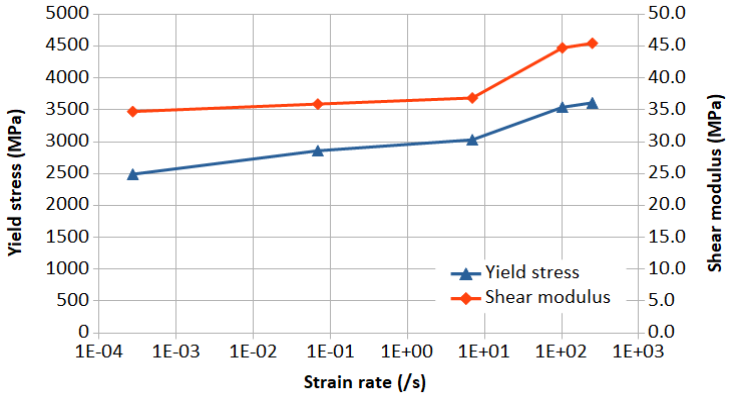

Figure 2: Evolution of shear modulus and yield stress with strain rate

A stiffening of the welded samples is observed for specimens composed of at least one $[45]_4$ substrate. The maximum force carried by the joint increases while the maximum elongation of the specimen tends to decrease for a growing loading speed. Moreover, these joints' shear strength (LSS in Eq. (1)) increases with the loading rate growth. An increase of 11.2% is noticed for SLJ $[45]_4/[45]_4$ and 22.9% for dissimilar assemblies $[0/45]_S/[45]_4$ between quasi-static and 7 m/s for loading speed. The same trend is observed for SLJ $[0/45]_S/[0/45]_S$ fracture force with a 19.5 % increase of LSS between quasi-static and 2 m/s loading speeds.

$$LSS = \frac{F_{max}}{S_{welded}} \quad (1)$$

Even if our study focuses on the cohesive fracture as it leads to the highest performance for the joint, different fracture mechanisms were observed during the experimental campaign for the welded specimens. A cohesive fracture refers to an interface fracture occurring along the welded surface, with fibre/matrix debonding and ductile resin fracture. Despite the evolution of loading speed, no change in the fracture mechanism was observed in the experiments. However, no purely cohesive fracture was observed for some testing conditions. In that case,

the specimen with a mixed cohesive/adhesive fracture was considered as the reference for the numerical simulation.

3.2 Numerical results

The laminate behaviour law was updated from the experimental results and was validated for strain rate from 10^{-4} s^{-1} to 250 s^{-1}. Figure 3 shows a satisfactory correlation between experimental and numerical results for the in-plane shear. The same validation was made on the laminate longitudinal behaviour tested in quasi-static.

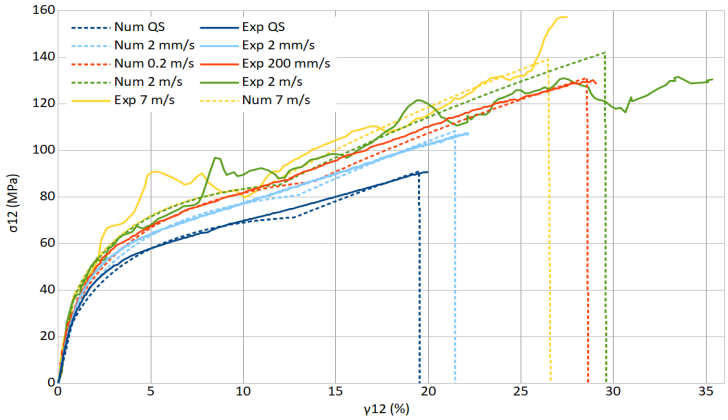

Figure 3: Comparison of experimental and numerical shear behaviour of four plies PA66/GF - tensile test on $[45]_4$ specimens

Parameters of the cohesive law were determined by inverse method for the several conditions tested in this study (orientation, loading speed). The experimental and numerical results were compared on the force-displacement (F-U) data, considering the extension of a virtual gauge. The numerical results presented in Figure 4, in quasi-static and at 7 m/s of loading speed, were obtained using the same values for traction-separation law parameters regardless of the loading speed. Both mode I and mode II parameters considerably affect the specimen behaviour.

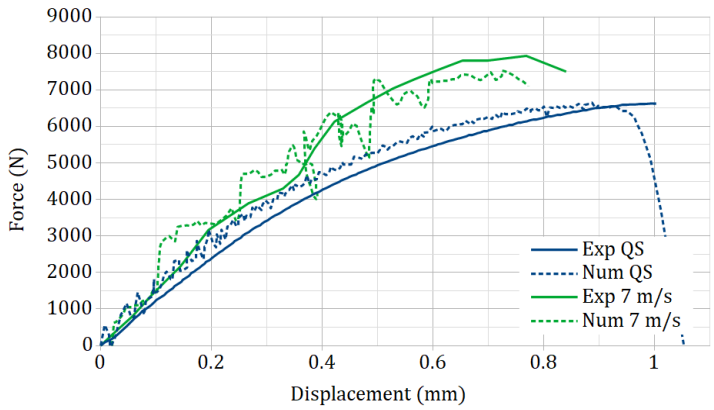

Figure 4: Experimental and numerical force-displacement curves of SLJ $[45]_4/[45]_4$ in quasi-static and at 7 m/s for the loading rate

Interface parameters identified for SLJ $[45]_4/[45]_4$ allow a suitable description of specimen behaviour until fracture with a softening due to the damage in the interface and the plasticity of substrates. Mode I is characterised by a lower initiation stress and fracture toughness than

mode II. The results are in line with the observations made by Machado et al. on bonded structures [19]. The rupture of $[45]_4/[45]_4$ and $[45]_4/[0/45]_S$ occurs when substrates get plasticised. For SLJ $[45]_4/[45]_4$, fracture arises when $[45]_4$ substrates reach 4% to 6% strain around the free edges of the overlap for quasi-static loading. For a higher loading speed, 6% to 8% strain is reached in the substrate. This result is consistent with the increase of laminate yield stress in shear. Finally, the interface fracture seems to coincide with the level of plastic deformation reached in the substrate. A plastic strain between 2% and 2.5% in the substrate is achieved when the interface breaks for the $[45]_4/[45]_4$ configurations. This critical value does not evolve significantly with the loading rate.

Numerical investigations were also made on the SLJ $[0/45]_S/[0/45]_S$. Interface parameters were defined for the quasi-static condition. However, this joint configuration suffers mixed fracture types at the highest loading speeds, with about 67% of the surface fractured cohesively. Thus, the force-displacement curve is highly affected by the welded zone surface with a loss of stiffness (2 m/s experimental curve in Figure 5). The partially welded surface was geometrically considered in the numerical model for defining the traction-separation law at 2 m/s loading speed. The interface parameters determined for this loading speed required higher fracture toughnesses to reach the experimental fracture force than quasi-static. Figure 5 shows that numerical results agree with experiments. Hence, considering the current cohesive fracture surface makes it possible to reproduce the stiffness loss between quasi-static and 2 m/s loadings.

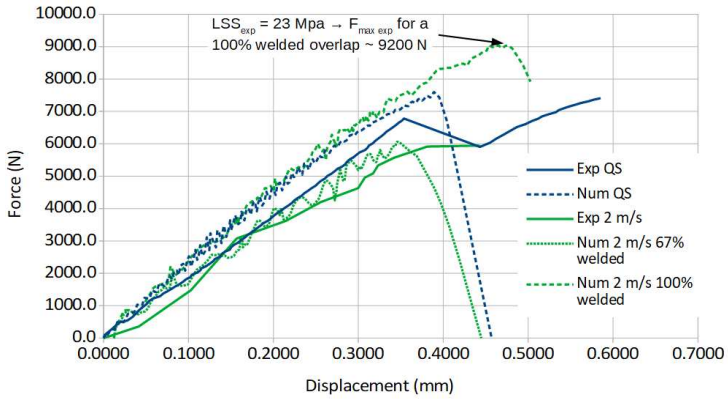

Figure 5: Experimental and numerical force-displacement curves of SLJ $[0/45]_S/[0/45]_S$ un quasi-static and at 2 m/s for the loading rate

In this joint configuration and for a similar fracture type (purely cohesive or mixed cohesive + adhesive), the F-U curves have the same stiffness but different fracture force depending on the loading speed (LSS increases). A fully welded overlap surface simulation is carried out at 2 m/s, with the interface parameters determined for the 67 % welded overlap. The numerical and experimental LSS showed about 3 % of relative error. Thus, it confirms that the mode I and II fracture toughnesses increase according to the loading speed for SLJ $[0/45]_S/[0/45]_S$. However, it is noticed that the error between numerical and experimental stiffness is more prominent for this configuration than for the SLJ $[45]_4/[45]_4$. It may result in the extraction of displacements from experiments that are relatively small but also from substrate stiffness as this stacking sequence was not tested in traction. Furthermore, the force loss was not observed numerically for quasi-static tests. It corresponds to the fracture initiation at the free edges.

The parameters identified vary depending on the substrate direction considered. The more ductile the substrate, the higher the fracture toughness of the welded joint. The higher stiffness observed in the experimental part for the SLJ $[45]_4/[45]_4$ at higher loading rate is achieved numerically only considering substrate stiffening. Moreover, the fracture forces observed experimentally were numerically reached without any change in initiation stress or fracture toughness of the interface with strain rate for SLJ $[45]_4/[45]_4$. For the SLJ $[0/45]_S/[0/45]_S$, the LSS increase is reproduced by increasing GIC and GIIC. A first set of parameters was determined here for SLJ $[45]_4/[45]_4$ and SLJ $[0/45]_S/[0/45]_S$ in quasi-static and dynamic. They still need to be optimised in the further course of this study.

4. Conclusion

An experimental campaign was conducted on the laminate and welded specimens to investigate their behaviour under several loading rates. This campaign was used as a reference for the welded interface modelling. Boundary conditions for the simulation were extracted from the experimental displacement fields. Numerical and experimental comparisons were made on the force-displacement data considered on a virtual gauge.

We proposed a model for the mechanical behaviour of welded joints based on cohesive elements. A simple bilinear traction-separation law, with a complete description of the substrate in-plane behaviour, permitted the modelling of single-lap joint $[45]_4/[45]_4$ specimens' behaviour at RH0 and ambient temperature; no viscous law is needed in the interface behaviour for this configuration. Moreover, the welded joint fracture coincides with a certain level of plasticity reached in the substrates. For the SLJ $[0/45]_S/[0/45]_S$, traction-separation evolves with the increase of loading speed. Higher fractures toughnesses are needed to reach experimental LSS.

As a perspective, polyamides are more sensitive to strain rate for an RH of 50% or 85%, with a ductile behaviour even for large strain rates (up to 35 /s at RH50 [6]). Then a study conducted at another relative humidity condition could underline a non-negligible influence of the strain rate on the interface behaviour of all the configurations tested here. Finally, the influence of loading rate on the interface behaviour of SLJ $[0/45]_S/[0/45]_S$ will be included in the interface behaviour with a user subroutine based on May et al. work [13].

Acknowledgements

The authors wish to thank IRT Jules Verne (French Institute in Research and Technology in Advanced Manufacturing Technologies for Composites, Metallic and Hybrid Structures) for supporting this study under the PERFORM program.

References

1. Ageorges C. Experimental investigation of the resistance welding of thermoplastic-matrix composites. Part II: optimum processing window and mechanical performance. Composites Science and Technology. 2000 Jun;60(8):1191–202.
2. Villegas IF. Strength development versus process data in ultrasonic welding of thermoplastic composites with flat energy directors and its application to the definition of optimum processing parameters. Composites Part A: Applied Science and Manufacturing. 2014 Oct;65:27–37.

  doi:10.5075/epfl-298799_978-2-9701614-0-0

3. Murray RE, Roadman J, Beach R. Fusion joining of thermoplastic composite wind turbine blades: Lap-shear bond characterisation. Renewable Energy. 2019 Sep;140:501–12.
4. Koutras N, Fernandez Villegas I, Benedictus R. Effect of ultrasonic welding process on the crystallinity at the welding interface of CF/PPS joints. ECCM 2018 - 18th European Conference on Composite Materials. 2020;
5. Rohart V, Lebel LL, Dubé M. Effects of environmental conditions on the lap shear strength of resistance-welded carbon fibre/thermoplastic composite joints. Composites Part B: Engineering. 2020 Oct;198:108239.
6. Dau AT. Elaboration d'un outil numérique reliant les échelles micro/méso d'un composite thermoplastique sensible à l'humidité et la température en quasi-statique. Ecole centrale de Nantes; 2019.
7. Zabala H, Aretxabaleta L, Castillo G, Aurrekoetxea J. Loading rate dependency on mode I interlaminar fracture toughness of unidirectional and woven carbon fibre epoxy composites. Composite Structures. 2015 Mar;121:75–82.
8. Machado JJM, Marques EAS, Campilho RDSG, da Silva LFM. Mode II fracture toughness of CFRP as a function of temperature and strain rate. Composites Part B: Engineering. 2017 Apr;114:311–8.
9. Blackman BRK, Kinloch AJ, Rodriguez-Sanchez FS, Teo WS. The fracture behaviour of adhesively-bonded composite joints: Effects of rate of test and mode of loading. International Journal of Solids and Structures. 2012 Jun;49(13):1434–52.
10. Machado JJM, Gamarra PM-R, Marques EAS, da Silva LFM. Improvement in impact strength of composite joints for the automotive industry. Composites Part B: Engineering. 2018 Apr;138:243–55.
11. Marzi S, Hesebeck O, Brede M, Kleiner F. A Rate-Dependent Cohesive Zone Model for Adhesively Bonded Joints Loaded in Mode I. Journal of Adhesion Science and Technology. 2009 Jan 1;23(6):881–98.
12. May M, Lässig T. Rate-dependent mode I delamination in ballistic composites – Experiment and simulation. Composite Structures. 2017 Nov 15;180:596–605.
13. May M. Numerical evaluation of cohesive zone models for modeling impact induced delamination in composite materials. Composite Structures. 2015 Dec;133:16–21.
14. Mbacke MA, Rozycki Pa. Non-linear constitutive law for a glass-pa66 fabric composite dedicated to numerical simulations in crash studies. In Athens, Grece; 2018.
15. Réthoré J. UFreckles. Zenodo; 2018. https://zenodo.org/record/1433776
16. Pivdiablyk I. Durability of mechanical performance of prestressed bolted composite joints in a hygro - thermo - mechanical environment. PhD thesis. Ecole centrale de Nantes; 2019. https://www.theses.fr/2019ECDN0068
17. ABAQUS/Standard User's Manual, Version 2019. Providence, RI: Dassault Systèmes Simulia Corp, 2019.
18. Camanho PP, Davila CG, de Moura MF. Numerical Simulation of Mixed-Mode Progressive Delamination in Composite Materials. Journal of Composite Materials. 2003 Aug;37(16):1415–38.
19. Machado JJM, Marques EAS, da Silva LFM. Adhesives and adhesive joints under impact loadings: An overview. The Journal of Adhesion. 2017 Mar 20;94(6):421–52

INVESTIGATION OF THE STRAINFIELD SURROUNDING COMPLEX-SHAPED LOCAL FIBER METAL HYBRIDS

Alexander, Herwig[a], Carsten, Schmidt[b], Sebastian Heimbs[a]

a: Institute of Aircraft Design and Lightweight Structures, Technische Universität Braunschweig, Stade, Germany – al.herwig@tu-braunschweig.de
b: Institute of Production Engineering and Machine Tools, Leibniz Universität Hannover, Stade, Germany

Abstract: *A methodology and visualisation concept for the structural influence of local fibre-metal hybrids is presented. By using strain increase factors the obtained results can easily be compared to similar research investigating the load introduction into thin-walled fibre reinforce plastic structures. The layered geometry of the investigated local fibre metal hybrid is derived in order to be compatible with the automated fibre placement (AFP) process. Additional restrictions are imposed on the layer thicknesses to minimise changes in the outer shape. For the investigated specimen geometry, the influence of the layer orientation, the size and shape of the metal sheets as well as the positioning of the material transitions is shown and the first failing component is determined.*

Keywords: fibre-metal laminate; insert; embedded load introduction; joints; open holes

1 Introduction

The establishment of common detachable joining methods and their improvement is an essential step to further increase the practicability and usability of fibre reinforced plastic (FRP) components. The project “Multi-Layer Inserts” (MLI) proposed a new design for inserts used in thin-walled carbon fibre reinforced plastic (CFRP) structures. The proposed insert consists of multiple thin metal sheets and is build up simultaneously with the laminate in a fully automated intrinsic hybridisation process. Thus, time-consuming post-processing steps are eliminated. Furthermore, at equal weight, such inserts greatly increase the bonding area between metal and CFRP in comparison to conventional inserts. This results in a significant increase of the loads that can be transmitted into the CFRP [1]. The detailed positioning of a single metal sheet in the laminate layers is shown in Figure 1a. The individual material layers of the local CFRP-metal-hybrid (CFRP, metal, adhesive) are very thin (0.04 to 0.25 mm) and form a multitude of adhesive connections with a pure metal area in the centre (Figure 1).

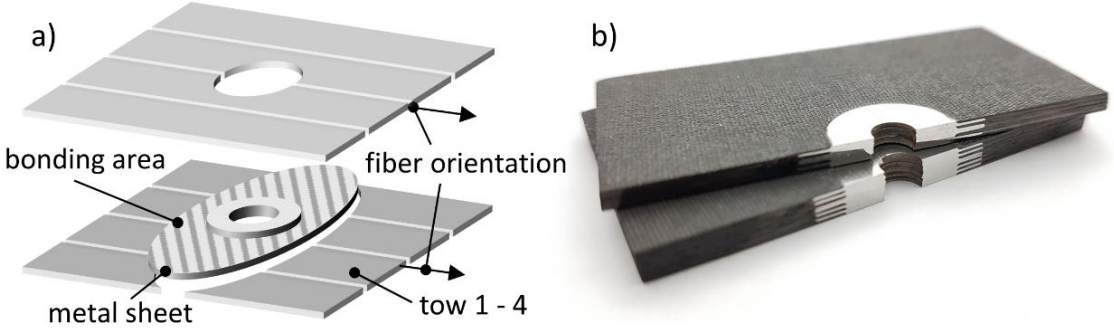

Figure 1: a) Schematic view [1] and b) cross section of a local fibre-metal hybrid laminate.

  doi:10.5075/epfl-298799_978-2-9701614-0-0

The presented investigation aims to provide a methodology and visualisation concept, which allow for a comparison of the structural influence of local fibre metal hybrids with different topologies. The strain of individual layers and material components is evaluated in order to compare geometric configurations as well as to determine the first failing component.

2 Experimental setup

Load introduction elements can be assessed by their load-bearing capability and their influence on the surrounding structure, which will be the focus of this investigation. In order to achieve a better comparability with published research [2–6] a common specimen geometry similar to the standard AITM 1-0007 [7] is chosen, see Figure 2. The ratio $W_{spec}/d_{hybrid} \approx 2$ is expected to induce a considerable load transfer towards the edges of the specimen, which would lead to undesired quantitative changes of the results. In the presented qualitative assessment of different geometric configurations, keeping the hybrid diameter constant, the effect can be neglected.

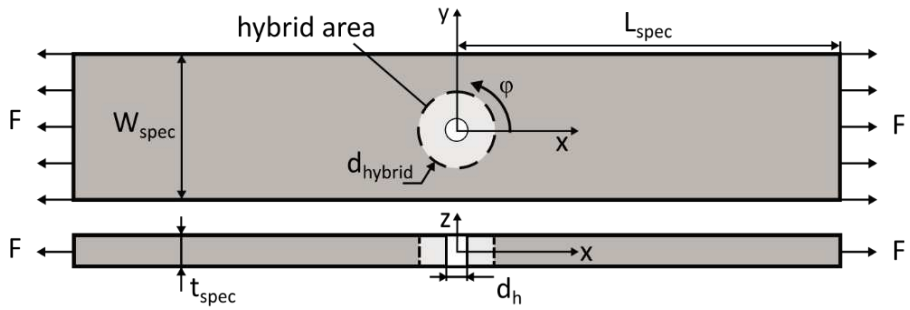

Figure 2: Geometry of coupon specimen with central hybrid area (not to scale).

2.1 Hybrid area

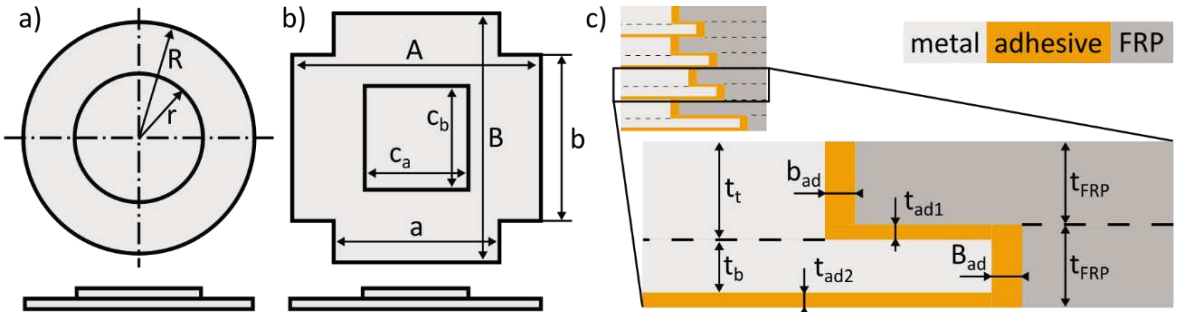

Figure 3: Top and side view of the investigated a) circular b) cross-shaped geometries. c) dimensions in the circumference of the hybrid area.

In this investigation a layered hybrid area consisting of FRP, adhesive and several metallic sheets is evaluated. Each circular or cross-shaped metal sheet spans two layers of FRP in its centre and is thinned outward. The shape parameters can differ for each layer, see Figure 3 as well as Table 1 and Table 2 for the geometric dimensions and material parameters used.

The circular metal sheets are a well-suited reference shape that is easy to manufacture and has no directional dependency with respect to the load introduction. The cross shaped geometry is motivated by restrictions that originate from the capabilities of the AFP manufacturing process.

  doi:10.5075/epfl-298799_978-2-9701614-0-0

Table 1: Reference values of geometric parameters.

specimen					
$W_{spec} = L_{spec}$	50	mm	$t_t = t_{FRP} + t_{ad1}$	0.26	mm
d_h	6.35	mm	$t_b = t_{FRP} - t_{ad1}$	0.24	mm
t_{FRP}	0.25	mm	$t_{ad1} = t_{ad2}$	0.1	mm
			$b_{ad} = B_{ad}$	0.5	mm
circular hybrid			cross shaped hybrid		
R	25.4	mm	$a = b = 3A/4$	19.05	mm
r	12.7	mm	$c_a = c_b$	12.4	mm
$A = B$	25.4	mm			

Table 2: Material parameters IM7 8551-7 [8], 1.4310 [9] and AF163-2 [10].

	IM7 8551_7		AF163-2		
$E_{\parallel}$	165,000	N/mm²	E	1,110 (161,000)	N/mm²(psi)
$E_{\perp}$	8,400	N/mm²	G	414 (60,000)	N/mm²(psi)
$\nu_{\parallel\perp}$	0.34	−	R	48.26 (7,000)	N/mm² (psi)
$\nu_{\perp\perp}$	0.5	−	S	40 (5,800)	N/mm²(psi)
$G_{\parallel\perp}$	5,600	N/mm²	ν	0.34	−
	1.4310				
E	210,000	N/mm²	$R_{p_{0.2}}$	888	N/mm²
ν	0.33	−	ν	0.34	−

In order to comply with the outer structure, the stacking of the hybrid area is placed under several constraints:

From the structure itself:

1. The orientation of the FRP layers has to be the same as in the surrounding laminate.
2. The sum of the layer thicknesses has to stay constant to avoid a local thickening.

The production process:

3. Edges have to be parallel to the fibre direction or at an acute angle in order to reduce the length of the tow cut.
4. The width perpendicular to the fibre direction should be a multiple of the tow width in order to avoid partly cut tows.

A shape and stacking following the stated restrictions is shown in Figure 3. The stacking is used for all specimen configurations within this investigation. According to the thickness constraint (2.), the thickness t_b of the metal sheet is reduced by the adhesive layers, while the thickness t_t is increased by t_{ad1}.

  doi:10.5075/epfl-298799_978-2-9701614-0-0

In order to minimise the number of additional cuts while forming the pockets in which the metal sheets are placed, the widths of the presented cross shaped specimen, are chosen as a multiple of the tow width. The gap between the metal sheet and the FRP layers is approximately 0.5-1.0 mm. The gaps in fibre direction can lead to a change in the local fibre volume content or a reduced local thickness due to moving fibres and resin flow during the curing process. The cuts perpendicular to the fibre direction can be performed by (single) tow cuts. The resulting gaps are typically bigger and depend on the layup speed. They also will be filled with adhesive or matrix material during the curing. Within this numerical investigation the gaps are assumed to be filled with adhesive but the local change in fibre volume content is not considered. This simplification should not influence the deduced general dependencies.

3 Numerical approach

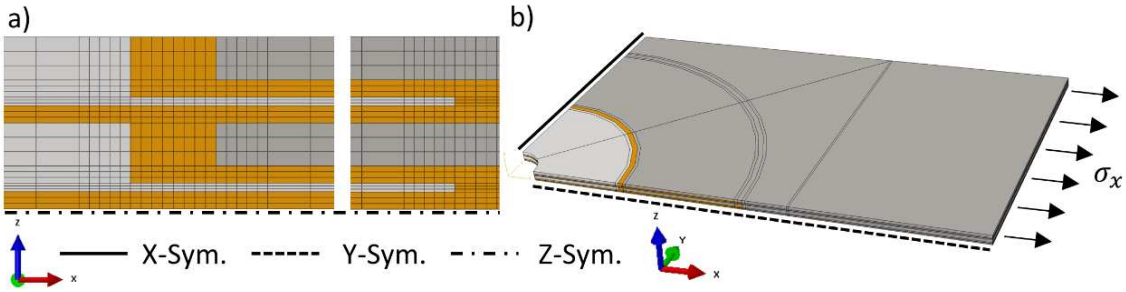

Figure 4 : Meshing of the material transitions and symmetric boundary conditions used in the triple symmetric model.

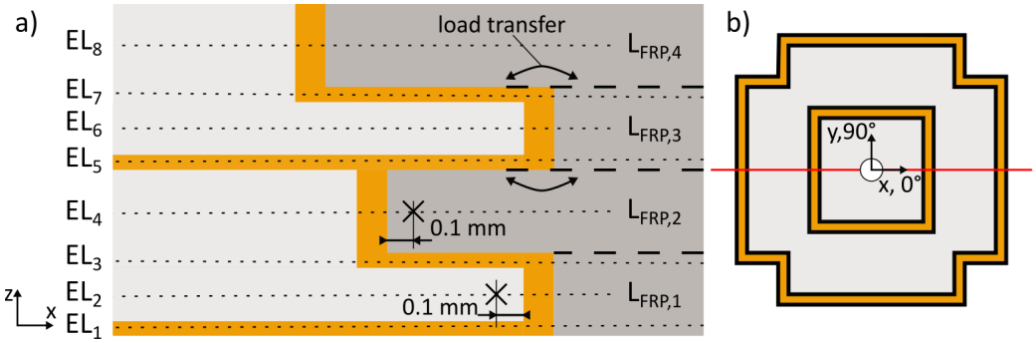

Figure 5 : a) Evaluation lines EL1-EL8 in the four layers of the top four FRP layers. The evaluation lines are placed in the centre of each layer. The evaluation points (cross) are placed at a distance of 0.1 mm from the material transition. b) exemplary location of a cross section in the XZ-plane at y=0 shown in a).

A configuration with a circular hybrid area, geometric parameters and stacking according to Table 1 is chosen as reference. Using the symmetry in geometry as well as the stacking the model can be reduced to 1/8th as shown in Figure 4. All Materials, the metallic sheets, the FRP as well as the adhesive are modelled discretely by separate material sections within one Abaqus part. The C3D8 element is used and each layer has at least three elements in thickness direction. Additionally, the mesh is refined to a size of 0.025 mm at the material transitions, leading to 1.27e6 degrees of freedom. The load σ_x is applied in a linear static step.

In order to evaluate the geometry variants, the von Mises stress (metal sheets) and Puck criterion (FRP and adhesive) are computed along the evaluation lines. The lines are placed in the centre of each layer and propagate through the hole specimen leading to eight evaluation lines

(EL) as shown for the stack of four FRP layers. The evaluation is performed within cross sections as well as along the circumference in a distance of 0.1 mm to a material transition, see Figure 5a.

4 Results and discussion

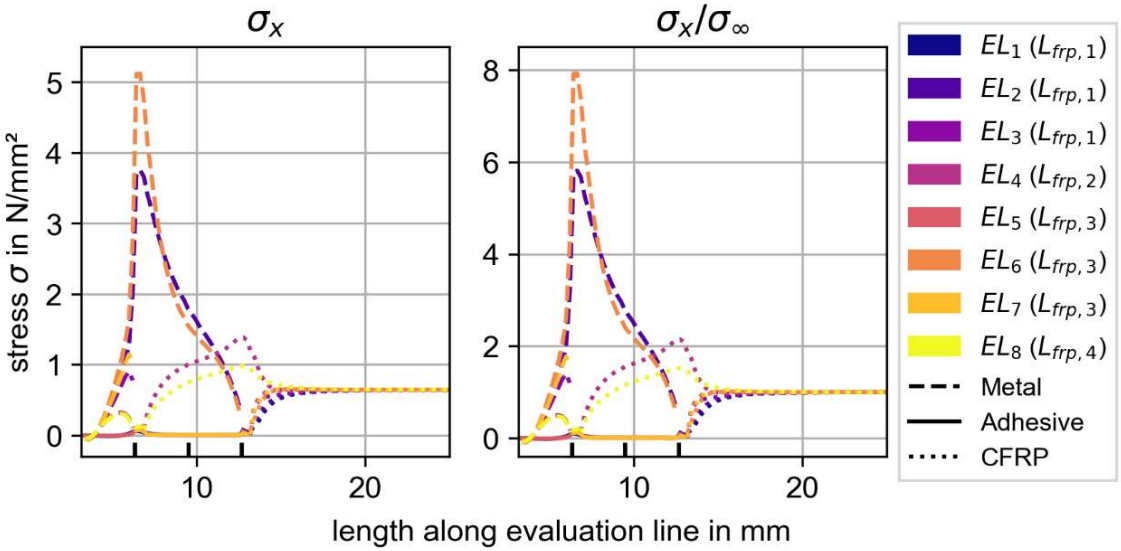

Figure 6: Stress σ_x (left) and normed stress (right) in along the evaluation lines displayed in Figure 5 for the cross-reference specimen reference with a $[0_8]$-stacking.

In order to familiarise with the evaluation methodology, the strain along the eight evaluation lines placed in the centre of each layer for a cross shaped specimen with unidirectional $[0_8]$ stacking at a load of $\sigma_x = 1$ N/mm² is shown in Figure 6. The evaluated cross section is placed in the XZ-plane at y=0 (red line in Figure 5). The curves are color-coded to differentiate the layers, while the line style is used to differentiate the material type.

The left graph shows the actual stress values σ_x that is equal for all layers in the undisturbed laminate. In the material transitions the load is transferred into the layers above and beneath the discontinued layer increasing the stress in these layers as a result. As expected for this load case, the highest stress is reached in the layers continuing through the material transitions: EL4 and EL8 (FRP) as well as EL2 and EL6 (metal). The highest stress values overall are reached in the metallic layers, which is also a result of the imposed geometric restrictions. Specifically, the "no thickening"-constraint, which results in a very thin outward metallic layers EL2 and EL6, while the FRP layer EL4 and EL8 retain their nominal thickness of 0.25 mm. This problematic can be mitigated by using thinner adhesive layers, thus allowing outwardly thicker metallic layers.

The difference in the stress values $\sigma_x(x = 25mm,\ y = 0) \approx 0.6$ N/mm² and $\sigma_x(x = 25\,mm,\ y = 12.5\,mm) \approx 1.2$ N/mm² (not depicted) along the load introduction indicates a less stiff hybrid area in comparison to the surrounding undisturbed CFRP. The load transfer can be compared to the load transfer surrounding an open hole, but is less severe since the stiffness is only (slightly) reduced. It is also visible that the layers closer to the symmetric plane exhibit a higher strain than the equivalent layer further away, e.g. EL3 and EL7.

In order to allow for a better comparison and produce transferable results, the values in the left graph of Figure 6 were normed by the stress value σ_∞ in the undisturbed surrounding. Thus, the depicted normed values on the right-hand site can be interpreted as strain increase factors. By

  doi:10.5075/epfl-298799_978-2-9701614-0-0

computing the normed value for each curve separately the geometrical effects and strain increase within the current cross section can be evaluated separately. This also improves the comparability between different cross sections by reducing the load transfer effects caused by the macro stiffness difference within the modelled hybrid plate.

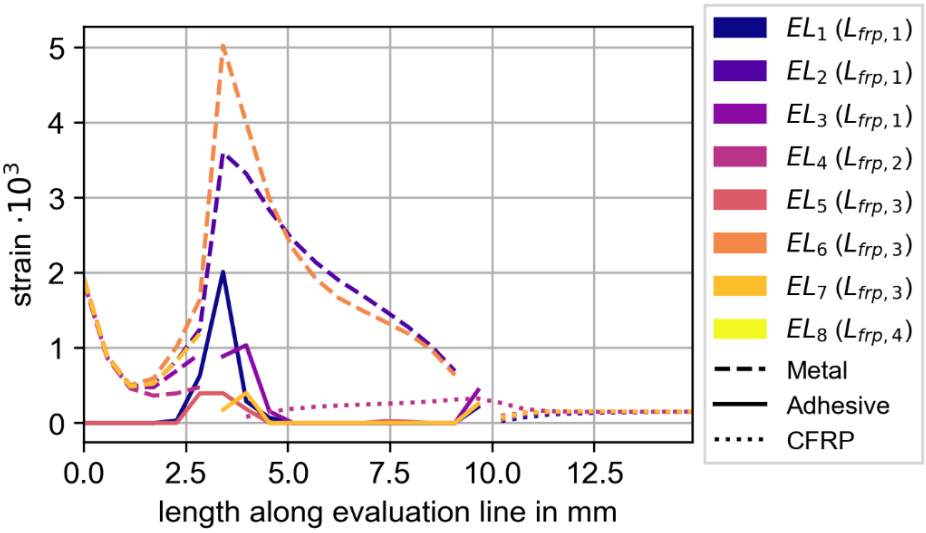

Figure 7 : Puck strain (FRP, adhesive) and von Mises strain (metal) along the evaluation lines displayed in Figure 5 for a load of $\sigma_x = 1$ N/mm².

Figure 7 shows the respective strain of EL1 to EL8. For the metal sheets the quotient of the von Mises stress and the yield point $R_{p_{0.2}}$ is used, while the Puck Interfibre Fracture (IFF) criterion is used for the adhesive. The FRP uses the maximum value of all Puck strain criteria, which is, for this exemplary specimen and load case, the fibre failure (FF). The strain curves support the indication of Figure 6: In this geometric configuration the first failure will take place in the metal sheets, more specifically in EL6 due to plastic deformation. Afterwards, the adhesive will fail in the inner material transition, while the FRP layers experience the lowest strain.

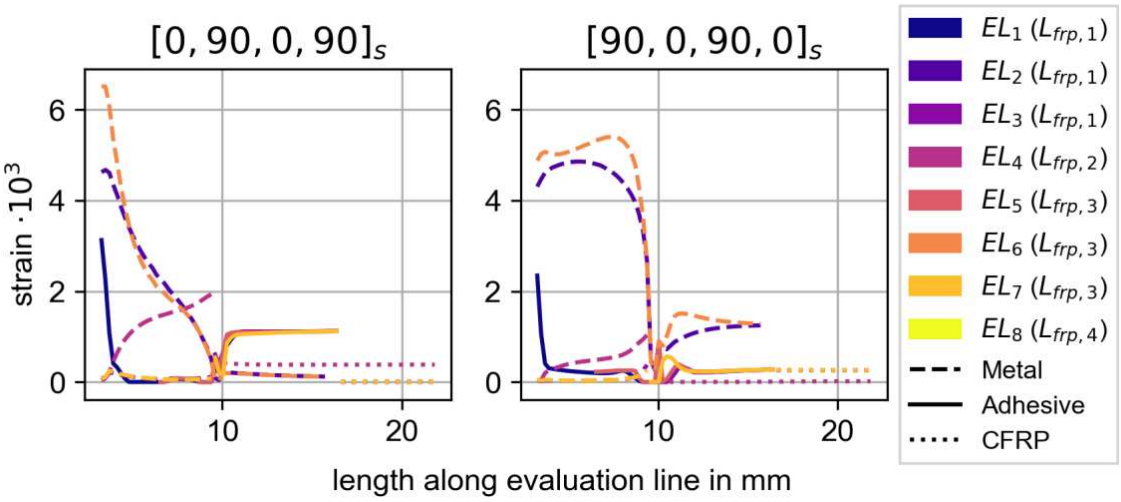

Figure 8 : Influence of the layer orientation on the strain values.

  doi:10.5075/epfl-298799_978-2-9701614-0-0

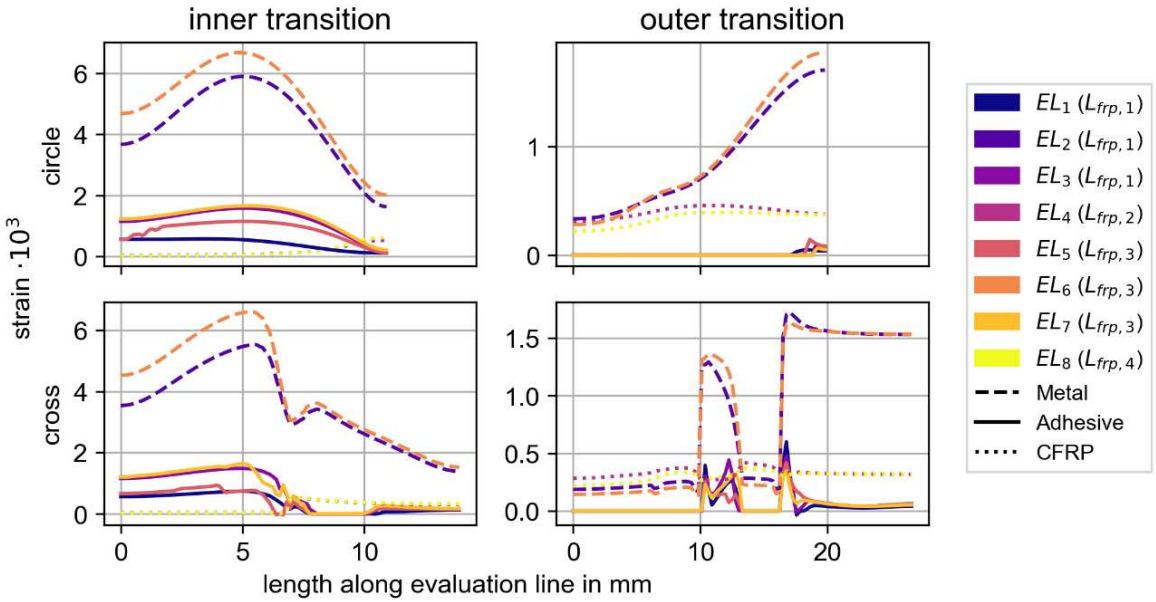

Figure 9 : Strain along the circumference of the material transition starting in the XZ-plane going counter clockwise.

The load transfer over the material transition is very sensitive to the chosen stacking. As can be seen in Figure 5, only every second FRP layer, in this case $L_{FRP,2}$ and $L_{FRP,4}$, traverse the outer material transition and can therefore be used for the load transfer. Figure 8 compares the resulting strain in case the traversing layers are placed in 0° or 90° orientation. An FRP layer with a 90° orientation is a much less stiff joining partner compared to the metal sheet and therefore increases the strain concentration at the beginning and end of the joint.

Additionally, the metal sheets in the reference configuration are of equal size, therefore the transitions are also placed in the same position. Thus, leading to an area in the cross section containing only the thin part of the metal sheets and the adhesive, which obviously should be avoided. The increased strain values of the metal sheets that carry nearly the whole load are shown in Figure 9 for both a circular and a cross specimens with a $[0_8]$ stacking. A suitable distance between transitions can for instance be derived from already existing ply-interleaving techniques used for instance for the joining of carbon and glass fibres [11].

5 Conclusions

A methodology using strain increase factors to assess and compare local fibre-metal hybrids was presented and applied to circular and cross-shaped reference geometries. The evaluation method was able to visualise the expected effects in reference load cases. By comparing the strain values within the individual layers, the first failure of the reference geometry was determined. Thin adhesive layers are advantageous and allow thicker outward metal sheets and thus increase the failure load. Also, the negative impact of disadvantageous layer orientation in combination with the stacking of multiple transitions close to each other was presented. Therefore, its recommended to use differently shaped metal sheets in each layer to distribute the material transitions. In the next step the methodology has to be applied within an optimisation study in order to find sets of geometric parameters that reach equal strain values in all components and therefore a good material utilisation including an experimental verification of the results.

  doi:10.5075/epfl-298799_978-2-9701614-0-0

Contributions

Conceptualisation: A.H; methodology: A.H.; formal analysis: A.H.; data curation: A.H; writing – original draft: A.H., writing – review & editing: A.H., C.S., S.H.; visualization: A.H.; supervision: C.S., S.H., project administration: S.H., funding acquisition, A.H., C.S.

Acknowledgements

This paper is based on investigations of the subproject 1 – 'Multilayer Inserts – intrinsic hybrid compounds for load introduction into thin walled high-performance CFRP-Structures' of the priority program 1712 'Intrinsic hybrid composites for lightweight load-bearings', which was kindly supported by the German Research Foundation (DFG).

6 References

1. Groß L, Herwig A, Berg DC, Schmidt C, Denkena B, Horst P, Meiners D. Production-based design of a hybrid load introduction element for thin-walled CFRP Structures. Prod. Eng. Res. Devel. 2018;12:113–20. doi:10.1007/s11740-018-0821-4.
2. Hu FZ, Soutis C, Edge EC. Interlaminar stresses in composite laminates with a circular hole. Composite Structures. 1997;37:223–32. doi:10.1016/S0263-8223(97)80014-1.
3. Gruber B, Hufenbach W, Kroll L, Lepper M, Zhou B. Stress concentration analysis of fibre-reinforced multilayered composites with pin-loaded holes. Composites Science and Technology. 2007;67:1439–50. doi:10.1016/j.compscitech.2006.08.018.
4. Camanho PP, Matthews FL. Stress analysis and strength prediction of mechanically fastened joints in FRP: a review. Composites Part A: Applied Science and Manufacturing. 1997;28:529–47. doi:10.1016/S1359-835X(97)00004-3.
5. Koord J, Stüven J-L, Petersen E, Völkerink O, Hühne C. Investigation of exact analytical solutions for circular notched composite laminates under tensile loading. Composite Structures. 2020;243:112180. doi:10.1016/j.compstruct.2020.112180.
6. Thoppul SD, Finegan J, Gibson RF. Mechanics of mechanically fastened joints in polymer–matrix composite structures – A review. Composites Science and Technology. 2009;69:301–29. doi:10.1016/j.compscitech.2008.09.037.
7. AITM 1-0007, Determination of plain, open hole and filled hole tensile strength, Issue 5 2016. Toulouse, France: Airbus.
8. Kaddour AS, Hinton MJ. Input data for test cases used in benchmarking triaxial failure theories of composites. Journal of Composite Materials. 2012;46:2295–312. doi:10.1177/0021998312449886.
9. Pavliuchenko P, Teller M, Hirt G. Analysis of influencing factors on the achievability of bistable fully closed shells by semi-analytical modelling 2021. doi:10.31224/osf.io/wyzx2.
10. 3M. Scotch-WeldTM Structural Adhesive Film - Technical Datasheet: AF 163-2; 11/2009.
11. Ahamed J, Joosten M, Callus P, John S, Wang CH. Ply-interleaving technique for joining hybrid carbon/glass fibre composite materials. Composites Part A: Applied Science and Manufacturing. 2016;84:134–46. doi:10.1016/j.compositesa.2016.01.010.

COMPUTATIONAL STUDIES OF THE INFLUENCE OF PARTICLE SHAPE ON ELASTIC PROPERTIES OF THE COMPOSITE

Pascal Alexander, Happ[a] and Romana, Piat[b]

[a] Faculty of Mathematics and Natural Sciences, Darmstadt University of Applied Sciences, Darmstadt, Germany - pascal-alexander.happ@h-da.de

[b] Faculty of Mathematics and Natural Sciences, Darmstadt University of Applied Sciences, Darmstadt, Germany

Abstract: *This work studies the influence of different design variables such as the particle surface, their undulations and volume fraction on the elastic properties of particle reinforced composites. The analytic functions of Laplace's Spherical Harmonics are used to approximate the particles derived from imaging techniques. The contributions of the particle shapes to the linear elastic properties of the homogenized composite are quantified. The proposed research identifies the crucial design variables that affect the linear elastic composite behavior. The obtained results can be used for the numerical microstructure design and optimization. This hybrid approach of numerical predictions and experimental validation can reduce the time and resource consuming experimental development process of particle reinforced composites.*

Keywords: Numerical Modelling; Finite Element Analysis; Composite Materials; Particle shape

1. Introduction

Industries such as aerospace, automotive and energy sector [1] heavily invest in continuous material research, as they need to meet high standards in regards to safety, efficiency and reliability during operations of their goods. Modern windmills, cars and aircrafts need to withstand the service conditions, be light weight and minimize the energy consumption during manufacturing, operations and recycling. This sets high, sometimes contradicting requirements for the deployed materials. Often, aluminum alloys are used for the intended application, but composite materials are starting to gain more importance.

Particle reinforced composites can specifically be designed on a microscopic level to achieve a prior defined, targeted material properties of the manufactured material. For this a thorough understanding of the influences of the microstructure onto the overall mechanical properties of the composite is needed as the microstructure directly relates to the mechanical behavior of the composite on the macroscopic level.

Usually, numerous material experimental tests are conducted to gain this thorough understanding of the material behavior under certain loading conditions. To achieve the desired material properties such as a specific elastic behavior, resistance against wear, crack growth behavior, several iterations of the composites are usually developed. This classical approach of material research bears the hallmarks of trial, error and repeat until certain criteria are met like achieving an overall satisfying material behavior. This rather costly and time intensive approach relies heavily on intuition and experiences of the research scientists.

A different path to finding appropriate material combinations for particle reinforced composites is provided by semi-analytic homogenization methods based on the solution proposed by Eshelby [2]. This homogenization method approximates the inclusions with ellipsoids. Using this, estimations about the composite material properties with two or more material constituents can be made. Different

  doi:10.5075/epfl-298799_978-2-9701614-0-0

variations of the semi-analytic methods were proposed by Benveniste [3] and other researchers. But the approximation of inclusions with ellipsoids, inherited through the aforementioned Eshelby solution, neglect irregular inclusions which account to a large number of possible particle shapes observed in scanning electron microscopy studies. This method is therefore not accurate enough for a sufficient prediction of the effective material properties of particle reinforced composites.

Computational methods and computational power matured enough so that composite materials with irregular particles can be assessed numerically. The computational homogenization methods utilize so called representative volume element (RVE), whose accurate determination is of high importance to the quality of results of the homogenization process. Methods to create a RVE can be found in [4]. These RVE's are then used for the homogenization process to predict the composite material behavior on a macroscopic level.

2. Particle Model Creation

Real world particles can possess very complicated shapes and vary vastly for the same kind of material (see Fig. 1a). Same can be said about pores [5]. The focus of the presented studies is not to exactly recreate some special particle shapes but to generate close representations by the use of analytic functions. These particles are then used for the computational simulations. The precise definition of the particle surface by the use of analytic function allows a thorough analysis, through deliberate variations of the function variables. A sensitivity analysis is thus possible.

The analytic functions of Laplace's Spherical Harmonics are used as described by Müller [6]. These functions allow creation of particles with undulations to represent rough surfaces. A large variety of different particle surfaces were created by the variation of the parameters of degree and order used in the Spherical Harmonics function. Examples of such are shown in Fig. 1b.

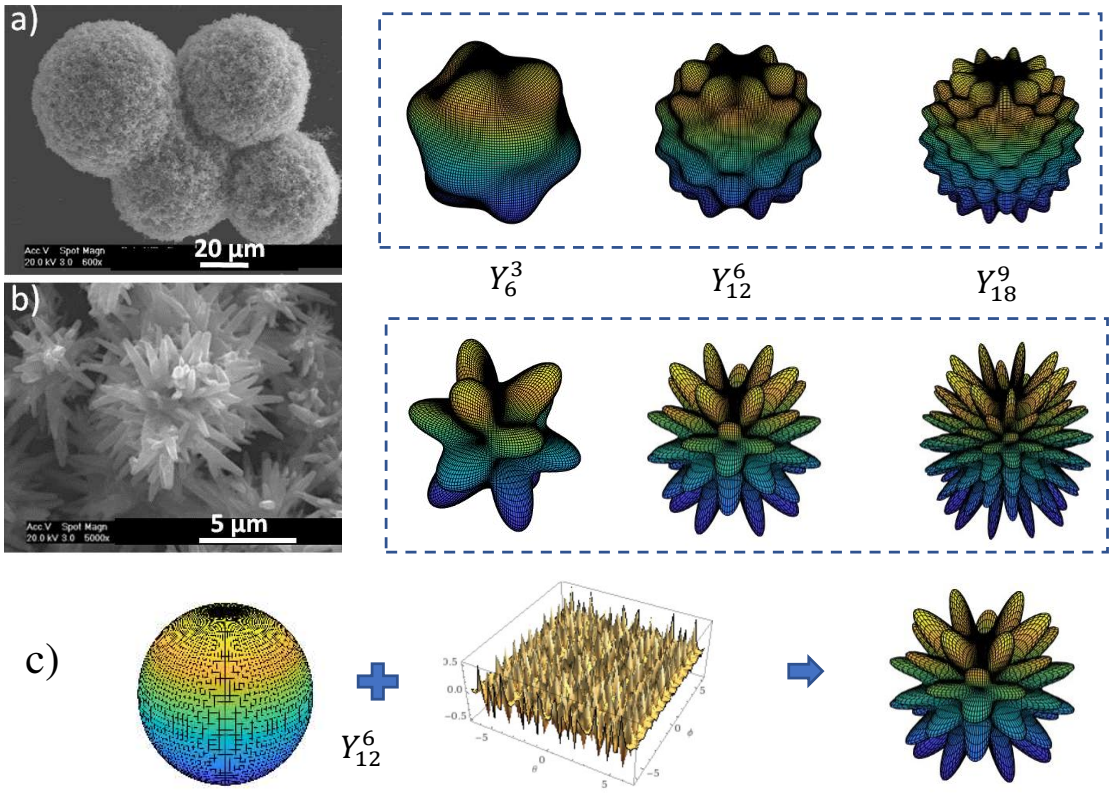

Figure.1. a) and b) Microscopic images of the real world particle with examples to the right of the approximation of particles using Laplace's Spherical Harmonics for different degrees and orders added

  doi:10.5075/epfl-298799_978-2-9701614-0-0

onto spheres with a base radius of R = 3 (upper row) and R = 0.6 (middle row); c) The creation process of the particles studied in this work is depicted in the bottom row.

The equation to describe the undulations as stated by Müller for the Laplace's Spherical Harmonics is written as the following:

$$Y_l^m(\theta,\phi) = \sqrt{\frac{2l+1}{2\pi}\frac{(l-m)!}{(l+m)!}} P_l^m(\cos\theta) e^{im\phi} \quad (1)$$

With P_l^m being an associated Legendre-Polynomial, l and m representing the degree and order respectively, $\theta \in [0,\pi]$ and $\varphi \in [0,2\pi)$.

The undulations are then added to a base sphere with a radius R, as depicted in of Fig. 1c. The particles with different amplitudes of the undulations are created by changing the base radius. The different particles depicted in Table 1 were created by the variation of degree, order and base radius.

Table 1. Particles created by Laplace's Spherical Harmonics Y_l^m for different values of degree (l) and order (m) added to spheres with different radii (R).

	R = 0.6	*R* = 0.8	*R* = 1.0	*R* = 1.5	*R* = 2.0	*R* = 2.5	*R* = 3.0
Y_6^3	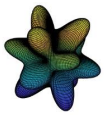	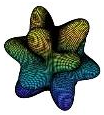	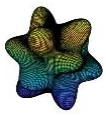	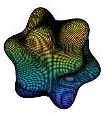	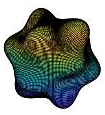	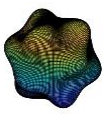	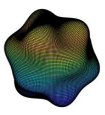
Y_8^4			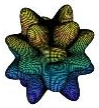	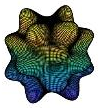	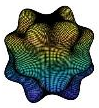	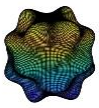	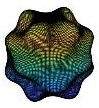
Y_{10}^5					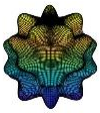	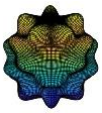	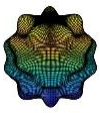
Y_{12}^6					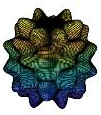	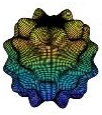	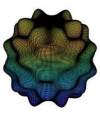
Y_{14}^7						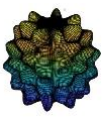	
Y_{16}^8						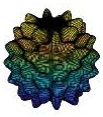	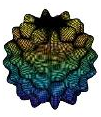
Y_{18}^9							

  doi:10.5075/epfl-298799_978-2-9701614-0-0

3. Estimation of the Overall Elastic Properties

The numerical evaluation of the particles' contribution to the overall linear elastic material properties of the particle reinforced composite were conducted as proposed by Trofimov et al. [7]. In the proposed study only one-particle-configurations were considered, to quantify the particle shape effect on the overall elastic properties. The effects of the particle-to-matrix interface were neglected as well, by assuming ideal bonding between the matrix and the particle. Furthermore only linear elastic material behavior was studied. A RVE representing the material statistically as proposed by Song et al. [8] consisting of two material phases was created. An example of the RVE created for this study is depicted in Fig. 2.

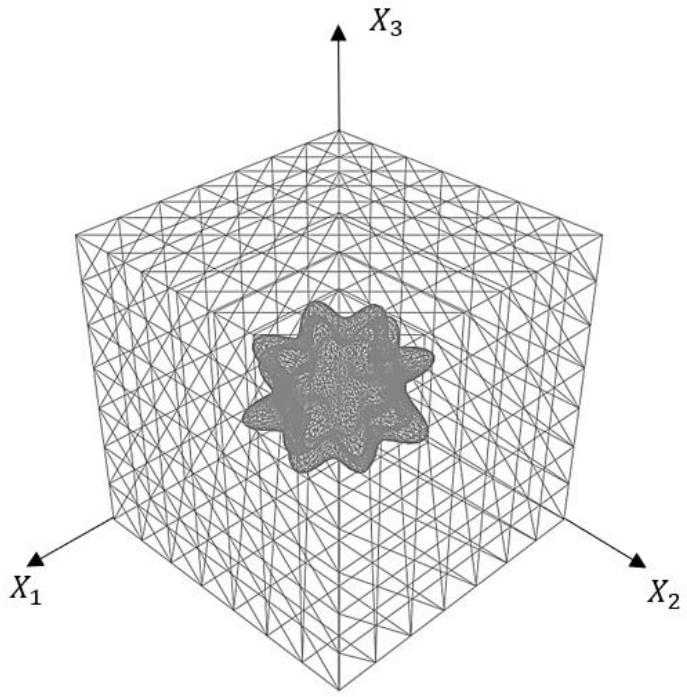

Figure2. An example of the one particle RVE used in the numerical simulations. The particle is embedded inside the cube consisting of the matrix material. Ideal bonding between matrix an particle was assumed. Periodic boundary conditions were applied.

Periodic boundary conditions were applied to the RVE, as proposed by Xia et al. [9].

$$u_i^{j+} = \bar{\epsilon}_{ik} x_k^{j+} + u_i^* \tag{2}$$

$$u_i^{j-} = \bar{\epsilon}_{ik} x_k^{j-} + u_i^* \tag{3}$$

Where $\bar{\epsilon}_{ik} x_k^{j+}$ is the linear displacement field, with $\bar{\epsilon}_{ik}$ being the average strain tensor. u_i^* is the periodic part considering the displacements of the boundary surfaces of the RVE. "$j+$" indicates the positive X_j-direction, "$j-$" the negative X_j-direction (see Fig. 2).

4. Mesh Studies

The numerical studies were carried out using the FE method employing the ABAQUS [10] Software for the calculations. Studies of the FE meshing effects on the numerical results, especially the Young's modulus of the particle reinforced composite were conducted, considering the influence of the element count, order and the meshing technique used in the calculation process. The particle shape described by a hyperbolic octahedron was utilized for this study, as the shape features numerous sharp

  doi:10.5075/epfl-298799_978-2-9701614-0-0 published under CC BY-NC 4.0 license

edges making it numerically difficult to evaluate (see Fig. 3). The equations to describe the hyperbolic octahedron can be found in [11].

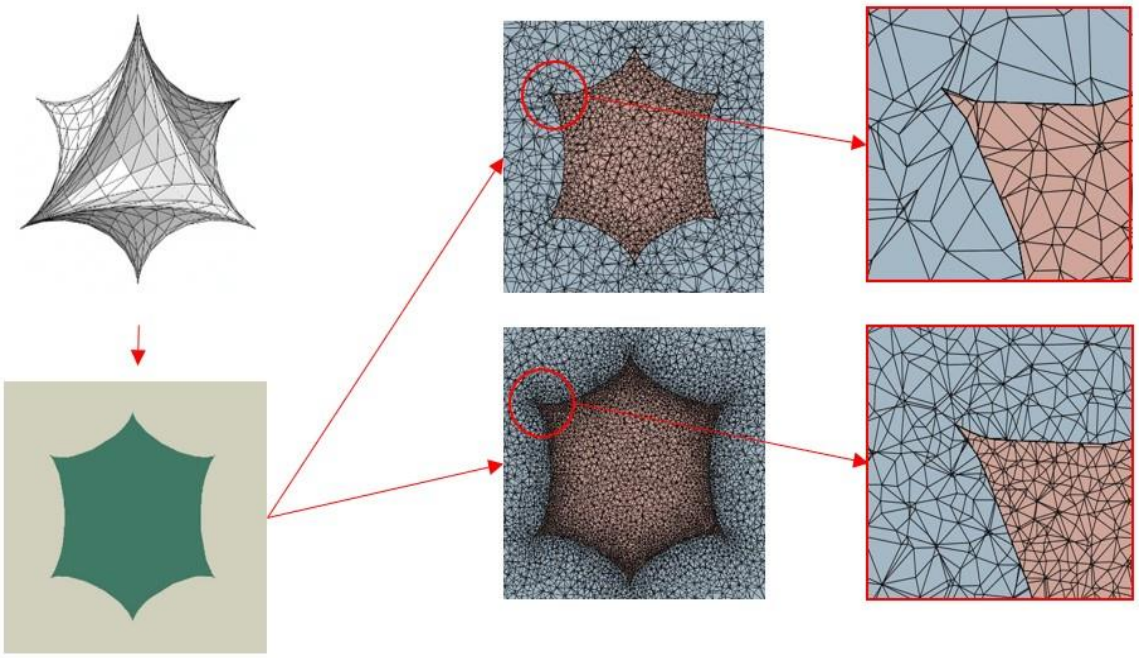

Figure.3. A hyperbolic octahedron was created (upper left) and embedded into the matrix material, considering ideal bonding (lower left). The RVE was then meshed assessing different meshing techniques. Image of the considered particle with standard meshing (upper part) and a refined mesh (lower part).

Tetrahedron elements of linear and quadratic order were considered. A RVE was created onto which different meshing algorithms were applied.

Table 2. Mesh study considering different element orders of tetrahedron elements, element count and meshing controls applied trough the ABAQUS UI and the effects on the material properties.

Order	Matrix Elements (Million)	Particle Elements (Million)	Total Elements (Million)	$\frac{E_{1c}}{E_{1i}}$	$\frac{E_{2c}}{E_{2i}}$	$\frac{E_{3c}}{E_{3i}}$	Mesh Controls
Linear	0.178	0.102	0.280	0.0248	0.0247	0.0248	No Controls Applied
Quadratic	0.178	0.102	0.280	0.0245	0.0244	0.0245	No Controls Applied
Linear	1.359	1.242	2.601	0.0246	0.0246	0.0246	Virtual Topology Refined Interface Mesh
Linear	2.569	2.803	5.372	0.0245	0.0242	0.0245	Virtual Topology Refined Interface Mesh
Quadratic	0.387	0.241	0.628	0.0245	0.0242	0.0245	Virtual Topology Refined Interface Mesh

The Young's moduli of the composite were evaluated numerically considering the listed parameters in Table 2. The results were then normalized by the Young's modulus of the particle material. The normalized Young's moduli of the composite vary only slightly, considering the different meshing

  doi:10.5075/epfl-298799_978-2-9701614-0-0 published under CC BY-NC 4.0 license

element count of around 280,000 using tetrahedron elements of quadratic order with no further restrictions to the applied meshing technique. 537,000 tetrahedron elements of linear order had to be used to achieve the same results using a virtual topology and a refined mesh at the particle-to-matrix interface.

5. Numerical Results for Different Particle Shapes

The particles presented in Table 1 are evaluated and their effects onto the overall linear elastic material properties are quantified. The particle volume fraction is kept constant throughout the numerical simulations. Furthermore, ideal bonding between the particle and the matrix is assumed and only the linear elastic behavior of the two phases is considered.

Periodic boundary conditions are applied for the calculations as described in (2)-(3). The surface-to-volume ratio for every particle was taken into account and evaluated the following way:

$$\psi = \frac{S_i}{\sqrt[3]{\pi(6V_i)^2}} \tag{4}$$

with S_i is the surface of the inclusion and V_i the volume of the inclusion. ψ is the surface-to-volume ratio, which is the inverse to the sphericity. The effects of the particle shapes on the overall elastic material properties of the composite were evaluated in this way.

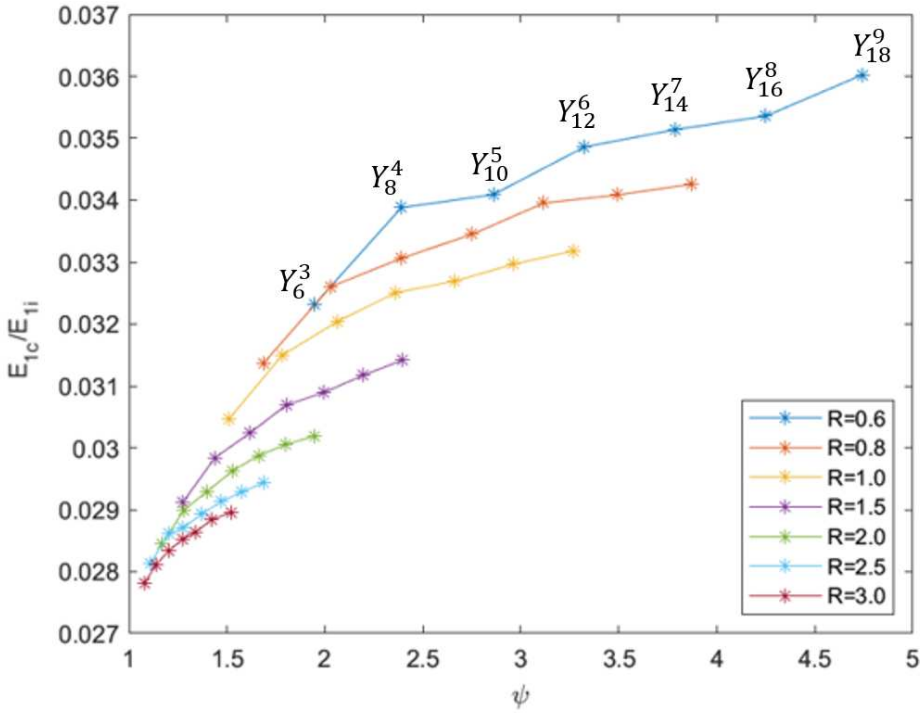

Figure 4. Correlation between the particle shape and the overall normalized $\frac{E_{1c}}{E_{1i}}$-modulus of the composite, for particles created by the use of Laplace's Spherical Harmonics. The undulations created for the following degrees and orders $Y_6^3, Y_8^4, Y_{10}^5, Y_{12}^6, Y_{14}^7, Y_{16}^8, Y_{18}^9$ were modeled onto the spheres of the following base radii R = 0.6, 0.8, 1.0, 1.5, 2.0, 2.5, 3.0.

The correlation between the particle shapes with different Y_l^m and normalized E1-Young's modulus is displayed in Fig. 4. The calculations are carried out considering spheres of the base radii R = 0.6, 0.8, 1.5, 2.0, 2.5, 3.0 with Spherical Harmonics $Y_6^3, Y_8^4, Y_{10}^5, Y_{12}^6, Y_{14}^7, Y_{16}^8, Y_{18}^9$ on the interface.

In the provided studies, the volume of the particle V_i was constant and only the surface area S_i was changed by varying the degree and order (l, m) of the spherical harmonics equation.

The contribution of the surface area to the linear elastic properties can be studied this way, without changing the volume of the particle. The increase in the obtained Young's modulus is thus a result of the waviness of the surface alone, which is impacted by the total number of waves modeled and therefore the amount of surface area onto the base sphere. The amplitude of the waves relative to the base sphere's radius, which effects the distribution of the reinforcing phase throughout the RVE, has a strengthening influence as well. Both can be specifically tuned by changing the base radius, degree and order considered by the Spherical Harmonics.

It can be seen in Fig. 4 that the effect of the approximation of the particle surface has a measurable influence on the obtained homogenized elastic material behavior. This variation cannot be addressed by the conventional method of ellipsoidal approximation.

6. Conclusion and Outlook

The shapes of the studied particles are created using Laplace's Spherical Harmonics. Different undulated surfaces are created by varying the parameters of Spherical Harmonics with the aim to understand the correlation between the particle shape and elastic properties of the particle reinforced composite.

Single particle inclusion RVEs are created with the particle volume fraction being kept constant, an optimized mesh applied and periodic boundary conditions utilized. The normalized Young's modulus of the homogenized material is evaluated along with the surface-to-volume ratio of the individual particle. The contributions of the different particle forms to the elastic properties of the composite material are compared with each other and with a sphere of the same particle volume fraction. The obtained results show (see Fig.4) that for sphere with some radii r and with increasing number of undulations (from Y_6^3 up to Y_{18}^9), the surface-to-volume ratio increases and corresponding effective E1-Young's modulus also increases. With decreasing the radius of the sphere while keeping the particle volume fraction constant, the effective E1-Young's modulus increases (compare the sequence of the graphs corresponding to the radii from the blue line with $R = 0.6$ down to the red line with $R = 3.0$). It can be concluded that the higher amplitude along with shorter wave lengths of the undulations on the particle's interface, results in larger surface area and higher effective Young's modulus of the particle reinforced composite.

It can be seen that the particle shape has a measurable impact on the effective properties of the composite and can result in a higher Young's modulus compared to a sphere of the same volume fraction. Particle approximations using spheres can therefore underestimate the reinforcing effect of the particles.

A mesh study is carried out and shows that the numerical results are independent of the applied mesh and a numerically stable calculation process is achieved.

In future, other particle surface parameters will be studied and e.g. correlation between the curvature and form of the particle edges and the composite properties will be calculated.

Acknowledgements

The financial support of the University of Applied Sciences Darmstadt and the Hessian Ministry of Higher Education, Research, Science and the Arts by Program "Forschung für die Praxis" is gratefully acknowledged. This research was funded by the Federal Ministry for Economic Affairs and Energy based on a decision of the German Bundestag.

  doi:10.5075/epfl-298799_978-2-9701614-0-0

7. References

1 Brøndsted P, Lilholt H, Lystrup A. Composite Materials For Wind Power Turbine Blades. Annu. Rev. Mater. Res. 2005; 35(1):505–38.
2 Eshelby JD. The determination of the elastic field of an ellipsoidal inclusion, and related problems. Proc. R. Soc. Lond. A 1957; 241(1226):376–96.
3 Benveniste Y. A new approach to the application of Mori-Tanaka's theory in composite materials. Mechanics of Materials 1987; 6(2):147–57.
4 Segurado J, Llorca J. A numerical approximation to the elastic properties of sphere-reinforced composites. Journal of the Mechanics and Physics of Solids 2002; 50(10):2107–22.
5 Drach B, Tsukrov I, Gross T, Dietrich S, Weidenmann K, Piat R et al. Numerical modeling of carbon/carbon composites with nanotextured matrix and 3D pores of irregular shapes. International Journal of Solids and Structures 2011; 48(18):2447–57.
6 Müller C. Spherical Harmonics. Berlin, Heidelberg: Springer; 1966. (Lecture Notes in Mathematics; vol 17).
7 Trofimov A, Drach B, Sevostianov I. Effective elastic properties of composites with particles of polyhedral shapes. International Journal of Solids and Structures 2017; 120:157–70.
8 Song W, Krishnaswamy V, Pucha RV. Computational homogenization in RVE models with material periodic conditions for CNT polymer composites. Composite Structures 2016; 137:9–17.
9 Xia Z, Zhang Y, Ellyin F. A unified periodical boundary conditions for representative volume elements of composites and applications. International Journal of Solids and Structures 2003; 40(8):1907–21.
10 ABAQUS. Providence, RI, USA: Dassault Systèmes (Simulia). Available from: URL: https://www.3ds.com/.
11 Krivoshapko SN, Ivanov VN. Encyclopedia of Analytical Surfaces. Cham: Springer International Publishing; 2015.

ANALYSIS OF FAILURE MODES AND IMPLEMENTATION OF DESIGN TOOLS FOR A REINFORCED METAL/COMPOSITE JOINT UNDER PULL-OFF LOADING

Paul Van Der Sypt [a], Christophe Bois[b], Jean-Philippe Léard [a], Hervé Wargnier[b], Michel Leroy [a]

a: ArianeGroup, Saint-Médard-en-Jalles, France – paul.van-der-sypt@ariane.group
b: I2M, UMR 5295, F-33400 Talence, France

Abstract: *The launcher industry is summoned by new competitors to radical changes. Cost and mass budget reduction is no more an option. Optimization of structures and new materials are used to cope with those specifications. But metal/composite assemblies are a challenge for designers. Out-of-plane loadings are complex to implement on composite joint ensuring satisfying mechanical properties without penalizing the mass. In 2010, Airbus Common Research & Technology proposed a new kind of Through-Thickness joints: the HYbrid Penetrative Reinforcement joints (HYPER joints). Obviously, the number and the pattern of pins will drive the mechanical response. In this study, experimental and numerical tools are implemented to determine the impact of the pin pattern and the number of pin of the joints in terms of mechanical strength and associated failure mode. To reduce the calculation time and perform sensitivity analysis, unit cells are defined from a reference model.*

Keywords: Hybrid joints; Simulation; Additive Manufacturing; Composite Laminate

1. Introduction

In the aerospace field, assemblies have to fulfill multiple functions such as: required mechanical performances, low cost and mass, and finally high stiffness. Moreover multi-material assemblies have always been a challenge for designers, particularly when one of the adherents is made of composite materials. The low out-of-plane strength limits the relevancy of numerous technologies. Nowadays, bolted joints are widely used and numerous studies have been carried out [1] [2]. The mechanical performances are satisfying if cautions are made in the designing process. Indeed drilling holes is required, generating stress concentration and may lead to composite damage [3] [4] [5]. Moreover, visco-elastic behavior of the resin requires torqueing fasteners several times to reach targeted preload [6]. Thus implementation of bolted solutions is costly and time consuming. Finally out-of-plane stiffness is a problem with this kind of technology. To sum up, bolted joint technology offers a compromise between the specifications imposed by the industrial design. Last decades have seen the emergence of a new kind of technology: the through-thickness reinforcement. For metal / composite assemblies, pins are manufactured on the top of metallic parts. Manufacturing process of the pins can differ depending on the technology chosen to manufacture the pins: wielding [7] [8], laser surface treatment [9] [10] [11] [12] or additive manufacturing [13] [14]. The technology chosen impacts directly the complexity of the pin shape. For instance, using additive manufacturing or the wielding technology allows the implementation of head on the top of the pins. Presence of heads induces a load transfer is performed by mechanical contact. Results have shown the anchorage tends to maximize the strength of the joint [8] [14].

  doi:10.5075/epfl-298799_978-2-9701614-0-0

This study focuses on a technology created and patented by Airbus Group: HYPER joints [15] (Figure 1). Pins are arrow shaped and manufactured using additive manufacturing. Pins are then inserted in the composite laminate while it is still uncured, allowing fibers to move around without breaking. Reticulation of the resin is made by autoclave, trapping the pins inside the composite laminate. Previous studies have demonstrated the potential of this technology, mainly under shear loading [16]. In order to implement such technology in an industrial framework, design tools need to be established to help choosing the appropriate configuration for a structure. This study proposes a methodology to develop such tools applied to simple configurations.

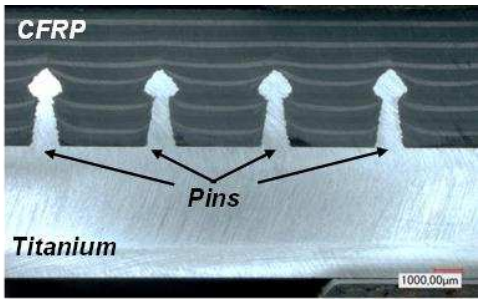

Figure 1. Transverse observation of HYPER joints

2. Overview

Design tools must predict the failure load and the failure mode independently of the chosen configuration. Additionally, it has to be clearly readable with fast utilization (the optimal configuration must pop-up). This study focuses on HYPER joints with a pull-off loading with pins placed on the same ring. The first step is to implement a reference model able to represent all failure modes with adequate failure loads. Therefore, an experimental approach is needed to identify the failure modes and damage location. Then a unit cell is identified to limit the time required to run the model and to allow performing a parametric analysis. Reference curves can be extracted from such parametric analysis. The methodology is summed up on Figure 2.

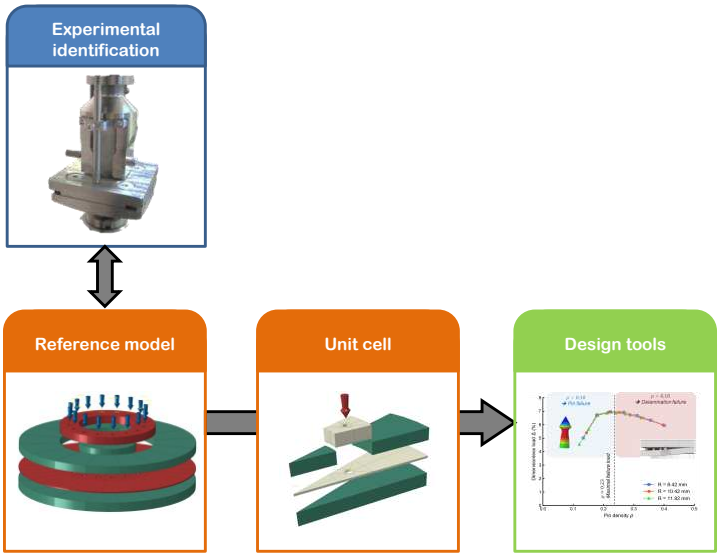

Figure 2. Overview of the methodology adopted

3. Experimental approach

3.1 Experimental set-up

The coupon used for this study is displayed on Figure 3(a). The metallic strip is made of TA6V with 16 pins circularly placed on top. The width of the strip is 25.4 mm (the section is square), and the height is 80 mm. The composite laminate is made of IMA/M21 with a quasi-isotropic lay-up (28 plies). The thickness is about 5 mm (0.185 mm for each ply). The composite part is 100 mm width (square section). The experimental set-up is displayed on Figure 3(b). A lug is implemented to impose a displacement to the metallic part, and a flange is used to maintain the composite laminate during the test. A window is set in the flange to let the metallic strip going through. A LVDT sensor is set up to measure the relative displacement between the lug and the flange. The displacement rate is imposed to 1 mm/min. Ultra-sound inspection is performed at different stages of the test to identify the damage scenario.

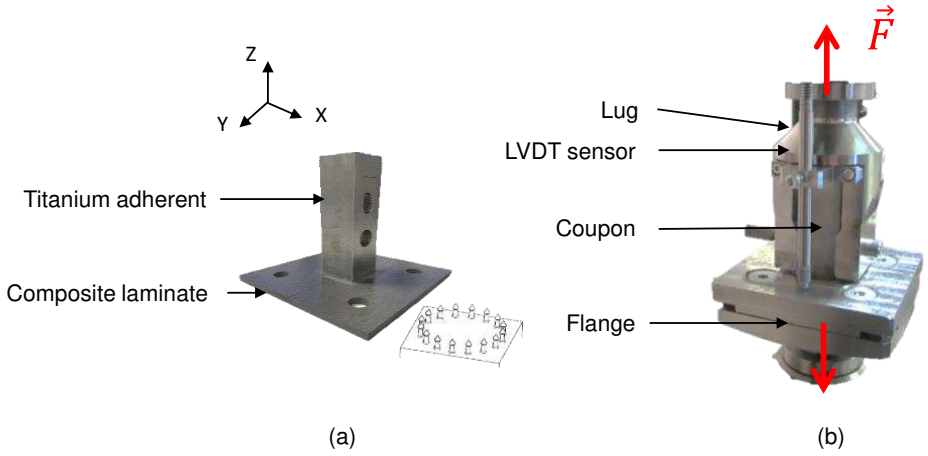

Figure 3. (a) Pull-off coupon, (b) Experimental set-up

3.2 Results and discussion

Figure 4 displays the curve load vs relative displacement. The configuration with 8 pins is driven by the plasticity of the pins, the response is firstly linear followed by a non-linear part driven by the elato-plastic behavior of the pins. The pin failure occurred at its minimal section. Head of pins remains inside the composite laminate and no composite damage has been observed. For the 16 pins configuration, the mechanical response is more complex. However, in an industrial framework, strength will be defined at first failure load. In this paper, damage scenario is thus only described up to the first failure drop (point noted "3" on Figure 4). The mechanical response is firstly linear (from point 1 to 2) and reached a first maxima F_1. Then a significant load drop occurs (from point 2 to 3). Ultra-sound inspection has shown that a delamination unstable propagation is responsible for this failure. This delamination appears at the maximal section of the pins.

The design tools must thus be able to consider both pin failure (observed for 8 pins) and delamination failure located at the maximal section (observed for 16 pins).

  doi:10.5075/epfl-298799_978-2-9701614-0-0

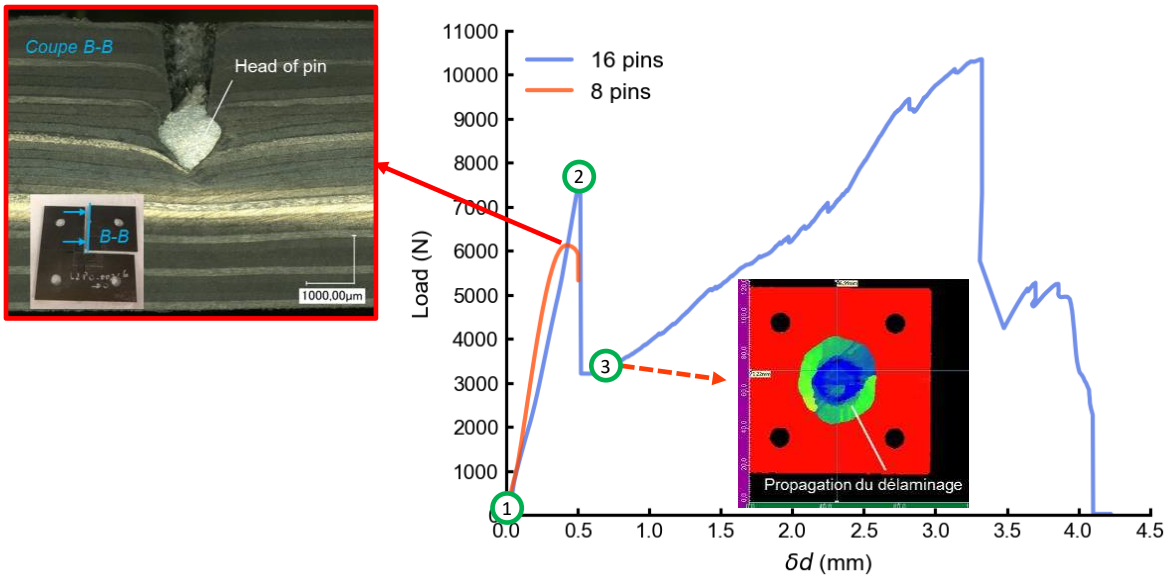

Figure 4. Identified damage scenario

4. Numerical modelling

4.1 Reference model

A reference model has been implemented (Figure 5). This model aims to represent the damage scenario described section 3. The outer surface of the coupon is encastre and a displacement is imposed to the root of the pins. The complex tri-dimension strain fields induced near the pins (composite compression, pin plasticity, delamination initiation) requires the use of volumic elements in this region. Plies are explicitly modeled with 1 element per ply. A linear law is implemented as no composite damage is observed before the first load drop. No ply waviness or resin pocket was introduced in the model. The elastic properties are summed up in [17]. The elasto-plastic law implemented for the pins was characterized from tensile coupons. The kinematic field further from the pin is simpler (bending of the composite laminate plate). Thus, the composite laminate located far from the pins is modeled using continuum shell elements. Delamination is modeled by the implementation of cohesive zone modelling with null thickness (CZM). Running several test cases have shown that implementing more than one interface penalizes the time calculation without significant effect on the failure load. Thus a unique interface is implemented right above the maximal section of the pins. A bilinear law is chosen and the interface parameters were identified using the linear fracture mechanics as presented in [17]. The plies adjacent to the interface are modeled using volumic elements to avoid any kinematic transition that could be responsible for premature numerical damage initiation. Mesh density has been determined based on the recommendations made by Turon [18] in his work.

  doi:10.5075/epfl-298799_978-2-9701614-0-0

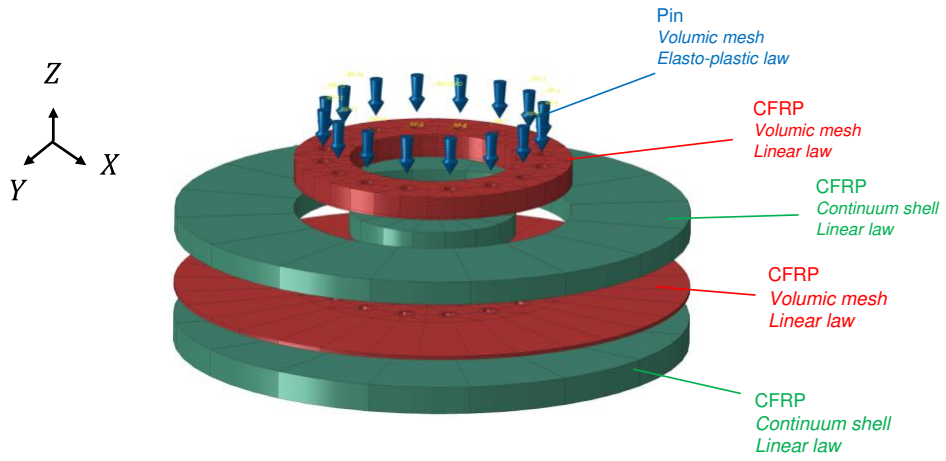

Figure 5. Reference model using continuum shell elements with volumic elements near the pins

The validity of the reference model was investigated by confronting the numerical results with the experimental data (section 3). Table 1 sums up the results obtained experimentally and thanks to the reference model for the 8 and 16 pins configurations. The agreement in terms of failure mode is satisfying. It is worth noting that the numerical damage scenario leading to a delamination failure always follow the same trend for a circular pattern of pins: (i) initiation of the delamination around each pins, (ii) delaminations grow circularly around each pins and finally (iii), coalescence of the delaminations leading to the load drop.

Table 1. Confrontation between the experimental and the model results

	Experimental		**Reference model**	
	Failure load (N)	Failure mode	Failure load (N)	Failure mode
8 pins (9 coupons)	6 128	Pin plasticity	5 985	Pin plasticity
16 pins (5 coupons)	8 024	Delamination	8 704	Delamination

4.2 Unit cell implementation

Optimization of joints is essential for industrial applications. This study proposes to use the model implemented to analyze the one ring configuration. Such pattern is driven by two parameters: the radius R of the ring and the number of pins N_p. It is worth noting that both parameters are dependent through the pitch p between the pins. The reference model does not allow a parametric study as the time required for each simulation is about 2 weeks (processor I7 with 64 Go of RAM). Therefore a unit cell is defined to limit the resources needed. The one ring configuration provides several symmetric planes in terms of geometry, loading (the load is uniformly distributed on each pin) and boundary conditions (if the number of pins N_p is pair). A unit cell is defined where the borders are based on those symmetric planes (Figure 6(a)). Symmetric boundary conditions are use at the external faces (S_{adj} and S_{adj}^{α} on Figure 6(b)). The unit cell permits to perform a simulation in about 1 hour (rather than 2 weeks for the reference model). The definition of the unit cell neglects the non-symmetric feature of the composite

  doi:10.5075/epfl-298799_978-2-9701614-0-0

layup. Comparison of responses obtained from the reference model and the unit cell for a 16 pins configuration has been made. Both responses are close enough to validate the unit cell.

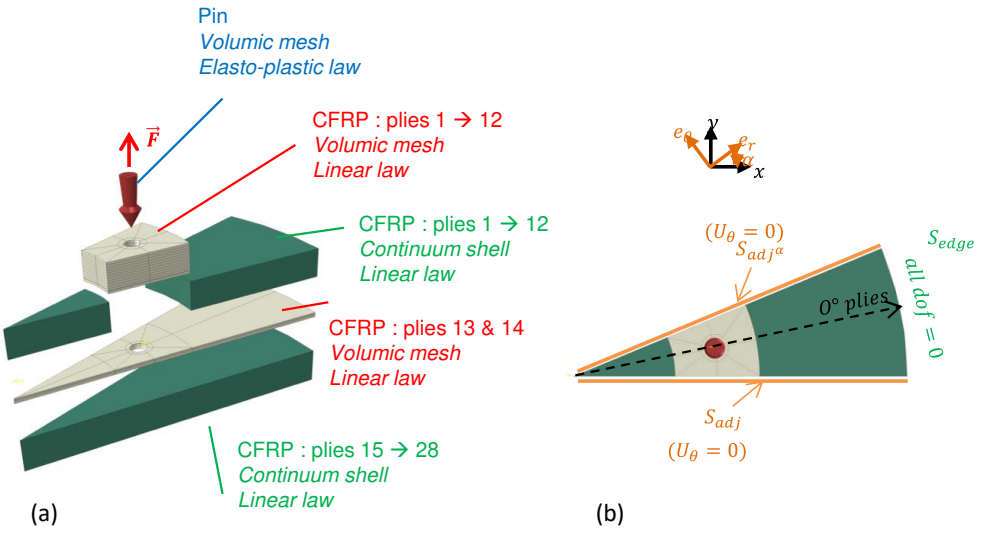

Figure 6. (a) Unit cell definition, (b) Boundary conditions

5. Implementation of design tools

In order to analyze the impact of the radius R of the ring and the number of pins N_P, a parametric analysis is carried out. Three radius R are considered (8.42, 10.42 and 11.92), and the number of pins N_p are increasingly implemented on each radius. To perform such study, unit cells are automatically generated by scripting (using the language PYTHON compatible with the commercial software Abaqus). The number of pins modelled is driven by the angular opening of the unit cell. Figure 7(a) displays the first failure load F_1 obtained for each configuration tested. The trend of the response is similar independently of the radius R. For a small number of pin, the failure occurs by plasticity of the pins. When the number of pins increases, the failure switches to a delamination failure. Indeed, the pins are close enough from each other to generate an interaction between the delamination initiated around each pin. For the same number of pins, raising the radius will spread the pins (raising the pitch). Thus the increase of the radius R tends to postpone the transition between the two failure modes as the interaction appears for a larger number of pins. After the transition to a delamination failure mode, increasing the number of pins N_p decreases the failure load F_1.

The curves introduced in the Figure 7(a) are attached to specific configurations (discrete values of radius and numbers of pins). It would be convenient to get a unique curve available to predict the failure load and failure mode in a one ring configuration (i.e. the coupling existing between the radius R and the number of pins N_p has to be removed). To do so, two parameters are introduced: the pin density ρ and the dimensionless load Δ. The pin density ρ represents the filling rate of the pins in the ring containing them. It is defined as the ratio between the sum of the surface of the pin at the maximal section and the surface of the ring, as expressed in the relation (1). The dimensionless load Δ is defined in the relation (2) and represents the ratio of the failure load F_1 and the strength of the ring if it would be made of bulk TA6V.

$$\rho = \frac{\sum_0^{N_p} S_{pin}}{S_{ring}} \quad (1)$$

$$\Delta = \frac{F_1}{\sigma_{TA6V} S_{ring}} \quad (2)$$

Where σ_{TA6V} is the strength of the TA6V.

Figure 7(b) displays the dimensionless curves obtained of the three radiuses R. It appears that the responses are identical. This approach reduces the analysis of a one ring configuration to a single parameter: the pin density ρ. A small density (ρ < 0.18) generates a pin failure. Whereas a high density (ρ > 0.18) leads to a delamination failure. An optimal configuration to maximize the failure load seems to appear for a density of 0.23 with a delamination failure.

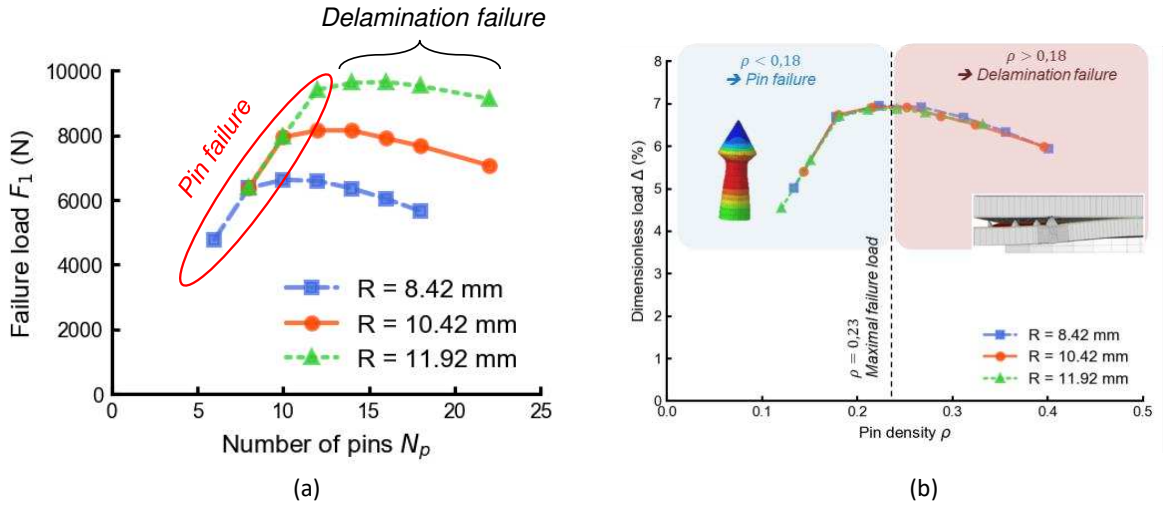

Figure 7. (a) Failure map for a one ring configuration

(b) Dimensionless failure map for a one ring configuration

6. Conclusion

This study aimed to propose a methodology for the implementation of a design tools. The requirement for this tool was to be fast of use, easily readable and able to predict the failure load and failure mode. First, tests were performed and two different damage scenarios were identified depending of the number of pins: pin failure or delamination failure. A reference model was thus implemented with an elasto-plastic behavior law for the pin and using cohesive zone modeling to represent the initiation and propagation of the delamination. A unit cell was defined by using the symmetric planes of the reference model to limit the time required to run each simulation. This unit cell has been validated by confronting the results obtained with the reference model. Finally, a parametric analysis was performed using the unit cell. A unique curve has been established to predict the load failure and the failure mode depending of the number of pins. Two dimensionless parameters had to be introduced: pin density and dimensionless strength. The results obtained allow the identification of the optimal number of pin to maximize the load failure.

  doi:10.5075/epfl-298799_978-2-9701614-0-0

In future work, scatter of experimental results can be taken into account in the tool. The delamination failure shows higher failure load than pin failure. However the high dispersion observed penalizes the confidence and will tend to apply design rules to ensure a failure by pin failure. A confidence interval could be introduced and then implemented inside the model (by degrading the interface properties for instance). Finally the present methodology should be extended to more complex cases (two rings of pins). The presence of a second ring will introduced new damage scenario possible as the interaction between the delamination will be able to occur not only inside the same ring, but also between each ring.

7. References

1. Hart-Smith, L.J. Bolted joints in graphite-epoxy composites. s.l. : NASA Contractor Report, 1973.
2. Camanho, P.P. et Matthews, F.L. A progressive damage model for mechnanically fastened joints in composite laminates. 1999, J. Compos. Mater., Vol. 33, pp. 2248-2280.
3. Gohorianu, G. Interaction entre les défauts d'usinage et la tenue en matage d'assemblages boulonnés en carbone/époxy. s.l. : Thèse de doctorat, Université de Toulouse III, 2008.
4. Persson, E., Eriksso, I. et Zackrisson, L. Effects of the hole machining defects on strength and fatigue life of composite laminates. 1997, Compos. Part Appl. Sci. Manuf., Vol. 28, pp. 141-151.
5. Surcin, L. Contribution à l'étude théorique et expérimentale du perçage de plaques composites minces. s.l. : Thèse de doctorat, Université Paul Sabatier, Toulouse III, 2005.
6. Caccese, V., et al. Influence of stress relaxation on clamp-up force in hybrid composite-to-metal bolted joints. 2009, Compos. Struct., Vol. 89, pp. 285-293.
7. Bianchi, F. Numerical modelling of through-thickness reinforced structural joints. s.l. : PhD Thesis, Cranfield University, 2012.
8. Ucsnik, S., et al. Experimental investigation of a novel hybrid metal-composite joining technology. 2010, Compos. Part Appl. Sci. Manuf., Vol. 41, pp. 369-374.
9. Buxton, A.L. et Dance, B.G.I.Surfi-Scult - Revolutionary surface processing with an electron beam. 2005. ASM International, ISEC Congress.
10. Dance, B.G.I et Kellar, J.C. Workpiece structure modification. International patent publication 2004028731 A1 2004.
11. Dance, B.GI. et Buxton, A.L. An introduction to Surfi-Scult technology - new opportunities, new challenges. 2007. 7th International Conference on Beam Technology.
12. Guild, F.J. COMELD joints: A novel technique for bonding composites and metal. 2017. ICCM.
13. Parkes, P. Metal-composite joining using hybrid penetrative reinforcement. s.l. : PhD Thesis, University of Bath, 2014.
14. Nguyen, A.T.T. Nature inspired aerospace Hybrid structural joint concepts realised by additive manufaturing. s.l. : PhD Thesis, RMIT University, 2018.
15. Meyer, J., Johns, D. Hybrid component. International number patent WO2010/112904A1 2010.
16. Parkes, P., et al. Static strength of metal-composite joints with penetrative reinforcement. 2014, Compos. Struct., Vol. 118, pp. 250-256.
17. Van Der Sypt, P. Analyse et modélisation des chemins d'effort et de la dégradation des liaisons de type "HYPER joints". s.l. : Thèse de doctorat. Université de Bordeaux, 2020.
18. Turon, A., et al. An engineering solution for mesh size effects in the simulation of delamination using cohesive zone models. 10, 2007, Eng. Frac. Mech., Vol. 74, pp. 1665-1682.

A NOVEL PROFILING CONCEPT LEADING TO A SIGNIFICANT INCREASE IN THE MECHANICAL PERFORMANCE OF METAL TO COMPOSITE JOINTS

Adam Whitehouse[a], Victor Medeau[a], Lorenzo Mencattelli[a], Bamber Blackman[b], Emile Greenhalgh[a], Silvestre Pinho[a]

a: Department of Aeronautics, Imperial College London, UK – adw15@ic.ac.uk
b: Department of Mechanical Engineering, Imperial College London, UK

Abstract: *In this work, we designed metal-CFRP joints with a profiled adherend termination to improve the mechanical performance. We have applied several profiles to the edge of titanium adherends which were adhesively bonded to CFRP substrates. We conducted finite element modelling and experimental 4PB (4-Point-Bend) testing to investigate how the geometry of the adherend edge profile effects the mechanical performance of the joint. This work shows that profiling of the metal adherend can result in increases of at least 27% in the peak load, and of at least 272% in the energy dissipated up to critical failure normalised by the mechanical energy.*

Keywords: Adhesive-Bonded Joints; CFRP; Joint Design; Stress Concentration; Erosion Shields

1. Introduction

Industry has increasingly made use of composite laminates [1] and consequently, designs include more interfaces between metal and composite components. Adhesive bonding provides a high joining strength and improved stress distributions relative to traditional mechanical joining methods [2]; however the discontinuity in stiffness at the joint edge means a stress concentration is still present, with higher stresses found along the edge of the joint [3].

Solutions to improve the performance of adhesive joints with composite adherends have been investigated in the literature [4]. The focus is predominantly on axial loading of the joints; however bonded joints may also be subjected to transverse loading. Bird strikes to laminate blades with adhesively bonded metallic erosion shields are one critical example.

In this work, we aim to improve the resistance to translaminar fracture of CFRP substrates with adhesively bonded metal adherends subjected to transverse loading as shown in Figure 1. To achieve this goal, we have taken the novel approach of systematically profiling the edge of the

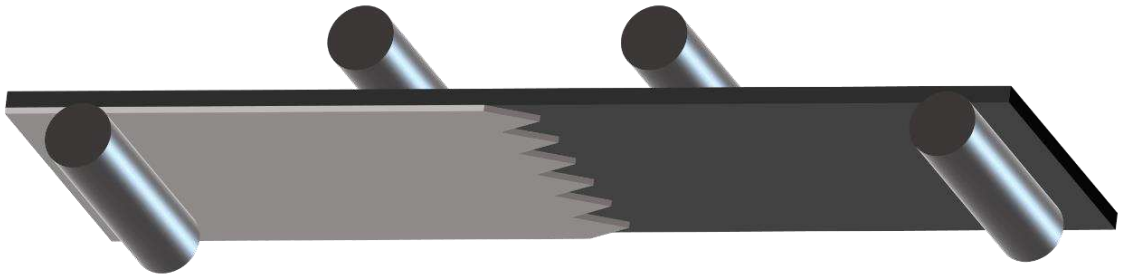

Figure 1. An example metal-CFRP 4PB test specimen with a profiled metal adherend.

  doi:10.5075/epfl-298799_978-2-9701614-0-0

metal adherend, in order to:

1. replace the discontinuous change in stiffness with a progressive change;
2. increase the effective length of the joint edge, hence increasing the load transfer area and reducing the stress concentration; and
3. deflect the straight translaminar fracture induced by a straight edge, thus increasing the energy dissipated during failure.

2. Finite Element Model

We developed a Finite Element (FE) model to guide the experimental study, as detailed further by Whitehouse et al. [5]. The model uses LaRC05 failure criteria [6, 7] to assess the propensity to failure of the laminate. We used the model to design a 4PB test coupon which would yield the failure mode of interest: laminate failure local to the bond edge for a straight edged specimen. We then modified the model to investigate the effect of the different adherend profiles. Figure 2 shows that profiling of the metal adherend effects the morphology of the failure indices within the laminate, resulting in isolation of the critically stressed areas.

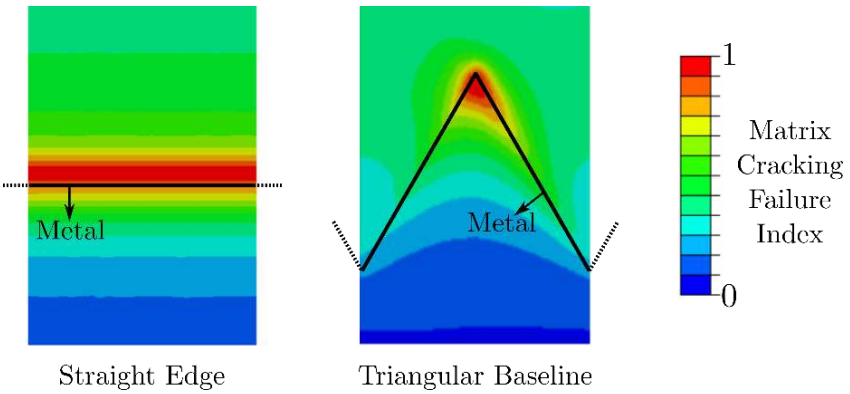

Figure 2. Matrix cracking failure index in a sub-surface ply, directly below the metal termination, at the onset of damage.

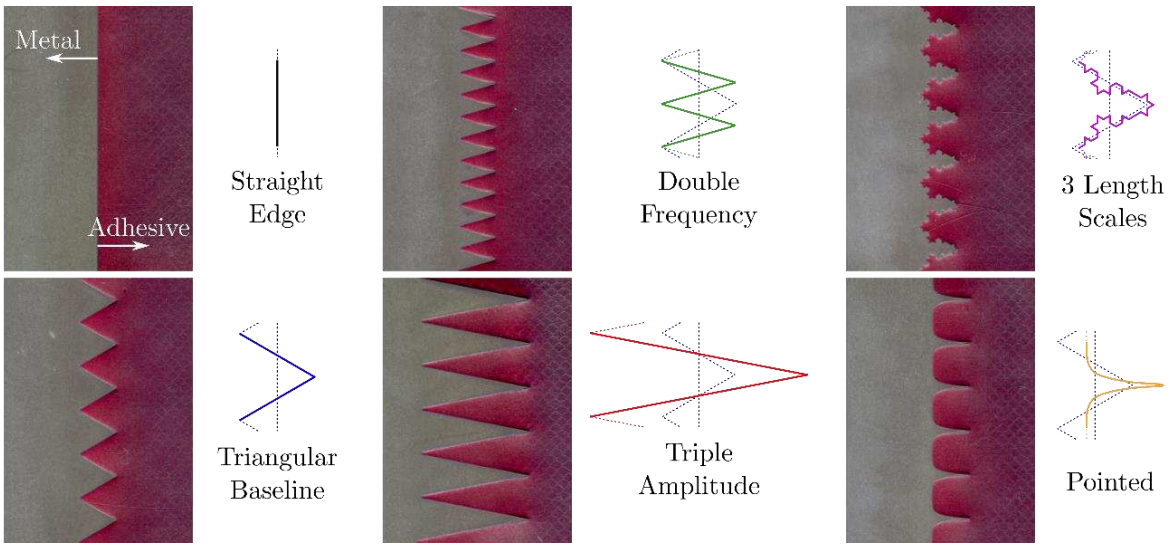

Figure 3. The profile patterns to be tested with their repeat units compared to the triangular baseline profile. The red film adhesive was extended beyond the edge of the metalwork such that a natural adhesive fillet formed at the profile edge.

  doi:10.5075/epfl-298799_978-2-9701614-0-0

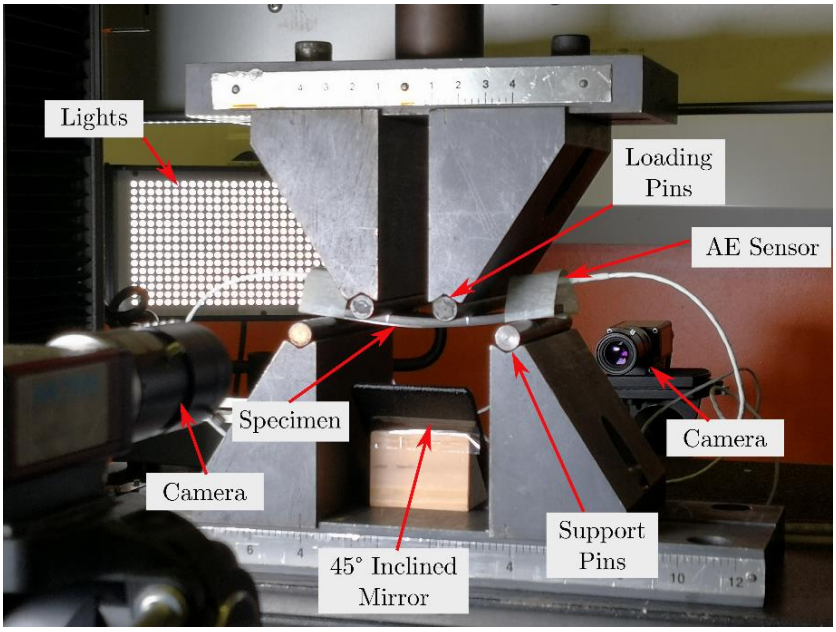

Figure 4. The experimental 4PB test set up.

3. Experimental Testing

3.1 Experimental Setting

In this work we vary the profile amplitude, profile frequency, number of length-scales, and profile geometry type, to investigate the effect of each on the mechanical performance of the adhesive joint. Figure 3 shows the different profiles considered. The test specimens are composed of a Titanium (TiAl6V4) adherend which has undergone a sodium hydroxide anodising surface treatment, and a IM7/8552 CFRP laminate substrate. They are adhesively bonded together using a AF163-2K film adhesive. We conducted quasi-static 4PB tests and used acoustic emission (AE) monitoring during the tests to assist with characterisation of failure modes via characteristic peak frequencies, as determined by Gutkin et al. [8]. The test set-up is displayed in Figure 4.

3.2 Results

A representative fracture surface for a straight edged specimen is shown in Figure 5a, whilst that of a triangular baseline profile specimen is shown in Figure 5b. Characteristic force versus displacement traces are shown in Figure 6 for each sample. Figure 7 displays the AE data

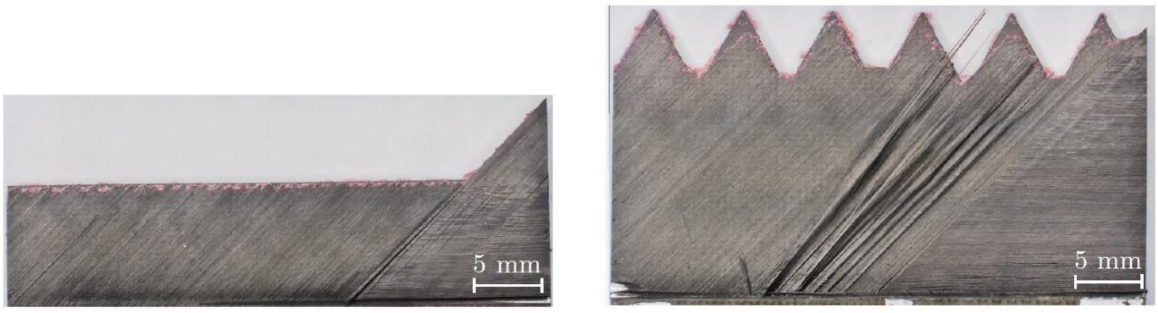

(a) Straight edged specimen (b) Triangular baseline specimen

Figure 5. Fracture surfaces on the underside of the titanium adherend.

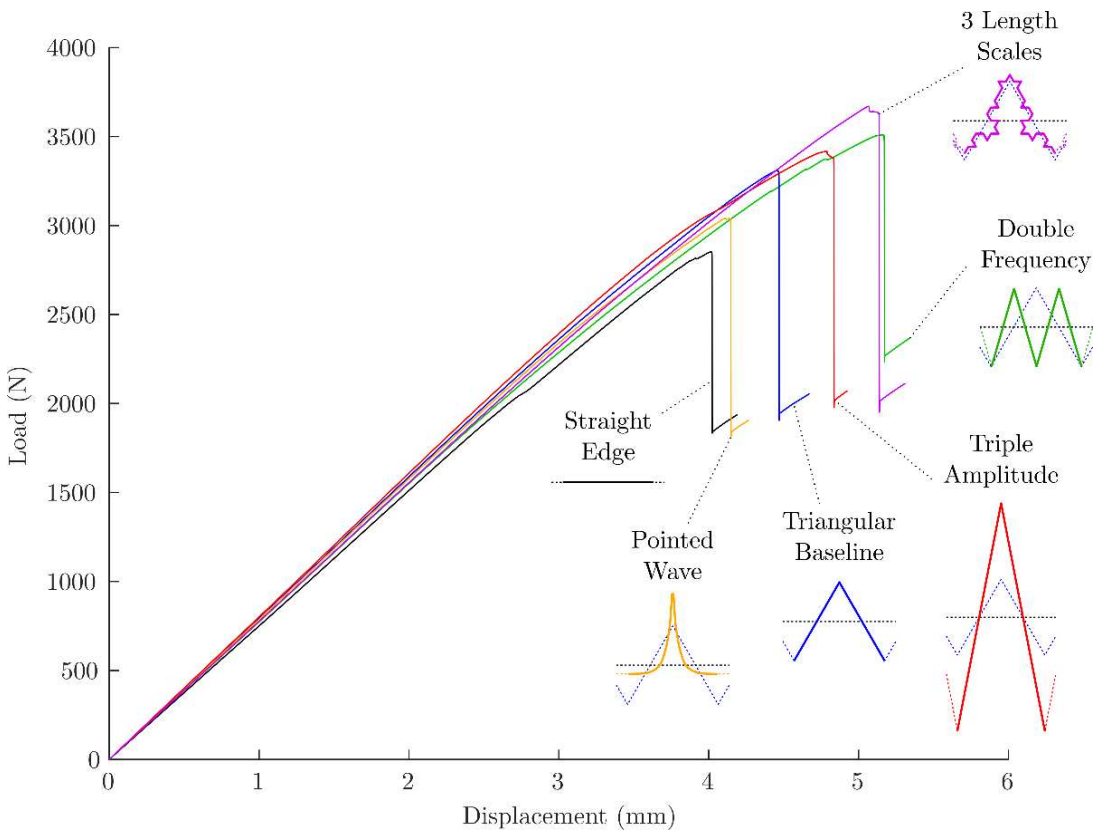

Figure 6. Representative load vs displacement traces for each sample.

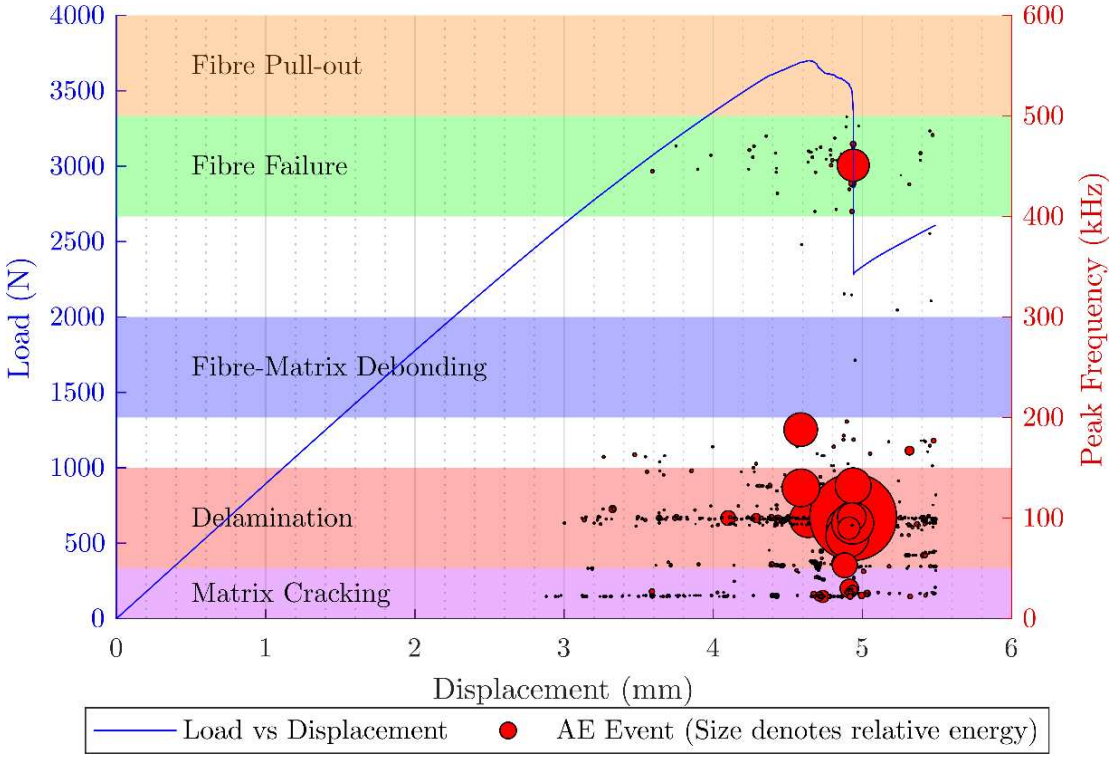

Figure 7. Force vs displacement and AE results of a double frequency specimen.

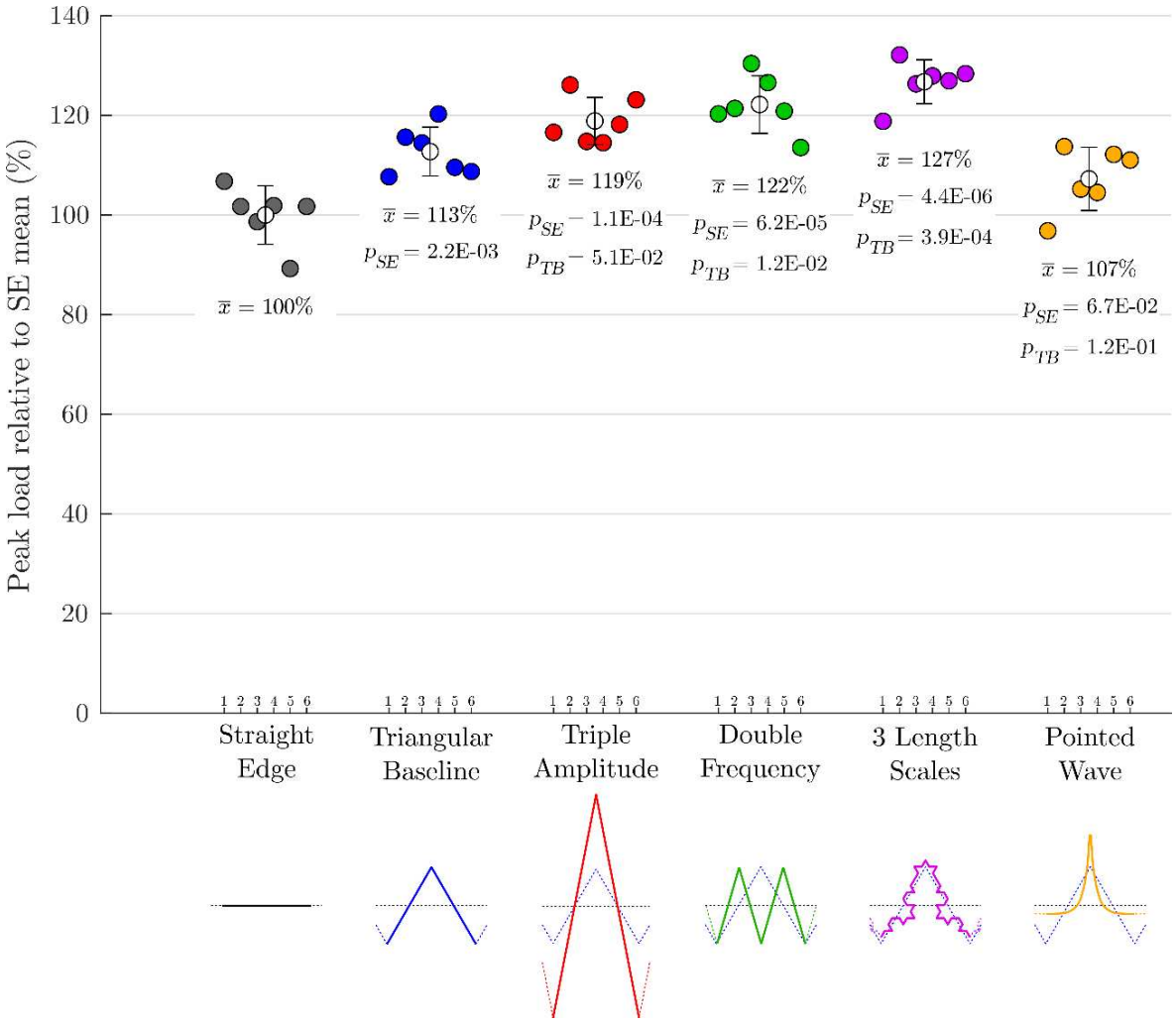

Figure 8. Peak load relative to a straight edged adherend. $\overline{x}$ indicates the sample mean, and p_{SE} & p_{TB} indicate the p-values compared to the straight edged and triangular baseline samples respectively.

overlaid on the loading trace for a double frequency profile specimen. The results for peak load, and dissipated energy normalised by the mechanical energy up to critical failure, are displayed in Figures 8 and 9 respectively. In order to judge the statistical significance of the results, the p-values have been calculated for each measure, relative to both the straight edge and triangular baseline samples, and are reported in Figures 8 and 9. A typical interpretation of p-values in the literature is that p ≤ 0.05 indicates statistically significant results.

4. Discussion

The specimens exhibited the failure mode of interest, translaminar fracture in the laminate local to the adherend termination, as shown in Figure 5. The acoustic emission results, such as that seen in Figure 7, suggest matrix cracking and delamination are the initial modes of failure, whilst fibre failure begins to occur later. The fracture surfaces in Figure 5 show, in support of the AE data, that failure occurred in the laminate with interlaminar, intralaminar and translaminar failure modes all present. The fracture surface in Figure 5b shows that the translaminar fracture of the 45° ply is seen to be deflected away from being a straight fracture in the profiled specimen.

  doi:10.5075/epfl-298799_978-2-9701614-0-0

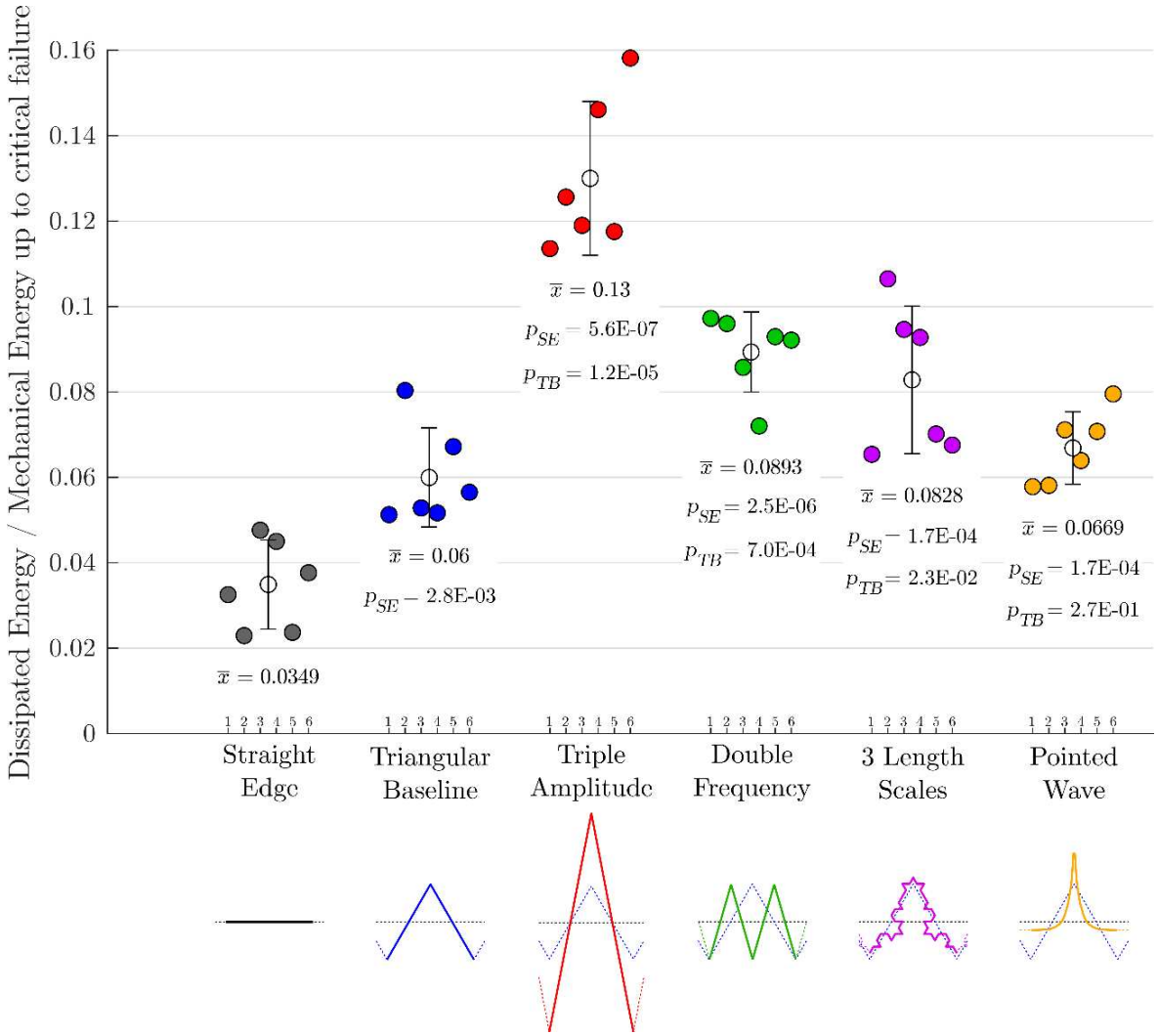

Figure 9. The ratio of dissipated energy to mechanical energy up to the critical failure. $\overline{x}$ indicates the sample mean, and p_{SE} & p_{TB} indicate the p-values compared to the straight edged and triangular baseline samples respectively.

Profiling of the adherend led to significant increases in mechanical performance. In the current work, the best improvements achieved relative to the straight edged sample were: a 27.0% increase in peak load ($p = 4.4 \times 10^{-6}$) achieved using a 3-length-scale profile; and a 272% increase in the ratio of dissipated to mechanical energy up to the critical failure ($p = 5.6 \times 10^{-7}$) achieved using a triple amplitude profile.

Further improvements could in principle be obtained using this profiling technique. The triangular baseline sample gave increases relative to the straight edge sample of 12.7% ($p = 2.2 \times 10^{-3}$) in peak load and 71.8% ($p = 2.8 \times 10^{-3}$) in the ratio of dissipated to mechanical energy up to the critical failure. Increasing the amplitude, frequency, and number of length scales in the pattern were all shown to further improve the performance as shown in Figures 8 and 9. Relative to the triangular baseline sample: increasing the number of length-scales from 1 to 3 led to an increase in peak load of 12.4% ($p = 3.9 \times 10^{-4}$), and an increase in the ratio of dissipated to mechanical energy up to the critical failure of 38.1% ($p = 2.3 \times 10^{-2}$); doubling the frequency of the profile led to an increase in peak load of 8.38% ($p = 1.2 \times 10^{-2}$), and an increase in the ratio of dissipated to mechanical energy up to the critical failure of 49.0% ($p = 7.0 \times 10^{-4}$); and tripling

  doi:10.5075/epfl-298799_978-2-9701614-0-0

the amplitude of the profile led to an increase in peak load of 5.46% ($p = 5.1 \times 10^{-2}$) which was only of marginal statistical significance, but it led to a highly significant increase in the ratio of dissipated to mechanical energy up to the critical failure of 117% ($p = 1.2 \times 10^{-5}$).

The alternative geometry profile, the 'pointed wave', was less successful than the other profiles tested. It showed an increase of 7.25% ($p = 6.7 \times 10^{-2}$) in peak load relative to the straight edged sample which was only marginally statistically significant, and an increase lower than for the triangular baseline profile sample. The pointed wave profile showed an increase in the ratio of dissipated to mechanical energy up to the critical failure of 91.6% ($p = 1.7 \times 10^{-4}$) relative to the straight edged sample, but when compared to the triangular baseline sample the increase of 11.5% ($p = 2.7 \times 10^{-1}$) was statistically insignificant.

5. Conclusions

This paper shows the effects of applying a profiled termination to the metal adherend of a metal-CFRP adhesive joint. Our results show that using a suitably defined pattern:

- the peak load can increase by at least 27.0%; and
- the energy dissipated up to critical failure normalised by the mechanical energy can increase by at least 272%.

The work also shows that this technique may be utilised to obtain further improvements by:

- increasing the profile amplitude (in our tests, tripling the amplitude resulted in a peak load increase of 5.46% and an increase of the energy dissipated up to critical failure normalised by the mechanical energy of 117%);
- increasing the profile frequency (in our tests, doubling the frequency resulted in a peak load increase of 8.38% and an increase of the energy dissipated up to critical failure normalised by the mechanical energy of 49.0%); and
- increasing the number of length scales (in our tests, incorporating 3 length-scales into the profile, rather than 1, resulted in a peak load increase of 12.4% and an increase of the energy dissipated up to critical failure normalised by the mechanical energy of 38.1%).

Acknowledgements

The authors would like to acknowledge the funding for this work from EPSRC DTP 2020-2021, grant reference no. EP/T51780X/1. The authors thank James Finlayson from Rolls-Royce for the helpful discussions on this work.

6. References

1. C Red. Advanced composites usage transitioning from market penetration to organic growth. In 4th Annual Aerospace Raw Materials & Manufacturers Supply Chain Conference, 2014.
2. A J Kinloch, C F Korenberg, K T Tan, and J F Watts. The durability of structural adhesive joints. Applied Science Publication: London, UK, 1983.

3. LJ Hart-Smith. Adhesive-bonded single-lap joints. Technical Report No. NASA-CR-112236, 1973.
4. X. Shang, E. A.S. Marques, J. J.M. Machado, R. J.C. Carbas, D. Jiang, and L. F.M. da Silva. Review on techniques to improve the strength of adhesive joints with composite adherends. Composites Part B: Engineering, 177:107363, 11 2019.
5. Adam Whitehouse, Victor Medeau, Lorenzo Mencattelli, Bamber Blackman, Emile Greenhalgh, and Silvestre Pinho. To Be Submitted. 2022.
6. ST Pinho, R Darvizeh, P Robinson, C Schuecker, and PP Camanho. Material and structural response of polymer-matrix fibre-reinforced composites. Journal of Composite Materials, 46(19-20):2313–2341, 9 2012.
7. ST Pinho, GM Vyas, and P Robinson. Material and structural response of polymer-matrix fibre-reinforced composites: Part B. Journal of Composite Materials, 47(6-7):679–696, 3 2013.
8. R. Gutkin, C. J. Green, S. Vangrattanachai, S. T. Pinho, P. Robinson, and P. T. Curtis. On acoustic emission for failure investigation in CFRP: Pattern recognition and peak frequency analyses. Mechanical Systems and Signal Processing, 25(4):1393–1407, 5 2011.

NUMERICAL MODELLING OF INTERFACE TRACTIONS OF A TRI-MATERIAL SCARF JOINT

Alexander Fu-My Thai[a,b], Erik Lund[a], Esben Lindgaard[a,b], Brian Lau Verndal Bak[a,b]

a: Department of Materials and Production, Aalborg University, Denmark – afmt@mp.aau.dk
b: The CraCS Research Group (cracs.aau.dk)

Abstract: *This paper investigates the numerical modelling and analysis of interface tractions in a tri-material scarf joint. The modelling procedure of the Abaqus scarf joint model, which includes zero thickness interface elements is detailed. The model is used to perform a study of an overlaminated scarf joint consisting of a carbon fibre-reinforced polymer core and glass fibre-reinforced polymer skin. Interface tractions and damage along the scarf interface are evaluated to examine the fracture process.*

Keywords: Adhesive joints; Scarf joint; Finite element analysis; Cohesive zone modelling; Abaqus; Python

1. Introduction

Manufacturing of modern wind turbines (WT)s faces several challenges driven by the growing complexity due to the increase in size and exacerbated by the high demand for wind energy due to recent crises. Therefore, tremendous pressure is put on existing blade manufacturing factories to increase manufacturing output and meet market demands. Conversely, wind turbine blades (WTB)s continue to be the target of technological improvements through improvements to designs, materials and manufacturing methods. Current manufacturing trends aim to increase material layup speeds by introducing a more automated design philosophy for blade subcomponents and, conversely, reduce manual labour. These trends include using preforms [1] and pultruded fibre-reinforced polymers (FRP)s [2], which ease the production process and guarantee a higher quality composite. However, even with these steps taken, the manufacturing of WTBs remains a predominantly manual process and more needs to be done [3].

Therefore, a solution is to advance automation strategies to encompass WTB subcomponents such as the spar cap. The use of sequential cast fibre-reinforced polymer (SC-FRP) is one such strategy, where prefabricated FRP are first produced on dedicated production equipment and subsequently joined together in a one-shot curing process in the full WTB mould (Figure 1). This creates a unique adhesive joint, where the resin doubles as a matrix material for the dry fabric and as an adhesive between prefabs. These types of adhesive joints are very susceptible to delamination due to the brittleness of the matrix, which weakens its peel strength. One key aspect of designing such joints is therefore to minimize the peel loads and maximize the load transferred through shear [4]. In this context, a scarf joint is a highly efficient joint configuration that also preserves laminate continuity and is suitable for thick laminates such as the spar cap [5]. Several approaches have been applied to study the stress fields and predict scarf joint strength.

  doi:10.5075/epfl-298799_978-2-9701614-0-0

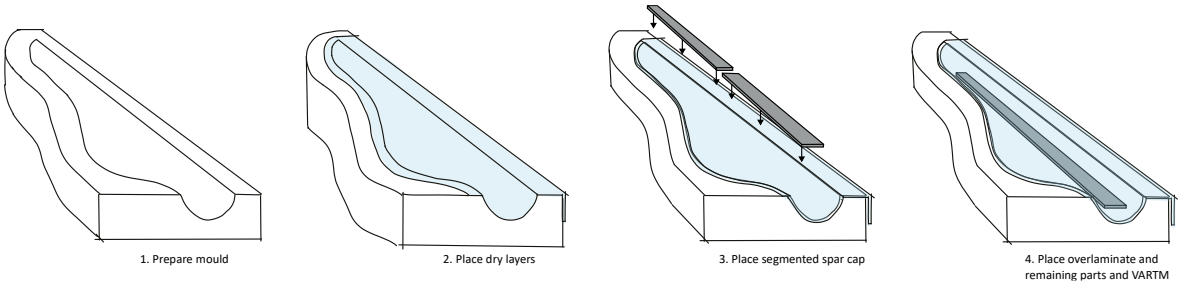

Figure 1. Sequential casting process applied to WTB spar cap.

Analytical solutions can be found in the works of [6–8]. However, increased complexity in layup, materials, and geometry means that numerical solutions such as the finite element method is more suited than analytical approaches. Several parametric studies on the scarf joint stress distribution have been conducted by [9–11] using finite element analysis. In recent decades cohesive zone modelling (CZM) has been employed to simulate the progressive damage evolution in [12–15]. Nonetheless, most of these studies have been limited to monolithic scarf joints and adhesives with finite thickness. The bi-and tri-material nature of spar cap laminate introduces severe stress concentrations, which become potential failure initiation points and addressing these weak points necessitates an accurate characterization of the stress distribution. Such a characterization is performed on a segmented spar cap of a WTB consisting of a pultruded carbon FRP core and glass FRP skin and joined by an overlaminated scarf joint.

In this work, a python script for Abaqus is built for the generation of the 3D-composite model of a scarf joint using solid elements combined with zero-thickness cohesive zone elements to capture non-linear behaviour. The model is parameterized with respect to geometrical, material and interface properties. An analysis of interface tractions for a simplified spar cap layup is carried out. These results are supplemented with damage development studies which aid the identification of critical points for damage initiation and damage evolution.

2. Methods

2.1 Cohesive Damage Model

A cohesive damage model formulation realized through cohesive interface elements have been adopted for the numerical work conducted within this paper. The constitutive response of the cohesive interface elements is based on a *bilinear traction-separation law* which is readily available in Abaqus [16]. The traction-separation law effectively describes the relation between the cohesive tractions, τ_i, and opening displacements, δ_i, and it is defined by the interfacial strength, $\tau_{o,i}$, the fracture toughness, G_{ic}, and an initial penalty stiffness, K_i for $(i = \mathrm{I}, \mathrm{II}, \mathrm{II})$. To complete the definition of the cohesive damage model, a quadratic stress criterion for damage initiation and a linear energetic criterion for crack propagation are established. The quadratic stress criterion is defined as follows:

$$\left(\frac{\langle \tau_I \rangle}{\tau_{o,I}}\right)^2 + \left(\frac{\tau_{II}}{\tau_{o,II}}\right)^2 + \left(\frac{\tau_{III}}{\tau_{o,III}}\right)^2 = 1 \tag{1}$$

where $\langle \cdot \rangle$ denote the MacAuley brackets. The propagation criterion is defined accordingly as:

$$\frac{G_I}{G_{IC}} + \frac{G_{II}}{G_{IIc}} + \frac{G_{III}}{G_{IIIc}} \geq 1 \quad (2)$$

The parameters used in the model are listed in the Table 1 and have been chosen so that the cohesive law is isotropic. This is done to simplify the analysis conducted in this study and limit the effects of mode mixity.

Table 1 : Quasi-static interface properties for numerical studies. Values are estimated from [17,18].

Interface properties		
$G_{Ic} = G_{IIc} = G_{IIIc}$	0.30	$[\mathrm{N/mm}]$
$\tau_{o,I} = \tau_{o,II} = \tau_{o,III}$	60	$[\mathrm{MPa}]$
$K_I = K_{II} = K_{III}$	6E5	$[\mathrm{N/mm^3}]$

2.2 Finite Element Model

The numerical tool that underpins the analysis is a user-written Python code which generates the full 3-D finite element model in Abaqus. This script is coded with the intent of performing parametric studies and many aspects of the model have therefore been parametrized. An outline of the code architecture is highlighted in Figure 2 to illustrate the capabilities of the script. The model is created by connecting several 3-D parts, where each part is parameterized with respect to geometrical and material parameters. Ultimately, this forms a model with the boundary conditions illustrated in Figure 3. Notably, surface-to-surface tie constraints are used to connect the cohesive elements to surrounding parts to allow for arbitrary refinement of the cohesive mesh and the use of both quadratic and linear elements in the bulk mesh. The overall meshing procedure follows a strict and structured mesh pattern and makes use of both wedge and hexahedral elements as showcased in Figure 4. Like other aspects of the model, the meshing procedure has also been parameterized to facilitate local refinement near the scarf region. For the purpose of this analysis, quadratic hexahedral (C3D20) and quadratic wedge (C3D15) are

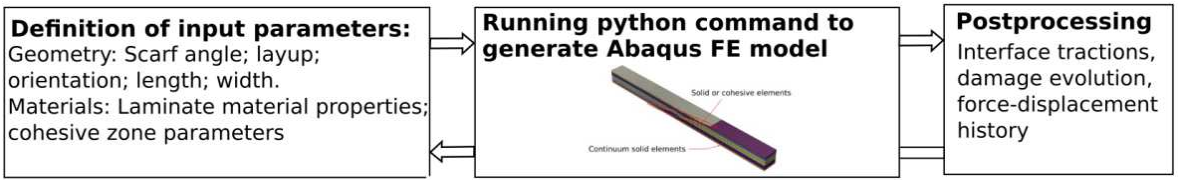

Figure 2. Flowchart of the code architecture.

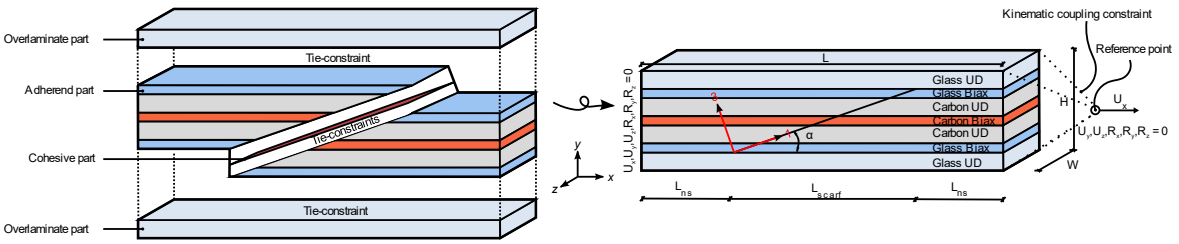

Figure 3. Elements of the model and model setup.

utilized in the bulk mesh to better capture the stresses near the scarf interface. This also necessitates the use of tie-constraints to connect the zero thickness cohesive elements (COH3D8) which are used to mesh the cohesive part. While the finite element model was made with the full 3-D spar cap in mind, the current model only has one element in the width direction. Doing this effectively creates a plane stress condition due to the model boundary conditions showcased in Figure 3. This was done to reduce computational time.

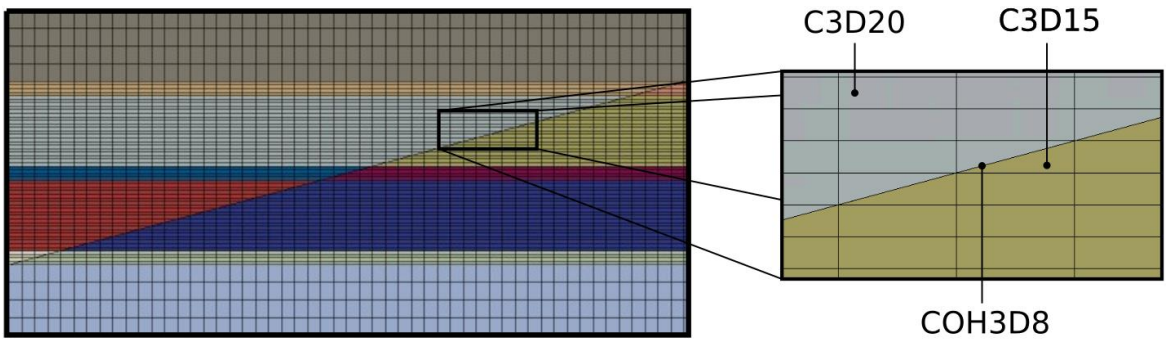

Figure 4. Mesh details near the scarf interface region.

Because of the complex material nonlinearity in the model, convergence issues are bound to be a problem. The analysis therefore utilizes automatic stabilization in Abaqus/Standard to aid convergence by applying damping forces to local regions that develop sudden instabilities. This is an alternative to applying viscous regularization of the cohesive zone damage variable often used together with cohesive zone interface elements. The latter is known to cause cohesive tractions to exceed the specified onset tractions, which may lead to traction oscillations.

3. Analysis and Results

The nonlinear geometrical analysis is carried out using the scarf joint dimensions as listed in Table 2, while the laminate layup is illustrated in Figure 3. Material parameters of the plies are omitted for the sake of confidentiality. A displacement of $U_x = 0.3\ [\mathrm{mm}]$ is applied to the reference point, which is connected to the rest of the model through a coupling constraint. The force-displacement history can then be extracted from this point and the maximum load P_{max} is recorded. Interface tractions, τ_{33}, τ_{31}, and the scalar stiffness degrading damage variable, $SDEG$, are sampled at the integration points of the cohesive elements.

Table 2 : Joint dimensions

Length: $L = 148.5\ [\mathrm{mm}]$	Glass UD thickness: $5\ [\mathrm{mm}]$
Non-scarf region length: $L_{ns} = 50\ [\mathrm{mm}]$	Carbon UD thickness: $5\ [\mathrm{mm}]$
Width: $W = 5\ [\mathrm{mm}]$	Carbon biax thickness: $1\ [\mathrm{mm}]$
Scarf angle: $\alpha = 15°$	Glass biax thickness: $1\ [\mathrm{mm}]$

  doi:10.5075/epfl-298799_978-2-9701614-0-0

3.1 Mesh Refinement Study

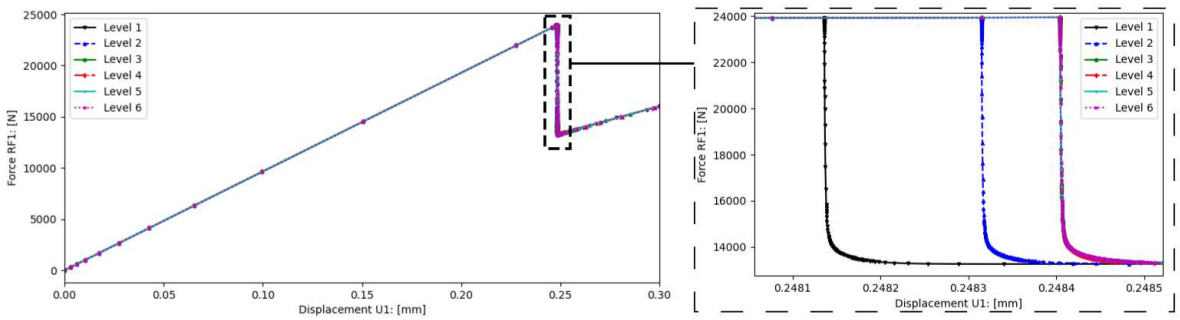

Figure 5. Mesh convergence study of the force-displacement response.

It is well known that modelling with cohesive zone interface elements often requires a very fine mesh resolution to resolve the damage process zone. A small mesh refinement study is therefore conducted to ensure that the studied quantities are mesh independent. Six levels of refinement are used following the mesh settings presented in Table 3, where the cohesive element lengths and corresponding relative errors are listed. Two cohesive elements are used per solid element in the bulk mesh, and the bulk mesh is also refined accordingly to maintain this relationship. The relative error is computed by Eq. 3 to obtain an error estimate over the interface, and it is sampled at a fixed specific time step to obtain a one-to-one comparison between individual refinement steps. The fixed time step is chosen such that damage has been initiated in all levels of refinement. Furthermore, due to the varying number of integration points between each refinement step, a linear re-interpolation has been applied to obtain a consistent number of sampling points and thereby vectors of same size. Most of the studied quantities, $P_{max}, \tau_{33}, \tau_{31}$ converge for the selected mesh parameters with variations below 1%. However, SDEG does not achieve this (Table 3). Further refinement of the mesh seemingly minimizes SDEG and confines it to a smaller area of the interface. This causes the relative error norm to remain very high for the chosen time step, since damage has not yet spread to other areas of the interface. The delay in damage between each refinement level is suspected to stem from the automatic stabilization, because a small amount of strain energy is dissipated.

$$(relative\ error\ norm) = \frac{||\boldsymbol{x}_6 - \boldsymbol{x}_i||}{||\boldsymbol{x}_6||}, (i = 1, \dots, 5) \tag{3}$$

Table 3 : Mesh refinement study of maximum load, interface tractions, and scalar stiffness degrading damage variable. All values are sampled at fixed time step, $t = 0.828$, for all mesh.

Refinement Level	Cohesive element length	Max. load P_{max}	Relative error in τ_{33}	Relative error in τ_{31}	Relative error in $SDEG$
	[mm]	$[N]$	$[-]$	$[-]$	$[-]$
1	0.4829	23928.46	1	1	386.367
2	0.2415	23945.64	0.999948	1.00004	386.361
3	0.1610	23954.17	0.020123	0.018948	4.14236
4	0.1207	23954.14	0.011692	0.010863	2.33751
5	0.0966	23954.15	0.005396	0.005098	0.99046
6	0.0805	23954.13	-	-	-

3.3 Interface Tractions and Damage Development

A stress analysis is performed on the scarf joint interface to study its distribution, identify the critical damage initiation points, and observe how the stress and damage develop. Figure 6 presents the results of these studies for three different stages of the analysis. Vertical lines are drawn to represent the ply division and serve as a visual aid for the reader. The first stage illustrates the linear elastic response of the scarf joint. Notably, significant transverse shear stresses develop across the interface, reaching a maximum value of 60 MPa corresponding to the specified onset traction. The significant difference in stiffness between the UD plies and the biax plies causes local stress concentrations at the ply transition regions. It is at these transition regions, damage also first initiates, as illustrated in the second stage. Once the damage has occurred, the tractions start to drop, and oscillations in the traction profiles are observed. These oscillations are likely attributed to numerical artefacts associated with automatic stabilization needed for convergence. Due to the presence of the outer biax layers and the overlaminates, damage suppression is observed at the scarf joint ends. Conversely, damage develops more quickly in the middle of the scarf interface. Full damage, therefore, occurs first in the middle region and propagates towards the biax layers as illustrated the final stage, where full damage has developed in some parts. While the results have been separated into three stages, it should be emphasized that the shift between the different stages occurs almost instantaneously once the model reaches the maximum load. This explosive crack growth stems from the low interface toughness of the scarf joint.

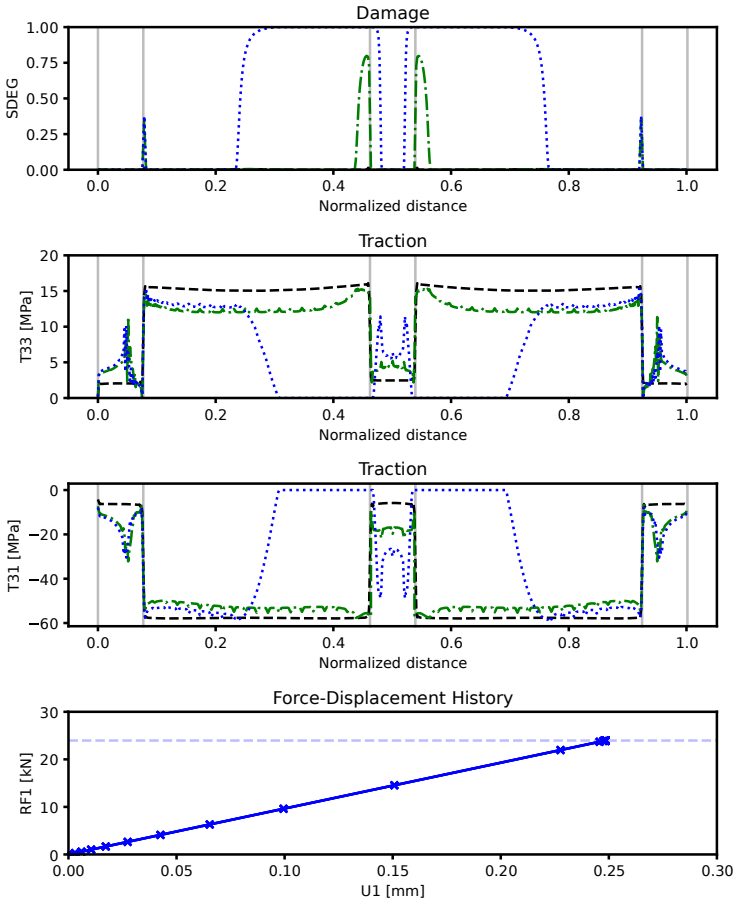

Figure 6. Evolution of tractions and damage in the scarf joint interface. Three stages of the analysis are showcased: No damage : — — —, Damage : — - -, More damage - - -.

4. Discussion and Concluding Remarks

The objective of this work is to analyze a sequentially casted tri-material scarf joint, with respect to interface tractions and damage development. Results from this study is part of on-going work which intends to improve SC-FRP adhesive joints. The manufacturing process yields interfaces with low toughness, which is reflected in the selected cohesive model parameters. In the stress analysis, large peak shear and peel stresses are observed due to the large stiffness change in the tri-material scarf joint. This causes damage to first occur in the UD ply interface close to the ply transition areas. As damage develops, it mostly remains confined within the connecting UD ply interface and the middle biax layer. This is due to the presence of the overlaminate which suppresses damage at the scarf joint ends. The low interface toughness causes interface failure to occur quite rapidly, and this leads to convergence difficulties in the Abaqus solver. Automatic stabilization is therefore needed in the current study. However, it is suspected that this also leads to observed oscillations in the traction profiles once damage has occurred. Future work therefore aims to rid the model of these inaccuracies.

Acknowledgements

This study was completed as part of the AIOLOS research project supported by the Innovation Fund Denmark, Grant no. 0224-00003A.

5. References

[1] Zangenberg J, Brøndsted P, Koefoed M. Design of a fibrous composite preform for wind turbine rotor blades. Mater Des 1980-2015 2014;56:635–41. https://doi.org/10.1016/j.matdes.2013.11.036.

[2] Wind blade spar caps: Pultruded to perfection? n.d. https://www.compositesworld.com/articles/wind-blade-spar-caps-pultruded-to-perfection (accessed April 10, 2022).

[3] Ohlendorf J, Richrath M, Franke J, Brink M, Thoben K. Towards automation of wind energy rotor blade production: a review of challenges and application examples 2020;6:173–90. https://doi.org/10.1080/20550340.2020.1838224.

[4] Hart-Smith LJ. Adhesively Bonded Joints in Aircraft Structures. In: da Silva LFM, Öchsner A, Adams RD, editors. Handb. Adhes. Technol., Berlin, Heidelberg: Springer; 2011, p. 1101–47. https://doi.org/10.1007/978-3-642-01169-6_44.

[5] Shang X, Marques EAS, Machado JJM, Carbas RJC, Jiang D, Silva LFM da. Review on techniques to improve the strength of adhesive joints with composite adherends. Compos Part B-Eng 2019;177:107363. https://doi.org/10.1016/j.compositesb.2019.107363.

[6] Hart-Smith LJ. Adhesive-bonded scarf and stepped-lap joints - NASA Technical Reports Server (NTRS) n.d. https://ntrs.nasa.gov/citations/19740005084 (accessed April 9, 2022).

[7] Mortensen F, Thomsen OT. Simplified linear and non-linear analysis of stepped and scarfed adhesive-bonded lap-joints between composite laminates. Compos Struct 1997;38:281–94. https://doi.org/10.1016/S0263-8223(97)00063-9.

[8] Gleich DM, Van Tooren MJL, De Haan PAJ. Shear and peel stress analysis of an adhesively bonded scarf joint. J Adhes Sci Technol 2000;14:879–93. https://doi.org/10.1163/156856100742942.

[9] Harman AB, Wang CH. Improved design methods for scarf repairs to highly strained composite aircraft structure. Compos Struct 2006;75:132–44. https://doi.org/10.1016/j.compstruct.2006.04.091.

[10] Gunnion AJ, Herszberg I. Parametric study of scarf joints in composite structures. Compos Struct 2006;75:364–76. https://doi.org/10.1016/j.compstruct.2006.04.053.
[11] Wang CH, Gunnion AJ. On the design methodology of scarf repairs to composite laminates. Compos Sci Technol 2008;68:35–46. https://doi.org/10.1016/j.compscitech.2007.05.045.
[12] Campilho RDSG, de Moura MFSF, Domingues JJMS. Stress and failure analyses of scarf repaired CFRP laminates using a cohesive damage model. J Adhes Sci Technol 2007;21:855–70. https://doi.org/10.1163/156856107781061477.
[13] Campilho RDSG, de Moura MFSF, Pinto AMG, Morais JJL, Domingues JJMS. Modelling the tensile fracture behaviour of CFRP scarf repairs. Compos Part B Eng 2009;40:149–57. https://doi.org/10.1016/j.compositesb.2008.10.008.
[14] Silva DFO, Campilho RDSG, Silva FJG, Carvalho UTF. Application a direct/cohesive zone method for the evaluation of scarf adhesive joints. Appl Adhes Sci 2018;6:13. https://doi.org/10.1186/s40563-018-0115-2.
[15] Sun L, Tie Y, Hou Y, Lu X, Li C. Prediction of failure behavior of adhesively bonded CFRP scarf joints using a cohesive zone model. Eng Fract Mech 2020;228:106897. https://doi.org/10.1016/j.engfracmech.2020.106897.
[16] Defining the constitutive response of cohesive elements using a traction-separation description n.d. https://abaqus-docs.mit.edu/2017/English/SIMACAEELMRefMap/simaelm-c-cohesivebehavior.htm (accessed April 12, 2022).
[17] Turon A, Costa J, Camanho PP, Dávila CG. Simulation of delamination in composites under high-cycle fatigue. Compos Part Appl Sci Manuf 2007;38:2270–82. https://doi.org/10.1016/j.compositesa.2006.11.009.
[18] Turon A, Davila CG, Camanho PP, Costa J. An engineering solution for mesh size effects in the simulation of delamination using cohesive zone models. Eng Fract Mech 2007. https://doi.org/10.1016/j.engfracmech.2006.08.025.

SERVICE STRENGTH ANALYSIS METHOD FOR ADHESIVELY BONDED HYBRID STRUCTURES UNDER MULTIAXIAL LOADING

Karsten Tittmann[a], Ilja Koch[a], Serkan Çavdar[b], Maik Gude[a], Gerson Meschut[b]

a: Institute of Lightweight Engineering and Polymer Technology (TUD-ILK), Technische Universität Dresden, Holbeinstraße 3, 01307 Dresden, Germany, karsten.tittmann@tu-dresden.de

b: Laboratory for Material and Joining Technology (LWF), Paderborn University, Pohlweg 47-49, 33098 Paderborn, Germany

Abstract: *Semi-structural adhesive joints with hyperelastic polyurethane adhesives and large adhesive layer thicknesses enable the realization of innovative hybrid lightweight designs with fiber reinforced plastic (FRP) composites. The design of these adhesively bonded joints with complex mechanical behavior requires a valid and efficient method for computational service life prediction. In this paper, a submodel-based service strength analysis method for adhesively bonded hybrid structures is presented and validated on sub component fatigue tests. The submodel strategy is generalized by periodic boundary conditions to evaluate failure relevant stresses and thus fatigue life in advance and independently from the global structure analysis.*

Keywords: hybrid adhesive joints; CFRP; service strength analysis; submodel-based method

1. Introduction

In the field of mobility, the hybrid design combining carbon fiber reinforced plastics (CFRP) and metals like aluminum (Al) offers favorable strength-to-weight ratios and thus reduction in energy consumption and CO_2 emissions. As a result, the joining technology gains importance and contrary requirements such as stiffness, strength, thermal expansion mismatch and reduction of stress concentrations are placed. In this context, hyperelastic adhesives with increased layer thickness show a unique performance with regards to manufacturing and structural integrity [1]. Efficient design of cyclically loaded bonded joints requires a valid and efficient method for service life prediction within the framework of the product development process. The complex mechanical behavior of hyperelastic adhesives and CFRP adherends as well as the need for compatibility with industrial modeling standards question the validity of existing fatigue life prediction concepts [2-3], which are mostly developed for structural adhesives.
In this contribution, a submodel-based service strength analysis method for adhesively bonded hybrid structures under multiaxial loading is presented and validated. After explaining the superordinate modeling strategy, the developed models are summarized. Later the submodel strategy with generalized periodic and kinematic boundary conditions is presented enabling the calculation of more realistic local stresses and strains compared to full structure level approaches (global model). In this study it is applied to the *Profile Sheet Specimen* and compared to different global models with varying modeling detail and to experimental results.

2. Theory

2.1 Submodel-based modeling strategy

To solve the challenges described above, a material- and practice-oriented method based on submodeling and homogenization techniques is developed that is compatible with existing

  doi:10.5075/epfl-298799_978-2-9701614-0-0

modeling standards for fatigue analysis of bonded vehicle structures. Central to this is a parameterized submodel with a high level of mesh refinement, which is generalized for selected types of bonded joints. Realistic local stress-strain fields are calculated for a large number of predefined boundary displacement combinations by applying suitable periodic boundary conditions (see 3.3.2) and using material models considering the hyperelastic deformation behavior of the adhesive. For fatigue life calculation, these stress states are evaluated separately using the fatigue life models developed by the authors for the CFRP [4, 5]) and for the adhesive [6, 7]. The selection of boundary displacement combinations (alternatively internal forces) to be analyzed is done by statistical design of experiments (DOE). A multidimensional load cycle dependent failure surface for arbitrary fatigue loads – boundary displacements – is generated from the precalculated fatigue lives using multivariate regression. The gained failure surface for the bonded joint can be used directly for the service strength analysis of different structures without having to refer to the submodels again. On the level of the full structure (e.g. car body) calculation, the boundary displacements at the bonded joints are calculated according to existing standards and evaluated against the load cycle dependent failure surface by linear damage accumulation.

2.2 Fatigue model CFRP – Unified Fatigue Model (UFM)

Numerous models have been developed previously for fatigue life prediction, mostly for constant amplitude loading [8-10]. However, the fiber composite joining partner in adhesively bonded hybrid structures is usually exposed to arbitrary fatigue loading with variable amplitudes and multiaxial stress states comprising significant out-of-plane stresses. For their reliable fatigue analysis, there are still significant challenges to be solved. The energy-based fatigue model used in this work overcomes some shortcomings of existing model approaches, such as the need of separated assumptions for constant life diagrams. As proposed in literature, the range of the elastic strain energy density (SED) ΔW is considered to be an adequate measure for describing the sensitivity of crack initiation to mean stresses in fiber composite materials [11-12]. By assuming linear elastic, ideally brittle material behavior and normalizing the actual SED to the SED at static failure the load cycle-dependent failure criterion can be derived as

$$\frac{\Delta\left(F^2\right)}{\Delta W^{\mathrm{c}}(N)} = 1. \tag{1}$$

Here, Δ denotes the range, F is the stress exposure and $W^{\mathrm{c}}(N)$ is the load cycle-dependent normalized critical strain energy density (SSED). The failure criterion is transferred to the unidirectional reinforced composite ply by assigning it to five fiber composite specific failure modes using an invariant formulation based on Cuntze [13]:

$$1 = \left(\frac{\Delta\left(\left(F^{\parallel\sigma}\right)^2\right)}{\Delta W^{c}_{\parallel\sigma}(N)}\right)^{\mathrm{m}} + \left(\frac{\Delta\left(\left(F^{\parallel\tau}\right)^2\right)}{\Delta W^{c}_{\parallel\tau}(N)}\right)^{\mathrm{m}} + \left(\frac{\Delta\left(\left(F^{\perp\sigma}\right)^2\right)}{\Delta W^{c}_{\perp\sigma}(N)}\right)^{\mathrm{m}} + \left(\frac{\Delta\left(\left(F^{\perp\tau}\right)^2\right)}{\Delta W^{c}_{\perp\tau}(N)}\right)^{\mathrm{m}} + \left(\frac{\Delta\left(\left(F^{\parallel\perp}\right)^2\right)}{\Delta W^{c}_{\parallel\perp}(N)}\right)^{m}. \tag{2}$$

In the achieved failure criteria in Eq. (2) $F^{\parallel\sigma}$, $F^{\parallel\tau}$, $F^{\perp\sigma}$, $F^{\parallel\perp}$ and $F^{\perp\tau}$ denote the five failure mode-specific exposures and m is the interaction coefficient which links probabilistically the failure-mode specific individual criteria. By solving Eq. (2), the fatigue life for arbitrary combinations of amplitudes and mean stresses can be determined for multiaxial cyclic loading situations triggering multiple interacting failure modes. More information on model features and validation are shown in [4]. Model calibration and application for the material considered in this study can be found in [5].

  doi:10.5075/epfl-298799_978-2-9701614-0-0

2.3 Fatigue model adhesive - Local Stress Concept (LSC)

The lifetime prediction of the adhesive layer under single-stage cyclic fatigue loading is based on the local maximum stress concept, which was empirically developed, verified and validated in [6, 7] based on experimental investigations using the considered adhesive system.

Based on load-controlled fatigue tests with so-called bonded basic test specimens, uniaxial tensile tests on the adhesive substance under quasi-static and cyclically increased loading (cf. section 3.1), the characteristic deformation behavior of the adhesive layer can be taken into account in the FE software Abaqus following [14] by a combination of the Marlow model [15] with a modified Ogden-Roxburgh model [16] and a Mises plasticity. The stress multiaxiality in the adhesive layer is considered with

$$\tau_{\mathrm{eq}} = \sqrt{J_2 + cI_1^2} \tag{3}$$

for $I_1 \geq 0$ under tensile stress by a combination of the second invariant of the stress deviator J_2 with the first invariant of the stress tensor I_1 using a hydrostatic weighting factor c. To avoid the influence of possible stress concentrations between adherends and adhesive, the evaluation is not carried out in the whole adhesive layer, but uniformly in the adhesive layer middle plane, cf. section 3.3.1. The comparison of the maximum equivalent upper stress with the master SN curve (identified based on fatigue tests under shear and tensile loading)

$$\tau_{\mathrm{eq.u}} = \tau_{\mathrm{u}}^{*}\, N^{-\frac{1}{k}} \tag{4}$$

with parameters $c_{\mathrm{i}} = 0.039$, $k_{\mathrm{i}} = 8.3$, $\tau_{\mathrm{u}}^{*} = 15.5\, MPa$ for crack initiation und $c_{\mathrm{f}} = 0.038$, $k_{\mathrm{i}} = 8.1$, $\tau_{\mathrm{u}}^{*} = 17.1\, MPa$ for failure leads to the predicted endurable load cycle N.

3. Materials and Methods

3.1 Materials

The investigations are performed on unidirectional prepreg material HexPly® M79/34%/UD300/CHS provided by Hexcel Corporation [17]. The *CFRP* sheet material is manufactured by an autoclave process and water cut in rectangular plates with dimensions 100 x 100 mm. A $[90/45/0/-45]_s$ layup is used and the mean thickness including peel plies is 2.31 mm. The fiber volume fraction is 58.8% for all plates. The quasi-static characterization of the in-plane and out-of-plane properties of the unidirectional single ply is described by the authors in [18]. Cyclic characterization including a summary of all tested static and cyclic properties is covered by the authors in [5].

Representative for a semi-structural *adhesive* bond with relevance for automotive applications, the present paper considers the visco-hyperelastic two-component polyurethane adhesive BETAFORCE™ 2850L [19] from DuPont de Nemours. Uniaxial tensile tests on the adhesive substance with tensile specimens (Fig. 1a) of type 1B according to [20], show a degressive nominal stress-strain curve under quasi-static loading until the tensile strength of 10.3 MPa is reached at a nominal strain of about 117 %. In true stresses and strains, on the other hand, an s-shaped curve results, which can be linearized in fatigue-relevant stress range of 2.8 MPa < σ_{n} < 6.75 MPa. Under cyclic load-increased loading, it can further be seen that the so-called Mullins effect [21] and a permanent set are superimposed on the hyperelasticity.

  doi:10.5075/epfl-298799_978-2-9701614-0-0

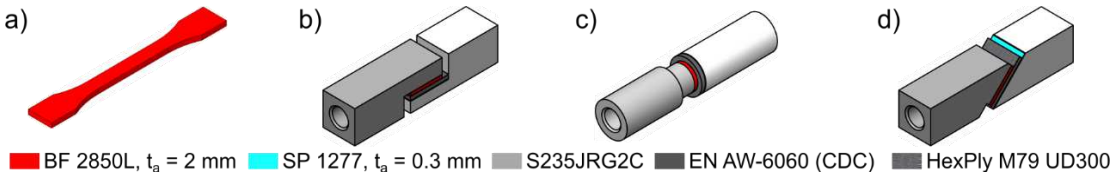

Figure 1: Basic adhesive test specimens, a) Tensile Test Specimen, b) Thick Adherend Shear Specimen, c) Butt Joint Specimen, d) Scarf Joint Specimen

Especially, load-controlled fatigue tests under pulsating tensile loading (load ratio R = 0.1 and load frequency f = 8 Hz) with Thick Adherend Shear, Butt Joint and Scarf Joint specimens made of aluminum and CFRP with an adhesive layer thickness of t_a = 2 mm (Fig. 1-d) are the basis of the master SN curve regarding adhesive failure and cracking described in section 2.3. In accordance with [6, 7], the cycles to crack initiation were identified inversely with an approximation of the amplitude compliance with a power approach.

3.2 Profile Sheet Specimen Test

In contrast to bonded specimens with stiff adherends, adhesively bonded sheet structures experience load-induced adherend deformation, which leads to inhomogeneous stress states in the adhesive layer. Thus, the component-like LWF Profile Sheet Specimen shown in Fig. 2b with adhesive layer thickness of t_a = 2 mm, overlapping length of l_o = 20 mm and an adhesive width of w_a = 100 mm is used.

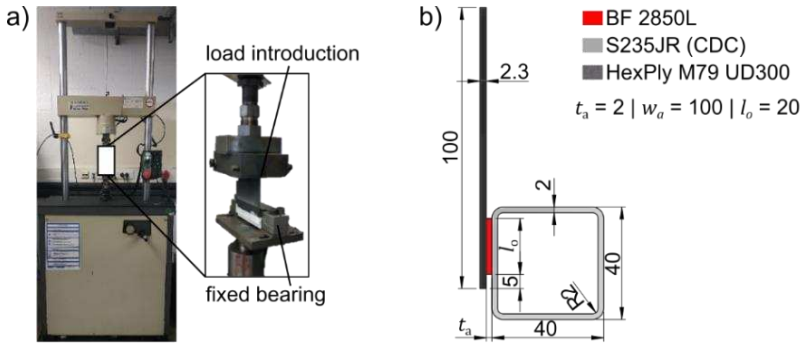

Figure 2 : Sub component tests, a) servo-hydraulic testing machine with specimen, b) geometry of LWF Profile Sheet Specimen

The load is applied via the CFRP sheet with a fixed bearing at the center of the square tube, that the adhesive layer is stressed shear dominated. The test results shown in Fig. 5 result from load-controlled fatigue tests under pulsating tensile loading (load ratio R = 0.1 and load frequency f = 8 Hz) on a servo-hydraulic testing machine (Schenk Hydropuls PSA, Fig. 2a) and, as shown representatively in Fig. 5, lead to a cohesive failure of the adhesive layer with intact adherend. More details and test results used here for concept validation are reported in [6].

3.3 Simulation

3.3.1 Global model for Profile Sheet Specimen

The FE modeling of the Profile Sheet Specimen is carried out with the FE software Abaqus following the common standards of the industry for the prediction of hybrid vehicle structures. The discretization of both adherends is done with fully integrated shell elements (type S4). The contact surfaces of the square tube to the steel insert is simulated with contact formulation (`*CONTACT; type=SURFACE TO SURFACE`). The insert is clamped with suppressed rotation

  doi:10.5075/epfl-298799_978-2-9701614-0-0

in accordance with the experimental condition. Load introduction by using kinematic couplings (*COUPLING_KINEMATIC) at a reference point is performed with suppressed rotation. The steel part is idealized with E = 210 GPa and ν = 0.3 linear elastic (*ELASTIC). The CFRP plate, idealized with shell elements, is defined with respect to the layer orientation using "Composite layup" and parameterized with the anisotropic material properties of the CFRP from [4, 18] using *COMPOSITE. The corresponding free length is 85 mm and the clamping length is 15 mm. For modeling of adhesive layer, three different approaches are followed and thus three different FE models are set up (cf. Fig. 4). The first modeling variant with one volume element (C3D20R) for the adhesive layer thickness and linear-elastic adhesive behavior corresponds to the current industrial standard (cf. Fig. 4 left). The young's modulus of the adhesive is assumed to be E_{lin} = 30 MPa. In the second variant (cf. Fig. 4, center), the nonlinear adhesive model presented in section 2.3 is used with one quadratic continuum element (C3D20R) for the adhesive layer thickness. Thus, it represents a suitable compromise between computational effort and modeling quality. The third variant exceeds the current standard in terms of mesh fineness and computation time. Thereby, nine elements (C3D8R) for the adhesive layer thickness are used in combination with the nonlinear adhesive description (cf. Fig 4, right). In all three variants, the adhesive layer is connected to the adherends with tied contacts (*TIE), which permits incompatible mesh size. The FE model is validated by comparing simulated force-displacement curves with quasi-static experiments in [6]. For the fatigue life prediction presented in the following, the upper forces from the fatigue tests resulting from the considered amplitude range 2.38 kN < F_{a} < 3.88 kN are used for the static simulation.

3.3.2 Generalized submodel

An essential part of the proposed method is the parameterized submodel, which is a representative narrow section of the linear bonded joint, cf. Fig. 3 upper left. In addition to requirements regarding compatibility for different material models and the efficient calculation for various load combinations, it is particularly important to ensure that the boundary conditions represent all relevant stresses in the adhesive joint. For this purpose, periodic boundary conditions are adapted for the boundaries with normal vectors in y-direction, as it known from the multiscale simulation with representative volume elements (RVE), cf. [22, 23]. The displacements of pairs of facing nodes (P_i^+, P_i^-) on the boundaries Γ^+ and Γ^- are linked by means of coupling equations. In doing so, displacement fluctuations $\Delta \mathrm{u}_{\mathrm{x,y,z}}$ are allowed, which are bound to the respective degree of freedom of the defined reference point RP_y:

$$\begin{pmatrix} u_x(P_i^+) - u_x(P_i^-) \\ u_y(P_i^+) - u_y(P_i^-) \\ u_z(P_i^+) - u_z(P_i^-) \end{pmatrix} = \begin{pmatrix} \Delta u_x(RP_y) \\ \Delta u_y(RP_y) \\ \Delta u_z(RP_y) \end{pmatrix}. \tag{5}$$

For loading the submodel, displacement boundary conditions are applied to the boundary faces of the joining partners (y-z plane). In order to represent the translational displacements and the rotations (corresponding to bending load), kinematic boundary conditions are used based on the Kirchhoff-Love plate theory [24]. Assuming that the cross-sections of the deformed plate remain flat, deformation kinematics are used to couple the nodal displacements on the submodel boundary face to the translations and rotations of a reference point (RP_1, RP_2, RP_3) defined on the mid-surface. The intersections to the joining partners are not placed directly at

the adhesive joints, but were spaced a small distance of one to three element edge lengths in order to exclude the overestimation of edge effects.

In order to ensure an efficient calculation of a large number of displacement combinations within the framework of the methodology and the FE software Abaqus, a Python script was developed for the automated creation of the coupling equations (here approx. 4200). In contrast to the global model, the adhesive as well as the CFRP is meshed with solid elements (C3D8I) using one element for each CFRP ply in order to represent occurring complex stress states with out-of-plane components as detailed as possible, see Fig. 3 bottom. Modeling of the adhesive is done identically to the fine global model described in sections 2.3 and 3.3.1, cf. V5 in Fig. 4. For the investigated Profile Sheet Specimen, a submodel width of 5 mm was shown to be adequate, resulting in a number of elements of 13848.

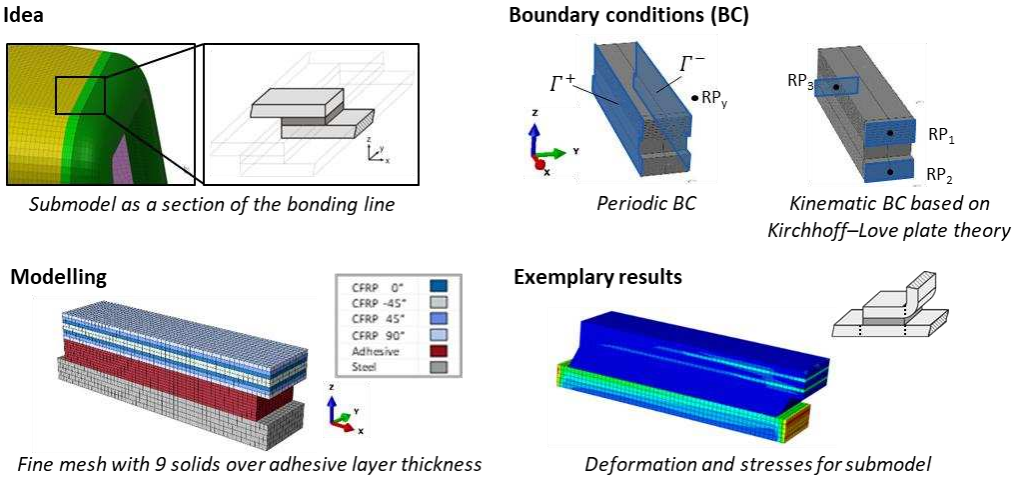

Figure 3. Submodeling approach

3.3.3 Simulation plan

Fatigue analysis of the LWF Profile Sheet Specimen is conducted with stresses gained from the generalized submodel as well from the global model and compared to experimental results for validation, see Fig. 4. Three different configurations of the global model with varying adhesive modeling are used, where the global model for V1/2 corresponds to the current standard in practice, the global model for V3/4 represents a good compromise between computational effort and modeling quality and the third model for V5/6 represents a significantly increased calculation effort compared to the current standard. See section 3.3.1 for more information. The CFRP plate is always modeled with shell elements following the industry standard.
The three global models are used to calculate and extract the stresses and displacements for five test load levels at different submodel positions. Here, the results for position 5 are presented exemplarily. For the standard variants V1, V3 and V5, the stresses are read directly from the global model (separately for CFRP and adhesive) and evaluated using the presented fatigue life models. Variants V2, V4 and V6 correspond to the novel proposed submodel based method, where the stress tensors for fatigue life evaluation are taken from the submodel. For this, the boundary deformations are extracted from the corresponding global model and, the stresses are read from pre-calculated and interpolated submodel results. For the fatigue life evaluation of the CFRP joining partner, the hot spot stress at the transition towards the bond line is used (integration point). Evaluation of the adhesive is carried out according to section 2.3 at the hot spot in the adhesive layer middle plane (centroid).

  doi:10.5075/epfl-298799_978-2-9701614-0-0

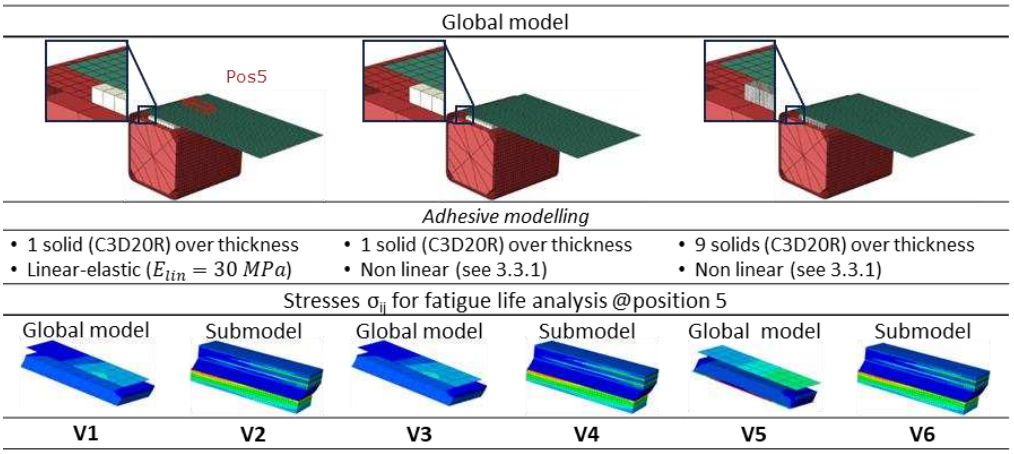

Figure 4. Simulation plan

4. Results

In Fig. 5, the predicted fatigue life of standard (top) and submodel-based variants (bottom) are compared to experimental results (gray). The fatigue life of the adhesive are marked in red and those for the CFRP in blue. The diagrams provide a good indication of the high utilization of the adhesive joint under cyclic loading.

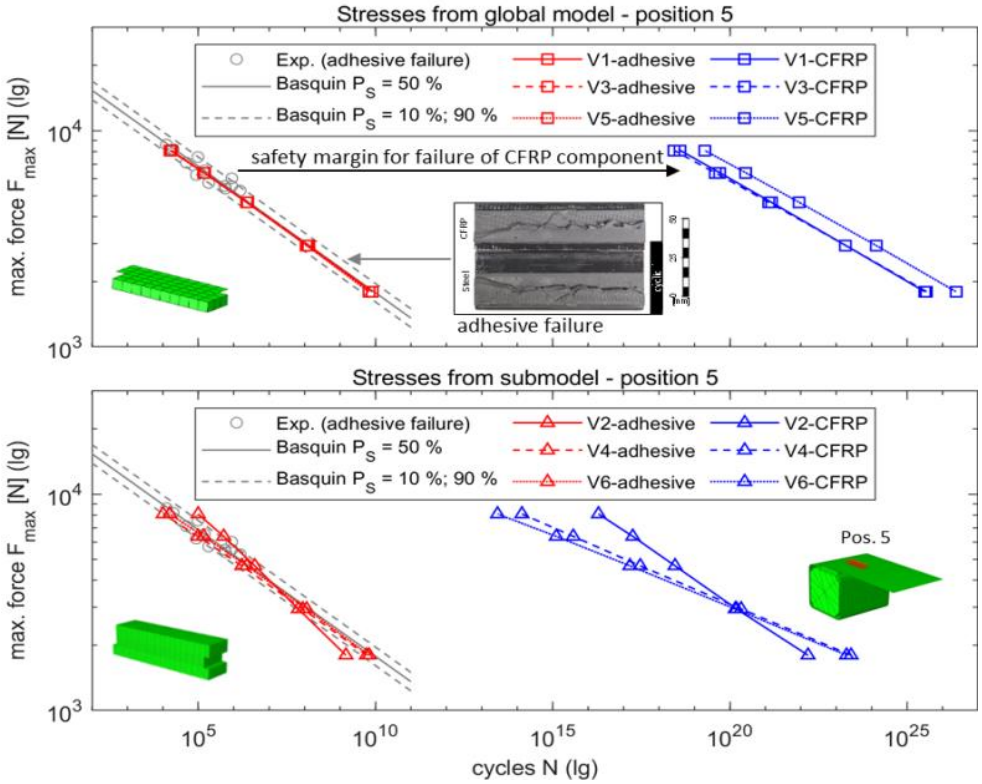

Figure 5. Fatigue prediction for pos. 5 based on stresses from global (top) and submodel (bottom)

Accordingly, only the failure of the adhesive layer is relevant for failure of the profiled sheet specimen. This is highlighted by the large safety margin for CFRP failure which is in good agreement with the experiments in which only adhesive failure was observed, cf. fracture pattern in Fig. 5. Comparably low stresses occur in the CFRP due to the loading situation, the low adhesive stiffness and the high adhesive layer thickness and width, leading to theoretical CFRP lifetimes in the range of 10^{13} to 10^{26} cycles.

  doi:10.5075/epfl-298799_978-2-9701614-0-0

The calculation results for the adhesive show - with the exception of V2 - very good agreement with the experimental results both for the standard calculation based on the stresses from the global model (V1, V3, V5) and based on the stresses calculated using the submodel (V4 and V6). The results are in the scatter band of the experiments. Here, even V1 with simple linear-elastic adhesive modeling gives satisfactory results, if correctly included during the calibration of the master SN curve, cf. [6, 7]. Only V2 leads to fatigue life predictions outside the scatter band and a deviating SN curve slope. This is caused by underestimated displacements due to the adhesive layer modeling with only one volume element and linear-elastic material behavior.
The comparison of the determined SN curves for CFRP failure shows that more conservative lifetime predictions result from the submodel (bottom) strategy than from the global model (top). Fine meshing of the CFRP with solid elements in submodel (V2, V4, V6) allows full and more detailed representation of the triaxial stress state, whereas the coarse shells of V1, V3, and V5 inherently represent only the in-plane stress components σ_1, σ_2 and τ_{12}. The UFM allows the evaluation of all components of the stress tensor through implemented interaction of all five CFRP-specifc failure modes [4, 5], resulting in more conservative predictions. However, it should be mentioned restrictively that a direct judgment of these results cannot be derived from the Profile Sheet Specimen experiments.

6. Conclusion

The presented fatigue life predictions of constant amplitude tests on Profile Sheet Specimen show very good agreement with the experimental results. The developed submodel and its generalized boundary conditions are suitable for efficiently calculating the complex triaxial stress and strain fields within hybrid hyper-elastic adhesive joints. This is particularly important for fatigue life prediction of the CFRP component, since its stress state is not sufficiently represented by the industry-standard modeling with coarse shell elements. The developed approach combines the advantages of both worlds, the detailed local stress state of the submodel and the fast calculation time of coarsely meshed full structures.
The used Unified Fatigue Model enables the material-specific and reliable fatigue life prediction of CFRP considering multiaxial stress states and mode interaction. Further it is shown that the Local Stress Concept is very well suited for reliable fatigue life prediction of hyper-elastic adhesives in semi structural joints. The calculated service life for the adhesive failure observed in the Profile Sheet Specimen experiment falls well within the experimental scatter band. The authors recommend the submodel-based analysis method V4 for service life prediction on level of full structure. It provides reliable predictions for both adhesive and CFRP failure, since triaxial stress states are calculated realistically for the adhesive layer and the adherends. Methods V1, V3, V5 are not recommended for hybrid adhesive joints since CFRP service life is systematically overestimated due to insufficient representation of three-dimensional stress states.
Future work will focus on further automatization of the presented method – e.g. fully automatic pre-calculation and regression of the load cycle dependent failure surface, automatized section-ing of the adhesive joint within the global model.

Acknowledgements

All shown results are taken from IGF research project 19187 BG by Research Association for Automotive Technology (FAT) and Research Association on Welding and Allied Processes (DVS), which have been founded by AiF under the program for promotion of industrial research (IGF) by the Federal Ministry of Economics and Energy based on a decision of the German Bundestag.

  doi:10.5075/epfl-298799_978-2-9701614-0-0

References

1. Lutz A, Droste A, Brändli C. Strukturkleben im Fahrzeugleichtbau: Eigenschaften und Haftungsspektrum moderner Strukturklebstoffe, Simulation und Anwendung im Karosserierohbau und in der Montage. Landsberg: Verl. Moderne Industrie. 2013.
2. Matzenmiller A, Hanselka H, Mayer B, et al. Schwingfestigkeitsauslegung von geklebten Stahlbauteilen des Fahrzeugbaus unter Belastung mit variablen Amplituden. Schriftenreihe Forschung für die Praxis P 796. Verlag und Vertriebsgesellschaft mbH. 2012.
3. Mayer B, Meschut G, Matzenmiller A, Hanselka H, et al. Analyse der Schwingfestigkeit geklebter Stahlverbindungen unter mehrkanaliger Belastung. Schriftenreihe Forschung für die Praxis P 1028. Verlag und Vertriebsgesellschaft mbH; 2020.
4. Tittmann K, Koch I, Gude M. Validation of an energy-based fatigue life model for fibre reinforced plastics under different stress ratios. 14th WCCM & Eccomas Congress 2020, 2021.
5. Wacker JD, Tittmann K, Koch I, Laveuve D, Gude M. Fatigue Life Analysis of Carbon Fiber Reinforced Polymer (CFRP) Components in Hybrid Adhesive Joints. Materialwissenschaft Und Werkstofftechnik 2021, 52; 11:1230–47. https://doi.org/10.1002/mawe.202100046.
6. S. Çavdar. Spannungsbasierte Lebensdauerberechnung von zyklisch beanspruchten Klebverbindungen mit hyperelastischem Deformationsverhalten. Dissertation, in Berichte aus dem Laboratorium für Werkstoff- und Fügetechnik, Bd. 152. Aachen: Shaker Verlag, 2021, ISBN: 978-3-8440-8084-1.
7. Çavdar S, Teutenberg D, Meschut G, Wulf A, Hesebeck O, Brede M, Mayer B. Stress-based fatigue life prediction of adhesively bonded hybrid hyperelastic joints under multiaxial stress conditions. International Journal of Adhesion and Adhesives 2020; 97:102483, doi: 10.1016/j.ijadhadh.2019.102483.
8. Vassilopoulos AP, Keller T. Fatigue of fiber-reinforced composites. Springer Science & Business Media, 2011.
9. Koch I, Zscheyge M, Tittmann K, Gude M. Numerical fatigue analysis of CFRP components. Composite Structures 2017; 168:392-401.
10. Hahne C. Zur Festigkeitsbewertung von Strukturbauteilen aus Kohlenstofffaser-Kunststoff-Verbunden unter PKW-Betriebslasten. Ph.D. Thesis, TU Darmstadt, Germany, 2014.
11. El Kadi H, Ellyin F. Effect of stress ratio on the fatigue of unidirectional glass fibre/epoxy composite laminae. Composites (1994) 25: 917-924.
12. Shokrieh MM, Taheri-Behrooz F. A Unified Fatigue Life Model Based on Energy Method. Composite Structures 2006; 75:444-450.
13. Cuntze RG. Efficient 3D and 2D Failure Conditions for UD Laminae and Their Application within the Verification of the Laminate Design. Composites Science and Technology 2006; 66:1081-1096
14. Govindarajan SM, Hurtado JA, Mars WV. Simulation of Mullins effect and permanent set in filled elastomers using multiplicative decomposition. Constitutive models for rubber V: Proceedings of the 5th European Conference on Constitutive Models for Rubber, Paris, 4.-7. Sep. 2007, A. Boukamel, L. Laiarinandrasana, S. Méo und V. Erwan, Hg., London: Taylor & Francis, 2008, S. 249–254, ISBN: 978-0-415-45442-1.
15. Marlow RS. A general first-invariant hyperelastic constitutive model. Constitutive models for rubber III: Proceedings of the third European Conference on Constitutive Models for Rubber, London, 15.-17. Sep. 2003, J. Busfield, Hg., Lisse: Balkema, 2003, S. 157–160, ISBN: 9058095665.

16. Bose K, Hurtado JA. Modeling of stress softening in filled elastomers. Constitutive models for rubber III: Proceedings of the third European Conference on Constitutive Models for Rubber, London, 15.-17. Sep. 2003, J. Busfield, Hg., Lisse: Balkema, 2003, S. 223–230, ISBN: 9058095665.
17. Hexcel Corporation, Product data sheet, HexPly® | M79/34%/UD300/CHS. Stamford, 2014.
18. Tittmann K, Wacker JD, Koch I, Gude M, Melz T. Testing and Modelling Strategy for Application-Oriented Service Strength Analysis of Composite Materials in Hybrid Adhesive Joints. ECCM 2018 - 18th Eur. Conf. Compos. Mater., Athens, Greece, June 24 - 28, 2018.
19. DuPont de Nemours Inc., Hg., „BETAFORCETM 2850L: Form No. 299-00228592en“. datasheet, Feb. 2015.
20. DIN EN ISO 527-2:2012-06, Kunststoffe - Bestimmung der Zugeigenschaften - Teil 2: Prüfbedingungen für Form- und Extrusionsmassen (ISO 527-2:2012); Deutsche Fassung EN ISO 527-2:2012, Deutsches Institut für Normung e. V., Berlin, Jun. 2012, doi: 10.31030/1860304.
21. Diani J, Fayolle B, Gilormini P. A review on the Mullins effect. European Polymer Journal 2009; 45:601–612. doi: 10.1016/j.eurpolymj.2008.11.017.
22. Kouznetsova VG. Computational homogenization for the multi-scale analysis of multi-phase materials. Dissertation. Technische Universiteit Eindhoven. 2002.
23. Hund AS. Hierarchische Mehrskalenmodellierung des Versagens von Werkstoffen mit Mikrostruktur. Dissertation. Stuttgart, Univ., 2007.
24. Altenbach H, Altenbach J, Naumenko K. Ebene Flächentragwerke: Grundlagen der Modellierung und Berechnung von Scheiben und Platten. Berlin, Heidelberg: Springer. 1998.

FRACTURE TOUGHNESS AND PERFORMANCE OF RESISTANCE-WELDED AND CO-BONDED THERMOSET/THERMOPLASTIC POLYMER COMPOSITE HYBRID JOINTS

Thomas, Maierhofer[*,a]*, Evripides G., Loukaides*[a]*, Thibault, Hernandez*[b]*, Craig, Carr*[c]*,*
Chiara, Bisagni[d]*, and Richard, Butler*[a]

a: Materials and Structures Centre, Dept. of Mechanical Engineering, University of Bath, UK
b: The ThermoPlastic Composites Research Centre, Netherlands
c: GKN Aerospace, Global Technology Centre, UK
d: Delft University of Technology, Faculty of Aerospace Engineering, Netherlands
*Corresponding author's e-mail: tam48@bath.ac.uk

Abstract: *Modern aerospace structures see increasing use of combinations of thermoplastic and thermoset composite components, requiring the development of efficient joining methods for dissimilar matrix materials. This study aimed to investigate the Mode I fracture toughness and performance of resistance-welded and co-bonded thermoset-thermoplastic composite joints for primary aerospace structural applications. Double cantilever beam and single lap shear trials were performed. It was found that using resistance welding, a significant improvement in the Mode I fracture toughness of approximately 360 % - 520 % over co-bonding can be achieved. Single lap shear tests did not allow any conclusion about the bond strengths due to thermoset laminate failure. Although, combined with optical microscopy of the fracture surfaces, it was possible to show that significant thermal degradation of the thermoset matrix can be avoided.*

Keywords: Hybrid joints; resistance welding; co-bonding; fracture toughness; thermoset-thermoplastic

1. Introduction

For improved design flexibility and structural efficiency, there is a growing interest in using a combination of thermoset composite (TSC) and thermoplastic composite (TPC) components for aerospace structures. Taking advantage of their different properties allows for increased design flexibility and further structural optimisation [1]. One of the main challenges is the efficient joining of composite components. Amongst other factors, structural efficiency, ease and cost of assembly, repairability and stringent certification regulations drive the selection of joining processes for aerospace applications [2].

Mechanical fastening and adhesive bonding are most commonly used for the assembly of TSC and TPC components. Mechanical fastening however is suboptimal for joining CFRP parts as fastener holes create stress concentrations or need complex fibre steering, add a significant amount of weight and require additional sealing [3]. The structural efficiency of thermoset adhesive joints is inherently better and they are much lighter than mechanically fastened joints. Though, thermoset adhesives often require long curing cycles, are permanent, cannot easily be repaired in field operations and require extensive surface preparation [4]. The performance of a bond is highly dependent on proper surface preparation. Current nondestructive inspection methods can detect voids and debonds. However, they cannot detect weak bonds (zero-volume debonds), thus making it difficult to predict the bond performance [5]. An alternative joining

  doi:10.5075/epfl-298799_978-2-9701614-0-0

method that can be readily applied to TPC is fusion bonding (welding). It offers significantly reduced cycle times and eliminates complex surface preparation whilst offering similar joint strength to traditional joining methods [6]. To make a TSC weldable, an established concept is to co-bond a thermoplastic film with an uncured TSC. Previous studies performed by Villegas et al. [7] have demonstrated that if the thermoset resin and thermoplastic coupling layer (CL) are chemically compatible and initially miscible, a reaction induced gradient diffused interface (interphase) forms. This interphase results in a strong bond between the thermoset resin and the CL via molecular entanglements [4]. Polyetherimide (PEI) is a strong candidate for the CL material for primary structural applications due to its compatibility with polyaryletherketones (PAEKs) and commonly used epoxy resins [7]. One of the most promising fusion bonding methods for joining TSC-TPC components is resistance welding. Ageorges et al. [8] and Zweifel et al. [9] have previously studied the applicability of resistance welding for creating TSC-TPC hybrid joints using single lap shear (SLS) tests. However, very limited research exists on the fracture toughness and performance of bonded TSC-TPC joints for aerospace applications.

This study focused on the evaluation and comparison of the Mode I fracture toughness of resistance-welded (RW) and co-bonded (CB) TSC-TPC hybrid joints, by conducting double cantilever beam (DCB) tests. Furthermore, SLS samples were tested to assess joint performance.

2. Experimental procedure

2.1 Manufacturing of adherends and heating elements

In this study, two different types of aerospace-grade carbon fibre reinforced TPC and one carbon fibre reinforced TSC were used. Both thermoplastic laminates consisted of 16-plies with a stacking sequence of $[0/90/0/90/0_3/90]_s$. A Cetex® TC1225/T700 laminate, with a low-melt PAEK matrix, was supplied by Toray Advanced Composites. The laminate was manufactured using a hot platen press, with a consolidated mean laminate thickness of 2.2 mm. APC® PEKK-FC/AS4D, with a polyetherketoneketone matrix, prepreg was supplied by Solvay and consolidated using the manufacturer's recommended autoclave cycle, by maintaining the maximum temperature of 377 °C at a pressure of 0.7 MPa for 20 min, resulting in a consolidated mean laminate thickness of 2.3 mm.

Thermoset laminates were made of 11-plies HexPly® AS4/8552 (CF/epoxy) with a stacking sequence of $[0/90/0/90/0/\underline{0}]_s$, tailored to match the bending stiffness of thermoplastic laminates. CF/epoxy laminates were autoclave cured using the manufacturer's recommended cycle by maintaining a maximum temperature of 180 °C under 0.7 MPa pressure for 120 min, with a cured laminate thickness of 2.2 mm. For thermoset laminates used for resistance welding, a 250 µm-thick PEI film (grade ULTEM 1000) was co-bonded on one surface with the uncured CF/epoxy. This created a thermoplastic rich, weldable surface. A strong bond between the epoxy matrix and the PEI film was formed via molecular entanglements resulting in a gradient thermoset-thermoplastic polymer interphase with a thickness of approximately 30 µm. The interphase thickness was measured on cross-section samples of co-bonded CF/epoxy-PEI laminates using optical microscopy (OM), as shown in figure 2.a.

For resistance welding, two different heating elements (HEs) were investigated. The primary HE used consists of a woven stainless steel (SS) mesh, with a wire thickness of 40 µm and an open gaps size of 87 µm, sandwiched between two plies of 8-harness satin weave glass fibre (GF) TC1225/EC6 (GF/PAEK), from Toray Advanced Composites. The second HE (uninsulated HE)

investigated consists of the same woven SS mesh sandwiched between two 50 µm thick PEI films (ULTEM 1000). This was only used to establish the feasibility of using an uninsulated HE. Both HEs were consolidated in a hot platen press at 350 °C under a pressure of 1.0 MPa for 20 min.

2.2 Adhesive co-bonding

Thermoset and thermoplastic laminates were cut into 200 mm x 155 mm panels for DCB samples and 300 mm x 101.6 mm panels for SLS samples. Thermoplastic laminates were mechanically abraded and surface wet wiped using Isopropyl alcohol, followed by Argon plasma treatment, using an atmospheric plasma torch. A 3M™ Scotch-Weld™ AF 555M epoxy film, with a thickness of 200 µm was used for co-bonding the uncured CF/epoxy laminate and the plasma-treated thermoplastic laminates. To minimise exposure of the surface-treated laminates, adhesive bonding was performed immediately after plasma treatment. Co-bonded hybrid joints were then cured in an autoclave, maintaining a maximum temperature of 180 °C and 0.2 MPa pressure for 120 min. As a pre-crack initiator for DCB samples, a 13 µm thick PTFE film was inserted at the joint interface between the epoxy film and the thermoset adherend. Figures 1.a and 1.b show an illustration and an OM image of the joint cross-section of co-bonded samples.

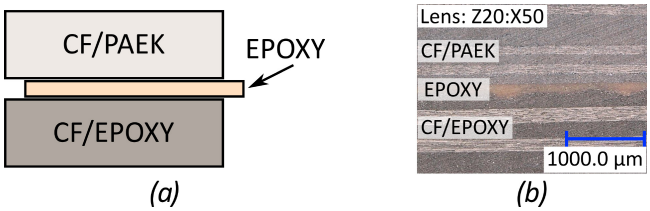

Figure 1. Co-bonded samples: (a) illustration of joint, (b) OM cross-section of joint.

2.3 Resistance welding

Resistance welding was performed at the ThermoPlastic composites Research Center (TPRC), NL, using an in-house developed welding rig. The power was supplied via a computer-controlled 6 kW power supply unit with a maximum DC voltage output of 45 V and a maximum current output of 140 A. The welding and clamping pressure to hold the specimen and connect the power source to the HE were provided via pneumatic actuators. The pressure was uniformly distributed across the specimens' surfaces via active air-cooled aluminium blocks. For DCB specimens, laminates were cut into 250 mm x 50 mm strips, with a heating element width of 25 mm and for SLS specimens laminates were cut into 250 mm x 101.6 mm adherends with a welded overlap of 25.4 mm. To introduce a pre-crack in DCB coupons, a 13 µm thick polyimide film was placed at the interface between the CF/epoxy adherend and the HE, as the crack propagation between the CF/epoxy and the PAEK matrix of the HE was investigated. In figure 2.a an illustration and in figure 2.b an OM image of the cross-section of welded samples is shown.

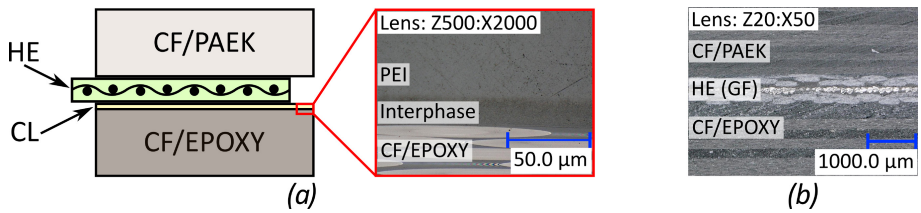

Figure 2. RW samples: (a) joint illustration and OM of interphase, (b) OM cross-section of joint.

To monitor the welding process and ensure fully welded joints, for every performed weld a K-type thermocouple was placed at the HE/CL interface, outside the specimen test region.

Additional welds were performed to determine the optimum welding parameters for the GF insulated HE. These welds had six K-type thermocouples bonded between the PEI CL and the thermoset laminate and two further K-type thermocouples placed between the HE and the PEI CL. To evaluate the applicability of an uninsulated HE, additional layers of 50 µm PEI film were added up to a total thickness of 350 µm on either side of the HE, aiming to prevent current leakage to the laminate. However, this was unsuccessful and current leaking to the fibres of the adherent could not be prevented. Therefore, achieving a uniform weld was impossible. Hence, only the primary GF insulated heating elements were used for producing the specimens. For the manufacturing of DCB and SLS specimens process parameters were chosen to achieve rapid heating of the interface to 350 °C and to maintain it for 30 s, ensuring a fully welded joint. This was achieved via a high initial current of 45 A which was reduced to approximately 30 A once the interface temperature reached 350 °C. The welding cycle is illustrated in figures 3.a and 3.b.

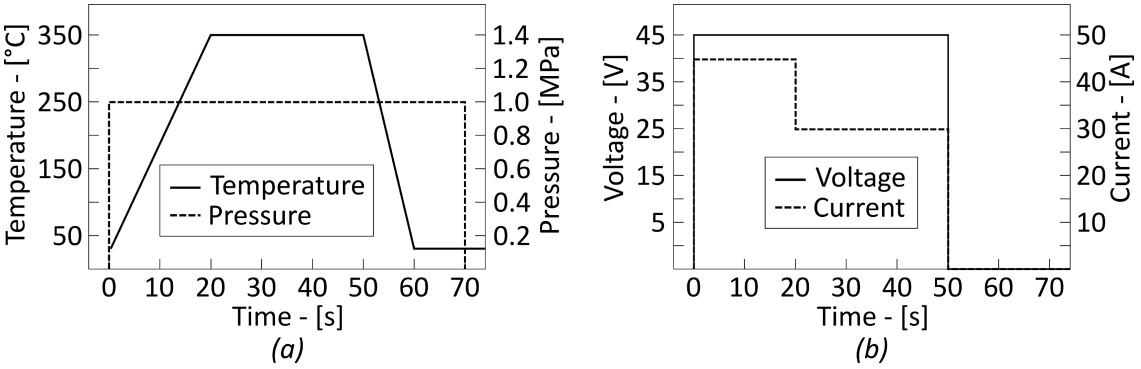

Figure 3. Resistance welding target cycle parameters: (a) interface temperature and welding pressure, (b) power supply: voltage and current.

2.4 Testing and performance analysis

SLS and DCB experiments were based on ASTM D5868 and ASTM D5528 standards respectively. SLS samples were cut into 25.4 mm wide specimens. DCB samples were cut into 160 mm x 21 mm specimens with a crack insert length of 52.5 mm. Tests were performed using an Instron 50 kN universal testing machine. For SLS and DCB specimens, load rates of 13 mm/min and 1 mm/min respectively were chosen, with all tests performed in standard laboratory conditions (23 °C and 50 % relative humidity). For all samples, the force and crosshead displacement of the testing machine were recorded. The side faces of DCB specimens were spray-painted with a thin layer of white acrylic paint. Crack front propagation on DCB specimens was recorded by bonding crack length gauges, with an accuracy of ±0.5 mm to both specimen side faces and recording crack growth using a 4K camera. For SLS samples, seven welded and five co-bonded specimens were tested per material combination. Six DCB tests were performed for each coupon configuration.

Lap shear strengths (LSS) were calculated by dividing the failure load by the bonded joint area of SLS experiments. The Mode I fracture toughness (G_{IC}) was calculated using the modified beam theory method, as it was observed to yield the most conservative fracture toughnesses for the majority of tested samples [10]. The Mode I fracture toughness was therefore calculated using:

$$G_{IC} = \frac{3P\delta}{2b(a+|\Delta|)} \quad (1)$$

The modified beam theory method accounts for the rotation at the crack front by increasing the crack length (a) to $a + |\Delta|$. Δ was determined for each specimen by creating a least-squares fit of the cube root of the compliance ($C^{1/3}$) against crack length, where C is the ratio of load point displacement vs. applied load.

3. Results and discussion

3.1 Lap shear strength

Lap shear strength values showed similar performance values for both hybrid co-bonded and hybrid resistance-welded samples, as outlined in table 1 and shown in figure 4.

Table 1: LSS, standard deviation (SD) and coefficient of variation (CV) of each sample type.

Sample type	LSS – [MPa]	SD – [MPa]	CV – [%]
CB-LMP	7.7	0.6	8.3
CB-PEKK	9.6	1.6	16.3
RW-LMP	11.7	0.9	8.1
RW-PEKK	10.2	1.5	15.1

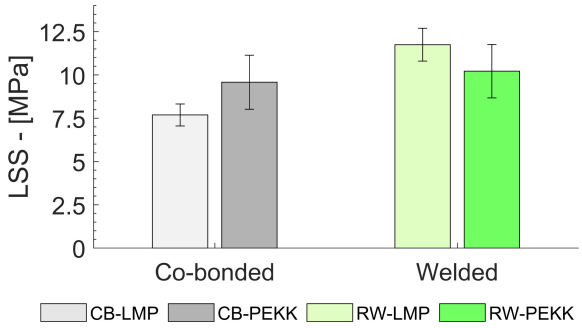

Figure 4. LSS comparison between co-bonded and resistance-welded hybrid joints.

The observed failure mode for all specimens, independent of coupon configuration was laminate failure between the first and second ply (0/90) interface of the thermoset adherend. As a result, the performed SLS tests do not allow any conclusion about the actual bond strength, apart from the joint being stronger than the thermoset laminate's interfacial strength. However, given that the heat-affected zone is focused around the joint interface, CF/epoxy plies closest to the joint interface are subject to the greatest risk of thermal degradation. Hence, as the observed LSS for CB and RW samples are comparable and failure occurred between the 1st and 2nd ply, it is concluded that thermal degradation of the thermoset matrix was successfully prevented.

3.2 Mode I fracture toughness

The main focus of this study was to investigate and compare the Mode I fracture toughness of resistance-welded vs. co-bonded TSC-TPC hybrid joints. Post bonding optical microscopic analysis showed that, due to resin flow during the bonding process, insert folds at the crack tip formed in most specimens. Therefore, specimens were loaded to an initial increment of crack growth, unloaded, and then reloaded to induce crack growth from a natural Mode I pre-crack.

  doi:10.5075/epfl-298799_978-2-9701614-0-0

For fracture toughness analysis, only G_{IC} values obtained from reloading cycles were evaluated. Table 2 and figure 5.a show the obtained mean initiation ($G_{IC,INIT.}$) and propagation ($G_{IC,PROP.}$) toughnesses, SDs and CVs for each sample type respectively. Example R-curves for a CB-LMP specimen and a RW-LMP specimen are shown in figure 5.b.

Table 2: Mean G_{IC} initiation and propagation toughnesses with respective SDs and CVs.

Sample type	$G_{IC,INIT.}$ – [J/m²]	SD– [J/m²]	CV – [%]	$G_{IC,PROP.}$ – [J/m²]	SD – [J/m²]	CV – [%]
CB-LMP	267	14.0	5.2	301	15.7	5.2
CB-PEKK	399	74.0	18.5	450	73.8	16.4
RW-LMP	1650	241.0	14.6	2097	242.7	11.6
RW-PEKK	1847	177.9	9.6	2246	129.9	5.8

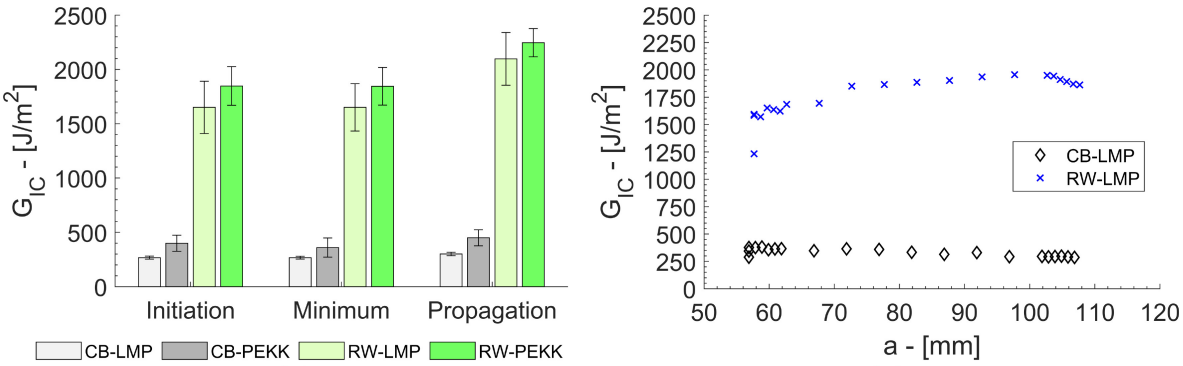

Figure 5. (a) Initiation, minimum and propagation G_{IC} values with respective SDs for all samples, (b) example R-curves for co-bonded and resistance-welded specimens.

In comparison to co-bonded joints, the resistance-welded joint interface is much more complex, as it consists of multiple different material systems. Thus, it is much more challenging to evaluate the fracture toughness for a specific joint configuration. However, resistance-welded samples show a Mode I fracture toughness increase of approximately 360 % - 520 % vs. co-bonded samples. This suggests that resistance welding may offer a significant performance improvement in addition to a much shorter manufacturing cycle time when compared to adhesive bonding.

The main failure mode of co-bonded samples was adhesive failure between the epoxy film adhesive and the thermoplastic adherend with partial thin layer cohesive failure being observed along the fracture surface. For most CB samples, a run-arrest crack extension was observed.

For welded samples, as the pre-crack insert was placed at the HE/CL interface, it was expected that the crack would propagate at that interface, with a risk of it extending into the thermoset laminate. Though in general, crack extension tended towards the midplane of the joint, which resulted in significant fibre bridging between the HE's GF insulation and the CL over a distinct length of crack extension. Fibre bridging significantly increased the local fracture toughnesses at a given crack length, as the load was partially transferred to the bridged GFs. This phenomenon is reflected in the R-curve shown in figure 6.a, with figure 6.b showing an example of fibre

bridging occurring shortly after crack initiation. The resulting toughness extrema were excluded from the data used to evaluate mean toughness values. Even though most specimens showed fibre bridging to some degree, due to the phenomenon being limited to a distinct crack extension, it is believed that the "true" Mode I fracture toughness can be extracted where no fibre bridging was visually observed. The primary failure modes observed were the cohesive failure of the CL and fibre-tear failure of the HE. Although initial results are promising further tests are recommended to determine whether an offset of the pre-crack insert from the joint mid-plane resulted in structural coupling hence resulting in mixed mode failure.

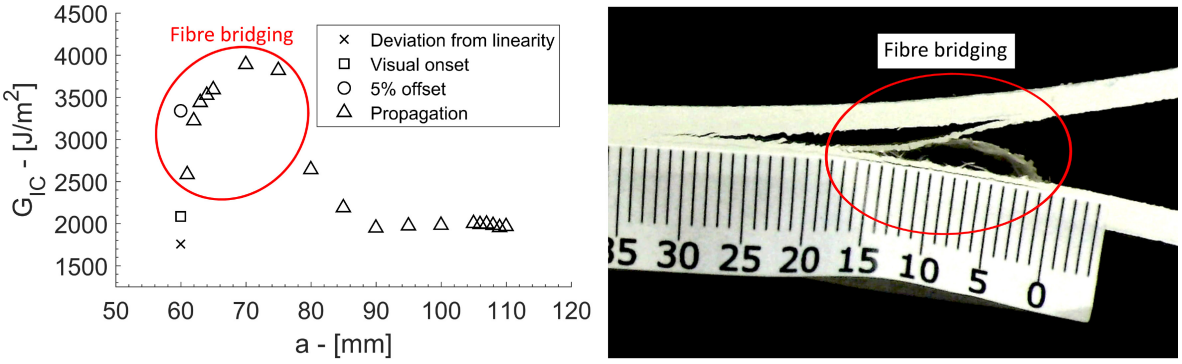

(a) *(b)*

Figure 6. (a) R-curve showing the effect of fibre bridging on G_{IC}, (b) fibre bridging between GF insulation of the HE and thermoplastic CL.

Two RW-PEKK specimens were exposed to prolonged high power heating, resulting in exceeding the required processing temperature and reaching interface temperatures above 500 °C. As a result, the epoxy matrix was expected to show signs of thermal degradation. Optical microscopy of the fracture surface allowed the identification of discoloured resin and a significant amount of epoxy sublimation-induced porosity trapped in the consolidated thermoplastic resin pool. Figures 7.a and 7.b show an extract of the fracture surface of both an overheated specimen and another produced following the target welding cycle shown in figure 3 respectively. Overheating resulted in a significant fracture toughness reduction of approximately 80 % (≈450 J/m^2).

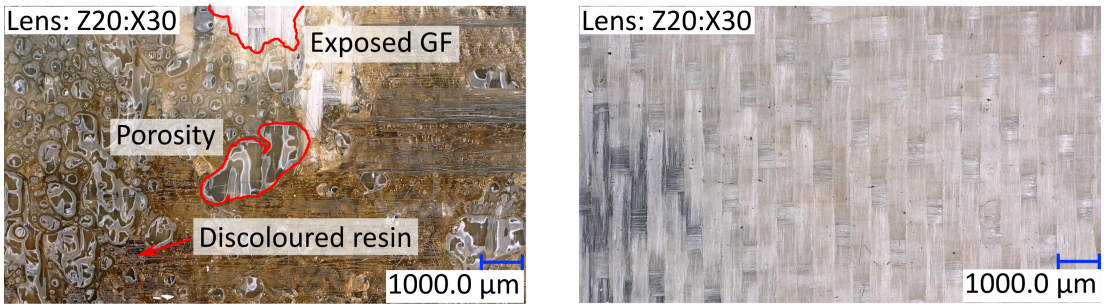

(a) *(b)*

Figure 7. RW DCB fracture surface: (a) overheated specimen, (b) target cycle specimen.

Conclusion

An experimental study on the Mode I fracture toughness and joint performance of co-bonded and resistance-welded thermoset-thermoplastic composite hybrid joints was performed. Four different sample configurations were investigated: two co-bonded (CB-LMP and CB-PEKK) and two resistance-welded (RW-LMP and RW-PEKK). Single lap shear tests were performed for which laminate failure was observed for all tested specimens. However, because the laminate failure

occurred between the first and second ply and comparable lap shear strengths were obtained for both joining methods, it is concluded that thermal degradation of the thermoset adherend can be avoided. When comparing resistance-welded with co-bonded samples, the obtained Mode I fracture toughness for resistance-welded samples were evaluated to be approximately 360 % - 520 % higher. However, failure of resistance-welded joints is much more complex, potentially making it difficult to achieve pure Mode I fracture.

Acknowledgements

The authors gratefully acknowledge GKN Aerospace UK for their continuous support and industrial guidance. Technical advice and manufacturing assistance provided by the ThermoPlastic composites Research Center (TPRC), NL, the Advanced Manufacturing Research Centre (AMRC), UK, and the National Composites Centre (NCC), UK, are greatly appreciated. The authors want to thank Toray Advanced Composites and Solvay for supplying the thermoplastic laminates and prepreg. Richard Butler holds the Royal Academy of Engineering - GKN Aerospace Research Chair. The research was gratefully supported by the EPSRC, UK, Programme Grant: "Certification for Design: Reshaping the Testing Pyramid" (CerTest, EP/S017038/1).

4. References

1. Quan D, Alderliesten R, Dransfeld C, Tsakoniatis I, Benedictus R. Co-cure joining of epoxy composites with rapidly UV-irradiated PEEK and PPS composites to achieve high structural integrity. *Compos. Struct.* 2020; 251:Article 112595.
2. Xiong X, Wang D, Wei J, Zhao P, Ren R, Dong J, Cui X. Resistance welding technology of fiber reinforced polymer composites: a review. *J. Adhes. Sci. Technol.* 2021; 35(15):1593-1619.
3. Ageorges C, Ye L, Hou M. Experimental investigation of the resistance welding for thermoplastic-matrix composites. Part I: Heating element and heat transfer. *Compos. Sci. Technol.* 2000; 60(7):1027-1039.
4. Deng S, Djukic L, Paton R, Ye L. Thermoplastic-epoxy interactions and their potential applications in joining composite structures - A review. *Composites Part A.* 2015; 68:121-132.
5. Campbell FC. *Manufacturing Processes for Advanced Composites*. Oxford: Elsevier Advanced Technology; 2003.
6. Tsiangou E, Teixeira de Freitas S, Fernandez Villegas I, Benedictus R. Ultrasonic welding of epoxy- to polyetheretherketone- based composites: Investigation on the material of the energy director and the thickness of the coupling layer. *J. Compos. Mater.* 2020; 54(22):3081-3098.
7. Fernandez Villegas I, van Moorleghem R. Ultrasonic welding of carbon/epoxy and carbon/PEEK composites through a PEI thermoplastic coupling layer. *Composites Part A.* 2018; 109:75-83.
8. Ageorges C, Ye L. Resistance welding of thermosetting composite/thermoplastic composite joints. *Composites Part A.* 2001; 32:1603-1612.
9. Zweifel L, Brauner C. Investigation of the interphase mechanisms and welding behaviour of fast-curing epoxy based composites with co-cured thermoplastic boundary layers. *Composites Part A.* 2020; 139:Article 106120.
10. ASTM. ASTM D5528-13(2021). Standard Test Method for Mode I Interlaminar Fracture Toughness of Unidirectional Fiber-Reinforced Polymer Matrix Composites. West Conshohocken (PA): ASTM International; 2021.

  doi:10.5075/epfl-298799_978-2-9701614-0-0

SELECTIVE INTERLAMINAR DELAMINATION PROCESS IN CFRP BY LASER SHOCK

Mohammad, Ayad [a], Marine, Scius-Bertrand [b], Selen Ünaldi [a] , Charlotte Michel [c], Laurent Berthe [a]

a: PIMM, UMR8006 ENSAM, CNRS, CNAM, 151 bd de l'Hôpital, 75013 Paris, France
b: Rescoll, 8 All. Geoffroy Saint-Hilaire, 33600 Pessac
c: DYNAS+, 5, Avenue Didier Daurat 31400 TOULOUSE, France

Abstract: *During the lifetime of an aircraft, different maintenance and routine checks should be established. One of the heaviest inspection is the D checks, which is called "heavy maintenance visit" that occurs every 6 – 10 years depending on the aircraft. During these checks, different inspection methods can be used to detect debonding in aircraft structures such as Liquid Penetrant, Magnetic Particle, Eddy Current. However, none of these Non-Destructive Testing (NDT) methods could detect the weak bond and its level except laser adhesion test (LASAT). Mastering wave propagation in Carbon Fiber Reinforced Polymer (CFRP) produced by laser shock allows us to control the maximum tensile stress zone within the composite. To that scope, material model of CFRP has been validated under high strain rate (up to 10^6 s^{-1}) by coupling experimental and numerical response of CFRP under laser shock. In addition, different laser configurations and parameters have been optimized to localize the maximum tensile stress at the desired location, which produce the delamination. We simulate the shock wave propagation using non-linear explicit code LS-DYNA, that we validate with experiments performed at Héphaïstos Laser facility, PIMM – ENSAM, Paris. This process is a key step towards the development of a selective and controlled laser shock adhesion test in composites.*

Keywords: CFRP; Laser Adhesion Test (LASAT); Laser shock; Dynamical simulation

1. Introduction

One of the biggest challenge in our decade is to decrease the CO_2 emission of air transport. This ambition of Climate-Neutral Aviation can be reached either by reducing the airplane mass or moving to hydrogen aviation. Airplane weight reduction is one of the crucial aspect in this domain [1], by using dissimilar parts [2] or composite materials, which are known by the big ratio of performance to structure weight [3]. Through the big advancement in the composite manufacturing and development, safety of the adhesive bonding still under investigation. Different non-destructive techniques (NDT) could be applied to verify if there is a deboning on the composite structure like ultrasonic, thermography or vibration-based inspection [4] or other methods like Liquid Penetrant, Magnetic Particle or Eddy Current [5].

Despite the numerous of the available NDT, none of the mentioned above could quantify the mechanical strength of a joint, and to identify the weak bonds or the extremely weak bonds as known as "kissing bonds" in the literature [6, 7]. One of the promising technique is the Laser Adhesion Test (LASAT), which has been proved capable to detect bonding strength in the desired location by the usage of the laser shock propagation.

  doi:10.5075/epfl-298799_978-2-9701614-0-0

The only available diagnostic at Héphaïstos laser facility is the Velocity Interferometer System for Any Reflector (VISAR) which measures the back face velocity of specimens. In order to better investigate all the phenomena involved, numerical simulation is required during the shock wave propagation. To simulate the shock wave propagation within the targets, the applied pressure by the created plasma should be modeled. Recently, by Scius-Bertrand et al. 2020 is provided analytical laws, which could be used in mechanical codes as an applied pressure [9]. Different material model has been used and developed to simulated composites under laser shock, which counts all mechanical regime (elasticity, plasticity, strain rate sensitivity, damage…) [6, 7, 8].

In this paper, we present the methodology, which is used to analyze the bonding strength in the stack of composite structures. To that scope, we use the Velocity Interferometer System for Any Reflector (VISAR) system under mono-shock configuration (Figure 1a) to measure the dynamical response of Carbon Fiber Reinforced Polymer (CFRP) under laser shock at Héphaïstos laser facility, PIMM-ENSAM-Paris as described in Section 2.1. In this study, we use LS-Dyna explicit solver to simulate the laser shock propagation through the composite structures, where the developed numerical model is described in Section 2.2. Simulation and experiments of mono shocks will be coupled on the studied CFRP sample of 10 plies in Section 2.3. The validated numerical model will be used to optimize the symmetrical impact (Figure 1b) in order to locate the maximum tensile stresses at the desired locations as the case of the matrix-fiber interface to evaluate the threshold of delamination or the bonding strength limit as described in Section 3. In Section 4, obtained results and conclusion can be found.

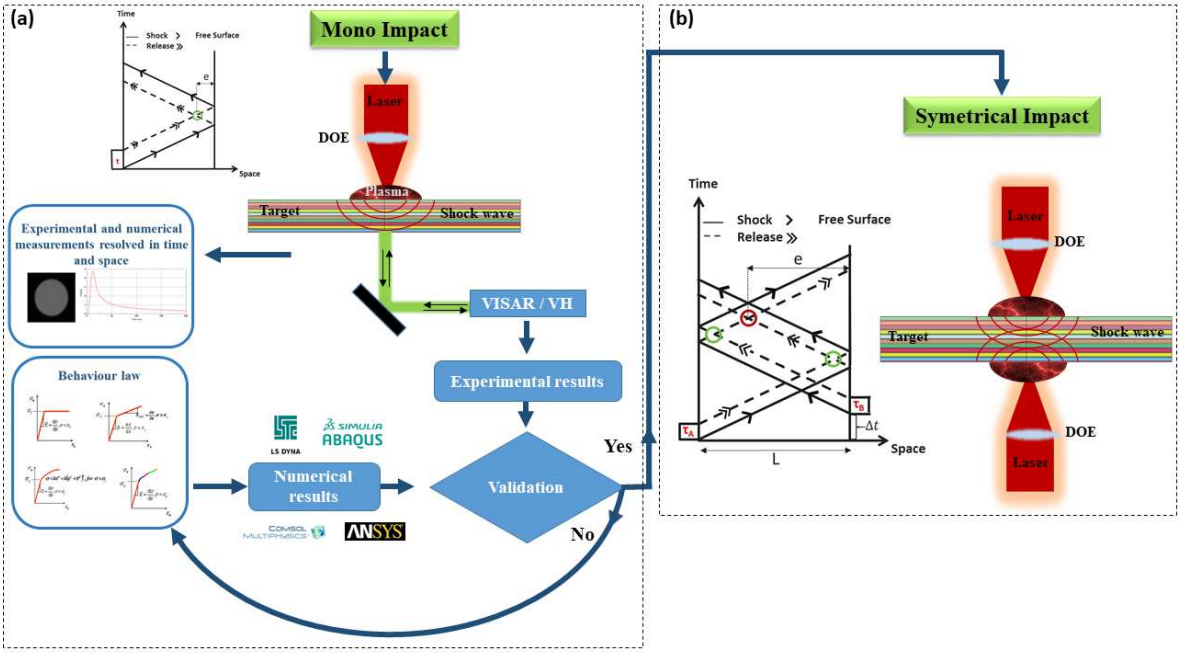

Figure 1. Laser shock application in mono impact (a) coupled with VISAR system and in symmetrical impact to study the desired bonding strength (b).

2. Experimental and numerical tools

2.1 Héphaïstos laser facility

A platform installed in the PIMM laboratory is the Héphaïstos platform which includes a laser system that delivers a Gaussian time pulse with a duration of 7.2 ns at full width at half maximum

  doi:10.5075/epfl-298799_978-2-9701614-0-0 published under CC BY-NC 4.0 license

(FWHM) in the green visible wavelength (532 nm), with an energy up to 14 J. It is composed of two laser beams called A and B (Figure 2). The two beams can be combined or separated to make single or double shots respectively (Figure 2a), or separated to make symmetrical shots (Figure 2b). Real-time resolved target free surface velocity profiles are measured by a laser velocimeter (VISAR) based on a Barker system [10, 11].

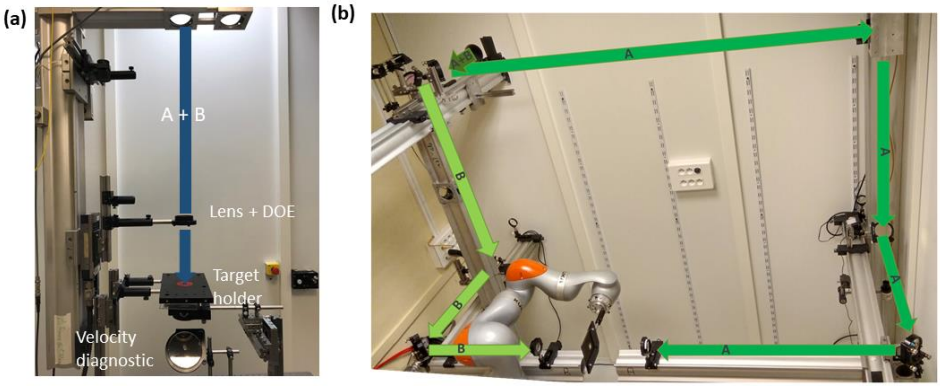

Figure 2. Héphaïstos laser facility with mono pulse (a) and symmetrical impact (b) [12].

2.2 Numerical modeling

In this work, we used the explicit solver LS-DYNA to simulate the shock wave in the composite plate. Our CFRP sample is of 1.473 mm thickness made of 10 unidirectional plies (UD). We used 2D axisymmetric mesh to model this sample, made of 2×10 [µm× µm] for the matrix (epoxy) mesh size and 4.9×10 [µm× µm] for the fiber mesh size as shown in Figure 3.

Figure 3. 2D mesh for 10 plies CFRP generated using LS-PrePost.

According to previous work of Perton et al., fibers and matrix could be simulated using elastic material model [6]. Therefore, in this work MAT_ELASTIC has been used for fibers and matrix separately, where corresponding parameters are shown in Table1.

Table 1: Fibers and matrix mechanical properties [6].

Material	ρ (g/cm^3)	E (GPa)	v
Epoxy	1.26	3.95	0.4
Carbon	1.66	10.8	0.35

  doi:10.5075/epfl-298799_978-2-9701614-0-0

2.3 CFRP response under mono laser shock

Laser shock has been applied on the plies of CFRP at Héphaïstos laser facility (Section 2.1), using 8 mm focal spot and 0.8 GW/cm² laser Intensity. Laser beam has been applied on the top face of the composite using water confinement, and back face velocity has been measured using the VISAR system (Section 2.1). The spatial and temporal pressure profiles used for simulation has been generated following the previous work of Ayad et al. 2022 as shown in Figure 4 [8].

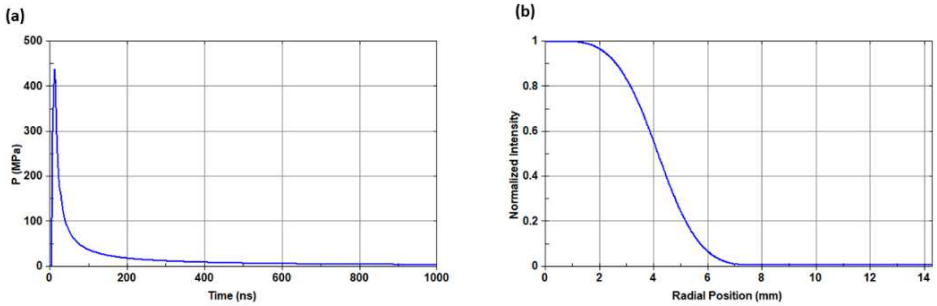

Figure 4. Temporal (a) and spatial (b) distributions of the applied pressure used in the numerical simulation.

Using the material properties mentioned in Table 1, and by applying the pressure distributions (described in Figure 4), in the numerical model described in Section 2.2, we simulated the CFRP behavior under laser shock which we compare and validate with the experimental results as shown in the Figure 5. What is more, we provide in Figure 5 the XT diagram, which shows the propagation of the axial stress in the CFRP plate under laser shock.

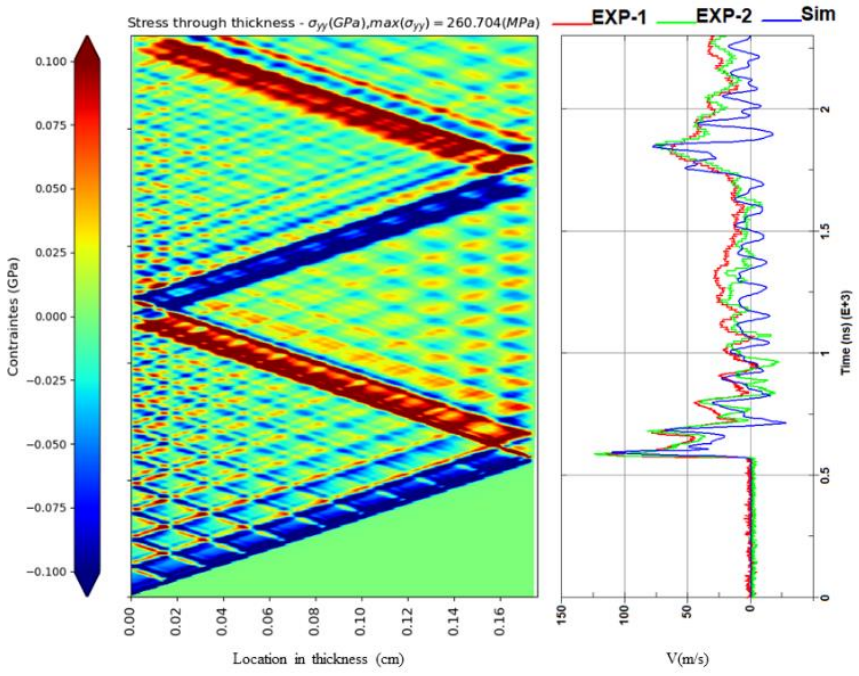

Figure 5. Propagation of the simulated axial stress σ_{yy} associated with the simulated back face velocity profile (Sim) compared to two experimental back face profiles (EXP-1 and EXP-2).

  doi:10.5075/epfl-298799_978-2-9701614-0-0

The comparison of simulated back face velocity (Sim: blue curve) with the experimental measurements (EXP-1 and EXP-2: red and green curves), shows good correlation between the experimental and the simulation which could validate the material models and the numerical boundary conditions with their relative pressure distributions.

3. Symmetrical laser shocks on CFRP

In this section, we will show the possibility to locate the maximum tensile stress at the desired location. In this study, we will optimize the delay between beam B and A until we obtain the biggest tensile at the interface between the Joint-3 bottom face (J3bf) and the Fiber-3 top face (F3tf). Therefore, the validated numerical model used in Section 2.3 will be re-used with the same applied pressure from both faces and by using both beams (A & B) with an optimized delay (α) to get the maximum tensile axial stresses in which will be located at the J3bf. From the Figure 5 (the obtained XT diagram), one can see the propagation of the axial stress through the CFRP under symmetrical shocks.

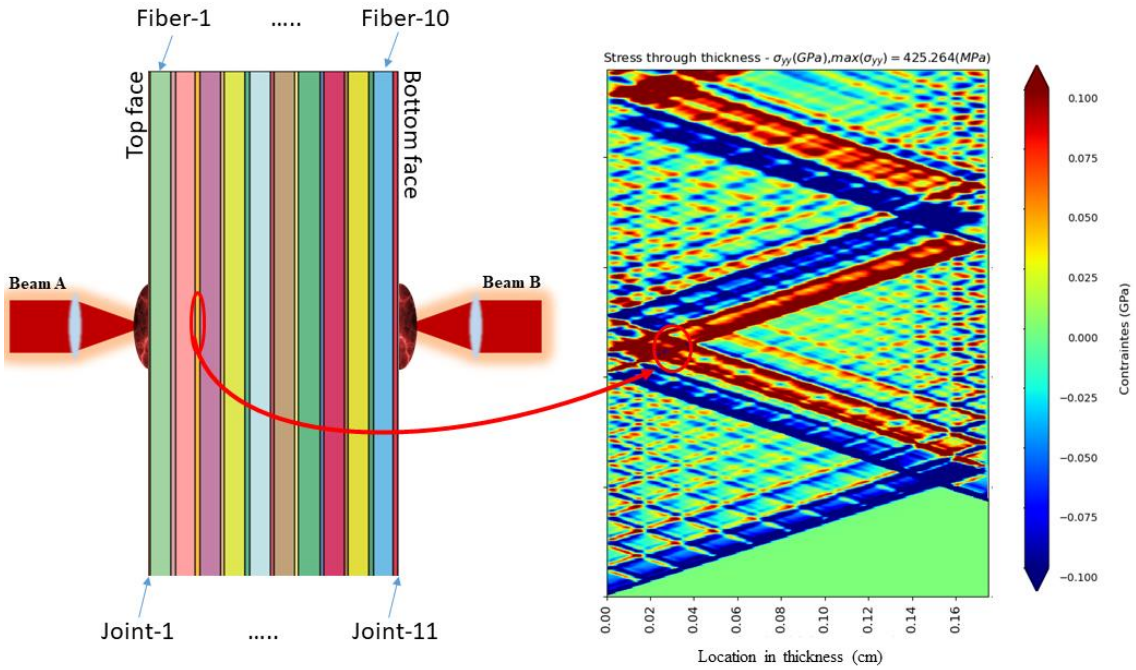

Figure 6. Propagation of the simulated axial stress σ_{yy} under symmetrical shocks of 430 ns delay between beam A and B.

As we can see from the XT diagram the release waves meets in the Joint-3, and the biggest tensile stress among all the joint has been found on J3bf (400 MPa). While the closest one was 296 MPa which has been obtained on the bottom face of Joint-2 (J2bf) and followed by 280 MPa on the top face of Joint-3 (J3tf).

  doi:10.5075/epfl-298799_978-2-9701614-0-0

4. Discussion and Conclusion

Experiments and simulation of laser shock have been performed on CFRP plate of 10 plies under 0.8 GW/cm² laser intensity. Elastic material model proves sufficient to model the CFRP behavior under this power density, by validating the experimental measurement of the CFRP dynamical response under laser shock and the numerical one obtained by LS-DYNA. The validated numerical model has been used for symmetrical shocks, where the optimization has been done on the delay between two laser beams until the biggest tensile occurs at the desired location. Simulation proved that the biggest tensile stress has been obtained at the desired interface J3bf by separating A & B laser beams by 430 ns delay (400 MPa ≈ 93.5 % of the maximum tensile stress in the sample). Verification has been made that other interfaces are subjected to less than 70% of this maximum). These results of simulation of symmetrical shocks should be coupled with experimental ones in order to obtain the threshold of each joint before delamination.

The used material model has been validated under this lower laser power density, material model taking into account plasticity, strain rate sensitivity and damage parameters should be used for higher power densities. In addition, laser has been applied in this work on the top face of the composites; experiments should be repeated using an ablative layer (Aluminum tape) which could reduce the uncertainty for the applied pressure.

Acknowledgements

The authors acknowledge the financial support from EU COST CA18120 Action for travel and accommodation costs to attend CERTBOND session during the ECCM20 conference. This work was supported by Délégation Générale pour l'Armement (DGA) Rapid during the Vanesses project.

5. References

1. Zhu L, Li N, Childs P. Light-weighting in aerospace component and system design. Propulsion and Power Research 2018; 7: 103–119.
2. Martinsen K, Hu S, Carlson B. Joining of dissimilar materials, CIRP Annals 2015; 64: 679–699.
3. Krzyżak A, Mazur M, Gajewski M, Drozd K, Komorek A, Przybyłek P. Sandwich Structured Composites for Aeronautics: Methods of Manufacturing Affecting Some Mechanical Properties. International Journal of Aerospace Engineering, 2016.
4. Katunin A, Dragan K, Dziendzikowski M. Damage identification in aircraft composite structures: A case study using various non-destructive testing techniques. Composite Structures 2015; 127: 1-9.
5. Cawley P. Non-destructive testing—current capabilities and future directions. Proceedings of the Institution of Mechanical Engineers, Part L: Journal of Materials: Design and Applications 2001; 215: 213-223.

  doi:10.5075/epfl-298799_978-2-9701614-0-0

6. Perton M, Blouin A and Jean Monchalin J-P. Adhesive bond testing of carbon-epoxy composites by laser shockwave. Journal of Physics D: Applied Physics 2010; 44.
7. Ecault R, Touchard F, Boustie M, Berthe L, Dominguez N. Numerical modeling of laser-induced shock experiments for the development of the adhesion test for bonded composite materials, Composite Structures 2016; 152: 382-394.
8. Ayad M, Lapostolle L, Rondepierre A, Le Bras C, Scius-Bertrand M, Ünaldi S, Trdan U, Rouchausse Y, Grassy J, Maillot T, Lapoujade V, Michel C, and Berthe L. Modeling of multi-edge effects in the case of laser shock loadings applied on thin foils: Application for material characterization of aluminum alloys, Journal of Applied Physics 2022; 131.
9. Scius-Bertrand M, Videau L, Rondepierre A, Lescoute E, Rouchausse Y, Kaufman J, Rostohar D, Brajer J, and Berthe L. Laser induced plasma characterization in direct and water confined regimes: New advances in experimental studies and numerical modelling, Journal of Physics D: Applied Physics 2020; 54.
10. Barker L M, Hollenbach R. Laser interferometer for measuring high velocities of any reflecting surface, Journal of Applied Physics 1972; 43: 4669-4675.
11. Barker L M, Schuler K W. Correction to the velocity-per-fringe relationship for the visar interferometer, Journal of Applied Physics 1974; 45: 3692-3693.
12. Scius-Bertrand M. "Endommagements maîtrises par chocs laser symétriques et désassemblages des collages". Submitted PhD Thesis. 2021.
13. Ecault R, Berthe L, Touchard F, Boustie M, Lescoute E, Sollier A, and Voillaume H. Experimental and numerical investigations of shock and shear wave propagation induced by femtosecond laser irradiation in epoxy resins. Journal of Physics D: Applied Physics 2015; 48.
14. Riedel W, Nahme H, and Thoma K. Equation of State Properties of Modern Composite Materials: Modeling Shock, Release and Spallation. AIP Conference Proceedings 2004; 706: 701-706.
15. See http://www.matweb.com for “Online materials information resource-matweb” (accessed 20 April 2022).
16. Minus M, Kumar S. The processing, properties, and structure of carbon fibers. JOM 2005; 57: 52–58.

  doi:10.5075/epfl-298799_978-2-9701614-0-0

DAMAGE MONITORING OF COMPOSITE BONDED JOINTS USING THE ELECTRICAL METHOD: MODELLING AND EXPERIMENTS

Carraro, Paolo Andrea[a], Panozzo, Francesco[a], Pontefisso, Alessandro[a], Quaresimin, Marino[a], Zappalorto, Michele[a]

a: Department of Management and Engineering, University of Padova – paoloandrea.carraro@unipd.it

Abstract: *The continuous health monitoring of bonded composite parts could significantly increase their level of safeness and reliability, assisting and broadening their application in several sectors, starting from the aviation industry. When conductive adherends are used (as for instance made of carbon fibers), together with a conductive adhesive, the initiation and propagation of a bondline crack cause an irreversible interruption of the conductive network across the crack faces. Therefore, the electric resistance of a bonded assembly increases. This can be measured by simply applying electrodes on the part surfaces, without the need of external additional sensors. In this work the possibility of monitoring the crack formation and propagation in bonded joints under cyclic loadings is explored. First, an analytical model was developed to correlate the resistance increase with the crack length for simple geometrical configurations, such as the single lap and double lap joints. It could be easily extended to other configurations such as T- or L-joints. The model was initially validated through electrically conductive Finite Element analyses and revealed the fundamental role of the main geometrical and material parameters, allowing their best choice for maximizing the accuracy and sensitivity of the monitoring method. Then, fatigue tests were carried out on single lap joints made of carbon/epoxy adherends and a CNT-modified adhesive. The specimen electric resistance and the crack length were periodically measured. The model predictions of the resistance increase versus the crack length were then compared to the experimental results, obtaining a satisfactory agreement.*

Keywords: Bonded joints; Health Monitoring; Damage; Electrical method; Fatigue

1. Introduction

The use of fiber-reinforced polymer composites for structural applications has been tremendously growing in the last years due to the thrust of dominating industrial fields like aerospace, automotive and wind energy. Structural applications of composite materials often involve joining different parts. Among the available joining techniques, adhesive bonding represents an excellent candidate as it leads to light and cheap connections. Indeed, it does not require drilling holes in the composite parts, this having the twofold disadvantage of decreasing the material performances and entailing high costs.

Designing bonded connections against the static and, mainly, fatigue failure is not a trivial task, and no standard is currently available for guiding the design and certification at an industrial level. Indeed, the fatigue behavior of composite bonded joints is a complex phenomenon that depends on several parameters. But what makes the problem even more challenging, hampering the certifiability of purely bonded connections in primary parts in the aviation industry, for instance, is the influence of defects. Some defects such as voids, pre-cracks or

cracks initiated during the service life can be detected by standard periodical inspection techniques and managed by proper design tools. But defects in the form of poor bonds, due for instance to the presence of contaminating agents, are impossible to detect, so that the integrity of a bonded connection cannot be proved in advance, leading to the impossibility of certifying purely bonded connections for primary parts in some industrial sectors (aviation in primis). These uncertainties force companies in several fields to use combined bonded/bolted joints, thus losing the great economical, weight and performance advantages of adhesive bonding. In this frame, companies should demonstrate that they can correctly simulate the fatigue damage initiation and evolution in bonded connections and that the presence of damage in the bond area can be detected and tolerated. For this reason, the search for efficient crack stopping mechanisms and Health Monitoring (HM) methods has increased in the recent years [1-4].
In this frame, the aim of this work is to develop models and methods for the continuous HM of bonded connections. Among the possible HM strategies, that based on the electrical method, which is recently giving promising results for monolithic composite parts [5-10], was chosen. This has the advantage of being a sensor-less technology, which only requires cabling properly positioned electrodes on the component, exploiting the irreversible resistance increase due to the formation of damage, i.e. of a bondline crack in bonded joints. Obviously, this method is subjected to the use of electrically conductive materials both for the adherends and the adhesive. Carbon fiber-based composites are conductive materials, whereas in the case of glass fibers, a matrix nano-modification through conductive fillers can be adopted. Conductive adhesives are widely available in the market, and new solutions could also be developed.
In this work, first a new analytical model is developed for correlating the bondline crack length and the joint electrical response. Then, experiments were carried out on a Single Lap (SL) joint under cyclic loadings, for validating the proposed methodology.

2. Analytical model

A model for the electric response of a SL joint with cracks at the bondline is developed. This can be considered a case study, valid for this particular geometry, but the method can be applied also to other geometrical configurations.
Consider a SL joint with cracks propagating from the two corners, subjected to a current I_x injected through the cross section, as in Figure 1.

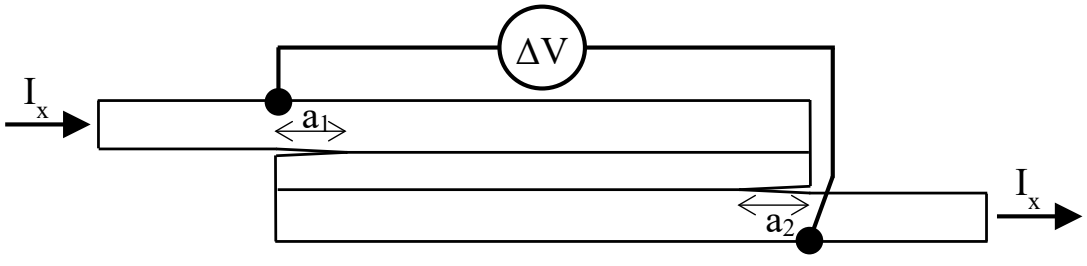

Figure 1. Geometry of the problem

As suggested in Refs. [9,10], the trend of the electric potential along the thickness of the different layers is approximated with polynomial functions. In particular, a parabolic function is used for the electric potential of the adherends, whereas a more flexible polynomial with a grade n > 1 is used for the adhesive layer:

$$\begin{aligned} V^{(i)}(z_i) &= a_i z_i^2 + b_i z_i + c_i \qquad \text{with } i = 1, 3 \text{ (adherends)} \\ V^{(2)}(z_2) &= a_2 z_2^n + b_2 z_2 + c_2 \qquad \text{(adhesive)} \end{aligned} \tag{1}$$

Z_i is the through-the-thickness coordinate starting from the bottom of the i-th layer. As in [9], by considering the continuity of the electric potential and the through-the-thickness current density, the following relationship can be obtained between the through-the-thickness averaged electric potentials and the z-direction current density at the interfaces (j_c, see Figure 2):

$$\begin{Bmatrix} \Delta V^{(1)} \\ \Delta V^{(2)} \end{Bmatrix} = \begin{Bmatrix} \overline{V}^{(1)} - \overline{V}^{(2)} \\ \overline{V}^{(2)} - \overline{V}^{(3)} \end{Bmatrix} = \begin{bmatrix} H_{11} & H_{12} \\ H_{12} & H_{11} \end{bmatrix} \begin{Bmatrix} j_c^{(1)} \\ j_c^{(2)} \end{Bmatrix} \tag{2}$$

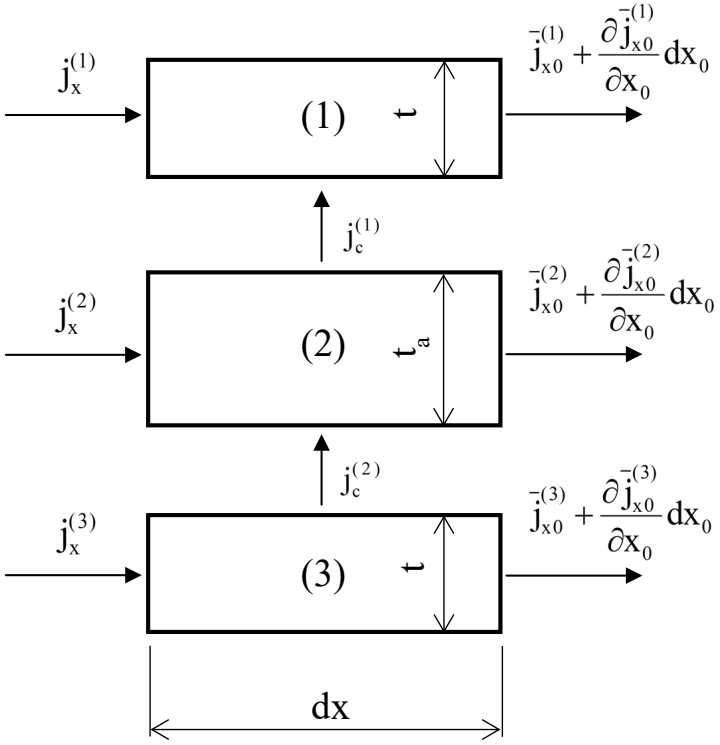

Figure 2. Current density on an infinitesimal length element of the overlap region

From figure 2, the following charge conservation equations can be written, involving the through-the-thickness averaged current densities along x and the interface current densities:

$$\begin{cases} \dfrac{\partial j_x^{(1)}}{\partial x} - \dfrac{1}{t} j_c^{(1)} = 0 \\ \dfrac{\partial j_x^{(2)}}{\partial x} - \dfrac{1}{t_a}\left(j_c^{(2)} - j_c^{(1)}\right) = 0 \\ \dfrac{\partial j_x^{(3)}}{\partial x} + \dfrac{1}{t} j_c^{(2)} = 0 \end{cases} \tag{3}$$

Differentiating Eq. (3), substituting Eq. (2) and considering the global charge conservation law, it is possible to obtain a system of second order differential equations. Solving the system and applying proper boundary conditions, the electric potential and current density fields are obtained, and so the potential drop ΔV (Figure 1), which increases as the crack grow.

3. Model Validation

To validate the model and the HM strategy, experiments were carried out on SL joints made of carbon/epoxy woven fabric adherends and a home-made CNT-modified epoxy adhesive. A schematic of the specimen and measurement configuration is shown in Figure 4. Glass/epoxy insulating tabs were glued at the specimen ends.
A cyclic load was applied in force control through an axial-torsional servo-hydraulic machine (MTS 809), with a load ratio of 0.1 and a frequency of 5 Hz.
Electrical measurements were carried out through a sourcemeter Keithley 2604B (Keithley Instruments, USA).

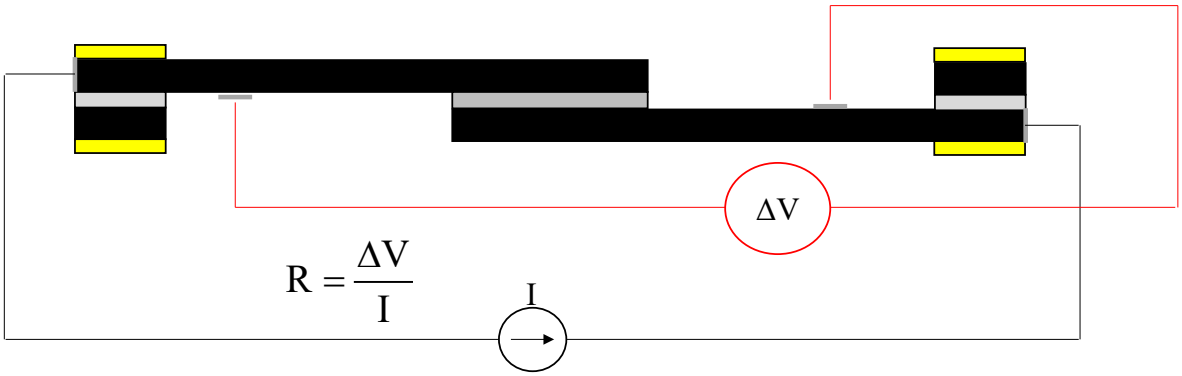

Figure 3. Schematic of the specimen configuration

During the test the joint resistance R was periodically measured, as well as the specimen stiffness, using the load cell and the machine LVDT.
Based on the measured resistance, the crack length was estimated through the analytical model. Then, Finite Element (FE) analyses were carried out simulating the entire specimen, with proper boundary conditions. In the FE model, a crack length equal to that estimated from the measured electric resistance was introduced. FE analyses were carried out with the ANSYS code, using parabolic plane elements, with an element size small enough to ensure the convergence of the obtained stiffness.
In Figure 4, the estimated stiffness, normalized to the initial value, K_0, is plotted and compared to that measured during the fatigue test. A fairly good agreement can be observed, even though the model underestimates the stiffness loss. This is probably due to the fact that the crack faces are not perfectly insulating, as assumed by the model, thanks to the presence of bridging fibers and bundles. This causes an underestimation of the crack length and, thus, the stiffness degradation.

  doi:10.5075/epfl-298799_978-2-9701614-0-0

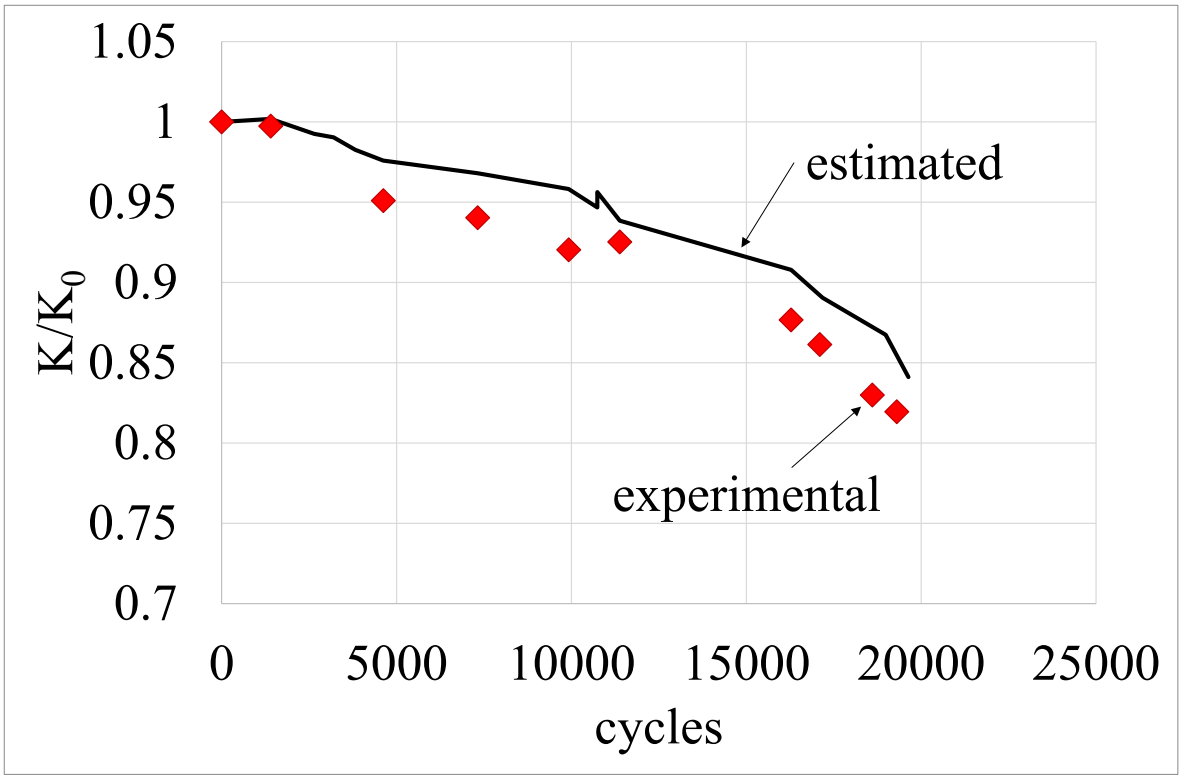

Figure 4: Experimental and predicted stiffness trend

4. Conclusions

The possibility of performing the HM of a bonded connection has been explored. A model was developed to assess the crack length based on electric measurements. Experiments were carried out on conductive SL joints. The model predictions, in terms of the crack-induced stiffness degradation, are in reasonable agreement with the experimental results, even though the possible presence of conductive bridging ligaments sho7uld be accounted for in the model to improve the predictions.

5. References

1. Tserpes KI, Peikert G, Floros IS. The Effectiveness of Corrugation as a Crack Stopper in Composite Bonded Joints, 4th International Conference of Engineering Against Failure (ICEAF IV), 24-26 June 2015, Skiathos, Greece.
2. Floros I, Tserpes KI. Numerical simulation of quasistatic and fatigue debonding growth in adhesively bonded composite joints containing bolts as crack stoppers, The Journal of Adhesion 2019; 97(7):1-23.
3. Yashiro S, Wada J, Sakaida Y. A monitoring technique for disbond area in carbon fiber–reinforced polymer bonded joints using embedded fiber Bragg grating sensors: Development and experimental validation, Structural Health Monitoring 2017; 16(2):185–201.
4. Sánchez-Romate XF, Sbarufatti C, Sánchez M, Bernasconi A, Scaccabarozzi D, Libonati F, Cinquemani S, Güemes A, Ureña A. Fatigue crack growth identification in bonded joints by using carbon nanotube doped adhesive films Smart Mater Struct 2020; 29(3):1-14.

5. Schulte K, Baron Ch. Load and failure analyses of CFRP laminates by means of electrical resistivity measurements. Compos Sci Technol 1989; 36:349–356.
6. Böger L, Wichmann MH, Meyer LO, Schulte K. Load and health monitoring in glass fibre reinforced composites with an electrically conductive nanocomposite epoxy matrix. Compos Sci Technol 2008; 68:1886-1894.
7. Fernberg SP, Joffe R. Damage detection in carbon fibre cross-ply laminates by aid of carbon nanotube doped resin. In: Proceedings of the 13th European Conference on Composite Materials ECCM13, Stockholm, Sweden, June 2-5 2008.
8. Gao L, Thostenson ET, Zhang Z, Chou TW. Sensing of damage mechanisms in fiber-reinforced composites under cyclic loading using carbon nanotubes. Adv Funct Mater 2009;19: 123–130.
9. Zappalorto M, Panozzo F, Carraro PA, Quaresimin M. Electrical response of a laminate with a delamination: modelling and experiments. Compos Sci Technol 2017; 143:31-45.
10. Carraro PA, Zappalorto M, Quaresimin M. Health monitoring of cross-ply laminates: Modelling the correlation between damage evolution and electrical resistance change. Compos Part A 2016; 82:151-158.

  doi:10.5075/epfl-298799_978-2-9701614-0-0

DURABILITY OF CFRP-CONCRETE BOND IN EBR AND NSM SYSTEMS UNDER NATURAL AGEING FOR A PERIOD OF THREE YEARS

Aloys Dushimimana[a], Luís Correia[a], Ricardo Cruz[a], João Miguel Pereira[a], José Sena-Cruz[a]

a: University of Minho, ISISE/IB-S, Guimarães, Portugal – aloysdushimimana@yahoo.fr

Abstract: *Carbon Fibre Reinforced Polymer (CFRP) composites have been shown to possess desirable properties for strengthening of reinforced concrete (RC) structures. The application of CFRP composites is mainly through Externally Bonded Reinforcement (EBR) or Near Surface-Mounted (NSM) techniques. The main objective of the present work was to provide insights on durability of bond between concrete and CFRP strips installed according to EBR and NSM techniques under the effects of ageing induced by outdoor conditions for a period of three years. Specimens were placed in four different outdoor environments (E3-E6) with ageing mainly induced by freeze-thaw attacks, carbonation, airborne chlorides, and elevated temperatures. Besides, the study included a reference environment (E1: ≈20 °C / 55% RH) and another environment (E2: ≈20 °C / water immersion). The bond test results for the specimens collected from the aforementioned environments showed a small degradation of the CFRP-concrete bond after three years.*

Keywords: *bond; EBR; NSM; durability; natural outdoor ageing*

1. Introduction

Carbon Fiber Reinforced Polymer (CFRP) composites possess desirable properties for strengthening of existing RC structures [1, 2]. CFRP composites can mainly be applied through EBR or NSM techniques [3]. In the former, the CFRP is applied on the surface of a RC element to be strengthened, while in the latter the CFRP is inserted in a groove cut into the concrete cover of the RC element. The adhesion between FRP and concrete substrate in EBR generally controls the ultimate capacity of the strengthened element [4]. However, the premature failure due to debonding will lead to underutilization of the materials [5]. On the other hand, NSM technique is an effective solution to increase cracking, yielding and ultimate loads of strengthened elements failing in bending [6]. Besides, experimental observations from different past studies have revealed that NSM has superior benefits than EBR [7, 8]. This is attributed to a better CFRP-concrete bond performance which leads to a more efficient use of CFRP strain [9].

Regarding the durability of the CFRP-concrete bond, the bond strength can be affected by various factors, mainly by ageing of the constituent materials, environmental exposure conditions, or due to loading conditions. Negligible variations of NSM CFRP-concrete bond strength were found after 240 days of exposure to water immersion, water immersion with chlorides, wet/dry cycles in tap water with chlorides, and freeze-thaw cycles [1]. However, the latter exposure changed the failure mode from debonding at the CFRP/adhesive to adhesive/concrete and cohesive failure of concrete [1]. Furthermore, some studies show that the glass transition temperature (T_g) of adhesive can significantly affect the failure mode [10], and the exposure to temperature cycles can improve the bond strength (due to post-curing phenomena), while temperatures higher than the T_g can reduce it [11, 12].

  doi:10.5075/epfl-298799_978-2-9701614-0-0

A comparative analysis on the bond performance using data from the available literature can contribute to further understanding of EBR and NSM systems when considering their service life and long-term benefits. Referring to existing data on accelerated ageing conditions, a comparative perspective in [1], showed a significant degradation of the bond strength up to 68% for EBR and 1.4% for NSM when exposed to moisture, and up to 25% and 5%, respectively, when exposed to freeze-thaw cycles. However, a comparable bond strength reduction was found when EBR and NSM were exposed to natural outdoor environments, but further studies were suggested for confirmation [1]. In fact, most of the existing studies on the durability of the CFRP-concrete bond have been conducted under laboratorial conditions using accelerated ageing protocols [13], and little is known on whether such conditions can provide an appropriate estimate of what normally happens in the real (natural) outdoor conditions. Hence, there is a need to conduct further studies under natural ageing conditions, perform comparative analysis, and gain an increased understanding on the behavior of EBR and NSM systems with time. In this regard, this work presents the durability of the EBR and NSM CFRP-concrete bond after three years of natural outdoor exposure to different aggressive environments, particularly, the maximum pull-out force and the type of failure mode are the main parameters investigated.

2. Materials and Methods

2.1. Description of materials, EBR and NSM specimens

A description of the materials involved in the preparation of the specimens for bond tests and the prepared specimens is provided in this section.

Materials: In this work, the commercial cold curing epoxy adhesive, trademarked as S&P Resin 220 epoxy adhesive by S&P® Clever Reinforcement Ibérica Lda. Company, was used as the bonding agent between the CFRP strip and the concrete substrate. The CFRP strips, also produced by the same company, with the trademark CFK 150/2000 were adopted to strengthen the specimens according to EBR and NSM techniques. In the latter technique, CFRP laminates with a cross-section of 50 × 1.4 mm^2 (L10) were adopted, while CFRP laminates with a cross-section of 50 × 1.2 mm^2 (L50) were adopted in the former. The concrete with C30/37 XC4(P) CL 0.40 d_{max} 12.5 S4 as per [14] was used to cast all the specimens from a single concrete batch of about 12 m^3. The average elastic modulus and compressive strength of concrete after 28 days were 29.1 GPa and 41.5 MPa, respectively. The elastic modulus and ultimate strength of CFRP and adhesive were approximately 170 GPa and 2000 MPa, 11.2 GPa and 29 MPa, respectively. Further details on the properties of the adhesive and CFRP used can be found in [13].

EBR specimens: 40 concrete prisms each with 400 × 200 × 200 [mm] and two CFRP laminate strips with a cross-section of L50 applied in opposite faces (parallel to the casting direction) were prepared from different environments for testing. A bond length of 220 mm was adopted, with 100 mm free from the extremity of the concrete prism to avoid premature failure by concrete rip-off ahead of the loaded end. According to [15], the used bond length (220 mm) should be higher than the theoretical effective length, L_e, of 101 mm.

NSM specimens: 40 concrete cubic blocks, each with 200 mm of edge and CFRP strip (L10) applied along a bond length of 60 mm, were prepared according to NSM system. The CFRP strip was inserted in the center of a groove with 15 × 5 [mm] opened at the surface of the concrete block.

  doi:10.5075/epfl-298799_978-2-9701614-0-0

2.2. Description of experimental stations

After the preparation of the EBR and NSM specimens, the specimens were placed in different regions of Portugal for ageing until three years of exposure, that is, the specimens were kept in two artificial environments (E1 and E2), and four outdoor environments (E3-E6). In E1, the specimens were placed in controlled hygrothermal conditions of 20 °C / 55% RH, while in E2 the specimens were continuously immersed in water under controlled temperature (approximately 20 °C). On the other hand, specimens were placed in E3 characterized by high levels of concrete carbonation (station near the International Airport of Lisbon), E4 characterized by freeze-thaw attacks (i.e., specimens placed at the highest mountain in Portugal), E5 characterized by high elevated service temperatures and lower relative humidity (i.e., specimens placed in Elvas), and E6 characterized by high levels of chlorides concentration and relative humidity (i.e. specimens placed near the Atlantic ocean). Additionally, sensors were installed close to the materials in order to control the temperature and relative humidity in each environment. Further details on the experimental stations can be found in [13]. Finally, each year, 2 specimens of EBR and 2 specimens of NSM were collected and tested in the laboratory of civil engineering, University of Minho. Details on the tests conducted in each of the consecutive three years (namely T1 for year1, T2 for year 2, and T3 for year 3) are provided in the next section.

2.3. Pull-out tests for EBR and NSM specimens

In order to perform the pull-out tests, the EBR specimens were placed horizontally on a steel plate with 70 × 300 × 550 [mm] identified as Support 1 (see Fig. 1), fixed to the stiff base of the testing steel frame system through eight M16 steel threaded rods. A steel plate identified as Support 2 was placed in the bottom front part of the concrete block to assure negligible horizontal displacements of the specimen in the loading direction during the test, which acted as a reaction element at a height of 50 mm. The Support 3, which is a prismatic steel plate, was placed in the rear top part of the specimen to minimize vertical displacements during the test. Support 2 and Support 3 were fixed to Support 1 through two M20 steel threaded rods. The tests were performed using a servo-controlled equipment and the applied force was measured through a load cell of 200 kN maximum load carrying capacity (linearity error of 0.05% F.S.), placed between the actuator and the grip was used to pull the CFRP laminate during the test. The relative displacement between the CFRP and the concrete (slip) at the loaded end section (s_l) and free end section (s_f) were measured using the linear variable displacement transducers (LVDT) LVDT1 and LVDT2, respectively, with a stroke of ±10 mm (linearity error of 0.24% F.S.). The tests were performed under displacement control at the loaded end through LVDT1 with a rate of 2 μm/s. Additionally, a series of four strain gauges TML BFLA-5-3-3L were placed along the CFRP laminate centerline to measure the longitudinal strains during the loading process.

  doi:10.5075/epfl-298799_978-2-9701614-0-0

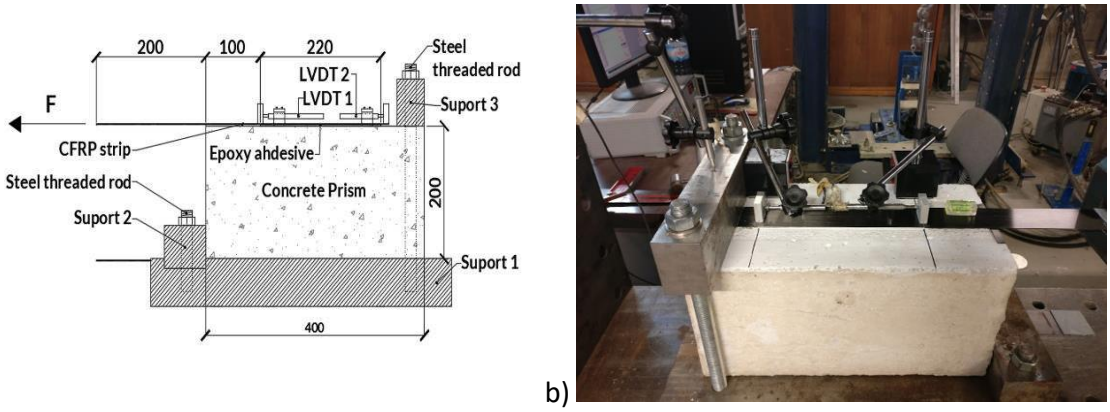

a) b)

Figure 1. (a) Specimen's geometry and test configuration, and (b) photograph of the EBR bond test. Note: all units in [mm]

On the other hand, the geometry of NSM specimens and the respective test configuration is shown in Fig. 2. A servo-controlled equipment was used to apply the load, and the slip at the loaded and free end, was measured using two LVDTs (range ±2.5 mm and linearity error of ±0.05% F.S.) i.e. LVDT1 and LVDT2, respectively. The load was measured by a load cell placed between the grip and the actuator, with a static load carrying capacity of 200 kN (linearity error of ±0.05% F.S.). These tests were also performed under displacement control at the loaded end section (LVDT1), at a rate of 2 µm/s.

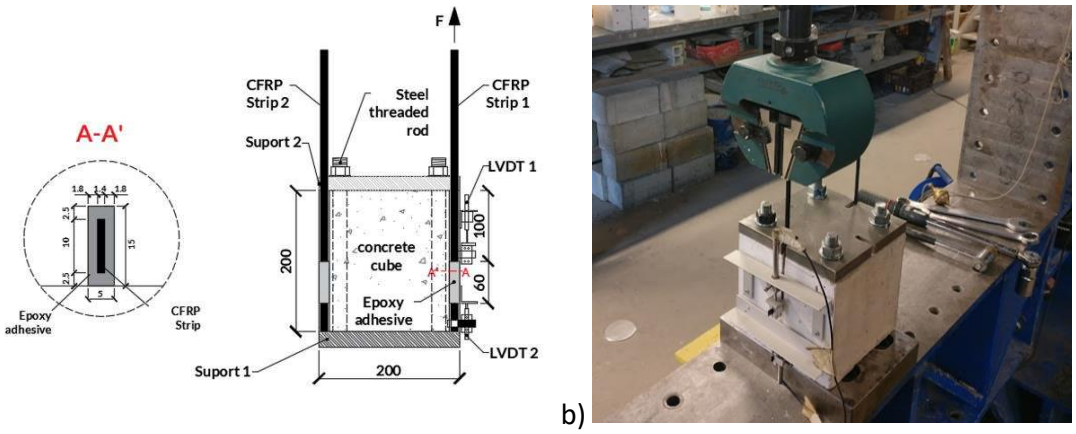

a) b)

Figure 2. (a) Specimen's geometry and test configuration, and (b) photograph of the NSM bond test. Note: all units in [mm]

3. Results and Discussion

The average curves for EBR force *versus* slip relation in each of the studied environments after T3 are presented in Fig. 3a. It can be seen that the E1 and E2 environments have the lowest maximum force, E5 shows the highest force and slip compared to other environments. When comparing the results for the maximum pull-out force (pullout strength) from T1 to T3 (Fig. 3b), it can be seen that there was an increase in the pullout force from T1 to T2, followed by a reduction from T2 to T3 in the environments E2-E4, while a reduction can be noticed from T2 to T3 in all environments. After T3, the force is generally lower than the initial value at T0, mainly in the artificial environments (E1 and E2), and a small degradation of bond strength can be seen in outdoor environments.

  doi:10.5075/epfl-298799_978-2-9701614-0-0

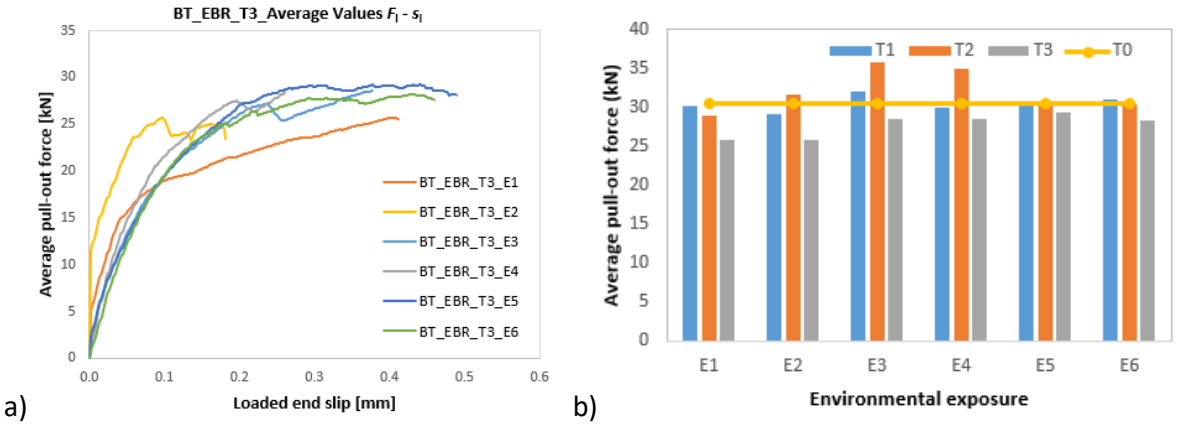

Figure 3. Results obtained from EBR systems for the different environments: (a) average curves for pullout force vs. slip for T3, (b) average values of pull-out force from T1 to T3

Looking at the results for NSM system in different environments (Fig. 4), it can be seen that specimens continuously immersed in water (E2) show the lowest maximum pull-out force, which can be attributed to the degradation caused by ingress of water through the constituent materials. On the other hand, the specimens collected in E6 exposed to airborne chlorides shows the highest pull-out force. After three years, a small degradation in E3-E5 and a slight increase in E1 and E6 can be noticed, while a significant degradation is observed in E2 (see Fig. 4b).

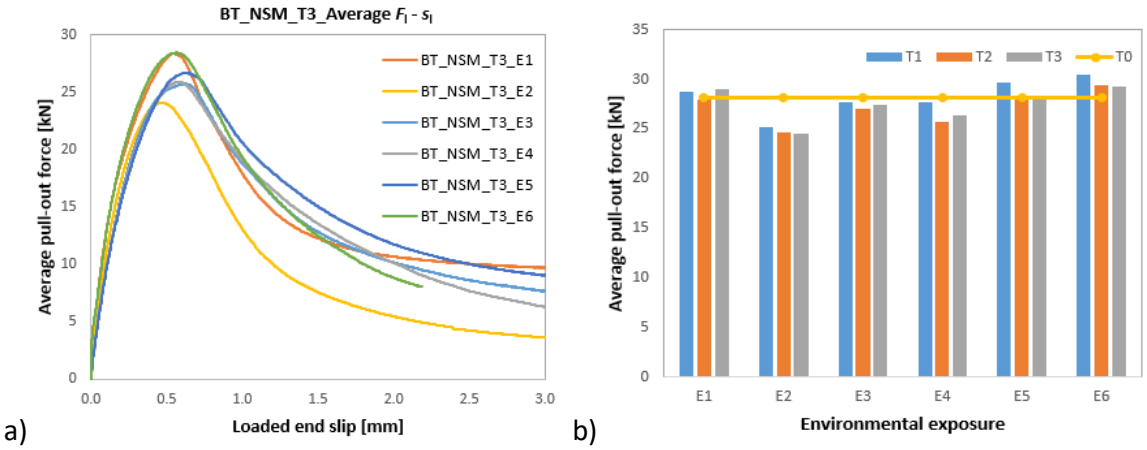

Figure 4. Results obtained from NSM systems for the different environments: (a) average curves for pull-out force vs. slip after T3, (b) average values of pull-out force from T1 to T3

In order to examine the cause of the strength variation in both EBR and NSM systems, the bond strength from EBR and NSM is plotted together with the tensile strength of the constituent materials (concrete, CFRP and adhesive) in Fig. 5 after 3 years. It can be seen that CFRP is immune against strength variation with time, while both concrete and adhesive tensile strengths tend to vary with time and environment. Mainly, the hybrid effect of the highest adhesive and concrete strength degradation is observed to cause the highest bond strength degradation for the specimens immersed in water (E2). Like what has been previously observed in [1], a comparable bond strength reduction is found between EBR and NSM systems when exposed to natural outdoor environments, except in E6.

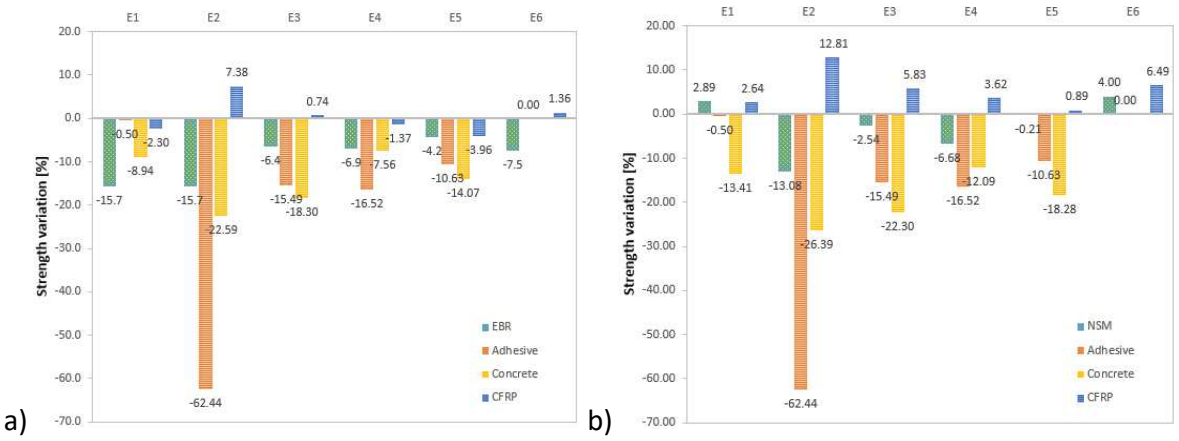

Figure 5. Comparison of strength variation between EBR (a) or NSM (b) bond strength and the constituent materials' strength in different environments after 3 years

Typical failure modes (FM) for both EBR and NSM systems are shown in Fig. 6. In the former system, the concrete cohesive failure is predominant in all environments, while in the latter the failure at CFRP-adhesive or at CFRP-adhesive combined with concrete cracking (or splitting) is predominant. In general, the failure mode is observed to vary with time and environments.

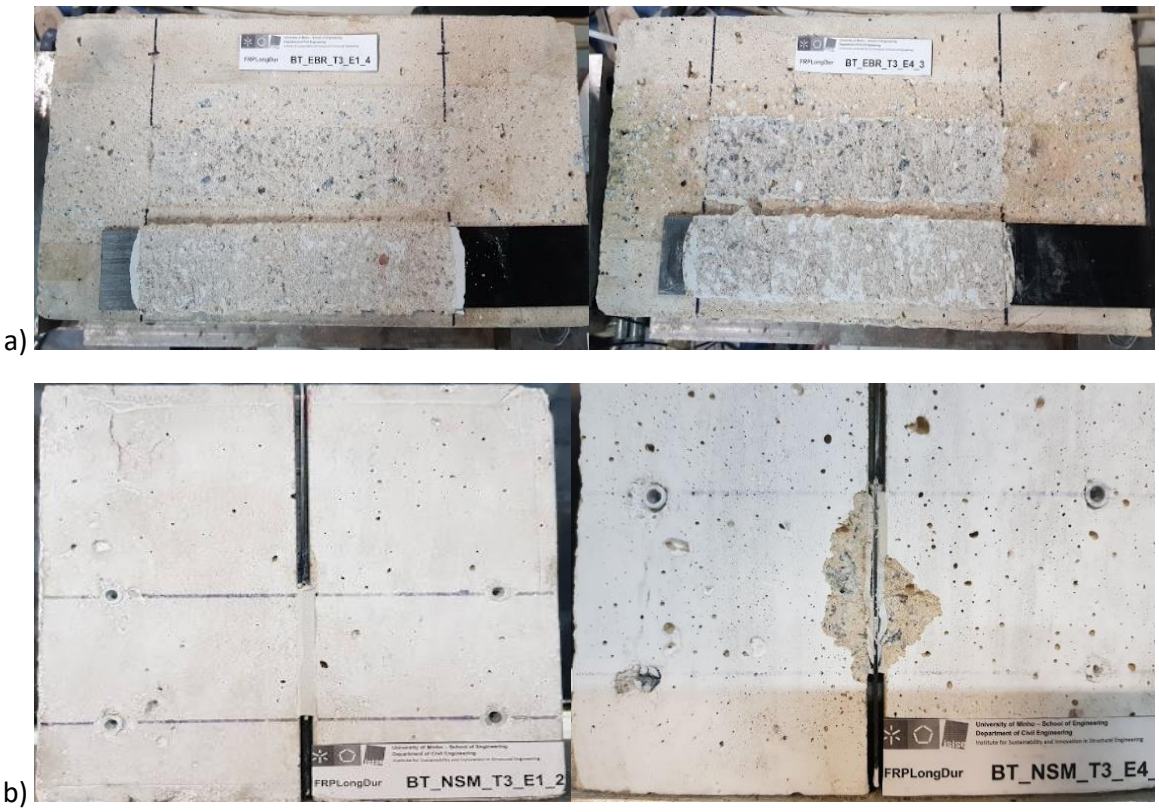

Figure 6. Typical failure modes observed after three years of exposure: (a) EBR specimens, (b) NSM specimens

4. Conclusions

In this work, pull-out bond tests were carried out for specimens strengthened according to EBR and NSM techniques. These specimens were previously placed in different environments (E1-E6) and then collected (each year) from these environments to be tested up to three years of exposure. The key findings from the tests are as follows.

1. Bond strength of both EBR and NSM systems had generally a slight variation after three years of natural exposure when compared to the value recorded at initial time. Besides, the maximum pull-out force in EBR specimens from outdoor environments tend to have a similar plateau after being exposed to different aggressive environments.
2. A slight increase in CFRP tensile strength is observed in all studied environments for NSM systems, while for the case of EBR a slight decrease is found in some environments. On the other hand, the tensile strength of both the concrete and adhesive showed a decrease in all environments, the most significant decrease being observed in specimens immersed in water.
3. The effect of strength variation of different constituent materials (CFRP, concrete, and adhesive) on the bond strength degradation in EBR and NSM systems is investigated. It is found that CFRP strength variation has no effect on the EBR or NSM strength degradation after three years of exposure. However, the effect of adhesive and concrete strength degradation tends to lead to slight degradation of bond strength for the specimens immersed in water, exposed to carbonation, freeze-thaw cycles and high temperatures. This shows that the above environments might have significant effect on the adhesive and concrete properties with time. Particularly, the immersion of epoxy adhesive in water is observed to severely affect its strength.
4. The failure modes for EBR and NSM systems are generally different. Also, the FM are found to change with time. In general, the EBR system shows cohesive failure of concrete as the predominant failure, whereas for the NSM system the failure at CFRP-adhesive or CFRP-adhesive combined with concrete cracking (or concrete splitting) are the observed predominant failures.

Acknowledgements

This work was carried out in scope of the project FRPLongDur POCI-01-0145-FEDER-016900 (FCT PTDC/ECM-EST/1282/2014) funded by national funds through the Foundation for Science and Technology (FCT) and co-financed by the European Fund of the Regional Development (FEDER) through the Operational Program for Competitiveness and Internationalization (POCI) and the Lisbon Regional Operational Program. This work is also financed by national funds through FCT under grant agreement [DFA/BD/08403/2021] attributed to the first author.

5. References

1. Fernandes P, Sena-Cruz J, Xavier J, Silva P, Pereira E, Cruz J. Durability of bond in NSM CFRP-concrete systems under different environmental conditions. Compos Part B Eng [Internet]. 2018;138(November2017):19–34. https://doi.org/10.1016/j.compositesb.2017.11.022

2. Cabral-fonseca S, Correia JR, Custódio J, Silva HM, Machado AM, Sousa J. Durability of FRP - concrete bonded joints in structural rehabilitation : A review. Int J Adhes Adhes [Internet].

2018;83(March):153–67. Available from: https://doi.org/10.1016/j.ijadhadh.2018.02.014

3. Bilotta A, Ceroni F, Di Ludovico M, Nigro E, Pecce M, Manfredi G. Bond Efficiency of EBR and NSM FRP Systems for Strengthening Concrete Members. J Compos Constr. 2011;15(5):757–72.

4. Bilotta A, Faella C, Martinelli E, Nigro E. Design by testing procedure for intermediate debonding in EBR FRP strengthened RC beams. Eng Struct [Internet]. 2013;46:147–54. Available from: http://dx.doi.org/10.1016/j.engstruct.2012.06.031

5. Torabian A, Isufi B, Mostofinejad D, Pinho Ramos A. Flexural strengthening of flat slabs with FRP composites using EBR and EBROG methods. Eng Struct. 2020;211(August 2019).

6. Dias SJE, Barros JAO, Janwaen W. Behavior of RC beams flexurally strengthened with NSM CFRP laminates. Compos Struct [Internet]. 2018;201(March 2017):363–76. Available from: https://doi.org/10.1016/j.compstruct.2018.05.126

7. Barros JAO, Dias SJE, Lima JLT. Efficacy of CFRP-based techniques for the flexural and shear strengthening of concrete beams. Cem Concr Compos. 2007;29(3):203–17.

8. Bilotta A, Ceroni F, Nigro E, Pecce M. Efficiency of CFRP NSM strips and EBR plates for flexural strengthening of RC beams and loading pattern influence. Compos Struct [Internet]. 2015;124:163–75. Available from: http://dx.doi.org/10.1016/j.compstruct.2014.12.046

9. Bianco V, Barros JAO, Monti G. Three dimensional mechanical model for simulating the NSM FRP strips shear strength contribution to RC beams. Eng Struct [Internet]. 2009;31(4):815–26. Available from: http://dx.doi.org/10.1016/j.engstruct.2008.12.017

10. Burke PJ, Bisby LA, Green MF. Effects of elevated temperature on near surface mounted and externally bonded FRP strengthening systems for concrete. Cem Concr Compos [Internet]. 2013;35(1):190–9. Available from: http://dx.doi.org/10.1016/j.cemconcomp.2012.10.003

11. Yu B, Kodur VKR. Effect of high temperature on bond strength of near-surface mounted FRP reinforcement. Compos Struct. 2014;110(1):88–97.

12. Firmo JP, Correia JR, Pitta D, Tiago C, Arruda MRT. Bond Behavior between Near-Surface-Mounted CFRP Strips and Concrete at High Temperatures. J Compos Constr. 2015;19(4):04014071.

13. Cruz R, Correia L, Dushimimana A, Cabral-Fonseca S, Sena-Cruz J. Durability of epoxy adhesives and carbon fibre reinforced polymer laminates used in strengthening systems: Accelerated ageing versus natural ageing. Materials (Basel). 2021 Mar 2;14(6).

14. IPQ. IPQ (Instituto Português da Qualidade). 1992. NP EN EN 1992-1-1. Eurocode 2: design of concrete structures - Part 1-1: general rules and rules for buildings, Instituto Português da Qualidade (IPQ). Caparica, Portugal; 2010.

15. CNR. Guide for the Design and Construction of Externally Bonded FRP Systems for Strengthening Existing Structures; CNR-DT 200 R1/2013,. Rome, Italy; 2013.

Composites Meet Sustainability – Proceedings of the 20th European Conference on Composite Materials,
ECCM20. 26-30 June, 2022, Lausanne, Switzerland

LASER SHOCK FOR NDT OF COMPOSITES MATERIALS AND BONDED JOINTS: RECENT ADVANCES

Nicolas Cuvillier[a], *Mathieu Ducousso*[a], *Eduardo Cuenca*[a,b,c], , *Laurent Berthe*[c], François Coulouvrat[b]

a: Safran Tech, Rue des jeunes Bois, 78114 Magny les Hameaux, France, nicolas.cuvillier@safrangroup.com
b: Sorbonne Université, Institut Jean Le Rond d'Alembert, UMR CNRS 7190, 4 place Jussieu, 75005 Paris, France
c: Laboratoire PIMM, UMR 8006, ENSAM, CNRS, CNAM, HESAM, 151 boulevard de l'Hôpital, 75013 Paris, France

Abstract: *Composite materials play an essential role in reducing greenhouse gas emissions in aircraft industry, notably thanks their lightweight but strong structural properties. However, their generalization in aircraft industry requires improving some related industrial processes, such as structural bonding. For instance, efficient ways must be found to control the structural mechanical strength of the bonding and to disassemble them. We present here some experimental and numerical works applied to titanium/composite bonding using laser-driven shock wave, to control and disassemble it.*

Keywords: Bonding; NDT;

1. Introduction

Sustainable fuel and electric propulsion are frequently presented as main issues for carbon emissions reduction in aviation. However, a probably equally important lever is on the side of the lightening of the structures. This can be achieve by increasing the use of high performance materials. With a higher specific strength and stiffness than many metals (for instance, x5 and x3 than aluminum alloys, respectively), carbon-fiber reinforced composites are often the better choice in aircraft lightweight design considerations. For such a material, structural bonding is the most efficient assembly method since welding is impossible and mechanical fasteners induce associated mechanical stress concentrations that limit the overall mechanical performances

The main limitation of structural bonding in the aircraft industry concerns the ability to certify in a non-invasive way the good quality of the bonding, *i.e.* to certify that it can resist up to a predefined strength value. To date, no industrial method for such certification has been demonstrated. Thus, there is a need to identify a quantitative non-destructive evaluation (NDE), able to certify the good quality of structural bonding, to allow further generalization of the use of composites in the transportation industry. Several NDE approaches have been investigated to enable such certification. However, as bonding quality depends on a variety of factors, including chemical (surface treatment, surface pollution…), physical (thickness, reticulation, anchorage…), and morphological (porosities and ageing), such evaluation is challenging.

Thermal, tomographic, electromagnetic, and optical methods have already been investigated, but presently none of them allows quantification of the mechanical strength of bonding. Intuitively, acoustic approaches appear to be more adapted to such quantification, as ultrasound

  doi:10.5075/epfl-298799_978-2-9701614-0-0

is a technique based on mechanical displacement. We recently demonstrated in Safran that laser-driven acoustic waves could be efficiently used to quantify the adhesion quality of industrial bonding by measuring temporal attenuation of local resonances [1] or by using plane wave synthesis to quantify interfacial stiffnesses in aluminum/aluminum bonding [2] [3]. For mixed bonding, such as the titanium leading edge bonded to the 3D woven composite Leap fan blade, we investigate the Laser Adhesion Test approach (LASAT). [4] [5]

LASAT consists of generating an intense shock wave (GPa intensity range) in the bonded structure by illuminating the surface using a laser pulse (in the GW/cm^2 intensity range). Using *ns*-scale laser pulses, it is found that the temporal duration of the plasma expansion – created by the laser-matter interaction- is similar to the laser pulse duration. Such plasma expansion induces an intense stress, which propagates into the material. The temporal profile and duration of the wave are similar to those of the plasma expansion at the surface. The amplitude of the stress depends mainly on the laser pulse energy and on the material at the surface of the target. In a finite thickness target, the shock wave is reflected from the back face of the material. Boundary conditions (amplitude free) induce a phase change at the reflection, and the compressive shock wave becomes a release shock wave. This release wave is used to test the quality—or the mechanical strength—of a bond. NDE, for example, ultrasonic inspection, must be performed after the experiments to detect any bonding failure that may have occurred. [4]

We recently demonstrated the relevancy of the LASAT approach on composite/titanium bonding. [5] In the following, we will quickly remind the main obtained results on simplified representative samples and we will then present some recent simulations to propose a new LASAT way for application on real Leap fan blade.

2. LASAT on flat Titanium / thin 3D woven composite bonding

2.1 Sample and Experiments

The samples used here are flat samples of 3.8 mm of 3D woven composite material bonded to a 0.4 mm titanium plate with a 0.15 mm thick layer of epoxy adhesive. Lateral dimension of the samples are 240x40 mm². We generated two different mechanical strengths of the bonding using two different polymerizations levels, at 90 and 50 %. Respective quantified mechanical strengths using normalized test (single-lap shear test and plot extraction) are between 35 and 39 MPa for the best bonding and between 10 and 15 MPa for the lower mechanical strength.

LASAT experiments were performed on the Hephaistos laser facility (PIMM Laboratory for Processes and Engineering in Materials and Mechanics, ENSAM ParisTech and CNRS). Two Gaïa HP lasers from THALES (Elancourt, France) emit two Nd:YAG synchronized or delayed laser pulses, both at 532 nm, with a repetition frequency of 2 Hz. Through a Gaussian temporal shape of 7 ns of duration [Fig. 2(a)], it is able to deliver an energy up to 14 J when both laser pulses are superposed (Gaussian spatial shape with diameter of around 6 mm). The applied laser energy started at 10% of the energy available on the Hephaistos facility and was increased per 10% steps up to the maximum available. Water confinement was used to increase the surface pressure. [4] This procedure was applied to the two bonding quality levels and with illumination of either the Titanium face or the composite face of the structure. After these experiments, a 15 MHz ultrasonic water tank inspection was performed allowing the identification of the laser intensity, which corresponds to the bonding damage threshold for each configuration (90% and

  doi:10.5075/epfl-298799_978-2-9701614-0-0

50% of reticulation, illuminating titanium and composite material). Results are presented on figure 1.

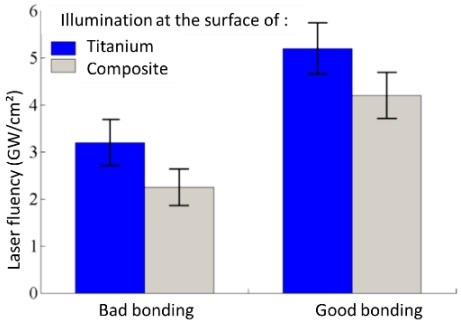

Figure 1. Damage threshold for each configuration (90% and 50% of reticulation, illuminating titanium and composite material).

The two bonding qualities are well discriminated: the debonding of the lowest mechanical strength appears for intensities around 2.7 ± 1 GW/cm^2 (composite illumination), while the highest bonding level debonds at intensities around 4.7 ± 1 GW/cm^2. We also note that around 1 GW/cm² more energy is required for when lighting the titanium than when lighting the composite for the two bonding qualities. This point will be explain by simulations.

2.2 Simulations

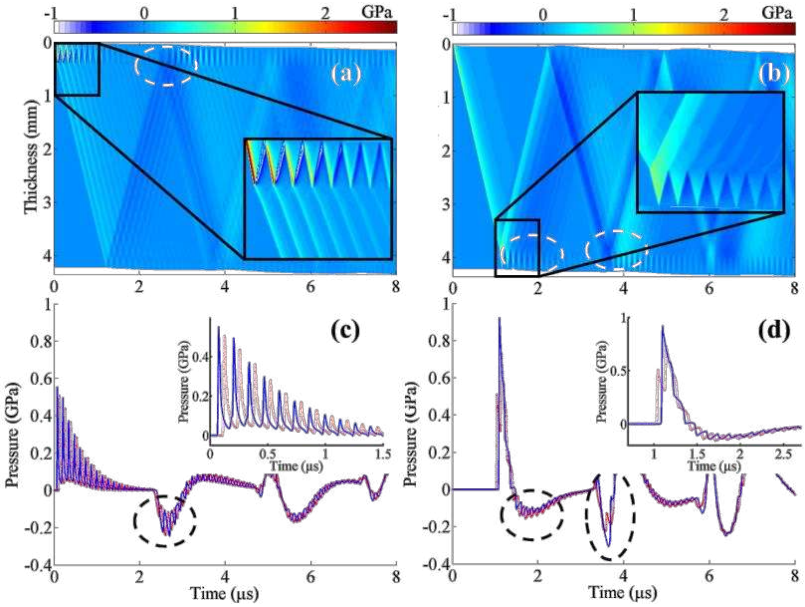

Figure 2. Time–position (X-t) stress diagram (a) and (b) of the shock wave propagation into Titanium/composite bonding, as a function of the illuminated material: Titanium on the left and composite on the right. Stress (c) and (d) at the composite/epoxy (red dotted line) and epoxy/TA6V4 (blue continuous line) interfaces for both illumination configurations, on the titanium or composite surfaces, are also presented. For each plot, a zoom is also presented into a 1 µs/1mm spatio-temporal window for plots (a) and (b) and 1.5 µs for plots (c) and (d). The two tiny irregular white bands along the horizontal edges of (a) and (b) are related to the 1D

  doi:10.5075/epfl-298799_978-2-9701614-0-0

nature of the ESTHER Lagrangian code, which cannot model boundary conditions at lateral borders and, thus, cannot model a recall force. Image from [5].

Simulations were performed using ESTHER software, developed by CEA. [6] ESTHER is a 1D Lagrangian code that describes both laser–matter interaction and shock propagation in materials. The laser energy deposition is calculated by solving the Helmholtz equation. Thus, it allows simulation of the induced pressure field in the target. Shock wave propagation into the multilayer is then simulated by the resolution of the continuity equations with an adapted equation of states to relate energy and stress. We used the Steinberg-Cochran-Guinan formalism for the TA64V19 and the Mie-Grüneisen formalism for the epoxy adhesive and the composite modeling. [5]

From these simulations, we found that different acoustic paths are involved before generating the release wave used to exert the LASAT process depending on the illuminated material. See [5] for details. Main results are the following : 1) Titanium/3D woven composite is a critical interface for the classical LASAT process as the acoustic transmission coefficient is around 10% ; 2) The 3D nature of the composite material makes the shock propagation very challenging in this material as significant scattering occurs due to material heterogeneities ; 3) These two first points are all the more important for the LASAT process as the mechanical strength of the considered bonding is very high (see static evaluation results).

We are finally, however, able to quantify a mechanical strength of the involved bonding in LASAT dynamic loading, at 250 MPa and 300 MPa for the 50% and 90% polymerized samples, respectively. These dynamic strengths have to be compared to the corresponding static strengths, 35 and 15 MPa respectively.

2.3 LASAT limitations for industrial use on the Leap fan blade

Because of the 3 points highlighted above, a classical version of the LASAT (*i.e.* a release traction on the adhesive layer generated by back face reflection of a compressive shock wave) seems not applicable on the leading edge of the Leap fan blade. Indeed, as illustrated on fig. 3, in addition to its curved geometry, the considered structure is a trilayer over most of the leading edge (Titanium-composite-titanium) and thus the titanium/composite interface has to be crossed twice before exerting the LASAT traction. Moreover, composite thickness can be significantly larger than 3.8 mm, as considered in the first work. Thus, finally, it seems very difficult to generate, in the adhesive layer, a release stress of 300 MPa using the classical LASAT configuration and a new way is now proposed.

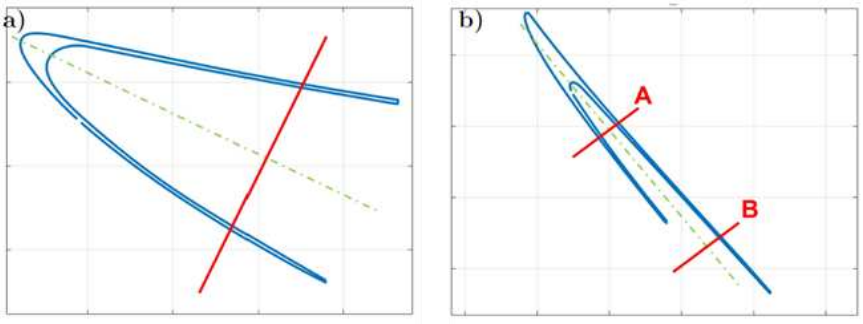

Figure 3. Cross section of the leading edge of the LEAP engine fan blade. The green discontinuous line represents the bisection of the angle between extrados and intrados. The red line is perpendicular to the bisection. (a) Cross section of the bottom part of the fan blade where the composite is thicker. (b) Cross-section of the top part of the fan blade.

3. Optimized LASAT configuration for the Leap fan blade inspection of disbonding.

3.1 Laser-driven shock wave propagation in a metallic part using a laser top-hat spatial profile

We consider here the laser-driven shock wave propagation in a homogenous metallic part, such as a titanium plate. This work has been recently discussed and modelled in detail, [7] thus we **remind** here only the main points necessary to understand our new LASAT approach. First, main and essential novelty with experiments presents in part 2 concern the spatial profile of the laser illumination.

In the experiments described in section 2, the spatial profile is Gaussian. Thus, only one longitudinal shock wave, propagating at a c_L velocity, is generated from center of the laser illumination. On the contrary, using a top-hat spatial profile generates more waves; see fig. 4(a): a main pressure wave (note P) is generated from the center of the illumination. This wave is similar to the wave generated using a Gaussian laser beam. However, due to diffraction induced by the discontinuity of the laser illumination (top-hat profile), a release longitudinal wave (R) is also generated all around the edge of the laser focal spot. This wave propagates from the edge of the focal spot with the same c_L velocity as the longitudinal pressure wave. Finally, a shear wave (S) is also radiated from the discontinuity at the spot edge but propagates slower, at a c_T velocity.

3.2 Single pulse LASAT optimization

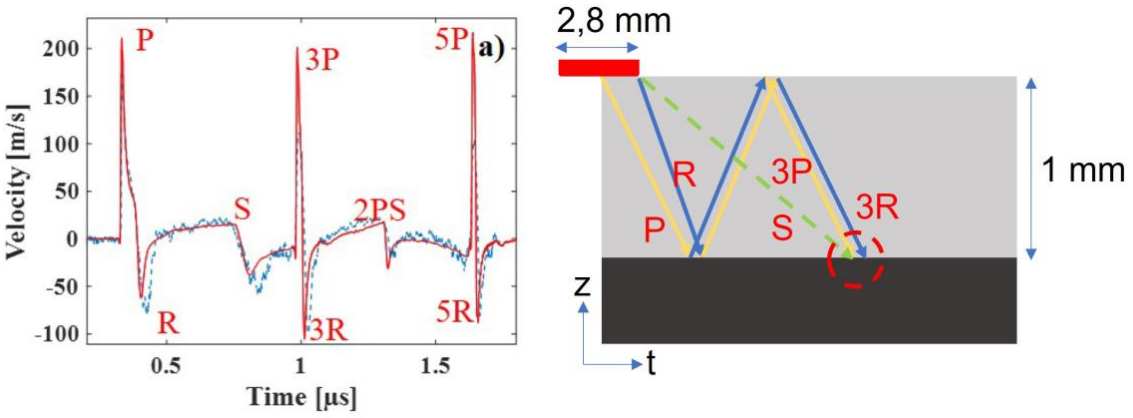

Figure 4. (a) Comparison between 3D numerical simulation (red continuous line) and VISAR measurement of the opposite free surface velocity (blue dashed line). (b) Time-space scheme of the optimization process. The yellow lines represents pressure shock waves and the blue ones the tensile shock waves. The polarization of the waves is indicated by the continuity of the arrows: continuous for the longitudinal ones and discontinuous for the shear ones. For this particular case, a 1 mm titanium plate, the optimized diameter of the laser spot is 2.8 mm. We

  doi:10.5075/epfl-298799_978-2-9701614-0-0

draw the origin of the release and the shear wave at the edge of the laser illumination merely for the sake of clarity.

The shear waves have two particularities that we can use to optimize the LASAT process in our case of interest. The first one is that their propagation velocity is slower that the pressure wave velocity, about 3200 m/s in the titanium compared to 6100 m/s for longitudinal waves. The second one is that, since they originate from the edge of the laser spot, tuning the source diameter allows tuning their arrival time (we consider here only the vertical of the epicenter of the illumination in the bulk of the material). Moreover, the shear waves have, in part, a tensile contribution.

Therefore, an optimization can be proposed by accumulating, in a small volume under the epicenter of the illumination and at the titanium/composite interface, the shear wave tensile contribution with the main release one, with time synchronization between the two waves. This optimization has been patented and is illustrated on fig. 4(b). The yellow arrows represent the compression shock waves, the blue ones the release waves and the green line the shear wave with compression and release contribution. The continuous arrows indicate longitudinal waves and the green discontinuous line the shear one. Letters P, R and S mark the pressure, release and shear waves, respectively. P wave is generated from the overall surface of the laser illumination, while R and S waves are generated from laser edge. The number 3 indicates waves having travelled three times through the titanium thickness and having reflected twice, once on the composite interface and once on the upper free surface. Since the shear wave propagates slower that the longitudinal one, it is possible to synchronize on the interface the arrival of the first tensile shear wave S with the second arrival 3R of the release wave.

A simple geometrical description allows the estimation of the laser radius required for that optimization, considering a titanium layer of thickness h:

$$r = \sqrt{\frac{h^2(9c_L^2 - c_T^2)}{c_L^2 - c_T^2}} \tag{1}$$

Thus, for example, if we consider a 0.75 mm titanium layer bonded to a semi-infinite composite, and if we want to optimize the tensile force at the interface by using the shear wave, given the longitudinal and shear velocities in the titanium, this yields a laser spot radius of equal to 1.1 mm.

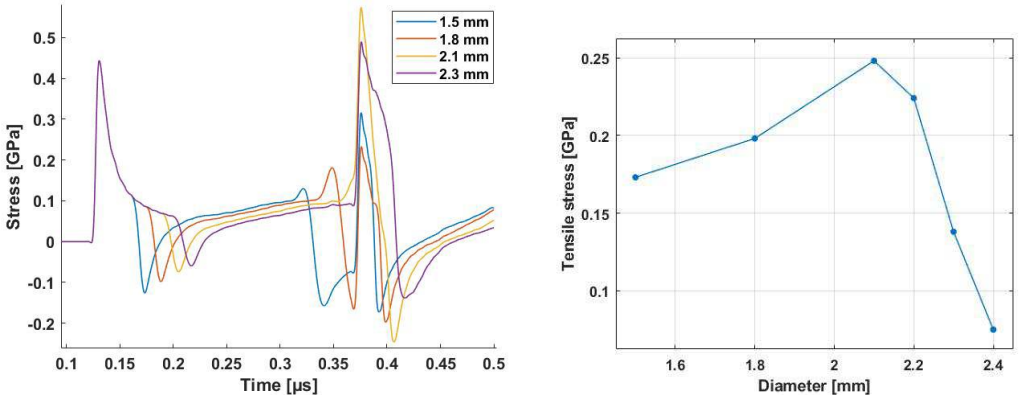

Figure 5. (a) Influence of the laser spot diameter on the axial stress component σ_{zz} at the interface of a 0.75 mm titanium - semi-infinite composite assembly. (a) Temporal profile of the stress at the interface. (b) Influence of the diameter of the source on the maximum (negative) value of the tensile stress at the interface.

Let us now simulate this configuration using a 3D elastodynamic model. [7] It allows the estimated value using Eq. (1) to be refined and to quantify the efficiency of the optimization. The displayed quantity is the stress component σ_{zz} where z is the direction through the material thickness, at the interface $z = h$ and at the center of the laser axis $r = 0$. We will keep for all the simulations the delivered energy per surface constant for an easier comparison.

On fig. 5(a), the shear wave *S* in the case of a 1.5 mm diameter configuration is easily observable since it arrives well before the second longitudinal shock wave 3P/3R. When the laser diameter increases, it arrives later and interferes first with the second shock 3P, thus decreasing its amplitude (1.8 mm case). In the optimal case (2.1 mm case), it is in-phase with the release wave 3R so that the amplitude of the tensile wave is maximized (240 MPa at time at 0.41 µs). This amplitude then decreases when further increasing the diameter and dephasing the two waves. This confirms that the shear wave can increase the traction at the interface with a proper tuning of the laser spot diameter. In figure 5(b) we represented the maximum value of the tensile stress at the interface, with a 43% increase between the 1.5 mm (170 MPa) and the optimal 2.1 mm configurations.

3.3 Double pulse LASAT optimization

Despite the optimization proposed in section 3.2, the release traction is not high enough in intensity to disbond the leading edge of the fan blade. Indeed, a release traction of 300 MPa is necessary while we are able to generate a release traction of 240 MPa using the previous optimization. One way to increase again the release traction is to use two laser pulses instead of one and to cumulate the release traction achievable using each pulse, adjusting the time delay between the two pulses, see fig. 6(a).

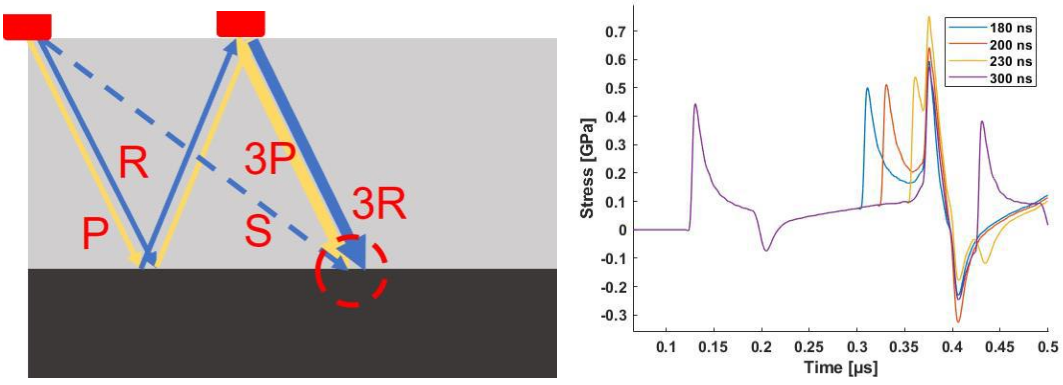

Figure 6. (a) Scheme of the double impulsion experiment, with same color code. The red boxes over the figure represent the delayed laser illuminations. The 3P and 3R lines are thicker because of the addition of the P and R waves from the second laser. (b) Axial (r = 0) stress component σzz of a 0.75 mm titanium - semi-infinite composite assembly illuminated by a laser spot of diameter 2.1 mm on the interface z = h. Influence of the delay between two successive identical illuminations.

  doi:10.5075/epfl-298799_978-2-9701614-0-0

In figure 6(b) we present the stress component σ_{zz} at the interface of the assembly and on the laser central axis ($z = h,\ r = 0$) in case of a double optimized illumination, as a function of the time delay between the two laser shots. All parameters are identical to the ones of the single shot optimized configuration, with a 0.75 mm-thick titanium layer and an optimized laser spot of 2.1 mm. Measured spatial top-hat and temporal laser pulse profiles are unchanged and the same for the two shots. The figure points out that a delay of 200 ns between illuminations is the optimal choice (for this thickness). We observe that the negative peak of the stress is about 320 MPa at the interface for the doubled optimal configuration. Compared to the optimized single illumination (240 MPa), this is a 33 % increase and the 300 MPa required value is reach.

4. Conclusion

To conclude we presented first results obtained using a classical LASAT procedure on a bonding of around 4 mm thickness (3.8 mm for the composite layer). This result allows the damage threshold of the bonding in a LASAT dynamic loading condition, at around 300 MPa to be quantified. This loading seems, however, not achievable using a classical LASAT scheme on the industrial LEAP fan blade. Thus, based on quantitative simulations of the process and using only the shock propagation in the metallic part of the assembly, we proposed a new method for the LASAT process which allows the generation of a high enough traction in the bonding to control or disbond it.

Acknowledgements

Authors would like to acknowledge L. Videau for simulations of laser loading using Esther. They also would like to acknowledge BPI France for funding through the FUI Monarque project.

References

[1] Hodé R, Raetz S, Blondeau J, Chigarev N, Cuvillier N, Tournat V. and Ducousso M, Nondestructive evaluation of structural adhesive bonding using the attenuation of zero-group-velocity Lamb modes, Applied Physic. Letter 2020; .116 (10):104101

[2] Hodé R, Ducousso M, Cuvillier N, Gusev V, Tournat V. and Raetz S, Laser ultrasonics in a multilayer structure: Semi-analytic model and simulated examples, Journal of the Acoustical Society of America 2021; 150(3):2065-2075.

[3] Hodé R, Raetz S, Blondeau J, Cuvillier N, Gusev V, Ducousso M. and Tournat V, Laser ultrasonics in a multilayer structure: Plane wave synthesis and inverse problem for nondestructive evaluation of adhesive bondings, Journal of the Acoustical Society of America 2021; 150(3):2076-2087

[4] Berthe L, Arrigoni M, Boustie M, Cuq-Lelandais J.P, Broussillou C, Fabre G, Jeandin M, Guipont V and Nivard. M, State-of-the-art laser adhesion test (LASAT), Nondestructive Testing and Evaluation 2011; 26(3-4):303-317.

[5] Ducousso M, Bardy S, Rouchausse Y, Bergara T, Jenson F, Berthe L, Videau L. and Cuvillier N, Quantitative evaluation of the mechanical strength of titanium/composite bonding using laser-generated shock waves, Applied Physic. Letter 2018; .112 (11):119904.

[6] Cuenca E, Ducousso M, Rondepierre A, Videau L, Cuvillier N, Berthe L. and Coulouvrat F, Propagation of laser-generated shock waves in metals: 3D axisymmetric simulations compared to experiments, Journal of Applied. Physics 2020; 128(24):249903.

  doi:10.5075/epfl-298799_978-2-9701614-0-0

BOND LINE DURABILITY EVALUATION IN A BUILDING INTEGRATED SOLAR THERMAL SYSTEM

Paulo, G. Lacerda[a,b], Saed, Raji[c], Pierre, Roger[c], Julien, Jumel[b]

a: Université de Bordeaux, CNRS, Arts et Métiers Institute of Technology, Bordeaux INP, INRAE, I2M Bordeaux, F-33400 Talence, France – pguimaraesla@u-bordeaux.fr
b: ENSTA Bretagne, UMR CNRS 6027, IRDL, F-29806 Brest Cedex 9, France
c: NOBATEK/INEF4, F-33100 Bordeaux, France

Keywords: solar thermal system; structural bonding; creep; hydrostatic stress; durability

Buildings are very energy-consuming, they account for 40% of the European Union's consumption and are responsible for 36% of all greenhouse gas emissions in 2020. For this reason, improving buildings' energy efficiency was selected as one of the main actions of the European Green Deal [1]. To tackle this problem researchers will play a main role in developing and deploying innovative solutions for renewable energy generation integrated into the buildings.

Solar Thermal Systems (STS) are responsible for harnessing solar energy to produce thermal energy (heat). Since most of the energy consumed in buildings is primarily used for heating and supply of hot water, STS are widely used. The main component of any STS is the solar collector. This apparatus absorbs the solar radiation and transfers the heat to a fluid flowing through the interior of the collector. There are many types of collectors in the market, each with its different advantages and disadvantages, and that can be applied to the buildings. One of these is called Flat-Plate Collector (FPC).

A typical FPC consists of a metallic frame well insulated at the back and the sides that will support an absorbing plate on its exposed surface. The radiation absorbed will be transferred to metallic tubes that are hidden behind the hot absorber plate and, thereafter, heat the fluid inside those tubes. FPC's greatest advantages are that they can be constructed easily with a relatively low manufacturing cost, and they are permanently fixed in the position since they collect both beam and diffusive radiations [2]. However, a key issue to the spreading of STS in architectural projects is its integration into the building structure since most STS are only roof-mounted and are frequently seen as a foreign element. As such, Nobatek-INEF4 developed and tested BATISOL®, an innovative building-integrated FPC [3].

The BATISOL® device innovates in both terms of façade integration and aesthetic design. This collector consists of an absorber plate and a backplate made of aluminium. As depicted in Figure 1, the two plates are bonded in a manner that the joints shape the circuit through which the transfer fluid will flow and, at the same time, will guarantee the system sealing. Indeed, the bond line as an alternative to the typical FPC tubes permitted this collector a major weight/thickness reduction, increasing its fitting to the façade structure. In addition, the bond line is "invisible", i.e., the bond line is hidden between both plates, while other assembly methods (e.g., fasteners, riveting) could be noticed on the façade if used, not to mention the

  doi:10.5075/epfl-298799_978-2-9701614-0-0

liquid leaking and corrosion concerns. Moreover, given that the only connection between both plates is the bond line, it is the bond line that will transfer the constant load deriving from the hydrostatic pressure of the water column within the system, guaranteeing the structural integrity of the FPC during service life.

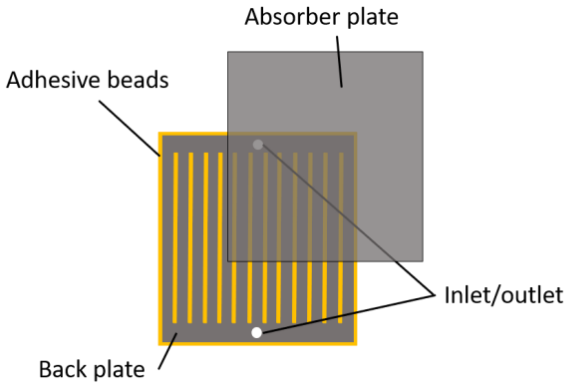

Figure 1 – BATISOL® FPC main components

As shown in Figure 2, the adhesive thickness presents the same order of magnitude as the thickness of the substrates (a few millimetres). Besides, the unbonded zones of the thin plates (fluid channels) will deflect under the hydrostatic pressure and will induce peel stresses in the adhesive joints. Therefore, the adhesive selected for this structural bonding must present non-sag high viscosity during manufacturing because of the gap-filling and relative flexibility for higher resistance to peel stresses in opposition to classic structural adhesives [4]. For this purpose, a methyl methacrylate (MMA) based adhesive was chosen for the preliminary design.

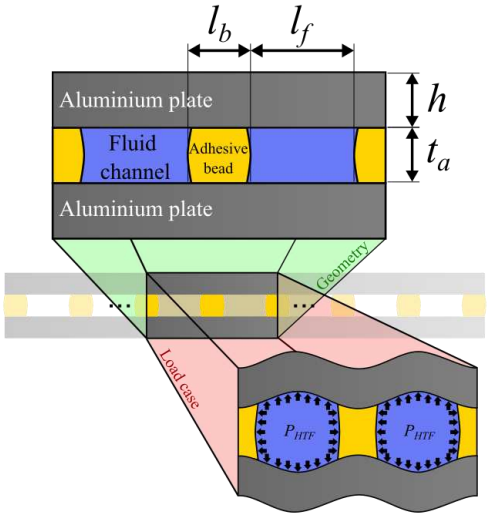

Figure 2 – BATISOL® assembly cross-sectional view

Structural adhesives exhibit a time-dependent mechanical behaviour. When submitted to high stresses at relatively high temperatures they exhibit viscoelastic and viscoplastic behaviour [5]. In the present study, this is the case for the MMA adhesive submitted to a constant long-term peel load at temperatures that can reach up to 60°C, falling within the range of glass transition temperatures for this type of adhesive [6]. In addition, the adhesive layer is constrained between substrates, thus, resulting in a hydrostatic stress state in the layer. For this reason, the contribution of the hydrostatic component of the stress tensor needs to be considered in the material's constitutive formulation for an accurate durability prediction of the assembly.

This work proposes a viscoplastic constitutive model to predict the creep strength of the MMA adhesive joints. For the yield criterion, equivalent stress as a function of both deviatoric stress and hydrostatic stress is used. The material parameters are determined experimentally from tensile creep tests using dog bone and butt-joint specimens (BJS). Subsequently, the constitutive equation is implemented in a commercial finite element analysis software (ABAQUS®). Intending to verify that our constitutive equation can predict the adhesive behaviour, both tensile creep test configurations are analysed using the finite element code.

In the future, the same constitutive formulation will be tested to analyse a more complex adhesive joint (linear bead configuration), as found in the BATISOL® device. Hence, an experimental set-up that allows the inflation and the maintenance at a constant pressure of a reduced-scale collector (one linear adhesive joint) is in development. The pressure and the displacements fields of the surface of the adherend will be acquired over time by a stereo Digital Image Correlation (s-DIC) system to detect the specimen failure. Finally, a failure criterion will be used simultaneously with the proposed constitutive equation to predict the experimental time-to-failure.

References

1. European Commission. Communication from the Commission to the European Parliament, the European Council, the Council, the European Economic and Social Committee and the Committee of the Regions - The European Green Deal [Internet]. Brussels: European Commission; 2019 [cited 10 April 2022]. 24p. Available from: https://eur-lex.europa.eu/resource.html?uri=cellar:b828d165-1c22-11ea-8c1f-01aa75ed71a1.0002.02/DOC_1&format=PDF
2. Kalogirou SA, Agathokleous RA. Solar thermal energy for building applications. In: Desideri U, Asdrubali F, editors. Handbook of Energy Efficiency in buildings: A life cycle approach. Oxford, United Kingdom: Butterworth-Heinemann is an imprint of Elsevier; 2019. p. 507–34.
3. Martinez RG, Goikolea BA, Paya IG, Bonnamy P, Raji S, Lopez J. Performance assessment of an unglazed solar thermal collector for envelope retrofitting. Energy Procedia. 2017;115:361–8.
4. Banea MD, da Silva LFM. Mechanical Characterization of Flexible Adhesives. The Journal of Adhesion. 2009 May 22;85(4-5):261-85.
5. Hu GK, Schmit F, Baptiste D, François D. Viscoplastic Analysis of Adhesive Joints. Journal of Applied Mechanics. 1996 Mar 1;63(1):21-6.
6. Jaillon A. Étude expérimentale et numérique du comportement à rupture des assemblages collés à épaisseur de couche adhésive variable [dissertation on the Internet]. Toulouse (FR): Université de Toulouse; 2020 [cited 16 Apr 2022]. Available from: https://depozit.isae.fr/theses/2020/2020_Jaillon_Agathe.pdf

PHYSICAL AND MECHANICAL CHARACTERIZATION OF POLYURETHANE FOAM CORE OF SANDWICH PANELS OF VARIOUS DENSITIES

Pier Giovanni, Benzo[a], Guilherme, L. Gontijo[a], Marco A., Abreu Filho[a], Aloys, Dushimimana[a], Sandra Cristina, Oliveira[b], Zlatan, Z. Denchev[b], João Miguel, Pereira[a], José, Sena-Cruz[a]

a: ISISE-IB/S, Department of Civil Engineering, University of Minho (PT) – glgontijo28@gmail.com
b: IPC, Polymer Engineering Department, University of Minho (PT)

Abstract: *Sandwich foaming is a manufacturing process in which a liquid monomer mixture is injected on the bottom face sheet of the sandwich panel where it polymerizes to form cross-linked polyurethane (PUR) foam providing an adhesive joint between the bottom and upper metal sheets. The single-step process avoids manual operations in the assemblage of the panel and the use of adhesive. However, the PUR foam in the core of the panel and at foam-to-face sheet interface may present fluctuations in the mechanical properties. The aim of this study is the mechanical and thermophysical characterization of PUR foam of various densities produced by sandwich foaming. Additionally, a qualitative assessment of the foam-to-face sheet interface is carried out based on the results of the flatwise tensile and shear tests.*

Keywords: Polyurethane foam; Steel sandwich panel; Flooring system; Digital image correlation; Thermogravimetric analysis.

1. Introduction

Polyurethane (PUR) foam is one of the most common core materials used in sandwich panels for civil engineering applications. Sandwich panels are made of two thin and stiff face sheets separated by a low-density core material that result in a structure with high stiffness-to-weight ratio. In the literature [1,2] the most common production method of sandwich panels involves two phases: i) prefabricated foam blocks must be cut and then ii) adhered to both face sheets by manual operation. These foams are manufactured in bulk and their properties are relatively well controlled [3]. On the other hand, the dust resulting from the machining of the foam blocks may weaken the bond quality between core and face sheets [4]. Steel face sheet sandwich panels are currently produced continuously. The liquid monomers of the PUR foam are injected on the bottom face sheet where they polymerize and cross-links providing an adhesive bond in a single-step process called sandwich foaming [5]. Promising results have emerged in the use of novel foam-filled metal structures [6,7]. However, [8] indicates that this sandwich foaming process may result in high variability in the foam and the foam-to-face sheet interface characteristics. The main objectives of this study are to provide experimental data on the mechanical properties of PUR foam of various densities to be used as structural core in a novel steel sandwich panel for flooring system [9] and to assess the influence of the single-step production technology on the molecular structure of the foam by means of thermogravimetric analysis (TGA).

  doi:10.5075/epfl-298799_978-2-9701614-0-0

2. Experimental program

The mechanical properties of the PUR foam are required to efficiently design and correctly predict the failure modes of sandwich floor panels. In the context of application of flooring system, the shear, tensile, and compressive properties are particularly relevant. The shear properties are required to assess the integrity of the foam during its service life as it is mostly subjected to this kind of stresses. The latter two properties are necessary to predict common failure modes of sandwich panels involving local buckling phenomena such as wrinkling [10]. The experimental campaign also included a study of the thermal stability and composition of the PUR foam by means of TGA.

The mechanical tests of the experimental program include flatwise tensile and compressive tests, as well as shear tests. Regarding the flatwise tensile and compressive tests, they are carried out on three sets of specimens with nominal density of 40, 50, and 60 kg/m^3 according to [11] and [12], respectively. The specimens are extracted from large-scale steel face sheet sandwich panel. The specimens are tested in tension and compression up to failure at a rate of 0.5 and 2.4 mm/min, respectively. The load is recorded by a load cell with a capacity of 25 kN (±0.005 kN) and the vertical displacement by 4 linear variable differential transformers (LVDTs), one for each side of the specimen. Furthermore, the displacement of one of the faces is monitored using the digital image correlation (DIC) technique. Concerning the shear tests, they are carried out on one series of specimens with nominal dimensions 360×115×30 mm^3 and nominal density of 40 kg/m^3. The test setup follows the recommendation of [13] and [14]. The load and relative displacement are recorded with a load cell of 200 kN (±0.12 kN) and 2 LVDTs, one for each side. The different test setups are illustrated in Figure 1 and can be consulted in detail in [15].

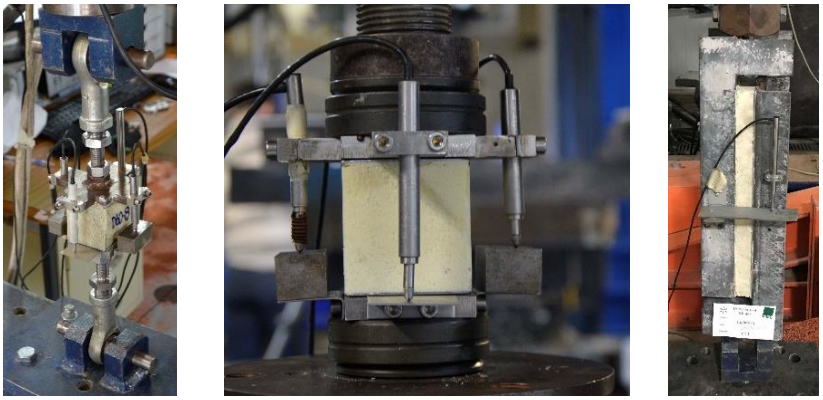

(a) (b) (c)

Figure 1. Mechanical test setups: (a) flatwise tensile test; (b) flatwise compressive test; (c) shear test

Thermogravimetric experiments were carried out according to [16] on specimens extracted from the cubic samples of the flatwise tensile and compressive specimens from three different levels across the thickness, namely top, middle, and bottom layer as shown in Figure 2. The tests are carried out in a TA Instruments SDT Q600 apparatus in a nitrogen atmosphere. The specimens' weight was approximately 2 mg, heated from 30°C to 700°C at a heating rate of 10°C/min, with a gas flow rate of 100 mL/min.

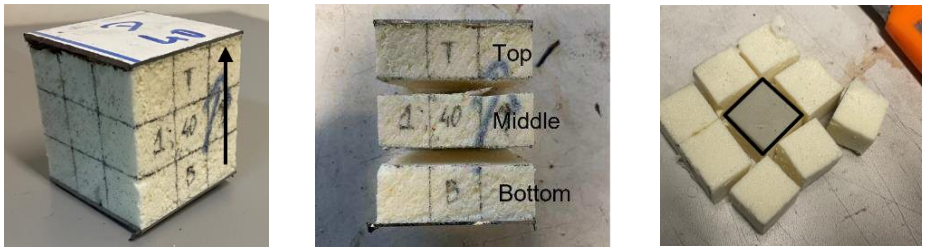

(a) (b) (c)

Figure 2. TGA specimen preparation: (a) foam rising direction; (b) top, middle, and bottom layers of the PUR foam specimen; (c) sample extraction location from one of the layers

3. Results and discussion

A summary of the mechanical properties of the PUR foam and their respective coefficients of variation is given in Table1. From the flatwise tensile and compressive tests carried out, the tensile strength (σ_t) and modulus (E_t), and the compressive yield strength (σ_c) and modulus (E_c) were obtained, respectively. The shear yield strength (τ) and modulus (G) were determined through the shear tests.

Table 1: Mechanical properties of the tested PUR foam

Density [kg/m^3]	σ_t [MPa]	E_t [MPa]	σ_c [MPa]	E_c [MPa]	τ [MPa]	G [MPa]
40	0.12 (±0.02)	5.7 (±1.4)	0.15 (±0.01)	5.9 (±0.6)	0.16 (±0.01)	2.9 (±0.3)
50	0.12 (±0.01)	2.8 (±0.3)	0.09 (±0.01)	3.2 (±0.3)	*	*
60	0.16 (±0.02)	3.5 (±0.3)	0.08 (±0.01)	2.8 (±0.5)	*	*

Note: (*) Shear tests are carried out only on the 40 kg/m^3 PUR foam due to the decrease in the mechanical properties with the increase of density

The stress-strain curves obtained in the flatwise tensile tests are illustrated in Figure 3a.

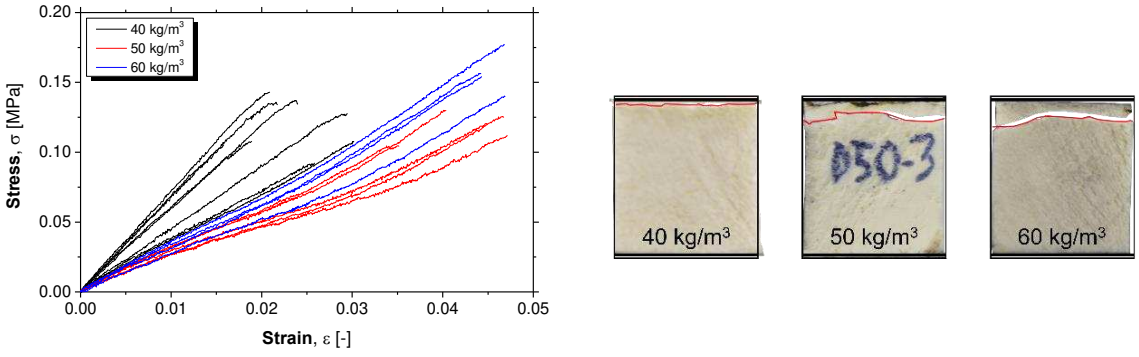

(a) (b)

Figure 3. Flatwise tensile test results: (a) stress-strain curves; (b) typical failure modes with tensile crack highlighted in red

All the specimens show a linear elastic behavior up to failure in tension. Slight strain-hardening may be noticed in the 50 kg/m^3 and 60 kg/m^3 specimens. The observed failure mode for all the densities is cohesive failure of the foam (see Figure 3b). This confirms the good quality of the foam-to-face sheet interface provided by the single-step production process. In Figure 4 the maximum principal strain field obtained from the DIC measurements prior to failure is illustrated for the 40 kg/m^3 and 50 kg/m^3 foams. The 40 kg/m^3 specimen shows a strain concentration in the top layer whereas the 50 kg/m^3 one shows a more distributed strain pattern in the middle and top layers. The 50 kg/m^3 and 60kg/m^3 foams show a similar tensile behavior.

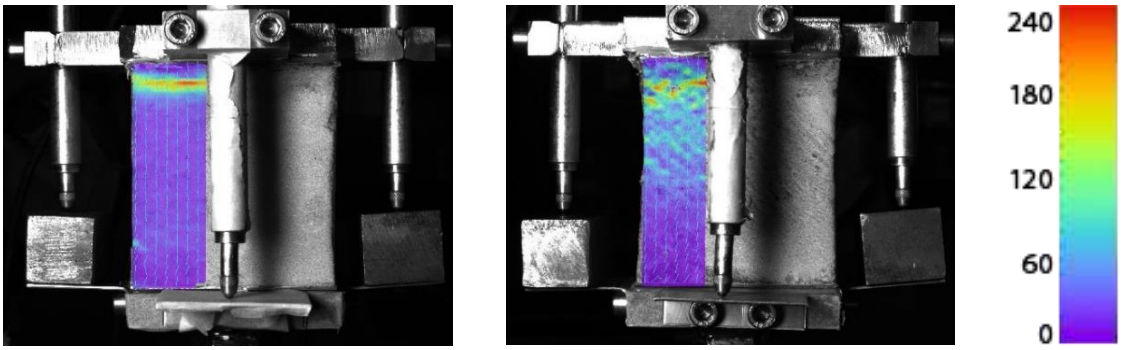

(a) (b)

Figure 4. DIC measurements in terms of maximum principal strain at yielding of flatwise tensile tests: (a) 40 kg/m^3; (b) 50 kg/m^3. All units in micro strain

For what concerns compressive behavior, the 40 kg/m^3 specimens show a stress-strain curve with three distinct regions: i) a linear elastic part, ii) a plateau of deformation at constant stress due to cell buckling, and iii) a strain-hardening part at large strain due to crushing of the cell walls. On the other hand, in the 50 kg/m^3 and 60 kg/m^3 series the plateau region is replaced by a longer strain-hardening part (see Figure 5). This may suggest that the 50 kg/m^3 and 60 kg/m^3 foams microstructure present strong imperfection [17].

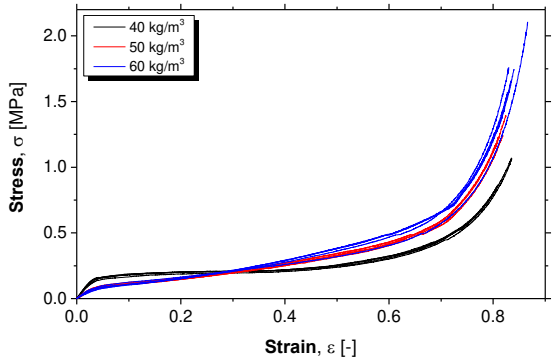

Figure 5. Flatwise compressive test results: stress-strain curves

In Figure 6 the maximum principal strain fields obtained from the DIC measurements at yielding are illustrated for the 40 kg/m^3 and 50 kg/m^3 foams. In the 40 kg/m^3 the deformation is concentrated in the top and bottom layers of the foam. The middle layer present lower deformation, and thus higher compressive modulus in agreement with [18] that locates the level with the highest mechanical properties at mid height. The 50 kg/m^3 specimen presents strain concentration in the top layer of the foam and negligible deformation in the bottom layer similarly to the 60 kg/m^3 foam. It is important to note that the 40 kg/m^3 foam generally present

higher tensile and compressive failure stress and Young's modulus values than the 50 kg/m^3 and 60 kg/m^3 foams. This result is contrary to the increase in mechanical properties with the density of the PUR foam. However, it is worth mentioning that the estimated density of the 50 kg/m^3 and 60 kg/m^3 foams were significantly lower than the nominal density, namely -6.7% and -14.9%. Thus, some differences in the chemical composition between the 40 kg/m^3 and the 50 kg/m^3, and 60 kg/m^3 are to be expected.

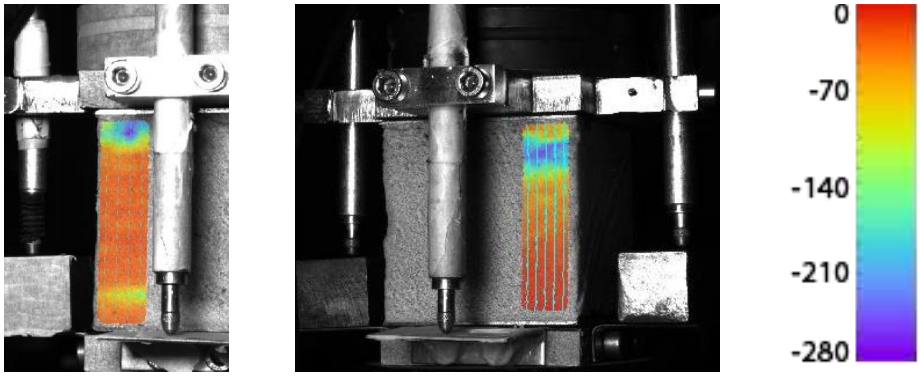

(a) (b)

Figure 6. DIC measurements in terms of minimum principal strain at yielding of flatwise compressive tests: (a) 40 kg/m^3; (b) 50 kg/m^3. All units in micro strain

The stress-strain curves obtained in the shear tests are illustrated in Figure 7a. All the specimens present an initial elastic behavior followed by a non-linear stage. Two failure mode were identified: i) cohesive shear failure of the foam with the formation of cracks oriented at 45° and ii) adhesive shear failure at the foam-to-face sheet interface with cracks parallel to the loading plate. The latter failure mode occurred in specimens where the presence of macropores at the interface has been observed after testing (see Figure 7b).

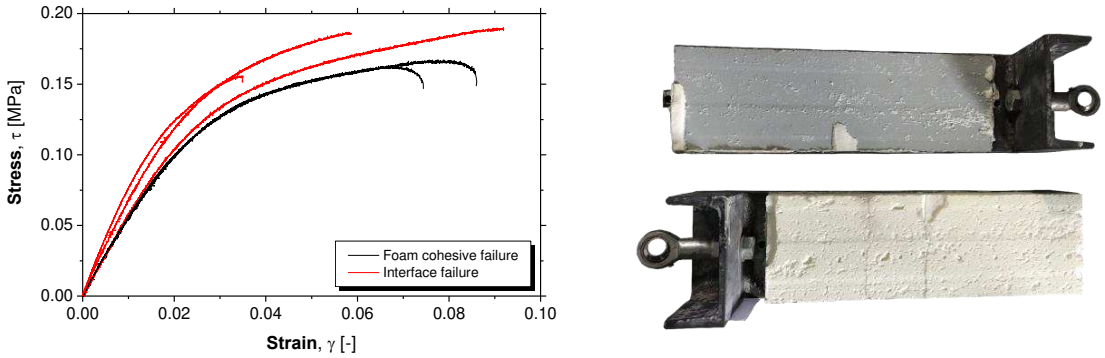

(a) (b)

Figure 7. Sher test results: (a) stress-strain curves; (b) macropores at the interface foam-to-face sheet

The weight and derivative of the weight, both as a function of temperature, obtained from the TGA are plotted in Figure 8. All the layers of every foam density present a two-stage degradation process [19]: i) the first has a maximum rate loss at 316°C during which the mass is reduced by approximately 50% and ii) the second has its peak at 468°C during which the mass reduction is equal to 25%. The largest differences between the curves are found in the amount of residue at 700°C. The residue gives an indication about the cross-linked fraction of the polymer.

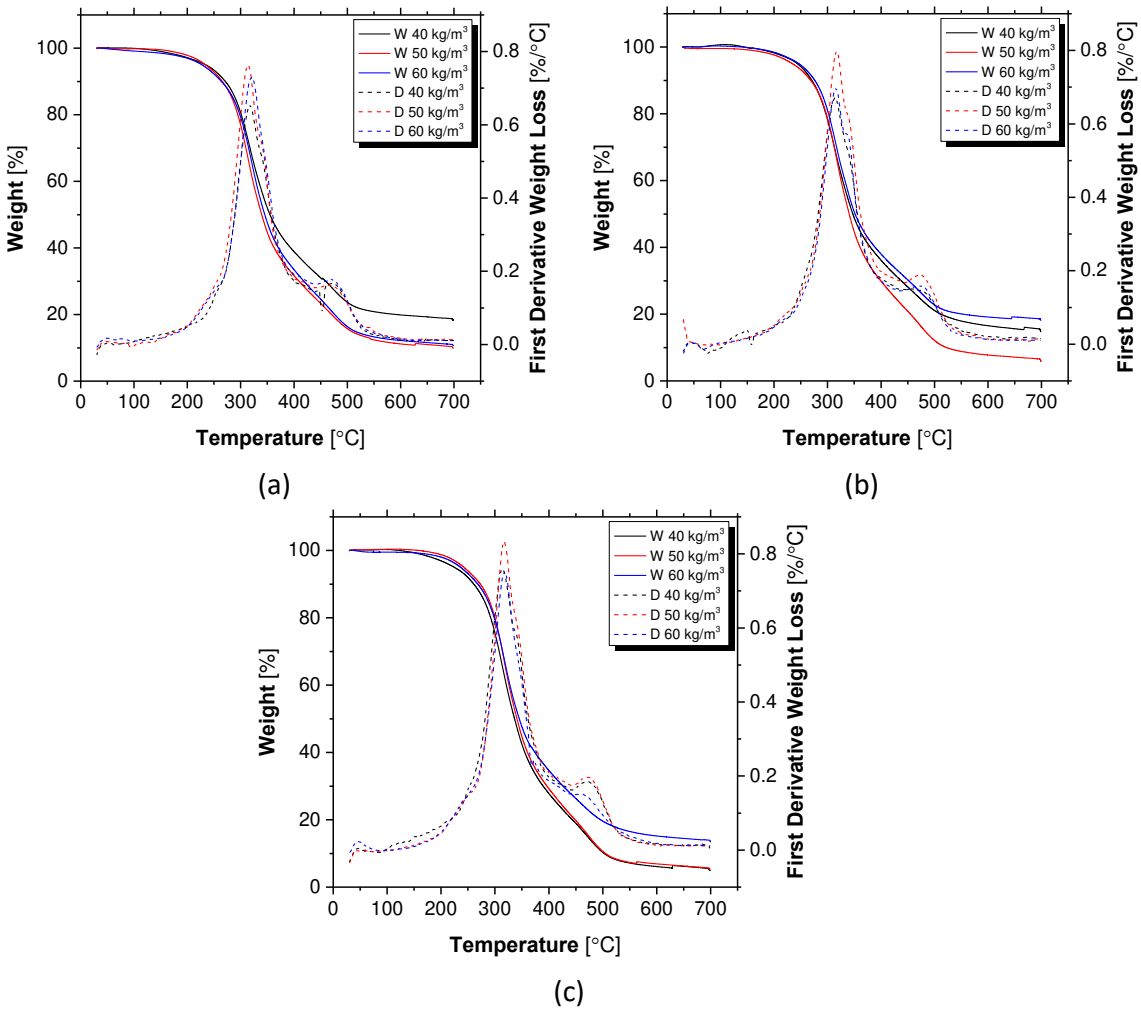

Figure 8. TGA results: (a) top layer; (b) middle layer; (c) bottom layer

It is a critical aspect in the production of thermoset foamed product [20] such as PUR foam. Low crosslinking speed may delay gelation time and provoke the foam structure to collapse. The top layer of the 40 kg/m^3 is the largest value among all layers and foam densities. The residue of the middle layer of the 50 kg/m^3 is smaller than those of the other foam densities. Finally, the bottom layer of the 60 kg/m^3 foam is larger than those of the 40 kg/m^3 and 50 kg/m^3 foams. In the 40 kg/m^3 PUR foam a residue gradient is observed across the thickness, reaching its peak in the top layer. The density of crosslinking is related to large elastic deformation in polyurethane rubbers [21]. This may explain the large strain concentration found in the top layer of the 40 kg/m^3 foam in the flatwise tensile test (see Figure 4a). On the other hand, discrepancies may be found between the TGA and mechanical test results of the 50 kg/m^3 and 60 kg/m^3 PUR foams. Nevertheless, their scattered carbonized residue values may suggest that crosslinking and blowing processes might be imbalanced, and thus resulting in a foam with non-optimized microstructure.

4. Conclusions

In this work, an experimental campaign is carried out to assess the mechanical and thermophysical properties of PUR foams of various densities to be used as core material in a novel flooring system based on sandwich panels. Additionally, a qualitative assessment of the

properties of the foam-to-face sheet interface is performed in terms of tensile and shear behavior. From the obtained results the following conclusions and a future topic of research are highlighted:

- The lowest density PUR foam (40 kg/m^3) generally exhibits the highest mechanical properties, i.e. a yielding tensile, compressive, and shear stress of 0.12 MPa, 0.15 MPa, and 0.15 MPa, respectively. It also shows the highest tensile, compressive, and shear modulus values, namely 5.7 MPa, 5.9 MPa, and 2.7 MPa, respectively.
- The DIC measurements provide insight on the mechanical behavior of the PUR foams. Two different strain fields are identified for the 40 kg/m^3 and the 50 kg/m^3 and 60 kg/m^3 foams: i) the former presents strain concentration at the top and bottom layers whereas ii) the 50 kg/m^3 and 60 kg/m^3 foams present a more uniform strain pattern.
- The foam-to-face sheet interface obtained through a single-step production process shows higher tensile strength than the PUR foam itself. On the other hand, the shear tests yielded both interface and PUR foam cohesive failure mode. This suggest that the presence of defects such as macropores is an influencing factor in the shear behavior of steel face sheet sandwich panel with PUR foam core.
- TGA measurements highlight the high heterogeneity of PUR foams produced continuously by injection on the bottom face sheet of sandwich panels. Additionally, the results suggest that other techniques, such as the scanning electron microscopy, may be required to further investigate the relation between mechanical behavior and foam microstructure.

Acknowledgements

This work was developed within the scope of the research project “Lightslab – Desenvolvimento de soluções inovadoras de lajes de painel sandwich”, supported by FEDER funds through the Operational Program for Operational Program for Competitiveness and Internationalization (POCI) and the Portuguese National Innovation Agency (ANI) – project no. 33865 [POCI-01-0247-FEDER-033865]. This work was partly financed by FCT/MCTES through national funds (PIDDAC) under the R&D Unit Institute for Sustainability and Innovation in Structural Engineering (ISISE), under reference UIDB/04029/2020. The first and second authors wish also to acknowledge the grants DFA/BD/8319/2020 and DFA/BD/07696/2021 respectively, provided by Fundação para a Ciência e a Tecnologia, IP (FCT), financed by European Social Fund and national funds through the FCT/MCTES.

5. References

1. Mastali M, Valente I, Barros J, Gonçalves D. Development of innovative hybrid sandwich panel slabs: Experimental results. Composite Structures 2015; 133:476-498.
2. Abdolpour H, Garzón-Roca J, Escusa G, Sena-Cruz J, Barros J, Valente I. Development of a composite prototype with GFRP profiles and sandwich panels used as a floor module of an emergency house. Composite Structures 2016; 153:81-95.
3. Kraus B, Das R, Banrjee B (2014) Characterization of an anisotropic low-density closed-cell polyurethane foam. Parresia Research Limited 2015; Report #20151007CI.01.

  doi:10.5075/epfl-298799_978-2-9701614-0-0

4. Shams A, Stark A, Hoogen F, Hegger J, Schneider H. Innovative sandwich structures made of high performance concrete and foamed polyurethane. Composite Structures 2015; 121:271-279.
5. Ashida K. Polyurethane and related foams. London: Taylor & Francis; 2007.
6. Briscoe CR, Mantell SC, Okazaki T, Davidson JH. Local shear buckling and bearing strength in web core sandwich panels: model and experimental validation. Engineering Structures 2012; 35:114-119.
7. Sagadevan R, Rao BN. Experimental and analytical study on structural performance of polyurethane foam-filled built-up galvanized iron members. Thin-Walled Structures 2020; 146.
8. Chuda-Kowalska M, Garstecki A. Experimental and numerical analyses of anisotropic behaviour of PU foam. In: 16th European Conference on Composite Materials, 2014 June 22-26; Seville.
9. Benzo PG, Pereira JM, Sena-Cruz J. Optimization of steel web core sandwich panel with genetic algorithm. Engineering Structures 2022; 253.
10. Zenkert D. The handbook of sandwich construction. Cradley Heath: Engineering Materials Advisory Services Ltd; 1997.
11. American Society for Testing and Materials. ASTM C 297/C 297M-04. Standard Test Method for Flatwise Tensile Strength of Sandwich Constructions. West Conshohocken: ASTM International; 2004.
12. American Society for Testing and Materials. ASTM C365-03. Standard Test Method for Flatwise Compressive Properties of Sandwich Cores. West Conshohocken: ASTM International; 2003.
13. Escusa G, Cruz F, Sena-Cruz J, Pereira E, Valente I, Barros J. Shear behaviour of polyurethane foam. In: 6th Asia-Pacific Conference on FRP in Structures, 2017 July 19-21; Singapore.
14. American Society for Testing and Materials. ASTM C273-00. Standard Test Method for Shear Properties of Sandwich Core Materials. West Conshohocken: ASTM International; 2000.
15. Benzo PG, Abreu M, Dushimimana A, Gontijo G, Sena-Cruz J, Pereira JM, Lourenço PB. Caracterização mecânica dos materiais. Universidade do Minho, Departamento de Engenharia Civil. Report number: D2.3, 2021.
16. American Society for Testing and Materials. ASTM E1131-08. Standard Test Method for Compositional Analysis by Thermogravimetry. West Conshohocken: ASTM International; 2008.
17. Hawkins M, O'Toole B, Jackovich D. Cell morphology and mechanical properties of rigid polyurethane foam. Journal of cellular plastics 2005; 41:267-285.
18. Ashby M. The mechanical properties of cellular solids. Metallurgical Transaction A 1983; 14: 1755-1769.
19. Garrido M, Correia J, Keller T. Effects of elevated temperature on the shear response of PET and PUR foams used in composite sandwich panels. Construction and Building Materials 2015; 76: 150-157.
20. Odian G. Principle of polymerization. 4th ed. New York: John Wiley & Sons; 2004.
21. Kontou E, Spathis G, Niaounakis M, Kefalas V. Physical and chemical cross-linking effects in polyurethane elastomers. Colloid & Polymer Science 1990; 268: 636-644.

EXPERIMENTAL AND ANALYTICAL ANALYSIS OF POINT FIXED TEMPERED LAMINATED GLASS PANELS

Afonso Mesquita[a], Eliana Inca[b], Sandra Jordão[c]

a: ISISE, Department of Civil Engineering, University of Coimbra, Portugal – acbdm@uc.pt
b: ISISE, Department of Civil Engineering, University of Coimbra, Portugal
c: ISISE, Department of Civil Engineering, University of Coimbra, Portugal

Abstract: *This work analyses the structural behaviour of point fixed tempered laminated glass panels subjected to wind action using a layout where the air pressure is orthogonally distributed to the panel's surface. The panels are fixed with stainless steel M14 bolts, which are bonded to the external glass surface using a structural adhesive. The analysis carried out includes results registered in panels with PVB, EVASAFE and SENTRYGLAS® interlayer films. A comparison study is presented with the available results obtained from previous tests when embedded and countersunk bolts are used. The global comparison is made with displacement values in the central point of panels, under the bi-direction bending effect, but also with stresses. The maximum experimental principal stress at the central point of each panel revealed a smaller magnitude compared with the design value (established by prCENTS_19100). The experimental principal stress at the same point for the laminated annealed glass panels was higher comparing with the correspondent design value.*

Keywords: Tempered laminated glass panels; interlayer film; experimental and design stresses.

1. Introduction

The types of point fixed systems for use on building facades and roofs have been widely used in a growing number of cases that reflect a diversified typology of constructions and structures. Such examples include the facades of office buildings, museums, airports, shopping centers, hospitals and other medical and health care buildings, as well as for use in a university or research context [1, 2]. Traditionally, the facades intend to reproduce the search for a greater elegance, in terms of geometry and architectural framework, to which the intention of the greatest possible environmental sustainability is nowadays added.

Among many solutions [1, 3], curtain facades stand out and those in which the covering of the several openings in the buildings that use them is used as wall and whose architectural projects (with a more contemporary configuration) include, in accordance with the luminosity, transparency, aesthetics and lightness characteristics provided by the structural glass [1, 2, 3]. However, in addition to the application of the point fixed glass façade system in new constructions, the aforementioned solution was also used in terms of the structural rehabilitation of previously existing buildings as in the case of hotels and even in several residential buildings. In fact, the options for glass walls as an alternative to systems with more conventional frames and contemplating the use of punctual mechanical fastenings capable of ensuring adequate resistance in the context of the safety required for the functioning of the glass combine the necessary resistance with an appealing aesthetic lightness. In this context, within certain criteria and with certain options, referring, among other possibilities, to the use

  doi:10.5075/epfl-298799_978-2-9701614-0-0

of the Fitechnic® system [4], the fastening elements are almost disguised in geometric terms at the level of the elevations in order to provide the same desired in/out visibility within the framework of structural facades with high technological performance. As examples, two facades and a roof with the mentioned structural glass system are shown in Figure 1, in which material and technology according to the Fitechnic® system were used [4]. In the example of Figure 1a) the building includes the point fixed glass panels system in the four facades.

a) Glass museum (Marinha Grande - Portugal) *b) IST – TagusPark (Oeiras - Portugal)* *c) Horta's Hospital (Faial - Portugal)*

Figure 1. Buildings with point fixed glass facades, Fitechnic® system by Pentagonal [1]

The connection required for the glass panels, which can be monolithic tempered, laminated tempered and double tempered, is, in practical terms, carried out by means of stainless steel connectors with hinged head (type AISI 316), whose typology is subdivided into countersunk bolt model, embedded and adhesive, mentioned in [1, 2, 5]. The first two as a mechanical fastening example and the third with a chemical connection, confer resistance to shear and to tension/compression, depending on the existence of the main regulated actions. Advantages and disadvantages exist in either case, referring for the first two situations the need to drill holes of 60 mm near to the corners of the glass panels with the consequent emergence of stress fields associated with the holes before the application of the glass panels. In the third situation, if the absence of holes is a huge advantage from the material point of view, the question arises about the effective long-term performance of the structural adhesives used for the bonding of stainless steel connectors to the glass faces. The potential danger of accessibility to the physical integrity of the connection itself, in terms of its conservation over time, must be taken into account.

The GF Seismic Project, with the support of the Portuguese Science and Technology Foundation [5], taking place at the Civil Engineering Department of the Faculty of Sciences and Technology of the University of Coimbra, is subdivided into two phases. The first has addressed the problem of the structural behaviour of each panel (individually evaluated) when subjected to a distributed load perpendicularly applied to the plane of the glass, such as that which corresponds to the wind action [5, 7]. A second phase foreseeing the testing of a sector of a facade with 9 full-scale panels and the study of the structural behaviour under the effect of the seismic action when it is affected to a standard reference building, previously analyzed according to the guidelines of the EC8 [6].

The experimental campaign includes a variation of elements inherent to the tempered laminated glass panels, considering, at the level of the respective film between each of the glass foils, the PVB, EVASAFE® and SENTRYGLAS® material. The threaded shanks of the connectors presented in Figure 2 are bolted into plates that are integrated in the layout system prepared

for the desired type of test, as reproduced in Fig. 3 inserted in point 2. With regard to the type of stainless steel connector before mentioned, panels with countersunk bolts (Figure 2a) and embedded (Figure 2b) but also with adhesive (Figure 2c) bolts have already been tested.

a) Countersunk (RE-12-21_M14)

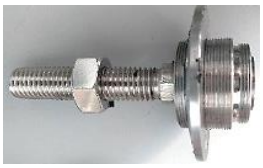

b) Embedded (RCE10-21/FTL_M14)

c) Adhesive (RCE-GL_M14)

Figure 2. Stainless steel bolts typology (AISI316) - Fitechnic®, according to [1, 2 e 4]

The incorporation of the stainless steel connectors with the hinged head identified above in the connections of the panels helps the structural system to be more flexible, facilitating the bending of the glass panel and its dimensional variation when subjected to different types of loads, avoiding, therefore, the appearance of premature stresses around the zone of holes. On the other hand, each panel is composed by the association of two monolithic glasses joined by interlayers of polymeric material such as polyvinyl butyral (PVB), EVASAFE® or SEN-TRYGLAS®. Such materials are selected taking into account their remarkable qualities of resistance, adherence and elasticity. It is recognized that the butyral/glass adherence is obtained by heat and pressure treatment, resulting in the final product with the same transparency as any other glass of similar thickness. However, in a situation of rupture, the small pieces of glass do not disintegrate from the butyral, remaining together inside the frame of the panel, providing, therefore, a safety effect by preventing or greatly limiting their projection, reinforcing, thus, the concept of safety in the application of that type of structural element in facades.

2. Laboratory tests, layout and used materials

In this work, the type of test underlying the presented results uses a layout according to the 3D scheme inserted in Figure 3. The glass panel is placed on the four supports materialized by the respective bolts, which are fixed on the plates of the corresponding beams, connected to two transversal beams bolted to the frame's columns. The lateral walls of the steel box (where the front panel is opened) are sealed *a posteriori* with a suitable silicone, what is accomplished according to the Sika® [10] recommendations, after the sliding movement. Taking into account the application of air pressure (as constant as possible) to simulate the effect of wind action (EC1 - Part 1-4, [8]) on an outward facing glass surface, in the context of a real building, it is possible to close the panel-air box assembly as long as the four joints between the edges of the panel. The procedure is previously systematized with the placement of the planned instrumentation (strain gauges) on the inner face of the panel, closing the box and application of silicone around the perimeter of the joints with 10 mm of width and a depth of approximately 17,5 mm. The external face of the specimen is also instrumented with strain gauges (Figure 3b). On this same surface are also positioned the displacement transducers (LVDT, in Figure 3b also), in order to be able to record the deformations that occurred at critical points during the load increase phase. Such load was previously identified through simple numerical models. Strain gages were arranged along horizontal axes (middle and aligned with bolts centers). Thus, it is possible to simulate the situation of an airtight box so that, by admission through the laboratory's compressed air system, the created air pressure will be capable of bending the simply supported panel (horizontally and vertically), as illustrated in Fig. 3a). Thus, it is possible to simulate the situation of an airtight box so that, by admission through the laboratory's compressed air

system, the created air pressure will be capable of bending the simply supported panel (horizontally and vertically), as illustrated in Fig. 3a).

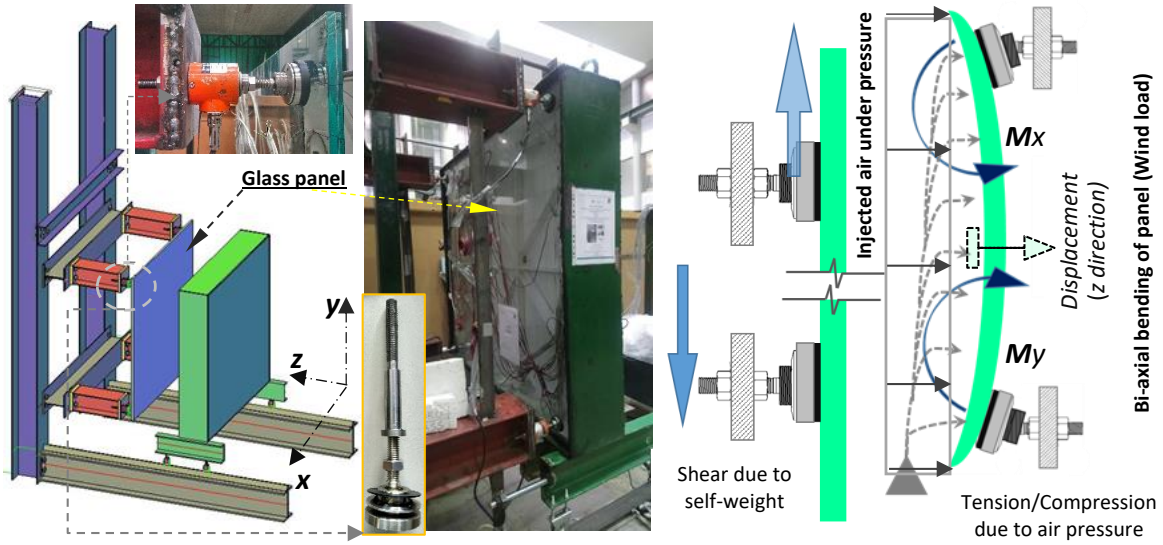

a) Frame reaction, test piece related to the glass panel and air box - forces due to the load

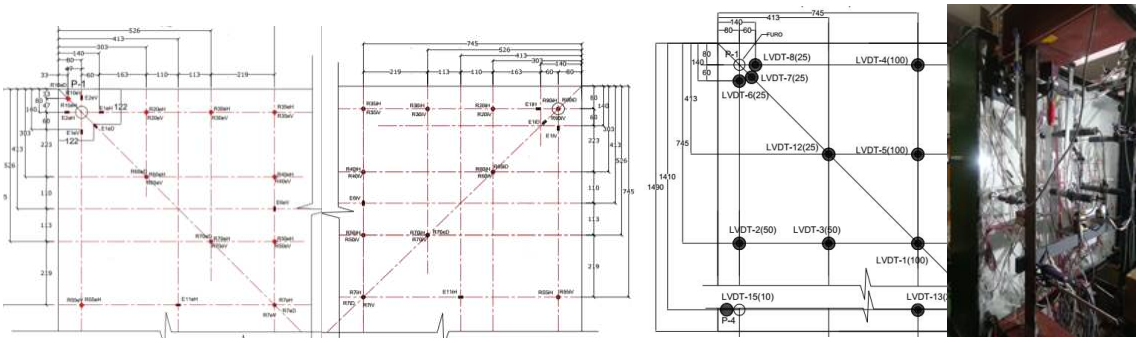

b) Strain gauges in both faces of panel and LVDTs on the face of the panel's thickest foil

Figure 3. Layout and instrumentation of glass panels referring to tests under wind action

In tests T08 to T28, the adhesive bolt option was used, following the procedures for the installation of stainless steel elements produced by Fitechnic®, according to [4], as well as those recommended by Sika® for the application of adhesive corresponding to the bi-component product SG-500, according to [10]. Such adhesive has a curing period of 7 days until the maximum resistant capacity is reached. In the T07 tests, the interlayer film was PVB, while in the T08/09/10 tests it was Evasafe, being of Sentryglas®Plus in the T15/T16 tests. Tests 11 to 14 included annealed glass with EVA and PVB interlayers. Tests T25/26 and T27/28 replaced T11/12 and T13/14 tests in what concerns to final statistic results for tempered glass panels.

3. Experimental results

3.1 General load-displacement results and panels' rupture modes

Table 1 presents a summary of the results obtained during the 24 tests carried out in the first phase of the current program. The value of the maximum load relative to the maximum air pressure reached inside the layout box (measured by means of a Campbell® datalogger) as well as the corresponding value of the maximum displacement at the central point of the panel (measured orthogonally to it through a TML® datalogger) are indicated. The failure mode

detected in each of the tests is also included as well as the average values of load and displacement referring to the association of results in homologous panels.

Table 1. Summary of results referring to the tests of the first phase with wind load

Nº	Test	Glass	Interlayer film	Máx Load [kN/m²]	Máx displ. [mm]	Rupture mode	Type of bolt	Average Load [kN/m²]	Average displ. [mm]
1	**T01**	Tempered	EVA	16,0	38,3	**Panel did not collapse. The WS-605S silicone cord collapsed**	Embedded	17,1	41,5
2	**T02**	Tempered	EVA	18,2	44,6				
3	**T03**	Tempered	EVA	17,1	41,5				
4	**T04**	Tempered	EVA	15,7	38,8	*Idem*	Counter-sunk	17,1	40,2
5	**T05**	Tempered	EVA	20,8	48,1				
6	**T06**	Tempered	EVA	14,8	33,7				
7	**T07_1**	Tempered *inner foil cracked due a chock	PVB	14,3	45,6	Panel did not collapse. The WS-605S silicone cord collapsed	Embedded	14,3 (10,3)	45,6 (34,4)
8	**T07_2***			7,6	24,8				
9	**T07_3***			9,2	31,0				
10	**T07_4***			10,1	36,3				
11	**T08**	Tempered	EVA	9,5	21,1	*Idem*	Adhesive	15,0	27,8
12	**T09**	Tempered	EVA	17,3	29,5	*Idem*	Adhesive		
13	**T10_1**	Tempered	EVA	19,5	36,3	*Idem*	Adhesive		
14	**T10_2**			13,9	24,8	*Idem*			
15	**T11**	Annealed	EVA	10,4	43,3	**Glass Panel collapsed**	Adhesive	11,7	34,0
16	**T12**	Annealed	EVA	12,9	24,6	Glass Panel collapsed	Adhesive		
17	**T13**	Annealed	PVB	11,1	84,5	Glass Panel collapsed	Adhesive	9,6	57,3
18	**T14**	Annealed	PVB	8,0	30,0	Glass Panel collapsed	Adhesive		
19	**T15**	Tempered	**SGP**	18,2	27,8	The WS-605S silicone cord collapsed	Adhesive	**20,0**	**29,8**
20	**T16**	Tempered	**SGP**	21,7	31,7	*Idem*	Adhesive		
21	**T25**	Tempered	EVA	15,5	31,0	*Idem*	Adhesive	16,2	35,0
22	**T26**	Tempered	EVA	16,9	39,0	*Idem*	Adhesive		
23	**T27**	Tempered	PVB	14,6	36,7	*Idem*	Adhesive	13,9	34,4
24	**T28**	Tempered	PVB	13,1	32,0	*Idem*	Adhesive		

Concerning the tempered glass panels tested under wind effects, Table 1, it was observed that the highest applied load was registered on a panel with SENTRYGLAS film (T16) and adhesive bolts. In relation to the first two trios of panels, the average maximum load reached was equal for both situations of embedded and countersunk bolts (17,1 kN/m^2) but the average maximum displacement was a slightly higher for the embedded one. In the case of panels with adhesive bolts (with structural silicone) and an EVASAFE-type interlayer film, a maximum load was reached in test T10_1 almost identical to that in test T05, which leads to very similar overall strength capacities for both bolts. The main differences between these tests are related with the deformations obtained, where the panel with adhesive bolts had a lower maximum displacement (36,3 mm) than the panel with countersunk bolts (48,1 mm). In average, the maximum displacement in the panels with Evasafe film and embedded bolts was 3,2% higher than the displacement of the panels with the same film, but countersunk bolts. The two tests with panels including Sentryglas® film and adhesive bolts achieves the higher global maximum load and the global lower deformation. The actual thickness of the silicone cords in the 4 joints influences the maximum rotation capacity of the panels, constituting the weakest link in the maximum deformation reached.

3.2 Load-displacement/stress and position-displacement/strain relations

Figure 4a) includes seven load-displacement diagrams overlapping the respective graphs for comparison. The greater stiffness evidenced by the panels with Sentryglas® film compared to panels with Evasafe and PVB can be seen. If the comparison is made between the panels with these last two films, those with PVB interlayers present lower stiffness compared to those that include Evasafe films, as can be seen in the tangent lines. Figure 4b) shows the overlap for the load-strain variation at the central point of the outer and inner sides of the panels, denoting predominantly linear relationships.

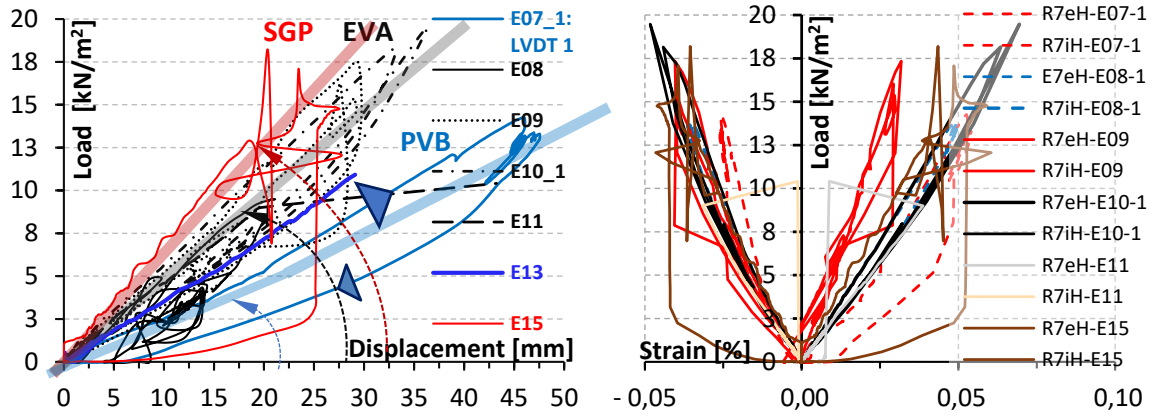

a) Load-orthogonal displacement *b) Load-horizontal strain*

Figure 4. Load-displacement/strain diagrams in panels' central point (int/ext)

It is presented in Figure 5 the position-displacement diagram along the mid-span line of the panel according to the horizontal direction (axis I-I) referring to test T08 for loads of 2 in 2 kN/m^2 up to the maximum load.

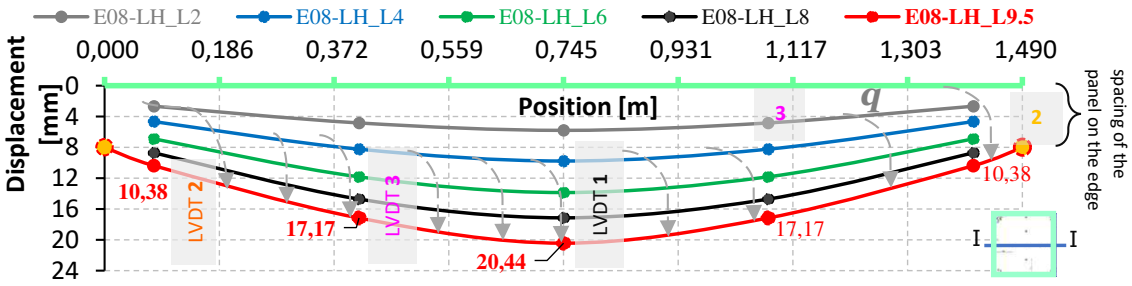

Figure 5. Position-displacement diagram for T08 (EVASAFE film and adhesive bolts)

4. Maximum stress evaluation

Laboratory research has allowed the identification of the mechanical properties that affect not only the glass itself, but also the interlayer films between sheets of the same material when inserted into laminated glass panels, such as tested in the research presented. Table 2 presents the elastic constants of the materials, reflecting the elastic behavior shown by the glass and its variation in the material behavior law. In the case of polymeric materials, they have a hyper-elastic behavior when considering quasi-static loads. Special careful needs to be taken when calculating Cartesian stresses as well as experimental principal ones.

Table 2. Mechanical properties of the materials used in the glass panels

Material	Young's Modulus [MPa]	Poisson's ratio, ν	$E_{equivalent}$ [MPa]	$\nu_{equivalent}$	f_y [MPa]	f_u [MPa]
Tempered laminated glass	70000	0,21	63927,57	0,231	-	≈ 120*
- EVASAFE	5 a 30	0,45			-	26,0
- PVB	2,23 a 11	0,43	63927,13	0,229	-	20,0
- SentryGlas®	200 a 400	0,49	-	-	-	34,5
Annealed glass	70000	0,21 a 0,27	-		-	≈ 40-45*
Stainless steel bolts	193000	0,27 a 0,3	-		290	580 **

* Bending strength | ** Uniaxial tensile resistance

Using a continuous section as an approximation of the real section, that includes two layers of glass and a film (interlayer) with reduced thickness (1.52 mm, which corresponds to only about 8.7% of the nominal total thickness of each panel, 17.52 mm), we can compute those stresses with the equations of the theory of elasticity. The alternative calculation implies the consideration of a homogenized section, and expressions for the equivalent longitudinal modulus of elasticity (E_{equiv}) and the equivalent Poisson's ratio (ν_{equiv}), respectively. In this case, the tendency for the order of magnitude of σ_x, σ_y, τ_{xy}, σ_1 and σ_2 would be a decrease since the modulus of elasticity would decrease in value, as indicated in Table 2.

Regarding the European standardization, and from a perspective of design and safety verification, the so-called EC10 has not been implemented yet. This will allow the continuation of the strategy approach and analysis of structural glass elements, similar to what is established with the first 9 Eurocodes referring to materials with structural function. However, according to the prCENTS_19100-1 [11], it is feasible to determine the value corresponding to the design stress at the central point of a glass panel subjected to the bending effect ($f_{g,d}$). In this way, such a parameter can be analytically determined by applying expression (1),

$$f_{g,d} = k_e . k_{sp} . \lambda_A . \lambda_L . k_{mod} . \frac{f_{g,k}}{\gamma_M} + k_p . k_{ep} . \frac{f_{b,k} - f_{g,k}}{\gamma_p} \quad (1)$$

The calculation of the resistant capacity referenced in [11] is performed by replacing the parameters of equation (1) by those suggested in Annex AA of [11] for both tempered laminated glass and annealed glass.

The maximum experimental principal stress (σ_1 at the central point of each panel - exterior face) took values between 40.8 MPa (T09) and 58.2 MPa (T10_1), in the case of tempered laminated glass panels (excluding T16 to T28). This largest value for σ_1 is clearly lower than the design value obtained by expression (1), equal to 95.1 MPa. In the case of annealed glass panels (standard situation indicated in the [11]) the maximum experimental stress at the same point varied between 32.8 MPa (T11) and 44.9 MPa (T13), which exceeds the corresponding calculation value of $f_{g,d}$, equal to 26.9 MPa. Hence, the failure observed in the annealed panels tested, with the same boundary conditions of the tempered panels, can be confirmed.

5. Conclusions

Following the study carried out, the main conclusions are highlighted:

i) Regarding the situation of the tests with the model of the 4 labeled supports, the panels with interlayer type EVASAFE showed greater resistance than those that included the PVB material. As for the rigidity, it was found that the panel with SGP film presented the highest

rigidity of the 3 options used. In addition, the thickness of the silicone cords constitutes the weakest link in the assembly.

ii) The bolts did not show very significant forces in the context of the tests performed, remaining with their shear and tensile strength clearly above the applied stresses.

iii) The tempered laminated glass panels were able to withstand about 2.7 times (on average) the design load established by the worst case scenario foreseen in Part 1-4 of EC1, without collapsing, recovering to its original configuration after removal of the applied air pressure. In the case of the panels with annealed glass, the corresponding average capacity was only about 1.6 times the same design load.

iv) It was found that the experimental stresses related to the panels with tempered glass reached about 50% of the respective design value of the flexural strength evaluated by the pre-standard prCENTS_19100 (2020), excluding T16 to T28. Regarding the annealed glass panels, it was found that the experimental stresses were higher than the corresponding design value by about 45%, thus proving the failure that occurred for the latter.

Acknowledgements

The authors express their gratitude to the Portuguese Foundation for Science and Technology (FCT) for the granted support within the research project GF SEISMIC POCI-01-0145- FEDER-032539. They also express their gratitude to the companies Pentagonal, Vidromax and Sika® Portugal for the granted facilities.

References

1. Pentagonal – Project Catalog. 2017. Available in https://pentagonal.com/projectos/.
2. Figueiredo F, “Point fixing glass facades – PFGF – Fitechnic® System”. Presentation on Structural Glass Subject – CMM Master Course, CED – FCT UC. Pentagonal – Projects Department. 2020.
3. Aguirregabiria, B L “Vidrio Estructural”. Escuela Técnica Superior de Arquitectura de Madrid – Universidad Politécnica de Madrid. 2018. (In Castilian)
4. Fitechnic® - Glass Fixing System: Point Fixing Catalog. V2.0. 2019.
5. Jordão S, Inca E, Mesquita, A. GF SEISMIC Project Annual Report: Structural Glass Façades Subjected to Seismic Loading. Submitted to the Portuguese Foundation for Science and Technology – POCI-01-0145-FEDER-032539. ISISE / DEC - FCTUC. 2020. (In Portuguese)
6. NP EN 1998 – 1. Eurocode 8 – Projecto de Estruturas para Resistência aos Sismos – Parte 1: Regras gerais, acções sísmicas e regras para edifícios. IPQ. 2010. (In Portuguese)
7. Jordão S, *et al.* “Painéis agrafados em vidro estrutural: Avaliação experimental”. XII Congresso de Construção Metálica e Mista. Coimbra. 1015-1024. 2019. (In Portuguese)
8. NP EN 1991 – 1 – 4: 2009. Eurocode 1 – Acções em Estruturas. Parte 1-4: Acções gerais – Acções do Vento. IPQ. 2010.
9. Product File: Sikasil WS-605 S – High performance sealant. Sika®. 2009.
10. Product File: Sikasil SG-500 – Silicone structural adhesive. Sika®. 2016.
11. Draft of Pr CEN/TS19100 – 1: 2020. Design of Glass Structures - Part 1: Basis of design and materials. CEN / TC 250/SC 11 N 572. 2020.
12. Mesquita A, Jordão S, Inca E. “Experimental and analytical evaluation of point fixed tempered laminated glass panels”. Proceedings of XIII Congress of Metallic and Mixed Construction. Coimbra, Portugal. 2021; 277-286. (in Portuguese)

  doi:10.5075/epfl-298799_978-2-9701614-0-0

ENHANCEMENT OF MODE I FRACTURE TOUGHNESS OF ADHESIVELY BONDED SECONDARY JOINTS USING LAYUP PATTERNING OF CFRP

R. A. A. Lima [a], A. Oswal [c], N. Roux [b], A. Bernasconi [a], M. Carboni [a], N. Carrere [c], S. Teixeira de Freitas [b]

[a] Department of Mechanical Engineering, Politecnico di Milano – Milan, Italy

[b] Faculty of Aerospace Engineering, Delft University of Technology – Delft, Netherlands

[c] ENSTA Bretagne, UMR CNRS 6027, IRDL, F-29200 – Brest, France

Abstract: *This work aims to analyse the influence of the CFRP layup patterning on the crack path of composite bonded joints and evaluate its effect on the mode I fracture toughness. An experimental program has been performed using Double Cantilever Beam tests with three different CFRP layup patterning and two adhesives. In addition, a finite element analysis was also implemented to further identify different damage mechanisms during the tests.*
The outcome shows that different substrate CFRP layup patterning results in distinct crack onsets and propagation paths during the tests, also influenced by the type of adhesive used. Furthermore, an enhancement of around 25% in the joint's onset fracture toughness was observed with the layup patterning compared to a reference joint (with unidirectional layup). Thus, the substrate's patterning morphology seems to be a promising method to increase the mode I fracture toughness of the studied secondary joints.

Keywords: CFRP patterning layups, fracture toughness, secondary bonded joints.

1. Introduction

Recently, with a worldwide demand to promote eco-friendly solutions to several industrial processes and products, the automotive and aeronautical sectors aim for lightweight structures. Consequently, multi-advanced materials such as new-modified steel alloys and composite materials are increasingly being used [1]. Adhesive joining technology is one of the most promising solutions to join multi-materials, especially composites, as it brings design flexibility, uniform stress distribution, and a limited impact on substrates' mechanical performance compared to traditional fasteners.

Nevertheless, adhesively bonded joints face challenges in ensuring reliability and safety during their operational life, as they tend to fail suddenly and show a limited tolerance to damage [2]. Consequently, to prevent catastrophic failure in safety-critical bonded joints, "back-up" rivets are used in current composite primary structures.

One promising solution to improve the reliability and safety of secondary bonded joints in primary structures is to enhance the joint's damage resistance and fracture toughness [3]. Different methods have been proposed in the literature to increase the fracture toughness of composite bonded joints: improving the adhesive's mechanical properties by modifications in the adhesive layer [4]; introducing Crack stoppers within the adhesive layer [5] [6]; interfacial

  doi:10.5075/epfl-298799_978-2-9701614-0-0

adhesion patterning over substrate's surface [7] [8]; and tailor the composite's stacking sequences [9][10].

Kupski *et al*. 2019 [11] investigated the effects of different stacking sequences and plies thickness on the mechanical behaviour of Single-Lap Joints (SLJ). It was observed that the crack propagates through different layers inside the composite when using a thin ply thickness instead of persuing single in-plane delamination when using a thicker ply thickness. As a result, multiple transverse matrix cracking co-occurs, increasing the energy dissipation and enhancing the SLJ strength for damage initiation.

Nonetheless, it is still unclear which mechanisms trigger the changes in the damage resistance of the SLJ due to their complex stress state. In the pursue to better understand the mechanisms related to enhancing adhesively bonded joints strength, this work aims to analyse the influence of different CFRP patterning layups on the fracture toughness of bonded joints and how the undergoing damage mechanisms can affect the crack propagation rate. Moreover, the Cohesive Zone Model (CZM) is used as a qualitative tool to understand the fracture mechanisms involved during Double Cantilever Beam (DCB) tests.

2. Materials and methods

2.1 Samples manufacturing

The Hexply 8552 – AS4, toughened epoxy resin supplied in prepreg unidirectional carbon fibres, was used to produce composites substrates with the following stacking sequences: $[0]_8$, $[0/90_2/0]_s$ and $[90/0_2/90]_s$. The curing of the composites laminated was performed in an autoclave under a total pressure of 7 bar and a temperature cycle of 180°C for 120 min.

Two different structural adhesives were used to join the CFRP substrates: a high toughness epoxy film adhesive with carrier 3M Scotch-weld™ AF163-2k (G_{IC} = 2416 J/m^2) [12] and a low toughness bi-component epoxy paste adhesive Araldite 2015/1 (G_{IC} = 640 J/m^2) [13], supplied by Hunstman International. The curing procedure for each adhesive is shown in Table 1.

Before the bonding procedure, the substrates' surfaces were sanded to ensure a uniform roughness, cleaned using acetone, and followed by a UV treatment for 7 minutes, as detailed in [12].

Each adhesive presented a different curing process, as described in Table 1.

Table 1: Description of adhesive's curing procedure.

Adhesive type	Temperature (°C)	Time (minutes)	Pressure (bar)	Method
Araldite 2015/1	80	60	-	Oven
AF- 163 2K	120	90	3	Autoclave

The dimensions of the CFRP adhesively bonded DCB specimens are detailed in Figure 1 (a). An initial crack length of 35 mm was guaranteed using Teflon tape. For AF163-2K, an inner carrier

  doi:10.5075/epfl-298799_978-2-9701614-0-0

ensured a nominal thickness of around 0.3 mm. For Araldite 2015/1, metallic spacers were used at both ends of the specimen to ensure the min thickness of 0.3 mm.

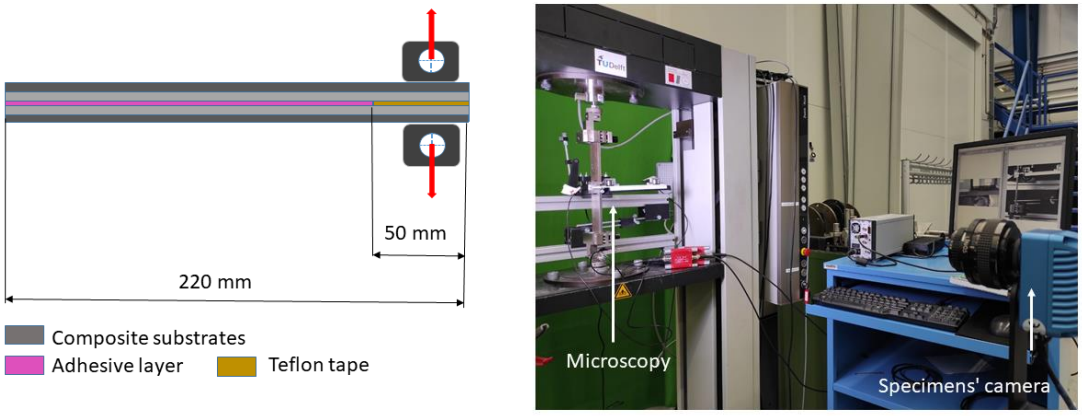

(a) (b)

Figure 1: (a) DCB dimensions and (b) testing set-up.

2.2 Experimental setup

DCB quasi-static mode I test were performed using an electro-mechanical Zwick testing machine with a Load cell of 1 kN. A testing speed of 4 mm/min was applied. At least four specimens of each type were tested, and their nomenclature is described in table 2.

Table 2: Specimens type and nomenclature.

Adhesive /CFRP layup	$[0]_8$	$[0/90_2/0]s$	$[0/90_2/0]s$
Araldite 2015/1	Araldite $[0]_8$	Araldite $[0/90_2/0]s$	Araldite $[0/90_2/0]s$
AF- 163 2K	AF – 163 2K $[0]_8$	AF – 163 2K $[0/90_2/0]s$	AF – 163 2K $[0/90_2/0]s$

Visual inspection was done on both lateral sides of the DCB specimens; on one side, using a microscope camera, and a regular camera on the other side, as shown in Figure 1(b). Both cameras were synchronised with load and displacement outputs from the testing machine. In addition, the photos were taken every four seconds.

The lateral surface used for regular camera photos was white painted to improve the contrast to track crack propagation. On the other side, the surface used for the microscopy camera measurements was kept natural to allow better visualisation of the crack path during the entire test.

  doi:10.5075/epfl-298799_978-2-9701614-0-0

3. Finite element analysis

Aiming to qualitatively simulate the crack propagation paths in the CFRP secondary bonded joints tested, a finite element model based on Cohesive Zone Modeling (CZM) was built.

A 3D finite element model for DCB specimens, under pure mode I, was set up in the ABAQUS software. In addition, a CZM with bi-linear traction separation law was applied. The substrates were modelled using eight-node brick elements (C3D8) and the cohesive elements with eight-node three—dimensional cohesive elements (COH3D8).

After a convergence study, a reasonable sweep mesh size of 0.5 mm was implemented for all the analyses.

To detect crack deflection and propagation in numerous possible paths, very thin cohesive element layers (5 microns thickness) were positioned at three different locations, as shown in Figure 2:

(1) in the middle of the adhesive layer to simulate cohesive failure.
(2) between each composite ply in a longitudinal direction to simulate delamination between composite plies.
(3) in the transversal direction next to the crack tip region to simulate transverse matrix cracking at the 90° lamina.

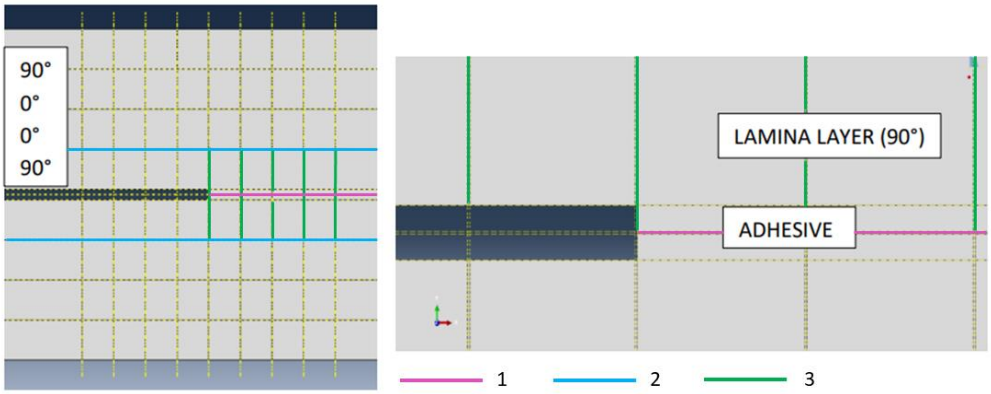

Figure 2: Scheme of the cohesive element layers distribution in the finite element analysis.

The distance between the cohesive element layers is equal to 0.375 mm. It is worth mentioning that each cohesive element layer had its properties correlated to the type of damage to be simulated represented (composite's matrix failure, delamination, or adhesive properties). The primary materials' properties used in the model are described in Tables 2 and 3.

  doi:10.5075/epfl-298799_978-2-9701614-0-0

Table 3: CZE properties used in cohesive interfaces of the FEA.

Material	E (MPa)	G (N/mm)	σ (MPa)
Araldite 2015/1	1.0E6	500	22
AF 163- 2K	1.0E6	2416	46
Hexply 8552 – AS4	1.0E6	500	64

Table 4: Composite material's properties used in the FEA.

Material	E_{11} (MPa)	E_{22} (MPa)	E_{33} (MPa)	V_{12} - V_{13}	V_{23}	G_{11} (MPa)	G_{22} (MPa)	G_{33} (MPa)
Hexply 8552 – AS4	141000	9750	9750	0.267	0.5	5200	5200	3190

4. Results

The load versus displacement curves of the DCB, and corresponding R-curves and fracture surfaces are shown in Figure 3. Moreover, specimens' onset fracture toughness and the crack onset location are presented in Table 4. The G_{IC} was calculated using the Corrected Beam Theory, as recommended by the standard ASTM D5528.

The specimens adhesively bonded with Araldite 2015/1 all showed cohesive failure independently of the substrates' layup ($[0]_{8,}$ $[0/90_2/0]$s and $[0/90_2/0]$s) and with maximum load values around 40-50N. The different stacking sequences did not affect the crack propagation paths, and no significant changes were observed in the onset fracture toughness. The average onset value of G_{IC} is around 600 J/m^2, and it is in accordance with the nominal fracture toughness of the Araldite 2015-1, which varies between 400 to 600 J/m^2.

On the other hand, specimens bonded with the film-adhesive AF 163- 2k showed different results depending on the substrates' stacking sequence. The $[0]_8$ layup showed a consistent cohesive crack propagation and an average onset fracture toughness of 2868 J/m^2. Moreover, an interesting bridging phenomenon triggered by the presence of the carrier inside the adhesive was observed [12]. This bridging phenomenon furtherly enhanced the adhesive's fracture toughness by around 20% as the crack further propagated along the specimen's lenght.

The specimens $[0/90_2/0]$s – AF163 – 2K showed a load versus displacement curves with a first peak that characterises the onset of damage without any visible crack, a 1st drop in the load values that corresponds to a matrix cracking at the 90-degrees ply (see Figure 4), a second peak related to a cohesive failure in the adhesive followed by a significant drop corresponding to delamination through the 0-degrees ply. In this case, it was possible to observe a crack competition between the initial cohesive failure and the matrix cracking. The last one promoted a crack deflection and final delamination at the 0-degree layer. Also, higher values of the joint's onset fracture toughness were obtained for these specimens compared to the $[0]_8$ with a total value of 3568 J/m^2 (25 % increase).

For specimens $[90/0_2/90]$ s – AF163 – 2K (Figure 3e), the crack onset deflected directly for the first 90-degree layer next to the adhesive layer, and a decrease in the joint's G_{IC} was obtained.

Through the numerical simulations, it was possible to observe that, for this specific case, the damage at the cohesive layer at the first composite layer next to the crack tip was significant and had a larger influence on the crack propagation path, as can be seen by the red colour (maximum degradation of the cohesive element) in Figure 4. Figure 3 (a) for this specimen also shows a non-smooth crack propagation, characterised by a stick-slip trend in the load-displacement curve that was not evident for the other specimens.

As shown in Table 4 and Figure 4, the finite element analysis could qualitatively predict the crack propagation paths in the specimens.

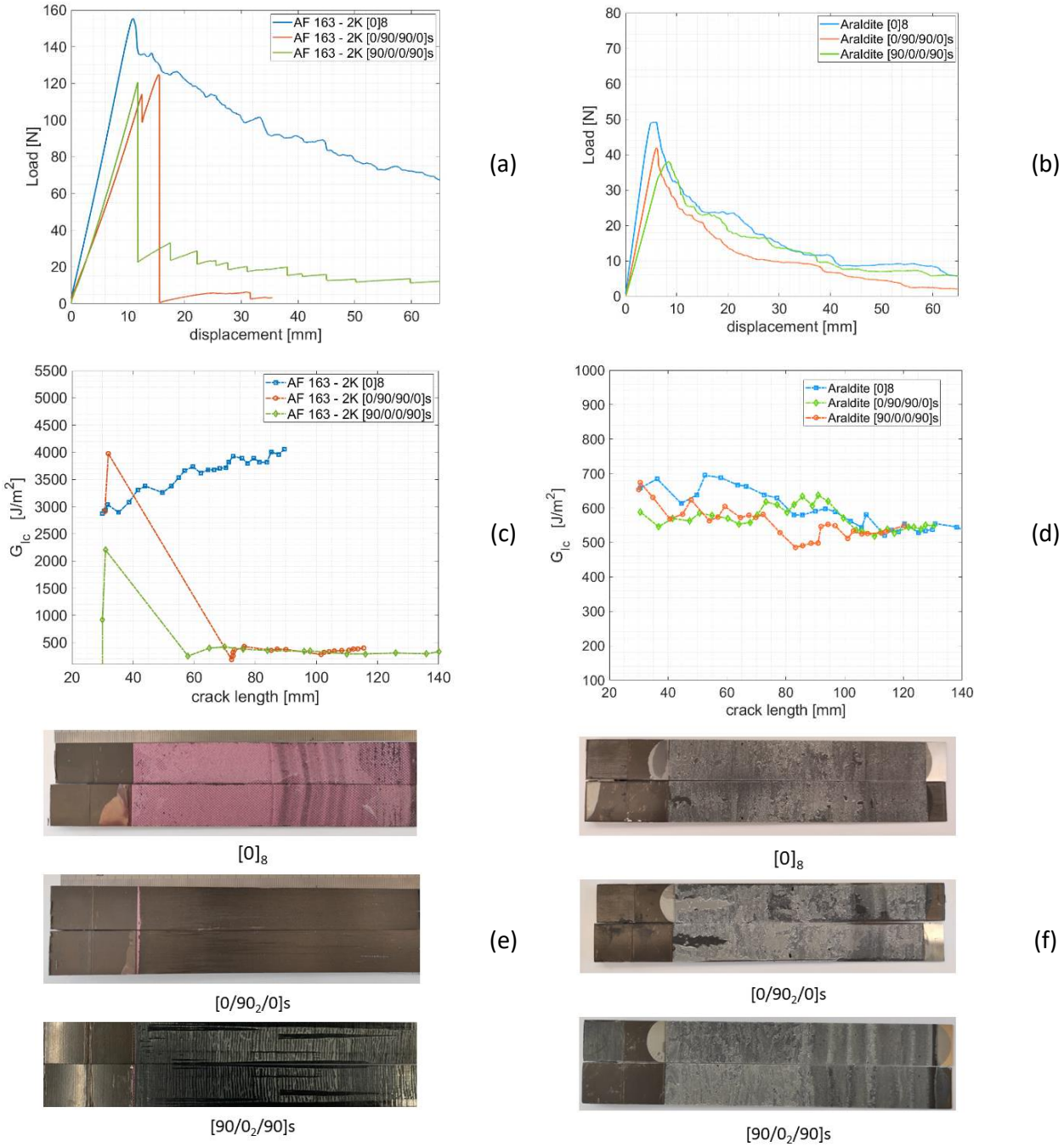

Figure 3:Load versus displacement curves (a) AF163-2K, (b) Araldite 2015/1, R- curves: (c) AF163-2K, (d) Araldite 2015/1, and fracture surfaces: (e) AF163-2k and (f) Araldite 2015-1.

Table 5: Mode I fracture toughness of each bunch of specimens and their crack onset observed experimentally and predicted by FEA.

Adhesive type	**CFRP stacking sequence**	**G_{IC} (J/m²) at crack onset**	**Crack onset** (experimental)	**Crack onset** (FEA)
AF 163 – 2K	$[0]_8$	2868	adhesive	-
	$[0/90_2/0]s$	3568	adhesive followed by matrix cracking	adhesive
	$[90/0_2/90]s$	2147	composite layup	Adhesive and composite layup
Araldite 2015-1	$[0]_8$	619.7	adhesive	-
	$[0/90_2/0]s$	563.9	adhesive	adhesive
	$[90/0_2/90]s$	600.1	adhesive	adhesive

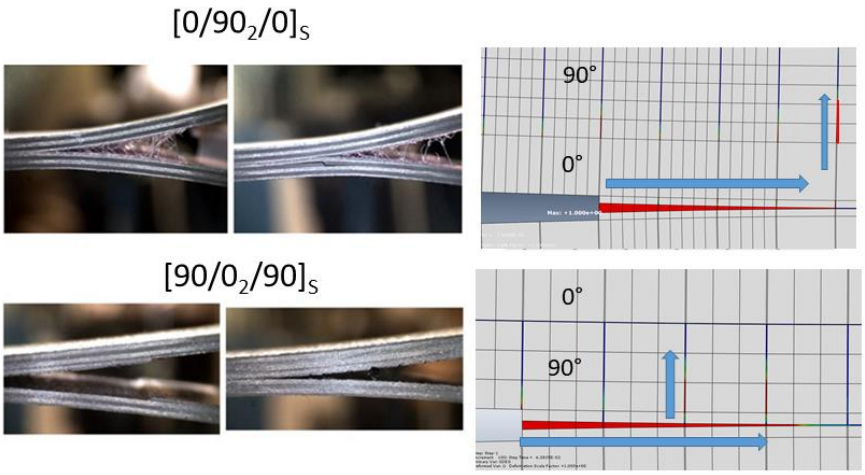

Figure 4: DCB specimens bonded with adhesive AF 163-2K with their crack paths visualised experimentally and by FEA.

5. Conclusions

This work studied the effects of CFRP layup patterning to enhance the secondary bonded joints' fracture toughness. The following conclusions could be drawn from the results:

  doi:10.5075/epfl-298799_978-2-9701614-0-0

When using a low toughness adhesive as the Araldite 2015/1 all fractures were cohesive, i.e., crack onset and propagations within the adhesive layer, indicating that the ultimate transverse strength of the CFRP plies was not exceeded. When using a high toughness adhesive as the AF 163-2K, , a crack competition was triggered between different crack locations (adhesive layer, matrix cracking, and delamination), influenced by different stress concentrations regions within the joint.

For the specimens bonded with the more tough adhesive, the CFRP patterning had a leading role in the G_{IC} of the studied joints. In particular, specimens $[0/90_2/0]s$ increased around 25% their onset fracture toughness compared to the unidirectional specimens. Moreover, the unidirectional specimens presented a bridging phenomenon triggered by an inner carrier that also lately enhanced their $G_{IC.}$ These results show promising solutions for enhancing the fracture toughness of mode I adhesively bonded joints.

Acknowledgements

This article/publication is based upon work from COST Action CA18120 (CERTBOND - https://certbond.eu/), supported by COST (European Cooperation in Science and Technology).

6. References

[1] M. D. Banea and L. F. M. Da Silva, “Adhesively bonded joints in composite materials: An overview,” *Proc. Inst. Mech. Eng. Part L J. Mater. Des. Appl.*, vol. 223, no. 1, pp. 1–18, 2009.

[2] M. Kadlec, R. Růžek, and P. Bělský, “Concurrent use of Z-pins for crack arrest and structural health monitoring in adhesive-bonded composite lap joints,” *Compos. Sci. Technol.*, vol. 188, no. December 2019, 2020.

[3] K. Maloney and N. Fleck, “Toughening strategies in adhesive joints,” *Int. J. Solids Struct.*, vol. 158, pp. 66–75, 2019.

[4] A. Buchman, H. Dodiuk-Kenig, A. Dotan, R. Tenne, and S. Kenig, “Toughening of Epoxy Adhesives by Nanoparticles,” *J. Adhes. Sci. Technol.*, vol. 23, no. 5, pp. 753–768, 2009.

[5] T. Kruse, T. Körwien, S. Heckner, and M. Geistbeck, “Bonding of CFRP primary aerospace structures - Crackstopping in composite bonded joints under fatigue,” *ICCM Int. Conf. Compos. Mater.*, vol. 2015-July, no. July, pp. 19–24, 2015.

[6] D. Quan, J. L. Urdániz, C. Rouge, and A. Ivanković, “The enhancement of adhesively-bonded aerospace-grade composite joints using steel fibres,” *Compos. Struct.*, vol. 198, pp. 11–18, Aug. 2018.

[7] R. Tao, X. Li, A. Yudhanto, M. Alfano, and G. Lubineau, “On controlling interfacial heterogeneity to trigger bridging in secondary bonded composite joints: An efficient strategy to introduce crack-arrest features,” *Compos. Sci. Technol.*, vol. 188, no. December 2019, p. 107964, 2020.

[8] R. Tao, X. Li, A. Yudhanto, M. Alfano, and G. Lubineau, “Laser-based interfacial patterning enables toughening of CFRP/epoxy joints through bridging of adhesive ligaments,” *Compos. Part A Appl. Sci. Manuf.*, vol. 139, no. September, p. 106094, 2020.

[9] S. Yin *et al.*, “Toughening mechanism of coelacanth-fish-inspired double-helicoidal composites,” *Compos. Sci. Technol.*, vol. 205, no. September 2020, p. 108650, 2021.

[10] J. Kupski, S. Teixeira de Freitas, D. Zarouchas, P. P. Camanho, and R. Benedictus, “Composite layup effect on the failure mechanism of single lap bonded joints,” *Compos. Struct.*, vol. 217, pp. 14–26, Jun. 2019.

[11] J. Kupski, D. Zarouchas, and S. Teixeira de Freitas, “Thin-plies in adhesively bonded carbon fiber reinforced polymers,” *Compos. Part B Eng.*, vol. 184, p. 107627, 2020.

[12] S. Teixeira de Freitas, D. Zarouchas, and J. A. Poulis, “The use of acoustic emission and composite peel tests to detect weak adhesion in composite structures,” *J. Adhes.*, vol. 94, no. 9, pp. 743–766, 2018.

[13] R. Lopes Fernandes, S. Teixeira de Freitas, M. K. Budzik, J. A. Poulis, and R. Benedictus, “From thin to extra-thick adhesive layer thicknesses: Fracture of bonded joints under mode I loading conditions,” *Eng. Fract. Mech.*, vol. 218, Sep. 2019.

Composites Meet Sustainability – Proceedings of the 20th European Conference on Composite Materials,
ECCM20. 26-30 June, 2022, Lausanne, Switzerland

NUMERICAL ANALYSIS OF BOLTED POINT FIXED LAMINATED GLASS PANELS SUBJECTED TO SEISMIC LOADS

Eliana, Inca[a], Sandra, Jordão[a], Chiara, Bedon[b], Afonso, Mesquita[a], Carlos, Rebelo[a]

a: University of Coimbra, Institute for Sustainability and Innovation in Structural Engineering (ISISE), Department of Civil Engineering, 3030-790 Coimbra, Portugal – e.inca.cabrera@uc.pt
b: University of Trieste, Department of Engineering and Architecture, 34127 Trieste, Italy

Abstract: *Pointed fixed glass façade systems have been used to fulfill the requirements for high transparency in modern structures, technological developments in glass production lead to an extent worldwide use. Nevertheless, structural designers face a void in regard to standardization for the current design practices, even for typical loads. Moreover, the overall response under seismic actions is not yet fully studied. This paper explores the seismic performance of bolted point fixed laminated glass façades fixed with stainless steel spider arms. The study focussed on the dissipative capacity of the system, and the influence of the spider clearances on the installation phase to accommodate the lateral drift, by allowing horizontal translation of the panels for in-plane loads. The characterization involves numerical models developed in ABAQUS software, benchmarked with ongoing experimental research.*

Keywords: Glass Façade Systems; Laminated Glass Panels; Seismic Analysis; Numerical Analysis; Point Fixed Glass Façade Systems.

1. Introduction

Technological developments in the production of glass panels lead to an extensive use of glass as structural material worldwide. The spectrum of construction includes a variety of applications from stairs, canopies, to complex facade systems for tall buildings and wide-open spaces. Particularly, point fixed glass facade systems (PFGFS), have been used to fulfill the requirements of transparency of facades in modern structures, the spider connection allows a reduction of area of steel in the systems in comparison to a clamped system (Figure 1).

(a)

(b)

Figure 1. (a)Example of pointed fixed glass façade, BIOCANT, Cruz de Oito, Portugal, 2006. (b)Example of spider arms. Cable car station, La Paz, Bolivia, 2020.

In contrast to the versatile construction with glass material, structural designers still encounter a void in regard to design standardization [1]. Thus, several glass systems have been designed

  doi:10.5075/epfl-298799_978-2-9701614-0-0

with piecewise procedures, including full scale testing and even complex numerical modeling, to support pioneer design. Particularly, the overall response of point fixed glass façade systems under seismic actions is not yet fully studied [2-3]. Some structural design standards, for example, would classify glass façades as merely secondary elements, disregarding the lateral load transfer from the main building, and therefore assuming no response from different façade systems to certain dynamic loads. This is a fundamental topic, given that although glass is surprisingly deformable and able to accommodate significant displacements, it is critically susceptible to harsh contact, which may occur during a seismic event at the panel contour (in supported panels), or at the connectors (in point supported façades).

This paper explores the seismic performance of bolted point fixed laminated glass panels with stainless steel spider arms. The spider plays the role of intermediary between the main structure and the bolt fitting fixed onto the glass panel, allowing the construction to enhance all its transparency. A typical spider-arm, located at a central façade panel (Figure 2a), includes four arms with circular holes to fix the fittings (Figure 2b). Among commercial products, spider-arms that include different clearances on each arm for the fittings (Figure 2c), shown a promising seismic dissipative solution, allowing horizontal translation of the panels for in-plane loads.

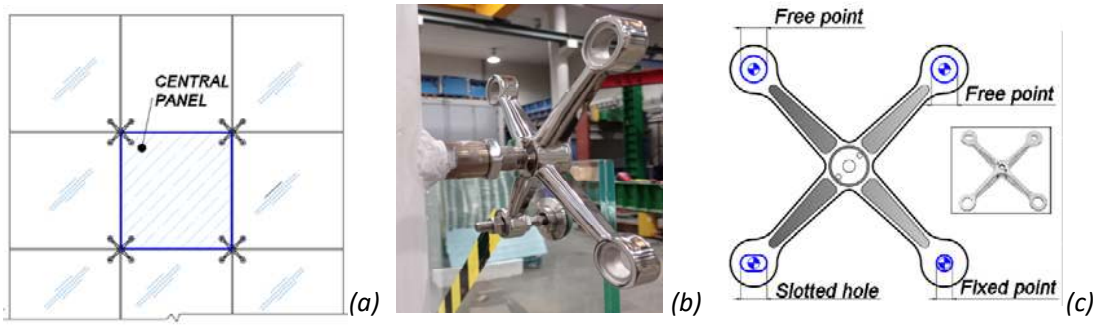

Figure 2. (a) Glass façade. (b) Example of spider arm fixing with circular holes [4]. (c) spider arm with different clearances [5]

2. Glass Façade Subjected to Seismic Loads

2.1 Material calibration of laminated glass panels with bolted point fixings

This paper reports on methodologies to numerically study the behavior of real scale pointed fixed laminated glass panels (PFLGP) for façade systems under cyclic loads, by means of finite element models. Prior to this study, the characterization of the structural behavior under uniform distributed loads for mechanical and bonded point fixed laminated glass panels was carried on. The numerical models were benchmarked with an experimental campaign, performed at the Laboratory of Structures, Structural Mechanics and Construction (LEMEC) of the civil engineering department (DEC), of the University of Coimbra (UC), to which it is associated the Laboratory of the Institute for Sustainability and Innovation in Structural Engineering (ISISE), under GF-Seismic research project [6]- focused on performance of PFLGP for façade systems subjected to seismic loads, in close collaboration with Portuguese companies of the glass industry.

Three different solutions of stainless-steel bolts were studied, embedded (laminated) bolt fixing and bonded fixings were part of the parametric variation of the work. Particularly in this work

  doi:10.5075/epfl-298799_978-2-9701614-0-0

countersunk fixings that transfer the out of plane and in plane loads directly through the bolt and glass interface are addressed. The glass panels were subjected to uniform distributed load, simulating wind pressure, applied incrementally in a closed and sealed steel box (Figure 3). Overall, eighteen specimens were tested, including variations on the type of interlayers (EVA, PVB and SentryGlas™). A section of a pointed fixed façade system will be tested under quasi-static cyclic in plane- load, allowing the overall behaviour of a full-scale façade systems to be assessed.

The numerical models allowed the calibration of the material properties, finite element configurations and interactions, which were used for the study of the isolated panel with spider arms subjected to in-plane lateral loads.

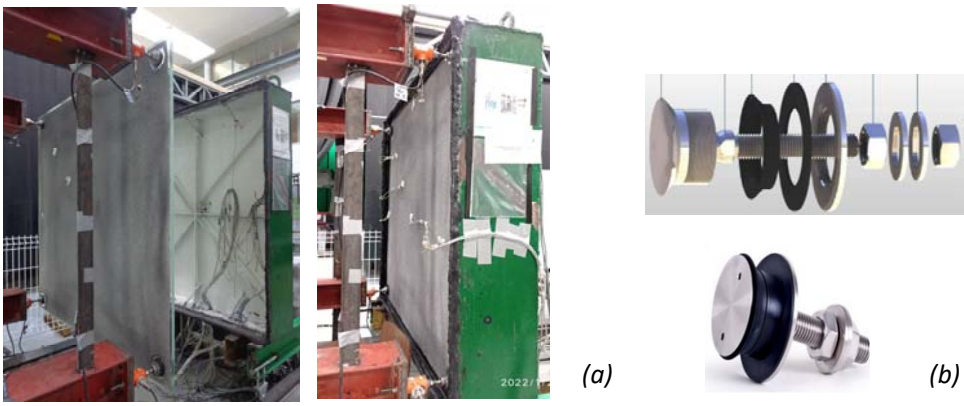

Figure 3. (a) Experimental layout of a tempered laminated glass panel with bolted point fixings at the corners, subjected to uniform distributed load. (b) Stainless steel countersunk bolt fixing

2.2 In plane quasi static-cyclic load pattern

The determination of the lateral load transferred by the primary structure to the facade system, involves several parameters. The major influencing parameters are the type of secondary support system, type of connections on top and bottom of the facade, the type of structural system, seismic performance of the building, and most importantly the local seismicity. The variability of the mechanisms that are involved regarding the type of façade system has led to a void in regard to standardized loading protocols.

The influence of the primary structure for the facade systems is the main interest of this study. More in detail, the study of a mid-height office building located in an active seismic region (Figure 4a), designed according to current standards EN 1998-1 design standard [7]. The criteria for maximum lateral drift for ductile non-structural elements was selected and limited to 0.75% of height of the typical stories. The maximum lateral displacements for both the perpendicular were obtained and transferred to the façade system (Figure 4 b and c).

In this work the in-plane lateral load transferred to the façade was explored. A system of 3 x 3 panel located at the top of the façade's building were selected and studied. An incremental cyclic load was applied with the objective to numerically study the structural behavior of the interaction between the spider-arm and the central laminated glass of the system.

  doi:10.5075/epfl-298799_978-2-9701614-0-0

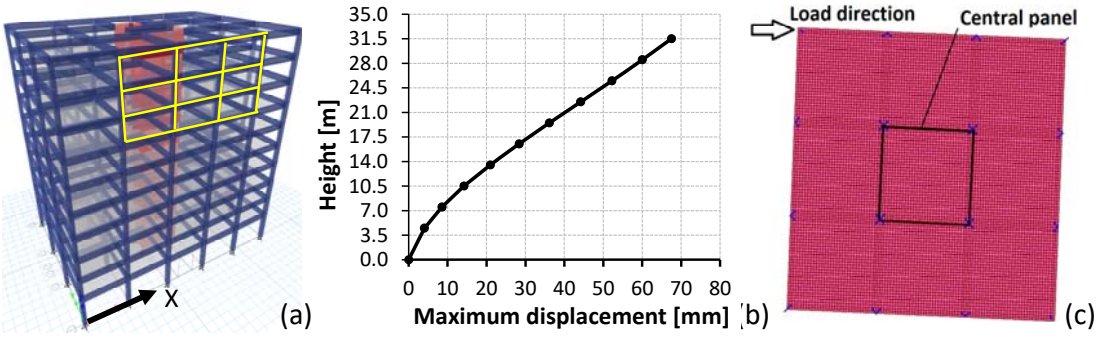

Figure 4. (a) Reference concrete building. (b) Maximum lateral displacement in X direction for each floor. (c) Load direction of a section of a façade 3 x 3 elements

3. Seismic behavior of pointed fixed façade systems with dissipative spiders arms

3.1 Numerical models for laminated glass panels with bolted point fixings

The complexity of the analysis of a laminated glass element lies on the interaction between different material properties. While the mechanical behavior of glass before fracture, is considered as a linear elastic material, the polymeric interlayers are viscoelastic materials, with a mechanical response dependent on the type of load, time and temperature. The large differences in stiffness, within polymeric interlayers and glass is almost 10000 times lower, leading to numerical problems when solving the systems. In this work, numerical models were developed with ABAQUS software [8].

For this study, linear elastic analysis was considered for the laminate. The material properties for the interlayer were correlated with experimental tests. The material properties for glass were defined by its nominal values for the modulus of elasticity (E_{glass} = 70 GPa) and Poisson ratio (ν_{glass} = 0.23). The panels included PVB interlayer, that was defined by a modulus of elasticity of E_{PVB} = 4 MPa and corresponding Poisson' ratio of ν_{PVB} = 0.45, finally the stainless steel type A316 for the bolts and spiders, were modeled with nominal values for modulus of elasticity (E_{steel} = 193 GPa) and Poisson ratio (ν_{steel} = 0.3).

Full-scale dimensions were used for the panel (1490 x 1490 mm square size), constituted of a layer of glass with 6 mm + 1.52 mm of interlayer + 10 mm of glass, fixed with four bolt fixings at 80 mm from the corners (Figure 4). The interaction between glass and interlayers were defined with a surface-to-surface interaction, to account for possible relative tangential dis-placement (penalty method), and a fully rigid hard normal contact behaviour (i.e. compenetration avoided) at the interface between glass and interlayers. A set of 2-node linear beam elements were used to characterize the rotation capacity of the bolt's head interacting with glass material, with a multi-point constraint (MPC constraints).

8-node solid brick elements with reduced integration and hourglass control were used for glass, steel and interlayers. The mesh arrangement included a minimum of 2 elements per thickness of the layers, and a 20 x 20 mm maximum element size. The outer face of the shaft was fixed in all degrees of freedom, given that during the experimental campaign these elements were fixed to the support frame (Figure 4).

  doi:10.5075/epfl-298799_978-2-9701614-0-0

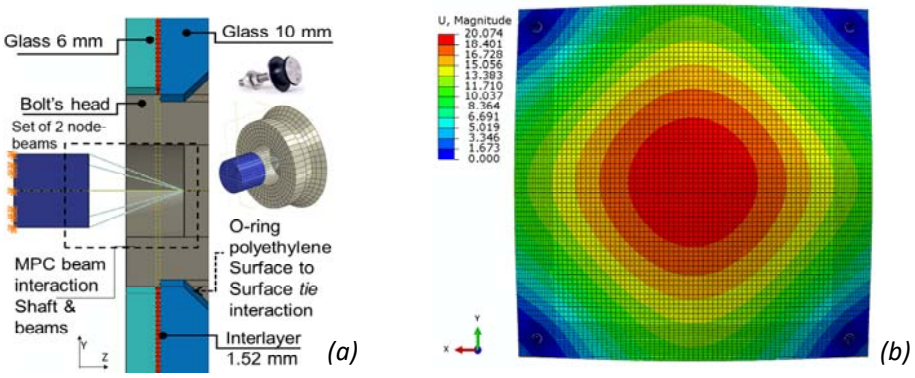

Figure 5. (a) Description of elements for the numerical model of countersunk bolt and laminated glass. (b) out-of-plane displacements for 8 kPa of distributed load for the pointed fixed laminated glass panel

3.3 Numerical model of stainless steel spiders

Numerical models of a laminated glass panel located at the center of a section of a façade (Figure 2a), fixed with spider arms attached to the secondary structure of the reference building's façade were developed. The objective of the study is to evaluate the structural response of the glass panels under quasi-static lateral loads using countersunk bolts, comparing the cases with spider arms with "dissipative" clearances (Figure 2c) and non-dissipative (without clearances) spider systems (Figure 2b).

For the dissipative spider element, each arm clearance allows a different boundary condition at each corner of the laminate. A typical central panel on a façade will follow the configuration shown in Figure 6. The system includes: one fixed point, one horizontal-translation free point, and two free points with horizontal and vertical translation. The clearances according to the systems described by [5], allow a ±10 mm clearances for the free-translation points. For the numerical models developed in ABAQUS software, the stainless steel bolts included different types of connector elements, between the bolt's head and shaft element (Figure 6) to accommodate a pre-set clearance according to the producer.

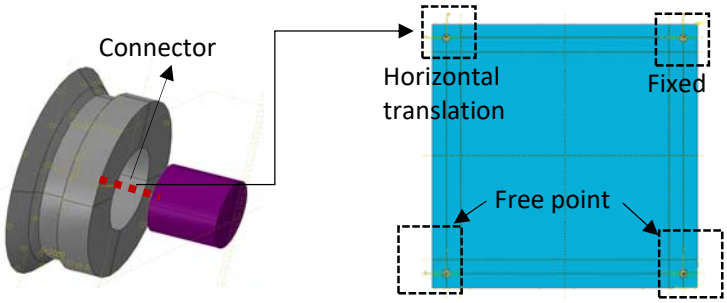

Figure 6.Countersunk bolt with connector properties different boundary conditions for spider arms

The laminates were studied under a quasi-static cyclic lateral load with increments of 10 kN, 50 kN and 100 kN with a minimum of 3 cycles per load (Figure 7a), until reaching the maximum displacement imposed at the top of the reference building. Three reference points were allocated on the inner face of the laminate, to compare the response for both spider arm systems, as presented in Figure 7b. Reference point 1 and 2 (Ref-1 & 2) located close to the

bolt's position on the inner layer of glass panel, and reference point 3 (Ref-3) located at the middle of the panel.

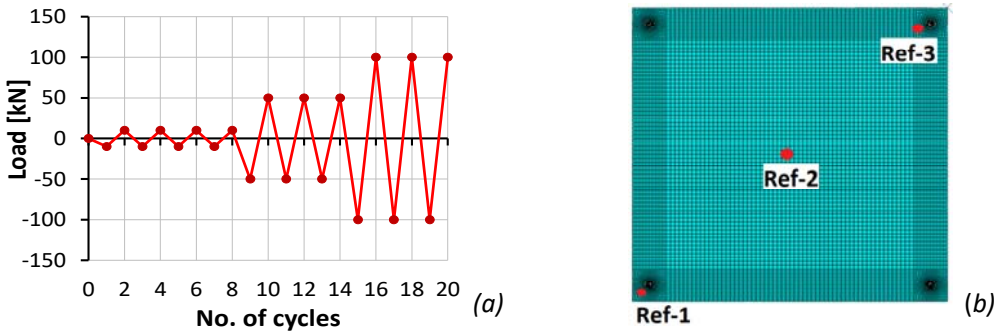

Figure 7. (a) Lateral load applied to analyses the section of a façade. (b) Reference points for comparison of numerical results

A damage limitation criteria was imposed for the laminates, considering the maximum stresses that will produce breakage on the tempered glass (σu=90 MPa) according to [9]. In Figure 8 a comparison of maximum displacements [mm] and stresses [MPa] for the 1st load cycle, corresponding to a lateral load of 10 kN. For the panels with spider arms including different clearances (dissipative spiders) and non-dissipative spiders (fixed) is presented. The stresses around the bolts are higher for the non-dissipative spider as expected, as a result of the limitation in lateral displacement.

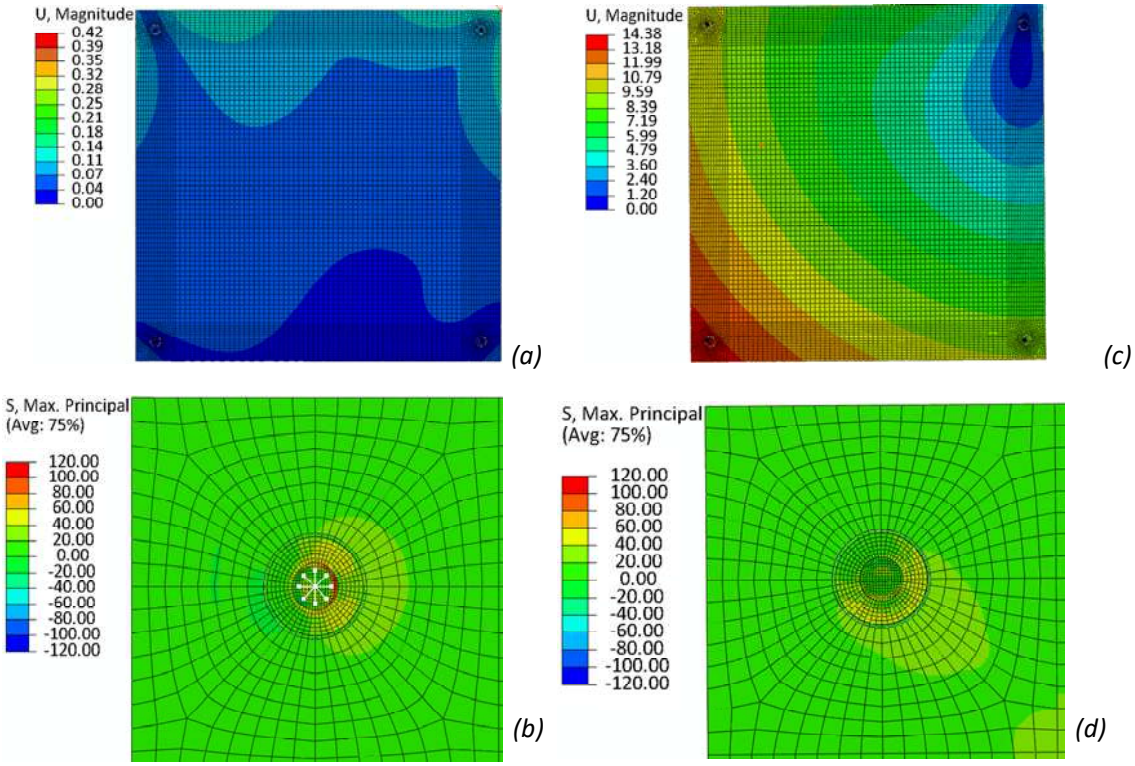

Figure 7. Results from the numerical model for non-dissipative (a & b) and dissipative spider arms (c & d), for maximum displacements [mm], and maximum stresses [MPa]

3.3 Results

The comparison between the dissipative and non-dissipative spider systems was performed by comparing the maximum displacement and stresses obtained in the numerical simulations, from three reference positions on the panel according to Figure 6b.

In Table 1, the results from the reference points are described, for different cycles of lateral load. It is observed that higher stresses are developed specifically close to the bolts for the non-dissipative spider system. The system allows lateral displacements given the different clearances for each spider arm, reducing at least 40% the stresses developed around the bolts and at critical points of the laminate.

Table 1: Comparison of results between numerical models with dissipative and non-dissipative spiders.

Reference	No. of cycles	Applied Load [kN]	Max. Stess [MPa]		Max. Displacement [mm]	
			Non dissipative	Dissipative	Non dissipative	Dissipative
Ref-1	1	10	19.55	0.22	0.118	13.79
Ref-2			0.35	4.65	0.0056	6.89
Ref-3			39.5	17.74	0.13	1.28
Ref-1	3	10	19.55	0.22	0.118	14.9
Ref-2			0.35	4.65	0.056	7.01
Ref-3			73.98	66.72	0.128	1.28
Ref-1	5	50	97.75	1.16	0.593	11.7
Ref-2			1.74	23.3	0.28	12..94
Ref-3			197	93	0.64	6.88

4. Conclusions

Besides being largely used in buildings, glass facades and glass structures still represent a challenging task for designers. In most of the cases, no specific design recommendations are given by standards, or even testing protocols, with significant issues for designers. Particularly prone to seismic action, glass facades are often considered as non-structural elements, which collapse may cause damage and high reparation costs. The current study explores the seismic performance of laminated glass panels with bolted point fixings using two types of spider arm fixations available in the market. Spider arms with pre-set clearances for the bolt fixation showed a “dissipative” structural response under lateral loads. Reducing the amount of stress concentration around the bolts in 40% in comparison to traditional fixed spider arms.

  doi:10.5075/epfl-298799_978-2-9701614-0-0

Acknowledgements

The Portuguese Foundation for Sciences and Technology (Fundação da Ciência e Tecnologia) under contract grant POCI-01-0145-FEDER-032539 (GF-Seismic | Structural Glass Facades Subjected to Seismic Load), and the first author's studentship under grant agreement 2021.06822.BD is gratefully acknowledged. The EU-COST Action CA18120 (CERTBOND, https://certbond.eu/) is also acknowledged for providing financial support to the first author to perform part of this work (STSM visitor at University of Trieste, Italy).

References

1. Bedon C, Zhang X, Santos F, Honfi D, Kozłowski M, Arrigoni M, Figuli L, Lange D. Performance of structural glass facades under extreme loads–Design methods, existing research, current issues and trends. Construction and Building Materials. 2018;;163:921-37.
2. Bedon C, Amadio C, Noé S. Safety issues in the seismic design of secondary frameless glass structures. Safety. 2019; 5(4):80.
3. Inca E, Jordão S, Rebelo C , Rigueiro C and Simões R. Seismic Behaviour of Point Fixed Glass Façade Systems: State of the Art Review. European Journal of Engineering Science and Technology 2019; 2(2):1-15.
4. Fitechnic® - Glass Fixing System. Technical catalogue of spider arms, rotules and complements for pointed fixed glass facades. V2.0. 2019. Retrieved from: //fitechnic.com/point-fixing/.
5. SADEV® classsic- Technical catalog. 2014. Retrieved from: https://www.sadev.com/products/building-envelopes/glass-spiders/s-3001-evo/
6. Jordão S, Rebelo C, Simões R, Constança R, Mesquita A, Inca E. GF Seismic project report: Structural glass façades subjected to seismic loading. FCT Portuguese Foundation for Sciences and Technology, POCI-01-0145-FEDER-032539, 2019.
7. Eurocode 8: Design of structures for earthquake resistance-part 1: general rules, seismic actions and rules for buildings. Brussels: European Committee for Standardization. 2005.
8. Simulia, ABAQUS v. 6.14 computer software and online documentation, Providence, RI, USA: Dassault Systems, 2016.
9. Draft of Pr CEN/TS19100 – 1: 2020. Design of Glass Structures - Part 1: Basis of de-sign and materials. CEN / TC 250/SC 11 N 572. 2020.

  doi:10.5075/epfl-298799_978-2-9701614-0-0

FRACTURE TOUGHNESS OF ELASTICALLY COUPLED LAMINATES: EVALUATION OF ANALYTICAL SOLUTIONS THROUGH DIGITAL IMAGE CORRELATION

Panayiotis Tsokanas [a], Theodoros Loutas [b], Anastasios P. Vassilopoulos [c]

a: Department of Mechanical Engineering and Aeronautics, University of Patras, Greece; panayiotis.tsokanas@gmail.com
b: Department of Mechanical Engineering and Aeronautics, University of Patras, Greece
c: Composite Construction Laboratory, École Polytechnique Fédérale de Lausanne, Switzerland

Abstract: *This paper presents some preliminary results of our ongoing work that elaborates on the idea of experimentally validating analytical expressions that can potentially be used as data-reduction equations. Two recent mechanical models are compared: the clamped crack tip model and the semi-rigid interface joint model. Firstly, the valuable expressions of these two models are collected and provided. Next, interlaminar fracture toughness experiments are performed using the double cantilever beam configuration and a glass fiber reinforced polymer laminate. The generalized displacements of the specimens during the experiments are captured using the digital image correlation (DIC) technique. The work compares the fracture toughness calculated by the two models and their predictions for the specimen displacements against the DIC measurements. To the best of our knowledge, this is the first attempt to experimentally validate explicit equations as potential data-reduction schemes of (elastically coupled) composite laminates.*

Keywords: composite laminate; bending-extension coupling; interlaminar fracture toughness; analytical solution; digital image correlation

1. Introduction

Delamination is among the most critical failure modes of laminated composites, making its study essential using theoretical and experimental methods. In recent decades, various analytical models for computing the energy release rate (ERR)—and sometimes the mode mixity—have been proposed in the literature, which are characterized by scalable complexity. Thus, it would be interesting to know which are the most realistic ones. However, how can two or more such models be compared? The ERR is not an experimentally measurable quantity, but it is obtained based on experimental measurements (*e.g.*, applied loading, crack length) and data reduction. Two other options are discussed below.

One way to validate the analytically calculated ERR is using a computational model (*e.g.*, finite element model). For example, in our recent works [1, 2], we performed finite element analyses to validate our previously developed analytical model for the computation of the ERR and mode mixity of elastically coupled laminates [3]. As it is logical, we based our numerical model on some assumptions—*e.g.*, how the two sublaminates are connected in their interface—that are *in line* with the corresponding assumptions of the analytical model. However, for comparing two analytical models based on one or more differentiated assumptions, the respective assumptions

  doi:10.5075/epfl-298799_978-2-9701614-0-0

introduced in the numerical model may prejudge closer agreement of the latter with one of the two analytical models.

An alternative idea for validating analytical models for the calculation of the ERR is based on measurements from a physical experiment; as known, the experiment is not subjected to assumptions for the specimen behavior. Among the mechanical quantities that can both be provided by an analytical model and be measured experimentally are the displacements (and rotations) of the specimen's lateral sides during the test. In particular, the digital image correlation (DIC) method seems to be able to provide reliable measurements of these quantities [4]. However, such experimental validations of analytical models in fracture mechanics are still rare [5]. Particularly for *non-standard* (*e.g.*, asymmetric, elastically coupled) specimens, there is no reference in the literature to the best of our knowledge.

The present paper aims to demonstrate the above conception of experimentally confirming analytical models for the calculation of the ERR through measuring, using DIC, the displacements of the specimen. To this end, we collect and outline below two recent, state-of-the-art models under consideration and some representative results of our ongoing work that will help us elaborate the idea.

2. Analytical expressions

2.1 The analytical models under consideration

As shown in Figure 1a, we consider a cantilever beam from a generally layered material—*i.e.*, exhibiting bending-extension coupling (BEC). The beam features an interfacial crack of length *a* that splits it into two sublaminates: the upper one and the lower one. Henceforth, we will refer to these sublaminates using the indices $i = 1$ and $i = 2$, respectively. Both sublaminates have arbitrary stacking sequences and are modeled as Timoshenko beams. Lastly, the specimen has a width (not shown in the figure) equal to b and is loaded at its cracked end by two equal and opposite forces, P.

The specimen is subjected to mixed-mode fracture because of the geometric and material asymmetry of the two sublaminates with respect to the interface plane. The available analytical models for determining the ERR and the induced mode mixity of specimens with BEC are rare (*e.g.*, [3, 6–11]). Among them, even fewer models provide explicit expressions for the displacements (and rotations) of the specimen. In this paper, we focus on two of the most updated of them: the clamped crack tip model [8] and the semi-rigid interface joint model [3, 6]. For these two models, we will employ the respective simpler names *clamped model* and *semi-rigid model*, and the superscripts *cl* and *s-r*. Figure 1b represents the difference in the kinematic assumptions of the two models. The semi-rigid model is relatively more refined but, at the same time, more complex than the clamped model as it does not constraint the displacements (and rotations) of the uncracked part of the specimen.

The rest of this section collects only the final, useful expressions from these two models, always concerning the double cantilever beam (DCB) configuration (Figure 1a). We start by presenting data-reduction expressions, which are adapted from [8] for the clamped model and from [3] for the semi-rigid model. Next, we summarize explicit equations for the generalized displacements, which are adapted from [8] for the clamped model and from [6] for the semi-rigid model.

  doi:10.5075/epfl-298799_978-2-9701614-0-0

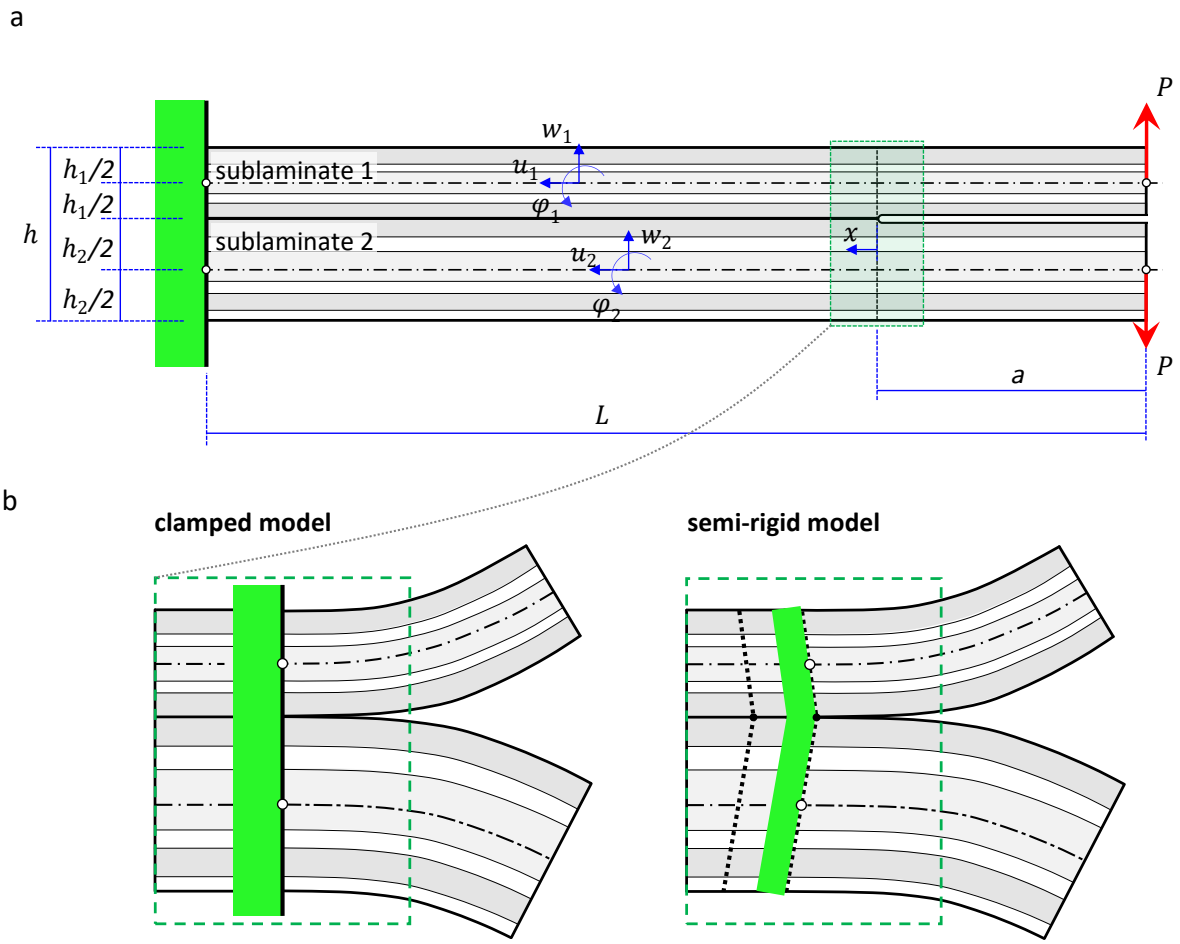

Figure 1. A schematic of two recent analytical models for bending-extension coupled laminates

2.2 Modal contributions to the energy release rate (ERR)

According to the clamped model, the final expressions for the mode I and mode II contributions to the ERR of the DCB configuration are

$$\mathcal{G}_{\mathrm{I}}^{\mathrm{cl}} = \frac{P^2}{2}\left\{\left[d_1 + d_2 - \frac{\left(b_1+b_2+d_1\frac{h_1}{2}-d_2\frac{h_2}{2}\right)^2}{a_1+a_2+b_1h_1-b_2h_2+d_1\frac{h_1^2}{4}+d_2\frac{h_2^2}{4}}\right]a^2 + c_1 + c_2\right\} \text{ and}$$

$$\mathcal{G}_{\mathrm{II}}^{\mathrm{cl}} = \frac{P^2}{2}\frac{\left(b_1+b_2+d_1\frac{h_1}{2}-d_2\frac{h_2}{2}\right)^2}{a_1+a_2+b_1h_1-b_2h_2+d_1\frac{h_1^2}{4}+d_2\frac{h_2^2}{4}}a^2, \quad (1)$$

respectively. In Eqs. (1), a_{i}, b_{i}, c_{i}, and d_{i} are the extensional compliance, BEC compliance, shear compliance, and bending compliance of sublaminate i, respectively. The total ERR is provided by the sum of the two modal contributions: $\mathcal{G}^{\mathrm{cl}} = \mathcal{G}_{\mathrm{I}}^{\mathrm{cl}} + \mathcal{G}_{\mathrm{II}}^{\mathrm{cl}}$. Following some simplifications, the final expression for the total ERR is

$$\mathcal{G}^{\mathrm{cl}} = \frac{P^2}{2}[c_1 + c_2 + (d_1 + d_2)a^2]. \quad (2)$$

According to the semi-rigid model, the final expressions for the mode I and mode II contributions to the ERR of the DCB test are

  doi:10.5075/epfl-298799_978-2-9701614-0-0

$$\mathcal{G}_{\mathrm{I}}^{\mathrm{s-r}} = \frac{P^2}{2}(c_1 + c_2)(1+\lambda a)^2 \text{ and } \mathcal{G}_{\mathrm{II}}^{\mathrm{s-r}} = P^2 \frac{\xi^2}{h_1\xi + 2\eta} a^2, \tag{3}$$

respectively. In Eqs. (3), the parameters λ, ξ, and η are functions of the compliances a_{i}, b_{i}, c_{i}, and d_{i} and the thicknesses h_1 and h_2 [3]. The total ERR is $\mathcal{G}^{\mathrm{s-r}} = \mathcal{G}_{\mathrm{I}}^{\mathrm{s-r}} + \mathcal{G}_{\mathrm{II}}^{\mathrm{s-r}}$.

2.3 Generalized displacements

Following the clamped model and based on the conventions shown in Figure 1a, the generalized displacements along the cracked region of the beam are

$$\begin{aligned}
u_1^{\mathrm{cl}}(x) &= -b_1 P\left(a + \frac{x}{2}\right)x, & u_2^{\mathrm{cl}}(x) &= b_2 P\left(a + \frac{x}{2}\right)x,\\
w_1^{\mathrm{cl}}(x) &= -c_1 P x + d_1 P\left(a + \frac{x}{3}\right)\frac{x^2}{2}, & w_2^{\mathrm{cl}}(x) &= c_2 P x - d_2 P\left(a + \frac{x}{3}\right)\frac{x^2}{2}, \text{ and}\\
\varphi_1^{\mathrm{cl}}(x) &= -d_1 P\left(a + \frac{x}{2}\right)x, & \varphi_2^{\mathrm{cl}}(x) &= d_2 P\left(a + \frac{x}{2}\right)x,
\end{aligned} \tag{4}$$

where $x \in [-a, 0]$.

Likewise, according to the semi-rigid model, the generalized displacements along the entire length of the beam are

$$u_1^{\mathrm{s-r}}(x) = \begin{cases} -b_1 P\left(a+\frac{x}{2}\right)x - \left(a_1 + \frac{\eta}{\xi}b_1\right)\frac{c_0}{\lambda}\left[1 - e^{-\lambda(L-a)}\right] & \text{if} \quad x \in [-a, 0^-] \\ \nexists & \text{if} \quad x = 0 \\ -\left(a_1 + \frac{\eta}{\xi}b_1\right)\frac{c_0}{\lambda}\left[e^{-\lambda x} - e^{-\lambda(L-a)}\right] & \text{if} \quad x \in [0^+, L-a] \end{cases},$$

$$w_1^{\mathrm{s-r}}(x) = \begin{cases} -c_1 P x + d_1 P\left(a+\frac{x}{3}\right)\frac{x^2}{2} + \left(b_1 + \frac{\eta}{\xi}d_1\right)\frac{c_0}{\lambda}\left[x - \frac{1}{\lambda} - e^{-\lambda(L-a)}\left(x - \frac{1}{\lambda} - L + a\right)\right] + \left(\frac{\eta}{\xi} + \frac{h_1}{2}\right)c_1 c_0\left[1 - e^{-\lambda(L-a)}\right] & \text{if} \quad x \in [-a, 0^-] \\ \nexists & \text{if} \quad x = 0 \\ \left[\left(\frac{\eta}{\xi} + \frac{h_1}{2}\right)c_1 - \frac{1}{\lambda^2}\left(b_1 + \frac{\eta}{\xi}d_1\right)\right]c_0\left[e^{-\lambda x} - e^{-\lambda(L-a)}\right] - \left(b_1 + \frac{\eta}{\xi}d_1\right)\frac{c_0}{\lambda}e^{-\lambda(L-a)}(x - L + a) & \text{if} \quad x \in [0^+, L-a] \end{cases},$$

$$\varphi_1^{\mathrm{s-r}}(x) = \begin{cases} -d_1 P\left(a+\frac{x}{2}\right)x - \left(b_1 + \frac{\eta}{\xi}d_1\right)\frac{c_0}{\lambda}\left[1 - e^{-\lambda(L-a)}\right] & \text{if} \quad x \in [-a, 0^-] \\ \nexists & \text{if} \quad x = 0 \\ -\left(b_1 + \frac{\eta}{\xi}d_1\right)\frac{c_0}{\lambda}\left[e^{-\lambda x} - e^{-\lambda(L-a)}\right] & \text{if} \quad x \in [0^+, L-a] \end{cases},$$

$$u_2^{\mathrm{s-r}}(x) = \begin{cases} b_2 P\left(a+\frac{x}{2}\right)x + \left[a_2 + \left(\frac{\eta}{\xi} + \frac{h_1+h_2}{2}\right)b_2\right]\frac{c_0}{\lambda}\left[1 - e^{-\lambda(L-a)}\right] & \text{if} \quad x \in [-a, 0^-] \\ \nexists & \text{if} \quad x = 0 \\ \left[a_2 + \left(\frac{\eta}{\xi} + \frac{h_1+h_2}{2}\right)b_2\right]\frac{c_0}{\lambda}\left[e^{-\lambda x} - e^{-\lambda(L-a)}\right] & \text{if} \quad x \in [0^+, L-a] \end{cases},$$

$$w_2^{\mathrm{s-r}}(x) = \begin{cases} c_2 P x - d_2 P\left(a+\frac{x}{3}\right)\frac{x^2}{2} - \left[b_2 + \left(\frac{\eta}{\xi} + \frac{h_1+h_2}{2}\right)d_2\right]\frac{c_0}{\lambda}\left[x - \frac{1}{\lambda} - e^{-\lambda(L-a)}\left(x - \frac{1}{\lambda} - L + a\right)\right] - \left(\frac{\eta}{\xi} + \frac{h_1}{2}\right)c_2 c_0\left[1 - e^{-\lambda(L-a)}\right] & \text{if} \quad x \in [-a, 0^-] \\ \nexists & \text{if} \quad x = 0 \\ -\left\{\left(\frac{\eta}{\xi} + \frac{h_1}{2}\right)c_2 - \frac{1}{\lambda^2}\left[b_2 + \left(\frac{\eta}{\xi} + \frac{h_1+h_2}{2}\right)d_2\right]\right\}c_0\left[e^{-\lambda x} - e^{-\lambda(L-a)}\right] + \left[b_2 + \left(\frac{\eta}{\xi} + \frac{h_1+h_2}{2}\right)d_2\right]\frac{c_0}{\lambda}e^{-\lambda(L-a)}(x - L + a) & \text{if} \quad x \in [0^+, L-a] \end{cases}, \text{ and}$$

$$\varphi_2^{\mathrm{s-r}}(x) = \begin{cases} d_2 P\left(a+\frac{x}{2}\right)x + \left[b_2 + \left(\frac{\eta}{\xi} + \frac{h_1+h_2}{2}\right)d_2\right]\frac{c_0}{\lambda}\left[1 - e^{-\lambda(L-a)}\right] & \text{if} \quad x \in [-a, 0^-] \\ \nexists & \text{if} \quad x = 0 \\ \left[b_2 + \left(\frac{\eta}{\xi} + \frac{h_1+h_2}{2}\right)d_2\right]\frac{c_0}{\lambda}\left[e^{-\lambda x} - e^{-\lambda(L-a)}\right] & \text{if} \quad x \in [0^+, L-a] \end{cases}. \tag{5}$$

The parameter c_0 appearing in Eqs. (5) is generally a function of the material properties, specimen geometry, and applied load [3]. For the specific problem of the present paper, $c_0 = -\frac{Pa}{\frac{h_1}{2} + \frac{\eta}{\xi}}$.

3. Experimental campaign

The idea of experimentally validating the above two analytical models is specified below based on measurements of the specimen displacements. Although the expressions presented can

  doi:10.5075/epfl-298799_978-2-9701614-0-0

tackle elastically coupled laminates, the experimental part of this short paper will be restricted to an uncoupled laminate for simplicity in the presentation.

3.1 Material and testing

We consider a glass fiber/epoxy composite consisting of the following materials: UD E-glass fiber fabrics EC 9-68, Biresin CR83 resin, and Biresin CH83-2 hardener. The engineering constants of the lamina are $E_1 = 40.71$ GPa, $E_2 = 11.62$ GPa, $G_{12} = 6.07$ GPa, and $\nu_{12} = 0.240$ [12]. Using this material, we produced specimens with stacking sequence [0°$_2$/90°$_2$/0°$_2$//0°$_2$/90°$_2$/0°$_2$]. The specimens consisted of two sublaminates with equal thicknesses ($h_1 = h_2 = h/2 = 2.05$ mm) and had a width $b = 40$ mm, length $L = 208$ mm, and initial crack length $a_0 = 50$ mm (notation in shown in Figure 1a).

A set of DCB experiments was performed at an MTS machine, following the guidelines of the ASTM D5528-13 standard. The experimental setup is shown in Figure 2. After the experiments, we determined the crack-initiation point in line with the NL, VIS, and 5%/max criteria of the ASTM standard.

3.2 Measurements using digital image correlation (DIC)

To experimentally extract the generalized displacements, u_i, w_i, and φ_i, we recorded the displacement field in one of the two lateral sides of the specimen. Before the tests, we painted the lateral side white and marked it with an appropriate speckle pattern (see Figure 2). Next, we used the ARAMIS v6.0.2-6 DIC-2D system to take and process the images. As can be shown in Figure 2, the camera lens was positioned to be vertical to the lateral side of the specimen, while the working distance between them was adjusted to about 1 m.

During the test, images were automatically recorded at 1 Hz. Load and displacement were also recorded at each instant when pictures were taken. Following the tests, the images were processed using the open-source software GOM Correlate to obtain the axial and vertical displacement fields. Using these data and some simple assumptions, we finally extracted the generalized displacements in the lateral side of the specimen.

4. Experimental evaluation of the analytical expressions

4.1 Total energy release rate (ERR)

Using the above DCB experiments, we calculate the ERR of the composite laminate at crack initiation by applying the clamped and semi-rigid models (see Eqs. [1]–[3]). Table 1 summarizes the results for the total ERR, $\mathcal{G}_{\mathrm{C,ini}}$; there is no mode mixity in our case, given that the specimen at hand has a symmetric layup. The calculations of $\mathcal{G}_{\mathrm{C,ini}}$ were performed for three experiments. In addition, from each experimental curve, three values of the crack-initiation load, P_ini, were determined based on the NL, VIS, and 5%/max criteria of the standard.

As shown in Table 1, the disagreement between the two models is minor following all criteria for crack initiation. This is strongly attributed to the specific problem under consideration. Specifically, the specimen is characterized by a high $(L - a)/h$ ratio, which reduces the effect of the deformability of the crack tip on the fracture toughness. In contrast, in cases of *thicker* specimens or *non-conventional* specimens (*e.g.*, specimens that contain asymmetries in

  doi:10.5075/epfl-298799_978-2-9701614-0-0

thickness or dissimilar materials), the difference between the two models is expected to be greater.

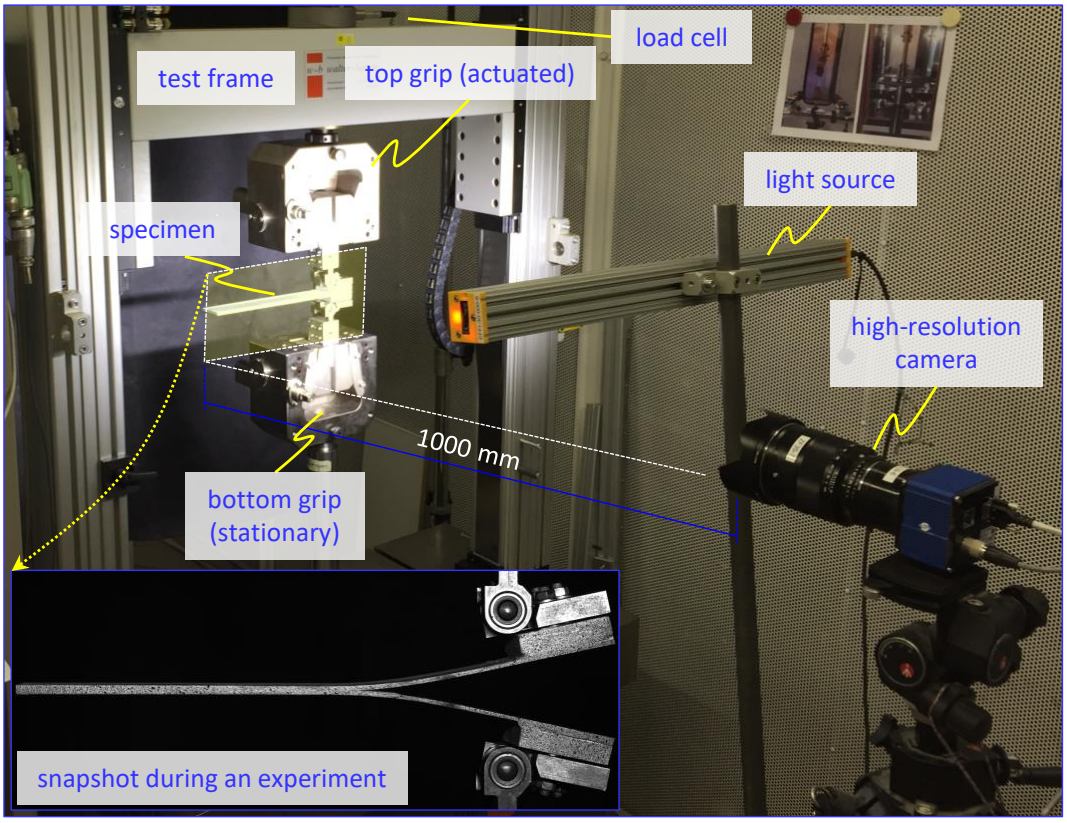

Figure 2. Experimental setup and a snapshot of the specimen during an experiment

Table 1: Total ERR at crack initiation, $\mathcal{G}_{\mathrm{C,ini}}$, from the performed DCB experiments.

Criterion	P_{ini} [N]	$\mathcal{G}_{\mathrm{C,ini}}$ [N/mm]	
		Clamped model	Semi-rigid model
NL	63.2 [±5.9]	0.207 [±0.038]	0.215 [±0.040]
VIS	59.4 [±3.0]	0.183 [±0.018]	0.189 [±0.019]
5%/max	87.2 [±0.1]	0.393 [±0.001]	0.407 [±0.001]

4.2 Generalized displacements

We now compare the predictions of the generalized displacements along specimen length by the clamped and semi-rigid models (see Eqs. [4] and [5]) versus the DIC measurements. Figure 3 reports the results only for the transverse displacements, w_{i}, given that the axial displacements are zero and the cross-sectional rotations are almost zero in our problem. In addition, the displacements in the figure concern the instant of one of the experiments at crack initiation. As shown in the figure, the disagreement between the clamped and semi-rigid models is slight. Moreover, a satisfactory agreement between the DIC measurements and analytical

results is obtained using both models. For the transverse displacement in particular, the results imply that the deformations of the specimen near the crack tip can be modeled adequately with both the simpler clamped model and the more refined (but also more complex) semi-rigid model.

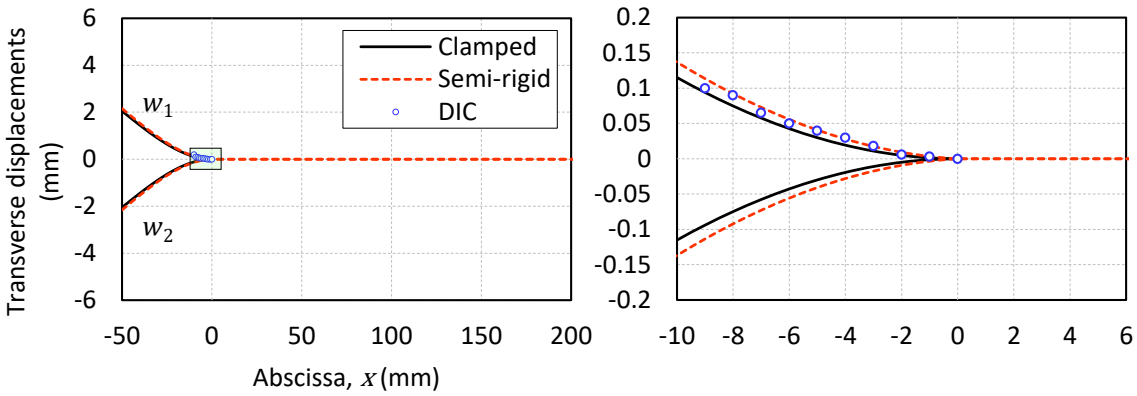

Figure 3. Transverse displacements-versus-abscissa following the two analytical models compared with the DIC predictions

The agreement of the two models regarding the generalized displacements matches their corresponding agreement regarding the total ERR presented above. However, for asymmetric or other *non-conventional* configurations, the two models are expected to show more significant discrepancies. It would be even more interesting to compare the analytical models based on DIC measurements in such cases.

5. Conclusion

The present paper aimed to *specify* the conception of experimentally validating analytical expressions to determine the ERR and the mode mixity of elastically coupled laminates. Firstly, the final, useful expressions of two state-of-the-art analytical models (clamped and semi-rigid models) were collected and reported. Next, a dedicated experimental campaign was performed using the DCB test. Without losing generality, the experimental data were presented for an uncoupled glass fiber/epoxy laminate. Specimen displacements during the experiment were measured using the DIC method. As a result, the paper compared the ERR calculated by the two models. In addition, it compared the predictions of these two models for the generalized displacements with the respective ones from the DIC. We found that the DIC predictions agree satisfactorily with both models.

To the best of our knowledge, this is the first paper to demonstrate the idea of comparing data-reduction equations based on experimental measurements. Our complete work on this topic will be presented in a forthcoming publication.

Acknowledgments

The first author acknowledges the European Cooperation in Science and Technology (COST)—COST Action CA18120—for the attributed Short Term Scientific Mission (STSM) grant (reference: ECOST-STSM-CA18120-45619). Moreover, the authors express their gratitude to the technical team of the Structural Engineering Platform of the École Polytechnique Fédérale de Lausanne

  doi:10.5075/epfl-298799_978-2-9701614-0-0

(EPFL) for the assistance in producing the specimens and executing the experiments. Lastly, the first author acknowledges the members of the Composite Construction Laboratory of the EPFL for their hospitality and support.

6. References

1. Tsokanas P, Loutas T, Kotsinis G, Kostopoulos V, van den Brink WM, Martin de la Escalera F. On the fracture toughness of metal-composite adhesive joints with bending-extension coupling and residual thermal stresses effect. Composites Part B: Engineering 2020; 185:107694.
2. Tsokanas P, Loutas T, Kotsinis G, van den Brink WM, Nijhuis P. Strain energy release rate and mode partitioning of moment-loaded elastically coupled laminated beams with hygrothermal stresses. Composite Structures 2021; 259:113237.
3. Tsokanas P, Loutas T. Hygrothermal effect on the strain energy release rates and mode mixity of asymmetric delaminations in generally layered beams. Engineering Fracture Mechanics 2019; 214:390-409.
4. Ben Salem N, Jumel J, Budzik MK, Shanahan MER, Lavelle F. Analytical and experimental investigations of crack propagation in adhesively bonded joints with the Mixed Mode Bending (MMB) test Part I: Macroscopic analysis & Digital Image Correlation measurements. Theoretical and Applied Fracture Mechanics 2014; 74:209-221.
5. Sun F, Blackman BRK. Using digital image correlation to automate the measurement of crack length and fracture energy in the mode I testing of structural adhesive joints. Engineering Fracture Mechanics 2021; 255:107957.
6. Tsokanas P, Loutas T. Closed-form solution for interfacially cracked layered beams with bending-extension coupling and hygrothermal stresses. European Journal of Mechanics – A/Solids 2022. (to appear)
7. Ševčík M, Shahverdi M, Hutař P, Vassilopoulos AP. Analytical modeling of mixed-mode bending behavior of asymmetric adhesively bonded pultruded GFRP joints. Engineering Fracture Mechanics 2015; 147:228-242.
8. Valvo PS. On the calculation of energy release rate and mode mixity in delaminated laminated beams. Engineering Fracture Mechanics 2016; 165:114-139.
9. Samborski S, Valvo PS. Numerical and analytical modeling of the end-loaded split (ELS) test specimens made of multi-directional coupled composite laminates. AIP Conference Proceedings 2018; 1922:030003.
10. Bennati S, Fisicaro P, Taglialegne L, Valvo PS. An elastic interface model for the delamination of bending-extension coupled laminates. Applied Sciences 2019; 9(17):3560.
11. Garulli T, Catapano A, Fanteria D, Huang W, Jumel J, Martin E. Experimental assessment of fully-uncoupled multi-directional specimens for mode I delamination tests. Composites Science and Technology 2020; 200:108421.
12. Jiang Z, Wan S, Keller T, Fang Z, Vassilopoulos AP. Influence of curved delamination front on R-curve of DCB specimen. Composite Structures 2019; 227:111311.

  doi:10.5075/epfl-298799_978-2-9701614-0-0

INFLUENCE OF TEMPERATURE AND DIFFERENT POST CURING CONDITIONS ON THE MECHANICAL BEHAVIOUR OF POLYURETHANE-BASED ADHESIVE FOR CIVIL ENGINEERING APPLICATIONS

Marco A., Abreu Filho[a], Guilherme, L. Gontijo[a], Sandra Cristina, Oliveira[b], Pier Giovanni, Benzo[a], Aloys, Dushimimana[a], Zlatan, Z. Denchev[b], João Miguel, Pereira[a], José Sena-Cruz[a]

a: ISISE-IB/S, Department of Civil Engineering, University of Minho (PT) – marcoabreufilho@hotmail.com
b: IPC, Polymer Engineering Department, University of Minho (PT)

Abstract: *Sandwich panels based on cold-formed-steel (CFS) face sheets and polyurethane foam (PUR) core were designed and manufactured to be used as a feasible solution for the rehabilitation of degraded floors. This panel is manufactured by a continuous process, whereby the polymerization and foaming of the PUR core is performed simultaneously with the face sheets assembling and their adhesive bonding in certain zones. A three-component polyurethane adhesive, manufactured with the same components as the PUR, is used on the bonding of these steel elements. However, the foaming process of the sandwich panel involves moderate heating at specific stages of its manufacture to enhance polymerization of the PUR, which may influence the adhesive mechanical response. This work intends to establish the best adhesive composition and its thickness to be used on this connection. Additionally, the influence of different curing and post-curing conditions on the shear response of the adhesive is assessed.*

Keywords: Polyurethane-based adhesive; Steel sandwich panel; Flooring system; Post-curing conditions.

1. Introduction

Historically, constructions in Europe (which precede the use of reinforced concrete and structural steel), were commonly composed by masonry walls and timber flooring systems [1]. The rehabilitation of these constructions requires special attention, since the existing timber floors often present high deformations (floor sagging) due to durability problems caused by biological attacks related to lack of maintenance [1,2]. This aspect, when combined to the demanding requirements stablished by current structural performance standards, usually results in the replacement of these floors by new flooring solutions. These could be new timber floors or new flooring systems composed by different materials (Reinforced concrete, structural steel or composite materials) [2]. In this context, the development of sandwich panel-based flooring systems, characterised by two relatively thin and stiff faces and a relatively thick and lightweight core, arise as potentially interesting solutions [3,4].

For such applications, within the scope of Lightslab R&D project, cold-formed steel (CFS) face sheets sandwich panel with polyurethane (PUR) foam core including longitudinal steel web reinforcements were designed and manufactured (as shown in Figure 1) [5]. Among the advantages of this flooring system, it can be highlighted its lightweight (which limits the dead load transmitted to the existing structure and consequently reduces the impact in terms of

  doi:10.5075/epfl-298799_978-2-9701614-0-0

seismic vulnerability) [4]. Moreover, its modular feature can minimize waste production and reduce overall construction/rehabilitation time, leading to a more sustainable construction [6].

In the manufacture process of these panels, the PUR foaming process takes place on the bottom face sheet, while the adhesive joint connects the webs with the top face sheet. For this connection, polyurethane adhesives can be adopted, as they are flexible, ductile and, due to their composition, present compatible properties with the core of the panels [5,7]. However, structural adhesives are sensitive to temperature and relative humidity (RH), both during their curing and service life [8]–[11], and the foaming process of the sandwich panel involves moderate heating at specific stages of its manufacture to enhance polymerization of the PUR. Thus, this work intends to establish the best adhesive composition and the layer thickness to be used on this connection, as well as to reproduce the temperature and RH conditions imposed on the adhesive during the sandwich panel manufacturing process, and furthermore, to assess the influence of different post-curing conditions on the adhesion of cold-formed-steel elements, namely the upper face sheet and the webs.

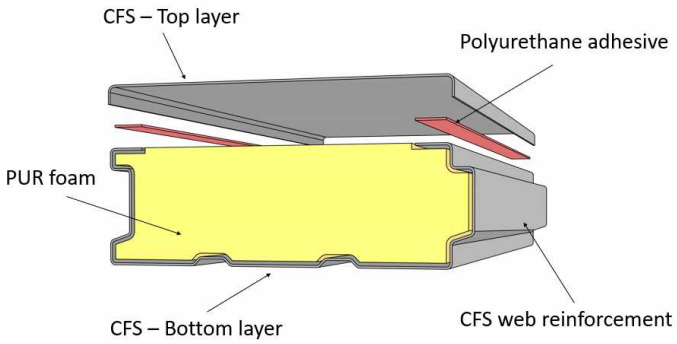

Figure 1. Schematic representation of the developed sandwich panel.

2. Influence of the adhesive's composition on their mechanical response

To maximize the mechanical performance of the three-component polyurethane-based adhesive, the influence of different proportion of components on their shear response was assessed in a preliminary experimental campaign. This assessment was done varying two different parameters: i) the proportion of the diIsocyanate component Voranate M 229 SH, by increasing it mass proportion from 25% to 50%, in respect to the total quantity of the polyol component Voratron EG711; ii) the proportion of the Voralast GM 817 catalyst increasing it in a rate from 0 to 0.8 wt.% of the total polyol quantity. The choice of these constituents for the adhesive was based on the PUR composition (same components).

The formation of the adhesive layer (i.e., curing) passes through a polycondensation reaction between optimized amounts of the diisocyanate and polyol components. The role of the catalyst (a clear, low-viscosity liquid) is to accelerate the curing time and limit the side reactions related to the formation of bubbles in the curing adhesive [3]. Summarizing, by the variation of the mass proportions of the three adhesive components it was possible to fine-tune the curing time and the shear strength of the bonded specimens.

The studied proportions were tested on lap shear strength tests performed on adhesively bonded specimens according to the ASTM D1002-2010 [12]. For this purpose, 10 different sets

  doi:10.5075/epfl-298799_978-2-9701614-0-0

of mixtures were experimentally assessed. For each set, tests were performed on 6 bonded specimens. For these tests, 120 steel specimens with nominal dimensions of 25.4×101.6×1.5 [mm³] were prepared and jointed in pairs with adhesive connection.

The procedure for assembling the specimens was as follows: i) the faces to joint were cleaned with acetone in order to remove any contaminants; ii) the pre-mixed adhesive were deposited over one of the metal specimens; iii) the opposite specimen is then assembled creating an overlap region of 12.7 mm; iv) A pressure equivalent to 1161.8 Pa/sample was applied over the joint; v) The assembled specimens (with the applied pressure) were left to cure under controlled conditions (temperature of 23°C, relative humidity of approximately 50%). The nominal thickness of the adhesive layer for this campaign was 0.12 mm.

This stage of the mechanical characterization tests was carried out using a universal tensile testing machine INSTRON 5969. The samples were attached to the machine by grips with a length of 25.4 mm and the distance between grips was 139.7 mm. The test occurred in quasi-static monotonic-instantaneous loading up to failure, under a displacement control rate of 1.3 mm/min. All the tests were carried out under the same conditions, being the adhesive composition used to bond both samples the only variable.

Table 1 summarizes the obtained results for the tests performed on adhesively bonded specimens with different proportions of polyurethane-based adhesive. The parameters analysed for the different mixtures were: i) the handling time of the adhesive; ii) the fixture/solidification time; iii) minimum ultimate shear strength for the set of 6 specimens; iv) maximum ultimate shear strength for the set of 6 specimens; and v) average ultimate shear strength obtained for the given set of specimens, with respective coefficient of variation (CoV). Note that the quantities of Isocyanate Voranate M 229 SH and Voralast GM 817 Catalyst are expressed as a percentage of the of the total Voratron EG711 mass.

Table 1: Solidification and shear strength obtained for different proportions of adhesive.

Isocyanate [%]	Catalyst [%]	Fixture/handling time [min]	Solidification time [min]	Min/Max Ultimate Strength [MPa]	Mean Ultimate Strength [MPa]	Coefficient of variation [%]
25.0	0	60-80	270	0.3 / 0.9	0.5	60.0
	0.25	25-30	45	0.5 / 1.9	1.0	70.0
	0.5	06-11	29	0.9 / 1.5	1.2	16.7
	0.8	07-10	30	1.1 / 1.4	1.3	15.4
31.3	0	30-50	190	1.8 / 2.1	1.9	10.5
	0.25	**16-23**	**48**	**3.0 / 4.0**	**3.5**	**14.3**
	0.5	05-07	17	3.2 / 4.9	4.5	15.6
50.0	0	27-48	180	1.4 / 2.0	1.6	18.8
	0.25	14-17	34	1.1 / 1.8	1.3	23.1
	0.5	06-08	16	2.0 / 2.8	2.3	17.4

As seen from Table 1, the experiments revealed that the adhesive composition comprising 31.3% M229 SH Iso and 0.5% of the GM817 Catalyst showed the best ultimate strength varying between 3.2 and 4.9 MPa. However, the handling time for this composition (5-7 min) was

considered inappropriate for the current industrial application (once the adhesive joint assembling is performed simultaneously to the core's PUR foaming process on the panels manufacture). For such, the adhesive composed by 31.3% M229 SH Iso and 0.25% of the GM817 Catalyst (highlighted in bold), which presents ultimate strength in a range from 3.0 to 4.0 MPa and handling time from 16 to 23 minutes, was considered the most adequate for this application. Therefore, this proportion of components was chosen to be used on the following tests.

3. Shear strength of bonded specimens

The best adhesive mixture solution obtained on the previous sections was also assessed in an in-depth shear strength experimental campaign. The first series of performed tests intended to identify the influence of the adhesive layer thickness on the shear response of the adhesive (section 3.1), and then the influence of different post-curing conditions (section 3.2).

The specimen's preparation and the bonding of the specimens was performed as described in section 2. Such as for the optimization of the adhesive composition, the shear strength experimental tests performed in this campaign followed the ASMT D 1002 [12]. However, in this investigation, modifications were done on the geometry of the samples to allow the fixing of 2 LVDTs to accurately monitor displacement during the tests (see Figure 2). The shear tests were performed with a universal testing machine, with 10 kN MicroTest loadcell.

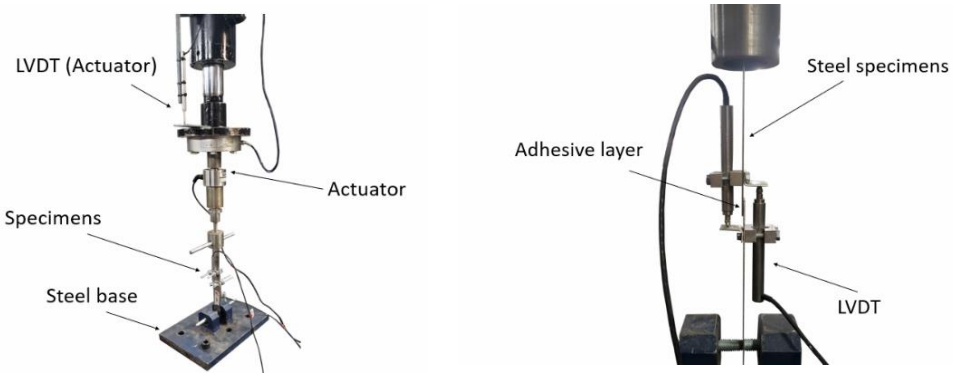

Figure 2. Test setup used for following shear strength experimental tests: a) overview and b) detail view of the test setup.

3.1 Influence of the adhesive layer thickness on their shear strength

Initially, this campaign was used to evaluate the influence of the layer thickness on the shear strength of the adhesives. Therefore, tests were performed on three sets of six specimens each with layer thickness of 0.1 mm (referred as PC0), 0.5 mm and 1.0 mm.

Figure 3a shows the ultimate shear strength obtained for each specimen of the different sets. From Figure 3a, one can see that an inversely proportional relationship can be stablished between the adhesive thickness and its ultimate shear strength. Specimens with 1.0 mm adhesive thickness presented an average ultimate strength of 0.89 MPa (CoV: 16.67%), while the average ultimate shear strength for specimens with 0.5 mm and 0.1 mm was 2.17 MPa (CoV: 8.89%) and 3.01 (CoV: 6.91%), respectively, with an increase of 143% and 238% when compared with 1.0 mm thickness. Furthermore, the decrease on the coefficient of variation with the reduction of the thickness suggests more regular and homogenous adhesive layers. This may be

related to a greater quality control over the thickness of the layer for the thinner specimens and this could be observed during the preparation of the specimens.

Figure 3b shows the evolution of the force vs. displacement curves obtained for the specimens with 0.1 mm thickness. Despite the differences on the ultimate shear strength for the three studied sets (depicted in Figure 3a) no major differences were observed on the evolution of the shear response curves for the different thickness of adhesive.

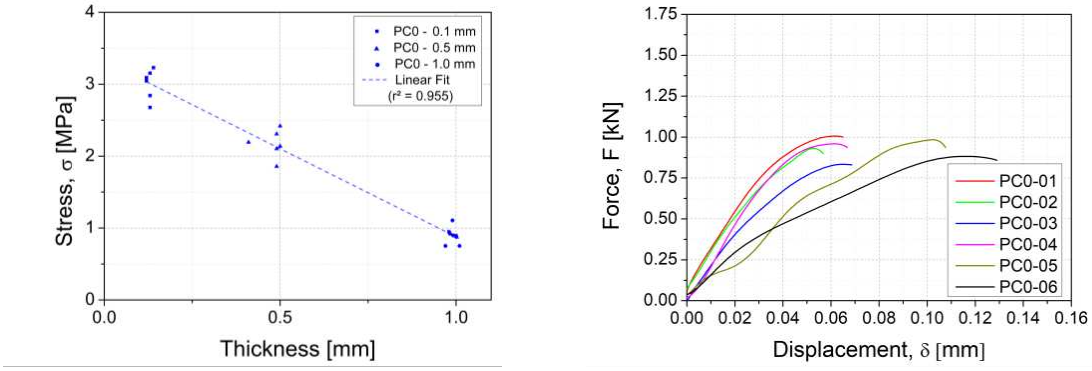

a) *b)*

Figure 3. Influence of the layer thickness: a) Ultimate shear strength for specimens with different layer thickness; b) force vs. displacement evolution obtained for specimens with 0.1 mm layer thickness.

Figure 4 shows that in all the specimens with 0.5 mm and 1.00 mm thickness, failures took place by debonding of the interface steel/adhesive, while one of the specimens with 0.1 mm thickness presented a mix between cohesive and debonding failure (specimen PC0-04).

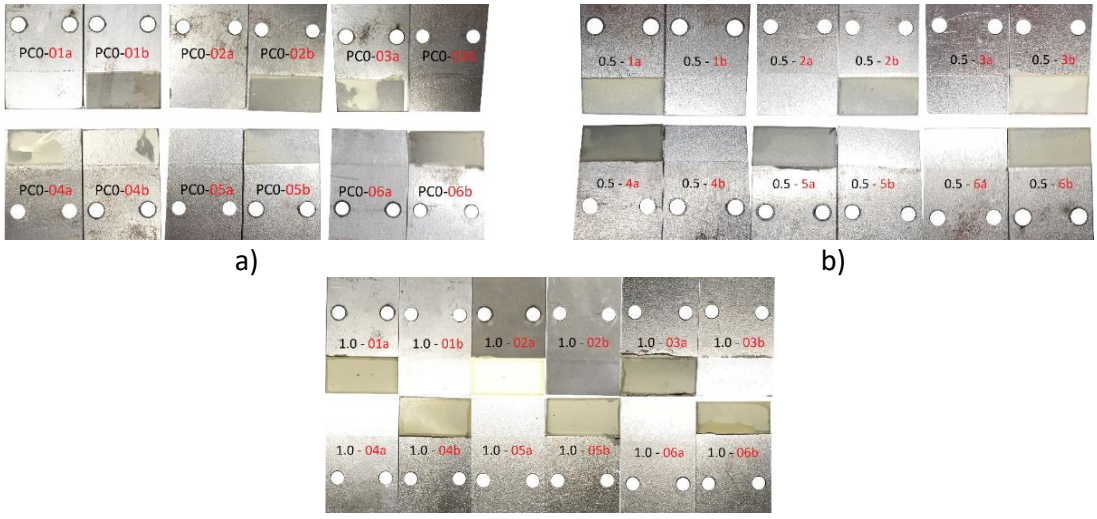

a) b)

c)

Figure 4. Aspect of the failure regions on specimens with different layer thickness: a) 0.1 mm; b) 0.5 mm; c) 1.0 mm.

3.2 Influence of post-curing conditions on the adhesive's shear strength

In a final stage of this investigation, two sets of specimens with 6 specimens each, bonded with the optimal layer thickness (0.1 mm) were manufactured and subjected to different post-curing conditions to assess its influence on their shear response. Therefore, three different post-curing

conditions were tested: i) values obtained on the previous campaign were used as a reference set (referred as PC0), without any additional post-curing procedures (despite being kept under controlled conditions); ii) a set (referred as PC1) subjected immediately after manufacture to 42 °C for 7 minutes (similar conditions as during manufacture of the panels); iii) a set (referred as PC2) subjected immediately after manufacture to 42 °C for 7 minutes, and additionally subjected to 80 °C for 12 hours after 3 days of manufacture, to reproduce eventual post-curing during the service life of the adhesive.

Figure 5 shows the relationships between force and displacement obtained for sets PC1 and PC2. Comparing these results with the reference set (Figure 3b) it can be seen that PC1 specimens present an increase on their shear stiffness (depicted by the increase on the curves slope). Likewise, PC2 specimens also presented a similar increase on their shear stiffness. Additionally, this set also revealed a considerable increase on their ultimate shear strength.

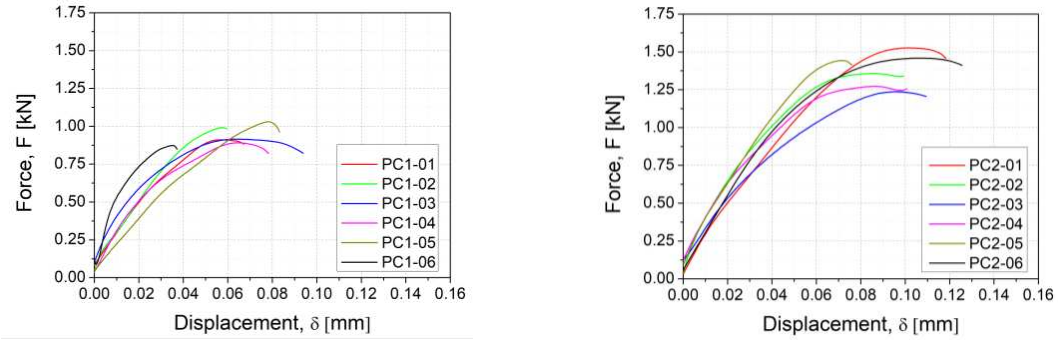

a) b)

Figure 5. Force vs. Displacement evolution obtained for specimens: a) PC1 set; b) PC2 set.

Figure 6 presents the failure modes obtained on this campaign. For the PC1 set, it can be noticed one of the specimens presented a mix of cohesive and debonding failure (PC1-04), and all other showed pure debonding failures (similarly as shown in Figure 4c for the reference set PC0). On the other hand, all the PC2 specimens presented a mix of cohesive and debonding failure, which reveals a stronger interface connection between the metal and the adhesive.

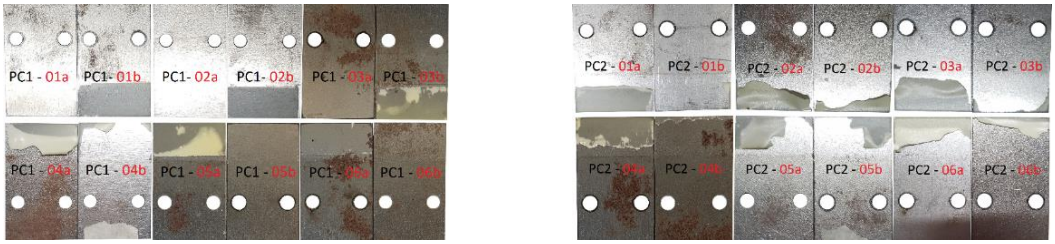

a) b)

Figure 6. Aspect of the failure regions on specimens subjected to different post-curing conditions: a) PC1; b) PC2.

Figure 7 summarizes the ultimate shear strength results obtained for specimens assembled with different adhesive thickness and subjected to different post-curing conditions. The average values for the shear strength of the sets were 3.25MPa (CoV: 11.10%) for set PC1; and 4.57MPa (CoV: 8.35%) for set PC2. These values, when compared to the obtained on section 3.1 and used as reference (3.01 MPa, CoV: 6.91%), represent an increase of 8% and 51% on the maximum shear strength for the two sets with specific post-curing procedures (PC1 and PC2, respectively).

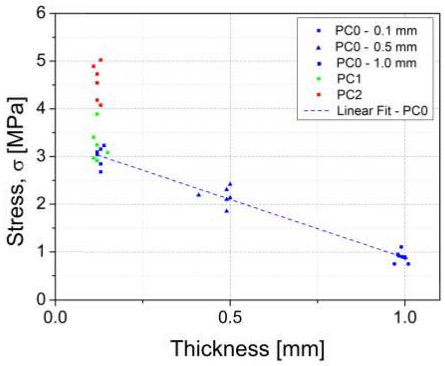

Figure 7. Ultimate shear strength for specimens with different layer thickness and subjected to different post-curing conditions.

4. Conclusions

This paper intended to assess the influence of different post-curing conditions on the mechanical response of polyurethane-based adhesive for civil engineering applications. For such, stepwise experimental campaigns were performed, in order to achieve a series of specific goals, namely: i) investigate the influence of different proportions of components on the adhesive; ii) investigate the influence of the layer thickness on the shear strength of the adhesive; and, finally, the main goal of the study, iii) investigate the influence of different post-curing conditions on the shear response of the adhesive.

From the different experimental campaigns of this work, it can be concluded that:

- The adhesive composed by 31.3% M229 SH Isocyanate and 0.25% of the GM817 Catalyst was considered the most adequate for this work, once it showed an ultimate strength in the magnitude of 3.0-4.0 MPa and 16-23 min of handling time (which is sufficient to allow the assembling of the CFS sheets simultaneously to the foaming of the PUR).
- Thinner layers increase the shear strength of the adhesive. An increase of 143% and 238% on the maximum shear strength for 0.5 mm and 0.1 mm thick specimens, respectively, was observed when compared to the values obtained for the 1.0 mm thick.
- Modifications on the adhesive layer thickness can modify the failure modes obtained on the shear strength tests. While for adhesive layers with 1.0 mm and 0.5 mm thick all the specimens failed by debonding on the steel/adhesive interface, one of the specimens with 0.1 mm thickness presented a mix of cohesive and debonding failure.
- Subjecting the panel to elevated temperatures during the curing of the polyurethane adhesives is an effective way to enhance their stiffness and shear strength. An increase of 8% on the maximum shear strength was observed for specimens of PC1 set. Likewise, specimens of PC2 set presented a 52% increase on their maximum shear strength when compared to the reference set.
- Post-curing conditions that encompass higher temperatures can also play an important role on the type of failure mode obtained on the tests. While for the PC1 set, 5 specimens presented debonding of the steel/adhesive interface failure modes and 1 presented a mixed failure (similarly as for the reference set), all specimens of PC2 set showed a mix of cohesive and debonding failure modes.

  doi:10.5075/epfl-298799_978-2-9701614-0-0

Acknowledgements

This work was developed within the scope of the research project "Lightslab – Desenvolvimento de soluções inovadoras de lajes de painel sandwich", supported by FEDER funds through the Operational Program for Operational Program for Competitiveness and Internationalization (POCI) and the Portuguese National Innovation Agency (ANI) – project no. 33865 [POCI-01-0247-FEDER-033865]. This work was partly financed by FCT/MCTES through national funds (PIDDAC) under the R&D Unit Institute for Sustainability and Innovation in Structural Engineering (ISISE), under reference UIDB/04029/2020. The second and fourth authors wish also to acknowledge the grants DFA/BD/07696/2021 and DFA/BD/8319/2020 respectively, provided by Fundação para a Ciência e a Tecnologia, IP (FCT), financed by European Social Fund and national funds through the FCT/MCTES.

5. References

1. Costa A, Guedes J, Varum H. Structural rehabilitation of old buildings. Springer. 2003.
2. Garrido M, Correia JR, Keller T, Branco FA. Adhesively bonded connections between composite sandwich floor panels for building rehabilitation. Composite Structures. 2015;134:255–68.
3. Davies JM. Lightweight Sandwich Construction. New York, USA: John Wiley & Sons; 2008.
4. Garrido M, Correia JR, Keller T, Branco FA. Connection systems between composite sandwich floor panels and load-bearing walls for building rehabilitation. Engineering Structures. 2016;106:209–21.
5. Benzo P, Sena-Cruz J, Pereira J. Multi-objective optimization assisting design of sandwich panels. In: Seventh Asia-Pacific Conference on FRP in Structures (APFIS). Australia; 2019. p. 4.
6. Tam VWY, Tam CM, Zeng SX, Ng WCY. Towards adoption of prefabrication in construction. Building and Environment. 2007;42(10):3642–54.
7. Weiss J, Voigt M, Kunze C, Sánchez JEH, Possart W, Grundmeier G. Ageing mechanisms of polyurethane adhesive/steel interfaces. International Journal of Adhesion and Adhesives. 2016 Oct 1;70:167–75.
8. Vallée T, Tannert T, Fecht S. Adhesively bonded connections in the context of timber engineering–A Review. Vol. 93, Journal of Adhesion. Taylor and Francis Inc.; 2017. p. 257–87.
9. Michels J, Sena Cruz J, Christen R, Czaderski C, Motavalli M. Mechanical performance of cold-curing epoxy adhesives after different mixing and curing procedures. Composites Part B: Engineering. 2016 Aug 1;98:434–43.
10. Czaderski C, Martinelli E, Michels J, Motavalli M. Effect of curing conditions on strength development in an epoxy resin for structural strengthening. Composites Part B: Engineering. 2012 Mar;43(2):398–410.
11. Śliwa-Wieczorek K, Zając B. Rigid and flexible double shear lap adhesive joint at elevated temperature—an experimental study. Polymers (Basel). 2021 Sep 1;13(17).
12. American Society for Testing and Materials. D1002- Lap Shear Strength of Adhesively Bonded Metal Specimens. 2010.

THE DURABILITY OF ADHESIVELY JOINTS IN SPACE STRUCTURE DURING INTERPLANETARY EXPLORATION

Gabin, Charpentier [a,b], Ugo, Lafont [c], Sofia, Teixeira De Freitas [a]

a: Faculty of Aerospace Engineering, Delft University of Technology, Kluyverweg 1, 2629 HS Delft, The Netherlands
b: ISAE ENSMA, Téléport 2, 1 Avenue Clément Ader, BP 40109, 86961 Futuroscope Chasseneuil, Cedex, France
gabincharpentier@gmail.com
c: European Space Agency, Keplerlaan 1, PO Box 299, 2200 AG Noordwijk, The Netherlands – ugo.lafont@esa.int

Abstract:

Spacecraft are subjected to very few mechanical loads but in the future with reusable spacecraft designed for interplanetary explorations and with the repetition of landing and takeoff, structures will be subjected to increased mechanical loads. The effect of space environment on the aging of adhesive materials used as joints in space structure is not well understood for such long-term application. In this study, two adhesives widely used in spacecraft assembly were investigated: Scotch-Weld™ EC-2216 and Scotch-Weld™ EC-9323-2. They were subject to two aging conditions: (1) high energetic electron irradiation using a Van de Graaf accelerator and (2) thermal vacuum cycling. The results related to the evolution of the intrinsic adhesive properties and adhesion to CFRP and aluminum adherents were investigated before and after environmental exposure with tensile tests, peel tests, double cantilever beam (DCB) tests and dynamic mechanical analysis (DMA).

Keywords: Adhesives; space environment; aging

1. Introduction

Spacecraft and satellites are subjected to very few mechanical loads in space, but in the future with reusable spacecraft, loads can become significant. Indeed, for spacecraft designed for interplanetary explorations and with the repetition of landing and take-off (on the Moon or Mars or some asteroids for instance) [1-2] the structure will be subject to more repetitive mechanical loads and thus even after long period of exposure toward space environment.

In such conditions, materials intrinsic properties will evolve. One of the first effect related to exposure to space vacuum is outgassing. Due to the vacuum, molecules from an organic component tend to be released into space [3-5]. However, minimizing and controlling such effect is mainly driven by the need to avoid molecular contaminants that can be release and later re-adsorbed by sensitive surface of a spacecraft like optics. Outgassing can be anticipated and countered prior to launch with using material that have very low outagassing and implementing bakeout strategy on ground prior launch phase. At this stage, the integrity of adhesives are not impacted by outgassing and can be discarded as relevant parameter. Radiation is also an integral part of the special conditions to which spacecrafts are subjected. This radiation

  doi:10.5075/epfl-298799_978-2-9701614-0-0

is broken down over the entire spectrum of light depending on the wavelength. Thus, a material expose to space is subjected to two types of radiation: energetic photons (UV-ray, X-ray, γ-ray) which come from the solar flux and charged particle (electrons, protons, nucleon) trapped by electromagnetic fields such as the van Allen belt around the earth [6]. The effect of different types of radiation on the materials mechanical properties may vary in the case of polymers. Radiation causes molecular chain scission and recombination or cross-linking in macromolecular chain leading to deformation, embrittlement, and discoloration, which affect the mechanical integrity of the polymer [7-8]. Another parameter of the space environment, specific to Low Earth Orbit and able to induce degradation of the materials is Atomic Oxygen (ATOX). Oxygen atoms are generated during the photo-dissociation of the oxygen molecules of the atmosphere by the solar electromagnetic radiation [7] leading to the breaking of the bond between two atoms. These very reactive species can interact with the surface of any exposed material and degrade it. Even if Atomic Oxygen is mostly present around Earth it can also be produced in other planetary environments, such as the Mars orbital environment, where oxygen is also present. It should be notice that although the effects of ATOX can induce severe material degradation like etching, pitting, it will not be considered in this study as adhesives are generally protected from direct exposure to atomic oxygen and are therefore not affected by this space environmental factor.

In terms of temperature, the space environment goes from very low to very high temperatures, so the adhesive must be resistant to its use [8-9]. With temperature gradients, thermal residual stresses can occur at the bond line between materials with different coefficients of thermal expansion. This can create stresses and therefore failures, damage, delamination, etc.

Furthermore, as detailed in the literature, one of the major issues related to adhesives is the differentiation between adhesion and material properties of the adhesive. On the one hand, adhesion represents the force that bonds a material to the adhesive and can be quantified through various adhesion mechanical tests [10-11], such as peel tests. The intrinsic material properties of the adhesive, on the other hand, are mainly determined by physical-chemical and mechanical tests of the adhesive material itself [12].

The choice of adherent is another important issue for adhesives. Indeed, in most spacecrafts more and more composite materials such as CFRP are used, as well as metal such as aluminum which is still widely used because of its lightness [13-14]. The literature provides numerous mechanical parameters on the durability of adhesives in contact with these two types of surfaces, for unaged specimens or specimens subjected to hydrothermal aging. However, the literature remains rather poor in information on durability of adhesion subjected to space environment.

The durability of the adhesive materials used as joints in space structure is not yet known for spacecraft subjected to repeated launching loads and several phases of exposure to space conditions (for a 10, 15, 20, ... years exploration). Thus, the challenging question is to anticipate the mechanical and physico-chemical properties degradation of adhesives after X years. The literature has no precedent for the aging of certain material properties related to space conditions. Furthermore, there is lack of adhesion assessment in space aging environment, using mechanical and physical testing. This study will therefore aim to determine the durability of adhesion-related properties, under space environment such as fracture toughness, peel load and surface failure modes. In addition, material properties such as glass transition temperature,

  doi:10.5075/epfl-298799_978-2-9701614-0-0

young's modulus, tensile strength and strain at break will be investigated. The objective is to complement the literature by providing new data on the aging of adhesives for long-term space exploration application.

In this research, we looked into the effect of thermal vacuum cycling and high energetic electron irradiation on the properties of two adhesives that are widely used for space application Scotch-Weld™ EC-2216 and Scotch-Weld™ EC-9323-2. Adhesive behavior for Composite-to-composite and Alumimium-to-aluminum joints were evaluated using double cantilever beam tests (DCB) and floating roller peel tests (FRPT), respectively. The evolution of the adhesive intrinsic properties like tensile strength, thermo-mechanical behavior were investigated by means of tensile tests and Dynamic Mechanical Analysis (DMA).

2. Materials and Methods

2.1 Materials

Two types of adhesives were investigated: Scotch-Weld™ EC-2216 and Scotch-Weld™ EC-9323-2. Their respective processing/curing temperature and time and the mixing ration between the two parts are reported in Table 1. Both adhesives are space qualified but are used in different applications. Having a low Tg, EC-2216 is used for bonding elements that have no structural application at high temperatures while EC-9323-2, having a higher Tg, is used mainly in structural applications.

Table 1: Adhesive materials and corresponding curing cycle.

Adhesive	Curing temperature [°C]	Curing time [mm/min]	Part A/B [Weight ratio]
EC 2216	66	120	7/5
EA 9323-2	65	120	1/2

To assess the adhesion to CFRP, Double Cantilever Beam specimens were produced using carbon fibers already pre-impregnated with epoxy resin. CFRP were prepared from a unidirectional pre-preg consisting of Hexply 8552 epoxy matrix in combination with AS4 carbon fiber (Hexcel Corporation, Stamford, Connecticut, USA). To produce the two-rigid adherent of a DCB samples, a lay-up of 8 plies [0°]s of approximately 1.6 mm was used. The laminate was cured for 120 min at 180 °C. Prior to bonding, the cured CFRP surfaces were prepared by mean of abrasion with sand paper and cleaned with acetone.

To assess the adhesion to aluminum, floating roller peel test specimens were produced using clad Alumimium alloy 2024. The aluminum surfaces were pre-treated by grit blasting, coated with Sol-Gel 3M AC-130-2 and sprayed with 3M Scotch-Weld™ Primer 3901. The flexible aluminum sheets were 0.6 mm thick and the rigid aluminum sheets were 1.6 mm thick.

2.2 Methods

For tensile tests, experimental procedure was based on the standard test method for tensile properties of plastics described in ASTM D638 [15]. Testing was carried out using Zwick machine (Zwick, Ulm, Germany) equipped with a load cell of 1 kN. For EC-2216, the test speed was 5

  doi:10.5075/epfl-298799_978-2-9701614-0-0

mm.min^{-1} and the crosshead displacement and load were recorded each 5 s and 0.42 mm. For EC-9323-2, the test speed was 0.5 mm.min^{-1} (to ensure a similar acquisition time before failure as the EC-2216 because the EC-9323-2 is a more brittle adhesive that breaks more quickly at imposed displacement) and the crosshead displacement and load were recorded for all 5 s and 0.042 mm. Displacement data were recorded using a DIC (Digital Image Correlation) setup.

For Dynamic Mechanical Analysis (DMA), experimental procedure was based on the standard test methods for glass transition temperature, loss modulus and storage modulus determination as described in ASTM D7028, E2254 and E2425 [16-18]. Testing was carried out using TA Instrument RSA G2 machine (TA Instrument, New Castle, Delaware, USA) with a temperature range between -40°C and 140°C, a ramp rate of 2°C.min^{-1}. The test were performed in flexion mode (3 point bending).

For floating roller peel test (FRPT), the experimental procedure was based on the standard test method described in ASTM D3167 [19]. Testing was carried out using Zwick machine (Zwick, Ulm, Germany) coupled with a load cell of 1 kN. The testing speed was 125 mm.min^{-1}.

For Double cantilever Beam (DCB), test procedure follows the standard method of determining fracture toughness described in ASTM D5528 [20]. For this purpose, a Zwick machine (Zwick, Ulm, Germany) coupled with a load cell of 1 kN was used. The testing speed was 2 mm.min^{-1}. The crack length propagation in the bond line was monitored using millimetric paper and camera observation.

2.3 Sample preparation

DMA and tensile test specimens were produced via machining of plates of pure adhesive material. These plates were produced by placing adhesive between two glass plates with a control thickness of 2 mm and cured in an oven (as per Table 1). The plates were then machined to cut out specimens of 12 x 56 x 2 mm for DMA specimens as described in ASTM E2254 and ASTM E2425 [17-18] and 20 x 150 x 2 mm as per ASTM D638 standard [18] (Figure 1).

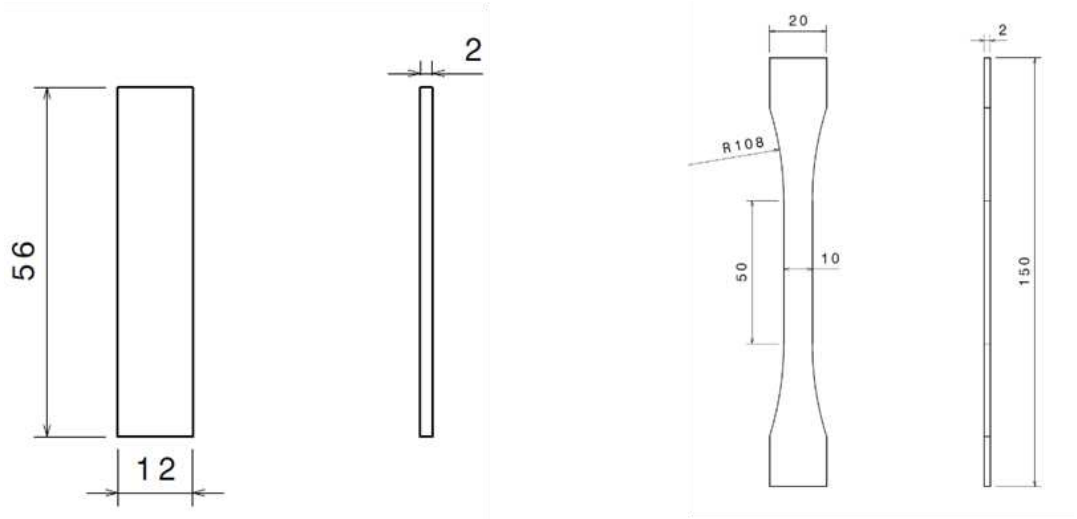

Figure 1: Sample shape and dimension for (Left) DMA and (Right) tensile testing

For FRTP specimens, after applying Teflon tape to the first 75 mm of the flexible adherent length (25 mm for the opening crack and 50 mm for the flexible adherent that protrudes from the rigid adherent, as shown on Figure 2). To control the adhesive bond line, 0.1% wt of glass beads of

250 microns in diameter were added to the mixture between part A and part B. The blend was then spread on the aluminum plates, which were then joined together using weights and cured in oven (as per Table 1). Floating roller peel test specimen dimensions were based on the standard test method ASTM D3167 [19] for floating roller peel resistance of adhesives. Specimens were 12.5 mm width and 350 mm long with a bond line thickness of 0.15 ± 0.05 mm.

For double cantilever beam specimens, Teflon tape was applied on the 50 mm of CFRP plates to create the crack opening, then similar glass beads were added with the same ratio as for floating roller peel test procedure and cured in an oven. Double Cantilever Beam specimen dimensions were based on the standard test method ASTM D5528 [20] for mode I interlaminar fracture toughness of unidirectional fiber-reinforced polymer matrix composites. Specimens were 25 x 220 mm with a 50 mm crack opening and a bond line thickness of 0.17 ± 0.06 mm.

Both aluminium-to-aluminium (FRTP test) and composite-to-composite (DCB test) products were then machined to cut out specimens with the desire dimension (Figure 2).

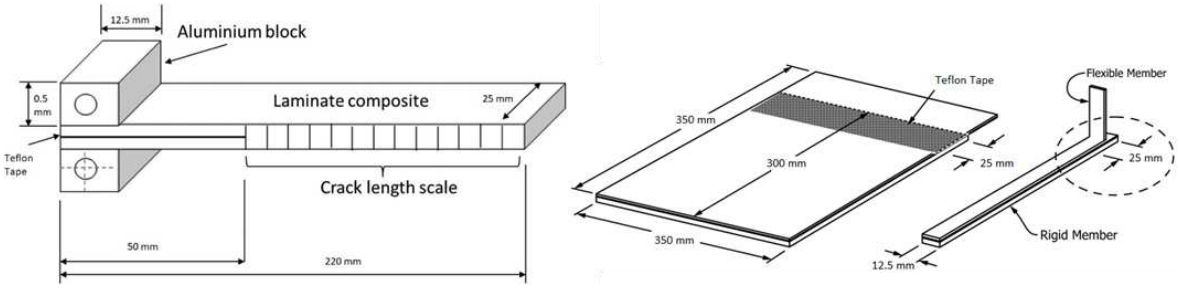

Figure 2: (Left) DCB and (Right) Peel test specimen dimension

2.3 Space environment exposure

In order to mimic space environment conditions, two different type of space environment were considered in this study: thermal vacuum cycling and irradiation with high energetic electrons. Thermal vacuum cycling test was carry out at ESA-ESTEC (Noordwijk, Netherlands) using a dedicated chamber for 25 cycles between -100°C and 100°C at 10^{-6} mbar. The period of each cycle was 4 hours and total duration was about 100 hours. Electron irradiation was performed at the Delft Reactor Institute (Delft, Netherlands) using a Van de Graaf accelerator. Samples were subjected to a total ionizing dose of 1 MGy using electron beam delivering 1.5 10^{12} $e^{-}.cm^{-2}.s^{-1}$ and an average dose of 47.4 $kGy.cm^{-2}$ for 3.5 h

For each characterization technique, five (N=5) specimens were tested per adhesive and configuration with the following conditions: (1) unaged/pristine, (2) after irradiation exposure and (3) after thermal vacuum cycling.

3. Results and Discussion

3.1 Effect space environment on adhesive intrinsic properties

In order to evaluate the aging effect on the adhesives, five parameters were derived from the experimental results: Young Modulus, Tensile strength and Strain at break (tensile tests), glass transition temperature (DMA and DSC tests) and heat flow (DSC tests).

  doi:10.5075/epfl-298799_978-2-9701614-0-0

Figure 3 shows the representative stress-strain curves obtained for both adhesives under the three conditions. The average values for Young's modulus, tensile strength and strain at break are given in Table 3.

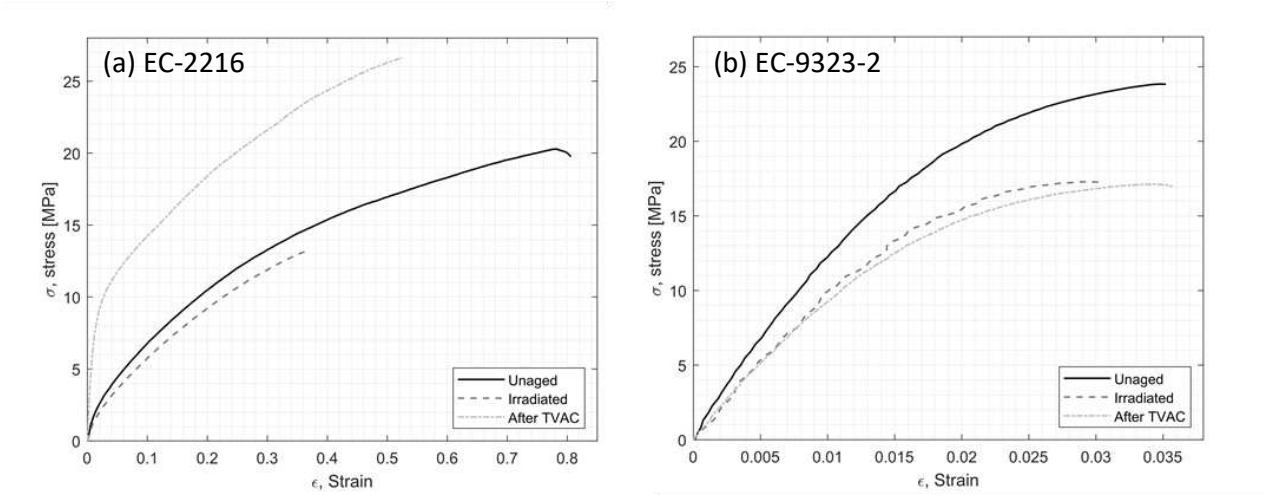

Figure 3: Typical tensile stress-strain of EC-2216 (Left) and EC-9323-2 (Right) as-produced (unaged), after irradiation and after Thermal vacuum cycling (TVAC)

For EC-2216 (Figure 3a) it can be noticed that behaviors are different after particle irradiation and TVAC. After particle irradiation the average Young's modulus drops from about 240 MPa for a non-aged sample to about 120 MPa for an irradiated sample. On the contrary, after Thermal Vacuum Aging Cycling (TVAC) the average Young's modulus increases to about 600 MPa. The stress-strain curve in its elastic zone, after TVAC, is much steeper in addition to presenting a larger elastic zone than for unaged material. This is also reflected in the tensile strength value that increases by almost 50% after TVAC, whereas it decreases by about 25% after irradiation. Finally, both types of aging have the same effect on elongation at break by decreasing its value, and therefore decreasing the ability of this adhesive to elongate prior to failure when subjected to tensile loading, even though particle irradiation decreases it more than TVAC. It is clear for EC-2216 that irradiation leads to a general decrease of the tensile properties whereas TVAC leads to an overall increase. Such improvement after TVAC can be attributed to a the post-curing effect occurring during the thermal cycling.

For EC-9323-2 (Figure 3b), the tensile behavior is similar after TVAC and particle irradiation. However, compare to the non exposed samples, modulus decreases by a factor 2 to from 2.2 GPa to 1.1 GPa for the pristine sample and the sample exposed to irradiation and TVAC, respectively. The same trend is observed in the tensile strength that also decreases after both aging conditions. The elongation of EC-9323-2 is almost unaffected after aging. However, the fracture surface of the sample reveals the presence of small voids for EC-9323-2 for all samples that were not present for EC-2216. Even if such inhomogeneity could have a negative effect on the general tensile properties, the EC-9323-2 tensile test reached a plateau as expected with respect to the mechanical behavior of such material. However, the strain might be not fully representative and shall not be considered. This difference of homogeneity between the 2 type of adhesive is related to the preparation process. In this study, the mixing process where identical for both adhesive and potentially not optimized. For space application, each bonding procedure is qualified and validated leading to a stable and reproducible process. This aspect

  doi:10.5075/epfl-298799_978-2-9701614-0-0

was not the focus of this study even if it is clear that is will have an impact on the optimum performance of the adhesive.

Table 2: Average tensile properties of EC-2216 and EC-9323-2 including standard deviation

Aging	Scotch-Weld™ EC-2216			Scotch-Weld™ EC-9323-2		
	E [MPA]	σ_{max} [MPA]	ε_{max}	E [MPA]	σ_{max} [MPA]	ε_{max}
Unaged	242 ± 48	19 ± 1.3	0.74 ± 0.08	2197 ± 703	20 ± 4.2	0.027 ± 0.007
Irradiated	123 ± 49	15 ± 3.3	0.53 ± 0.29	1026 ± 267	17 ± 2.2	0.026 ± 0.008
After TVAC	606 ± 130	28 ± 1.5	0.61 ± 0.07	1042 ± 198	18 ± 1.0	0.033 ± 0.008

DMA (Dynamical Mechanical Analysis) was performed to investigate the visco-elastic behavior and the glass transition temperature (Tg). The elastic storage modulus (E') which is proportional to the energy fully recovered per deformation cycle, the loss modulus which is proportional to the net energy dissipated in heat per cycle (E'') and tan δ the loss factor which represents the damping during dynamic deformation are plotted in Figure 4. The Tg was extracted at the temperature at which tan δ is maximum. Tg values are reported in Table 3.

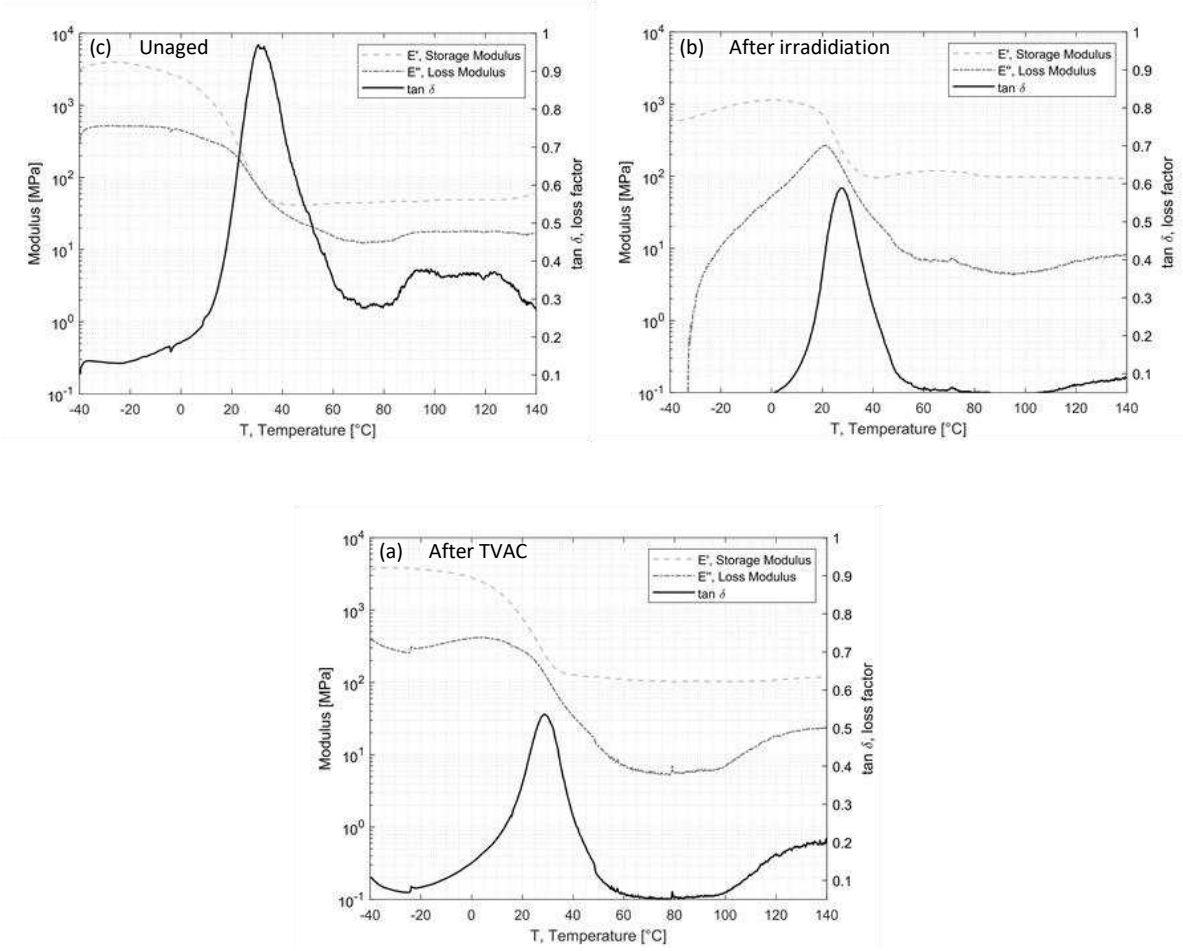

Figure 4: Evolution of storage and loss modulus, tan δ for EC-2216 (a) before aging and after (b) irradiation and (c) TVAC (c)

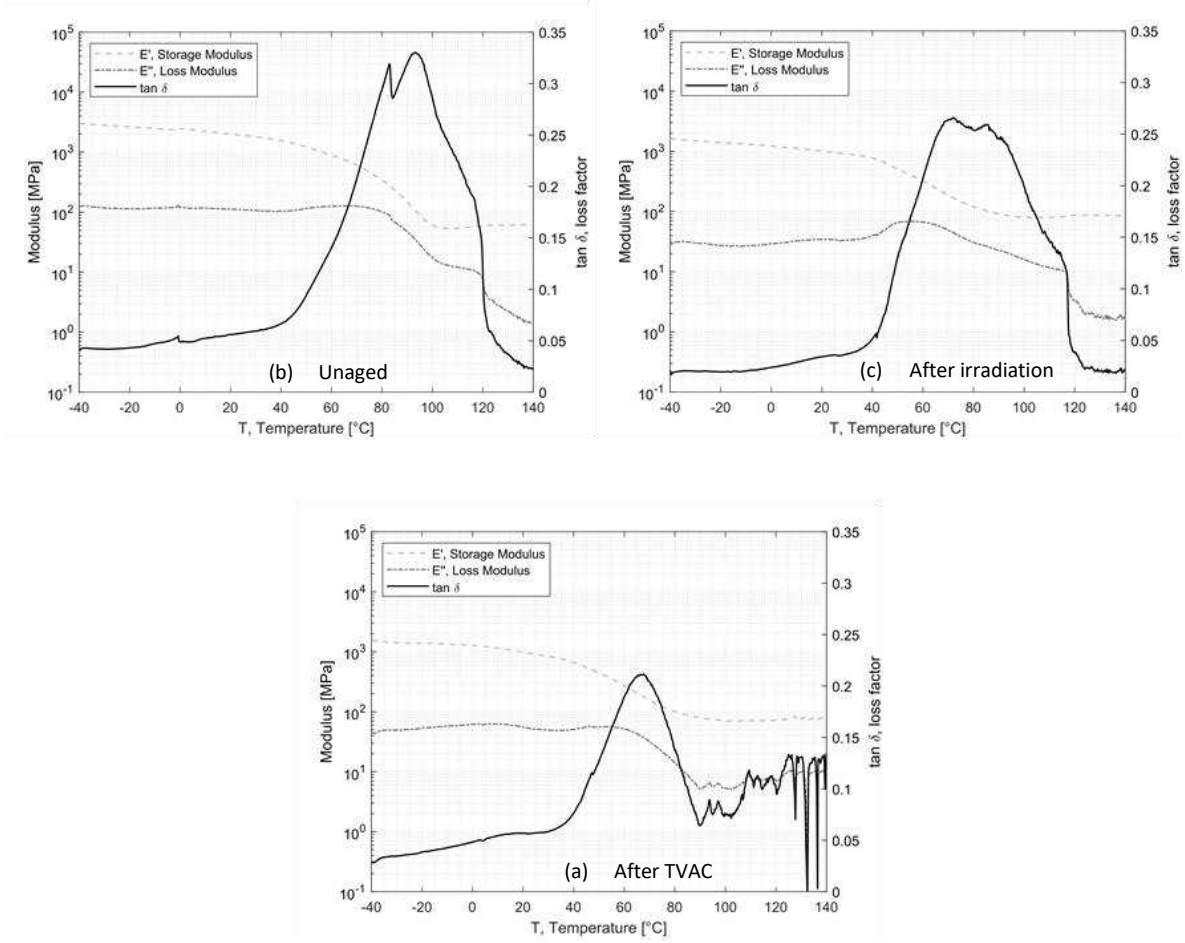

Figure 5: Evolution of storage and loss modulus, tan δ for EC-9323-2 (a) before aging and after (b) irradiation and (c) TVAC

Table 3: Average glass temperature evolution as function of the environmental exposure

Aging	T_g from max Tan δ [°C]	
	Scotch-Weld™ EC-2216	Scotch-Weld™ EC-9323-2
Non Aged	28 ± 1.1	91 ±7.4
Irradiated	30 ± 2.2	72 ± 3.6
After TVAC	30 ± 1.8	68 ± 7.8

For EC-2216, it can be seen that after irradiation or TVAC exposure the Tg increases by 2 °C in comparison to the pristine/unaged material. This change is not very significant taking into the standard deviation. However, the value of the maximum of tan δ which is around 1 for unaged sample, drops around 0.6 after TVAC and irradiation. This means that the ability of the adhesive to dissipate energy into heat after aging is lower. This could be explained by the average diminution of Loss Modulus with the aging. Indeed, in Figure 4b, it can be seen that after irradiation over the temperature range of -40 °C to 20 °C the loss modulus increases from almost zero to a peak at about 300 MPa, in contrast to unaged where it gradually decreases throughout

the temperature range. After TVAC, the loss modulus follows the same pattern as for unaged sample except that it increases significantly from 100 °C to 140 °C. These increases mean that over the relevant intervals the EC-2216 experiences an increase in net energy dissipated per cycle. The storage modulus, which is proportional to the total energy recovered per deformation cycle, does not change significantly after aging. It can also be noticed that the glassy state, the glass transition range and the rubbery plateau are not changing in a major way for unaged and irradiated sample as they are respectively between -40 °C and 0 °C, 0 °C and 60 °C, 60 °C and 100 °C. After TVAC (i.e. 25 cycles between -100 °C and 100 °C) the glass transition range is between -30 °C and 60 °C. Furthermore, the tan δ is decreasing between -40 °C and -30 °C which suggests a flow region for lower temperatures.

For EC-9323-2, the glass transition zone extends from 40 °C to 120 °C for unaged and irradiated samples. After TVAC, this range is again modified but this time with a decrease from 40 °C to 90 °C. After this zone there is no longer rubbery plateau which is replaced by a zone of great instability created by TVAC, as shown in Figure 5c. Moreover, for this adhesive the irradiation exposure does not change the general behavior of E' and E''. The main change concerns the Tg as shown in Table 3. Indeed, initially situated around 91 °C, the latter drops to 72 °C after irradiation and 68 °C after TVAC. As irradiation creates chain splitting and cross-linking which are two opposing phenomena, it is necessary to carry out additional tests to determine which of these phenomena predominates in the adhesives concerned and whether or not they have an impact on the Tg.

3.2 Impact of space conditions on adhesion properties

For DCB test, using DIC (Digital Image Correlation) periodic image recordings, the crack growth is obtained. With these values the opening Mode I interlaminar fracture toughness G_{Ic} is determined using equation (1).

$$G_{I_c} = \frac{3\,P\,\delta}{2b(a+|\Delta|)} \quad (1)$$

Where P is the applied load, a the delamination length, b the width of the DCB specimen, δ the load point displacement and Δ be determined experimentally by generating a least squares plot of the cube root of compliance, as a function of the delamination length using equation (2) as reported in the Modified bean theory (Figure 6).

$$C^{\frac{1}{3}} = \left(\frac{\delta}{\mathrm{P}}\right)^{\frac{1}{3}} \quad (2)$$

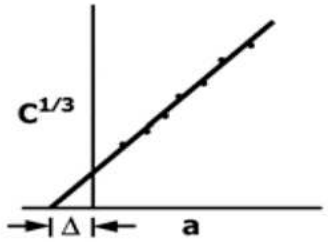

Figure 6: Modified beam theory

  doi:10.5075/epfl-298799_978-2-9701614-0-0

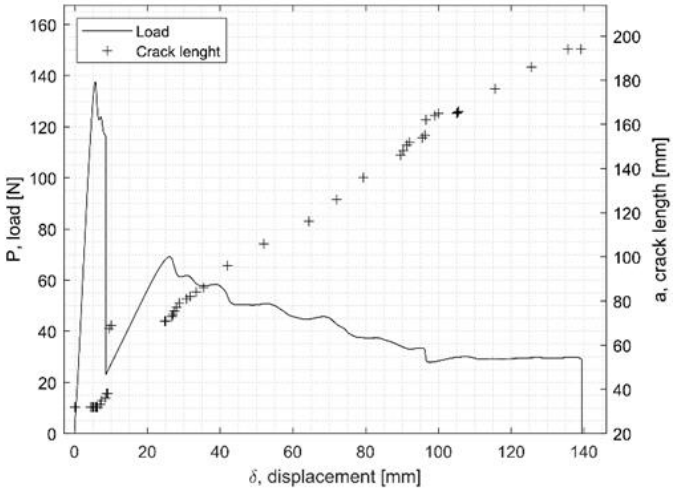

Figure 7: Example of load displacement curve for EC-2216 unaged DCB specimen

Figure 7 shows an example of a load displacement curve as well as the crack growth for EC-2216. Figure 8 shows the evolution of fracture toughness G_{Ic} (R-curve) and the corresponding fracture surface of the specimen.

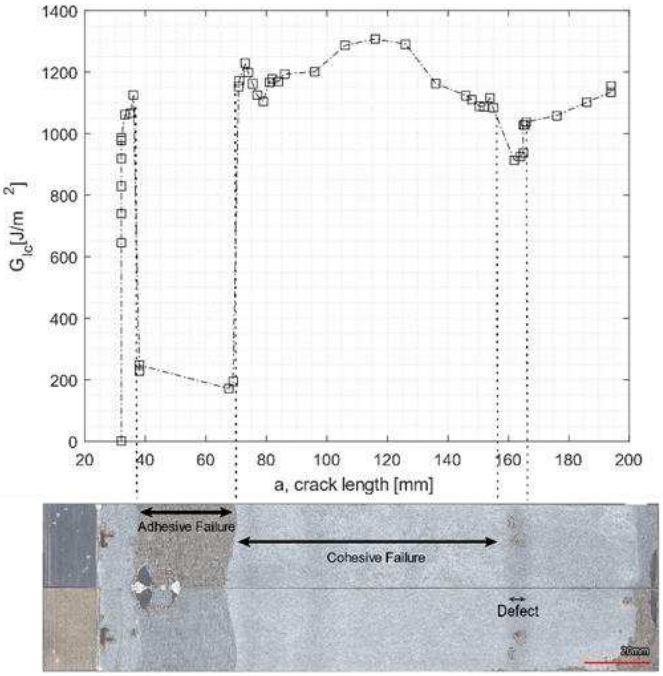

Figure 8: R-curve for EC-2216 unaged DCB sample and the correspondent failure surface of both adherent

From Figure 8 it can be seen that a drop in the value of the fracture toughness corresponds to an adhesive failure. In addition, a second drop in the G_{Ic} appears, due to a change of failure mode created by manufacturing defect, which also cause G_{Ic} drops.

  doi:10.5075/epfl-298799_978-2-9701614-0-0

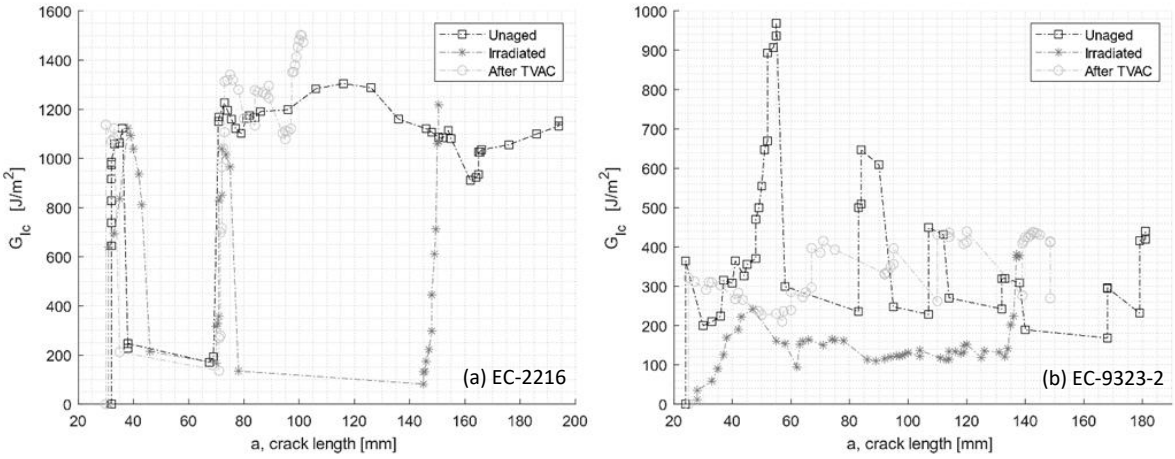

Figure 9: R-curves of DCB test for unaged, after irradiation and after TVAC for (a) EC-2216 and (b) EC-9323-2

Concerning the evolution of the G_{Ic}, the two aging conditions affect differently the adhesives performance. For both adhesives the average value of fracture toughness decreases after particle irradiation. The drop is however more significant for EC-9323-2 with a decrease of almost 50%, while the value of EC-2216 drops by only 5%. In contrast, after TVAC the G_{Ic} value for EC-9323-2 increases by 8% and for EC-2216 by 12% in average. It is interesting to note that TVAC also increased the tested parameters (here fracture toughness) of EC-2216 as it does for the tensile test values. TVAC also increases the G_{Ic}, values for EC-9323-2 but due to significant manufacturing defects in this adhesive samples, the results are less representative than EC-2216.

Table 4: Double Cantilever bean test result with evaluation of cohesive (CF) and adhesive (AF) failure mode

Aging	Scotch-Weld™ EC-2216			Scotch-Weld™ EC-9323-2		
	G_{Ic} [J/m^2]	*Failure mode*		*G_{Ic} [J/m^2]*	*Failure mode*	
	(on CF)	*CF (%)*	*AF (%)*	*(on CF)*	*CF (%)*	*AF (%)*
Non Aged	1203 ± 52	61 ± 15	39 ± 15	280 ± 100	10 ± 10	90 ± 11
Irradiated	1142 ± 79	41 ± 23	59 ± 23	142 ± 11	0.5 ± 1	100 ± 1
After TVAC	1348 ± 130	31 ± 13	69 ± 13	302 ± 33	0 ± 0	100 ± 0

Concerning the failure type, for EC-2216, both aging processes increase the area of adhesive failure and therefore decrease the proportion of cohesive failure. This means that exposure to space environment related conditions significantly deteriorates the adhesion. For EC-9323-2, the area of adhesive failure also increases. However, samples manufactured with this adhesive have more manufacturing defects.

The floating roller peel test load-displacement curves for unaged, irradiated and post-TVAC conditions are reported in Figure 10. Pictures of the fracture surface of the rigid adherent are displayed below each load-displacement curve. As expected, there is an intimate relation between the peel load and the type of failure. For each of the two surface images, the top

sample is the unaged sample, the middle one is the irradiated sample and the bottom one is the sample subjected to TVAC. In addition, the average peel load values and different failure mode proportions (CF, AF and MD [Manufacturing Defect]) were collected and recorded in Table 5.

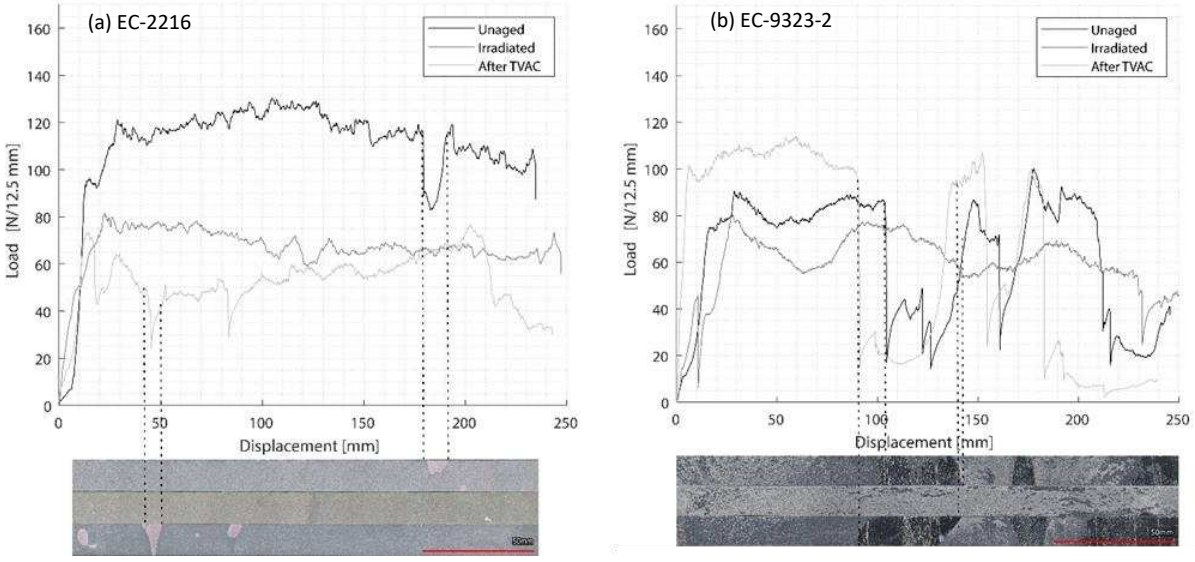

Figure 10: Load displacement curves for peel-test sample non-aged, after irradiation and TVAC for each adhesive and the correspondent failure surface of rigid adherent for (a) EC-2216 and (b) EC-9323-2

EC-2216 shows very few manufacturing defects and a failure 97% cohesive for non-aged samples, which shows the very good quality of the bond line for this adhesive. After radiation of EC-2216, the average peel load decreases by 38% compared to unaged, and after TVAC decreases about 55%. Moreover, irradiation has not significant effect on the failure mode (93 % cohesive failure), however after TVAC, the adhesive failure increases significantly to approx. 30 %. Although results from DCB and tensile tests show that after TVAC for EC-2216, mechanical properties increase, this does not hold true for the floating roller peel tests results.

Table 5: Average peel load and failure mode identification

Aging	Scotch-Weld™ EC-2216				Scotch-Weld™ EC-9323-2			
	F_{ave} [N/12.5 mm]	Failure mode			F_{ave} [N/12.5 mm]	Failure mode		
		CF (%)	*AF (%)*	*MD (%)*		*CF (%)*	*AF (%)*	*MD(%)*
Non Aged	111 ± 6.4	97 ± 2.2	0.8 ± 1.1	2 ± 1.3	87 ± 8	54 ± 27.2	0 ± 0	46 ± 27.2
Irradiated	68 ± 3.5	93 ± 6.1	6 ± 6.5	0.4 ± 0.8	62 ± 5.5	63 ± 23.9	2.2 ± 8	35 ± 26.2
After TVAC	53 ± 6	63 ± 17.7	30 ± 20	7 ± 1.4	105 ± 5	50 ± 7.3	0 ± 0	49 ± 7.3

Figure 11 shows 2D and 3D profile of the rigid adherent of EC-2216, unaged, after irradiation and TVAC. It is shown that after TVAC the adhesive thickness remaining on the rigid adherent part is much higher than for other aging. This indicated the fractured occurred closer to the interface in the case of TVAC than for unaged and irradiation. Indeed, the surface of the

  doi:10.5075/epfl-298799_978-2-9701614-0-0

specimen after TVAC (Figure 10) is slightly pink, which corresponds to the color of the primer applied to the aluminum during the surface treatment. This means that the crack has propagated within the primer and not within adhesive. Peel load values after TVAC are therefore not only representing peel load created by the adhesive but also peel load created by the primer. This value is still quite usable as it qualifies the ability of the sample to resist peeling after thermal aging in vacuum.

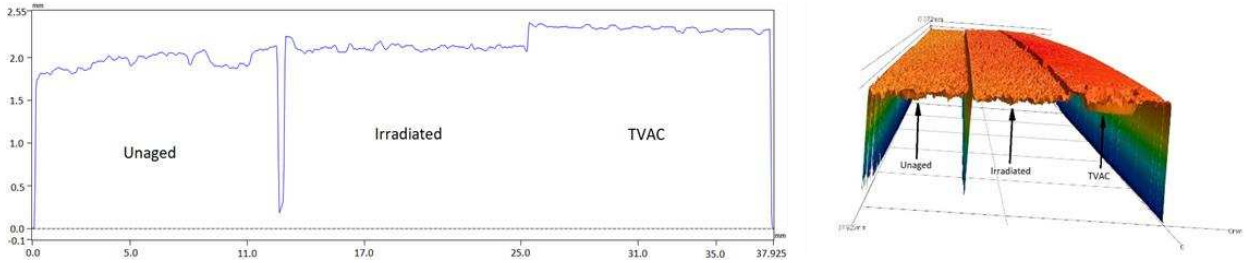

Figure 11: 2D and 3D profiles of EC-2216 thickness present on rigid adherent after testing (unaged on the left, irradiated in the centre and TVAC on the right)

A third failure mode must be considered for peel tests: Manufacturing Defect (MD). The latter is mainly present on EC- 9323-2 specimens. It is represented through a very particular effect on the surface: each of the two faces has adhesive on it, which could suggest a cohesive failure at first sight, but these areas are shiny, which indicates that there has been no bonding between the two faces in this area. The defects are similar to those obtained in the DCB tests with the same adhesive. This reinforces the hypothesis that the entire process used for this adhesive was not optimized specially related to the work life. It was witnessed that during the mixing an exothermic reaction occurs and that the curing reaction starts before the bonding. Thus, the quality of the bond line is reduced.

4. Conclusion

The material properties and adhesion properties to CFRP and to aluminum of EC-2216 and EC-9323-2 under space aging conditions (thermal vacuum and particle irradiation) were evaluated using tensile tests, DMA, DCB tests and floating roller peel tests.

For the Scotch Weld EC-2216 the effect of electron irradiation and thermal vacuum cycling do not influence the Tg. If both cases, decrease in the peel strength occurs with reduction of 50% and 39% for the sample subjected to Thermal vacuum cycling and irradiation, respectively. The DCB test performed using CFRP adherent lead to small increase after TVAC (+12%) and a small decrease after irradiation (-5%) of the G_{Ic}. The tensile properties are positively affected after TVAC with a very strong increase of the modulus and the tensile strength but a decrease of the tensile properties is observed after irradiation.

For Scotch Weld EC-9323-2, the Tg is decreasing after TVAC and irradiation. In both cases, the tensile modulus is negatively impacted with a decrease reaching 50%. TVAC have a positive effect on the G_{Ic} (+8%) value and peel strength (+20%) but a strong negative effect on these values is witnessed after irradiation leading to a decrease of 50% for G_{Ic} and 30% for the peel strength.

  doi:10.5075/epfl-298799_978-2-9701614-0-0

The understanding of many of the macroscopic phenomena induced by space environment conditions can be observed and quantified through the results of this study. However, the results on the impact of space aging conditions on the molecular behavior of adhesives do not allow any interpretation. Further detailed study of these behaviors would allow, in addition to the results of this study, to create a predictive model under space aging condition of the degradation of adhesive and adhesion properties. Thus, the durability of the adhesive joints could be quantified enabling lifetime prediction leading to more robust and adequate design and for long-term missions.

Acknowledgements

The authors would like to acknowledge the support of Delft Reactor Institute and ESA-ESTEC for providing access to testing facilities, and of the technical team of the DASML laboratory at TU Delft.

5. References

1. Braunand RD, Manning RM. Mars Exploration Entry, Descent and Landing Challenges 2006; 1.
2. Martin AA. Model Predictive Control for Ascent Load Management of a Reusable Launch Vehicle. Massachusetts Institute of Technology. 2002.
3. Chen J, Ding N, Li Z, Wang W. Organic polymer materials in the space environment 2016; 5.
4. Justiz CR, Sega RM, Dalton C, Ignatiev A. DSMC and bgk-based calculations for return flux contamination of an outgassing spacecraft. Journal of Thermophysics and Heat Transfer 1994; 8:802–803.
5. Laikhtman A, Verker R, Gouzman I, Noter Y, Grossman E. Outgassing effects of a kapton acrylic adhesive tape. Technical report.
6. Zimmermann J, Sadeghi MZ, Schroeder KU. The effect of γ-radiation on the mechanical properties of structural adhesive. International Journal of Adhesion and Adhesives 2019; 93, 9.
7. Dagras S, Eck J, Tonon C, Lavielle D. Adhesives in space environment 2018; 5.
8. Silverman EM. Space environmental effects on spacecraft: Leo materials selection guide. Nasa contractor report 4661. 1995.
9. Stevenson R, Chisabas S, Loureiro G, De Oliveira Lino C, Paola J, Zabala O, Fernando D, Salamanca C. Development of a thermal-vacuum chamber for testing in small satellites. 2017.
10. Teixeira de Freitas S, Banea MD, Budhe S, de Barros S. Interface adhesion assessment of composite-to-metal bonded joints under salt spray conditions using peel tests. Composite Structures 2017 ; 164:68–75, 3.
11. Teixeira de Freitas S, Zarouchas D, Poulis JA. The use of acoustic emission and composite peel tests to detect weak adhesion in composite structures. Journal of Adhesion 2018; 94:743–766, 7.
12. Lee-Sullivan P, Dykeman D. Test method guidelines for performing storage modulus measurements using the TA instruments DMA 2980 three-point bend mode 1 amplitude effects. 2000.
13. Teixeira De Freitas S, Sinke J. Adhesion properties of bonded composite-to-aluminium joints using peel tests. Journal of Adhesion 2014; 90(5-6):511–525, 6.
14. Benzarti K, Chataigner S, Quiertant M, Marty C, Aubagnac C. Accelerated ageing behaviour of the adhesive bond between concrete specimens and CFRP overlays. 2010.
15. ASTM D638. Standard test method for tensile properties of plastics. 2014.

  doi:10.5075/epfl-298799_978-2-9701614-0-0

16. ASTM D7028. Standard test method for glass transition temperature of polymer matrix composites by dynamic mechanical analysis. 2015.
17. ASTM E2254. Standard test method for storage modulus calibration of dynamic mechanical analyzers. 2018.
18. ASTM E2425. Standard test method for loss modulus conformance of dynamic mechanical analyzers. 2016.
19. ASTM D3167. Standard test method for floating roller peel resistance of adhesives. 2017.
20. ASTM D5528. Standard test method for mode 1 interlaminar fracture toughness of unidirectional fiber-reinforced polymer matrix composites. 2013.
21. Huang G, Ni Z, Chen G, Zhao Y. The influence of irradiation and accelerated aging on the mechanical and tribological properties of the graphene oxide/ultra-high-molecular-weight polyethylene nanocomposites. 2016.
22. Sahu SK, Badgayan ND, Samanta S, Rama Sreekanth PS. Dynamic mechanical thermal analysis of high-density polyethylene reinforced with nanodiamond, carbon nanotube and graphite nanoplatelet. Materials Science Forum 2018; 917:27-31.
24. Williamson JR, Semprimoschnig C, Simon-Boutemen P, Levan L, Van Eesbeek M. Use of model free kinetic lifetime values to evaluate mechanical performance of a high temperature polyimide composite. Proceeding of 11th ISME 2009
25. Space product assurance adhesive bonding for spacecraft and launcher applications. ECSS-Q-ST-70-16C ESA-ESTEC requirements and standards section. 2020.
26. ASTM D3418. Standard Test Method for Transition Temperatures and Enthalpies of Fusion and Crystallization of Polymers by Differential Scanning Calorimetry. 2021

  doi:10.5075/epfl-298799_978-2-9701614-0-0

WIDE SINGLE LAP SHEAR SAMPLES FOR EXAMINATION OF ENVIRONMENTAL EFFECTS OF BONDED REPAIRS

Jelena Ravic[a], *Gregor Peikert*[a], *Patrick Böhler*[a], *Marc Gubser*[a]

a: ZHAW, Zurich University of Applied Sciences, CH-8401 Winterthur, Switzerland

Abstract: *In the frame of the EU FP7 BOPACS (Boltless Assembling of Primary Aerospace Structures) project, the new Wide Single Lap Shear (WSLS) specimen was developed to test a more realistic application scenario for bonded joints. It represents a typical high load transfer configuration as e.g. a fuselage longitudinal joint or a repair joint. The implementation of artificial disbonds and different crack stoppers were part of the validation concept.*

The concept of this test sample was presented during ECCM17. Derived from the Single Lap Shear and the Cracked Lap Shear Coupon, the Wide Single Lap Shear (WSLS) specimen was developed. It marked the next level test setup beyond the basic coupon level for demonstration and investigation of crack growth behavior in bonded joints. [1]

In the BOPACS project two different sizes of WSLS specimens were used. While the test samples for validation tests were made with a width of 500mm, a smaller sample with only 180mm width was developed at ZHAW in order to allow parameter studies at lower cost. The small WSLS is used only for crack growth investigations on a comparative basis. However further work has been performed at ZHAW to develop this set up into a useful examination tool.

Keywords: Composites; Crack; Adhesive; Joint

1. Introduction

In the frame of the EU FP7 BOPACS project, several shear test coupons were examined and compared. To study the effect of crack stoppers the new wide single lap shear (WSLS) specimen was developed to test a more realistic application scenario for bonded joints. It represents a typical high load transfer configuration in Mode II with the option of including damages or crack stoppers.

One of the key elements of the WSLS concept is the crack propagation direction which is perpendicular to the load direction.

In the BOPACS project two different sizes of WSLS specimens were used. While the test samples for validation tests were made with a width of 500mm, a smaller sample with only 180mm width was developed by ZHAW in order to allow parameter studies at lower cost. The small WSLS does not provide an equal load distribution and is therefore used only for crack growth investigations on a comparative basis. Further work has been performed at ZHAW and is presented in this paper.

  doi:10.5075/epfl-298799_978-2-9701614-0-0

This paper focuses on:

- the sample lay-out, stress distribution and crack growth
- crack growth detection with Ultrasonic testing
- the damage introduction process using a combination of an artificial defect as crack inhibitor and subsequent impact damage as a real crack
- test parameters for the cyclic fatigue testing

Based on the defined test parameters, environmental studies were performed to demonstrate its capability to examine effects like:

- humidity and liquid water intrusion in the impact disbond
- effect of freezing of the water in the impact disbond

The results demonstrate that the small WSLS samples is a useful tool to study detrimental effects of environment etc. on crack growth on a bonded high load transfer joint.

2. Background / BOPACS project (2012-2016)

The BOPACS project aimed at developing means to stop or at least control the growth of a crack or disbond in a bondline.

Application as described in BOPACS project: longitudinal joint of fuselage sections. More recent application scenarios target at large repairs in shell structures.

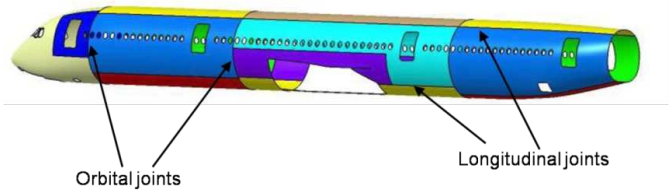

Figure 1. Application case BOPACS: fuselage joint [BOPACS consortium]

The following validation concept was followed within BOPACS:

The target within BOPACS is to demonstrate a secured crack stopping under fatigue loads in case of the presence of a local defect as e.g., a weak bond.

For comparison of the individual crack arresting capability of different design features the Cracked Lap Shear (CLS) test hast been selected. The CLS specimen features a mixed mode load (in plane shear & peeling).

To demonstrate a more realistic application scenario the wide single lap shear (WSLS) specimen has been developed within BOPACS. Figure 2 shows the principal of the WSLS sample. The bondline is 5-10x wider than the overlap, the center section is prepared with an initial disbond. As a consequence of the force F, the disbond grows perpendicular to the direction of the force F.

  doi:10.5075/epfl-298799_978-2-9701614-0-0

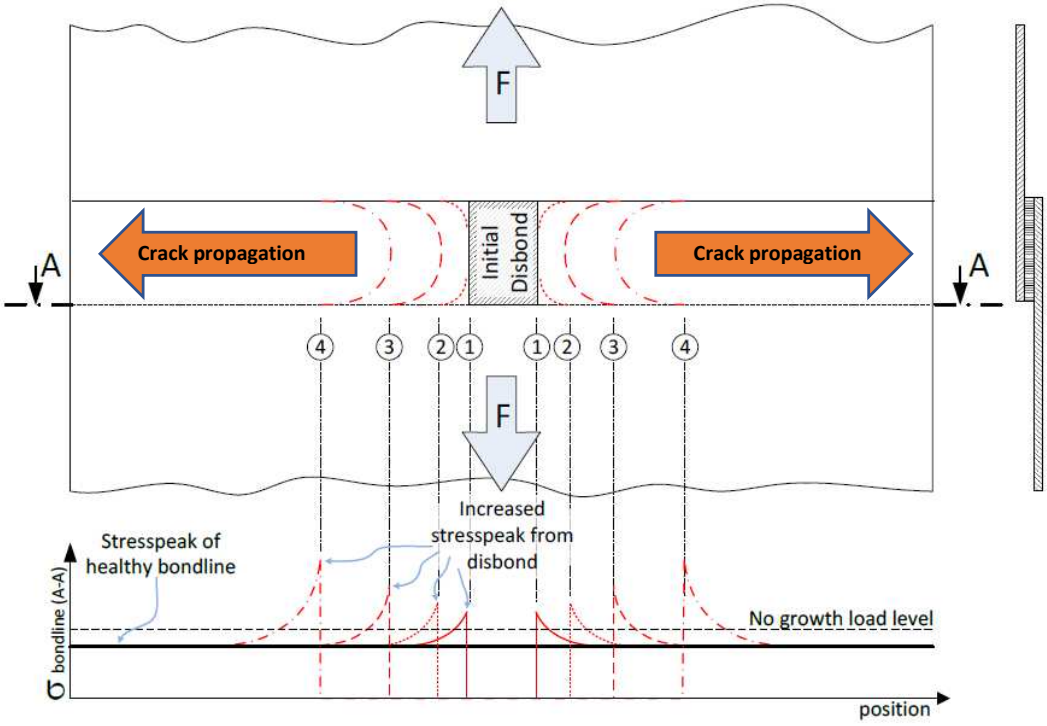

Figure 2. Structure mechanic principle on high load transfer (HLT) joints as applied in the WSLS test coupon, modified from [1], Th. Kruse, Th. Körwien and R. Ruzek, ECCM17.

3. Initial development of WSLS samples at ZHAW (2013)

Screening testing of WSLS samples began in 2013 at ZHAW complementary to CLS samples for crack growth research. While local loads in the CLS samples are rather low and dominated by Mode I and Mode II, the crack grows slowly under quasi-static loading, the effect of crack stoppers or the influence of damages in the bondline can easily be recorded.

A completely different behavior was observed with WSLS samples. Due to the dominating Mode II, the sample bears very high static loads, up to 100kN. This high load is only slightly reduced when damages are introduced. As soon as a crack starts, the sample ruptures immediately and crack growth cannot be investigated.

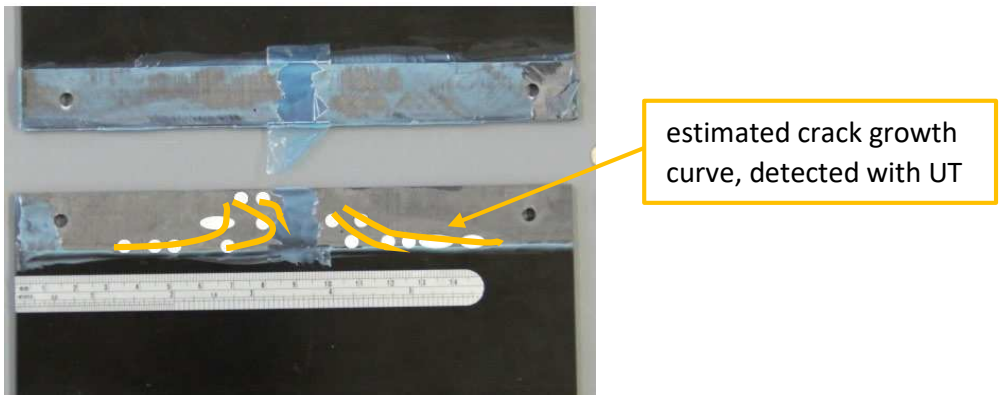

Figure 3. First WSLS sample with centered artificial disbond (blue film) and successful crack growth perpendicular to load direction under cyclic loading. [ZHAW, BOPACS, 2014]

Only the change from static to cyclic fatigue loading resulted in a steady slow crack growth. Figure 3 shows one of the first samples with detectable crack growth. Based on this success the WSLS sample was continuously improved. Major improvements were reached with introduction of a taper (inner and outer) on the adherends to reduce the stress peak in load direction. The single-film disbond was replaced by a double-layer disbond to ease NDT inspection. Finally, a rather constant crack growth could repeatedly be produced which allowed positioning of crack stoppers and studying their effect regarding crack growth speed.

The successful demonstration of crack growth perpendicular to the load direction led to the decision to develop, manufacture and test WSLS on a large scale.

4. Development of large WSLS samples in BOPACS

Highly loaded single lap shear joints shall mainly act in Mode II. The large WSLS sample was designed for Mode II and an even load distribution over the whole joint length. As a consequence, the load introduction is very massive which results in very large sample dimensions and complex clamping in the tensile testing machine. The height of the large WSLS samples is approx. 2m, including the load introduction adapter. However as soon as an initial disbond is introduced in the sample the load distribution is not even anymore as shown in figure 4. As a result of the disbond, stress concentrations arise just next of the disbond. The stress increases, the larger the crack grows. Bearing this in mind the small WSLS sample was designed with a simpler clamping design, using standard 60mm wide clamping devices.

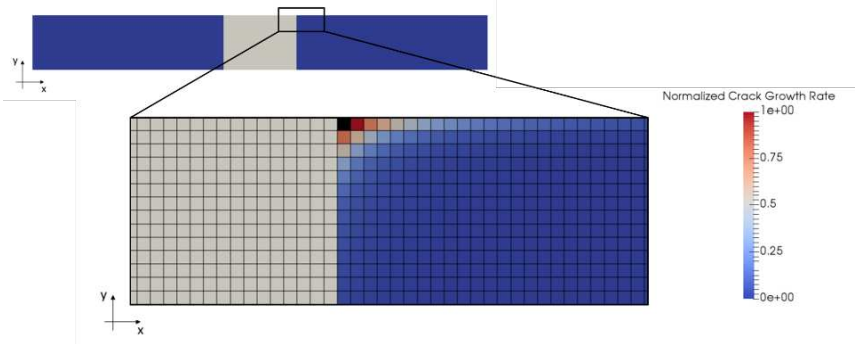

Figure 4. Simulation of crack propagation in WSLS samples showing stress peak (red colour) in corner area of the bondline, from [3], M. Santaniello.

In the ECCM 17 results of the large WSLS samples were presented.

The crack growth starts in the upper and lower corner, as analyzed by FEM, and grows continuously until the two cracks meet in the middle and start to form a uniform round crack line. The wide single lap shear test setup has proven to be suitable for evaluating the crack arresting capability for high load transfer joints. Also the general assumed and theoretically predicted crack growth behavior transverse to the load direction of a WSLS configuration has been validated [2].

  doi:10.5075/epfl-298799_978-2-9701614-0-0

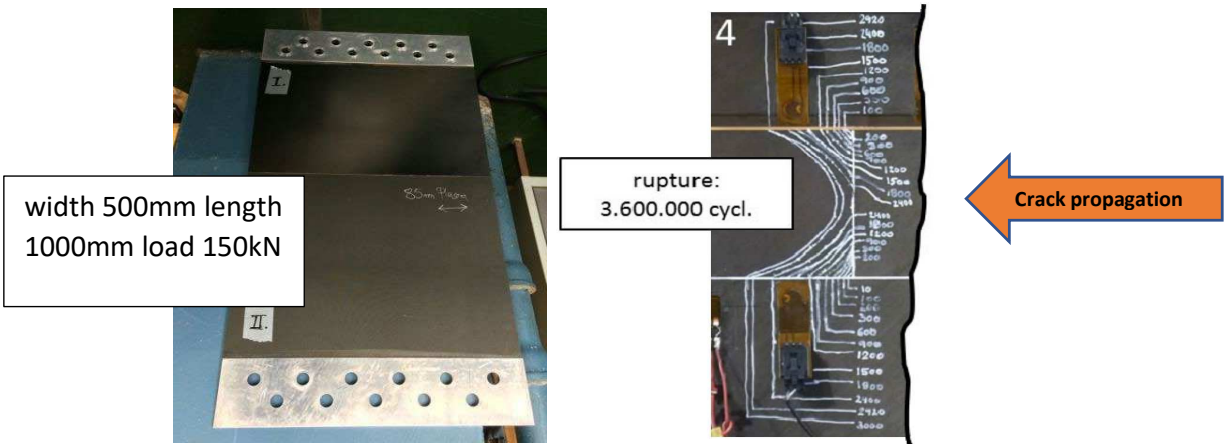

Figure 5. Pictures presenting a large WSLS sample prior to testing (left) and crack propagation detected with Ultrasonic Testing and indicated with white paint. [1]

5. Comparison between large and small WSLS samples

The main difference between the large WSLS samples and the smaller version used at ZHAW besides the dimensions is the stress distribution. The stress distribution of the undamaged large WSLS sample is rather equal over the whole bondline width. This is achieved with a large and sturdy adapter plate. However, as soon as an artificial disbond is introduced, a stress peak occurs as demonstrated in figure 2. The smaller WSLS samples is simply clamped with standard tensile test machine grips and therefore the stress distribution is very uneven over the sample width. A FEM analysis was performed at EPFL in Lausanne showing the stress distribution. As with the large WSLS samples a stress peak arises close to the artificial disbond. This means, that in both sample configuration a stress peak near the disbond is present and that both samples show comparable crack growth behavior. Yet the large sample cracks more evenly and the curved crack growth front line is more symmetric. This seems not achievable with the small samples, but for comparative tests, the small sample design seems appropriate.

Additionally, the small WSLS are designed with a taper which covers half of the overlap length. This complicates the UT (Ultrasonic Testing) investigation, since the first crack start is not detectable with impulse-echo UT. Through transmission testing of this section is foreseen.

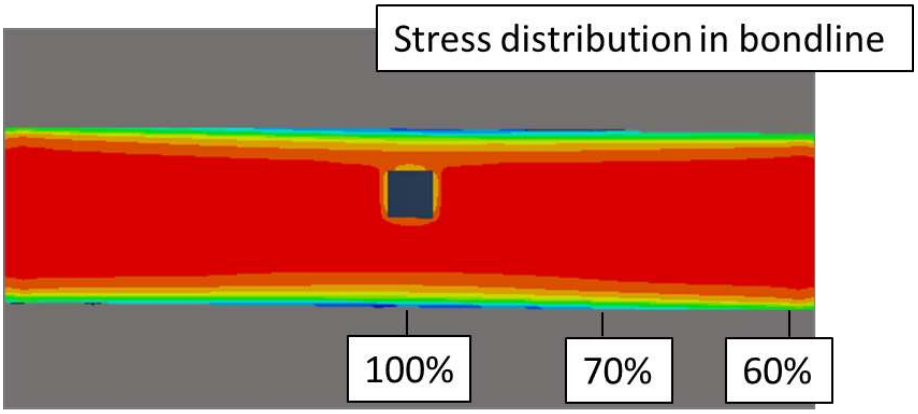

Figure 6. Stress distribution on the small WSLS sample with damage zone, D. Vadugappatty Srinivasan EPFL.

  doi:10.5075/epfl-298799_978-2-9701614-0-0

6. Improvements of small WSLS at ZHAW

Smaller test coupons are considerably cheaper and allow more testing. They can be considered one level lower in the test pyramid. More testing also means, more material combinations to compare, more defect types to study, more environmental conditions to examine, etc.

One important development was achieved through changing from release film disbonds to the creation of real cracks. Artificial disbond using release film do not behave like real cracks, since real cracks have a sharper crack tip. Therefore, the release film disbond was reduced in size and acts now as a crack inhibitor for an impact damage. The goal was to develop a process which repeatedly results in an impact damage with dimension of 20-30mm.

The WSLS sample with 180mm width and a real disbond resulting from an impact damage is considered as the new baseline sample configuration. From this starting point investigations like influence of humidity, liquid water, temperature changes etc. can be investigated.

7. Current Status: WSLS samples with impact damage

7.1 Test coupon description

Adherends: UD-prepreg cmp UD HTS45E, 150gsm, layup: quasiisotropic, starting with 45°. Thickness: 3.35 mm. Adhesive: Loctite EA 9394 AERO; dimensions shown in figure 7:

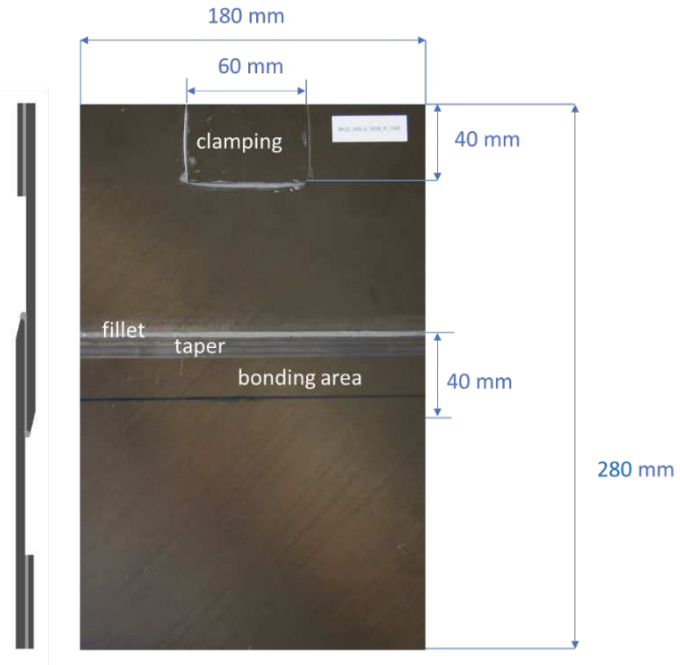

Figure 7. Dimensions of small WSLS coupon. The fillet is controlled with the bonding jig.

7.2 Impact damage process

WSLS samples are used to investigate crack growth in the disbond; hence they must be manufactured with a crack starter. ZHAW investigated several crack starter ideas during the BOPACS project. The WSLS samples are made with a simple square release film (double for NDI

reason), followed by an impact, which cracks the release film spot into a realistic impact damage with reasonable size. The aim was to produce an impact which is about 15-to 20% of the bondline area.

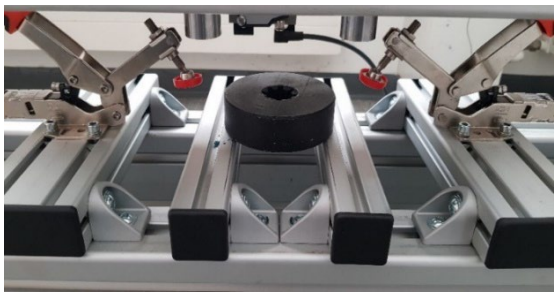

Figure 8. For the drop tower impact, a round steel plate with 30mm bore hole is used as hard support and the WSLS sample is fixed using clamps as shown.

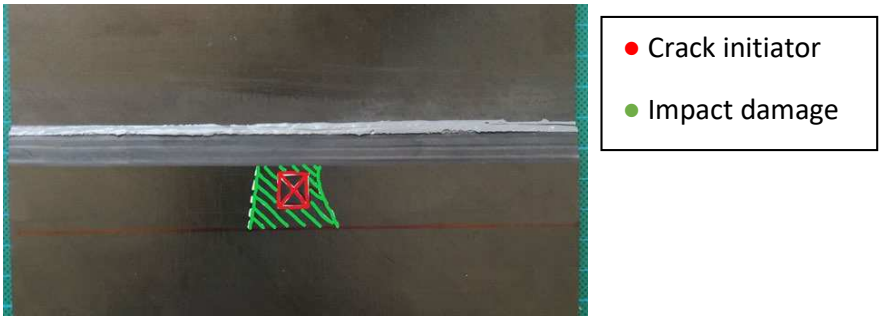

Figure 9. Damage of approx. 15 % bondline width, achieved with impact energy of 7 Joule.

7.3 UT determination of damage growth

A Krautkrämer USM36 UT detector was used in pulse-echo mode for the determination of the disbonded area. This limits the inspectable area to the parallel section of the bondline. The zone with the taper cannot be inspected. This is a disadvantage since the crack start in the corner cannot be detected. Therefore through-transmission mode would be more appropriate. This will be applied in the coming period of the project. Testing under load, for easier determination of open crack size is also possible, if allowed by security restrictions.

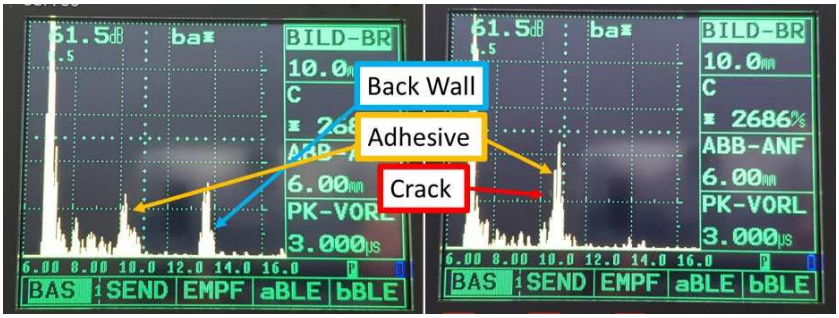

Figure 10. UT-Scans on the WSLS-samples. Left: measurement on bonded area with visible adhesive- and more intensive back wall-echo. Right: measurement on a large crack without back wall-echo due to disbond.

  doi:10.5075/epfl-298799_978-2-9701614-0-0

8. Recent results from ZHAW

Following a discussion with aircraft industry, ZHAW performed studies with the goal to expand the capability of the WSLS test with environmental exposures targeting at adhesively bonded repairs. Starting with impacted samples, tested dry at room temperature (RT), followed by testing with liquid water in the impacted area, followed by testing in the frozen state with ice in the impacted zone and finally combined with intermittent high peak loads.

8.1 Reference coupons with impact at room temperature

The load level for the dynamic testing was determined by increasing the load until first signals for crack growth could be detected. That load level could be found at 25kN. For further tests the load was kept on this level. The R-value for fatigue testing was always kept at 0.1.

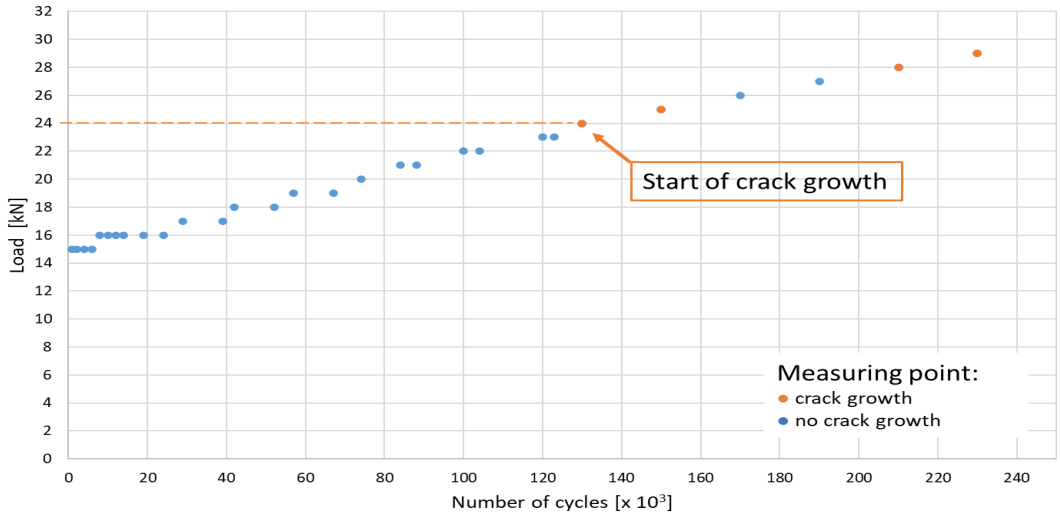

Figure 11. Load-cycle plot showing how the test load was defined, starting at 15kN and increasing the load until a crack growth could be recorded.

Based on this pretest, the load level for further tests was set to 25kN (constant amplitude, R=0.1, 0.3Hz). Yet this is still a rather low load level, and cracks grow very slowly, resulting in time consuming tests. Shorter tests with faster crack grow were run at 30kN.

8.2 Intrusion of liquid water into the damaged zone

To be able to inject water into the impacted and disbond zone, the sample had to be impacted multiple times with less energy. This procedure did not increase the damaged size, but it allowed to slightly open up the disbond. Afterwards 3 small holes were drilled into the adherend and water was injected with a syringe in one hole until the water spilled out of the other holes. The complete filling of the disbond area was confirmed with UT.

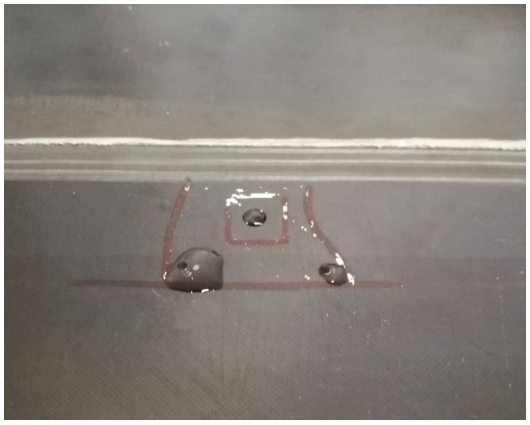

Figure 12. Water injection in impact damaged adhesive joint.

Water usually masks the crack when scanning with UT. Subsequently the water needs to be evaporated prior to the NDI check each time.

Cycling of WSLS coupons with water in the disbond was demonstrated. Scientific investigations to study the influence are not yet planned.

8.3 Intrusion of liquid water, freezing and testing at cold temperature

WSLS test coupons with liquid water were deep frozen and tested at RT and also at cold temperature for demonstration purpose. Again, the current procedure for each UT check is to warm up the coupon and to evaporate the water.

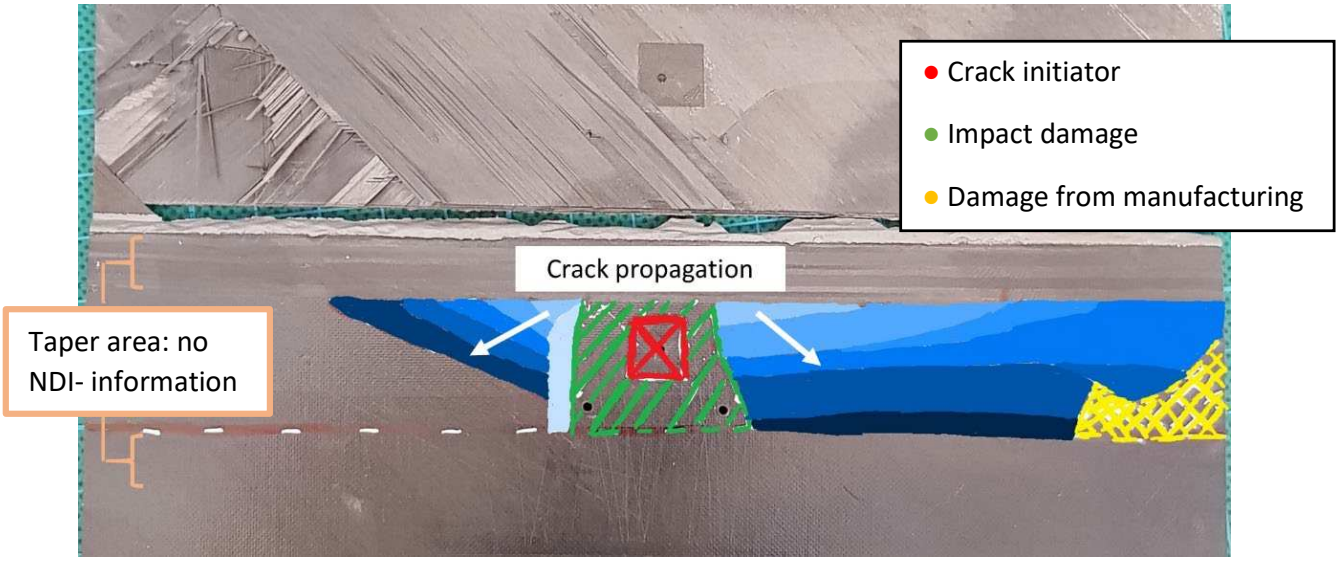

Figure 13. WSLS sample after rupture at 30kN after 114'000 cycles, tested at RT, following several freezing cycles at -28°C with water/ice in the disbond. The crack grows from light- to dark blue, initial crack start area is not indicated (not detected with UT in the taper).

9. Outlook

The work performed so far demonstrates that a real impact crack can repeatedly be produced and its growth under environmental influence of water and ice can be studied.
The concept of small WSLS-samples was proven to work but it is evident that the large WSLS samples used during the BOPACS showed a more symmetric and steadier crack growth. Currently the crack propagation in the tapered area is unknown. The lack of information must be minimized by upgrading the NDI e.g., with trough transmission method using a second US-sensor.

10. Way toward standardization of WSLS samples

The current status of sample definition, impact generation and fatigue testing is quite mature and provides a good starting point for individual investigations. Cooperation with partners is welcome. The standardization of the test can be considered.

Acknowledgements

SNF: funded by Swiss National Science Foundation
EU-COST Action CA18120
EPFL for cooperation

References

1. Th. Kruse, Th. Körwien and R. Ruzek; Fatigue Behaviour and Damage Tolerant Design of Composite Bonded Joints for Aerospace Application, ECCM17, 2016.
2. Th. Kruse, Th. Körwien, Th. Meer, Matthias Geistbeck; Certification by means of Disbond Arrest Features and Results (EU-FP7 Project BOPACS)
3. M. Santaniello; Numerical Assessment of Defects Effect on Boltless Composites Longitudinal Joints

  doi:10.5075/epfl-298799_978-2-9701614-0-0

Composites Meet Sustainability – Proceedings of the 20th European Conference on Composite Materials,
ECCM20. 26-30 June, 2022, Lausanne, Switzerland

PROMOTING EXTRINSIC BRIDGING OF ADHESIVELY-BONDED CFRP JOINTS THROUGH THE ADHESIVE LAYER ARCHITECTURE

Ran, Tao[a b], Gilles, Lubineau[a], Sofia, Teixeira De Freitas[b]

a: Mechanics of Composites For Energy and Mobility Lab, Mechanical Engineering Program, Physical Science and Engineering Division, King Abdullah University of Science and Technology (KAUST), Thuwal 23955-6900, Kingdom of Saudi Arabia
b: Structural Integrity & Composites, Faculty of Aerospace Engineering, Delft University of Technology, Delft, 2629 HS, the Netherlands
Presenter email: r.tao@tudelft.nl

Abstract: *Toughening and arresting crack propagation in secondary adhesive bonding of carbon fiber-reinforced polymers (CFRPs) are critical to their safety applications. Our previous work utilized the adhesive ligament bridging by alternatively patterning the mating surfaces, which successfully arrested the crack propagation under mode I loading. However, a large portion of the required energy is stored elastically in the stretching ligaments, which lead to sudden catastrophic debonding after the failure of ligaments. Two improvement methods are summarized in this work to further promote energy dissipation and slow down the catastrophic debonding. Integrating polyamide wires within the epoxy adhesive layer introduced complex failure mechanisms and bridging of embedded wires, while adopting a more ductile adhesive could largely extend the size of the bridging zone. Both methods are promising to soften the damage behavior when the bridging ligaments fail, and thus they both improve the reliability and damage tolerance of adhesively bonded joints.*

Keywords: CFRP; adhesive bonding; extrinsic bridging; wire reinforcement; mode I energy release rate;

1. Introduction

Carbon fiber-reinforced polymers (CFRPs) have widely attracted the aerospace and automotive industries due to high stiffness and lightweight. Secondary adhesive bonding of CFRPs is one of the most promising joining technologies to fully explore CFRP potential in full-scale structures where joints are inevitable. However, multiple challenges have limited the further application of adhesively-bonded composite joints since it is difficult to inspect the premature debonding, which leads to catastrophic failure once initiated. Thus, it is crucial to introduce crack arrest features, to slow down (or even stop) the crack growth and achieve progressive failure.

Various methods have been reported to introduce crack arrest features, including z-pins and corrugated substrates. Our previous work directly utilized the adhesive layer to bridge the separating CFRP parts, through the extrinsic bridging of adhesive ligaments [1]. The bridging adhesive ligaments are triggered by the patterning of distinct surface treatments. These extrinsic bridging ligaments largely enhance the energy release rate (ERR) and successfully arrest the crack propagation. However, due to the brittleness of the thermoset epoxy adhesive layer, the stored energy is released all at once after the failure of bridging ligaments, exaggerating the unstable crack propagation. Such safety concern will be elevated as the adhesive thickness increases, since more elastic energy will be stored, and then released, in thicker bridging

  doi:10.5075/epfl-298799_978-2-9701614-0-0

ligaments, which aligned with the analysis conducted in the previous work about the snap-back instability [2].

In this work, we modified the conventional brittle epoxy adhesive layer to further promote ERR and slow down the fast catastrophic crack propagation. By promoting the plastic energy dissipation, the bridging, stretching, and failure of generated adhesive ligaments could result in tougher and safer joints. To do so, two methods were summarized in this work. The first method is to integrate a ductile phase to the epoxy adhesive layer. In particular, various nylon (PA) wire structures were embedded into the epoxy adhesive layer and their effects on ERR were investigated experimentally under mode I double-cantilever beam (DCB) tests. The bonding CFRP substrates were alternatively patterned by two distinct surface treatments to achieve different interfacial strength and toughness values. The second method is to directly adopt an alternative adhesive material which exhibit a more ductile behavior, such as a methyl methacrylate adhesive (MMA) [3]. Numerical investigations were conducted to compare the influence of brittle epoxy and ductile methyl methacrylate adhesive (MMA) materials. Both experimental and numerical results showed that, with the alternative patterning surface treatment technique, a more ductile adhesive layer could further improve ERR and stabilize the crack propagation, leading to a toughened and safe adhesive joint.

2. Material and methods

2.1 Surface patterning on CFRP substrates

Unidirectional $[0]_8$ CFRP substrates (2 mm thick) were used in this work. Once cured, a surface patterning was applied to CFRP substrates, where the arrest interfaces, b=5 mm, were placed at a gap distance of 5 mm on top of the baseline interface, as shown in Figure 1. This type of patterning treatment on CFRP substrates aims to trigger adhesive ligaments during fracture tests, as already investigated in detail in our previous work [1]. In particular, in the experimental investigation for the first method, we used the pulsed CO_2 laser (PLS6.75 Laser Platform, Universal Laser Systems) to alternatively treat CFRP surfaces. Baseline interfaces were obtained using laser ablation (LA), which had pulse fluence of F_p=1.2 J/cm^2. While a lower fluence, F_p=0.4 J/cm^2, was deployed to slightly clean CFRP substrates (LC). LC regions feature better adhesion and therefore, so they were considered as arrest regions [4]. After laser-based patterning, CFRP substrates were immersed in acetone bath for a 10-min ultrasonic cleaning and then dried at 60°C in oven for 30 mins.

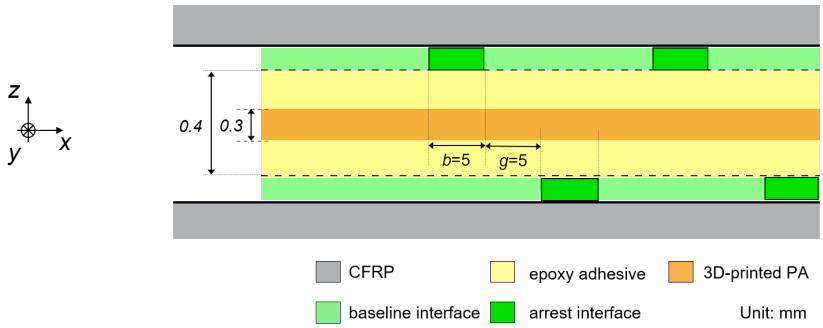

Figure 1. Schematic of the adhesive bonding with alternative patterning on CFRP substrates and 3D-printed PA wires (side view). The unit is mm in the schematic.

  doi:10.5075/epfl-298799_978-2-9701614-0-0 published under CC BY-NC 4.0 license

2.2 Integrating PA wires within epoxy adhesive

After the surface patterning, CFRP substrates were bonded using a hybrid adhesive layer, which consisted in a 3D printed PA structure embedded into an epoxy layer. The two-component epoxy adhesive was mixed at a weight ratio of 10:4 (resin versus hardener), and then it was applied to all CFRP substrate and PA surfaces to avoid voids. The PA wires were 3D-printed using fused filament fabrication. An example of 0.3-mm thick wire structure is shown in Figure 2 (a), where the printing was made along *x*-direction to ensure a high failure strength during the stretching. The adopted PA wires had a fixed width of 1 mm and three different spacing distances, as summarized in Table 1. As a comparison, we also tested a baseline configuration without inserting PA wires into the epoxy adhesive layer.

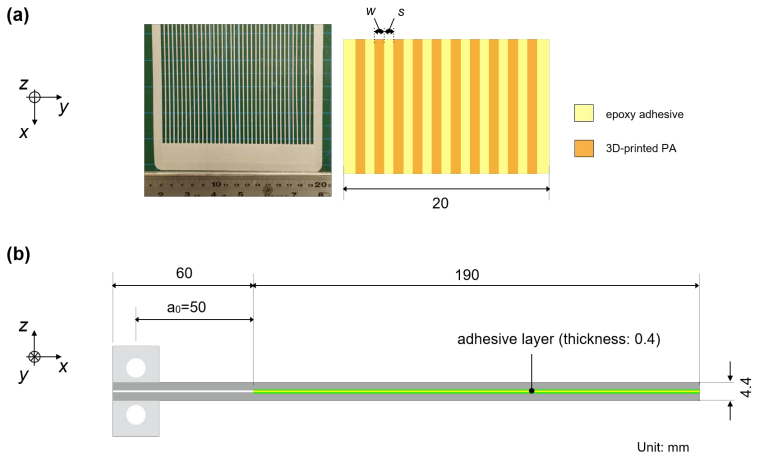

Figure 2. (a) Optical observation and schematic of 3D-printed PA wires. (b) Schematic of DCB specimen 20 mm wide. The unit is mm in the schematics.

Table 1: Three PA wires adopted in the work.

Batch	Wire width w [mm]	Spacing s [mm]	Wires per DCB sample [-]
wn2	1	9	2
wn5	1	3	5
wn10	1	1	10

2.3 Mode I fracture testing through DCB configurations

In order to evaluate the toughening effect resulting from the PA inserts, mode I fracture tests were carried out using the DCB configuration. To introduce a pre-crack, a non-sticky polyethylene (60-mm long) was positioned between the bonding of the two treated substrates. The DCB specimens were in the vacuum-oven under 60°C for 3 hours with a mechanical pressure to ensure a full adhesive-CFRP contact. The curing temperature was selected based on the thermal properties characterized in our previous work to achieve a good PA-epoxy interaction and avoid PA discoloration [5]. The thickness of the entire adhesive layer was controlled to be 0.4 mm. After curing, we cut the bonded plate into a size of 250x20 mm^2, following the

  doi:10.5075/epfl-298799_978-2-9701614-0-0

recommendations of ASTM D5528-13 standard [6]. At last, aluminum loading blocks were bonded to the specimens to apply the end peel loading by a universal testing machine (Instron 5882, Instron, Massachusetts, USA), as shown in the schematic in Figure 2 (b).

Six DCB specimens were tested for each configuration under the displacement control at a rate of 0.5 mm/min. On the side of each DCB specimen, we manually drew a scale to identify the crack propagation length, which was recorded through a high-resolution camera. The energy release rate (ERR, G_I) was obtained to analyze the failure mechanisms of the integrated PA structures. In this work, the compliance calibration (CC) data reduction method was used to determine ERR [6].

2.4 2D FEM simulation of brittle and ductile adhesive material

To compare two different adhesive material properties, 2D finite element (FE) simulations were performed using a DCB configuration, shown in Figure 3 (a). In this model, the unidirectional CFRP substrates were 1 mm thick with the following orthotropic properties based on the datasheet of Hexply 8552 AS4: E_x=141 GPa, E_y=E_z=10 GPa, G_{xy}=G_{xz}=3.3 GPa, G_{yz}=3.6 GPa, ν_{xy}= ν_{xz}=0.3, and ν_{yz}=0.38. Three different thickness values of the adhesive layer were modeled 0.5 mm, 1 mm, and 2 mm. Figure 3 (b) plots the Mises stress-strain curves adopted for the two distinct adhesive material types in [3]. It is clear that epoxy adhesive is brittle but has a higher strength, while MMA adhesive is much more ductile at the cost of lower strength. When both adhesives reach their strength values, the same damage behavior is assigned. Both the substrates and the adhesive were modeled using approximately 41000 2D plane strain elements CPE4R. The mesh convergence was validated in the previous work [7].

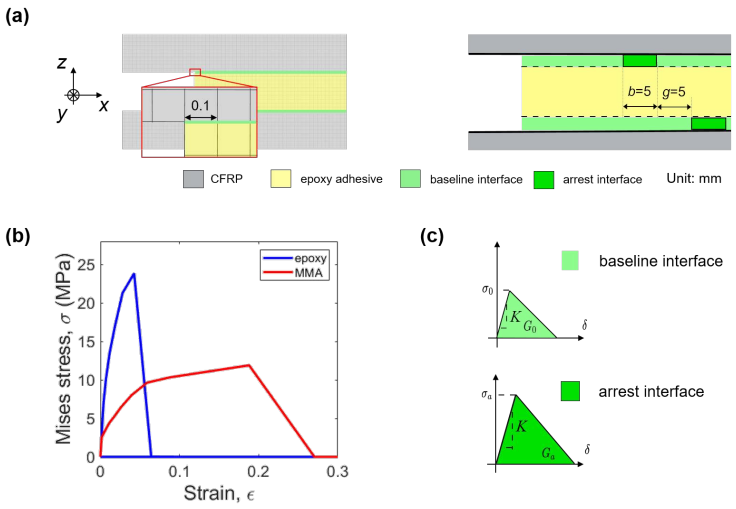

Figure 3. (a) Example of simulation mesh and schematics of DCB surface patterning (in mm). (b) Stress-strain curve of two adopted adhesive materials: brittle epoxy adhesive and ductile MMA adhesive. (c) Schematics of the traction-separation laws of baseline and arrest interfaces.

Similar to the experimental investigation, alternative patterning treatment was applied at the CFRP/adhesive interfaces, where two arrest interfaces were alternatively placed on the bottom and top baseline interfaces. The arrest size b is 5 mm and the gap between them is also 5 mm, as illustrated in Figure 3 (a). A bilinear traction-separation law was chosen for the two cohesive layers, which had 2200 COH2D4 elements (Figure 3 (c)). The baseline cohesive strength σ_0,

  doi:10.5075/epfl-298799_978-2-9701614-0-0

toughness G_0, arrest strength σ_a, and toughness G_a are based on the previous work [3], and the exact values are summarized in Table 2. Although mode I was the major fracture mode [7], the built-in quadratic traction-based criterion was employed to initiate the crack propagation. To stabilize the simulation when large load drop happens, a small viscosity value, 10^{-5}, was assigned to the cohesive element control [7]. An opening displacement was imposed on both loading blocks to simulate the opening load of the DCB testing, as indicated in Figure 3 (a).

Table 2: Interfacial properties of both configurations with epoxy and MMA adhesive materials.

Adhesive	σ_0 [MPa]	G_0 [kJ/m^2]	σ_a [MPa]	G_a [kJ/m^2]
epoxy	5	0.2	20	0.6
MMA	2	0.2	10	2.4

3. Experimental evaluation of integrated PA wires

Typical load-displacement responses, corresponding ERR curves, and fracture surface observations of DCB specimens with three integrated PA wires are shown in Figure 4. Typical curves of DCB specimens with only epoxy adhesive layer (without PA) are also plotted in light grey for comparison. For the DCB specimen without PA, the obtained ERR reaches the peak at nearly 100-mm crack length and then catastrophic brittle fracture happens to the entire joint for an extended debonding. Therefore, no average ERR could be obtained, since no plateau region could be identified in the ERR curve. Severe safety concerns may arise due to such catastrophic brittleness of bonded composite joints, limiting the application of our surface patterning strategy in a thick adhesive layer.

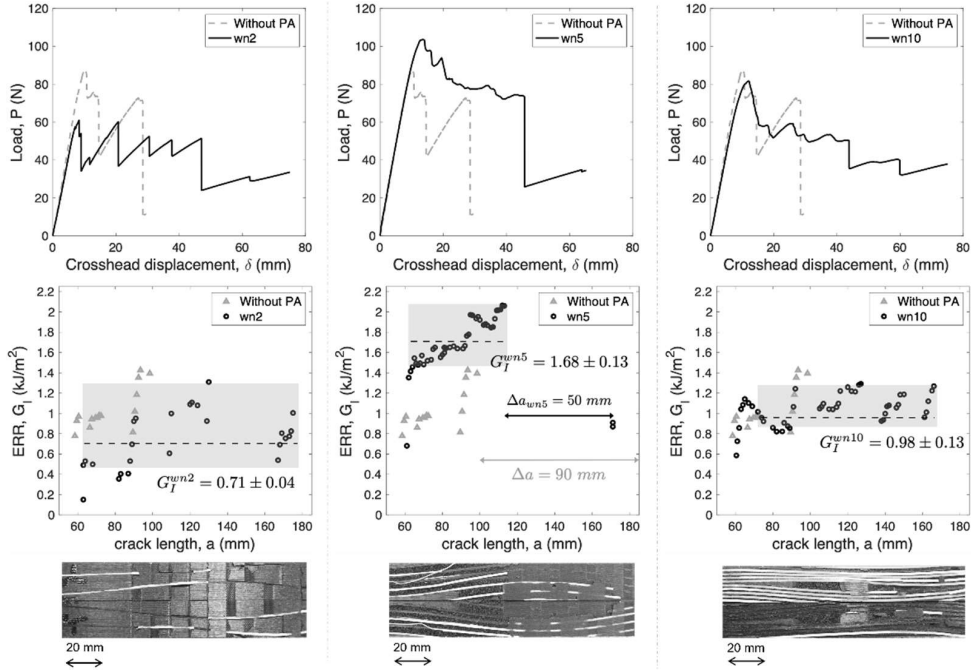

Figure 4. Typical load-displacement responses, corresponding ERR curves, and fracture surfaces of DCB configurations integrated with wn2, wn5, and wn10.

  doi:10.5075/epfl-298799_978-2-9701614-0-0

On the contrary, all specimens with integrated PA wires demonstrate a more stable softening behavior. With only two PA wires integrated within the adhesive layer (wn2), we could see a clear stick-slip load-displacement curve. The plateau of ERR is scattering and a relatively low average value (0.71 kJ/m^2) is obtained by averaging the plateau region in ERR curves of all tested specimens (highlighted by the grey areas in Figure 4). No catastrophic fast crack propagation is viewed compared to that without PA wires. Based on the optical fracture surface, adhesive ligaments were triggered, and PA wires started to hold after the failure of epoxy ligaments. Only two integrated PA wires are not strong enough to further hold the separating arms, which is consistent with the large ERR scattering and relatively low ERR.

When integrating five wires in a DCB specimen (wn5), the obtained ERR is largely enhanced up to 1.68 kJ/m^2. A large load drop is observed in the load-displacement curve of wn5, indicating the presence of an extensive debonding due to the release of stored energy. However, compared to without PA configuration, wn5 demonstrates a higher ERR and a smaller growth of the debonding (50 mm instead of 90 mm in Figure 4), illustrating a better toughening and a more progressive damage. During loading of wn5, large scale bridging of PA wires could be viewed, associated with a large improvement in ERR. Apart from crack jumps at CFRP/epoxy interfaces, fracture surface of wn5 also shows cohesive failure of epoxy. Moreover, bridging PA wires are highly stretched, largely plastic deformed, and finally fractured. Therefore, multiple damage mechanisms are responsible of the enhancement of ERR in this configuration.

Further increasing the number of integrated wires, wn10, could not improve such toughening effect. wn10 only reaches a similar load and ERR level as that without PA, lower than that of wn5. However, its plateau region of ERR is more stable than that of wn2 and exhibits a higher average value of 0.98 kJ/m^2. Besides, the fracture surface illustrates that the main crack propagates at PA/epoxy interfaces, with detached PA wires and cohesive failure of epoxy. Therefore, the alternative surface patterning on CFRP substrates is deactivated in this configuration. The integrated PA wires acted like a carrier within a commercial adhesive film, as already reported in Heide-Jørgensen's work [8].

4. Numerical comparison of brittle and ductile adhesive materials

Simulated load-displacement responses, corresponding ERR curves, and bridging observations of DCB specimens with epoxy adhesive with three thickness values are shown in Figure 5. The locations of arrest interfaces are highlighted in green in the observations. Simulation results show that the adhesive thickness affects the generation of the adhesive ligament, and the bridging of epoxy adhesive ligament is limited. When the thickness is 0.5 mm and 1 mm, the crack jumps from the bottom to the top interface, but the bridging epoxy ligament fractures quickly without a large-scale extrinsic bridging. While 2-mm thick adhesive layer will entirely eliminate the bridging of ligament, and the elevated ERR is due to the detaching from the arrest region G_a. Such observations echoed the limitation of brittle epoxy adhesive, and they also indicate the motivation for embedding PA fibers: to hold the joint after the early failure of the epoxy layer.

As for a more ductile MMA adhesive, simulation showed a distinct behavior. When the thickness is 0.5 mm and 1 mm, a clear extrinsic bridging ligament is generated. Obtained ERR illustrated two increase stages. At the first stage, the crack propagation is arrested by the green arrest interface till the crack jumps from the bottom to the top interface. Different from the epoxy

  doi:10.5075/epfl-298799_978-2-9701614-0-0

adhesive, where ERR starts to drop back to the baseline G_0 after the crack jump, MMA adhesive ligament gradually extends the bridging length up to 4 mm, leading to a second rising stage of ERR curve. Therefore, thanks to the plastic energy dissipation, ERR could experience an extra enhancement and further slowdown the crack propagation. In the case of 2-mm thick MMA adhesive layer, the simulation stops before the crack jump due to the convergence issue. If the length of the arrest interface increases to 10 mm, a similar extrinsic bridging ligament as those in 0.5-mm and 1-mm thick adhesive layer is expected. Further work is needed to analyze this relationship and maximize the extrinsic toughening when using the MMA adhesive.

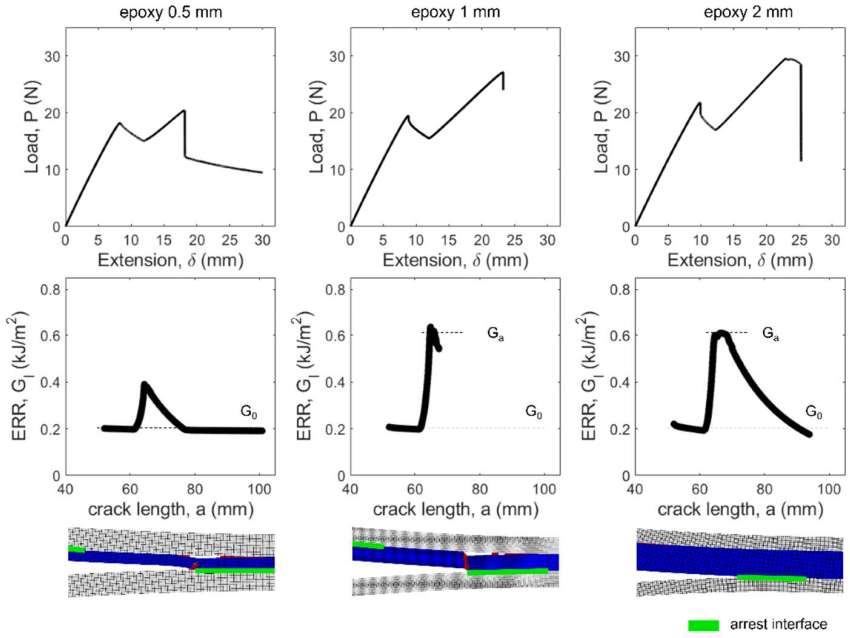

Figure 5. Simulated load-displacement responses, corresponding ERR curves, and bridging observations of DCB with adopted epoxy adhesive with 0.5 mm, 1 mm, and 2 mm thickness.

5. Conclusions

In this work, two methods to further promote ERR and slow down crack propagation of secondary adhesive bonding of CFRP is summarized. The first method is to integrate PA wires within the epoxy adhesive layer. Experimental DCB results indicated that embedded PA wires introduced complex failure mechanisms, softening the joint damage behavior. The second way is to directly adopt a more ductile MMA adhesive material. Numerical investigations showed that, by promoting plasticity, extrinsic bridging could be extended and ERR would be further increased when using MMA instead of epoxy adhesive. Therefore, a more ductile adhesive layer could further improve ERR and stabilize the crack propagation, leading to a toughened and more damage tolerant adhesive joint.

Acknowledgements

The research reported in this publication was supported by funding from both King Abdullah University of Science and Technology (KAUST) Office of Sponsored Research (OSR) under award number OSR-2017-CRG6-3388.01 and Delft University of Technology (TU Delft).

  doi:10.5075/epfl-298799_978-2-9701614-0-0

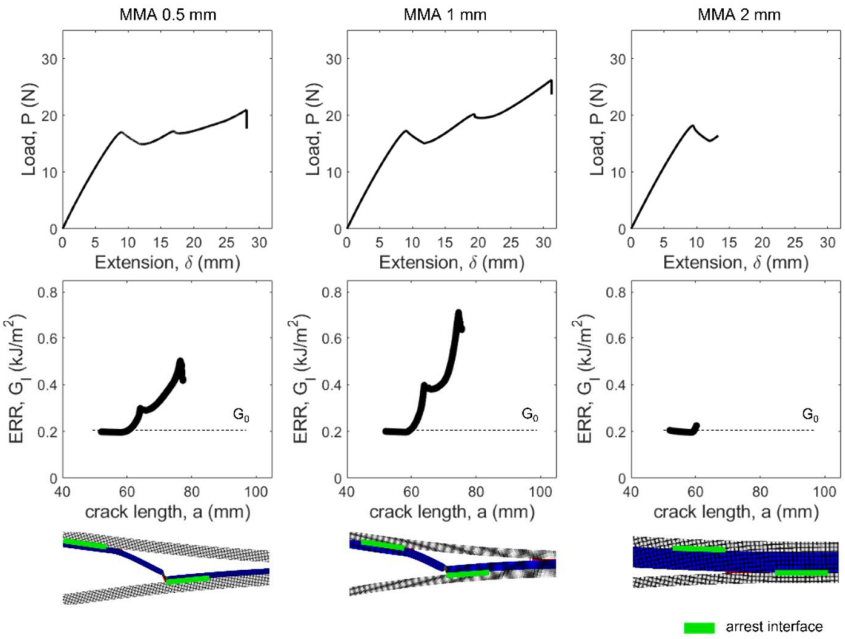

Figure 6. Simulated load-displacement responses, corresponding ERR curves, and bridging observations of DCB with adopted MMA adhesive with 0.5 mm, 1 mm, and 2 mm thickness.

6. References

1. Tao R, Li X, Yudhanto A, Alfano M, Lubineau G. Laser-based interfacial patterning enables toughening of CFRP/epoxy joints through bridging of adhesive ligaments. Composites Part A: Applied Science and Manufacturing 2020; 139:106094.
2. Li X, Lu S, Lubineau G. Snap-back instability of double cantilever beam with bridging. International Journal of Solids and Structures 2021; 233:111150.
3. Saleh MN, Budzik MK, Saeedifar M, Zarouchas D, De Freitas ST. On the influence of the adhesive and the adherend ductility on mode I fracture characterization of thick adhesively-bonded joints. International Journal of Adhesion and Adhesives 2022; 115:103123.
4. Tao R, Alfano M, Lubineau G. Laser-based surface patterning of composite plates for improved secondary adhesive bonding. Composites Part A: Applied Science and Manufacturing 2018; 109:84-94.
5. Yudhanto A, Almulhim M, Kamal F, Tao R, Fatta L, Alfano M, Lubineau G. Enhancement of fracture toughness in secondary bonded CFRP using hybrid thermoplastic/thermoset bondline architecture. Composites Science and Technology 2020; 199:108346.
6. Standard test method for mode I interlaminar fracture toughness of unidirec- tional fiber-reinforced polymer matrix composites, ASTM Internat. 2014.
7. Tao R, Li X, Yudhanto A, Alfano M, Lubineau G. On controlling interfacial heterogeneity to trigger bridging in secondary bonded composite joints: An efficient strategy to introduce crack-arrest features. Composites Science and Technology 2020; 188:107964.
8. Heide-Jørgensen S, de Freitas ST, Budzik MK. On the fracture behaviour of CFRP bonded joints under mode I loading: Effect of supporting carrier and interface contamination. Composites Science and Technology 2018; 160:97-110.

  doi:10.5075/epfl-298799_978-2-9701614-0-0

TOWARDS THE DEVELOPMENT OF A LASER SHOCK-BASED DISASSEMBLY PROCESS FOR ADHESIVELY BONDED TI/CFRP STRUCTURAL PARTS: EXPERIMENTS AND NUMERICAL SIMULATION

Panagiotis, Kormpos[a], Selen, Unaldi[b], Mohammad, Ayad[b], Laurent, Berthe[b], Konstantinos, Tserpes[a]

a: Laboratory of Technology & Strength of Materials (LTSM), Department of Mechanical Engineering & Aeronautics, University of Patras, Patras 26504, Greece
b: PIMM, UMR8006 ENSAM, CNRS, CNAM, 151 bd de l'Hôpital, 75013 Paris, France

Abstract: *The objective of this paper is to develop a disassembly process for adhesively bonded Ti/CFRP materials based on laser plasma induced shock waves. To this end, an integrated experimental-numerical work has been performed. Laser shock tests have been conducted by PIMM Lab in Paris, France, while numerical simulations by LTSM in Patras, Greece. During tests, the back face velocity has been measured on the specimen by the VISAR method and after the tests, C-scan tests were conducted to detect damage in the specimen. Disassembly simulations are using a custom Python script that is calling the LS-DYNA explicit FE code for subsequent simulations. The data produced by the experimental procedure along with the C-scan inspection were used to describe the shock wave propagation and validate the numerical model. Both experimental and numerical results have shown no damage on the bondline, which leads to conclusion that the one-sided single laser shock is not capable to disassemble the specific configuration. On the contrary, additional simulations have shown that the symmetrical laser shock is capable of breaking the bondline, however, this remains to be verified experimentally.*

Keywords: Laser shock; Composites disassembly; Adhesive bonding; Finite element analysis

1. Introduction

The end-of-life of composite aircraft structures involves several environmental and technical issues. Among the major technical difficulties, are the lack of an environmentally friendly and non-destructive disassembly process and the low efficiency of the available recycling processes [1]. All current recycling processes require materials to be sorted and separated efficiently. Material separation and dismantling consists of various strategies, that are using a combination of disassembly and cutting (shredding, smart shredding, gross cutting, detail cutting, smart disassembly etc.) in order to achieve the best cost-benefit process [2]. While disassembly is not the best cost-effective solution for material separation, it yields to the best material segregation, while it enables a reuse approach that is best suited for composites.

Bonded multi material structures like the Ti/CFRP hybrid that is studied in this work, do not have a clear strategy to be dismantled or disassembled. That prevents the recycling process from producing high quality and usable products. For that reason, a novel disassembly technique is being developed using a known laser induced shockwave technique. This technique can create localized tensile stresses that have the ability to break a bondline between the materials involved. The principal of the method has been established by studies for laser shock adhesion testing (LASAT) that were able to break weak bonds between composite structures [3].

  doi:10.5075/epfl-298799_978-2-9701614-0-0

additionally, destructive applications of the laser shock technique have been studied to create controlled delaminations in composites [4] and selective paint striping from Aluminum substrates [5,6]. The goal is to use this process is to completely debond the Titanium and composite with minimum to no damage in the composite. To achieve this result, the process must be calibrated. Using an explicit finite element code to simulate the shock propagation it is possible to test laser parameters, as well as laser set-ups. Experiments are also conducted to observe the behavior of the structure under laser shock, which are providing back face velocity measurements that can be used to validate the simulations.

2. Laser-Shock

Laser-shock is a technique based on laser matter interaction. When an intense laser is focus over the surface of the target material, it ablates its surface over a thickness of 1.7-3 µm changing superficially the material into dense plasma. A transparent material, such as water, is used to confine the expansion and further increase the surface pressure induced by the expanding plasma [7]. That results in a compressive shockwave generation in the bulk of the material. The shockwave propagates inside the material depending on its properties, specifically its density and sound speed. When it reaches the back face of the material the shock front is reflected into a release wave due to the presence of a free surface. That release wave is propagating in the opposite direction of the initial wave and it coincides with the release wave created by the front surface unloading. The coincidence of the two release waves is resulting in a tensile stress that can be used for testing purposes [3] or in that case for damaging a bond for disassembly. The generation and propagation of the shock wave into the Ti/CFRP specimen is schematically described in Fig. 1.

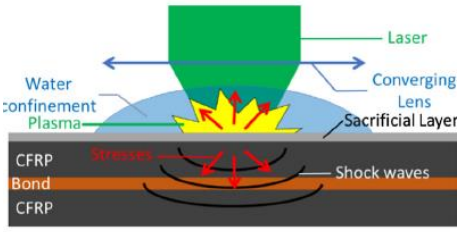

Figure 1. Schematic illustration of the laser shock disassembly process.

3. Experimental

3.1 Materials and specimens

The specimen size is 10 cm x 4 cm x 1.06 cm. The thickness of the CFRP is 10.36 mm, the thickness of the Ti layer is 100 µm and the thickness of the bondline is 140 µm. The specimen's dimensions as well as the layers can be seen in Fig. 2.

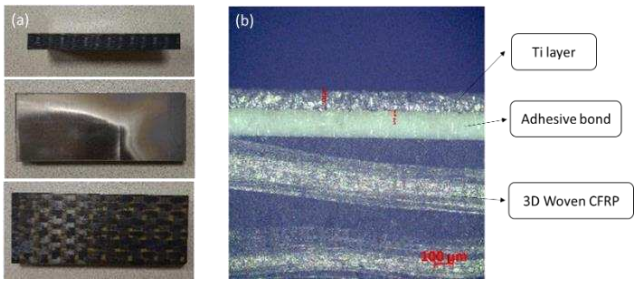

Figure 2. Different views of the Ti/CFRP specimen.

3.2 Laser shock testing

  doi:10.5075/epfl-298799_978-2-9701614-0-0

The first experimental series for the development of the disassembly process comprises laser shots on bonded Ti/CFRP specimens conducted in the Hephaistos facility (energy up to 14 J at 532 nm wavelength laser, pulse duration: 7 ns) while particle velocity is being measured on the back face of the material. The velocity is measured by a non-contact optical diagnostic tool called VISAR (Velocity Interferometer for Any Reflector). VISAR is an interferometer that makes possible to measure the Doppler shift in the wavelength of a probe laser that is being reflected on the target back face that is moving due to the shock wave [7]. The back face velocity measurements can be used to explain the behavior of the material under shock as it is unique for each specimen. Velocity curves can be also extracted from the numerical simulations and used for model validation.

As shown in Table 1 this experimental series is consisting of shots done in both Ti and CFRP side and laser intensity in the range of 1.2 GW/cm^2 to 6 GW/cm^2. Each specimen was shot with the same laser intensity in ten spots and ten back face velocities were obtained for each side. The spot diameter is 4mm, which is a typical spot diameter and has been used in the Hephaistos facility for past experimental series [3,5,6,8].

Table 1: Conducted experiments.

Experiment	Number of specimens	Laser Intensity	Number of Shots	Use
Titanium side shots with VISAR for backface velocity measurements	4	▪ 1.2 GW/cm^2 ▪ 3 GW/cm^2 ▪ 4.5 GW/cm^2 ▪ 6 GW/cm^2	40 (10 / specimen)	Model Validation
CFRP side shots with VISAR for backface velocity measurements	4	▪ 1.2 GW/cm2 ▪ 3 GW/cm2 ▪ 4.5 GW/cm2 ▪ 6 GW/cm2	40 (10 / specimen)	Model Validation
CFRP side double shot with VISAR for backface velocity measurements	2	▪ 4.5 GW/cm^2 ▪ 6 GW/cm^2	6 (3 / specimen)	Damage case validation

The CFRP side of all specimens were covered by a thin Aluminum tape. This was done for two reasons. For the titanium side shots, the aluminum is acting as a reflecting surface for the VISAR to be able to measure the back face velocity (no measurements can be taken directly from the CFRP). For the CFRP side shots, the aluminum acts as a protective layer to the CFRP as well as an ablation layer, because the pressure that is being generated directly from shooting the CFRP is not as well defined as it is for the aluminum. The titanium was providing a good reflection surface and there was no need to cover it with the aluminum tape. Water is used as a confinement regime in all the shots. The experimental set-up of the laser shock tests is shown in Fig. 3 (a). Fig. 3(b) shows the specimen covered with aluminum tape.

For each laser intensity, ten shots were performed on each specimen. The reason for that is the uncertainty that the non-homogeneous 3D woven CFRP is creating. VISAR is a very high precision measurement device, focusing on a small spot at the surface of the sample, local deviations of thickness and stiffness might change the measured back face velocity. The shots where centered two centimeters apart from each other, that distance being ten times the radius is considered to be far enough so that any previous shot is not affecting the next one. This can be observed in previous simulations [9] and also in experimental testing [4].

  doi:10.5075/epfl-298799_978-2-9701614-0-0


(a)
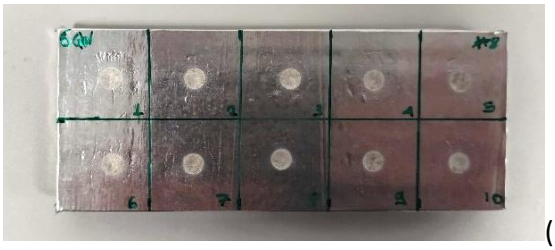
(b)

Figure 3. (a) Experimental Setup, (b) Specimen covered with aluminum tape

4. Numerical model

The laser shock process, in every application needs to be guided by simulations. The complex phenomena that are happening in a small increment of time makes the laser shock problems hard to solve by experimental means. It is essential that the laser parameters (Intensity, time delay, different set-ups) are calibrated and studied through simulations in order to produce a usable method. Different applications and materials have already been simulated [3,6,7]. In this work the disassembly process is being simulated using LS-DYNA explicit finite element code. The disassembly process requires multiple instances in order to achieve a full debonding, for that reason an iterative method has also been developed [9] and implemented using a python script to automate the process. The output of one simulation is used as the input for the next simulation, while transferring all the loads and history variables from one simulation to the other.

4.1 Finite element model

For the simulation, the LS-DYNA explicit finite element code was used. The geometry was modeled using constant stress solid elements, which in LS-DYNA is ELFORM 1, for the Titanium and the Composite parts, and 8-noded, 4-point cohesive elements (ELFORM 19) for the bond. The element size is gradually smaller towards the center of the specimen's geometry where the loading is applied. In the center a rectangular area with element size of 100 μm is designed so that the model is capable of simulating a moving spot for the disassembly. The element thickness is constant, at 10 μm. Fig. 4 shows the FE mesh of the specimen.

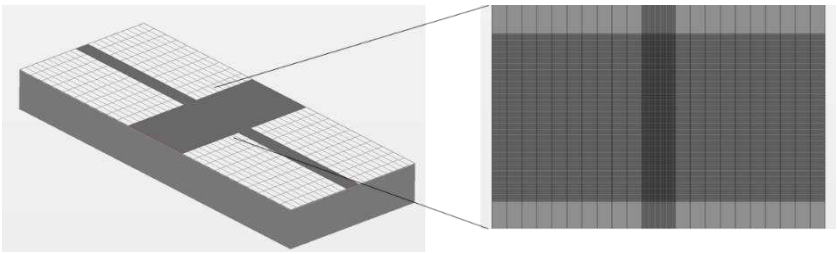

Figure 4. Model geometry and mesh

4.2 Material models

The Titanium part of the model was simulated using the Johnson-Cook material model in combination with the Grüneisen equation of state. Titanium is a well-studied material and Johnson-Cook as well as Grüneisen parameters were obtained by literature [10]. For the bond the cohesive zone modeling method is being used and the properties are also obtained from literature [11].

  doi:10.5075/epfl-298799_978-2-9701614-0-0

For the 3D woven CFRP, MAT_162 is being used. This is a progressive damage model with options for unidirectional and woven composites. For the time being full material characterization is in progress and until real properties are obtained, literature properties are being used [12,13].

Table 2: Material properties and parameters

Johnson-Cook		**Mat_162 Properties**	
Density, ρ(kg/m^3)	4430	Density, ρ(kg/m^3)	1500
Elastic Modulus, E (GPa)	110	Elastic Modulus, Ea (GPa), Eb (GPa)	117, 115
Shear Modulus, G (GPa)	69	Elastic Modulus, Ec (GPa)	11.5
Poisson's ratio, ν	0.33	Shear Modulus, Gab, Gbc, Gca (GPa)	4.5
A (MPa), B(MPa)	862, 331	Longitudinal tensile strength, Sat (MPa)	2800
n, C	0.34, 0.012	Longitudinal compressive strength, Sac (MPa)	2000
T_{melt} (^{o}C)	1630	Transverse tensile strength, Sbt (MPa)	290
Specific heat, Cp (J/kg^{o}C)	670	Transverse compressive strength, Sbc (MPa)	290
Grüneisen equation of state		Through thickness tensile strength, Sct (MPa)	87
Bulk sound speed, C (m/s)	5130	Crush strength, Sfc (MPa)	290
Slope in Vs versus Vp diagram, S	1.028	Fiber mode shear strength, SFS (MPa)	120
Grüneisen coefficient, γ_0	1,23	Matrix mode shear strength, Sab, Sac, Sca	42

4.3 Pressure calculations

The ablation pressure applied in the model is defined by the maximum pressure P_{max} (GPa), which is calculated by Eq. (1) [14]

$$P = 0.01 \sqrt{\frac{a}{2a+3}} \sqrt{zI_0} \quad (1)$$

$$Z = 2\frac{Z1\,Z2}{Z1+Z2} \quad (2)$$

where I_0 (GW/cm^2) is the Laser's intensity, α is the part of the energy being used for the ionization and Z (g cm^{-2}/s^{-1}) is the relative acoustic impedance where $Z1$, $Z2$ the acoustic impedance of the material and confinement respectively.

5. Results

5.1 Experimental results

Fig. 5 compares back-face velocity profiles from different shots on different locations on the same specimen. Some small deviations are visible in the resulting curves that can be explained by the local thickness and stiffness variation. Although the back-face velocity measurements showed no clear indication of damage to the specimen, C-scan inspection was performed to validate that the deviation between the back face velocity curves did not occur due to CFRP or bond damage. Indeed, the c-scans showed that no damage was created, even at the higher intensities. This was expected, as 3D woven CFRP has enhanced through thickness properties compared to unidirectional or woven CFRP. No damage was observed at the bondline either, this is due to the specimen dimensions. The Titanium is very thin and the bond between the two materials is very close to the face of the specimen, where the coincidence of the release

waves is not possible. This is good for the validation process because it provides clear curves on many laser intensities. Different laser set-ups are required for bond damage, like symmetrical laser [4,15] or double laser. Both of those set-ups require simulations to be calibrated, because the time delay between the two laser beams is a crucial parameter for the location of the generated tensile stress.

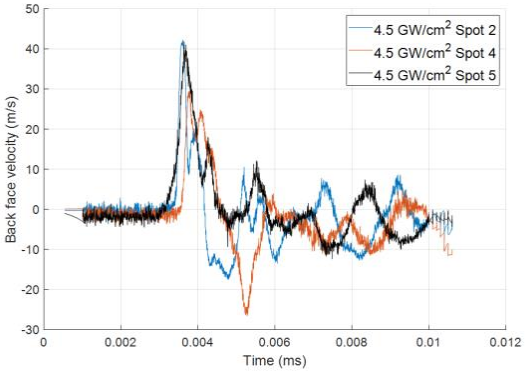

Figure 5. Back-face velocity measurements taken from different shots on the same specimen for 4.5 GW/cm²

5.2 Simulation results – Model validation

Before the simulation of the disassembly process, the model needs to be validated. This is possible by comparing the back face velocities of experimental curves with those that are obtained from the simulations. First the Titanium is being compared with literature laser shock experiments [7] for the validation of the Johnson-Cook and Grüneisen. As can be seen in Fig. 6, the model describes well the behavior of Titanium under shock.

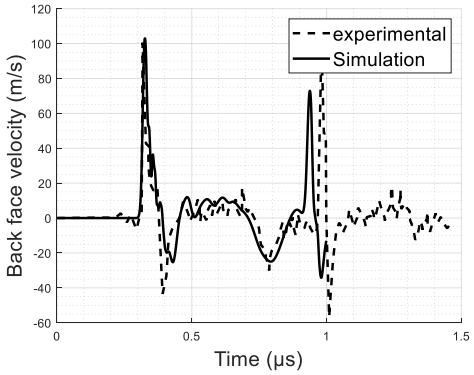

Figure 6. Comparison of experimental and numerical back-face velocity measurements taken on the Ti surface

The Ti/CFRP specimen simulation is conducted for the 4.5 GW/cm² Laser intensity and the back face velocity is being compared with the experimental data. The model is capable to predict the behavior of the Ti/CFRP assembly. Using a custom MATLAB application, the shockwave propagation is being visualized from LS-DYNA output data (Fig. 7). The differences observed in the back face velocity measurements are assumed to be originated by the uncertainty of material properties, especially for the CFRP. As mentioned, full material characterization in being conducted and is going to be used in simulations. Still, the model is capable of predicting the stress field and that is enough to proceed with the disassembly simulation.

  doi:10.5075/epfl-298799_978-2-9701614-0-0

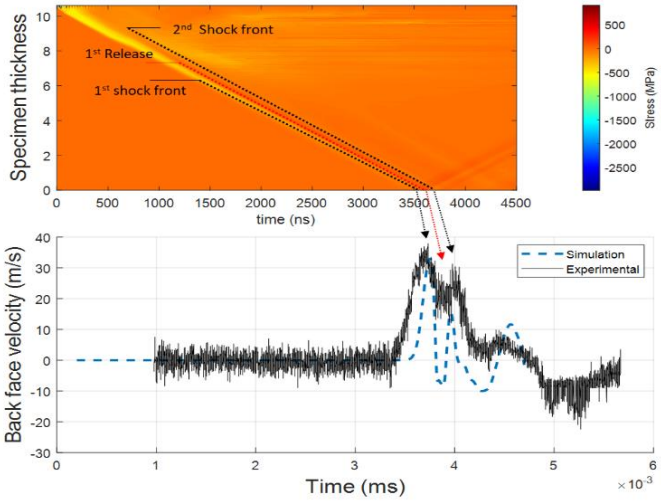

Figure 7. Ti/CFRP shock-wave propagation and back-face velocity comparison

5.3 Disassembly simulation

From the experimental data it is obvious that a single top loading, of either face of the specimen is not creating the required stress field in order to disassemble the bond. For that reason, a different loading scenario is simulated to provide the required stress field. A symmetrical loading case, which has been used as a bond testing method [15], where one shot is fired from each side of the specimen, is being simulated. Using a time delay between each shot it is possible to guild the wave coincidence at the bond line. In this case the time delay was calculated as 3.42 μs, the laser intensity that was used was 4.5 GW/cm^2. As shown in Fig. 8(a), the fist symmetric shot is indeed initiating the debonding on the CZM, the fringe is showing the damage that has been done to the CZM as a ratio, where 1 meaning element deletion. For the second shot the spot was moved by 2 mm aiming to propagate the initiated damage area, Fig. 8(b) shows the damaged area after 2 shots.

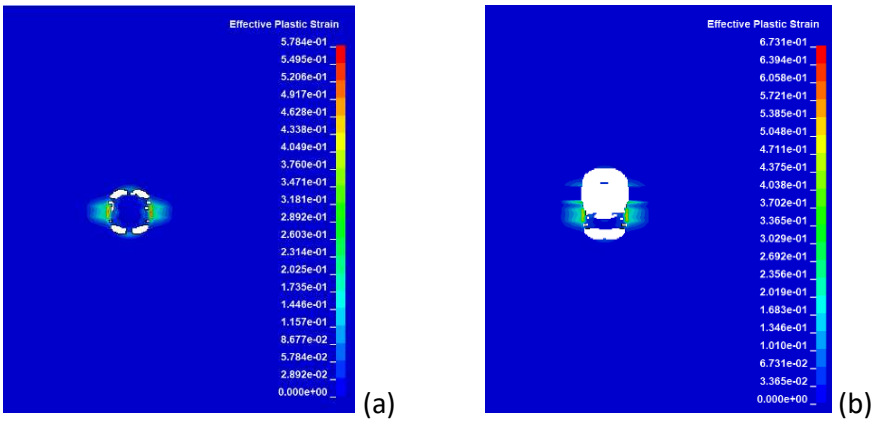

Figure 8. CZM damage: (a) After the first shot and (b) after the second shot

6. Conclusions

A disassembly process for adhesively bonded Ti/CFRP materials based on one-sided single laser shock waves was developed by conducting tests and performing simulations. For the simulations a customized Python script that is calling the LS-DYNA explicit FE code for multiple subsequent simulations was developed. The experimental and numerical results show that the

  doi:10.5075/epfl-298799_978-2-9701614-0-0

bondline remains intact, which reveals that the one-sided single laser shock is not capable to disassemble the Ti/CFRP specimen. However, additional simulations have shown that the symmetrical laser shock is capable of breaking the bondline.

Acknowledgement


This project has received funding from the European Union's Horizon 2020 research and innovation programme under grant agreement No 101006854

Bibliography

1. Pantelakis S, Tserpes K, editors. Revolutionizing aircraft materials and processes. Cham: Springer; 2020. 403 p.
2. Sabaghi M, Cai Y, Mascle C, Baptiste P. Sustainability assessment of dismantling strategies for end-of-life aircraft recycling. Resour Conserv Recycl. 2015 Sep;102:163–9.
3. Ecault R, Touchard F, Boustie M, Berthe L, Dominguez N. Numerical modeling of laser-induced shock experiments for the development of the adhesion test for bonded composite materials. Compos Struct. 2016 Sep;152:382–94.
4. Ghrib M, Berthe L, Mechbal N, Rébillat M, Guskov M, Ecault R, et al. Generation of controlled delaminations in composites using symmetrical laser shock configuration. Compos Struct. 2017 Jul;171:286–97.
5. Ünaldi S, Papadopoulos K, Rondepierre A, Rouchausse Y, Karanika A, Deliane F, et al. Towards selective laser paint stripping using shock waves produced by laser-plasma interaction for aeronautical applications on AA 2024 based substrates. Opt Laser Technol. 2021 Sep;141:107095.
6. Tserpes K, Papadopoulos K, Unaldi S, Berthe L. Development of a Numerical Model to Simulate Laser-Shock Paint Stripping on Aluminum Substrates. Aerospace. 2021 Aug 24;8(9):233.
7. Cuenca E, Ducousso M, Rondepierre A, Videau L, Cuvillier N, Berthe L, et al. Propagation of laser-generated shock waves in metals: 3D axisymmetric simulations compared to experiments. J Appl Phys. 2020 Dec 28;128(24):244903.
8. Scius-Bertrand M, Videau L, Rondepierre A, Lescoute E, Rouchausse Y, Kaufman J, et al. Laser induced plasma characterization in direct and water confined regimes: new advances in experimental studies and numerical modelling. J Phys Appl Phys. 2021 Feb 4;54(5):055204.
9. kormpos P, Tserpes K, Floros G. Towards simulation of disassembly of bonded composite parts using the laser shock technique. IOP Conf Ser Mater Sci Eng. 2022 Jan 2;1226(1):012081.
10. Zhang Y, Outeiro JC, Mabrouki T. On the Selection of Johnson-cook Constitutive Model Parameters for Ti-6Al-4V Using Three Types of Numerical Models of Orthogonal Cutting. Procedia CIRP. 2015;31:112–7.
11. Floros IS, Tserpes KI, Löbel T. Mode-I, mode-II and mixed-mode I+II fracture behavior of composite bonded joints: Experimental characterization and numerical simulation. Compos Part B Eng. 2015 Sep;78:459–68.
12. Koumpias AS, Tserpes KI, Pantelakis S. Progressive damage modelling of 3D fully interlaced woven composite materials: PROGRESSIVE DAMAGE MODELLING OF 3D WOVEN FABRICS. Fatigue Fract Eng Mater Struct. 2014 Jul;37(7):696–706.
13. Tehrani M, Yari Boroujeni A, Al-Haik M. Modeling and simulation of impact and perforation in fiber reinforced composites. 2014.
14. Fabbro R, Peyre P, Berthe L, Scherpereel X. Physics and applications of laser-shock processing. J Laser Appl. 1998 Dec;10(6):265–79.
15. Sagnard M, Ecault R, Touchard F, Boustie M, Berthe L. Development of the symmetrical laser shock test for weak bond inspection. Opt Laser Technol. 2019 Apr;111:644–52.

  doi:10.5075/epfl-298799_978-2-9701614-0-0

MODE I ICE ADHESION OF A COMMERCIAL CYANATE ESTER AND A CORRESPONDING POLYMER BLEND

Zoe, Fielden-Stewart[a], Marie-Laure, Pervier[b], Hugo, Pervier[b], Anastasios, Toulitsis[c], Rob, Backhouse[c], Ian, Hamerton[a,d]

a: Bristol Composites Institute, University of Bristol, Bristol, BS8 1TR, UK – zf17676@bristol.ac.uk
b: Cranfield University, Cranfield, MK43 OAL, UK
c: Rolls-Royce, Filton, Bristol, BS34 6QA, UK
d: National Composites Centre, Bristol & Bath Science Park, Emersons Green, Bristol BS16 7FS, UK

Abstract: *Accretion of ice on aircraft components can be detrimental to flight. Inlet gas-turbine components can be susceptible to icing whilst dormant on the runway but must also have good temperature performance, due to high operational temperatures. Cyanate ester resins have excellent thermal performance but, prior to this study, have not been investigated for their ice adhesion properties. Thus, the ice adhesion of a commercial cyanate ester (Primaset® PT-30) and a novel cyanate ester ternary blend has been characterized through the measurement of mode I ice fracture energy for both rime and glaze ice. A comparison was made with an industry-standard titanium alloy sample, Ti-6Al-4V. In both ice cases, both the commercially available cyanate ester and the cyanate ester blend performed significantly better than the titanium sample; both yielding lower ice fracture energy values.*

Keywords: Mode I ice adhesion; cyanate ester; aerospace; icephobicity.

1. Introduction

Ice accretion on aircraft components poses significant risk to flight by altering the aerofoil profile and disrupting the aerodynamics, such as lift and drag [1]. Traditional de-icing methods are energy intensive, involving bulky heating elements that can add to overall component weight and decrease aircraft efficiency, de-icing solvents that require heating and spraying under high pressure before flight. Front-end gas turbine components therefore have a requirement for an environmental coating that protects against icing, as well as erosion from débris and potential bird strike. Through reducing the ice adhesion of the component material, the need for other de-icing methods is reduced, increasing the efficiency of the de-icing process and achieving a more sustainable process (without resorting to environmentally harmful solvents). Understanding the ice adhesion behaviour is therefore advantageous.

Aircraft engine components are progressing from traditionally metallic to advanced composite materials due to their superior specific strength and stiffness, in order to reduce component weight and increase overall aircraft efficiency. Cyanate ester resins have become increasingly popular for high-temperature aerospace applications due to their excellent thermal mechanical performance, which is attributed to their high cross-link density [2], however this is the main cause of their inherent brittleness. The incorporation of flexible chain moieties in the polymer network can improve the fracture toughness and therefore impact resistance of the cured system. Thus, Koh *et al.* [3] improved both the curing and thermal mechanical performance of

  doi:10.5075/epfl-298799_978-2-9701614-0-0

a cyanated novolac, (similar in chemical structure to the PT-30 cyanate ester) through blending the material with LECy cyanate ester and 2,2'-bis(3-allyl-4-hydroxyphenyl)isopropylidene (DBA). This approach was first demonstrated in the Matrimid 5292 toughened bismaleimide that was originally marketed by Ciba Geigy, based on the same toughening component [4].

In 2016 Golovin *et al.* [5] published a breakthrough study on the design of icephobic coatings, describing a phenomenon called interfacial cavitation, wherein the mechanism occurs due to the difference in hardness of the substrate material (in this case, elastomers) and ice. This leads, in turn, to crack propagation along the material-ice interface, with bigger differences facilitating propagation and hence lowering ice adhesion. Theoretically, a more elastic material should increase the difference in hardness, creating larger stress concentrations along the material-ice interface and thus reducing the force required to remove the ice. This formed the basis of the current study where the incorporation of flexible chain polymers within a more brittle cyanate ester was proposed to reduce the ice adhesion of the cured polymer blend.

For the reasons stated, cyanate ester resins are typically used in high-temperature applications, and their ice adhesion characteristics have not previously been reported. In this study, the mode I ice adhesion of a commercial cyanate ester, Primaset® PT-30 and a corresponding ternary polymer blend based on PT-30 was measured in terms of ice fracture energy, for two distinct ice types. An industry-standard titanium, Ti-6Al-4V was also tested to provide baseline data for comparison.

2. Methodology

2.1 Materials

Primaset® PT-30 trifunctional novolac cyanate ester and Primaset® LECy cyanate ester (based on 1,1'-bis(4-cyanatophenyl)ethylidene) were supplied by Arxada AG (Visp, Switzerland). 2,2'-Bis(3-allyl-4-hydroxyphenyl)isopropylidene (DBA) was purchased from Sigma-Aldrich (Darmstadt, Germany). All reagents were used without further purification.

2.2 Specimen preparation

The cyanate ester blend consisted of a combination of PT-30:LECy:DBA, which was prepared by blending all three constituents at 90°C for 40 min with constant stirring. PT-30 and the ternary blend were then cured at 160°C for 1 hr, 200°C for 3 hr, and post-cured at 250°C for 1 hr, with a ramp rate of 1°C/min between isothermal temperature dwells. The materials were cured between two borosilicate glass plates clamped around a PTFE mould insert to produce 4 mm thick parallel resin plaques of both materials. Disk specimens (30 mm diameter with a central 4 mm diameter hole) were machined from both cured resin plaques.

An industry-standard titanium alloy Ti-6Al-4V (plate thickness 2 mm), was provided by Cranfield University for testing, from specimens were machined and polished to a mirror finish (R_a = 0.01 μm).

2.3 Mode I test principle

Testing occurred in the Cranfield Ice and Wind Tunnel (CIWT) [6], which contains a test rig that is based on blister test initially reported by Andrews and Lockington [7] and modified by Hammond [8]. The test principle is shown in Figure 1. The material specimen disk is fixed to a cylindrical metal platform, both with a 4 mm central hole. A small plastic disk covers the hole of the specimen to act as a crack initiation site between the ice and specimen interface. Ice is accreted on the specimen surface and then subsequently removed by applying pressurised gas. The fracture energy of ice is calculated from the measured gas pressure required to remove the ice from the specimen surface, named the critical pressure (*Pc*), the Young's modulus of ice (*Ei*), the Poisson's ratio of ice (*vi*), the radius of the flaw (*c*) and the thickness above the flaw (*h*) as stated by the two expressions established by Andrews and Lockington [6]. Three cases can occur upon ice removal: completely adhesive, where all ice is removed from the specimen surface; completely cohesive, where crack propagation occurs through the ice and leaves a layer of ice covering the entire specimen surface; or mixed, which is a combination of cohesive and adhesive. In the case of cohesive fracture, the fracture energy is denoted by 2τ. If the fracture is adhesive, the fracture energy is denoted by θ. Therefore, fracture energy is expressed as

$$2\tau = \frac{P_c^2 c}{E_i \times f_1} \tag{1}$$

$$\theta = \frac{P_c^2 c}{E_i \times f_2} \tag{2}$$

where f_1 and f_2 are

$$f_1 = \frac{1}{1-v^2}\left(\frac{3}{32}\left[\left(\frac{c}{h}\right)^3 + \left(\frac{c}{h}\right)\frac{4}{1-v}\right] + \frac{1}{\pi}\right)^{-1}$$

$$f_2 = \frac{1}{1-v^2}\left(\frac{3}{32}\left[\left(\frac{c}{h}\right)^3 + \left(\frac{c}{h}\right)\frac{4}{1-v}\right] + \frac{2}{\pi}\right)^{-1}$$

If a mixed case of fracture occurs, the percentage of adhesive fracture, x, is visually estimated and the fracture energy, FE, is expressed as

$$FE = \frac{100-x}{100} \times 2\tau + \frac{x}{100} \times \theta \tag{3}$$

Ice thickness must be a minimum of 15 mm to ensure plain strain conditions to satisfy Eq. (1), (2) and (3).

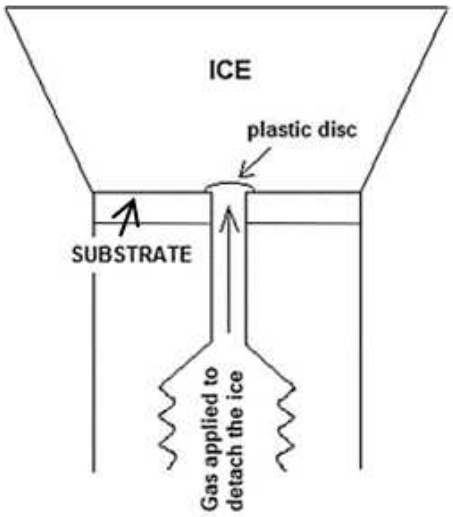

Figure 1. Mode I test principle. Adapted from [6].

2.4 Ice parameters

Two ice types were considered: glaze and rime ice. Rime ice occurs when supercooled droplets freeze instantly upon impact with the substrate surface, resulting in trapped air and therefore produces ice that is opaque in appearance. Glaze ice occurs when supercooled droplets hit the surface and partially freeze, with the liquid water flowing across the substrate surface first before freezing, resulting in very little trapped air and therefore a translucent appearance, yet a more irregular profile. To produce the two distinct ice types in the CIWT for testing, the tunnel temperature was set to -5°C for glaze ice conditions, and to -20°C for rime ice conditions. The remaining parameters of tunnel wind speed, a cloud liquid water content (LWC), and droplet median volume diameter (MVD) were kept constant. All tunnel parameters are summarised in Table 1.

Table 1: CIWT parameters for glaze and rime ice types.

Ice type	Tunnel temperature [°C]	Tunnel wind speed [m/s]	LWC [g/m^3]	MVD [µm]
Glaze	-5	50	0.4	20
Rime	-20	50	0.4	20

2.5 Test procedure

The material specimens were fixed to the metal platforms with an adhesive and assembled on the testing rig within the CITW (Figure 2). During each experiment, a total of 8 specimens were tested. A PTFE disc with a thickness of 50 µm was held over the central hole with a vacuum. The supercooled droplet spray was then started under the specific tunnel conditions for the ice type and ice was accreted on the specimen surface until an ice thickness of approximately 20 mm was achieved. Pressurised nitrogen was then applied to the ice through the hole at a rate of 10 bar/s, corresponding to a strain rate of 10-4s^{-1}. The critical pressure, P_c, was recorded. The ice

removal type was estimated by eye as a percentage of adhesive failure immediately after removal.

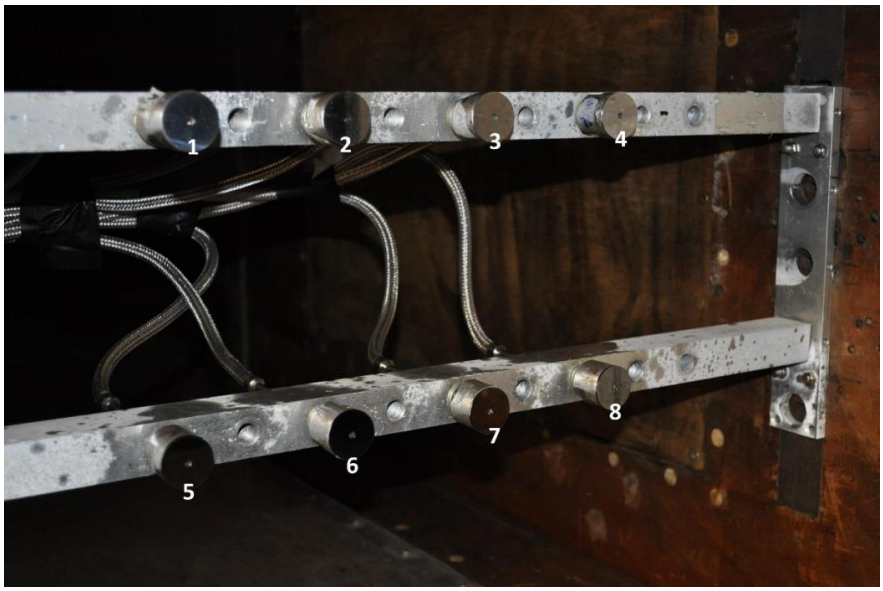

Figure 2. 8 empty sample platforms positioned on the testing rig within the CIWT labelled with the position number.

A total of 11 repeats were tested for both PT-30 and the ternary blend and 7 repeats for the Ti-6Al-4V, to ensure the validity of average values calculated for each material. The assumptions were made that the Young's modulus and the Poisson's ratio were constant for both ice types and were taken as 8.5 GPa and 0.31 respectively. A 10% error of estimation of the adhesive fracture % occurs, resulting in an error on the fracture energy of approximately 0.01 J/m^2.

3. Results and discussion

Both tests conducted on the cyanate ester resins resulted in 100% adhesive fracture, with the exception of one test resulting in 90 % adhesive fracture for rime ice on PT-30. This was deemed an outlier as was outside a two standard deviation margin from the mean value. In the case of Ti-6Al-4V, all the glaze ice tests resulted in adhesive failure, however two rime ice tests resulted in adhesive percentages of 30 and 75 %. Ice adhesion was calculated in terms of ice fracture energy using Eq. (1), (2) and (3). Mean fracture energy values and standard deviation were calculated using a two-parameter Weibull distribution, due to the brittle nature of ice [9].

In the glaze ice tests, the average fracture energies of PT-30 and the ternary blend were calculated as 0.48 J/m^2 and 0.26 J/m^2 respectively (Figure 3). These demonstrated significant reductions (34% and 57% respectively) in ice adhesion in comparison to Ti-6Al-4V, which had a calculated fracture energy of 0.61 J/m^2. The ternary blend showed a large reduction in the scatter (σ = 0.08 J/m^2), with a slight reduction also observed for PT-30 (σ = 0.17 J/m^2).

  doi:10.5075/epfl-298799_978-2-9701614-0-0

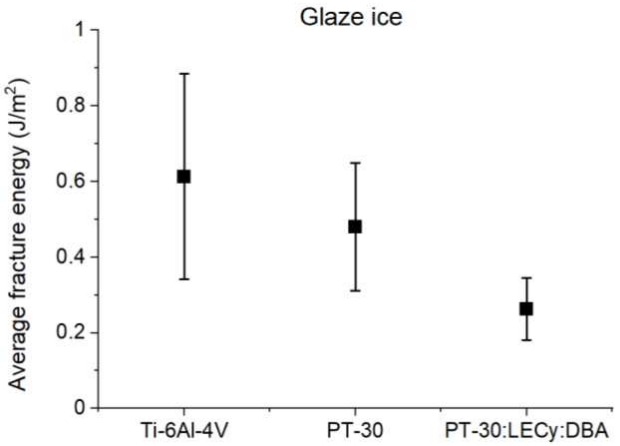

Figure 3. Average fracture energy of glaze ice (J/m^2).

The rime ice tests for Ti-6Al-4V showed that the average rime ice fracture energy had increased slightly to 0.70 J/m^2, in comparison to glaze ice. Furthemore, the cyanate ester resins showed further reductions in the ice adhesion under these conditions, with the average fracture energy of PT-30 being calculated at 0.38 J/m^2 (a reduction of 46%) and that of the ternary blend at 0.24 J/m^2 (a reduction of 66 %) (Figure 4). The same trend for the scatter was also seen for rime ice, with the titanuim alloy producing the largest scatter in data (σ = 0.30 J/m^2), with a slight reduction observed for PT-30 (σ = 0.22 J/m^2) and the lowest scatter observed for the ternary blend (σ = 0.07 J/m^2).

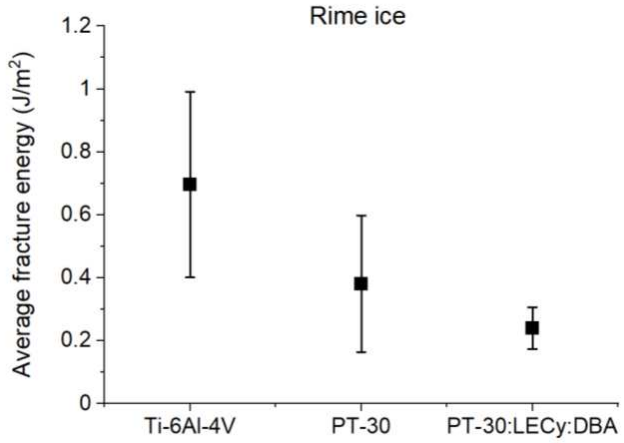

Figure 4. Average fracture energy of rime ice (J/m^2).

Table 2: Average fracture energy values for glaze and rime ice types.

Material	Glaze ice fracture energy [J/m^2]	Rime ice fracture energy [J/m^2]
PT-30	0.48	0.38
PT-30:LECy:DBA	0.26	0.24
Ti-6Al-4V	0.61	0.70

As Ti-6Al-4V was used as an industry-standard comparison, a reference factor (RF) was calculated by dividing the average fracture energy of the reference material by the average fracture energy of the material for comparison. This was plotted to directly compare the cyanate ester materials with the titanium alloy (Figure 5). In the case of PT-30, the material performed better by a factor of 1.3 compared with the titanium in glaze ice conditions and 1.8 in rime ice conditions. The ternary blend showed a further improvement in reducing the ice adhesion, performing better than the titanium alloy by a factor of 2.9 in rime ice conditions and 2.3 in glaze ice conditions.

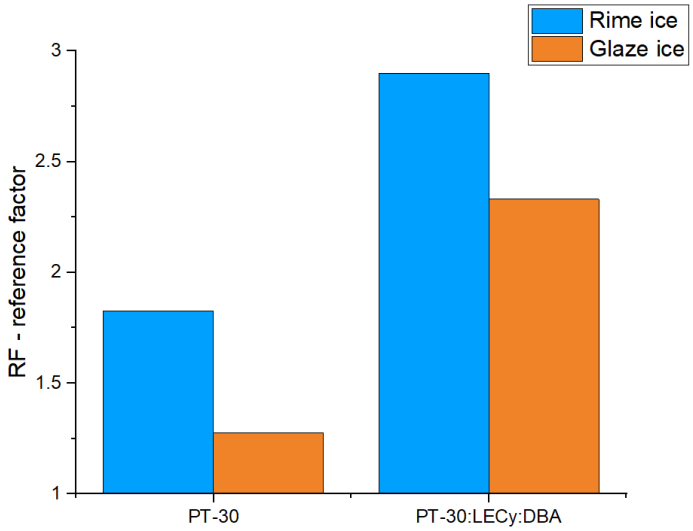

Figure 5. RF values of average rime and glaze fracture energy values for PT-30 and PT-30:LECy:DBA in comparison to Ti-6Al-4V.

4. Conclusion

The mode I ice adhesion screen test has been successfully conducted in order to compare the ice adhesion of a commercial cyanate ester, Primaset® PT-30, and a corresponding ternary cyanate ester blend, with the behaviour exhibited by an industry standard titanium alloy, Ti-6Al-4V. The ice adhesion was characterised through calculating the fracture energy of both rime and glaze ice types accreted on to the material specimen surface. Both PT-30 and the ternary polymer blend showed lower ice adhesion for both ice types in comparison to Ti-6Al-4V, with both reducing the ice fracture energy by a factor of at least 1.3 and, in the best case, a factor of 2.9. This study has given valuable initial insights into the icing behaviour of cyanate ester resins, providing baseline material data for further gas turbine component development.

Acknowledgements

We thank Rolls-Royce plc and the Engineering and Physical Sciences Research Council (EPSRC) for financial support through the Industrial Doctoral Centre (EP/L015102/1). The authors thank Arxada AG, Switzerland, for providing Primaset®PT-30 for the testing.

  doi:10.5075/epfl-298799_978-2-9701614-0-0

5. References

1. Gent RW, Dart NP, Cansdale JT. Aircraft icing. Philosophical Transactions of the Royal Society B 2000; 359:2873-2911.
2. Hamerton I. Chemistry and Technology of Cyanate Ester Resins. I Hamerton (Ed.) Blackie Academic and Professional. 1994.
3. Koh HCY, Dai J, Tan E. Curing behaviour and thermal mechanical properties of cyanate ester blends. Journal of Applied Polymer Science 2006; 5:4284-4920.
4. Takao I, Nishina T, Fukuda W, Tomoi M. Effect of matrix compositions on modification of bismaleimide resin by *N*-phenylamide-styrene copolymers. Journal of Polymer Science 1996; 60:37-45.
5. Golovin K, Kobaku SPR, Lee DH, DiLoreto ET, Mabry JM, Tuteja A. Designing durable icephobic surfaces. Science Advances 2016; 2:e1501496.
6. Pervier MLA, Hammond DW. Measurement of the fracture energy in mode I of atmospheric ice accreted on different materials using a blister test. Engineering Fracture Mechanics 2000; 214:223-232.
7. Andrews EH, Lockington NA. The cohesive and adhesive strength of ice. Journal of Materials Science 1983; 18:1455-1465.
8. Hammond DW. Microstructure and mechanical properties of some small impact ice accretions. 7th international workshop on atmospheric icing of structures. 1996.
9. Jayatilaka A. Fracture of engineering brittle materials. Applied Science Publishers. 1979.

  doi:10.5075/epfl-298799_978-2-9701614-0-0

BRAIDING CHARACTERISATION AND OPTIMISATION: COMPLEX GEOMETRIES

B.Grimes[1,2], M.Thompson[2], P.Giddings[1], N.A Warrior[2]

1: National Composites Centre, Bristol, UK – beth.grimes@nccuk.com
2: Composites Research Group, The University of Nottingham, Nottingham,UK

Abstract: *For simple prismatic geometries, such as cylinders, the addition of a twist to fibre tows at the pre-braiding, bobbin winding stage is seen to result in beneficial changes in the fibre architecture of a braided preform. This research considers the effects of braiding on a non-prismatic, frusto-conical cross-section by analysing the key process metrics of tow width, braid angle and braid thickness. The present study demonstrates that whilst some variabilities were observed, adding twist to fibre does not make a significant difference to braid architecture for non-prismatic geometries, but does reduce processing-induced tow damage and is therefore of benefit in improving the final part quality.*

Keywords: Braiding, twist, complex geometry

1. Introduction

Braid architecture simulations are built on generalised assumptions for the tow geometry[1]. This results in discrepancies between key process variables such as cover factor and braid thickness of the designed braid and manufactured preform.

Localised variations in braid architecture and process-induced tow damage are detrimental to the final quality of the manufactured preform. One of the ways tow widths can be influenced is by adding twist to the fibre during the rewinding stage of the process. Torun et al determined that increasing the number of twists reduces the tow diameter producing a more compact structure[2] and that a small number of additional twists offered favorable processability benefits.

It is well accepted that the tow rewinding stage of the braiding process is critical to resultant product quality[3]. State-of-the-art rewinding machines can control multiple parameters including rewinding speed, rewinding tension and tow twist to produce a high-quality bobbin package. Torun et al recommended no more than 10 twists per metre (Tpm) to reach a compromise between tow diameter and friction benefits for a 12K carbon fibre tow.

A geometrical cross-sectional change in the component has been shown to increase the level of variability in braid architecture, for example Du and Popper demonstrated an increase in preform uniformity when section gradient is converging [4]. The authors' previous work has demonstrated that the inclusion of an additional twist during the bobbin rewinding stage reduces braided tow geometry variability [5]. This present research builds on [5] by investigating the effects of fibre tow twist on the braid architecture of a component with changing cross section. The information in this study is aimed at improving the quality and performance of braided composites.

  doi:10.5075/epfl-298799_978-2-9701614-0-0

2. Methodology

2.1 Material Bobbin Rewinding

Standard modulus HST45 12K carbon fibre was wound using the CEZOMA VLS87 winding machine and accompanying Eurocarbon Twist Cabinet at the National Composites Centre (NCC). Three different sets of bobbins were wound with three different levels of twist: 0, 5 twists and 7 twists per metre (Tpm). The rewinding tension was maintained for each set of bobbins and the rewinding speed was constant at 1000 rpm. Anticlockwise bobbins were wound in an anticlockwise direction (or Z-twist) and clockwise bobbins were wound with a clockwise twist (S-twist) to produce a balanced braided preform.

2.2 Preform Manufacture

Two sizes or scales were considered. For the large-scale study, preforms were manufactured using the 192-carrier axial Eurocarbon braider at the NCC. For the small-scale study the preforms were manufactured on the 48-carrier Steeger braider at the UoN.

The fibres were braided onto a continuous axisymmetric mandrel incorporating two stages – a cylindrical section and a frusto-conical section with a transition angle of 10°. For the large-scale study nominal mandrel diameter was 200mm and maximum diameter 350mm, for the small-scale study 50mm and 87.5mm respectively. By switching the located end of the mandrel in the gantry, the transition therefore becomes either a converging (reducing) or diverging (increasing) cross-section. Manufacturing trials were completed with the mandrel in both orientations. The braiding machine was operated in a fully loaded configuration to create a biaxial braid with a regular braid pattern. The process parameters, carrier speed and take-up speed were varied to produce single layer preforms with a constant braid angle of 45°

In the large-scale study braids were single ply and in the small-scale study multi-ply preforms of four layers were manufactured.

2.3 Braid Architecture Measurement

An Apodius RS6 Scanner was used to measure the thickness of layers in the small-scale braided preforms.

Manual images and images taken using the in-process monitoring system at the NCC were used to monitor the characteristics of the braid architecture. Parameters such as braid angle and tow width were measured using image processing software ImageJ.

3. Results

The outputs from the investigation are summarised in the following section. The results highlight the importance of tow material preparation on the resulting fibre architecture of the braided preform.

3.1 Tow Width Variability

Tow widths for the constant, increasing or decreasing cross-sectional change are shown in Figure 1. The twisted fibre tows generally resulted in a smaller tow width than the untwisted tow (roughly 2mm compared to 3.5mm), with a significantly reduced variability (roughly ± 0.3mm

  doi:10.5075/epfl-298799_978-2-9701614-0-0

compared with more than ± 0.6 mm). No clear trends for the effects in cross section change were seen - differences between prismatic, diverging and converging sections were within the range of observed variability. The variability of the tow width leads to localised defects in the braid architecture, this results in irregularity in cover factor which in turn leads to inconsistent mechanical properties.

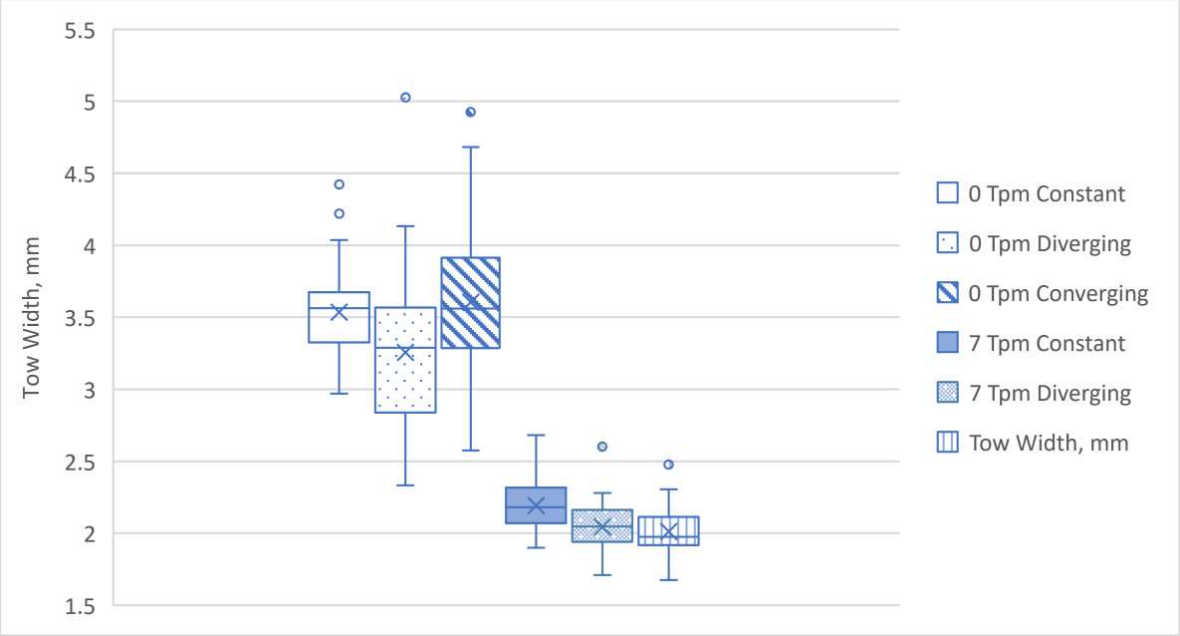

Figure 1 Tow width range for different cross-section changes

3.2 Braid Architecture Variability

Figure 2a and Figure 2b demonstrate the influence of the direction of transition, increasing or decreasing (2b) diameter on the braid angle (for the programmed constant braid angle of 45 degrees), where the yellow orange and red lines represent the converging cross-section and the three blue lines represent the diverging section and where the sloped section of the component is between 200-600mm of the axial length.

Figure 2a shows that for untwisted fibres, braiding on a diameter of decreasing, converging cross-section achieves a more consistent braid angle closer to the programmed braid angle, within ± 2 degree. The braid angle deviation for the diverging cross-sectional diameter was notably higher, reaching 4 degrees at its peak.

Figure 2b shows that for twisted fibres, braiding on a diameter of decreasing, converging cross-section also achieves a more consistent braid angle - within ± 1 degree of the programmed angle. For the diverging cross-section, the braid angle deviation was again higher, reaching 6 degrees.

A braid angle variation of ± 1 degree is generally perceived to be a tolerable range in aerospace manufacture.

  doi:10.5075/epfl-298799_978-2-9701614-0-0

(a)

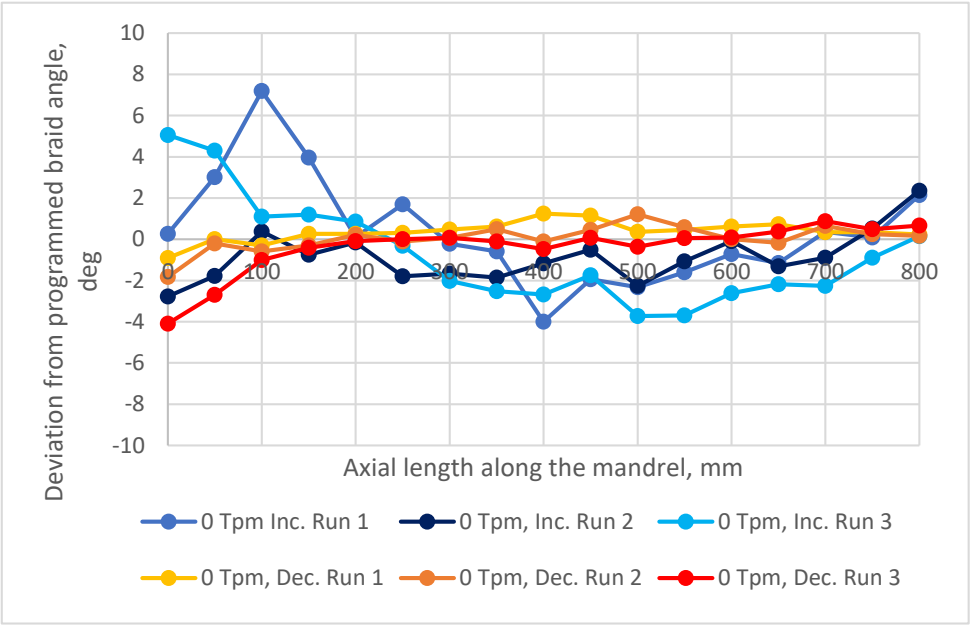

(b)

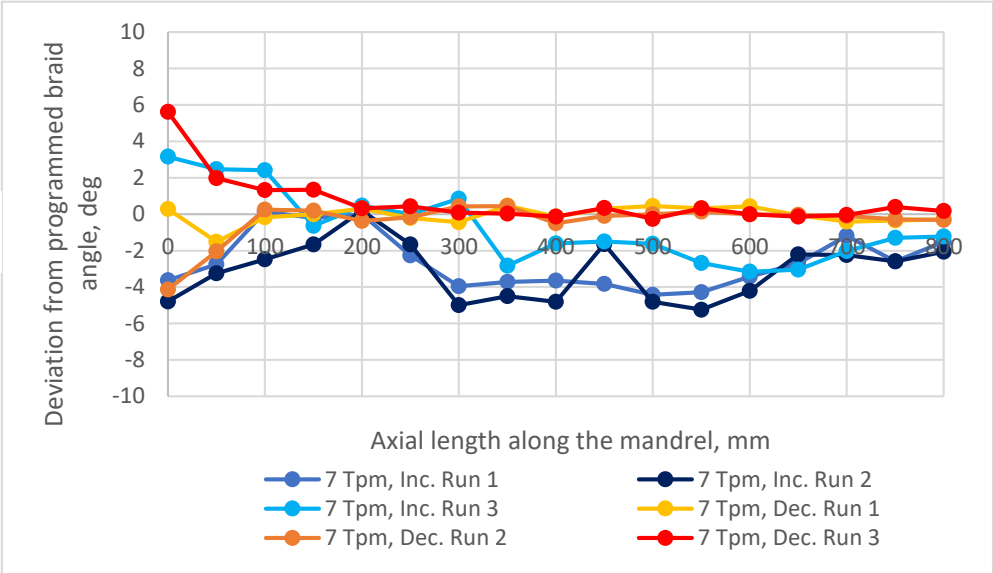

Figure 2 Deviation from programmed braid angle : (a) untwisted fibre tows, (b) twisted fibre tows

3.3 Layer Thickness

In the small-scale study, multi-ply preforms of four layers were manufactured. Table 1 shows the average layer thickness recorded for each layer. An increase in layer thickness was seen in the twisted preforms, 0.668 mm ± 0.067 compared to 0.570 mm ± 0.074 for the diverging transition and 0.689 mm ± 0.076 compared to 0.584 mm ± 0.141 for the converging sections. However, the overlap in standard deviation suggests that these differences were not statistically significant. The variability in layer thickness showed no difference for either the inclusion of a twist or the direction of the transition. The additional twist to fibres did not appear to influence the nesting of the subsequent layers with each additional layer in a 0.2-0.4 mm increase in preform thickness.

Table 1 Average layer thickness of braided preform

Number of Layers	0 Tpm Diverging	0 Tpm Converging	5 Tpm Diverging	5 Tpm Converging
1	0.570 ± 0.074	0.584 ± 0.141	0.668 ± 0.067	0.689 ± 0.076
2	0.813 ± 0.069	0.820 ± 0.087	1.017 ± 0.334	0.959 ± 0.108
3	1.213 ± 0.008	1.058 ± 0.096	1.386 ± 0.104	1.300 ± 0.065
4	1.430 ± 0.006	1.364 ± 0.104	1.700 ± 0.079	1.521 ± 0.035

3.4 Fibre Processability

Figure 3 shows examples of the accumulation of processing defects for the untwisted preform. The images highlight the visible fibre damage shown by the red boxes.

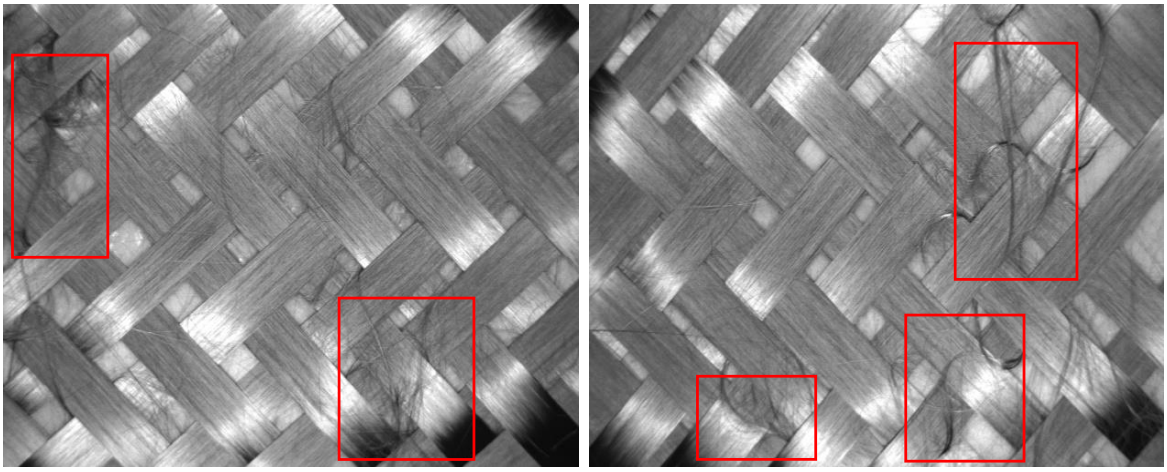

Figure 3 Images from the in-process monitoring system of untwisted preforms

Figure 4a and 4b shows a visual comparison of the impact of adding twist to carbon fibre tows. Figure 4a demonstrates the preform manufactured with 0 Tpm fibres and Figure 4b demonstrates the preform manufactured with twisted fibres. Greater visible damage such as filamentation and fibre breakage (fuzz) is noticeable in Figure 4a.

Figure 4 Images of the braided preforms (a) untwisted, (b) twisted

Figure 5 demonstrates a collection of images taken during the manufacturing process on the 192-carrier braider. Image (a) and (b) show significant levels of filamentation in the braid cone, (c) demonstrates the influence of inconsistent tension levels and (d) shows filamentation causing process interruptions. These filaments catch on the mechanisms of the machine which cause the level of fibre damage to escalate. This results in inconsistent tow tension which leads to tow breakages.

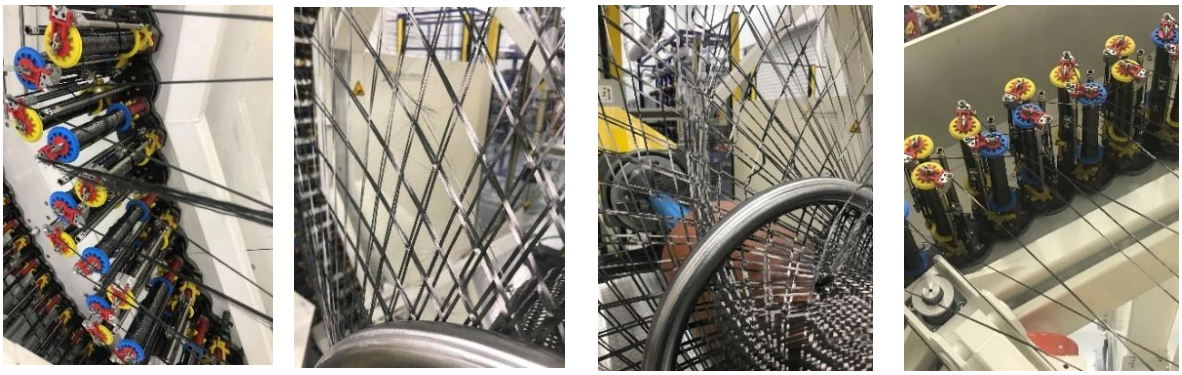

(a) (b) (c) (d)

Figure 5 Images of processability problems

4. Conclusions

This research investigates the influence of the addition of a twist to carbon fibres during the rewinding process and its resultant impact of the manufacture of a frusto-conical preform. Two different manufacturing set-ups were both considered: small scale (48-carrier) and large scale (192-carrier). Two different levels of twist were used in each configuration: 0 and 5 Tpm for the small-scale manufacture and 0 and 7 Tpm for the larger machine. Changes in tow width and braid angle were measured to analyse the variability of the braid architecture. The observations and the key points are outlined below summarised in terms of tow geometry, braid architecture variability and fibre processability.

- Tow Geometry:
  - Direction of the slope influenced the spread of the tow for the untwisted fibre. On a diverging cross-section change the tow width reduced and a converging cross-section changed the tow spread.
  - The tow width of the twisted tow remained constant for both straight and changing geometrical features.
  - Variability of the tow width increased for the untwisted fibres on the geometrical change in cross-section.
- Braid Architecture Variability:
  - Braiding on a converging cross-sectional change produced a more repeatable braid angle, close to the programmed value of 45 degrees.
  - The addition of twist to the fibres had no discernible impact on the braid angle of the preform.
- Layer Thickness:

  - The initial layer of the braid saw an increase in thickness with twisted fibres.
  - The direction of transition did not influence the magnitude or variability of the thickness of the braided preform.
- Fibre Processability:
  - Surface 'fuzz' caused by fibre filamentation during braiding was seen in the untwisted preforms, resulting in visible processing defects and a greater number of fibre breakages and entanglements.

Acknowledgements

This research work was supported by contributions from the National Composites Centre, the ESPRC Centre for Doctoral Training in Composites Manufacture (Grant EP/L015102/1) and the EPSRC Future Composites Manufacturing Research Hub (Grant EP/P006701/1).

References

1. J. H. Van Ravenhorst, "Design Tools for Circular Overbraiding of Complex Mandrels," Degree of Doctor Dissertation, University of Twente, 2018
2. Torun A, Hoffmann G, Mountasir A, Cherif C. Effect of twisting on mechanical properties of GF/PP commingled hybrid yarns and UD-composites. Journal of Applied Polymer Science. 2011;123(1):246-256
3. C. Ebel, M. Brand and K. Drechsler, "Effects of fiber damage on the efficiency of the braiding process," in *TexComp-11*, Leuven, Belgium, 2013.
4. Du GW, Popper P. Analysis of a Circular Braiding Process for Complex Shapes. J Text Inst [Internet]. 1994 [cited 2019 Jun 18];85(3):316–37. Available from: http://www.tandfonline.com/action/journalInformation?journalCode=tjti20.
5. Grimes B et al, The effect of twist on braid architecture and stability, SAMPE Europe 2021

MANUFACTURING ADVANCED STRUCTURAL COMPOSITES FROM SUSTAINABLE PREPREGS

Jack Holyoak[ab], Alix Sauget[a], Lee Harper[b]

a: SHD Composite Materials Ltd, Sleaford, Lincolnshire, NG34 7BY, UK
b: Composites Research Group, University of Nottingham, Nottingham, NG7 2RD, UK

JHolyoak@shdcomposites.com

Abstract: *Sustainability has become an essential element in the design and manufacture of fibre reinforced polymer (FRP) composites, prompting research and development into alternative resin systems and optimisation of associated composite manufacturing processes. This project investigates high volume manufacturing processes, utilising more sustainable prepreg materials, including natural and recycled fibres and bio-based resins.*

Keywords: Prepreg; Bio-resin; Double Diaphragm Press Forming

Introduction

The SHD Group manufactures and develops a wide range of prepreg materials for advanced composite tooling and components, supplying globally from their manufacturing sites in the UK, Europe, and USA. At their head office and centre for Research & Development in the UK, SHD have been actively responding to the shift toward utilising raw materials from increasingly sustainable sources.

As SHD begin to integrate these novel bio-based prepregs materials into their product lines, they must verify that they can also be processed effectively and efficiently. In conjunction with the University of Nottingham, this 4-year Engineering Doctorate (EngD) project is investigating prepreg compression moulding, which has the potential to produce structural components at sufficient rates for high volume manufacturing. A double diaphragm arrangement is used to constrain the plies during forming to avoid potential defects, but also to eliminate the need for release agents and to aid rapid part ejection.

1. Sustainability: The challenge

Defining sustainability within advanced composites is challenging. Composites light-weighting has successfully been proven to improve fuel efficiency in the transport sector and facilitate the construction of large renewable energy structures, such as wind turbines. However, the energy consumed in the production of fibre reinforced polymer materials (FRP) can be very high, so it is important to consider the complete lifecycle, not just the energy savings during the use phase. Whilst carbon fibres offer greater weight savings than glass fibres for example, due to higher specific properties, the embodied energy during the fibre manufacturing phase is much higher. The embodied energy is reported to be somewhere between 171 and 771 MJ/kg [1,2], depending on the grade, compared with 13-32MJ/Kg for glass fibre [3]. In combination with an epoxy or polyester resin, with embodied energies in the range 63-80MJ/Kg [3], the total energy usage to create a composite material can be ten times higher than that of steel [4,5]. However,

  doi:10.5075/epfl-298799_978-2-9701614-0-0

this worst-case scenario does not consider the specific property benefits of composites, alongside optimised design freedoms, and energy saving in service. This project will strive to establish sustainability targets through the entire process, benchmarking with respect to manufacturing rate, cost, and part performance.

Fundamentally, traditional composite materials are synthetic and are produced from non-renewable sources. Therefore, the most logical approach to producing more sustainable products, with lower embodied energy, is to increase the use of renewable materials and renewable energy sources.

This project will investigate the processing of a range of carbon, glass, and natural fibres in combination with SHD's bio-resin formulations. Polyfurfuryl alcohol (PFA), is a fully bio-based thermosetting polymer with excellent natural fire and heat resistance. With the global electric vehicle (EV) market currently amid rapid growth, these prepregs are suitable for providing heat and fire containment for battery boxes. The substitution of conventional metal alloys for these lightweight composite battery boxes can help to maximise the energy density of the battery; in turn, improving range, performance, and life span, which are just some of the major challenges faced by the current EV market.

SHD have also developed a range of epoxy prepregs with 30% bio-based content, which will be increased in the future. Furthermore, the ambient storage of these prepregs has been verified to 6 months – reducing the embodied energy of the final product, by avoiding freezer storage.

Combining these resin systems with natural fibre reinforcements, such as flax and hemp, further increases the overall bio-based content of the composite, significantly reducing its carbon footprint (10 to 50%) against a functionally comparable fossil fuel-based composite [6]. Furthermore, if carbon storage is included, where the quantity of carbon dioxide removed from the air during growth is also considered, the carbon footprint reduction is consistently higher (30 to 70%) [6]. Using bio-derived materials is an essential place to start for addressing the global sustainability challenge for advanced composites, but it does not ensure circularity. Perhaps composite prepreg will never become fully circular, but many small progressions will continually accumulate towards this goal. To address the circularity problem more closely, it is hoped that there will also be scope within this project to make use of the University of Nottingham's end-of-life fibre reclamation facilities, where re-purposed prepreg could be made suitable for compression moulding.

2. Double Diaphragm Press Forming

For Double Diaphragm Press Forming (DDPF) to be successful with thermoset prepregs, suitable diaphragm materials and heating mechanisms are required. The flat material stack is sandwiched between two polymeric diaphragm films, secured by a series of aluminium frames, allowing it to be easily heated by an overhead infrared device or heated tooling elements. Pre-heating the material prior to forming reduces the viscosity of the resin, which acts as a lubricant during forming to provide lower inter-ply friction.

A vacuum is pulled between the diaphragms to prevent wrinkles from appearing between the film and the material stack. This transfer of tension controls the draping process and helps to prevent the formation of out of plane wrinkles during forming [7].

  doi:10.5075/epfl-298799_978-2-9701614-0-0

Process simulations will be carried out to capture the effects of intra-ply shear with respect to changing the forming temperature and hence the viscosity of the matrix. Characterising the friction at all diaphragm interfaces will also be investigated. Understanding the diaphragm interaction with the stack will be pivotal to identifying and eliminating wrinkles within the final part.

A generic tool installed in the University of Nottingham's Langzauner press will be used, [Figure 1], which was designed to have complex features to challenge the prepreg draping process, without the requirement for darting the plies around the perimeter. It also includes a recessed channel around the base which, if laminating by hand, would be difficult to achieve a component without fibre bridging or introducing resin rich areas. [7]

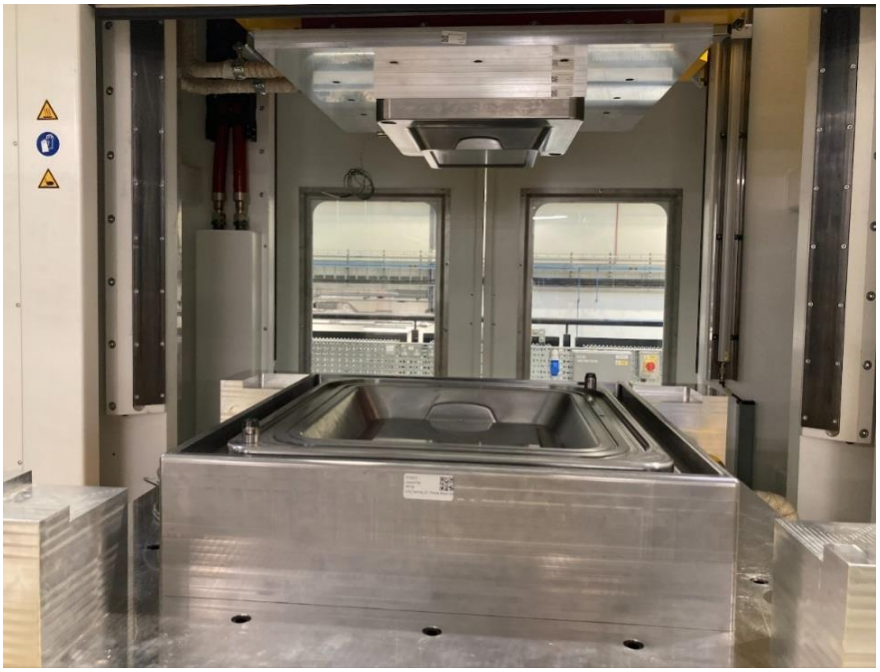

Figure 1: Generic press tool at the University of Nottingham, within 3000kN Langzauner Press

A pre-heat station needs to be designed, in conjunction with a user-friendly shuttling method for the frames into the press. Ideally, the frames will also shuttle out of the rear of the press after curing to simulate a production line for high volume applications.

3. Sustainable Manufacturing

For processing technology to be adopted in industry, the cycle time and scrap rate need to be minimised for both sustainable and economic reasons. Ordinarily, scrap rates are higher within compression moulding than with traditional autoclave vacuum bagging processes, but the autoclave can act as a bottle neck for high volume manufacture. Despite this, correctly applying a well understood DDPF approach will enable plies to be constrained effectively to avoid defects during forming – thus reducing scrap rates. Detailed studies of the matrix rheological development are required to understand the effects of prepreg tack, inter-ply friction and intra-ply shear during forming. Rheological and cure kinetic modelling will enable optimal temperatures and forming speeds to be identified to meet component quality, cycle time and mechanical performance expectations.

  doi:10.5075/epfl-298799_978-2-9701614-0-0

The DDPF technology has likely benefits for producing EV battery boxes from PFA-based prepregs, not only because it can meet the cycle-time demand set by the industry, but it also eliminates issues with part/tool release. Furthermore, cure consumables can potentially be re-used and so the overall process waste is minimised. Once cycle times have been optimised, the embodied energy of the process can be calculated and compared against metallic parts manufactured for the same application.

4. References

1. Dér, A., et al., Modelling and analysis of the energy intensity in polyacrylonitrile (PAN) precursor and carbon fibre manufacturing. Journal of Cleaner Production, 2021. 303: p. 127105.
2. Tapper, R.J., et al., An evaluation of life cycle assessment and its application to the closed-loop recycling of carbon fibre reinforced polymers. Composites Part B: Engineering, 2020. 184: p. 107665.
3. Composites UK. Embodied Energy [Internet]. Composites UK [cited 2022 Mar 14]. Available from: https://compositesuk.co.uk/composite-materials/faqs/embodied-energy
4. Wiesen, K. and M. Wirges, From cumulated energy demand to cumulated raw material demand: the material footprint as a sum parameter in life cycle assessment. Energy, Sustainability and Society, 2017. 7(1): p. 13.
5. Kim, H.C. and T.J. Wallington, Life-Cycle Energy and Greenhouse Gas Emission Benefits of Lightweighting in Automobiles: Review and Harmonization. Environmental Science & Technology, 2013. 47(12): p. 6089-6097.
6. Beus, N. d., & Carus, M. (2019). Carbon Footprint and Sustainability of Different Natural Fibres for Biocomposites and Insulation Material. Hurth (Germany): Nova Institute.
7. Corden T, Dickinson C, Hewison R, Swait T, Wells D. Double Diaphragm Compression Moudling. SAMPE Journal March/April 2021.

  doi:10.5075/epfl-298799_978-2-9701614-0-0

THE BENEFITS AND CHALLENGES OF AN ACCURATE LIFETIME PREDICTION MODEL FOR LEADING EDGE EROSION OF WIND TURBINE BLADES

Robbie Herring [a, b], Kirsten Dyer [a], Carwyn Ward [b]*

[a] Offshore Renewable Energy Catapult, Offshore House, Albert Street, Blyth, NE24 1LZ, UK.
[b] Department of Aerospace Engineering, Queen's Building, University of Bristol, Bristol, BS8 1TR.
* Corresponding Author: Robbie.Herring@ore.catapult.org.uk.

Abstract: *Harsh environments and high blade tip speeds have caused leading edge erosion to become a serious problem for the offshore wind industry. Materials used to protect the blade do not currently last the turbine lifetime and require frequent repair. Erosion tests exist but there is uncertainty in predicting in-situ lifetime from the results. Successful achievement of this would provide support to the industry in the development and identification of improved materials. However, there are several different aspects to a lifetime prediction model and several challenges need to be overcome to unlock its benefits in combatting leading edge erosion.*

Keywords: Wind Energy; Leading Edge Erosion; Protection Materials; Prediction Models

1. Introduction

Composite materials have been a key driver in the growth of the wind industry, with their structural efficiencies enabling increased blade lengths and increased power generation. However, composites have a low resistance to perpendicular impacts and can have poor resistance to environmental conditions. These attributes, coupled with harsh offshore environments and high blade tip speeds, have caused Leading Edge Erosion (LEE) to develop into a significant issue for the offshore wind industry [1]. Raindrops and hailstones impacting the Leading Edge (LE) of the blade cause material to be progressively removed from the surface. This forms an unplanned roughening topology, that degrades aerodynamic performance and impacts structural integrity. It is estimated that this LEE costs each turbine £1.3 million over its 25-year lifetime [2] and it is therefore an expensive problem for the industry. The operators of wind turbines try to protect the at-risk section of the blades by applying Leading Edge Protection (LEP) systems to them, in the form of polymeric coatings and tapes, but these do not last the lifetime of the turbine and require regular replacement.

Typically, a protection system is experimentally evaluated using a Rain Erosion Test (RET) rig, where a sample is fixed to the end of an arm and rotated through an erosion field at high speed. However, it is often seen that LEP systems with good test results do not translate into having good in-situ performance; leaving material developers and turbine operators with limited information on the best materials to use and so risk turbine blades being poorly protected. Given the clear impacts of LEE, selecting and developing suitable LEPs is now more important than ever and to enable this, a methodology that can accurately compare LEP systems, quantify the progression of erosion, and predict their in-situ lifetime for a given wind farm is required [3]. Successful achievement of this methodology would: a. Allow developers to identify the best LEP product for their specific wind farm; b. Provide LEP manufacturers with quantitative information on their product's in-situ performance and how to further develop their products, and; c. Inform

  doi:10.5075/epfl-298799_978-2-9701614-0-0

wind farm operators with guidance on scheduling maintenance periods, enabling erosion to be repaired early and minimising unexpected downtime and lost aerodynamic performance.

Ultimately this methodology will contribute towards preventing LEE and so reduce wind energy industry costs. A successful translation would be highly beneficial to the wind industry, although an inaccurate one would be detrimental as it would lead to unexpected turbine downtime and the promotion and lock-in of unsuitable LEPs. Furthermore, if the methodology overlooks an important erosion driver, it could lead to the rejection of the step change LEPs that the industry requires. It is therefore essential that any translation is accurate and appropriately validated. To inform the generation of such a methodology and support the realisation of its benefits, an investigation into the different areas of a lifetime prediction methodology between RET results and in-situ performance has been conducted. This paper reviews each area in turn and highlights the challenges that need to be overcome.

2. Lifetime Prediction

To predict an LEP systems in-situ lifetime, it's response to erosion loading and the probability of the loading occurring need to be understood. Response to loading is found through: i. A damage model, and; ii. RET. Probability of loading is found from: iii. The offshore environment, and; iv. A particle impingement model. Any methodology must be: v. Validated, to correctly support LEP identification, development, and inform maintenance periods. Each of these five areas has been examined with the challenges and research gaps identified.

2.1. Damage Model

A damage model will estimate the number of droplet impacts under a given impact condition to reach the end of the erosion incubation period, and is central to any lifetime prediction. The Springer model [4], developed in 1975 for the aerospace industry, is the most commonly used approach. It combines the mechanical properties from several materials into an analytical model, and fits the output against the respective material's RET results. Thus it determines two fitting constants, forming a semi-empirical model to predict the number of impacts to failure.

Experimental testing and materials used by Springer focus on the aerospace industry, so are not representative of those currently used within the wind energy industry [5]. For example at the time of model development, the aerospace industry was interested in erosion at supersonic speeds [6] and explored local velocities of 223-966 m/s; significantly higher than the limit of 100 m/s tip speeds of current wind turbine blades. Furthermore, Springer used a combination of aluminium, polyester, and epoxy as the substrate, whereas turbine blade LE's are presently glass fibre reinforced plastic. LEP systems have recently moved to highly viscoelastic coatings, with a filler and primer layer, and so the coating systems used by Springer are now outdated as the analytical model does not include those layers and assumes that the coating and substrates are perfectly elastic. By ignoring the main damping benefit of viscoelastic materials, the Springer model is outdated for the current wind industry and should not be used for erosion lifetime predictions.

Alternate detailed computational models that include multiple layers and viscoelastic damping effects have been developed. Domenech [7, 8] developed a 1D model that examines the shock wave propagation through the thickness of an LEP, whilst Mishnaevsky [9] and Doagou-Rad [10] produced Finite Element models that examine the stresses caused from a single droplet impact.

  doi:10.5075/epfl-298799_978-2-9701614-0-0

To include viscoelastic damping, models such as Kelvin-Voight [11] need to be used. All of these models remain limited by material characterisation, which is highly challenging for viscoelastic materials, requiring large numbers of mechanical tests to be performed across a range of temperatures, strains, and strain rates. Uncertain material properties introduce significant uncertainty to model outputs, and so no computational model has been sufficiently validated. As a result, confidence in computational models is limited and, despite its severe limitations, the simplistic Springer model is still preferred by industry.

2.2. Rain Erosion Testing

A successful LEP system is expected to work for several years, making evaluations at normal operating conditions unrealistic. Given this, and needing to observe failure to better understand and improve performance, RET techniques for accelerated testing have been developed. The industry dominant RET test rig design is the whirling arm erosion test rig [12]. In this test a sample is mounted on an arm and rotated at high speed through a uniform rain field until erosion occurs. A testing practice developed by DNV [13] in 2018 - DNVGL-RP-0171 (2018) - endorsed this method as the recommended industry design and provides guidance on its operation. Whilst this has provided a central testing mechanism for the industry, Bartolomé [14] states that the testing process has not been completely standardised and that comparing results between different test facilities is difficult. Fraisse [15] also highlights the issue with reproducibility between test setups. Both claim this is due to a lack of restrictions and control over the different test parameters, such as droplet size distributions, temperature, and turbulence, whilst there is no common guidance on slice length and inspection periods. Consequently, Bartolomé concludes that current erosion experimental results are unsuitable for understanding the operational life of an LEP system. This agrees with Dyer [16], who points out that good test performance does not always correlate to good in-service performance. To aid the experimental evaluation of LEP systems and translate to their in-situ performance, greater guidance on the various test parameters is therefore required.

An alternative method is the pressure jet erosion test [17]. In this test water is ejected from a nozzle under high pressure onto the sample. The jet can be continuous or cut by a rotating body [18]. In both cases the impacting droplet is unstable and not representative of the actual impact conditions, as accelerating a droplet onto a stationary material causes it to impact as a slug; risking damage mechanisms that are unrepresentative. The different impact mechanisms also make it challenging to compare results to the whirling arm erosion test rig [19]. However, the better versions of whirling arm erosion tests are expensive and largely limited to industry use. Therefore the pressure jet erosion test rig is still widely used - such as [20, 21] - to offer indications of an LEP systems erosion performance.

2.3. Offshore Environment

Prediction methodologies aim to translate test results into the normal operating conditions, and for an offshore wind turbine, this is the offshore environment that it is situated within. Consequently a thorough understanding of the offshore conditions and their frequency is required. Up to the rated power, where the turbine rotational velocity is capped, the wind speed governs the blade tip speed, and therefore dictates the velocity of the impacting particles. The wind resource at a particular site forms a key part of the wind farm planning process, and is typically understood from an early stage [22]. Wind speed measurements can be captured by

installing anemometers on tall meteorological masts or with recent remote sensing techniques [23], with the frequency of different wind speeds normally projected using Weibull probability distributions [24]. The inherent importance of the offshore wind speed to a wind turbine's performance has resulted in offshore wind speeds being widely understood.

A precipitation environment is represented by the frequency of the precipitation intensities; type of impacting particles - termed hydrometeors, and; rain Droplet Size Distribution (DSD). As the distribution of rain droplet diameters varies with precipitation intensity, DSDs are given as intensity functions. Various studies investigate onshore precipitation environments [25–27] but there is limited work on offshore environments, with comparisons simply showing precipitation environments to differ. Hasager [28] investigated precipitation environments at five coastal and three inland weather stations in Denmark, with the coastal sites found to have a much higher frequency of heavy rain than the inland sites. Hasager surmised there is a lack of knowledge of the offshore environment with the amount, type, and intensity of precipitation not being well quantified at this point. Suh [29] observed that rain in typhoons consisted of smaller diameters than other types. The reduced droplet size is likely caused by the high-speed winds breaking up the droplets. Typhoon wind speeds are extreme and therefore the conclusion may not translate entirely to the higher wind speeds offshore than onshore, but the research implies that the wind speed has an influence on droplet sizes. Given the prominence of offshore erosion, further research into the offshore precipitation environment is clearly essential. Towards this, ORE Catapult have started to characterise the offshore precipitation environment [30] through an anemometry hub located three nautical miles off the coast of Northumberland, UK, and at their Levenmouth Demonstration Turbine. These datasets provide the first known measurement of the offshore precipitation environment and will offer a valuable contribution towards understanding a wind turbine's environment.

The influence of Ultraviolet (UV) radiation on LEE is uncertain [31]; although it is known that UV ages the LEP, degrades mechanical properties, and negatively affects rain erosion performance. For example, Claus [32] conducted RET on a coating material before and after 1500 hours of UV ageing, finding a noticeable reduction in the erosion performance of the coating. At present there is very little other research on the degrading effect of UV and how to include it into lifetime predictions remains uncertain.

2.4. Impingement Characterisation

Stresses and strains introduced into the LEP system are determined by how many hydrometeors in the environment impact the blade and their impingement characteristics. Papadakis [33] investigated the droplet impingement dynamics on aerofoil sections. Using a wind tunnel and visualisation techniques, droplet impingement data was collected across four different aerofoil sections at a freestream velocity of 78 m/s, with a range of droplet sizes and angles of attack also explored. The fraction of droplets that impact the blade was observed to be dependent on the droplet diameter with larger droplets impinging with a greater efficiency and smaller droplets more influenced by aerodynamics and deflected. Iuliano [34] developed a computational model to investigate droplet impingement, finding a good correlation between model predictions and the experimental results.

Blade curvature may influence the droplet impingement characteristics. Verma [35] analytically investigated the effect of blade curvature on the compressible stage of a droplet impact. By

exploring the curvature of open-source blades ranging 750 kW to 10 MW, it was found that the kinematics of the impact are influenced by the curvature, with the effect becoming more significant for smaller blades under larger droplet impacts. Figure 1 highlights the difference in curvature between a typical RET sample and the tip of the DTU 10 MW blade [36]. RET is performed on narrow aerodynamic samples with the results used to update a damage model and extrapolate to the in-situ turbine blade. Whilst the curvature effects on the stresses and strains that the droplet introduces is not yet provided, Verma's findings suggest that there may be a large change in the damage response between the test sample and the field. Thus the effect of the curvature difference between test sample and blade should be understood and, if significant, included in any lifetime prediction.

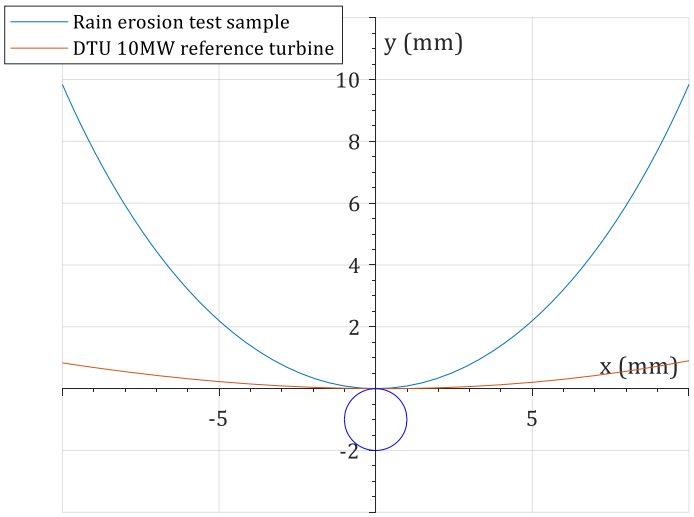

Figure 1. *The difference in curvature between a rain erosion test sample and the DTU 10 MW blade* [36]*. A droplet diameter of 2mm has been included for reference.*

2.5. In-situ Validation

To have confidence in any lifetime prediction and its benefits in enabling effective development of LEP systems, and/or scheduling of maintenance periods, it is crucial that any prediction methodology is validated against in-situ data. ORE Catapult have started a trial on their Levenmouth Demonstration Turbine to address this need. Three different commercial LEP systems have been applied to separate blades of the turbine. ORE Catapult have complete knowledge of the operation of the turbine and the environment in which it is situated. The trial will provide valuable information on LEE and should be able to provide the required validation data.

3. Conclusion

LEE has become a key challenge for offshore wind energy over the past decade, with the eroded blades causing a loss in aerodynamic performance and requiring expensive in-situ repairs. The LEP systems currently used by operators are unable to last the lifetime of the turbine and improved systems. An accurate and validated lifetime prediction methodology would support the selection of suitable LEP systems, provide manufacturers with guidance on improvements, and inform farms on scheduling maintenance periods for repairing erosion. It would therefore provide considerable benefits in yielding improved systems and mitigating the effects of LEE. An

  doi:10.5075/epfl-298799_978-2-9701614-0-0

accurate lifetime prediction model will rely on several key inputs, namely: i. A damage model; ii. RET; iii. The offshore environment; vi. The impingement characteristics, and; v. Validation against in-situ data. Each input has been reviewed in this paper, and Table 1 summarises the different components and their challenges. Addressing these challenges will provide a significant step change in erosion lifetime prediction methodologies, ultimately enabling an accurate lifetime prediction model that will reduce the costs associated with LEE of wind turbine blades.

Table 1. *Key components in a lifetime prediction methodology and their respective challenges.*

Lifetime Prediction Component	Challenge
Damage Model.	Uncertainty in the material characterisation of viscoelastic material inputs introduces uncertainty.
Rain Erosion Testing.	Good test performance does not always result in good in-situ performance and greater guidance on appropriate test conditions is required.
Offshore Environment.	Limited knowledge on offshore precipitation environment and UV radiation.
Impingement Characteristics.	The influence of curvature on hydrometeor impingement characteristics has not been understood.
In-situ Validation.	There is a lack of available in-situ datasets.

Acknowledgements

This work was supported by the Engineering and Physical Sciences Research Council through the Industrial Doctorate Centre in Composites Manufacture (grant EP/K50323X/1), project partner the Offshore Renewable Energy Catapult - https://ore.catapult.org.uk [last accessed: 21 March 2022]; and the Future Composites Manufacturing Hub (EP/P006701/1). The authors would also like to thank the Wind Blade Research Hub for their support in the delivery of this paper. All data necessary to reproduce the results and support the conclusions are included within this paper.

References

[1] R. Herring, K. Dyer, F. Martin, and C. Ward, “The increasing importance of leading edge erosion and a review of existing protection solutions,” *Renewable and Sustainable Energy Reviews*, vol. 115, p. 109382, Nov. 2019.

[2] ORE Catapult, “Develop alternative leading edge protection solutions for repairing existing blades in service,” 2018. https://ore.catapult.org.uk/work-with-us/smes/innovation-challenges/develop-alternative-leading-edge-protection-solutions-for-repairing-existing-blades-in-service/ (accessed Jan. 01, 2021).

[3] H. M. Slot, E. R. M. Gelinck, C. Rentrop, and E. van der Heide, “Leading edge erosion of coated wind turbine blades: Review of coating life models,” *Renewable Energy*, vol. 80, pp. 837–848, Aug. 2015.

[4] G. S. Springer, C.-I. Yang, and P. S. Larsen, “Analysis of Rain Erosion of Coated and Uncoated Fiber Reinforced Composite Materials.” Air Force Materials Laboratory, Dayton, Ohio, USA, 1974.

[5] R. Herring *et al.*, “Assessment of a Wind Turbine Blade Erosion Lifetime Prediction

  doi:10.5075/epfl-298799_978-2-9701614-0-0

Model with Industrial Protection Materials and Testing Methods," *Coatings*, vol. 11, no. 7, p. 767, Jun. 2021.

[6] G. F. Schmitt, "Research for Improved Subsonic and Supersonic Rain Erosion Resistant Materials." Air Force Materials Laboratory, Dayton, Ohio, USA, 1968.

[7] L. Domenech, V. García-Peñas, A. Šakalytė, D. Puthukara Francis, E. Skoglund, and F. Sánchez, "Top Coating Anti-Erosion Performance Analysis in Wind Turbine Blades Depending on Relative Acoustic Impedance. Part 2: Material Characterization and Rain Erosion Testing Evaluation," *Coatings*, vol. 10, no. 8, p. 709, Jul. 2020.

[8] L. Domenech, J. Renau, A. Šakalytė, and F. Sánchez, "Top Coating Anti-Erosion Performance Analysis in Wind Turbine Blades Depending on Relative Acoustic Impedance. Part 1: Modelling Approach," *Coatings*, vol. 10, no. 7, p. 685, Jul. 2020.

[9] L. Mishnaevsky, S. Fæster, L. P. Mikkelsen, Y. Kusano, and J. I. Bech, "Micromechanisms of leading edge erosion of wind turbine blades: X-ray tomography analysis and computational studies," *Wind Energy*, vol. 23, no. 3, pp. 547–562, Mar. 2020.

[10] S. Doagou-Rad and L. Mishnaevsky, "Rain erosion of wind turbine blades: computational analysis of parameters controlling the surface degradation," *Meccanica*, vol. 55, no. 4, pp. 725–743, Apr. 2020.

[11] A. Morro, "Modelling of viscoelastic materials and creep behaviour," *Meccanica*, vol. 52, no. 13, pp. 3015–3021, Oct. 2017.

[12] C. Mackie, D. Nash, D. Boyce, M. Wright, and K. Dyer, "Characterisation of a Whirling Arm Erosion Test Rig," in *2018 Asian Conference on Energy, Power and Transportation Electrification (ACEPT)*, Oct. 2018, pp. 1–6.

[13] DNV-GL, "DNVGL-RP-0171: Testing of rotor blade erosion protection systems," Bærum, Norway, 2018.

[14] L. Bartolomé and J. Teuwen, "Prospective challenges in the experimentation of the rain erosion on the leading edge of wind turbine blades," *Wind Energy*, vol. 22, no. 1, pp. 140–151, Jan. 2019.

[15] A. Fraisse *et al.*, "Impact fatigue damage of coated glass fibre reinforced polymer laminate," *Renewable Energy*, vol. 126, pp. 1102–1112, Oct. 2018.

[16] K. Dyer and P. Greaves, "Futureproofing the Next Generation of Wind Turbine Blades," *Ingenia*, no. 70, pp. 30–35, Mar. 2017.

[17] S. Zhang, K. Dam-Johansen, S. Nørkjær, P. L. Bernad, and S. Kiil, "Erosion of wind turbine blade coatings – Design and analysis of jet-based laboratory equipment for performance evaluation," *Progress in Organic Coatings*, vol. 78, pp. 103–115, Jan. 2015.

[18] T. Obara, N. K. Bourne, and J. E. Field, "Liquid-jet impact on liquid and solid surfaces," *Wear*, vol. 186–187, no. PART 2, pp. 388–394, Aug. 1995.

[19] E. F. Tobin, T. M. Young, D. Raps, and O. Rohr, "Comparison of liquid impingement results from whirling arm and water-jet rain erosion test facilities," *Wear*, vol. 271, no. 9–10, pp. 2625–2631, Jul. 2011.

[20] A. S. Verma, S. Di Noi, Z. Ren, Z. Jiang, and J. J. E. Teuwen, "Minimum Leading Edge Protection Application Length to Combat Rain-Induced Erosion of Wind Turbine Blades," *Energies*, vol. 14, no. 6, p. 1629, Mar. 2021.

[21] E. F. Tobin, T. M. Young, and D. Raps, "Evaluation and correlation of inter-laboratory results from a rain erosion test campaign," *28th Congress of the International Council of the Aeronautical Sciences, ICAS*, 2012.

[22] D. Menezes, M. Mendes, J. A. Almeida, and T. Farinha, "Wind Farm and Resource Datasets: A Comprehensive Survey and Overview," *Energies*, vol. 13, no. 4702, pp. 1–24, Sep. 2020.

[23] R. J. Barthelmie, H. Wang, P. Doubrawa, and S. C. Pryor, "Best practice for measuring wind speeds and turbulence offshore through in- situ and remote sensing

technologies." Cornell University, Ithaca, New York, USA, 2016.
[24] M. J. M. Stevens and P. T. Smulders, "Estimation of the Parameters of the Weibull Wind Speed Distribution for Wind Energy Utilization Purposes.," *Wind Engineering*, vol. 3, no. 2, pp. 132–145, 1979.
[25] H. MacDonald, D. Infield, D. H. Nash, and M. M. Stack, "Mapping hail meteorological observations for prediction of erosion in wind turbines," *Wind Energy*, vol. 19, no. 4, pp. 777–784, Apr. 2016.
[26] F. Letson, R. J. Barthelmie, and S. C. Pryor, "Radar-derived precipitation climatology for wind turbine blade leading edge erosion," *Wind Energy Science*, vol. 5, no. 1, pp. 331–347, Mar. 2020.
[27] E. A. Brandes, G. Zhang, and J. Vivekanandan, "Experiments in Rainfall Estimation with a Polarimetric Radar in a Subtropical Environment," *Journal of Applied Meterology*, vol. 41, no. 6, pp. 674–685, 2002.
[28] C. Hasager, F. Vejen, J. I. Bech, W. R. Skrzypiński, A.-M. Tilg, and M. Nielsen, "Assessment of the rain and wind climate with focus on wind turbine blade leading edge erosion rate and expected lifetime in Danish Seas," *Renewable Energy*, vol. 149, pp. 91–102, Apr. 2020.
[29] S.-H. Suh, C.-H. You, and D.-I. Lee, "Climatological characteristics of raindrop size distributions in Busan, Republic of Korea," *Hydrology and Earth System Sciences*, vol. 20, no. 1, pp. 193–207, Jan. 2016.
[30] R. Herring, K. Dyer, P. Howkins, and C. Ward, "Characterisation of the offshore precipitation environment to help combat leading edge erosion of wind turbine blades," *Wind Energy Science*, vol. 5, no. 4, pp. 1399–1409, Oct. 2020.
[31] G. Leishman, "Creation of a single water droplet FEA model for rain erosion and observations of coating property changes during rain erosion testing," *International Symposium on Leading Edge Erosion of Wind Turbine Blades*, 2020.
[32] C. E. Claus, "Effects of leading edge erosion on wind turbine efficiency & innovative erosion protection solutions," *Wind Power Monthly - Blade Inspection, Damage and Repair*, 2013.
[33] M. Papadakis, S.-C. Wong, A. Rachman, K. E. Hung, G. T. Vu, and C. S. Bidwell, "Large and Small Droplet Impingement Data on Airfoils and Two Simulated Ice Shapes." NASA, Withita, Kansas, USA, 2007.
[34] E. Iuliano, G. Mingione, F. Petrosino, and F. Hervy, "Eulerian Modeling of Large Droplet Physics Toward Realistic Aircraft Icing Simulation," *Journal of Aircraft*, vol. 48, no. 5, pp. 1621–1632, Sep. 2011.
[35] A. S. Verma, S. G. P. Castro, Z. Jiang, W. Hu, and J. J. E. Teuwen, "Leading edge erosion of wind turbine blades: Effects of blade surface curvature on rain droplet impingement kinematics," *Journal of Physics: Conference Series*, vol. 1618, no. 5, p. 052003, Sep. 2020.
[36] C. Bak *et al.*, "DTU 10MW Reference Wind Turbine." DTU, Rosekilde, Denmark, 2013.
[37] D. Snieckus, "Global offshore wind players join forces for blade erosion project," *Recharge*, 2019. https://www.rechargenews.com/wind/global-offshore-wind-players-join-forces-for-blade-erosion-project/2-1-667298 (accessed Jan. 01, 2022).

  doi:10.5075/epfl-298799_978-2-9701614-0-0

REAL TIME REMOTE APPROXIMATION OF NIP POINT TEMPERATURES IN AUTOMATED TAPE PLACEMENT

Anastasios, Danezis [a, b], David, Williams [b], Alex, Skordos [a]

a: School of Aerospace, Transport and Manufacturing, Cranfield University, MK43 0AL, UK
b: Heraeus Noblelight Ltd., Cambridge Science Park, Milton Road, Cambridge, CB4 0GQ, UK
Corresponding author's email: a.danezis@cranfield.ac.uk

Abstract: *The complexity of automated tape placement (ATP) necessitates fast analysis tools allowing monitoring and control of the process throughout production. A strategy for on-line estimation of the nip point temperature in ATP is put forward based on an approximate analytical solution of the heat transfer in ATP, formulated to accept temperature data on the tool surface as an input. An inverse solution is introduced to approximate the acting irradiance on the composite tapes based on the tool surface temperatures. The performance of the scheme is examined against predictions of a validated 2D finite element model of ATP for a range of velocities, substrate thicknesses and tool materials. The analytical predictions show good agreement with an average error of 15°C. The scheme presents advantages compared to complex FE analysis in terms of computational time, number and complexity of inputs and the capability to deal with variations introduced during the process.*

Keywords: Polymer-matrix composites, Process modelling, Process monitoring, Tape placement

1. Introduction

Automated tape placement (ATP) is an advanced manufacturing method of composites which deploys robotic deposition of material tapes onto a tool. Despite significant effort has been made towards in-situ consolidation of the part using thermoplastic composites, quality on par with conventional methods is yet to be accomplished due to process complexity.

Manufacturing composites with ATP is challenging due to the number of parameters influencing the final quality. The temperate history has a critical role on bond strength, crystallinity levels, void content, and thermal degradation [1]. As a result, numerous studies have developed heat transfer models of ATP. Three-dimensional models have been presented [2], but in most cases the domain is reduced to two dimensions [3,4]. Further simplifications are made by neglecting the heat diffusion in the placement direction based on the dominance of heat transfer due to advection [4]. Analytical solutions for the simplified one-dimensional heat transfer problem have been derived [5]. Thermal simulations coupled with material reaction models [6], as well as surrogate models and neural networks [7,8], have been used for process optimisation.

Solely predictive studies yield results based on ideal process conditions and material properties. Given the complexity of ATP, process monitoring and control are necessary to counteract variations throughout the part production. Thermography and laser-vision systems have been deployed to identify placement defects [9]. Optical fibre Bragg grating sensors have been used to monitor the temperature and strain during ATP [10]. These methods act as on-line inspection rather than process control systems. Utilisation of thermal measurements in conjunction with

  doi:10.5075/epfl-298799_978-2-9701614-0-0

inverse methods to identify process parameters has been put forward for the curing stage of thermosetting composites [11]. Similar methodologies are not currently available for ATP, due to the difficulty of obtaining temperature measurements during the process. The bonding zone is out of sight under the compaction roller and the viewing angle can vary with the robot head movements, or being limited over convex geometries, influencing emissivity. Integrating sensors in the part is only viable in experimental setups for research purposes due to the additive nature of the process and large dimensions of typical parts produced. The concept of a closed loop control system using temperature readings and approximate process model has been described [6], but its development has not been carried out.

In this study, a monitoring strategy is presented based on a 1D analytical solution of the heat transfer in ATP which receives temperature data on the tool surface as input to estimate values of nip point temperature. The method integrates an inverse solution to approximate the incident irradiance delivered by the heater on the composite tapes and improve the accuracy of the estimations. The accuracy of the method is evaluated against outputs of a validated 2D finite element model for a wide range of velocities, substrate thicknesses and tool materials.

2. On-line estimation of nip point temperature

2.1 Heat transfer modelling

The analytical solution for the remote estimation of the nip point temperature is derived from the general energy balance of ATP, when a Eulerian frame is attached to the moving head:

$$\rho c_p \left(\frac{\partial T}{\partial t} + u_x \frac{\partial T}{\partial x} + u_y \frac{\partial T}{\partial y}\right) = \dot{q} + \frac{\partial}{\partial x}\left(k_x \frac{\partial T}{\partial x}\right) + \frac{\partial}{\partial y}\left(k_y \frac{\partial T}{\partial y}\right) \quad (1)$$

where T is the temperature, ρ the density, c_p the specific heat capacity, $\dot{q}$ the heat rate, k_x and k_y the conductivities in the longitudinal and thickness direction and u_i the velocities.

The latent heat due to crystallisation and melting of the thermoplastic matrix is assumed negligible compared to the power delivered by the heater. The domain is simplified further if the ATP is represented as shown in Fig.1. The substrate and tow are treated as a single slab of material which undergoes equivalent temperature evolution, has a thickness (d) equal to the total thickness of substrate and incoming tow, and length (L) equal to the size of the irradiation zone. Further simplification of Eq. (1) can be made using that the process Peclet number in the placement direction is high, indicating that heat diffusion is negligible compared to the heat transport due to advection. In addition, the through-thickness diffusion is much slower than the heat transport in the placement direction due to the high velocities. These assumptions lead to:

$$c_p u_x \frac{\partial T}{\partial x} - \dot{q} = 0 \quad (2)$$

which can be integrated, with $\overline{\dot{q}_{eff}}$ being the average heat rate across the path of the tape from irradiation zone entry to the nip point:

$$T_2 = T_1 + \frac{L\overline{\dot{q}_{eff}}}{\rho c_p u_x} \quad (3)$$

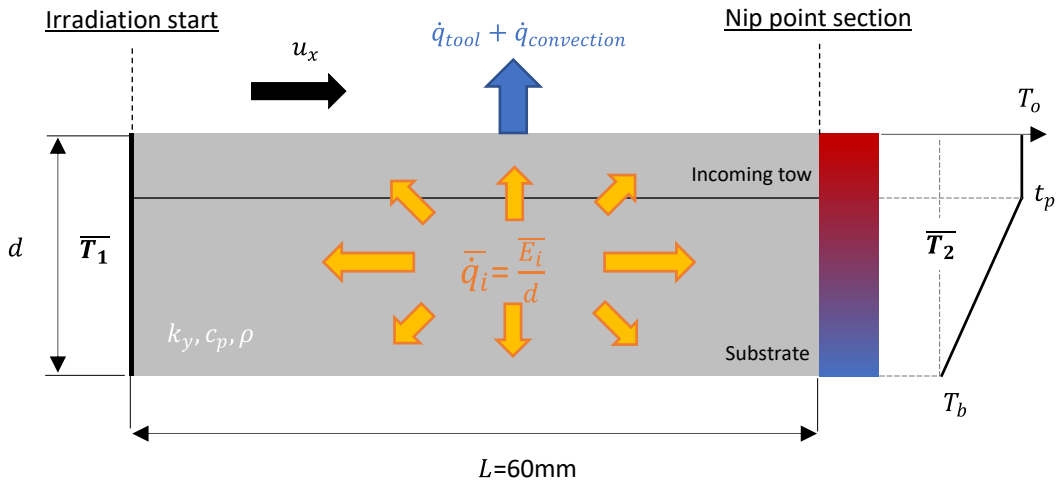

Figure 1. Simplification of ATP geometry to a single slab of composite material with equivalent boundary conditions and a bilinear temperature profile at the nip point section.

During placement, the temperature close to the surface is expected significantly higher than the rest of the section, rendering the average temperature values of Eq. (3) not representative of the actual profile. To account for this, the temperature profile through the thickness at the nip point location is assumed to have a bilinear shape (Fig. 1). The nip point is located at the interface between the incoming tow and substate at one ply depth (t_p). T_2 is calculated as:

$$T_2 = T_o \frac{t_p + d}{2d} + T_b \frac{d - t_p}{2d} \tag{4}$$

The average power losses per unit volume due to contact with the tool can be estimated as the average heat transfer by conduction, assuming a linear increase of T_o and T_b across the irradiation length:

$$\overline{\dot{q}_{tool}} = -k_y \frac{T_o - T_b}{d - t_p} \frac{1}{2d} \tag{5}$$

Similarly, the losses to air due to convection to ambient temperature T_a are approximated:

$$\overline{\dot{q}_{convection}} = -h \left(\frac{T_1 + T_o}{2} - T_a\right) \frac{2}{d} \tag{6}$$

The average volumetric power input due to radiative heating by the heat source is:

$$\bar{\dot{q}}_i = \bar{E}_i \frac{1}{d} \tag{7}$$

Combining Eqs. (3)-(7):

$$T_o = \frac{2\,d\rho c_p u_x T_1 + 2\bar{E}_i L + hL(4\,T_a - 2T_1) + \left[\frac{k_y L}{d - t_p} - \rho c_p u_x (d - t_p)\right] T_b}{\rho c_p u_x (d + t_p) + \frac{k_y L}{d - t_p} + 2hL} \tag{8}$$

The physics of the problem approach that of a semi-infinite solid with a heat flux ($\bar{\dot{q}_s}$) applied to its surface as the part is built up and thickness increases. The solution of a steady semi-infinite [12] is adjusted to ATP process at the nip point position as a function of the through-thickness position (y) and time (t). The nip point temperature at t_p depth is given:

$$T_{oo} = \frac{T_1 + \frac{(\bar{E}_i + 2hT_a - hT_1)}{k_y}\left[2\sqrt{\frac{k_y L}{\pi\rho c_p u_x}}e^{\frac{-t_p{}^2\rho\, c_p u_x}{4k_y L}} + t_p\left(erf\left(\frac{t_p\sqrt{\rho c_p u_x}}{2\sqrt{k_y L}}\right) - 1\right)\right]}{1 + h\left[2\sqrt{\frac{k_y L}{\pi\rho c_p u_x}}e^{\frac{-t_p{}^2\rho\, c_p u_x}{4k_y L}} + t_p\left(erf\left(\frac{t_p\sqrt{\rho c_p u_x}}{2\sqrt{k_y L}}\right) - 1\right)\right]} \tag{9}$$

The approximations represented by Eqs. (8) and (9) are effective for thin and thick composite substrates respectively. The transition between the physics is predicted by the instantaneous Fourier number, which expresses the ratio between conductive transport and power storage:

$$F_o = \frac{k_y L}{\rho c_p u_x d^2} \tag{10}$$

Conductive transport is dominant for low thicknesses and low speeds ($F_o > 1$), whilst power storage for thick parts ($F_o < 1$) and fast processes. A continuous transition in behaviour is ensured by a smooth step using the logistic function is selected between the two solutions:

$$T = T_o + \frac{(T_{oo} - T_o)}{1 + e^{C(F_o - 1)}} \tag{11}$$

2.2 Strategy for on-line estimation of nip point temperatures

The strategy for on-line estimation of nip point temperatures involves a number of sensors mounted at positions of interest across the process tool during the placement. Each sensor captures the tool surface temperature (T_b) during the placement of a new layer, which is then used to approximate the nip point temperature at that location using Eq. (8). The working algorithm uses the position of the placement head to identify the sensor involved, post-process the data and feed the controller which carries out the calculations. Based on the estimated nip point temperature, the processing parameters can be adjusted to achieve desired values.

To estimate the incident irradiance ($\bar{E}_i$) required in Eqs. (8)-(9), an inverse solution is introduced based on the direct 1D analytical solution of a two-layered body under a power-law varying surface flux [13]. The spatial heat flux acting on the substrate surface prior to the nip point can be translated to a time-varying boundary condition on an 1D body. The interface between the two materials coincides with the sensor position during the 2nd ply deposition at $y = t_p$ relative to the substrate surface. The irradiance on the tapes typically follows an asymmetric bell shape and can be approximated by a time-varying triangular profile as shown in Fig.2. The interface temperature is the result of the superposition of these segments acting for their corresponding timings. An Evolutionary Algorithm in the Solver of Microsoft Excel deployed to identify the optimal set of parameters which satisfies:

$$[q_o, t_o, t_m, t_\infty\,] = argmin\ \textstyle\sum_i [T(q_o, t_o, t_m, t_\infty, t_i) - \bar{T}(t_i)]^2 \tag{12}$$

where the summation is over all the measured temperature ($\bar{T}$) acquired at times t_i. Then the average irradiance acting on the composites on the ATP cavity is:

$$\bar{E}_i = b\ \frac{1}{t_\infty - t_o} \int_{t_o}^{t_\infty} q(0,t)\ dt \tag{13}$$

where parameter b accounts that $\bar{E}_i$ is the total incident irradiance on the substrate and incoming tow, whilst the method identifies only the portion delivered to the substrate.

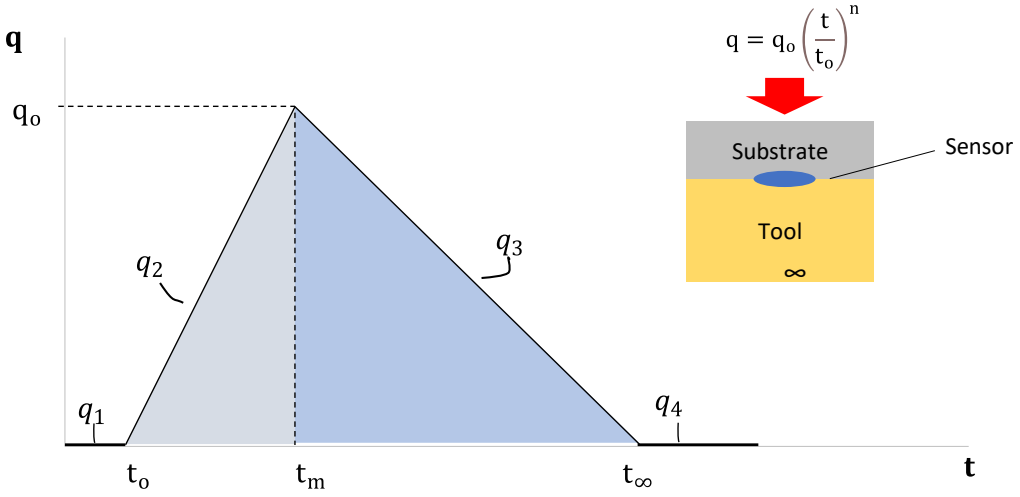

Figure 2. The triangular irradiance profile assumed for the inversion and the configuration of the direct 1D solution used [13].

Table 1: Tool material properties and the average composite values used in the 1D model

	Specific heat capacity (J/kg/K)	Thermal conductivity k_y (W/m/K)	Density (kg/m$^{3)}$
Metallic tool	950	237	2700
Insulating tool	1500	0.25	1500
PEEK/AS4 (1D model)	1500	0.6	1500

3. Methodology

Predictions from an experimentally validated 2D finite element model of the placement of AS4/PEEK in ANSYS APDL [4] are utilised to examine the performance of the approximation. A metallic tool and an insulating one are examined to test the application of the scheme on different setups. The temperature dependent thermal properties of the AS4/PEEK prepreg are detailed in [4], whilst the tool values and averaged ones of the composite for use in the 1D calculations are reported in Table 1. The tool thickness is set at 1.5 cm which is sufficient for behaving as a semi-infinite body (Eq. 10). A Heraeus Noblelight humm3 system of 4.4 kW average power acts as a heater, delivering 2.25 ms long pulses at 50 Hz. Although the simulation data are generated under a pulsed source, similar nip point values are expected for a continuous one [4]. As a result, the performance assessment of the analytical scheme and application of inverse solution is valid for both continuous and pulsed sources.

4. Results and discussion

4.1 Inverse estimation of irradiance

The temperature profiles on the tool given by the FE model for the 2nd ply deposition at 100 mm/s are plotted in Fig.3 for both tools. The low conductivity of the insulating tool decreases the energy dissipation away from the layup, resulting in significantly higher temperatures. To simulate typical noisy temperature sensor data, a Gaussian noise of zero mean value was added to the FE profiles. The standard deviation was set at 2°C for the metallic tool and 20°C for the insulating one, being 10% of the maximum temperature reached in each case.

The recovered triangular irradiance profiles by the inverse solution are given in Fig. 1b. The inversion yields an error of 9% for the metallic tool data with noise, whilst the inversion on the original data results in 5% deviation from the FE profile. The error for the insulating tool is higher at 16% due to the significant amount of noise added. Overall, the inverse solution provides satisfactory results even when significant noise is incorporated in the temperature data. The use of a strong function for the shape of the spatial irradiance has a regularizing effect on the ill-posed problem. This method is advantageous because it incorporates variations and parameters not accurately known in offline strategies such as the heater efficiency or material absorptivity.

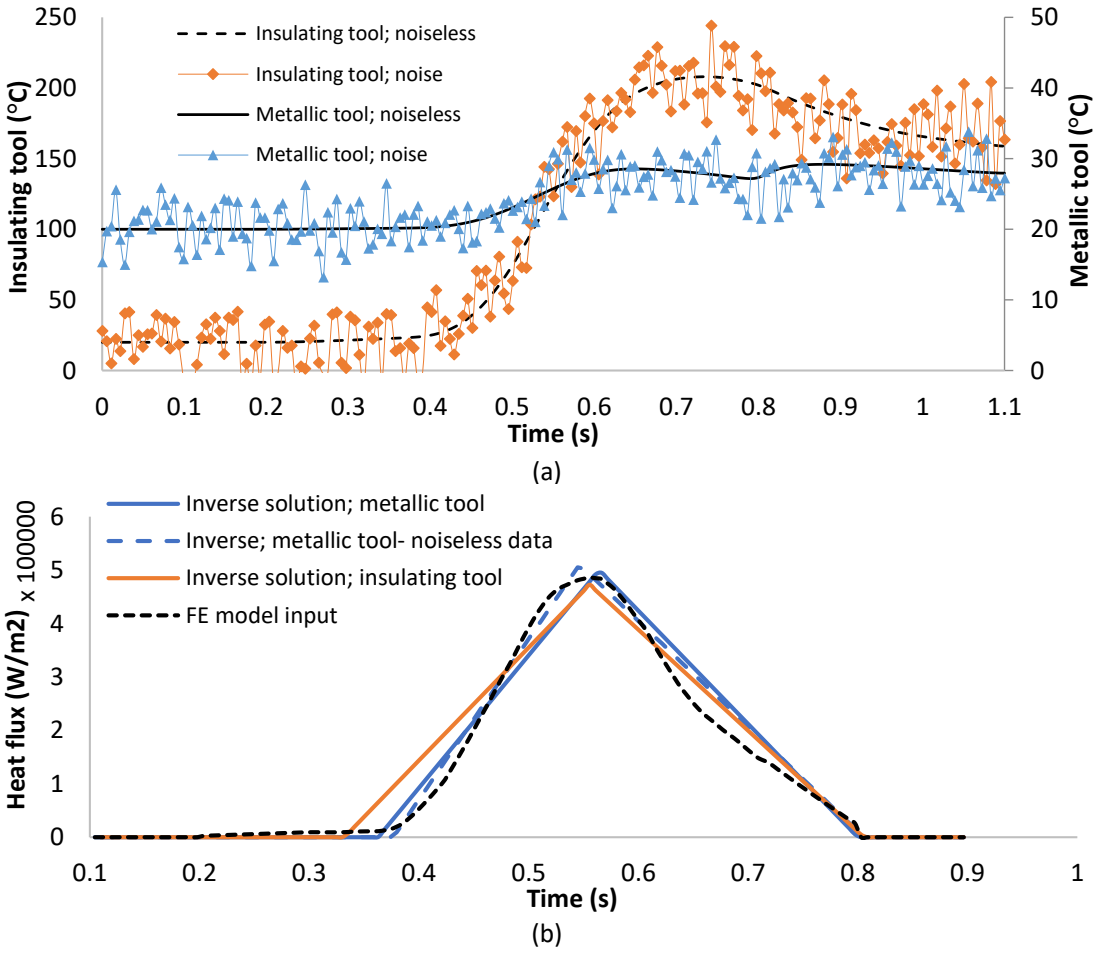

Figure 3. Inverse solution: (a) temperature profiles (FE model) on tool for the 2nd ply deposition at 0.1 m/s; (b) recovered irradiance distribution versus the FE model profile.

4.2 Nip point temperature estimation

The comparison of the FE and 1D model predictions is given in Fig.4. The approximation is in good agreement with the FE results with over 80% of the cases presenting an error lower than 30°C. Approximately 50% of the scenarios present an error lower than 10°C. The maximum deviation across all cases is 50°C, encountered in only 4 cases at the lowest speed of 0.025 m/s for both tool materials. These are attributed to the constant thermal properties in the analytical calculations in contrast to the temperature dependence in the FE model. The average conductivity used in the approximation is 0.6 W/m/K for all scenarios which corresponds to 150°C in the FE model [4]. The temperatures achieved at 0.025 m/s and 0.2 m/s differ from this value, at 400 and 120°C respectively. As a result, the analytical predictions correlate well at temperature levels around the temperature value of the average thermal properties and deviate at temperatures away from the average point used. Predictions at 0.025 m/s are overestimates whilst predictions at 0.2 m/s are underestimates, due to the lower and higher conductivity values used respectively.

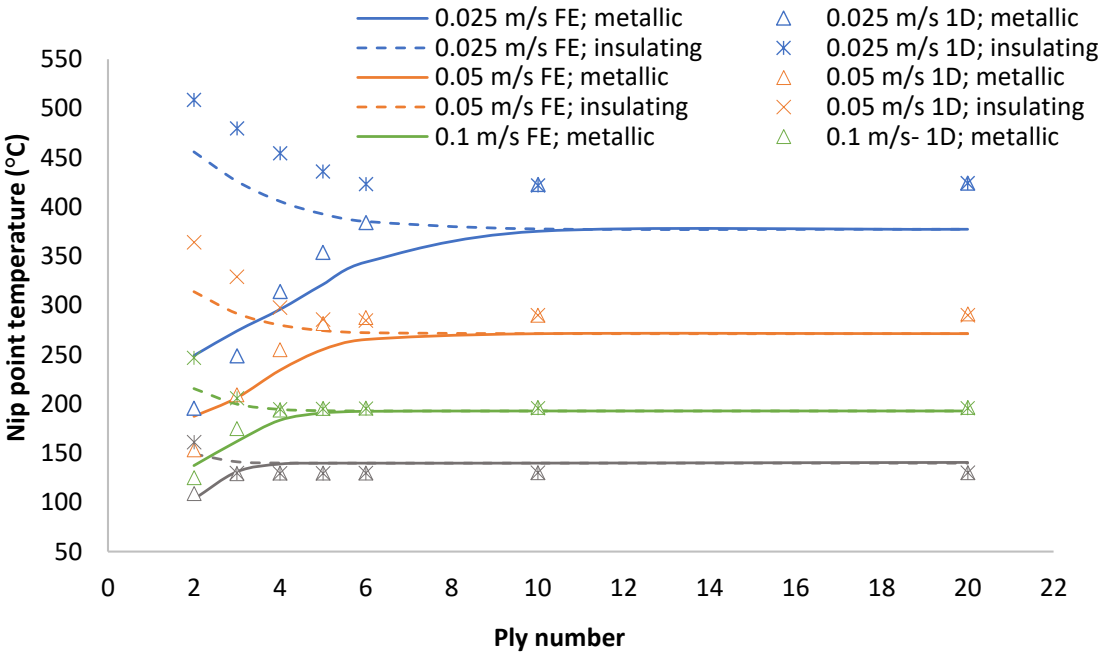

Figure 4. Comparison of FE and analytical model predictions for a range of velocities, number of layers and tool materials

5. Conclusions

An analytical scheme of two 1D solutions was developed for online estimation and monitoring of nip point temperatures in ATP. An inverse solution was combined to offer estimations of effective power input from the source. Despite the simplifications in geometry and heat transfer effects, the analytical scheme presents good predictive capability for a wide range of process conditions. It provides predictions of nip point temperature regardless of tool material due to the use of a monitoring input in the form of tool temperature which compensates for the approximations made. For this reason, this methodology is appealing for application in a manufacturing environment where changes to processing conditions and materials can be reflected in the monitoring signals and included in the solution indirectly. This capability offers

significant advantages over fully predictive FE analysis that requires a large number of inputs and operates under ideal conditions, whilst also unlocks the potential for process control.

6. Acknowledgements

This work was supported by the Engineering and Physical Sciences Industrial Doctorate Centre in Composites Manufacturing [grant number EP/L015102/1] and Heraeus Noblelight Ltd. Discussions with Professor Jay I. Frankel of New Mexico State University on the heat flux identification are gratefully acknowledged.

7. References

1. Rosselli F, Santare MH, Güçeri SI. Effects of processing on laser assisted thermoplastic tape consolidation. Compos Part A: Appl Sci Manuf 1997; 28: 1023–1033.
2. Toso YM, Ermanni P, Poulikakos D. Thermal phenomena in fiber-reinforced thermoplastic tape winding process: computational simulations and experimental validations. J Compos Mater 2004; 38: 107–135.
3. Agarwal V, Guçeri SI, Mccullough RL, Schultz JM. Thermal characterization of the laser-assisted consolidation process. J Thermoplast Compos Mater 1992; 5(2): 115–35.
4. Danezis A, Williams D, Edwards E, Skordos AA. Heat transfer modelling of flashlamp heating for automated tape placement of thermoplastic composites. Compos Part A: Appl Sci Manuf 2021; 145, 106381.
5. Weiler T, Emonts M, Wollenburg L, Janseen H. Transient thermal analysis of laser-assisted thermoplastic tape placement at high process speeds by use of analytical solutions. J Thermoplast Compos Mater 2017; 31: 311-38.
6. Sonmez FO, Akbulut M. Process optimisation of tape placement for thermoplastic composites. Composites A: Appl Sci Manuf 2007; 38: 2013-23.
7. Schaefer PM, Gierszewski D, Kollmannsberger A, Zaremba S, Drechsler K. Analysis and improved process response prediction of laser-assisted automated tape placement with PA-6/carbon tapes using Design of Experiments and numerical simulations. Compos A Appl Sci Manuf 2017; 96: 137–146.
8. Heider D, Gillespie JW. A neural network model-based open-loop optimization for the automated thermoplastic composite tow-placement system. Compos Part A: Appl Sci Manuf 2003; 34: 791-99.
9. Shadmehri F, Ioachim O, Pahud O, et al. Laser-vision inspection system for automated fiber placement (AFP) process. In: 20th International Conference on Composite Materials. Copenhagen, July, 2015.
10. Oromiehie E, Prusty BG, Compston P, Rajan G. In-situ simultaneous measurement of strain and temperature in automated fibre placement (AFP) using optical fibre Bragg grating (FBG) sensors. Adv Manuf Polym Compos Sci 2017; 3(2): 56–51.
11. Tifkitsis KI, Skordos AA. Real-time inverse solution of the composites' cure heat transfer problem under uncertainty. Inverse Probl Sci En 2020; 28: 1011-30.
12. Azad H, Mustafa MT, Arif A. Analytic solutions of initial-boundary-value problems of transient conduction using symmetries. Appl Maths Comp 2009; 215: 4132-40.
13. Cole KB, Beck JV, Woodbury KA, Monte F. Intrinsic verification and a heat conduction database. Int. J. Thermal Sciences 2014; 78 :36-47.

  doi:10.5075/epfl-298799_978-2-9701614-0-0

THE EFFECT OF STITCH DIRECTION ON NON-CRIMP FABRIC FORMING FOR AEROSTRUCTURES

Claudia Jimenez Martin[a,b], Vincent Maes[b], Turlough McMahon[a], James Kratz[b]

a: Airbus UK – claudia.jimenezmartin@bristol.ac.uk
b: University of Bristol – claudia.jimenezmartin@bristol.ac.uk

Abstract

The increased production rate targets of the aerospace industry have driven the development of dry fibre infusion processes. Biaxial Non-Crimp Fabrics (NCFs) are considered in this work due to their potential high deposition rates and higher mechanical performance to woven fabrics. Parameters defining NCF architecture, such as stitching, have been observed previously in uniaxial loading using bias extension tests for example. This paper presents an experimental study into this parameter on a large scale (2 metres in span) geometry. The change in stitch direction relative to the geometry leads to distinctive out-of-plane wrinkling. The effect of this parameter on resulting preform quality is observed using 3D scans. Results show differing preform quality in terms of wrinkling phenomena, showing the importance of stitch direction to load for material drapability tests at an industrial scale.

Keywords: Non-Crimp Fabric; forming; dry fibre process

1. Introduction

Out-of-autoclave dry fibre technology is one of the processes that has the potential to meet the increase in production rate targets for industries like aerospace. A key step prior to curing is the forming of the reinforcement material into the final part geometry [1]. In-plane shear is the dominant deformation mechanism in forming [2], resulting in large rotations in the fibre direction and a change in the net shape of the material [3]. Non-Crimp Fabrics (NCFs) are chosen for their higher mechanical properties by comparison to conventional woven fabrics [2], due to their fibres being stitched instead of woven. However, this architecture affects the shear behaviour, as the 'cross-over points' between tows around which rotation occurs are not present in stitched NCFs. One effect of the stitching is the asymmetry introduced when loading the fabric in different orientations to the stitch direction. This study investigates this parameter in relation to single diaphragm forming over a representative geometry for aerostructures.

2. Literature Review

Several studies exist in the literature investigating the effect of parameters defining Non-Crimp Fabric architecture [4]. These include: fibre orientation, areal weight and binder type, as well as those related to the stitch architecture: stitch type, length and tension. The asymmetry introduced by the stitching has been shown in both uniaxial test set-ups, like bias extension tests [4] and hemispherical punch set-ups with blank holders applying planar forces to the ply being punched through [5]. Chen et. al. even removed the stitching from a material sample in an attempt to show this as the driving factor, showing the stitch-less fabric becoming symmetric in both loading conditions. Figure 1(a) is taken from Bardl et. al.'s bias extension testing, showing

  doi:10.5075/epfl-298799_978-2-9701614-0-0

the difference in force required to shear a specimen with the stitch aligned in the load direction versus aligned perpendicular to the load. Figure 1(b) shows the results of a hemispherical punch test with a 45°/135° pillar stitch NCF showing the same principle in a three dimensional set up. A shorter distance (or extension) is seen from corner to corner in the stitch direction than perpendicular to it. This is because as equal load is applied to the perimeter of the ply, the 0° direction does not shear as much as the 90° direction, as shown in the bias extension shear force curve.

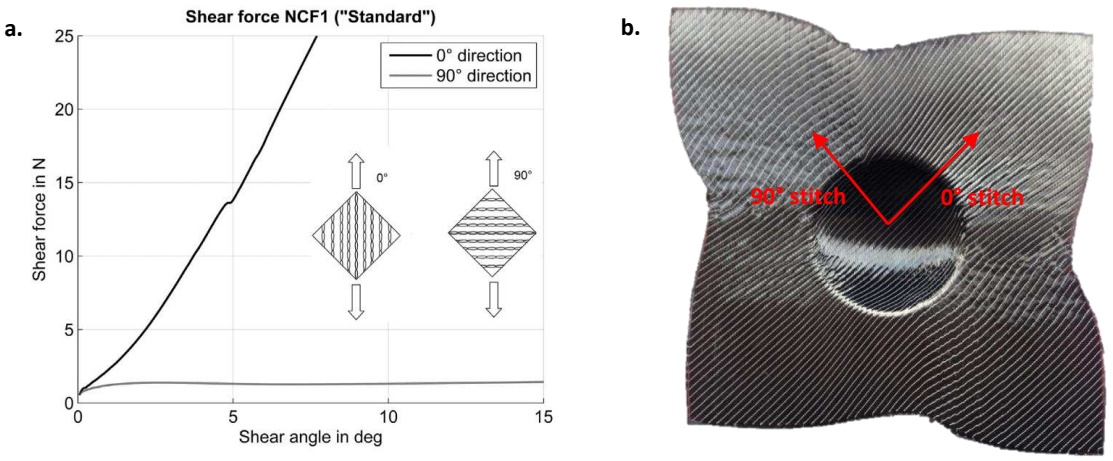

Figure 1. (a) Taken from [4]*: force shear curves for varying stitch direction to load (b) Taken from* [5]*: Biaxial +45/-45 NCF with a pillar stitch preform result in hemisphere forming process*

Both of these cases, however, show the effect of stitch to load in a controlled uniaxial loading test set-up. Whereas the results are important to characterise and understand NCF behaviour better, it is not clear whether they are applicable to processes where the loading is multiaxial and complex, such as single diaphragm forming. Figure 2 shows the forces acting on a preform in a single diaphragm forming process over two common geometry features, relevant to this study: a concave or female radius and a convex or male radius. As can be seen, the forces don't only act along the 'preform plane' but also perpendicular to it. There are not as many studies available using diaphragm processes by comparison to those using matched tool or punch and die forming. Those that do, for example Hallander's diaphragm forming of C-spars [6], are limited in size. This study aims to show the effect of stitching under representative complex loading using a single diaphragm forming process and on a large scale.

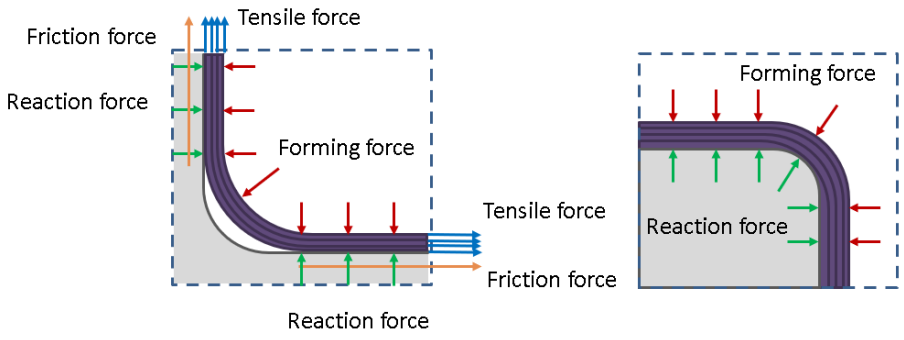

Figure 2. Adapted from Chen et. al. [7]*: force schematic for a female radius (left) and male radius (right) in a single diaphragm forming set up*

  doi:10.5075/epfl-298799_978-2-9701614-0-0

3. Methodology

Forming experiments were carried out on the geometry shown in Figure 3. The geometry contains two ramps with a gradient of 1:40 receding towards the centre of the geometry creating an excess in fabric length. Ramps are common in aerostructures for weight and loading optimization of the structure. The length of the geometry is approximately 2 m, a sizeable increase from any forming geometries currently available in the literature. Table 1 shows a list of dimensions. The NCF material was placed on the geometry upper surface and left to drape over the vertical web and rest on the lower surface under its own weight. A non-reusable diaphragm was sealed around four raised edges surrounding the geometry. This set-up ensures the kinematics of the diaphragm remain the same throughout the different trials. The diaphragm contacts the top surface first, followed by the male or convex radius and outside edge of the bottom surface. The last surface the diaphragm meets is the female or concave radius. The preform surface was scanned while still under vacuum with a Hexagon Absolute Arm and interrogated for wrinkle dimensions using Polyworks software.

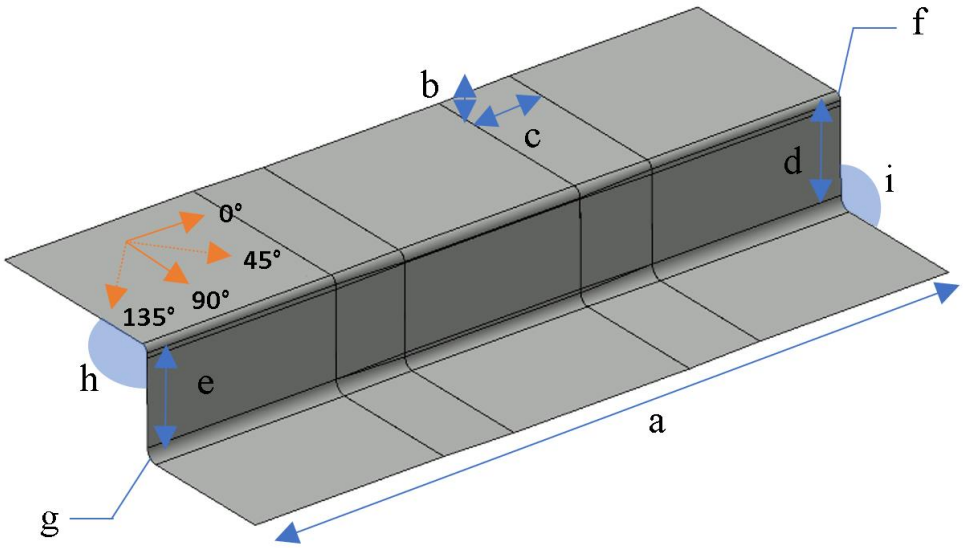

Figure 3. Geometry used for forming trials

Table 1: Geometry dimensions

Dimension	Number
Length [a] (mm)	2000
Ramp height to length ratio [b:c]	1:40
Web height ratio [d:e]	1:1
Convex to concave corner radius ratio [f:g]	1:2
Top surface / web to bottom surface / web angle ratio [j:k]	1:1

  doi:10.5075/epfl-298799_978-2-9701614-0-0

The preforms were assessed qualitatively through photographs and preform scans. Preform wrinkling was assessed through:

- Wrinkle colour maps showing the distribution of out-of-plane wrinkle heights
- Average direction of wrinkles relative to geometry features (corner radii and ramp location).

Two NCF orientations were used to create the preforms. The specification of each is shown in Table 2.

Table 2: NCF specification

ID	Orientation	Stitch type	Stitch size	Binder type
NCF1	0°/90°	Tricot	5.1 mm	Polyamide
NCF2	0°/45°			

Using these NCFs, the matrix of trials documented in Table 3 was carried out. Six plies were placed all at once on the geometry. This number was chosen to show significant wrinkling used to assess the effect of the parameter change. The stitch direction is given according to the rosette shown in Figure 3. The 90° stitch trials (T2 and T4) were carried out with the same NCF as that for the 0° stitch trials (T1 and T3) but with the ply rotated 90° on the geometry tooling to align the stitching correctly. This however meant the fibre directions relative to the geometry also changed. Whereas for T1 and T2, the orientation remained 0°/90°, T4 changed from 0°/45° a 90°/135° relative to the geometry. An asterisk on T4 is used to highlight this.

Table 3: Matrix of trials

Trial ID	NCF Ply sequence	Stitch direction to geometry
T1	$[0°/90°]_6$	0°
T2		90°
T3	$[0°/45°]_6$	0°
T4*		90°

4. Results & Discussion

The scanned preform results are shown in Figure 4. Colour maps show the distribution of out-of-plane heights along the wrinkle, with the scale adjusted for each scan for viewing purposes. Vertical lines show the start and end of both left and right ramps on the geometry. All preforms show wrinkling initiating on the outer edge of the ramps near the upper male radius and descending into the centre at an angle. The 0°/45° ply with stitch at 90° produces a much steeper angle than all other layups, however this may not only be an effect of the change in stitch direction but the change in fibre direction from 0°/45° to 90°/135° relative to the tool. This shows the importance of the choice in fibre orientations for biaxial NCF formats, with some pairs

forming better than others. Overall higher-out-of-plane wrinkle heights are observed when the stitch direction is aligned at 90° to the geometry. The wrinkling is approximately symmetric in appearance, though there are differences in overall wrinkle heights between left and right wrinkles, with the 0°/45° layups showing the least symmetry. This suggests if the geometry and laminate share a symmetry plane (e.g. 0°/90° plies), the resultant defect may also be symmetric.

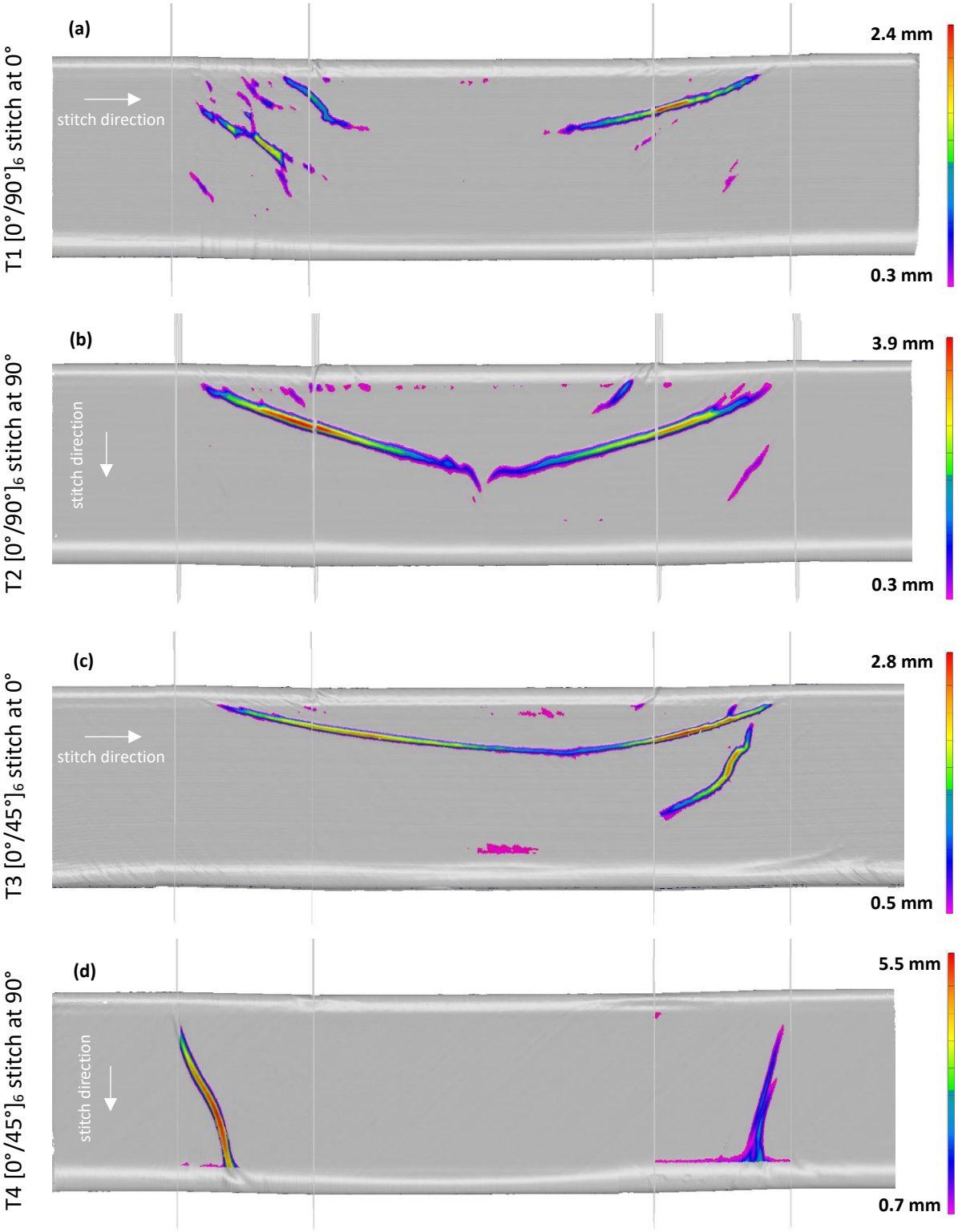

Figure 4. Frontal web view of 3D preform scans showing wrinkle height colour maps and location relative to ramps on geometry

The measured angles for both left and right wrinkles for the four trials carried out are given in Table 4. Angles were measured relative to the upper male radius or top of the tool and measured clockwise for left wrinkles and anti-clockwise for right wrinkles. Angles have been colour coded with green showing smaller angles and red showing larger angles to the horizontal (upper male radius). The 0°/45° layup with the stitch angled at 90° showed the biggest angle values, with the wrinkle approaching the stitch direction, as seen in Figure 4(d).

Table 4: Wrinkle angle results

Trial ID	NCF Ply sequence	Stitch direction to geometry	Left wrinkle angle	Right wrinkle angle
T1	$[0°/90°]_6$	0°	38°	20°
T2		90°	21°	19°
T3	$[0°/45°]_6$	0°	14°	18°
T4		90°	69°	74°

As well as characterising the wrinkling phenomena, this study can help better understand the loading applied by the diaphragm during the forming process. The literature review pointed at studies involving bias extension or punch tests, equipped with load gauges to obtain force shear profiles as shown in Figure 1. Though load was not measured in this study – using wrinkles instead as a proxy measure for drapability of the fabric – an assumption can be made on the 'principal loading directions', based on the kinematics of the diaphragm. It should be noted, though labelled as 'loading', this is not equivalent to mechanical loading applied in a tensile test. As described in the methodology, the diaphragm contacts first on the upper surface and upper male radius, followed by the outer edge of the bottom surface. With the top and bottom surface 'secured' on to the geometry by the diaphragm, an assumption is made that the principal loading direction within the plane of the geometry web is as drawn in Figure 5 below. This means the as labelled 0° direction stitch is aligned perpendicular to this load direction and vice versa for the 90° direction stitch.

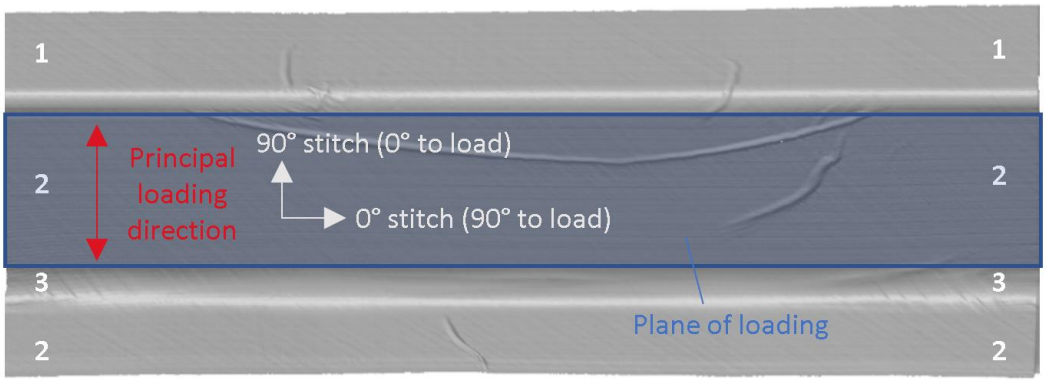

Figure 5. Diagram of drape sequence and resulting 'principal' load paths on geometry

Comparing this to Chen et. al.'s result of a biaxial NCF on a hemisphere punch can help explain why the 0° stitch trials (T1 and T3) showed overall lower wrinkling. Based on the assumption of the principal loading direction following the bag kinematics, the stitch in T1 and T3 is aligned perpendicular (at 90°) to the load, resulting in higher shearing by comparison to T2 and T4 (stitch aligned at 0° to the assumed load). The NCF's fabric ability to shear in the former two leads to a lower out-of-plane wrinkle amplitude. Trials T2 and T4 on the other hand are restricted in shear by the stitch direction running along the load path leading to higher wrinkle amplitudes. The differences in absolute wrinkle height values between T1 and T3, and T2 and T4, respectively are likely due to the resultant bending stiffness properties of the fibre orientations combined to make the biaxial formats. This property change between T3 and T4 (from 0°/45° to 90°/135°) is likely the biggest driver for the difference in wrinkling observed, neglecting the effect of stitch direction by comparison to T1 and T2 (both maintaining a 0°/90° orientation relative to the geometry).

5. Concluding Remarks

The effect of stitch orientation to load has been shown in the literature for dry fabric samples in uniaxial loading scenarios. This study has shown this effect on a much larger scale on a geometry with representative complex loading for a single diaphragm forming process. Results show that whereas the angle of the wrinkle direction is mostly driven by the fibre direction, the wrinkle height or amplitude is driven by stitch direction. The importance of the choice in fibre orientations to combine for biaxial NCF formats is highlighted, with some pairs draping better than others. Overall, this study shows a tooling geometry and method with the potential to study further NCF material parameters, relevant to an industrial material characterisation campaign.

Acknowledgements

The research presented was supported by Airbus, part funded by the UK's Aerospace Technology Institute, and the EPSRC through the Centre for Doctoral Training in Composites Manufacture (EP/L015102/1) and the Programme Grant 'Certification for Design – Reshaping the Testing Pyramid' (CerTest, EP/S017038/1). The support received is gratefully acknowledged.

6. References

1. Turk MA, Vermes B, Thompson AJ, Belnoue JPH, Hallett SR, Ivanov DS. Mitigating forming defects by local modification of dry preforms. Compos Part A Appl Sci Manuf [Internet]. 2019;(October):105643. Available from: https://doi.org/10.1016/j.compositesa.2019.105643

2. Lomov S. Non-Crimp Fabric Composites: Manufacturing, Properties and Applications. Woodhead Publishing Series in Composites Science and Engineering; 2016.

3. Thompson AJ, Said B El, Belnoue JP, Hallett SR. Modelling process induced deformations in 0 / 90 non-crimp fabrics at the. Compos Sci Technol [Internet]. 2018;168(January):104–10. Available from: https://doi.org/10.1016/j.compscitech.2018.08.029

4. Bardl G, Nocke A, Hübner M, Gereke T, Pooch M, Schulze M, et al. Analysis of the 3D draping behavior of carbon fi ber non-crimp fabrics with eddy current technique. Compos Part B [Internet]. 2018;132:49–60. Available from:

  doi:10.5075/epfl-298799_978-2-9701614-0-0

https://doi.org/10.1016/j.compositesb.2017.08.007

5. Chen S, Mcgregor OPL, Harper LT, Endruweit A, Warrior NA. Composites : Part A Defect formation during preforming of a bi-axial non-crimp fabric with a pillar stitch pattern. Compos Part A [Internet]. 2016;91:156–67. Available from: http://dx.doi.org/10.1016/j.compositesa.2016.09.016

6. Hallander P, Akermo M, Mattei C, Petersson M, Nyman T. An experimental study of mechanisms behind wrinkle development during forming of composite laminates. Compos Part A Appl Sci Manuf [Internet]. 2013;50:54–64. Available from: http://dx.doi.org/10.1016/j.compositesa.2013.03.013

7. Chen S, McGregor OPL, Endruweit A, Elsmore MT, De Focatiis DSA, Harper LT, et al. Double diaphragm forming simulation for complex composite structures. Compos Part A Appl Sci Manuf [Internet]. 2017;95:346–58. Available from: http://dx.doi.org/10.1016/j.compositesa.2017.01.017

THE EFFECT OF TEST PARAMETERS ON THE MICROCRACKING BEHAVIOUR OF CARBON COMPOSITE LAMINATES DURING CRYOGENIC CONDITIONING

Huw, Edwards[ab], Janice, Dulieu-Barton[a], Byung Chul, Kim[a], Daniel, Galpin[b], Marcus, Walls-Bruck[b]

a: Bristol Composites Institute,
University of Bristol,
Bristol, BS8 1TR
UK
huw.edwards@bristol.ac.uk

b: National Composites Centre
Bristol and Bath Science Park
Emersons Green
Bristol
BS16 7FS

Abstract: *The work outlined in this paper investigated the impact of test parameters on the microcracking behavior of carbon composites laminates during cryogenic cycling. Previous studies have not defined a standard test method and have used a range of cooling methods with different cooling rates, cycle temperatures and coupon geometries, the results of which can be difficult to compare. In this paper the impact of cycling composites with different heating and cooling rates, and coupon sizes, to both liquid nitrogen (77 K) and liquid hydrogen (20 K) temperatures is investigated for two composite materials with different matrix compositions. The overarching aim being to develop a consistent testing methodology to identify candidate composite materials suitable for the manufacture of LH2 storage tanks.*

Keywords: Hydrogen; Pressure-Vessels; Cryogenic, Microcracking

1. Introduction

Liquid hydrogen (LH2) is increasingly being considered as a zero-carbon fuel for commercial aviation. LH2 is stored at low pressures (< 10 bar) and low temperatures (20 K). Designing lightweight LH2 tanks is a rapidly growing area of interest and the high specific strength and stiffness of carbon fibre-reinforced polymer (CFRP) composites, along with their anisotropic properties, have made composites an attractive proposition.

Significant challenges exist when applying CFRPs to LH2 storage. When cooled to cryogenic temperatures, internal stresses build up within the composite, caused by differential expansion and contraction of the constituent fibre and matrix materials. The primary mode of failure of CFRPs when cooled to cryogenic temperatures is microcracking. Microcracking can reduce the structural properties of the CFRP and create permeation paths that allow leakage of hydrogen through the structure.

The screening and characterisation of composites for use in cryogenic environments down to 20 K is an under researched area and work is needed to develop applicable test methods. Coupon geometry, cooling rates and cycle temperatures all can have an impact on the propensity for a composite to microcrack.

To thermally cycle coupons there have been numerous studies in literature that use liquid nitrogen (LN2), however this limits the lower temperature of the thermal cycle to 77 K. To achieve

  doi:10.5075/epfl-298799_978-2-9701614-0-0

temperatures below 77 K, liquid helium (LHe) can be used. It is significantly less challenging to test with LN2 when compared to LHe due to scarcity of helium and additional energy required to liquify it. However thermal stress continues to increase with a decrease in temperature so a true picture of material behaviour at 20 K cannot be found without testing below LN2 temperatures. Some prior studies have used liquid helium with a temperature of 4 K [2, 3].

Coupons can be cooled by direct immersion in cryogenic liquids, which gives the highest cooling rates when compared to cold gas or cold-head based cooling. For warming the coupons, the highest heating rates are through immersion in warm water, although warming in ambient air or in an oven is common. High cooling rates can cause thermal shock within the coupon where there is a temperature differential across the coupon causing internal stress. Investigations have shown reducing thermal shock can reduce microcracking during thermal loading [4].

The impact of coupon size has been investigated numerically and it can be shown that near the edge of flat laminated plates the stress field can change, causing behaviour that would not be seen in cylindrical tanks [5]. Coupon sizes in literature vary, with edge lengths varying from 150 mm [6] to 12 mm [7]. There has been no clear guidance on the size and shape of the coupon suitable for thermal cycling tests.

2. Experimental Methods

2.1 Materials

For the experimental work, two materials systems were used in order to test materials with different expected levels of microcracking. Laminates with two different matrix systems were tested: a standard aerospace type toughened epoxy system and the same aerospace epoxy system without toughening agents to reduce quality and induce microcracking. Both unidirectional prepreg systems included intermediate modulus carbon fibres of approximately 200 g/m^2 areal weight.

For the layup, both the ply orientation and stacking sequence have been shown to have an influence on microcracking behaviour. The most comprehensive study from Grogan [8] compared cross-ply and quasi-isotropic layups over a range of laminate thicknesses. It was found that increasing ply thickness increased microcracking. Quasi-isotropic layups had increased levels of microcracking when compared to a cross ply equivalent.

In choosing a laminate for cryogenic testing there is a choice between having a laminate that triggers microcracking and a laminate for optimal performance. For test method development, triggering microcracking is important to enable comparison of variables so the plies were blocked in pairs to increase the apparent ply thickness in this work. A quasi-isotropic laminate was chosen as this is more reflective of the number of angles likely to be used in a tank design. The layup design for all coupons is a 16 ply quasi-isotropic $[0_2/45_2/\text{-}45_2/90_2]_s$.

To process the material systems into coupons, panels with dimensions of 1 m x 1 m were manufactured. The panels were manufactured by hand layup and cured between two caul plates with a cure cycle of 180 °C for 133 minutes with a 2 °C/min heating and 3 °C/min cooldown rates.

After curing the panels were inspected using ultrasound, the unmodified toughened system showed low porosity and with and the modified untoughened system showed high porosity. The untoughened coupons were sectioned to provide pairs of coupons of matched quality for each test variable.

  doi:10.5075/epfl-298799_978-2-9701614-0-0

The panels were then sectioned into coupons of three different sizes (25 mm x 25 mm, 75 mm x75 mm and 150 mm x 150 mm) using a water-cooled diamond bladed panel saw to reduce any edge damage. Two perpendicular edges of the coupons were then polished on a rotary polisher in preparation for optical microscopy.

2.2 Cryogenic Thermal Cycling

Two methods of cooling were used: direct immersion in LN2, and cooling in cold helium (He) vapour. Direct immersion in LN2 is the most common method of cooling as it is relatively low cost and commonly available. Cooling in He vapour enabled controlled rate cooling down to 20 K.

To cool the coupons in liquid nitrogen, an open Dewar of the appropriate size was filled with LN2

The coupons were suspended in a copper cage and immersed rapidly into the LN2. Upon immersion, the LN2 boils rapidly at the interface between the surface of the coupon and liquid in a process called film boiling. Once the boiling has subsided, the coupon stabilised at 77 K within 15 seconds. The coupons were left in the fluid for a minimum of one minute after boiling had subsided.

The coupons were then removed from the fluid and left in ambient lab conditions to warm. The humidity from the atmosphere led to a build-up of frost on the coupons. As the coupons continued to warm, the frost transitioned to moisture on the surface. The phase change of the condensation indicated the surface of the coupon was above 273 K and the coupons were then moved to an oven at 323 K to dry. The coupons were then left in the oven for a minimum of 5 minutes. The coupon was then removed from the oven and the thermal cycle completed.

For the 20 K testing a LHe Dewar with a dipping probe was used to cool the coupons in the cold vapour of the helium. An image and schematic of this set-up is given in Figure 1. There was a thermal gradient within the Dewar in the gaseous phase of the helium, rising from 4 K at the surface of the liquid helium to ambient temperature at the top of the Dewar. By using a dipping probe, the coupon was lowered from the entrance at the top through the thermal gradient in the gaseous phase. By controlling the elevation of the coupon in the Dewar, both rate of heat transfer and temperature can be controlled.

The coupon was also warmed to above freezing at a controlled rate in the dipping probe before being heated in an oven. By warming the coupon to above freezing before allowing it to contact with atmospheric conditions, frost was prevented from forming on the surface of the coupon and condensation was minimised.

A comparison of cooling rates and temperatures can be seen in Figure 2, based on thermocouple measurements from the 25 mm coupons. For the immersion testing, a thermocouple was embedded in the centre of the laminate upon manufacture. For the slow cooling, the thermocouple was attached to the end of the probe in contact with the coupon.

  doi:10.5075/epfl-298799_978-2-9701614-0-0

2.3 Inspection of Microcracking

An inverted reflected light microscope was used to take the images of the coupons at 5X magnification. Images were taken of two perpendicular edges. For the 25 mm coupons it was possible to capture the entire edges. For the larger coupons, only the areas that met on the polished corner were captured, this equated to approximately 35 mm along the edges.

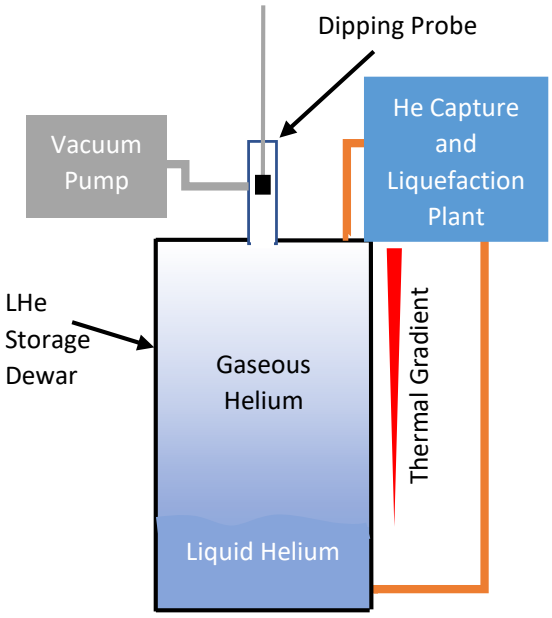

Figure 1: Schematic of bucket cryostat and dipping probe.

The coupons were cycled up to 20 cycles with images taken at 0, 1, 5, 10, and 20 cycles to track microcrack progression.

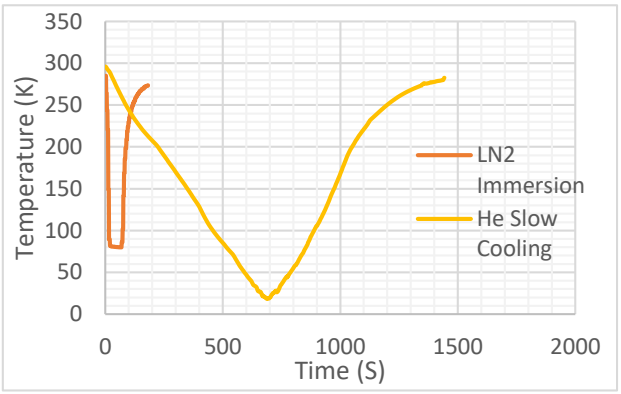

Figure 2: Time temperature graph of LN2 immersion compared to controlled rate He cooling for 25 mm coupons.

3. Results & Discussion

The results for coupon material, coupon size, and cooling method trials, are discussed below.

Material - For the two materials, in general there is more microcracking in the coupons with untoughened matrix than that with toughened matrix. This trend is most visible in LN2 25 mm coupons when compared with the other cooling rates and coupon sizes. The images for the LN2 25mm coupons are shown in Figure 3 and Figure 4.

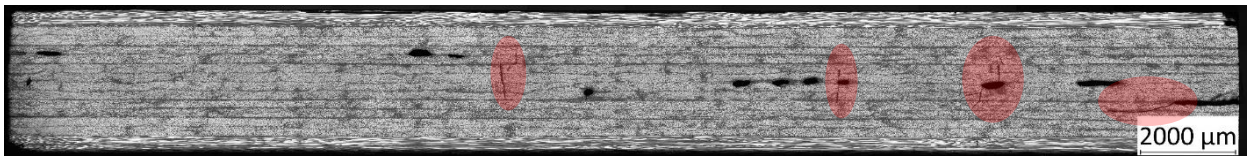

Figure 3: 25 mm untoughened coupon after 20 LN2 cycles

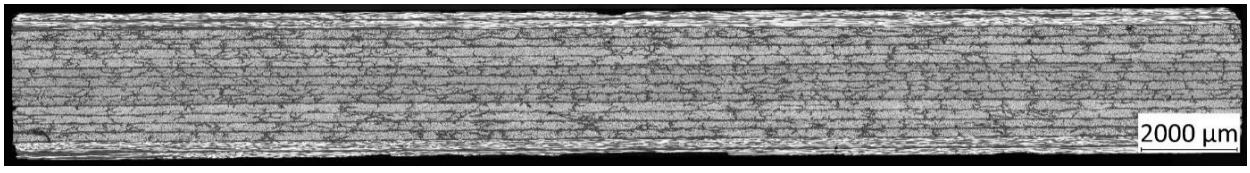

Figure 4: 25 mm toughened coupon after 20 LN2 cycles

It was apparent that in the untoughened coupons microcracks are present predominantly originating from the areas with voids. It is possible that the voids are acting as stress concentration points and / or crack initiation sites. In the toughened coupons there is no microcracking present in most coupons.

  doi:10.5075/epfl-298799_978-2-9701614-0-0

Coupon size - Three coupon sizes were chosen for this work: 25 mm, 75 mm, and 150 mm.

The highest density of microcracking is observed in the 150 mm coupons, with the least occurring in the 75 mm coupons and the 25 mm coupons having intermediate levels.

The microcracking in the 150 mm coupons appears to be uniformly distributed along the length of the coupon. In comparison in the 25 mm coupons the microcracking appears to be predominantly around voids.

The effect of size is most clear in the untoughened material, per the images shown below in Figure 5, Figure 6, and Figure 7.

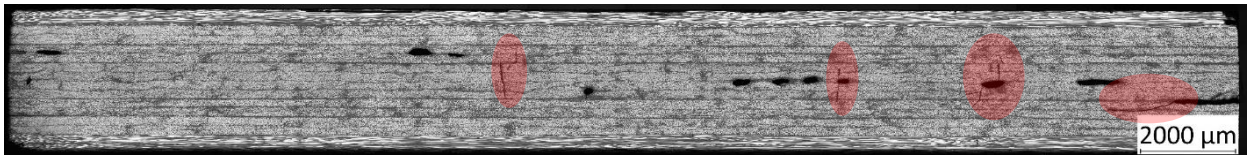

Figure 5: 25 mm untoughened coupon after 20 LN2 cycles

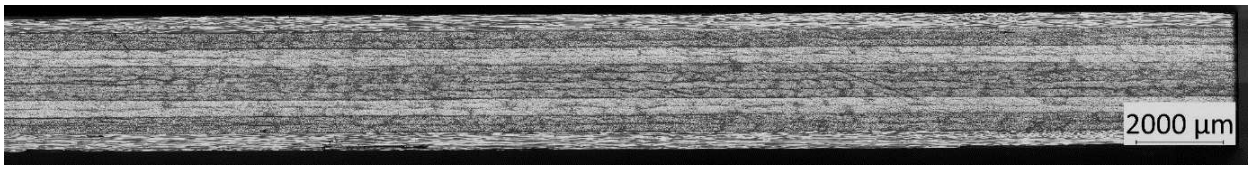

Figure 6: 75 mm untoughened coupon after 20 LN2 cycles

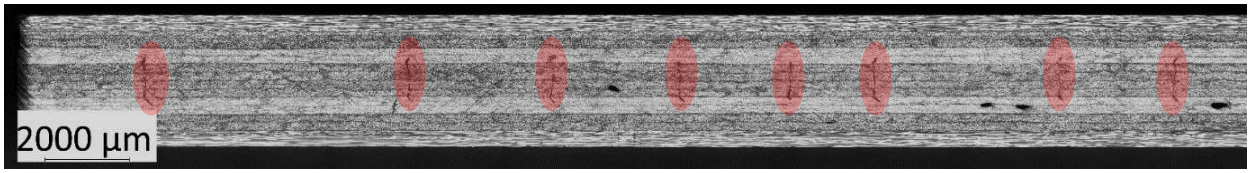

Figure 7: 150 mm untoughened coupon after 20 LN2 cycles

It is possible that edge effects may dominate the microcracking in the 25 mm coupons, providing more initiation sites than in the large coupons.

For the 150 mm coupons it appears that there was a temperature gradient across the coupon when cooled in LN2. This was visible as the film boiling subsided from the edges to the centre in a square pattern as shown in **Figure 9**. This could be due to a greater in-plane thermal conductivity than through thickness thermal conductivity. There could also be a through thickness thermal gradient as the vapour layer could be insulating the bottom surface of the coupon as the gas has to move from coupon centre to edges as shown in Figure 8, which can increase the thickness of the gas layer. A temperature gradient across the coupon will also act to add stress to the coupon and could be the initiator of microcracking.

  doi:10.5075/epfl-298799_978-2-9701614-0-0

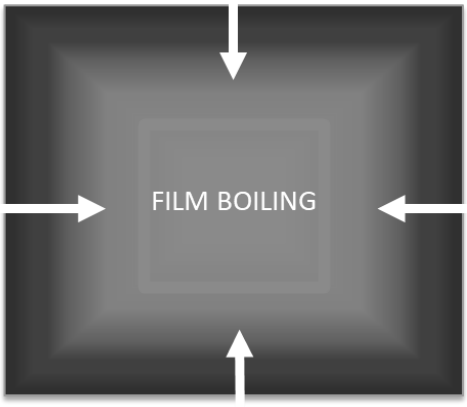

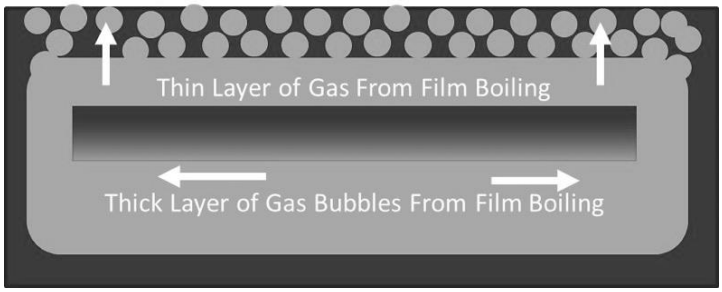

Figure 9 & Figure 10 : Film boiling recedes on top surface from edges to centre in rectangular pattern & gas migration across lower surface of coupon providing increased insulation

Cooling method - The effects of cooling rate and minimum temperature could only be compared in combination with each other due to the choice of cooling methods. Results are available for the 25 mm coupons. At this coupon size it appears that rapid cooling has a more damaging effect on microcracking than minimum temperature.

Results are shown for untoughened coupons in Figure 11 and Figure 12.

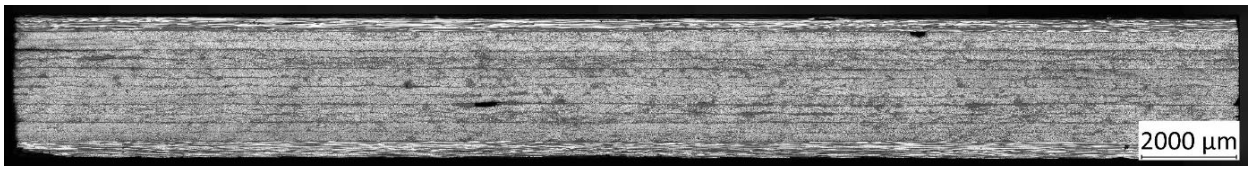

Figure 11: 25 mm untoughened coupon after 20 LHe cycles

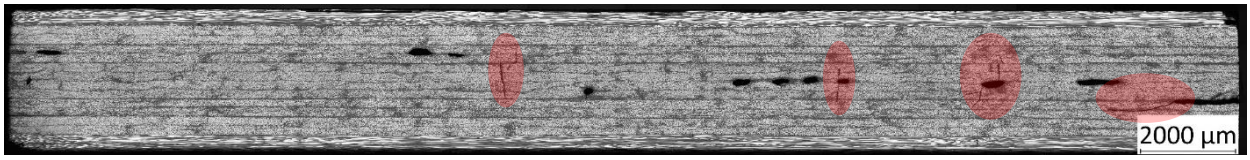

Figure 12: 25 mm untoughened coupon after 20 LN2 cycles

4. Conclusions

Work carried out so far indicates that there was a difference in microcracking behaviour across epoxy matrix systems with different levels of toughening. There are also indications that voids and porosity within the laminate can increase levels of microcracking through providing microcrack initiation sites and increasing local stresses. This finding highlights the importance of manufacturing quality and inspection.

Coupon size had a large impact on microcracking, with the trend that microcracking decreases between an edge length of 25 mm to 75 mm but then increased on larger 150 mm edge length coupons potentially due to the thermal gradient within the coupons. When designing thermal cycling test methods consideration should be given to the impact of film boiling and the potential of thermal gradients in coupons.

Finally, fast cooling in liquid nitrogen to 77 K appeared to induce more microcracking than slow cooling in helium gas to 20 K, so could be a practical way to accelerate the microcracking for relative comparison between different materials.

Work is ongoing to investigate the initial findings further across more materials to provide increased confidence in the trends that are seen. Experiments are underway to decouple the impact of cooling rate and lower temperature and will be completed later in the year.

  doi:10.5075/epfl-298799_978-2-9701614-0-0

References

1. Grogan, D.M., et al., *Damage characterisation of cryogenically cycled carbon fibre/PEEK laminates.* Composites Part A: Applied Science and Manufacturing, 2014. **66**: p. 237-250.

2. Kessler, S.S., T. Matuszeski, and H. McManus. *Cryocycling and mechanical testing of CFRP for the X-33 liquid H2 fuel tank structure*. in *Annual Technical Conference of the American Society for Composites*. 2001.

3. Whitley, K. and T. Gates, *Thermal/Mechanical Response and Damage Growth in Polymeric Composites at Cryogenic Temperatures*, in *43rd AIAA/ASME/ASCE/AHS/ASC Structures, Structural Dynamics, and Materials Conference*. 2002.

4. Oh, B., et al., *An Experimental Investigation of the Effect of Thermal Shock on Damage in Cryogenic Composite Laminates*, in *47th AIAA/ASME/ASCE/AHS/ASC Structures, Structural Dynamics, and Materials Conference
 14th AIAA/ASME/AHS Adaptive Structures Conference
 7th*. 2006.

5. Wang, A. and F.W. Crossman, *Edge effects on thermally induced stresses in composite laminates.* Journal of Composite Materials, 1977. 11(3): p. 300-312.

6. Bechel, V., *Permeability and Damage in Unloaded Cryogenically Cycled PMCs*, in *46th AIAA/ASME/ASCE/AHS/ASC Structures, Structural Dynamics and Materials Conference*. 2005.

7. Park, C.H. and H.L. McManus, *Thermally induced damage in composite laminates: Predictive methodology and experimental investigation.* Composites Science and Technology, 1996. 56(10): p. 1209-1219.

8. Grogan, D.M., *Damage and permeability in linerless composite cryogenic tanks*. 2015.

The research described in the paper was supported by the Engineering and Physical Sciences Industrial Doctorate Centre in Composites Manufacturing (EP/L015102/1) and the National Composites Centre.

  doi:10.5075/epfl-298799_978-2-9701614-0-0

DEVELOPMENT OF FORMING SIMULATION CAPABILITIES FOR USE IN LARGE-SCALE NEXT-GENERATION COMPOSITE AEROSPACE STRUCTURES

Lachlan M. Williams, Adam J. Thompson, Stephen R. Hallett and Jonathan P-H. Belnoue[a]

a: Bristol Composites Institute, University of Bristol, Queen's Building, BS8 1TR, Bristol, UK – lachlan.williams@bristol.ac.uk

Abstract: *Non-Crimp Fabrics (NCFs) are a textile of interest in future aerospace structures requiring a high rate of manufacture. NCFs pose unique challenges to forming simulation due to the presence of deformation mechanisms which were not active in traditional woven textiles, most significantly, tow sliding. This contribution presents early developments in a contact approach to modelling stitch effects within NCFs. The stitch model is separated from the material model and evaluated as a virtual entity within the contact evaluation procedure. Further consideration is given to robust model testing informed by practical experience and the additional tools required to extract use from forming simulation capabilities.*

Keywords: Non-Crimp Fabric; Forming; Manufacturing Process Simulation

1. Introduction

Application of advanced composites in the aerospace industry is not new. Where the timeline begins can be debated, but the Airbus A340-600 has flown a primary structure made of composites, a keel beam, since 2001. Composites have not stood still. New technologies and applications thereof to reduce cost and improve production rate while maintaining or possibly improving mechanical performance are in strong demand. One candidate technology is the application of Non-Crimp Fabrics (NCFs) to advanced aerospace composites, via dry fibre forming and subsequent resin infusion. In today's context, where decarbonization and cost pressure pushes us towards challenging geometries with higher integration, insight into the forming process is required to offset increased risk of defect generation.

Simulation based prediction of ply conformation of dry fibre composites when formed from the material stock onto a tool surface now has a multi-decade history [1,2]. The forming simulation field has demonstrated modelling of physical materials via Finite Element (FE) implementations which use characterized material models. These methods can take account of manufacturing process, defect generation and as manufactured fibre orientation [3]. The presented contribution details early work on NCF material modelling and application of forming simulation.

2. Non-Crimp Fabric Forming Simulation

A core requirement of composite textiles is to ensure handleability during manufacturing processes. Non-Crimp Fabrics (NCFs) are composed of multiple layers of fibrous reinforcement at selected fibre orientations which are then stitched through the thickness to provide handleability. The stitching process minimally affects the state of the fibres.

This stands in contrast to traditional weaving technology which perturbs the tows out of plane, inducing 'crimp' at the crossover point. While the crimp is undesirable from a mechanical

  doi:10.5075/epfl-298799_978-2-9701614-0-0

performance perspective, it enforces a boundary condition between tows which is analogous to a no-slip condition at the crossover points. This condition is of great practical use when creating material models and therefore has heritage in forming simulation dating back to pin-jointed net kinematic forming.

In [4] it is demonstrated by experiment that while NCF eliminates undesirable crimp, stitching fundamentally permits tow sliding through the stitch constraint. The work also demonstrated an ability to simulate the mechanism. Tensile stitch forces are modelled by through thickness bar elements, affixed to each constituent unidirectional fiber mesh within an NCF via a contact with a modified anisotropic Coulomb friction law which permits sliding in the fiber orientation once a tension threshold has been met. The use of a contact enables a formulation which permits large tangential displacements at the interface between fibre layers.

The presented work expands upon this approach by moving all stitch considerations from the primary modelling space into a single contact formulation. By modelling stitch effects within the contact formulation, the stitch problem is conveniently separated from the reinforcement material model. It is also made possible to take advantage of the contact procedure's distribution of contact stresses across the contact area associated with an individual proximity point. By extension, this makes the contact formulation agnostic to the structure of the mesh which comprises the individual unidirectional fibre layers of a ply. This distributive feature of the approach is expected to be advantageous when applied to very large forming problems. Further, the contact search operation is computationally expensive. The outlined procedure extends the functionality of existing proximity points which are required to enforce normal contact between the UD plies. Therefore, it maintains the same number of total contact search operations to be conducted at each increment, eliminating propagation of an expensive operation.

This approach results in the following contributions at the contact evaluation:

$$\boldsymbol{\sigma_C}(\boldsymbol{\delta_C}) = \begin{bmatrix} \sigma_{C,n} \\ \sigma_{C,t1} \\ \sigma_{C,t2} \end{bmatrix} = \begin{bmatrix} \sigma_{P,n} \\ 0 \\ 0 \end{bmatrix} + \begin{bmatrix} 0 \\ \sigma_{F,t1} \\ \sigma_{F,t2} \end{bmatrix} + \begin{bmatrix} \sigma_{S,n} \\ \sigma_{S,t1} \\ \sigma_{S,t2} \end{bmatrix} \quad (1)$$

Where $\boldsymbol{\sigma_C}$, σ_P, σ_F and σ_S are the contact stresses, and stress contributions due to penetration, friction and stitching respectively. $\boldsymbol{\delta_C}$ are the contact displacements. Subscripts n, $t1$ and $t2$ are the normal, first and second tangential axis of the local contact coordinate system.

For the purpose of a proof of concept, to resolve the stresses from the stitch, a simple function, $\boldsymbol{\sigma_S}(\boldsymbol{\delta_c})$, was implemented in Abaqus using a virtual truss element representing the through thickness components of the NCF stitch, the effect of which is analogous to a linear-elastic no-separation condition and pseudo-friction. The reinforcement was modelled by a unidirectional shell-membrane implementation of HypoDrape [3]. Figure 1 shows the effect of the stitch constraint. When formed over an ellipsoid 'rugby ball' shape (see figure 2) in the absence of stitch effects, the constituent UniDirectional (UD) fibrous layers corresponding to a worse case scenario, a [0°,45°] NCF ply, are fee to adopt their preferred lowest stored energy deformed shape. With the stitch component active, a compromise global net shape between the two isolated shapes is achieved, as expected.

Current work focuses on advancing the stitch stress evaluation to $\boldsymbol{\sigma_S}(\boldsymbol{\delta_c}, \boldsymbol{f})$, a function of contact displacements and local fiber orientations, $\boldsymbol{f}$ (see figure 3), to gain functional parity with

  doi:10.5075/epfl-298799_978-2-9701614-0-0

the literature [4]. However, the literature shows that stitch effects are complex. In [5] it was shown that under shear deformation the stitch yarn can be, but is not always, highly mobile in the fibre bed. This implies in some states the stitch yarn redistributes rather than imposing constraining forces on the fibrous tows as intended. It is well documented in the literature that some stitching patterns at particular orientation to the fibre orientations can produce an asymmetric shear response [6]. In combination with the aforementioned presence of tow sliding in the NCF, these examples portray the result of the stitch response to NCF ply deformation as a compliant, conditional constraint. How and if to represent such mechanisms in $\boldsymbol{\sigma_S}$, with what inputs, $\boldsymbol{\sigma_S}(\boldsymbol{\delta_c}, \boldsymbol{f}, \dots)$, while considering the sensitivity of the final formed ply shape to these mechanisms and by extension their practical relevance, is a core activity of this research.

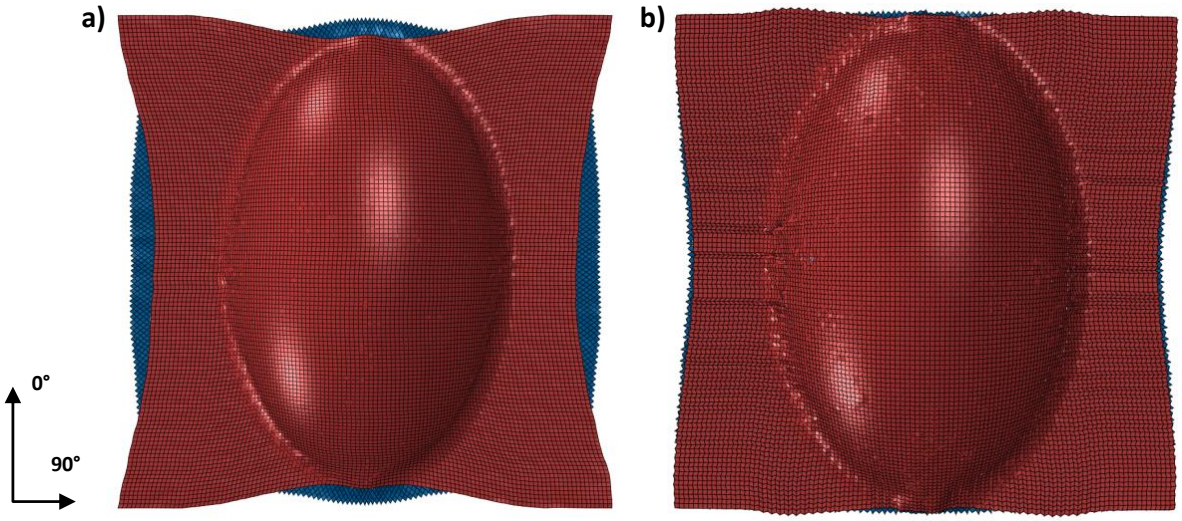

Figure 1. Proof of concept demonstration in Abaqus of an NCF stitch model implemented via VUINTERACTION subroutine on a [0°,45°] NCF, formed over an ellipsoid. Red upper ply and blue lower ply 0° and 45° respectively. a) Simulation result with friction only contact between constituent plies displaying independent conformation. b) Simulation result with active stitch model in contact between constituent plies displaying compromise NCF net shape.

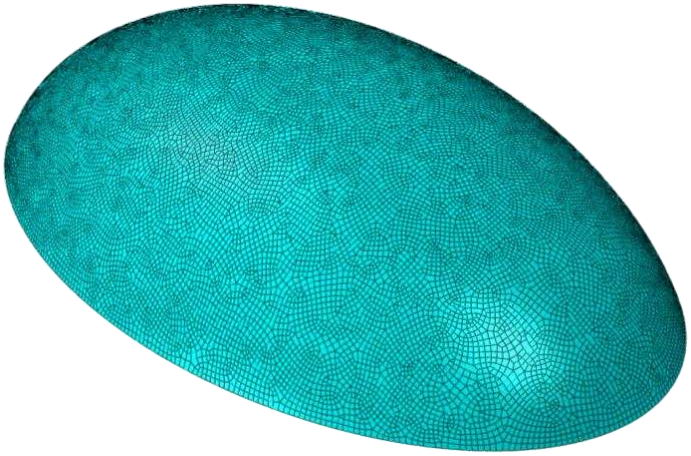

Figure 2. The ellipsoid 'rugby ball' tool which performed the forming action in the simulation shown in figure 1.

  doi:10.5075/epfl-298799_978-2-9701614-0-0 published under CC BY-NC 4.0 license

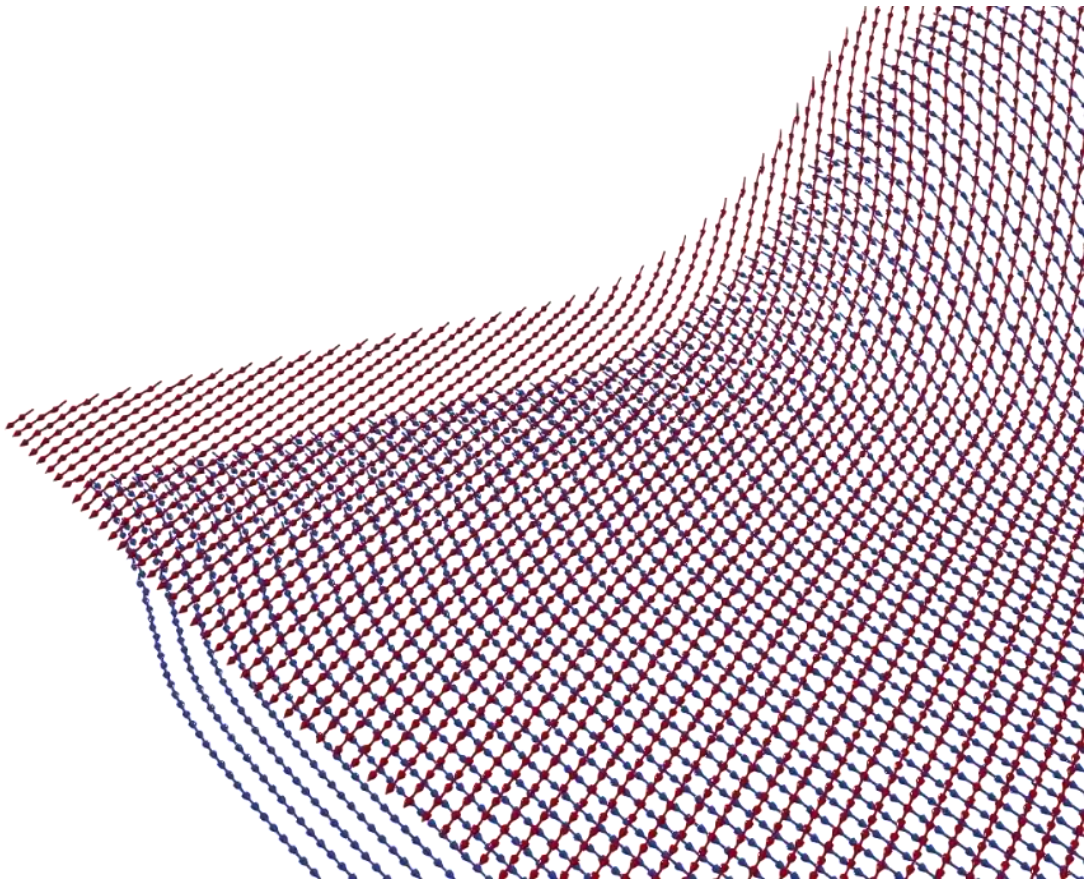

Figure 3. Visualization in Paraview of local fibre orientations of two constituent plies of an NCF, initialized at 45 degrees separation from one another. Fibre orientations were extracted from an Abaqus contact subroutine during a simulation.

The high degree of design freedom inherent to the NCF architecture via the stitching process has many potential benefits. However, formability and therefore dependent part quality attributes are highly sensitive to architecture, in particular stitch design. Material selection generally occurs early via physical test, an example of freezing a significant proportion of the design space before most engineering challenges have been solved or encountered. A sophisticated stitch model could support evaluation of the inherent trade-offs in textile architecture in the context of intended geometries during early conceptual design, long before tooling is available for physical test.

3. Observations in Making Useful Tools

An accurate material model is not sufficient to make a tool useful. It has been observed that the model creation and analysis process can be time consuming. This lowers the productivity of costly engineering professionals and by extension reduces the impact of forming simulation. The scope of the presented research includes practical deployment and therefore consideration of the software toolchain which may be required to enable useful implementation of FE forming simulation in the industrial setting. Tools developed for this purpose are presented in figure 4.

Some considerations are straightforward, such as routines which prepare material models for the solver. Others are complex, such as pursuing automation in the model building process

  doi:10.5075/epfl-298799_978-2-9701614-0-0

which must account for the diverse nature of tools and manufacturing processes, where we normally rely on the expert knowledge of engineers.

The accumulation of code for a growing toolchain is often met with concern, especially regarding maintainability. In response to this, this research activity has made great effort to write good quality code which does useful, general things, even if only intended for a narrow application. In the beginning this slowed down the rate of progress, but now it is an accelerant. New problems can often draw on the existing code base to quickly produce a prototype or are able to reuse a technical core entirely**.**

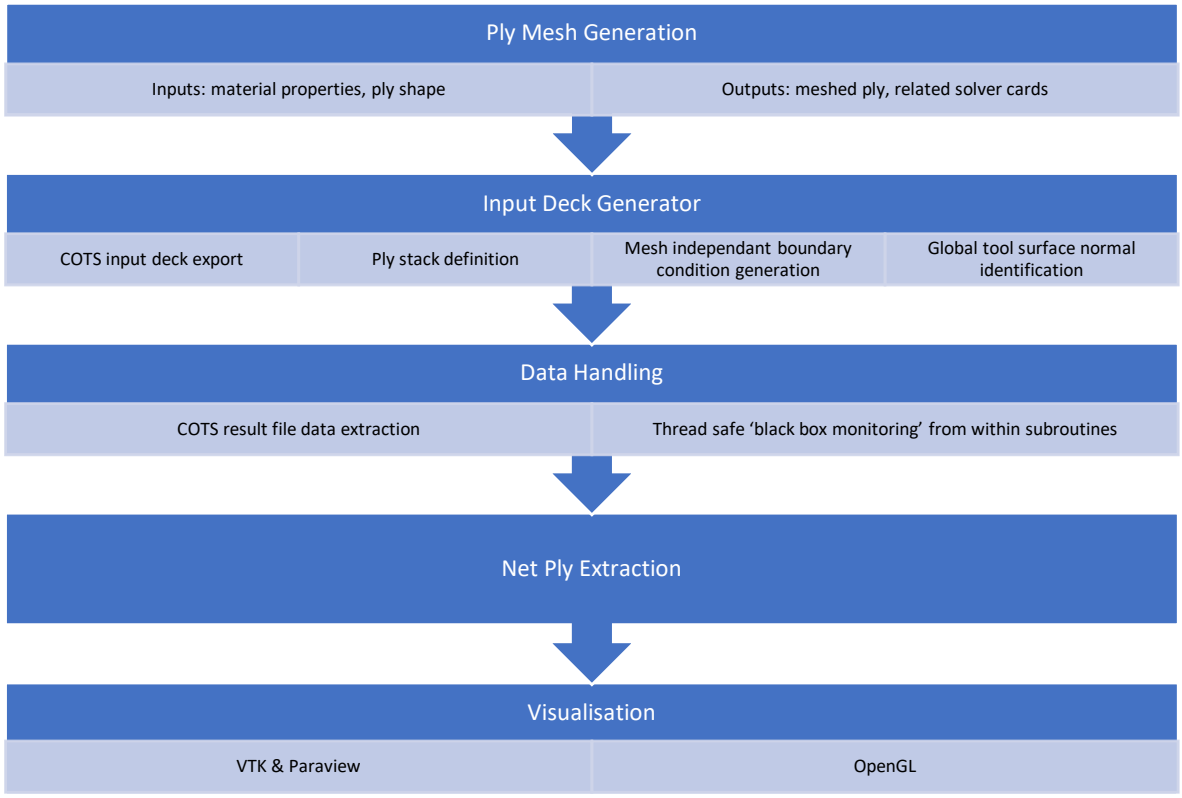

Figure 4. A coarse chart depicting the software toolchain developed around the core forming simulation capability to enable useful analysis.

4. Testing for Robustness

Practical experience of FE forming simulation has shown that stability can be hard to achieve. Widespread use of explicit solvers in lieu of implicit indicates the difficulty experienced in attaining solutions when considering the tradeoff with inherent risk of loss of accuracy in an explicit scheme applied to quasi-static analysis. Difficulty in attaining solutions results in issues of trustworthiness and practical deployability. Constant tweaking of simulation parameters to attain results, for computationally expensive simulations, constitutes a considerable tax on productivity. Such a requirement is incompatible with unsupervised simulation, i.e. automated forming simulation coordinated by MBSE driven design practice. Finally, bugs in complex software are virtually inescapable, COTS FE software being no exception. Experience has shown they can be easily missed without diverse and intensive testing.

  doi:10.5075/epfl-298799_978-2-9701614-0-0

To investigate this issue, preliminary investigation of developing an automated test framework which is able to intensively exercise the test model has been investigated. This is intended as a verification of computational procedure integrity, not as a validation of model accuracy. In essence, when subjected to an application representative, diverse set of stimuli, can the simulation complete without unexpected failure or behaviour? To this end, figure 5 shows simple test forming surfaces randomly generated using single or double curvature and ramp topologies.

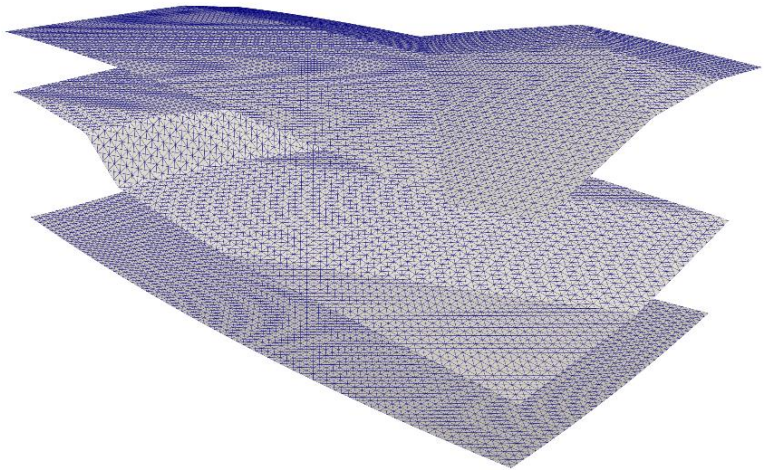

Figure 5. Randomly generated test forming surfaces employing simple single or double curvature and ramp topologies, as a proof of concept.

5. Conclusion

This contribution has presented early work on the development of a contact-based FE forming simulation approach to resolving stitch effects in NCFs. This includes demonstration of a proof of concept and outlining potential future work. For example, consideration of local fibre orientation and the ply state during the contact evaluation. Characterisation and validation were not discussed but should be regarded as core challenges. In response to challenges observed in model robustness, first steps towards a test framework for forming simulation have been shown. Finally, the suite of tools which are used to create and analyse simulations, and the implications thereof on the development process has been considered.

6. Acknowledgements

This work was funded by the Engineering and Physical Sciences Research Council (EPSRC) through the Industrial Doctorate Centre in Composites Manufacture (grant no. EP/K50323X/1) and the platform grant “Simulation of new manufacturing Processes for Composite Structures (SIMPROCS)” (grant no. EP/ P027350/1).

7. References

1. Tam AS, Gutowski TG. The kinematics for forming ideal aligned fibre composites into complex shapes. Composites Manufacturing. 1990;1(4):219–28.

2. Golden K, Rogers TG, Spencer AJM. Forming kinematics of continuous fibre reinforced laminates. Composites Manufacturing. 1991;2(3–4):267–77.

  doi:10.5075/epfl-298799_978-2-9701614-0-0

3. Thompson AJ, Belnoue JPH, Hallett SR. Modelling defect formation in textiles during the double diaphragm forming process. Composites Part B: Engineering. 2020 Dec 1;202:108357.

4. Bel S, Hamila N, Boisse P, Dumont F. Finite element model for NCF composite reinforcement preforming: Importance of inter-ply sliding. Composites Part A: Applied Science and Manufacturing. 2012 Dec 1;43(12):2269–77.

5. Colin D, Bel S, Hans T, Hartmann M. On the inter-stitch interaction in biaxial non-crimp fabrics. AIP Conference Proceedings. 2018 May 2;1960(1):020004.

6. Yu WR, Harrison P, Long A. Finite element forming simulation for non-crimp fabrics using a non-orthogonal constitutive equation. Composites Part A: Applied Science and Manufacturing. 2005 Aug 1;36(8):1079–93.

  doi:10.5075/epfl-298799_978-2-9701614-0-0

TOWARDS DATA-DRIVEN AUTOMATED FIBRE PLACEMENT WITH CAM IN THE LOOP

Philip Druiff[a], Amit Visrolia[a], Carwyn Ward[b]

a: National Composites Centre
Bristol, United Kingdom
b: Department of Aerospace Engineering, University of Bristol
Bristol, United Kingdom
E-mail: philip.druiff@bristol.ac.uk

Abstract: *Automated Fibre Placement (AFP) lay-up quality is dependent on multiple process parameters and their interactions. The data-driven approach aims to predict output quality through capturing process variability, using in-process sensor-collected data to train predictive machine learning models. Within this study, a number of process parameters, such as compaction force, lay-up speed and nip-point temperature, are measured continuously during manufacture and are used to train and deploy machine learning models.*

Additionally, AFP is often used to manufacture complex 3-dimensional components, the quality of which is also significantly impacted by geometrical factors. These factors can affect decisions during tape path planning, a compromise between design intent and lay-up quality.

This study proposes a methodology for machine learning model deployment in conjunction with tape path programming. These methods aim to reduce the requirement for physical development trials of complex AFP-manufactured components, resulting in time and cost savings.

Keywords: Manufacturing; Automated Fibre Placement; Machine Learning; Data-Driven

1. Introduction

Automated Fibre Placement (AFP) is a composite manufacturing process by which thin, continuous composite tapes are deposited onto a layup tool in a collimated band. Heat is applied by an external heat source during lay-up and compaction pressure is transmitted through a compliant roller in order to aid tack and consolidation [1][2]. These bands are deposited in layers (plies) according to a lay-up strategy, aided by specialised Computer-Aided Manufacturing (CAM) software.

The capability to control individual tow speed also enables the lay-up of curvilinear paths on complex tool surfaces [3]. CAM software algorithms are utilised for path planning and optimisation, outputting information about the position and attitude of the placement head roller into an AFP machine-compatible motion control file. Post-processing algorithms also verify the placement paths and estimate the impact of that path on the ply [4].

Decision making during tape-path definition often entails a compromise between minimisation of defects while maintaining the intended fibre direction. Unintended features such as bridging and steering wrinkles can be produced as a result of this compromise, potentially reducing component strength [3]. Insufficient consolidation during layup can also lead to fibre waviness in the cured preform, causing a severe knockdown in mechanical properties [5]. In order to

  doi:10.5075/epfl-298799_978-2-9701614-0-0

validate fibre path simulations, physical development trials are often required to reach an acceptable solution, which can be costly and time-consuming.

It has been shown that the quality and consistency of AFP manufactured components is largely dependent on layup parameters and their interactions, such as layup speed, temperature and consolidation force [2][6][7][8]. However, optimising these parameters can be extremely challenging, with over 50 independent parameters potentially influencing the process [2][6]. The complexity of the process also provides a challenge for physics-based modelling, with examples thus far proving computationally costly and difficult to adapt [9].

Capable of handling large amounts of data and high dimensionality, Machine Learning (ML) is increasingly being utilised in advanced manufacturing and has recently extended into composites [9]. Applications for tape placement include inspection of in-process defects [9], maintaining process conditions [10] and predicting performance based on these conditions. The ML approach has demonstrated its ability to predict mechanical properties of flat laminates, such as elastic modulus and Inter-Laminar Shear Stress (ILSS), with a high degree of accuracy [6][11].

ML models have also been trained to predict consolidation in complex 3D components, in the form of local preform thickness, from data captured during the AFP process [2]. These predictions can give an indication of process and geometric factors that could lead to poor consolidation. This study aims to use ML model predictions, trained using data captured in-process, to predict the location of poor-consolidated areas in a complex 3D perform. These predictions can be used to facilitate and inform layup strategies in order to mitigate consolidation issues without the need for significant physical manufacturing trials.

2. Methodology

Figure 1 shows the data-driven process flow during the AFP process (grey), with an additional step to feed predictions from the process capability model into a CAM program (green). Machine toolpath and kinematics data from CAM and process variable data collected during the manufacture of multiple preforms were fed into a data warehouse. An assessment of quality; local preform thickness, was also provided. This dataset is then pre-processed and contextualised into the tool's coordinate system, and aligned into a single dataset, from which process parameters can be visualised. This process of data capture, pre-processing and visualisation is described in detail in Druiff et al. [2].

Throughout this study, process data was captured during the manufacture of 12, 8-ply complex 3-D components, with a quasi-isotropic lay-up sequence of [0/-45/45/90]s, and processed using the method shown in Figure 1. Bindered dry carbon fibre tows were deposited onto a deposition tool with multiple complex features by a Coriolis Composites robotic AFP machine. Heat was supplied by a head-mounted diode laser and local preform thickness was measured, following each ply, using a portable laser scanner measurement arm [2]. Kinematics and tool path data were also extracted from the CAM software.

The dataset, once pre-processed, was split into test and training datasets, and a k-fold cross validation was carried out within the training dataset in order to reduce the impact of bias during model training [2][12]. ML models in Python were then generated from the training dataset in order to predict local preform thickness. The highest-performing regressor from a selection of

popular methods, assessed by coefficient of determination (R^2) using the test dataset, was then tuned via the 'random grid search' method.

Using the test dataset, thickness predictions from the tuned model were visualised in order to identify likely high thickness regions. These visualisations could then be converted into a format compatible with the CAM software. Finally, programming strategies were modified within the CAM software in order to improve consolidation in these areas. These modifications resulted in an 'improved' programming strategy; a lay-up program equal in ply number, orientation and geometry to the original, but adapted in strategic places in order to reduce the occurrence of poor consolidation.

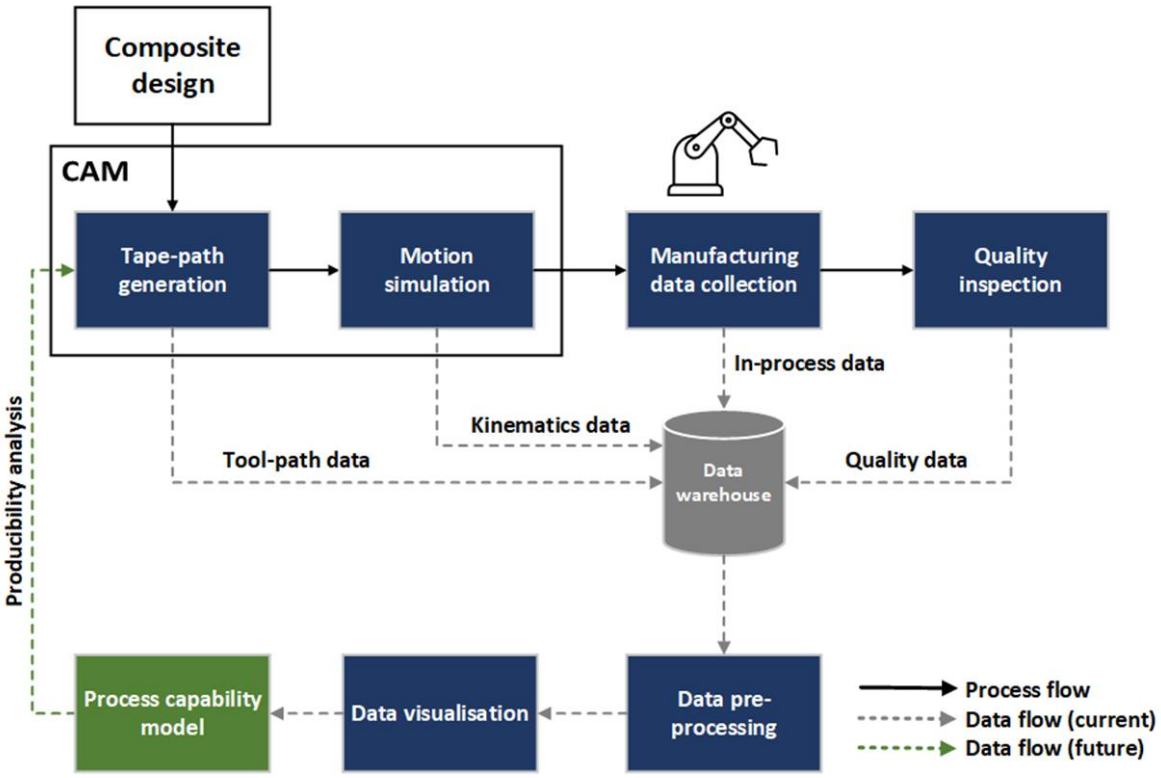

Figure 1: Data process flow during the data-driven approach to AFP. Green arrows represent an additional step to communicate ply surface predictions into CAM software

Bridging can be one such cause of high thickness; material can sperate from the tool surface in concave surfaces with tight radii, in part due to tension in the AFP feed system [3][13]. To aid the ML model in predicting the occurrence of bridging and other geometry-related features, a metric was introduced to indicate local curvature severity across the tool surface. Discrete mean curvature was the selected metric for its ability to distinguish between convex (positive) and concave (negative) curvature.

Mean curvature was calculated for each data point on the tool surface using the 'trimesh' library in Python, as defined by Steiner and Morvan [14]. Figure 2a) shows the mean curvature distribution across the chosen component, measured at the tool surface. Figure 2b) shows thickness measurements across a 90° ply as a comparison. Areas of negative mean curvature seem to correlate well with high thickness, likely due to bridging [13].

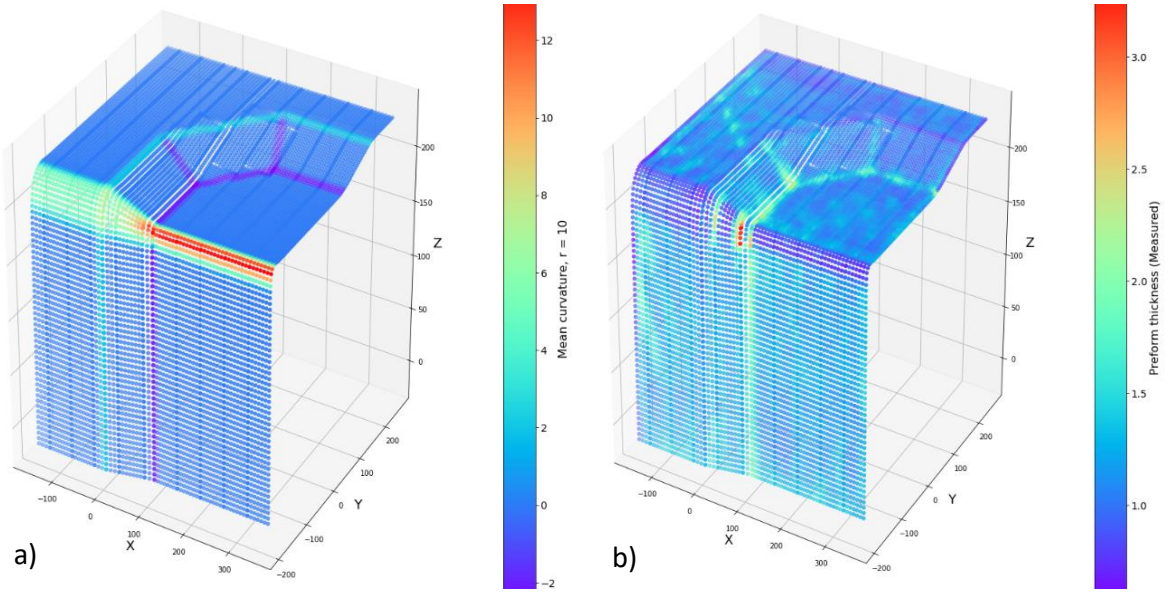

Figure 2: a) Mean curvature distribution across the tool CAD surface. b) Preform thickness distribution after ply 4 (90°) of an example preform

3. Results and discussion

Figure 3 shows the coefficient of determination (R^2) for a number of regressors, trained using the training dataset and assessed using the test dataset. As a baseline, a linear regressor was also trained using the 'ply number' feature only, achieving an R^2 of 0.88. The eXtreme Gradient Boosting (XGBoost) algorithm [15], along with Light Gradient Boosting Machine (LGBM) algorithm performed highest, and XGBoost, using the 'gbtree' booster, was selected for hyperparameter tuning, resulting in an R^2 of 0.94. This represents a clear improvement on the simple linear model and shows that the data-driven approach to AFP can improve the accuracy of predicted preform thickness in complex 3D preforms.

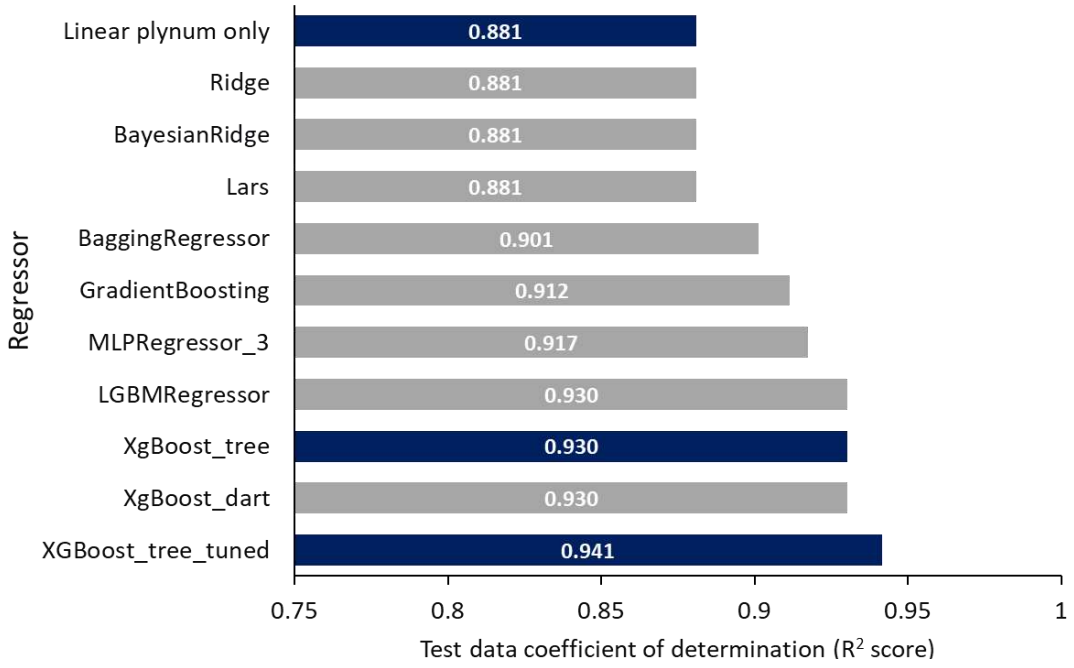

Figure 3: Coefficients of determination for multiple regressors in comparison with a basic linear model, assessed on the test dataset

Represented by a series of coloured dots, a SHAPely value (SHAP) summary plot, Figure 4, provides insight into how each feature's value affects its contribution to the model output; preform thickness. Produced using the tuned model, each dot represents a single datapoint for each feature. The x position of the dot denotes the impact of the feature on the output (SHAP value), and the colour of the dot represents the value of that feature [16]. Ranked for feature importance, with highest importance at the top, the highest contributing factor to thickness is the ply number; increasing the number of plies will manifestly increase the thickness. The feature of second highest impact is the calculated 'mean curvature', with a strong indication that lower (more concave) curvature leads to higher thickness, likely caused in-part by bridging.

Other geometrical factors also rank highly, including the global coordinates in x, y, z; indicating that thickness build-up is correlated to specific areas in the tool. This result implies that thickness predictions are significantly impacted by geometrical factors such as bridging. Providing a prediction of ply thickness at the tape definition stage can facilitate feature-based lay-up optimisation, potentially reducing the likelihood of poor consolidation without the need for physical development trials.

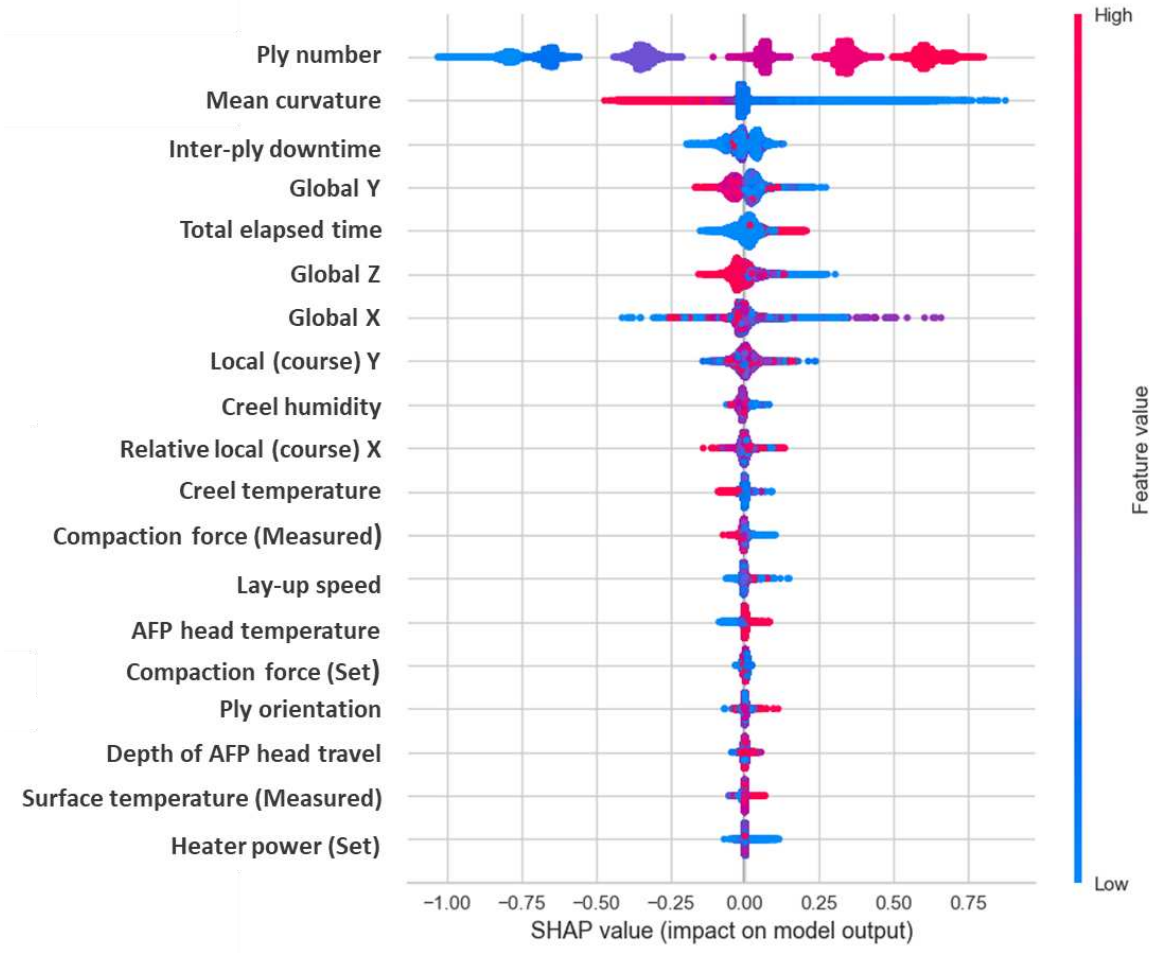

Figure 4: SHAP summary plot showing feature contribution on the output for each data point in the test dataset

Thickness predictions from the tuned model were then visualised for each ply orientation; examples of which are shown in Figure 5. Figure 5 a) highlights areas of poor consolidation for plies 1 and 8 (0°). These areas correlate with the section of tows deposited after the AFP machine's cut operation. After cutting the tows, the machine has little control over the tape

placement for a length of tow equal to the minimum tow length, typically approximately 40mm. Tows can therefore deviate from their intended path, which can lead to overlaps, among other issues [17][18]. During this study, these issues are represented by increased thickness, as shown in Figure 5 i). Therefore, when defining the improved programming strategy, these courses were extended to move the post-cut length outside the edge of the final part.

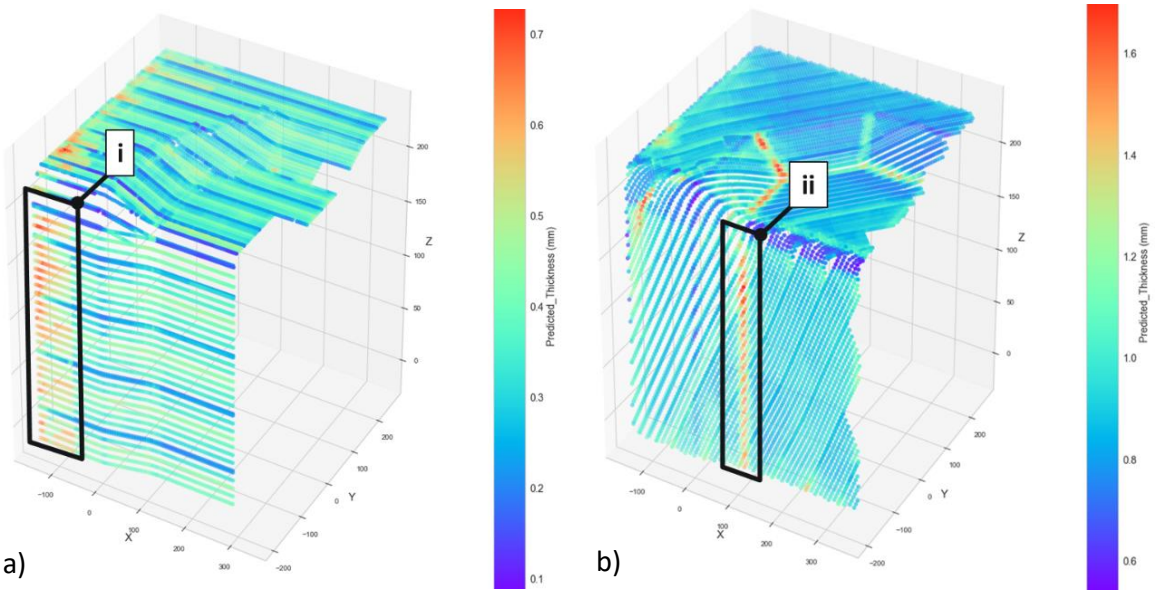

Figure 5: Preform thickness predictions for a) ply 1 (0°), b) ply 3 (45°). Examples of high thickness regions are highlighted in i and ii. The lay-up direction is from right to left in both cases

Figure 5 b) shows an example of a 45° ply, deposited from right to left. Thickness is significantly higher than average in region ii), which may be caused by bridging, due to the challenge of maintaining contact between roller and preform in that particular lay-up direction [13]. Reducing lay-up speed and increasing compaction force in this area may reduce this occurrence [6]. However, Figure 6 indicates that lay-up speed and compaction force have a relatively low impact on local thickness for this component. While defining the improved programming strategy, compaction force was increased for all ±45° plies, and lay-up speed was reduced within the area defined by Figure 5 b) ii).

The improved programming strategy is expected to reduce preform thickness in regions i) and ii), highlighted in Figure 5. In the next phase of the study, 3 preforms of each programming strategy, 'original' and 'improved', will be manufactured. Local preform thickness will be measured in regions i) and ii) of Figure 5 to determine any improvement in consolidation. This will demonstrate the effectiveness of the strategy to include CAM in the loop of data-driven manufacturing.

4. Conclusions and further work

Machine learning models were trained on a dataset of complex 3D preforms manufactured by AFP, in order to predict an output quality metric: preform thickness. These models, once tuned, achieved an accuracy of $R^2 = 0.94$ on a separate test dataset, demonstrating that the data-driven approach to AFP can generate accurate quality predictions in complex 3D preforms.

  doi:10.5075/epfl-298799_978-2-9701614-0-0

Predictions of local preform thickness from these models were then visualised for a series of plies, indicating areas of poor consolidation. This information was used to inform lay-up strategy decisions at the CAM stage, in a step towards data-driven AFP with CAM in the loop.

If this approach is successfully validated, it can be used to facilitate CAM-based consolidation predictions, informing lay-up strategy decisions based on real-world data. Further, it can facilitate feature-based lay-up optimisation, reducing the occurrence of poor consolidation without the need for physical development trials.

Acknowledgements

This work is supported by the Engineering and Physical Sciences Research Council through the EPSRC Centre for Doctoral Training in Composites Manufacture (grant: EP/L015102/1) and The Future Composites Manufacturing Hub (grant: EP/P006701/1). The authors acknowledge the National Composites Centre and Bristol Composites Institute (ACCIS) for their support of this research. All data necessary to reproduce the results and support the conclusions can be accessed through the named corresponding author. The author would also like to thank Philippe Monnot for his significant contributions towards the methods used within.

5. References

1. Lukaszewicz DHJA, Ward C, Potter KD. The engineering aspects of automated prepreg layup: History, present and future. Composites Part B: Engineering. 2012;43(3):997–1009.
2. Druiff P, Dell'Anno G, Visrolia A, Arruda M, Ma K, Palardy-Sim M, et al. A Smart Interface for Machine Learning Based Data-Driven Automated Fibre Placement. In: Composites and Advanced Materials Expo, CAMX 2021. Dallas, Texas; 2021. p. 704–18.
3. Lozano GG, Tiwari A, Turner C, Astwood S. A review on design for manufacture of variable stiffness composite laminates. Vol. 230, Proceedings of the Institution of Mechanical Engineers, Part B: Journal of Engineering Manufacture. 2016. p. 981–92.
4. Zhang L, Wang X, Pei J, Zhou Y. Review of automated fibre placement and its prospects for advanced composites. Journal of Materials Science. 2020;55(17):7121–55.
5. Belnoue JPH, Nixon-Pearson OJ, Thompson AJ, Ivanov DS, Potter KD, Hallett SR. Consolidation-driven defect generation in thick composite parts. Journal of Manufacturing Science and Engineering, Transactions of the ASME. 2018;140(7).
6. Wanigasekara C, Oromiehie E, Swain A, Prusty BG, Nguang SK. Machine Learning Based Predictive Model for AFP-Based Unidirectional Composite Laminates. IEEE Transactions on Industrial Informatics. 2020;16(4):2315–24.
7. Oromiehie E, Prusty BG, Compston P, Rajan G. The influence of consolidation force on the performance of AFP manufactured laminates. In: ICCM International Conferences on Composite Materials. 2017.
8. Brüning J, Denkena B, Dittrich MA, Hocke T. Machine Learning Approach for Optimization of Automated Fiber Placement Processes. In: Procedia CIRP. 2017. p. 74–8.
9. Sacco C, Baz Radwan A, Anderson A, Harik R, Gregory E. Machine learning in composites manufacturing: A case study of Automated Fiber Placement inspection. Composite

  doi:10.5075/epfl-298799_978-2-9701614-0-0

Structures. 2020 Oct 15;250:112514.

10. Römer M, Bergers J, Gabriel F, Dröder K. Temperature Control for Automated Tape Laying with Infrared Heaters Based on Reinforcement Learning. Machines. 2022;10(3):164.

11. Oromiehie E, Prusty BG, Rajan G, Wanigasekara C, Swain A. Machine learning based process monitoring and characterisation of automated composites. In: International SAMPE Technical Conference. 2017. p. 398–410.

12. Anguita D, Ghio A, Ridella S, Sterpi D. K-Fold Cross Validation for Error Rate Estimate in Support Vector Machines. International Conference on Data Mining. 2009;(June 2014):291–7.

13. Lichtinger R, Lacalle J, Hinterhölzl R, Beier U, Drechsler K. Simulation and experimental validation of gaps and bridging in the automated fiber placement process. Science and Engineering of Composite Materials. 2015;22(2):131–48.

14. Cohen-Steiner D, Morvan JM. Restricted delaunay triangulations and normal cycle. In: Proceedings of the Annual Symposium on Computational Geometry. 2003. p. 312–21.

15. Chen T, Guestrin C. XGBoost: A scalable tree boosting system. In: Proceedings of the ACM SIGKDD International Conference on Knowledge Discovery and Data Mining. 2016. p. 785–94.

16. Meng Y, Yang N, Qian Z, Zhang G. What makes an online review more helpful: An interpretation framework using xgboost and shap values. Journal of Theoretical and Applied Electronic Commerce Research. 2021;16(3):466–90.

17. Oromiehie E, Prusty BG, Compston P, Rajan G. Automated fibre placement based composite structures: Review on the defects, impacts and inspections techniques. Vol. 224, Composite Structures. Elsevier; 2019. p. 110987.

18. Wu KC, Tatting BF, Smith BH, Stevens RS, Occhipinti GP, Swift JB, et al. Design and manufacturing of tow-steered composite shells using fiber placement. In: Collection of Technical Papers - AIAA/ASME/ASCE/AHS/ASC Structures, Structural Dynamics and Materials Conference. 2009.

WARPAGE PREDICTION FOR LARGE THERMOPLASTIC COMPOSITE OVERMOULDED AEROSTRUCTURES

Will Darby [a, b], Matt Etchells [b], Ole Thomsen [a], Sean Cooper [b]

a: Bristol Composites Institute, University of Bristol, will.darby@nccuk.com
b: National Composite Centre (NCC), Bristol, UK

Abstract: *Aerostructures manufactured via thermoplastic composite overmoulding can benefit from high structural performance due to the use of continuous fibre composite laminates, combined with injection moulded composite parts to stiffen the structure as well as for the addition of functional features to increase part complexity. The aim of the OBStruct project is to demonstrate the suitability of overmoulded structures through optimizing the manufacture of a demonstrator component. During manufacturing trials, significant amounts of warpage were observed after the demoulding of the demonstrator part. The aim of this research was to simulate the filling, packing, cooling and warpage of the OBStruct demonstrator using commercial injection moulding simulation software, where the simulation took into account the composite inserts.*

Keywords: Overmoulding; Warpage; Thermoplastic composites

1. Introduction

The use of high-performance thermoplastic composite offers several advantages, including recyclability and the potential for high-rate manufacture. Overmoulding can utilise thermoplastic composite properties whilst making complex geometries. Overmoulding combines thermoforming of continuous fibre thermoplastic laminates, with injection moulding of short fibre reinforcements. The process can be fully automated and enables net shape components to be manufactured with short cycle times. However, currently there is a lack of manufacturing expertise as well as limited experimental data and models that can support wide-spread adoption in the industry [1] – [3].

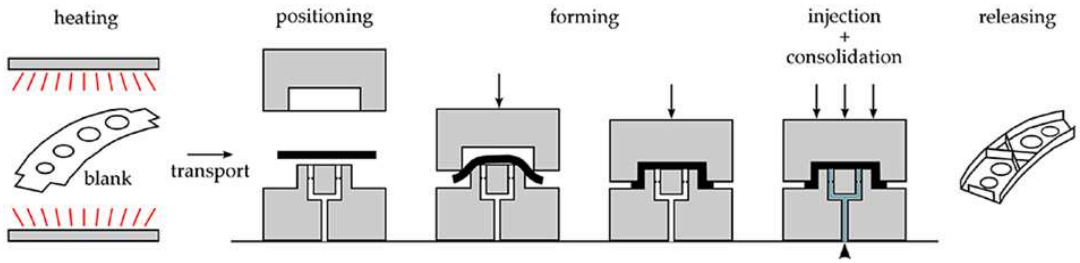

Figure 1. Schematic diagram of the overmoulding process [3]

The ability to increase part complexity can allow for a reduction in the number of parts for sub-assemblies and the number of adhesives and rivets used. Allowing for a quicker assembly and a reduced overall sub-assembly weight. A good example of this is a butt-jointed stringer stiffened panel. Traditionally stingers are bonded or riveted to the panel, both of which are labour-intensive assembly processes. Overmoulding has the ability to combine the stringer and panel during manufacture, not only saving time but also weight [4] – [6].

  doi:10.5075/epfl-298799_978-2-9701614-0-0

The Overmoulding of Butt Jointed Aerostructures 3 (OBStruct 3) project is part of the National Composite Centre's (NCC) core research programme (2021-2022). The aim of the project series is to demonstrate that an overmoulded butt-jointed T-stringer stiffened panel can be designed and manufactured, to significantly reduce manufacturing cycle time, whilst meeting the quality and repeatability requirements of the aerospace industry. The OBStruct demonstrator component can be seen in Figure 2.

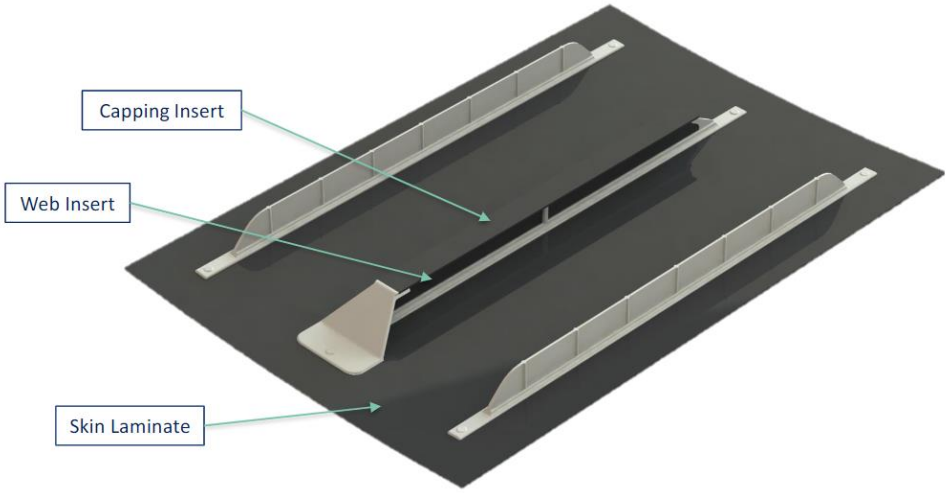

Figure 2. CAD render of the OBStruct demonstrator component

During previous manufacturing trials, it was clear that the manufactured components experienced significant amounts of warpage along the length of the ribs. Warpage in injection moulded parts is caused by a variation in shrinkage across the part. Variation in polymer shrinkage is caused by fluctuations in the densification of the molten polymer throughout the part during cooling. This creates internal stresses within the part. Shrinkage is influenced by temperature and pressure history, frozen layer growth, flow induced orientation of the molecular chains and flow induced crystallisation for semi-crystalline polymers. Shrinkage can be limited by an effective packing phase, where more material is forced into the injection cavity to compensate for shrinkage [7] – [10].

The addition of composite inserts can influence the amount of warpage experienced during injection overmoulding due to the composite being an insulator, thus reducing the cooling rate along the interface. This is beneficial for forming a strong interfacial bond but increases the variation in cooling rates across the component. For semi-crystalline polymers, like PEEK, this variation in cooling rate can result in an increased variation in shrinkage throughout the part and therefore increase the amount of warpage in the component. This is because the degree of crystallinity is heavily dependent on the cooling rate, with a faster cooling rate resulting in less crystallinity within the polymer. The density of a crystalline phase is significantly greater than that of an amorphous phase. This results in regions with a higher degree of crystallinity experiencing more shrinkage. There is also a difference in CTE between the injected polymer and composite inserts, which will contribute to the warpage of the component [9], [11] – [13].

2. Simulation Method

Existing injection moulding software packages offer the ability to predict the warpage of thermoplastic composite. Z. Zou et al [(14]) and Z. Fan et al [(15]) incorporated the orthotropic

  doi:10.5075/epfl-298799_978-2-9701614-0-0

properties of composite inserts within a three-dimensional finite element model in Moldflow. Various simple and complex geometries were investigated and were able to predict the warpage of overmoulded components. However, this approach was not validated against manufactured parts. [14], [15]

A similar approach to what Z. Zou et al [(14]) and Z. Fan et al [(15]) was chosen to predict the warpage of the OBStruct demonstrator part, with Moldex3D used as the software package to simulate the filling, packing, cooling and warpage of the demonstrator component. For the composite laminate push rod dilatometry was used to determine the co-efficient of thermal expansion (CTE) in the 0°(X) direction, 90°(Y) direction & through thickness (Z) direction. Three repeats were taken for each direction with the results measured via dimension change vs temperature.

The material undergoes a thermal transition between 140 and 170 °C. This likely to be due to the polymer matrix going through its glass transition temperature (Tg) during this temperature range, from the data sheet it is stated that the Tg is 147 °C [16]. CTE values were obtained by fitting a line of best fit through the linear regions before and after the transition region. These can be seen in Table 1. The results show that the CTE in the X and Y directions are similar, which is expected due to the composite laminate being symmetrical and balanced. The CTE in the Z direction is drastically different, caused by the fact that there is no carbon fibre reinforcement in the Z direction. Moldex3D allows for only one value for each principal direction. The largest CTE values were used for each direction, to represent the worst-case scenario in terms of the amount of shrinkage within the composite insert.

	CTE (31 to 140°C) (µm/m.°C)			CTE (166 to 268°C) (µm/m.°C)		
Direction	X	Y	Z	X	Y	Z
Average	1.840	1.849	36.919	1.286	1.748	182.683

Table 1: Average CTE results via push rod dilatometry in the X, Y and Z directions

The equivalent laminate mechanical properties were estimated using classical laminate theory (CLT), using the mechanical properties of a single ply from the material datasheet. For the mechanical properties in the through thickness (Z) direction the properties were taken as the 90° degree properties from a single ply [[(16].)

Within the Moldex3D model the injection cavity, composite inserts, some tooling features, cooling channels with hose attachments and hot runner geometry, seen in Figure 3.

  doi:10.5075/epfl-298799_978-2-9701614-0-0

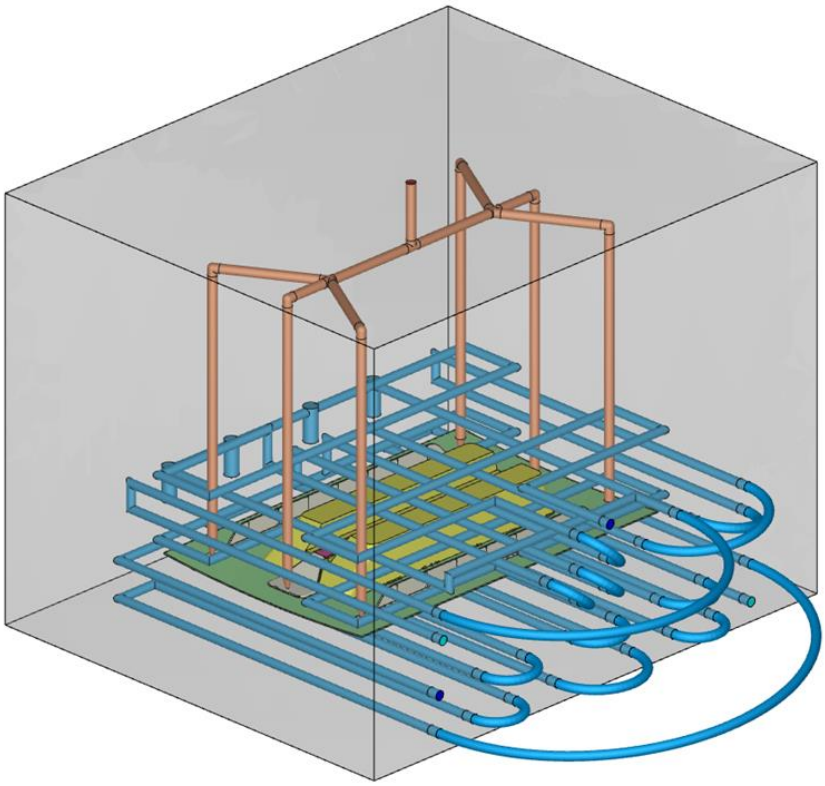

Figure 3. Moldex3D model of the OBStruct demonstrator part and tooling geometries

Within the meshing parameters the part and part insert mesh type had been set to tetrahedral with 3 layers BLM. The hot runner gates and cooling channel have a tetrahedral mesh type with 5 layers BLM. The compression zone was set at pure tetra. It is recommended by Moldex3D for simulating overmoulding that a face matching mesh is used between the part and the part insert. Face matching enables the nodes and elements to be at the same points on each contacting surface meshes. The mesh of the two lifting blocks, highlighted in yellow in Figure 3, was face matched as well because of the large area of contact between them and the demonstrator part [(17,18].)

The processing parameters were defined by equipment capabilities at the NCC and the material information within Moldex3D. Initial filling simulations were carried out to optimise the fill of the component. Two different PEEK compounds were used as the injected polymer within this study. An unfilled PEEK similar to what was used in previous manufacturing trials and a 30% short carbon fibre (CF) filled PEEK. The effect of the fibre orientation of the CF filled PEEK was considered within the simulation.

3. Results

The simulation was able to predict the filling, packing, cooling and warpage of the demonstrator part for both materials. From visual inspection the warpage displacement from the simulation of the unfilled PEEK is comparable to the warpage of the manufactured demonstrator component using an unfilled PEEK, with the maximal displacement occurring in the same region of the component.

  doi:10.5075/epfl-298799_978-2-9701614-0-0

The amount of total warpage is significantly greater in the unfilled PEEK compared to the CF filled PEEK. This can be seen in Figure 4, with the maximum displacement in the unfilled PEEK being 36.6 mm compared to 8.83 mm in the CF filled PEEK. The amount of volumetric shrinkage in the two different polymer compounds is drastically different. The cause of this difference is down to the fact that the unfilled polymer has significantly more volumetric shrinkage and a larger distribution of shrinkage than the CF filled PEEK. The large amounts of shrinkage in the larger cross-sectional areas like the stringer runouts and the bottom of the external stringers are the main cause of the large amounts of warpage seen in the unfilled PEEK. The predicted shrinkage from the simulation can be seen in Figure 5.

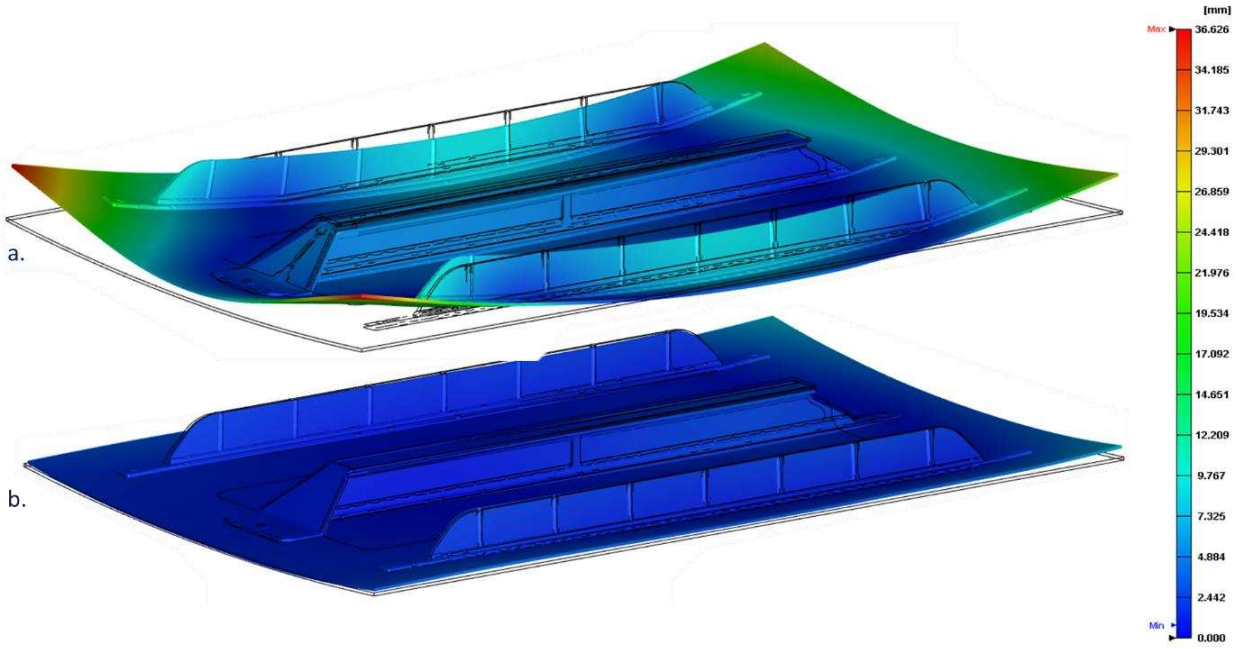

Figure 4. Total warpage displacement of the unfilled PEEK (a.) and 30% CF filled PEEK (b.)

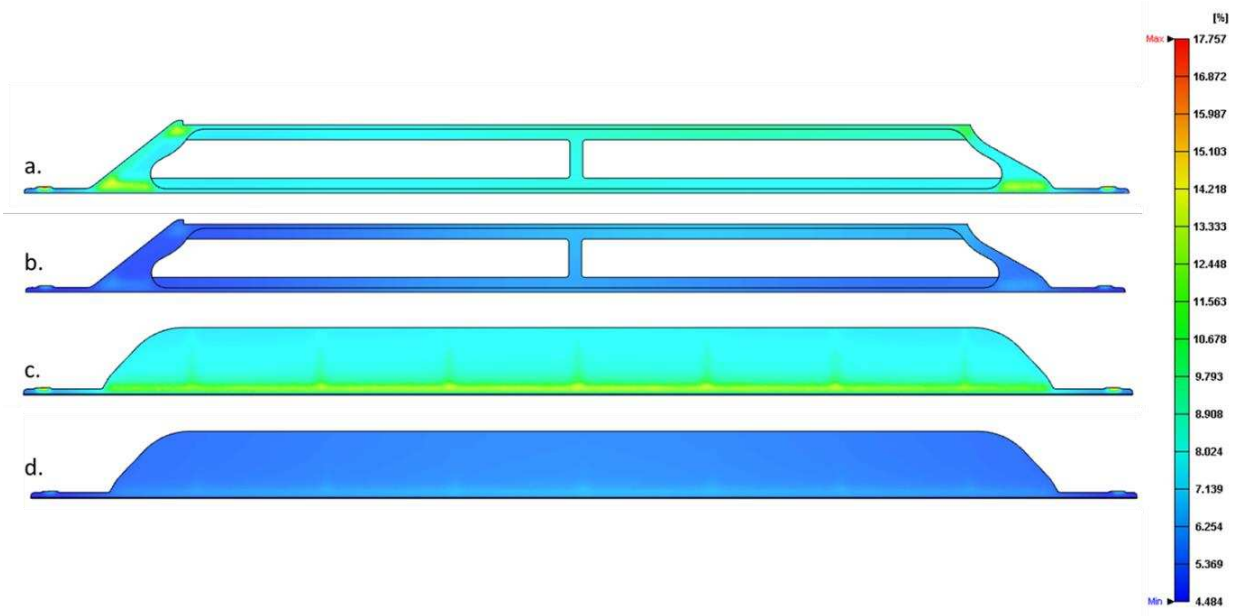

Figure 5. volumetric shrinkage of the unfilled and CF filled central (a. and b.) and external stringers (c. and d.)

4. Conclusions and future work

The unfilled injected PEEK sees considerably higher amounts of volumetric shrinkage and warpage compared to the CF filled PEEK. The large amount of shrinkage is caused by a poor packing phase. The packing phase is not effective in preventing the shrinkage due to several factors, namely the part geometry, the high melt viscosity of the injected polymer and high frozen layer ratios at the end of filling. Less shrinkage is predicted when using the CF filled PEEK because there is less polymer injected due to the presence of the short carbon fibres. there is then less injected polymer that shrinks during cooling.

Currently the change in polymer density between the injection barrel and mould is not currently considered within the model. The change is due to differences in temperature and pressure between the barrel and mould and is known as barrel compressibility. The aim is to include this within the model and see how this affects the results seen above.

The accuracy of this method on predicting warpage of thermoplastic composite overmoulding will be validate against manufactured demonstrator components using a 30% CF filled PEEK.

Acknowledgements

The research presented was supported by the EPSRC Industrial Doctoral Centre in Composites Manufacture (EP/L015102), Bristol Composites Institute, University of Bristol and the National Composites Centre, Bristol, UK. The support received is gratefully acknowledged.

References

[1] "Further Airbus Production Rate Increase 'Very Likely,' Faury Says | Aviation Week Network." https://aviationweek.com/air-transport/aircraft-propulsion/further-airbus-production-rate-increase-very-likely-faury-says (accessed Feb. 01, 2022).

[2] "Overmolding as enabler for composites, aerospace to automotive | CompositesWorld." https://www.compositesworld.com/articles/overmolding-as-enabler-for-composites-aerospace-to-automotive (accessed Jul. 23, 2021).

[3] R. Akkerman, M. Bouwman, and S. Wijskamp, "Analysis of the Thermoplastic Composite Overmolding Process: Interface Strength," *Frontiers in Materials*, vol. 7, p. 27, 2020, doi: 10.3389/fmats.2020.00027.

[4] J. W. van Ingen, P. Lantermans, I. Lippers, and F. Aerostructures, "Impact behavior of a butt jointed thermoplastic stiffened skin panel," 2012.

[5] S. Francis, "No Title," *Composites World*, 2019. ENGEL unveils IR robotic cell for large-series production of lightweight thermoplastic composites (accessed Jul. 22, 2021).

[6] M. Cetin and M. Thienel, "Large-series Production of Thermoplastic Door Module Carriers," *Lightweight Design worldwide 2019 12:5*, vol. 12, no. 5, pp. 12–17, Oct. 2019, doi: 10.1007/S41777-019-0052-1.

[7] P. Kennedy and R. Zheng, "Flow Analysis of Injection Molds," *Flow Analysis of Injection Molds*, pp. I–XXIX, Jan. 2013, doi: 10.3139/9781569905227.FM.

[8] R. Kent, "Processing," *Energy Management in Plastics Processing*, pp. 211–318, Jan. 2018, doi: 10.1016/B978-0-08-102507-9.50005-2.

[9] A. I. Isayev and K. Kwon, "Volumetric and Anisotropic Shrinkage in Injection Moldings of Thermoplastics," *Injection Molding*, pp. 779–808, May 2009, doi: 10.3139/9783446433731.019.

[10] P. Kennedy, "Development of Injection Molding Simulation," *Injection Molding*, pp. 553–598, Jan. 2009, doi: 10.3139/9783446433731.014.

[11] M. Divekar, V. R. Gaval, A. Wonisch, and G. Jadhav, "Advancement in warpage prediction of thermoplastic glass filled material through integrative simulation approach," *Materials Today: Proceedings*, vol. 44, pp. 4216–4222, Jan. 2021, doi: 10.1016/J.MATPR.2020.10.535.

[12] S. Kulkarni, "Properties of Polymers and Plastics That Influence Injection Molding," *Robust Process Development and Scientific Molding*, pp. 13–45, Jan. 2017, doi: 10.3139/9781569905876.002.

[13] N. Mills, M. Jenkins, and S. Kukureka, "Semi-crystalline polymers," *Plastics*, pp. 49–66, Jan. 2020, doi: 10.1016/B978-0-08-102499-7.00004-7.

[14] Z. Zuo, Z. Fan, F. Costa, and D. Astbury, *WARPAGE SIMULATION OF INJECTION OVER-MOLDING PLASTICS ON CONTINUOUS FIBER REINFORCED COMPOSITES*. 2016.

[15] "(PDF) Three Dimensional Cooling and Warpage Simulation for the Injection Overmolding Process." https://www.researchgate.net/publication/333745164_Three_Dimensional_Cooling_and_Warpage_Simulation_for_the_Injection_Overmolding_Process (accessed Mar. 03, 2022).

[16] "Toray Cetex ® TC1225".

[17] "More Customized BLM Options for Insert Components in Moldex3D | Blog | Moldex3D | Plastic Injection Molding Simulation Software." https://www.moldex3d.com/blog/tips-and-tricks/more-customized-blm-options-for-insert-components-moldex3d/ (accessed Mar. 01, 2022).

[18] "Properly Match the Mesh Elements of Multi-Component Molding to Attain High-accuracy Analysis | Blog | Moldex3D | Plastic Injection Molding Simulation Software." https://www.moldex3d.com/blog/tips-and-tricks/properly-match-the-mesh-elements-of-multi-component-molding-to-attain-high-accuracy-analysis/ (accessed Mar. 01, 2022).

  doi:10.5075/epfl-298799_978-2-9701614-0-0

REDUCING THE LENGTH OF RECYCLED CARBON FIBRES TO IMPROVE DISPERSION BEHAVIOUR AND ENABLE HIGHLY ALIGNED CARBON FIBRE MATERIALS

Patrick Sullivan[a,b], Stephen J. Eichhorn[a], Ian Hamerton[a,b], Vicky Summers[b],

a: Bristol Composites Institute, University of Bristol, Queen's Building, University Walk, Bristol, BS8 1TR, U.K.
b: National Composites Centre, Bristol & Bath Science Park, Emersons Green, Bristol BS16 7FS, U.K.

patrick.sullivan@bristol.ac.uk

Abstract: *Work has been conducted to reduce the length of reclaimed carbon fibres from 60-100 mm to a target of 4 mm using a manually operated guillotine for use in dispersion based reformatting technologies to produce second life materials for manufacture. The fibre length distribution of a chopped sample was determined using the FASEP 3E Eco high-resolution scanner system.*

Fibre length is critical for successful dispersion of discontinuous fibres ahead of the alignment process. Through analysing the guillotine chopping method, two peak distributions of fibre length have been identified, at 0.6 mm and 4.3 mm. A small number were 6 mm or greater, totalling 2 % of the volume frequency of the sample. The longest fibre measured was 9.2 mm. While any fibres over 6 mm could cause issues to dispersion quality, the result indicates they would be minimal for the sample.

Keywords: Reclaimed fibres; Discontinuous fibres; Fibre length distribution; HiPerDiF; Sustainable composites

1. Introduction

Commercial aircraft are typically decommissioned after an operational life of 20-30 years [1]. The current generation of aircraft reaching the end of their operational lives, therefore, includes the Boeing 777 series and Airbus A320, and is soon to include the Boeing 787 series. The fibre reinforced composite composition of the airframe in the 777 and A320 is 12% and 25% respectively by weight [2], while in comparison the 787 airframe design incorporates 50% of composite materials by weight and represents a key step change in the aerospace industry. 12 years on from the first flight of the 787, there is now a greater focus on the management of waste materials, most prominently on the recycling and circularity of those with high embodied energy associated with their production, such as the carbon fibre reinforced polymers (CFRP) that feature heavily in modern aircraft structures. Examples of methods to reclaim carbon fibres (CFs) for input into new recycled materials can be widely found in the literature and industrial reports [3]. There is a growing need, however, to characterise the fibres after reclamation for them to be successfully introduced into downstream processes and be effective in second life manufacture.

  doi:10.5075/epfl-298799_978-2-9701614-0-0

Reclaimed carbon fibres (rCF) from aircraft structures typically form aggregates of discontinuous filaments and, unlike virgin carbon fibre products, it is a challenge both to separate and align rCFs or ensure a consistent areal weight. The HiPerDiF (high performance discontinuous fibre) technology was discovered and patented at the University of Bristol and now forms the basis of a new company, Lineat Composites. The process produces highly aligned thin tapes and includes a water-based dispersion step to separate the individual filaments prior to alignment [4]. The fibre length is key to successful dispersion of the CFs: longer fibres flocculate and block the system, while fibre lengths of 3-6 mm have so far shown good dispersion behaviour for the HiPerDiF system.

Future CF waste could come from multiple sources: end-of-life cured composites, prepreg waste, or dry fibre waste. Therefore, it is expected that rCF products, such as those produced using HiPerDiF, will have to prepare fibres from mixed sources with different characteristics. A new capability is needed to reduce the length of rCFs to 3-6 mm accurately and consistently.

The following study proposes a method to characterise the fibre length distributions of recycled carbon fibres that have been chopped to shorter lengths. By characterising the fibre length distribution and analysing samples corresponding to later processing outcomes, relationships and guidance can be defined between length reduction techniques and the influence of fibre length on the success of dispersion and other downstream processes.

2. Methodology

2.1 Materials and reclamation process

The fibres used in the work were sourced and reclaimed from carbon fibre reinforced polymer (CFRP) extracted from an end-of-life aircraft component. Two vertical tailplanes (VTPs) were sourced from an aircraft salvage company (see Fig. 1), and CFRP panels, each around 400 mm × 400 mm in size with a thickness between 2 and 4 mm, were cut out of the components. The VTPs came from two Airbus A320 aircraft which had been in service for 12 and 19 years respectively. The matrix of the CFRP was assumed to be a toughened epoxy typically seen in civil aerospace. The CFs were then reclaimed from the CFRP panels using a commercial pyrolysis process and chopped to a nominal length of 80 ± 20 mm.

Figure 1. The two end-of-life vertical tail planes from which the carbon fibres were reclaimed and subsequently chopped for analysis

  doi:10.5075/epfl-298799_978-2-9701614-0-0

The resulting fibres from the reclamation showed variability; many fibres remained in tow format with undegraded matrix or char from the pyrolysis process, keeping them bundled rather than as individual filaments. The fibres were manually sorted into those remaining in tow format and those as individual filaments, and the tows were disregarded for the following work. This step is to ensure the results of the fibre length distribution relates only to the chopping of samples of discontinuous filaments, the format typically expected from reclaimed carbon fibres.

2.2 Size reduction of reclaimed fibres

A sample of the fibres was reduced from a range of fibre lengths (60-100 mm) to a target of 4 mm using a manually operated guillotine and a manual fabric rotary cutter.

The cutting process using these tools is highly reliant on the eyesight and competence of the user, with no control mechanism on the resulting fibre lengths. A sample of the chopped fibres totalling approximately 5 grammes was then taken for measurement and analysis.

2.3 Measurement and analysis of fibre length distribution

The fibre length distribution of the sample of the chopped rCF was analysed using the FASEP 3E Eco system, previously used primarily to measure higher diameter glass fibres [5][6]. The sample was prepared with a 500ml water solution with a few drops (around 1ml) of acetic acid before being placed in a petri dish and into the high-resolution scanner and lightbox for imaging. The software then identifies and measures individual fibres from the high contrast image (see Fig. 2). In the following work, the same scan input was exported as both 2400 dpi and 4800 dpi images to assess the sensitivity of the software to the image resolution.

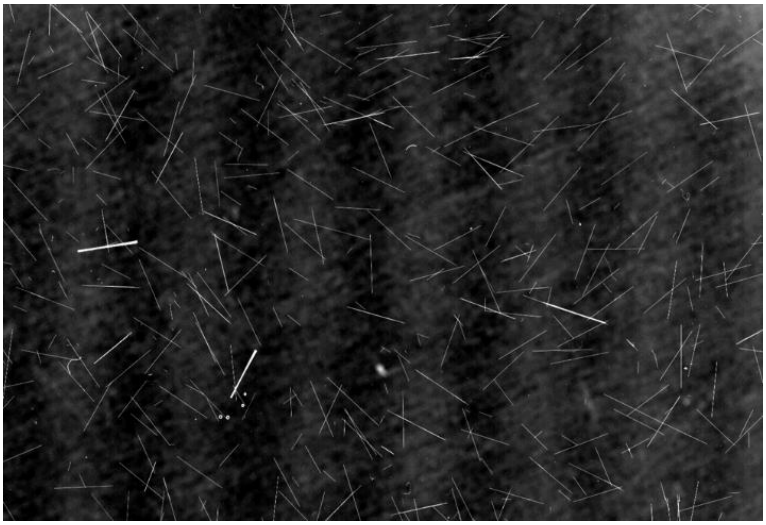

Figure 2. A typical high contrast image produced of the chopped fibre used for analysis using the FASEP 3E Eco fibre analyser.

A key user defined setting within the FASEP analysis is the minimum width criterion. The software filters out detected objects in the image based on the criterion and allows the user to remove dust particles that may skew the fibre length distribution analysis. In the work presented, two analyses with different minimum width criterions for fibres have been processed (see Tab. 1). The first has a minimum width criterion of 15 µm and the second has a minimum width criterion of 20 µm. The maximum width criterion is another user defined setting that instead aims to filter out clusters of fibres that are not single filaments after the preparation for

scanning via dispersion. The first sample has been analysed with a maximum width criterion of 70 µm and the second sample 100 µm.

Table 1: Analysis set-up parameters for the FASEP fibre length distribution software

Analysis ref	Image resolution [dpi]	Fibre count	Min width [µm]	Max width [µm]
1	2400	660	15	70
2	4800	8202	20	100

The FASEP 3E Eco system produces an output result of fibre length distribution with automated software interpreting the image. The fibre length distribution can be used to assess whether the chopping method of discontinuous, recycled fibres meets the input requirements for reformatting processes, such as the HiPerDiF machine.

3. Results and discussion

Analysis 1 produces a single peak fibre length distribution by volume (see Fig. 3). 8 % of the total sample volume has been measured between 3960 and 4032 µm and 9 % measured between 4032 and 4104 µm. The peak therefore indicates reasonable precision of the manual operator cutting to a target of 4000 µm. A high quantity of fibres has been detected below the 3000 µm minimum guidance for HiPerDiF, 41% of the cumulative volume frequency or 75% of the quantity frequency of the fibre sample. The longest fibre detected and measured by the FASEP software is 5764 µm, 4 % below the 6000µm maximum guidance for HiPerDiF. The analysis output is a unimodal distribution that could be used to evaluate operator competency of the manual cutting process or to compare cutting techniques.

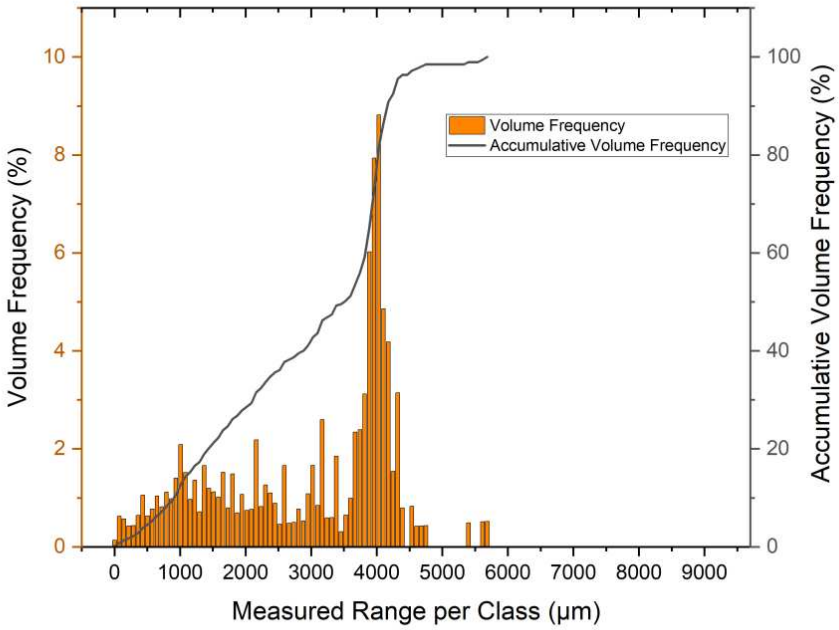

Figure 3. The volume frequency of fibre length distribution of reclaimed carbon fibre in Analysis 1 as a percentage of the total sample volume, along with the cumulative volume frequency of the fibre length distribution

  doi:10.5075/epfl-298799_978-2-9701614-0-0

Compared to Analysis 1, the fibre count detected by the FASEP 3E Eco system during Analysis 2 is considerably higher (see Tab. 2). The software detected 8202 fibres within a width criterion of 20-100 µm when analysing the higher resolution image of 4800 dpi compared to 660 fibres at 2400 dpi within a width criterion of 15-70 µm. The higher resolution image, despite being exported from the same sample, means there is greater detail and definition in the image for the software to detect samples. The importance of scanning and exporting the scans into high resolution images for more detailed and accurate analyses is clear from the results.

Table 2: Fibre detection count results for the two analyses performed using the FASEP system

Analysis ref	Image resolution [dpi]	Fibre count
1	2400	660
2	4800	8202

Analysis 2 has two peak distributions of fibre length (see Fig. 4). The first and highest intensity distribution has a mean centred around 600 µm, whereas the mean position of the second is around 4300 µm and within 10% of the target length. There is also a small number of fibres measured at 6000 µm or greater, above the maximum length HiPerDiF guidance, totalling 2% of the volume frequency of the sample. The longest fibre detected was measured at 9.2mm.

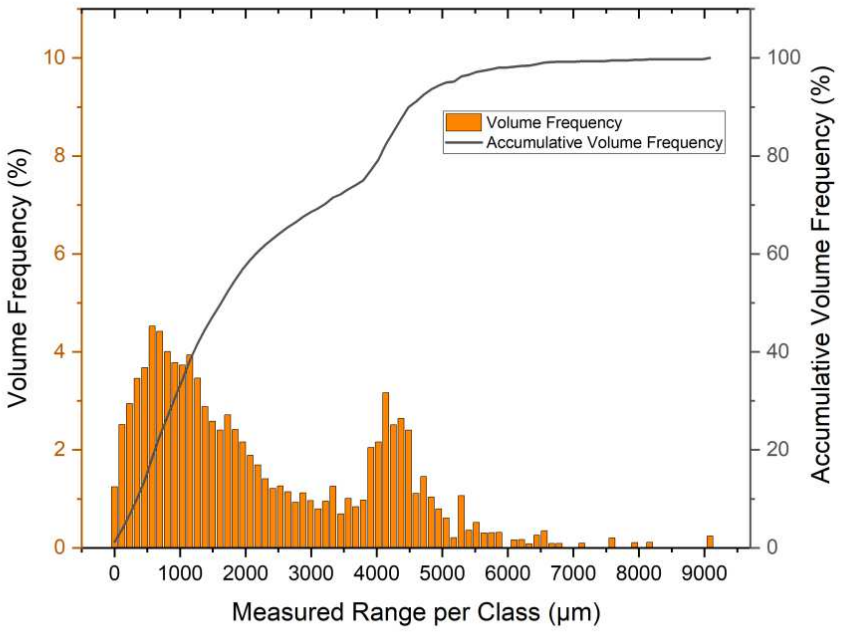

Figure 4. The volume frequency of fibre length distribution of reclaimed carbon fibre in Analysis 2 as a percentage of the total sample volume, along with the cumulative volume frequency of the fibre length distribution

The most notable result of Analysis 2 is the higher distribution of fibres measured at less than 1000 µm (or 1mm) with the higher image resolution. The software is detecting and measuring smaller carbon fibres or dust particles than in Analysis 1, even when a higher minimum width criterion of 20 µm is applied compared to 15 µm. The results and inclusion of smaller fibres or

dust disrupts the analysis of the cutting technique by skewing the peak distribution towards lower values and leading to the resulting graph output to be a bimodal distribution.

The fibre length distribution is further skewed towards lower values when evaluated as a quantity frequency distribution rather than a volume frequency distribution (see Fig. 5).

The majority (93%) of the fibres measured in Analysis 2 are shorter than 3000 µm with 90% below 2185 µm. The result confirms the existence of many short fibres within the sample after manual chopping. The shearing effect while using a guillotine or rotary cutter to chop fibres is likely to cause a high amount of fibre breakage at the point of cutting. Therefore, the significant presence of shorter fibres could be reduced by adapting the length reduction technique. Areas to explore in future work could include blade sharpness, the use of motorised rotary cutters, and the use of die cutters. The inclusion of shorter fibres in downstream processes and materials produced using recycled carbon fibre may also affect the mechanical performance. It is recommended that the FASEP system and the process outlined here be used in future to define the relationship between fibre length distribution of discontinuous recycled carbon fibre samples and the mechanical performance and other properties of composite materials manufactured using them.

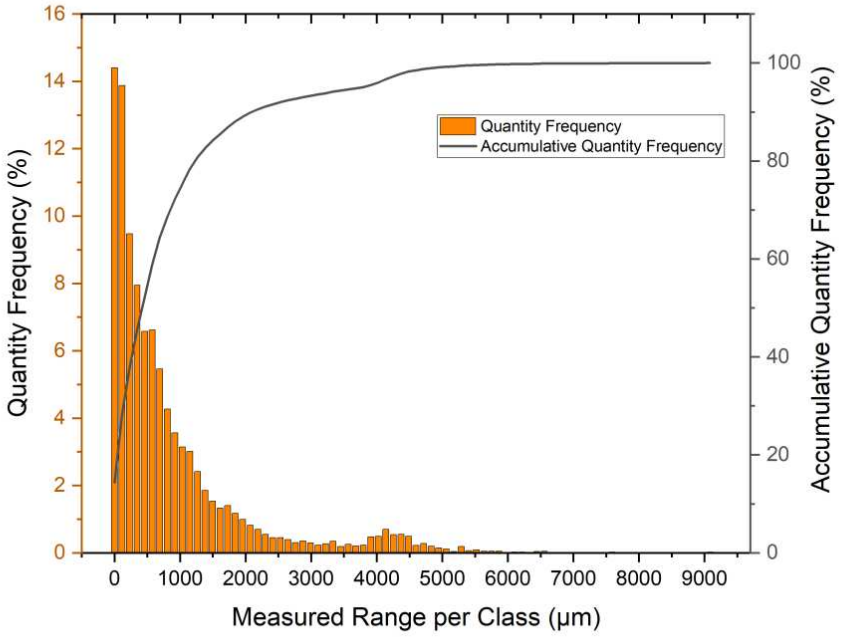

Figure 5. The quantity frequency of fibre length distribution of reclaimed carbon fibre in Analysis 2 as a percentage of the total sample, along with the cumulative quantity frequency of the fibre length distribution

Although a less notable result, Analysis 2 also detected and measured longer fibres than in Analysis 1, which demonstrates the importance of the width criterion in the set-up of the FASEP software. In Analysis 2, a maximum width criterion of 100 µm was defined rather than the 70 µm used in Analysis 1. When analysing the width measurements produced by the FASEP software for Analysis 2, 5 % of the total volume frequency of the sample was measured between

70 and 100 µm. The mean width measured was 25 µm by volume frequency, and the mode was 21 µm. The results suggest that the higher width fibres being detected are clusters of fibres in the sample which overlap and measured as if a single fibre. Depending on how they overlap as the scan is being taken, the fibre length measured by the FASEP software from the image could be significantly higher than a single fibre length in the sample. In future, an array of maximum width criteria could be considered for higher resolution images in order to define the most accurate representative of the sample as well as to note the influence of the set-up parameter.

4. Conclusion

The two analyses using the FASEP 3E Eco system to measure fibre length distribution demonstrate the application of the process for characterising recycled carbon fibre and how the outputs can be used to assess the performance of length reduction techniques. In the case of the manual operation of a guillotine and rotary cutters analysed here, the technique and operator achieved peak distributions close to the target length of 4 mm and there were few fibres longer than the maximum length guidance of 6 mm. While any fibres longer than 6 mm could still cause issues for the HiPerDiF process, the result indicates the issues would be minimal for the sample.

The results from the two analyses also demonstrate the importance of setting up the FASEP system and the influence of the following parameters: image resolution, minimum width criterion and maximum width criterion. An image resolution of 4800 dpi led to the software detecting a far greater number of fibres in the sample which better represented the high presence of shorter fibres and dust. These could increase the level of discontinuity in remanufactured carbon fibre composite materials using the reclaimed fibres to the detriment of their mechanical performance.

  doi:10.5075/epfl-298799_978-2-9701614-0-0

Acknowledgements

The research described in the paper was supported by the Engineering and Physical Sciences Industrial Doctorate Centre in Composites Manufacturing (EP/L015102/1) and the National Composites Centre.

The authors acknowledge the contributions of Helga Mayr from IDM Systems for their support with the FASEP system and the preparation of chopped fibre samples for measurement.

The authors acknowledge the support of the NCC Core Programme and the supporting members from which the materials analysed have been provided.

5. References

1. SGI Aviation. Aircraft Decommissioning Study. Available from: https://www.sgiaviation.com/wp-content/uploads/2020/03/IATA_Aircraft_Decommissioning_Study_May-2018.pdf [Accessed 22 April 2022]. 2018.
2. Griffiths B. Boeing sets pace for composite usage in large civil aircraft. Composites World; 5 January 2005. [Online]. Available from: https://www.compositesworld.com/articles/boeing-sets-pace-for-composite-usage-in-large-civil-aircraft. [Accessed 20 December 2021]. 2005.
3. Karuppannan Gopalraj S, Kärki T. A review on the recycling of waste carbon fibre/glass fibre-reinforced composites: fibre recovery, properties and life-cycle analysis. SN Applied Science; 2:433. 2020.
4. Longana M, Yu H, Hamerton I, Potter K. Development and Application of a quality control and property assurance methodology for reclaimed carbon fibers based on the HiPerDiF (High Performance Discontinuous Fibre) method and interlaminated hybrid specimens. Advanced Manufacturing: Polymer & Composite Science 2018; 4(2): 48-55. 2018.
5. Hartwich M, Höhn N, Mayr H, Sandau K, Stengler R. FASEP ultra-automated analysis of fibre length distribution in glass-fibre-reinforced products. Proceedings of SPIE 7389 Optical Measurement Systems for Industrial Inspection VI; 7389(21). 17 June 2009.
6. Nagel U, Yang L, Kao C C, Thomason J L. Effects of thermal recycling temperatures on the reinforcement potential of glass fibers. Polymer Composites; 39(4): 1032-1040. 2018.

  doi:10.5075/epfl-298799_978-2-9701614-0-0

DEVELOPMENT OF A "DIGITAL TWIN" OF THE AUTOMATED FIBRE PLACEMENT (AFP) LAYUP OF LM-PAEK THERMOPLASTIC MATERIAL USING A PULSED XENON FLASHLAMP HEAT SOURCE

Michael Edwards[a], David Williams[a], Martin Brown[a], Guillaume Fourage[b]

a: Heraeus Noblelight, Unit 163 Cambridge Science Park, Milton Road, Cambridge, CB4 0GQ, UK – michael.edwards@heraeus.com
b: ESTIA Compositadour, Parc Technocité, 1 rue Pierre-Georges Latécoère, 64100 Bayonne, France

Abstract: *Xenon flashlamps have emerged as an alternative heat source to the laser in Automated Fiber Deposition (AFP) of thermoplastics. A Xenon Flashlamp system, consisting of a flashlamp, reflector and light guide, has been shown to reach the temperatures required to process thermoplastic composites in a similar response time to a laser with reduced safety burden. To quickly determine good process parameters for TC1225 LM-PAEK, an opto-thermal simulation model has been created. Two simulation techniques optical ray tracing and finite element analysis (FEA) were used to characterize the flashlamp source and predict the resultant processing temperature respectively. Using these simulation tools, pulse parameters can be chosen more quickly to achieve a desired processing temperature without a significant number of physical trials.*

Keywords: Automated Fiber Deposition; digital twin; pulsed Xenon flashlamp; ray tracing; FEA

1. Introduction

An optical-thermal simulation tool for predicting AFP processing or "nip point" temperature for pulsed xenon flashlamp systems with heated tooling has been developed for end users. This tool allows the prediction of nip point temperature from system parameters before starting layup. This will allow the system user to more quickly determine the most optimal system parameters, reducing setup time and maximizing the time available for laying-up good-quality thermoplastic material. There are a lot of constituent material parameters and validation experiments required to reach a point where the simulation tool is at a point where the end user can use the tool with confidence.

Goniometric, optical materials and surface models, as well as energy level validation work was covered in a previous publication [1]. This paper covers the follow up work namely validation of the irradiance distribution, measurement of thermal parameters, comparison of the initial version of the "digital twin" with AFP layup experiments and investigations into radiative heating effects originating from the quartz light guide.

2. Experimental Validation of the Irradiance Distribution

Since previous work demonstrated the optical energy output of the simulation aligns with the integration sphere measurements [1], the distribution of energy exiting the block end modified for AFP from the simulation was subsequently experimentally validated. Figure 1 (a) shows the predicted energy distribution from the optical simulation and figure 1 (b) is an image of the

  doi:10.5075/epfl-298799_978-2-9701614-0-0

energy output estimated from photosensitive burn paper. The distributions look similar but required experimental measurement.

Measuring the energy distribution or surface irradiance was not straight forward with available equipment, but a method for estimating the irradiance was determined using a thermal camera and the test setup in figure 1 (c). A Micro Epsilon TIM640 thermal camera with a refresh rate of 133 Hz was used for the measurements. The high refresh rate was required to ensure that the temperature measurement was as close to the peak as possible. A single pulse from the xenon flashlamp system of 200 V and 2.5 ms duration was directed at the thermoplastic surface whilst the camera was recording. The thermoplastic sample was then left to cool for approximately one minute before another pulse was directed at the sample, with this process repeated until there were several decent pulse measurements available. Thermal image stills were captured immediately before and after each pulse, where figure 1 (d) captures a post-pulse image.

As can be seen in figure 1 (d), a line was plotted along roughly the center of the irradiated zone and was used to capture datasets of temperature measurements. For each pulse, the post-pulse temperature was subtracted from the pre-pulse temperature from the entire dataset along the line. These results for three pulses are plotted in figure 1 (e) and show that all the lines have the same reproduceable behavior, with deviations in dT due to the camera frame rate and pulse start time not being synchronized. The thermal plot in figure 1 (e) also shows evidence of five fringe artifacts, which help with the validation process.

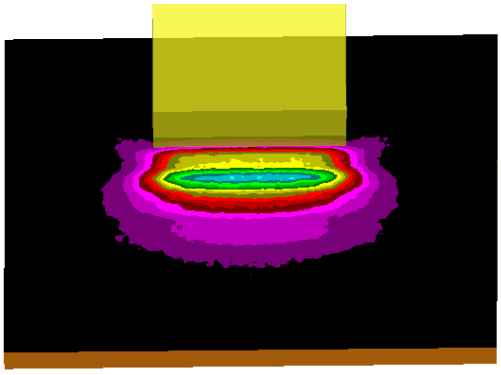

(a)

(b)

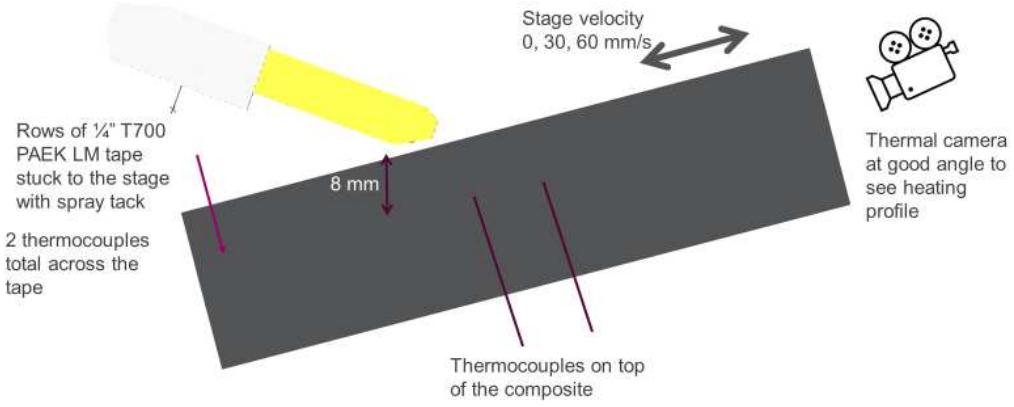

(c)

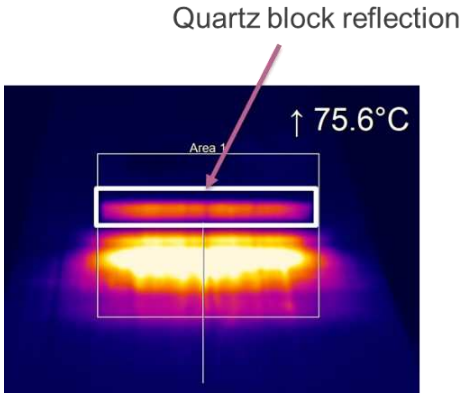

(d)

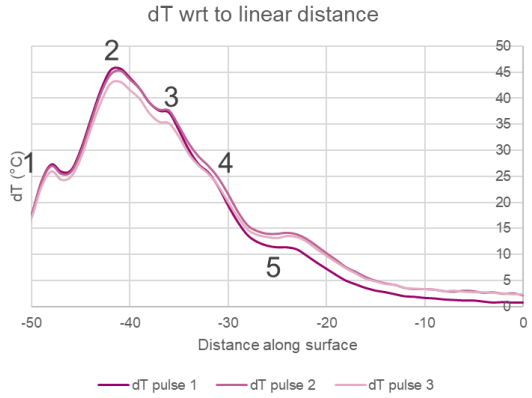

(e)

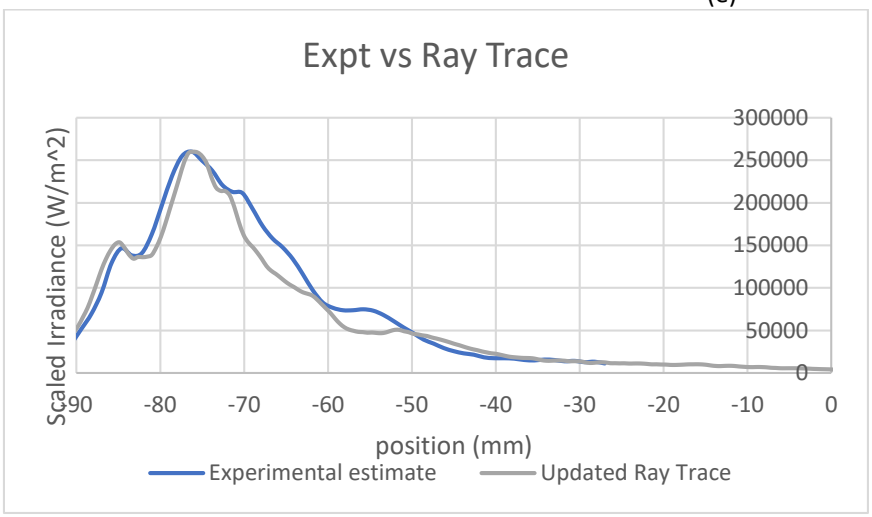

(f)

Figure 1: (a) image of ray tracing prediction of the validation experiment. (b) Burn paper capture of energy exiting the quartz block. (c) Schematic diagram of experimental test setup used to validate the optical simulation output. (d) Thermal camera still of TC1225 PAEK LM tape after a single pulse. (e) Change in temperature with respect to distance plot for a single pulse. (f) Comparison between experimental estimate of irradiance

The next part of the validation was to convert the dT plot data in figure 1 (e) into irradiance, q using a simplified version of Fourier's equation for surface boundaries shown in (1). Since the pulse duration is short and the experiment is static, both the convective and advective terms can be neglected. For the purposes of this estimation, the partial derivative in y can be approximated as the penetration depth as indicated in (2). The thermal diffusivity α is given in (3). The specific heat c, thermal conductivity λ, and thermal diffusivity α values are shown in figure 3.

$$\frac{\partial T}{\partial t} = -\frac{1}{\rho c}\frac{\partial q}{\partial y} \quad (1)$$

$$\frac{\partial}{\partial y} = \sqrt{\frac{\alpha}{\pi f}} \quad (2)$$

  doi:10.5075/epfl-298799_978-2-9701614-0-0

$$\alpha = \frac{\lambda}{\rho c} \tag{3}$$

The comparison between the simulation and experimental estimate of irradiance is shown in figure 1 (f) and agreement appears to be excellent with energy levels of the two peaks and fringe positions appearing to line up. This appears to validate the energy profile produced by the optical simulation. The key outcome is that the optical simulation gives an excellent representation of the actual optical output of the system.

3. Optical Simulation Output

For AFP layup systems, the geometry of the systems is important for the optical simulation because the irradiance received is proportional to the distance between the end of the light guide and the target surface. For the AFP system used in experimental trial, the geometry was as shown in figure 2 (a). Based upon the validated optical simulation from this work and [1], the simulated irradiance absorbed at maximum averaged energy for the substrate and tow tapes is given in figures 3 (b) and (c) respectively. These results were converted into pulsed heat flux boundary conditions that were read by an ANSYS transient thermal simulation.

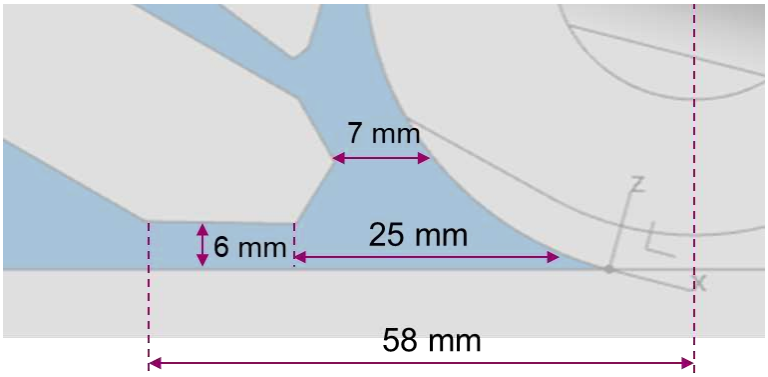

(a)

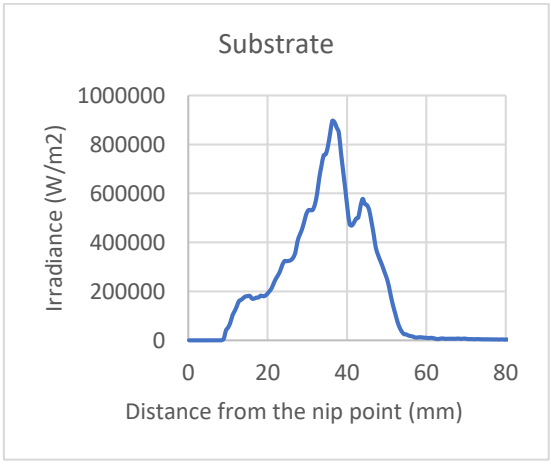

(b)

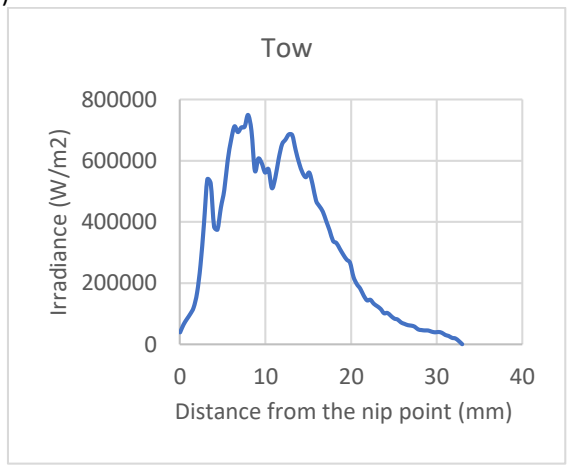

(c)

Figure 2 (a) CAD schematic of AFP layup system used for trials. Optical simulation irradiance outputs along the central axis of the source at maximum averaged power for (b) substrate and (c) tow in AFP trials arrangement.

  doi:10.5075/epfl-298799_978-2-9701614-0-0

4. Development of Transient Thermal FE Model and Comparison between initial Opto-Thermal Simulation and AFP layup trials

Samples of TC1225 PAEK LM tape were sent to external laboratories for external characterization by laser flash analysis (LFA) and differential scanning calorimetry (DSC). LFA directly measures the through-plane thermal conductivity and thermal diffusivity of a material, and the specific heat was directly measured by DSC. Using these measurements and the relationship between the quantities given in (3), a full thermal model of the thermoplastic composite was built. One point of uncertainty is that the thermal conductivity measurements were performed on fully consolidated samples and materials processed by AFP only are likely to be partially consolidated, meaning the effective through-plane thermal conductivity of the substrate tape will likely be lower than the values indicated here for cases greater than one ply thick.

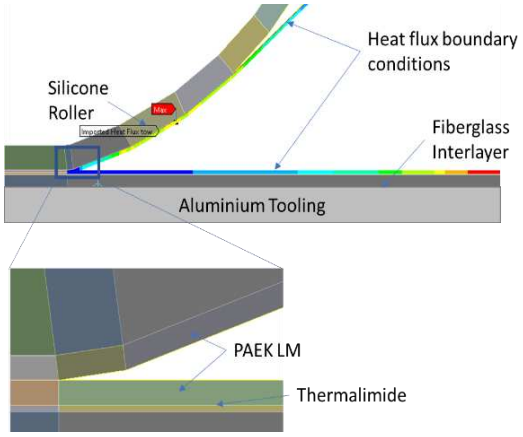

(a)

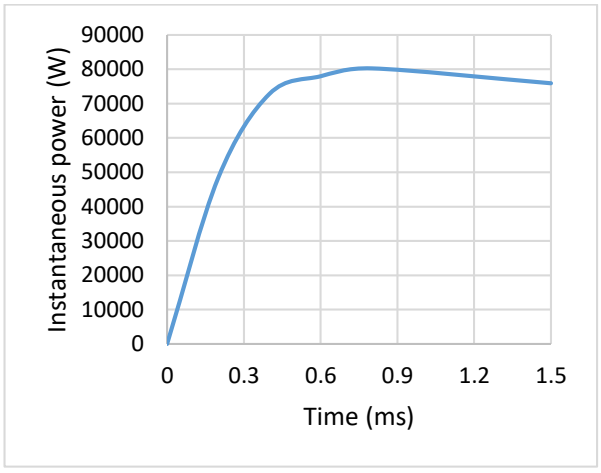

(b)

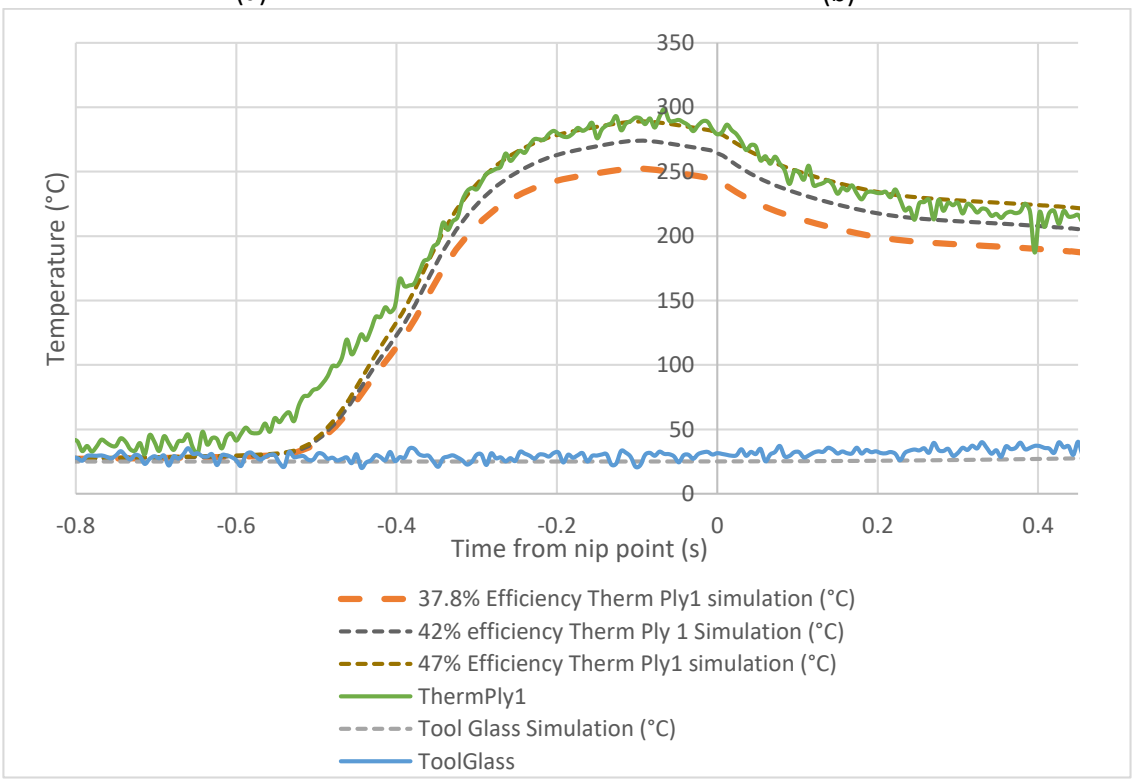

(c)

  doi:10.5075/epfl-298799_978-2-9701614-0-0

Figure 3 (a) Schematic of transient thermal FE simulation with constituent materials. (b) Oscilloscope measurement of instantaneous electrical power for a single pulse with same parameters as that used in the AFP trial. (c) Comparison between thermocouple measurements and the digital twin from the initial trials for a two-ply quasi-isotropic (QISO) layup on an ambient tool with pulse parameters of 250V 90 Hz 1.5 ms 75 mm/s.

Since the optical aspect of the simulation is valid and the key thermal diffusivity parameters measured, a finite element (FE) simulation was built within ANSYS Mechanical with supplemental ADPL scripts using the methodology described in [2]. The simulation is Eulerian with an advective term added to the heat flow equation as shown in (4) and solved as a transient thermal problem over a period of 1.5s to ensure a quasi-equilibrium state. The validated optical simulation output results shown in figure 2 were imported into the FE simulation as pulsed heat flux boundary conditions as shown in figure 3 (a), with the LFA and DSC measurements used to describe the PAEK LM film. The IV behavior of individual pulses was measured using a Tektronix MDO 3024 oscilloscope, as shown in figure 3 (b), giving an electrical pulse energy and this was converted to an optical pulse energy using the 37.6% efficiency value determined in [1].

In parallel to the development of the thermal simulation, AFP layup trials were performed using a commercial 6kW pulsed Xenon flashlamp system built by Heraeus attached to a Coriolis C1 robot. Layup was performed on an aluminium table with a 1 mm thick fiberglass interlayer and a 0.05 mm thermalimide film, below the fist ply of PAEK LM material. Layup was performed in QISO orientation and system parameters of 250V 90 Hz 1.5 ms 75 mm/s were used to perform the AFP process. Thermocouples were placed between the thermalimide and first ply of PAEK LM film and the tooling and fiberglass, providing reliable thermal measurements. The data from the thermocouple measurements, as well as predictions from the thermal simulations are plotted together in figure 3 (b). As figure 3 (b) demonstrates, the initial thermal simulation appears to closely match the shape of the heating curve: but the overall result is conservative. A further simulation runs at both 42% and 47% assumed conversion efficiency suggests that the tape is starting to heat earlier than predicted and there is an additional heating effect that heats samples before the main Xenon flashlamp heating process commences.

5. Investigation into Radiative Heating Effects

(a)

  doi:10.5075/epfl-298799_978-2-9701614-0-0 published under CC BY-NC 4.0 license

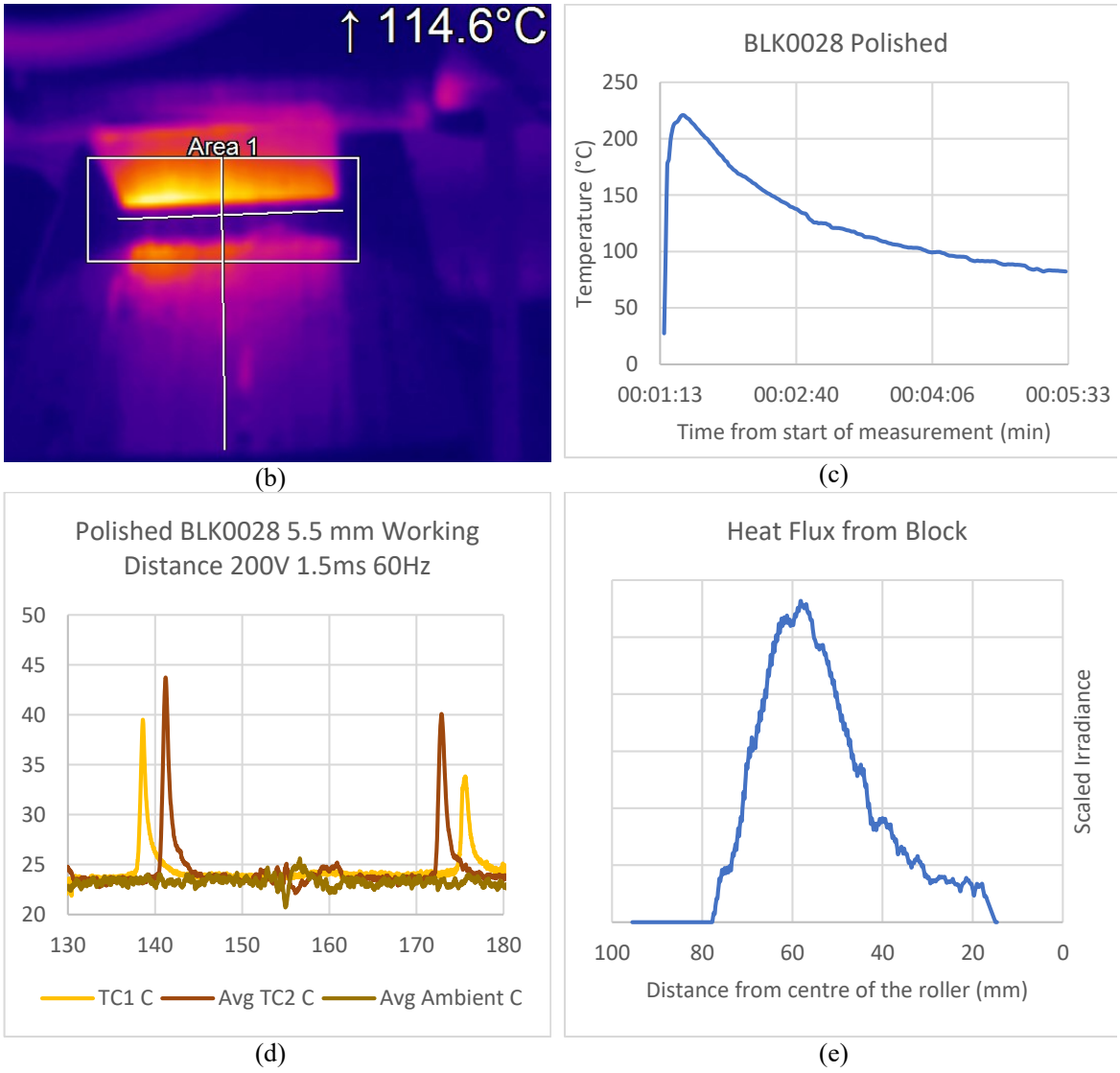

Figure 4: (a) Schematic of experiment designed to prove existence of radiative heating of the substrate tape from the light guide. (b) Thermal camera still capturing the heating of the quartz block after 60s of operation at 200V 1.5 ms 60 Hz for a 6 kW system. (c)Thermocouple measurement of a block cooling after operating in the same conditions as (b). (d) Thermocouple measurements on the surface of the PAEK LM material after pulsing was completed, confirming radiative heat transfer. (e) Estimated heat flux from block heating deduced by running the thermal simulation in "reverse".

Further analysis showed that an additional radiative heating process originates from the quartz block, which functions as a light guide, heating up whilst the system is powered and this heat transferring to the composite tapes via radiation. This requires characterization so that the thermal model is less conservative. A schematic of the test sample is shown in figure 4 (a) and to characterize the additional radiative heating effect, a 6kW pulsed xenon flashlamp system ran at 200 V 1.5 ms 60 Hz for one minute under observation of a thermal camera. Once pulsing was completed, a thermocouple was placed on the surface of the quartz block and sample of PAEK LM composite material with two thermocouples on the surface was run under the system at 30 mm/s with the end of the light guide being 5.5 mm above the thermoplastic sample. As the

  doi:10.5075/epfl-298799_978-2-9701614-0-0 published under CC BY-NC 4.0 license

thermal camera and thermocouple measurements of the block show in figures 15 (b, c), it can reach several hundred degrees on the surface and can potentially be locally hotter on the surface close to the back facet interface that appears to be a heating source. Cutting the quartz will cause surface imperfections at facet edges, preventing a small amount of energy escaping as light. This energy will be converted into heat at this edge, providing the mechanism for heating the block and subsequent radiative heat transfer. Figure 4 (d) contains the sample surface thermocouple results and shows that the heating effect will heat the tapes even if the system has finished pulsing. This shows that this effect will need to be accounted for in any simulation tool, unless the block heating can be minimized via surface finish or AR coatings.

Finally, by running the thermal simulation in reverse, to was possible to obtain an estimate for the surface irradiance from the radiative block heating as shown in figure 4 (e) and this looks reasonable based on solutions with an additional heat flux boundary condition. 3D radiation simulations built in ANSYS Mechanical with the same geometry, with a thermal heating boundary condition up to a maximum of 1000°C show similar curves to figure 4 (e). This suggests that with careful thermal characterization of the quartz light guide during operation, an integrated simulation tool with a 3D thermal radiation simulation can be used to provide accurate estimates of nip point temperature.

6. Conclusion

Presently, a conservative “digital twin” has been produced to describe the AFP process with a pulsed Xenon flashlamp system. The reason why the simulation under-predicts “nip point” temperature is understood and is the result of IR radiation originating from the quartz light guide, used to direct optical energy, as it heats up during processing. Current effort is going into characterizing this effect so that it can be understood, possibly mitigated against, and included in an already good digital twin and improve its accuracy further.

7. Acknowledgements

This project has received funding from the Clean Sky 2 Joint Undertaking under the European Union’s Horizon 2020 research and innovation programme under grant agreement No 886549.

8. References

1. Edwards M, Page A, Williams D, Danezis A, Schilling M, Jenek T, Optimization of Xenon flashlamp heating in Thermoplastic Automated Fibre Placement, Proceedings of Composites and Advanced Materials Expo 2021, CAMX 2021, October 19-21 2021, https://www.researchgate.net/publication/358978544_OPTIMIZATION_OF_XENON_FLASH LAMP_HEATING_IN_THERMOPLASTIC_AUTOMATED_FIBRE_PLACEMENT
2. Danezis A, Williams D, Edwards M, Skordos A, Heat transfer modelling of flashlamp heating for automated tape placement of thermoplastic composites, Composites Part A: Applied Science and Manufacturing, Volume 145, 2021, 106381

  doi:10.5075/epfl-298799_978-2-9701614-0-0

VOID TRANSPORT IN LIQUID RESIN TRANSFER FLOW THROUGH DUAL-SCALE FIBRE REINFORCEMENTS

João M. Machado[a], Masoud Bodaghi[b], Pedro P. Camanho[a], Suresh G. Advani[c], Nuno C. Correia[a]

a: Institute of Science and Innovation in Mechanical and Industrial Engineering, Porto, Portugal – jmmachado@inegi.up.pt
b: IMT Nord Europe, CERI Materials & Processes (CERI-MP), 59508, Douai, France
c: Department of Mechanical Engineering, University of Delaware, Newark, United States

Abstract: *In Liquid Composite Molding (LCM), voids are defects that can be generated during mold filling and degrade the mechanical properties of the composite part. Understanding the dynamics behind the formation and removal of these defects during the manufacturing stage can lead to substantial improvements regarding part performance, as well as the process reliability and repeatability. Several approaches have been proposed to minimize the void content inside composite parts manufactured by LCM, however, a more profound comprehension surrounding void transport is needed to enable the design of more efficient void removal strategies. By means of experimental analysis, this study aims to characterize void transport inside fiber tows, using a scaled 3D printed geometry resembling a fiber tow. Results suggest that the statistical distribution of the cross-sectional aera of voids that cannot be purged follows a Weibull distribution.*

Keywords: Liquid Composite Molding; Voids

1. Introduction

In the context of Liquid Composite Molding (LCM), since preforms are composed by several textile layers, the fibrous preform is not a porous medium with uniform porosity distribution but a medium with two different porous length-scales: the meso-scale porosity, which is located in between the fiber tows, and the micro-scale porosity, which is located inside the fiber tows (in between the fibers). The existence of two different porous length-scales creates two predominant types of pressure driven flow inside the preform: capillary pressure driven flow inside the fiber tows (micro-scale), and hydrodynamic pressure driven flow in between the fiber tows (meso-scale).

In turn, the imbalance between capillary and hydrodynamic pressures forms a lead-lag flow effect that leads to void formation by air encapsulation. If the flow is driven by the capillary pressure, air encapsulation occurs in between the tows as the lag-flow occurs at the meso-scale. On the contrary, if the flow is driven by the hydrodynamic pressure, air encapsulation occurs inside the tows, as the lag-flow occurs at the micro-scale.

This competition between capillary forces (predominant at the micro-scale) and viscous forces (predominant at the meso-scale) can be quantified by the capillary number, in Eq. (1), which is a dimensionless relation between the fluid flow velocity v, the fluid viscosity μ and the surface tension σ.

  doi:10.5075/epfl-298799_978-2-9701614-0-0

$$Ca = \frac{v\,\mu}{\sigma} \quad (1)$$

Several studies established a correlation between the capillary number and the generated void content in composite laminates, where the optimal Ca was found to be approximately 10^{-3} [1–4]. Since void formation can be minimized but not completely avoided, the study of void transport has also been an active research topic, as a means to devise post-fill strategies that provide a more efficient void removal.

Experimental works [5,6] regarding void mobilization through constricted capillary tubes provided close results to the adapted Young-Laplace equation, which in a generic form, this model states that in order to mobilize a void, the hydrodynamic pressure across its length must overcome the capillary pressure around it. Therefore, the critical pressure differential, required for void mobilization can be written as Eq. (2):

$$P_c = 2\gamma\left(\frac{cos\theta_R}{R_1} - \frac{cos\theta_A}{R_2}\right) \quad (2)$$

Where P_c is the critical pressure differential, γ is the surface tension, θ_R and θ_A are the receding and advancing contact angles and R_1 and R_2 are the void radius and constriction radius.

A conclusion that can be taken from this model is that the reduction of R_1, increases the pressure gradient required to mobilize the void through the constriction. This also means that micro-voids will be more difficult to mobilize than meso-voids. Experimental works regarding experiments of void mobilization [4,7,8] agree with this rationale. The relevance of the study and characterization of this type of void is therefore relevant to LCM processing, as due to the increased removal difficulty, this type of void is often found in laminates.

This study explores void transport at the microscale, using 3D printing technology to manufacture a random fiber packing geometry resembling the fiber arrangement inside a fiber tow, scaled to the order of millimeters. An experimental setup has been designed to allow for the accurate control of the resin flow rate inside the fibrous geometry, along with the visual monitoring of the experiment. The results obtained in this study should prove useful in designing process conditions in which voids can be further removed from parts manufactured by LCM.

2. Methodology

2.1 Experimental setup

The experimental setup was devised in a way to allow the visual monitoring of the flow through the porous medium, as well as the subsequent flowrate calculation. The flow was imposed by drawing vacuum in one end of the circuit using a vacuum pump, while the inlet was connected to a test-fluid reservoir. A leak-proof chamber, depicted in Figure 1, was designed to contain the porous medium during the flow experiments, allowing video recording, through a transparent acrylic window. The chamber hollow cavity dimensions were adjusted to the porous medium dimensions, to minimize the occurrence of racetracking around the porous medium. Additionally, a mass scale was positioned below the test-fluid reservoir in order to allow the calculation of mass-flowrate throughout the experiment. A schematic of the experimental setup is depicted in Figure 2.

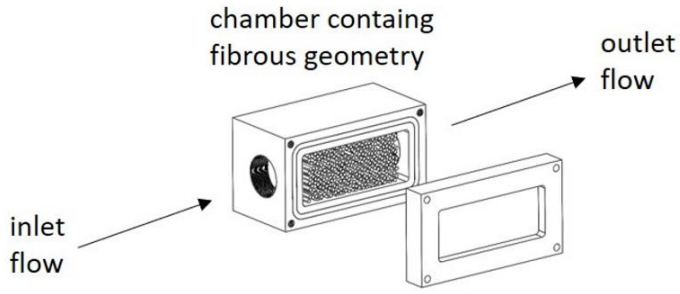

Figure 1. Schematic of the chamber containing the porous medium

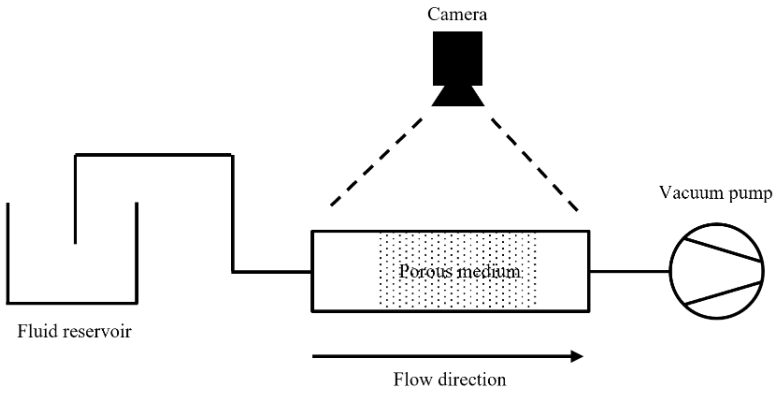

Figure 2. Schematic of the experimental setup

The test-fluid used in this study consists of a mixture of corn-syrup with water, at a mass concentration of 80% corn-syrup. The mean rheologic properties of the fluid measured at 20°C, are summarized in Table 1.

Table 1: Properties of the test-fluid at 20°C.

Viscosity [Pa.s]	Surface tension [N/m]	Contact angle [°]	Density [kg/m^3]
0.287	0.08	64.7	1300

An in-house developed artificial vision algorithm based on convolutional neural networks [9] was applied to process the video recordings, classifying each frame pixel into belonging to a void or background. An example of a frame semantic segmentation is depicted in Figure 3. In all experiments, the voids were generated naturally by the flow front advancement.

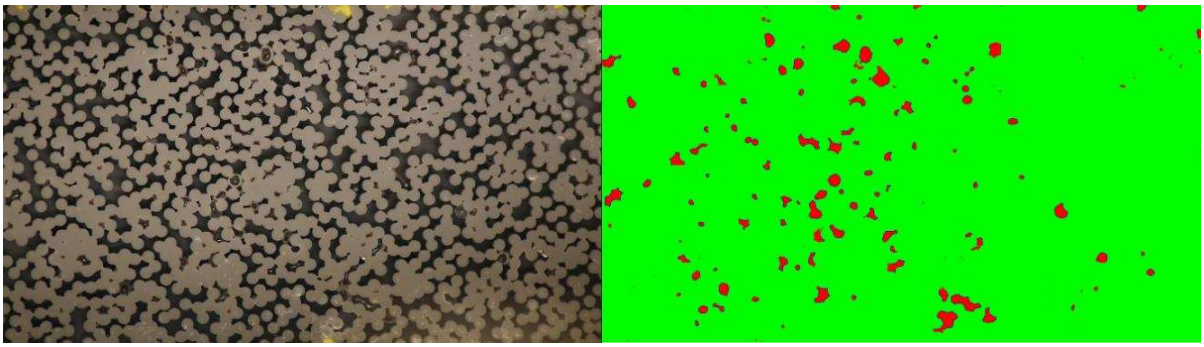

Figure 3. Example of a video frame semantic segmentation by the algorithm (red: void; green: background)

  doi:10.5075/epfl-298799_978-2-9701614-0-0

2.2 3D printed porous medium

Prior to the generation of the porous medium CAD geometry, a necessary step was to understand which size the geometry would have to acquire, to be considered representative. In fiber tows the interstitial spaces between fibers have a stochastic nature, hence, to generate a representative element (RVE) of a fiber tow, it needs to possess a minimum size, by which its geometrical variability is similar to the variability of a fiber tow. The RVE generation was done using an in-house algorithm based on [10]. Due to computational constraints, the RVE sizes considered range from $N_f = 16$ to a maximum of $N_f = 140$, where N_f is the quotient between the length of the RVE and the radius of the fibers.

Using the derived probability distributions of the 12th nearest neighbor fiber distances, it was possible to conduct a statistical convergence analysis, where the minimum RVE size was determined to be $N_f = 70$. This convergence can be observed by the derived coefficients of variation depicted in Figure 4, for RVEs containing different fiber volume fractions. The coefficient of variation is the quotient of the derived standard deviation by the mean. For this study, an RVE with a size of $N_f = 70$ was used to conduct the experiments.

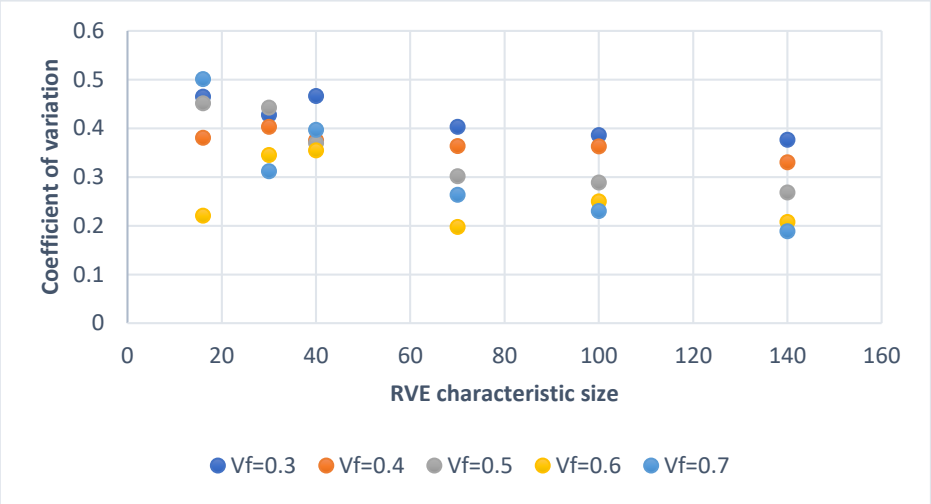

Figure 4. Coefficient of variation of the measured 12 nearest neighbor filament distances for different RVE sizes and fiber volume fractions

3. Results

Two experiments were conducted at two different flowrates, by adjusting the vacuum level. Steady-state flow was achieved in all experiments after a few seconds, while the experiment was conducted for a few minutes. The steady-state capillary numbers for the experiments are presented in Table 2. The 3D printed porous medium porosity was kept at 50% in all experiments.

Table 2: Capillary number in experiments.

Experiment	Flowrate [m^3/s]	Capillary number
1	6.15e-8	0.0032
2	9.42e-8	0.0050

Both void transport and void entrapment phenomena were captured during the experiments, however, due to limitations in the artificial vision system, only the entrapped voids could be analyzed. Regarding the latter, using the artificial vision algorithm it was possible to measure the cross-sectional area of all voids present in a video frame. The frame was captured when all mobile voids had exited the porous medium, by which all the remaining voids were entrapped. Using the void cross-sectional areas extracted from both experiments, it was possible to conduct a frequency analysis, shown as a histogram, in Figure 5 and Figure 6. In turn, the derived probability distributions for both experiments follow a gamma distribution, which fitting is represented in red.

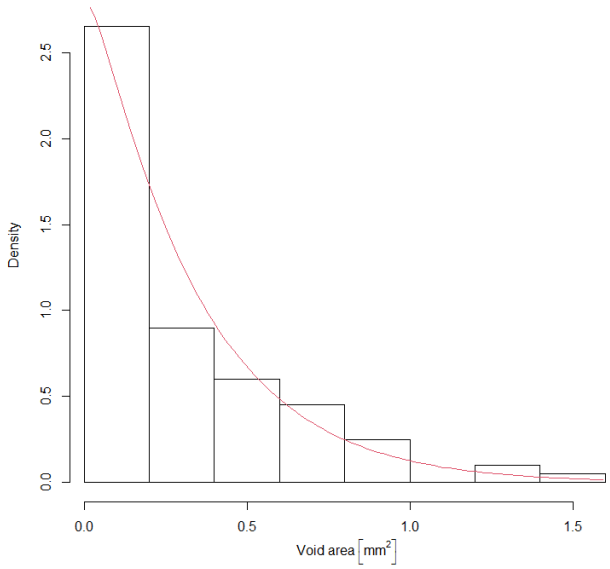

Figure 5. Histogram of void cross-sectional areas found in experiment 1

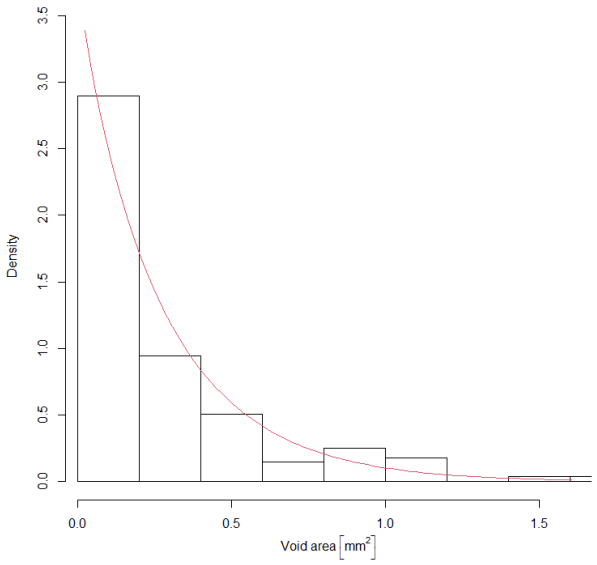

Figure 6. Histogram of void cross-sectional areas found in experiment 2

3. Conclusions

In this study, void transport phenomena inside fiber tows were studied, in the context of LCM. A 3D printed porous medium composed by a random cylinder packing was used to provide a scaled geometry resembling a fiber tow, allowing the visual monitoring of void transport phenomena. To this effect, a machine learning based artificial vision algorithm was employed to enable the post-processing of the recordings of experiments in an automatic fashion. It was demonstrated that the underlying distribution of void cross-sectional areas follows a Weibull distribution, independently of the flowrate at which the experiments were conducted. Future work should explore the effect of higher capillary numbers on void cross-sectional area distribution, as well as the effect of fiber volume fraction variation on void entrapment.

Acknowledgements

The authors would like to acknowledge the support from the Associated Laboratory for Energy, Transports and Aeronautics (LAETA) under the Research Grant UIDB/50022/2020.

4. References

1. Chung Hae Park, Woo L. Modeling void formation and unsaturated flow in liquid composite molding processes: a survey and review. Fu S-Y, Mai Y-W, Du S-Y, editors. J Reinf Plast Compos [Internet]. 2011 Jun 16;30(11):957–77. Available from: http://journals.sagepub.com/doi/10.1177/0731684411411338

2. Leclerc JS, Ruiz E. Porosity reduction using optimized flow velocity in Resin Transfer Molding. Compos Part A Appl Sci Manuf [Internet]. 2008;39(12):1859–68. Available from: http://dx.doi.org/10.1016/j.compositesa.2008.09.008

3. Zingraff L, Michaud V, Bourban P-E, Månson J-AE. Resin transfer moulding of anionically polymerised polyamide 12. Compos Part A Appl Sci Manuf [Internet]. 2005 Dec;36(12):1675–86. Available from: https://linkinghub.elsevier.com/retrieve/pii/S1359835X05001284

4. Rohatgi V, Patel N, James Lee L. Experimental investigation of flow-induced microvoids during impregnation of unidirectional stitched fiberglass mat. Polym Compos. 1996;17(2):161–70.

5. Lundström TS. Bubble transport through constricted capillary tubes with application to resin transfer molding. Polym Compos [Internet]. 1996 Dec;17(6):770–9. Available from: http://doi.wiley.com/10.1002/pc.10669

6. Shih CH, Lee LJ. Analysis of void removal in liquid composite molding using microflow models. Polym Compos. 2002;23(1):120–31.

7. Patel N, Lee LJ. Modeling of void formation and removal in liquid composite molding. Part II: Model development and implementation. Polym Compos [Internet]. 1996;17(1):104–14. Available from: http://doi.wiley.com/10.1002/pc.10595

8. Kang K, Koelling K. Void transport in resin transfer molding. Polym Compos. 2004;25(4):417–32.

9. Machado JM, Tavares JMRS, Camanho PP, Correia N. Automatic void content assessment of composite laminates using a machine-learning approach. Compos Struct

[Internet]. 2022 May;288:115383. Available from: https://linkinghub.elsevier.com/retrieve/pii/S0263822322001830

10. Catalanotti G. On the generation of RVE-based models of composites reinforced with long fibres or spherical particles. Compos Struct [Internet]. 2016;138:84–95. Available from: http://dx.doi.org/10.1016/j.compstruct.2015.11.039

MINIMISATION OF THE NUMBER OF SENSORS FOR DEFECT DETECTION IN RESIN TRANSFER MOULDING

Mikhail Matveev[a], Andreas Endruweit[a], Marco Iglesias[b], Michael V. Tretyakov[b]

a: Composites Research Group, Faculty of Engineering, University of Nottingham, UK,
Mikhail.Matveev@nottingham.ac.uk
b: School of Mathematical Sciences, University of Nottingham, UK

Abstract: *Resin Transfer Moulding (RTM) is often employed in composites manufacturing when high dimensional accuracy of components is important. In RTM, defects of a reinforcement that arise from local variations of fibre volume fraction, such as race tracking or wrinkles and folds of fibre reinforcement, may result in incomplete impregnation or excessive void content. Once a defect is detected, it can be mitigated by controlling the resin injection process. Therefore, a defect detection algorithm that reliably can predict position of defects, their magnitude and severity is required. The accuracy of the defect detection depends on the number of sensors available for in-process monitoring and their positions. Minimising the number of sensors is desirable to reduce maintenance costs. A detailed study on the effect of sensor density on the relative precision of defect detection is presented in this work.*

Keywords: Resin Transfer Moulding; defect detection; sensors.

1. Introduction

Resin Transfer Moulding (RTM) is one of the frequently used methods in composites manufacturing. While offering benefits over other methods like vacuum infusion or prepreg layup, RTM also has some drawbacks such as higher tool cost as well as being prone to defects related to the resin flow through a fibre reinforcement. In particular, local changes and variability in the reinforcement porosity and permeability can lead to unpredicted and undesirable resin filling scenarios such as dry spots [1]. These scenarios can be avoided by employing a process control system that can detect defects and offer a way to mitigate the effect of these defects on the resin flow. This work concentrates on the first component of such control system, an in-process defect detection.

Flow through a porous reinforcement is often modelled using Darcy's law that defines the average flow velocity, $\mathbf{v}$, as [1]:

$$\mathbf{v} = -\frac{\mathbf{K}}{\mu\Phi}\nabla p\,, \tag{1}$$

where $\mathbf{K}$ is the permeability tensor of the reinforcement, Φ is its porosity, μ is the resin viscosity, and ∇p is the pressure gradient.

The defects of the reinforcement are manifested in local changes in permeability and porosity. Therefore, most in-process defect detection methodologies are aiming at estimating local values of these two quantities. One of the approaches relies on matching the in-process data to one of the pre-computed scenarios or their combination [2, 3]. This methodology provides good results

  doi:10.5075/epfl-298799_978-2-9701614-0-0

in case of race-tracking defects that have preferential positions along the edges of the mould. However, it may be less adequate for analysing the cases that deviate from the pre-computed scenarios.

The second type of the in-process defect detection aims to minimise the difference between the experimental data and simulations of the process with a defect. For example, it was shown that this methodology can be used to estimate both local porosity and permeability of random mat as well as race-tracking present in the experiment [4]. While these approaches are more versatile than those based on pre-computed scenarios, they come at a cost because the minimisation procedure relies on a computationally expensive algorithm e.g. a non-linear optimisation algorithm [4] or a probabilistic inversion algorithm [5]. The latter is employed here.

The defect detection in this work relies on an inverse method that employs experimental data from an array of pressure sensors. Precision of the defect detection is compared using a specially constructed characteristic. The presented methodology can be used to minimise the number of sensors required for detecting defects of a given size in a general case.

2. Defect detection methodology

2.1 Bayesian inversion algorithm (BIA)

Defect detection in RTM is based on using available experimental data, typically fluid pressure measurements and observations of the flow front via arrival sensors during the resin filling. Once the experimental data are obtained, it is possible to employ an inverse method. A Bayesian inversion methodology [5, 6] that was validated with lab experiments is used in this work.

The Bayesian inversion algorithm (BIA) employed here starts with an initial guess, a prior distribution, of local porosity and permeability. This distribution is based on available prior knowledge of porosity and permeability, i.e. target values and estimated variability. The distribution is represented by an ensemble of samples of these material properties weighted with their probabilities. Each sample is created using a three-level parametrisation that allows to describe defects of random shape and aspect ratio.

The RTM process needs to be simulated for every sample of porosity and permeability to obtain pressure values at specified locations. This can be done by any numerical solver as the algorithm uses the solver in a black-box fashion. Based on the obtained simulation results, the distributions of porosity and permeability are updated using Bayes' rule so that the calculated pressure values become consistent with the experimental data. The numerical implementation of BIA iteratively updates the ensemble of samples. Details of the BIA implementation of are given in [6].

It should be noted that BIA employed here estimates the distribution of the porosity and permeability. This makes it possible to assess the uncertainty of the defect detection in absence of rich experimental data.

2.2 Metrics of defect detection

The defect detection algorithm estimates the local mean and standard deviation of porosity and permeability. These estimations are consistent with the experimental data and can be used to reconstruct the defect in the preform.

For comparing the reconstructed and the actual defects, a range of characteristics should be considered in order to compare the size and position of the defects as well as the values of the porosity and permeability. The first of the characteristics, intersection over union, is often used for benchmarking computer vision algorithms [7]. It is used for describing what portion of the detected defect overlaps with the actual defect and its ratio to the size of defects combined. This can be written as:

$$\varepsilon_1 = \frac{|S_{actual} \cap \bar{S}_{estimated}|}{|S_{actual} \cup \bar{S}_{estimated}|}, \tag{2}$$

where S_{actual} is a two-dimensional set representing the actual defect and $\bar{S}_{estimated}$ is a two-dimensional set representing the reconstructed defect computed as an average over an ensemble of samples using in the BIA.

The second characteristic is used for comparing local values of the estimated porosity with the values of the porosity in the actual defect. Normalised root mean square error is used for this purpose:

$$\varepsilon_2 = \frac{\sqrt{1/N \sum_{i=1}^{N} (\Phi_i - \bar{\Phi}_i)^2}}{1/N \sum_{i=1}^{N} \Phi_i} \tag{3}$$

where Φ_i and $\bar{\Phi}_i$ are the local porosities in the actual and estimated porosity fields at points $i = 1,..,N$. All points used to compute this error belong to the defect only.

The characteristic ε_3, which is identical to the one defined by Eq. (2), is introduced for the area outside the defect. Finally, a characteristic that considers variability in the estimations is considered as well. This is also defined as a normalised root mean square error:

$$\varepsilon_4 = \frac{\sqrt{1/N \sum_{i=1}^{N} (\overline{\sigma\Phi}_i)^2}}{1/N \sum_{i=1}^{N} \Phi_i} \tag{4}$$

where $\overline{\sigma\Phi}_i$ is the estimated variance of the porosity at point i.

The characteristics ε_j, $j = 1,..,4$, are combined with the equal weights to create a new quantity called *the relative precision of the detection* that takes value of 0 for an absolutely precise detection and value of 1 when the defect is not detected at all. The relative precision can be written as:

$$\varepsilon = \left(1 - \frac{\varepsilon_1 + \varepsilon_2 + \varepsilon_3 + \varepsilon_4}{4}\right) \tag{5}$$

The relative precision defined by Eqs. (2)-(5) will be used for comparing different defect detection scenarios.

3. Material properties

A glass fibre non-crimp fabric, Hexcel FGE 247, with an areal density of 411 g/m^2 is used in this work. In-plane permeability of the reinforcement was measured using a radial injection setup

  doi:10.5075/epfl-298799_978-2-9701614-0-0

[ref]. The permeability was characterised at several porosity values. This allowed to approximate relationship between porosity and permeability with a power law:

$$K_i = a_i(1 - \Phi_i)^{b_i}\,, \tag{6}$$

where Φ_i is the porosity, and a_i and b_i are the power law parameters.

The in-plane permeabilities, K_1 and K_2, of the reinforcement along with the parameters a_i and b_i are shown in Figures 1 and 2. These material properties were used for the virtual experiments in the next section.

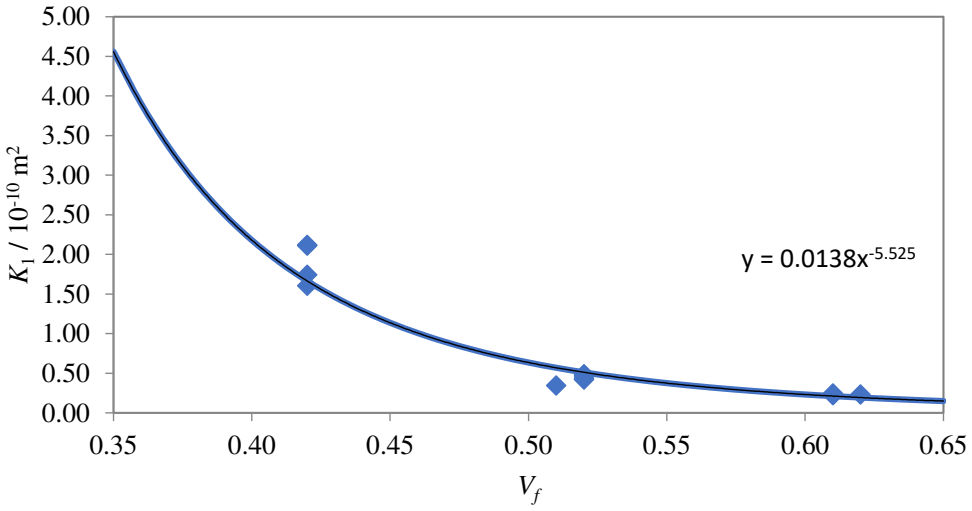

Figure 1. Principal permeability K_1 of FGE 247 reinforcement

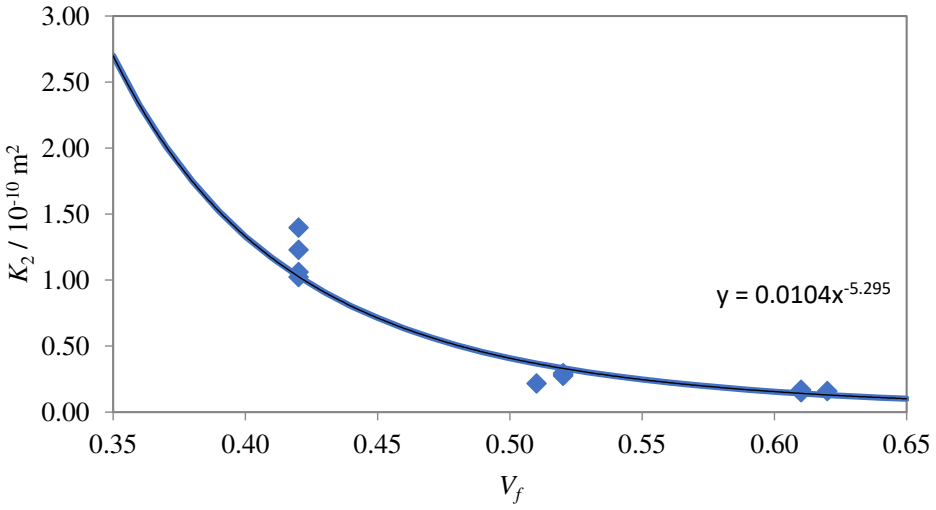

Figure 2. Principal permeability K_2 of FGE 247 reinforcement

4. Virtual experiments

4.1 Methodology

To determine the optimum number of sensors, a series of virtual experiments are carried out. Each of the experiments represents a simulation of resin injection into a preform with a random

defect, collection of experimental data, and use of this data for defect detection as described above. Using the relative precision of the detection, the estimated permeability and porosity are compared to the permeability and porosity that were used to generate the experimental data.

The experiments are repeated for different number of sensors and different arrangements. For every sensor arrangement, a Monte Carlo experiment is run to generate statistics for the defect detection.

4.2. Simulation setup

Resin injection into a square mould with dimensions of 0.3 m x 0.3 m is simulated using Ansys Fluent. A two-phase flow is simulated where the resin phase displaces air in the mould. Solver settings used for the simulations can be found in [6]. The geometry of the mould is discretised in a regular mesh of 100×100 elements that was found to be sufficient to resolve the defects considered in this work.

The resin inlet and the vent are located on two opposite sides of the mould (full length). The injection pressure is set at 1 bar and the vent pressure is set at 0 bar. The preform is assumed to have an alternating 0°/90° layup that has isotropic permeability equal to $(K_1(\Phi) + \mathrm{K}_2(\Phi))/2$ for any given porosity value, where $K_i(\Phi)$ is the function defined by Eq. (6).

For simulating defects and variability in the reinforcement, porosity and permeability of the preform are split into two regions – defect and background. The background represents nominal properties of the preform, i.e. as-designed properties, along with the inherent variability of the reinforcement properties. The average nominal porosity for the preform is 0.55, corresponding to an average nominal permeability of 0.937×10^{-9} m^2. The variability of these nominal values is set to 2.5%.

The defect regions are generated as circles with centres at random positions and their radius being a random value from an interval [0.027; 0.033] m. This creates defects that take less than 1% of the mould area. Permeability and porosity of the defects are random values from the intervals [0.125; 0.194] $\times10^{-9}$ m^2 and [0.35;0.4], respectively.

4.3 Sensor arrangements

Only pressure sensors are considered in this study. The sensors are simulated as point sensors in Ansys Fluent. Output from all sensors is written to a text file at a required frequency.

It is assumed that defects can appear anywhere in the mould with equal probability. Therefore, the sensors should cover the mould uniformly. The mould is split into equal areas and the sensors are placed in the centres of these areas. Examples of such splits are shown in Figure 3.

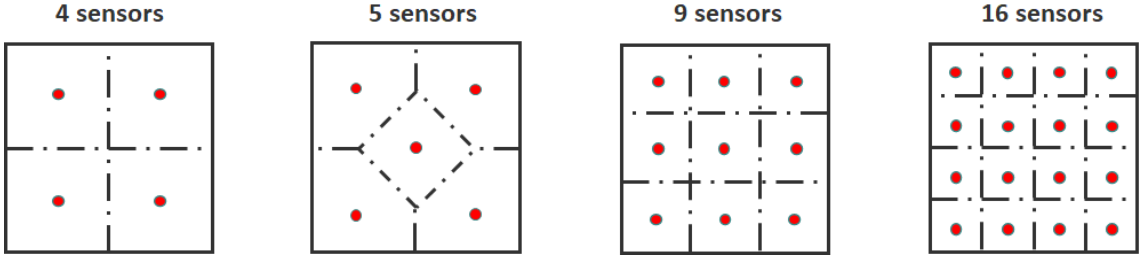

Figure 3. Four possible sensor arrangements

4.4 Results

The sensor arrangements with 4, 9 and 16 sensors were analysed. Each of the arrangements was used to analyse 10 preforms with random defects generated as outlined above. Two examples of the defect detection are given in Figure 4. It can be seen that even 4 sensors can detect the presence of the defect, but the size of the defect is not detected correctly. Obviously, increasing the number of sensors leads to better estimations.

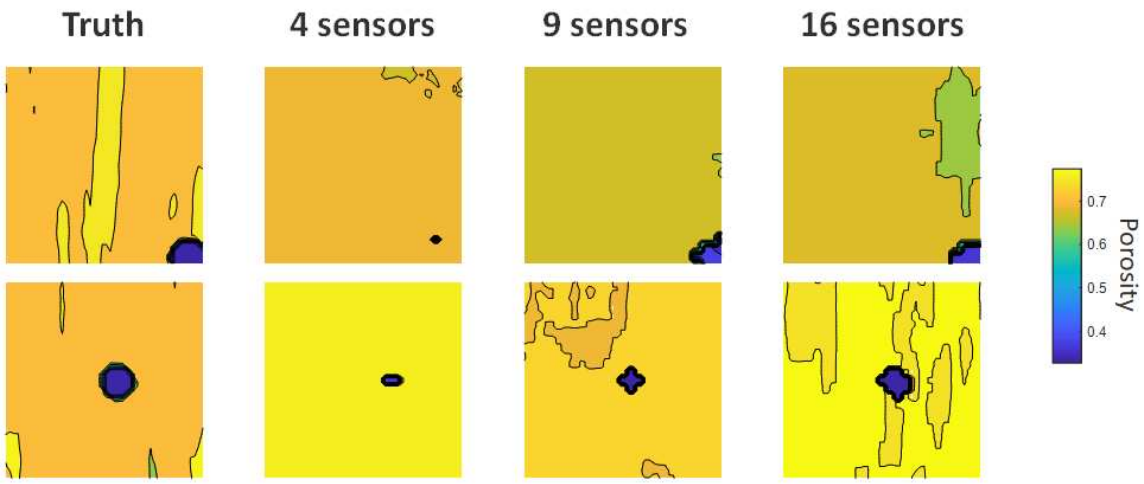

Figure 4. Two examples of defect detection with different number of sensors

Results of the Monte Carlo simulations for three sensor arrangements are given in Figure 5. The relative precision of the defect detection was calculated using Eq. (5). The relative precision plateaus after 9 sensors which indicates that this is a sufficient number of sensors for the given size of the defect, which is a circle with an average radius equal to 10% of the mould length.

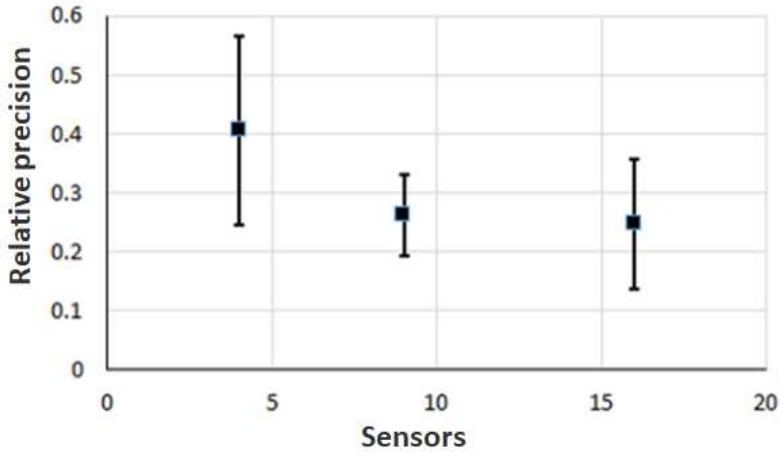

Figure 5. Relative precision of defect detection with different number of sensors

5. Conclusions

The methodology for detecting defects in the resin injection phase of the RTM process is presented here. The methodology is based on a Bayesian inversion algorithm (BIA) that was validated in lab experiments in an earlier work [6]. This study aims to minimise the number of pressure sensors required for detecting a defect of a given size. A relative precision of the defect

  doi:10.5075/epfl-298799_978-2-9701614-0-0

detection is quantified using a specially constructed characteristics that compare the size and position of the reconstructed defect as well as the porosity values with those of the actual defect.

It was found that even 4 sensors give sufficient precision in terms of detecting the presence of the defects. The relative precisions of the configurations with 9 and 16 sensors are close to each other. Lack of improvement between these two cases is explained by the sensor spacing being already comparable to the defect size considered here. Thus, any further increase in the sensor density does not lead to significant improvement in the relative precision. Therefore, the configuration with 9 sensors is the optimum for the considered case.

Acknowledgements

This work was supported by the Engineering and Physical Sciences Research Council [grant number EP/P006701/1]; though the EPSRC Future Composites Manufacturing Research Hub.

6. References

1. Advani SG, Sozer EM. Process modeling in composites manufacturing. CRC press. 2010.
2. Hsiao KT, Advani SG. Flow sensing and control strategies to address race-tracking disturbances in resin transfer molding. Part I: design and algorithm development. Composites Part A: Applied Science and Manufacturing, 2004; 35: 1149–1159.
3. Siddig NA, Binetruy C, Syerko E, Simacek P, Advani S. A new methodology for race-tracking detection and criticality in resin transfer molding process using pressure sensors. Journal of Composite Materials, 2018; 52: 4087–4103.
4. Caglar B, Salvatori D, Sozer EM, Michaud V. In-plane permeability distribution mapping of isotropic mats using flow front detection. Composites Part A: Applied Science and Manufacturing, 2018; 113: 275 – 286.
5. Iglesias M, Park M, Tretyakov MV. Bayesian inversion in resin transfer molding. Inverse Problems, 2018, 34(10): 105002.
6. Matveev MY, Endruweit A, Long AC, Iglesias MA, Tretyakov MV. Bayesian inversion algorithm for estimating local variations in permeability and porosity of reinforcements using experimental data. Composites Part A: Applied Science and Manufacturing, 2021; 143: 106323.
7. Rezatofighi H, Tsoi N, Gwak J, Sadeghian A, Reid I, Savarese S., Generalized Intersection Over Union: A Metric and a Loss for Bounding Box Regression. 2019 IEEE/CVF Conference on Computer Vision and Pattern Recognition (CVPR), 2019; 658-666

  doi:10.5075/epfl-298799_978-2-9701614-0-0

TRANSVERSE LIQUID COMPOSITE MOULDING PROCESSES AND LUBRICATION EFFECTS IN ADVANCED COMPOSITES MATERIAL MANUFACTURING

Jeeeun Lee[a], Miro Duhovic[b], Tom Allen[c], Piaras Kelly[a,c]

a: Department of Engineering Science, University of Auckland – jlee874@aucklanduni.ac.nz
b: Leibniz-Institut für Verbundwerkstoffe GmbH, Technische Universität Kaiserslautern
c: Centre for Advanced Composite Materials, University of Auckland

Abstract: *In a recently developed transverse Liquid Composites Moulding (LCM) process termed Resin Transfer Pressing (RTP), compaction drives the resin from a saturated carrier material into a dry reinforcement material. In transverse resin infusion processes, the complex coupling between fluid flow and preform deformation induces a non-homogeneous fibre volume fraction distribution through the thickness. Additionally, wet fabrics typically require lower stresses to compact than dry fabrics due to lubrication effects, causing the compaction behaviour to change as a dry fabric becomes saturated. In this work, a comprehensive model has been developed to simulate the RTP process and simpler transverse LCM processes, including resin injection into a dry preform and Compression Resin Transfer Moulding. For all transverse processes, the dry compaction behaviour has a more significant influence on the fill time, whereas the wet compaction behaviour determines the thickness and fibre volume fraction of the final product.*

Keywords: Compression Resin Transfer Moulding; Resin Transfer Pressing

1. Introduction

Liquid Composites Moulding (LCM) refers to a family of composite manufacturing methods in which the fibrous material is filled and bound by a polymeric resin. There are numerous variations of LCM processes, with improvements made to reduce manufacturing time and cost. Transverse (through-thickness) impregnation variants of LCM processes result in relatively fast fill times since the flow path is reduced to the material thickness. In these transverse processes, the fluid flows in the same direction as the preform deformation, so the complex coupling between fluid flow and deformation leads to hydrodynamic compaction of the preform stack [1]. The fluid pressure gradient can cause the fibrous material to deform, and the deformation can influence the fluid flow. The fibre volume fraction distribution in the saturated region is non-homogeneous because the fluid pressure drops from the injection pressure to atmospheric pressure along the flow path. The material will relax to a homogeneous state when the injection pressure is removed. Many studies have neglected the hydrodynamic compaction effects in the past [2,3,4,5]. A few studies have modelled the hydrodynamic compaction effects for simpler transverse processes such as constant pressure injection into a dry preform [6], compression of a saturated preform [7,8] and saturated transverse permeability measurement systems [9].

In Compression Resin Transfer Moulding (CRTM), the resin is injected into a gap between the upper piston tool and the dry fibre preform, and compression drives the resin through the preform [2,10]. Resin Transfer Pressing (RTP) is a recently developed LCM process that involves the through-thickness transfer of resin from a saturated carrier material to a dry reinforcement via compression [11,12]. A basic initial model has been developed by Duhovic et al. [11].

  doi:10.5075/epfl-298799_978-2-9701614-0-0

Wet fabrics generally require lower stresses to compact than dry fabrics due to fibre lubrication [13]. For example, the wet layer of a nonwoven fabric is much thinner than the dry layer in an RTP experiment [12]. Recent studies show continued interest in characterising the different wet and dry compaction behaviour, such as the recent international benchmark exercise carried out on a woven and non-crimp fabric [14]. Most previous studies have assumed that the compaction behaviour of wet and dry fibre reinforcement is identical in transverse LCM process models. In studies that incorporate the lubrication effect, the flow and deformation are not coupled.

Modelling of transverse processes involving more than one material is limited. Shojaei [5] modelled the CRTM process for a multi-layer preform. However, hydrodynamic compaction was ignored, assuming homogeneous fibre volume fraction through the thickness. Simulations capable of modelling more than one material type would be beneficial to determine the thickness of carrier material required, compare the performance of different materials and predict process times in an RTP process. Multi-layered material stacks with combinations of two or more material combinations could also be considered.

In this work, a comprehensive model has been developed to predict the preform deformation, resin impregnation and fibre stresses of the RTP process and other simpler transverse LCM processes, including transverse resin injection into a dry preform and CRTM. The general simulation model applies to the entire family of transverse resin infusion processes. The study focuses on hydrodynamic compaction behaviour, flow through multiple different materials, and the lubrication effects in transverse resin infusion processes. The numerical results are used to show how the different wet and dry compaction behaviour influences the flow.

2. Modelling of transverse impregnation processes

The infiltration of an incompressible fluid through a deformable porous solid is governed by the conservation of mass of fluid and solid, Darcy's law, Terzaghi's Law and constitutive equations for permeability and fibre compaction stress. A Lagrangian coordinate system fixed to the solid results in the flow front being the only moving boundary [6,7]. It is assumed that there is no in-plane flow or compaction. The reinforcement is modelled as a non-linear elastic material. Full saturation in the wet region and a sharp flow front are assumed under the slug-flow approximation. The resulting one-dimensional governing equation of the wet region is the non-linear transient diffusion equation:

$$\frac{\partial}{\partial X}\left(D(e)\frac{\partial e}{\partial X}\right) = \frac{\partial e}{\partial t} \tag{1}$$

with the non-linear diffusion coefficient given by:

$$D(e) = -\frac{(1+e_0)^2}{\mu}\left[\frac{K(e)}{1+e}\frac{\partial \sigma_{eff}(e)}{\partial e}\right] \tag{2}$$

where e is the voids ratio given as the fluid volume fraction divided by the fibre volume fraction, μ the viscosity, K the permeability, σ_{eff} the effective stress, X the Lagrangian coordinate measured from the top of the preform stack, and e_0 the voids ratio in the reference configuration (at zero stress). A complete derivation of Eq. (1) can be found in a previous work [11]. The model was solved using a Finite Element Method (FEM) scheme coded in Python. For processes that involve filling, the time step is taken to be equal to the time taken for the flow front to advance to the next node, which is evaluated by applying Darcy's Law at the flow front:

  doi:10.5075/epfl-298799_978-2-9701614-0-0

$$\frac{dX_f}{dt} = -\frac{1}{e_f} D\left(e_f\right) \frac{\partial e}{\partial X}\Big|_{X=X_f} \approx \frac{L}{\Delta t} \tag{3}$$

where X_f is the flow front position, e_f is the voids ratio at the flow front, Δt is the time step required to fill the next element and L is the length of the next element. The entire family of transverse impregnation processes can be modelled by applying the appropriate initial and boundary conditions to Eq. (1). Initially, the preform can be saturated or dry, and fully relaxed or pre-compacted to a given fibre volume fraction.

2.1 Inlet and outlet boundary conditions

If the material is free to relax into the pressurised fluid, the voids ratio on the inlet surface corresponds to zero stress for the wet material:

$$e(0,t) = e_0^{wet} \tag{4}$$

If the piston is in contact with the material, the velocity of the solid, fluid and piston are the same at the piston surface. At the piston or mould wall:

$$\frac{\partial e}{\partial X}(0,t) = 0 \tag{5}$$

A process can be driven by direct compression via a piston or by a fluid injected at a certain pressure or velocity. For a pressure-driven process, the effective stress at the flow front or outlet is equal to the applied pressure:

$$e\left(X_f, t\right) = e_c(t) \tag{6}$$

where e_c is the voids ratio corresponding to the driving pressure $P_{in}(t) = \sigma_{eff}^{wet}\left(e_c(t)\right)$. For a velocity-driven process, the derivative of the voids ratio at the flow front or outlet, using Darcy's law and mass conservation is:

$$\frac{\partial e}{\partial X}\left(X_f, t\right) = -\frac{1+e_0}{D\left(e_f\right)}\left(v_{in} - v_s\left(X_f, t\right)\right) \tag{7}$$

where v_{in} is the driving velocity and v_s is the solid velocity.

2.2 Material interface conditions

The mass and momentum must be conserved across the interface between two materials. Ignoring inertial terms, momentum conservation is satisfied by stress continuity:

$$\sigma_{eff}^{(1)}\left(e^{(1)}\right)\Big|_{X=X_b} = \sigma_{eff}^{(2)}\left(e^{(2)}\right)\Big|_{X=X_b} \tag{8}$$

where the material interface is at $X = X_b$ and $\sigma_{eff}^{(1)}$ and $\sigma_{eff}^{(2)}$ represent the effective stress for material 1 and material 2 respectively. By combining the conservation of mass of solid and fluid, the total mass conservation can be given as the continuity of composite velocity:

$$v_c^{(1)}\Big|_{X=X_b} = v_c^{(2)}\Big|_{X=X_b} \tag{9}$$

where v_c is the composite velocity given by:

$$v_c = \frac{v_s + e v_f}{1+e} \tag{10}$$

  doi:10.5075/epfl-298799_978-2-9701614-0-0

and v_f is the fluid velocity. The composite velocity can be calculated using Darcy's law:

$$v_c = v_s - D(e)\frac{1}{1+e_0}\frac{\partial e}{\partial X} \tag{11}$$

2.3 Flow front interface conditions

Modelling the lubrication effect involves a transition from dry to wet material properties as the material becomes saturated. The dry and saturated fabric on either side of the flow front can be modelled as two different materials, with the boundary between the two materials moving with the flow. Stress continuity is enforced using Eq. (8). However, mass conservation cannot be satisfied using Eq. (9) since there is no fluid flow in the dry region. By balancing the mass flow rate of the mixture as a whole across the flow front [6,15,16]:

$$[\![\rho_m(v_m - v_{front})]\!] = 0 \tag{12}$$

where v_{front} is the velocity of the flow front, and ρ_m and v_m are defined as the mixture density and mixture velocity respectively, given by:

$$\rho_m = \rho_s\phi_s + \rho_f\phi_f, \tag{13}$$

$$v_m = \frac{\rho_s\phi_s v_s + \rho_f\phi_f v_f}{\rho_m} \tag{14}$$

where ρ_s and ρ_f are the solid and fluid densities, and ϕ_s and ϕ_f are the fibre and fluid volume fractions. The flow front is the material surface for the fluid, so the flow front velocity is equal to the fluid velocity at the flow front [6,17]. From the jump condition Eq. (12):

$$\phi_s^{wet}(v_{front} - v_s^{wet}) = \phi_s^{dry}(v_{front} - v_s^{dry}) \tag{15}$$

where the superscripts "wet" and "dry" represent the quantities at the flow front in the wet and dry regions respectively. Since the fibre volume fraction is discontinuous from Eq. (8), it is evident that the wet and dry solid velocities will be different at the boundary. For velocity-driven processes, v_s^{wet} is required in the outlet boundary condition (Eq. (7)). In the dry region, the preform is uniformly compacted by the applied pressure. By integrating the conservation of mass, the dry solid velocity is given as:

$$v_s^{dry}(X,t) = \frac{1}{1+e_0}\frac{de^{dry}}{dt}(X - l_0) \tag{16}$$

where l_0 is the initial length of the preform stack. By transforming the flow front velocity from the moving domain to the fixed Lagrangian domain and combining with Eq. (15), it follows that:

$$\frac{dX_f}{dt} = \frac{1+e_0}{1+e^{dry}}(v_{front} - v_s^{dry}) \tag{17}$$

By rearranging Eq. (15) and expressing in terms of voids ratio, v_s^{wet} is given by:

$$v_s^{wet} = \frac{1}{1+e^{dry}}\left[v_{front}(e^{dry} - e^{wet}) + v_s^{dry}(1+e^{wet})\right] \tag{18}$$

where v_s^{dry} is calculated using Eq. (16) and v_{front} using Eq. (3) and (17).

2.4 Constitutive equations

  doi:10.5075/epfl-298799_978-2-9701614-0-0

Material data of a glass fibre 2/2 twill weave woven fabric (Hexcel 295 g/m^2) and chopped strand mat (CSM) material were obtained by the Centre for Advanced Composite Materials and Leibniz-Institut für Verbundwerkstoffe. The data for the woven fabric was collected as part of the compaction [14] and out-of-plane permeability [18] benchmark studies. An exponential curve was fitted to the compaction data,

$$\sigma(e) = c_1[\exp(-c_2 e) - \exp(-c_2 e_0)] \tag{19}$$

and a modified Carman-Kozeny relation to the permeability [19]

$$K(e) = \frac{1}{d}\ \frac{e^{k+1}}{1+e} \tag{20}$$

It is assumed that the saturated and unsaturated permeability are equal. The parameter values for the constitutive equations are summarised in Table 1.

Table 1: Parameters for the compaction stress and permeability constitutive equations.

Material		c_1	c_2	e_0	d	k
Woven	Dry	7.01e6	4.91	2.27	6.62e11	2
	Saturated	4.90e6	4.89	2.21	6.62e11	2
CSM	Saturated	6.09e9	3.18	5.66	7.47e10	1.66

3. Results and discussion

In the following section, the total dry initial stack height is 10 mm, and the resin viscosity is taken as 0.1 Pa.s. A constant piston/inlet velocity of 0.2 mm/s is applied for velocity-driven processes, and a smooth ramp-up to 0.1 MPa in 10 seconds is applied for pressure-driven processes.

3.1 Resin injection into a dry preform

In resin injection, the preform is initially fully dry and relaxed. The resin is injected into the top surface, and the bottom is a draining surface. The effect of implementing different wet and dry compaction behaviour is investigated by running simulations using only dry data, only wet data, and combined wet and dry data in the corresponding wet and dry regions of the entire stack. The top boundary and flow front node positions for these simulations are shown in Fig. 1a) for pressure-driven, and Fig. 1b) for velocity-driven injection. The “wet only” simulations have a smaller initial height due to the higher fibre volume fraction at zero stress. The flow fronts for the “dry only” and “wet and dry” simulations are almost identical in both plots. The top surface for the “wet and dry” simulation initially follows the “dry only” and then approaches the “wet only” simulation as the preform becomes saturated. Implementing only dry material properties will overestimate the final stack thickness, and only wet properties will underestimate the fill time for velocity-driven processes. The fill times for the pressure-driven simulations are not significantly different. The analytic fill time t_{fill} for velocity-driven injection can be determined from the conservation of mass between the wet and dry regions, following the methodology of Ambrosi [17]:

$$t_{fill} = e_i l_0 / \big(v_{in}(1 + e_0)\big) \tag{21}$$

The fill time only depends on the initial stack thickness l_0, inlet velocity v_{in}, the reference voids ratio e_0, and the initial voids ratio e_i. Therefore, the difference in the voids ratio at zero stress between wet and dry fabric will determine the difference in fill time. Using the input parameters from the simulations, the analytic fill times for initial voids ratios of 2.27 (dry) and 2.21 (wet) are 34.7s and 33.8 s, respectively, which matches the fill times in Fig. 1b).

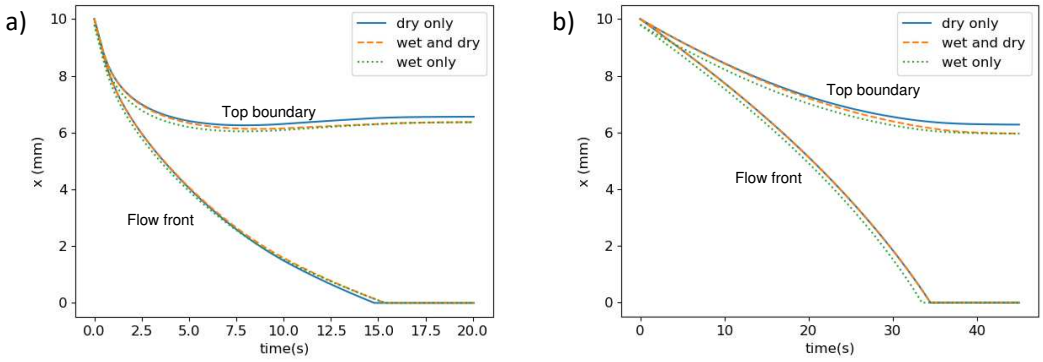

Figure 1. Top boundary and flow front development for only dry, wet and dry, and only wet material properties for: a) pressure-driven, and b) velocity-driven injection into a dry preform.

3.2 Compression Resin Transfer Moulding

For the CRTM simulations, the initial piston position is 13.3 mm and 12 mm for the pressure and velocity-driven simulations, respectively. For the velocity-driven process, the stack is held at constant thickness once it reaches 5 mm. The top boundary and flow front positions are given in Fig. 2a) for pressure-driven, and Fig. 2b) for velocity-driven. The flow front positions are similar to the resin injection simulations (Fig. 1). The time to gap closure differs for all simulations. For pressure-driven, the top boundary for the "wet and dry" simulation starts the same as the "dry only" and approaches the "wet only", similar to Fig. 1a). For velocity-driven, once the gap closes, the thickness is the same for all simulations; however, the fibre volume fractions through the thickness are different.

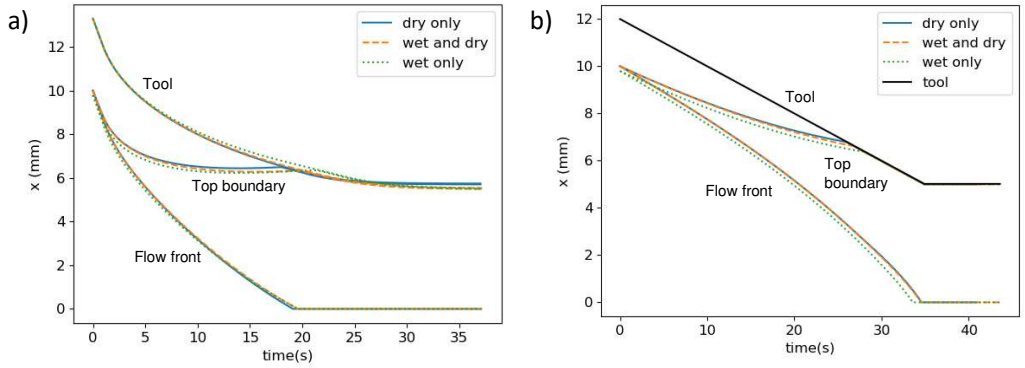

Figure 2. Top boundary, tool position and flow front development for simulations using only dry, wet and dry, and only wet material properties for: a) pressure-driven, and b) velocity-driven CRTM.

3.3 Resin Transfer Pressing

In the RTP simulations, the carrier material is 6 mm, and the reinforcement material is 4 mm. The stack is held at a constant thickness when the stack reaches 70% of the initial total stack

978/1151 ©2022 Lee et al. doi:10.5075/epfl-298799_978-2-9701614-0-0 published under CC BY-NC 4.0 license

thickness. Results from a velocity-driven RTP simulation are given in Fig. 3. A constant piston velocity of 0.2 mm/s was applied, (Fig. 3a)) and the corresponding pressure profile is shown in Fig. 3b). Fig. 3c) gives the normalised node positions and flow front with time and Figs. 3d), e) & f) illustrate the fluid pressure, effective stress and fibre volume fraction contours, respectively. The effective stress contours (Fig. 3e)) indicate that compression starts at the outlet and decreases towards the top. Due to the lubrication effect and different compaction behaviour of the carrier and reinforcement, the fibre volume fraction contours are discontinuous at the flow front and the material boundary, whereas the effective stress and fluid pressure contours are continuous. There is a reduction in the piston pressure once the stack is held at constant thickness because the preform relaxes and approaches a homogeneous through-thickness fibre volume fraction.

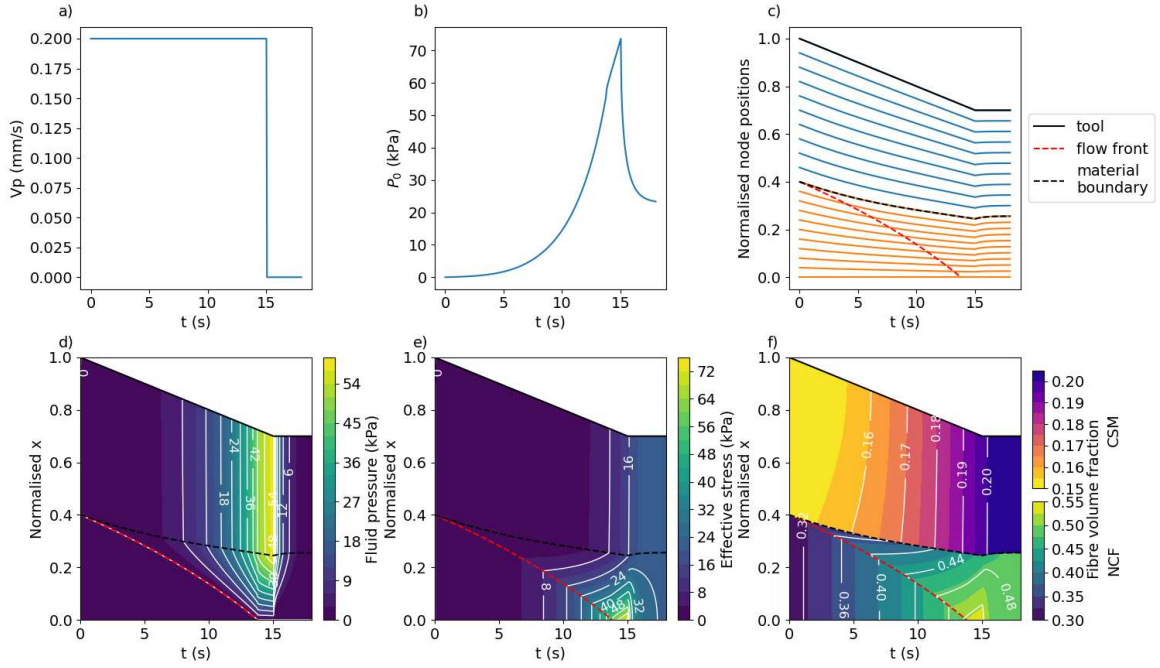

Figure 3. Velocity-driven RTP for a CSM/woven stack: a) constant applied piston velocity, b) resulting piston pressure, c) node positions in space over time, and contour plots of d) fluid pressure, e) effective stress and f) fibre volume fraction, plotted over normalised x and time t.

4. Conclusions

In this paper, a fully coupled, transient numerical model of general transverse compression and impregnation processes is developed. Hydrodynamic compaction effects and the transition from dry to wet properties during filling have been included. The compression and impregnation of a stack consisting of more than one material have also been modelled. This model can predict the fluid pressure, effective stress, fibre volume fraction distribution, flow front progression and process time. In general, it is shown that, for all transverse processes, the dry compaction behaviour influences the fill time, whereas the wet compaction behaviour determines the final thickness and fibre volume fraction. It is essential to implement the lubrication effect into simulations for materials with significantly different wet and dry compaction behaviour. Future work could involve implementing more complex material models, such as plastic or viscoelastic models. A comprehensive numerical model is helpful for a deeper understanding of transverse flow processes and can assist in developing and analysing new advanced processes.

  doi:10.5075/epfl-298799_978-2-9701614-0-0

5. References

1. Willenbacher B, Kabachi A, May D, Mitschang P, Ermanni P. Flow induced sample deformations in out-of-plane permeability measurement. In: ECCM. 24-28 June. Athens, Greece; 2018.
2. Bhat P, Merotte J, Simacek P, Advani SG. Process analysis of compression resin transfer molding. Comp A 2009;40:431–41.
3. Simacek P, Advani SG, Iobst SA. Modeling flow in compression resin transfer molding for manufacturing of complex lightweight high-performance automotive parts. J Comp Mat 2008;42(23):2523-2545.
4. Kang MK, Lee WI. Analysis of Resin Transfer/Compression Molding process. Polym Comp 1999;20(2):293-304.
5. Shojaei A. Numerical simulation of three-dimensional flow and analysis of filling process in compression resin transfer moulding. Comp A 2006; 37:1434–50.
6. Billi L, Farina A. Unidirectional infiltration in deformable porous media: Mathematical modelling and self-similar solution. Quart Appl Math 2000;58(1):85–101.
7. Farina A, Cocito P, Boretto G. Flow in deformable porous media: Modelling and simulations of compression moulding processes. Math Comput Model 1997;26(11):1–15.
8. Danzi M, Klunker F, Ermanni P. Experimental validation of through-thickness resin flow model in the consolidation of saturated porous media. J Comp Mat 2017;51(17):1–9.
9. Klunker F, Danzi M, Ermanni P. Fiber deformation as a result of fluid injection: modeling and validation in the case of saturated permeability measurements in through thickness direction. J Comp Mat 2015;49(9):1091–105.
10. Merotte J, Simacek P, Advani S. Resin flow analysis with fiber preform deformation in through thickness direction during Compression Resin Transfer Molding. Comp A 2010; 41:881–887.
11. Duhovic M, Kelly P, May D, Allen T. Simulating Compression-Induced Resin Transfer from a Saturated Non-Woven into a Dry Fiber Structure. Proceedings of ICCM22, Melbourne, Australia; 11-16 August 2019.
12. Goergen C, May D, Mitschang P. Integration of rCF in resin transfer pressing process. J Reinf Plast Comp 2020; 39(9-10):361-372.
13. Kelly P, Wijaya W. Transverse compression properties of composite reinforcements, In Composite Reinforcements for Optimum Performance (Second Edition), Woodhead Publishing. 2021. 333-374.
14. Yong A, Aktas A, May D, Endruweit A, Lomov S, Advani S, et al. Experimental characterisation of textile compaction response: A benchmark exercise. Comp A 2021;142:106243.
15. Ambrosi D, Preziosi L. Modeling injection molding processes with deformable porous preforms. SIAM J Appl Math 2000;61(1):22–42.
16. Gurtin ME, Fried E, Anand L. The Mechanics and Thermodynamics of Continua. Cambridge University Press. 2010. 216-218
17. Ambrosi D. Infiltration through deformable porous media. ZAMM 2002;82(2):115–24.
18. Yong A, Aktas A, May D, Endruweit A, Advani S, Hubert P, et al. Out-of-plane permeability measurement for reinforcement textiles: A benchmark exercise. Comp A 2021;148:106480.
19. Bickerton S, Kelly PA. Compression resin transfer moulding (CRTM) in polymer matrix composites. In: Manufacturing Techniques for Polymer Matrix Composites (PMCs). Woodhead Publishing. 2012. 348–380.

  doi:10.5075/epfl-298799_978-2-9701614-0-0

PARAMETRIC STUDY OF AFP LAY-UP PROCESS PARAMETERS EFFECT ON THE AIR PERMEABILITY OF THERMOPLASTIC COMPOSITES AND THEIR SUITABILITY FOR OUT OF AUTOCLAVE POST-PROCESSING BY A NEW METHOD

Sasan, Karimi [a,b,c], Ali, Barzegar[a,b,c], Mehmet, Yildiz[a,b,c], Hatice S. , Sas[a,b,c]

a: Integrated Manufacturing Technologies Research and Application Center, Sabanci University, Tuzla, Istanbul, 34956, Turkey- sasankarimi@sabanciuniv.edu

b: Composite Technologies Center of Excellence, Sabanci University-Kordsa, Istanbul Technology Development Zone, Pendik, Istanbul 34906, Turkey

c: Faculty of Engineering and Natural Sciences, Department of Manufacturing Engineering, Sabanci University, Tuzla, Istanbul, 34956, Turkey

Abstract: *Structural thermoplastic composites manufacturing by automated fiber placement (AFP) needs a secondary process to ensure perfect bonding between plies and remove all interlaminar voids and pores. Regarding the drawbacks of the autoclave as a conventional post-processing method of composites and the growing demand for aerospace-grade thermoplastics, out of autoclave post-processing methods such as vacuum bag only (VBO) getting more and more attention. Since the VBO process depends on the evacuation of internal air from components and filling them with resin flow under high temperature, the inherent air permeability of composite structure is the key parameter in the VBO process efficiency and final part quality. This study aims to find a correlation between the permeability of CF/PEKK thermoplastic composite structure and AFP lay-up process parameters. The air permeability is measured for coupons from components by the pulse-pressure decay method. Among studied parameters, high compaction force and high lay-up velocity result in low air permeability.*

Keywords: AFP manufacturing; thermoplastics prepreg; void content; gas permeability; vacuum bag only process

1. Introduction

Automated fiber placement (AFP) started a new era in automated composite manufacturing. AFP process utilizes a robotic arm with a placement head to laminate prepreg tapes layer by layer to fabricate different geometries. Lamination direction can be adjusted to optimize the directional strength of final composite components for specific loading and applications.

One of the main issues with AFP fabricated composites is interlaminar void in final components after fabrication. The voids prohibit successful in-situ consolidation during AFP lay-up. AFP roller compaction force and lay-up velocity are two major process parameters that determine the final void content and mechanical performance of the fabricated component. The function of roller compaction force is to ensure proper adhesion of incoming tow to substrate after high temperature applied by AFP heat source (1). The average void fraction of the fabricated samples decreases as compaction force is increased(2). The lay-up velocity (lamination head velocity) is

  doi:10.5075/epfl-298799_978-2-9701614-0-0

another effective parameter. Under constant consolidation force and heat flux, many studies concluded that higher lay-up velocity results in inadequate heat transfer and higher void fraction in laminates (2–5).

The presence of interlaminar voids makes it necessary for the post-processing of AFP components to ensure the standard level of final void content for different applications. The autoclave is the conventional post-processing method for AFP fabricated composites which utilizes high pressure and high-temperature environment to squeeze the voids and obtain high-quality final components. However, high capital cost, time-consuming and expensive process and restriction on large parts can be listed as some cons of autoclave (6). Vacuum bag only (VBO), as one of the promising out-of-autoclave (OOA) processes for thermoplastics, presents some advantages over autoclave such as low capital and operational cost, flexibility for processing components with different geometries and sizes, and high energy efficiency(7). VBO relies on interlaminar air evacuation and consolidation of laminates with the aid of atmospheric pressure and high temperature. Hence, the air permeability of composite components plays a crucial role in the success of the VBO process. As a result, the permeable composite components are more suitable for VBO post-processing.

In this study, at first, thermoplastic samples are fabricated by the AFP machine under different lay-up process parameters. After that, coupons are cut from different locations of fabricated samples, and they are mounted in epoxy. Generally, the coupon mounting is used to create microscopy photos of composite samples but in this study, as a dual application, the air permeability of the same coupons also is measured with the Pulse-pressure decay method. Based on the author's best knowledge, the air permeability of AFP fabricated thermoplastic components for the VBO process was not studied in the literature previously. The correlation between the AFP lay-up process parameters and air permeability is studied and discussed.

2. Material and Methods

2.1 Material

The thermoplastic prepreg tape, CF/PEKK (PolyEtherKetoneKetone) is supplied by Toray Cetex®. The tapes have a fiber volume fraction of 66 wt%, the glass transition temperature of 160 °C, melting temperature of 337 °C, and nominal thickness and width of 0.15 mm, and 6.35 mm, respectively (8).

2.2 AFP lay-up

Figure 1 shows the (AFP) machine used to manufacture three thermoplastic plates namely, samples A, B, and C, with the length and width of 650 mm and 100 mm, respectively. All plates consist of two unidirectional layers with a [0°/0°] stacking sequence. Two different lay-up velocities, v=100 mm/s and v=400 mm/s, and two compaction forces, F=300 N and F= 600 N, are considered to study the individual effect of the major AFP lay-up parameters on the air permeability of each sample. Table 1 shows the setpoints for lay-up parameters of each sample. Figure 2 shows the lamination parameters variation during fabrication. The compaction force is constant during fabrication while lamination velocity is increased until set velocity and then decreased until the end of the lamination.

  doi:10.5075/epfl-298799_978-2-9701614-0-0

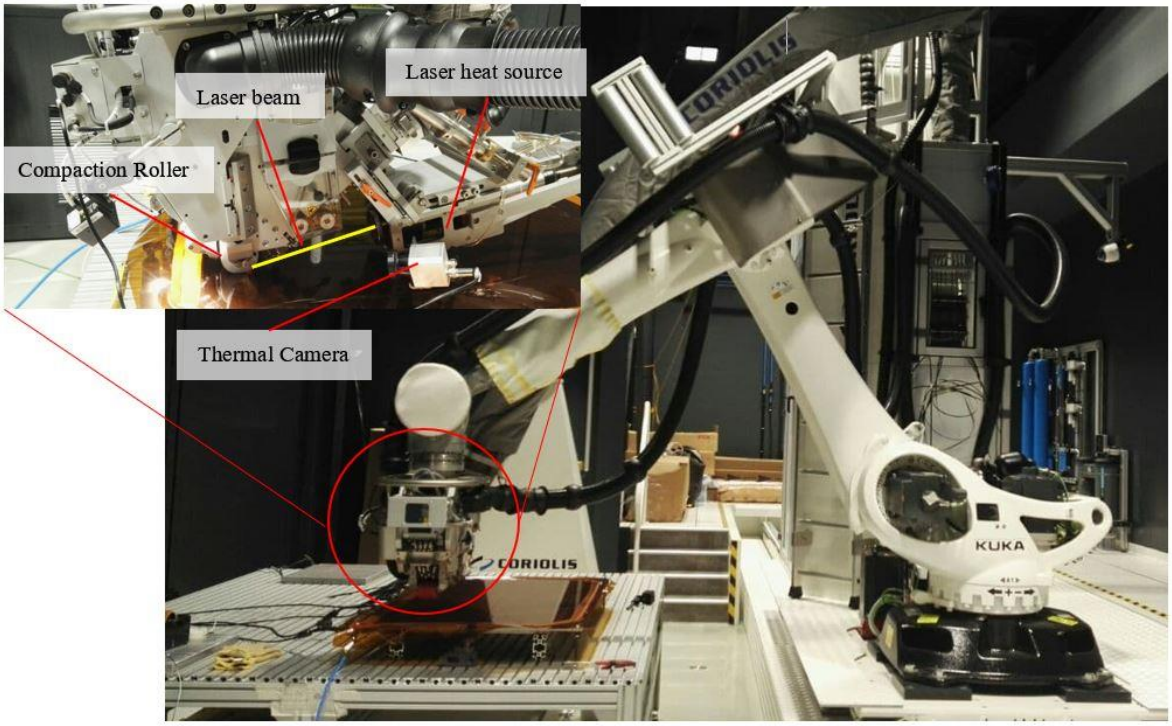

Figure 1. AFP machine with main components of lamination head

Table 1: Setpoint process parameters for samples

	Sample A	Sample B	Sample C
Compaction Force (N)	300	300	600
Lay-up Velocity (mm/s)	100	400	100

2.3 Coupon mounting and sample preparation

Six coupons are cut from each sample as Figure 3(a) shows. Regarding the almost symmetric lay-up velocity profile in Figure 2, coupons are cut from the first middle of plates to represent better the air permeability of different locations under different lay-up velocities. Coupons are cold mounted by using EpoFix Kit 1, Epoxy resin, and hardener, from Struers®. After epoxy curing inside a mold, the mounted samples are polished automatically by the Struers® polishing machine. Sandpapers with 280, 320, 500, 2500, and 4000 grits in European FEPA scale are used respectively during polishing for all mounted samples. **Error! Reference source not found.** represents all the procedures for preparing the samples. Polishing is done for both sides of molds to ensure the coupons are open from both sides to create permeable path through coupons.

2.4 Air Permeability Measurement, experimental and numerical method

Generally, the voids can be categorized into two groups: isolated voids and interconnected voids (9). interconnected voids work as microchannels which create the air permeability and can be used to evacuate the internal air of composite components. The more connected voids create higher air permeability and make the composite part more suitable for VBO post-processing.

  doi:10.5075/epfl-298799_978-2-9701614-0-0

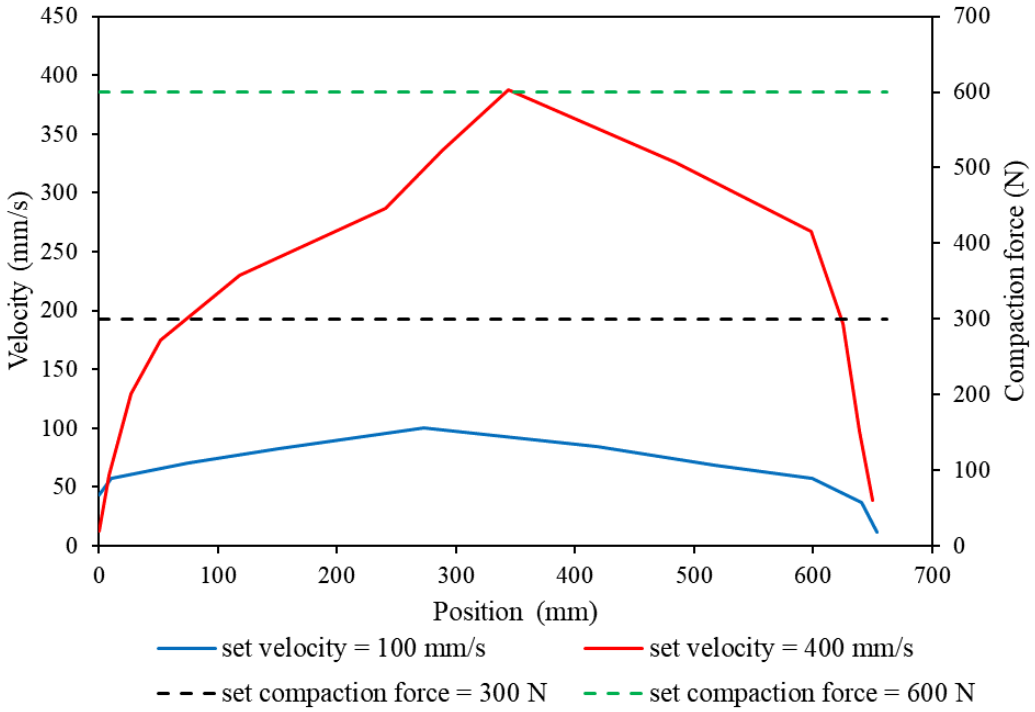

Figure 2. AFP head velocity and compaction force profile during sample fabrication

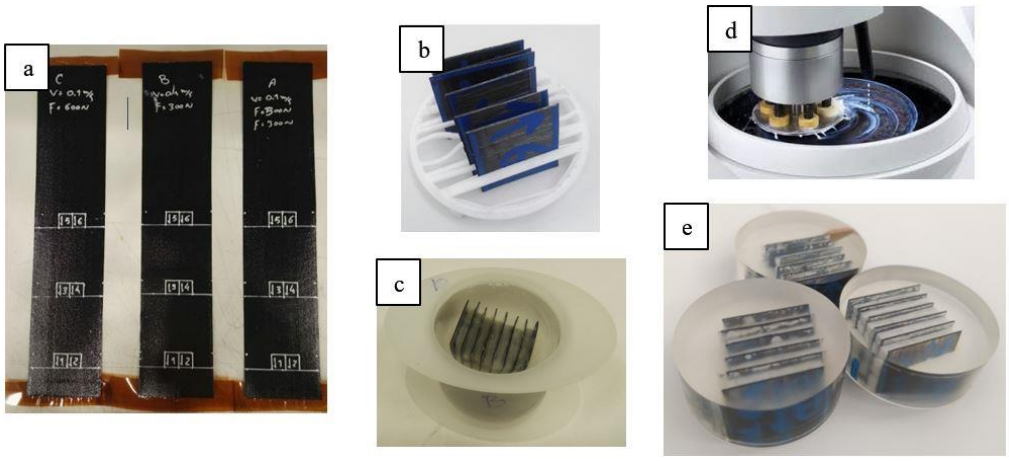

Figure 3. sample preparation and coupon mounting stages from fabricated plates.

Figure 4 schematically represents the two kinds of voids and their connectivity by micropores in mounted coupons.

Figure 5 shows the designed and fabricated experimental setup for air permeability measurement of mounted coupons. The measured air permeability is attributed to all six coupons from each plate to just obtain the average air permeability and corollate the overall air permeability to fabrication process parameters.

For experimental data, as Figure 5 shows, the mounted coupons are sealed by tacky tapes between two parts of the experimental setup, the upper part is connected to the pressure sensor and the lower part to the vacuum line which creates a constant vacuum.

  doi:10.5075/epfl-298799_978-2-9701614-0-0

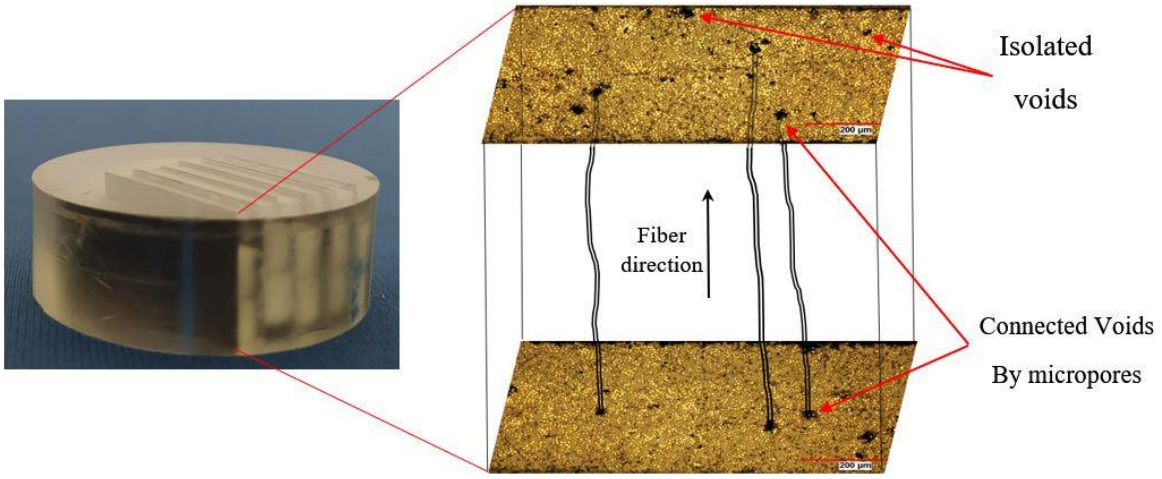

Figure 4. Representation of isolated voids and connected voids by micropores inside the AFP fabricated sample

The air moves from the upper side to the downside through mounted coupons. The pressure is measured just on the upper side and the pressure drop profile reveals the air permeability of coupons. If the pressure drops immediately the air permeability will be higher for coupons. The vacuum line in the laboratory with 0.07 absolute bar pressure is connected to the experimental setup to create a vacuum during tests. A GDH 200- 07 barometer from GHM Messtechnik GmbH® is used for pressure decay measurement. Figure 6 shows the recorded pressure versus time data for three samples. All the permeability measurements are done at room temperature, 20 °C. Since thermoplastics do not show viscous behavior at this temperature, fixed pore structures, and material porosity during the experiments are valid assumptions.

For numerical data, the compressible continuity equation in porous media with considering volume average Darcy's velocity and ideal gas law assumption was solved to obtain governing PDE. The obtained equation is non-dimensionalized with the following equations where L is the length of the domain (here the length of coupons), P_i is the initial pressure equal to atmospheric pressure, and P_f is the final pressure equal to vacuum pressure: ΔP = P_i - P_f.

$$\hat{x} = \frac{x}{L}, \quad \hat{P} = \frac{P - P_f}{\Delta P}, \quad \hat{P}_s = \frac{P_f + b}{\Delta P}, \quad \hat{t} = \frac{t}{t_c} \tag{1}$$

Characteristic time, t_c, was defined to normalize time, b is Klingenberg parameter, Ø is porosity, and K_i is liquid permeability.

$$t_c = \frac{\emptyset \mu L^2}{K_i \Delta P} \tag{2}$$

The dimensionless form of the governing PDE which gives the numerical solution is:

$$\frac{\partial \hat{P}}{\partial \hat{t}} = \frac{\partial}{\partial \hat{x}}\left(\left(\hat{P} + \hat{P}_s\right)\frac{\partial \hat{P}}{\partial \hat{x}}\right) \tag{3}$$

Klingenberg analytically derived a correlation factor (1+ $\frac{b}{P}$) which relates to the gas permeability K_g to the liquid permeability K_i (Equation 4) (10). The gas permeability depends on pore diameter, higher pore diameter results in a lower b value, so b and K_g are interrelated.

  doi:10.5075/epfl-298799_978-2-9701614-0-0

$$K_g = K_i\left(1 + \frac{b}{P_f}\right) \quad (4)$$

K_g represents the air permeability in this study. By dividing both sides of Equation 4 to porosity (Ø), the gas permeability over porosity ($K_g/Ø$) for each sample can be obtained. $K_g/Ø$ was reported for samples and the porosity of the samples in this study was not reported. Cender et. al.'s (11) methodology for calculation of air permeability by pulse-decay method is applied in this study. $\hat{P}_s$ and t_c are two unknowns in Equation 1. The t_c scales the experimental pressure decay data and $\hat{P}_s$ determines the shape of the pressure decay diagram for numerical solutions. Based on Cender method, when, for each sample, two experimental and numerical diagrams are matched, corresponding values are found for $\hat{P}_s$ and t_c. Finding the $\hat{P}_s$ and t_c gives us the Klingenberg parameter, b, and liquid permeability over porosity, $K_i/Ø$ by Equation 1 and Equation 2, respectively.

3. Results and Discussion

Figure 6 presents the experimental data for three batches of coupons from three AFP fabricated plates. As it is clear, Sample C does not show any variation in the pressure-decay diagram, or at least, the pressure sensor cannot record any pressure decay. Because the Pulse-pressure decay is based on the pressure-decay profile, we can conclude zero permeability for sample C, and for Klingenberg parameter, b, we cannot report any value. Sample A shows a much sharper pressure decay profile than Sample B and as an initial conclusion, Sample A has higher air permeability and a Klingenberg parameter, b, value smaller than that for Sample B. Figure 7 shows the comparable numerical and experimental nondimensional pressure-time, $\hat{P} - \hat{t}$, diagrams for sample A and Sample B. Sample C is not studied because experimental data shows zero permeability for it. These diagrams are used to calculate $\hat{P}_s$ from numerical data and t_c from experimental data based on Cender method (11). Table 2 summarizes the lay-up process parameters and obtained liquid and gas permeability parameters from Figure 7.

4. Conclusion

Sample C shows zero permeability so it can be concluded, that high roller compaction in AFP fabrication of unidirectional composite components removes all microchannels and results in zero permeability. We can conclude most of the voids in Sample C are isolated types and VBO will not be a proper post-processing method for samples fabricated with high compaction pressure. For Sample A the air permeability over porosity is higher than that for Sample B. If we assume the porosity of both Sample A and Sample B in the same order, then sample A will have higher gas permeability than Sample B. Higher permeability makes the component more suitable for vacuum bag only process. In another main conclusion, high lay-up velocity does not create more micropores, or at least created porosity is not open porosity. Klingenberg parameter for sample A is larger than that for Sample B and this reveals a larger pore diameter in Sample A. In conclusion, high compaction pressure during fabrication removes most of the open pores in the final components, and among studied velocities, higher velocity does not create higher porosity in the final components. As a general result, the process parameters should be adjusted properly if the final components will be post-processed by the VBO process instead of the autoclave. Coupon scale samples can be used for porosity study besides their main application for microscopy imaging and this dual application was discussed in this study.

  doi:10.5075/epfl-298799_978-2-9701614-0-0

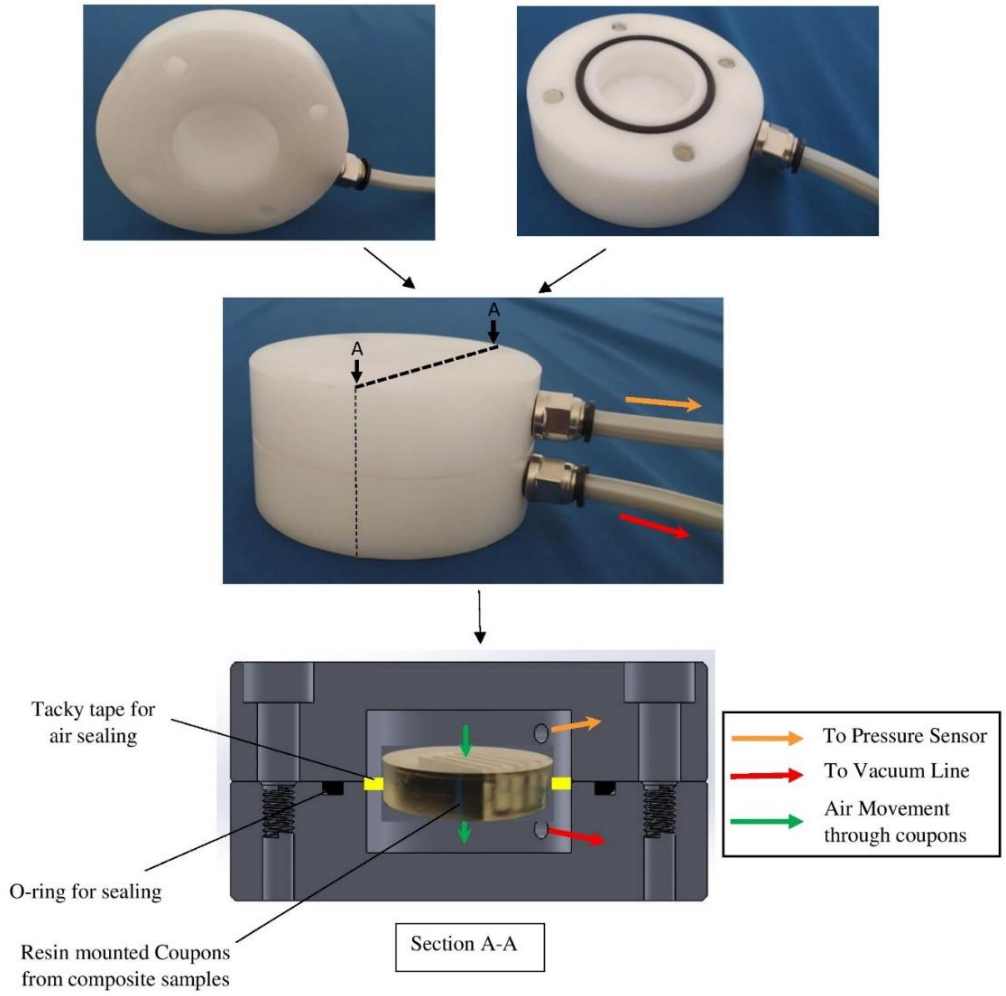

Figure 5. Experimental setup for air permeability measurement of mounted coupons

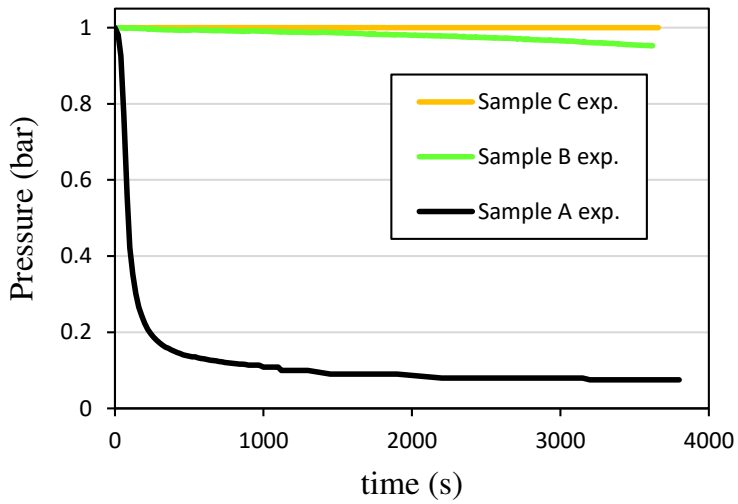

Figure 6. Experimental pressure decay data for three samples.

  doi:10.5075/epfl-298799_978-2-9701614-0-0

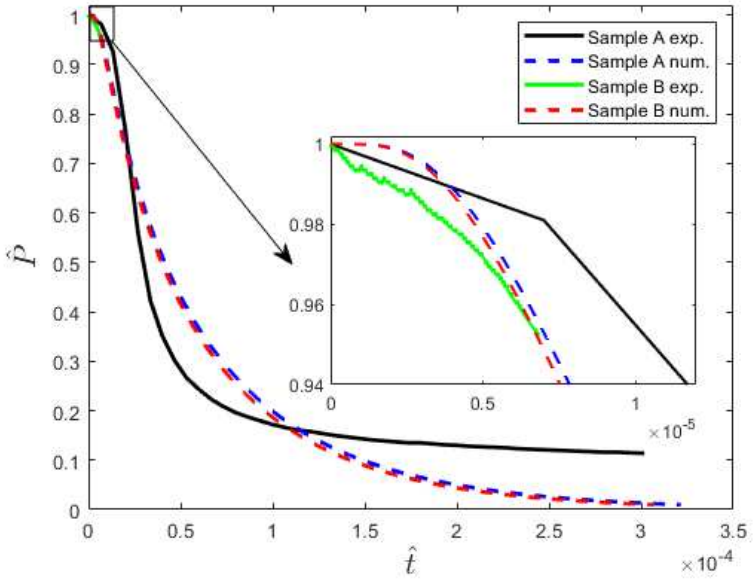

Figure 7. Numerical and experimental nondimensional pressure-time diagrams for in-situ consolidated AFP samples, Sample A and Sample B.

Table 2: Fabrication parameters and permeability parameters for in-situ consolidated AFP samples

	Lay-up velocity (mm/s)	Compaction force (N)	$K_i/\emptyset$ (m^2)	b (kPa)	$K_g/\emptyset$ (m^2)
Sample A	100	300	1.45E-20	8.20E-01	3.69E-20
Sample B	400	300	8.20E-23	8.60E-01	2.14E-22
Sample C	100	600	0.00	-	0.00

5. References

1. Brasington A, Sacco C, Halbritter J, Wehbe R, Harik R. Automated fiber placement: A review of history, current technologies, and future paths forward. Compos Part C Open Access [Internet]. 2021;6(June):100182. Available from: https://doi.org/10.1016/j.jcomc.2021.100182

2. Khan MA, Mitschang P, Schledjewski R. Tracing the void content development and identification of its effecting parameters during in situ consolidation of thermoplastic tape material. Polym Polym Compos. 2010;18(1):1–15.

3. Tierney J, Gillespie JW. Modeling of Heat Transfer and Void Dynamics for the Thermoplastic Composite Tow-placement Process. J Compos Mater. 2003;37(19):1745–68.

4. Khan MA, Mitschang P, Schledjewski R. Parametric study on processing parameters and resulting part quality through thermoplastic tape placement process. J Compos Mater [Internet]. 2013;47(4):485–99. Available from: https://doi.org/10.1177/0021998312441810

5. Lamontia MA, Gruber MB, Tierney J, Gillespie JW, Jensen B, Cano R. In Situ Thermoplastic ATP Needs Flat Tapes and Tows with Few Voids. 30th Int SAMPE Eur Conf. 2009;2009(30):1–8.

6. Lee J, Ni X, Daso F, Xiao X, King D, Gómez JS, et al. Advanced carbon fiber composite out-of-autoclave laminate manufacture via nanostructured out-of-oven conductive curing. Compos Sci Technol. 2018;166:150–9.

7. Vernejoux C, Fischer X, Deseur S, Duc E. Influence of A Aut utomat omated ed Fiber Placement P Par aramet ameters ers on Thermoplastic Composit Composite e Blank s Used on Stamp F Forming orming Pr Process ocess 1 Intr Introduction oduction. 2021;02:1–11.

8. Toray. Toray Cetex ® TC1320 PEKK PRODUCT DATA SHEET. 2019;31(0):1–3. Available from: www.toraytac.com

9. Boon Y Di, Joshi SC, Bhudolia SK. Review: Filament winding and automated fiber placement with in situ consolidation for fiber reinforced thermoplastic polymer composites. Polymers (Basel). 2021;13(12).

10. Di Francesco M, Valverde MA, Ward C, Giddings PF, Dell'Anno G, Potter K. Influence of layup speed on the quality of thermoplastic preforms manufactured by laser-assisted automated fibre placement. ECCM 2016 - Proceeding 17th Eur Conf Compos Mater. 2016;(June).

11. Cender TA, Simacek P, Davis S, Advani SG. Gas Evacuation from Partially Saturated Woven Fiber Laminates. Transp Porous Media. 2016;115(3):541–62.

  doi:10.5075/epfl-298799_978-2-9701614-0-0

ACCOUNTING FOR THE VARIABILITY IN 3D INTERLOCK FABRIC PERMEABILITY THROUGH FLUID FLOW SIMULATIONS

Morgan Cataldi [a,b], Yanneck Wielhorski [b], Nicolas Moulin [a], Monica Francesca Pucci [c], Pierre-Jacques Liotier [d]

a: Mines Saint-Étienne, Univ Lyon, CNRS, UMR 5307 LGF, 158 Cours Fauriel 42023, Saint-Étienne, France – morgan.cataldi@emse.fr
b: Safran Aircraft Engines, Rond-point René Ravaud, Réau, 77550 Moissy-Cramayel, France
c: IMT Mines Alès, Univ Montpellier, LMGC CNRS, 6 Avenue de Clavières 30100, Alès, France
d: IMT Mines Alès, Univ Montpellier, PCH, 6 Avenue de Clavières 30100, Alès, France

Abstract: *Resin Transfer Moulding (RTM) processes used to manufacture high performance composite parts require an estimation of the fabric permeability and its variability. The value given to a constant intra-yarn permeability is thus a key parameter among many others studied in literature. To go further, the effect of variability into the intra-yarn permeability field onto 3D interlock fabric permeability is investigated. Reinforcements unit cells are modelled through material forming simulations which provide an intra-yarn fibre volume fraction (iy-FVF) field. The latter is used to locally compute an intra-yarn transversely isotropic permeability tensor field. Numerical simulations of dual-scale Stokes-Darcy coupled fluid flows between and within the yarns are performed with a monolithic approach by a Finite Element Method (FEM).*

Keywords: 3D interlock fabric; numerical permeability; intra-yarn permeability distribution; flow simulations; Stokes-Darcy coupling

1. Introduction

3D interlock fabrics are filled with an organic resin through RTM (Resin Transfer Moulding) processes to create high performance composite materials with designed mechanical properties. Due to their light weight compared to their mechanical properties, they are well suited for aeronautics. Ensuring composites mechanical properties implies a precise monitoring of the manufacturing. The fabric permeability is a key parameter of this process and thus needs to be characterised accurately. Fluid flow experiments or simulations within the fabric can be performed to compute its permeability. However, such a value comes along with its associated variability resulting from many factors. Among them, the variability of the intra-yarn permeability is of particular interest, since the weaved yarns are also porous materials which permeability is linked to its fibres local microstructure.

3D woven models generation [4-5] is widely used in the literature, and our simulations are performed on these models. Some works on the effect of the intra-yarn permeability onto the overall one have been conducted on whether idealized woven patterns as in Wang et al. [1] or X-ray micro-tomographies as in Ali et al. [2]. In such cases, a constant permeability tensor is generally given to all the yarns as in Geoffre et al. [3]. However, the yarns undergo a local compaction during the simulation of the forming process of the fabric. Consequently, the intra-yarn fibre volume fraction (iy-FVF) is locally computed all along the yarns, thus allowing the

  doi:10.5075/epfl-298799_978-2-9701614-0-0

calculation of an intra-yarn permeability field. The effect of its variability, induced by the fabric forming process, on the overall fabric permeability is studied.

The dual-scale fluid flow problem within and between the yarns can be modelled in several ways. Among them, Brinkman equation [6] is generally convenient to use through giving a very high artificial permeability value to the free space between the porous media [7-8]. In our simulations, the fluid flow is modelled by the Stokes-Darcy coupled problem and solved by a mixed velocity – pressure Finite Element (FE) formulation with a monolithic approach, which is detailed in previous works [9]. Its stability is ensured by a Variationnal Multiscale Method (VMS) named Algebraic SubGrid Scale (ASGS) method.

2. Materials and Methods

2.1 Materials

The material used is a 3D angle-interlock woven fabric simulated with the software Multifil [10]. The unit cell is composed of 27 yarns and its dimensions are 18.9 x 18.9 x 4.9 (mm^3). This 3D fabric is computed with the woven pattern and the yarn features (the number of carbon fibres per yarn, their mechanical properties and their twist) as inputs. The yarn deformations are then computed by taking into account an enriched kinematics beam model and contact-friction interactions. Finally, the output unit cell contains both the meso-scale yarn morphology and the iy-FVF field which up-scales the microscopic intra-yarn morphology as shown in Figure 1. Yarns are described as consecutive sections attached and oriented along their neutral fibres.

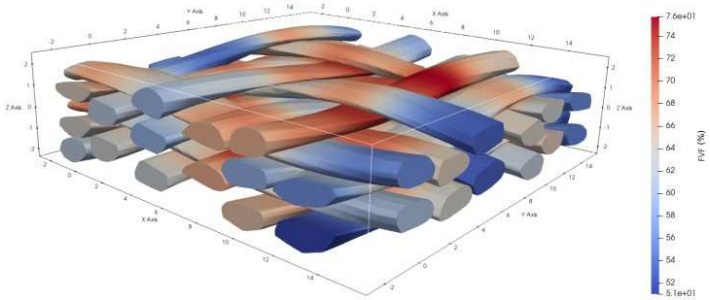

Figure 1. 3D interlock unit cell and its iy-FVF field

The unit cell thus describes the fabric at the mesoscopic scale where yarns are homogeneous porous media characterized by a permeability tensor. This allows considering both flow scales: within (microscopic scale) and between (mesoscopic scale) the yarns. The intra-yarn permeability tensor is assumed transversely isotropic and described in its principal coordinate system shown in Figure 2 by its eigenvalues K_I, K_{II} and K_{III}.

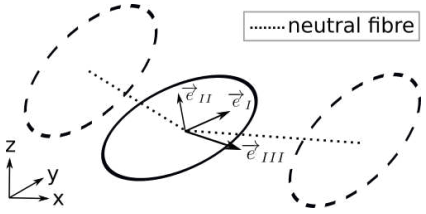

Figure 2. Coordinate system of a yarn section, with K_I, K_{II} and K_{III} its permeability components

  doi:10.5075/epfl-298799_978-2-9701614-0-0 published under CC BY-NC 4.0 license

Then, their numerical values can be calculated from a iy-FVF value V_f through the Gebart's law (Eq. (1) and (2), with the fibre radius R = 2.6e-3 mm), detailed in [11], for transverse $K_I = K_{II} = K_T$ and longitudinal $K_{III} = K_L$ permeabilities in relation to fibre orientation in a hexagonal arrangement. The mean values of K_T and K_L are respectively 2.03e-14 m^2 and 9.73e-14 m^2.

$$\mathrm{K}_T = \frac{16R^2}{9\pi\sqrt{2}}\left(\sqrt{\frac{\pi}{2\sqrt{3}V_f}} - 1\right)^{2.5} \quad (1)$$

$$\mathrm{K}_L = \frac{8R^2}{53}\frac{(1-V_f)^3}{V_f^2} \quad (2)$$

The fluid injected within the preform is supposed to have a Newtonian behaviour and its dynamic viscosity is set to a constant value of μ = 0.2 Pa.s for all simulations performed in the present work. This value corresponds to the dynamic viscosity at 120°C of an epoxy resin.

2.2 Methods

The following steps are needed to compute the permeability of the previous unit cell. Firstly, it has to be meshed with tetrahedra and that should have conformal interfaces between Stokes (inter-yarn region) and Darcy (intra-yarn region). Then, finite element simulations of the dual-scale steady-state fluid flow within it are performed. Finally, the resulting velocity and pressure fields are post-processed to compute the homogenized permeability of the unit cell.

Both yarns and spaces between them are meshed with tetrahedra forming an unstructured grid. This kind of mesh was chosen instead of a structured grid because it allows to mesh more efficiently complex geometries such as those involved in this work. The unit cell is firstly meshed with voxels [12-13], and then remeshed by Mirax with tetrahedra [14]. Moreover, the mesh is conformal, meaning that nodes belonging to elements from both parts of an interface are matching on the interface itself. So, this feature allows an explicit description of the different regions within the unit cell. The results of both steps are shown in Figure 3. The characteristic size of the voxels is 100 μm, thus leading to a tetrahedral mesh with 2.8 million nodes and 16 million elements.

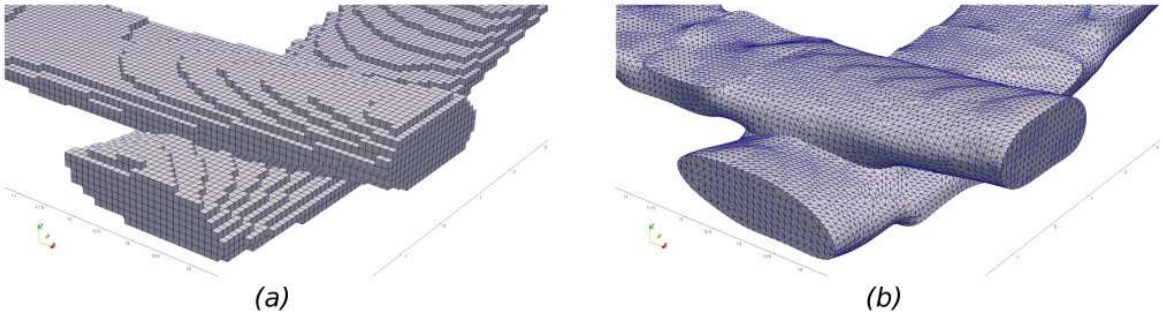

Figure 3. Meshed 3D interlock unit cell with voxels (a) and tetrahedra (b)

Finite element simulations are performed with the Z-set software [15]. The steady-state fluid flow is modelled as incompressible and laminar (*ie:* for small Reynolds numbers Re<<1). The fluid has a Newtonian behaviour with a constant dynamic viscosity. The fluid flow within the inter-yarn domain is then modelled by the Stokes problem shown in Eq. (3).

  doi:10.5075/epfl-298799_978-2-9701614-0-0

$$\begin{cases} \mu \Delta \vec{v} = \vec{\nabla} p \\ \vec{\nabla} . \vec{v} = 0 \end{cases} \quad (3)$$

Whereas the yarns are assumed to be porous and considered as homogeneous equivalent media. Hence, they can be characterized by a permeability tensor and fluid flow within the yarns is modelled by the Darcy problem as follows Eq. (4).

$$\begin{cases} \vec{v} = -\frac{1}{\mu} \underline{\underline{K}} . \vec{\nabla} p \\ \vec{\nabla} . \vec{v} = 0 \end{cases} \quad (4)$$

The fluid flow problem on the whole domain is then modelled by the coupled Stokes-Darcy problem. A mixed velocity-pressure finite element formulation is used through the entire unit cell and P1/P1 elements are used to approximate piecewise linearly both velocity and pressure fields. Such formulation is not stable, so Variational Multi-Scale (VMS) method, especially the Algebraic Sub-Grid Scale (ASGS) technique, is used to stabilise the coupled problem. Moreover, one simulation per direction needs to be performed to compute the effective permeability tensor of the unit cell. A pressure drop $\Delta P = P_e - P_s$ is applied respectively in the X, Y and Z directions, while for the other unit cell boundaries a null normal velocity condition is given, as shown in Figure 4. Note that no periodic boundary condition can be applied on this unit cell since it is not periodic. The pressure values assigned in this work are $P_e = 1$ Pa and $P_s = 0$ Pa.

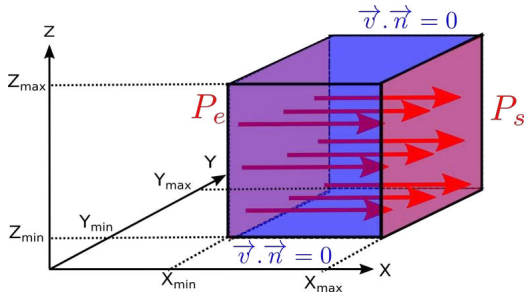

Figure 4. Boundary conditions applied on the unit cell for a main flow in the X direction

The effective permeability of the unit cell is post-processed through the 3D-generalized Darcy law shown in Eq. (4) by using the software Paraview [16]. No assumptions are made on this tensor, so all its components are computed. All the flow rate values involved are computed by integrating the velocity field component normal to the planes of abscissa $X = X_{max}$, $Y = Y_{max}$ and $Z = Z_{max}$ respectively. All the pressure values involved are computed as the mean value of the pressure over the corresponding unit cell boundary.

3. Results

3.1 Pressure and velocity fields resulting from the simulations

Finite element simulations of the fluid flow along the three main directions X, Y and Z have been performed. The resulting pressure and velocity fields for a main flow along the X direction are shown in Figure 5. The pressure field decreases linearly in average through the unit cell but with local variations due to the intra-yarn permeability. Differences in the velocity field highlight the global alignment of velocity vectors with the main flow direction. The fluid velocity has an average of 1.4e-2 $mm.s^{-1}$ in our simulations, with those specific boundary

  doi:10.5075/epfl-298799_978-2-9701614-0-0 published under CC BY-NC 4.0 license

conditions. Nonetheless, the numerical permeability computed from a steady-state flow should not depend on the fluid velocity.

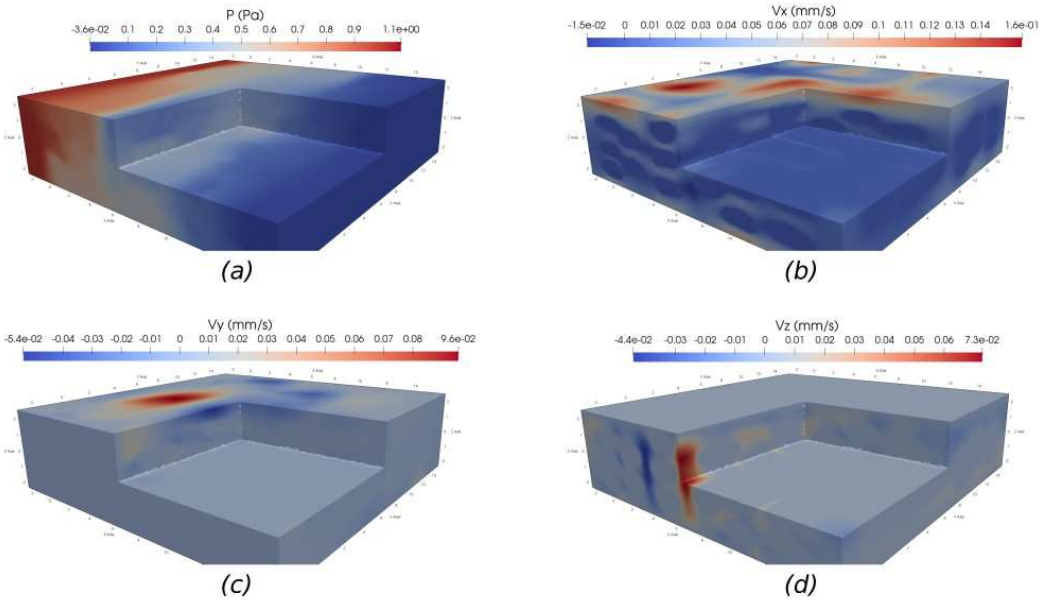

Figure 5. (a) pressure and velocity fields - (b) v_x, (c) v_y and (d) v_z - for a main flow in the X direction

However, preferential flow channels located close to the unit cell boundaries will lead to an overestimation of the fabric numerical permeability. This phenomenon is intrinsic to our mesoscopic unit cell and so it has the same significance for all the present simulations. Still, the results obtained in this first approach cannot be easily extended to unit cells without preferential flow channels.

It is also interesting to have a look at flow paths to get a qualitative idea of the balance between the inter- and intra-yarn flows. Figure 6 shows that most of the streamlines flow around the yarns and do not penetrate them. This can be explained by the relatively low yarns permeabilities compared to the relatively wide flow channels between them. Nevertheless, some streamlines penetrate the yarns, but with much smaller velocities. Therefore, the inter-yarn meso-scale flow is more significant in our unit cell than the intra-yarn micro-scale flow. Thus, the fabric permeability is mainly determined by its meso-scale morphology than by its intra-yarn permeabilities.

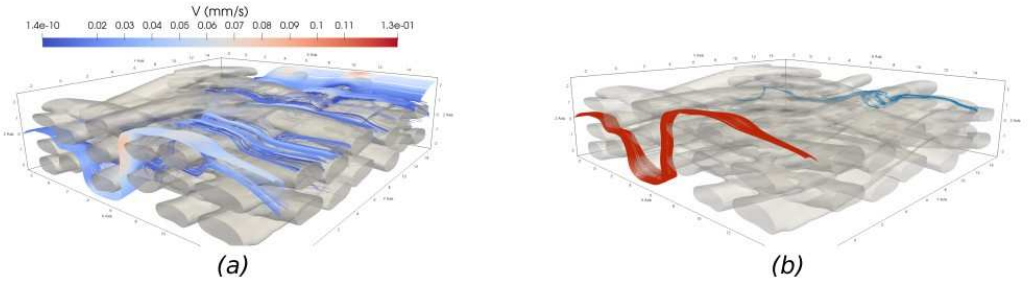

Figure 6. Streamlines from the inlet boundary $X = X_{min}$ at $Z = 0$ mm: (a) all the streamlines and (b) a non-penetrating group (red) and a penetrating group (blue) of streamlines

  doi:10.5075/epfl-298799_978-2-9701614-0-0

3.2 Effect of the intra-yarn fiber volume fraction field variability on the fabric permeability

A fibre volume fraction is used to characterise each yarn section. This leads to a higher level of details on the micro-scale yarn characteristics. This field has been averaged for each yarn, thus giving a iy-FVF value per yarn, but also averaged over all the yarns, thus giving a global iy-FVF value for all the yarns, see Figure 7. The aim is to investigate how much the iy-FVF field level of definition changes the fabric permeability. Then the permeability tensor is calculated through Gebart's laws as explained previously, the finite element simulations are performed, and the computed fabric permeability tensors are expressed in Eq. (5) in m^2.

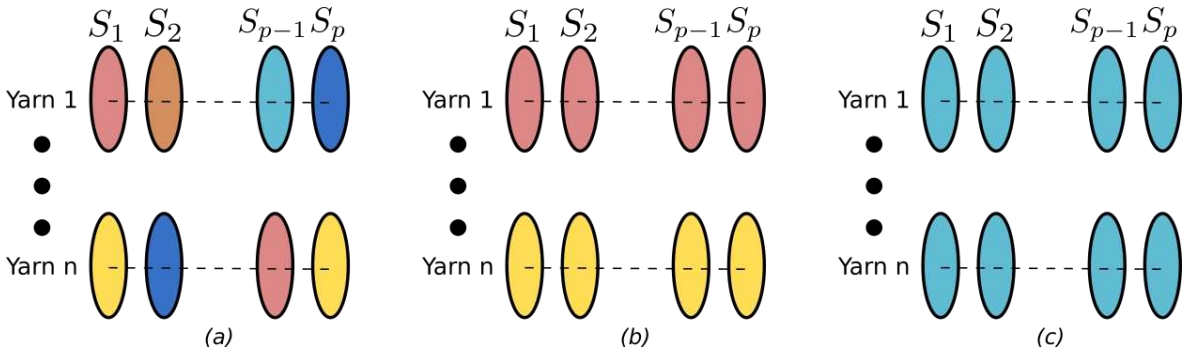

Figure 7. iy-FVF field levels of definition (colors representing different iy-FVF values): (a) section, (b) yarn and (c) global

$$\underline{\underline{K}}_{section} = \begin{pmatrix} 5.65 \times 10^{-8} & -5.80 \times 10^{-10} & -2.16 \times 10^{-10} \\ -1.77 \times 10^{-9} & 8.80 \times 10^{-8} & -5.11 \times 10^{-10} \\ -6.11 \times 10^{-9} & 3.51 \times 10^{-9} & 2.19 \times 10^{-8} \end{pmatrix}$$
$$\underline{\underline{K}}_{yarn} = \begin{pmatrix} 5.65 \times 10^{-8} & -5.80 \times 10^{-10} & -2.15 \times 10^{-10} \\ -1.77 \times 10^{-9} & 8.80 \times 10^{-8} & -5.13 \times 10^{-10} \\ -6.11 \times 10^{-9} & 3.51 \times 10^{-9} & 2.19 \times 10^{-8} \end{pmatrix} \quad (5)$$
$$\underline{\underline{K}}_{global} = \begin{pmatrix} 5.65 \times 10^{-8} & -5.79 \times 10^{-10} & -2.14 \times 10^{-10} \\ -1.77 \times 10^{-9} & 8.80 \times 10^{-8} & -5.15 \times 10^{-10} \\ -6.11 \times 10^{-9} & 3.51 \times 10^{-9} & 2.19 \times 10^{-8} \end{pmatrix}$$

It appears that the computedfabric permeability tensors are diagonally dominant since their non-diagonal terms are one or two orders of magnitude smaller than their diagonal terms. Computation of the tensors eigenvectors supports the idea that their principal directions are well aligned with the fabric directions X, Y and Z. The relative difference between the permeability tensors with regards to a iy-FVF field defined per yarn section is computed by Eq. (6) by using the spectral norm defined in Eq. (7), where ρ is the spectral radius of the tensor.

$$\frac{||\underline{\underline{K}}_i - \underline{\underline{K}}_{section}||_{2,2}}{||\underline{\underline{K}}_{section}||_{2,2}} \quad \text{with:} \quad i \in \{yarn, global\} \quad (6)$$

$$||\underline{\underline{K}}||_{2,2} = \sup_{||\overrightarrow{x}||_2 \leq 1} ||\underline{\underline{K}}\,\overrightarrow{x}||_2 = \sqrt{\rho\left({}^t\underline{\underline{K}}\,\underline{\underline{K}}\right)} \quad (7)$$

The result is a relative difference of 2.54e-5 and 5.10e-5 for the yarn and global iy-FVF definition levels respectively. So, there is no meaningful effect of the iy-FVF field variability on our unit cell permeability. An explanation can come from the analysis of the flow paths, which conclusion was that the fabric permeability is more affected by its meso-scale morphology

  doi:10.5075/epfl-298799_978-2-9701614-0-0

than by its iy-FVF field, and so by its intra-yarn permeability field. As such, intra-yarn characteristics variability is of little impact on the flow within the unit cell, and so on the fabric permeability.

This result is applicable only in the particular conditions of this first approach which are: unit cells with preferential flow channels and a steady-state flow. Consequently, a first area to investigate in the future would be unsaturated flows. The variability of intra-yarn characteristics on the flow paths and the filling time is thought to be more impacting in such cases than in steady-state flows. The second area would be to study the same unit cell, but truncated, hence avoiding the preferential flow channels. Moreover, different unit cells corresponding to several compaction levels of the same fabric will be investigated. This allows to change the contribution ratio of the micro-scale flow compared to the meso-scale flow by reducing the inter-yarn space in whole the unit cell related to the compaction level.

4. Conclusion

Finite element simulations of the dual-scale flow within a 3D interlock unit cell were performed in order to compute the fabric permeability tensor without prior assumptions made on its nature. The Stokes-Darcy coupled problem was solved by a monolithic approach stabilized by the ASGS method. The unit cell resulting from a material forming simulation is described at the meso-scale by its yarns morphology, and at the micro-scale by an intra-yarn fibre volume fraction field. The latter was averaged in two steps in order to investigate the effect of its variability, and thus the intra-yarn permeability field variability, on the fabric permeability tensor. The result is that there is no meaningful impact for the unit cell studied here, which has some preferential flow channels. These are thought to increase the weight of the meso-scale inter-yarn flow compared to the micro-scale intra-yarn flow. That is why further works will broaden this study to 3D interlock unit cells without preferential flow channels. The aim is more widely to explore different relative weights of meso- and micro-scale flows in order to observe in what cases the iy-FVF field variability affects the fabric permeability. Afterwards, such study will be extended to unsaturated flows.

5. References

1. Wang Q., Mazé B., Tafreshi HV., Pourdeyhimi B. A note on permeability simulation of multifilament woven fabrics. Chemical Engineering Science. 2006 dec; 61 (24).
2. Ali MA., Umer R., Khan KA., Cantwell WJ. XCT-scan assisted flow path analysis and permeability prediction of a 3D woven fabric. Composites Part B: Engineering. 2019 nov; 176.
3. Geoffre A., Wielhorski Y., Moulin N., Bruchon J., Drapier S., Liotier PJ. Influence of intra-yarn flows on whole 3D woven fabric numerical permeability: from Stokes to Stokes-Darcy simulations. International Journal of Multiphase Flow. 2020 aug; 129.
4. Wielhorski Y., Mendoza A., Rubino M., Roux S. Numerical modeling of 3D woven composite reinforcements: A review. Composites Part A: Applied Science and Manufacturing. 2022 mar; 154.
5. Lomov SV., Huysmans G., Luo Y., Parnas RS., Prodromou A., Verpoest I., et al. Textile composites: modelling strategies. Composites Part A: Applied Science and Manufacturing. 2001 oct; 32 (10).

  doi:10.5075/epfl-298799_978-2-9701614-0-0

6. Brinkman HC. A calculation of the viscous force exerted by a flowing fluid on a dense swarm of particles. Flow, Turbulence and Combustion. 1949 dec; 1 (1).
7. Shou D., Ye L., Tang Y., Fan J., Ding F. Transverse permeability determination of dual-scale fibrous materials. International Journal of Heat and Mass Transfer. 2013 mar; 58 (1-2).
8. Syerko E., Binetruy C., Comas-Cardona S., Leygue A. A numerical approach to design dual-scale porosity composite reinforcements with enhanced permeability. Materials & Design. 2017 oct; 131.
9. Abou Orm L., Troian R., Drapier S., Bruchon J., Moulin N. Stokes–Darcy coupling in severe regimes using multiscale stabilisation for mixed finite elements: monolithic approach versus decoupled approach. European Journal of Computational Mechanics. 2014 jul; 23 (3-4).
10. Durville D., Baydoun I., Moustacas H., Périé G., Wielhorski Y. Determining the initial configuration and characterizing the mechanical properties of 3D angle-interlock fabrics using finite element simulation. International Journal of Solids and Structures. 2018 dec; 154.
11. Gebart BR. Permeability of Unidirectional Reinforcements for RTM. Journal of Composite Materials. 1992 aug; 26 (8).
12. Schneider J., Hello G., Aboura Z., Benzeggagh M., Marsal D. A meso-fe voxel model of an interlock woven composite. In: Proceeding of the international conference in composite materials 17th (ICCM17), Edinburgh, Scotland; 2009.
13. Hello G., Schneider J., Aboura Z. Numerical simulations of woven composite materials with voxel-fe models. In: Proceedings of the 16th European Conference on Composite Materials; 2014. p.22–26.
14. Rassineux A. Robust conformal adaptive meshing of complex textile composites unit cells. Composite Structures. 2022 jan; 279.
15. Missoum-Benziane D., Chiaruttini V., Garaud JD., Feyel F., Foerch R., Osipov N., et al. Z-set/ZeBuLoN : une suite logicielle pour la mécanique des matériaux et le calcul de structures. In: 10e colloque national en calcul des structures. Giens, France; 2011. p.8.
16. Ahrens J., Geveci B., Law C. Paraview: An end-user tool for large data visualization. The visualization handbook. 2005; 717 (8).

  doi:10.5075/epfl-298799_978-2-9701614-0-0

CAPILLARY PRESSURE ESTIMATION DEPENDING ON FABRIC, LIQUID AND FIBRE VOLUME FRACTION FOR LIQUID COMPOSITE MOULDING (LCM) PROCESSES

H.N. Vo[1,2], M.F. Pucci[3], S. Drapier[1] and P.J. Liotier[4]

[1] Mines Saint-Etienne, Université de Lyon, CNRS, UMR 5307 LGF, Centre SMS, 158 Cours Fauriel, 42023 Saint-Etienne, France

[2] Department of Chemistry, College of Natural Sciences, Can Tho University, Campus II, 3/2 street, Nink Kieu District, Can Tho City, Vietnam

[3] LMGC, IMT Mines Ales, Université de Montpellier, CNRS, 6 Avenue de Clavières, 30100 Ales, France

[4] Polymers Composites and Hybrids (PCH), IMT Mines Ales, 6 Avenue de Clavières, 30100 Ales, France

Abstract: *Liquid Composite Moulding processes are considered as promising and effective to manufacture structure composite parts reinforced with synthetic and natural fabrics. The main novelty of this work is the estimation of capillary pressure (Pcap) for both fabrics at different fibre volume fractions (Vf) and with different liquids. From the previous works, the Pcap was defined as the equivalence between Washburn's equation and Darcy's law while our novel model for the capillary wicking could predict very well the swelling behaviour of natural fabrics. The combination of our Pcap definition and our novel model was explored in this study. Linear trends, thresholds and extremums of Pcap at different conditions were found for the first time. These results are relevant to estimate the importance of capillary effects during Liquid Composite Moulding processes and extremely valuable for numerical models at the fibrous scale to predict voids formation.*

Keywords: Capillary pressure, Permeability, LCM processes

1. Introduction

In LCM processes, the impregnation of fabric by resin is commonly driven by a pressure gradient. More precisely, low pressure gradients are used to avoid fibre misalignment, meaning that all other forms of pressure such as capillary pressure (Pcap) cannot be neglected. This is because such pressure can contribute to the overall pressure gradient to drive flow front movement and an error in calculation of the overall pressure gradient can occur if the capillary pressure is not considered. Pcap is, here, a homogenized representation of local wetting effects that depends on the morphology of the medium and its interaction with the liquid. The Pcap was fundamentally estimated using the Laplace's equation where some shape factors appear to consider the flow. The Laplace's equation was used coupled with the Darcy's law, measuring simultaneously the Pcap with the permeability. Authors have estimated the Pcap under a constant applied pressure gradient and at a constant flow rate, but shape factors are difficult to measure, and results strongly dependent on such parameters [1].

Other works focused on the spontaneous capillary wicking to determine the Pcap, where no external driving pressure was applied during impregnation. The test velocity was thus non-constant allowing to define a homogenized value of Pcap, independent from the flow. In this case the Pcap is defined thanks to an equivalence between Washburn's equation and Darcy's

  doi:10.5075/epfl-298799_978-2-9701614-0-0

law. The Pcap thus depends on parameters accounting for the geometry of the porous medium, the fluid-solid interactions and the medium permeability. All parameters can be evaluated independently by experimental methods [2].

On the other hand, natural fibres have not a stable morphology during wicking that makes difficult the determination of Pcap. In this work, a model was developed to predict the capillary wicking in flax fabrics at different fibre volume fractions (Vf), considering the multi-scale swelling effects of the elementary fibres and the individual yarns [3]. Then the Pcap was estimated in carbon fabrics and in flax fabrics. The main novelty of this approach resides in two aspects: the study of Pcap in natural fabrics and the correlation between the Pcap and the Vf, for both types of fabrics (carbon vs flax) and with different liquids (n-hexane vs water).

2. Materials

Carbon and flax fabrics used in this study are quasi-unidirectional woven fabrics. Carbon fabrics were supplied by Hexcel with material code 48580□. Such fabrics contain 3% in volume of glass tows in weft direction. They have an areal weight of 541 g/m2 and a density of 1.8 g/m3. Flax fabrics were provided by Libeco under the commercial designation FLAXDRY UD 180□. Their areal weight is 180 g/m2 and density is 1.45 g/m3. Both types of fabrics were used in our previous works dealing with wicking [4,5,6].

3. Theory and experiments

2.1 Equivalence law for capillary pressure (Pcap)

Assuming that fibre bundles inserted into a hollow cylinder can be approximated as a pack of capillary tubes [4] and according to the conventional Washburn's equation, the linear evolution of squared mass gain as a function of time should be obtained in constant porous medium. This can be expressed as follows neglecting gravity effects [7]:

$$m^2(t) = \left[\frac{(c\bar{r})\varepsilon^2(\pi R^2)^2}{2}\right]\frac{\rho^2\gamma_L cos\theta_a}{\eta}t \quad (1)$$

where c is a parameter taking into account tortuosity, $\bar{r}$ is the mean porous radius, ε is the porosity, which is considered as 1 – Vf (Vf: the fibre volume fraction), and R is the radius of a hollow cylinder. ρ, γL and η are the liquid density, surface tension and viscosity respectively and θa is the apparent advancing contact angle. For constant medium porosity (related to geometric product $c\bar{r}$), Eq. 1 fits very accurately the experimental data for synthetic fabrics over time [4,6].

The flow of liquid in a porous medium can also be described by the Darcy's law [8]. This equation relates an equivalent fluid velocity νD to a pressure drop with the help of permeability K, characterizing the ability of a porous medium to be crossed by a liquid of viscosity η:

$$v_D = -\frac{K}{\eta}\frac{dP}{dh} \quad (2)$$

In the case of wicking of fibre bundles into a hollow cylinder, Eq. 2 was rewritten considering the porosity ε and introducing a negative Pcap in the pressure gradient. Integrating linearly the Darcy's law and rewriting this expression as a function of the squared mass gain, a linear relation over time was obtained [4]:

$$m^2(t) = \frac{2K\varepsilon\rho^2(\pi R^2)^2 P_{cap}}{\eta}t \quad (3)$$

  doi:10.5075/epfl-298799_978-2-9701614-0-0

where R is the radius of the cylindrical sample holder and ρ is the liquid density.

In order to give a physical meaning to the Pcap, it is thus possible to state the equivalence between the Washburn (Eq. 1) and the Darcy (Eq. 3) equations describing the wicking of porous medium. The resulting expression is:

$$P_{cap} = (c\bar{r})\varepsilon\frac{\gamma_L cos\theta_a}{4K} \quad (4)$$

The Pcap thus depends both on the porous medium morphology (a parameter related to tortuosity c, mean capillary radius $\bar{r}$, porosity ε and the medium permeability K) and parameters taking into account the interactions between the fluid and the porous medium (surface tension of the fluid γL and the apparent advancing contact angle θa).

2.2 The interpretation of capillary pressure calculation

In this work, the Pcap values of carbon and flax fabrics are calculated using Eq. 4. The porosity ε is considered as 1 – Vf and the surface tension of the fluid γL is taken from [6]. This means that the medium permeability K, the geometric product $c\bar{r}$ and the apparent advancing contact angle θa need to be determined in order to determine Pcap.
Based on regularly ordered and aligned filaments, equation of permeability along the fibres K// was derived by Gebart [9]:

$$K_{//} = \frac{8R_f^2}{\varsigma}\frac{(1-V_f)^3}{V_f^2} \quad (5)$$

where Rf is the fibre radius (3.5 μm for carbon fibre and 10 μm for flax fibre are the mean values that are considered in this study) and ς is the shape factor with the value of 53 for a hexagonal arrangement [9].
The geometric product $c\bar{r}$ and the apparent advancing contact angle θa are determined by capillary wicking test using Eq. 1. In the constant porous medium, e.g. carbon fabrics, the evolution of squared mass gain as a function of time was linearly observed with both n-hexane and water as described in conventional Washburn's equation. The geometric product $c\bar{r}$ is first determined with n-hexane. Such liquid is considered as a totally wetting liquid which has an apparent equivalent advancing contact angle of 0°. Once $c\bar{r}$ is known, it can be substituted into Eq. 1 again. Hence, the apparent advancing contact angle θa can be calculated through a wicking test with water.

2.3 Adaptation to dual scale swelling of natural fibres

However, for natural fibres, the porous medium changes over time during wicking of water, due to fibre swelling. In this case, the wicking test with n-hexane can only be used to determine the initial non-swollen geometrical parameter of the fibrous medium $(c\bar{r})$. In a previous study of the authors [3], Washburn's model was modified, taking into account the fibre swelling at two scales, i.e. elementary fibres and individual yarns. The $(c\bar{r})$ can now be expressed as a function of the surface ratio $(\emptyset_{yarn})$ of yarn in a section of a fabric made of natural fibres:

$$c\bar{r} = c\left(\left(1-\emptyset_{yarn}\right)\bar{R} + \emptyset_{yarn}\bar{r}'\right) \quad (6)$$

where $\bar{R}$ is the inter yarn mean pore radius and $\bar{r}'$ the intra yarn mean pore radius [6].
During swelling of fibres and the associated swelling of yarns, the mean pore radiuses decrease along with the swelling rate of both fibres and yarns. Those two parameters have been identified in authors previous work as linear[3]. Eq. 7 and Eq. 8 can thus be written:

$$(c\bar{r})(t) = c\left(\left(1-\emptyset_{yarn}\right)(\bar{R}_0 - bt) + \emptyset_{yarn}(\bar{r}_0' - at)\right) \quad (7)$$

  doi:10.5075/epfl-298799_978-2-9701614-0-0

$$(c\bar{r})(t) = (c\bar{r})_{ini} - ct\left(\left(1 - \emptyset_{yarn}\right)b + \emptyset_{yarn}a\right) \quad (8)$$

where $\bar{R}_0$ and $\bar{r}_0'$ are the initial pore radiuses, and a and b are the respective apparent swelling rates of fibres and yarns. Then it is possible to insert those assumptions in the modified Washburn equation of wicking in reinforcements undergoing swelling [5] to be able to describe the deviation to Washburn's original law (Eq. 3):

$if\ (c\bar{r})(t) > (c\bar{r})_{fin}$

$$(c\bar{r})(t) = (c\bar{r})_{ini} - ct\left(\left(1 - \emptyset_{yarn}\right)b + \emptyset_{yarn}a\right) \quad (9)$$

$else$

$$(c\bar{r})(t) = (c\bar{r})_{fin} \quad (10)$$

The proposed model satisfactorily fits experimental results from capillary tests at different Vf, allowing to obtain the apparent advancing contact angles θa for flax fabrics with water. Figure 1 shows a wicking test for the flax fabrics with water and the fit of this non-linear trend with model proposed in Vo et al. 2020 [3, 6][40].

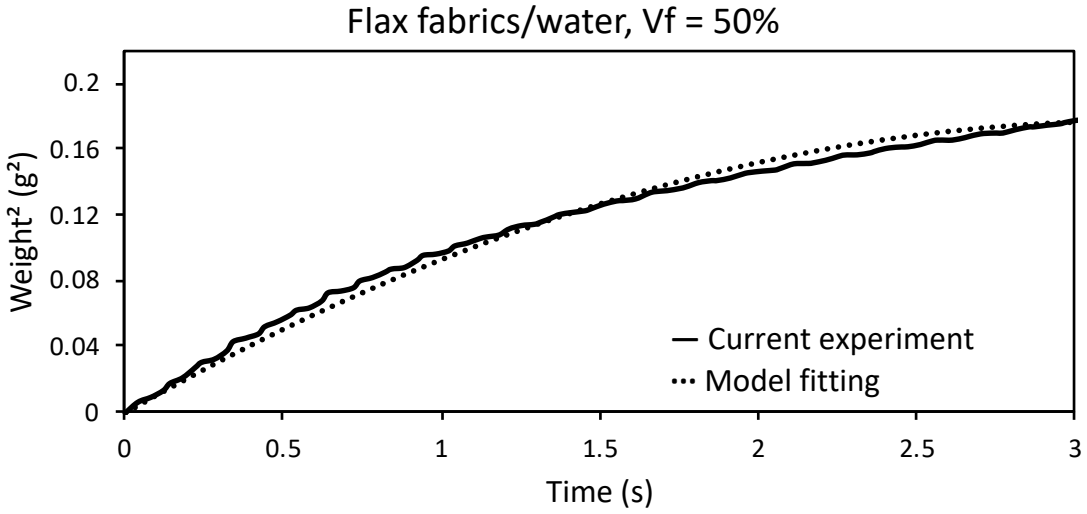

Figure 1. Fitting of experimental wicking data with the model proposed in Vo et al. 2020 [3,6] at 50% Vf.

4. Results and discussions

4.1 Permeability calculation

An important parameter to determine the Pcap is the magnitude of permeability K. According to Gebart [9], this parameter depends on the fibre radius and fibre volume fraction, as shown in Eq. 5. Table 1 presents the values of permeability of carbon and flax fabrics at different Vf. K decreases as Vf increases and the magnitude of permeability of carbon fabrics is much lower than that of flax fabrics. This is logical because the radius of carbon fibre is much smaller than the one of flax fibre at the same Vf.

4.2 Wicking in fabrics

Examples of mass gain during wicking are given in Fig. 2 and 3. Fig. 2 presents data acquired with the carbon/n-hexane couple which is the one that has the best correlation with Washburn law and Fig. 3 depict the different that appears with the couple flax/water due to swelling and modification of the capillary radius in the Washburn equation as modelled in previous works [3,6]

  doi:10.5075/epfl-298799_978-2-9701614-0-0

Table 1 : Magnitude of permeability of carbon and flax fabrics with hexagonal packing at different Vf, according to Gebart [9]

V_f (%)	$K_{//}$ of carbon fabrics (µm^2)	$K_{//}$ of flax fabrics (µm^2)
30	7.0	57.5
35	4.1	33.8
40	2.5	20.4
50	0.9	7.5
55	0.6	4.5
60	0.3	2.7
65	0.2	1.5

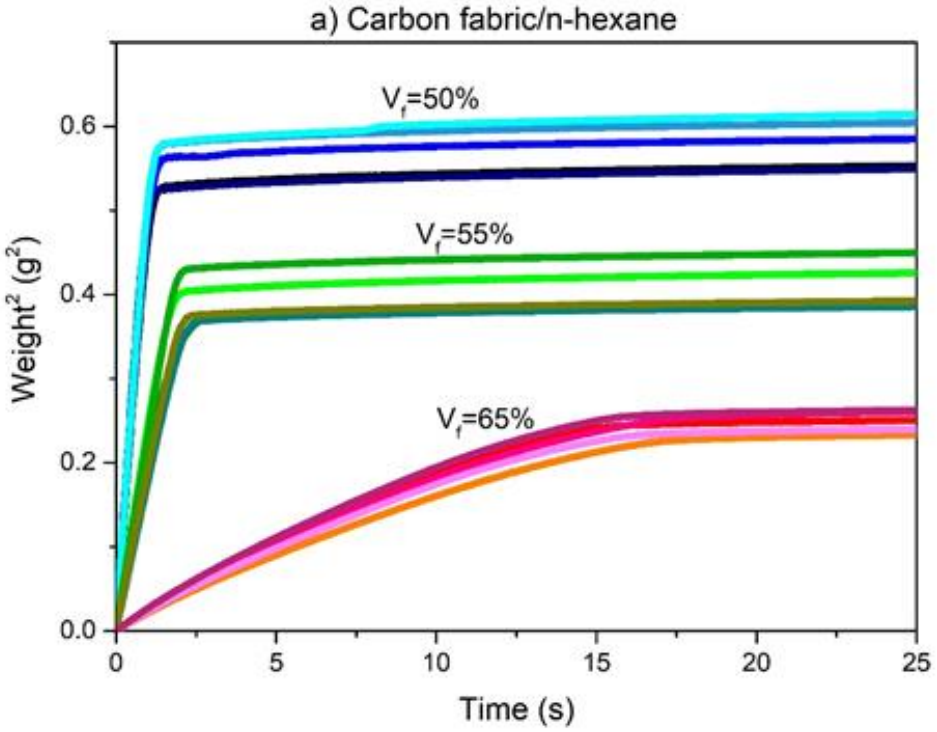

Figure 2. Wicking curves in warp direction of carbon fabrics with (a) n-hexane at 50, 55 and 65% Vf.

The table 2 summarize data obtained from three published papers [3,5,6] and shows that the model predicting the swelling of flax during wicking of water allows a reliable determination of Washburn parameters from experimental data. Using the definition of capillary pressure described by Eq. 4 [5], it is thus possible to express this parameter using.

  doi:10.5075/epfl-298799_978-2-9701614-0-0

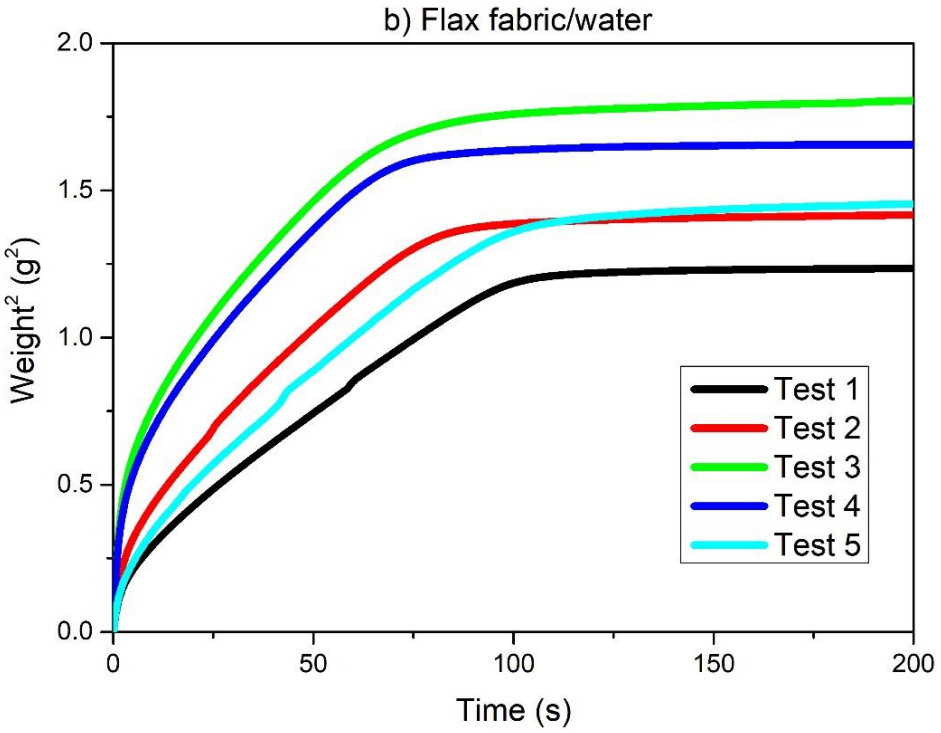

Figure 3. Wicking curves in warp direction of flax fabrics with distilled water at 50% Vf.

Table 2. Average wicking parameters of carbon and flax fabrics at different Vf [6].

Fabrics	V_f (%)	$c\bar{r}$ (µm)	θ_a (°)
Carbon	40	28.3 ± 2.4	82.7 ± 0.9
	50	13.0 ± 0.7	75.9 ± 1.5
	55	6.4 ± 0.8	68.7 ± 1.4
	60	2.3 ± 0.4(1)	55.4 ± 3.8(1)
	65	0.9 ± 0.1	56.5 ± 4.9
Flax	30	14.2 ± 0.8(2)	87.0 ± 0.3(3)
	35	13.4 ± 1.3(2)	76.5 ± 0.4(3)
	40	12.2 ± 1.4(2)	76.5 ± 1.0(3)
	50	5.7 ± 0.8	74.5 ± 7.7(3)
	60	3.8 ± 0.4(1)	68.3 ± 4.2(3)

(1) Data taken from Vo et al. 2020 [3].

(2) Data taken from Pucci et al. 2016 [5].

(3) Data obtained through the previous model [3].

4.3 Determination of the equivalent capillary pressure

Using parameters from Table 2, capillary pressures at the mesoscale of the fabrics have been calculated as a function of liquids and fiber volume fraction. Results are summarised in Fig. 4. It can be noted that an extremum appears in some cases but not for all the fabric/liquid couples.

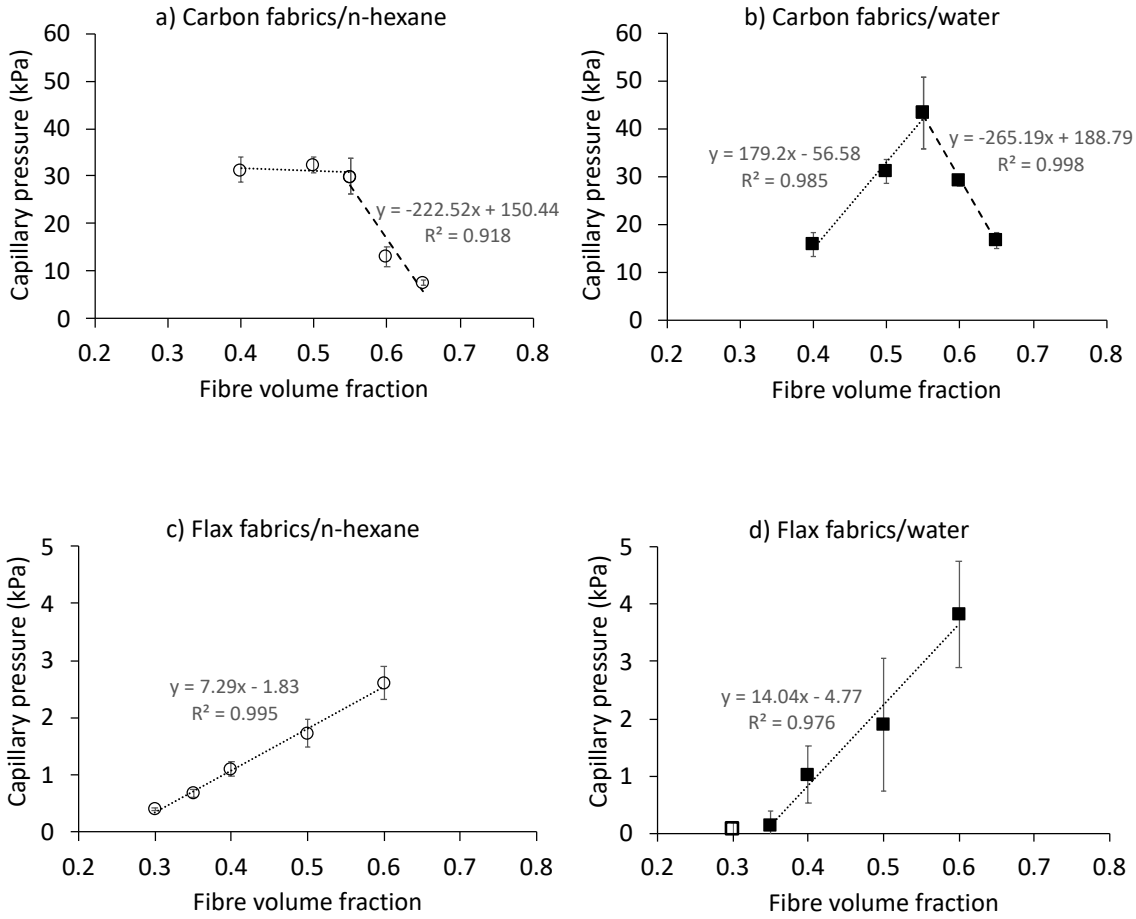

Figure 4. Capillary pressure in carbon fabrics with n-hexane a) and water b); in flax fabrics with n-hexane c) and water d) at different Vf.

5. Conclusions

The presented work proposes a significant extension of methods previously published [,5,6,10] confirming the large range of validity of the Pcap defined through wicking. The main novelty can be summarised in three principal conclusions.

The first one is that the Pcap depends on the tested liquid. It is the first time that the Pcap is also calculated for n-hexane. The second one is linked to the reliability of the model developed to consider the swelling of natural fibres. It was proved with the present results that the model is able to provide Washburn's equivalent advancing contact angles that can be used to calculate relevant Pcap with water in flax fabrics. The third and main novelty of this work resides in the study of the influence of Vf on Pcap for different liquids and fabrics. The principal conclusions obtained here are the linear trend of the Pcap as a function of Vf and that it can reach a maximum. Indeed, it was demonstrated that the Pcap could either be constant or vary linearly, depending on the type of fabrics (synthetic or natural) and liquids. A threshold value at which the trend is modified has been shown at 55% in carbon fabrics, while such a threshold could not be reached in flax fabrics. This might be due to the values of Pcap that are significantly lower in flax (ten times lowers).

The results obtained in the present study are of first interest for composite manufacturing simulation [10,11] and a major concern for complex part and 3D reinforcements [12].

  doi:10.5075/epfl-298799_978-2-9701614-0-0

Formulating an analytical description of the change of Pcap with Vf is thus the next step to be included in further numerical studies along with the understanding and predicting the occurrence of the threshold in further experimental studies.

6. References

[1] Verrey et al., Dynamic capillary effects in liquid composite moulding with non-crimp fabrics. Compos Part A Appl Sci Manuf 2006;37:92–102.

[2] Pucci et al., Capillary wicking in a fibrous reinforcement - Orthotropic issues to determine the capillary pressure components. Compos Part A 2015;77:133–41.

[3] Vo et al. Capillary wicking in bio-based reinforcements undergoing swelling – Dual scale consideration of porous medium. Compos Part A 2020;134:105893.

[4] Pucci MF, Liotier PJ, Drapier S. Capillary wicking in a fibrous reinforcement - Orthotropic issues to determine the capillary pressure components. Compos Part A Appl Sci Manuf 2015;77:133–41. .

[5] Pucci MF, Liotier PJ, Drapier S. Capillary wicking in flax fabrics - Effects of swelling in water. Colloids Surfaces A Physicochem Eng Asp 2016;498:176–84. https://doi.org/10.1016/j.colsurfa.2016.03.050.

[6] Vo, H. N., Pucci, M. F., Drapier, S., & Liotier, P. J. (2022). Capillary pressure contribution in fabrics as a function of fibre volume fraction for Liquid Composite Moulding processes. Colloids and Surfaces A: Physicochemical and Engineering Aspects, 635, 128120.

[7] Washburn EW. Note on a Method of Determining the Distribution of Pore Sizes in a Porous Material. Proc. Natl. Acad. Sci. U. S. A., 1921, p. 115–6. https:// https://dx.doi.org/10.1073%2Fpnas.7.4.115.

[8] Darcy H. Les fontaines publiques de la ville de Dijon: exposition et application des principes à suivre et des formules à employer dans les questions de distribution d'eau. Victor Dalmont; 1856.

[9] Gebart BR. Permeability of Unidirectional Reinforcements for RTM. J Compos Mater 1992;26:1100–33. https://doi.org/10.1177/002199839202600802.

[10] Andriamananjara K, Moulin N, Bruchon J, Liotier P-J, Drapier S. Numerical modeling of local capillary effects in porous media as a pressure discontinuity acting on the interface of a transient bi-fluid flow. Int J Mater Form 2019;12:675–91. https://doi.org/10.1007/s12289-018-1442-3.

[11] Chevalier L, Bruchon J, Moulin N, Liotier PJ, Drapier S. Accounting for local capillary effects in two-phase flows with relaxed surface tension formulation in enriched finite elements. Comptes Rendus - Mec 2018;346:617–33. https://doi.org/10.1016/j.crme.2018.06.008.

[12] Geoffre A, Wielhorski Y, Moulin N, Bruchon J, Drapier S, Liotier P-J. Influence of intra-yarn flows on whole 3D woven fabric numerical permeability: from Stokes to Stokes-Darcy simulations. Int J Multiph Flow 2020;129:103349.

DEVELOPMENT OF AN EXPERIMENTAL SETUP TO DETERMINE THE PERMEABILITY OF A SINGLE TOW

Maximilian Steinhardt[a], Benno Böckl[a], Anna Denk[a], David Techmer[a], Dennis Bublitz[a], Klaus Drechsler[a]

a: Technical University of Munich, TUM School of Engineering and Design, Chair of Carbon Composites, Boltzmannstr. 15 85748 Garching
E-Mail: maximilian.steinhardt@tum.de

Abstract: *For the optimization of liquid composite molding processes (LCM), the use of filling simulations is widely spread. In these simulations, the porosity of the dry fibrous textiles is usually represented by a homogenized permeability of the textile on a macroscale. In reality, the flow inside the textile can be divided into the micro flow inside the tows and the macro flow between the tows. However, some flow induced defects such as entrapped air between the tows can only be predicted with simulations on smaller scales. Actually, only few experimental studies on the flow inside a single tow have been published. This micro flow is influenced by capillary effects, whilst the interaction of the injection pressure and capillary effects has not been well examined yet. In this study, a new test setup was developed to determine the permeability of a single tow. It can be used to investigate the flow inside the tow. The results show a good correlation with analytical models for permeability estimation from literature. The test rig allows to validate simulation models for the microflow and to further investigate influencing parameters, such as the capillary effects.*

Keywords: permeability; microscale; tow; roving

1. Introduction

Liquid composite molding processes offer the possibility to produce fiber reinforced parts in high volumes. Filling simulations are often used to ensure a fast and homogenous filling of the part and to reduce defects such as voids. Therefore, the resin flow through the textiles has to be understood correctly considering the macroscopic flow as well as the microscopic flow. Whilst the macroscopic flow is mainly driven by process parameters such as the pressure gradient, the microscopic flow is also influenced by capillary effects. To conduct a filling simulation the impregnation behavior of the porous textile structure is usually characterized by determining its permeability. This is usually done by experiments on a macroscopic scale. Some microscopic effects which take place inside the tow are usually not considered in these experiments.

Various test setups have been developed to determine the permeability of textiles in in-plane directions as well as for out-of-plane measurements. The test results are strongly influenced by the test equipment and the handling of the material. Several international benchmark studies have been conducted showing the difficulties in the permeability determination and a rather large scatter of the results [1–4]. Whilst these setups mostly focus on the filling on a macro scale, only few studies focus on an experimental characterization of the intra tow flow. Simacek et al. used the translucent properties of wet glass fiber tows to investigate their impregnation behavior [5]. A sample of assembled rovings was used by Bezerra et al. and Sandberg et al. to

  doi:10.5075/epfl-298799_978-2-9701614-0-0

measure its permeability [6–8]. Godbole et al. analyzed the transversal tow permeability for the development of a semi-analytical permeability model [9].

In this study, a test setup is presented which is capable of characterizing the microscopic flow isolated on a single tow. This flow is influenced by the surface tension of the materials and the fiber volume content of the tow.

2. Experimental method

2.1 Materials

In this study, a Pyrofil TRW40 50L tow with a number of 50 000 filaments was used for the measurements. This tow was selected, because it is suitable to evaluate the design of the test stand due to its high number of filaments. The silicone used for sealing of the edges of the tow was REPLISIL 32 N. It was selected because of its short curing time of 20 minutes and therefore reduces the time effort for each test. The test fluid used for the experiments was sunflower oil.

2.2 Measurement principle

Figure 1 schematically shows the experimental setup for the determination of the longitudinal tow permeability. To evaluate the flow through the tow, race tracking at the edges of the tow has to be prevented. Therefore, a tool was designed which enables a controlled two-step infiltration. At first, the high viscosity silicone is injected and cured to seal the edges of the roving without impregnating them. In the next step, the roving is infiltrated with the test fluid. The infiltration of the tow is driven by a pressure gradient using a pressure pot at the inlet and atmospheric pressure at the outlet. For postprocessing, a matlab code was developed using digital image correlation to detect the flow front from images taken by an industrial camera. The permeability is calculated using pressure and viscosity values based on Darcy's law.

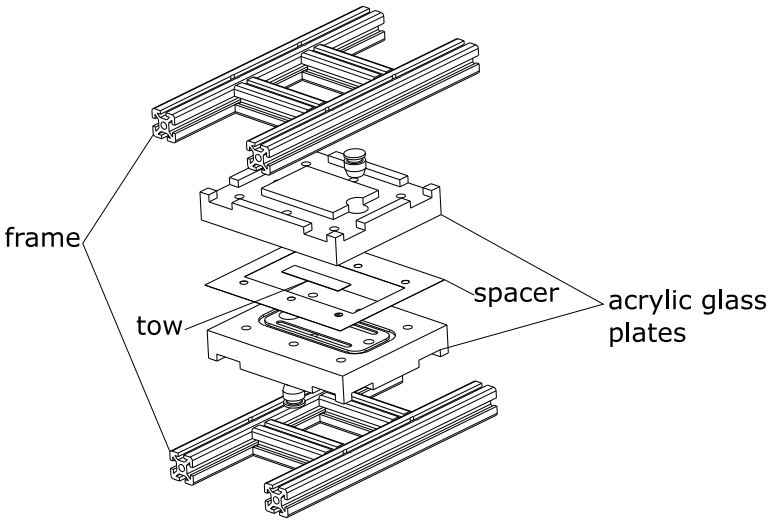

Figure 1 : Components of the test setup for the permeability measurements of a tow

2.3 Test procedure

At first, the roving is cut into a length of 60 mm. While cutting, the roving has to be fixed to prevent the development of gaps, which would lead to an uneven flow of the test fluid in the tow. This is done by clamping the roving between two plates. Then, the tow and a spacer, which enables a defined cavity height, are placed between two acrylic glass plates. A frame is used to

create a homogenous closing force on the mold which is applied by six screws. This leads to a compaction of the roving and a high fiber volume content. After closing, silicone is injected through the inlets at each side of the roving.

Before conducting the experiment, the silicone, which has flown at the inlet and outlet side of the roving, has to be removed. This enables a homogenous flow in the tow.

The experiment is conducted with sunflower oil as test fluid. As the viscosity depends on the temperature during the experiment, a sensor is used to measure the temperature of the oil. A temperature dependent viscosity curve is determined for each batch of oil using a rheometer. The mold is placed in a box with illumination and an industrial camera for image acquisition (Figure 2). The images are taken with a frequency of 1 Hz.

Figure 2: Test rig for the optical analysis of the impregnation

For determining the permeability of the tow according to Darcy's law, the pressure gradient has to be determined. A sensor at the inlet measures the pressure of the test fluid before entering the mold. At the outlet, ambient pressure is assumed.

2.4 Postprocessing

For the post processing of the experimental data, a matlab routine was developed which uses digital image correlation. As for local variations in the roving, such as small gaps and varying local fiber volume contents, the flow front is not distributed equally along the tow width. In Figure 3 an example of the differences in the propagation of the flow front are shown.

  doi:10.5075/epfl-298799_978-2-9701614-0-0

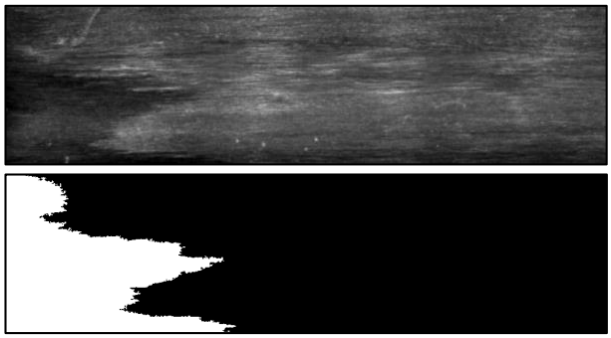

Figure 3: Flow front during experiment and result of the image correlation using the matlab routine

Therefore, the flow velocity is calculated for each line of pixels and a mean value of the overall permeability is calculated for each time step according to Darcy's law:

$$u = -\frac{K}{\mu} * \Delta p. \tag{1}$$

Where u is the fluid velocity, K the permeability, μ the dynamic viscosity of the test fluid and Δp the pressure gradient between inlet and outlet. The pressure gradient and the viscosity are calculated from the sensor data. A least square fit method is used to calculate the overall permeability of the experiment.

3. Results

3.1 Evaluation of the impregnation of the tow

To analyze the impregnation of the tow, the experiment was also conducted using an epoxy resin system CR80 from Sika. The tow was removed from the acrylic glass plates after the resin was cured. The tow then was embedded in resin and polished before microscopic images were taken.

At first, the effect of the sealing at the tow edges by the silicone was analyzed. Figure 4 shows the edge of the roving. The silicone (blue) surrounds the tow edge and penetrates the roving at the outer fibers. This leads to a sealing of the outer area and successfully prevents race tracking during the experiment. The penetration depth of the silicon was analyzed using a microscope. The maximum depth was less than 45 µm. This ensures that this method effectively seals the edge without influencing the impregnation behavior in the remaining tow.

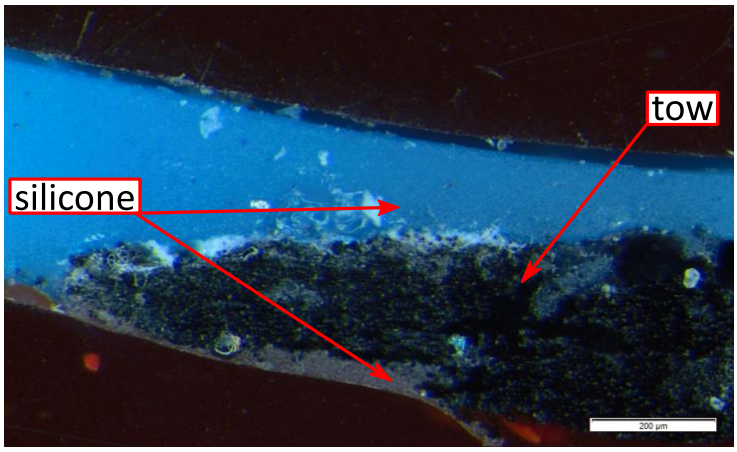

Figure 4: Micrographic analysis of the interface between silicone and tow

  doi:10.5075/epfl-298799_978-2-9701614-0-0

To analyze the flow inside the roving, additional images were taken with higher resolution, as seen in Figure 5. It shows the fiber distribution with local variations and gaps. Dark areas represent porous zones where the impregnation was not successful. These zones can be seen in various parts of the tow and they implicate that the resin did not fully impregnate the roving. This can be explained by the fact that the experiment was stopped when the resin reached the outlet side of the roving for the first time. Due to the local variability in fiber distribution, the test fluid did not reach every part of the roving at this moment. Nevertheless, the micrographs do not show a development of flow channels, so the resin can be assumed to flow through the tow in a representative manner.

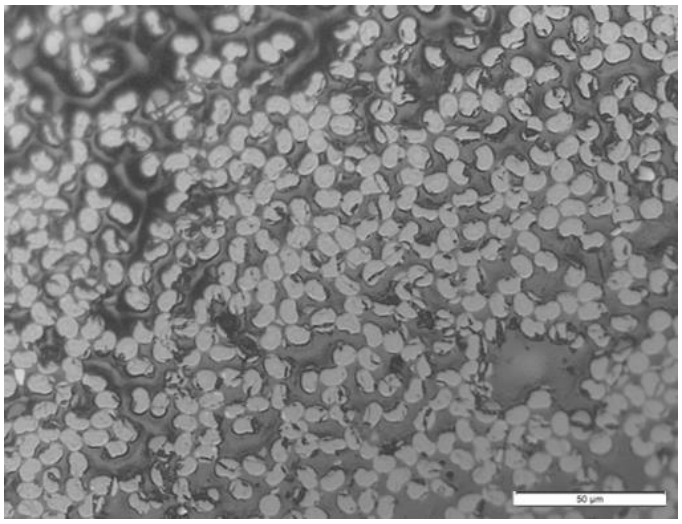

Figure 5: Micrograph of the tow with porous segments

3.2 Permeability results

Several repetitions of the experiment were conducted. For a successful experiment, it is crucial that the material is handled carefully, otherwise gaps will emerge and lead to flow channels and a nonuniform impregnation of the tow. With an inlet pressure of 0.5 bar, five successful experiments were conducted. The results show a mean permeability of $2.43 * 10^{-13}\ \mathrm{m}^2$ in the longitudinal direction of the roving. They are compared to Gebart's model [10], which allows to estimate the permeability of the tow using geometrical properties of the tow.

$$K_{||} = \frac{8R^2}{c} \frac{\left(1 - V_f\right)^3}{V_f^2} \tag{2}$$

For the experiments a global fiber volume content V_f of 65% was assumed, based on the geometrical parameters of the tow and a fiber radius R of $3.5\ \mu m$. A hexagonal packing of the fibers was assumed ($c = 57$). This results in a longitudinal permeability of $1.88 * 10^{-13}\ \mathrm{m}^2$. The results are displayed in Figure 6 and show a good compliance between the experiments and the analytical model.

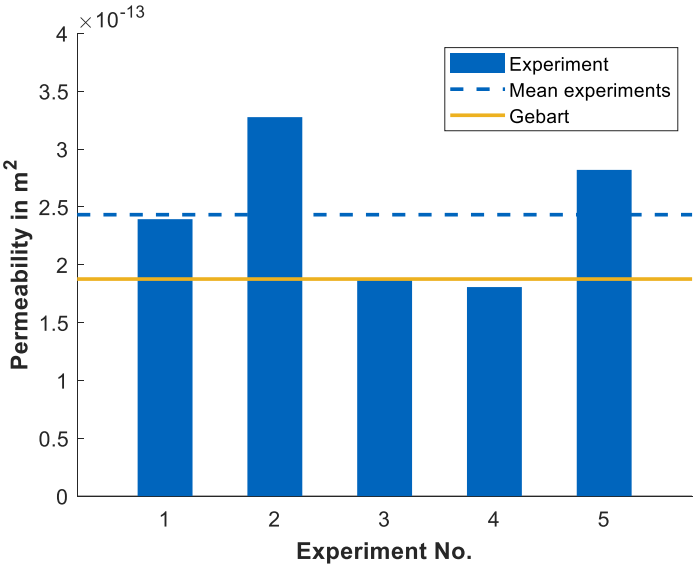

Figure 6: Results from the experiment and comparison with the Gebart model

2 Conclusion

The described test setup proves to be a promising method to analyze the impregnation of a single fiber tow and the flow on a microscopic level. The results correlate well with the analytical model and therefore serve as a proof of concept. Nevertheless, a higher number of repetitions has to be performed due to the scatter of the results. In addition, the impregnation behavior during the experiment needs to be investigated in more detail. In future, comprehensive experimental studies have to be performed by varying the inlet pressure, the fiber volume content as well as the fiber material. The experiments can also be used to analyze capillary effects, for example by determining the capillary pressure inside a tow. For the characterization of the microscopic flow in fiber textiles, the flow in transversal fiber direction has to be investigated as well. The design of the test stand allows to investigate this flow direction by only applying minor changes to the setup. The results of these studies will help to better understand the flow phenomena inside tows and to validate simulations on the microlevel.

Acknowledgements

The present work has been funded by the German Federal Ministry for Economic Affairs and Energy under the project “Hybrider SMC-TFP Hinterradrahmen (HySTHra)”.

4. References

1. Vernet N, Ruiz E, Advani S, Alms JB, Aubert M, Barburski M et al. Experimental determination of the permeability of engineering textiles: Benchmark II. Composites Part A: Applied Science and Manufacturing 2014; 61:172–84.

2. Arbter R, Beraud JM, Binetruy C, Bizet L, Bréard J, Comas-Cardona S et al. Experimental determination of the permeability of textiles: A benchmark exercise. Composites Part A: Applied Science and Manufacturing 2011; 42(9):1157–68.

  doi:10.5075/epfl-298799_978-2-9701614-0-0

3. Yong AXH, Aktas A, May D, Endruweit A, Advani S, Hubert P et al. Out-of-plane permeability measurement for reinforcement textiles: A benchmark exercise. Composites Part A: Applied Science and Manufacturing 2021;148(1):106480.

4. D. May, A. Aktas, S.G. Advani, D.C. Berg, A. Endruweit, E. Fauster et al. In-plane permeability characterization of engineering textiles based on radial flow experiments: A benchmark exercise. Composites Part A: Applied Science and Manufacturing 2019; 121:100–14.

5. Simacek P, Neacsu V, Advani SG. A phenomenological model for fiber tow saturation of dual scale fabrics in liquid composite molding. Polym Compos 2010;31(11):1881–9.

6. Bezerra R, Wilhelm F, Henning F. Compressibility and permeability of fiber reinforcements for pultrusion. 16th European Conference on Composite Materials, ECCM 2014 2014.

7. Bezerra R, Henning F. Modelling and simulation of the pultrusion process with closed injection and impregnation molds. ECCM 2016 - Proceeding of the 17th European Conference on Composite Materials 2016.

8. Sandberg M, Kabachi A, Volk M, Bo Salling F, Ermanni P, Hattel JH et al. Permeability and compaction behaviour of air-texturised glass fibre rovings: A characterisation study. Journal of Composite Materials 2020; 54(27):4241–52.

9. Godbole MG, Purandare R, Harshe R, Hood A, Gururaja S, Joshi M et al. Influence of filament distribution on transverse tow permeability: Model predictions and experimental validation. Composites Part A: Applied Science and Manufacturing 2019; 118:150–61.

10. Gebart BR. Permeability of Unidirectional Reinforcements for RTM. Journal of Composite Materials 1992; 26(8):1100–33.

  doi:10.5075/epfl-298799_978-2-9701614-0-0

DUAL-SCALE VISUALIZATION OF RESIN FLOW FOR LIQUID COMPOSITE MOLDING PROCESSES

Helena Teixidó[a], Baris Caglar[b], Véronique Michaud[a]

a: Laboratory for Processing of Advanced Composites (LPAC), Institute of Materials (IMX)
Ecole Polytechnique Fédérale de Lausanne (EPFL), 1015 Lausanne, Switzerland
helena.teixidopedarros@epfl.ch
b: Aerospace Manufacturing Technologies, Faculty of Aerospace Engineering, Delft University of Technology, Kluyverweg 1, 2629HS Delft, the Netherlands

Abstract: *Visualization of resin flow progression through fibrous preforms is often sought to elucidate flow patterns and validate models for filling prediction for liquid composite molding processes. Here, conventional X-ray radiography is compared to X-ray phase contrast technique to image in-situ constant flow rate impregnation of a non-translucent unidirectional carbon fabric. X-ray attenuation of the fluid phase was increased by using a ZnI_2-based contrasting agent, leading to enough contrast between the liquid and the low density fibers. We proved the suitability of conventional X-ray transmission to visualize fluid paths by elucidating different flow patterns, spanning from capillary to viscous regimes and a macro-void entrapment phenomenon.*

Keywords: Liquid Composite Molding (LCM); Resin flow; Saturation curve; Process monitoring; X-ray imaging.

1. Introduction

Liquid Composite Molding (LCM) techniques belong to infiltration processes whereby a liquid matrix is forced to flow in between the open pore space of a fibrous reinforcement placed inside a closed mold. Textiles used in composite processing exhibit a highly anisotropic network of pores, generally with a dual scale comprised of intra- and inter-tow spaces resulting in a dual-scale flow leading to a void entrapment mechanism. At the flow front, there is a constant competition between viscous and capillary forces; depending on the extent of viscous/capillary flow and the textile architecture, the fluid pattern as well as the amount of entrapped voids properties will vary. The dimensionless capillary number is used to define the relative influence of viscous and capillary flow regimes:

$$Ca = \frac{u_l \eta}{\gamma_{la}} \quad (1)$$

where u_l, η, and γ_{la} are the fluid velocity, viscosity and surface tension respectively. Researchers converged on the existence of an optimal capillary number for which capillary and viscous forces compensate each other and the amount of the voids is minimal. However, its value is specific for a given resin/fabric system and no one to date has been able to predict it quantitatively (1).

Multiphase flow and progressive saturation of the preforms have received much attention during the past decades with the aim to better understand the flow behavior and predict optimum fibrous preform impregnations (2). In practice, flow studies couple an in-situ flow visualization to mathematical models and numerical simulations to explore unsaturated flows

  doi:10.5075/epfl-298799_978-2-9701614-0-0

and void formation mechanisms. Nevertheless, flow visualization is still a difficult task and often reserved to optically translucent reinforcements such as glass fibers and few studies have been performed on observing flow patterns through non-translucent preforms. One of the proposed methods relies on the inclusion of sensors in-between stacked preforms (3,4). However, imaging techniques that do not require embedding additional materials are in general preferred to detect realistic flow paths. For example, ultrasound techniques (5,6) and Magnetic Resonance Imaging (MRI) have been investigated as potential techniques to visualize dual scale-flows (7). However, either spatial or time resolutions remain the limiting factors.

Nowadays, X-ray based techniques are gaining interest for fluid tracking and analysis given their fast time resolution. Bréard et al. (8) proposed to use conventional X-ray radiography to visualize the ingress of silicon oil into a thick glass preform. However, the low absorption coefficient of carbon and flax limits the resulting contrast with the fluid phase for an accurate liquid/fabric distinction. X-ray micro computed tomography (µCT) systems have enabled the observation of dual-scale flows at unprecedented resolutions (9,10). Recently, Castro el al. (11) used synchrotron radiation computed laminography to image 3D in-situ dual scale flows with micron-scale resolution at an acquisition rate of 1.8 minutes per tomogram. This method allows to locally study void distribution and flow patterns at a small scale when compared to real composite impregnation scales; however, the flow kinetics should remain well below the industrially relevant range.

In Ref. (12), we proposed to use an X-ray phase contrast device (13) to assess the progressive saturation of several distinct fibrous preforms even with conventional resins with acquisition rates below 10 seconds per radiograph. This technique is sensitive to the ultra-small angle scattering and allows to enhance the contrast between materials with low density but with enough microscale heterogeneities. In some cases, a sufficient contrast to elucidate clear flow patterns was not achieved. To overcome this limitation, we explored the use of contrasting agents in the fluid phase to enhance the fluid/fabric contrast in conventional absorption images. The benefits and limitations between the two methods for elucidation of dynamic patterns and entry data for mathematical models are addressed.

2. Materials and Methods

2.1 Materials

The unidirectional carbon fiber reinforcement from Suter Kunststoffe AG (A_w=270 g/m^2), previously employed in Ref. (12) was selected as non-translucent porous media. The fabric contains thin E-glass threads in the weft direction to hold in place and tightly pack carbon tows resulting in inconspicuous space between the tows. Two tests fluids based on an aqueous solution of poly(ethylene glycol) (PEG) (Mw=35 kDa, Sigma Aldrich) were used. The first fluid had a concentration of 16.7 wt% of PEG and in the second one a ZnI_2-based contrasting solution (14) was added to the first solution, resulting in the following formulation: 67.9 wt% of water, 8.2 wt% of PEG, 20.4 wt% of ZnI_2 and 3.5% wt% of Kodak PhotoFlow 200. The properties of the mixtures are listed in Table 1. The viscosity was measured in continuous shear mode in a concentric rheometer (AR2000ex, TA Instrument) by means of a Peltier Couette setup at a constant shear-rate of 10 s^{-1}. The surface tension in air at ambient temperature was assessed by means of the pendant drop method with a Drop Shape Analyzer (DSA30, Krüss).

  doi:10.5075/epfl-298799_978-2-9701614-0-0

Table 1: Properties of tests fluids measured at 20°C.

Fluid	Viscosity [Pa·s]	Density [g/ml]	Surface tension [mN/m]
PEG 16.7%	0.103	1.026	56.5
PEG solution with ZnI_2	0.087	1.276	32.7

2.2 Flow experiments

Flow experiments were performed with the setup from Ref. (12). Fabric layers were accurately hand-cut to a dimension of 4.95 ± 0.05 cm x 15 ± 0.10 cm. Then, nine layers were fitted into the PMMA mold with a 3 mm cavity, leading to a fiber volume fraction of approximatively 45%. A silicon joint was used to prevent race-tracking. Close to the fluid inlet, a Keller Series 35XHTT sensor was placed to monitor the fluid pressure and temperature. Vertical constant flow rate experiments were carried out, the capillary number thus stays constant along the test and the fluid velocity was estimated by measuring the average front velocity. Three experiments were conducted at different flow rates to obtain a range of flow regimes spanning from capillary to viscous dominated. A summary of the experimental campaign is given in Table 2, three flow rates were set and repeated using both fluids.

Table 2: Impregnation experiments.

#	Fluid	Flow front velocity [mm/s]	Ca (10^{-3})
1	PEG 16.67%	0.08	0.15
2	PEG 16.67%	0.26	0.47
3	PEG 16.67%	0.38	0.69
4	PEG solution with ZnI_2	0.08	0.21
5	PEG solution with ZnI_2	0.26	0.69
6	PEG solution with ZnI_2	0.38	1.01

The phase contrast X-ray apparatus developed in (13) was employed to image the flow front for the different tests. As explained in (12), this device allows obtaining three different images: absorption, refraction and scattering images. An imaging area of around 70 mm × 70 mm per acquisition was obtained and the apparatus incorporates a moving platform whose movement can be synchronized with the scanning routine. Image size was 1334 x 1331 pixels and the resulting pixel size about 50 µm. Images were taken at an averaged time of 9.2 s per acquisition and in order to entirely image the impregnation, six different stage positions were defined; then, depending on the fluid speed the number of acquisitions per positions was adapted.

3. Experimental results

3.1 Observation of flow regimes by X-ray phase contrast

Test #1, #2 and #3 correspond respectively to capillary, balanced and viscous flows and the images recorded by X-ray-phase contrast are shown Figure 1. As already reported in (12), the

  doi:10.5075/epfl-298799_978-2-9701614-0-0

higher fabric/fluid contrast is obtained in scattering images. In test #3, viscous fingering and unsaturated length are clearly depicted in the scattering images. Absorption, refraction and scattering images show a rather balanced flow for impregnation #2. However, for experiment #1, although the flow front position is clearly identified in the scattering images, the intra-tow capillary fingering is not elucidated. Absorption and refraction images show a large unsaturated area and a flow preferentially filling the tows, though, the interpretation of the flow front in these images is hampered by the low contrast obtained. To overcome this limit, we thus investigated the potential benefit of a contrasting agent in the solution to increase the effect of the fluid on the attenuation signal and thus observe the flow progression in absorption images.

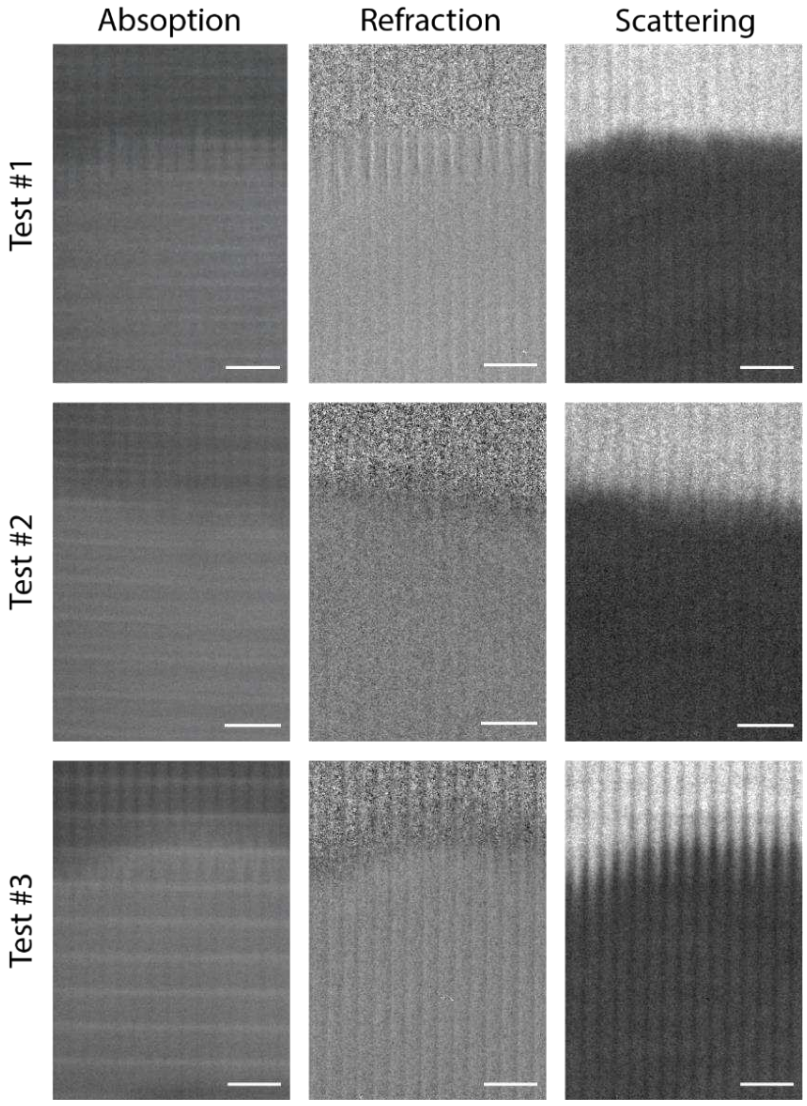

Figure 1. Absorption, refraction and scattering images obtained for tests #1, #2 and #3. The scale bar corresponds to 5 mm.

3.2 Observation of flow regimes by X-ray transmission

Flow front images obtained for experiments #4, #5 and #6 are shown Figure 2. The different flow domains of experiments #4, #5 and #6 are clearly identified in absorption images: capillary and viscous fingering are observed for tests #4 and #6 respectively with a large unsaturated area and as expected, test #5 is a rather balanced flow with a small unsaturated zone. Moreover, inter-tow meso-voids resulting from strong capillary effects are apparent for test #4. In this case, the

  doi:10.5075/epfl-298799_978-2-9701614-0-0

flow front is almost flat due to the domination of homogeneous diffusion inside the tows whereas in test #6, it is less sharp since it is highly influenced by fabrics layup resulting in an irregular meso-porosity network. By employing a contrast agent, a high resolution and fluid/fabric contrast are obtained in absorption images whereas little information can be extracted from refraction and scattering images in which the flow front is disturbed by the fluid composition, affecting the refraction properties.

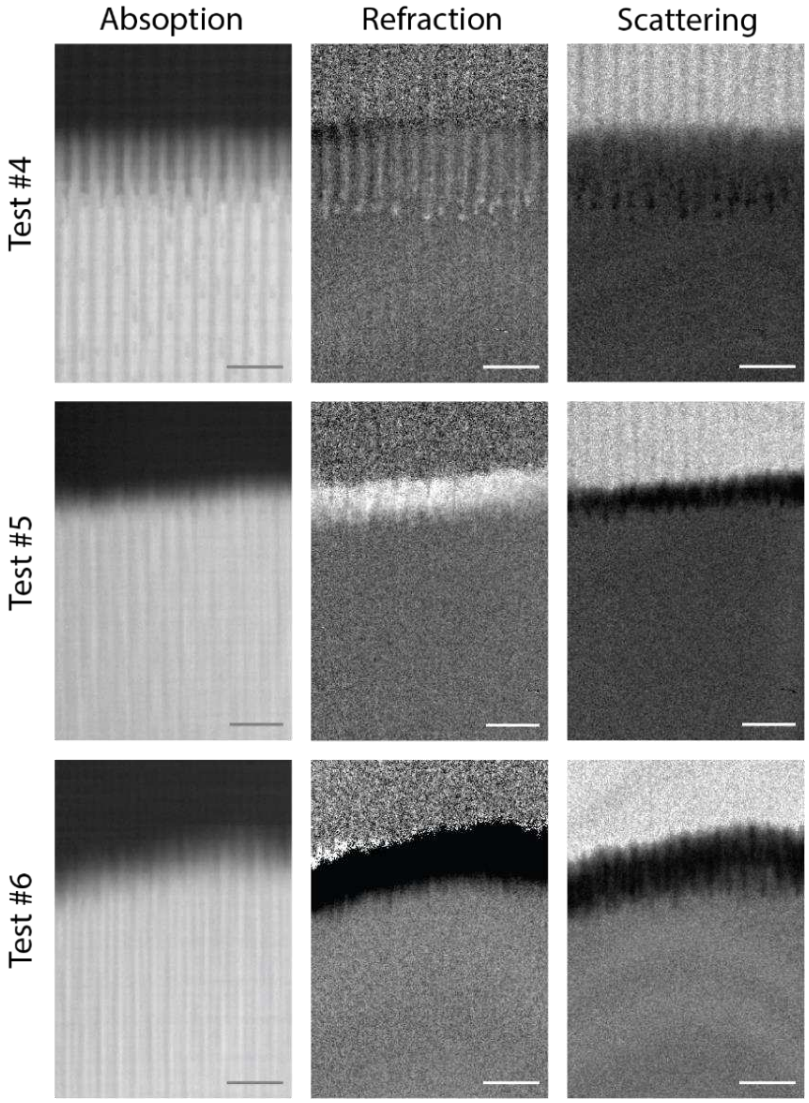

Figure 2. Absorption, refraction and scattering images obtained for tests #4, #5 and #6. The scale bar corresponds to 5 mm.

In addition, the fabric architecture and in particular the presence of horizontal glass stitches was found to significantly affect the flow pattern. In the capillary-driven case, those fiber bundles create “pools” which lead to macro-void entrapment as shown in the sequence of images in Figure 3 and explained in Figure 4. In the viscous case, they form large porosity areas within the fibrous preform leading to a stabilization of the flow as shown in Figure 4.

  doi:10.5075/epfl-298799_978-2-9701614-0-0

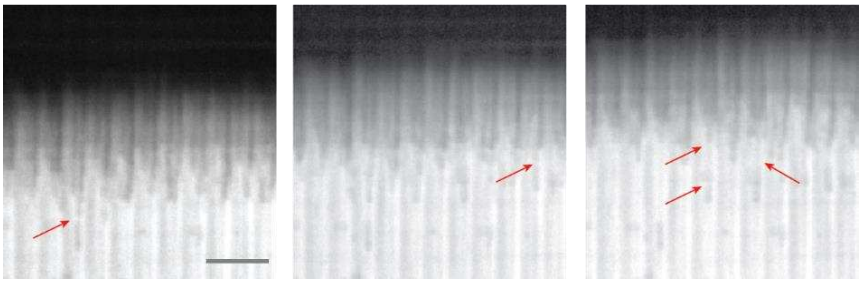

Figure 3. Macro-void formation in impregnation #4. From left to right the images correspond to the times 614.7 s, 634.7 s and 643.8 s. Red arrows show some examples of void entrapment due to the horizontal stitches. The scale bar corresponds to 4 mm.

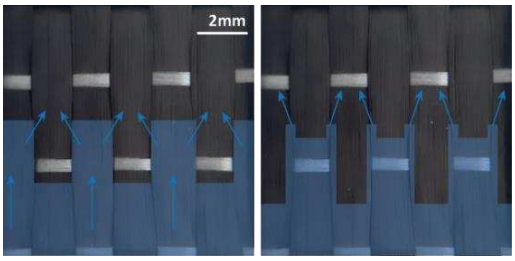

Figure 4. Influence of the fabric architecture on capillary (right) and viscous (left) flow patterns.

3.3 Visualization methods comparison

We evaluated the visualization of flow patterns by X-ray phase contrast imaging (impregnation carried out with a model fluid) and by conventional X-ray radiography (using a ZnI_2-based contrasting solution). Figure 5 shows the histograms of the different images presented in Figures 1 and 2 for tests #2 and #5. For the absorption image, peaks of dark and light grays are clearly differentiated with the use of contrasting agents. Moreover, the pixel intensity range for fluid and fabric is narrower when compared to the scattering images histogram which leads to a better differentiation between materials. This simplifies the image interpretation and analysis since the objective is to build the dynamic saturation curve for each experiment following the grayscale analysis method presented in (12) and thereupon model the progressive saturation with a two-phase flow model adapted from soil science. Finally, Table 3 presents the main advantages and disadvantages of the two approaches.

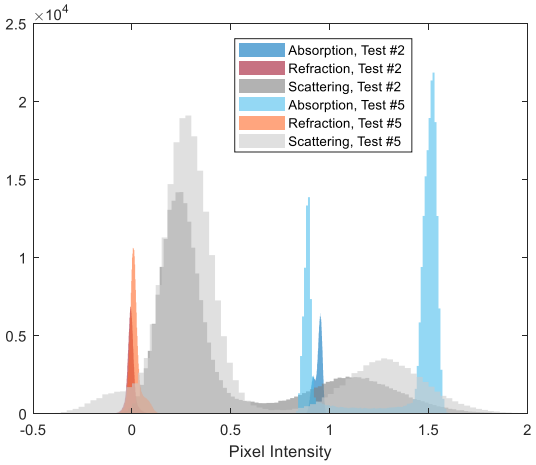

Figure 5. Histogram of absorption, refraction and scattering images of tests #2 and #5.

Table 3: Advantages and disadvantages between visualization methods.

	Advantages	Disadvantages
X-ray phase contrast	Scattering images can be used to track flow paths at a real scale even with conventional resins. Additional information of the flow type can be extracted from refraction images.	Scattering image resolution is not sufficient to extract flow patterns. For example, capillary fingering is hindered by the scattering images. Time of acquisition can be too long for fast flows observation.
X-ray transmission	Fine detail is obtained and the flow patterns can be clearly depicted. Since the grating movement specific for scattering and refraction images is not needed, the time of acquisition can be reduced.	Need of contrasting agents to visualize flow patterns, slightly modifying the fluid properties.

4. Conclusions

The present results show that conventional X-ray radiography is a suitable technique for in-situ flow analysis for Liquid Composite Molding studies and in particular for non-translucent preforms. Despite the low density of carbon fabrics, by adding contrast agent we were able to enhance the fluid/fabric contrast in absorption images and elucidate fluid paths at a real impregnation rate with a satisfactory resolution. The flow front for different impregnation conditions was successfully tracked for a unidirectional carbon preforms. Capillary to viscous fingering were clearly identified and the location and shape of meso-porosity for the capillary case was even observed. However, some hurdles need to be overcome to fully complete the flow analysis: (i) for viscous flows, the flow displacement per image acquisition can be too significant leading to a slight error when building the saturation curve, to overcome this, it is sought to reduce the time of acquisition; (ii) a complete analysis of the final saturation state (accurate measurement of the residual porosity) is needed to properly describe the flow behavior for the modeling; (iii) micro-void formation and location is hardly identified with this method.

Acknowledgements

This work was supported by the Swiss National Science Foundation (SNF n° 200021_182669).

5. References

1. Teixidó H, Staal J, Caglar B, Michaud V. Capillary Effects in Fiber Reinforced Polymer Composite Processing: A Review. Frontiers in Materials. 2022;9:1–24.

2. Michaud V. A Review of Non-saturated Resin Flow in Liquid Composite Moulding processes. Transport in Porous Media. 2016;

  doi:10.5075/epfl-298799_978-2-9701614-0-0

3. Konstantopoulos S, Fauster E, Schledjewski R. Monitoring the production of FRP composites : A review of in-line sensing methods. Express Polymer Letters. 2014;8(11):823–40.

4. Caglar B, Esposito W, Nguyen-Dang T, Laperrousaz S, Michaud V, Sorin F. Functionalized Fiber Reinforced Composites via Thermally Drawn Multifunctional Fiber Sensors. Advanced Materials Technologies. 2021;6(3):1–8.

5. Thomas S, Bongiovanni C, Nutt SR. In situ estimation of through-thickness resin flow using ultrasound. Composites Science and Technology. 2008;68(15–16):3093–8.

6. Konstantopoulos S, Grössing H, Hergan P, Weninger M, Schledjewski R. Determination of the unsaturated through-thickness permeability of fibrous preforms based on flow front detection by ultrasound. Polymer Composites. 2018;39(2):360–7.

7. Endruweit A, Glover P, Head K, Long AC. Mapping of the fluid distribution in impregnated reinforcement textiles using Magnetic Resonance Imaging : Application and discussion. Composites Part A. 2011;42(10):1369–79.

8. Bréard J, Saouab A, Bouquet G. Dependence of the reinforcement anisotropy on a three dimensional resin flow observed by X-ray radioscopy. Journal of Reinforced Plastics and Composites. 1999;18(9):814–26.

9. Vilà J, Sket F, Wilde F, Requena G, González C, Llorca J. An in situ investigation of microscopic infusion and void transport during vacuum-assisted infiltration by means of X-ray computed tomography. Composites Science and Technology. 2015;119:12–9.

10. Castro J, Sket F, González C. S-XCT experimental determination of local contact angle and meniscus shape in liquid moulding of composites. 2020;199(April).

11. Castro J, Sket F, Helfen L. In situ local imaging and analysis of impregnation during liquid moulding of composite materials using synchrotron radiation computed laminography. Composites Science and Technology. 2021;215(August).

12. Teixidó H, Caglar B, Revol V, Michaud V. In-operando dynamic visualization of flow through porous preforms based on X-ray phase contrast imaging. Composites Part A: Applied Science and Manufacturing. 2021;149.

13. Gresil M, Revol V, Kitsianos K, Kanderakis G. EVITA Project : Comparison Between Traditional Non-Destructive Techniques and Phase Contrast X-Ray Imaging Applied to Aerospace Carbon Fibre Reinforced Polymer. Appl Compos Mater. 2017;24:513–24.

14. Sket F, Enfedaque A, Alton C, González C, Molina-Aldareguia JM, Llorca J. Automatic quantification of matrix cracking and fiber rotation by X-ray computed tomography in shear-deformed carbon fiber-reinforced laminates. Composites Science and Technology. 2014;90:129–38.

THE COMPARISON OF DIFFERENT MACHINE LEARNING METHODS TO PREDICT THE TYPE OF FLUID FLOW FRONT SHAPE IN THE COMPOSITE MANUFACTURING PROCESS IN THE PRESENCE OF RACE-TRACKING WITH DIFFERENT PROPERTIES

Keayvan Keramati[a, b], Joaquin Fernández-León[a,c], Davide Mocerino[a], Luis Baumela [c], Carlos Miguel Giraldo[d], Carlos González[a, b]

a: IMDEA Materiales, C/Eric Kandel 2, 28906, Getafe, Madrid, Spain
keayvan.keramati@imdea.org
b: Departamento de Ciencia de Materiales, Universidad Politécnica de Madrid, E.T.S. de Ingenieros de Caminos, 28040, Madrid, Spain
c: Departamento de Inteligencia Artificial, Universidad Politécnica de Madrid, E.T.S. de Ingenieros Informáticos, 28660, Madrid, Spain
d: Airbus Operations S.L., Paseo de John Lennon s/n, 28906, Getafe, Madrid, Spain

Abstract: *Fiber-reinforced polymer composites (PMCs) are broadly used in applications that require lightweight materials such as those found in aerospace, automotive, energy, healthcare sectors, and others. However, the dependence of processing on external factors or disturbances is still remarkable, which means that the number of parts to be inspected and either rejected or reworked produces a considerable impact on the final cost distribution.*

Different supervised machine learning models were developed to determine the type of race tracking region in liquid composites molding during the injection process by the installed pressure sensors on the RTM mold surface. Four fluid flow front patterns were assumed due to race tracking shapes in two edges of the RTM mold. Race-tracking affects the pressure evolution in pressure sensors' position with five parameters, the permeability of fabric, the length of race-tracking in 2 edges, and their permeability.

Keywords: Machine learning; Mould filling simulations; Composite Materials; Liquid Molding

1. Introduction

Nowadays, Fiber-reinforced polymer composites (PMCs) are widely used in applications that require lightweight materials, such as those found in aerospace, automotive, energy, healthcare sectors, and sports. However, the dependence of processing on external factors or disturbances is still remarkable in some strategic areas such as aeronautics, aerospace or the automotive sector, which means that the number of parts to be inspected and either rejected or reworked produces a considerable impact on the final cost distribution. With that in mind, the cumulative and recurrent costs for the non-implementation of the appropriate diagnosis manufacturing policies that could allow recovery from failure will undoubtedly negatively impact the competitiveness of the industrial sector.

Within the family of manufacturing methods for structural composites, liquid molding (LM) and, more precisely, resin transfer molding (RTM) emerged as the out-of-autoclave technique that

  doi:10.5075/epfl-298799_978-2-9701614-0-0

best provides high-quality parts at optimized costs. The RTM process starts with a dry fabric preform draped and placed into a mold for its impregnation with a liquid resin driven by a pressure gradient (Advani & Hsiao, 2012) and (Rudd, Long, Kendall, & Mangin, 1997). After the part is totally impregnated, the resin is cured, generally by the action of heat sources, until the part becomes solid and can be demolded. However, one of the major drawbacks associated with RTM arises from the inherent uncertainty regarding the flow patterns produced during impregnation, which are seriously affected by processing disturbances that lead to dry spots and void formation. Such dry spots are generated by unexpected resin channels at mold edges, known as race-tracking channels (Bickerton, 1999)and (Devillard, Hsiao, Gokce, & Advani, 2003), resulting in non-homogeneous resin flow diverted directly to the outlet gates. In addition, resin velocity variations, mainly attributed to local values of permeability and viscosity, may induce void formation due to unbalanced capillary and viscous forces in textile reinforcements. In the last two decades, efforts have been made to propose automated systems that perform corrective actions after detecting manufacturing disturbances in RTM. The concept of online filling in RTM developed by Advani and co-researchers is an excellent example of such a philosophy (Lawrence, et al., 2002), (Siddig, Binetruy, Syerko, Simacek, & Advani, 2018). These strategies rely on the intelligent use of sensors for flow and pressure detection (Fratta, Klunker, & Ermanni, A methodology for flow-front estimation in LCM processes based on pressure sensors, 2013), (Fratta, Koutsoukis, Klunker, & Ermanni, 2016) distributed over the surface of the mold.

AI is opening revolutionary opportunities across engineering disciplines such as continuum mechanics (Bock, et al., 2019) and fluid mechanics, (Brunton, Noack, & Koumoutsakos, 2020) as well as manufacturing (Meng, et al., 2020). However, the permeation of practical knowledge in manufacturing is still limited, and applications are at an initial stage (Wang, Fu, & Gao, 2019).

The main purpose of this work is to provide a first experimental exploration of ML methods to detect automatically flow disturbances caused by the presence of race-tracking channels in RTM. The detection capabilities of the model fall on the analysis of pressure changes recorded by a distributed network of only five sensors. The model was developed to address the problem of the presence of race-tracking regions in a squared flat RTM mold.

2. Materials and experiments

Resin injection experiments were carried out by using a 600*300 mm^2 closed mold, as shown in Figure 1. The upper half of the mold was manufactured with transparent polymethyl methacrylate (PMMA), providing optical access to the interior, while the other half was steel-made as a typical RTM mold. Injection experiments were performed by imposing an overall uni-axial flow between the inlet and outlet gates. The geometry of such a channel as race-tracking was created simply by cutting the fiber edges. The effective fabric dimensions inside the mold were L=300*300mm^2, as shown in Figure 1 b.

The inlet was connected to a pressure pot in which fluid pressure was controlled externally with a compressed-air line. Fluid pressure in the panel was measured with five pressure transducers. Four of them, namely P_1 to P4, were distributed equally in a uniform square array, while a fifth sensor, P_0, was placed at the fabric entrance. An additional sensor was used to control the electro-valve activity of the pressure pot, avoiding line pressure disturbances during the tests. All the tests were performed by applying a constant pressure at the injection pot of p_{in}=0.7bar.

  doi:10.5075/epfl-298799_978-2-9701614-0-0

The pressure sensor signals were recorded by using a Catman Quatum HBM data acquisition system. A video camera installed on the top of the mold was used to track the flow front evolution for direct comparison with the simulations.

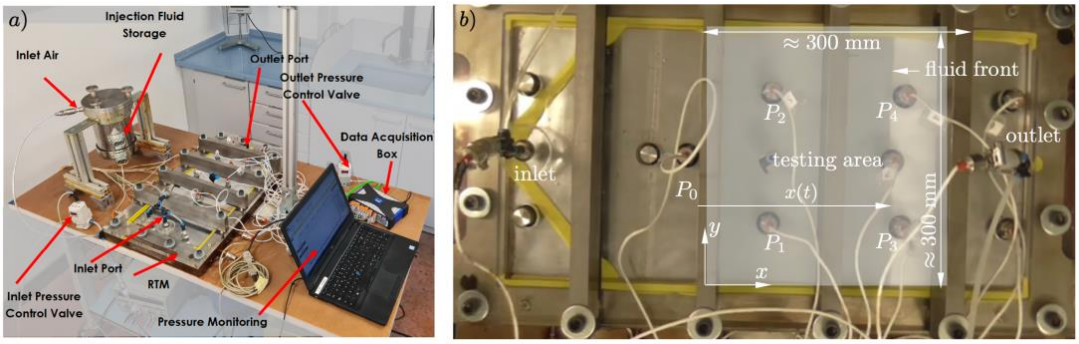

*Figure 1 a) General overview of the RTM testing system, b) RTM mold for experimental tests and pressure sensor locations P_0 to P_4. The testing area corresponded to L=300*300mm² square*

A blend of corn syrup with water at average concentrations of 70%-30% was used as an injection fluid for all the experiments. The fluid's viscosity was measured individually and immediately before the experiments were performed. The viscosity values measured ranged between 130-200 mPa.s for all the experiments, corresponding to slight blend variations and daily laboratory temperature.

The fabric lay-up involved stacking four plies of a polyethylene terephthalate (PET) non-woven felt of 280 g/m^2 areal. Race-tracking was induced by cutting with lateral blade channels along the flow direction. In this work, four types of race-tracking types were studied, as shown inFigure 2. In all the cases, race-tracking channels were introduced at the edges parallel to the flow direction. *Type 1* and *2* can be considered the same race-tracking type but flipped concerning the flow direction axis. *Type 3* race-tracking contains the two channels starting from the fabric entrance. *Type 4* was generated by producing centered channels totally disconnected from the entrance and exit of the panel. *Type 0* is a reference scenario without race-tracking to calculate the fabric permeability and compare flow patterns concerning the other scenarios.

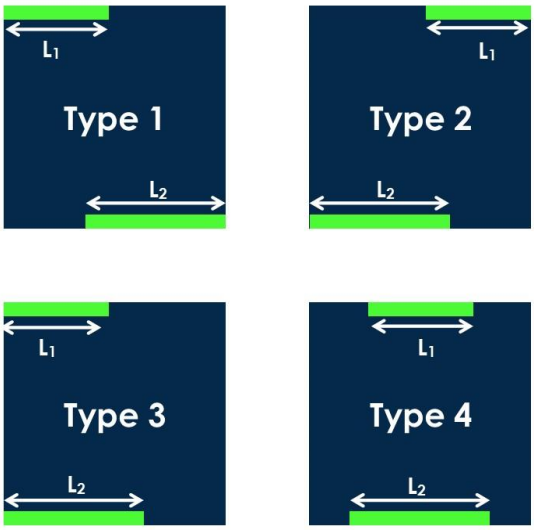

1023/1151 ©2022 Keramati et al. doi:10.5075/epfl-298799_978-2-9701614-0-0 published under CC BY-NC 4.0 license

Figure 2 Race-tracking scenarios for classification

By using the mentioned method, five experimental tests were carried out. One test for each scenario. For permeability calculation, *test 1* as a reference test was considered. You can see the geometrical properties of each experimental test in *Table 1*:

Table 1 RT Experimental tests for classifier validation

	RT Type	L1(cm)	L2(cm)
Test1	RT0	0	0
Test2	RT1	7.5	15
Test3	RT2	15	7.5
Test4	RT3	7.5	22.5
Test5	RT4	15	7.5

1. Numerical method

Open-Foam (Open source Field Operation And Manipulation), a free, open-source computational fluid dynamics (CFD) software, is used to calculate the flow evolution. In this case, an interFoam solver was employed for two-phase incompressible, isotherm, and immiscible fluids. The geometry of the model corresponds to a fabric of 300mm ×300mm ×3mm divided into 50 ×50 ×1 cubic elements. The velocity profile of the flow in the z-direction is linear, so it's possible to assume 2D simulation and mesh in-depth only with one element. The pressure evolution in sensors' position in simulations is shown in Figure 3 for one of the random normalized simulations for race-tracking *type 1* with *L1 = 7.5 cm* and *L2 = 15 cm.*

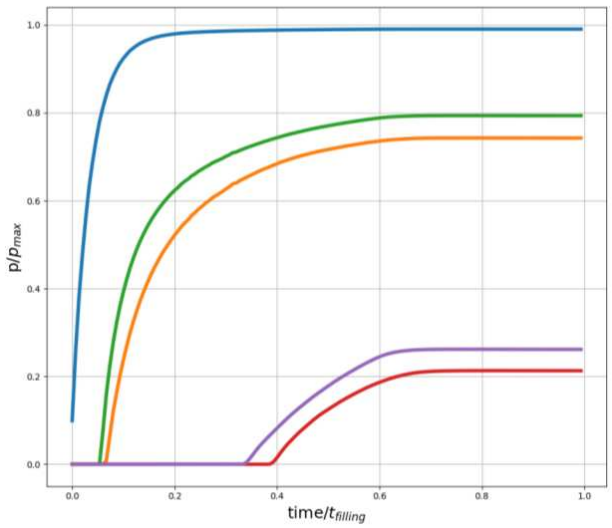

Figure 3 Pressure evolution in normalized simulation

Figure 4 shows the response of the first column of pressure sensors in the presence of race-tracking. As you can see, there is a meaningful difference between pressure evolution and the type of race-tracking. With the progress of flow front and touching the race-tracking channels,

the pressure is changing regarding the type of race-tracking, so if we can see this difference with naked eyes, the neural network models could train with this type of data-sets.

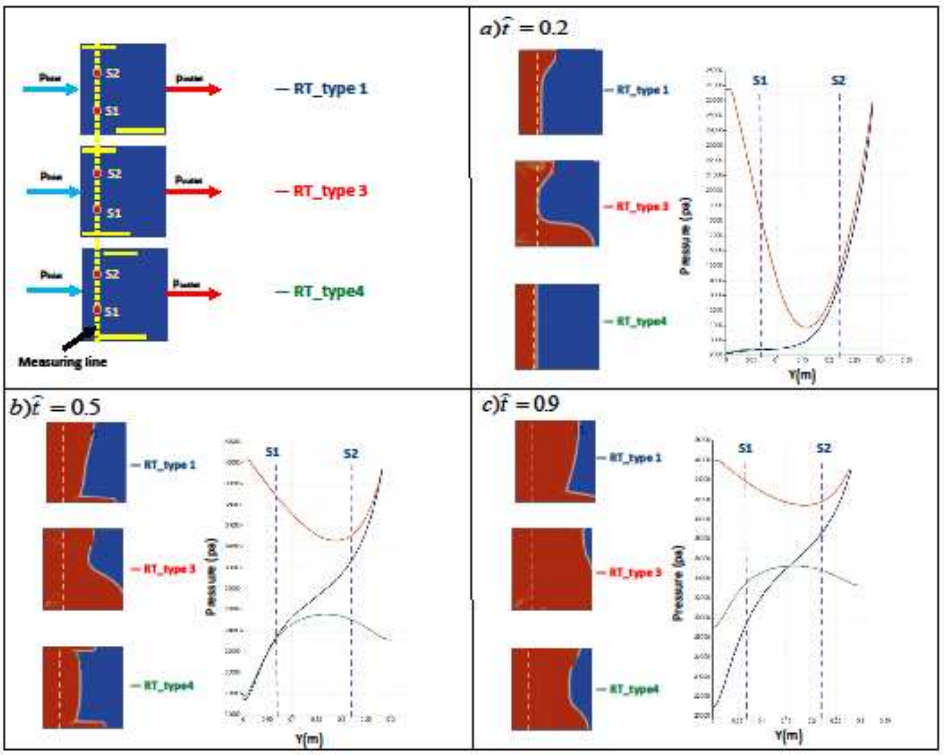

Figure 4 Race-tracking presence effect on pressure evolution at the first column of pressure sensors line and flow pattern a) pressure evolution and flow pattern at $\hat{t} = 0.2$, b) pressure evolution and flow pattern at $\hat{t} = 0.5$, c) pressure evolution and flow pattern in $\hat{t} = 0.9$

3. Result and Discussion

3.1 Neural Network training process

In the training of deep learning models, to have a generalized model, the prediction accuracy should be considered, and the classification prediction probability must be taken into account.

The cross-entropy error is chosen as a metric to compare the ResNet and DenseNet classification accuracy. For instance, Figures 5 and 6 show the training learning rate, cross entropy, and accuracy for ResNet and DenseNet for 3000 subset sizes. The learning rate decreases in both model training processes from 0.1 to 0.001.

In Figure 5, ResNet cross-entropy plot, the minimum cross-entropy for training data is 9.52e-7, and the minimum value for validation data is 2.9e-7. The validation cross-entropy is less than the training cross-entropy.

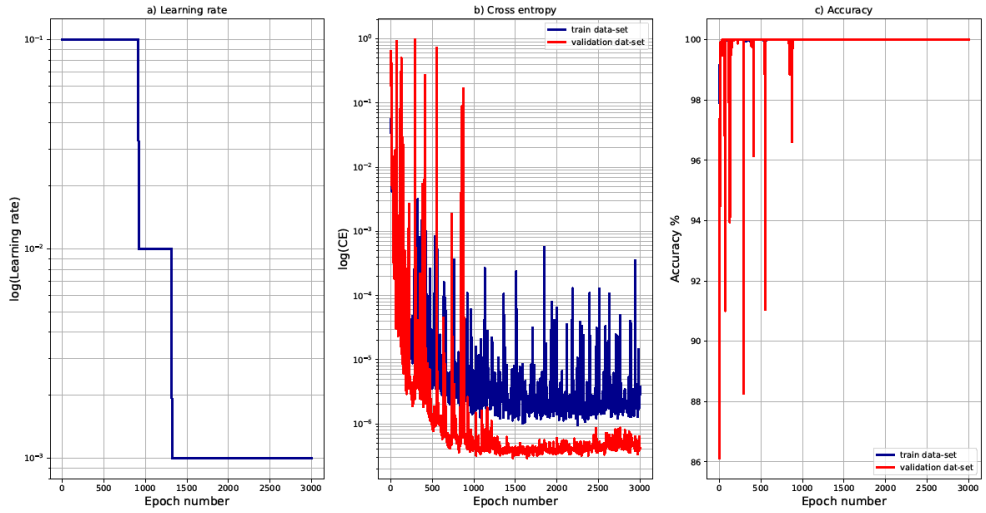

Figure 5 ResNet training curves

In Figure 6, DenseNet Cross entropy plot, The minimum cross-entropy for training data is 1.026e-5, and the minimum value for validation data is 3.031e-5. The validation data-set cross-entropy is higher than the training cross-entropy in the Densenet model.

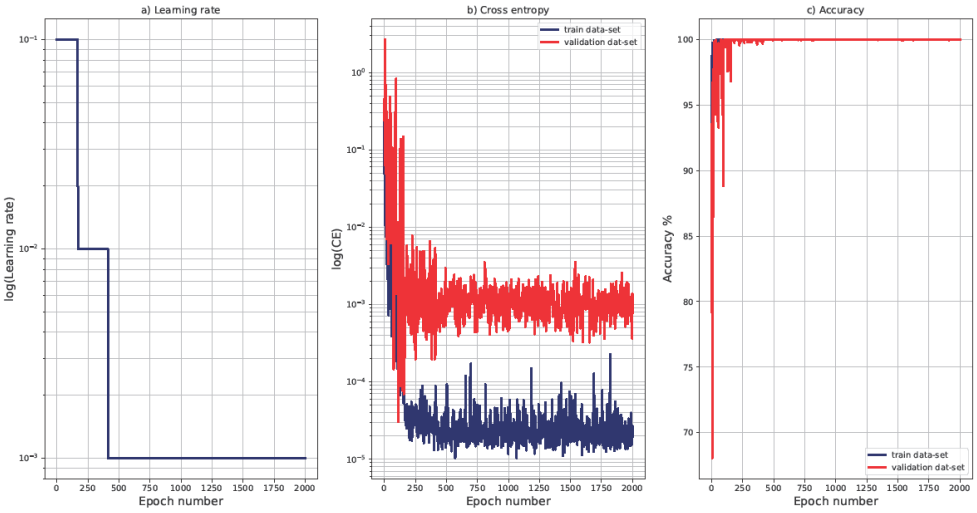

Figure 6 DenseNet training curves

The correct type prediction probability is always higher than 99 percent in both trained NN models. In the end, the accuracy of prediction in ResNet and DensNet is almost 100 percent

3.2 The compression of Cross-Entropy for different numbers of data-sets

The subset of 100, 500, 1000, 2000, and 3000 were randomly selected from the whole simulated data-set to show the dependency of CE on data-set size. As mentioned in the training prepossess, all the models were trained healthily. The correct prediction probability increases in both ResNet and DenseNet models by increasing the number of data-set. The ResNet models probability is higher than the DenseNet models in all cases. As you can see in Figure 7, the cross-entropy of the ResNet model for different number of subsets are always less than the DensNet, but we should take into account the result of experimental prediction to complete the comparison of the ML models

  doi:10.5075/epfl-298799_978-2-9701614-0-0

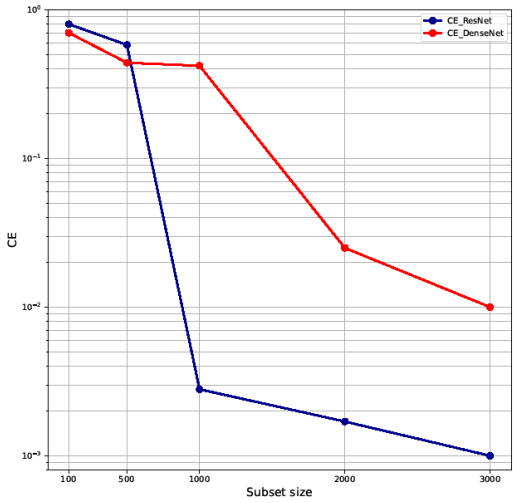

Figure 7 Compression of classification Cross-Entropy Error for ResNet and DenseNet

3.3 ResNet and DenseNet probability comparison for experiment data-set

For mentioned experimental data-set, both models are applied. The accuracy of the models for the experimental data-set is 80 percent in both ResNet and DenseNet models, but there is a difference in wrong prediction scenarios and the probability values.

In the case of ResNet, the model is predicting the scenarios *type 1*, *type 2,* and *type 4* perfectly, and the probability is almost 1. The model couldn't predict the *type 3* experimental test as a correct scenario. On the other hand, the correct probability of race-tracking *type 0* is 0.77, which means that even by predicting this test as a type 0, there is a conflict with other scenarios.

In the DenseNet prediction, the model could predict all experimental tests with a probability of almost 1 except *type 0*. The model predicted a *type 0* experimental test as a *type 4* scenario.

4. References

1. Advani, S. G., & Hsiao, K.-T. (2012). Introduction to composites and manufacturing processes. Introduction to composites and manufacturing processes, 1-12. Elsevier. doi:10.1533/9780857096258.1.1

2. Bickerton, S. (1999, November). Characterization and modeling of race-tracking in liquidcomposite molding processes. Composites Science and Technology, 59(15), 2215-2229. doi:10.1016/S0266-3538(99)00077-9

3. Bock, F. E., Aydin, R. C., Cyron, C. J., Huber, N., Kalidindi, S. R., & Klusemann, B. (2019, May). A Review of the Application of Machine Learning and Data Mining Approaches in Continuum Materials Mechanics. Frontiers in Materials, 6. doi:10.3389/fmats.2019.00110

4. Brunton, S. L., Noack, B. R., & Koumoutsakos, P. (2020, January). Machine Learning for Fluid Mechanics. Annual Review of Fluid Mechanics, 52(1), 477-508. doi:10.1146/annurev-fluid-010719-060214

5. Devillard, M., Hsiao, K.-T., Gokce, A., & Advani, S. G. (2003, September). Online Characterization of Bulk Permeability and Race-Tracking During the Filling Stage in Resin Transfer Molding Process. Journal of Composite Materials, 37(17), 1525-1541. doi:10.1177/0021998303034459

6. Fratta, C. D., Klunker, F., & Ermanni, P. (2013, April). A methodology for flow-front estimation in LCM processes based on pressure sensors. Composites Part A: Applied Science and Manufacturing, 47, 1-11. doi:10.1016/j.compositesa.2012.11.008

7. Fratta, C. D., Koutsoukis, G., Klunker, F., & Ermanni, P. (2016, September). Fast method to monitor the flow front and control injection parameters in resin transfer molding using pressure sensors. Journal of Composite Materials, 50(21), 2941-2957. doi:10.1177/0021998315614994

8. Lawrence, J. M., Hsiao, K.-T., Don, R. C., Simacek, P., Estrada, G., Sozer, E. M., . . . Advani, S. G. (2002, July). An approach to couple mold design and online control to manufacture complex composite parts by resin transfer molding. Composites Part A: Applied Science and Manufacturing, 33(7), 981-990. doi:10.1016/S1359-835X(02)00043-X

9. Meng, L., McWilliams, B., Jarosinski, W., Park, H.-Y., Jung, Y.-G., Lee, J., & Zhang, J. (2020, June). Machine Learning in Additive Manufacturing: A Review. JOM, 72(6), 2363-2377. doi:10.1007/s11837-020-04155-y

10. Rudd, C. D., Long, A. C., Kendall, K. N., & Mangin, C. G. (1997). 1 - Introduction to liquid composite moulding. 1 - Introduction to liquid composite moulding, 1-37. (C. D. Rudd, A. C. Long, K. N. Kendall, & C. G. Mangin, Eds.) Woodhead Publishing. doi:https://doi.org/10.1533/9781845695446.1

11. Siddig, N. A., Binetruy, C., Syerko, E., Simacek, P., & Advani, S. (2018, December). A new methodology for race-tracking detection and criticality in resin transfer molding process using pressure sensors. Journal of Composite Materials, 52(29), 4087-4103. doi:10.1177/0021998318774829

12. Wang, J., Fu, P., & Gao, R. X. (2019, April). Machine vision intelligence for product defect inspection based on deep learning and Hough transform. Journal of Manufacturing Systems, 51, 52-60. doi:10.1016/j.jmsy.2019.03.002

USING LIGHT TO STEER THE RESIN FLOW IN LIQUID COMPOSITE MOULDING PROCESSES

Andreas Endruweit[a], Mikhail Matveev[a], Mikhail Tretyakov[b]

a: Composites Research Group, Faculty of Engineering, University of Nottingham, UK – andreas.endruweit@nottingham.ac.uk
b: School of Mathematical Sciences, University of Nottingham, UK

Abstract: *A Vacuum Infusion process was implemented to produce composite specimens from a random glass filament mat and an acrylic modified polyester resin curable upon irradiation with ultraviolet (UV) light. Through localised irradiation with UV light during the reinforcement impregnation, the viscosity of the flowing resin was increased selectively. This allowed converging-diverging flow patterns with defined inclusions to be realised and racetracking along reinforcement edges to be suppressed. The approach is based on radical photopolymerisation, where the degree of cure and the viscosity of the resin increase under direct irradiation, such that the resin gels and the flow stalls in a matter of seconds. They remain unchanged in areas covered with an opaque mask. While this study is concerned with the feasibility of the process, potential practical applications are in flow control for Liquid Composite Moulding, i.e. compensation for local variations in the fibre volume fraction and permeability of reinforcements.*

Keywords: Liquid Composite Moulding; Resin flow; Viscosity; Photopolymerisation

1. Introduction

In Liquid Composites Moulding (LCM) processes, long-range flow develops during the impregnation of the dry fibrous reinforcement with a liquid resin system. The resin flow front, which separates the dry from the impregnated part of the reinforcement, propagates at a velocity

$$\mathbf{v}_f = -\frac{\mathbf{K}}{\Phi\,\eta} \cdot \nabla p \,. \tag{1}$$

Here, $\mathbf{K}$ describes the (directional) permeability of the reinforcement, Φ is the porosity of the reinforcement, η is the viscosity of the resin, and ∇p is the gradient in fluid pressure. The porosity is related to the fibre volume fraction, V_f, through

$$\Phi = 1 - V_f . \tag{2}$$

The permeability is a function of the porosity. It depends also on the fibre arrangement in the reinforcement. The flow front propagation determines the quality of the component (in terms of complete reinforcement impregnation) and the process cycle time.

Local variability in Φ and $\mathbf{K}$, particularly related to edge flow (racetracking) [1], reinforcement forming (drape) [2] or stochastic variability in the reinforcement structure [3], can result in irregular resin flow patterns. As this may lead to the formation of dry spots, particularly if a low-permeability zone is surrounded by high-permeability zones, in-process control of the flow front

  doi:10.5075/epfl-298799_978-2-9701614-0-0

propagation can be implemented to prevent the potential formation of defects in the composite.

While different approaches for process control in LCM have been proposed, based on control of the pressure gradient [4] or the local fibre volume fraction [5], Eq. (1) implies that local variations in $\mathbf{K}/\Phi$ can be compensated for by varying η locally by the same factor. Reducing the resin viscosity through localised temperature control has been discussed [6]. A problem with this approach is that heat conduction in the composite and in the tooling makes it difficult to control the resin temperature and viscosity locally. Increasing the temperature to reduce the viscosity also results in an increased curing rate, i.e. a faster increase in resin viscosity, which limits the time window for the flow process. Other resin systems cure when exposed to ultraviolet (UV) light, but not when heated. These resins can be cured locally to increase the viscosity where they are exposed to UV light and kept uncured where they are shielded from irradiation [7]. On the other hand, the temperature can be increased (globally) to reduce the viscosity without inducing the curing process.

In the work presented here, the feasibility of controlling the resin flow front propagation through localised UV irradiation and local manipulation of the resin viscosity is assessed experimentally for a LCM process combined with UV curing.

2. Theory

Most UV-curable resins are based on acrylates, which undergo free radical polymerisation [8]. In this polymerisation mechanism, a photoinitiator, which is added to the base resin, is decomposed to produce free radicals upon irradiation with UV light. This initiates a chain growing reaction, which ceases as soon as the irradiation stops. Hence, the resin cures only under direct UV irradiation and remains uncured in the shadow.

Unlike in thermosetting resins, it is possible to completely separate the reinforcement impregnation and the resin cure. This can be an advantage, particularly in LCM processes. As long as the resin is not exposed to UV light during impregnation of the reinforcement, the degree of cure (i.e. the viscosity) does not increase, and the resin does not gel prematurely. Once the reinforcement is completely impregnated, the resin can be irradiated and cured in a second step. Without affecting the degree of cure, the resin can be heated to reduce the viscosity during processing and to aid the impregnation of the reinforcement.

The degree of cure of a UV-curable resin system increases with radiant exposure, i.e. the total radiant energy incident on a surface per unit area. This is the product of the irradiance, i.e. the radiant power incident on a surface per unit area, and the irradiation time (assuming that the irradiance is constant). This means that the degree of cure depends on the light source, which determines the radiant power, and increases with time.

In LCM processes, the pressure-driven flow of a UV-curable resin under UV irradiation can be described by substituting a relation for the dependence of the viscosity on the degree of cure and on the temperature in Eq. (1). If the irradiance and the temperature are given, the degree of cure and the viscosity of the flowing resin do not only depend on the time but also on the position. Hence, the resulting equation needs to be solved numerically to determine the flow front propagation. It can be shown that the lengths covered by the moving flow front before the resin gels

  doi:10.5075/epfl-298799_978-2-9701614-0-0

- decreases if the pressure gradient driving flow in the given time prior to gelation is reduced;
- decreases if the irradiance is increased, i.e. the time to gelation is reduced;
- increases if the temperature is increased, i.e. the initial viscosity is decreased.

3. Materials and methods

A Vacuum Infusion (VI) process was implemented to impregnate a continuous glass filament mat with random fibre orientation (Unifilo) and a measured superficial density of approximately $220\ \mathrm{g/m^2}$ with a commercial UV-curable resin (Solarez acrylic modified polyester). Unless stated otherwise, reinforcement specimens were rectangular with a length, l, of $280\ \mathrm{mm}$ and a width, w, of $115\ \mathrm{mm}$, and consisted of 6 layers of the glass fibre mat. To obtain uni-directional flow, a linear resin inlet and a linear vent were created by placing polypropylene flow mesh along the short edges of the specimens. A nylon film with $50\ \mu\mathrm{m}$ thickness was used as vacuum bag. No flow medium (and peel ply) was used on top of the reinforcement in the vacuum bag lay-up.

For UV curing, a $400\ \mathrm{W}$ flood light (Dymax 2000 PC) with a metal halide "D" bulb was used. Major emission peaks of the bulb lie at wavelengths of approximately $365\ \mathrm{nm}$ and $440\ \mathrm{nm}$, i.e. in the UV-A and visible blue range of the electromagnetic spectrum. The irradiance on the specimen surface was adjusted by setting the distance from the light source (Beer-Lambert law).

In infusion experiments with selective local irradiation, masks cut from corrugated cardboard were placed on the surface of the vacuum bag to shield defined areas from UV light. To avoid curing of resin in the feed line and vacuum line during the infusion process, both were wrapped in aluminium foil. To stop an infusion, the feed line was clamped off, and the cardboard mask was removed so that the resin was cured everywhere in the impregnated part of the reinforcement.

In preparation of the infusion experiments, the irradiance in a plane corresponding to the surface of the vacuum bag was measured in the UV-A band, using a UV201-UVA Radiometer (Macam Photometrics Ltd.). In addition, the UV light transmission of all materials used in the infusion experiments was measured [9]. Results are listed in Table 1.

Table 1: Transmission in the UV-A band, measured for different materials.

material	transmission
corrugated cardboard	0 %
aluminium foil, $10\ \mu\mathrm{m}$ thick	0 %
nylon vacuum bag, $50\ \mu\mathrm{m}$ thick	82 %
polypropylene flow mesh, 4 layers	~68 %
glass filament mat, 6 layers, impregnated with resin and compacted in vacuum bag	< 1 %
glass filament mat, 1 layer, dry, not compacted	20 % - 33 %

  doi:10.5075/epfl-298799_978-2-9701614-0-0

For the reinforcement, the dependence of the fibre volume fraction on the compaction pressure and the dependence of the permeability on the fibre volume fraction were characterised. This allows the fibre volume fraction ($V_f = 0.23$) and the permeability ($K = 8\times10^{-10}$ m^2) to be estimated for a specimen compacted in a vacuum bag (at a compaction pressure of 10^5 Pa).

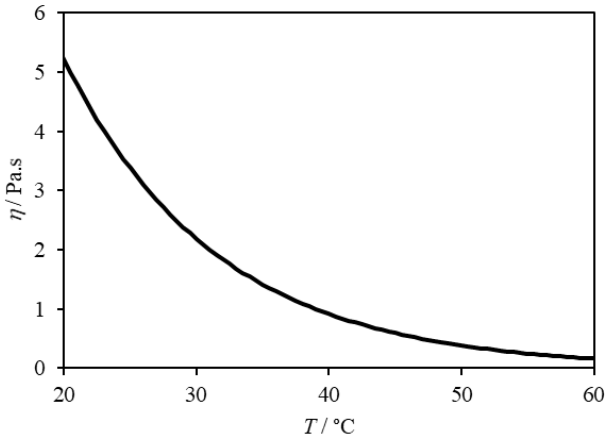

Figure 1. Viscosity, η, as a function of the resin temperature, T, for uncured resin.

The viscosity of the uncured resin was measured as a function of the temperature (Figure 1) using a Brookfield viscometer (DV II+). The viscosity at room temperature is in the order of 5 Pa.s, which means that this specific resin would need to be heated for use in VI processes, as otherwise fill times would be infeasibly long for practical application. The viscosity could not be measured as a function of the radiant exposure (at constant temperature), as the degree of cure will not be uniform in a larger volume of irradiated resin as required for the viscometry.

As an upper limit to the flow time at given irradiance, the time for the resin to gel was estimated. For different radiant exposures, the Barcol hardness (ASTM D2583) was measured on the top (directly exposed to irradiation) and bottom surface of the specimen. The results show that cure is faster on the top surface than on the bottom surface of the specimen, because light transmission through the impregnated reinforcement is limited. On the top surface, the resin gels after approximately 9 s of irradiation. On the bottom surface, the time for the resin to gel was estimated as 19 s.

4. Results

4.1 Reference experiments

VI experiments were conducted with no UV irradiation (i.e. the viscosity did not change during the infusion) at temperatures of 22 °C and 43 °C. The times for complete impregnation of the reinforcement were approximately 1440 s and 320 s, respectively.

The viscosity of the uncured resin is approximately 4.4 Pa.s at T = 22 °C and 0.7 Pa.s at T = 43 °C (Figure 1). Using the values Φ = 0.77, K = 8×10^{-10} m^2, Δp = 10^5 Pa and l = 0.28 m, and the analytical solution of the uni-directional flow problem,

$$t = \frac{\Phi\,\eta}{2K\Delta p}\,l^2, \tag{3}$$

fill times of 1660 s and 264 s can be calculated for the two temperatures. Relative differences between calculated and experimental fill times for both temperatures are smaller than 20 %.

  doi:10.5075/epfl-298799_978-2-9701614-0-0

Considering that the process parameters can only be controlled with limited accuracy in VI, this indicates that the results from the infusion experiments are consistent with the measured dependence of the resin viscosity on the temperature.

4.2 Combination of temperature and cure effects

Infusions were conducted at two temperatures with localised UV irradiation. Here, the specimens were rectangular with dimensions $140\ \text{mm} \times 115\ \text{mm}$. The infusion set-up was the same as described in Section 3. A cardboard mask was used to cover the surface of the reinforcement specimens in three rectangular areas with different lengths, separated by rectangular gaps where the reinforcement was exposed to irradiation. The measured resin temperatures for the experiments were $T = 20\ °\text{C}$ and $T = 43\ °\text{C}$.

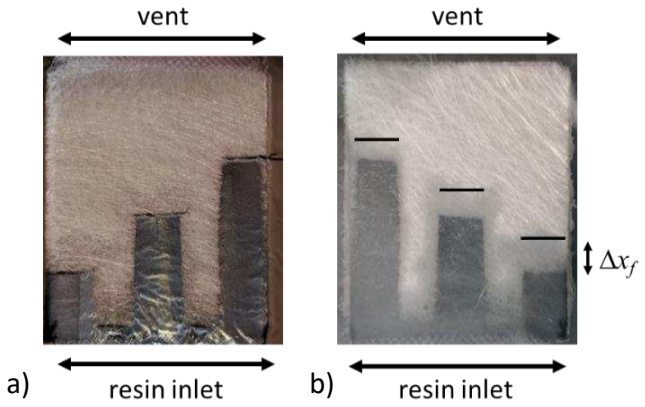

Figure 2. VI experiments with UV irradiation; reinforcement covered with a mask; a) impregnated specimen after removal of mask (top surface); b) impregnated specimen after removal of mask (bottom surface).

Table 2: Flow lengths in irradiated part of the specimen for different mask lengths and different infusion temperatures, T.

length of mask / mm	Δx_f / mm	
	$T = 20\ °\text{C}$	$T = 43\ °\text{C}$
30	20	32
60	17	32
90	10	25

At both infusion temperatures, the flow front does not propagate beyond the edges of the mask on the top surface of the irradiated area, where the flowing resin gels fast (shown in Figure 2a for $T = 20\ °\text{C}$). On the bottom surface, resin gelation is delayed because of the limited UV transmission through the reinforcement (Table 1). Hence, the resin can flow beyond the edges of the mask before it gels (Figure 2b). The flow length in the irradiated part of the specimen, Δx_f, was measured for each covered rectangular area (Table 2) as a measure for the accuracy of controlling the flow front propagation. The values of Δx_f decrease (i.e. the accuracy increases)

1033/1151 ©2022 Endruweit et al. doi:10.5075/epfl-298799_978-2-9701614-0-0 published under CC BY-NC 4.0 license

with increasing length of the masked area, as the effective pressure drop at the edge of the mask decreases with increasing distance from the resin inlet. The values increase (i.e. the accuracy decreases) with increasing temperature, which corresponds to a longer time for gelation.

4.3 Racetracking

Infusion experiments with racetracking were carried out at room temperature. Unlike in the reference experiments, a channel with a width of approximately $10\ \mathrm{mm}$ was created along one long edge of the reinforcement using 4 layers of flow mesh.

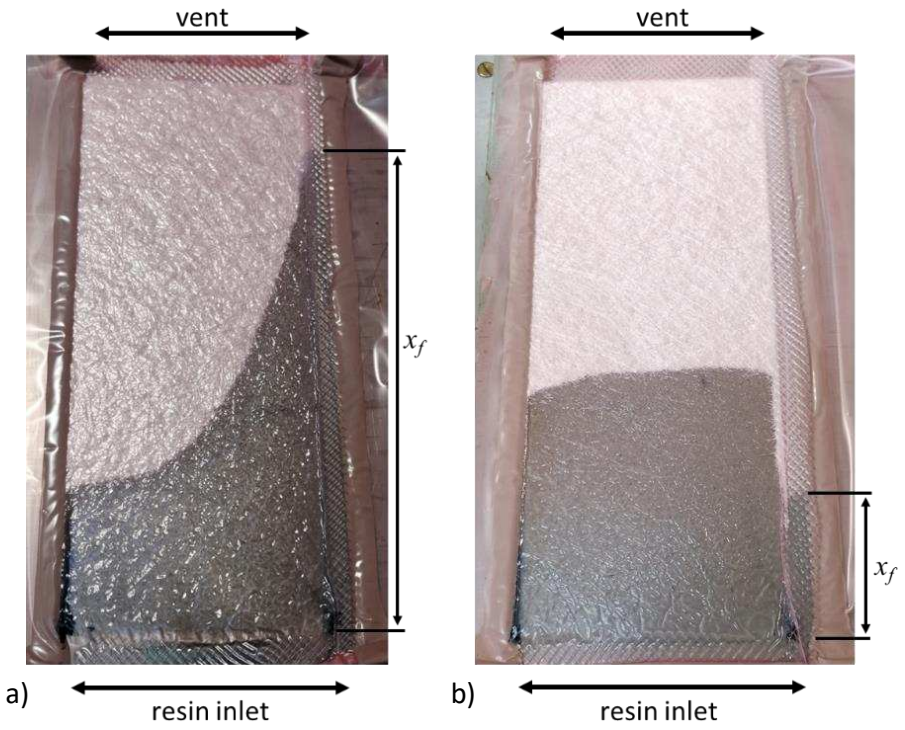

Figure 3. Vacuum infusion experiments with racetracking; a) no UV irradiation; b) UV irradiation on racetracking channel only.

Without UV irradiation, the resin flow front propagates faster in the channel than in the reinforcement, as the permeability of the flow mesh is greater than the permeability of the reinforcement (racetracking). As a result, a transverse pressure gradient develops which results in a curved flow front shape (Figure 3a). Using the same set-up, infusion with UV irradiation was studied. The reinforcement was covered with a cardboard mask, such that only the channel was exposed to irradiation. After an infusion time of 5 minutes, the flow front position in the channel is $74\ \mathrm{mm}$ (from the resin inlet), while the flow front position in the reinforcement is $135\ \mathrm{mm}$ (Figure 3b). The flow front shape in the reinforcement is not affected by flow in the channel, indicating that the flow in the channel is separated from the flow impregnating the reinforcement. It can be concluded that suppressing racetracking by stopping flow in the channel through the change in viscosity and gelation is feasible.

4.4 Different flow patterns

Infusions were carried out at room temperature, using the same geometry as in the reference experiments.

  doi:10.5075/epfl-298799_978-2-9701614-0-0

- For one example, the reinforcement was covered with a cardboard mask with a triangular cut-out. Only a triangular area along the right edge was exposed to UV light. Figure 4a shows that a converging-diverging flow develops during the infusion process.
- In a second example, a cardboard mask was used to create a narrow flow path with a rhombic inclusion along the axis of the geometry. Figure 4b shows that splitting and merging flow fronts develop during the resin infusion.

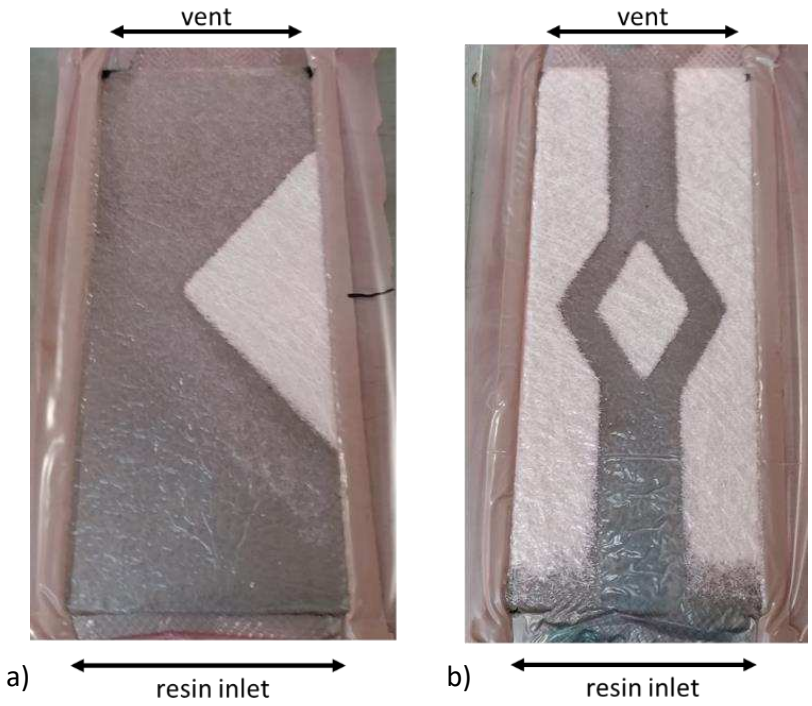

Figure 4. Vacuum infusion experiments with UV irradiation; reinforcement covered with masks; a) mask with triangular cut-out; b) mask with rhombic inclusion.

These examples show that complex flow paths can be realised using localised UV irradiation. As observed in Section 4.2, the length of penetration of resin into irradiated areas is approximately zero on the top surface of the specimens and increases through-thickness. On the bottom surface, it is longer near the resin inlet and decreases with increasing distance. This shows again that the accuracy of flow control is lower near the resin inlet and increases with increasing distance from the inlet.

5. Conclusions

Composite specimens from a random glass filament mat and a UV-curable acrylic modified polyester resin were produced in a VI process. During the reinforcement impregnation, the resin viscosity was increased selectively through localised irradiation with UV light to control the resin flow and realise different flow patterns. Here, opaque cardboard masks were used to create defined irradiation patterns. This approach is based on radical photopolymerisation, where the resin cures only under direct irradiation and remains uncured in areas covered with a mask. Hence, the viscosity of the flowing resin is constant in masked areas. It increases in areas exposed to UV light until the resin gels and the flow stalls in a matter of seconds.

Theoretical considerations show that the distance covered by the moving resin flow front in exposed areas prior to resin gelation decreases with increasing UV irradiance, decreasing

  doi:10.5075/epfl-298799_978-2-9701614-0-0

applied pressure gradient and decreasing resin temperature. In experiments, the resin flow front did not propagate beyond the boundaries of the masked areas on the top surface of the specimens. On the bottom surface, resin was observed to flow into irradiated areas. As the transmission of UV light through the impregnated glass fibre reinforcement is limited, the irradiance is lower on the bottom surface than on the top surface of a specimen. As a result, the time for resin gelation is longer and the flow front propagates further on the bottom surface than on the top surface. Because of the dependence on the pressure gradient, flow lengths in the irradiated area decrease with increasing distance from the resin inlet.

Despite the minor uncertainties in the flow patterns on the bottom surface, it was possible to steer the flow along converging-diverging paths with inclusions and to suppress racetracking along reinforcement edges. Practical applications of the process studied here could be in process control, i.e. compensation for local variations in fibre volume fraction and permeability of fibrous reinforcements. Selection of other combinations of suitable resin systems and UV light sources may help to optimise the process. Its applicability is limited by the need for UV transparency of the reinforcement and the tool. It would need to be considered in process planning that the photocuring process is irreversible.

Acknowledgements

This work was supported by the Engineering and Physical Sciences Research Council [grant number EP/P006701/1]; though the EPSRC Future Composites Manufacturing Research Hub.

6. References

1. Bickerton S, Advani SG. Characterization and modeling of race-tracking in liquid composite molding processes. Composites Science and Technology 1999; 59(15): 2215-2229.
2. Smith P, Rudd CD, Long AC. The effect of shear deformation on the processing and mechanical properties of aligned reinforcements. Composites Science and Technology 1997; 57(3): 327-344.
3. Endruweit A, Zeng X, Long AC. Multiscale modeling of combined deterministic and stochastic fabric non-uniformity for realistic resin injection simulation. Advanced Manufacturing: Polymer and Composites Science 2015; 1(1): 3-15.
4. Modi D, Correia N, Johnson M, Long A, Rudd C, Robitaille F. Active control of the vacuum infusion process. Composites Part A: Applied Science and Manufacturing 2007; 38(5): 1271–1287.
5. Alms JB, Advani SG, Glancey JL. Liquid Composite Molding control methodologies using Vacuum Induced Preform Relaxation. Composites Part A: Applied Science and Manufacturing 2011; 42(1): 57-65.
6. Johnson RJ, Pitchumani R. Enhancement of flow in VARTM using localized induction heating. Composites Science and Technology 2003; 63(15): 2201–2215.
7. Endruweit A, Johnson MS, Long AC. Curing of composite components by ultraviolet radiation: A review. Polymer Composites 2006; 27(2): 119–128.
8. Green AW. Industrial Photoinitiators - A Technical Guide. CRC Press. 2010.
9. Endruweit A, Ruijter W, Johnson MS, Long AC. Transmission of ultraviolet light through reinforcement fabrics and its effect on ultraviolet curing of composite laminates. Polymer Composites 2008; 29(7): 818–829.

  doi:10.5075/epfl-298799_978-2-9701614-0-0

PROCESS MONITORING USING LIQUID THERMOPLASTIC RESIN AND 2D NANOMATERIAL-BASED FABRIC SENSORS

Tayyab Khan[a], Muhammad Shafiq Irfan[a], Muhammad Abdullah Ali[a], Kamran Ahmed Khan[a], Kin Liao[a], Rehan Umer[a]

a: Department of Aerospace Engineering, Khalifa University of Science and Technology, Abu Dhabi, UAE.

Abstract: *In this study, an online and in-situ process monitoring system based on graphene-coated glass fabric sensors was developed to monitor different stages of Vacuum-Assisted Resin Transfer Molding (VARTM) process for liquid thermoplastic resin (Elium®)/glass fiber composites. The nanomaterial was coated on the glass fabrics via solution coating method. The coated glass fabric sensors were embedded at different locations within the laminate in the form of strips. The piezoresistive changes in the smart sensors were monitored and resultant electrical resistance was continuously recorded using a multichannel Data Acquisition system. The relative change in the overall resistance of the sensors was utilized to successfully monitor various steps during the VARTM process including the reinforcement compaction response under vacuum, resin impregnation and resin gelation and cure. It was found that the coating quality, dimensions and spatial position of the sensors within the laminate influenced the sensor performance.*

Keywords: Process monitoring; Graphene Oxide; Resin Infusion; Smart Sensors; Thermoplastics.

1. Introduction

Fiber-reinforced polymer (FRP) composites are commonly used in multiple industries such as aerospace, automotive, marine, construction, wind energy, etc. owing to their high strength-to-weight ratio, load-bearing capacity, lightweight and corrosion resistance (1–3).Among different composite manufacturing techniques, VARTM is one of the most cos-effective liquid composite molding (LCM) techniques suitable for manufacturing large composite structures with complex geometries(4). Typically in a VARTM or resin infusion process, a low viscosity thermoset resin is injected into the fabric preform covered with a flexible vacuum bag. It has been well-established that the flexibility of the vacuum bag leads to pressure and thickness variation throughout the mold during VARTM manufacturing. Consequently, the dimensions and the quality of the composite parts manufactured through the VARTM process are not very consistent (5,6).

There has been significant research in recent years on monitoring and mitigating the process-induced defects encountered during the VARTM manufacturing process through timely detection by using different kinds of process-monitoring sensors. Timely detection of the undesirable flow provides an opportunity for altering the inlet and outlet conditions to control the flow pattern. As a result, these process-induced defects such as dry spots and unsaturated regions can be eliminated during the early stages of the infusion cycle and can further ensure process optimization, faster production rates and high-quality end products.

In recent years, highly piezoresistive carbon nanomaterial coated fabrics have emerged as one of the most promising alternatives to conventional sensors such as fiber-optic sensors, dielectric

  doi:10.5075/epfl-298799_978-2-9701614-0-0

sensors and fiber Bragg grating (FBG) sensors. These carbon-coated fabric sensors are capable of self-sensing, in-situ continuous process monitoring and quantifying health states by virtue of excellent mechanical robustness and structural non-invasiveness. Based on their superior electrical properties, carbon-based nanomaterials such as graphene and carbon nanotubes form an interconnected conductive network once deposited on the fibers. Any external stimulus such as pressure, force, heat, resin flow, etc. causes a disruption in this conductive path, triggering a change in the overall resistance of the sensors.

In this study, graphene-coated piezo-resistive fabrics were used as sensors for process monitoring of composites based on liquid thermoplastic resin (Elium®) by conducting a number of well-defined experiments. Multiple sensor strips of graphene-coated piezo-resistive glass fabrics were used as sensors. The experiments were conducted in a VARTM setup with a multilayer 2D glass fabric. The sensing strips were placed transverse to the flow direction and were electrically connected to a DAQ system for continuous resistance measurement. These sensors were then used to monitor the entire infusion cycle in terms of compaction response, resin flow detection and cure monitoring.

2. Materials and methods

2.1 Materials

Plain weave E-glass fabrics, supplied by Gurit®, UK with an areal weight of 202 g/m^2 were used as the substrate material as well as the reinforcement material for manufacturing the composite laminate. The sensors were prepared by coating reduced graphene oxide (rGO) on rectangular glass fabric strips having an area of 100 × 250 mm^2. The novel infusible thermoplastic resin i.e. Elium® 188-O supplied by ARKEMA, China, was used as resin for manufacturing the composites. As per manufacturer's advice, 2 wt.% Luperox® ATC50 benzoyl per oxide, supplied by Sigma Corporation, USA was used as an initiator for the polymerization of the thermoplastic resin.

2.2 Methods

2.2.1 Resin flow and cure monitoring

The thermoplastic based composite laminates consisted of 8 fabric layers having an area of 100 × 250 mm^2. Three sets of rectangular rGO coated sensors (top, middle and bottom), having an area of 10 × 100 mm^2, were placed at five different equidistant locations throughout the mold from the inlet to the outlet. The arrangement of the sensors within the fabric layer is shown in Figure 1. The fabric sensors were connected from both ends using electrical wires and adhesive copper tape. The Keysight DAQ970A data acquisition (DAQ) system was utilized to continuously measure and record the resistance of the sensors throughout the infusion process. The acquired data was then exported for post processing. During the post processing, the relative change in resistance (%$\Delta R/R_0$) was used as a measure of the piezoresistivity of the fabric sensors. The relative change was calculated by the following formula:

$$\%\frac{\Delta R}{R_0} = \left(\frac{R-R_0}{R_0}\right) \times 100 \quad (1)$$

where R_0 is the initial reference resistance at the start of the experiment and R is the instantaneous resistance.

  doi:10.5075/epfl-298799_978-2-9701614-0-0

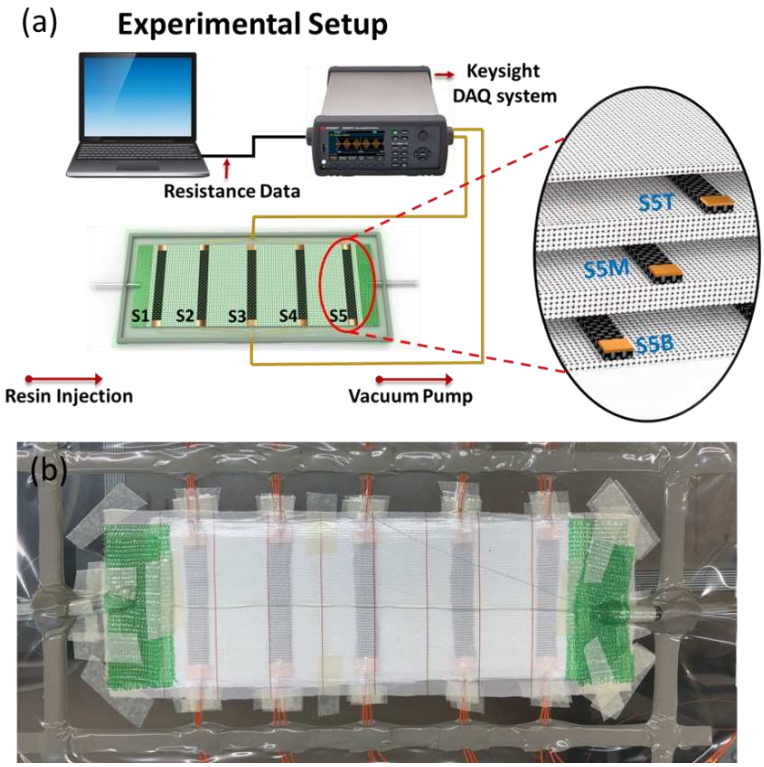

Figure 1. (a) Schematic illustration of the infusion setup, data acquisition setup and graphene coated sensor layout, and (b) experimental setup for resin infusion.

2.2.2 Vacuum compaction

In order to investigate the sensitivity and accuracy of the fabric sensors, the preform was subjected to cyclic compaction experiments within the resin infusion mold using vacuum. The primary purpose of the compaction tests was to calculate the resistance values corresponding to the vacuum levels in an actual infusion cycle. Once the preform containing the sensors was covered by the vacuum bag, the mold was carefully sealed and the inlet pipe was clamped. Full (100%) vacuum was created instantaneously by opening the outlet valve while keeping the inlet pipe clamped. The pressure inside the mold cavity was kept constant for 2 minutes and then the vacuum was released through the release valve and outlet valve was simultaneously closed to reduce the pressure inside the mold cavity to atmospheric level (0% vacuum). The resistance values from all the sensors were observed for another 2 minutes and the compaction test was repeated 5 times.

2.2.3 Infusion, cure and post-cure

The compacted fabric preform with the sensors was infused with the thermoplastic resin by unclamping the inlet pipe and allowing the resin to completely fill the mold cavity. The vacuum pressure was monitored throughout the infusion cycle using a pressure gauge attached to the vacuum pump. Once steady-state pressure was achieved, the vacuum pump was turned on and the infusion process was started. A flow mesh was used at both ends of the infusion setup to ensure uniform flow front pattern and resin distribution through all the sensors placed at different locations of the preform. The entire process was continuously monitored by measuring the resistance of all the sensors.

  doi:10.5075/epfl-298799_978-2-9701614-0-0

3. Results and discussion

The response of all the sensors in terms of electrical resistances was recorded during the vacuum compaction, resin flow and curing stages. All these stages were analyzed in terms of relative changes in the resistances of the sensors. Only the results for the middle layer sensors during compaction, infusion and curing stages are presented here in detail as similar trends were observed for top and bottom plies as well.

3.1. Vacuum compaction

The compaction results for five consecutive cyclic loading and unloading cycles for all the middle ply sensors i.e., S1M-S5M are shown in Figure 2. It can be observed that the relative resistance of all sensors returned to the same value in the fully compacted state at the end of each loading cycle. No major differences in terms of the overall resistance values was observed for different cycles in the fully compacted state. However, the resistance values showed a minor variation at the end of each unloading cycle, especially after the first cycle due to permanent deformation. These differences in the unloaded state can also be due to the relaxation of the fabrics. It is also important to note that even though cyclic compaction from atmospheric pressure to 100% vacuum or vice versa is an abrupt phenomenon, the inlet and the outlet sensors were highly sensitive to record a clear lag in the response during both loading and unloading conditions.

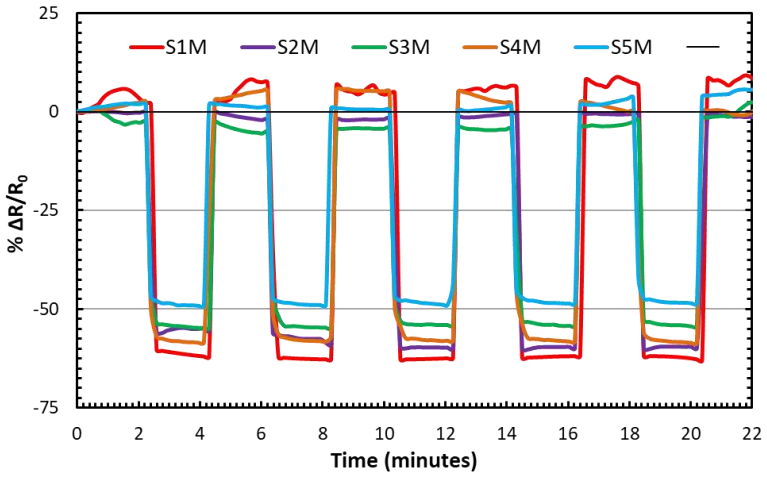

Figure 2. Relative change in the resistance of the middle sensors during cyclic compaction.

3.2. Resin flow monitoring

During resin infusion, the fluid pressure also contributes to the piezo-resistive response of the sensors in addition to the vacuum compaction and resin conductivity. As demonstrated in the previous section, the vacuum compaction enhances the piezoresistivity of the fabric sensors. On the contrary, the fluid pressure increases the resistance since the fluid pressure and fiber preform follow Terzaghi's principal (7) and resist the stress caused by vacuum compaction. Therefore, the effective stress on the fibrous medium is reduced due to spring back effect, disrupting the conductive paths formed at higher stress. The overall resistance change is determined by the most dominant of these two stimuli (i.e., conductivity of the resin or the effective stress).

The relative change in resistance during the resin infusion process only showed only two distinct responses of the sensors, (i) instantaneous drop in resistance of all sensors as the Elium® resin

  doi:10.5075/epfl-298799_978-2-9701614-0-0

made initial contact with the sensors, and (ii) a sharp rise in resistance at the inlet sensors only due to spring-back effect. Once Elium® resin was injected, it was observed that all the sensors (S1M-S5M), including the top and bottom ply sensors at the inlet (S1T and S1B), exhibited a sharp decrease in resistance value at initial contact with Elium® resin. This sharp decrease represents the location of the resin flow front as it makes its initial contact with the coated fabrics. After that, a sharp rise in resistance of the inlet sensors was observed due to pressure build up and the rise in the vacuum bag at the inlet (8). It was observed that the conductivity of the thermoplastic resin was more dominant during the resin flow and overshadowed the spring-back effect and the sensors exhibited a steady response in terms of relative resistance and post-filling phase i.e. after clamping the injection line after approximately 20 minutes of infusion. Nevertheless, the initial drop in resistance due to contact with Elium® resin corresponds to the flow front location, as shown in Figure 3.

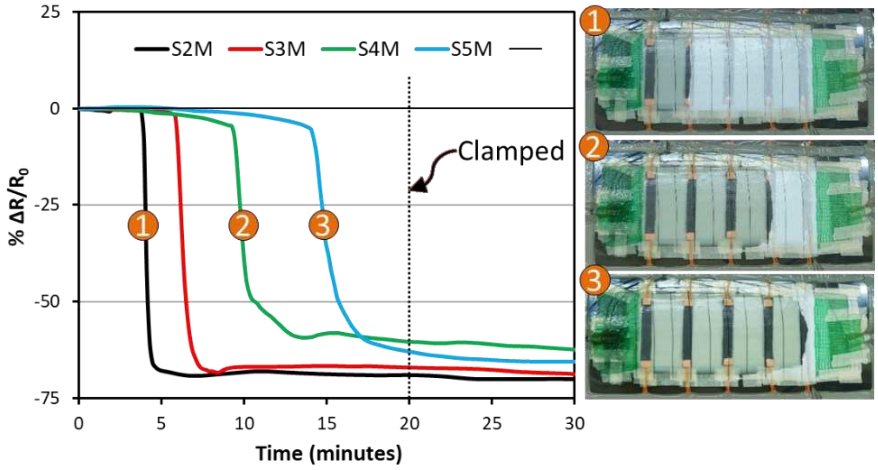

Figure 3. Time vs. percent resistance change during thermoplastic resin flow at the middle and end sensors along with photographs of the resin flow front.

As the sensors in the current size were unable to detect the effect of pressure-driven flow, an additional experiment was conducted by using a wider strip of coated fabric sensor (S6). The wider sensor (S6) exhibited a very low initial resistance value (0.57 MΩ) as compared to the other sensors (in the range of 20 MΩ to 70 MΩ). The infusion process was repeated in which the wider sensor (S6) having an area of 30 × 100 mm^2 was also embedded in the top layer along with the middle sensors to detect the pressure-driven resin flow (Figure 4a).

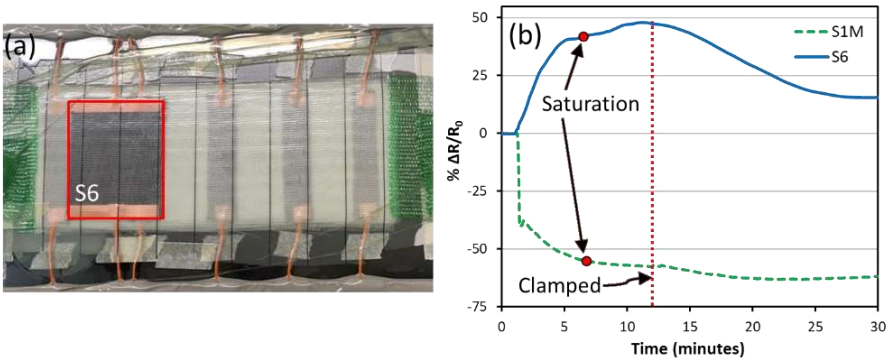

Figure 4. Time history of change in resistance during thermoplastic resin flow (a) experimental setup with wider sensor and (b) results for the inlet sensors.

  doi:10.5075/epfl-298799_978-2-9701614-0-0

The newly embedded wider sensor (S6) successfully detected the pressure-driven flow overshadowing the effect of conductivity of the Elium® resin. Figure 4 shows that the resistance of the wider sensor kept on increasing due to the pressure-driven flow and started to stabilize after clamping at around 13 minutes. Such a response is primarily attributed to the low initial resistance of the wider sensor and its high piezoresistive sensitivity compared to the other sensors.

3.3. Cure monitoring

During the post-filling stage, a sharp increase in the resistance of all the sensors was observed due to the polymerization of the thermoplastic resin. The change in relative resistance for sensors S3M and S4M during the polymerization of thermoplastic resin is demonstrated in Figure 5. It can be observed from Figure 5 that the response of the sensors kept on increasing after the post-filling stage. The bulk of the polymerization in case of the thermoplastic resin takes place within 1 – 2 hours as seen by the peak of time-rate of resistance change shown in Figure 5. However, the time-rate curve continues to stabilize for next 5 hours.

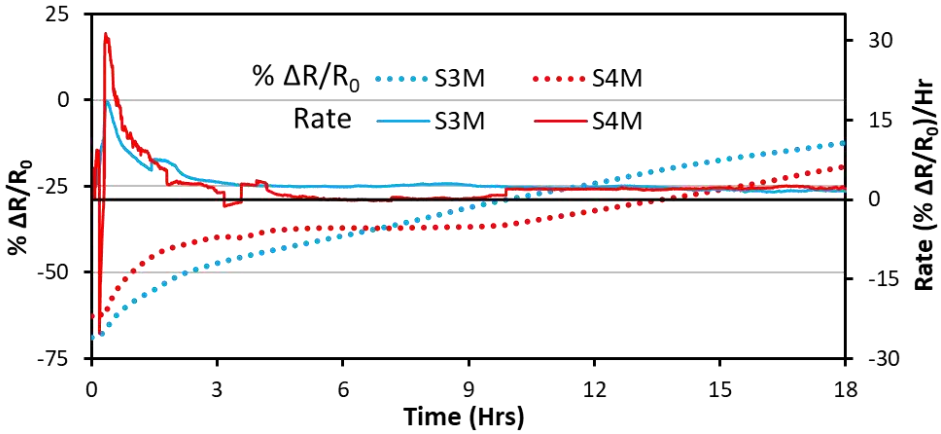

Figure 5. Time vs percent resistance change and time-rate of resistance change during polymerization of the thermoplastic resin.

4. Conclusions

In this study, rGO was coated on nonconductive glass fabric substrate to prepare highly piezoresistive sensors using the dip-coating process. These smart sensors were then utilized to monitor a comprehensive compaction response of the fabrics under vacuum by conducting multiple cyclic compaction experiments. The piezoresistive sensors were observed to be highly sensitive to accurately depict the lag between different sensors based on their locations with respect to the inlet and outlet. Similarly, it was then demonstrated that these sensors were capable of in-situ process monitoring in the resin infusion experimental setup using a novel thermoplastic resin i.e. Elium®. The on-line electrical response of the piezoresistive sensors was utilized for comprehensive process monitoring during the complete infusion cycle in terms of detecting the vacuum pressure, resin flow progression and resin phase changes during cure/polymerization. The sensors were able to precisely detect the resin flow front based on their locations. Furthermore, these smart sensors also successfully detected the pressure-induced flow, preform saturation and stabilization in the post-filling stages. As a future study, the size and the initial resistance of the fabrics can be optimized for effective results, especially in the process monitoring during the post-filling stages of the novel thermoplastic resin.

  doi:10.5075/epfl-298799_978-2-9701614-0-0

Acknowledgements:

This publication is based on work supported by the Khalifa University of Science and Technology internal grants CIRA-2020-007 and FSU-2019-08.

5. References:

1. Reis PNB, Neto MA, Amaro AM. Effect of hostile solutions on stress relaxation of carbon/epoxy composites. Polymer Degradation and Stability. 2019 Jul 1;165:60–7.

2. Behera A, Behera RK, Sahu P, Swain RR, Mahapatra TR. Tensile and Failure Behavior of Kevlar Fiber Reinforced Epoxy Matrix Composite Exposed to Different Environmental Conditions. Materials Today: Proceedings [Internet]. 2018;5(9):20250–6. Available from: https://linkinghub.elsevier.com/retrieve/pii/S2214785318315232

3. José-Trujillo E, Rubio-González C, Rodríguez-González J. Seawater ageing effect on the mechanical properties of composites with different fiber and matrix types. Journal of Composite Materials [Internet]. 2019 Sep 12;53(23):3229–41. Available from: http://journals.sagepub.com/doi/10.1177/0021998318811514

4. Ali MA, Umer R, Khan KA, Samad YA, Liao K, Cantwell W. Graphene coated piezo-resistive fabrics for liquid composite molding process monitoring. Composites Science and Technology. 2017;148:106–14.

5. Govignon Q, Bickerton S, Kelly PA. Simulation of the reinforcement compaction and resin flow during the complete resin infusion process. Composites Part A: Applied Science and Manufacturing [Internet]. 2010 Jan 1 [cited 2020 Oct 12];41(1):45–57. Available from: https://linkinghub.elsevier.com/retrieve/pii/S1359835X09002292

6. Govignon Q, Bickerton S, Morris J, Kelly PA. Full field monitoring of the resin flow and laminate properties during the resin infusion process. Composites Part A: Applied Science and Manufacturing. 2008 Sep 1;39(9):1412–26.

7. Terzaghi K. Theoretical Soil Mechanics [Internet]. Theoretical Soil Mechanics. Hoboken, NJ, USA: John Wiley & Sons, Inc.; 1943 [cited 2021 Jun 7]. Available from: https://onlinelibrary.wiley.com/doi/book/10.1002/9780470172766

8. Rousseau G, Wehbe R, Halbritter J, Harik R. Automated Fiber Placement Path Planning: A state-of-the-art review. Computer-Aided Design and Applications [Internet]. 2018 Aug 13 [cited 2020 Aug 10];16(2):172–203. Available from: https://doi.org/10.14733/cadaps.2019.172-203

  doi:10.5075/epfl-298799_978-2-9701614-0-0

IDENTIFICATION OF SATURATED AND TRANSIENT TRANSVERSE PERMEABILITY OF CARBON FIBER FABRICS

Paul Baral[a], Giuseppe Pedoto[a], Sylvain Drapier[a]

a: Mines Saint-Etienne, Univ Lyon, CNRS, UMR 5307 LGF, Centre SMS, Saint-Etienne, France – paul.baral@emse.fr

Abstract: *Saturated and unsaturated transverse permeability of quasi-unidirectional carbon fiber fabric have been measured with a new test bench equipped with micro-thermocouples. A temperature gradient is detected when the cold fluid enters in contact with the thermocouples. The developed methodology allows tracking the flow front with accuracy in a sample stack which does not exceed 3 mm. Saturated and unsaturated permeability are compared for different fiber volume fractions, between 43 % and 64 %. The decrease of permeability with increased fiber volume fraction is coherent with the Kozeny-Carman's relation. Thanks to the high resolution in pressure measurement, transient effects can be evidenced in a single ply.*

Keywords: transverse permeability; transient effects; experimental characterization; thermocouple

1. Introduction

The transverse permeability characterization of fibrous reinforcements is of crucial importance for modelling Liquid Composite Moulding (LCM) processes, particularly when transverse flows are promoted or unavoidable such as when manufacturing thick composite parts or for infusion-driven processes. Some experimental set-ups have been proposed so far to identify the saturated permeability in transverse direction and provide reliable data – *see* [1] for instance. However, although it is admitted that transient permeability can largely differ from saturated permeability in the longitudinal direction [2,3], very little attention has been paid to transverse permeability, which however exhibits the same saturated/transient contrast [3]. The main difficulty raising in the characterization of transient transverse permeability is to obtain the position of the fluid front *in situ*, through small distances (thicknesses) and without disturbing the local flow. This front tracking can hardly rely on optical measurement like in planar permeability for instance [3,4]. Recently, some authors propose to use ultrasonic wave propagation to detect the flow front [5]. In this study, we propose to use micro-thermocouples to track the flow front through temperature gradient within the plies stack.

2. Experimental set-up

2.1 Transverse permeability test rig

The transverse permeability test rig is composed of a cylinder where the fluid – here, cold water – is collected and flows through the sample. A pressurized reservoir is used to inject the fluid in the cylinder and a flow control valve is added between the reservoir and the cylinder. A pressure sensor is placed in the cylinder, upstream of the sample. This sensor has a measurement range of 0-350 mbar of differential pressure and a precision of 3.5 mbar. Micro-thermocouples are placed between each ply to detect the flow front progression in the sample. Synchronous

  doi:10.5075/epfl-298799_978-2-9701614-0-0

acquisition of the signals is performed by a multimeter Hioki LR8431-20 at a sampling frequency of 100 Hz.

Figure 1.a represents a complete view of the cylinder supporting the sample. A detailed view of the positioning of the thermocouple is proposed Figure 1.b. The thermocouples are placed, at the center of the cylinder, between each ply during the pile-up of the sample stack. The thermocouple wires are then guided out of the sample through a small channel (see Figure 1.b). Figure 1.c displays a sectional view of the same cylinder for the sake of clarity.

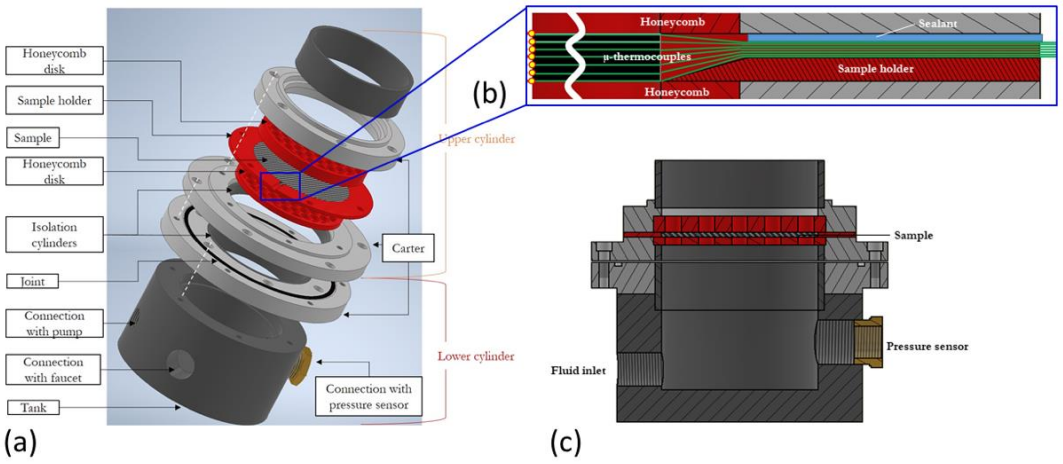

Figure 1 Transverse permeability test rig: (a) detailed view of the sample and measurement support; (b) micro-thermocouples placement within the plies and the sample support; (c) sectional view of the sample support.

2.2 Material

The tested material is a quasi-unidirectional carbon fabrics from Hexcel Corp. For this study, each ply is rotated 90° from the previous ply. The samples are cut from the fabric roll using a ring-shape cutting tool of 98 mm diameter. The tool is pressed on the fabric with a manual press and the samples are carefully cut to avoid as much as possible the separation of carbon tows from the sample edges. The fabric is impregnated with a binder which improves the resin adherence to the fibers. In order to test the material closer to industrial infusion conditions, each ply of fabric is tested only once. Three different fiber volume fractions are tested by varying the number of ply at a fixed sample height. The total sample height is 3 mm and 4 to 6 plies stacks are tested. The equivalent fiber volume fractions V_f are given in Table 1.

Note that the fiber volume fraction is calculated from the following equation [6]:

$$V_f = \frac{m}{Ah\rho} \tag{1}$$

where m is the total sample mass, A is the sample area , h the height of sample and ρ the bulk density of the fiber material. In the proposed experiments, the area of the fabric is 7.53x10^3 mm^2 the sample height is 3 mm and the bulk density is 1800 kg/m^3.

  doi:10.5075/epfl-298799_978-2-9701614-0-0 published under CC BY-NC 4.0 license

Table 1: Sample and experiment specifications.

ID number	1	2	3	4	5	6	7	8	9	10	11	12
Number of plies	4	4	4	4	5	5	5	5	6	6	6	6
Volume fraction V_f	0.43	0.43	0.43	0.43	0.53	0.53	0.53	0.53	0.64	0.64	0.64	0.64
v_{flu} (mm/min)	118	101	69	49	122	90	59	45	84	65	46	14

2.3 Flow front tracking

Following some work proposed by Drapier *et al.* [2] who used optical fibres to detect the fluid front advancement in stitched blanket stacks, our transverse permeability rig allows for a local detection of the flow front *in situ* by using more convenient and robust sensors, namely thermocouples. The flow front is determined from a rapid change in the local temperature measured (*see* Figure 2.a) – *i.e.* typically with a cold fluid in a room temperature test.

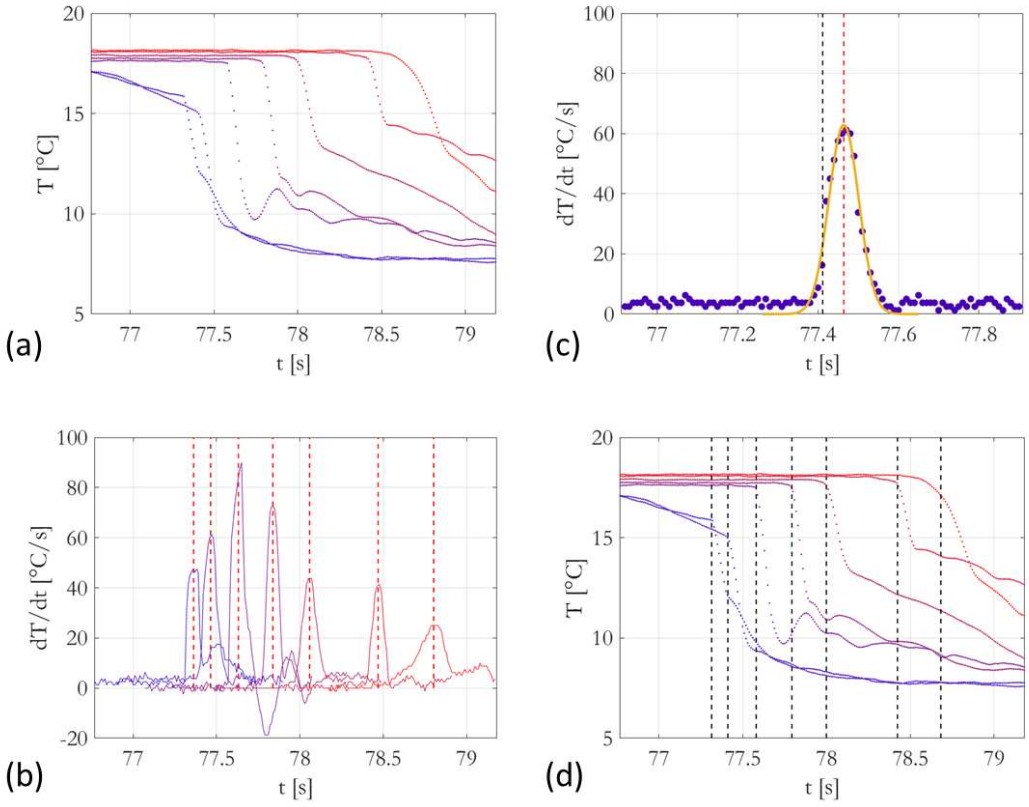

Figure 2 Flow front detection methodology based on temperature change between the air (at room temperature) and the cold water (at 7 °C): (a) thermocouples signal when the water cross the sample stack; (b) derivative of the temperature as a function of time for each thermocouple with a peak location detection, displayed with red dashed line; (c) example of fitting to obtain the peak width and determine the first point of contact between the thermocouple and water and (d) detection location of the flow front in time (sample 11).

Figure 2.b displays the temperature derivative with time. One can clearly observe the strong peaks associated with abrupt temperature decreases. To obtain more accurately the instant were the cold fluid enters in contact with the thermocouple, each peak on fig. 2.b is fitted with a Gaussian equation (*see* Figure 2.c) and the width of the peak is extracted. The maximum of the

derivative is not the meaningful parameter is terms of timing; instead, we use the maximum location minus the Gaussian half-width (represented as a black dashed line on fig. 2.c). Finally, the flow front advancement is represented in time-scale on fig. 2.d were black dashed lines correspond to the fluid first contact with each thermocouple.

3. Results

3.1 Pressure measurement

The pressure measurement is performed upstream of the sample and is compared with the flow front position deduced from the thermocouple signal. This allows quantifying the differential pressure needed to travel across a single ply. Figure 3 displays the pressure evolution as a function of time superimposed to the thermocouple signals. The green curve with open circles highlight the pressure delta associated with each ply. One can see that this pressure delta is not constant even if the plies are identical. Several effects could lead to such variability:

- First, the flow front may not be perfectly flat, this induces an uncertainty on the time correlation between pressure and temperature signals. The pressure signal being an average response of the fluid/sample interface while the thermocouple signal is a local measurement (typically at the center of the ply).
- The velocity of the fluid within the sample decreases with time, which also induces a pressure variation.

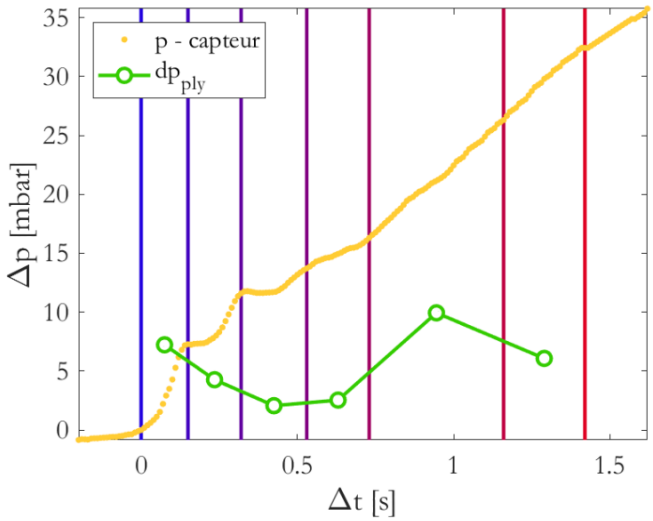

Figure 3 Pressure evolution within the sample. The yellow dots represent the pressure measured upstream minus the initial pressure at the contact of the first thermocouple. Vertical colored lines represent the thermocouple detection. The green open circles represent the delta pressure induced in each ply. (Sample 11)

3.2 Fluid velocity inside the fabric

Within the sample, three fluid velocities can be expressed. One which is related to the fluid velocity before any interaction with the sample v_{flu}, one related to the average fluid velocity during the flooding of the sample, named v_{wet} and one related to the flow front velocity in the sample named v_{dry}.

The velocity of the fluid in the cylinder, before entering in contact with the sample, v_{flu} is calculated from the pressure variation (due to the mass of the fluid column, $p = \rho g z$). This

velocity is given as a reference but might evolve when the fluid reach the sample because only the inlet pressure is kept constant. The average fluid velocity in the wet section of the sample is calculated such as:

$$v_{wet} = \frac{\Delta z_{wet,i}}{\Delta t_{wet,i}} \tag{2}$$

with $\Delta z_{wet,i}$ the cumulative sample height in the fluid – *i.e.* product of the number of saturated plies with individual ply thickness h_{ply} – and $\Delta t_{wet,i}$ the corresponding cumulative time for the number of ply i to be wetted. Finally, the flow front velocity is given by:

$$v_{dry} = \frac{h_{ply}}{\Delta t_i} \tag{3}$$

with h_{ply}, the individual ply thickness and Δt_i the corresponding time for the i^{th} ply to be saturated.

Figure 4 shows an example of the evolution of the fluid velocity as a function of the flow front advancement within the sample stack, compared with the inlet fluid velocity. The fluid velocity v_{wet} is significantly larger than the inlet fluid velocity due to the reduced (porous) efficient surface at iso-flow rate. Also, the average flow front velocity v_{wet} tends to decrease with fluid advancement due to increased pressure resistance.

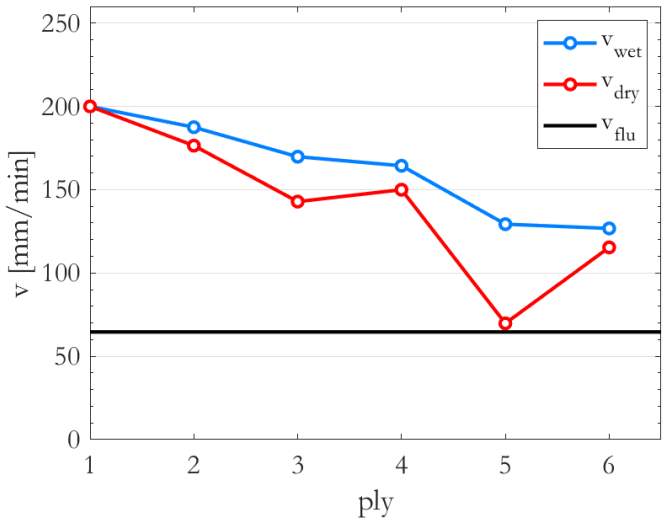

Figure 4 Fluid velocity within the sample stack as a function of the position in the sample for sample 11.

3.3 Saturated and unsaturated permeability

The saturated permeability is expressed from the 1D Darcy's law through the following expression [3, 8]:

$$k_{z\,sat} = \frac{\mu h v_{out}}{\Delta p_{tot}}, \tag{4}$$

with μ the fluid dynamic viscosity, h the sample stack thickness, v_{out} the flow front velocity downstream of the sample and Δp_{tot} the pressure gradient, both in steady state flow. The flow front velocity v_{out} is calculated, once steady state is reached, from a linear fit of the pressure evolution (since the pressure variation is only due to the mass of the fluid column after the sample is saturated). The total pressure gradient Δp_{tot} is calculated by differentiating the

  doi:10.5075/epfl-298799_978-2-9701614-0-0 published under CC BY-NC 4.0 license

pressure at steady state flow to the pressure once the flow is interrupted. Finally, the viscosity of water is adjusted for each experiment considering the temperature of the fluid at steady state flow. Results of the saturated permeability are displayed in Figure 5.b as a function of fiber volume fraction.

The unsaturated permeability is expressed as follow [3, 8]:

$$k_{z\,unsat} = \frac{(1-\mathrm{V_f})\mu z(t)^2}{2\Delta p(t)t}, \tag{5}$$

with z the fluid position in the sample, Δp the pressure gradient in the sample and t the time for the fluid to saturate the considered sample thickness z. In order to obtain quantitative estimation of the unsaturated permeability, we propose to fit Equ. 5 to the flow front position obtained by the thermocouples – i.e. square of flow front position vs. time multiplied by pressure gradient. A linear fit is performed without taking into account the last thermocouple signal since the positioning error in the z-direction is not perfectly known (the thermocouple might be slightly above the ply free surface) (*see* Figure 5.a). The results are displayed on Figure 5.b as a function of fiber volume fraction. The error bar represents the standard deviation calculated on four experiments.

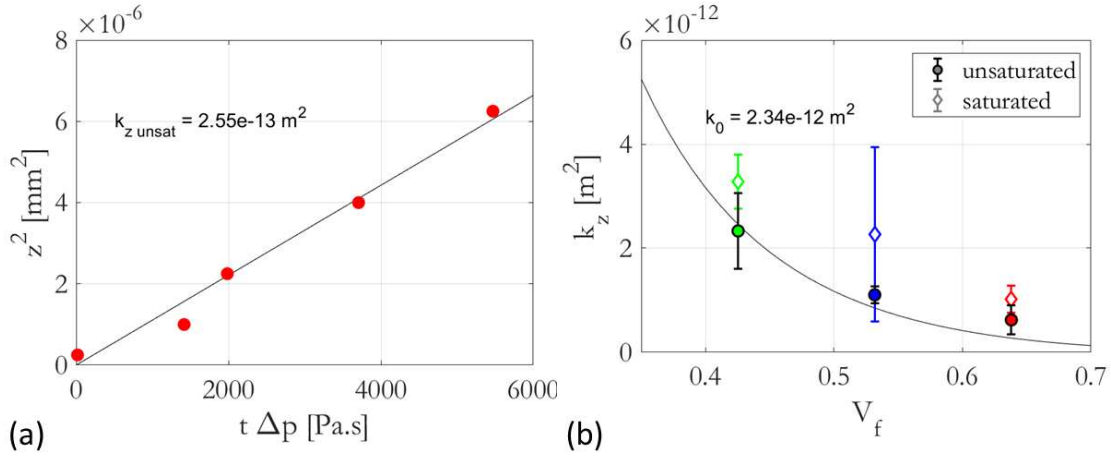

Figure 5 Unsaturated permeability calculation: (a) fit of Equ. 4 on the set of data (sample 12) without taking the last thermocouple signal (each data point correspond to a thermocouple detection signal) ; (b) Average unsaturated permeability as a function of fiber volume fraction. The error bar represents the standard deviation calculated on 4 experiments. The black line represents Eq. 6 best fit to the data.

The analytical Kozeny-Carman's equation, which relates the permeability to the volume fraction, is given in [7]:

$$k_z = k_0 \frac{(1-\mathrm{V_f})^3}{\mathrm{V_f^2}}, \tag{6}$$

with k_0 a coefficient of permeability. The fitted coefficient to the unsaturated permeability is equal to 2.34x10^{-12} m^2 and the obtained curve is plotted as a black line in Figure 5.b.

4. Discussion

The ratio $k_r = \frac{k_{z\,unsat}}{k_{z\,sat}}$ is equal to 0.61, 0.49 and 0.71 for V_f equal to 0.64, 0.53 and 0.43, respectively. This is in good agreement with the range reported by Park and Krawczak [3] who relate the ratio k_r to the degree of saturation (presence of air bubbles during the unsaturated

  doi:10.5075/epfl-298799_978-2-9701614-0-0

flow). This assumption leads to the conclusion that unsaturated permeability is smaller that saturated permeability, as seen in our experiments [3].

In addition to classical permeability measurements, an interesting pressure evolution for each ply is evidenced as shown in Figure 6, for two distinct fluid inlet velocities. Statistically, the position of the inter-ply detected by the thermocouples is located at the end of the steep increase in pressure and just before the plateau. This would imply that the transient pressure within one ply is first composed of a low pressure increase (or decrease) followed by a steep increase until it reaches the top of the ply. At this stage of our work, it is not possible to decipher the cause of this complex variation. It could be due to the fiber fraction volume difference between the inter-ply (lower fraction) and in the ply (higher fraction). Further investigations are needed to elucidate these observations. However, this phenomenon seems to persist at fluid velocity from 14 to 120 mm/min and independently of the fiber volume fraction, within the range tested.

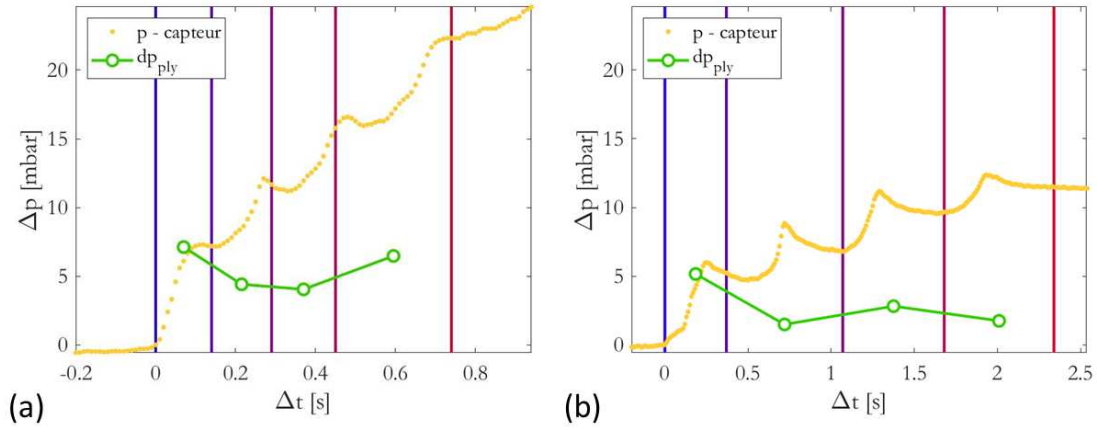

Figure 6 Pressure evolution as a function of time within the sample: (a) test on 4 plies stack sample with a fluid inlet velocity of 118 mm/min (Sample 1) and (b) 69 mm/min (Sample 3).

5. Conclusions

We developed a new transverse permeability test rig for the measurement of saturated and unsaturated regimes based on thermocouple detection of the fluid flow front. The use of water as test fluid allows a great experimental ease and improves the repeatability of the test by reducing cleaning complications. The main results obtained from this study are:

- Permeability measurements are consistent with the Kozeny-Carman's equation on the range of fiber volume fraction tested.
- The ratio of unsaturated to saturated permeability k_r is around 0.6 - 0.7, for this carbon UD fabric infused with water.
- Some very particular pressure evolution can be evidenced in each ply. Which are still under investigation at this stage.

The sensibility of the sensors allows following small-scale variations in the pressure profile and correlating them to statistically probable location within the stack. This work is preliminary and more experiments will certainly bring some new insights in the understanding of transient permeability.

  doi:10.5075/epfl-298799_978-2-9701614-0-0

Acknowledgements

The authors acknowledge the technical support provided by Eric Garrigou to the development of this test bench.

6. References

1. R. Nunez, Problématique de la mesure de la perméabilité transverse de préformes fibreuses pour la fabrication de structures composites. PhD thesis Mines Saint-Etienne, 2009.
2. S. Drapier, J. Monatte, O. Elbouazzaoui, and P. Henrat, Characterization of transient through-thickness permeabilities of Non Crimp New Concept (NC2) multiaxial fabrics, Composites Part A: 36(7) 877-892, 2005.
3. C.H.Park and P. Krawczak, Unsaturated and saturated permeabilities of fiber reinforcement: Critics and suggestions, Front. Mater. 2:38, 2015.
4. R. Arbter, et al., Experimental determination of the permeability of textiles: A benchmark exercise, Composites Part A, 42 (9) 1157-1168, 2011.
5. F. Lionetto, F. Montagne and A. Maffezzoli, Out-of-plane permeability evaluation of carbon fiber preforms by ultrasonic wave propagation, Materials. 13:2684, 2020.
6. A. Yong, et al., Out-of-plane permeability measurement for reinforcement textiles: A benchmark exercise, Composites Part A: Applied Science and Manufacturing 148 106480, 2021.
7. P.C. Carman, Fluid flow through granular beds. T I Chem Eng-Lond, 15:150–6, 1937.
8. D. Salvatori, B. Caglar, H. Teixido and V. Michaud, Permeability and capillary effects in a channel-wise non-crimp fabric, Composites Part A: 108 41:52, 2018.

  doi:10.5075/epfl-298799_978-2-9701614-0-0

TIME RESOLVED IN-SITU CT SCANNING OF NON-CRIMP FABRIC FORMING

Claudia Jimenez Martin[a,b], Ronan Smith[c], Mark Mavrogordato[c], Sebastian Rosini[c], Vincent Maes[b], Ian Sinclair[c], Turlough McMahon[a], James Kratz[b]

a: Airbus UK – claudia.jimenezmartin@bristol.ac.uk
b: The Bristol Composites Institute, University of Bristol – claudia.jimenezmartin@bristol.ac.uk
c: µ-VIS X-Ray Imaging Centre, University of Southampton – muvis@soton.ac.uk

Abstract

A better understanding of wrinkle development in dry fibre forming processes can help select the most appropriate material and process parameters. This paper shows the evolution of wrinkles occurring in a single diaphragm forming process using novel time-resolved in-situ CT scanning. Forming trials were carried out using a representative curved C-spar geometry and a [0°/45°] Non-Crimp Fabric layup. A custom walk-in X-ray CT system allowed for the detailed 3D visualisation of the evolution and formation of subsurface defects. Results showed correlation between the waviness observed in the preform during partial vacuum and that in the fully vacuum and consolidated state. Overall, this study proves a methodology for in-situ CT scanning of a preforming process and shows the potential for time resolved in-situ CT to provide detailed information on the behaviour of dry fabrics during forming.

Keywords: Non-Crimp Fabric; forming; in-situ CT

1. Introduction

The increased production rate targets of the aerospace industry have driven the development of dry fibre processes. Biaxial Non-Crimp Fabrics (NCFs) are considered in this work due to their potential high deposition rates and higher mechanical performance over their woven counterparts. Forming is an integral step prior to infusion and curing [1]. Understanding the forming behaviour of NCFs is therefore key to achieving high quality parts. For forming over double curvatures or corner radii where shearing is required, this may lead to wrinkling in the fabric and a subsequent knockdown on the mechanical performance of the final component.

Composite parts are made up of several layers or 'plies' of NCFs. Out-of-plane defects arising during forming may show in the outer-most visible ply. Identifying the initiation point of the defect and its propagation through the ply stack can help understand the influence of layup on preform quality. Tracking the evolution of a wrinkle in a dry fibre forming process is one way to do this. For this to happen, imaging techniques that help visualise the internal structure of the sample are required. This paper explores the use of in-situ X-ray CT to track wrinkles as they develop during a single diaphragm forming process over a representative curved spar geometry.

  doi:10.5075/epfl-298799_978-2-9701614-0-0

2. Literature Review

2.1 Time resolved in-situ CT – the current state-of-the-art

X-ray Computed Tomography (XCT) is a well-established method for damage detection and characterisation in composite parts. Its ability to obtain detailed 3D volumes of components with full sub surface visualisation has led to a variety of applications, including in forming, as seen in the micro-CT wrinkle scans of Hallander et al. [2]. Hallander's work as well as most others in the literature employ CT to scan the final formed and cured part. This means that subsequent manufacturing steps after the forming may affect and change the physical wrinkle characteristics. Information on how the wrinkle develops throughout the forming is also not possible to extract in these scans.

Industrial CT scanners rotate the sample through 360° while exposed to X-rays to extract a 3D volume of the relative material densities. The scanning time is dependent on the number of projections per scan and the exposure time of each. Multiple hour scans are the norm for static composite samples, as this improves signal to noise ratio in the reconstructed image. However in order to capture the changes in a forming process, as the preform transitions from an almost flat position to a 3D geometry, a very short scan time is needed [3]. Advances in X-ray Imaging Systems have allowed for shorter scan times. In turn, this has enabled industrial CT scanners to track the changes in samples over time, capturing both spatial and temporal information.

Most in-situ CT studies are focused on the curing stage due to the introduction of defects such as voids in the sample [3]. For these studies, the size of the defect means micro-CT is most appropriate and generally leads to high resolution projections of the sample due to the small volume size. Pickard et al. [3] focused on tracking tow gaps that were 2 mm wide and 2 plies deep – an order of magnitude larger than those focusing on voids. The size of the wrinkle defects in this study are even larger - spanning the web height of the geometry used (up to 10cm). This places this study as one of the first of its kind to observe in-situ defect formation in element scale geometries. The increased scan volume offered by the CT system at the µ-VIS X-ray Imaging Centre at the University of Southampton made this possible.

3. Materials & Methods

The experimental set up is shown in Figure 1 with the sample under vacuum and formed on to the geometry. To raise the geometry and region of interest to an appropriate height for the beam, a support table was built on the rotation stage. A foam support base was then used with a smooth sealable top to seal the vacuum on to. The support base was covered with breather to aid with the vacuum distribution. The vacuum pipe was fed through the centre of the rotate stage, to allow the sample to rotate 360° and remain out of the field of view between the X-ray gun and detector. The software was set to counter-rotate the sample back to the start position before the next scan, so the vacuum hose does not become entangled. No vacuum port was used to avoid any metallic parts obstructing the X-rays. The pipe was fed into the CT scanner from the vacuum pump outside.

  doi:10.5075/epfl-298799_978-2-9701614-0-0

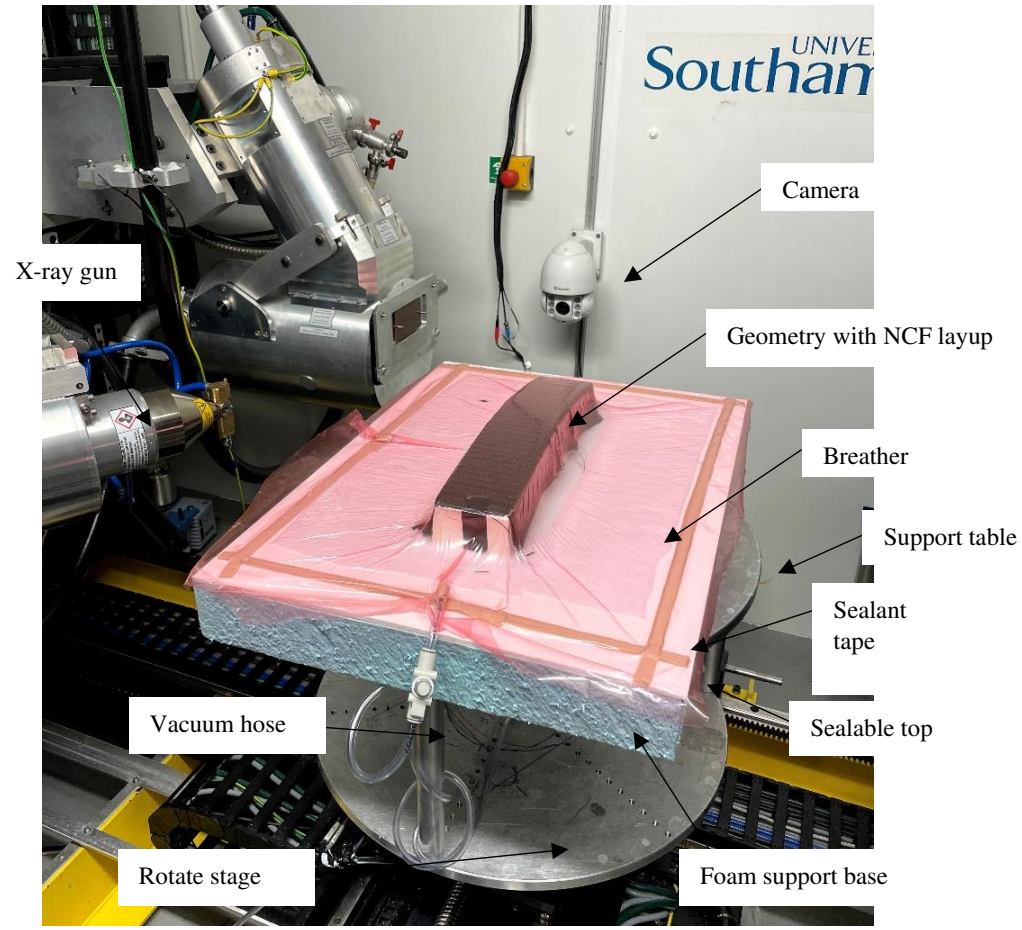

Figure 1. Experimental set up in CT scanner

A flow control valve was used to regulate the speed at which vacuum was pulled. This was necessary as the change in shape of the preform had to be slower than the scan time (54 seconds per scan), in order to capture the quasi-static state. The vacuum sequence is described in Table 1.

Table 1: Sequence of vacuum for forming trial

Projection number	Vacuum stage
0	No vacuum, vacuum pump turned on but valve closed, preform resting on geometry
1	Valve opened 2 turns
5	Valve opened 4 turns
10	Valve opened fully, preform fully formed
12	Vacuum pump turned off
20	No vacuum, preform relaxes

  doi:10.5075/epfl-298799_978-2-9701614-0-0

The aim of the presented work is to help further understand the mechanisms behind wrinkling of NCF preforms. A curved spar causing compression and buckling of the fibres on the geometry's flanges is used to this effect. The geometry was made out of high density foam in order to avoid attenuation of the beam. The geometry dimensions (see Figure 2) were chosen based on the minimum distance required from the source to the sample to achieve appropriate voxel resolution that would cover the wrinkle defects expected. The dimension of a common defect was estimated as the tow width x 1 cured ply thickness (5 mm x 0.5mm). Assuming 3 voxels are needed to resolve a feature, this led to a 200µm voxel size. The plies were laid up on the 'top' or web of the geometry and left to drape either side under their own weight. The plies were secured on to the shorter sides of the geometry with tape to avoid slip. Vacuum was applied through a non-reusable diaphragm membrane secured on to the sealable top of the foam support base.

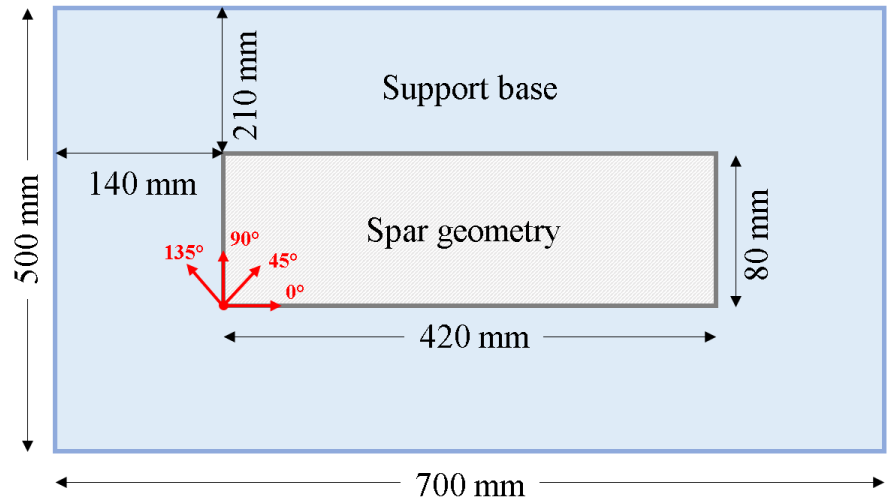

Figure 2. Representative curved C-spar geometry tool and set up

The CT scanner was a custom walk-in Nikon X-ray CT system with a 225kVp Microfocus source, running at 160kVp and 32W. In total, 360 projections were taken for each scan with an exposure time of 0.67 seconds, giving a temporal resolution of 54 seconds when allowing for overheads. These were reconstructed, producing a volume 20cm across with a voxel size of 200µm. This allowed for a detailed 3D visualisation of the evolution and formation of subsurface defects. Extraction of image modalities from XCT projection data and subsequent reconstruction was performed using Nikon software.

Table 2: Scanning parameters

CT- sytem	Voltage (kVp)	Power (W)	Projections	Exposure Time (s)	Temporal resolution (s)	Voxel size (µm)
Nikon 225kVp Hutch	**160**	**32**	**360**	**0.67**	**54**	**200**

The specification for the NCF material used is shown in Table 3. To investigate the effect of defect propagation through the stack, six plies were laid up at a time.

  doi:10.5075/epfl-298799_978-2-9701614-0-0

Table 3: NCF specification

ID	Orientation	Stitch type	Stitch size	Binder type
NCF1	0°/45°	Tricot	5.1mm	Polyamide

The preform results were assessed qualitatively as well as numerically using the following metrics: wrinkle amplitude versus wavelength and inner ply excess length versus outer ply excess length. Figure 3 shows how these are defined in a wrinkle observed in the sample.

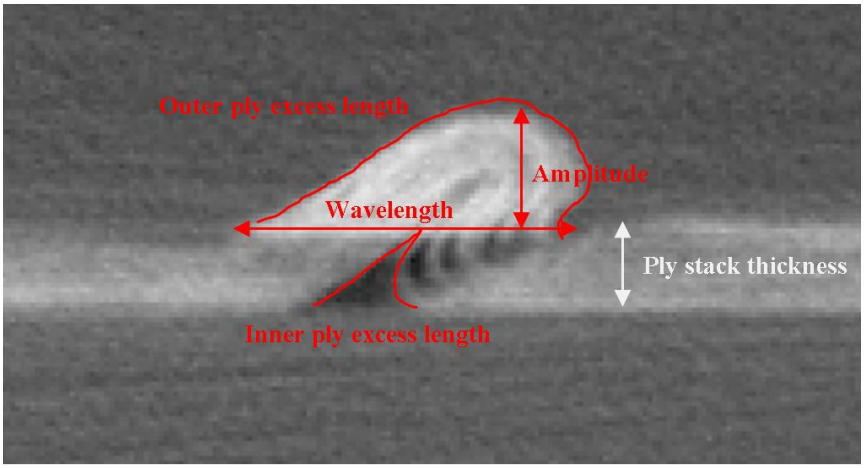

Figure 3. Wrinkle metrics extracted from an example wrinkle shown in a CT scan slice

4. Results & Discussions

4.1 Fully formed preform results

Wrinkling was observed in the preform along the vertical flanges. This clearly points to the wrinkling being geometry driven. The combination of the curved upper web and corner radii leads to an excess length in the 0° fibres. As these are stitched together with 45° fibres to create a biaxial NCF format, both orientations buckle out-of-plane in the form of wrinkling. Figure 4 shows isometric and side on views as seen in the CT scan of the fully formed preform. Results show that the wrinkle direction is influenced by the fibre orientation stitched to the 0° fibres (e.g. 90° for a 0°/90° ply). This is clearly seen in the side on view, the diagonals of the wrinkles on either side oppose each other (one tending towards 45° and the other towards 135°). However, wrinkle angles look steeper than the NCF's 135 fibres suggesting this angle is also partially geometry driven. The 0° fibres can be seen to follow the curve of the geometry web along the flanges.

The side on view also shows the position of the wrinkling along the 0° fibre direction on one side of the geometry does not match the other, even though the tool is symmetric about two planes going through the centre and both perpendicular to the bottom face of the tool. This phenomenon has been observed previously in the literature with the forming of NCF's over a hemisphere – also a symmetric tool shape. Chen et al. [4] explained this behaviour with the asymmetry introduced by the stitching of the NCF. In the case of the 0°/45° plies, the preform is not only asymmetrical due to the stitching but also due to the direction of the two fibre orientations relative to each other (45° clockwise and 315° counter-clockwise or vice-versa

  doi:10.5075/epfl-298799_978-2-9701614-0-0

rather than 90° for a 0°/90° or 45°/135° format). Though the stitching may influence the asymmetric wrinkling pattern, the variability of the ply in its 'natural drape' state at the beginning of the form is likely the biggest influence on wrinkle positioning. This is discussed further in section 4.2.

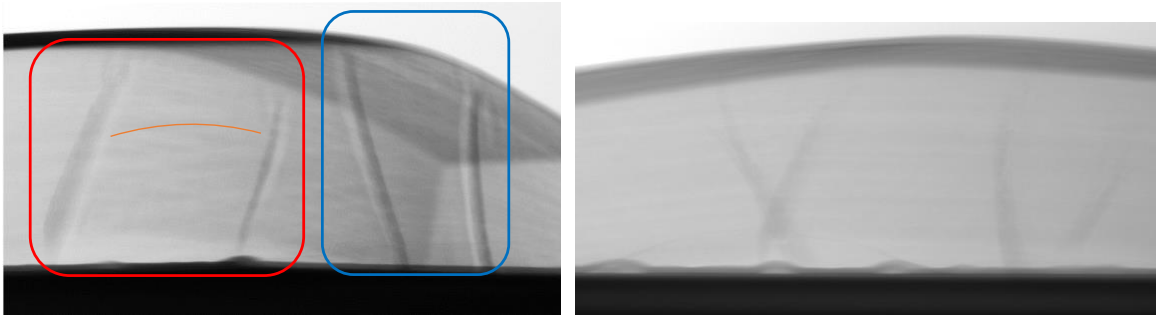

Figure 4. Isometric and side on projections of fully formed preforms with wrinkles on one side labelled in blue and on the other in red. Orange line traces 0° fibres.

Results for maximum wrinkle amplitude versus wavelength and maximum inner ply excess length versus outer ply excess length are shown in Figure 5. Each data point corresponds to a wrinkle on the preform. Data points have been colour coded according to where they are located on the geometry, labelled F1 and F2 for flange 1 and 2 respectively. To extract the maximum values, a slice or plane closest to the bottom of the flanges was taken, as wrinkles increased in severity from the upper corner radius down the flanges. No significant difference was observed between wrinkles on flange 1 or 2, with all wrinkles showing similar wrinkle aspect ratios (amplitude / wavelength). One wrinkle showed higher absolute values for inner and outer ply excess lengths due to a larger area of air trapped beneath (top left wrinkle shown in Figure 6).

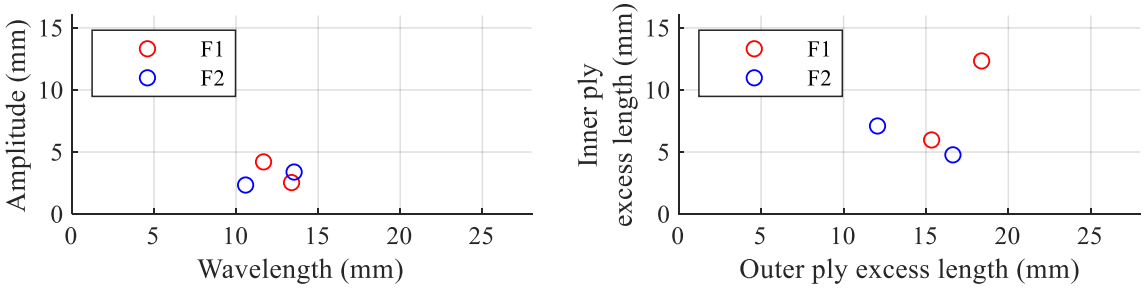

Figure 5. Plots of the maximum wrinkle amplitude vs wavelength and maximum inner & outer ply excess length for the five ply sequences tested.

4.2 In situ results

This section shows results gathered during the forming process as part of the in-situ proof of concept. The effect of the ply in its 'natural drape' state prior to forming has been highlighted in the previous section. The in-situ CT scans allowed the capture of the ply in its various states prior to consolidation under full vacuum. Figure 6 shows CT scan slices as seen from above the curved upper surface of the C-spar. The appearance of the ply stack during the forming as vacuum

  doi:10.5075/epfl-298799_978-2-9701614-0-0

increases is compared to that in its fully formed state at maximum vacuum. The waviness of the 'during forming' preform visually correlates to that at the 'fully formed' state: the closest point of contact of the preform to the geometry during the forming corresponds with the point where a wrinkle forms in the fully formed state.

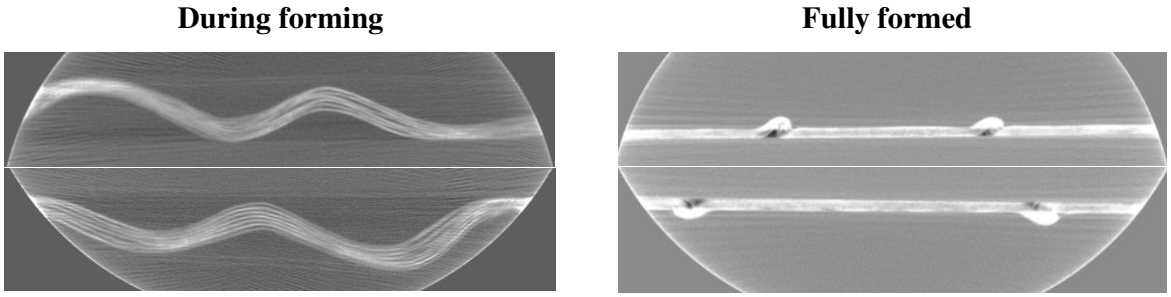

Figure 6. CT scan slices showing the preform during the forming (left) as vacuum is increasing and fully formed (right) at maximum vacuum

The temporal results for wavelength and wrinkle aspect ratio are shown in Figure 7. Three data points are shown corresponding to three scans of the preform in three different quasi-static states: two during the forming and one fully formed. Data points shown were chosen every two scans up until the fully formed scan, resulting in a 108 seconds time interval between data points (54 seconds multiplied by 2). Vacuum increases non-linearly with time. Results show that whereas wavelength decreases by an order of magnitude, as is clear in Figure 6, wrinkle aspect ratio remains relatively constant, as the bending stiffness of the material remains the same, regardless of vacuum being applied. This shows the correlation between the preform during the in-process state to the final consolidated shape.

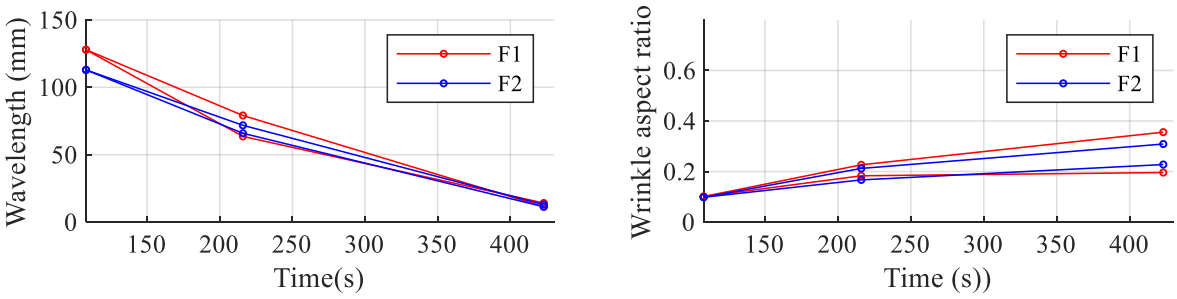

Figure 7. Plots of the development in time of wavelength and wrinkle aspect ratio for the five ply sequences tested.

5. Concluding Remarks

This study has shown insights into the development of wrinkle defects common in dry fibre forming processes. Though the NCF material and geometry of choice make it relevant to aerospace applications, the learning on NCF wrinkle mechanisms can be applied in any other industry and adds to the current state-of-the-art in the literature. The combination of temporal and spatial information has enabled characterisation of the preform during the process of forming and related this to its final consolidated shape. This study has also proven the success of a time-resolved in-situ CT scanning technique for a dry fibre preforming process.

  doi:10.5075/epfl-298799_978-2-9701614-0-0

Acknowledgements

The research presented was supported by Airbus, part funded by the UK's Aerospace Technology Institute, and the EPSRC through the Centre for Doctoral Training in Composites Manufacture (EP/L015102/1), the Programme Grant 'Certification for Design – Reshaping the Testing Pyramid' (CerTest, EP/S017038/1), and the National Research Facility for Lab X-ray CT (EP/T02593X/1). The support received is gratefully acknowledged.

6. References

1. Turk MA, Vermes B, Thompson AJ, Belnoue JP-H, Hallett SR, Ivanov DS. Mitigating forming defects by local modification of dry preforms. Compos Part A Appl Sci Manuf [Internet]. 2019;(October):105643. Available from: https://doi.org/10.1016/j.compositesa.2019.105643

2. Hallander P, Akermo M, Mattei C, Petersson M, Nyman T. An experimental study of mechanisms behind wrinkle development during forming of composite laminates. Compos Part A Appl Sci Manuf [Internet]. 2013;50:54–64. Available from: http://dx.doi.org/10.1016/j.compositesa.2013.03.013

3. Pickard LR, Smith K, Kratz J, Potter K. Tracking the evolution of a defect, characteristic of AFP layup, during cure with in-process micro-CT scanning. ICCM Int Conf Compos Mater. 2017;2017-Augus(August):20–5.

4. Chen S, Mcgregor OPL, Harper LT, Endruweit A, Warrior NA. Composites : Part A Defect formation during preforming of a bi-axial non-crimp fabric with a pillar stitch pattern. Compos Part A [Internet]. 2016;91:156–67. Available from: http://dx.doi.org/10.1016/j.compositesa.2016.09.016

  doi:10.5075/epfl-298799_978-2-9701614-0-0

IMPROVING MECHANICAL PROPERTIES WITH AFP-BASED FIBER ARCHITECTURE

Julian Schuster, Lazarula Chatzigeorgiou, Prof. Klaus Drechsler

Julian.schuster@igcv.fraunhofer.de

Abstract: *Automated Fiber Placement (AFP) is a well-known advanced manufacturing method for production of high-performance composite structures using precise layup of unidirectional slit-tapes to ensure mechanical and weight efficiency.*

This approach will provide a new design tool to composite engineers, enabling to deviate from the classical way of constant angle orientations for composite design towards an optimization of fiber deposition design harmonized with best manufacturing opportunities. Therefore, Iterations between design, analysis and manufacturing can be dramatically reduced with improved part quality, respecting manufacturing oriented fiber courses at part dimensioning process.

Keywords: AFP; Automated Fiber Placement; gap management; surface cover ratio; tool path optimization

  doi:10.5075/epfl-298799_978-2-9701614-0-0

1. Introduction

Fiber reinforced plastics offer various advantages over conventional structural materials, mainly in view of stiffness-to-weight ratio and strength-to-weight ratio. The anisotropic material behavior and the characteristic of being additively manufactured from individual layers, each of which potentially with different orientation and size, opens up a wide range of opportunities to meet design requirements.

Nonetheless, different manufacturing methods bring their own limitations respectively to which fiber architecture can be realized as close as possible to the mechanical optimum value.

Especially for complex shapes and curved fiber paths, Automated Fiber Placement (AFP) with its capability to cut and feed on demand and to lay up small increments of unidirectional preimpregnated slit-tapes (tows) with designated repeat accuracy renders possible the highest structural results achievable in an industrial scale.

Mechanical downgrades mainly go into effect, when radii are too small to be laid and therefore fiber architecture deviates from the desired path, when fiber bending leads to laminate defects or in case the design requirements induce a discontinuity of the deposited tape width, namely triangle gaps and overlaps. In addition, composite laminates tend to be designed in a traditional fashion with fixed angle plies and a small range of possible orientations, subsequently effecting the formerly mentioned triangle gaps/overlaps.

In this paper, a novel design approach focused on providing AFP-ready fiber architecture is discussed. Instead of taking fixed orientations into account only, it is proposed to use parallel curves as a priority design basis instead, leading to continuous fiber courses and a reduction of triangle gaps and overlaps.

2. Notching effect of in-ply cuts

To illustrate the downgrading effect of in-ply cuts, resulting in triangle shaped discontinuities, a pressure vessel like geometry will be examined as case study. The dimensions are generic and allow for Fiber Placement typical defects to appear within the spherical dome area. With 50.6mm wide tapes, consisting of 8 1/4'' tows, and the given part dimensions, a 45° layer contains 43 tapes evenly distributed in the circumferential direction.

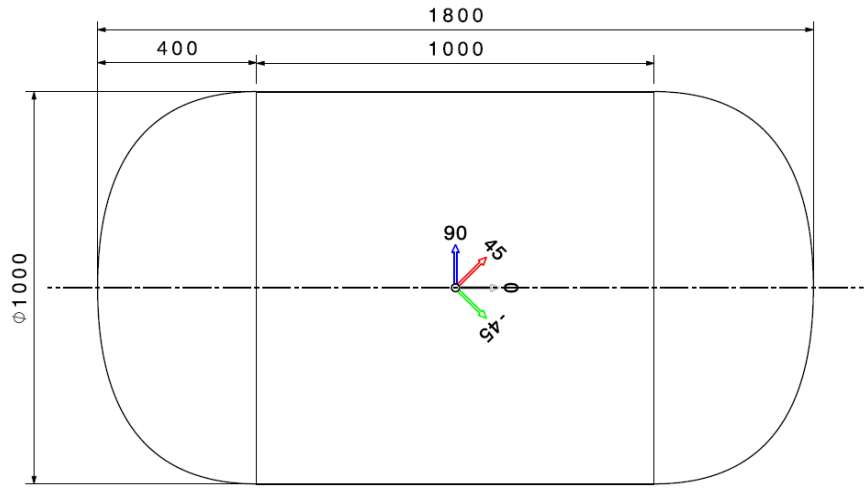

Figure 1: Rotational case study geometry, shape and dimensions

1061/1151 ©2022 Schuster et al. doi:10.5075/epfl-298799_978-2-9701614-0-0 published under CC BY-NC 4.0 license

The distance between the tapes is approximately 0.8mm in the cylindrical part. Furthermore, the tapes were generated with an overlap ratio of 0% to simulate a laminate without unintended thickening.

As seen in **Fehler! Verweisquelle konnte nicht gefunden werden.**, the decrease of diameter results in a systematic reduction in the number of tows per tape, creating circular arrays of voids. With a typical stacking consisting of numerous plies of different orientations and taking lateral gap staggering into account, such void arrays add up to a continuous thickness step and therefore to a discontinuity in stiffness. Furthermore, overlying layers experience increasing ondulations due to the abrupt change in substrate height, which in itself also induces a local defect due to angular deviation in the undulating layers.

An immediate solution would be to vary the gap/overlap ratios throughout the stacking in addition to lateral gap staggering, but this can lead to considerable additional effort in manual process development and also only distributes the discontinuities that still exist.

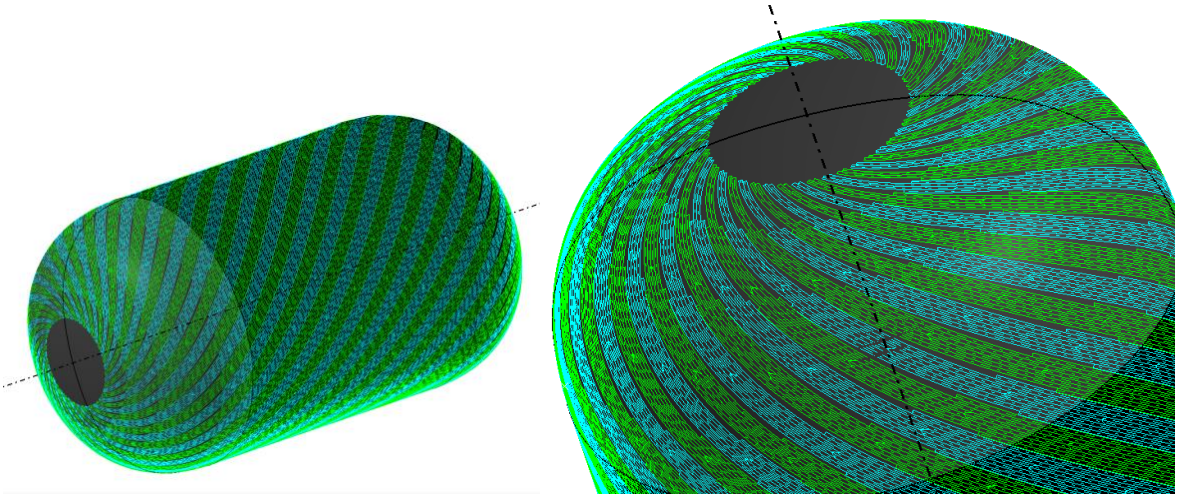

Figure 2: 45° fixed angle layer on spherical shape with circular rows of triangle gaps

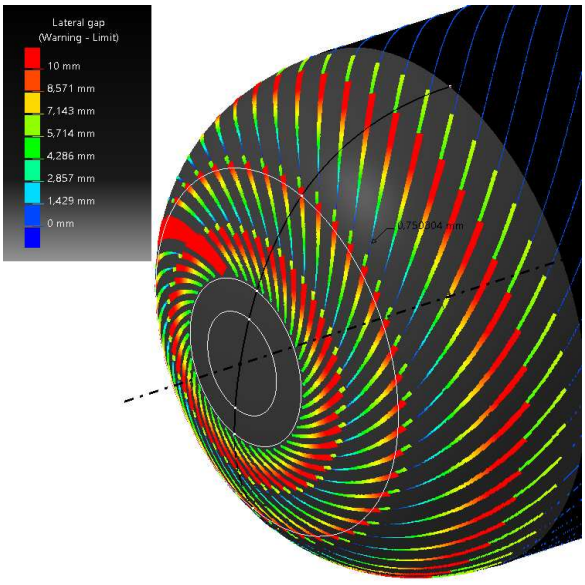

Figure 3: 45° fixed angle; lateral gap analysis

  doi:10.5075/epfl-298799_978-2-9701614-0-0

Another, less obvious option is to modify the reference curve to compensate for the circumferential drop according to a trigonometric relationship by raising the fiber angle α relatively to the 90° reference fiber. For a constant gap width in between the tapes, the orientation α in relation to the initial orientation α0 can for a high amount of tapes approximately be calculated as relation between initial radius R0 and current radius R:

$$\sin(\alpha) / \sin(\alpha\_0) = D\_0/D \quad (1)$$

In the following sections, an exact description of the function just mentioned for plane geometries is explained and an application to three-dimensional use case geometry is discussed.

3. Fixed tape width curve for flat geometries

In order to derive a first classification of the fiber architecture, which allows a constant tape width at a constant angle in the intersection to the reference curve, a further, strongly simplified use case is defined. **Fehler! Verweisquelle konnte nicht gefunden werden.** shows a two-dimensional surface with a constant curved neutral fiber (NF) in the center. Furthermore, three curves are shown, all passing through the same point at half the diameter of the NF and intersecting the NF at the same angle b = 45°.

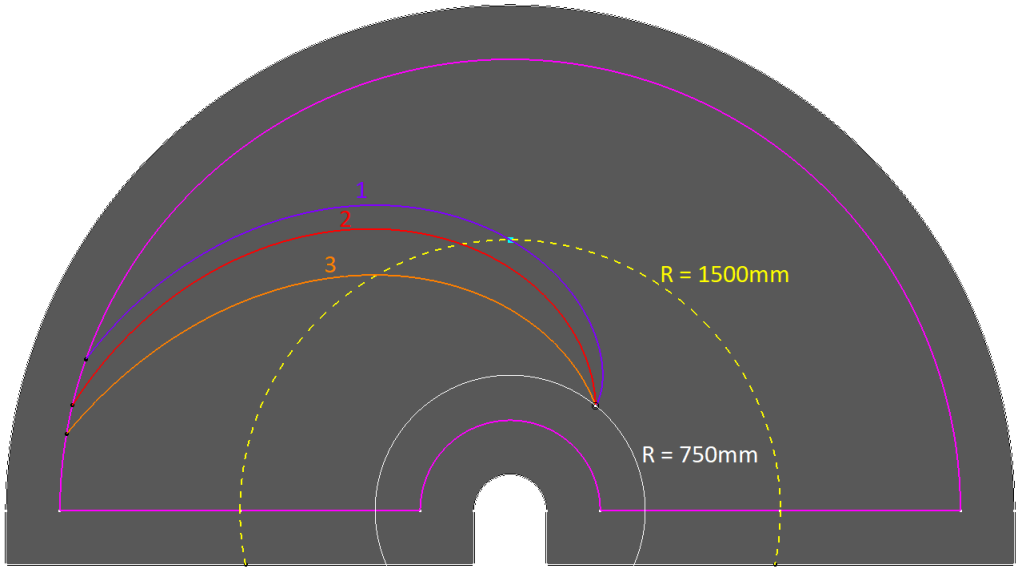

Figure 4: Flat geometry with constant radius reference curve R = 1500mm; cut by different curves in 45° angle

- Curve 1: In the case of a circle, its involute, constructed at any point, represents the parallel curve of every other involute of the same circle. Accordingly, this curve represents the function sought in the present case, provided that the radius of the auxiliary circle is chosen so that the involute intersects the neutral fiber at the desired angle.
- Curve 2: The Archimedean spiral is often mistakenly ascribed the property of consisting of a curve with a constant distance to itself. However, when rotating around the axis of the NF, two curves are created which increasingly diverge towards the outside, which is why it is not suitable for the present application.
- Curve 3: Strictly following the design requirement of a fixed angle orientation leads to a logarithmic spiral. A rotational displacement of the curve around the axis of the

1063/1151 ©2022 Schuster et al. doi:10.5075/epfl-298799_978-2-9701614-0-0 published under CC BY-NC 4.0 license

neutral fiber generates a distance increasing directly proportional to the radius and thus also triangle gaps / overlaps.

It is striking here that the circular involute is perpendicular to the neutral fiber for exactly half of its radius. However, the relationship already described in equation (1) coincides with this result and thus additionally validates the procedure.

Fehler! Verweisquelle konnte nicht gefunden werden. shows the radius of curvature t of the individual curves plotted against their arc length s. Clearly recognizable is the linear increase of the radius for the logarithmic spiral, furthermore the root-shaped relationship for the involute is apparent. Specifically, the relationship between arc length s and radius of curvature t can be described by the following equation:

$$t = \sqrt{2} * s \tag{2}$$

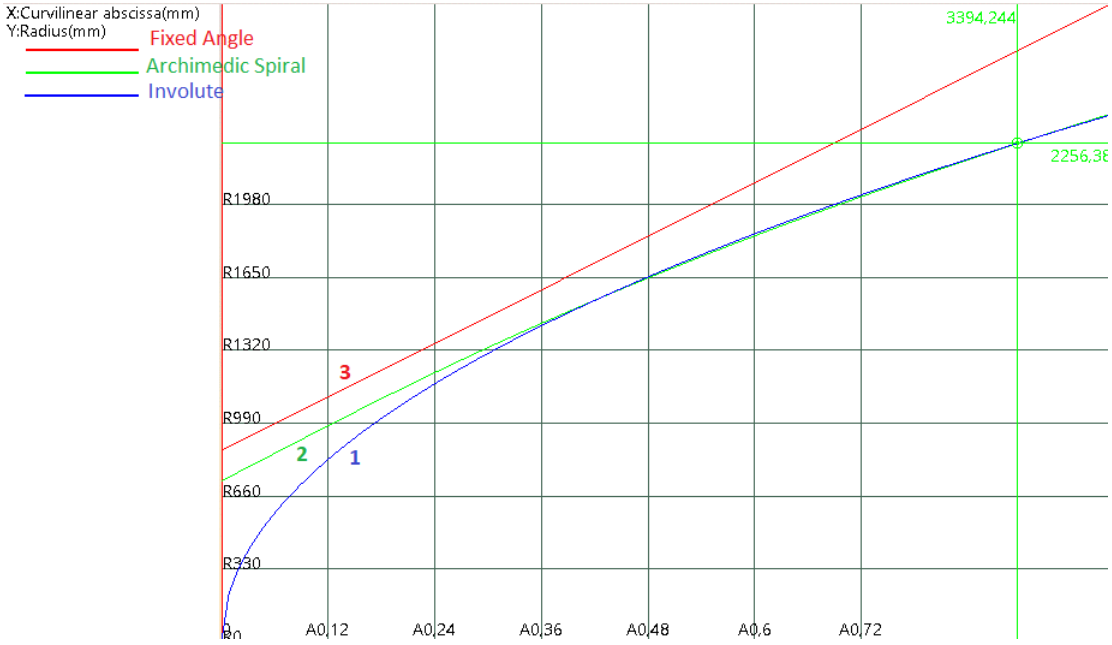

Figure 5: local radius of the different curves relatively to their curvlinear abscissa

  doi:10.5075/epfl-298799_978-2-9701614-0-0

4. Fixed tape width curve on 3D shapes

Based on the former results, a three-dimensional curve was constructed on the pressure vessel use case with the same property of cutting the reference curve in a certain angle and being parallel to its own rotationally shifted copies. The parallelism only applies for the geodesic type, which means the distance is calculated as shortest distance over the surface. **Fehler! Verweisquelle konnte nicht gefunden werden.** shows the large polar opening of the layer, not being possible to be decreased any further due to the curves characteristics without inducing overlaps. Nonetheless, it's always possible to define a second reference curve closer to the axis to allow for different angles and to cover a larger percentage of the dome area.

Analogous to the two-dimensional case, the angle in the spherical region increases relative to the reference curve from 45° to 90°, which is reached for a diameter $D/D_0 = \sin(45°)$.

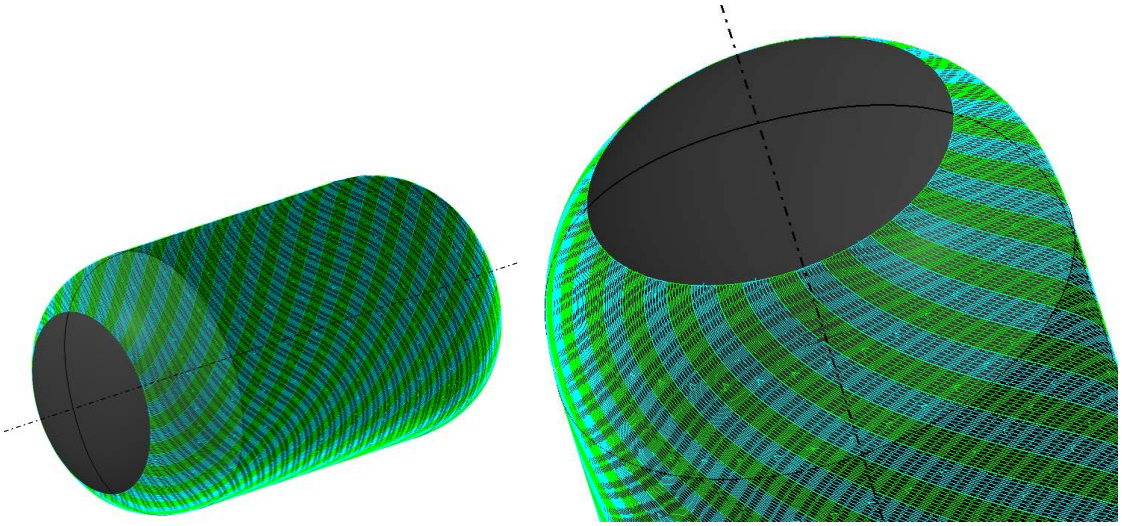

Figure 6: 45° involute style layer; equator diameter 1000mm, polar opening 707mm

Modifying the fiber architecture in favor of uniform coverage only comes at the expense of various compromises, which in turn can severely limit manufacturability. First and foremost is the steering radius, which falls below the critical value for the process for a slightly larger distance to the axis than in the case of the fixed angle curve. **Fehler! Verweisquelle konnte nicht gefunden werden.** shows an example of the comparison of the steering analyses with material parameters typical for aerospace applications. When smaller radii are deposited, there is a risk of introducing defects relevant to structural mechanics into the laminate.

1065/1151 ©2022 Schuster et al. doi:10.5075/epfl-298799_978-2-9701614-0-0 published under CC BY-NC 4.0 license

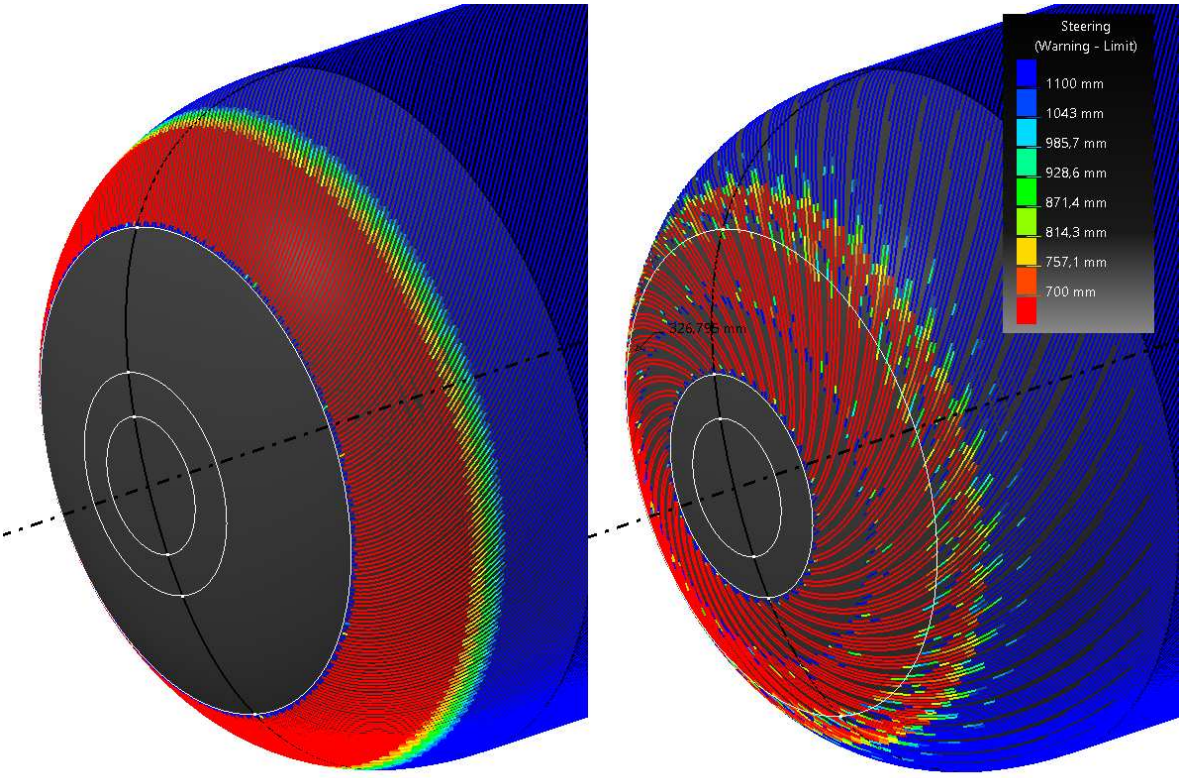

Figure 7: Steering analysis with 1100mm warning and 700mm limit; 45° fixed tape width and 45° fixed angle

Another aspect to be considered is the strong fiber angle deviations, seen in **Fehler! Verweisquelle konnte nicht gefunden werden.**, which do not allow FRP laminates to be engineered in the traditional way. Rather, a revision of the engineering philosophy is advisable, which is directly oriented to the chosen manufacturing method.

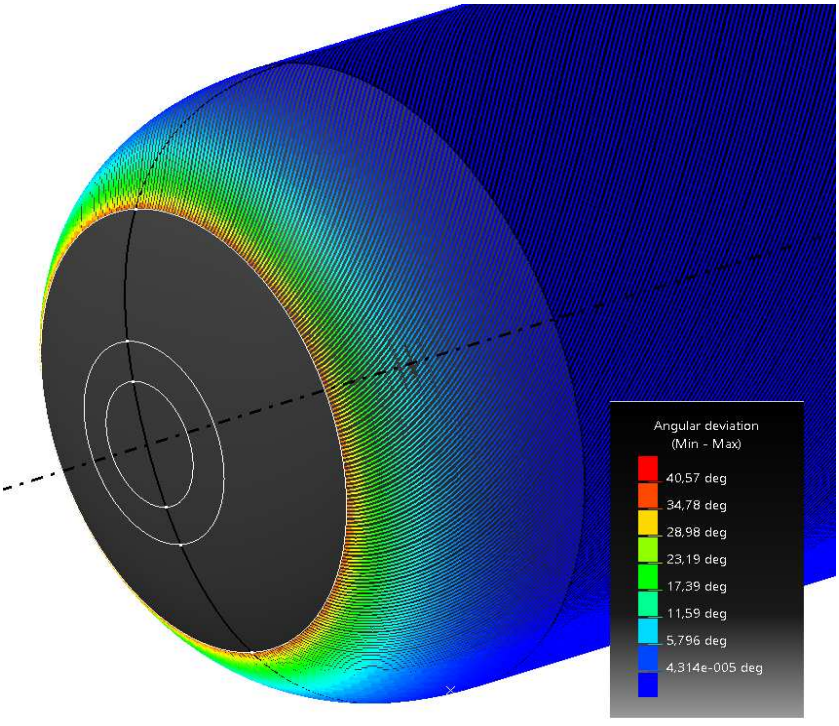

Figure 8:45° fixed tape width; angular deviation relative to 45° fixed angle

  doi:10.5075/epfl-298799_978-2-9701614-0-0

5. Conclusion

- A motivation for designing fiber pathes for reduction of discontinuities within fiber placement laminates was presented
- For a simplified model of a general use case of rotational symmetric fiber architecture a method of constructing parallel curves was proposed
- The formerly proposed method was applied on a three-dimensional geometry to discuss the pros and cons of such fiber architecture

  doi:10.5075/epfl-298799_978-2-9701614-0-0

ROBOTIC ADDITIVE MANUFACTURING OF CONTINUOUS CARBON FIBER THERMOPLASTIC COMPOSITES

Alberto Pedreira, Elena Rodriguez, Adrian Rodriguez, Paula Rodriguez

AIMEN Technological Centre – alberto.pedreira@aimen.es

Abstract:

Fused Filament Fabrication (FFF) technology is one of the most popular 3D printing processes and interest in direct manufacturing of functional parts is growing. For this reason, both techniques and feedstock materials require improvements to meet the mechanical requirements of load-bearing components. In this sense, this work is focused on the robotized FFF process of continuous carbon fiber thermoplastic composites. It includes an analysis and comparison of the developed FFF robotic 3D printing process with the conventional process, as well as the development of robotic 3D printing equipment for the manufacture of continuous fiber reinforced composites and the characterization of the printing process developed to print the new filaments based on the thermoplastic matrix and reinforced with continuous carbon fiber. The material was analysed by microscopic analysis, and the manufacturing specimens were characterized by mechanical tensile and flexural tests.

Keywords: Fused filament fabrication (FFF); 3D printing; Carbon fiber; composites; thermoplastic matrix

Introduction

Additive manufacturing is a fast manufacturing process from Computer Aided Design (CAD) model without geometry limitation, capable to handle complex shapes with great design flexibility and with little waste.

Among the many 3D printing technologies that exist today, the Fused Filament Fabrication (FFF), is one of the most popular process. Although this technique has been mainly used for rapid prototyping, interest is growing in direct manufacture of functional parts. For widespread applications of 3D additive manufacturing, both techniques and feedstock materials require improvements to meet the mechanical requirements of load-bearing components.

For this reason, in recent years new materials have been developed for FFF with short fibers, and also, more recently, with continuous fibers. The use of these reinforcing fibers in conventional FFF printers has made it possible to obtain, depending on the amount of charges material and the mixing ratio of the fibers used, improvements in tensile stress and elastic modulus, compared to parts produced with the same technique without filler material. Even so, despite the improvements, the mechanical properties are still not comparable to that manufactured by conventional continuous fiber reinforced composites processes such as Autoclave, RTM or press process [1]. The fibers are the main ones in charge of transferring loads in the composites, so maintaining their continuity would allow increasing the mechanical properties of the manufactured parts. For this reason, the additive manufacturing of continuous fiber composites is a field of great interest and in a state of growth. The CFRTPCs have gained considerable attention in automotive and aeronautics applications due to their attractive

  doi:10.5075/epfl-298799_978-2-9701614-0-0

strength-to-weight ratio, enabling energy and recyclability to be saved as suitable end-of-life scenario. The quest for printed parts with high mechanical performance led to the development of innovative FFF processes where continuous fibers are incorporated into printed structures [2 3 4].

On the other hand, three-axis additive manufacturing machines are associated with strict layer by layer manufacturing to create the three-dimensional parts, the combined use of multi-axis robot systems and additive manufacturing technologies offers the possibility for multi-axis additive manufacturing and the fabrication of complex geometries in different manufacturing environments [5]. In this sense, this work is focused on the robotized FFF process of continuous carbon fiber thermoplastic composites. It includes from the development of the new filaments based on the thermoplastic matrix and the embedded continuous carbon fiber, as well as the development of the equipment needed for the 3D printing process. The material was analysed by microscopic analysis, and the manufacturing specimens were characterized by mechanical tensile and flexural tests.

1. Materials and Methods

1.1 Materials

In this study, thermoplastic filaments of two different matrices such as polyamides (PA) and polysulfones (PPS) were used. The non-fiber filaments are commercial NANOVIA brand filaments and the continuous fiber reinforced filaments were developed from pellets (same matrix as the filaments) and continuous carbon fiber through the co-extrusion process. The filament matrices 3d printing properties are presented in Table 1.

Table 1 Filament matrices 3d printing properties

Material	Nozzle Tª (°C)	Printing Speed (mm/s)	Bed Tª (°C)	Filament diameter (mm)
PA6	250	50-70	80-100	2.75
PPS	340	30	100-130	2.75

A wide variety of filaments reinforced with continuous fiber were developed to achieve the appropriate percentage of fiber and considered optimal for the development of the study. These filaments were made with 3K, 4K and 6K carbon fibers. Table 2 shows the most relevant parameters of the developed filaments.

Table 2. Parameters of continuous carbon fiber reinforced filaments

Material	Fiber	Filament diameter (mm)	Fiber mass %
PA6-CCF	3K	0.98	26.9
	4K	0.82	26.4
	6K	0.81	53.5
PPS-CCF	3K	0.73	57.7
	4K	0.76	65.3
	6K	0.72	66.4

1069/1151 ©2022 Pedreira Estévez et al. doi:10.5075/epfl-298799_978-2-9701614-0-0 published under CC BY-NC 4.0 license ToC

1.2 3D printing equipment: ROBOTIC SYSTEM

The tests were developed using a commercial printer and a custom robotic 3D printing system. In order to characterize and compare the quality of the conventional FFF process with the developed robotic process, specimens were printed in both equipment. The commercial equipment is a printer model FFF 3NTR A2V4 from the manufacturer 3ntr.

The robotic 3D printing equipment for the manufacture of continuous fiber reinforced composites consists of a robotic 3D printing cell composed of the following elements.

- 6 axis industrial robot
- Specific print head made up of two high-temperature nozzles, one for printing polymer filaments and the other for printing filaments reinforced with continuous fiber, equipped with a fiber cutting system.
- Heated print bed
- Printing software. Parametric CAD/CAM system (CAx).
- Global control system.

The *Figure 1* shows the 3D printing cell developed with each of the elements that participate in the process:

Figure 1. Robotic 3D printing cell developed.

On the other hand, specific software was developed to be able to process the parts in the robotic 3D printing cell. The software automatically generates the robot routines necessary for printing the different parts. The software works from STL files (Standard Triangle Language) and allows parameterizing the process and defining which parts are made with polymer and which with continuous fiber.

2. Process characterization

The characterization process was divided into two phases:

- First phase: Printing of polymer filaments without reinforcement. In this phase, the conventional 3D printing process was characterized and compared with the robotic 3D printing process.

-Second phase: Printing of continuous fiber reinforced filaments. In this phase, the robotic 3D printing process of the continuous fiber filament was printed and characterized.

2.1 Mechanical testing

The following tests were defined for both phases:

- Tensile tests according to UNE-EN ISO 527 standards. The specimens are manufactured with dimensions and geometry according to the standard.

- Flexural tests according to standards UNE-EN ISO 178 for polymer and

- ILSS test, interlaminar shear strength, according to UNE-EN-2563 for filaments reinforced with continuous carbon fiber.

2.2 Micrographic analysis

Finally, the cross section of the manufactured samples was analysed by optical microscopy. With this analysis, the microstructure of the samples is analysed to evaluate the failure mode and the consolidation between layers, and in the case of continuous fiber printing, the fiber-matrix adhesion after its deposition by FFF.

3. Results and Discussion

3. 1 First phase: Printing polymer filaments without reinforcement

- Mechanical properties

In this first phase, tensile and flexural specimens were manufactured with commercial PA6 and PPS filaments. To compare both printing processes, the parameters defined in the robotic process were replicated in the conventional printer, so that the process is as comparative as possible. As different software is used in each of the equipment, the calculations and deposition routes are different, which may affect the print quality and the results obtained. To minimize variables, the specimens were manufactured using the same nozzle diameter, same temperatures (nozzle, bed and environment) and that the central lines of the specimens are unidirectional (specimen rupture area).

Table 3 and Table 4 show the results of the tensile and flexural tests of the specimens manufactured in the robotic 3D printing cell and in the conventional FFF printer, with the commercial PA6 and PPS filaments, respectively.

Table 3. Mechanical properties of PA6 filament.

PA6 filament without reinforcement		Conventional 3D printer	Robotic 3D printing
Tensile	Strength (MPa)	59	55
	Modulus (GPa)	1.9	2.2
Flexural	Strength (MPa)	95	98
	Modulus (GPa)	2.3	2.2

  doi:10.5075/epfl-298799_978-2-9701614-0-0

Table 4. Mechanical properties of PPS filament.

PPS filament without reinforcement		Conventional 3D printer	Robotic 3D printing
Tensile	Strength (MPa)	52.8	44
	Modulus (GPa)	3.1	2.9
Flexural	Strength (MPa)	106.8	97.6
	Modulus (GPa)	2.6	2.2

The results show that there is hardly any difference between both processes. It should be noted that the robotic system presents a slightly higher deviation, but with a tensile load and a bending stress of the same order of magnitude. This represents a good result for the validation of the FFF robotic process, since the polymer properties are preserved during processing by the new developed technology.

- Micrographic analysis

Finally, the specimens of both processes were analysed by optical microscopy. Figure 2 shows a cross section of the central part of the specimens obtained by robotic process and Figure 3 shows the specimens obtained by conventional FFF process.

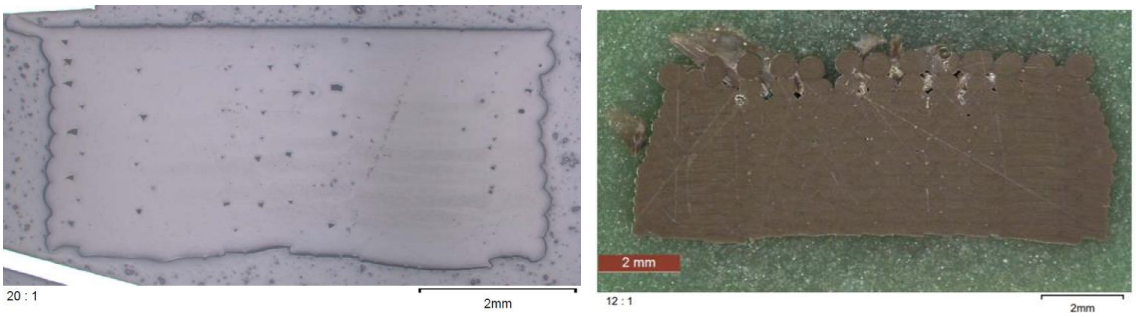

Figure 2. Micrograph of the cross section of the PA6 (left) and PPS (right) specimen manufactured by robotic 3D printing.

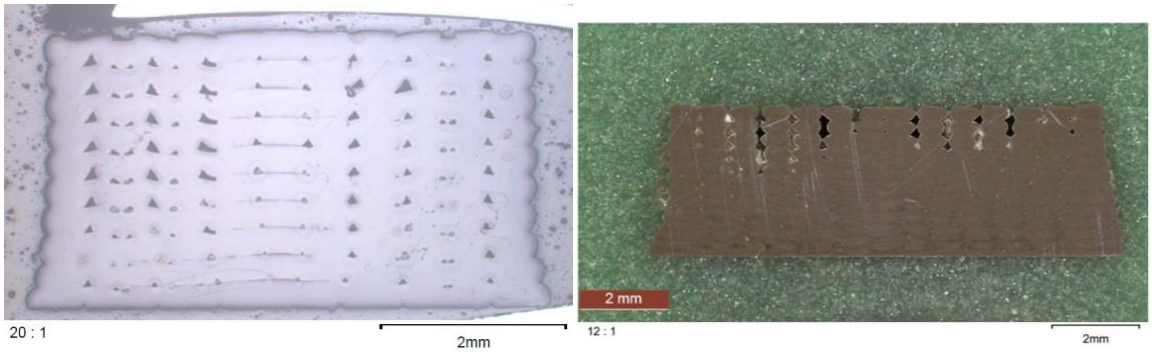

Figure 3. Micrograph of the cross section of PA6 (left) and PPS (right) specimens manufactured by conventional 3D printing.

The micrographs of the specimens show as both processes present internal voids between the intersection of 4 threads, two of them deposited in parallel in the same layer and the other two deposited just in the upper or lower layer of the same. These voids can be caused by poor thread

overlap or reduced material flow. This problem is increased in the conventional printer than in the specimens made by the robotic process. These differences between processes may also be due to the difference between the software used.

Another aspect is the geometry of the specimens that show the precision of the conventional process is greater than the robotic process, where technical aspects of repeatability and precision of the robot influence.

3.2 Second phase: Printing continuous fiber reinforced filaments

In this second phase, the printing of the continuous fiber reinforced filament was parameterized in the robotic system. The development of the equipment and software was defined and updated during the tests given the novelty of the technology and the continuous fiber printing process. Among the peculiarities of this equipment, the need to implement a cutting system, special nozzles, new deposition strategies, preferential trajectories and adaptations to the fiber, among others, was observed.

After characterizing the system, the optimum layer height for printing the fiber used is 0.3mm and the printing speed is 10mm/s. With the width obtained, overlap tests between threads were realized to obtain the correct value.

The vertices or the angles are a critical point, the geometry itself and the properties of the fiber limit the generation of sharp edges, leaving these slightly rounded. The speed has an important influence on the quality of the vertices. At high speeds the fiber moves with the movement of the head, while at low speeds it consolidates and achieves better quality and definition. Examples of continuous fiber print results are shown in Figure 4.

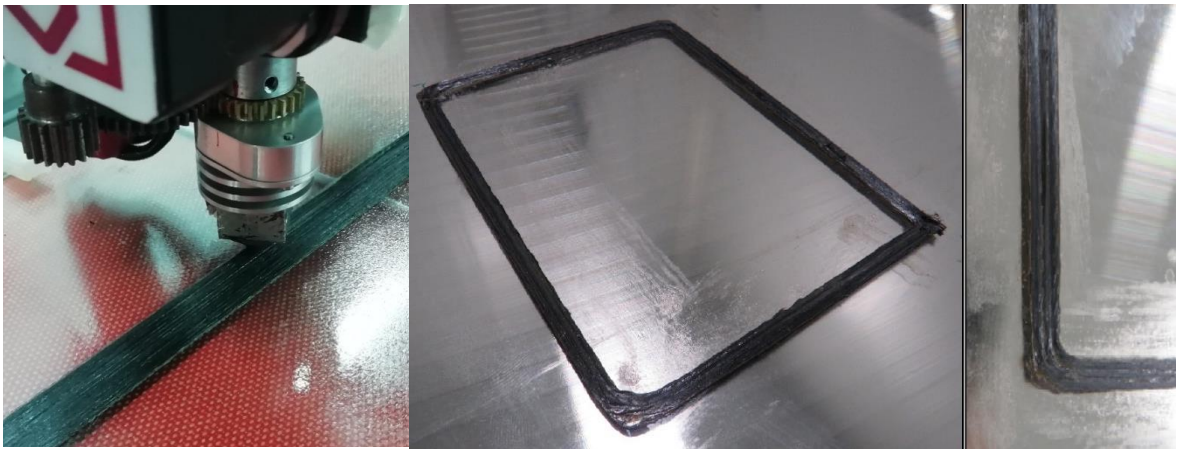

Figure 4. Robotic 3D printing process of continuous carbon fiber reinforced filament.

- Mechanical properties

The printing process and the PA6-CCF and PPS-CF continuous fiber filaments developed were characterized by tensile tests according to ISO 527 and ILSS tests according to UNE-EN-2563. The results of the tested specimens are presented in Table 5.

  doi:10.5075/epfl-298799_978-2-9701614-0-0

Table 5. Mechanical properties of PA6-CCF and PPS-CCF filaments

		PA6 - CCF	PPS - CCF
Tensile	Strength (MPa)	162.8	239
	Module (GPa)	22	52.4
ILSS	Force (N)	290	281
	Interlaminar shear strength (MPa)	7.4	6.3

Comparing the tensile values with the results obtained from the polymer filaments without reinforcement, it was observed that the tensile load in the case of PA6 presents an increase of up to three times more, going from 55 MPa to 162 MPa; while in the case of the PPS it has presented an increase of up to five/six times more, going from 44.6MPa to 239MPa. This shows that the increased load is due to the effect of the continuous fiber of the filament. Similarly, the effect of the fiber, the quality of the material and the printed piece, is reflected in the modulus that goes from 2.2GPa to 22.1GPa for PA6 and from 2.9GPa to 52.4GPa for PPS, among to 10 and 20 times more, respectively.

Analysing the failure mode of the specimen, it was observed that most of the break occurred in the adhesive of the tabs, and therefore the resistance and modulus were not correctly measured and the value of could be higher. In addition, the lack of an adequate and specific standard to test this type of composite materials manufactured by 3D printing complicates the interpretation and comparison of results with similar materials and processes.

- Micrographic analysis

The specimens of both materials were analysed by optical microscopy. Figure xxx shows a cross section of the central part of the specimens obtained by continuous fiber 3D printing robotic process.

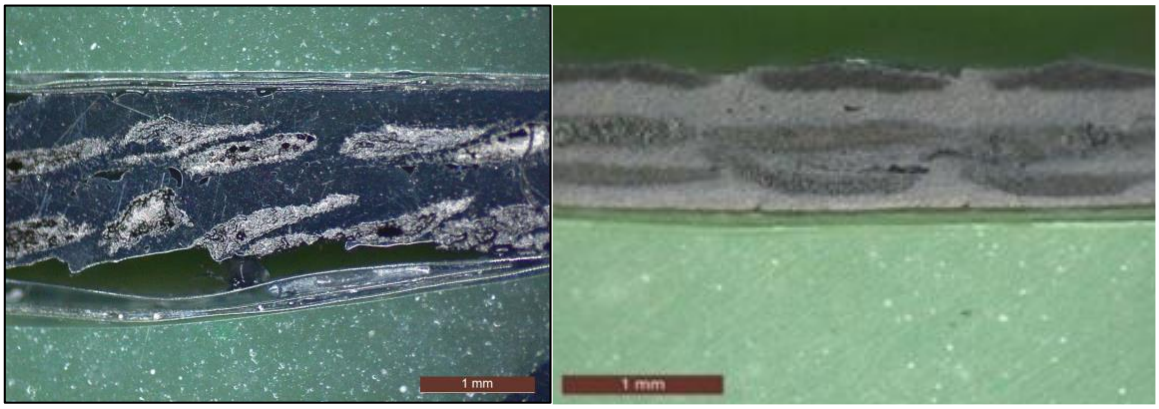

Figure 5. Micrograph of the cross section of PA6-CCF (left) and PPS-CCF (right) specimens manufactured by conventional 3D printing.

The micrographs show the consecutive deposition of the filament threads that were deposited layer by layer during the additive manufacturing process. It also shows how the threads are deformed during the 3D printing process with both materials, going from a circular section to a practically rectangular section.

In this case, the cohesion between threads and layers is more homogeneous, they present a higher quality and with fewer voids, inclusions and cavities compared to the conventional process.

4. Conclusions

In this work, the robotic FFF process developed with the conventional 3D printing process was analysed and characterized. The results of the tensile and flexural showed that under the same processing conditions the properties of the materials are not diminished.

On the other hand, it was possible to print continuous fiber filaments using a custom-developed print head. In addition, the material and the process were characterized by tensile and ILSS tests, the lack of an adequate and specific standard to test this type of composite materials manufactured by 3D printing complicates the interpretation and comparison of results with similar materials and processes. Also, it is a novel technology, which still has a lot to develop and investigate in order to implement improvements in the manufacturing process as well as in the quality of the starting materials.

Another relevant aspect is the printing software. For this type of filament, specific printing software is necessary that takes into account the particularities of the fiber.

For now, all the printing tests were on planar surfaces, but the objective of a robotic system is printing on non-planar surfaces and be able to locally reinforce parts in any direction. This will be another paradigm to study in future works, since it requires higher software development, which allows reading the surfaces and detecting the areas in which fiber or polymer needs to be deposited following the surface.

References

5. References

1. Peng Zhuo, Shuguang Li, Ian Ashcroft, Arthur Jones, Jing Pu. 3d_printing_of_continous_fibre_reinforced_thermoplastic_composites. School of Mechanical, Materials, Manufacturing Engineering, University of Nottingham, UK. Composites Science and Technology Division, AVIC Composites Corporation, Ltd., China
2. Fatemeh Mashayekhi, Julien BardonOrcID, Vincent Berthé, Henri PerrinOrcID, Stephan Westermann and Frédéric Addiego. Fused Filament Fabrication of Polymers and Continuous Fiber-Reinforced Polymer Composites: Advances in Structure Optimization and Health Monitoring. Department Materials Research and Technology (MRT), Luxembourg Institute of Science and Technology (LIST), ZAE Robert Steichen, 5 Rue Bommel, L-4940 Hautcharage, Luxembourg. Polymers 2021, 13(5), 789; https://doi.org/10.3390/polym13050789
3. Mori K., Maeno T., Nakagawa Y. Dieless. Forming of Carbon Fibre Reinforced Plastic Parts Using 3D Printer. Procedia Eng. 2014;81:1595–1600. doi: 10.1016/j.proeng.2014.10.196
4. Matsuzaki R., Ueda M., Namiki M., Jeong T.K., Asahara H., Horiguchi K., Nakamura T., Todoroki A., Hirano Y. Three-dimensional printing of continuous-fiber composites by in-nozzle impregnation. Sci. Rep. 2016;6:1–7. doi: 10.1038/srep23058.
5. Pinar Urhal, Andrew Weightman, Carl Diver, Paulo Bartolo. Robot assisted additive manufacturing: A review. School of Mechanical Aerospace and Civil Engineering, The University of Manchester, UK.

EXPERIMENTAL CHARACTERISATION OF TWO STRUCTURAL BONDED COMPOSITE REPAIRS

Nathalie Barrière[a], Laetitia Minier[a], Thomas Duval[b], Fabien Degrigny[b], Irène Maillet[a]

a: DGA TA - 47, rue Saint-Jean, CS 93123, 31130 Balma
b: SIAé AIA-CF - 161, av du Brézet – CS70501 – 63028 Clermont-Fd cedex 02
nathalie.barriere@intradef.gouv.fr

Abstract: *Composite structures are used on military aircrafts because of their light weight and high mechanical performance, but they are sensitive to impact damage. Structural repairs are essential to restore mechanical properties after impact event, but they rely on fasteners because bonding repairs are difficult to certify. To have a better understanding of the behaviour of bonded repairs, the authors investigated two types of bonded repairs under several loading conditions: tension, compression and fatigue on carbon epoxy laminate panel. The initial damage, a hole of 75 mm diameter and 10 plies depth is repaired either by a flush repair with a dry fabric and a film adhesive or an external pre-cured patch made with the same material as the parent. Static results are slightly better for the flush repair, but the fatigue results demonstrated that flush repair can withstand higher fatigue load without any damage initiation detected by lock-in thermography analysis.*

Keywords: Composite material; bonded repair; wet lay up; external patch

1. Introduction

Structural repairs are required to restore mechanical properties of damaged composite parts, including their ultimate strength, durability, and damage tolerance. Main repair techniques of primary structures consist in either bolted or bolted and bonded (hybrid repair) because of the lack of non-destructive technique able to detect weak bond [1]. However, simply bonded repairs offer some advantages: weight saving and more uniform load transfer and avoid stress concentration around fastener holes [2]. New approaches have been proposed to meet the certification requirements [3, 4, 5].

Investigation of the behavior of bonded repair are necessary to understand their failure mechanism but are often limited to joints or coupons [6, 7, 8, 9]. Very few experimental studies focus on mechanical performance of repairs on monolithic composite panel [10, 11, 12]. To have a better understanding of the behavior of bonded repairs, two repair strategies have been investigated. The first repair is a wet lay up repair with a dry fabric and a film adhesive. The second one is an external pre-cured patch pasted with the same film adhesive.

2. Experimental work

2.1 Objective and methodology

An experimental program has been set up to study the mechanical behaviour of monolithic panels with the two types of circular repairs under tensile, compressive and fatigue load. The

  doi:10.5075/epfl-298799_978-2-9701614-0-0

wet layup repair was a flush repair, which offered an aerodynamically smooth surface but less mechanical performance because of the low mechanical properties of the fabric compared to the pristine material. The external repair was a pre-cured patch made with the same material as the pristine material.

The composite panels may be representative of wing cover, which works mainly in tension and compression. To avoid buckling of the panel during compression, out of plane displacement was constrained in some area. Fatigue tests were conducted à R=0.1 to propagate an eventual damage and then panels were submitted to compressive residual test.

2.2 Specimen preparation

The parent composite panels were made of 24 plies of UD tape of carbon fiber /epoxy pregreg cured in autoclave at 180°C. The size of the panels was 400mm x 400 mm without tabs. The initial damage was a machined hole of 75 mm diameter and 10 plies depth.

For the flush repairs, steps of 6 mm were made with conventional machining and then smoothly ground to achieve a correct surface preparation. Then G806 fabric and Redux 312L film adhesive were laid up. Additional plies were added during the stacking sequence due to the difference of ply cured thickness between the parent and repair materials (Figure 1). An over-ply was added on the top of the repair to provide protection and stiffness at joint tips, but also to reduce peak stress [10]. The repair was cured at 110°C after a first step at 70°C with a thermal blanket and a portable device, which enable temperature and vacuum control during the whole process.

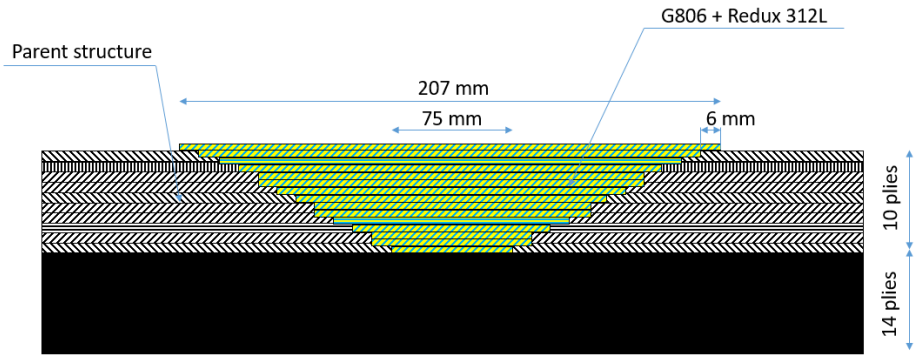

Figure 1. Flush repair with step machining and wet lay up (not to scale)

External patches were made with the same material as the parent but the stacking sequence has been modified to obtain a symmetrical layup. They were cured in autoclave with the same process as the parent material. The hole in the parent structure was filled with Ly5052 and then the patch is bonded with a film of Redux 312-5 adhesive with a thermal blanket with the same cured cycle used for the flush repair (Figure 2). The carrier inside the film adhesive enable to achieve a controlled thickness along the bond line of 0.2 mm.

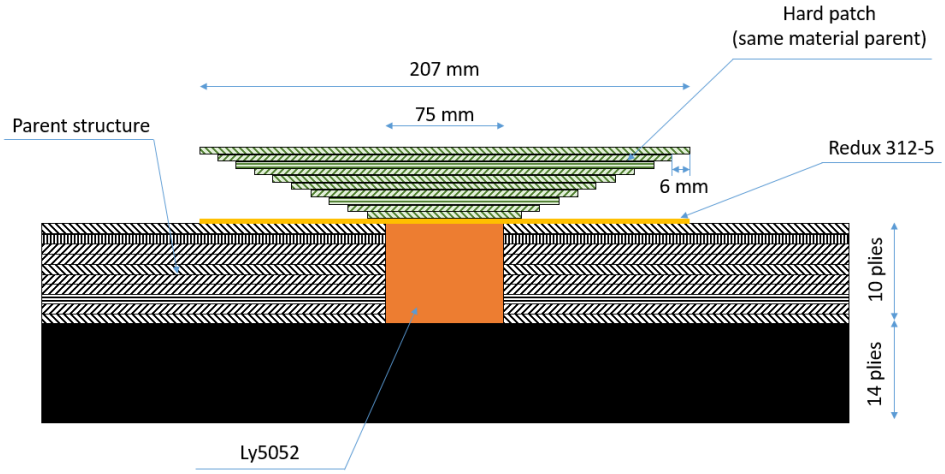

Figure 2. External repair with a pre-cured patch (not to scale)

2.3 Tensile tests

Tensile tests were run on 3 pristine panels and 3 repaired panels of each configuration at room temperature on a Schenk test machine with a 1000kN load cell. The loading speed was 1 mm/min. The specimen side with the repair was painted for measurement by a 3D digital image correlation (DIC) system (Aramis by GOM). The DIC post processing software was used to calculate in-plane and out of plane displacements and strain fields. At the rear side of specimen, 4 acoustic emission sensors (R15) were pasted to follow damage evolution in the specimen. A LVDT sensor measured length change of the specimen. Strain gages are used to follow strain field on the specimen.

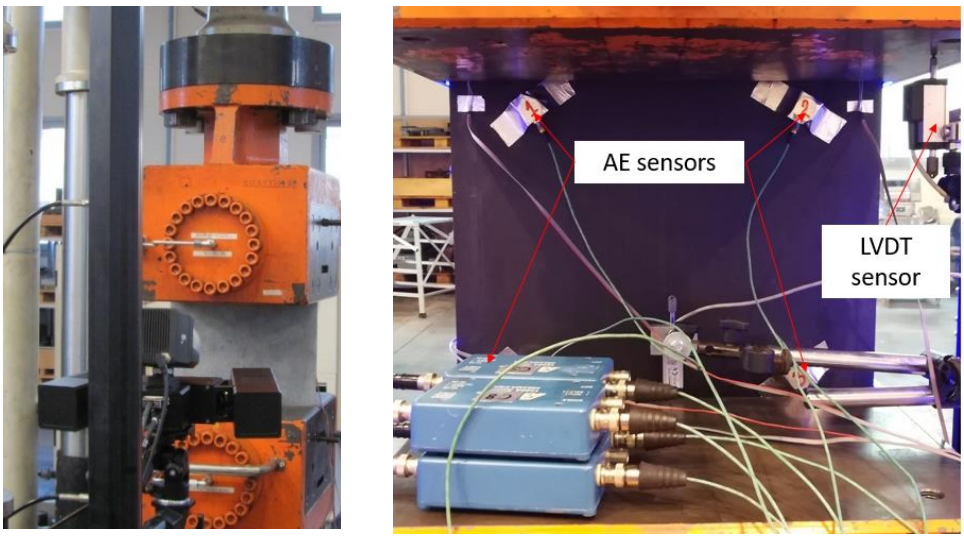

(a) (b)

Figure 3. Experimental set up for tensile tests. (a) Front size (face with the repair) with DIC measurements and (b) AE sensors on the rear side.

The failure load and the stiffness of the repaired panels obtained for the static tensile tests are compared to the pristine panels (Table 1). Even if the dry fabric has quite low mechanical properties (strength and stiffness), the flush repair offer the highest strength recovery with 87%, and a small loss of stiffness (2%). The external patch repair increases the stiffness of the panel

(+6%), which may be detrimental on a real composite structure because it may change the load path and generate a stress concentration around the repair.

Table 1: Test results for different panel configuration tested in tension

Specimen	Mean failure load F [kN]	Std Dev.	Strength recovery	Mean Stiffness [kN/mm]	Std Dev.	Stiffness recovery
Pristine	570	10.0	-	121	1.5	-
Flush repair	497	20.5	87%	119	1.7	98%
External patch	474	26.1	83%	128	0.9	106%

The acoustic events (AE) recorded during the test show damage initiation starts very early in the panel repaired with the external patch (about 30% of the failure load in Figure 4). For the flush repair, the tensile failure has been reached in two stages. After the first load until 452 kN, the panel has been unloaded and inspected with ultrasonic device to detect potential damages (in particular disbond between repair and panel). Then the panel has been loaded again until failure. AE initiated at a higher load (about 65% of the failure load) for the flush repair. However, as soon as the damage process started the damage evolution increased dramatically until failure.

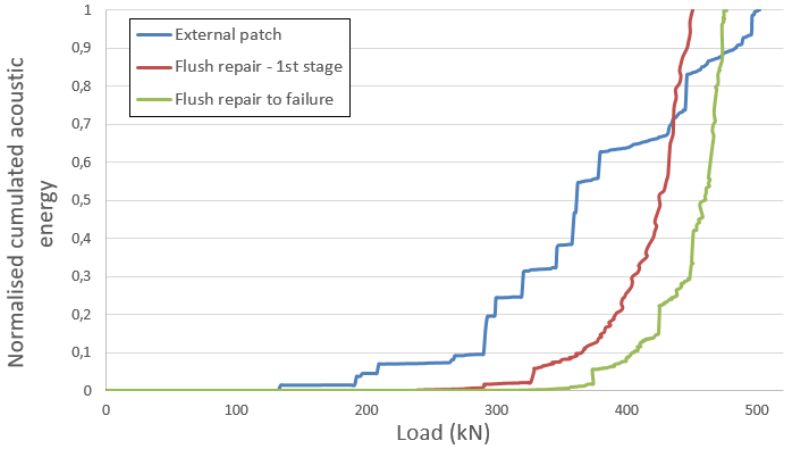

Figure 4. Normalised cumulated acoustic emission absolute energy of the two types of repaired panels

2.4 Compressive tests

Compressive tests were performed on a S-MOH test machine with a 3000 kN load cell and a constant displacement rate of 0.5 mm/min (Figure 5). For each repair configuration, 3 tests specimen were run at ambient temperature and 3 pristine panels were also tested as reference. An anti-buckle device constrained out of plane displacement in the centre of the specimen and the edges of the specimen to prevent premature failure because of global buckling of the panel.

  doi:10.5075/epfl-298799_978-2-9701614-0-0

The compressive tests were also multi-instrumented with LVDT sensors, DIC measurements, acoustic emission recording and strain gages.

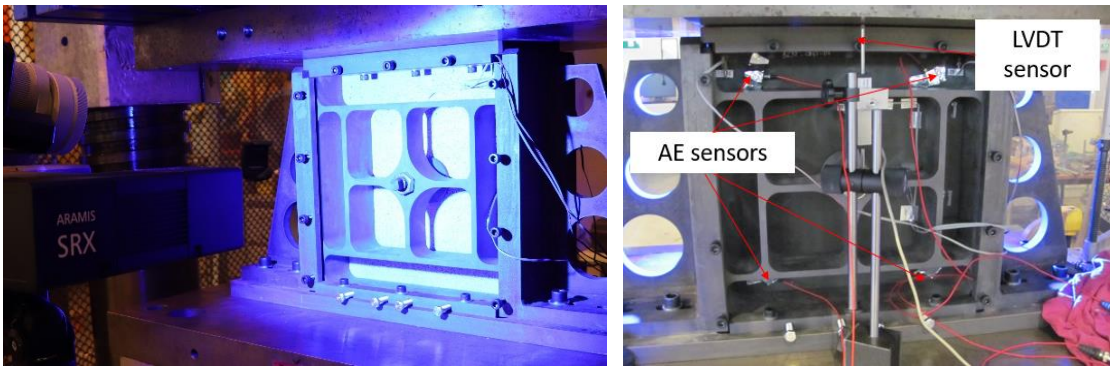

Figure 5. Experimental set up for compressive tests

Results of the compressive tests are summarized in the Table 2. The strength and the stiffness recovery can be considered as equivalent for both type of repairs because of the high standard deviation. The set up of specimen in the compressive device may have been difficult to reproduce from one specimen to another.

Table 2: Test results for different panel configuration tested in tension

Specimen	Mean failure load F [kN]	Std Dev.	Strength recovery	Mean Stiffness [kN/mm]	Std Dev.	Stiffness recovery
Pristine	-355	9.9	-	154	7.5	-
Flush repair	-353	19.8	99%	145	3.5	94%
External patch	-372	3.9	105%	144	12.8	93%

For the external patch, damage initiation start at very low compressive load (less than 30% of failure load), as it was already mentioned for tensile tests. The damage evolution presents two stages of very slow damage evolution before a fast increase until failure (Figure 6). For the flush repair, as soon as damage appeared in the panel (about 76% of the failure load), it rises rapidly until failure. The pristine panel has a more continuous damage evolution after the apparition of damage (same level as the flush repair, about 75% of the failure load).

1080/1151 ©2022 Barriere et al. doi:10.5075/epfl-298799_978-2-9701614-0-0 published under CC BY-NC 4.0 license

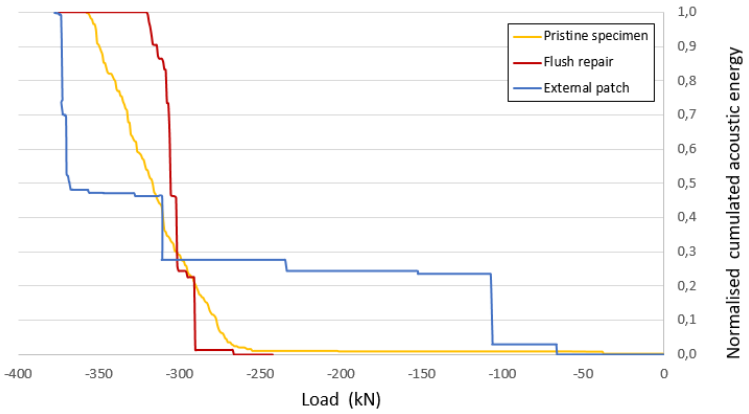

Figure 6. Normalised cumulated acoustic emission absolute energy of the two types of repaired panels

2.4 Fatigue tests

Fatigue tests were performed at a constant load ratio R=0.1 and at f=2Hz on a Schenk test machine with a 1000kN load cell. They were paused after the occurrence of three events of high amplitude recorded by an A.E sensor to perform a lock-in thermography (LT) analysis with a CEDIP Jade LW camera to detect damage initiation in the repair panel (Figure 7). The lens was a LW 2.0 Jade lens with a 25mm focal distance and a spectral band 8-12µm. Samples were heated by the use of two halogen lamps of 1000W square wave modulated with a frequency of 0.062Hz. Thermal images were collected at a frame rate of 5Hz. At the beginning of the fatigue test, LT analysis was also run to ensure the absence of any defect. For the fatigue campaign, there were 3 pristine specimen and 3 specimen for each repair configurations. The fatigue load of the 1st specimen was chosen at 60% of the tensile failure load of pristine specimen, then for the two next specimen, the fatigue load was decreased to achieve 5.10^5 cycles without any damage.

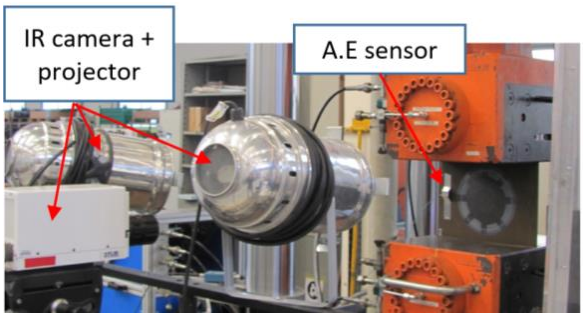

Figure 7. Experimental set up for fatigue tests

Fatigue results are presented in the Table 3. For the highest fatigue load (60% of failure load), both repair configurations showed a very fast damage initiation: about few hundred cycles for the external patch and about 10 000 cycles for the flush repair, leading to a failure of the panel before 100 000 cycles. The flush repair can withstand 40% of the failure load without any damage detected for 5.10^5 cycles, whereas the load has to be reduced at 20% for the external patch to undergo 5.10^5 cycles without damage. Fatigue behaviour are consistent with static results since damage initiation starts at very low stress for the external patch repair which lead to rapid damage propagation leading to the failure of the panel.

1081/1151 ©2022 Barriere et al. doi:10.5075/epfl-298799_978-2-9701614-0-0 published under CC BY-NC 4.0 license

Table 3: Test results for different panel configuration tested in fatigue tests

Specimen	% failure load of pristine panel	% failure load of repaired panel	Observations
Pristine-1	60%	-	5.10^5 cycles without failure but delamination in the tabs.
Pristine-2	50%	-	5.10^5 cycles without failure.
Pristine-3	40%	-	5.10^5 cycles without failure.
Flush repair-1	60%	67%	Disbond of the repair at ~ 10 000 cycles. Failure at 91 800 cycles.
Flush repair-2	50%	57%	Disbond of the repair at 126 000 cycles. Test stopped at 5.10^5 cycles without failure.
Flush repair-3	40%	46%	5.10^5 cycles without any damage detected via LT.
External patch-1	60%	68%	Disbond of the repair at ~ 100 cycles. Failure at 85 800 cycles.
External patch-2	40%	48%	Disbond of the repair at 164 000 cycles. Test stopped at 5.10^5 cycles without failure
External patch-3	20%	24%	5.10^5 cycles without any damage detected via LT

3. Conclusion

Two types of repair have been investigated on carbon epoxy panels of 4.5 mm thick under static and fatigue loadings. A pre-cured external patch with the same material as the parent has been compared to a flush repair, with 6 mm steps and a wet lay up of dry fabric and film adhesive. Both tensile and compressive results show slightly better mechanical performance (strength and stiffness) of the flush repair, but the AE revealed large difference in damage initiation and propagation between the two configurations. Indeed, in the external patch repair damage initiation starts at very low loads, followed by a slow damage evolution. These results are consistent with fatigue results which demonstrated that even low fatigue loads lead to failure of the external patch repair.

Acknowledgements

Authors are greatly thankful to the divisions TF and BE-Calc of AIA Clermont Ferrand and also the division MT of DGA TA, who have contributed to this work.

  doi:10.5075/epfl-298799_978-2-9701614-0-0

4. References

1. K.B. Katnam et al. Bonded repair of composite aircraft structures: A review of scientific challenges and opportunities, Progress in Aerospace Sciences. 2013; 61: 26–42
2. Duong C. N., Wang C. H., Composite repair, Theory and design. Elsevier. 2007.
3. Ecault R. Experimental and numerical investigations on the dynamic behaviour of aeronautic composites under laser shock - Optimization of a shock wave adhesion test for bonded composites, PdD, 2013.
4. Baker A., Gunnion A.J., Wang J., Chang P. Advances in the proof test for certification of bonded repairs – Increasing the Technology Readiness Level, International Journal of Adhesion & Adhesives 2016; 64: 128–141
5. Zhou W., Ji X., Yang S., Liu J., Ma L., Review on the performance improvements and non-destructive testing of patches repaired composites, Composite Structures 2021; 263.
6. Campilho R.D.S.G., de Moura M.F.S.F., Pinto A.M.G. , Morais J.J.L. , Domingues J.J.M.S. Modelling the tensile fracture behaviour of CFRP scarf repairs, Composites: Part B. 2009; 40: 149–157
7. Truong V-H., Yoo J_S., Kim C-H., Park M-Y., Jin-Ho Choi J-H., Kweon J-H. Failure load prediction of laminates repaired with a scarf-bonded patch using the damage zone method. Advanced Composite Materials 2016.
8. Han Q., Liu B., Xie W. The tension failure mechanisms of composite stepped bonding repairs and joints for the aircraft primary load bearing structures. Journal of Adhesion Science and Technology. 2019.
9. Wang S., Xie Z., Li X.: On adhesively bonded stepped scarf joint: an analytical model and its validation. Mechanics of Advanced Materials and Structures. 2019.
10. Breitzman T.D., E.V. Iarve, Cook B. M., Schoeppner G.A., Lipton R. P. Optimization of a composite scarf repair patch under tensile loading. Composites: Part A. 2009. 40: 1921–1930
11. Cheng P., Gong X-J., Aivazzadeh S., Xiao X. Experimental observation of tensile behavior of patch repaired composites, Polymer Testing. 2014. 34: 146–154.
12. Ghazali E., Dano M-L. , Gakwaya A., Amyot C-O. Experimental and numerical studies of stepped-scarf circular repairs in composite sandwich panels. International Journal of Adhesion and Adhesives. 2018. 82 : 41–49

  doi:10.5075/epfl-298799_978-2-9701614-0-0

DEVELOPING A NEW TYPES OF FIBER-REINFORCED COMPOSITES MANUFACTURING SYSTEM: MULTI-DROP FILLING PROCESS

Seung In, Kang[a], Jung Jae, Yoo[a], Min Gyoung, Kim[a], Dong Gi, Seong[a,b*]

a: School of Chemical Engineering, Pusan National University, Busandaehak-ro 63beon-gil 2, Geumjeong-gu, Busan, Republic of Korea

b: Department of Polymer Science and Engineering, Pusan National University, Busandaehak-ro 63beon-gil 2, Geumjeong-gu, Busan, Republic of Korea

First/presenting author : Seung In, Kang (brad1024@pusan.ac.kr)
Corresponding author : Dong Gi, Seong (dgseong@pusan.ac.kr)

Abstract: We suggest a new liquid composite molding process (LCM) called the multi-drop filling process (MDF). The newly proposed MDF includes a programmable resin dosing system that allows dropping an accurate amount of resin at the pre-designated location. Carbon fiber-reinforced plastic (CFRP) with both complex geometry and simple plate shape specimens were fabricated by the suggested MDF and the vacuum-assisted resin transfer molding (VARTM). MDF's advanced impregnability and filling time were proved by comparing parameters such as tensile, compressive, flexural, short-beam strengths as well as void contents with VARTM. In the case of plate shape specimens, all parameters showed a similar level in both groups, while the void content at corner regions of the MDF fabricated complex-shaped specimen showed a significant reduction as well as cycle time decreased. Obtained results proved that the newly developed MDF has the ability to mass-produce the customized complex-shaped composite parts, overcoming conventional LCM limitations.

Keywords: Carbon fibers; Liquid composite molding; Resin flow; Resin transfer molding

1. Introduction

Nowadays, most countries in the world are implementing carbon reduction policies to deal with environmental problems such as global warming, and many industries are suggesting various methods to meet such regulations. Among many solutions, the carbon-fiber-reinforced plastics (CFRPs) which are light-weighted materials and have high specific strengths have been highlighted as the primary solution to decrease carbon emissions and increase fuel efficiency. In particular, automobile industries had adapted plastics as their vehicle interior materials and have started to manufacture automobile bodies with Composite materials like CFRPs after they faced some limitations using metals [1-5].

Various composite material industrial fields have applied LCM as the manufacturing system that has versatile potential in production speed and cost. Approaching ideas of designing the present LCM is different from the old-fashioned autoclave molding-based manufacturing process which requires a long cycle time and high production costs that were not suitable for mass production [6]. After the development of the resin transfer molding (RTM), the set-up cost, and the production time of the manufacturing system have been reduced. For further improvements, diverse methods have been derived by adding additional suitable conditions such as High-pressure RTM (HP-RTM) and VARTM, etc. However, improvement was selectively

  doi:10.5075/epfl-298799_978-2-9701614-0-0

made, and side effects occurred according to each method. The HP-RTM, the suitable mass production method for manufacturing automobile parts, guarantees excellent productivity and adequate quality [7-9], however, it needs high capacity facilities such as resin injectors and a press which increase the equipment cost. In the case of the VARTM, the method has the advantage of being relatively simple and having fewer limitations for the product sizes, however, a strong dependence on the vacuum pressure increased the possibility of occurring unimpregnated areas and restricted the fiber volume fraction of the final product which determines the mechanical properties [10].

Many studies have been conducted to overcome the aforementioned limitations and to relieve a kind of trade-off relationship between productivity and product quality caused by resin impregnation. The wet compression molding (WCM) and the compression RTM (C-RTM) were the representatives of developed advanced LCM during the kind of research. These processes have been improved in many parts, such as proper production cost, high productivity, and maintaining high impregnation ability that leads products to be high quality, etc. [11-13], but these advantages are only applied to the flat shape products, not for complex shape and 3-dimensional geometries.

In this study, we developed a novel LCM that can cover the conventional LCM problems. The process called MDF has been developed and established on a laboratory scale. The MDF has adopted the programmable resin dosing system which combined remarkable points of WCM and multi-gate RTM [14] to dose the accurate amount of resin to a pre-designated location which leads the MDF to shorten the cycle time and fabricate high-quality products through superior impregnation ability and combined curing-compression stage. Furthermore, the designed automatic process has the advantage to minimize human labor and the waste of resources. To verify the superiority of the MDF, simple flat shapes and complex-shaped CFRPs were fabricated by the MDF and the VARTM [15]. Tensile, compressive, flexural, short-beam strengths, and void contents of produce samples were measured and compared to each other [16]. As a result, a shortened cycle time of the MDF and improved impregnation ability at the corner of the complex-shaped CFRPs were shown without any mechanical property damages.

2. Experiments

2.1 Material

A plain woven fabric with 3K tow of carbon fiber, labeled WSN 3KY, which has a fiber areal weight of 208 g/m^2 was supplied by Hyundai Fiber Co., Korea. Epoxy grades of KFR-120V and KFH-163 produced by Kukdo Chemical Co., Ltd. were used as the matrix resin and hardener, respectively.

2.2 Equipment

The MDF process was designed to minimize the unimpregnated section by dosing an accurate amount of resin at the pre-determined location (Fig. 1a). To implement the required resin-dosing system (Fig. 1b), an ENKIT 1000 with TRX 48 produced by WIKAN (Fig. 1d) was modified to achieve a dosing function with 3-axis movements. A pre-determined dosing region in this laboratory scale system is 215 mm X 180 mm X 40 mm for x, y, z axis respectively, and can be scaled up to the larger size adaptable to the desired products. An automated heating plate produced by QMESYS (Fig. 1e) was introduced to sequentially cure after impregnating the resin by compressive force (Fig. 1c).

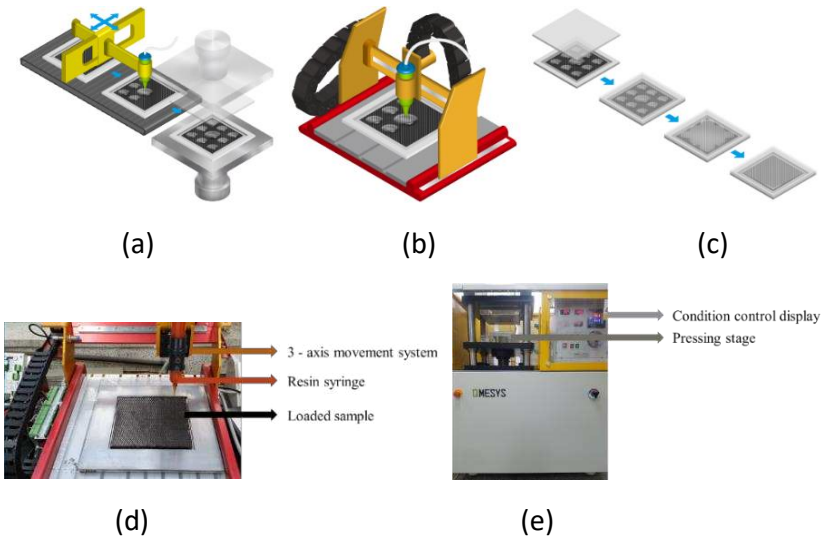

Figure 1. Schematic diagrams of MDF: (a) full process, (b) dosing system, (c) pressing system and implemented equipment: (d) dosing system, (e) hot pressing systems

2.3 Process optimization

To acquire the adequate MDF process window, rheological behavior of the selected resin was tested through a non-isothermal scan (Fig. 2a) and an isothermal scan (Fig. 2b) conducting at 10 ℃/min and with 20 ℃ intervals, respectively, by the Anton paar rheometer MCR-302. The hot press system and the dosing system were progressed through repetitive experiment. Obtained results were used to optimize the temperature, pressure, and cycle time of the MDF.

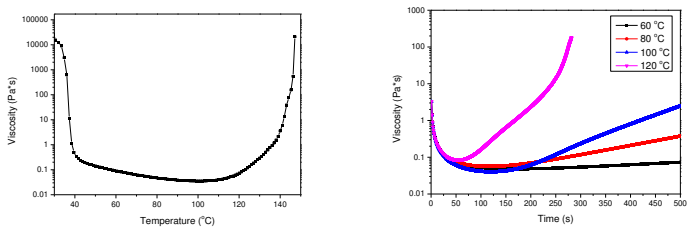

Fig. 2. Results of viscosity measurement: (a) non-isothermal and (b) isothermal scans of the epoxy resin

2.4 CFRPs fabrication

After the process optimization, the CFRPs samples were fabricated. The targeted plate sample with 50% of fiber volume fraction size was $150\ \text{mm} \times 150\ \text{mm} \times 2\ \text{mm}$ (length × width × thickness). The samples were prepared by MDF and VARTM and preparation procedures were illustrated in Fig. 3 and Fig. 4 respectively.

First, WSN 3KY carbon fabrics were cut into an designed size and dried in an oven at 100 ℃ for 24 hours to remove humidity. The nine plies of cut carbon fabric was stacked on a release agent coated mold (Fig. 3a, Fig. 4). The required number of fabrics was calculated by Equation (1) as follows:

$$V_f = (FAW \times N)/(\rho \times t). \quad (1)$$

Where V_f indicates the fiber volume fraction, *FAW* means the fiber areal weight (g/m^2), *N* is required number of stacked fiber, ρ is the fiber density (1.8 g/cm^3), and the *t* is the thickness of

  doi:10.5075/epfl-298799_978-2-9701614-0-0 published under CC BY-NC 4.0 license

the CFRP sample. In the case of the matrix, the resin and hardener was mixed in a 10:3 weight ratio for 1 min, and degassed in a vacuum oven at 60 ℃ for 20 min [17-18].

From the treatment of the resin mixture, the progress becomes different. For the MDF, a degassed resin matrix was placed into a dosing cylinder, and the cylinder is equipped with a dosing system (Fig. 3b). The dosing system was processed following the programmed pattern and 30 ml of resin was dropped onto the stacked fabric (Fig. 3c). After the resin drop was done, the upper mold was placed on the lower mold to keep the resin dropped area airtight. This makes the entire load applied to the mold uniformly in the hot press system (Fig. 3d). The curing and pressing stage was conducted for 45 min (Fig. 3e), then the mold was removed and cooled at room temperature. After successful demolding of the samples, a CFRPs sample was obtained.

In the case of the VARTM, peeling layers and flow media were piled onto the prepared fabrics to secure a smooth and uniform flow front. A few breather sheets were placed next to the piled fabric to ensure vacuum condition under all areas of the mold. Sealant tape was attached to the mold corner, and a bagging film covered the top of the mold to seal the experiment areas. A vacuum pump was operated to inject the resin into the stacked carbon fabric, and inlet and outlet pipes were locked when the resin reaches the outlet pipe securing the vacuum state in the experiment areas. The process was paused for a few minutes to settle the uniform thickness of the samples. After flattening the sample, the mold was moved into a 100 ℃ oven to cure the epoxy resin for 1 hour and cooled down at room temperature. Finally, a sample was removed from the mold (Fig. 4).

(a) (b) (c) (d) (e)

Fig. 3. CFRP sample preparation using the MDF process: (a) preforming, (b) preform loading on the dosing system, (c) matrix dosing, (d) finished d osing system, and (e) pressing and curing using the hot press system.

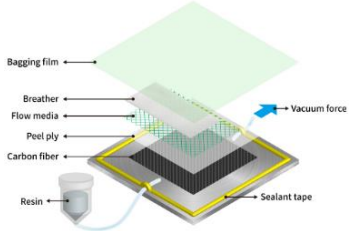

Fig. 4. Schematic diagram of the used VARTM process

Furthermore, complex shapes including bottle-neck, T-shaped, inserted areas were designed to prove the applicability of the MDF (Fig. 5a). The proposed 2-dimensional complex shape is a very harsh condition to fabricate the CFRPs due to the resin unimpregnation not only at the corner of T-shaped, and inserted areas but also in bottle-neck areas which narrows the resin flow channel. The fabric was cut and prepared in the designed complex shape and pre-proceeded the VARTM to record and observe the resin flow in the complex shaped fabrication (Fig. 5b-5g). After observing the unimprngatable risky areas, we programmed the resin dosing system of the MDF to drop the resin onto the areas and proceed with the MDF following the beforementioned progress and the sample was fabricated (Fig. 6a-6f) [19].

  doi:10.5075/epfl-298799_978-2-9701614-0-0

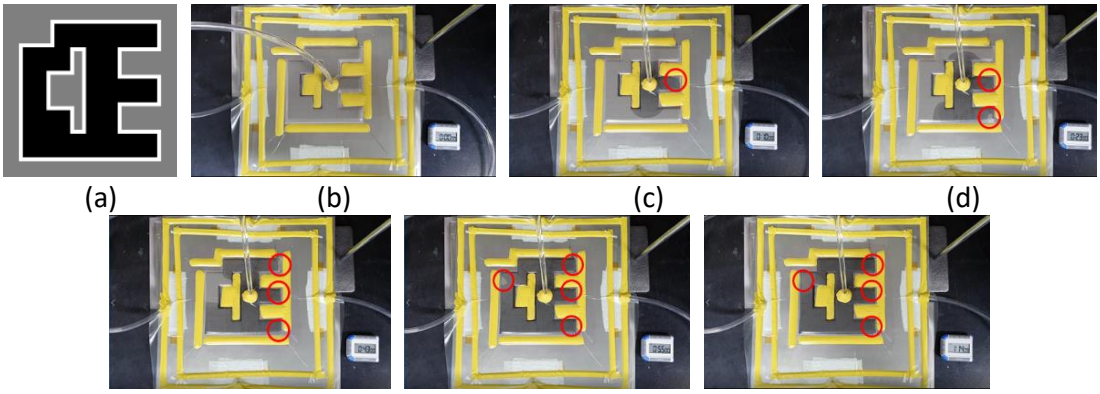

(a) (b) (c) (d)

(e) (f) (g)

Fig. 5. The complex shaped mold and the recorded resin flow in VARTM: (a) Geometry of the complex shaped mold, (b) VARTM preparation, (c) startup of resin flow initiation and the first air entrapment zone, (d) the second air entrapment zone, (e) the third air entrapment zone, (f) the fourth air entrapment zone, (g) the total expected air entrapment zone after finishing process

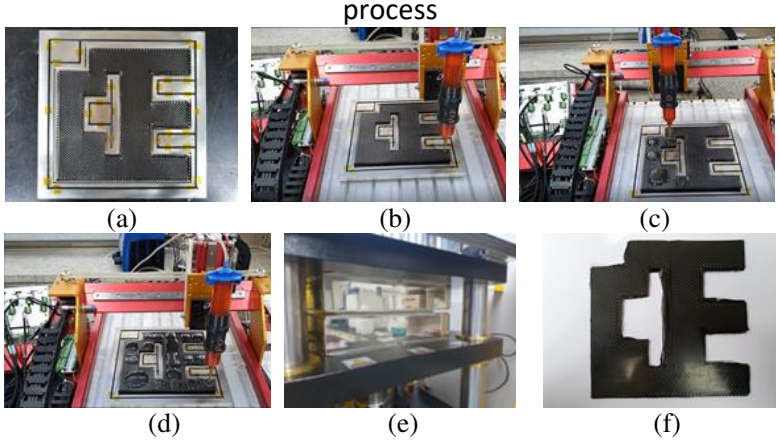

(a) (b) (c)

(d) (e) (f)

Fig. 6. Complex shaped sample preparation using MDF: (a) Preforming, (b) preform loading on the dosing system, (c) resin dosing, (d) completed dosing process, and (e) pressing and curing using the hot press system, (f) the fabricated sample

3. Results and discussion

3.1 CFRP fabrication

According to section 2.4, the CFRPs samples were fabricated through the optimized MDF and the VARTM. In this stage, we experimentally got an adequate dropping pattern for plate shape sample fabrication after several trials. The fabricated sample condition is shown in Table 1. Due to the additional compressive mold filling stage of the MDF system, the thickness of the fabricated samples was 1.98 mm, which was slightly thinner than that of the VARTM sample.

Table 1: Conditions of fabricated CFRPs

Process	MDF	VARTM
Average thickness (mm)	1.98	2.03
Fiber volume fraction	52.52%	51.23%

3.2 Mechanical properties and void content measurement

Tensile, compressive, flexural, and short-beam strengths of processed plate shape CFRPs were measured according to the proper ASTM methods. The results were shown in Fig. 7. In the case

of the tensile and short-beam strengths, the MDF samples showed 3.9% and 3.1% higher values respectively than the VARTM samples (Fig. 7a, 7d), while the VARTM samples showed each 8.1% and 3.1% higher compressive and flexural strengths than that of the MDF's (Fig. 7b, 7c).

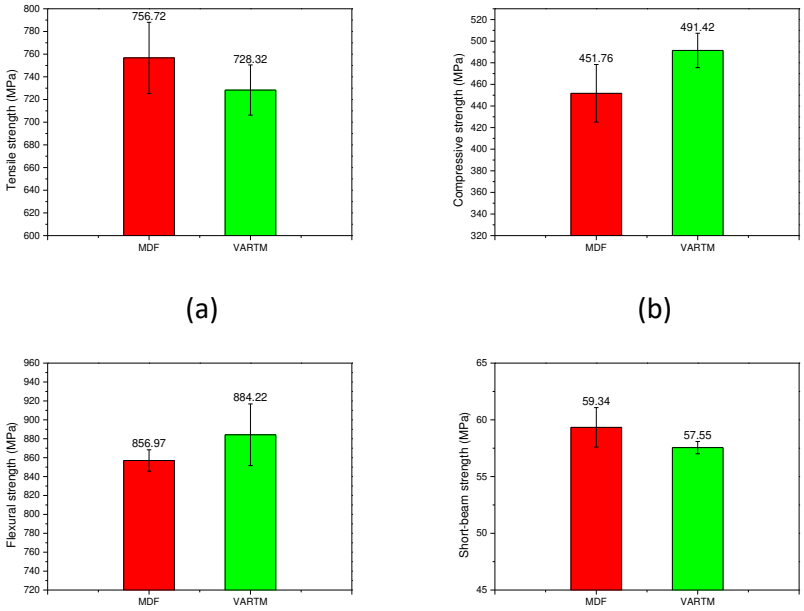

Fig. 7. Comparison of mechanical properties: (a) tensile, (b) compressive, (c) flexural, (d) and short-beam strengths

Some of the processed sample cross-section was observed by optical microscope through the mounting and polishing stages. The observed image was then analyzed by comparing the contrast ratio, the tool of the Image J software. As illustrated in Fig. 8, the VARTM sample had 0.3% of very low void content on average, while the MDF had a relatively high 1.2%.

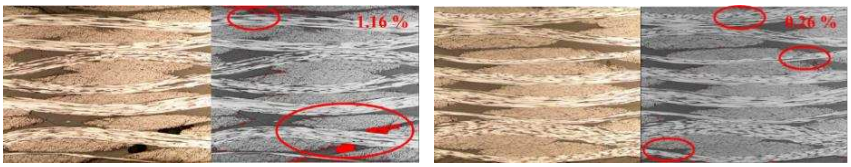

Fig. 8. Void contents measured using contrast ratio: (a) MDF and (b) VARTM products

In the case of the complex-shaped CFRPs, predicted unimpregnatable areas were processed into the specimens (Fig. 9a) and the average void content was calculated through the as same step as the plate shape CFRPs have done. As shown in Fig. 9b and 9c, the results have reversed. The MDF sample showed 0.1% of the void contents when the VARTM showed 0.77%.

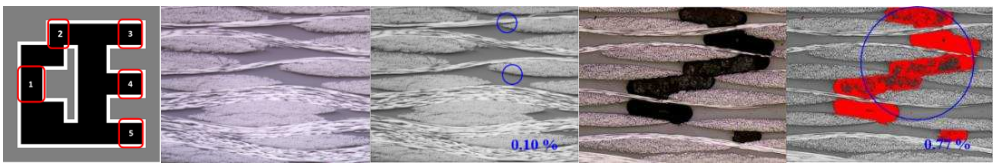

Fig. 9. Selected cut section for optical microscope observation (a) and void contents measure using contrast ratio, (b) MDF, and (c) VARTM products in section 3.

  doi:10.5075/epfl-298799_978-2-9701614-0-0

3.3 Discussion

According to the different four mechanical properties measurement results, both the MDF and the VARTM sample showed a similar level of value although there were some different behaviors. Fig. 7a and 7d showed that the MDF sample had better tensile and short-beam strengths. This behavior is pretended to be the properties are directly affected by the volume fraction of fiber reinforcements. As shown in Table 1, the MDF sample had a slightly thinner thickness which causes the higher volume fraction of the carbon fabric. By contrast, the VARTM sample had higher compressive and flexural strengths. In this case, void content in the sample affects more than that of fiber volume fraction and can cause early breakage due to the stress concentration. Illustrated in Fig. 8, the VARTM had a lower level of void content than the MDF sample. Moreover, the impregnation ability in the complex shaped CFRPs fabrication was analyzed. Both the MDF and the VARTM showed a very low level of void content at an expected risky zone of the samples. However, the MDF showed 0.1% of the void content while the VARTM showed 0.77%. The higher void content in the VARTM sample was caused by the vortex occurring in the corner of the mold and, the permeability difference between the empty mold and the fiber reinforcement makes the large void.

4. Conclusion

To summarize, we successfully developed and established the novel LCM called the MDF. The programmable resin dosing system that drops the accurate amount of the resin onto the pre-designated areas is equipped and also the hot press system which makes the MDF sustain the high productivity without losing its mechanical properties. Two adapted system makes the MDF to has the advantage of minimizing the labor intensity and resource wastes by the process to be automatic.

The conventional VARTM was used as the reference for comparing with the MDF. Four mechanical properties, void content, and impregnation ability in the complex-shaped fabrication of CFRPs samples were compared. Obtained results verified that the MDF has superior impregnation ability without losing any mechanical properties.

In conclusion, the MDF has the superb possibility of commercialization and is able to propose a better condition when additional research will be done such as numerical simulation in the future.

Acknowledgement

This research was supported by the National Research Foundation of Korea (NRF) Grant funded by the Basic Science Research Program (2018R1D1A1B07045211) and the Industrial Strategic Technology Development Program funded by the Ministry of Trade, Industry & Energy(MOTIE, Korea) (K_G012001095002)

5. Reference

1. Holbery J, Houston D. Natural-fiber-reinforced polymer composites in automotive applications. JOM 2006;58(11):80-86.
2. Hosseinzadeh R, Shokrieh MM, Lessard LB. Parametric study of automotive composite bumper beams subjected to low-velocity impacts. Composite Structures 2005;68(4):419-427.
3. Lee J, Kim B, Ko D. Development of vacuum-assisted prepreg compression molding for production of automotive roof panels. Composite Structures 2019 1 April 2019;213:144-152.

  doi:10.5075/epfl-298799_978-2-9701614-0-0

4. Mallick PK. Fiber-reinforced composites: materials, manufacturing, and design. : CRC press; 2007.
5. Mamalis A, Manolakos D, Demosthenous G, Ioannidis M. The static and dynamic axial collapse of fibreglass composite automotive frame rails. Composite Structures 1996;34(1):77-90.
6. Maffezzoli A, Grieco A. Optimization of parts placement in autoclave processing of composites. Applied Composite Materials 2013;20(3):233-248.
7. M. Yamashita, T. Sakagawa, F. Takeda, F. Kimata, Y. Komori. Development of advanced vacuum assisted resin transfer molding technology for use in an MRJ empennage box structure. Technical Review 2008;45(4):1-4.
8. Verma KK, Dinesh BL, Singh K, Gaddikeri KM, Sundaram R. Challenges in Processing of a Cocured Wing Test Box Using Vacuum Enhanced Resin Infusion Technology (VERITy). Procedia Materials Science 2014 2014;6:331-340.
9. Seong DG, Kim S, Um MK, Song YS. Flow-induced deformation of unidirectional carbon fiber preform during the mold filling stage in liquid composite molding process. J Composite Mater 2018 04/01; 2022/04;52(9):1265-1277.
10. Correia NC, Robitaille F, Long AC, Rudd CD, Šimáček P, Advani SG. Analysis of the vacuum infusion moulding process: I. Analytical formulation. Composites Part A: Applied Science and Manufacturing 2005 December 2005;36(12):1645-1656.
11. Bhat P, Merotte J, Simacek P, Advani SG. Process analysis of compression resin transfer molding. Composites Part A: Applied Science and Manufacturing 2009 April 2009;40(4):431-441.
12. Poppe C, Albrecht F, Krauß C, Kärger L. A 3D Modelling Approach for Fluid Progression during Process Simulation of Wet Compression Moulding – Motivation & Approach. Procedia Manufacturing 2020 2020;47:85-92.
13. Kim SJ. The automotive stabilizer bars prepared by the third-generation method of composite fabrications. Functional Composites and Structure 2019;1(025005):1-11.
14. Kang MK, Jung JJ, Lee WI. Analysis of resin transfer moulding process with controlled multiple gates resin injection. Composites Part A: Applied Science and Manufacturing 2000 1 May 2000;31(5):407-422.
15. Bodaghi M, Cristóvão C, Gomes R, Correia NC. Experimental characterization of voids in high fibre volume fraction composites processed by high injection pressure RTM. Composites Part A: Applied Science and Manufacturing 2016 March 2016;82:88-99.
16. Alms JB, Glancey JL, Advani SG. Mechanical properties of composite structures fabricated with the vacuum induced preform relaxation process. Composite Structures 2010 November 2010;92(12):2811-2816.
17. Labordus M, Hoebergen A, Soderlund J, Astrom T. Avoiding voids by creating bubbles-Degassing of resin for the vacuum injection process. Innovative process and material solutions for creative design effectiveness 2000:47-58.
18. Patel N LL. Modeling of void formation and removal in liquid composite molding. Part II: Model development and implementation. Polym Compos 1996;17(1):104-114.
19. Kang SI, Yoo JJ, Kim MG, Seong DG. A new variant of liquid composite molding process based on multi-drop resin filling. Materials Today Communications 2022 June 2022;31:103363.

  doi:10.5075/epfl-298799_978-2-9701614-0-0

FUNCTIONAL MATERIAL BASED APPROACHES FOR REACTIVE RESIN TRANSFER MOLDING OF CARBON FIBER REINFORCED THERMOPLASTIC COMPOSITES

Dong Gi, Seong[a,b], Jae Hyo, Lee[a], Jung Jae, Yoo[a], Seung Mo, Son[a], Kyung Hyun, Song[c]*

a: School of Chemical Engineering, Pusan National University, Busandaehak-ro 63beon-gil 2, Geumjeong-gu, Busan 46241, Republic of Korea
b: Department of Polymer Science and Engineering, Pusan National University, Busandaehak-ro 63beon-gil 2, Geumjeong-gu, Busan 46241, Republic of Korea
c: School of Materials Science and Engineering, Ulsan National Institute of Science and Technology (UNIST), UNIST-gil 50, Ulju-gun, Ulsan 44919, Republic of Korea
Presenting & Corresponding author: Dong Gi, Seong (dgseong@pusan.ac.kr)

Abstract: *Thermoplastic polymer based carbon fiber composites have received great attentions as a lightweight structural material due to the superior advantages over the thermoset based ones in recyclability, cost effectiveness as well as good mechanical properties including impact resistance. Thermoplastic resin transfer molding using ε-caprolactam monomer has been developed as a promising high speed reactive process for mass-production of carbon fiber reinforced polyamide 6 composites. However, it still has some difficulties to be successfully applied to industries. In this study, several examples on functional materials introduced into the ε-caprolactam monomer are presented to improve the critical problems in the thermoplastic resin transfer molding such as flow instability caused by very low viscosity of monomer, moisture induced termination of polymerization during the process, and property degradation by moisture absorption of the final composite. It is expected to help the thermoplastic composite manufacturing process being successfully launched for industrial applications.*

Keywords: Reactive resin transfer molding; Thermoplastic; Function material; Polyamide 6; Moisture

1. Introduction

As environmental regulations in the automotive industry become tighter, many efforts have been made to reduce the weight of automotive structural parts. Carbon fiber reinforced composite is one of the promising lightweight material with superior mechanical properties for the applications to automotive industries which often require the fast production system of composite parts with low costs [1]. Liquid composite molding has been regarded as an efficient process for mass production of fiber reinforced composite parts, because it makes it possible to fabricate 3 dimensional structural parts by directly impregnating thermoset or thermoplastic resin into the dry fiber preform. It enables us to make composite parts only in several minutes by using a fast cure type epoxy resin or reactive monomer for thermoplastic resin [2].

Thermoplastic polymer based carbon fiber composites have received great attentions as a lightweight structural material due to the superior advantages over the thermoset based ones in recyclability, cost effectiveness as well as good mechanical properties including impact

  doi:10.5075/epfl-298799_978-2-9701614-0-0

resistance [3]. Thermoplastic resin transfer molding using ε-caprolactam monomer has been developed as a promising high speed reactive process for mass-production of carbon fiber reinforced polyamide 6 composites. However, it still has some difficulties to be successfully applied to industries. In this study, several examples on functional materials introduced into the ε-caprolactam monomer are presented to improve the critical problems in the thermoplastic resin transfer molding such as flow instability caused by very low viscosity of monomer, moisture induced termination of polymerization during the process, and property degradation by moisture absorption of the final composite. It is expected to help the thermoplastic composite manufacturing process being successfully launched for industrial applications.

2. Experimental

2.1 Materials

Plain woven carbon fibers (WSN 2KY, Hyundai Fiber CO. LTD, South Korea) were used to manufacture the composites. A monomer (ε-caprolactam, C2204, Sigma-Aldrich, USA), a catalyst (ethylmagnesium bromide, 189871, Sigma-Aldrich, USA), an activator (N-acetylcaprolactam, 283010, Sigma-Aldrich, USA) are used for synthesis the polyamide 6. In the manufacturing step of the composites, another activator (hexamethylene diisocyanate, 52650, Sigma-Aldrich, USA) that can slow the polymerization rate was used to improve the impregnation of the resin.

2.2 Experiments

To fabricate the polyamide 6-based CFRTP through reactive resin transfer molding, ε-caprolactam was melted in a 75 °C flask. After the melting process, the catalyst was injected. After 30 min of degassing was conducted, the initiator was injected with stirring for 1 min. Finally, the resin was injected into the prepared mold, which was heated to 150 °C in a hot-press machine (QM900A, QMESTS). After synthesizing the matrix in the hot-press machine for 1 h, the polyamide 6-based CFRTP sample was obtained.

Three kinds of functional materials were introduced during the reactive resin transfer molding. Porous ceramic particle was used as moisture absorbing material, polyamide oligomer was used for improving flow instability, and polyamide copolymer was introduced for protecting the degradation of polyamide 6 by moisture absorption.

3. Results and discussion

3.1 Effect of porous ceramic particle

Water remained in ε-caprolactam is known as terminating the polymerization and resulting in low conversion and molecular weight of polyamide 6. Figure 1 shows that 0.357 mol% of water decreases conversion of ε-caprolactam from 89.0% to 27.5% and viscosity average molecular weight from 53512 to 13465 g/mol. It is why very low moisture content should be maintained in reactive resin transfer molding of ε-caprolactam. Although successful control of moisture requires high level of sealing technique in a whole process equipment and the additional desiccating system, it is difficult and can be a big burden to process engineers. Introduction of

water absorbing porous ceramic particle improved monomer conversion to 85% and viscosity average molecular weight to 43441 g/mol in the condition of 0.357 mol% water, as shown in figure 1. The effect of the porous particle was also verified by measuring viscosity change during polymerization of ε-caprolactam in figure 2. Particle added resin showed the increase of viscosity even in a high-humidity condition, which indicated that inhibition of polymerization was improved by the water absorbing particle.

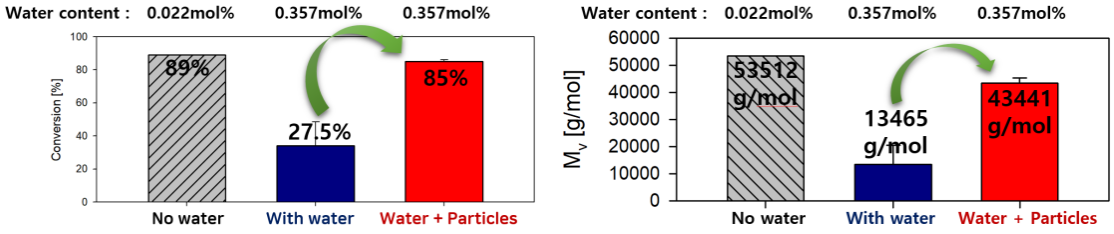

(a) *(b)*

Figure 1. (a) Monomer conversion, and (b) viscosity average molecular weight of polyamide 6 with and without water and porous particle

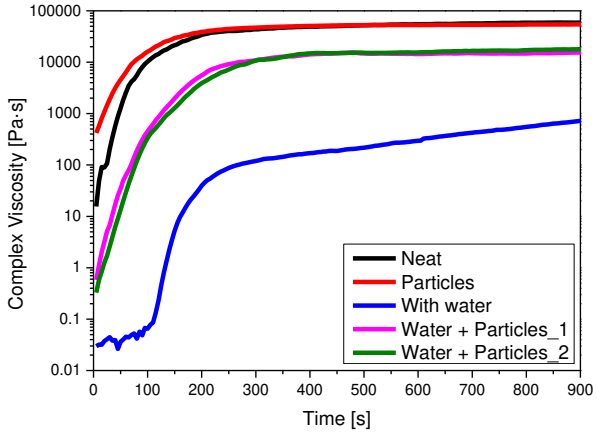

Figure 2. Viscosity behavior during progress of polymerization in the high-humidity condition by adding water absorbing particle

3.2 Effect of polyamide oligomer

To compare the void contents between neat ε-caprolactam- and polyamide oligomer (C-PA6O) based composite materials, they were fabricated under the same conditions and analyzed the cross-section of composite. As shown in figure 3, the C-PA6O-based composite material displayed more evenly impregnated with lower void contents than the neat ε-caprolactam-based composite material. It is because PA6O has a higher hydrophobicity than ε-caprolactam as previously discussed, playing a role to enhance the hydrophobicity of the existing resin. This may induce the interfacial interaction between the fiber preform and the resin, which can increase the capillary force and simultaneously decrease the contact angle between the fiber and the resin, showing high-quality impregnation. In contrast, due to an excess viscous force,

several unoccupied sections in the intra-tows were more found in the neat caprolactam-based composite material, demonstrating the formation of microvoids.

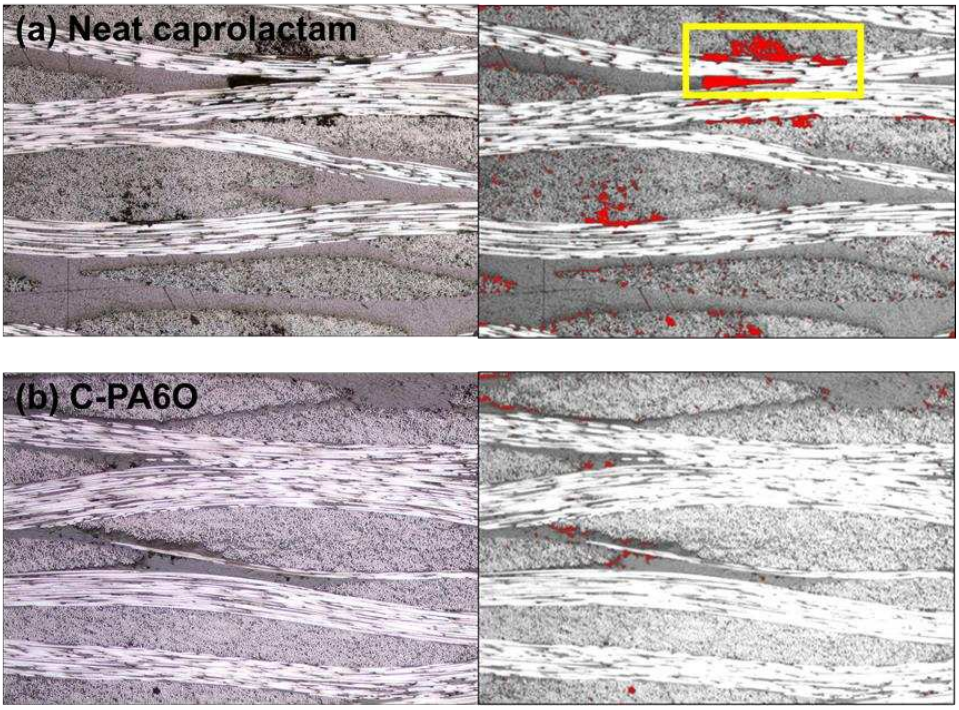

Figure 3. Optical microscopic images of the cross-sections of the CFRPs with (a) neat ε-caprolactam, and (b) C-PA6O resin to observe the void contents

3.3 Effect of polyamide copolymer

As shown in figure 4, the polyamide copolymer matrix absorbed a remarkably lower amount of water than the PA6 matrix, with only 43% of the water absorption of PA6 after 6 h of immersion. However, as the immersion time increased, the gap in the water absorption data between the two samples decreased, until they finally showed similar values after 8 h of immersion. As the immersion time increased in the water absorption test of PA6, a decrease in the water absorption occurred, which finally accounted for the similarity of the water absorption amount with that of the copolymer as the hydrolysis of the PA6 chain occurred. Therefore, the mechanical properties of the composite were estimated after 6 h of immersion in a 60 °C water bath to verify the effectiveness of the copolymer system. The contact angles of the PA6-based composite and copolymer-based composite were estimated to analyze the hydrophilicities of the two matrices. Contact angles of 54.59° and 86.41° were estimated, confirming the decreased hydrophilicity of the copolymer. Such a decrease in the contact angle was due to the lower hydrophilicity of the copolymer.

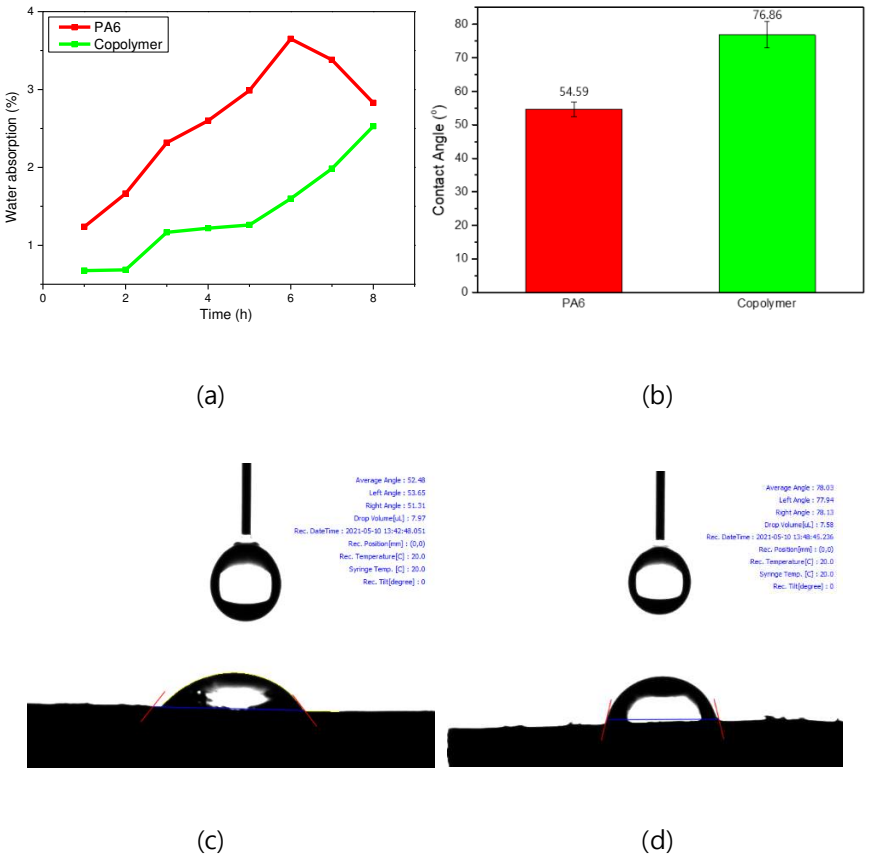

Figure 4. (a) Water absorption data of PA6 and copolymer, (b) contact angle data of two matrices, (c) contact angle image of PA6-based composite, and (d) contact angle image of copolymer-based composite

The void content was calculated using an image processing method with images obtained by optical microscopy as represented in figure 5. As a result, a 2.08% void content was observed in the PA6 composite. In addition, a void content of 0.88% was observed in the copolymer CFRP, which was less than half of the void content in the PA6 CFRP. Such a decrease in void content was expected to originate from the affinity between the matrix and carbon fiber due to hydrophilicity. Because conventional PA6 has a low affinity to carbon fiber, micro-voids formed in the tow of the carbon fiber were observed. However, when the ε-caprolactone oligomer was added to the resin of the composite, it could easily be mixed with the carbon fiber to fill the inter-tow region of the carbon fiber with lower hydrophilicity and finally obtain a lower void content than the PA6 matrix. Furthermore, such a decrease in the void content could contribute to the enhancement of the mechanical properties of the composite.

  doi:10.5075/epfl-298799_978-2-9701614-0-0

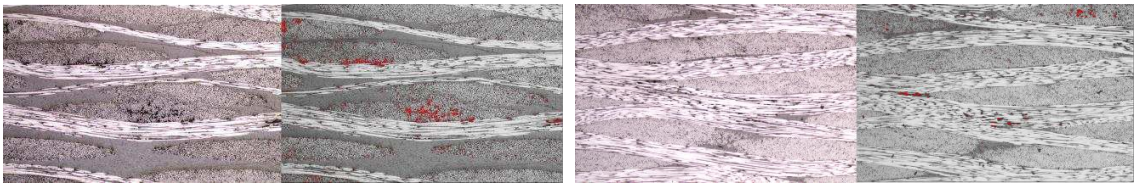

(a) (b)

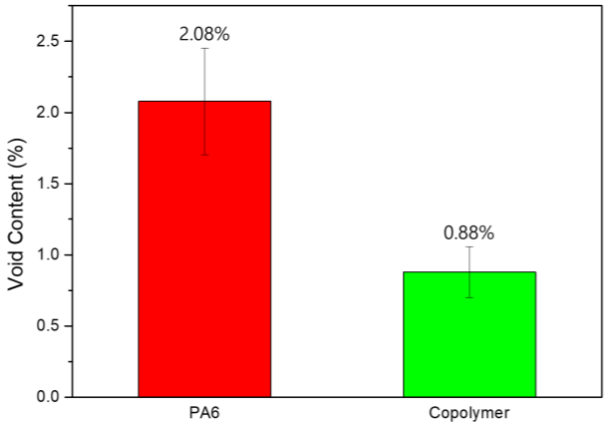

(c)

Figure 5. (a) Optical microscope image of (a) PA6-based CFRTP, (b) copolymer-based CFRTP, and (c) void content of composite

4. Conclusions

In this study, three kinds of examples on functional materials introduced into the ε-caprolactam monomer are presented to improve the critical problems in the thermoplastic resin transfer molding such as flow instability caused by very low viscosity of monomer, moisture induced termination of polymerization during the process, and property degradation by moisture absorption of the final composite. Porous ceramic particle was introduced to absorb the remained water in the ε-caprolactam, which resulted in preventing from terminating the polymerization of polyamide 6. Flow instability of ε-caprolactam was improved to decrease the void content of polyamide 6 composite by adding polyamide oligomer. The degradation of polyamide 6 in the composite by water immersion was remarkably improved by introducing polyamide copolymer with the higher hydrophobicity. The use of these functional materials is expected to help the reactive molding process of thermoplastic composite being successfully launched for industrial applications.

Acknowledgements

This research was supported by the National Research Foundation of Korea (NRF) Grant funded by the Basic Science Research Program (2018R1D1A1B07045211) and the Industrial Strategic

Technology Development Program funded by the Ministry of Trade, Industry & Energy(MOTIE, Korea) (K_G012001095002).

5. References

1. Muhammad P, Suhara P, Birat KC, Mohini S, Jimi T. Emerging trends in automotive lightweighting through novel composite materials. Materials Science and Applications. 2016; 7, 26–38.

2. Seong DG, Kim S, Um MK, Song YS. Flow induced deformation of unidirectional fiber preform during the mold filling stage in liquid composite molding process. Journal of Composite Materials. 2018; 52, 1265–1277.

3. Kim BJ, Cha SH, Park YB. Ultra-high-speed processing of nanomaterial-reinforced woven carbon fiber/polyamide 6 composites using reactive thermoplastic resin transfer molding. Composites Part B: Engineering. 2018; 143:36-46.

  doi:10.5075/epfl-298799_978-2-9701614-0-0

VARTM OF NATURAL FIBER COMPOSITE DOME USING INLAY KNIT FABRICS

Mami Sano[a], Kodai Kobayashi[a], Satoshi Tamaki[b], Junji Noda[a]

a: Kindai University – 2233730014e@waka.kindai.ac.jp
b: Shima Seiki MFG., LTD.

Abstract: *The continuity and excellent draping properties of knitted materials are expected to improve the formability and high strength of three-dimensional structures in natural fiber composites (NFC). However, composites using inlay-type knitted material as reinforcement have not been used in the field of composite yet. Therefore, the purpose of this study is to establish a forming method for NFC domes using inlay knit fabrics, and to evaluate their mechanical properties. In order to evaluate the formability of the NFC domes, VaRTM under various conditions were conducted. In addition, we evaluated the compressive capacity of the NFC dome by on-Axis compressive tests to observe the fracture mechanism.*

Keywords: VaRTM; NFC; dome; Inlay knit fabrics

1. Introduction

Recently, natural fiber composites (NFC) have attracted attention from the viewpoints of environmental considerations. In Europe, NFC is widely used as interior materials for automobiles, and these are made by injection molding [1]. These NFC parts made by injection molding are reinforced with short fibers, so the productivity and drape property is prioritized in exchange for the decrease in stiffness and strength. For the construction of sustainable society, it is required to develop a NFC reinforced with continuous fibers having high stiffness, strength and draping. Since the natural fiber has a high failure strain, the woven and knit structure using natural fibers have been used from a long time ago. Inlay knit fabric is one of knit structures, that is, weft threads called inlays are inserted into the knit to keep the outline of clothes. Inlay knit fabric has the high modulus along inlay straight thread and the good draping due to stitch structure. From the above, it was considered possible to molding NFC structures with complex shapes by using flax inlay knit, which has not been used in the field of composite yet. In this study, we aimed to establish a molding method for NFC dome, using inlay knit fabrics, and to evaluate their mechanical properties. NFC domes were molded by VaRTM under various conditions to evaluate their formability. In addition, the fracture mechanisms of NFC dome consisted of inlay knit fabric were investigated by conducting on-axis compressive tests to evaluate the compressive capacity.

2. Materials, structure and VaRTM

The reinforcement for the NFC dome was an inlay knit fabrics made of flax fibers. The flax inlay knit of dome was produced on WHOLEGARMENT knitting machine (SWG091N_2, Shima Seiki, Japan), which allows in 3D shape knitting without seams. In this study, unidirectional flax yarn with an inlay yarn of 2.6 was used with a knit yarn of 7.2 flax yarn. A knit substrate with a loop length of 9 mm was used.On the NFC dome fabric, the inlay thread was folded back at various places to keep that continuity. The used NFC dome fabric in this study was shown in Figure 1.

  doi:10.5075/epfl-298799_978-2-9701614-0-0

Epoxy resin (EPOLAM5015 resin and hardener, AXSON) was used as the matrix. The mixing ratio is 10:3. This matrix was cured at room temperature for 48 hours.

In this study, VaRTM was used for molding NFC domes. In general, VaRTM molding is performed using a bagging film to keep vacuum. However, it was difficult to keep a vacuum condition in the case of VaRTM of 3D structures due to bagging film's non-stretchability. Therefore, two types of VaRTM conditions were investigated, using bagging film and silicon mold as shown in Figure 2. The mold was made of silicon (RTV-2 MSR9200) and VaRTM was performed. In addition, VaRTM was performed using sealant tape (AT-200Y, AIRTECH) and bagging film (WL7400-.002”-60”-1000”-SHT, AIRTECH).

VaRTM using silicon was performed three times, and VaRTM using bagging film was performed two times. Table 1 shows the molding conditions and evaluation of formability. In the following, VaRTMs using the silicon mold denoted as S1, S2, and S3. In S3, a drying oven was used to accelerate the curing of the resin.The VaRTM using bagging film is denoted as B1 and B2. Formability was evaluated by the vacuum condition was maintained until the resin cured and by the amount of voids in the NFC dome. For S1, S2, S3, and B1, VaRTM was performed using bagging films with the resin inlet at the zenith and the outlet at the edge of the dome.For the molding conditions of B2, the resin inlet and outlet were placed at the edge of the dome at one point each, and VaRTM was performed using bagging film.

Silicon was used for S1 and VaRTM was performed. The inlets were set at the zenith and the outlets were set at the edge of the dome.The silicon used in S1 could not maintain the vacuum condition until the resin cured. Therefore, in S2, the silicon used in S1 was coated with silicone to improve its ability to keep the vacuum condition. However, it could not keep the vacuum condition until the resin cured due to the silicon mold floating after 5 hours at the resin impregnation. In addition,NFC dome contained many voids. In S3, curing of the resin was accelerated using a drying oven. After the resin impregnation, the dome was placed in a drying oven with the resin inlet and outlet clipped to prevent air from entering. But it could not keep the vacuum condition until the resin cured due to floating silicone mold. In addition, the resin impregnation of the NFC dome was unsatisfactory. In B1, the vacuum condition could be kept until after the resin cured. However, there were voids in the molded product and more resin in the zenith position. It is thought that this is due to the resin remaining in the hose at the zenith falling by gravity.The reason for more cavities in the molded product waswas considered to the effect of molecular diffusion. Molecular diffusion is a phenomenon in which a void expands due to a pressure difference . In this case, it was considered that molecular diffusion affected the molded product due to the pressure difference caused by inlet at the zenith and outlet at the edge. Therefore, in B2, the position was changed to the opposite side of the resin outlet from the zenith of the resin inlet. Figure 3 shows the molded product of B2. In B2, when the resin reached the resin outlet, there were areas of unimpregnated areas due to accelerated resin impregnation on the edge side of the domes. However, all fibers were impregnated the resin after 1 minute. Furthermore, the vacuum condition could be kept until the resin cured. The B2 had fewer voids in the molded product than B1. Therefore, it was considered that VaRTM of condition B2 is suitable for inlay knit NFC domes among the five conditions.

The inlay spacing, fiber volume fraction (Vf), and thickness of the NFC dome were measured to investigate the structure of the NFC dome. As shown in Figure 4, the tape was adhered at intervals of 30˚ in the directions vertical in the inlays and various parameters along this line were

  doi:10.5075/epfl-298799_978-2-9701614-0-0

measured. The spacing of inlays was measured by measuring the number of inlays and perimeter at ±60˚, ±30˚, and 0˚, with 0˚ as the area passing through the zwnith. Vf and thickness measurements were observed by scanning electron microscopy on a cross-section of the molded NFC dome. An example of the image is shown in Figure 5. The measurement results are shown in Table 2. An example of the image is shown in Figure 5. Also, the measurement results are shown in Table 2. The inlay spacing tended to increase in the order of 0˚, ±30˚, and ±60˚. In addition, it was found that Vf was decreased in the order of 0˚, ±30˚, and ±60˚.

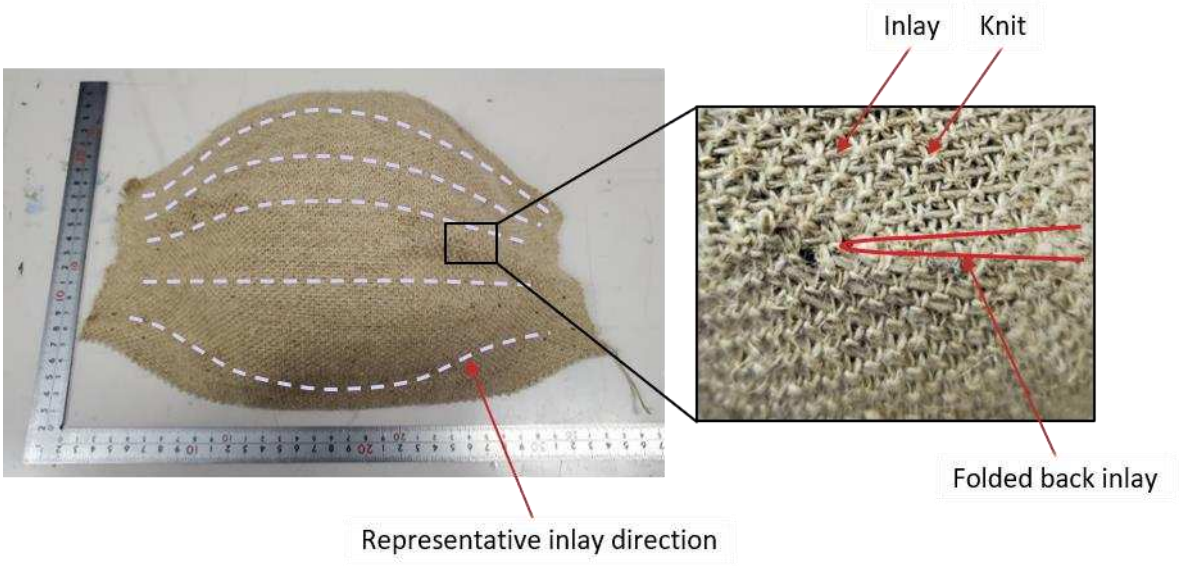

Figure 1. Flax knit

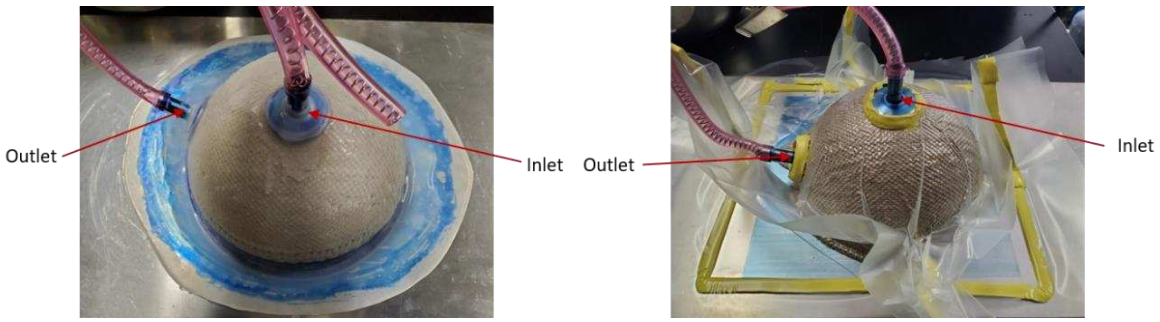

(a) Silicon *(b) Bagging film*

Figure 2. Vacuum arrangement

Table 1: Molding condition.

Abbreviation	Upper mold	Inlet	Drying oven	Vacuum	Formability
S1	Silicon	Zenith	×	×	△
S2	Silicon	Zenith	×	×	×
S3	Silicon	Zenith	○	×	×
B1	Bagging film	Zenith	×	○	△
B2	Bagging film	Side	×	○	○

Figure 3. Mold article （B2）

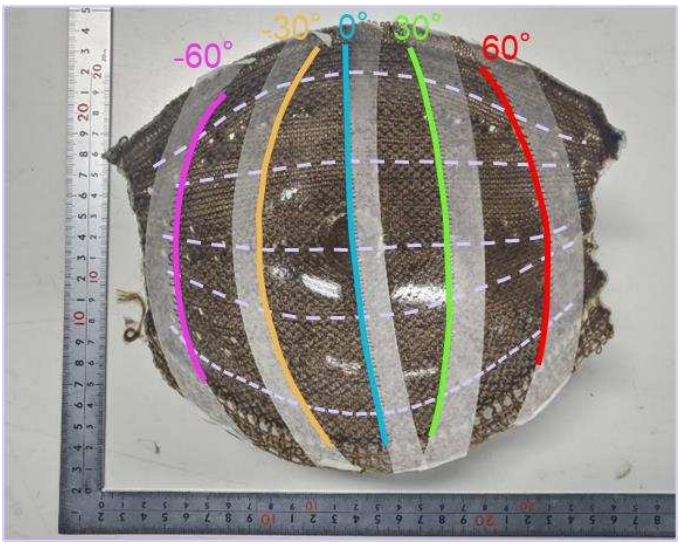

Figure 4. Angle distribution of a hemisphere

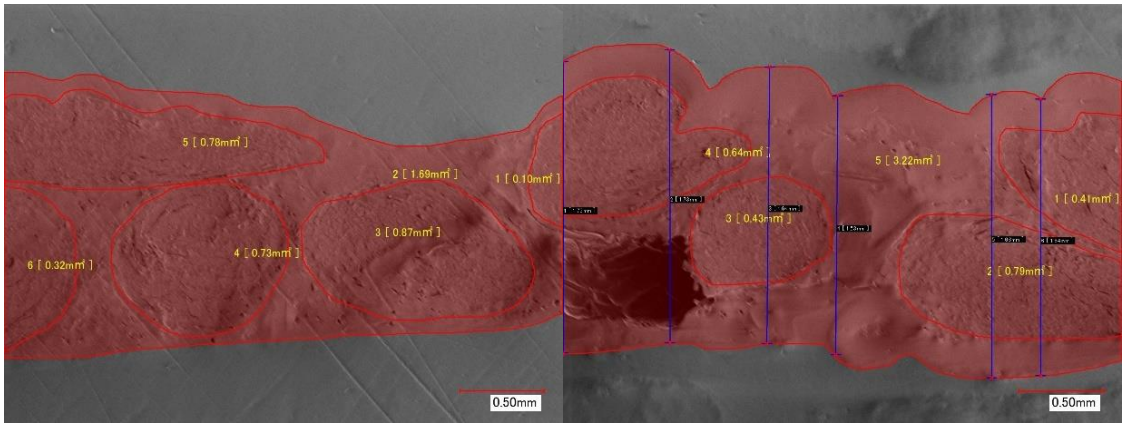

(a) Fiber volume fraction *(b) Thickness*

Figure 5. SEM images for structure measurement

Table 2: Measurement result of Inlay structure in NFC dome.

Angle [°]	Inlay interval [mm]	Vf [-]	Thickness [mm]
-60	2.69	0.39	1.38
-30	2.32	0.46	1.31
0	1.86	0.48	1.49
30	2.51	0.44	1.29
60	2.43	0.38	1.62
AVE.	2.32	0.43	1.42
C.V.	0.12	0.09	0.09

3. On-axis compressive test

On-axis compressive tests were conducted to evaluate the structural compressive capacity of the NFC dome. A small tabletop testing machine was used for the compressive tests, and a micro dynamic strain recorder was used to record the loads and strokes. The jig was set in the small testing machine, and the NFC dome structure was compressed at a rate of 3 mm/min to a maximum load of 1000 N, after which the machine was stopped.

On-axis compressive tests were conducted three times to evaluate the structural compressive capacity of NFC domes molded by B1 and B2 conditions. We marked the folded position of the inlay because it was predicted that stress concentrations occur as the space was larger than at other positions. The load-stroke diagrams are shown in Figure 6. Figure 7 shows the NFC dome after the test. The NFC dome buckled at the folded position of the inlay. As a result, it was determined that the buckling position of the inlay knit fabrics NFC dome. Also, it was found that all tests could withstand up to 1000 N. The stroke of B2 was 32.5 mm at 1000 N. It is thought that the stiffness was lower due to the more voids contained. The stroke of B1 was 20.2 mm and that of B2 was 18.2 mm when 1000 N was reached, it was found that B2 was stiffer than B1. The

  doi:10.5075/epfl-298799_978-2-9701614-0-0

results suggest that load-stroke relations depends on formability. However, there was no significant difference between B1 and B2 as compressive tests were conducted in a small testing machine up to a maximum load of 1000 N. To confirm the fracture mechanism of B1 and B2, we plan to conduct a compressive test up to the failure using a large testing machine with a maximum load of 250 kN.

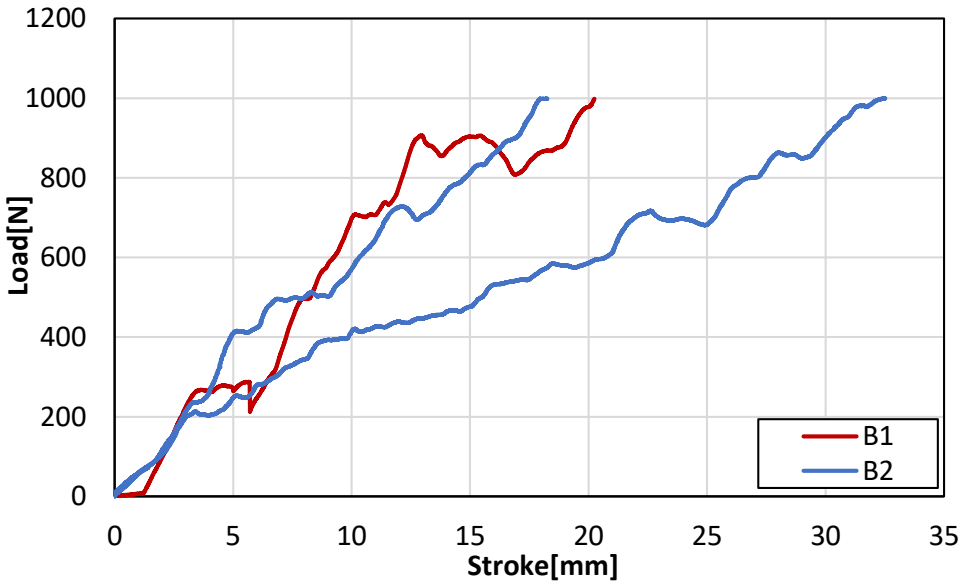

Figure 6. Load-stroke relation diagrams of NFC dome

Figure 7. Final failure

4. Conclusion

The purpose of this study is to establish a molding method for NFC domes using inlay knit fabrics and to evaluate the structural mechanical properties. Therefore, VaRTMs were conducted under various conditions to evaluate their formability of NFC dome. In addition, to

  doi:10.5075/epfl-298799_978-2-9701614-0-0

observe the fracture mechanism, on-axis compressive tests were conducted to evaluate the structural compressive capacity. In this study, using VaRTM for molding NFC domes. Two types of VaRTM conditions were investigated, using bagging film and silicon mold. As a result, it was considered that the VaRTM of the inlay knit NFC domes is best under conditions where the resin inlet and outlet are positioned at the edge of the NFC dome and using a bagging film. The NFC dome buckled at the folded position of the inlay. As a result, it was determined that the buckling position of the inlay knit fabrics NFC dome. Also, it was found that a single-layer NFC dome with a thickness of 1.42mm could withstand up to 1000 N. However, there was no significant difference between B1 and B2 as compressive tests were conducted in a small testing machine up to a maximum load of 1000 N. To confirm the fracture mechanism of B1 and B2, we plan to conduct a compressive test up to the final failure using a large testing machine with a maximum load of 250 kN.

5. References

1. Furtado S C, Araújo A L, Silva A, Alves C, Ribeiro A M R. Natural fiber-reinforced composite parts for automotive applications Int J Automotive Compos. 2014; 1(1):18-38.

  doi:10.5075/epfl-298799_978-2-9701614-0-0

LIGNIN AS A GREEN ADDITIVE FOR 3D PRINTING APPLICATIONS

Shammi Sultana, Nisha [a], Mostafa, Nikzad [a], Mohammad, Al Kobaisi [a], Fareed, Tamaddoni Jahromi [a], Masoud, Bodaghi [b]

a: School of Engineering, Swinburne University of Technology, Melbourne, Australia
b: IMT Lille Douai, CERI Materials & Processes (CERI-MP), Douai, France

Abstract: *In this study, low-cost protic ionic liquid (IL) is used for the extraction of lignin from two native Australian sources, namely Acacia mangium and Pinus radiata. The recovery of green lignin was achieved by the Ionosolv pre-treatment method as ionic liquid lignin solution, which further introduced into resin systems directly for 3D printing applications. Two 3D printing techniques of stereolithography (SLA) and fused deposition modelling (FDM) are evaluated for the development of 3D printable lignin-based composites. In SLA technique, IL-lignin based methacrylate photoreactive resin (MPR) composites with enhanced flexural properties were printed. Incorporating up to 2.5 wt.% IL-Lignin in the photoreactive resin improves the flexural strength of the composites by 16.9% while preserving its printability. FTIR spectroscopy is used to confirm coupling of the ammonium-based IL and lignin to enhance the polymerisation effects during the 3D printing on SLA platform which results in improved mechanical properties. Chemical structural analysis of the IL-Lignin based MPR composites, and the control resin showed no significant changes in the functional groups of the matrix. TGA analysis of these IL-Lignin composites and the control resin shows a slight increase in the thermal stability. Thermal and mechanical properties of printed Alkali-Lignin based PLA composites, processed via FDM technology was also explored and some preliminary observations are reported here.*

Keywords: Lignin; Green Additive; PLA; Photoreactive resin; SLA; 3D printing

1. Introduction

Lignin is a natural polymer composed of phenylpropanoid units in a complex three-dimensional structure. This structural characteristic makes it a highly resistant material to degrade and hydrolyse in chemical and microbial processes (1). An efficient quantitative extraction and separation of lignin from lignocellulosic biomass is needed to make this material viable for the largescale fabrication of value-added products. Conventionally, extreme conditions, such as strong base or mineral acids, are utilized in the extraction of the lignocellulosic materials. In these processes, the extracted fractions are harshly and irrevocably altered, changing the nature of the materials, at the same time causing a great concern due to resultant waste materials and environmental pollution. Furthermore, traditional processes cannot make full use of non-cellulose biopolymers, i.e. lignin and hemicelluloses (2). The demonstration that ionic liquids (ILs) can dissolve cellulose in several reports offers another method to process lignocellulosic biomass(3, 4). ILs are organic salts composed of cations and anions that exist in liquid phase at low temperatures (≤100 ◦C). ILs are green solvents characterised by chemical stability, negligible vapor pressure, and excellent thermal stability within the range from 200 to 450 °C (3, 4). Their use can provide a solution to the problem arising from the use of volatile organic solvents around human safety, toxicity, and environmental hazards. Several reports demonstrated the advantages of utilizing lignin in thermoset and thermoplastic composites (1, 5, 6). However, the use of IL treated lignin in composite materials is a new concept and has its own challenges. Though lignin-based materials are widely studied in the traditional fabrication methods of

  doi:10.5075/epfl-298799_978-2-9701614-0-0

thermoset, thermoplastic, biodegradable, rubber, and foam composites (1, 5, 6), their use as potential additives for the development of 3D printable bio composites solutions offers new scopes to be explored. Resins that are designed for additive manufacturing (AM) processes are complex mixtures. One of the first additive manufacturing techniques developed for 3D printing is stereolithography (SLA). Several materials are used as enhancing fillers in SLA printing to give high-performance mechanical properties. Previous studies demonstrated that the addition of lignin as a filler in polymer composites can improve physical properties, such as, UV absorption, flame retardation, and antiaging (7). Of promising potentials of lignin is as bio-renewable additive in development of thermoplastic filament material for Fused Deposition Modelling (FDM) as a leading additive manufacturing (AM) technology. These allow for fabrication of new composites when mixed with other naturally derived thermoplastics polymers to then fabricate parts with advantages in the design and optimization of models with complex geometries, great design flexibility, recyclability, and low material waste and minimisation of environmental impacts. Despite the variety of printing polymers available, their mechanical properties such as stiffness and strength are naturally low due to spacing between rasters left in the material bulk produced using this process, limiting the applicability of printed components (8). Research on polymer matrix reinforced composites for 3D printing has recently grown to broaden the potential of FDM processable materials (8). The addition of lignin is expected to improve the mechanical and thermal properties of the 3D printed biodegradable matrix such as Polylactic acid (PLA). The current study aims to design a facile means of producing composites using ionic liquid – lignin and thermoset as well as thermoplastic polymers, with focus on the isolation processes of lignin from two native Australian biomass sources as green additives. The properties of the extracted ionic liquid–lignin is further studied to develop lignin-based photocurable composites and PLA based composites that can be processed via SLA and FDM as the two leading methods of 3D printing polymer composites.

2. Materials and Method

2.1 Materials

Methacrylate photoactive resin (thermoset polymer) was supplied by Formlabs. Polylactic acid (PLA), pearl white in color, was supplied by Imaginable Australia. Lignin was extracted from two types of Australian biomass sources, Acacia Mangium and Pinus Radiata. The commercial alkali lignin was purchased from Sigma-Aldrich and used as control material. The protic ionic liquid was prepared from triethylamine and sulphuric acid, which were purchased from Sigma-Aldrich. Tetrahydrofuran was supplied by Sigma-Aldrich, and acetone and absolute ethanol were obtained from ChemSupply.

2.2 Characterisation Methods

FTIR spectra were obtained in the Attenuated total reflection (ATR) mode using a Thermo Scientific Nicolet iS5 FT-IR spectrometer with 64 scans being performed per specimen in the 600 – 4000 cm^{-1} range. AFM was used to study the topography features of the surface of the samples at the nanoscale in tapping mode using an Innova scanning probe microscope (Bruker, Billerica, MA, USA), and silicon cantilever (Cont20A, Bruker, Billerica, MA, USA) with spring constant of 0.9 Nm^{-1} and resonance frequency ranging between 18 – 24 kHz. Measurements and roughness analysis were performed over 10 µm × 10 µm and 2 µm × 2 µm areas of the samples. Thermal gravimetric analysis (TGA) measurements were performed using Q50 TGA instrument (TA

  doi:10.5075/epfl-298799_978-2-9701614-0-0

Instruments, USA). Approximately 5 ± 0.5 mg of powdered samples was used to carry out the test up to 600 °C at 5 °C/min rate under nitrogen flow of 40 ml/min. Flexural test of the sample was carried out using 3-point bending setup in Zwick/Rowell Universal Testing Machine. The distance between the two supports was fixed to be 40 mm, samples dimensions according to ASTM D790 standards were 64 mm × 13 mm × 3 mm. Load was applied at the centre with a rate of 10 mm/min. At least 3 samples were tested for each composition. IZOD impact testing without a notch was used for determining the impact energy of the specimen according to the ASTM D638 standards.

2.3 Lignin Extraction Process and Sample Preparation using SLA and FDM methods

IL-Lignin solution was prepared from *Acacia mangium* and *Pinus radiata*, as described by Gschwend et al (9). Pure lignin was precipitated from the extracted IL-Lignin solution using ethanol and THF and centrifuged to collect solid lignin and dried for further analysis. In stereolithography technique, a CAD file with all the required dimensions was created by CREO Parametric. Printing was done at room temperature while orientation and layout remained the same and 100µm layer thickness was selected. The printed samples were then post-cured in the Form Cure Chamber for 60 mins at 60°C. For the 3D printed PLA and Alkali Lignin-based PLA sample Ultimaker^3 printer has been used. The printing parameters has been tabulated below in Table 1.

Table 1: Printing parameters for 3D printed Alkali lignin-based PLA composites.

Parameters	Values
Print Speed	30 mm/min
Layer height	0.15mm
Infill	100%
Infill Pattern	45°, -45°
Build Plate temperature	60°C
Printing temperature	205°C

3. Results and discussion

3.1 Characterisation of Extracted Lignin and IL-Lignin Based Composites

The optical microscopic image of IL-Lignin deposited on a glass substrate in Figure 1a showed the presence of extracted lignin in IL solution. Height and amplitude AFM images were studied to explore the dispersion of lignin within the IL solution and showed in Figure 1c. From this image, the particle size distribution of lignin was studied by Gwyddion software and showed in Figure 1b. It shows that the average particle size length of lignin is 273.80 nm. FTIR analysis in Figure 2 showed that IL extracted Acacia lignin presented the vibration of O-H stretching at 3332 cm^{-1}, and C-H stretching in -CH_2- and -CH_3 group at 2924cm^{-1} and 2847 cm^{-1}, respectively, as well as the C=O group stretching of carbonyl group that showed peaks at 1701 cm^{-1}. The difference between peaks obtained from Acacia lignin and pine lignin was that Acacia lignin showed no syringyl bands, S ring breathing, and aromatic C-H in plane deformation (S) (10), while syringyl units were found with stronger band intensities (1619, 1308, and 1157 cm^{-1}), aromatic skeletal vibrations (1442 cm^{-1}), and aromatic C-H in plane deformation (G > S) (1032) cm^{-1}) in pine lignin. For the O-H vibrations of lignin, an extensive vibration band lies in the range associated with

  doi:10.5075/epfl-298799_978-2-9701614-0-0

3200–3500 cm^{-1} as reported by Ji et al (10). The absorption band of the O-H vibration of the Alkali lignin is 3309 cm^{-1}, while this vibration for Pine and Acacia lignin shifts to a higher wavenumber 3322 and 3332 cm^{-1}, respectively. This could be attributed to the reason that during dissolution and regeneration process the intramolecular interactions of lignin are weakened which could increase its heterogeneity and affect its chemical resistance towards processing of this feedstock for further commercial applications. The spectrum of the IL- Lignin

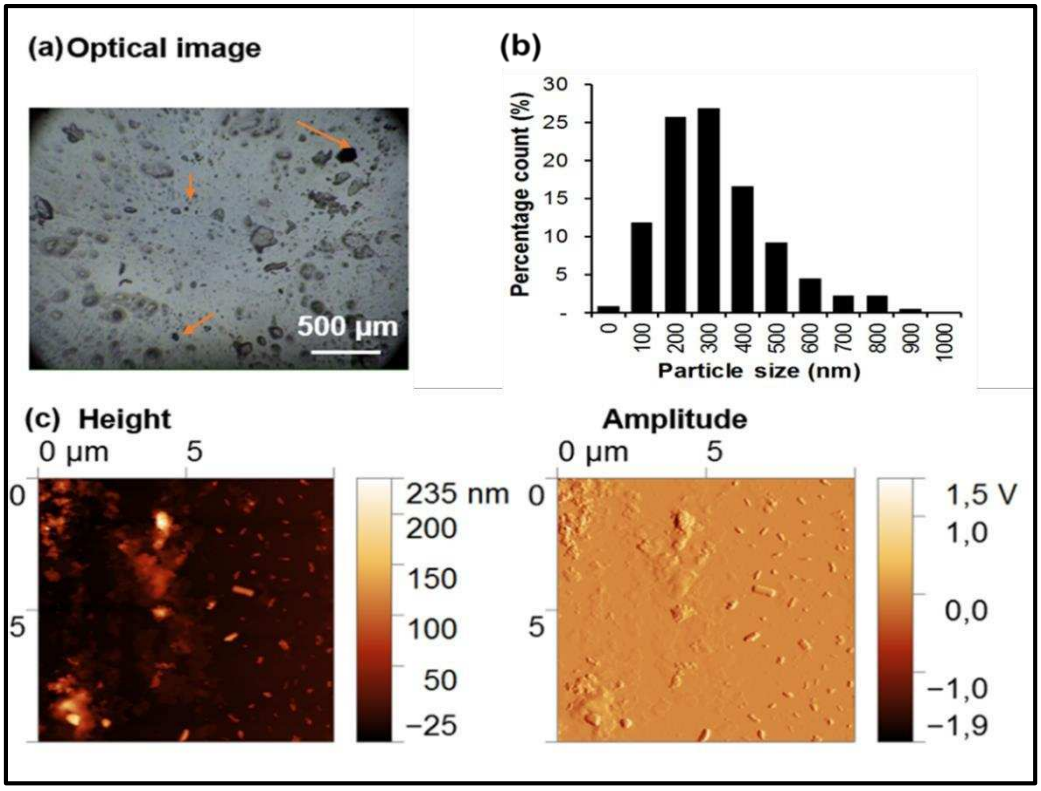

Figure 1. (a)The optical microscopic image of IL-Lignin surface (the arrows show the presence of lignin in IL). (b) Particle size distribution of lignin in IL surface. (c) Height and amplitude AFM images (10 µm×10 µm area) of IL-Lignin.

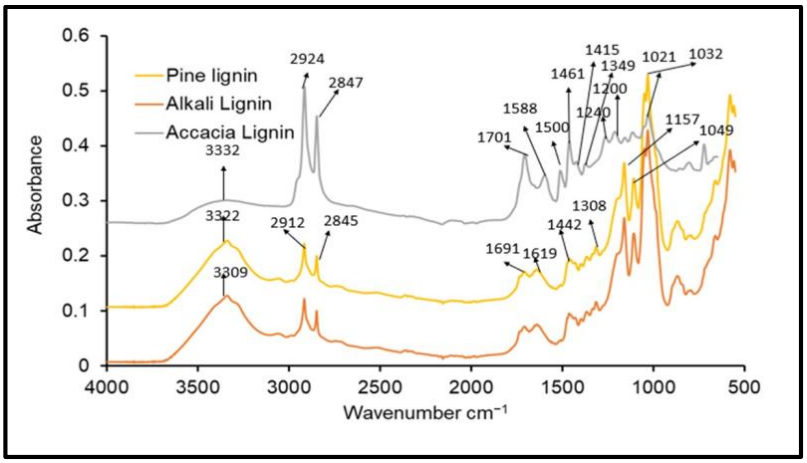

Figure 2. Comparison of FTIR spectrum of Alkali lignin, Acacia lignin and Pine Lignin.

solution showed (Figure 3) the hydroxyl, carbonyl, and aromatic vibrations of the Ionosolv pre-treated lignin at 3395, 1630, and 1473 cm^{-1}, respectively. The presence of guaiacyl ring in

aromatic region observed at 1156 cm^{-1}. The uncured neat MPR sample showed peaks at 3346 cm^{-1} for -OH stretching. The neat MPR sample also showed peaks at 2871–2953 cm^{-1} for C-H and CH_3 stretching, at 1700 cm^{-1} for C=O stretching and at 1368–1387 cm^{-1} for the asymmetric O=C-O stretching (Figure 3). The peaks for the C–H and CH_3 of the polymer chain were observed at 2919 and 2847 cm^{-1} for the printed sample, respectively (Figure 3a). For the printed samples, the peaks formation at 3305 and 1700 cm^{-1} were responsible for the –OH stretching and C=O stretching, respectively, which appears due to the presence of lignin. A slight difference was observed for -OH and C=O stretching at 3305 cm^{-1} and 1700 cm^{-1}, respectively. There was an insignificant shift from 3346 cm^{-1} to 3305 cm^{-1} of the -OH band present in neat MPR and its printed composites. The increasing amount of IL-Lignin (5 wt.%) content also decreased the band intensity (Figure 3b). When a free OH group of IL-Lignin reacted with the MPR matrix, the shift of the -OH band wavenumber was usually occurred in the system. The increasing amount of IL-Lignin content up to 5 wt.% also responsible for the decrease of C=O peak intensity. After postcured, the esterification reaction occurred between the -COOH group in the MPR matrix and the free -OH group of the IL-Lignin and the presence of this ester group is responsible for the changes in the IR peaks. However, the agglomeration of IL-Lignin at higher concentration (5 wt.%) within the MPR matrix is responsible for the decrease of the reaction efficiency, which also decrease the band intensity of asymmetric O=C-O stretching and C=O stretching. These slight changes in printed samples suggested that the increasing amount of lignin restricted the polymerization of MPR resin in SLA printing process.

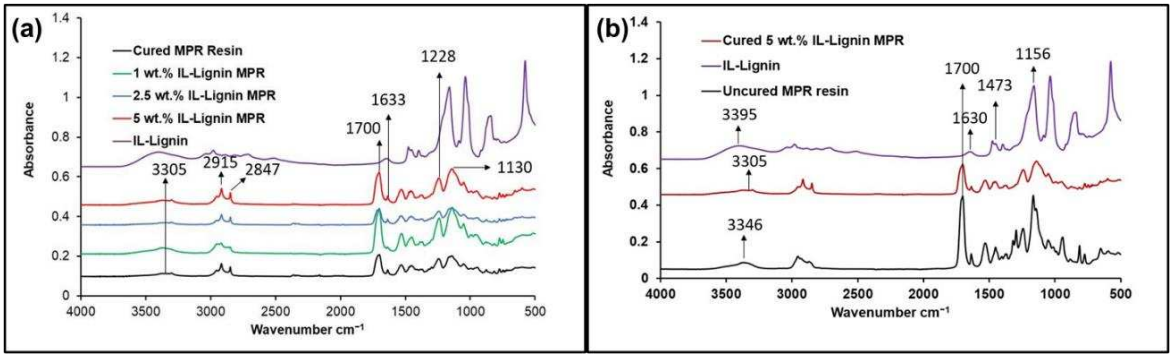

Figure 3. FTIR spectrum of (a) cured MPR and IL-Lignin MPR composites with various concentration, and (b) uncured MPR and cured 5wt.% IL-Lignin MPR composites.

3.2 Thermogravimetric Analysis of Lignin Based Composites

Figure 4a shows temperature derivative of TG curves (DTG) for MPR composites sample and figure 4b shows the DTG curves for PLA composite samples. All SLA printed composites samples showed a two-step slow degradation over a range of temperature from 270 to 600°C with onset temperature of 243°C. The first degradation peak was appeared at 366 °C and at (240°C to 375°C) for neat MPR sample and IL-Lignin based MPR composites, respectively, in which the vinyl chain units were decomposed. The second degradation step was appeared in the range from 375°C to 500°C, which caused by random chain scission of the C-C bonds present in the polymer backbone of MPR chains. The maximum degradation temperature was shifted from 366 °C for neat MPR to 356 °C for 5 wt.% of IL-Lignin, indicating that IL-Lignin advances the degradation of the nanocomposites (7). This phenomenon occurred because of the presence of degradation products in IL-lignin, such as sulphate groups. The presence of this group decreased the thermal stability (11) by a dehydration reaction and accelerated the

  doi:10.5075/epfl-298799_978-2-9701614-0-0

decomposition in the printed composites. The TG of the lignin sample shows a one step slow degradation over a range of temperature from 100-600°C. The first and second degradation peak were at 270 °C and 510 °C for lignin, respectively, therefore, the decrease in the degradation peak of the composite samples may be attributed to the presence of IL-Lignin, which can be confirmed by the chemical analysis of the FTIR spectra mentioned in the last section. The presence of Alkali Lignin in the PLA system didn't affect the degradation of 2.5 wt.% and 5 wt.% of Alkali lignin-based PLA composites. The first and second degradation peak for Alkali lignin PLA composites appeared around 365-369°C and 447°C, respectively.

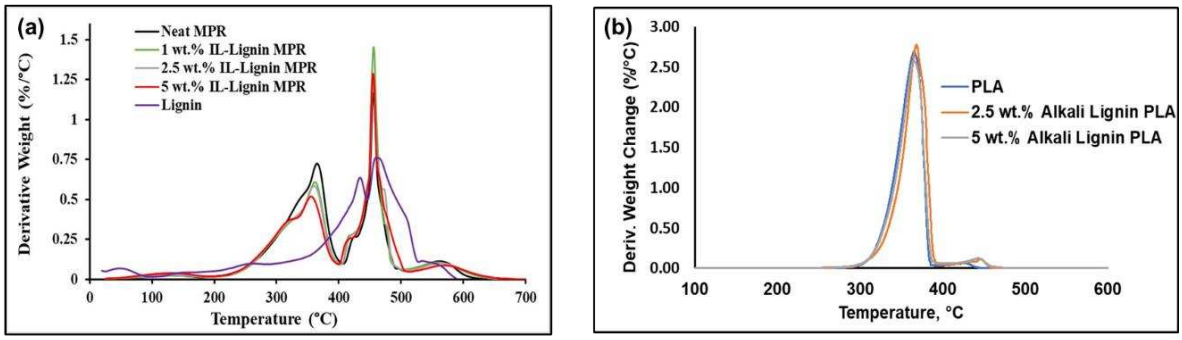

Figure 4. DTG curves (a) of the photocured IL-Lignin MPR samples, and (b) Alkali lignin-based PLA samples.

3.3 Mechanical Properties Analysis of Lignin Based Composites

The data for flexural strength and elastic modulus are documented in Table 2 with impact strength data gathered from impact test for further analysis. The data shows that, 1 and 2.5 wt.% IL-Lignin based samples exhibited noticeable increase in the maximum flexural strength within the range from 80 to 85 MPa (8×10^7 to 8.5×10^7 Pa) with 12.8 and 16.92% increment, respectively, compared to neat sample. The 5.0 wt.% IL-Lignin composites sample showed a decrease in flexural strength at break at 74 MPa (7.4×10^7 Pa) due to the hindering effect of the lignin during the photopolymerization of the resin. The elastic modulus was increased by 10% from 1.91 (1.91×10^9 Pa) to 2.10 GPa (2.10×10^9 Pa) with the addition of 2.5 wt. % IL-Lignin. But the addition of 5 wt. % IL-Lignin slightly decreased the modulus up to 1.84 GPa (1.84×10^9 Pa). The improved elasticity modulus is a result of the resin curing process modification. Any incorporation of a filler, with a surface rich in hydroxyl –OH groups, may cause an additional catalytic effect resulting in the creation of additional segments of curing network (12). The reason for lowering elastic modulus values for composites containing 5 wt.% of IL-Lignin, could be a random arrangement of filler particles and a hindered degassing of highly viscous compositions. The impact strength increased from 3.82 kJ/m^2 to 5.64 kJ/m^2 and 5.78 kJ/m^2 for 1 wt.% and 2.5 wt.% IL-Lignin concentration. There is a significant increase in impact strength for 5 wt.% IL-Lignin MPR composites which is 86.8 % increase than neat MPR composites. However, the impact strength decreased from 16.23 kJ/m^2 to 8.97 kJ/m^2 and 7.62 kJ/m^2 for 2.5 wt.% and 5 wt.% Alkali Lignin PLA composites. For the Alkali Lignin based PLA composites (figure 5b), flexural strength (F_{max}) and Elastic modulus of the Alkali lignin/PLA composites decreased with increasing Alkali lignin content up to 5 wt.%. This declining trend in flexural strength of the PLA-based composites likely results from poor dispersibility and interfacial adhesion between the Alkali lignin domains and PLA matrix (13). The stress vs strain curves (figure 5a) showed that the presence of Alkali lignin without any surface modification

  doi:10.5075/epfl-298799_978-2-9701614-0-0

produced brittle 3D printed sample compared to the neat PLA samples. The presence of 2.5 wt.% Alkali lignin dropped the maximum flexural strength by half compared to the neat PLA printed samples. The elastic modulus of the 2.5 wt.% Alkali Lignin based printed samples also dropped by 30% compared to the neat PLA printed sample.

Table 2. Flexural strength and elastic modulus of the printed Lignin based composites

Sample name	Flexural Strength (F_{max}) (MPa)	Elastic Modulus (GPa)	Impact strength (KJ/m^2)
Neat MPR	72.7± 3.2	1.91±0.09	3.82± 1.20
1 wt.% IL-Lignin MPR	82± 1.23	2.02±0.06	5.64±0.75
2.5 wt.% IL-Lignin MPR	85±2.65	2.10±0.10	5.78±0.72
5 wt.% IL-Lignin MPR	74±3.03	1.84±0.20	7.10±0.76
Neat PLA	105.33±2.08	3.60±0.03	16.23 ± 3.50
2.5 wt.% Alkali Lignin PLA	46.70±6.36	2.21±0.03	8.97 ± 0.01
5 wt.% Alkali Lignin PLA	43.65±4.66	1.91±0.01	7.62 ± 2.12

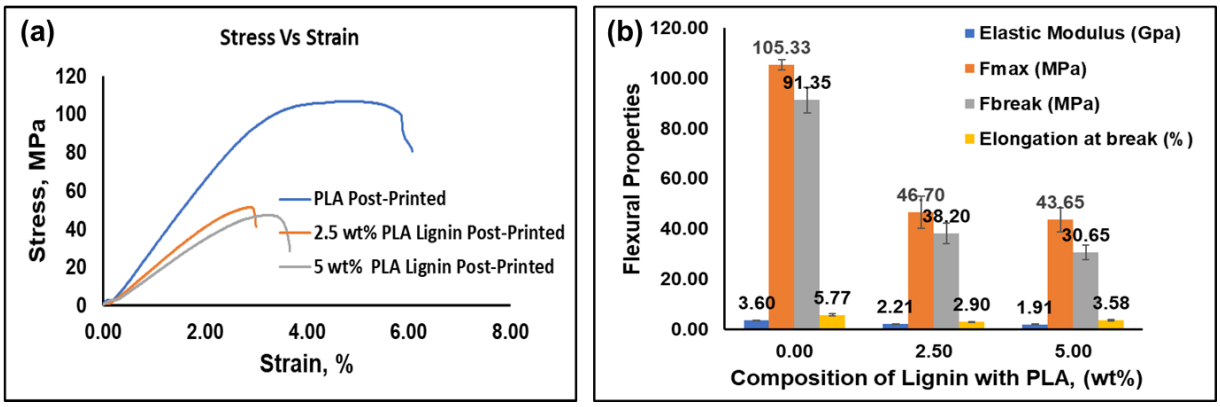

Figure 5. (a) Flexural stress-strain curves and (b) properties of the 3D printed samples via FDM method

4. Conclusions

The chemical and morphological studies of Acacia and Pine lignin extracted as pristine additives concludes that Ionosolv pre-treatments yields in production of lignin particles by preserving its native structure. From end-use point of view, this is a noteworthy advantage for obtaining a green additive through this process alongside the possibility to fully recover the solvent content.

Composites of lignin and commercially available resins were 3D printed through SLA and FDM processes. Chemical, thermal, and mechanical properties of these composites were analysed. For samples printed through SLA, a slight change was observed between the uncured neat sample and the cured composites for -OH and C=O at 3305 cm^{-1} and 1700 cm^{-1}, respectively. The addition of lignin up to 2.5 wt.% enhanced the flexural strength of the composites by 16.92% when processed through SLA 3D printing platform. Samples of Alkali Lignin- PLA composites

were also printed through FDM to demonstrate processability via this low-cost and widely used extrusion-based printing process. Thermal degradation analysis of printed Lignin-PLA composites didn't show any significant changes on degradation peaks with addition of up to 5 wt.% of Alkali Lignin. The initial assessment of the mechanical properties, however, shows the presence of Alkali lignin results in reduction of properties of the thermoplastic matrix pointing towards needs for lignin surface modification to enable realisation of its full potential as a green additive for 3D printing thermoplastic-based composites.

5. References

1. Laurichesse S, Avérous L. Chemical modification of lignins: Towards biobased polymers. Progress in Polymer Science. 2014;39(7):1266-90.

2. Tarasov D, Leitch M, Fatehi P. Lignin–carbohydrate complexes: properties, applications, analyses, and methods of extraction: a review. Biotechnology for Biofuels. 2018;11(1):269.

3. Xu CC, Z. Thermal Stability of Ionic Liquids: Current Status and Prospects for Future Development. Processes. 2021;9:337.

4. Gupta KM, Jiang J. Cellulose dissolution and regeneration in ionic liquids: A computational perspective. Chemical Engineering Science. 2015;121:180-9.

5. Jawerth ME, Brett CJ, Terrier C, Larsson PT, Lawoko M, Roth SV, et al. Mechanical and Morphological Properties of Lignin-Based Thermosets. ACS Applied Polymer Materials. 2020;2(2):668-76.

6. Sahoo S, Misra M, Mohanty AK. Enhanced properties of lignin-based biodegradable polymer composites using injection moulding process. Composites Part A: Applied Science and Manufacturing. 2011;42(11):1710-8.

7. Sutton JT, Rajan K, Harper DP, Chmely SC. Lignin-Containing Photoactive Resins for 3D Printing by Stereolithography. ACS Applied Materials & Interfaces. 2018;10(42):36456-63.

8. Wang S, Daelemans L, Fiorio R, Gou M, D'hooge DR, De Clerck K, et al. Improving Mechanical Properties for Extrusion-Based Additive Manufacturing of Poly(Lactic Acid) by Annealing and Blending with Poly(3-Hydroxybutyrate). Polymers. 2019;11(9).

9. Au - Gschwend FJV, Au - Brandt A, Au - Chambon CL, Au - Tu W-C, Au - Weigand L, Au - Hallett JP. Pretreatment of Lignocellulosic Biomass with Low-cost Ionic Liquids. JoVE. 2016(114):e54246.

10. Ji W, Ding Z, Liu J, Song Q, Xia X, Gao H, et al. Mechanism of Lignin Dissolution and Regeneration in Ionic Liquid. Energy & Fuels. 2012;26(10):6393-403.

11. Roman M, Winter WT. Effect of Sulfate Groups from Sulfuric Acid Hydrolysis on the Thermal Degradation Behavior of Bacterial Cellulose. Biomacromolecules. 2004;5(5):1671-7.

12. Nguyen NA, Bowland CC, Naskar AK. Mechanical, thermal, morphological, and rheological characteristics of high performance 3D-printing lignin-based composites for additive manufacturing applications. Data in Brief. 2018;19:936-50.

13. Hong SH, Park JH, Kim OY, Hwang SH. Preparation of Chemically Modified Lignin-Reinforced PLA Biocomposites and Their 3D Printing Performance. Polymers (Basel). 2021;13(4).

DESIGN OF ADDITIVELY MANUFACTURED COMPOSITE ELEMENTS WITH LONG AND SHORT FIBER REINFORCEMENTS FOR IMPROVED STAB PROTECTION

Dominik Muenks[a], Anna Mona Sprenger[a], Yordan Kyosev[a]

a: Chair of Assembly Technology for Textile Products, Institute of Textile Machinery and High Performance Material Technology (ITM), TU Dresden, Germany – dominik.muenks@tu-dresden.de

Abstract: *Introduced are the development steps of a new generation of stab protection equipment manufactured using FFF (Fused Filament Fabrication) printing technology. A polyamide-based thermoplastic polymer with micro Carbon fibers and high-performance fibers such as Aramid and Carbon as reinforcing fibers provided the material basis for creating protective elements for the new development. These protective elements were printed in combination on textile to further support the protective effect. The resulting fiber composites were tested in accordance with the VPAM (Association of Testing Institutes for Attack Resistant Materials and Structures) - KDIW 2004 standard. The right use of materials, thickness and printer settings for the additively manufactured protective elements made it possible to achieve the protection class.*

Keywords: stab protection; fiber reinforcement; additive manufacturing; 3D printing; Carbon;

1. Introduction

According to the Federal Situation Report 2020 of the German Federal Criminal Police Office, 84,831 police officers were victims of violent acts directed against them. Compared to the previous year, this represents an increase of 5.9%. The long-term trend shows a continuous increase in documented cases since 2013, with the exception of 2017 [1]. Crimes with sharp objects and knives have also increased in recent years. Due to the annually increasing number and intensity of attacks as well as the easy accessibility of stabbing weapons, personal protective equipment is therefore becoming increasingly important.

So far, there are two types of stab protection equipment. Firstly, there is hard stab protection, in which heavy, inflexible metal plates are used, and secondly, there is soft stab protection. This is achieved via the number of textile layers, which, depending on their thickness, can also be heavyweight and also offer little thermophysiological comfort. The demand for a new generation of stab protection equipment that combines the flexible textile component with the protective function of hard panels is therefore high. The versatile additive manufacturing offers new possibilities for stab protection equipment. Particularly worthy of mention are the design diversity and the possibility of targeted fiber reinforcement and individual adaptation to the individual user.

  doi:10.5075/epfl-298799_978-2-9701614-0-0

2. Material and Methods

Initially, two test sample variants, a round and a flat version, were designed in SolidWorks. Both variations have the same diameter of 50 mm. The thickness was adjusted in the course of the study. The measurement is based on the study of Sitotaw and colleagues [2]. Figure 1 shows both samples and their dimensions. The round geometry is hollow inside. The test samples are used to investigate the behavior and the depth of the knife penetration with different material combinations and thicknesses.

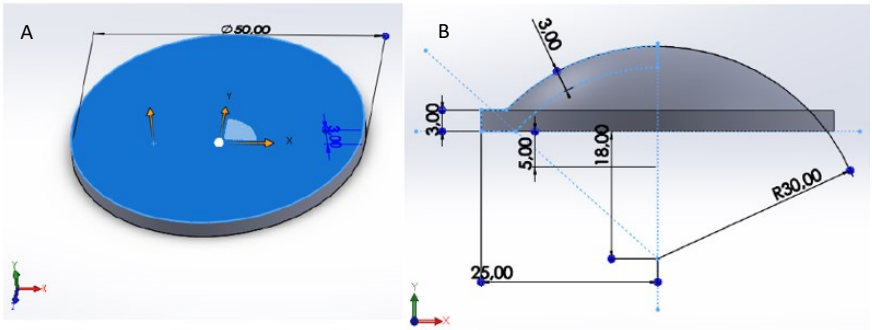

Figure 1. Flat (A) and round (B) test sample and the corresponding dimensions, which serve as the basis for the knife penetration test

In the next step, the test samples were printed using the Fused Filament Fabrication (FFF) printing process with a Mark Two™ 3D printer from the manufacturer Markforged. The special printer allows components to be printed from a base material together with composite material. This is achieved using two different nozzles. In the study, the base material Onyx™ was used. The filament is a Nylon filled with short Carbon fiber. Additional composite material made of Aramid or Carbon (both used in this study) can be used to additively produce resistant and highly compliant components [3, 4]. The slicer (Eiger) allows the test samples to be sliced accordingly. Additionally, the fiber orientations of the composite material can be defined. As shown in Figure 2, the fiber orientation was always rotated to the next layer at a 45 degree angle. This results in a reinforced fiber build-up at angles of 0°;45°;90° and 135° and then again starting from the beginning until the final height has been reached. The fibers are always embedded on the top and bottom with two layers of the Onyx™ base material. The slicer provides many default settings (print temperature, layer height, etc.), which are not changeable and were therefore taken over. The layer height of all prints is 0.125 mm.

  doi:10.5075/epfl-298799_978-2-9701614-0-0

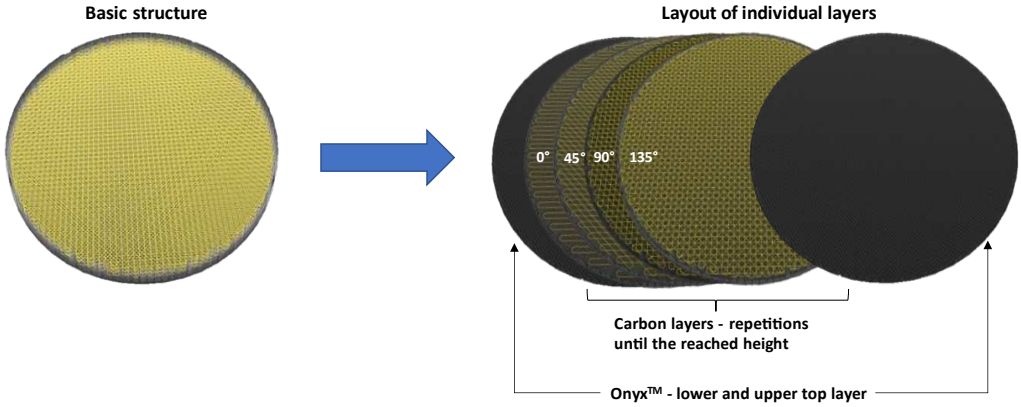

Figure 2. (A) Construction of the test (fiber deposit shown in yellow)
(B) The fiber orientations of the individual layers.

The micrograph in Figure 3 shows an additive print made of the base material Onyx™ and additional Carbon fiber as composite material. The individual layers of Onyx™ and the additionally imprinted Carbon fiber are very clearly visible. The lower and upper layers of Onyx™ and in the middle the Carbon fiber have been imprinted in different orientations. The Carbon fiber can be seen through the light areas. Since the composite base material Onyx™ also contains a micro Carbon fiber in the filament, the Carbon parts can also be recognized by bright white dots.

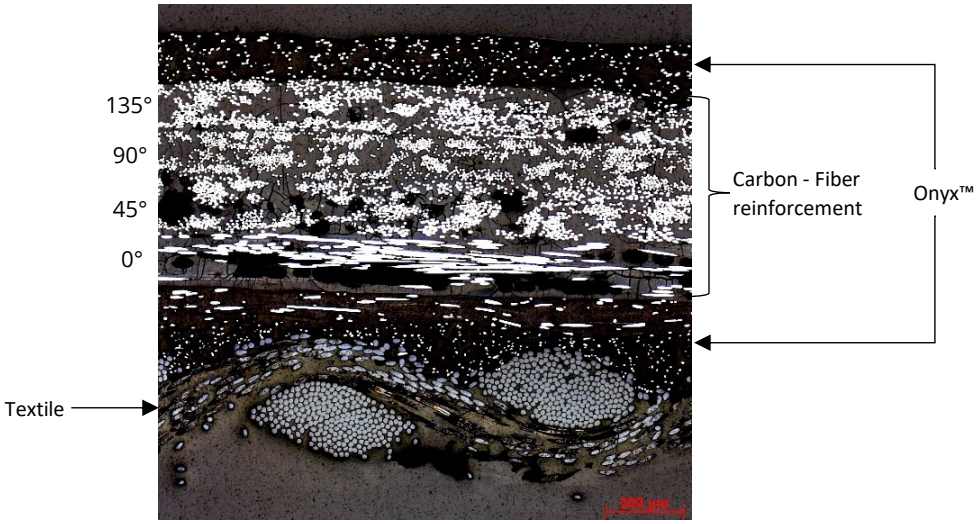

Figure 3. Micrograph of layers - top and bottom 2 layers of Onyx™ in the middle Carbon fiber in different orientations

After printing the test samples with different thicknesses, they were then tested on the institute's own test stand in accordance with the German VPAM (Association of test laboratories for bullet resistant materials and constructions) standard. The test was performed according to Class K1 (KDIW 2004 - Edition 18.05.2011) [5]. The standard specifies that a standardized knife with an impact energy of 25 joule is not allowed to penetrate a sample by more than 20 mm.

  doi:10.5075/epfl-298799_978-2-9701614-0-0

3. Results and Discussion

Different additively manufactured test specimen variants as already presented in Figure 1 (flat and round) were printed. The test samples made of different materials and volume amounts of matrix and fiber reinforcement and were tested on the institute's own drop test rig. Different penetration depths were found.

The flat test specimen variant made of Onyx™ without any additional fiber reinforcement is not sufficient to prevent a knife penetration of 20 mm with 25 joules of impact energy. Test samples were penetrated to the maximum of the measurable (50 mm) Consequently, a pure print of Onyx™ is not sufficient. Fiber reinforcement is necessary. The combination of Onyx™ and fiber reinforcement of aramid also did not provide sufficient protection. The average puncture is 45.3 mm, but within the measurable range. The best results were achieved with the combination of Onyx™ and Carbon fiber reinforcement. By adjusting the thickness, the fiber volume fraction of the Carbon fiber reinforcement was increased. With a thickness of 4 mm of Onyx™ matrix with additional Carbon fiber reinforcement, the puncture is 14.9 mm and is below the required 20 mm of the standard. Figure 4 shows a penetration test performed after impact of the knife on the flat 4 mm sample.

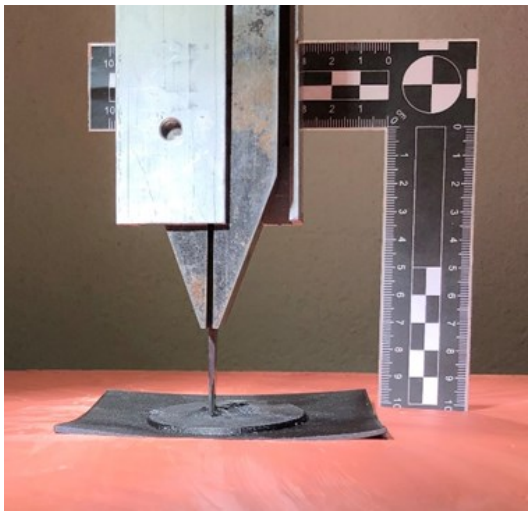

Figure 4. After a penetration test of a test sample (4 mm thickness) with an enlarged contact surface for fixing the sample

In material combination of Onyx™ and additional Carbon reinforcement and thickness, the round geometry (Figure 1b) was also subjected to a puncture test. It was tested to what extent a round geometry absorbs the impacting energy better and thus minimizes the puncture. With a thickness of 4 mm, the puncture is 14.9 mm for the flat and 15.6 mm for the round. Both results are very close to each other. From this it can be concluded that the geometry (round or flat) has practically no influence on the plunge depth.

The results are summarized in Figure 5. The results of the material combination of Onyx™ and Carbon are shown for different thicknesses of the respective geometries. The limit value is 20 mm in the VPAM standard and is shown as the maximum penetration depth.

  doi:10.5075/epfl-298799_978-2-9701614-0-0

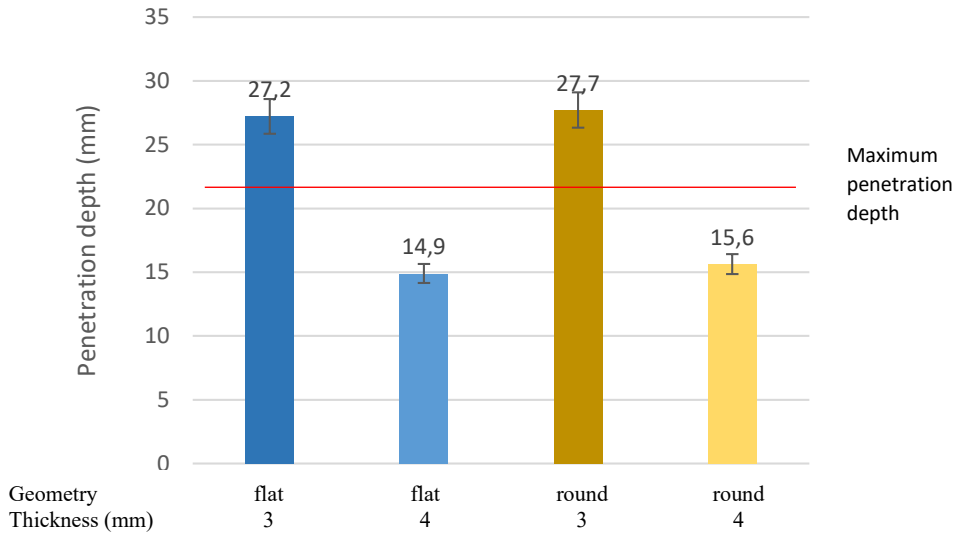

Figure 5. Material combination of Onyx™ and Aramid - influence of geometry (round/flat) and thickness on the penetration depth of the knife

The previous results of the material combination and thickness were used to design a scale-like protective surface and to print it with the corresponding FFF printing parameters. The goal is an overlapping protective surface and interlocking scale structure, as shown in Figure 6, is to achieve a high level of comfort while providing a high level of protection. In the design, the thickness of 4 mm and the fiber reinforcement in slicing were taken into account and printed directly onto para-Aramid fabric.

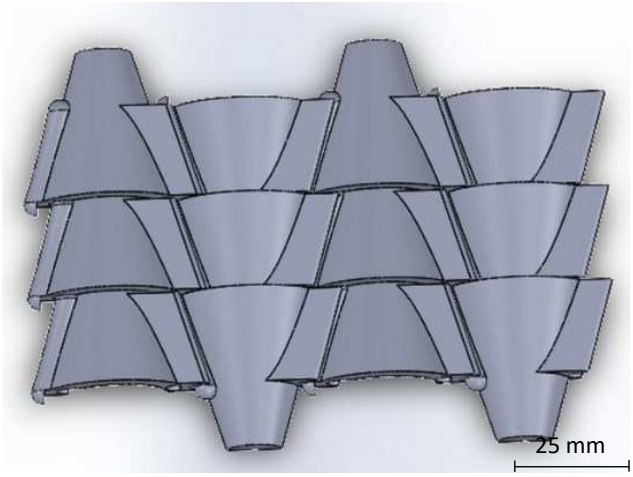

Figure 6 Interlocking and overlapping designed scale structure

Figure 7 shows the printed scale geometry with fiber reinforcement inside. A printed sample was then also subjected to a puncture test. In total, the sample was subjected to the test 6 times. The knife tip did not penetrate more than 20 mm on the reverse side in any test. On average, the puncture was 6.8 mm. The maximum of 20 mm was not reached. This demonstrated that the tests of the flat and round geometry can also be transferred to other geometries and are suitable for scale-like protective surfaces.

  doi:10.5075/epfl-298799_978-2-9701614-0-0

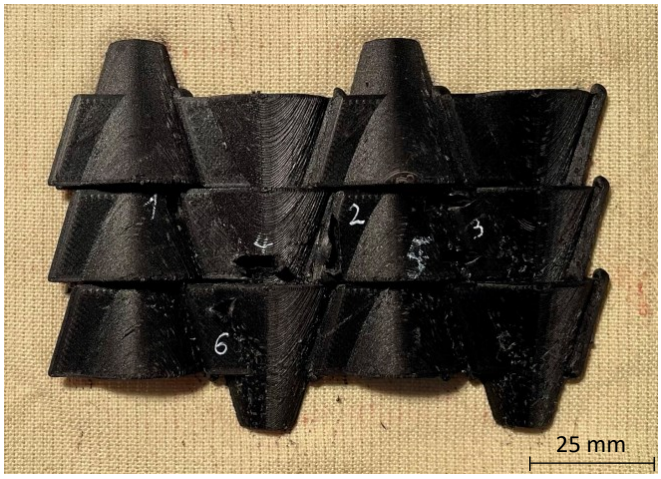

Figure 7 Interlocking and overlapping printed protective surface after 6 times puncture test

4. Conclusion and Outlook

The study shows that additive printing technology (FFF) with composite material can be used to print protective objects for protective clothing and provide sufficient protection. A knife attack can be defended against using a combination of Onyx™ and imprinted Carbon composite fibers with a thickness of 4 mm. It should be pointed out that the geometry thickness has a significant influence on the knife penetration. The geometry, whether flat or round, has no critical influence. The results were used to construct an interlocking and overlapping structure, which was also tested. The results show a value well below the maximum puncture.

In the future, these results can be used to apply the advantages of additive manufacturing to personal protective equipment as well. The interlocking and overlapping structures are further developed and scaling is used to optimally adapt the structures to the body shape. This would make it possible to produce customized protective clothing from the 3D printer, tailored to the body proportions of the respective wearer.

Acknowledgements

The IGF research project 21622 BR of the Forschungsvereinigung Forschungskuratorium Textil e. V. is funded through the AiF within the program for supporting the „Industriellen Gemeinschaftsforschung (IGF)“ from funds of the Federal Ministry for Economic Affairs and Climate Action on the basis of a decision by the German Bundestag.

References

1. Lagebilder - Bundeslagebild Gewalt gegen Polizeivollzugsbeamtinnen und Polizeivollzugsbeamte 2020: Bundeslagebild 2020; 2021 [cited 2022 Feb 26]. Available from: https://www.bka.de/SharedDocs/Downloads/DE/Publikationen/JahresberichteUndLagebilder/GewaltGegenPVB/GewaltGegenPVBBundeslagebild2020.html.

  doi:10.5075/epfl-298799_978-2-9701614-0-0

2. Sitotaw DB, Ahrendt D, Kyosev Y, Kabish AK. Investigation of Stab Protection Properties of Aramid Fibre-Reinforced 3D Printed Elements. Fibres & Textiles in Eastern Europe 2021; Nr 3 (147):67-73. Available from: http://yadda.icm.edu.pl/baztech/element/bwmeta1.element.baztech-65378316-15a7-4de6-a412-c4655f4348a7.
3. Kevlar 3D Printing - Specialized Continuous Fiber; 2022 [cited 2022 Feb 10]. Available from: https://markforged.com/materials/continuous-fibers/kevlar.
4. Sitotaw DB, Ahrendt D, Kyosev Y, Kabish AK. Additive Manufacturing and Textiles—State-of-the-Art. Applied Sciences 2020; 10(15):5033. Available from: https://www.researchgate.net/publication/343147680_Additive_Manufacturing_and_Textiles_-_State-of-the-Art.
5. Association of test laboratories for bullet resistant materials and constructions. Test Standard - Stab and Impact Resistance: Requirements, classifications and test procedure; 18.05.2011. Available from: https://www.vpam.eu/wp-content/uploads/2020/06/2011-05-18_KDIW2004_englisch.pdf [cited 2022 Mar 07].

  doi:10.5075/epfl-298799_978-2-9701614-0-0

AN ENGINEERING VIEW OF USING RESEARCH RESULTS TO INCREASE THE DESIGN WINDOW AND AVOID MANUFACTURING DEFECTS

Per Hallander [a, b], Tommy Grankäll [a, b], Mikael Petersson [a], Malin Åkermo [b]

a: Saab AB, Bröderna Ugglas gata, SE-581 88 Linköping, Sweden –
per.hallander@saabgroup.com
b: Department of Engineering Mechanics, KTH Royal Institute of
Technology, Teknikringen 8, SE-100 44 Stockholm, Sweden

Abstract: *The design freedom of composite parts is often limited by the material and/or manufacturing process. When approaching the limits of the processing window, manufacturing robustness is lost, and defects occur. Most common defects are out of plane laminate wrinkles, voids, porosities, delamination, thickness deviations and fibre angle misalignments. The process settings resulting in defects needs to be translated into hard limitations. The research community has during the years added excellent contributions to the understanding of defect generation. In this work we will present the engineering adoption of these results into industrial practice to further improve the composite manufacturing. This work is focusing on corner thickness deviations during manufacturing of carbon/epoxy parts out of Uni-Directional prepreg.*

Keywords: Composites; manufacturing; prepreg; defects; thickness deviation

1. Introduction

Corner thickness deviation can be introduced already during hand-layup due to bridging plies in concave areas and tensioned plies in convex areas. These defects will accelerate during cure due to factors as pressure deviations [1-2], bulk factor [3], wrinkling, interply friction [4], resin rheology [5], fibre direction [6], fibre content, well described in research. The engineering approach towards efficiency and improved robustness during hand lay-up includes lamination strategies related to geometrical aspects in combination with pairwise or multilayer lamination. However, the root cause for the cure related thickness deviation is often local pressure differences in the cure assembly. The solution is differentiated baging strategies to even out the pressure in the cure assembly [2, 7].

Introduction of automation in terms of multi-stack forming also comes with corner thickness deviations, in this case mainly radius thinning over convex corners [1]. The phenomenon is dependent on consolidation mechanisms such as squeeze flow due to increased pressure in the corner area. Increasing the material friction or viscosity will decrease the corner thinning, but this kind of material manipulation often results in other manufacturing issues [4, 7, 8].

While the industrial methods to reduce corner thickness deviations are different depending on which process step it focuses on, an approach attacking a single process step is seldom enough. Relying on counteracting effects in different steps may be tempting but dangerous. Adjusting the root cause is always a better alternative. To reach tight tolerances and manufacturing robustness, the overall process must be adjusted with a set of improvements targeting each processing step differently.

  doi:10.5075/epfl-298799_978-2-9701614-0-0

The aim of this paper is to review different generations of experimental research performed by the authors and connected research groups and compare it with manufacturing data from different generation of production methods that have translated the gained research knowledge into engineering solutions. This paper is especially focusing on the cure assembly, however influences from material, tool geometry, lay-up and heat distribution are also presented.

2. Method

Corner thickness deviation are influenced by several parameters. In this chapter state-of the art for each parameter are presented together with the parameter settings used in the study.

2.1 Materials

Carbon fibre/epoxy uni-directional prepreg materials containing thermoplastic toughener particles are today established on the market. The main reason for introducing these materials were improved impact properties. The thermoplastic particles have great influence on both the morphology and the interply friction [4]. Dodwell et al. [8] show that the friction can prevent the prepreg plies from conforming to the mould which effects the corner compaction. The friction coefficient can differ with a factor ten between different prepreg systems [4]. The morphology of the prepreg itself can also have effect on the compaction behavior, including bleeding flow and squeezing flow [6]. Nixon-Pearson et al. [9] show that M21 prepreg containing thermoplastic particles have an inhibiting effect on this flow mechanism. The effect on the corner thickness deviation from the mechanisms above are well described by Levy and Hubert in [10].

In this paper three different prepreg systems are used to describe the influence of the material on the corner thickness deviation. Hexply M21/T700 (268g/m2) and M21 (134g/m2) containing thermoplastic toughener particles, Cycom 977-2/HTS (134g/m2) with a relatively low viscous profile and 6376/HTS (134 g/m2) with a viscous profile comparable to M21 (according to the supplier material data sheet). The 977-2 and 6376 resins do not contain toughener particles.

2.2 Tool geometry

Tool geometry naturally have great influence of the corner thickness variation. Concave or convex tooling surfaces are most common [10]. Corner sections manufactured on convex tooling influences from the friction between part and tool and the radius size itself are therefore important. The radius to thickness ratio also introduce a pressure deviation in the radius during the cure cycle [2]. Corner sections manufactured on concave tools influences from the lay-up procedure [11], the bulk factor [3], the cure assembly [7] and are also affected by the radius to thickness ratio. The variation of the part cross section in a double curved geometry also has an influence on the corner thickness variation [12]. This is mainly related to the forming process. Different kinds of engineering solutions could also be applied to the tool geometry with the purpose to avoid lay-up defects such as compression of the plies. Geometrical compensation improves aying up on a convex tool and curing on concave tool, as described in chapter 2.3. This has been shown in a novel work by Grankäll et al. [13].

In this paper results from part geometries with constant cross section are presented. Convex radius of 2, 3 and 6 mm are used as well as concave radius of 5 and 8 mm.

2.3 Lay-up

For the lay-up the engineering knowledge and operator skills have great influence on corner thickness. The lay-up technique itself indeed have an impact on the corner thickness variation, especially for Uni-Directional (UD) prepregs. For convex tooling different lay-up techniques could be used such as Hand-Lay-up (HLU), Pairwise Hand Lay-up (PHLU), Pairwise Vacuum forming (PVF), Hot Drape Forming (HDF), Press Forming and Automated Fibre Placement (AFP). When using HLU and UD prepreg, placing one ply at the time, the plies with fibre direction along the radius can be separated/split in-between fibres. An engineering approach to solve this item is to lay-up a pair of plies (with different fibre direction) flat and then form them, like a woven fabric, to the tool. This can even be extended to use vacuum forming to apply the paired plies to the tool (PVF) in order to reach a more uniform lay-up, with no un-necessary tension, to avoid in-plane separation of plies. The PVF also avoids the extra de-bulking operations needed to prevent corner wrinkling described by [8, 14] and depending on the difference of the lay-up thickness and the cure ply thickness (that is, the bulk factor). The simplest form of automation is to lay up the complete stack flat manually or with machine followed by vacuum forming at an elevated temperature (HDF). The drawback with HDF is that corner thickness deviation has been shown to originate from forming operation [1] as well as from the curing. This effect was primarily found to depend on the squeeze flow of the prepreg layer in the fibre direction perpendicular to the forming direction, depending on the pressure gradient in the spar corner. The pressure gradient was dependent on forming force appearing in the radius when tensioning the forming rubber over the radius. The pressure gradient also depended on the difference between inner and outer radius periphery when forming on a convex mould.

The lay-up of a part on concave tooling is often limited to HLU or PHLU. However the same extended lay-up features as for the convex tooling could be used if the lay-up is performed on a convex tool and then using the concave tool only for the curing operation. The risk with HLU in a concave tool is tacking of the plies on both sides of the radius before the correct form of the radius have been reached (see figure 1a). This is often mentioned as bridging of plies. The bridging can introduce unwanted forming mechanisms during debulk or cure [11] or pressure drops in the cure assembly [15] which affects the corner compaction [10]. The engineering approach to limit this well-known problem is to apply lay-up strategies including of where to start the lamination and temporarily introduce consumables between critical areas of the plies. In figure 1b one strategy for lay-up of a u-spar on a concave tool is presented.

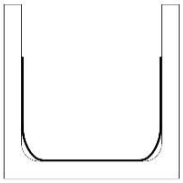

Figure 1a. Tacking at both sides of radius.

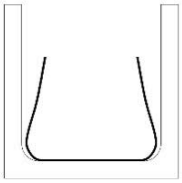

Figure 1b. Lay-up start at web middle.

The lay-up is starting in the middle of the web area followed by carefully work with the corner area often supported with a hand-tool. The ply is then carefully tacked from corner to the edge of the flange. De-bulk is performed with a vacuum bag at least every fourth ply.

For material with high level of interply friction such as M21, de-bulk of the lay-up is critical to avoid the defects described in [8, 14]. This type of material might require a hot compaction with vacuum bag in an oven or even sometimes with pressure in an autoclave.

In this paper corner thickness results from lay-up with HLU, PHLU, PVF, HDF, PHLU and HDF on a convex tool combined with cure in a concave tool as well as pressure forming with 400 bars in terms of Quintus Press Forming (QP) [16] is used.

2.4 Cure assembly

A great part of the corner thickness deviation are developed during the cure cycle and therefore the cure assembly (vacuum bag) has the possibility of limiting this. The main purpose of the vacuum bag is to even out the pressure over the part surface during the cure cycle. However a bad design of the cure assembly might introduce different kind of disturbances. Corner thinning in a convex radius is effected by the bag stretching over the corner creating a forming situation such as described in 2.2 for HDF. Corner thickening in a concave radius is affected by a bridging bag which is causing a pressure drop in the corner.

A traditional way of bagging a spar is to place the spar tool on a flat plate and then seal the bag to the plate. This reduces the complexity and size of the mould tool but lead to a risk of bridging the bag in the corner between the spar flange and the plate. The autoclave pressure will push the bag into the corner and the bag can stretch over the convex radius between the spar web and flange as shown in figure 2.

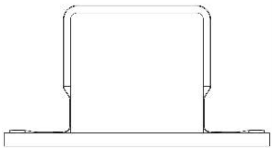

Figure 2. Stretch of bag in convex radius.

The classic engineering approach to relax the force from the bag is to put a bag film fold or a pleat in the corner between the plate and the tool as shown in figure 3a. During application of the vacuum the bag film and the pleat must be carefully worked down in the corner to reach a minimum of bridging. When autoclave pressure is applied, the friction in the bag will prevent further “opening” of the fold. However even when using this technique, bridging is still a risk as the breather consumable is going through compaction during the cure cycle. The engineering approach to minimize the effect of compaction in the consumables is to use thinner breathers, 4 oz or less, see figure 3b. Adding another pleat in the radius between spar web and flange provides more flexibility of the film during apply of vacuum. On the other hand, a pleat at a convex corner might also cause a small pressure drop in the corner which might cause a resin ridge in the radius. This technique can naturally also be used for a hat-profile geometry.

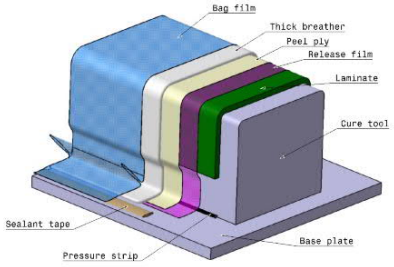

Figure 3a. Classic vacuum bag.

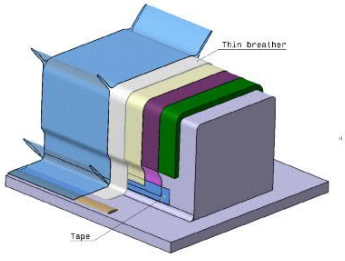

Figure 3b. Improved vacuum bag.

To further relax the stretch of the bag film in the spar radius an envelope bag could be used or even better, a simplified bag sealed with sealant tape on the spar tool flange, see figure 4a. An envelope bag makes the cure assembly less sensitive to breather compaction.

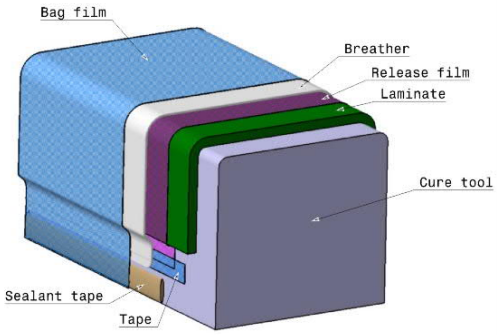

Figure 4a. Simplified bag, convex mould.

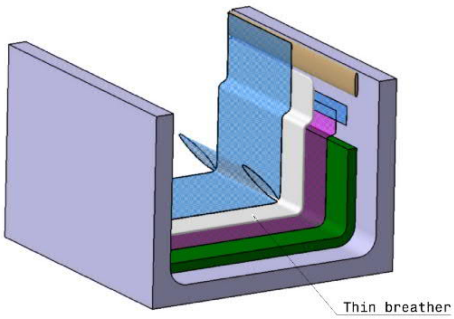

Figure 4b. Simplified bag, concave mould.

For a concave tool, the bagging technique to avoid bag film bridging in the radius is equal to the strategies used for a convex tool radius in terms of using a pleat in the radius, using a thin breather and also placing the sealant tape in the flange area in case of a u-spar tool (see figure 4b). The engineering experience is that a concave radius of 9 mm is possible to bag and cure, in serial production while still obtaining an acceptable level of radius thickening. With a skilled operator this limit can be stretched to 6 mm radius. For a smaller radius the bag must be complemented by some kind of pressure intensifier. Grankäll et al. [17] presents a novel idea how to use a 3D-printed bag support tool (outside the bag) to enable reaching concave radius with good quality 6 mm and beyond. This is proven to be a preferred engineering solution compared pressure intensifiers and caul plates [2] since these kind of solutions can either cause dents in the laminate or in worst case be misplaced and cause defects during compaction in the cure cycle.

In this paper the classic and improved bag showed in figure 3 are used as well as envelope bag and simplified bag (figure 4). All laminates were sealed with release film and tape to avoid unnecessary transport of resin out of the laminate.

2.5 Heat distribution

The compaction behaviour includes both bleeding flow and squeezing flow [11]. However Nixon Pearson et al. [9] showed that below a specific temperature, commonly between 30°C and 60°C (dependent on material), the degree of compaction depends mainly on temperature and consequently resin viscosity. A lower temperature might therefore be beneficial for the corner thickness control, which is in favour for Hand Lay-up (HLU) and Pairwise Vacuum Forming (PVF). However, when introducing Hot Drape Forming (HDF) or pressurized forming, elevated temperature between 45°C and 70°C is needed to avoid flange wrinkling [18, 19]. This also involves preheating of the tool. In work by Grankäll et al. [20] and Hallander et al. [21] it has been shown that both corner thickness control and flange forming could be achieved using non-isothermal forming and tailoring the temperature distribution. Some results from this are presented for HDF and pressure forming at 400 bars in terms of Quintus Press Forming (QP). In both cases the tool was kept at room temperature. Results from experimental studies on HLU, PVF and HDF also reveals the tool preheating effect.

  doi:10.5075/epfl-298799_978-2-9701614-0-0

2.6 Evaluation

In the presented study, some radius measurements are performed with microscope on cross sections from cut-up parts and all radius thicknesses from manufacturing trials are measured using a micrometer from Mitutoyo. The allowable radius thickness deviation differs depending on which defects are considered and translated into knock-down factors for the specific composite part. A too thin radius might lead to stiffness loss and a too thick radius might include resin pockets which can introduce micro cracks. As an example, for aerospace composite parts the allowable thickness variation/deviation can be ±10%.

3. Results and Discussion

Results from radius thickness measurements on different generations of experimental studies are presented in Table 1 together with comparing data from different generations of composite part manufacturing at Saab AB.

Table 1: Research data compared with manufacturing data for corner thickness deviations.

a) Data from HLU= hand lay-up on a hat profile performed in [12]
b) Production data from PHLU= pairwise hand lay-up spar manufacturing at SAAB AB
c) Data from PVF= pairwise vacuum forming performed on a spar performed in [1]
d) Production data from HLU spar manufacturing at SAAB AB
e) Production data from HDF= hot drape forming spar manufacturing at SAAB AB
f) Data from QP= Quintus press forming performed on a spar in [17]
g) Data from QP with tailored heat distribution on a spar performed in [22]
h) Data from HDF with heat distribution on a convex spar and cure in a concave mould [21]
i) Production data from PHLU on a convex spar and cure in a concave mould at SAAB AB

ID number	Material	Lay-up	Cure assembly	Tool feature	Tool radius [mm]	Part thickness [mm]	Corner thickness deviation [%]
1	977-2	HLU	Classic	Convex	6	4	-13 [a]
2	M21 (268)	HLU	Classic	Convex	6	4	0 [a]
3	977-2	HLU	Improved	Convex	6	4	-1 [a]
4	M21 (268)	HLU	Improved	Convex	6	4	0 [a]
Prod 1	Ref	PHLU	Improved	Convex	6	4	-8 [b]
5	977-2	HLU	Classic	Concave	8	4	+66 [a]
6	M21 (268)	HLU	Classic	Concave	8	4	+31 [a]
7	977-2	HLU	Improved	Concave	8	4	+25 [a]
8	M21 (268)	HLU	Improved	Concave	8	4	+12 [a]
9	6376	PVF	Envelope	Convex	2	4	-7 [c]
10	6376	PVF	Envelope	Convex	6	4	-5 [c]
Prod 2	Ref	HLU	Simplified	Convex	6	5	-1 to -4 [d]
11	6376	HDF	Envelope	Convex	2	4	-19 [c]
12	6376	HDF	Envelope	Convex	6	4	-4 [c]

Prod 3	Ref	HDF	Simplified	Convex	6	4	-1 to -6 [e]
13	6376	QP	Envelope	Convex	2	4	-30 [f]
14	6376	QP	Envelope	Convex	6	4	-16 [f]
15	6376	QP heat dis	Envelope	Convex	2	4	-8 [g]
16	6376	QP heat dis	Envelope	Convex	6	4	-4 [g]
17	M21 (134)	QP heat dis	Envelope	Convex	2	4	-5 [g]
18	M21 (134)	QP heat dis	Envelope	Convex	6	4	0 [g]
19	6376	HDF heat dis	Simplified	convex	3	8	-4 [h]
20	6376	HDF heat dis	Simplified	concave	13	8	-4 [h]
Prod 4	Ref	PHLU	Bag support tool	concave	7	4	Max 5 [i]

The research data from sample 1 to 4 show that both material and cure assembly had an impact on the thinning of a convex radius. However, when modifying the bag technique the influence from material selection was limited to a minimum. In a real production situation, it is probably not possible to change material. On the other hand, the bag technique can be always be altered and this is reflected in the Prod 1 result using the improved bag technique.

10 to 15 years ago, the work with thinner breather and improved positioning of the bag with pleats in the radius resulted in a stable radius thinning at 8% (Prod 1) which was within the limit of ±10%.

The research data from sample 5 to 8 showed increased radius thickness with a slurry of fibres in the radius for the low viscosity 977 material and resin pockets in the radius for the M21 material. The improved bag clearly affected the radius thickening. However the limit of ±10% thickness deviation was not reached. In this case, the bag-side radius was 4 mm which reflects the engineering statement at the time that a radius beyond 6 mm could only be achieved with acceptable thickness deviation if a pressure intensifier or a caul plate was used. This has never been considered as an optimal solution.

The research sample 9 to 18 used an envelope bag to minimize the effect of stretching the bag over the convex radius (see figure 2). In a real production situation this type of bagging is impractical and an engineering approach is therefore the simplified bag. Prod 2 and Prod 3 reflects the manufacturing situation today with a corner thinning in manufacturing on a convex mould that is equal to -6% or less.

Sample 9, 10 and 11, 12 uses different lay-up techniques in terms vacuum forming at room temperature (PVF) and vacuum forming at an elevated temperature of 65°C (HDF). The difference in temperature and lay-up technique results in varying thickness deviations depending on the size of the radius. The influence of lay-up technique and tool temperature was also reflected in Prod 2 and 3 showing a difference between Hand-lay up (HLU) with a radius thinning of -1% to -4% and Hot Drape Forming (HDF) with a radius thinning of -1% to -6%. Research sample 13 to 19 further investigates the influence of tool temperature on the radius thinning. Both forming pressure (represented by method), radius size, material and tool

temperature have an impact on the radius thinning. However, tool temperature has a dominant effect.

In research sample 19 and 20 Grankäll et al. is challenging the engineering statement of concave bag radius below 6 mm. The technique of forming on a convex radius and curing on a concave mould is used to avoid bridging of plies in the radius. The mould was geometrically compensated [13] to improve the fitting between part and mould. The forming was also performed at a low temperature (only heating the flanges). A simplified bag with an as thin breather as possible was also used. The result shows that the radius thinning gained in the forming also remains after the cure. Using this technique in production, combining it with a 3D printed bag positioning tool [17], as in Prod 4, that shows that a corner thickness deviation of maximum 5% can be achieved even at a bag radius of 3 mm.

4. Conclusions

All manufacturing steps (until curing) have an impact of the final corner thickness deviation. However, influence from factors such as radius size and material can be reduced with a developed bag technique. Pre-heating of the lay-up tool influences the thickness deviation and should therefore if possible be avoided. Small concave radii could be achieved without using pressure intensifiers or caul plates.

5. References

1. Sjolander J. Improving forming of aerospace composite components through process modelling. Doctoral Thesis in Aerospace Engineering, Stockholm, Sweden, 2018, ISBN 978-91-7729-881-6.
2. Fernlund G, Griffith J, Courdji R, Poursartip A. Experimental and numerical study of the effect of caul-sheets on corner thinning of composite laminates. Composites Part A: Applied Science and Manufacturing. 2002;33(3):411 – 426.
3. Hallander P. Åkermo M. Mattei C. Petersson M. Nyman T. An experimental study of mechanisms behind wrinkle development during forming of composite laminates. Composites: Part A 2013;50:54-64.
4. Larberg YR, Åkermo M. On the interply friction of different generations of carbon/epoxy prepreg systems. Compos Part A 2011;42(9):1067–74.
5. L. W. Davies, R. J. Day, D. Bond, A. Nesbitt, J. Ellis, and E. Gardon, “Effect of cure cycle heat transfer rates on the physical and mechanical properties of an epoxy matrix composite,” Compos. Sci. Technol., vol. 67, no. 9, pp. 1892–1899, 2007, doi: 10.1016/j.compscitech.2006.10.014.
6. Hubert P. Poursartip A. Aspects of the compaction of composite angle laminates: an experimental investigation. J Compos Mater 2001;35(2):2–26.
7. Svanberg JM. Hallander P. and Nyman T. Variation in shape distortion due to corner thinning/thickening of prepreg. Proceedings of 17th International conference of composite materials, Edinburgh, Scotland; 2009.
8. Dodwell TJ, Butler R, Hunt GW. Out-of-plane ply wrinkling defects during consolidation over an external radius. Compos Sci Technol 2014;105:151–9.
9. Nixon-Pearson O. Belnoue J. Ivanov D. Potter K. Hallet S. An experimental investigation of the consolidation behaviour of uncured prepregs under processing conditions. Journal of Composite Materials 2017;51(13):1911-1924

10. Levy A. Hubert P. Vacuum-bagged composite laminate forming processes: Predicting thickness deviation in complex shapes. Composites Part A 2019; 126: 105568
11. Lightfoot J. Wisnom M. Potter K. A new mechanism for formation of ply wrinkles due to shear between plies. Composites: Part A 2013;49:139-147
12. Hallander P. Sjölander J. Åkermo M. Interface manipulation towards wrinkle-free forming of stacked UD prepreg layers. Composites Part A: Applied science and Manufacturing 2016;90:340-348
13. Grankäll T. Hallander P. Åkermo M. Geometric compensation of convex forming tools for successful final processing in concave cure tools – an experimental study. Composites Part A 2019;116:187-196
14. Belnoue J. Hallett S. A rapid multi-scale design tool for the prediction of wrinkle defect formation in composite components. Materials & Design 2020;197: 108388
15. Wells J. Kay J. Poursartip A. Lane M. Fernlund G. Surface and bulk porosity in Out-of-Autoclave prepregs. Proceedings of 20th International conference of composite materials, Copenhagen, Denmark; 2015.
16. Hallander P. Sjölander J. Petersson M. Andersson T. Åkermo M. Fast forming of multi-stacked UD prepreg using a high-pressure process. Polymer Composites 2019;40(9):3550-3561
17. Grankäll T. Tooling and processing for efficient and high tolerance prepreg composites manufacturing. Doctoral Thesis in Aerospace Engineering, Stockholm, Sweden, 2022
18. Pandey RK and Sun CT. Mechanisms of wrinkle formation during the processing of composite laminate. Compos Sci Technol 1999; 59: 405–417
19. Farnand K, Zobeiry N, Poursartip A, et al. Micro-level mechanisms of fiber waviness and wrinkling during hot drape forming of unidirectional prepreg composites. Compos Part A Appl Sci Manuf 2017; 103: 168–177
20. Grankäll T. Hallander P. Åkermo M. Vacuum assisted hot forming with tailored temperature. Applied Composite Materials DOI 10.1007/s10443-020-09858-8
21. Hallander P. Grankäll T. Eriksson M. Petersson M. Åkermo M. Using tailored temperature variations to obtain flawless forming of multi-stacked UD prepreg. Journal of Composites Materials 2020;54(26):3999-4009

EFFECTS OF ION IRRADIATION ON MICROSTRUCTURE AND MECHANICAL PROPERTIES OF AUTOMATED FIBRE PLACEMENT BASED THERMOPLASTIC COMPOSITES

E.Oromiehie[a],V. Nair[b], K.Short[c], D.Bhattacharyya[c,d], B.G. Prusty[a]*

a: ARC Training Centre for Automated Manufacture of Advanced Composites, School of Mechanical and Manufacturing Engineering, UNSW Sydney, NSW 2052, Australia
b: School of Mechanical and Manufacturing Engineering, UNSW Sydney, NSW 2052, Australia
c: Australian Nuclear Science and Technology Organization (ANSTO), NSW 2234, Australia
d: School of Materials Science and Engineering, UNSW, Sydney, NSW 2052, Australia

Abstract: *In recent years, there has been increasing interest in carbon fibre reinforced material poly-ether-ether-ketone (PEEK) composite for application in aerospace industry because of its many attractive properties including recyclability, low density, high strength, high wear resistance, and continuous operating temperature of up to 260 °C. However, the resistance to radiation damage has not been studied extensively, although this is an important property to be assessed if these materials are to be used in aerospace applications, as all components in spacecraft are subject to a high radiation environment once they escape the earth's atmosphere. Among the many kinds of radiation, these materials are exposed to α particles and protons which are two of the major types of ionizing radiation that can impact their properties and service life. This is a major concern for long duration space travel over several months or years. The aim of this study is to understand the effect of high-energy α particles on the microstructure and properties of the PEEK material manufactured using automated fibre placement (AFP) under different processing conditions. Samples of carbon fibre reinforced PEEK material have been radiated with 5 MeV He ions in two directions using an energy degrader wheel to create a layer with relatively uniform damage. These samples have then been characterized using optical and scanning electron microscopy and their hardness measured with nanoindentation. The results have been analyzed taking into account the fibre directions. It was observed that radiation has caused significant hardening of the material, and that the change in hardness varied with the fibre direction.*

Keywords: Thermoplastic composites; Automated Fibre Placement; Irradiation

1. Introduction

Carbon fibre polymer reinforced composites (CFRP) are of great interest for application in aerospace and aviation industries, as they compare favourably to conventional metal structures due to their specific strength to weight ratio [1]. Among them, the poly-ether-ether-ketone (PEEK) based CFRP composites are superior due to their excellent mechanical properties, chemical inactivity, high resistivity to heat, wear, and ease in industrial processing [2, 3]. Hence, understanding their behavior under extreme conditions of long-term irradiation combined with thermal shock is necessary [4]. These materials would be subjected to two types of radiations, ionising and non-ionising. The former includes α (He^{2+}) and β (e^-) particles that may cause more damage to the material as they penetrate through the material causing the nearby atoms in their path to ionise and be displaced from their original positions, leaving vacancies and

  doi:10.5075/epfl-298799_978-2-9701614-0-0

interstitials. These can then form clusters, resulting in changes in microstructure and mechanical properties. Recent investigations have shown that irradiation can change the structure of the fibers and resin system, consequently changing their physical and chemical properties [5].

Nanoindentation testing is an advanced method for measuring the mechanical properties of all kinds of materials, including polymers and nanocomposites, before and after irradiation. Hence, It has been implemented by many researchers to study the elastic modulus and hardness [5].

To understand the relationship between the ion energy, damage peak depth and hardness peak depth, a nanoindentation test was conducted on ion-irradiated SS316 samples (using He^{+2} ions having 1, 2 and 3 MeV beam energies) by one of the present authors in a previous work [6]. From the obtained radiation-induced hardness (ΔH) curves, it was observed that the peaks of the hardness curves are at a much shallower depth than those of the displacement damage curves, and the hardness peaks appear at increasing depths with increasing ion energies. This is caused by the large size of the plastic zone in ductile metals, and the increasing penetration of ions at higher energies.

It is shown that, N^{+}-ion irradiation results in diameter change and morphology of the carbon fibre due to ion sputtering, ion implantation and chemical reaction between CF and nitrogen atoms in the fluence range 10^{17}–10^{19} cm^{-2} [5].

Similarly, the effect of ion irradiation on the tensile properties of pure Ni single crystals was investigated using an in situ micromechanical testing device inside an SEM. The results show that the peak strength increases from ~230 MPa for the unirradiated material to ~370 MPa and ~500 MPa for the materials irradiated with 6MeV He^{+2} ions to peak damage of 10 displacements per atom (dpa) and 19 dpa, respectively [7].

Effects of ion irradiation on microstructures and mechanical properties of SiOC nanocomposites containing β-SiC nanocrystals and turbostratic graphite have been investigated under a series of radiation conditions (4 MeV Kr ions, to the maximum fluence of 1×10^{14}, 2×10^{14}, 1×10^{15} ions/cm^2). It was shown that ion irradiation leads to rearrangement of the Si-containing tetrahedral units with more formation of mixed-bonded units in the amorphous matrix, and disordering of the turbostratic graphite, but the crystallinity of the β-SiC is preserved. More severe radiation condition results in higher variations in the amorphous SiOC matrix and more damage in the graphite. However, the surface morphologies and mechanical properties show little change under the applied radiation conditions, indicating the macro-property stability of the materials [8].

The radiation damage and thermal shock response of carbon-carbon (C/C) composites and carbon fiber reinforced molybdenum-graphite compounds (MoGRCF) to intense proton beams (120-200 MeV) and long-term irradiation also have been investigated [9]. The E-951 BNL experimental results (using 24-GeV proton tight beam pulses) confirmed that the C-C composite can withstand the thermal shock better than graphite. The study revealed the similarity between the effects of fast neutrons and of energetic protons on the microstructure of C/C and graphite composites, around the threshold fluence of $\sim 5 \times 10^{20}$ cm^{-2}. The modest irradiation levels of $\sim 6 \times 10^{18}$ p/cm^2 have been shown to induce significant changes in the microstructure of MoGRCF. Also, the impedance properties of MoGRCF tested in the Large Hadron Collider (LHC) beam collimation exhibit a significant decrease in post-irradiation load-displacement behavior even after low dose levels ($\sim 5 \times 10^{18}$ p/cm^2).

In another study, atomic force nanoindentation technique was used to investigate the effect of strain rate on the PEEK. It has shown that the average hardness and elastic modulus of PEEK

follow a linear model (from 263.9 MPa/1.377 GPa to 323.1 MPa/2.477 GPa) with respect to logarithm of strain rate from (0.012 s^{-1} to 1 s^{-1}) [10]. This technique was also used to investigate the microscopic and mechanical properties of pure PEEK versus CF-PEEK. It has been shown that the load-displacement curves of pure PEEK have superior uniformity, repeatability and consistency at different nano-indentation depths compared to CF-PEEK [3].

Nanoindentation and nanoscratching responses of PEEK-based composites reinforced with short carbon fibre (CF) and nano-silica has been investigated and show a significant increase in hardness and elastic modulus due to the presence of reinforcing agents. Incorporation of short carbon fibres (6 mm) and 2 wt.% of nano-SiO_2 particles into pure PEEK and conventional composite (PC) results in 143% and 44% improvement in the reduced elastic modulus [2].

A recent study on the nanomechanical characterisation of unidirectional CF-PEEK composites manufactured with AFP using different processing conditions shows that the nano hardness, elastic modulus, and creep resistance either in the polymer matrix or fibre/matrix interface of the samples that were manufactured at higher consolidation force and processing temperature are higher than those which are manufactured at lower values of these parameters. The nano hardness values in polymer matrix and fibre-matrix interface of CF-PEEK composites manufactured at 950 °C with 350 N consolidation force were about 188.8 and 1297.7 MPa while these values for composites manufactured at 650 °C using the same consolidation force (350 N) were about 173.2 and 1077.6 MPa, respectively [11].

To date, there have been no investigations on the effects of ion irradiation on CFRP composites, especially CF-PEEK manufactured using AFP. Thus, the aim of this research is to understand the effect of high energy α particles on the microstructure and properties of CF-PEEK composites manufactured under different processing conditions. The tests would be carried out on unirradiated as well as the radiated samples using nanoindentation techniques followed by microstructural analysis using scanning electron microscopy (SEM).

2. Experimentation

2.1 Sample preparation

In this experimental program, two composite panels with an overall dimensions of 160 mm x 60 mm x 6 mm were manufactured using Automated Dynamics built AFP machine. The panels comprised 40 plies of (UD) thermoplastic prepreg CF-PEEK (AS4-APC2), supplied by Solvay. To study the effect of ply orientations, $[90_4/30_3/60_3/90/–60_3/–30_3/90_3/90_3/-30_3/-60_3/90/60_3/30_3/90_4]$ lay-up sequence was implemented, where the subscripts mean the number of plies in each orientation. The prepreg tape has 6.35 mm width and thickness of 0.15 mm. The other material properties including density, elastic modulus, shear modulus, Poisson's ratio and fibre volume fraction (V_f) are 1570 kg/m^3, 138 GPa, 5 GPa, 0.28 and 0.6 respectively.
During the lay-up process the prepreg plies were processed simply by heating and cooling cycle. The panels were manufactured using different processing conditions. The deposition rate was kept constant at 76 mm/s for manufacturing all samples while the temperature and consolidation force were varied (Table 1). Only two samples (a: HGT temperature = 850 °C, consolidation force =250N; b: HGT temperature = 750 °C, consolidation force = 450N) were used in the present study. The panels were cut to coupons (5 mm x 5 mm x 2 mm) using Low Speed Cutting machine (150 rpm) as shown in Figure 1- (b). The cut samples then proceeded for polishing and grinding process using Struers Labo-Pol 60 machine. The top and cross-sectional surfaces of the cut samples are polished and ground initially using a 320-4000 grit size silicon carbide (SiC) paper / colloidal silica.

  doi:10.5075/epfl-298799_978-2-9701614-0-0

The final surface finish of polished samples was close to < 1 µm. As a preliminary investigation, the ion-irradiation was performed on samples “a” and “b”.

Table 1: AFP processing conditions.

Sample No.	Processing conditions		
	HGT Temperature (°C)	Nip-Point Temperature (°C)	Consolidation Force (N)
a	850	~415	250
b	750	~315	450

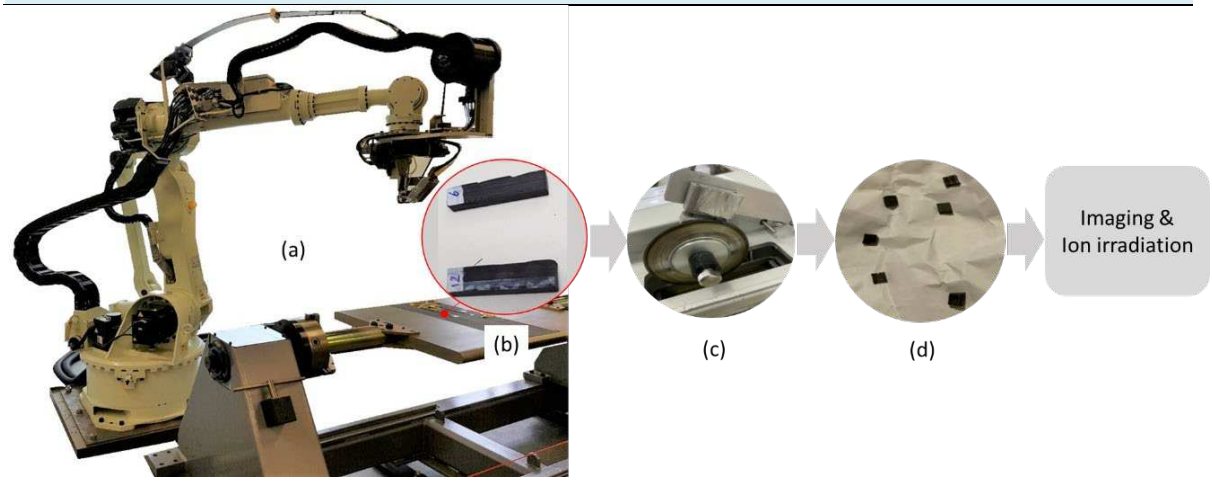

Figure 1. (a) Manufacturing Thermoplastic panels with AFP; (b) Small samples cut using diamond saw; (c) Low Speed Cutting Machine; (d) Coupon samples before polishing.

2.2 Ion-irradiation

The STAR accelerator at ANSTO was used to irradiate the material with α particles. SRIM or Stopping and Range of Ions in Matter [12], a quantum mechanics based simulation program, was used to estimate the depth of penetration and damage caused by the He ions in the composite target It performs the calculations by treating the target as amorphous and all collisions as binary interactions. The SRIM simulations showed that the radiation damage layer is shallow (up to ~25 µm for 6 MeV He, 38 µm for 2 MeV protons). For the present experiments, the polished samples were irradiated with an beam of 5 MeV He^{2+} ions to a fluence of $1e^{17}$ ions/cm^2 using a degrader wheel in the STAR accelerator, as shown in Figure 2.

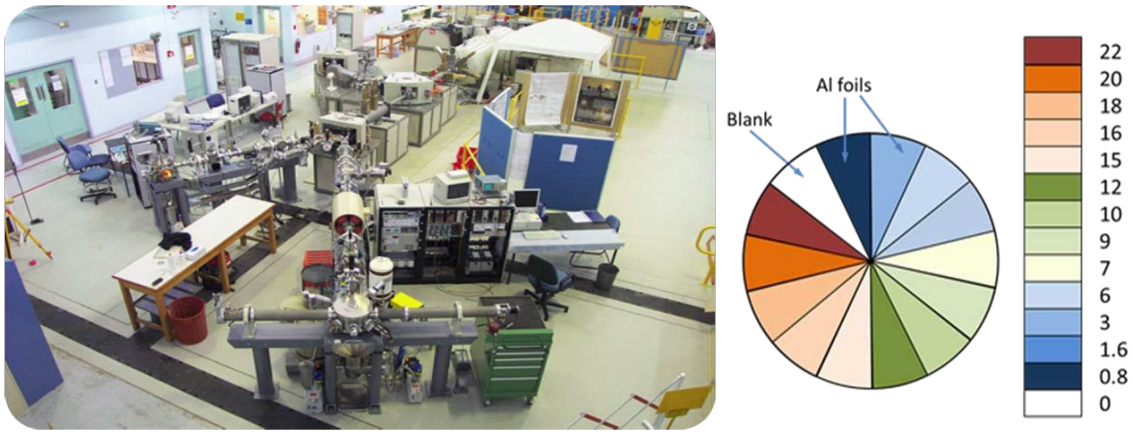

Figure 2. (a) 2MV STAR particle accelerator at ANSTO; (b) Degrader wheel showing sectors of Al foil with different thicknesses in microns.

The degrader wheel consisted of 20 sectors made of Al foils of increasing thickness, which led to the attenuation of the beam energy to varying degrees, thus leading to a more uniform damage through the depth of the ion range, as shown in the results section.

2.3 Image acquisition

Structural analysis of prepreg tape were carried out using a Zeiss® Optical Microscope (OM) and Zeiss® UltraPlus™ Scanning Electron Microscope (SEM). The SEM was run at a voltage of 10 kV and the secondary electron detector was used to image the sample, which was painted on the side with C paste to make it conductive for SEM characterization .

SEM analysis provided information on the diameter, shape and aspect ratios of the fibres which helped in the determination of orientation across the regions of varying hardness within the material using Eq. (1 and 2).

$$Aspect\ ratio = \frac{Major\ axis}{Minor\ axis} \tag{1}$$

$$cos\ \theta = \frac{1}{Aspect\ ratio} \tag{2}$$

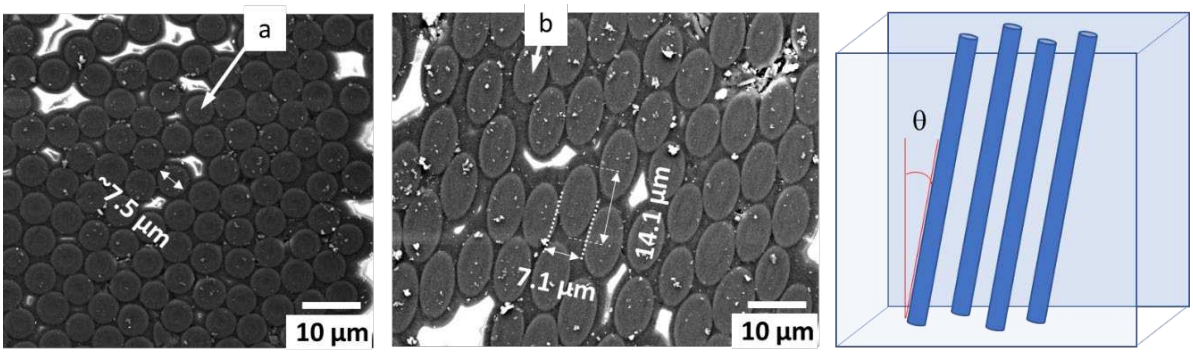

Figure 3. SEM images for determination of fibre orientation: (a) Aspect ratio of ~ 1 means angle of fibre to surface = 90 °; (b) Aspect ratio of ~ 2 means angle of fibre to surface = 60 °.

2.4 Nanoindentation

Nanoindentation analysis was carried out using an Agilent® / MTS® G200™ available at the NMDC research facility at ANSTO. The nanoindentation was carried out with a Berkovich diamond tip at maximum loads of 50 mN and 250 mN, respectively, and along linear arrays parallel to the traces of the fibre plies in the cross-section of the composite blocks. It was a load-controlled indentation that was carried out for both samples. For the correlation of the indents with the measured hardness values at the respective sites, the nanoindenter setup used an inverted XY coordinate system. Thus, the reference markers were used where the indent spacing was maintained at 100 µm. The hardness of the material was determined using the Eq. (3) [25],

$$H = \frac{P_{max}}{A_c} \tag{3}$$

where P_{max} is peak loading force achieved and A_c is projected contact area. As the indenter tip had a triangular pyramid structure, the area of cross-section is related to the indentation depth by Eq. (4),

$$A_c = 25.4xd^2 \tag{4}$$

  doi:10.5075/epfl-298799_978-2-9701614-0-0

where d is indentation depth and 25.4 is the area function for a Berkovich indenter with tip angle approximately 67˚.

3. Results and discussion

The optical microscope (OM) images in Figure 4- (a & b) show that the carbon fibre composite layers were laid out on top of one another. From OM images it was observed that the indents are more visible when 25 gf are applied. With the application of 5 gf, the materials tend to recover the holes generated by the indenter with time.

SEM analysis also provides information on the diameter, shape and orientation of the fibres which helped in the determination of aspect ratios, fibre density across the varying hardness within the material, Figures 4- (c &d). Moreover, in certain regions the fibres looked to retain a certain core-shell structure as shown in Figure 4-(d). This might happen because of the polishing process, as the wear rate of PEEK material is greater in comparison to the embedded carbon fibres. The bright white spots that are observed in the sample during the SEM investigation are the regions of continuous electron deposition i.e., the regions are seen to be charging and also highlight the presence of epoxy in the mixture, Figures 4- (c &d).

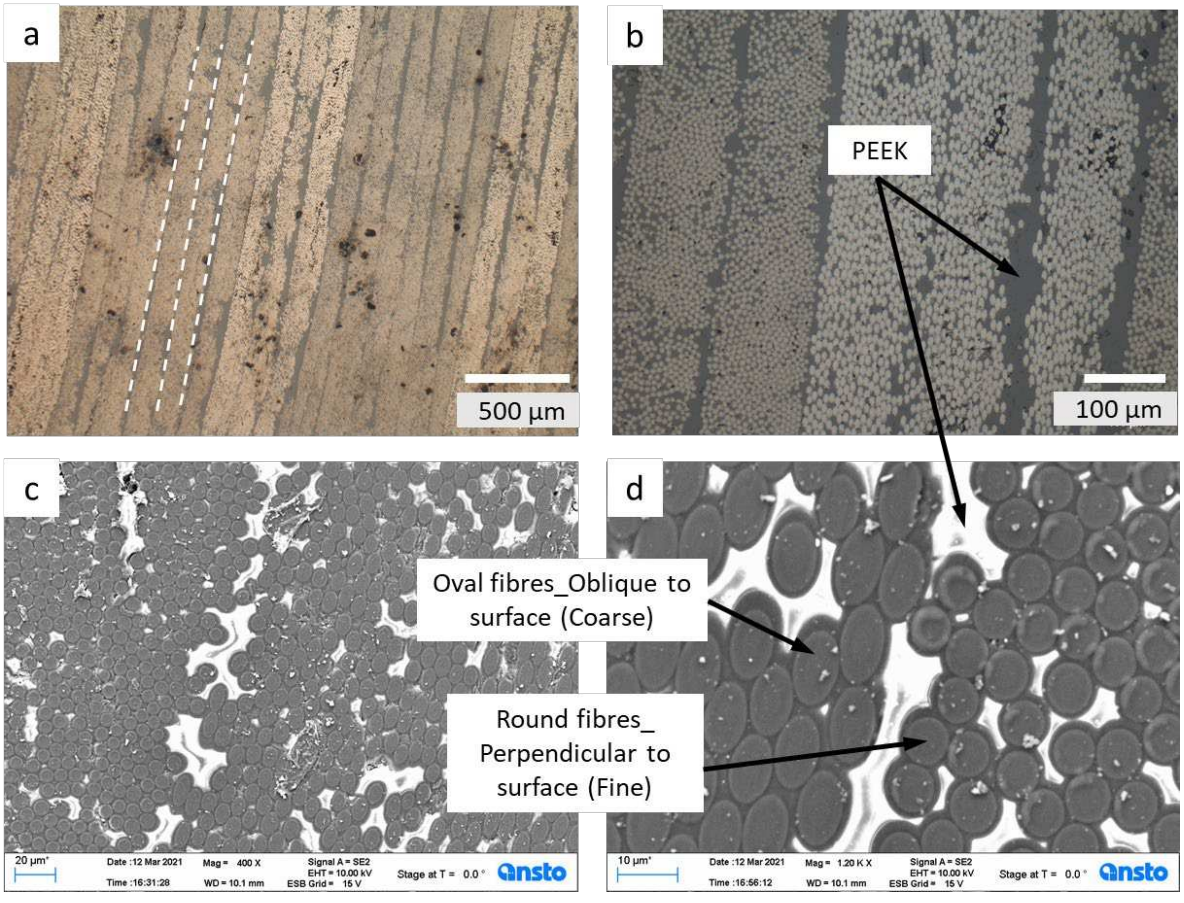

Figure 4. (a) Optical microscopy image of sample "a" at 50x magnification; (b) Optical Image at 200x to show the circular structures at center; SEM image of (c) Sample "a" at 400x; (d) Sample "a" at 1200x magnification.

The effects of fibre orientation on the hardness was also studied. The results show that hardness decreases with increasing inclination of fibres from the surface normal. The non-linear

correlation in the graph is influenced by the density of packing of the fibres in the region, Figure 5-(b).

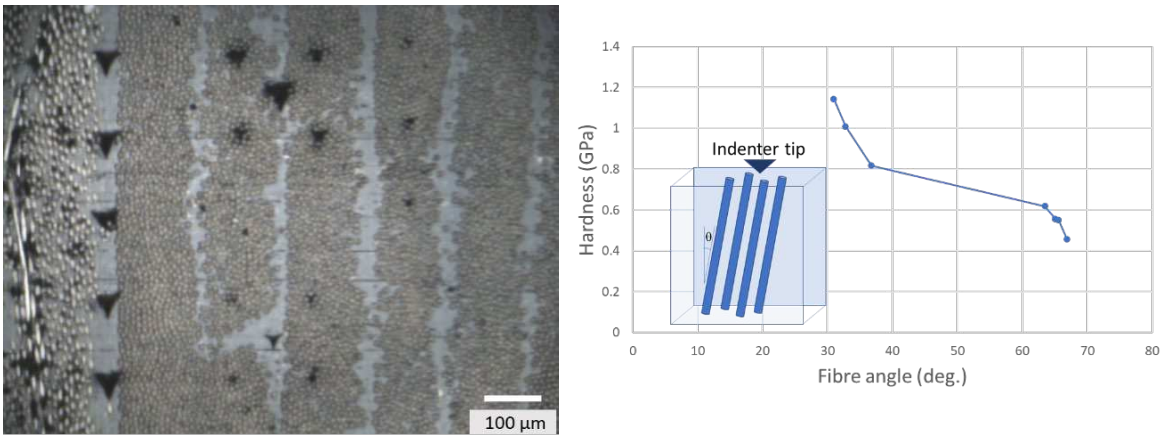

Figure 5. (a) Indents in the PEEK region for sample "b" and the markers for reference at 200X; (b) correlation between the hardness and ply angle in unirradiated sample.

As mentioned above, the SRIM software was used to identify the extent of penetration of α-particles and the resultant displacement damage in the different regions of samples. SRIM showed that α-particles penetrated to different regions of the modelled composite material (CF-PEEK) on varying the incoming ion energy, as shown in Figure 6. A higher incoming ion energy causes greater penetration into the target.

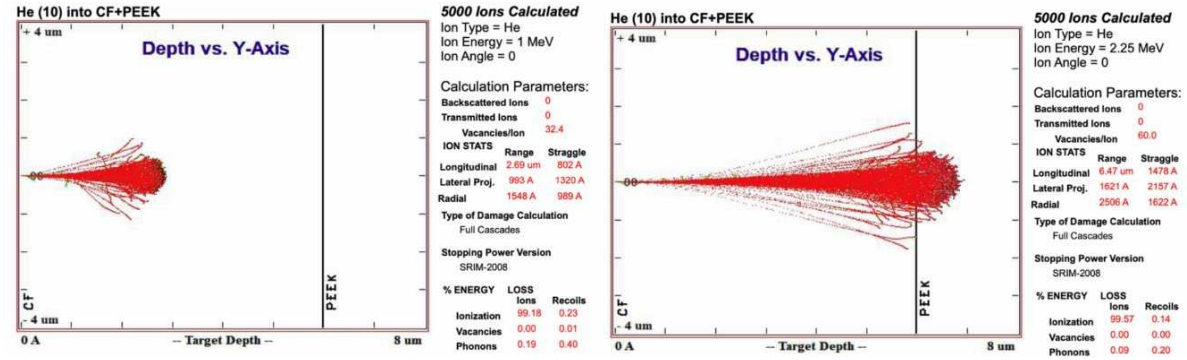

Figure 6. He ion irradiation and SRIM calculations.

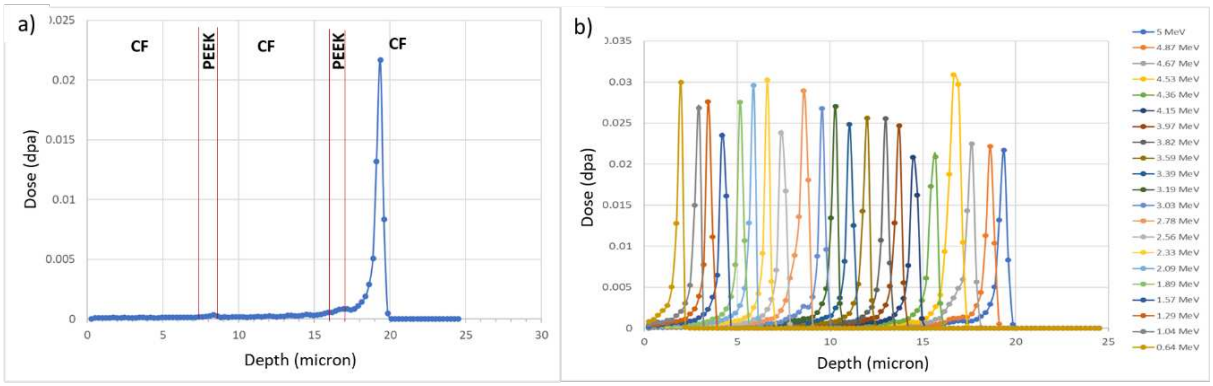

Figure 7. (a) Displacement damage dose (dpa) due to single He ion energy of 5 MeV; (b) Displacement *damage dose (dpa) due to multiple energies after ion beam passes through degrader wheel.*

  doi:10.5075/epfl-298799_978-2-9701614-0-0 published under CC BY-NC 4.0 license

Figure 7-(a) shows the simulated displacement damage dose (dpa) due to single He ion energy of 5 MeV while the doses (dpa) due to multiple energies after the ion beam passes through the degrader wheel are shown in Figure 7-(b). The sample was simulated as a multilayer composite of alternating C fibres of 7.5 µm thickness and PEEK layer of 1 µm thickness.

The simulated total displacement damage curve for 5 MeV He ions passed through energy degrader wheel for the first five layers of the composite, consisting of alternating C fibre and PEEK material, shows that multiple peaks in the total dpa curve makes the damage more uniform. The average dose is about 0.02 dpa which is much less than conventional structural materials such as steel, which would get about 0.4 dpa with the same fluence in MA57 steel [13] and about 0.1 dpa in SA508 [14].

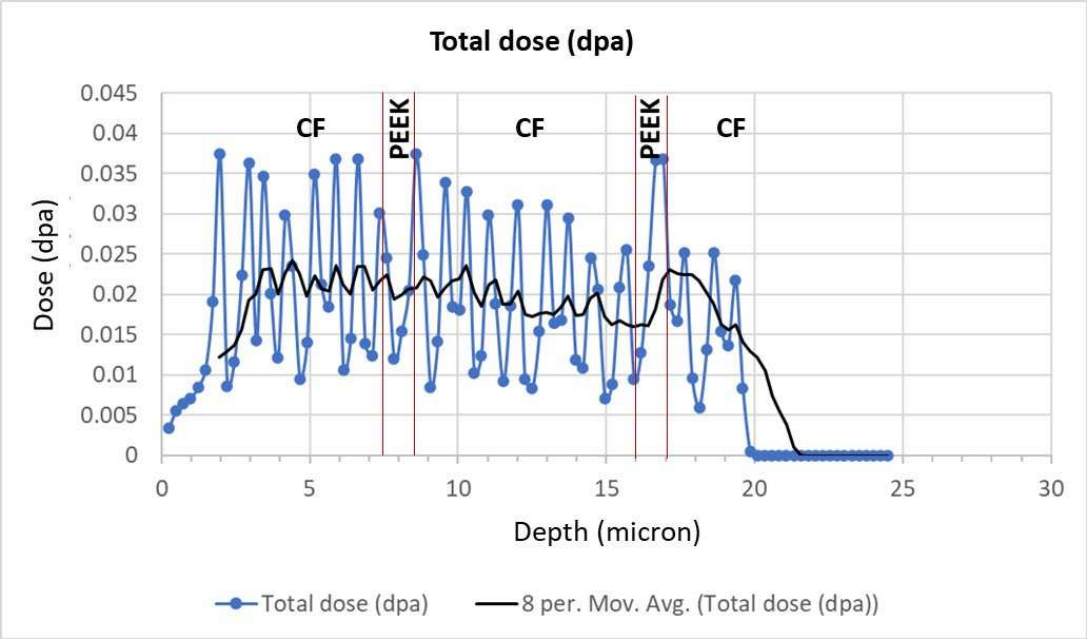

Figure 8. Total displacement damage dose due to all the foils, showing a more even distribution than a single energy (The black curve shows moving average).

The average hardness values for samples “a” and “b” were obtained for both radiated and unirradiated samples.

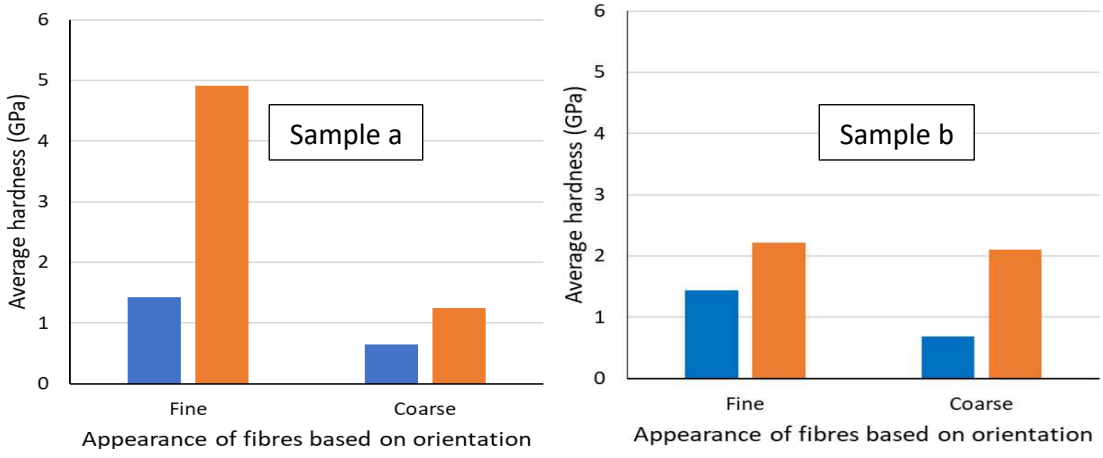

Figure 9. Comparison between the hardness of irradiated and unirradiated samples. Blue – Unirradiated, Orange – He ion irradiated

  doi:10.5075/epfl-298799_978-2-9701614-0-0

As can be seen in Figure 9, the areas of “fine” fibres or perpendicular orientation are harder than “coarse” fibres or oblique orientation in both unirradiated and irradiated condition for both sample “a” and “b”. Also, the average hardness of radiated samples in both “fine” and “coarse” areas [refer to Figure 4 –(d)] are higher than unirradiated samples. The “fine” area in sample “a” shows the greatest irradiation hardening while the “coarse” area shows least absolute hardening. Further analysis is required to distinguish different orientations and fibre packing densities in “fine” and “coarse” appearance.

4. Conclusion

In this study, the effect of high energy α particles on the microstructure and properties of CF-PEEK composites manufactured using AFP under different processing conditions was investigated. The tests were carried out on unirradiated as well as the radiated samples using nanoindentation techniques followed by microstructural analysis using SEM.

Some of the conclusions from these tests are as follows:

(i) The hardness depends on the orientation of fibres and the orientation perpendicular to the surface is the hardest.

(ii) SRIM simulations were used to estimate the damage caused by 5 MeV He ions using a degrader wheel in a composite modelled by 3 layers of 7.5 µm carbon fibres alternating with 2 layers of 1 µm thick PEEK. It was found that, the average damage dose for 1 x 10^{17} ions /cm^2 was about 0.02 dpa through a depth of ~ 20 µm and there was not much difference in damage between the carbon fibre and PEEK

(iii) Irradiation by He atoms causes hardening of the CF-PEEK composite, ranging from 0.7 GPa to 3.5 GPa, depending on the processing condition and fibre orientation. This level of hardening is very high with respect to the low dose when it is compared with the hardening observed in metals.

Future work:

Further analysis of hardness with respect to both orientation and fibre density is required to separate their effects. Future work will also involve through micro-tensile testing of FIB milled samples in both unirradiated and irradiated layers. The dependence of strength and fracture toughness on fibre orientation and irradiation, found using the nanoindentation tests, will be compared with the micro-tensile tests to obtain a comprehensive understanding of the combined effects of fibre orientation and radiation dose on mechanical properties.

Acknowledgements

The authors would like to thank Dr. Tao Wei for his assistance with the ion irradiation experiments. In addition, the authors would like to acknowledge the following funding:

ARC LIEF: Australasian facility for the automated fabrication of high-performance bespoke components (LE140100082).

ARC ITTC: ARC Training Centre for Automated Manufacture of Advanced Composites (IC160100040).

  doi:10.5075/epfl-298799_978-2-9701614-0-0

5. References

1. Yang B, Huang Y and Cheng L. Defect detection and evaluation of ultrasonic infrared thermography for aerospace CFRP composites. Infrared Physics & Technology. 2013/09/01/ 2013;60:166-173.
2. Molazemhosseini A, Tourani H, Naimi-Jamal MR and Khavandi A. Nanoindentation and nanoscratching responses of PEEK based hybrid composites reinforced with short carbon fibers and nano-silica. Polymer Testing. 2013/05/01/ 2013;32(3):525-534.
3. Rosselli F and Santare MH. Comparison of the short beam shear (SBS) and interlaminar shear device (ISD) tests. Composites Part A: Applied Science and Manufacturing. 1997/01/01/ 1997;28(6):587-594.
4. Rojdev K, O'Rourke MJE, Hill C, Nutt S and Atwell W. Radiation effects on composites for long-duration lunar habitats. Journal of Composite Materials. 2014/03/01 2013;48(7):861-878.
5. Ivanov MB, Gavrilov NV, Belyh TA, et al. Irradiation effects in carbon fibers after N+-ion irradiation. Surface and Coatings Technology. 2007/08/05/ 2007;201(19):8326-8328.
6. Saleh M, Zaidi Z, Ionescu M, et al. Relationship between damage and hardness profiles in ion irradiated SS316 using nanoindentation – Experiments and modelling. International Journal of Plasticity. 2016/11/01/ 2016;86:151-169.
7. Reichardt A, Ionescu M, Davis J, et al. In situ micro tensile testing of He+2 ion irradiated and implanted single crystal nickel film. Acta Materialia. 2015/11/01/ 2015;100:147-154.
8. Niu M, Wang H, Gao H, et al. Effects of ion irradiation on microstructures and mechanical properties of SiOC nanocomposites. Journal of Nuclear Materials. 2022/01/01/ 2022;558:153383.
9. Simos N, Zhong Z, Ghose S, et al. Radiation damage and thermal shock response of carbon-fiber-reinforced materials to intense high-energy proton beams. Physical Review Accelerators and Beams. 11/16/ 2016;19(11):111002.
10. Yang Y. Sensitivity of nanoindentation strain rate in poly(ester-ester-ketone) using atomic force microscopy. Polymer Testing. 2016/08/01/ 2016;53:85-88.
11. Gain AK, Oromiehie E and Prusty BG. Nanomechanical characterisation of CF-PEEK composites manufactured using automated fibre placement (AFP). Composites Communications. 2022/04/01/ 2022;31:101109.
12. Ziegler JF and Biersack JP. SRIM - The Stopping and Range of Ions in Solids: James Ziegler 2009.
13. Xu A, Susanto I, Wei T, Ionescu M, Daniels J and Bhattacharyya D. Investigation of mechanical property changes in He2+ ion irradiated MA957 through nanoindentation and in situ micro-tensile testing. Journal of Nuclear Materials. 2021/04/15/ 2021;547:152819.
14. Gasparrini C, Xu A, Short K, et al. Micromechanical testing of unirradiated and helium ion irradiated SA508 reactor pressure vessel steels: Nanoindentation vs in-situ microtensile testing. Materials Science and Engineering: A. 2020/10/07/ 2020;796:139942.

  doi:10.5075/epfl-298799_978-2-9701614-0-0

DRILLING INDUCED DELAMINATION IN AERONAUTICAL CARBON FIBRE REINFORCED POLYETHERKETONEKETONE (CF/PEKK) COMPOSITE

Jia Ge [a], Giuseppe Catalanotti [a,b], Brian G. Falzon [a,c,d], John McClelland [e], Colm Higgins [e], Jean-Aubin Thiebot [e], Yan Jin [a], Dan Sun [a]*

a: School of Mechanical and Aerospace Engineering, Queen's University Belfast, Belfast, BT9 5AH, UK jge02@qub.ac.uk

b: Escola de Ciências e Tecnologia, Universidade de Évora, 7000-671 Évora, Portugal

c: RMIT Space Industry Hub, STEM College, RMIT University, Melbourne, Victoria, 3000, Australia

d: Aerospace Engineering and Aviation, School of Engineering, RMIT University, Melbourne, Victoria, 3000, Australia

e: Northern Ireland Technology Centre (NITC), Queen's University Belfast, Belfast, BT9 5AH, UK

Abstract: *The excellent mechanical and thermal properties of thermoplastic carbon fibre/polyetherketoneketone (CF/PEKK) composite has led to its increased utilisation in various manufacturing sectors, particularly in the aeronautical industry. However its machining performance, especially the performance under drilling, has rarely been reported. In this study, the drilling performance of CF/PEKK composite is investigated in detail. The effect of different feed rates on the resulting thrust force, machining temperature and delamination damage has been elucidated. Through monitoring of thrust force and machining temperature, the effect of thermo-mechanical interaction on the delamination damage formation was revealed. This study provides an important insight into the damage mechanism in drilling of CF/PEKK and can provide parametric guidance on practical drilling of such material in aircraft manufacturing industry.*

Keywords: CFRTP; Aeronautical composites; Drilling; CF/PEKK; Delamination damage

1. Introduction

In recent years, continuous carbon fibre-reinforced thermoplastic (CFRTP) composites have received much attention in a wide range of industrial applications, such as aircrafts, automobiles, wind energy and sport equipment. Compared to traditional carbon fibre-reinforced thermosetting plastic (CFRP), CFRTP exhibits higher toughness, faster manufacturing turnover and improved recyclability [1], hence is considered as a more sustainable composite material for future aircraft and automobile manufacturing.

Mechanical joining through riveting is the still most deployed joining method for load bearing composite structures [2], especially in aircraft assembly. However, the studies in the literature mainly focus on investigating the drilling performance of thermoset CFRP, especially CF/epoxy composites. Andreas Haeger et al. [3] conducted a comparative experiment on the effect of the drill point angle on the delamination factor using twist drills with point angles of 70°and 100°. Results showed that the delamination factor of the CFRP drilled with 70° drill bits is 30% smaller compared to that with a point angle of 100°. Tsao and Hocheng [18] compared the influence of different drill bit geometries on the delamination of CFRP using Taguchi analysis. The

  doi:10.5075/epfl-298799_978-2-9701614-0-0

experimental results revealed that the saw drill and brad spur drill resulted in a reduced delamination factor compared to conventional twist drill bit. The influence of step drill on the delamination factor was investigated by Qiu et al. [4] and a corresponding relationship between the ratio of the pilot section diameter to the sizing section diameter and delamination was obtained. Ramirez et al. [5] conducted drilling experiments on unidirectional (UD) CFRP and found the surface roughness deteriorated for fibre orientation of $\theta = 135° \pm 18°$. This can be explained by the uncut fibres around 135 ° fibre orientation. Similar results were also demonstrated by others [5–8]. This can be explained by the material removal mechanism in the region with a fibre orientation of $90° < \theta < 180°$. The bending and subsequent breaking of carbon fibres resulted in voids and pits on the finished surface. Apart from drill bits geometries and fibre orientation, cutting speed and feed rate are two significant factors that considerably influence the hole quality in drilling of CFRP. Heidary et al. [9] and Krishnaraj et al. [130] revealed that the feed rate has a greater influence on the drilling delamination factor as compared to the cutting speed. Similar results were reported by Krishnaraj et al. [10] where contribution of feed rate on push-out delamination (51.4%) was much greater than that of the spindle speed (35.42%) during high speed drilling of CFRP. Eneyew and Ramulu [8] conducted drilling experiment in UD CFRP and a lower surface roughness can be obtained when employing higher cutting speed and lower feed rate. Liu et al. [11] further validated such correlation using finite element analysis (FEA) method.

Compared to the large body of works available on drilling of CFRP, only a few studies have been carried out on drilling of CFRTP. In this paper, the drilling performance of thermoplastic carbon fibre reinforced polyetherketoneketone (CF/PEKK) composite is reported. The effect of different feed rates on the resulting thrust force, machining temperature, delamination damage will be discussed.

2. Experiment setup

2.1 Materials and drilling experiment

CF/PEKK laminates used in this study were fabricated from 22 lies of unidirectional prepregs with a stacking sequence of $[0/90]_{11}$ and a nominal thickness of 3 mm. The coupons used for drilling experiment has a dimension of 120 mm x 120 mm x 3 mm.

Two-flute 6 mm diameter drill bits (point angle = 104°) with TiAlN coating were supplied by Changzhou Aitefasi Tools Co. Ltd. Drilling experiment were carried out under dry condition with Deckle FP3A 3 axis CNC machine, at different feed rates shown in Table 1. During drilling, the thrust force was measured with a Kistler 9272 dynamometer and the hole wall temperature was captured by a FLIR A6751 thermal camera. Three holes were produced for each set of parameters to endure repeatability.

Table 1Drilling parameters used in this study

Parameters	Values
Feed rate F (mm/rev)	0.025, 0.05, 0.1, 0.15, 0.2
Cutting speed V_c (m/min)	50

The hole delamination damage was analysed using Alicona infinite focus G5 microscope (Uruker, UK) and quantified by delamination factor F_{da} following established method [15].

3. Results and discussion

3.1 Thrust force and hole temperature

For drilling of CF/PEKK, thrust force is the main reason causing delamination damage at the hole exit, as a result of Mode-I opening fracture [16]. On the other hand, the high machining temperature can soften the CF/PEKK plies and induce thermal-related damage to the hole. The thrust force and hole temperature at different drilling feed rates are shown in Figure 1. The results showed that the thrust force significantly increased with feed rate, while the hole wall temperature followed the opposite trend which showed a clear decline with feed rate.

The thrust force in drilling of CF/PEKK showed 224% increase when the feed rate increased from 0.025 mm/rev to 0.2 mm/rev. The drastic increase can be attributed the thicker material removed per tool revolution under the higher feed rate. The thrust force showed a linear correlation with feed rate, which is similar to the report by Guo et al. [19] in their thrust force mathematical models for drilling of CF/epoxy composite. The hole wall temperature decreased from 201 ℃ to 85 ℃ as the feed rate increased from 0.025mm/rev to 0.1 mm/rev. The hole wall temperature stabilized at ~ 80 ℃ for feed rate > 0.1 mm/rev. The decrease of hole wall temperature can be attributed to the reduced tool-workpiece contact time at high feed rate, which creates less thermal energy accumulation.

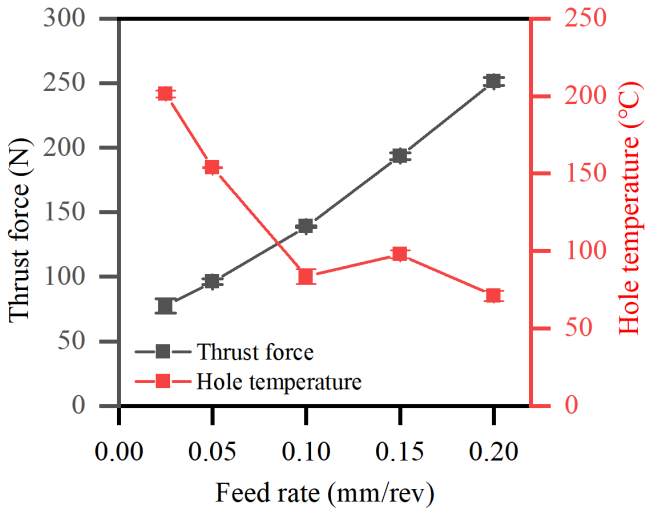

Figure 1 Thrust force and hole wall temperature at different drilling feed rates

3.2 Delamination damage

Delamination damage is mostly induced at the last uncut ply of the laminate during the drilling process, due to lack of mechanical support underneath. Hole delamination can weaken the components' strength and reliability, and therefore should be controlled and minimized whenever possible. Table 2 shows the delamination damage of CF/PEKK at hole-exit under different feed rates. The variation of delamination factor with feed rate is shown in Figure 2. The delamination factor F_{da} first decreased from 1.16 to 1.02 with the feed rate increasing

from 0.025 mm/rev to 0.1 mm/rev. Then F_{da} started to show increasing trend with feed rate and reached the highest value 1.47 at the highest feed rate F = 0.2 mm/rev.

The initial declining trend seen for delamination damage can be associated to the decreasing trend of the hole wall temperature. Under a low feed rate (F < 0.025 mm/rev), the high machining temperature can soften the CF/PEKK ply and weaken its resistance to bending deformation. Under high feed rate (F > 0.1 mm/rev), the high trust force can cause severe Mode-I opening fracture and take over the predominant influence on the delamination damage. As such, the delamination damage in drilling of CF/PEKK is strongly influenced by the thermal-mechanical interaction at the tool-workpiece interface.

Table 2 Typical hole exit delamination image produced under different feed rates

Feed rate (mm/rev)	0.025	0.05	0.1	0.15	0.2
CD					

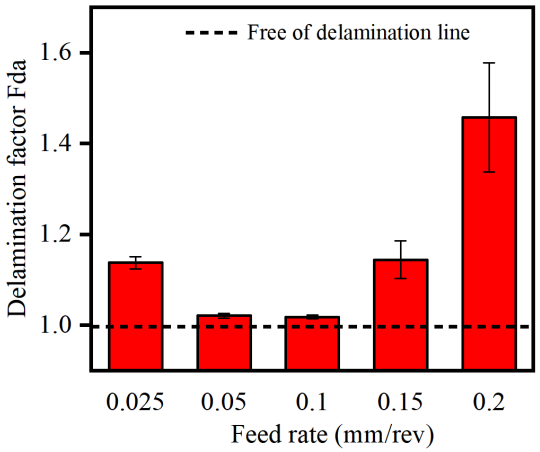

Figure 2 Variation of delamination factor F_{da} with feed rate

4. Conclusions

This paper investigated the drilling characteristics of high-performance thermoplastic CF/PEKK composite. The effect of feed rate on the resulting thrust force, machining temperature and hole delamination damage has been revealed. Experimental results suggested that drilling thrust force increases significantly with feed rate while machining temperature showed clear decreasing trend with feed rate. The composite's delamination damage is a result of combined mechanical –thermal interaction caused by the thrust force and high machining temperature.

Acknowledgements

The funding support from EPSRC projects EP/P025447/1 and EP/P026087/1 is acknowledged. This project has also received funding from the European Union's Horizon 2020 research and innovation programme under grant agreement No 734272.

5. References

[1] Ge J, Catalanotti G, Falzon BG, McClelland J, Higgins C, Jin Y, et al. Towards understanding the hole making performance and chip formation mechanism of thermoplastic carbon fibre/polyetherketoneketone (CF/PEKK) composite. Compos Part B Eng 2022:109752. https://doi.org/https://doi.org/10.1016/j.compositesb.2022.109752.

[2] Xu J, Mansori] M [El. Experimental study on drilling mechanisms and strategies of hybrid CFRP/Ti stacks. Compos Struct 2016;157:461–82. https://doi.org/https://doi.org/10.1016/j.compstruct.2016.07.025.

[3] Haeger A, Schoen G, Lissek F, Meinhard D, Kaufeld M, Schneider G, et al. Non-destructive Detection of Drilling-induced Delamination in CFRP and its Effect on Mechanical Properties. Procedia Eng 2016;149:130–42. https://doi.org/https://doi.org/10.1016/j.proeng.2016.06.647.

[4] Qiu X, Li P, Niu Q, Chen A, Ouyang P, Li C, et al. Influence of machining parameters and tool structure on cutting force and hole wall damage in drilling CFRP with stepped drills. Int J Adv Manuf Technol 2018;97:857–65. https://doi.org/10.1007/s00170-018-1981-2.

[5] Ramirez C, Poulachon G, Rossi F, M'Saoubi R. Tool Wear Monitoring and Hole Surface Quality During CFRP Drilling. Procedia CIRP 2014;13:163–8. https://doi.org/https://doi.org/10.1016/j.procir.2014.04.028.

[6] Geier N, Szalay T, Takács M. Analysis of thrust force and characteristics of uncut fibres at non-conventional oriented drilling of unidirectional carbon fibre-reinforced plastic (UD-CFRP) composite laminates. Int J Adv Manuf Technol 2019;100:3139–54. https://doi.org/10.1007/s00170-018-2895-8.

[7] Geier N, Szalay T. Optimisation of process parameters for the orbital and conventional drilling of uni-directional carbon fibre-reinforced polymers (UD-CFRP). Measurement 2017;110:319–34. https://doi.org/https://doi.org/10.1016/j.measurement.2017.07.007.

[8] Eneyew ED, Ramulu M. Experimental study of surface quality and damage when drilling unidirectional CFRP composites. J Mater Res Technol 2014;3:354–62. https://doi.org/https://doi.org/10.1016/j.jmrt.2014.10.003.

[9] Heidary H, Karimi NZ, Minak G. Investigation on delamination and flexural properties in drilling of carbon nanotube/polymer composites. Compos Struct 2018;201:112–20. https://doi.org/https://doi.org/10.1016/j.compstruct.2018.06.041.

[10] Krishnaraj V, Prabukarthi A, Ramanathan A, Elanghovan N, Kumar MS, Zitoune R, et al. Optimization of machining parameters at high speed drilling of carbon fiber reinforced plastic (CFRP) laminates. Compos Part B Eng 2012;43:1791–9.

https://doi.org/https://doi.org/10.1016/j.compositesb.2012.01.007.

[11] Liu H, Xie W, Sun Y, Zhang J, Chen N. Investigations on micro-cutting mechanism and surface quality of carbon fiber-reinforced plastic composites. Int J Adv Manuf Technol 2018;94:3655–64. https://doi.org/10.1007/s00170-017-1110-7.

[12] Hocheng H, Puw HY. On drilling characteristics of fiber-reinforced thermoset and thermoplastics. Int J Mach Tools Manuf 1992;32:583–92. https://doi.org/10.1016/0890-6955(92)90047-K.

[13] Xu J. Drilling characteristics of carbon / epoxy and carbon / polyimide composites 2020.

[14] Xu J, Huang X, Davim JP, Ji M, Chen M. On the machining behavior of carbon fiber reinforced polyimide and PEEK thermoplastic composites. Polym Compos 2020;41:3649–63. https://doi.org/10.1002/pc.25663.

[15] Davim JP, Rubio JC, Abrao AM. A novel approach based on digital image analysis to evaluate the delamination factor after drilling composite laminates. Compos Sci Technol 2007;67:1939–45. https://doi.org/https://doi.org/10.1016/j.compscitech.2006.10.009.

[16] Hocheng H, Pwu HY, Yao KC. Machinability Of Some Fiber-Reinforced Thermoset And Thermoplastics In Drilling. Mater Manuf Process 1993;8:653–82. https://doi.org/10.1080/10426919308934872.

INFLUENCE OF THE INNOVATIVE PROCESS OF PRODUCTION OF EPOXY COMPOSITES FILLED WITH MICROCELLULOSE ON THE MECHANICAL PROPERTIES OF THESE COMPOSITES

Jana, Novotná[a], Blanka, Tomková[a]

a: Technical University of Liberec, Dep. Of Material Engineering, Studentská 2, 46117 Liberec, Czech Republic, Email: jana.novotna3@tul.cz

Abstract: *The effect of Alba-Fiber®C-200 short recycled cotton fibers on the mechanical properties of cotton fibers/epoxy composites were investigated.*

As the application of cellulose in epoxy is complicated due to powerful attraction between the fibers (agglomeration of particles), surface treatment must be used prior to the cellulose mixing into the selected matrix. In this paper, new methods of cellulose surface treatments were used with fillers concentrations of 0 %, 1 % and 10 % by weight. The first method is without using degassing; the second method uses degassing for 10 minutes. In the third method, the micro cellulose particles were dried at 100 °C for 60 min and, after that added and mixed with hardener for 60 min before cure.

The mechanical properties, represented by three-point bending (3PB), were analyzed on the prepared samples. It was demonstrated that the compatibility between micro cellulose and epoxy resin could be maintained due to an innovative production process and improved epoxy composite mechanical properties.

Keywords: fibers reinforced epoxy composites (FRE); cotton fibers; three-point bending (3PB).

Highlights

- FRE with and without micro cellulose filler was prepared.
- Three types of preparing methods were used to improve the composites system.
- Mechanical properties of composites were analyzed.

1. Introduction

Cotton is an important crop for the textile industry with a long history. These fibers have been used in the clothing industry for a long time. The cotton fibers are white in colour and have a matte sheen. The main building block of cotton fiber is cellulose. Moisture in standard conditions (65% RH) is 8 %, moisture in a humid atmosphere (95% RH) is higher 25 %, fibers tend to swell (1). Due to its low density, cotton or micro cellulose is an ideal material suitable for use as a filler in epoxy resins (compare selected properties of the materials used in Table 1).

It is known that the shape, size, volume fraction, and specific surface area of the added particles in polymer have been found to affect the mechanical properties of the composites significantly greatly (2)(3).

The test 3PB provides important design information on the bending behaviour of polymeric materials, which is persistent stresses (beams, roof structures, cladding materials and others).

  doi:10.5075/epfl-298799_978-2-9701614-0-0

The bending test allows the modulus of elasticity to be determined for materials for which this is not possible with sufficient accuracy determined from tensile or compressive tests. Based on knowledge of composite materials with short fiber reinforcement, the tested samples have low ductility. When pulling, the applied tensile force would act mainly on the material matrix and reinforcement from recycled micro fibers would not significantly help tensile strength. The advantage is achieving significant bending moments even with a small loading force (4).

To correct for deficiencies in these materials, reinforcing fibers can be modified by physical and chemical methods, especially to impart bonding and adhesion and dimensional stability (5). Usually are, surface modifications of natural fibers used to optimize the properties of the fiber-matrix interface. While in this work, the fibers are not chemically treated; they are only pre-dried in a drier, using knowledge of their considerable moisture content.

2. Materials and method

2.1. Material

The low molecular weight epoxy resin based on bisphenol A CHS-EPOXY 455 without phthalates and hardener T 0492, which reduces the heat generation during the reaction and is suitable for prolonging the processing time, was chosen as the matrix), mixing ratio 100:23 by weight (6). Selected properties of epoxy and used fibers, see Tab. 1. The diameter of the fibers was 20 µm, length 50 – 300 µm.

Tab. 1 Selected material properties Cotton Fiber (5) *and epoxy* (7)

Material	Density [g/cm^3]	E [GPa]	Tensile strength [MPa]	Moisture absorption [%]
Cotton	I.51	12	400	8-25
EP	I.25	2-3	30-50	-

As fillers were used, short recycled cotton fibers Alba-Fiber®C-200, see Figure 1. The fibers were added in 0 wt.%, 1 wt.% and 10 wt.% concentrations. Samples were prepared by magnetic stirring for 10 min. Micro cellulose was stored in closed containers before use to avoid moisture uptake from the surroundings.

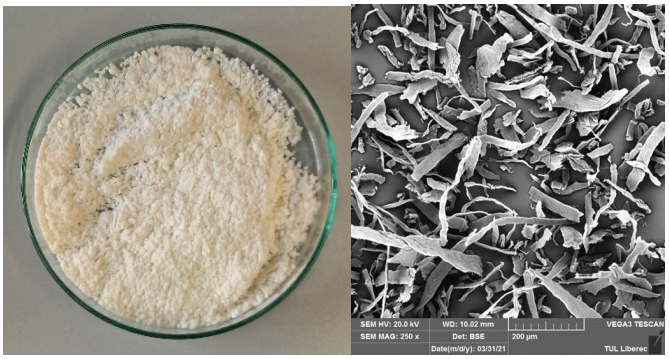

Figure 1. Makro and micro (SEM) photo of Microcellulose

2.2. Methods of preparing samples

It was used three different methods for preparing composite samples; an overview of the sample preparation methods used is given in Table 2. The first method is without using

  doi:10.5075/epfl-298799_978-2-9701614-0-0

degassing; the second method uses degassing for 10 minutes. In the third method, the micro cellulose particles were dried at 100 °C for 60 min and, after that, added and mixed with hardener for 60 min before cure.

Tab. 2 Methods of preparing samples

Method	Time of degassing [min]	Time of fiber drying at 100 °C [min]	Time of action of hardener and fibres [min]
A	-	-	-
B	10	-	-
C	10	60	60

2.3. Testing methods

The specimens of each material with randomly oriented micro cellulose fibres were tested in three-point bending according to EN ISO 14125 (8) in a universal testing machine, Tiratest 2300, at a displacement rate of 2 mm/min. Five tests were performed for each specimen. The radius of supports and loading noses were: supports RA = 9.9 mm; loading noses RC = 30 mm.

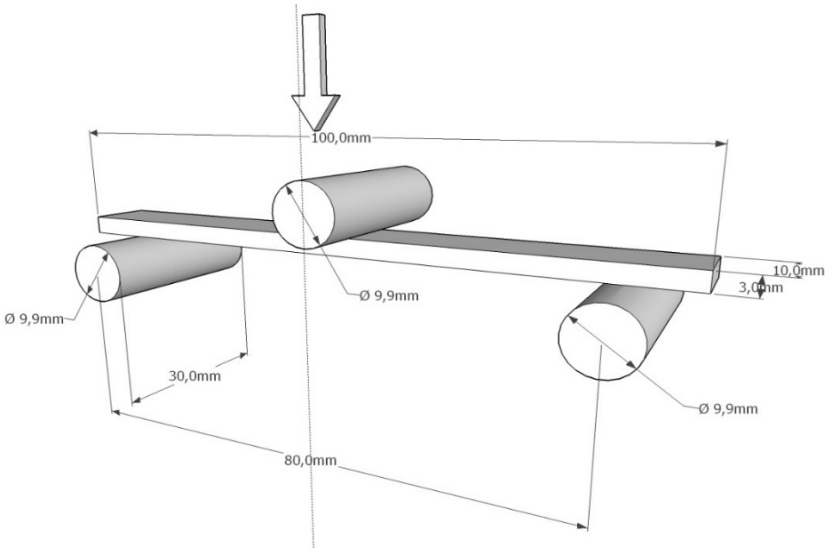

Figure 2. Three-point bending test configuration

Flexural stress was calculated according to:

$$\sigma = \frac{3 \cdot F \cdot l}{2\, a \cdot b^2} \quad (1)$$

where σ is the flexural stress [MPa], F is the load [N], l is the span [mm], a is the specimen width [mm] and b is the specimen thickness [mm].

Flexural modulus was calculated according to:

$$E = \frac{F \cdot l^3}{4 \cdot X \cdot a \cdot b^3} \quad (2)$$

  doi:10.5075/epfl-298799_978-2-9701614-0-0

where *E* is the flexural modulus [MPa], *l* is the span [mm], *a* is the specimen width [mm], *b* is the specimen thickness [mm], and *X* is the slope of the linear region of the load-displacement curve. All tests were repeated at least 5 times, and the results were recorded and plotted, see Fig. 4.

3. Results

Fig. 3 (a) shows the fracture surface of the composites specimen for pure epoxy. In Figs. 3(b)-(d), morphological observations on fractured surfaces from the ten FRE samples with 10 wt.% prepared by the method A, B and C are shown. It can be seen that the microcellulose fibers are uniformly dispersed in the sample. The filler-filled composites fracture is a brittle mechanism-type failure. Figure 3 (b) shows a large number of air bubbles, which are caused by the sample preparation technology, as the samples were not degassed.

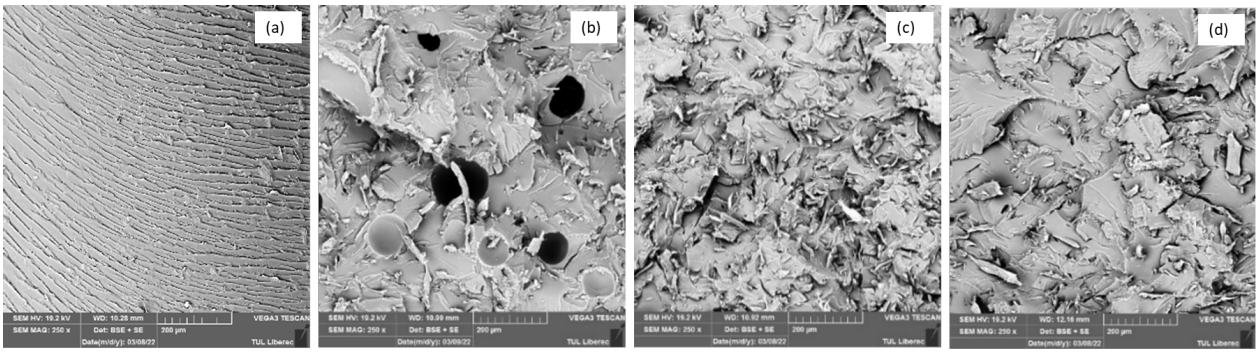

Figure 3. SEM images of fracture surface of RCF/epoxy composites with Micro cellulose content (a) 0 wt.%, (b) 10 wt.% prepared by the method A, (c) 10 wt.% prepared by the method B and (d) 10 wt.% prepared by the method C

The effect of fibre content on the flexural stress of FRE reinforced with epoxy composites is shown in Figure 4. It is found that the flexural stress decreases with increasing the fibre content increases. The significant reduction in flexural strength at higher microcellulose content is due to the increased stress transferred to the fibres due to insufficient bonding to the interface between the fibre and the matrix. The problem of agglomeration of the filler occurs at higher ratios of nanofiller, as pointed out by (9)and (10).

As the fillers increased the stiffness and stiffness behaviour of the polymer composite, the content of flexural modulus increased with the increasing amount of filler. The highest flexural modulus values were achieved for composites with a micro filler content of 10 wt.% prepared by method C.

Lam et al. (3) investigated different particle size effects and achieved better dispersion with minor particle fillers. Increasing the particle size and filler ratio caused difficulties inhomogeneous dispersion of the fillers, resulting in poor dispersion of the fillers. Based on these recommendations, in the future, it would certainly be interesting to conduct a similar study with smaller microcellulose particles, e.g. ground cellulose

  doi:10.5075/epfl-298799_978-2-9701614-0-0

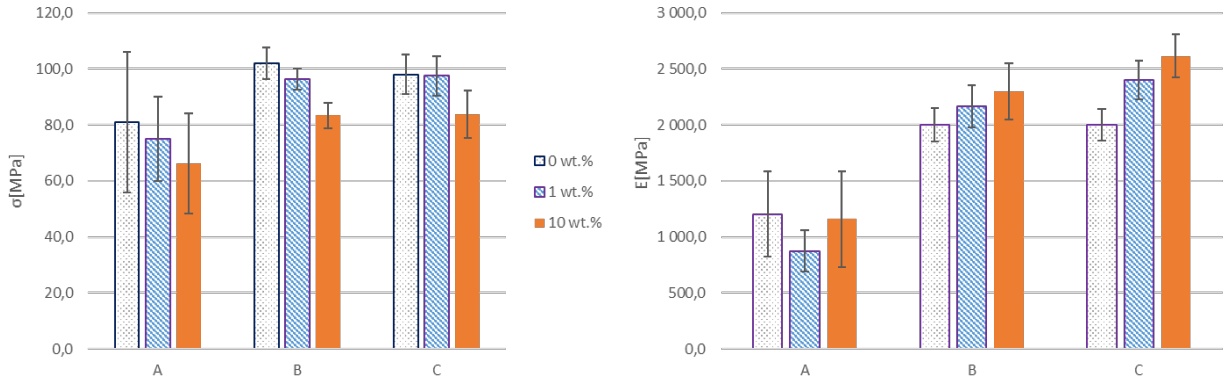

Figure 4. Effect of fibre content and type of specimen preparation on flexural stress and Young's modulus

4. Conclusion

The results show that the flexural strength of composites decreased while the flexural modulus increased with the increasing micro cellulose content ratio. Small amounts of microparticles in epoxy substantially affect flexural strength results; these results agree with the results reached by (11).

In summary, using pre-drying the micro cellulose fibers and pre-application of the hardener into the fibers prior to application to the epoxy component of the matrix is cost-effective and straightforward. The pre-dried micro cellulose particles showed many advantages such as limited agglomeration, improved hydrophobicity, and homogeneous dispersion in the matrix. Micro cellulose fibers treated in this manner could be used in an epoxy matrix and provide successful reinforcement at only 1 wt.% loading. The results showed that 1 wt.% micro cellulose reinforcement was good for improving the elastic modulus suggesting that there might be an optimum density of crosslinks between the cellulose and the epoxy matrix. Using recycled materials, epoxy micro cellulose composites could benefit the polymer industry by incorporating waste materials into new environmentally friendly products.

Acknowledgements

This work was supported by the project ‘Advanced structures for thermal insulation in extreme conditions’ (Reg. No. 21-32510M) granted by the Czech Science Foundation (GACR).

References

1. Baffes J. The “Cotton Problem.” World Bank Res Obs. 2005;20(1):109–44.
2. Satheesh Raja R, Manisekar K, Manikandan V. Study on mechanical properties of fly ash impregnated glass fiber reinforced polymer composites using mixture design analysis. Mater Des. 2014 Mar 1;55:499–508.
3. Lam CK, Cheung HY, Lau KT, Zhou LM, Ho MW, Hui D. Cluster size effect in hardness of nanoclay/epoxy composites. Compos Part B Eng. 2005 Apr 1;36(3):263–9.
4. Mujika F. On the effect of shear and local deformation in three-point bending tests. Polym Test. 2007 Oct 1;26(7):869–77.

  doi:10.5075/epfl-298799_978-2-9701614-0-0

5. Wallenberger TF, Weston N. Natural Fibers, Plastics and Composites. 2004. 370 p.
6. Chemex [Internet]. 2018. Available from: http://www.chemex.cz/
7. Ehrenstein WG. Polymerní kompozitní materiály. Scientia; 2009. 351 p.
8. ISO. 14125 Fibre-reinforced plastic composites - Determination of flexural properties. ISS; 1998. p. 18.
9. Okubo K, Fujii T, Yamashita N. Improvement of Interfacial Adhesion in Bamboo Polymer composite. JSME Int J. 2005;48(4):1–6.
10. Oliveira AD de, Beatrice CAG. Polymer Nanocomposites with Different Types of Nanofiller. In: Nanocomposites - Recent Evolutions [Internet]. 2018. p. 230. Available from: https://www.intechopen.com/chapters/64843 doi: 10.5772/intechopen.81329
11. Ozsoy I, Demirkol A, Mimaroglu A, Unal H, Demir Z. The Influence of Micro- and Nano-Filler Content on the Mechanical Properties of Epoxy Composites. J Mech Eng. 2015;61(10):601–9.

  doi:10.5075/epfl-298799_978-2-9701614-0-0

ECCM
26-30 JUNE
2022
LAUSANNE
SWITZERLAND

ECCM20 - Proceedings

ISBN: 978-2-9701614-0-0
DOI: 10.5075/epfl-298799_978-2-9701614-0-0